Velocity Measurement of Supersonic Ammonia and Nitrogen/Hydrogen-Mixture Plasma Jets

H. Tahara[1], M. Demizu[1], Y. Ando[2] and T. Yoshikawa[1]

[1] *Graduate School of Engineering Science, Osaka University, Osaka, Japan*
[2] *Department of Mechanical Engineering, Ashikaga Institute of Technology, Tochigi, Japan*

Abstract

Mach probe measurement was carried out in order to evaluate ion Mach numbers and velocities of plasma flows for a supersonic direct-current arc plasma jet generator in a low pressure environment. The plasma flow velocity increased by adding hydrogen compared with the cases with only nitrogen. Accordingly, the high plasma flow enthalpy with mixtures of nitrogen and hydrogen is considered to enhance nitriding effect in addition to efficient chemical reaction of NH radicals.

1. Introduction

The direct-current arc plasma jet generator is a promising plasma device suitable for economically assisting material processing in which a high throughput of material is desired. In low pressure plasma spraying, an arc jet generator with a supersonic expansion nozzle is useful for spraycoating hard and large-area films adhering strongly to substrates. In surface treatment such as nitriding, a supersonic plasma jet in a low pressure environment also has benefits of efficient plasma treatment by using irradiation of highly excited and/or chemically active particles in the thermodynamical nonequilibrium plasma in addition to large-area and uniform treatment[1],[2].

In our previous study, ammonia and mixtures of nitrogen and hydrogen were used for nitriding processing[1],[2]. Since these gases were chemically active, the processing efficiency was enhanced. However, plasma properties of ammonia and mixtures of nitrogen and hydrogen are unknown because of complicated chemical reactions among many fragmented particle species. Particularly, plasma characteristics near substrates are hardly clear because the existence of substrates influences the plasma features. Therefore, spectroscopic and electrostatic probe measurements were made to examine plasma characteristics near substrate plates[3]-[8]. Heat fluxes into substrates were also measured[9]-[11]. The relationships between the plasma and heat flux characteristics and the substrate nitriding characteristics were discussed.

In the present study, Mach probe measurement is carried out in order to evaluate ion Mach numbers and velocities of plasma flows for a supersonic direct-current arc plasma jet generator in a low pressure environment. The influence of plasma flow velocity on the nitriding characteristics is discussed.

2. Experimental Apparatus

Figure 1 shows the cross-sectional views of the supersonic direct-current arc plasma jet generator used for this study. A constrictor of a convergent-divergent nozzle throat has a diameter of 6 mm and a length of 7 mm. A divergent nozzle has an exit diameter of 34 mm and is inclined at an angle of 52 deg. The ratio of the cross-sectional area of the nozzle exit to that of the constrictor is 32.1. A cylindrical cathode made of 2% thoriated tungsten has a diameter of 10 mm. The gap between the electrodes is set to 2 mm. Ammonia and mixtures of nitrogen and hydrogen are used as the working gas. In the mixture of N_2+nH_2, the H_2 mole fraction n is varied from 0 to 3, in which mole fractions of 0 and 3 correspond to pure nitrogen and simulated ammonia, respectively. The working gas is injected tangentially from the upstream end of the discharge chamber. The arcjet generator is operated with input powers of 3-12 kW at discharge currents of 70-150 A. The arcjet generator, as shown in Fig.2(a), is located in a vacuum tank 0.8 m in diameter and 1.5 m long, which is evacuated using a mechanical booster 1600 l/s connected in series with a rotary pump 160 l/s.

Mach probe measurement is carried out in order to evaluate ion Mach numbers and velocities of plasma flows. The probe, as shown in Fig.2(b), mainly consists of two wires 0.5 mm in diameter, and their end surfaces are parallel and perpendicular to flow. The ion Mach number can be estimated from the ratio of the two ion saturation currents, and then the flow velocity is predicted from the ion Mach number, and electron and ion temperatures obtained by means of Langmuir probe and spectroscopic measurements[12],[13],[6]-[11]. Particularly, the ion temperatures are assumed to equal rotational temperatures of NH or N_2 obtained by emission spectroscopic measurement.

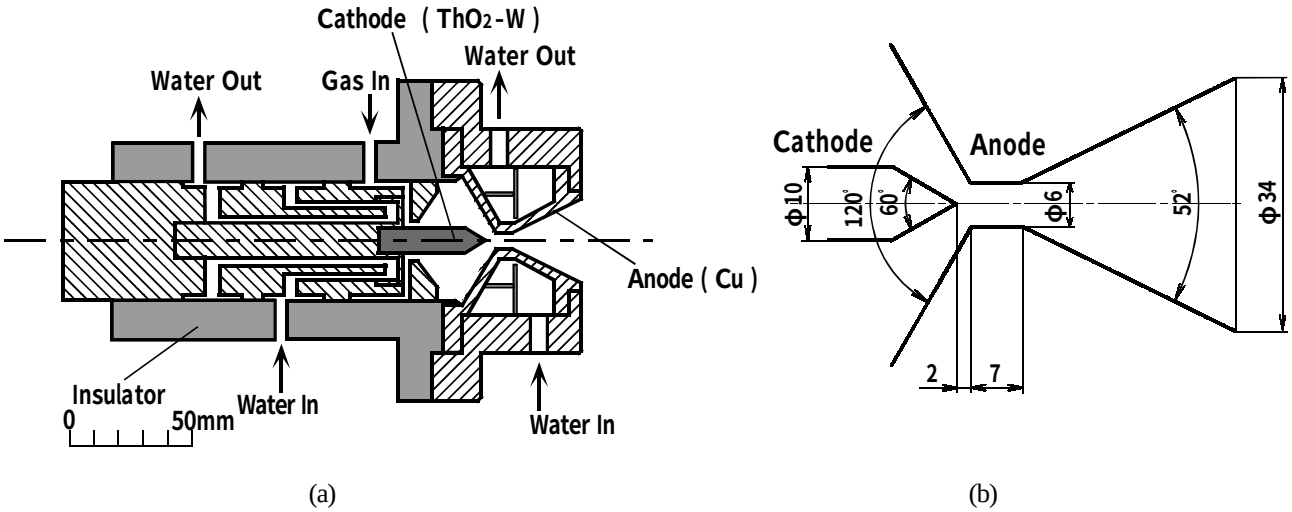

(a) (b)

Fig.1 Cross-sectional views of 10-kW-class water-cooled direct-current arc plasma jet generator with supersonic expansion nozzle. (a) Configuration of arcjet generator. (b) Arrangement of electrodes.

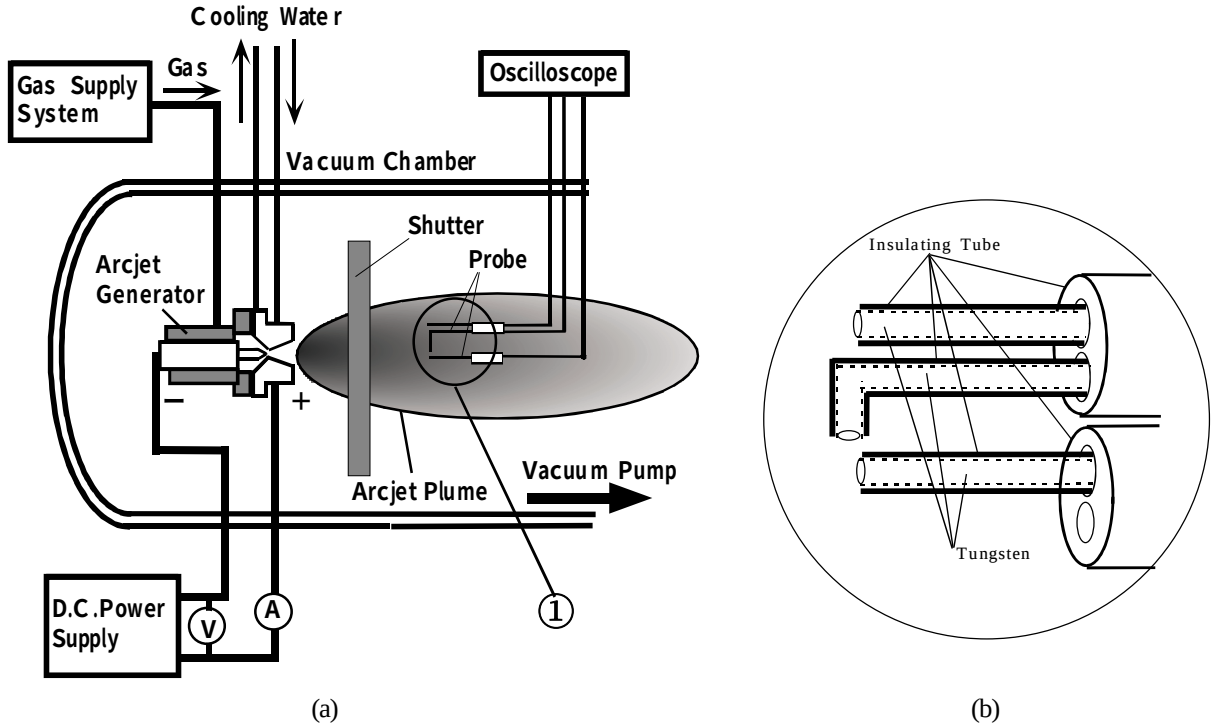

(a) (b)

Fig.2 Mach probe measurement apparatus. (a) Experimental system. (b) Mach probe.

3. Results and Discussion

In all experiments, the discharge current and the mass flow rate are fixed to 150 A and 0.21 g/s, respectively. The input power and the tank pressure are 6.3 kW and 34 Pa for N_2, 9.45 kW and 82 Pa for N_2+H_2, 10.8 kW and 150 Pa for N_2+2H_2, and 11.85 kW and 205 Pa for N_2+3H_2, respectively.

Figure 3 shows the axial variations of ion saturation current for the two wires parallel and perpendicular to plasma flows on the central axis. The ion saturation current gradually decreases downstream. At a constant axial position, the current for N_2 is the largest of all gas species, and an increase in H_2 mole fraction increases the current. This is expected because for N_2 the degree of ionization is relatively high with the small particle number flux at the lowest tank pressure and because for mixtures of N_2 and H_2 more intensive thermal pinch occurs with increasing H_2 mole fraction, resulting in enhanced ionization.

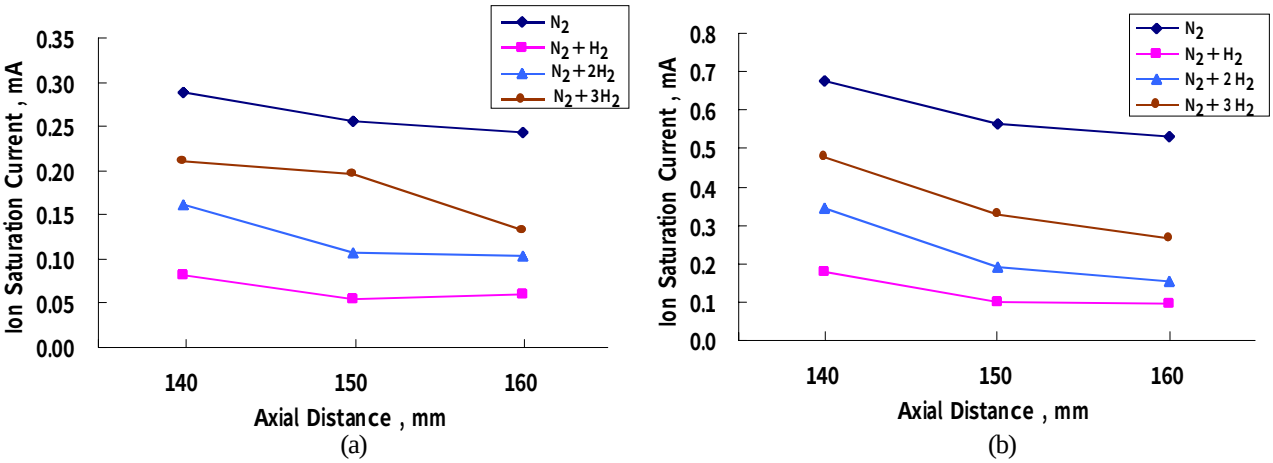

Fi.g.3 Axial variations of ion saturation current for wires parallel and perpendicular to plasma flows on central axis. (a) Parallel. (b) Perpendicular.

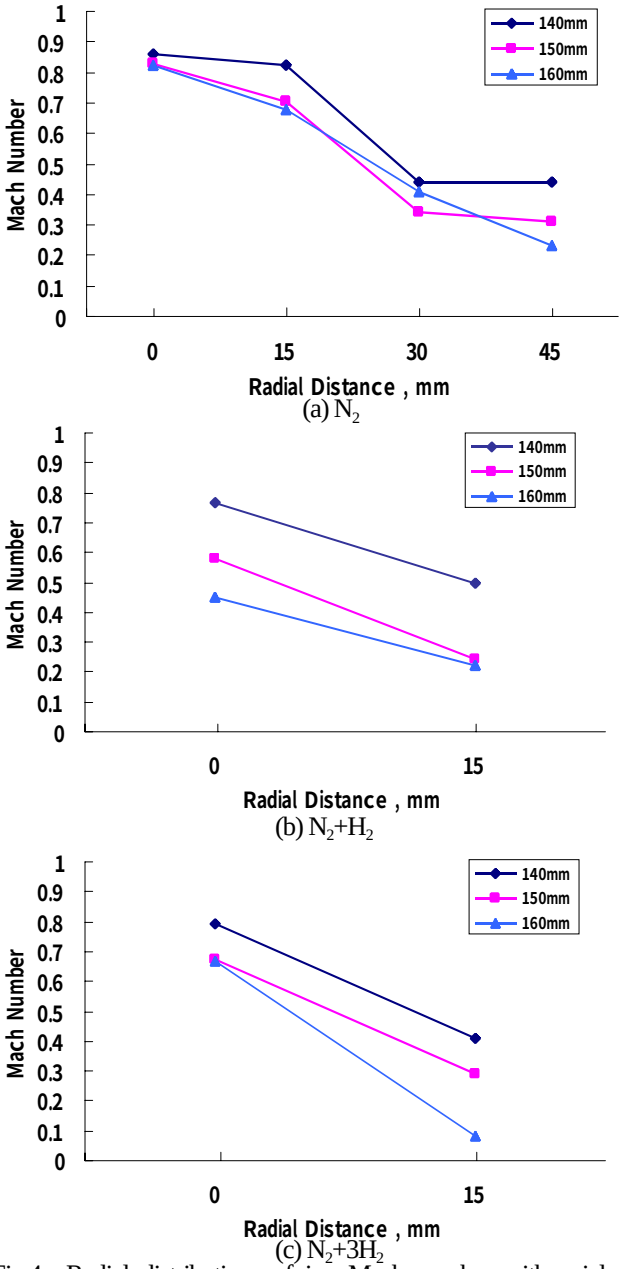

Fig.4 Radial distributions of ion Mach number with axial positions of 140, 150 and 160 mm from nozzle exit for N_2, N_2+H_2 and N_2+3H_2.

Figure 4 shows the radial distributions of ion Mach number with axial positions of 140, 150 and 160 mm from the nozzle exit for N_2, N_2+H_2 and N_2+3H_2. For N_2+H_2 and N_2+3H_2, the ion Mach number at large radial positions of 30 and 45 mm could not be evaluated because of too small ion saturation currents; that is, because plasma is concentrated on the central axis due to thermal pinch effect. The ion Mach number for N_2 gradually decreases radially-outward, and at a constant radial position the Mach number at 140 mm is the highest. For the mixture gases, the Mach number rapidly decreases radially-outward compared with that for N_2, and at a constant radial position the Mach number decreases downstream.

Figure 5 shows the axial variations of ion Mach number on the central axis with varying gas species. Although the ion Mach number decreases downstream regardless of gas species, the rate of decrease for N_2 is very small, and for mixtures of N_2+H_2 and N_2+2H_2 the rate is relatively large. For N_2+3H_2, the Mach number rapidly decreases at axial positions from 140 to 150 mm, and then the characteristic is almost flat enough

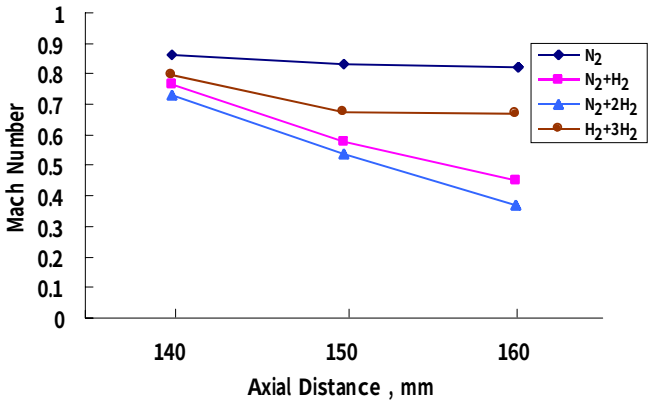

Fig.5 Axial variations of ion Mach number on central axis with varying gas species.

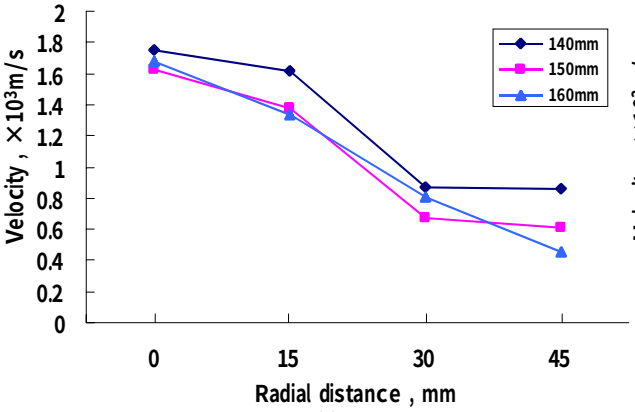

(a) N_2

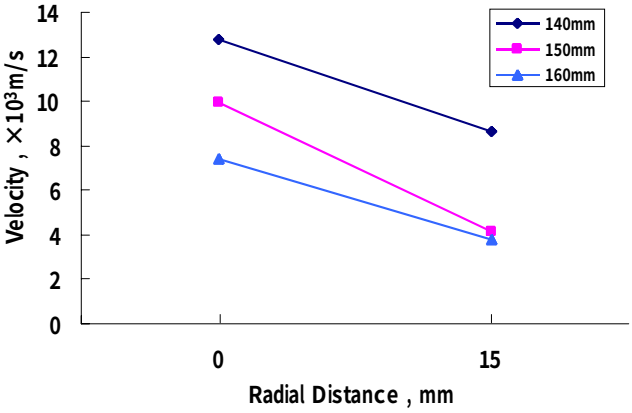

(b) N_2+H_2

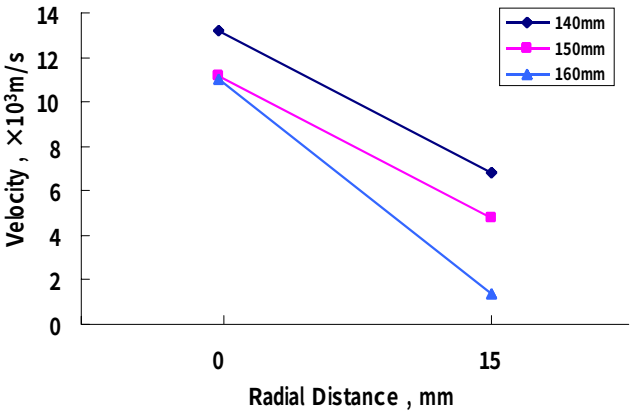

(c) N_2+$3H_2$

Fig.6 Radial distributions of flow velocity with axial positions of 140, 150 and 160 mm from nozzle exit for N_2, N_2+H_2 and N_2+$3H_2$.

downstream. At a constant axial position, the Mach number for N_2 is the highest of all gas species because of intensive expansion with the lowest tank pressure. For the mixture gases, the Mach number for N_2+$3H_2$ is the highest because of intensive acceleration by enhanced thermal pinch even with the highest tank pressure.

Figure 6 shows the radial distributions of flow velocity with axial positions of 140, 150 and 160 mm from the nozzle exit for N_2, N_2+H_2 and N_2+$3H_2$. The

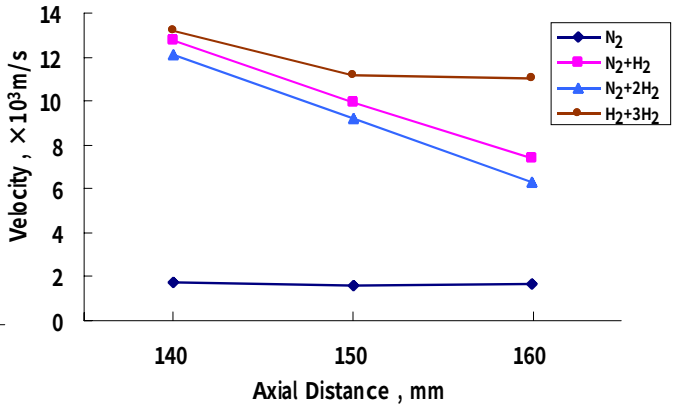

Fig.7 Axial variations of flow velocity on central axis with varying gas species.

flow velocity characteristics agree with the ion Mach number characteristics mentioned above.

Figure 7 shows the axial variations of flow velocity on the central axis with varying gas species. Although the ion Mach number for N_2 is the highest of all gas species, the flow velocity is the lowest. This is because the particle mass of N_2 is smaller than the average particle mass for mixtures of N_2 and H_2. The flow velocity for N_2 ranges from 1.63 to 1.75 km/s and for the mixture gases from 6.28 to 13.21 km/s. Accordingly, the high plasma flow enthalpy with mixtures of N_2 and H_2 is considered to enhance nitriding effect in addition to efficient chemical reaction of NH radicals[1],[2].

4. Conclusions

Mach probe measurement was carried out in order to evaluate ion Mach numbers and velocities of plasma flows for a supersonic direct-current arc plasma jet generator in a low pressure environment. Mixtures of N_2 and H_2 were used as the working gas. In the mixture of N_2+nH_2, the H_2 mole fraction n was varied from 0 to 3, in which mole fractions of 0 and 3 corresponded to pure nitrogen and simulated ammonia, respectively. Although the ion Mach number decreased downstream regardless of gas species, the rate of decrease for N_2 was very small, and for N_2+H_2 and N_2+$2H_2$ the rate was relatively large. For N_2+$3H_2$, the Mach number rapidly decreased near the nozzle exit, and then the characteristic was almost flat enough downstream. At a constant axial position, the Mach number for N_2 was the highest of all gas species because of intensive expansion with the lowest tank pressure. For the mixture gases, the Mach number for N_2+$3H_2$ was the highest because of intensive acceleration by enhanced thermal pinch even with the highest tank pressure. Also, the ion Mach number for N_2 gradually decreased radially-outward although for the mixture gases it rapidly decreased. As a result, the flow velocity for N_2 ranged from 1.63 to 1.75 km/s and for the

mixture gases from 6.28 to 13.21 km/s. The flow velocity for N_2 was the lowest of all gas species. Accordingly, the high plasma flow enthalpy with mixtures of N_2 and H_2 is considered to enhance nitriding effect in addition to efficient chemical reaction of NH radicals.

References

[1] H. Tahara et al., Proc. of Int. Symp. Designing, Processing and Properties of Advanced Eng. Materials, 1997, 523-528.
[2] Y. Andoh et al., Proc. of UTSC, 1999, 234-239.
[3] H. Tahara et al., IEEE Trans. Plasma Sci., **22**(1994), 58-64.
[4] H. Tahara et al., IEEE Trans. Plasma Sci., **24**(1996), 218-225.
[5] H. Tahara et al., IEEE Trans. Plasma Sci., **26**(1998), 1307-1313.
[6] H. Tahara et al., Proc. of UTSC, 1999, 720-725.
[7] H. Tahara et al., Proc. of 14th ISPC, **2**(1999), 563-568.
[8] H. Tahara et al., Proc. of 1st ITSC, 2000, 21-28.
[9] H. Tahara et al., Proc. of 15th ISPC, **1**(2001), 205-210.
[10] H. Tahara et al., Proc. of 3rd ITSC (ITSC2002), 2002, 771-776.
[11] H. Tahara et al., IEEE Trans. Plasma Sci., 2003, in press.
[12] J. French, Institute of Aerphysics, UTIA No.79.
[13] P.C. Stangeby et al., Plasma Physics, 6.

A novel approach to cathode / anode modelling for high-current AC arcs

G.Sævarsdottir[1], M. T. Jonsson[1], J.A. Bakken[2]

[1] *Department of Mechanical Engineering, University of Iceland, Reykjavik, Iceland. gudrunsa@hi.is, magnusj@hi.is.*
[2] *Department of Materials Technology, Norwegian University of Science and Technology, Trondheim, Norway. jabakken@nt.ntnu.no*

Abstract
Boundary conditions at cathode and anode are crucial when electric arcs are simulated. In the case of high current industrial AC arcs with currents ~100 kA, phase voltages ~100 V and total furnace power ~10 – 60 MW, the surfaces that the arc attaches to, receive enormous amounts of energy from the arc. Therefore a novel approach has been made to the cathode and anode simulation. Radiation from the arc is taken into account. An energy balance for the space charge sheath, isolated from the arc, is omitted whereas an overall energy balance for the arc-cathode-anode system is fulfilled. The result is a *diffuse* arc attachment.

1 Introduction

The arc simulation models require knowledge about conditions at the cathode and anode. However, it is preferable that assumptions are kept to a minimum. As arc behaviour is very sensitive to the boundary conditions at cathode and anode, considerable work has been put into the development of cathode sub-models for high-current AC arcs. In fact three different models have been developed. The first model, here called *the classic model* was based on the assumption that the cathode spot is self-sustained with energy, and that the cathode fall voltage is constant all over the cathode spot, which in turn requires the cathode spot to deliver excess energy to the arc. The second model called *the variable u_C model* allows the cathode fall voltage to vary over the cathode spot, but assumes that an energy balance is fulfilled in each element of the cathode. The weakness of this model is that when energy transfer by radiation from the arc to the cathode is taken into account, the integrated current density from the model is much higher than the total arc current. Therefore measures must be taken to reduce the total integrated current. The third model which is presented in this paper, *the diffuse spot cathode / anode model*, is different from the first two in that it does not require the energy balance in the ionization sheath to be fulfilled as there is an abundance of energy from the electric arc that enters this layer in the form of radiation or energetic plasma electrons.
In this paper only the diffuse spot model will be presented. The cathode fall voltage is assumed constant over the cathode surface and determined by the requirement that the total current from the electrode should be equal to the imposed arc current. The anode is treated in the same way as the cathode. This model is the most promising of the three in the case of a high-current industrial arc which corresponds to the limit of an arc dominated cathode spot.

2 General cathode spot theory

2.1 The plasma sheath

If there initially is a wide body of LTE plasma and suddenly a part of it is surrounded by an isolating wall, the wall will initially be bombarded and charged up by fast moving plasma electrons. The negatively charged wall will then repel approaching plasma electrons and attract ions, thus forming a *space charge sheath* that shields the plasma gas from the effect of the negatively charged wall. Approaching plasma electrons will not notice the wall before they enter the space charge sheath, but as they penetrate the ion layer the shielding effect is reduced and they are slowed down by the electric field. For an isolating wall the potential drop in the sheath must be exactly high enough to ensure zero total current. When a net current is applied upon a plasma contained between two walls, it is natural to assume that the potential fall is adjusted such that the there is a net charge exchange between the plasma and the wall consistent with the applied current. The thickness of this space charge sheath is approximately $25\lambda_D$ which is close to 1 μm and orders of magnitude smaller than the thermal boundary layer, which in the case of an industrial arc is close to 500 μm.

2.2 General expressions

The AC Cathode/Anode Sub-Model (CASM) to be described is based on the following assumptions: The cathode current density j is composed of three components: Thermionically emitted electrons j_e, ions from

the plasma that reaches the cathode surface j_i, and finally plasma electrons that pass through the potential barrier and reach the surface j_{epl}. The models are to a certain extent based on ideas appearing in Neumann's theory [1] and Benilov's model [2] for low-current DC arc cathodes.

When a body is sufficiently hot, a fraction of its electrons have kinetic energy high enough for them to overcome the energy barrier called the work function ϕ which traps them in the body. The thermionic emission current density is given by Richardson-Dushman's equation :

$$j_e(T_C) = 1.2 \cdot 10^6 T_C^{\,2} f \exp\left(\frac{e(\varphi + \Delta\varphi)}{k_B T_C}\right) \tag{1}$$

where T_C denotes the cathode surface temperature, e is the electronic charge, ϕ the thermionic work function, k_B is Boltzmann's constant and $\Delta\phi$ is the Shottky correction. The factor f in the Richardson-Dushman equation is a scaling factor accounting for the fact that a thermionically emitted current with the theoretic value of $f = 1$ has never been observed. According to Pfender et al.'s [3] estimate, $f = 0.5$, which is used in this work. The hot plasma gas contributes with electrons that diffuse over the cathode fall potential u_C and enter the cathode. *The counter-diffusing plasma electron current* is given by:

$$j_{epl} = \frac{1}{4} e n_{e0} c_e e^{-eu_c / k_B T_c}$$

$$c_e = \sqrt{\frac{8 k_B T_e}{m_e \pi}} \tag{3}$$

where n_{e0} is the electron density at the edge of the space charge sheath, and c_e is the mean electron velocity in each direction. Benilov *et al* [2] reported a solution for the plasma sheath equation that leads to the following expression for the current density of *plasma ions* towards the surface:

$$j_i = n_{i\infty} \frac{0.8}{2 + \alpha} \sqrt{\frac{k_B (T_C + T_e)}{M_i}}$$

$$\alpha = \sqrt{\frac{k_B T_h}{m_i D_{ia\infty} k_r n_{i\infty}^2}} \tag{4}$$

where $D_{ia\infty}$ is the ion-atom diffusion coefficient, k_r is the ion-electron recombination rate coefficient and T_h the heavy particle temperature, all evaluated at the edge of the ionization layer. In conventional cathode models it is assumed that the energy balance for the ionization of atoms by emitted electrons is fulfilled in the ionization layer all over the cathode spot, then the radially dependent cathode fall voltage $u_C(r)$ can be determined:

$$j_e\left(u_C + 2\frac{k_B T_C}{e} - 3.2\frac{k_B T_e}{e}\right) = j_i\left(U_i + 2\frac{k_B T_i}{e} + 3.2\frac{k_B T_e}{e} - 2\frac{k_B T_C}{e}\right)$$

$$+ j_{epl}\left(u_C + 2\frac{k_B T_e}{e} - 3.2\frac{k_B T_e}{e}\right) \tag{5}$$

Here j_e and j_i represent the electron and ion current densities in the near cathode layer and U_i is the ionization potential. The thermionically emitted electrons are accelerated over the space charge sheath potential fall u_C,. The thermionic electrons are emitted with their two-dimensional enthalpy in equilibrium with the cathode body, but need to be heated up to the plasma temperature to be in thermodynamic equilibrium. The energy supplied by the thermionic electrons is used to ionize atoms, and bring the electrons excited from the atoms to equilibrium with the arc plasma. The counter-diffusing electrons must overcome the space charge potential, and carry a two-dimensional enthalpy to the cathode.

An extension to AC is accomplished by imposing a periodically varying arc current. The non-steady two-dimensional axi-symmetric Fourier equation is solved for the electrode body using the heat flux in Equation 6 as a boundary condition, to obtain a periodically varying cathode surface temperature $T_c(r,t)$. The computational domain is assumed large compared to the cathode spot radius (0.1 m) in the radial direction and to the thermal penetration depth of 50 Hz temperature oscillations (1 mm) in the axial direction. As a boundary condition we need an expression for the cathodic heat flux:

$$\dot{q}_c = j_i(u_c + 2\frac{k_B T_i}{e} - 2\frac{k_B T_C}{e} + U_i - \phi) - j_e\left(2\frac{k_B T_C}{e} + \phi\right) + j_{epl}\left(\frac{k_B T_e}{e} + \phi\right) + \dot{s}_{rad} \quad (6)$$

Radiation from the arc as well as energy contributed by the particle impact on the surface during the anodic half-period is considered, and calculated values from the MFD model are used. However, ohmic heating in the electrode is disregarded as it is judged as insignificant as compared to the heat input from the arc and the particle impact in the cathode spot. The electromagnetic equations are not solved for the electrode body, and the current density within the electrode is not known. In the present results sublimation of the electrode body has not been taken into account, but the introduction of a *maximum temperature* ensures that the sublimation temperature is not surpassed.

3 The Diffuse Spot Cathode/Anode Sub-Model

The diffuse spot cathode/anode sub-model (CASM) is based on the observation that in a relatively short high-current industrial arc, the energy supply from the arc is so overwhelming that it is not possible to divide the cathode and the arc into two separate energy domains that do not exchange energy. It cannot be required that thermionically emitted electrons accelerated through the cathode fall supply all energy required to sustain the arc spot as the radiation from the arc and the abundance of much more energetic plasma electrons is sufficient to ionize neutral atoms and equilibrate colder electrons. This means that instead of *two separate energy balances*, Equation 5 on the one side, and the *MFD* transport equations for the arc on the other, an energy balance for the whole system must be solved *within the MFD model.* In the *CASM* only the energy balance for the electrode itself, using boundary conditions in Equation 6 will be considered. The heat flux into the cathode/ anode body must be tapped from the arc by a boundary condition for the arc model. In this new model cathode and anode are considered to be formally identical, and the total current balance

$$I(t) = 2\pi \int_0^{r_{\max}} j_e(r,t) r dr + 2\pi \int_0^{r_{\max}} j_{isat}(r,t) r dr - 2\pi \int_0^{r_{\max}} j_{epl}(r,t) r dr \quad (7)$$

is fulfilled at any time for both electrodes. This means that the cathode as well as the anode thermionically emit electrons consistently with their temperatures, and that they are both bombarded with plasma electrons and ions dependent on the temperature of the plasma next to the electrode. The difference between cathode and anode is only that the net current is negative in the cathodic half-period and positive in the anodic half-period. The cathode/anode fall voltage, here termed u_C for consistency, is determined by solving Equation 7 for the given current at each timestep. This means that the potential fall is adjusted such that the there is a net charge exchange between the plasma and the wall consistent with the applied current. Radiation fluxes and plasma temperatures are obtained from arc simulations. For this model to be optimal it will be necessary to couple the MFD arc model and the cathode /anode sub-model and solve both models simultaneously. This has not been possible within the time frame of this work, but an iterative procedure is used. In the simulations it is assumed that the cathode/anode body is a good current conductor as compared to plasma. It is also assumed in this model that u_C is constant over the surface.

The abundance of energy provided by the electric arc is such that the energy balance in Equation 5 is not fulfilled, separated from the arc. But as the heat flux by particle impact in Equation 6 includes heat transport due to ambipolar diffusion and heat flux due to current, the boundary condition for heat transport in plasma must be set up correspondingly in the *MFD* arc model. The source term is included in the cells next to the cathode/anode surfaces. This source term then has the form:

$$\dot{q}_{bound} = -j_i\left(2\frac{k_B T_i}{e} - 2\frac{k_B T_C}{e} + U_i\right) - j_e 2\frac{k_B T_C}{e} - j_{epl} 2\frac{k_B T_e}{e} + j u_C \quad (8)$$

Notice that the thermionic work function ϕ terms have been removed as ϕ is exclusively a material property, which determines the energy of an electron within the material as compared to a free electron. The electric arc is not directly affected by the work function except by the work function's effect on the current density of emitted electrons. Also note that the term $j_i u_C$ has disappeared and been replaced with $j u_C$. This is because the power generated by the total current over the cathode fall voltage, $p_{uC} = j u_C$ has to be taken into account. The same equations apply at the anode.

.

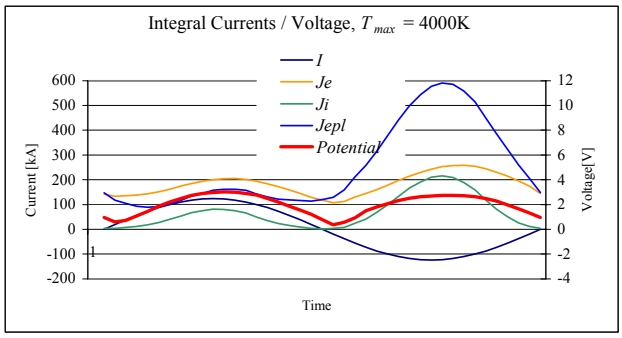

Figure 1: Integral current components and cathode/ anode fall voltages. The first half period is the cathodic and the second is the anodic half-period. The maximum material temperature is 4000 K.

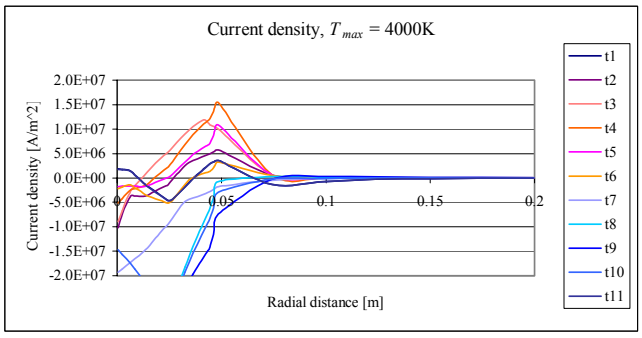

Figure 2: Current distributions for T_{max}= 4000 K at even time intervals through an AC period. The reddish curves refer to the cathodic half-period and the blue curves to the anodic half-period.

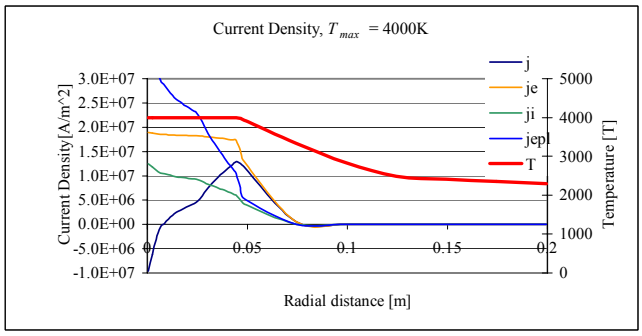

Figure 3: The current density distributions of the three current components at peak current in the cathodic half-period as well as the resulting total current density and the cathode temperature profile. T_{max}= 4000K

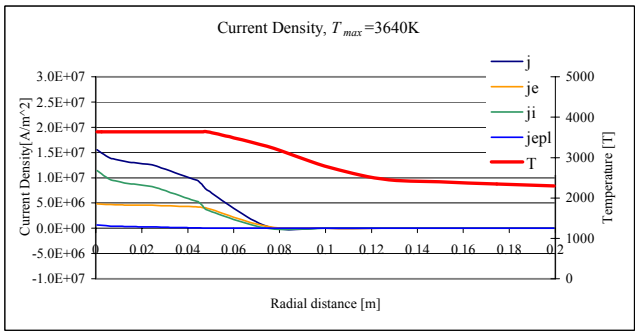

Figure 4: Same as Figure 3 in the case of T_{max}= 3640 K .

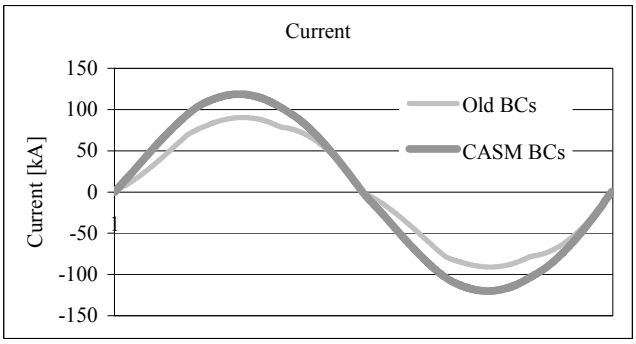

Figure 5: Current waveforms calculated for a 5 cm long industrial arc with the old type of boundary conditions as compared to CASM boundary conditions, for both one phase and three phase simulations

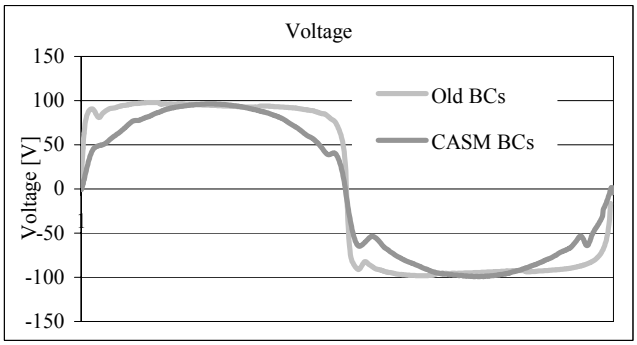

Figure 6: Voltage waveforms corresponding to the current waveforms in Figure 9.

Table 1: The maximum values of the various current densities [A/m^2] components at two maximum electrode material temperatures. The cathode fall voltage [V] is shown as well.

Max. cathode temperature	4000 K	3640 K
u_c	2.9	5.8
$j\ (r = 0)$	$-1.00 \cdot 10^7$	$1.50 \cdot 10^7$
$j_e\ (r = 0)$	$1.90 \cdot 10^7$	$0.50 \cdot 10^7$
$j_{epl}\ (r = 0)$	$3.98 \cdot 10^7$	$0.05 \cdot 10^7$
$J_i (r = 0)$	$1.08 \cdot 10^7$	$1.07 \cdot 10^7$

Table 2: Results of MFD simulations of industrial arcs. The corresponding current and voltage waveforms are shown in Figures 13 and 14.

Data	Old BCs	CASM-BCs
I_{rms} [kA]	64.5	84.6
U_{rms} [V]	90.1	78.4
P [MW]	5.4	6.5

3.1 Simulation results

When the energy balance is omitted and the potential drop u_C is assumed constant, u_C decreases, and thereby the plasma electron current density j_{epl} increases exponentially. This leads to a much lower total current density in the cathode (anode) spot dependent on the plasma temperature. If the plasma temperature is high enough, that results in a negative current density in a part of the arc spot. The resulting total current is composed of three components, two of which have a much higher total value than their difference. Figures 1 display the time variation in the total current and the integral current components as well as the cathode and anodic fall voltages for maximum cathode temperatures 4000 K. It is seen that the three current components are each larger, and in the anodic half-period much larger, than the resulting total current. Another result is that the potential fall required to hamper the flow of plasma electrons in the anodic half-period is only about 0.3 V lower than the cathode fall voltage in the case of the 'hot' electrode. In the cathodic half-period the voltage reaches a maximum at 3.0 V and in the anodic half-period the maximum voltage is 2.7 V. All this only demonstrates the necessity of coupling together the MFD arc model and the cathode / anode model to get more reliable values for the plasma temperature at the surface. It should be kept in mind that between the two half periods the overall arc voltage has changed sign, so that the anode fall voltage is indeed *subtracted* from the arc voltage – we have a *negative* anode fall. Let us now consider the current distribution at the surface. The plasma temperature at the electrode varies with the distance from spot center. The potential fall is, however, constant over the surface, so inevitably, the current density distribution is strongly varying. Figure 2 shows the time-varying cathode current density as a function of radius with a maximum cathode temperature of 4000 K. It is seen that the current density is negative in the center of the arc spot both in the anodic and cathodic half-periods.

Figures 3 and 4 show the radial distributions of the current density components at peak current with a maximum cathode surface temperature of 4000 K and 3640 K, respectively. The cathode radial temperature distribution is shown as well. The most obvious difference between the two sets of current densities is that all densities are lower for the colder cathode. Lower cathode surface temperatures naturally lead to lower thermionic emission of electrons j_e, and therefore a higher cathode fall voltage is needed to hamper the flow of plasma electrons towards the cathode surface. The cathode fall voltage is thereby increased from 2.9 V up to 5.8 V. The plasma electron current density j_{epl} is insignificant for the colder cathode, and therefore the resulting current density is a rather smooth curve with its highest value at the cathode spot center. The hotter cathode emits thermionically a larger amount of electrons. Therefore it must receive more plasma electrons to keep the balance, and the voltage is half of that of the colder electrode. As a result, the total current density is negative at the center of the cathode spot, while it is positive over the main part of the cathode. Such a current density profile is rather unphysical and would probably not occur if the electromagnetic equations were solved for the electrode body, and the energy balance for the entire arc/cathode system were properly fulfilled. These results are summed up in Table 1

3.2 Effect on industrial arc simulations

MFD simulations have been performed on the high-current AC arcs expected to exist in the craters of a 30 MVA three-phase submerged-arc furnace for production of *silicon metal*. The crater gas was assumed to consist of SiO and CO in molecular ratio 1:1 with or without Al and Ca contaminants. The computational domain again corresponds to the assumed shape and size of the crater cavity of the industrial furnace. The arc length was varied from 5 to 20 cm. It was soon found that arc lengths of 5 – 10 cm gave the best fit to industrial data. The available transformer secondary voltage is not high enough to sustain e.g. a 20 cm long arc. As an example, Figures 5 and 6 show the simulated current and voltage waveforms for a 5 cm long arc in pure SiO-CO gas. The results shown here are for three-phase calculations using both the traditional boundary conditions (Old BCs) with a constant parabolic cathode current density with a mean value of $j_c = 1.4 \cdot 10^7 A/m^2$ and the new BCs obtained by the cathode / anode sub - model (CASM).

Neglecting parallel charge conduction, the calculated RMS currents for a 5 cm long arc varies from 64.5kA for the arc using the older type of boundary conditions, up to 84 kA for the boundary conditions based on the cathode / anode sub-model (CASM). A normal RMS electrode current for the furnace in question is around 80 kA, and the measured voltage between electrode holder and furnace bottom 100 V. That corresponds to approximately 80 V over the arc, when phase reactance has been accounted for. In an industrial furnace under normal operation it is generally believed that a considerable part of the electrode current bypasses the arc and goes through the charge material surrounding the electrode. That will lead to a larger electrode current at the same voltage than shown here for the pure arc. The recent CASM boundary conditions that considerably reduce the arc resistance actually allow a longer arc. Simulations of a 10 cm long arc using the recent boundary condition give a RMS current of 56 kA and a RMS voltage of 110V. If a charge current is taken into account, realistic electrode currents and voltages are obtained.

4 Discussion and conclusions

The diffuse spot model deviates in important aspects from cathode models that have been reported in the literature. Most existing models have been made for low-current DC arcs, where the cathode spot must be energetically self-sustained, and no energy is extracted from the arc itself. This novel model represents the other limit: The cathode/anode spot is dominated by energy impact from the arc, and must be included in the energy balance for the arc. Although the CASM has not yet been fully integrated into the MFD arc model, the tentative iterative results indicate a much lower cathode current density than previously assumed and a much smaller cathode fall voltage, which indeed has the same sign in the anodic half-period. This means that in the voltage considerations for the total arc-cathode-anode system, the voltages for the cathode and anode almost cancel out! A *negative* anode fall voltage has previously been suggested by Pfender, but the standard assumption is that cathode and anode fall voltages add up. The relatively low current density gives rise to a *diffuse* cathode spot, wider than the part of the arc attached to it. Such diffuse cathode spots have been observed and discussed on many occasions.

This diffuse arc spot also leads to a smaller resistance in the arc itself. Changing the arc boundary conditions in this direction in fact allows us to lengthen the arc from 5 to 10 cm and maintain a reasonable phase resistance *neglecting the charge conduction*. Taking charge conduction into account, assuming that for example half of the current passes through the charge, the arc resistance may be increased and the arc itself lengthened accordingly, but still the order of magnitude is the same. The arc length is not much more than 15 cm.

5 REFERENCES

[1] W. Neumann,"The mechanism of the thermoemitting arc cathode", Akademi-Verlag, Berlin, 1987.

[2] M.S. Benilov, " The ion flux from a thermal plasma to a surface", J.Phys. D: Applied Phys. 28, 1995, pp.286-294.

[3] E. Pfender, M. Boulos, P. Fauchais, "Methods and Principles of Plasma Generation", Plasma Technology in Metallurgical Processes, pp. 27-47, ISS-1987

[4] M.S. Benilov, G.V. Naidis, "Ionization layer at the edge of a fully ionized plasma", Physical Review E, Vol 57, No 2, Feb 1998.

[5] G.A. Sævarsdottir, J.A. Bakken, V.G. Sevastyanenko, Liping Gu, "Arc Simulation Model for Three-Phase Electro-Metallurgical Furnaces", INFACON 9, June2001, Quebec City, Canada. In proceedings pp.253-263.

[6] R. Bötticher, W. Bötticher, "Numerical modeling of arc attachment to cathodes of high-intensity discharge lamps", J.Phys D: Appl. Phys. 33(2000), pp. 367-374.

[7] Ahmed Kaddani, Said Zahrai, Oliver Simon, "Kinetic model for the space charge zone in the cathode region of electric arcs", ABB Technical report SECRC/KB/TR-95/244E, Vesterås, Sweden, 1995.

Decomposition of HCl and Chlororganics in RF Plasma

G. Paskalov

Department of Physics, University of California, Los Angeles, USA

Abstract
Plasma decomposition of HCl, C_6H_5Cl, and $C_6H_2Cl_4$ were studied. A RF plasma reactor was constructed to study the fundamental reaction kinetics and thermodynamics for decomposition of HCl and chlororganics at atmospheric pressure. The experiments were performed in a mixture of HCl and Chlororganics with Ar and H_2O at different ratios. It was shown that dissociation of HCl is efficient only at plasma temperatures higher than 5000K.

1. Introduction

Industries manufacturing chlorohydrocarbons such as tetrachloroethylene (PCE), 1, 2 dichloroetan (EDC), trichloroethylene (TCE), vinyl chloride (VCM), diphenyl methane (DME), fluorochemicals and fluoropolymers typically produce anhydrous hydrogen chloride as a by-product. When manufacturing fluorochemicals, generally via halogen exchange reaction, the resulting reaction product mixture is distilled allowing for the recovery of anhydrous HCl.

The thermal decomposition of HCl was studied in [1, 3]. The experiments were performed in a mixture containing 1.4 to 3800 ppm HCl diluted in Ar in a temperature range 2500K to 4600 K. A rate coefficient for the reaction HCl + Ar = H + Cl + Ar , was determined. The elementary reaction of HCl with H and Cl were studied in the temperature range 240 K to 1000 K by a different group. High temperature data are not available. HCl pyrolysis was performed in two shock tubes as described in [1]. The measurements were made using ARAS and IR Diode Laser Spectroscopy.

Hydrogen Chloride is very aggressive and thermally stable gas. Its dissociation energy is 4.48 eV. This is not very high compared to the dissociation energy for the Hydrogen - 14.48 eV. The dissociation process starts only at the temperatures higher than 2000 K. The needed constants for the evaluation of HCl conversion can be obtained from the following classical reaction:

$$H_2 + Cl_2 = 2HCl + 44\ kCal.$$

The reaction rate constant K_r is expressed as

$$K_r = p^2 [HCl] / (p [H_2] \times p [Cl_2])$$

Thus, $K_r = 9554/T - 0.533 \times lgT - 2.42$ or $K_r = 4x (1 - \alpha)^2 / \alpha^2$, where α is the dissociation degree of the HCl. The following table shows the dependence of α from temperature, T.

T, ^oC	20	400	700	1200	1700	2200
α	$3x10^{-17}$	$4.4x10^{-8}$	$0.9x10^{-5}$	$5.2x10^{-4}$	$3.8x10^{-3}$	$1.2x10^{-2}$

To understand the problems with HCl dissociation one has to analyze the process of HCl synthesis. The synthesis of the HCl is a simple chain reaction. The reaction is initiated by the quantum lights in the visual spectrum. This was confirmed by Nernst in the 19th century and the photo synthesis of HCl can be described by the following reaction:

$$Cl_2 + h\nu = Cl + Cl^* ;\ Cl^* + H_2 = HCL + H^* ;\ H^* + Cl_2 = HCl + Cl^*$$

The number of chain reactions that can reach 10^5, i.e. one quantum of light can create 10^5 molecules of HCl. This reaction speed can be increased by using the water vapor, coal, quartz and titanium. Thus, the dissociation of the HCl can be achieved if the following conditions occur:

1. adjust the dissociation temperature, so that $\alpha = 1$
2. stop the recombination process

2. Thermo-dynamic evaluation of the HCl dissociation

The thermodynamic evaluation of the dissociation reaction of HCl is performed in the temperature range from 2000K to 6000K. This lowest limit of temperature was chosen based on the value of α equals 0.0122. This temperature characterizes the beginning of the dissociation of HCl. Thermodynamic calculations were made based on the minimization system of all of the thermodynamic functions of HCl. We evaluated the reaction product, such as Cl_2, Cl, H, and H2. Fig. 1 presents the changes in the number of moles of HCl, H_2, H, Cl dependent on the temperature. The changes in Cl_2 are not shown, because they are so small at temperatures higher than 2000K ($< 10^{-2}$). The data, which is shown on fig.1, needs to be matched to the degree of conversion, α, vs. temperature (fig.2).

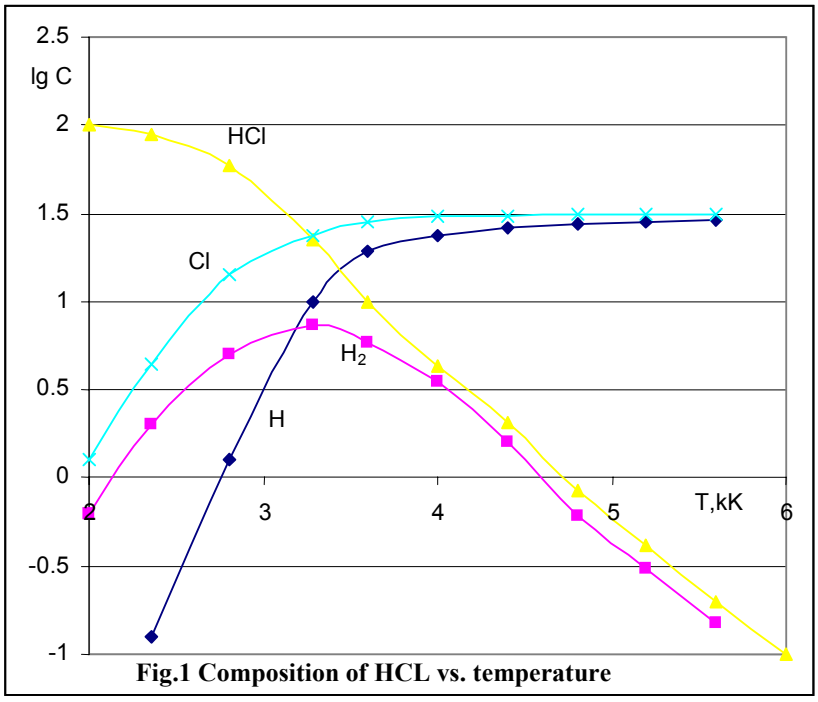

Fig.1 Composition of HCL vs. temperature

Analysis of the data from fig.1 and fig.2 shows that the effective dissociation of HCl should be at temperatures higher than 5500K. At the above temperature Δ approaches 100%. At temperatures higher than 5500K the plasma gas consists only of the Hydrogen and Chlorine atoms. However, thermodynamic evaluation is not enough to evaluate the speed of recombination and the conversion process itself.

3. **Kinetics of the dissociation of HCl**

Calculations of the thermal dissociation of HCl are made between temperatures of 4000 – 7000K based on the coefficient of the reaction

$$K = A\, T^n\, E / kT, \quad \text{where}$$

E – is the dissociation energy; T – temperature, A,n – parameters.

This calculation was made based on the model, which described in the following reaction [3]

$$HCl + Ar == H + Cl + Ar$$

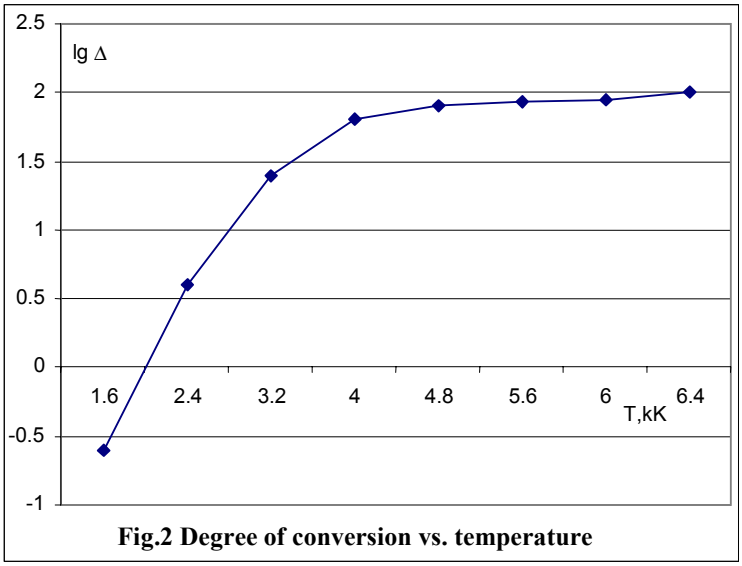

Fig.2 Degree of conversion vs. temperature

The calculation results are shown on fig 3 for two values of n: 0 and 0.5.

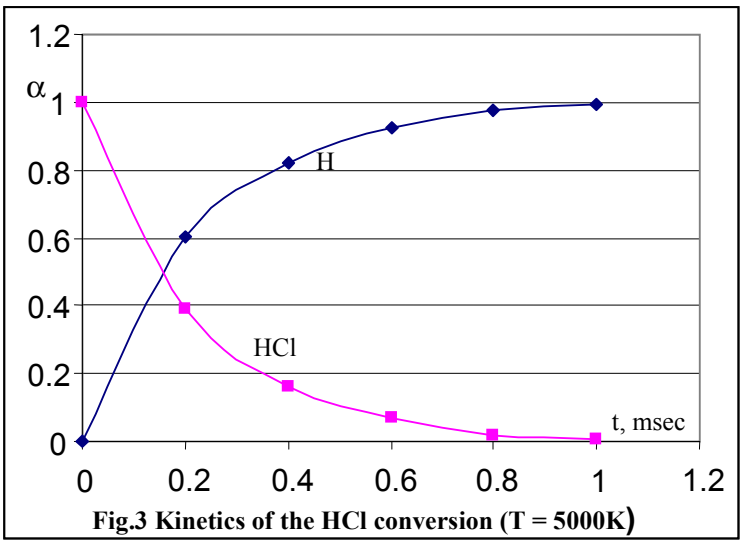

Fig.3 Kinetics of the HCl conversion (T = 5000K)

Comparison of the thermodynamic and kinetic calculations shows that dissociation temperature, which was calculated above, is higher then real. At this temperature the full dissociation is achieved at 7×10^{-3} sec for n = 0. For n = 0.5 the dissociation time is near 0.5×10^{-3} sec. The analysis shows that the treatment time can be achieved in the 0.01 – 0.2 meters long discharge chamber at an average plasma velocity of 30 m/sec.

4. Experimental Set-Up

The experimental diagram is shown on fig.4.

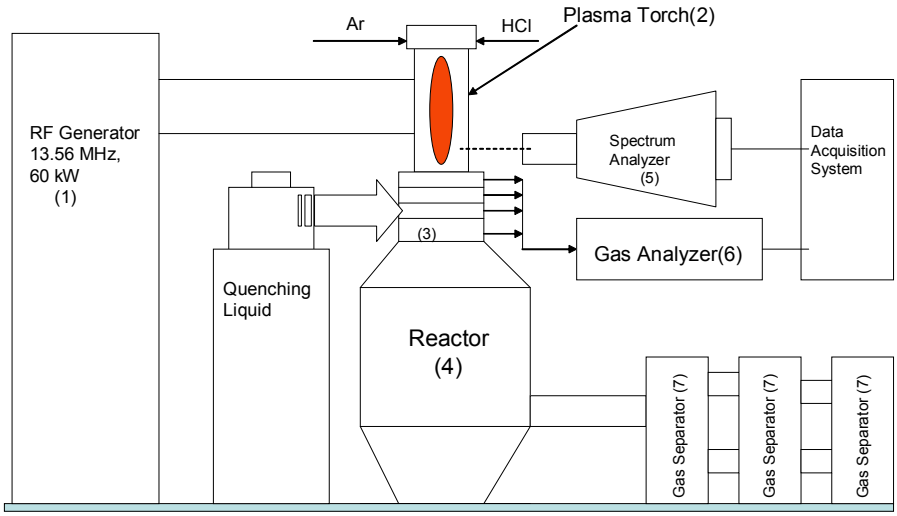

Fig.4 Experimental Set-Up

The Plasma Unit consists of a 60 kW RF generator(1) at 13.56 MHz working frequency, a hybrid plasma torch (2), a quenching device (3), a reactor (4), a spectrometer (5), a gas analyzer (6), and gas separators (7). The average gas temperature was 6000K at 10 kW discharge power. The plasma temperature didn't change within the range of a plasma gas rate between 0.25 l/sec and 10 l/sec. The plasma spectrum was obtained using an industrial spectrometer within a 220nm – 900 nm range with a linear dispersion of 4 Angstroms per mm. The gas was analyzed by a RGA -300. Samples were taken just after the quenching device.

Hydrogen Chloride was introduced to the plasma torch as a feed mixture using Argon as the plasma forming gas. Recombination of the Chlorine and Hydrogen ions into molecular H_2 and Cl_2 was achieved by cooling the product stream in the quenching device at different quenching rates (10^3 K/sec - 10^7 K/sec).
A high yield of Cl_2 and H_2 (typically 90 – 95% by weight) was obtained by plasma conversion of HCl as well as by cooling the gas product stream. Gaseous H_2 and Cl_2 do not react at normal temperatures in the absence of the light. However, at the temperatures above 300^0C, or in the presence of sunlight or artificial light (~ 470 nm wavelength), they combine explosively. The explosive limits of this mixture of pure gases are approximately an 8 % vol. of H_2 and a 12% vol. of Cl_2. This limit depends on temperature, pressure and concentration, additives, etc. Converted hydrogen and chlorine are separated after the quenching device by standard method (membranes).

5. Results and Discussion

The experimental data shows that the processes of HCl dissociation can be realized using RF plasma discharge and a small amount of Argon. The full dissociation of HCl to Hydrogen and Chlorine can be achieved with the following conditions: a plasma gas consisting of a mixture of Ar and HCl at a ratio of 1:1; a plasma gas rate = 1 liter per second; discharge power = 10 kW. These results are confirmed by gas analysis of the product before and after the quenching device. The plasma spectrum consists only of Argon, Chlorine and Hydrogen exited lines (Bulmer series). The intensity of Ar lines decreases with the increase of HCl ratio. At the same time the intensity of Hydrogen and Chlorine lines increases. The most sensitive "indicator" of the efficiency of the dissociation process are the Hydrogen lines (Bulmer series), especially, the H_α line (α =

6562.81 Angstrom). In this spectrum we observed the Chlorine lines, such as ClI (6531.43A), ClI(6434.80A), ClI(4363.3A), ClI4369.52A and ClI(94389.76A). The plasma spectrum between H_γ and H_δ (λ = 4101.74A) consists only of Argon lines. Also, we observed some very weak lines that are matched to impurities from the reactor's wall. The control of dissociation of HCl can be organized based on the analysis of the intensity of H_α, group of Cl lines in the range between 4370A and 4490A, as well as the Argon spectrum lines between H_δ and H_γ.

The analysis of the gas mixture in the reactor shows that they contain Argon, Chlorine and Hydrogen in molecular form. Fig. 5 shows the dependence of the HCl contents, C, in the plasma product mixture vs. RF plasma power.

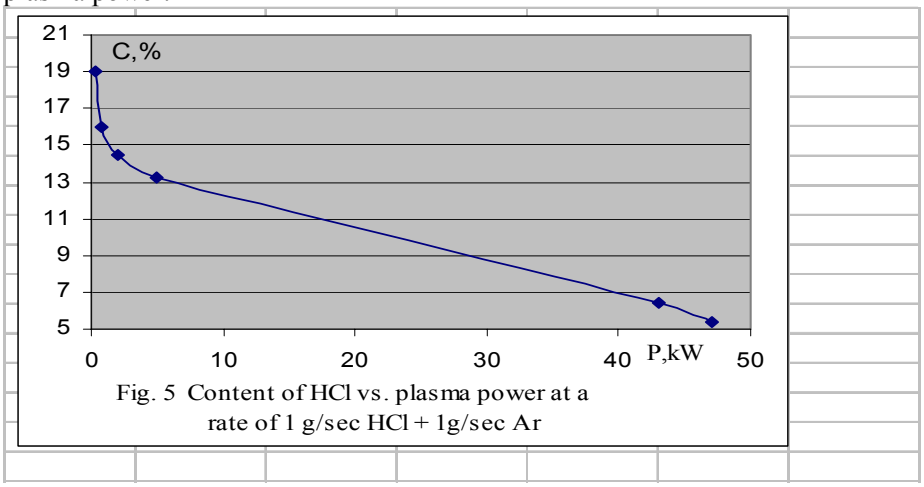

Fig. 5 Content of HCl vs. plasma power at a rate of 1 g/sec HCl + 1g/sec Ar

The dissociation of the C_6H_5Cl and $C_6H_2Cl_4$ was performed in the capacitive plasma discharge in the presence of water vapor. Fig. 6 shows the dependence of the destruction temperature vs. the specific plasma power.

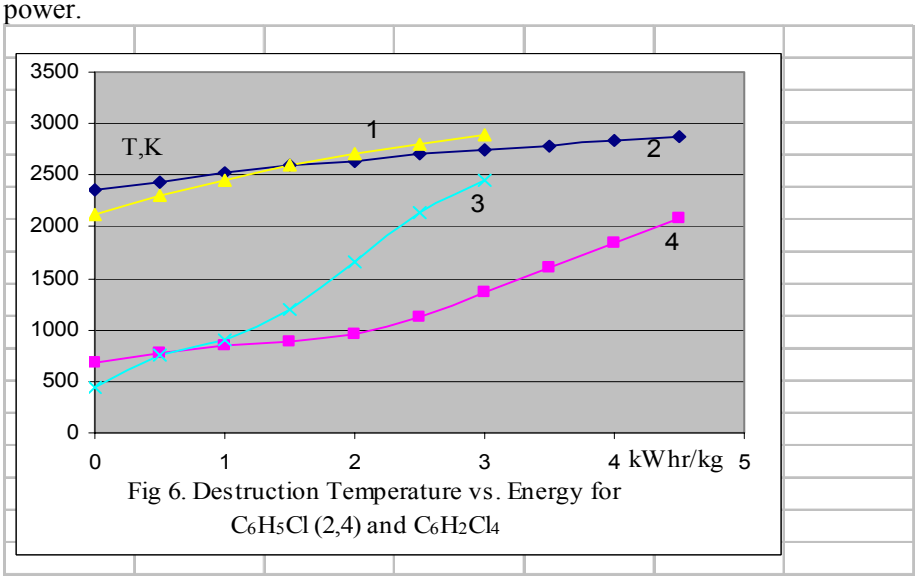

Fig 6. Destruction Temperature vs. Energy for C_6H_5Cl (2,4) and $C_6H_2Cl_4$

The advantage of capacitive plasma discharge over an inductive discharge is the higher stability of the operation at a lower discharge power due to a lower minimum sustained power [2]. Also, the electron temperature is considerably higher than the temperature of heavy particles that leads to an increase in the rate of dissociation (fig 7).

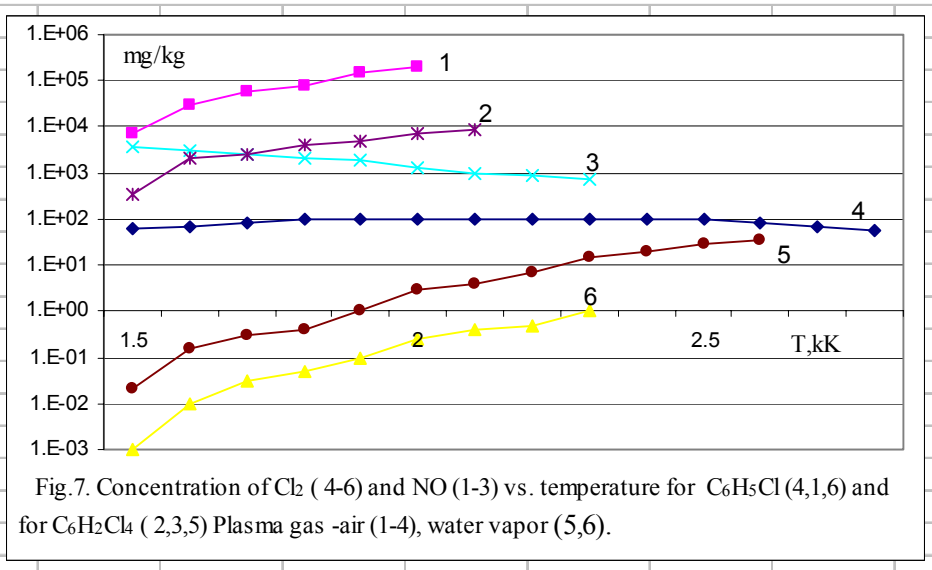

Fig.7. Concentration of Cl_2 (4-6) and NO (1-3) vs. temperature for C_6H_5Cl (4,1,6) and for $C_6H_2Cl_4$ (2,3,5) Plasma gas -air (1-4), water vapor (5,6).

Using the water vapor as plasma gas allows one to increase the discharge power while helping to decrease the by-products, like NO etc.

6. Conclusion:

1. The dissociation of HCl within the RF plasma discharge with the temperatures above 6000K has a thermodynamic character that is described above. Based on reactor design (the distance between discharge and quenching device was about 10 cm) the processing time was around $3x10^{-3}$ sec. According to our theoretical calculations for processing time $3x10^{-3}$ sec at T = 6000K, we can achieve 95% conversion (parameter n =0). This is close to our experimental results. The difference arises because the temperature profile is not uniform.
2. An important factor is the Argon. Argon was chosen for two reasons:
   -The ignition and stabilization of the RF discharge at atmospheric pressure is not difficult - Argon is an inert gas and can be recycled.
   It is known that fast argon ions Ar^+ can create a stable complex of $\{ArH\}^+$ and Cl during the collisions of Ar^+ and HCl [3-4]. The dissociation energy of the above complexes is around 2 eV. The existence of the above complexes was confirmed at low pressure and with fast ions in the discharge. The following reactions take place:

   $$Ar + e \text{ ---- } Ar^+ + 2e;$$
   $$Ar^+ + HCl \text{ -----} \{ArH\}^+ + Cl$$

   With RF plasma at high pressure in equilibrium the level of fast Ar^+ is relatively low. Thus, the probability of getting $\{ArH\}^+$ is also is very low. The same dissociation mechanism can be observed in the mixtures with other noble gases.

References

1. G.N. Schading and P. Roth Combustion and Flame 99: 467 – 474 (1994)
2. Low Temperature Plasma (RF and UHF plasma torches)v.6 Novosibirsk:Nauka,1992
3. Gluchkov A.G. The dissociation energy and electron affinity M.:Nauka, 1979

CLUSTERING PROPERTIES OF RARE GAS ATOMS ON AROMATIC MOLECULES

A. Zoppi[a], M. Becucci[a], G. Pietraperzia[a], E. Castellucci[a],
A. Riganelli[b], M. Alberti[b,#], and A. Lagana[b]
[a]Dipartimento di Chimica e LENS, Università di Firenze, Firenze (Italy)
[b]Dipartimento di Chimica, Università di Perugia, Perugia (Italy)
[#]Departament de Química Física, CERQT, Universitat de Barcelona, Barcelona (Spain)

Abstract

The behaviour of rare gas atoms bound to aromatic molecules has been investigated by means of experimental and computational techniques. Experimental results are reported for aniline-neon and –argon systems, while theoretical results showing the importance of using realistic interaction potentials to rationalize the stereo dynamics of this type of systems is discussed for the model benzene-argon clusters.

Introduction

The behaviour of rare gas atoms bound to aromatic molecules was investigated experimentally by measuring the 0-0 band of the $S_1 \leftarrow S_0$ electronic transition of several van der Waals complexes formed in a molecular beam using high resolution electronic spectroscopy [1]. The analysis of the rotationally resolved spectra allowed us to determine the rotational constants and, therefore, to estimate the effective value of the various components of the moment of inertia for these systems. From these data it was also possible to determine, in special cases, the equilibrium value of the rare gas atom coordinates and the amplitude of the zero point motion.
Experimental results can be compared with theory by working out an interaction potential and performing a molecular dynamics (MD) simulation. To carry out meaningful MD simulations it is essential to use realistic representations of the potential energy surface. The difficulties arising in the description of the interaction of heterogeneous clusters and the sensitivity of the potential energy minima and transition states to the value of the parameters of the adopted functional form stress out the importance of providing an accurate description of the force field of the system [2]. In particular, for strongly anisotropic systems, like the benzene-rare gas ones, the atom-atom pairwise additive functional form has serious difficulties in describing geometries other than the most stable one. Nevertheless, these additional less stable geometries are very important since at certain temperatures they are accessible and make the system isomerize by transforming between different isomers via unstable geometries. Despite the fact that, as shown in several contexts, pairwise additive potentials give a poor description of inter- and intra-molecular forces, many MD studies of clusters of aromatic molecules and rare gas atoms have been performed using these potentials. There are basically two main reasons for this. First, pairwise additive potentials are easy to evaluate, allowing thus, faster computations. Second, it is difficult to obtain realistic estimates of the potential energy surface for complexes dominated by long range interactions using *ab initio* techniques.
In this paper we present experimental results for the aniline-neon and aniline-argon systems and we discuss the use of alternative formulations of the interaction by considering the prototype benzene-Ar system.

Experimental

Experimental studies on van der Waals complexes have been carried out at the Molecular Beam facility of LENS in Florence [1]. The apparatus for high resolution electronic spectroscopy consists of a 50 microns diameter nozzle that allows the flow of a high pressure gas mixture (sample and carrier gas; the total pressure is typically 600 KPa) into a vacuum chamber (pumped by a 6000 l s^{-1} diffusion pump). In the expansion process the collisions cool the sample gas down to a few Kelvin degrees. The expanded gas is then spatially filtered by a skimmer and enters in a second high vacuum chamber (10^{-4} Pa during the experiment) pumped by a 2000 l s^{-1} diffusion pump. The resulting molecular beam consists of very cold molecules travelling in the direction of the expansion in a collision free environment. Therefore, weakly bound intermolecular van der Waals complexes formed during the expansion can live long enough to be studied. By crossing the

molecular beam with a laser beam in a 90° configuration and by detecting with large aperture optics the total fluorescence emission from the excited molecules, we have set up a Doppler free molecular beam laser spectrometer working in the visible-ultraviolet region of the spectrum. The laser source is a single mode, frequency stabilized, ring dye laser (a modified Coherent 699-21, 1 MHz bandwidth, up to 2W mission round 590 nm) pumped by a large frame argon ion laser (up to 9W at 514.5nm). The dye emission is frequency doubled in a BBO crystal placed in an external optical resonator. In this way a laser beam of 40mW having a wavelength around 295 nm is generated. The instrumental frequency resolution of the spectrometer is about 15 MHz in a Gaussian profile, dominated by the residual Doppler broadening.

Results

The laser induced fluorescence spectra of the van der Waals complex of aniline with rare gas atoms obtained with a full rotational resolution (see Figure 1) have been analysed using custom software.

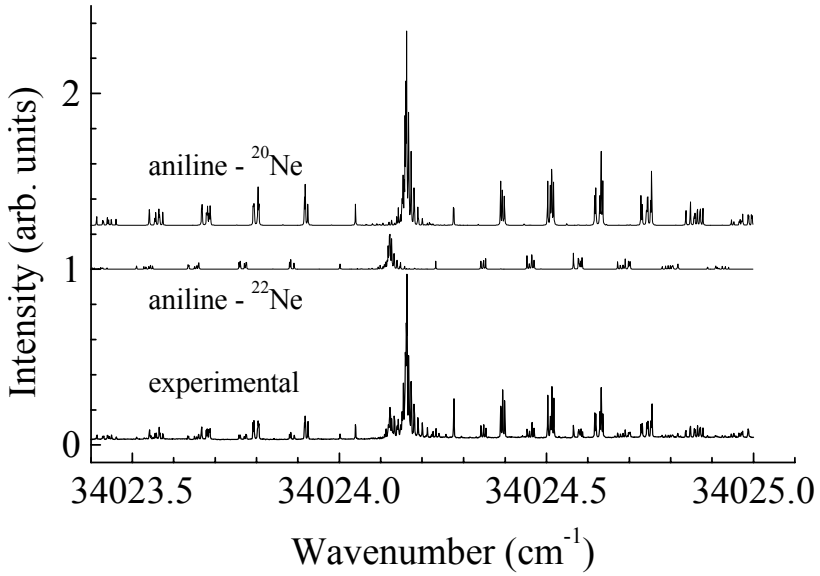

Figure 1: A comparison of the measured (lower curve) high resolution LIF spectrum of the 0_0^0 $S_1 \leftarrow S_0$ vibronic transition of the aniline-neon complex with its simulations (upper curves) calculated using the parameters of Table 1.

The pattern of the rovibronic spectrum has been simulated using the Hamiltonian of a rigid rotor by a trial and error procedure. This allowed us to assign a large set of transitions and to adjust the value of the ground and upper state rotational constants by a least square fit. The rotational constants offer a direct measure of the vibrationally averaged value of the various components of the inertia tensor. The related coordinate values are *effective* coordinates. The information contained in the rotational constants is in fact of the type $\langle X^2 \rangle$ whilst the structure is related to $\langle X \rangle$, with X being a generic coordinate of the complex. However the two quantities are related to the following equation

$$\langle X^2 \rangle = \langle X \rangle^2 + \langle \delta X \rangle^2$$

where $\langle \delta X \rangle$ is the mean vibrational displacement. Relevant data for the investigated systems are given in Table 1 where the ground and the excited state rotational constants of the aniline-neon and aniline-argon complexes are given.

Table 1: Ground and upper state rotational constants[a] of the aniline–neon and aniline–argon van der Waals complexes.

	A”	B”	C”	A’	B’	C’
Aniline–^{22}Ne	0.06100(2)	0.05537(1)	0.04182(2)	0.06043(2)	0.05478(3)	0.04251(9)
Aniline–^{20}Ne	0.06184(2)	0.05750(1)	0.04359(1)	0.06138(3)	0.05672(3)	0.04432(9)
Aniline-Ar	0.060029(8)	0.038265(2)	0.031023(2)	0.059306(9)	0.039083(2)	0.031989(2)

[a] Units: cm^{-1}; the standard deviation of the fit is reported in parentheses in units of the last significant digit.

In the case of the van der Waals complexes formed by aromatic molecules and rare gas atoms, the binding energy is so small (typically below 500 cm^{-1}) to consider the internal coordinates of the aromatic molecule unchanged after the formation of the complex. Therefore, the inertia tensor of the complex can be easily written using the rotational constants of the isolated aromatic molecule.

$$\begin{Bmatrix} k/A_0 + \mu(Y^2 + Z^2) & -\mu X\,Y & -\mu X\,Z \\ -\mu X\,Y & k/B_0 + \mu(Z^2 + X^2) & -\mu Y\,Z \\ -\mu X\,Z & -\mu Y\,Z & k/C_0 + \mu(X^2 + Y^2) \end{Bmatrix} \quad (1)$$

In equation (1) μ is the reduced mass of the complex, *X*, *Y* and *Z* are the Cartesian coordinates of the rare gas atom in the original reference frame of the aromatic molecule, and *k* is the proportionality constant $h / (8\pi^2 c)$ (in units of cm^{-1} amu $Å^2$) [3]. The effective values of *X*, *Y* and *Z* can be analytically derived by diagonalization of the inertia tensor, using the so-called Kraitchmann equations[4]. The reference frame has been placed on the aniline center of mass with the *XZ* plane coinciding with the symmetry plane of aniline (C_s symmetry) and the aromatic ring placed on the *XY* plane. The values of the vibrationally averaged coordinates obtained from the analysis of the inertia tensor are reported in Table 2.

Table 2**:** Ground (") and upper (') state effective coordinates[a] of the rare gas atom with respect to the center of mass of aniline (see the text for further information on the axis orientation).

	X"	Y"	Z"	X'	Y'	Z'
Aniline–^{22}Ne	0.2088(18)	0.2582(23)	3.40(3)	0.2203(10)	0.1660(8)	3.38(2)
Aniline–^{20}Ne	0.1807(15)	0.1279(11)	3.41(3)	0.1986(9)	0.1188(6)	3.38(2)
Aniline-Ar	0.2852(1)	0.2797(1)	3.504(1)	0.3434(2)	0.3541(3)	3.514(2)

[a] Units: Å; the standard deviation is reported in parentheses in units of the last significant digit.

The most significant information is provided by the effective value of the *Y* coordinate that represents the mean vibrational displacement of the rare gas atom out of the aniline plane of symmetry (C_s configuration). The value determined for the effective coordinate *Z* is also of relevance since it mainly reflects the average distance of the rare gas atom from the aromatic ring ($\langle Z \rangle >> \langle \delta Z \rangle$). The effective coordinate *X*, instead is less informative. In fact, it is impossible to disentangle the equilibrium and the vibrational terms which are both expected to be non zero and not differ by orders of magnitude.

Dynamical Calculations

As already mentioned, dynamical calculations were carried out for the model benzene-Ar(n) system. For this system some dynamical studies were performed in the past using pairwise additive potentials[5-7]. In our study, the potential proposed by Wales et al.[8] (obtained by summing the relevant Lennard-Jones (12-6) diatomic contributions (PES1)) was used. Preliminary results of our dynamical calculations for benzene-Ar(2) are given in references[9].
Recently, a realistic analytical potential energy surface (PES2) for benzene-rare gas systems, explicitly dealing with the dependence of the potential energy from the collision angles has been proposed[10]. This functional form, $V(R,\theta,\phi)$, is expressed as the product of a Morse-Swithing-van der Waals radial term times the spherical harmonics (expressed in terms of Legendre and associated Legendre polynomials[11]) describing the angular dependence of the interaction

$$V(R,\theta,\phi) = V_0^0(R) + V_2^0(R)P_2(\cos\theta) + V_4^0(R)P_4(\cos\theta) + \\ + V_6^0(R)P_6(\cos\theta) + V_6^6(R)P_6^6(\cos\theta)\cos(6\phi) \quad (2)$$

where the first radial term, $V_0^0(R)$, represents the isotropic component on the interaction and the remainder terms describe the overall anisotropy.
The parameters of the functional are optimised to the reproduction of crossed molecular beam data. The $V_0^0(R), V_2^0(R)$ and $V_4^0(R)$ radial terms have been parameterized switching a Morse function at short and intermediate distances and with a van der Waals dispersion attraction at long range. $V_6^0(R)$ and $V_6^6(R)$ have been parametrized switching an exponential function at short range with a simpler long range dispersion attraction.
In Figure 2 we show the coordinate system used to describe the benzene-rare gas complex adopted in this work.

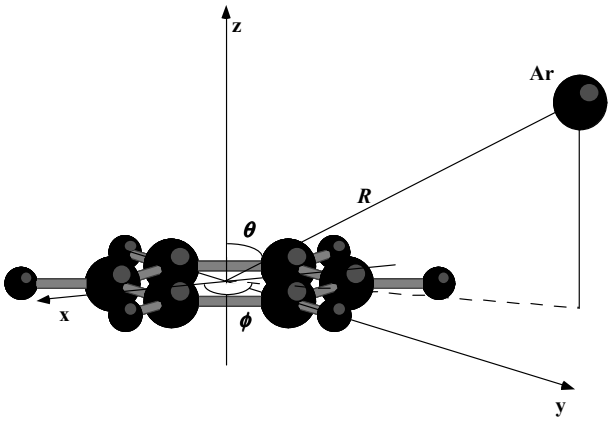

Figure 2. Coordinate system for the benzene-rare gas complex.

The value of the parameters of PES1 are given in Table 3 while those of PES2 are given in reference [10].

Table 3: Lennard- Jones parameters of PES1.

Atom pair	σ/ Å	ε / kcal mol^{-1}
Ar-C	3.42	0.11494
Ar-H	3.21	0.09435

A comparison of the properties of the two PESs is given in Figure 3 where the potential energy is plotted as a function of the angle θ for a given value of R and ϕ. The figure clearly shows that PES1 and PES2 have quite different properties near the in-plane configuration. (θ=90 degrees). Indeed, the energy barrier appearing when the system approaches to planar structures is much more pronounced for PES1 than for PES2.

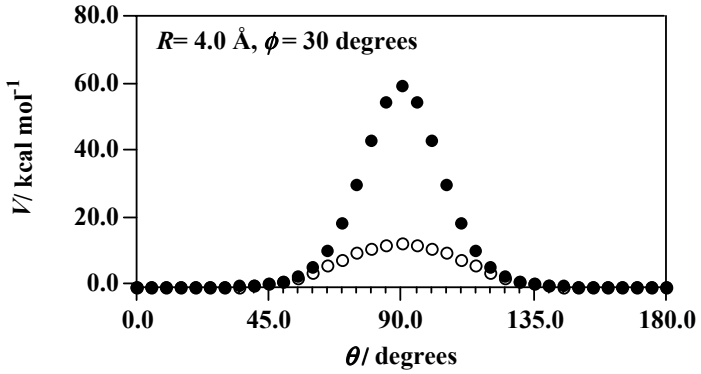

Figure 3. Potential energy *vs* angle θ. Solid circles (PES1), open circles (PES2).

It is interesting also to note that, as can be observed in Figure 4, the two PESs show non negligible differences also for geometries away from in-plane configurations ($\theta \neq 90$ degrees).

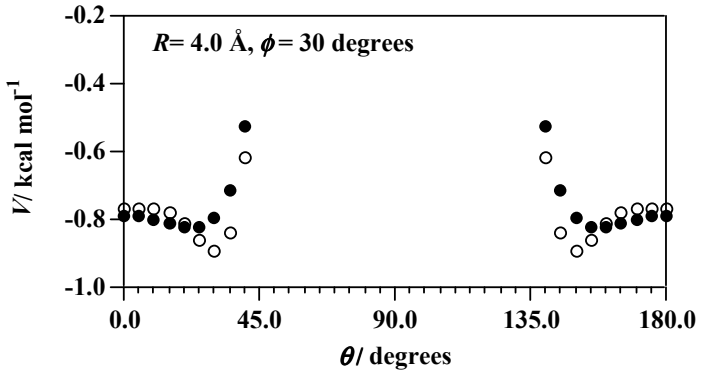

Figure 4. Potential energy *vs* angle θ. Solid circles(PES1), open circles (PES2).

As it can be seen in Figure 5, significant differences between PES1 and PES2 have been also found for the dependence of the potential energy on the ϕ angle. As a matter of fact the two curves show an opposite phase (i.e. a minimum for PES1 corresponds to a maximum for PES2 and *vice versa*). The behaviour of PES2 agrees with accurate *ab initio* calculations[12] predicting a minimum of energy when the Ar atom approaches C_6H_6 at the middle of the C-C bonds.

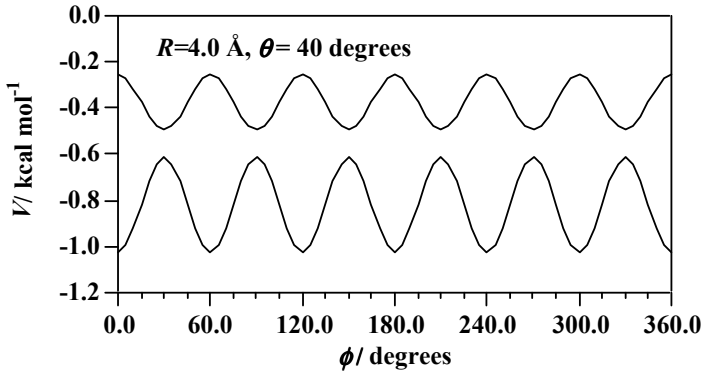

Figure 5. Potential energy *vs* angle ϕ. Dotted line (PES1), continuous line (PES2).

To carry out a dynamical test of the PES2 functional form, calculations were carried out using the DL-POLY suite of programs[13]. The temperature of the benzene-Ar system was set at 15 K and 25 K by taking the benzene molecule frozen at its equilibrium configuration. To introduce PES2 in DL-POLY an extended customization work was necessary. To this end, the interaction between the Ar atom and the centre of mass of the benzene molecule (once the molecule is correctly placed in the *XY* plane) is treated as an interaction bond by adding a dummy atom at the centre of mass of C_6H_6. The rotation of the system, needed to calculate the potential energy and the corresponding derivatives, was treated using the quaternion matrix representation. The forces were calculated by working out an analytical expression for the first derivatives of the potential.

This preliminary study shows that PES2 is appropriate for use in dynamical calculations. Dynamical simulations in the microcanonical ensemble during 100 ns allow to test the conservation of the total energy.

However, evidence was also obtained for the need of further improving the formulation of the potential functional. To this end work is being carried out on the development of a pseudo additive pair potential based on bond order coordinates[14,15].

Conclusions

The study of clustering properties of rare gas atoms and aromatic molecules is both an important experimental application and a challenging theoretical problem.

In this paper the experimental work carried out using the Molecular Beam apparatus at LENS has shown that it is possible to obtain from the experiment valuable information on the structure of the adducts.

From the theoretical point of view, the work pointed out some critical features of the interaction and the need for working out more accurate functional representations of the potential energy surface.

Acknowledgments

Financial support from the Italian Space Agency (ASI) and the MIUR is acknowledged. M. Albertí thanks the generous support from the Ministerio de Educación, Cultura y Deporte (Programa para la movilidad de profesores españoles y extranjeros: PR2002-0014). The Spanish DGICYT (Projects PB97-0919 and BQU2001-3018) and the Generalitat de Catalunya (CUR 20001SGR-00041) are also acknowledged.

References

[1] E. R. Th. Kerstel, M. Becucci, G. Pietraperzia, E. Castellucci, *Chem. Phys.*, **199** (1995) 263
[2] A. Dullweber, M.P. Hodges, D.J. Wales, *J. Chem. Phys.,* **106** (1997) 1530
[3] M. Becucci, G. Pietraperzia, N. M. Lakin, E. Castellucci and Ph. Brechignac, *Chem. Phys. Lett.*, **260** (1996) 87
[4] J. Kraitchman, *Am. J. Phys*., **21** (1953) 17
[5] J. Vacek; P. Hobza, *J. Phys. Chem.*. **98** (1994) 11034
[6] J. Vacek; P. Hobza, J. Jortner, *J. Phys. Chem.*. **102** (1998) 8268
[7] V. Bernshtein, I. Oref, *Chem. Phys. Letters* **300** (1999) 104
[8] D. J. Wales, P.L.A. Popelier, J. Stone, *J. Chem. Phys.* **108** (1995) 5551
[9] A. Riganelli, M. Memelli, A. Laganà, *Lecture Notes in Computer Science,* **926** (2002) 2331
[10] F. Pirani, M. Porrini, S. Cavalli, M. Bartolomei, D. Cappelletti, *Chem. Phys. Letters* **367** (2003) 405
[11] J.S. Gradshteyn, I.M. Ryzhik, Table of Integrals, Series and Products, Academic Press, New York, 1980
[12] H. Koch, B. Fernández, J. Makarevicz, *J. Chem. Phys.* **111** (1999) 198
[13] http://www.dl.ac.uk/TCSC/Software/DL-POLY
[14] A. Laganà, *A Molecular Dynamics Metalaboratory in Theory of the Dynamics of Elementary Chemical Reactions* NATO ARW Workshop, Balantofoldvar, 2003
[15] E. García, A. Rodríguez, M.L. Hernández, A. Laganà, *J. Phys. Chem.* (submitted)

The Influence of the Surface State on the Glow-to-Arc Transition at Reduced Pressure

B. Juettner[1], and C. H. Wu[2]

[1]*Humboldt-University Berlin, Institute of Physics, Hausvogteiplatz 5/7, D-10117 Berlin, Germany*
[2]*Max-Planck-Institute for Plasma Physics, D-85748 Garching, Germany*

Abstract
The paper reports experiments on the glow-to-arc transition in deuterium in the pressure region 1-12 mbar. Rectangular high voltage pulses have been applied to electrodes of various materials at gap distances of 5-10 mm and in the presence of magnetic fields of 0-0.4 T in various configurations. The transition to the arc manifests itself by formation of cathode spots. The transition was analysed by high speed imaging with time resolution of 100 ns. It has been found that the formation of arc cathode spots is preceded by an enhancement of the particle density near the cathode. This can be reached by the formation of anodic plasmas (anode spots) prior to the occurrence of the cathode spots or by gas desorption from the cathode surface. If the latter is reduced by heating the cathode, the pulse voltage necessary for the transition is considerably increased. Also, conditioning effects can be explained by the role of adsorption. Admixture of 1 % oxygen to the gas strongly reduced the transition voltage for some materials. The consequence of these findings is that for the transition the electric field at the cathode is more important than the surface temperature.

1. Introduction

The transition of a glow discharge into an arc is an important issue of gas discharge physics. This phenomenon takes place at breakdown and after transient extinction of burning arcs. In spite of its widespread occurrence it is poorly understood. Since arcs with cold electrodes need cathode spots to exist, the transition means the generation of such spots where surface material is molten, evaporated and transformed into a surface plasma. So a general opinion is that contraction of the glow discharge plasma must enhance the energy transport to the surface until local melting takes place [1]. The present paper examines this question experimentally.

2. Experimental setup

The electrodes consisted of half-spheres of 10 mm diameter made of graphite, or of hairpins of tungsten or molybdenum made of wires of 1 mm diameter. They were placed in glass tubes connected to a clean vacuum system with base pressure 10^{-8} mbar. Spectrally pure gases could be introduced, especially deuterium, hydrogen and oxygen. The hairpin electrodes could be heated up to 2000 K by passing a current from a battery. Magnetic fields parallel or perpendicularly to the electrode axis could be produced by using coils or permanent magnets with an induction of 0.1–0.4 T. Figure 1 shows a section of the glass tube placed inside the coils. The upper electrode is the graphite anode, the lower electrode is the heated tungsten cathode. Rectangular high voltage pulses of 0.5-15 kV were applied to the electrodes via a series resistor of 110 Ohm. This resulted in a glow discharge, followed by the transition into an arc at sufficiently high voltage. The discharges were registered (i) by the high speed camera IMACON 468 having seven frame channels that use the same optical axis [1], (ii) by the sensitive color camera SENSICAM, and (iii) by a four channel digital oscilloscope having a bandwidth of 1 GHz.

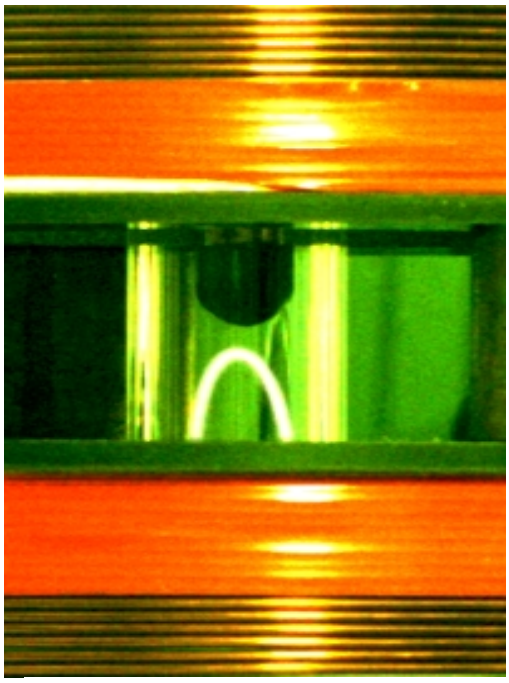

Figure 1: Discharge tube with electrodes, placed inside magnetic field coils. Upper electrode: graphite, 10 mm diameter. Lower electrode: hot tungsten hairpin.

3. Results

Figure 2 shows a discharge between graphite electrodes in 1 mbar deuterium with magnetic field parallel to the electrode axis. The magnetic field confines the glow discharge to a column with a diameter of the electrode size. The arc is characterized by a cathode spot and a luminous column. Figure 3 gives a time resolved sequence of the phenomenon. Here the glow-to-arc transition lasts 200-400 ns. Without magnetic field this transition is preceded by the formation of anode spots as demonstrated in figure 4. In frame 2 the glow discharge constricts itself at the anode, leading to anode spots after about 200 ns, frames 3-7. Another 200 ns later a cathode spot appears, frame 4. It produces surface plasma that expands against the ambient gas, frames 4-7. Thus, if there exits no magnetic field that confines the plasma, additional plasma must be generated at the anode to support the formation of cathode spots.

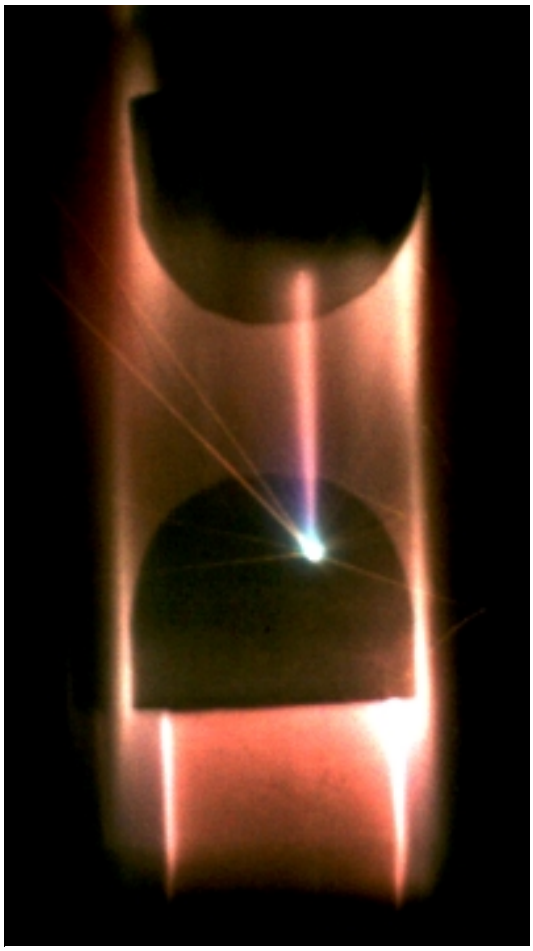

Figure 2: Glow-to-arc transition in deuterium between graphite electrodes. Electrode distance 7 mm, magnetic field (0.12 T) parallel to the electric field, pressure 1 mbar.

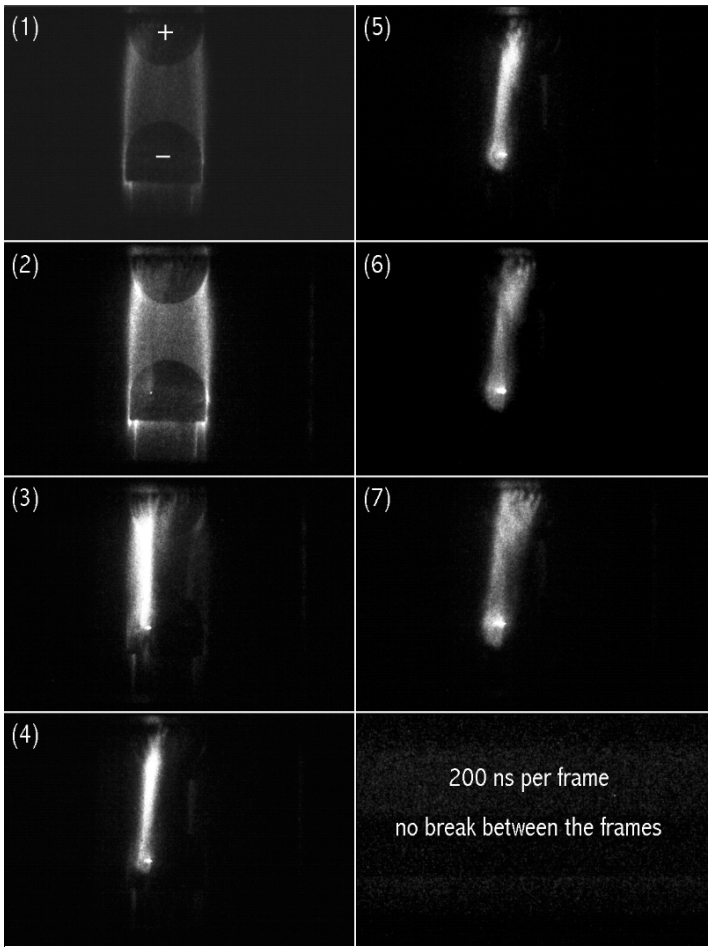

Figure 3: High speed photograph of a glow-to-arc transition at conditions equal to figure 1. Frame sequence down the columns, exposure time 200 ns, no break between the frames.

In a second experiment, the probability of unipolar spot formation (i.e. arcing by the contact of a floating electrode with a hot plasma) has been studied with a hot hydrogen plasma. The device has been described in ref. [2]. Here the plasma parameters were measured by Langmuir probes. As shown in figure 5, the probability rises strongly with the electron density.

Indirectly, another phenomenon could be identified that is important for the ignition of cathode spots, viz. the desorption of gases at the cathode. It manifests itself by conditioning effects and the influence of the cathode temperature. Figure 6 shows the arcing probability to decrease strongly as a function of the number of applied pulses for graphite electrodes. Figure 7 shows the pulse voltage necessary for 50% arcing probability as a function of the temperature of a molybdenum cathode. At about 1000 K there occurs a steep increase of the curve, reaching saturation at about 1400 K. Figure 8 demonstrates a combination of heating and conditioning effects. The arcing probability decreases by heating and by the repetition of the discharges.

After each curve the cathode was allowed to cool down, and the following curve started again with high arcing probability. Finally, admixture of oxygen reduced the arcing voltage as listed in Table 1.

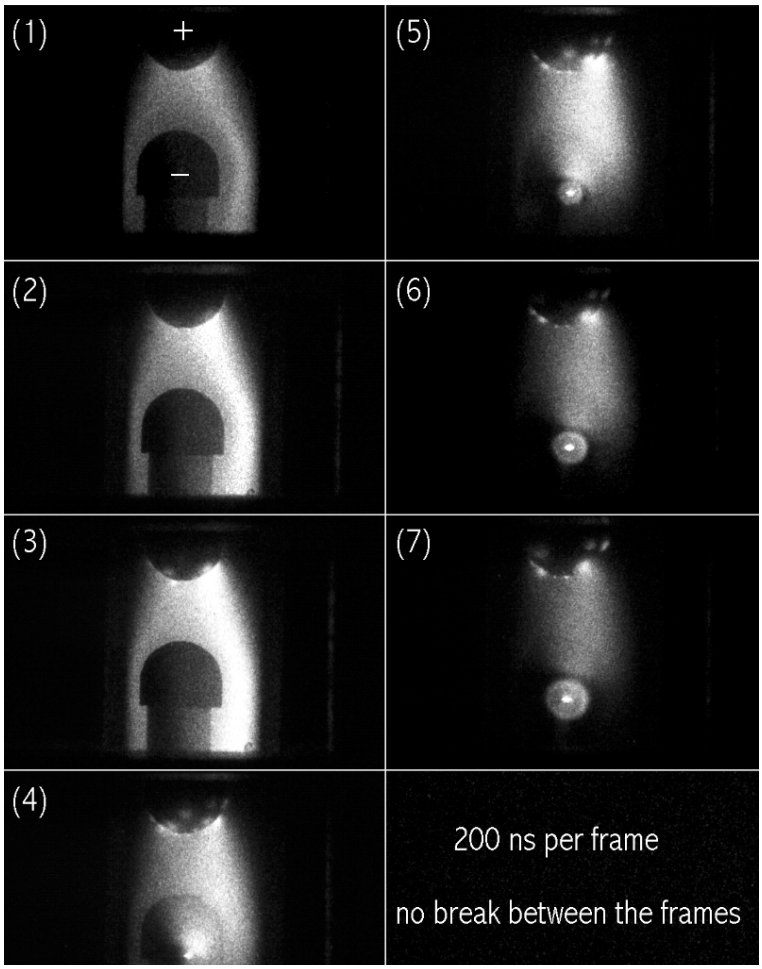

Figure 4: Analogous to figure 3, but without magnetic field.

Table 1**:** Voltage for 50% arcing probability after conditioning

Material	1 mbar D_2	1 mbar D_2 +1% O_2
Graphite at room temperature	2.3 kV	2.2 kV
Mo at room temperature	7.5 kV	5.9 kV
W at room temperature	13.5 kV	5.2 kV
Mo, W at 1400K	>15 kV	-

4. Discussion

The experiments show that cathode spot formation must be preceded by an increase of the particle density near the cathode. This can be achieved by the action of anode spots or by desorption of gases from the cathode surface. The latter explains the decrease of the arcing probability during conditioning (figures 6, 8) or the increase of the necessary pulse voltage as a function of cathode temperature (figure 7). As indicated in Table 1, adsorption of oxygen plays an important role. Such adsorbates have a high binding energy, so temperatures around 1000 K are necessary for desorption, in agreement with figure 7.

The steep curve in figure 5 demonstrates that the electron density is a very critical parameter. The effect must be due to the electric field in the space charge sheath rather than by the surface temperature. Otherwise the arcing probability would grow with the temperature. However, as figure 7 demonstrates, the breakdown

voltage increases strongly with the cathode temperature. From figure 8 it can be concluded that conditioning is more effective at high temperatures.

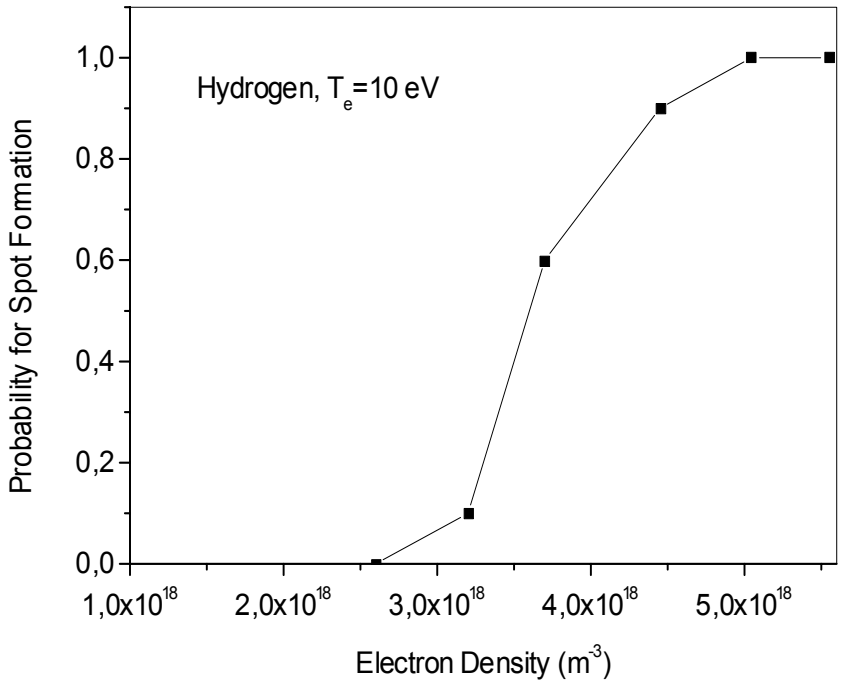

Figure 5: Probability of unipolar arcing in hot hydrogen plasma as a function of the electron density.

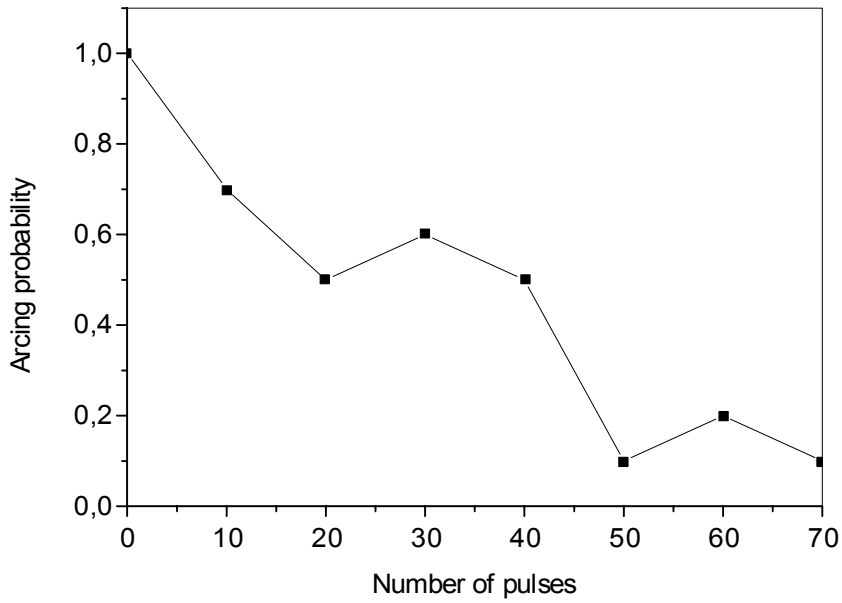

Figure 6: Arcing probability for graphite electrodes in deuterium (1 mbar) as a function of the number of applied pulses with an amplitude of 1.6 kV.

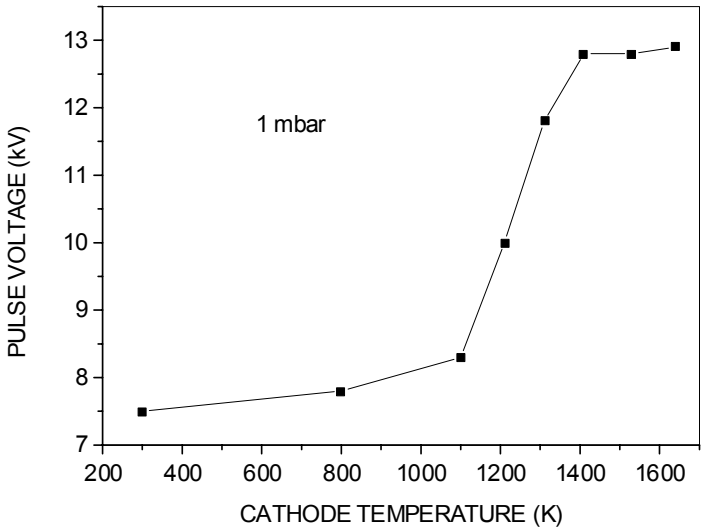

Figure 7: Pulse voltage necessary for 50% arcing probability as a function of the temperature of the molybdenum cathode.

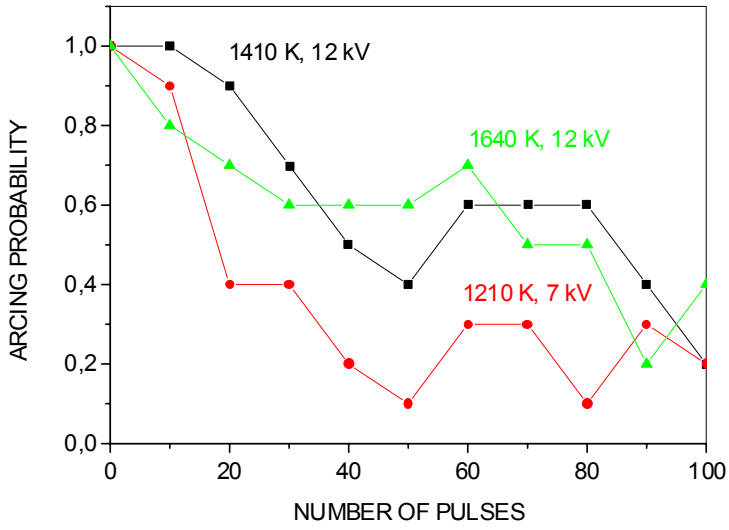

Figure 8: Decrease of the arcing probability as a function of the number of applied pulses at various temperature of a hot molybdenum cathode.

In a simplified form, the space charge field F at the cathode reads

$$F \approx \frac{kT_e}{e\lambda_{D,e}}\left(\frac{eV_c}{ZkT_e}\right)^{1/4}$$

where T_e and $\lambda_{D,e}$ are temperature and Debye length of the plasma electrons, respectively, Z is the ion charge, and V_c is the cathode fall voltage. With plausible values of plasma temperature and density, this formula yields fields $<10^7$ V/m, more than two orders of magnitude smaller than required by the Fowler-Nordheim equation for noticeable field electron emission. However, this does not mean that such emission is not possible. A similar

discrepancy is known from experiments with vacuum breakdowns. Here electron emission can be measured at similarly small fields (e.g. ref. [3]). Still another analogy is the vacuum-microelectronics where arrays of field emitters are produced by well defined solid-state techniques. For such systems Obraztsov et al. [4] found high emission at microfields that are by 1-2 orders of magnitude smaller than expected from the Fowler-Nordheim-equation. According to these authors the surface barrier is more complicated than assumed in the theory, so the tunneling probability is markedly increased.

5. Conclusions

At reduced pressures the glow-to-arc transition is controlled by the particle density at the cathode rather than by the local surface temperature. This points at the role of cold field electron emission for the initiation of cathode spots. Estimated values of the electric surface field indicate that this emission cannot be described by the classical Fowler-Nordheim-equation, a situation which is similar to phenomena of prebreakdown electron emission in vacuum.

References

[1] Yu. P. Raizer,"Gas Discharge Physics", Springer Berlin, 1991.
[2] V. A. Ivanov, B. Jüttner, and H. Pursch, "Time-Resolved Measurements of the Parameters of Arc Cathode Plasmas in Vacuum", IEEE Trans. Plasma Sci., **PS-13**, 334-336 (1985).
[3] B. Jüttner, "Instabilities of prebreakdown currents in vacuum II: the nature of the emitting sites", J. Phys. D: Appl. Phys., **32**, 2544-2551 (1999).
[4] A. N. Obraztsov, A. P. Volkov, K. S. Nagovitsyn, K. Nishimura, K. Morisawa, Y. Nakano and A. Hiraki, "CVD growth and field emission properties of nanostructured carbon films", J. Phys. D: Appl. Phys., **35**, 357-362 (2002).

Experimental investigation on puffing exploding wire vapor plasma

Rahmani Bouabdallah[1], Yasuoka Kouiti[2] and Ishii Shozo[2]

1- Institute of Electronics, University of Sciences and Technology of Oran (U.S.T.O), B.P.1505 Mnaouer, Oran, ALGERIA
Email:brrahmani@caramail.com
2- Department of Electrical and Electronic Engineering
Tokyo Institute of Technology (T.I.T)
2-12-1 O-Okayama, Meguro-ku, Tokyo, JAPAN

A simple experimental method is proposed to investigate the radiation emitted from the boundary layer, which is formed near the insulator wall. This method consists of a fast-pulsed exploding aluminum wire set on the Low-Density PolyEthylene (LDPE) flat wall. Two phases have been observed in the intensity shape of the aluminum and the carbon atoms lines showing an enhancement during the collisionless interaction regime. The photoablation of LDPE wall was occurred during the plateau as observed in the temporal behavior of the intensity of the carbon atom line, which agree with the observed peak value in the UV radiation emission.

Deposition of High Density Aligned Carbon Nanotubes by Pulsed Plasma

L. Valentini[1], I. Armentano[1], J. M. Kenny[1], S. Santucci[2]

[1]*Materials Engineering Center, Università di Perugia, 05100 Terni - Italy*

[2]*Dipartimento di Fisica - Unità INFM, Università dell'Aquila, 67010 Coppito (AQ) - Italy*

Abstract

The growth of uniform films of well-aligned carbon nanotubes using pulsed plasma enhanced chemical vapor deposition is here reported. So, it is demonstrated that nanotubes can be grown on a certain critical catalyst film thickness and that their alignment is primarily induced by pulsed plasma excitation time. It is, in fact, found that switching the plasma source for 0.1s effectively turns the alignment mechanism on, leading to a sharp transition between the pulsed plasma-grown straight nanotubes and continuous plasma-grown curly nanotubes.

References

[1] S. Iijima, T. Ichihashi, Nature 363 (1993) 603.

[2] D.S. Bethune, C.H. Kiang, M.S. deVries, G. Gorman, R. Savoy, J. Vazquez, R. Beyers, Nature 363 (1993) 605.

[3] A. Thess, R. Lee, P. Nikolaev, H. Dai, P. Petit, J. Robert, C. Xu, Y.H. Lee, S.G. Kim, D.T. Colbert, G. Scuseria, D. TomaÂnek, J.E. Fischer, R.E. Smalley, Science 273 (1996) 483.

[4] M. Terrones, N. Grobert, J. Olivares, J.P. Zhang, H. Terrones, K. Kordatos, W.K. Hsu, J.P. Hare, P.D. Townsend, K. Prassides, A.K. Cheetham, H.W. Kroto, D.R.M. Walton, Nature 388 (1997) 52.

[5] Z.F. Ren, Z.P. Huang, J.W. Xu, J.H. Wang, P. Bush, M.P. Siegal, P.N. Provencio, Science 282 (1998) 1105.

[6] S.L. Sung, S.H. Tsai, C.H. Tseng, F.K. Chiang, X.W. Liu, H.C. Shih, Appl. Phys. Lett. 74 (1999) 197.

[7] N. Hamada, S. Sawada, A. Oshiyama, Phys. Rev. Lett. 68 (1992) 1579.

[8] J.W. Mintmire, et al., Phys. Rev. Lett. 68 (1992) 631.

[9] T.M. Whitney, J.S. Jiang, P.C. Searson, C.L. Chien, Science 261 (1993) 1316 .

[10] M.S. Dresselhaus, G. Dresselhaus, P.C. Eklund, Science of Fullerenes and Carbon Nanotubes (Academic Press, San Diego, 1996), (Chapter 19) and references therein.

[11] M.M.J. Treacy, T.W. Ebbesen, J.M. Gibson, Nature 381 (1996) 678.

[12] P. Delaney, H.J. Choi, J. Ihm, S.G. Louie, M.L. Cohen, Nature 391 (1998) 466.

[13] W.A. de Heer, A. Chatelain, D. Ugarte, Science 270 (1995) 1179.

[14] S.J. Tans, R.M. Verschueren, C. Dekker, Nature 393 (1998) 49.

[15] S.J. Tans, R.M. Verschueren, C. Dekker, Nature 386 (1997) 474.

[16] C. Journet, W.K. Maser, P. Bernier, A. Loiseau, M.Lamy de la Chapelle, S. Lefrant, P. Deniard, R. Lee, J.E. Fischer, Nature 388 (1997) 756.

[17] W.Z. Li, S.S. Xie, L.X. Qian, B.H. Chang, B.S. Zou, W.Y. Zhou, R.A. Zhao, G. Wang, Science 274 (1996) 1701.

[18] C. Bower, W. Zhu, S. Jin, and O. Zhou, Appl. Phys. Lett. 77 830 (2000).

[19] L. Valentini, I. Armentano, J. M. Kenny, L. Lozzi, S. Santucci, J. Appl. Phys. 92 6188 (2002).

[20] L. Valentini, I. Armentano, J. M. Kenny, L. Lozzi, S. Cantucci, Mater. Sci. and Eng. C (2003 in press).

[21] Y.H. Lee, S.G. Kim, D. Tomanek, Phys. Rev. Lett. 78 (1997) 2393.

[22] C.J. Lee, D.W. Kim, T.J. Lee, Y.C. Choi, Y.S. Park, W.S. Kim, Y.H. Lee, W.B. Choi, N.S. Lee, J.M. Kim, Chem. Phys. Lett. 312 (1999) 461.

[23] Y. Y. Wei, G. Eres, V. Merkulov, and D. H. Lowndes, Appl. Phys. Lett. 78 1394 (2001)

[24] M. Yudasaka, R. Kikuchi, Y. Ohki, E. Ota, and S. Yoshimura, Appl. Phys. Lett. 70 1817 (1997).

[25] M. Yudasaka, R. Kikuchi, Y. Ohki, E. Ota, and S. Yoshimura, Appl. Phys. Lett. 67 2477 (1995).

[26] M. Chhowalla, K. B. K. Teo, C. Ducati, N. L. Rupesinghe, G. A. J. Amaratunga, A. C. Ferrari, D. Roy, J. Robertson, and W. I. Milne, J. Appl. Phys. 90 5308 (2001).

[27] C. Riccardi, R. Barni, M. Fontanesi, P. Tosi, Chem. Phys. Lett. 329 66 (2000).

[28] L. Delzeit et al. J. Appl. Phys. 91 6027 (2002).

[29] G. J. Vandentop, M. Kawasaki, R. M. Nix, I. G. Brown, M. Salmeron, G. A. Somorjaj, Phys. Rev. B41 3200 (1990).

[30] Y. Choi, D. Bae, Y. Lee, B. Lee, G. Park, W. Choi, N. Lee, J. Kim, J. Vac, Sci. and. Technol. A 18 1864 (2000).

[31] Y. Choi, D. Bae, Y. Lee, B. Lee, G. Park, W. Choi, N. Lee, J. Kim, Synth. Metals 108 159 (2000).

I. Introduction

Carbon nanotubes (CNTs), synthesized by different methods - arc discharge [1,2], laser vaporization [3], pyrolysis [4], plasma-enhanced chemical vapor deposition (CVD) [5,6] - have been extensively investigated for its unique physical and chemical properties [7-12] and for applications in nanoscale devices [13-15]. The main issues in this field are the synthesis in large quantities, reproducibility, controllability of diameters and lengths, selective growth and its further applications in nanoscale devices such as field emission displays, electrodes for secondary batteries, fuel cells, memory devices and so on [13-16]. In order to apply nanotubes to field emission displays, in situ growth of vertically aligned nanotubes in a large area of substrates is always desirable, since it does not require complex sample-preparation processes. For this purpose, vertically aligned nanotubes have been grown on glass [5] and on porous media [17], although the growth mechanism is still far from being clearly understood. Recently Zhou and coworkers [18] used a microwave methane/hydrogen plasma and clearly showed that the plasma enabled a vertically oriented growth of MWNTs. This encouraging results suggest that low temperature plasmas, particularly those with independent control of the substrate bias, can be useful in the growth of nanotubes with vertical alignment. In this paper, the growth of vertically aligned CNTs using a pulsed radiofrequency plasma enhanced chemical vapour deposition (PECVD) glow discharge system on a Ni catalyst layer is reported and a detailed parametric study of the various factors influencing the growth of CNTs is performed. Specifically, we investigated the effects of the timing of plasma excitation and catalyst layer thickness on the nanotube growth. The nanotubes are characterized using field emission scanning electron microscopy (SEM), atomic force microscopy.

II. Experimental Details

CNTs films were grown on (100) silicon substrates by pulsed plasma enhanced chemical vapor deposition of CH_4 plasma. Thin films (3 and 5 nm) of Ni catalyst were deposited onto Si_3N_4/Si substrates using thermal evaporation. With the plasma discharge in the off position prior to initiating the deposition, the substrates were heated to 650°C and held at this temperature for 15 minutes to induce the clusters formation of the catalyst layer before the activation of the CNTs plasma deposition.

Substrates were positioned onto the heated cathode, capable of reaching a maximum temperature of 850°C, connected to the radiofrequency (RF) power supply. For pulsed-PECVD runs, a peak RF power of 100W was applied during on-time excitation. In our experiment we used an on-time excitation of 0.1s with the duty cycle, defined as a fraction of the total time during which the power was applied, fixed at 50%.

The CNTs depositions were carried out with deposition pressure and temperature fixed at 53 Pa and 570°C, respectively. The total precursor (CH_4) gas flow rate was kept constant at 40 sccm. The film deposition was performed with a rf bias voltage fixed at –150V.

Atomic Force Microscopy (AFM) measurements were performed to evaluate the surface morphology of the films on a Digital Instrument (Model D5000) using the contact mode technique. The scanning electron microscopy investigation was performed on a field emission scanning electron microscope LEO 1530 operated at 5 kV.

III. Results and Discussion

Figure 1 shows AFM images of Ni films of varying thickness (3-5nm) after annealing at 650°C. It was seen that the annealed Ni forms small islands and that the island size depends on the thickness of the initial Ni films; in particular the higher the initial Ni layer thickness the larger the island diameter [19]. The XPS spectra of Ni 2p and O 1s core levels indicate the presence of oxygen physisorbed on Ni due to sample exposure to atmosphere after thermal evaporation [20].

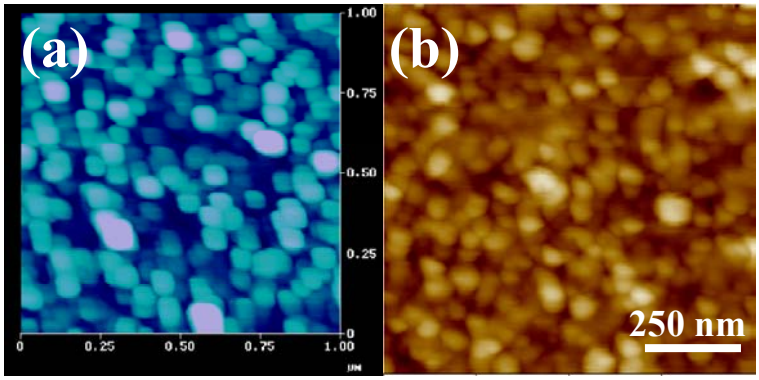

Figure 1: AFM images of Ni films with varying thickness, (a) 5 nm and (b) 3 nm, after annealing at 650°C.

Figure 2 shows high-resolution field emission SEM images of CNTs grown by plasma continuous mode on annealed Ni layers of different initial thickness. From the white spots in this figure it is clear how all nanotubes tips are terminated by the metal particles at the top. This strongly suggests, according to previous reports [21,22], that the metal particles play a crucial role as catalyst for the growth of the carbon nanotubes. With a catalyst layer thickness of 5 nm (Figure 2a) the density of nanotubes is low and amorphous carbonaceous particles are observed with nanotubes. As the catalyst layer thickness decreases to 3 nm the density of nanotubes increases with an average diameter of ≈30nm (Figure 2b). In both cases (Figs. 2a) and 2b) the nanotubes were seen to grow in a random and curly fashion.

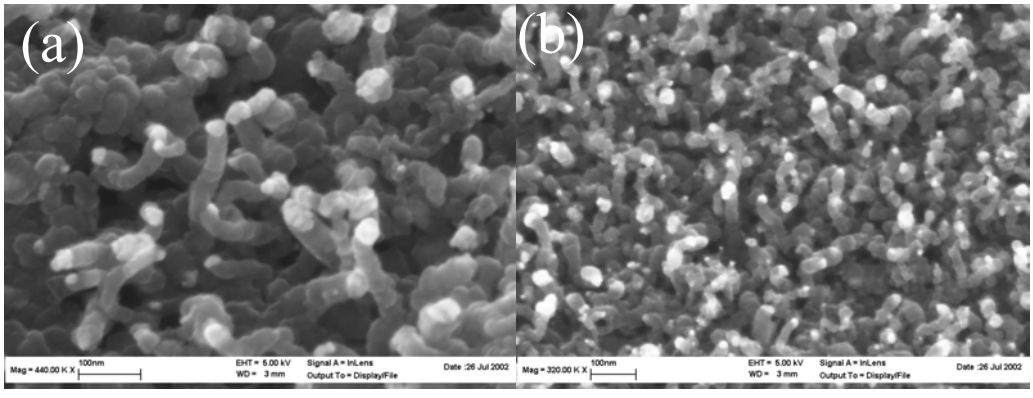

Figure 2: High resolution SEM photograph of CNTs grown by continuous plasma mode on (a) 5 nm and (b) 3 nm Ni catalyst layer thickness.

The micrographs of CNTs deposited with pulsed plasma are plotted in figure 3. Figure 3b) shows that well aligned CNTs can be grown on a Ni thickness of 3 nm. Figure 3b) also shows that the density of the tubes

increases with respect to that reported for the same sample deposited in continuous mode. As the catalyst layer thickness increases to 5 nm, the SEM image shows (Figure 3a) that the tubes appear always aligned but with a lower density.

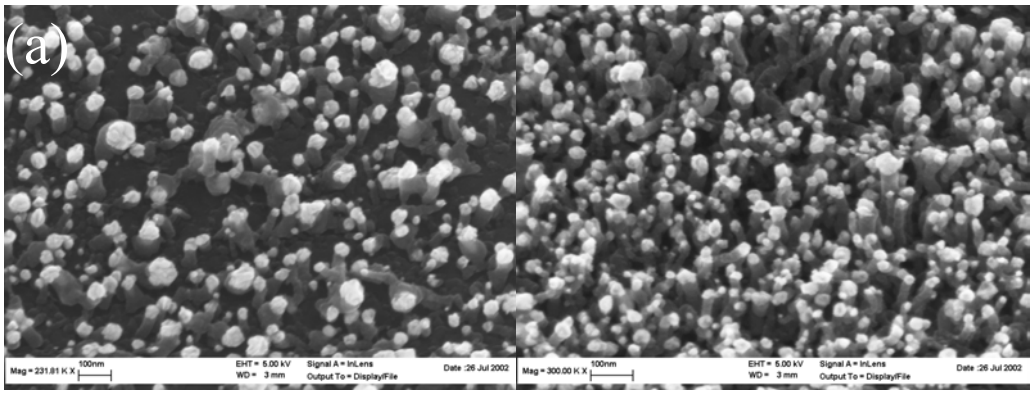

Figure 3: High resolution SEM photograph of CNTs grown with 0.1s on-time plasma excitation on (a) 5 nm and (b) 3 nm Ni catalyst layer thickness.

From the results reported here, two different carbon structures can be identified, depending on the plasma excitation mode: i) randomly oriented CNTs, which are formed by continuous plasma and ii) well aligned CNTs obtained with pulsed plasma.

The effects of the catalyst layer thickness seem to indicate a growth mechanism of CNTs similar to that reported in references [23-25]; in particular that the carbonaceous gas decomposes on the surface of the catalyst particle, the carbon diffuses across the particle and then, the carbon precipitates outwardly. As carbon atoms are further supplied, a carbon-metal eutectic alloy can be formed, decreasing the melting temperature of the alloy. The formation of carbon-Ni eutectic enhances the diffusion of carbon in the metal alloy, initiating carbon aggregations which act as a nucleation seed for nanotube growth. The carbon diffusion is limited by the domain size within the metal particles and thus the diameter of nanotubes should be smaller than the domain size. As the nanotube grows further, part of the metal domain is pushed upward, forming a metal cap. When the nanotube growth is initiated on the larger droplets, the force required to detach and raise them from the substrate is higher than that required for smaller Ni particles. This mechanical pulling of the larger Ni particle could be the origin of the observed round shape of graphite embedded in an amorphous carbon matrix [26].

Since all the carbon nanotubes are graphitic, and therefore conductive, two morphologically identical tubes will be subjected to the same electrostatic force without regard of the catalyst particle. Nevertheless, the images in Figs. 2 and 3 indicate that the magnitude of the electrostatic force on the CNTs is not the only determining factor in the nanotubes alignment. While the formation of a CNT can be explained by the formation of Ni droplets, uniform orientation is probably related to the different energy and flux of ion bombardment. In the case of deposition by continuous mode with analogous pure methane plasmas, it has been reported that the most abundant species are neutral species like CH_4, CH_3, C_2H_2, C_2H_4 and atomic hydrogen [27,28]. These neutrals species move in random directions, whereas the electric-field lines govern

the direction of travel for the ions. We noted that in our case, the Debey shielding distance is of the order of 100 μm. This distance is significantly larger than the CNT height and therefore, CNTs are located in the dark space of the glow discharge. If the etchant species are absent, then, in addition to the vertical growth process, carbon begins to precipitate also at the wall of the growing CNT. As a result, co-deposited amorphous carbonaceous particles are not removed selectively. Thus, in this case the excess of methane leads to a higher carbon deposition rate. On the contrary, in the case of deposition by pulsed plasma, the scenario for nanotube formation is quite different. In particular, according to Vandentop et al. [29], by pulsing the cathode to large negative voltages during the deposition, in addition to the primary ions CH_3^+ and CH_4^+ which are species produced by electron impact ionization of methane, secondary ions are present in relatively high ratios when the cathode is grounded (i. e. off-time excitation). These secondary ions, such as CH_5^+ and $C_2H_5^+$ are produced through ion molecule reaction. Furthermore, since the self-bias potential is proportional to the mass of the ions [$V=(kT_e/2e)\ln(m_i/2.3\ m_e)$] where k is Boltzmann's constant, T_e is the electron temperature, e is the charge of the electron, and m_i and m_e are the mass of ions and electrons respectively, the production of heavier ions by means of pulsed plasma is helpful in establishing a stronger local field at the surface, compared with other types of much lighter-mass ions produced by a continuous plasma. The electrostatic force would then induce these one-dimensional tubular structures to align in the field direction.

IV. Conclusions

To summarize, we have demonstrated that aligned carbon nanotubes can be obtained using pulsed plasma enhanced chemical vapor deposition with pure methane precursor. The nanotubes obtained by pulsed plasma grow always perpendicular to the local substrate surface regardless of the Ni catalyst layer thickness. Moreover, the use of this technique does not require the presence of etchant species in the plasma to reduce the formation of amorphous carbon during the deposition of the carbon nanotubes as reported for continuous plasma processes [19,30,31]. The electrical pulsed self-bias imposed on the substrate surface appears to be the primary mechanism responsible for the conformal alignment. In particular, by turning off the plasma source with an excitation time of 0.1s, which effectively turns on the alignment mechanism, a transition can be introduced between a pulsed plasma-grown straight nanotube and a continuous plasma-grown curly nanotubes.

Spectroscopic Diagnostics of Atmospheric Argon Radio Frequency Inductively Coupled Plasma

G. Gao[1], J. Mostaghimi[1], and L. Pershin[1]

[1] *Department of Mechanical & Industrial Engineering, University of Toronto, Toronto, Canada*

Abstract

An experimental study was conducted to determine the property fields of radio frequency inductively coupled plasma using optical emission spectroscopy. Various spectroscopic methods were checked for the measurement of non-equilibrium plasma fields. The Boltzmann plot method was proved to be still valid to obtain the plasma temperature. The electron density was estimated by the continuum emission method. Emission asymmetry of plasma close to the coil zone was also investigated and solved.

1. Introduction

Ever since Babat's discovery in 1942 [1], radio-frequency (RF) inductively coupled plasma (ICP) has found many applications in a number of different disciplines. It is used in analytical chemistry as a source of atomic excitation; in spray coating of metals and ceramics; and in nucleation and growth of submicron powders; etc. The distinguishable advantages of the ICP over other types of plasmas are that the plasma can be operated both in reduced and above atmospheric pressure, and because of the lack of electrodes, the discharge is contaminant free, and thus, its chemical composition can be precisely controlled. Furthermore, since the size of the plasma depends on the applied frequency and power of the induction current, it comes in a broad range of powders and sizes.

ICP is formed within a quartz tube by applying a radio frequency current across a load coil wound around the tube (Fig.1). Q_1 represents the carrier gas flow, Q_2 represents the plasma gas flow and Q_3 is the sheath gas flow. Depending on the application, the operating pressure may vary between 50 Torr to above atmospheric pressure; induction frequency from 0.2 to 100 MHz; plate power from 0.5 to more than 500 kW; and torch diameter from 13 to 200 mm. The choice of the plasma gas(es) depends on the type of application and any gas and/or mixture of gases can be excited by the RF fields.

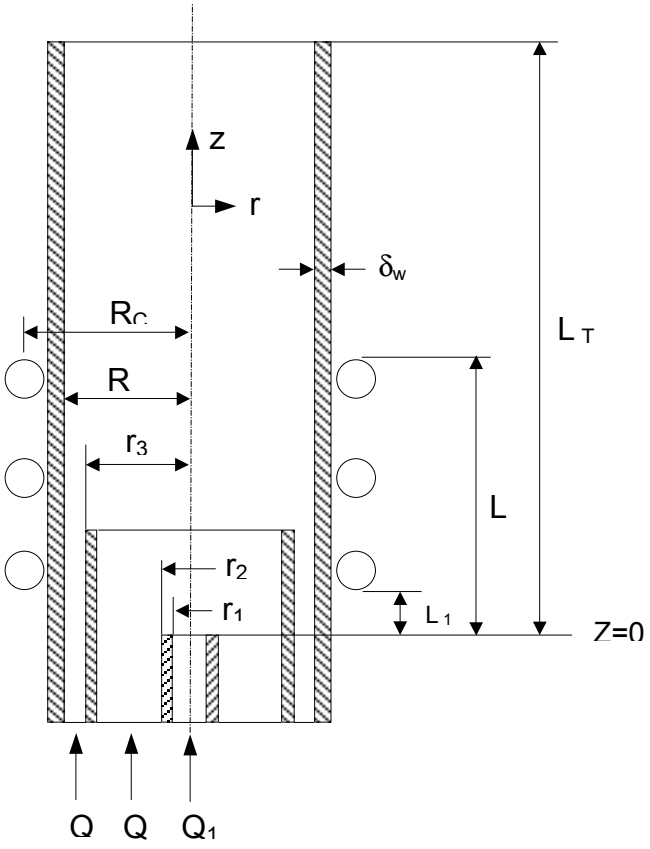

Figure 1 Schematic of a typical rf-ICP torch

The success of the applications of RF ICP depends to a large extent on our ability to control the conditions in the discharge. To have a complete understanding of the plasma processing and validate the mathematical model, the measurement of the crucial features of plasma is required. As is well known, the plasma temperatures, electron number densities, atom and ion emission intensities, number densities of analyte and argon species, and spectral line widths are generally considered to be the fundamental parameters of plasma.

We built a 40 MHz RF ICP in our lab running at atmospheric pressure with argon gas. For this high frequency, the size of the plasma torch can be quite small. The diameter of torch is 18 mm. However, in the small plasma area, the high temperature of heavy particles such as atoms and ions can reach 6000 K, while the electron temperature can be up to 8000 K. Due to the extremely high temperature and small size of the plasma torch, it is almost impossible to apply any intrusive measurement. The atomic emission spectroscopy (OES) method has been extensively used for plasma property measurements in the past

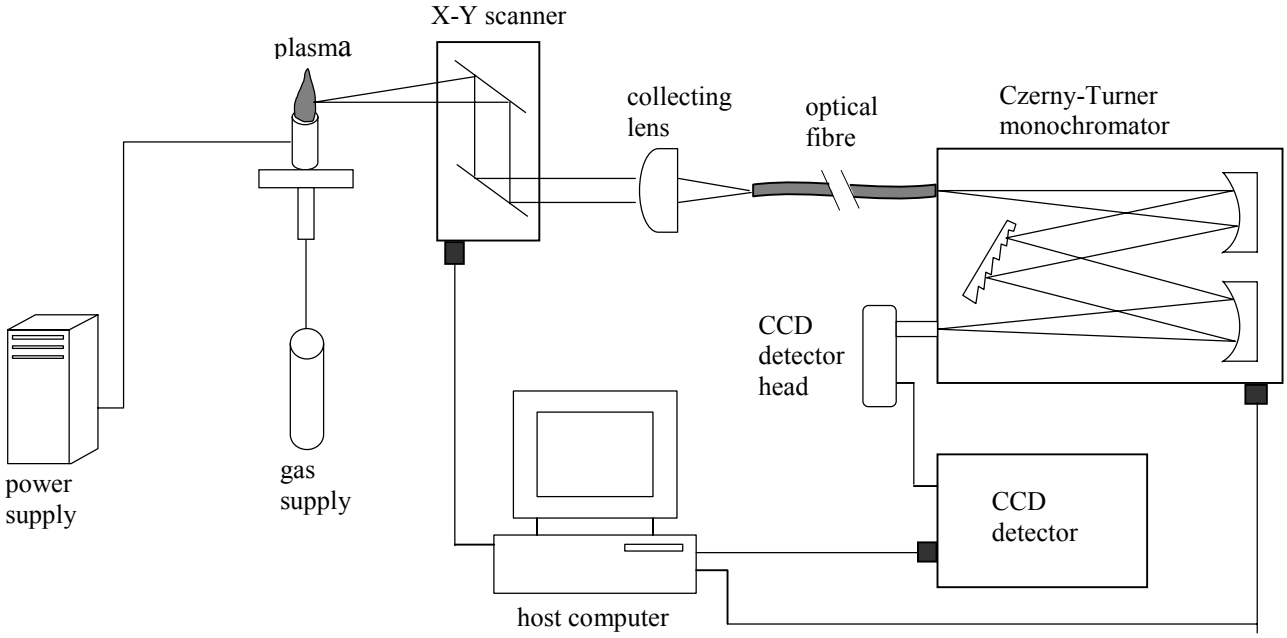

Figure 2 Setup of plasma emission spectroscopic diagnostics

decades. Although the measurements of plasma properties may rely on the equilibrium assumption in most cases and optically thin plasmas, emission spectroscopy remains one of the most powerful techniques for plasma diagnostics. It is still the most popular non-invasive diagnostic technique for temperature measurements, especially in axially symmetric plasmas. We established a fully computer controlled AES measurement system and measured the emission of argon RF ICP. The plasma temperature and electron number density were then obtained using different methods.

2. Experiment Facility

The equipment used for this study in our laboratory includes a radio frequency plasma generator, an OES measurement system, and a data acquisition system. The experimental setup for spectroscopic measurements of plasma fields is schematically shown in Figure 2. The 40MHz RF plasma torch was operated at the input power of 0.1 ~ 1 kW and under atmospheric pressure. The working gas was pure argon. The optical spectroscopic system includes a monochromator fitted with a CCD detector, a mirror scanner, and optical focusing lenses. The spectroscopic measurements were performed using a Jobin-Yvon monochromator. It has 0.025nm Resolution with 1200 g/mm grating. A 2-D electro-optical scan head and a digital scanning controller (DSC) from General Scanning Inc. were used for the sampling of optical emissions from any desired location in the plasma and can precisely scan a portion of the plasma radially and axially. A host computer controlled device operation and data acquisition. A calibrated quartz tungsten halogen (QTH) lamp from Thermo Oriel was used for absolute calibration of spectral intensities.

3. Spectroscopic methods

Most spectroscopic methods require the plasma is in equilibrium state in certain level such as local thermal equilibrium (LTE), local Saha equilibrium (LSE), etc. However, the plasma in our study is in strong non-equilibrium state. Therefore it is essential to find methods still valid under this condition. The spectroscopic methods we used require that the plasma is at least in the state of partial local Saha equilibrium (PLSE), in which electrons in higher exicted states are in equilibrium with free electrons and their distribution is given by Saha-Boltzmann relation characterized by a temperature equal to the electron temperature. And the electron is allowed to differ from the temperature of heavy particles. For temperature measurement, we checked several methods

Provided populations of excited states obey Boltzmann distribution, the emission coefficient ε_{pq} of an atomic line corresponding to a transition from a level p to a level q can be written in the form

$$\ln\left(\frac{\varepsilon_{pq}\,\lambda_{pq}}{g_{pq}\,A_{pq}}\right)=-\frac{E_p}{kT}+\ln K(T) \qquad (1)$$

where λ_{pq}, A_{pq}, E_p, and g_p are the wavelength of the spectral line, Einstein transition probability, statistical weight and excitation energy of the upper level respectively, and $K(T)$ includes parameters independent of the transition. Plotting $\ln(\lambda\varepsilon/Ag)$ versus E_p using emission coefficients of measured atomic lines forms the Boltzmann plot. The excitation temperature T_{exc} is then obtained from a slope of the straight line fitted to the points in the Boltzmann plot.

As a variation of this technique, two line intensities with sufficiently different excitation energies can be used to determine the temperature directly from

$$T=\frac{E_2-E_1}{k\ln\left(\frac{\varepsilon_1\lambda_1 A_2 g_2}{\varepsilon_2\lambda_2 A_1 g_1}\right)} \qquad (2)$$

where λ, A, E, and g are the wavelength of the spectral line, Einstein transition probability, statistical weight and excitation energy of the upper level of two spectral lines respectively.

4. Results

For one spatial position, we let the AES system do one test and obtain the spectrum at certain wavelength. Line and continuum emission intensities and spectral line width were recorded for this scanning point. By moving the mirrors of the electro-optical scanner, we can collect the spectra of all the positions within the plasma area.

Due to the ability of rapid diagnostics of our system, we can collect the 2D spatial emission distribution profiles in minutes. Figure 3 shows the lateral line emission profile at 696.54 nm of argon plasma. Usually we only need to measure half of the plasma region in order to get the local emission coefficient as long as the axisymmetry assumption is valid. In our experiment, we scanned the whole plasma area. The interesting

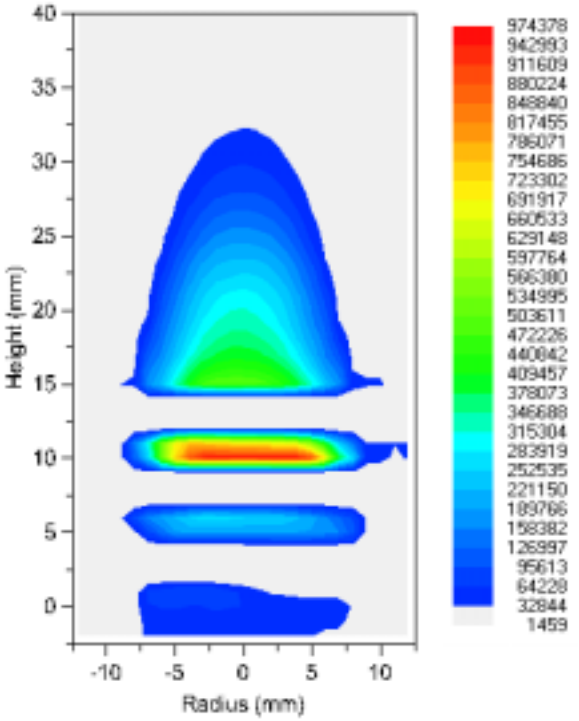

Figure 3 Lateral line emission profile at 696.54 nm

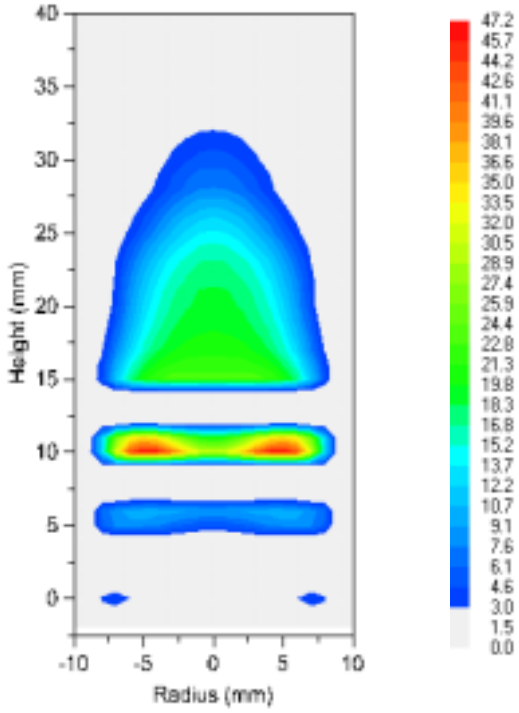

Figure 4 Local line emission coefficient at 696.54 nm

thing we found is that there was obviously non-axisymmetry existing within the load coil zone, while outside of the coil zone the emission distribution appeared to be symmetric. Abel inversion is popularly used to obtain the local emission coefficients but it is only valid for axisymmetric emission distributions. Figure 4 shows the local emission coefficient profile at 696.54 nm obtained by applying Abel inversion.

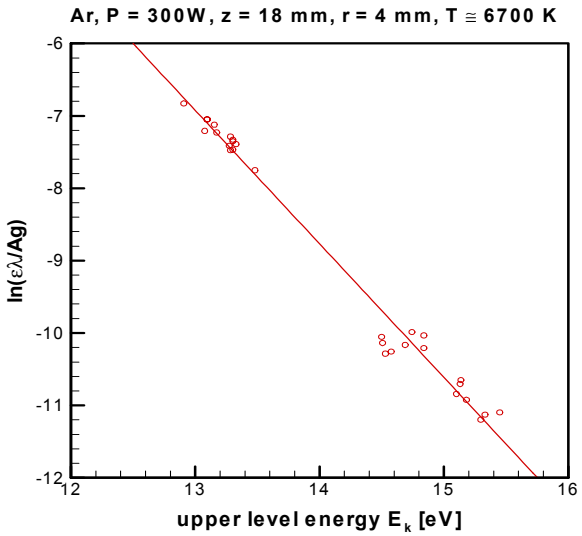

Figure 5 Boltzmann plot

Without knowing the electron number density at first, the Boltzmann plot is a method for getting the plasma temperature. However, the Saha-Boltzmann relation is not always valid in the Ar ICP. So we need to check the Boltzmann plot for both different position and different temperature range. To cover the most part of atomic argon state distribution, we selected about 30 spectral lines with wavelengths between 415 and 912 nm. All atomic properties were taken from [2]. A typical Boltzmann plot is shown in Figure 5. As we can see, the resulting Boltzmann plot is of quite high quality with the slope of the linear relationship through the data producing an unambiguous plasma temperature. The Boltzmann plots obtained from different regions of the plasma demonstrate a good capability to measuring temperatures over a wide range between 2500 K and 10000 K. Two Ar-I emission lines at wavelengths λ_1 = 696.54 nm and λ_2 = 518.77 nm were chosen for rapid diagnostic use of the line-intensity ratio method for plasma temperature measurement. This selection was based on the stronger intensities of these lines compared to others as well as the sufficiently different excitation energy levels of these transitions as indicated in Figure 5.

Figure 6 shows the measured plasma temperature by two wavelengths at 696.54 nm and 518.77 nm. According to the comparison between the measured temperature and the prediction of the Two-temperature

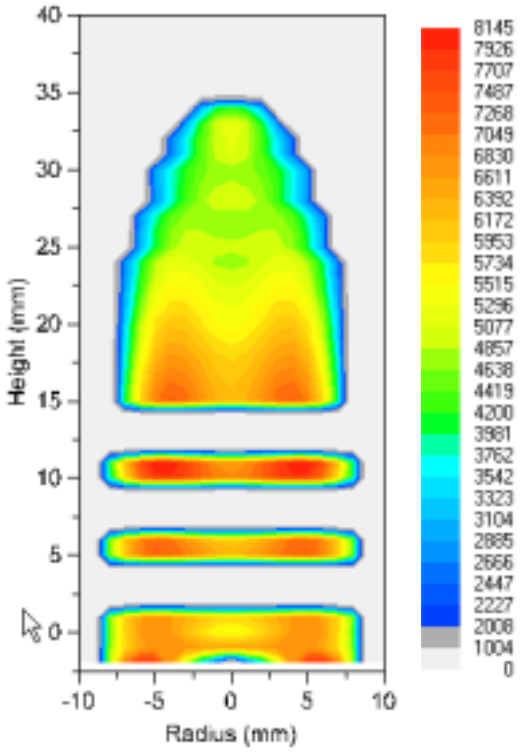

Figure 6 Measured temperature by line-intensity ratio method with wavelengths at 696.54 nm and 518.77 nm

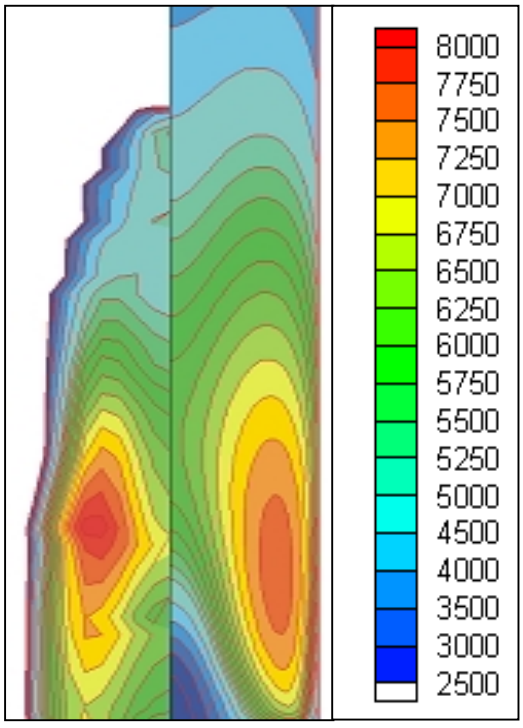

Figure 7 Comparison between measurement and prediction from the mathematical model

model, as shown in Figure 7, good agreement between measurement and calculation exists within the plasma torch. The difference at the downstream area may be caused by the assumed "infinite long tube" boundary condition used in the model. Plus, at the outlet of the tube, pure argon gas is mixed with cold air, mostly the nitrogen, which cools the plasma flow much faster than that estimated in the model.

Besides the Boltzmann plot method, the other methods of temperature measurement, however, were proven to be not suitable for the non-equilibrium plasma in our study.

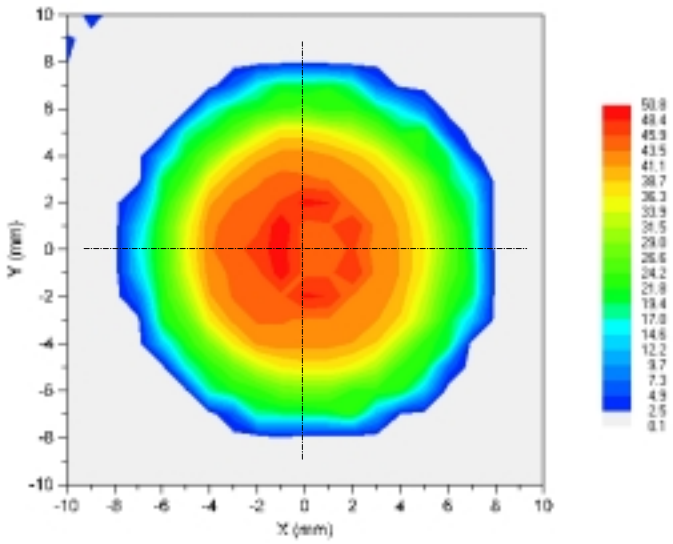

Figure 8 Top view of plasma line emission at 696.54 nm

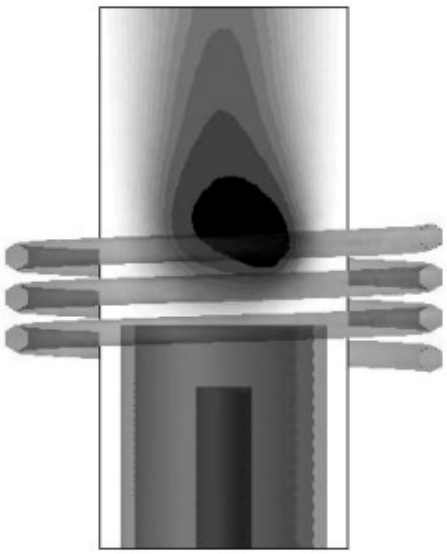

Figure 9 Schematics of induction coil configuration

To investigate the non-axisymmetry emission of plasma, we measured the emission from the top of the plasma torch. As shown in Figure 8, the line emission at 696.54 nm clearly shows the non-axisymmetry. Although it is the integral of the local emission along the axis direction, the measured emission still represents the asymmetry of the plasma temperature field. We figured that the asymmetry distribution is due to spiral configuration of the induction coil. As shown in Figure 9, the each turn of coil doesn't remain in the same flat surface. This results in the non-axisymmetric electric field and consequently the plasma fields.

Since the Abel inversion is not valid any more for non-axisymmetric emission distribution, we need to find other effective way to obtain the local emission under this situation. Fortunately, the asymmetry happens mostly in the regions within or close to the coil zone. Above the coil zone, we still can apply Abel inversion.

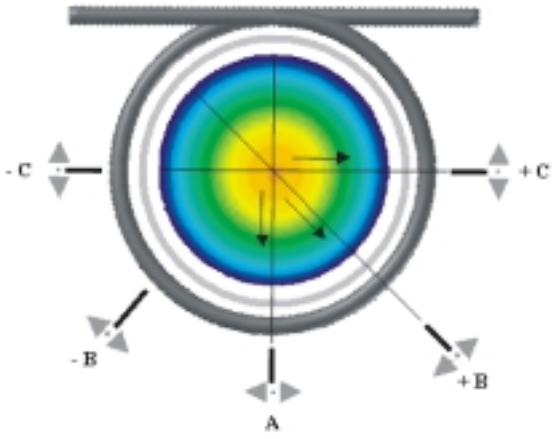

Figure 10 Definition of directions of the side-on measurement

We applied emission tomography method to calculate the non-axisymmetric local emission coefficient based on the lateral emission profiles measured at different directions around the plasma torch. As shown in Figure 10, we measured several lateral emission profiles at A, ±B, and ±C directions. Some of them show nearly symmetry, while others don't. Firstly, we assume an axisymmetric local emission coefficient as initial guess. Then we use each measured lateral emission to correct the original profile. When the procedure finally comes to convergence, we will obtain the 2D local emission $\varepsilon(r,\theta)$, which fits all the lateral emission profiles.

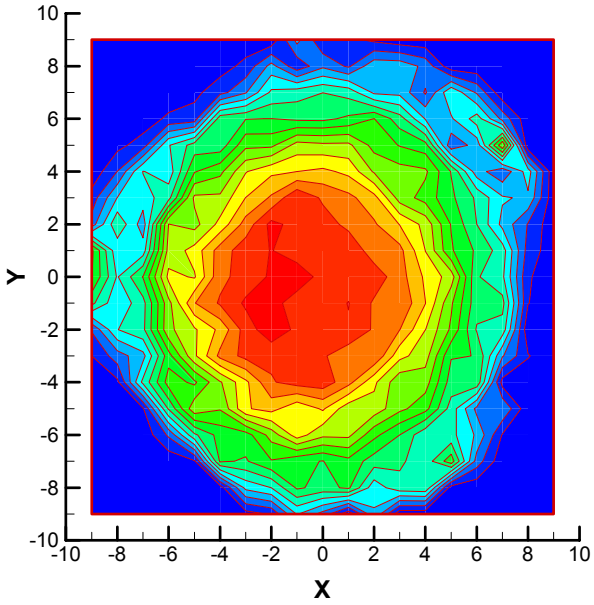

Figure 11 2D local emission coefficient profile obtained by applying the emission tomography method

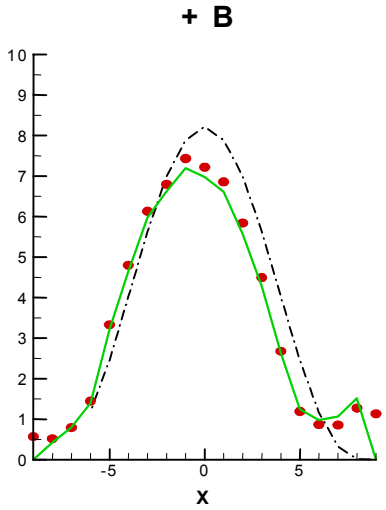

Figure 12 Comparison of lateral emission among symmetric initial guess (black dash-dot line), measurement (red points), and calculated profile based on the 2D local emission in Figure 12 (green solid line).

Figure 11 shows the calculated the local emission profile at height z=16 mm (just above the coil zone) by applying emission tomography method. From this distribution, we can calculate the lateral emission at each projection direction. As shown in Figure 12, the calculation at "+B" direction is in great agreement with measurement.

5. Conclusions

A fully computer-controlled optical emission spectroscopic (OES) measurement system for plasma studies was established. The emission coefficients of line and continuum radiation and spectral line width were measured for each spatial position within the plasma area. Based on the emission profiles, different methods were applied to calculate the plasma temperatures and electron number density. The Boltzmann plot was checked for different positions and different temperature ranges. The results show that the Saha relation exists in the plasma studied. Therefore the line-intensity ratio method provides reliable temperature without knowing the electron density. The non-axisymmetric emission of plasma was investigated. And the emission tomogrphy method was proven to be a effective way to obtain the 2D local emission profile.

References

[1] T. B. Reed - Journal of Applied Physics, **32**, 821- 824 (1961).
[2] NIST Physics Laboratory - Physical Reference Data: Atomic Spectroscopic Data.
[3] D. Hofsaess - Journal of Quantitative Spectroscopy Radiative Transfer, **19**, 339 (1978).
[4] V. M. Lelevkin, D. K. Otorbaev, and D. C. Schram -Physics of Nonequilibrium Plasmas, North-Holland, Amsterdam, Chap. **8 (**1992).
[5] J. R. Fincke - Plasma Chemistry and Plasma Processing, **6**, No. 2, 127 (1986).
[6] A. V. Likhachev, and V. V. Pikalov - Optics and Spectroscopy, **88**, No. **5**, 667 (2000).
[7] Richard Gordon - IEEE Transaction on Nuclear Science, **NS-21**, 78 (1974).

Surface Treatment of Polymers in Low-Pressure Plasma with Control over the Ion Energy and Flux

J.W. Bradley[1], M. Dhayal[1], K.L Parry[2] and R.D.Short[2]

[1] *Dept. of Physics, UMIST, PO Box 88, Manchester, U.K, M60 1QD*
[2] *Dept. of Engineering Materials, University of Sheffield, Sheffield, UK, S1 3JD*

Abstract
We have developed a new 'two-mesh' low-pressure plasma reactor for the surface treatment of polymeric materials, in which the electron temperature (and therefore ion energy) and ion flux can be controlled independently in the range 0.2 to 5.6 eV, and 0.2 and 5.4 x 10^{18} m^2 s^{-1} respectively. XPS analysis of treated PS samples show that the surface O/C ratio rises from 20% to 29%, with increasing ion dose from 1 to 5 x 10^{20} m^{-2} at an ion energy of 21 eV. However, our preliminary results indicate that the O/C ratios are insensitive to changes in the ion energy between 1.5 and 21 eV.

1. Introduction

There is currently much interest in developing low-pressure plasma discharges with greater control over the plasma parameters, for instance, the electron energy distribution function (eedf), so that the ion energy and flux at a material substrate or work-piece can be tailored, to provide selectability in the surface process.

One method to alter the eedf is to separate the plasma into two parts: a main plasma, which is sustained through electrical excitation and a diffuse process plasma which is maintained by transport of particles from the main discharge. This has been done using a single fine electrically biased separating mesh [1 - 5], allowing T_e to be changed from about 0.2 to 5 eV, however it is difficult to independently control the ion flux Γ. For instance, with increased negative mesh bias, both T_e and Γ fall substantially in much of the usual mesh bias range, say –20 to +30 V. Some independent control over T_e and Γ has been achieved with the single mesh technique [6], however, it is necessary to vary either the discharge power and pressure simultaneously or the substrate location. Recently, the technique has been extended to the use of two meshes instead of one [7], in which both meshes are biased separately, giving greater control over both T_e and Γ downstream. The important feature employed in all these techniques is that the secondary plasma has no plasma sustaining electric field across it and the emerging electrons can cool through collisions with the gas. Here, we develop the two-mesh discharge and treat polystyrene surfaces in it over arrange of independently controllably plasma parameters.

2. The experimental set-up

The two-mesh separated discharges configuration is shown in figure 1. It consists of an RF plasma source separated from the downstream process chamber plasma by an assembly containing the two electrically biased fine meshes. A turbo-molecular pump unit was used to pump the system to a base pressure of 10^{-3} Pa. The system is described in more detail in [7]. An electrostatic double probe [8] have been used to determine the plasma parameters (T_e, Γ) at a distance of 15 mm downstream of the mesh in the process chamber, for different bias potentials on mesh 1 (5-30 V) and mesh 2 (-20 to +30 V). In this study, the pressure was fixed at 2.6 Pa, and an RF plasma power of 20 W was used. Contour maps of T_e and Γ are shown in figure 2. For the surface treatment work, the polystyrene samples (1 cm diameter coated glass cover slips) were processed 15 mm from the second mesh in a specially constructed sample holder. The holder was equipped with a special draw, which was opened after the plasma discharge was allowed to settle down for approximately 10 minutes prior to treatment. The open face of the polystyrene samples were orientated upwards, perpendicular to the meshes, so as to reduce the vacuum ultra violet radiation (VUV) bombardment from the source plasma, i.e. to block the line-of-sight with the RF plasma source.

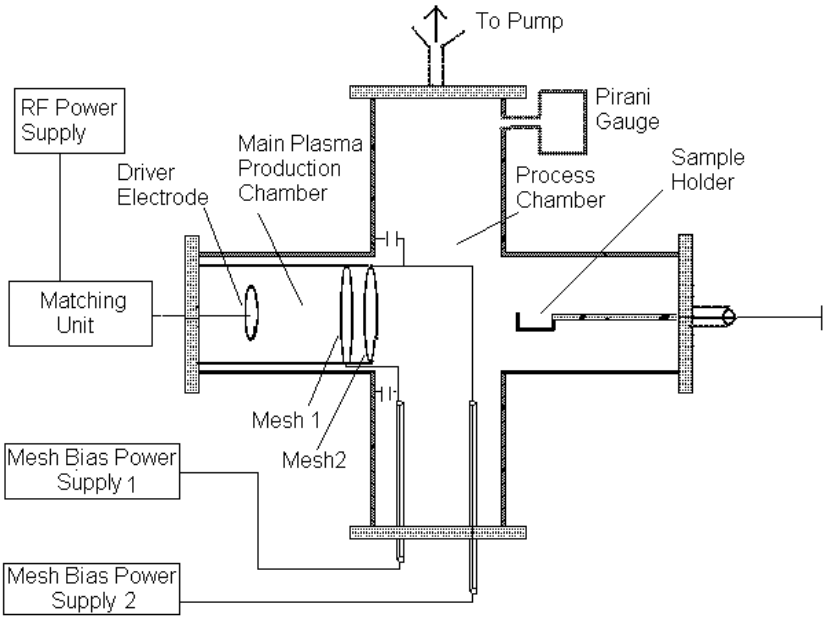

Figure 1: A schematic diagram of the two-mesh-separated plasma discharge, and the sample holder.

3. Results and Discussion

The double probe results (figure 2) show that through grid biasing, the electron temperature in this discharge can be varied from 0.2 to 5.6 eV. Given that there is no RF field in the discharge, and assuming idealised argon plasma, this corresponds to bombarding ion energies in the range 1 to 29 eV. This calculated from 5.2 x T_e (in eV) for argon plasma [10]. The probe results also show to an electrically isolated surface, the ion bombarding fluxes can be controlled between 0.2 and 5.4 x 10^{18} m^2 s^{-1}. Importantly, through grid control, (the line $V_{mesh\ 1}$ = +20 V), the electron temperature varies by an order of magnitude while ion flux varies by only a factor of two.

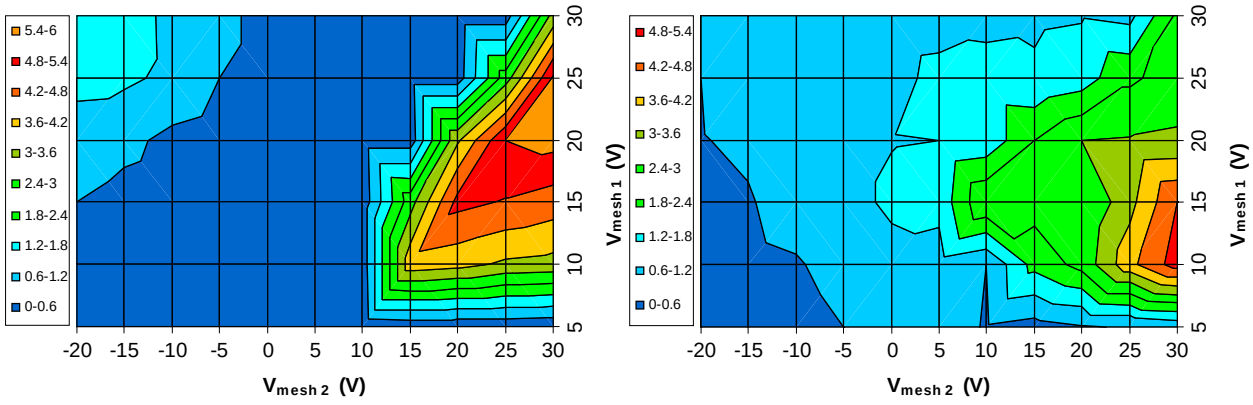

Figure 2: Contour plots of a) electron temperature T_e (eV), b) the ion flux Γ (x 10^{18} particles $m^{-2}s^{-1}$) at a position 15 mm from the mesh in the process chamber, for a variation in mesh biases, $V_{mesh\ 1}$ and $V_{mesh\ 2}$. The pressure is 2.6 Pa and the main plasma power is 20 W.

Figure 3 shows the oxygen to carbon ratios (O/C) measured in the top surface by XPS after the samples were exposed to atmospheric oxygen, (i.e. post-treatment) against the total ion dose to the

surface (flux x treatment time). The treatment time was 120 seconds in each case. Through biasing the meshes we have varied the ion bombarding flux for two different electron temperatures, 0.26 and 4 eV respectively, corresponding to approximately 1.5 and 21 eV ion bombarding energies. In the high-energy case, the O/C ratios clearly increase with dose as expected [11], however it is difficult to judge the trend for the low ion energy case due to the lack of data points taken in these preliminary experiments. The results do show however, similar treatment levels for the high and low ion energy cases, and we may tentatively suggest that the O/C ratios are independent of ion energy in this energy range.

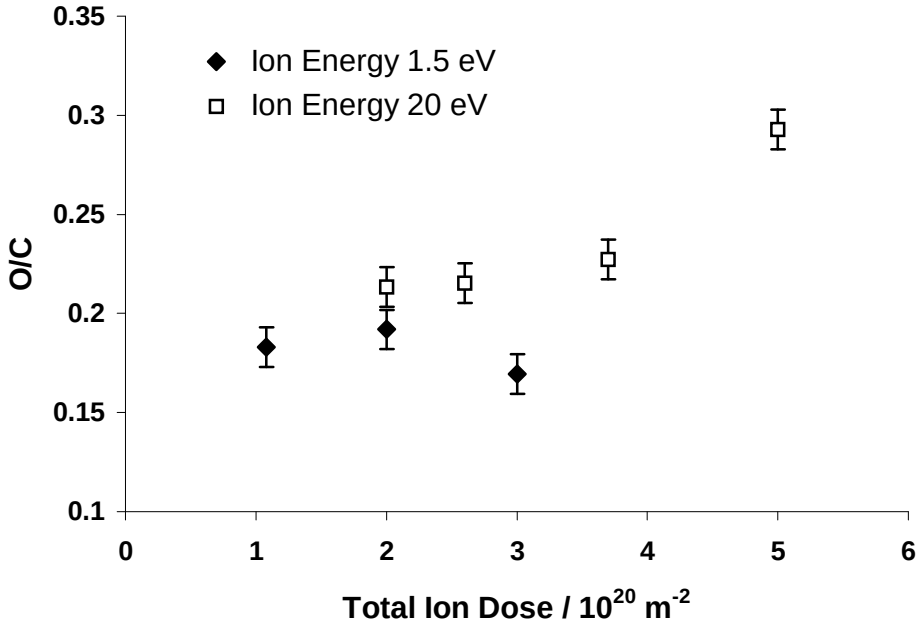

Figure 3. The O/C ratios measured by XPS, against total ion dose (flux x treatment time) for two different ion energies, 1.5 and 21 eV.

4. Conclusions

We have developed a two-mesh separated plasma discharge in which the electron temperature and ion flux can be well controlled through the variation of the DC bias on both meshes. Using the discharge we have treated polystyrene surfaces for a range of plasma conditions and measured the O/C ratios in the top surface, post exposure to air using XPS.

For ion energies of about 21 eV, we find the O/C ratios increase with ion dose (flux x time), rising from about 20 % at 1 x 10^{20} m^{-2} up to about 29 % at 5 x 10^{20} m^{-2}. At low ion energy (1.5 eV), the results are inconclusive, however the treatment level is similar to that at higher energy. These preliminary results suggest that the O/C ratios are independent of ion energy in this energy range, however clearly more work is needed to confirm this.

With refinement of the discharge, this technique for plasma control may prove particularly useful in advanced studies of the plasma treatment of polymeric materials, both from a practical but also scientific point of view. It may also have applications in plasma polymerisation of chemically functional materials, through control of the electron energies, which determine the dissociation and ionisation of the monomer gases molecules. In future studies, the possible effect of the VUV radiation in the surface treatment should be evaluated, although here we have taken steps to reduce its flux to the polymer surface.

Acknowledgements. The Authors would like to thank the EPSRC for their funding support. This work is part of the COST 527 programme.

References

1] G Ganguly, T Ikeda, I Sakata and A Matsuda, Mat. Res. Soc. Symp. Vol.420 (1996) 347
2] KH Bai, JI Hong, CW Chung SS Kim and HY Chang Phys. Plasmas **8** (2001) 3498
3] JI Hong, SH Seo SS Kim, NS Yoon CS Chang and HY Chang Phys. Plasma Vol 6 **3** (1999) 1017
4] KH Bai JI Hong SJ You k Choi and HY Chan, Physic of Plasmas Vol 9 **3** (2002) 1025
5] K Kato, S Iizuka and N Sato, Appl. Phys. Lett. **65** (1994) 816
6] M Dhayal, D Forder, K Parry, RD Short, D Barton and JW Bradley, Surf. Coat. Technol, Vol 162, **2-3** (2003) 294
7] M Dhayal, D Forder, RD Short and JW Bradley, Vacuum Vol 70 **1** (2003) 67
8] 'Electrical Probes for Plasma Diagnostics', J D Swift and M J R Schwar (1970) Iliffe, London
9] Bradley JW, Thompson SM, and Aranda Gonzalvo Y, Plasma sources Sci. Technol. **10** (2001) 490
10] MA Liebermann and AJ Lichtenberg (1994) Principles of Plasma Discharges and Materials
11] DA Steele, 'Radio Frequency Plasma Used for the Surface Modification of Polymers: A Physical and Chemical Investigation' – PhD Thesis, University of Sheffield (2000)

Use of HMDS/Hexane Plasma Deposition for Obtaining Low Cost Selective Membrane

Nicole R. Demarquette[a] , Ing H. Tan[a], Maria Lucia P. da Silva[b],

Escola Politécnica- Universidade de São Paulo, Av. Prof. M. Moraes 2463, 05508-900 São Paulo, Brazil.
a)Depto. de Engenharia Metalurgica e de Materiais, b) Depto. de Engenharia Eletrica

Abstract

In this work, filter paper was coated with plasma depositions of hexamethyldissilazane (HMDS), and double layers of HMDS and n-hexane. All coating films formed adhered well to the substrate, and resulted in water repellent paper surfaces with apparent water contact angles above 100 degrees and water adsorption around 15 g/m^2. The porosity of paper was not altered showing that all depositions were conformal. The paper was tested successfully as a selective membrane for water and hydrocarbons of different chain length.

Introduction

The hydrophilic character of cellulose is a desirable property for some paper applications such as utilities, but is a problem for applications like liquid recipients, printing, or other applications where dimensional stability is important. It is known that in 50% relative humidity environments, cellulose adsorbs about 5% of water [1]. Due to its fibre network structure, paper is a porous material, and can be covered by polymer films in order to make it impermeable to water. In some applications however, it is desirable that the system be permeable to air but water repellent. Therefore, making cellulose fibres hydrophobic can be interesting in applications such as printing with non-water based inks. Currently, water repellence is accomplished using solvents and organic reagents, mostly wax emulsions, quaternary ammonium salts and hydrophobic resin finishes, which requires discarding and can cause environmental problems [2].

Cold plasma processing is already a well known and widely used technique for etching and surface modification in electronics industry. Plasmas create extremely reactive species like ions, free radicals and metastable species, which allow reactions to occur at much lower temperatures than in conventional methods, or even reactions that would not occur at all, unless the reagents are under plasma conditions. Low quantities of reagents are used and discarded in plasma processing since treatment times are very short (a few minutes for deposition and even seconds in activation processes), and low pressures are used. Furthermore, low energies are used in most processes making them economically attractive.

Plasma polymerisation of hydrocarbon monomers like ciclohexane [3] has been demonstrated to make cellulose surfaces hydrophobic. However, the treated paper in this case looses its porous structure due to the film's bridging over the fibres. Plasma polymerisation of carbon tetrafluoride[4] and fluorine alkyl silanes [5,6] have also been studied leading to high contact angles as a result of intense surface fluorination. However, the use of CFCs and other compounds containing fluorine, is not an environmentally friendly process owing to the hazardous effects on, for example, the atmosphere's ozone layer. Organic silicon compounds are commonly used for plasma depositions in microelectronics, optics and surface protection industries [7,8]. One of their great advantages is the ease of manipulation, since they are liquids of low toxicity [7,9,10]. Plasma deposition of Hexamethyldisilazane (HMDS) presents interesting characteristics owing to: 1) the presence of Si-N-Si bonds, creating the possibility of forming silicone type structures, 2) the presence of silicon in the molecule and its strong affinity to oxygen atom of various substrates such as cellulose [11,12], alumina[13] etc. 3) the presence of CH_3 groups which can modify the surface properties of the coated material making it hydrophobic, 4) its high resistance to strong inorganic acids and bases[14], 5) the possibility of using it as an adhesion promoter for the deposition of n-hexane to obtain a hydrophobic surface at low cost[11]. All these characteristics make HMDS deposition interesting to obtain material surface with taylored properties.

The objective of this work was to study the hydrophobic protection of paper that can be obtained by plasma deposition of HMDS, and by the deposition of a double layer HMDS and n-hexane, with an intermixing layer in between. n-hexane was chosen as a second reagent since it is easily polymerised in plasma conditions, requiring low energy and low reagent flux [15]. Deposition of n-hexane with HMDS was attempted to lower costs, with a first layer of HMDS functioning as an adhesion promoter. An HMDS-n-

hexane interface layer is expected to have two polymers bonded either chemically (by Si-C bonds) or by Van der Waals interactions. A two layer deposition was chosen since previous experiments[16] demonstrated deposition difficulties when two reagents were used simultaneously. Filter paper was chosen as the cellulose substrate since it is the most hydrophilic type of paper. The modified paper was then tested as a membrane for water and hydrocarbon compounds.

Materials and Methods

Silicon wafers (<100>, p type, 10-20 Ωcm, 3"diameter) were used as substrates for profile meter and FTIR analysis of the films. High purity filter paper with less than 0,007% ash content from Binzer & Munktell was used as cellulose substrate, in 5cmX5cm samples. This type of paper was used because it does not contain non cellulosic components. Therefore, the contact angles values reported here do not depend on surface chemical heterogeneity. The reagents used were HMDS (Hoescht, industrial use) and n-Hexane (chromatographic grade).

The equipment used for plasma depositions was a parallel plate capacitively coupled reactor powered by a 40 kHz source. The reactor had two 20 cm diameter stainless steel electrodes, 3cm apart, one of them grounded and used as substrate holder. Base pressures of 20 mTorr could be reached within a few minutes with a rotary pump. Monomers were injected by pressure gradient at room temperature, with the working pressure controlled by changing the aperture of the pumping valve, and consequently the pumping speed. Figure 1 shows a schematics of the reactor used. Two types of depositions were made: 1) HMDS alone (called HMDS in the remaining of the text); 2) double layers of HMDS and n-hexane (called hexane in the remaining of the text). For double layered films, HMDS was first deposited for two minutes, after which the second monomer (n-hexane) was injected simultaneously for 30 seconds (the intermixing period). The HMDS reservoir valve was then closed, and the second monomer deposition for 6 minutes.

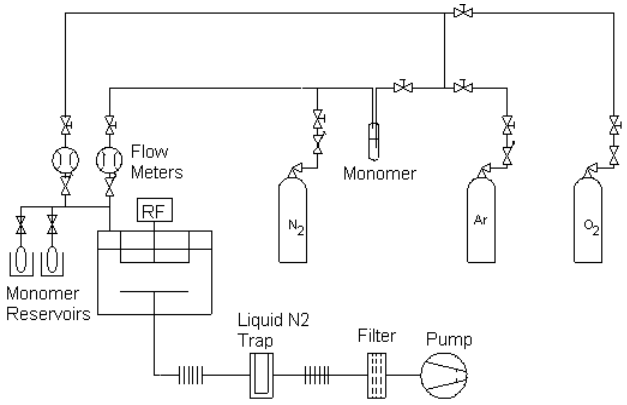

Figure 1: Schematics of the Plasma Reactor Used

A profile meter (model Dektak 3030) was used to measure the step height when part of a silicon wafer was covered during deposition, giving the film's thickness. The deposition rates of HMDS and Hexane were respectively 2200 A/min and 200Amin.

The morphological modifications on the paper surface were verified by scanning electron microscopy (Cambridge Instruments, Stereoscan 240). The porosity of the paper was evaluated by mercury porosimetry using a Micromeritics 92-10.

Apparent water contact angles were measured using a Rame-Hart goniometer after plasma treatment, and after tests of ultraviolet light and chemical resistance. The accuracy of the measurement was ± 2° and the dispersion of the data (five to six measurements were made for each sample in different positions) was around ± 7°. Water adsorption was tested using the Cobb method, which consists of placing a column of water on the treated paper for 20 minutes and measuring the water adsorbed by mass difference.

The deposited hydrophobic layers are intended mainly to protect documents and other applications of paper used in indoor conditions. Therefore, resistance to ultra-violet light was tested exposing the treated samples to filtered UV light, according to the international standard ISO 105-B02. This is a test of colour fastness of textiles to artificial light (Xenon arc fading lamp test), which is representative of the effects of indoor ultraviolet light, to which documents are typically subjected, in contrast to the much harsher outdoor

conditions. The samples were exposed for 8, 50 and 100 hours using a Hanau's Xenotest model 150 (1500W of lamp power, with lamp-sample distance of 65mm).

In order to test the treated paper as a separation membrane for water and hexane, ciclohexane, heptane, dodecane, benzene, silicon oil poly(dimethylsiloxane), Dow Corning 200 ® Fluid, 350 cs), carbon tetrachloride, acetophenon or phenol (all PA reagents) the following procedure was used: 2 ml of these different organic liquids were mixed to 1 ml of 1.5 wt% $CuSO_4$ aqueous blue solution. The 3 ml mixture was manually agitated and filtered by the treated paper. $CuSO_4$ aqueous solution was used instead of water for better visualisation of the liquids. Care was taken so that the organic liquid and water would not evaporate during the experiment by placing a cellophane film above the funnel in which the paper was located.

Results and Discussion

Infrared spectra of films deposited on silicon wafers showed Si-CH_3 (850-840 cm^{-1}), N-H (1180-1175 cm^{-1}), Si-CH_2-Si (1090-1020 cm^{-1}) and Si-N-Si (900-830 cm^{-1}) bonds for HMDS films[6], and C-Hn bonds only for n-hexane depositions. Measuring contact angles formed by drops of water of an unmodified filter paper is literally impossible as water penetrates rapidly the paper owing to its porous structure which makes it absorbent. We observed that the deposition of hexadimethylsilasane (HMDS) and double layers of HMDS and n-hexane, made the paper repellent to water and that stable drop forms were obtained to measure contact angles. Apparent contact angles around 120^o were measured. Water adsorption of around 15 g/m^2, a very good result for filter paper (untreated paper adsorbs normally around 300g/m^2), showed that for both deposition conditions the paper samples became water repellent.

The adhesion of the films to the substrate was tested by dipping the treated samples in the same acid and basic solutions for 5 seconds and measuring the apparent contact angles. It was still possible to measure an apparent contact angle as stable drop forms were still obtained. All apparent angles were unchanged (well above 90°) showing good adhesion of all films to the paper substrate, as expected.

Table 1 also shows the apparent water contact angles and water adsorption a) after the treated samples had been immersed in a strong basic solution for 15 minutes b) after immersion in strong acid solution (H_2SO_4) for 15 minutes and c) after UV exposure for different time duration. It can be seen that both the water apparent contact angles and water adsorption were not affected by strong basic or acidic immersion nor by EV exposure. The water adsorption decreased for HMDS samples, probably due to crosslinking induced by UV light.

Table 1: Water adsorption and contact angle

	Contact Angle	Water adsorption (g/m^2)
As coated		
HMDS	124	15
n-hexane	120	12
After immersion in a strong basic solution		
HMDS	118	20
n-hexane	112	25
After immersion in strong acidic solution		
HMDS	112	15
n-hexane	112	15
After UV exposure		
HMDS	120	10
n-hexane	115	15

The decrease in water adsorption of the HMDS film exposed to UV light was an interesting result, and was investigated in more detail by depositing the same film on silicon wafer and examining the FTIR spectrum before and after the sample was exposed to unfiltered ultra-violet light. The film was exposed to UVA light (a 22W lamp, with a wavelength of 350 nm, distant 5cm from the sample) for 20 hours and to UVC light (same parameters, but with a wavelength of 250 nm) for 5 hours. Table 2 shows the relative intensities of FTIR spectra obtained by exposure of HMDS films to UVA (Table 2a) and UVB (Table 2b)

light. Similar results were obtained for both tests: Si-CH_2-Si bonds increased if compared to Si-N-Si bonds, indicating that UV light is favouring crosslinks through carbon radical reactions. For UVA light a maximum in Si-CH_2-Si intensity was observed after 3 hours. However, the Si-CH_2-Si band showed traces of Si-O-Si bonds (both species have peaks in the same spectrum region) in both experiments, indicating that oxidation reactions occurred simultaneously. It should be noted that solar radiation consists mainly of UVA, some UVB and no UVC radiation. The fact that UVC, the most energetic of the three types of radiation, causes mainly crosslinkings after up to 3 hours of exposure, indicates that besides being resistant to indoor UV radiation, HMDS films could be used as a protection layer for paper in outdoor applications as well.

Table 2a: Relative intensities of FTIR spectrum of HMDS film exposed to UVA light. I(x/y) represents the relative peak heights between x and y species.

Relative Intensities of FTIR spectrum				Time
I(Si-CH_3/Si-N-Si)	I(N-H/Si-N-Si)	I(Si-O-Si/Si-N-Si)	I(Si-CH_2.Si/Si-N-Si)	(min)
0,83	0,28	-	0,37	0
0,81	0,23	-	0,43	10
0,86	0,26	-	0,45	95
0,88	0,18	Traces	1,1	190
0,80	0,25	Traces	0,6	600
0,47	0,14	Traces	0,35	1200

Table 2b: Relative intensities of FTIR spectrum of HMDS film exposed to UVC light. I(x/y) represents the relative peak heights between x and y species.

Relative Intensities of FTIR spectrum				Time
I(Si-CH_3/Si-N-Si)	I(N-H/Si-N-Si)	I(Si-O-Si/Si-N-Si)	I(Si-CH_2.Si/Si-N-Si)	(min)
0,81	0,27	-	0,44	0
0,86	0,27	-	0,76	15
0,88	0,23	trace	0,93	75
0,96	0,23	trace	1,16	275

Figure 2 shows the cumulative porosity of paper as a function of pore diameter for both treated and untreated paper. It can be seen that the pore distribution of the sheet of paper was not altered by the PECVD of HMDS and n-Hexane. Also the overall porosity of the untreated paper and treated paper were 68 and 71 % respectively which is the same within experimental error. Therefore, the chemical deposition did not modify the porous structure of paper.

Figure 2:Porosity of the paper before and after treatment

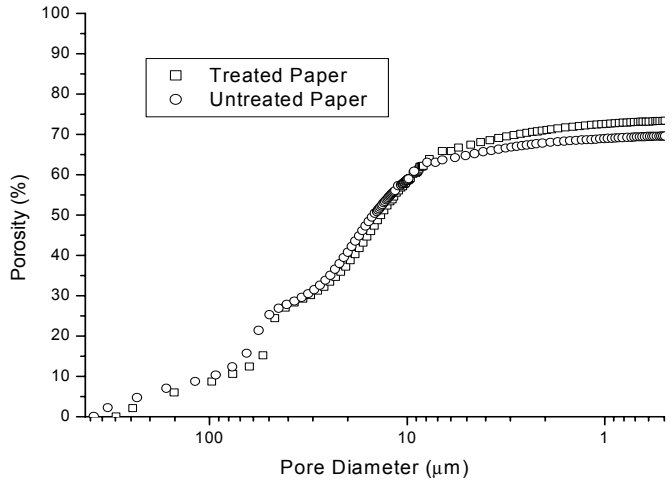

Table 3 shows a summary of separation experiments conducted. It can be seen from Table 3 that all the non polar liquids were filtered by the paper whereas the polar compounds (acetophenon, phenol and carbon tetrachloride) were not. It can also be seen that for all the non polar liquids only around 1 ml out of 2 ml was filtered indicating that some organic liquid stayed trapped in the paper or in the solution above the filter. This can be explained as follows: all the non polar liquids tested have a lower density than water. Therefore, when poured in the funnel they form a ring above a cone of water. Owing to its affinity with the double layer, the non polar liquid starts to percolate through the paper with which it is in contact. Once there is no more contact between the non polar liquid and the paper, the solution stops percolating. This was confirmed by the fact that once the liquid to be filtered was removed from the filter only a wet ring could be observed, the remaining of the paper being totally dry. The data reported in Table 3 also indicate that the time to filter is a function of viscosity; the time to filter the total quantity that percolated through the paper, Q_o, is increasing when the chain length of the organic compound is increasing and is much greater for poly(dimethyl siloxane). The results shown in Table 3 seem to indicate that the coated paper can be used as a phase separator between water and non polar organic compounds, if a mixing mechanism to enhance paper/non polar compounds contact is used.

Table 3: Separation Experiments

Organic liquid	Q_o: Quantity of liquid that passed through the paper (ml)	Time to filter the Q_o (minutes)	Time to start filtering (seconds)
n-Hexane	1.2	5	Immediate
Ciclohexane	1.0	5	Immediate
Heptane	1.2	5	Immediate
Dodecane	1.2	8	30
Benzene	1.2	8	30
Poly(dimethyl siloxane)	1.0	30	300
Acetophenon	0 after 30 minutes	-	-
Phenol	0 after 30 minutes	-	-
Carbon Tetrachloride	0 after 30 minutes	-	-

Conclusions

We have demonstrated that plasma deposition of hexamethyldissilazane (HMDS) is an efficient method for making paper surfaces hydrophobic, while still maintaining its porous structure. This deposition is resistant to strong bases and acids, as well as to indoor ultraviolet light. The deposition of a double layer of HMDS followed by n-hexane is an alternative to lower costs, resulting in a protection layer with the same characteristics as of HMDS alone. The HMDS layer functions in this case as an adhesion promoter of n-hexane to the cellulose substrate. The resistance of HMDS films to ultra-violet light through crosslinkings could make this process suitable for paper applications in more aggressive atmospheric conditions like outdoor panels. A filter paper modified by plasma enhanced chemical vapor deposition of a double layer of HMDS/Hexane was tested successfully as a membrane for water and hydrocarbon compounds.

Acknowledgements

We would like to thank the Laboratory of Molecular Spectroscopy of the Chemistry Institute of the University of São Paulo for the Raman Microscopy analysis. This work was supported by FAPESP (Fundação de Amparo à Pesquisa do Estado de São Paulo, process numbers 95/9287-0, 96/06947-2 and 97/06071-6).

References

[1] J. Kroschwitz in *Concise Encyclopedia of Polymer Science and Engineering*, Wiley & Sons, N. Y, 704, (1990)

[2] A. M. Schwartz, in *Advances in Textile Processing*, ed. J. E. Lynn and J.J. Press, 1961, **1** ,263, (1993)

[3] Tu, X., R. A Young, F.Denes, *Cellulose*, **1**, 87, (1994);

[4] F. Denes, Z. Q. Hua, E. Barrios, R. A. Young, *J. Macromolecular Science – Pure Appl. Chem.*, **A32**, 1405, (1995).

[5] A. Hozumi and O. Takai, *Thin Solid Films*, **303**, 222, (1997)

[6] A. Hozumi, N. Kakinoki, Y. Asai and O. Takai, *J. Mater. Sci. Lett.*, **15**, 675, (1996)

[7] R. d'Agostino, "Plasma Deposition, Treatment, and Etching of Polymers", Academic Press, Inc.(1990)

[8] G. Lucovsky, D. V. Tsu, *J. Vac. Sci. Technol.,* **A5**, 2231, (1987).

[9] R. Gonzáles-Luna; M.T. Rodrigo, C. Jiménez, J.M. Martínez-Duart, *Thin Solid Films*, **317**, 347 (1998)

[10] M. T. Kim, J. Lee , *Thin Solid Films,* **303**, 173, (1997).

[11] I. H. Tan, M. L. P. Silva, N. Demarquette, *J. Mat. Chem.*, 11, 1019, (2001)

[12] Patent Pending "Processo de deposição química a vapor para a hidrofobização de papel" INPE NPI9903097-7

[13] G. J. Pereira, M. L. P. Silva, I. H. Tan, D. Gouvea, *J. Mat. Chem*., **10**, 259, (2000).

[14] S. Nogueira, M. L. P. Silva, I. H. Tan, ISPC-14 Symposium proceedings, Prague, 1393, (1999)

[15] H. Yassuda, in *Plasma Polymerization*, Academic Press, Chapter 9, (1985)

[16] I. H. Tan, N. Demarquette, M.L. da Silva, F. T. Degasperi, R. Dallacqua, *Proc. 14th Int. Conference on Plasma Chemistry*, Praha, Czech Republic, vol. IV, 1907, (1999)

Microwave plasma chemical vapour deposition of nanocrystalline diamond films from CH_4/N_2 mixtures

C. Popov[1], M. Jelinek[2], J. Bulir[2], W. Kulisch[1]

[1] *Institute of Microstructure Technologies and Analytics (IMA), University of Kassel, Kassel, Germany*
[2] *Institute of Physics, Academy of Sciences of the Czech Republic, Prague, Czech Republic*

Abstract
Nanocrystalline diamond films have been prepared by microwave plasma chemical vapour deposition from methane/nitrogen mixtures and the influence of the gas phase composition on the properties of the deposited films was investigated. The increase of the methane concentration up to 17 % resulted in a gradual change of morphology and topography, from a layer composed of ball-shaped clusters of nanocrystals to a uniform film of amorphous matrix with embedded nanocrystallites.

1. Introduction

Diamond possesses various unique properties such as extreme hardness, low friction coefficient, chemical inertness, high electrical resistance, excellent thermal conductivity and good biocompatibility [1]. Upon doping it becomes a large band-gap semiconductor with an extremely high breakdown voltage and a high carrier mobility. It is transparent over a wide wavelength range and can withstand high electromagnetic radiation power fluxes from X-ray or laser sources. These outstanding properties make diamond of potential interest for a wide spectrum of applications including wear resistive and transparent protective coatings for optical components, heat spreaders, novel semiconductor devices, etc. However, the diamond coatings prepared by chemical vapor deposition techniques (CVD) are in most cases rough and nonuniform over large areas. The high surface roughness is a major problem for wear resistant applications of diamond films [2], for example in optical coatings, since it causes attenuation and scattering of the transmitted light. It also hinders the application of polycrystalline diamond films as coatings for bioimplants.
The deposition of diamond-related films, e.g. diamond-like carbon (DLC), tetrahedral amorphous carbon (ta-C) or nanocrystalline diamond (NCD) can overcome the roughness problem [3]. These films are much smoother and at the same time extremely hard, not reaching, however, the hardness of diamond. The first two types of films (DLC and ta-C) are prepared by ion-assisted methods leading to high compressive stresses [4]. The stress in the films directly affects their adhesion to the substrate and causes delamination. Moreover, the wear resistance is not high enough for biomedical applications. NCD films can be deposited by CVD techniques, i.e. without ion impact on the growing films. In such a way the stress problem can be solved to a great extent [5].
In general, there are two main approaches for deposition of NCD films:
(i) „the polycrystalline diamond route“ based on standard low pressure techniques for diamond deposition (especially MWCVD) [6-8]. In order to interrupt the crystal growth and to enhance the rate of secondary nucleation (leading finally to nanocrystallites) one or more of the process parameters should deviate from the standard values for polycrystalline diamond growth: lowered working pressure; higher methane concentrations; partial or complete substitution of H_2 by N_2 or Ar; application of bias voltage during the entire process.
(ii) „the DLC and ta-C route“ based on ion assisted techniques such as sputtering [9] or rf plasma-enhanced CVD [10]. By using high pressures, increased concentrations of Ar in the plasma as well as addition of H_2 and providing sp^3-rich underlayers, it is possible to achieve diamond nanocrystals in an amorphous matrix.
From the existing literature it is evident that the NCD films possess the high hardness, the high wear resistance and the good biocompatibility of diamond combined with low roughness, low compressive stress and good adhesion which make them very perspective for a number of applications.
We report on the deposition of NCD films by MWCVD from CH_4/N_2 gas mixtures with methane concentrations up to 17%. The influence of the gas phase composition on the properties of the deposited NCD films was investigated and they were compared to that of polycrystalline diamond films.

2. Experimental

The MWCVD set-up (*Plasma Technology*) used in the present study consists of a stainless steel reactor with water-cooled walls. The reactor is connected to turbomolecular and rotary pumps which provide a base pressure of about 10^{-4} Pa. Monocrystalline silicon wafers (3 inch) were used as substrates placed on a movable graphite holder inside the chamber which was inductively heated by a copper coil within the holder. In order to achieve continuous films by MWCVD, the substrate surface was pretreated with a suspension of diamond powder in n-pentane in an ultrasonic bath. The working gases (CH_4 and N_2) were introduced in the upper part of the chamber (above the substrate holder) and their flows were regulated by MFCs. The signal from the microwave plasma generator (*Astex Inc.*, 1.5 kW, 2.45 GHz) was introduced by an antenna with variable length into the chamber through a quartz window at the top of the reactor. A scheme of the deposition set-up is shown in Fig. 1.

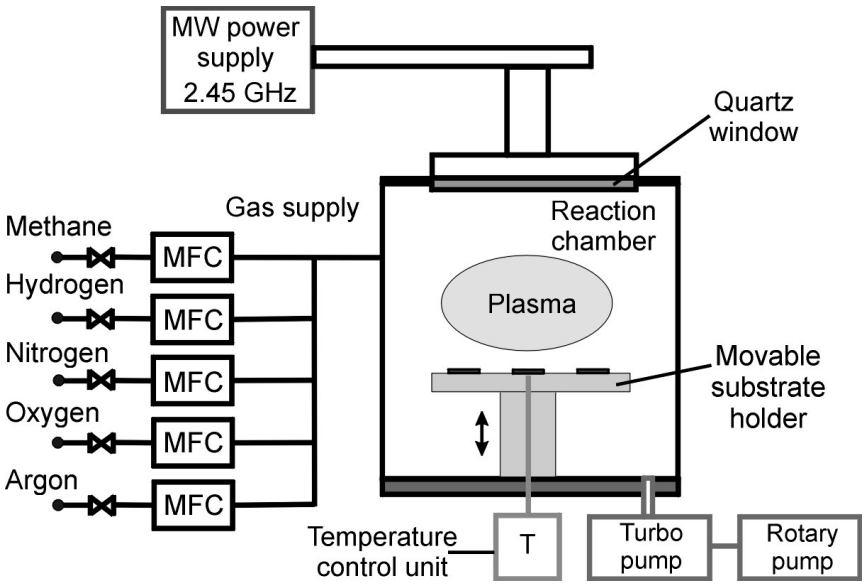

Fig. 1. Schematic drawing of the MWCVD set-up

Three series of samples were prepared by MWCVD: nanocrystalline diamond films from CH_4/N_2 precursor mixtures with 9% and 17% methane and polycrystalline diamond films from CH_4/H_2 with 1% methane, which were used as references. The substrate temperature (1043 K), the substrate position in the chamber, the input microwave power (800 W) and the working pressure (2600 Pa) were maintained constant during the deposition process.

The morphology and thickness of the deposited films were investigated by scanning electron microscopy (SEM). Atomic force microscopy (AFM) was used to derive information about the topography of the diamond coatings. The structure of the films was studied by X-ray diffraction (XRD) using the 0.514 nm CuK_α line, Raman spectroscopy with an Ar^+ laser at 514 nm, and Fourier transform infrared (FTIR) spectroscopy.

3. Results and discussion

The SEM pictures show the influence of the gas phase composition on the morphology of the layers – from large well-formed crystalline facets for polycrystalline diamond films through rounded nodules of sub-micron size, which entirely cover the substrate surface for the films deposited with 9% methane, to smooth and uniform NCD layers prepared with 17% methane (Fig. 2). The gas phase composition affects the growth mechanism and subsequently the structure of the films. Due to the absence of large amounts of hydrogen in the gas mixture, carbon dimers, C_2, appear to be the major nucleation and growth species instead of methyl radicals, CH_3^*, in the case of standard polycrystalline diamond deposition [11]. Higher methane concentrations lead to higher C_2 fractions which result in higher nucleation and growth rates (from 0.11 μm/h to 0.57 μm/h) and changes in the morphology (from sub-micron ball-shaped clusters of nanocrystals grown from the initial nuclei at the film-substrate interface (Fig. 2a) to uniform and smooth films (Fig. 2b)).

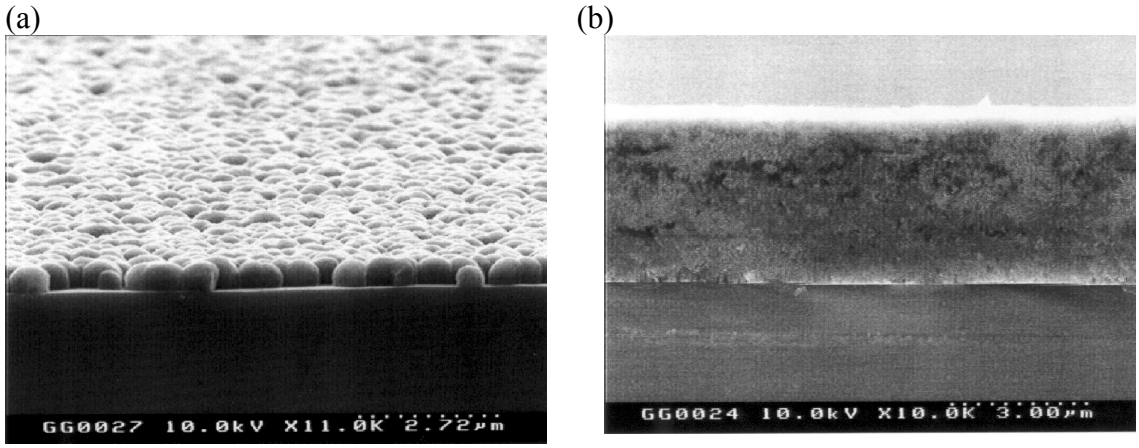

Fig. 2. Cross-section SEM micrographs of NCD films prepared by MWCVD from CH_4/N_2 mixtures: (a) 9% CH_4; (b) 17% CH_4

The surface roughness and topography of the NCD films are also dependent on the gas phase composition, as revealed by AFM investigations (Fig. 3). The topography changes with the CH_4 content from ball-shaped clusters of nanocrystals to smooth films with nanometer sized diamond inclusions. The rms roughness of the films and the grain heights decreases from 34 nm to 12 nm and from 380 nm to 43 nm, respectively, when increasing the methane concentration up to 17%. The obtained roughness is in the range of typical values for NCD films deposited by MWCVD [7,12].

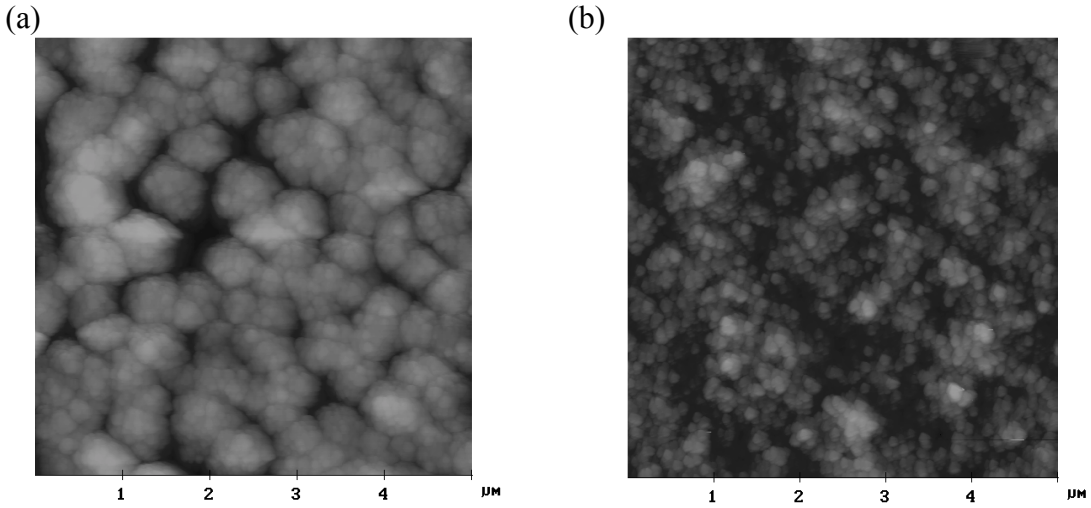

Fig. 3. AFM images of NCD films prepared by MWCVD from CH_4/N_2 mixtures: (a) 9% CH_4 (Z-scale 180 nm); (b) 17% CH_4 (Z-scale 50 nm)

The FTIR spectra of the NCD films showed significant absorption bands in the region 2800-3000 cm^{-1} attributed to superimposed CH_x asymmetric and symmetric stretching vibrations (Fig. 4). The hydrogen originate from the methane molecules since no H_2 was added to the gas mixtures. In general, sp^3-carbon atoms bonded to 1, 2 or 3 hydrogen atoms give rise to stretching modes in the region below 3000 cm^{-1}, while the sp^2-CH_x bonds are located above 3000 cm^{-1} [13]. In our case the C-H band is mainly below 3000 cm^{-1} suggesting that the hydrogen is predominantly bonded to sp^3-carbon, e.g. at the grain boundaries of the diamond nanocrystallites. The intensity of the infrared C-H band is greater for the films prepared with higher methane concentrations, suggesting a higher hydrogenation of the layers as a result of the increased hydrogen content in the gas phase.

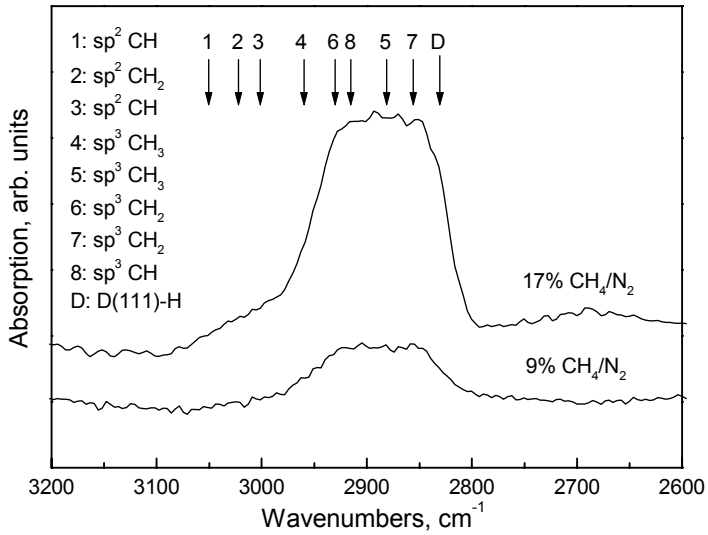

Fig. 4. FTIR spectra of NCD films prepared by MWCVD from CH_4/N_2 mixtures in the region of C-H stretching vibrations

The Raman spectra of the NCD films were fitted using four Gaussian peaks with variable parameters for peak width, position and area (Fig. 4); the results of the deconvolution are summarized in Table I. The attempt to deconvolute the raw spectra with three Gaussians did not give a sufficiently good fit, especially for the films prepared with 17% methane. The first band around 1160 cm^{-1} can be assigned to the presence of a nanocrystalline diamond phase, as well as the band around 1470 cm^{-1} [5,8,12,14]. Although the origin of these bands is controversially discussed in literature [15], a number of investigations of nanocrystalline diamond powder and films attributed these bands to the nanocrystallinity of the diamond, i.e. to the crystallite size. The other two broad bands, at about 1345 and 1560 cm^{-1} are attributed to the *D* and *G* bands of sp^2-bonded carbon, respectively. The diamond peak at 1336 cm^{-1} observed in the Raman spectrum of the polycrystalline films cannot be seen in the spectra of NCD films indicating, in agreement with the SEM observations that the films no longer consist of large, micron-size crystals. Rather, the Raman spectra suggest a mixture of diamond nanocrystallites and a sp^2-bonded graphitic phase.

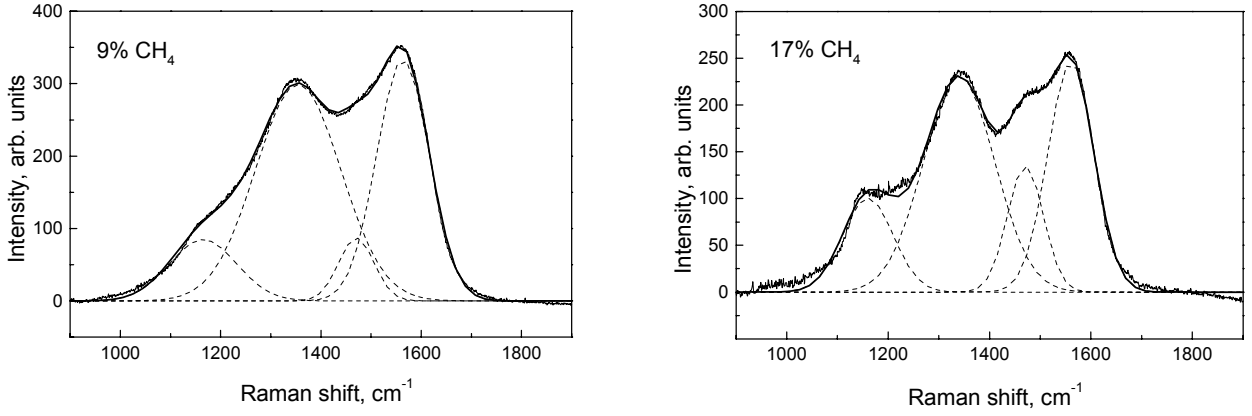

Fig. 4. Raman spectra of NCD films prepared by MWCVD from CH_4/N_2 mixtures with different methane concentrations

The I_D/I_G ratio remains the same while the intensity of the bands assigned to NCD $(I_{NCD}+I_{NCD*})/(I_D+I_G)$ increases with the increase of the methane concentration which, as already discussed, leads to smaller diamond crystallite sizes. Other trends observed from the deconvolution data are the decrease of the width and the downward shift of all bands with the increase of the CH_4 content in the gas mixture. However, in

order to draw further conclusions for the influence of the gas phase composition, the characteristics of the Raman spectra have to be correlated with some macroscopic properties of the films, like hydrogenation, density, hardness, optical gap, etc.

Table I. Analysis of Raman spectra deconvolution

	9% CH_4				17% CH_4			
	NCD	*D*	*NCD**	*G*	*NCD*	*D*	*NCD**	*G*
Peak position, cm^{-1}	1165	1345	1471	1564	1161	1340	1470	1560
FWHM, cm^{-1}	133	170	71	104	99	141	70	91
Peak intensity	14 170	63 786	7 726	43 877	12 592	40 536	12 024	28 085
I_D/I_G	1.45				1.44			
$I_{NCD}+I_{NCD*}/I_D+I_G$	0.20				0.36			

4. Conclusions

Nanocrystalline diamond films were prepared by MWCVD from CH_4/N_2 mixtures in which the methane concentration was increased up to 17 %. The complete substitution of hydrogen by nitrogen in the gas phase and the higher methane contents resulted in an increase of the deposition rate and changes in the film structure, morphology and topography. Gas mixtures with 9% CH_4 yield layers composed of ball-shaped clusters of nanocrystals, while at 17% a uniform film of diamond nanocrystallites embedded in an amorphous matrix was obtained. The coatings prepared with 17% methane were smooth with a rms roughness of 12 nm. The Raman spectra showed that a higher methane concentration leads to smaller grain sizes and higher fractions of the sp^2-bonded graphitic matrix in the films. Hydrogen, originating from the methane molecules, was present in the films, predominantly bonded to sp^3-carbon atoms.

Acknowledgements

The authors gratefully acknowledge the financial support of the German Ministry of Education and Research (BMBF) under the WTZ Program (Contract CZE 02/010); they would also like to thank Dr. M. Schreck from the University of Augsburg for the Raman measurements.

References

[1] W. Kulisch - *Deposition of Superhard Diamond-Like Materials*, Springer, Tracts on Modern Physics, Heidelberg, Berlin (1999).
[2] A.K. Gangopadhyay, M.A. Tamor - Wear **169**, 221 (1993).
[3] M. Chhowalla, Y. Yin, G.A.J. Amaratunga, D.R. McKenzie, T. Frauenheim - Appl. Phys. Lett. **69**, 2344 (1996).
[4] R.G. Lacerda, F.C. Marques - Appl. Phys. Lett. **73**, 617 (1998).
[5] T. Sharda, M. Umeno, T. Soga, T. Jimbo - J. Appl. Phys. **89**, 4874 (2001).
[6] N. Jiang, K. Sugimoto, K. Eguchi, T. Inaoka, Y. Shintani, H. Makita, A. Hatta, A. Hiraki - J. Crystal Growth **222**, 591 (2001).
[7] D. Zhou, D.M. Gruen, L.C. Qin, T.G. McCauley, A.R. Krauss - J. Appl. Phys. **84**, 1981 (1998).
[8] K. Wu, E.G. Wang, J. Chen, N.S. Xu - J. Vac. Sci. Technol. B **17**, 1059 (1999).
[9] S.N. Kundu, M. Basu, A.B. Maity, S. Chaudhuri, A.K. Pal - Mater. Lett. **31**, 303 (1997).
[10] G.A.J. Amaratunga, A. Putnis, K. Clay, W.Milne - Appl. Phys. Lett. **55**, 634 (1989).
[11] D. Zhou, A.R. Krauss, L.C. Qin, T.G. McCauley, D.M. Gruen, T.D. Corrigan, R.P.H. Chang, H. Gnaser - J. Appl. Phys. **82**, 4546 (1997).
[12] D.M. Gruen, X. Pan, A.R. Krauss, S. Liu, J. Luo, C.M. Foster - J. Vac. Sci. Technol. A **12**, 1491 (1994).
[13] B. Dischler, A. Bubenzer, P. Koidl - Solid State Commun. **48**, 105 (1983).
[14] M.N. Gamo, T. Tachibana, K. Kobashi, I. Sakaguchi, K.P. Loh, K. Yamamoto, T. Ando - Diamond Relat. Mater. **7**, 783 (1998).
[15] A.C. Ferrari, J. Robertson - Phys. Rev. B **63**, 121405 (2001).

Continuous Emission of O- Anion Radical from C12A7

Yoshifumi Torimoto *1, Masateru Nishioka *2, Quanxin Li *2 And Masayoshi Sadakata*2

*1 Production Technology Institute of Kao Coprporation,1334 Minato, Wakayama ,640 8405, Japan

*2 Dept. of Chemical System Engineering, School of Engineering, The Univ. of Tokyo, 7-3-1, Bunkyo-ku,Tokyo, 113-8656

Negative ions have become to gain a considerable attention recently, because they have great potential for applications ranging from material syntheses and modifications such as charge-free ion plantation to artificial formation of neuron- network[1-2]. The O- negative ion is one of the most active and useful radical for applications. The method conventionally used to generate O- is the attachment of a free low-energy electron to a molecule reaction, which can occur in a plasma process. We have proposed a simple method by using a solid electrolyte as an O- emitter. This approach is expected to obtain a high purity and sustainable ionic radical beam due to good ion conductivity. Although the sustainable and pure O- emission can be implemented by a Y_2O_3-stablized ZrO_2 (YSZ) electrolyte, we can not achieve a high-intensity of O- flux. In this letter, we present a strong and pure O- emission from the crystal 12CaO・Al2O3（C12A 7）, which is about three orders of magnitude higher than the O- current density from YSZ surface. A μA/cm2-level of O- emission from C12A7 has been achieved at the surface temperature of 800℃ and the extraction field over 1000V/cm. The mass signals of negative ion from C12A7 can be analyzed by time of flight (TOF) mass spectrometer. The dominant peak of TOF mass spectrum is the mass number 16 shown in Fig.1, which corresponds to the O- anion radical. We revealed that the emission features from C12A7 and YSZ electrolytes are significantly different because the strong O- emission from C12A7is likely to originate from a direct migration of O- through the C12A7 cage by the filed enhanced thermal diffusion. The comparison of absolute current density of O- between C12A7 and YSZ at 800℃ is shown in Fig.2.

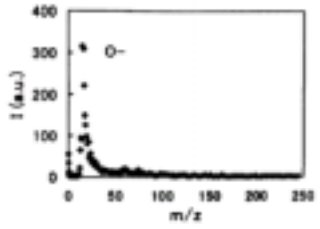

FIG. 1. Typical TOF spectrum measured at 750 °C. The strong peak corresponds to the O⁻ emitted from the C12A7 surface.

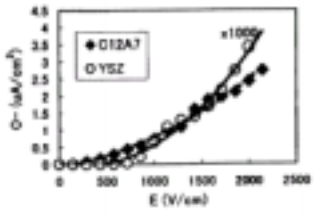

FIG. 2. Comparison of absolute current densities of O⁻ between C12A7 and YSZ at 800 °C. The emission current density from the C12A7 surface is about three orders of magnitude higher than that from the YSZ surface.

1: J.Ishikawa, Rev. Sci, Instrum. 67. 1410(1996)

2:J.Ishikawa, Rev.Sci.Instrum.71,1036(2000)

Preparation and Properties of SiNx-based Nitride Films by Liquid Injection Plasma CVD

S. Shimada and K. Tsukurimichi

Graduate School of Engineering, Hokkaido University, Sapporo 060-8628 Japan

Abstract

SiNx-based nitride films including monolithic SiNx films and composite and compositionally graded SiNx-TiN films were prepared on a Si wafer at 700 ^{o}C by a plasma chemical vapor deposition technique designed to inject ethanol solution of alkoxides (hexa-methyl-disiloxane and titanium tetra-ethoxide at a feed rate of 0.05 – 0.3 ml min^{-1} into a thermal Ar/H_2/N_2 plasma.

1. Introduction

Titanium nitride (TiN) has low resistivity (several tens μΩ cm), good hardness and chemical stability, and high melting point (> 3000 ^{o}C). TiN films are used as coatings on cutting tools, because they are harder than alumina and thermally stable to 3000 ^{o}C [1-3]. A disadvantage of TiN is its tendency to oxidize rapidly above ～500 ^{o}C to form TiO_2 that causes a drastic degradation of its wear resistance. Silicon nitride (Si_3N_4) exhibits high thermal conductivity and high oxidation resistance. Composite Si_3N_4-TiN films are thus useful because of their improved oxidation resistance at elevated temperatures and expected to exhibit higher hardness compared with the monolithic nitride.

The preparation of monolithic Si_3N_4 films by plasma-enhanced CVD (PECVD) has been reported by several authors [4,5], whereas there have been a very few reports on the preparation of composite SiNx-TiN films [6]. In previous papers, one of the authors (S.S.) has established the preparation of TiN and AlN films by injecting the solutions of titanium tetra-ethoxide ($Ti(OC_2H_5)_4$, TTEO) and aluminum tri-butoxide solution, respectively, into a thermal Ar/H_2/N_2 plasma, by a novel liquid injection PECVD (LI-PECVD) [7] and extended this work to the preparation of composite $(Ti_{1-x}Al_x)N$ films from the mixed solutions [8]. He has also made the compositionally graded (CGed) TiN-AlN films from the respective alkoxide solutions; the Ti and Al or Si complementarily change in depths in the films 1 - 2 μm thick [9]. Since it was found possible to prepare monolithic SiNx films from HMDS solution by LI-PECVD method, this method provides an alternative promising technique to make SiNx-based composite films using HMDS solution as the starting source. The present report describes the preparation of monolithic SiNx and SiNx-based films including composite and CGed SiNx-TiN films from HMDS and the mixed solutions of HMDS and TTEO by LI-PECVD. These films are characterized from viewpoints of impurity content, phase evolution, microstructure, micro-hardness, and electrical resistivity.

2. Experimental Procedures

The HMDS was used as the starting material for the preparation of monolithic Si_3N_4 films and dissolved in dried ethanol at a molar ratio of 1:1.7. The solution was fed into Ar/N_2/H_2 gas plasma using a

HPLC pump (GULLIVER PU-980, JASCO corporation) at a rate of 0.05 – 0.3 ml min^{-1}. Tri-ethanol amine (TEA) was used to stabilize TTEO solution. Ethanol solution of TTEO containing TEA was mixed with that of HMDS. The mixed solution with various mole ratios of TTEO and HMDS was fed at a total rate of 0.1 ml min^{-1} for 15 min into the plasma to make the composite TiN/Si_3N_4 films. The substrate used for film preparation was a 100 Si wafer, which had been treated with 46% HF solution for 10 min, followed by ultrasonic cleaning in acetone, ethanol, and deionized water. The substrate temperature was at 700 ^oC.

Each alkoxide solution of HMDS and TTEO was dissolved in dried ethanol at a molar ratio of 1:1 to 1:3. The CGed SiNx-TiN films were prepared; SiNx and TiN deposited on the surface and substrate, respectively, with complementary change of Si and Ti in the film (designated SiNx//TiN). For the CGed films to be prepared, the feeding rate of the two alkoxide solutions was complementarily changed with time, maintaining the total feeding rate at 0.1 ml min^{-1} using two HPLC pumps. The detailed procedures were reported elsewhere [9]. The substrate used in this experiment was also the (100) face of Si wafer.

Phases formed on the film were identified by thin film X-ray diffractometry (XRD) with CuKα radiation. The chemical states of Si, Ti, N, O, and C were determined by X-ray photoelectron spectroscopy (XPS). The relative atomic ratios of the elements (N, O, C) to Si were calculated from their XPS peak areas. The surface and cross section of the film was observed by scanning electron microscopy (SEM). The electrical resistivity of the composite films was measured by a four-probe method at room temperature and the relative Vickers micro-hardness was determined at a load of 1 fg.

3. Results and discussion

Figure 1 shows Si_{2p} spectra of the silicon nitride films on a Si wafer obtained at 700 ^oC from the HMDS solution at feed rates of 0.05 – 0.3 ml min^{-1}. It is obvious that the films made at a feed rate of 0.3 ml min^{-1} possess a main peak at a binding energy of 100.2 eV, which is due to SiC. The decreasing feed rate from 0.3 to 0.05 ml min^{-1} shifts the peak to the Si-N bond at 101.7 e V. Since the XRD patterns of these films gave no diffraction peaks, the films with the Si-N bond are designated as amorphous SiNx. The influence of the feed rate on the relative atomic ratios of N, O, and bonded/free C to Si in SiNx films was examined. At a feed rate of 0.3 ml min^{-1}, the films contained the N less than 0.7, although much bonded C was included in addition to free C and O. A feed rate of 0.2 ml min^{-1} did not remove the carbon and oxygen impurities. Lowering the feed rate to 0.1 ml min^{-1} increased the N content to about 1.0 with decreasing the bonded C and O. At 0.05 ml min^{-1}, the films possessed the N/Si = 1.35 near the composition of Si_3N_4 (N/Si = 1.33) with the lower free/bonded C and O contents.

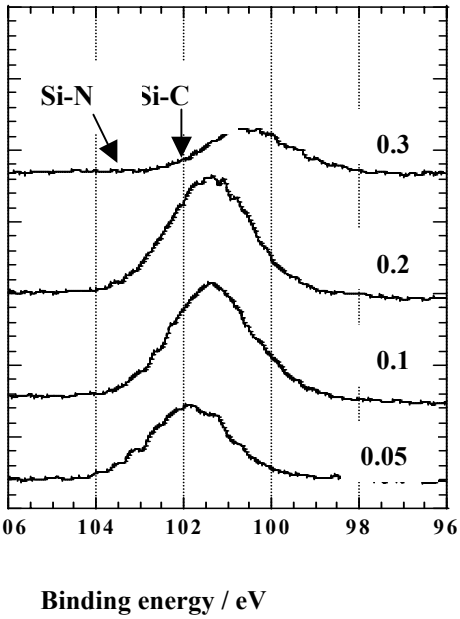

Figure 1 Si2p XPS spectra of SiNx films at feed rates of 0.05 – 0.3 ml min^{-1}

The surfaces of the SiNx films obtained at feed rates of 0.3 – 0.05 ml min^{-1} were observed by SEM. The films obtained at 0.05 ml min^{-1} is about 0.5 μm thick and show the formation of fine packed particles of 0.1 μm in size, with 0.4 μm-sized particles on the top. The films obtained at 0.1 ml min^{-1} exhibited relatively densely packed layer consisting of about 1 μm-sized particles, with larger particles of 2 – 7 μm in size sparsely on the top. Cross-sectional observation of the films showed several thin layers to be piled up to about 1 μm thick. The optimum feed rate for producing SiNx films was found to be 0.05 ml min^{-1} at which the films possess the composition near Si_3N_4 with the less free and bonded C and O impurities and exhibit the microstructure consisting of regularly 0.1 μm sized particles in bulk.

Composite SiNx-TiN films were prepared on a Si wafer at 700 ^oC by feeding the mixed solutions of HMDS and TTEO containing stabilizing TEA at a rate of 0.1 ml min^{-1}. Figure 2 shows the XRD patterns of composite SiNx-TiN films with various mole ratios of Ti to Si in the mixed solution. No peaks related to Si_3N_4 are seen at all the mole ratios, which is not contradictory to the XRD results of amorphous monolithic SiNx films. Very small broad peaks of TiN appear at a mole ratio of Ti:Si = 3:7, and increase with increasing the ratio. At 100 % Ti, sharp peaks of TiN are observed, similarly to those reported in a previous paper [7].

The relative atomic percentages of the Si, Ti, N, O, and total C (bonded and free C) elements determined from the respective XPS peak areas are

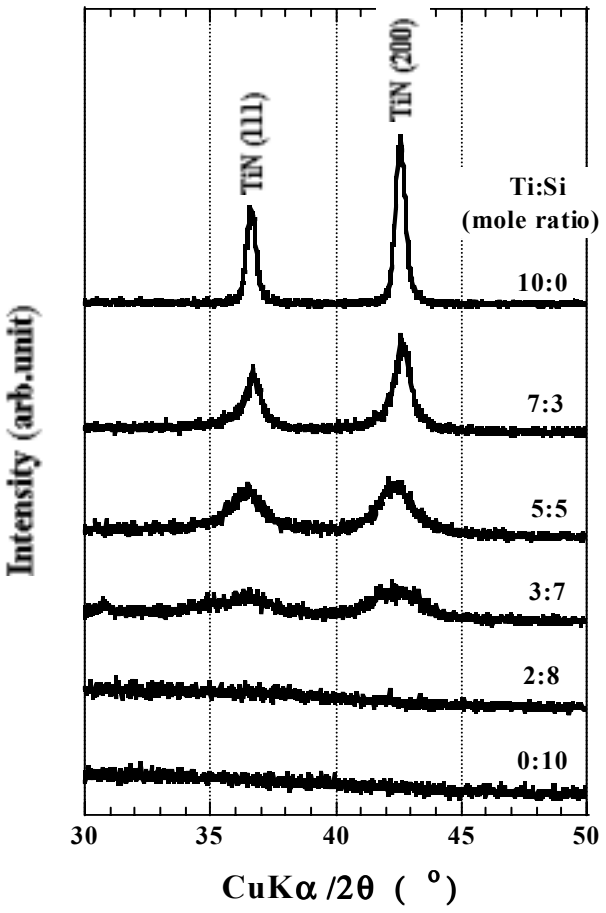

Figure 2 XRD patterns of composite SiNx-TiN films.

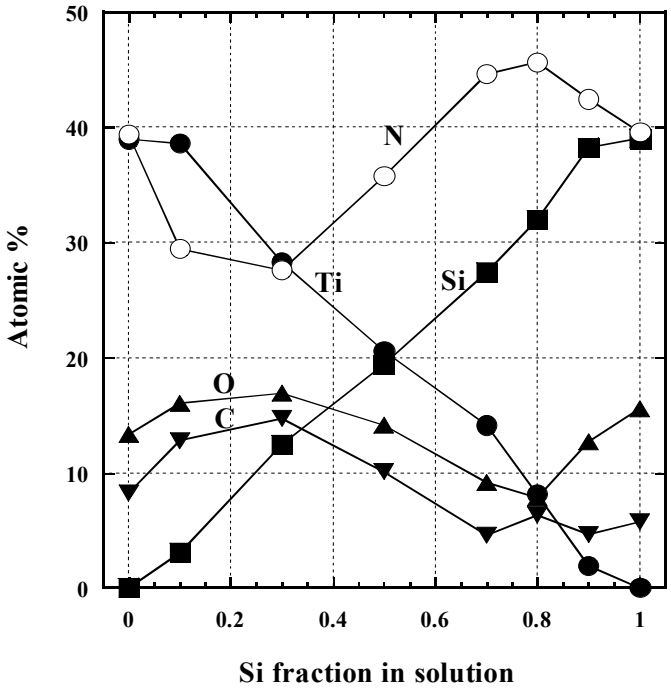

Figure 3 Change of atomic % of Si, Ti, N, O, and C in composite SiNx-TiN films

shown in Fig. 3 . The N content is relatively small (30 – 35 at. %) at a Si fraction of 0.1 – 0.5, while that is 40 – 45 at. % at Si fractions above 0.5. The total content of Ti and Si is around 40 at. %, each Ti and Si changing linearly and complementarily with the solution composition. This indicates that the respective Ti and Si component is effectively deposited from the solution without their selective etching or removal in the plasma. Approximately 10 – 15 at. % oxygen and carbon impurities are incorporated in the film at Si fractions of 0 – 0.5, whereas these impurities decrease to < 10 at.% at Si fractions above 0.5. The increase and decrease of the N content correspond to the reverse decrease and increase of the O and C impurities, suggesting that the O and C impurities replace the N atoms in the TiN or SiNx structure; the C impurity exists partly as free carbon. It is concluded that the SiNx-TiN composite films were successfully prepared on a Si wafer at 700 ^{o}C by injecting the mixed ethanol solutions of HMDS and TTEO containing TEA into a thermal $Ar/H_2/N_2$ plasma.

The surface and cross-section of the composite SiNx-TiN films were observed by SEM (Fig. 4). Monolithic SiNx film obtained at a feed rate of 0.1 ml min^{-1} was already explained above. Compact monolithic TiN film is formed, with angular particles of 200 nm in size (Fig. 4(a)), which slightly increased to the sizes of 300 to 400 nm at a Si fraction of 0.1. At Si fractions higher than 0.3 ((b) – (e)), particles are consolidated to be 1 to 2 μm in size, consisting of uniformly 200 – 300 nm sized particles, under which a layer with uniformly packed particles of 200 – 300 nm

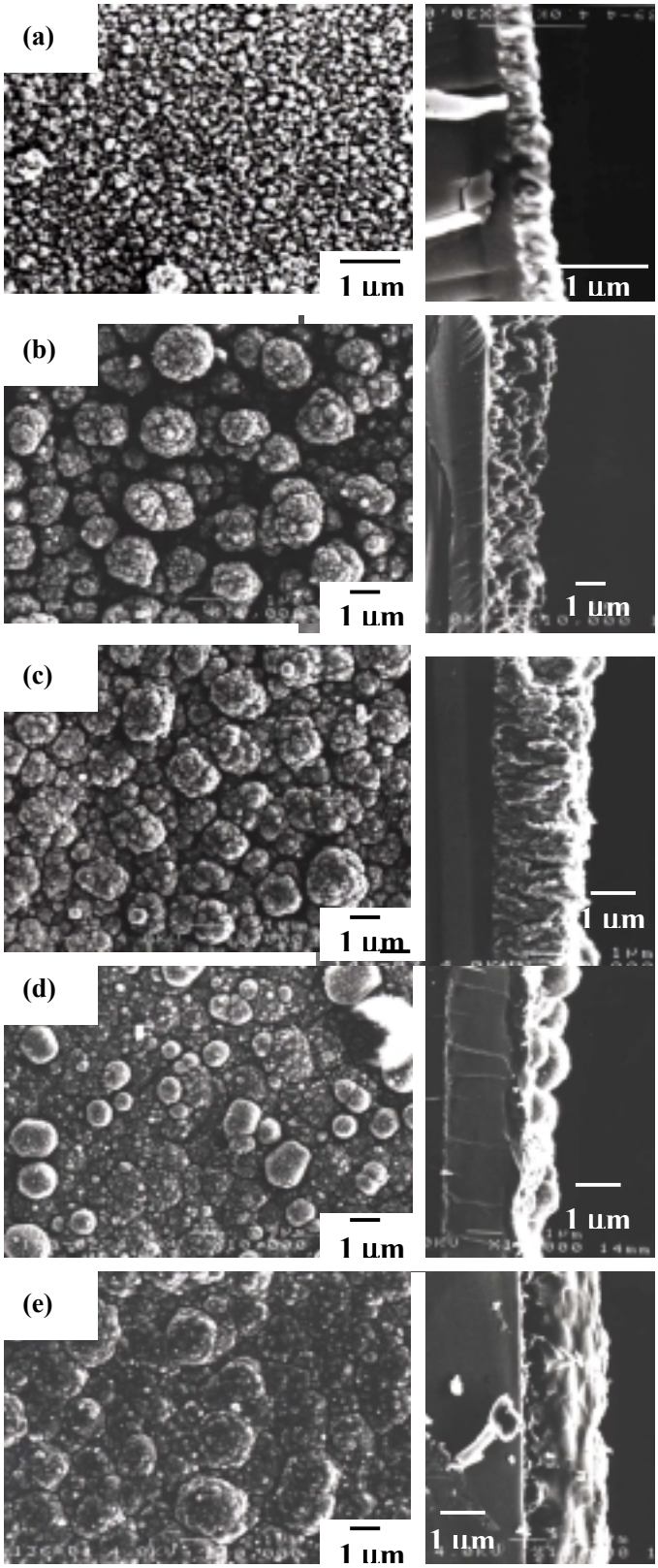

Figure 4 SEM of surface and cross-section of composite SiNx-TiN films. The atomic ratio of Ti:Si (a) 10:0, (b) 7:3, (c) 5:5, (d) 3:7.

size is seen. Consolidated particles slightly decrease to 1 μm size at 0.7 Si fraction, but increase again at 0.8 fraction. Films obtained at 0.9 Si fraction showed a microstructure similar to that prepared at 1.0 Si. From cross-sectional observation, the film is 0.4 μm thick for the TiN and thickens slightly with increasing Si fraction, up to about 1.5 μm thick at a Si fraction of 0.3 – 0.8. Further increase of Si fraction to 0.9 and 1.0 maintains a thickness of 1 – 1.5 μm. It is observed that columnar structures are formed normal to the substrate at Si fractions lower than 0.5, consisting of 200 – 300 nm grains, which are perpendicularly connected ((a) to (c)). At the higher fractions, flattened spherical particles of 1 μm size are observed on the top of the surface, under which dense layer is formed ((d) to (e)).

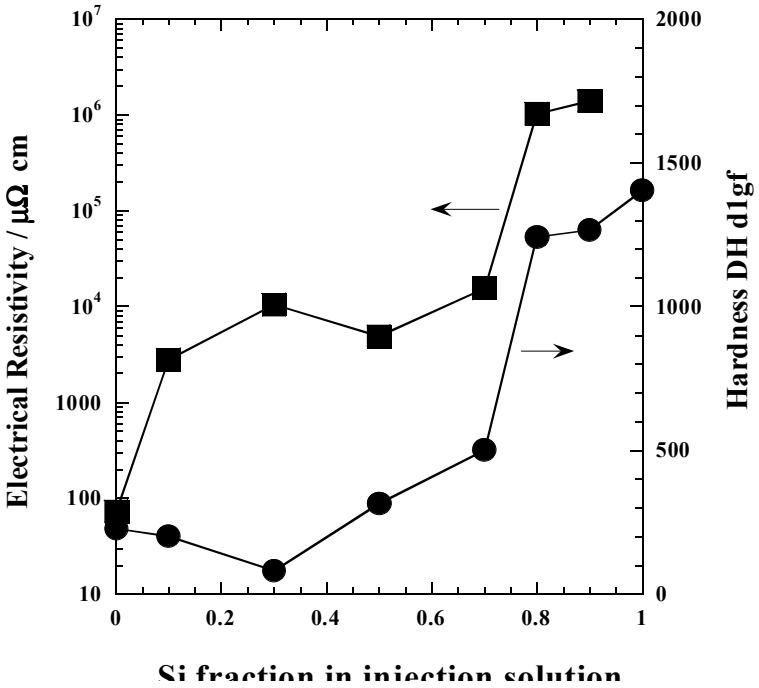

Figure 5 Relationship between electrical resistivity /microhardness and Si fraction in composite SiNx-TiN films.

The electrical resistivity and micro-hardness of the SiNx-TiN films, measured as a function of the Si content of the solution, are shown in Fig. 5. Since the surface of the films is rather rough, it was difficult to determine their absolute values, but the measured values are compared with each other. The resistivity of the films is low (80 μΩ cm) for the TiN film and suddenly increases to 2 x 10^3 μΩ at 0.1 Si fraction. The resistivity slightly increases to 10^4 μΩ cm at 0.3 –0.7 Si. It is believed that paths for electric current are maintained in the films up to this Si content. It is noted that the films at 0.7 Si fraction show still lower electrical resistivity (about 10^4 μΩ cm), compared with the value prepared by the magnetron sputtering (10^7 μΩ cm) and that obtained by the arc ion plating (10^8 μΩ cm). SiNx-rich films with 0.8 and 0.9 Si fractions showed resistivities of an order of magnitude of 10^6 μΩ cm; the value of SiNx films was too high to measure. The relative micro-hardness of the SiNx-TiN films were measured to levels off at the relative value of 250 at Si fractions of 0 - 0.3 and increases greatly with increasing Si content. The pure SiNx film shows a value of 1400.

It was found that the compositionally graded SiN_x//TiN films can be formed by liquid injection plasma CVD method using the alkoxide solutions. Changes of the concentrations of N, Si, Ti, O, and C with depth in the are shown in Fig. 6. The first 10 minutes of etching removed the concentrated impurities O and C from the SiN_x surface. After removal of the impurities, the N content increases to 46 at. %, becoming constant with depth. Concomitantly, the Si content rises to 38 at. %, then gradually decreases from 30 at. % over two-thirds of the film depth towards the substrate. The Si content then drops steeply to 3 at. %, in contrast to the Ti which concomitantly increases to 35 at. % near the substrate. The O and C impurities occur at less than 6 at. % over most of the film depth, but increase slightly near the substrate.

Surface and cross-sectional bservations of SiN_x//TiN films are shown in Fig. 7. Spherical particle 3 μm in size are formed on the outermost surface of the SiN_x//TiN film, beneath which ≦1 μm particles are seen. The cross-section shows the film to be 3 μm thick and dense, containing particles piled up from the substrate and growing larger toward the surface.

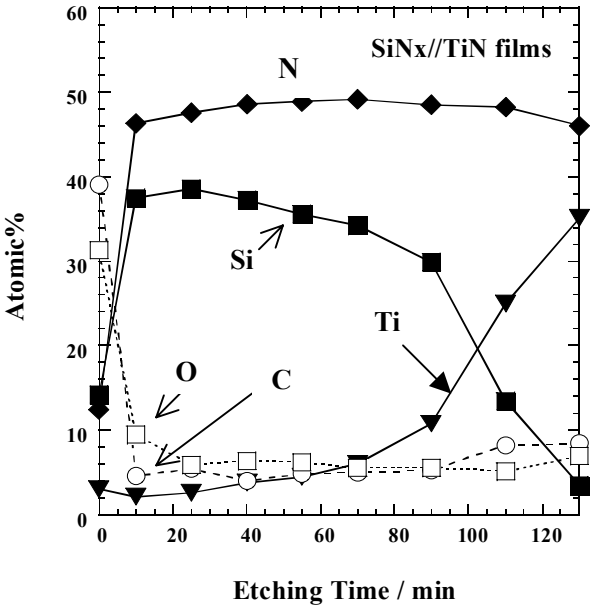

Figure 6 Changes in the depth direction of atomic % of N, Ti, Si, O, and C in the SiNx//TiN films

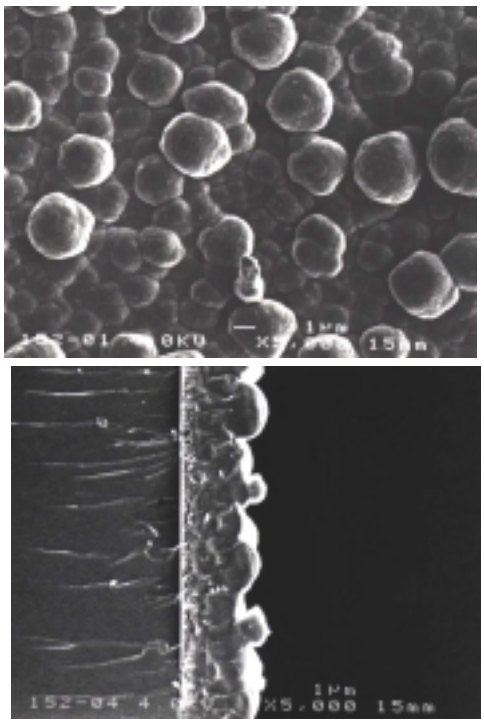

Figure 7 SEM photographs of surface and cross-section of SiNx//TiN films.

References

[1] S. Laimer, P. Braun, H. Stori, F.Viehbock, P. Rodhammer, K. Kailer, Mikrochimica Acta, Suppl. **10**, 177 (1983).

[2] A. Weber, C.-P. Klages, M.E. Gross, R.M. Charaton, and W.L. Brown, J. Electrochem. Soc., **142**, L79 (1995).

[3] A. Intemann and H. Koerner, J. Electrochem. Soc., **140,** 3215 (1993).

[4] D-H. Kuo and D-G. Yang, Thin Solid Films, **374** , 92 (2000).

[5] T. Aoki, T. Ogishima, A.M Wrobel, Y. Nakashima, and Y. Hatanaka, Vacuum, **51**, 747 (1998).

[6] B.H. Park, Y-H. Kim. and K.H. Kim, Thin Solid Films, **348,** 210 (1994).

[7] S. Shimada, M. Yoshimatsu, H. Nagai, M. Suzuki, and H. Komaki, Thin Solid Films, **370**, 137 (2000).

[8] S. Shimada and M. Yoshimatsu, Thin Solid Films, **370**, 146 (2000).

[9] S. Shimada, K. Tsukurimichi, Y. Takada, J. Takahashi, and M. Nagai, J. Ceram. Soc. Jpn. , **110,** 444 (2002).

Study of properties and preparation conditions of the plasmochemical SiO_2 films.

V.M. Izgorodin, Yu.V. Tolokonnikova, A.A. Aushev, A.I. Vasil'eva,
V.G. Gogolev, A.F. Kovylov, E.G. Orlikova and I.G. Sevrugin

Russian Federal Nuclear Center—All-Russian Scientific Research Institute of Experimental Physics (RFNC-VNIIEF)
Russia, 607190, Sarov, Nizhni Novgorod reg., Mir str., 37

ABSTRACT.
Plasmochemical SiO_2 film was carried out by decomposition of the tetraethoxycilane vapor by the electrical discharge with the frequency of about 18 kHz. The excessive products of decomposition were pumped out with maintenance of the tetraethoxycilane vapor and argon pressure of about 0.2 Torr. The study of element structure has shown that the film represents Si_xO_y with $x \approx 1$ and $y \approx 2$ and contains an impurity of organic inclusions. This method is applied for preparing of the covering with uniform thickness on glass microspheres used as targets in laser fusion experiments on the installation "Iskra-5".

1. INTRODUCTION.

For a number of applications it are required transparent hollow microspheres with a wide set of diameters and wall thickness, and also with added various elements as impurity in wall. Manufacturing such microspheres from a glass with a diameter up to 1-1.5 mm now is possible with wall thickness up to 1-3 microns. It is rather inconvenient to receive spheres with the greater thickness of wall. The input in glass of tracer elements also requires the large technological work on a blend preparation, suitable for process of formation of hollow microspheres.
Earlier for the decision of these tasks we have tried to use usual thin-walled glass microspheres as substrates, on which the homogeneous covering of required thickness with composition and structure close to glass is deposited. Most suitable there was a film of silicon dioxide. For deposition of covering we used a plasmochemical method, by which it is possible to make a homogeneous on thickness covering on sphere [1-3]. Besides we hoped, that this method will allow entering into the basic matrix of a film an impurity of wide set of elements.
As basic substance we used tetraethoxycilane (TEC), which at decomposition in plasma provides fragments of SiO_2 forming the basic matrix [4]. This method does not give also strong heating of substrate. That is important at deposition of covering on ready sphere. This substance has an optimum vapor pressure for our installation at room temperature. Films were formed by decomposition of TEC vapor in a mix with argon 0.5: 0.5 (sample 1) or with argon and oxygen 0.5: 0.25: 0.25 (sample 2) in the glow discharge of alternating current with frequency ~ 18 kHz. The flowing mode was carried out both by continuous submission of initial substance and pumping out argon and volatile products of decomposition.

2. PROCESS OF SILICON DIOXIDE LAYER FORMATION.

Film deposition was carried out on flat and spherical substrates of glass, polished crystal NaCl, titanium, aluminum, cupper and gold. The thickness of layer achieved 25 microns. As a gas atmosphere the TEC vapor with argon or mix argon and oxygen were used.
The experiments have shown [3] that the thickness of formed SiO_2 film is practically linear function from time and from the TEC expense. The deposition velocity depends on a material of substrate. The least velocity was observed on the NaCl substrate, greatest velocity - on metal substrate. In Fig. 1a and 1b the dependences of film thickness from the deposition time and from the TEC expense are given for a case, when the glass spheres with diameter of ~ 300 microns were used as substrate. The deposition velocity did not depend practically on a partial pressure of Ar and O_2.

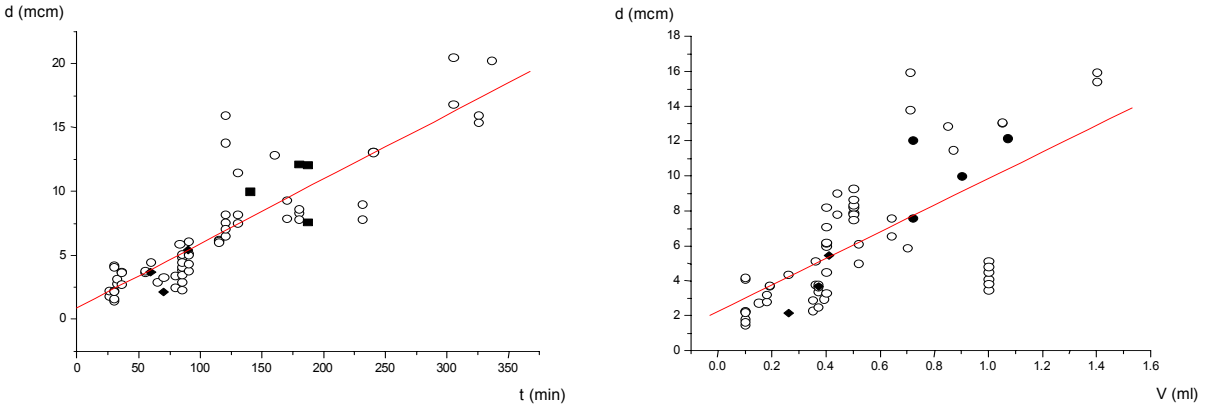

a) b)

Fig. 1. Dependence of SiO_2 film thickness on the deposition time a) and expense of tetraethoxycilane b) in a various gas atmosphere: o - points received in mix of vapor of TEC + Ar + O_2 (Ar: O_2 = 1:1); ♦ - points received in mix of vapor of TEC + Ar + O_2 (Ar: O_2 = 3:2); ● - points received in mix of vapor of TEC + Ar.

2. COMPOSITION OF FILMS.

2.1. Element composition.

The research of element composition was made by the following methods:

- qualitative analysis by mass-spectrometer with evaporation of a sample by laser pulse;
- quantitative analysis of elements with nuclear number Z>7 on the X-ray microanalyzer with excitation of a sample by an electronic beam;
- quantitative analysis of the contents of carbon and hydrogen by a method of reactionary gas chromatography (decomposition of a sample at presence of the oxidant catalyst) and by burning a sample in a current of oxygen at the presence of the catalyst with subsequent gravimetric measurement of formed products of burning (CO_2 and H_2O) after them settling to an absorber.

The analysis has shown, that the covering consists mainly of silicon, oxygen, carbon and hydrogen with gross - formulas

$$SiO_{1.85}C_{2.12}H_{3.54}$$

at excitation of plasma in the mix of TEC vapor and argon and

$$SiO_{1.97}C_{1.83}H_{3.53}$$

at excitation of plasma in the mix of TEC vapor, argon and oxygen (Ar:O_2= 1:1).

2.2. Molecular composition.

The molecular composition was investigated by registration and processing of IR-spectra of transmission, and also Raman spectra. In Fig. 2 the IR- spectra of films, prepared in mixes of TEC vapor + argon and TEC vapor + argon + oxygen, and in Fig. 3 Raman spectra of films are given. Here the appropriate spectra of initial substance (liquid tetraethoxycilane) and fused quartz are given [5].

The analysis of IR-spectra of plasmochemical films (Fig. 2) has shown, that they have two characteristic for amorphous SiO_2 stripes of absorption - wide intensive stripe with a maximum of ~ 1070 cm^{-1} and less intensive stripe with a maximum of 790 cm^{-1} [6,7]. Besides there are stripes connected with valence (wide stripe of 3600-3200 cm^{-1} and narrow stripe of 3570 cm^{-1}) and distortion (1690-1710 cm^{-1}, 960 cm^{-1}) vibrations of connections O—H [6,8]. There are also stripes of absorption caused by valence (2970-2880 cm^{-1}) and distortion (1445-1370 cm^{-1}) vibrations of the connection C—H in alkane [9]. In spectra of absorption the presence of connections C-Si-C (650-690 cm^{-1}) is visible. It is possible also existence of connections Si-H and defective centers of a type E′H. It worsens of strength property and loosens structure.

In Raman spectrum the stripes, characteristic for fused quartz, and lines caused by the connection C—H are visible.

Thus, the spectra show, that the structure of silicon oxygen films received by TEC decomposition in the decaying low-frequency electrical discharge by mixes of TEC vapor and argon (0.5: 0.5), and also TEC vapor, argon and oxygen (0.5: 0.25: 0.25), corresponds to stochiometric SiO_x at x ~ 1.8. Both films contain significant amount of an organic impurity as groups CH, CH_2 and CH_3, and also of hydroxyl groups.

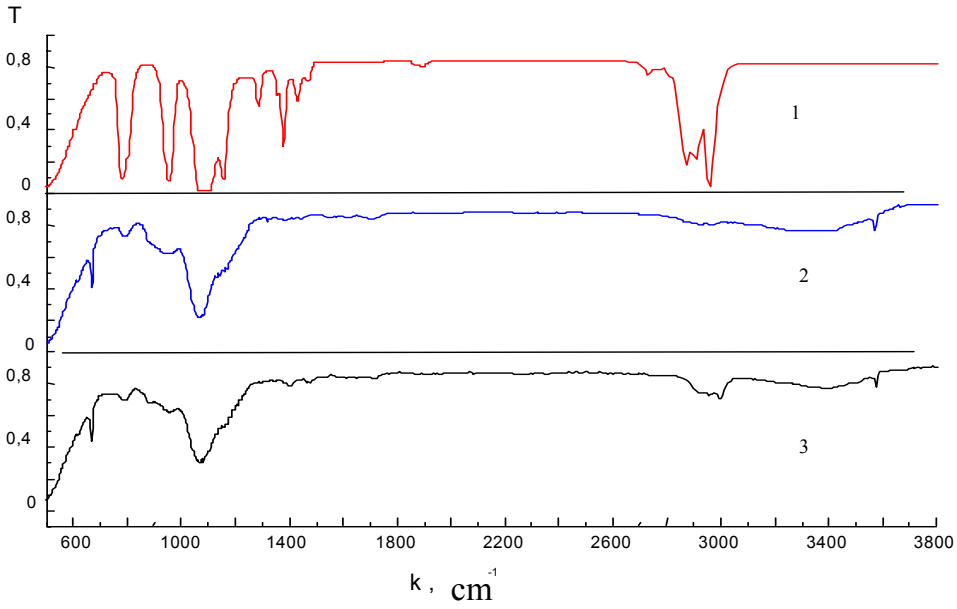

Fig. 2. IR-spectra of absorption of liquid TEC and plasmochemical silicon dioxide films.
1 - TEC; 2 - film prepared by mix of TEC vapor, argon and oxygen (0.5: 0.25: 0.25); 3 - film prepared by mix of TEC vapor and argon (0.5: 0.5).

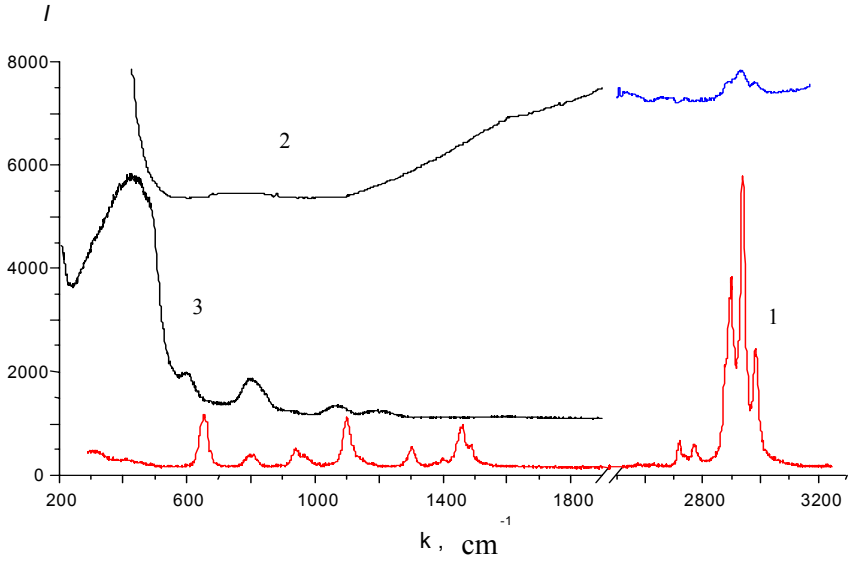

Fig. 3. Raman spectra of liquid TEC (1), plasmochemical silicon dioxide films (2) and fused quartz (3).

3. PHYSICAL PROPERTIES OF COVERING.

3.1. Density.

Density of a covering was determined by division of the substrate weight increase after deposition in comparison with the weight before deposition on volume of covering. Volume was determined as the sum of products of the elementary areas on covering thickness in middle of these areas. The thickness was determined on microinterferometer. The summation was carried out on all surface of a substrate. The values of density are equal

2.34 ± 0.03 g/cm^3

for discharge in mix of TEC vapor and argon and

2.17 ± 0.05 g/cm^3

for discharge in mix of TEC vapor, argon and oxygen ($Ar:O_2$= 1:1).

3.2. Factor of refraction.

The measurement of factor of refraction was carried out on microinterferometer by measurement of a difference of optical ways for beams, past through a layer of known thickness (2) and outside this layer (1). The scheme of measurements is submitted in Fig. 4. The measured value of refraction factor of films is

$$n = 1.46 \pm 0.02$$

independently of ratio of auxiliary gases in discharge (Ar and O_2).

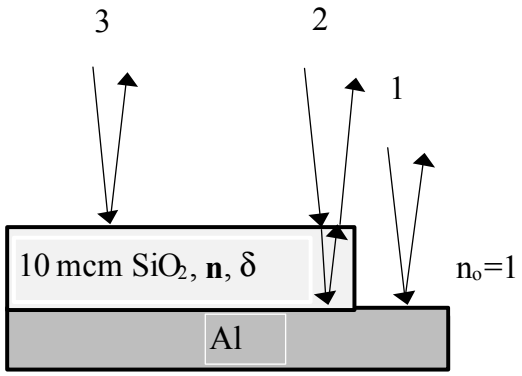

Fig. 4. The scheme for determination of refraction factor of SiO_2 deposition by interferometer method.

3.3. Structure and surface properties.

The X-structural analysis has not found out in films a crystal structure.

The image of a surface was received with the help of carbonic replica of surface on electronic microscope and on the microanalyzer in reflected electrons. Films received in pure argon (auxiliary gas) have a very smooth surface; at use of a mix argon-oxygen on a film surface the ledges or infringements of structure are observed. At work electronic microscope in a mode electron diffraction any diffraction picture was not observed, that also speaks about amorphous film condition. The images of a surface are given in Fig. 5.

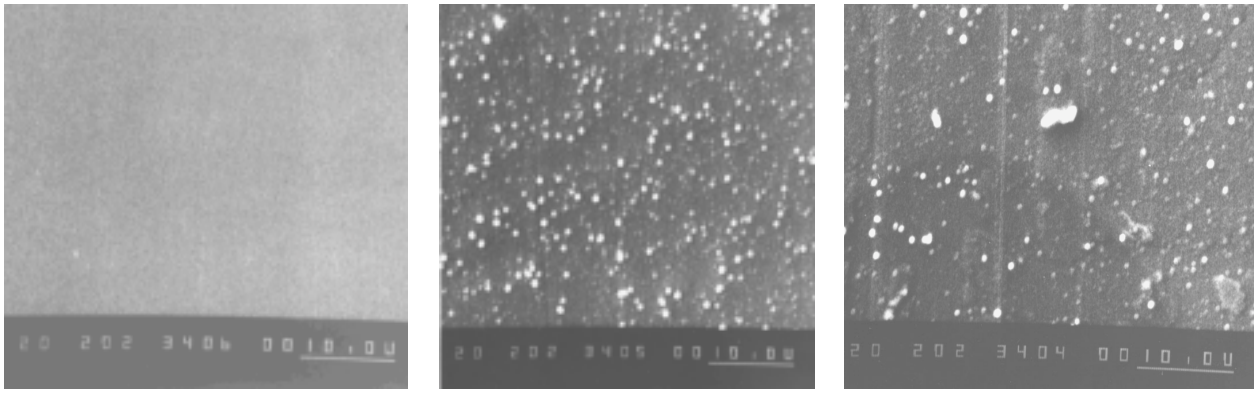

a) b) c)

Fig. 5. Photomicrography of plasmochemical film surfaces with increase x 2000, length of marker - 10 microns; a) – film deposited in TEC and argon, b) – film deposited in TEC and argon with oxygen in the ratio 2:1, c) – film deposited in TEC and argon with oxygen in the ratio 1:1.

4. USE OF PLASMOCHEMICAL METHOD OF SiO_2 FILM PRECIPITATION FOR DEPOSITION HOMOGENEOUS ON THICKNESS OF A LAYER ON GLASS MICROSPHERES.

We apply the given method for jointing of wall thickness of glass microsphere filled by gaseous mix. The manufacturing of glass microspheres with thickness more than 5 - 10 microns at a diameter of > 300 microns is a difficult task. We took the glass microspheres filled with a gas mix and having small wall thickness as a substrate and deposited homogeneous on thickness SiO_2 covering. Optical interferogram of such sphere is given in Fig. 6 [2,10]. Good concentricity of interference rings speaks about high uniformity of thickness.

Fig. 6. Optical interferogram of glass shell received by displacement interferometer. On surface of glass microsphere the layer of plasmochemical silicon dioxide is put. Common thickness of wall together with a covering is 11 microns.

5. INPLANTATION OF IODINE.

We have begun experiments on deposition of plasmochemical covering of silicon dioxide with an impurity of iodine. Iodine was entered in the plasmochemical chamber as vapor. The partial pressure corresponded to pressure of saturated iodine vapor at room temperature. The film is received, in which the iodine presence is stably registered. In Fig. 7 is given mass-spectra of one of aria of a plasmochemical SiO_2 covering with an iodine impurity.

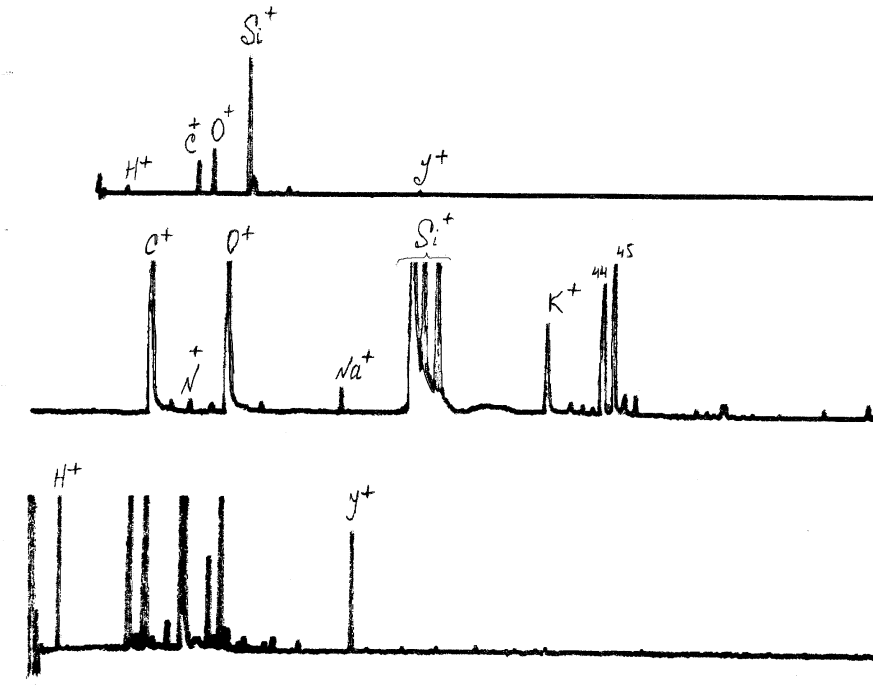

Fig. 7. Mass-spectra of one of area of a plasmochemical SiO_2 covering with an iodine impurity.

6. CONCLUSION.

Thus, the received covering represents a homogeneous amorphous silicon dioxide with good stochiometry containing significant amount of organic impurity. Density and refractive index are 2.34-2.17 g/cm^3 and 1.46 depending on composition of gas formed plasma - argon or mix argon with oxygen. Probably, there is a possibility of halogen introduction, in particular of iodine, in a plasmochemical SiO_2 film.

REFERENCES.

[1] V.V. Tkatchuk, V.M. Kolotirkin. Receipt of thin polymeric films from gaseous stage. Chimija, M. (1977).

[2] Yu.V. Andramanova, A.A. Aushev, N.L. Zolotuhina, V.M. Izgorodin, A.F. Kovylov, N.A. Lisovenko, G.P. Nikolaev, M.A. Pavlovskaya and I.V. Sevrugin. "Coating glass microspheres in tetraethoxysilane vapor discharge." *J. Moscow Phys. Soc*.,.**9**, No. 2, p. 159 (1999).

[3] V.M. Izgorodin, Yu.V. Tolokonnikova, A.A. Aushev, E.G. Orlikova, and I.V. Sevrugin. "Low-frequency glow discharge deposition of a silicon dioxide film onto the surface." *High Energy Chemistry*, **35**, No. 2, p. 152 (2001).

[4] K.A. Osipov, Ju.N. Lozinski G.E. Folmanis. " Receipt of SiO_2 films in high frequency discharge." Nonorganic materials, **5**, No. 4, p. 791 (1969).

[5] V.M. Izgorodin, Yu.V. Tolokonnikova, A.A. Aushev, A.F. Kovilov, N.L. Zolotuchina. *High Energy Chemistry*, **36**, No. 6, p. 1 (2002).

[6] A.N. Lazarev. Vibration spectra and structure of silicate. Nauka, L. (1968).

[7] E.P. Domashevskaja, N.N. Makeeva, V.A. Terekhov, D.M. Bodnar. "Silicon dioxide films received by plasmochemical and pyrolytic methods." Nonorganic materials, **31**, No. 3, p. 333 (1995).

[8] V.A. Mironov, S.A. Jankovski. Spectroscopy in organic chemistry. Chimija, M. (1985).

[9] L.J. Bellamy. The infra-red of complex molecules. Methuen & Co. LTD., London (1963).

[10] Yu.V. Andramanova, A.V. Veselov, N.V. Zhidkov, I.A. Ivanin, Yu.V. et al. "The technology of indirectly irradiated targets for inertial fusion researches at the Russian Federal Nuclear Center – VNIIEF. *Proc. Int. Conf. Inertial Fusion Sciences and Applications 99*, Bordeaux, France, 12-17 Sept. (1999).

Comprehensive Study of Polymer Fiber Surface Modifications - Low temperature plasma treatment

Joanne Yip[1], Kwong Chan[1*], Kwan Moon Sin[1], Kai Shui Lau[2]
[1]*Institute of Textiles & Clothing, The Hong Kong Polytechnic University, Hong Kong*
[2]*Department of Applied Physics, The Hong Kong Polytechnic University, Hong Kong*
**Tel.: +852-2766-6429; Fax: +852-2773-1432*
E-mail address: tcchank@inet.polyu.edu.hk (K. Chan)

Abstract
In this study, polyamide fiber was treated with low temperature oxygen plasma. Morphological changes of the resulting samples were characterized by scanning electron microscopy (SEM) and tapping mode atomic force microscopy (TM-AFM). Chemical modifications by plasma treatment were studied by x-ray photoelectron spectroscopy (XPS) and time-of-flight secondary ion mass spectrometry (Tof-SIMS).

1. Introduction
Recently, there has been great interest in physico-chemical surface treatments for modifying polymer surfaces [1-5]. The low temperature plasma (LTP) technique is widely used to modify polymer and textile materials. It is regarded as an environmentally friendly process since no larger volumes of waste chemical are involved [6-8]. By controlling the working parameters of plasma, such as the nature of the plasma gas, the discharge power, the pressure, and the exposure time, a great variety of surface effects can be generated. In this study, the effects of plasma treatment on polyamides were studied by using different characterization techniques.

2. Experimental
2.1 Low temperature plasma treatment
A glow discharge generator (SPP-001, Showa Company of Japan) was employed for the plasma treatment of the samples with oxygen gas. The applied discharge power and gas flow rate were 50-200 W and 50 cm^3min^{-1} respectively. The exposure time was varied from 5 to 30 minutes.

2.2 Morphological study
The morphology of the samples was investigated by scanning electron microscope, SEM (Lecia Stereoscan 440), for untreated and laser treated samples. All of the samples were gold coated prior to SEM examination. Tapping mode atomic force microscopy TM-AFM study was performed with a NanoScope III (Digital Instruments) under ambient conditions (24 ± 2 °C, 45 ± 5% relative humidity). The images were recorded with typical scan speed of ½-1 line/s.

2.3 Surface chemical study
The surface chemical composition of laser treated nylon 6 samples was analyzed by X-ray photoelectron spectroscopy, XPS (Physical Electronic PHI 5600) with an Al $K\alpha$ source under conditions of 14 kV and 25 mA. Time-of-flight secondary ion mass spectrometry, Tof-SIMS experiments were performed using a Physical Electronics PHI 7200 ToF-SIMS. The examined area was 200 μm x 200 μm for each sample.

3. Results and Discussion
3.1 SEM study
Figure 1 shows the nylon 6 filaments subjected to oxygen plasma treatments with different treatment parameters. It can be observed that the filaments treated with a low discharge power and for a short duration of time are smoother than the untreated filament (see Figure 1b, c and e). The *surface cleaning* results can be attributed to plasma species that bombard the sample surface and remove some uneven places [9]. *Surface etching* occurs when the filament is subjected to a higher discharge power and longer treatment time. Granules and ripple-like

structures of sub-micrometer size are found on the treated surface perpendicular to the fiber axis (see Figure 1d, f, h and i). It should be mentioned that a further increase in the treatment time to 30-minute might cause *surface melting* of the material (see Figure 1g, h) [3]. The previously developed ripple structures merge together, leaving some micro cracks on the sample's surface.

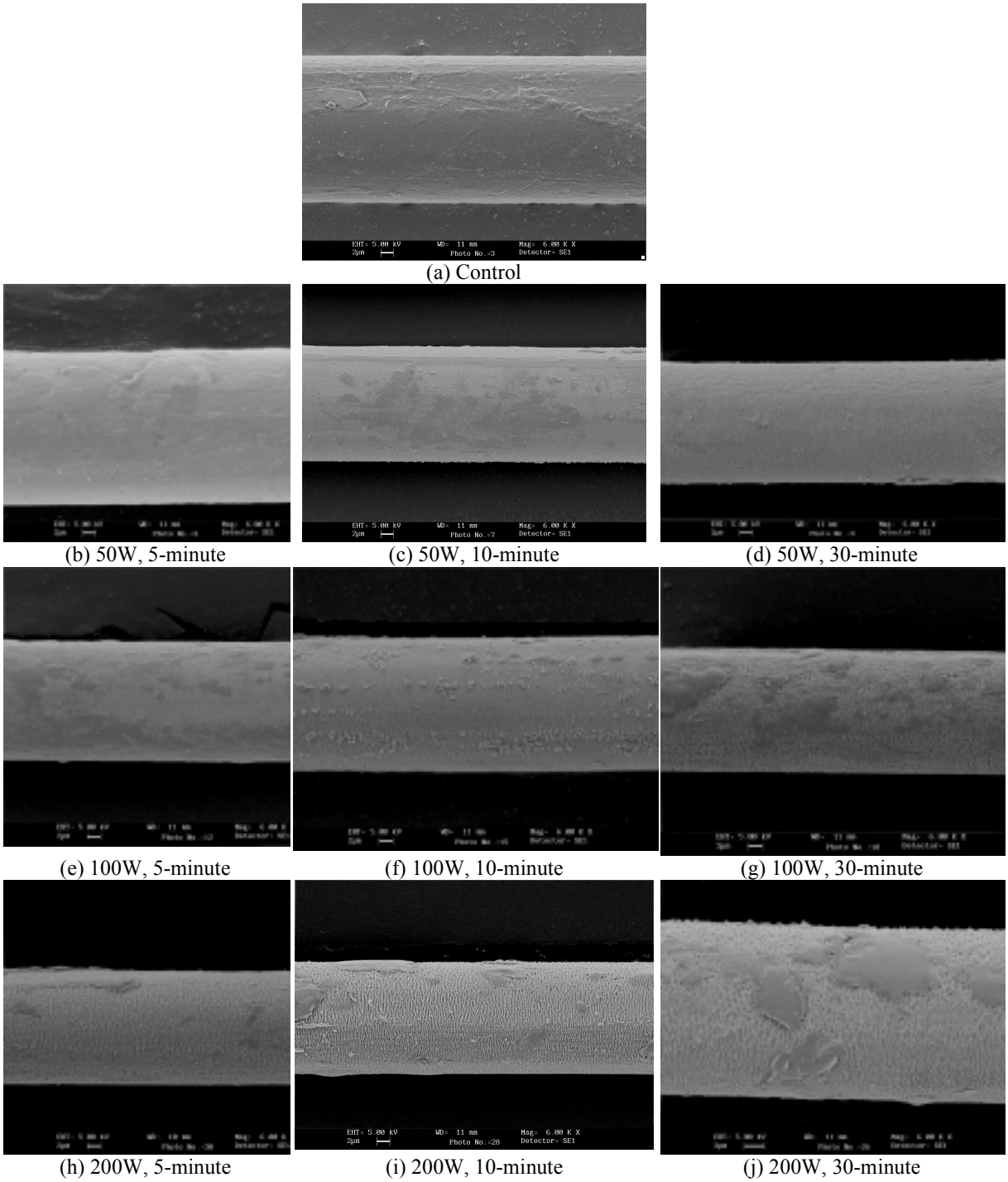

(a) Control

(b) 50W, 5-minute (c) 50W, 10-minute (d) 50W, 30-minute

(e) 100W, 5-minute (f) 100W, 10-minute (g) 100W, 30-minute

(h) 200W, 5-minute (i) 200W, 10-minute (j) 200W, 30-minute

Figure 1 Morphological features of oxygen LTP treated nylon 6 filaments with various input powers and exposure times

3.2 TM-AFM study

Comparisons of the AFM images of untreated and oxygen plasma treated surfaces are shown in Figure 2 (5 μm x 5 μm size, top view). The images on the right hand side are phase images corresponding to the height images show on the left hand side. Oxygen plasma treatment produces a "fibrous" structure, leaving no trace of the original surface morphology. It is observed that the extent of plasma etching increases by increasing the discharge power. The plasma induced surface roughness is found to be on the sub-micron scale, leading to enhancements of the surface area.

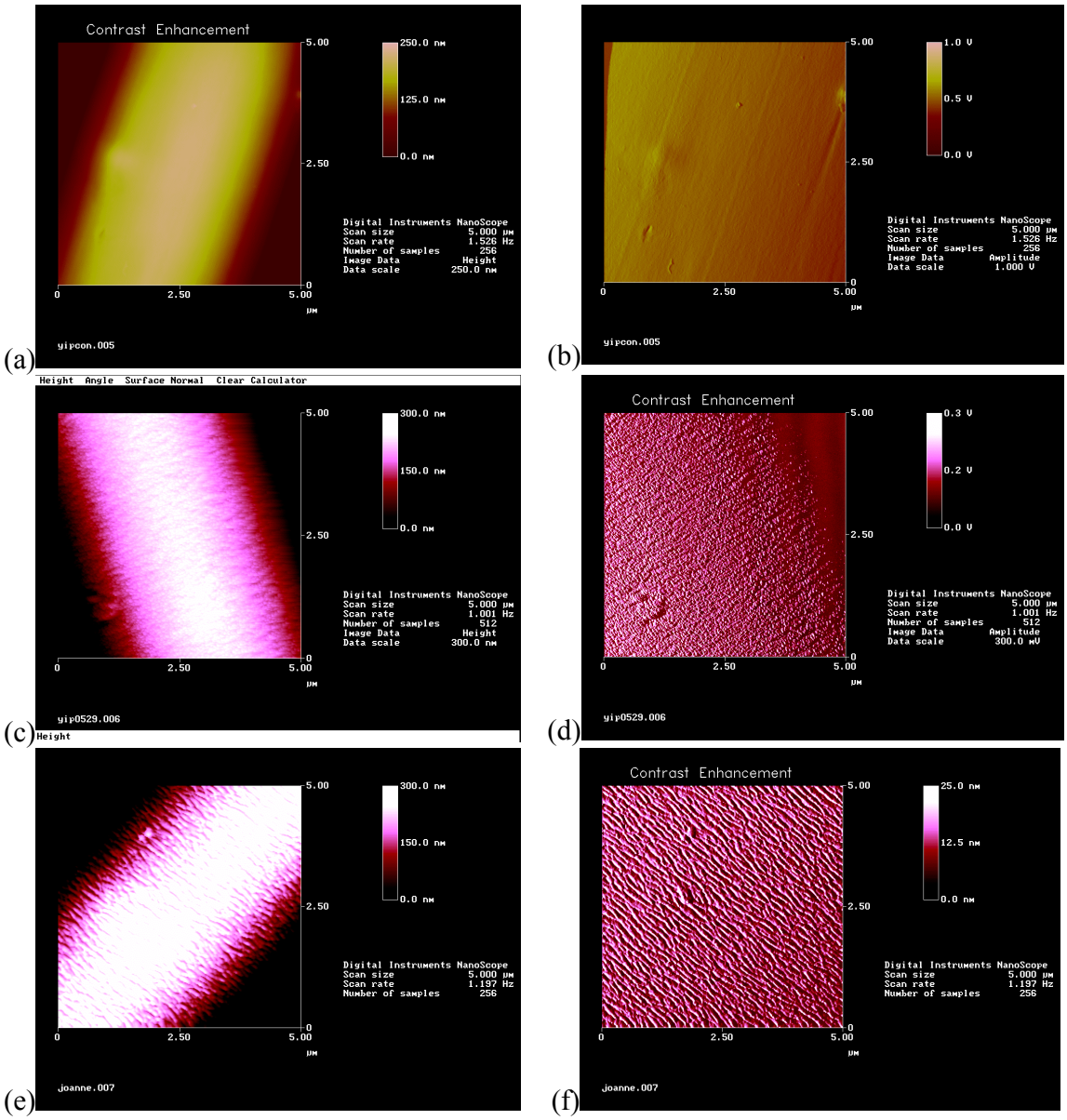

Figure 2 Surface morphology of polyamide fiber at the micrometer scale (5 μm x 5 μm)
(a) Untreated (b) A phase image corresponding to part a.
(c) 100 W, 10-min Oxygen plasma treated (d) A phase image corresponding to part c.
(e) 200W, 10-min oxygen plasma treated (f) A phase image corresponding to part e.

3.3 XPS study

The O_{1s}/C_{1s} and N_{1s}/C_{1s} atomic ratios for untreated and 100-W oxygen plasma treated samples are shown in Table 1. The results show that after plasma treatment O_{1s}/C_{1s} and N_{1s}/C_{1s} ratios increase with increasing treatment time. It is suggested that oxidation has occurred and oxygen atoms are incorporated onto the surface of nylon.

Table 1 Elemental composition analysis of nylon 6 treated with O_2 plasma determined by XPS measurements

RELATIVE INTENSITIES OF CHEMICAL COMPOSITION	OXYGEN PLASMA TREATMENT DISCHARGE POWER: 100 W			
	Untreated	5 minutes	10 minutes	30 minutes
O_{1s}/C_{1s}	0.208	0.400	0.534	0.548
N_{1s}/C_{1s}	0.134	0.138	0.161	0.171

Figure 3 summarizes carbon 1s signals of the XPS spectra for both untreated and oxygen-plasma treated (100 W; 10-minute) nylon 6. It can be observed that the relative peak areas of sub-components change significantly after the treatment (see Table 2). The most obvious is the C_{1s} curve that rises from its minimum at about 289 eV after the treatment. This new peak at 289 eV can be assigned to a C5 (-**C**OOH) peak. The results also reveal that both peaks of C2 (-**C**H_2-C=O-) and C4 (-NH-**C**=O-) components have decreased. It is suggested that oxygen plasma treatment induced carboxylic acid groups in the polymer, either in hydrocarbon or carbonyl groups, which finally increases hydrophilicity of the polymer.

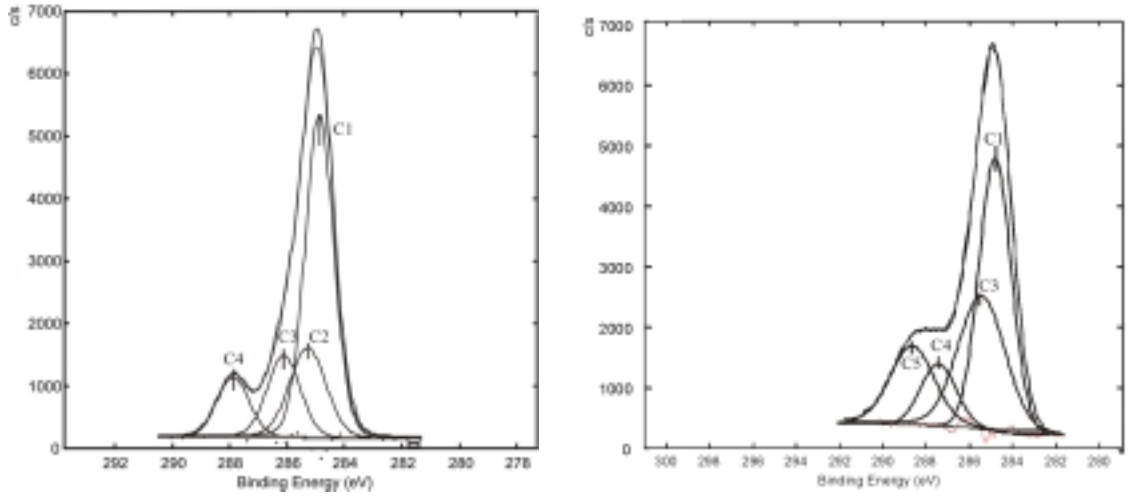

(a) Untreated nylon 6 (a) 100 W, 10-min O_2 plasma treated

Figure 3 Different chemical states of C_{1s} atom obtained by XPS measurements
C1 (–**C**H_2-), C2 (-**C**H_2-C=O-), C3 (-**C**H_2-NH-) C4 (-NH-**C**=O-) C5 (-**C**OOH)

Table 2 Relative peak area of chemical component (at %) of nylon 6 surface treated with oxygen low temperature plasma

	Relative peak area of chemical component (%)				
	C1	C2	C3	C4	C5
Control	54.88	17.77	16.46	10.89	0
Oxygen-plasma treatment (100 W; 10 minutes)	59.99	0	25.14	6.69	8.18

3.4 ToF-SIMS study

The characteristic positive and negative ions as well as their normalized intensities for both untreated and oxygen plasma (100W, 10-minute) treated nylon 6 are summarized in Table 3 and 4, respectively. It is observed that the intensities of most hydrocarbon secondary ions decrease and those of all hydroxyl or carboxyl-containing ions increase after the treatment. For example, the positive ions *m/z* = 31, 45, 133 and 149 correspond to CH_3O^+, $C_2H_5O^+$, $C_5H_9O_4^+$ and $C_6H_{13}O_4^+$ increase significantly after oxygen plasma treatment. It should be noticed that not all oxygen-containing peaks increase after the treatment: let us consider the positive ions at *m/z* = 114 ($C_6H_{12}NO^+$) and 227 ($C_{12}H_{23}NO^+$); negative ions at *m/z* = 31 (CH_3O^-) as well as 45 ($C_2H_5O^-$), these ions contain carbonyl groups have decreased obviously after the plasma treatment. The results reveal that oxygen plasma can induce many hydroxyl (-OH) and carboxylic acid (-COOH) functional groups. These groups replace mainly hydrocarbon or carbonyl groups in nylon and finally change the normalized intensities of the particular peaks.

Furthermore, the positive ions correspond to CH_4N^+ and $C_3H_6N^+$ (contain nitrogen atom) have increased after the treatment. The results can be attributed to ions bombardment by the plasma treatment. The treatment breaks the long polymer chain (C-N bond) and therefore increases the number of amine end-groups. Decrease in *m/z* =114 and 227 positive ions of treated sample (from 5.03 x 10^{-3} to 0.567 x 10^{-3}) are in good agreement with the above suggestion.

Table 3 Characteristic positive ions and the normalized intensity for untreated and oxygen-plasma treated (100 W; 10 minutes) nylon 6. The intensity of the peaks is normalized with respect to the total intensity of the selected spectra.

m/z	Positive ions	Normalized intensity (10^{-3})	
		Untreated	O_2 plasma-treated
15	CH_3^+	9.57	5.50
29	$C_2H_5^+$	57.6	33.3
30	CH_4N^+	6.07	12.4
31	CH_3O^+	0.126	3.23
45	$C_2H_5O^+$	1.59	21.1
56	$C_3H_6N^+$	10.1	12.5
83	$C_6H_{11}^+$	14.5	11.6
114	$C_6H_{12}NO^+$	7.84	7.17
133	$C_5H_9O_4^+$	0.095	0.257
149	$C_6H_{13}O_4^+$	0.027	0.05
227	$C_{12}H_{23}NO^+$	5.03	0.567

Table 4 Characteristic negative ions and the normalized intensity for untreated and oxygen-plasma treated (100 W; 10 minutes) nylon 6. The intensity of the peaks is normalized with respect to the peak at *m/z* = 25

M/z	Negative ions	Normalized intensity (10^{-1})	
		Untreated	O_2-plasma treated
12	C^-	6.24	5.48
13	CH^-	18.6	18.9
14	CH_2^-	3.66	3.47
16	O^-	23.0	32.4
17	OH^-	15.7	25.6
26	CN^-	9.34	9.22
31	CH_3O^-	0.345	0.307
42	CNO^-	1.81	8.58
45	$C_2H_5O^-$	1.29	0.643
71	$C_3H_3O_2^-$	2.79	0.364
113	M^- / $C_6H_{11}NO^-$	0.0941	0.209
115	$C_6H_{13}NO^-$	0.278	0.035
163	$C_6H_{13}NO_4^-$	0.249	0.0353
225	$(2M-H)^-$ / $C_{12}H_{21}N_2O_2^-$	0.406	0.0415

3.5 Adhesion property

Table 5 shows the mean ultraviolet protection factor (UPF) of *uncoated* and *aluminium coated* polyamide fabrics with various duration of plasma treatment. It can be observed that aluminium coating does not cause significant improvement in blocking UV radiation. However, the UPFs increase dramatically after the plasma treatment. A 10-min plasma treated fabric give excellent protection of UV light. The results can be attributed to the increased surface area and functional groups induced by plasma treatment.

Table 5 The Ultraviolet protection factor (UPF) of uncoated and aluminium coated polyamide fabrics with various duration of plasma treatment

Treatment	Untreated, Uncoated	Untreated, Coated	1-min plasma treated, Coated	3-min plasma treated, Coated	5-min plasma treated, Coated	10-min plasma treated, Coated
Ultraviolet Protection Factor (UPF)	16.3	18.2	28.7	38.5	59.6	66.4

4. Conclusion

Low temperature plasma treatment has become an important process for modifying polymer surfaces. The capability of plasmas to alter physical and chemical surface properties without affecting the bulk properties (especially mechanical properties) of the base material is advantageous in the design, development and manufacturing polymeric fibers. In this study, the effects of plasma treatment on polyamides were studied by using different characterization techniques.

Topographical results illustrated that changes in the surface morphology of the oxygen plasma treated polyamide correlate well with the discharge power and treatment time. The effects can be categorized into three groups: surface cleaning resulting in smoother surface, surface etching with formation of ripple-like structures in sub-micrometer size, and surface melting with material downgraded. Chemical studies showed that the surface oxygen content of polyamide increases after oxygen plasma treatment. The treatment induces many hydroxyl (-OH) and carboxylic acid (-COOH) functional groups. These groups mainly replace the hydrocarbon or carbonyl groups in polyamide. It was found that there is a strong interfacial interaction in the plasma treated polymer-coated particles. The adhesive properties and surface metallization of the modified material were significantly improved due to the increased surface area and functional groups.

References

[1] Yip J., Chan K., Sin K.M. and Lau K.S., Applied Surface Science. **205** (2002) p.151-159
[2] Yip J., Chan K., Sin K.M. and Lau K.S., Color. Technol. **118** (2002) p. 26-31.
[3] Yip J., Chan K., Sin K.M. and Lau K.S., J. of Materials Processing Technology, **123** (2002) p.5-12
[4] Yip J., Chan K., Sin K.M. and Lau K.S., Mater Res Innov, **6(2)** (2002) p.44-50
[5] Yip J., Chan K., Sin K.M. and Lau K.S., Mater Res Innov, **6(2)** (2002) p.73-78
[6] Bhat NV and Benjamin YN, Indian Journal of Textile Research, **14**:1 (1989).
[7] Subbulakshmi MS and Kasturiya NH, The Indian Textile Journal, **109**(1):12 (1998).
[8] Wong W, Chan K, Yeung KW, Tsang YM and Lau KS, J. Mater. Process. Tech. **103**:225 (2000).
[9] Anderson, F.R. and V.F. Holland, Journal of Applied Physics, **31(9)** (1960) p. 1516-1518.

SHORT RESIDENCE TIME HIGH-DENSITY INDUCTIVE PLASMA ETCHER FOR SiO_2 AND LOW-K

H. HATTORI, Y. HIRANO, A.KELLY, A. KURODA, V. MENAGARISHVILI, Y.TAKAHASHI, and G. VINOGRADOV

FOI Corporation, 6-38-28 Kamiasao, Asaoku, Kawasaki 215-002, JAPAN

Abstract

A novel compact narrow-gap flat ICP source (GROOVY™) for advanced high-density plasma etch of SiO_2 and Low-k materials on 300-mm wafers has been developed and successfully tested for a variety of materials and patterns. The groovy configuration overcomes the main problem of uniformity control in the plasma sources with flat inductive applicators.

1. Introduction

Plasma etching equipment utilizes the most advanced technologies known in semiconductor industry. However, there is presently only one type of 300-mm plasma processing chambers for highly selective SiO2 etch, especially for high aspect ratio contact holes (HARC): parallel-plate capacitive discharges. Inductively coupled plasma sources, usually referred to as ICP, realized in flat compact configurations do not provide necessary level of radial process uniformity, because of the basic toroidal structure of inductively excited plasmas. An increase of the discharge gap does improve the uniformity but decreases selectivity to photoresist at the same time. This trade-off between the narrow-gap parallel-plate capacitive and wide-gap inductive discharges was not overcome yet in favor of both plasma uniformity and process selectivity relied upon the short gas residence time in the discharge zone.

FOI Corporation has developed and manufactured new inductively coupled plasma sources with essentially flat narrow-gap geometry for advanced oxide etch and processing of a wide range of organic and inorganic Low-k materials. We present here process results obtained with our 300-mm etchers in order to show principal advantages and exclusive controllability of the new manufacturing equipment over traditional capacitive etchers. Such results are yet unachievable for other inductive etchers.

2. Experimental

300-mm GROOVY™ plasma source incorporates three geometrically separate and independently adjustable ring-shape inductive plasma sources designed as annular grooves in a flat roof made of monocrystalline i-type silicon or ceramics depending on the etching application. **Fig. 1** shows a cross-section view of the groovy roof with three inductive coils and an electrostatic chuck in a process chamber. Every coil has its own RF power supply. The coils and RF matching system are specially designed in order to avoid power interference between annular discharges in the grooves thus achieving full controllability over the radial sputtering profiles. Coils are not sensitive to each other for a wide range of RF power and operate as independent ICP sources in the integrated flat plasma source.

The silicon or ceramic roof incorporating inductive coils is temperature stabilized by a top metal plate attached to the roof and connected to a chiller/heater. High temperature condition favorable for carbon-rich plasmas and effective in HARC silicon oxide etch are thus established. Silicon as a roof materials is essentially good in terms of purity and low level of generated particles. The side wall of the process chamber (inner ring) is temperature stabilized for the same purpose.

Every groove in the roof, or every plasma ring in other words, has its own gas supply system for independent adjustment of chemicals in every ring discharge, and hence, the radial etch profile.

Consequently, GROOVY™ has two powerful and substantially independent means for profile/uniformity adjustment: rate of physical sputtering and density of chemically active components. Thus, the new plasma source allows independent distributions of physical and chemical plasma parameters without compromising damage issues caused by attempts to compensate one non-uniform parameter by another. Maximum inductive RF power in the roof is up to about 6 kW at the standard 13.56 MHz RF frequency.

Uniform process operation range for oxide and low-k etch is within about 5-60 mTorr gas pressure. Moreover, the integrated plasma source is also capable of oxygen discharges up to 2 Torr gas pressure, which is useful for free-radical dry chamber cleaning and in-situ ash.

The roof assembly is mounted with about 40-mm separation gap over the RF biased temperature stabilized electrostatic chuck. The bias RF power is up to about 5 kW. The process chamber of about 50-cm inner diameter has a temperature stabilized hot wall (inner ring) in order to supress polymer deposition and increase mean time between maintenance. Wafer transfer platform is capable of 200- or 300-mm wafers.

Commercial Langmuir probe system was used for spatial estimation of plasma parameters at the mid-plane of the discharge gap. The results were used only for inductive plasma uniformity evaluation, since the probe does not work well under the high RF bias power condition in a narrrow discharge gap.

Etching processes are well characterized on a number of bare and patterned production wafers with different materials: photoresists (KrF, ArF), silicon oxide (TEOS), organic and inorganic low-k materials like SiLK, SiOC, polyimidazole derived, fluorinated polymers, and silicon.

3. Results and discussion.

a) Low-power discharge ignition;

One of the most valuable features of the GROOVY™ is its ability for extremely low power ignition because of quasi-immerse nature of the induction coils. It is well known that large commercial etchers have essentially high power ignition of about hundred watts. Moreover, the ignition in very low-pressure etchers is usually performed at substantially higher gas pressure (50-100 mTorr) than the process level of a few millitorrs.

Fig. 2 shows the dependence of minimum ignition power with a groovy roof made of ceramics on the gas pressure for pure oxygen gas, which is known for rather difficult discharge ignition. A 100 W RF power is enough for discharge ignition at 10-mTorr gas pressure in case of the roof made of silicon, which is relatively higher than for ceramics but still very low absolutely. Therefore, it is not necessary to switch pressure levels between the ignition and process regimes as in many commercial etchers. Low-power ignition prevents production wafers from specific plasma damages typical for capacitive etchers.

b) Uniform plasma density;

Fig. 3 shows electron density distribution in the mid-plane of 40-mm discharge gap as measured with a movable Langmuir probe. There is no RF bias in this case: only inductive discharge was excited in the groovy roof. Plasma density is constant within the level of experimental errors over 300-mm wafer surface. There are no bumps or valleys at the grooves or between them.

Excellent sputter uniformity;

Oxide etchers operate under the highest RF bias power among all etchers. Therefore, the uniformity of sputter rate distribution over the wafer surface is vitally important for advanced processing. Fig. 4 shows three-dimensional sputter patterns for the separate ring discharges in the grooves (Coil 1, Coil 2, or Coil 3). Every individual sputter pattern demonstrates very good azimuthal uniformity and substantial axial symmetry. The ring discharges excited altogether, make flat uniform sputter rate distribution over the whole wafer. Typical example of normal three-coil discharge sputter distribution is shown in **Fig. 5**. The sputter rate non-uniformity of the GROOVY™ is below about 5% over the widest range of process conditions. It is certainly an excellent level of sputter uniformity taking into consideration that chemical factors in a real oxide etch process improve uniformity. There is no problem with the edge non-uniformity typical for a number of capacitive and ICP etchers

Independent controllability of radial plasma/sputter profiles is an essential feature of GROOVY™. Indeed, the process window of usual etchers is essentially limited with only a few external discharge parameters being controlled: power, pressure, flow rate, gas mixture. No one of these parameters is usually adjustable over the wafer radius. There is a narrow parameter range producing a flat etch profile: step up or step down changes the etch ratio center/edge. GROOVY™ overcomes this principal limitation by independent adjustment of the edge/center etch profile thus essentially expanding the process window.

c) Etch uniformity on bare wafers;

Etch rate distributions on bare wafers (no pattern) for different materials are quite uniform. Oxide

etch non-uniformity at about 5 mTorr pressure is within ±1.4% ([MAX-MIN]/[2xAVE]). Typical etch non-uniformity for organic (SiLK) or inorganic low-k materials at the discharge pressure of about 30 mTorr are within about ±2%. Even at 60 mTorr, the uniformity level is better than ±5%. It shows the widest process window of GROOVY™. Radial plasma density and process rate profile control relies upon independent RF power and gas flow control in the grooves. The developed plasma source practically excludes any self-redistribution of the RF power from one coil to another. **Fig. 6** shows typical dependence of the RF current in one coil fed with a constant RF power on the variable RF power in the adjacent coil. All three coils and corresponding inductive ring discharges operate as virtually independent plasma sources. It guarantees exceptionally wide process window in comparison with parallel-plate capacitive discharges, where radial profiles cannot be optimized for a range of different process conditions without substantial modification of hardware, for example, by gap control. Usual ICP etchers (wide-gap) of any configuration do not enter into advanced oxide etch processing at all, because of long gas residence time.

d) High aspect ratio contact etch;

In order to characterize an advanced oxide etcher, HARC holes are usually etched. An example of such processed pattern is shown in **Fig. 7** and **8**. Fig. 7 shows 80 nm hole pattern with aspect ratio 20. Oxide to photoresist etch selectivity of about 119 (bulk) and about 7.1 (facet) is easily achievable as Fig. 8 shows for partial deep oxide etch.

GROOVY™ plasma source demonstrates excellent performance in a wide range of process conditions including a very low-pressure condition of about 5 mTorr. Process conditions can be varied from "clean" etch mode to polymer deposition mode, which is preferable for highly selective etch in respect to the polymer resist.

e) Etching of Low-k materials;

GROOVY™ outperforms capacitive etchers in etching of Low-k materials. Indeed, its basic physical difference from capacitive discharges is the possibility to work under no-bias condition in principle unachievable for capacitive discharges due to their very nature. Therefore, GROOVY™ can smoothly operate in the widest range of RF bias conditions: from extremely high, typical for oxide etchers, down to extremely low, typical for pure inductive discharges. This unique combination of so many different, and incompatible in usually capacitive etchers, properties in one process chamber sets a new industrial standard for a Low-k etcher. This unique combinations of process parameters allows excellent multi step multi processing of newly developed structures with organic/inorganic low-k insulators and SiO2, SiC, or SiOC hard masks, spacers, and stoppers in one chamber. Obviously, such processing brings about essential improvement in overall quality, throughput, and reduces cost of ownership for end users.

Fig. 9 shows organic Low-k pattern (SiLK) with SiO2/SiC or SiOC hard masks processed in GROOVY™. It is seen, that there is no micro trenching in the low-k layer in a half-etched pattern, while the taper angle in the completed sample is 89 degree.

f) Comparison

Comparing capacitively coupled, conventional inductive, and GROOVY plasma sources, one inevitably concludes that GROOVY integrates the best features of capacitive and ICP sources. Indeed, it is a narrow-gap low gas residence time similar to a capacitive oxide etcher plasma source. At the same time, it is a wide pressure and power range ICP source. Moreover, it is an integrated plasma source with adjustable radial distributions of both RF power and gas flow rate. It is well seen that GROOVY plasma source represents a converging landmark of capacitive and inductive plasma technologies for advanced etching. The best features of narrow-gap capacitive and wide-gap inductive plasma sources have been implemented in one planar geometry.

4. Conclusion

A new integrated narrow-gap flat ICP plasma source has been developed and successfully implemented in advanced 300-mm etching technology. It is shown, that the new etcher has substantially wider process window in comparison with commonly used narrow-gap capacitive discharges. The new etcher demonstrates excellent process results for deep silicon oxide and low-k etch.

Fig. 1.

GROOVY ICP plasma source.

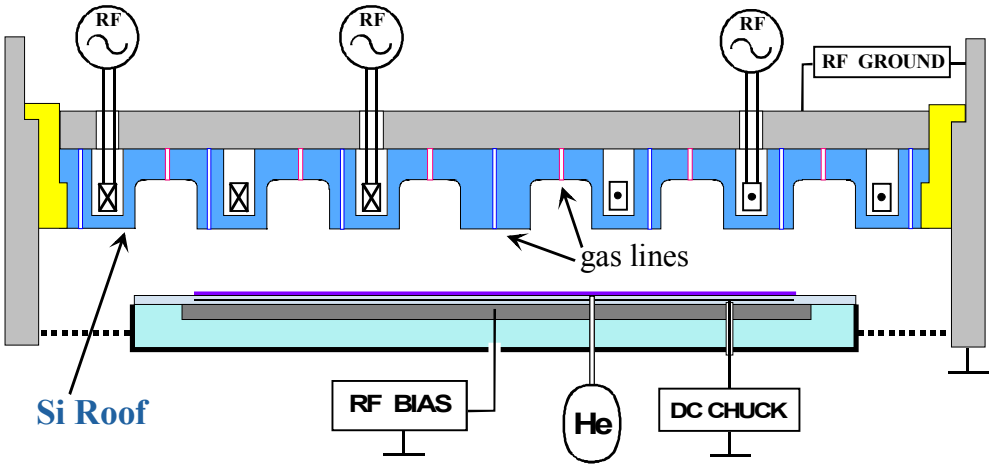

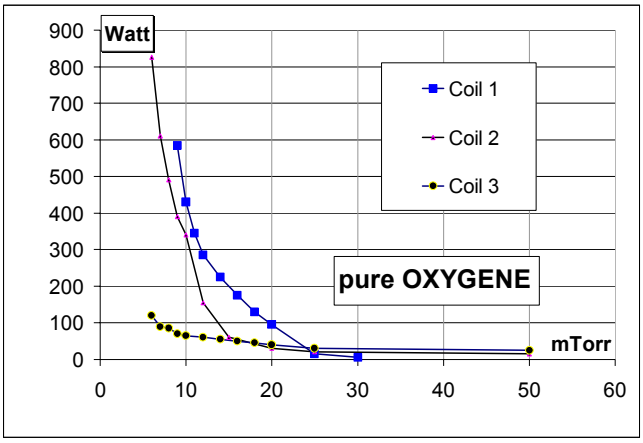

Fig. 2.

Minimum ignition RF power for every separate coil (No. 1 is central).

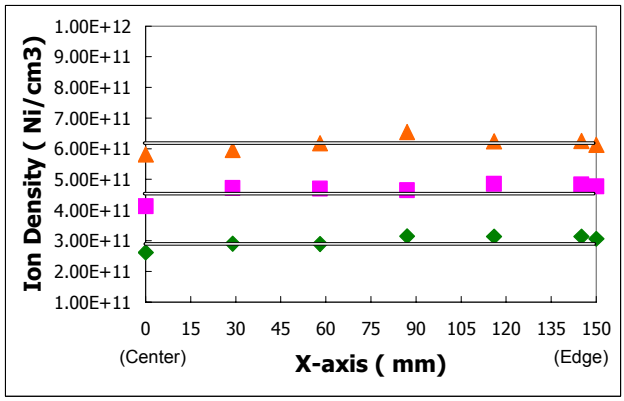

Fig. 3.

Midplane radial distributions of plasma density over 300-mm wafer for 1.6; 2.4; and 3.2 kW RF power: Ar, 10 mTorr.

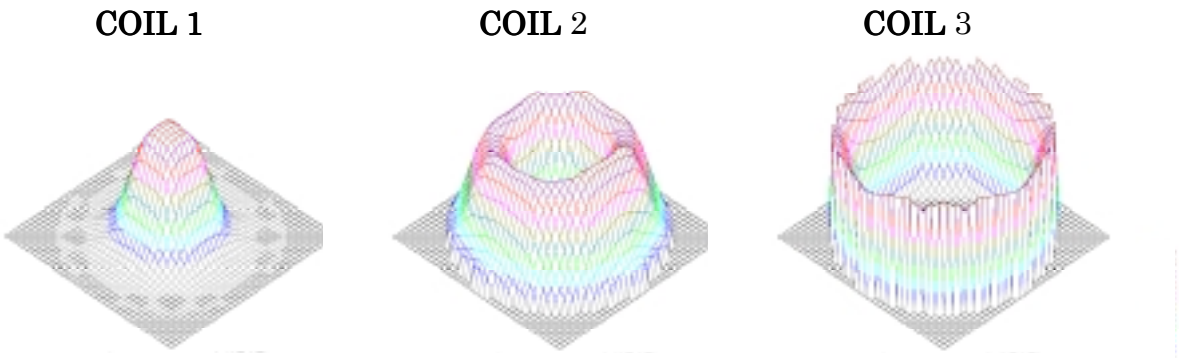

Fig. 4.

Three-dimensional sputter profiles produced on the 300-mm wafer by the discharges generated with separate induction coils. Left to right: center-to-edge.

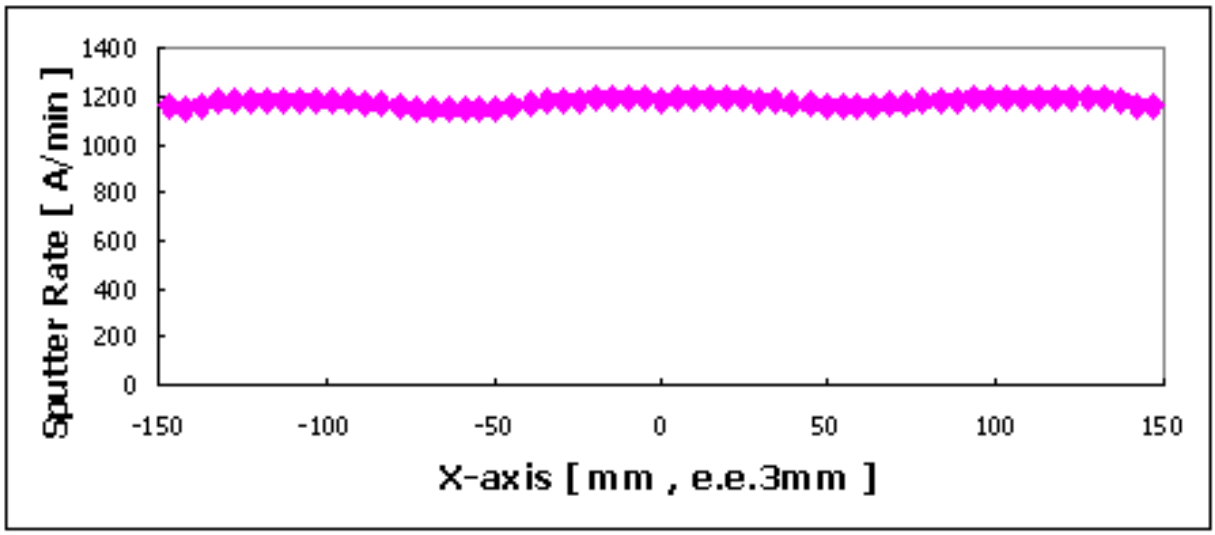

Fig. 5.

Radial sputter profile over 300-mm wafer. **Ar** 500 sccm, 10 mTorr, non-uniformity 2.5% (range).

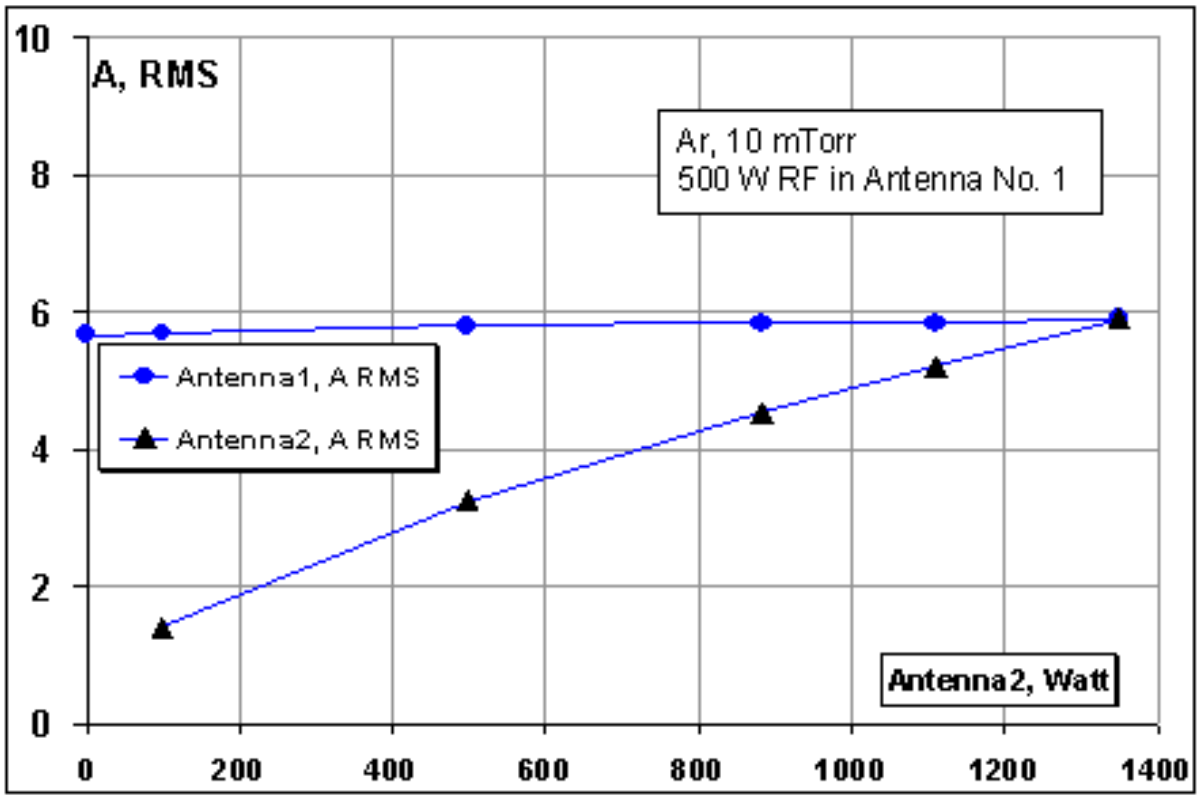

Fig. 6.

RMS RF current in adjacent induction coils No.1 (center) and No. 2.
RF power in No. 1 coil is constant: 500 W; RF power in No. 2 coil is variable.

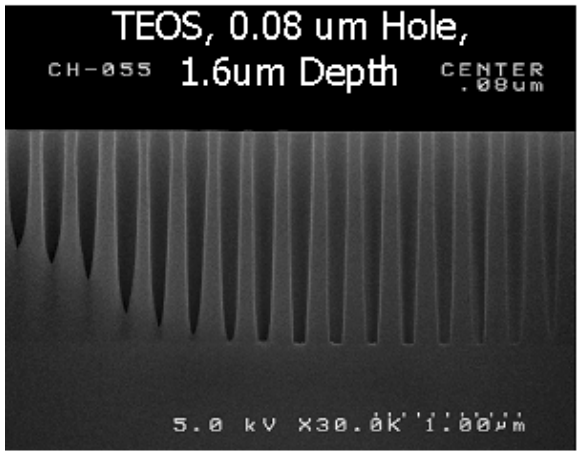

Fig. 7. Etching of HARC holes in **SiO2**.

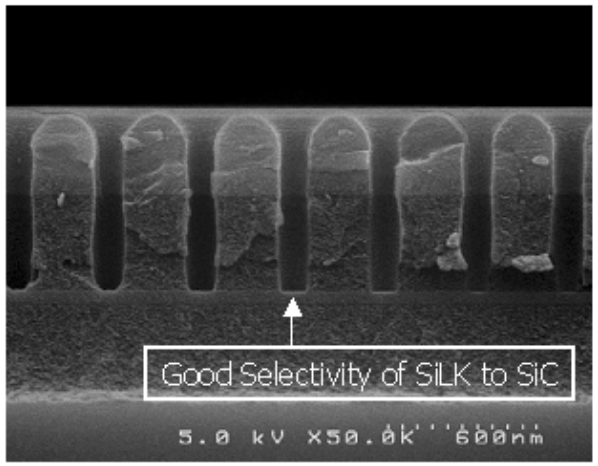

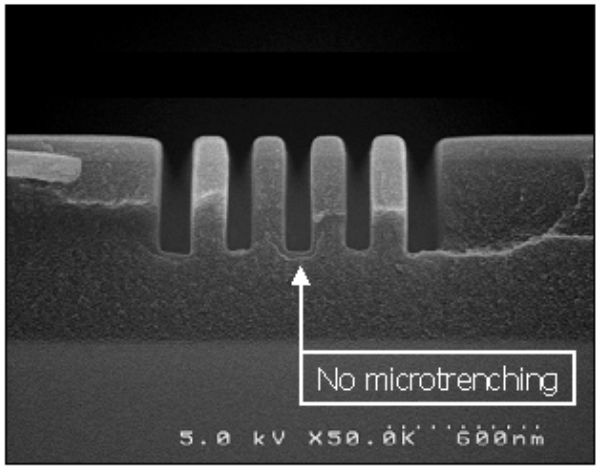

Fig. 9. Etching of **SiLK** of 0.12 um: (a) via-first dualdamascene pattern using **SiO2/SiC** hardmask to **SiC** etch stop midlayer; and (b) trench pattern using **SiOC** hardmask showing partial etch profile: no microtrenching.

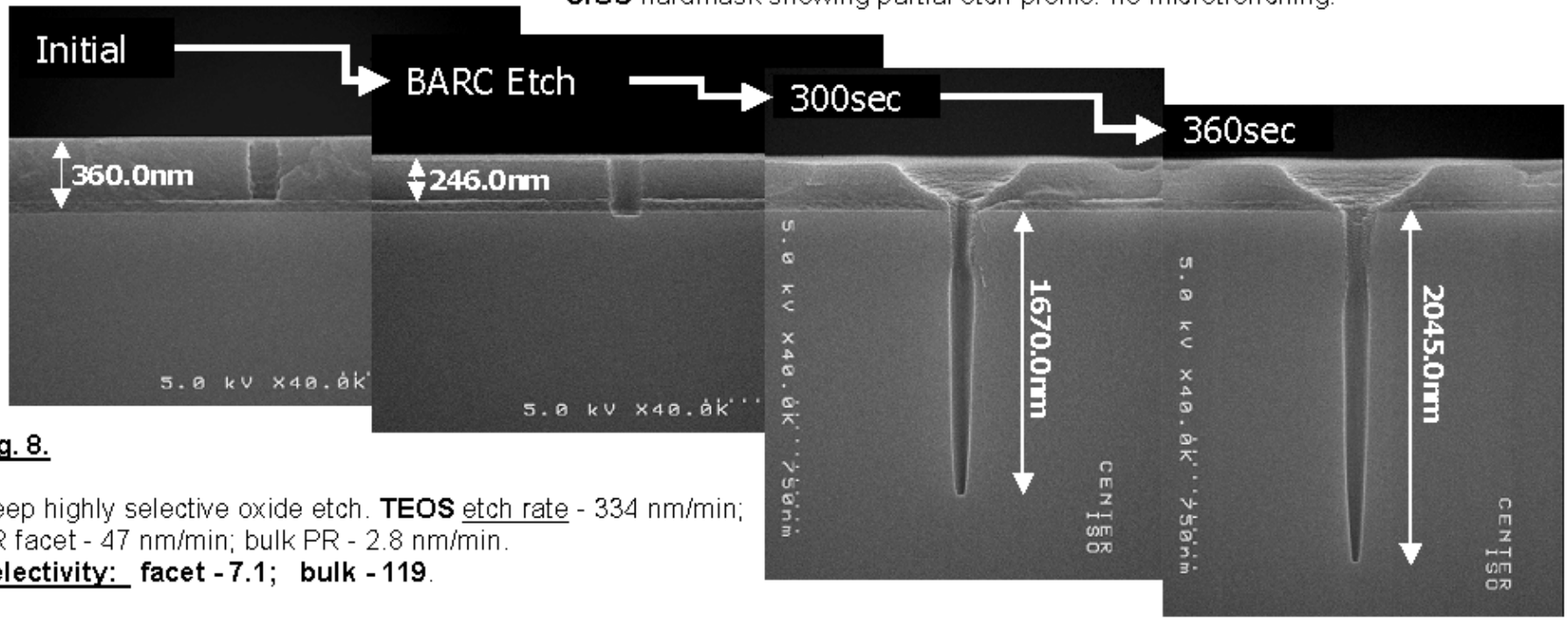

Fig. 8.

Deep highly selective oxide etch. **TEOS** etch rate - 334 nm/min; PR facet - 47 nm/min; bulk PR - 2.8 nm/min.
Selectivity: facet - 7.1; bulk - 119.

Production of carbon nanostructures ranging from carbon black over fullerenes to nanotubes by thermal plasma

L. Fulcheri[1], G. Flamant[3], F. Fabry[2], T. M. Gruenberger[1], J. Gonzalez-Aguilar[1], N. Probst[2], E. Grivei[2], J.C. Charlier[4], H. Okuno[4]

[1]*Cenerg, Ecole des Mines de Paris, Sophia-Antipolis, France*
[2]*Erachem-Europe, Brussels, Belgium*
[3]*IMP-CNRS, Odeillo, France*
[4]*UCL, Louvain, Belgium*

Abstract
The plasma technology for the production of carbon nanoparticles has been one of the major research areas developed by a consortium composed of Ecole des Mines de Paris, CNRS and ERACHEM for about ten years. The plasma technology has shown a very high versatility and it has been demonstrated that the very same technology can be used for the production of a wide range of carbon nanostructures ranging from Carbon Black over Fullerenes to carbon nanotubes with a high product selectivity.

1. Introduction
The total world production of carbon black is about 6 million tons per year, most of this production being applied in the rubber, plastics, inks, batteries industries [1],[2]. Although the partial combustion processes are able to produce at very low price carbon blacks, satisfying the present demand, it remains that the operating conditions are limited by thermodynamic reactions. Depending on the feedstock and on the quality of the product, the furnace process achieves poor carbon yields raging between 30 to 50 % and is characterised by a high level of atmospheric emissions. While the legislation in different countries will become more and more stringent, it will be an increase necessity, for CB industry, to take into account these environmental aspects [3],[4]. The carbon black industry also faces problems with the availability of adequate raw materials as highly aromatic hydrocarbons are required for the production of most carbon blacks.
Discovered in 1985, by Smalley, Curl and Kroto, the Fullerenes, a family of pure carbon cage molecules [5], moved from "laboratory curiosities" to stakes materials for a wide number of applications such as chemistry, biology, electronics, electrochemistry, materials, optics, energy science,…The availability of these new nanostructures in reasonable quantities, typically the order of several kilograms, is a compelling necessity for the development of future applications. Present production methods can only provide very limited quantities of the order of a few grams per hour !!!.. Currently known processes for fullerene synthesis use either of the following methods: Arc [6], laser [5], solar [7] or combustion method [8]. The first three processes, all of them based on the ablation of a solid carbon at reduced pressure have many things in common. The combustion method takes a slightly special position among the other three as the carbon precursor is derived from a hydrocarbon source. All these methods have in common a very low fullerene production capacity. This is in the end the critical parameter when it comes to the production of large quantities of fullerenes. In addition, attempts to upscale these processes have so far been of only limited success. The fullerene contents in the individual soot samples lie typically between 5 and 10 %-wt., whereby isolated fullerene yields of up to 40 % are reported for the arc process [9].
Finally, the carbon nanotubes (CNT), discovered by Iijima in 1991, [10] offer also exciting possibilities in the material, chemical and physical sciences and again, the production methods can be classified into two main categories : those using very high temperature (arc, laser, solar concentrated) and those using the catalytic decomposition of hydrocarbons [11] . For the methods belonging to the first group, the above limitations listed for the fullerenes are also valid.
Fundamentally new approaches can be developed using thermal plasma. Indeed, plasma technologies are particularly adapted to the production of nanoparticles. Being highly flexible they allow the use of a wide range of carbon feedstock (solid, liquid, gaseous, alone or associated with a catalyst element), the access to

very high temperatures and enthalpies densities unreachable with conventional combustion processes. Finally, the use of any plasma gas allows the control of the atmosphere (inert or reactive).

2. Plasma technology and diagnostics

Since 1993, a new 3-pase AC plasma technology for producing new carbon black grades and hydrogen has been under development [12], [13], [14]. The principle of the new process consists in replacing the incomplete combustion by directly splitting the hydrocarbon into carbon black and hydrogen thanks to an external electric energy supply.. The overall process illustrated in Figure 1 is composed of : a plasma power supply : 3-phase, 600 Hz, 0-400 A, 263 kVA maximum power. It supplies electricity to 3 graphite electrodes located at the top of the reactor, a high temperature chamber which upper part is equipped with a graphite nozzle where the hydrocarbon (HC) is introduced, a tail filter with PTFE bags where carbon and gas are separated and collected, gas and water networks develop to provide cooling fluid to the external kiln of the reactor which is double walled and water cooled.

This technology, initially designed for the treatment of hydrocarbons, was adapted in order to treat solid carbon powders [15]. The overall process is illustrated in Figure 2. In this case, solid powder is transported together with the plasma gas to the arc zone. The main difference with the classical arc process for fullerene and nanotube synthesis is that the input carbon rate is not limited to the electrodes erosion but can be controlled totally independently. In addition, a system was specially designed for the sampling of the species inside the reactor, their quenching and their transport up to a filter. This system is mainly composed of a water cooled suction pipe, a set of modular cooling pipes and a filter / gas recycle system.

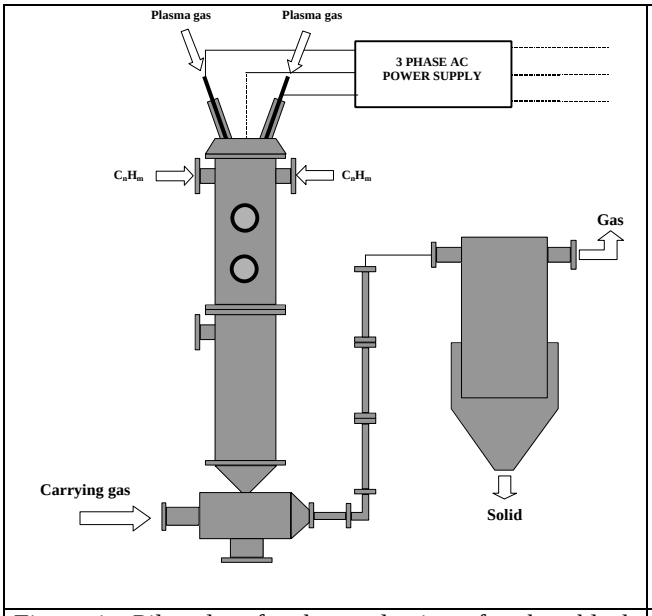

Figure 1 : Pilot plant for the production of carbon black (configuration 1)

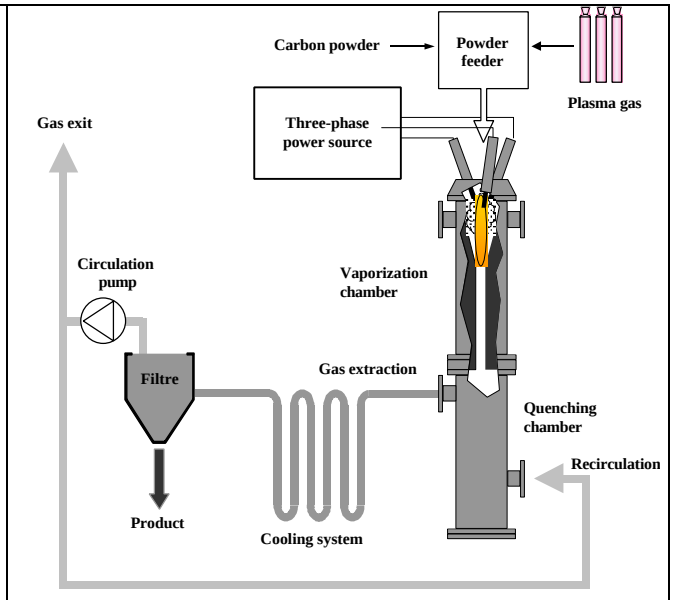

Figure 2 : Pilot plant for the production of fullerenes and nanotubes (configuration 2)

Flow and wall temperatures were measured along the reactor. In the high temperature zones, the measurements were carried out by optical emission spectroscopy (OMS) and optical pyrometry, whereas R-type and K-type thermocouples were placed in the low temperature regions. OMS was used for the plasma diagnosis. A quartz window located in the upper part of the reactor allowed the observation of the arc zone. By using an optical system composed of a lens, an optical fibre and a 3 dimensional measurement bench, the light emitted by the plasma is directed to the entrance of a monochromator (600 mm focal distance, with a 1200 lines/mm grating) with a 1024x256 photodiodes matrix detector. This device allows a quasi-instantaneous analysis in a spectral range in the order of 30 nm with a spectral resolution of 0,029 nm per photodiode. At the same time, the axial exploration of the plasma was also possible with the optical system. The pyrometic measurements were carried out by a bichromatic infrared pyrometer sighted on a graphite tube immersed in the plasma flow. A FT-IR spectrometer was also used for the on-line analysis of the off-gas composition. The sampling system was connected to the reactor exit.

3. Operating conditions

All the experiments were carried out at atmospheric pressure. For the production of carbon black, the experimental set-up was installed in configuration 1, while configuration 2 was used for the synthesis of fullerenes and carbon nanotubes.

	Parameter		**Operating conditions**	
Carbon Black	Precursor	Flow rate	CH_4, C_2H_4, PFO[1], C_8H_8, Colza oil	0.5-3 $kg.h^{-1}$
	Injection		Axial or radial	
	Plasma gas	Flow rate	N_2, Ar, He, Ar/H_2 , CO	50-220 $Nl.mn^{-1}$
	Electrical power		25-200 kW	
Fullerenes	Precursor	Flow rate	Acetylene Black, Carbon black, graphite powder	0.1-1 $kg.h^{-1}$
	Injection		Axial or radial	
	Aspiration zone		Upper[2] or Lower[3]	
	Plasma gas	Flow rate	Ar, He	50-150 $Nl.mn^{-1}$
	Electrical power		40-60 kW	
N**anotubes**	Carbon precursor	Flow rate	Acetylene Black, Carbon black, graphite powder, C_2H_4	0.1-0.3 $kg.h^{-1}$
	Metal catalyst	$\%_{mass}$	Ni, Co, Y, mixtures	1-15 %
	Injection		Axial or radial	
	Aspiration zone		Upper or Lower	
	Plasma gas	Flow rate	N_2, Ar, He	50-150 $Nl.mn^{-1}$
	Electrical power		50-100 kW	

Table 1 : Operating conditions for the production of the different nanostructures

4. Characterization of the carbon nanostructures

Carbon black samples were analysed by TEM and SEM together with the two major carbon black parameters: Nitrogen specific surface area BET and DBP-absorption and the crystallographic parameters. In addition, the carbon black samples were evaluated by standardised procedures in the following domains : polymer composites, rheological behaviour, tensile properties, hardness. A detailed description of the characterisation procedures can be found in [19].

For each Fullerenes sample, Soxhlet Toluene extraction was performed and the extract was analysed by UV-Vis spectrophotometry. The extract concentration in fullerenes C_{60} and C_{70} was evaluated from the two characteristic absorption peaks at 330 10^{-9} m and 470 10^{-9} m [16], [17], [18]. In addition, specific analysis were carried out on a limited number of samples in order to confirm the results : mass spectroscopy analysis, High Pressure Liquid Chromatography (HPLC) and TEM. A detailed description of the characterisation procedures can be found in [20].

For each Nanotubes sample SEM and TEM analyses were systematically performed. In addition, specific analyses by HRTEM, XPS, X-ray diffraction and Auger spectroscopy were carried out on a limited number of samples.

5. Results

The plasma technology allows the production of materials which can be classified as carbon blacks. The results have shown that the technology allows the adjustment of the two main morphological properties: specific surface area and DBP absorption (Table 2). In addition, the rubber compounded data confirm that these carbon blacks behave like all other blacks and obey to similar rules.

[1] Pyrolysis Fuel Oil

[2] 30 cm downstream the electrodes bottom. This position corresponds to a high temperature zone (T>2500°C) and a high quenching velocity

[3] 1 m downstream the electrodes bottom. This position corresponds to a low temperature zone (T < 1100°C) and a low quenching velocity

Feedstock	CH_4	C_2H_4	C_8H_8	PFO	Colza oil
Spec. Surf. Area (m^2/g)	50-90	30-80	50-90	70-90	50-80
DBP Absorption (ml/100 g)	90-210	100-250	150-190	150-220	100-250

Table 2 : Main morphological characteristics of the plasma carbon blacks

As expected, the materials produced by this process have shown no porosity as no oxygen is present in the reaction zone. Carbon blacks have also been investigated by TEM. These analyses have shown a smoother particle shape in the case of the lower energy input and an apparently higher graphitic nature at higher energy input. For some very high energy input, HRTEM pictures show hollow structures similar to electrical conductive grades.

Concerning fullerene synthesis, best yields of 5 % extractible fullerenes have been obtained with flow rates of 150 $g.h^{-1}$ what corresponds to a production capacity of 7.5 $g.h^{-1}$. The main results including the yield dependence on the most sensitive process parameters have been presented in [21]. The nature of the plasma gas and the distances between the three electrodes appear to be the most critical ones. Yields have been found to be about one order of magnitude higher when using helium as plasma gas rather than argon or nitrogen, a fact generally known for the arc or laser process. The nature of the carbon precursor, showed no drastic influence on the process performance. Almost all carbon types showed similar results apart from one carbon black grade showing significantly lower fullerene yields.

At the time being, more than 300 “nanotubes samples” have been produced. Their analysis is not yet achieved and this task will still take several years. However, as expected, it has been demonstrated that a very wide diversity of carbon nanotubes : MWNT[4] and SWNT[5], could be synthesised. In a lot of samples as shown on Figure 3 tubular structures were observed. These structures are generally found as deposit on the electrodes and on the graphite walls. High yields are obtained when Nickel is used as catalyst alone or associated with another catalyst. Their typical length is ranging from 1 ? m up to several tens ? m and their diameter is ranging between 10 to 100 nm. Some of this tubes appear being open (left) while others are terminated by catalyst particle (right).

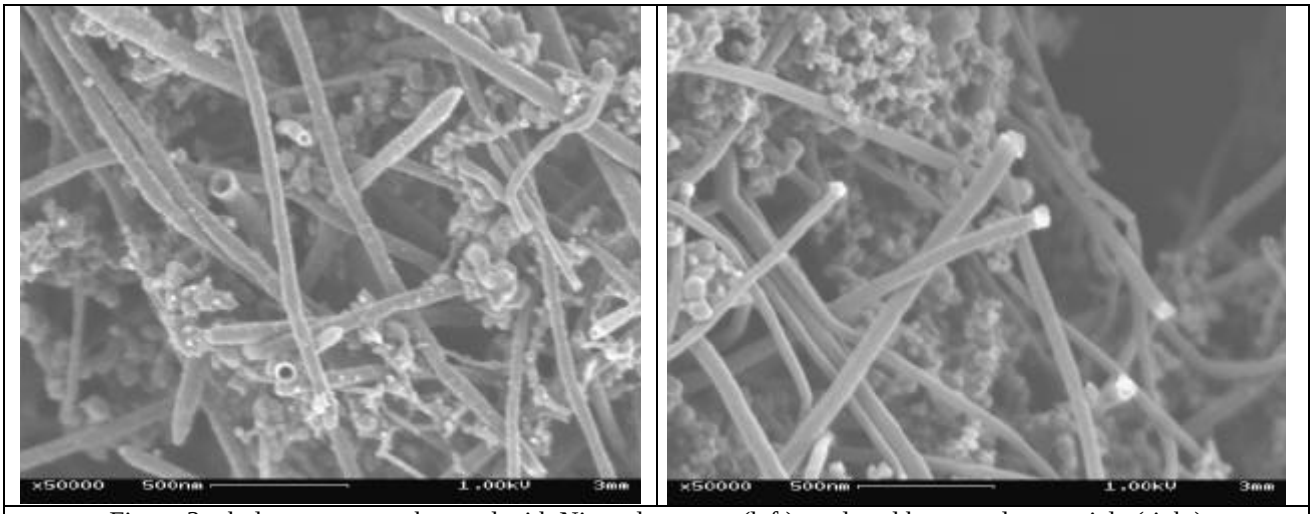

Figure 3 tubular structures observed with Ni catalyst open (left) or closed by a catalyst particle (right)

TEM observation show that these structures are composed of multi wall « bamboo like » structures, each element being composed of approximately 20 graphite sheets (Figure 4). The most commonly growth model proposed by [11] and [22] is represented in the Figure 5. The dissolved carbon diffused into the bottom of the Ni needle. After the graphitic layers is formed, the Ni particle is probably pushed out the Ni needle may be the stress accumulated in the graphtic sheath ; the segregation of carbon from the inside of the sheath brings a compressive stress on the Ni needle. The stress would be released by pushing out the Ni needle. This process is similar to that proposed by Oberlin et al. [23] for carbon fibers prepared by thermal

[4] Multi Wall NanoTube
[5] Single Wall NanoTube

decomposition of hydrocarbons. However, the lengthening of tubes proceeds intermittently for the bamboo-shaped tubes while it is continuous for pyrolytic fibers.

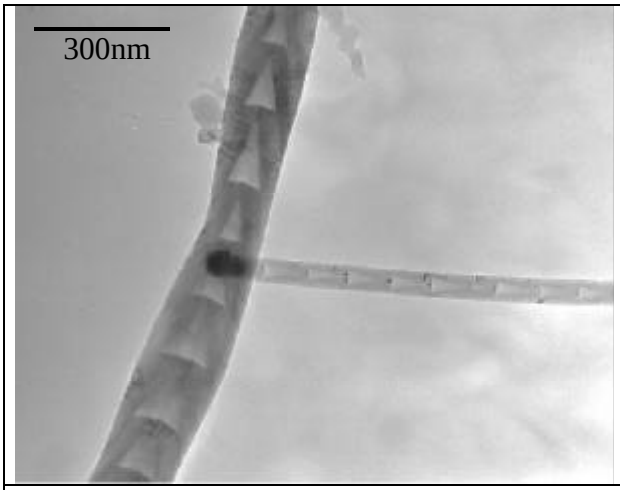

Figure 4 : TEM Observation of a « bamboo like » growth starting from a catalyst particle

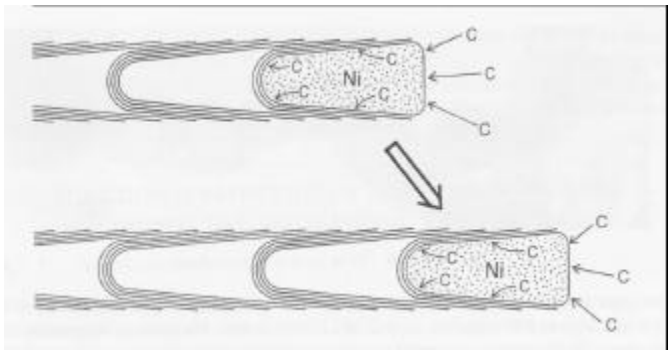

Figure 5 : Growth Model of « bamboo like » structures

As mentioned above, SWNT and other more "exotic" structures such like "carbon necklaces" have also been found in different samples but their complete characterisation is not yet completed. As example, Figure 6 and Figure 7 represent respectively SEM and HRTEM observations of a typical sample obtained by plasma under an helium atmosphere.

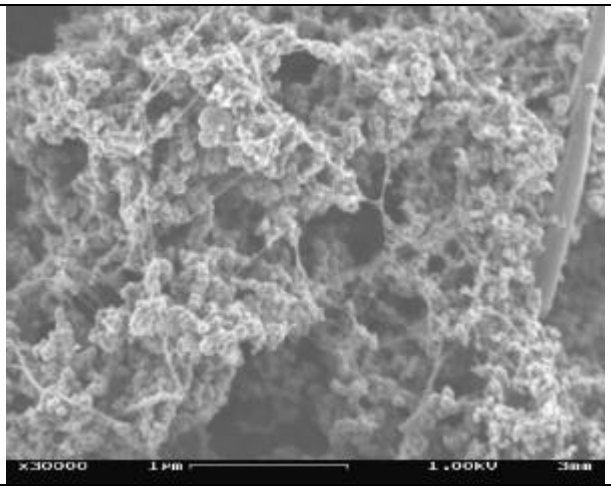

Figure 6 : SEM observation of a SWNT "web" together with amorphous carbon obtained by plasma

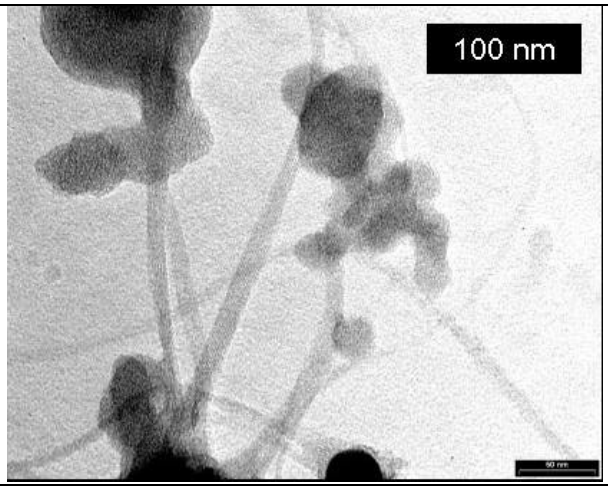

Figure 7 : HRTEM Observation of bundles of SWNT obtained by plasma

Conclusion

The plasma process opens a totally new area for the production of carbon nanostructures. In the conventional carbon black market, it will bring new carbon blacks thanks to thermodynamic conditions unreachable by conventional means. The plasma process will allow the use of new raw materials: waste oils, vegetable oils,…since it appears that any hydrocarbon can be used if enough energy is given. It will allow a more rational use of the raw material (100 % carbon yield), the production of carbon black free from CO_2 emission on the site and the production of hydrogen as by-product.

In the emerging domains, the plasma process will allow the production of novel materials of nano-size structure, which are without any doubt amongst the most promising resources for future industrial applications and systems. Moreover, nanomaterials based on carbon as fullerenes, nanotubes, nanofibers are classified as one of the major R&D goals in the scientific politics in material sciences and engineering,

giving rise to a whole new branch in nanotechnologies and nanosciences and the unrestricted availability of these materials at a reasonable price is a real challenge and opportunity for the plasma community.

The authors thank the EC for their support in the frame of the following projects : JOE3-CT97-0057, G5RD-CT-1999-00173, HPRN-CT-2000-0037

References

[1] Ulmann's Encyclopedia of Industrial Chemistry, VCH Verlags Gesellschaft mbH, Vol. A5, 140, 1986.
[2] Donnet J.B, Bansal R.P., Wang M.J., Carbon Black, Science and Technology, Marcel Dekker, Inc, second edition.
[3] G. Kühner, Carbon black and industry - Economical and Ecological Aspects, Intertech Conferences, CB world 96, 4-6 March 1996, Nice France.
[4] Boyd J.W., Air Quality Issues for Carbon Black, Intertech conferences, The Global Outlook for Carbon Black, February 23-24, 1993, Houston, Texas USA. Intertech Conferences, 170 US Route one, Portland Maine 04105 USA.
[5] Kroto, H. W., Heath, J. R., O'Brien, S. C., Curl, R. F., and Smalley, R. E., *Nature* 318, 162 (1985).
[6] Krätschmer, W., Lamb, L. D., Fostiropoulos, K., and Huffmann, D. R., *Nature* 347, 354 (1990).
[7] Guillard, T., Flamant, G., Laplaze, D., Robert, J.-F., Rivoire, B., and Giral, J., "Towards the large scale production of fullerenes and nanotubes by solar energy", Solar Forum 2001, Washington, DC, April 21-25 (2001).
[8] Howard, J. B., McKinnon, J. T., Makarovsky, Y., Lafleur, A. L., and Johnson, M. E., *Nature* 352, 139 (1991).
[9] Parker, D. H., Wurz, P., Chatterjee, K., Lykke, K. R., Hunt, J. E., Pellin, M. J., Hemminger, J. C., Gruen, D. M., and Stock, L. M., *Journal Am. Chem. Soc.* 113, 7499 (1991).
[10] Iijima, S., Nature (London), 350, 320 (1991).
[11] Ebbesen, T.W., Carbon nanotubes, Preparation and properties, Polymer Chemistry-Materials Science and Engineering, CRC Press (1997).
[12] L. Fulcheri, Y. Schwob, From Methane to Hydrogen, Carbon Black and,...Water, International Journal of Hydrogen Energy, vol 20, N° 3, pp. 197-202, 1995.
[13] L. Fulcheri, et. Al., A 3-Phase AC Plasma Process for Carbon Black Production from Methane, Thermal Plasma Processes, 19-21 Sept. 94, Aachem Germany, VDI BERICHTE NR 1166, pp 525-532, 1995.
[14] L. Fulcheri, et al., Characterization of a 3-phase AC plasma reactor for carbon black synthesis from natural gas, ISPC 12, August 21-25 1995, Minneapolis, MINNESOTA USA, vol III, pp 1159 - 1164.
[15] Procédé pour la Fabrication de Carbone 60, BF 97 07 011.
[16] Hare JP, Kroto HW, Taylor R, Chem. Phys. Lett. 177, 1991. p. 394.
[17] Ajie H, Alvarez MM, Ans SJ, Beck RD, Diedderich F, Fostiropoulos K, Huffman DR, Krätschmer W, Rubin Y, Schriver KE, Sensharma D and Wetten RL, J. Phys. Chem. 94, 1990. p. 8630.
[18] Catalan J, Saiz JL, Laynez JL, Jagerovic N, Elguero J, Angew. Chem. Int. Ed. Engl., 34, 1995. p. 105.
[19] L. Fulcheri, N. Probst, G. Flamant, F. Fabry, E. Grivei, X. Bourrat, Plasma processing: a step towards the production of new grades of carbon black, Carbon 40 (2002) 169-176.
[20] L. Fulcheri , Y. Schwob, F. Fabry, G. Flamant, L.F.P. Chibante, D. Laplaze, Fullerene Production in a 3 - Phase AC Plasma Process, Carbon 38 (2000) N°5, pp 797-803.
[21] T. M. Gruenberger, et al., Continuous Production of Fullerenes and Other Carbon Nanomaterials on a Semi-Industrial Scale using Plasma Technology, KIRCHBERG 2002.
[22] Saito, Y. and Yoshikawa, T., J. Cryst. Growth, 134, 154, 1993.
[23] Oberlin, A., Endo, M. and Koyama, T., J. Cryst. Growth, 32, 335, 1976.

Surface Fluorination of Nitrile Butadiene Elastomers

A. Tressaud, E. Durand, C. Labrugère, H. Benalla

Institute of Condensed Matter Chemistry of Bordeaux (ICMCB-CNRS), 87 Avenue du Dr. A. Schweitzer, 33608 Pessac Cedex, France.

Abstract - This work is devoted to surface treatment of thin NBR nitrile gloves using either plasma-enhanced fluorination in rf plasmas of fluorinated gases (CF_4, CHF_3) or direct fluorination (10% F_2-gas diluted in N_2). The mechanisms of fluorination of these co-elastomers are proposed on the basis of the assignment of the different components of the XPS spectra. When the treatments are carried out at room temperature a gradual fluorination occurs : monofluorinated CF groups are the species most found at the surface and perfluoro groups CF_n are present in lower amount. An addition reaction takes thus place at the $-(CH=CH)-$ double bonds of the polybutadiene entities, leading to $-(CHF–CHF)-$ units with large amounts of unfluorinated domains.
When the reaction is thermally activated at 90°C, an important increase of the fluorinated surface is noted from the elemental surface analysis, with a mean F/C ratio higher than 1.5. C1s spectra exhibit a maximum shifted of + 6.8 eV with respect to the starting material which can be assigned to CF_2 groups with first C neighbours bound to one F atom, for instance CF_2–CHF groups. Additional contributions at higher BE correspond to CF_2 groups with CF_2 first neighbours, as in PTFE, and to CF_3 groups . Similar trend is found in F1s XPS spectra.The relationships between fluorination experimental parameters and surface reactions will be discussed.

1. Introduction

Because of the outstanding characteristics of F_2 molecule, i.e. extreme reactivity and oxidizing power, F^- ion exhibits utmost electronegativity and hardness, in particular towards hydroxyl groups. Therefore fluorine and fluorinated gases constitute exceptional tools for modifying the surface properties of materials. In particular the fluorination of polymers has received wide spread attention and several review papers on this subject have appeared [1-3]. The surface modification of these materials can be achieved either during or after the manufacture process. Several advantages can be indeed outlined, when compared to more conventional methods : [i)] low temperature reaction (even at room temperature), [ii)]chemical modification limited to surface only without modifying the bulk properties, [iii)] possible non-equilibrium reactions. Depending on the type of starting materials and employed techniques, the improved properties may concern wettability, adhesion, chemical stability, permeation, electrical conductivity, biocompatibility, grafting, mechanical behaviour, etc.

The present work deals with the effect of fluorination on the surface of co-elastomers, which have been scarcely studied [4]. It is devoted to the surface treatment of thin nitrile gloves [made of carboxylated nitrile butadiene rubber latex (NBR)] using either plasma-enhanced fluorination (PEF) in rf cold plasmas using fluorinated gases (CF_4, CHF_3) or direct fluorination by 10% F_2-gas diluted in N_2. The mechanisms of fluorination of these co-elastomers will be proposed on the basis of the assignment of the different components of the XPS spectra.

2. Experimental procedure

Fluorination procedure

The experiments in rf plasma conditions were carried out in a S.E. 80 Barrel Plasma Technology System. CF_4 gas was excited by a rf source at 13.56 MHz. The chamber was thermostatically controlled and maintained either at room temperature or at about 90°C during the process. Taking into account previous plasma-enhanced fluorination (PEF) experiments on various types of carbon materials [5, 6], the optimized conditions could be established with the following parameters : CF_4 gas flow rate: Q = 8 ml min^{-1} ; total pressure: p = 300 mTorr ; rf power: P = 80 W. After the fluorination treatment, the samples were generally handled and kept in a glove box under an Ar atmosphere.

Elastomer samples

The thin nitrile gloves submitted to fluorination have a thickness of 100 µm. They were made by dipping a porcelain former previously coated with calcium nitrate into a latex compound, leaching in warm water, drying and curing the form at elevated temperature, and then stripping the gloves. The compound comprises carboxylated nitrile butadiene rubber latex (XNBR) having about 40 % dry rubber content and zinc oxide (1-2%).

XPS Characterization

XPS analysis were performed with a VG 220 i-XL ESCALAB. The radiation was a Mg non-monochromatized source (1253.6 eV) at 200 W. Surveys and high resolution spectra were recorded, then fitted with a Eclipse processing program provided by Vacuum Generators. Each C1s component was considered as having similar full width at half maximum (FWHM), i.e. 1.3eV. This procedure appeared to be the most reliable one, as previously proposed in investigations on fluorinated carbon materials [6]. A good agreement between the experimental curve and the full calculated envelope was obtained, explaining in addition subtle distinctions between the proportion of fluorinated components.

3. Results and discussion

On the XPS survey spectrum of the surface of NBR rubber, it can be noticed, besides the components of the polybutadiene and polyacrylonitrile backbone of the material (C, O, N), the presence of other elements which have been introduced during the different steps of the elaboration process of the glove : Ca, Na, S, Si, K, Zn, Cl. Oxygen which is present in large amount in pristine gloves occurs as carboxyl, carbonyl, hydroxyl groups or as pollution element. Because of the low contents of most of these components, we will only deal in the following with those elements which are able to provide an insight into the fluorination mechanisms, i.e. C and F.

Room temperature fluorination treatments

PEF treatments using CF_4 rf plasma at room temperature for treatment durations up to 120 min do not bring important modifications of C 1s spectra, as shown in Fig. 1a.

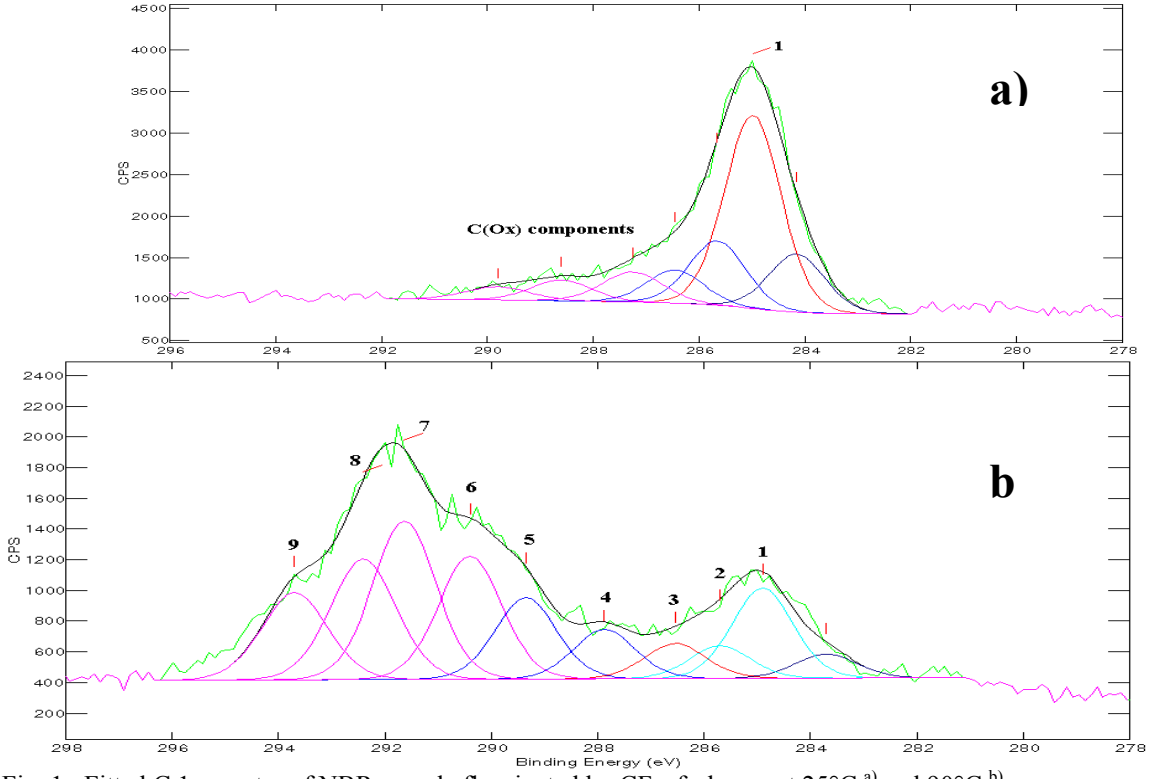

Fig. 1- Fitted C 1s spectra of NBR sample fluorinated by CF_4 rf-plasma at 25°C [a] and 90°C [b].

The main peak is located at 284.6 eV, as for the starting material, and corresponds therefore to CH or CH_2 bonds that are present in both starting PBD and PAN. A component can be noticed on the lower BE side of the C 1s envelope, which can be fitted at about -1eV relative to this peak. This contribution could arise from the presence in the samples of different types of hydrocarbon surface pollution and non-fluorinated domains with different levels of charging effect. The high energy shoulder which is found between 287 and 289 eV is mostly due to carboxyl and carbonyl groups whose BE fall in the 287-288.5 eV range. Small amounts only of CF bonds are formed and are attributable to CHF-CHF groups. On the other hand, 5 to 10% of F are found at the surface depending on the studied sample. Among the three contributions of the F 1s spectrum (Fig. 1b), the weakest one at 687.3 eV (10 %) corresponds indeed to the formation of C-F bonds while the two major components can be attributed to those of « inorganic » fluorides, in which fluorine is bound to inorganic elements that are present in the gloves: CaF_2 for the one at 684.3 eV, ZnF_2 or complex fluorides to the one at 685.3eV.

Thermally activated fluorination treatments

The effect of thermal activation is illustrated in Fig. 1b and 2b which show C 1s and F 1s spectra of the surface of NBR gloves treated in a CF_4 rf plasma at 90°C. In the survey spectrum, the F 1s peaks have considerably increased, with a mean F/C atomic ratio reaching 1.6. In this case, the C 1s spectra exhibit 2 clear maxima : one at a BE similar to that of the starting material, and another one with a shift of + 6.8 eV. If we take the same procedure as previously used, this second maximum can be assigned to CF_2 groups with first C neighbours bound to one F atom, for instance CF_2 – CHF groups.

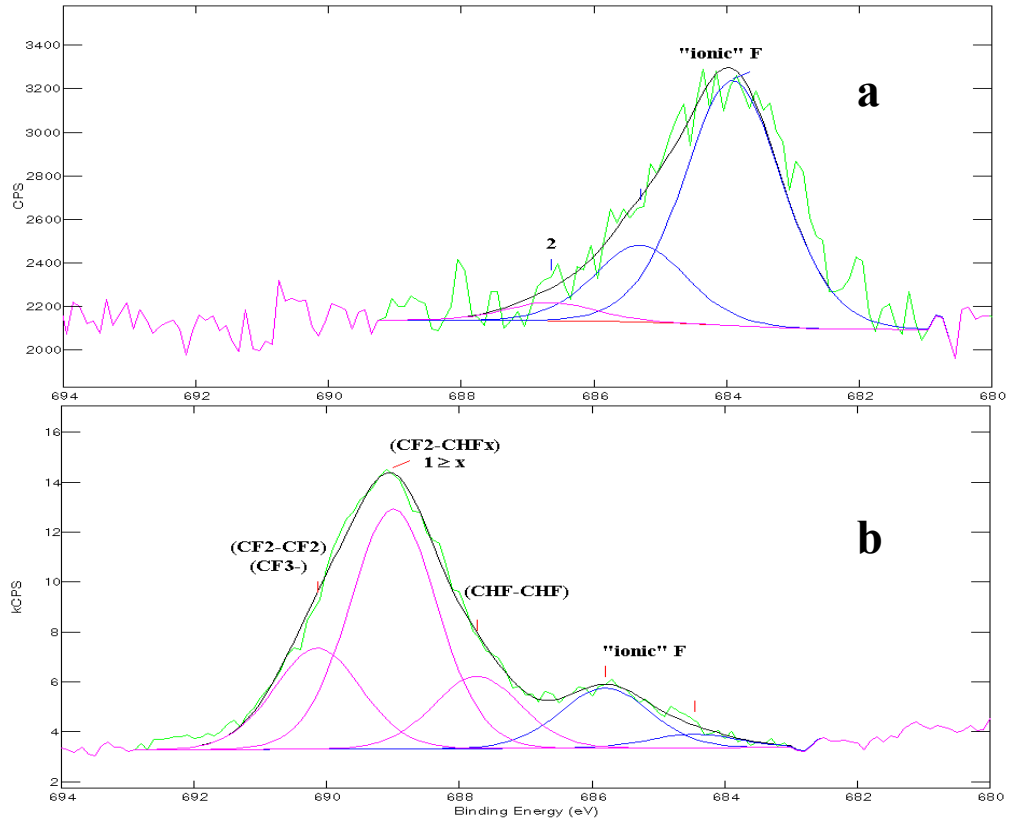

Fig. 2- Fitted high-resolution F 1s XPS spectra of NBR sample fluorinated by CF_4 rf-plasma at 25°C [a)] and 90°C [b)], and by F_2-gas at 25°C [c)].

Another feature of the spectrum which is consistent with an increase of surface fluorination is the presence of two more contributions at higher BE. The one with a shift at + 8.0 eV corresponds to CF_2 groups with CF_2 (or CF_3) first neighbours, or to CF_3 groups with non-fluorinated neighbours. The contribution with a shift of 9.1 eV can be assigned to terminal CF_3 groups with fluorinated neighbours. It can be noted that most of BE are shifted of 0.8 eV relative to the room-temperature experiments due to higher fluorination levels and increase of the insulating character of the sample. The same trend is

found in the F 1s spectrum, as shown in Fig. 2b. Although the amount of « inorganic » fluorides is more or less similar (12%), the maximum value of the envelope corresponding to the F-C components is shifted of about 1 eV towards higher BE. As previously stated, the value of the maximum at 688.7 eV should correspond to $CF_2 - CH_2$, or $CH\underline{F} - CF_2$ units. At lower BE, the CHF – CHF component at 687.3 eV is weaker (15%). In addition, a further component occurs from the fitting procedure at 689.8 eV, which can be assigned to perfluorinated CF_n groups, in particular PTFE-like $CF_2 - CF_2$ units and terminal CF_3 groups.It can be noted that similar results are obtained for shorter fluorination times, 30 min for example.

Comparison with direct F_2-gas fluorination

The direct F_2-gas fluorination process was performed at room temperature in a "fluorine line" using handling procedures previously described. The samples were set in a Ni boat which had been passivated. F_2 gas 10% diluted in N_2 (Air Products) was used at room pressure. The reaction duration did not exceed 120 min. At the end of the experiment, F_2-gas was eliminated from the container and substituted by N_2.

Fig. 3 shows the C 1s XPS spectra for 5, 30, and 120 min treatments. The high resolution C 1s spectra exhibit an envelope spread over 10 eV. For 30 min fluorination durations or higher, the maximum of the envelope is located at 288.1 eV, with a shift of 3.5 eV relative to the 284.6 eV reference. This value being similar to those of CHF-CHF groups in poly(vinylene fluoride), we can assume that the main effect of fluorination is to open the double bond of PBD with a subsequent addition of a F atom on both C atoms. A second important contribution is located at a chemical shift of + 5.5 eV, which could be attributed to of $-(CF_2 - CH_2)-$ units coming from the substitution of F for H, or alternatively C-F bond with highly fluorinated neighbors, such as CF_2 groups or terminal CF_3 groups. Further contributions can be assigned to CF_2-CHF and CF_2-CF_2 groups, respectively. The assignments of the different components are given in Table 1.

The F 1s peak, shown in Fig. 2c, is displaced of about 4 eV toward higher BE, when compared with that of room-temperature PEF experiments. The FWHM is also much larger, reaching 3 eV, which points out the presence of several contributions. The « inorganic » part of the spectrum (CaF_2, ZnF_2) with components at BE ~ 685 eV is very weak and corresponds to less than 10%. The maximum of the peak, at 687.6 eV, can be ascribed to a F-C bond with first carbon neighbours presenting also C-F bonds, i.e. (CHF-CHF) groups, which is in good agreement with the C 1s spectrum. The contribution at lower BE, that is 686.5 eV, should correspond to F-C bonds with non-fluorinated C neighbours, i.e. ($CHF-CH_2$) groups. On the other side, the contribution at higher BE, that is 688.8 eV, can be assigned to C-F bonds with CF_2 groups as first neighbours or alternatively to CF_2 groups with CH_2 or CHF units as first neighbours (unfortunately the only literature data on F 1s BE of (CF_2 – CHF) groups (BE = 690.1 eV) [7] is known to be too high [6].

4- Conclusions

The above results clearly show that in the fluorination of NBR rubbers several mechanisms can be observed depending on the experimental conditions. When CF_4 rf-plasma treatments are carried out at room temperature a gradual fluorination occurs: monofluorinated CF groups are the species most found at the surface and perfluoro groups CF_n are present in lower amount, most fluorine species reacting with inorganic cations such as Ca^{2+}. Thermal activation yields an increase of the amount of surface perfluoro groups that finally leads to a coating mostly formed of perfluorinated $-(CF_2)-$ groups and terminal $-CF_3$ groups. This trend is found in both C 1s and F 1s spectra. On the other hand, direct F_2-gas fluorination is more active, even at room temperature: the addition reaction takes place at the $-(CH = CH)-$ double bonds of the PBD, leading to $-(CHF - CHF)-$ units, whereas perfluoro groups CF_n are present in a lower amount.

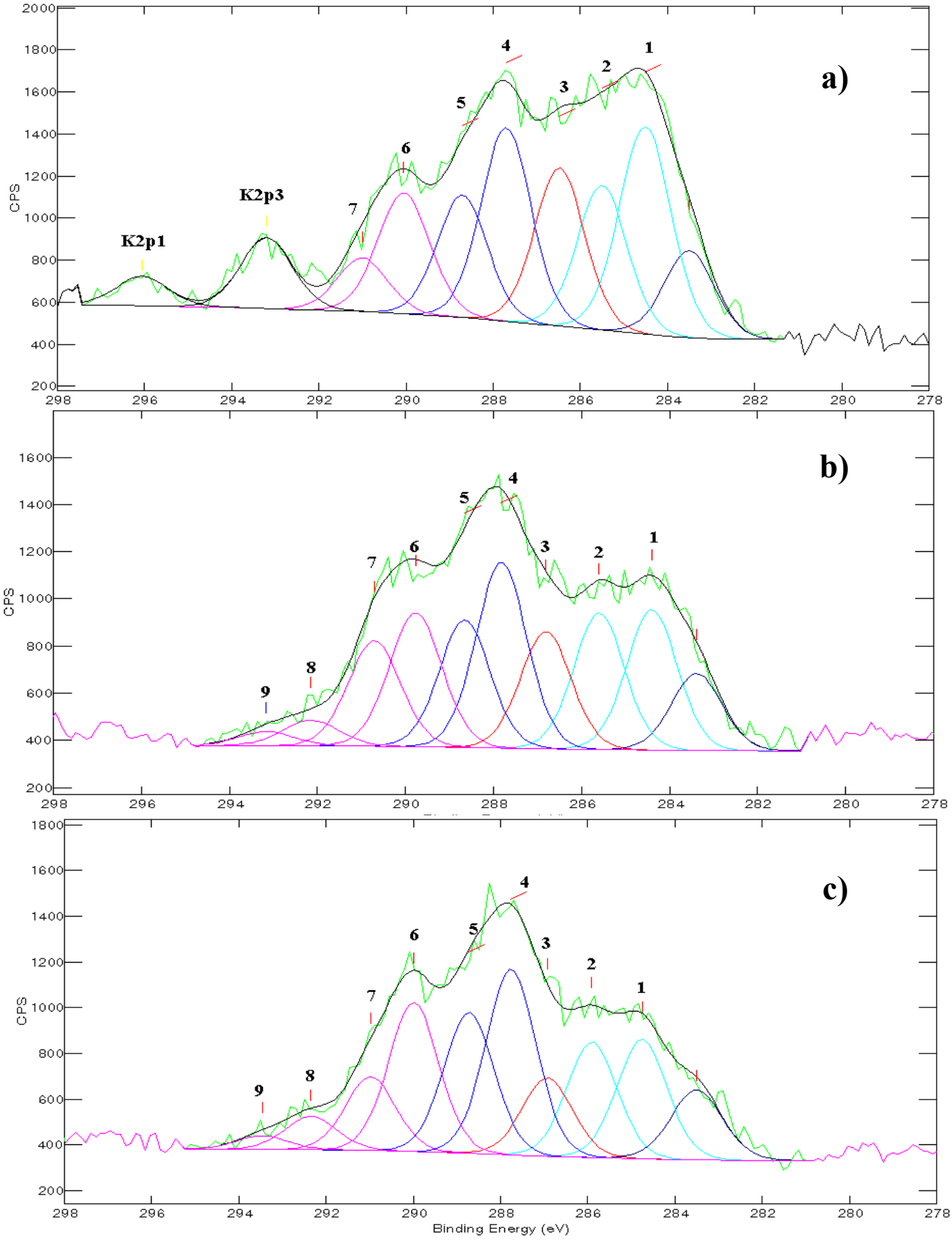

Fig. 3- Fitted high-resolution C 1s XPS spectra of NBR sample fluorinated by F_2 - gas at 25°C during 5 min [a)], 30 min [b)], 120 min [c)].

Table 1 - Assignments of the different components of the XPS spectra

N°	Chemical Bond	Shift (eV)
1	CH_n	-
2	$\underline{C}H_2$-CHF	0.7 - 1.1
3	$\underline{C}H_2$-CF_2	2.0
4	$\underline{C}$HF-CH_2 CHF-CHF	3.0 - 3.5
5	$\underline{C}$HF-CF_2	4.5
6	CF_x-$\underline{C}$F-$CF_{x'}$ (x, x'=2, 3) $\underline{C}F_2$-CH_2	5.3 - 5.5
7	$\underline{C}F_2$-CHF	6.2 - 6.8
8	CF_2-CF_2	7.8
9	$\underline{C}F_3$-CF_x	9.1

Acknowledgments - Mapa-Hutchinson [M. Renaud, Centre Technique, Liancourt, France] is acknowledged for interest and financial support.

References

[1] "Plasma Deposition, Treatment and Etching of Polymers", R. d'Agostino Ed., Academic Press, Boston (1990), and articles herein.

[2] "Plasma Surface Modification of Polymers : Relevance to Adhesion", M. Strobel, GS. Lyon, K.L. Mittal, VSP, Utrecht (1994), and articles herein.

[3] F.J. du Toit, R.D. Sanderson, J. Fluorine Chem. **98,** 107 (1999).

[4] G. Legeay, F. Epaillard, J.C. Brosse in "Second International Conference of Plasma Chemistry and Technology", H.V. Boenig Ed., Technomic Publ. Co. p 29 (1985).

[5] C. Cardinaud, A. Tressaud, Chapter 14, "Advanced Inorganic Materials", T. Nakajima, A. Tressaud, B. Žemva, Eds., Elsevier (2000).

[6] G. Nansé, E. Papirer, P. Fioux, F. Moguet, A. Tressaud, Carbon **35,** pp. 175, 371, 515 (1997).

[7] D.T. Clark, W. Feast, D. Kilcast, W. Musgrave, J. Polym. Sci. Polym. Chem. Ed. **11,** 389 (1973).

Different performance of Ar, O_2 and CO_2 RF Plasmas in the Adhesion of Thermoplastic Rubber Towards Polyurethane Adhesive

A.B. Ortiz-Magán, M.M. Pastor-Blas, J.M. Martín-Martínez

Adhesion and Adhesives Laboratory, Department of Inorganic Chemistry, University of Alicante, 03080 Alicante, Spain.

Abstract

RF plasma treatment has been used to improve the adhesion of synthetic vulcanized rubbers to polyurethane adhesives as an environmentally friendly alternative to the currently used chemical surface treatments. In this study, a non vulcanized (thermoplastic) styrene-butadiene-rubber -S0- was treated with argon, oxygen and carbon dioxide plasmas and the surface modifications were analyzed. Surface analysis of the failed surfaces after peel tests showed that the loci of failure was dependent on the gas plasma.

1. Introduction

Synthetic styrene butadiene (SBS) rubbers are thermoplastic elastomers which consist of block segments of a hard an rigid thermoplastic block polymer (styrene) and a soft and flexible elastic polymer (butadiene). The main advantage of thermoplastic rubbers over the thermoset elastomers is that upon heating above melting temperature of the hard phase, they melt and therefore they may be processed by conventional thermoplastic forming techniques. For this reason in a variety of applications, the thermoplastic elastomers have replaced the conventional thermoset elastomers. Typical uses for the SBS rubbers include automotive components, shoe soles and heels, sporting goods, medical barrier films and protective coatings, and they find application as components in sealants, caulking and adhesives. However, due to the non-polar nature of these rubbers, poor adhesion is produced with polyurethane adhesives. Consequently a surface treatment is required to chemically modify the rubber surface and produce suitable joints [1-3].

The most widely used surface treatment for SBS rubbers is halogenation with organic chlorine donors (trichloroisocyanuric acid or chloramine) which improves the wettability of these rubbers and enhances their adhesion properties [4]. However, this treatment involves the use of organic solvents, the chlorinating solutions have a limited stability and evolution of chlorine is a potential threat. Thus, an environmentally friendly treatment -RF plasma- has been proposed as an alternative to halogenation for thermoplastic SBS rubbers. Recent studies [5-7] have shown the effectiveness of RF plasma treatment in the treatment of rubbers. The energetic environment of the plasma creates surface free radicals as well as produces cleaning, ablation, crosslinking and chemical modifications on the rubber surface. However, these effects are greatly dependent on the gas used to generate the plasma. In this study the RF plasma treatment of an non vulcanized thermoplastic styrene butadiene rubber has been investigated. The effectiveness of different gas atmospheres (argon, oxygen and carbon dioxide) has been considered and the surface modifications and adhesion properties of the surface modified S0 rubber have been studied.

2. Experimental.

A block copolymer synthetic thermoplastic styrene-butadiene-styrene rubber (S0) has been used in this study. A simplified structure is given in Figure 1. The S0 rubber, which was provided by REPSOL QUÍMICA (Santander, Spain), does not contain oils, plasticizers or fillers but a small amount of antioxidant. The rubber samples were obtained by injecting the polymer into a heated mold at 150ºC, and test samples of 30 mm width, 150 mm length and 6 mm thick were obtained. The styrene block content of the S0 rubber is 30%, its tensile strength is 17 MPa and the Shore A hardness is 72º.

The S0 rubber was treated under low pressure RF plasma using argon, carbon dioxide and oxygen atmospheres for 1 to 15 minutes. The surface modifications produced on the S0 rubber were assessed by contact angle measurements, ATR-IR spectroscopy, XPS and SEM. Adhesion was evaluated from T-peel strength measurements of joints produced between two similarly treated S0 rubber samples bonded with a polyurethane (PU) adhesive in solution. The adhesive solution (18 wt% PU pellets in MEK + 5 wt% isocyanate) was applied to the rubber surface immediately after the treatment was carried out. Failed surfaces

after peel tests were characterized using ATR-IR spectroscopy to accurately assess the locus of failure of the joints.

3. Results and Discussion

As received S0 rubber shows (Figure 2) a high contact angle value (water, 25ºC), indicating a poor wettability due to its non polar nature. ATR-IR spectrum of the as received S0 rubber (Figure 3a) shows typical absorption of styrene (3010-3080, 1480, 915, 760, 696 cm^{-1}) and butadiene (2920, 2850, 1448, 1380, 968). Plasma treatment for 1 minute produced a noticeable increase in wettability of S0 rubber (Figure 2) with the three gases considered (oxygen, argon and carbon dioxide), being this increase more important when argon plasma was used. Besides, an extended plasma treatment (up to 15 minutes) produced a further decrease in contact angle on the Ar-plasma treated S0 rubber. Surface energy was evaluated using the Owens and Wendt approximation [8] (Figure 4). A noticeable increase of the polar component (γ^p) (Figure 4c) and a decrease of the dispersive component (γ^d) (Figure 4b) of the total surface energy (γ) (Figure 4a) was produced when the S0 rubber was treated with Ar plasma. This behavior can be explained on the basis of different surfaces modifications. ATR-IR spectra of plasma treated S0 rubber (Figure 3) show a decrease of hydrocarbon absorption (2920, 2850, 1448 cm^{-1}) and a decrease of C=C absorption (3080-3010, 915 cm^{-1}) when the S0 rubber was treated in Ar plasma. This corresponds to the decrease of the dispersive component of the surface energy (Figure 4b). However the treatment in O_2 or CO_2 plasmas produced the increase of the hydrocarbon absorption (2920, 2850, 1448 cm^{-1}) which is in agreement with the increase of the dispersive component of the surface energy (Figure 4b).

XPS allowed to restrict the depth of analysis from approximately 5 μm (ATR-IR) to the outermost 5 nm. As received S0 rubber is mainly composed (Table 1) of carbon and some oxygen and silicon (likely from a mold release agent, *i.e.* a silicone). Besides, some degree of oxidation of the surface rubber might be favored when the plasma treated rubber is exposed to the air. The plasma treatment for 3.5 min produced an increase of oxygen on the surface of the S0 rubber. This increase was more important when the S0 rubber was treated in Ar-plasma compared to CO_2 and O_2 plasmas, which is in agreement with the more pronounced increase in the polar component of the surface energy (γ^p) on the Ar-plasma treated S0 rubber (Figure 4c). Curve fits of the C 1s and O 2p photopeaks (Tables 2 and 3) show the creation of C-O, C=O and R-O-C=O moieties on the plasma treated S0 rubber, which contribute to increase the polar component of the surface energy (γ^p). Besides, C=O and Si-O moieties are removed from the S0 rubber surface (Table 3) when treated in plasma, this removal being more important with CO_2 and Ar plasmas. These findings suggest that CO_2 and O_2 plasmas produce ablation of the rubber surface and partially remove hydrocarbon and silicon moieties from the S0 rubber surface. On the other hand, Ar plasma does not produce such degree of ablation, consequently, hydrocarbon and silicon moieties are not such effectively removed and a more important degree of oxidation was achieved.

Ablation of the S0 rubber surface was monitored by SEM (Figure 5). Topography of the S0 rubber was modified by the plasma treatment. Thus, removal of surface layers (ablation) was produced mainly with CO_2 and O_2 plasmas. The increase in the length of plasma treatment produces a smoothing of the rubber surface (Figure 6) due to further ablation produced by an extended plasma treatment. This explains the decrease in the dispersive component of the surface energy (γ^d) when S0 rubber is treated wih Ar and CO_2 plasmas for 15 min (Figure 4b). Thus, the increase of the length of CO_2 and O_2 plasma treatments produce ablation of a previously oxidized rubber surface. On the other hand, Ar plasma oxidizes S0 rubber surface but is not sufficiently aggressive to remove this oxidized rubber surface. In consequence, oxidized polar moieties remain on the Ar-plasma treated S0 rubber surface producing an increase in the polar component of the surface energy (γ^p) (Figure 4c).

The different surface modifications produced by the several gas plasma treatments were expected to affect differently the adhesion properties of the S0 rubber. Adhesion was evaluated from T-peel test measurements in joints produced between two identically treated rubber strip test pieces bonded by a polyurethane (PU) adhesive. The non polar nature of the as received S0 rubber as well as the presence of a mold release agent (*i.e.* a silicone) on the rubber surface are responsible for the lack of adhesion of the joints produced with the

as received S0 rubber. The plasma treatment of the S0 rubber produced a noticeable increase of adhesion with all the plasmas irrespective of the length of treatment (Figure 7). Thus the T-peel strength values do not reflect the different chemical and morphological surface modifications produced by the different plasma treatments. This suggest that additional factors might affect the adhesion performance of treated S0 rubber. For this reason, the loci of failure of the joints were analyzed by ATR-IR spectroscopy on the failed surfaces after the T-peel test. ATR-IR spectra of the PU adhesive and the as received S0 rubber are included in Figure 8 and the absorption peaks are shown in Table 1 for comparison with those of the failed surfaces (Figures 9-11)

The ATR-IR spectra of the failed surfaces of the joint produced with the as received S0 rubber (Figure 9) show absorption from the rubber on the surface that visually corresponded to the rubber after the peel test (R-surface) and absorption from both the PU adhesive (3390, 2942, 2863, 1730, 1200-1100 cm^{-1}) and the S0 rubber (2920, 2850, 1480, 968, 915 cm^{-1}) on the failed surface that visually corresponded to the adhesive (A-surface). This suggest that a mixed failure mode (mainly adhesional) is produced. A cohesive failure mode was observed (Figure 10) in joints produced with S0 rubber treated in CO_2 plasma for a short time (1 min). Thus, a short treatment time is sufficient to produce an adequate adhesion of the S0 rubber. The increase in the length of plasma treatment did not affect the adhesion properties but modified the loci of failure of the joints. Thus, the treament of the S0 rubber in CO_2 or O_2 plasmas for 3.5 min produced a mixed failure mode (mainly adhesional) (Figures 11 and 12). This is consistent with the ablation of the outermost rubber surface by both the O_2 and the CO_2 plasmas prior to bonding. However, the Ar plasma treatment of S0 rubber for 3.5 min produced a mixed failure mode mainly cohesive in a thin rubber layer: there is rubber and PU absorption on the A-surface and absorption from the rubber on the R-surface (Figure 13). The mechanical properties of this thin crosslinked rubber layer, where the failure of the joint is located, are determining the peel value.

4. Conclusions

The Ar, CO_2 and O_2 plasma treatments produced an increase in adhesion of the S0 rubber toward a PU adhesive due to chemical and morphological modifications on the S0 rubber surface. Ar plasma created polar moieties on the rubber surface and a consequent increase of the polar component of the surface energy. Thus wettability was increased. On the other hand, CO_2 and O_2 plasma treatments produced ablation of the previously oxidized crosslinked outermost S0 rubber surface.

Short plasma treatment times are enough to produce adequate T-peel strength values and a cohesive failure was obtained with CO_2 plasma treatment for 1 minute. The increase in the length of treatment or the use of another gas plasma atmosphere did not affect adhesion properties but modified the loci of failure of the joints. Thus, with Ar plasma no ablation was produced so the failure of the joints was located within a crosslinked oxidized rubber surface. CO_2 and O_2 plasma treatments removed the previously oxidized thin rubber layer in such a way that no transference of hydrocarbon moieties from the rubber to the A surface was produced during peel test and a mixed failure mode (mainly adhesional) was produced.

Acknowledgements

Financial support form CICYT (project MAT 98-0611) and COST S27 Action of the European Commission are gratefully acknowledged.

References (Times 11, bold)

[1] J. Royo, Manual de Tecnología del Caucho, Consorcio Nacional de Industrias de Caucho, Madrid (1985).
[2] Handbook ofAdhesives. I. Skeist (Ed.), 3rd ed., Van Nostrand, New York (1990).
[3] Polymeric Materials Encyclopedia **vol. 10**, J.C. Salamone (Ed.), CRC, Boca Raton (1996).
[4] M.M. Pastor-Blas, M.S. Sánchez-Adsuar - J. Adhesion **8(10)**, 1093 (1994).
[5] M.M. Pastor-Blas, J.M. Martín-Martínez, J.G. Dillard - Surf. Int. Anal. **26**, 385-399 (1998).
[6] M.M. Pastor-Blas, T.P. Ferrándiz-Gómez, J.M. Martín-Martínez - Surf. Int. Anal. **30**, 7-11 (2000).
[7] A.B. Ortíz-Magán, M.M. Pastor-Blas, T.P. Ferrándiz-Gómez, C. Morant-Zacarés, J.M. Martín-Martínez - Plasmas & Polymers **6(1,2)**, 81-105 (2001).
[8] D.K. Owens, R.C. Wendt. *J. Appl. Polym. Sci.* **13**, 1741 (1969).

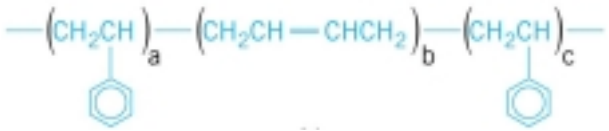

Figure 1. Structure of styrene-butadiene-styrene block copolymer (SBS rubber)

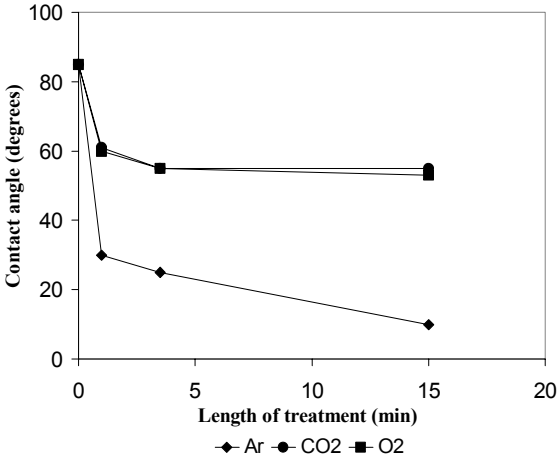

Figure 2. Contact angle values (water, 25ºC) of as-received and plasma treated S0 rubber.

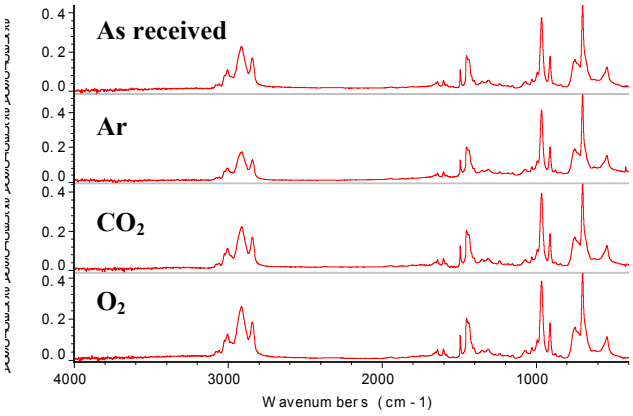

Figure 4. ATR-IR spectra of as-received and plasma treated S0 rubber for 3.5 min

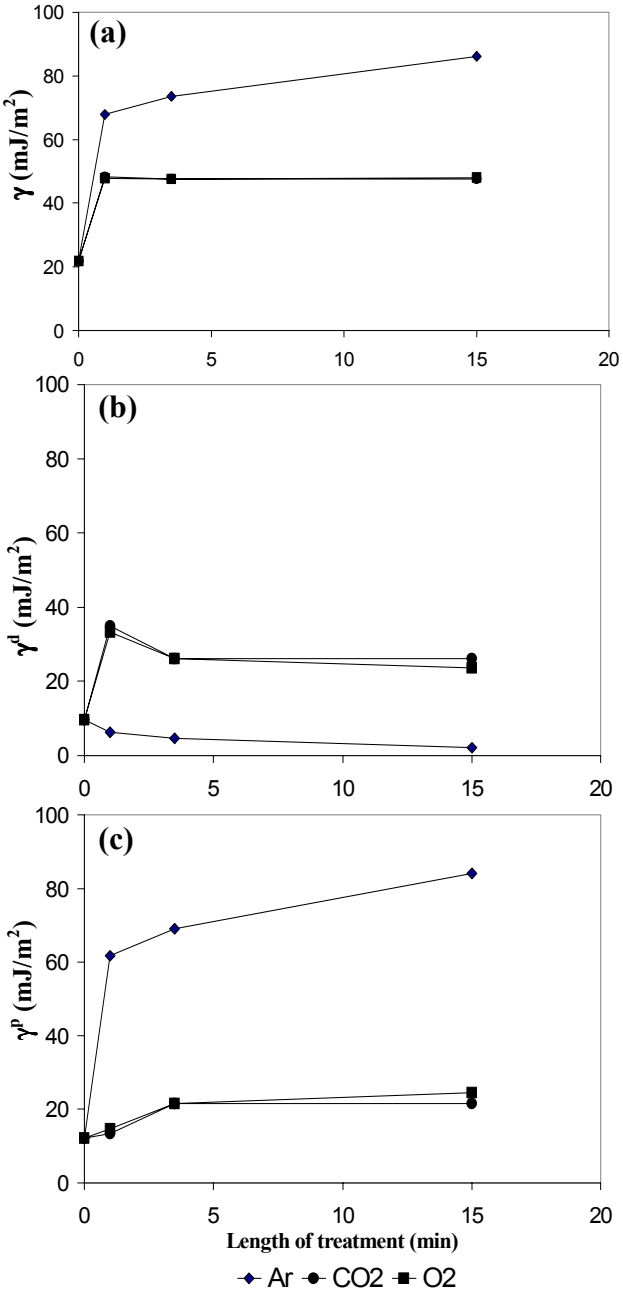

Figure 4. Surface energy of as-received and plasma treated S0 rubber: (a) total (γ); (b) dispersive (γ^d); (c) polar (γ^p).

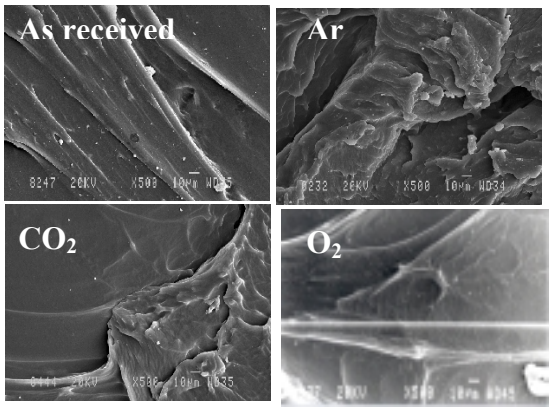

Figure 5. SEM micrographs of as-received and plasma treated S0 rubber for 3.5 min. x500.

Table 1. XPS atomic percentages (at %) of as-received and plasma treated S0 rubber

Binding energy (eV)	Element	As-received S0	Plasma treated S0 rubber (3.5 min)		
			Ar	CO_2	O_2
285.0	C 1s	94.2	71.6	73.6	75.4
532.0	O 1s	4.7	26.0	22.5	21.6
398.3	N 1s	---	1.2	1.4	1.0
99.6	Si 2p	1.1	1.2	2.5	2.0
532.0/285.0	O/C	0.05	0.36	0.31	0.29

Table 2. XPS atomic percentages (at %) of C1s curve fitting of as-received and plasma treated S0 rubber.

Binding energy (eV)	Species	As-received S0	Plasma treated S0 rubber (3.5 min)		
			Ar	CO_2	O_2
285.0	C-C, C-H	96.3	65.0	74.9	78.9
286.5	C-O	3.7	27.6	20.3	16.5
288.0	C=O	---	4.5	2.9	2.7
289.2	RO-C=O	---	2.9	1.9	1.9

Table 3. XPS atomic percentages (at%) of O 2p curve fitting of as-received and plasma treated S0 rubber

Binding energy (eV)	Species	As-received S0	Plasma treated S0 rubber (3.5 min)		
			Ar	CO_2	O_2
532.2	C=O, Si-O	74.3	62.9	51.1	61.8
533.6	C-O	25.7	37.1	48.9	38.2

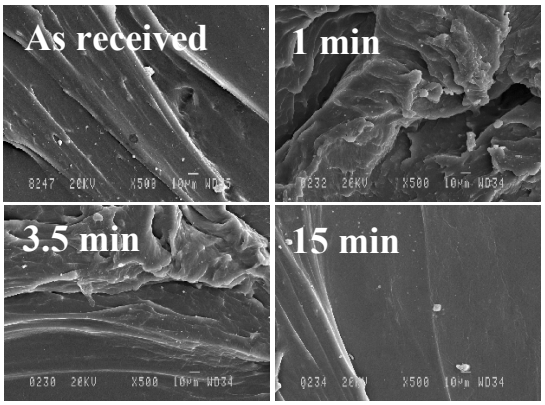

Figure 6. SEM micrographs of as-received and CO_2 plasma treated S0 rubber for different times

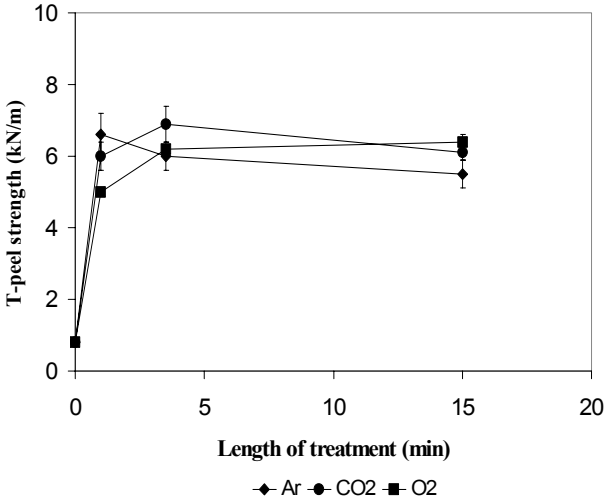

Figure 7. T-peel strength measurements (kN/m) of as-received and plasma treated S0 rubber/PU adhesive/S0 rubber joints.

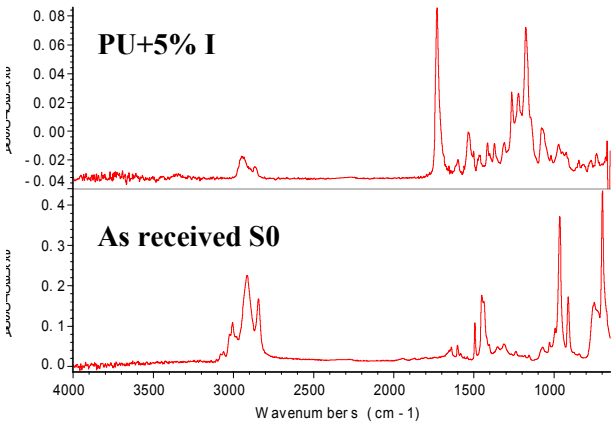

Figure 8. ATR-IR spectra of the raw materials: (a) adhesive (PU + 5% isocyanate); (b) as-received S0 rubber.

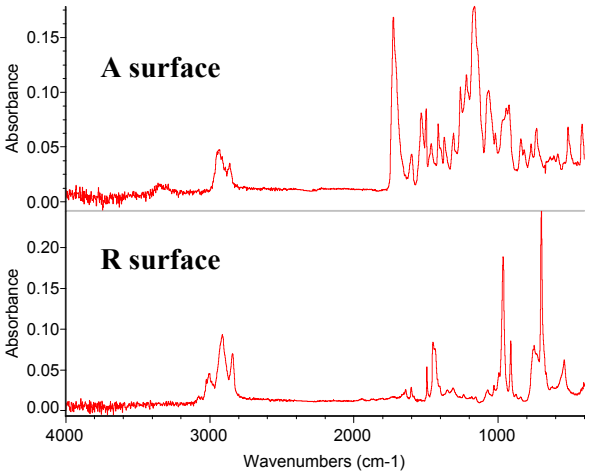

Figure 9. ATR-IR spectra of failed surfaces after T-peel test of joints between as-received S0 rubber and a PU adhesive.

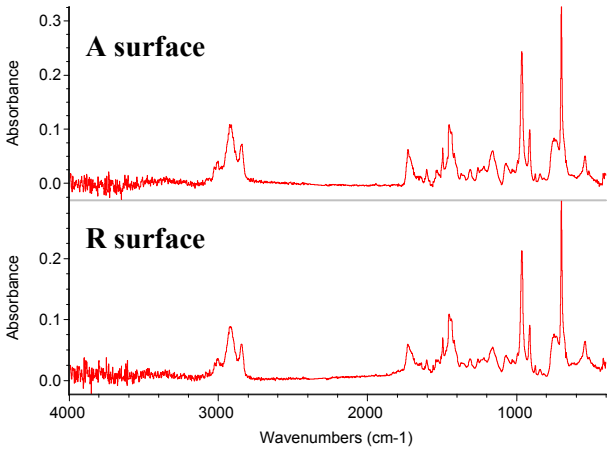

Figure 10. ATR-IR spectra of failed surfaces after T-peel test of joints between CO_2 plasma treated S0 rubber (1 min) and a PU adhesive.

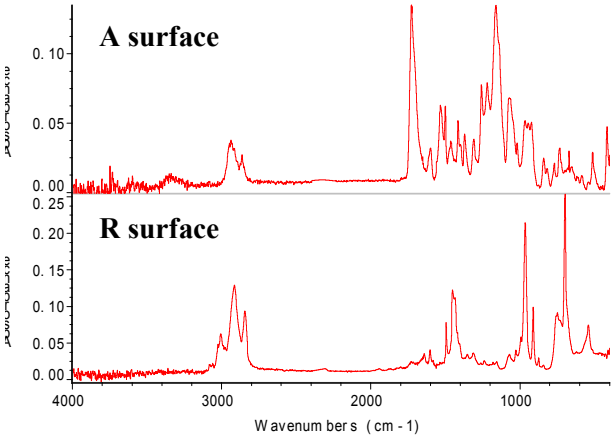

Figure 11. ATR-IR spectra of failed surfaces after T-peel test of joints between CO_2 plasma treated S0 rubber (3.5 min) and a PU adhesive.

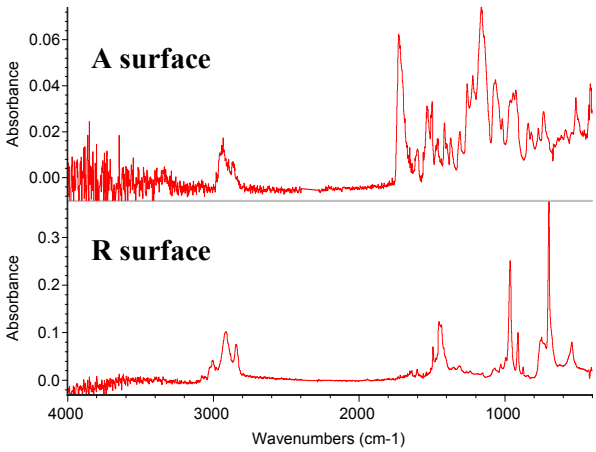

Figure 12. ATR-IR spectra of failed surfaces after T-peel test of joints between O_2 plasma treated S0 rubber (3.5 min) and a PU adhesive.

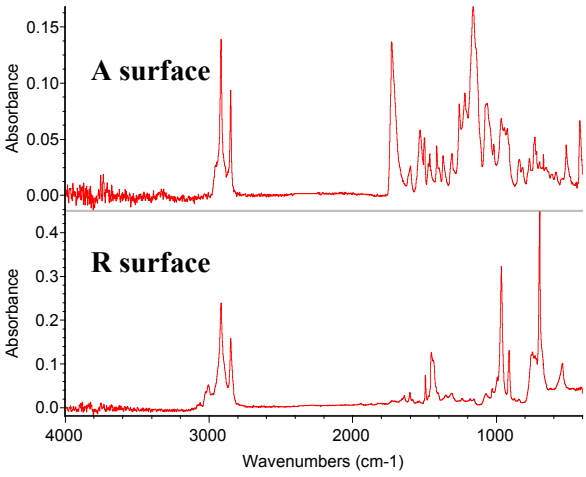

Figure 13. ATR-IR spectra of failed surfaces after T-peel test of joints between Ar plasma treated S0 rubber (3.5 min) and a PU adhesive.

Consequences of non-uniform RF plasma potential in large-area capacitive reactors

J. Ballutaud[1], Ch. Hollenstein[1], A.A. Howling[1], L. Sansonnens[1], H. Schmidt[1] and J.P.M. Schmitt[2]

[1] *Centre de Recherches en Physique des Plasmas, Ecole Polytechnique Fédérale de Lausanne, Switzerland*
[2] *Unaxis-France SA, Displays Division, 5 Rue Léon Blum, F-91120 Palaiseau, France*

Abstract
It is conventionally assumed that the plasma potential is the same everywhere in the plasma bulk. However, the non-zero plasma resistivity means that this is not true for the RF plasma potential in large area reactors. The spatial variation in plasma potential due to asymmetric electrode areas is described in terms of a telegraph equation, and the predictions of the model are compared with measurements using electrical probes mounted in the ground electrode of two large area RF plasma reactors.

1. Introduction

In small area capacitive reactors, the RF and DC components of the plasma potential can be assumed to be uniform over all the plasma bulk. In large area reactors, however, the RF plasma potential can vary over a long range across the reactor due to the finite plasma conductivity. A perturbation in RF plasma potential, due to electrode edge asymmetry or the boundary of a dielectric substrate, propagates along the resistive plasma between capacitive sheaths. This study consists of theoretical and experimental sections. In the first part, we develop a model based on a telegraph equation to show how the plasma potential is affected in large area reactors. Perturbations in potentials and currents due to the edge effects of the electrodes will be demonstrated by means of a simple analytical model assuming sinusoidal plasma potential and Langmuir-Hertz sheaths. In the second part we present measurements of the DC current and potential using an array of Langmuir probes in the ground electrode of two large area reactors, one cylindrical and the other rectangular. These measurements are used to test some predictions of the telegraph model.

2. The telegraph equation applied to large area reactors

At the edge of the RF plasma reactor represented in Fig. 1, the electrode areas are asymmetric because of the sidewall. In order to preserve RF current continuity, the RF sheath voltage at the larger area electrode will locally be less than the RF sheath voltage at the smaller electrode, the sum of the potentials being equal to the applied RF voltage. In the middle of the reactor, however, the electrode areas are symmetric and both RF sheath voltages would be expected to equal half of the RF voltage V_{RF}. The different sheath potentials in these two zones can be reconciled by allowing the RF plasma potential to vary across the reactor with a characteristic damping length Λ due to the non-zero plasma resistivity [1]. The redistribution of the sidewall RF current is represented by a lateral RF current in the simplified 1D equivalent circuit model in Fig. 1.

In the presence of a perturbation $\underline{V}(x,t)$ due to the sidewall, the ground sheath RF potential is

$$\underline{\tilde{U}}(x,t) = \frac{V_{RF}}{2} \cdot e^{i\omega t} + \underline{V}(x,t).$$

A lateral current $\underline{I}(x,t)$ flows through R and L, the plasma resistance and inductance per unit length, where

$\frac{\partial \underline{V}}{\partial x} = -R\underline{I} - L\frac{\partial \underline{I}}{\partial t}$, and

$\frac{\partial \underline{I}}{\partial x} = -C\frac{\partial \underline{V}}{\partial t}$, where C is the combined sheath parallel capacitance per unit length. We therefore obtain

$\frac{\partial^2 \underline{V}}{\partial x^2} = LC\frac{\partial^2 \underline{V}}{\partial t^2} + RC\frac{\partial \underline{V}}{\partial t}$ which is the telegraph equation.

The damping term dominates if $R/\omega L = \nu_m/\omega >> 1$ (high pressure, low excitation frequency).

In 1D Cartesian coordinates, with $\underline{V}(x,t) = \underline{V}(x)e^{i\omega t}$, the particular solution is

$$\underline{V}(x,t) = \underline{B}\exp\left(\frac{\pm x}{\underline{\Lambda}}\right)e^{i\omega t} = \underline{B}e^{\pm x/\Lambda}e^{i(\omega t \pm x/\Lambda)} \text{ where } \underline{\Lambda} = \frac{\Lambda}{(1+j)} \text{ and } \Lambda = \sqrt{\frac{2}{\omega RC}} = \omega_{pe}\sqrt{\frac{ag}{\omega\nu_m}}$$

with a the sheath width, g the plasma bulk height, ν_m the electron-neutral collision frequency, and ω_{pe} the electron plasma frequency. The voltage perturbation is a strongly-damped wave; the value of Λ increases with electron density, sheath thickness and bulk plasma height, and decreases with higher excitation frequency and collision frequency (higher pressure). If inductance is included, the damping length increases and the wavelength decreases. The boundary condition at the sidewall is

$$\left.\frac{\partial \tilde{U}}{\partial x}\right|_{x=L} = -I_{sidewall} R = -\underline{\tilde{U}}(L) j\omega C_W R \quad \text{where } C_W \text{ is the sheath capacitance at the sidewall.}$$

Note that this simple model assumes the plasma to be a uniform slab. The RF plasma potential is the same as the ground sheath RF voltage in this simple model where the impedance of the bulk plasma is neglected compared to the sheath impedance. The combination of a reduced and augmented sheath potential at the asymmetric edge results in a net increased power deposition at the edge. Comparison between this solution and solution of Maxwell's equations for the voltage distribution in a lossy dielectric shows that the telegraph model is a good approximation.

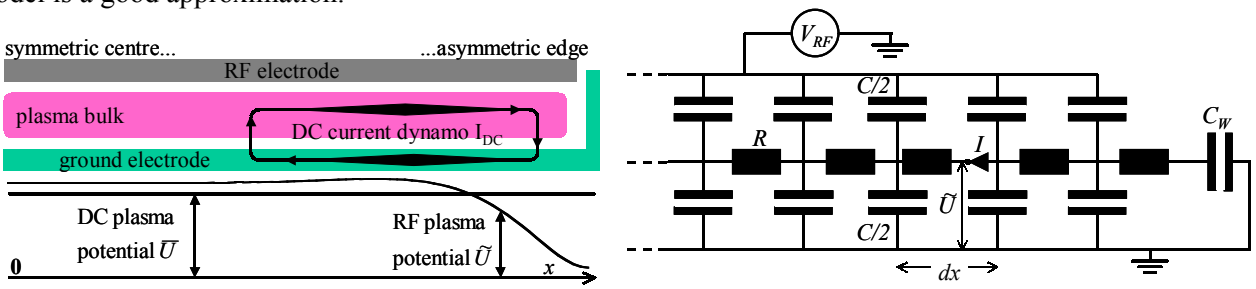

Figure 1. Left: schematic cross-section of an asymmetric reactor, from the centre to the right hand sidewall, showing profiles of the RF and DC components of the plasma potential, and the 'dynamo' of DC current between the ground electrode and the plasma. Right: the equivalent circuit used for the telegraph description. The sidewall sheath capacitance is represented by C_W.

3. Consequences of non-uniform RF plasma potential

Since the DC plasma potential is uniform across the plasma, and a conducting electrode is an equipotential surface (in absence of a dielectric substrate), a consequence of the non-uniform RF plasma potential is that local ambipolarity cannot be satisfied over all the electrode surface. This is because the RF and DC sheath voltages, $\tilde{U}$ and $\bar{U}$ respectively, cannot everywhere simultaneously satisfy the self-rectification condition [2] for zero DC current flow, which is $\bar{U} = \frac{T_e}{2}\ln\left(\frac{M_i}{2.3m_e}\right) + T_e \ln\left[I_o\left(\frac{\tilde{U}}{T_e}\right)\right]$ (a sinusoidal plasma potential, and therefore sinusoidal sheath voltages, have been assumed for the sake of convenience in this simplified model). Any spatial variation in the plasma RF potential will necessarily lead to time-averaged current flow across the sheaths. However, the reactor is capacitively coupled which prevents any DC current in the external circuit. Therefore, any DC current which flows across the sheaths must circulate through the plasma and return via the conducting surface of the electrode, so that the integral of the DC current over the electrode area is zero. The DC plasma potential adjusts to satisfy this condition at the ground electrode, and the self-bias of the RF electrode adjusts to satisfy this condition at the RF electrode. Consequently, the reactor asymmetry drives DC current 'dynamos' within the reactor as shown in Fig. 1. These DC sheath currents can be measured with grounded probes in the ground electrode surface, as shown in the following sections. These probes measure the local DC current density $j(\underline{x})$ to the ground electrode. The DC floating potential of the surface probes can also be used to give an indirect indication of the spatial variation of the plasma RF potential amplitude: in the previous equation, where the plasma potential is not equal to the value necessary for local ambipolarity, a floating probe in the electrode surface will have the time-averaged voltage:

$$\bar{V}_f(\underline{x}) = \bar{U} - T_e \ln\left[I_o\left(\frac{\tilde{U}(\underline{x})}{T_e}\right)\right] - \frac{T_e}{2}\ln\left(\frac{M_i}{2.3m_e}\right) \neq 0 \text{ because the grounded surface is not floating.}$$

$$\text{In the limit } \tilde{U}(\underline{x}) >> T_e : \bar{V}_f(\underline{x}) \approx \bar{U} - \tilde{U}(\underline{x}) + \frac{T_e}{2}\ln\left(2\pi\frac{\tilde{U}(\underline{x})}{T_e}\right) - \frac{T_e}{2}\ln\left(\frac{M_i}{2.3m_e}\right), \text{ therefore } \Delta\bar{V}_f(\underline{x}) \approx -\Delta\tilde{U}(\underline{x}).$$

i.e. the negative of the ground electrode probe floating potential $\overline{V}_f(\underline{x})$ is approximately equal to the variation in plasma potential amplitude $\widetilde{U}(\underline{x})$ across the reactor. To summarise: the experimental measurements in this work are made with probes mounted in the ground electrode. The current to a grounded probe represents the DC current density flowing to ground; and the negative of the probe floating potential represents approximately the deviation of the RF plasma potential amplitude from the value necessary for local ambipolarity.

4. Experimental results and comparison with a telegraph model in a cylindrical reactor

Figure 2 shows the measured radial profiles, across the one metre diameter of a cylindrical reactor, of the optical emission intensity, the DC current density, and the probe floating potential (the probes were mounted in the surface of the ground electrode). In this reactor, the grounded sidewall (1 cm high) is smaller than the sidewall of the RF electrode (2 cm high), therefore the grounded electrode has the smallest area, opposite to the case shown in Fig. 1. These radial profiles were cylindrically symmetric, as shown in the figure, provided that the sidewall height was precisely the same around the reactor circumference.

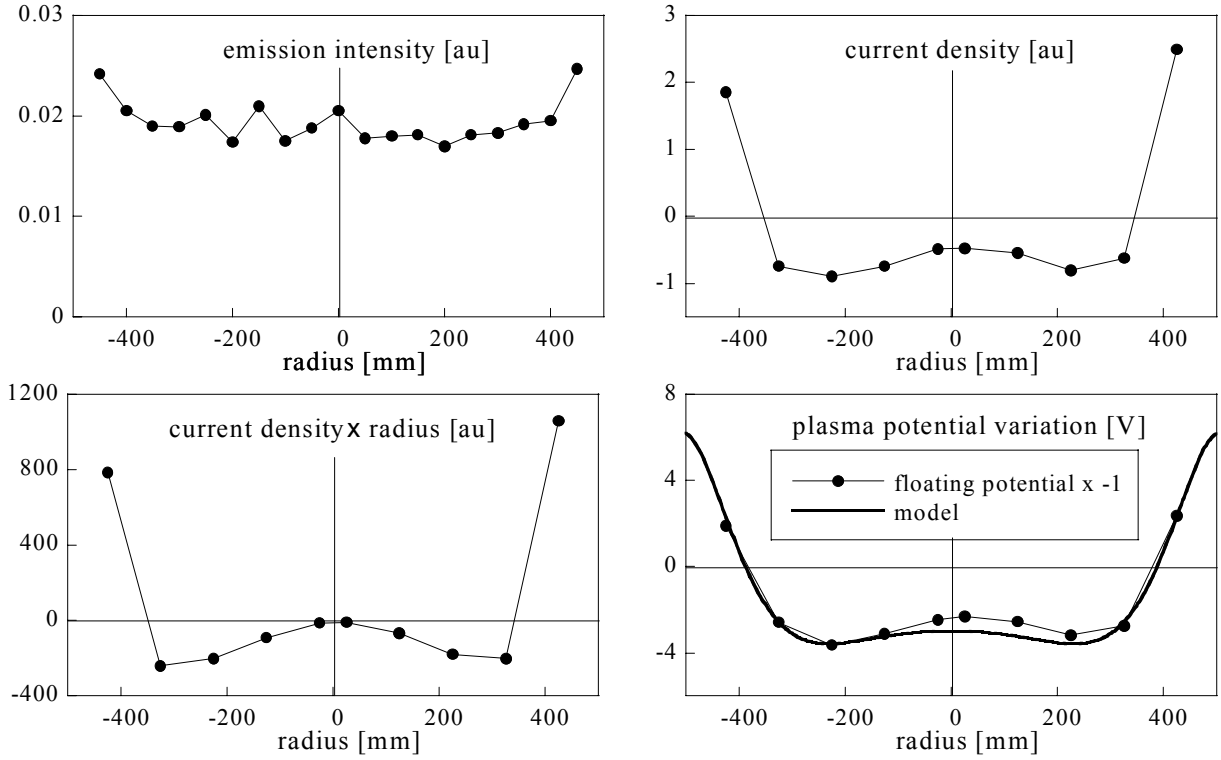

Figure 2: Measured profiles of emission intensity, DC current density, DC current, and floating potential profiles for probes mounted along a 1 m diameter of the cylindrical reactor. The DC current balance is approximately satisfied; and a comparison of the deduced RF plasma potential amplitude profile with a numerical solution of the telegraph equation (Λ=0.06 m) is also shown. Electrode gap 3 cm, grounded sidewall 1 cm high, RF sidewall 2 cm. Plasma parameters: argon/hydrogen flow ratio 2:1, 13.56 MHz, pressure 100 mTorr, 200 W RF power.

The damping length Λ is estimated to be a few cm [1] for the plasma parameters given in the caption to Fig. 2. At 13.56 MHz, any standing wave non-uniformity is negligible since the RF wavelength is much larger than the machine. The edge plasma non-uniformity can be seen on the emission intensity profile. The plasma power is higher towards the reactor edge, in agreement with the telegraph model. The radial profiles of the DC current density and floating potential are both bipolar, with the zero crossing point at the same radius as expected. This radius is the null point about which the DC dynamo rotates from larger to smaller radii. DC current from probe to plasma is defined as positive throughout this work. The surface integral $2\pi\int_0^R j(r)\,dr$ of the current density $j(r)$ shows that the net DC current to the ground electrode is indeed zero (within experimental error due to the limited number of probes defining the DC current profile) as expected for the capacitively-coupled reactor. The DC current density near the wall is majority electron current, being

balanced by a majority ion current within the radius of zero current; this corresponds to the current flow in Fig. 1 for the smaller (upper) electrode.

The negative profile of the probe DC floating potential is compared with a numerical solution of the telegraph equation for the RF plasma potential amplitude in cylindrical geometry. Given the approximations made and the assumption of uniform plasma resistivity and sheath capacitance in the telegraph model, there is reasonable agreement for a value of Λ = 0.06 m. Note that the deduced envelope of the RF plasma potential amplitude increases towards the wall, which corresponds to Fig. 1 for the smaller (upper) electrode.

When the sidewall height asymmetry was reversed (grounded sidewall larger than the RF electrode sidewall), the DC current and floating potential profiles were inversed, as expected. If the sidewall height differed by a few mm around the perimeter, the cylindrical symmetry was broken and the profiles became skewed with a marked slope across the diameter, demonstrating that the sidewall geometry can have a strong influence on the plasma uniformity, even across the entire 1 m diameter. However, when the RF and grounded sidewalls were accurately equalised (equal effective sidewall areas for the ground and RF electrodes), then the measured values of probe current density and floating potential were strongly reduced along the whole diameter, indicating that there was no systematic variation in RF plasma potential, and the plasma emission intensity was uniform. Any remaining edge non-uniformity is due to fringing fields which are localized close to the junction between the sidewalls.

As a supplementary demonstration of the experimental method, it is interesting to consider measurements performed at a higher RF frequency where standing wave effects become important, and even dominate edge effects. Figure 3 shows the same profile measurements as for Fig. 2, but at 67.8 MHz. In contrast to a telegraph model at low frequency, the plasma profile is dominated by a central peak. The RF voltage amplitude has the Bessel function radial distribution $J_o\left(k_{eff}\, r\right)$, where k_{eff} is the effective wavenumber due to the plasma permittivity [1]. This voltage profile is a solution of Maxwell's equations in parallel plate cylindrical geometry, and is independent of plasma resistivity effects. Nevertheless, any phenomenon which causes the RF plasma potential to be non-uniform (in the presence of a uniform DC plasma potential) will cause DC currents to circulate for the same reasons as given in the previous section. Figure 3 shows that the current density profile, as measured by the grounded probes, integrates approximately to zero. Furthermore, the negative floating potential profile approximates to a Bessel profile, shifted by a DC value corresponding to the DC plasma potential. This shows the probe method used in a different context independently of the telegraph effect.

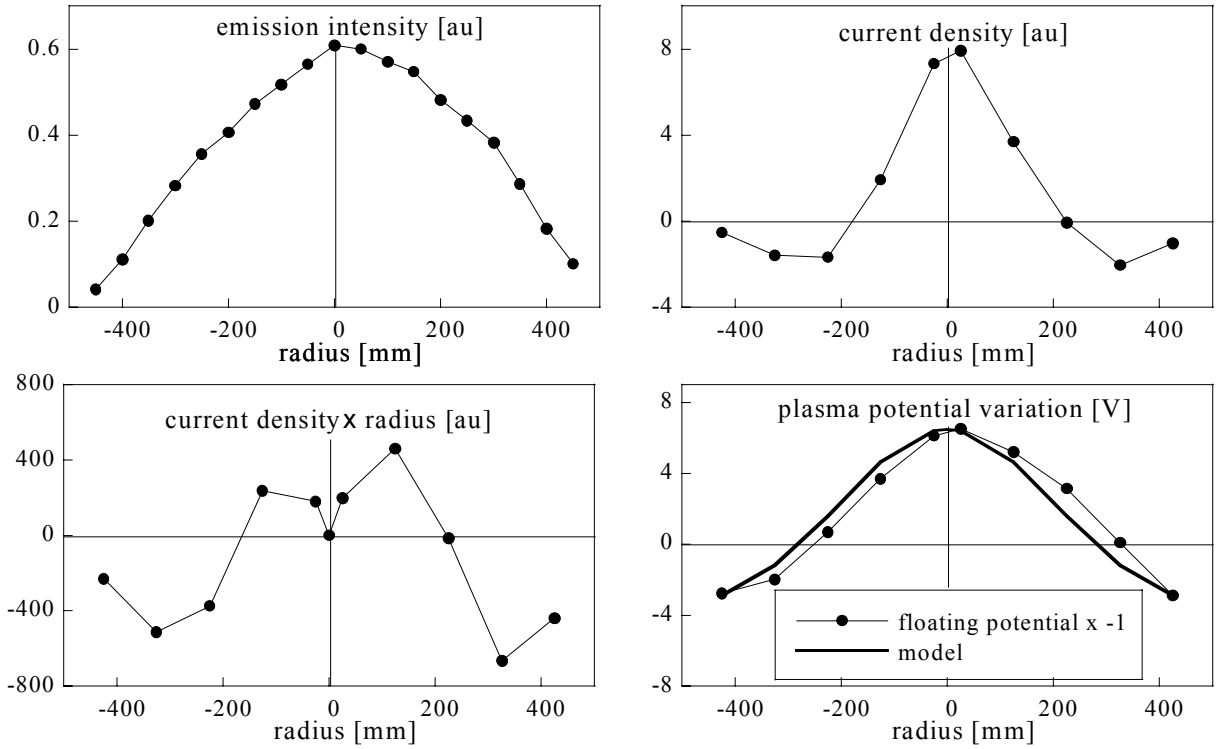

Figure 3: The same cylindrical reactor as for Fig. 2, but at 67.8 MHz, Ar 250 mTorr, 300 W. The RF plasma potential amplitude profile, deduced from the probe floating potential profile, is compared with a Bessel function solution for the standing wave. The standing wave effect is seen to dominate the edge asymmetry effect at this high frequency.

5. Experimental results and comparison with a telegraph model in a rectangular reactor

The rectangular reactor has electrode dimensions 47 cm by 57 cm, with a grounded sidewall of height 2.5 cm. The grounded electrode now has the largest area, corresponding to Fig. 1, which is the opposite case to the cylindrical reactor in the previous section. An array of surface probes is mounted in the ground electrode along a line from the reactor axis towards the sidewall (see Fig. 5 for the probe positions) with another probe in the sidewall itself. In Fig. 4(a) we see that the sign of the current density is inversed (with majority DC electron current contribution this time on the interior of the grounded electrode surface) with respect to Fig. 2 because the electrode area asymmetry is reversed. In contrast to the data presented up to now with no substrate, Fig. 4(c) shows the DC current density measurement in presence of a centrally-positioned glass substrate 37 cm x 47 cm, leaving a 5 cm gap between the substrate edge and the sidewall. The insulating substrate now constrains the DC current dynamo to circulate in the 5 cm gap between the sidewall and the substrate. The DC plasma potential and the RF electrode self-bias voltage adjust to maintain global ambipolarity. The integral of the DC current $\int_0^L j(x)\,dx$ is still roughly zero although accurate values are difficult to obtain because the current density in the vicinity of the sidewall is not measured with sufficient spatial resolution.

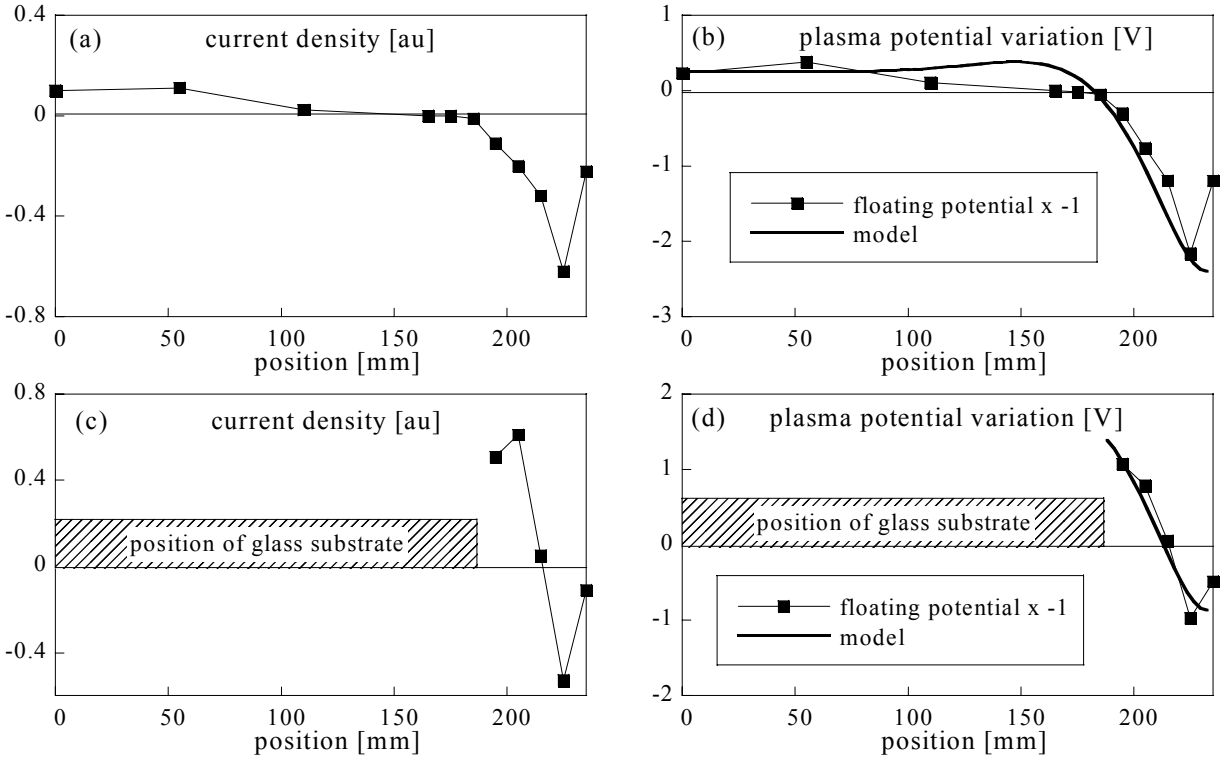

Figure 4: Measured DC current density and DC floating potential profiles for probes mounted along the 0.235 m halfwidth of a rectangular reactor. Top: no substrate. Bottom: with a glass substrate to 5 cm from the sidewall. The DC current balance is approximately satisfied in both cases; and comparisons of the deduced RF plasma potential amplitude profile with a telegraph solution (Λ=0.02 m) are also shown. Hydrogen plasma parameters: 40.7 MHz, 0.6 mbar, 60 W.

The envelope of the RF plasma potential, inferred from the negative of the DC floating potential profile, decreases towards the wall, also opposite to the behaviour for the previous results in Fig. 2 for the same reason of reversed electrode area asymmetry. This fall-off in amplitude is to reduce the RF current contribution from the grounded sidewall. The negative profile of the probe DC floating potential is compared with the analytic expression for the RF plasma potential amplitude in Cartesian geometry. There is reasonable agreement between the measurement and the telegraph 1D profile using a damping length distance Λ = 0.02 m, provided that the sidewall current is 2-3 x smaller than the extrapolated value, as observed experimentally. It seems reasonable that this is due to imperfect contact of the plasma with the sidewall. It is interesting to note that the condition for local ambipolarity above a thin insulating substrate can cause its surface potential to be maintained at a negative value – this would be impossible if the plasma potential were unique. The consequent negative charging of a hot glass substrate has been measured in many

different conditions [3], and is supporting evidence for the telegraph effect. The DC sheath potential then varies over a dielectric substrate resulting in a non-uniform ion bombardment energy.
The experimental parameters were purposely chosen to obtain a damping length much smaller than the reactor width, because otherwise a one-dimensional treatment is not justified. Fig. 5 shows 2D solutions of the telegraph equation in the reactor geometry for Λ = 0.03 m and 0.1 m. For Λ = 0.1 m, the voltage perturbation extends over a large distance, and the enhanced area asymmetry due to the corner sidewalls influences the DC current dynamo flow far from the corners, to the extent that all the probes measure a positive DC current density (unipolar profile), as observed, and the negative DC current density is concentrated in the corners. For Λ = 0.03 m and less, the range of influence of the corners is restricted, and, for most of the reactor perimeter, the perturbation can be described by the 1D model as used in Fig. 4.

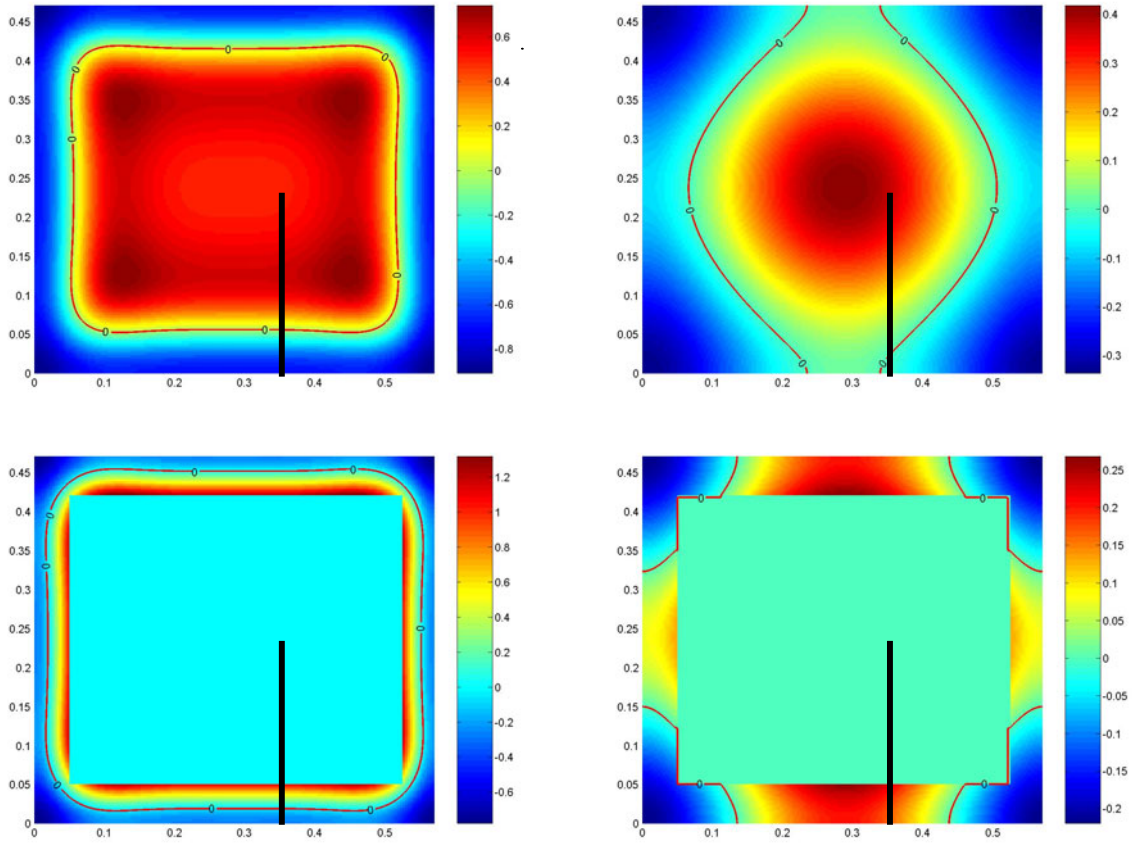

Figure 5: 2D colour contour plots of the RF current density solutions of the telegraph equation for damping lengths Λ = 0.03 m (left) and 0.1 m (right). Above: no substrate; below: with glass substrate. The location of the probe array is shown by the bar. The contour of zero DC current is indicated. For Λ = 0.03 m, the 1D description along the halfwidth at the probe positions is a good approximation. For Λ = 0.1 m, the current density everywhere is strongly influenced by the corner sidewalls.

6. Conclusions

Model and measurements with surface probes show that non-symmetric electrode areas cause a spatial variation in the RF plasma potential which can be described by a telegraph equation. This leads to non-uniform RF sheath voltages and RF power density. The non-uniform RF plasma potential in presence of the uniform DC plasma potential results in non-ambipolar currents circulating through the plasma and along conducting surfaces. If the electrode sidewall areas are accurately equalized, then the RF plasma potential amplitude and the power density are uniformalised.

References

[1] J. Schmitt, M. Elyaakoubi and L. Sansonnens – Plasma Sources Sci. Technol. **11**, A206 (2002).
[2] K.-U. Riemann – J. Appl. Phys. **65**, 999 (1989).
[3] A.A. Howling, A. Belinger, P. Bulkin, L. Delaunay, M. Elyaakoubi, Ch. Hollenstein, J. Perrin, L. Sansonnens, J. Schmitt and E. Turlot – 15th Int. Symp. Pl. Chem. July 9–13 (2001) Vol. I pp33-39.

Anti-corrosive properties of thin films produced on metal surfaces by cold atmospheric plasma of glidarc type

B. Benstaali[1], N. Benderdouche[1], A. Addou[1], B. G. Cheron[2], J.L. Brisset[3]

[1] *Laboratoire des Sciences et Techniques de l'Environnement et de la Valorisation (STEVA), Faculté des Sciences de l'Ingénieur, Université de Mostaganem. 27000 Mostaganem, ALGERIA*
[2] *CNRS UMR 6614-CORIA, Technopole du Madrillet, BP 12 76801, St Etienne du Rouvray Cedex, France*
[3] *Laboratoire d'Electrochimie Interfaciale et de Chimie Analytique (LEICA), Faculté des Sciences, Université de Rouen, 76821 Mont-Saint-Aignan, France*

Abstract
The electrochemical properties of oxide thin films produced by non thermal plasma of glidarc type on austenitic 304L and 316L stainless steel surfaces are investigated and compared to plasma treated pure iron samples by means of analytical techniques. The combined electrochemical, gravimetric and galvanic results of the stainless steels and iron samples lead to conclude that the iron (III) oxide formed enhances the material resistance in aggressive media and could have important future applications.

1. Introduction

The exposition of austenitic 304L and 316L stainless steel alloys to a humid air plasma of the gliding arc type provokes modification of the surface by forming a thin oxide film [1]. The identification of the iron hydroxide $Fe(OH)_3$ on the treated surface using electrochemical methods is confirmed by its characteristic reduction peak at –1.18 V/SCE in a NaOH solution (pH = 11.7). X-ray investigation of these samples shows the simultaneous presence of austenitic (γ-Fe) and ferric (α-Fe) phases where the former phase is predominant [2]. The exposure of the austenitic samples to the humid air plasma induces phase modifications. The observed decrease in the reduction peak intensities of the ferric (α-Fe) phase may suggest the contribution of the (α-Fe) phase in the hydroxide formation. The anticorrosive properties of the hydroxide were investigated using Tafel measurements performed in nitric acid solutions (10^{-2} $M.L^{-1}$) which show that the corrosion potential of 304L and 316L austenitic stainless steel surfaces increases and reaches a saturation step after a 30 minute treatment time.
Since identical iron (III) oxide thin films are grown on pure iron substrates when exposed to a humid air glidarc plasma for different exposure times, their properties are investigated by looking at different analytical techniques to those imposed to the austenitic samples. Plasma-treated iron surfaces are immersed in 3.5% NaCl solutions in order to simulate their behaviour in corrosive and aggressive marine environments such as inland industrial chemical processes, boats and off-shore petroleum equipment. Gravimetric measurements show that the mass loss linearly varies with the immersion time. The corrosion rates are deduced from the relevant slopes. The increase in the plasma treatment time of the iron electrode leads to lower slope values and consequently to lower corrosion rates.

2. Experimental procedures

2.1 Experimental set-up

The gliding arc reactor is described elsewhere [3]. A high voltage is applied across two diverging electrodes. Water saturated air flows between the electrodes gap. An electrical arc sets up at the shortest electrodes gap and spreads away towards the electrodes tips. It provokes electronic collisions with the air compounds and various chemical reactions including one or more air compounds occur, which generates highly reactive neutral species $OH^{\bullet}$ and $NO^{\bullet}$. These species are determined by their optical signals analyzed by emission spectroscopy in the 230–650 nm range and correspond to the $OH^{\bullet}\left(A^2\Sigma^+ - X^2\Pi, \Delta v = 0\right)$ and $NO^{\bullet}\left(A^2\Sigma^+ - X^2\Pi, \Delta v = -1\right)$ systems [4]. The electrical arc length increases towards the wider non equilibrium zone and breaks down before the cycle resumes.
Density measurements of the radicals show constant values along the whole non thermal plasma zone but the $OH^{\bullet}$ value is much higher than $NO^{\bullet}$, which confers oxidising properties to the plasma. Samples are exposed to the reactive radicals at a fixed distance d = 4.5 cm from the neck of the electrodes at a constant air flow rate Q = 16.25 $L.min^{-1}$.

2.2 Samples preparation

Pure iron and austenitic (304L and 316L) stainless steel discs (1.5 cm in diameter and 0.5 cm thick) are polished using various grinding papers (400, 800, 1200) and finished by a Mecaprex self-adhesive polishing disc using 3µm diamond paste. They are cleaned with acetone and nitrogen dried before being exposed at the electrodes limit to the non thermal zone of the glidarc.

The rectangular pure iron electrodes of total surface 2 cm^2 are mechanically polished, rapidly cleaned in 8% hydrogen chloride solution, degreased in trichloroethylene. The copper electrode receives the same polishing and cleaning procedure as the iron electrode but the copper/iron surface ratio is maintained at 3:1 throughout the investigation.

2.3 Analytical techniques

Stainless steel samples are investigated using electrochemical analysis (linear sweep voltammetry and Tafel plots) in a suitable solvent, while rectangular iron electrodes are studied in 3.5% sodium chloride solution.

- **Linear sweep voltammetry and Tafel**

The electrochemical investigation is carried out using a Potentiostat/Galvanostat Model 273 coupled to an IBM PC. The electrochemical cell is fitted with a platinum auxiliary and a SCE reference electrodes. The electrolyte is a 25 $mmol.L^{-1}$ NaOH solution ($pH = 11.7$). It is purged before each run for nearly 1h with nitrogen. The potential sweep is fixed to 1 $mV.s^{-1}$ for all runs. The characteristic current intensity (µA) is plotted straightaway vs. potential (mV).

The Tafel curves were recorded from –300 mV to +300 mV/SCE at a rate of 1 $mV.min^{-1}$ with (10^{-2} $M.L^{-1}$) nitric acid solutions as the electrolyte. The current intensity versus the potential variations define the corrosion potential E_{corr} of the sample. The intersection of the linear sections of the Tafel curves determines the corrosion potential E_{corr} and the corrosion current I_{corr} .

- **Immersion tests**

The influence of the rectangular iron electrodes treatment by the humid air plasma is investigated by looking at the electrodes mass loss and the galvanic current resulting. The iron electrodes are immersed in a cell filled with an aerated, non stirred 3.5% sodium chloride solution maintained at a constant temperature (30°C). They are kept inside the solution for increasing immersion periods (up to 6 hours) and different exposure times to the plasma. Liquid losses by evaporation are minimized by using a condenser. Gravimetric measurements were performed with an analytical weighing apparatus (A&D ER-180A) after every hour of immersion time. Corrosion rates are obtained from the curves of mass loss per unit area of the iron sample versus the immersion time for different plasma treatment times. The galvanic current is also monitored every hour using a digital, high internal resistance microammeter (PHYWE 0713200). It establishes on forming a galvanic cell, when the iron electrode is electrically coupled with a cleaned copper electrode disposed in the same electrolyte solution. The copper/iron surface ratio is maintained at 3:1. The purpose of using such a large ratio is to create a large anodic current density which in turn enhances the corrosion rate.

3. Results and discussions

3.1 Linear sweep voltammetry

The linear sweep voltammograms obtained during the scanning range [-1.0 to -1.4 V/SCE] show a reduction potential peak at –1.26 V/SCE in NaOH solution for the iron samples (Fig. 1). Plasma treated stainless steels samples show similar reduction peaks, which may suggest that presumably identical iron (III) hydroxide $Fe(OH)_3$ forms on the treated surfaces when dipped in NaOH solution. The slight difference between the reduction potential of the couple $Fe(OH)_3/Fe(II)$ (E = -1.168 V/SCE) [5] which is pH dependant is presumably due to the electrode overpotential. The intensity of the reduction peaks obtained increases with the plasma treatment times. As the current intensity depends only on the quantity of transformed matter and concerns only the same sample (constant geometry), we can put forward that the thickness of the oxide produced is a linear function of the treatment time.

On the other hand, RX diffraction shows a remarkable decrease in the ferric (α-Fe) phase lines intensity for short exposure times (≈ 30 min) for the 316L alloy, while long exposure times (≈ 8 hours) are needed to observe similar effects for the 304L alloy.

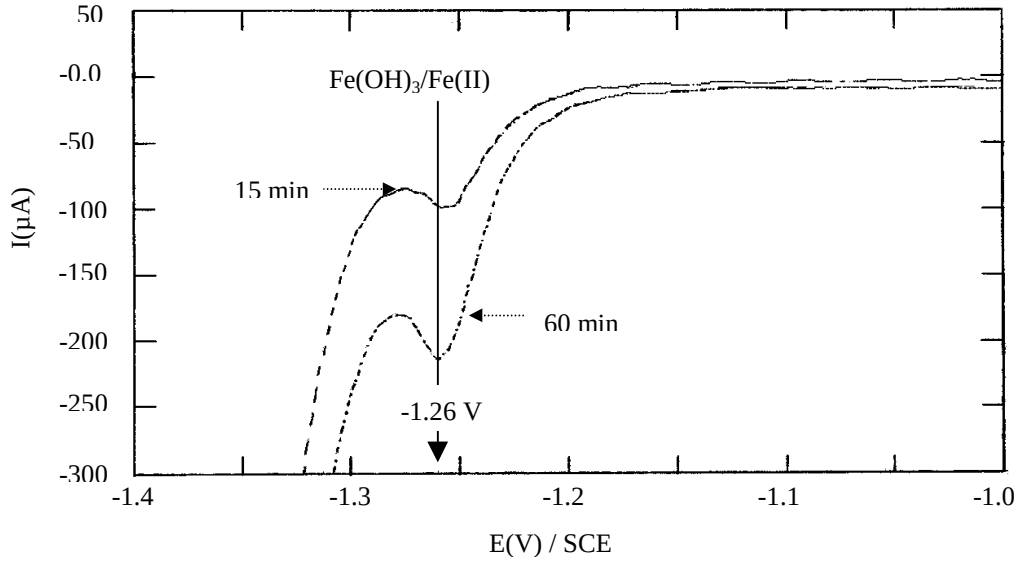

Fig. 1 : Voltammograms of plasma treated iron samples, in a NaOH solution of pH = 11.7, for exposure times 15 min and 60 min.

3.2. Tafel method

Non treated austenitic stainless steel samples show different corrosion potentials E_{corr} (-161.5 mV/SCE for the 304L and -186.6 mV/SCE for the 316L) in nitric acid solutions (10^{-2} $M.L^{-1}$). The high value of E_{corr} observed for 304L is probably due to the composition variation in chromium content: (≈18%) present in the 304L while (≈17%) in the 316L, or in nickel content: (≈ 9%) in the 304L while (≈ 12.5%) in the 316L or complete absence of molybdenum in 304L and 2% in 316L. Tafel measurements performed on plasma treated stainless steels show that the corrosion potential is influenced by the plasma interaction with the surface. The values of the corrosion potential E_{corr} of the treated austenitic stainless steel samples 304L and 316L increase with the increasing exposure time to the plasma. A sharp increase of the corrosion potential values is observed till 30 minutes followed by a rather plateau-like behavior close to a saturating value of –36 mV/SCE and –88 mV/SCE for the 304L and 316L alloys respectively. The values of the 304L stay higher than those of the 316L. Some values of the corrosion potentials are given in Table 1.

TABLE 1. Some corrosion potential values at critical exposure times.

E (mV/SCE)	$E_{t=0}$	$E_{t=30min}$	$E_{t=1h}$	$E_{t=2h}$	$(E_{t=2h}- E_{t=0})/ E_{t=0}$
304L	-161.5	-35.8	-34.1	-36.0	78 %
316L	-186.6	-102.8	-95.4	-87.8	53 %

The plasma treatment efficiency which could be expressed in terms of percent increase in corrosion potential is estimated at 78 % for 304L and 53 % for 316L whereas the corrosion current decrease is nearly 80% for the 304L and only 45 % for the 316L.

3.3. Gravimetric measurements

The iron corrosion rate is deduced from the linear mass loss *vs* immersion time curve. The untreated iron samples suffered the largest corrosion rate (17.84 $mg.cm^{-2}.hr^{-1}$) in 3.5% NaCl solutions while it diminishes with plasma exposure time. The corrosion rate of iron decreases as the exposure time to the plasma increases. The corrosion rate depends on whether the iron electrode is coupled or not to some more noble metal electrode, such as copper, in order to enhance corrosion effects. The mass loss decreases with the exposure time and depends also on whether only one face of the rectangular sample is treated or both. This is expressed by the percentage 50% and 100% surface area treated. Fig. 2 shows the mass loss of the iron electrode coupled to a copper electrode with one or both sides treated for 2 hours.

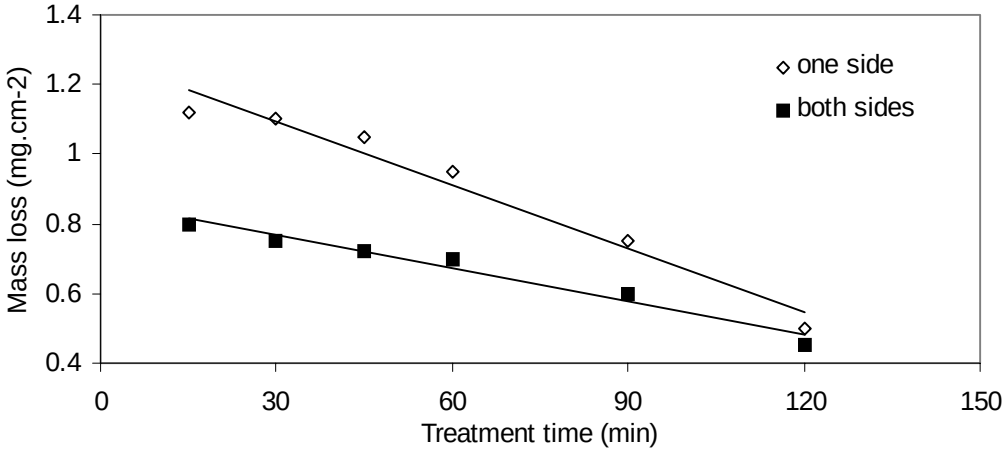

Fig. 2. Coupled iron mass loss versus immersion time : one side (50%), both sides (100%), treatment time 2 hours.

When both sides are treated, they are both oxidized to a higher potential and contribute less to the mass loss. This attains 5 and 4.5 $mg.cm^{-2}.h^{-1}$ for 2 hours treatment time for one and both sides respectively. The interaction of humid air plasma with the substrate surface results in a modification of the latter properties as the resulting hydroxide layer formed contributes to protection and then less corrosion is observed. When exposed to the humid air plasma, the iron samples start loosing less mass than untreated sample and the corrosion rate is deduced from the linear slope of Fig. 2. All the values of the corrosion rates for different plasma treatment times are shown in Fig. 3.

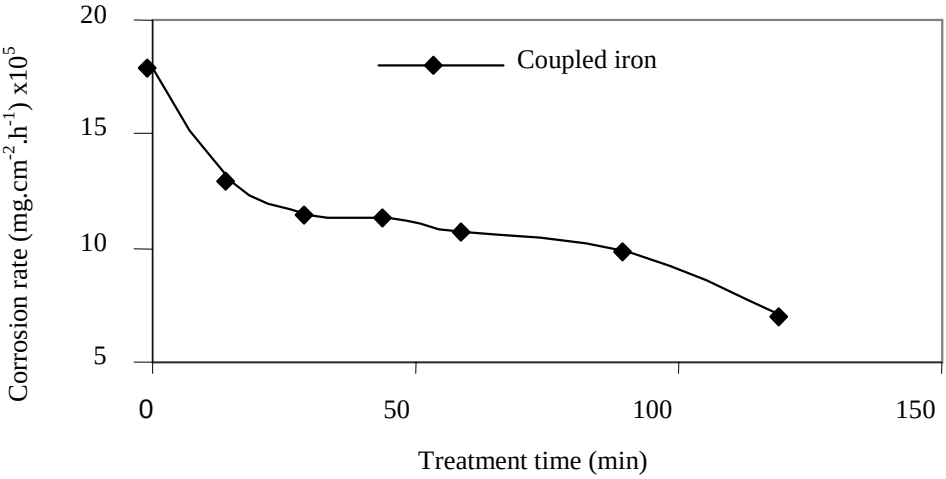

Fig. 3. Iron corrosion rate variation versus treatment time .

The rate decreases rather rapidly for the first 30 minutes and slightly less for the 60 minutes afterwards. It decreases even more for two hours treatment time, which may suggest that the all metal surface is oxidized and covered by an oxide film.

3.4. Galvanic current measurements

The galvanic current density between the iron sample and the copper electrode was measured in the 3.5% NaCl cell during the immersion tests. A slight decrease in the current is seen during the first thirty minutes exposure to the plasma as shown in Fig. 4.

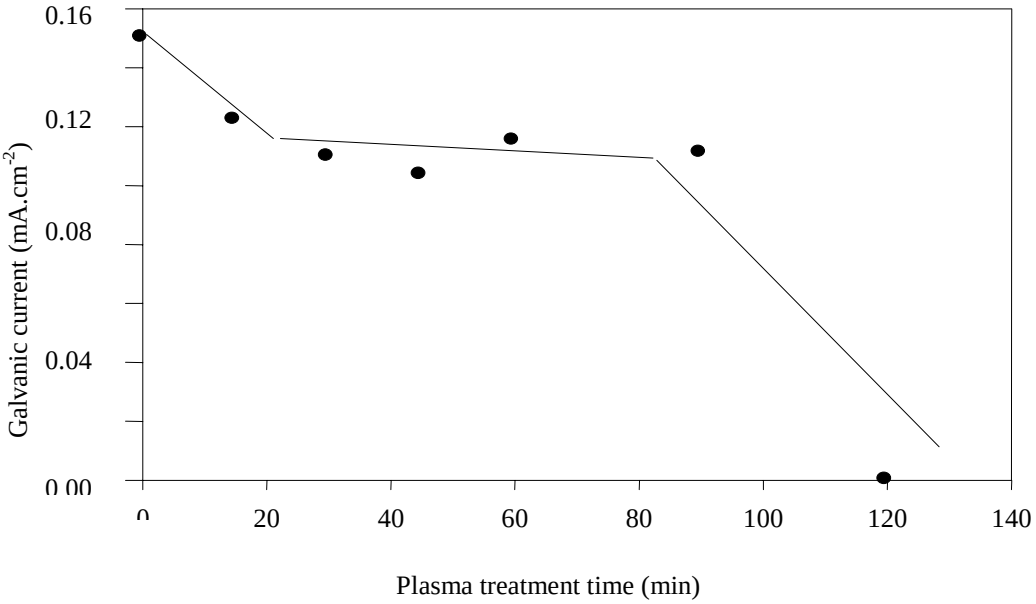

Fig. 4 : Galvanic current variation with the plasma treatment time of iron electrode.

The galvanic current decreases from 150 µA.cm^{-2} for the untreated specimen, to around 120 µA.cm^{-2} for the specimen treated for 60 minutes, and finally a sharp drop (to a few µA.cm^{-2}) around 120 min treatment time is observed. A constant current plateau-like behaviour follows during an hour of treatment time. It decreases sharply to an approximately zero value which means that the electronic drain from the treated iron electrode virtually ceases and can be attributed to the formation of a strengthened oxide film on the metal surface which firmly adheres to the substrate. The galvanic current is 100 times higher than the corrosion current I_{corr} (less than 1 µA.cm^{-2} for untreated samples) observed in the austenitic stainless steels specimens. These results can be explained by the fact that the processes involved during the interaction plasma-iron surface result in an effective protective and passivating layer of ferric oxide for long exposure times. Gravimetric and galvanic current measurements performed in the cell show a net decrease in the corrosion rate of the plasma-treated iron electrode.
The results show that the longer the iron surface is exposed to the gliding arc plasma in humid air, the lesser the mass is lost in the saline solution and the weaker is the galvanic current when iron is coupled to copper forming a galvanic cell.

4. Conclusion

The humid air plasma treatment produces surface modifications of easily corroded iron and highly corrosion resistant austenitic stainless steels 304L and 316L. The combined electrochemical methods with gravimetric and galvanic measurements show an increase in anticorrosive properties of the treated surfaces, which could be assigned to the formation of iron oxide thin film formed on the surface. The occurrence of iron (III) hydroxide is related with the basic nature of the electrolyte. As long as the iron hydroxide layer firmly adheres to the treated surface, it becomes a reliable protective layer, which could in the future widen its application field in more aggressive environments.

References

[1] B. Benstaali, J. M. LeBreton, B. G. Chéron, A. Addou and J. L. Brisset, Phys. Chem. News **5,** 87 (2002)
[2] B. Benstaali, A. Addou, J. L. Brisset, Mat. Chem.Phys. **78**, 214 (2002).
[3] H. Lesueur, A. Czernichowski, J. Chapelle, Brevet français N°2639172, (1988)
[4] B. Benstaali, P. Boubert, B. G. Cheron, A. Addou, J. L. Brisset, Plasma Chem. Plasma Proc., **22**, 553 (2002).
[5] J. Sarrazin, M. Verdaguer, L'oxydoréduction, Concepts et expériences, Ellipses, Paris (1991).

Plasma Processes for 2-D Photonic Crystal of C-S-Au Film

Yukinori Hirano, Chikao Yamasaki, Md. Abul Kashem, Masaki Matsushita and Shinzo Morita

Department of Electronics, Graduate School of Engineering, Nagoya University

Abstract

Photonic crystal introduced by E. Yablonovitch, S. John etc. in 1987 is expected to be a new and important optical element. For 2-D photonic crystal, C-S-Au (carbon-sulfur-gold) film formed by co-operation process of plasma CVD and sputtering was used as large refractive index (max 3.7) material which can be etched by oxygen plasma RIE (reactive ion etching). After the process of 2-D photonic crystal of C-S-Au film by an electron beam lithography, the 2-D photonic crystal surface was flattened by filling spin coated polymer, such as PMMA and then an organic EL was formed on the crystal surface to use as a light source for a photonic IC (integrated circuit).

1. Introduction

Photonic crystal was introduced by E. Yablonovitch and S. John etc. in 1987 [1,2]. The crystal has a periodic refractive index distribution in 1-D, 2-D, 3-D structure. By using the 2-D or 3-D photonic crystal, curved optical waveguide is expected to be fabricated in small size, where the optical waveguide can be formed by introducing defects linearly in the 2-D or 3-D photonic crystal. Additionally, 2-D photonic crystal acts as traps and emitters of photons depending on the size at the wavelength level if point defect is introduced near the waveguide in the 2-D photonic crystal [3].

For the photonic crystal, large refractive index material must be used. In this work, C-S-Au (carbon-sulfur-gold) film was developed, which is optically transparent in visible wavelength range and has process compatibility for oxygen plasma etching.

The C-S-Au film was fabricated by co-operative process of plasma CVD and sputtering with using CH_4, SF_6 and Ar mixture gas and Au plate discharge electrode.The optimized film was formed, which has refractive index of 3.5 and transmittance of 51 % at a wavelength of around 500 nm.

Using the C-S-Au film, 2-D photonic crystal was designed and fabricated by an electron beam lithography with using two-layer resist system of negative resist and evaporated Al film which works as an oxygen plasma etching stopper.

2. Experimental

C-S film and C-S-Au film were formed by plasma CVD reactor (ULVAC CPD-1108), which has a parallel plate electrode of 20 cm diameter and 1.5 cm gap distance. In order to eliminate impurity from the discharge electrode, the upper electrode was made of graphite plate and connected to RF power source. The reactive gas was introduced from the upper discharge electrode through numerous small holes. Substrates of Si wafer were set on the lower discharge electrode grounded and electrically connected to the reactor vessel of stainless steel.

The RF discharge frequency was 13.56 MHz. The deposition condition was kept to be constant at a pressure of 0.1 Torr, a discharge power of 100 W, and a discharge duration of 30 min. The flow rates of CH_4

and Ar were kept to be constant to 10 SCCM and SF_6 flow rate was varied from 2 to 25 SCCM. To form the C-S-Au film, an Au plate with area of 50×50 mm^2 was set on the upper electrode. The C-S-Au film was characterized by measuring the thickness and the refractive index using an ellipsometer, atomic compositions using ESCA measurements and transmittance using spectro-photometer.

2-D photonic crystal was fabricated as following. After Al film was evaporated on the C-S-Au film, which works as etching stopper, negative resist (SHIPLEY SAL601) was spin coated on the Al film by 4000 rpm and cured at 105 °C for 1 min. Then electron beam patterning apparatus (JEOL JBX-6000SG) was used for patterning of 200 nmϕ poles at three apex of triangle with 500 nm sides as a single cell shown in Fig. 1 at an acceleration voltage of 50 kV and a current of 100 pA. After development of delineated pattern on the resist, Al film was etched through the resist pattern by mixing liquid of HNO_3 5%, HF 3% and H_2O 92%, and the C-S-Au film with around 1 μm thickness was etched through the Al patterns by oxygen plasma with using RIE (SAMCO RIE-1C) at 13.56 MHz. The etching rate of this film was measured at oxygen flow rate of 10 SCCM and a pressure of 0.09 Torr as a function of discharge power.

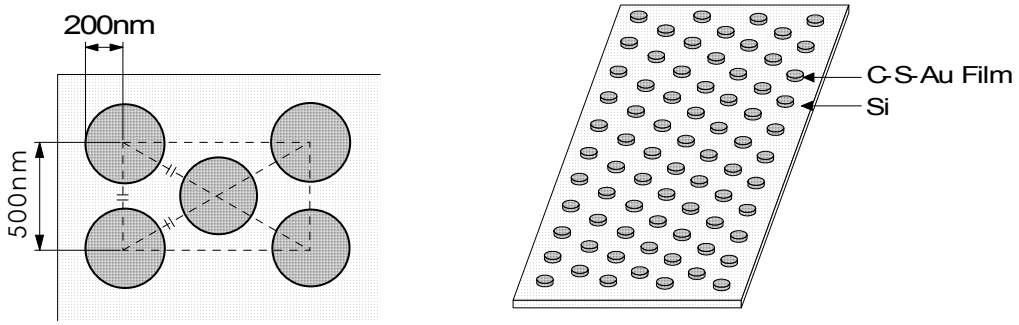

Fig. 1. The design of a photonic crystal

3. Results and Discussions

The C-S-Au film was formed in the co-operation process of plasma CVD and sputtering. The mechanism of Au mixing in the film was referred to the sputtering of Au plate on the discharge electrode, because the discharge electrode was self-biased to the negative potential during the plasma CVD[4].

As shown in Table 1, the sulfur content in the C-S and C-S-Au film was increased with increasing SF_6 flow rate. But Au content show the opposite tendency compared to the sulfur. Au atom density showed the maximum at 2 SCCM of SF_6 in this experiment and the value was 2.12 atomic%. The Au content was very small compared to other works reported [4-7]. They performed the deposition at one order lower pressure compared to our case. This may be a main reason why they obtained higher Au content in the film because Au sputtering will be enhanced at lower pressure. It is concluded that Au mixing in the film was realized under suppressed sputtering condition.

Table 1. Atomic composition and refractive index of the films (C-S & C-S-Au)

(CH_4: 10 SCCM, Ar: 10 SCCM, Pressure 0.1 Torr, Duration 30 min.)

Flow of SF_6 [SCCM]	C-S film				C-S-Au film			
	Atomic Composition [%]			Refractive Index	Atomic Composition [%]			Refractive Index
	C	S	Au		C	S	Au	
2	98.88	1.12	0	1.72	96.02	1.86	2.12	1.94
5	93.10	6.90	0	1.75	96.07	3.22	0.71	2.20
10	93.20	6.80	0	1.95	93.45	5.84	0.71	2.40
15	90.60	9.40	0	1.98	88.37	11.62	0.01	2.70
20	85.20	14.80	0	2.17	85.90	14.01	0.11	2.80
25	79.30	20.70	0	2.41	81.09	18.79	0.12	3.66

The refractive indexes for the C-S and C-S-Au films were measured by an ellipsometer at 628 nm. The refractive index of C-S film was increased simply from 1.7 to 2.4 with increasing the SF_6 flow rate from 2 to 25 SCCM. For the C-S-Au films, the refractive index was increased also simply from 2.0 to 3.7 for the same gas flow rate change of SF_6. For the photonic crystal, the large refractive index extends the photonic band gap wavelength range. To increase the refractive index, the increase of atomic content of Au and S in the film is effective according to the dielectric theory. However, the optical transmittance was decreased with increasing the atomic content of Au and S atom as shown in Fig.3. Whereas, Au and S atom content must be optimized on the optical transmittance and the refractive index. The optimization of C-Au-S film was realized by controlling the deposition condition, where the refractive index of 3.5 and the optical transmittance of 51% at 500nm were attained.

The etching rate of C-S-Au film and negative resist were measured in the RIE reactor as shown in Fig. 2. The etching rate was increased for the discharge power from 10 to 40 W. In this experiment, the etching rate of C-S-Au film at a discharge power of 25W was 263 nm/min and the negative resist showed the etching rate of 213 nm/min at the same plasma etching condition. So the etching time C-S-Au film was 4 min for the film thickness of about 1μm, and the negative resist was etched off at 70 sec for the resist thickness of about 250 nm. Therefore negative resist was etched completely before the C-S-Au film was processed, whereas we adopted the etching stopper of evaporated Al between C-S-Au film and negative resist.

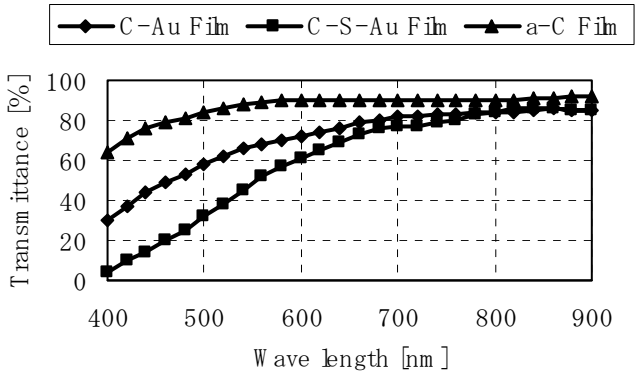

Fig. 2. Optical transmittance of C-Au, C-S-Au and a-C film as a function of wavelength.

(Pressure 0.09 Torr, Oxygen flow rate 10 SCCM)

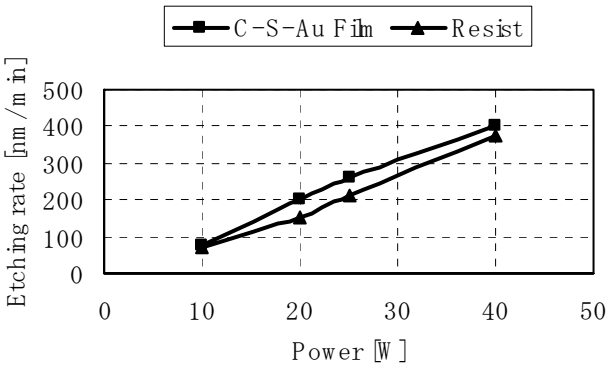

Fig. 3. Etching rate of C-S-Au film and resist

2-D photonic crystal fabricated by an electron beam lithography and oxgen plasma RIE are shown in Fig. 4 and 5. As shown in Fig. 4 after Al etching, 200 nmϕ poles at three apex of triangle with 500 nm sides as a single cell is observed. And Fig. 5 shows the photograph of the C-S-Au film after oxygen plasma etching, where the columns are arranged periodically. The etching duration was 5 min.

The photonic crystal structure of C-S-Au film was successfully processd even if chemically inert Au atom was included. In this process, carbon, sulfur and gold atom were expected to be etched forming volatile materials like as CO_2, SO_2 and $Au(CO)_x$ in oxygen plasma.

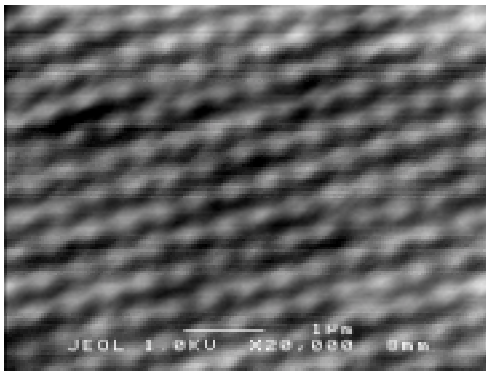

Fig. 4. The SEM photograph after Al etching

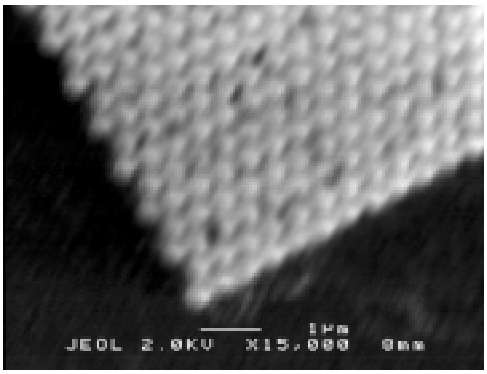

Fig. 5. The SEM photograph of the C-S-Au film etched by oxygen plasma

4. A light source for a photonic IC

To form organic EL on 2-D photonic crystal, the 2-D photonic crystal surface must be flattened by filling lower refractive index material. So PMMA is spin coated on the 2-D photonic crystal. After that transparent conducting layer will be formed on the crystal. Basic concept is shown in Fig. 6. Additionally how to take out the light from the sample is shown in Fig. 7.

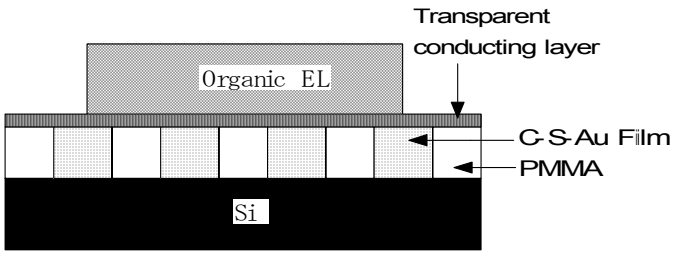

Fig. 6. Basic concept of connection

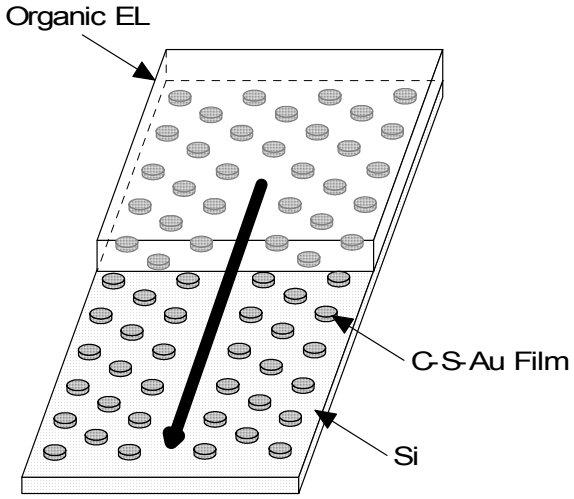

Fig. 7. Propagation of light from Organic EL

5. Conclusion

The C-S-Au film was synthesized by co-operation process of plasma CVD and sputtering with using methane, SF_6 and Ar mixture gas and gold plate on the discharge electrode. The refractive index was measured for the C-S and C-S-Au film. The refractive index increased as the sulfur content increased. By adding small amount of Au atom in a film, a refractive index was observed to increase largely. We found that the C-S-Au film was etched by oxygen plasma RIE. The etching rate was 263 nm/min. The 2-D photonic crystal of C-S-Au film and air space was successfully fabricated by using two layer resist system for oxygen plasma RIE. Finally the method of connection between the photonic crystal and organic EL was proposed.

Acknowledgement

A part of works was performed at Center for Cooperative Research in Advanced Science and Technology, Nagoya University.

References

[1] E. Yablonovitch - Phys. Rev. Lett. **58**, 2059 (1987).

[2] S. John - Phys. Rev. Lett. **58**, 2486 (1987).

[3] S. Noda, A. Chutinan and M. Imada - NATURE **407**, 608 (2000).

[4] E. Kay - Z. Phys. **D3**, 251 (1986).

[5] H. Biederman - Vacuum **37**, 367 (1987).

[6] H. Biederman, L. Martinu, D. Slavinska and I. Chudacek - Pure Appl. Chem. **60**, 607 (1988).

[7] L. Martinu - Solar Energy Materials **15**, 21 (1987).

Antimicrobial and Electrically Conductive Silver Coated Fabrics by Plasma-Based Techniques

Dominic Tessier,[1] Martin Filteau,[1]
CTT Group, 3000 Boullé, Saint-Hyacinthe (Quebec), Canada, J2S 1H9

Claude Côté,[2] Andranik Sarkissian[2]
[2] Plasmionique Inc, 1650 boul. Lionel-Boulet, Varennes (Quebec), Canada, J3X 1S2

Abstract
Silver-coated antimicrobial fabrics are often used for skin wound dressings (burn or chronic), after-surgery masks, and pressure-controlled garments. Other specific silver fabric applications, especially against biological hazards, include active antimicrobial sterile fabrics or dressing for prevention of infections. A knitted fabric consisting of a Nylon 6-Spandex (74:26) was plasma treated prior to the silver coating deposition carried out by magnetron sputtering. Silver sputtered fabric, after acid treatment, showed very high antimicrobial activity.

1. Introduction

Cold plasma technology offers a versatile, environmentally friendly and energy cost effective method for treatment and/or development of fabrics with applications in medical, hygiene, and protection markets. Such applications for protective clothing include fabrics exhibiting antimicrobial, electroconductivity or electrostatic dissipation properties, as presented in Figure 1. Silver-coated antimicrobial fabrics (or laminates) are often used for skin wound dressings (burn or chronic), after-surgery masks, and pressure-controlled garments. Other specific silver fabric applications, especially to counteract biological hazards, may include active antibacterial or antimicrobial sterile fabrics or dressing for prevention of microbial infections.

	Personal protection	***Transport and architecture***
Electrostatic risks or discharges	Anti-static garments for military, medical, electronic, police, fire workers and civils	Light weight composites (for substitution)
Microwave radiation	Uniforms for soldiers against microwave detection	Web, laminated or membrane structure for camouflage
Interactive device	Smart clothing incorporating alarm or sensor for soldiers and civils	
CB Threats	Anti-microbial or anti-bacterial suits	Fabrics for shelters, tents

Figure 1. Applications of silver coated fabrics in protective clothing.

Deposition of antimicrobial metals (like silver) on textile fabrics often requires complicated multi-step chemical process to provide useful antimicrobial properties to the fabric and sufficient durability. Furthermore, such chemical process may result in chemical pollution and variability of the quality of the silver coating, leading to reproducibility and quality control problems; therefore, new deposition technologies for antimicrobial silver fabrics need to be developped. Alternative technologies include physical vapor deposition, such as magnetron plasma sputtering which provide good adhesion and uniformity of the coating while allowing precise control of the nanostructural properties.

2. Deposition method

In this work, a knitted fabric consisting of a Nylon 6-Spandex (74:26) fabric was plasma treated prior to the silver coating deposition. A mixture of Argon and Nitrogen gas was used for plasma removal of silicone contaminants (used as lubricants in the knitting process) and plasma surface activation. Thus, plasma treatment resulted in a cleaner and more reactive fabric surface prior to deposition. The silver deposition was carried out with a magnetron sputtering system, as presented in Figure 2.

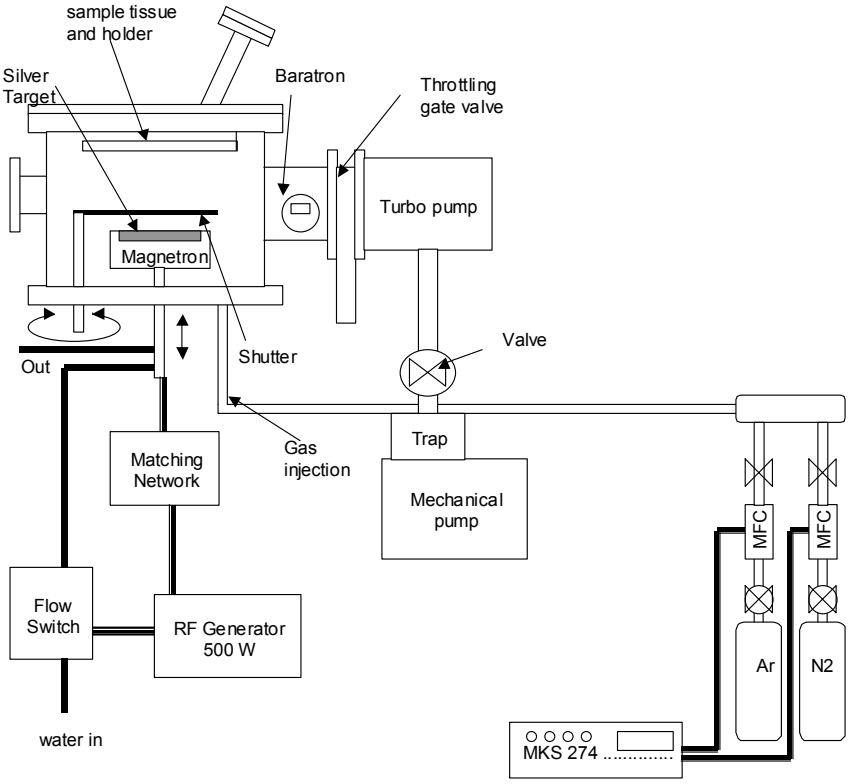

Figure 2. Magnetron sputtering system for silver deposition.

Following the silver deposition (by magnetron plasma sputtering), the knitted fabric was dipped in nitric acid solution using various acid concentrations and incubation time to improve further the antimicrobial properties of the coating.

3. Results

SEM photomicrographs of the virgin and silver treated fabrics are shown in Figure 3, where the virgin fabric is used as a control. While the virgin fabric appears to have a fiber surface relatively clean and smooth, the silver treated fabric depict a rough but uniform surface with visible silver particulates that form the coating.

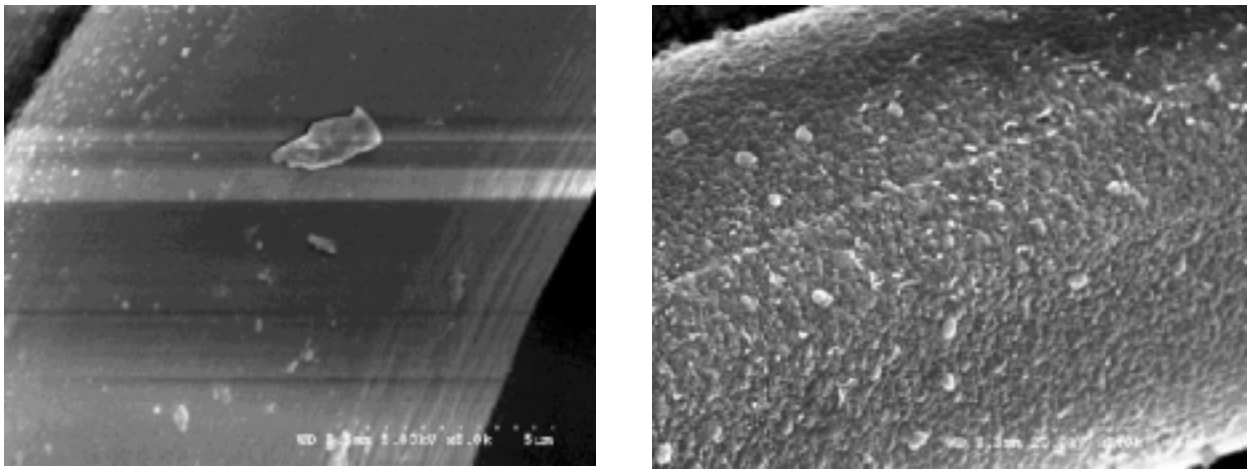

Figure 3. SEM photomicrographs at 8000 X magnification of the virgin (left) and acid-treated and sputtered silver fabric (right).

Antimicrobial testing (AATCC Test Method 147-1998) using gram positive and gram negative bacterias, S. Aureus and K. Pneumoniae respectively, revealed that the antimicrobial activity of the sputtered silver fabric was moderate. Results indicate that bacteria inhibition was observed only for bacteria in direct contact to – beneath- the fabric and no clear zone of inhibition beyond its edge was detected. However, a simple nitric acid treatment significantly improved the area of inhibition around the silver coated fabric's edge (inhibition zone, in mm). The initial experiments demonstrate that the acid-treated and sputtered silver fabric depicts a significantly higher inhibition zone, e. g. 2.0 to 6.0 mm and more, than the commercially available chemically-deposited silver fabric which possess a typical inhibition zone of 1.0 to 2.5 mm.

Other antimicrobial, metal-coated materials can be developped, using plasma-based techniques, such as woven fabrics, multilayer composites, laminates, non wovens and membranes.

4. Acknowledgements

Authors would like to thank Claude Côté and Andranik Sarkissian from Plasmionique Inc., Varennes (Quebec) for their technical contribution and also the Ministère de l'Éducation du Québec (MEQ) and Canadian Foundation for Innovation (CFI) for their financial support.

Modification of PET Surfaces with RF CF_4 Plasma

Chun-Hsiang Wen, Miao-Ju Chuang, Tzong-Shing Cheng , Ging-Ho Hsiue*
Materials Research Laboratories, Industrial Technology Research Institute, Hsinchu, Taiwan, 310, R.O.C.
**Department of Chemical Engineering, National Tsing Hua University Hsinchu, Taiwan, 300, ROC.*

E-mail: mjchuang@itri.org.tw

Abstract
Double side surface modifications of PET film by roll-to-roll RF plasma system are described. The changes of chemical structure and composition of PET film treated by low-pressure CF_4 plasma was characterized by X-ray photoelectron spectroscopy (XPS), atomic force microscopy (AFM) and water contact angle (CA). XPS and CA results revealed that the increasing of relative intensity of CF_2 and CF-CF_n species in the C (1s) spectrum could enhance the hydrophilic characteristic of the polymer surface. Nevertheless, the surface property would be hydrophobic when CF_3 species is detected from XPS C (1s) spectrum, even the relative intensities of CF_2 species increased to 23.45 %. Additionally, longer treating time and higher RF power (12 minutes, 600W), the surface wettability of both side of PET film appeared the division into two opposite extremes. One side is super-hydrophilic, 7.56^o, and another side is hydrophobic, 108.63^o. Furthermore, we will discuss the modified PET surface dynamics upon dipping into the potassium hydroxide water solution.

Introduction
Low temperature plasmas are ionized gases generated at pressures between 10^{-3} and 1 torr.
Plasma treatments have been widely used for the surface modifications of various materials; such as promoted the adhesion between the polymer and the metal or changed the wettability of materials. [1-5] Furthermore, modified the polymer surface can improve its permeability, biomedical compatibility or bacterial resistant without varying its bulk properties. [6-9] In this paper, we studied the effect of polyethylene terephthalate (PET) film exposed to RF CF_4 plasma. The changes of chemical structure and composition of PET film surface were characterized by X-ray photoelectron spectroscopy (XPS), atomic force microscopy (AFM) and water contact angle (CA). Moreover, we also studied the dynamics behavior of the plasma treated surface. The surface dynamics of PET denote concentration-dependent characteristic (e.g. upon dipping into the different concentrations of sodium hydroxide solution).

Experimental
The materials used in this study are the commercial polyethylene terephthalate (PET) film. (188μm, DuPont Teijin Films) Plasma treatments were carried out in a roll-to-roll system (from AST Products) with two internal electrodes, and fitted with a gas inlet, pressure gauge, vacuum system, and matching network for capacity coupling of a 13.56 MHz radio frequency (RF) source. The pumping system consists a combination of a roots pump and a one-stage rotary vane pump. We used CF_4 as operating gas. The operating pressure and power were fixed at 0.35torr and 300-600W respectively. The treating time were varied from 0.5min to 12min. The chemical natures of the plasma treated PET films were characterized by X-ray photoelectron spectroscopy (XPS). XPS analyses were carried out on VG MicroLab MKIII spectrometer at a base pressure lower than 10^{-9} torr with non-monochromatized Mg Kα (1253.6 eV) radiation.

The changes of surface roughness for before and after plasma-treated PET film were measured on atomic force microscope (AFM). An atomic force microscope "Auto Probe CP " designed by Park Scientific

Instrument was used in the contact mode for the surface roughness investigation. The measurement of water contact angles used the sessile drop method with an automatic apparatus and deionized water. For each sample, the contact angle here is the mean of five measurement points, which located uniformly on the films. The deionized (DI) water and KOH solutions are used to recognize the effect of hydroxyl ion concentration on the plasma-treated films. Each sample was dipped into the solution within 1.5 min at room temperature and then rinsed with deionized water for another 1.5 min.

Results and Discussion

The water contact angle of modified PET films at various RF power are shown in Figure 1, while a working pressure of 0.35 torr and the treatment time of 2 min. From figure 1 we can find that contact angle of both side of PET film decrease with the increasing of RF power. But the "front side" (surface-facing cathode) almost keep constant contact angle when the RF power is above 400 W. Further, the "back side" contact angle still decreased almost linearly with the RF power.

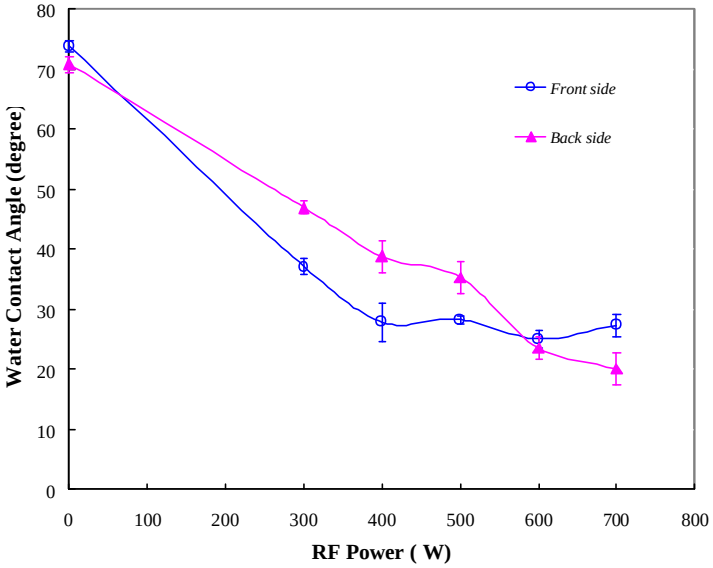

Figure 1. The water contact angle as a function of RF power (Plasma treated time: 2 min.; Working pressure: 0.35 Torr)

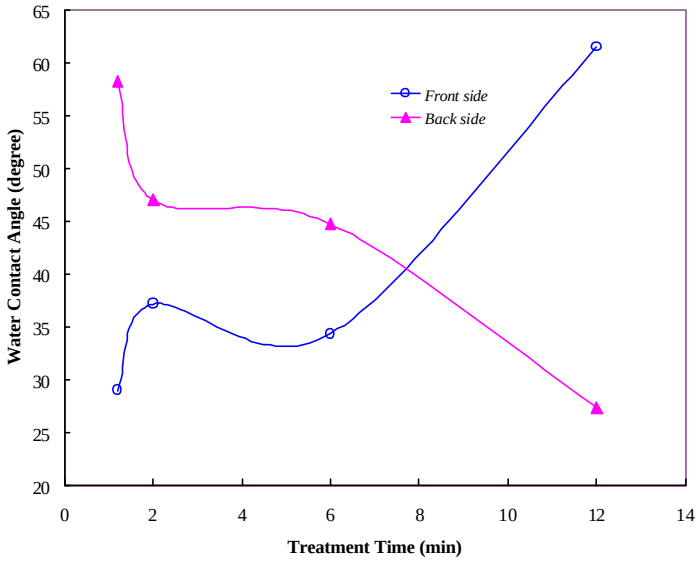

Figure 2. The water contact angle as a function of plasma treatment time. (RF power, 300 W; Working pressure: 0.35 Torr)

The contact angle as a function of treating time at RF power 600 W is given in figure 2. We can find that 1.2 min treatment time the difference of CA between "front side" and "back side" is above 30 ° and "front side" is more hydrophilic than "back side" and then both side CA will closed to 40 °. Above 6 min, the "back side " CA still keeps decreasing but the "front side" increasing with time. After 12 min treatment, "back side" decreased to 27.5° and front side increased drastically to 61.45 °. Furthermore, we can also find that "front side" contact angle nearly keep constant with increasing plasma treated time. And then it increases above 6 min treatment.

The C (1s) spectrum of untreated PET [Figure 3(a)] can be fitted to carbon environments corresponding to the carbon atoms in phenyl ring at 284.6 eV, the methylene carbon atoms singly bond to oxygen at 286.1 eV, the ester carbon bond at 288.6 eV, and the π-π* shake up peak at 290.6 eV. [10-11] The C (1s) spectra of plasma treatment on both sides of the PET surface are shown in Figure 3(b)(c). CF_4 plasma treated PET resulted in an enormous amount of fluorine incorporation at the surface. There is a dramatic change in the C (1s) XPS envelope, which can be attributed to formation of fluorinate carbon functionalities: $\underline{C}$-CF_n at 286.6 eV, $\underline{C}F$ at 287.8 eV, CF-CF_n at 289.3 eV, $\underline{C}F_2$ at 291.2 eV and $\underline{C}F_3$ at 293.6 eV. [10,12] Table 1 shows the relative peak areas of curve-fitted spectra for C (1s).

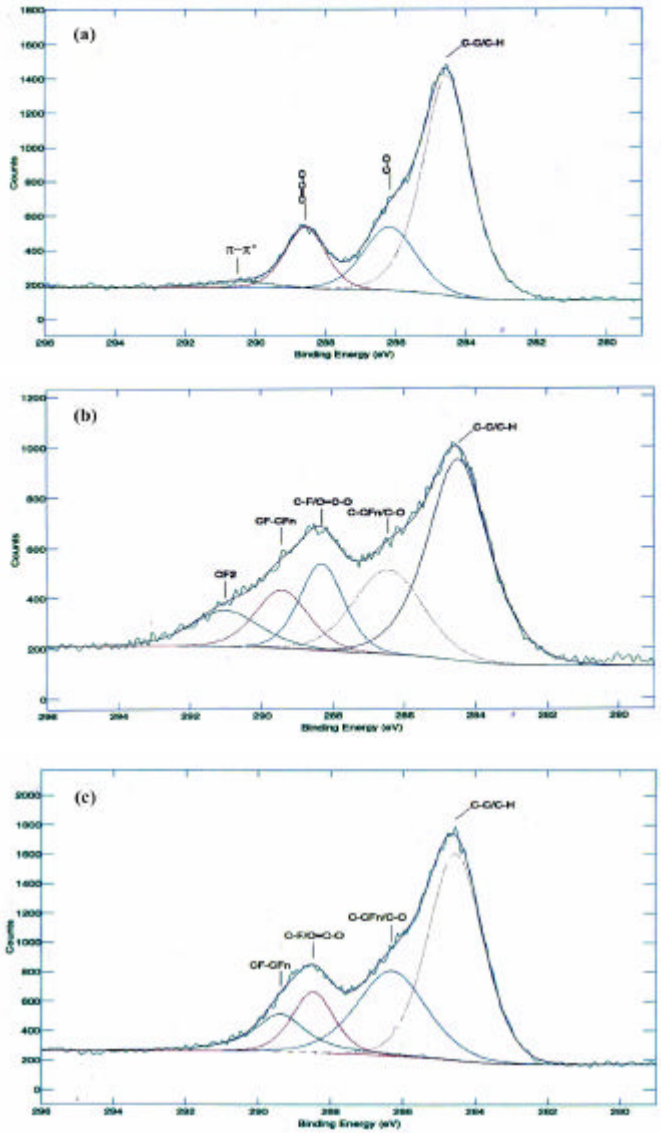

Figure 3. C (1s) XPS spectra of PET surface, (a) Untreated PET, and 600 W RF power plasma treated PET at treatment time 2 min onto the (b) Front side and (c) Back side.

Table 1: XPS data and Contact Angle data for the CF_4 plasma treatment PET

Treatment (rf power, Treatment time)		Untreated PET	300W, 2 min	300W, 2 min	600W, 2 min	600W, 2 min	600W, 12 min	600W, 12 min
			Front side	Back side	Front side	Back side	Front side	Back side
Water Contact Angle (degree)		73.8 ± 1.28	37.10 ± 1.04	46.96 ± 1.29	25.02 ± 1.83	23.54 ± 1.52	108.63 ±2.47	7.567 ±1.44
	F/C	0.00	0.00	0.00	0.58	0.11	1.44	1.05
% C (1s)	C-C/C-H	64.40	63.69	62.11	45.87	51.02	23.69	18.76
	C-O/C-CF_n	19.30	23.57	26.09	20.64	26.53	20.37	19.47
	O=C-O/CF	14.20	12.74	11.80	13.76	11.73	11.84	22.8
	CF -CF_n	-	-	-	11.00	10.72	10.9	15.2
	CF_2	-	-	-	8.72	-	23.45	23.75
	CF_3	-	-	-	-	-	9.71	-

According to the figure 3 and table 1, when PET is exposed to CF_4 plasma with lower RF power (e. g. 300W), the C (1s) spectrum does not change significantly. However, as the RF power increase, the relative peak areas of the curve-fitted C (1s) lines change and additional peak is observed at 600W. In a low-pressure plasma, electrons are accelerated by the oscillating field collide with CF_4 molecules, and cause bond cleavage and ionization. The predominant reactive components of CF_4 plasma are reported to be F atoms and relatively low concentrations of CF_n (n = 1,2,3) radicals. [6,13-14] With a low CF_n/F ratio, CF_4 does not polymerize in plasma, it can produces fluorination through a direct grafting of F atoms onto polymer surface. [15-18] Therefore, the fluorine atoms in the CF_4 plasma undergo hydrogen abstraction and substitution reaction at the PET surface yield CF, CF-CF_n, CF_2, and CF_3functionalties. The presence of CF_3 moieties signifies chain ends. [16] In comparing Figure1, 2 and Table 1, a clear distinction is observed in the shape of the corresponding to CF_2 and CF-CF_n which increasing the CF_2 and CF-CF_n can relatively enhance the hydrophilic characteristic of the polymer surface. Nevertheless, the surface property is hydrophobic when CF_3 species is detected from XPS C (1s) spectrum, even the relative intensities of CF_2 species increase to 23.45 %. On the other hand, as RF power increases to 600 W and treating time increase to 12 min., the wettability of both sides PET surface appeared the division into two opposing extremes. Water contact angle the faced cathode side of PET film is 108.63^o and opposite side is 7.56^o for example.

To understand the change of surface physical nature of PET after plasma treatment, AFM analysis was performed with both the treated and untreated PET. The results of comparative AFM surface roughness measurements for treated and untreated PET film are shown in Table 2. By increasing operating power and treating time will cause the surface smoothly. On the other hand, the roughness on front side is always smoother than the opposite side after plasma treatment.

The significant XPS data of CF_4 plasma treated PET after dipping into different KOH solution are summarized in Table 3. It is seen that the F/C ratio decreases with increasing OH^- concentration for both sides of PET surfaces. In addition to, the front side after dipping into the OH^- concentration of 0.1 M, it was found that the intensity of CF_3 and CF_2 in the C (1s) spectrum decreases from 9.71% to 0% and from 23.45% to 5.1 % respectively. However, CF_2 in the C (1s) spectrum decreases from 23.75 % to 0 % on the backside.

In a plasma-modified surface, the chain scission reaction can produce low molecular weigh compounds (e.g. oligomers). [19] By comparing table1 and 3, it was fount that the intensity of C-C/C-H peak in the C (1s) spectrum is increasing from 23.69% to 61.2% on front side and from 18.76% to 62.56 % on back side by dipping into the solution contains hydroxyl ion.

Table 2: Summary of AFM Measurents

Treatment		R_{p-v} (Å)	R_{rms} (Å)	R_{ave} (Å)
Untreated PET		570	40.9	25.6
300W, 2 min.	Front side	408	20.4	14.3
	Back side	319	34.5	24.4
600 W, 2 min.	Front side	206	16.8	12.4
	Back side	471	27.7	20.1
600 W, 12min.	Front side	110	3.49	2.42
	Back side	177	16.8	13

Table 3. Summary of XPS data for the CF_4 plasma treatment of PET before and after dipping into different concentration of OH^-

Treatment		*CF4 plasma teatmed PET		Dipping into water $[OH^-]$: 1×10^{-7} M		Dipping into KOH solution $[OH^-]$: 1×10^{-4} M		$[OH^-]$: 0.1 M	
		Front side	Back side	Front side	Back side	Front side	Back side	Front side	Back side
% C (1s)	F/C	1.438	1.05	0.823	0.084	0.786	0.0635	0.31	0.042
	C-C/C-H	23.69	18.76	49.7	36.9	55.97	62.56	61.2	62.5
	C-O/C-CF_n	20.37	19.47	17.25	24.72	17.81	19.55	18	23.44
	O=C-O/CF	11.84	22.8	7.31	20.3	6.1	9.78	7.7	8.85
	CF -CF_n	10.9	15.2	11.4	12.55	6.36	8.11	5	5.21
	CF_2	23.45	23.75	11.4	5.54	11.9	-	5.1	-
	CF_3	9.71	-	2.93	-	2.54	-	-	-

* Plasma treatment conditions: working pressure= 0.35 torr, RF power = 600 W, Web speed = 0.5 ft/min.

Conclusions

The interested result of CF_4 plasma treated PET in a roll-to-roll plasma system, water contact angle of one side is super-hydrophilic (7.56°) and another side is hydrophobic (108.63°), shows the wettability of both PET surfaces appeared two divisions of opposite extremes. The XPS analysis results are showing different functional group on both side PET surfaces. The CF_3 species in C (1s) spectrum can rather enhance the surface hydrophobic, no matter even the relative intensity of CF_2 increased to 23.45 %.

Furthermore, the surface dynamics of PET denote concentration-dependent characteristic that is dipping the sample into different $[OH^-]$ solutions exhibit the F/C ratio decreases upon the concentration of hydroxyl ion increase.

References

[1] Q. T. Le, J. J. Pireaux and J. J. Verbist, *Surf. Interface Anal.* 22, 224 (1994).

[2] M. K. Shi, A. Semani, L. Martinu, E. Sacher, M. R. Wertheimer and A. Yelon, *J. Adhesion Sci. Technol.* 8, 1129 (1994).

[3] N. Inagaki, S. Tasaka and K. Hibi, *J. Adhesion Sci. Technol.* 8, 395 (1994).

[4] M. D. Duca, C. L. Plosceanu and T. Pop, *Polym. Degrad. Stabil.*, 61, 65 (1998).

[5] X. Xie, T. R. Gengengach and H. J. Griesser, *J. Adhesion Sci. Technol.* 6, 1411 (1992).

[6] J. Hopkins and J. P. S. Badyal, *Langmuir*, 12, 3666 (1996).

[7] S. Marais, M. Métayer, M. Labbé, J. M. Valleto, S. Alexandre, J. M. Saiter, F. Poncin-Epaillard, *Surf. Coat. Technol.* 122, 247 (1999).

[8] J. Thome, A. HollAnder, W. Jaeger, I. Trick and C. Oehr, *Abstract, 8th international conference on plasma surface engineering, Garmisch-Partenkirchen, Germany*, p.74 (2002).

[9] F. Garbassi, M. Morra, and E. Occhiello, *Polymer surface*, Ch.12, John Wiley & Sons, New York (1994).

[10] J. F. Moulder, W. F. Stickle, P. E. Sobol and K. D. Bomben, In *Handbook of X-ray Photoelectron Spectroscopy*; Jill Chastain Ed.; Perkin-Elmer Corporation, Physical Electronics Devision, Minnesota (1992)

[11] L. J. Gerenser, *J. Adhesion Sci. Technol.* 7, 1019 (1993).

[12] T. R. Gengenbach and H. J. Griesser, *Surf. Interface. Anal.* 26, 498 (1998).

[13] M. Strobel, P. A. Thoms, and C. S. Lyons, *J. Polym. Sci.: Part A Polym. Chem.*, 25, 3343 (1987).

[14] J. Hopkins and J. P. S. Badyal, *J. Phys. Chem*., 99, 4261 (1995).

[15] J. W. Coburn and H. F. Winters, *J. Vac. Sci. Technol.*, 16, 391 (1979).

[16] J. Wang, D. Feng, H. Wanf, M. Rembold, and F. Thommen, *J. Appl. Polym. Sci*., 50, 585 (1993).

[17] M. Strobel, S. Corn, C. S. Lyons, and G. A. Korba, *J. Polym. Sci. Polym. Chem Ed*., 23, 1125 (1985).

[18] Y. Iriyama and H. Yasuda, *J. Polym. Sci. Part A Polym. Chem.*, 30, 1731 (1992).

[19] A. Holländer, J. E. Klemberg-Sapieha, and M. R. Wertheimer, *J. Polym. Sci*.: *Part A Polym. Chem.*, 34, 1511 (1996).

Temporal evolution of the electron energy distribution function in the nitrogen afterglow

V. Guerra[1], P. A. Sá[2] and J. Loureiro[1]

[1] *Centro de Física dos Plasmas, Instituto Superior Técnico, 1049-001 Lisboa, Portugal*
[2] *Dep. De Física, Faculdade de Engenharia, Universidade do Porto, 4200-465 Porto, Portugal*

Abstract
In this work we present a theoretical study of the time-relaxation of the electron energy distribution function (EEDF) in the nitrogen afterglow. An equilibrium between the vibrational distribution function (VDF) of ground-state molecules $N_2(X,v)$ and low energy electrons is quickly established and the EEDF reaches a quasi-stationary state. Collisions of highly excited $N_2(X,v>35)$ molecules with N atoms are in the origin of a maximum in the electron density occurring downstream from the discharge. Slow electrons remain in the post-discharge for very long times and can be involved in electron stepwise excitation processes.

1. Introduction

Different plasma-chemical applications, such as N atoms production for metallic nitriding and polymer surface treatments, require the control of the plasma parameters in the nitrogen flowing afterglow. The knowledge of the basic processes occurring in these medium is therefore of primary importance. One essential aspect is the knowledge of the temporal evolution of the electron energy distribution function (EEDF), since it provides information relative to the electron energy and density relaxations and gives the characterization of the electron energy loss and gain mechanisms.

One interesting phenomenon exhibited by the post-discharge in nitrogen is the no-monotonic variation of the electron density n_e. More precisely, it has been shown that the electron density has an initial stage of decay, but then an increase occurs during a relatively long period, after which the plasma finally dies out [1,2]. The same behavior is presented as well by some heavy-particles in the post-discharge, like the $N_2(A\ ^3\Sigma_u^+)$ and $N_2(B\ ^3\Pi_g)$ electronically excited states [2] and $N_2^+(B\ ^2\Sigma_u^+)$ ions [3].

In this work we present a theoretical investigation of the time-dependence of the EEDF in the nitrogen afterglow of a $\omega/2\pi$=433 MHz flowing discharge at p=3.3 Torr, in a tube with inner radius R=1.9 cm. For these conditions the electron density in the beginning of the afterglow is estimated to be $n_e(0)=3\times10^{10}$ cm^{-3}, which corresponds approximately to the critical value for surface-wave propagation. Our analyses includes a self-consistent description of the discharge which allows to determine the EEDF and the concentrations of the different heavy species at the end of the discharge. The EEDF thus obtained is then used as the initial distribution at the beginning of the afterglow, where we solve the time-dependent Boltzmann equation – including a term describing the continuous reduction of the space-charge field [4] and a term for creation of new electrons in associative/Penning reactions – coupled to a system of rate balance equations for the heavy particles.

2. Theoretical model

The theoretical model used to investigate the evolution of the EEDF in the afterglow is largely based on the one presented in [4]. The study starts with a self-consistent description of the discharge, since it is the discharge that establishes the initial conditions for the afterglow. The discharge model accounting for the electron and heavy-particle kinetics in N_2 was described in detail in [5,6]. Briefly, the homogeneous electron Boltzmann equation is solved together with a system of rate balance equations for the population of the most important neutral and ionic species in the discharge, $N_2(X\ ^1\Sigma_g^+, v)$, $N_2(A\ ^3\Sigma_u^+, B\ ^3\Pi_g, C\ ^3\Pi_u, a'\ ^1\Sigma_u^-, a\ ^1\Pi_g, w\ ^1\Delta_u, a''\ ^1\Sigma_g^+)$, $N(^4S, ^2D, ^2P)$, N_2^+ and N_4^+. The electric field sustaining the discharge is obtained from the requirement that under steady-state conditions the total ionization rate must compensate exactly for the electron losses by electron-ion recombination and ambipolar diffusion to the wall. Ionization takes place by electron impact both from the ground-state and electronically excited N_2 molecules, as well as via the Penning/associative reactions [5]

$$\begin{aligned} N_2(A) + N_2(a') &\rightarrow N_2 + N_2^+ + e \\ &\rightarrow N_4^+ + e \end{aligned} \qquad (1)$$

and

$$N_2(a') + N_2(a') \rightarrow N_2 + N_2^+ + e$$
$$\rightarrow N_4^+ + e\,. \qquad (2)$$

The input parameters for the discharge model are the field frequency $\omega/2\pi$, tube radius R, gas pressure p and the electron density at the end of the discharge $n_e(0)$.

Once the EEDF at the end of the discharge is obtained, its time-evolution in the afterglow is obtained by the solution of the time-dependent Boltzmann equation, as described in [4]. The EEDF is normalized in the afteglow to the electron density, *i.e.* $\int F(u,t)\, u^{1/2}\, du = n_e(t)$, where $F(u,t)$ denotes de EEDF and u the electron energy. The electron Boltzmann equation is solved assuming zero electric field in the afterglow, and taking into account inelastic collisions for the excitation of electronic and vibrational states of N_2, superelastic collisions with the vibrational levels $N_2(X,v)$, elastic collisions, excitation of the rotational levels, electron-electron collisions, as well as the terms for loss of electrons by electron-ion recombination and by diffusion to the wall, using an effective diffusion coefficient to describe the transition from the ambipolar to free diffusion regimes [4]. The Boltzmann equation further includes the terms for creation of electrons by reactions (1) and (2) [7], in order to describe the increase in n_e after the initial stage of decay, as observed in [1,2].

Inspection of equations (1) and (2) reveal the need to know the time-dependent concentrations $[N_2(A)](t)$ and $[N_2(a')](t)$ in the afterglow. To this purpose, we described the relaxation of the heavy-particles that have been previously considered in the discharge, using the discharge calculated populations as initial conditions for the afterglow, by solving the corresponding rate balance equations. The detailed analysis of the heavy-particle kinetics is beyond the scope of the present work and can be found in [8]. Nevertheless, it is worth to note that the metastable states $N_2(A\ ^3\Sigma_u^+)$ and $N_2(a'\ ^1\Sigma_u^-)$ are created in the afterglow in collisions of N_2 vibrationally excited molecules in very high v-levels with N atoms, through the reactions

$$N_2(X, v \geq 39) + N(^4S) \rightarrow N_2(A) + N(^2D) \qquad (3)$$

and

$$N_2(X, v \geq 38) + N(^4S) \rightarrow N_2(a') + N(^4S)\,. \qquad (4)$$

The high vibrational levels of the VDF, which do not present a significant concentration under discharge conditions, can be effectively populated in the afterglow as a consequence of the so-called V-V pumping up mechanism [9]. After a certain time, these high v-levels become thus available to participate in reactions in the post-discharge. Therefore, there is a local production of the states $N_2(A\ ^3\Sigma_u^+)$ and $N_2(a'\ ^1\Sigma_u^-)$ in the afterglow, which will be subsequently involved in the production of new electrons via reactions (1) and (2). We note that reactions (3) and (4) correspond to a vibration-electronic (V-E) energy transfer, a mechanism that has been recently identified to occur in CO [10].

The calculated time-dependent populations of $N_2(A\ ^3\Sigma_u^+)$ and $N_2(a'\ ^1\Sigma_u^-)$ metastables are then introduced into the time-dependent Boltzmann equation, which is finally solved to obtain the EEDF and all its integrals. According to the calculations from [8], the populations of the vibrational levels $N_2(X,v \leq 10)$ has been kept constant during the resolution of the Boltzmann equation, which for the present conditions is certainly a good approximation for times lower than $\sim 10^{-2}$ s.

3. Results and discussion

All the calculations have been carried out for the conditions described above ($\omega/2\pi$=433 MHz, p=3.3 Torr, R=1.9 cm and $n_e(0)=3\times10^{10}$ cm^{-3}), to which correspond an effective electric field $E_e/N = 4.6\times10^{-16}$ V.cm^2 and a characteristic vibrational temperature of ground-state molecules $T_V \approx 6200$ K.

Figure 1 shows the EEDF $f(u,t)$ during the afterglow, with t in seconds. f is normalized to unity, so that $F(u,t) = f(u,t)n_e(t)$. It can be seen that the EEDF is largely modified in the first instants of the afterglow ($t < 10^{-6}$ s), as a result of inelastic collisions. On the other hand, for longer times the EEDF reaches a quasi-stationary state, which is due to an equilibrium achieved between the EEDF and the VDF, where the superelastic collisions of electrons with vibrationally excited molecules compensate for the inelastic vibrational losses.

Figure 2 shows the EEDF in the first instants of the afterglow, $t=10^{-9}$, 10^{-8} and 10^{-7} s. The rapid depletion of the high-energy tail is a consequence of inelastic collisions of electrons with ground-state molecules. We recall that the first electronically excited state is the metastable $N_2(A\ ^3\Sigma_u^+)$, with an energy threshold of about 6.2 eV. One interesting feature exhibited on figure 2 is the formation of a dip around u = 4 eV for afterglow times in the range $10^{-8} - 10^{-7}$ s. This is a consequence of the particular shape of the electron cross sections for excitation of the vibrational levels $N_2(X,v)$, which present a strong maximum at $u \approx 2$ eV and vanish for $u \geq 4$

eV. The mechanisms leading to the formation of this dip can be understood by inspection of figure 3, where we plot the frequency $\nu(u)$ of gain (ν positive) or loss (ν negative) of electrons with a certain energy u. It can be seen that the behavior of electrons with energies $u \leq 4$ eV is essentially determined by the inelastic and superelastic electron-vibration (e-V) collisions. Therefore, there is a loss of electrons in the energy range $2 \leq u \leq 4$ eV (where the vibration cross section is important) and a gain in the $0 \leq u \leq 2$ eV one. However, electrons with energies $4 \leq u \leq 6$ eV do not lose significantly their energy, since all the inelastic cross sections are zero in this region, which explains the formation of the dip at 4 eV. The formation of a similar dip was observed experimentally in [11].

The dip on the EEDF at 4 eV does not get deeper and deeper with time simply because the frequency $\nu(u)$ is not constant in time. As the electrons lose and gain energy in inelastic and superelastic e-V collisions the EEDF and the VDF attain an equilibrium, so that $\nu(u)$ becomes vanishing small for $0 \leq u \leq 4$ eV. When this happens, the electron temperature T_e of the $0 \leq u \leq 4$ eV electrons simply corresponds to the vibration temperature T_V. The effect is illustrated on figure 4, where $\nu(u)$ is depicted for three instants in the afterglow. As it is readily seen, the equilibrium between the EEDF and the VDF is established at times of the order of $t \sim 10^{-7}$ s.

In order to check the correctness of the present calculations, figure 5 shows the comparison of the calculated EEDF and the measured one for $t = 6.5\times10^{-3}$ s. The measured EEDF was taken from [7,12]. The excellent agreement between the calculated and measured EEDFs confirms the attainment of an EEDF/VDF equilibrium and gives an indication of the correctness of our calculations under discharge conditions, in particular of the calculated VDF. As mention before, the slope of the EEDF for $0 \leq u \leq 4$ eV essentially reflects the value of T_V, which remains constant from the discharge [8].

Figure 6 shows the electron density calculated from the time-dependent Boltzmann equation, by including (full curves) and neglecting (dashed curves) the creation of new electrons in reactions (1) and (2), together with the interferometry measurements from [2] (open circles) and the probe measurements from [7] (black squares). The agreement between the calculations and both measurements is quite good when the production of secondary electrons is considered. In particular, the no-monotonic behavior for n_e, previously observed in [1,2] is obtained as a result of the formation of the metastables $N_2(A\ ^3\Sigma_u^+)$ and $N_2(a'\ ^1\Sigma_u^-)$ through reactions (3) and (4), followed by ionization via (1) and (2).

In the previous figure we have shown that electrons remain in the afterglow for very long times. Therefore, it is important to quantify the possible importance of electron processes in the afterglow. Figure 7 shows the calculated electron kinetic temperature as a function of the afterglow time, with the same notation as in figure 6. It can be confirmed that in spite of the very fast equilibrium between low energy electrons and the VDF, which settles for $t \sim 10^{-7}$ s, a quasi-stationary EEDF in the full range of energy only establishes itself at $t \sim 10^{-6}$ s (see also figure 1). When this happens we have $T_e \approx T_V \approx$ *constant*.

From figures 1, 6 and 7 we can infer that, although the processes of direct electron impact on ground-state molecules are not effective in the afterglow, electron stepwise processes with low energy threshold may take place. This idea is indeed confirmed by figure 8, where we depict the rate coefficients for electron stepwise excitation of states $N_2(B\ ^3\Pi_g)$ and $N_2(C\ ^3\Pi_u)$ from $N_2(A\ ^3\Sigma_u^+)$. Since both coefficients remain significant at least up to times $t \sim 10^{-2}$ s, these processes can play a non-negligible role in nitrogen post-discharges.

4. Conclusions

In this work we have presented a theoretical study of the temporal evolution of the EEDF in the nitrogen afterglow. The electron Boltzmann equation has been solved taking account the creation of new electrons in the Penning/associative reactions (1) and (2). The concentrations $[N_2(A)](t)$ and $[N_2(a')](t)$ were obtained using a detailed kinetic model describing the relaxation of the heavy-particles.

It has been shown that an equilibrium between the vibrational distribution function (VDF) of ground-state molecules $N_2(X, v)$ and low energy electrons is rapidly established, in times of the order of 10^{-7} s, since in this time interval the energy of the electrons is determined by the balance between the heating and cooling due to de-excitation and excitation electron-vibration (e-V) processes. In these early instants of the afterglow the EEDF presents a dip around 4 eV, as it was experimentally observed in [11]. The EEDF reaches a quasi-stationary state for $t \geq 10^{-6}$ s, although the electron density still continues to decrease beyond this instant.

The very high vibrational levels of the VDF, as high as $v \sim 35$, can be effectively populated in the afterglow as a consequence of the V-V pumping up mechanism. Therefore, these high vibrational levels become

available to participate in reactions in the post-discharge, such reactions (3) and (4) that form $N_2(A)$ and $N_2(a')$ metastables.

The mechanism described by reactions (1)–(4) explains the existence of a maximum in the electron density occurring downstream from the discharge at times of the order of 10^{-2} s, detected experimentally in [2] for the same conditions as in this study. The metastable states locally produced in reactions (3) and (4) subsequently ionize the gas via (1) and (2), which in turn leads to the observed increase in n_e.

As a consequence of the long characteristic times for ambipolar diffusion and for creation of new electrons, slow electrons remain for very long times in the post-discharge, as long as 10^{-3}–10^{-2} s, and can be involved in electron stepwise processes with energy thresholds typically smaller than ~2–3 eV.

References

[1] L. S. Bogdan, S. M. Levitskii and E. V. Martysh, *Tech. Phys.* **38** (1993) 532.

[2] N. Sadeghi, C. Foissac, and P. Supiot, *J. Phys. D:Appl. Phys.* **34** (2001) 1779.

[3] D. Blois, P. Supiot , M. Barj, A. Chapput, C. Foissac, O. Dessaux and P. Goudmand, *J. Phys. D:Appl. Phys.* **31** (1998) 2521.

[4] V. Guerra, P. A. Sá, and J. Loureiro, *Phys. Rev. E* **63** (2001) 046404–1.

[5] V. Guerra and J. Loureiro, *Plasma Sources Sci. Technol.* **6** (1997) 361.

[6] V. Guerra, E. Tatarova and C. M. Ferreira, *Vacuum* **69** (2003) 171.

[7] V. Guerra, F. M. Dias, J. Loureiro, P. A. Sá, P. Supiot, C. Dupret and Tsv. Popov, *IEEE Trans. Plasma Sci.* (2003) accepted for publication.

[8] V. Guerra, P. A. Sá and J. Loureiro, *Plasma Sources Sci. Technol.* **12** (2003) accepted for publication.

[9] C. E. Treanor, J. W. Rich, and R. G. Rehm, *J. Chem. Phys.* **48** (1968) 1798.

[10] E. Plönjes, P. Palm, J. W. Rich, I. Adamovich and W. Urban, *Chem. Phys.* **279** (2002) 43.

[11] T. Kimura, K. Ohe, and M. Nakamura, *J. Phys. Soc. Japan* **67** (1998) 3443.

[12] F. M. Dias and Tsv. Popov, *Vacuum* **69** (2003) 159.

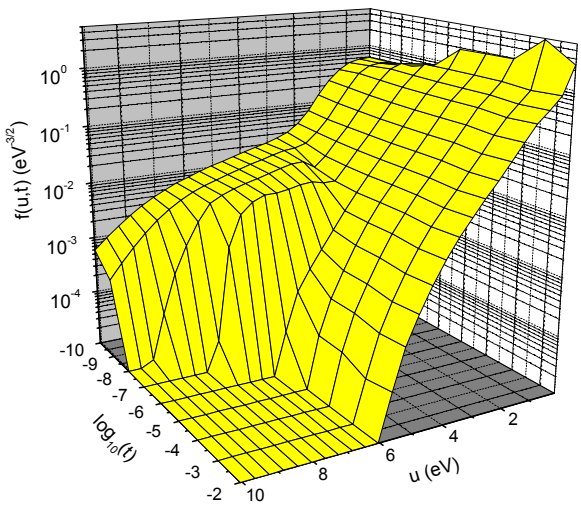

Fig.1: Calculated EEDF in the nitrogen afterglow. The afterglow time t is expressed in seconds.

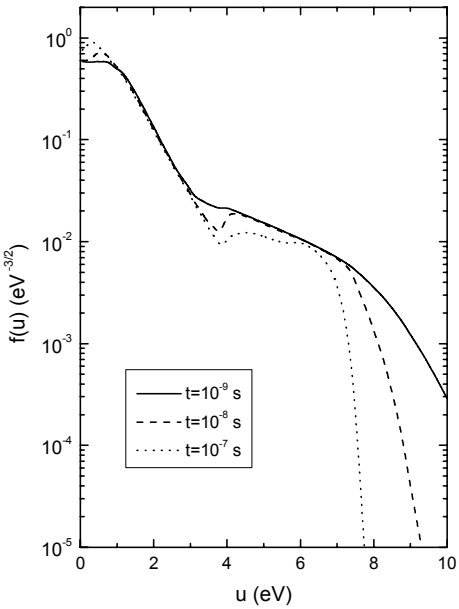

Fig. 2: Calculated EEDFs in the first instants of the afterglow (10^{-9}, 10^{-8} and 10^{-7} s).

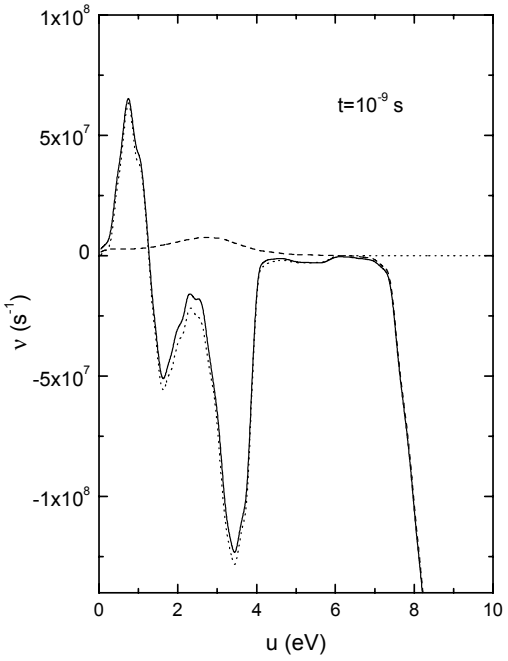

Fig.3: Frequency of gain or loss of electrons, for t = 10^{-9} s: due to vibrational excitation and de-excitation (dotted curve); due to the excitation of electronically excited states (dashed curve); total frequency (full curve).

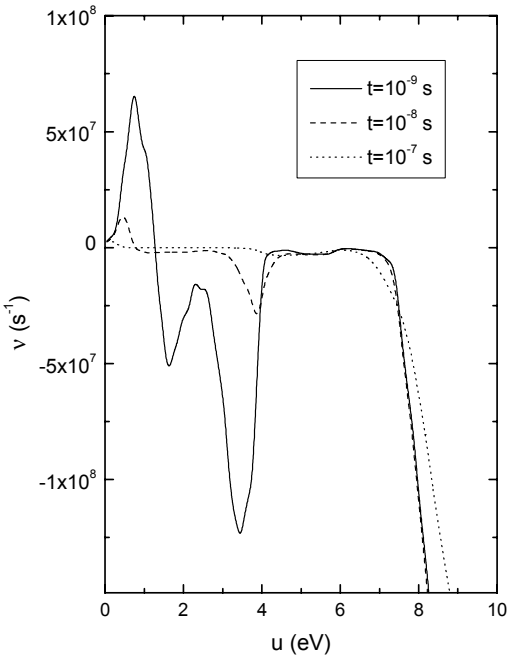

Fig. 4: Total frequency of gain or loss of electrons, for t = 10^{-9} s (full curve), t = 10^{-8} s (dashed curve) and t = 10^{-7} s (dotted curve).

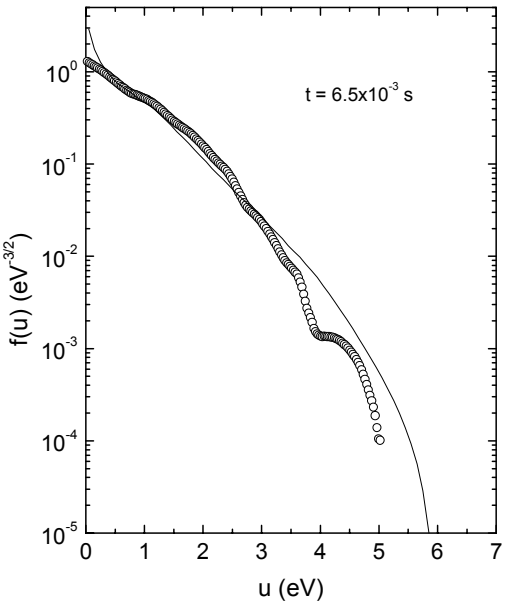

Fig.5: Measured (o) and calculated (full curve) EEDFs at $t = 6.5\times10^{-3}$ s.

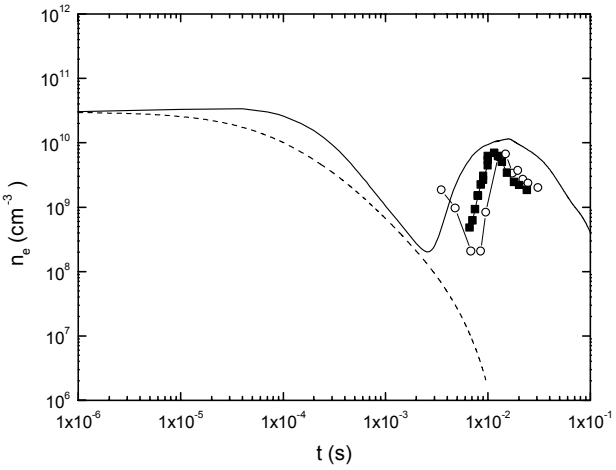

Fig. 6: Temporal evolution of the electron density, as calculated from the model including (full curves) and neglecting (dashed curves) reactions (1) and (2). The data points correspond to the measurements from [2] (■) and [7] (○).

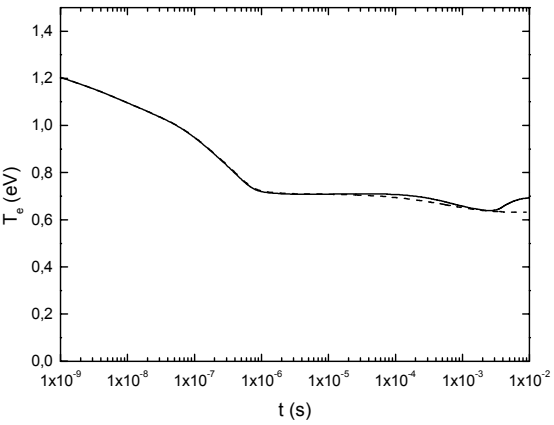

Fig.7: Temporal evolution of the electron kinetic temperature, for the same notation as in figure 6.

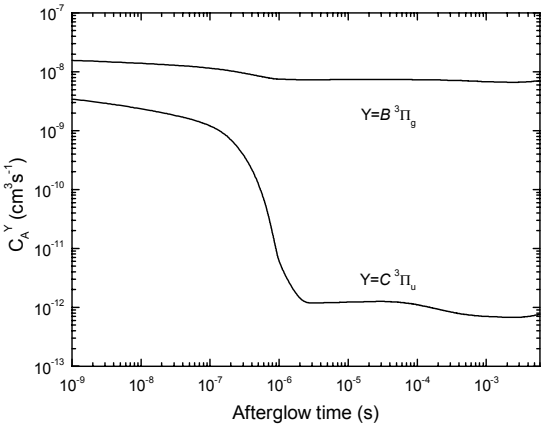

Fig. 8: Electron impact rate coefficient for excitation of states $N_2(B\ ^3\Pi_g)$ and $N_2(C\ ^3\Pi_u)$ from $N_2(A\ ^3\Sigma_u^+)$.

Spectroscopic Measurement of Electron Temperature and Density in Argon Plasmas Based on Collisional-Radiative Model

Katsuhiro Kano and Hiroshi Akatsuka

Research Laboratory for Nuclear Reactors, Tokyo Institute of Technology, Tokyo, Japan

Abstract

The paper describes a spectroscopic method for determining electron temperature T_e and density n_e in argon plasmas on the basis of Collisional-Radiative model. We measure T_e and n_e in a positive column of an argon DC arc discharge by the method developed. The results of T_e agree roughly with those by the probe. However, the limitation of our method for obtaining n_e is found. We also measure T_e and n_e of an expanding arc-jet, for which the results agree roughly with those by the probe.

1. Introduction

There exist several methods for obtaining electron temperature T_e and density n_e in plasmas from line spectra. Conventional methods, however, have the disadvantage that they are applicable only if atoms or ions are in particular equilibrium states, such as corona model or LTE. In the present study, we propose a method for determining T_e and n_e simultaneously based on Collisional-Radiative model (CR model). This method allows us to determine T_e and n_e from line spectra intensity where no specific equilibrium is assumed.

The principle of the method developed in the present study is to solve steady-state rate equations on the assumption that T_e and n_e are unknown quantities. Compared with the existing methods, the essential advantage of our method lies in its applicability not only to ionizing plasmas but also to recombining plasmas. This is because our method resolves T_e and n_e from equilibria of electronic transitions of excited levels by using a CR model directly, and accordingly it does not depend on whether the source of electronic transition is ground levels (ionizing plasmas) or ions (recombining plasmas). Historically, a number of atomic models for the measurement of plasma parameters have been proposed; there are, however, quite a few methods that actual measurement by the models has not been performed. For above reasons, it is worth developing a method for determining T_e and n_e in argon plasmas based on CR model, and examining its validity through measurement by the method.

The objective of the present article is to review our spectroscopic methods for determining T_e and n_e in two kinds of argon plasmas based on a CR model of argon. Another objective is checking its applicability by performing measurements. In this paper we review two simplified atomic models of the argon plasmas. One is a DC arc discharge plasma with its discharge pressure several Torr, used for fundamental research for isotope separation, as an example of an ionizing plasma [1]. The other is an arc-heated magnetically trapped expanding plasma jet, where an arc discharge plasma generated under atmospheric pressure is expanding into a lower pressure [2]. We check the suitability of the models and applicability of the method, by comparing T_e and n_e obtained by the spectroscopic method with those obtained by the probe measurement [3].

2. Spectroscopic Measurement of a DC Arc Discharge Argon Plasma in a Thin Capillary

2.1. Principle for a DC arc discharge argon plasma

An argon plasma treated in this section is a positive column of DC discharge, a typical ionizing plasma. Probe measurement showed that T_e and n_e ranged from 0.8 – 2.0 eV, and from 1.0×10^{14} – 1.0×10^{15} cm^{-3}, respectively, and the discharge pressure ranged from 4.0 to 31.6 Torr [4].

When the range of the electron temperature to be measured is relatively low, the electrons in the high-energy tail of electron energy distribution function (EEDF) play an important role in the electron-impact excitations and de-excitation [5]. In the present discharge plasma, we already found $V - I$ negative characteristics of the discharge, and hence, the discharge is considered to be an arc discharge [1]. This fact is considered to be equivalent to sufficient relaxation of electron gas. Therefore, we presume Maxwellian EEDF when calculating rate coefficients for electron-impact collisional transitions. The outline of the CR model is as follows: In this CR model, an Ar atom has 65 effective levels. Atom-atom inelastic collisions, diffusion losses of the metastables along with the electron-atom inelastic collisions, and radiative processes are taken into account. The model is available to study how the populations of the excited levels are effected

by the various set of parameters, such as electron temperature T_e, the gas temperature T_a, electron density n_e, the density of the ground state N_1, the plasma radius R, and optical escape factors [6]. In this section, the radius of the plasma is set to be 1.8 mm, and the gas temperature is derived from the empirical formulation [7]. The density of the ground state atom is approximated by the law of ideal gases.

The principle of our method for determining T_e and n_e based on the CR model is to solve steady-state rate equations describing electronic transitions on the assumption that T_e and n_e are unknown quantities. The rate equations comprising all the transitions become complicated. However, we can simplify them, since electronic transitions in atoms or ions of ionizing plasmas can be well described by specific transitions [8]. From now on, the levels of Ar atom is referred to by the level number defined in [6].

For input parameters $0.8 \le T_e$ [eV] ≤ 2.0, $10^{14} \le n_e$ [cm^{-3}] $\le 10^{15}$ and $5 \le P$ [Torr] ≤ 31.6, we have made a simplified model describing electronic transitions of the level from $i = 2$ (4s[3/2]$_2$) to $i = 30$ (7p') in such a way that the atomic model contains at least 80 % of all the electronic transition of the level defined in the CR model. As a result, we have found that T_e and n_e can be determined from the balance of electronic transition of the level $i = 20$ and $i = 7$, respectively. To determine T_e, the governing equations are as follows;

$$F_{25,20}N_{25} + F_{27,20}N_{27} = (C_{20,25} + C_{20,27})N_{20} \quad \text{for } 0.8 \le T_e \text{ [eV]} < 1.2, \tag{1}$$

$$C_{18,20}N_{18} = C_{20,23}N_{20} \quad \text{for } 1.2 \le T_e \text{ [eV]} < 2.0, \tag{2}$$

where N_i is the number density of the level i, C_{ji} and F_{ij} is the rate coefficient of electron impact excitation from the level j to i and its reversal de-excitation from the level i to j, respectively. It is found that the specific transitions in Eqs. (1)-(2) approximate the real electronic transition of the level $i = 20$. A solution to Eqs. (1) or (2) allows one to determine T_e. In both equations, unknown quantity is T_e only, if we have known population densities N_{18}, N_{20}, N_{25} and N_{27} by spectroscopic measurement prior to solving those equations.

Electron density is determined from the equilibrium of electronic transitions of the level $i = 7$. Equilibria of the electronic transition used for obtaining n_e require a radiative transition which is not negligible compared to electron-impact transitions. The equations to obtain n_e are expressed by the following simultaneous equations, which are population balance equations of the levels 7, 2, 3 and 5, respectively;

$$(C_{2,7}N_2 + C_{3,7}N_3 + C_{5,7}N_5 + F_{18,7}N_{18})n_e = (A_{7,2} + A_{7,3})N_7 + (C_{7,13} + C_{7,16} + C_{7,18} + C_{7,25})n_eN_7, \tag{3}$$

$$C_{1,2}N_1 + F_{3,2}N_3 = (C_{2,3} + C_{2,6} + C_{2,7} + C_{2,16})N_2, \tag{4}$$

$$C_{1,3}N_1 + F_{7,3}N_7 + C_{2,3}N_2 = (C_{3,6} + C_{3,7} + C_{3,16} + F_{3,2})N_3, \tag{5}$$

$$C_{1,5}N_1 = (C_{5,7} + C_{5,8} + C_{5,14} + F_{5,2} + F_{5,3} + F_{5,4})N_5, \tag{6}$$

where $A_{i,j}$ is the rate of radiation transition from the level i to j. In Eqs. (3)-(6), the unknown quantities are n_e, N_2, N_3 and N_5. The three latter number densities cannot be measured by the visible spectroscopic observation. To solve these equations, we need to know the densities N_7 and N_{18} by the spectroscopic examination in addition to N_1 and T_e. The details of the rate coefficients are given in [6]. More detailed discussion on the determination of Eqs. (1)-(6) is given in [1, 3]. We have found that the present model of atomic processes can predict T_e and n_e with accuracy of ± 39 % and ± 90 %, respectively [1, 3].

2.2 Experimental

Figure 1 shows the schematic view of our experimental arrangement [1]. The probe measurement was performed on the axial point at 1 cm out of the anode, as shown in Fig. 1. When performing spectroscopy, the probe was taken out from the discharge tube so that it did not disturb the plasma. In this study, spectroscopic measurement was also performed at the same point as the probe measurement. Because the spatial resolution of the optical system was 6 mm, the optical system measured emission from the entire plasma volume at the axial position.

An optical fiber was employed to guide the emission from the plasma to a visible monochromator system, whose wavelength resolution was 0.2 nm. The output from the monochromator was detected by a photo-multiplier tube, and signals from the photo-multiplier tube was recorded by a computer. The wavelength dependence of the sensitivity of the detection system is calibrated with a standard halogen lamp and a white standard reflectance plate as a diffuse reflector [9].

To obtain population densities N_7, N_{18}, N_{20}, N_{25} and N_{27} of Ar I, five wavelengths of 763.5 nm (4p[3/2]$_2$ → 4s[3/2]°$_2$), 436.4 nm (5p[1/2]$_1$ → 4s[3/2]°$_2$), 739.3 nm (6s[3/2]°$_1$ → 4p[3/2]$_2$), 360.7 nm (6p[1/2]$_0$ → 4s[3/2]°$_1$), and 699.2 nm (5d[1/2]°$_0$ → 4p'[1/2]$_1$) were chosen for their measurement,

respectively. In this study, radiative transitions are assumed to be perfectly optically thin except for the transitions to the ground level in the CR model. Vlček and Pelikán [10] have performed the CR calculation of atmospheric and sub-atmospheric pressure arc plasmas under this assumption, and they have presented that both population densities by the CR calculation and those obtained in their experiment agree well. The measured line intensities between excited states, however, might be affected by the opacity. We estimated optical escape factors with the aid of the CR calculation for the range of $0.8 < T_e$ [eV] < 2.0, $1.0 \times 10^{14} < n_e$ [cm^{-3}] $< 1.0 \times 10^{15}$ and $4.0 < P$ [Torr] < 31.6 [11]. The result is that the optical escape factor for the emission of 763.5 nm is larger than 0.97, and those for the rest of emissions are larger than 0.99. Consequently, it shows the appropriateness of our assumption that the spontaneous emissions between excited states are optically thin. However, we could not measure population densities N_{18} and N_{25} of our plasma due to absorption by cooling water that surrounded the discharge tube. For this reason, we estimated N_{18} by extrapolation and N_{25} by interpolation by excitation temperature determined from population densities N_{20} and N_{27}, respectively [12].

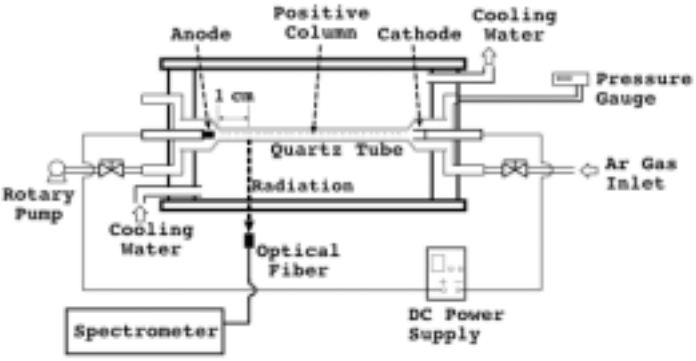

Figure 1. Schematic view of the experimental arrangement. The region where spectroscopic measurement was performed is also shown. Gas pressure of argon is measured with a pressure gauge connected to the cathode region.

2.3 Results and discussion

Figure 2(a) shows dependence of T_e on the gas pressure when the discharge current is 4 A. Closed plots and opened plots denote T_e obtained by the spectroscopic method developed in the present study and that with the probe, respectively. Error bars indicate ± 39 % deviation points from the plots. The uncertainty of spectroscopic measurement arising from photon counting error is negligible compared with the error originating from the simplification of the atomic process. For this reason, error bars owing to experimental uncertainty are not shown in Fig. 2(a).

The result of T_e obtained by the spectroscopy also indicates the usual linear decrease in the temperature as a function of the logarithm of the gas pressure throughout the current range 2 – 8 A. This characteristic agrees with those obtained by the probe measurement. Strictly speaking, T_e obtained by the spectroscopy should be lower than that with the probe, since the former result corresponds to volumetrically averaged T_e and the latter to the local value on the axis of the discharge tube. In Fig. 2(a), there are some plots that do not obey this principle. Our spectroscopic method based on the CR-model, however, can predict T_e within the ranges of the error bars. We have found from the experiment that our spectroscopic method has feasibility for determining T_e in the range from 0.8 to 2.0 eV. The range of the feasibility of our spectroscopic method for determining T_e is small (± 0.6 eV) and is not much larger than the measurement uncertainty. Although we have not surveyed whether it could be applied in other range of T_e, the method for obtaining T_e could be also useful in other systems.

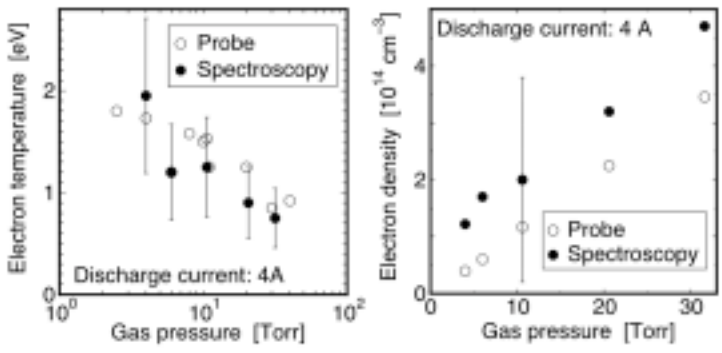

(a) (b)

Figure 2. Electron temperature (a) and density (b) obtained by the spectroscopic measurement based on the proposed model of atomic processes (closed circles) and that by probe (open circles) as a function of discharge pressure [Torr]: discharge current is 4 A. Gas pressure is measured with a pressure gauge at the cathode shown in Fig. 1.

Figure 2(b) shows the results of n_e obtained by the spectroscopic method and those measured with the probe as a function of gas pressure when the discharge current is 4 A. Closed plots and opened plots denote n_e obtained by the spectroscopic method and with the probe, respectively. Error bars indicate 90 % deviation points from the plots. Generally, electron density measured with the probe [4] increases linearly with the gas pressure. On the other hand, this feature does not hold for n_e determined by the spectroscopy

when n_e is higher than 2×10^{14} cm^{-3}, especially for other discharge current shown in Fig. 2(b).

Electron density determined by the spectroscopy should be also lower than that with the probe since the former result corresponds to volumetrically averaged n_e and the latter to the local one on the axis of the discharge tube. However, the result for n_e by spectroscopy does not posses the characteristic. This discrepancy is ascribable to the fact that the radiative transition of the level $i = 7$ does not have a large fraction enough to obtain n_e with high precision. Another reason of the discrepancy is that n_e is affected by the accuracy of determining T_e since n_e is calculated after T_e is determined.

We might be able to determine n_e more precisely from the balance of the electronic transition of the level $i = 3$ or 5 in this study, since lower levels contain a larger fraction of radiative transition. However, since spontaneous emission from the level $i = 3$ or 5 is in the range of ultraviolet, we could not measure them by our apparatus. Therefore, we had tried to measure n_e by using the balance of population of the level $i = 7$, and consequently, found the limitation of our spectroscopic method for the plasma whose electron density was higher than 2.0×10^{14} cm^{-3}. If n_e is lower than 10^{14} cm^{-3}, the fraction of the radiative transition of the level $i = 7$ is larger than 10 %, and this leads to a more precise measurement of n_e. Therefore, the method for determining n_e should be applied to Ar plasma whose electron density is lower than 1.0×10^{14} cm^{-3} [1, 3].

3. Spectroscopic Measurement of a Recombining Argon Plasma, an Expanding Argon Plasma Jet

3.1 Principle for an expanding argon plasma jet atomic model

We examined the argon arc jet plasma as the next objective to be observed, by the probe measurement prior to the spectroscopic observation, and found that T_e ranges from 0.3 eV to 0.9 eV and n_e from 10^{12} cm^{-3} to 10^{14} cm^{-3}, with the background pressure about $P_c = 22.6$ Pa. Next, we performed CR calculations on the assumption that the gas temperature $T_a = 1000$ K [2], $R = 3$ cm and the ion density $n_i = n_e$. The density of the ground state, N_1, is estimated from the law of ideal gases. The EEDF of the plasma should be Maxwellian, at least when it is generated by arc discharge. In the downstream expansion region, it is considered to be no electric field to maintain the discharge. Therefore, we can consider the EEDF of the recombining argon plasma should be Maxwellian.

The principle of our method for determining T_e and n_e based on the CR model is, again in this section, to solve the steady-state rate equations describing electronic transition on the assumption that T_e and n_e are unknown quantities. We found that T_e and n_e are determined from balance of the level $i = 18$ (5p) and the level $i = 7$ (4p$[3/2]_{1,2}$, $[5/2]_{2,3}$) respectively, within the ranges considered. The approximated balance equation of the transitions of the level $i = 18$ is given by

$$C_{7,18}N_7 + F_{20,18}N_{20} + F_{25,18}N_{25} = (F_{18,7} + C_{18,20} + C_{18,25})N_{18}. \quad (7)$$

It is found that the specific transitions in Eq. (7) approximate more than 80 % of the actual electronic transitions of the level. The population densities N_7, N_{18}, N_{20} and N_{25} in Eq. (7) can be obtained by the spectroscopic measurement in the visible range of light. In Eq. (7), the unknown quantity is solely T_e, if we know population densities N_7, N_{18}, N_{20} and N_{25} by the spectroscopic measurement.

On the other hand, the electron density is determined as solutions to the following simultaneous equations, namely, four population balance equations of the levels 7, 2, 3 and 13, and three LTE-like relationships of the sufficiently highly-excited level pairs (16, 18), (20, 23) and (23, 29) [8]:

$$\begin{aligned}
&A_{16,7}N_{16} + n_e(F_{13,7}N_{13} + F_{16,7}N_{16} + F_{18,7}N_{18} + F_{25,7}N_{25} + C_{2,7}N_2 + C_{3,7}N_3) \\
&\qquad = \{(A_{7,2} + A_{7,3}) + n_e(F_{7,2} + C_{7,13} + C_{7,16} + C_{7,18} + C_{7,25})\}N_7, && (8)\\
&n_eC_{1,2}N_1 + A_{7,2}N_7 + n_eF_{3,2}N_3 = n_e(C_{2,3} + C_{2,7})N_2, && (9)\\
&n_eC_{2,3}N_2 + (n_eF_{7,3} + A_{7,3})N_7 = \{n_e(F_{3,2} + C_{3,5} + C_{3,7}) + A_{3,1}\}N_3, && (10)\\
&A_{23,13}N_{23} + A_{29,13}N_{29} + n_e(C_{7,13}N_7 + F_{16,13}N_{16} + F_{18,13}N_{18} + F_{23,13}N_{23}) \\
&\qquad = \{A_{13,7} + n_e(F_{13,7} + C_{13,16} + C_{13,18} + C_{13,23})\}N_{13}, && (11)\\
&C_{16,18}N_{16} = F_{18,16}N_{18}, && (12)\\
&C_{20,23}N_{20} = F_{23,20}N_{23}, && (13)\\
&C_{23,29}N_{23} = F_{29,23}N_{29}, && (14)
\end{aligned}$$

Unknowns of Eqs. (8)-(14) are n_e, N_2, N_3, N_{13}, N_{16}, N_{23} and N_{29}. In the level 7, since there exists a large fraction of radiative transition, the electron density can be determined with good precision, which quite

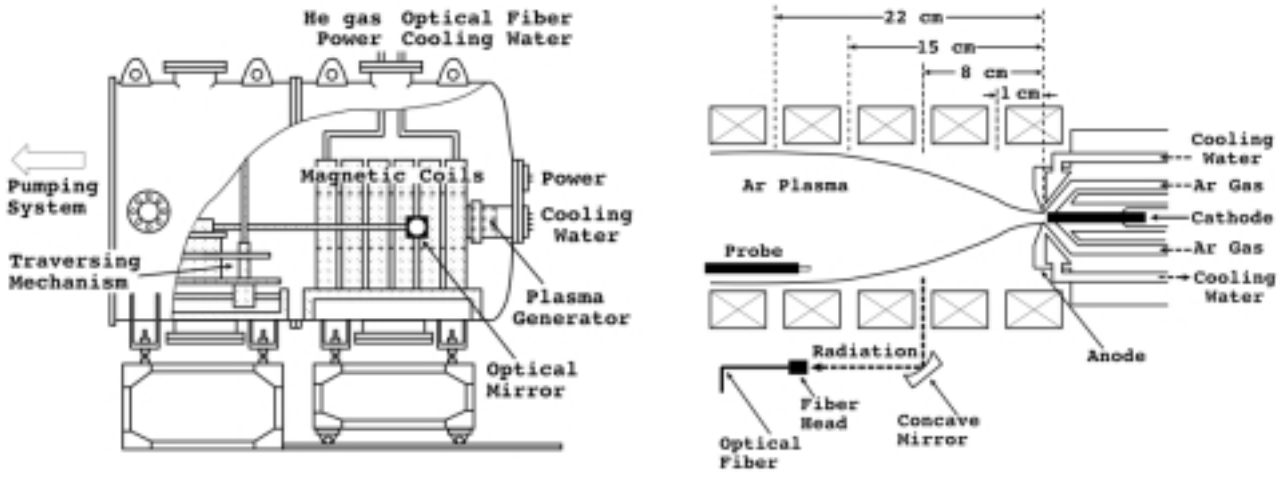

(a) (b)

Figure 3. Cross-sectional view of (a) a plasma jet apparatus, and (b) electrodes, magnetic coils, and argon plasma.

differs from the previous section. It is confirmed that the specific transitions in Eq. (8) approximate more than 80 % of the actual electronic transitions of the level $i = 7$. To solve these equations, we need to know the densities N_7, N_{18}, N_{20} and N_{25} by the spectroscopic examination in addition to T_e. The details of the rate coefficients are given in [6]. More detailed discussion on the determination of Eqs. (8)-(14) is given in [2,3].

3.2 Experimental

Figure 3(a) shows the schematic view of the plasma jet apparatus [2]. The apparatus consists of a plasma generator, magnetic coils, traversing mechanism for an optical fiber terminal assembly. These components are placed in a rarefied gas chamber of 1.2 m in diameter and 2 m in length. The chamber is evacuated with a 12-inch mechanical booster pump, and the ultimate pressure in it becomes as low as 0.74 Pa. Figure 3(b) shows the cross-sectional view of the electrodes for generating the plasma and the expanding plasma from the nozzle, which is opened on the anode. In the wind tunnel, there exist six coils of 80 mm in inner diameter for confining the plasma. The strength of the magnetic field is 0.15 T. The discharge conditions are the following: arc voltage V_{arc} = 18 V, discharge current I_{arc} = 120 A, pressure in the wind tunnel P_c = 22.6 Pa, gas flow rate is 650 SCCM.

To obtain population densities N_7, N_{18}, N_{20} and N_{25}, four wavelengths, 763.5 nm ($4p[3/2]_2 \rightarrow 4s[3/2]^\circ_2$), 430.0 nm ($5p[5/2]_2 \rightarrow 4s[3/2]^\circ_2$), 693.8 nm ($4d[1/2]_0 \rightarrow 4p[1/2]_1$) and 360.7 nm ($6p[1/2]_0 \rightarrow 4s[3/2]^\circ_1$) were chosen, respectively. We could not, however, measure population density N_{25} of our plasma since the intensity of 360.7 nm emission was very weak. For this reason, we estimated N_{25} by interpolation by excitation temperature determined from densities N_{20} and N_{27}, respectively [12]. We measured N_{27} from the line intensity of 545.2 nm ($7s[3/2]^\circ_2 \rightarrow 4p[1/2]_1$).

3.3 Results and discussion

Figure 4(a) shows the radial distributions of T_e measured by the present spectroscopic method at the longitudinal position 15 cm. Abel inversion has been carried out to deduce spatial distribution of population densities, N_7, N_{18}, N_{20} and N_{27} from the averaged value along the line of sight. It is found that T_e becomes lower as axial distance r and longitudinal distance z increase. This characteristic is similar to the results by the probe measurement. The discrepancy between the result by the spectroscopic measurement and that by the probe measurement is smaller than ± 0.1 eV. Since the range of T_e considered in the

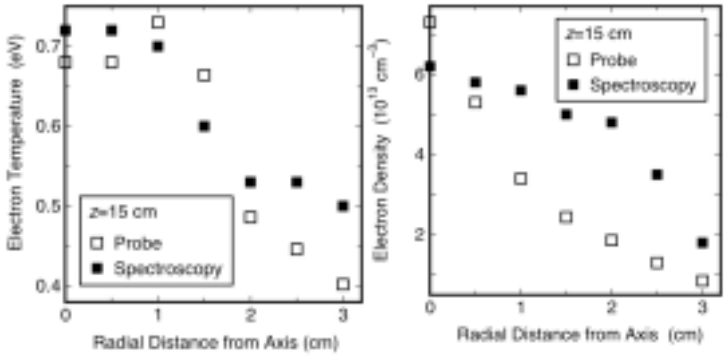

(a) (b)

Figure 4. Radial profiles of (a) electron temperature T_e and electron density n_e measured by the present spectroscopic method (filled squares) and by the probe method (open squares) wherethe longitudinal distance from the nozzle z is 15 cm.

present study is 0.3 eV through 0.9 eV, we should expand the availability of the range to apply the spectroscopic method to other plasmas. However, it is also found that we can determine T_e with good accuracy by the spectroscopic measurement based on the CR model, and that the present atomic model is an appropriate for obtaining T_e.

Figure 4(b) shows the radial distribution of n_e measured by the present spectroscopic method where z is 15 cm. Electron densities obtained by the CR model is about twice as higher as those by the probe method when $r > 1$ cm at $z = 8$ and 15 cm. The spectroscopic method for determining n_e cannot avoid the dependence on the result for T_e. The electron density obtained by the present spectroscopic method, however, agrees roughly with that by the probe. The spectroscopic method, therefore, is also feasible for knowing n_e of the wide range from 10^{12} cm^{-3} to 10^{14} cm^{-3} [2, 3].

4. Concluding Remarks

In the present study, we proposed a spectroscopic method for determining T_e and n_e from radiation intensities based on CR model. First, we measured these parameters of an ionizing plasma and compared them with the result obtained with a Langmuir probe. The experimental results show that the method developed has feasibility for determining T_e in the range from 0.8 eV to 2.0 eV. As for the measurement of n_e in the plasma, the limitation of the method was also found, since radiative transition became negligible compared to electron-impact ones due to its high electron density [1]. Second, we measured these parameters of a recombining argon plasma and compared them with the result obtained with a Langmuir probe. The experimental results show that the method developed has feasibility for determining T_e in the range from 0.3 eV to 0.9 eV, and n_e in the wide range from 10^{12} cm^{-3} to 10^{14} cm^{-3} [2].

We can apply the present method to many different kinds of argon discharge plasmas in principle. If we know approximate range of T_e and n_e of the argon plasmas by probe analysis, we can extract dominant processes to determine excited states populations by the CR model. After that, we can obtain simultaneous equations to describe population balances of the states, where T_e and n_e are unknowns. In order to solve the equations, number densities of excited states become necessary, and consequently, we should measure the number density by the spectroscopic examination. Sometimes, the simultaneous equations contain the number densities of excites states which cannot be measured spectroscopically. Then, all we have to do is to increase the number of the simultaneous equations that contain the densities of the unobservable levels, till the number of simultaneous equations becomes the same with that of the unknowns.

Fortunately, the EEDF of the argon plasmas examined in the present review is almost Maxwellian, and consequently, the rate coefficients are easily calculated as functions of the electron temperature. If the EEDF depends on the discharge conditions, it seems difficult to apply the present spectroscopic method. However, when the EEDF can be approximated by some function with a few unknown parameters, such as by Druyvesteynian or bi-Maxwellian, we can obtain the unknown parameters, since at this time again, the rate coefficients become functions of the unknown parameters instead of the electron temperature [3].

Acknowledgments

We thank Professor J. Vlček of University of West Bohemia for his excellent argon CR model code.

References

[1] K. Kano, M. Suzuki, H. Akatsuka – Plasma Sources Sci. Technol. **9**, 314 (2000).
[2] K. Kano, M. Suzuki, H. Akatsuka – Contrib. Plasma Phys. **41**, 91 (2001).
[3] K. Kano, H. Akatsuka – *Ch.3, Advances in Plasma Physics Research Vol. 3*, Ed. F. Gerard, Nova Science Publishers, Inc., New York (2002).
[4] H. Akatsuka, N. Ohtsuki, A.N. Ezoubtchenko, M. Suzuki – Contrib. Plasma Phys. **39**, 557 (1999).
[5] A. Bogaerts, R. Gijbels, J. Vlček – J. Appl. Phys. **84**, 121 (1998).
[6] J. Vlček – J. Phys. D: Appl. Phys. **22**, 623 (1989).
[7] A.N. Chester – Phys. Rev. **169**, 184 (1968).
[8] T. Fujimoto – J. Phys. Soc. Jpn. **47**, 265 (1979); **47**, 273 (1979); **49**, 1561 (1980); **49**, 1569 (1980); **54**, 2905 (1985).
[9] H. Akatsuka, M. Suzuki – Plasma Sources Sci. Technol. **4**, 125 (1995).
[10] J. Vlček, V. Pelikán – J. Phys. D: Appl. Phys. **23**, 526 (1990).
[11] T. Fujimoto – J. Quant. Spectrosc. Radiat. Transfer **21**, 439 (1979).
[12] M.M. Mohamed, T. Tchida, S. Minami – Appl. Spectrosc. **43**, 794 (1993).

Deposition of a-Si:H films of high stability by cluster-suppressed plasma CVD

Yukio Watanabe, Kazunori Koga, Atsushi Harikai, Takanori Ogata, and Masaharu Shiratani

Department of Electronics, Kyushu University, Fukuoka, Japan

Abstract

Reduction of cluster amount in silane discharges is a key to a considerable decrease of micro-structure parameter R_α of a-Si:H films deposited with the discharges. The cluster amount is found to be reduced more than one order of magnitude using 60 MHz discharges instead of 28 MHz ones or using an H_2 dilution of H_2/SiH_4 ratio of 5. Cluster-suppressed plasma CVD using 60 MHz discharges realizes deposition of a-Si:H films of $R_\alpha \approx 0$ at a rate of 0.55 nm/s.

1. Introduction

A-Si solar cells have three issues to be solved: 1) a low stabilized efficiency of 9%, 2) light-induced degradation of efficiency, and 3) a low deposition rate of 0.2 nm/s for the best quality films, although they will play a considerable role as one of clean, sustainable electricity sources in this century [1]. Clusters smaller than a few nm in size formed in silane discharges employed for a-Si:H film deposition are one of causes of light-induced degradation of the films [2-4]. Previously, we have systematically studied growth kinetics of clusters by using two in situ cluster detection methods which are named double-pulse-discharge (DPD) [5, 6] and photon-counting laser light scattering (PCLLS) methods [7-13]. Based on the results, we have developed a cluster-suppressed plasma CVD method and by using the method together with the PCLLS method, we have shown that reduction of cluster amount in silane discharges is a key to a considerable decrease of micro-structure parameter R_α of a-Si:H films, leading to a high stabilized fill factor of a n^+Si/a-Si:H/Ni Schottky solar cell [14, 15].

These results motivate us to study effects of discharge frequency and H_2 dilution on amount of clusters incorporated into depositing films, since VHF discharges and H_2 dilution are often employed to deposit device quality films at a high deposition rate. In this paper, we will report these new experimental results together with some previous important ones. After a description of the reactor and experimental methods in the next section, we will present the effects of discharge frequency and H_2 dilution on cluster amount in section 3.1 and 3.2, and then we will describe dependence of microstructure parameter on deposition rate in section 3.3.

2. Experimental

Experiments were carried out using two capacitively-coupled high frequency discharge reactors A and B: the reactor A is of the cluster-suppressed plasma CVD type and employed for examining dependence of microstructure parameter on deposition rate; the reactor B is of conventional type and employed for studying effects of discharge frequency and H_2 dilution on the amount of clusters incorporated into depositing films.

The reactor A was developed by applying cluster suppression methods in which the growth of clusters were suppressed by using gas viscous force, thermophoretic force, as well as by reducing gas stagnation regions [14, 15]. Figure 1 shows the reactor A. For this reactor, a powered stainless steel mesh electrode of 120 mm in diameter and a grounded plane electrode of 120 mm in diameter, were placed 20 mm apart in a stainless steel vessel of 315 mm in diameter and 250 mm in height. Gas of SiH_4 was supplied towards the center axis of

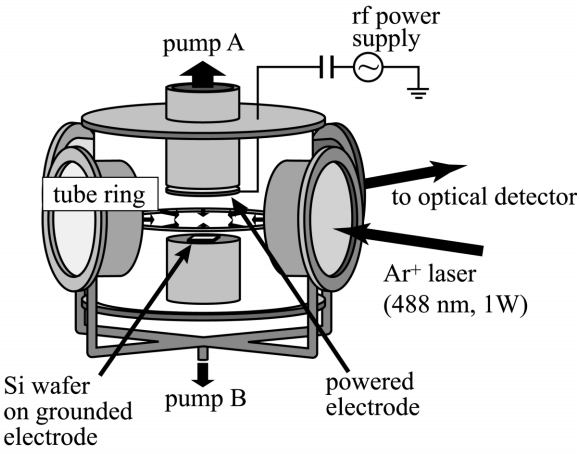

Fig. 1. Reactor A.

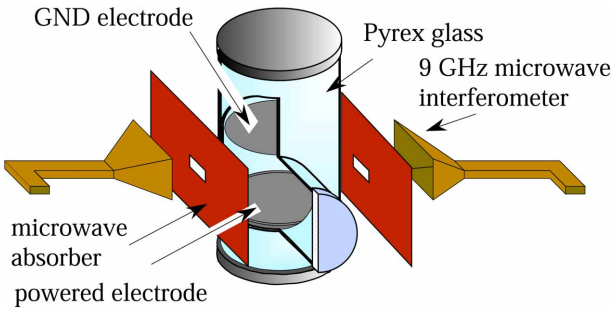

Fig. 2. Reactor B.

the discharge column from a tube ring of 240 mm in diameter, having 44 nozzles of 1mm in diameter directed to the center of the ring, which was placed at 10 mm above the grounded electrode as shown in Fig. 1. The flow rate and pressure were 5-30 sccm and 9.3 Pa, respectively. The discharge frequency and power were 28-60 MHz and 2-15 W (0.018-0.13 W/cm^2) respectively. Gas was pumped out through the powered electrode by a mechanical booster pump (pump A) and through four ports on the side wall by a rotary pump (pump B). Gas flow through the powered electrode contributes to reduce cluster growth in the radical generation region around the plasma/sheath boundary. When the grounded electrode is heated up to about 250˚C, gas temperature gradient drive clusters above a few nm in size to the powered electrode of room temperature. The pump B was employed to reduce accumulation of clusters due to their reflection at the wall and stagnation of gas flow.

The reactor B was described in detail elsewhere [12, 13]. Figure 2 shows the reactor B. For this reactor, two stainless steel plane electrodes of 85 mm in diametaer were placed at a separarion of 50 mm in a Pyrex glass vessel of 94.5 mm in inner diameter, and they were at room temperature. Pure SiH_4 gas was fed into the reactor at a flow rate of 5 sccm and a pressure of 13.3 Pa. The discharge frequency used was 13.56, 40 or 60 MHz, and the power was 10W (0.18 W/cm^2) for 13.56 and 40 MHz or 20W (0.35 W/cm^2) for 60 MHz, respectively.

Langmuir probe and 9 GHz microwave interferometer were employed for measuring densities of plasma ions and electrons [11]. The DPD and the PCLLS methods were employed to detect clusters in silane discharges [5-7]. For the DPD method, the size and density of clusters are determined by using both the density decay of clusters due to their diffusion and that of plasma electrons due to their attachment to clusters after turning off the discharge. For the PCLLS method, the size and density of clusters are determined by using time evolution of intensity of laser light scattering (LLS) from clusters due to their coagulation and diffusion after turning off the discharge. In order to obtain information on radical generation rate, emission intensities from Si and SiH, were measured with an optical detection system composed of apertures, lens and a monochromator.

For deposition experiments, two kinds of Si wafers were placed on the grounded electrode in the reactor A. One is Si (111) wafer with a high resistivity (1000-5000 Ωcm) for the measurement of microstructure parameter R_α of a-Si:H film, which is defined as the ratio of absorption intensity at 2100 cm^{-1} (Si-H_2 stretching mode) to that at 2000 cm^{-1} (Si-H stretching mode) which are measured by Fourier-transform infrared (FTIR) spectroscopy. In order to obtain a high sensitivity for R_α, the FTIR measurements were carried out in a vacuum with averaging more than 64 spectra, and also baseline determination and wave-form separation of the

FTIR results were made carefully. The other is n^+Si (100) wafer for the measurement of fill factor (FF) of a n^+Si/a-Si:H/Ni Schottky solar cell, which is defined as the ratio of the maximum power of the cell to the product of the short-circuit current and the open-circuit voltage. The FF was measured by irradiating an AM 1.5 solar spectrum light of 100 mW/cm^2. For the FTIR and FF measurements, the a-Si:H films of 1 μm in thickness were deposited at a substrate temperature of 250˚C.

3. Results and Discussion

3.1 Effects of discharge frequency on cluster amount

To study effects of discharge frequency f on growth of clusters, time evolution of their size and density was measured for f= 13.56, 40 and 60 MHz. The results together with time evolution of electron density n_e are shown in Fig. 3. The maximum n_e value increases from 1.7x10^9 cm^{-3} for 13.56 MHz to 1.3x10^{10} cm^{-3} for 60 MHz. The n_e value falls to a quasi-steady state value of about 1.5x10^9 cm^{-3} for 40 and 60 MHz, whereas ion densities for all f values (not shown here) and n_e for 13.56 MHz are nearly constant. Kinetic energy of electrons in a low energy bulk regime of an electron energy distribution, corresponding to the electron temperature T_e, becomes lower for the higher f and, hence, electron attachment to cluster becomes notable for the higher f, because the attachment cross section increase considerably with decreasing the electron energy. Therefore, the n_e value begin to decrease when clusters become detectable at around 2-3 ms after the discharge initiation for 40 and 60 MHz. Optical emission intensities of Si 288 nm and SiH 414 nm become high for a higher discharge frequency (not shown here), indicating a higher radical genaration rate or a higher depostion

Now, we focus our attention to cluster growth. For three cases, small clusters have an almost constant size of 0.5 nm and their density is about 1x10^{11} cm^{-3} in steady state of T_{on}> 100 ms. Large clusters are nucleated at T_{on}≈5 ms for 40 and 60 MHz, and ≈10 ms for 13.56 MHz. For three f's, they grow at an almost

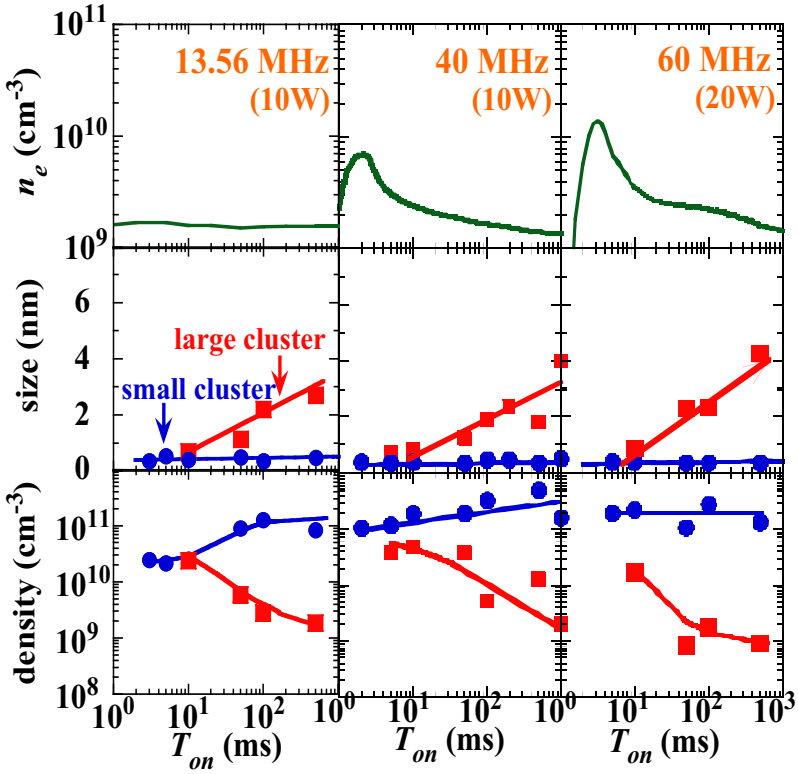

Fig. 3. Time evolution of electron density n_e, as well as size and density of clusters as parameter of f. Experimental conditions: SiH_4 (100%), 5 sccm, 13.3 Pa.

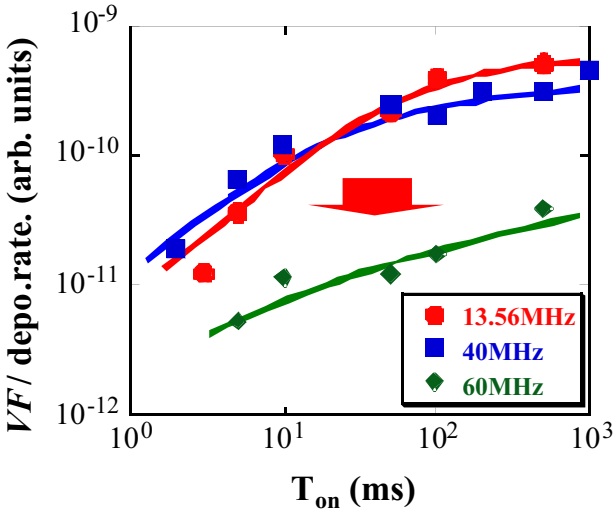

Fig. 4. Time evolution of volume fraction of clusters normalized by deposition rate. Experimental conditions: SiH_4 (100%), 5 sccm, 13.3 Pa.

same growth rate of about 4 nm/s. Their steady state density is about $1x10^9$ cm^{-3}.

Effects of f on the amount of clusters, incorporated into depositing a-Si:H films, were studied by evaluating a ratio of volume fraction of all clusters to a deposition rate, since most clusters generated in the discharge space are neutral and hence their amount is proportional to that of clusters incorporated into the films, if a sticking probability of clusters to the films is insenstive to the dischrage frequency and cluster size. The results are shown in Fig. 4. While the ratios for 13.56 and 40 MHz are almost the same, the ratio for 60 MHz is 1/10 of those for 13.56 and 40 MHz respectively. The result suggests that the incorporation of clusters is drastically suppressed for 60 MHz.

3.2 Effects of H_2 dilution on cluster amount

Effects of H_2 dilution on cluster amount was studied by the DPD method, since the dilution is often employed to deposit device quality films at a high deposition rate. The results are shown in Fig. 5. While n_e is almost the same value for the three P_{SiH4} values, large clusters cannot be detected for P_{SiH4}=20 and 50%. Moreover, the density of small clusters for P_{SiH4}=20% is 1/10 of those for P_{SiH4}=50 and 100%, whereas their size of 0.5 nm is insensitive to P_{SiH4}.

Effects of H_2 dilution on the amount of clusters, incorporated into depositing a-Si:H films, were studied by evaluating a ratio of volume fraction of all clusters to a deposition rate. The results are shown in Fig. 6. The

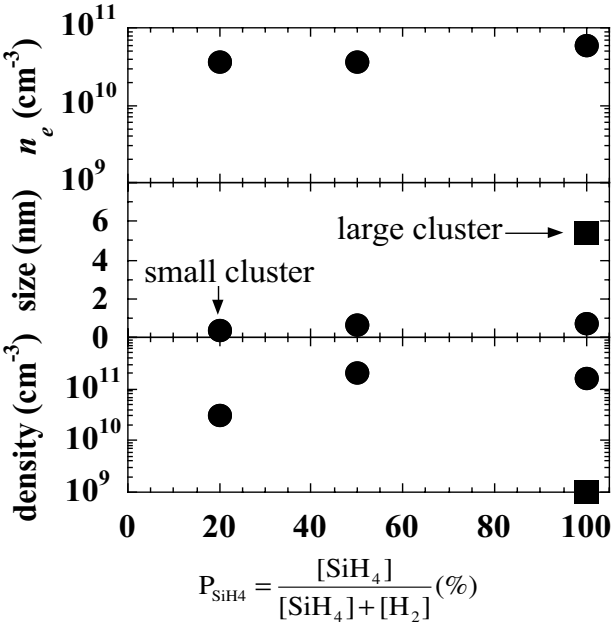

Fig. 5. Dependence of n_e, and size and density of clusters on P_{SiH4}.

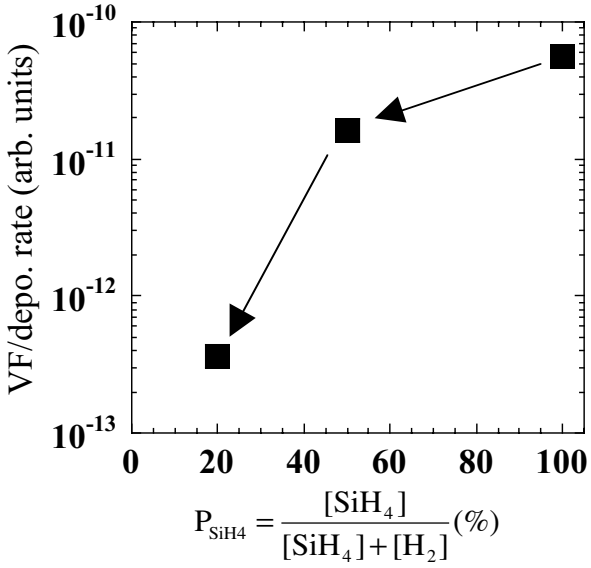

Fig. 6. Dependence of volume fraction of clusters normalized by deposition rate on P_{SiH4}.

ratios decreases drastically with decreasing P_{SiH4} value. The result suggests that the incorporation of clusters is drastically suppressed by employing an appropriate H_2 dilution.

3.3 Dependence of microstructure parameter on deposition rate

Gas flow near the powered electrode was found to have a great influence on R_α by using the powered electrodes 1 and 2: the electrode 1 was designed without considering the gas flow, while the electrode 2 was carefully designed for reducing gas stagnation regions near the powered electrode. Figure 7 shows dependence R_α on deposition rate. Solid circles and squares indicate results for the powered electrode 1. The value of R_α=0.084 at a high deposition rate of 0.74 nm/s for 60 MHz still remains low compared to R_α=0.115 at a rate of 0.38 nm/s for 28 MHz. Open squares in Fig. 7 show results for the electrode 2. The R_α values are notably low compared to those for the electrode 1. Especially, a-Si:H films of $R_\alpha \approx 0$ is deposited at 0.55 nm/s for the electrode 2. These results show that the VHF discharge and reduction of gas stagnation region are effective in reducing R_α.

Finally, we examine dependence of light-induced decrease of fill factor FF of a n^+Si/a-Si:H/Ni Schottky cell on SiH_2 concentration in a-Si:H films. Figure 8 shows our results (solid squares) together with the results of AIST (open cicles)[3]. Reduction ΔFF due to light irradiation tends to decrease with decreasing the SiH_2 concentration in a-Si:H films. Since the R_α value is proportional to the SiH_2 concentration and R_α=0.1 corresponds to a SiH_2 concentration of 1 atomic %, the results indicate that suppression of cluster amount brings about reduction of light-induced decrease in a-Si:H solar cell efficiency, which is proportional to FF.

4. Conclusions

The cluster amount is found to be reduced more than one order of magnitude using 60 MHz discharges or using H_2 dilution of H_2/SiH_4 ratio of 5. We have shown that the combination of the cluster-suppression

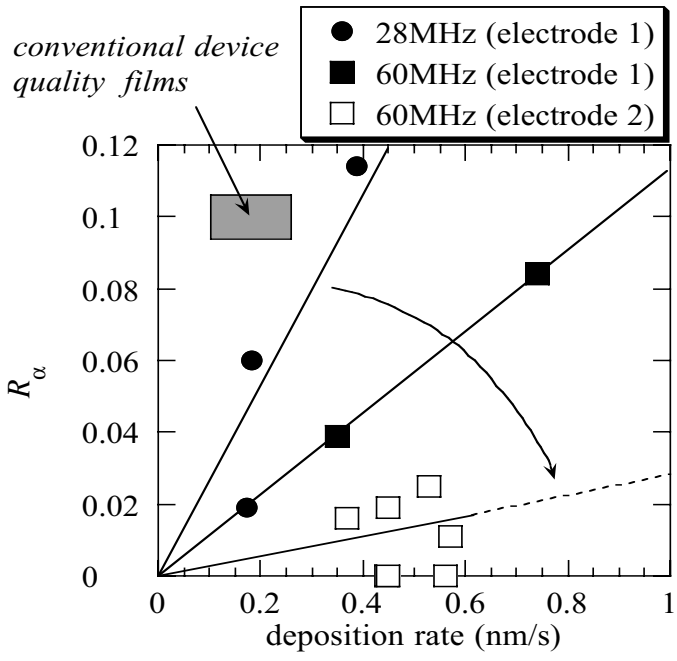

Fig. 7. Dependence of microstructure parameter on deposition rate.

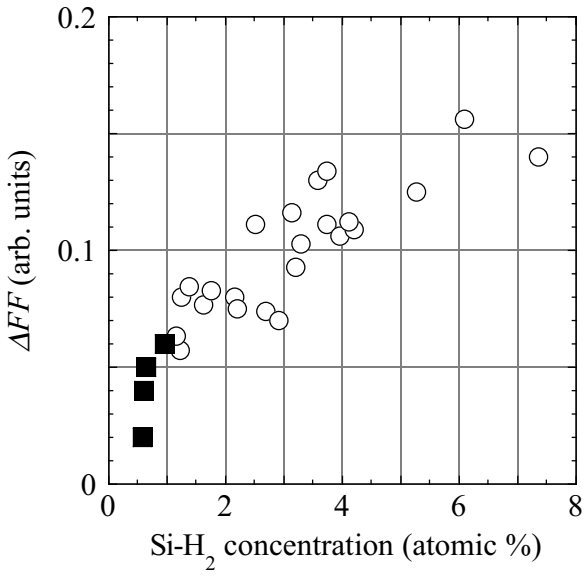

Fig. 8. Dependence of light-induced decrease of fill factor on SiH_2 concentration in a-Si:H films.

method and the VHF discharge is effective in depositing a-Si:H films of $R_{\alpha} \approx 0$ at 0.55 nm/s . The key for reducing the light-induced degradation is suppression of cluster amount in silane high frequency discharges for a-Si:H film deposition.

Acknowledgments

This work was partly supported by a Grant-in-Aid for Scientific Research (A) from the Japan Society of the Promotion of Science (KAKENHI 14205047). We would like to acknowledge the assistance of Mr. T. Kinoshita who contributed greatly to the preparation of the experimental set-up.

References

[1] G. Bruno, P. Capezzuto, and A. Madan, Plasma Deposition of Amorphoous Silicon-Based Materials, pp. 1-62 , Academic Press, San Diego (1995)

[2] M. Takai, T. Nishimoto, T. Takagi, M. Kondo, and A. Matsuda, J. Non-Cryst. Solids **266**, 90 (2000).

[3] T. Nishimoto, M. Takai, M. Kondo, and A. Matsuda, Proc. of 28th IEEE Photovoltaic Specialists Conference vol. 28, pp. 876- 880, IEEE, Alaska, 2000.

[4] H. Miyahara, M. Takai, T. Nishimoto, M. Kondo, A. Matsuda, Solar Energy Materials And Solar Cells **74**, 351, (2002).

[5] K. Koga, Y. Matsuoka, K. Tanaka, M. Shiratani, and Y. Watanabe, Appl. Phys. Lett.**77**, 196 (2000).

[6] K. Koga, M. Shisratani, and Y. Watanabe, Proc. Nano-technology Workshop, pp. 13-20, Dejun, Korea, Feb. 2002.

[7] M. Shiratani, and Y. Watanabe, Rev. of Laser Eng. **26**, 449 (1998).

[8] M. Shiratani, T. Fukuzawa, and Y. Watanabe, Jpn. J. Appl. Phys. **38**, 4525 (1999).

[9] Y. Watanabe, M. Shiratani, T. Fukuzawa, and K. Koga, Journal of Technical Physics, **41**, 505 (2000).

[10] M. Shiratani, S. Maeda, K. Koga, and Y. Watanabe, Jpn. J. Appl. Phys. **39**, 287 (2000).

[11] M. Shiratani, T. Fukuzawa, K. Eto, Y. Watanabe, Jpn. J. Appl. Phys. **31**, L1791 (1992).

[12] Y. Watanabe, M. Shiratani, K. Koga, Plasma Sources & Sci. Tech. **11**, A229 (2002).

[13] Y. Watanabe, A. Harikai, K. Koga, and M. Shiratani, Pure Appl. Chem. **74**, 483 (2002).

[14] K. Koga, M. Kai, M. Shiratani, Y. Watanabe, and N. Shikatani, Jpn. J. Appl. Phys. **41**, L168 (2002).

[15] M. Shiratani, M. Kai, K. Koga, and Y. Watanabe, Thin Solid Films **427**, 1 (2003).

SURFACE MODIFICATION OF 8620 STEEL BY PULSE PLASMA TECHNIQUE AFTER PRIOR CARBURISATON PROCESS

Y.Yaralı, M.Durman, H.Akbulut

Sakarya University Engineering Faculty Department of Metallurji and Materials Eng.

The Pulse-plasma technology allows to produce surface strengthening of parts of machines and tools, and deposition of high performance coating from oxides and carbides. The technology and equipment are developed for modifying surface of tools and other pieces. The pulse-plasma technology and equipment for the high-energy of coating from metal oxides and hard alloys have been developed. The offered pulse-plasma technology provides a low consumption of alloying elements and electric power in combination with high productivity and the technology. These make it possible to treat only working (cutting) surfaces, which solves the problem of increasing wear resistance without any change in structural state of the entire workpiece.

In our study, the wear behaviour of detonation pulse plasma treated AISI 8620 steel was evaluated. The conventional carburizing steel was subjected to prior surface hardening by using two different carburisation routes. After a carburisation for 2 hours at 900 °C the first group of samples was quenched by air. The second group of the carburized steel was quenched into an oil bath which heated to 250 °C. The surfaces of these two group of samples were modified by nitrogen and argon gases by using plasma pulse technique appling two different battery capacities of 800 and 1000 C, μF. and, three different sample-plasma gun nozzle distances of 60, 80 and 100 H,mm. The surface modified steels were subjected to a ball-on-disc wear test and the wear rates and the friction coefficient values were determined.

Yıldız Yaralı
E.mail: yyarali@sakarya.edu.tr
tel. 0 264 346 03 53 (339)
GSM: 0 533 214 64 14
Adr. Sakarya University Engineering Faculty Deparment of Metallurji and Materials Eng. 54187 Esentepe Campüs
Serdivan/Sakarya
Turkey

Prof.Dr.Mehmet Durman
E.mail.durman@sakarya.edu.tr
Tel.0 264 346 03 50
Adr.Sakarya University Engineering Faculty Deparment of Metallurji and Materials Eng
54187 Esentepe Campüs
Serdivan/Sakarya
Turkey

Doç.Dr.Hatem Akbulut
E.Mail.akbulut@sakarya.edu.tr

On the plasma chemistry in H_2-Ar-N_2-microwave discharges with admixtures of hydrocarbons

F. Hempel[1], D. Loffhagen[1], L. Mechold[1*], J. Röpcke[1], P.B. Davies[2]

[1] *Institute for Low-Temperature-Plasma-Physics (INP), Friedrich-Ludwig-Jahn-Straße 19, D-17489 Greifswald, Germany*

[2] *Department of Chemistry, University of Cambridge, Lensfield Road, Cambridge, CB21EW, U.K.*

**present address: Laser Components, Postfach 1129, D-82133 Olching*

Abstract

Tuneable infrared diode laser absorption spectroscopy has been used to detect the methyl radical and nine stable molecules, CH_4, CH_3OH, C_2H_2, C_2H_4, C_2H_6, NH_3, HCN, CH_2O and C_2N_2, in H_2-Ar-N_2 microwave plasmas containing up to 7 % of methane or methanol. It was found that HCN and NH_3 are the main final products of plasma chemical conversion. The fragmentation rates of methane and methanol and the respective conversion rates to HCN and NH_3, CH_4, C_2H_2, C_2H_4 and C_2H_6 have been determined for different H_2 to N_2 ratios. A model of the chemical reactions in the H_2-N_2-Ar-CH_4 plasma has been developed.

1. Introduction

Plasmas containing hydrocarbon precursors are used in a variety of plasma enhanced chemical vapour deposition (PECVD) systems to deposit thin films with advantageous mechanical, electrical or optical properties. By varying the plasma parameters coatings with a wide range of chemical and physical properties can be produced to open up new fields of application. This is a challenging subject for plasma technology. The key to an improved understanding of plasma chemistry and kinetics in such chemical active discharges is the analysis of the fragmentation of the precursor and the monitoring of transient or stable plasma reaction products, in particular the measurement of their ground state concentrations. This can be done by specific diagnostic methods using absorption spectroscopy. The decomposition of hydrocarbons in non-equilibrium plasmas containing reactive species has been the subject of a variety of experimental and theoretical studies. Some recent examples with nitrogen admixture shall be given here; a more comprehensive discussion related to oxygen admixtures can be found in [1-4].

Tuneable infrared diode laser absorption spectroscopy (TDLAS) in the mid infrared spectral region between 3 and 20 µm is a non-invasive technique for measuring number densities of stable molecules and radicals. TDLAS can also be used to determine neutral gas temperatures [1] and to investigate dissociation processes [2-4]. Due to their small laser line width (about 10^{-4} cm^{-1}) the lead-salt diode lasers used in the mid infrared region are well suited for high resolution spectroscopy purposes, e.g. of low molecular weight free radicals and molecular ions [5,6].

The TDLAS method allows also time resolved measurements with repetition rates exceeding 1 kHz. The time dependence of the conversion of methane to the methyl radical and three stable C-2 hydrocarbons was studied e.g. in surface wave plasmas [3]. Recently new compact and transportable TDLAS systems for plasma and gas phase process diagnostics and control have been developed. These use up to four diode lasers operating simultaneously and independently with a time resolution as short as ten microseconds [7,8].

2. Experimental

A detailed description of the experimental arrangement of the absorption cell and the discharge system can be found elsewhere [2]. A multi-pass optical arrangement was added to the planar microwave plasma source to improve the dynamic range by about one order of magnitude. The discharge configuration in planar microwave discharges has the advantage of being well-suited for end-on spectroscopic observations because a considerable homogeneity can be achieved over relatively long plasma path lengths (figure 1). The dimensions of the vessel used here were 150 × 21 × 15 cm^3. As described in ref. 2 the measurements were performed at a microwave frequency of 2.45 GHz and a power of 1.5 kW in an unpulsed plasma regime, corresponding to a power flux in the TDLAS observation plane of about 10 W cm^{-2}. Investigations were done under flowing and static discharge conditions. The gas flows were measured on mass flow controllers and then the gases mixed before entering the reactor. They were pumped out via a port in the reactor wall. The gas mixture supplying the reactor consisted of *x* sccm H_2+ 60 sccm Ar + *y* sccm N_2 + *z* sccm CH_4 or

CH_3OH. The total flow rate and pressure were kept constant at 555 sccm and 1.5 mbar respectively. For both methane and methanol containing gas mixtures four different flow rates (*z*) were selected: 5, 15, 25 and 40 sccm corresponding to 0.9, 2.7, 4.5 and 7.2 % of the total flow rate, respectively. When nitrogen was added the proportion of hydrogen was reduced correspondingly to maintain a constant flow rate.

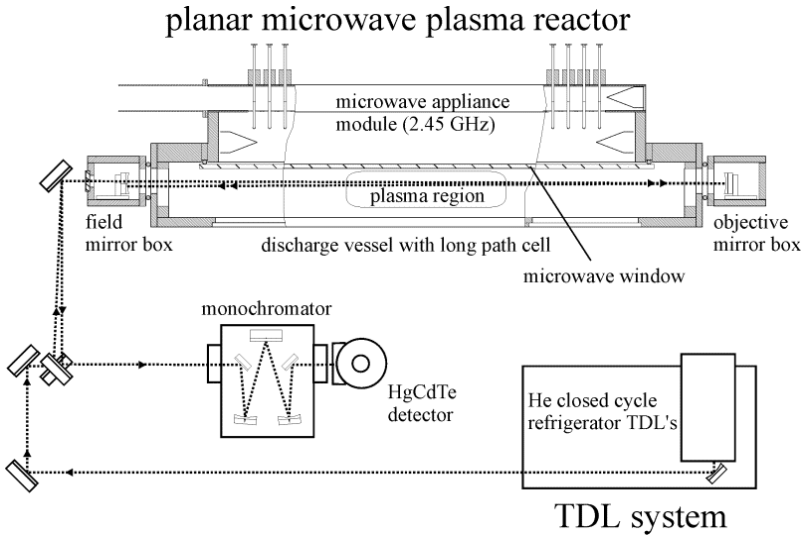

Figure 1: Experimental arrangement of the planar microwave plasma reactor (side view) with White cell multiple pass optical arrangement and tuneable diode laser infrared source. The laser beam path is indicated by dotted lines.

A representative TDL absorption spectrum of a H_2-Ar-N_2-CH_3OH microwave plasma with lines due to methanol and the methyl radical is shown in figure 2. The identification of lines and the measurement of their absolute positions were carried out using well documented reference gas spectra and an etalon of known free spectral range for interpolation. Absolute species concentrations are determined by non-linear least square fitting the measured lines and integrating the area under the transition. This data acquisition was carried out by a special software package described in detail in [7,8].

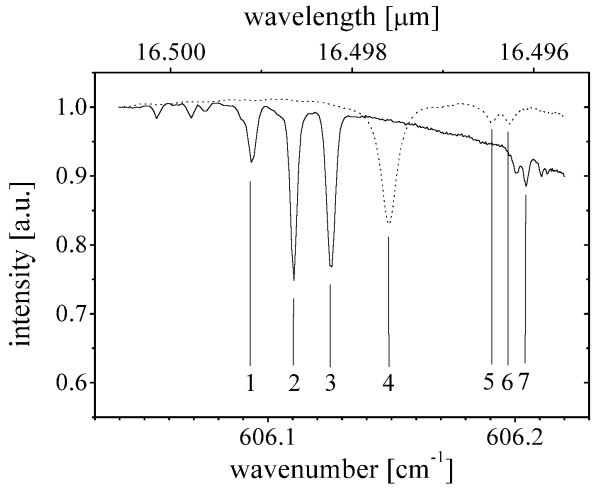

Figure 2: TDL absorption spectra of some methyl and methanol lines in a H_2-Ar-N_2-CH_3OH discharge (1,3,7 – CH_3; 2 – CH_3OH; 4,5,6 – N_2O). The dotted lines due to N_2O are from a reference gas cell placed in the beam path.

3. Results

General features

TDLAS has been used to detect the methyl radical and nine stable molecules, CH_4, C_2H_2, C_2H_4, C_2H_6, CH_3OH, CH_2O, NH_3, HCN and C_2N_2 in H_2-Ar-N_2 microwave plasmas containing up to 7.2% of methane or methanol. The concentrations of these species measured at nitrogen flows of up to 455 sccm are shown in figure 3 and 4 for flowing gas discharge conditions. The initial flow used in these figures for methane and methanol (40 sccm) was selected to represent typical flows used in practical CVD reactors.

The wide range of concentrations measured for the different species provides a convenient means for detailed discussions below. The degree of dissociation of the hydrocarbon precursor molecules varied between 20 and 97 %. It was determined from their concentrations measured before starting and in the discharge. The highest concentrations are for the precursor molecules and the major products HCN and NH_3 presented in figure 3, followed by the stable and unstable hydrocarbon products (C_2H_2, C_2H_4, C_2H_6 and CH_3, figure 4). Both HCN and NH_3 concentrations rise under flowing conditions rapidly as the proportion of nitrogen reaches 25 % and then they are approximately constant. In the case of methanol admixture methane is the dominant hydrocarbon product. Besides, C_2H_6 and C_2H_2 are produced with concentrations of 10^{13}-10^{14} molecules cm^{-3}. The CH_3 radical concentration was found to be in the range of 10^{13}-10^{14} molecules cm^{-3} too. Under all circumstances, C_2H_4 showed lower concentrations than the other hydrocarbons. For methanol in the gas flow H_2CO was observed as the prior dissociation product.

In contrast to the other species for the admixture of methane C_2N_2 rises steadily with the amount of nitrogen admixture in the plasma up to the maximum proportion of nitrogen. C_2N_2 was the species with the lowest concentration of all those studied.

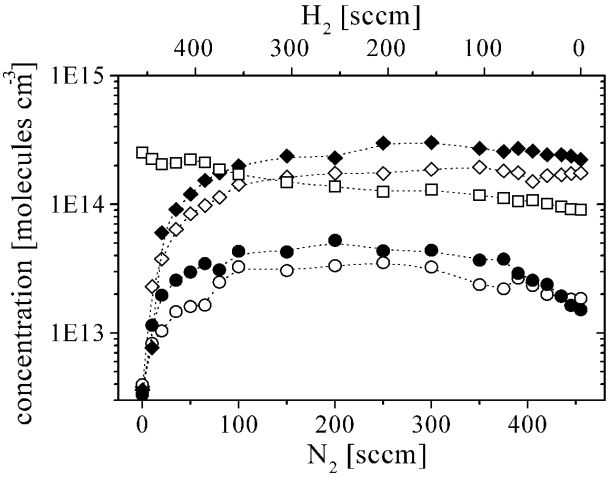

Figure 3: Molecular concentrations of final products under flowing discharge conditions over the nitrogen flow rate for methane (closed symbols) and methanol (open symbols) admixture. (Λ,M - HCN, ●,○ - NH_3, □ - CH_4).

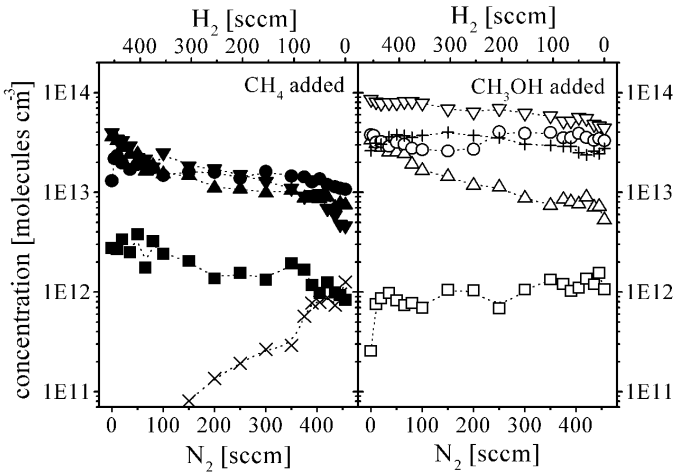

Figure 4: Molecular concentrations of hydrocarbons produced under flowing discharge conditions for methane (closed symbols) and methanol (open symbols) admixture over the nitrogen flow. (▲,△ - C_2H_2, ■,□ - C_2H_4, ▼,▽ - C_2H_6, ●,○ - CH_3, × - C_2N_2, + - CH_2O).

Fragmentation and Conversion Rates

To gain further insight into plasma chemical conversion the experimental data concerning methane and methanol dissociation was used to estimate absolute fragmentation rates of methane and methanol and conversion rates to the measured main products CH_4, HCN and NH_3. These rates are normalised on the discharge power.

The fragmentation rate R_F of the hydrocarbon precursor molecules methane and methanol is introduced by analogy to [3] as

$$R_F = \Phi_P \; 1/60 \;\; D/100 \;\; N_o/P$$

where R_F has the units of molecules J^{-1}, Φ_P is the precursor flow (sccm), D is the degree of dissociation of the precursor molecules given in percent, N_o is the number of molecules per cm^{-3} at norm conditions (2.69×10^{19} molecules) and P is the power (W).

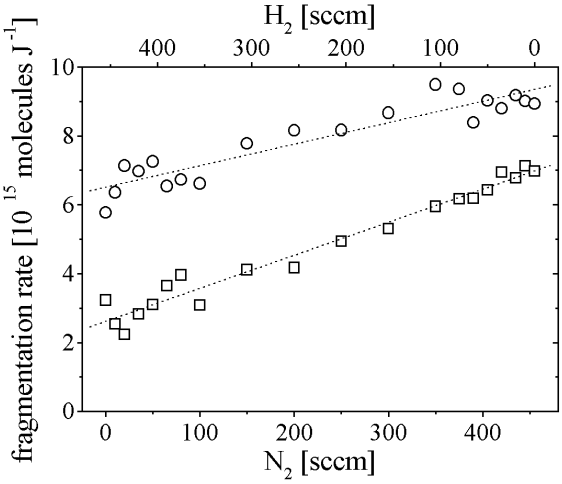

Figure 5: The rate of fragmentation of methane (□) and methanol (○) under flowing discharge conditions for various H_2 / N_2-ratios (CH_3OH, CH_4: 40 sccm).

Figure 5 shows the respective rate of fragmentation of methane and methanol for increasing nitrogen flows containing 7.2 % of the precursor gas and for flowing conditions. In nitrogen-free plasmas the rate of fragmentation of methanol ($R_F(CH_3OH) \approx 6 \times 10^{15}$ molecules J^{-1}) is twice as high as for methane ($R_F(CH_4) \approx 3 \times 10^{15}$ molecules J^{-1}). Adding nitrogen to the plasma, while keeping the total gas flow and the discharge pressure constant, i.e., varying the ratio of H_2 to N_2, both rates of fragmentation increase nearly linearly up to about 7×10^{15} molecules J^{-1} for methane and about 9×10^{15} molecules J^{-1} for methanol. Similar

results have been obtained for other admixtures of hydrocarbon precursors. In general smaller admixtures of hydrocarbons resulted in lower fragmentation rates. The values of the fragmentation rates of methane at high nitrogen flow rates presented here are near to those found in a H_2-CH_4 surface wave discharge at a comparable high total gas flow rate [3].

The conversion rate R_C to plasma product molecules is expressed analogously as

$$R_C = n_{molecule} \ \Phi_{total}/60 \ 10^3/p \ 1/P$$

where R_C has the units of molecules J^{-1}, $n_{molecule}$ is the measured molecular concentration in molecules cm^{-3}, Φ_{total} is the total gas flow in sccm, p is the pressure in mbar and P is the power (W).

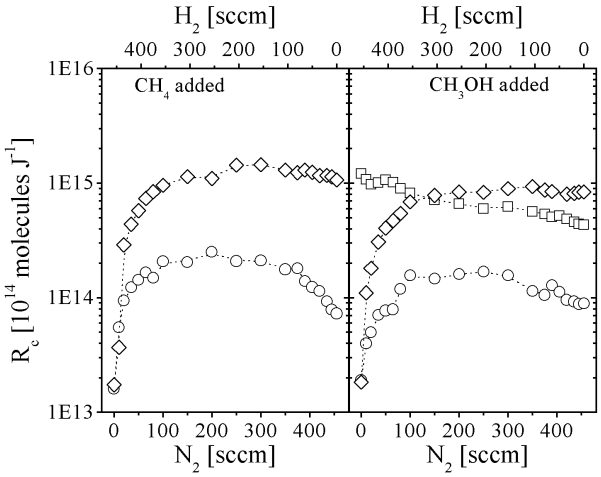

Figure 6: The rates of conversion to HCN (M), to NH_3 (–) and to CH_4 (∀) under flowing discharge conditions for various H_2 / N_2-ratios (CH_3OH, CH_4: 40 sccm).

Figure 6 shows the rates of conversion to HCN and NH_3 in H_2-Ar-N_2 microwave plasmas containing methane as well as the corresponding conversion rates, including that to CH_4, for plasmas containing methanol. The rates of conversion to particular reaction products are based on the measurements of their absolute concentrations. They range between 10^{14} to 10^{15} molecules J^{-1}. The conversion rate to HCN is about one order of magnitude higher than that of NH_3. H_2-Ar-N_2 microwave plasmas with methane as precursor tend to show slightly higher conversion rates compared to the methanol case. Both rates of conversion rise steeply to a maximum at the ratio of H_2 to N_2 of 1:1. Thus, CH_4 was detected in methanol containing plasmas, its conversion rate decreases from 12 – 4 x 10^{14} molecules J^{-1} with increasing nitrogen flow rate.

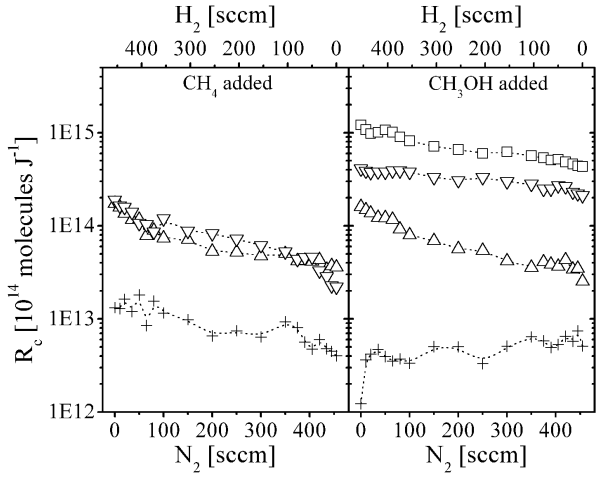

Figure 7: The rates of conversion to CH_4 (∀), to C_2H_2 (8), to C_2H_4 ( ) and to C_2H_6 (X) under flowing discharge conditions for various H_2 / N_2-ratios (CH_3OH, CH_4: 40 sccm).

Conversion rates to hydrocarbon products are presented in figure 7. While the values for C_2H_2 and C_2H_4 are similar for methane and methanol as precursor, the conversion rate to C_2H_6 is in the methanol admixture case by a factor of about 4 higher. A major difference in comparison with ref. 3 is that in the present work for high flow rates and methane as precursor hydrocarbon similar conversion rates to C_2H_2, C_2H_4 and C_2H_6 were found. These values are by a factor of about five smaller. This is mainly caused by the additional conversion to HCN and NH_3 under the presence of nitrogen in the actual gas mixtures.

Plasma Chemistry Model

The experiments were accompanied by model calculations of the kinetic processes in a plasma under static discharge conditions. The model established for a typical mixture composition of 73 / 9 / 11 / 7 % of H_2 / N_2 / Ar / CH_4 includes 22 species with 30 electron impact dissociation processes and 78 chemical reactions. Various rate coefficients for electron impact dissociation needed were determined by solving separately the time-dependent electron Boltzmann equation for given values of the reduced electric field, microwave frequency, mixture composition and recommended cross section data until approaching the periodic state. The data for neutral chemical reaction rate coefficients were taken from literature.

In principle the 22 species included in the model can be gathered into five different groups. First, there are the precursor molecules and their electron impact dissociation products. These eventually form NH_3, HCN and CH_4 or C_2H_6 by thermal reactions in the discharge volume. Species containing the CN group are mainly formed by the interaction of hydrocarbons with nitrogen or with species of the NH_3-group. In contrast, the production of NH_3 or hydrocarbons was found to be relatively independent of the hydrocarbon chemistry.

A comparison of calculated and measured species concentrations is shown in figure 8. A satisfactory agreement within the order of magnitude of the errors of the measurements was found for the species, which have been monitored by TDLAS. Moreover, concentrations of further species, in particular of important transient species, e.g. CH_2, C_2H_5, NH and NH_2, can be estimated from the result of the model calculations.

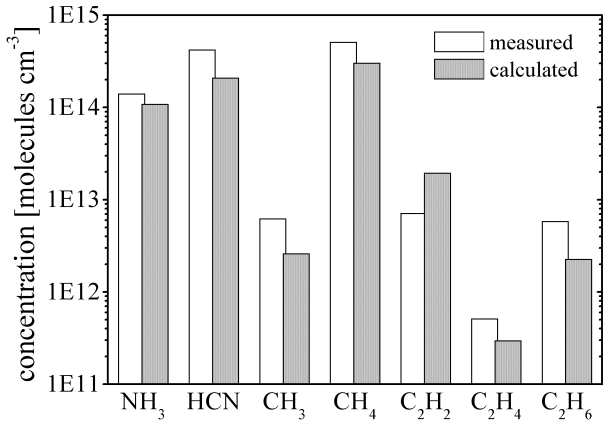

Figure 8: Comparison of measured and calculated species in a H_2-N_2-Ar-CH_4-plasma.

4. References

[1] W.Y.Fan, P.F.Knewstubb, M.Käning, L.Mechold, J.Röpcke, P.B.Davies - J. Phys. Chem. A **103,** 4118 (1999).

[2] J.Röpcke, L.Mechold, M.Käning, W.Y.Fan, P.B.Davies - Plasma Chem. Plasma Process. **19,** 395 (1999).

[3] L.Mechold, J.Röpcke, X.Duten, A.Rousseau - Plasma Sources Sci. Technol. **10,** 52 (2001).

[4] C.Busch, I.Möller, H.Soltwisch - Plasma Sources Sci. Technol. **10,** 250 (2001).

[5] F.Hempel, J.Röpcke, A.Pipa, P.B.Davies - Molecul. Phys. **101** 589 (2003).

[6] Z.Liu, P.B.Davies - J. Chem. Phys. **105,** 3443 (1996).

[7] J.Röpcke, L.Mechold, M.Käning, J.Anders, F.G.Wienhold, D.Nelson and M.Zahniser - Rev. Sci. Instrum. **71,** 3706 (2000).

[8] J.B.McManus, D.Nelson, M.Zahniser, L.Mechold, M.Osiac, J.Röpcke and A.Rousseau – Rev. Sci. Instrum. in press (2003).

Atmospheric Pressure Afterglow Plasma In Argon

Navin Muthuswamy[1], Bijan Pashaie[2], and Shirshak Dhali[1]

[1]*Department of Electrical Engineering, Southern Illinois University, Carbondale, IL 62901*
[2]*Department of Engineering Physics, Southeast Missouri State University, Cape Girardeau, MO63701*

Abstract

An RF driven atmospheric pressure plasma source is discussed. The plasma produces an afterglow, which can be used for plasma chemical reactions under ambient conditions. The light intensity measurement shows that the discharge is continuous in time unlike low frequency discharges, which are intermittent in nature. The gas temperatures are near ambient and the afterglow temperatures do not exceed 180 ^{o}F.

1. Introduction

At atmospheric pressures, there are two popular methods for producing non-thermal plasmas; (1) a corona discharge and (2) a barrier-type ac discharge. Although corona discharges have found

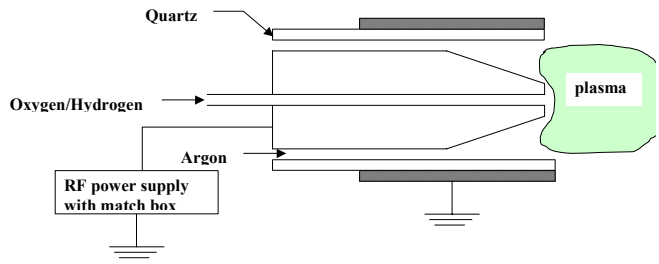

Fig. 1: Schematic of the atmospheric pressure discharge,

numerous applications, they are not particularly suitable for large surface or volume gas phase plasma processing [1]. The dielectric-barrier discharge, also known as a silent discharge or a partial discharge, is widely used in industry for ozone synthesis. These discharges are best characterized by streamers, which are a result of space charge dominated transport at high electric fields [2]. A

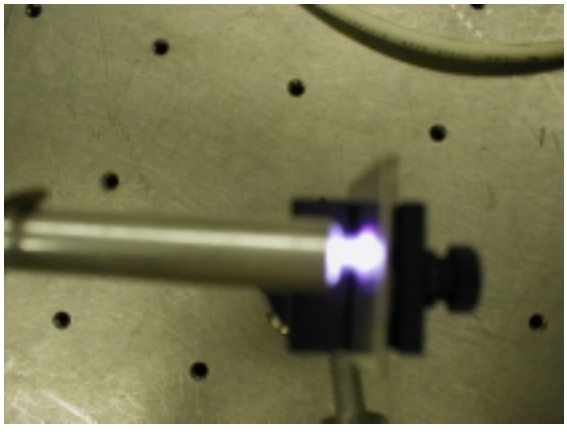

Fugure2: The picture of an atmospheric afterglow in a radio frequency Argon discharge.

disadvantage of existing plasma sources is that the specific energy (energy per unit volume of the processing gas) is low. This is a major shortcoming for adaptability to manufacturing processes. We have taken a different approach for the generation of plasma under ambient conditions. The discharge

has been used to treat metal surfaces prior to coating. Peel test, and XPS results show that Ar/H_2 and Ar/O_2 plasma are effective in cleaning the metal surface and produce superior coatings.

In plasma chemical devices, the aim is to produce desired radicals to carry out a particular reaction. The main thrust for atmospheric pressure plasma for our application is the production of H and O radicals and Ar ions. For efficient cleaning the production of radicals rather than gas heating is important. The ambient afterglow discharge is a cold discharge with most of its energy being utilized for the production of excited species. In $Ar/He/H_2/H_2O$ plasma the following electron impact processes will be present

$$Ar + e \rightarrow Ar^+ + 2e \text{ and } Ar^* + e$$

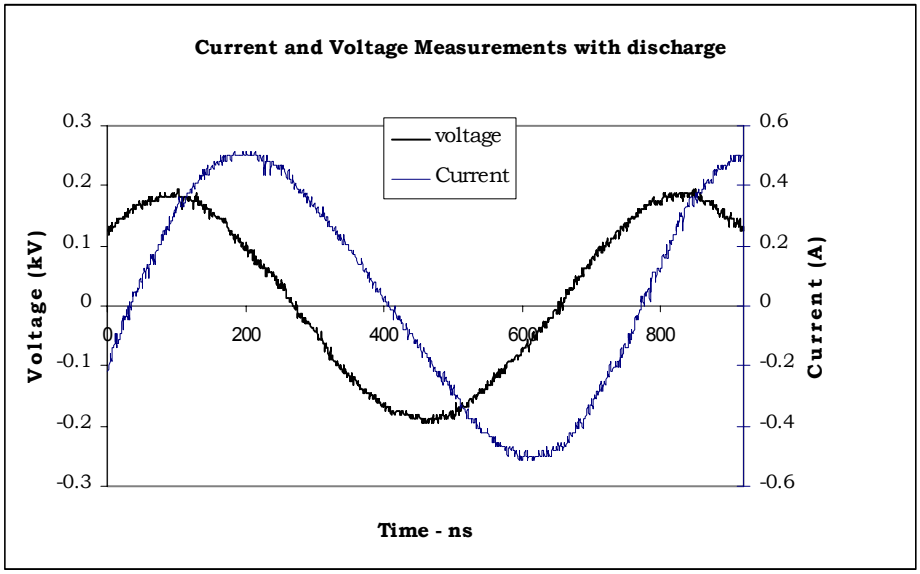

Fig 3. RF current and voltage waveforms at 13.56 MHz.

$$H_2 + e \rightarrow 2H + e$$

$$He + e \rightarrow He^+ + 2e \text{ and } He^* + e$$

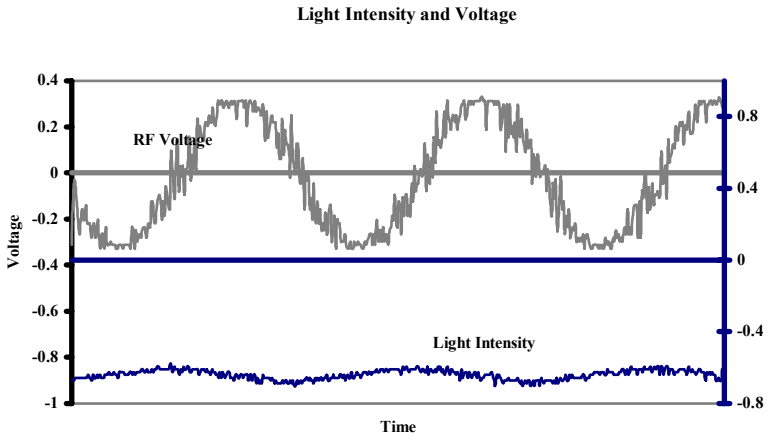

Figure 4: The integrated light output (relative) along with RF voltage as a function of time.

2. Results and Discussions

Shown in Fig. 1 and Fig.2 are the schematic and the picture of the plasma source. In the

configuration shown, the discharge is "struck" in the noble gas (Argon) and the reactive gas is added to the afterglow. The centered electrode is bored to allow the reactive gases to flow into the afterglow. This is critical for the stability of the discharge: Gases like H_2 and O_2 are attaching and change the physical characteristics of the discharge. Due to increase in breakdown voltage, even for concentration of reactive gases in few percentages, it is difficult to strike a discharge using radio frequency (RF). RF is the most suitable power source because it can be tuned to the load easily compared to low frequencies: Low frequency discharges have very high capacitive current, which is difficult to correct. Similar discharges at radio frequency are being investigated [3]. The discharges

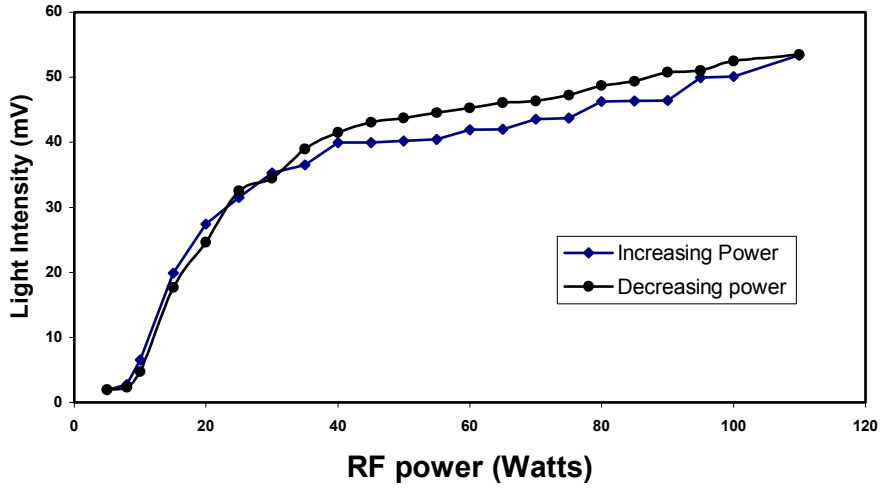

Figure 5: The light intensity as a function of RF power input.

by Park et al. produce a narrow plasma jet and are stabilized by very high flow of helium at 600 Torr. Our approach does not depend on high gas flow, but uses a dielectric to stabilize the discharge.

Figure 3 shows the RF current through the discharge and the voltage across the discharge. The RF current was measured with IPC CM-10-M (0.1 V/A into 50 Ω) current monitor. The current waveform is sinusoidal indicating a temporally uniform discharge. Figure 4 shows the total light intensity along with the voltage waveform. Again, the light is uniform in time therefore the discharge at 13.56 MHZ is temporally uniform. At low frequencies the dielectric barrier discharge is

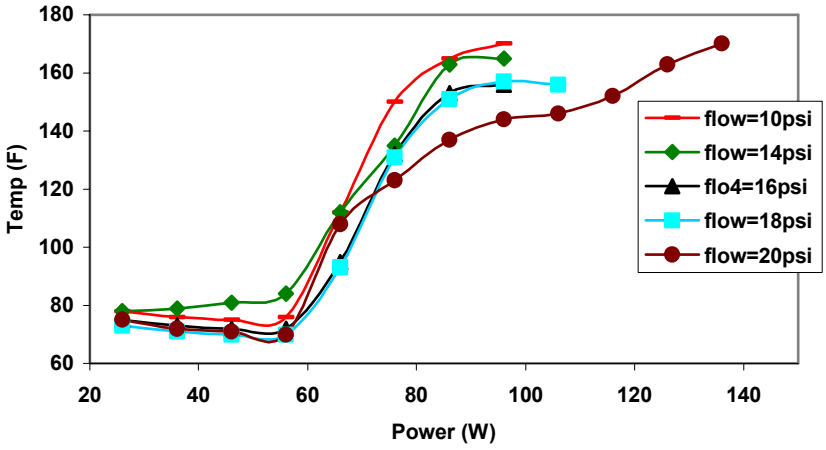

Figure 6: The afterglow temperature on axis at the exit of the discharge.

intermittent unlike Fig. 4 [4].

The afterglow was investigated by optical spectroscopy In an Ar/H_2 discharge the H_α and the H_β lines increase with increasing discharge power. In Ar/O_2 plasma, the dissociated oxygen line shoed a strong emission line. Figure 5 and 6 show the total light output and the gas temperature at the exit as a function of RF power. The temperature profile of the afterglow was obtained and the maximum

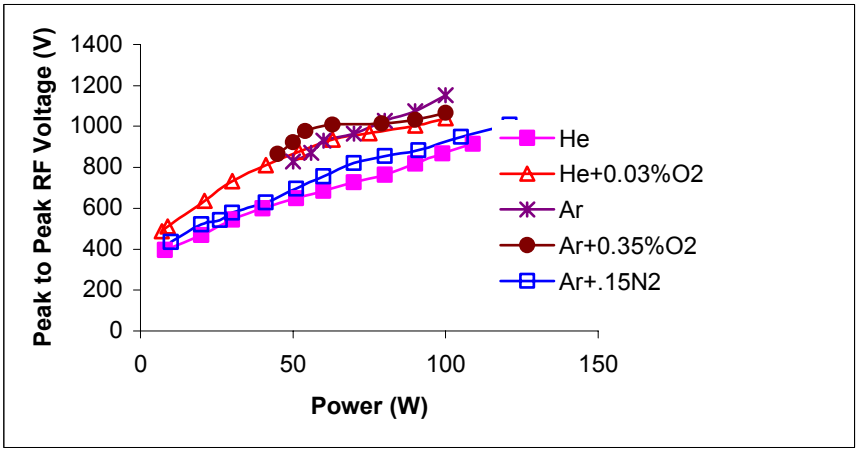

Figure 7: Voltage versus power for different gas composition.

value found on axis was about 60^0 C. With increasing RF power, the light intensity stars to saturate whereas, the gas temperature increases rapidly. It is clear that energy partitioning at higher powers favor gas heating as opposed to other nonelastic processes.

The discharge power, P, in a dielectric-barrier type discharge is given by [4][5]

$$P = 4fV_c'[c_d V_p - (c_g + c_d)V_c] = 4fV_c' c_d [V_p - \frac{(c_g + c_d)}{c_d} V_c] \qquad (1)$$

where f is the power frequency, c_g and c_d are the gap and dielectric capacitance respectively, v_p, v_c', and v_c are the peak to peak applied voltage, the critical gap voltage required to sustain a discharge, and the critical voltage at which the gap breaks down, respectively. The RF discharge discussed in this paper, the c_g=4.1 pF and c_d=7.7 pf. The voltages v_c and v_c' are nearly equal, however we have observed that v_c' tends to be lower than v_c [4]. This equation shows that the power input to a dielectric type discharge has a linear dependence on voltage. At low frequencies, dielectric-barrier discharges show this characteristics for all gases [4] [5]. Shown in Fig. 7 is the measured relationship between the discharge power and voltage for the RF discharge. For pure monatomic gases, the linear relationship predicted by the equation 1 is observed. The slope of the pure He and Ar depends on the critical field required for breakdown. However with trace amount of molecular gases the voltage starts to saturate with power. Due to the continuous nature of discharge, the vibratioanlly excited molecules, especially nitrogen, lower the critical voltage required for maintenance of discharge. This discharge is more pronounced at higher powers.

3. Conclusions

An ambient afterglow plasma source driven by RF power source has been demonstrated. The discharge at RF is continuous and behaves like a dielectric-barrier discharge. However at higher powers, the vibrationally stored energy in trace amounts of molecular gases start to influence the discharge.

4. References

[1] B. Eliason, and U. Kogelschatz. 1991. Nonequilibrium Volume Plasma Chemical Processing. IEEE Tran. On Plasma Science. Vol. 19, pp1063(1991).

[2] S. K. Dhali and A. K. Pal. Numerical simulation of streamers in SF_6, Journal of Applied Physics. 63:1355(1988).

[3] J. Park, I Hennis, W. H. Herman, G. S. Selwyn, J. Y. Jeong, R. F. Hicks. Discharge phenomena of an atmospheric pressure radio-frequency capacitive discharge source, J. Appl. Physics, vol. 89, 20(2001).

[4] R. Sankaranarayan, B. Pashaie, and S. K. Dhali. Characteristics of Barrier Discharge in monatomic and molecular gases, App. Phys. Let. Vol. 74, pp3199, (1999).

[5] H. D. Park and S. K. Dhali. Generation of Atmospheric Pressure Plasma with Duel-Chamber Discharge, App. Phys. Lett. Vol. 77, pp2112 (2000).

Atmospheric Pressure Plasma for Metal Surface Preparation

P. Nuamatha[1], J. K. Madella[1], Sanghamitra Dhali[1], S. K. Dhali[1] , and B. Dave[2]

[1]*Department of Electrical and Computer Engineering, Southern Illinois University, Carbondale, IL, USA*
[2]*Department of Chemistry, Southern Illinois University, Carbondale, IL, USA*

Abstract

The results of using ambient plasma for cleaning and treating metal surfaces are presented. Metal surfaces are cleaned with atmospheric pressure argon/hydrogen or argon/oxygen plasma. The cleaned surface was characterized by XPS and was found to consist of exposed metal with very low carbon content. Profilometry and optical imaging results show that plasma are very effective in removing oil and paint coatings from the surface of metals. New sol-gel coatings on metal surfaces were investigated for their corrosion properties.

1. Introduction

There are various types of corrosion that can occur on the surface of steel: direct oxidation, atmospheric corrosion, electrochemical corrosion, stress corrosion, and galvanic corrosion. To prevent rusting or corrosion, ferrous metals must either be isolated from the environment or coated in such a way that the corrosion reactions are neutralized. Good protection is associated with good adhesion, and this requires a clean surface.

The basic principle of treatment processes for steel is chemical reaction of the metal surface to produce a compound, which is more resistant to corrosion than the metal itself. Very thorough cleaning of the steel surface necessarily precedes the coating processes. The conventional methods of cleaning consist of blast cleaning, flame cleaning, acid pickling, solvent wipe, and vapor degreasing [1]. The conventional methods produce substantial toxic waste, which are difficult to dispose. As noted in the Waste Management Research Center (WMRC TN98-043) fact-sheet, industries have begun to look for alternatives to chlorinated and organic solvents [2]. For specific types of contaminants, alternatives such as aqueous cleaners, semi-aqueous cleaners, and liquid carbon dioxide have found limited use [2]. Chlorinated solvents, despite their adverse environmental effects, are still used in critical cleaning of metal parts. Various less or non-hazardous metal parts cleaning processes for the preparation/masking of parts and metal surfaces for electroplating are currently under development. However, these processes tend to be either costly or less effective compared to the chlorinated solvent processes. Hence the search for a cost effective and efficient cleaning process continues.

Plasmas can produce a clean and activated surface, which can produce chemical conversion coating with sol-gels. Chemical reactions under plasma state are very specific and can be controlled. It can be easily manipulated to produce a reducing or oxidizing atmosphere by the proper choice of additives (H_2, O_2, H_2O, and H_2O_2). Therefore plasma is very effective in cleaning and pre-treating surfaces prior to coating and electroplating.

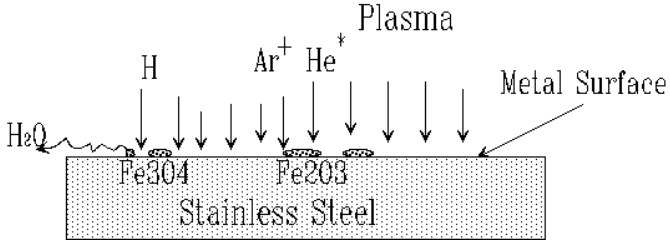

Fig. 1. Interaction of the plasma with the metal surface.

At atmospheric pressures, there are two popular methods for producing non-thermal plasmas; (1) a corona discharge and (2) a barrier-type ac discharge. Although corona discharges have found numerous applications, they are not particularly suitable for large surface or volume gas phase plasma processing [3][4]. The dielectric-barrier discharge, also known as a silent discharge or a partial discharge, is widely used in industry for ozone synthesis. These discharges can best be characterized as streamers, which are a result of space charge dominated transport in high electric fields [5].

In plasma chemical devices, the aim is to produce desired radicals to carry out a particular reaction. The main thrust for atmospheric pressure plasma for our application is the production of H and O

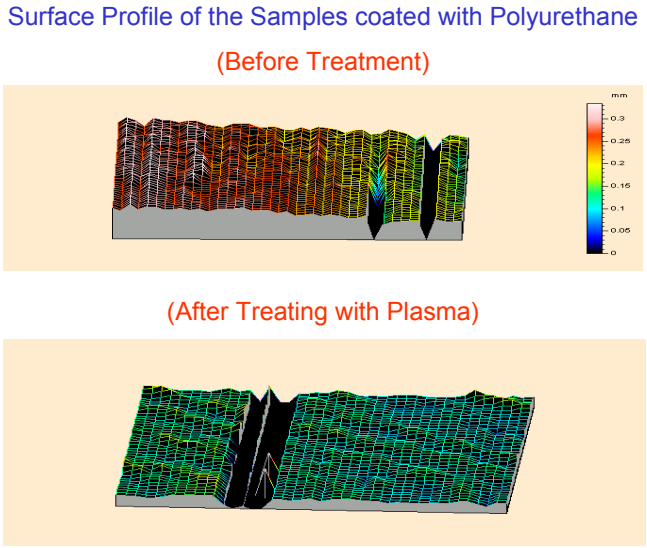

Figure 2: Results of Argon/Oxygen plasma treatment on a polyurethane coating on steel for 30 sec.

radicals and Ar ions. For efficient cleaning the production of radicals rather than gas heating is important. The ambient afterglow discharge is a cold discharge with most of its energy being utilized for the production of excited species. In $Ar/He/H_2/H_2O$ plasma the following electron impact processes will be present

$$Ar + e \rightarrow Ar^+ + 2e \text{ and } Ar^* + e$$
$$H_2 + e \rightarrow 2H + e$$
$$He + e \rightarrow He^+ + 2e \text{ and } He^* + e$$
$$H_2O + e \rightarrow H + OH$$

Modification of solid surface arising from interaction with non-thermal plasma can be broadly classified as surface cleaning and alteration, chemical alteration, etching, film deposition and texturing [6]. Non-thermal plasmas are used to remove trace contaminants and to produce rearrangement of atomic or molecular configuration, usually in preparation for further processing of the surface. The chemical composition of surface and near surface regions can also be altered by interactions with plasmas.

The interaction of the plasma with the metal surface is depicted in Fig. 1. The H atoms reduce the iron oxide along with physical sputtering by the heavy Ar^+ ions. It is expected that M-OH type of bonds will be introduced which will improve the binding properties of coating. However, the ion bombardment is not as intense as in a low-pressure discharge due to short mean free paths at high pressures. In addition to the neutral radicals, the plasma is also a rich source of UV and visible radiation. However the additional important species are the Argon metastables. These species are

long lived and have energies in 8-10 eV (electron volts). These species are capable of inducing surface reactions and break up bonds.

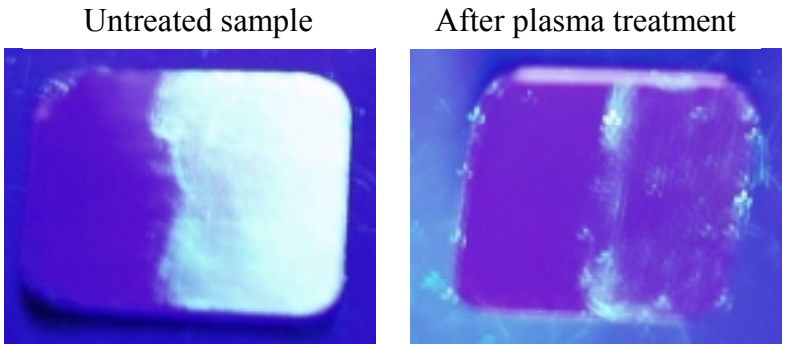

Figure 3: The bright area on the samples shows machine oil with a UV fluorescent dye. After plasma treatment of the same sample in Argon/Oxygen plasma for 30 seconds most of the oil has been removed.

A plasma treated surface can remove scaling and irregularities by hydrogen etch. This will be helpful in better adhesion of the further coating materials as well prevent corrosion of the metal surface itself by making the surface more homogeneous. Such a surface is likely to be resistant to corrosion due to removal of chemically active steps and other microdistortions [7].

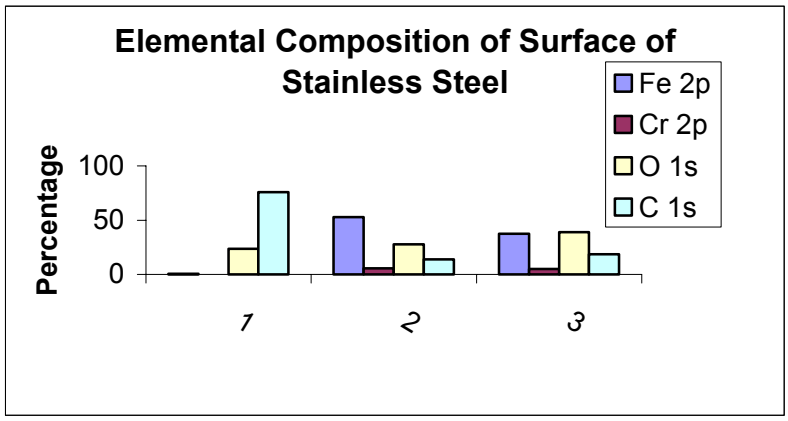

Figure 4: XPS analysis of stainless steel surface. The blank sample of steel has a coating of adhesive on it. (1) The surface composition of the blank. (2) The surface after 30 seconds of Ar/H_2 plasma treatment. (3) The surface composition after 30 seconds of He/H_2 plasma.

2. Results and Discussions

A survey of currently used methods for the removal of coatings suggests that plasma processing can be competitive due to pollution prevention. Preliminary results of plasma treatment of polyurethane on steel are shown in Fig. 2: Polyurethane is a hard durable coating and difficult to remove. The removal in Fig. 2 suggests that oxygen plasma can be very effective for removal of coatings. Traditional methods for the removal of coatings, from aircraft structures and components involve the use of chemical formulations containing strong solvating chemicals such as methylene chloride and methyl alcohol activated with strong organic acid or base materials. Scraping and/or sanding were required between applications of the strippers to remove the blistered and loosened coating. This

process involved the release of Ozone Depleting Chemicals, Volatile Organic Compounds, Hazardous and Toxic vapors, Hazardous Air Pollutants as well as the production of large volumes of contaminated wastewater from the rinsing process that is required [8].

Results from simple qualitative experiment demonstrate the effectiveness of plasma in removing contaminants. Shown in Figure 3 is a sample, which is partially coated with oil and subsequently treated with plasma. An oil soluble fluorescent dye was added to the oil to photograph the oil film.

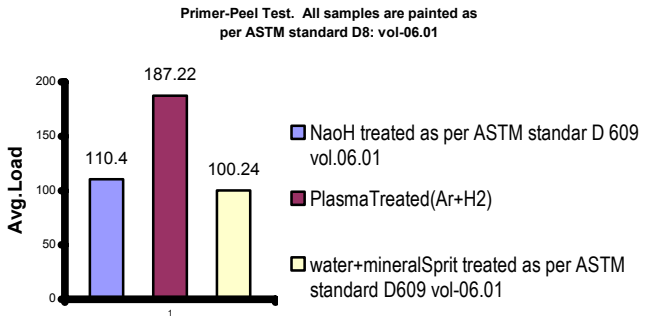

Figure 5: Peel strength for a zinc-based primer on steel.

The sample treated with Argon-Oxygen plasma for 30 seconds shows the nearly complete removal of oil from the surface of the metal. Machine oil is a silicone based organic that is high temperature resistant and stable under most chemical attack. However, an oxygen plasma removes the oil film by plasma chemical reaction through the O^* radicals to produce volatile compounds.

XPS analysis of a stainless steel surface (the surface had a layer of adhesive from a protective backing) treated with and without plasma is shown in Figure 4. The plasma used was hydrogen/argon. The untreated surface shows primarily carbon and oxygen from ester type adhesive compound. The plasma treatment removes majority of the carbon and exposes the iron and chromium. From the energy shift of the $O^1(s)$, it can be concluded that the O is bonded as OH groups to the metal on the surface. Macroscopic analysis such as contact angle adhesion of coatings and microscopic analysis such as XPS and infrared spectroscopy were used to characterize the surface and understand the cleaning mechanism.

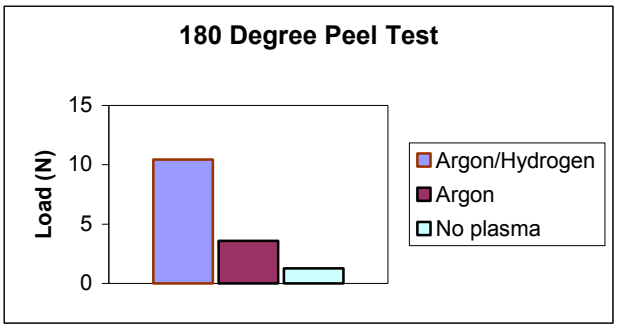

Figure 6: Peel test results of polyurethane coating on stainless steel samples. The treatment with Ar/H_2 plasma for 30 seconds shows the best peel strength.

The results presented are significant for this project as it validates the technical feasibility of the

proposed method. Figure 5 shows the results of peel strength of zinc oxide primer on steel. The Ar/H_2 plasma treatment for 30 s produces coatings, which are over 50% stronger, compared to two ASTM standards [9]. Results of polyurethane coating are even more dramatic for surfaces that are plasma cleaned compared to untreated samples. As shown in Figure 6, there is significant improvement in peel strength with plasma cleaning prior to polyurethane coating on stainless steel. The results are shown for samples, which were untreated and treated under various conditions. Treatment with Ar/H_2 plasma is most effective in cleaning compared to Ar plasma alone. The H_2 in the plasma produces the highly reactive H atoms that attack organic compounds from adhesives, grease and oil and produce volatile products.

3. Conclusions

This technique is a non-polluting alternative to surface treatments that currently use chemicals/solvents. In addition the plasma has been shown to improve the binding properties by uniformly hydroxylating the surface. The results from this research will allow the integration of plasma processes into manufacturing of metal parts.

4. References

[1] Morgans, W. M. 1990. Outlines of Paint Technology, Halsted Press, New York.

[2] Waste Management Research Center, fact sheet, Alternative to Solvents, TN98-043, Champaign Illinois, 1998, http://www.wmrc.uiuc.edu/pdf/98-043.pdf.

[3] Eliason, B. and U. Kogelschatz. 1991. Nonequilibrium Volume Plasma Chemical Processing. IEEE Tran. on Plasma Science. Vol. 19, pp1063.

[4] Masuda, S. and H. Nakao. 1990. Control of NO_x by positive and negative pulsed corona discharges. IEEE Tran. on Industrial Applications, vol. 26, pp374.

[5] Dhali, S. K., and A. K. Pal. 1988. Numerical simulation of streamers in SF_6. Journal of Applied Physics. 63:1355.

[6] Winters, H. F., R. P. H. Chang, C. J. Mogab, J. Evans, J. A. Thornton, and H. Yasuda. 1985. Coatings and surface modification using low pressure non-equilibrium plasmas, Materials Science and Engineering, vol. 70, 53-77.

[7] Gutman, E. M. 1994. Mechanochemistry of Solid Surfaces. World Scientific. New Jersey.

[8] Reinhart T. J., 2000 "Rapid Removal of Radar Absorbing Coatings," Project Report, Air Force Research Laboratory, Wright Patterson AFB, OH, UDR-TR-2000-00031.

[9] Annual Book of ASTM Standards (1996), vol. 02.05, American Society for Testing and Materials, West Conshohocken, PA.

Addition of oxygen to liquid fuel oils by means of non-equilibrium plasmas

Pedro Patiño

Escuela de Química, Facultad de Ciencias, Universidad Central de Venezuela,
P.O. Box 47102, Caracas 1041A, Venezuela

Abstract
The oxidation of 6 model liquid hydrocarbons, mixtures of them, and 3 commercial diesel fuels, by means of low pressure high-voltage oxygen plasmas was studied. O_2 pressure was 0.2 mbar, applied power was 35 W and reaction times ranged from 1 minute to 23 hours. Olefins were the most reactive with ground-state atomic oxygen, $O(^3P)$. Addition of 4.7 to 7.8% wt of oxygen was achieved for the diesels, depending on the particular composition.

Introduction
The use of oxygenate compounds as additives in fuel formulations improves the combustion process in engines because they diminish particulate emissions (PE), non-burnt hydrocarbons and carbon monoxide[1]. Recently, various types of oxygen containing compounds have been tested in engines to determine the effects of oxygenates on exhaust emissions[2-4]. Among 7, tripropylene glycol mono-methyl ether and dibutylmaleate have been the most promising for diesel engine testing[5-6]. PE has been 26.1% below that of the base fuel for 7% wt. of oxygen.
Oxidation of fuel oils has also been performed classically by means of methodologies based on $KMnO_4$ and $K_2Cr_2O_7$ with catalysts and pH adjustment[7-9]. More recently, O_2 low pressure plasmas have been employed to increase the cetane number of a light diesel fuel by 66%[10].
The interaction of plasmas with gases and solids has been studied extensively, leading to numerous syntheses techniques[11] and methods for surface modifications[12]. Under certain conditions, electrical discharges through molecular oxygen produce predominantly ground state atomic oxygen, $O(^3P)$. This species in turn reacts with liquid organic compounds[13-19].
This paper is devoted to the oxidation of commercial diesels by means of low pressure high-voltage oxygen plasmas. In order to fully understand the contribution of the different fractions forming part of every diesel, the oxidation of n-heptane, 1-octene, toluene, *cis*-decahydronaphthalene, mixtures of them, 4-phenyl-1-butene and 1,2,3,4-tetrahydronaphthalene have been investigated separately.

Experimental
The reactions were carried out by allowing the oxygen plasma to reach the low vapour pressure liquid substrate. The plasma was produced by means of a high voltage discharge. A diagram of the experimental assembly is shown elsewhere[17]. The reactor was a glass vessel of ca. 300 ml, supplied with two electrodes made of aluminium and Teflon. O_2 was introduced through one of the electrodes, which was hollow. Applied power was 35 W for all experiments. The liquid (2 ml) was placed in the reactor, cooled by means of a methanol-liquid nitrogen bath, and magnetically stirred. The system was connected to a vacuum line; one trap was used to collect any volatile product. The O_2 flow was measured with a 247 B-MKS flow meter and the pressure was monitored with a Leybold-Heraeus TM111 thermotron. The products of the reactions were identified and quantified by using the following: a Varian 3800 GC/Saturn 2000 MS system; a Perkin Elmer FTIR 1700X spectrometer; a JEOL ECLIPSE 270 MHz NMR spectrometer.

Results
Model compounds
1-Octene
The oxidation of 1-octene was studied as a function of the oxygen pressure in the reactor, at a constant temperature of –90°C. The shape of the curve is very similar to that obtained for the optical emission signal of the $3p\ ^3P \rightarrow 3s\ ^3S$ (λ=844.6 and 844.7 nm) transition[10], that can be

correlated to the population of O I (2p ^{3}P), the ground state of atomic oxygen. The results confirm that O(^{3}P) is the most relevant oxidant species in the plasma. In fact, the production of oxygen atoms by electron impact with O_2 is scarce at the side of low pressure. When the latter is increased more atoms are produced but, at a certain pressure, the frequency of collisions between electrons and oxygen molecules becomes great enough to reverse the tendency. The electrons are not sufficiently accelerated by the electric field and hence most of them do not acquire enough energy to produce the dissociation of O_2. The pressure for maximum production of O(^{3}P) is somewhere between the two extremes.

Total conversion was maximum at about 0.2 mbar. At –90°C, the vapour pressure (*vp*) of 1-octene is 0.0022 mbar, thus the pO_2/vp ratio was 90.9, i.e., in agreement with earlier works[17,18]. Products were 1,2-epoxioctane (39.0% of the mixture) and octanal (21.0%) for 60 minutes of reaction; 2-octanol, 2-octanone, octanoic acid and compounds with two oxygenate groups were byproducts. No evidence of singlet O_2 ($a^1\Delta_g$) was detected in the optical emission spectrum under the conditions of the discharge. The corresponding hydroperoxide, product of the reaction of singlet oxygen with olefins, was not observed in the reaction mixtures.

Toluene

By fixing pO_2 at 0.2 mbar, oxidation of toluene was studied versus its temperature, for 60 minutes. Conversion reached a maximum of 16.0% at –95°C, *vp* of toluene being 0.0011 mbar, i.e., $pO_2/vp = 182$. *o*-Cresol represented 12.6% of the mixture while *p*-cresol and *m*-cresol were 2.3% and 1.1% respectively. By increasing the temperature more toluene molecules evaporate. Therefore these molecules, much bigger than O_2, compete advantageously with it for the electrons and the amount of O(^{3}P) in the plasma decreases. Due to this, the conversion of toluene decreases too. If the temperature is too high, then collisions between electrons and toluene dominate the plasma and fragmentation plus condensation products, arising from oxygen-free organic radicals, are the main products. From the point of maximum conversion to lower temperatures, the reactivity decreases. Close to the freezing point of the hydrocarbon, the interaction becomes one between oxygen atoms and a solid. It is well known that the reactivity in this case is negligible[17].

n-Heptane

The study of n-heptane had been performed earlier at lower power[17]. In order to explore the conditions for the mixture of hydrocarbons, its oxidation was repeated at –88°C, 0.2 mbar of oxygen ($pO_2/vp = 33$) and 60 minutes. Total conversion was 26.0%, products distribution being 3-heptanol > 2-heptanol > 4-heptanol > 3-heptanone > 2-heptanone > 4-heptanone. None of the ketones was among the products in the mixture at 15 minutes of reaction, thus confirming that these compounds are produced by successive oxidation of the alcohols[17].

cis-Decahydronaphthalene

cis-Decaline was studied at similar conditions used for the previous compounds, except for its temperature which was –40°C ($pO_2/vp = 20$). Total conversion was 10.1%, the most important products being *cis*-10-decahydronaphtol (36.9%), *trans*-10-decahydronaphtol (3.2%), 1-decahydronaphtol (4.8%), *cis*-1-decalone (5.8%), *trans*-1-decalone (3.4%), 2-decahydronaphtol (12.6%), *cis*-2-decalone (6.0%), *trans*-2-decalone (4.7%), 1,10-deca-hydrodinaphtol (2.2%) and 5,10-decahydrodinaphtol (4.1%).

4-Phenyl-1-butene

This is an interesting model for it contains olefinic, aromatic and paraffinic fractions. The working conditions different from those for previous compounds were temperature, –63.0°C ($pO_2/vp = 46$), and time of reaction: 1, 2, 3, 4, 5, 30, 60 and 120 minutes, respectively. The objective was to determine how the different fractions reacted with O(^{3}P). At 1 minute, all signals in the ^{13}C NMR spectrum were assigned to 4-phenyl-1,2-epoxibutane. Four more signals appeared at 2 minutes, assigned to 4-phenylbutanal. By increasing the time of reaction these signals became stronger, and four new signals were observed after 30 minutes. They were due to 4-phenyl-2-butanone. Two more, weaker than the latter, assigned to 4-phenyl-2-butanol, were

observed after 60 min. There was no evidence of reaction on the benzene ring, nor on the 2 paraffinic $–CH_2–$. This result confirms that olefins are more reactive with $O(^3P)$ than alkanes and aromatics[10]. Total conversion was 45% at 60 minutes, main products being the epoxide (48.0 %), the aldehyde (38.3 %), 4-phenyl-2-butanone (9.4 %), and 4-phenyl-2-butanol (2.3 %).

1,2,3,4-Tetrahydrohaphthalene

Tetraline possesses 4 different carbons that can be attacked by $O(^3P)$, two in the aromatic ring and two in the naphthenic fraction. It was oxidized at –28°C, i.e, $pO_2/vp = 22$. Total conversion rate was 19.0% at 60 minutes of reaction. The main products were 1-hydroxi-1,2,3,4-tetradydronaphthalene (*A*), 2-hydroxi-1,2,3,4-tetradydronaphthalene (*B*), 7-hydroxi-1,2,3,4-tetradydronaphthalene (*C*), and 8-hydroxi-1,2,3,4-tetradydronaphthalene (*D*), the proportion *C:B:A:D* being 1:1:1.23:2.29. This means that the aromatic fraction was ca. 1.47 times more reactive than the naphthenic fraction, in agreement with the ratio toluene/*cis*-decaline ≅ 1.58.

Fuel oils

Some properties of the three diesel fuels are given in Table 1, together with those of LCGO, a light gas oil product of a coking process, previously studied[17]. They are commercial fuels with particular specifications. In order that the $p(O_2)/vp$ ratio of each fuel was >20, each sample was cooled down to a temperature close to its freezing point, thus guaranteing that the amount of hydrocarbon molecules in the gas phase was low enough to avoid homogeneous gas-phase reactions. The working temperatures are given in the first raw of Table 1. All samples were treated at an oxygen pressure of 0.2 mbar for 23 hours.

The main feature in the IR spectra of the three diesels, after treatment with the oxygen plasma, was the appearance of the bands at 1100, 1750 and 3400 cm^{-1}, due to the –C–O, –C=O and –O–H stretchings respectively. This was the first evidence of the addition of oxygen to the fuels.

The three diesels had in common ^{13}C NMR signals in the regions (ppm): 9-48 (aliphatic) and 121-148 (aromatic). Olefinic signals, around 3.8-5.2 ppm in the ^1H NMR spectra, showed an integrated area of less than 1% of the aromatic ones. After 23 hours of reaction, new signals appeared in the ^{13}C NMR spectra, at 50-75 ppm and 90-122 ppm, corresponding to carbons α to OH groups, and CH α and β to OH. Week signals due to carbonyl groups were observed around 200 ppm. Signals at 118 ppm, due to phenols, were not observed.

Table 1. Properties of fuel oils and percentage of oxygen added with the plasma

Property	10% Aromatics (TPCA) -32 °C	Ultra low sulfur (ULS) -38 °C	Low sulfur (LS) -35 °C	LCGO[10]. -40 °C
API gravity	34.24	39.77	36.21	33.80
Distillation (°C)	167.2-344.0	183.1-352.5	-	180.7-273.8
Cetane number	54.2	46.0	50.2	37.7 (62.6)[§]
Alkanes (% vol.)	92.5	73.9	90.6	62.1
Naphthenes (% vol.)	32.3	1.1	12.8	38.8
Olefins (% vol.)	<0.1	<0.1	<0.1	3.1
Aromatics (% vol.)	7.5	26.1	9.4	34.8
Carbon content* (% wt.)	86.5 (82.0)	85.0 (81.4)	86.0 (80.4)	86.2 (72.0)
Hydrogen content* (% wt.)	13.0 (12.7)	14.0 (13.0)	13.2 (12.1)	11.8 (10)
Oxygen content (% wt.)	7.8	4.7	7.0	16.8
Treatment time (hours)	23	23	23	3

*Prior and (after treatment). Oxygen was not detected for any original sample and nitrogen was the balance element. [§]After treatment.

Mixtures

Four mixtures were studied representing LCGO[10] and the three diesel fuels respectively. n-Heptane, *cis*-decahydronaphthalene, 1-octene and toluene were mixed to simulate them. LCGO was the most widely studied. The compositions of the simulated mixture and the original gas

oil, prior and after treatment, are given in Table 2. The amount of the olefinic fraction in the synthetic sample was higher (4.5%) than in the original one (3.1%). That is the reason why the former needed a shorter time to be oxidized. Samples treated for 10 minutes only showed some signals of products arising from the olefin, i.e., 1,2-epoxioctane and octanal, in the ^{13}C NMR spectrum. At 60 minutes, the conversions of the four components were: 1-octene (100%), n-heptane (49.7%), toluene (40.6%) and *cis*-decahydronaphthalene (12.8%).

Table 2. Properties of original and simulated LCGO prior and after treatment

Property	Original	Original treated –40 °C, 120 min	Simulated	Simulated treated, -90 °C, 60 min
Alkanes (vol %)	62.1	73.9	61.4	73.9
Aromatics (vol %)	34.8	26.1	34.1	26.1
Olefins (vol %)	3.1	0.0	4.5	0.0
Carbonyl index (%)*	0.0	6.0	0.0	2.4
Alcohols and epoxide Index (%)*	0.0	4.4	0.0	6.5

*Calculated from NMR spectra

Table 3 shows the results for the treatment of the three simulated diesel fuels, namely Ten Per Cent Aromatics (TPCA), Ultra Low Sulphur (ULS) and Low Sulphur (LS). The calculated $p(O_2)/vp$ ratio of each mixture was higher than 20 at –90 °C. TPCA fuel was the synthetic sample that gave the highest conversion with the oxygen plasma, in agreement with its highest original percentage of paraffins. The higher contents of oxygen in the treated simulated samples compared to those of the original ones could be related to the fact that no poly-aromatic compounds were employed in the mixtures. These species are less reactive than mono-aromatics becasuse of the lower number of C-H bonds per carbon atoms in the former.

Table 3. Total conversions of simulated fuel oils treated with the oxygen plasma (0.2 mbar) for 23 hours. Temperature: -90 °C

Parameter	**TPCA**	**ULS**	**LS**
Paraffins (%)	60.1	74.7	77.3
Naphthenes (%)	32.5	2.0	13.2
Aromatics (%)	7.4	23.3	9.5
Total conversion (%)	35.0	28.3	33.5
Oxygen (% wt.)	12.1	9.4	11.0

Discussion

Among the different kind of hydrocarbons studied, olefins have shown to be the most reactive with $O(^3P)$. This is due to the electrophilic character of $O(^3P)$, the most accepted mechanism for the reaction with olefins involving the formation of a diradical triplet transition state[20-22].

The mechanism for the reaction of $O(^3P)$ with alkanes is the abstraction of an H atom to produce an alkyl and an OH radicals, followed by their recombination to produce the alcohol[17].

The results for toluene are similar to those for other aromatic compounds[18], and they all agree with the proposed mechanism for reaction of $O(^3P)$ with olefins. The situation has been quite different when oxidation of toluene has been studied in a radio frequency homogeneous plasma, i.e., by introducing mixtures of oxygen and gaseous toluene in the reactor[24]. In this case, the product is a mixture of benzaldehyde, benzyl alcohol, phenol, *o-, m-,* and *p*-cresol, and bibenzyl.

The most important result of this study has been the successful addition of oxygen to LCGO and the three diesel fuels. They are difficult to oxidize by classical means with inorganic agents.

According to expectations, LCGO showed the highest reactivity, due to its highest percentage of olefins. The amount of this kind of hydrocarbons was meaningless in the three diesel fuels. The lowest oxygen percentage of the treated ULS fuel can be associated with the higher percentage of aromatics in its composition. This fraction has shown to be less reactive than paraffins. The

different reactivity of the three fuels could be understood after deeply analyzing their ^{13}C NMR spectra. This technique was used to calculate the proportions of the different kinds of carbon atoms in each fuel. This parameter should be more suitable than the whole amount of hydrocarbons to be correlated with the conversion of each fuel. The 5-60 ppm region of the ^{13}C NMR spectra of non-treated TPCA, LS and ULS fuels, presented in Figure 1, corresponds to the aliphatic carbons. The regions of aromatic carbons (110-150 ppm) of LS and ULS show similar signals while that of TPCA is much simpler, indicating the presence of a higher percentage of mono-aromatic structures in this fuel. This observation favours the latter, in the reaction with $O(^3P)$, respect this kind of hydrocarbons. The spectra show sharp signals at 14.2, 22.8, 29-30 and 32.0 ppm, due to linear alkanes. It has been shown that the integration of their areas permits to determine the relative percentage of this kind of structures in the respective fuel[25]. Results are given in Table 4. They show a higher amount of aliphatic carbons (95.75%) and lower amount of aromatics in TPCA fuel. This is in good agreement with the fact that this fuel added the highest amount of oxygen. Although LS and ULS fuels contain similar amounts of aliphatic and aromatic carbons, the ^{13}C NMR spectrum of the former shows well defined signals at 11, 19, 27, 37 and 40 ppm, assigned to branched-paraffins. These sharp signals are not observed in the spectrum of ULS fuel. The complexity and higher dispersion of the many weaker bands observed in the latter are indicative of hydrocarbons with poly-ringed naphthenic structures. These two observations, particularly the first, could explain the higher conversion of LS fuel compared to ULS fuel. It has been demonstrated that the different C–H of alkanes react with $O(^3P)$ in the order tertiary > secondary >> primary. This is due to the average bond strengths, 92, 95 and 100 kCal/mol respectively. As an illustration, n-heptane and 4-methylheptane have both 5 carbons potentially reactive with $O(^3P)$ at short to moderate times, that is not taking into account the methyl groups which react at times as long as 120 minutes[10,17]. Their treatment with the plasma, at 0.2 mbar of oxygen for 30 minutes, produced total conversions of 14.1 and 39.9% respectively, i.e., the conversion per reactive carbon was 2.8% for n-heptane and 8.0% for 4-methylheptane. This is obviously due to a 25.8% extra reaction on the tertiary C–H respect to the methylenes.

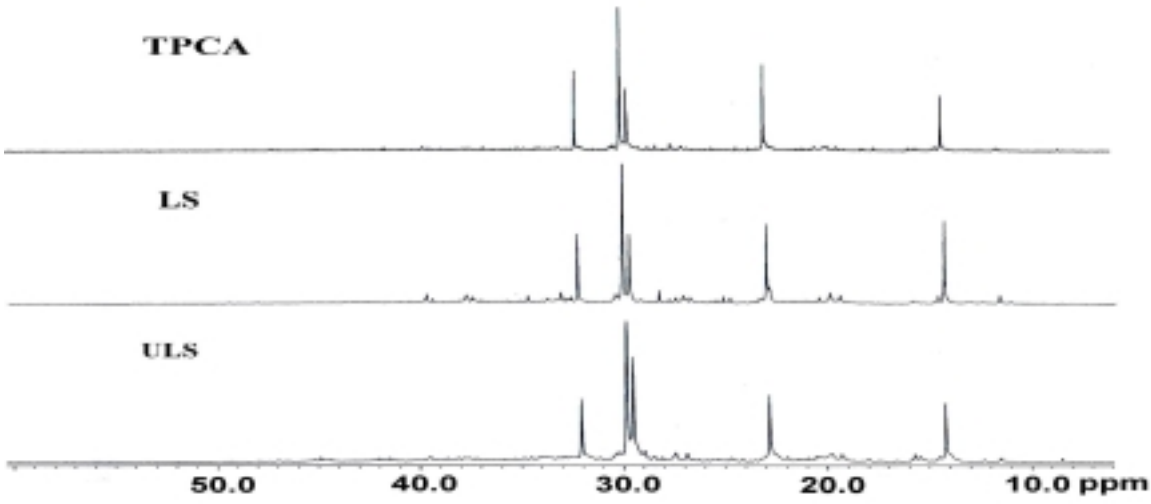

Figure 1. 75.4 MHz ^{12}C NMR spectra of the TPCA, LS and ULS fuel oils. Only the aliphatic region is shown.

Table 4. NMR percentages of different types of carbon in the diesel fuels.

Fuel	Aliphatic C (%)	Aromatic C (%)	n-Paraffinic C (%)
TPCA	95.75	4.25	34.38
LS	84.82	15.18	24.25
ULS	84.86	14.54	28.64

Conclusions

Once again, low pressure oxygen plasmas have proved to be an efficient tool to oxidize liquid hydrocarbons in one-step process. Addition of oxygen to commercial diesel fuels by this technique is comparable to mix them with commercial oxygenate compounds. This should traduce in improving automotive engine performance and reducing exhaust emissions.
Olefins are more reactive with $O(^3P)$ than the other kinds of hydrocarbons.

Acknowledgements. Funding for this research has been provided by Fondo Nacional de Investigaciones Científicas (FONACIT) through Grant 97003740.

References

1 I.K. Karas, H.S. Jr. Kesling, F.J. Liotta, M.K. Nandi, *ACS Division of Fuel Chemistry Preprints* 1994, **39**(2), 316.
2 R.L. McCormick, J.D. Ross, M.S. Graboski, *Environ. Sci. Technol*. 1997, **31**, 1144.
3 T. Litzinger, M. Stoner, *International Journal of Engine Research* 2000, **1**, 57.
4 F. Takahashi, I. Glassman, *Combustion Sci. and Technol*. 1984, **37**, 1.
5 M. Natarajan, E.A. Frame, D.W. Naegeli, T. Asmus, W. Clark, J. Garbak, M.A. González-D., E. Liney, W. Piel, J. P. III. Wallace, Society of Automotive Engineers, Inc. Paper N° 01FL-576, 2000.
6 M.A. González-D., W. Piel, T. Asmus, W. Clark, J. Garbak, E. Liney, M. Natarajan, D.W. Naegeli, D. Yost, E.A. Frame, J.P. III Wallace, Society of Automotive Engineers, Inc. Paper N° 01FL-577, 2000.
7 Ch. Venkat, N.J. Bellemead, D.E. Walsh, P. Richboro, United Stated Patent Nº 4494961, 1985.
8 W.F. Taylor, N.J. Mountainside, United States Patent N° 4723963, 1988.
9 A. Chertkov, E.A. Kunina, T.I. Kirsanova, *J. Appl. Chem. of URSS* 1980, **53**(7), 1245.
10 G. Gambús, P. Patiño, B. Méndez, A. Sifontes, J. Navea, P. Martín**,** P. Taylor, *Energy & Fuels* 2001, **15**, 881.
11 H. Suhr, *Plasma Chem. Plasma Process.* 1983, **3**, 1.
12 R. d'Agostino (Ed.) *Plasma Deposition, Treating, and Etching of Polymers,* Academic Press, Inc., San Diego, Ca, 1990.
13 S. Hirokami, R.J. Cvetanovic, *J. Am. Chem. Soc.* 1974, **96**, 3738.
14 E. Zadok, D. Amar, Y. Mazur, *J. Am. Chem. Soc*. 1980, **102**, 6369.
15 R. Klein, M.D. Scheer, *J. Phys. Chem.* 1969, **73**, 1598, R. Klein, M.D. Scheer, *ibid.* 1970, **74**, 613, M.D. Scheer, R. Klein, *ibid.* 1970, **74**, 2732.
16 H. Suhr, H. Schmid, H. Pfeundschuh, D. Iacocca, *Plasma Chem. Plasma Process.* 1984, **4**, 285.
17 P. Patiño, F.E. Hernández, S. Rondón, *Plasma Chem. Plasma Process*. 1995, **15**, 159.
18 P. Patiño, M. Ropero, D. Iacocca, *Plasma Chem. Plasma Process*. 1996, **16**, 563.
19 P. Patiño, N. Sánchez, H. Suhr, N. Hernández, *Plasma Chem. Plasma Process*. 1999, **19**, 241.
20 S. Sato, R.J. Cvetanovic, *J. Am. Chem. Soc.* 1959, **81**, 3223.
21 R.J. Cvetanovic, *Can. J. Chem*. 1960, **38**, 1678.
22 R.J. Cvetanovic, *Adv. Photochem*. 1963, **1**, 115.
23 P. Andresen, A.C. Luntz, *J. Chem. Phys.* 1980, **72**, 5842.
24 M. Tezuka, T. Yajima, *Plasma Chem. Plasma Process*. 1996, **16**, 329.
25 M.U. Hasan, A. Bukhari, M.F. Ali, *Fuel* 1995, **64**, 839.

Plasma diagnostic of a pulsed MSIP-process by energy-resolved mass spectroscopy

E. Lugscheider, N. Papenfuß-Janzen
Materials Science Institute, RWTH Aachen University, Aachen, Germany

Abstract
Reactive Magnetron Sputter Ion Plating (MSIP) is a conventional process for the coating of tools. Nowadays, the coating of machine parts against wear and corrosion is an application of this process, as well. To produce homogeneous coatings and to achieve a higher efficiency, especially for the coating with insulating materials, the pulsed MSIP was developed. In this article, plasma diagnostic measurements of a pulsed MSIP process of TiAlN is presented using energy resolved mass spectroscopy showing the advantages of this process.

1. Introduction

Ceramic coatings show a good protection against wear and corrosion. Thus, they are commonly used to increase the life cycle of tools and machine parts. A coating process that is suitable for this application is magnetron sputter ion plating (MSIP). In this process, a target is mounted on a magnetron cathode where material is sputtered by impacting process gas ions, e.g. argon, produced by a low pressure glow discharge plasma. A thin ceramic compound forms at the metallic target, the substrate and the reactor walls during reactive MSIP. In this process mode, an reactive gas, e.g. oxygen or nitrogen, is supplied to the reactor in addition to the process gas. Due to the insulating behavior of a number of ceramics, e.g. Al_2O_3, a dc-voltage power supply to the cathodes is not suited for those materials. Instead of this, radio frequency (rf) plasmas are used to overcome this effect. The rf-MSIP process shows its potential in producing very homogeneous coatings, but it has only a low coating efficiency.
Within the last few years, the pulsed plasma technology has become an increasing importance. This technology shows the advantages of both process variations, the dc-MSIP and the rf-MSIP. Pulsed plasma MSIP is suitable for insulating coatings [1, 2] as well as for high quality, homogeneous coatings. Different types of pulsed plasma MSIP processes have been developed: sinusoidal and dc-voltage, single cathode and dual cathode mode, unipolar, bipolar, symmetric and asymmetric charged.
In this article, energy resolved mass spectroscopy measurements are presented. The reactive MSIP process of the well known coating material (Ti, Al)N was chosen for this purpose[3]. The mass spectrum in the sims mode (secondary ion mass spectroscopy) is shown and the titanium ion energy distribution for dc-MSIP is compared to the pulsed MSIP for different cathode power. The reason for the good performance of the pulsed process will be pointed out. At the end of the article, concluding remarks and an outlook to further research will be given.

2. Mass Spectroscopy

For the presented work a HIDEN EQP 300 mass spectrometer (Figure 1) was used. An excellent description of this diagnostic tool was given by Budtz-Jørgensen [4] and is sketched below. It was applied to a glow discharge sputtering unit to understand the argon-hydrogen plasma as well as the argon-nitrogen plasma in a plasma nitriding process. First measurements of the MSIP process to produce TiN coatings and TiWN were presented by Mišina et al. [5].
The HIDEN EQP 300 consists of five main sections. The functions of those sections should briefly be explained. The extraction section consists of the extractor and the lens 1. In this part the ions and neutrals that pass the orifice have to be directed towards the detector. The ionization source is only needed when measurements in the RGA mode are conducted. Then neutral particles are ionized by a dual-filament electron impact ionization source. The deceleration section consists of the axis, the lens 2 and the quadrupole lens. This section is needed to decelerate the ions to an energy of about 40 eV. Only at this low kinetic energy ions can pass the 45° bend to the analyzer. The energy filter is a 45° sector field energy analyzer, where ions are deflected by an electric field depending on their kinetic energy when the particles enter the section field. The last part of the HIDEN EQP 300 is the mass filter. This filter is a quadrupole mass spectrometer consisting of four metal rods with a superposed dc and rf voltage. Only particles with a special

mass-to-charge ratio can pass this filter and can be detected, while the other m/q ratios are removed by the rf-field and the dc-field, respectively.

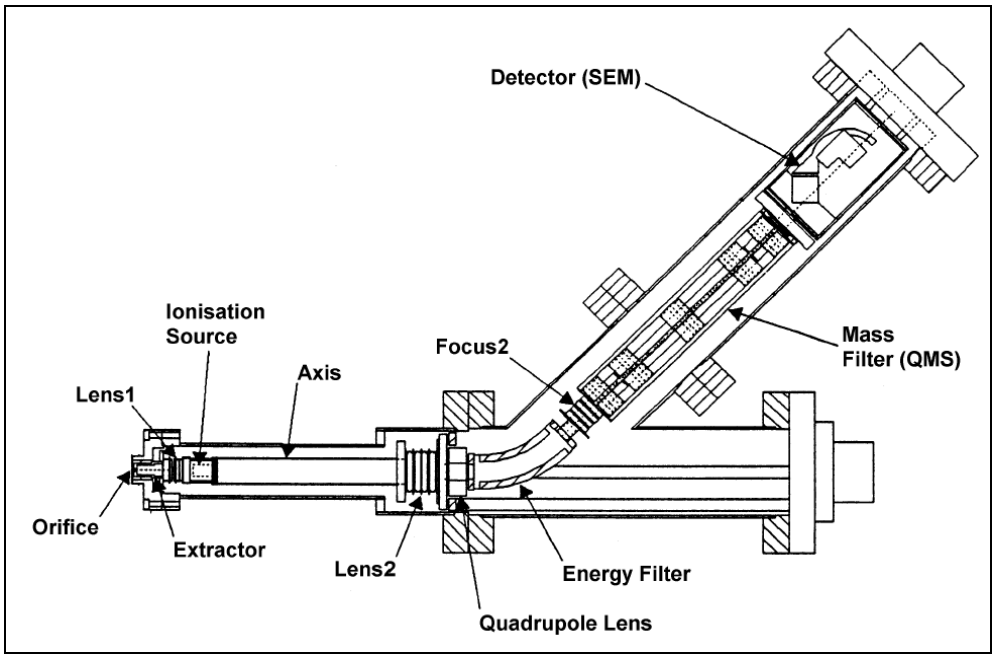

Figure 1: Assembly of the HIDEN EQP [4]

3. Experimental Details

The measurements were carried out with a HIDEN EQP 300 energy resolved mass spectrometer at the Materials Science Institute at the Aachen University on an industrial MSIP coating unit of the type CemeCon CC 800®/9 with four cathodes CST 288. The mass spectrometer was positioned parallel to the cathode with a distance of about 600 mm for the presented experiments. The observed coating material was (Ti, Al)N, produced by magnetron sputtering of two-component-Ti-Al-targets with nitrogen as a reactive gas. Argon and krypton were used as process gases.

The pulsed plasma experiments were conducted by using two sinusoidal pulsed power supplies of the type PE II by Advanced Energy Industries. These supplies operate in a dual cathode mode as shown in Figure 2. Two cathodes get a sinusoidal negative voltage, while the corresponding cathodes are discharged. The output frequency is 40 kHz. First results concerning the use of this technology on (Cr, Al) N coatings were presented, recently [6, 7].

The mass spectroscopy measurements were conducted in the sims mode. Therefore, only ions were detected and no further ionization of neutral particles was forced by high energy electrons.

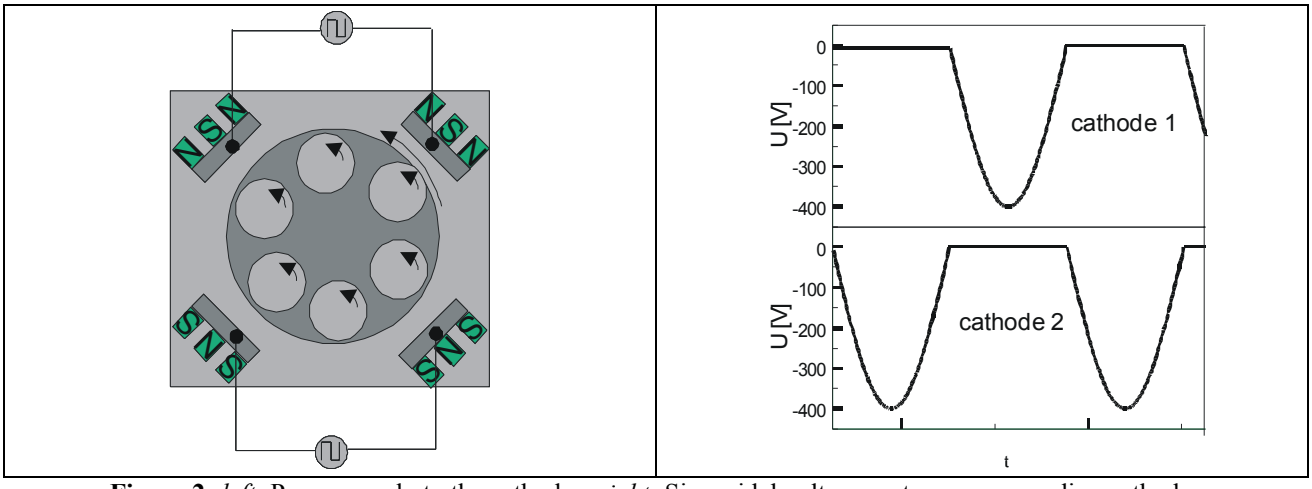

Figure 2: *left:* Power supply to the cathodes; *right:* Sinusoidal voltage on two corresponding cathodes

4. Results

First, a mass spectrum was taken in the dc-process as well as in the pulsed process with fixed gas flows and a power per cathode of 4 kW (Figure 3). It can be seen, that the spectra only differ slightly. Mainly, ionized gas atoms and molecules are detected (N^+, N_2^+, Ar^+, Kr^+). The ionization of the metal components Ti and Al is lower than the one of gases. It can be observed, that more titanium ions are detected than aluminum ions, which corresponds to the fact, that the sputter rate of titanium is much higher than the one of aluminum in the reactive mode. In this experiment, the ionization does not depend on the type of the power supply.

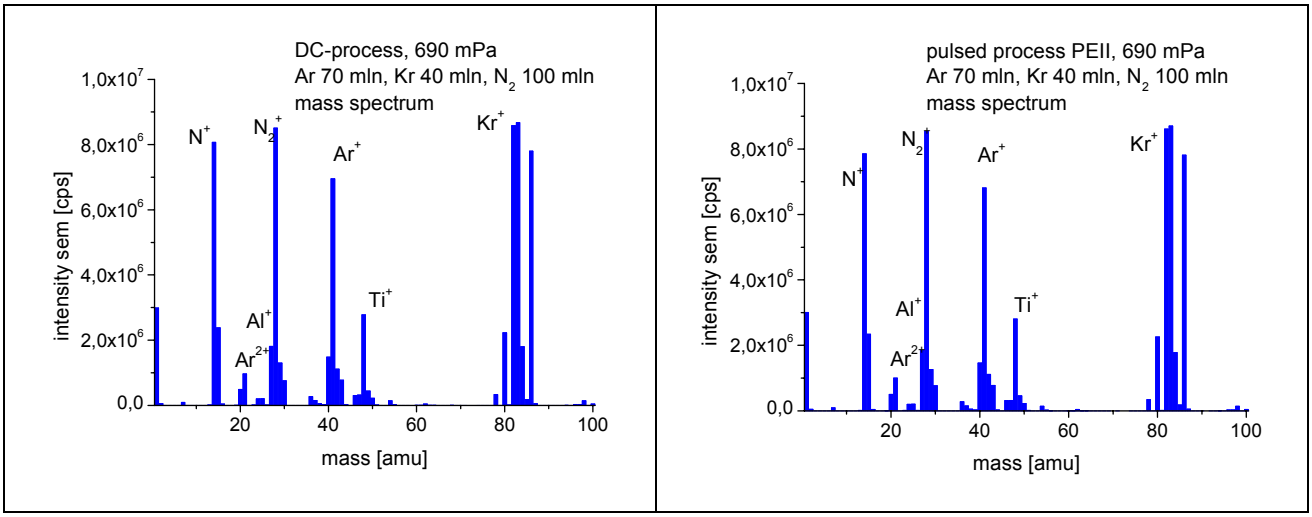

Figure 3: Mass spectra of a (Ti, Al)N coating process; *left:* dc-process; *right:* pulsed process

The energy distribution of Ti^+ 48 ions for different cathode powers is presented in Figure 4. In the dc-process, the maximum of the distribution is at about 5 eV. It can be seen, that there is a strong influence on the power per cathode on the intensity at the maximum. The increase of the detection intensity from 1 kW to 3 kW is more than one order of magnitude. However, the width of the distribution is only small (0-13 eV).
The ion energy distribution of the pulsed process shows a different behavior. The maximum of the distribution is at about 10 eV with only a slight increase of the intensity due to increasing cathode power. At 1 kW/per cathode a second maximum is observed at about 25 eV. With an increasing cathode power this maximum is flattened, but a broader distribution can be seen up to ion energies of 45 eV.

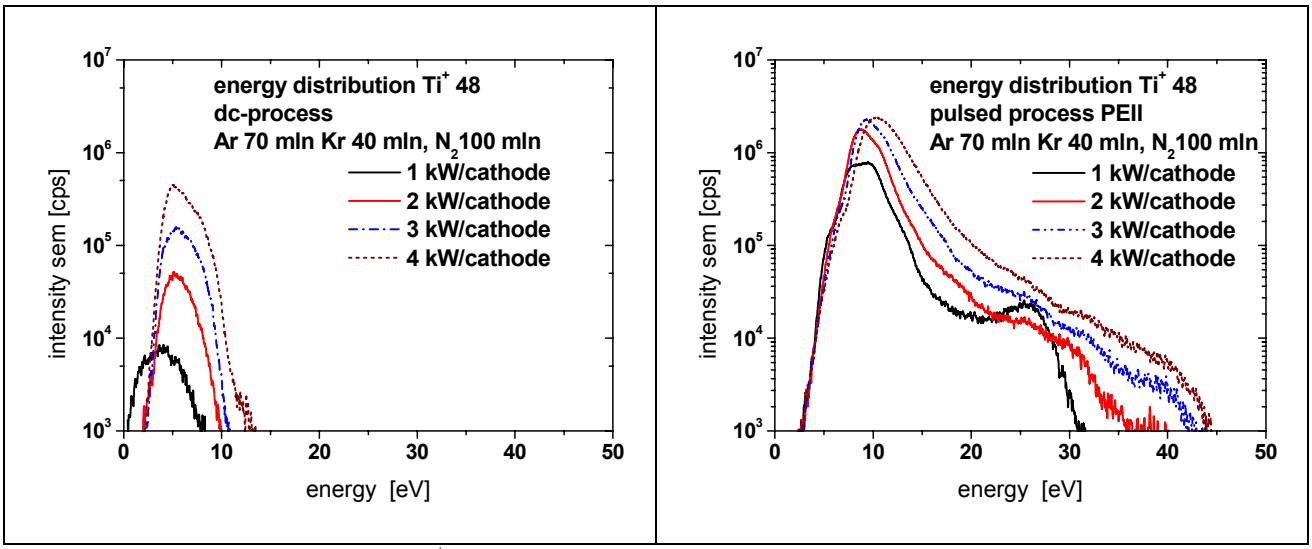

Figure 4: Energy distribution if Ti^+ 48 depending on the cathode power; *left:* dc-process; *right:* pulsed process

A characteristic value for the ion energy consumption is the integral of the distribution. The dependency of this integral on the cathode power is shown in Figure 5. Even with the lowest cathode power (1 kW/cathode) ions in the pulsed process have a higher energy than in the dc-process. Furthermore, a different behavior of the energy depending on the cathode power can be observed. While the pulse process exhibits an almost linear behavior, the energy increases superproportional with an increasing cathode power in the dc-process.

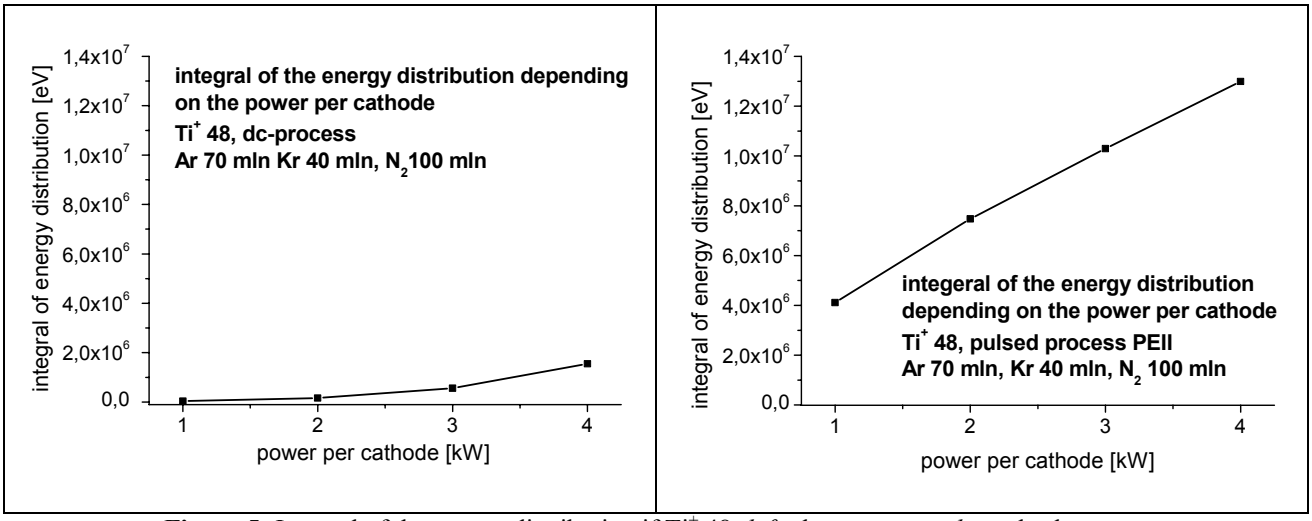

Figure 5: Integral of the energy distribution if Ti^+ 48; *left:* dc-process; *right:* pulsed process

5. Discussion

The results presented above underline the great potential of the pulsed MSIP process. It was shown, that the same cathode power in the pulsed process leads to a higher energy of ions. Thus, it can be explained why coatings from pulsed processes exhibit a more homogeneous structure.

In dc-processes the energy of the impacting ions and atoms is usually not sufficient to force the coating atoms to find the absolute minimum of the energy potential. Thus, the atoms stay in local potential wells forming a columnar crystalline structure. However, with the higher impact energy in the pulsed process the particles have a higher kinetic energy when they are caught at the substrate. The particles have a higher statistical probability to leave the local potential well to find the global minimum and form a homogeneous, crystalline structure. This is an effect that is observed in dc-processes. Coatings show a better quality when a higher cathode power was used for this process. However, coating processes with high cathode power are connected with a great amount of thermal energy input into the facility. This requires an increasing heat transfer out of the coating unit and it leads to a significant thermal load on the substrates.

Therefore, hard coatings can be applied at a low temperature with the pulsed process, because the energy is sufficiently high even with low cathode power. Due to the low power, the temperature load on the substrate is small compared to the load in the dc-process with an equivalent ion energy. This makes the pulsed process interesting for the coating of temperature sensitive substrates, e.g. machine parts or plastics.

6. Conclusion

In this article, a plasma diagnostic comparison between dc-MSIP and pulsed MSIP was presented. It was shown, that the composition of the plasma does not dependent on the process mode, whereas the energy is strongly connected with the process. It was observed, that the particles in the pulsed process have a much higher energy than in the dc-process. This may be one reason for the significant better quality of pulsed coatings with equivalent cathode power. Therefore, the use of the pulsed MSIP for low temperature processes with good coating performances is possible.

In future work, the behavior of other coating materials has to be observed. Especially, the energy of aluminum ions is of high interest, because the aluminum fraction in the coating is much smaller than the titanium fraction. To develop coatings with a greater aluminum fraction the knowledge of the dependencies between the ion energy and the process parameters is crucial.

In addition to this, the influence of the coating parameters pressure, gas flow composition, bias voltage has to be investigated. For the use in process control and process simulation, a spatial resolution of the plasma is

necessary. The energy resolved mass spectroscopy then would be able to measure required boundary conditions to conduct plasma simulation and thus to improve the knowledge about the process.

7. Acknowledgement
The authors gratefully acknowledge the Deutsche Forschungsgemeinschaft (DFG) for the financial support within the collaborative research center SFB 442 and the project Lu 232/74-1.

References

[1] R. Cremer, M. Witthaut, D. Neuschütz, G. Erkens, T. Leyendecker, M. Feldhege - Surf. Coat. Tech. **120-121**, 213 (1999)
[2] A. Schütze, D.T. Quinto - Surf. Coat. Tech. **162**, 174 (2003)
[3] S. PalDey, S.C. Deevi - Mat. Sci. Eng. **A342**, 58 (2003)
[4] C.V. Budtz-Jørgensen - Studies of Electrical Plasma Discharges, PhD-Thesis, Aarhus University (2001)
[5] M. Mišina, L.R. Shaginyan, M. Maček, P. Panjan - Surf. Coat. Tech. **142-144**, 348 (2001)
[6] E. Lugscheider, K. Bobzin, M. Maes - Low Temperature Deposition of CrAlN Coatings for the Application on Machine Parts, Proceedings ICMCTF 2003, San Diego, (submitted)
[7] E. Lugscheider, K. Bobzin, M. Maes - Increasing the AlN Amount in Magnetron Sputtered $Cr_{1-x}Al_xN$ PVD Coatings for High Temperature Applications by means of Pulsed Power Supplies, Proceedings ICMCTF 2003, San Diego, (submitted)

Chemical Kinetic Modeling of Tar Removal from Biomass Derived Fuel gas by Pulsed Corona Discharges

S.A.Nair[1], K.Yan[1], A.J.M.Pemen[1], E.J.M.van Heesch[1], G.J.J. Winands[1], K.J.Ptasinski[2], A.A.H. Drinkenburg[2]

1-Faculty of Electrical Engineering, 2- Faculty of Chemical Engineering, Eindhoven University of Technology, P.O.Box 513, 5600 MB Eindhoven, The Netherlands.
Phone: *+31 40 247 4492,* ***Fax:*** *+31 40 245 0735,* ***Email:*** *S.A.Nair@tue.nl*

Tar (heavy hydrocarbon or PAH) removal from biomass derived fuel gas is one of the biggest obstacles in its utilization for power generation. We have investigated pulsed corona as a method for tar removal. Experimental results have indicated the energy density requirement to be about 400 J/L for naphthalene removal (model tar compound) from synthetic fuel gas (CO, CO_2, H_2, CH_4, N_2) at temperatures of 200 ^oC [1]. For the process to be competitive and economical, the energy consumption needs to be reduced. This requires an understanding of the chemical processes involved. In previous studies, we have investigated the primary processes at temperatures of 200 ^oC [2]. The present study aims to identify the main reactions involved by means of a sensitivity analysis

1. Introduction

Pulsed corona induced non-thermal plasma processes for pollution control applications have been investigated for over a decade [3]. One significant advantage of such a process is its ability to perform the necessary function at less stringent conditions. Typical example is that of PAH (PolyAromatic Hydrocarbon), dioxin etc. removal, which can be facilitated at atmospheric conditions. Research is directed towards both fundamental understanding [4] as well as developing dedicated equipment for the purpose [5]. In any case, to implement a new technology or method, it has to be competitive in terms of economics over the existing methods, or it should be the only method available to achieve a certain task. Perhaps one of the most widely investigated processes by using non-thermal plasma techniques would be combined NO_x and SO_x removal. In addition, this would be the most likely process to bridge the gap between research and industrial application [5,6]. Out of the several milestones regarding research in this area, one of the crucial turning points was the understanding of process chemistry involved [7]. Although several investigations have been made into understanding the fundamentals of gas discharges, several open questions remain. For example, one still needs to investigate the relation between power source properties and the streamer behavior. Several directions or indications are available which are used as design criteria (or thumb rules) [5], but lack of concrete understanding still hinders the transfer of knowledge from one system to another. Hence, each system has to be considered as a stand-alone system from an information point of view. As was stated before, understanding of process chemistry (in the area of NO_x, SO_x control) proved to be decisive in manipulating the process to one's needs. Fundamental reactions were outlined [7]; therefore, one could study the influence of addition of additives, catalysts, changing process conditions (temperature, gas composition)[8] and thereby reduce the energy consumption. In principle, any non-thermal plasma chemical process can be considered to take place in 4 discrete steps at various time scales

(a) Electron energy distribution (ps ~ ns)
(b) Physical processes leading to generation of radicals (ns ~ μs)
(c) Free radical chemistry (μs ~ ms)
(d) Ground state chemistry (ms ~ s)

The first three steps can be considered as a source for the last step. Since all the radicals and excited species that are generated by means of collisions between energetic electrons (> 5eV) and molecules and that survive the quenching process will act as reaction initiators for the purpose to be achieved. The design related to power source properties and electrode geometries is aimed at increasing the radical density. However, high local radical densities would lead to more quenching. The question related to "what is too much" varies from process to process and most often, it is to be obtained experimentally. A detailed streamer model is necessary to obtain the initial radical density, a question which remains unsolved in the area of non-

thermal plasmas. The present work related to kinetic modeling for tar/poly aromatic hydrocarbon removal from biomass gasification is aimed at developing a comprehensive yet brief set of reaction scheme, largely governing the process. Gasification of biomass produces a low calorific value gas typically 4 ~5 MJ/Nm^3, gas compositions as mentioned in table 1.

Table 1: Producer gas quality from two types of atmospheric, air blown gasifier [10]

Material		Downdraft	CFB[1]
Fuel Moisture	wt %	5~20	13~20
Particles	g/Nm^3	0.1~8	8~100
Tars	g/Nm^3	0.01~6	2~30
H_2	Vol %	15~21	15~22
CO	Vol %	10~22	13~15
CO_2	Vol %	11~13	13~15
CH_4	Vol %	1~5	2~4
C_nH_m	Vol %	0.2~2	0.1~1.2
N_2	Vol %	Rest	Rest

Non-thermal plasma processing or pulsed corona processing (in this case) of the above gas can occur via several routes leading to various chemical processes. On a more global level, the energy requirements for removal of representative compounds have been established experimentally. Results indicate energy requirements to be about 400~500 J/L for naphthalene removal to 900~1000J/L for phenol removal. Experiments have also been conducted for removal of these compounds in various gas mixtures to establish the chemical pathways. However, a detailed kinetic scheme is necessary to establish the secondary processes.

2. Method of Investigation:

The aim of the calculation is to

1) Have a chemical kinetic reaction scheme developed that can adequately describe the process.
2) To identify termination & competitive reactions

The short description below explains the method adopted for the purpose.
In general, to reach conditions in an actual process, one needs to have a “perfect” streamer model to describe the distribution of the species produced in both the axial and radial directions. However, this is far from reality. Hence, to achieve this a fitting parameter is used which physically means the amount of radicals necessary for the desired conversion of tar as observed experimentally. Radical production in reality is pulsed, that is, radical generation takes place during a period much shorter than the period between two pulses. In effect, it can also be said that radical concentration decays to zero between two pulses (Fig.1)
Another option that is followed is to have a continuous model instead of a discrete model as is described in the above case [11]. Here radical production is incorporated in the rate constant of the process. Therefore, both phases in the reactor, viz. the plasma phase as well as the bulk gas phase are well mixed; hence, the model can be termed as a pseudo-homogenous model.
The reactor used for the experiments is a tubular flow reactor or a differential reactor and it forms a part of a closed loop system [1,2]. Hence, the overall configuration represents a well-mixed system (Fig.2).
We assume,

1) Radicals produced are well mixed with the reactants.
2) Radicals once produced are uniformly distributed within the whole volume, i.e. a zero-dimensional model.
3) Chemistry of the process is solely described by radical behavior; ion chemistry is not taken into account.

For description of the chemical reactions, 106 reactions[#] and 15 species are taken into account viz. O, OH, H, CO, N, CH_3, O_2, H_2O_2, HO_2, HCO, CH_4, CH_2O, naphthalene, toluene, and phenol.

The general reaction scheme and the format of the mass conservation equation is:

[1] Circulating Fluidised bed gasifier
[#] can be provided if needed.

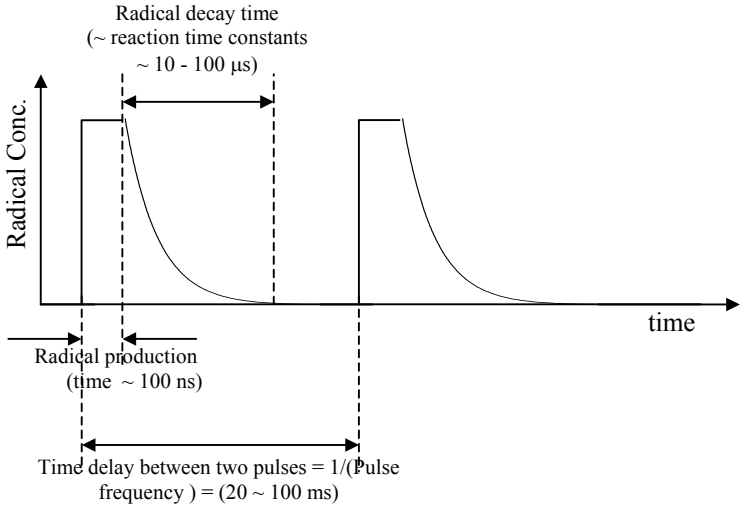

Fig.1. Time dependence vs. radical concentration profile

$$M \rightarrow R \qquad \text{…….(1)}$$

$$R + X \rightarrow \text{products} \qquad \text{…….(2)}$$

$$\frac{\partial R_i}{\partial t} = G_R \cdot E_p \cdot f. - \sum k \cdot [R_i] \cdot [X_i] \qquad \text{…….. (3)}$$

where, G_R = Radical production per Joule per m^3 ($mol.J^{-1}m^{-3}$)

$= K_R * [M]$

where, K_R = dissociation constant (J^{-1})

M = bulk species concentration (mol/m^3)

E_p = Energy per pulse (J/pulse)

f = Pulses per second (pulse/second)

k = reaction rate constant (s^{-1})

X, R = species concentration (mol/m^3)

Hence $G_O = K_{CO2} * [CO_2]$

$G_{OH} = K_{H2O} * [H_2O]$

$G_H = K_{H2} * [H_2] + K_{H2O} * [H_2O]$

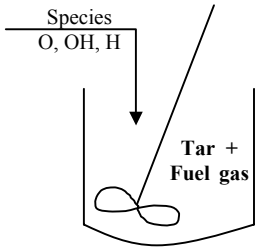

Fig.2 Well-mixed Reactor

Equation (3) presents a mass balance of radicals, with the first term on the right hand side indicating the production term and the second term indicating the formation or consumption of radicals by reactions. K_R is used as the fit parameter, and the value is adopted to achieve a good fit between the calculated and the experimental value. In principle, this value has to be obtained from an adequate streamer model, which as described before is not included into the present case. The G value or the radical yield can be evaluated from the above since

$$G\ (\text{molecules}/100\text{eV}) = G_R * V * 1.6\text{e-}17 \qquad \text{…… (4)}$$

where V = Volume of reactor (m^3)

and the conversion factor, 1eV = 1.6 e-19 J

The experiments are performed for near about 99.99 % conversion, and the equivalent time is about for the calculation purpose.

For eg: Naphthalene removal occurs at energy density of about 400 ~ 600 J/L, this is used to determine the calculation time.

$$\Delta T = \frac{E_D * V}{E_p * f} \qquad \text{……..(5)}$$

where ΔT = time for calculation (time for 99 % conversion)

E_D = Energy Density (J/L)

The calculations yield naphthalene removal as a function of time, which is reconverted to the adequate units by eq.5 and plotted to compare with the experimental results. However, because of the simplicity associated with the above calculations, the interpretations of the results are only valid within the experimental conditions. Since, for e.g. if the gas temperature changes, although change in the gas density have been incorporated, the resulting effect on the gas discharge phenomena is not taken into account. This may affect the value of the fit parameter or the apparent dissociation rate constant. Similarly, all factors related to the influence of the pulse power source cannot be investigated, because of lack of incorporation of a streamer model. However all parameters, which are influenced by the kinetics of the process or rather the chemistry can be investigated.

3 Experimental conditions:

The experimental set-up has been explained in detail elsewhere [1,2]. However, important details are summarized in table 2.

Table 2: Experimental conditions

Experimental operation: Batch wise			
Temperature = 200 ~ 210 °C			*Pulse power properties*
Pressure = 1 bar			70 ~ 80 kV
Biogas composition		*Tar Components*	20 ns rise time, 100 ns pulse width
CO	20 %	Naphthalene	50 ~ 80 MW peak power
CO_2	12 %	Toluene	1 ~1.2 J/pulse
H_2	17 %	Phenol	50 pulses per second
CH_4	1 %		80 % efficiency (from mains to corona)
N_2	Rest		

4 Results:

(a) Estimation of G-value

The first step is to reach the "right" value of the fit parameters. For this case naphthalene removal from fuel gas is taken as a reference and then further on, compared with the experimental results for the removal of other compounds It is assumed that for such a gas composition the primary step is the dissociation of CO_2 to produce O species. This is based on the previous experimental observations [2]. Based on a trial and error procedure, a reasonably good fit (Fig.3) with the experimental results was obtained for the values of

K_{CO2} = 2.5e-7 ➔ G_O = 4.654e17 mol/m^3/J

K_{H2} = 1.5e-9 ➔ G_H = 3.956e15 mol/m^3/J

Therefore, the radical yield can be estimated to be (reactor volume of 0.189 Nm^3)

G_O (G-value) = 1.41 mol /100 eV

G_H (G-value) = 0.012 mol/100 eV.

Fig.3 indicates a comparison between the calculated results using the above fit parameter with the experimental results.

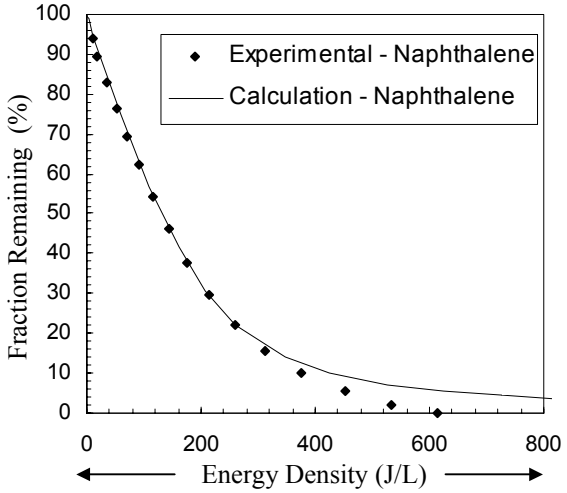

Fig.3 Comparison of experimental and calculated results

(b) Verification of parameters:

The estimated value of the parameter can be verified by comparing it with the experimental results for removal of toluene as well as for phenol. The experiments are performed under the same conditions as that for naphthalene. Fig.4 (a & b) shows comparison for the calculated as well as experimentally obtained results for the case of toluene and phenol.

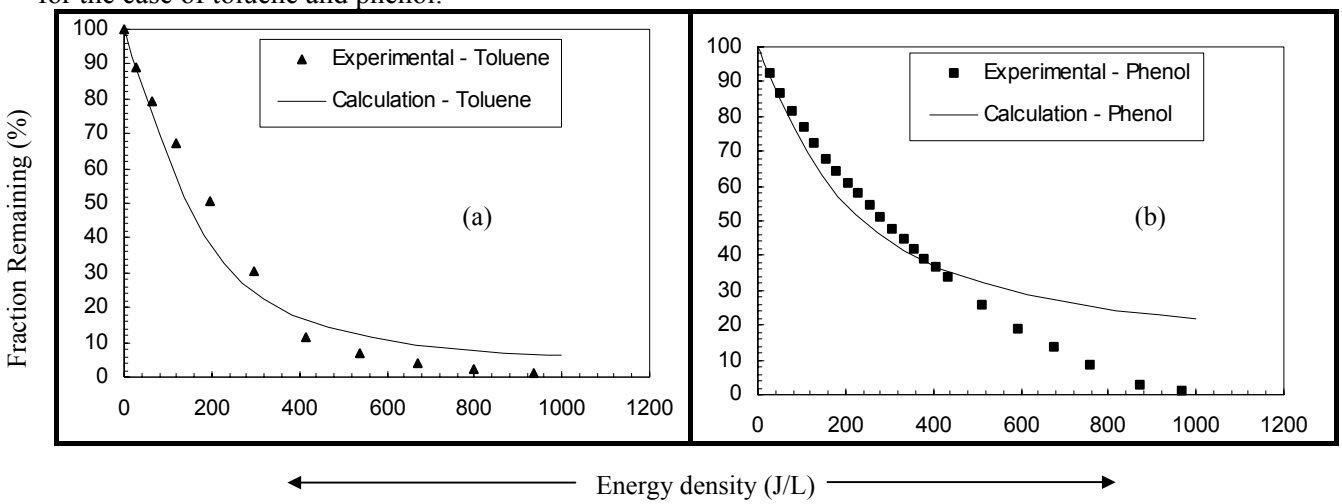

Fig.4. Verification of fit parameters (a- Toluene, b-Phenol)

The calculations show good agreement for the case of toluene and for the case of naphthalene. Deviations are seen for the last remaining fraction in the case of phenol. This may be due to one of the following factors or a combination of both

a) Phenol removal due to thermal dissociation can also be a factor (since in the calculation only removal due to reactions initiated by corona plasma is taken into account.)
b) Chemical reactions to describe phenol removal may not be complete, which suggests that the products formed after the breakdown play an important role.

Nevertheless, good fit is obtained with the values of the fit parameter for the case of naphthalene removal. Since further experiments for determining, the mechanisms are done only with naphthalene as the model compound as well as for the purpose of sensitivity analysis.

5 Sensitivity Analysis

The aim here is to isolate the main reactions that are more likely to effect the process from the "pool". This was performed as indicated in eq.6.

Every reaction rate constant was changed by about 50% of its value, and correspondingly its effect on naphthalene removal was observed. Evidently, those reactions, which showed an effect on the removal in terms of the energy density, are more likely to influence the process.

As can be expected, the calculations are sensitive to the value of the fit parameter, and thereby the gas composition, if changed by an order of magnitude. In addition, in the case of the rate constants, small changes to the values, to the extent of 5% do not influence the calculations.

The sensitivity analysis indicated the following reactions to be more critical than the others:

$$
\begin{array}{lcllcl}
O & + & \text{Naphthalene} & \rightarrow & \text{Products} & \\
H & + & \text{Naphthalene} & \rightarrow & \text{Products} & \\
OH & + & \text{Naphthalene} & \rightarrow & \text{Products} & \\
O & + & CO + M & \rightarrow & CO_2 + M & \\
O & + & H_2 & \rightarrow & OH + H & \\
O & + & CH_4 & \rightarrow & CH_3 + OH & \\
O & + & CH_3 & \rightarrow & CH_2O + H & \\
O & + & CH_2O & \rightarrow & HCO + OH & \\
HCO & + & M & \rightarrow & H + CO + M & \\
O & + & H_2 + M & \rightarrow & H_2O + M &
\end{array}
$$

$$\frac{\partial X}{\partial t} = \sum k \cdot [R] \cdot [X]$$

$$t = \frac{E_D * V}{E_p * f}$$

$$\partial t = \partial E_D * \left(\frac{V}{E_p * f} \right) \qquad \ldots\ldots\ldots (6)$$

$$\left(\frac{E_p * f}{V} \right) \frac{\partial X}{\partial E_D} = \sum k.[R].[X]$$

$$\frac{\partial}{\partial k_i} \left\{ \left(\frac{E_p * f}{V} \right) \frac{\partial X}{\partial E_D} = \sum k.[R].[X] \right\}$$

Based on the above analysis, it is now possible to start outlining the chemical scheme at the experimental conditions, and subsequently investigate the effects of additives and varying conditions.

5. Conclusion:

A chemical reactions database has been set up which can describe the process of tar removal from fuel gas. The adopted method produces result that agrees with the experimental observation within the conditions of investigation. Deviations do exist from the experimental results. In addition, a chemical scheme can be outlined based on the sensitivity analysis performed.

References:

[1]. S.A. Nair, K. Yan, A.J.M. Pemen, E.J.M. van Heesch, K.J. Ptasinski, A.A.H. Drinkenburg, "Tar removal from biomass derived fuel gas by pulsed corona discharges", paper submitted to FUEL PROCESSING TECHNOLOGY (Accepted, Jan 2003)

[2]. S.A. Nair, K. Yan, A.J.M. Pemen, E.J.M. van Heesch, K.J. Ptasinski, A.A.H. Drinkenburg, "Chemical Processes in tar removal from biomass derived fuel gas by pulsed corona discharges", paper submitted to PLASMA CHEMSITRY AND PLASMA PROCESSING (Accepted, Dec, 2002)

[3]. S.Masuda, "Pulsed corona induced plasma chemical process: a horizon of new plasma chemical technologies", Pure and applied Chemistry, Vol. 60 (5), Pg. 727-731, 2002

[4]. A.A.Kulikovsky, "Production of chemically active species in the air by a single positive streamer in a nonuniform field", IEEE transactions on plasma science, Vol.25 (3), Pg. 439-446, 1997

[5]. Yan.K. *Corona Plasma Generation*, Ph.D. Thesis, Eindhoven University of Technology, 2001.

[6]. C.R.McLarnon, V.K.Mathur, "Nitrogen Dioxide decomposition by barrier discharge", Ind.Eng.Chem.Res., Vol. 39, Pg. 2779-2787, 2000.

[7]. Yan.K., Kanazawa.S., Ohkubo.T., Nomoto.Y., "Oxidation and reduction processes during NOx removal with corona plasma", Plasma Chemistry and plasma processing, Vol.19, Pg. 421-443, 1999.

[8]. E.A. Filimonova, R.H. Amirov, S.H. Hong, Y.H. Kim, Y.H. Song, "Influence of temperature and hydrocarbons on removal of NOx and SO_2 in a diesel exhaust gas activited by pulsed corona discharge", Pg.337, HAKONE VIII (Proceedings of International Symposium on High Pressure Low Temperature Plasma chemistry), Puhajarve, Estonia, 2002.

[9]. Eliasson.B., Egli.W., Kogelschatz.U., "Modelling of dielectric barrier discharge chemistry", Pure & Appl. Chem., Vol. 66, Pg. 1275-1286, 1994

[10]. Van Paasen.S.V.B. "Biogas treatment with pulsed electric fields", EUT-SAI report, ISBN 90-5282-940-3, Eindhoven, April 1999.

[11]. B.Eliasson, F.G.Simon, W.Egli, "Hydrogenation of CO_2 in a silent discharge", *Non-Thermal plasma techniques for pollution control*, Part B, Pg. 321-337, 1992.

The Influence of Work Function on Electrode Erosion

I.R. Jankov[1], R.N. Szente[2*], I.D. Goldman[1]
[1] *Physics Institute, USP, Cidade Universitaria, São Paulo- SP, Brazil, CEP: 05508-900*
[2] *Mechanical and Electrical Department, IPT, Cidade Universitaria, São Paulo- SP, Brazil, CEP: 05508-901*
* corresponding author - Email: szente@ipt.br

Abstract
The erosion of a cathode in a plasma torch is related to its surface condition, particularly with respect to its composition. An experimental and theoretical approach was developed in order to study the work function changes of copper (material mostly used for electrodes in plasma torches) induced by ion implantation. The Cu substrates were implanted with low energy P and Cs ions; the surfaces before and after implantation were analysed in terms of crystalline structure, composition, surface topography and work function changes.

1. Introduction

Plasma generator or plasma torch is an essential tool for various industrial processes, such as: production of new materials, refining of metals, applications for environmental issues (treatment of hospital and toxic industrial wastes) and others. Recently the use of plasma torches has been expanded into the field of treatment of soil contaminated with oil and the production of silicon for solar cells. The understanding of the electrode erosion of plasma torches used for those processes is essential in expanding even further the present applications.

The electron emission for electrodes in plasma torches is believed to be controlled by the Thermo-Field (TF) mechanism. This mechanism of electron emission uses the concepts developed originally by Fowler-Nordheim [1] with the thermionic concepts expressed by the Richardson equation modified by the Schottky effect [2]. The general equation describing the TF emission was first described by Murphy and Good [3]; many modifications to this original work have been suggested ever since. In general, the electron emission current density depends on the surface temperature, on the electric field above the surface and on the work function of the surface. Higher temperature and electric field, but lower work function, result in higher electron current densities, or in other words, in higher and easier emission of electrons. A lower current density and/or lower residence time of the arc on one spot of the cathode surface, which also depends on the work function, will decrease the erosion of the cathode [4-6].

An extensive experimental study on electrode erosion in a concentric cylinder geometry with magnetically driven electric arcs, simulating a plasma torch, was conducted in the past by one of the present authors; the study focused on the behaviour of the cathodes, since those electrodes are the ones presenting the more severe erosion in normal industrial applications. The addition from ppm to a few percent of polyatomic gases (N_2, O_2, CO, Cl_2, CH_4, H_2S) to inert gases (Ar or He) caused large variations in the arc velocities, arc voltage, in the arc movement and cathode erosion when compared with experiments using pure inert gases. It was determined that the contamination of the cathode surface, caused by the decomposition of the polyatomic gases by the electric arc and plasma jet, and the consequent attraction of the positive ions towards the cathode, was the cause for the observed changes. The change of the work function of the cathode material, due to the change in the surface composition, was determined for selected experiments using Kelvin Probe technique. More details can be seen in Refs. [6-9].

Since the contamination of the cathode surface was not controlled in those experiments, a more systematic study of the changes occurring on the cathode surface when it is contaminated with different elements needed to be conducted. An experimental and theoretical approach was developed here in order to study the changes of the work function of copper (copper is mostly used as electrode material for plasma torch) when small and controlled amounts of contaminants were placed on the surface by ion implantation [10,11]. The aim of the work is to understand the main phenomena controlling the emission of electrons from a metallic surface for future use of that material as cathodes in plasma torches. It is presented here some of our experimental and theoretical results obtained in the ongoing effort for understanding those phenomena.

2. Methodology

The methodology for the study of work function change of copper caused by ion implantation process is formed of two parts: theoretical and experimental.

The theoretical approach adopted in this work consisted of simulating the implanted surfaces using SRIM (Stopping and Range of Ions in Matter), version 2003.10, [12] and TB-LMTO-ASA (CPA) (Tight Binding – Linear Muffin Tin Orbital – Atomic Sphere Approximation (Coherent Potential Approximation)) [13] programmes. The SRIM programmes provide, among other parameters, the ion range distribution and sputtering yield (defined as the mean number of sputtered target atoms per incident ion) of surface components, which were used to estimate the concentration of implanted ions on the surface.

The TB-LMTO-ASA (CPA) programmes simulate the electronic structure of the surface, which was used to estimate the work function change of copper due to the presence of implanted ions on the surface. In this method, the crystal is considered to be totally filled out with spheres centred at individual nuclei (Atomic Sphere Approximation – ASA). The radius of each sphere is determined so that the sum of the volumes of all the spheres equals the volume occupied by all the atoms in the material. In the case of a material with just one atom type, the Wigner-Seitz radius of the solid is used as the sphere radius. At each sphere, a potential which is spherically symmetrical inside the sphere and constant outside (such potential is called Muffin-Tin - MT), is set. The radial solution of the Schrödinger equation for the system, which can be written as a linear combination of energy independent basis functions (Linear Orbitals – LO), inside the sphere (spherically symmetric potential) depends on the form of the solution outside the sphere (constant potential) through the boundary conditions of continuity of the base functions and their first derivations. The Tight Binding - TB basis, commonly used for the problem of imperfections in the metallic surfaces is obtained in such a way that the interactions between the neighbouring sites have the smallest possible range. The procedure used in the TB-LMTO-ASA (CPA), the method adopted here, can be summarised in two main steps:

1. The electronic density is calculated through the surface Green function method adapted for the TB-LMTO-ASA. In the case of the presence of random alloys or impurities without symmetry in the metallic surfaces, the average electronic density is calculated using Coherent Potential Approximation (CPA);

2. In the Density Functional Theory – DFT calculations, which assumes the existence of a functional of energy with a minimum value for the correct electronic density, the electronic density obtained in the previous step is used, thus providing variables necessary for the description of the properties of the solids (in our case, the work function).

The experimental approach consists in bombarding a target surface (made of copper) with certain ions, in a controlled manner and study the variation that the implantation of those ions cause on the surface of the target. In order to accomplish that, a mechanical mask was specially designed and manufactured; during the ion implantation process this mask is positioned above the substrate. The main objective for using a mechanical mask on the top of the sample undergoing an ion implantation process is to create, on the sample surface, a determined pattern of implanted and non-implanted regions; this allows the determination of changes induced by the process without the need for the reference sample (i.e., the non-implanted areas on the same sample serve as the reference). The mask had rectangular-shaped holes (rectangular area of $50x100\mu m^2$ with spacing of 10μm between them) through which the ions were able to pass and thus, the same pattern of implanted regions was created on the sample surface. The mechanical mask is made of silicon and silicon oxide; more details of the method for producing the masks can be seen elsewhere [10].

Two types of copper substrates were used in the study: polycrystalline copper sheets and thin film of deposited copper on silicon wafers. The sample preparation procedures for both substrates are presented below. The samples were produced in pairs so that one sample can be analysed exclusively by Kelvin Probe Force Microscopy (surface topography and work function measurements) and other techniques of interest.

The polycrystalline copper substrates were obtained by cutting an electrolytical copper rod into disks (1cm in diameter, 1mm of thickness); the disks were alternatively rinsed in ethanol and polished with diamond pastes, each time diminishing the diamond grain size (reaching 1μm grain size). The surface topography of the obtained substrates was examined using AFM (*Nanoscope IIIa*, *Digital Instruments*); the maximum topography difference, determined in those measurements, was of the order of 250nm. One pair of polished copper substrates were implanted with phosphorus ions with acceleration voltage of 39keV and with a dose of $3.4x10^{16}ions/cm^2$.

The copper thin film substrates were obtained by depositing copper on silicon wafer using the electron beam technique. The mean value for the deposition rate was 3Å/s and the thickness of the deposited

film was approximately 2000Å (determined by *Alpha-Step*). The crystalline structure of the film was obtained with XrD technique and it was determined to be similar to the polycrystalline copper substrate. The surface topography, determined with AFM, exhibited maximum topographic difference of the order of 100nm. One pair of copper film substrates were implanted with caesium ions with the acceleration voltage of 50keV and with a dose of $3.0x10^{15}$ions/cm^2.

The surfaces before and after implantation were analysed in terms of composition (Auger Electron Spectroscopy - AES), work function changes (Kelvin Probe Atomic Force Microscopy - KPFM), surface topography (Atomic Force Microscopy – AFM) and several other parameters (using different techniques such as Rutherford Backscattering Spectroscopy - RBS, X-ray Diffraction – XrD and others).

3. Results

In this section, the results obtained in the work, both experimental and theoretical, are presented.

The calculated range distribution of implanted ions for both ion types (i.e., P with acceleration voltage of 39keV and Cs with acceleration voltage of 50keV) were obtained with SRIM programmes (100,000 ions were used in the simulations) and are shown in Figure 1. The ion density at a certain depth can be obtained by multiplying the respective value on the right-hand axis with the implanted ion dose (i.e., $3.4x10^{16}$ions/cm^2 for P and $3.0x10^{15}$ions/cm^2 for Cs); the density of polycrystalline copper is approximately $8.45x10^{22}$at/cm^3.

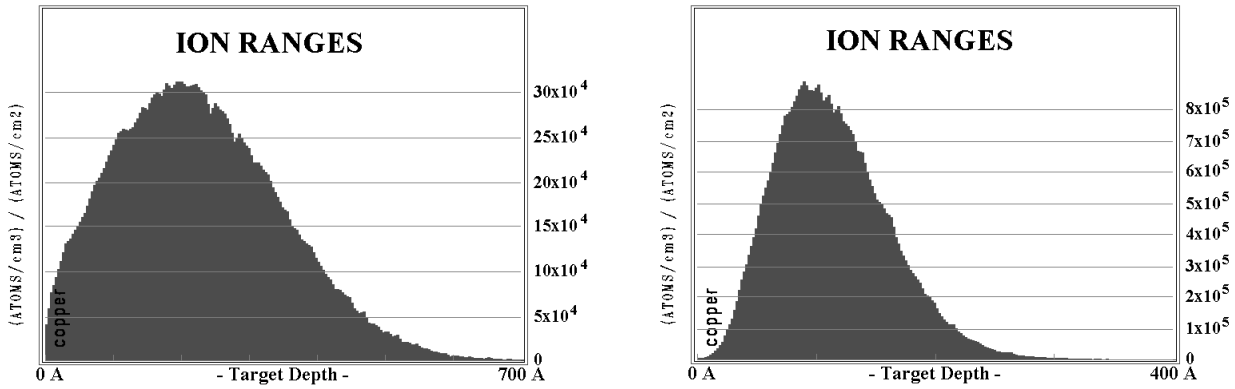

Figure 1a. Cu implanted with P (39keV) Figure 1b. Cu implanted with Cs (50keV)

Figure 1. Simulation of the Ion Range Distribution

Sputtering yield for copper was estimated for the case of phosphorus and caesium implantation using SRIM programmes and the values were 6.7at/ion and 12.7at/ion, respectfully. Therefore, a dose of $3.4x10^{16}$ions/cm^2 of P with acceleration voltage of 39keV should remove $2.28x10^{17}$ of copper atoms, which corresponds to approximately 270Å (i.e., there should be a step of 270Å between the implanted and non-implanted regions) and a dose of $3.0x10^{15}$ions/cm^2 of Cs with acceleration voltage of 50keV should remove $3.84x10^{16}$ of copper atoms, which corresponds to approximately 45Å. From Figure 1a., the surface concentration of phosphorus (estimated using the phosphorus concentration at 270Å) should be 10.9%. From Figure 1b., the surface concentration of caesium (estimated using the caesium concentration at 45Å) should be 1.3%.

A measure of surface composition was obtained in the present experiments from the peak-to-peak height of the P(LMM), Cs(MNN) and Cu(LMM) Auger lines plotted in the derivative mode. The P(LMM) Auger transition corresponds to a 120eV electron, the Cs(MNN) corresponds to a 563eV electron and the Cu(LMM) corresponds to a 920eV electron. The surface concentration of contaminants (C, N, O, S, Cl) was determined by comparing their respective representative Auger transition peak with the Cu(LMM). The analysis of the Auger spectra of implanted and non-implanted regions (for implantation processes of both ion specie, i.e., P and Cs) showed that the variation of the surface concentration of contaminants was within experimental error and that the implanted ions were detected only in the implanted regions. In the results presented in this article, the contaminant concentration was ignored and the percentage of implanted ion on the surface was calculated as if only copper atoms and implanted ions were present on the surface.

All Auger spectra reported here were obtained using primary beam energy of 3keV. In Figure 2a. the Auger spectrum for Cu implanted with P is shown. The form of the P(LMM) peak (at 120eV) is different

from the one in AES manual and therefore, its height could not be determined precisely. Consequently, the obtained phosphorus concentration of 2% on the surface should be taken with certain caution. In Figure 2b. the Auger spectrum for Cu implanted with Cs is shown. The obtained caesium concentration was 6%. Contrary to the case of phosphorus, the form of the Cs(MNN) peak was according to the AES manual.

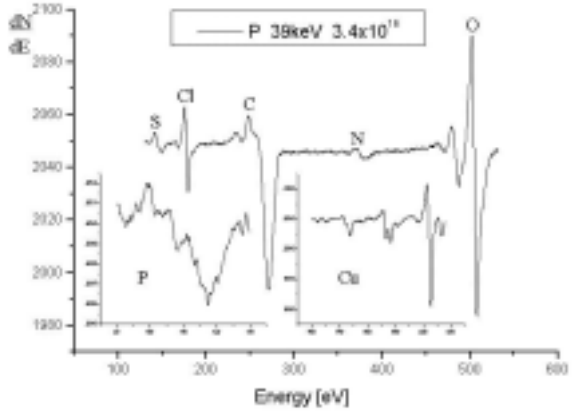

Figure 2a. Cu implanted with P (39keV)

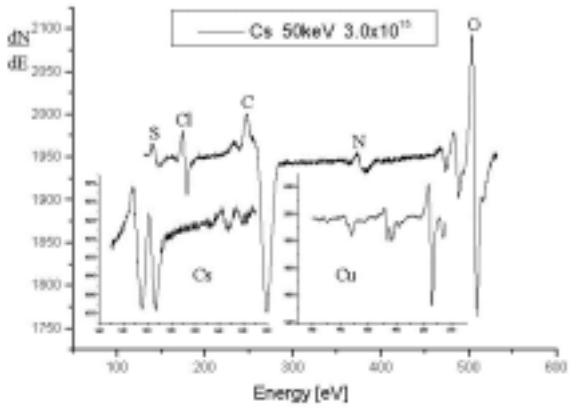

Figure 2b. Cu implanted with Cs (50keV)

Figure 2. Auger spectra of the implanted samples

RBS analyses were conducted in this work in order to determine how many ions were actually present in the sample after the ion implantation process (i.e., what is the "effective" ion implantation dose). The polycrystalline copper sheets (implanted with phosphorus) could not be analysed with this technique, since the copper signal "masks" the presence of all the elements with Z lower than 29. For the copper film samples, the detected dose of implanted caesium ions was approximately $1.3x10^{15}$ions/cm^2, which is less than half of the original dose ($3.0x10^{15}$ions/cm^2).

The KPFM measurements, which provide the work function change (determined by comparison of the surface potential of implanted and non-implanted regions) were performed on 5 different areas (100x100μm^2 for the P/Cu and 70x70μm^2 for Cs/Cu) within each sample. Typical results of copper sheets implanted with phosphorus and copper thin films implanted with caesium are shown in Figure 3.

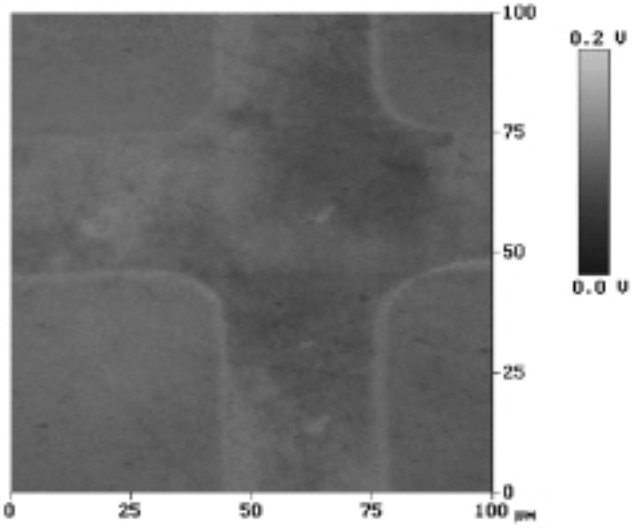

Figure 3a. Cu implanted with P

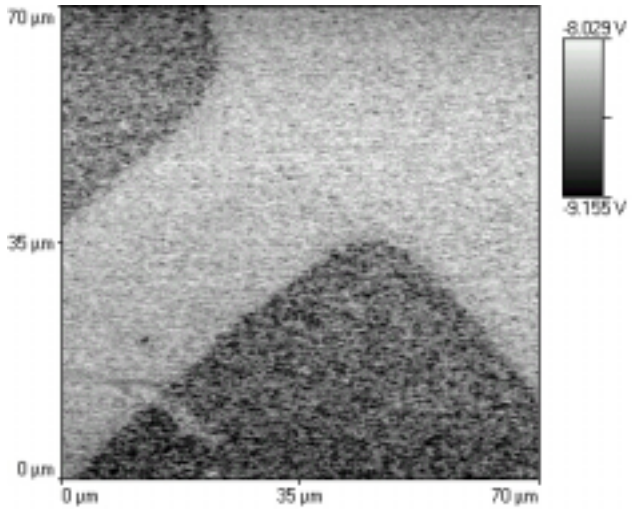

Figure 3b. Cu implanted with Cs

Figure 3. Typical results for KPFM measurements of the implanted copper substrates

As it can be seen, the implanted (rectangular) regions were brighter in the case of P/Cu and darker in the case of Cs/Cu than the non-implanted regions, indicating that the implantation of phosphorus increased the work function and the implantation of caesium decreased the work function in comparison with the

(pure) copper surface. In the case of phosphorus, the work function increased by approximately 50±30mV and in the case of caesium the work function decreased by approximately 400±100mV (the mean value of 10 different measurements within one area (100x100μm^2 for P/Cu and 70x70μm^2 for Cs/Cu case) was obtained (area mean value); this process was repeated for all the measurements performed on one sample (5 measurements) and the final value for one sample (sample mean value) was calculated as the mean value of all the areas). The error associated with the results are the maximum deviation of area mean values from the sample mean value.

The topography analyses (the equipment for KPFM simultaneously measures the change in the surface potential as well as the surface topography) of the samples revealed that the level of the implanted regions were lower compared with the level of the non-implanted regions; in the case of P/Cu, the step (between implanted and non-implanted region) was approximately 280±80Å and in the case of Cs/Cu, the step was approximately 70±30Å. Also, the analysis of the surface structure indicated that there was an increase in surface roughness of implanted regions (comparing with the non-implanted ones).

The surface obtained experimentally by implantation of Cs ions into copper film substrate was simulated, using TB-LMTO-ASA (CPA) programmes, by one monolayer of surface alloy (containing 6% of Cs and 94% of Cu) placed on top of Cu(111) crystalline facet. Preliminary theoretical results showed the decrease of approximately 240mV comparing to the work function value of pure copper, which is in relatively good agreement with obtained experimental value (400±100mV). This value decreased even further if the increase of the surface roughness, which occurs in the implanted regions due to the process of sputtering, was taken into account in simulations. The theoretical study of Cs/Cu system is being continued and the results will be published elsewhere [16]. The TB-LMTO-ASA (CPA) programmes are specially designed for purely metallic systems and, therefore, the P/Cu system could not be simulated with them.

4. Discussion

The fact that the surface concentration of contaminants was within experimental error (indicating that there was no change in the surface concentration of contaminants due to the ion implantation process) and that the implanted ions were detected only in the implanted regions (confirming that the mechanical mask produced here was indeed thick enough to stop all the ions and thus protect the substrate surface underneath) prove that the described methodology is appropriate for the studies conducted in this work. One can conclude that if there are some changes in the work function between the implanted and non-implanted regions this can be attributed to the presence of implanted ions on the sample surface and/or change in the surface roughness induced by ion bombardment.

The experimental results (obtained by AES) for the surface concentration of implanted ions (2% of P and 6% of Cs) were different than the values estimated with SRIM programmes (10.9% of P and 1.4% of Cs). The calculation based on the Kinchin-Pease formalism, used in SRIM simulations for a fast estimative of the damage induced by ion implantation, may not be appropriate for the samples investigated in this work. The sputtering, which occurs during the ion implantation process, changes the ion range distribution by broadening the peak and, upon prolonged implantation processes, by depletion of the implanted ion specie in the near surface region. Another mechanism which can significantly change the surface concentration of implanted ion is migration. At thermodynamic equilibrium, the surface composition of an alloy corresponds to the lowest possible surface free (Gibbs) energy. However, in a radiation environment, other processes start to influence the surface composition, such as: preferential sputtering, displacement mixing, radiation-enhanced diffusion, etc. [14,15]. Also, it should be considered the formation of compounds (changes in the phosphorus peak form indicates that a compound was formed during the ion implantation process) for a precise surface composition analysis. The experimental results indicate that the processes mentioned above indeed play a significant role in determining the surface concentration of elements in implanted copper. Further experiments and theoretical studies are being conducted in order to gain better understanding of the processes which control the surface composition of P/Cu and Cs/Cu systems.

The sputtering yield is very sensitive to the surface binding energy (in the simulation presented in this work, the value for copper of 3.52eV was used). For real surfaces, this changes under bombardment due to surface roughness, and also changes due to surface stoichiometry for compounds. Further, sputtering involves mostly the upper monolayer of the target. For targets such as copper the electronic energy loss of a target atom moving through the last monolayer is of the order of the surface binding energy, so even

monolayer roughness will change the sputtering yield. In spite of the arguments mentioned above, the values for the step estimated by SRIM programmes (270Å in the case of P/Cu and 45Å in the case of Cs/Cu), although slightly lower than the values obtained with KPFM, are still within the experimental error.

5. Conclusions

Two quite distinctive cases of ion implantation in copper were studied primarily in terms of surface composition and work function change; as substrate- copper polycrystalline sheets and deposited copper films were used, as ion specie- one light element (P) and one heavy element (Cs) were implanted with two different doses. The comparison between the surface composition analysis of implanted and non-implanted regions showed that there was no change in the concentration of contaminant elements (C, N, O, S, Cl) due to the ion implantation process and that the implanted ions were only present in the implanted regions, indicating that the adopted is appropriate for the experiments conducted in those studies. The detected concentration of phosphorus in P/Cu system was 2% and of caesium in Cs/Cu system was 6%. For both cases, work function changes were observed; for the case of polycrystalline copper sheets implanted with phosphorus, there was an increase of 50mV and for the case of thin copper films implanted with caesium, there was a decrease of 400mV. Topography analysis of the samples showed a lowering of the implanted regions (in comparison with the level of non-implanted regions) of 280Å for P/Cu system and of 70Å for Cs/Cu system and an increase in the surface roughness for the implanted region.

Using SRIM programmes, the value of sputtering yield was estimated and found to be close to the values found experimentally. However the ion range distribution, obtained with SRIM programmes cannot be used in a straightforward way to estimate the surface concentration of implanted specie; other considerations (Gibbsian segregation, radiation-induced processes, surface stoichiometry for compounds) should be taken into account.

Preliminary theoretical results, using TB-LMTO-ASA (CPA) programmes, show the decrease of the work function value of copper in presence of small amounts of Cs on the surface, with the value in relatively good agreement with one obtained experimentally. The agreement is even better if, in simulations, the increase of the surface roughness, which occurs in the implanted regions due to the process of sputtering, was taken into account. The studies are being continued, both theoretical and experimentally, for different elements, doses and substrate compositions.

Acknowledgements
The financial support of FAPESP for this project, grant number 99/03779-0, is greatly appreciated. One of the authors, I.R. Jankov, would like also to thank FAPESP for granting him a scholarship (process number 00/09681-0).

References

[1] R.H. Fowler, L.W. Nordheim - Proc. Roy. Soc. Lond. A119, 173 (1928)
[2] C. Herring, M.H. Nichols, Rev. Mod. Phys. 21(2), 185 (1949)
[3] E.L. Murphy, R.H. Good, Phys. Rev. 102(6), 1464 (1956)
[4] J.E. Daalder, J. Phys. D: Appl. Phys. 8, 1647 (1975)
[5] J.E. Harry, J. Appl. Phys. 40(1), 265 (1969)
[6] R.N. Szente, R.J. Munz, M.G. Drouet, J. Phys. D25, 1193 (1990)
[7] R.N. Szente, R.J. Munz, M.G. Drouet, Plasma Chem. Plasma Proc. 12(6), 327 (1992)
[8] R.N. Szente, R.J. Munz, M.G. Drouet, Pure Appl. Chem. 64(5), 657(1992)
[9] R.N. Szente, R.J. Munz, M.G. Drouet, J. Phys. D27, 1443 (1994)
[10] I.R. Jankov, I.D. Goldman, R.N. Szente, M.N.P. Carreño, R. Landers, Bras. J. Phys. 31(4), 552 (2001)
[11] I.R. Jankov, I.D. Goldman, R.N. Szente, Vacuum 65, 547 (2002)
[12] J.F. Ziegler, J.P. Biersack, U. Littmark, *The Stopping and Range of Ions in Solids* (Pergamon Press, New York, 1985)
[13] I. Turek, *et al.*, *Electronic Structure of Disordered Alloys, Surfaces and Intefaces* (Kluwer Academic Publishers, Amsterdam, 1997)
[14] R.A. Johnson, N.Q. Lam, Phys. Rev. B13, 4364 (1976)
[15] N.Q. Lam, H. Wiedersich, J. Nucl. Meter. 103/104, 433 (1981).

Electrode Erosion Studies for Plasma Torches

A. C. F. Baratelli[1], R. N. Szente[2]* L. B. Souza[2], J. D. T. Capocchi[1]
1Metallurgical and Materials Department
Escola Politécnica – University of São Paulo, Cidade Universitária, São Paulo-SP, Brazil
2 IPT, Mechanical and Electrical Division
Cidade Universitaria, CEP 01064-970, São Paulo- SP, Brazil
*corresponding author – Email: szente@ipt.br

Abstract
In the present work, electrode erosion studies were performed using a chamber that simulates a plasma torch. Several different types of gases and cathode materials were studied, as well as different magnetic fields and arc currents. The first results obtained on this on going project can be summarized as follows: i) preliminary results obtained here for similar conditions are almost identical to ones published by other authors, validating the equipment and procedures adopted here; ii) use of industrial argon resulted in the contamination of the surface; iii) Cu/Ni alloys showed similar behavior as pure when copper cathodes were used.

I. Introduction

Thermal plasma technology is playing an important role in the production of new materials, in the destruction of toxic wastes and in the development of safer and more efficient processes. One of the remaining problems inhibiting the further industrial application of plasmas is related to the plasma generator or plasma torch. Short electrodes lifetimes, unreliable torch performance, and lack of flexibility in torch operation are all directly or indirectly due to a still lack of fundamental knowledge of the role of the electrodes in the plasma generating process.

Although considerable advances have been made by torch manufacturers, electrode erosion still limits the application of thermal plasma technology to industrial processes. The erosion of the cathode is generally more severe (for non refractory materials) and therefore has been more studied. In the absence of direct chemical reaction, erosion is primarily due to the volatilization of electrode material by local overheating.

There are two significant classes of heat sources on the cathode surface: an external one, caused by particle impact on the surface (ion bombardment) and an internal one due to the passage of the electric current within the volume of the cathode (Joule heating). The other sources of heating, radiation from the arc and convection from the plasma gas have too low a flux to be important in erosion [1-3].

The erosion of the electrodes, in particular of the copper cathodes used in industrial plasma torches operating at atmospheric pressure, is probably the major problem for a broader use of plasma torches. Some of the factors suggested as important in determining cathode erosion rates are: arc velocity [4-7], water cooling rate for the cathode [8], transverse magnetic field strength [9], thickness of the oxide layer on the cathode [10], time duration of the experiment [11], plasma gas composition [12-14], and others. Previous studies [15-17] conducted by one of the authors, strongly appointed to the importance of the surface composition on cathode erosion rates; the composition of the electrode surface was directly affected by the type of plasma gas or mixture of gases used.

In the present work, an experimental chamber was built in order to simulate concentric electrodes of a plasma torch; experimental results were obtained for the effect of arc velocity, magnetic field strength, plasma gas composition and gas flow rate on copper cathode erosion in magnetically driven arcs.

II. Equipment and experimental procedures

A schematic representation of the test chamber is shown in Fig. 1. The DC arc was ignited by a high-frequency pulse and powered by a welding power supply. The arc was driven by an external magnetic field generated by a water-cooled coil external to the chamber and mounted coaxially with the electrodes. The arc rotation frequency was monitored using a light probe located in the chamber, and the mean arc velocity was calculated at the cathode surface. The current, voltage and velocity of the arc were monitored by an acquisition data program installed in a portable computer (one measurement per second).

The gas flow rate was 20 liters/min for all the experiments presented here; the pressure inside the chamber was always kept at 1.1 atm. Before an experiment, the electrodes were cleaned using a sequence of washings with dilute nitric acid and distilled water. The erosion rates reported here were obtained from the difference in weight of the electrodes before and after the experiments. Before the second weighing, the electrodes were again cleaned with the dilute nitric acid and distilled water to remove any contaminant layer that was formed during the experiments. After installing the test electrode, the chamber was purged with argon for 5 min. The electric arc was initiated in argon, and then after other gases could be used.

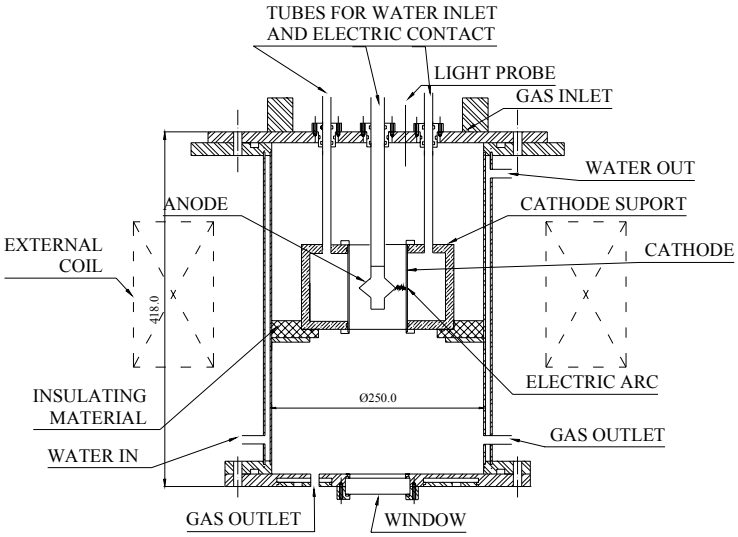

Fig. 1. Schematic representation of the test chamber

III. Results

The experimental results are summarized in the tables below. Each set of results is the mean value of at least three individual experiments carried out under identical conditions.

In the present work three different types of copper material were used (all of them were purchased as electrolytic quality copper from different suppliers). In Table I it is shown the composition of one of those materials, that was used more extensively for the experiments conducted here; the analysis were done using XRF.

Table I- Composition of the electrolytic copper obtained by XRF analyses.

ELEMENT	Electrolytic Copper (%)
Al	0.07
Si	0.15
P	0.07
S	0.03
Cl	0.06
K	--
Ca	<0.01
Fe	0.05
Cu	99.5
Pb	--
Sn	0.04

III.1 Preliminary results

In Table II it is shown two sets of results, one obtained here and a second one obtained by different authors using similar equipment and operating conditions. No difference was obtained when used industrial or ultra pure nitrogen (added to the argon main stream in the amount indicated in Table II).

Table II – Comparison of the results

---	Gas	Cathode Material	Erosion (μg/C)	Arc Velocity (m/s)	Magnetic Field (G)	Current (A)	Voltage (V)	Gas flow rate (l/min)
This work	Ar + 1.25% N_2	Cu 99.5%	3.5	43	1000	156	37-38	20
Ref. (16)	Ar + 1.25% N_2	Cu 99.9%	3.4	35	1000	100	39	20

In this work, the minimum value of current that can be obtained is 156 A for those operating conditions (arc voltage in particular). Since the arc current used in the other work was 100 A, in order to compared directly the arc velocities of the two studies is necessary to use a converting equation, proposed by Szente et al (16):

$$\text{Arc Velocity} \propto I^{0,56} \quad (1)$$

When that equation is used, the arc velocity of the experiment conducted here would be 34,4 m/s (instead of the value indicated in Table II, 43 m/s).

III.2 Formal Experimental results

Different experiments were performed, varying the composition of the plasma gas and of the copper material used for the cathode. In Tables III to VI the different results obtained for those various conditions are shown (the title of each Table characterizes the set of experiments conducted).

Table III – Results obtained varying the plasma gas composition.

---	Gas	Erosion (μg/C)	Arc Velocity (m/s)	Current (A)	Voltage (V)
1	Ar industrial	4.4	49	156	36
2	Ar Ultra Pure (UP)	7.6	16	156	38
3	Ar UP + 1.25% N_2 industrial	3.5	43	156	38
4	Ar UP + 1.25% N_2 UP	3.5	44	156	38
5	Ar UP + 0.3% N_2 industrial	3.6	38	158	36
6	Ar industrial + 0.3% N_2 industrial	4.2	39	158	36
7	N_2 industrial	1.7	104	200	65-70
8	He	1.2	190	210	49

All the results shown in Table III were obtained using a gas flow rate of 20 l/min, a magnetic field of 1000 G and for the cathode material, electrolytic copper (see Table I).

Table IV – Results obtained varying the cathode material .

----	Cathode Material	Erosion (μg/C)	Arc Velocity (m/s)	Current (A)	Voltage (V)
1	Cu	4.5	41	156	41-38
2	CuNi 90/10	4.3	26	158	36-32

All the results shown in Table IVI were obtained using ultra pure argon as the plasma gas, gas flow rate of 20 l/min and magnetic field of 1000 G.

Table V - Results obtained varying the gas composition for CuNi cathodes.

---	Gas	Cathode Material	Erosion (μg/C)	Arc Velocity (m/s)	Current (A)	Voltage (V)
1	Ar industrial	CuNi 90/10	3.9	37	158	30
2	Ar U.P.	CuNi 90/10	4.3	26	157	37-32
3	Ar industrial + 2.5% O_2	CuNi 90/10	5.5	22	196	40
4	Ar industrial + 0.3% O_2	CuNi 90/10	7.7	19	158	36
5	N_2	CuNi 90/10	1.9	93	200	52-58

All the experiments above (Table V) were conducted using a gas flow rate of 20 l/min and a magnetic field of 1000 G.

Table VI – Results obtained varying the magnetic field.

---	Magnetic Field (G)	Erosion (μg/C)	Arc Velocity (m/s)	Current (A)	Voltage (V)
1	160	15.8	23	180	34-35
2	1000	4.4	49	156	35.5

All the experiments were conducted using a gas flow rate of 20 l/min, industrial argon as the plasma gas and electrolytic copper for the cathode (Table I).

It is shown below, in Figure 2, photographs of the electric arc and plasma formed during different experiments, using a high speed photographic camera (exposition time of around 0.1 ms). In Figure 3 it is shown a schematic representation of the arc + plasma formed between the concentric electrodes, for different conditions (the representations shown in Figure 3 are based on high speed photographs).

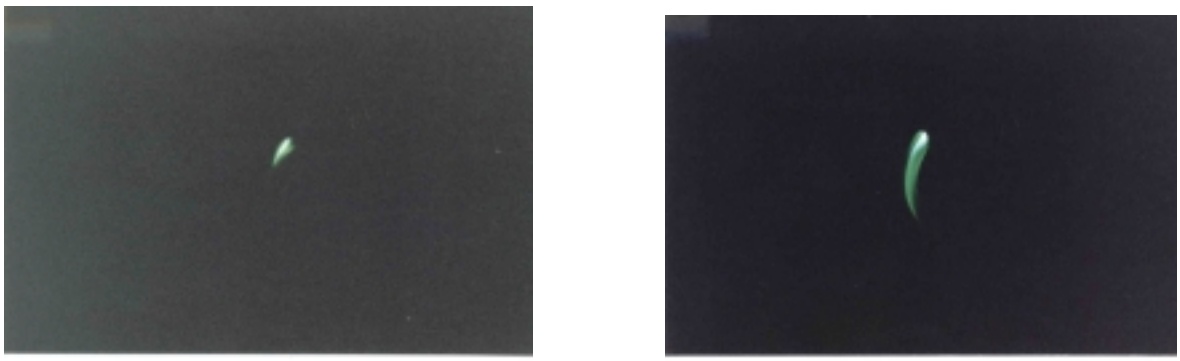

a) b)

Fig. 2 High speed photography of the electric arc and plasma a) in Ar + 0.3%N_2 plasma, b) in UP Ar plasma.

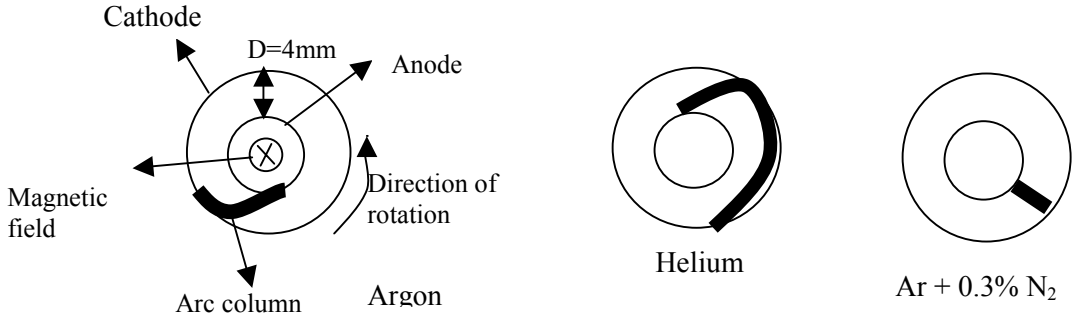

Fig. 3 Schematic representation of the electric arc and plasma between the electrodes, for different conditions

IV. Discussion

As it can be seen in Table II, the results obtained in the present work are very similar, for the same operating conditions, to the results obtained by other authors using similar equipment, validating the experimental procedures adopted here.

In general terms, the erosion of the cathode is higher for lower arc velocities (the arc stays longer over a same region, increasing the amount of material volatilized), which is affected by the surface conditions (work function in particular).

It has been reported [20], that the use of polyatomic gases or noble gases contamined with polyatomic gases contaminates the copper cathode surface and affects the arc caracteristics (arc velocity, arc residence time, arc voltage at the surface). In the present work, this has been also observed when comparing the results obtained using industrial and ultra pure argon, as well as when using argon + % of nitrogen (Table III).

The results obtained using industrial argon and electrolytic copper (experiment 1 in Table III) are very different than the ones reported by other researchers (19), who obtained, for otherwise similar conditions, an erosion rate of the cathode of 13.5 μg/C, arc velocity of 2 m/s and arc voltage of 44 V. The differences could be due to a contamination of the industrial argon used here or possible copper composition differences. The surface composition changes (caused by the use of mixtures of gases or copper alloys) would cause differences in work function among others, and this could change dramatically the behavior of the electric arc and plasma (see for instance Ref.19).

Comparing experiments 1 and 2, of Table III, it can be seen that the use of ultra pure argon indeed resulted in values closer to the ones obtained in (19), indicating that the industrial argon used here, although specified as 99.9 % pure, can have some contaminants that would cause a surface contamination (see above) which would result in a higher arc velocity, lower erosion rate (due to the high velocity) and lower voltage (less stretching of the electric arc, see for more details (16)). Analysis of the argon gases are current being conducted.

Comparing experiments 3 to 6 (Table III) it can be seen that the use of industrial or ultra pure argon, once % of nitrogen has been added to the argon main stream, did not result in significant differences, indicating that the level of contamination of the industrial argon is probably less than 0.3 % and that after a certain level of contamination of the surface is reached, the addition of more nitrogen did not cause substantial differences (up to a certain level, after what the nitrogen present in the argon stream would result in variations in all parameters, as it can be seen comparing experiments 3, 6 and 7 of Table III). The behavior of the arc adding nitrogen to a main argon gas stream observed here is similar to the ones obtained by other authors (19).

Experiment 8 (Table III) was conducted using industrial helium. The absolute values of the results obtained are different than the ones obtained by Szente (16) (who obtained lower arc velocity (20 m/s), similar erosion rate (1 μg/C) and higher voltage (110 V)), although the general trend, when comparing argon and helium was the same for both cases. Therefore comparing results 2 and 10 with the equivalent ones published previously (19), there is a strong indication that the copper material used here, although purchased as electrolytic copper, has composition differences when compared to the material used in the previous study. Analysis of the copper material used here, shown in Table I, indeed show the presence of several contaminants that could in principle cause variations in the properties of the surface (work function in particular) that would explain the differences found when comparing the results obtained here and the ones by Szente et al.

In Table IV it is shown the results obtained using different copper materials for the cathode, using ultra pure argon as the plasma gas. It can be seen that the use of copper-nickel alloy did not result in significant differences in erosion rate and arc velocity when comparing with the electrolytic copper. In Table V, the results obtained using the copper-nickel alloy for different gases, showed again similar results to the ones obtained using electrolytic copper. The use of the copper-nickel alloy may be important for other plasma gases, such as hydrogen; this is being investigated at the moment.

The decrease in the magnetic field strength (Table VI) resulted, as expected, in a decrease in the arc velocity (after correcting for the different arc currents used, the arc velocity for the lower magnetic field would be around 20 m/s) and an increase in the erosion rate.

The high speed photographs obtained in the present work show that the electric arc present similar characteristics to the ones published previously (19). The electric arc and plasma are longer for cleaner surface conditions (when using ultra pure argon, for instance), resulting in higher arc voltages.

V. Conclusion

Cathode erosion on copper electrodes by magnetically driven arcs was studied at atmospheric pressure by varying different parameters (B, I, type of plasma gas and purity of the electrode materials). The experimental results presented here will be used to further understand erosion phenomena. It was shown that the use of industrial gases affects the erosion rate and electric arc velocities due to contaminants present in the gases. The use of commercial electrolytic copper, for making cathodes, also revealed that there is an important level of contamination, which affects the overall behavior of the electric arc. Using copper-nickel alloys, as cathode material, did not result in significant differences when compared to electrolytic copper; however those alloys could be important for some plasma gases, such as hydrogen. Further experiments are being conducted in order to determine the effect of using industrial electrolytic copper and different plasma gases on the overall electric arc and plasma behavior.

Acknowledgement

The financial support of Fapesp for this project, grant number 99/03779-0, is greatly appreciated.

References

[1] J. Prock, IEEE Trans. Plasma Sci, PS-14, 482 (1986).
[2] E. Hantzsche, Plasmaphysick 2, 59 (1979).
[3] J. Miterrauer and P. Till, IEEE Trans Plasma Sci PS-15, 488 (1987).
[4] F. M. Lehr and M. Kristiansen, IEEE Trans. Plasma Sci. 17, 811-817 (1989).
[5] A. E. Guile and A. H. Hitchcock, J. Phys. D: Appl. Phys. 7, 597-606 (1974).
[6] J. E. Harry, J. Appl. Phys. 40, 265-270 (1969).
[7] A. H. Hitchcock and A. E. Guile, "Erosion of Copper Cathodes by moving arcs at currents of 45-800A" Proc. IEE 122, 763-764 (1975)
[8] A. E. Guile and A. H. Hitchcock, "Effect of water cooling on erosion of the copper cathode of a rotating arc", Proc. IEE 122, 579-580 (1975).
[9] A. E. Guile and A. H. Hitchcock, "Effect of transverse magnetic field on erosion rate of cathodes of rotating arcs", Proc. IEE 128, 117-122 (1981).
[10] A. E. Guile and A. H. Hitchcock, "Effect of copper oxide thickness on the number and size of arc-cathode emitting sites", Proc. IEE 124, 148-152 (1977).
[11] A. E. Guile and A. H. Hitchcock, J. Appl. Phys. 49, 4275-4276 (1978).
[12] R. N. Szente, R. J. Munz and M. G. Drouet, Plasma Chem. Plasma Proc. 7, 349-364 (1987)
[13] A. P. George and A. L. Hare, "Arc heater operating characteristics on oxygen and nitrogen, an interim report", Proc. ISPC-6, IUPAC, Montreal, Paper A-5-2, (1983), pp. 144-147.
[14] D. R. Porto, C. W. Kimblin and D. T. Tuma, J. Appl. Phys. 53, 4740-4749 (1982)
[15] R. N. Szente, "Cathode erosion in magnetically rotated arcs", M. Eng. Thesis, McGill University, Montreal, Canada, (1986).
[16] R. N. Szente, "Erosion of plasma torches electrodes", PhD Thesis, McGill University, Montreal, Canada, (1989).
[17] R. N. Szente, R. J. Munz and M. G. Drouet, Plasma Chem. Plasma Proc. 12, 327-343 (1992).
[18] J. E. Kwak and R. J. Munz, Plasma Chem. Plasma Proc. 16, 577-603, (1996).
[19] R. N. Szente, R. J. Munz and M. G. Drouet, J. Phys. D: Appl. Phys. 23, 1193 –1200 (1990).
[20] R. N. Szente, R. J. Munz and M. G. Drouet, Plasma Chem. Plasma Proc. 9, 121-132 (1989).
[21] D. Heskett, A. Baddorf, E. W. Plummer, "Nitrogen induced reconstruction of Cu (110): Formation of a surface nitride", Surface Science, vol. 30, n.6, 3124-3130, (1984).

A combined mass spectrometry and thin film deposition study of pulsed C_4F_8 plasmas

D. Theirich, F. Osenberg, J. Engemann

Forschungszentrum Mikrostrukturtechnik - fmt, University of Wuppertal, Wuppertal, Germany

Plasma polymerization of C_4F_8 was used to deposit teflonlike thin films. These films are used for example to control diffusion and the wettability of surfaces or as chemically inert and anti-sticking coatings. Besides other applications they are increasingly used in growing fields like biotechnological applications, sensors and nano systems. Important for theses films is the amount of CF_2 bonds inside the film which indicates how close the structure of the plasma deposited film comes to the structure of conventional teflon. Recently pulsed plasmas have been frequently used to influence and to control the plasma chemistry of molecular gas plasmas, especially pulsed plasmas have been used to control the degree of retention of the monomer structure during plasma deposition.

In this study pulsed C_4F_8 plasmas have been used to deposit thin films. XPS and FTIR analyses of these films were used to determine the film structure. A plasma monitor was used to perform neutral mass spectrometry, appearance mass spectrometry and time resolved mass spectrometry of C_4F_8 deposition plasmas in order to correlate the resulting film structure with the amount of different molecular fragments in the plasma. Mass spectrometry was also used to determine the essential reaction paths, which are influenced by pulsing the plasma. A capacitively coupled parallel plate rf plasma source (13.56 MHz) was used for the experiments. The upper electrode was a mesh connected to the rf generator. The lower electrode was grounded and used as substrate holder, which was held at a constant temperature of 20°C. The spacing between the electrodes was 3 cm. The monomer gas was supplied above the upper mesh electrode and transported to the mesh through a funnel shaped gas flow guiding.

The deposited films showed an increasing relative amount of CF_2 bonds under conditions of decreasing mean rf power, decreasing pulse-on times and increasing pulse-off times. Especially at constant mean power a decreasing pulse-on time results in an increasing CF_2 content in the films. Results from mass spectrometry showed the overall dissociation of C_4F_8 and the C_2F_6 content of the plasma is affected only by the mean rf power, whereas the content of fragments with larger carbon chains like C_4F_7 can also be influenced by the pulse parameters under conditions of constant rf power. Under these conditions the increasing C_4F_7 content in the plasma is correlated to an increasing relative amount of CF_2 bonds in the deposited films. Thus the results indicate that C_nF_{2n-1} fragments which may be produced by reactions of the type $C_3F_5 + nCF_2 \rightarrow C_nF_{2n-1}$ may contribute to the plasma deposition of fluorocarbon films with a large content of CF_2 bonds.

Modelling of a Microwave Flowing Post-Discharge in N_2-O_2 for Plasma Sterilization

C.D. Pintassilgo[(1)], T.Belmonte[(2)], J.Loureiro[(3)] and V.Guerra[(3)]

[(1)] *Dep. Física, Faculdade de Engenharia, Univ. Porto, 4200-465 Porto, Portugal*
[(2)] *Laboratoire de Science et Génie des Surfaces, Ecole des Mines, 54042 Nancy, France*
[(3)] *Centro de Física dos Plasmas, Instituto Superior Técnico, 1049-001 Lisboa, Portugal*

Abstract
The aim of the present work is to give an insight into the kinetics of a low pressure afterglow of a microwave discharge in a N_2-x%O_2 mixture (x=0.2 and 2%). First, we calculate the conditions at the end of the discharge by solving the homogeneous Boltzmann equation for the electrons coupled with an appropriate set of rate balance equations. Once the concentrations of species are obtained, their temporal relaxation in the near afterglow is described by a 1D model. Then, we use a hydrodynamic 2D model to describe the flow in the sterilization vessel.

1.Introduction

Recently, gas plasma sterilization in hospitals has appeared as very promising alternative to conventional sterilization process, in particular for materials, essentially polymer based, that are heat sensitive. Among the proposed solutions to achieve sterilization using an afterglow plasma [1], it was shown that a N_2-2%O_2 mixture, within the pressure range 1-7 Torr and gas flow 0.5-3 slm, is a good candidate for such purposes [2]. In that paper an experimental study was realized on the operating conditions, pointed out the role played by O atoms and ultraviolet (UV) photons in spore inactivation. However, no modelling studies have been carried out to determine the concentrations of the various active species produced in the discharge, as well in the transport of the species in the post-discharge reactor. In this work, we present the results from a kinetic model for a microwave discharge at $\omega/2\pi$=915 MHz and its afterglow in a N_2-x%O_2 mixture with x=0.2 and 2%. The discharge model is based on the solution of the Boltzmann's equation for the electrons coupled to a set of rate balance equations for the various molecular and atomic species produced in the discharge, including ions and the vibrational distribution of $N_2(X^1\Sigma_g^+,v)$ molecules, in which the sustaining electric field is self-consistently determined [2]. Once the concentrations of the various neutral and ionic species are obtained, the time-evolution of the concentrations is analysed in the post-discharge by considering the relaxation of a set of coupled time-varying kinetic master equations for all heavy species. An analysis of the populating and depopulating mechanisms is then carried out for every species, with emphasis on $O(^3P)$ atoms, $NO(A^2\Sigma^+)$ and $NO(B^2\Pi_r)$ molecules, the later two being responsible for the UV emission of NOγ and NOβ system bands.
In parallel with this 1D analysis, a hydrodynamic 2D model for the afterglow taking into account the proper dimensions of the sterilizer vessel, has also been considered to determine the concentrations of O atoms and other active species near the sample to be sterilized. The hydrodynamic model is based on the solutions of the coupled transport equations, corresponding to the conservation of mass, the conservation of momentum and the conservation of heat.

2.Kinetic Model

Our work involves the kinetic study of two main different regions: the plasma source and the afterglow chamber, where the objects to be sterilized are placed (see figure 1). The plasma source includes the discharge tube and its connection to the sterilization chamber. In this intermediate zone a short-lived afterglow occurs. We start our analysis by the discharge, where we consider a steady-state kinetic model, based on the solutions to the homogeneous Boltzmann's equation coupled to a system of rate balance equations for the most populated neutral and ionic species present in a N_2-O_2 microwave discharge [2].

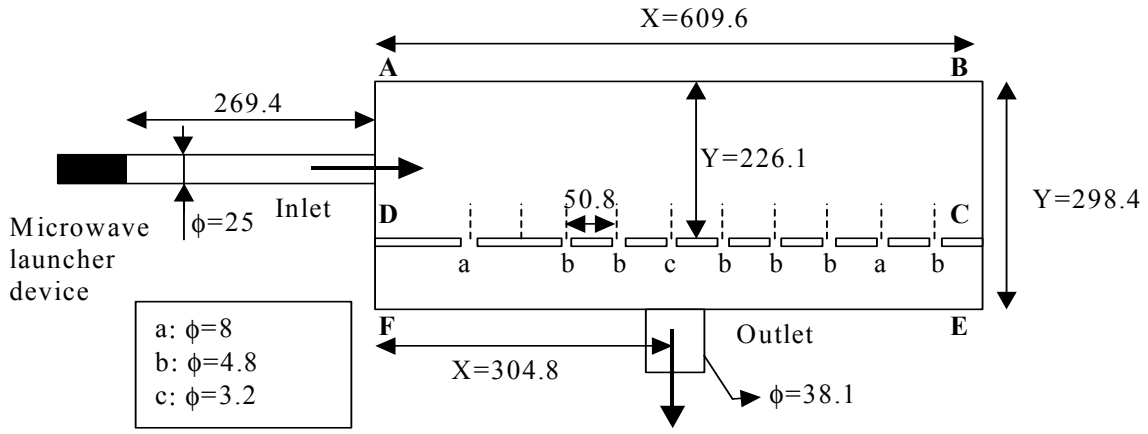

Fig.1 : Schematic of the sterilizer reactor. Units are in mm.

The reduced sustaining electric field in the plasma is self-consistently calculated using the requirement that under steady state conditions the total rate of ionization must compensate exactly for the rate of electron loss by diffusion to the wall plus the electron-ion recombination. In this analysis, we have considered two improvements in the model presented in [2]. First, we have included the kinetics of the atomic metastables $N(^2D,^2P)$, as it was recently proposed [3]. Secondly, within the purposes of this work, we have introduced the kinetics of NO(A) and NO(B) molecules, where we have added the reactions presented in table 1.

Table 1 : Reactions considered for the species NO(A) and NO(B).

$N_2(A)+NO(X) \rightarrow N_2(X,v=0)+NO(A)$	[4]	$NO(A)+N_2 \rightarrow NO(X)+N_2$	[8]
$N+O+O_2 \rightarrow NO(X)+O_2$	[5]	$NO(A)+O_2 \rightarrow NO(X)+O_2$	[8]
$N+O+(M) \rightarrow NO(B)+(M)$, $M=N_2, O_2$	[6]	$NO(A)+NO(X) \rightarrow NO(X)+NO(X)$	[9]
$NO(B)+N_2 \rightarrow NO(X)+N_2$	[7]	$NO(B) \rightarrow NO(X)+h\nu$	[9]
$NO(B)+O_2 \rightarrow NO(X)+O_2$	[8]	$NO(A) \rightarrow NO(X)+h\nu'$	[10]
$NO(B)+NO(X) \rightarrow NO(X)+NO(X)$	[8]		

Once the concentrations for the neutral and ionic species produced in the microwave discharge are obtained, we must investigate their temporal evolution until they reach the sterilization chamber. This is done by considering a system of coupled time-varying kinetic master equations for the most important heavy species, including ions and the vibrational distribution of $N_2(X^1\Sigma_g^+,v)$, where we assume the calculated concentrations in the discharge as initial conditions.

After these calculations, we can describe in detail the concentrations of active species in the sterilization vessel, by assuming the former as the concentrations at the entry of the reaction chamber. The modelling of this reactor has been done using or not the pumping grid (noted CD in Fig. 1). Thus, two geometries have been considered. They are represented by the two volumes ABCD and ABEF in Fig. 1. This 50-liter sterilizer (aluminum frame) is described as providing better spatial uniformity of the active species in the afterglow chamber [11]. A more detailed development of the equations solved, the boundary conditions and the finite volume method used herein is provided in [12].

3.Results and Discussion

The calculations of our work have been carried out for typical operating conditions of a microwave discharge at $\omega/2\pi$=915 MHz in a N_2-x%O_2 mixture (x=0.2 and 2) with p=8 Torr and a gas temperature T_g=1000K in a discharge quartz tube of inner radius R=1.3 cm. The electron density in the discharge is assumed to be equal to the critical value for surface-wave mode propagation, $n_e=5.196\text{x}10^{10}\text{cm}^3\text{s}^{-1}$, since the values calculated in the

discharge constitute the initial conditions at the beginning of the afterglow. Further, we have assumed a gas temperature T_g=500 K in the near afterglow.

The results concerning the temporal evolution in the near afterglow are presented in figures 2 to 5. Figure 2 and 3 report, respectively, the temporal evolution of the concentrations of $[N(^4S)]/[N_2]$,$[O(^3P)]/[N_2]$, $[NO(X)]/[N_2]$ and $[NO(A)]/[N_2]$, $[NO(B)]/[N_2]$ for N_2-0.2%O_2.

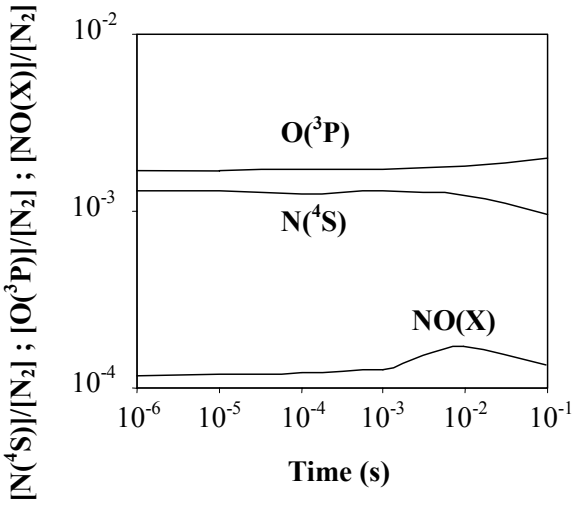

Fig. 2 : Temporal evolution of $[N(^4S)]/[N_2]$, $[O(^3P)]/[N_2]$ and $[NO(X)]/[N_2]$ in the near afterglow of a N_2-0.2%O_2 microwave discharge, with $\omega/2\pi$=915 MHz and p=8Torr.

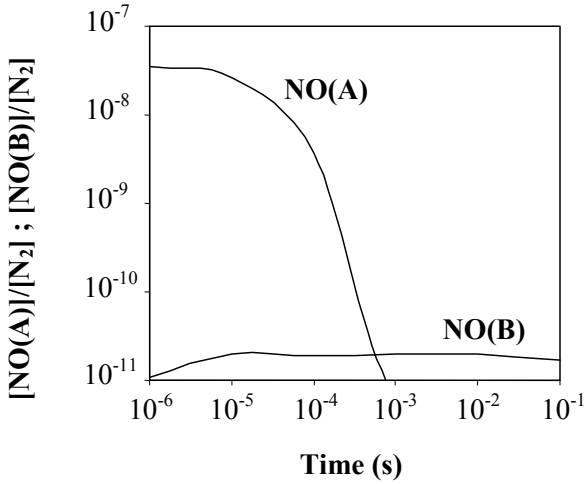

Fig. 3 : Temporal evolution of $[NO(A)]/[N_2]$ and $[NO(B)]/[N_2]$ in the near afterglow of a N_2-0.2%O_2 microwave discharge, with $\omega/2\pi$=915 MHz and p=8Torr.

Figs 4 and 5 show the same information as in Figs 2 and 3, but for the case of a higher O_2 initial concentration in the mixture, i.e. 2%O_2.

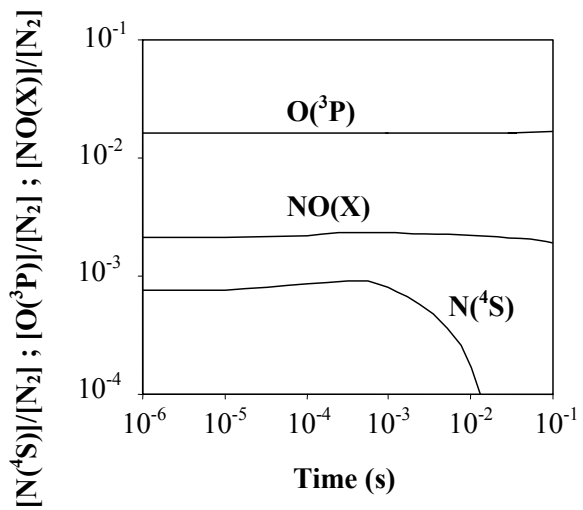

Fig. 4 : As in Fig.2, but for a N_2-2%O_2 mixture.

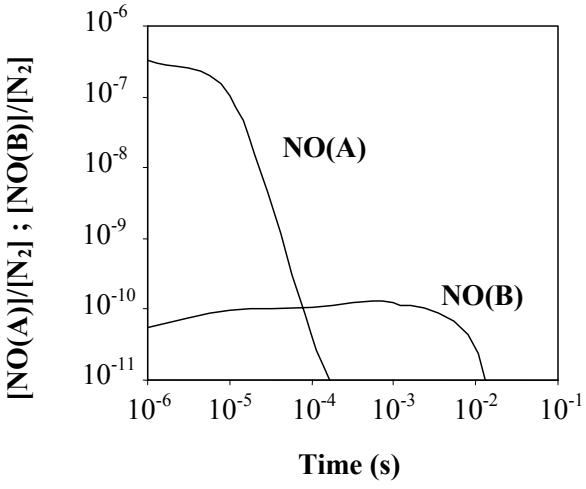

Fig. 5 : As in Fig.3, but for a N_2-2%O_2 mixture.

Figure 2 and 4 show that the relative concentrations $[N(^4S)]/[N_2]$, $[O(^3P)]/[N_2]$ and $[NO(X)]/[N_2]$ remain practically unchanged during the short-lived afterglow, with the exception of $N(^4S)$ for times $t \geq 10^{-2}$s in the case

of 2%O_2. For these larger values of *t*, the main mechanism of creation for N(^{4}S) is the reaction $N_2(X,v\geq13)+O\rightarrow NO+N$, whose rate becomes smaller in a N_2-2%O_2 mixture, as a result of a stronger depletion of the higher vibrational levels not shown here.

Figures 3 and 5 show a faster decay of NO(A) and NO(B) concentrations in the short-lived afterglow when the initial oxygen concentration increases. The NO(A) state is destructed more efficiently in a N_2-2%O_2 mixture via the reaction $NO(A)+O_2 \rightarrow NO(X)+O_2$. On the other hand, the NO(B) concentration remains almost constant in a N_2-0.2%O_2 afterglow and has a very fast decay for times $t\geq10^{-2}$s in a N_2-2%O_2 mixture. Since NO(B) is only created through the three body reaction, $N+O+M\rightarrow NO(B)+M$ (M=N_2 and O_2), and [O(^{3}P)] remains unchanged during the afterglow, we can conclude that the NO(B) decay follows that of N(^{4}S).

Using the data available from the 1D post-discharge model after a 0.1 s flow in the 25 mm ID quartz tube (see Fig. 1), calculations have been performed to understand the flow of the active species in the sterilization chamber. The set of chemical reactions considered in the present calculation is available in [12].

The chemistry of the post-discharge strongly evolves when the amount of oxygen in the initial gas mixture increases from 0.2 to 2%. For example, nitrogen atoms are no longer present at 2%. To account for such changes, the set of reactions considered in the late post-discharge has been adapted from the one presented in [12] to the two cases considered herein (0.2 and 2%). The influence of NO_2 has also been considered, contrary to the 1D model. Its concentration has thus been assumed to be null at the entrance of the reactor.

The temperature of the gas at the entrance of the sterilizer has been chosen equal to 500 K, whereas the temperature of the walls has been assumed to stay at room temperature. The pumping configuration being extremely important to distribute the active species around the samples, the two geometries previously presented have been studied using the two mixtures N_2-0.2%O_2 and in N_2-2%O_2. The velocity maps are depicted in Fig. 6 and 7. The improvement due to the grid noted (DC) in Fig. 1 is of major importance, since the flow no longer presents strong recirculation when it is used (only one remains in the upper right side of the vessel). Only this geometry will be retained hereafter.

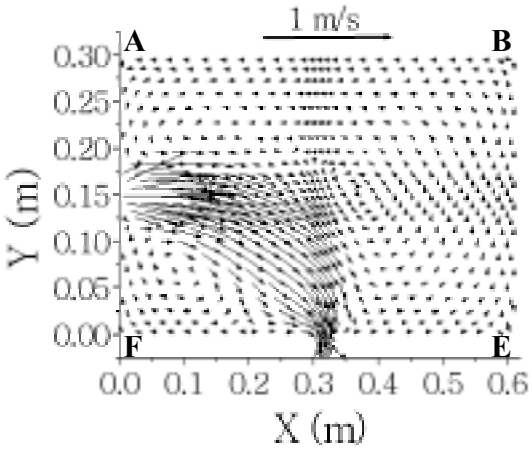

Fig. 6 : Velocity map in the (ABEF) volume of the reactor (see Fig. 1 for the meaning of the letters)

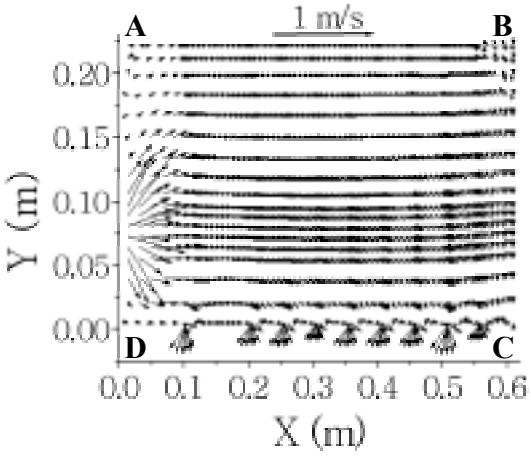

Fig. 7 : Velocity map in the (ABCD) volume of the reactor (see Fig. 1 for the meaning of the letters)

Only species with meaningful variations are represented in Fig. 8 to 11.

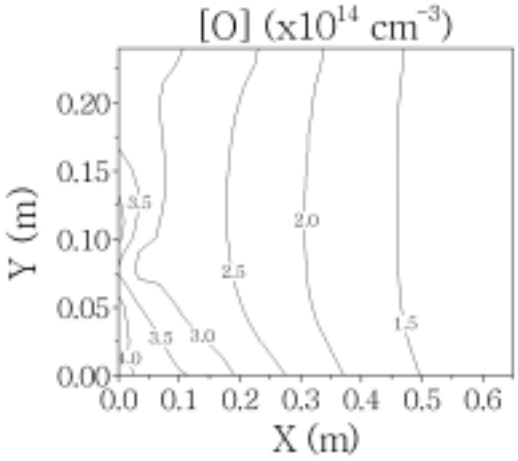

Fig. 8 : Density map of atomic oxygen in a late N_2-0.2%O_2. Reactor geometry : (ABCD).

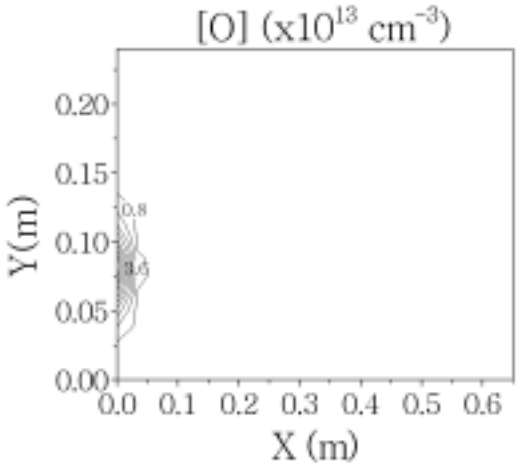

Fig. 9 : Density map of atomic oxygen in a late N_2-2%O_2. Reactor geometry : (ABCD).

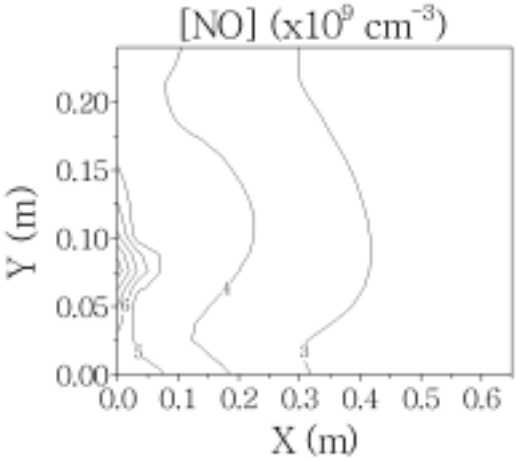

Fig. 10 : Density map of nitrogen monoxide in a late N_2-0.2%O_2. Reactor geometry : (ABCD).

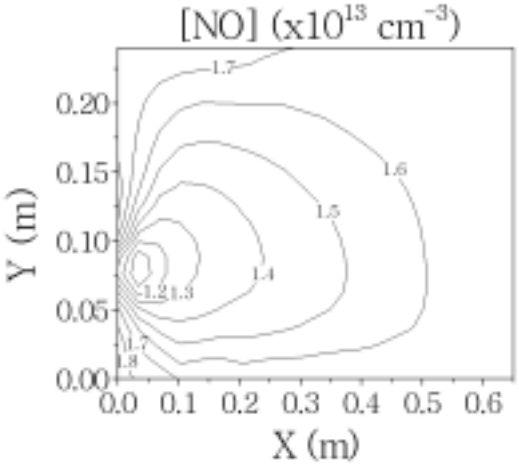

Fig. 11 : Density map of nitrogen monoxide in a late N_2-2%O_2. Reactor geometry : (ABCD).

The density of oxygen atoms strongly decreases at the entrance of the reactor. Their repartition is affected when the initial amount of oxygen in the gas varies. It is mainly due to the creation of NO_2 from NO molecules. This reaction is much less efficient in the N_2-0.2% O_2 mixture where the density of NO molecules is much lower (Figs. 10 and 11). The NO radical also evolves significantly from a N_2-0.2% O_2 mixture to a N_2-2% O_2 mixture but in an opposite way. To interpret the slight increase in NO density in Fig. 11, one must keep in mind that the temperature decreases in the reactor from 500 K at the entrance to 300 K at the walls. Thus, such an increase corresponds in fact to a weak consumption of matter in a temperature gradient. The evolution of the density of O_3, which is not represented herein, is not significantly affected by the change in the oxygen concentration. It is close to $2x10^{12}$ cm^{-3} mainly distributed near the walls. Thus, one can think from these results that the mechanisms responsible for the sterilization, which is efficient in both cases, are not the same. New experiments are in progress to confirm the first trends revealed by the present models.

References

[1] M. Moisan, J. Barbeau, S. Moreau, J. Pelletier, M. Tabrizian, L.H. Yahia, Int. J. Pharmaceutics, **226** 1 (2001)
[2] V.Guerra, J. Loureiro, Plasma Sources Sci. Technol., **8** 110 (1999)
[3] V. Guerra, E. Tatarova, C. M. Ferreira, Vacuum, **69** 171 (2003)

[4] L.G.Piper, L.M.Cowles and W.T.Rawlings, J.Chem.Phys. **85** 3369 (1986)
[5] I.A.Kossyi, A.Yu Kostinsky, A.A.Matveyev and V.P.Silakov, Plasma Sources Sci.Technol. **1** 207 (1992)
[6] R.W.F.Gross and N.Cohen, J. Chem. Phys. **48** , 2582 (1968)
[7] G.Black, R.L.Sharpless, and T.G.Slanger, J.Photochem. **5** 435 (1976)
[8] G.A.Raiche and D.R.Crosley J.Chem.Phys. **92** 5211 (1990)
[9] H.Zacharias, J.B.Halpern and K.H.Welge, Chem.Phys.Lett. **43** 41 (1976)
[10] L.G.Piper, T.R.Tucker, W.P.Cummings, J.Chem.Phys. **94** 7667 (1991)
[11] N. Philip, B. Saoudi, M.C. Crevier, M. Moisan, J. Barbeau, J. Pelletier, IEEE-Transactions-on-Plasma-Science, **30** 1429 (2002)
[12] T. Belmonte, T. Czerwiec, A. Ricard, H. Michel, XXIII International Conference on Phenomena in Ionised Gases (ICPIG), Toulouse, France, IV (1997) 198-199.

Metallized Polyimide for a new Generation of Flexible Electronic Circuit Boards

P. Gröning[1] and B. Kindle-Hasse[2]

[1]*Swiss Federal Laboratories of Testing and Research, Überlandstrasse 129, CH-8600 Dübendorf, Switzerland*
[2]*ROWO Coating, Allmendstrasse 7, D-79336 Herbolzhein, Germany*

Abstract
On long (30 – 60 sec.) plasma pre-treated polyimide (UPILEX) Cu/Cr films show high initial adhesion strengths, but also a significant loss in the adhesion strength of up to 40 % after thermal aging at 150°C and 250 hours. Short (3 – 6 sec.) plasma pre-treated samples have initially a 20% lower adhesion strengththan the long pre-treated samples, but show no reduction of the adhesion strength after thermal aging. The different long-term stability behavior of the short and long plasma pre-treated samples can be explained by relaxation processes inside the plasma modified surface layer of the polymer.

1. Introduction

The continuing trend towards miniaturization of electronic devices requires also development of cost-effective, environmentally friendly materials and processes for the interconnection techniques. The gap between chip production, now producing 80 nm lines and spaces, and the interconnection techniques able to producing electronic circuit boards with 60 µm structures, must inevitably shrink. Laser direct patterning (LPD) is a new possibility to structure ultra-thin metallic films laid onto polyimide foils [1]. By using a KrF UV eximer laser (λ = 248 nm) the light penetrates the ultra-thin (d ~ 50 nm) metal film and cracks the chemical bonds at the metal-polymer interface. The resulting plasma plume lifts off the metal film in a mini explosion. With this technique, structures less than 15 µm can be produced on 1 cm^2 by a single millisecond long laser shot.

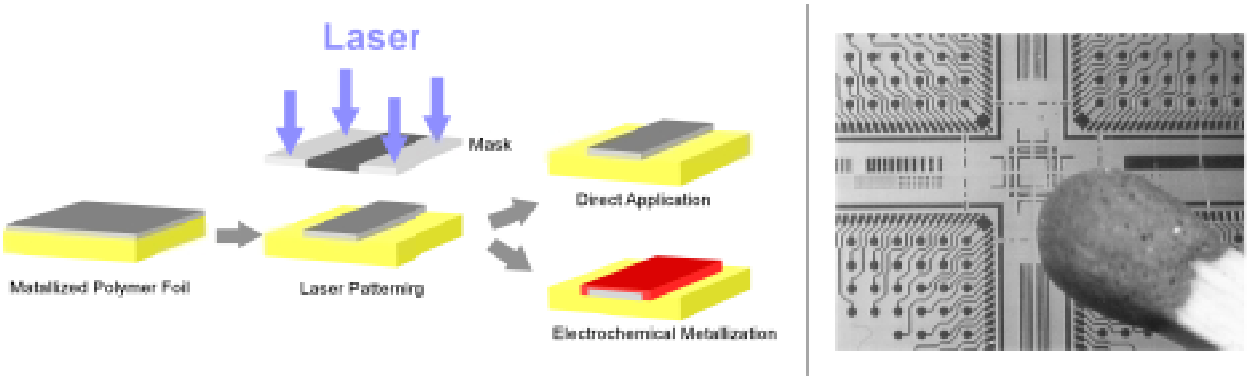

Figure 1
Principle of the direct laser pattering (LPD) process, together with a picture showing electronic interconnects produced by LPD on a thin polyimide foil. The finest lines and spaces are 15 µm wide.

For electronic applications very strong and durable adhesion of the metallization is required. The IPC-FC-241/18 norm dictates adhesion strength higher than 7 Ncm^{-1} after deposition and 5.2 Ncm^{-1} after thermal aging at 150°C and 1000 hours. These very strong adhesion requirements demand an activation of the polymer substrate surface. Plasma treatment is one of the more recent technologies to improve the adhesive properties of polymers. The plasma activation of a polymer surface is related to surface cleaning by ablation of low-molecular-weight materials, crosslinking and formation of polar functional groups, resulting in a

change of the surface energy γ. According to the Dupré relation an increase in surface energy will result in a higher reversible thermodynamic work of adhesion W_A given by:

$$W_A := E_i - E_f = (\gamma_A - \gamma_B) - \gamma_{AB} \qquad \text{Dupré relation}$$

Where E_i is the energy of the initial sate given by the sum of the surface energies γ_A, γ_B of the body A and B and E_f the energy of the final state given by the interface energy γ_{AB} of the two bodies in contact.
In the present contribution we will show that the adhesion performance between a metal film and a plasma modified polymer is in generally rather limited by the cohesion of the polymer near the plasma modified surface than by the adhesion at the metal-polymer interface. X-ray photoemission spectroscopy (XPS) data from the fracture surfaces after peel test reveal that the critical zone limiting the adhesion behavior of the metal film is located ~ 2 nm inside the polymer and not at the metal-polymer interface. A phase separation process of the plasma modified polymer chains and the bulk polymer can explain the formation of this new interface inside the polymer.

2. Experimental

The polyimide used was a commercial UPILEX foil. Figure 2 shows the XPS reference spectra together with the repeating structural unit of the UPILEX. Prior metallization the UPILEX surfaces was activated by Ar/O_2 RF-plasma at p = 2 x 10^{-2} mbar. Subsequently a 10 nm thin Cr adhesion layer followed by a 50 nm thick Cu film were sputtered onto the plasma activated polymer surface "in-situ". Finally a 50 µm thick Cu film was deposited electrochemically onto the sputtered Cu film. The adhesive strengths were determined by a standard 90° peel test. X-ray photoelectron spectroscopy (XPS) was performed in an Omicron Fullab equipped with an EA-125HR electron analyser. Analysis were carried out with non-monochromatized MgKα (hν = 1253,6 eV) radiation. The instrument was calibrated to the $Au4f_{7/2}$ signal at the binding energy of E_B = 84.0 eV and the $Cu2p_{3/2}$ signal at E_B = 932.7 eV. The mean free path λ_e for inelastic scattering of 1.0 keV electrons in polymers is about 30 Å [2], which results in a XPS probing depth of about 100 Å for electron emission normal to the surface. Charging of the samples, due to the photoemission process, was corrected by setting the binding energy of the main carbon component (-CH_2- component) in the C1s spectrum to 284.8 eV.

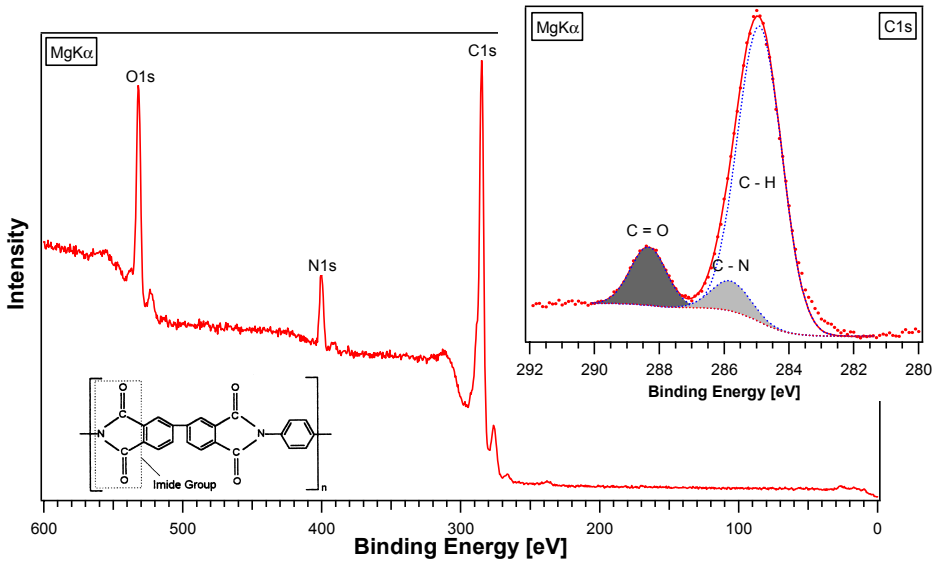

Figure 2
Reference XPS spectra together with the repeating structural unit of the untreated UPILEX surface.

3. Results and Discussion

For UPILEX treated for 30 – 60 sec. in Ar/O_2 RF-plasma we measured initial (as deposited) adhesion forces of 9.2 – 13.8 Ncm^{-1}. This is significant higher than the 7.0 Ncm^{-1} provided by the IPC-FC-241/18 norm. After thermal aging at 150 °C for 100 hours and 250 hours the adhesion forces reduce to 6.1 – 7.8 Ncm^{-1} and 4.6 – 5.9 Ncm^{-1} respectively. With this values we are not able to fulfil the 5.2 Ncm^{-1} after 1000 hours thermal aging provided by the IPC-FC-241/18 norm. XPS analysis of the fracture surfaces (Fig. 3) suggest that the loss in the adhesion force during thermal aging is associated to a change in the fracture behavior. The overview spectrum of the fracture surface from the Cu/Cr-side peel test fragment of the as deposited sample shows apart from the C1s, N1s and O1s signals from the UPILEX no additional signals from the underlying metal Cr adhesion layer. This indicates that the cohesive fracture is at least 100 Å (XPS probing depth) underneath the metal/polymer interface inside the polymer. After thermal aging Cr signals from the adhesive layer appear in the XPS spectra of the Cu/Cr-side peel test fragments, indicating that the fracture becomes closer and closer to the metal/polymer interface with increasing aging time, but still cohesive. For the 250 hours thermal aged samples we determined using the Toogaard procedure [3], we determined an average thickness of 20 Å for the polymer layer sticking on the Cr film, which indicates the cohesive nature of the fracture. The C1s detail spectra from the UPLEX-side fracture surfaces are for all samples identical with the reference spectrum of the untreated UPILEX (Fig. 2). In opposition to that shows the C1s detail spectra of the Cu/Cr-side fracture surfaces an increase in the intensity of the C = O component with increasing aging time. The increase of the C = O component indicates the presents of plasma modified polymer chains. From this observation we conclude that during the thermal aging process a new interface inside the polymer is formed by a phase separation of the plasma modified polymer chains from the bulk polymer, and the fracture propagates along this new interface.

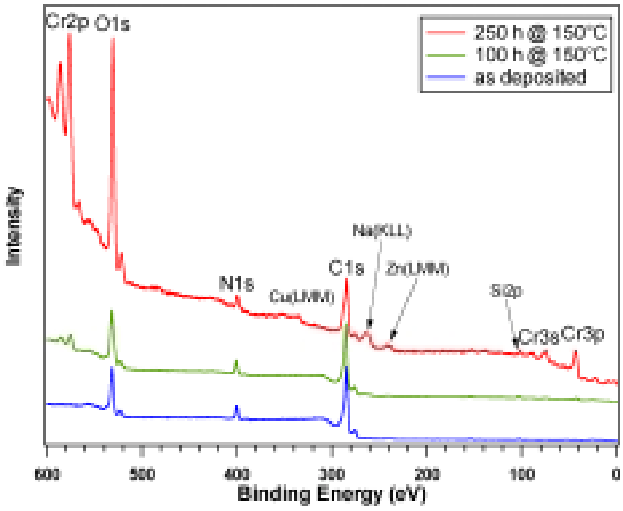

Figure 3

XPS overview spectra from the fracture surface of the Cu/Cr side peel test fragment, peel tested after deposition and after thermal aging at 150 °C for 100 and 250 hours, respectively. The UPILEX surface was pre-treated for 30 sec. in Ar/O_2 plasma.

On polymers the plasma treatment is not restricted to the surface. The thickness of the polymer surface layer strongly modified by plasma treatments is about 100 Å [4 – 6]. This plasma modified surface layer is initially in a highly excited state and tends to relax. In the presence of a reactive metal on the surface (Cr layer) the functional groups inside in the modified surface layer have the tendency to migrate at the surface and forming chemical bonds with the metal. This thermal driven process becomes equal to a phase separation process between the plasma-modified polymer chains and the bulk polymer, resulting in the formation of a new interface with low cohesive strength. The formation of this new polymer/polymer interface is in generally the limiting factor for the long-term stability of the adhesion of metal films on plasma modified polymers. As stronger the plasma modifications (polar bonds, chain secession) inside the polymer are as faster the phase separation process occurs. Consequently, in regard to the long-term stability of the adhesion, it is very important to reduce the plasma modifications in the surface region of the polymer as much as

possible. A confirmation of this conclusion can be found in the work of Gong et al. [7]. They studied the effect of sticker groups (–COOH) on the fracture energy of Al – cPBD interface (cPBD: carboxylated polybutadiene (PDB)) and found that a small amount of sticker groups improves the fracture energy considerably. They found a critical concentration around 3 mol% to give a maximum bond strength. Higher concentrations of sticker groups show lower bond strength. Further they showed that the concentration of sticker groups was much higher at the interface as in the bulk polymer, indicating the migration of the sticker groups to the interface. To proof our idea that relaxation processes inside the plasma activated polymer surface region are important for the long-tern stability of the adhesion we reduced the plasma pre-treatment time by a factor of ten to 3 – 6 seconds. The initial adhesion forces of the Cu/Cr film on such plasma pre-treated UPILEX was between 8.0 and 9.1 Ncm^{-1}. These values are about 20 % lower than for the samples with 30 – 60 seconds plasma exposure time, but still higher than the 7.0 Ncm^{-1} dictated by the IPC-FC-241/18 norm. The type of fracture for the short pre-treated samples is mixed adhesive/cohesive, indicated by the presence of the Cr signals in the overview spectrum and the Cr-C component in the C1s spectrum of the Cu/Cr side fracture surface (Fig. 4).

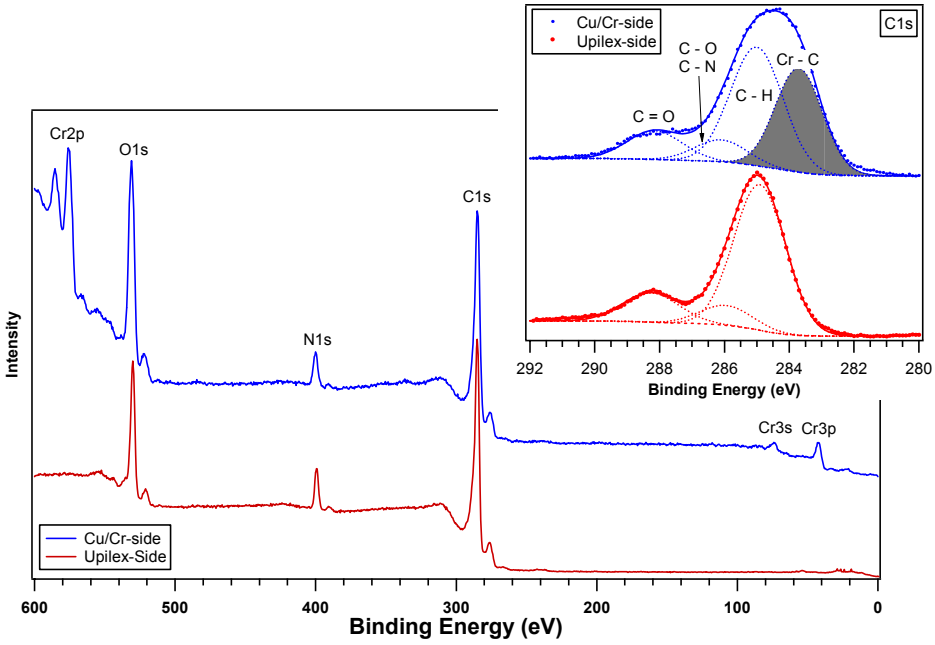

Figure 4
XPS spectra from the fracture surfaces from as deposited Cu/Cr-UPILEX sample.
The UPILEX surface was pre-treated for 5 sec. in Ar/O_2 plasma.

The mix-fracture can be associated to the structure of UPILEX consisted by crystalline and amorphous regions. Due to the stretching in the manufacturing of thin foils the crystalline regions are oriented parallel to the surface. The cohesive strength perpendicular to the surface is therefore very low for the crystalline regions at the surface. Consequently, the crystalline parts do practically not contribute to the adhesion of the metal film. The type of fracture in the crystalline regions is in generally cohesive. In the amorphous regions the type of fracture can be adhesive or cohesive depending on the surface activation. In our case the fracture is cohesive in the amorphous regions for long plasma pre-treatment and adhesive for short plasma pre-treatment. This explains the perfect cohesive fracture for the sample with long plasma pre-treatment and the mixed adhesive/cohesive fracture for the short plasma pre-treated samples (Fig. 5).
In contrast to the long plasma pre-treated samples show the samples with short plasma pre-treatment no losses in the adhesive strength during thermal aging. In the ideal case the adhesive strength even increases after thermal aging up to values of 10.5 Ncm^{-1}. Behind this effect are the same processes which are responsible for the weak layer formation in samples with long plasma pre-treatment. The migration of polar bonds inside the plasma modified surface region to the metal/polymer interface increases the number of

metal/polymer bonds and consequently the adhesion at the interface, but not to a phase separation and consequently to the formation of weak boundary layer as proposed for the long plasma pre-treated sample.

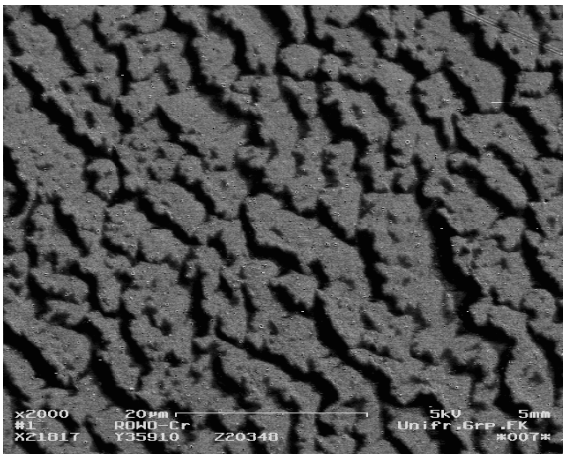

Figure 5
SEM picture of the Cu/Cr side fracture surface from a sample with short plasma pre-treatment.
The dark (polymer) and bright patches (Cr) illustrate the mixed adhesive/cohesive fracture of the sample.

4. Conclusion

For polymers, plasma treatments can not be considered as a classical surface effect. The surface region on polymer modified by plasma treatments is at least 100 Å thick. This plasma modified surface region is initially in a highly excited state and tends to relax. In the presence of a reactive metal on the surface (Cr layer) the functional introduced by the plasma have the tendency to migrate to the metal/polymer interface and forming chemical bonds with the atoms from the metal film. If the amount of adhesive sites inside the plasma modified surface region is to high the migration process becomes to phase separation process of the plasma modified polymer chains and the bulk polymer. This results in the formation of new interface inside the polymer with a low cohesive strength. For long plasma treated samples the formation of this new interface is factor limiting the long-term stability of the adhesion. For short plasma pre-treatments the amount of modifications inside the polymer is not high enough to trigger the phase separation process, which explains the good long-term stability of the adhesion. Our investigations have shown that the relaxation of the plasma activated polymer surface region may have strong effects on the long-tern stability of the adhesion of metallized films and must be considered in the optimization of the adhesion behavior of plasma modified polymer surfaces.

Acknowledgement

We acknowledge generous financial support from the “Deutschen Bundesstiftung Umwelt”.

References:

[1] LPKF Laser & Electronics, Osteriede 7, D-30827 Garbsen, Germany, http://www. lpkf.de
[2] R.F. Roberts, D.L. Allara, C.A. Pryde, D.N.E. Buchmann, and N.D. Hobbins, Surf. Interf. Anal. **2**, 5 (1980).
[3] S. Tougaard, Surf. Interf. Anal. **11**, 453 (1988)
[4] P. Gröning, O.M. Küttel, M. Collaud Coen, G. Dietler, and L. Schlapbach, Appl. Surf. Sci. **89**, 83 (1995).
[5] P. Gröning, M. Collaud, G. Dietler, and L. Schlapbach, J. Appl. Phys. **76**, 887 (1994).
[6] P. Gröning “Cold Plasma Processes in Surface Science and Technology” in Handbook of Thin Film Materials, edited by H.S. Nalwa, Vol. **1**, 219 (2002), Academic Press.
[7] L. Gong, A.D. Friend and R.P. Wool, Macromolecules **31**, 3706 (1998).

Plasma Functionalisation of the Carbon Nanofibres Surface

G. Marginean, W. Brandl

Department of Materials Science, University of Applied Sciences Gelsenkirchen, Gelsenkirchen, Germany

A selected plasmachemical treatment is utilised to improve the surface properties of carbon fibres used for fibre-reinforced composites. Compared to other methods for modifying the fibres surface the plasma treatment has many advantages [1]. Plasma processing presents, besides the advantage of a dry and clean process, also the advantage of the non-significantly diminishing of the fibre mechanical and physical properties [2].
In this study differerent plasma functionalisations of Vapour Grown Carbon-Nanofibres (VGCNF) surface are presented. The VGCNFs have a diameter of 50-200 nm and a length of 100-200 μm and are produced by the cathalytic decomposition of gaseous carbon precursors. Depending on the plasma parameters and functionalising gases (O_2, NH_3, N_2), an enhancement of the fibre surface energy occurs. Those surface treatments are doubly important in composites because they optimise the adhesion between the fibre and the polymer matrix which conducts to the improvement of the mechanical and physical properties of the composite. The morphology and the properties of the carbon nanotubes as well as of the fibre/polymer composites (before and after the plasma functionalisation) were characterised by scanning electron microscopy (SEM), contact angle measurements, electrical conductivity measurements and testing of the tensile strength of the obtained composites.

Keywords: plasma surface treatment, carbon nanofibres, polymer composites

[1] J.-B. Donnet, Carbon Fibres, 145-205, (1990)
[2] C.U. Pittman et al., Carbon 36, No. 1-2, 25-37, (1998)

Prediction of anode arc root position in a DC arc plasma torch

He-Ping Li[1], E. Pfender[1], Xi Chen[2]

[1] *Department of Mechanical Engineering, University of Minnesota, Minneapolis, MN 55455, USA*
[2] *Department of Engineering Mechanics, Tsinghua University, Beijing 100084, P. R. China*

Abstract
Modeling results are presented concerning the 3-D flow and heat transfer inside a non-transferred DC arc plasma torch using two different electric potential boundary conditions, i.e. anode iso-potential condition and the Steenbeck minimum principle. The computed results show that although the predicted anode arc root positions by the two approaches are almost the same, using the Steenbeck minimum principle can predict more precisely the anode arc root shape and the local high temperature region near the anode arc spot.

1. Introduction

Although DC arc plasma torches have been widely used over the past decades, understanding of the complex physical and chemical processes occurring inside plasma torches are still incomplete. The complex interactions between electromagnetic fields, gas flow and arc self-induced flow fields and temperature fields make modeling a formidable task. Transient behavior of the arc, non-local thermodynamic equilibrium (non-LTE) effects near electrodes, three-dimensional (3-D) effects inside the torch add further to this complexity [1]. In this paper, we will focus on the 3-D effects inside a non-transferred DC arc plasma torch.

The complex physical phenomena inside a DC arc plasma torch can be described by a complete set of magnetohydrodynamic (MHD) equations. Previously, many researchers used the two-dimensional (2-D) MHD equations to simulate the temperature, flow and electromagnetic fields inside the torch [2-7]. Although some useful information can be obtained by 2-D modeling, 3-D effects are entirely ignored. For example, the predicted arc voltage for the turbulent regime is much higher than measurement indicated, and the calculated anode arc root position at the anode surface is also much farther downstream than actually observed [6, 7]. A 3-D MHD model was proposed in Refs. [7, 8] to simulate heat and flow patterns inside a DC arc plasma torch. And physically reasonable anode arc root positions at the anode surface were obtained for a few operating parameters [7, 8].

As indicated in Ref. [4], the Steenbeck minimum principle [9] is a very useful tool to predict anode arc root positions at the anode inner surface. This principle is compatible with Maxwell's equations, and thus, it is not an independent law [10]. The goal of this paper is to compare the 3-D heat and flow patterns inside a non-transferred DC arc plasma torch by employing the Steenbeck minimum principle with those using the previous 3-D MHD model presented in Refs. [7, 8].

2. Mathematical model

2.1 Basic assumptions

In this paper, the following assumptions are employed for the 3-D modeling:

(1) The flow inside the plasma torch is quasi-steady, turbulent, having temperature-dependent properties;
(2) The plasma is in LTE state outside the electrode boundary layers and optically thin;
(3) The viscous dissipation and the pressure work terms in the energy equation are neglected;
(4) The working gas (argon) is injected into the plasma torch in axial direction, i. e., without any swirling velocity component of the gas at the torch inlet;
(5) The induced electric field $\vec{V}\times\vec{B}$ is negligible in comparison with the electric field intensity $\vec{E}$.

2.2 Governing equations

Based on the foregoing assumptions, the governing equations for the 3D quasi-steady numerical simulations can be written in (r,θ,z) coordinates as follows:

$$\nabla\cdot\left(\rho\vec{V}\right)=0 \tag{1}$$

$$\nabla\cdot\left(\rho\vec{V}\vec{V}\right)=\nabla\cdot\left(-p\vec{I}+\vec{\tau}\right)+\vec{j}\times\vec{B} \tag{2}$$

$$\nabla \cdot \left(\rho c_p \vec{V} T\right) = \nabla \cdot \left(\Gamma_T \nabla T\right) + j^2/\sigma + \frac{5}{2}\frac{k_B}{e}\vec{j} \cdot \nabla T - S_R \tag{3}$$

$$\nabla \cdot \left(\sigma \nabla \phi\right) = 0 \tag{4}$$

In the preceding equations, $\vec{V}$, p, T and ϕ are the velocity, pressure, temperature of the gas and the electric potential, respectively. $\vec{\vec{I}}$ and $\vec{\vec{\tau}}$ are unit tensor and shear stress tensor, respectively. The current density vector $\vec{j}$ relates to the electric potential ϕ as

$$\vec{j} = -\sigma \nabla \phi \tag{5}$$

$\vec{B}$ is the magnetic induction, which is obtained by

$$\vec{B} = \nabla \times \vec{A} \tag{6}$$

and by using this equation in the actual modeling work speeds up the iteration process [7]. In Equation (6), $\vec{A}$ is the magnetic vector potential, which satisfies the following equation

$$\nabla^2 \vec{A} = -\mu_0 \vec{j} \tag{7}$$

with

$$\vec{A}(x, y, z) = \frac{\mu_0}{4\pi}\int_{V'}\frac{\vec{j}(x', y', z')}{r}dV' \tag{8}$$

as the boundary conditions, where μ_0 is the permeability in vacuum. The boundary conditions for the magnetic vector potential employed in this paper are very different from those employed in Ref. [11].

The standard $K-\varepsilon$ two-equation turbulence model is employed in this study. The turbulent kinetic energy and its dissipation rate equations are

$$\nabla \cdot \left(\rho \vec{V} K\right) = \nabla \cdot \left(\Gamma_K \nabla K\right) + G - \rho\varepsilon \tag{9}$$

$$\nabla \cdot \left(\rho \vec{V} \varepsilon\right) = \nabla \cdot \left(\Gamma_\varepsilon \nabla \varepsilon\right) + \frac{\varepsilon}{K}\left(c_1 G - c_2 \rho\varepsilon\right) \tag{10}$$

The turbulent generation term G appearing in Equations (9) and (10) is expressed as

$$G = \mu_t\left\{2\left[\left(\frac{\partial v_z}{\partial z}\right)^2 + \left(\frac{\partial v_r}{\partial r}\right)^2 + \left(\frac{\partial v_\theta}{r\partial\theta} + \frac{v_r}{r}\right)^2\right] + \left(\frac{\partial v_z}{\partial r} + \frac{\partial v_r}{\partial z}\right)^2 + \left(\frac{\partial v_\theta}{\partial z} + \frac{\partial v_z}{r\partial\theta}\right)^2 + \left(\frac{\partial v_r}{r\partial\theta} + \frac{\partial v_\theta}{\partial r} - \frac{v_\theta}{r}\right)^2\right\} \tag{11}$$

where v_r, v_θ and v_z are the components of the velocity vector $\vec{V}$ in r-, θ- and z-directions, respectively. All the physical quantities in the foregoing equations are their time-averaged values. ρ, c_p, σ and S_R are the temperature-dependent mass density, specific heat at constant pressure, electric conductivity and the radiation power per unit volume of an argon plasma, respectively. k_B is the Boltzmann constant, e is the elementary charge. The effective 'diffusion' coefficients are the combination of laminar and turbulent values in the transport equations.

2.3 Calculation domain and boundary conditions

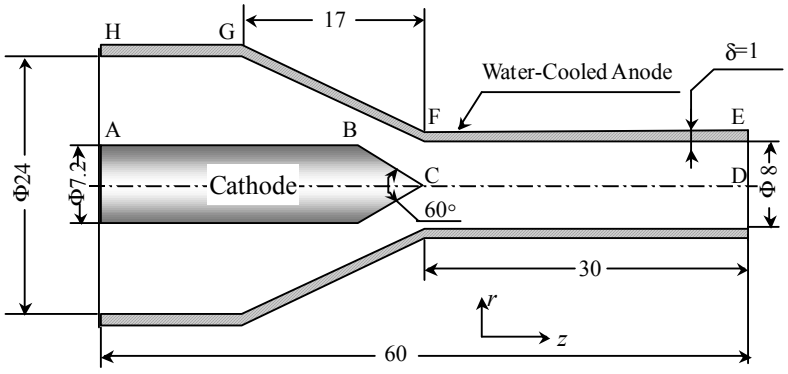

Figure 1. Calculation domain.

The calculation domain, as shown in Figure 1, is formed by the rotation of the region ABCDEFGHA about the torch axis with the indicated geometric dimensions. In this paper, the copper anode, the thickness of

which is in order of 1 *mm*, is included in the computational domain for getting a reasonable prediction of the temperature distribution on the anode. The boundary conditions are listed in Table 1, where Q is the volumetric flow rate of the working gas, A is the inlet cross-section area of the torch, while Φ_i are the values of the variable Φ at the grid points on the small circle nearest to the centerline ($\Phi = v_r, v_z, T, K, \varepsilon, \phi$). At the cathode surface, the temperature (T_c) and current density ($\vec{j}_0$) distributions are specified as shown in Figure 2 according to the experimental data presented in Ref. [12]. Then, the potential gradient is calculated as

$$\vec{j}_0(r) = -\sigma \frac{\partial \phi}{\partial n} \tag{12}$$

where $\vec{j}_0(r)$ is the current density vector at the location of the cathode arc root. This vector is perpendicular to the cathode surface and a function of the radial distance (r) and the axial distance from the cathode tip (z_c), while n indicates the normal direction of the cathode surface from the inner side to the outer side of the cathode. On the symmetry plane [$\theta = 0\,(2\pi)$], a periodic boundary condition is employed as follows [7]:

$$\Phi_{b_1} = \Phi_{b_2} \approx \frac{1}{2}\left(\Phi_{a_1} + \Phi_{a_2}\right) \tag{13}$$

where $\Phi = v_r, v_\theta, v_z, T, K, \varepsilon, \phi$. The subscripts b_1 and b_2 indicate the grid points located on the symmetry plane, while a_1 and a_2 indicate the nearest inner grid points to the symmetry plane located on both sides of this plane in the calculation domain.

Because the outer side of the anode is immersed in the cooling water, the third kind of boundary condition is employed in the present paper, i. e.,

$$-k \left.\frac{\partial T}{\partial r}\right|_w = h(T_w - T_\infty) \tag{14}$$

where the subscript "*w*" indicates the interface between the anode and the cooling water, h is the heat transfer coefficient, which is in order of $10^5\ W/\left(m^2 \cdot K\right)$, T_∞ is the temperature of the cooling water.

Table 1. Boundary conditions for 3D modeling of non-transferred DC arc plasma torch.

	ABC	CD	DE	EFGH	HA	$\theta = 0\,(2\pi)$
v_r	$v_r = 0$	$v_r\big\|_{r=0} = \frac{1}{N}\sum_{i=1}^{N} v_{r,i}$	$\partial v_r/\partial z = 0$	$v_r = 0$	$v_r = 0$	On the symmetry plane, periodic boundary conditions, [Eq. (13)], are employed.
v_θ	$v_\theta = 0$	$rv_\theta = 0$	$\partial v_\theta/\partial z = 0$	$v_\theta = 0$	$v_\theta = 0$	
v_z	$v_z = 0$	$v_z\big\|_{r=0} = \frac{1}{N}\sum_{i=1}^{N} v_{z,i}$	$\partial v_z/\partial z = 0$	$v_z = 0$	$v_z = Q/A$	
T	Assumed Fig. (2b)	$T\big\|_{r=0} = \frac{1}{N}\sum_{i=1}^{N} T_i$	$\partial T/\partial z = 0$	Eq. (14)	300 K	
K	Wall Function Method	$K\big\|_{r=0} = \frac{1}{N}\sum_{i=1}^{N} K_i$	$\partial K/\partial z = 0$	/	$0.005v_z^2$	
ε		$\varepsilon\big\|_{r=0} = \frac{1}{N}\sum_{i=1}^{N} \varepsilon_i$	$\partial \varepsilon/\partial z = 0$	/	$0.1K^2$	
ϕ	$\vec{j}_0(r) = -\sigma\frac{\partial \phi}{\partial n}$	$\phi\big\|_{r=0} = \frac{1}{N}\sum_{i=1}^{N} \phi_i$	$\partial \phi/\partial z = 0$	See Section 2.3	$\partial\phi/\partial z = 0$	

In this paper, two approaches are employed to deal with the electric potential boundary condition on the anode surface, which are described as follows:

CASE I: Specified arc-root position boundary condition. With this approach, the anode arc-root position is specified in advance with $\phi = 0$ as boundary condition, and no current passes through the remaining parts of the anode. Thus, the total arc voltage can be obtained through solving the governing equations mentioned above. In our modeling work, we can obtain different arc voltages

by specifying different anode arc-root locations. And then, according to Steenbeck's minimum principle, the physically reasonable position of the anode arc-root should correspond to the position with minimum value of the arc voltage for a certain set of operation parameters.

CASE II: Iso-potential boundary condition. It means that the values of the electric potential are equal on the whole outer surface of the anode. This boundary condition is physically reasonable because of the very large electric conductivity of the anode material (copper), and was employed in Refs. [7, 8].

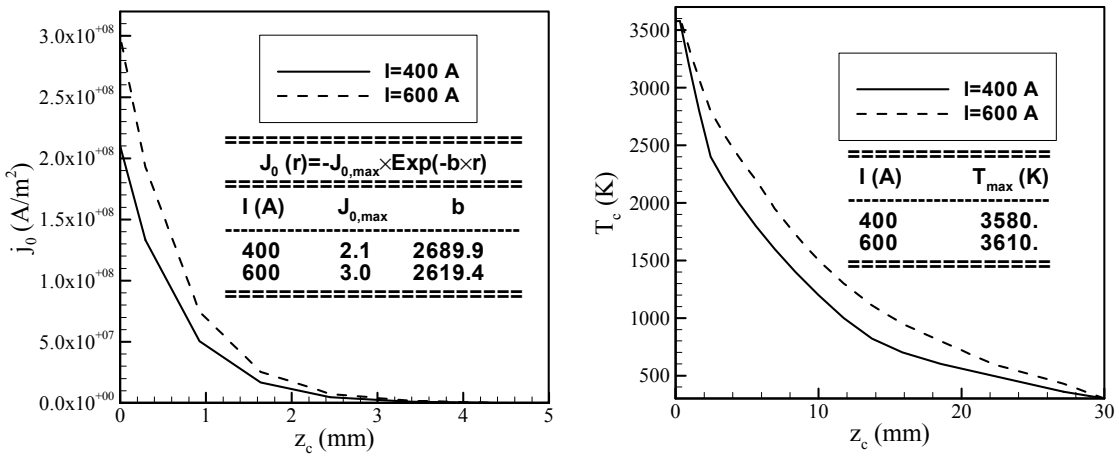

(a) (b)

Figure 2. The assumed current density (a) and temperature (b) distributions on the cathode surface.

3. Modeling results and discussions

In this paper, the SIMPLE algorithm [13] is employed to solve the non-linear equations (1)~(4), (7), (9) and (10) simultaneously with the new version of the non-commercial software FAST-3D (Fluid Analytical Simulation Tools—Three Dimensional) [14]. A 3-D, body-fitted, non-uniform mesh $32\,(z)\times 22\,(r)\times 11\,(\theta)$ is adopted for the 3-D modeling of a plasma torch in the present paper [7].

3.1 Modeling results and discussions

In CASE II, we assume that the anode arc-root positions are as L_{Arc}=2.32, 3.29, 4.47, 5.86, 7.53 and 9.54 *mm*. The calculated arc voltages as a function of the arc length L_{Arc} are plotted in Figure 3, which shows that for a given set of operation parameters (e. g., I=400 *A*, Q=2.0 STP m^3/hr), the arc voltage V_{Arc} varies with the increase of the arc length L_{Arc} as a V-shaped curve, and there exists a position corresponding to the minimum value of the arc voltage among the different assumed anode arc-root positions along the anode surface. Thus, according to Steenbeck's minimum principle, this position should be the real position of the anode arc-root attachment during torch operation. In our calculation, the arc length determined by Steenbeck's minimum principle is L_{Arc}=5.86 *mm*.

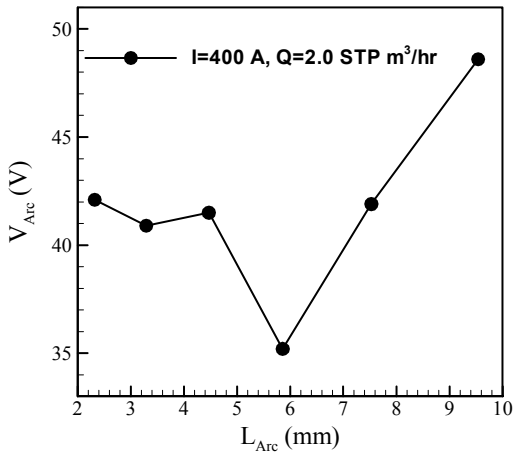

Figure 3. Arc voltage variations with different assumed anode arc-root positions.

The corresponding temperature distributions inside the plasma torch at $0-\pi$ plane and the iso-contours of the radial current density component at the inner surface of the anode are plotted in Figures 4(a) and 5(a), and compared with their counterparts for CASE I as shown in Figures 4(b) and 5(b), respectively. From Figures 4 and 5, we can find that although the predicted anode arc-root attachments in CASE I and CASE II are almost the same ($L_{Arc} \approx 5.9\,mm$), the temperature distributions near the anode arc-root attachment in Case I are very different from that in Case II. In CASE I, the anode arc root is confined to a certain spot, and

as a consequence, there is a higher temperature region near this spot, related to the anode jet formation as described in Ref. [15]. While in CASE II, such local characteristics of the arc cannot be predicted, and the maximum local current density is also much smaller than that in CASE I because the anode arc root distributes over a larger area in CASE II. The calculated average maximum values of the temperature and axial velocities at the torch exit are 12,650 *K*, 426 *m/s* and 12,738 *K*, 461 *m/s*, for CASE I and CASE II, respectively. The corresponding relative discrepancies for the averaged maximum temperature and axial velocity component between these two cases are 0.7% and 7.6%, respectively (both smaller than 10%). Similar results are also obtained for the case *I*=600 *A*, *Q*=2.0 STP m^3/hr.

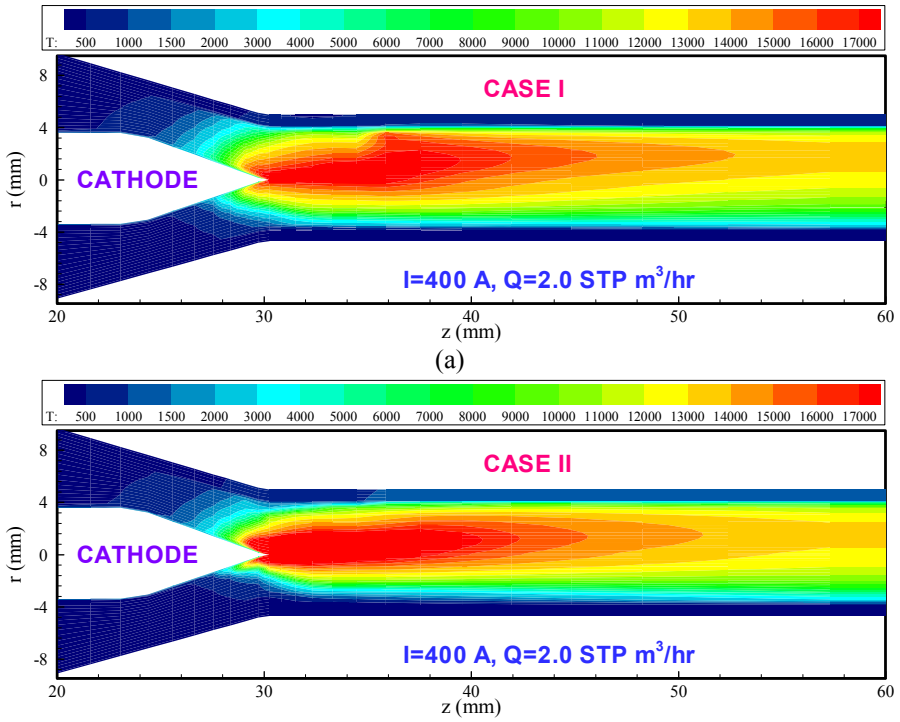

Figure 4. The temperature distributions inside the plasma torch for CASE I (a) and CASE II (b).

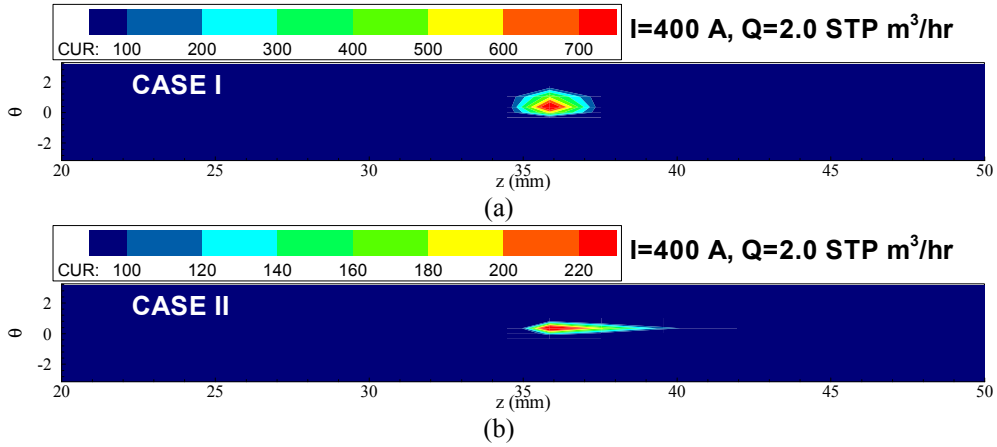

Figure 5. the iso-contours of the radial current density component at the inner surface of the anode for CASE I (a) and CASE II (b).

3.2 Comparison with experimental observations

As discussed in Section 3.1, Steenbeck's minimum principle used in this study can predict the anode arc-root position and the arc shape more precisely than the method with an iso-potential boundary condition.

The typically calculated arc contours for CASE I and II (*I*=400 *A*, *Q*=2.0 STP m^3/hr) and a photograph of the arc in steady mode of operation [15] are shown in Figure 6. The calculated arc shape (CASE I in Figure 6) is similar to the experimentally observed arc shape (lower part in Figure 6), while by using a uniform potential

boundary condition at the outer surface of the anode [7, 8], instead of using Steenbeck's minimum principle, the local characteristics of the arc near the anode arc-root cannot be well predicted.

4. Conclusions

In this paper, the 3-D heat transfer and flow patterns inside a non-transferred DC arc plasma torch are simulated. Two different electric potential boundary conditions are employed to determine the position of the anode arc root. The main conclusions are as follows:

(1) The 3-D effects inside the non-transferred DC arc plasma torch are significant.

(2) The predicted anode arc root positions by either the iso-potential boundary condition or the application of Steenbeck minimum principle are almost the same.

(3) The predicted anode arc root shape by using Steenbeck's minimum principle is more precise than that predicted by using an iso-potential boundary condition.

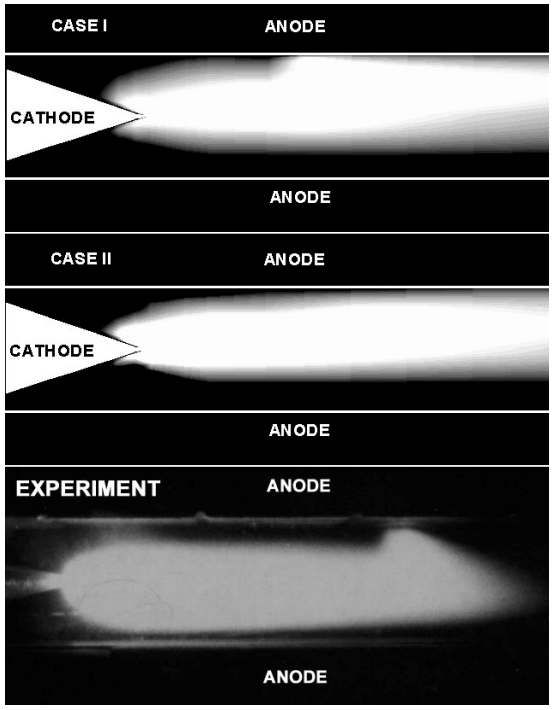

Figure 6. Comparison of the typically calculated arc temperature distribution inside the DC arc plasma torch (upper part) with the photograph of argon arc in steady mode of operation (lower part, [15]).

Acknowledgement

This work was partly supported by the National Natural Science Foundation of China (grant No. 50176024). The first author has been supported through a postdoctoral fellowship by the Department of Mechanical Engineering, University of Minnesota. The support through a supercomputer grant by the University of Minnesota Supercomputing Institute is gratefully acknowledged.

References

[1] P. Fauchais, A. Vardelle - Plasma Physics and Controlled Fusion **42**, B365 (2000).

[2] D. A. Scott, P. Kovitya, G. N. Haddad - Journal of Applied Physics **66**, 5232 (1989).

[3] R. Westhoff, J Szekely - Journal of Applied Physics **70**, 3455 (1991).

[4] S. Paik, P. C. Huang, J. Heberlein, E. Pfender - Plasma Chemistry and Plasma Processing **13**, 379 (1993).

[5] J. M. Bauchire, J. J. Gonzalez, A. Gleizes - Plasma Chemistry and Plasma Processing **17**, 409 (1997).

[6] Peng Han - Ph. D. Thesis, Department of Engineering Mechanics, Tsinghua University (1999, In Chinese).

[7] He-Ping Li - Ph. D. Thesis, Department of Engineering Mechanics, Tsinghua University (2001, In Chinese).

[8] He-Ping Li, Xi Chen - Journal of Physics D: Applied Physics **34**, L99 (2001).

[9] W. Finkelnburg, H. Maecker - "Electric Arcs and Thermal Plasmas" in Encyclopedia of Physics, Vol. XXII, Springer-Verlag, Berlin (1956).

[10] Ming-Lun Xue, Yun-Ming Chen - Acta Mechanica Sinaca **11**, 96 (1979, In Chinese).

[11] P. Freton, J. J. Gonzalez, A. Gleizes, F. C. Peyret, G. Caillibotte, and M. Delzenne - J. Phys. D: Appl. Phys. **35**, 115 (2002).

[12] Xin Zhou - Ph. D. Thesis, Department of Mechanical Engineering, University of Minnesota (1995).

[13] S. V. Patankar - *Numerical Heat Transfer and Fluid Flow*, Hemisphere Publishing, Taylor and Francis, (1980).

[14] J. Zhu - *An Introduction and Guide to the Computer Program FAST-3D*, Institute for Hydromechanics, University of Karlsruhe, Report No. 691 (1992).

[15] S. A. Wutzke - Ph. D. Thesis, Department of Mechanical Engineering, University of Minnesota (1967).

Wettability of Ion Bombarded Plasma Polymer Films

E. C. Rangel, R. Y. Honda, R. C. C. Rangel and N. C. Cruz

Departamento de Física e Química, UNESP - Guaratinguetá, SP, Brazil

The deposition of a film onto a surface can drastically alter its performance in certain applications. Thus, lubricating, hard, adhesive, biocompatible and wear resistant thin films are of great interest for mechanical and electronic engineering, food industry and biomedical devices [1-4]. In this work, the surface properties of plasma polymer films treated by PIII (Plasma Immersion Ion Implantation) were investigated. The effect of the treatment time on the wettability and free surface energy of the films was determined.

The system employed in the film deposition and PIII experiments is composed by a stainless steel vacuum chamber, fitted with two parallel plate electrodes. The upper electrode is connected to a radiofrequency (13.56 MHz) supply via a matching circuit. For the film deposition, the lower electrode is grounded and used as substrate holder. For the PIII experiments, chamber walls are grounded and the holder is biased with pulsed voltage (- 25 kV). Using this equipment, films were deposited from low-pressure acetylene/argon or hexamethyldisiloxane (HMDSO) glow discharges. Treatment plasmas were generated from nitrogen or helium, while biasing the samples with 25 kV negative tooth saw–like pulses. Exposure time to the plasma treatment (t) varied from 0 to 7200 s. Sample wettability was investigated by contact angle (θ) measurements, using de-ionized water. The stability of the modifications induced by ion bombardment was investigated through the temporal evolution of θ. Free-surface energy was derived from contact angle data acquired using water and methylene iodide.

Figures 1a and b show respectively, the contact angle of HMDSO and acetylene plasma polymer films as a function of the exposure time to the PIII. As can be noticed, θ drops after the bombardement for all the samples. However, the fall is more pronounced in films deposited from organosilicon compounds. Indeed, θ does not vary significantly with t in the hydrocarbon prepared samples.

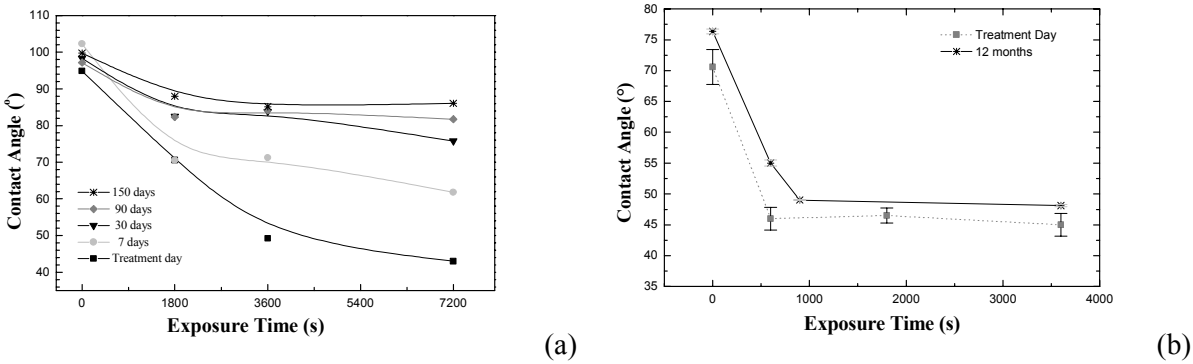

(a) (b)

Fig.1. Contact angle of HMDSO (a) and acetylene-argon (b) plasma polymer films as a function of t. Different curves correspond to data acquired at different days after the treatment.

The evolution of θ with the aging can be accessed comparing the different curves in the pictures, which correspond to θ values measured at different days after ion implantation. Treated hydrocarbon samples demonstrated higher stability of θ than the bombarded organosilicon. Such behavior is ascribed to the different abilities to crosslink of each material.

[1]. H. Grünwald, R. Adam, J. Bartella, M. Jung, W. Dicken, S. Kundel, K. Nauenburg, T. Gebele, S. Mitzlaff, G. Ickes, U. Patz, J. Snyder, Surf. Coat. Technol. **111**, 287 (1999).
[2]. R. Suchentrunk, G. Staudigl, D. Jonke, H. F. Fuesser, Surf. Coat. Technol. **97**, 1 (1997).
[3]. J. S. Cho, Y. Beag, S. Han, K. Kim, J. Cho, S. Koh, *Surf Coat. Technol.* **128-129,** 66 (2000).
[4]. P. Favia, R. d'Agostino, Surf. Coat Technol. **98**, 1102 (1998).

Treatment of Conventional Polymers by Plasma Immersion Ion Implantation

E. C. Rangel, W. C. A. Bento, M. A. Algatti, R. C. C. Rangel and N. C. Cruz

Departamento de Física e Química - UNESP - Guaratinguetá, SP, Brazil

Polymeric materials are becoming increasingly attractive to a series of applications so far dominated by metals, semiconductors and ceramics. The main reason for that is the possibility of surface selective modification while keeping bulk characteristics unchanged. For instance, the adhesion of metal films to polymers, subject of great concern in food packaging, flexible cables and connectors in microelectronics, is fairly improved as the free-surface energy augment [1]. Besides, activated polymers are being used as base for tissue integration, cell seeding and bacterial growth [2-4]. In this work, polyurethane (PU) and polytetrafluoroethylene (Teflon) were submitted to plasma immersion ion implantation. It was investigated the effect of the ion mass on the wettability, surface energy and plastic resistance parameters of the polymers.

Commercially pure polymer sheets were first cleaned and then exposed to helium, nitrogen or argon glow discharges (13.56 MHz, 70 W, 0.53 Pa). Simultaneously to the plasma ignition, the sample holder was biased with 25 kV tooth saw-like negative pulses. Total exposure time to the PIII treatments was 3600 s. Contact angle measurements, using de-ionized water or methylene iodide droplets, allowed the determination of the wettability and surface energy of the polymers. The stability of the modifications was investigated monitoring periodically the contact angle (θ) after the treatment. Mechanical resistance of the treated layer (R) was evaluated through the plastic resistance parameter, using data acquired by nanoindentation.

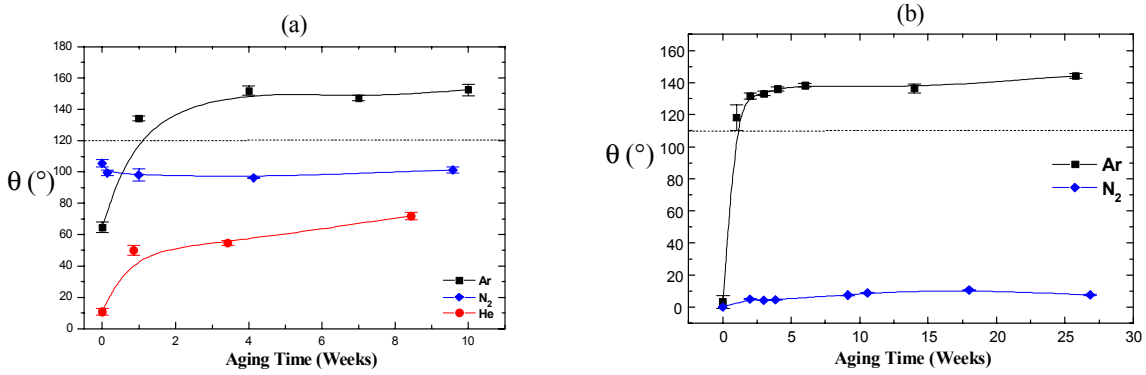

Fig.1. Temporal evolution of the contact angle of Teflon (a) and Polyurethane (b) bombarded with different ions.

In a general way, ion bombardment decreases the contact angle of the polymers. The reduction rate, however, depends on the mass of the implanted ion and also on the composition of the target material (Teflon or PU). In some cases θ was reduced to less than 1% of its original value. Despite of the intensity of such modifications, they were not stable, once θ tends to recover its initial character. Figures 1 (a) and (b) show respectively the temporal evolution of θ for Teflon and PU bombarded with different ions. It is interesting to note that the same material can become hydrophilic or hydrophobic depending on the mass of the implanted ion. After aging, Teflon implanted with argon and PU bombarded with nitrogen attained stable contact angles of 152 ° and 10 °, respectively.

There was improvement in the plastic resistance parameter of the polymer bombarded with argon. Treatments with helium and nitrogen, on the other hand, decreased R. Interpretation is proposed in terms of the ion energy loss mechanisms.

[1]. J. S. Cho, Y. Beag, S. Han, K. Kim, J. Cho, S. Koh, *Surf Coat. Technol.* **128-129,** 66 (2000).
[2]. J. McGuire and V. Krisdhasima, *J. Adhesion Sci. Technol* **3,** 195 (1993).
[3]. K. S. Birdi, *J. Theor Biol*. **93,** 1 (1981).
[4]. R. Daw, S. Candan, A. J. Beck, A. J. Devlin, I. M. Brook, S. MacNeil, R. A. Dawson and R. D. Short, *Biomaterials* **19,** 1717 (1998).

5H-polytype of sp^3-bonded boron nitride prepared by plasma-packets-assisted pulsed laser deposition: an ultraviolet light-emitter at 225 nm

Shojiro Komatsu, Keiji Kurashima, Hisao Kanda, Katsuyuki Okada, Mamoru Mitomo, Yusuke Moriyoshi[a)], Yoshiki Shimizu[a)], Masaharu Shiratani[b)], Toshiki Nakano[c)], and Seiji Samukawad)

Advanced Materials laboratory, National Institute for Materials Science, 1-1 Namiki, Tsukuba, Ibaraki, 305-0044, Japan,

[a)]College of Engineering, Hosei University, 3-7-2 Kajino-machi, Koganei, Tokyo 184-8584, Japan

[b)]Department of Electronics, Kyushu University, Hakozaki, Fukuoka 812-8581, Japan

[c)]Department of Electrical and Electronic Engineering, National Defense Academy, 1-10-20 Hashirimizu, Yokosuka 239-8686, Japan

d)Institute of Fluid Science, Tohoku University, 2-1-1 Katahira, Aoba-ku, Sendai 980-8577, Japan

Highly crystalline 5H-polytypic form of sp^3-bonded boron nitride (BN) was grown by pulsed-laser-vaporization of BN, where synchronous reactive-plasma packets assisted the crystal growth in the vapor phase. The structure of the product crystallites (~5 micrometers) was confirmed by using transmission electron diffraction and electron energy loss spectroscopy. This material proved to have a sharp and dominant band at 225 nm by cathodeluminescence at room temperatures and corresponding monochromatic images revealed that they uniformly emitted the ultraviolet light. Considering that cubic BN has already been doped as p- and n-type semiconductors, this material may be applied to the light-emitting devices working at almost the deepest limit of the UV region that is functional without vacuum.

References

(1) S.Komatsu, K.Kurashima, H.Kanda, M.Mitomo ,Y.Moriyoshi, Y.Shimizu, K.Okada, M.Shiratani, T.Nakano, S.Samukawa, Appl.Phys.Lett. Dec.9th issue (2002).

(2) S.Komatsu, Y.Shimizu, Y.Moriyoshi, K.Okada, and M.Mitomo, J.Appl.Phys. 91(9), 6181-6184(2002).

(3) S.Komatsu, Y.Shimizu, Y.Moriyoshi, K.Okada, and M.Mitomo, Appl.Phys.Lett.79(2), 188-190(2001).

Hot wire plasma deposition of N-doped carbon films on fluorocarbon polymers to improve their biocompatibility.

Vasilets V.N.[1], Yang Q.[2], Singh A.[2], Sammynaiken R.[3], Shulga Yu.M.[4], Vasin S.L.[1], Sevastianov V.I.[1], Hirose A.[2]

[1] *The Research Center for Biomaterials, Research Institute of Transplantology and Artificial Organs, Shukinskaya 1, 123182 Moscow, Russia*
[2] *Plasma Physics Laboratory, Univ. of Saskatchewan, 116 Science Place, Saskatoon, SK, S7N 5E2 Canada*
[3] *Department of Chemistry, Univ. of Saskatchewan, 110 Science Place, Saskatoon, SK, S7N 5C9, Canada*
[4] *Institute of Problems of Chemical Physics, Chernogolovka, Moscow reg., 142432, Russia*

Abstract
Carbon films doped with nitrogen and oxygen were deposited on polytetrafluoroethylene (PTFE) support by hot wire plasma sputtering of graphite target in the mixture of Ar with 5% air. The composition and structure of carbon films were determined by XPS, FTIR and Raman spectroscopy. A comprehensive platelet adhesion analysis demonstrates improved haemocompatibility of doped carbon coatings in comparison with untreated PTFE.

1. Introduction

Plasma assisted deposition of amorphous carbon and diamond-like carbon (DLC) films on polymer substrates is one of the promising techniques for modification of the substrate surface. Due to a combination of superior mechanical and chemical properties including hardness, low friction coefficient, high wear and chemical resistance, carbon deposition holds promise in different applications and particularly in biomedical field [1]. Although amorphous and isotropic carbon as well as pyrolitic graphite have been applied for modification of implants for a long time [2], the potency of DLC films as a bio- and haemocompatible material has been proved only recently [3].
Fluorocarbon polymers are widely used now in the field of biomaterials for cardiovascular surgery. The haemocompatibility of polytetrafluoroethylene (PTFE) vascular grafts with small diameter (< 6 mm) is a problem that has to be resolved for wider applications. Our approach was to use hot wire plasma sputtering of graphite in the mixture of Ar with air to deposit carbon layer containing nitrogen and oxygen groups onto PTFE. The hot wire plasma causes heating and softening of the polymer surface layer thus stimulating the growth of carbon film with high adhesion to the polymer support. Doping of carbon layer with nitrogen and oxygen containing groups usually present in biological substances could improve haemocompatibility and used for further immobilization of biomoleculars.

2. Experimental details

2.1. Preparation of samples.
The substrate materials were polytetrafluoroethylene $-[CF_2\text{-}CF_2]_n-$ (PTFE) films (thickness 60 microns) and Si (100) wafers used as a witness samples. The size of PTFE and Si samples was 20 mm×10mm. All samples were cleaned in ultrasonic bath with methanol and distillate water before deposition.
2.2. Plasma deposition technique.
The PTFE samples were exposed to deposition in dc glow discharge plasma by sputtering a graphite target in the flow of Ar with 5% air. The gas flow and pressure in the plasma chamber were maintained at 25 sccm and 5×10^{-2} torr respectively. The square graphite target (25 mm × 25 mm) was located at 10 mm from round sample holder (diameter 50mm). The temperature of sample holder during deposition was measured by chromel/alumel thermocouple and ranged between 180-210 C depending on plasma conditions. The temperature of hot wire was controlled by Micro Optical Pyrometer (Pyrometer Instr. Co., USA) and varied in the range 1950 – 2100 K depending on the filament current. The deposition time was varied from 15 min to 3 hour. In each run, polymer and Si wafer were deposited simultaneously.
2.3. Surface characterization
The surface chemical composition before and after deposition were analysed by XPS spectroscopy (Kratos Axis Ultra spectrometer, USA). The XPS spectra were obtained with 90 degree take-off angle by using monochromatised Al K_α source. The charge neutraliser was on for all the analysis.

The Raman spectra were measured using 633 nm excitation wavelength of helium neon laser. The scattering light was collected in backscattering with CCD camera, using Renishaw Model 2000 Raman spectrometer. The incident laser power on the sample was 0.3 – 1.2 mW.
The surface morphology of the samples was examined by scanning electron microscopy (SEM) using secondary and backscattered electrons, 5 kV accelerating voltage, and magnification up to 5000 (JSM T330, JEOL, Japan).
The carbon films deposited on Si wafer were smooth enough and the crater depth after Ar^+ ion beam etching could be measured accurately using a profilometer Alpha Step 500 (Fencor Inc. USA). From these data the thickness of carbon films and the rate of deposition under typical deposition conditions (75 A/min) were determined.
2.4. Platelet adhesion technique.
The study of platelet adhesion was performed with informed consent of the donors. Five volunteers were included in the series of repeated experiments. Ten milliliters of blood was anticoagulated 1:9 with sodium citrate [4]. Platelet-rich plasma (PRP) was obtained by centrifugation of the whole blood at 100 g for 20 min at room temperature. The small PRP drops (50 μl) were placed onto sample surfaces and incubated in humid atmosphere for different periods (from 5 to 30 min). The samples incubated with PRP for 15 min were chosen for further analysis. The number of platelets adhered to the surface during this time interval was appropriate for quantification, and the platelets did not form large thrombus-like structures. The samples were rinsed in normal saline to remove unadsorbed plasma proteins and weakly adhered platelets and then fixed in 2.5% glutaraldehyde and dehydrated in a series of ascending ethanols by the standard technique [4].

3. Results and discussion
3.1. Characterization of deposited film
Figure 1 shows XPS survey spectra of PTFE film before and after deposition of carbon layer. For untreated PTFE film the XPS spectrum consists of F1s peak (688.2 eV) and less intensive C1s peak (291.4 eV). In the XPS spectrum of the film obtained after 15 min deposition one can see intensive C1s peak (285.0 eV) as well as O1s (532.1 eV) and N1s (399.8 eV) peaks.

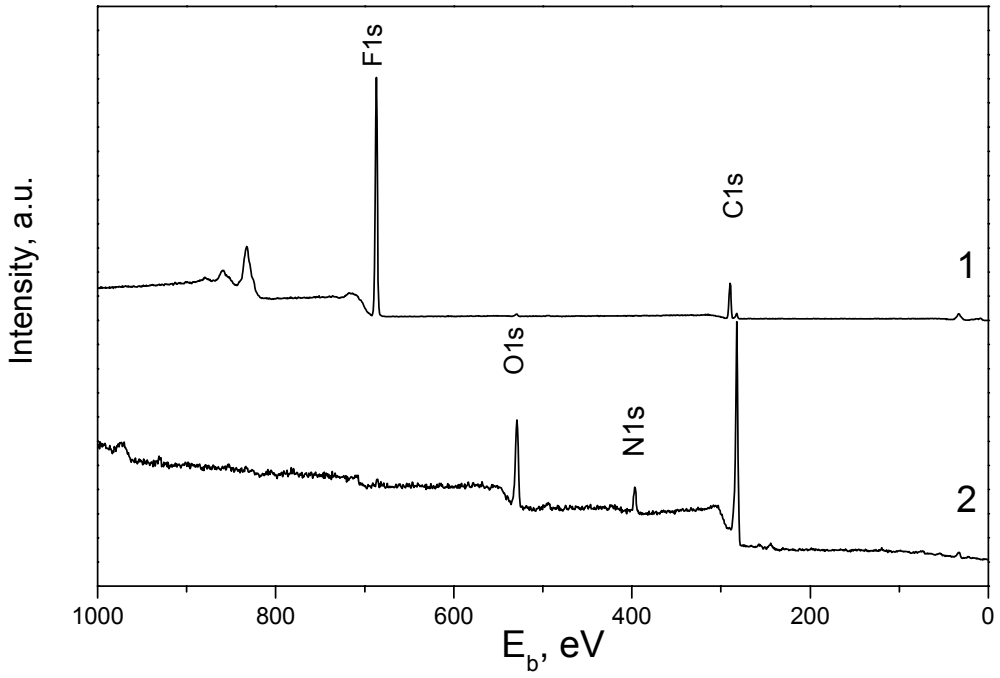

Figure 1 The XPS survey spectra of PTFE support before(1) and after plasma deposition of carbon film (2).

The important point is that no significant F1s peak was observed in the XPS spectrum of carbon film obtained after 15 min carbon deposition. It means that pin-hole-free carbon layer with the thickness more then 30 Å (depth of free electron path for 800 eV [5]) is formed on the PTFE surface already after 15 min of

graphite sputtering. The atomic surface concentrations calculated from measured integral intensities of XPS peaks for as deposited carbon film are: 72.2at% C, 10.5at% N and 14.0at% O. The appearance of relatively high concentration of oxygen on the surface of carbon layer may be explained by the surface contamination and/or bonding of oxygen in post reactions with carbon free radicals formed during plasma deposition. After a few minutes of Ar^+ ion sputtering oxygen content decreased in three times while the nitrogen concentration only slightly changed. The chemical composition measured after ion etching was: 86.8at%, 8.7%N, 4.5%O.
The surface morphology of PTFE support and carbon film formed on the support after 1 hour of deposition are shown in Fig.2. A complex fibril-type 1-2-micron regular structure could be observed on the surface of carbon layer.

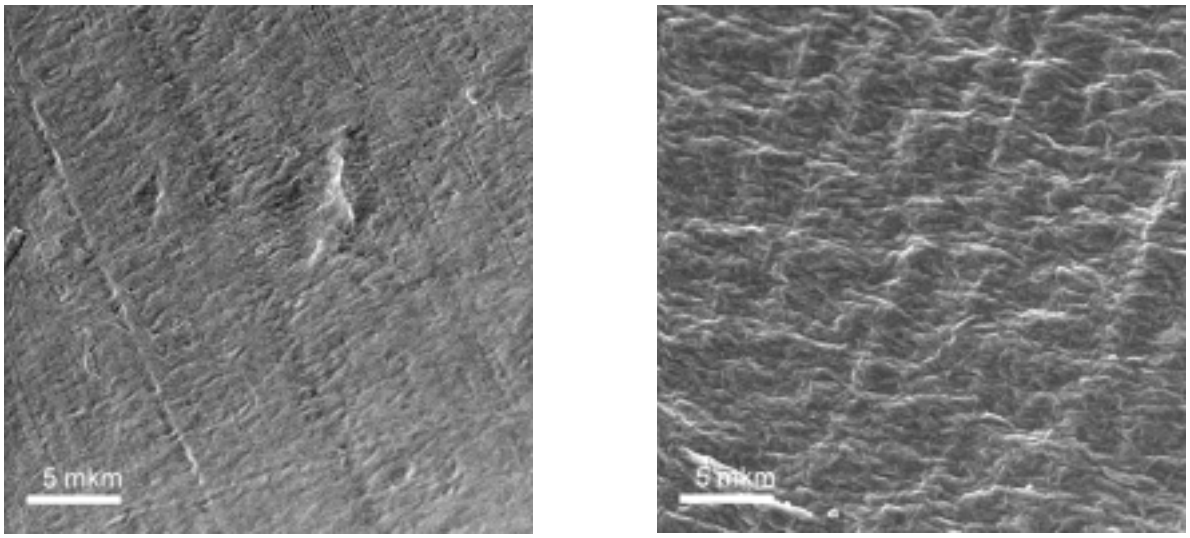

a b

Figure 2 Scanning electron microscope images of PTFE support before (a) and after (b) 1 hour of carbon deposition.

The adhesion of carbon film was checked by scotch tape test [6]. No visible peeling of the deposited film was observed after scotch tape strip off.
The Raman spectra of PTFE films before and after deposition of carbon layer with different thickness are shown on Figure 3. The characteristic bands of PTFE support: at 734 cm^{-1} assigned to stretching vibration of C-F, and two bands at 387 cm^{-1} and 293 cm^{-1} attributed to deformation vibration of C-C in polymer chains, are still detectable through the carbon film with the thickness 225 nm deposited during 1 hour but did not appear in the spectra after deposition of carbon layer with the thickness 450 nm (2 hours of deposition). This result is in agreement with the optical probing depth for Raman spectroscopy d determined by absorption coefficient α for carbon layer at our excitation wavelength 633 nm $d=1/(2\alpha)$. Taking the optical constants for different carbons [7] we can estimate the Raman probing depth in our case as 100 – 200 nm that is much higher then XPS analyzing depth (about 3 nm [5]).
The Raman spectrum of our carbon film consists of two broad bands at 1575 cm^{-1} and 1360 cm^{-1} which are usually detected in amorphous and diamond-like carbon films [8,9,10]. According to Wagner's model [11] developed for Raman scattering of carbon and polycrystalline diamond films, peak at 1575 cm^{-1} has to be assigned to graphite-like sp^2 bonded carbon (G peak) while the scattering in low frequency region around 1300 cm^{-1} has to be interpreted in terms of scattering by sp^3 –bonded carbon plus possible contribution of disordered sp^2 -bonded carbon (D peak).
Figure 4 shows FTIR spectra for carbon films of different thickness deposited on Si wafer. Broad main band in the region 1000 – 1700 cm^{-1} increases with the increase of film thickness. The IR absorption in this range covers the frequency range of stretching vibration of both CN and CC bonds which is often observed in carbon nitride films [12]. Usually CC bonds in pure carbon films are not active in the IR absorption but only detected by Raman spectroscopy. Kaufman et al. [13] analyzed IR spectra of carbon films doped with different amount of nitrogen and have found that Raman-active G (1575 cm^{-1}) and D (1360cm^{-1}) CC bonds become IR-active due to the nitrogen replacement of carbon which breaks the symmetry in six-fold carbon

ring structure. The nitrogen replacement gives rise to a net dipole moment and makes active IR absorption. The presence of C-N groups is indicated by the small IR absorption at 1230 cm^{-1}. Liu et al. [14] found that Raman and IR spectra of nitrogen containing carbon films deposited by dc magnetron sputtering are almost identical, and attributed the peaks at 1557 cm^{-1}, 1337 cm^{-1} and 1269 cm^{-1} to the G peak, the D peak and the single C-N bond respectively.

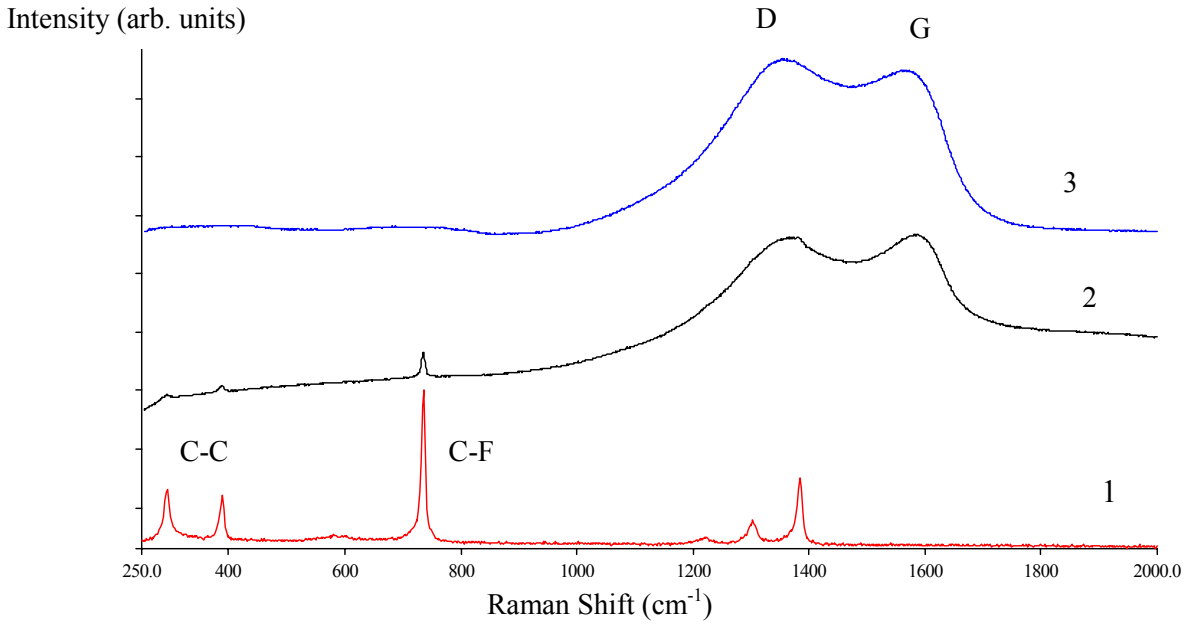

Figure 3 Raman spectra of PTFE support before (1) and after carbon deposition during 1hour(2) and 2 hour (3).

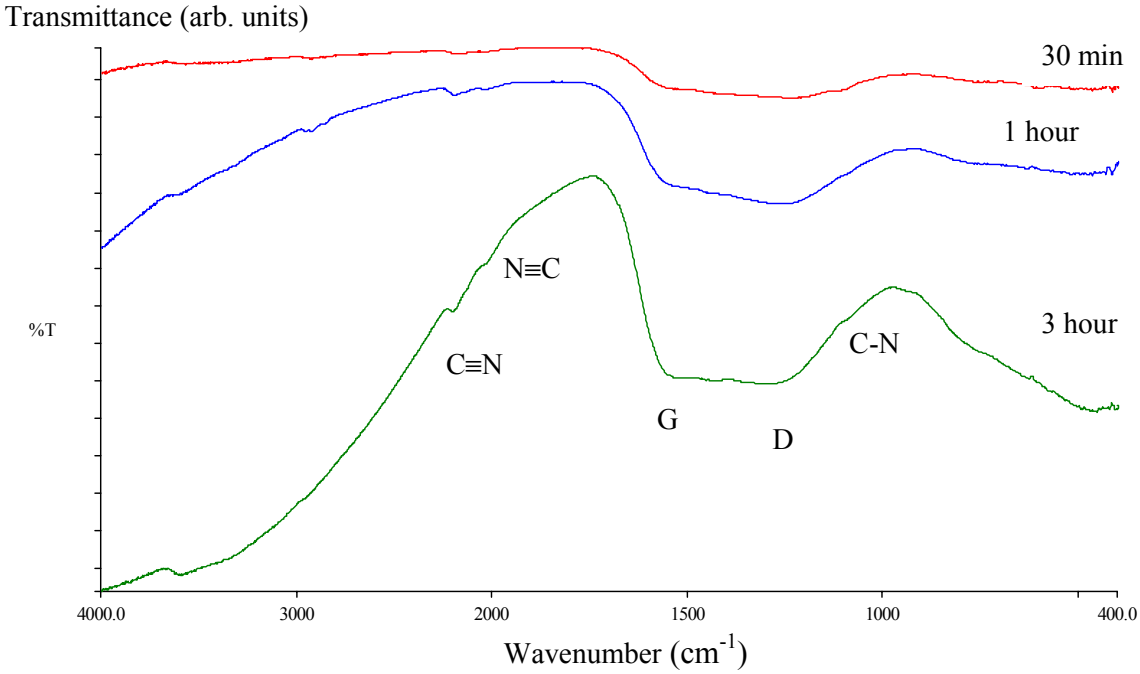

Figure 4. FTIR spectra of carbon film deposited on Si wafer

In the IR spectra range 1700 – 3000 cm^{-1} an additional bands at 2050cm^{-1} and 2200 cm^{-1} can be observed and assigned to the stretching vibration of nitrile -C≡N and isonitrile -N≡C groups respectively. A small amount of oxygen was detected in the film by XPS spectroscopy. But IR absorption bands in the range 1100-1300

cm^{-1} characteristic for C-O groups could not be observed due to the overlapping with the broad main carbon band at 1000 – 1700 cm^{-1}.

3.2. Platelet adhesion

Platelet adhesion patterns were investigated by SEM. All samples were decorated with copper (thickness~30 nm). For each sample 25 areas of 400 μm^2 were randomly chosen on the surface contacting with PRP. Then we qualified the total platelet number N_{tot} and platelet numbers N_i in the following four morphological classes [15] (Fig. 5a)

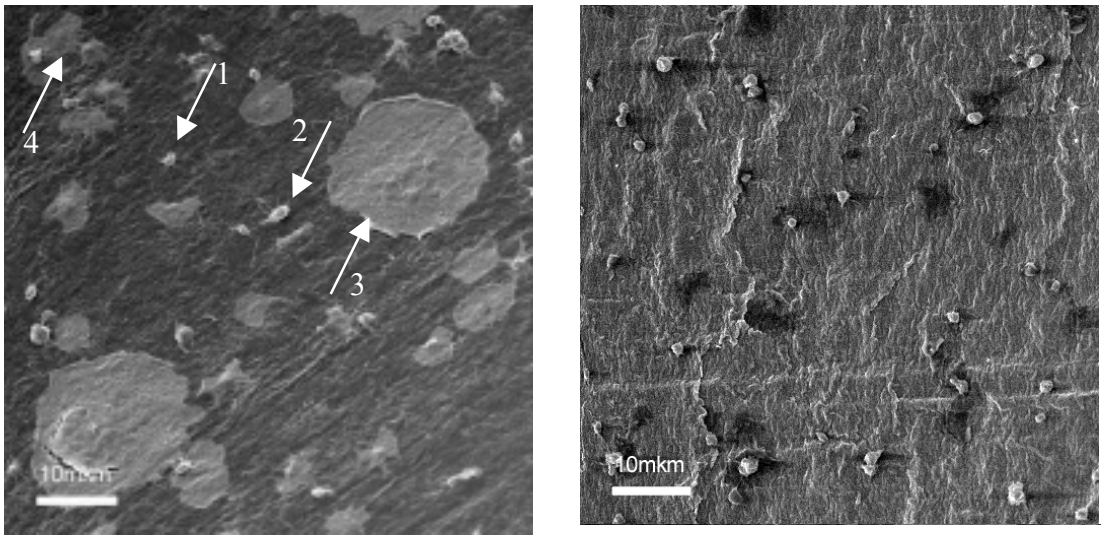

a b

Figure 5. Scanning electron microscope images of platelet adhesion on PTFE support before (a) and after (b) 1 hour of carbon deposition:

1. Single – non-activated cells
2. Slightly activated deformed cells and pseudopodical cells.
3. Spread – fully spread platelets.
4. Aggregates –aggregates of two or more platelets.

Adhesion process is believed to run in several stages: platelet attachment to the surface, activation, pseudopodia development, spreading and aggregate formation (see Fig. 5a) [16]. The release of intracellular components from adhered or fully spread platelets (ADP, Ca^{2+}, serotonin, etc.) promotes further platelet adhesion, aggregation and finally thrombus formation. [17]. One can estimate the activation of adhered platelet by their morphology. The more severe the impact of material on platelets, the more adhered cells are activated spread or aggregated. Usual approach for quantitative investigation of platelet adhesion consists in calculation of relative index of platelet adhesion (RIPA) for different morphological classes of adhered platelets. Presented on Figure 6 are RIPA values for carbon coatings in comparison with that of untreated PTFE. From this point of view, all carbon coatings seem more preferable for contact with platelets than untreated PTFE. Onto all coatings the numbers of slightly activated cells, spread cells and cell aggregates were lower but number of single cells was higher than that of the surface of unprocessed PTFE. It is noteworthy that the total number of platelets was also lower on carbon coated surface for all three samples. Assuming the existence of the adhesion stages, it can be suggested that platelet transition to later stages of activation was much slower on carbon coatings than on untreated PTFE.

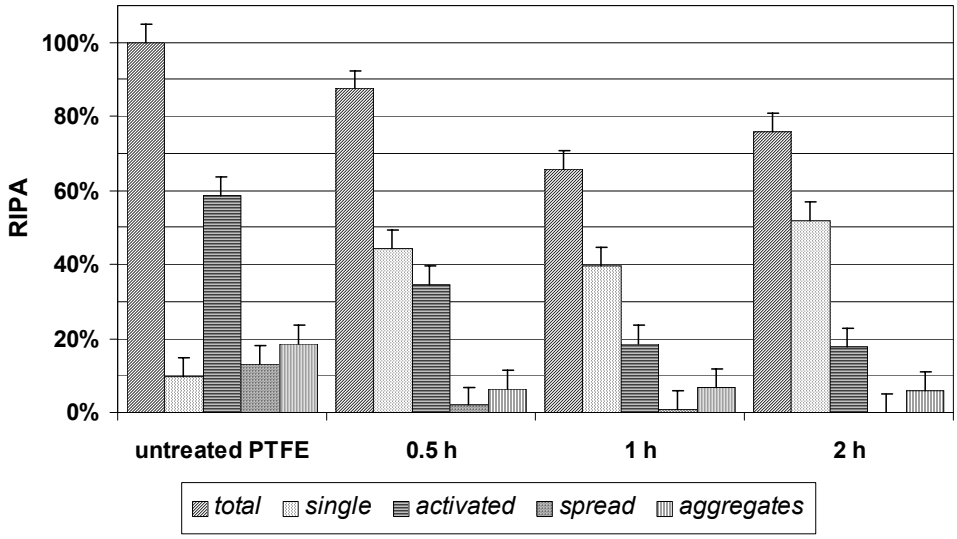

Figure 6. Diagram representing relative platelet quantities (RIPA) for different morphological classes observed by SEM for untreated and carbon coated PTFE (time of deposition 0.5, 1, 2 hours; RIPA=100% for the total number of adhered platelets on untreated PTFE)

4. Conclusions

The PTFE films were successfully modified with highly adhesive carbon layer using hot wire plasma sputtering of graphite in the mixture of Ar and 5% air. The platelet adhesion tests demonstrate that deposition of structured carbon layer containing oxygen and nitrogen groups promotes the minimization of platelet's reactions on foreign body thus considerably extending the haemocompatibility of PTFE film.

Acknowledgements

This research has been sponsored by the Canada Research Chair Program and by the Natural Science and Engineering Research Council of Canada.

References

1. M.S. Sheu, D.M. Hudson, I.K. Loh, In Encyclopedic Handbook of Biomaterials and Bioengineering, Part A, vol.1, D.L. Wise, D.J. Trantolo, D.E. Altobelly, M.J. Yaszemski, J.D. Gresser, E.R. Shwartz (eds). Marcel Dekker, New York, 865, (1995).
2. H.S. Shim, N.K. Agarwal, A.D. Haubold: J. Bioeng., **1**, 45 (1976)
3. H.J. Steffen, J. Schmidt, A. Gonzales-Elipe: Surf. Interface Anal., **29**, 386 (2000)
4. L.V. McIntire (ed): Guidelines for Blood-Material Interactions. Report of the National Heart, Lung, and Blood Institute Working Group. U.S. Department of Health and Human Services. Public Health Service. National Institutes of Health. (NIH Publication No.85-2185), 1985, Appendix 1.
5. D. Briggs, M.P. Seah (eds.), Practical Surface Analysis by Auger and X-ray Photoelectron Spectroscopy, Wiley, Chichester (1983).
6. I.S. Trakhtenberg, O.M. Bakunin, I.N. Korneyev., S.A. Plotnikov, A.P. Rubshtein, K.Uemura: Diamond and Related Materials, **9**, 711 (2000)
7. J. Wagner, P. Lautenschlager: J. Appl. Phys. **59**, 2044 (1986)
8. E. Braca, J.M. Kenny, D. Korzec, J. Engemann: Thin Solid Films **394**, 30 (2001)
9. A.C. Ferrari, J. Robertson: Phys. Rev. B **64**, 75414 (2001)
10. D. Liu, T. Ma, S.Yu, Y. Xu, X. Yang: J. Phys D: Appl. Phys. **34**, 1651 (2001)
11. J. Wagner, M. Ramsteiner, Ch. Wild, P. Koidl: Phys. Rev. **40**, 1817 (1989)
12. A. Laskarakis, S. Logothetidis, M Gioti: Phys. Rev. B, **64**, 125419 (2001)
13. J.H. Kaufman, S. Metin, D.D. Saperstein: Phys. Rev. B, **39**, 13053 (1989)
14. Y. Liu, C Jiaa, H. Do: Surf. Coat. Technol., **115**, 95 (1999)
15. S.L. Goodman: J.Biomed. Mater. Res. **45**, 240 (1999)
16. S.L. Goodman: K.S. Tweden, M. Albrecht: J.Biomed. Mater. Res. **32,** 249 (1996)
17. L.M. Waples, O.E. Olorundare, S.L. Goodman, Q.J. Lai, R.M. Albrecht:. J.Biomed. Mater. Res. **32**, 65, (1996)

GlidArc-assisted removal and/or upgrading of Hydrogen Sulfide or Methyl-Mercaptan

A. Czernichowski[1], P. Czernichowski[2*], and M. Czernichowski[2]

[1.] *Department of Physics, University of Orleans, Orleans, France*
[2.] *Etudes Chimiques et Physiques (ECP), La Ferté Saint Aubin, France*

Abstract
Diluted or concentrated (up to 100%) H_2S and air-diluted (up to 0.1%) CH_3SH are processed in various GlidArc discharge reactors at up to 70 m^3/h flow rate and 5 kW scales. These powerful high-voltage discharges produce non-thermal plasma directly generated in the processed gases. They activate some oxidation reactions in the case of air-diluted sulfides. Concentrated H_2S or H_2S+CO_2 mixtures are preferably dissociated into H_2 or H_2+CO (synthesis gas) at very low energy consumption.

1. Introduction

Hydrogen sulfide and mercaptans are unwanted compounds that have to be removed in many industrial processes. Moreover H_2S is also an abundant source for potentially the cheapest Hydrogen. Many hydrocarbon gas reserves contain large amounts of hydrogen sulfide frequently mixed with CO_2. The petroleum industry spends hundreds million of dollars per year to produce Hydrogen for Sulfur removal from crude oils and refinery products. This creates more than 6 million tons of concentrated H_2S in which very weakly bonded hydrogen is then stupidly burned to water (*via* 113-years old Claus process) making it unavailable for further use.
Burning of H_2S and/or mercaptans is also practices when their concentration is low. Such combustion gives another strong pollutant: SO_2. However at low concentrations the sulfides cannot burn themselves so that an extra fuel (and air) must be added. It brings the Nitrogen ballast into the flue gas and asks for much bigger washing installation in which SO_2 is removed in the presence of CO_2 issued from added fuel. Therefore several processes propose a low-temperature oxidation, particularly in aqueous phase, which end either in the production of water and Sulfur or sulfuric acid. Catalysts must often assist these reactions. All such processes require considerable volumes of equipment subjected to corrosion by aggressive solutions, hence high investment and maintenance costs. They present the further drawback of consuming a considerable amount of various chemical reagents that raises environmental problems created by some final products of these processes.
Since 1876' works of Marcelin Berhelot (France) the plasma-assisted H_2S destruction or upgrading has been quite largely studied. We are presenting that history in the papers [1] and [2] where our previous experimental contribution is also described. For more recent plasma-related works one can see contributions from ABB [3], Kurchatov Institute [4], or Argonne National Laboratory [5] – amongst others.

2. GlidArc-assisted processing of concentrated H_2S

2.1. Chemistry

It is worth to repeat that Hydrogen is very weakly bound in the H_2S molecule so it is so pity to convert it to water through the classical Claus process. In theory, the energetic requirement for 1 mole H_2 production from such dissociation:

$$H_2S \rightarrow H_2 + S \qquad (1)$$

is only 20.1 kJ, which is 14 times less than that of H_2 from an ideal water electrolysis. An extraction of Hydrogen would be therefore worthwhile when H_2S concentration in a waste gas is high enough. Also, the total upgrading of H_2S + CO_2 mixtures (called "acid" or "sour" gas) can be done *via* a low endothermic reaction:

$$H_2S + CO_2 \rightarrow H_2O + CO + S \qquad (2)$$

for the theoretical price of only 61.3 kJ per mole CO. Carbon monoxide is H_2-equivalent *via* the water-shift exothermic process:

$$CO + H_2O \rightarrow H_2 + CO_2. \qquad (3)$$

---

[*] *Presently with WESCO, Conroe, Texas 77301, USA*

From H_2S + CO_2 direct plasma processing one obtains therefore, after Sulfur and water precipitation, a mixture of the CO + H_2 (synthesis gas).

2.2. Our previous tests

First tests [6] were performed using a "controlled" transferred arc at 3 – 6 kW DC power, a kind of GlidArc precursor. Up to 71% of H_2S dissociation rate was observed but the energetic expense for 1 m^3(n) of Hydrogen was as high as 19 kWh. Some tests on simulated sour gas processing were also done: at 2 – 4 kW power applied to the gas containing 36 - 69% of H_2S (the ballast being CO_2) and at 0.75 - 0.83 m^3/h gas flow rate we got as high as 64 - 99% H_2S conversion rates. The energetic expense for 1 m^3(n) H_2+CO mixture was however in the 12 kWh range. Moreover, the cathode section of the reactor needed an Argon-flow protection that was a serious drawback for an industrial application of this proposed technology that we started to call "SulfArc".

The GlidArc reactors that we started developing in 1987 have largely opened a new way of a direct plasma-chemical processing of almost any gas mixtures. Our first results [7] on pure H_2S splitting in 6-electrode GlidArc reactor at 1.4 m^3(n)/h input flow rate and 0.73 kW AC power were quite encouraging as the energetic expense was equal to 7.9 kWh per 1 m^3(n) of produced Hydrogen. Too low (6.6%) H_2S dissociation rate was however observed for these conditions. Much better results were obtained at those time when processing a simulated sour gas containing 41% of H_2S and 59% of CO_2: at 2.6 m^3(n)/h input gas flow rate and 0.93 kW power: the energetic expense was equal to only 2.4 kWh per 1 m^3(n) of produced H_2+CO at quite reasonable 39% H_2S dissociation rate for one pass.

Further tests [8] were performed using another 3-electrode GlidArc reactor to split pure H_2S as well as some H_2S+CO_2 mixtures for different gas composition, pressure, flow-rate, dissipated power, electrode material and electrode gap. Up to 45% dissociation rate of pure H_2S was observed for that one-pass reactor without any gas preheating. The best result of 4.0 kWh per 1 m^3(n) of produced H_2 was obtained at 3-mm electrode gap but much lower energy expenses were expected with a complementary ignition system allowing a larger gap. Two sour gas mixtures containing 60 or 25% H_2S were also tested. The results indicated a minimal requirement of 5.5 kWh per 1 m^3(n) of H_2 + CO product in a pressure range of 0.5 - 0.7 bar.

Fig. 1. Three-step GlidArc-I reactor.

Figure 1 presents our 3-steps GlidArc pilot reactor built for an acid gas processing. The gas was issued from a natural gas cleaning plant near Zmigrod, Poland [9]. Figure 2 shows also the principle of the reactor implementation for the whole SulfArc process.

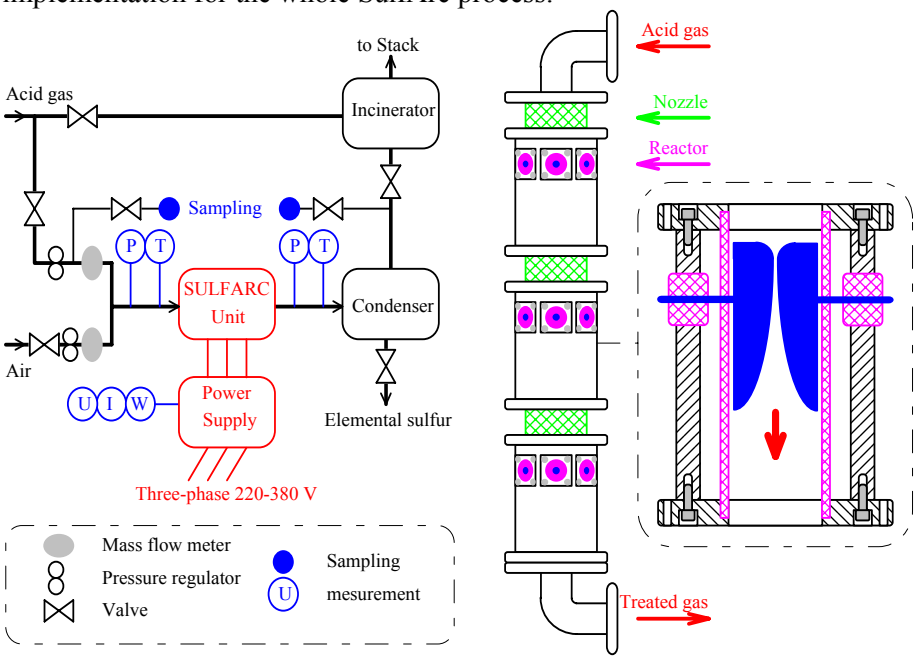

Fig. 2. Schematic view of a pilot installation of SulfArc for 60 m^3/h sour gas processing.

Some preliminary field tests of the sour gas (25% H_2S, 70% CO_2, and 5% light hydrocarbons) processing were satisfactory at 60 m^3/h scale: almost total destruction of H_2S was observed. No further field tests were however possible as the plant was going to close.
In 1997 we started to develop an alternative way of gliding discharges generation using so-called GlidArc-II principle. In an abstracts [10] we shortly mentioned this new reactor application for H_2S processing.

2.3. New developments
Using one or more rotating central electrodes and "connecting" them, *via* high-voltage AC discharges, to several stationary electrodes located around the central electrodes we have obtained a new GlidArc-II device. Figure 3 presents the principle of the GlidArc-II.

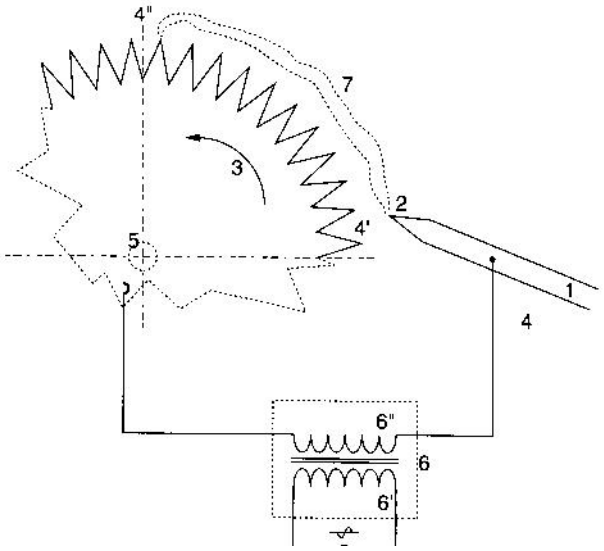

Fig. 3. Principle of the GlidArc-II device: 1 – stationary electrode, 3 – rotating electrode, 6 – power supply, 7 – high-voltage discharge filaments.

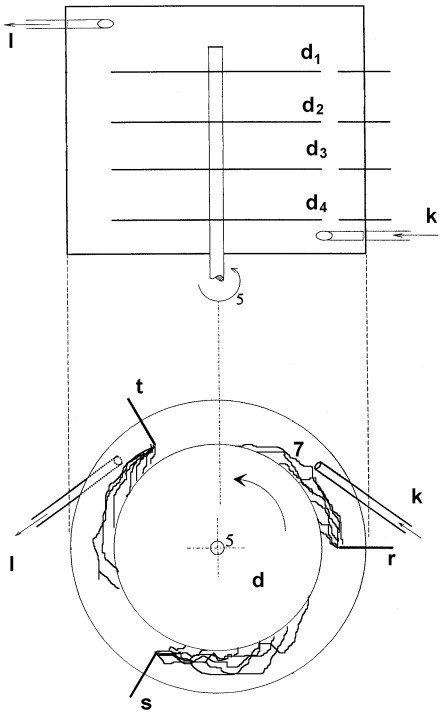

Fig. 4. Multiple-stages and multiple-electrodes GlidArc-II reactor: r, s, and t – three-phase-supplied stationary electrodes, k and l – input and output of the processed gas, d – rotating electrodes.

There are multiple advantages of the new structure. The high voltage discharges generation and the processed gas flow rates are no more self-dependent so that even a very low gas flow can now be accepted at any power as there is no more need to accelerate the gas at the proximity of electrodes. The mobile electrodes rotate in the range of 50 – 1000 rad/s, which are acceptable speeds. The discharges can "touch" several times the same gas flux without any obligation to push the gas between the stages (as it was previously needed for the reactor presented on the Fig. 1 and 2). The reactor is quite compact for even large gas flows. For example one can realize three 5 A and 2 kV = 30 kW discharges for one stage. When adding 4 stages it makes us a 120 kW reactor realized in a 0.3 m diameter cylinder of 0.5 m length (30 L of volume). Such reactor can process roughly up to 2400 m^3/h of gas.
The decomposition of pure H_2S has been first tested at the atmospheric pressure in relatively small GlidArc II reactor [11]. It has only one toothed steel disk of 15 cm diameter and three stationary steel electrodes (bent-knives-shaped) placed symmetrically around the rotating disk electrode. Every stationary electrode is connected to one of the three phases of a high-voltage transformer (5 kV, 50 Hz) and the disk is connected to the neutral point of the transformer. The processed H_2S is continuously introduced below of the vertical axis of the disk and the products are extracted above of the disk. A small electric motor rotates the disk (100 rad/s). A refractory glass closes the space in which our "cold" discharges strike the gas. This reactor can work under a pressure up to 1.5 bars and at the injected electric power of less than 1 kW. The power is controlled while activating one, two or three stationary electrodes, each one injecting the current limited to 0.12 either 0.25 A. We obtain the following performances:

- For an electric energy of 1 kWh injected into 1 m^3(n) of H_2S (initially at the ambient temperature) we are producing 0.31 m^3(n) of Hydrogen, which indicates an energy consumption of 3.1 kWh per 1 m^3(n) of Hydrogen.
- The conversion of a 40/60 mixture of H_2S/CO_2 has also been tested in the same reactor under 1 bar. For an electric energy of 1 kWh injected initially into this mixture at the ambient temperature we got the synthesis gas ($CO+H_2$) at the specific energy expense of 2.5 kWh/m^3(n). A side reaction towards the COS (3% in the products) should not present an obstacle for the process because it is sufficient to wash the products with water that splits COS towards initial H_2S and CO_2.

A 60-L stainless steel SulfArc reactor was recently built by ECP for H_2S-related streams processing. The reactor contains 9 stages, each of them being powered by 3 stationary electrodes so that 36 active electrodes are present. At the time of this ISPC-16 Poster Session we hope to present our first results on a larger scale H_2 extraction from pure H_2S and some sour gases.

3. GlidArc-assisted processing of air-diluted H_2S or CH_3SH

3.1. Chemistry

Direct injection of an active energy through our gliding discharges allows us to avoid the problem of additional fuel injection for conversion of so badly smelling sulfides into less smelling SO_2. Up to 100% conversion of the sulfides into SO_2 can be obtained at quite low energy expense … but we do not seek for such a high conversion! Using a very simple water-washing column, which saturates with the produced SO_2 (and some plasma-synthesized NO_x) and then captures unprocessed H_2S *via* a wet-Claus reaction, we are cutting the process' energy expense by factor of three, avoiding a SO_2 emission to the atmosphere and obtaining non-toxic elemental Sulfur as unique product of such depollution technology described by the following exothermal reactions:

$$3\ H_2S + 1.5\ O_2 = 2\ H_2S + SO_2 + H_2O = 3S + 3\ H_2O. \quad (4)$$

Indeed, the reactions (4) show that only 33% conversion rate of H_2S into SO_2 is needed for the full removal of the initial pollutant while the remaining amount of H_2S is simply destroyed by its oxidation product: SO_2!

3.2. Our previous tests [12]

3.2.1. One-stage reactor

Experiments were performed using a GlidArc-I reactor shown in Fig. 5. It contained three main electrodes (2 mm thick steel) as well as one central thin ignition electrode connected to a 50/150 Hz, 2/12 kV, 3-phase power supply. The electrodes were put inside a glass tube of 80/5 mm diameter and 50 cm length.

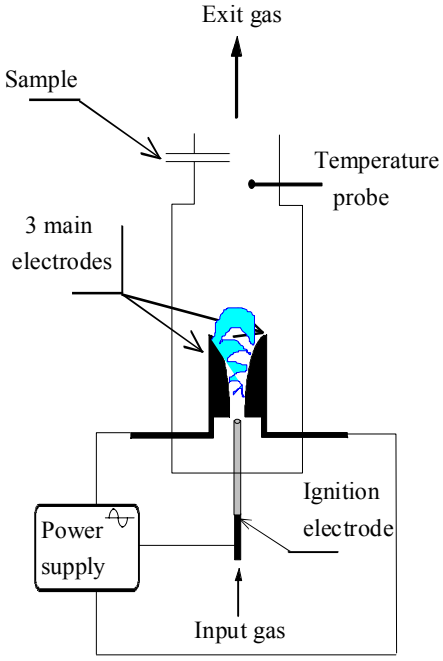

Fig. 5. Schematic view of the one-stage GlidArc-I reactor.

A stream of compressed air (about 20% RH at ambient temperature and pressure) was mixed with a controlled flow of a Nitrogen-diluted H_2S and then injected into the reactor through a nozzle. A Specific Energy Input (SEI, in kWh per 1 m^3(n) of the entering gas mixture) was determined for each run. Chemical analyses of entry and exit gas streams were performed using gas chromatography with a photometric determination of the S_2 emission at 394 nm; this provides detection and accuracy limits of 0.1 ppm.

Our washing tower is schematically shown in the Fig. 6. It consists of a 1.8 m height pipe of 8 cm of diameter. The tower is filled with a packing in order to enhance the gas-liquid contact. The liquid, initially tap water, flows into the top of the tower *via* a small pump (0.5 kg/min) and is recovered on the bottom. Only 2 kg of water is in continuous re-circulation.

More than 30 experiments were conducted to evaluate the influence of several parameters on H_2S destruction. We varied: the initial concentration of the H_2S (5 to 174 ppm), air flow rate (3.6 to 11 m^3(n)/h), power (1.1 to 1.7 kW), SEI (0.10 to 0.45 kWh/m^3(n)), and other.

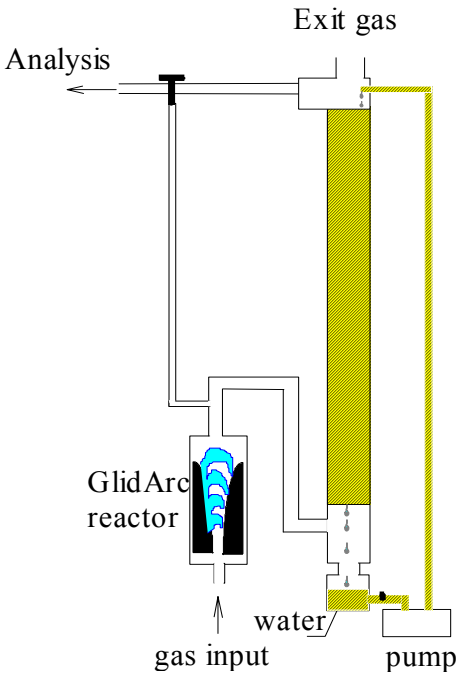

Fig. 6. Schematic view of the washing tower.

The reactor operated several hours without the electrodes deterioration. The destruction rate of H_2S was in the range of 60 - 100% so that complete removal of H_2S was possible even without using the water wash tower. The rate of the H_2S removal increased as a linear function of the SEI injected to the processed gas. The energy expense of pollutant removal was a strong inverse function of its initial concentration. It varied in the range of 0.77 – 44 MWh per kg of Sulfur, which seems very high. However, if related to the energy needed to cleanup 1 m^3(n) of polluted air we have obtained a very low value of around 0.05 kWh independently on initial pollutants' concentration in the range from 1 ppm to 1%.

The concentrations of NO_x at the reactor exit were at 0.3% level. Such strong oxidant plays a positive role in H_2S or mercaptan destruction in the plasma reactor as well as in the washing tower where a large improvement of the gas cleanup was observed: Initially neutral tap water becomes quickly acidified down to pH ~ 3 and stayed at that level up to the end of a run. After several runs we could observe opalescence due to colloidal Sulfur in water. Instead of 60 - 92% removal rate observed without gas wash we observed rather 93 - 98.5% removal with gas washing.

3.2.2. Four stages reactor

Experiments were also performed using a 4-stages serial reactor shown in Fig. 7. Each stage of that pilot contained the same GlidArc-I segment already described in the section 3.2.1. The gas transfer between the stages was organized through large nozzles, which allowed an acceleration of the gas near the electrodes. The exit gas washing was not applied. Four independent power supplies were used, each for one stage. A stream of ambient air was polluted with a controlled flow of pure H_2S or a CH_3SH-N_2 mixture and then injected to the reactor by the first large nozzle. The SEI was determined for each run. Gas flow rate metering and the chemical analyses at the entry and exit were based on gas chromatography.

Twenty runs were conducted in order to evaluate the influence of several parameters on H_2S or CH_3SH destruction. We varied: initial concentration of the H_2S (95 ppm to 1%) or CH_3SH (110 to 930 ppm), polluted air flow rate (from 48 to 67 m^3(n)/h), injected power (1.0 to 4.6 kW when one, two, three or four reactor's stages were running), and other.

As the results of the gas processing in this pilot we reported the destruction rates of H_2S or CH_3SH up to 39% or 65%, respectively. Removal rates of both H_2S and CH_3SH increased as linear functions of the specific energy (SEI) injected to the GlidArc-processed air.

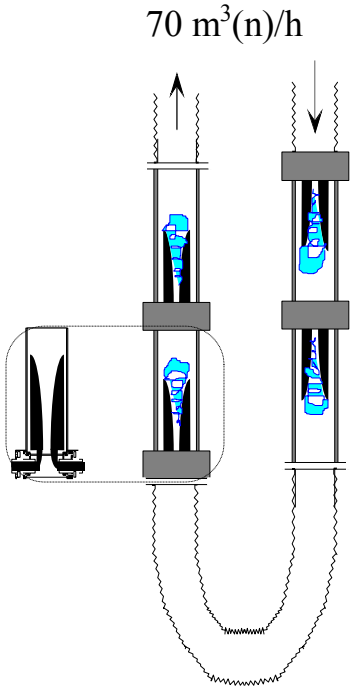

Fig. 7. Schematic view of the four-stage reactor.

Depending on initial pollutant concentration, roughly 1 MWh of energy was needed to withdraw 1 kg of converted Sulfur at 100 ppm of H_2S, and only 10 kWh for 1% initial H_2S in air. Similar energy expenditures were observed in the case of CH_3SH-air mixtures. Such energy expense for the unitary amount of pollutants removal is therefore a strong inverse function of their initial concentrations. But again, if accounted as the energy needed to clean 1 m^3(n) of polluted air, we have obtained a very low value of 0.05 kWh independently on initial pollutants' concentration in the range from 1 ppm to 1%.

3.3. New developments [11]

Several tests of air cleaning from sulfide molecules have been performed in GlidArc-II pilot reactor similar to that presented on Fig. 3 and 4. The reactor is composed of four toothed steel disks of 14 cm diameter and of 12 stationary steel electrodes placed symmetrically, three by stage, around the disks attached to the same rotation axis. For every stage of the reactor, each of the 3 stationary electrodes is connected to one of the three phases of a 5 kV, 50 Hz transformer. The disks are connected to the neutral point of the transformers (there are 4 identical transformers, one per disk). All mobile and stationary electrodes are inside a heat-resistant tube of the inner diameter of 20 cm and the length of 30 cm. Two plates close the tube and lodge: the system of the axis rotation (by a small electric motor), glass portholes, the entrance and the exit of the gas, and some probes (pressure, temperature). The reactor permits to work at pressures going from 0.1 to 5 bars. The regulation of the electric power injected to the reactor takes place while activating one, two or three stationary electrodes by stage (each electrode injecting the current limited to 0.12 or 0.25 A). The maximal electric power of the reactor is set to 4 kW.

All tests confirmed our previous results. The energy expense is weak, almost identical for various sulfide pollutants: while spending 1 kWh of electric energy we can completely clean out about 20 m^3 of air containing between 1 ppm and 1% of H_2S or CH_3SH.. Our observations indicate that the heavier sulfide molecules oxidize more easily thanH_2S.

Already mentioned 60-L GlidArc-II reactor, recently built by ECP for H_2S-related streams processing, is going to be used also for some tests on diluted H_2S and mercaptan destruction. At the time of this ISPC-16 Poster Session we hope to present our preliminary results.

4. Conclusion

Conditions are united to advance towards new GlidArc-I or -II processes of the concentrated H_2S upgrading into Hydrogen (or Synthesis Gas) as well as the destruction of diluted H_2S and/or mercaptans. We have demonstrated such feasibilities in laboratory as well as at the pilot scale of 70 m^3/h gas flow rate. An extrapolation of these reactors to process bigger flows will be easy as a result of very recent development of our so-called "Multi-Cluster" GlidArc (an electric powering system of dozens or hundreds of Gliding Discharges from unique ordinary High Voltage transformer) [13]. Advantages of the gliding discharges and here-described processes are the following:

- Utilization of the electricity as unique source of energy so that the process products do not contain ballasts of added reactants; it makes much easier all operations of their final treatment like washing, extraction, separation.
- No chemical reagents added (except water and air).
- No catalysts (except those generated spontaneously by the electric discharges).
- Final products are no poisonous nor pollutants: H_2O, Sulfur, and CO_2.
- Versatile treatment capacity (nature and quantity): the processes do not depend on the chemical composition nor the purity of products to treat. Accordingly, one can also treat weak quantities of sulfides produced by small industrial units that otherwise could not be valorized or cleaned out by the traditional processes.
- Energy expense of the pollutant processing is low.
- Very compact reactors and comfortable maintenance.
- Reactors have no thermal inertia and can therefore answer very quickly to control signals.
- Reactors have a good resistance of materials to corrosion.

The energy consumptions, already low, can certainly be further improved. All range of parameters asks for a further fine-tuning. Several further tricks can still be applied like heat recycling, Oxygen addition, and other. The compromise GlidArc + Claus could also present also some advantages…

* * * * *

Can one imagine plasma-chemical reactors and their powering simpler and cheaper?

References

[1] A. Czernichowski, Plasmas pour valorisation totale ou partielle des gaz contenant de l'H_2S, Revue de l'Institut Français du Pétrole, vol. **53**(2), 163-179 (1998).

[2] A. Czernichowski, Plasmas pour la destruction de l'H_2S et des mercaptans, Oil & Gas Science and Technology, **54**(3), 337-355 (1999).

[3] U. Kogelschatz, E. Killer, and B. Eliasson, Decomposition of Hydrogen Sulfide in a Dielectric-Barrier Discharge, 52nd Annual Gaseous Electronics Conference, October 1999, Norfolk (Virginia), USA, see an abstracts on http://www.eps.org/aps/meet/GEC99/baps/abs/S326010.html
[4] B.V. Potapkin, V.D. Rusanov, and V.K. Jivotov, Microwave discharges for the environmental protection; Chapter 13 in: *Electrical Discharges for Environmental Purposes. Fundamentals and Applications,* Nova Science Publishers, Inc., New York, 2000, p. 345-375, see http://www.kiae.ru/rus/inf/pabl/p_hepti.htm
[5] Microwaves split toxic hydrogen sulfide into valuable products at fraction of disposal cost, Argonne National Laboratory, USA, see http://www.techtransfer.anl.gov/highlights/9-1/misha.html
[6] A. Czernichowski, P. Jorgensen, J. Chapelle, and K. Meguernes, Plasma-chemical valorisation of H_2S, ISPC-9, Pugnochiuso, Italy, 1989, p. 687-692.
[7] A. Czernichowski, H. Lesueur, T. Czech, and J. Chapelle, Plasma assisted gas or steam depollution from Hydrogen Sulfide or Mercaptans", ISPC-10, 1991, Bochum, Germany, paper no. 3.2.22, 6 pp.
[8] S.V. Sanijuk, S.S. Kingsep, V.D. Rusanov, and A. Czernichowski, Complete valorisation of H_2S or $H_2S + CO_2$ waste gases in a gliding arc reactor, ISPC-11, Loughborough, England, 1993, p. 740-745.
[9] H. Lesueur, A. Czernichowski, and M. Granops, Discharge plasma reactor for partial H_2S valorisation or destruction, ibid., p. 752-757.
[10] A. Czernichowski, P. Czernichowski, J. Ruszniak, and M. Mlotek, Comparative study of GlidArc-I and GlidArc-II assisted destruction of some Volatile Organic Compounds and H_2S, ISPC-14, Prague, Czech Republic, 1999, p. 2631-2.
[11] A. Czernichowski and P. Czernichowski, French Patent No.2775864.
[12] A. Czernichowski, Plasma assisted removal of H_2S and methyl-mercaptan, Second North American Conf. "Clean Air '96", Orlando, Florida, USA, 1996, 8 pp (CD-edition).
[13] A. Czernichowski and M. Czernichowski, French Application No.02.08648.

GlidArc-assisted reforming of carbonaceous feedstocks into synthesis gas. Detailed study on Propane

A. Czernichowski[1], M. Czernichowski[2], and P. Czernichowski[*]

[1.] *Department of Physics, University of Orleans, France*
[2.] *Etudes Chimiques et Physiques (ECP), La Ferté Saint Aubin, France*

Abstract
Natural gas, commercial propane, gasoline and various diesel oils as well as other carbonaceous feeds are converted into synthesis gas using GlidArc-assisted Partial Oxidation reactors. We produce up to 8 m^3(n)/h of Nitrogen-diluted syngas containing up to 26% of H_2 and up to 23% of CO. It corresponds to 9 kW of electric power when such syngas is converted in an ideal Fuel Cell (FC). Power requirement for GlidArc assistance of such non-catalytic reforming is below 2% of the FC output.

1. Introduction

Fuel Cell manufacturers have been concentrating on readying their products for commercial applications. In parallel, efforts have been made to supply these Cells with appropriate Fuels. Presently, only very pure Hydrogen can be consumed in so called Proton Exchange Membrane cells while two other FCs (Solid Oxide or Molten Carbonate referred as SOFC or MCFC) can also directly "burn" the syngas. Neither H_2 nor CO is naturally present on our Planet so that they need to be produced somehow. It appears that in the near- to medium-term future most of these applications will involve systems with FCs operating rather on fossil fuel derived CO and/or H_2. Some new horizons open as concerns a bio-derived syngas.

Reforming of fossil Hydrocarbons (HC) and bio-related feeds (carbohydrates, alcohols, vegetable oils, oils and gases from biomass pyrolysis, biogas from biomass or bio-waste fermentation, etc.) is therefore an important process for the FC and other Hydrogen- or syngas-related industries. Small-scale reforming would allow using of these feeds in widely distributed power generation systems and would require a development of small- and medium-scale reformers.

Conventional reformers' technologies require careful attention to heat management, feed introduction, specific catalysts as well as combustion know-how, and entails solution of a set of difficult problems. For example, diesel oil reforming is a problem; due to its complex composition (long HC chains and cycles) and Sulfur content it represents one of the hardest fuels to reform. Natural gas, propane, gasoline, quite "dirty" diesel oils and jet fuels are however the most available fuels through a very dense chain of distribution. One should add to this list a myriad of easily available vegetable oils, alcohols, sugars, molasses etc. So should one remove first all poisoning additives or molecules from such feeds to make them compatible as regards a catalyst? Or apply a non-catalytic reforming?

Instead of using a catalyst we run our reforming process in a presence of high-voltage and low-current GlidArc discharges that assist the Partial Oxidation (POX) of various carbonaceous feedstocks into the syngas without their prior cleaning. Electric power of this non-catalytic reformer can be as low as 5% of a typical FC electric power output so that a recycling of such a small portion of the electric power produced in a FC is, in our opinion, an acceptable compromise allowing an implementation of such a specific plasma-assisted technology into the FC chain. Very active (and also very simple) GlidArc discharges play there a role of igniters and homogeneous phase catalysts; they also stabilize a post-plasma zone of our reformer. For the sake of simplicity and economics, our unique oxidant source is atmospheric air.

This contribution firstly presents some of our initial tests with pure cyclohexane, heptane, toluene, and the tests with pipeline grade natural gas as well as commercial gasolines and diesel oils. The last ones can contain up to 4% of Sulfur. The ability to reform "dirty" diesels (and similar feeds like naphtha and jet fuel) for their use in FCs is critical for industrial and military operations in many parts of the world where only off-specification feedstocks are available.

More results are then presented here below on our newest detailed study on propane reforming while our current experiments on GlidArc-assisted reforming of such "green" carbonaceous fuels as rapeseed oil and

---

[*] *Presently with WESCO, Conroe, Texas 77301, USA*

biogas (a mixture of CH_4 and CO_2 from anaerobic digestion of organic wastes) will be presented during this ISPC-16 Poster Session.

2. Experimental

2.1. GlidArc-assisted reformers

The GlidArc-assisted reformers for Natural Gas into syngas conversion, a part of our Gas-to-Liquid (clean diesel and gasoline) advanced technology [1], have proved to be also excellent reformers for other fuels. Our here-presented test work has been based on small reactors, similar to those described in [2]. The reformer is shown schematically on the Fig. 1.

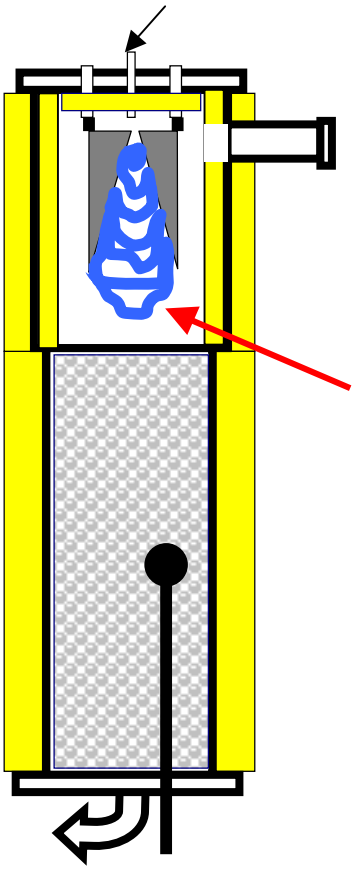

Fig. 1. Schematic view of GlidArc-assisted reformer.

The reactor contains three or six knife-shaped electrodes. The electrodes delimit a cone-shaped volume filled with gliding discharges. A feed + air premix is blown into that space through a simple tube and flows along the diverging electrodes. The plasma space (chamber) is thermally isolated in order to limit heat loses. Two flanges close the tubular reactor. The upper one supports the electrodes isolated electrically with high voltage connections. The other flange closes the reactor's bottom and comprises a product output tube. The entire structure is tight; it can support higher pressures but for the present runs we only worked at atmospheric pressure**.**

The gliding discharges ionize the gas mix. Given the moderate temperature of the electrodes (not cooled) and a very short contact time of the discharge roots with the electrodes, we do not observe any deterioration (even at a high Sulfur presence) that may prevent the gliding of these current-limited (0.1 A) discharges.

A perforated plate separates the plasma chamber and a post-plasma zone filled with packing. The plate makes it possible to transfer the products of partial reforming in plasma to the post-plasma zone. The whole reactor is externally insulated by a ceramic felt. In addition we thermally insulate the inner walls of the post-plasma zone of the reactor with a ceramic tube and a felt in order to keep it as hot as possible.

The total inside volume the reactor is 1 L (in our earlier experiments we also used a 2-L reactor). No part of the reactor is cooled in a forced manner. Two extra holes in the bottom flange provide for the insertion of two thermocouples measuring the post-plasma zone temperatures T_1 and T_2 respectively at 13 cm and 6 cm above the lower flange.

Almost punctual injection of the premixed feed + air between the electrodes provokes a phenomenon of re-circulation of the reactants in the plasma zone. The plate reinforces this recirculation. The flow of partially converted reactants containing long-living active radicals (and other catalytic species resulting from the gas excitation by gliding electric discharges) crosses the plate and, in the post-plasma zone, the conversion is thus completed in the presence of the packing where all the species deactivate. The luminous zone of the gliding electric discharges is observed through a window in order to verify the operation of the plasma chamber. A 10-kV power supply provides both ionization of the premix and then a transfer of electric energy into the discharges. The 3-phase supply is composed of commercial neon-light transformers. The time-averaged electric power is measured using a 3-phase kWh-meter and a chronometer. The averaged net GlidArc power during our runs was up to 0.8 kW.

A syngas sample crosses a white mineral wool in order to check if soot is present. Other sample is analyzed on-line using a 2-channels micro-gas chromatograph (μ-GC) dedicated to H_2, N_2, O_2, CH_4, CO for one channel, and CO_2 as well as some light HCs (C_2H_4, C_2H_6, C_2H_2, and C_3H_8+C_3H_6) for the second one. The gas product can be analyzed every 3 minutes.

2.2. Our previous preliminary tests [3]

As the test feeds we took several liquid HCs such as Cyclohexane, Heptane, Toluene, commercial Gasoline 95 and Diesel Oil (DO), and a pipeline-grade Natural Gas (NG). The reactor was fed by controlled flows of compressed air and HCs. Both flows were simply mixed together before their injection into the reactor. Some input/output data for these completely non-sooting experiments are presented in Tab. 1.

Table 1. Some input/output data of our first tests

Feed			C_6H_{12}	C_7H_{16}	C_7H_8	G-95[1]	DO[2]	NG[3]
Flow rate input	air	L(n)/min	42	35	47	77	91	81
	HC	cm^3/min	14	15	12	22	20	(23)
O/C atomic ratio @ input			1.0	0.9	1.2	1.2	1.4	1.3
Electric power injected		kW	0.33	0.37	0.33	0.44	0.28	0.79
Output gas conc. (vol.%)		CH_4	3.1	6.7	1.0	2.4	1.5	4.5
		C_2H_6	0.0	0.2	0.0	0.0	0.0	0.02
		C_2H_4	0.2	1.8	0.0	0.0	0.04	0.0
		CO_2	2.1	2.3	3.0	3.0	3.3	4.0
		CO	21	18	23	21	19	13
		H_2	21	18	15	19	14	26
		N_2	52	53	58	55	62	51
Output gas flow rate in m^3(n)/h		Total	3.8	3.2	3.8	6.6	6.9	7.4
		Syngas	1.6	1.1	1.4	2.6	2.2	2.9
kWh spent to produce 1 m^3(n) of H_2+CO			0.20	0.33	0.24	0.17	0.12	0.27
Output power* from syngas		kW	5.3	4.0	4.7	8.4	7.4	9.2
kW produced* per kW injected			19	11	20	19	26	12

* An ideal chemical-into-electric conversion of a FC is used; it takes into account the Lower Heating Value (LHV) of the produced H_2+CO mixture

[1] Gasoline: Aromatics 26.7%, Olefins 15.2%, Saturated 58.1%, and no Oxygenates; d = 0.73 g/cm^3; continuous run times of 6 h 31 min and 2 h 52 min

[2] d = 0.85 g/cm^3, 300 ppm of Sulfur; 3 main runs totalizing almost 11 hours

[3] CH_4 84.5%, C_2H_6 10.4%, C_3H_8 2.2%, C_4H_{10} 0.7%, C_{5+} 0.1%, N_2 1.6%, and CO_2 0.6%; continuous run times of 2 h 40 min and 9 h 20 min; the flow rate input is in L(n)/min

All feeds were totally reformed. We got a good energetic efficiency (defined in the bottom of the Tab. 1): always more than 10 times of chemical enthalpy contained in the syngas with respect to the electric energy injected into the GlidArc. We had no problem to reform such a cyclic compound as Toluene that is quite fragile. No soot was observed even in this case as well as when the commercial DO (containing a significant amount of Benzene, Toluene and Xylenes) was used as feed at a sufficient O/C ratio.

During the preliminary tests on the slightly Sulfur-polluted DO some H_2S in the syngas was detected. A simple way to remove it from the syngas can be, for example, a ZnO cartridge. We note therefore that our technology does not require clean feed and that our non-catalytic GlidArc-assisted reformer can accept some Sulfur-contaminated feeds. Based on that we performed a testing of some highly S-charged DO. Such fuels are widely spread over the world and therefore considered, for example, as logistic fuels for a local production of the electric energy on the battlefields. Our tests [presented orally as "Reforming of high-Sulfur diesel oil into synthesis gas in a plasma-assisted reactor", *3rd Department of Defense Conference on "Logistic Fuel Reforming"*, Panama City Beach, Florida, 2002] confirm that such dirty (up to 4% of S) and quite heavy fuel (end-point of distillation at 600°C) can be converted totally at no soot appearance and no harm to our compact reactor and electrodes (we worked several hours) at a 5-10 kW level of a FC output.

2.3. New detailed study of Propane reforming

2.3.1. Introduction

General availability of propane (also known as Liquefied Petroleum Gas LPG) designs it as an excellent candidate for an on-board or on-site POX reforming. Such process can provide the syngas for a direct feeding of the SOFC or MCFC. Otherwise, one can extract pure Hydrogen from the "water-shifted" syngas in which CO is partially or totally steam-converted to H_2. Hydrogen can then supply other types of FCs or can be used for other applications like chemical, petrochemical, metallurgical, and space. Small and medium size reformers running on propane/LPG can supply some FC powered buses, boats, homes, retail sales points etc. reducing therefore costs of the pure Hydrogen distribution. We contribute to such idea realization through our simply, GlidArc plasma-assisted reformer avoiding a need of poison-resistant catalysts or prior feedstock cleaner.

Generally, commercial propane can contain up to 300 ppm of Sulfur. Much higher Sulfur may be found in crude LPG or other light HC streams in refineries and gas processing plants. All such feedstock must be first cleaned (mostly desulfurized) in order to avoid the catalytic reformers poisoning (while some SOFCs can accept Sulfur-polluted syngas). For example only high purity propane (99.999%) can be reformed on a ceria-supported platinum catalysts [4].

2.3.2. Experiments

Our new experiments are performed using a short, 1-L, three-electrode GlidArc reactor. Commercial propane + air premix is blown into the plasma space through a simple 4-mm (I.D.) tube and flows along the diverging metallic electrodes. This time the averaged GlidArc assisting power was set to only 120 W.

Seven runs were preformed at various operating conditions. At the accumulated runtime of 25 hours we never changed any part of the reformer. The process was always very stable. When soot was starting to appear at an insufficient air/propane ratio we just put more air (or less propane) to establish the non-sooting conditions. Some characteristics of the runs are presented in Tab. 2.

When starting with a cold reactor it takes us less than 15 min to preheat it (a full combustion at a low propane flow) and then to collect the syngas at much stronger propane flow and proper reformer's temperatures. A regulation of the air/propane ratio and the GlidArc power are then applied as a function of reformer's temperatures during next fraction of hour after what the reforming could be left alone for an undetermined yet time. However we preferred to "play" various changes of input parameters to learn about the reformer productivity, efficiency, etc. To finish the run we simply cut all inputs letting the reformer to cool down in a natural manner.

Table 2. Some parameters of performed runs

Run	Air input $m^3(n)/h$	Propane input kg/h	H_2S added
A	1.9	0.41–0.49	0
B	1.9	0.35–0.42	0
C	3.0	0.46–0.72	0
D	4.2	0.86	0
E	3.0	0.53–0.78	0
F	1.9–4.2	0.5–0.83	0–8%
G	1.9–2.5	0.42–0.44	0 or 1000 ppm

Such hot reformer could be started again without any problem at a much shorter time. The reformer can also be left at reduced flows of air and propane as well as at limited electric assistance that keep it at appropriate temperature so that a re-start of reforming can be done in about 1 minute. Figure 2 shows an example of T_1 and T_2 temperatures evolution during the Run B.

The atomic ratio of Oxygen to Carbon in the feed should theoretically be equal to 1 according to the propane POX reaction:

$$C_3H_8 + 1.5\ O_2 = 3\ CO + 4\ H_2 \quad (1)$$

but such ideal POX cannot provide enough heat to keep the reaction going fast so that a combustion process must run in parallel. It may be presented as additional propane consumption:

$$C_3H_8 + 5\ O_2 = 3\ CO_2 + 4\ H_2O_{vap} \quad (2)$$

asking for extra Oxygen.

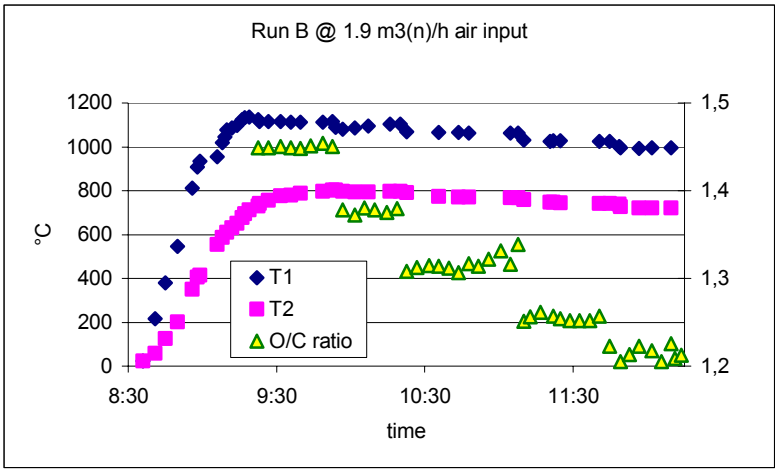

Fig. 2. T_1 (upper) and T_2 (lower) temperatures inside the post-plasma zone during the Run B as a function of time and air/propane input ratio (presented as an atomic O/C ratio on the right axis).

As shown on Fig. 2 (where for the constant flow rate of air a decrease of the O/C ratio means an increase of the propane input) the both temperatures decrease. We seek for a compromise between as low as possible O/C ratio and as fast as possible reforming kinetics that avoids at the same time the soot production according to exothermic parasite reaction:

$$2\ CO = CO_2 + C. \qquad (3)$$

Such a compromise is quite easy to find in the presence of the GlidArc. Moreover as the propane input increases the produced syngas flow increases at less pronounced reaction (2) due to a higher thermal loading of the reformer.

Precise mass balances show where the best compromise between the reactions (1) and (2) is located for the given reformer and wanted syngas outflow. The Figures that follow show some results of selected runs. The mass balances are based on the conservation of Nitrogen (totally inert gas in the reforming conditions) and total Carbon in the syngas (as no soot is present for an appropriate O/C ratio).

Figures 3 and 4 present the output flow rate of 100% syngas (H_2 + CO only) in m^3(n)/h and in kW units for Run B and integrated Runs C+E, respectively. In fact, the syngas is always diluted by Nitrogen as we use air to perform the reforming. The N_2 concentration at the output is typically in the range of 50-65 vol.% (dry basis), depending on O/C ratio applied for the given test. The H_2+CO flow rate in the output can also be presented as the potential thermal output power for the case this two components supply an ideal SOFC or MCFC where they are electrochemically converted into the steam and CO_2. Such a power is therefore assimilated to the LHV.

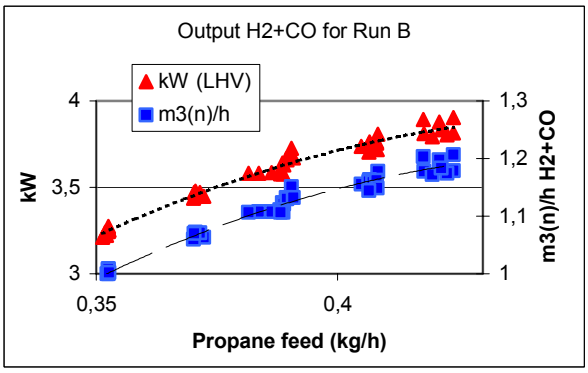

Fig. 3. Output flow rate of 100% syngas (H_2 + CO only) in m^3(n)/h and in kW units for Run B at constant air flow rate input of 1.9 m^3(n)/h.

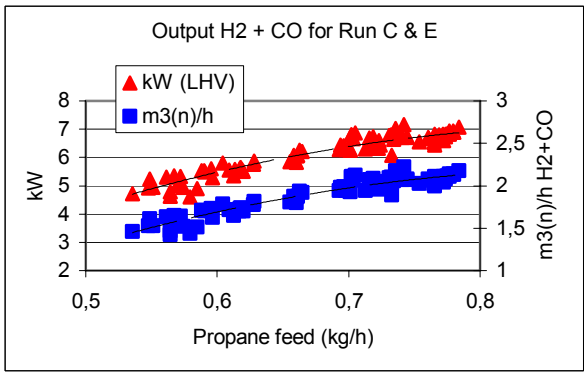

Fig. 4. Output flow rate of 100% syngas (H_2 + CO only) in m^3(n)/h and in kW units for integrated Runs C and E at constant air flow rate input of 3.0 m^3(n)/h.

In a short Run D at 4.2 m^3(n)/h air flow rate and 0.86 kg/h propane input we got the Nitrogen diluted syngas outflow corresponding to 2.7 m^3(n)/h of pure H_2 + CO mixture that is equivalent to LHV output power of 8.6 kW. This run was not yet optimized but it indicates that the maximal output of our 1-L reformer at atmospheric pressure is close to 9 kW or 3 m^3(n)/h of pure syngas. Higher outputs are expected for elevated pressures.

Having the output power we can calculate a thermal efficiency of the process. Such efficiency is defined here as a ratio of the LHV output power of the H_2+CO leaving the reformer with respect to the LHV input power of propane calculated from the reaction (2). The efficiency is shown on Fig. 5 and 6 as a function of O/C atomic ratio for the Run B and for integrated Runs C&E, respectively. On the same graphs we show also the H_2+CO concentration in the syngas as the function of O/C ratio deduced from relative flows of the air and

propane. At these O/C ratios the concentration of pure syngas in the output gas is around 36 to 44 vol.% (dry basis).

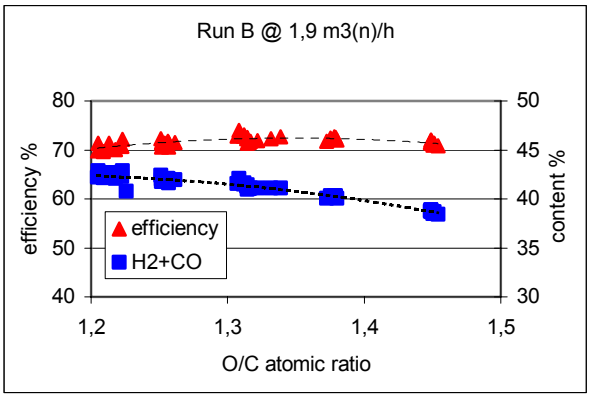

Fig. 5. Thermal efficiency of the propane reforming and the pure syngas concentration in output gas as a function of O/C atomic ratio for Run B at 1.9 m^3(n)/h air input flow rate.

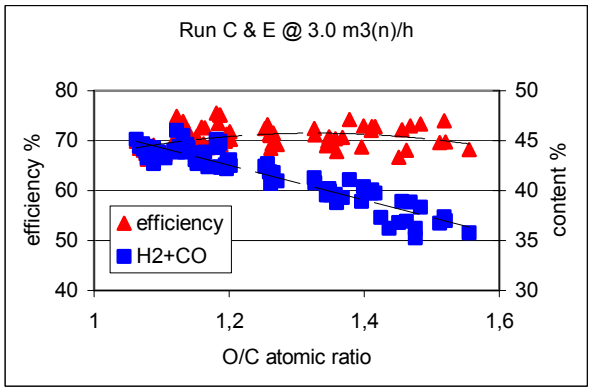

Fig. 6. Thermal efficiency of the propane reforming and the pure syngas concentration in output as a function of O/C atomic ratio for integrated Runs C and E at 3.0 m^3(n)/h air input flow rate.

Better than 70% thermal efficiency is obtained in the range of atomic ratio O/C ~ 1.2 to 1.4 (or otherwise O_2/C ~ 0.6 to 0.7 ratio) at no sooting conditions. Moreover, this quite high efficiency is based on only standard enthalpy heat (at 25°C) of output H_2+CO combustion to CO_2 and steam (LHV) with respect to the standard enthalpy heat of combustion (LHV) of entering C_3H_8. Such efficiency does not therefore take into account any sensitive heat content in the gas leaving the reformer at > 700°C. A part of that heat can certainly be reused to preheat entering HC feed and air so that a part of total propane combustion (2) could be limited and the thermal efficiency increased. No such heat exchange was however used in this study.
In order to show again our *pro*-Sulfur technology we have also performed Runs F and G adding a mass-controlled flow of pure H_2S into air/propane mixture. Especially Run G has simulated a quite dirty feed at 1000 ppm of H_2S. We did not observe any harm to our reformer and/or process. All collected reforming performances were the same when switching several times from "no H_2S" to "with H_2S" flows or *vice versa*. During the Run F where up to 8% of H_2S was added all went well but we could not yet make the full mass balances before identification of some unknown GC picks and their calibration.

3. Conclusion

This contribution presents firstly some of our preliminary tests on pipeline natural gas, gasoline 95 and diesel oils (including high-Sulfur containing ones) as well as some pure HC compounds: Heptane, Cyclohexane, and Toluene. These feeds were completely converted into syngas in our GlidArc-assisted reformer at atmospheric pressure and at low electric power assistance.
We are then appending these tests with more detailed study of propane as a representative of light HC feeds. The main operating parameters of the process: reforming temperature, air/propane ratio, GlidArc assisting power, etc. have been identified and set at their quasi-optimal levels. The results show the total propane conversion. No structural modifications of the whole converter or its parts are observed. As detailed and general conclusions we note:

- Propane is reformed at better than 70% energetic efficiency. Better efficiencies are expected when using heat exchangers.
- Soot is not produced if a sufficient O/C atomic ratio (and consequently some H_2O and CO_2 products) is accepted as compromise.
- 1000 ppm of Sulfur content in propane is not harmful for our reactor and process. Other high-Sulfur feeds were also successfully reformed so that GlidArc assisted technology opens the way for much simpler integrated reformer/SOFC units without prior removal of sulfur or other additives. This greatly expands the market potential to include military logistic fuels and/or other highly sulfur-polluted fuels.
- The flow rates of produced Hydrogen and Carbon Monoxide can be kept constant by fine-controlling the flow rates of entering propane and air. The syngas output can also match an actual need by regulating the rates of fuel and air.

- The temperature profile of the reactor is self-controlled by the process and by the GlidArc assistance. Frequent start-ups or quite drastic changes of syngas output can be done in a fraction of minute so that an integrated power-generation system can be much easier developed.
- Here presented 1-L (and not yet optimized reformer) can produce up to 3 m^3(n)/h of pure syngas (N_2 and other components not accounted). It can generate an amount of syngas corresponding to 9 kW of electric power (when syngas is fully converted in an ideal SOFC or MCFC). Further ECP's developments are in progress including systems to generate the syngas equivalent to 30 m^3(n)/h of pure H_2+CO mix corresponding to the LHV power of 100 kW.
- Electric power consumption assisting our reforming is less than 2% of the LHV power of produced syngas stream. Such a low power recycling level (or an import from outside) is, in our opinion, a worthy compromise. Instead of using a delicate catalyst that asks for a very clean fuel we dedicate an almost negligible part of produced syngas power to electrically support a non-catalytic reforming of almost any dirty fuel.
- No water or steam circuits, heaters, etc. are necessary. The process starts with compressed air (of any quality), a fuel, and the GlidArc. No special vaporizer/fuel injector unit is needed. The syngas appears after a short warm-up. If the reformer is kept hot than the full operation of our reformer can start after about 1 min.

These steps of ECP's self-financed project guarantees the development of a compact and reliable fuel processor fed by propane/LPG as well as other HC feeds. It can be used on-board of a SOFC vehicle or on-site for syngas or Hydrogen production for various applications.

* * *

Some qualitative tests were recently performed in our laboratory on the commercial rapeseed oil, 96% ethanol, and concentrated sugar solution in water. We got a soot-free syngas and the total feed conversion. It opens an opportunity to upgrade also other farm-issued products like molasses, residual or waste oils from various human activities. Other tests indicate that crude petroleum oils, heavy bitumen, and petroleum wastes can also be directly converted in our reformers… Large multiple-electrode ("GlidArc Multicluster", ECP's pending patent [5]) reformers are under development for a large-scale syngas production from almost any gaseous or liquid carbonaceous feed.

References

[1] M. Czernichowski and A. Czernichowski, French Patent No. 2824755.

[2] A. Czernichowski, GlidArc assisted preparation of the synthesis gas from natural and waste hydrocarbons gases, *Oil & Gas Science and Technology - Revue de l'IFP*, vol. **56**(2), 181-98 (2001).

[3] A. Czernichowski, M. Czernichowski, and P. Czernichowski, Non-catalytical reforming of various fuels into syngas, *France - Deutschland Fuel Cell Conference on "Materials, Engineering, Systems, Applications"*, Forbach, France, 2002, p. 322-8.

[4] A. Vita, M. Cordaro, M. Laganà, L Pino, and V. Recupero, V., Hydrogen generation by autothermal reforming of Propane on a ceria-supported platinum catalysts for PEFC, *14th World Hydrogen Energy Conference, Montreal,* 2002, CD Proceedings, 6 pp.

[5] A. Czernichowski and M. Czernichowski, French Application No.02.08648.

Gas-jet electron beam plasma chemical vapor deposition of silicon thin films

R. Sharafutdinov[1], S. Khmel[2], V. Schukin[1], O. Semenova[2], B. Kolesov[2], A. Buldygin[2]

[1] *Institute of Thermophysics, Novosibirsk, Russia*
[2] *Institute of Semiconductor Physics, Novosibirsk, Russia*

Thin films of amorphous, microcrystalline and epitaxial silicon are finding increasing application in solar sell fabrication. For industrial aims a deposition method are required which allows to grow both a-Si:H and μc-Si:H thin films under high rate on large area substrates for a-Si:H/ μc-Si:H tandem solar cells. Epitaxial Si growth at low temperatures of less than 650°C is required for production of thin-film monocrystalline solar cells. In this paper we present the results of the application of the gas-jet electron beam plasma CVD (GJ-EBP-CVD) method for deposition of amorphous, microcrystalline and epitaxial Si thin films. Our method has already demonstrated not only very high deposition rates for a-Si:H [1], μc-Si [2] and epitaxial Si [3], but also the capability of large area deposition [4].

The GJ-EBP-CVD method was described in detail elsewhere [2, 4]. The method is based on activation of gas mixture jet by electron beam plasma and fast convective transfer of generated radicals by the supersonic free jet to a substrate. The method has the following main features. Firstly, the electron beam plasma, in comparison to the discharge plasma, contains much more electrons with the effective energy enough for generation of radicals and ions. Secondly, a fast convective transfer of active particles from the activation zone to the substrate by the jet inhibits undesirable gas-phase processes. These two features ensure a high deposition rate of films and low power inputs on the process. At last, the jet protects the substrate from atoms and molecules of background gases, therefore one can use standard vacuum chambers and a low vacuum even for growth of epitaxial layers

In this work, the free jet of the gaseous mixture of 1-10 % of SiH_4 with Ar was activated by the electron beam with energy 1-2 keV and current 100-500 mA. The total flow rate of the mixture was up to 13500 sccm. Substrate temperatures were changed from 100 to 650 °C. A pumping system included booster oil-diffusion pumps. The base pressure in the growth chamber was about 10^{-4} Torr, the resulting pressure during growth process was $\approx 2\times10^{-2}$ Torr. Five kinds of substrate are used in the present work: stainless steel (20×20 cm^2), mono-Si wafers *n*-type (100)-oriented for homoepitaxy, mono-Si samples covered by SiO_2 layer for measure of photosensitivity, sapphire for optical absorption spectra study and ceramics.

The method was used for deposition of amorphous, microcrystalline and epitaxial silicon thin films under high rates up to 15 – 20 nm/s. The optical, electrical and structural properties of the films are systematically studied.

The structures of the films are significantly affected by the substrate temperature. Films deposited at 250 ºC were amorphous ones and have a low dark conductivity and a photosensitivity of 10^5. For samples deposited at 430 °C the crystalline fraction in the film is almost 100%. The films have a columnar structure perpendicular to the interface and the average grain size is about 300 nm [2]. SEM-investigation of the surface of μc-Si films shows that the surface roughness is in the range of 0.1-1 μm, that providing excellent light trapping as confirmed by spectroscopic ellipsometry measurement [2]. Carrier lifetime is measured in the range of 1-2 μs for μc -Si films deposited on ceramics substrate at 640 °C by means of microwave photoconductivity decay method at a bias light. Films deposited at 640 ºC on mono-Si wafers *n*-type (100)-oriented were epitaxial ones.

All results show that Si films grown by the gas jet method are suited for solar cell processing which is currently under development.

[1] R.G. Sharafutdinov, A.V.Skrynnikov, A.V.Parakhnevich, B.M.Ayupov, A.M.Badalian, O.V.Polyakov, M.R.Baklanov, K.P.Mogilnikov, S.A.Biryukov. – J.Appl.Phys. **79**, 7274 (1996).

[2] R. Sharafutdinov, S. Khmel, O. Semenova, S. Svitasheva, R. Bilyalov, J. Poortmans. – Proc. 29th IEEE Photovoltaic Specialists Conference, 2002, New Orleans, USA.

[3] S.Ya.Khmel, R.G.Sharafutdinov, V.M.Karsten, O.I. Semenova, A.G. Cherkov, L.D. Pokrovsky. – Abstracts of 8 Intern. Conf. on Plasma Surface Engineering, 2002, Garmish-Partenkirchen, Germany. P.181.

[4] R.G. Sharafutdinov, V.M.Karsten, A.A. Polisan, O.I. Semenova, V.B. Timofeev, S.Ya. Khmel – Acc. application on Russian patent #2002103408, Pr.12.02.2002.

Measurement of ion temperature in Ar/N_2 ECR plasma

M. Koga[1], S. Iwata[1], H. Muta[1], A. Yonesu[2] and Y. Kawai[1]

[1] *Interdisciplinary Graduate School of Engineering Sciences, Kyushu University, Kasuga, Fukuoka 816-8580, Japan*
[2] *Department of Electrical and Electronics Engineering, Faculty of Engineering, University of the Ryukyus, 1, Senbaru, Nishihara, Okinawa 903-0213, Japan*

Abstract
An ion temperature in ECR plasma is measured with high-resolution optical emission spectroscopy of Doppler profiles of Ar and Ar^+ transition. It is found that the Ar ion temperature is about 0.6eV in pure Ar plasma, and it decreases drastically as the nitrogen gas concentration is increased. The radial profile of the electron density becomes flat with adding the nitrogen gas. These results suggest that the cooling of the ion temperature due to the decreasing of the radial electric fields.

1. Introduction

An electron cyclotron resonance (ECR) plasma [1-3] has been actively used in the field of plasma etching and deposition processes for semiconductor manufacturing, because of its attractive features that high plasma density (10^{13} cm^{-3}) can be obtained at low gas pressures (a few mTorr).

Especially in plasma etching process, an ion temperature in plasma is one of the most important parameters. The ion temperature affects the rate of surface reaction, the etch rate and the selectivity. Moreover, the ion temperature determines the quality of etching. If the ion temperature is low, the incident angle of ions is narrow and, as the result, most of ions hit the bottom of the feature. On the other hand, if the ion temperature is high, the incident angle of the ions broadens and degradations of the feature such as the mask undercut, bowing and so on, occur. Recently, the ultra large-scale integrated circuit becomes smaller and high aspect ratio features with narrower width (<0.25 μ m) is required from industry. Thus, the production of the low ion temperature plasma is one of the most important subjects in plasma processing.

In addition, there is a growing interest in the characteristics of nitrogen plasma because of their potential use in the synthesis of nitride thin films, such as GaN, and in the surface modification of various materials. In these plasma CVD processes, the ion temperature may also affect the quality of thin films. Thus, the measurement of the ion temperature in Ar/N_2 plasma is also necessary for understanding these processes.

However, there are few works about measurements of the ion temperature in plasma for application, since the high-resolution measurement system is necessary. An energy analyser is inappropriate for ion temperature measurements because its resolution is as low as 1eV. In the previous work, we measured the ion temperature in Ar ECR plasma with high-resolution optical emission spectroscopy and found that the ion temperature in low gas pressure plasma was considerably higher than that expected [4].

In this paper, we measured the ion temperature in Ar/N_2 ECR plasma and investigated the effect of adding the nitrogen gas.

2. Experimental set up

Fig.1 shows a schematic diagram of the experimental apparatus. The experiments were performed using a stainless-steel vacuum chamber with an inner diameter of 290 mm and length of 1200 mm. The chamber was evacuated using a rotary pump and a 2000 l/s turbo molecular pump to a base pressure of less than 10^{-7} Torr. The six magnetic coils with a thickness of 100 mm and inner diameter of 320 mm were placed adjacent to the chamber to form magnetic mirror fields. 2.45 GHz microwaves were launched into the chamber through a tapered waveguide and a quartz window as a circular TE_{11} mode. 915MHz microwaves were launched into the

chamber as a circular TM_{11} mode. The incident and refracted microwave power was measured using a power monitor connected to the directional coupler and the refracted microwave power was minimized by adjusting the three-stub tuner. The substrate holder was placed at 550 mm from the quartz window. The gases used were Ar and N_2. The flow rate of these gasses was adjusted by each mass flow controller. The plasma parameters were measured with a 1 mm-diameter cylindrical single Langmuir probe. The probe was connected to 2D motor drive and moved along pallarel and perpendicular directions to the magnetic fields.

The optical measurement system consisted of a Czerny-Turner type monochromator, a photomultiplier tube, an optical fiber and an electronics system for photon count processing. The monochromator was equipped with 2400-groove/mm grating brazed at 300 nm and scanned in 0.0002 nm steps. The focal length of the monochromator was 1.5 m and the slit width was kept at 14 μ m. The line broadening due to instrument was determined from the measurement of a spectral profile of Hg-lamp light (HAMAMATSU L937-02) at 313.18 nm. The measured instrumental broadening was 0.0030 nm. The effects of the instrument width were removed from the raw data through deconvolution calculations. Optical emissions in the ECR plasma were collected along the radial direction through a viewing port using a lens-optical fiber combination. The viewing port was positioned 170 mm downstream from the ECR point. The emissions entered monochromator were analysed by the photon counting method.

3. The measurement of ion temperature

The emission line profile observed in plasmas may be broadened by many factors, such as natural broadening and Zeeman broadening. The expected Zeeman effect was approximately 0.001nm at the presence of the static magnetic fields about 1kG [5]. The expected Zeeman broadening at measured point was less than the instrument broadening, and was neglected. In our experiment, the natural broadening was also neglected.

Assuming that the ion velocity distribution function is Maxwellian, the emission line profiles is as follows:

$$I(\Delta\lambda) = \frac{I_0}{\pi^{\frac{1}{2}}\Delta\lambda_D} \exp\left[-\left(\frac{\Delta\lambda}{\Delta\lambda_D}\right)^2\right] \tag{1}$$

Here I_0 is total intensity of the spectrum, $\Delta\lambda$ is the divergence from the wavelength of radiation λ_0. $\Delta\lambda_D$ is the width of the Doppler broadening and defined as follows:

$$\Delta\lambda_D = \frac{\lambda_0}{c}\sqrt{\frac{2kT_i}{M_i}} \tag{2}$$

Using a full width at half maximum $\Delta\lambda_{D\frac{1}{2}} = 2(\ln 2)^{\frac{1}{2}}\Delta\lambda_D$, we obtain

$$T_i = 1.67\times10^8 \times A\left(\frac{\lambda_{D\frac{1}{2}}}{\lambda_0}\right)^2 [eV] \tag{3}$$

, where A is the mass number. $\Delta\lambda_{D\frac{1}{2}}$ was obtained from a Gaussian fit of the experimental data.

4. Results and discussion

Fig. 2 shows the dependence of the Ar ion temperature on the nitrogen gas concentration. The measured spectrum was 434.81 nm. The nitrogen gas concentration α was determined as follows; $\alpha = S_{N2}/(S_{N2}+S_{Ar})$. Here S_{N2} and S_{Ar} mean the gas flow rate of Ar and N_2, respectively. The total gas pressure was kept at 2.0mTorr and the incident microwave power was 2.4kW. As shown in Fig. 2, the ion temperature is 0.6eV in pure Ar plasma and it decreases drastically as the nitrogen gas concentration is increased. Fig. 3 shows the dependence of the electron temperature and the electron density on the nitrogen gas concentration. It is found that the electron

temperature slightly increases with increasing the nitrogen gas concentration. This result is valid for physical picture that the loss of the plasma increases with increasing the nitrogen gas concentration because the mass of the nitrogen is lighter than that of argon and, as the result, the electron density decreases and the electron temperature increases to sustain the plasma. Usually, it is considered that ions are heated by electrons through electron-ion collisions. However, as shown in Fig. 2 and Fig. 3, the dependence of the ion temperature on the nitrogen gas concentration is different from that of the electron temperature. Thus, it is concluded that the decrease of the ion temperature is not caused by electrons.

Fig. 4 shows the dependence of the ion temperature on the nitrogen gas concentration for 915MHz microwaves. It is found that the ion temperature also decreases with increasing the nitrogen gas concentration and it is lower than that of 2.45GHz ECR plasma. It has been reported that the electron temperature in 915MHz ECR plasma is lower than that in 2.45GHz ECR plasma [6]. Actually, as shown in Fig. 5, the measured electron temperature in 915MHz ECR plasma is lower than that in 2.45GHz ECR plasma. These results suggest that the lower electron temperature leads to the lower ion temperature.

The charge exchange collision is thought of as the reason for decreasing the ion temperature. When the nitrogen gas is added, the following charge exchange is caused; $Ar^{+}*+Ar \rightarrow Ar^{+}+Ar*$. This charge exchange makes Ar ions cool and energetic Ar neutrals are produced. To verify this effect, we measured Ar neutral temperature. Fig. 6 shows the dependence of the neutral temperature on the nitrogen gas concentration, where the measured spectrum was 434.81 nm. The total gas pressure was 2.0mTorr and the incident power of 2.45GHz microwaves was 2.4kW. It is found that the neutral temperature slightly decreases with increasing the nitrogen gas concentration. This result indicates that the charge exchange collisions is not dominant and the decrease of the neutral temperature is due to the decrease of the ion temperature thorough ion-neutral collisions. However, the ionisation rate of the ECR plasma was so low as 2~3% that the number of neutral particle was much larger than that of ions. Therefore, the number of energetic neutrals was too small to measure.

There are many works about the acceleration of ions due to increase of the ambipolar electric field [7-9]. The same effect may occur along the radial direction. Fig. 7 shows the radial profile of the electron density with varying the nitrogen gas concentration. The measured point was the same as the viewing port position and the experimental condition was the same as Fig. 6. It is found that the radial distribution of the electron density becomes flat by adding the nitrogen gas. Usually, electrons in a magnetic mirror plasma behave as the Boltzman distribution. Therefore, the density distribution implies the plasma potential distribution. If the plasma potential distribution becomes flat, the radial electric field becomes small, and as the result, the transverse ion temperature is considered to decrease. Muta et al. calculated the ion temperature with self-consistent calculation using the hybrid model [10]. The simulation was run for the cases where radial density was peaking and relatively flat. It was found that, when the radial profile of the electron density was peaking, the average of the ion temperature was high, while it was low when the radial density profile was flat. From these results, it is concluded that the radial electric field is an influential factor for decreasing the ion temperature.

5. Summary

The dependence of the Ar ion temperature on the nitrogen gas concentration was investigated. It was found that the ion temperature decreased with increasing the nitrogen gas concentration, while the electron temperature slightly increased. In addition, it was found that the radial distribution of the electron density became flat by adding the nitrogen gas. This change of the plasma density may cause the change of plasma potential and, as the results, the decrease of the radial electric fields make the ion temperature lower.

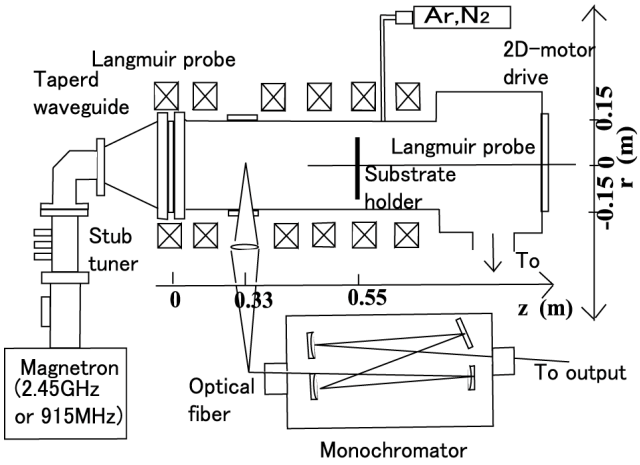

Fig. 1. Schematic diagram of the experimental set up.

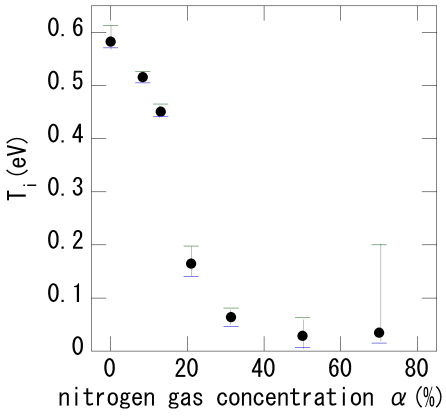

Fig. 2. The dependence of the ion temperature T_i on the nitrogen gas concentration. The total gas pressure was 2.0mTorr and the incident microwave power was 2.4kW.

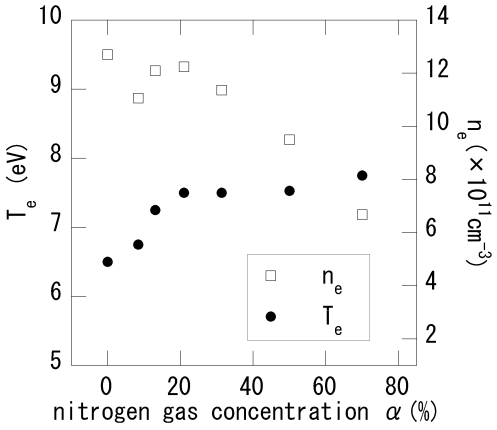

Fig. 3. The dependence of the electron temperature T_e and the electron density n_e on the nitrogen gas concentration.

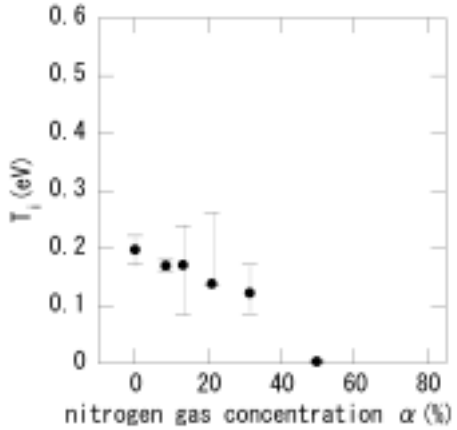

Fig. 4. The dependence of the ion temperature T_i on the nitrogen gas concentration when 915MHz microwaves were used. The total gas pressure was 2.0mTorr and the incident microwave power was 2.4kW.

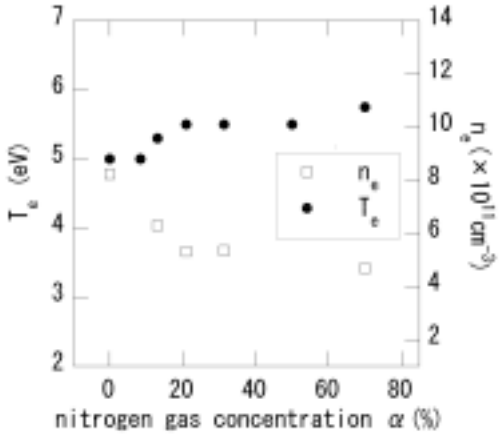

Fig. 5. The dependence of the electron temperature T_e and electron density n_e on the nitrogen gas concentration when 915MHz microwaves were used. The total gas pressure was 2.0mTorr and the incident microwave power was 2.4kW.

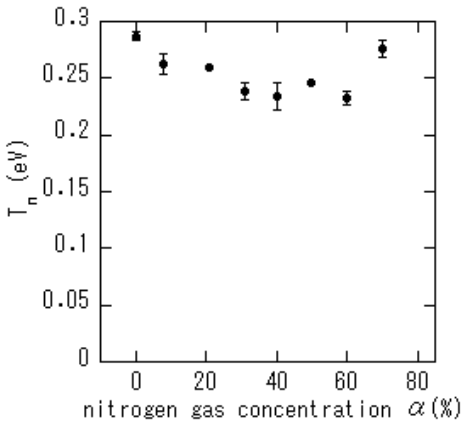

Fig. 6. The dependence of the neutral temperature T_n on the nitrogen gas concentration. The total gas pressure was 2.0mTorr and the incident microwave power was 2.4kW.

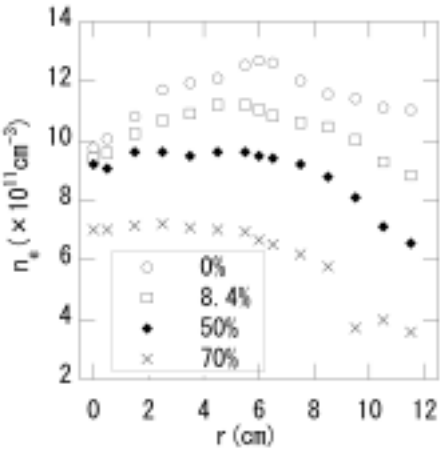

Fig. 7. The radial profile of the electron density with varying the nitrogen gas concentration. The total gas pressure was 2.0mTorr and the incident microwave power was 2.4kW.

References

[1] N. Sakudo, K. Tokiguchi, H. Koike, I. Kanomata, Rev. Sci. Instrum. **48** 762 (1977).
[2] K. Suzuku, S. Okudaira, N. Sakudo, I. Kanomata, Jpn. J. Appl. Phys. **16** 1979 (1977).
[3] S. Matsuo, M. Kiuchi, Jpn. J. Appl. Phys. **22** L210 (1983).
[4] M. Koga, T. Yoshizawa, Y. Ueda, A. Yonesu, Y. Kawai, Appl. Phys. Lett. **79** 3041 (2001).
[5] H. R. Griem, Principle of Plasma Spectroscopy, Cambridge (1997).
[6] N. Itagaki, S. Kawakami, N. Ishii, Y. Kawai, Vacuum **66** 323 (2002).
[7] J. Foster, C. C. Kleeper, L. A. Berry, S. M. Gorbatkin, J. Vac. Sci. Technol. **A 10** 3114 (1992).
[8] J. A. O'Neill, M. S. Barnes, J. H. Keller, J. Appl. Phys. **73** 1621 (1993).
[9] J. S. McKillop, J. C. Forster, W. M. Holber, Appl. Phys. Lett. **55** 30 (1989).
[10] W.Cronrath, M.D.Bowd
en, K.Uchino, K.Muraoka, H.Muta, M.Yoshida, J. Appl. Phys. **81** 2105 (1997).

Dissociation and hydrogen exchange reactions in water plasma monitored by emission spectroscopy

I. G. Koo, J. H. Shim, and W. M. Lee

Department of Molecular Science and Technology, Ajou University, Suwon, Korea

Abstract

We have studied the hydrogen exchange and water dissociation reactions in H_2/D_2O, D_2/H_2O, D_2O and H_2O plasma excited by hollow cathode discharge using emission and infrared spectroscopy. When the electrical power for the discharge, the flow rate of the gas system, and the reactor temperature were maintained at 1 W, 150 ml min^{-1}, and 100^oC, respectively, the reacting gas of one atmospheric pressure underwent about 30% of the hydrogen exchange reaction.

1. Introduction

Plasma, both thermal and non-thermal, is used as one of the major methods in removing environmental pollutants, replacing catalysts in many gaseous reactions, and altering chemical reaction paths [1-5]. Among many applications of the plasma method, we investigated the hydrogen isotope exchange reactions in water/hydrogen plasma [6].

Heavy water (D_2O) used as a coolant in nuclear reactors is partly transformed into DTO when the molecules capture neutrons. Among the many tritium recovery processes, the catalytic exchange of DTO with D_2 to produce DT and D_2O, or electrolysis of D_2O/DTO to D_2/DT and O_2 followed by cryogenic distillation of the hydrogen isotopes, appears feasible and promising [7,8]. But such exchange reactions require the use of expensive novel metals. When the hydrogen isotope exchange reactions occurring in (H_2O, D_2) or (D_2O, H_2) reacting system were carried out in a DC electrical discharge, it was revealed that the discharge method was far more effective in facilitating the exchange reaction than was the conventional catalytic method [6]. In this study the hollow cathode discharge method was employed instead of a typical DC discharge method relying on a point-plane geometry. Allowing gas flow through arrays of microhollow cathode holes and applying power between the electrodes could generate large area uniform and stable plasma [9-11]. The advantage of such large area plasma is obvious from the possibility of an increase in the energy efficiency defined by the extent of wanted chemical reactions per dissipated electrical energy. The advantage is even more pronounced considering a potential large increase in the treating capacity by the stable atmospheric plasma.

The plasma was monitored mainly using plasma emission spectroscopy (PES) and using the infrared spectroscopy (FTIR) as an auxiliary tool. The extent of the exchange reaction was determined by measuring in real time the OH or OD emission intensity or the IR absorbance of the HDO molecule, major products of the reaction. The progress of the reaction was studied as a function of the temperature, the current density and the composition of the reactants while the pressure of the system was maintained at the atmospheric pressure.

2. Experimental

The schematic experimental setup is illustrated in Fig. 1. The experimental setup used in this study consists of three major sections: the electrode assembly and the plasma reactor, the gas supply and regulating

lines, and the spectroscopic diagnostic system. The reactor included a thermocouple for temperature measurement, a pressure gauge, UV-grade quartz window for transmitting the emitted light, and CaF_2 windows (4000~1000 cm^{-1}) for transmitting infrared light. The emitted light from the plasma reactor was collected and transmitted through an optical fiber to the monochromator, the 750 mm Czerny-Terner monochromator (Model DM 702) attached to the Andor CCD camera (Model DB401-UV). The spectroscopic resolution of the emitted light for the 200-1000 nm ranges was made using a grating 1200 gr/mm, 2400 gr/mm with the resolution of 0.05, 0.01nm. The IR measurements of the reacting species were acquired using the FTIR spectrometer (Nicolet Magna-IR) in the form of a single beam with a resolution of 2 cm^{-1} and scan number of 1 in an IR detection range of 4000~800 cm^{-1}.

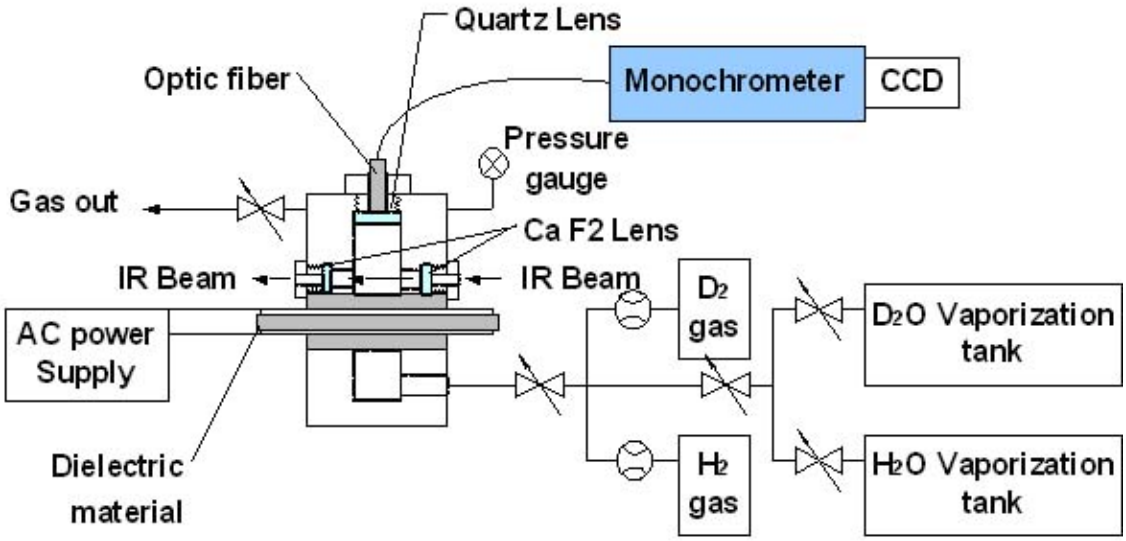

Fig. 1 Experimental setup

The electrode design for generating large-area atmospheric plasma is illustrated in Fig. 2. The electrodes basically consisted of two aluminum disks of 200 μm thickness separated by an alumina sheet of 1 mm thickness. A mechanical driller was used to bore many holes of 300 μm diameter through this electrode assembly. A 60 Hz AC power supply was connected to the cathode and the anode. Gas or gas mixture having composition such as He, H_2, D_2, H_2O, D_2O, H_2/D_2O or D_2/H_2O was allowed to flow through this assembly to generate atmospheric plasma.

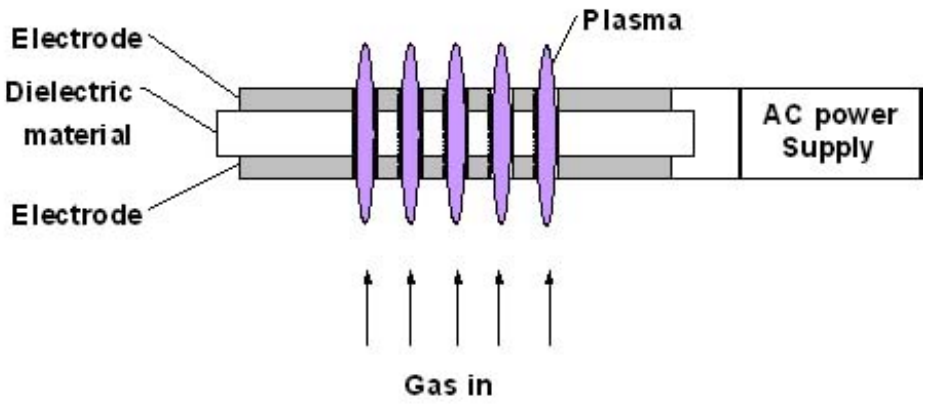

Fig. 2 Hollow cathode plasma generation

The transfer of the water vapor into the reactor and the regulation of its flow rate were accomplished by the following procedures. First, the reactor was pumped down to ~10^{-2} Torr by a cold-trapped rotary pump (Edward E2M1.5 double stage). The water reservoir was heated to reach a pre-set temperature and the saturated H_2O or D_2O vapor was introduced into the reactor. Second, during the reaction period the water loss at the reservoir was measured as a function of the temperature to determine its flow rate (250 sccm at 80°C). Concurrently with the introduction of water vapor the H_2 or D_2 gas was also allowed to enter the chamber with the help of a mass flow meter (100 sccm) and needle valve (Sierra series 820 Top-trak™). The total pressure of hydrogen gas plus water vapor and the chamber temperature were maintained at the atmospheric pressure and 100°C, respectively. The pressure was measured with the diaphragm manometer gauge (Baratron 268A model).

3. Results and discussion

AC discharge in pure hydrogen gas or water vapor or their mixture was able to generate stable large area plasma at a pressure of 760 Torr when the gas flew through the micro-cathode assembly. The success is quite remarkable in that no noble gas was used and the pressure reached the atmospheric pressure. It is quite well attributed to the unique geometry displayed in the micro cathode assembly. The characteristic α-emission line of atomic hydrogen obtained from pure hydrogen or deuterium gas plasma is shown in Fig. 3. The wavelength difference of the α-line between hydrogen and deuterium atom is about 0.3 nm that was also reported previously [12]. Such an extremely close occurrence of the atomic lines of the hydrogen isotopes makes it difficult to use such lines as the reference for monitoring the species containing H or D atoms.

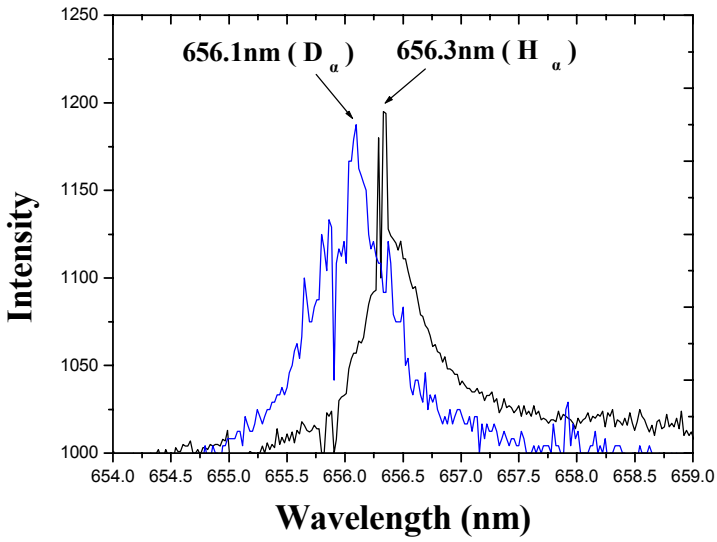

Fig. 3 The H-α or D-α line observed from the discharge in H_2 or D_2 gas

The emission spectrum of water vapor plasma is shown in Fig. 4. The characteristic lines of OH or OD radical are appearing in the range of 307 to 310 nm and much weaker hydrogen-α line is also showing up. But when the discharge was made in water/hydrogen gas mixture, the OH lines almost completely disappeared as shown in Fig. 5 while very weak hydrogen-α line appeared. It is surprising that OH or OD lines are almost completely subdued when hydrogen gas is added to the system. This is an indication that the lifetime of OH radical is very short during the discharge in the presence of hydrogen atom or molecule.

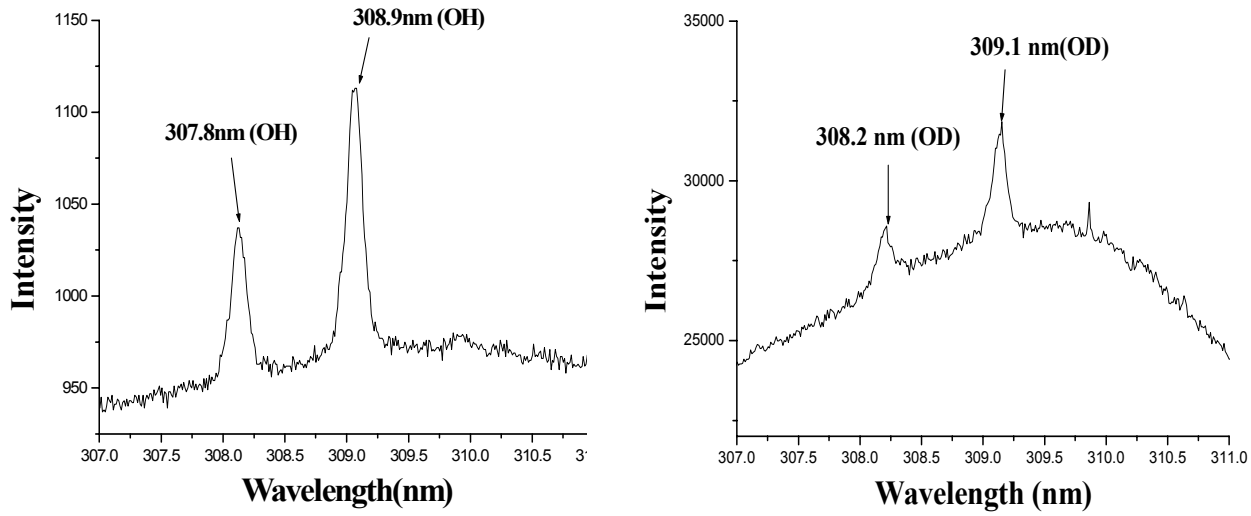

Fig. 4. The emission spectra of H_2O or D_2O plasma

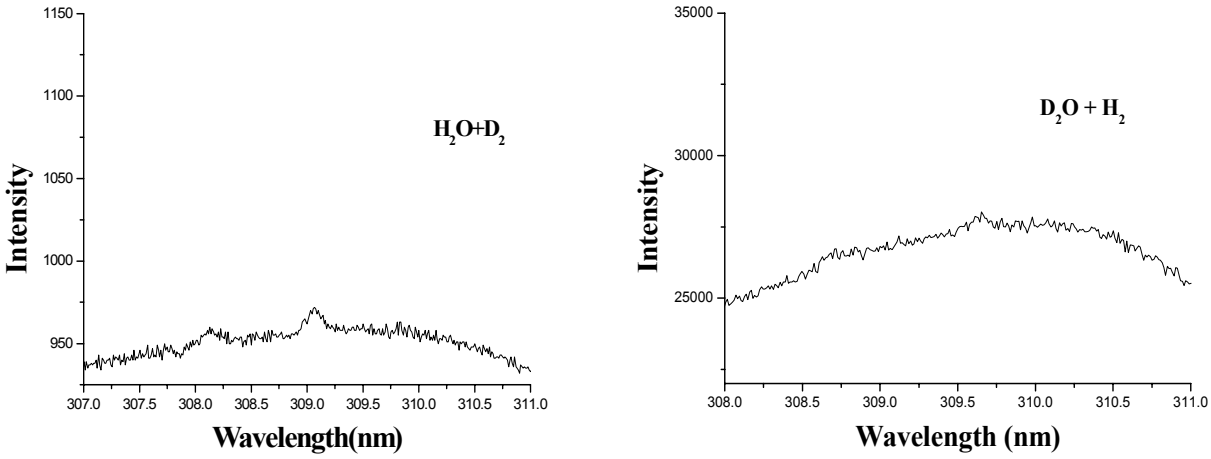

Fig. 5. The emission spectra of (H_2O/D_2) or (D_2O/H_2) plasma

But the emission spectra of water/hydrogen plasma obtained in a flowing system do not tell us directly the extent of the hydrogen isotope exchange reaction in a system such as (H_2O/D_2) or (D_2O/H_2). In order to determine the extent we have to resort to IR spectroscopy since this method renders it possible to obtain the information on the concentration of the exchange reaction product HDO. For example, measurements of the absorbency (or transmission) of the vibrational characteristic lines of D_2O or HDO molecules during the discharge in (D_2O/H_2) system gives out direct information on the advance of the exchange reaction. The exact determination of the advance of the exchange reaction in a flowing system requires that the reactor be closed at an arbitrary time during the steady discharge and then the measurement should follow in the closed system regarding the intensity of the vibrational peaks of the involved species. But in this study we assumed that the region of the reactor from which the optical signal was collected could represent the advance of the exchange reaction in the flowing system. Under this assumption the intensity of the flowing system can be compared with that measured in the closed system to determine the advance of the reaction. The vibrational

characteristic lines of HDO and D_2O molecules in D_2O/H_2 system are shown in Fig. 6. By comparing the intensity of the lines of D_2O in the flowing D_2O/H_2 system with those in the closed system, we were able to determine the advance of the reaction in the system. The advance of the exchange reaction in the closed D_2O/H_2 system, representable by the decrease in the number density of D_2O molecules, is plotted in Fig. 7 as a function of the discharge time. It turned out that the discharge with the given flow rate of the reacting gas accomplished about 30 % of exchange reaction when the power was maintained under 2 W.

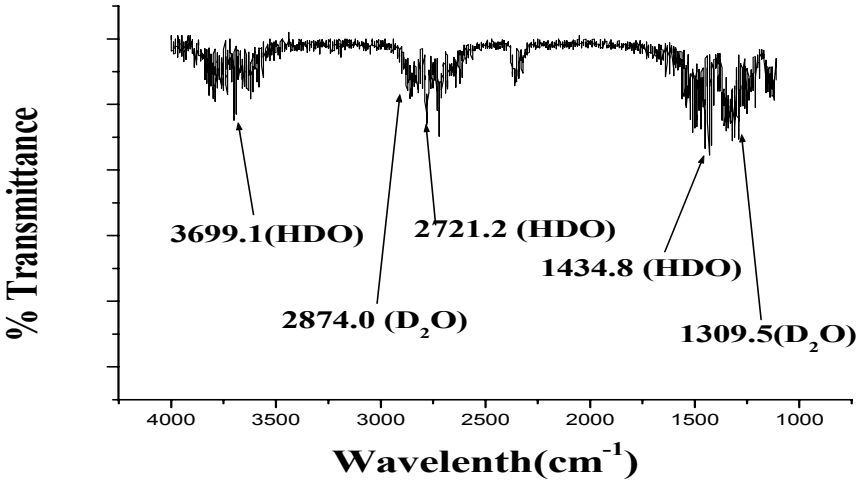

Fig. 6. FTIR spectra of D_2O/H_2 system

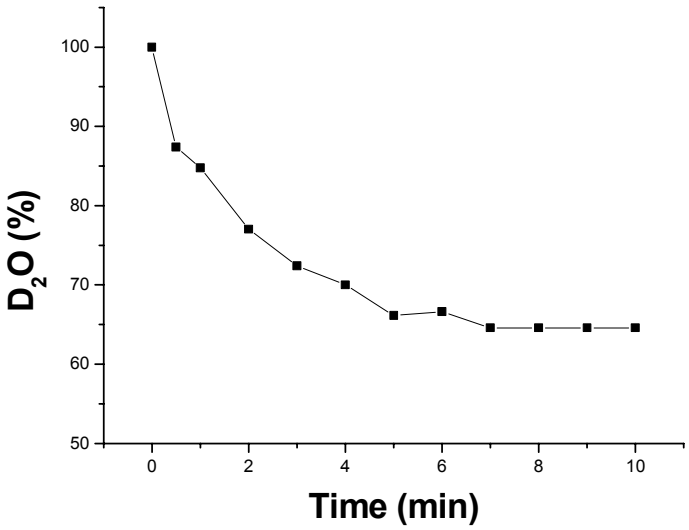

Fig. 7. The extent of the hydrogen isotope exchange reaction in a closed D_2O/H_2 system

Acknowledgements

This work was supported by the Mid- and Long-term Nuclear R&D Fund provided by the Ministry of Science and Technology, Republic of Korea.

References

[1] A. R. Hochstin -*Kinetic Processes in Gases and Plasma*, Acad. Press (1969).
[2] B. M. Penetrante and S. E. Schultheis - *Non-Thermal Plasma Techniques for Pollution Control*, Springer-Verlag, Berlin (1993).
[3] B. D. Blaustein - *Chemical Reactions in Electrical Discharge*, Adv. In Chem. Ser., No. **80**, ACS (1967).
[4] J. Lawton and F. J. Weinberg - *Electrical Aspects of Combination*, Clarendon Press, Oxford (1969).
[5] J. R. Hollahan, A. T. Bell - *Techniques and Applications of Plasma chemistry*, John Wiley & Sons, New York (1974).
[6] H.J. Kim, Y.D. Park, W.M. Lee - Plasma Chem. Plasma Process. **20**, 259 (2000)
[7] J. P. Butler, J. H. Rolston, and W. H. Stevens - *Proceeding of the symposium on "Separation of Hydrogen Isotopes"*, H. K. Rae ed., *ACS Symp*. - Ser No. **68**, 93 (1978).
[8] J. H. Rolston, J. den Hartog, J. P. Butler - *J. Phys. Chem.*, **80**, 1064 (1976).
[9] K.H. Schoenbach, R. Verhappen, T. Tessnow, F.E. Peterkin, W.W. Byszewski - Appl. Phys. Lett. **68**, 13 (1996)
[10] K.H. Schoenbach, A. El-Habachi, M.M. Moselhy, W. Shi, R.H. Stark - Phys. Plasmas **7**, 2186 (2000)
[11] Y. Guo and F. C. Hong - Appl. Phys. Lett. **82**, 337 (2003)
[12] Charlotte E. Moore, Jean W.Gallagher - Table of Spectra of Hydrogen, Carbon, Nitrogen, and Oxygen Atoms and Ions, CRC Press (2000).

GC-MS Investigation of Glow Discharges fed with Hexamethyldisiloxane-O_2 for PECVD of SiOx Thin Films.

A. Fornelli, R. d'Agostino, F. Fanelli, F. Fracassi, F. Palumbo

Dipartimento di Chimica Università degli Studi di Bari - IMIP CNR, via Orabona 4, 70126 BARI- (Italy)

Abstract

The results reported in this work have been obtained in HMDSO-O_2-Ar RF glow discharges, sustained in a capacitively coupled, parallel plate reactor. The exhaust gases has been sampled by means of a cold trap and analyzed using gas chromatography-mass spectrometry (GC-MS). The effect of feed composition, RF input power, and pressure on the concentration of unreacted HMDSO and of its conversion products has been investigated by means of qualitative and absolute quantitative analyses. HMDSO undergoes conversion to many different linear and cyclic compounds, containing from one to five silicon atoms. The results seams to indicate that under the experimental conditions investigated, HMDSO is not activated by reactions with oxygen but mainly by electron collisions. On the contrary, oxygen seams to have an important role in the plasma chemistry.

Introduction

Plasma Enhanced Chemical Vapor Deposition (PECVD) of silicon dioxide (SiO_2-like) thin films has many large-scale applications because of the interesting properties of the coatings: insulating characteristics[1], good abrasion resistance[2], low gas and moisture permeability[3,4,5], resistance to chemicals, optical transparency[3], etc... SiO_2-like thin films have been extensively applied in semiconductor industry and now they find applications in many other fields, like packaging, biomaterials, corrosion protection, etc.

In recent years, many organosilicon compounds like hexamethyldisiloxane (HMDSO) or tetraethoxysilane (TEOS) mixed with oxidants (O_2, N_2O) and/or noble gases (Ar, He), are used as SiO_2 precursors. Organosilicon monomer fed plasmas are complex reactive systems and a great deal of work has been produced to understand their chemistry, nevertheless the deposition mechanism is not yet completely known and for this reason many investigations are directed to the identification of the main film precursors and to clarify the plasma-surface interaction. An overall general deposition mechanism, reporting some of the possible reaction paths can be proposed according to Figure 1[6,7,8].

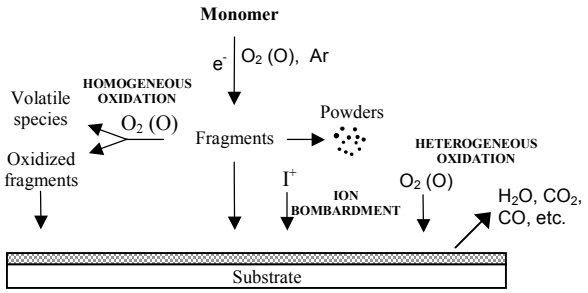

Figure 1. General deposition process in organosilicon plasma.

The organosilicon monomer is activated by electron collision and/or reaction with oxygen and/or excited Ar or He, the fragments can form powders or undergo homogeneous oxidation reactions with formation of partially or totally oxidized species. The intermediates are then adsorbed on the substrate surface where they can experience ion bombardment as well as heterogeneous (gas-surface) oxidations with release of water and other oxidized compounds.

The identification of the reaction steps relevant for the deposition process and the correlation with the chemical composition and properties of coatings is one of the most important research task.

Many diagnostic techniques such as Fourier Transform Infrared Absorption Spectroscopy (FTIR-AS), Optical Emission Spectroscopy (OES), Mass Spectrometry (MS), etc. have been utilized to study organosilicon containing plasmas[6,7,8,9,10], among them gas chromatography with mass spectrometric detection

(GC-MS) has shown to be a very powerful gas phase indirect diagnostic technique[11,12,13,14,15]. When coupled to other direct diagnostics, GC-MS can improve the understanding of organosilicon fed plasmas since it allows for the quali-quantitative determination of stable by-products formed by plasma activation. Unfortunately GC-MS does not allow a continuous monitoring of exhaust composition, since it is not compatible with on line continuous sampling, but requires a suitable discrete gas sampling system, such as a cold trap located between the plasma chamber and the pump.
GC-MS has been extensively utilized by Wróbel et al. to investigate PECVD and remote plasma chemical vapor deposition processes carried out with different organosilicon monomers (i. e. siloxanes, silanes and silazanes)[11,12,13,14].
In the present work we report the results of GC-MS investigation of RF glow discharges fed with HMDSO-O_2-Ar. The effect of the feed composition, input power and pressure on the monomer depletion and on the concentration of by-products have been investigated. The results allow for a clarification of some aspects of the overall deposition mechanism under the experimental conditions utilized for the study.

Experimental
The experimental apparatus consists of a stainless steel parallel-plate reactor with an asymmetric electrode configuration, at 13.56 MHz RF, pumped by a turbomolecular-rotary pumping system. The gas flow rates are controlled with MKS mass flow controllers while HMDSO vapor flow rate is controlled by means of MKS Vapor Source Controller (a commercial vapor delivery system maintained at constant temperature and equipped with a flow meter). A throttle valve allows the working pressure regulation.
Glow discharges were fed with HMDSO-O_2-Ar mixtures at the total flow rate of 23 and 78 sccm. HMDSO (Sigma Aldrich, 99 % purity) flow rate was kept constant at 3 sccm, while the O_2-to-HMDSO ratio was in the range 0 ÷ 25 (the Ar content in the feed gas was changed to keep the total flow rate at the selected value). The input power was changed in the range 50 ÷ 200 W and the working pressure was set at 100 and 500 mTorr. A stainless steel liquid nitrogen trap, located between the reactor and the turbomolecular pump (Figure 2), allows for the retention of the exhaust gases of the plasma process: i.e. unreacted HMDSO and products derived from recombination of plasma intermediates.
The exhaust gas was sampled at the liquid nitrogen temperature (78 K) for 20 minutes, then the trap was

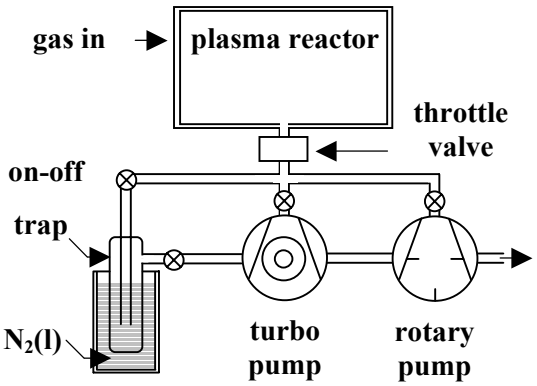

Figure 2. Schematic of the sampling apparatus.

isolated from the system and vented with Ar. The condensate was dissolved in acetone (50 ml), filtered and than analyzed with a GC 8000 Top GC-MS (Thermoquest Corporation) apparatus, equipped with an Alltech AT^{TM}-5MS capillary column of fused silica, coated with 0.25 μm of 5% phenyl and 95% methyl polysiloxane (length of 30 m, i.d. of 0.25 mm). The analyses have been performed with 2 sccm of He as carrier gas, injector temperature of 200˚C, and column temperature programmed from 30 to 200˚C (1 min at 30˚C, linear heating rate of 10 ˚C min^{-1}, 1 min. at 200˚C). Separated products were analyzed with a Voyager quadrupole Mass-Spectrometer, Thermoquest Corporation, at the interface and source temperatures of 250 and 200˚C respectively. Mass spectra were recorded in the m/z range: 15 ÷ 450 u.m.a. at the standard ionizing electron energy of 70 eV. The products were identified by means of available libraries[15] and, in particular for quantified products, by the comparison of retention time and mass spectra with standard compounds.

The quantitative analysis of some identified species was performed utilizing nonane (Sigma Aldrich, 99% purity) as internal standard (IS) through the calculation of calibration curves in the linear range. The amounts of quantified compounds have been converted in flow rate, Φ (sccm), by means of Eq. 1 assuming the ideal gas behavior:

$$\Phi(\text{sccm}) = \frac{\text{mass(g)}}{\text{MW}(\text{g}\cdot\text{mol}^{-1})} \cdot 22400\,(\text{cc}\cdot\text{mol}^{-1}) \cdot \frac{1}{\text{t}_{\text{sampling}}\,(\text{min})} \qquad (1)$$

where MW is the molecular weight and $t_{sampling}$ the collecting time of the exhaust in the LN_2 trap. The extent of monomer conversion has been evaluated by dividing the flow rate of HMDSO in the exhaust at plasma on with that introduced into the reactor at plasma off according to (2):

$$\%_{\text{HMDSO}} = \frac{\text{HMDSO}_{\text{plasma on}}\ (\text{sccm})}{\text{HMDSO}_{\text{plasma off}}\ (\text{sccm})} \cdot 100 \qquad (2)$$

The higher is $\%_{HMDSO}$ the lower is the monomer depletion. It is also verified that the collection of exhaust gases in the trap was quantitative and reproducible.

Result and descussion

Figure 3 shows two typical chromatograms of the by-products sampled with HMDSO containing plasma, the identified species are reported in Table 1.

Table 1. Identified species detected in HMDSO containing plasmas.

	Compound	**Formula**	**Molecular weight (u.m.a.)**
	Hexamethyldisiloxane (HMDSO) *	$Me_3SiOSiMe_3$	162
1	Tetramethylsilane (TMS)*	Me_4Si	88
2	Ethyltrimethylsilane (ETMS)	$EtMe_3Si$	102
3	Trimethylsilanol (TMSOH)*	Me_3SiOH	90
4	Pentamethyldisiloxane (PMDSO)	$Me_3SiOSiHMe_2$	148
5	Ethoxytrimethylsilane (EOTMS)	$EtOMe_3Si$	118
6	Trimethylsilylformate (TMSF)	$HCOOSiMe_3$	118
7	Ethylpentamethyldisiloxane (EPMDSO)	$EtMe_2SiOSiMe_3$	176
8	Hexamethylcyclotrisiloxane(HMCTSO)*	$(Me_2SiO)_3$	222
9	Octamethyltrisiloxane (OMTSO)*	$Me\text{-}(Me_2SiO)_2\text{-}SiMe_3$	236
10	Octamethylcyclotetrasiloxane (OMCTSO)*	$(Me_2SiO)_4$	296
11	Decamethyltetrasiloxane (DMTSO)*	$Me\text{-}(Me_2SiO)_3\text{-}SiMe_3$	310
12	Dodecamethylpentasiloxane (DMPSO)	$Me\text{-}(Me_2SiO)_4\text{-}SiMe_3$	385

(*) *absolute quantification with standard compounds available*

It is reasonably to assume that the heavier compounds are not sampled for their low volatility, while light species, e.g. CO, CO_2, CH_4, etc. are lost during manipulation of the condensed for their high volatility. It can be appreciated that HMDSO undergoes conversion to many different linear and cyclic compounds, containing up to five silicon atoms.

The simplest species detected, i.e. tetramethysilane (TMS) and trimethylsilanol (TMSOH), are very interesting because they give evidence of HMDSO fragmentation while the presence of species containing the dimethylsiloxane ($-Me_2SiO-$) repeating unit confirms the occurrence of oligomerization processes: e.g. chain propagation, ring formation and expansion, those bring to linear and cyclic compounds with general formulas $Me\text{-}(Me_2SiO)_n\text{-}SiMe_3$ (n = 1-4) and $(Me_2SiO)_n$ (n = 3,4), respectively.

The working conditions affect, both qualitatively and quantitatively, the composition of sampled mixtures along with HMDSO depletion; but in all the experimental conditions investigated, the most abundant species is the unreacted monomer.

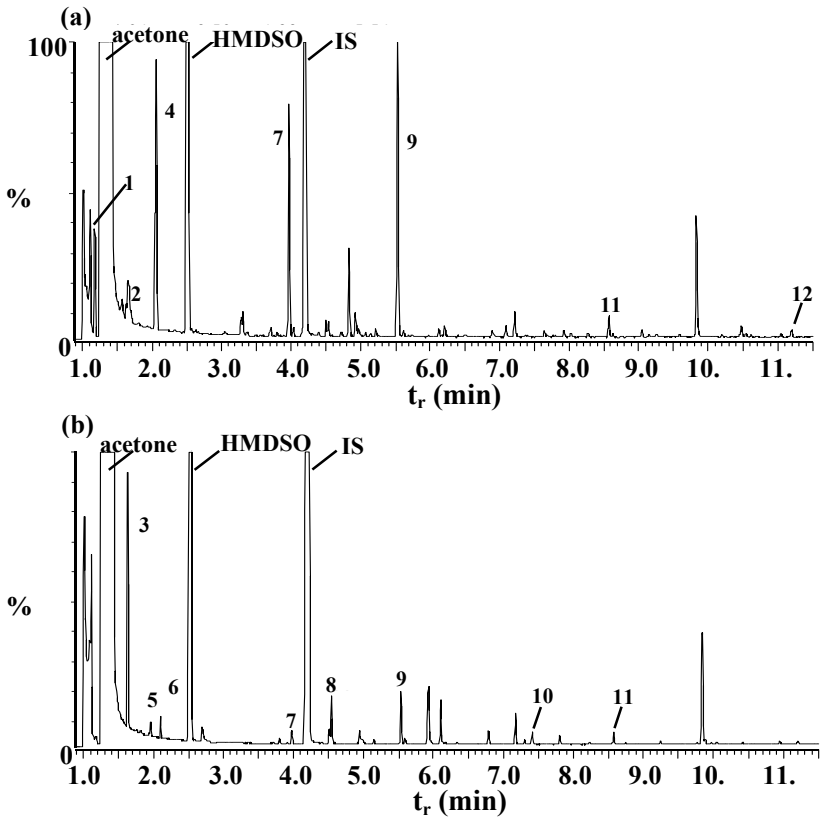

Figure 3. Typical gas-chromatograms of exhaust: (a) O_2/HMDSO = 0; (b) O_2/HMDSO = 25. The peaks without number indicate species not identified.

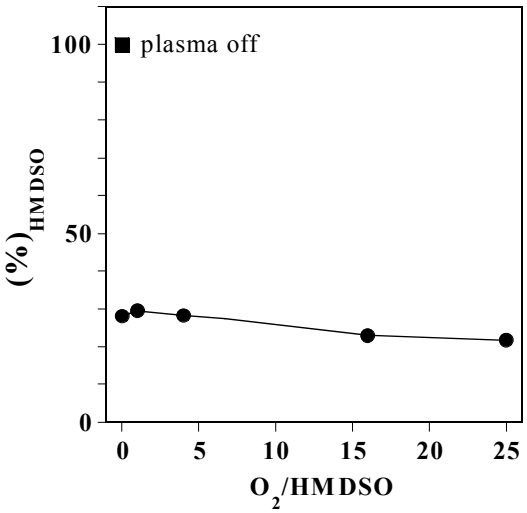

Figure 4. Concentration trend of (HMDSO) *vs.* the O_2-HMDSO ratio in the gas feed. Total flow rate = 78 sccm, 200 mTorr, 100 W).

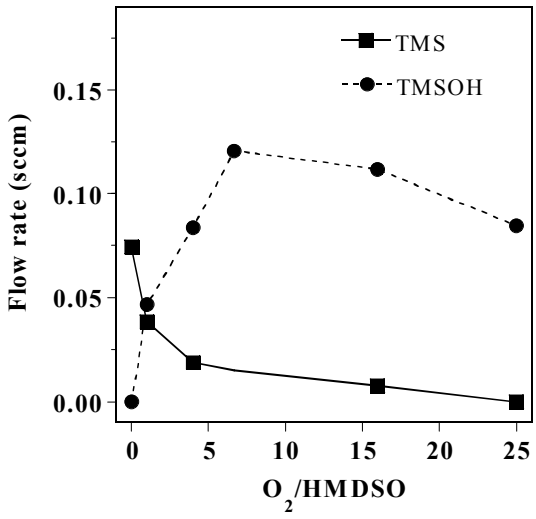

Figure 5. Concentration trends of (TMS) and (TMSOH) *vs.* the O_2-HMDSO ratio in the gas feed Total flow rate = 78 sccm, 200 mTorr, 100 W).

As shown in figure 4, $\%_{HMDSO}$ does not depend significantly on the feed composition even if the O_2-to-HMDSO flow rate ratio is varied in a wide range (0 ÷ 25).

By increasing the oxygen content of the feed the unreacted fraction of the monomer decreases very slowly: from about 28-30% for O_2/HMDSO = 0-1 respectively to about 20% for O_2/HMDSO = 25. This indicates

that under the experimental conditions explored, oxygen does not have a fundamental role in the activation of the monomer, a different conclusion respect to what reported by other authors under different conditions (see for instance ref. [14]).
On the contrary, feed composition affects the distribution of the by-products generated for plasma activation.

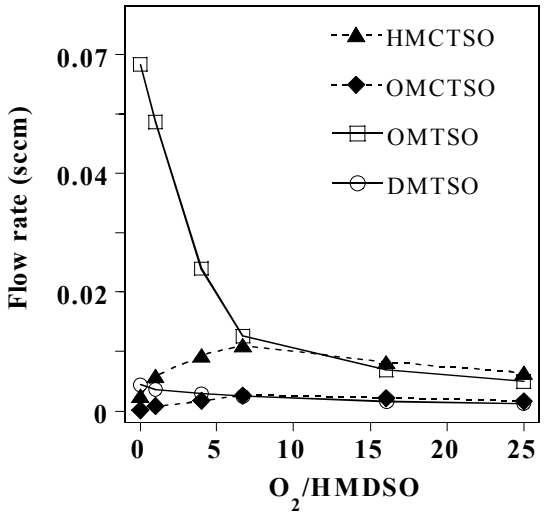

Figure 6. Concentration trends of OMTSO, HMCTSO, DMTSO and OMCTSO *vs.* the O_2-HMDSO ratio in the gas feed (total flow rate = 78 sccm, 200 mTorr, 100 W)

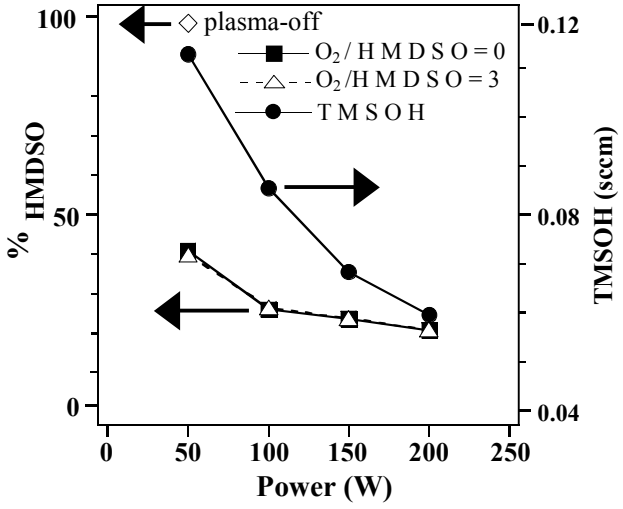

Figure 7. Concentration trends of HMDSO in the exhaust *vs.* the input power at O_2-to-HMDSO ratio of 0 and 3; concentration trend of TMSOH in the by-products *vs.* the input power at O_2-to-HMDSO ratio of 3 (total flow rate = 23 sccm, 100 mTorr).

Figures 5 and 6 show that increasing the oxygen content of the feed gas the trend of tetramethylsilane and of linear oligomers concentration decrease while the trends of trimethylsilanol and cyclic oligomers show a maximum at O_2-to-HMDSO ratio of 7, approximately.
The maximum can be reasonably explained considering that oxygen promotes the formation of trimethylsilanol and cyclic oligomers, but at high O_2 content the oxidation reactions prevail.
In order to study the effect of working pressure on the concentration of by-products, the total flow rate has been reduced to 23 sccm and consequently the O_2-to-HMDSO flow rate ratio has been varied in a narrower range (0 ÷ 7). Two sets of experiments have been performed at 100 and 500 mTorr. The trends of by-products concentration *vs.* O_2-to-HMDSO ratio are similar but the absolute values of concentration, as well as that of the $\%_{HMDSO}$, are always lower at 500 mTorr than at 100 mTorr. In particular, as a function of the other working conditions, the extent of unreacted monomer was found to vary in the range 40-30% and 15-10% at 100 and 500 mTorr, respectively. The effect of input power has been examined, at 100 mTorr, in the range 50 - 200 W at O_2-to-HMDSO ratio of 0 and 3.
The concentration of HMDSO in the exhaust decreases with the input power at both feed compositions without appreciable differences (figure 7), the main change is observed passing from 50 to 100 W. In oxygen containing feed, by-products concentration generally shows a decreasing trend with input power.

Descussion and conclusion
The results shown in the previous section allow a better definition of the general deposition scheme reposted in Figure 1, in particular for HMDSO activation (i.e. the first step of the overall reaction) which is directly linked to monomer depletion. When the organosilicon compound is fed directly into the plasma, as in the case under discussion, activation can occur through reactions with oxygen (atoms or excited molecules), with excited Ar, or by means of electron collisions. Since the variation of the feed composition results in modest changes of $\%_{HMDSO}$ (Figure 4), while input power has a more evident effect (Figure 7), it appears reasonable to assume that, under the experimental conditions explored, electron collision is the main monomer activation channel. Electron collision is more efficient when the input power is raised, i.e. when the electron

energy and density become higher. The importance of direct plasma dissociation by electron impact has been already reported by other authors.[16]

If oxygen addition has a negligible effect on monomer activation, on the contrary it seems to have an important role in plasma chemistry. In fact, oxygen addition affects the concentration of the organosilicons formed by recombination of reactive species in gas phase, although it has a remarkably different effect on linear and cyclic compounds. The important role played by oxygen addition in the overall discharge chemistry can be also stressed considering that the effect of power on by-products concentration is more evident when the feed gas contains oxygen.

The concentration trend of trimethylsylanol (TMSOH) is of particular importance. The marked decrease of trimethylsylanol concentration when the input power is raised (Figure 7) is in agreement with the concentration trend of Si-OH groups in the coating: by increasing the input power the content of Si-OH groups decreases and a more stable, inert and resistant film is obtained[16].

By considering the structure of the by-products revealed by GC-MS (Table 1) and the fact that many compounds in the gas chromatogram have not been identified by mass spectrometry, it can be concluded that despite the unit -Me_2SiO- is the most important building block for the formation of cyclic and linear heavy oligomers, other units shall also be considered. If -Me_2SiO- reasonably derives from the fragmentation of HMDSO (Me_3Si-O-Si Me_3), the other units (e.g. ethyl or ethoxy groups) are not contained in the structure of starting organosilion monomer and therefore the contemporaneous occurrence of different reactions should be considered.

The chemistry of the plasma phase and the distribution of by-products concentration is also affected by the working pressure. It has been reported in the previous section that at 500 mTorr the concentration of unreacted HMDSO and of by-products is lower than at 100 mTorr. It can be therefore concluded that at high working pressure by-product oxidation, and powder or deposit formation are favoured, otherwise as a consequence of the increased monomer depletion a higher concentration of by-product should be detected.

Further investigations by coupling GC-MS results with Infrared Absorption and Optical Emission Spectroscopies will be carried out for a better comprehension of the deposition mechanism.

Acknowledgements

The financial support of the Italian **"***Ministero dell'Università e della Ricerca Scientifica e Tecnologica*" (DM n. 10 del 23 gennaio 2001) and of the European Community (NANOMAG – V FP) is acknowledged.

References

[1] T. S. Ramu, M. R. Wertheimer, and J. E. Klemberg-Sapieha, *IEEE Trans. Electr. Insul.* E1-21, 549 (1986).
[2] K. S. Chen, N. Inagaki, and N. Katsuura, *J. Appl. Pol. Sci.*, **27**, 4655 (1982).
[3] J. Felts Airco, in Proc. to Society of Vacuum Coaters 36th Annual Conference 1993, 324-332.
[4] R. J. Nelson, in Proc. to *The Society for the research of polymerized compound surfaces*, Fukui City Japan 9 July 1993
[5] Adam Rizika, *Airco Coating Tecnology*, Pack Expo '92 Conference.
[6] F. Fracassi, R. d'Agostino, and P. Favia, *J. Electrochem. Soc.*, **139**, 9 (1992).
[7] D. Magni, Ch. Deschenaux, Ch. Hollestein, A. Creatore, and P. Fayet, *J. Phys. D: Appl. Phys.*, **34**, 87-94 (2001).
[8] M. Creatore, F. Palumbo, R. d'Agostino, *Plasmas Polym.*, **7**(3), 291 (2002).
[9] M. R. Alexander, F. R. Jones, and R. D. Short, *Plasmas Polym.*, **2**, 4 (1997).
[10] M. R. Alexander, F. R. Jones, and R. D. Short, *J. Phys Chem. B*, **101**, 3614-3619 (1997).
[11] A . M. Wròbel, *Plasma Chem. Plasma Process.*, **7**, 4 (1987).
[12] A. M. Wròbel, G. Czeremuszkin, H. Szymanowski, and J. Kowlaski, *Plasma Chem. Plasma Process.*, **10**, 2 (1990).
[13] A. M. Wròbel, and A. Walkiewicz-Pietrzykowska, *J. Electrochem. Soc.*, **145**, 8 (1998).
[14] A. M. Wròbel, A. Walkiewicz-Pietrzykowska, Y. Hatanaka, S. Wickramanayaka, and Y. Nakanishi, *Chem. Mater.*, **13**, 5 (2001).
[15] NIST and Wiley libraries in *MassLab Release 1.4 (GC/MS Data System Software), Finngan*
[16] F. Fracassi, R. d'Agostino, F. Palumbo, E. Angelini, S. Grassini, F. Rosalbino, *Surface and Coating Technology*, in press.
[17] C. Rau, W. Kulish, *Thin Solid Films*, 249 (1994) 28.

Numerical Prediction of Population Inversion in a Fast -Axial- Flow CO_2 Laser

F. Siserir and D. Louhibi

Centre de Développement des Technologies Avancées,Baba Hassen BP17, Algiers, Algeria

Abstract
A six temperature kinetic model is used to predict the performance of a high power fast axial flow CO_2 laser, pumped by a longitudinal electric discharge. At an emission wavelength of $\lambda = 10.6$ µm, a typical output power of 1kW/m can be extracted from such lasers, with electrical efficiencies exceeding 30 percent. The spatial distributions of vibrational levels populations are determined through the numerical resolution of a set eight coupled differential equations. The results obtained are in satisfactory agreement with experimental data.

1. Introduction

The aim of the present paper is to apply a six-temperature kinetic model describing the behavior of fast- axial -flow CO_2 laser, electrically pumped by a longitudinal self-sustained glow discharge, in a linear cavity configuration. Quantitative predictions about laser operating characteristics are made. Such lasers generate more than 1 kW of 10.6 µm cw radiation per meter of tube length, with electrical efficiencies in excess of 30 percent. They are extremely useful in a number of industrial tasks involving materials processing like cutting, drilling, welding and surface treatment.

The model consists of a set of eight coupled differential equations [1]. It takes into account the effects of electrical excitation, energy transfer processes between vibrational and translational degrees of freedom, thermal energy transport, as well as laser light intensity amplification and losses inside the active medium. Using a numerical method to solve the system, we determine the distribution along the tube axis of the vibrational level population and population inversion in the laser process. We deduce the laser output power under given geometrical and pumping conditions [2]. The results of our simulation are compared to experimental performances achieved with devices described in the literature [3]-[4].

2. Presentation of the model

2.1. Geometrical configuration of the cavity

A linear cavity configuration was considered, as shown in Fig.1. The electric discharge region (positive column, lying between z= 0 and z = l_{pc}) is followed by a drift zone between z = l_{pc} and z= l_{flow} where population inversion, though decreasing, remains positive and contributes thus to additional light amplification.

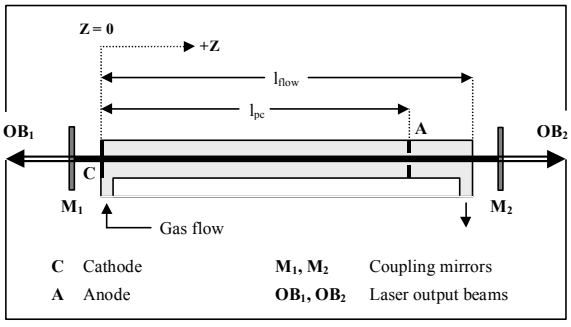

Figure 1. Geometrical configuration of the considered axial -flow CO_2 laser cavity.

2.2. Notations and assumptions

- Population distribution among the vibrational levels of a given mode β can be described by means of a Boltzmann vibrational temperature T_β. In fact, the energy redistribution process between those levels is fast enough for the mode to be considered in local Boltzmann equilibrium [5].

- The five Boltzmann factors $\mathrm{Exp}[-hc\nu_\beta / kT_\beta]$ which we will denote by β (β = s, b, a, n, w) thus constitute a good description of the state of population on the various vibration modes.
- The gas kinetic temperature T determines population distribution among the rotational sub-levels of a given vibrational level, because of the strong coupling between translation and rotation in the present operating conditions [6], [7].
- Our calculation is based on the P(20) laser transition in the $00^01 \rightarrow 10^00$ (10 μm) band, that particular vibration-rotation line being dominant in the considered gas temperature range.
- The high gas flow velocity (~100m.s^{-1}) is such tat one can neglect pressure variations along the tube, as well as molecular dissociation effects.
- All operating parameters are considered as functions of the only axial coordinate z, their dependence with respect to radial coordinates being neglected. There is experimental evidence that for this kind of lasers, the approximation is fairly good [8].

2.3. Differential equation system

The evolution along the tube axis of the five Boltzmann factors s, b, n, w, the gas temperature T and the light intensities I^+ and I^- can be modeled through a set of eight coupled differential equations [1]. The system reads as follows:

$$\frac{v}{(1-s)^2}\frac{ds}{dz} = R_{sb}\frac{(b^2 D_{s,b} - s)}{(1-b)^2(1-s)} + \Gamma + U_s \tag{1}$$

$$\frac{2v}{(1-b)^2}\frac{db}{dz} = -3R_{ab}\frac{(b^3 D_{a,b} - a)}{(1-b)^3(1-a)} - 2R_{sb}\frac{(b^2 D_{s,b} - s)}{(1-b)^2(1-s)} - R_{bw}\frac{(b D_{w,b} - w)}{(1-b)(1-w)} + 2R_b\frac{(\bar{b} - b)}{(1-b)} + U_b \tag{2}$$

$$\frac{v}{(1-a)^2}\frac{da}{dz} = R_{an}\frac{(n D_{a,n} - a)}{(1-n)(1-a)} + R_{aw}\frac{(w D_{a,w} - a)}{(1-w)(1-a)} + R_{ab}\frac{(b^3 D_{a,b} - a)}{(1-b)^3(1-a)} - \Gamma + U_a \tag{3}$$

$$\frac{v}{(1-n)^2}\frac{dn}{dz} = -R_{na}\frac{(n D_{a,n} - a)}{(1-n)(1-a)} + R_{nw}\frac{(w D_{n,w} - n)}{(1-w)(1-n)} + R_n\frac{(\bar{n} - n)}{(1-n)} + U_n \tag{4}$$

$$\frac{v}{(1-w)^2}\frac{dw}{dz} = -R_{wa}\frac{(w D_{a,w} - a)}{(1-w)(1-a)} - R_{wn}\frac{(w D_{n,w} - n)}{(1-w)(1-n)} + R_{wb}\frac{(b D_{w,b} - w)}{(1-b)(1-w)} + R_w\frac{(\bar{w} - w)}{(1-w)} + U_w \tag{5}$$

$$\frac{N_0}{N_A}\left(f_c C_c + f_n C_n + f_h C_h + f_w C_w\right) v_0 \frac{dT}{dz} = -h(\nu_a - \nu_n) N_a R_{an}\frac{(n D_{a,n} - a)}{(1-n)(1-a)} - h(\nu_a - \nu_w) N_a R_{aw}\frac{(w D_{a,w} - a)}{(1-w)(1-a)}$$

$$- h(\nu_a - \nu_b) N_a R_{ab}\frac{(b^3 D_{a,b} - a)}{(1-b)^3(1-a)} - h(\nu_s - \nu_b) N_s R_{sb}\frac{(b^2 D_{s,b} - s)}{(1-b)^2(1-s)} - 2h\nu_b N_b\frac{(\bar{b} - b)}{(1-b)} + F_e \tag{6}$$

$$\frac{dI^+}{dz} = \left(\alpha - \alpha_{sc}\right) I^+ \tag{7}$$

$$\frac{dI^-}{dz} = -\left(\alpha - \alpha_{sc}\right) I^- \tag{8}$$

2.4. Boundary conditions

At z=0, the gas temperature T is equal to T_0 , and Boltzmann factors are evaluated on the basis of Boltzmann temperatures equal to the gas kinetic temperature T_0, since no pumping has occurred yet . Hence:

$$\beta(0) = \exp[-hc\nu_\beta/kT_0] \quad \text{with } \beta = s, b, a, n, w. \tag{9}$$

As regards I^+ and I^- , they have to fulfil the following conditions, imposed by the output mirrors reflectivities:

$$I^+(0)=r_1 I^-(0)= (1-\alpha_1-\tau_1) I^-(0) \tag{10}$$

$$I^-(l_{flow})= \tau_2 I^+(l_{flow})= (1-\alpha_2-\tau_2) I^+(l_{flow}) \tag{11}$$

2.5. Computational method used

We use a numerical method where a set of equally spaced points $z= i\,\Delta z$($0 \le i \le N_p$ is generated along the interval $[0, l_{flow}]$ with a step size $\Delta z = l_{flow}/N_p$. Any z-dependent parameter p will be determined as an array of values $p_i=p(z_i)$, In differential equations $\frac{dp}{dz}(z_i)$ is replaced by $\frac{p(z_{i+1})-p(z_i)}{\Delta z}$ The step size Δz is progressively reduced, increasing the number N_p of data points to be handled. We stop the process when a stationary solution is reached, in the sense that any further reduction of Δz that any further reduction of doesn't change the obtained parameters distributions.

3. Results and discussion

The present simulation was performed using parameters listed in table.I. The gas mixture proportions, pressure and entrance flow velocity have been set identical to those in the experimental set-up described by Sugawara *et al* .[2], with slightly reduced tube dimensions.

We adopt a very commonly used value of $3\ 10^{-16}$ V cm^2 for the self-sustained reduced electric field strength E/N. it guarantees an optimal energy transfer from the discharge to the upper level (00°1 of CO_2) through efficient population of N_2 vibrational level v=1. In a such configuration, the discharge electrons have an average energy $E_{e(av)}$ of 1.2 eV. On that basis, their number density N_e can be estimated using formula $N_e = 4i/(\pi d^2 e v_{drift})$, where v_{drift} is the electrons drift velocity taken as $(2E_{e(av)}/m_e)^{1/2}$, m_e being the electron rest mass. Here, $v_{drift} = 6.5\ 10^5$ m s^{-1}, and $N_e = 5.910^8$ cm^{-3} , while the gas mixture number density N is $6.6\ 10^{17}$ molecules per cubic centimetre.

Table I: Operating specifications of the simulated setup

Considered laser transition line	P(20), 10,6 µm
Tube length l_{flow}	60 cm
Positive column length l_{pc}	50 cm
Tube diameter d	5 cm
Coupling mirrors transmittivities (τ_i) and absorptivities (α_i)	
$M_1 : \tau_1 = 0, \alpha_1 = 0$ $\quad M_2 : \tau_2 = 0.2, \alpha_2 = 0$	
Scattering loss per unit length α_{sc}	0
Entrance gas mixture pressure P_0	20 Torr
Entrance gas flow velocity v_0	100 m s^{-1}
Entrance gas mixture temperature T_0	293 K
$CO_2/N_2/He/H_2O$ gas mixture proportions	
$f_c = 0.04$ $\quad f_n = 0.4$ $\quad f_h = 0.56$ $\quad f_w = 5\ 10^{-5}$	
Discharge parameter E/N	$3\ 10^{-16}$
Discharge current intensity i	120 mA

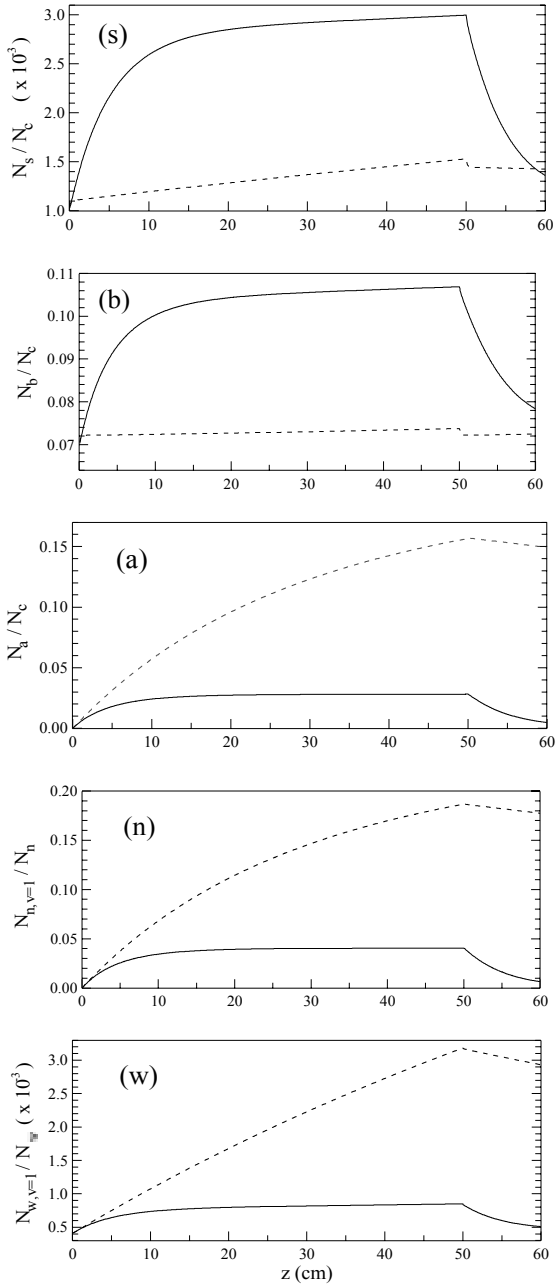

Figure 2. Relative first vibrational level population distribution along the tube, for each of five the vibrational modes s, b, a, n, and w. Dashed-line curves indicate the unsaturated regime case.

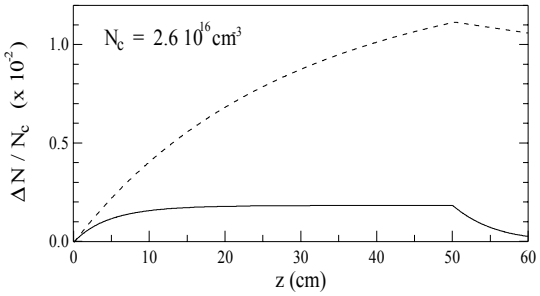

Figure 3. Distribution of CO_2 population inversion ratio along the tube, in both unsaturated (dashed –line curve) and oscillation (solid-line curve) regimes.

The obtained five Boltzmann factors distributions (s, b, a, n and w) lead to relative first vibrational level population profiles displayed in Figure 2. For each modeβ, the characteristic temperature $\theta_\beta = hc\nu_\beta/k$ is indicated. The relative first vibrational level populations $N_{\beta,v=1}$ /$N_{species}$ are respectively given by the expressions: $s(1-s)(1-b)^2$ (1-a), $2b(1-s)(1-b)^2(1-a)$, $a(1-s)(1-b)^2$ (1-a), n(1-n) and w(1-w).

The evolution along the tube axis of population inversion density ΔN between CO_2 laser levels 00°1 and 10°0, divided by the CO_2 number density N_c , is shown in Figure 3. Absolute population inversion density $<\Delta N>$ is $2.01x10^{14}$ cm^{-3} (resp. $3.90x10^{13}$), the average CO_2 number density $< N_c >$ being $2.61x10^{16}$ cm^{-3}. Our results concerning $< \Delta N >$ in the unsaturated regime compares to measurements performed by the authors of ref. [9], who found $2.5x10^{15}$ cm^{-3} in similar experimental conditions (3/38/59 $CO_2/N_2/He$ gas mixture with P= 50 mbar, d = 19 mm and i = 50 mA).

It is interesting to note the proportions of vibrationally excited molecules in the active medium. In the case of CO_2, the proportions is given by $[1-(1-s)(1-b)^2(1-a)]$, while it is simply represented by Boltzmann factors n and w for N_2 and H_2O. We find respective averaged proportions of excited CO_2 ,CO_2, N_2 and H_2O of 0.140, $3.46x\ 10^{-2}$ and $7.79x\ 10^{-4}$ (resp. 0.227,0161 and $2.10x\ 10^{-3}$) in the oscillation (resp. unsaturated) regime. The proportions of excited CO_2 molecules in pure vibration modes s, b are expressed as $s(1-b)^2(1-a)$, b(2-b)(1-s)(1-a) and a $(1-s)(1-b)^2$. Their respective average values, are found to be $2.59\ x10^{-3}$, 0.109 and $2.39\ x10^{-2}$ (resp. $1.34x\ 10^{-3}$, $7.83x\ 10^{-2}$ and 0.133) in oscillation (resp. unsaturated) regime.

Conclusion

We report on the application of six-temperature kinetic model predicting the operational characteristics of a fast –axial –flow CO_2 laser in a linear cavity configuration. The active medium consists of a $CO_2/N_2/He/H_2O$ Gas H_2O gas mixture and is pumped by a longitudinal self-sustained electric discharge.
We determine the evolution along the tube axis of the state of population in each of the five vibration modes involved in the laser process (the three normal modes of CO_2, the N_2 mode and the H_2O bending mode).
A system of eight coupled differential equations is numerically solved for that purpose. The gain spatial distribution and the laser power extracted from the cavity are deduced. Comparison of the results of our simulation to reported experimental performance achieved with similar lasers [2]-[4] is quite satisfactory.

References

[1] R. E. Beverly III, "kinetic modeling of a fast-axial-flow CO_2 laser" Opt. Quant. Elect., **14**, 25 (1982)
[2] H. Sugawara, et al, Rev. Laser Eng. (Laser Soc. Japan) **9**, 21 (1981)
[3] S. Müller and J.Uhlenbusch, "Influence of turbulence and convection on the output of a high-power CO_2 laser with a fast axial flow", J. Phys.D: Appl. Phys**. 20**, 697 (1987)
[4] M.G. Baeva and P.A Atanasov, "Numerical investigation of cw CO_2 laser with a fast turbulent flow" J. Phys. D: Appl. Phys. **26**, 546 (1993)
[5] R. K. Preston and R. T. Pack, "Mechanism and rates of rotational relaxation of CO_2 (001) in He and Ar*"* J. Chem. Phys**.,69**, 2823 (1978)
[6] J. E. Lambert,Vibrational and Rotational Relaxation in Gases, (Oxford: Clarendon Press, (1977)
[7] B. P. Lavrov and D.K. Otorbaev "Relation between the rotational temperature and gas temperature in a low-pressure molecular plasma", Sov. Tech.Phys. Let., **4**, 574, (1978)
[8] C. Carlhoff, et al Proc.Gas Flow and Chemical Lasers, 621 (New York: Plenum, 1984)
[9] M. Spiridonov et al , " Investigation of the active medium of a direct –current-excited fast –axial-flow CO_2 laser using a tunable diode laser,", J. Phys.D: Appl. Phys., **27**, 962 (1994).

Plasma processing at atmospheric pressure using a dielectric barrier discharge (DBD)

G. Borcia, N. M. D. Brown and C. A. Anderson

Surface Science Laboratory, University of Ulster, Coleraine, Northern Ireland, UK

Abstract

The effects of the air dielectric barrier discharge on surface treatment are reported for various polymer materials in the form of thin films and fabrics. XPS, contact angle/wickability measurement and SEM techniques were used in the study of the surface properties. The stability of the modified samples was monitored for two weeks after the treatment. The influence of the discharge parameters is discussed and related to the surface characteristics, allowing optimisation of the parameters used for treatment in the DBD.

1. Introduction

Chemical processes occurring in cold non-equilibrium discharge plasmas find increasing applications in various materials processing technologies. Among these techniques the dielectric barrier discharge (DBD) is one of the most effective non-thermal plasma sources, with an effective conversion of electric field to chemical and physical processes in gases or on surfaces for many applications. Importantly, it offers the major advantage of inducing significant surface chemical modifications on a material exposed to the discharge at atmospheric pressure.

For most of the industrial applications concerned barrier discharges are operated in the filamentary mode. In the past much effort has been dedicated to obtaining DBDs running in the homogenous glow regime. While it has been demonstrated that homogenous diffuse discharge behaviour can be obtained in barrier discharge configurations, special, quite restrictive conditions are required. Indeed, until recently it has been difficult and tricky to control reliably homogeneous glow discharges running at atmospheric pressure. Such diffuse discharges have obviously advantages over the more common filamentary type, especially for the uniform activation of material surfaces on the entire area exposed to the discharge.

However, the filamentary DBD is demonstrably an excellent source of microdischarges containing energetic electrons and ions. Discharges of this type, for which reliable control and significant average power densities can be achieved more easily, provide a chemically mild and mechanically non-destructive means of modifying surface properties targeting improved performance of materials. Moreover, ways can be found to ensure that the apparent inhomogeneity of the filamentary DBD does not lead to operational disadvantage.

Taking into account these issues, we describe here a surface treatment technique using a DBD of random filamentary type as a very convenient tool for the controlled activation of various categories of material surfaces. Remarkably uniform treatment and stable modified surface properties result on the entire treated area of the test surfaces. Moreover, the experimental set-up allows the simulation of continuous high speed processing of samples associated with in-line applications.

2. Experimental

The in-house designed and built dielectric barrier discharge system used is presented schematically in Figure 1. The sample is mounted on an electrically grounded, precision bearing mounted, aluminium cylinder. During the treatment a motor rotates the grounded electrode, so allowing the materials to be treated to pass through the discharge region between the electrodes with linear speeds in the range 60-9500cm/s. Experiments have shown that DBD treatments even as short as a few rotations (i.e. fractions of a second exposure time) can modify markedly the surface properties of the treated specimen.

The discharge is generated via a low frequency (80KHz) high voltage (peak-to-peak values in the 10-20KV range) power supply. The high voltage is applied between the cylinder and a spiral-shaped stainless steel electrode fitted inside a water-cooled quartz tube mounted above the grounded electrode. The inter-electrode gap is adjustable within a range $\leq$ 2.2mm. The latter is the practical upper limit that ensures a uniformly distributed random discharge over the width of the test sample.

The discharge region thus created ensures uniform treatment (as will be shown) over the entire surface (i.e. about 10 x 30 cm^2) of both porous and non-porous test samples, even though the DBD in the present electrode configuration is clearly of the random micro-filamentary type.

The discharge was characterised, when the power supply is optimally tuned, by means of the energy deposited at the electrodes during one cycle of the DBD. Measurements performed over the range of variation of the high-voltage input and for various values of the inter-electrode gap showed that the resulting energy surface density in the present experimental arrangement is of the order of $10\text{-}10^2 \mu J/cm^2$.

An extended series of treatments was performed on various types of commercial polymer films (Goodfellow Ltd., Cambridge), chosen from two main categories: a) polymers which do not contain oxygen in their chain: ultra-high density poly(ethylene) (UHMW PE), high density poly(ethylene) (HDPE), low density poly(ethylene) (LDPE), poly(styrene) (PS), poly(methylpentene) (PMP); poly(tetrafluorethylene); b) polymers which already contain structurally bonded oxygen in their chain: poly(amide) 6 (PA 6), poly(amide) 6,6 (PA 6,6), poly(amide) 12 (PA 12), poly(ethylene terephthalate) (PET). Woven commercial polyester (PET) and Nylon 6,6 fabrics (Clark & Sons, Ltd, UK) were also treated.

Treatments were systematically performed for two different values of the energy of the discharge (the energy deposited by the DBD during one cycle of the high-voltage), i.e. 3.5mJ and 5.0mJ, and various treatment times between 0.1s and 5.0s. A first series of treatments, on poly(ethylene) films, performed for different values of the inter-electrode gap, showed no significant influence of this parameter on the surface properties. For all other experiments the gap was fixed at 1.8 mm.

During treatment the samples were placed either directly on the grounded aluminium cylinder or on an additional thin polymer (polyethylene) film intimately contacting the cylinder. These two experimental configurations, as is shown later, led of to very different consequences in respect of the outcome of the treatment on samples of woven fabric.

The modification of the surface properties of the treated samples has been studied using X-ray photoelectron spectroscopy (XPS), contact angle/wickability measurement and scanning electron microscopy (SEM). The stability of the modified samples was monitored for two weeks after the treatment.

3. Results and discussions

Figure 2 shows an example of the values of the contact angle measured on a UHMW PE film treated for a set of fixed discharge parameters (5.0mJ energy, 1.8mm gap) and various treatment times, as a function of the ageing time. The contact angle observed is found to change from 103.6º for the untreated sample to the lowest value of 49.3º associated with the 5.0s treated sample, i.e. more than 50% reduction from the initial value.

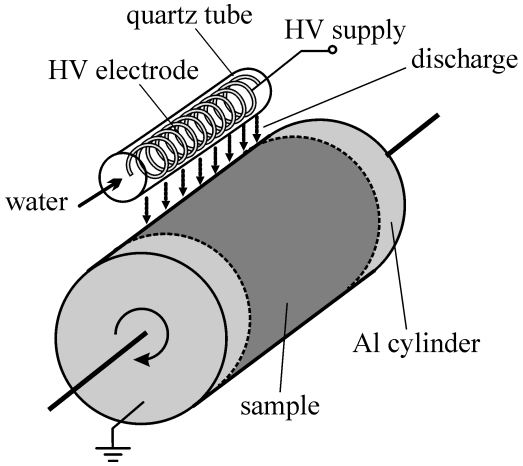

Figure 1. DBD set-up.

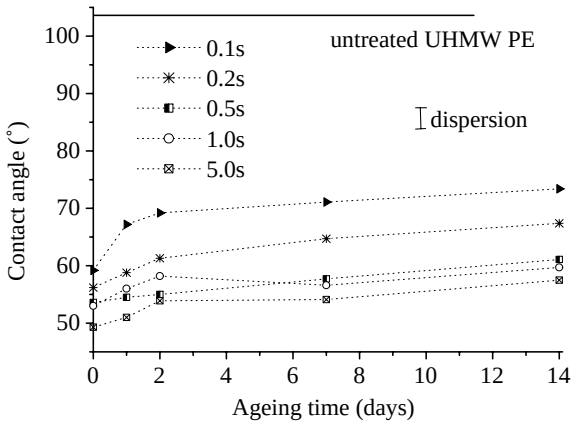

Figure 2. Contact angle of water on UHMW PE film vs. treatment time and ageing (5.0mJ discharge energy).

The steep diminution of the contact angles on treated samples compared to the non-treated PE shows the strongly increased wettability induced by the air-DBD even after such short treatment times. This behaviour can be attributed to strong surface oxidation. The molecular oxygen in the contacting air is activated, ionised and dissociated in the discharge to give extremely reactive oxygen species that react readily with the substrate surface.

The same behaviour is observed for all the various polymer films treated (Table 1). Even polymer surfaces that are quite “polar” before treatment, as with the polyamide (PA) or poly(ethylene terephthalate)

(PET) films (of intrinsically lower contact angles for the untreated surface compared to that of the other polymers examined), show much increased wettability after DBD treatment.

The surface modification reaches a steady level after only 0.1-0.2s of treatment, suggesting the modification of the outermost layer of the surface be extremely fast under the present experimental arrangement and discharge conditions. For most of the treated polymers the level of additional modification of the surface wettability achieved for treatment times greater than 1.0s is not significant. Even if lower contact angles were measured in a few cases after increased DBD exposure, i.e. 5.0s, the recovery of the surface, post-treatment, leads to comparable levels of wettability for all surfaces treated for more than 1.0s.

Here the particular behaviour of the PTFE films should be stressed, showing a rather low degree of wettability improvement after DBD exposure (Table 1). Complementary treatments on PTFE films extended up to 20s still showed a very low degree of modification. This is not too surprising, given that PTFE films generally are held to be very resistant to plasma modification.

It follows, therefore, that the DBD regime presented here induces significant modifications of the surface properties of the substrates so treated at a very high rate within the first few fractions of second. Treatments longer than 1.0s do not seem justified in terms of cost and duration of processing, as further modification at the surfaces examined takes place at a diminished rate and, thereafter, actual surface degradation processes are very likely to interfere.

Another important outcome concerns the spatial uniformity of the DBD surface treatment. The dispersion of the contact angle values measured over extended areas of all the treated polymer film samples is of only 3-4°, which is within experimental error, and leads to the conclusion that the surface treatment is remarkably uniform.

Referring to Figure 2, the treated poly(ethylene) film partly recovers after treatment. The contact angle reverted by 5º - 10º towards that of the untreated state over a period of several days. As expected, the material never fully returns to the untreated state, i.e. any necessary storage post-processing for significant times is not seen as an operational problem.

Moreover, since all the treated polymer surfaces show a notably low extent of recovery post-processing during ageing (with measured contact angles still having a similar low dispersion) it was concluded that the surface is not degraded after such short treatments and the resultant modification of the surface properties is stable with time.

Furthermore, topographical images obtained by atomic force microscopy (AFM), but not further discussed here, confirmed that treatments of up to a few seconds duration do not lead to damage at the surface by the etching effects alluded to above.

The XPS technique was used to elaborate the previous results, which suggested a strong oxidation level at the surface of the DBD treated samples, i.e. increased hydrophilicity followed DBD treatment in air.

Figure 3 shows, as an example, the C(1s) XPS band of a UHMW PE sample before and after surface processing for 1.0s in the DBD where the obvious changes in the band profiles reflect the effects of the oxidation of the sample surface.

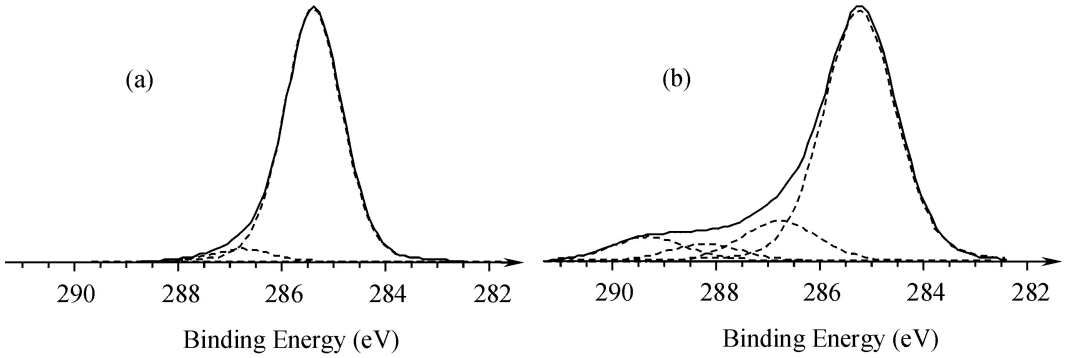

Figure 3. Carbon (1s) XPS spectra for (a) untreated and (b) 1.0s (5mJ energy) treated UHMW PE film.

The C(1s) band of the untreated sample can be fitted with two peaks. The hydrocarbon signal shows a peak at 285.0eV. The second peak at 286.5eV represents the intrinsic low-level oxidised carbon centres on the PE surface, attributed to carbon singly bonded to oxygen. The atomic elemental composition yields an O/C ratio of 0.05/1, ~5% carbon bound to oxygen.

Following DBD treatment, the higher binding energy carbon species increase and additionally oxidised species also start to appear. Thus, the C(1s) band now shows a long tail extending to ~291.5eV to the high-energy side. At the same time, the total oxygen content also increases, yielding an O/C ratio up to about 1/1. The C(1s) envelope of the modified surface can now be fitted with four peaks, by introducing two new, more oxidised, carbon species, i.e. ketone [-(C=O)-] and/or acetal [-(O-C-O)-] carbons at 288.0eV, and carboxyl carbon [-(C=O)-O-] at 289.6eV.

For the same duration of treatment the extent of oxidation further increases the higher the energy deposited by the discharge. Correspondingly, with increasing processing times the oxidised carbon components continue to increase then level off with overly extended treatment.

The same increase in the level of surface oxidation with increasing treatment parameters (energy and time) is observed for most of the other polymer films processed (Table 2). In all cases, the most marked parameter dependence is on the duration of the DBD treatment.

Surface oxidation after DBD processing is particularly strong in the case of polymers that do not initially contain oxygen in their monomer unit. As expected, the increase in the oxygen content is less important for the more "polar" polymers, i.e. those which already contain structurally bound oxygen before DBD treatment. Nevertheless, it is clear that the DBD treatment creates oxidised functional groups even on these surfaces.

Here again the particular behaviour of the PTFE film is noted. Very limited modification is apparent in the XPS data concerned, even less than that indicated by contact angle measurement. After treatment as extended as 20s the oxygen level on the surface is found never to reach more than 1%.

On all the other types of polymers addressed here (even those already containing oxygen in their monomer unit) the initial rate of bound oxygen uptake for the untreated surfaces processed for 0.1s is very high compared to the subsequent uptake for treatments of up to 5s.

This behaviour correlates with the contact angle measurements and confirms that treatments with duration of one second to maximum a few seconds represent an optimum for acquiring major surface modifications. Surfaces which cannot be processed within such short intervals arguably will not show further change in their surface properties after more extended treatment.

	untreated	0.1s	0.2s	0.5s	1.0s	5.0s
UH PE	103.6	59.2	55.6	55.0	53.0	49.3
HDPE	108.1	63.6	63.1	58.6	54.3	52.5
LDPE	102.2	66.1	63.0	58.8	57.7	54.3
PMP	113.2	83.4	72.6	70.0	68.1	65.0
PS	91.1	52.7	49.8	48.5	45.6	42.8
PTFE	124.8	103.8	99.8	96.0	95.1	89.4
PA 6	69.4	32.4	31.3	27.5	26.3	25.3
PA 6,6	80.6	40.7	35.3	28.3	27.6	20.3
PA 12	101.7	65.1	56.8	52.9	43.6	38.6
PET	84.9	61.9	42.5	40.0	39.0	37.3

Table 1. Contact angle of water (θº) on the various polymer films vs. treatment time (5mJ energy).

	untreated	0.1s	0.2s	0.5s	1.0s	5.0s
UH PE	0.5	21.9	29.1	36.9	40.5	45.9
HDPE	2.5	20.4	24.6	30.2	33.1	40.4
LDPE	0.2	22.8	25.6	31.0	35.4	40.4
PMP	0.2	18.9	22.0	27.0	28.4	32.5
PS	0.1	21.8	24.5	24.5	25.2	27.0
PTFE	0.0	0.6	0.6	0.8	0.8	0.9
PA 6	13.5	19.3	19.9	20.6	20.7	24.8
PA 6,6	11.7	21.1	21.9	22.4	22.6	25.0
PA 12	10.3	14.4	21.8	22.4	23.7	29.6
PET	33.4	39.3	40.2	40.7	42.9	44.0

Table 2. Oxygen content (in atom %) on the various polymer films vs. treatment time (5mJ energy).

The conclusions drawn from the results obtained by wickability measurement on treated fabric samples (Table 3) were very similar to those obtained from the wettability data of polymer films.

For example, the water rise time on the polyester fabric (measured as the rise time of distilled water up to 2cm on the vertically positioned sample) is found to decrease from 19.0s for the untreated sample, to the lowest value of 7.0s associated with the 5.0s treated sample, representing about a 60% reduction from the initial value. The increase in wickability for the Nylon fabrics is even more dramatic, emphasised by water rise times of about 10-20s on the treated samples, in marked contrast to the rise level of not more than 0.5cm reached (over more than 15min) on an untreated vertically positioned sample. This steep diminution of the rise time compared to the non-treated fabric shows the strong increase of the wickability induced by the DBD exposure after very short treatment times and also confirms the very high rate of surface modification within the first 0.1-0.2s of treatment on fabric samples. Any subsequent modification for longer treatment (more than ~1.0s) is less important.

Wickability measurements repeated two weeks after the treatment on DBD-treated fabrics stored under ambient conditions showed no evidence of significant recovery of the surface properties in that the stored samples then having a wickability comparable with that evaluated immediately after DBD processing.

Note here again that during treatment the fabric samples were placed either directly on the grounded aluminium cylinder or on an additional thin polymer (polyethylene) film intimately contacting the cylinder. Importantly, XPS analysis was performed on both sides of the fabric samples, i.e. the one directly exposed to the discharge and the other side facing the grounded electrode during treatment.

As already noted, the polyester and the Nylon (PA 6) are intrinsically oxygen-rich materials prior to DBD treatment. Nevertheless, it is clear that the DBD treatment creates additional oxidised functional groups (not discussed further here) on the side of the fabric directly exposed to the discharge, i.e. the total oxygen content is shown to increase (Table 4). The initial rate of oxygen uptake of the untreated fabric for the 0.1s treated sample is very rapid, while the subsequent uptake for treatments up to 1.0s is practically negligible.

	polyester						nylon					
Substrate	untreated	0.1s	0.2s	0.5s	1.0s	5.0s	untreated	0.1s	0.2s	0.5s	1.0s	5.0s
on cylinder	19.6	11.5	9.0	8.5	7.5	7.0	>15min	57	48	42	22	19
on polymer	19.6	10.0	10.0	9.5	8.0	7.5	>15min	28	25	22	15	9

Table 3. Wickability of fabric samples (estimated as the water rise time to 2cm on the vertical positioned fabric, in seconds), vs. treatment time and the substrate placed (see text) on the grounded electrode (5.0mJ discharge energy).

The evolution shown in the behaviour of the side of the sample facing the grounded electrode during treatment is also very interesting. This side too is oxidised. In this case the amount of oxygen on the surface was found also to increase with increasing processing time. In contrast, when the fabric is processed with the additional polymer film in place, the degree of oxidation on the side directly exposed to the discharge levels out after 0.2-0.5s of treatment, behaviour mirrored in the fabric face contacting the electrode.

	Substrate	0.1s		0.2s		0.5s		1.0s		5.0s	
		top face	bottom face	top face	bottom face	top face	bottom face	top face	bottom face	top face	bottom face
polyester (34.9% at. O)	cylinder	43.2	34.0	45.4	35.7	46.8	39.6	48.8	43.6	49.4	45.2
	polymer	40.0	38.3	46.4	39.9	46.0	46.4	49.7	48.2	50.1	49.5
Nylon (18.4% at. O)	cylinder	29.6	18.9	31.5	20.7	32.6	24.2	33.2	29.7	34.1	31.4
	polymer	27.4	22.5	32.1	28.4	33.5	31.8	34.0	33.3	34.9	34.2

Table 4. Oxygen content (in atom %) on the fabric surface, as a function of the treatment time and the substrate placed on the grounded electrode (5.0mJ discharge energy), with and without the interposed polythene film present (see text).

This behaviour is a consequence of the dielectric properties of the polymer film in contact with the aluminium cylinder. In this configuration, as alluded to above, the additional dielectric surface spreads the micro-discharge channels into surface discharges covering a much larger local area than do the original discharge channels present when the bare grounded aluminium alone supports the fabric.

For porous materials, such as the textile fabrics, rapid treatment (fractions of a second) on both sides of the sample appears to be ensured, i.e. the discharge readily permeates the fabric weave.

It should be noted that the behaviour of the polyester and Nylon fabrics discussed here is very similar to the behaviour, under the same DBD treatment, of compact film variants of the same polymeric materials - polyester PET and Nylon 6,6 (PA 6,6) films, respectively - showing the same trend in the evolution of the surface composition.

The SEM analysis of the fabrics gave valuable supplementary information on the role of the additional polymer film placed on the grounded electrode during surface processing (Figure 4).

Images show that for samples placed during treatment directly on the grounded aluminium cylinder a very localised strong degradation of the fabric takes place, with fibres melting at the locations were the bundles of fibres are crossing each other (Figure 4.b). The effect is most probable due to the non-homogeneity of the discharge, with the micro-discharges tending to localise on spots where they can reach directly the grounded electrode directly. This behaviour can be seen as a type of corona effect where the channels at the

yarn crossover points in the fabric promote a localised more energetic discharge than the norm. The degradation is readily visible even using very short treatment times, showing locally the violent effect of the DBD discharge. For extended treatment, longer than about one second, the degradation is "complete", i.e. all crossing locations are attacked and the fibres in the yarn contiguous with these points melt (Figure 4.b).

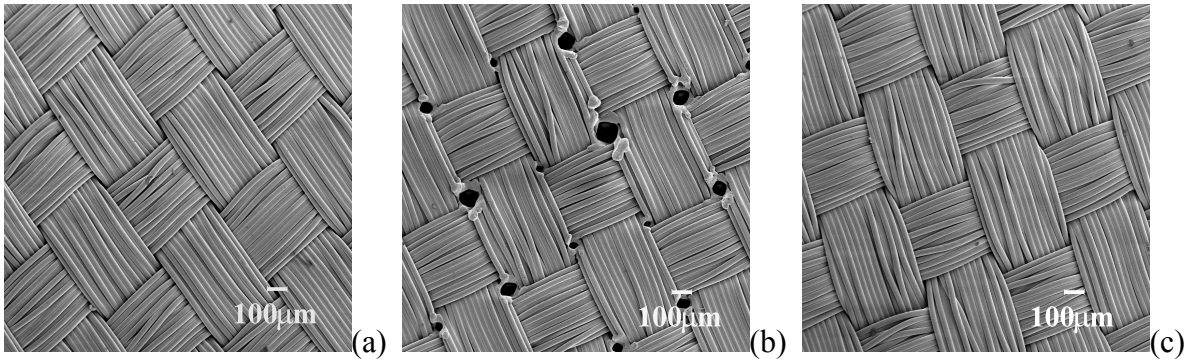

(a) (b) (c)

Figure 4. SEM images of nylon fabric: (a) untreated, (b) 1.0 s air-DBD treated, placed directly on the grounded cylinder, (c) 1.0s air-DBD treated, placed directly on the additional polymer film.

The results are very different for the fabric samples placed on the additional thin polymer (polyethylene) film, so the grounded electrode is electrically isolated from the discharge. In this case no visible degradation of the fabric takes place. Samples show no visual difference compared to the untreated case (Figure 4.a), even for extended treatment duration, e.g. 1.0s (Figure 4.c).

This result offers a very attractive perspective for controlling the physical modification of non-compact materials and also shows that uniform, mild and efficient modification of surface properties can be obtained by DBD processing for samples with various texture, porosity etc.

4. Conclusions

The experiments show that air dielectric barrier discharge (DBD) surface treatments exert significant effects on the surface characteristics of various polymer films and on polymer fabric materials.

The results obtained underlined the utility of this type of surface processing for modifying the surface properties of materials, as the present experimental arrangement shows a highly efficient ability to modify in a very *uniform* way the surface of all the materials so far examined in detail. The surface properties, such as wettability, wickability and the level of oxidation appear to be increased markedly within the first 0.1-0.2s of treatment; moreover, any subsequent modification for longer treatment times (> 1.0s) is less important. The modification of the surface properties also appears to be stable with time, as minimal change (recovery) of the surface properties is shown on ageing post-exposure to the discharge.

The behaviour in respect of oxidation of the thin film polymers studied here in woven fabric form is found to be very similar under DBD treatment, to that of the same materials as thin films.

For porous materials, such as the textile fabrics examined, rapid, efficient and simultaneous treatment (fractions of a second) of both sides of the sample appears to be ensured.

The processing system also offers the attractive prospect of controlling the physical modification of non-compact materials of various texture, porosity etc., as the samples placed on an additional polymer film and treated in the DBD show no evidence of physical damage under the processing conditions used. In contrast, at higher power levels, evidence for a local melting phenomenon is found with woven materials if treated using a bare metal grounded electrode.

Taking into account the above commentary, the present surface treatment technique, using a DBD of random filamentary type, offers a convenient, reliable and economic alternative for the controlled surface modification (so far, largely dependent on surface oxidation) of different types of materials. Remarkably uniform treatment and markedly stable modified surface properties result over the entire area of test surfaces exposed to the DBD even at transit speeds simulating those associated with continuous processing expectations even at relatively high speeds. DBDs thus provide chemically mild and mechanically non-destructive means of altering surface properties targeting improved surface characteristics.

Authors acknowledge support for this work from Invest Northern Ireland.

ON THE ROLE OF PLASMA FORMATION GAS AND DISCHARGE CHAMBER GEOMETRY ON CHARACTERISTICS OF THE D.C. ARC PLASMA TORCH WITH HOLLOW CYLINDRICAL ELECTRODES

A.F. Bublievsky[1], D.A.Bublievsky[1,2],. E.I. Urinok[1]

[1] *The Luikov Heat & Mass Transfer Institute NANB, Minsk, Rep. Belarus*
[2] *Instituto de Física, Universidade Estadual de Campinas, Campinas, São Paulo, Brazil*

In spite of wide application of the plasma torches with hollow cylindrical electrodes, the methods applied for their designing are imperfect due to the phenomena complexity. The methods of physical modeling, based on similarity theory, using an experimental data, are applied widely in this case. However, during the selection of similarity numbers, the sufficiently subjective methods of dominant processes determination are usually used. In present work, for this limitation overcoming, the statistical treatment methods together with a wide original selection of generalized parameters are applied, thus taking into account all processes affected on arc characteristics.

The data statistical treatments for air, nitrogen, hydrogen, helium and argon demonstrated that obtaining of single generalized characteristic for all gases with high accuracy is quite difficult. Reducing accuracy requirements, it is possible to find the arc generalized current-voltage characteristics (CVC) with one independent variable (convective heat transfer), with two ones (convection and turbulence) or, if discharge chamber geometry was considered, with three independent variables. The appropriate generalized CVC have next forms:

$$\frac{\sigma_0 UD}{I} = 2{,}5\left(\frac{\sigma_0 h_0 GD}{I^2}\right)^{0{,}610}, \text{ SE} = 0.335 \qquad (1)$$

$$\frac{\sigma_0 UD}{I} = 1{,}46\left(\frac{\sigma_0 h_0 GD}{I^2}\right)^{0.398}\left(\frac{\rho_0\sigma_0 h_0^{1.5} D^3}{I^2}\right)^{0.218}, \text{ SE} = 0.207 \qquad (2)$$

$$\frac{\sigma_0 UD}{I} = 1.475\left(\frac{\sigma_0 h_0 GD}{I^2}\right)^{0.400}\left(\frac{\rho_0\sigma_0 h_0^{1.5} D^3}{I^2}\right)^{0.208}\left(\frac{d}{D}\right)^{0.151}, \text{ SE} = 0.193 \qquad (3)$$

where U - voltage; I - electric current; G - gas flow-rate; D, d - internal and external electrode diameter, respectively; h - enthalpy; λ - heat conductivity; ρ - density; σ - electric conductivity; SE – regression standard error; index "0" means characteristic value.

In consequence of gas properties variation, the numerical estimate of inadequacy, using Fisher variances ratio, can be made for expressions (1)-(3). This parameter for expression (1) is $F_{inadeq} = 19.9$, for (2) $F_{inadeq} = 32.5$ and for (3) $F_{inadeq} = 30.2$. The values of allowed upper limits for combination of separated expressions into one are 1.95/2.53, 1.76/2.21 и 1.67/2.05, respectively, for case (1), (2) and (3) (numerator is referred to five-percentage probability level, denominator is referred to one-percentage one). Thus the combination into single generalized CVC of plasma torch with hollow cylindrical electrodes for different gases is inadequate.

The generalized dependences for every gas, having considerably higher accuracy then (1)-(3), are obtained too. The effect of discharge chamber geometry on CVC is analyzed.

EXPERIMENTALLY-STATISTICAL STUDY OF D.C. ELECTRIC ARC OPERATING IN THE PLASMA TORCH WITH TUBE ELECTRODES AND AIR

A.F. Bublievsky[1], D.A.Bublievsky[1,2],. E.I. Urinok[1]

[1] *The Luikov Heat & Mass Transfer Institute NANB, Minsk, Rep. Belarus*
[2] *Instituto de Física, Universidade Estadual de Campinas, Campinas, São Paulo, Brazil*

The analysis of physical processes in d.c. plasma torches with two tube electrodes (one of electrodes is closed cathode with diameter D, anode diameter is d) is realized by the methods of physical modeling and mathematical statistic using ridge regression.

The selection of dominant processes is made by the statistical analysis methods using present-day software for PC compatible computer. The wide range experimental data for electrode diameter ($D(d) = 8 - 40$ mm), power ($N = 3.7 - 320$ kW), current ($I = 20 - 760$ A) and gas flow-rate $G = 0.8 - 40$ gs^{-1}) are analysed. Both same electrode diameters $D = d$ and different ones ($D/d = 1.0 - 4.375$) are used for experiments.

It is determined, that the heat transfer processes have dominant role for arc current-voltage characteristics (CVC) formation. The gas-dynamic factors, taken into account by Reynolds number, are insignificant (the standard regression coefficient is about 10 %). At the same time, heat transfer processes (convection, conduction, radiation, turbulent heat transfer) have strong correlation. It is possible to simplify generalized CVC, considering only most effective processes (convection and conduction). The discharge chamber geometry does not affect significantly on CVC, but make difficult generalized characteristic formation.

The generalized CVC, obtained by statistical analysis using ridge regression, have very complex form. If from three correlate independent variables (π_{turb}, π_{cond} and π_{rad}) use only single one, for example, π_{cond} and standard regression, it is possible to simplify expression. The standard error of such regression is SE=0.095, and Fisher variances ratio is $F_{(3.347)} = 6256.6$. The corresponding CVC have next form:

$$\frac{UD\sigma_0}{I} = 3.630\left(\frac{GD\sigma_0 h_0}{I^2}\right)^{0.516}\left(\frac{\sigma_0\lambda_0 T_0 D^2}{I^2}\right)^{0.120}\left(\frac{D}{d}\right)^{0.322}. \qquad (1)$$

By reducing accuracy, it is possible to obtain CVC with one independent variable:

$$\frac{UD\sigma_0}{I} = 1.835\left(\frac{GD\sigma_0 h_0}{I^2}\right)^{0.656}; \qquad \text{SE=0.192,} \qquad F_{(1,349)}=4328.5. \qquad (2)$$

Here, U - voltage; T - temperature; h - enthalpy; λ - heat conductivity; σ - electric conductivity; index "0" means characteristic value.

For quantitative comparison, two groups of experimental data, with the same and different electrode diameters, were separated. The corresponding generalized relations and their analysis are presented.

Non-equilibrium plasma processing of hydrocarbons

K. Schmidt-Szałowski, J. Sentek, K. Krawczyk, J. Ruszniak and K. Radomyska

Faculty of Chemistry, Warsaw University of Technology, Warszawa, Poland

Keywords: Dielectric-barrier discharges; Methane conversion

Abstract

The methane transformation was examined under dielectric barrier discharge (DBD) conditions using a new developed laboratory reactor operated at frequency of 50 Hz. The growth of overall methane conversion and methane conversion rate was observed in the presence of granular dielectrics: quartz-glass and silica gel, in CH_4+Ar gas mixtures at ambient temperature. Ethane and hydrogen were found to be the main gas products. It was concluded that under the conditions of DBD, the methane transformations can be terminated after one of the first steps of the chain reaction where ethane is produced.

1. Introduction

The profits, gained by natural gas (NG) processing, are the reason for a number of searches undertaken on plasma techniques application in the field of hydrocarbon conversion. The hydrogen cyanide manufacturing (developed commercially by I. Mościcki in Switzerland and in Poland) [1] and the acetylene synthesis were the first plasma processes successfully used for the processing of gaseous and liquid hydrocarbons. The arc-process for acetylene production has been implemented in large scale, particularly in Germany (the Huels process) and in the United States (Du Pont). It was highly improved when the modern technique of plasma torch was applied. However, this production has lost some of its importance, over the recent decades, owing to the decreasing demand of acetylene from the industry of chemicals, and the increasing price of electric energy. Taking into account the high energy demand for hydrocarbon processing in arc discharges and plasma torches, other plasma sources, such as low frequency glow and microwave discharges, coronas and dielectric-barrier discharges (DBD), or gliding arc (Glid-Arc) have been investigated. In those discharges, under non-equilibrium plasma conditions, reaction rates are relatively high even at low gas temperatures. The energy of electrons generated in non-equilibrium plasmas is sufficient for transformation of stable hydrocarbon molecules [2-6].

In the last years, a number of investigations were performed on methane processing with DBD as a source of non-equilibrium plasma. The reactions of methane (both pure and in mixtures with helium or ethane were examined at ambient temperature [7] using a simple flat DBD reactor of capacity about 200 cm^3, at low frequency (50 Hz). Considerable methane conversion was observed (more than 20 % with pure CH_4, and about 30 % in mixtures with helium), ethane, ethylene, propane and butane being the reaction products. The methane transformation yield increased in the presence of ethane. It is to note that no acetylene formation was found in these experiments. Also the reactions of methane with carbon dioxide in DBD were studied [8-11]. The experiments [12] were performed in a tubular reactor 54 mm in diameter, 310 mm long, with the discharge space 1 mm wide, at frequencies of 15 to 20 kHz. Methanol was obtained (up to 0.5%) with traces of CH_3OCH_3 in CH_4+O_2 mixtures and ethane (2%) in CH_4+CO_2 mixtures. Various products, such as C_2 hydrocarbons (mainly ethane) and oxygenated ones (formaldehyde, ethylene oxide, dimethyl ether etc.) were obtained, depending on the CH_4/CO_2 ratio in the starting mixture [13]. As has been found [14,15], a direct synthesis of methanol from methane and water vapour may proceed in DBD when ultra-short voltage pulses were applied. The yield of this reaction was, however, very low (<1%). From those examples one can conclude that a number of valuable products may be obtained from methane under the DBD conditions, but it is difficult yet to attain satisfactory yield.

2. Experimental

The methane conversion into higher hydrocarbons was examined under DBD conditions using a new developed laboratory flow reactor operated at atmospheric pressure and the frequency of 50 Hz. The reactor (Fig. 1) was made of a quartz-glass tube (being a dielectric barrier) with an inner metal (aluminium) high voltage electrode. The discharge gap distance was about 3 mm. The outer grounded electrode was made of

aluminium foil adjacent to the quartz tube surface. Inter-electrode voltage was maintained constant at the 18 kV level and the temperature of the reactor was about 45 ^{O}C. The methane conversion was examined in the presence of dielectric materials in the discharge gap: granular quartz-glass and silica gel (the grain size of 1-2 mm). It was found that those materials did not influence the current-voltage characteristics of the discharge. Methane 99,5 % and argon 99,999% were the only components for the starting gas mixtures. The inlet and outlet gas compositions were determined using gas chromatography (GC Agilent 6890N).

3. Results and discussion

The results of experimental series with CH_4+Ar mixtures of 7.5 and 10% methane content, for the gas flow rate 2.7 - 16 Nl/h, are presented (Figs. 2- 6) using the following quantities:

W - flow rate of CH_4+Ar mixture [mmol/h]

$W[CH_4]$ - flow rate of CH_4 [mmol/h]

$W[CH_4]^*$ - flow rate of CH_4 in outlet [mmol/h]

P - discharge power [W], constant for all the measurements (5 W)

Overall methane conversion $$X = \frac{W[CH_4] - W[CH_4]^*}{W[CH_4]} \cdot 100\%$$

Methane conversion rate $$Y = X\, W[CH_4] \cdot \frac{1}{100}$$

Overall specific energy $$E_V = \frac{3600\,P}{W} \quad [J/mmol\ (CH_4+Ar)]$$

Specific energy per methane unit $$E_R = \frac{3600\,P}{W[CH_4]} \quad [J/mmol\ CH_4]$$

Energy efficiency $$\eta_E = \frac{Y}{3600\,P} \quad [mmol\ CH_4/J]$$

The growth of overall methane conversion X and methane conversion rate Y were observed using the packing of granular dielectrics: quartz-glass and silica gel. The energy efficiencies η_E were also increased in the presence of both packing materials. The influence of the packing on the overall methane conversion and conversion into C_2H_6 is shown in Table 1 for the CH_4+Ar mixture (7.5% CH_4) and flow rate 2.7 Nl/h.

Table 1. The influence of the packing on the overall methane conversion and conversion into C_2H_6 for CH_4 + Ar mixture (7.5% CH_4)

Packing	Overall CH_4 conversion X [%]	CH_4 conversion into C_2H_6 [%]
None	33.8	8.4
Quartz-glass	43.5	9.2
Silica gel	38.9	9.2

Under the action of barrier discharges in CH_4+Ar mixtures, ethane and hydrogen were generated as the main gas products with small addition of unsaturated hydrocarbons C_2 (C_2H_2 and C_2H_4). However, a significant part of methane was transformed into non-volatile products - macromolecular compounds or soot (not identified). The overall conversion of methane was evidently higher than the conversion into gaseous (C_2) hydrocarbons. From the fact that the contents of ethane in the gas products were found to be much higher than that of unsaturated hydrocarbons C_2, one may conclude that, for a part of methane involved, after the first steps of the chain reaction (shown in Table 2) while ethane was generated, the transformation path was terminated. There are some points to be considered as a reason for that. The filamentary feature of DBDs seems to be one of them taking into account the action of tiny, short-living microdischarges in surrounding cool gas reagents. On the other hand, it may be the solid surfaces (electrode, wall) acting as chain stoppers which take part in the deactivation of high-energy particles (radicals, excited molecules) in fast heterogeneous processes. It should be added that the high selectivity of ethane formation was observed earlier when methane was converted under the conditions of DBD [7,13] and corona [17].

When granular dielectric packing is present in the discharge gap, the current - voltage characteristics of the discharges are similar to those without packing. However, it should be taken into account that the feature of

the discharges may be modified because of surface discharges occurring on the packing grains. One can conclude that heterogeneous processes on the surfaces of quartz-glass and silica grains paticipate in the overall methane transformation, resulting in the growth of methane conversion rate (not neglecting the role of solid surface as a chain stopper).

Table 2. Chain reactionns of methane [16]

CH_3 radicals and atomic hydrogen formation	$CH_4 + e^- = CH_3^{\cdot} + H^{\cdot} + e^-$
Ethane generation	$CH_4 \rightarrow CH_3^{\cdot} + H^{\cdot}$ $CH_4 + H^{\cdot} \rightarrow CH_3^{\cdot} + H_2$ $2\,CH_3^{\cdot} \rightarrow C_2H_6$
Ethylene generation	$C_2H_6 \rightarrow 2\,CH_3^{\cdot}$ $C_2H_6 + H^{\cdot} \rightarrow C_2H_5^{\cdot} + H_2$ $C_2H_6 + CH_3^{\cdot} \rightarrow C_2H_5^{\cdot} + CH_4$ $C_2H_5^{\cdot} \rightarrow C_2H_4 + H^{\cdot}$
Acetylene generation	$C_2H_4 + H^{\cdot} \rightarrow C_2H_3^{\cdot} + H_2$ $C_2H_4 + CH_3^{\cdot} \rightarrow C_2H_3^{\cdot} + CH_4$ $C_2H_3^{\cdot} \rightarrow C_2H_2 + H^{\cdot}$

Acknowledgement

This work was supported by the State Committee for Scientific Research (KBN);
grant No PZB/KBN/018/T09/99

References

1. R.E. Kirk, D.F. Othmer (ed.), *Encyclopedia of chemical technology*, **4**, (1949), 691
2. A. Czernichowski, *Pure & Appl. Chem*. **66**, (1994),1301
3. C.-J. Liu, R. Mallinson, L. Lobban, *Appl. Catalysis* A: General **178,** (1999), 17
4. M. Okumoto, A. Mizuno, *Catalysis Today* **71,** (2001), 211
5. X. Zhang, B. Dai, A. Zhu, W. Gong, Ch. Liu, *Catalysis Today* **72**, (2002), 223
6. T. Jiang, Y. Li, C.-J. Liu, G.-H. Xu, B. Eliasson, B. Xue, Catalysis Today **72**, (2002) 229
7. K. Thanyachotpaiboon, S. Chavadej, T.A. Caldwell, L.L. Lobban, R.G. Malinson; *AIChE Journal (Reactors, Kinetics&Catalysis)* 44/10, (1998), 2252
8. K.V. Kozlov, P. Michel, H.-E. Wagner; *Proc. Hakone'98 - VI International Symposium on High Pressure Low Temperature Plasma Chemistry, Cork, Ireland* (1998) 78
9. K.V. Kozlov, P. Michel, H.-E. Wagner, *Proc. Hakone'2000 - VII Greisfwald, Germany* (2000), 262
10. K.V. Kozlov, P. Michel, H.-E. Wagner, *Czechoslovak Journal of Physics*, **48** (1998), No. 10
11. B. Eliasson, W. Egli, U. Kogelschatz, *Pure & Appl. Chem*. **66,** (1994), 1279
12. U. Kogelschatz, B. Eliasson, Proc. *Hakone'96 – V International Symposium on High Pressure Low Temperature Plasma Chemistry, Milovy, Czech Republic* (1996), 47
13. D.W. Larkin, L.L. Lobban, R.G. Malinson, *Catalysis Today* **71,** (2001), 199
14. K. Okazaki, T. Kishida, *Proceedings 14 ISPC, Praha* (1999), 2283
15. M. Okumoto, A. Mizuno, *Catalysis Today*, **71,** (2001), 211
16. A.Holmen, O. Olsvik, O.A. Rokstad; *Fuel Process. Technol*. **42,** (1995), 249
17. C. Liu, A. Marafee, R. Mallinson, L. Lobban, *Appl. Catalysis* **164,** (1997), 21

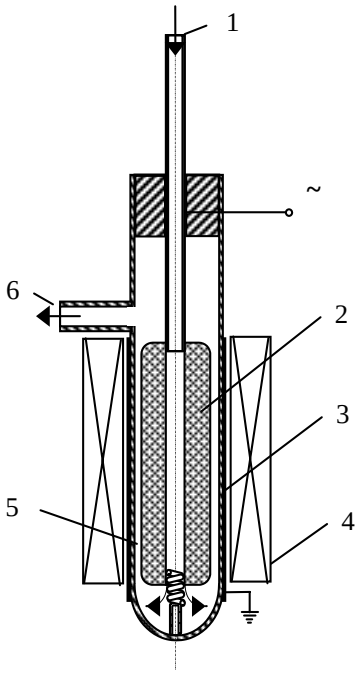

Fig. 1. DBD reactor: 1 – connector pipe of the gas inlet, 2 – high voltage electrode, 3 – grounded electrode, 4 – electric heater, 5 – discharge gap, 6 - gas outlet.

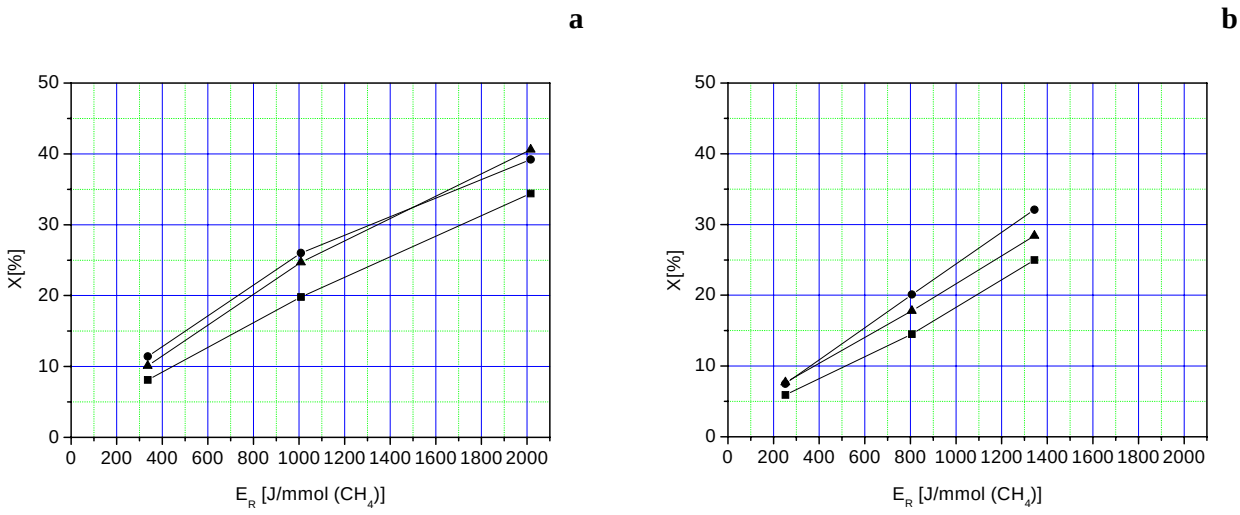

Fig. 2. Overall conversion X vs. specific energy per CH_4 unit E_R for CH_4 + Ar mixtures: a – 7.5 % CH_4, b – 10 % CH_4, ■ – without packing, ● – quartz-glass, ▲ – silica gel

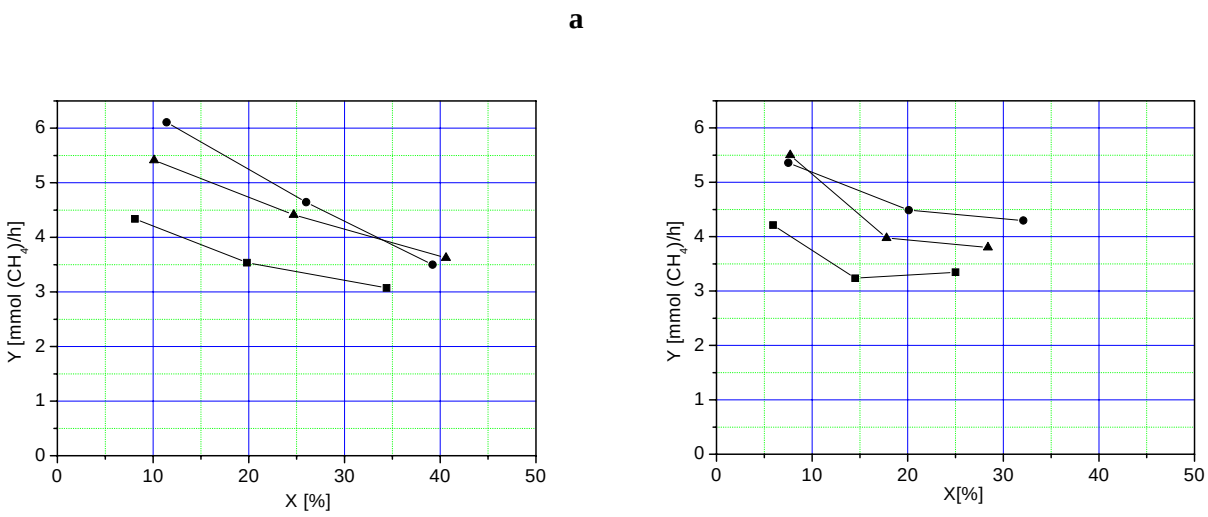

Fig. 3. Methane conversion rate Y vs. overall conversion X for CH_4 + Ar mixtures:
a – 7.5 %, CH_4 b – 10 % CH_4, ■ – without packing, ● – quartz-glass, ▲ – silica gel

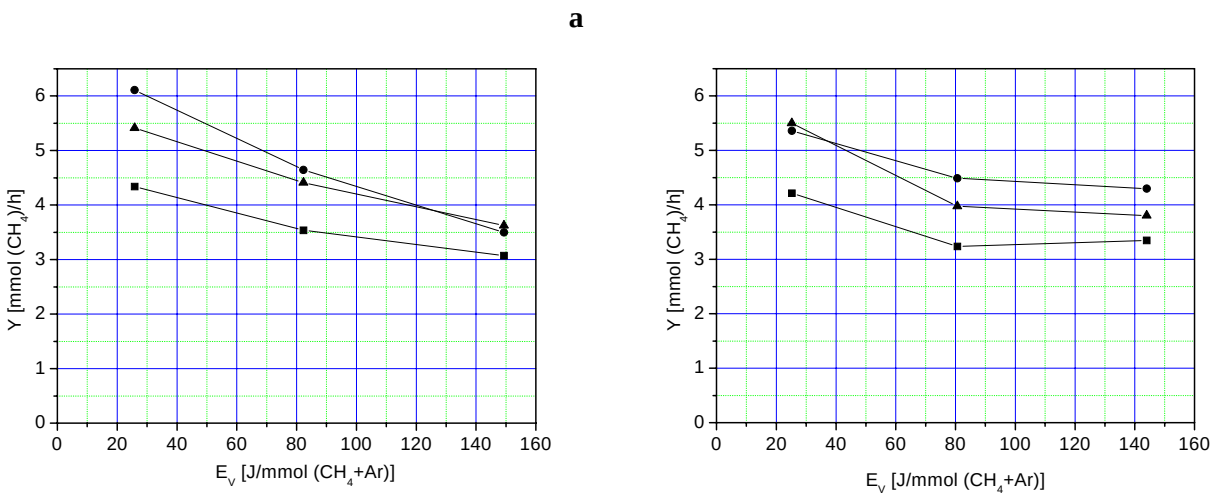

Fig. 4. Methane conversion rate Y vs. specific energy E_V X for CH_4 + Ar mixtures:
a – 7.5 %, CH_4 b – 10 % CH_4, ■ – without packing, ● – quartz-glass, ▲ – silica gel

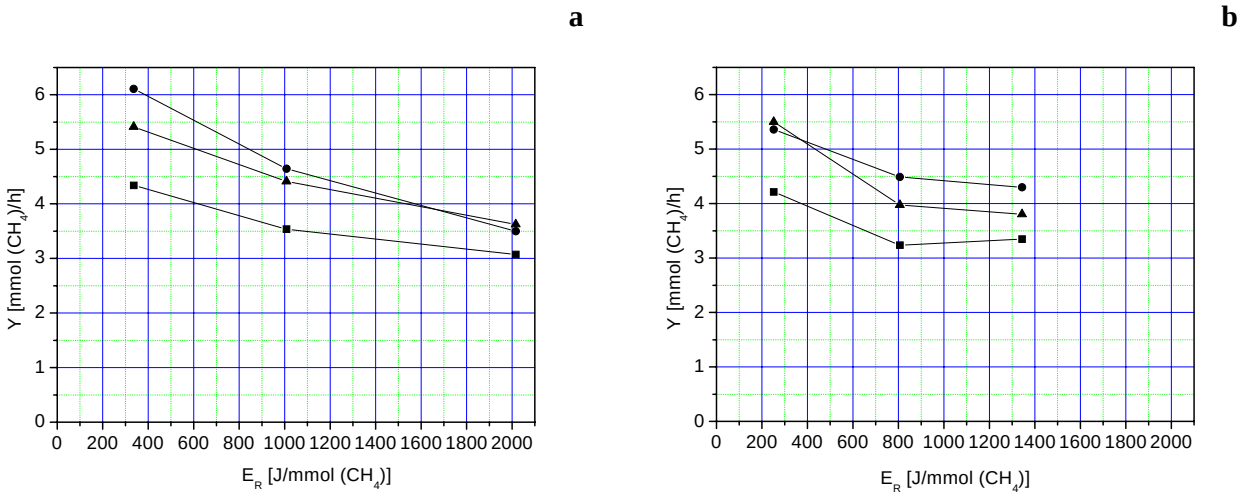

Fig. 5. Methane conversion rate Y vs. specific energy per CH_4 unit E_R for CH_4 + Ar mixtures:
a – 7.5 %, CH_4, b – 10 % CH_4, ■ – without packing, ● – quartz-glass, ▲ – silica gel

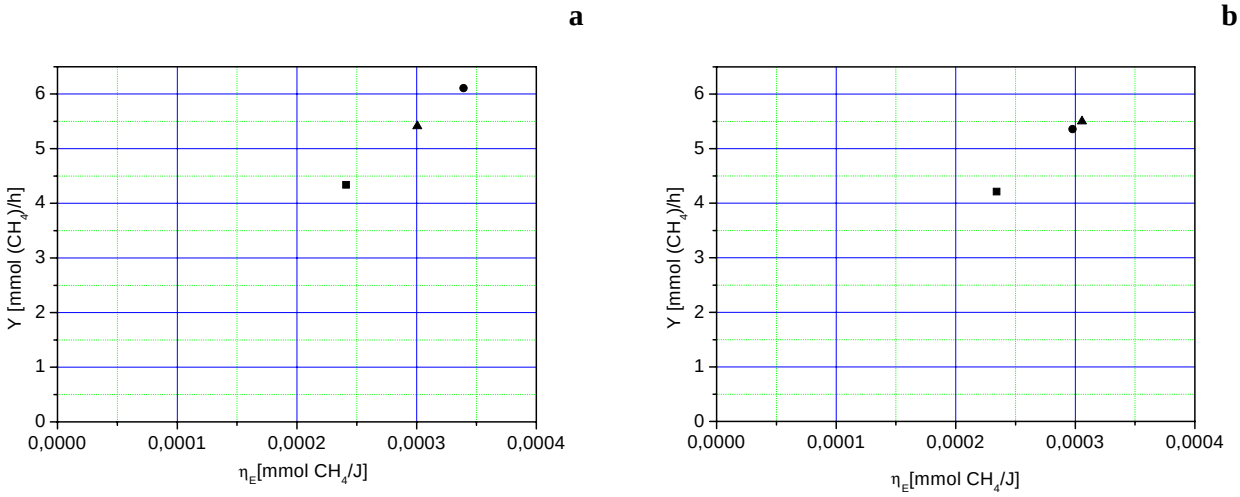

Fig. 6. Methane conversion rate Y and energy efficiency η_E for CH_4 + Ar mixtures:
a – 7.5 %, CH_4; E_R = 336 J/mmol CH_4, b – 10 % CH_4; E_R = 252 J/mmol CH_4
■ – without packing, ● - quartz-glass, ▲ – silica gel

Plasma Production and Control at Atmospheric Pressure Using Dielectric Materials

A. Hallac[1], G. E. Georghiou[2] and A. C. Metaxas[3]
[1] *Electricity Utilisation Group, Department of Engineering, University of Cambridge, Cambridge CB2 1PZ, UK*
[2] *Electronics and Computer Science Department, University of Southampton, Bld 21, Faraday Tower, Highfield, Southampton, SO17 1BJ, UK*
[3] *St John's College, University of Cambridge, Cambridge CB21TP, UK*

Abstract

In this paper a potential plasma source at atmospheric air is analyzed. The production of a corona discharge in air at atmospheric pressure is achieved by using a needle-plane configuration with a gap length of 1 mm. The needle-plane is surrounded by a hollow dielectric, which influences the plasma density, its shape and duration. The effect of the dielectric material and shape on the discharge development and stabilization is investigated using a model based on the drift-diffusion equations.

1. Introduction

Conventional plasma-processing tools are essentially based on parallel-plate discharges [1], in which a voltage is applied between two electrodes to break down the gas and sustain the generated discharge. Plasmas generated in this method are usually used in high-plasma-density processing at lower gas pressures needing specialized applicators [2]. Recently the study of atmospheric non-thermal plasmas has received much interest because of the elimination of expensive vacuum systems. This leads to system simplification and cost reduction. The possibility arises therefore to create low-power, cold non-equilibrium plasma at atmospheric pressure. At the moment the best-known example is a micro-discharge, i.e. plasma constricted to the size of 10 - 100 mm by using very small electrodes [3]. Although the power density in these plasmas is of the same order as in larger discharges, the total consumed power is very low (of the order of mW) due to the small volume involved. Moreover, since gas heating in plasmas is a volume effect, micro-discharges remain cold. These micro-plasmas, arranged in an array, are intended for applications in modern display technology, to obtain improved TV screens [4]. Another possibility of obtaining non-equilibrium plasma is limiting the plasma operation time to microsecond range (i.e. by pulsing the plasma power supply). In this case electrons in the plasma have enough time to gain energy and create active species, but not to heat the ambient gas.

In this paper we focus on the modeling and simulation of low power, cold non-equilibrium plasmas (micro-discharges) at atmospheric pressure, which may find many useful applications ranging from the treatment of skin cancer and removal of decayed dental surfaces [5] to material processing of low-cost polymers and semiconductors [6]. Another growth area is the use of mercury free excimer lamps employing dielectric barrier discharges [7]. The current major challenge is producing, stabilizing and controlling non-thermal plasma at atmospheric pressure in air, thus avoiding the use of expensive helium or argon gases at lower voltage and power levels. This challenge can only be overcome with a fuller understanding of plasma processes at atmospheric pressure and the factors that control their stabilization.

Modeling and numerical simulations of plasma processing can be useful in many ways. An improved understanding of a plasma-processing system can be achieved by comparing predictions from numerical simulations with experimental observations. The optimization of existing processes or the development of new plasma processes that offer better processing results may follow such an understanding. Additionally, such modeling and simulations can also be used in the computer-aided design (CAD) of new process systems and to optimize manufacturing processes within the framework of existing processing systems. The ultimate goal may be the numerical solutions of the Boltzmann equation under general conditions, which is a very difficult computational problem. One scheme that can be used to solve the equation exactly is the convective scheme [8]. A more widely used alternative method is the particle in cell (PIC) method [9]. However direct numerical simulations are very costly comparing with continuum models [10].

The solution of continuum models is predominantly carried out using the finite-difference (FD) method in conjunction with the Flux Corrected Transport (FCT) algorithm for the stabilization of the convective terms (coupled with the Poisson's equation). The structured nature of the grids used in FD results in a large number of unknowns for complex configurations which leads to long calculations. Unstructured

grid methods such as finite volume (FV) and finite element (FE) methods have been applied to discharge problems and their many advantages are reported in recent publications [11,12,13]. Due to the efficiency of FE method for the solution of Poisson's equation it is advantageous to use FE for the solution of the complete coupled system [12].

The aim of this paper is to present fundamental aspects of plasma-process modeling based on relevant physical/chemical mechanisms. The plasma generation of point plane structures is analyzed using the FE-FCT method in a two-dimensional (2D) axis symmetric model [11,13]. The effect of secondary processes such as photo-ionization, photoemission and background ionization on gas discharges is added to the numerical simulations very accurately using methods presented in [14]. More specifically, the avalanche and streamer phase of corona development is presented. For the control of plasma (homogeneity in density profiles) the effect of various dielectric configurations is added to the point plane configurations.

2. Numerical (Continuum) Model

If the neutral-gas pressure is sufficiently high, collisional processes dominate the dynamics of the plasma. The drift-diffusion equations are "condensed" equations derived from the well-known fluid equations (i.e., mass- and momentum-conservation laws) for ions and electrons under the assumption of high collision frequencies [14]. Within this framework the simplest set of equations containing the basic physics necessary for streamer formation and propagation are the continuity equations for particle species, coupled with Poisson's equation. If the values of the mobility and diffusivities are given, we need equations only for the electron and ion densities and the electric field E to fully define the system. This can be achieved by the following formulation:

$$\frac{\partial N_e}{\partial t} + \nabla \cdot (\Gamma_e) = S_e \tag{1}$$

$$\frac{\partial N_p}{\partial t} + \nabla \cdot (\Gamma_p) = S_p \tag{2}$$

$$\frac{\partial N_n}{\partial t} + \nabla \cdot (\Gamma_n) = S_n \tag{3}$$

where t is the time, N_e, N_p and N_n are the charge densities for electrons, positive ions and negative ions. Γ_e, Γ_p, Γ_n , S_e, S_p and S_n are the associated fluxes and source terms respectively and can be written as:

$$\Gamma_e = N_e W_e - D_e \nabla N_e \,,\; \Gamma_p = N_p W_p \,,\; \Gamma_n = N_n W_n \tag{4}$$

$$S_e = N_e \alpha |W_e| - N_e \eta |W_e| - N_e N_p \beta_{ep} + S_{sc} \tag{5}$$

$$S_p = N_e \alpha |W_e| - N_e N_p \beta_{ep} - N_n N_p \beta_{np} + S_{sc} \tag{6}$$

$$S_e = N_e \eta |W_e| - N_e N_p \beta_{np} \tag{7}$$

where W_e, W_p and W_n are the corresponding drift velocities and D_e is the electron diffusion coefficient. The symbols α, η, β_{ep} and β_{np} denote the ionization, attachment and recombination coefficients respectively. The value of the rate constants of these processes is taken [15] as a function of the local value of the reduced electric field and extracted from experimental data. The term S_{sc} is the source term due to secondary effects such as photo-ionization and surface emissions. Poisson's equation is given by:

$$\nabla \cdot (\varepsilon_r \nabla V) + \frac{e}{\varepsilon_0}(N_p - N_n - N_e) = 0 \tag{8}$$

where ε_0 is the dielectric constant of free space, ε_r the relative permittivity, e the electron charge and **V** the electric potential. The electric field E is computed using:

$$E = -\nabla V \tag{9}$$

In addition, ions and electrons are also lost at the walls and electrodes that contain the plasma. Some electrons are also created at the walls and the electrodes due to secondary-electron emission and photoemission. These effects must be incorporated in the boundary conditions. The other boundary conditions may be given as follows: for typical parallel-plate DC and RF discharges, the potential at the anode and wall boundaries may be set to zero, whereas the potential at the cathode may be set to the applied voltage. Depending on the physical conditions, there are a variety of choices for boundary conditions for electron and ion fluxes. Here we used the boundary conditions given in [14].

3. Numerical Results

It is well known that streamers and arcs move towards high field regions that generally occur on sharp metallic and dielectric material edges. Numerical modeling of high-pressure discharges considering the effects in the presence of dielectrics has been reported to a limited extent. Allen and co-workers [16] have studied the streamer propagation on insulator surfaces and have observed that for a given dielectric constant, the streamers spread along a dielectric surface with a constant separation layer between the dielectric surface and the streamer. The separation of the streamers varies with the dielectric strength of the material. This channeling effect reduces the damage caused by the streamer and eases the breakdown mechanism of the system by spreading charged particle species in close proximity to the dielectric surface.

Numerical simulation of such effects may be useful for the design of homogeneous distributed and stable plasma production systems. To demonstrate the effect the dielectric insertions have on streamer propagation, an axisymmetric model shown in figure 1 is employed. Numerical results were obtained for a 50 μm spherical radius point, 1 mm from a plane in air at atmospheric pressure, with a positive voltage of 3 kV applied to the needle. In this axisymmetric model the dielectric material has a hollow cylindrical geometry with curved edges to ensure numerical stability. From previous experience it has been observed that the numerical load increases proportionally with increasing dielectric constant. Four types of dielectric insertions have been simulated, namely, ε_r=2.2, 3.2, 4.2 and 6.2, as well as the case of no dielectric insertion.

The current characteristics are shown in figure 2. The magnitude of the current increases considerably with increasing dielectric constant. This is mainly due to the high electric field occurring at the dielectric material interface. This leads to high ionization rates and the spread of charged particles in a large area approaching the dielectric surface. It is also observed that the peak in the current characteristics occurs in earlier times as the dielectric constant increases. For example, with ε_r=2.2 the maximum peak is at t=1.2 ns whereas, for ε_r=6.2 it occurs at 0.75 ns.

The electron charge density distributions are shown in figure 3. From this figure it is clear that the streamer is not attached to the dielectric surface and there is a constant separation distance between the streamer and the dielectric. When the dielectric constant increases, this separation layer reduces. Moreover figures 3(f), 3(j), 3(k) and 3(l) show the calculated electron density when the streamer reaches the cathode and it is evident that the streamer bridges the gap at different times. Figure 4 shows a plot of the time the streamer takes to reach the cathode versus the dielectric constant. This clearly demonstrates that the streamer propagates faster as the dielectric constant increases, which may lead to corona discharges at lower voltages.

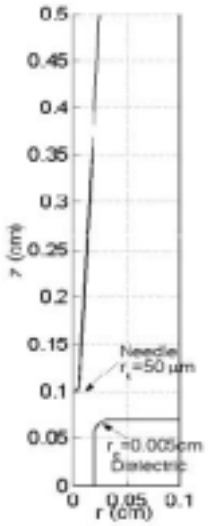

Figure 1: 2D axisymmetric model of a point plane dielectric model. Needle has a radius of curvature r_c = 50 μm and a dielectric edge of curvature r_c= 0.005 cm

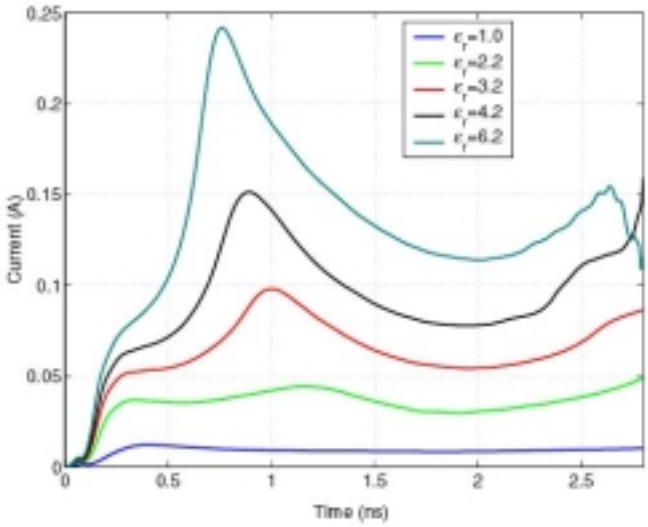

Figure 2: Current characteristic of four different types of dielectric when positive potential of 3 kV is applied to the needle.

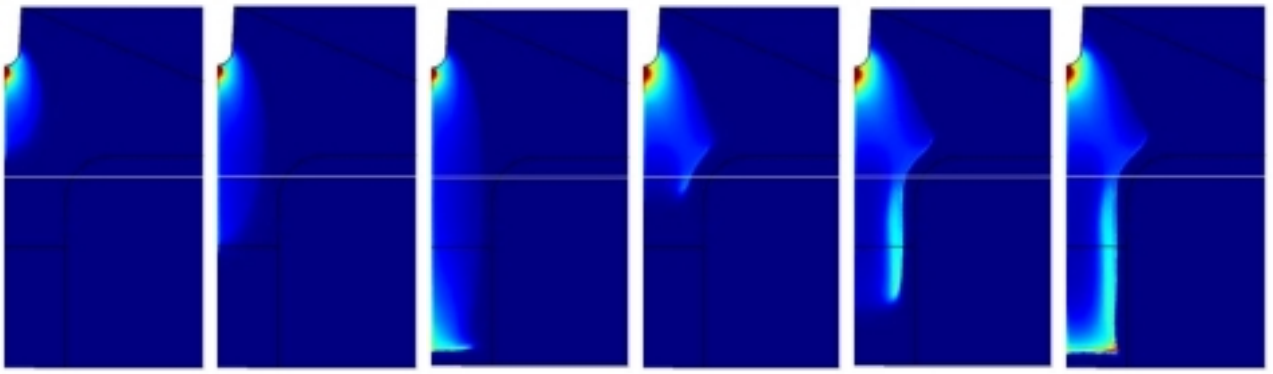

(a) ε_r=1.0 at t=1.6 ns | (b) ε_r=1.0 at t=3.2 ns | (c) ε_r=1.0 at t=4.3 ns | (d) ε_r=2.2 at t=1.6 ns | (e) ε_r=2.2, t=2.7 ns | (f) ε_r=2.2, t=3.2 ns

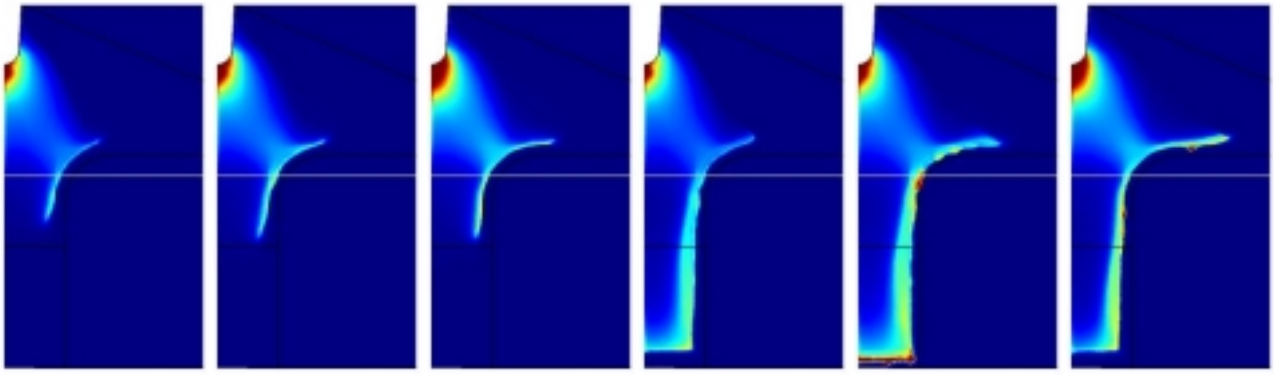

(g) ε_r=3.2 at t=1.5 ns | (h) ε_r=4.2 at t=1.4 ns | (i) ε_r=6.2 at t=1.3 ns | (j) ε_r=3.2 at t=2.7 ns | (k) ε_r=4.2 at t=2.2 ns | (l) ε_r=6.2 at t=2.0 ns

Figure 3: Electron density distribution for point plane geometry. Applied voltage is 3 kV.

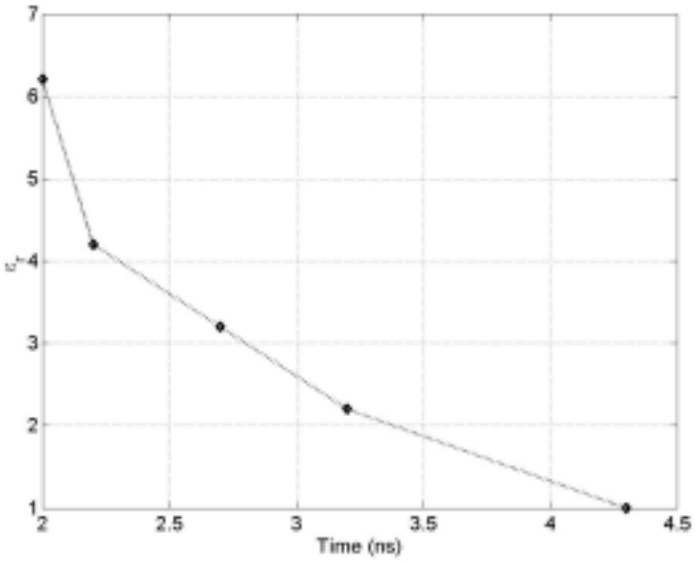

Figure 4: Time duration for the streamer to reach the cathode. The applied voltage is 3 kV for all dielectric materials.

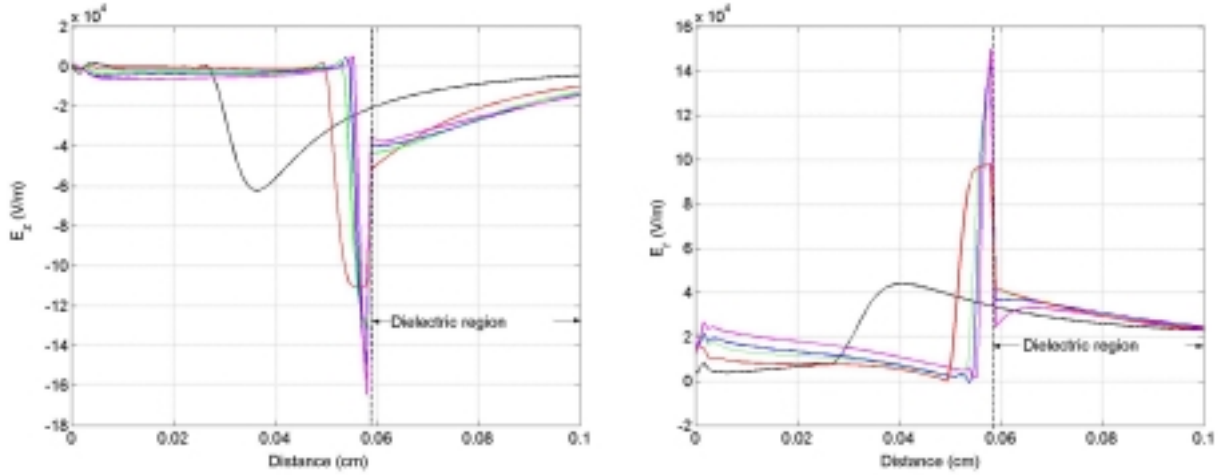

(a) (b)

Figure 5: 1D axisymmetric electric field distributions between point r=0 cm, z=0.1 cm and point r=0.07 cm, z=0 cm. (a) Axial electric field. (b) Radial electric field. Black: ε_r=1.0, red: ε_r=2.2, green: ε_r= 3.2, blue: ε_r=4.2 and magenta: ε_r=6.2.

Radial and axial 1D cross-section electric field distributions are shown in figures 5(a) and 5(b). It is interesting to note that, the electric field is nearly constant in the free space. A high gradient field occurs at the dielectric air interface, which increases the plasma density and the streamer speed.

4. Conclusion

In this paper the FE-FCT algorithm has been applied to the solution of high pressure gas discharge problems in the presence of dielectric insertions. Results suggest that the streamers spread along the dielectric surface with a separation layer, which depends on the dielectric permittivity and the applied potential.

Simulation of the streamer channel evolution for different dielectric constants shows that the streamer speed is not constant in the presence of dielectric material. This is a very important mechanism for the application of low tempareture plasmas to very small surfaces such as very small size biological tissues. The simulations suggest that carefully designed dielectric layer configurations may reduce the breakdown voltage.

References

[1] B. N. Chapman, “Gas Discharge Physics”, John Wiley and Sons, Inc. (1980)
[2] O. A. Popov, “Glow Discharge Processes”, Park Ridge. (1995)
[3] Takaki and T. Fujiwara, “Multipoint barrier discharge process for removal of NOx from diesel engine exhaust”, IEEE Transactions on Plasma Science, 29(3) 518-523, (2000).
[4] H. C. Kim and M. S. Hur and S. S. Yang and S. W. Shin and J. K. Lee, “Three-dimensional fluid simulation of a plasma display panel cell”, Journal of Applied Physics, 91(12) 9513-9520, (2002).
[5] E. Stoffels, A. J. Flikweert, W. W. Stoffels and G. M. W. Kroesen, “Plasma needle: a non-destructive atmospheric plasma source for fine surface treatment of (bio)materials, Plasma Sources Sci. Technol, 11, 383-388, (2002).
[6] C. P. Klages, K. Hoepfner, N. Klaeke, and R. Thyen, “Surface functionalisation at atmospheric pressure by DBD-based pulsed plasma polymerisation”, Plasmas and Polymers, 5(2), 79-89, (2000).
[7]R. P. Mildren and R. J. Carman, “Enhanced performance of a dielectric barrier discharge lamp using short-pulsed excitation”, J. Phys. D: Applied Phys. **34**, L1-6 (2001)
[8] T. J. Sommerer, W. N. G. Hitchon, R. E. P. Harvey and J. E. Lawler, “Self-consistent kinetic calculations of helium rf glow discharges”, Phys. Rev. A. **43**, 4452-4472 (1991)
[9] C. K. Birdsall and A. B. Langdon, “Plasma Physics Via Computer Simulation”, McGraw-Hill Book Co., (1985)

[10] V. Nikonov and R. Bartnikas and M. R. Wertheimer, “The Influence of Dielectric Surface Charge Distribution Upon the Partial Discharge Behaviors in Short Air Gaps”, IEEE Transaction on Plasma Science. IEEE Transaction on Plasma Science, 29(6), 866-874 (2001)
[11] A. Hallac, G.E. Georghiou and A.C. Metaxas, “Three-dimensional simulation of transient gas discharge phenomena - Validation”, XIV Gas Discharges Conference and their Applications, Liverpool, UK, Sept. 1-6, Vol 1, p315-318, 2002
[12] G. E. Georghiou and R. Morrow and A.C. Metaxas, “Theory of Short-Gap Breakdown of Needle Point-Plane Gaps in Air Using Finite Difference and Finite Element Methods”, J.Phys. D:Appl. Phys, 32, 1370-1385 (1999)
[13] R. Lohner and K. Morgan and M. Vahdati and J. P. Boris, “Theory of Short-Gap Breakdown of Needle Point-Plane Gaps in Air Using Finite Difference and Finite Element Methods”, Commun. Appl. Numer. Meth, 4, 714-730 (1988)
[14] A. Hallac, “Hybrid Methods for Microwave Heating”, PhD Thesis, University of Cambridge, 2003.
[15] R. Morrow and J.J. Lowke, “Streamer propagation in air”, J.Phys.D: Applied Phys, 30, 614-627, (1997)
[16] L. S. Pritchard and N. L. Allen, “Streamer propagation along profiled insular surfaces”, IEEE Trans. on Dielectrics and Electrical Insulation, 9, 371-380, (2001)

Surface reactions in the presence of gas atoms: role of the vibrational excitation of the adlayers

E.Molinari and M.Tomellini

Dipartimento di Scienze e Tecnologie Chimiche, Università di Roma Tor Vergata, Roma,, Italy

Abstract. In the presence of gas atoms the reactive adlayer is likely to be found in vibrationally excited quasi steady states. Non-Boltzmann vibrational distribution functions of the adspecies characterize the adlayer, and exert a profound influence on the kinetics of the surface reaction by modifying rates and activation energies.

It has been shown, in a series of recent contributions [1-4], that the current, tacit assumption that adspecies present at a catalytically active surface, or at a reactive gas-solid interface, are in It has Boltzmann equilibrium at the surface temperature T_S , should be replaced, by a non-equilibrium picture of the reactive adlayer, where vibrational distribution functions (vdf) of the adspecies can be approximated by a Treanor vdf , well known in the chemical physics of gas plasmas and lasers[5],

$$\ln\left(\frac{n_\nu}{n_0}\right) = -\frac{\nu E_{10}}{RT_s}\left[\frac{T_s}{T_1} - \delta(\nu - 1)\right] \qquad (1)$$

which coincides with a Boltzmann vdf only if $T_1=T_S$. With the non-equilibrium parameter $(T_S / T_1) < 1$, vibrational levels with $\nu>0$ are over-populated with respect to an equilibrium distribution, the more so the lower the (T_S / T_1) ratio. The possibility of non-equilibrium quasi steady states in a reactive adlayer stems from the inclusion in a surface reaction scheme of fast (V-V) up-pumping processes, similar to those described by Treanor in the gas phase, and bound to the anharmonicity of the vibrational levels of mobile surface species. This up-pumping process competes with the vibrational relaxation of the adspecies $A_s(\nu)$ to the solid lattice ((V-L) relaxation), and the possibility of establishing a non-equilibrium quasi steady state at the surface is controlled by the ratio **K** between the constants of these competing processes.

The consequences of replacing a Boltzmann vdf by eq. (1) can be far reaching.

Let us select, as an example, the catalytic oxidation of CO by either molecular, $O_{2(g)}$, or atomic, $O_{(g)}$, gaseous oxygen on noble metal catalysts. It is a well-established fact that the surface reaction $CO_{(s)} + O_{(s)} \Rightarrow CO_{2(g)}$ is the rate-determining step of the heterogeneous oxidation of carbon monoxide on metallic surfaces [6] (subscript (s) denotes a chemisorbed species). Fig. 1 gives qualitative profiles for chemisorbed oxygen (a) and of chemisorbed CO (b) with the corresponding anharmonic vibrational levels $\nu=i$ and $\nu=j$ respectively. The very initial step of $O_{(g)}$ chemisorption corresponds to a *pump* process *populating the* upper i^* level of the $(S-O)$ species: $O_{(g)} \Rightarrow O_{(s)}(i = i^*)$, chemisorption of $O_{2(g)}$ pumps a lower i^+ level (fig.2a): $O_{2(g)} \Rightarrow 2O_{(s)}(i = i^+)$ chemisorption of $CO_{(g)}$ populates the upper j^* level of the vibrational ladder of the $(S-CO)$ species: $CO_{(g)} \Rightarrow CO_{(s)}(j = j^*)$(Fig.2b).

The vibrational energy pumped into these excited vibrational levels by the chemisorption processes is redistributed over the entire vibrational manifolds of the adspecies by (V-V) and by (V-L) processes.

For a non resonant (V-V) exchange among **mobile** surface anharmonic oscillators $O_{(S)}$ or $CO_{(s)}$, one writes:

$$O_{(S)}(\nu = 1) + O_{(S)}(\nu) \underset{P_r}{\overset{P_f}{\rightleftharpoons}} O_{(S)}(\nu = 0) + O_{(S)}(\nu + 1) \qquad (2)$$

and similarly for $CO_{(s)}$.. Application of detailed balancing to this reaction yields $P_f > P_r$, i.e. up--pumping, is

faster than reverse pumping, P_r, with the net result of over-populating the vibrational levels with respect to a Boltzman distribution.
For (V-L) relaxation one has:

$$O_{(S)}(v) + Lattice \underset{K_r}{\overset{K_f}{\rightleftarrows}} O_{(S)}(v-1) + Lattice^* \quad . \tag{3}$$

In this case $K_f > K_r$ and the system is driven towards a Boltzmann distribution. The condition for attaining a *quasi* steady state non-equilibrium vibrational distribution is that rate coefficients $P_{f,r}$ and $K_{f,r}$ in eqs.(3) and (5) respectivly, should obey the inequality $P_{f,r} n >> K_{f,r}$ with n total surface density of the adspecies, or $\mathbf{K} = (K_{fr} / P_{fr}\, n) << 1$. If this inequality is obeyed, the distribution functions at quasi steady state will be approximated by the Treanor vdf.
For a Langmuir-Hinshelwood mechanism involving vibrationally excited adspecies one writes

$$CO_{(s)}(j) + O_{(s)}(i) \xrightarrow{K(i,j)} CO_{2(g)}^* \langle i,j \rangle + 2S, \tag{4}$$

i.e. a reaction between the adspecies $(S-CO)$ in its jth vibrational level and the adspecies $(S-O)$ in its ith level , giving a vibrationally, rotationally and translationally excited gaseous $CO_{2(g)}^*$ molecule. The $\langle i,j \rangle$ symbol remarks that $CO_{2(g)}^* \langle i,j \rangle$ originates from the encounter of two adspecies in their ith and jth state respectively.
The rate of this reaction should be written:

$$\frac{dn_{CO_{2(g)}^* \langle i,j \rangle}}{dt} = K(i,j) n_1(i) n_2(j) \quad , \tag{5}$$

with $n_1(i), n_2(j)$ surface densities (molecule cm^{-2}) of $O_{(s)}$(i) and of $CO_{(s)}$(j) respectively.
The *total* rate of production of $CO_{2(g)}$ will then be given by:

$$\frac{dn_{CO_{2(g)}}}{dt} = \sum_{i,j} K(i,j) n_1(i) n_2(j) \tag{6}$$

The consequence of the presence of an activation energy $E^{\#}$ for the formation of the product $CO_{2(g)}$ from $CO_{(s)}$ and $O_{(s)}$ is that $\frac{dn_{CO_{2(g)}^* \langle i,j \rangle}}{dt}$, becomes appreciable only for (i,j) couples satisfying the condition $\left[E_1(i) + E_2(j)\right] \geq E^{\#}$. The sum over the *(i,j)* couples satisfying this constraint will be denoted $\sum_{i,j}^{\#}$ and contains a *lower cut-off*. With $\frac{dn_{CO_2}}{dt} = k(n_1 n_2)$, the expression for the overall rate constant is

$$k = \overline{K} \left[\frac{\sum_{i,j}^{\#} P_1(i) P_2(j)}{\sum_{i,j} P_1(i) P_2(j)} \right] \tag{7}$$

a function of $E^{\#}, T_s, (T_s/T_1)$, with $P(i) = n(i)/n(0)$

One can now analyse the dependence of the dimensionless rate constant for CO oxidation $\kappa = k / \overline{K}$, on $E^{\#}, T_s, (T_s/T_1)$ .Fig.2 shows log κ. for the reaction in atomic oxygen, plotted against (T_s/T_1) at different T_S and two different values of $E^{\#}$(95 kJ mol^{-1}, (full lines) and 50 kJ mol^{-1}, (dotted lines)). log κ at 300 K for the reaction in molecular oxygen is also shown for comparison (thick lines).The temperature dependence of log κ derived from fig,2 at constant (T_s/T_1), can be fitted by Arrhenius equations with slopes decreasing with decreasing (T_s/T_1). From these slopes one receives the 'non-equilibrium activation energies' $E_{NE}{}^{\#}$, which have been plotted in fig.3 vs. (T_s/T_1). Figs.2 and 3 allow a comparison to be made between non-equilibrium and Boltzmann dimensionless rate constants : the ratio between rate constants corresponding to 'true' activation energies $E^{\#}$ of 50 and of 95 kJ mol^{-1} are the following for Boltzmann vdfs ((T_s/T_1)= 1): (κ_{50}/κ_{95})=7 10^7, 8 10^3, 4 10^2 at 300 K, 600 K and 900 K respectively. At (T_s/T_1)=0.3 these ratios become (κ_{50}/κ_{95}) = 7, 3 , 1.5

The interpretation of these results is straightforward; it simply reflects the increased populations of (i,j) couples satisfying the constraint $[E_1(i)+E_2(j)] \geq E^{\#}$ and connected with a decrease of (T_s/T_1) in the Treanor vdfs of the $(S-CO)$ and$(S-O)$ surface species. The influence of T_S on these populations is therefore also expected to decrease with a decrease of (T_s/T_1), and κ becomes temperature independent ($E_{NE}{}^{\#}$=0) at values of $(T_s/T_1)$of about 0.1 because essentially all(i,j) couples will now satisfy the constraint in the whole range of temperatures considered (300-900 K). The influence on the reaction rates of oxygen atoms in the gas phase can therefore be attributed to a decrease of (T_s/T_1) with respect to the reaction in molecular oxygen, which follows from the observation that atomic oxygen populates, with no activation energy, the upper vibrational level *i**, while molecular oxygen pumps,with an activation energy, a lover level i^+ (fig 1).

The influence of oxygen atoms is nicely shown by the different vibrational distribution functions of the gaseous CO_2 molecules leaving the catalytic surface [7], which can be fitted [3] using the non-equilibrium scheme outlined above.(fig.4). Vibrational distribution functions of H_2 leaving the Ta surface after atom recombination [8] or abstraction can similarly be accounted for [2] (fig.5)

Impingement of energetic (4-8 eV) Xe atoms on coadsorbed $CO+O$ on Pt (111) at 100 K induces both formation of $CO_{2(g)}$ and desorption of O_2 below the surface temperature where any thermal reaction occurs and the reaction probability per incident Xe atom increases with the kinetic energy of the atom, above a 3-4 eV threshold [9]. When high energy gaseous Xe atoms hit the surface, efficient (T-V) energy transfer from the very fast Xe to coadsorbed $CO+O$ becomes possible and it has been shown in ref.[2] that additional pumping over all levels shifts the vdf's from a Treanor parabola to Treanor-like functions corresponding to higher degrees of vibrational excitation. In the low temperature (85 K) CO oxidation triggered by gaseous D-atoms incident on a $CO_S + O_S$ adlayer on Pt (111)[10] the pump process might well be represented by the highly exotermic reaction proposed by the authors $D_{(g)} + O_{2(s)} \Rightarrow O_{(s)} + OD_{(s)}$ and the oxidation reaction will again proceed at rates determined by the non-equilibrium vdf's of $O_{(s)}$, $OD_{(s)}$ and $CO_{(s)}$, pumped by this process.

An important observation stems from fig.2, namely that catalysts with widely different 'true' activation energies $E^{\#}$ can exhibit an equal κ, at the same T_S, provided (T_s/T_1) is properly selected for each system .In figs.2 and 3 Boltzmann rates represent but a limiting case, (T_s/T_1)=1, of a more general non-equilibrium picture showing that two parameters, besides T_S, are now necessary to define the non-equilibrium rate constant κ, namely $E^{\#}$ and (T_s/T_1).. Chemisorption of the reactants and the successive reaction steps on the surface, which are normally considered as independent from one another (one of them is rate determining), actually become closely coupled in this non-equilibrium picture in that the adsorption flux now controls the rate constants of successive steps via (T_s/T_1) [1,4].

Two examples of classical catalytic reactions influenced by the presence of atoms in the gas phase that can, at least qualitatively, be interpreted within the outlined framework of vibrational non-equilibrium, are the

following: 1)-*NH_3 oxidation on Pt -Rh and on Co O in the presence of $O_{(g)}$.[11]* .Oxidation of NH_3 on a *Pt -Rh* gauze was investigated in the temperature range 350 - 750 K in the presence of both $O_{2(g)}$ and of $O_{2(g)}$ + *10 % $O_{(g)}$* mixtures [11a]. *NO and H_2O* were, in both cases, the only reaction products . An ignition temperature marking the transition from a kinetic to a diffusional regime characterizes this reaction. First order kinetic rate constants can be extracted from the observed rates and plotted accoding to Arrhenius. The influence of $O_{(g)}$ is the following: a)-the ignition temperature is lowered from 525 K to 400 K, b) the activation energy derived from the Arrhenius plots is lowered from 54±12 to 29±4 kJ mol^{-1}, c)- these plots merge at a 'isokinetic temperature' Θ=890±20 K.The same technique was used with a cobalt oxide catalyst, grown on a copper gauze, in the temperature range 450-700 K[11b]. Reaction products are now N_2 and *NO* besides H_2O . The results parallel those obtained with a *Pt -Rh* gauze: in the presence of $O_{(g)}$ the activation energy is lowered from 125±16 to 38±4 kJ mol^{-1}, with an 'isokinetic tempe- rature' Θ= 750±20 K. The selectivity $s = [N_2]/[NO]$ decreases with increasing temperature and is systematically lower in the presence of $O_{(g)}$. 2) -*NH_3 decomposition on W in the presence of $H_{(g)}$ [12]*. Mixtures of NH_3 and H_2 of variable composition were flown across a tungsten wire spiral in a temperature range around 1300 K, yielding N_2+H_2 at rates *decreasing* with increasing partial pressure of H_2 . Addition of $H_{(g)}$ to these mixtures entrains an *increase* of the rate of NH_3 decomposition at all compositions and temperatures investigated.

One might then conclude that any analysis of surface reaction schemes in the presence of gas plasmas should duly take into account the existence of vibrational excitation in the reactive adlayer.

References

E.Molinari and M.Tomellini, [1] Chem.Phys. **253** (2000) 367; [2] Chem.Phys. **270** (2001) 439;
[3] Chem.Phys. **277** (2002) 373 ; [4] Catalysis Lett. **83** (2002) 71
5-Non-Equilibrium Vibrational Kinetics, M. Capitelli (Ed), Top.Curr. Phys. **39** (1986)
6- C. T.Campbell, G. Ertl, H. Kuipers, J..Segner, J.Chem.Phys.73 (1980)5862 ; J.Segner, C. T. Campbell, G. Doyen, G. Ertl, J.Chem.Phys. **100** (1984) 505
7-C.Wei, G. L. Haller, J.Chem.Phys. **105** (1996)810
8-R.I. Hall, I. Cadez, M. Landau, F: Pichou, C. Schermann, Phys. Rev. Lett. **60** (1988)337
9-C. Akerlund, I. Zoric, B. Kasemo, J. Chem. Phys. **104** (1996) 7359
10- J. Y.Kim,J. Lee, J. Chem. Phys. **109** (1998) 869
11- a) E.Molinari, F. Cramarossa, A.Pullo, L. Triolo, J.Catal. **4** (1965); b)E. Molinari, F.Cramarossa, M. Capitelli, A. Pullo, Atti Acc. Naz. Lincei **38** (1965) 531
12- E. Molinari, F.Cramarossa, M. Capitelli, A. Mercanti, Ric.Sci. **36** (1966)109

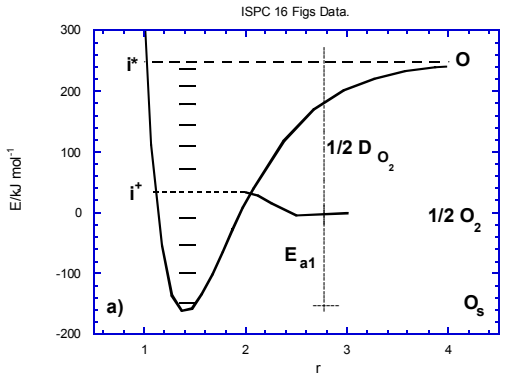

fig.1 a)-Energy diagram of adspecies O_s

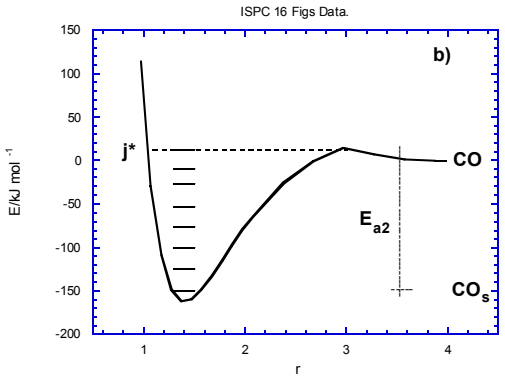

fig.1 b)-Energy diagram of adspecies CO_s

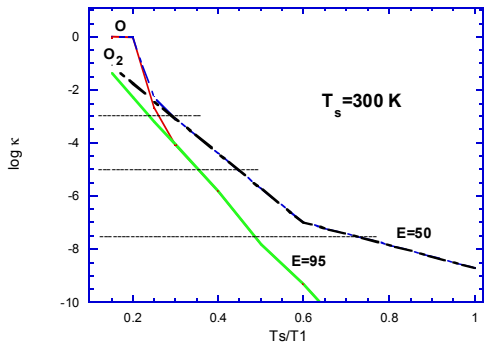

fig.2- Dimensionless non-equilibrium rate constant κ vs.(T_s /T_1) calculated for two 'true' activation enegies E .(Thick lines O_2, , thin linea O)

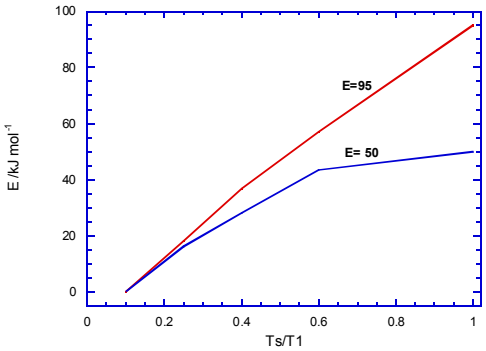

fig.3-Non-equibrium activation energies vs.(T_s /T_1) ('true'E/kJ mol^{-1}=95, 50)

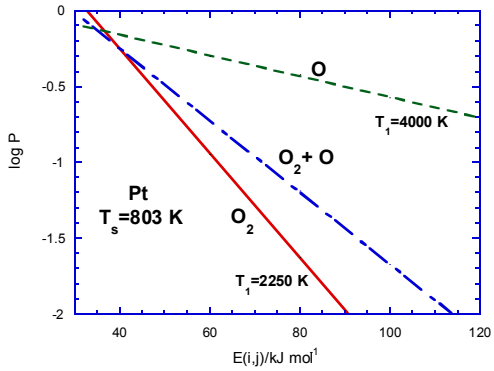

fig.4- Total energy distribution functions of CO_2 gas, formed in CO oxidation by O_2,O_2+O, O, on Pt.

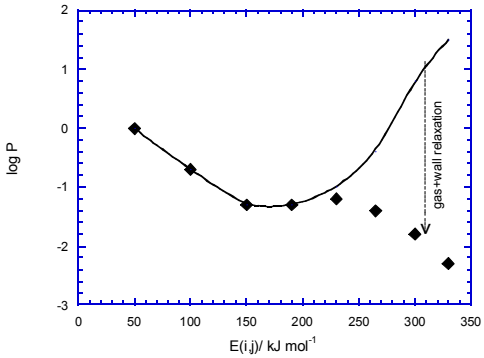

fig.5- Observed and calculated total energy distribution functions of H_2 gas formed by recombinative desorption from Ta. (T_s=300K , T_1= 1650 K)

DEEXCITATION CROSS SECTIONS OF Ne($^3P_1$) AND Ne($^3P_2$) BY Ar, Kr, Xe AND N_2

D. B. Khadka[1], N. Kouchi[2] and Y. Hatano[2]

[1]*Central Department of Chemistry, Tribhuvan University*
Kirtipur, Kathmandu, Nepal
[2]*Department of Chemistry, Tokyo Institute of Technology,*
O-okayama Campus, Meguro-ku, 152 Tokyo, Japan

Collisional deexcitation of excited rare gas atoms by atoms and molecules is of great importance in both fundamental and applied sciences, which provides the essential features of chemical reactions, in particular, those including electronic energy transfer. The collisional deexcitation is a key also to understand fundamental processes in the interaction of ionizing radiation with matter and the phenomena in ionized gases such as reactive plasmas and upper atmosphere. Excited neon atoms have a large amount of internal energy enough to ionize Ar, Kr, Xe and N_2 at thermal energy.

Collisional deexcitation processes of excited neon atoms have not been extensively studied in comparison with those of excited helium atoms, the collisional deexcitation of Ne($^3P_1$) and Ne($^3P_2$) by Ar, Kr, Xe and N_2 has been studied in detail in this experiment. The temperature dependence of the rate constants for the deexcitation has been measured in the temperature range from 133K to 295K using a pulse radiolysis method and thus the collisional energy dependence of the deexcitation cross sections is obtained. The deexcitation cross sections are in the range of 10 -26 Å^2 and 6-20 Å^2 for Ne($^3P_1$) and Ne($^3P_2$), respectively, and increase slightly with increasing the collisional energy. The absolute experimental cross sections for the Ne($^3P_1$) deexcitation are larger than but close to those of Ne($^3P_2$). Moreover, the calculated optical model cross sections show that an electron-exchange interaction plays an important role in the deexcitation of Ne($^3P_1$) in collisions with Ar, Kr, Xe, and N_2. The comparison between the present experimental and calculated cross sections indicates that the deexcitation processes for Ne($^3P_1$) and Ne($^3P_2$) are dominated by collisional ionization induced by an electron exchange interactin, although the deexcitation cross sections for Ne($^3P_1$) are slightly enhanced by a weakly allowed dipole-dipole interaction. The details will be discussed at the conference.

Semicondactive polymer films obtained by plasma polymerization

A. Drachev, A.Gilman, and A. Kuznetsov

N. S. Enikolopov Institute of Synthetic Polymeric Materials, Russian Academy of Sciences, Moscow, Russian Federation

Polymerization of aniline, pyridine, and thiophene in the high-frequency discharge plasma was used for the preparation of the thin polymer films with semicondacting properties [1–4]. The bulk conductivity of the non-doped samples did not exceed 10^{-9}Ohm^{-1}cm^{-1} and only after doping reached 10^{-5}-10^{-4}Ohm^{-1}cm^{-1}.

In this work, polymer films based on 1-amino-9,10-anthraquinone (AAQ) were synthesized by polymerization in dc discharge.

Polymerization was carried out in vacuum tubular reaction chamber 30-cm long with a diameter of 10 cm. The upper part of the chamber was placed in an electric furnace, which provided heating to 400˚C controlled by a thermocouple. Two horizontal planar-parallel electrodes with a diameter of 50 mm were placed in the chamber, and a ceramic cup with the starting substance was placed on an anode. Polymerization was performed for 5-120min at 240°C in a discharge current of 5-15mA under pressure of 2.10^{-2}Pa.

Under DC discharge, a deposition of black polymeric layer with specific metallic luster on the cathode was observed. The thickness of polymeric layer could be varied from 1 to 9μ by changing duration of deposition. The cathode film did not dissolve in any organic solvents, acids and alkalis. The layer deposited on the anode was of red color and was easily soluble in acetone. The thickness of the layer deposited on the anode was less than 1μm.

Polymer films obtained on the cathode and the anode found to differ essentially in their electrical properties. The film deposited on the anode had the specific conductivity of 10^{-16}Ohm^{-1}cm^{-1} (20°C). The film deposited on the cathode had a conductivity of $\sigma = 10^{-5}$–10^{-4}Ohm^{-1}cm^{-1} (20°C). Repeated heating on air from 20 up to 300°C with a rate of 0,5 degree/min was found to have no effect on the value of conductivity.

In range of film thickness from 1 to 9μ, no dependence of the electrical resistance on the film thickness obtained on the cathode was found. This means that the basic part of electrical resistance of a sample falls to the near-electrode layer. The surface conductivity of the film deposited on the cathode was found to be equal $3{,}7.10^{-14}$ Ohm^{-1}, i.e. a value typical for dielectrics. These results are the evidence of pronounced electrical anisotropy of polymeric films deposited on the cathode.

Obviously, semi-conductive properties of polymeric film deposited on a cathode are due to polyconjugated structure. One could suppose two routes led to formation of polyconjugated chain from AAQ, the first one being the polycondensation of amino groups with AAQ carbonyl groups, the second one being 1,4–polyaddition, i.e. a process similar to an oxydative polycondensation of aniline [4]. If the first mechanism would be predominant, the content of the oxygen atoms in polymer should decrease compared to that in AAQ. This supposition is in a controversy with the ESCA data showed that the film from cathode did not differ in element composition from the monomer. So, the second mechanism seems to be more acceptable. In this case, polyconjugated chain can be formed by means of 1,4-polyaddition an AAQ cation–radical to the negatively charged end fragment of growing polymer chain and anthraquinone fragment is involved into main chain of polymer. Presence of strong C=N absorption bands and peaks of polycyclic quinone structure in a FTIR spectrum cathode deposition film are in accordance with hypothesis of 1,4-polyaddition reaction.

The results obtained by FTIR–spectroscopy suggest that the film deposited on a cathode has a polyconjugated structure and can be considered as polyaniline derivative containing in chain basically anthraqunone moieties.

References

[1] G.J. Cruz, J. Morales, M.M. Castillo–Ortega, and R. Olayo – Synthetic Metals. **88,** 213 (1997).
[2] H. Goto, K. Iino, K. Akagi, and H. Shizakawa – Synthetic Metals. **85,** 1682 (1997).
[3] N.V. Bhat, D.S. Warahal – J. of Appl. Polym. Sci. **70**, 203 (1998).
[4] R. Hernandez, A.F. Diaz, R. Waltman, and J. Bargon – J. Phys. Chem. **88,** 3333 (1984).

Deposition of Amine Containing Films from Hyperthermal Silazane Ions

A. Choukourov[1], H. Biederman[1], E.R. Fuoco[2], S. Tepavcevic[2], and L. Hanley[2]

[1]*Department of Macromolecular Physics, Charles University, Prague, Czech Republic*
[2]*Department of Chemistry, University of Illinois at Chicago, Chicago, IL, 60607-7061 USA*

Abstract
This work examines films deposited from mass-selected 5 - 200 eV $Si_2NC_8H_{19}^+$ (silazane) ions onto aluminum and silicon substrates. Film chemistry including amine content, film aging, and film morphology are examined as a function of ion energy and fluence using x-ray photoelectron spectroscopy and atomic force microscopy

1. Introduction

Polyatomic ion deposition at ion impact energies below 200 eV is an effective method for the growth of thin organic films on polymer, metal, and semiconductor surfaces. We have previously shown that SO_3^+, CF_3^+, $C_2F_4^+$, $C_3F_5^+$, $Si_2O(CH_3)_3^+$, and $C_4H_4S^+$ ions can be employed for the growth and modification of organic thin films on polymer, semiconductor, and metal surfaces [1-4]. These films are often similar in chemical composition to plasma polymers, due at least in part the presence of large, hyperthermal positive ions in many plasmas. This work deposits beams of mass-selected 5 - 200 eV $Si_2NC_8H_{19}^+$ (silazane) ions onto aluminum and silicon substrates. Silazane ions are produced by electron impact ionization of 1,3-divinyltetramethyldisilazane. These ion-deposited films are analyzed by x-ray photoelectron spectroscopy (XPS) and atomic force microscopy. Chemical functionalization prior to XPS analysis permits the unique identification of primary and secondary amine groups. Secondary amine containing films are shown to form at low silazane ion energies whereas the higher ion energies lead to formation of more inorganic, silico-carbo-nitride-like films. Effects of film aging in air are also discussed.

2. Experimental

1,3-divinyltetramethyldisilazane, CH_2=CH-Si$(CH_3)_2$-NH-Si$(CH_3)_2$-CH=CH_2 (M=185), referred to below as silazane, was used as the ion precursor. The most abundant ion formed by electron impact appeared at m/z 170 ($C_7Si_2NH_{16}^+$) and was chosen for deposition. The m/z 170 silazane ion corresponds to the molecular ion minus one methyl group. Some deposition was also performed with the siloxane ion counterpart at m/z 171, formed from divinyltetramethyldisiloxane (CH_2=CH-Si$(CH_3)_2$-O-Si$(CH_3)_2$-CH=CH_2). The siloxane ion differs from the silazane ion in the replacement of the NH group by an oxygen atom ($C_7Si_2OH_{15}^+$). All ion depositions were performed with ion kinetic energies varying from 5 to 200 eV; ion currents of 25 to 35 nA; and ion fluences of 1.4 to 6.8×10^{15} ions/cm^2. Aluminum foil and silicon wafers were used as substrates, the latter after etching with 5% HF to produce a hydrogen-terminated surface with a minimum of oxide [3]. XPS of the aluminum substrate prior to ion deposition found an elemental content of 30% Al, 59% O and 11% C. The Si substrate prior to ion deposition displayed an elemental content of 10% C, 4% O, and 86% Si. Films noted "as-deposited" correspond to those directly transferred to the XPS without any air exposure. Initial XPS were recorded with monochromatic Al-Kα radiation and analyzed as previously described [5]. All XPS peaks are referenced to aliphatic C 1s (C-C, C-H) at 284.5 eV, chosen to take into account a considerable amount (~20%) of silicon in the coatings which shifts the carbon binding energy downwards slightly [6]. The peak positions vary with accuracy of 0.1 eV. Atomic force microscopy was recorded in air using the tapping mode, as previously described [3]. The average RMS roughness was calculated from 5 μm x 5 μm and 1 μm x 1 μm overlapping areas scanned for each sample. All work was performed at the University of Illinois at Chicago.

3. Results and Discussion

Fig. 1 displays the high-resolution Si 2p (left) and C 1s (right) XPS core levels of a silazane film deposited from 15 eV ions on a silicon substrate, without air exposure (as-deposited). The silazane film is thin enough to observe the substrate signal, consisting of the two Si 2p spin orbital peaks: $2p_{3/2}$ at 100.4 eV and $2p_{1/2}$ at 100.9 eV. The broad peak at 102.7 eV corresponds to silicon bound within the silazane film to carbon, nitrogen, and oxygen. Oxygen from the substrate appears in the films in the amount of several percent,

despite its absence in the silazane precursor ion. Unfortunately, the difference in the Si 2p chemical shift produced by nitrogen and oxygen is too small to be resolved here. Si 2p binding energies of SiN and SiC species range from 101.3 to 102.8 eV [7-13].

The broad Si 2p peak of the siloxane film appears at 103.2 eV (not shown), is 0.5 eV higher binding energy than the silazane film peak. This indicates that SiN is a major component of the silazane film, with smaller contributions from SiO and SiC environments. This SiN assignment is supported by elemental analysis (see below), which displays higher concentrations of nitrogen than oxygen across the entire range of the energies. The N 1s peak is centered at 396.9 eV, lower than usually found for many CN groups [6]. This lower N 1s binding energy is attributed to the predominance of nitrogen as Si_xN. The C 1s spectra in Fig. 1 (right) is featureless and is fit with an aliphatic and SiCN component (shown as solid underlying lines in Fig. 1), consistent with the above arguments and as discussed further below.

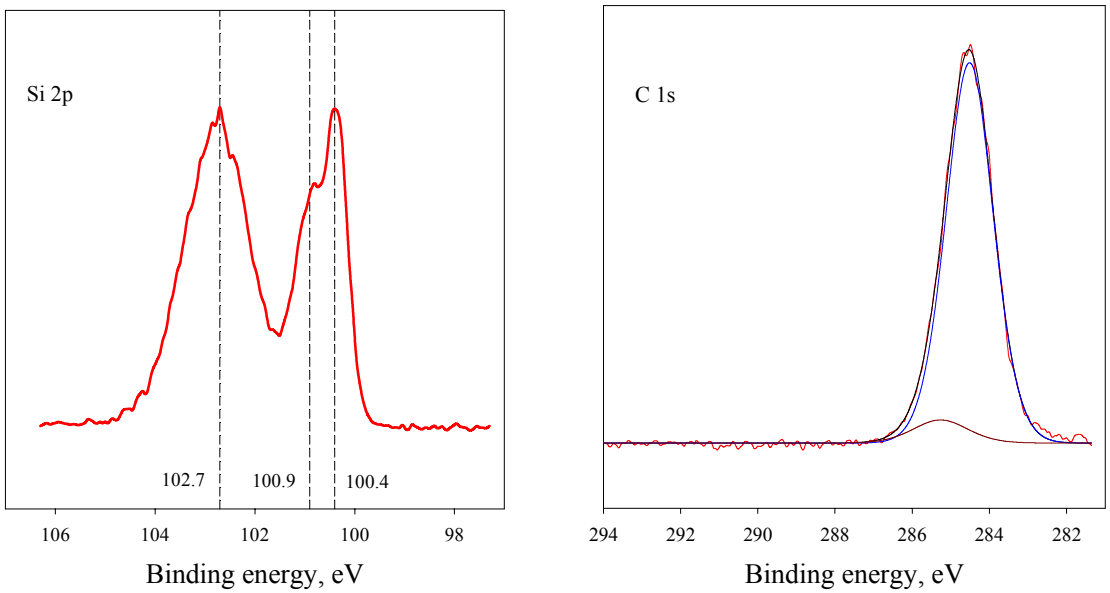

Fig. 1. The high-resolution Si 2p (left) and C 1s (right) XPS core levels of silazane films as-deposited by 15 eV ions on a hydrogen terminated Si substrate.

The elemental composition of the as-deposited silazane films on silicon is shown in Fig. 2a. The horizontal reference lines correspond to the element concentrations of the precursor ion $C_7Si_2NH_{16}^+$: 70% of carbon, 20% of silicon and 10% of nitrogen. There is evident dependence of the element composition on incident ion energy. With increasing ion energy the amount of carbon decreases and the concentration of silicon and nitrogen grows. The oxygen content for this set of experiments is nearly constant at ~4%. It has been reported that $Si\text{-}CH_3$ bonds are most vulnerable to cleavage in organosiloxane films deposited from plasmas [14]. It is similarly argued here that the $Si\text{-}CH_3$ dangling bonds are more easily broken than $Si\text{-}CH{=}CH_2$ or Si-NH-Si backbone bonds. It follows that the higher ion energy would favor cleavage of the $Si\text{-}CH_3$ bonds and formation of volatile CH_x species, leaving the film rich in silicon and nitrogen components. By contrast, low-energy ions should lead to films more similar to the monomer. The elemental contents in Fig. 2a are consistent with low-energy ions forming more organic polymer-like structures and the high-energy ions forming more inorganic SiCN coatings, as observed previously for $Si_2O(CH_3)_5^+$ ion deposition [2]. Slightly higher concentrations of carbon and lower concentrations of nitrogen and silicon are due to the initial carbon contamination of the substrate. The ion energy trend is similar in the case of the aluminum substrate (data not shown). However, the oxygen content of 10-18% is much higher, consistent with the high initial oxygen content on the aluminum substrate. The film thickness is on the order of several nanometers, allowing observation of oxygen signal from the aluminum substrate.

The elemental ratios vs. incident ion energy for the deposited silazane films are plotted in Fig. 3a. The broken lines at C/N=7, C/Si=3.5 and Si/N=2 ratios correspond to the precursor ion. The Si/N ratio remains nearly constant across the range of ion energies and is within experimental error of the precursor value. The decrease in C/N and C/Si ratios with ion energy at the expense of carbon is consistent with the loss of CH_x species. As mentioned above, the low binding energy of the N 1s peak confirms that nitrogen in the film

remains bound to silicon. Possible Si-N-Si structures include Si-NH-Si, Si=N-Si, Si=NH, Si-NH-C, Si-N=C, Si-NC-Si (the absence of primary amines will discussed below). The presence of SiCN binding environments is seen in a slight asymmetry of C 1s spectrum, shown for example in Fig. 1 (right). The small C 1s component is shifted ~0.8 eV below the primary aliphatic component, with ~7% of the total peak area. This minor component is assigned to SiCN species with some contribution from CO. Nitrogen bound only to carbon might also contribute to the C 1s, but there is no evidence of CN structures in the N 1s spectrum. Large fractions of SiC species are also unlikely.

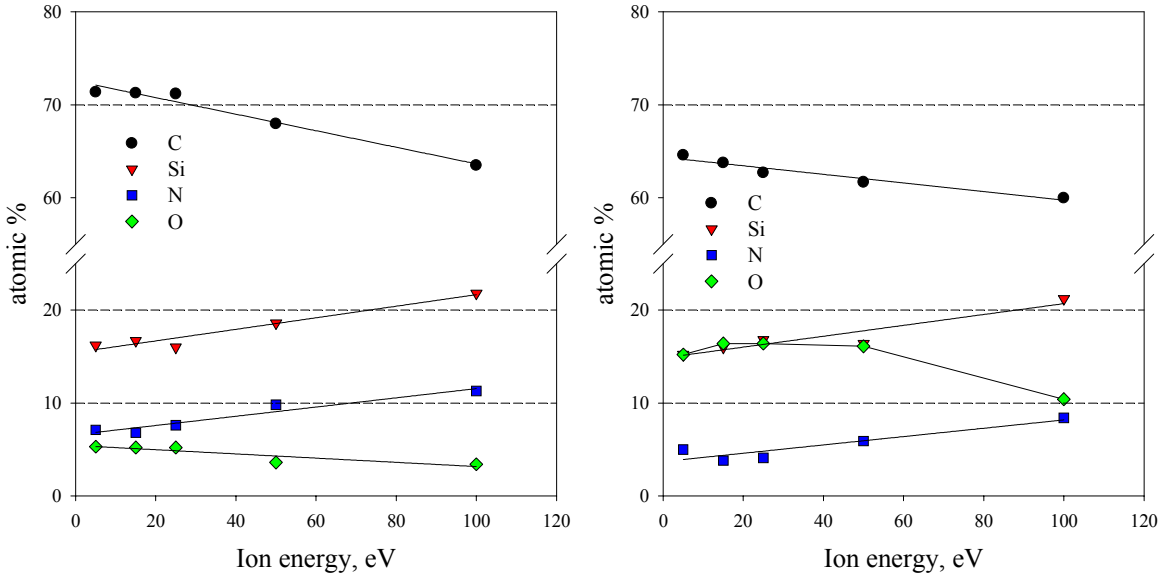

Fig. 2. Elemental composition of: a) as-deposited silazane films on Si; b) 7 day aged silazane films on Si.

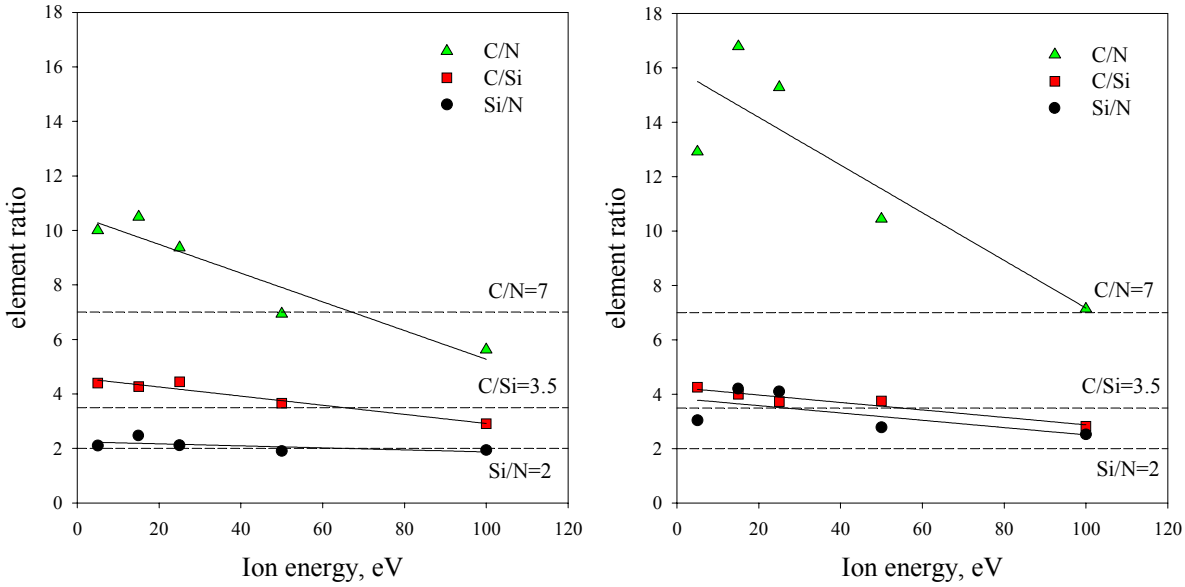

Fig. 3. Change of elemental ratios with ion energy for: a) as-deposited silazane films; b) 7 day aged silazane films.

The film samples were also stored in air for 7 days, then the XP spectra were again acquired. Chemical derivatization was applied to determine the concentration of primary and secondary amine on the aged samples. Trifluoromethyl benzaldehyde (TFBA, a) and trifluoroacetic anhydride (TFAA, b) were used as chemical agents to detect primary and secondary amines, as indicated in Fig. 4 [15]. XPS was immediately applied after treatment with TFBA or TFAA to determine the fluorine content, which was then related to the amine content. TFAA is also sensitive to hydroxyl groups, as discussed further below.

a) $-NH_2+O=CH-C_6H_5-CF_3 \rightarrow N=CH-C_6H_5-CF_3+H_2O\uparrow$ b) $-NH_2+(CF_3-CO)_2O \rightarrow -NH-CO-CF_3+CF_3COOH\uparrow$

$>NH+(CF_3-CO)_2O \rightarrow >N-CO-CF_3+CF_3COOH\uparrow$

Fig. 4. Derivatization reactions for primary (NH_2) and secondary (NH) amine analysis: a) NH_2 with TFBA; b) NH_2 and NH (and OH) with TFAA.

15 - 200 15 eV silazane films on aluminum were treated with TFBA and the lack of fluorine signal indicate an absence of primary amines. The same films on both on aluminum and silicon samples were then treated with TFAA, with the results shown in Fig. 5. The secondary amine content was calculated as [F]/3. TFAA may also react with hydroxyl groups which are likely present in the film as a result of oxidative reactions or hydrolysis during storage on air. So, the value of [F]/3 is referred to as the total amount of NH and OH on the film surface.

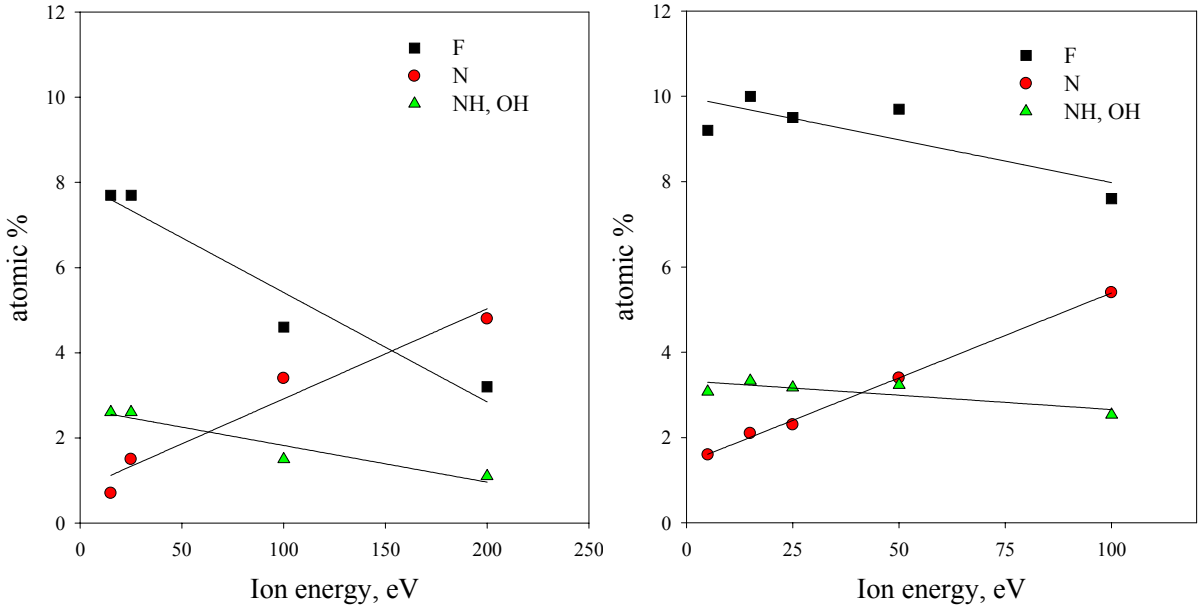

Fig. 5. Concentration of F, total N, and NH, OH (sum) after the derivatization with TFAA of films on a) Al and b) Si.

It is interesting to compare the behavior of the total nitrogen content (N) and the NH curves (NH, OH). The high-energy ions form films with higher nitrogen concentration, but the secondary amine concentration is the lowest. The collision of the silazane ions with the surface likely results in fragmentation of the secondary amine, leaving nitrogen bound mainly to silicon. In the case of 200 eV ions (aluminum substrate) the secondary amines constitute only ~20% of total nitrogen, but this rises to ~50% for 100 eV ions. The situation changes as the ion energy decreases. The values of [F]/3 are even higher than the nitrogen content for 15 and 25 eV ions. The curves follow the same trend for the films on the silicon substrates, except that the nitrogen and fluorine concentrations are slightly higher. However, [F/3] and total nitrogen curves intersect at about 50 eV ion energy for both substrates. The fact that the [F/3] values are higher than total nitrogen for the low-energy ions films is explained by the contribution from OH groups. A 15 eV film treated with TFAA immediately after extracting the sample from the vacuum system gave values of 2.5% total nitrogen and 2.7% [F]/3. This supports the argument that most nitrogen in the low-energy films is secondary amine, with oxidation in air leading to the formation of some surface hydroxyl groups.

The composition of the aged silazane films is shown in Fig. 2b. The aged samples have lower concentrations of carbon, silicon, and total nitrogen and much higher concentrations of oxygen than the as-deposited films. Aging effects were less for films deposited at higher ion energies. The oxygen content increased from 4% to 10% upon aging of 100 eV films, while it increased from 5% to 17% for aging of ≤25 eV films. The dependence of element ratios of the aged films on ion energy (Fig. 2b) reveals that C/N and Si/N ratios increase and C/Si stays at the same level as in the as-deposited coatings. Gengenbach [9] investigated the aging of plasma polymerized diaminopropane and considered the hydrolysis of imines with elimination of ammonia: $R-CH=NH + H_2O \rightarrow R-CH=O + NH_3\uparrow$. Given that the concentration of secondary amines is the highest for the low-energy ions films (see above), ammonia elimination can explain the unusual aging behavior of silazane films. The hydrolysis reaction runs slower in 100 eV films, in which only about half of the nitrogen atoms are in NH form.

The morphology of silazane films, kept after the deposition for 1-2 weeks on air, was investigated by AFM in tapping mode. To minimize the influence of substrate on resulted images silicon wafer with roughness of about 0.15 nm was chosen as a substrate (Fig. 6a).

a) Si wafer, Ra=0.13 nm

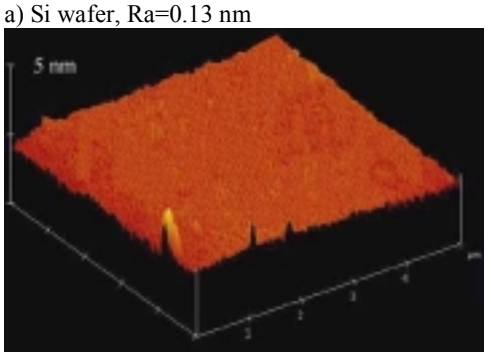

b) 15 eV, 33 nA, 7 h Ra=0.54 nm

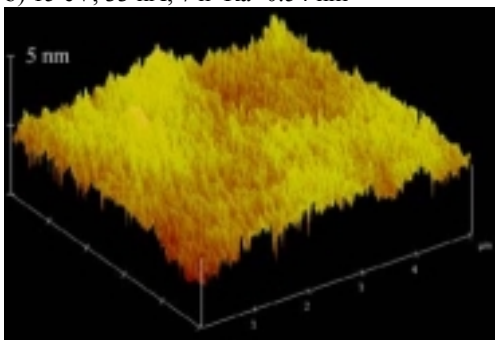

c) 15 eV, 33 nA, 10 h Ra=0.71 nm

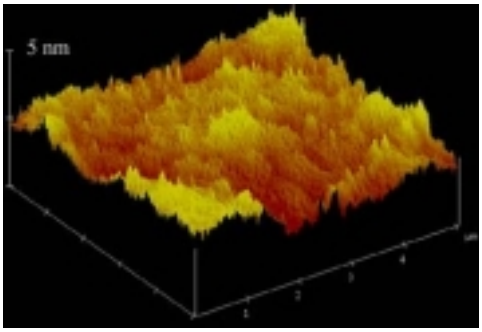

d) 100 eV, 35 nA, 3 h Ra=0.48 nm

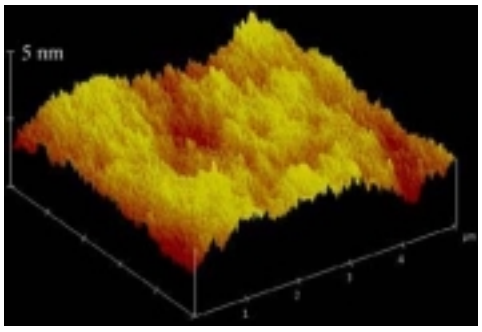

e) 100 eV, 35 nA, 4.5 h Ra=0.73 nm

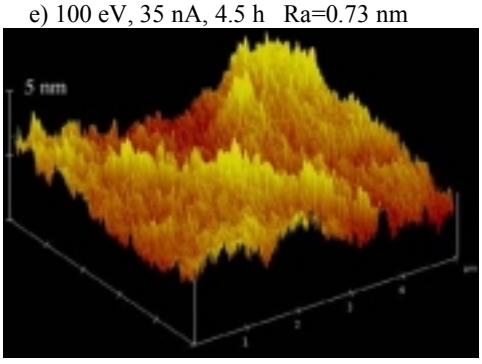

Fig. 6. AFM images of silazane films of equal thickness deposited by 15 and 100 eV silazane ions.

The films were deposited with 15 and 100 eV ions at 33-35 nA current with different deposition times. In order to analyze the morphology of different coatings, it is important to compare films of similar thicknesses. The very thin films yielded complex Si 2p XPS peaks, with both a silazane component (102.3 eV) and a substrate silicon component (100.0 - 101.0 eV), as depicted in Fig. 1 (left). Comparison of the relative peak areas of these different Si 2p components was used to grow films of similar thicknesses by 15 and 100 eV ions. The deposition rate for 100 eV silazane ions was thereby found to be ~2.3 times higher than that of 15 eV ions: deposition within 3 hours by 100 eV ions corresponded to 7-hour deposition by 15 eV ions; 4.5 hour, 100 eV deposition corresponded to 10 hours of 15 eV deposition.

The comparison of morphology of 15 and 100 eV ions films of equal thickness is given in Fig. 6. The only significant difference in roughness was observed for films of different thickness, with thicker coatings prepared at either energy (Figs. 6c and 6e) appearing rougher (~0.7 nm RMS) than thinner films (Figs. 6b and 6d, with ~0.5 nm RMS). Films of similar thicknesses at prepared at different energies displayed similar roughnesses, within experimental error.

4. Conclusion

The polyatomic ion deposition of 1,3-divinyltetramethyldisilazane occurs via fragmentation of the silazane ions colliding with the surface, followed by successive recombination of species in the film. The process occurs with preferential cleavage and elimination of methyl groups. The film composition depends strongly upon ion energy. Low energy ions produce more organic deposits with the highest concentration of carbon. As-deposited films are similar in composition to the original ion. Most of the nitrogen atoms in these films are in the NH form. The ions of higher energy form films with higher percentages of silicon and nitrogen, and reduced carbon content. Higher ion energy also leads to decomposition that reduces the amount of NH functionalities. The films deposited by the ion deposition of silazane are very smooth, with roughnesses less <1 nm (RMS). The roughness of the films depends more on their thickness, being higher for the thicker coatings. No strong difference in morphology between low- and high-energy films is found, in contrast to the case for films grown on polymer surfaces [16]. When exposed to air, silazane films age, which leads to oxygen concentration increase. One of the probable mechanisms of oxygen uptake is hydrolysis of imines with elimination of nitrogen as volatile ammonia. Low-energy ion films are more susceptible to aging because of higher NH concentration.

5. References

[1] L. Hanley and S.B. Sinnott, Surf. Sci. **500** (2002) 500.

[2] P.N. Brookes, S. Fraser, R.D. Short, L. Hanley, E. Fuoco, A. Roberts, and S. Hutton, J. Elec. Spect. Rel. Phenom. **121** (2001) 281.

[3] E.R. Fuoco and L. Hanley, J. Appl. Phys. **92** (2002) 37.

[4] S. Tepavcevic, Y. Choi, and L. Hanley, J. Amer. Chem. Soc. **125** (2003) 2396.

[5] M.B.J. Wijesundara, Y. Ji, B. Ni, S.B. Sinnott, and L. Hanley, J. Appl. Phys. **88** (2000) 5004.

[6] G. Beamson and D. Briggs, *High Resolution X-Ray Photoelectron Spectra of Organic Polymers: The Scienta ESCA300 Database*. New York: John Wiley, 1992.

[7] F.J. Gomez, P. Prieto, E. Elizade, and J. Piqueras, Appl. Phys. Lett. **69** (1996) 6.

[8] J.R. Yang, Y.P. Zhao, Y.Z. Hu, T.P. Chow, and R.J. Gutman, Thin Solid Films **333** (1998) .

[9] T.R. Gengenbach and H.J. Griesser, Polym. **40** (1999) .

[10] K. Tanaka, A. Tsuge, M. Takiyarna, and R. Shimuzu, Surf. Interf. Anal. **27** (1999) .

[11] H. Lutz, M. Bruns, F. Links, and H. Baumann, Surf. Coat. Technol. **116-119** (1999) .

[12] T. Seino, T. Matsuura, and J. Murota, Surf. Interf. Anal. **34** (2002) .

[13] Z.W. Deng and R. Souda, Diam. Rel. Mater. **11** (2002) .

[14] M.R. Alexander, F.R. Jones, and R.D. Short, J. Phys. Chem. B **101** (1997) 3614.

[15] A. Chilkoti and B.D. Ratner in *Surface Characterization of Advanced Polymers*, L. Sabbatini and P. G. Zambonin, Eds. Weinheim: VCH, 1993, pp. 221.

[16] L. Hanley, Y. Choi, E.R. Fuoco, F.A. Akin, M.B.J. Wijesundara, M. Li, A. Tikhonov, and M. Schlossman, Nucl. Instr. Meth. Phys. Res. B (2003) in press.

FUNCTIONAL PLASMA POLYMER COATINGS ON POWDERS

Sheyu Guo [1], Jiangang Zhao [2], Wim van Ooij [2] and Saswati Datta [1]

[1] *Procter & Gamble , Corporate Engineering Laboratories*
West Chester , OH 45069
And
[2] *Department of Materials Science and Engineering*
University of Cincinnati, Cincinnati OH

Plasma polymer coatings have been studied extensively on flat substrates such as paper, fabrics, glass and metal surfaces. Such coatings have been demonstrated to alter surface properties such as wettability and non-fouling characteristics. Applications of these coatings to powder surfaces, however, have additional challenges, and only limited studies have been done in applying these coatings to powders and particulates. This study focuses on the design and application of a plasma reactor for applying plasma polymer coatings on powders of various sizes. Plasma polymer coatings have been generated on powder substrates that provide such industrially important effects as moisture resistance, controlled dissolution and improved dispersion into solvent. The paper will discuss the process as well as chemistry used to generate various types of plasma polymer coatings on powders and particulates.

PLASMA POLYMERIZATION IN A MICROWAVE REACTOR AT ATMOSPHERIC PRESSURE

V. Shanov [1] , S. F. Miralai [2] , S. M. Mukhopadhyay [2] , Pratik Joshi [2] , and S. Datta [3]

[1] *University of Cincinnati , Department of Materials Science and Engineering*
Cincinnati , OH 45221

[2] *Wright State University, Mechanical and Materials Engineering Department*
Dayton , OH 45432 , USA

[3] *Procter & Gamble , Corporate Engineering Laboratories*
West Chester , OH 45069

Microwave plasmas at low pressures have been extensively studied in the literature and are known for their high chemical activities due to the high generation rate of reactive species. In contrast Microwave discharges at high pressures is relatively new, and has been used mainly as excitation source for dissociative processes and spectrochemical analysis for use in environmentally oriented applications such as abatement of CFCs and NOx destruction, due to their high temperatures. In this paper we will investigate a new application of atmospheric microwave discharges, namely post-discharge plasma polymerization of Fluorocarbon monomers, for production of hydrophobic coatings. In our study the bulk chemistry of the coatings was determined by using FTIR analysis, while the surface chemistry and function retention was investigated by X-ray photoelectron spectroscopy XPS. The coatings were found to replicate the structure of the monomer as shown by FTIR analyses. The deposition thickness and topology of the coatings are estimated by AFM while surface energy determination using sessile drop technique exhibited hydrophobic polymer coatings with low surface energy. The variation of the surface energy as a function of the applied power is discussed in terms of the CF2/CF3 ratio and the functional retention.

FLUOROCARBON PLASMA POLYMER FORMATION IN A DIELECTRIC BARRIER DISCHARGE REACTOR AT ATMOSPHERIC PRESSURE

S. F. Miralai [1] , S.M. Mukhopadhyay [1] , Pratik Joshi [1] and S. Datta [2]

[1] *Wright State University, Mechanical and Materials Engineering Department*
Dayton , OH 45432 , USA

[2] *Procter & Gamble , Corporate Engineering Laboratories*
West Chester , OH 45069

Dielectric Barrier discharges (DBD) are gaining increased attention as an economical and reliable method for generating non-equilibrium plasma conditions in atmospheric pressure gases. This has led to a number of important applications including industrial ozone generation, excitation of CO2 lasers, surface modification of polymers and large area plasma flat panel displays. This paper deals with a new topic in the spectum of applications of DBDs, namely plasma polymerization. Plasma polymerization of Fluorocarbons is studied in a parallel-plate dielectric barrier discharge (PPDBD) as a function of different plasma operating parameters. The chemical composition of the deposited films has been determined by X-ray photoelectron spectroscopy (XPS). The coating is found to be of a similar structure than the monomer as shown by FTIR analyses. The deposition thickness and topology of the coatings are estimated by AFM while surface energy determination using contact-angle measurements exhibits hydrophobic polymer coatings with very low surface energy. The retention of different functionalities and the influence of the ratio CF2/CF3 as a function of power are discussed and correlated to the surface energy of the coatings.

Combinatorial Synthesis of Conducting Oxides by Plasma-enhanced Chemical Vapor Deposition

C. A. Wolden, C. Fry, J. Esteban, and J. J. Robbins

Department of Chemical Engineering, Colorado School of Mines, Golden, CO 80401 USA

Abstract
Transparent conducting oxides (TCOs) are primarily doped oxides. Next generation applications require TCOs with improved conductivity and tailored properties. In this paper we will describe our combinatorial approach to rapidly evaluate new materials and process chemistries. The experimental reactor is described, as well as the characterization techniques used for both screening and formal evaluation. Examples are provided from a number of oxide systems, including tin–zinc, tin–antimony, and gallium–zinc.

1. Introduction (Times 11, bold)

Transparent conducting oxides (TCOs) are used extensively as transparent electrodes in photovoltaic and display applications. It is becoming clear that as photovoltaic, electrochromic, display and other technologies reliant on TCOs continue to advance the properties of existing TCOs are impacting the performance of the final device. To achieve superior performance the TCO community must discover new and improved materials since the existing ones have been highly optimized during the past three decades [1]. The TCO phase space is shown in Figure 1 [2]. The commercial TCOs are derived from the vertices of Figure 1: F-doped tin oxide (SnO_2:F), tin-doped indium oxide (ITO), and aluminum-doped zinc oxide (ZnO:Al). Despite some recent encouraging results, the elemental TCO phase space (Zn-In-Sn-Ga-Cd) remains largely uncharted.

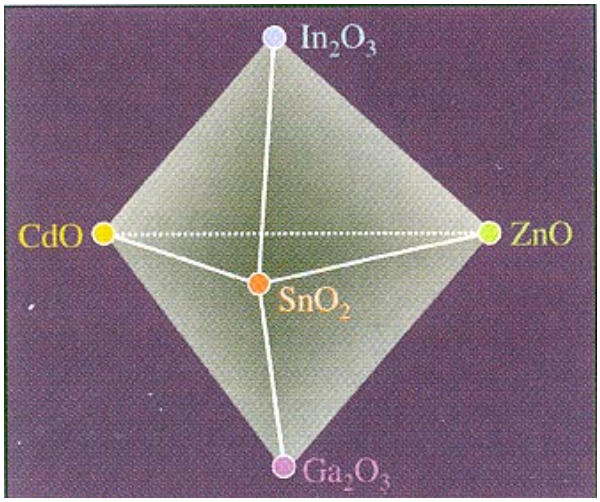

Figure 1. The TCO phase space [2].

The primary synthesis techniques for TCOs have been either physical vapor deposition (sputtering, pulsed laser ablation) or thermal chemical vapor deposition. Sputtering is the pre-eminent technique for the deposition of two widely used TCOs, ITO and ZnO. It has a demonstrated track record for producing high quality films at low temperature. It has some drawbacks, particularly the cost and reproducibility of forming new targets, which limits its suitability for exploring new compounds. An additional handicap is the inability to incorporate volatile compounds like N or F into targets. Atmospheric pressure chemical vapor deposition (APCVD) is an economical, high throughput technology that is employed for the synthesis of SnO_2:F. A kinetic process, it is capable of incorporating light atoms into film growth. Unfortunately APCVD has been restricted to tin oxide, mainly due to limitations on precursor volatility, reactivity, and compatibility. To make an alloy by thermal CVD is challenging since one must find precursors that have compatible volatility and reactivity. For example, the temperatures employed for CVD of ZnO [3] and SnO_2 [4] differ by several hundred degrees .

Plasma-enhanced chemical vapor deposition has a number of advantages over these techniques, particularly for the synthesis of alloys and functionally graded materials. In PECVD the initial chemistry is driven by electron impact reactions, which are very fast regardless of precursor. The low operating pressures ($P < 1$ torr) of the PECVD environment mitigate issues associated with low precursor volatility. To explore the phase space shown in Figure 1 by PVD would require numerous targets. In contrast, a wide range of compositions may be easily evaluated in a continuous manner through PECVD by simply adjusting flowrates. A further advantage of PECVD is that steps such as plasma cleaning and modification of surfaces may be performed *in-situ*. These steps are often used to improve adhesion on foreign substrates and to create

clean interfaces. In previous work we have established PECVD as an alternative technique for the synthesis of high quality tin oxide [5, 6] and zinc oxide films [7]. For both tin oxide and zinc oxide the best resistivity values achieved were $\rho \sim 10^{-3}$ Ω-cm, among the best values obtained for intrinsic films by any deposition method [1]. Further improvements in conductivity require the addition of dopants or alloy formation [8].

A drawback of plasma system is that the chemistry is complex, and not well understood. Combinatorial chemistry has established itself as the premier approach for the synthesis of materials as varied as new drugs and novel catalysts [9]. The essence of this approach involves the ability to *generate* and *evaluate* a large number of chemical compounds in an efficient manner. Originally developed by organic chemists to order peptide sequences into pharmaceuticals with therapeutic properties, the technique has recently been extended to solid-state materials synthesis. Particular success has been achieved with complex oxides, such as high temperature superconductors and ferroelectrics [10, 11]. For TCOs researchers have relied on sputtering to find new compounds using multiple targets [12, 13]. In this paper we describe a PECVD reactor that has been modified for combinatorial synthesis of TCOs. We also detail the techniques employed for both screening and detailed characterization. Results are presented from a number of materials systems.

2. Experimental

Since the plasma chemistry is quite complex and not well understood, an efficient means to screen potential precursors was developed. A custom-built, capacitively coupled PECVD reactor was used for this work. Additional details on the experimental setup may be found in the literature [5, 6]. The PECVD reactor was modified as shown schematically in Figure 2. Gaseous precursors were directed into the chamber through one of three sources: (*i*) a uniformly perforated showerhead, (*ii*) a single ¼" hole at the center of the showerhead, or (*iii*) through multiple ports on the exterior of the parallel plates. This combinatorial setup produced films with a radial gradient in composition. Figure 3 shows a photograph of a typical film produced with the combinatorial setup. Transparent throughout, the circular interference fringes are due to variations in thickness. The films all demonstrate radial symmetry, as one would expect from the setup shown in Figure 2. Three systems have been investigated to date: antimony-doped tin oxide (SnO_2:Sb) using $SnCl_4$ and $SbCl_5$, gallium-doped zinc oxide (ZnO:Ga) using diethyl zinc (DEZ) and trimethyl gallium (TMG), and alloy formation in the tin-zinc system using $SnCl_4$ and DEZ. In these studies the dopant was introduced through the center hole (Gas 2), and the base precursor was supplied through the showerhead (Gas 1).

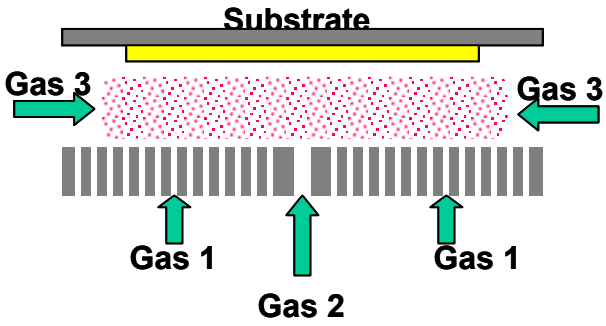

Figure 2. Schematic diagram of the PECVD setup.

The typical bottleneck to any combinatorial approach is property evaluation. For TCOs the primary metrics of interest are transparency and sheet resistance. Visual observation provided convenient screening of transparency, while a four point probe was used for expeditious evaluation of electrical properties with mm resolution. The sheet resistance is a function of both thickness and intrinsic resistivity, $R_s = \rho/t$. The thickness of the film across the glass substrate may vary by up to 50% in these combinatorial syntheses, which is the source of the interference fringes that may be seen in Figure 3. However, the electrical properties can vary by orders of magnitude. Thus, this technique provides an adequate first order assessment of electrical performance. As such a great range of process chemistries were examined with just a handful of deposition experiments. After screening, promising precursors and chemistries are examined in more detail.

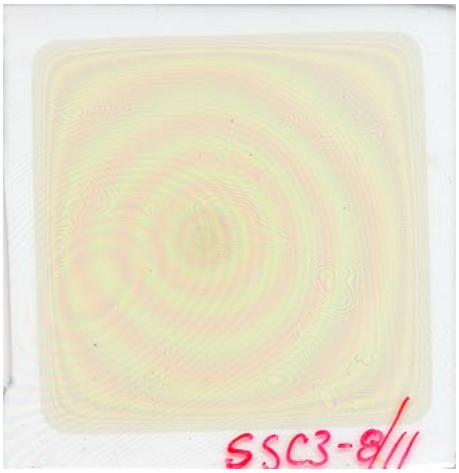

Figure 3. Optical photograph TCO film produced by the combinatorial setup.

The complete set of materials characterization included film, thickness, transmittance, resistivity, Hall mobility, and carrier concentration measurements, crystal structure, and film morphology. Film thickness was accurately measured using a Woolam WVASE32 variable angle spectroscopic ellipsometer. For our measurements the thickness and index of refraction the glass substrate were fixed; a standard file for Corning 7059 glass was used for the substrate index of diffraction. A parameterized Lorentz model was used for the film. Film transmittance was determined by a Cary 5G UV-VIS-NIR spectrophotometer over a wavelength range from 200 – 2500 nm. The values reported here reflect film properties only, since the contributions from the glass substrate were subtracted out during calibration. For visible transmission, the spectra were integrated over the 400-800 nm wavelength range, and the average value is reported. Film resistivity, electron mobility, and carrier concentration were determined using a Bio-Rad HL5500PC Hall Effect Measurement System using the square van der Pauw geometry. Structural measurements were made on several films using X-ray diffraction (XRD) and atomic force microscopy (AFM). XRD patterns were obtained by rotating the sample over a angle of incidence range of 20° to 70° using a Rigaku system. A Digital Instruments Nanoscope III scanning probe microscope was used to examine morphology and quantify surface roughness.

3. Results

The first property that was screened was optical transparency. The results were binary: either the film had excellent transparency (>85%), or it failed catastrophically. Figure 4 contrasts representative photographs of each case. Failure modes included both poor transmission or poor adhesion. The photograph on the left in Figure 4 is an example of a poor film that exhibited both failure modes. If a film had good transparency, it was next screened for electrical conductivity using the four point probe.

Figure 4. Comparison of films with poor (left) and good (right) optical transparency.

The three systems that have been investigated to date: antimony-doped tin oxide (SnO_2:Sb) using $SnCl_4$ and $SbCl_5$, gallium-doped zinc oxide (ZnO:Ga) using diethyl zinc (DEZ) and trimethyl gallium (TMG), and alloy formation in the tin-zinc system using $SnCl_4$ and DEZ. Figure 5 shows radial profiles of sheet resistance obtained for these three strategies. The dopant was highest in the center (r = 0), and in each case the electrical properties of the films at the edge of the substrate (r ~25 mm) were similar to that of undoped material.

In Figure 5 one can see antimony had a dramatic influence on the electrical properties of tin oxide. However the effect was detrimental, increasing the sheet resistance by more than 3 orders of magnitude. Similarly the electrical properties of alloys in the tin-zinc system were inferior to the individual oxides. However we did synthesize the ternary spinel, Zn_2SnO_4, which is also insulating. The most promising results were clearly achieved with gallium doping of zinc, and this system was investigated in more detail as described below.

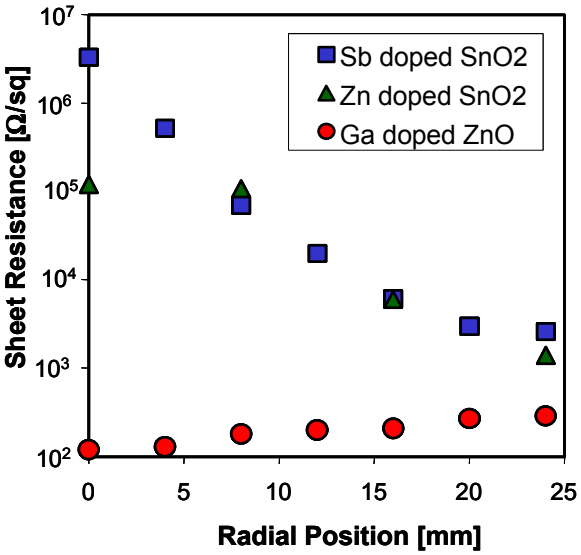

Figure 5. Radial profiles of sheet resistance from different screening experiment .

The structural features of the three films produced by combinatorial experiments are shown in Figures 6- 8. Figure 6 shows the XRD patterns from the tin-antimony systems. The major peak at 2θ ~26.6º is the (110) orientation of SnO_2. The crystallinity is best at the edge, and gradually deteriorates as one progresses towards the center of the film, where high levels of antimony were present. The structural data is consistent with the electrical properties shown in Figure 5.

The selection of dopant has a profound impact on the orientation of the base oxide. Figure 7 shows zinc-doped tin oxide. At the edge the two broad peaks at 34.5º and 52º correspond to the (101) and (211) orientations of tin oxide. Note that the prominent (110) peak that dominated the antimony-doped patterns is not present. At the center of the zinc-doped film the zinc stannate phase (Zn_2SnO_4) is formed, as identified by the (220) peak located at 2θ ~29.5º. The mixed oxide phases were not found to be beneficial for conductivity.

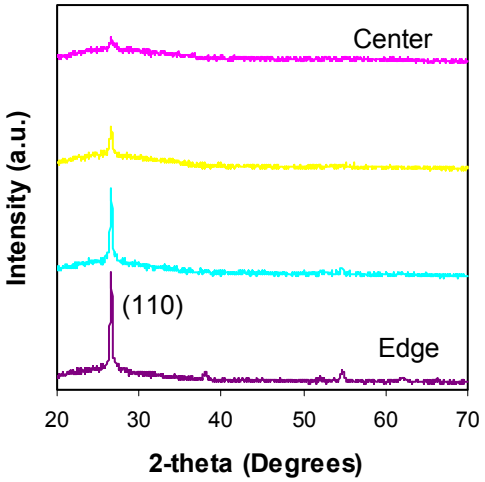

Figure 6. XRD patterns from a Sn-Sb-O film as a function of radial position.

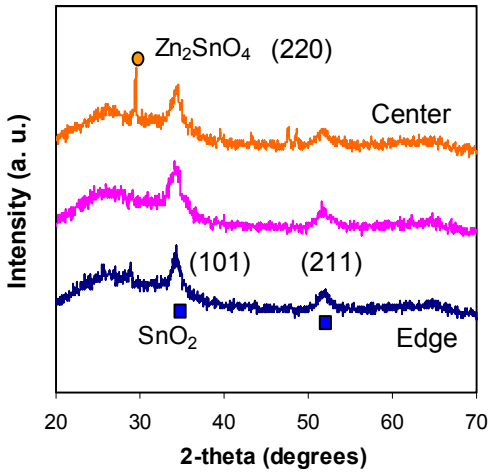

Figure 7. XRD patterns from a Sn-Zn-O film as a function of radial position.

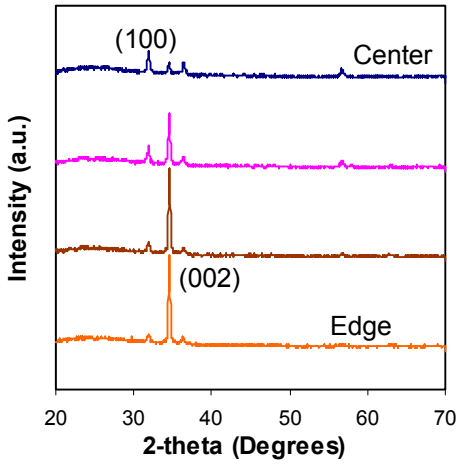

Figure 8. XRD patterns from a Zn-Ga-O film as a function of radial position.

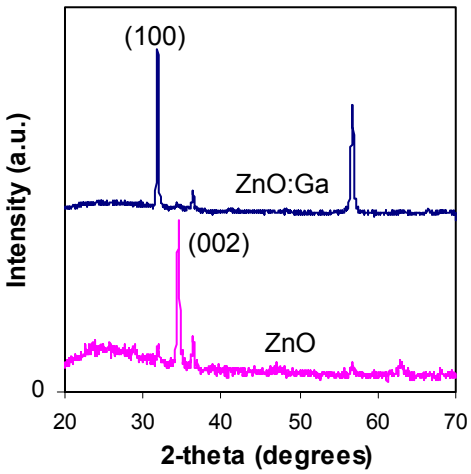

Figure 9. XRD patterns from optimized ZnO and ZnO:Ga films.

The final system examined was gallium-doped zinc oxide. The XRD patterns obtained from the screening experiments are shown in Figure 8. All of the peaks in Figure 8 were positively attributed to zinc oxide. At the edge of the film the ZnO demonstrated a preferred orientation in the (002) direction. As the gallium density was increased towards the center of the film it was observed that (002) at 2θ ~34.5º decreased, and the film shifted towards an (100) orientation identified by the peak at 2θ ~31.9º. As shown in Figure 5 the

inclusion of gallium was beneficial to the electrical conductivity. As such this reaction chemistry was pursued extensively. Films have been grown that span the ZnO – Ga_2O_3 phase space. The DEZ/TMG ratio was found to have a dramatic impact on the plasma chemistry, benefiting both rate and conductivity in a synergistic fashion. Details will be forthcoming [14], however at this point we have obtained commercial caliber TCO films with sheet resistance values ~ 15 Ω/square and visible transmission values > 85%. Figure 9 shows XRD patterns from undoped ZnO and gallium doped ZnO:Ga under optimal conditions. The undoped material is highly oriented in the (200) direction, while the doped film is dominated by the (100) orientation. These are the same features that were identified in the initial screening experiment shown in Figure 8. Work continues using this reactor to screen plasma chemistries for both oxide doping and alloy formation.

4. Conclusions

A system has been described for combinatorial synthesis of oxide films by plasma-enhanced chemical vapor deposition. It has been applied to examine doping and alloy formation for TCO thin films. Simple techniques were used to rapidly screen the optical and electrical performance of TCO films. A number of plasma chemistries were studied. This approach was used to identify the promising nature of diethyl zinc/trimethyl gallium mixtures. This system was further optimized to produce TCO films with very low sheet resistance and high optical transparency. Structural characterization of the films revealed the synthesis of the hard to form zinc stannate phase. It also showed that selection of dopant has a profound influence on the orientation of the base oxide.

Acknowledgements

The authors acknowledge financial support for this work from the National Science Foundation through awards No. DMII-9978676 and CTS-0093611.

References

[1] A. L. Dawar, H. L. Hartnagel, A. K. Jain, and C. Jagadish, in *Semiconducting Transparent Thin Films*. (Institute of Physics Publishing, Philadelphia, 1995).
[2] T. J. Coutts, D. L. Young, and X. Li, MRS Bulletin **25** (8), 58 (2000).
[3] J. Hu and R. G. Gordon, J. Appl. Phys. **72** (11), 5381 (1992).
[4] A. Al-Kaoud, T. Wen, A. Gilmore, V. Kaydanov, T. R. Ohno, C. A. Wolden, L. Feng, J. Xi, *NCPV Photovoltaics Program Review*, (Eds. M. Al-Jassim, J. P. Thorthon and J. M. Gee), American Institute of Physics, Woodbury, NY (1999) p. 212-217.
[5] J. J. Robbins, R. T. Alexander, M. Bai, Y.-J. Huang, T. L. Vincent, and C. A. Wolden, J. Vac. Sci. Technol. A **19**, 2762 (2001).
[6] J. J. Robbins, R. T. Alexander, W. Xiao, T. L. Vincent, and C. A. Wolden, Thin Solid Films **406**, 145 (2002).
[7] J. J. Robbins, J. Esteban, C.Fry, and C. A. Wolden, J. Electrochem. Soc. *under review* (2003).
[8] T. Minami, Mat. Res. Soc. Bull. **25** (8), 38 (2000).
[9] N. K. Terrett, *Combinatorial Chemistry*. (Oxford University Press, Oxford, UK, 1998).
[10] J. Wang, Y. Yoo, C. Gao, I. Takeuchi, X. Sun, X.-D. Xiang, and P. G. Schultz, Science **279**, 1712 (1998).
[11] H. Chang, C. Gao, I. Takeuchi, Y. Yoo, J. Wang, P. G. Schultz, X.-D. Xiang, R. P. Sharma, M. Downes, and T. Venkatesan, Appl. Phys. Lett. **72**, 2185 (1998).
[12] T. Minami, J. Vac. Sci. Technol. A **17** (4), 1765 (1999).
[13] J. D. Perkins, J. A. Del Cuento, J. L. Alleman, C. Warmsingh, B. M. Keyes, L. M. Gedvilas, P. A. Parilla, B. To, D. W. Readey, and D. S. Ginley, Thin Solid Films **411**, 152 (2002).
[14] J. J. Robbins and C. A. Wolden, *in preparation* (2003).

On-line study of collagen immobilization utilizing a wet cell system

Y. D. Wu, J. D. Liao*, C. C. Weng,

Dept. Materials Science & Engineering, National Cheng Kung University, Tainan, Taiwan

R. Klauser,

Synchrotron Radiation Research Center, Hsinchu, Taiwan

M. C. Wang,

Dept. Biomedical Engineering, Chung Yuan Christian University, Taoyuan, Taiwan

*(*Corresponding author: jdliao@mail.ncku.edu.tw)*

This study utilized nitrogen downstream microwave plasma to react with the well-packed self-assembly monolayers (SAMs) of 1-Octadecanethiol ($HS-(CH_2)_{17}-CH_3$, ODT) adsorbed on Au(111) or Ag(111) substrate. Plasma processing was applied to create polarizable groups for subsequent graft copolymerization with diluted acrylic acid (AAc) monomer. The functional group of AAc, O=C-OH, was purposely formed on the plasma-treated surface without obvious damage to the S/metal bonds. SAMs of 11-mercaptoundecanoic acid ($HS-(CH_2)_{10}-COOH$, MUA) on Au or Ag surface was taken as the reference. Collagen type III was subsequently immobilized on these two types of surface under a custom-made well cell system (Fig. 1). Synchrotron soft X-rays combined with high-resolution X-ray Photoelectron Spectroscopy (XPS) were then utilized to characterize the variations of chemical structures. Experimental result has demonstrated that using MUA/Au, Ag as the substrates, collagen immobilization process in wet cell system or in atmospheric environment does not have significant difference, qualitatively or quantitatively. The well cell system is therefore feasible to carry out on-line collagen immobilization process in vacuum (Fig. 2). Similar result has been found as MUA/Au, Ag changed to the plasma-treated ODT/Au, Ag surface with subsequent AAc-grafting, but their collagen immobilized quantities. The most pronounced processes are the participation of oxygen to the plasma-treated ODT surface, highly oxidative groups, including O=C-OH group from AAc, are likely to bind with protein molecules. Overall, this work has completed a combined collagen immobilized process in the wet cell system with on-line XPS characterization. Fundamental studies on reactive mechanism for biomedical applications are perspective.

Fig. 1: A custom-made wet cell system for on-line collagen immobilization.

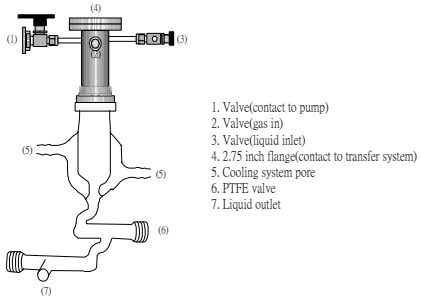

Fig. 2: Collagen immobilization on the plasma-treated SAMs, measured by synchrotron based XPS (The C 1s and S 2p spectra were shown.).

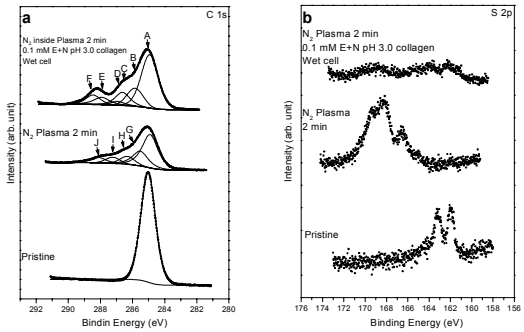

Reference:

[1] Ulman A., *Chem. Rev.*, 96, 1533-1554, 1996.

[2] Liao J. D., Wang M. C., Weng C. C., Klauser R., Frey S., Zharnikov M. and Grunz M., *J. Phys. Chem. B*, 106, 77-84, 2002.[3] Tyan Y. C., Liao J. D., Klauser R. K., Wu I. D. and Weng C. C., *Biomaterials*, 23, 65-76, 2002.

Interfacial reactions of downstream nitrogen plasma to alkanethiolate self-assembly monolayers

C. C. Weng, Y.D. Wu, J. D. Liao*
Dept. Materials Science & Engineering, National Cheng Kung University, Tainan, Taiwan
R. Klauser
Synchrotron Radiation Research Center, Hsinchu, Taiwan
M. C. Wang, H. W. Yang
Dept. Biomedical Engineering, Chung Yuan Christian University, Taoyuan, Taiwan
M. Zharnikov
Lehrstuhl für Angewandte Physikalische Chemie, Universität Heidelberg, Germany
(*Corresponding author: jdliao@mail.ncku.edu.tw)

This work utilizes synchrotron light source to study self-assembled monolayers (SAMs) using thiols ($HS-(CH_2)_{11}CH_3$) as sulfur anchor group from solution onto Au(111) or Ag(111) surface. In this experiment, downstream N_2 microwave plasma is generated by 80W under 1torr; plasma-induced chemistries on the ODT/Au and ODT/Ag surface are studied. Using *Langmuir* probe, the state of electron temperature and the electron (or ionization) density are statically measured; it provides valuable information to adjust fluctuating condition in practical plasma applications. Experimental result has indicated that current downstream plasma provides plasma density of *ca.* $1.38\times10^6 N/cm^3$ or electron temperature of *ca*. 0.46eV; it is regarded as low-density plasma. Surface analyses using synchrotron base high resolution X-ray photoelectron spectroscopy has demonstrated that the alkyl chains are reactive with N_2/O_2 plasma species, the C-O, C-N and C=O bonds are identified (Fig. 1). The N, O-containing structures mostly result from chemical reactivity of free radials in plasma. Sulfur anchor onto Ag(111) surface is much resistant to the reactive plasma species, compared with that onto Au(111) substrate (Fig. 2). The consequences may result in relatively high binding strength of the S/Ag.

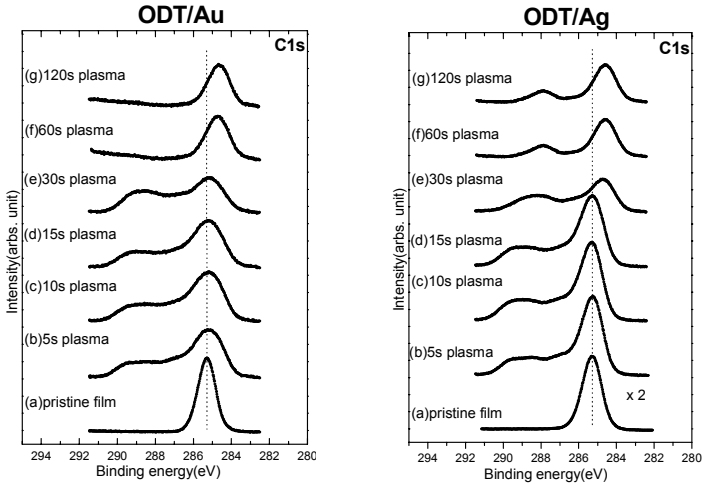

Fig.1: C 1s spectra of ODT/Au, ODT/Ag after 0-120sec plasma treatment.

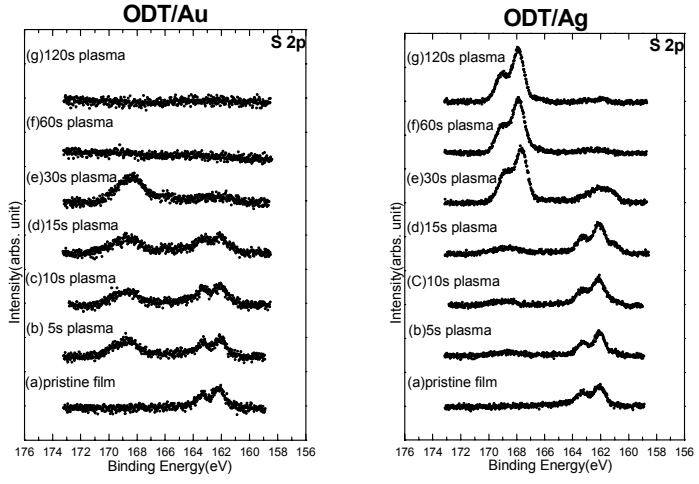

Fig.2: S 2p spectra of ODT/Au, ODT/Ag after 0-120sec plasma treatment.

Reference

[1] J.-D. Liao, M.-C. Wang, C.-C. Weng, R. Klauser, S. Frey, M. Zharnikov, M. Grunze, *J. Phys. Chem. B*, 106, 77-84, 2002.

[2] M.-C. Wang, J.-D. Liao, C.-C. Weng, R. Klauser, M. Zharnikov and M. Grunze, *J. Phys. Chem. B*, 106, 6220-6226, 2002.

Carbon Metal Sulfide by Co-operation Process of Plasma CVD and Sputtering

Md. Abul Kashem, Shinji Goto, Masaki Matushita and Shinzo Morita
Department of Electronics, Graduate School of Engineering, Nagoya University
Nagoya 464-8603, Japan

Abstract
Carbon metal sulfide was synthesized by co-operation process of plasma CVD and sputtering with using CH_4, SF_6 and Ar mixture gas and metal plate discharge electrode. Gold (Au) and copper (Cu) plate was used as a discharge electrode to fabricate carbon gold sulfide (C-Au-S) and carbon cupper sulfide (C-Cu-S) film respectively. The maximum refractive indexes of both C-Au-S and C-Cu-S film were measured as 3.5. The gold and cupper atom in the carbon metal sulfide is considered to be uniformly distributing in the film.

1. Introduction

Photonic crystal is expected to be very important for optical devices like as optical wave-guides and others [1]. Optically transparent and large refractive index material is necessary to fabricate the photonic crystal with a wide photonic band gap. GaAs, SiO_2 and other materials are utilizing to form the crystal [2,3]. However, we are interesting in C-Au-S material for fabrication of photonic crystal, which is expected to be optically transparent and has a large refractive index and process compatibility.

CuS_2 is known as a superconducting material, which was synthesized at a high pressure of 50 kber and high temperature of 800^0K [4,5]. Recently Yahoo reported superconductor of carbon copper sulfide (C-Cu-S) material at a high temperature of 77^0K was applied for a patent to European patent office [6].

Whereas, polymer-metal films are attracted much attention due to their high potential in basic and technological applications. Metal species can dramatically influence on both chemical and physical properties of resultant polymer [7]. Metal atom can be incorporated into the plasma polymerized film matrices in several ways. The co-operation process of plasma CVD and sputtering is a well-known technique to fabricate metal containing carbonaceous film [8,9]. The carbonaceous gold sulfide is also formed by above process with using similar reactor with a parallel plate electrode system, where the upper electrode was connected to RF power source and the lower electrode was grounded with the stainless steel vessel. Therefore the upper electrode causes the development of negative self-bias potential with respect to plasma during the plasma CVD. The upper electrode materials are sputtered under negative self-bias potential condition and the metal containing film can be synthesized. When CH_4 and SF_6 were used as reactive gases, H and F atoms are dissociated from CH_4 and SF_6 by forming HF in the plasma, and then carbon sulfide was synthesized [10]. If the upper electrode material is metal, synthesized carbon metal sulfide can also be deposited on the lower electrode. The purpose of this paper is to study chemical and optical properties of polymer-metal film. An approach leading to the uniform dispersion of metal atom in the film is also discussed in this work.

2. Experimental

Carbon metal sulfide was synthesized by co-operation process of plasma CVD and sputtering with using CH_4, SF_6 and Ar mixture gas and metal plate discharge electrode. Where the discharge was performed by a parallel plate electrode system of 20 cm diameter and 1.5 cm gap distance between the electrodes. The upper electrode was a graphite plate connected to the RF power source at 13.56 MHz and the lower electrode was grounded with the reactor vessel of stainless steel. The graphite plate has a large number of holes to supply the gas uniformly. Sample substrates were set on the lower electrode. The graphite electrode was adopted to

eliminate the contamination, which is induced by sputtering the discharge electrode under negative self-bias potential. However the sputtering phenomenon was utilized to mixing metal atoms in the deposited plasma CVD film of carbon sulfide. Therefore carbon-gold-sulfide (C-Au-S) and carbon-copper-sulfide (C-Cu-S) were synthesized with using gold and copper sheet (50x50 mm^2) on a graphite electrode respectively. Si wafer and glass were used as substrates, where glass substrate was cleaned by ethanol and acetone and Si wafer was immersed into liquid HF for 5 minute to etch off the oxidized layer. The deposition was performed at two different discharge pressures of 0.07 or 0.1 Torr, which was kept constant by controlling evacuation rate. The discharge power and deposition duration were 100 W and 30 min respectively for the each cases. The characterizations of deposited films were performed using thickness and refractive index by ellipsometer, atomic compositions by ESCA apparatus, optical transmittance by spectro-photometer and X-ray diffraction data by X-ray diffraction analyzer.

3. Results and discussions

Thicknesses of the films were ranged from 1000 to 800 nm formed at the pressure of 0.1 and 0.07 Torr. The growth rate was decreased with decreasing the deposition pressure.

The atomic compositions for each sample were evaluated by ESCA measurements after cleaning the surface by Ar sputtering for 1 min. For C-S-Au film, C, S, Au, F and O atoms are identified by the C(1s), S(2p), Au($4f_{5/2}$) , Au($4f_{7/2}$), F(1s) and O(1s) photoelectron-energy chemical shift peak. Table 1 shows atomic compositions and refractive index "n" of C-Au-S film respectively formed at a pressure of 0.1 Torr. Oxygen was not included in the source gas but small amount of oxygen was detected in the films. Probably it will be referred to the contaminated oxygen, which was introduced by the reaction with leaked oxygen gas in the reaction vessel and/or by the oxidization in the air or the adsorption of water. The origin of F atom in the film was referred to the residual F atom, because, SF_6 was not dissociated perfectly by the reaction with hydrogen from methane in the plasma by forming HF [10]. However, the content of the F is negligibly small compare to C, Au and S atom.

For C-Au-S film formed at 0.1 Torr, Au atom content was only 1.9-2.1 atomic %, but the S atom was 8.1-9.5 atomic %, the maximum value of refractive index was measured to be 3.5.

The Au mixing with the film is referred to a sputtering of Au plate on the upper electrode, which is coupled to the RF power supply through a blocking capacitor and a matching circuit. The sputtering is induced by Ar ion bombardment under a negative bias potential, which is formed automatically in this discharge electrode configuration after the discharge initiation [11]. Our interest is a form of Au atom in the film. Previously Martinu reported existence of Au cluster in the film at a large Au content of 25-50 volume %, which was deposited at 10 mTorr. 10 mTorr is one order lower pressure than our experimental condition [11]. In order to increase the Au content, the deposition was performed at a lower pressure of 0.07 Torr. Table 2 shows the atomic compositions of C, S, Au, O and F atom of C-Au-S film formed at 0.07 Torr. Atomic % of Au was increased remarkably due to decreasing deposition. The maximum Au and S atom content were 10.5 and 3.6 atomic %. The maximum refractive index of C-Au-S film was 3.3, however the values are smaller than 3.4-3.5 for the film formed at 0.1 Torr.

Table 3 showed the atomic compositions and refractive indexes of C-Cu-S films formed at a deposition pressure of (a) 0.1 and (b) 0.07 Torr. Atomic % of Cu was increased with decreasing deposition pressure. The refractive index of C-Cu-S film was also decreased for the film of large Cu atomic compositions.

Table.1. Atomic compositions and refractive index of C-Au-S film
CH_4: 10, SF_6: 10 SCCM, Pressure 0.1 Torr

Flow of Ar (SCCM)	Atomic composition					n
	C (%)	S (%)	Au (%)	F (%)	O (%)	
10	89.4	8.1	2.1	0.0	0.4	3.4
15	88.3	9.5	1.9	0.0	0.3	3.5

Table.2. Atomic compositions and refractive index of C-Au-S film
CH_4: 10, SF_6: 10 SCCM, Pressure 0.07 Torr.

Flow of Ar (SCCM)	Atomic composition					n
	C (%)	S (%)	Au (%)	F (%)	O (%)	
10	86.8	2.6	10.5	0.0	0.1	2.5
15	86.7	3.6	9.5	0.1	0.1	3.3

Table 3. Atomic compositions and refractive index of C-Cu-S film, CH_4: 10, Ar: 10 SCCM

Flow of SF_6 (SCCM)	(a) Pressure 0.1 Torr					(b) Pressure 0.07 Torr.				
	Atomic composition				n	Atomic composition				n
	C (%)	S (%)	Cu (%)	O (%)		C (%)	S (%)	Cu (%)	O (%)	
10	84.8	4.3	9.6	1.3	2.2	75.5	5.8	17.5	1.2	2.1
15	87.4	11.3	0.9	0.4	3.5	88.7	6.8	4.0	0.5	2.8

Martinu reported the calculated refractive index for a large Au containing film was only 2.8. Where the Au atoms were existed in the form of cluster. The refractive index of our C-Cu-S film formed at 0.1 Torr was larger than that of Martinue's C-Au film. In order to understand the difference, x-ray diffraction spectra on the C-Au and C-Au-S films were measured as shown in Fig.1 and 2 where the films were formed at 0.1 and 0.07 Torr. The x-ray diffraction spectrum measurements were carried out by using CuKα radiation source. Fig. 1 and 2 represents the x-ray diffraction (XRD) spectra of C-Au and C-Au-S film respectively, where big peak at $2\theta = 56.2^0$ is referred to Si wafer substrate. In Fig. 1, Peak at $2\theta = 38.2^0$ was increased with increasing Au atom density which is referred to Au cluster. Another peaks at $2\theta = 44.4^0$, $2\theta = 64.6^0$ and 77.6^0 in Fig.1(b) were also referred to Au cluster structure. However, there is no peak except the peak of Si wafer in Fig. 2. This means that the Au atom did not form polycrystalline structure in the C-Au-S film. X-ray diffraction spectra of the C-Cu-S film also showed similar tendency with the C-Au-S film.

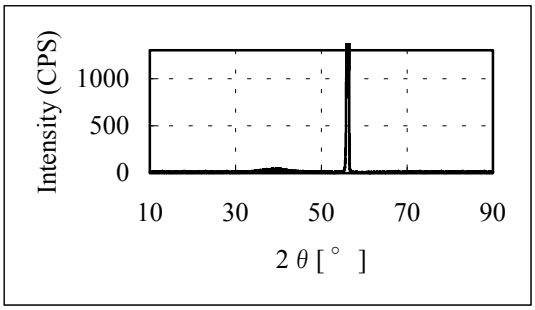

(a)

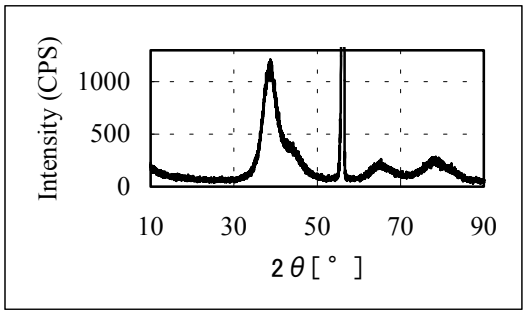

(b)

Fig.1. XRD spectra of C-Au films carried out by CuKα radiation source; (a) Pressure 0.1 Torr, Au: 5.5 %, (b) Pressure 0.07 Torr, Au: 12.3 %.

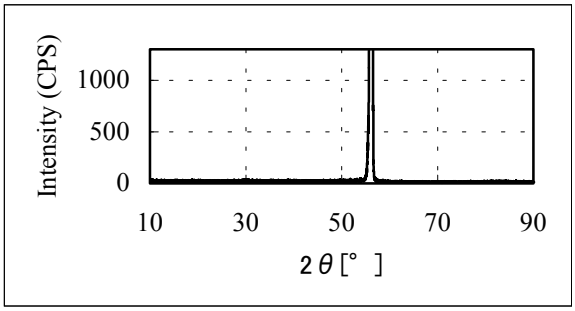

(a)

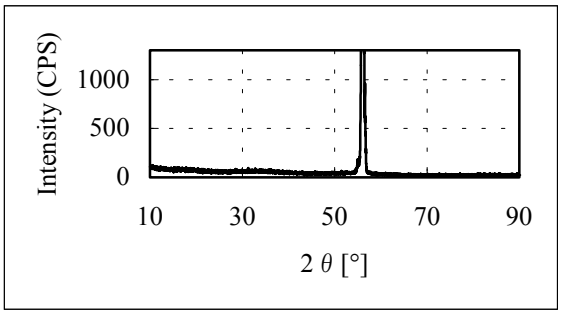

(b)

Fig. 2. XRD pattern of C-S-Au film carried out by CuKα radiation source; (a) Pressure 0.1 Torr, Au: 2.1 % (b) Pressure 0.07 Torr, Au: 10.5 %.

It is well known that the metallic atom have a tendency to form a cluster or crystallized structure when the metallic atom content is increased more than a few atomic % and the x-ray diffraction spectra shows broad peak usually [12]. It is also known that Au atom forms bonds with sulfur [13]. Therefore the Au atom in the C-Au-S film is considered to distribute uniformly by reacting with sulfur at a high Au atom content [14]. As shown in Table 1-3, the refractive indexes of metal containing film were decreased at a higher metal containing films. The smaller refractive index for the film of larger metal content is inconsistent properties on the carbon-metal-sulfide film. A possible explanation is referred to conductive properties of molecular structure like as C-Au-S or C-Cu-S. In the conductive molecules, each atom cannot contribute on the refractive index independently because the electronic polarizability of each atom is muffled by the electron cloud in the conductive molecules like as metallic cluster.

For the large refractive index properties of carbon-metal-sulfide film, fabrication of photonic crystal is more profitable applications. Figure 3 shows optical transmittance of C-Au, C-Au-S and a-C film. At a shorter wavelength region, the transmittance was decreased with sulfur and Au content. By optimizing transmittance and refractive index, carbon-metal-sulfide can be used as photonic crystal dielectrics.

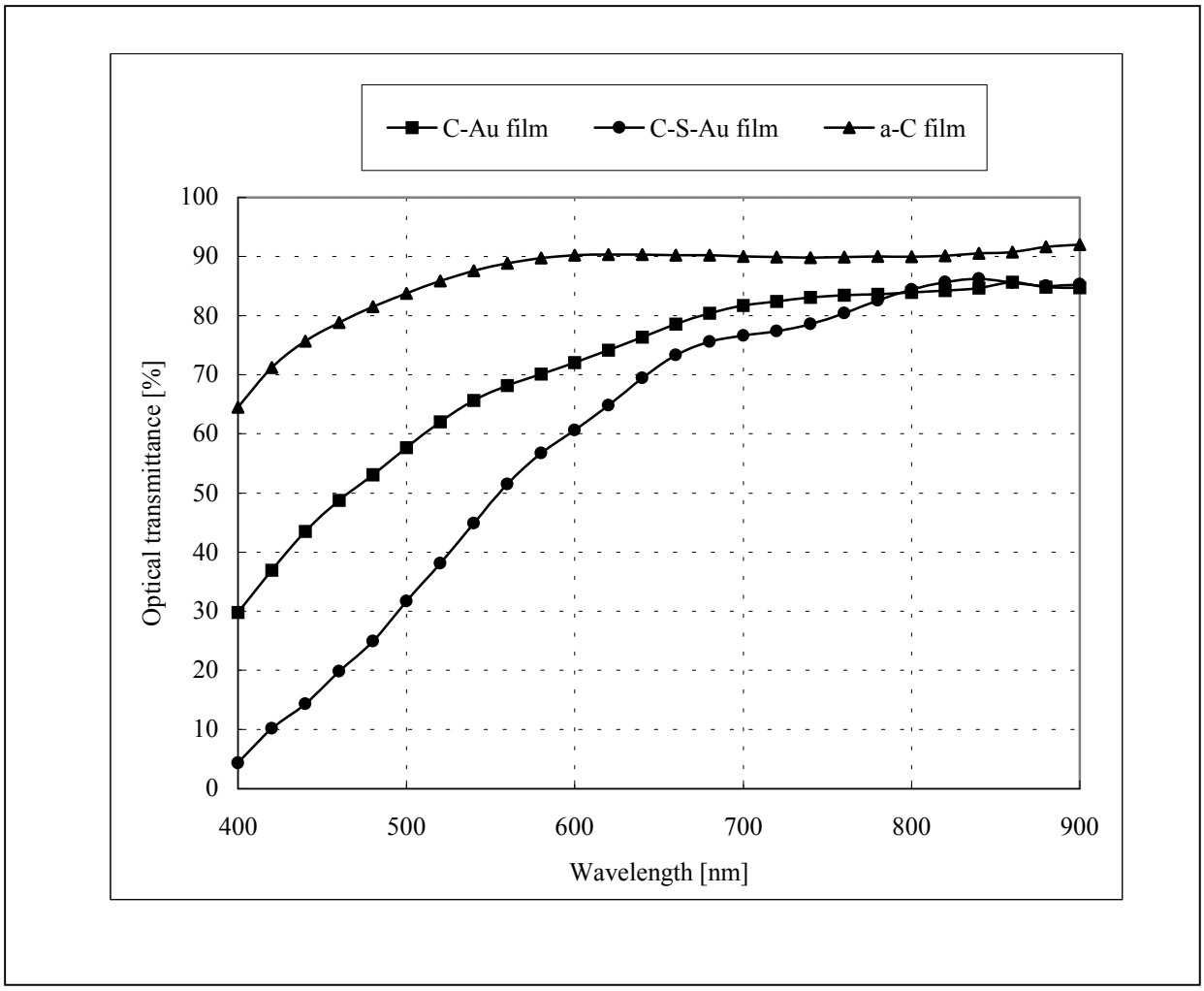

4. Conclusion

C-Au-S and C-Cu-S film were formed by plasma CVD and sputtering. By decreasing deposition pressure, atomic % of Au and Cu in the film was increased. Larger refractive index was realized for a few atomic % of Au and Cu containing film. Au atom forms cluster structure when atomic % of Au increased more than a few atomic % in the C-Au film, but it was atomically distributed in the carbon metal sulfide film even at higher atomic % of Au, where chemical bond between S and metal atom was expected to be formed. The film is transparent in a visible light wavelength range but it shows an insulating property because the metal content is still small.

5. Acknowledgement

The works were performed partly at the Center of Co-operative Research in Advance Science and Technology (CCRAST), Nagoya University. The refractive index and optical transmittance was measured at Yasuda and Tsunashima laboratory respectively. We express our thanks to the respective persons at the laboratories.

References

[1] M.D.B. Charlton, M.E. Zoorob and G.J. Parker, Mat. Sci. Eng. **B74** pp.17-21 (2000).
[2] D. Cassagne, C. Jouanin, and D. Bertho, Phy. Rev. **B53** 11 p.7134 (1996).
[3] H. Kosaka, T. Kawashima, A. Tomita et. al., Phy. Rev. **B58** 16 pp.10096-10099 (1998).
[4] T. A. Bither, C. T. Prewitt, J. L. Giillson, P. E. Bierstedt, R.B. Filippen and H.S. Young, Solid State Communications, **4** pp.533-535 (1966).
[5] M. Kontani. T. Turui, T. Morikawa and T. Mizukoshi; Physica **B, 284-288** pp.675-676 (2000)
[6] European Patent, Appl. No. EP02090016.3
[7] Eric Kay and M Hecq, J. Appl. Phys. **55**, 2 p.370 (1984)
[8] L. Marutinu, Solar Energy Materials **15**, p.21 (1987).
[9] R. d'Agostino, Ed*., "*Plasma Deposition*,* Treatment*,* and Etching of Polymers*",* Academic Press, (1990).
[10] M. Matsushita, Md. Zalid Bin Harum, Md. Abul Kashem and S. Morita; J. Photopol. Sci. and Tech*.,* **12,** 1 pp.11-14 (1999).
[11] H. Biederman and L. Martinu; Plasma Deposition, Treatment and Etching of Polymers, Edited by R. d'Agostino, Chap. 4, Academic Press, Boston, p.269 (1990).
[12] I. Dutta, C.B. Munns, G Datta; Thin Solid Films **304** pp.229-238 (1997).
[13] K.Ishikawa, T. Isonaga, S. Wakita and Y. Suzuki; Solid State Ionics **79** pp.60-66 (1995)
[14] M. Matsushita, Md. Abul. Kashem and S. Morita; J. Photopol. Sci. and Tech*.,* **14,** 1 pp.123-126 (2001).

Investigation of excited species in a carbon ablation plume in nitrogen gas environment

M.A. Bratescu, D. Yamaoka, Y. Sakai, Y. Suda and H. Sugawara

Hokkaido University, Division of Electronics and Information Engineering, Sapporo, 060-8628, Japan
maria@eng.hokudai.ac.jp

Abstract

In this work we investigate a carbon plasma plume produced by laser ablation of a graphite target in nitrogen gas environment. The XPS analysis of film deposited was explained in connection with the spatial distribution and velocities of excited particles (C, N, C_2 and CN) in the expanding plasma. The chemical reactions in the ablation plume in the vicinity of the Si substrate could be understood using spatial distributions of atoms, molecules and radicals.

1. Introduction

A laser ablation method for thin film deposition offers many advantages compared with traditional deposition techniques, due to the possibility to control the impurities and to deposit high refractory elements as well as different compounds with superior properties produced by chemical reaction.

In the last decade, interest in carbon nitrides was increased because this crystalline phase exhibits interesting properties like hardness combined with high elasticity [1]. Understanding of the mechanism of CN_x film formation could improve the film quality. The film quality depends on laser-induced plasma parameters, i.e. the velocity, temperature, number density of ablated species in the plume and chemical composition, and could be controlled if we measure these data. The quality of CN_x film is determined by the type of bonding between nitrogen and carbon atoms in connection with the plasma composition and dynamics of various species in the plume [2, 3].

2. Experimental set-up

Fig.1 shows the experimental set-up along with the arrangement of laser beams from excimer laser and diode laser (DL) on a target. A pulsed laser deposition (PLD) chamber is almost the same as the one given in Ref. [4]. An ArF excimer laser beam

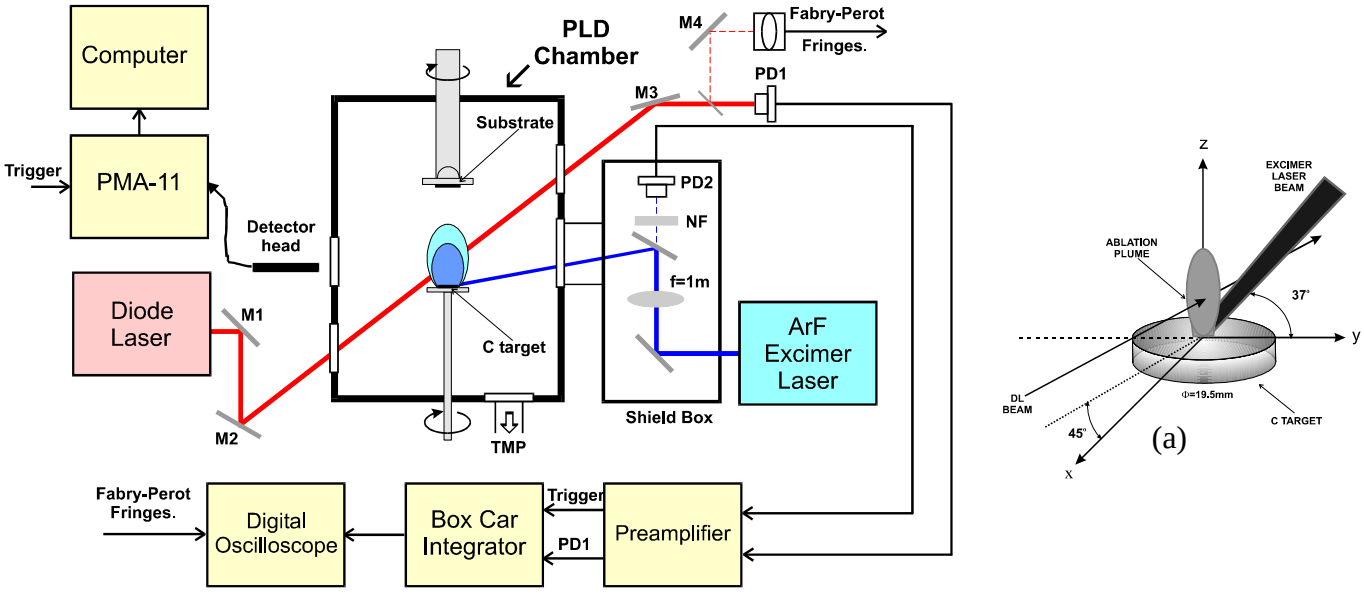

Fig. 1. Experimental set-up for carbon ablation plume diagnostics by laser absorption spectroscopy and by emission spectroscopy

(Lambda Physik COMPex205) was focused onto a crystal graphite target at an incidence angle of 53°. The pulse duration of the laser is 20 ns and the fluence is adjustable in the range of $E = 2 – 4.7$ J/cm^2.

A set-up for the laser absorption diagnostics of the number densities of excited atoms, C($3^1P_1^o$) and N($3^4P_{5/2}$) in a plume was realized with two distinct diode lasers (DL; Hitachi 8325G; 40 mW maximum output with the 830 nm central wavelength at 25°C). DL were tuned to the resonance absorption of C ($3^1P_1^0 \rightarrow 3^1S_0$) at λ_0^C = 833.7 nm or tuned to the resonance absorption of N ($3^4P_{5/2} \rightarrow 3^4P_{5/2}^0$) at λ_0^N = 821.859 nm. To acquire the absorption signal of excited atoms in the ablation plume we used a digital oscilloscope. The signal to noise ratio (*S/N*) of the absorption signals was about 10^3. The temporal absorption signal detected by PD1 simultaneously recorded with temporal signal of excimer laser light emission aquired by PD2 offers information about decay and expansion velocity of the excited atom in the plume.

DL beam was focused at different positions *z* from the target surface (see Fig. 1(a)). The spatial resolution of the DL beam was about 0.05 mm. A boxcar integrator (Standford SRS250) that is connected with an oscilloscope in acquisition mode to record the data accomplishes integration of the absorption signal of C and N by PD1.

When DL was scanned with a frequency of ~ 5 mHz over the resonance wavelength of the atomic transition, the time-integrated absorption signal was simultaneously recorded with the Fabry – Perot fringes of the 1.5 GHz free spectral range, in order to measure the line width of the absorption line ($\Delta\nu$).

The emission spectrum of the ablation plume was spectrally analyzed in a visible range between 300 and 800 nm using a Hamamatsu PMA-11 (Photodiode Multi-channel Analyzer). The PMA detector head was set in a (*y, z*) plane parallel with the (*y, z*) plane of the plume (fig. 1(a)). An XPS study characterizes the N and C bonds on the film deposited in different experimental conditions.

The nitrogen pressure (*p*) was varied from 0.1 to 13 Torr, the absorption signal and emission spectrum were measured at the vertical distance (*z*) from the carbon target surface from 0 to 25 mm. A Si(100) substrate was set in the plume at different distances *z* from the target. Measurements were done with and without substrate.

3. Results and discussion

From the absorption signal amplitudes the excited nitrogen N($3^4P_{5/2}$) number density (N_N) or the excited carbon C($3^1P_1^o$) number density (N_C) were calculated following the relation [4]:

$$N = \frac{8\pi^2 g_1}{g_2} \cdot \frac{\Delta\nu \cdot \ln\left(\frac{I_0(0)}{I_0(L)}\right)}{\lambda_0^2 \cdot A_{21} \cdot L} \qquad (1)$$

where $I_0(L)$ represents the DL intensity after passing through the plume, $I_0(0)$ the incident DL beam intensity, when the DL wavelength is fixed at the resonance absorption value λ_0 (λ_0^C or λ_0^N), $g_{1,2}$ are the corresponding statistical weights of the excited atom levels, A_{21} is the Einstein spontaneous emission coefficient, L is the mean absorption length through the plasma plume. $\Delta\nu$ is the absorption line width.

We measured the density of C excited atoms on $3^1P_1^o$ level at 7.5 eV and N excited atoms on $3^4P_{5/2}$ level at 10.3 eV in the carbon ablation plume in the vicinity of a Si(100) substrate introduced at different distances from the target surface. The presence of the substrate perturbs the density of nitrogen and carbon, as can be seen in Fig. 2. In the presence of substrate, an interesting effect, i.e. the increase of N_N with ~ 70%, was observed. This can be explained by a secondary plume excitation at the substrate surface, which may indicate film sputtering, and consequently an increasing of excited nitrogen in this region [3].

The N_2 pressure *p* can control densities of different species in different regions of the plume. The maximum number density of N($3^4P_{5/2}$) was $N_N = 7\times10^{10}$ cm^{-3} for p = 13 Torr at z = 1.8 mm (Fig. 3). Generally N_N increases as *p* increases and decreases with *z* if $z > 4$ mm. N_C was ~ 10^{11} cm^{-3} at z = 2 mm in vacuum, and decreases as *p* increases. In order to compare different results the laser fluence was kept at about E = 3.2 Jcm^{-2}.

From the delay (τ) of the absorption signal of the excited atom in the ablation plume, relative to the excimer laser light pulse, the mean expansion velocity of C($3^1P_1^o$) and N($3^4P_{5/2}$) atoms was calculated. Fig. 4 shows the delay of nitrogen atoms (τ_N) in the plume in different nitrogen pressures p = 1, 5 and 10 Torr.

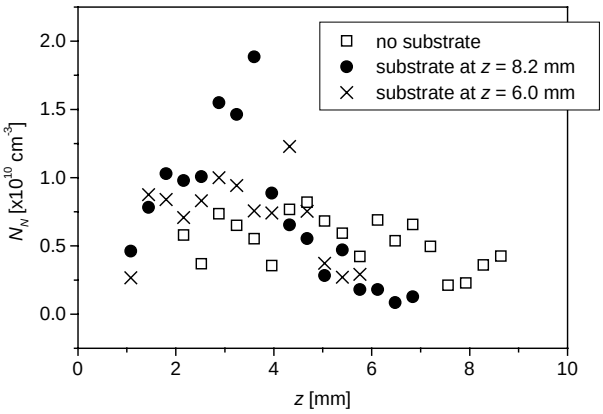

Fig. 2. N_N dependence on z with and without substrate, p = 1 Torr, E = 3.1 J/cm^2.

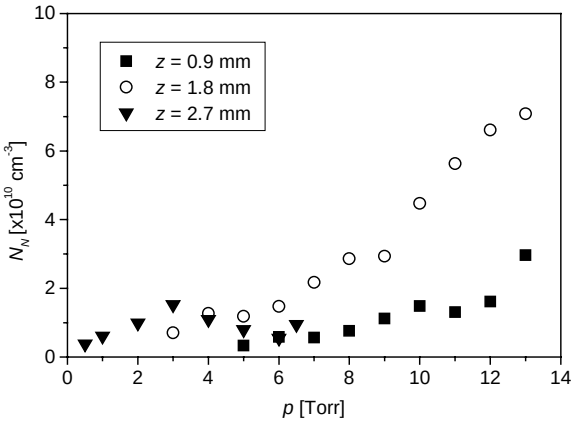

Fig. 3. N_N dependence on p for different z and E = 3.25 J/cm^2.

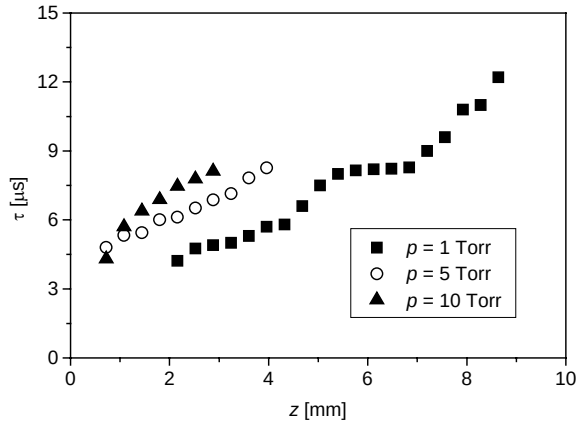

Fig. 4. τ_N dependence on distance in the ablation plume for different pressures p and E = 3.2 J/cm^2.

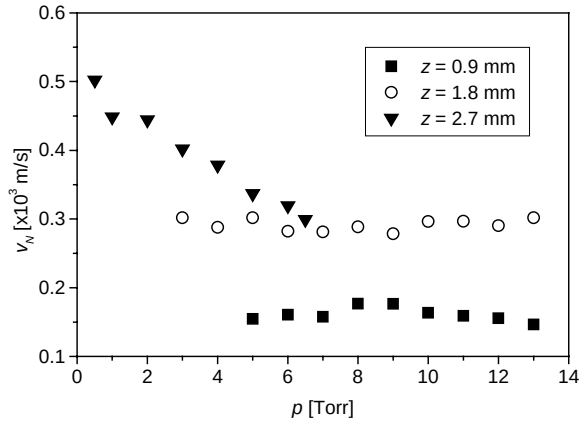

Fig. 5. v_N dependence on pressure for different z and E = 3.25 J/cm^2.

Space and pressure dependences of N($3^4P_{5/2}$) velocity (v_N) can explain expansion, collision and chemical reaction between N and C atoms. The N($3^4P_{5/2}$) velocity near the target surface was ~ 5×10^4 cm s^{-1}, while C($3^1P_1^o$) velocity was ~ 10^6cm s^{-1}, because carbon atoms were ablated from the target surface by ArF laser. The N($3^4P_{5/2}$) velocity near the target surface (~ 1 mm) was higher than that at z=~ 3 mm, and the N($3^4P_{5/2}$) velocity depended strongly on the pressure (Fig. 5). In the vicinity of the target surface the ablated particles have high kinetic energies and collide with the buffer gas molecules and atoms. Therefore N($3^4P_{5/2}$) atoms have higher velocity in this region than far. The excited atoms N($3^4P_{5/2}$) may be produced in the plume by N_2 dissociation and excitation. The N($3^4P_{5/2}$) velocity was slightly dependent on p for z > 2 mm. The N($3^4P_{5/2}$) velocity decreased with z due to plume expansion.

Expansion of laser-induced plasma could be described by a drag model for N($3^4P_{5/2}$) at p = 1 Torr, just after ablation, for z < 6 mm. For z > 6 mm, reaction between N and C atoms occurs [2] and this model is no longer valid.

In the vicinity of the surface substrate τ_N is almost constant as can be seen in Fig. 6. We can explain that by the release of nitrogen atoms from the substrate surface (as is shown in Fig. 2) produces an increased density of nitrogen atoms in this region (as is shown in Fig. 2).

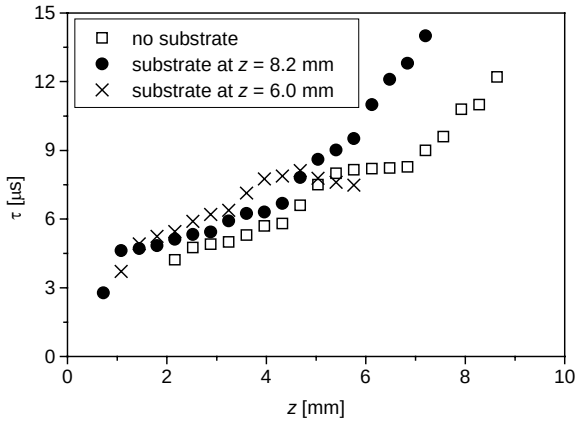

Fig.6. τ_N dependence on z in the ablation plume with and without substrate when p = 1 Torr and E = 3.1 J/cm^2.

CN radical molecular bands dominate the emission spectrum of the carbon ablation plume in nitrogen atmosphere. C_2 and N_2 molecules emission bands have intensities about five times less than CN emission bands intensities (Fig. 7).

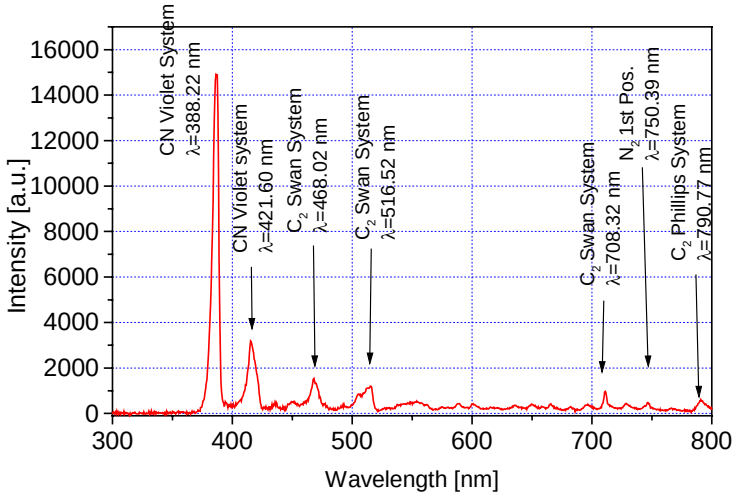

Fig. 7. Typical emission spectrum of C ablation plume in p = 5 Torr of nitrogen, E = 3.5 J/cm^2.

The highest density of C_2 excited molecule on $d^3\Pi_g$ level at 3 eV, produced by direct ablation from target surface is at z ~ 5 mm far from the target surface at pressures in the range of p = 1 – 5 Torr, where high density of N_2 excited molecule on $B^3\Pi_g$ level at 8 eV and CN radical on $B^2\Sigma$ at 3.2 eV could be found (Fig. 8). The appearance of CN radical excited on $B^2\Sigma$ level could be explained by the following chemical reactions in the plume:

$$C_2\left(d^3\Pi_g\right)\rightarrow C\left(^3P\right)+C\left(^3P\right)$$
$$N_2\left(B^3\Pi_g\right)\rightarrow N\left(^4S^0\right)+N\left(^2D^0\right)$$
$$C\left(^3P\right)+N\left(^4S^0\right)\rightarrow CN\left(B^2\Sigma\right)$$
$$C\left(^3P\right)+N\left(^2D^0\right)\rightarrow CN\left(B^2\Sigma\right)$$

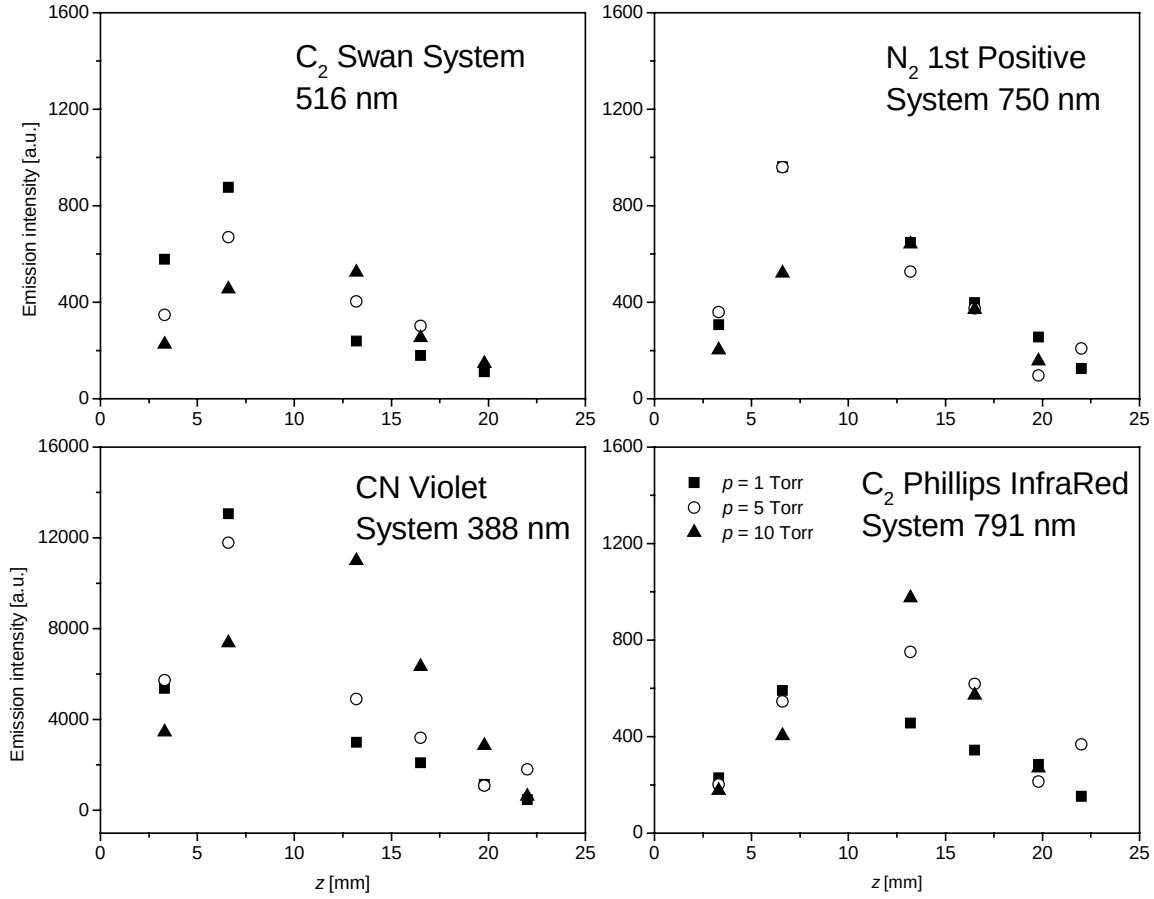

Fig. 8. Emission intensities of C_2 molecule at 516 nm (Swan system) and at 791 nm (Phillips infrared system), N_2 molecule at 750 nm (First positive system) and CN radical at 388 nm (Violet system), for different pressures in the carbon ablation plume (E = 4.5 J/cm^2)

C_2 molecular band at 791 nm (Phillips system) (Fig. 8), corresponding to the electronic level $b^1\Pi_u$ at 8 eV, has the maximum emission intensity at z = 13 mm in the plasma plume as explained by recombination of carbon atoms on excited electronic levels followed by de-excitation [5]. But laser absorption spectroscopy measurements of C($3^1P_1^o$) and N($3^4P_{5/2}$) densities shows a maximum at z = 2 mm far from the target surface due to the high electron density and electron temperature in this region [4]. Emission intensities in spectrum are higher if excimer laser fluence is higher because electron energy and temperature increase with E.

The results of XPS analysis of the film deposited on Si(100) substrate introduced in the carbon ablation plume are presented in Table I. The de-convolution of XPS spectra of carbon films deposited in nitrogen atmosphere in different conditions shows two main components: first component at 284.1 eV (line width ~ 1.0 eV) corresponding to

Table I

p [Torr]	z [mm]	A_{sp3}/A_{sp2}
1	6	0.046
1	10	1.439
1	15	0.512
10^{-8}	6	0.715
10	6	1.814

sp^2 carbon atoms (graphite) and the second component at 285.5 eV (line width ~ 1.1 eV) corresponding to sp^3 carbon atoms (diamond). A small intensity peak was also obtained by de-convolution of the XPS spectra, at 286.5 eV and corresponds to CO, which could be present on the film surface [6]. These results show that a high density on C_2 and CN is necessary to obtain high content of sp^3C by carbon ablation in nitrogen gas. In vacuum, sp^3C content relative to sp^2C content can be compared with the composition in the film obtained in p = 1 Torr nitrogen and z = 15 mm , but the substrate should be placed close to the target surface at z = 6 mm.

4. Conclusions

Optical methods, emission and laser absorption spectroscopy, are powerful tools for diagnostics of physical and chemical processes in plasmas used for thin films deposition.

The high content of sp^3C on the Si substrate set in the carbon ablation plume at 6 mm from the target surface, in 10 Torr nitrogen pressure, was explained by the high molecular (C_2, N_2, CN) density in this region. Close to the target surface the electron density and temperature are high and maximum values of atomic nitrogen and carbon were obtained. Here dissociation and excitation processes have higher probability than far to the target where de-excitation, diffusion and recombination processes become dominant.

References

[1] H. Sjostrom, S. Stafstrom, M. Boman, and J. –E. Sundgren, Phys. Rev. Lett., **75** (1995) 1336 – 1339

[2] S. Acquaviva, and M. L. De Giorgi, J. Phys.B: At. Mol. Opt. Phys., **35** (2002) 795 – 806

[3] A. A. Voevodin, J.G. Jones, J. S. Zabinski, and L. Hultman, J. Appl. Phys., **92** (2002) 724 –735

[4] M. –A. Bratescu, Y. Sakai, D. Yamaoka, Y. Suda, and H. Sugawara, Appl. Surf. Sci., **197** (2002) 257 – 262

[5] S. S. Harilal, R. C. Issac, C. V. Bindhu, V. P. N. Nampori, C. P. G. Vallabhan, J. Appl. Phys. **81** (1997) 3637 – 3643

[6] P. Merel, M. Tabbal, M. Chaker, S. Moisa, J. Margot, Appl. Surf. Sci., **136** (1998) 105 – 110

Acknowledgement

This work was supported in part by a Grant-in Aid for Scientific Research (C) of JSPS No.70312379

Investigations on wire arc spray process by analysis of the frequency and amplitude of the arc characteristics and correlation with the coating properties

M. Planche[1], H. Liao[1], T. Le Ba[2], C. Coddet[1]

[1]*LERMPS, University of Technology of Belfort–Montbeliard, Belfort, FRANCE*
[2]*Corrosion and metal protection, Institut of Tehnology of Hanoï, VIETNAM*

Abstract
Wire arc spray is a process to produce coatings and forms structures through the deposition of metal droplets. Droplets are then produced at the arc heated wires end, they are eventually atomized and accelerated towards the substrate by the gas stream. Our research focuses on the investigation of the wire arc spray process trough an understanding of the interaction between the process parameters and the coating properties using the frequency and amplitude spectrums. Since arc fluctuations may have a strong effect on droplets formation and therefore on coating properties, such fluctuations were recorded by measuring arc voltages synchronized with current and luminosity signals. Some relationships between arc characteristics and coating properties can be pointed out.

Introduction
Electrical arc spraying with dual wires is an economical coating process which finds different industrial applications today. With this process, a cold gas jet across the arc atomizes and drives the molten droplets from the electrode tips [1]. Then, the melting behaviour of the consumable wire electrodes, giving rise to the formation of the droplets, is influenced by the arc stability which in turn is dependent on the input parameters, i.e. gas flow rate, current intensity and voltage [2]. It is now proved that arc fluctuations are due to the periodic removal of molten droplets from the wire tips by the atomizing stream. Because the dynamic forces of the atomizing air stream act on the arc, these fluctuations are characteristic of the wire arc spraying process and that leads to the formation of droplets with different sizes. That determines finally the coatings properties [3]. In this study, arc spraying of alumina wires is considered in order to establish correlations between input parameters and coating properties such as porosity, microstructure and adhesion in relation with the arc characterization too. Thus, the TAFA 9000^{TM} gun is used for these experiments; the air flow rates and current intensities were changed in order to understand the fundamental mechanisms of the wire arc spraying process. Concerning the arc characterization, the technique involves the recording of time resolved signals, i.e. arc voltage, current and luminosity. This way, the corresponding arc voltage across the consumable electrodes and the current have been simultaneously recorded by an oscilloscope as the luminous fluctuations of the jet have been recorded using a system including a photodiode and connected to the oscilloscope. After the process, the data processing has been performed using a specific application developed via Labview software. These fluctuations have been analyzed using the Fourier Transform for determining the frequency of the maximum peak as well as its corresponding amplitude. Because the turbulence can be estimated by the waveforms of the voltage fluctuations and the velocity of the droplets can be estimated by the frequency and the amplitude spectrum of the voltage fluctuations [4], the voltage spectral peak and voltage standard deviation have been correlated with operating conditions. That denotes the different phenomena occurring during this process. Finally, these analyses are combined with quantitative materials characterization to study the effect of each input parameter on the coating properties.

Experimental procedures

1. Operating conditions
The schematic of the TAFA 9000^{TM} arc spray system is represented in figure 1. On the TAFA equipment, voltage and current intensity can be adjusted independently and the current is directly related to wire feed rate. As a consequence, the feedstock increases with the current increase. For all the experiments, the voltage was fixed at 30V, compressed air was used as the atomizing gas, the flow rates were between 90 and 120 m^3/h and the current intensity was fixed at 100, 150 and 200 A. Alumina wires, referenced TAFA01T, were used as spraying materials and contain 99,5% in weight aluminium.

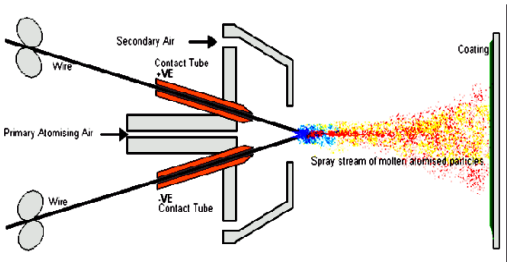

Figure 1 : Diagram of the wire arc spray process

2. Process diagnostics

During the spray, the corresponding arc voltage and current between the two consumable electrodes have been simultaneously recorded with an oscilloscope. The arc voltage is directly measured at the electrical connexions of the gun as the current intensity is measured using a Hall effect clip. The detection of light fluctuations of the jet was ensured by a PIN type photodiode. This photodiode with a 0,5 mm² surface was placed at the gun exit and connected to the oscilloscope as shown in the schematic of the experimental set up given in figure 2. Finally, the time resolved voltage signals were recorded giving directly the relationships with the intensity by the Ohm law.

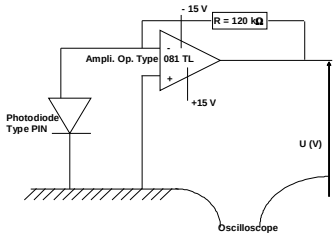

Figure 2 : Schematic of the set up used for the luminosity signals

For all these diagnostic methods, measurements are in real time. Time resolved traces are obtained using a digital oscilloscope connected to a PC operating with Labview® Software. During the process, the signals can be observed on the PC monitor control. Each signal contain 2500 points whatever the sampling rate. These signals can be real time processed and stored in the workstation in order to proceed to the future treatment of the data.

3. Data acquisition and treatment

All the data are then processed to find correlations between the arc parameters and the input conditions. For each set of operating conditions, the same data are collected several times in order to obtain an average value and a standard deviation of the characteristics of the wire arc spray process. Labview® software can conveniently perform Fourier Transforms from which the power and amplitude spectra can be determined.

4. Coatings analysis

The wire arc spray was fixed onto a ABB IRB4400^{TM} robot to ensure repeatable kinetic motion to build coatings. Coatings have been built onto a 316L steel plates, with dimensions of 2,5 cm diameter and 1 cm thick. Specimens were fixed on a drum with 380 mm in diameter, rotating with a speed 60 turns per minute. The transverse speed was 10 mm/s while the stand off distance was 250 mm. For each set of operating parameters, the same 300 µm thickness was obtained for the coating. For the resulting coatings, microstructure, porosity and adhesion have been determined. Optical micrographs are obtained on polished cross sections, using a reflected light microscopy. Image analysis are performed to determine porosity of polished coating cross sections. The analysis of grey levels enables to distinguish the different features of coating microstructures (Graftek^{TM} software). Average results have been obtained by measuring porosity at three random locations for each sample. The coating adhesion is also determined using the traction test method.

Results on arc characteristics

1.Time resolved measurements

Figures 3 and 4 represent the typical signals corresponding to real time measurements of arc voltage, current and luminosity obtained with a 90 m^3/h air flow rate and a 150 A current intensity.

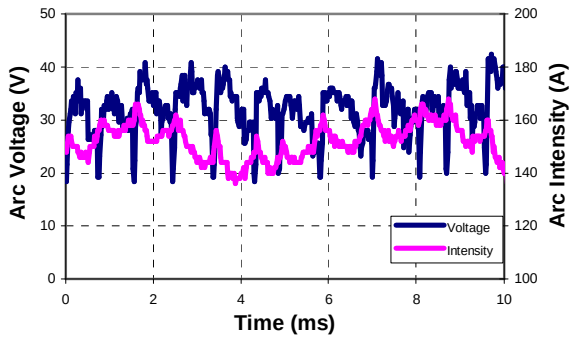

Figure 3 : Voltage and current fluctuations with a 90 m^3/h air flow rate and 150 A current intensity

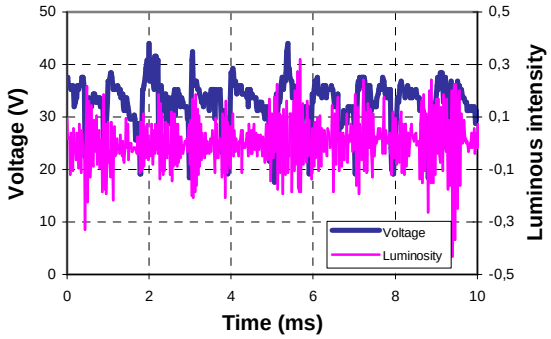

Figure 4 : Voltage and luminosity fluctuations with a 90 m^3/h flow rate and 150 A current intensity

One can notice that the arc voltage shows important and fast fluctuations, the current and the light display strong fluctuations as well. A repeating event is observed in the three signals : a sharp dip in the voltage occurs about every millisecond and is associated to a sudden variation in current and luminosity. Moreover, as it can be observed an important dip in luminous fluctuations directly related to voltage variation, some very rapid and small fluctuations follow this event, which are not present in voltage or current signals. According to what has been observed by Sheard & Co [5], it is assumed that this event is a key point in the droplet formation process. It can be assumed too that the voltage dip corresponds to the situation when the distance between the wire tips is a minimum value leading finally to the formation of large molten metal droplets. The molten wire tips are blown away by the compressed atomizing air flow leading to the renewed formation of the arc. It appears that at a certain instant, the compressed atomizing gas stream extends the arc voltage beyond a value which can not be sustained by the power supply. At this point the arc extinguishes and reignites after the advancing consumable wire tips make contact, leading initially to a high current flow and rapid melting of the consumable wire tips. This process leads to periodic fluctuations of the arc voltage, the arc current and the droplet size as shown previously and is also dependent of the input parameters. For example, in figure 5, time resolved signals of arc voltage are presented for the two different air flow rates, 90 m^3/h and 115 m^3/h.
It can be observed that the shape of the time resolved measurements is influenced by the experimental parameters. When the flow rate increases, the dips in voltage become in large number as their amplitudes become smaller. According to the phenomena involving in the wire arc spray process, the arc flow removes the droplets from the arc region and pushes the arc to the arc gun exit. Smaller droplets are then produced at higher flow rate of the atomizing gas because increasing the atomizing gas flow rate breaks the molten droplets more finely during the flight [6]. These results suggest that higher velocities of the atomizing gas can be correlated firstly with higher frequencies of the voltage fluctuations corresponding to smaller particle sizes and secondly with smaller amplitudes characteristic of more stable arcs. Then, the distance between the consumable wire and the arc nozzle determines the fluid velocity in the arc region.

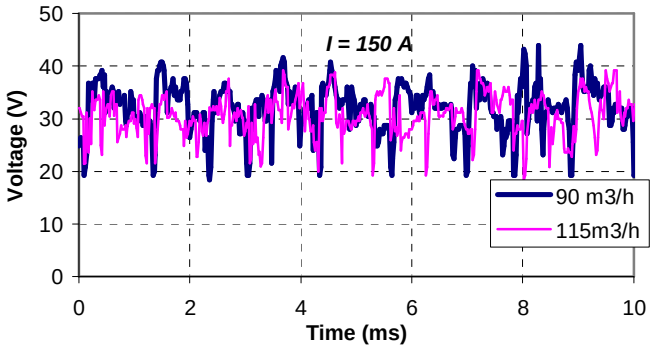

Figure 5 : Voltage fluctuations with a 90 m^3/h and a 115 m^3/h air flow rate

2. Power spectrum analysis

A typical example of the results of power spectrum obtained by Fourier Transform is given in figure 7. These results of respectively voltage, current and luminosity power spectrum correspond to 115 m^3/h air flow rate and a 200 A current intensity input parameters.

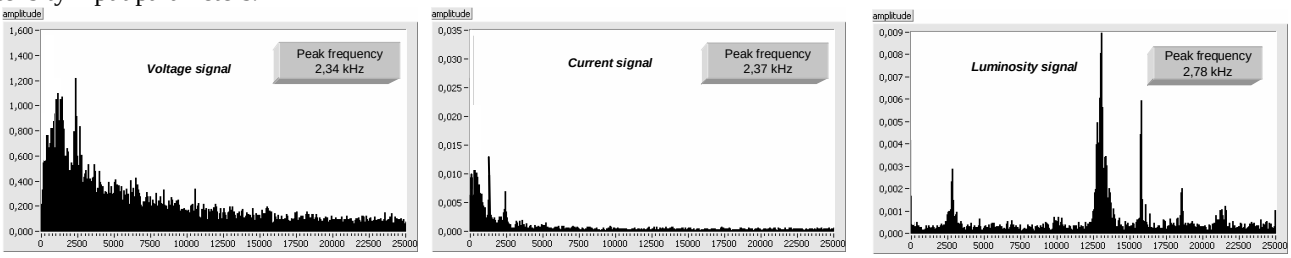

Figure 7 : Power spectrum of voltage, current and luminosity fluctuations at 115 m^3/h and I = 200 A

Very well defined peaks occur in all figures. The voltage waveforms indicate a clear periodicity at a dominant frequency, about 2,5 kHz in this case. This peak is detected in the power spectrum of current and light too but do not correspond to their maximum peak. Moreover, a group of peaks appears in the power spectrum of the light at much higher frequencies, around 12,5 kHz for the maximum peak frequency which do not appear in the voltage and current spectra. It can be thought that these peaks can be associated with a large scale turbulence of light due to numerous and different size particles which are produced using arc spray process [2].In order to point out the difference of the turbulence of the jet, the comparison of the power spectrum obtained with two different air flow rates is given in figure 8. As the peaks are really well defined in the case of the highest flow rate, a much larger dispersion appears when the flow rate is minimum. Because the light is due to the particles emission, that indicates why the particles produced by the spray are much more homogeneous in size with a high flow rate.

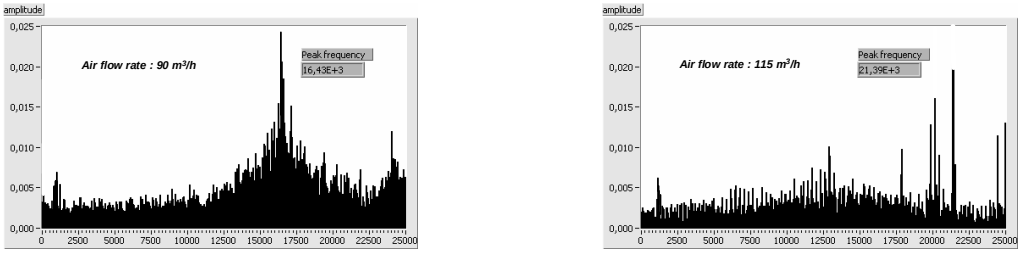

Figure 8 : Power spectrum of luminosity fluctuations at I = 150 A for 90 and 115 m^3/h

3. Average values of frequency and amplitude versus the input parameters

Several acquisitions of data have been performed for each set of input parameters. Figure 9 corresponds to the average value and to the standard deviation of the maximum peak frequency detected in voltage and intensity power spectrum in the case of a 150 A current intensity and air flow rates varying from 90 m^3/h to 115 m^3/h. Figure 10 gives the evolution of the corresponding amplitudes of voltage and intensity for the same input conditions.

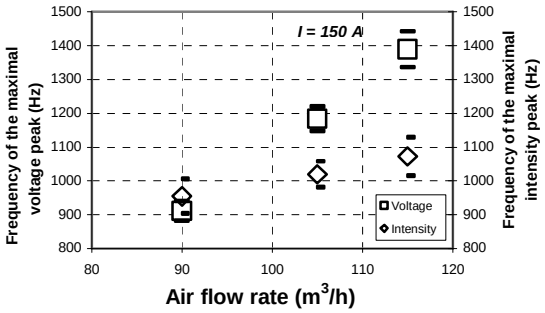

Figure 9 : Evolution of the maximum peak frequency of voltage and intensity versus air flow rate.

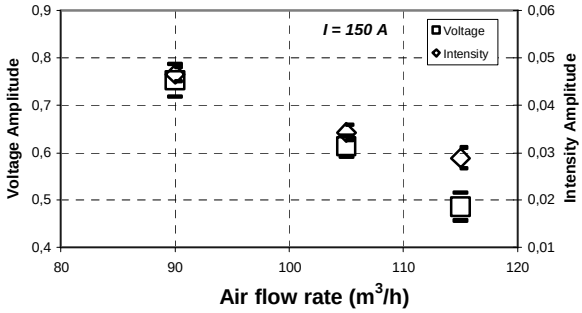

Figure 10 : Amplitude of voltage and intensity corresponding to the maximum peak detected versus air flow rate.

In figure 9, it can be noted an increase in voltage and intensity frequency respectively from 900 Hz to 1400 Hz and from 984 Hz to 1064 Hz versus the flow rate. As a consequence, the characteristic frequency of the voltage fluctuations corresponding to a periodic shortening of the arcing gap, higher frequencies with lower amplitudes can be associated to the generation of particles in a large number with smaller diameters. Then, it can be deduced that higher velocities and less turbulence in the wire arc spray process exist leading to more stable arcs when the flow rate increases. It is confirmed by the results obtained on the particles characteristics through the DPV measurements showing an important decrease in the standard deviation of in-flight particle characteristics as the flow rate increases [7]. More homogeneous arcs in terms of particles size and velocity are produced in such a case. Concerning the evolution of voltage and intensity frequencies and amplitudes, figures 11 and 12, corresponding to a variation of the current intensity from 100 to 200 A for a constant 115 m^3/h air flow rate, the rise of current intensity leads to increase the frequency of the maximum peak and to decrease the amplitude of this peak.

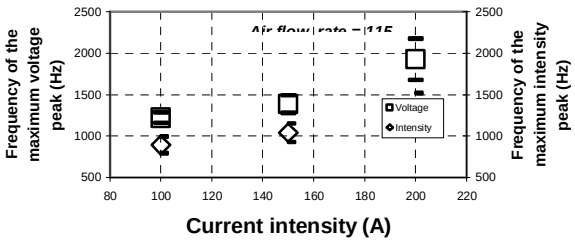

Figure11 : Evolution of the maximum peak frequency of voltage and intensity versus current intensity.

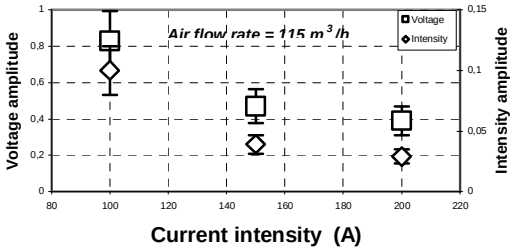

Figure 12 : Amplitude of voltage and intensity corresponding to the maximum peak detected versus current intensity.

Results on coating properties

1. Coating microstructures

Figure 13 presents the micrographs of the cross section of aluminium coatings elaborated with a 100A current intensity and three different air flow rates : 90, 105 and 115 m^3/h

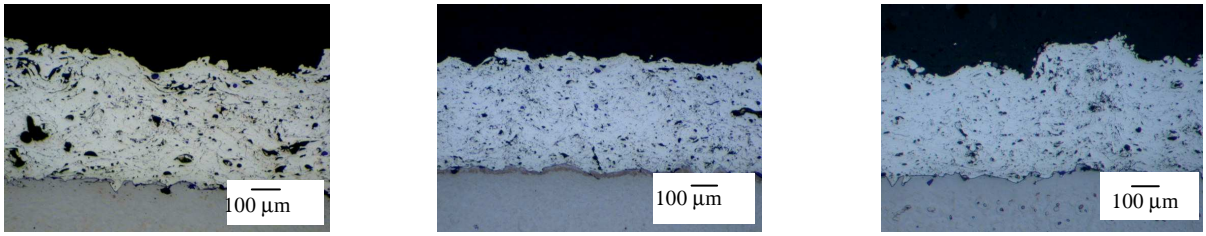

90 m^3/h and 100A *105 m^3/h and 100A* *115 m^3/h and 100A*

Figure 13 : Evolution of coating microstructures versus air flow rate

When the flow rate is changed, the coating lamellae are very different in terms of thickness and pores. According to the evolution of arc characteristics, higher frequencies with smaller amplitudes can be observed which can be associated to smaller particles with higher velocity when increasing the flow rate. Then, the quicker shearing of molten particles, the thinner lamellae. In such a case, all parameters contribute to a better accommodation of the particles to each other at the impact leading finally to smaller dimensions of the pores in the deposit [8]. Because the deformation on the impacted particles becomes better, the coating density increases.

2. Coating porosity

The determination of the coating porosity has been performed using images analysis obtained on the cross section of the deposits. The treatment, realized by Scion Image software, corresponds to the threshold presented in figure 14. The variations detected on the luminosity are due to the presence of pores (dark zone) and to the presence of oxydes (light zone).

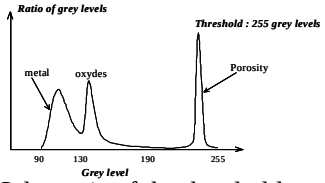

Figure 14 : Schematic of the threshold treatment

The evolution of the porosity versus the flow rates is given in figure 15.

A decrease of the coating porosity from 2,5 to 0,5 % can be noted when the flow rate increases. Then, higher air flow rates lead to lower coating porosity which can be attributed to higher impact particle velocities as well as smaller particle sizes. Then, higher gas velocities result in higher frequencies and smaller amplitudes of the voltage and in smaller molten droplets leading to coatings with lower porosity. Finally, lower turbulence levels at the electrode tips result in more periodic waveforms with a lower frequency content and in a lower porosity of the coatings.

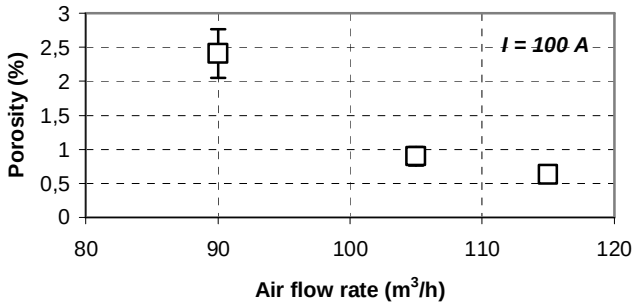

Figure 15 : Evolution of the coating porosity versus air flow rate

3. Coating adhesion

The adhesion measurements have been performed using ESCOTET^{TM}50 machine system following the ASTM C 663-79 standard. The 25mm diameter specimens are arranged like presented in figure 16 in order to avoid the shearing phenomena during the tests. The FM100 glue has been used due to its high mechanical resistance characteristic.

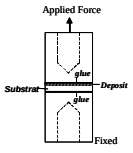

Figure 16 : Experimental set up for adhesion measurements

Figure 17 corresponds to the evolution of the coating adhesion in function of the air flow rate.

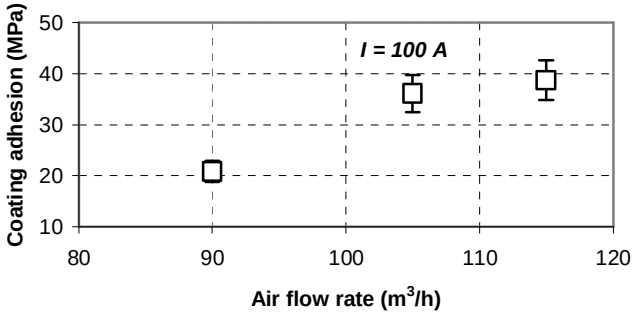

Figure 17 : Evolution of the coating adhesion versus air flow rate

In accordance with the previous results, the coating adhesion increases with the flow rate mainly due to the fact that higher velocity resulting in higher frequency and smaller amplitude of the voltage fluctuations leads to smaller molten droplets. Then, less turbulence at the electrode tips resulting in periodic waveforms of the voltage fluctuations leads to a lower porosity of the coatings in such a case.

Conclusion

Aluminium wires have been sprayed with air using the TAFA^{TM} 9000 gun. Arc fluctuations due to periodic narrowing and widening of the gap between the electrode tips have been investigated in order to point out the effects on the droplet formation therefore on the coating properties such as microstructure, porosity and adhesion. This way, arc characteristics i.e. voltage, intensity and luminosity were recorded using an oscilloscope for different input conditions. Accordingly, time resolved signals of voltage, intensity and luminosity fluctuations have been analyzed by Fast Fourier Transform and by amplitude analysis. The obtained results show that increasing the flow rate of the atomizing gas leads to increase frequency and to decrease amplitude of the voltage fluctuations. The same evolution was observed with the current intensity. As a consequence, the arc stability increases and a more homogeneous jet in terms of particle size is formed. In relation with the arc characteristics, the frequency and the amplitude as well as the waveform of the arc fluctuations are regarded as important parameters for the indication of the droplet characteristics : when increasing the flow rate, the higher the frequency, the smaller the amplitude corresponding finally to smaller particles with a higher velocity. Concerning the coating properties, a strong influence of air flow rates can be noted on the microstructure, porosity and adhesion. When increasing the flow rate, the coating becomes more dense which could be related to the particles size and velocity. In such a case, the porosity decreases due to a better accommodation of the particles between themselves at the impact. The coatings with a lower porosity are produced by the smaller droplets. Finally, velocity and turbulence are important functions for the coatings properties. In wire arc spray process, an increase in air flow rate leads to increase the homogeneity of the coating because the peaks of arc characteristics are well defined.

References

[1] M. Thorpe, “Thermal spray : Industry in transition”, in Advanced Materials and Processes, Vol 143, n°5, 1993, p.50-60

[2] T. Watanabe, X. Wang, J. Heberlein, E. Pfender, W. Herwig, "Voltage and current fluctuations in wire arc spraying as indications for coating properties", in Thermal Spray : Practical solutions for engineering problems, published by ASM International, Matreials Parks, Ohio – USA, (1996), p577-583

[3] X. Wang, J. Heberlein, E. Pfender, W. Gerberich, „Effect of nozzle configuration, gas pressure and gas type on coating properties in wire arc spray”, in Journal of Thermal Spray Technology, Vol 8, n°4, 1994, p.565-575

[4] N. Hussary, J. Heberlein, “Investigations of arc behaviour and particle formation in the wire arc spray process using high speed photography”, in Thermal Spray : Surface Engineering via Applied Research, (ed) C. Berndt, published by ASM Int., Material Parks, OH, Montreal, 2000, p.737-742

[5] J. Sheard, J. Heberlein, K. Selson, E. Pfender, "Diagnostic development for control of wire arc spraying", in Thermal Spray : A united Forum for scientific and technological Advances, (ed) C. Berndt, published by ASM International, Materials Park, Ohio, USA, (1997), p. 613-618

[6] G. Jandin, M.P. Planche, H. Liao, C. Coddet “Relationships between in-flight particles characteristics and coating microstructure for the twin wire arc spray process”, In Proc. Thermal Spray 2002, (ed) E.F. Luchscheider, published by ASM Int., Materials Park , OH , Essen 2001, p.954-959

[7] M.P. Planche, A. Lakat, H. Liao, C. Coddet, “Investigations of in-flight particle characteristics through DPV measurements and correlation with impact analysis and coating properties”, In Proc. Thermal Spray, (ed) F. Moreaux, C. Berndt, published by ASM Int., Material Parks, OH, Orlando 2003 (to be published)

[8] H. Steffens, K. Nassenstein, “Influence of the spray velocity on arc sprayed coating structures”, in Journal of Thermal Spray Technology, Vol 8, n°3, 1999, p.454-460

Non-equilibrium chemistry of Li atoms in laser-produced plasmas from ablation of $LiNbO_3$ crystals in gas atmospheres

F. J. Gordillo-Vázquez[1] and C. N. Afonso[1]

[1] *Instituto de Óptica (CSIC), Serrano 121, 28006 Madrid, Spain*

A precise knowledge of the non-equilibrium chemistry of the laser-produced plasmas typically found in Pulsed Laser Deposition (PLD) experiments is important for having a complete understanding of the growth process of thin solid films of technological interest. In particular, the homogeneous (plasma) and heterogeneous (plasma-surface) reactions partially control the plasma composition and, consequently, that of the growing films.

The use of PLD has proven to be one of the most successful techniques in growing complex oxide materials [1]. However, the thin films of $LiNbO_3$ (used in optoelectronic and photonic applications) deposited by laser ablation of $LiNbO_3$ in vacuum or low pressure (< 1 Torr) atmospheres are often found Li deficient [2]. However, when the films are grown at a pressure of about 1 Torr, independently of the nature of the used ambient atmosphere (either inert, Ar, or reactive, O_2), the $LiNbO_3$ films grow stoichiometrically [3]. Although the latter result has been understood in the frame of the blast-wave model [3], which describes the plasma expansion in a gas environment at a sufficiently high pressure, the detailed kinetics together with the species concentrations in the laser-produced plasma have not been modeled up to date.

The objective of this contribution is to develop a collisional-radiative model to determine the influence of Ar and O_2 atmospheres (at 1 Torr) on the electron-driven kinetics of ground and excited Li atoms (up to the 3^2D level) within the laser-generated plasma. It is found that whereas the Li atom population densities in the plasma produced in gas are, in general, higher than those found in vacuum, they are similar in vacuum and Ar close to the substrate, though lower than in O_2. In addition, it is suggested that the reabsorption of radiation by the plasma is more important within O_2 than in Ar since the absorber (ground Li) concentration is higher in O_2 environments. In this regard, a very reasonable qualitative agreement is found when comparing the Li I-670.8 nm spectral line emission intensity predicted by the model with that obtained experimentally in Ar and O_2 atmospheres.

Finally, the kinetic model proposed here provides quantitative information on the relative loss and gain electron-driven mechanisms contributing to, respectively, populate and depopulate the different energy levels of Li atoms present in the laser-produced plasmas of interest here.

[1] C. N. Afonso, in *Materials for Optoelectronics: New Developments*, edited by F. Agulló-López (World Scientific, Singapore, 1995), Chap. 1, and references therein.
[2] S. B. Ogale, R. Nawathey-Dikshit, S. J. Dikshit, and S. M. Kanetkar, J. Appl. Phys. **71**, 5718 (1992).
[3] J. A. Chaos, J. Gonzalo, C. N. Afonso, J. Perrière, and M. T. García-González, Appl. Phys. A **72**, 705 (2001).

On the origin of the structural properties of PECVD silica.

H. Caquineau[1], M. Chayani[1], B. Despax[1] and J. P. Couderc[2]

[1] *Laboratoire de Génie Electrique de Toulouse, Université Paul Sabatier, Toulouse, France*
[2] *Laboratoire de Génie Chimique, Ecole Nationale Supérieure des Ingénieurs en Arts Chimiques et Technologiques, Toulouse, France.*

Abstract
In this paper, a study of the PECVD of close-to-stoechiometry silicon oxide is proposed with a special focus on how the material structures itself. Indeed, depending on the operating conditions, a wide range of material properties can be achieved even for films close to stoechiometry. Based on physico-chemical analysis results (wet etch-rate, ellipsometry, XPS, FTIR, Raman spectroscopy) and on modeling results, the origin of such differences for almost similar materials is inferred from a structural point of view.

1. Introduction

Silicon oxide is a material of major importance for the microelectronics industry and is commonly used as an intermetal or interlayer dielectric. Among the various processes available to deposit silicon dioxide thin films, PECVD processes offer the possibility to operate at low temperature which is of great interest when the substrate is thermosensitive. Nevertheless, these processes have some drawbacks and often do not allow the reproducibility of thermal CVD. The properties of the material deposited using PECVD are changeable for a given process and changes from one process to the other as testify by the various results available in the literature. In this paper dedicated to films having a composition close to that of silica, i. e. SiO_2, a study of the structural properties of PECVD silicon oxide using various physico-chemical analysis tools is first proposed. More particularly, these properties are shown to depend on the position in the reactor. A mass transfer model has been used to establish which are the film precursors as a function of this position and so to propose relationships between the precursors and the film structure. At the end of this paper, the interest of helium dilution of the reactive gas mixture is also discussed and put in perspective with the help of the preceding analysis.

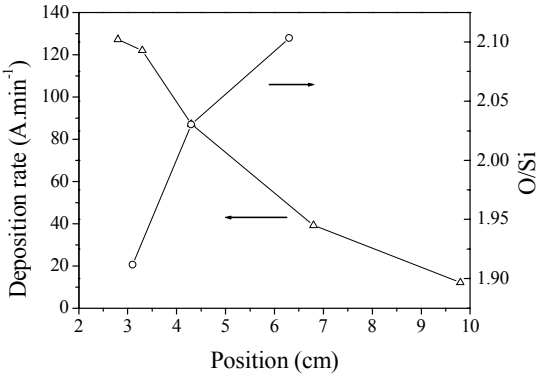

Figure 1 : Deposition rate and O/Si ratio as a function of the position

2. Experimental

Silicon oxide was deposited in a parallel-plate RF (13.56 MHz) reactor with the gas entrance on one end of the inter-electrode space and the exit on the opposite end. The utilized gas was a mixture of 1 % silane diluted in excess N_2O. With such a low dilution, the obtained films were close to the stoechiometry of silica in the reference condition (P= 0.5 Torr, T = 503 K) used throughout this paper as shown in figure 1. The O/Si ratio was measured by XPS. At the moderate power used under this reference condition (5 $mW.cm^{-2}$), an important decrease of the deposition rate is observed (figure 1).

3. Film analysis

Several analyses were carried out on our films. A special attention was dedicated to FTIR results. The spectra of our films presented the usual peaks of amorphous silica with some variations depending on the position in the reactor. First, Si-OH bonds were present in our films, but no Si-H bonds. Isolated Si-OH and associated ones can be distinguished as it was done by Theil [1]. In our reference conditions, it can be seen in figure 2 that the amount of associated OH decreases from the entrance of the reactor to its exit while that of isolated OH remains steady. Meanwhile, as shown in figure 3, the position of the peak corresponding to the stretching of Si-O-Si bridges changed from 1063 down to 1050 cm^{-1} and the Full Width at Half Maximum (FWHM) increases. The position of this peak is representative of the mean Si-O-Si angle and its FWHM of the angle distribution :the higher the position, the higher the angle and the higher the FWHM, the wider the

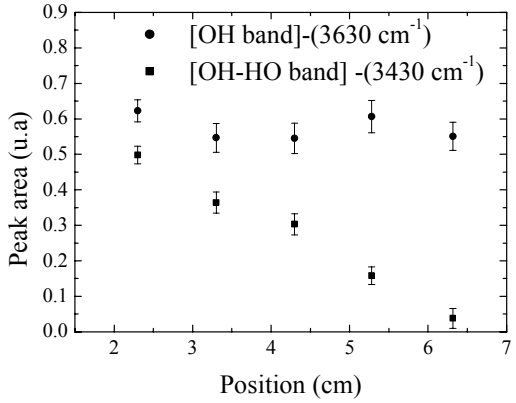

Figure 2 : Normalized area of isolated and associated OH IR peak as a function of position

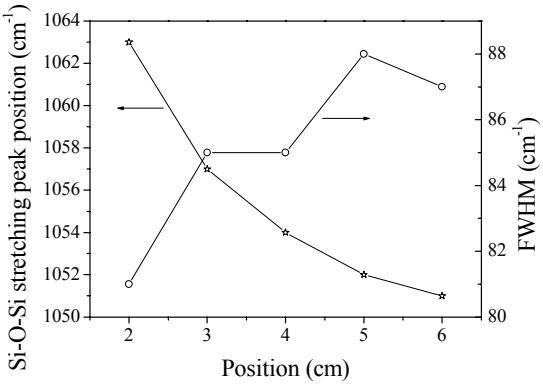

Figure 3 : Position of the IR Si-O-Si stretching peak and its FWHM as a function of position

distribution. First, it should be underlined that the normal position of this stretching peak in thermal silica is 1075 cm^{-1}. Therefore, the mean angle in our films is lower than in thermal silica and thus probably more constrained. The evolution along the position in the reactor of the energy of the IR peak is a signature of a lowering of this mean angle. Remarking that this decrease of the mean angle is accompanied by a similar evolution of the amount of associated OH makes us think that the material at the entrance is relaxed by water reaction with the more constrained bridges as suggested by Theil [1] and Brunet-Bruneau [2].

We suppose that these relaxation reactions open the more constrained Si-O-Si bridges to give birth to associated Si-OH bonds, which can explain that associated OH are present at the positions where the Si-O-Si mean angle is the highest. Such a process was also evidenced by Theil [1]. This hypothesis is supported by ageing experiments at the ambiant atmosphere which show that the films containing numerous associated OH are more prone to hydrolysis than the others. This leads us to think that the formation of associated OH is a post-venting effect.Then, it could be anticipated that before this ex-situ action of water, the mean angle of the film at the entrance and thus their peak position might be lower than the one we actually measured. The evolution of the FWHM is also coherent with the hypothesis of a relaxation by water. Indeed, the film which are the more relaxed have the narrower angle distribution.

At this stage, considering the preceding explanations, it can be quite surprising that the films around 6 cm are almost inert toward water, since they have a low mean angle and therefore Si-O-Si bridges which are potentially reactive. Nevertheless, these films have a wet etch-rate close to that of thermal silica and much lower than that of the films at the entrance (figure 4), which can result from a high compactness for these low-angle films. Several other facts come as a support to a higher compactness of these films. First, their refractive index is higher than the index of thermal silica (1.461 at 630 nm) as presented in figure 4. Besides, Raman spectroscopy showed that the behaviour of our films can be compared to pressure-densified silica. This matter is described more thoroughly in [3]. As far as the refractive index is concerned, most of our films have a refractive index higher than that of thermal silica, but in the case of the associated-OH containing films, this could be the result of a dense matrix containing pores partially filled by water, just as in [2]. Although none of our films when observed by TEM at a nanometric resolution presented pores and although no water was detected by FTIR, we think that subnanometric voids 'containing' the associated Si-OH bonds could give our films similar refractive properties as in [2].

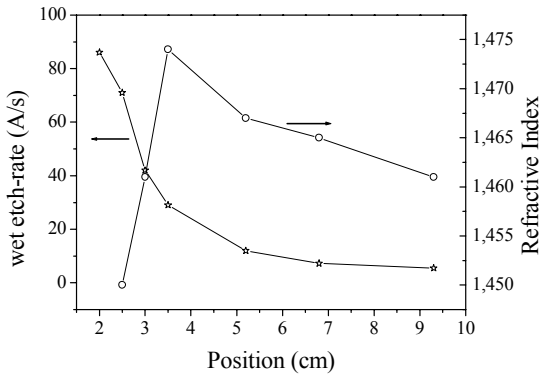

Figure 4 : wet-etch rate and refractive index as a function of the position

Back to the films which are almost associated-OH free, althought they are close to the stoechiometry of thermal silica, when compared to this last material, these films have a lower mean angle for the Si-O-Si bridges, the Si-O-Si angle distribution is larger (the

FWHM of thermal silica is about 65 cm^{-1}), their matrix seems to be denser and their wet etch-rate is comparable. The caracteristics of the Si-O-Si stretching peak of these films had already been observed in irradiated silica films [4, 5]. More particularly, Douillard and Duraud [5] attributed the evolution of this peak to a structural rearrangement process occuring during the ion implantation in silica which they studied. The energetic bombardment results in the creation of defects, mainly E' center and non-bridging oxygen centers. When reaching a sufficient amount of defects, new Si-O-Si bonds form. In fact, a steady state is reached between the defect creation and the rearrangement process which finally lead to a stable material with constrained bond. This process is called metamictization.

In the light of these information, we will now propose a film growth mechanism which could explain the observed structural properties of our films.

4. Film growth mechanism

It is well-known that in PECVD processes, the precursor species to the deposit are radical species. Moerover, at the low operating temperature used in this work, the sticking species have a reduced mobility and react with their immediate neighborood. In these conditions, defects can easily appear during the film growth. We just have explained how the presence of defects can lead to a deposit rearrangement which could explain the structure of the films around 6 cm. Nevertheless, the question of why the film structural properties are so changeable as a function of the position remains an open case. In order to answer this question, a mass transfer model coupled with an electrical model was used. The chosen chemical mechanism is quite simple and is described in details in [6]. In a nutshell, SiH_4 is mainly decomposed by $O\cdot$ which results from the electronic impact on N_2O. Afterwards, a radical propagation occurs and leads to SiH_xO species. This model allowed us to explain the drastic decrease of the deposition rate (figure 1) which is a direct consequence of the silane consumption along the flow. Indeed, the sticking silicon-containing radical are short-living species, which induces that the deposition rate at a given position is rather directly linked to the local silane concentration. Beyond that, in figure 5, the contributions of the different precursors to the film are given as a function of the position in the reactor. The analysis of this graph in combination with that of the deposition rate is a path toward the understanding of the obtained different structures. In the entrance zone, the silyl radical contributes substantially to the deposit and a large part of the oxidation occurs at the film surface. Moreover, at this place, the deposition rate is rather high, which implies that the time left to a deposited species to find a neighbor in a correct configuration is limited. In this condition, it can be anticipated that the defects can easily appear, may be rearrange in highly constrained bond and also that these defects and constrained bonds can be rapidly buried. Such a film can then be subjected to the water post-venting effect described above. When getting further in the reactor, the precursors become more and more oxided and the deposition rate decreases. As a consequence, the precursors which already contains an Si-O bond, have more time once sticked to the surface and before their burial to be oxided by gas phase $O\cdot$ or to react with other gas phase species. Then, the amount of defects is probably lower than in the entrance zone and gives place to a metamictization-like process. It should be also noticed here that due to the silane consumption, the $O\cdot$ concentration increases along the flow direction and so does the surface oxidation of the growing film. Besides, The higher contribution of SiH_3 in the entrance zone can also explain the lower O/Si ratio measured there (figure 1).

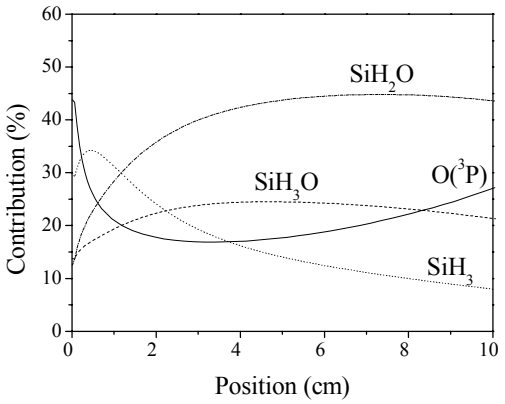

Figure 5 : Contribution of the deposit precursors as a function of position

Let us add a few words on SiH_2O which plays a major part in the deposition process, at least with the chemical mechanism we proposed. This species is known to react easily with itself with almost no activation barrier to form a species containing a $(Si\text{-}O)_2$ ring [7]. It is then possible that whether in the gas phase or directly on the surface SiH_2O could be at the origin of small $(Si\text{-}O)_n$ rings containing constrained Si-O-Si bridges in the material.

Based on the consideration given above on how the film structures itself, new conditions which could lead to associated OH free and stable material will now be studied. More particularly, our interest will focus on a

process where the SiH_4/N_2O mixture is diluted in helium. Indeed, diluting the reactive gas mixture results in a lowering of the active species concentration and by the way, of the deposition rate.

5. Effect of helium dilution

For these experiments, the pressure was set at 1 Torr and the N_2O and SiH_4 flow rates were kept at the same values as before. The dilution rate by helium was taken at 75 %. The consequence of this dilution was not only to decrease the reactant concentration but also to increase the gas velocity between the two electrodes. Both these effects reduces the deposition rate heterogeneity observed in figure 1. This is logical since silane is less rapidly consumed in the reactor. Also, the helium dilution lowers the wet etch-rate and increases the refractive index, probably due to an increase of the film compactness. More interestingly, the position of the Si-O-Si stretching peak stays about 1050 cm^{-1}, with a very low amount of associated Si-OH bonds. One can rapidly think that this is a direct consequence of the low deposition rate which let the time to the depositing species to be oxided. Nevertheless, we can wonder if the benefit of the helium dilution only comes from the lowering of the deposition rate. To investigate this, a film containing associated OH was exposed to a pure He plasma. This exposure results in the disappearance of the associated OH and to a shift the Si-O-Si stretching peak from 1063 cm^{-1} to 1055 cm^{-1}. This behavior could correspond to the formation of Si-O-Si bonds sharper than in thermal silica upon water departure from the film. Indeed, He plasma are known to produce energetic UV photons which could be at the origin of these modifications of the films. Obviously, such a process can also take place while the film is growing in SiH_4/N_2O/He plasma. Furthermore, two other experiments we carried out consisted in depositing films at 623 K in a SiH_4/N_2O mixture and in a diluted mixture, while keeping all the other parameters constant. Both the obtained films are under the detection limit of associated OH, which shows that at this temperature a thermal release of water happen. However, whereas the Si-O-Si stretching peak position in the diluted mixture is 1055 cm^{-1}, its position in the other case is 1065 cm^{-1}, closer to its position in thermal silica. This clearly shows that the water removal and the Si-O-Si bridge closure action of He is quite different from a thermal relaxation. This might explain why Batey [8] observed that when silicon oxide is deposited from He diluted plasma its electrical properties are improved as compared to process with no dilution. In fact, the helium dilution leads to structural modifications of the films.

6. Conclusion

In this work, the structural properties of silicon oxide films deposited using PECVD were studied using various physico-chemical analysis tools. Our interest mainly focused on films where the O/Si ratio is close to 2. It was shown that depending on the position in the parallel-plate PECVD reactor used for this work the properties of our films changed. The analysis of FTIR results and ageing experiments showed that the post-venting effect of water affect the amount of associated OH present in the films. It is inferred that the PECVD growth of the films lead to constrained Si-O-Si bridges which can interact with atmospheric water to form associated Si-OH bonds. Nevertheless, the films which have the highest O/Si ratio (around 2) are insensitive to water although their mean Si-O-Si angle is lower than in thermal silica. We proposed that during a film growth under plasma conditions, the growing films are subjected to a metamictization-like process. Metamictization is a rearrangement process which is caused by the defect induced when silica is irradiated. As the properties of our films are variable depending on the position in the reactor, a mass transfer model was used to identified the change of the deposit-precursor species with the position. This brought to the fore the role of the deposition rate on the film structure as well as that of the oxidation level of the precursor. The best conditions to obtain a stable material is to operate at a low deposition rate in order to let it the time to grow properly, which is easier when Si-O bonds already exist in the sticking species and to be oxided by O gas phase radicals. The effect of helium dilution have also been studied, since it led to low deposition rate. The structure of the films were actually interesting, and we found that this results not only from the low deposition rate but also from a possible action of the UV photons emitted by the helium-containing plasma. Future work will be dedicated to the electrical properties of our films essentially for those which are water-inert and more particularly for those obtained under helium dilution of the gas mixture. Besides, models will also be developed to reach a further understanding of the chemistry of the process, once again, especially under helium dilution.

References

[1] J. A. Theil, D. V. Tsu and G. Luckovsky, J. of Electronics Materials, 19, 209 (1990).
[2] A. Brunet-Bruneau, D. Souche, S. Fisson, V. Nguyen Van, G. Vuye, F. Abeles and J. Rivory, J. Vac. Sci. Technol. A, 16, 2281 (1998).
[3] M. Chayani, H. Caquineau, B.Despax, J. Bandet and R. Berjoan, submitted to Thin Solid Films.
[4] R. A. B. Devine, Nucl. Instr. Meth. Phys. Res. B,. 91, 378 (1994).
[5] L. Douillard, J. P. Duraud, Nucl. Instr. Meth. Phys. Res. B,. 107, 212 (1996).
[6] K. Radouane, L. Date, M. Yousfi, B. Despax and H. Caquineau, J. Phys. D : Appl. Phys., 33, 1332 (2000).
[7] M. R. Zachariah and W. Tsang, J. Phys. Chem., 99, 5309 (1995).
[8] J. Batey and E. Tierney, J. Appl. Phys., 87, 2807 (1986).

RF plasma deposition of SiO_x and a-C:H as barrier coatings on polymers

D. Hegemann, H. Brunner, C. Oehr

Fraunhofer Institute for Interfacial Engineering and Biotechnology IGB, Nobelstr. 12, 70569 Stuttgart, Germany; www.igb.fraunhofer.de

Abstract

RF discharges of O_2/HMDSO and CH_4 were used to deposit SiO_x and a-C:H barrier coatings on PET foils using a symmetrical and an asymmetrical plasma reactor, respectively. Both processes were found to be radical-dominated since the reaction parameter *W*/*F* determines the film growth. Surface processes driven by ion bombardement result in rival ablation/deposition processes leading to a broadened interphase on PET. This inorganic/organic interphase was found to posses no barrier properties, whereas inorganic/inorganic interphases in two-layer systems of SiO_x/a-C:H contribute to the barrier properties.

1. Introduction

Siloxane- or hydrocarbon-based plasma films have been extensively studied, for example as protective or barrier coatings [1-4]. By using organic precursors like hexamethyldisiloxane (HMDSO) or methane (CH_4), the film properties can be varied from polymer-like to quartz- and diamond-like, respectively, at near room temperature. Thus, these films can be deposited on polymers for example with different wetting properties or gas permeation rates [5, 6]. However, optimized deposition conditions often depend strongly on the reactor geometry used. In particular for barrier coatings on polymers, surface roughness, adhesion, internal stresses, flexibility, and transparency – beside the permeation rates – must be considered. Barrier properties of flexible packagings are required for example in food packaging, for solar modules, LEDs and OLEDs.
Therefore, this work investigates the plasma deposition process of SiO_x and a-C:H films regarding deposition rate, plasma potentials, and film properties, using compact plasma reactors which can be scaled up. Moreover, the "interphase" formation (broadening of the substrate/coating transition) of inorganic, hard coatings on soft polymers during the first stage of film growth is examined. While this interphase enhances the adhesion of PECVD-derived coatings on polymers compared to PVD coatings, it seems to limit the critical film thickness needed for good barrier qualities. Therefore, OTR and WVTR values are compared for single layers and two-layer coatings of SiO_x and a-C:H on PET foils.

2. Experimental

Capacitively coupled RF discharges (13.56 MHz) with plane parallel electrode configuration were used in this study to deposit barrier coatings on polymers. For SiO_x films, a symmetrical reactor with an electrode size of 29 x 39 cm^2 was developed, whereas for the deposition of a-C:H films, an asymmetrical plasma reactor with an electrode size of 24 x 39 cm^2 was used to attain an additional bias voltage. Both reactors have a gas feeding system inside the top electrode to generate a uniform, vertical gas flow towards the bottom electrode where a homogeneous deposition over large areas is obtained. The lower (substrate) electrode is powered. A V/I probe (ENI Model 1065) measures applied voltage, current and phase angle.
The precursor hexamethyldisiloxane (HMDSO), $C_6H_{18}OSi_2$, used as obtained by FLUKA was thermo-stabilized and vaporized outside the apparatus. Oxygen as carrier gas is mixed with HMDSO and fed together into the plasma chamber. Power was varied between 50 and 400 W, HMDSO flow between 10 and 100 sccm, O_2 flow between 50 and 220 sccm and pressure between 10 and 35 Pa. SiO_x films were deposited near room temperature.
For the deposition of a-C:H coatings, methane, CH_4, was used as precursor alone. The parameter set was varied between 50 and 500 W for power, 20 and 100 sccm for CH_4 flow, and 10 and 35 Pa for pressure. Due to ion bombardement, the substrate temperature raised during deposition, but was always below 80° C.
To determine the deposition rate, Si wafers (100) were coated. The mass deposition is obtained by weighing the substrates immediately before and after the coating procedure (Sartorius Balance H110; precision:

0.1 mg). It was proven, that the deposition rate depends linearly on time. Additionally, thickness is measured on film edges via atomic force microscopy (PSI Autoprobe CP). Film density is calculated from mass and volume of the coatings. As substrate material 23 µm thick PET foils (Hostaphan RD) were coated.
X-ray photoelectron spectroscopy (KRATOS Axis Ultra) with Mg k_α excitation and a 110 µm spot and Auger electron spectroscopy (PHI 545C) were used to determine the chemical composition. For the depth profiles the samples were sputtered with 5 keV Ar ions at an incident angle of 90°.
Oxygen (OTR) and water vapor transmission rates (WVTR) were measured by Mocon Oxtran and Permatran devices at 23° C, 50% r.h. (DIN 53380-3) and 23° C, 85% to 0% r.h. (DIN 53122-1), respectively.

By measuring the excitation voltage V_0, bias potential V_{bias} and average thickness of the plasma sheath d_{sh} in front of the electrodes, the potential distribution can be given (Fig. 1) by using a simple model described in the literature [7, 8].

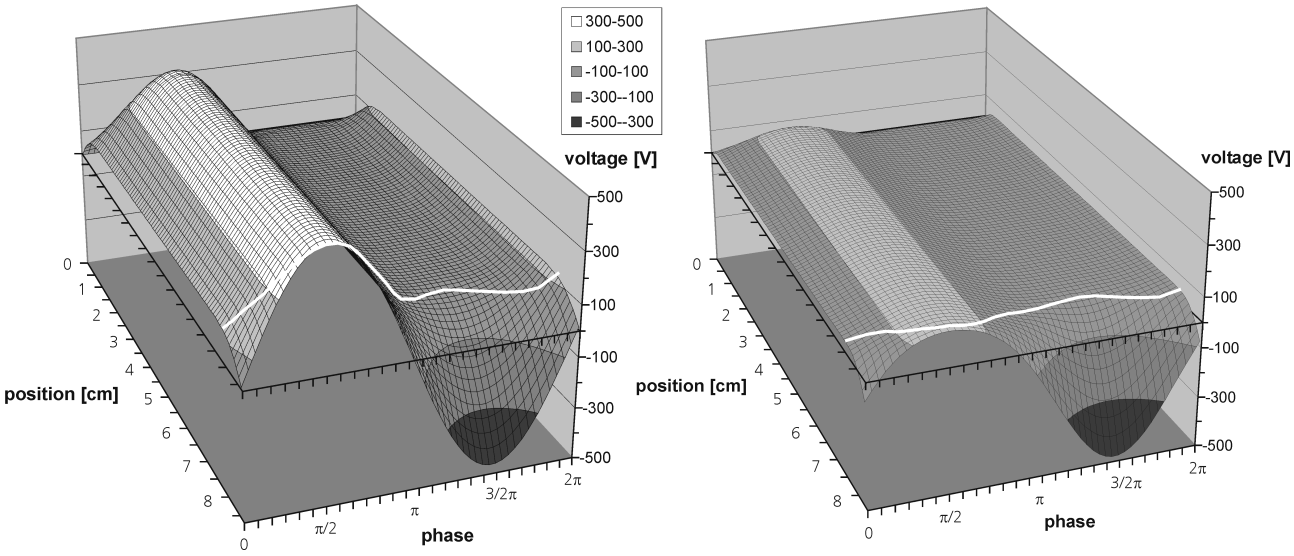

Fig. 1: Potential distribution over one RF cycle for the symmetrical (left; O_2/HMDSO 350 W 0.2 mbar) and the asymmetrical plasma reactor (right; CH_4 300 W 0.2 mbar). Both processes yield comparable potential drops across the plasma sheath (RF electrode in front). The white, bold line indicates the oscillation of the plasma sheath.

It can be seen that although there is no bias voltage in the symmetrical reactor, a sheath potential of about 190 V ($V_{sh} \approx 0.39\ V_0$) is applied on average in front of the powered electrode at typical parameters used to deposit SiO_x barrier coatings. On the other hand, the potential drop in the asymmetrical reactor is an addition of plasma potential and negative (average) bias potential ($V_{sh} \approx 0.39\ V_0 - 0.73\ V_{bias}$). Again about 190 V is obtained for typical conditions to generate a-C:H barrier coatings.

3. Results and Discussion

According to the work of Yeh, Shyy and Yasuda the mass deposition rate R_m for radical-dominated discharges depends on power input W, monomer gas flow F_m, and a geometrical, reactor depending factor G [9], thus that

$$\frac{R_m}{F_m} = G \exp\left(-\frac{E_a}{W/F_m}\right). \qquad (1)$$

It was found that W/F_m was the unique reaction parameter controlling the conversion of monomer in the gas phase to the plasma polymer in the solid phase primarily by activation of molecular bonds, where E_a is the apparent activation energy [10].

Only recently, it could be shown by our group that this concept also holds when oxygen is added to HMDSO as a reactive carrier gas [6, 11]. It was approved that power per gas flow still determines the deposition rate (Fig. 2), where the total gas flow F_{mc} is now an addition of monomer flow and carrier gas flow as

$$F_{mc} = F_m + aF_c \,. \tag{2}$$

The factor a was found to be 0.6, i.e. smaller than 1. This in turn means that keeping the total gas flow and the power input constant, the energy density W/F_{mc} raises with increasing O_2/HMDSO ratio. Thus, the addition of oxygen supports the film growth, since it contributes to the radical formation in the gas phase.

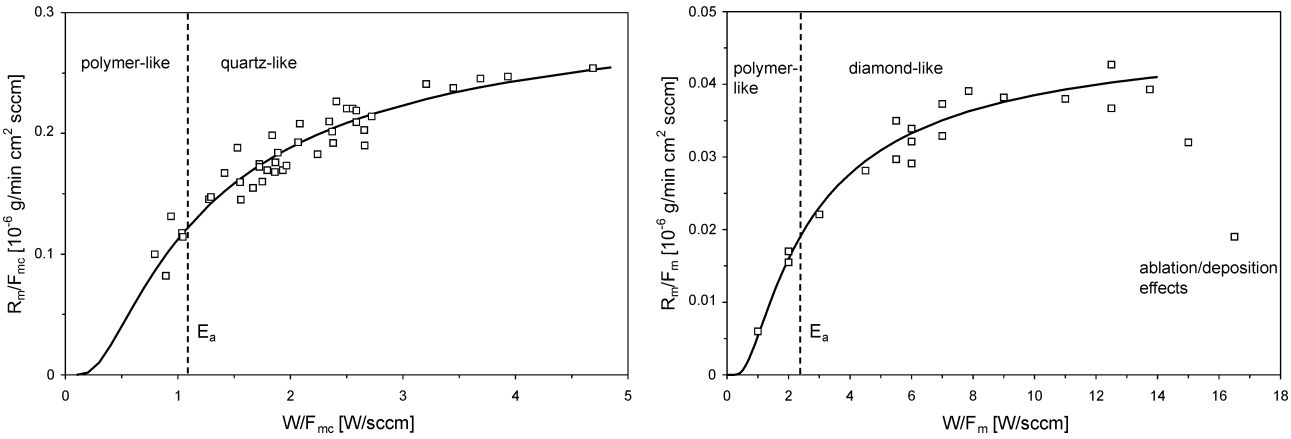

Fig. 2: Mass deposition rate per gas flow for O_2/HMDSO (left) and pure CH_4 (right) discharges depending on the reaction parameter W/F. The apparent activation energy E_a divides the energy density into a polymer-like and a quartz-like, respectively diamond-like, regime. A third regime occurs for a-C:H coatings at high energy densities due to rival ablation/deposition processes. The bold line represents the fit corresponding to eq. 1 and 2.

As long as ion bombardement does not prevail, the film growth is thus determined by gas phase processes such as fragmentation and generation of radicals. Nevertheless, ions accelerated across the plasma sheath by the potential drop V_{sh} supports cross-linking of the growing films. But V_{sh} also scales with the internal stresses in the SiO_x and most of all a-C:H films, whereby increased internal stresses result in a reduction of the barrier properties [6]. Hence, the two parameters, W/F and V_{sh}, which determine the plasma volume and surface processes, provide evidences for the optimum deposition conditions. It was found that an energy density of 2-3 times the activation energy E_a yields the optimum barrier properties (table 1). Compared to SiO_x films, a-C:H films are more flexible and smoother, but show higher oxygen permeation rates and internal stresses. Adhesion on polymers and transparency can be improved by applying the minimum film thickness required for barrier coatings.

Table 1: Oxygen (OTR) and water vapor (WVTR) transmission rates of SiO_x and a-C:H coatings on PET foil.

Material combination	OTR [cm^3/m^2 d bar]	WVTR [g/m^2 d]
23 µm PET	51	11
PET / 40 nm SiO_x	0.35	1.1
PET / 20 nm a-C:H	2.4	0.33
PET / 40 nm SiO_x / 20 nm a-C:H	0.21	0.29
PET / 40 nm SiO_x / 10 nm a-C:H	0.24	0.3
PET / 20 nm a-C:H / 40 nm SiO_x	0.23	0.28

Using the obtained deposition rates for SiO_x and a-C:H coatings, ultra-thin layers can be deposited. This can then be used to examine interphase formation of these coatings on polymers or in multi-layer systems. At first, ~14 nm thick SiO_x coatings were deposited on smooth Si wafers (R_{rms} = 0.5 nm; R_{ave} = 0.3 nm) using

the optimized plasma conditions for barrier coatings without a plasma pre-treatment. Depth profile analyses by XPS and AES were performed by sputtering through the SiO_x layer. As can be seen in Fig. 3 for both methods an interphase width of about 5.5 nm were detected. Due to the difficulty of getting the AES sensitivity factor of oxygen in oxide layers [12], the absolute chemical composition of the AES spectra was normalized with the XPS measurement, which was calibrated using a quartz standard. However, this has no influence on the sputtering depth. Assuming the real interphase width to be 1-2 nm due to Si–O bonds at the interface SiO_x/Si [13], a broadening of the interphase of about 4 nm occurs which can be assigned to the information depth of AES and XPS measurements [14]. Mixing effects might not play an important role with these ultra-thin coatings.

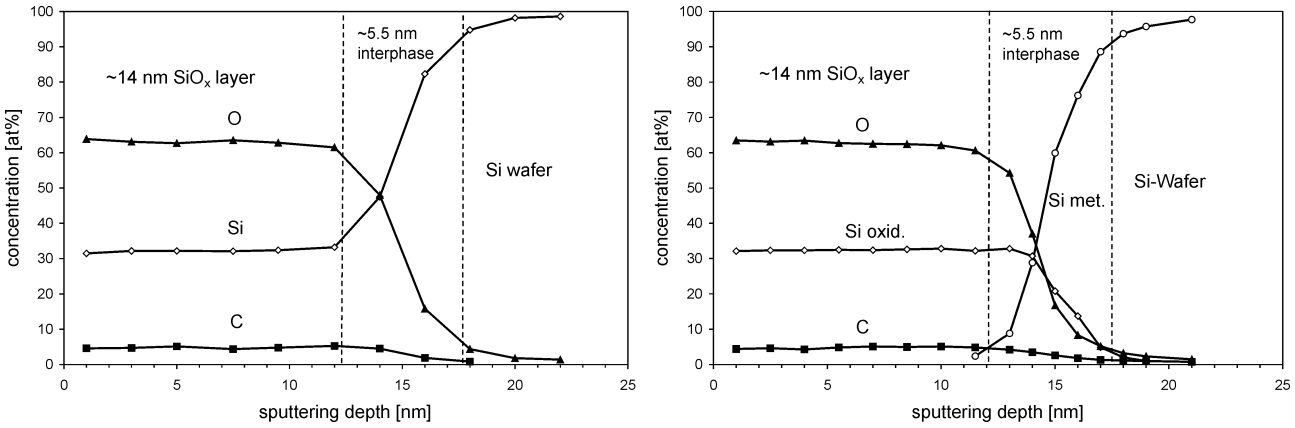

Fig. 3: Depth profile analyses by means of AES (left) and XPS (right) of ultra-thin SiO_x layers on Si wafers. With both methods the interphase width can be detected yielding comparable results. XPS can also differentiate the oxidic and metallic Si component.

With these findings, the interphase of a ~14 nm SiO_x layer on smooth PET foils (R_{rms} = 0.6 nm; R_{ave} = 0.45 nm) can be analyzed (Fig. 4). The apparent interphase width is around 8 nm, i.e. the real interphase might be ~4 nm derived in analogy with the SiO_x/Si interface. Hence, the deposition of SiO_x layers on PET leads to a broadened interphase formation due to ablation/deposition effects as long as the polymer surface is concerned through the plasma interaction [15]. To our understanding, the finding of thicker interphases might be attributed to an enhanced roughness of the polymer substrate [16]. This broadening of the interface yields a fairly good adhesion as long as the SiO_x layer does not become too thick. Then, the internal stresses of the films must be adopted to the polymer properties via a gradient layer [11].

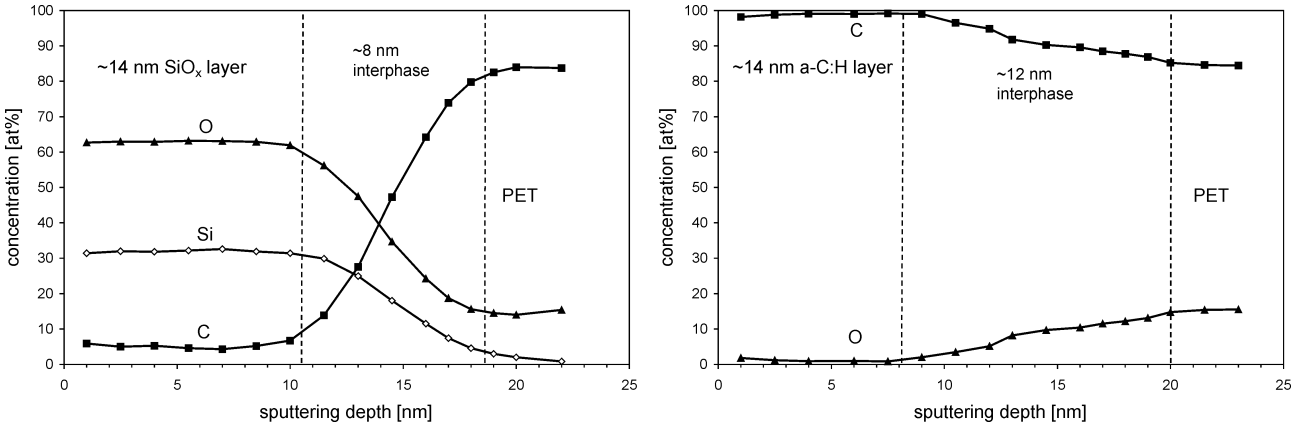

Fig. 4: Depth profile analyses by means of XPS of ultra-thin SiO_x (left) and a-C:H (right) layers on PET foils. The interphases are broadened due to rival ablation/deposition processes during the first stage of film growth.

Furthermore, it was found that a minimum thickness of about 15 nm is required to achieve barrier properties of the SiO_x coatings, that means to obtain dense, closed films [3]. Similar findings were obtained for a-C:H

barrier coatings. Nevertheless, due to an increased ion bombardement during deposition (mainly H^+ ions), a further broadening of the interphase (~8 nm) was detected and the minimum barrier layer thickness required is thus about 20 nm.

Next, two-layer systems of SiO_x and a-C:H were investigated. By depositing the a-C:H layer on top of the SiO_x layer, a corrected interphase width of about 6 nm was observed (Fig. 5). However, on inorganic SiO_x even 10 nm a-C:H were found to be sufficient to achieve good barrier properties (table 1). Therefore, it can be concluded that the inorganic interphase itself contributes to the enhancement of the barrier properties, whereas the organic/inorganic transition of the barrier layers on polymers does not.

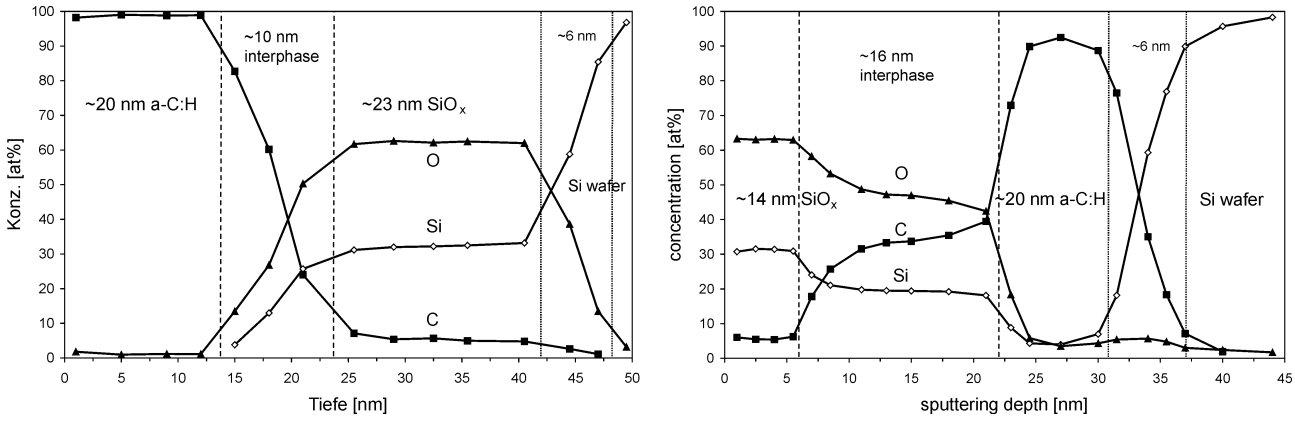

Fig. 5: Depth profile analyses by means of AES of a-C:H on top of SiO_x (left) and SiO_x on top of a-C:H (right) layers on Si wafers. The interphases are broadened due to rival ablation/deposition processes during the first stage of the second film growth. Due to chemical etching, this is particularly pronounced when depositing SiO_x on a-C:H.

When depositing the SiO_x layer on top of the a-C:H layer on the other hand, a noticeably broader interphase formation (~12 nm) can be observed (Fig. 5). Here, a strong interaction of the oxygen plasma with the a-C:H surface through chemical etching occurs, resulting in rival ablation/deposition processes. However, the adhesion of both two-layer systems were proven to be excellent. Moreover, since both combinations of SiO_x and a-C:H on PET exhibit comparable OTR and WVTR values (table 1), the interphase SiO_x/a-C:H can also be regarded to posses barrier qualities. However, considering the barrier improvement factors [17], these interphases add no additional or synergetical effects for improving the barrier properties, and WVTR (OTR) is hardly improved by SiO_x on top on a-C:H (a-C:H on SiO_x). The latter depends on the rather limited barrier properties of plasma polymerized a-C:H for oxygen and SiO_x for water vapor, respectively.

4. Conclusions

By evaluating the mass deposition rates of O_2/HMDSO- and CH_4-derived RF plasma coatings, it appears that the deposition of SiO_x and a-C:H barrier layers is a radical-dominated process since the reaction parameter power per gas flow W/F determines the deposition rate. The resulting apparent activation energy E_a gives hints to find the optimum deposition conditions. Nevertheless, the interaction of fast ions and neutrals with the growing film is needed to attain dense, closed films with a low defect rate. On the polymer substrate rival ablation/deposition effects thus lead to a broadening of the interphase SiO_x/PET and a-C:H/PET with an interphase width of about 4 nm and 8 nm, respectively. We suppose that these interphases do not contribute to the barrier properties, but enhance the adhesion of the layers. To obtain barrier properties on PET, a layer thickness of about 15 nm for SiO_x and 20 nm for a-C:H is required. On the other hand, when depositing a-C:H on top of a SiO_x layer, already 10 nm are sufficient to improve the barrier properties. Therefore, it can be concluded that the inorganic interphase itself contributes to the enhancement of the barrier properties, whereas the organic/inorganic transition of the barrier layers on polymers does not. However, synergetical effects, like healing of defects, did not occur in the two-layer system of plasma polymerized SiO_x and a-C:H coatings.

Acknowledgement

We thank Dr. H.-C. Langowski and A. Melzer, Fraunhofer IVV, Freising, Germany for the gas permeation measurements within the Fraunhofer alliance POLO ("Polymere Oberflächen").

References

[1] H. Chatham, Surf. Coat. Technol. **78**, 1 (1996).
[2] C.-P. Klages, A. Dietz, T. Höing, R. Thyen, A. Weber, P. Willich, Surf. Coat. Technol. **80**, 121 (1996).
[3] A.S. da Silva Sobrinho, M. Latrèche, G. Czeremuszkin, J.E. Klemberg-Sapieha, M.R. Wertheimer, J. Vac. Sci. Technol. **A16**, 3190 (1998).
[4] E.M. Moser, R. Urech, E. Hack, H. Künzli, E. Müller, Thin Solid Films **317**, 388 (1998).
[5] D. Hegemann, H. Brunner, C. Oehr, Plasmas Polym. **6**, 221 (2001).
[6] D. Hegemann, H. Brunner, C. Oehr, Surf. Coat. Technol. (2003), in press.
[7] M.A. Lieberman, A.J. Lichtenberg, Principles of Plasma Discharges and Materials Processing, John Wiley & Sons, Inc., New York, 1994.
[8] Y.P. Raizer, M.N. Shneider, N.A. Yatsenko, Radio-Frequency Capacitive Discharges, CRC Press, Boca Raton, 1995.
[9] Y.-S. Yeh, I.-N. Shyy, H. Yasuda, J. Appl. Polym. Sci.: Appl. Polym. Symp. **42**, 1 (1988).
[10] H. Yasuda, Plasma Polymerization, Academic Press, New York, 1985.
[11] D. Hegemann, H. Brunner, C. Oehr, Proc. 45th SVC Conf., 174 (2002).
[12] J.P. Deville, B. Lang, P. Raynaud, Appl. Surf. Sci. **137**, 136 (1999).
[13] K. Koh, H. Niimi, G. Lucovsky, Surf. Coat. Technol. **98**, 1524 (1998).
[14] M.R. Alexander, R.D. Short, F.R. Jones, M. Stollenwerk, J. Zabold, W. Michaeli, J. Mat. Sci. **31**, 1879 (1996).
[15] G. Dennler, A. Houdayer, P. Raynaud, I. Séguy, Y. Ségui, M.R. Wertheimer, Plasmas Polym. **8**, 43 (2003).
[16] D. Hegemann, U. Vohrer, C. Oehr, R. Riedel, Surf. Coat. Technol. **116-119**, 1033 (1999).
[17] H.-C. Langowski, A. Melzer, D. Schubert, Proc. 45th SVC Conf., 475 (2002).

Electrical Characteristics and Heat Balances of a Novel Atmospheric Pressure Pulsed Plasma Torch

A.A. Barba[1], S.A. Nair[2], K. Yan[2], E.J.M. van Heesch[2], A.J.M. Pemen[2], K.J. Ptasinski [3]

[1] *Department of Chemical and Food Engineering, University of Salerno, Italy*
[2] *Department of Electrical Engineering, Eindhoven University of Technology, The Netherlands*
[3] *Department of Chemical Engineering and Chemistry, Eindhoven University of Technology, The Netherlands*
Email: aabarba@unisa.it; phone: +31 40 247 4494; fax: +31 40 245 0735

Abstract
This paper presents some issues on a novel atmospheric pressure pulsed plasma torch. A high-voltage pulse generator is used to induce transient plasma in a gas flow (air) under different conditions of pulse repetition rates, energizing levels and mass flow rates. A dedicated multi-torch reactor, with rod-to-rod electrode type, was built to perform studies on electrical behavior and thermal effects of the generated pulsed plasma.

1. Introduction

The efficient use of the energy sources and the feature of a low-impact on environment are crucial points for industrial production of most modern countries. Thus, the sustainable development of emerging processes or enhancement of traditional technologies, passes under restrictive conditions such as high efficiency, reduced waste products, affordable costs.
Plasma technology appears promising to satisfy the rules of potential sustainable new techniques for producing, processing and environmental protection applications [1].
Plasma generation processes are most widely performed using partial electrical breakdown of neutral gas in the presence of an external electric field. Depending on type of source and operational conditions, generated plasmas are differentiated in *thermal plasma* (*equilibrium plasma*) and *cold plasma* (*non-equilibrium plasma*), on the bases of thermal properties (ions temperature) of the gas ionized state. Traditional thermal plasma generation methods are high-frequency inductively coupled plasma torches, DC transferred and non-transferred arcs. These plasmas usually generate very high temperature or high heat flux. Cold plasmas are often produced under low-pressure conditions using low power radio frequency or microwave or dc sources. Both plasma types suffer from high costs for electrical energy consumptions and, often, their characteristics do not satisfy required fundamental processing conditions.
Pulsed plasmas technology seems to solve or reduce the reported problems [2]. Basically, a pulsed system is able to supply high-voltage to discharge phenomena in a discontinuous manner. Discharges can occur in very short time using a storage capacitor component, repetitively charged by a resonant circuit. Much attention, in the last ten years, was devoted to high-voltage pulsed power for many kinds of potential applications that this type of plasma source can perform [3], [4]. These applications extend from environmental purposes (gas and waste water cleaning, odor control), to biological treatments (inactivation of microorganisms) [5], and chemical processes and synthesis [6], [7]. In particular, non-thermal pulsed plasma appears as an emerging advanced technology especially for environmental and industrial chemistry applications [8], [9], [10]. The reasons of this increasing attention are the advantages that pulsed plasma systems show in comparison to continuous discharge plasma generators. Furthermore, the ability to obtain a non-thermal pulsed plasma at atmospheric pressure gives to this new technology a wide scientific interest.
The advantages of the pulsed technology over continuous arc discharges are to be further discussed in detail. They regard: costs/efficiency, spatial distribution of plasma parameters (homogeneity), output quality, reliability and size.
The main characteristic of plasma torches operating under arc discharge mode is the extremely high temperature (several thousand degree centigrade) confined in small volume. High temperatures during the discharge phenomena are very useful in some processes such as incineration treatments [11], [12] but in other applications, such as chemical processes, the impossibility (or the limitation) to control thermal effects can lead to undesired by-products. Often, the use of a non-reactive gas such as argon or a cooling system can reduce some of the problems related to high temperature (electrode-life and the reactor thermal stresses) but, at the same time, reduces the heating efficiency.

Pulsed technology presents the advantages of a tunable power supply with control by a variable duty cycle of active plasma and plasma afterglow (energy efficiency). The immediate consequence of this is the major homogeneity of the plasma characteristics since pulsed energization in conjunction with rapid gas exchange among pulses can promote heat and mass transfer between plasma boundary and the plasma center. This latter is an important feature especially in presence of chemical reactions since transport phenomena can play a key role in selectivity pattern (output quality).
Non-continuous discharges pulsed at high repetition rate are intrinsically stable and this together with the use of a new multiple switch concept for the realization of multiple plasma torches can give larger reactor volume for processing (reliability and size). Pulsed technology, thus, seems to solve the scale-up problems of the plasma sources since changing the linear dimension of conventional plasma sources, keeping the same proprieties, is not simple.
Finally repetitive pulsed power appears also able to generate a new kind of plasma, the *transient plasma* (not thermal plasma, not cold plasma), which the thermo-physic properties depend on the electric and temporal features of the discharge stages.

In this work a lab-scale plasma processing system, realized to observe transient plasma induced in a gas flow (air) at atmospheric pressure, is presented. The pulsed plasma torch is achieved in plug-flow like reactor under turbulent conditions of the gas flow. The electrical behavior of the induced plasma and the heat transferred to the gas stream under imposed discharge stages are also reported.

2. Bench-scale plasma torch equipment components

The realized lab-scale plasma processing system is composed of two main parts: repetitive pulsed power source and torch reactor. The pulsed power system consists of low-voltage and high-voltage circuits. The high-voltage capacitor C and the high-voltage transmission line with an impedance of Z are resonantly charged to around 20-30 kV in a three-step process described in the following. Figure 1 shows a circuit topology for a single transient thermal plasma torch. Detailed discussions on the circuit principle were reported in [13].

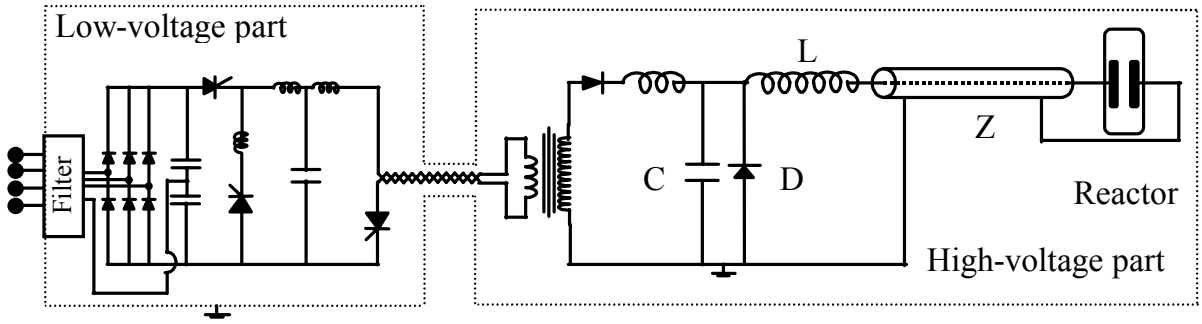

Figure 1. Schematic diagram of the main electrical circuit for a single transient thermal plasma torch.

For this study, a multiple plasma torch reactor is realized in a column (Figure 2). The plasma is induced in air flowing inside a channel with rectangular cross section. The column consists of ceramic walls (refractory material) and a transparent like-glass window. The torch electrodes, rod-to-rod type, are 60 mm long and are made in steel and mounted on the surface of the ceramic walls. The electrode pairs (four independent pairs) are connected to the high voltage and ground connection of four parallel transmission lines. The pairs are fixed at distance of about 100 mm in order to prevent interaction when powered.
The flow channel is 50 mm x 15 mm and 830 mm long. Gas flows in the reactor from the bottom side to reach the torch electrodes (Figure 2 (d)). It leaves the reactor at the top of the column via a tube which is connected to a temperature monitoring system.
Figure 2 shows the outline and the photo of the column reactor with the particulars of the channel cross-section and of the gas flow path.

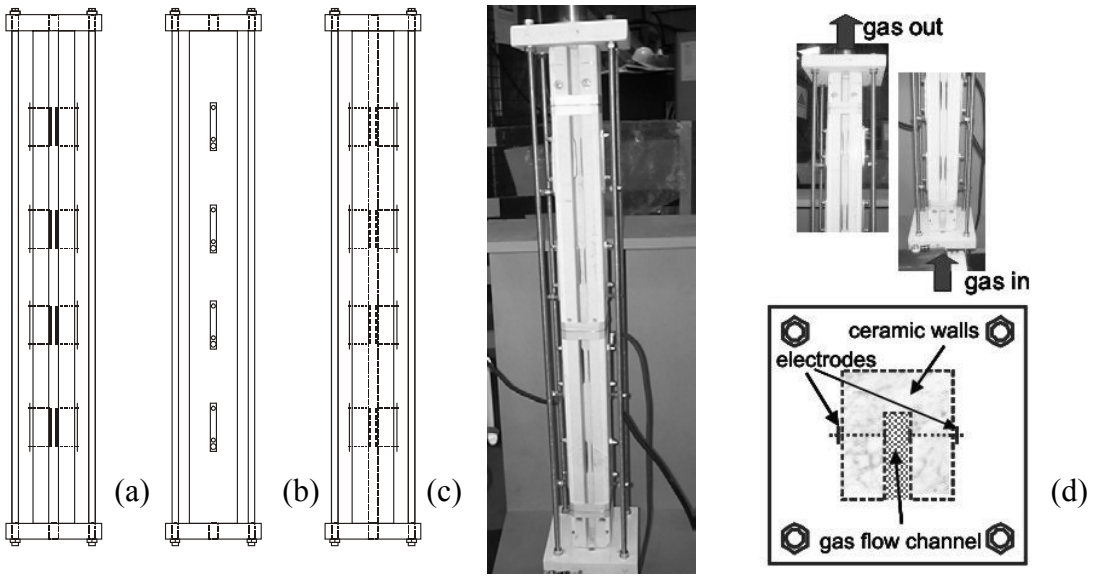

Figure 2. Scheme (*a,* front view; *b,* lateral view; *c,* back view; *d* top view) and photo of the multiple plasma torches.

3. Electrical behavior of the induced plasma

Initially the single plasma torch electrical behavior is investigated using the circuit scheme reported in Figure 1 (only one electrode is connected via one transmission line - Z -). Figure 3 shows the waveforms of the various electrical parameters collected during the transient plasma generation process. The electrical signals are recorded with a digital oscilloscope (*HP Infinium Oscilloscope*) having an analog bandwidth of 500 MHz and a maximum sampling rate of 1 GS/s. The measurements are performed at room temperature, atmospheric pressure and an electrodes gap distance of 8 mm.

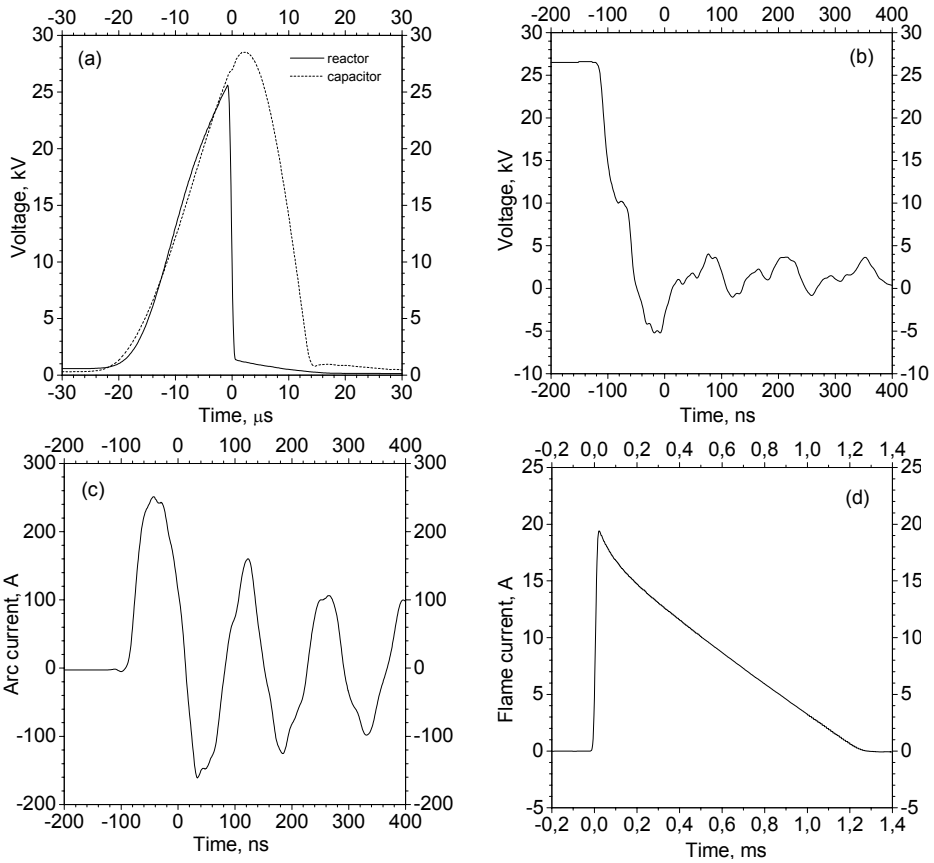

Figure 3. The voltage waveforms (a) on the plasma reactor and on the high-voltage capacitor; the voltage (b) and current (c) waveforms for arc discharge; the current waveform (d) for the flame like plasma.

Three stages are distinguishable in this kind of plasma generation process. Within the first stage, as shown in Figure 3 (a), the plasma reactor is resonantly charged to a maximum voltage of around 20-30 kV in about 20 μs. In a second stage, as shown in Figure 3 (b), (c) an arc discharge occurs inside the reactor. The voltage drops to about around 100 V in about 50-100 ns, and at the same time, the reactor is energized with a large peak current within a few hundred nanoseconds. In the last stage, called flame-like plasma, the voltage on the reactor is almost constant during about 1.2 ms with a peak current of around 20 A (Figure 3 (d)). The peak arc current, in the arc plasma, depends on the maximum charging voltage and the characteristic impedance of the transmission line where the energy is stored. During the flame-like plasma stage, the peak current depends on the maximum charging voltage on the capacitor and the circuit impedance $(L/C)^{1/2}$ since this stage is generated by the discharge of the high-voltage capacitor via the inductor L. Finally, the plasma duration depends on the plasma resistance and the inductor.

In order to transfer the transient thermal plasma process towards industrial applications, the possibility to achieve larger processing volumes must be considered. For this purpose a new circuit topology has also been developed and used to energize multiple plasma reactors.
Figure 4 shows the modified circuit topology reported in Figure 1 for two transient thermal plasma torches. Similar to the synchronization of multiple-switches [14], the two transmission lines synchronize the two transient plasmas. As a general circuit principle, multiple plasma reactors are inter-connected to a set of transmission lines, where the lines are connected in parallel at the input side. Investigations with two, three and four plasma reactors in air are performed. Coherent features of two pulsed plasma torch in terms of typical arc current waveforms are also shown in Figure 4. It is possible to observe that the two plasmas are generated within a time delay of around 2 ns.

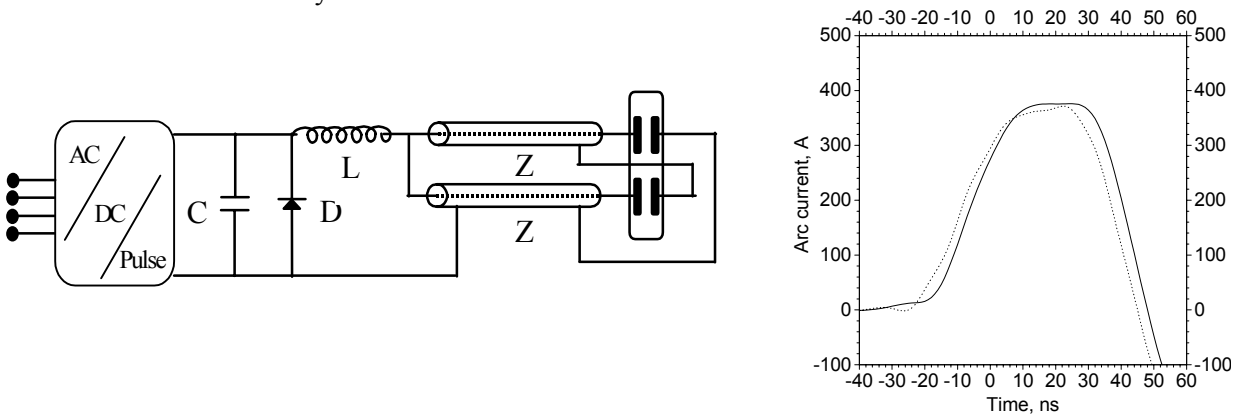

Figure 4 A circuit topology for generation of multiple (two) transient thermal plasmas (on the left); typical arc current waveforms for two pulsed plasmas (on the right)**.**

4. Heat Balances of the Pulsed Plasma

To understand the relations between discharge properties and thermal effects of the transient plasma torch, a preliminary overall energy balance is carried out by temperature measurements of the flowing gas under different operational conditions. In particular, heat transfer phenomena are studied changing gas flow rate, pulse repetition rate and energy per pulse.
Five different gas velocities are imposed for the gas flow. Since the Reynolds number of the gas flow in the reactor channel is always near 4600, a turbulent regime is achieved. Pulse repetition rates are varied in the range of 10-100 Hz; energies of 1 to 5 J per pulse are obtained by changing the capacitor values.
Gas flow rate and temperature measurements are performed by a *Pitot tube* and by a K-thermocouple, respectively. The two different probes are inserted in the tube outside the torch reactor.
To avoid electromagnetic interference the temperature equipment is shielded. Electrical parameters (voltage and current) are also monitored by an oscilloscope.
In Figure 5 the results are reported about the temperature increase of the air flow, using a single plasma torch and an energy per pulse level of 2 J/pulse. As reported above, temperature measurements are performed in the exhaust about twenty centimeters from the discharge point. To minimize thermal losses this part of the gas flow path is thermally insulated.

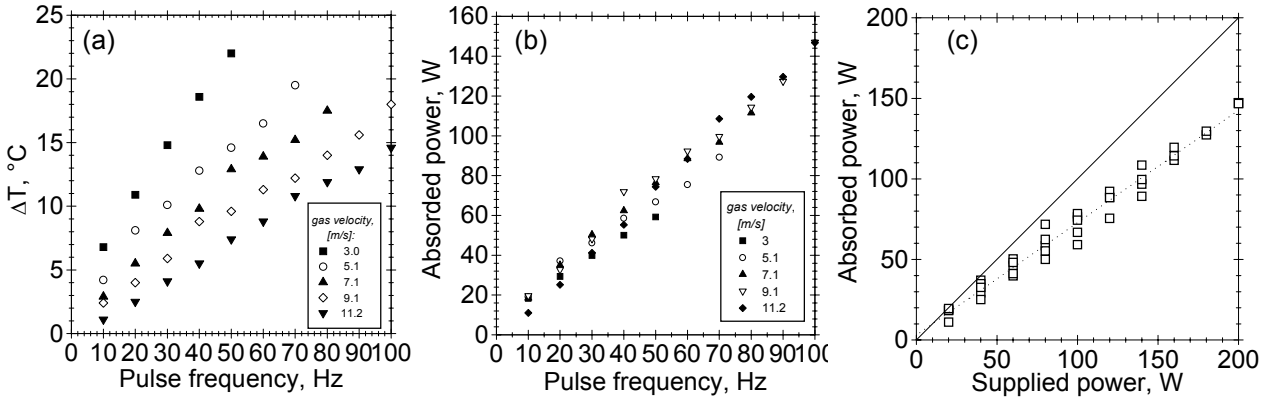

Figure 5. Temperature increase as a function of pulse repetition rates at different gas velocities (a); adsorbed power in different gas flows as a function of pulse repetition rate (b); thermal energy conversion as a ratio between absorbed and the supplied power (c).

Figure 5 (a) shows temperature increases in the gas for different air flow rate. Temperature increases have a linear trend with respect to the pulse repetition rates.

The absorbed power, plotted versus pulse repetition rates in Figure 5 (b), is calculated by the product $\dot{m} \cdot cp \cdot \Delta T$ where $\dot{m}$ is the mass flow rate [kg/s], cp is the specific heat [J/kg °C] and ΔT is the temperature increase achieved [°C]. Data collected show that, under the investigated hydrodynamic conditions, the absorbed power is independent from the flow rate.

The thermal effects of the transient plasma are studied by means of ratio between the absorbed and the supplied power at different conditions of mass flow rate (Figure 5 (c)). Supplied power is calculated on the bases of the supplied energy per pulse and the frequency value (pulse per second). For all performed runs, these ratio values are about 0.7. Overall consideration is that the main part of the supplied energy is transferred into temperature increases of the flowing gas.

Similar results in terms of: i) absorbed power proportional to frequency and independent upon hydrodynamics, and ii) absorbed energy at about 70% of input energy, independent upon hydrodynamics, have been also obtained when working with different values of the energy per pulse, in the range between 1 and 5 J per pulse.

5. Conclusions

In this work first studies on the physical characteristics of a novel atmospheric pressure pulsed plasma torch are performed. In particular, the realized high-voltage pulse generator system can induce a plasma torch in a gas flow at atmospheric pressure.

Electrical behavior studies on the torch energization process show that by changing either the high-voltage capacitor or the transmission line, the energy transfer ratio for the arc and flame-like plasmas can be easily controlled.

The thermal behavior of the transient plasma torch are studied by a preliminary overall energy balance. In particular, under different operational conditions, temperature measurements in the gas flow are performed. Preliminary runs have shown that the heating of the bulk flow is independent of the gas velocity and has a linear trend with respect to the furnished energy. Overall consideration on heat balances is that the main part (70%) of the supplied energy is transferred into temperature increases of the flowing gas.

Further work is in progress to equip the bench-scale plasma torch system with diagnostic instruments. In particular, studies on the active species produced (and temperature achieved too) during the plasma generation in the gas flow and on the composition of the exhaust flow are needed in view of industrial applications of atmospheric pulsed torch.

References

[1] G. van Oost, C. Leys, M. Joos, B. van Heesch, M. Hrabovský, P. Šunka - Czechoslovak Journal of Physics, **52**, Suppl. A, (2002).

[2] H. Conrads, M. Schimdt - Plasma Sources and Technology, **9**, 4 (2000).

[3] K. Yan, E.J.M. van Heesch, S.A. Nair, A.J. M. Pemen - Journal of Electrostatics, **57**, 1 (2003).
[4] S. Yao, E. Suzuki, A. Nakayama - Thin Solid Films, **390** (2001)
[5] S. Lerouge, M.R. Wertheimer, L.H. Yahia - Plasma and Polymers, **6,** 3 (2001).
[6] S. Yao, A.Nakayama, E. Suzuki - Catalysis Today, **71** (2001).
[7] S. Yao, A.Nakayama, E. Suzuki - AIChE Journal, **47**, 2 (2001).
[8] S. Yao, A.Nakayama, E. Suzuki - AIChE Journal, **47**, 2 (2001).
[9] S.L. Yao, E. Suzuki, A. Nakayama - Plasma Chemistry and Plasma Processing, **21**, 4 (2002).
[10] A. P. Napartovich - Plasmas and Polymers, **6**, 1-2 (2001).
[11] G. Bonizzoni - Pure Appl. Chem., **71**, 10 (1999).
[12] G. Bonizzoni, E. Vassallo – Vacuum, **64**, (2002).
[13] K. Yan, Corona plasma generation, Ph.D Dissertation, Eindhoven University of Technology, The Netherlands;- http://alexandria.tue.nl/extra2/200142096.pdf.-; (2001).
[14] K. Yan, S. Kanazawa, T. Ohkubo, Y. Nomoto Y. - Trans. IEE Japan, **119-A**, (1999).

Electrochemical Estimation of Coverage of Oxide Layer at Platinum Metal Surface Treated by RF Plasma

Tatsuhiko Yajima[1], Mikio Akasaka[1], Naomi Harada[1], Yoshio Okabe[1], and Kazuo Sugiyama[2]

[1]*Department of Marerials Science and Technology, Graduate School of Engineering, Saitama Institute of Technology, Okabe, Saitama 369-0293, Japan*
[2]*Department of Applied Chemistry, Saitama University, Saitama 338-0825, Japan*

Platinum has promise as an ultra-micro electrode material because of it's intrinsic Nernstian potential response to pH [1-4]. As mentioned in previous paper,[5] such potential behavior may be due to the formation of an oxide layer at the platinum surface.

From thermodynamic considerations, the Nernst equation is given as eq (1), where R, F and T are the gas constant, the Faraday constant and the absolute temperature, respectively. Since pH is defined by -log[H^+], it can be rearranged to eq (2), which shows the pH-potential response of the electrode. The intercept E_o' in the eq (2), which is independent on pH, can be written as the eq (3). This equation can be rearranged to the eq (4) with the constant term of E_o" as the water concentration [H_2O] is approximately constant.

$$Pt + H_2O \rightleftharpoons PtOH + H^+ + e^-$$

$$E = E_o + 2.303(RT/F)\log([PtOH][H^+]/[Pt][H_2O]) \quad (1)$$

$$E = E_o' - 2.303(RT/F)pH \quad (2)$$

$$E_o' = E_o + 2.303(RT/F)\log([PtOH]/[Pt][H_2O]) \quad (3)$$

$$E_o' = E_o'' + 2.303(RT/F)\log([PtOH]/[Pt]) \quad (4)$$

$$E_o' = E_o'' + 2.303(RT/F)\log(\theta/1-\theta) \quad (5)$$

The ratio [PtOH]/[Pt] in the second term of the eq (4) can be represented as a function of θ which represents the coverage of the oxide layer at the uppermost surface of platinum, that is, [PtOH]/[Pt]= θ/(1-θ). Then, the eq (5) arises [5]. The last equation indicates that E_o' in the eq (2) is determined only by the surface coverage of oxide layer when T is constant. The slope of the eq (5) is theoretically calculated to ca. 59.2 mV at 25°C. In this study, the relationship of the eq (5) was verified quantitatively by X-ray photoelectron spectroscopy (XPS) especially with the Pt4f spectrum analysis involving peak separation between a pair of metallic $Pt4f_{5/2}$ and $Pt4f_{7/2}$ peaks and a pair of oxygen-binding $Pt4f_{5/2}$ and $Pt4f_{7/2}$ peaks and consequently the coverage of oxide layer at platinum surface could be estimated.

Platinum wires (0.5 mm in diameter by 5 cm length) with different oxidation states at their surface, which means θ values are different from each other, were prepared easily by low temperature plasma oxidation and reduction technique with O_2 and H_2 gases. The plasma apparatus used consisted of a 13.56 MHz radio-frequency (RF) generator (Creative Design Co. Ltd., type T847A), an RF power meter (TRIO, type PF-810), a tuner, a copper coil tubing and a Pyrex reactor tube. A platinum wire was set in the reactor tube in parallel with the O_2 gas flow to be treated by an inductive RF plasma. Typical plasma treatment parameters were RF power, P= 40 W; flow rate of gas, r_g= 2.0 mmol min^{-1}; gas pressure, p_g= 1-100 Pa and treatment time, t_{TR}= 2.0-6.0 min. A direct current (D.C.) microvolt ammeter (TOA Electronics Ltd., type PM-18U) was used to measure electric potentials of platinum wires versus a saturated calomel reference electrode (SCE) at 22±1 °C. The pH potential measurements involved preparing solutions with pH 5, 7 and 9 by adding 1.0 M acetic acid to 100 ml of 0.01 M NaOH aq., immersing the tip of the plasma treated or untreated platinum wires in those solutions prerviously prepared to measure their electric potentials. X-ray photoelectron spectroscopy (XPS) was carried out using PHI Quantum 2000 Scanning ESCA Microprobe spectrometer equipped with a spherical capacitor analyzer (SCA) with monochromatic 200 mm diameter Al Kα X-ray radiation (1486.6 eV). Sputtering for depth profile was performed under the following conditions: ion energy, 2 kV; sputtering rate, 9 nm min^{-1} reduced to SiO_2 basis; and total sputtering time, 10.2 min.

References

[1] Nowak, F. W. Schultz, M. Umana, H. Abruna and R. W. Murray, J. Electroanal. Chem., 94, 219 (1978).
[2] Oyama, T. Hirokawa, S. Yamaguchi, N. Ushizawa and T. Shimomura, Anal. Chem., 59, 258 (1987).
[3] Ballarin, C. J. Brumlik, D. R. Lawson, W. Lian, L. S. Van Dyke and C. R. Martin, Anal. Chem**.,** 64, 2647 (1992).

[4] Yajima, Surface & Coatings Technology, 112, 80-84 (1999).

Characteristic structure of ZnO particle produced by flash evaporation in RF plasma

T. Sato[1], T. Tanigaki[1], H. Suzuki[1] Y. Saito[2], O. Kido[1], Y. Kimura[1], C. Kaito[1], A. Takeda[3] and S. Kaneko[4]

[1] *Department of Nanophysics in Frontier Project, Ritsumeikan University, Shiga 525- 8577 Japan*
[2] *Department of Electronics and Information Science, Kyoto Institute of Technology, Kyoto 606- 8585 Japan*
[3] *ISI. Ltd., Motobuto 5- chome 40- 6, Saitama-shi, Saitama Pref., 336- 0004 Japan*
[4] *Hitachi Instruments Service Co., Ltd., Yotsuya 4- chome, Shinjuku- ku Tokyo, 160- 0004 Japan*

Abstract

ZnO particles were produced by dropping Zn powder on the heated boat which was set into the plasma in the mixture gas of argon (9.75 Torr) and oxygen (0.25 Torr). The structure of ZnO particle produced by the present method was the characteristic structure with tetrapod configuration having the [0001] short four needles.

1. Introduction

Zinc oxide (ZnO) is widely used in various applications such as cosmetic material [1], ultraviolet (UV) absorption substance [2] and gas sensors [3]. One of the problems on the production of ZnO particles is the size control and the shape control, or may be contained the ionic compound. By the use of flash evaporation technique in the gas evaporation, structure and morphology of ZnO particles can be controlled and elucidated the characteristic of infrared (IR) spectra [4]. Furthermore, it was found that the condition of the cubic ZnO particles predominantly produced by the flash evaporation method [4].

On the other hand, by using of the passing metal and/or semiconductor smoke particles through the plasma field, these particles were changed to the nitrogen particles in spite of the nitrogen gas pressure of 0.25 Torr [5]. The size of the order of 50 nm of these particles did not change after passing through the plasma field. Therefore, by using plasma field during production of the smoke particle, the compound particle of nanometer size can be produced in a low partial pressure of reactive gas.

In this study, the flash evaporation technique was used in the plasma field and ZnO particles were produced in the mixture gas of argon (9.75 Torr) and oxygen (0.25 Torr) by controlled evaporation of Zn. The comparison with and without plasma have been also presented.

2. Experimental method

The work chamber for the production of ZnO particle was a glass cylinder 17 cm in diameter and 33 cm in height. The plasma field which was set in the work chamber was shown in Fig. 1 schematically. The used electrodes were stainless steel of 5 cm in diameter and 5 cm in height. RF plasma with a frequency of 13.56 MHz was used. Zn powder was dropped into the heated boat at 1000°C which was set below the plasma field in a mixture gas of argon (9.75 Torr) and oxygen (0.25 Torr). The dropping rate of the Zn powder was about 10^{-2} m/sec. Dropped Zn powder into the heated boat was evaporated and passing through the plasma field with accompanying to the exothermic reaction of Zn vapor with oxygen gas. The color of the plasma field changed from the red-violet to the brilliant blue, i.e., oxidation of Zn vapor occurred [6]. The produced specimens were examined using transmission electron microscopic (TEM), high resolution TEM (HRTEM) method.

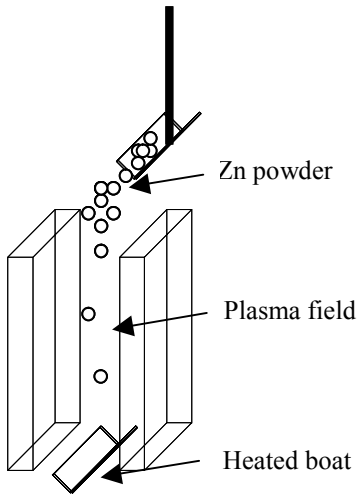

Figure 1: Schematic representation of the flash evaporation in plasma

3. Results and Discussion

Figure 2 shows the characteristic growth of ZnO particles produced by the general gas evaporation method of Zn in a mixture gas of argon (95 Torr) and oxygen (5 Torr) from nichrome boat. The characteristic needle crystal with the tetrapod shape can be seen. If the flash evaporation method was used in this gas pressure, the cubic ZnO particles with the size of 30 nm can be produced as shown in Fig. 3. The electron diffraction (ED) pattern shows clearly the growth of the cubic phase [4].

Figure 4 shows the characteristic ZnO particles produced by flash evaporation in plasma. Each particle can be seen spherical, but high magnified image showed tetrapod configuration. The size of ZnO was about 30 nm. As can be seen in Fig. 4, the dispersion state of ZnO particles was very good. The ED pattern of the present specimen showed the hexagonal structure of ZnO.

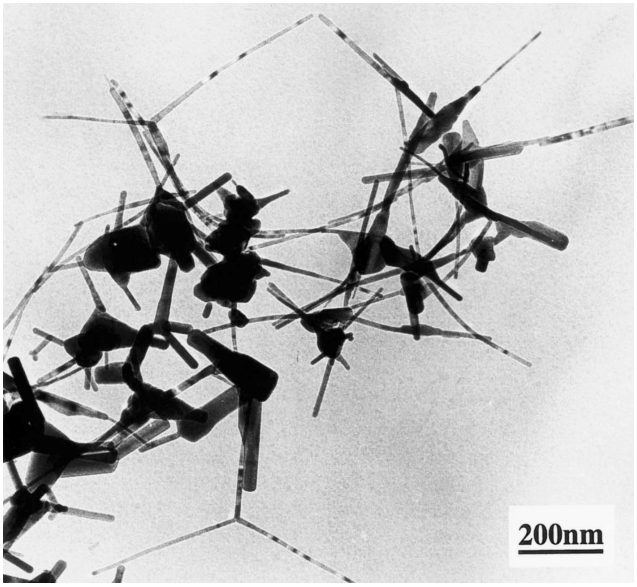

Figure 2: Elcetron microscopic image of ZnO produced by general evaporation method.

The HRTEM image of one ZnO particle is shown in Fig. 5. Lattice fringes of needle part are identified ($10\bar{1}0$) plane of the hexagonal ZnO particle as indicated by an arrow. The lattice image at the center of a particle is identified as crossed {$10\bar{1}0$} planes, as shown in Fig. 5. Therefore, the hexagonal [0001] axis for the central part is the incident electron beam direction. The dotted line as shown in Fig. 5 indicated {$11\bar{2}0$} planes of the interface between the central part of the ZnO particle and the needle parts. This corresponds to the projection of the {111} plane of the cubic nucleus, i.e., tetrapod growth starts from the cubic nucleus. Since ZnO particles were polar crystals, four {111} planes composed of Zn atoms at the top surfaces grew in Zn-rich atmosphere [7].

If the oxygen partial pressure were 0.25 Torr with the same total pressure as in Fig. 2, and only the flash evaporation technique were used without the plasma field, the morphology of the grown particle was drastically change and Zn crystals were included, as shown in Fig. 4. Therefore plasma is important factor on the growth of ZnO particles.

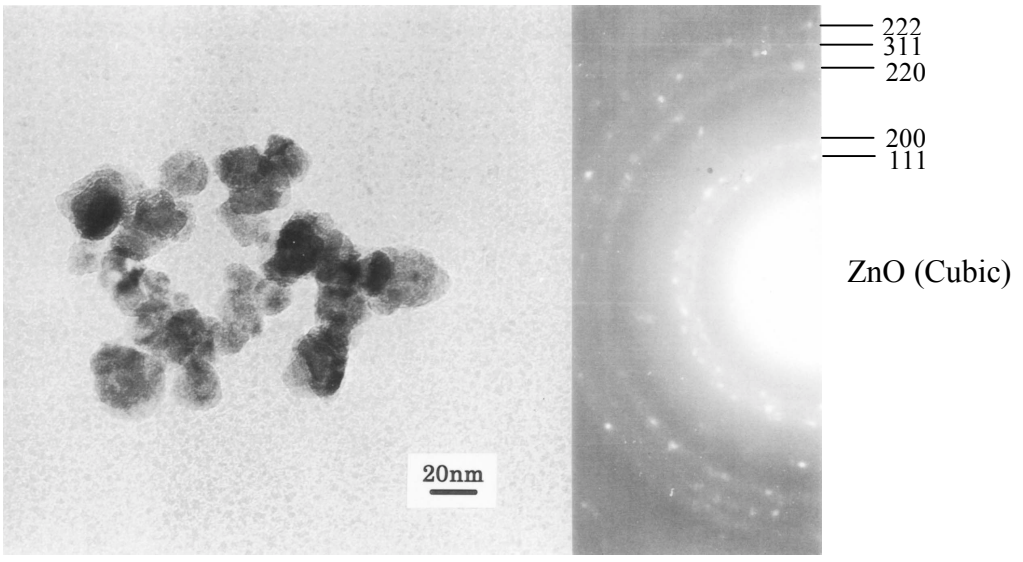

Figure 3: EM image and ED pattern of cubic ZnO particles

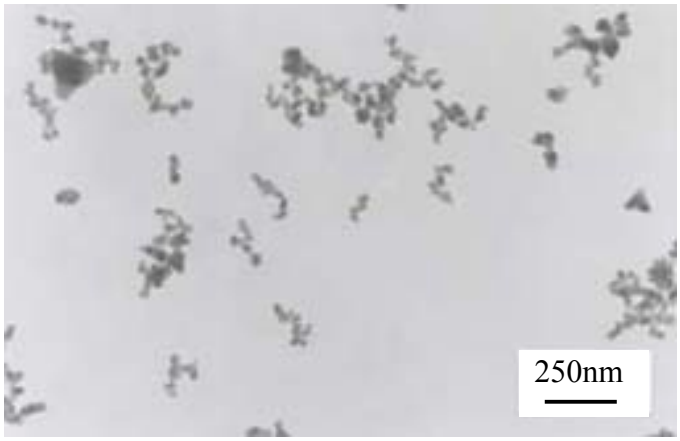

Figure 4: TEM image of the ZnO particles produced by flash evaporation in plasma

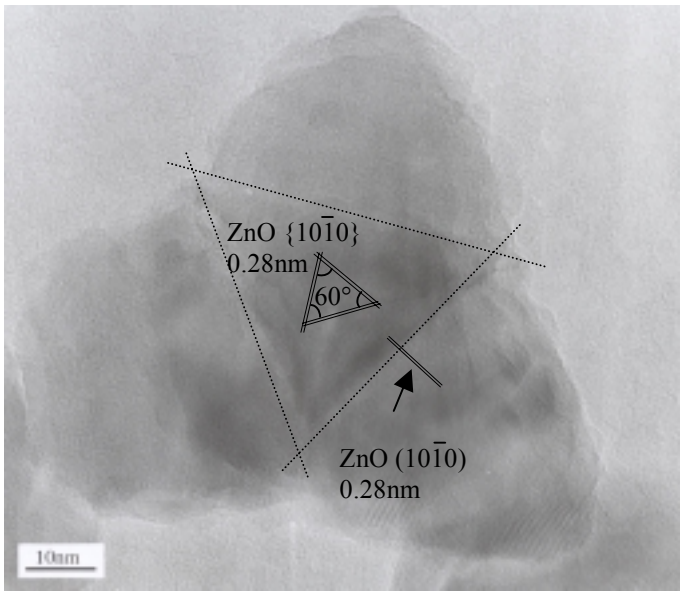

Figure 5: The HRTEM image of ZnO particle with tetrapod configuration

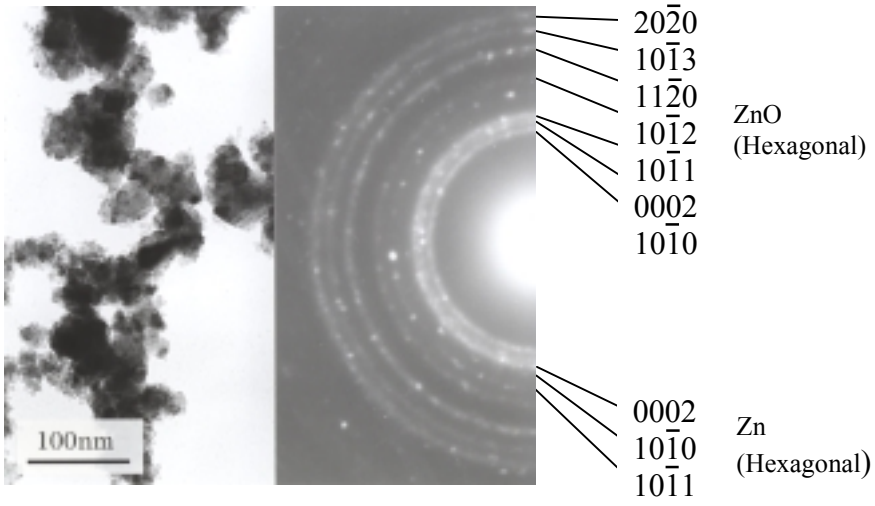

Figure 4: EM image and ED pattern of the particles produced by the flash evaporation technique

4. Summary

ZnO particle size, shape and dispersion can be controlled by preparation method. The morphology of ZnO particle shows the characteristic structure with very short needle parts and the dispersion state of each particle was very good in the plasma field. These results indicate that electric charge in the plasma field controlled by the coalescence growth of the particle and crystal growth of the particle was influenced by the plasma effect. By the flash evaporation method in the plasma field, the particles of the size of the nanometer can be obtained in the low gas partial pressure. The present particles may be used as the characteristic absorbance at 3.2 eV without Mie scattering.

References

[1] T. Mori, K. Tanaka, T. Inomata, A. Takeda and M. Kogoma - Thin Solid Films. **316**, 89 (1998).
[2] N. Kollias - Arch. Dermatol. **135**, 209 (1999).
[3] P. Mitra, A. Chatterjee and H. Maiti - Mater. Lett. **35**, 33 (1998).
[4] T. Tanigaki, S. Kimura, N. Tamura, C. Kaito - Jpn. J. Appl. Phys. **41**, 5529 (2002).
[5] T. Sato, Y. Saito and C. Kaito - Surface Review and Letters. in press (2003).
[6] C. Kaito, N. Shiba, A. Sakagami, S. Kimura, N. Suzuki, N. Tsuda, C. Koike, Y. Saito - Jpn. J. Appl. Phys. **35**, 4736 (1996).
[7] M. Shiojiri and C. Kaito - J. Crystal Growth. **52**, 173 (1981).

Stability of plasma treated amorphous SiO_2 layer on TiO_2 and ZnO particles

T. Tanigaki[1], T. Sato[1], H. Suzuki[1], O. Kido[1], Y. Kimura[1], C. Kaito[1], A. Takeda[2] and S. Kaneko[3]

[1] *Department of Nanophysics in Frontier Projects, Ritsumeikan University, Shiga 525- 8577 Japan*
[2] *ISI. Ltd., Motobuto 5- chome 40- 6, Saitama- shi, Saitama Pref., 336- 0004 Japan*
[3] *Hitachi Instruments Service Co., Ltd., Yotsuya 4- chome, Shinjuku- ku Tokyo, 160- 0004 Japan*

Abstract

Stability of SiO_2 thin layer designed as the functional particles such as TiO_2 and ZnO have been elucidated by the heating experiment. When these particles were path through the plasma field in He gas at 80 Torr, SiO_2 layer were crystallized and broken due to the density change of the film. The heating experiment showed the crystallization at 650°C (TiO_2) and 600°C (ZnO). In the case of TiO_2, SiO_2 layer was dissolved into TiO_2 particle. In the case of ZnO, the small crystallites of Zn_2SiO_4 were formed on the surface.

1. Introduction

Titanium oxide (TiO_2) and Zinc oxide (ZnO) particles are able to use in various applications, for example, a white pigment of cosmetic material and ultraviolet (UV) absorption substance respectively. In order to improve safety and the dispersion of each particle, the method of covering the particle surface with thin SiO_2 layer has been developed with the aid of plasma treatment [1]. However, the stability and the state of the SiO_2 layer which was produced on the particle were hardly examined.

In this study, the stability by heating and the more RF plasma (13.56 MHz, 300 W) treatment process of the TiO_2 and ZnO particles which were covered with an amorphous SiO_2 layer of a few nanometers was examined by transmission electron microscopic (TEM) introducing the in situ observation method.

2. Experimental

In this experiment, two types of particles covered with an amorphous SiO_2 layer were prepared to compare the stability of heat treatment with plasma treatment. Commercial ZnO powder (ISI. Ltd.) was used as ZnO particles covered with thin amorphous SiO_2 layer, which produced by the aid of plasma [1].

TiO_2 particles were produced by burning Ti powder charged on a tantalum boat in a gas mixture of Ar (13.5 kPa) and O_2 (1.7 kPa). The Ti can be evaporated by heating the tantalum boat and Ti vapor was oxidized and condensed near the boat. Then, TiO_2 particles rise with convection flow like a smoke [2-5]. As same as TiO_2, SiO_2 particles were produced by evaporating SiO powder in the mixture gas [6]. The evaporation source of SiO_2 was set above 50 mm from the evaporation source of Ti. Since SiO_2 vapor existed around the evaporation source of SiO, produced TiO_2 particles passed through the SiO_2 vapor and were covered with an amorphous SiO_2 layer, as proposed in a previous paper [7]. In this experiment, these covered TiO_2 particles were dropped in a plasma field.

These samples were observed by Hitachi H- 7100 and H- 900NAR. In situ observation was done using a special heating holder in the high resolution electron microscope to confirm the stability of the SiO_2 layer on the TiO_2 and commercial ZnO particles. The dynamic behavior of the surface layer has been recorded directly on a video tape.

3. Results and Discussion

3.1 Stability of heat treatment of covered SiO_2 layer on TiO_2 and ZnO particles

Typical example of TiO_2 particles produced without SiO_2 vapor is shown in Fig. 1. Most of the particles are anatase, which is the low temperature phase, and small amounts of brookite and rutile are produced. When SiO_2 vapor introduced to the particles flow, TiO_2 particles uniformly covered with an amorphous SiO_2 layer were predominantly produced, as shown in Fig. 2. The SiO_2 layer is less than 10 nm on the TiO_2 particles with the size of the order of 100 nm. Using plasma at room temperature, the surface of TiO_2 particles was not covered uniformly by the SiO_2 layer [1].

These particles covered by the SiO_2 layer produced by this method were heated in the electron microscope. By heating at 650°C, the smooth surface layer of SiO_2 become rough due to the small black contrast on the particles with sizes of 5- 8 nm, as indicated by an arrow in Fig. 3. Lattice image of the contrast show the existence of β - quartz layer of 2 nm thickness which is stable phase at high temperature on the surface of

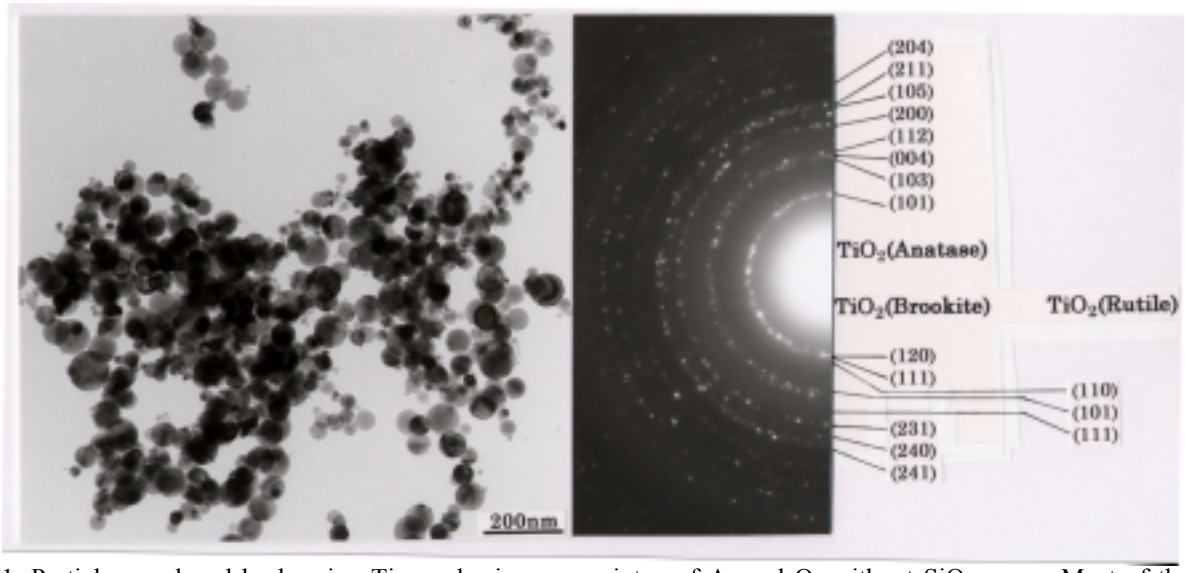

Fig. 1. Particles produced by burning Ti powder in a gas mixtue of Ar and O_2 without SiO_2 vapor. Most of the particles were rtile and a small amount of brookite and rutile partilces.

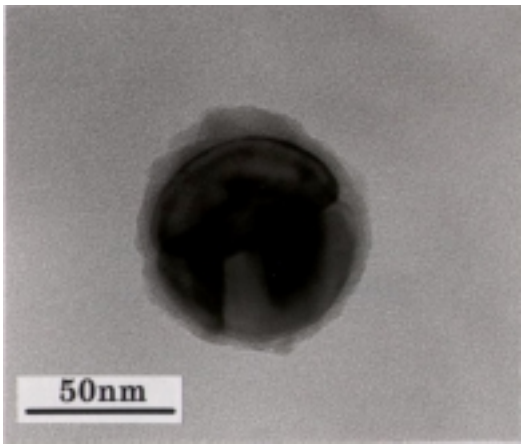

Fig. 2. TiO_2 particles covered with amorphous layer. Thickness of the layers is less than 10 nm.

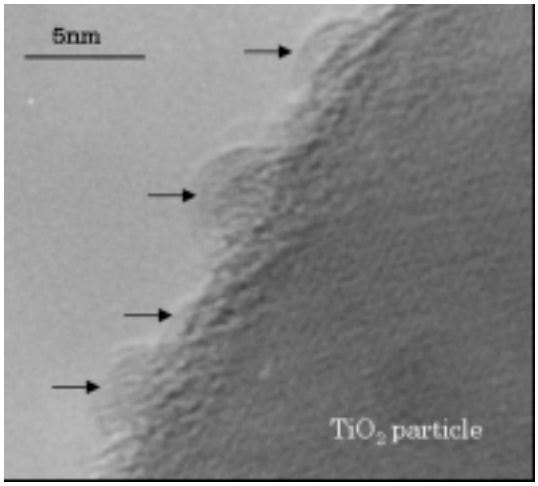

Fig. 3. HREM image of the surface of TiO_2 covered with SiO_2 layer which passed through plasma field. SiO_2 nanocrystallites are indicated by arrows.

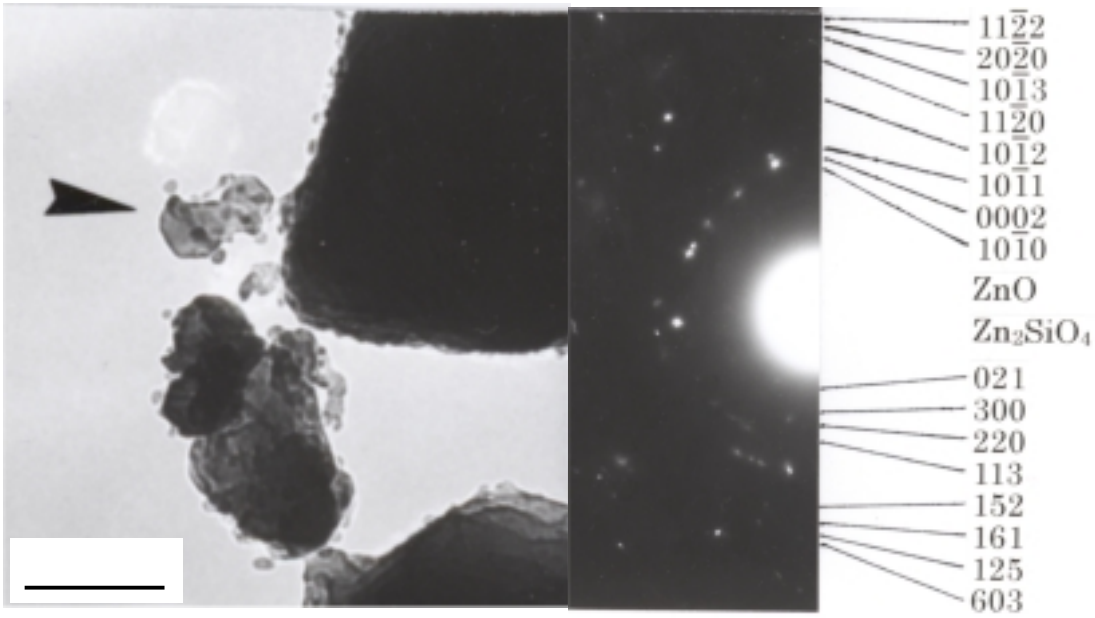

Fig. 4. Surface layer of ZnO particles produced by the aid of plasma became rough by heating at 700°C. Projections of the surface of ZnO were Zn_2SiO_4 crystallites indicated by arrow.

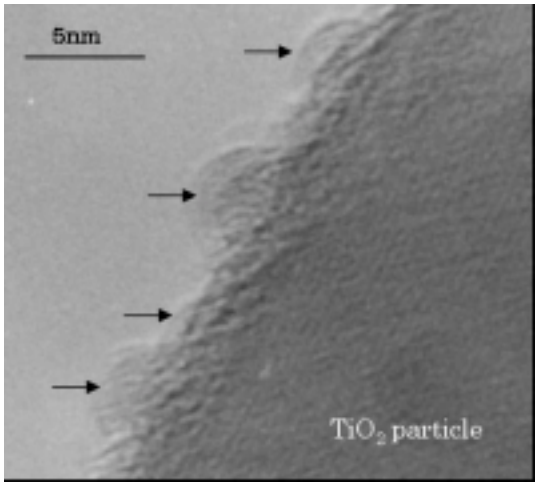

Fig. 5. HREM image of the surface of TiO_2 covered with SiO_2 layer which passed through plasma field. SiO_2 nanocrystallites are indicated by arrows.

TiO_2 particle. The β - quartz layer dissolved into TiO_2 particles on heating at 700°C and was disappeared completely on the particles at 750ºC [7]. This phenomenon means that the empty columns in TiO_2 are important in dissolving the SiO_2 molecules.

In the case of amorphous SiO_2 layer on ZnO particles, SiO_2 layer crystallized upon heating at 600°C. Upon heating at 700°C, the small crystallites of Zn_2SiO_4 were formed on the surface of ZnO particle, as shown in Fig. 4. This shows that the reaction of ZnO and SiO_2 also started above this temperature. Furthermore, the coalescence growth of these small crystallites started above 700°C.

3.1 Plasma treatment of covered SiO_2 layer on particles

TiO_2 particles covered with an amorphous SiO_2 layer was also crystallized by passing through the RF helium gas plasma field at 80 Torr. Fig. 5 shows the high resolution electron microscopic (HREM) image of the surface changed to the SiO_2 nanocrystallite of the order of 3 nm as indicated by arrows. The surface layer became uneven and didn't cover uniformly. Thus, the treatment of on the surface SiO_2 layer in plasma destroys the coverage of SiO_2, i.e., protected layer was destroyed.

In the case of heat treatment, the SiO_2 layer crystallized on heating at 650°C and dissolved into TiO_2 particles on heating at 700°C. Since the surface SiO_2 layer crystallized in the case of plasma treatment,

adequate energy to crystallize was accepted from plasma, i.e., the plasma treatment corresponded with over 650°C of the heat treatment. In the plasma field at high gas pressure, kinetic energy of electron is larger than the ion. Electric charge of electron in the plasma field accelerates the crystallization of amorphous SiO_2 layer.

In the case of ZnO particles, the small crystallites of Zn_2SiO_4 were formed on heating at 700°C. As same as TiO_2 particle, the surface SiO_2 layer on ZnO particles became rough and black contrast partly appeared on the particles in the case of plasma treatment. However Zn_2SiO_4 crystallites did not existed. Thus, the plasma treatment corresponds with less than 700°C. It is concluded that the plasma treatment corresponds between 650°C and 700°C of the heat treatment. If the power of the plasma becomes higher, the reaction growth of Zn_2SiO_4 may be occurred.

References

[1] T. Mori, K. Tanaka, T. Inomata, A. Takeda, M. Kogoma - Thin Solid Films. **361**, 89 (1998).
[2] R. Uyeda - Morphology of Crystals. part B, Ed., I. Sunagawa. p. 369 (Terra, Tokyo, 1987).
[3] K. Kimoto, Y. Kamiya, M. Nonomiya, R. Uyeda - Jpn. J. Appl. Phys. **2**, 702 (1963).
[4] K. Kimoto, I. Nishida - Jpn. J. Appl. Phys. **6**, 1047 (1967).
[5] C. Kaito, K. Fujita, H. Shibahara, M. Shiojiri - Jpn. J. Appl. Phys. **16**, 697 (1977).
[6] C. Kaito, R. Shoji, K. Fujita - Jpn. J. Appl. Phys. **26**, L965 (1987).
[7] Y. Atou, H. Suzuki, Y. Kimura, T. Sato, T. Tanigaki, Y. Saito, C. Kaito - Physica E. 16 179 (2003).

Density measurements of ammonia formed in N_2-H_2 plasma

J.H. van Helden, W. Wagemans, P. Vankan, T. Rutten, D.C. Schram and R. Engeln

Center for Plasma Physics and Radiation Technology (CPS), Department of Applied Physics, Eindhoven University of Technology, P.O. Box 513, 5600 MB, Eindhoven, The Netherlands

Abstract

In this contribution we focus on the formation of new molecules by wall association of atoms from atomic particle sources, investigating the efficiency and formation mechanism. We show that by using an atomic nitrogen and hydrogen source, ammonia can be formed efficiently, i.e. 11% of the total background pressure is measured to be ammonia. The measurements indicate that the ammonia is formed via plasma-surface interactions. The density of the produced ammonia is measured by cavity enhanced absorption spectroscopy.

Introduction

In applications in which plasma is used for chemical conversion, but also for surface treatment or deposition, newly formed stable molecules are often detected in the background gas. It has been acknowledged for quite some time that plasma-surface interactions are of great importance in the production of these new stable molecules. For example, in 1975 Eremin [1] reported that the synthesis of ammonia was increased by a factor of 3, when platinum was used as coating for the quartz wall of a plasma reactor in which discharges in N_2-H_2 mixtures were created. In 1989 [2], it was reported that zeolite added to the downstream plasma in high-frequency discharges facilitated the ammonia production, which was ascribed to the surface reaction of NH_x radicals adsorbed on the zeolite with hydrogen atoms. The formation of ammonia is still not completely understood and could depend on plasma conditions, but it is believed that it is due to plasma-surface interactions.

To gain a better knowledge of the plasma-surface interactions that take place during the formation of stable molecules, we have chosen to investigate the formation of ammonia in N_2-H_2 plasma in more detail. We show a new way of generating ammonia, i.e. via plasma-activated catalysis [3]. In this process fluxes of hydrogen and nitrogen radicals are produced in a high-density plasma source with high dissociation degree. The plasma then expands into a low-pressure vessel, where most of the atomic radicals will arrive at the surface at which they will adsorb. At the surface new molecules can be generated which subsequently may desorb. In this way the dissociation in the plasma source is geometrically separated from the production zone of the molecules. Since the plasma is used to produce the radicals for the ammonia production and the wall is used as a catalyst, the process is called plasma-activated catalysis.

We will present results of the production of ammonia in expanding plasma generated from mixtures of atomic hydrogen and nitrogen obtained by cavity enhanced absorption spectroscopy (CEA) [4]. In this technique, a narrow band (cw) light source is used in combination with a high-finesse optical cavity to perform sensitive high-resolution, direct absorption measurements. To study the influence of the geometry of the vessel on the ammonia production, measurements of the ammonia density obtained by mass spectrometry will be shown for a vessel with a larger surface to volume ratio. In the case the plasma is generated from a mixture of hydrogen and nitrogen, a significant amount of ammonia density is measured.

Experimental set-up

The plasma is created in a so-called cascaded arc source [5], which generates a direct current thermal plasma in mixtures of N_2 and H_2 at a typical pressure of 0.5 bar, a current of 55 A and a power of 5 kW. The plasma expands from the nozzle of the cascaded arc into a stainless steel vacuum vessel, which is kept at a pressure between 10 and 200 Pa. The expansion into the vessel is first supersonically and then, after a stationary shock, subsonically.

A scheme of the experimental set-up used in the cavity enhanced absorption measurements is depicted in Fig. 1. A continuous wave (cw) diode laser (New Focus, Model 6262, up to 5 mW) is used as a

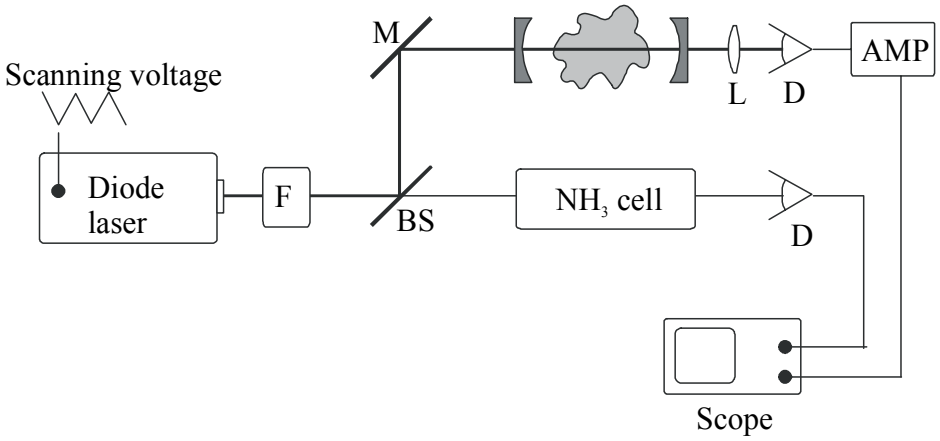

Figure 1: Scheme of the cavity enhanced absorption set-up.

light source, which is tunable in the 1520-1560 nm region. During all experiments, the laser is repeatedly scanned at a rate of 32 Hz over a spectral range of typical 1 cm^{-1}. A Faraday isolator is used to minimize the optical feedback to the laser. A beam splitter directs 10% of the laser light into a reference cell, which is filled with 5 mbar of ammonia. The absorption cell is used for absolute calibration of the frequency of the laser. The radiation that passes the beam splitter is coupled into a high-finesse, optically stable cavity with a length of 1.1 m, formed by two plano-concave mirrors with a diameter of 25 mm, a radius of curvature of -1 m and a reflectivity of R = 0.994. The mirrors are directly flanged onto the stainless steel vessel in which the plasma expands. The light that is leaking out of the cavity is detected by an InGaAs photodiode (New Focus, Nirvana 2017). The detector signal is amplified with a 0.1 ms rise time amplifier and integrated over 1 ms (spectral equivalent 0.06 cm^{-1}) and subsequently displayed on one of the channels of a digital oscilloscope (10 bits, 300 MHz). A second channel is used to record simultaneously the signal of the photodiode behind the reference cell. The data on the scope are transferred to a PC via GPIB for further analysis.

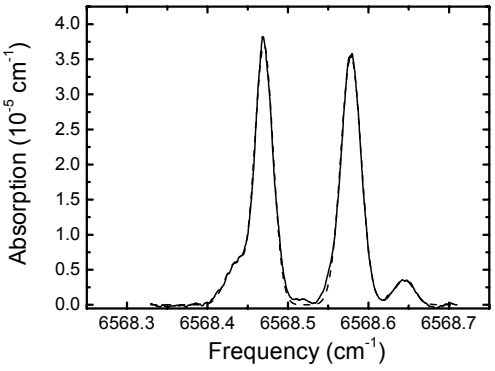

Figure 2: Typical NH_3 CEA spectrum measured in a vessel in which a N_2-H_2 plasma expands. The dashed line is a fit assuming four Gaussian line profiles. The background pressure was 20 Pa.

In the CEA technique the laser is continuously scanned over the same spectral range. Via accidental coincidences of the frequency of one of the cavity modes with the laser frequency light couples into the high-finesse optical cavity. During each scan different laser frequencies can be coupled into the cavity leading to a so-called interleaved sampling. After several scans, all frequencies will be sampled. The intensity of the light coupled into the cavity is determined by the overlap between the laser mode and the matching cavity mode, the scanning rate of the laser and the jittering and finesse of the cavity. Especially the scanning rate of the laser has a large influence on the measurements and is subject to several limitations. The maximum scanning rate is determined by the fact that the laser mode has to stay in resonance with the cavity mode sufficiently long, resulting in maximum intensity. The maximum intensity that can be reached inside the cavity is proportional to the overlap of the laser and the profile of the cavity mode. The spectral profile of the cavity mode is approximated by a Lorentzian profile with a width proportional to $1/\tau$, i.e. proportional to the total cavity losses, and the maximum of the Lorentzian profile is proportional to τ^2. The convolution of the laser profile and the Lorentzian profile has a maximum intensity that is directly proportional to the ring down time τ. One can show that the time-integrated intensity is also proportional to the ring down time τ, which is given by:

$$\tau = \frac{d}{c(1-R+\kappa(\nu)d)}, \qquad [1]$$

where d is the absorption path length, c the speed of light, R the reflectivity of the mirrors and $\kappa(\nu)$ the absorption coefficient.

There is also a lower limit to the scanning rate due to the requirement that all cavity modes should be in resonance with the laser frequency equally long. Therefore, the scanning rate of the laser must be significantly higher than the rate at which the cavity modes are changing.

An ammonia spectrum is measured in the plasma reactor and averaged over 1000 scans, i.e. about 30 s of acquisition time. The recorded spectrum however is a relative absorption spectrum expressed in loss of the empty cavity per round trip, i.e. (1-R)/d. The spectrum can be put on an absolute scale by measuring the CEA spectrum of a known amount of water. Using the transition strength [6] and the known density of the ground-state water molecules the factor (1-R)/d is determined as $(5.5 \pm 0.5)\cdot 10^{-5}$ cm^{-1}. The absolute absorption can be determined by using the formula:

$$\kappa(\nu) = \left(\frac{S_0(\nu)}{S(\nu)} - 1\right)\left(\frac{1-R}{d}\right), \qquad [2]$$

where $S(\nu)=I_0\tau$ is the time-integrated intensity with absorption in the cavity and $S_0(\nu)=I_0\tau_0$, is the signal in an empty cavity, i.e. the baseline, with I_0 the laser intensity inside the cavity. In Fig. 2, a typical measured ammonia spectrum is shown. The observed transitions of ammonia are strong lines from the combination band $\nu_1 + 2\nu_4$ reported by Lundsberg-Nielsen *et al.* [7]. Of the four transitions shown in Fig. 2, three are reported in literature with the line positions 6568.299, 6568.401, and 6568.463 cm^{-1}, and absorption coefficients, $7.556\cdot 10^{-4}$, $7.602\cdot 10^{-4}$, and $0.948\cdot 10^{-4}$ cm^{-1} Torr^{-1}

Results

Three different experimental situations have been studied. In the first experimental situation, the plasma is created with 2.0 SLM N_2 flowing through the arc, delivering a substantially dissociated and partially ionised (5%-10%) nitrogen flow. Simultaneously a varying hydrogen flow between 0 and 1.45 SLM is injected in the background of the vessel. The absolute density of ammonia as a function of the relative flow rate of hydrogen with respect to the total flow rate is shown in Fig. 3 for a background pressure of 100 Pa. The measured ammonia density first increases with increasing hydrogen flow and then saturates at a maximum of $2.5\cdot 10^{19}$ m^{-3}. This means that at T = 600 K, which is determined from the Doppler width of the measured ammonia transitions, 0.2% of the background gas is ammonia. The saturation of the ammonia density can be understood by noting that the hydrogen molecules, which are injected in the background, can only be

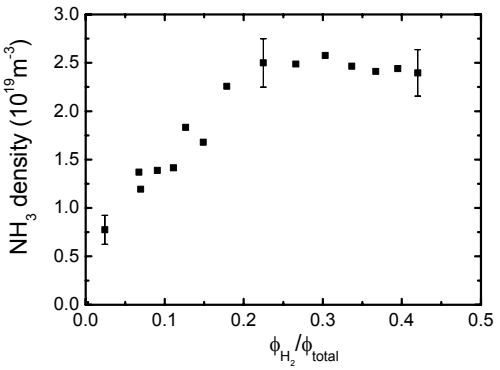

Figure 3: Ammonia density as function of the hydrogen flow rate relative to the to the total flow rate of nitrogen and hydrogen. The nitrogen is applied through the arc, while the hydrogen is injected directly into the vessel into which the nitrogen plasma expands. The background pressure is kept constant at 100 Pa.

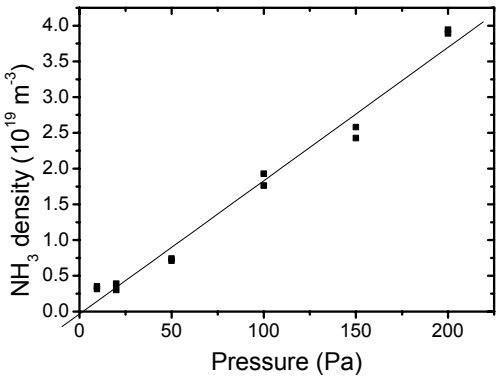

Figure 4: Ammonia density as function of the background pressure in the vessel. The plasma is created with 2.0 SLM N_2 flowing through the arc and 1.0 SLM H_2 injected in the background.

dissociated by the N^+ ions emanating from the arc. The H production will increase until all N^+ ions are consumed, which deliver two H atoms via the non-symmetric charge exchange reaction $N^+ + H_2 \rightarrow NH^+ + H$, followed by the dissociative recombination reaction $NH^+ + e \rightarrow N + H$. Adding more H_2 molecules will not lead to the production of more H atoms, and thus no extra NH_3 is produced.

In the second experiment, the ammonia density under the conditions of maximum NH_3 production, i.e. 1.0 SLM H_2 injected in the background, has been measured as function of the background pressure, i.e. from 10 to 200 Pa as shown in Fig. 4. The measured ammonia density shows a linear dependence on the pressure. Assume now that only N and H are necessary for the production of ammonia. Then the ammonia production rate is:

$$\frac{dn_{NH_3}}{dt} = n_H n_N k \,, \qquad [3]$$

where n_{NH3} is the ammonia density, n_N the atomic nitrogen density, n_H the atomic hydrogen density and k the reaction rate coefficient. The total ammonia density at a specific pressure in the vessel, i.e. at a certain residual time τ, can be calculated by:

$$\int_0^{\tau} \frac{dn_{NH_3}}{dt} = \int_0^{\tau} n_H n_N k dt \qquad [4]$$

This leads to:

$$n_{NH_3} = n_H n_N k \tau \qquad [5]$$

Under the experimental conditions used, n_N, n_H and k are constant and only τ is linear dependent on the pressure. In that case, the above shows that the ammonia density should be linear with the pressure. Starting from atomic radicals, volume production of ammonia would require reactions, i.e. three particle reactions, which are too slow to lead to any significant production under the experimental conditions used. Furthermore, the production would then show a stronger than linear dependence on the pressure, which is not observed. Moreover, under all conditions, the density of ammonia proved to be independent of the lateral position in the plasma jet at which the CEA spectrum was taken. All measurements have been performed at about 20 cm downstream from the exit of the arc. This shows that the ammonia is not produced in the plasma jet. This indicates that ammonia is mainly produced at the vessel wall.

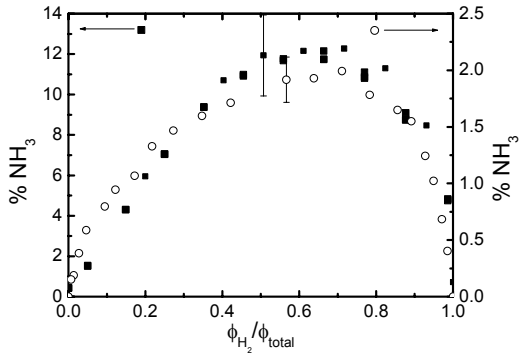

Figure 5: Density of ammonia as function of the hydrogen flow rate relative to the total flow of nitrogen and hydrogen (o CEA measurements, ■ mass spectrometry). Both nitrogen and hydrogen are applied through the arc at a total flow rate of 2 SLM. The background pressure is kept constant at 20 Pa.

In the third case, the plasma is produced while both nitrogen and hydrogen are flowing through the arc with a total flow of 2 SLM. In Fig. 5, the ammonia density as function of the relative H_2 flow rate to the total flow rate is presented as measured with cavity enhanced absorption spectroscopy. The maximum ammonia density under these plasma conditions is at $\phi(H_2)$ = 1.44 SLM and $\phi(N_2)$ = 0.56 SLM, which is close to the stoichiometric ratio of hydrogen and nitrogen in NH_3. The maximum density of NH_3 at 20 Pa background pressure is about $4 \cdot 10^{19}$ m^{-3}, which is 2% of the background gas at a temperature of 600 K.

If the production of ammonia is due to plasma-surface interactions a larger surface to volume ratio should lead to more ammonia production. This is confirmed by measurements on a different set-up, with a larger surface to volume ratio. The results are also depicted in Fig. 5, showing an ammonia density of 11%, measured with mass spectrometry. This is a remarkable result if one compares this with the total ammonia one could get under the conditions used. A maximum is detected around the stoichiometric ratio of hydrogen and nitrogen in NH_3. This means that one has 3 hydrogen atoms per 1 nitrogen atom. If one now takes all possible reactions into account leading to stable molecules, the maximum amount of ammonia one could make is 21%. The measured relative ammonia density as function of the relative hydrogen flow rate to the

total flow rate as shown in Fig. 5, is also measured in a low-pressure N_2-H_2 flowing discharge [8] and predicted fairly well from a self-consistent model assuming that NH_3 is mainly formed at the vessel wall [9].

The pressure in the vessel during the experiments is also monitored. With a starting background pressure of 0.220 mbar, a relative pressure decrease is found with a maximum of 11% as shown in Fig. 6. This decrease is not due to the pumping system as the pumping capacity is constant and independent of the gas type. Secondly, it is not caused by a temperature change, because the pressure is observed to change almost instantaneously after adjustment of the flows. The pressure is also observed to be equal for the pure hydrogen and nitrogen case. It seems that the decrease of the pressure as function of the relative H_2 flow rate to the total flow rate is a measure of the ammonia density. Consider the production of ammonia from nitrogen and hydrogen by the reaction: $N_2 + 3H_2 \rightarrow 2NH_3$. This means that if one molecule of NH_3 is formed from $\frac{1}{2}N_2$ and $1\frac{1}{2}H_2$, the total numbers of molecules decreases with one. Since the pressure in the vessel is linear dependent on the number of molecules, the pressure decrease in the vessel can be a measure of the ammonia density. Therefore, it is concluded that there is an ammonia density of 11% at a relative flow rate of hydrogen of 0.5 with respect to the total flow rate.

Now, we try to model the numbers of different molecules produced in the vessel with a very simple model using very basic statistics. It is assumed that just the relative amount of N and H determines the probability of a reaction. Furthermore, the formed N_2 or H_2 are assumed to undergo no further reactions and only four-atom molecules are considered as end product. So starting with one N or H will give N_2, NH, HN and H_2 with respectively a chance of $P_N^2P_H^0$, $P_N^1P_H^1$, $P_N^1P_H^1$ and $P_N^0P_H^2$, where P_N and P_H are the fractions of atomic nitrogen and atomic hydrogen, assuming a constant dissociation degree of the molecular hydrogen and nitrogen flows through the arc. This can be extended to statistics for all possible four-atom molecules. Now, two limitations are examined. In both H_2 and N_2 are formed, and in one case all possible four-atom molecules are formed and in the other only NH_3 is formed.

Both cases are plotted versus the measured ammonia production in Fig. 7. The model in which only N_2, H_2 and NH_3 are formed fits the measured ammonia density reasonable well. This indicates that at the wall the formation of NH_3 is favourable above the formation of other molecules. The calculated NH_3 fraction is rescaled because not all N_2 and H_2 molecules are dissociated, or because there are other processes that are not taken into account here. One possible cause is that due to the large difference in mass, a hydrogen plasma beam diverges more than a nitrogen plasma beam. This so-called mass-defocusing effect has been reported in Ar-H_2 and pure H_2 plasma expansion [10,11]. This mass-defocusing leads to an effective cross-section where both molecules are in a mixture, which is smaller than the total cross-section. In view of this effect the production efficiency of 11% is remarkably high.

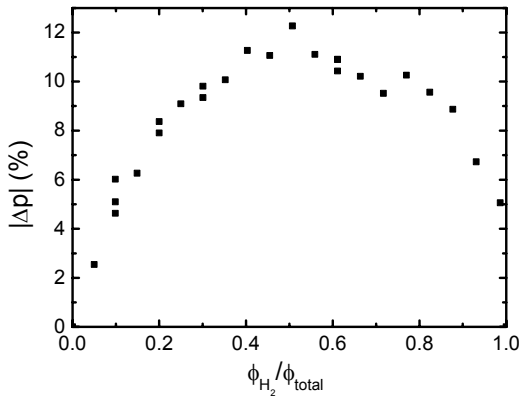

Figure 6: Relative decrease of the pressure as function of the hydrogen flow rate relative to the to the total flow rate of nitrogen and hydrogen.

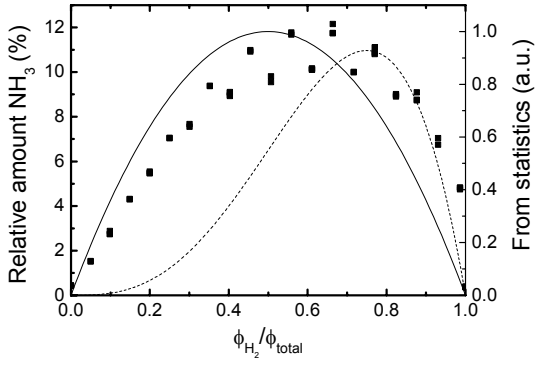

Figure 7: The ammonia density as measured with the mass spectrometer as function of the hydrogen flow rate relative to the total flow rate of nitrogen and hydrogen. The solid line is the calculated production from statistics assuming only reactions in which N_2, H_2 and NH_3 are formed. The dashed line is the calculated production assuming all possible reactions in which four-atom molecules are formed.

Conclusions

We have shown that by using high fluxes of atomic nitrogen and atomic hydrogen radicals, produced from N_2-H_2 plasma, ammonia is mainly produced at the vessel wall with high efficiency. Since the plasma is used to produce the radicals, and the wall acts as catalyst, the process is called plasma-activated catalysis. The results show that cavity enhanced absorption spectroscopy is a promising plasma diagnostic technique, which can supply fast and accurate density information.

Furthermore, Fourier transform (FT) spectroscopy with a thermal plasma as a broad-band light source, is currently installed on the set-up to be able to measure all different kind of molecules simultaneously. As FT spectroscopy is an absolute method, it can be used to complement the more indicative mass spectrometry technique and the absorption measured in a very narrow wavelength range with cavity enhanced absorption spectroscopy. The combination of these diagnostic techniques described above enables us to study the production of other molecules via plasma-activated catalysis.

By tuning the plasma parameters and choosing the right wall material, plasma-activated catalysis could be a promising new way for small-scale selective production of molecules, starting from their atomic constituents. It will be extended to hydrazine, N_2H_4, and later to organic molecules like methanol. In the latter example one could start from natural gas and oxygen [12].

This work is part of the research program of the "Stichting voor Fundamenteel Onderzoek der Materie (FOM)", which is financially supported by the "Nederlandse Organisatie voor Wetenschappelijk Onderzoek". We acknowledge the technical assistance of Ries van de Sande, Jo Jansen, Herman de Jong and Bertus Hüsken.

References

[1] E.N. Eremin - Russ. J. Phys. Chem. **49**, 1112 (1975).
[2] H. Uyama, O. Matsumoto - Plasma Chem. Plasma Process. **9**, 13 (1989).
[3] P. Vankan, T. Rutten, S. Mazouffre, D.C. Schram, R. Engeln - Appl. Phys. Lett. **81**, 418 (2002).
[4] R. Engeln, G. Berden, R. Peeters, G. Meijer - Rev. Sci. Instrum. **69**, 3763 (1998).
[5] M.C.M. van de Sanden, J.M. de Regt, G.M. Jansen, J.A.M. van der Mullen, D.C. Schram, B. van der Sijde - Rev. Sci. Instrum. **63**, 3369 (1992).
[6] HITRAN (high resolution transmission molecular absorption) database (http://www.hitran.com).
[7] L. Lundsberg-Nielsen, F. Hegelund, F.M. Nicolaisen - J. Mol. Spectrosc. **162**, 230 (1993).
[8] J. Amorin, G. Bavarian, G. Sultan – Appl. Phys. Lett. **68**, 1915 (1996).
[9] B. Gordiets, C.M. Ferreira, M.J. Pinheiro, A. Ricard – Plasma Sources Sci. Technol. **7**, 379 (1998)
[10] S. Mazouffre, M.G.H. Bogaarts, J.A.M. van der Mullen, D.C. Schram – Phys. Rev. Lett. **84**, 2622 (2000)
[11] S. Mazouffre, P. Vankan, R. Engeln, D.C. Schram – Phys. Rev. E **64**, 066405 (2001)
[12] C.E. Taylor, R.P. Noceti - Catal. Today **55**, 259 (2000).

CATALYCITY STUDY OF CNES/NASDA TPS SAMPLES AT THE CORIA INDUCTIVE PLASMATRON FACILITY

A. Desportes[1], P. Vervisch[1]

[1] *UMR 6614 CNRS CORIA, University and INSA of ROUEN, Saint Etienne du Rouvray, France*

Abstract

In the development of Reusable launchers technology, to explore the behaviour of TPS material in re-entry conditions is quite essential. At CORIA, an 100 kW class inductive plasmatron is implemented with a sample holder that allows tests on samples similar to Orex heat shield. Different working points are explored, simulating the whole area of the vehicle re-entry phase. To the date, the IPM method for γ determination is based on comparison between calculation of the boundary layer and measurements made on the surface sample. These measurements have been made on the OREX TPS material at CORIA. The final objective of this work is to contribute to the evaluation of the relevance of plasmatron facilities to determine the catalycity of thermal protection materials.

1. Introduction

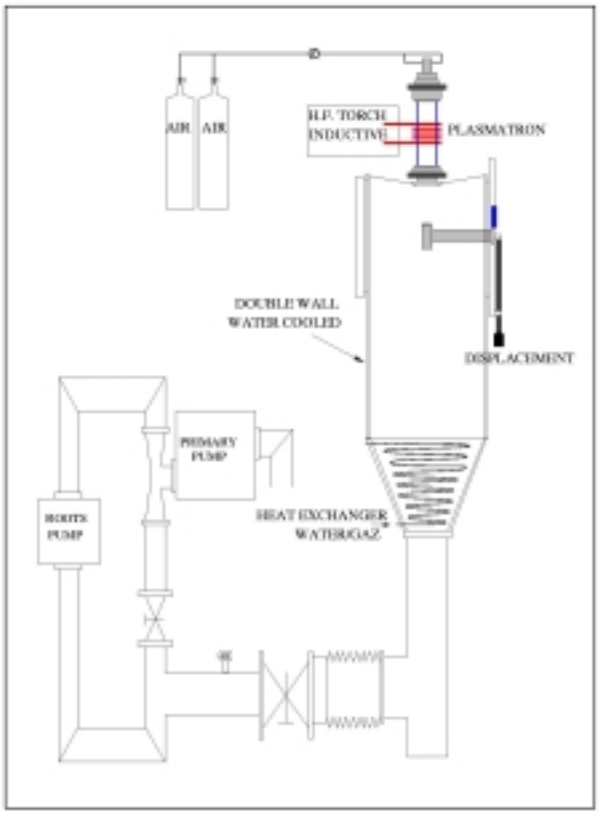

Fig 1. ICP torch at CORIA : IPWT

The catalycity parameters of a material cannot be obtained by direct measurements. In fact, this could be possible only with the knowledge of all the species concentration. Thus, the determination of the catalycity is a combination of experiments on the material and numerical simulations of the flow.

The samples that are to be tested are parts of heat shields of space vehicles. The aim of the tests is to prove that the material can resist or not to the atmospheric re-entry and reusability. In those conditions, the material has to be exposed to the same heat flux than the atmospheric re-entry.

These simulation conditions can be found in some plasma wind tunnels. One of the CORIA facilities was especially designed to produce such high enthalpy flows. The inductive 90 kW plasma generator can produce flows with various gases; the main interest of this kind of generator is the lack of electrodes which provides a high purity plasma jet.

1.1 Wind tunnel at CORIA : Description

The ICP torch is shown in Fig 1. There are three main parts :

- The generator : which can deliver a power up to 90 kW (9A 10 kV)
- The channel discharge : the place where the working gases confined in a quartz tube are ionised by the electro-magnetic field induced by the five turn coil.
- The test chamber : where is performed the interaction between the sample and the plasma. The pressure in the test chamber can vary from 1 mbar to 50 mbar.

2. Temperature and flux measurements on the samples

The total heat load of heat flux is one of the most important parameter during the atmospheric re-entry of the vehicle. It is primary determined by the convective part. Furthermore the catalytic behaviour of the surface of the thermal protection system can influence the heat flux to the vehicle.

The heterogeneous recombination of O and N atoms species and excited molecules can significantly increase the heat flux at the TPS material. The probabilities for wall recombination of O and N atoms γ_O and γ_N are the representative parameters to qualify this catalytic contribution. Information about these parameters are generally derived by the IPM procedure [2][3]. This method combine both experimental and numerical tools. The experiments give the sample surface temperature and the total heat flux received by the sample when it is placed in the plasma flow. These measurements are the input data to a numerical code that simulates the flow and the boundary layer around the sample. The gamma value is deduced for each tested material with a known gamma. Generally this reference sample is cold copper which is fully catalytic with $\gamma = 1$.

In this manner a macroscopic γ value is obtained where accommodation effects are integrated. However several hypothesis are underlying before to employ this method :

- Chemical equilibrium at the boundary layer edge
- $\gamma_N \cong \gamma_O$, weak variation with temperature and the ratio O/N

The deexcitations of metastable molecules at the wall are neglected.

To ascertain the reliability of theses assumptions, measurements in the boundary layer above the sample have to be performed. However in a first step, heat flux on the sample and its temperature level have to be primary determined.

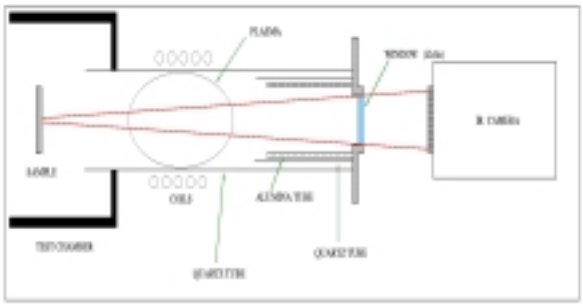

Fig 2. Experimental set-up for wall temperature and heat flux measurements

For surface temperature measurements, Infra-Red camera is used assuming a sample emissivity value. Experimental arrangements allow to explore the sample brightness at right angle, in order to prevent any mistakes due to the angle correction. Therefore the measurement is made in the axis through the plasma creation areas as shown in the **Fig 2**. This diagnostic is possible due to the specific wavelength used by the infrared camera (THERMACAM PM595 FLIR) which integers the emitted signal between 7 and 13 μm. Hopefully, there is no emission of the plasma in these wavelength.

The radiation Heat flux of the sample is given by the Stephan-Boltzmann laws as :

$$\Phi = \varepsilon.\sigma.T_w^{\,4} \quad (1)$$

The radiative flux focused on the camera can be written :

$$\Phi_{\,received} = \tau_{\,ZnSe} \,.\varepsilon\,.\sigma\,.T_{\,w}^{\,4} \quad (2)$$

Where σ is the Stephan-Boltzmann constant and τ_{ZnSe} the transmitivity of the ZnSe window equal to 0.68. The value of the heat fluxes are thus given thanks to the emissivity of the sample.
The total heat flux is the sum of the radiative flux and the transmitted flux on the sample.

$$\Phi_{TOTAL} = \Phi_R + \Phi_{TR} \quad (3)$$

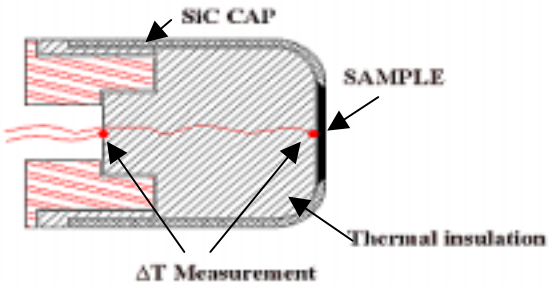

Fig 3. Experimental setup for transmitted heat flux measurements

Φ_{TR} is determined by the temperature difference between two thermocouples on the axis behind the sample (see **Fig 3**). This gradient depends on the thermal conductivity λ of the insulator holding the two sensors.
The ratio Φ_{TP}/Φ_R plotted against sample temperature is reported in **Fig 4**. The experimental point falls approximately on straight line. These measurements are able to estimate the loss of accuracy when Φ_{TR} is neglected. In the explored temperature range its contribution remains low.

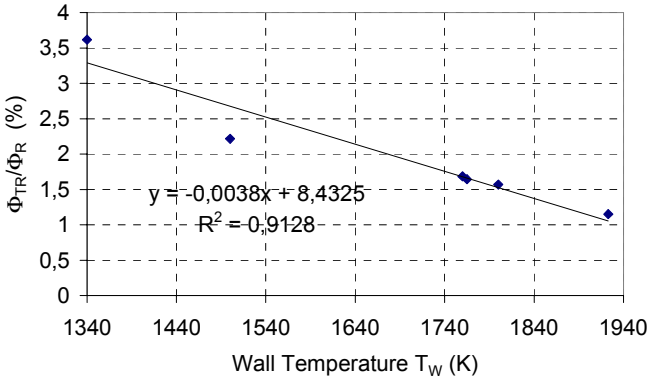

Fig 4. $\Phi_{TR}/\Phi_R = f(T_w)$

2.1 Infrared spectroscopy

As you can see on **Fig 4** the sample temperature range that have been explored is between 1340 and 1940 K. So the maximum intensity of the black body radiation for such temperatures is comprise between 1.5 and 3 µm. As discussed earlier, the infrared camera integers the wavelength between 7 and 13 µm. For example, we consider a black body with a temperature of 1500 K. The percentage of energy taken by the infrared camera is about 6 %. It is clear that an excellent calibration of the camera is needed otherwise the uncertainties will be so important that no temperature can be determined. In this way, we have replaced the camera by an infrared spectrometer. The experimental set-up is shown

on **Fig 5**. We use a parabolic off axis mirror rather than classical lens to get rid of the varying focal length with the wavelength. The spectrometer used is a Jobin-Yvon HR320 with a 300 grooves/mm grate. The wavelength range studied is 1-5µm. So the detector placed at the exit of the spectrometer is PbS or PbSe captor. The main drawback of this set-up is the time needed for a complete acquisition (description of the sample radiation between 1-5 µm will take about 10 min), whereas a picture taken with the camera is done in only 5 seconds. Furthermore the picture taken with the camera is a 2D picture of all the sample surface whereas with the spectrometer coupled with PbS or PbSe detector the information is 1D. On the other hand, the main advantage of this set-up, is the determination of the sample emissivity for plenty of wavelength comprised between 1-5 µm. In fact, ε_λ can be obtained by comparison between the black body radiation and the acquisition done. Furthermore, in order to obtained emissivity varying with temperature, this experimentation will be repeated for different wall temperatures. These measurements are underway.

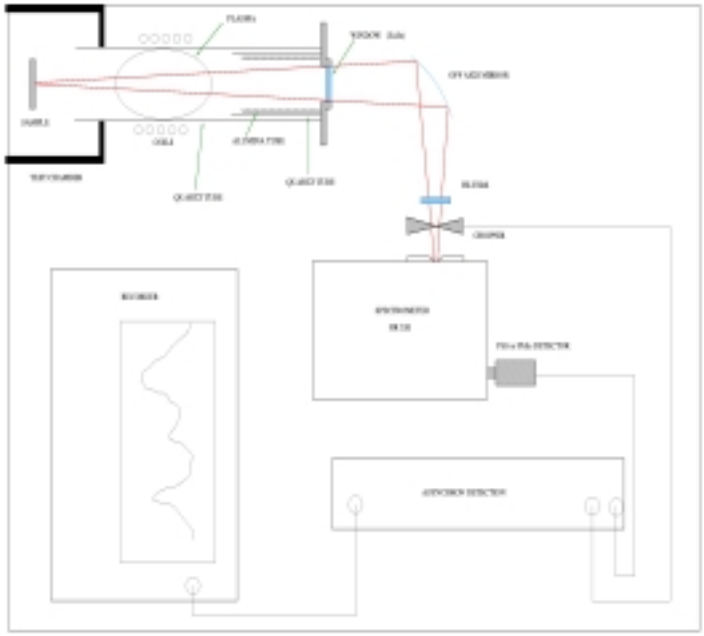

Fig. 5 Experimental set-up for infrared spectroscopy

3. Cold wall measurements

As discussed earlier, the IPM method for determination of catalycity needs a calibration with a material that has a tabulated gamma. In our case, this calibration is derived by the measured flux on a fully catalytic ($\gamma = 1$) copper sample.

The experimental set-up of the sample holder with the copper cold wall is described in **Fig 6**. The measured fluxes with this apparatus correspond of course to the highest fluxes available in our facility.

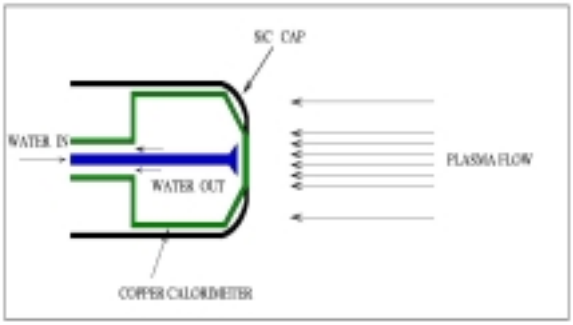

Fig 6. Copper calorimeter

Tab 1

Temperature measured on C/C sample	Φ_R	Corresponding heat flux on cold wall
3000 Pa		
1920 K	612.5 KW	1370 kW

To illustrate the abilities of the facility, typical results are reported in **Tab 1**. They are obtained for the following input conditions :

- 3.6 g.s-1 air mass flow rate
- 9 kV, 8 A anode power

4. Measurements technics : free jet and boundary layer

For an experiment-modelling comparison, the confidence of the deduced conclusions is related to the set of available measured parameters. In this direction, a special effort has to be made to measure as complete set of parameters as possible : temperature, velocity, species concentrations ….
For this purpose, several measurements techniques have been implemented on the experiment or are underway.

4.1 Spectroscopic measurement

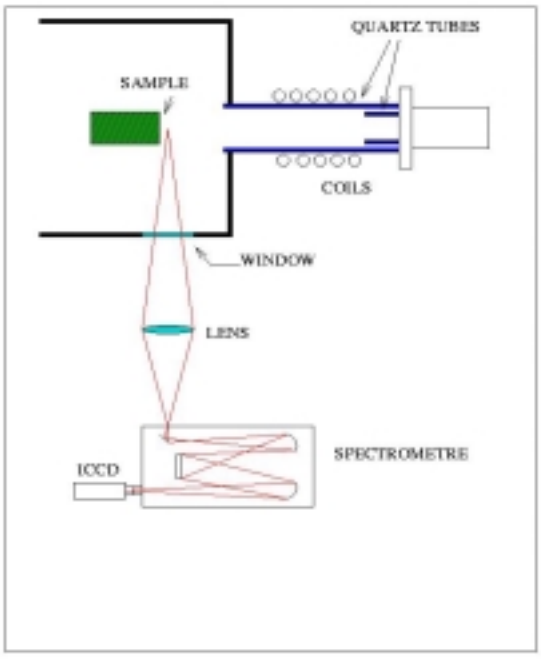

Fig 7. Experimental set-up for spectroscopic measurements

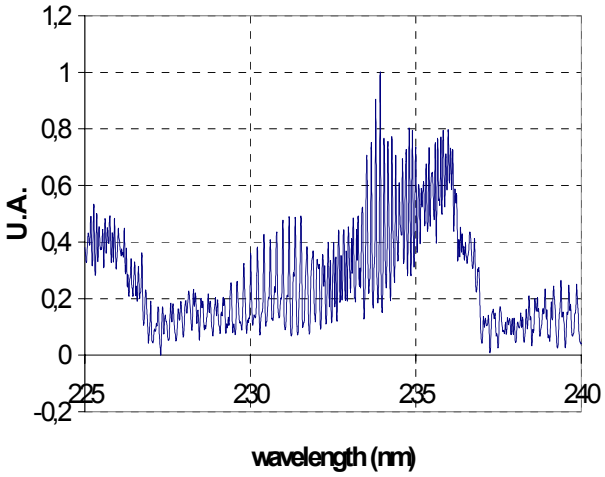

Fig 8. Emission spectra of the NOγ band.

For emission measurement, usual optical devices have been implemented on the experiment (**Fig 7**). The plasma image on the entrance slit of a 750 mm focal length Acton spectrometer, was produced by a quartz lens. An intensified CCD Camera (Princeton Instrument PI-MAX) designed for the UV wavelength range is used for the detection. The **Fig 8** shows the typical plasma emission in the wavelength range of the Noγ band. Temperature measurements can be achieved by fitting these experimental spectra with a calculation [1]. The experimental spectrum pictured in **Fig 8** correspond to a rotational temperature of about 5700 K. In present pressure conditions, rotational temperature can be equate to heavy particle temperature. The so measured axis temperature is reported on **Tab 2** for five typical working conditions. These measurements have been performed at 200 mm from the coil exit. To derive reliable γ value with IPM method, input conditions above the sample have to be as homogeneous as possible. Radial temperature behaviour (**Fig 9**) shows this required condition is approximately verified since the temperature change is about 10 % over 1.5 cm.

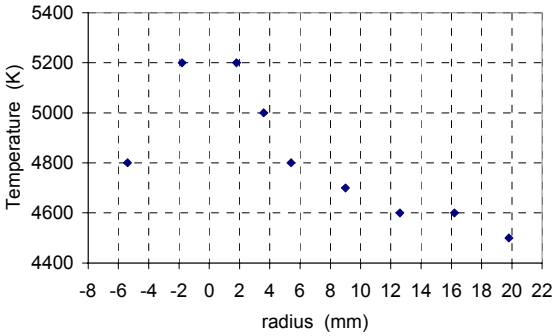

Fig 9. Temperature profile in the free plasma jet

Tab 2

Working Points			T_{kin} (K)
Pressure (mbar)	Anode Intensity (A)	Gas Mass Flow Rate (g/s)	
30	7,5	3,6	5300
30	6,8	3,6	5200
20	7,5	3,6	5600
20	6,7	4,3	4900
20	6,7	6,1	4800

4.2 Pitot probe measurements

In this kind of flow, difficulties are encountered to measure velocity. The velocity range being too low to derive its value by LIF (Doppler shift) and the temperature too high to employ PIV method. Then even if in plasma flow it is not easy to deduce reliable value with Pitot probe, this measurement technique have been implemented on the experiment. In the literature we find several theoretical works which study the determination of the velocity by dynamic pressure measurements [4][5][6]. But its are not available in our working conditions (low pressure, cone shape of the Pitot probe, low Mach number ……)

So, we assume that the impact pressure is :

$$\Delta P = \tfrac{1}{2}\rho_{\infty}U_{\infty}^{2} \qquad (4)$$

By this way, we have an order of magnitude of the velocity in a plasma jet section. An example is given for the same working point than the temperature profile (see **Fig 10**).

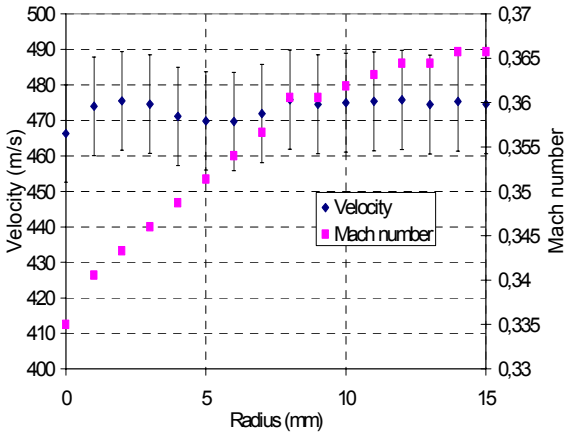

Fig 10. Velocity profile in the free plasma jet

We can see that the velocity profile is quite homogeneous on all the sample surface (the sample diameter is 26.5 mm).

4.3 LIF measurements

Thanks to an OPO laser, some LIF measurements are underway to obtain boundary layer profile for :

- NO, with a 226 nm excitation wavelength
- O , with a two photon LIF at 226 nm excitation wavelength
- N , with a two photon LIF at 211 nm excitation wavelength

5. Conclusion

We have seen that usual measurement techniques for γ determination have been implemented on IPWT. By the way of the IPM method (coupling between experimental results and a boundary layer numerical code) we are able to determine the γ parameter of TPS, like the OREX one. Furthermore, to complete the knowledge of the plasma jet, several measurement techniques have been used, like emission spectroscopy, Pitot probe and some LIF measurements are underway to get the species densities. This set of data will be very useful for the numerical code, and the so deduced γ will be more precise. In this way, we also want to improve the surface temperature measurement of the sample. This is a very important point, because this measurement is the base of the γ determination, and the new technique apply can lead us to the emissivity of the sample under re-entry conditions.

[1] Boubert P., *Méthodes spectroscopiques appliquées aux plasmas et aux milieux à haute enthalpie,* Thèse de doctorat, Université de Rouen, 1999

[2] Kolesnikov A.F., Yakushin M.I., *Modeling convective nonequilibrium heat transfer of bodies with hypersonic flows at induction plasmatrons,* Teplofizika Vysokikh Temperatur, vol 26, N° 4, 1987, pp 742-750

[3] Kolesnikov A.F., Pershin I.S., Vasil'evskii S.A., Yakushin M.I., *Study of quartz catalycity in dissociated carbon dioxide subsonic flows,* Journal of Spacecraft and Rockets, vol 37, N°5, 2000, pp 573-579

[4] Porterie B., Larini M., Loraud J-C., Jestin L., *Colled pitot tube in plasma jet : an impact prssure recovery model,* Journal of Thermophysics and heat transfer, vol. 8, N°3 ,1994, pp 385-392

[5] Magin T., Degrez G., *Cooled pitot probe in inductive air plasma jet: what do we measure ?*

[6] Chazot O., Vanden Abeele D. and Carbonaro M., *Comparison of experimental and numerical results for the dynamic pressure in an inductive plasma flow.*

Simulation of the decomposition reduction in composite layers by computer supported optimisation.

E. Lugscheider, N. Papenfuss-Janzen, W. Varava
Material Science Institute, Aachen University of Technology, Aachen, Germany

Abstract
A multi-component APS powder spraying process is formalized and analyzed. A mathematical model to estimate the influence of the injector parameters on the powder's decomposition is built. The model is based on an optimization procedure of a multi-injector system, which maximizes the relative mass quantities of the powders in the intersection area of the powder spots. The decomposition optimisation allows layers designing with a desirable component mass distribution and should supply improving their thermo-physical properties.

1. Introduction

Application of multi-layer sprayed coatings, particularly graded coatings, plays more and more important role in industry and medicine. Metals, ceramics and synthetic materials can be used as components of powders, applied to produce a functionally graded coating. Among other things, these complicated coatings are used in implant medicine, production of abradables for turbine blades and corrosion protection of light weight constructions. Graded coatings are applied to substrates by atmospheric- and shrouded plasma spraying (APS/SPS) as well as by physical- and chemical vapour deposition (PVD/CVD). The component's mass distribution is one of the most important characteristic of a graded coating quality. A determined grading of a multi-component powder should supply desirable mass distribution to achieve decisive advantages, concerned to the most important physical properties of the coating.
Based on above consideration, building of a mathematical model for graded processes simulation, provided direct and inverse calculation of input and output parameters, plays an important role. A developed mathematical model should be put to the numerical and experimental tests in order to validate it.

2. Problem description

A determined powder mass distribution by the fabrication of abradables for gas turbine blades is required. The modern powders, widely used for the production of abradables, consist in majority of the three following components: MCrAlY, BN and Polyester. The thicknesses of the turbine blade abradable coating are usually in the range of 1,5 – 2 mm. Because of technical and exploitation reasons, the BN and polyester fractions in the coating must be increased and MCrAlY fraction must be decreased in the direction to the contact surface. Therefore, the coating's thermo-mechanical properties strongly change towards the thickness coordinate. Required mass fraction dependences can be obtained by a graded spraying process. The same problem takes place in medicine implant fabrication, where the grading of Titan (Ti) and Hydroxylapatit (HAp) supplies the necessary functional properties [2]. Therefore, the matters concerning optimal mass distribution are discussed in the presented article. In addition to above, the graded coatings should supply the following features [3]:

- Jump decreasing in thermo-mechanical characteristics in the system substrate – coating;
- Improving the chemical compatibility in the system substrate – coating;
- Supplying needed hardness.

Based on above discussion, the problem statement can be formulated as: to obtain a predetermined mass fractions distribution depending only on the thickness coordinate.

3. Mathematical Model

The presented mathematical model is developed for the simulation of APS graded processes exclusively (the other cases are not taken into account). The investigated physical system includes an unloaded plasma jet, particle injectors, and particles. Its parts have the following borders: plasma gun outlet, calculation domain surface, and substrate surface. The powder injection takes place at the same time by a number of injectors, located at different positions.

The following input parameters are used in the presented model:

1. Parameters related to plasma jet (field values):

They are the field values like temperature-, velocity- and pressure distributions at the outlet of plasma gun as well as inside unloaded plasma jet. These fields will be following considered as steady state and known. Besides of them, the particles' influence on the plasma jet is neglected. The accepted assumption very well corresponds to reality for a wide range of metallic and ceramic materials [4]. The interaction between the particles in the plasma jet can be considered as insignificant for technical applications, what is validated by a number of experimental and theoretical investigations. The fields are calculated for fixed plasma gun – **F4 - Sulzer Metco –** and for fixed cold plasma forming gas mixture – Argon 93%, Hydrogen 7% – in the ambient air under atmospheric condition by CFD software PHOENICS [1].

2. Parameters related to the particles:

The particle diameter is a random variable. Because of a great amount of particles (N > 7,5e+04 part/sec) in plasma spraying, it is possible to consider the particle diameter as a continuous random variable. Gauss probability density is assumed for this random variable approximately:

$$p_D(d) = \frac{1}{\sqrt{2\pi}\,\sigma(D)} \exp^{-\frac{(d - M(D))^2}{2\sigma(D)^2}}$$

$$d \in [d_{\min}; d_{\max}] = [M(D) - 3\sigma(D); M(D) + 3\sigma(D)] \quad , \qquad d_{\min} > 0 \qquad (1)$$

where: D is a random particle diameter; d is a realisation of random particle diameter; $d_{\min}$, $d_{\max}$ are the minimal and maximal realisation of a particle diameter, respectively; $\mathbf{M}(D)$ is the particle diameter mean value; $\boldsymbol{\sigma}(D)$ is the particle diameter standard deviation; $p_D\ (d)$ is the probability density of the particle diameter.

3. Parameters related to injector and particles:

The particle initial position is a random variable. Uniform probability density is assumed for this random variable:

$$p_{\underline{R}_0}(\underline{r}_0) = p_{R_0,\Phi}(r_0, \varphi) = \frac{1}{A_I} = \frac{1}{\pi R_I^2} \qquad (2)$$

where: $p_{\underline{R}^0}(\underline{r}_0)$ is the probability density of the particle initial position; A_I , R_I are the injector outlet area and injector radius, respectively.

The particle initial position and its diameter is assumed to be stochastic independent:

$$p_{D,\underline{R}_0}(d, \underline{r}_0) = p_D(d)\, p_{\underline{R}_0}(\underline{r}_0) \qquad (3)$$

where: $p_{D\ ,\underline{R}^0}(d, \underline{r}_0)$ is the common probability density of the particle diameter and of the particle initial position.

Particle initial velocity is assumed to be independent on the initial position and the particle diameter is a deterministic value. [5]:

$$\underline{V}_0 = \underline{V}_0(D, \underline{R}_0) = \underline{V}_0 = const \qquad (4)$$

In addition, the initial velocity is assumed to be perpendicular to injector outlet and depends linearly on the carrier gas flow rate [5]:

$$\underline{V}_0 = const \cdot \dot{m}_{TG} \qquad (5)$$

where: $\dot{m}_{TG}$ is the carrier gas flow rate. The carrier gas flow rate is a deterministic steady-state value.

4. Parameters related to injector:

The situation of the injector surface with respect to the plasma gun outlet position $\underline{\boldsymbol{C}}$, the injector outlet surface A_I and mass particle flow rate $\dot{m}$ are deterministic input parameters.

The following output parameters are used in the presented model:

1. Parameters related to particle

The particles are considered as a mass point in the frame of the presented model, and the assumption is used to solve the dynamic equation for the particle. The particle position vector depends continuously on the initial conditions and the coefficients of the dynamic differential equation, therefore it also continuously depends on input parameters like particle diameter, initial position and initial velocity. According to the consideration above, the particle-hit position on the substrate is introduced as output variable that follows from its trajectory. This variable is a random variable depending on input random variables.

2. Parameters related to coating

Because of the great amount of particles and the great area flattening rate (can reach 150-200 for ceramic particles at its melting point and velocities about 150-200 m/s), the average spot area is introduced as an output parameter, so it is possible to say that the material distributes continuously inside the spot.
An area of the coating on the substrate can be considered as the spot, obtained by a motionless plasma gun. The studying of input parameters influence shows that the particle diameter distribution, the initial velocity, the injector outlet area and its position strongly influence on spot area, but the particle flow rate and the initial particle position have no influence.
The common dependence of spot area can be presented as

$$A_F = A_F(p_D(d), \underline{V}_0, A_I, \underline{C}) \qquad (6)$$

The two following output parameters can be introduced because of continuous mass distribution in the spot: coating thickness (ρ_{su}) and normalized coating thickness (p_{Rsu}), both of them should be related in respect to a time unit. ρ_{su} depends on all input parameters introduced before; in the mean time p_{Rsu} doesn't depend on particle mass flow rate that plays a big role by the following model building. The common dependence of both output parameters considered before can be presented as follows:

$$\rho_{SU} = \rho_{SU}(p_D(d), \underline{V}_0, p_{\underline{R}0}(r_0), \dot{\Theta}, A_I, \underline{C}) = \frac{d\dot{\Theta}}{dA} \qquad (7)$$

$$p_{\underline{R}SU} = p_{\underline{R}SU}(p_D(d), \underline{V}_0, p_{\underline{R}0}(r_0), A_I, \underline{C}) = \frac{1}{\dot{\Theta}}\frac{d\dot{\Theta}}{dA} \qquad (8)$$

where: ρ_{SU} is the coating thickness related in respect to a time unit; p_{RSU} is the normalized coating thickness;

p_{Rsu} can be interpreted as a probability density of the particle hit position on the substrate for each of the powder component accordingly expression (8). For the chosen problem statement a mathematical model based on optimisation technique is proposed:

It is required to maximize all powder fractions in common coating spot.

In that way, the simultaneous probability of the particle hit position for all powder components will be used as a goal function. The following independent variables will be introduced as optimisation variables: the

particle diameter mean value **M**(D); the particle diameter standard deviation **σ**(D); the initial particle velocity $\underline{\mathbf{V_0}}$; the injector outlet position $\underline{\boldsymbol{C}}$ and the injector outlet area A_I.
In particular for two-injector design, the goal function can be expressed as follows:

$$\mathbf{P}\left(\tau_1 \wedge \tau_1 \in A_{12=21}\right) = \int_{A_{12}} p_1\, dA \bullet \int_{A_{12}} p_2\, dA \xrightarrow{\text{in Designvariables}} max \quad (9)$$

$$p_1 = \dot{\Theta}_1^{-1}\rho_1 = \dot{\Theta}_1^{-1}\frac{d\dot{\Theta}_1}{dA} \quad ; \quad p_2 = \dot{\Theta}_2^{-1}\rho_2 = \dot{\Theta}_2^{-1}\frac{d\dot{\Theta}_2}{dA} \qquad (10)$$

where: p_1, p_2 are the normalized coating thickness for the first and the second powder component, respectively; ρ_1, ρ_2 are the coating thickness for the first and the second powder component, respectively; $\dot{\theta}_1$, $\dot{\theta}_2$ the volume particle flow rate for the first and the second powder component, respectively.

4. Adaptation of PLASMA 2000 software and first results

At present PLASMA 2000 software is used to solve particle dynamic and heating problems with taking evaporation into account [6]. The software is adapted to solve the graded coating problem by the means of an optimisation model. The following modification steps was done:

- definition of variation range for all input parameters;
- extension up to two injection system;
- build a new program module in frame of PLASMA 2000 called TOPO-model;
- choosing the NELDER-MEAD method as restriction free optimisation procedure [7];
- looking for start point to optimisation with non zero goal function value (MODUL_START);
- finding of satisfying number of test particle (MODUL_PARTICLE).
-

The TOPO-model is used to define the area of each powder, the intersection area of the spots as well as to calculate the goal function. The operation results of TOPO-model are illustrated in Figure.1 for the input parameter set, defined in Table 1.

Table 1. Spraying design 1-2 (one injector – two powders)

Plasma design		Injection design		Powder properties	MCrAlY	BN
Current, A	650	Velocity , m/s	12	Density, kg/m^3	8000	2300
Voltage, V	50	Injector area, mm^2	1,78	Mean diameter, µm	70	110
Power (effective), kW	25,3	Axial distance, mm	6,3	Standard deviation, µm	10	20
Argon flow rate, slpm	41	Radial distance, mm	8,5	Number of test particles	30x30	30x30
Hydrogen flow rate, slpm	10	Angle, °	180			

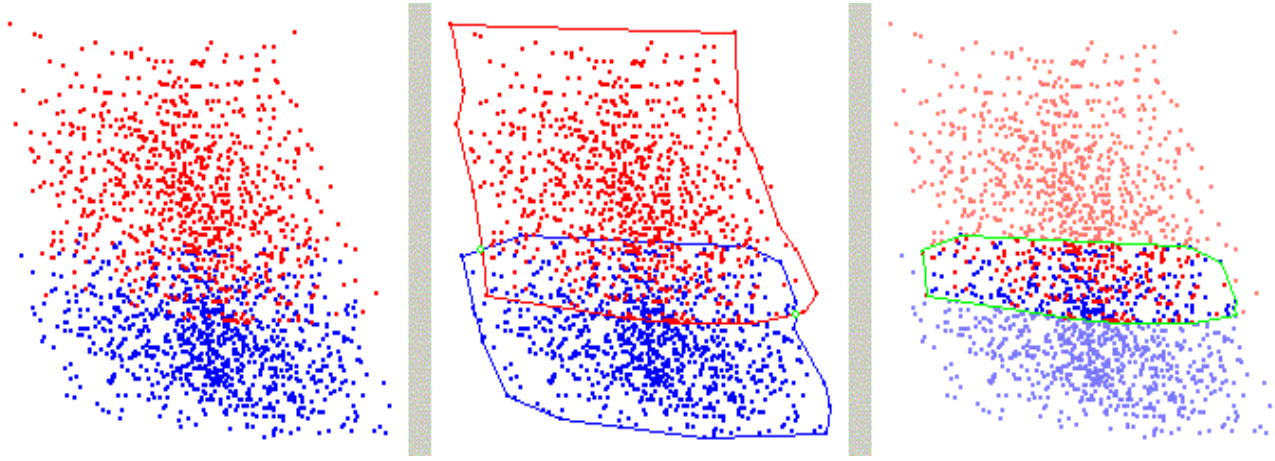

Figure 1. TOPO-model for spraying design 1-2

It is possible to observe quiet a big decomposition of the powders, which is represented by a relative little value of the goal function (P=0,057). It corresponds to the mean volume efficiency for each powder about 22%. The spot areas are equal to 8,55 mm^2 for McrAlY (red), 6,03 mm^2 for BN (blue) and 2,23 mm^2 for the intersection area.
Operation results of MODUL_PARTICLE are illustrated in Table 2.

Table 2. The deviation of spot areas and goal function (60x60 Particles)

Experiment, $N^{\underline{0}}$	**Goal, *P***	**Area 1, m^2 A_1 x 10^{-6}**	**Area 2 , m^2 A_2 x 10^{-6}**	**Intersection area, m^2 A_O x 10^{-6}**	**(MEAN ; STD), P , A_1 , A_2 , A_O , e**
1	0.9892	1.4783	1.5010	1.4419	μ (***P***) = 0.9869
2	0.9892	1.4835	1.5064	1.4454	
3	0.9844	1.5180	1.4098	1.3936	σ (***P***) = 0.0016 ; e = 0.16
4	0.9851	1.4725	1.4905	1.4220	
5	0.9856	1.4622	1.4637	1.4203	μ (***A1***) = 1.4683
6	0.9856	1.4134	1.4731	1.3696	
7	0.9869	1.4727	1.4767	1.4187	σ (***A1***) = 0.0261 ; e = 1.78
8	0.9855	1.4748	1.4828	1.4151	
9	0.9869	1.4468	1.4733	1.4089	μ (***A2***) = 1.4760
10	0.9875	1.4469	1.4796	1.4127	
11	0.9893	1.4583	1.4895	1.4335	σ (***A2***) = 0.025 ; e = 1.69
12	0.9868	1.4774	1.4897	1.4276	
13	0.9860	1.4650	1.4361	1.3870	μ (***AO***) = 1.4179
14	0.9873	1.5115	1.4730	1.4448	
15	0.9885	1.4428	1.4954	1.4268	σ (***AO***) = 0.0215 ; e = 1.42

The numerical results show, that the number of the test particles up to 4000 is enough to hold the deviation of the goal function in a 1% range.
Finally, the attention should be paid to the fact, that the particle heating part is neglected in the frame of the developed model, because the influence of the particle heating on particle dynamic process is insignificant and particle-heating calculation can be carried on separately for the optimal design. This assumption can hold the time for the calculation in reasonable limits.
In addition, some analytical expressions are obtained concerning graded spraying process.

Mean coating thickness:
$$\bar{h} = \bar{h}_1 + \bar{h}_2 = \kappa_1 \frac{\dot{\Theta}_1}{v_B \Delta x} + \kappa_2 \frac{\dot{\Theta}_2}{v_B \Delta x} = \frac{1}{v_B \Delta x}\left(\kappa_1 \frac{\dot{m}_1}{\rho_1} + \kappa_2 \frac{\dot{m}_2}{\rho_2}\right) \qquad (13)$$

Graded concentration ratio:
$$Q = \frac{\bar{h}_1}{\bar{h}_2} \qquad (14)$$

where: v_B is the plasma gun velocity; Δx is the maximal projection size in the direction perpendicular to the of plasma gun motion; $\bar{h}_1, \bar{h}_2$ are the mean coating thicknesses for the first an the second powder, respectively; $\dot{\theta}_1, \dot{\theta}_2, \dot{m}_1, \dot{m}_2$ are the particle volume and mass flow rate for the first an the second powder, respectively; κ_1 , κ_2 are the deposition efficiencies for the first an the second powder, respectively; ρ_1 , ρ_2 are the mass densities for the first an the second powder, respectively.
If the grading optimal design satisfies to technical requirements, the goal function is approximately 1. In this case it is possible to calculate particle mass and volume flow rates for defined elementary mean coating thickness and graded concentration ratio. The calculation and the spraying are carried on step-by-step up to the moment, when desirable whole thickness and concentration distribution will be reached.

5. Conclusion

The optimised graded spraying of few powders can improve thermo-physical properties of the coating. In this article, the mathematical model to calculate the controlled coating growth based on an optimisation technique developed by NELDER-MEAD is presented. This model is related to the problem formulation and shows advantages in the numerical solution procedure.

The optimisation procedure does not include the calculation of derivatives, only needs a limited amount of memory capacity and requires a small number of control parameters. The numeric testing of this procedure shows good stability and not sensibility to numerical errors, taking place at the goal function calculation [7].

The developed modules MODUL_START and MODUL_PARTIKEL allow to find an appropriate start design with a non-zero goal function value and to adjust the proper number of the test particles to hold the goal function deviations in a permissible range. The optimisation procedure combined with above described modules makes possible integrated numeric estimation of the optimal design for two or more powders, which helps to configurate appropriate graded spray equipment and to control the growing of the coating. High flexibility and possibility to vary the number of optimisation parameters are important advantages of the developed model too. The first presented numerical results combined with the analytic ones show the possibility to control the graded spraying by injector parameters.

Insignificant complication of the graded spraying process and injection equipment should lead to better coating quality.

In future work, some essential steps in order to develop further the model can be divided in the following groups: theoretical (taking into account particle influence on the plasma jet in the case of high loaded plasma; taking into account non stationery cases), numerical (extending and testing of the optimisation software, optimal design calculation for different material combination; dimension reduction of design variable space), and, the most important, detailed experimental investigations of the graded coating quality (metallography, radiography, hardness testing and tribology) to validate the developed model. It allows getting new knowledge and experience about the control and the structure of the graded coating process.

Acknowledgement

The authors gratefully acknowledge the Deutsche Forschungsgemeinschaft (DFG) for the financial support within the project Lu 232/70-1.

Reference:

[1] E. Lugscheider, C. Barimani, P. Eckert, U. Eritt - Modelling of the APS Plasma Spray Process, Proceeding of the 5th International Workshop on Computational Modelling of the Mechanical Behaviour of Materials, Aachen (1995)

[2] E. Lugscheider, S. Kyeck - Funktionell gradierte Materialien – Ein neuer Werkstoff für den Einsatz in der Medizintechnik, FDS Workschop, Tübingen (1998)

[3] N. Schimoda, S. Kitaguchi, T. Sailo, H. Takigawa, M. Koga - Production of Functionally Gradient Materials by Applying Low Pressure Plasma Spray, First International Symposium on Functionally Gradient Materials, Sendai Japan, 10 (1990)

[4] M. I. Boulos, P.Fauchais, A. Vardelle, E. Pfender - Fundamentals of Plasma Particle Momentum and Heat Transfer, Plasma Spraying Theory and Applications World Scientific (1993)

[5] U. Eritt - Entwicklung und Validierung von Simulationsmodellen zur Optimierung der Prozessführung bei der Herstellung plasmagespritzter Wärmedämmschichten ; Werkstoffwissenschaftliche Schriften-reihe, Band 40, Aachen (2000)

[6] V. Hurevich, L. Pawlowski, I. Smurov - Heating of porous particle in plasma flame; Proceeding of the International Thermal Spray Conference, Essen (2002)

[7] G. E. P. Box, N. R. Draper - Evolutionary Operation, Wiley (1969)

Transport coefficients in two-temperature argon-helium thermal plasmas

V. Rat, J. Aubreton, M.F. Elchinger, and P. Fauchais

SPCTS –CNRS UMR 6638, University of Limoges, 123 av. A. Thomas, 87060 Limoges cedex, France

Abstract

Transport coefficients in argon-helium plasmas at atmospheric pressure are calculated assuming that the kinetic electron temperature T_e is different from that of heavy species T_h. The influence on transport coefficients (electrical conductivity, viscosity and thermal conductivity) of the non-equilibrium parameter $\theta=T_e/T_h$ is investigated. The plasma composition shows that the increase of the non-equilibrium parameter θ gives rise to a shift of the ionisation of heavy species to lower heavy species temperatures. This results in a decrease of the viscosity at T_h fixed, as θ increases. Electrical conductivity is shown to be weakly dependent on θ, contrary to thermal conductivity.

1. Introduction

Departures from local thermal equilibrium (LTE) in many plasma processes have been highlighted, such as thermal plasmas in vacuum conditions, close to electrodes of electric arcs, in plasma jets as soon as a cold gas or a liquid is injected. Non-equilibrium plasmas, for which the kinetic electron temperature T_e can be different from that of heavy species T_h, are extensively studied and modelled.

Plasma processes modelling requires two-temperature transport coefficients in order to solve with accuracy conservation equations with their boundary conditions (see for example lately [i,ii,iii]). Very recently, Rat et al. [iv,v] proposed a modified approach of the Chapman-Enskog method applied to a two-temperature thermal plasmas in order to calculate non-equilibrium transport coefficients. Unlike Burm et al. [vi] who describe the plasma with reduced variables (depending on pressure and electron number density) and two non-LTE parameters, transport coefficients are basically obtained from the knowledge of plasma composition, the pressure, the temperature T_e and T_h. The non-equilibrium parameter $\theta = T_e/T_h$ is fixed for each calculation.

Many plasma processes use argon-hydrogen mixtures because argon and hydrogen respectively improve the momentum and energy transfers [vii,viii]. Argon-helium is also widely used because on the one hand, helium increase the plasma enthalpy and, on the other hand, the mixture exhibits a higher viscosity over 10000 K at equilibrium due its high ionisation energy [ix]. Besides its well known transport and thermodynamic properties, helium can present departures from LTE at atmospheric pressure, depending on experimental conditions as explained by Jonkers *et al.* [x], because of its high excitation potential of the first excited states and its light mass which facilitate its diffusion.

This paper is therefore aimed at calculating transport coefficients in argon-helium thermal plasmas, where the kinetic temperature of electrons T_e is different from that of heavy species T_h by using the approach of Rat *et al.* [iv,v]. First, plasma composition is calculated and the influence of $\theta = T_e/T_h$ on the latter is investigated. Second, results of two-temperature transport coefficients are shown and discussed as function of $\theta = T_e/T_h$.

2. Plasma composition

Considering a mixture of only atomic species, the modified equilibrium constant method of van de Sanden *et al.* [xi] is used to obtain the number density of each species up to T_e = 30,000 K.

Plasma composition is determined for 7 species, namely the electrons, Ar, Ar^+, Ar^{2+}, He, He^+ and He^{2+} using the conservation of pressure, the molar fraction ratio Ar/He and the electrical neutrality. The electron temperature T_e is used in the modified equilibrium constants for ionisation reactions of Ar, Ar^+, He and He^+.

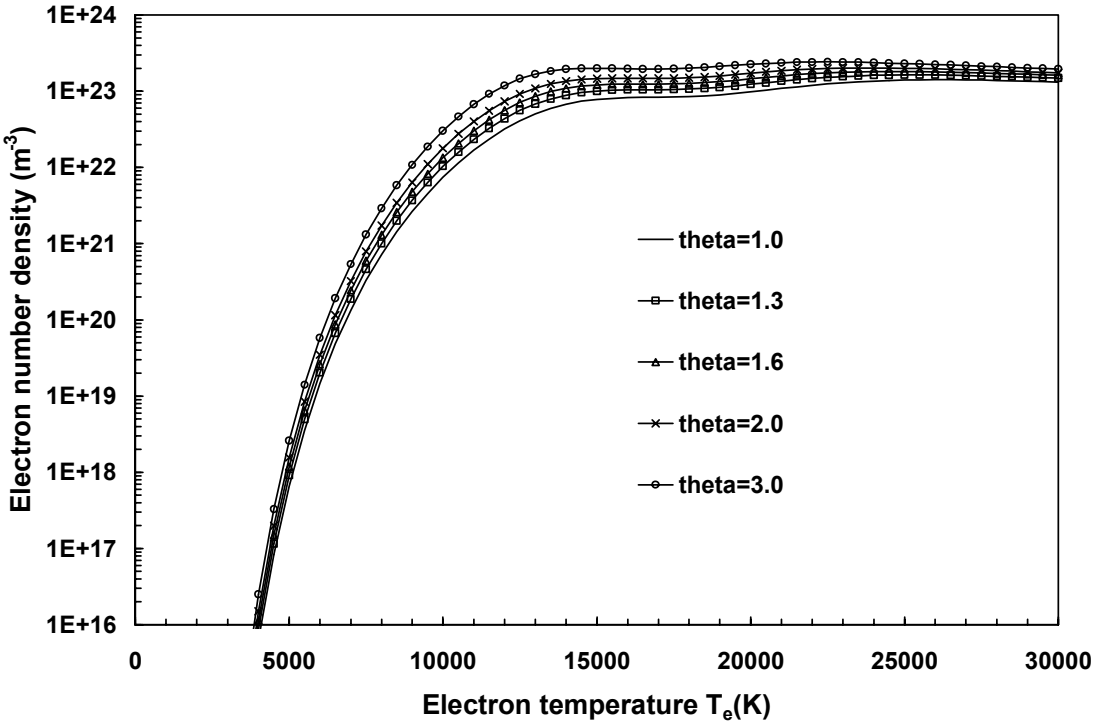

Figure 1: Dependence on electron temperature of the number densities of electrons of an argon-helium mixture (25mol % Ar) for different values θ at atmospheric pressure.

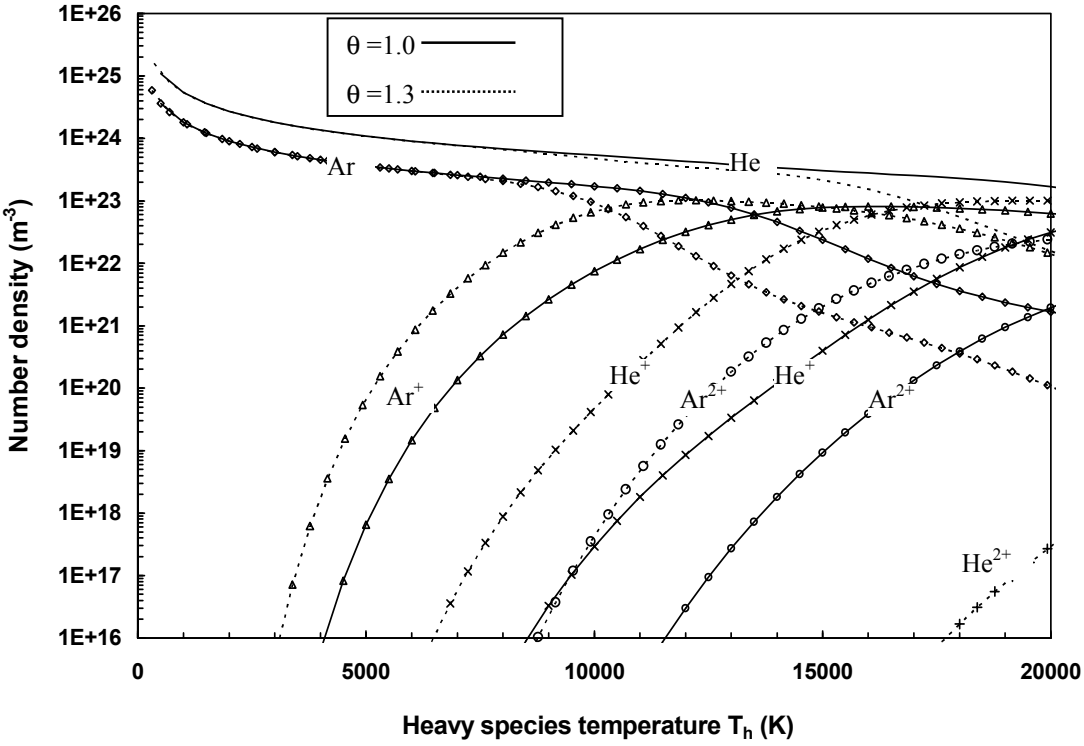

Figure 2: Dependence on heavy species temperature of the number densities of Ar, He, Ar^+, He^+, Ar^{2+} and He^{2+} species of an argon-helium mixture (25mol % Ar) for $\theta = 1.0$ and 1.3 at atmospheric pressure.

In order to illustrate the influence of the non-equilibrium parameter $\theta = T_e / T_h$ on plasma composition, Figure 1 shows the dependence on electron temperature of the number densities of electrons of an argon-helium mixture (25mol % Ar) for different values $\theta = T_e / T_h$.

It can be observed that electron density becomes almost constant over 15,000 K. The electron number density slightly increases with θ at fixed Te. However, in Figure 2, which depicts the dependence on heavy species temperature T_h of Ar, He, Ar^+, He^+, Ar^{2+} and He^{2+} species of an argon-helium mixture (25mol % Ar) for $\theta = 1.0$ and 1.3, the number densities of heavy species are strongly dependent on θ. For example, at 10,000 K, the number density of Ar^+ ions increases by one order of magnitude from equilibrium to $\theta = 1.3$. Similar observations can be carried out for He^+, Ar^{2+} and He^{2+} ions. Thus, it can be observed that the ionisation of heavy species is much more efficient in non-equilibrium conditions, resulting in a shift of ionisation to the lower heavy species temperatures. The non-equilibrium values are always higher than those obtained at equilibrium. Actually, plasma composition is dominated by the modified Saha equations calculated at T_e, which favour the ionisation of species.

Moreover, the number density of argon and helium atoms decreases over a heavy species temperature range smaller in the non-equilibrium case than at equilibrium. This means that the heavy species temperature range, over which the neutral-neutral and neutral-charged interactions dominate, decreases as θ increases, favouring the Coulomb interaction regime instead. Consequently, it is expected that transport coefficients should be deeply affected by the shift of ionisation to the lower heavy species temperatures, especially for the viscosity and combined diffusion coefficients, as it will be highlighted in section 3.

3. Plasma transport properties

Two-temperature transport coefficients are calculated at atmospheric pressure for different values of the non-equilibrium parameter θ.

Figure 3 shows the dependence on electron temperature of the electrical conductivity of an argon-helium mixture (25mol% of argon). It can be observed that, at electron temperature fixed, the electrical conductivity increases with θ. This behaviour is closely linked to that of the number density of electrons, which is also weakly dependent on θ as already shown in Figure 1. For a strong non-equilibrium parameter $\theta = 3.0$, the electrical conductivity indeed increases by only 17 % with respect to equilibrium.

However, the dependence on θ of the viscosity is much more pronounced, as shown in Figure 4, which depicts the viscosity of an argon-helium mixture (25mol% of argon) as a function of the heavy species temperature for different values of the non-equilibrium parameter θ at atmospheric pressure. The viscosity has been plotted as a function of heavy species temperature since it is well known that it is governed by heavy species. The part of non-equilibrium curves which overlap the equilibrium one corresponds to the neutral-neutral interactions regime, i.e. before a real efficient ionisation. The study of the plasma composition shows that ionisation is especially favoured as θ increases. This means that the ionisation temperature of heavy species is smaller than at equilibrium, inducing a shift to the lower heavy species temperatures of ionisation. A shift of viscosity curves to the lower heavy species temperature is therefore observed. It can be noted that the temperature range between both peaks of ionisation is drastically reduced as θ increases.

Figure 5 shows the dependence on electron temperature of the thermal conductivity of an argon-helium mixture (25mol% of argon) for different values of the non-equilibrium parameter θ at atmospheric pressure. It has to be emphasized that the thermal conductivity includes the translational (electrons and heavy species), reactional and internal contributions [xii]. This total thermal conductivity has been arbitrarily defined with respect to the temperature gradient of heavy species [viii]. At low temperature, the translational contribution of heavy species is dominant. Below 10,000 K, it can be seen that, at fixed T_e, the thermal conductivity, depending mainly on the heavy species temperature, decreases as θ increases due to a shift of curves plotting. However, as soon as ionisation occurs, above 10,000 K, a first peak corresponds to the ionisation of argon atoms, and a second one to the ionisation of helium atoms and Ar^+ ions. At high temperatures, the translational contribution of electrons seems to deeply dominate the behaviour of the thermal conductivity, especially as θ increases. However, it has to be focused that the translational contribution of electrons is θ times higher with respect to the heavy species temperature gradient than with respect to the electron temperature gradient.

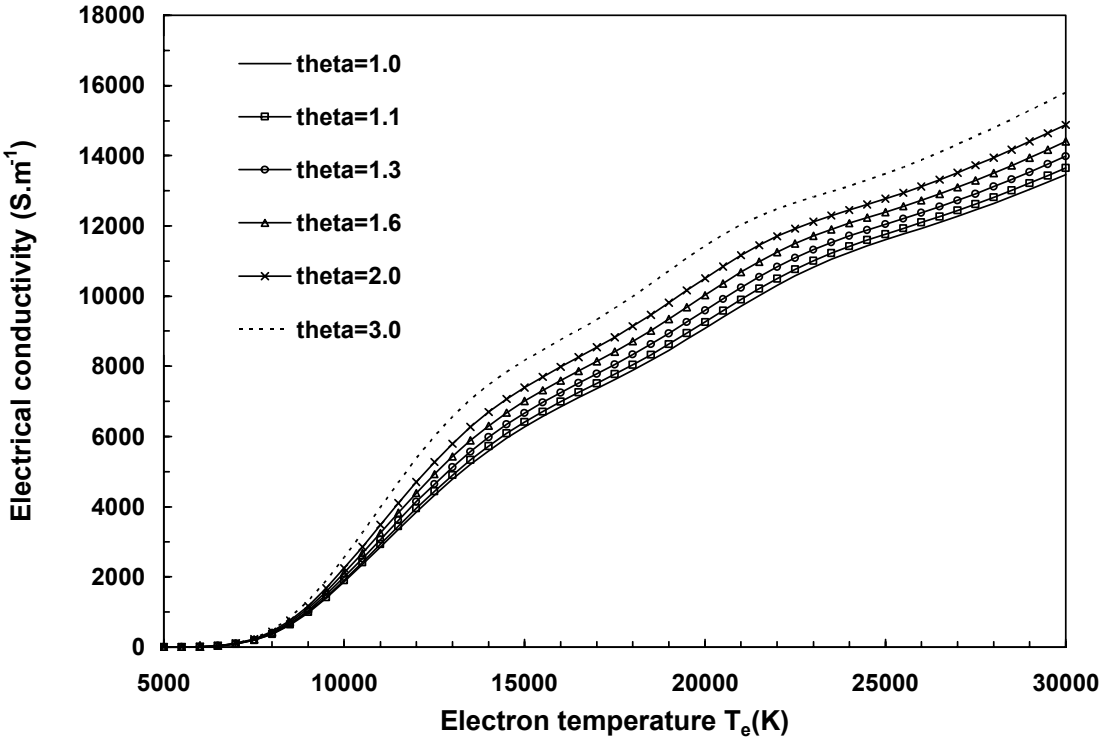

Figure 3: Dependence on electron temperature of the electrical conductivity of an argon-helium mixture (25mol% of argon) for different values of the non-equilibrium parameter θ at atmospheric pressure.

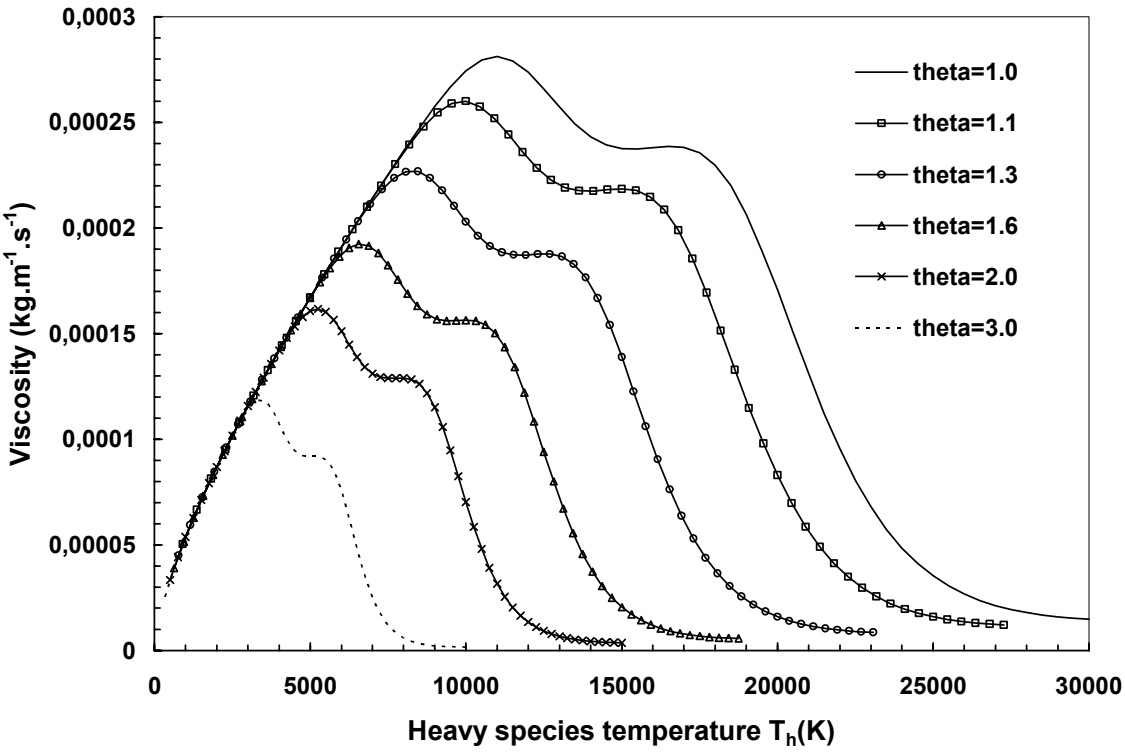

Figure 4: Dependence on heavy species temperature of the viscosity of an argon-helium mixture (25mol% of argon) for different values of the non-equilibrium parameter θ at atmospheric pressure.

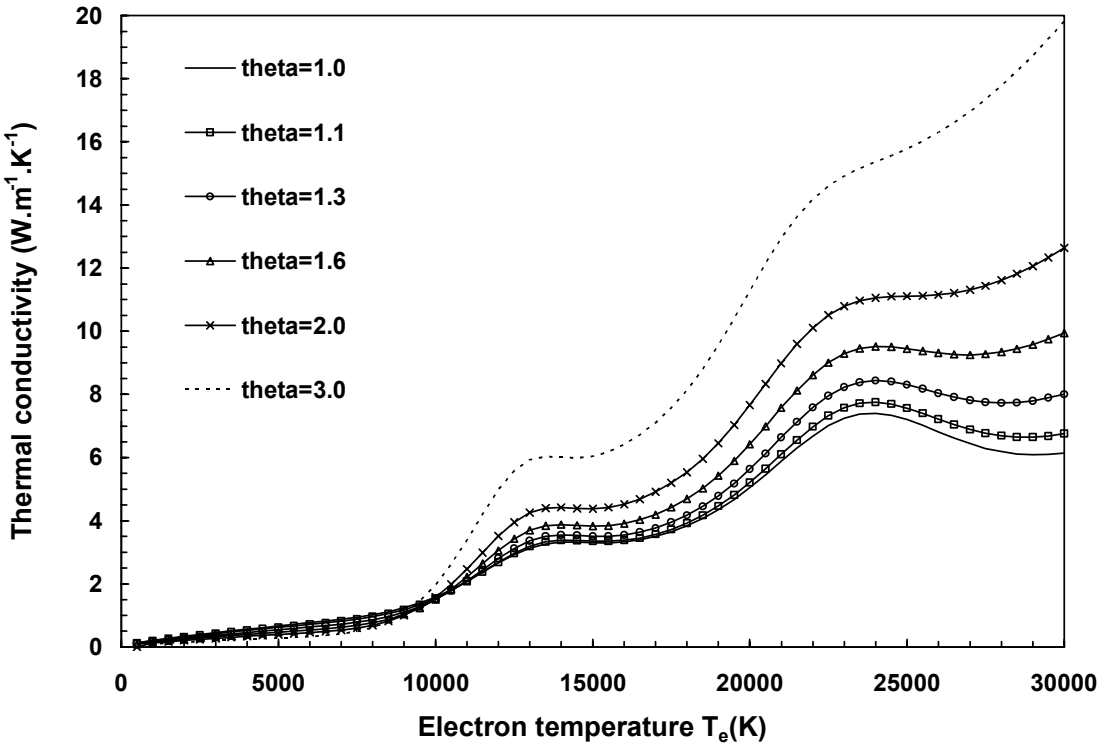

Figure 5: Dependence on electron temperature of the thermal conductivity of an argon-helium mixture (25mol% of argon) for different values of the non-equilibrium parameter θ at atmospheric pressure.

4. Conclusion

This paper is devoted to the calculation of two-temperature transport coefficients in argon-helium thermal plasmas at atmospheric pressure, where the kinetic electron temperature T_e is supposed to be different from that of heavy species T_h. To perform these calculations, first, plasma composition has been obtained using the modified equilibrium constants method of van de Sanden *et al.* [xi].

Two-temperature electrical conductivity, viscosity, and thermal conductivity have been calculated using a modified Chapman-Enskog method applied to a two-temperature thermal plasma [iv,v].

The analysis of the plasma composition has highlighted that the increase of the non-equilibrium parameter $\theta = T_e/T_h$ tends to shift the ionisation of atomic species to lower heavy species temperature. This behaviour is similar to that obtained by reducing the pressure. Numerous equilibrium calculations of transport coefficients (see for example [xii]) have indeed shown that a decrease of pressure moves dissociation and ionisation peaks to lower temperatures according to the Le Chatelier's law.

In a mixture consisted of only atomic species, an ions-dominated regime occurs all the more quickly as θ is high, and strongly influences transport coefficients, particularly through Coulomb collision integrals. The change of collision integrals from neutral-neutral interactions to charged-charged interactions drastically diminishes transport coefficients since the Coulomb integral collisions are two to three orders of magnitude higher than collision integrals of neutral species. The transport coefficients are then affected by displacing the maximum of viscosity and that of combined diffusion coefficients to the lower heavy species temperature. It can be noted that a shift of peaks of ionisation in thermal conductivity is expected if the latter is plotted as a function of heavy species temperature. Moreover, the electrical conductivity was observed to be weakly θ dependent.

[i] P. Chapelle, J.P. Brellot, A. Jardy, and D. Ablitzer, J. Phys. D: Applied Phys. **35**, 137 (2002).
[ii] Y. Bartosiewicz, P. Proulx, and Y. Mercadier, J. Phys. D: Applied Phys. **35**, 2139 (2002).
[iii] S.E. Selezneva and M.I. Boulos, J. Appl. Phys. **91**, 2622 (2002).
[iv] V. Rat, P. André, J. Aubreton, M.F. Elchinger, P. Fauchais, and A. Lefort, Phys. Rev. E **64,** 26409 (2001).
[v] V. Rat, J. Aubreton, M.F. Elchinger, P. Fauchais, and A. B. Murphy, Phys. Rev. E **66**, 56407 (2002).
[vi] K.T.A.L. Burm, W.J. Goedheer, and D.C. Schram, Plasma Chem. Plasma Process. **22**, 413 (2002).
[vii] V. Rat, P. André, J. Aubreton, M.F. Elchinger, P. Fauchais, and A. Lefort, Plasma Chem.Plasma Process. **22**, 453 (2002).
[viii] V. Rat, P. André, J. Aubreton, M.F. Elchinger, P. Fauchais, and A. Lefort, Plasma Chem. Plasma Process. **22,** 475 (2002).
[ix] A.B. Murphy, IEEE Trans. Plasma Sci. **25**, 809 (1997).
[x] J. Jonkers, M. van de Sande, A. Sola, A. Gamero, and J. van der Mullen, Plasma Sources Sci. Technol. **12**, 30 (2003).
[xi] M.C.M. Van de Sanden, P.P.J.M. Schram, A.G. Peeters, J.A.M. van der Mullen, and G.M.W. Kroesen, Rev. A **40**, 5273 (1989).
[xii] M.I Boulos, P. Fauchais, and E. Pfender, *Thermal Plasmas: Fundamentals and Application*, vol 1, Plenum, New York (1994).

Methane reforming with low energy electron beams

T. Kappes[1], T. Hammer[1], A. Ulrich[2]

[1] *Siemens AG, Corporate Technology, D-91052 Erlangen, Germany*
[2] *Technische Universität München, Fakultät für Physik E12, D-85747 Garching, Germany*

Abstract
Low energy electron beams with an acceleration voltage of up to 14 kV were used to initiate methane reforming reactions with CO_2, O_2 and H_2O for hydrogen generation. Electron beams were generated in a compact electron gun system comprising a very thin electron extraction window, which separates the vacuum from the atmospheric pressure gas mixture to be treated. A maximum CH_4 conversion of about 6 % at a total flow rate of 5 ml/min was achieved with specific energy requirement of 2 MJ/mol H_2.

1. Introduction

Hydrogen is supposed to play a more and more important role in the world-wide energy supply. Hydrogen-fueled fuel cells offer the possibility for very efficient generation of electrical energy practically without contaminating emissions. Furthermore, hydrogen-enriched fuels for conventional combustion processes allow the operation under leaner conditions, increasing the efficiency of the process and at the same time reducing noxious emissions. However, due to the difficulties which still arise from hydrogen transport and storage, on-site hydrogen generation from hydrocarbons is preferred for the applications mentioned above.

In addition to conventional catalytic reforming processes for hydrogen generation from hydrocarbons, various plasma-based techniques have been described in literature [1-6], among them both thermal arcs and non-thermal plasma techniques such as dielectric barrier discharges (DBD), corona discharges, and microwave discharges. Plasma methods are characterised by a short response time on load change, and they are uncritical in terms of fuel impurities and soot deposition.

Steam reforming experiments with DBD have shown that the dissociation of methane in the discharge is strongly favoured. With the mean electron energy which can be achieved under DBD conditions the cross section for the electron collision dissociation of water is significantly lower than that for methane (Fig. 1). A great part of the electron energy is spent on vibrational excitation of water which is likely to be dissipated as heat during the relaxation of the excited molecules and does not contribute substantially to the formation of the desired reaction products. This results in a high energy requirement for hydrogen generation [7]. The mean electron energy in a DBD depends for a given gas mixture on the discharge gap and the gas pressure, i. e. to increase the electron energy it is necessary to reduce either the gap or the pressure. Both of these measures are unfavourable for a process scale-up with the need to increase throughput by high pressure and to reduce the flow resistance by increasing the flow cross section. Another disadvantage of DBD is the need for pulsed high voltage which is more challenging to obtain, especially for high power levels.

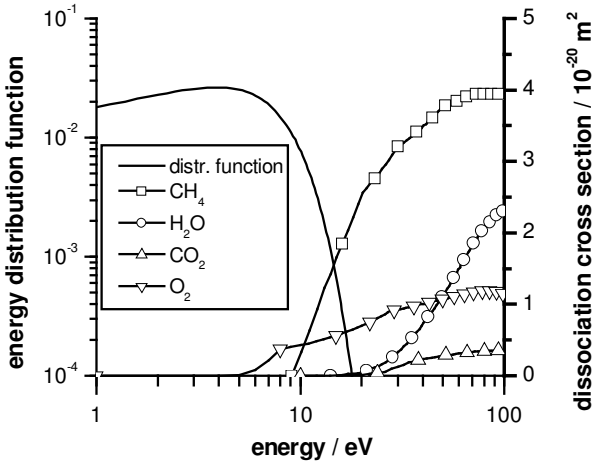

Fig. 1 Electron collision cross sections of CH_4, H_2O, CO_2 and O_2 as function of the electron energy and electron energy distribution function of DBD in a CH_4-H_2O-mixture at 400 °C at the moment of ignition.

Electron beams are an alternative method to gas discharges for the generation of a non thermal plasma. In a vacuum tube, free electrons are released from a suitable source, are accelerated in an electrical field and shot through a thin membrane into the gas phase, where they generate radicals, ions and secondary electrons and induce reactions of the gas components. The generation of accelerated electrons takes place outside the gas phase and is therefore independent of the conditions therein like gas composition, pressure and the reactor geometry. This means that it is easier to transfer the method to a large scale process. This is also true with regard to the power supply. Electron beams work with DC voltage and do not require pulsed power devices which are expensive and available only up to a certain power output level. Large scale electron beam systems with beam powers up to several hundred kW have successfully been tested for the treatment of large volume waste gases in power stations [8,9]. Surface treatment of various materials is another established industrial scale application of e-beams [10].

The transition from the vacuum into the gas mixture at atmospheric pressure requires an extraction window, which is on the one hand able to withstand the pressure difference and on the other hand sufficiently permeable for electrons in this low energy range to reduce the energy loss. For high energy electron beams (E > 100 keV) these requirements are fulfilled by thin metal foils, e. g. made of titanium. Low energy electron beams, however, require very thin window membranes to limit the energy loss in the material. Such thin membranes, which are at the same time mechanically and thermally stable, can be made of ceramic material like SiN using photolithographic techniques. These thin membranes have previously been used for e-beam ultraviolet light sources [11] and their application as ionisation method for mass spectrometry [12]. E-beam with an electron energy of 10-20 kV have a penetration depth in the order of 1 cm in gases composed of light elements at atmospheric pressure, and they generate a plasma zone with an approximately spherical shape. By that means a relatively high power density (~ 1W/cm^3) can be achieved.

In a first step we carried out experiments on e-beam activated methane reforming using a compact electron gun system generating a low energy electron beam with an acceleration voltage in the range of 10-14 kV and beam currents up to 30 µA.

2. Experimental

The electron beam was generated in the vacuum by a cathode ray tube which is built of a heated BaO cathode, various control and focussing electrodes and an electromagnetic system for beam alignment (Fig. 2). The transition of the electron beam from the vacuum into the gas mixture at atmospheric pressure required an extraction window, which is on the one hand able to withstand the pressure difference and which is on the other hand sufficiently permeable for electrons in this low energy range without a significant energy loss. A silicon plate containing a SiN membrane with a size of 1×1 mm and a thickness of about 300 nm was used in our electron gun system set-up to close the vacuum tube at the opposite wall. Due to the limited e-beam energy this system did not require any special X-ray shielding precaution.

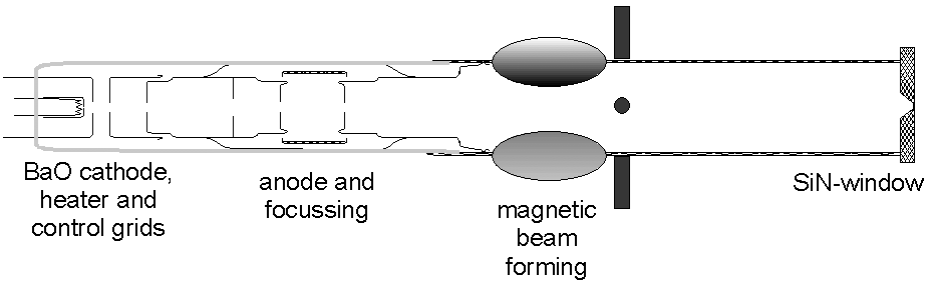

Fig. 2 Electron beam source

The gas to be treated passed the electron extraction window in a continuous flow. Two different gas flow cell designs were used, which are shown in Fig. 3. In the cell type A, the gas flow passed the electron beam in transverse direction. The reactor cell was divided into an inlet room and an outlet room separated by a wall with a small gap in front of the extraction window, which forced the all the gas to the volume reached by the electron beam. In the gas cell type B the gas flow entered the chamber radially nearby the extraction window and left axially opposite to the membrane. The cylindrical reaction chamber was formed by an exchangeable insert for easy change of the chamber diameter and length. Three different inserts were used with a diameter

d and a length l of 6, 8 and 10 mm. These inserts were electrically insulated from the reactor body for direct measurement of the effective beam current.
Methane reforming reactions were studied with three different oxidant components, particularly CO_2 (dry reforming), O_2 (partial oxidation) and H_2O (steam reforming). The gases were premixed with stoichiometric mole ratios regarding synthesis gas as reaction product including the water shift reaction in the case of steam reforming, in detail: CH_4:CO_2 1:1, CH_4:O_2 2:1 and CH_4:H_2O 1:2. Dry reforming and partial oxidation were carried out at ambient temperature with a total gas flow of 5 ml/min in the gas flow cell type A. The cell of type B was used for steam reforming with 15 ml/min at 110 °C and was therefore equipped with a heating coil. The reaction products were analysed with a gas chromatograph (Shimadzu GC14b) equipped with a thermal conductivity detector and a flame ionisation detector.

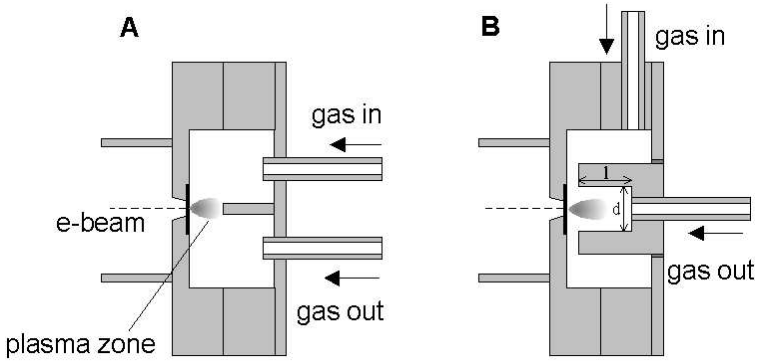

Fig. 3 Gas flow cells, type A: transverse flow, type B: radial/axial flow

3. Results and Discussion

Due to the low energy of the e-beam, the primary electrons penetrating the gas phase are retarded by ionising collision processes within a very low distance, typically a few millimetres in the voltage range of 10-15 kV at atmospheric pressure, and as a consequence, a very high power density in the reaction volume can be achieved, which results in a high density of reactive particles. The power density increases with decreasing acceleration voltage and with increasing pressure. The power output of the electron beam system is limited by the current density the extraction window can withstand without a destructive heat dissipation inside the membrane. With our system a maximum beam current of 33 µA could be achieved with an acceleration voltage of 14 kV. Thus the maximum e-beam power was 462 mW. On the other hand, the gas flow rate could not be reduced to any desired value in order to guarantee a precise gas manipulation and analysis. Therefore The conversions of methane and the oxidants achieved with this energy input are shown in Fig. 4, as a function of the e-beam power and the gas mixture. With dry reforming at 273 mW power (U = 13 kV, I = 21 mA), 5 % methane conversion was observed. However, the CO_2 conversion was lower by a factor 10. This can be explained by the significantly higher electron collision cross section of methane as shown in Fig. 1. By increasing the beam power to 462 mW the methane conversion rises to 6.6 % while the CO_2 conversion is nearly doubled. With partial oxidation the conversion ratio between methane and the oxidant is reverse. The oxygen conversion is about 8 %, almost twice as high as the methane conversion. According to Fig. 1 the oxygen cross section is significantly higher for low electron energy levels, i. e. between 5 and 10 eV. Thus one can suppose that the mean electron energy in the plasma zone is approximately in this energy range. Compared to dry reforming, the molar methane conversion is nearly the same, keeping in mind the higher methane concentration in the starting gas mixture. Steam reforming shows a similar behaviour to dry reforming, with the H_2O/CH_4 conversion ratio slightly higher than the CO_2/CH_4 conversion ratio, reflecting the proportions of the corresponding cross sections. The conversion rates increase linearly with the e-beam power, the maximum values at 420 mW are 1.6 % for methane and 0.4 % for water conversion.
the energy density in the gas was limited to 5.5 kJ/l.

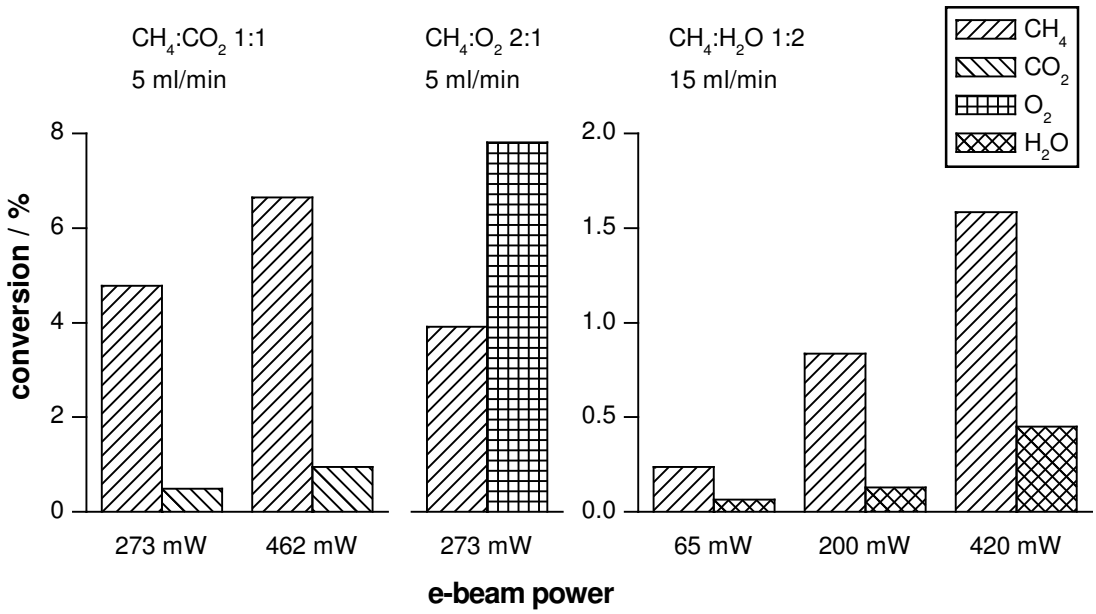

Fig. 4 Conversions of the starting compounds

The inhomogeneous activation of the different compounds by the electron beam has obviously also a strong influence on the secondary reactions and therefore on the composition of the reaction products. Fig. 5 shows the product yields depending on the e-beam power and the gas mixture. For dry reforming and steam reforming the main reaction products are hydrogen and saturated hydrocarbons, mainly ethane and propane. This is the consequence of the preferred methane dissociation which generates CH_3 and H radicals. The subsequent recombination reactions result in the formation of H_2 and C_2H_6, according to the following equations:

$$CH_4 + e^- \rightarrow H + CH_3 + e^- \quad (1)$$

$$CH_4 + H \rightarrow H_2 + CH_3 \quad (2)$$

$$CH_3 + CH_3 \rightarrow C_2H_6 \quad (3)$$

Compared to this the formation of oxygenated compounds like CO – and CO_2 in the case of steam reforming – plays a minor role due to the lower activation of CO_2 and H_2O. The e-beam power seems not to have a visible influence on the reaction pathways.

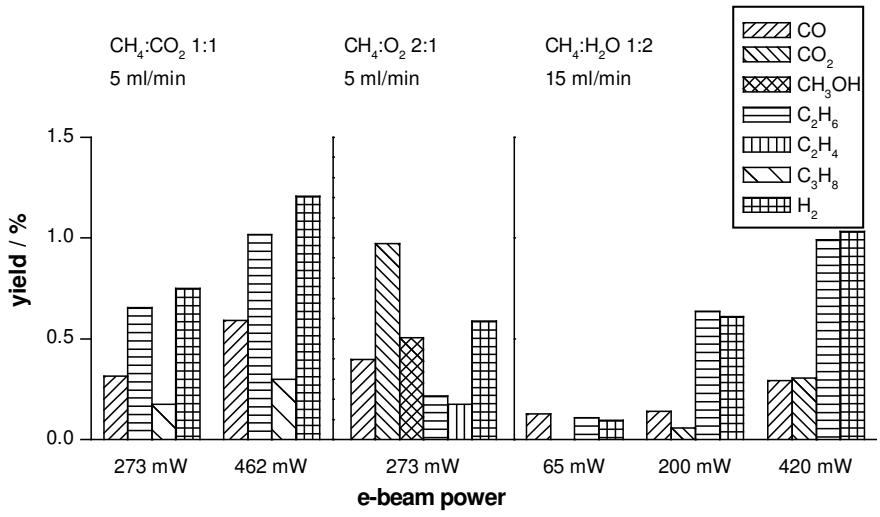

Fig. 5 Yields of reaction products

However, the product spectrum of partial oxidation is significantly different. The formation of oxygenated compounds is clearly favoured with CO_2 as the most important reaction product, due to the high dissociation rate of O_2. Also the hydrogen yield is lower than with dry reforming and steam reforming at the same power level. Although it was not possible to determine the amount of water in the product gas with the available equipment, one can expect that complete oxidation of methane plays an important role. An interesting aspect is the relatively high methanol yield, and also the formation of the unsaturated hydrocarbon ethylene.

In order to estimate the extension of the gas zone which is treated by the electron irradiation, another series of steam reforming experiments were carried out with the flow cell type B using various reaction chamber inserts. Both methane and water conversion increase by a factor 2 with the chamber diameter increasing from 6 mm to 10 mm keeping the specific energy unchanged. Apparently, with chamber diameters lower than 10 mm, a substantial fraction of the electron beam energy is dissipated directly to the chamber walls without inducing gas reactions. Thus, the diameter of the reactive plasma zone is estimated to be at least in the range of 10 mm, possibly even higher.

The specific energy requirement for hydrogen generation was in the order of 10 MJ/mol H_2 for dry reforming and partial oxidation, however, for steam reforming this value was only 2 MJ/mol H_2, and therefore by a factor 4 lower than the energy requirement of DBD steam reforming at low temperatures.

4. Conclusions

Hydrogen generation by methane reforming using low energy electron beams has been studied based on three different reforming reactions: dry reforming, partial oxidation and steam reforming. Electron beams were generated with a compact electron gun system including a ultra thin SiN membrane which allows the irradiation of the e-beam into the gas phase at atmospheric pressure with low energy loss.

The reaction products and therefore the preferential reaction path turned out to be quite different for partial oxidation on the one hand and for dry reforming and steam reforming on the other hand, due to the different electron collision cross sections of the corresponding oxidant molecule. While for partial oxidation the oxygen conversion is higher than the methane conversion and oxygenated reaction products prevail, in the case of steam reforming and dry reforming, the preferential reaction is the dissociation of methane and the formation of hydrogen and hydrocarbons. The energy requirement of the steam reforming reaction could be reduced by a factor 4 compared with previous DBD steam reforming experiment at low temperature.

Hydrogen yields were still relatively low – in the order of 1 % – due to the limited power output of the electron beam source and the small extraction window. The next experimental step should be to increase the cross section of the extraction window to be able to increase the power output while maintaining a low electron energy and hence high power density. Anyhow, there is the potential for scaling up to large reactor volumes, pressures and mass flows, as already demonstrated in power station flue gas cleaning applications.

References

[1] L. Bromberg - Energy & Fuel, **12,** 11-18 (1998)
[2] A.I. Babaritskii - High Energy Chemistry, **33**, 404-408 (1999)
[3] R.G. Mallinson - AIChE Journal, **44**, 2252-2257 (1998)
[4] U. Kogelschatz - Plasma Chemistry and Plasma Processing, **18**, 375-393 (1998)
[5] W. Schiene, T. Kappes and T. Hammer - Proc. 15th International Symposium on Plasma Chemistry, Orléans, pp. 701-706 (2001)
[6] W. Schiene - Nichtthermische Plasmaverfahren zur Erzeugung von Wasserstoff aus Kohlenwasserstoffen, Ph.D. Thesis, University of Bochum (2002)
[7] T. Kappes, W. Schiene, T. Hammer. - Proc. 8th International Symposium on High Temperture, Low Pressure Plasma Chemstry (HAKONE VIII), Pühajärve, Estonia, pp. 196-200 (2002).
[8] G. Häßler, H. May, W. Schikarski, H. Voos, S. Wittig - VGB Kraftwerkstechnik, **68**, 425 (1988)
[9] V.L. Auslender - Proc. NATO Advanced Workshop on the Modern Problems of Electrostatics with Applications in Environment Protection., Bucharest, pp.199-217 (1999)
[10] J. Hiley, P.M. Fletcher - Power Engineering Journal, **6**, 111 (1992)
[11] J. Wieser, D.E. Murnick, A. Ulrich, H.A. Huggins, A. Liddle, W.L. Brown - Rev. Sci. Instrum., **68**, 1360-1364 (1997)
[12] F. Mühlberger, J. Wieser, A. Ulrich, R. Zimmermann - Anal. Chem. **74**, 3790-3801 (2002)

Filamentary and homogeneous dielectric barrier discharges in He/N_2 mixtures at atmospheric pressure

N.K. Bibinov and K. Wiesemann

Ruhr-Universität Bochum, Experimentalphysik insbes. Reactive Plasmen, 44780 Bochum, Germany

Abstract

In He/N_2 dielectric barrier discharges at atmospheric pressure we studied the conditions for the appearance of filamentary and homogeneous (APGD) discharges. By analysing the emitted light measured time and space resolved we found that the afterglow phase is dominant for both types of discharges. We discuss our findings by means of a kinetic model of the processes occurring at the different conditions in a DBD.

1. Introduction

Dielectric barrier discharges (DBD) are high-pressure non-equilibrium discharges controlled by one or two dielectric barriers in the discharge gap. In the present work we discuss processes in He/N_2 DBD plasma. For this mixture the reaction model, the spectroscopic parameters of the excited particles and the rate constants for excitation and de-excitation processes are well known. Therefore, one can use efficiently spectroscopic methods for studying plasma processes in this discharge [1,2]. Two types of DBD modes in He/N_2 mixtures are known, namely filamentary and homogeneous (APGD) discharges [3]. Filamentary discharges are a consecution of short microdischarges ($\tau \approx 1$ μs in He/N_2) randomly distributed in space and time. The microdischarge radius is below 30 μm [1]. The APGD mode looks homogeneous along the electrodes. The discharge occupies sometimes totally sometimes only partly the gas gap. The spatial structure of the light emission from these discharges looks like the structure of glow discharges at low pressures [3]. The transition from the filamentary to the homogeneous mode occurs either at constant gas pressure when increasing the frequency of the applied voltage or at constant frequency of the power supply when decreasing the nitrogen partial pressure.

In the present work we study DBDs in both modes by means of spectroscopic measurements with time and space resolution.

2. Experiment

The discharge cell consists of two parallel plane electrodes (5.5×5.5 cm^2) with one single 0.2 cm thick dielectric glass plate on one of the electrodes. The He and nitrogen flows are controlled by mass flow controllers. The width of the gas gap is varied in the range 0.03-0.5 cm. The width of the gas gap is varied in the range 0.03-0.5 cm.

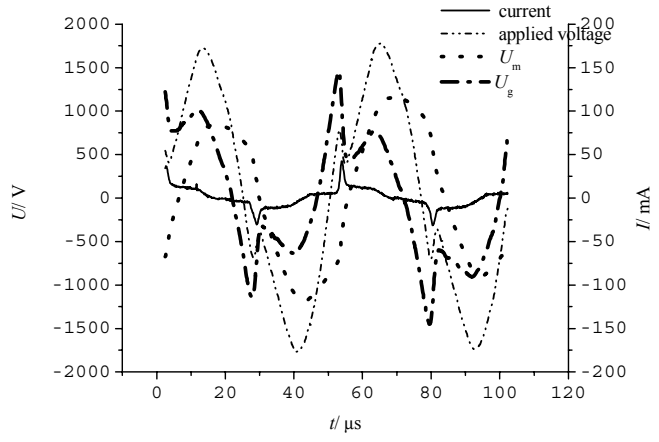

Fig.1 Measured applied voltage and current in the homogeneous mode of a He/N_2 DBD and calculated gas gap voltage .

An ac-generator with the frequency 19.7 kHz served as power supply. The applied voltage U_A and the current of the power supply I_d are measured by means of a digital oscilloscope TEKTRONIX 2440 either directly or via a 50 Ω resistor connected in series to ground. The voltage on the gas gap U_g is determined as

$$U_g(t) = U_A(t) - U_m(t) \quad (1)$$

$$U_m(t) = \frac{1}{C_d}\int_{t_0}^{t} I_d(t)dt + U_m(t_0). \quad (2)$$

One can see in fig. 1 that at our experimental conditions the gas gap voltage U_g at the time of discharge ignition is about two times higher than the applied voltage.
This difference U_m is caused by charges on the surface of the dielectric created during discharges in the previous half-cycle of the applied voltage.
For measuring emission spectra we used a SpectraPro-500i® spectrometer with up to 0.04 nm spectral resolution. From the rotational structure of the N_2^+(B-X) and OH(A-X) bands we determined the gas temperature. The resolution of the spectrometer allows determining the gas temperature with an accuracy of about ±5 K and ±10 K for N_2^+(B-X) and OH(A-X) respectively. By means of interference filters with a spectral resolution of $\Delta\lambda \approx 10$ nm we studied the emissions of N_2^+(B-X), N_2(C-B) and helium atoms space and time resolved. Time and spectrally resolved photographs of the discharge we obtained with an intensified CCD triggered by the discharge voltage – see fig. 2.

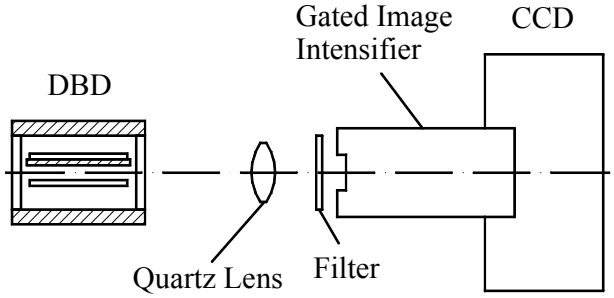

Fig.2 Experimental set-up for measuring space and time resolved distributions of the plasma emission for optical transitions of interest

3. Results

According to [1,2] the rotational temperature in the emission spectra of N_2^+(B-X) is 100-250 K higher than the rotational temperature in the N_2(C-B) and OH(A-X) bands. It was supposed in [1,2], that the emission of the nitrogen ions occurs in heated microdischarge channels, while the N_2(C-B) and OH(A-X) emissions are excited in the cool ambient gas by reactions of metastable nitrogen molecules:

$$N_2(A) + N_2(A) \rightarrow N_2(C) + N_2(X) \quad (3)$$

$$N_2(A) + OH(X) \rightarrow OH(A) + N_2(X) \quad (4)$$

For proving these assumptions we have measured the N_2^+(B-X) and N_2(C-B) emissions with spatial and time resolutions in the filamentary mode - see figs. 3 and 5. At relatively low nitrogen partial pressure the micro-

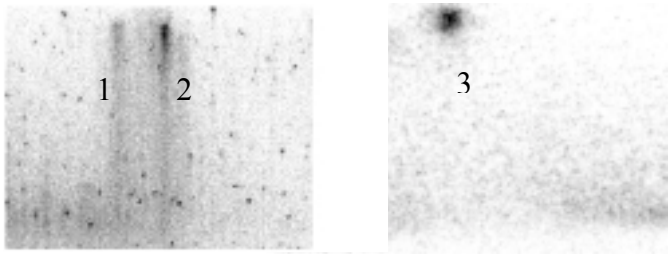

Fig.3 Photographs of He/N_2 DBDs in the light of the N_2^+(B-X) emission. The cathode is on top, the dielectric on bottom. Gas gap width 5 mm; p_{He}= 101 kPa, p_{N2}= 1.17 kPa.

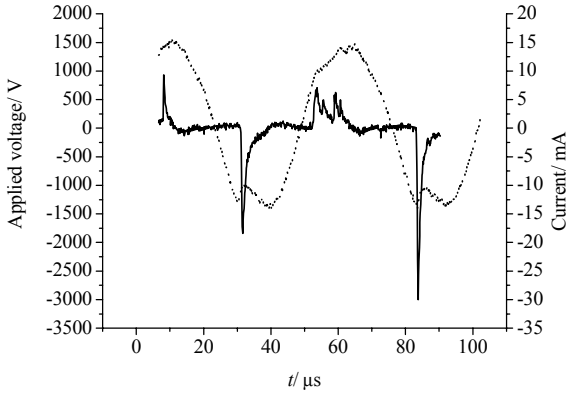

Fig. 4. Applied voltage (dotted) and discharge current (full line) in the filamentary mode (p_{He}= 101 kPa, p_{N2}= 1.17 kPa)

discharges are randomly distributed in space and time and one can detect in the photographs all discharge phases occurring simultaneously – see fig. 3.
For determining the order of the discharge phases we used photographs at 101 kPa He and 3.9 kPa nitrogen. At these gas conditions and for a low amplitude of the applied voltage only one microdischage is ignited per half-cycle of the applied voltage. It appears always at the same place. Thus we could determine the discharge phase order by varying the photographs' delay. Because of the high quenching rate at these conditions the intensity of the N_2^+(B-X) emission is very small while the intensity of the N_2(C-X) is so much higher that our filter was not sufficient selective for separating these emissions. Nevertheless we could work out the succession of the different discharge phases. We found three phases of the microdischarges in the filamentary mode - see the numbers in fig. 3. The first phase consists of an uniformly emitting narrow channel across the gas

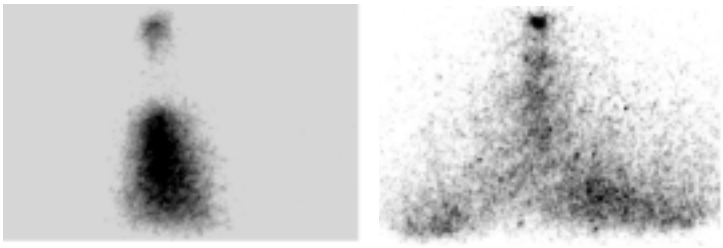

Fig.5. Photograph of a He/N_2 DBD in the light of the N_2(C-B) emission. The cathode is on top, the dielectric on bottom. Gas gap width 5 mm, pressure like in Figs. 3 and 4. The right photograph corresponds to a later phase.

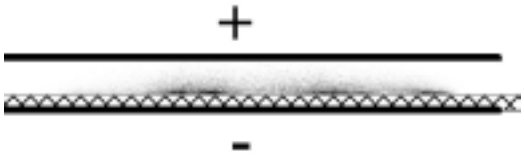

Fig.6. Photograph of a He/N_2 DBD in the light of the N_2^+(B-X) emission. Gas gap width 5 mm, pressures like in Figs. 3 and 4

gap. In the third phase the nitrogen molecular ions emit only from a point like area near the cathode. The second phase is an intermediate case - one can see there the transition between the two others.

The emission of N_2(C-B) originates from a broad area around the narrow channel defined by the emission of the nitrogen ions - see fig. 5. This area represents a cone with a base spreading out with time - similar to pictures published by Gherardi et al. [4] In the later phase the emission intensity exhibits a minimum near the anode in the middle of the discharge area. At this very position the intensity is maximum in the early phase.

The emission of nitrogen ions has a different temporal behaviour when the dielectric is on the cathode. One can see in fig. 4 that the discharge current has only one peak with a high maximum value. In time and space resolved photographs we find only an emission from a narrow area near the dielectric. This is shown in fig. 6.

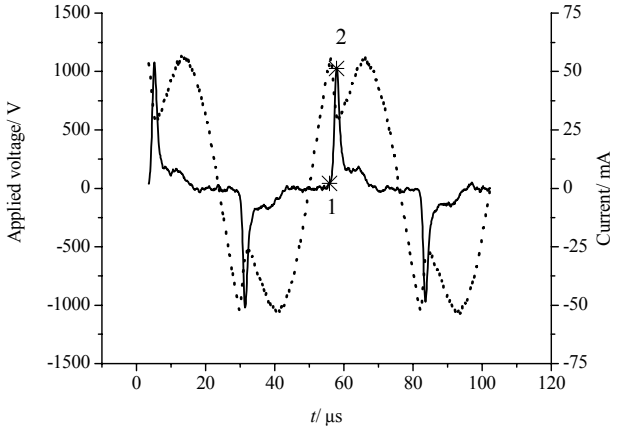

Fig.7. Applied voltage and discharge current in the homogeneous mode of a DBD (p_{He}= 101 kPa)

In the first phase of a homogeneous discharge (corresponding to the point number 1 in fig.7) the very weak emission of nitrogen ions and helium atoms extends along the total gas gap length - see fig.8. A photograph taken at the maximum of the current shows an intense emission near the cathode and no emission in the other areas - see fig. 9.

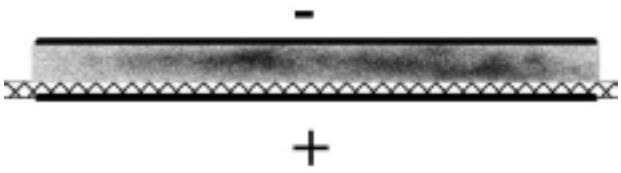

Fig.8. Photograph of a He/N_2 DBD in the light of the N_2^+(B-X) emission at the beginning of the discharge current pulse. Gas gap width 5 mm; p_{He}= 101 kPa. The grey background is caused by the high gain necessary to detect the low emission intensity.

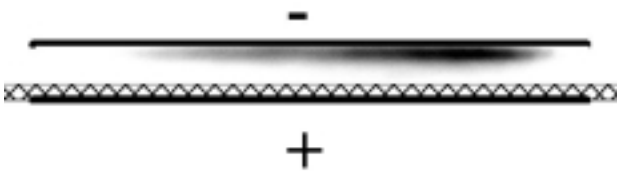

Fig.9. Photograph of a He/N_2 DBD in the light of the N_2^+(B-X) emission at the maximum of the discharge current. Gas gap width 5 mm; p_{He}= 101 kPa.

4. Discussion

The charge on the surface of the dielectric plays a key role for the filamentary mode as well as for the homogeneous mode. In the filamentary mode the charge density on the surface is irregular because of the random space distribution of the microdischarges. Because of this charge the gas gap voltage may locally increase

and microdischarges may ignite there at a value of the applied voltage below the ignition voltage. At very low amplitudes of the applied voltage this effect enables just one single microdischarge to ignite in every half-cycle again and again at the same place of the discharge gap.

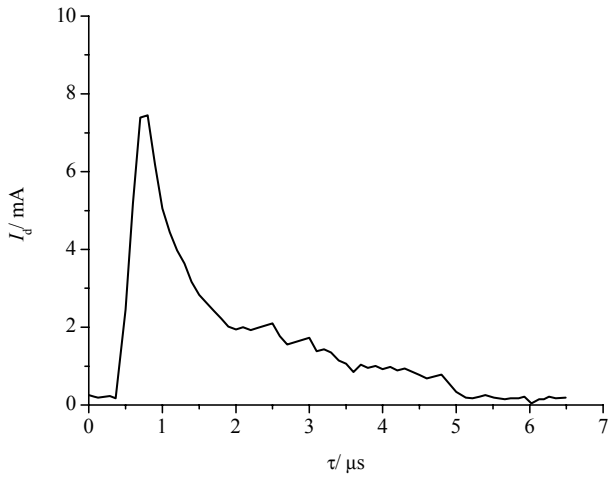

Fig.10. Measured discharge current in the filamentary DBD mode (p_{He}= 101 kPa, p_{N2}= 1.17 kPa).

From the characteristic time for a single transit of a primary electron from cathode to anode at a constant drift velocity the duration of a microdischarge in the filamentary mode can be estimated. For a free electron in a 101 kPa gas mixture predominantly consisting of He the drift velocity is about $2.1*10^6$ cm/s under the influence of a field strength of E≈3000 V/cm, the typical breakdown field at our experimental conditions. Thus the free electron transit time amounts to about $2.4*10^{-7}$ s for a 5-mm gap. This value agrees well with the time of the discharge current increase of about $3*10^{-7}$ s - see fig. 10.

For the conditions at discharge ignition we have calculated the excitation rates of He metastable and the ionisation rate. At our experimental conditions the rate of metastable excitation at the discharge ignition is about 60 times higher than the ionisation rate. At a nitrogen partial pressure of p_{N2}=1.17 kPa the characteristic time for Penning ionisation amounts to about $3*10^{-8}$ s. That is ten time shorter than the free electron transit time. When the primary electron avalanche reaches the anode, the electron density in the channel is maximum. Thus the gap field drops. The start of new avalanches in this area of the gap is inhibited because of a decrease of the surface charge density on the dielectric after surface discharges (Lichtenberg figures). But free electrons in the microdischarge channel drift to the anode and a region of high electric field, a cathode layer or "cathode fall" forms. When the electric field in this area reaches the ignition limit new avalanches start. Outside the high field region the electron drift more slowly to the anode. This finding is in agreement with model calculations of Braun et al. [5] for N_2 where the same succession was found, however, on a different time scale because the electron drift velocities are higher in the case considered there.

One can see in fig.10 that the discharge current decreases with a characteristic time of about 1 µs, which corresponds to a drift velocity of about $5*10^5$ cm/s. Such a drift velocity can be obtained from a field of about E≈300 V/cm. This field strength corresponds to a non-self-sustained discharge that is to afterglow conditions. These conditions correspond to the third phase of the filamentary mode shown in fig.3. Under these circumstances only lower excited states of nitrogen like N_2(A) can be populated and the emission due to the de-excitation of these states is observed – see fig. 5. During this discharge phase the dielectric surface is charged up. Due to the increase of the surface charge density the gap electric field changes and the surface charge saturates. Thus the discharge has to move to neighbouring areas otherwise the electric current stops. This produces the conical shape seen in fig.5.

When the polarity of the applied voltage reverses we observe only one intense current pulse during that half-cycle of the power supply. Probably, free surface electrons can be extracted from the dielectric. As a result of this "preionization" the formation of filaments in the gap is inhibited [6]. Primary avalanches produced by the extracted electrons reach the metal anode. Then a cathode layer forms and a discharge ignites near the cathode as seen in fig. 6.

To ignite a homogeneous DBD we stopped the nitrogen flow. However, adsorbed nitrogen atoms exist on the surface of the electrode and the dielectric. Because of the narrow and long shape of the gas gap nitrogen atoms move off very slowly even at the high He gas flow of 10^3 sccm. On the surfaces of the gas gap free nitrogen atoms recombine with adsorbed ones to form nitrogen molecules during the discharge. By a high Penning ionisation rate high nitrogen molecule concentrations cause an increase of the electron concentration and the ignition of filaments as mentioned above. Therefore, it is important to determine the nitrogen molecule concentration when studying the homogeneous DBD mode. For this purpose, we measured the temporal behaviour of the integral intensity of the emissions of nitrogen molecular ions and helium atoms. At our experimental conditions N_2^+(B) nitrogen ions are produced mainly by Penning ionisation.

The intensity distributions in the measured emission spectra of helium atoms testify that excited states of rare gas atoms are populated in the following recombination processes

$$He^+ + 2He \rightarrow He_2^+ + He, \quad (5)$$

$$He_2^+ + e \rightarrow He^* + He. \quad (6)$$

In the framework of this model (see Tab.1) we have calculated the temporal behaviour of the N_2^+(B-X) and He atom emissions and fitted these dependences to the measured ones - see fig.11. As fit parameters we used the duration of the active discharge (where metastables and ions are produced) and the partial pressure of nitrogen. From this fit we obtained partial pressures of nitrogen in the range 10-40 Pa and found that the measured discharge current reaches its maximum 0.5-1 μs later than the current of the active discharge. We conclude from these findings that the characteristic time of Penning ionisation is of the order of 1 μs – much longer than the transit time of free electrons. Thus the electron density in the channel of the primary avalanches increases only slightly and the low avalanche current cannot alter strongly the surface charge density on the dielectric. The small change of surface charging is compensated by the applied voltage increase and new avalanches start. Therefore, the discharge extends through the entire gap at the beginning of the current pulse and the emission intensity remains very low - see fig. 8. If the internal resistance of the power supply is high or the applied voltage rises too slowly to compensate for the changes of surface charging, starting of new avalanches is interrupted. In this case the discharge occupies only part of the volume between the electrodes. This latter case is shown in fig. 8.

Tab.1. Main processes and rate constants for excitation and de-excitation of molecular nitrogen ions and excited helium atoms

Process	Rate Constant
$He^+ + 2He \rightarrow He_2^+ + He$	$1.5*10^{-31}$ cm^6s^{-1}
$He_2^+ + e \rightarrow He^* + He$	$9*10^{-9}$ cm^3s^{-1}
$He^+ + N_2 \rightarrow$ quenching	$1.2*10^{-9}$ cm^3s^{-1}
$He_2^+ + N_2 \rightarrow N_2^+(B)$	$8.3*10^{-10}$ cm^3s^{-1}
$He_2^+ + N_2 \rightarrow$ quenching	$2.7*10^{-10}$ cm^3s^{-1}
$He^*(met) + N_2 \rightarrow N_2^+(B)$	$2.8*10^{-11}$ cm^3s^{-1}
$He^*(met) + N_2 \rightarrow$ quenching	$7.1*10^{-11}$ cm^3s^{-1}

When owing to Penning ionisation about 1 μs after ignition the electron density increases in the gap the electric field drops, free electrons drift to the anode, a cathode layer forms and new avalanches start near the cathode - see fig. 9. At our conditions the partial pressure of the nitrogen molecules is relatively low and thus the probability of the pooling reaction (3) is very low too. Therefore, we could not detect any emission from the area outside the cathode layer.

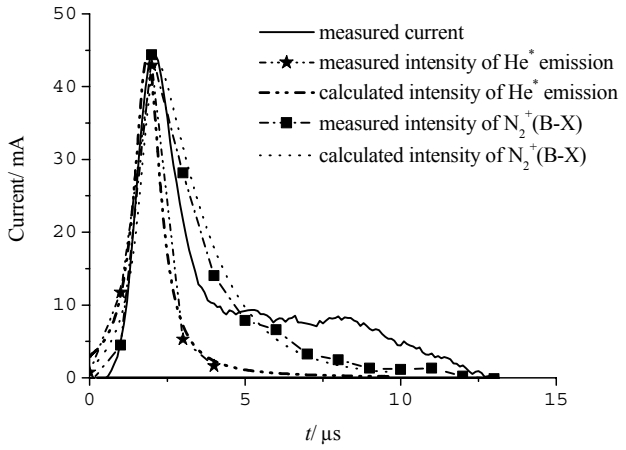

Fig.11. Measured and calculated emissions of nitrogen ions and helium atoms and discharge current of a homogeneous DBD; p_{He}=101 kPa, p_{N2}= 40 Pa (from fit).

In the channels of the microdischarges the gas is heated mainly when positive ions move rapidly. As the electric field strength is low in the area outside of cathode layer (in the "positive column") the gas temperature in this area is lower than in the cathode layer. We have measured the rotational structures in the N_2^+(B-X) and OH(A-X) emissions of nitrogen ions and OH-radicals. In the homogeneous DBD mode these structures correspond to the gas temperature in the microdischarge channel and in the ambient gas respectively - see fig. 12. Here the OH(A-X) emission is excited by absorption of the VUV helium emission by water molecules. Near the electrodes we measured about 400 K gas temperature. At the same time the temperature in the middle of the gas gap is notably lower- about 340 K and compares with the temperature of the ambient gas, which we determined to about 310 K by means of the OH(A-X) emission.

The drift velocity of the positive ions in the area of the cathode layer depends on the electric field strength, which in turn depends on the gas gap length in the following way [7]. The length of the cathode layer area and the electric field strength depend weakly on the distance between the electrodes if this distance is much longer than the thickness of the cathode layer area. But the field strength increases rapidly if the distance between the electrodes becomes comparable with this thickness. According to calculations of the spatial

evolution of the electric field in the homogeneous DBD mode in 101 kPa of helium [3] the cathode layer thickness amounts to about 0.03 cm.

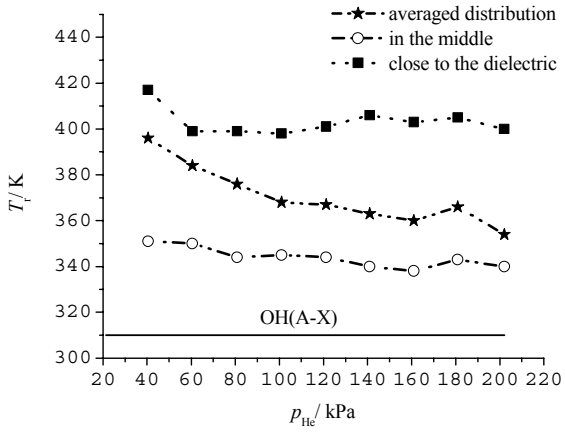

Fig.12 Rotational temperatures obtained from the nitrogen ion (curves with markers) and the OH–radical emissions in a homogeneous mode DBD. Gas gap width is 0.5 cm.

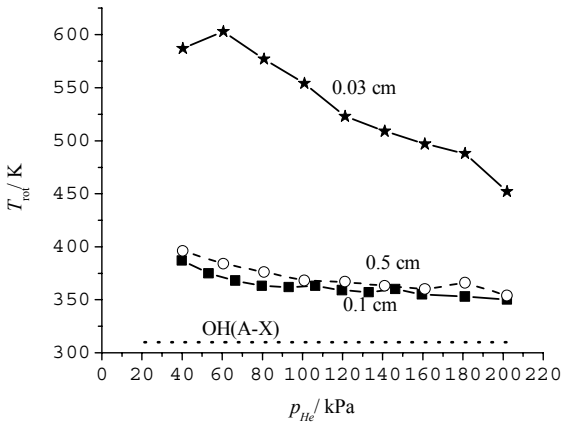

Fig. 13 Rotational temperatures obtained from the nitrogen ion (curves with markers) and the OH–radical emissions in a homogeneous mode DBD. Parameter is the gap width.

We have measured the gas temperatures at different gas gap widths. At large electrode separations the measured discharge gas temperature is practically independent of the gap width - see fig. 13 - but increases dramatically at small widths. At the same time the OH-radical rotational temperature and thus the temperature of the ambient gas is constant - about 310 K. Assuming the electrical energy of one current pulse to be totally dissipated we calculated the gas volume, which can be heated by this energy to the temperature corresponding to the nitrogen ion rotational temperature. This volume turned out to be more than two orders of magnitude smaller than the volume occupied by the cathode layer. Thus the difference between the values of the gas temperatures measured by means of the nitrogen ions respective the OH-radicals can be explained only if we assume that the homogenous discharge consists also of a multitude of microdischarges.

5. Conclusion

In atmospheric pressure He/N_2 dielectric barrier discharges (DBD) we have studied the conditions for the appearance of filamentary and homogeneous discharges. In both DBD modes we found an afterglow phase of the active discharges. During this phase the surface of the dielectric is charged. In both modes the active discharges consist of two phases: a discharge bridging the entire gas gap and a discharge restricted close to the cathode after formation of a cathode layer. From the temporal behaviour of the emissions of nitrogen ions and helium atoms we could determine the partial pressure of nitrogen in the rare gas flow. At our experimental conditions the homogeneous DBD mode consist of a multitude of microdischarges. The gas temperatures in the channels of these microdischarges are 50 - 300 K above the temperature of the ambient gas.

References

[1] N.K. Bibinov, A.A. Fateev, K. Wiesemann, Plasma Sources Sci.Technol.**10,** 579 (2001)
[2] N.K. Bibinov, A.A. Fateev, K. Wiesemann, J. Phys. D: Appl .Phys., **34**, 1819 (2001)
[3] F. Massines, A. Rabehi, P. Decomps, R. Ben Gadri, P. Segur, C. Mayoux, J. Appl. Phys. **83**, 2950 (1998)
[4] N. Gherardi, G. Gouda, E. Gat, A. Ricard, F. Massines, Plasma Sources Sci. Technol. **9,** 340 (2000)
[5] D. Braun, V. Gibalov, G. Pietsch, Plasma Sources Sci. Technol. **1**, 166 (1992)
[6] J.I. Levatter, S.C. Lin, J. Appl. Phys. **51**, 210 (1980)
[7] Y.P. Raizer, Gas Discharge Physics, 1. ed. 2. correct. print., Springer: Berlin, Heidelberg, 1997, p. 169

EXPERIMENTAL STUDY OF THE EFFECTIVE EFFICIENCY IN A CERAMIC COATED DIESEL ENGINE

[*]I. Taymaz, M.Gur and A. Mimaroglu.

[*]*Faculty of Engineering, Unıversity of Sakarya, Esentepe Kampusu, Adapazarı-Turkey*
Tel: +90-264-3460353, Fax:+90-264-3460351, Email:taymaz@sakarya.edu.tr

The quest for increasing the efficiency of an internal combustion engine has been going on ever since the invention of this reliable workhorse of the automotive world. In recent times, much attention has been focused on achieving this goal by reducing energy lost to the coolant during the power stroke of the cycle. A cursory look at the internal combustion engine heat balance indicates that the input energy is divided into roughly three equal parts: energy converted to useful work, energy transferred to coolant and energy lost to exhaust The reduction in, or the elimination of, in-cylinder heat transfer to either the coolant and/or the environment does not violate the second law of thermodynamics and, moreover, according to the first law, has the potential of producing more work. Added to this, another important advantage of the concept is the great reduction in parasitic losses due to elimination of cooling system, thus increasing the brake horsepower of the engine. These prospects of improving the design and performance have generated impetus to active research on adiabatic or more appropriately, low heat rejection (LHR) or insulated engines.

Since the 1970s, substantial interest has been focused on the development of the low heat rejection engine (LHRE) and the use of ceramic materials to insulate the metals of the combustion chamber (pistons, valves, cylinder head). Insulating an engine is not simply the means to an end. Reducing heat losses from the engine cylinder makes minimal changes to the efficiencies of existing engines. It does reduce the need for cooling systems and their costs, reducing weight, and reducing the complexity of the system. As in any IC engine, a tremendous amount of energy escapes from a diesel engine. It has been estimated that up to an equivalent of 87% of the amount of shaft work exits the engine in the form of waste heat. In a standard engine a large percentage is wasted through the cooling system. By thermally insulating the engine's piston, cylinders, and cylinder heads this heat energy could be directed to the exhaust gases. It then can be harnessed to increase the net power output of the system, thus raising thermal efficiencies and decreasing specific fuel consumption.

The main purpose of this study is to evaluate the effective efficiency at different engine loads and speeds with and without ceramic coated diesel engine. Experiments were conducted with six cylinders, direct injected, turbocharged, intercooled diesel engine. First, this engine was tested at different speeds and loads conditions without coating. Then, combustion chamber surfaces (cylinder head, valves and piston crown faces) was coated with ceramic materials using plasma spraying technique. Ceramic layers were made of $CaZrO_3$ and $MgZrO_3$ and plasma coated onto base of the NiCrAl bond coat. The ceramic coated research engine was tested at the same conditions as the standard (without coating) engine. The results showed a reduction in heat losses to the coolant and an increase in effective efficiency.

Characterization of Atmospheric Pressure Mixed-gases TIG Arc Plasmas

C. Fanara[(1)], L. O. Vilarinho[(2)]

[(1)] *School of Industrial and Manufacturing Science - Cranfield University c.fanara@cranfield.ac.uk*
[(2)] *Laboratory for Welding Process Development, Universidade Federal de Uberlandia, Brazil*

Abstract
Thermal plasma at atmospheric pressure used in industry are often made of inert gas mixtures. Changes in structure and properties of these arcs due to variation of the Ar-He mixture composition are presented for currents selected in the range 50-200 *A*. Emission spectroscopy provides temperature maps with isotherms variable in shape and location. Langmuir probes provide voltage, electrical radii whereas (Abel inverted) ion saturation currents give hints on changes of the width of the arc current carrying region.

1. Introduction

Thermal plasma technologies based on arcs at atmospheric pressure are used in industry for cutting, heat surfacing and welding. In these processes, multi-component plasmas are employed in form of inert gas mixtures. The structure and properties of the arc are altered with respect to pure gases. *Demixing* [1-4] from originally homogeneous mixtures takes place which separates the component gases in different regions of the arc. The present work is aimed at the characterization of the arc structure when two chemical species are present in form of an Ar-He mixture (1% to 10% He in mass fraction). Diagnostic techniques include Emission Spectroscopy and Langmuir probes. From the first, temperature maps are presented [5, 6], showing change of the argon isotherm shape and location upon variations in the impurity concentration. The use of Langmuir probes in atmospheric pressure plasmas, although problematic due to flow [7], high collisionality and spatial non-homogeneity [8], can still shed light on the electrical structure of the arc [9, 10]. A multi-probe apparatus for the study of TIG welding arcs constructed to operate in the range 50-200 *A*, provides voltage, axial electric field and electrical radii for pure argon and argon-helium mixtures as well as ion current densities obtained upon Abel inversion of the individual probe signals [9, 11]. The apparatus is summarized in section 2 whereas results are presented in section 3.

2. Experimental details and procedures

A detailed description of the apparatus, both the optical and of the probe system have been reported elsewhere [5, 6, 8, 10, 12]. Figure 1 left shows the vacuum vessel and some ancillary equipment.

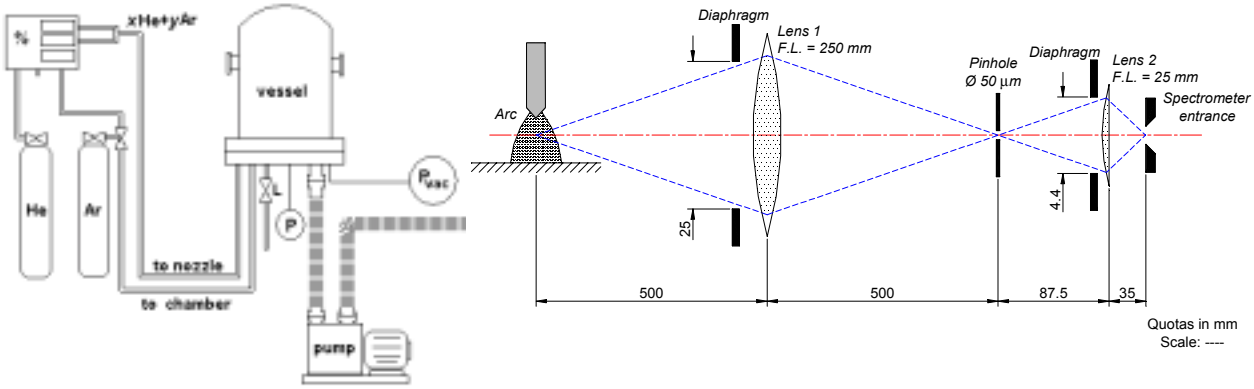

Figure 1 Chamber (left) and emission spectroscopy experiment Set up (right)

Of the two gas lines, one is dedicated to the filling of the chamber (usually with Argon), the other leads to the cathode nozzle (torch). The mass flow of the gases is controlled down to 1% by means of a mass flow controller capable of delivering up to 40 *slm* (full scale) on both the *Ar* and *He* channels (1 *slm* = 2.97 $\cdot 10^{-5}$

Kg s^{-1} of argon). The optical setup, leading to the Czerney-Turner 1 *m* focal length monochromator and CCD detector, is shown in figure 1 on the right. Figure 2 left depicts the complete probe system whereas on the right a photograph of the probe system is reported showing the torch and few probes (copper, Ø 250 µ*m*, length 58 to 60 *mm*). The arc is struck in the typical point-plane geometry and except where explicitly indicated the arc length is 5 *mm*.

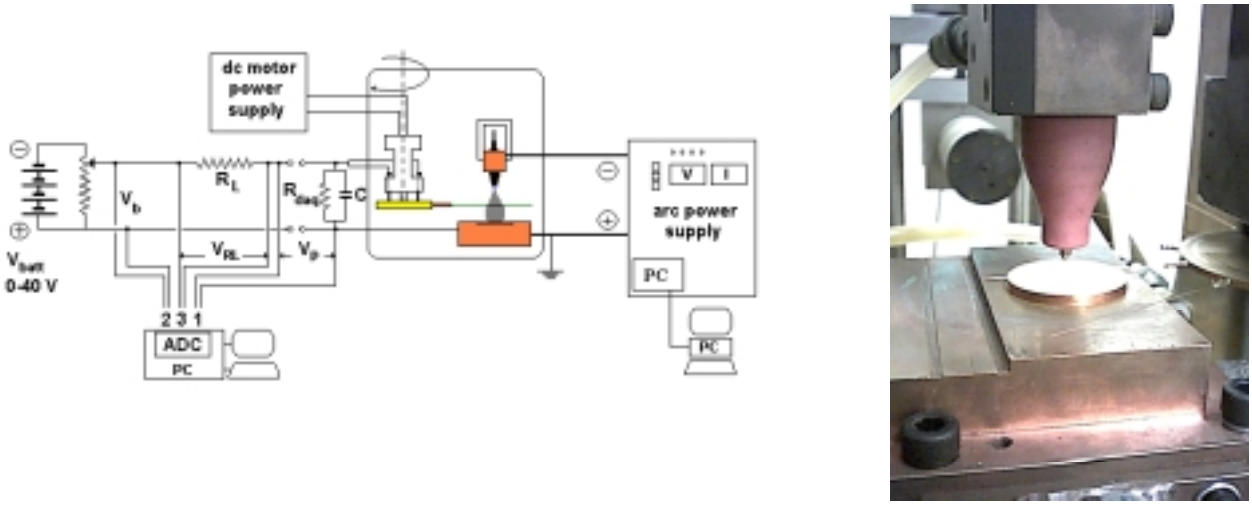

Figure 2, setup for the Langmuir probe. The probe disk sweeps probes through the arc (in between cathode and anode shown in orange). Right, torch nozzle with W tip, and copper anode. A portion of the multi probe disk with protruding probes is shown

3. Results

Effects of helium addition can be visualized by emission spectroscopy and electrical measurements. As an illustration, a selection of arc characteristic curves, optical temperature maps, probe characteristic curves (V-I), current distributions, electrical radii and probe voltages is shown.

3.1 Arc characteristic curves

Characteristic curves are shown (figure 3) obtained from the fixed arc current by measuring the total arc voltage fall for varying Ar-He mixture fraction. On the right, the corresponding electrical power input is also shown. Monotonicity in both the total arc voltage fall increase and in the electrical input power can be observed.

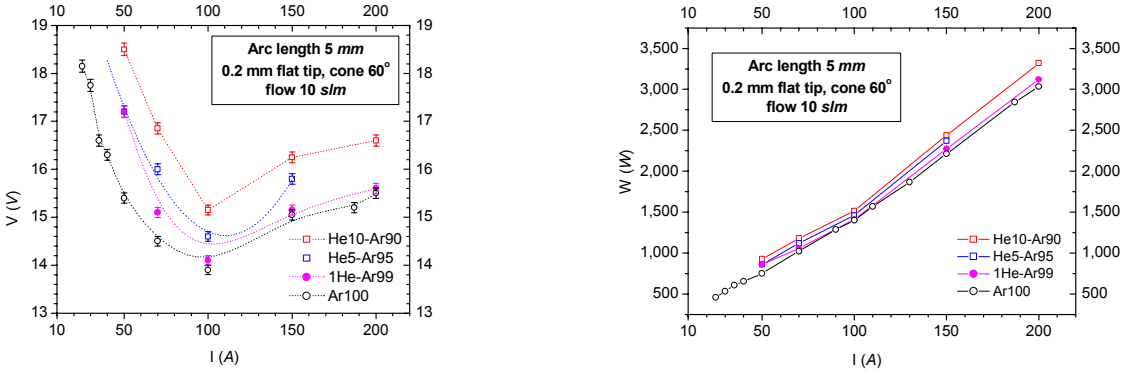

Figure 3, arc IV curve (left) and electrical power input (right) at varying Ar-He mixture compositions

3.2 Optical temperatures

Temperature maps obtained using the Fowler-Milne method are shown in figure 4. It was not possible to use the *modified* Fowler-Milne method [13] which requires separate measurement of emission lines for the pure argon and pure helium arcs. Limitations of the cooling system did not permit to record helium lines for more than few minutes before anode melt down. Therefore, the isotherms of figure 4 refer always to argon

emission lines. Limiting to high currents arcs, the assumption of a system not far form LTE, is sustainable even for mixtures [4] so that the argon electron temperature can be assumed to characterize the arc plasma as a whole. The difference between pure argon and 1*He*-99*Ar* in the upper half of figure 4 is at the limit of detectability.

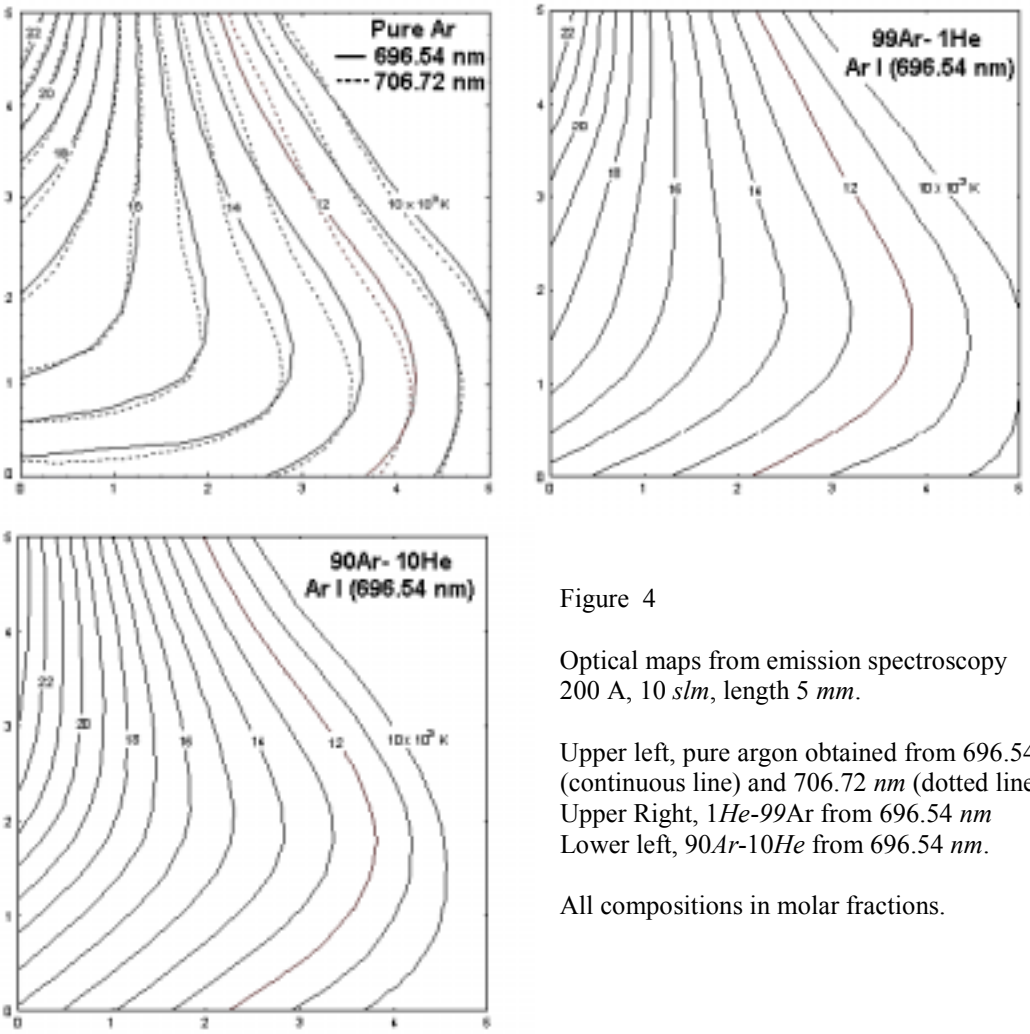

Figure 4

Optical maps from emission spectroscopy
200 A, 10 *slm*, length 5 *mm*.

Upper left, pure argon obtained from 696.54 *nm* (continuous line) and 706.72 *nm* (dotted line).
Upper Right, 1*He-99*Ar from 696.54 *nm*
Lower left, 90*Ar*-10*He* from 696.54 *nm*.

All compositions in molar fractions.

In fact, in this region the difference between the two pure argon determinations (lines at 696.54 and 706.72 *nm,* figure 4 left) is comparable with the difference between either of these two and the 1*He*-99*Ar* (figure 4 right). However, the isotherms for the pure argon show enhanced curvature towards the axis, especially in the lower region. The 10*He*-90*Ar* shows contraction of the outer part of the column at all arc heights. Extension of the highest isotherms toward the anode along the axis is also visible. This agrees with previous predictions and observations [2, 14]

3.3 Probes V-I curves

A selection of V-I curves is presented in figure 5 for some probes and increasing helium concentration. The effect of helium addition is to decrease the probe (ion) current at the same probe voltage especially close to the electrodes; whereas at mid arc (*cf z*=2.03 *mm*) the effect is minimal. Moreover, when ion saturation occurs (from mid arc downwards), the corresponding current decreases.

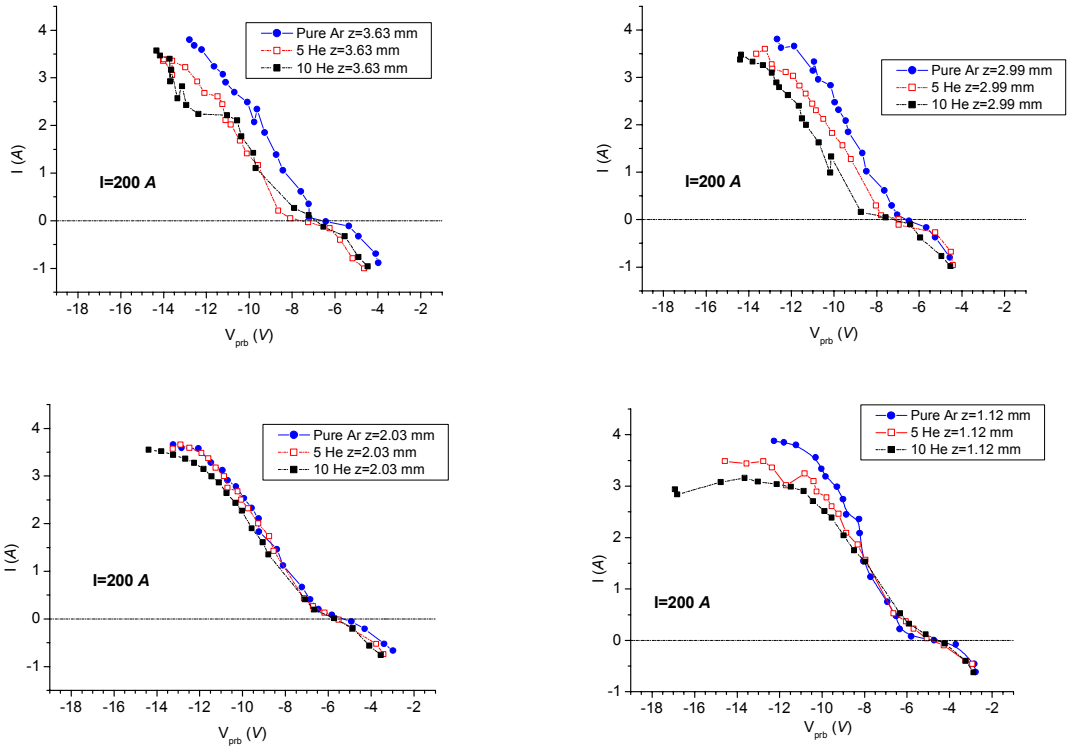

Figure 5, I=200 *A*. Central characteristic curves for selected probes for pure argon, 5He-95Ar and 10He-90Ar

Irrespective of the interpretative model chosen, this influences the electron temperature, when determined from the ion saturation portion of the V-I curve [11]. The current-temperature relationship is not monotonic over the range of interesting currents, therefore the prediction of whether an *apparent* cooling or heating occurs is not straightforward. Also, a reduction of the current could lead to a reduction of the number density and, within the appropriate temperature range, this implies a reduction of the electron temperature. The comparison with optical maps is possible only once corrections are performed that account for the recombinative cooling [11] occurring in the fluid flow perturbation region around probes [11, 15].
Figure 5 also suggests that helium additions change the location of the floating potential on the V-I curve (more exactly, the probe voltage in floating conditions). This change is monotonic with respect to helium addition.

3.4. Electrical radii

The notion of electrical radius has been anticipated in earlier works [10, 11, 16]. Helium addition tends to lower the absolute value of the ion current (figure 6 left), whose radial structure however, seems preserved. The radius of the current carrying region (*ccr*), defined by the intercept of the radial current distribution with the abscissa is enhanced for helium addition with respect to the pure argon case. This can be seen in figure 6 right in the *ccr* at high position in arc (errors on radii are 2.5% of the order of the symbols); this agrees with previous indications about dominance of the effect in the vicinity of the cathode region [17], although its *radial* dependency is shown for the first time here. The arc external boundary, corresponding to the interception of the peak edges in *floating conditions*, when the current is virtually zero, identifies the *halo* region. These radii correspond to a region where no current is flowing, although charge concentration is sufficiently high to be detected by probes. The apparent radial contraction of the halo upon helium increase is more difficult to assess due the scattering of the data.

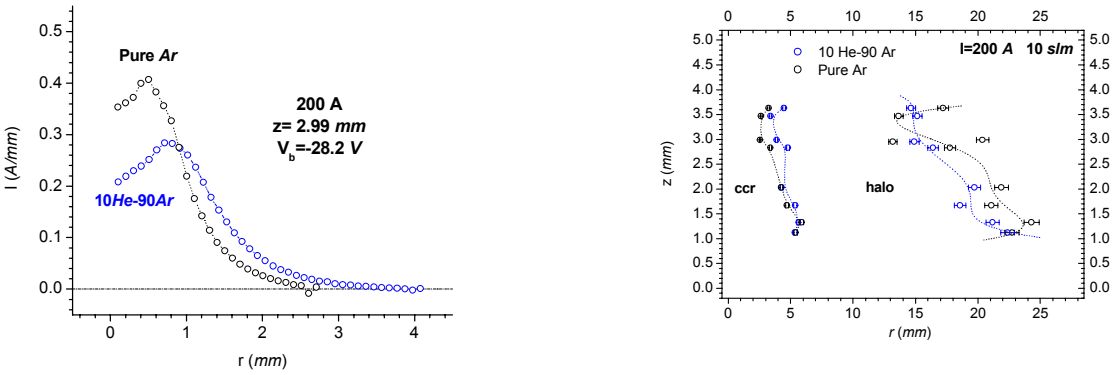

Figure 6 Left, comparison of the inverted current signals at ion saturation for pure Ar and 10He-90Ar. Right, comparison between the radius of the current carrying region, *ccr*, and of the arc external boundary identifies the electrical *halo*

3.5 Probe voltages

The increase of the electric potential for a given current and height within the arc is clearly detected in figure 7. Note that here a range of mixture fraction is shown broader than in figure 5.

Figure 7

Probe voltages in unbiased (but not floating) conditions, versus probe height in 5.2 *mm* arc. Arc currents 150 A. He molar fraction from 0 to 50%

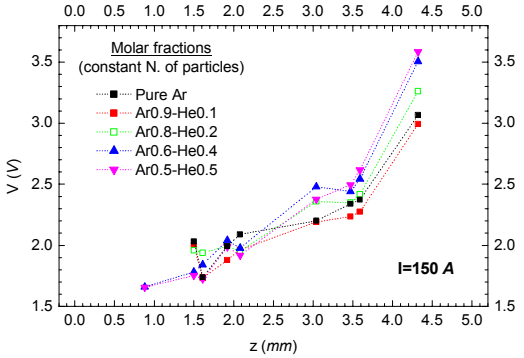

The voltage increases for increasing helium molar fraction. As previously indicated [17], there is a tendency for the phenomenon to occur in the cathode region, as shown by the highest He fraction. The effect is less clear in the column of the arc, so it is not possible to infer a voltage inversion which would suggest increased helium concentration along the arc height.

4. Summary and conclusions

Emission spectroscopy shows temperature maps variations for concentration variations of a few %. Perhaps 1% can be considered as the lowest limit as shown in the discussion following figure 3.

Contrary to previous beliefs, sensitivity of probes versus helium concentration appears of the order of 10% or less, as shown by the variation of several quantities: the shape of the V-I curves, the values of the ion saturation currents, the electrical radii (current carrying and halo), probe voltage along the arc height. The latter can be compared with previous values [17, 18]. For the V-I curves it is not known why only a limited portion of the retarding region was previously used [17].

These results require further analysis, in fact:

1. Quantitative analysis of the V-I curves (central as well as local) and attempts to obtain a probe determined temperatures, in analogy with work carried out for pure argon arcs [11], are currently under way at Cranfield
2. Careful analysis is required to verify variations in potential gradients and therefore in electric fields, once the way of determining the plasma potential is clarified.

3. The current carrying region structure obtained from ion saturation currents needs comparison with electron current density if the plasma potential can be attained experimentally by probes at all probe heights.
4. Finally, signals obtained in floating conditions [11], not shown here for reasons of space, suggest the possibility of unveiling charge distribution variations.

Acknowledgments
This work was funded under EPSRC grant Nr. L8 2281.

References

1. Murphy, A.B., *Demixing due to frictional forces in electric arc.* Physical Review Letters, 1994. **73**(13).
2. Murphy, A.B., *The influence of demixing on the properties of a free-burning arc.* Applied Physics Letters, 1996. **69**(3).
3. Murphy, A.B., *Cataphoresis in electric arcs.* Journal of Physics D: Applied Physics, 1998. **31**(23): p. 3383-3390.
4. Murphy, A.B., *Thermal plasmas in gas mixtures.* Journal of Physics D: Applied Physics, 2001. **34**: p. R151-R173.
5. Fanara, C., Vilarinho, L.O. *Optical and electrical measurements in atmospheric pressure arcs: a comparison*. in *Annual Gaseous Electronics Conference (GEC02)*. 2002. Minneapolis, MN, USA, October 15-18 2002.
6. Vilarinho, L.O., *Optical Emission Spectroscopy*. 2002, Internal Report Cranfield University: Cranfield.
7. Fanara, C., Vilarinho, L.O., *Measurement of the Perturbation Region thickness around probes in atmospheric pressure arc plasmas.* in press, 2002.
8. Fanara, C., Richardson, I.M., *A Langmuir multi-probe system for the characterization of atmospheric pressure plasmas.* Journal of Physics D: Applied Physics, 2001. **34**: p. 2715-2725.
9. Fanara, C., *Langmuir probe in atmospheric arc plasmas: a review, Technical report N.2, June*. 2001, Cranfield University.
10. Fanara, C. *Electrical characterization of atmospheric pressure arc plasmas*. in *EMRS Symposium A - TPP7 (Thermal Plasma Processes) - poster presentation, Ref. Nr. 0356A -Strasbourg, France, 18-21June 2002. Editors, Prof. J. Amouroux and P. Fauchais*. 2002.
11. Fanara, C., *A multi-langmuir probe for the characterization of atmospheric pressure plasmas, Ph.D. Thesis.* March 2003.
12. Fanara, C., Vilarinho, L.O., *Spectroscopic and Langmuir probe measurements in an atmospheric pressure arc plasma.* In press, 2002.
13. Murphy, A.B., *Modified Fowler-Milne method for the spectroscopic measurement of temperature and composition of multielement thermal plasmas.* Review of Scientific Instruments, 2000. **65**(11): p. 3423-3427.
14. Murphy, A.B., *Prediction of gas tungsten arc welding properties in mixtures of Argon and Hydrogen.* IEEE Transactions on Plasma Science, 1997. **25**(5): p. 809.
15. Fanara, C., Vilarinho, L.O., *Measurement of the Perturbation Region thickness around probes in atmospheric pressure arc plasmas.* in press, 2003.
16. Allum, C.J., *Power dissipation in the column of a TIG arc.* Journal of Physics D: Applied Physics, 1983.
17. Zijp, J., Hiraoka, K., *Basic parameters of heat transport in argon-helium mixed gas arcs.* Welding International, 1994. **8**(7): p. 518-524.
18. Hiraoka, K., Sakuma, N. and Zijp, J., *Energy Balance in Argon-helium Mixed Gas Tungsten (TIG) Arcs. Study of Characteristics of Gas Tungsten Arc Shielded by Mixed Gases (3rd Report).* Welding International, 1998. **12**(5): p. 372-379.

PLASMA EQUIPMENT and TECHNOLOGIES for HARDENING and REPAIR of WHEELSETS

Petrov S.V., Saakov A.G.

RPE TOPAS Ltd., Kiev, Ukraine

Abstract.

The work solves the package of problems associated with hardening and repair of wheelsets. Plasma equipment and technologies have been developed and tested. They meet contradictory requirements to different zones of a wheel during its life time. These are two methods which provide a constant shape of the wheel flanges, i.e. plasma surface hardening and deposition of wear-resistant coatings, plus tempering of the surface layer of increased hardness prior to re-profiling. All the three processes are applied using the UVPZ-2M machine.

1. Introduction

Local heat treatment is justifiable in many cases in terms of technology and cost effectiveness, where only the most loaded working surface is subjected to hardening, while the bulk of a material remains untreated. Plasma surface hardening allows wear to be decreased and service life of heavy-loaded machine parts to be extended 2-5 times. The novel method of plasma hardening is technically and economically preferable for heat treatment of a large number of parts. One example of its application is high-speed surface hardening of all types of passenger, freight and locomotive train wheelsets. Tests show that in all cases the amount of wear of the wheelset ridges after plasma hardening is much lower (2.5-3.0 times) than that of the ridges after standard heat treatment. The new approach to making machines for high-speed plasma surface hardening has been developed based on utilization of the variable-composition mixture of gas and air and the stabilized elongated electric arc that burns in a plasmatron and is adapted to meet the technology requirements.

2 Modelling of the plasma hardening process

The key task of the mathematical support realized in the form of the specialized software package based on modern computer facilities is to optimize the hardening process through selection of such heating-cooling conditions which would provide the desirable strength properties for a given material (steel grade) within the preset space area of heat treatment.

Fulfilment of this task is associated with a possibility of having a reliable prediction of the material structure to be produced, based on the selected thermal effect parameters. Considering complexity of the latter, the total work on development of the software was divided into three inter-related and, at the same time, sufficiently independent stages.

Stage 1 involved solution of the problem associated with computation of thermal cycles for an arbitrary micro-volume within the treatment area for the preset type of a material (density of a material, as well as temperature dependence of thermal conductivity and specific heat are considered to be known). External effects which can vary over a wide range include consumption, initial temperature and thermal-physical properties of the plasma, size of the zone to be heated, character of relative displacement, speed of displacement of the material treated, degree of preheating-cooling, cooling conditions upon leaving the plasma treatment zone, etc.

It should noted, however, that the latter approach is associated with a large scope of preliminary experimental studies, while reliability of the results obtained dramatically decreases even with a slight deviation of parameters outside the range studied.

Optimization of the technology is reduced to making special precautions to produce the preset configuration of the plasma flow and to proper selection of the required conditions of the hardening process. Reliable prediction of structures and residual stresses formed in the hardened layer can be made only in the case of using a non-linear mathematical model. Allowance for non-linearity of thermal-physical parameters of the plasma and material treated makes it possible to determine local extrema of rates of variations in temperature of certain micro-volumes within certain time intervals.

Further increase in level of service properties of a part being hardened can be achieved through improvement of the hardening technology, which is eventually reduced to ensuring the optimal thermal

cycle (heating-cooling), proceeding from regularities in structural, phase and polymorphic transformations of the material hardened.
Stage 2 of the work involved development of the software for modelling the processes of structural, physical and chemical transformations occurring in the material studied, under substantially non-equilibrium conditions of rapid heating and cooling, proceeding from the fundamental up-to-date concepts of the processes being investigated. In principle, occurrence of these processes and variations in thermal conditions of the material treated are a single process. Thus, they should be computed simultaneously, because structural, phase and chemical
transformations are related in this or that way to absorption or release of latent heat. However, based on the fact that the available reliable literature data on thermal-physical properties of the material treated implicitly make allowance for the above processes (e.g. the data on specific heat include values of the effective apparent heat capacity, and the same applies to thermal conductivity) as well as that under the considered conditions of rapid heating and cooling the diffusion processes substantially lag behind the thermal ones, the above separation of the procedures of computation of thermograms and transformations in the material treated seems justifiable.
Difficulties of stage 2 are associated firstly with the absence of a common opinion concerning the process of formation of austenite during heating and its decomposition during cooling. Secondly, in the majority of the available literature sources describing investigations into the hardening processes for certain classes of materials, the data given are in the best case the result of mathematical processing (plots, tables) of experimental studies. And as a rule it is very difficult to get from them the information concerning mechanisms of the processes occurring and quantitative estimates of the processes taking place in an individual micro-volume, which are important for description.
For this paper the authors selected as a reference point a relatively small number of works, where all variations taking place in micro-volumes are described on the basis of fundamental concepts of the material and energy conversion processes.
The problem of modelling of the heat treatment process consists in computation of the quantity of austenite formed during the period of heating (in compliance with the thermogram plotted for a given micro-volume) and, accordingly, the percentage of that quantity of austenite which remains non-decomposed by the moment of achieving the martensitic transformation temperature at a stage of cooling.
Mathematical description of these transformation processes is based on the diffusion equation of the following form:

$$\partial C/\partial \tau = \partial[D(t)\cdot\partial C/\partial x]/\partial x,$$

where C is the carbon concentration, D(t) is the carbon diffusion coefficient depending upon the temperature t, x is the space coordinate, τ is the time recorded for each of the micro-volume structures allowing for their boundary conditions.
The latter depend upon the type of steel considered, whether it is hypueutectoid (containing ferrite and pearlite), eutectoid (containing only pearlite) or hypereutectoid (containing pearlite and cementite). In this case the conditions for free ferrite and ferrite which is part of pearlite are different. This is equally true for cementite. In addition, the type of the boundary conditions greatly depends upon the a priori simplified assumptions of the morphological peculiarities of individual structural elements of the micro-volume.
As an example, consider the case of hardening of eutectoid steel following the preset thermogram:

$$t=t(\tau), \qquad 0\le\tau\le T$$

where T is the total hardening time. In this case τ_1 is the moment of achieving the martensitic transformation temperature at the stage of heating, τ_2 is the moment of achieving a temperature of 727 °C at the stage of heating, τ_3 is the moment of achieving a temperature of 727 °C at the stage of cooling and τ_4 is the moment of achieving the martensitic transformation temperature at the stage of cooling:

$$T\ge\tau_1 + \tau_2 + \tau_3 +\tau_4$$

For the process of formation of austenite as a result of decomposition of cementite of the pearlite grain ($\alpha-\gamma$ transition), the following boundary and initial conditions ($\tau_2 < \tau \le\tau_3$) are valid:

at the cementite-austenite boundary

$$C(\tau,\xi_1) = C_{max}(t),\ D(t)\cdot\partial C/\partial x|x = \xi_1 = (0{,}0667 - C_{max}(t))\cdot d\xi_1/d\tau,\ \ 0 \le x \le \xi_1$$

at the austenite-ferrite boundary

$$C(\tau,\xi_2) = C_{min}(t),\ \ D(t)\cdot\partial C/\partial x|x=\xi_2 = (0{,}0002 - C_{min}(t))\cdot d\xi_2/d\tau,\ \ \xi_1 \le x \le \xi_2 \le \xi_{2max}$$

$$\xi_1(\tau_2) = 0.5\cdot\delta Ce(\tau 2);\ \ \xi_2(\tau_2) = 0.5\cdot\delta Ce(\tau_2) + \delta A(\tau_2);$$

$$\xi_{2max} = 0.5\cdot(\delta F + \delta Ce + \delta A)$$

Here:
$C_{min}(t)$ is the equilibrium carbon concentration in austenite at the boundary with ferrite (GS curve in the constitution diagram);
$C_{max}(t)$ is the equilibrium carbon concentration in austenite at the boundary with cementite (SE curve in the constitution diagram);
ξ_1 is the austenite-cementite boundary coordinate;
ξ_2 is the austenite-cementite boundary coordinate;
D(t) is the coefficient of diffusion of carbon into austenite;
δF, δCe, δA, $\delta F(\tau)$, $\delta Ce(\tau)$, $\delta A(\tau)$ are the thicknesses of the ferrite, cementite and austenite layers within the pearlite zone at the initial moment ($\tau=0$) and arbitrary moment τ, respectively;
δA is determined from the value of the initial martensite content of steel.
For the stage of decomposition of austenite within the $\tau_1 < \tau \le \tau_2$ and $\tau_3 < \tau \le \tau_4$ ranges, it holds that:
at the cementite-austenite boundary:

$$C(\tau,\xi_1) = C^*_{max}(t),\ \ D(t)\cdot\partial C/\partial x|x = \xi_1 = (0{,}0667 - C^*_{max}(t)) - d\xi_1/d\tau,\ \ 0 \le x \le \xi_1$$

at the austenite-ferrite boundary:

$$C(\tau,\xi_2) = C^*_{min}(t),\ \ D(t)\cdot\partial C/\partial x|x = \xi_2 = (0{,}0002 - C^*_{min}(t)) - d\xi_2/d\tau,$$

$$\xi_1 \le x \le \xi_2 \le \xi_{2max},\ \ \xi_1(\tau_1) = 0.5\cdot\delta Ce;\ \ \xi_2(\tau_1) = 0.5\cdot\delta Ce + \delta A;$$

where $C^*_{max}(t)$ and $C^*_{min}(t)$ are the continuations of the SE and GS curves into the range of temperatures below 727 °C, respectively.
Problems of stage 3 concerning development of the software, associated with construction of correlation models of the type of "material structure - physical-mechanical properties" are not considered within the frames of this paper.

3 Process equipment

Milestones in improvement of equipment are associated primarily with development and realization of new approaches, and in recent years with using measurement and control digital devices. Based on the above ideology, RPE TOPAS Ltd. developed and started up manufacture of a number of new high-tech plasma machines to implement new technologies.
To realize this idea, the Company developed plasmatrons designed for different power levels, as well as hardware for high-speed surface hardening of various parts.
The set of equipment for plasma hardening includes:
1.High-speed surface hardening machine UVPZ-2M (Fig.1),
2. A semi-automatic line for hardening of wheelsets with wheeling out (Fig. 2)
The UVPZ-2M machine is equipped with an independent optimization unit to provide:
- in-process programming of conditions and parameters, indication of the current condition of the controlled process parameters, recording and storing of parameters of the process of plasma surface

hardening of wheelsets in permanent memory and output of the information accumulated to a personal computer;

- processing of analogue signals from the "TOPAS-Smotrich" pyrometer, the "Plasma-TOPAS" plasmatron power supply and pressure sensors, as well as input discrete signals from the final control mechanisms and formation of output commands for programmed control.

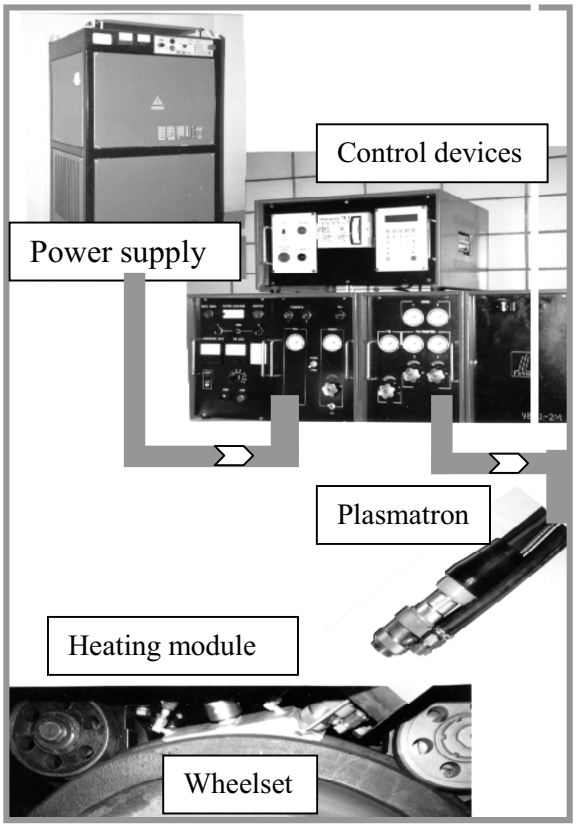

Fig. 1. High-speed surface hardening machine UVPZ-2M

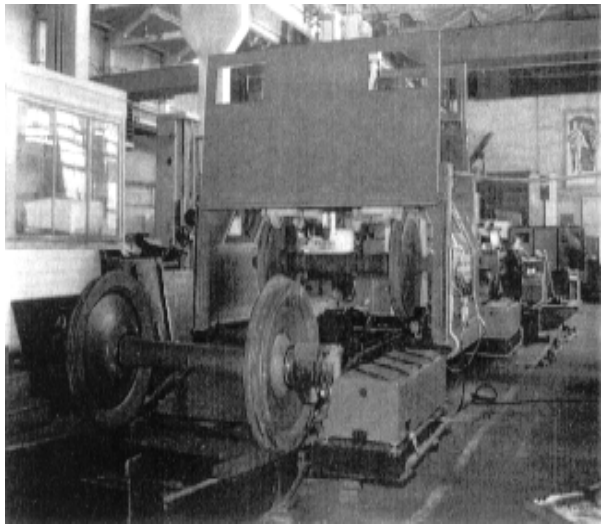

Fig. 2. A semi-automatic line for hardening of wheelsets with wheeling out

4. Results of wheelsets hardening

The technology of plasma surface hardening of TOPAS Ltd. is characterized by new capabilities in terms of increasing contact-fatigue strength and, therefore, increasing reliability of traction for locomotive wheelsets. Intensity of wear of the wheelset ridges after plasma hardening is much lower than that of the traditionally treated ones (2.5-3 times). The developed technology for hardening of the wheelsets has two peculiar features: 1.local (within the zone of the highest wear) surface hardening of the wheel ridge to a depth of 2.5-3 mm and width of 35 mm, ensuring an increase in hardness from 280 HB (in the base metal) to 450 HB. This provides an optimal relationship in hardness of the wheel and rail surfaces in contact; 2) change in structure of the hardened wheel zone from a ferrite-pearlite mixture with initial grain size of 30-40 μm to a mixture of fine-acicular or structureless martensite with a rosette-type troostite in a ratio of 50:50 %. This produces improvement of mechanical properties (including decrease in friction coefficient in contact of the ridge and the side surface of the rail) and increase in crack resistance of the wheel material within the plasma hardening zone.

Locomotives with the wheels plasma hardened by the TOPAS technology were first put into experimental operation at the Lviv-Zapad shed early in March 1996, and the cars - at the Kyiv-Passenger shed in summer that same year. Comparison of the plasma hardened wheel ridges of electric locomotives with the traditional ones under the same service conditions of the Lviv railway proved by the end of April 1996 the expected two-fold decrease in rate of wear. After that a decision was made to expand the scopes of application of plasma hardening of the wheelset ridges. It was for that purpose that the new specialized two-module high-speed plasma hardening machine UVPZ-2M was developed. Its application initiated the arrangement of workshops for plasma hardening of wheelsets without wheeling out from under a locomotive, which was completed in 1997. This was done using the KZh-20 machine tool at the Znamenka shed. Similar workshops for plasma hardening with wheeling out were arranged in Osnova,

Kharkiv. Workshops for plasma hardening of the wheelset ridges without wheeling out, based on the KZh-20 machine tool, were built at the Kazatin shed, those based on the K-40 machine tool were built at the Lviv-Zapad, Osnova (Kharkiv), Kotovsk, Nizhnedneprovsky junction, etc. (Fig. 3). The car wheels are hardened using the specialized production line with wheeling out at Kyiv, Kherson, Dneprodzerzhinsk and other car sheds.

The final outcome of more than 5 years operation of locomotives and cars with the plasma hardened wheelset ridges is as follows. 1.Plasma hardening is a highly productive efficient method for 2- or 3-fold extension of service life of the wheelsets, which can be applied under conditions of a typical car shed. The accepted technology provides a very high safety factor for operational reliability of the wheelsets. 2. The guaranteed reproducibility of the best indicators of operational reliability, and wear resistance is ensured by keeping precisely to the prescribed hardening parameters for every wheel.

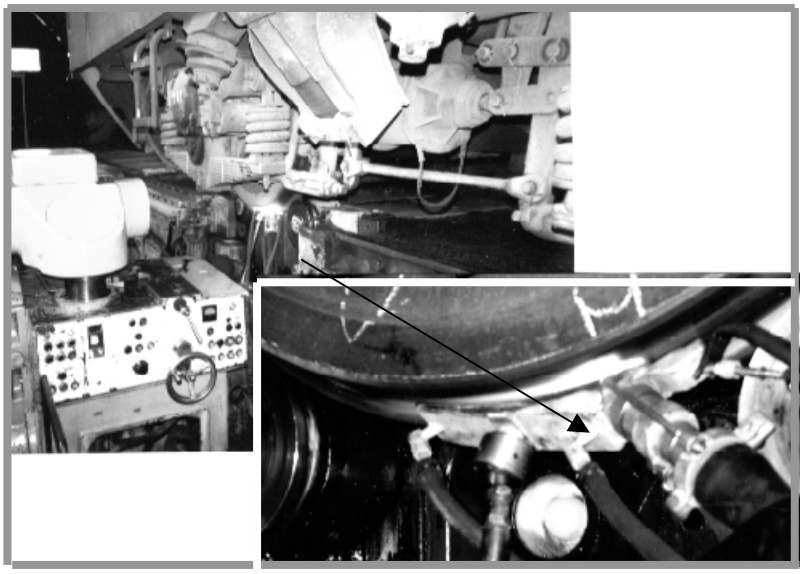

Fig.3. Plasma hardening of wheelsets without wheeling out from under a locomotive

5.Tempering of flats

A new technology for high-speed plasma tempering of cold-worked (hardened) roll surfaces of wheelsets has been developed on the basis of the UVPZ-2M machine. This technology has been successfully applied at a number of depots (Fig.4) Hardness of the surface layer of metal of wheels is increased due to cold working during movement from 285 HB to 350 HB, while on flats formed in braking with blocked wheels the hardness value may amount to 50-55 HRC.

In this situation tempering of the surface layer of metal prior to re-profiling the roll surface of wheels make the work of cutting tools and a lathe much easier. This enables the rate of turning to be increased and a substantial saving to be achieved.

6. Plasma Spraying of Resistant Coatings on Wheel Flanges

Constant shape of a wheel flange is ensured by deposition of wear-resistant coatings. This solves a contradictory problem, i.e. maintaining a sufficiently high coefficient of friction between the roll surface and rail to improve transfer of longitudinal forces and decreasing friction in the zone of pressing of the lateral face of the flange to the rail.

Wear-resistant coating of a self-fluxing material with an addition of carbides or carbonitrides (Fig.5) is deposited on the wheel flange in one pass with a simultaneous surface melting. Thickness of the coating is 1-2 mm, width of the coated strip is 25-30 mm. This is done using the TOPAS rotators, or rotators for wire deposition of the flanges, as the spray surface should be in a horizontal position. Wear-resistant coatings with simultaneous surface melting can be deposited using the UVPZ-2M plasma equipment for surface hardening, subjected to upgrading.

Materials which provide the following properties were selected for deposition of the coatings:

- high toughness and deformability of the deposited layer;
- special properties of the coating material the friction coefficient of which corresponds to a minimum probability of derailment;

- low wear of the rail-wheel system;
- high strength of adhesion of the coating to the substrate material;
- homogeneous structure of the coating;
- long service life of the coating;
- possibility of repeated deposition without preliminary machining.

Such a coating will provide a 5-10 times extension of life of the flange and a decrease of 50-100 % in the coefficient of friction of the working surface of the flange with the rail.

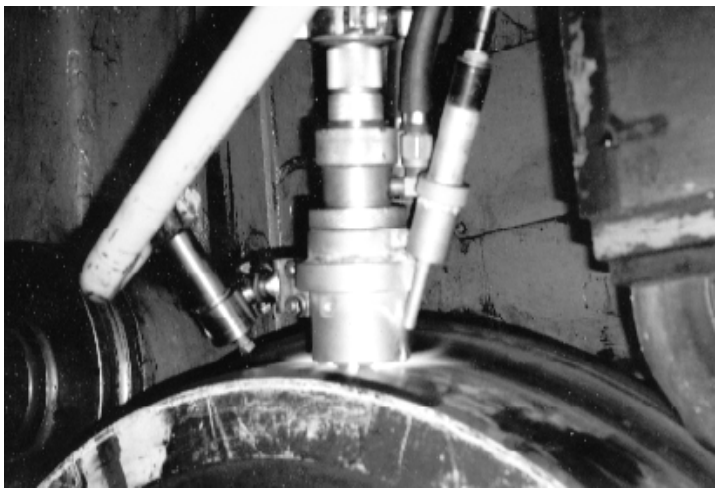

Fig.5. Tempering of flats

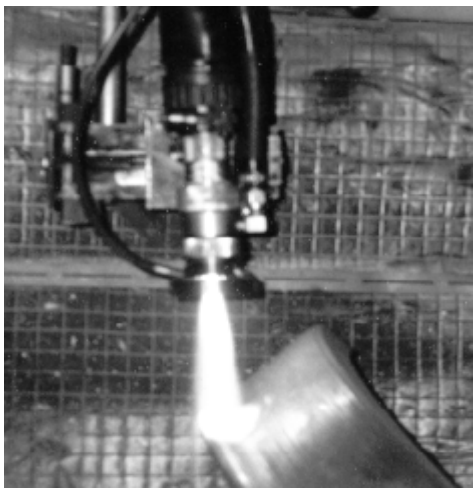

Fig.6. Plasma Spraying of Resistant Coatings on Wheel Flanges

Investigation of Surface Roughening of Advanced Photoresists During Low-Pressure Plasma Etching

Li Ling[1], Xuefeng Hua[1], G. S. Oehrlein[1], and E. A. Hudson[2]

[1]*Department of Materials Science & Engineering and Institute for Research in Electronics and Applied Physics, University of Maryland, College Park, Maryland 20742*

[2]*Lam Research Corp., 4650 Cushing Pkwy., Fremont CA 94538*

Plasma exposure of advanced resists during the pattern transfer step is often accompanied by resist surface roughening and line edge roughening due to factors which are not well understood. The roughness features so produced can be transferred into the underlayer and appear as sidewall striations. In the present work we have studied the evolution of surface roughening in advanced resists by ellipsometry in real time during plasma processing. We also have developed an optical model of the modified resist layer which is used to interprete the results of the real-time optical surface diagnostics. Using this methodology, we have investigated the relative importance of key plasma-surface interactions parameters, e.g. maximum ion energy, total energy flux, and plasma chemistry, in producing resist surface roughening, and also investigated chemical changes in the resist materials. A comparison of 248 nm resist with 193 nm resist shows that significantly more surface roughness is introduced in the 193 nm resist for all plasma processing conditions investigated. We also find a dramatic dependence of surface roughening on the chemistry of the plasma process, e.g. for Ar/C_4F_8 a rough resist surface layer with an extent of about 50 nm is produced in 193 nm resist, whereas for C_4F_8 discharges much less surface roughening is seen for otherwise similar conditions. We find that the thickness of the rough surface layer does not show a strong time dependence, but that the intensity of the roughness increases continuously with plasma exposure time. A comparison of the results of the real-time optical data with atomic force microscopy and x-ray photoelectron spectroscopy data obtained when interrupting the plasma process will also be reported. The mechanistic implications of the present results are discussed in the context of designing better resist materials/plasma processes, in particular for the development of 157 nm technology.

Characteristics of Broad-Band Frequency Low Pressure Inductively Coupled Plasma Used for Nanostructured Carbon Deposition

Katsuyuki Okada, Shojiro Komatsu, and Seiichiro Matsumoto

Advanced Materials Laboratory, National Institute for Materials Science
1-1 Namiki, Tsukuba, Ibaraki 305-0044, Japan; okada.katsuyuki@nims.go.jp

Abstract

We have developed a broad-band frequency (10-60 MHz) low pressure inductively coupled plasma system used for nanostructured carbon deposition by properly adjusting an antenna and an impedance matching network. The plasma characteristics {plasma potential (Vp), electron temperature (Te), plasma density (Ne), and electron energy distribution function (EEDF)} were investigated by an optical emission spectroscopy (OES) and an RF compensated Langmuir probe. We have found that the Vp and Te decrease with increasing pressure, whereas the Ne increases, and that the Vp and Ne also increase with increasing frequency, whereas the Te tends to be saturated in higher frequency. The EEDF at lower frequency exhibits a deviation from Maxwellian distribution, in which the population of electrons in the high-energy tail above 13 eV drops, whereas the high-energy tail grows at higher frequency and the almost straight line of the EEDF indicates Maxwellian distribution.

1. Introduction

Low pressure plasmas driven at very high frequency (VHF; 30-300 MHz) have recently attracted considerable attention [1] because they may have higher plasma density and lower electron temperature compared with those of conventional 13.56 MHz radio frequency (RF) plasma. In the VHF range, high plasma densities can be generated with low applied voltages, suggesting that high process rates can be realized with low damage. Sheath thickness also decreases with increasing frequency, reducing the number of collisions an ion experiences in the sheaths and improving anisotropy at a fixed pressure. These characteristics are considered to be appropriate for plasma process, e.g. deposition of thin films or etching. There are up to now many reports on capacitively coupled VHF discharge. In a conventional parallel-plate capacitive discharge, the applied voltage is essentially dropped across the electrode sheaths, and ion energies at the electrodes must increase along with the plasma density. This coupling between plasma density and ion energy is a serious limitation of conventional parallel-plate electrode reactors. On the other hand, in an inductively coupled discharge, the RF power is coupled to the plasma across a dielectric window, rather than by direct connection to an electrode in the plasma, as for a capacitive discharge. This noncapacitive power transfer enables one to achieve low voltages across all plasma sheaths at electrode, and independent control of the ion/radical fluxes and the ion bombarding energy is possible [2]. Therefore inductively coupled VHF discharge is considered to be the most suitable plasma source for processing. However there is few report on inductive VHF discharge.

We have recently developed a broad-band frequency (10-60 MHz) low pressure inductively coupled plasma (ICP) system used for nanostructured carbon deposition. We report on the plasma characteristics {plasma potential (Vp), electron temperature (Te), plasma density (Ne), and electron energy distribution function (EEDF)} measured with an optical emission spectroscopy (OES) and an RF compensated Langmuir probe [3,4] in this study.

2. Experiment

Figure 1 illustrates the schematic diagram of the experimental setup. A low pressure ICP was generated in a water-cooled quartz tube by applying VHF power to a loop antenna. The frequency was varied from 10 to 60 MHz. The maximum input power was 1 kW. The reflected power was always maintained at less than 10% of the forward power by properly adjusting an antenna and an impedance matching network consisting of two vacuum-dielectric variable capacitors. The total inductance of the antenna was always kept

less than 0.3 μ H.

The light emitted from a plasma was fed to an optical multi-channel analyzer (OMA) [Jobin Yvon HR-320 monochromator, 512 channels Photodiode-array] through an optical fiber. An RF compensated Langmuir probe [3,4] (Scientific Systems; Smart Probe) was mounted on the side flange of the chamber. The RF fluctuations of the plasma potential were compensated by self-resonant inductors, and the reference probe automatically compensated for the plasma-ground sheath impedance, fluctuations in the plasma sheath impedance, plasma potential shifts, and low frequency noise [3].

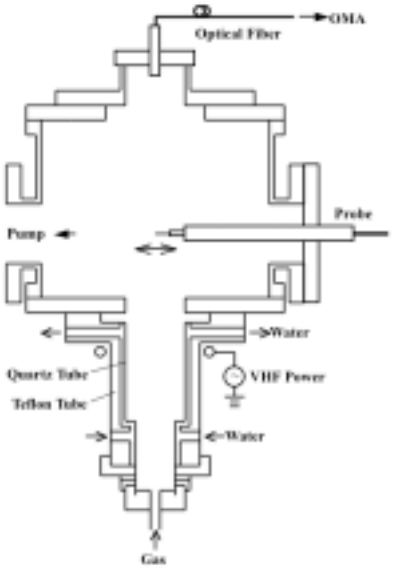

FIG. 1 Schematic view of the broad-band frequency low pressure ICP system.

3. Results and Discussion

Figures 2 and 3 show the OES profiles of an Ar and a H_2 plasma with 200 W in plasma power and 20 mTorr in pressure as a function of frequency, respectively. The absolute emission intensity of the both plasmas remarkably increased with an increase of frequency. The OES profiles of an Ar plasma exhibit that the relative intensities of ArI[4s'$(1/2)^0_1$-4p'$(1/2)_0$] at 750.4 nm become strong with an increase of frequency. The energy of the excited state of 4p'$(1/2)_0$ corresponds to 13.48 eV. Thus it is expected that the electron energy distribution around13.5 eV is relatively increased with increasing frequency. The OES profiles of a H_2 plasma exhibit that the relative intensities of H β at 486.1 nm become strong with an increase of frequency, and that the superimposed background due to H_2 molecules are lowered with increasing frequency. It was previously reported [5] that significant emission due to H_2 molecules appears in addition to H atomic transitions in a VHF H_2 plasma, and [6] that the intensity ratio of H_2/H α negatively correlates with the Te. The electron impact dissociation of hydrogen molecules is considered to proceed with increasing frequency. These features reveal that the excited states levels of chemical species in plasma largely depend on plasma driven frequency.

Figure 4 shows the radial distribution of the plasma potential Vp, the electron temperature Te, and the electron density Ne of an Ar plasma with 500 W in plasma power and 50 mTorr in pressure. The Vp and Ne have a similar shape, which has a peak at the center axis and decreases outward in the radial direction. The nonuniform profiles reflect the characteristics of diffusion-dominated plasmas [2,7]. On the other hand, the radial distribution of the Te is different from that of the Vp or the Ne. The Te is almost constant within the radius of 20 mm and then slightly decreases toward the chamber wall. The flatness of the Te around the

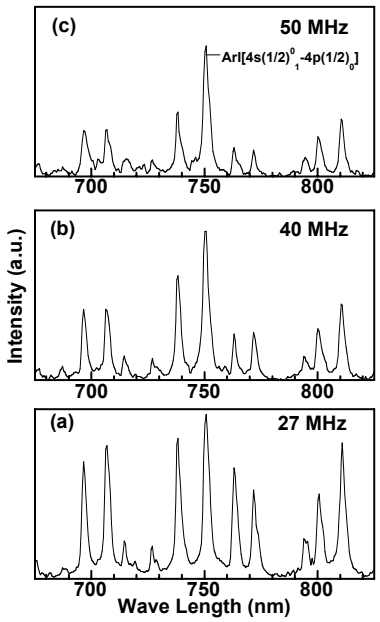

FIG. 2 OES profiles of an Ar plasma of 200 W at 20 mTorr as a function of frequency: (d) 27 MHz, (e) 40 MHz, and (c) 50 MHz.

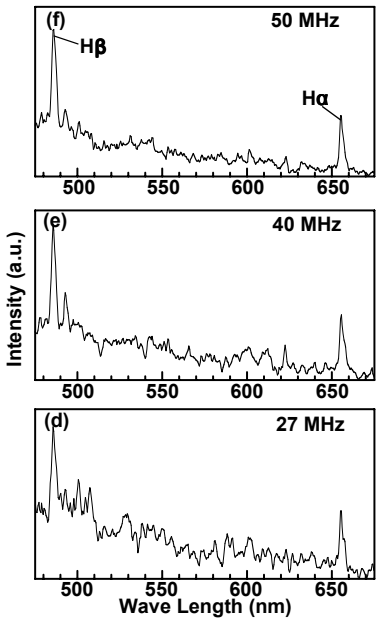

FIG. 3 OES profiles of a H_2 plasma of 200 W at 20 mTorr as a function of frequency: (d) 27 MHz, (e) 40 MHz, and (c) 50 MHz.

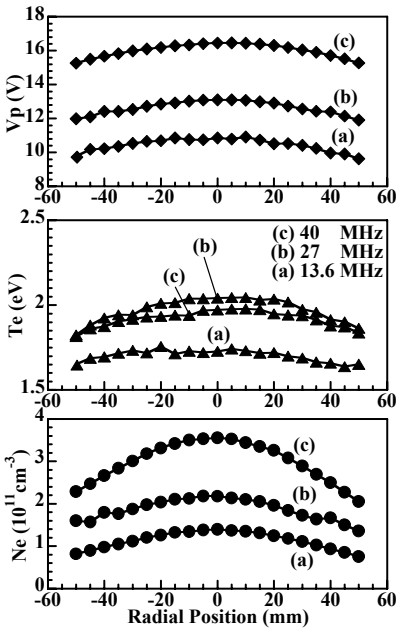

FIG. 4 Radial distribution of the Vp, Te, and Ne of an Ar plasma of 500 W at 50 mTorr: (a) 13.6 MHz, (b) 27 MHz, and (c) 40 MHz.

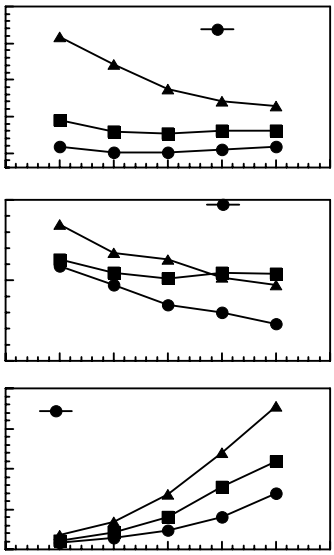

FIG. 5 Vp, Te, and Ne of an Ar plasma of 500 W at 13.6, 27, and 40 MHz as a function of pressure.

center axis is presumably due to the large mean free path of the electrons at low pressures [8], and the decrease of the Te at radii larger than 20 mm is caused by volumetric expansion [9]. The frequency does not affect these features of plasma parameters.

Figure 5 shows the Vp, Te, and Ne of an Ar plasma at 13.6, 27, and 40 MHz with 500 W in plasma power as a function of pressure. With an increase of pressure, the Ne also increases while the Vp and Te decrease. These variations with pressure are consistent with the previous results of 13.56 MHz ICP plasma [4,7]. The lower rate of inelastic electron-heavy particle collisions leads to the increase of the Te with decreasing pressure. This in turn increases the Vp because the rate of high-energy electrons escaping to the wall increases and brings about a loss of negative charge. The increase of Ne with increasing pressure is in agreement with the power balance relation [2], which indicates that the plasma density varies inversely with the effective plasma area.

With an increase of frequency, the Vp and Ne also increase, whereas the Te tends to be saturated in higher frequency. It was shown experimentally [5] that the electron density scales as the square of the frequency in an Ar VHF plasma. It was reported on a capacitive VHF plasma that the Vp decreases with an increase of frequency [10]. The opposite tendency in this study is presumably due to inductive discharge.

Figure 6 shows the EEDF of an Ar plasma with 500 W in plasma power and 50 mTorr in pressure. The population of electrons in the high-energy tail above 13 eV drops at lower frequency and the EEDF exhibits a deviation from Maxwellian distribution, whereas the high-energy tail grows at higher frequency and the almost straight line of the EEDF indicates Maxwellian distribution. This is consistent with the OES profile indicating that the electron energy distribution around 13.5 eV is relatively increased with increasing frequency. According to the theoretical investigation [11,12], the shape of the EEDF depends strongly on the ratio ν / ω, where ν is the frequency of energy transfer by electron-neutral collisions and ω is the angular excitation frequency of the applied VHF field. The EEDF tends toward a Maxwellian distribution as ν / ω decreases, whereas the EEDF is similar to a Druyvesteyn distribution in the low frequency limit ($\nu / \omega \rightarrow \infty$). Therefore, the high-energy tail of the EEDF is enhanced at higher frequency. The resultant EEDF profiles in this study are in agreement with the theory.

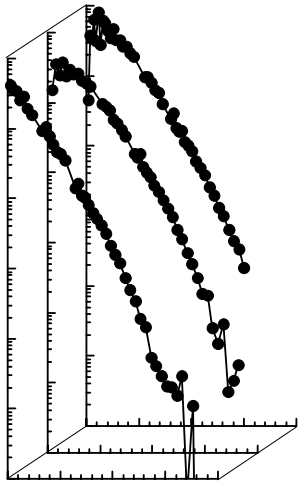

FIG. 6 EEDFs of an Ar plasma of 500 W at 50 mTorr as a function of frequency:(a) 13.6 MHz, (b) 27 MHz, and (c) 40 MHz.

4. Conclusions

We have investigated the plasma characteristics of a broad-band frequency (10-60 MHz) low pressure ICP. The OES profiles of an Ar plasma exhibit that the relative intensities of ArI[$4s'(1/2)^0_1$-$4p'(1/2)_0$] at 750.4 nm become strong with an increase of frequency. It suggests that the electron energy distribution around 13.5 eV is relatively increased with increasing frequency. The OES profiles of a H_2 plasma exhibit that the relative intensities of H β at 486.1 nm become strong with an increase of frequency, and that the superimposed background due to H_2 molecules are lowered with increasing frequency.

The Vp and Ne have a similar shape, which has a peak at the center axis and decreases outward in the radial direction, whereas the Te is almost constant within the radius of 20 mm and then slightly decreases toward the chamber wall. With an increase of pressure, the Ne also increases while the Vp and Te decrease. With an increase of frequency, the Vp and Ne also increase, whereas the Te tends to be saturated in higher frequency.

The EEDF at lower frequency exhibits a deviation from Maxwellian distribution, in which the population of electrons in the high-energy tail above 13 eV drops, whereas the high-energy tail grows at higher frequency and the almost straight line of the EEDF indicates Maxwellian distribution. This is consistent with the theory and the OES profile indicating that the electron energy distribution around 13.5 eV is relatively increased with increasing frequency.

References

[1] M. J. Colgan and M. Meyyappan, *High Density Plasma Sources,* edited by O. A. Popov, Noyes Publications, New Jersey, pp. 149-190, 1995.

[2] M. A. Lieberman and A. J. Lichtenberg, *Principles of Plasma Discharges and Materials Processing,* Wiley, New York, pp. 387-411, 1994.

[3] M. B. Hopkins, J. Res. Natl. Inst. Stand. Technol. **100**, 415 (1995).

[4] K. Okada, S. Komatsu, and S. Matsumoto, J. Vac. Sci. Technol. **A17**, 721 (1999).

[5] S. Oda, Plasma Sources Sci. Technol. **2**, 26 (1993).

[6] K. Kondo, K. Okazaki, H. Oyama, T. Oda, Y. Sakamoto, and A. Iiyoshi, Jpn. J. Appl. Phys. **27**, 1560 (1988).

[7] A. Schwabedissen, E. C. Benck, and J. R. Roberts, Phys. Rev. **E55**, 3450 (1997).

[8] U. Kortshagen, I. Pukropski, and M. Zethoff, J. Appl. Phys. **76**, 2048 (1994).

[9] P. A. Miller, G. A. Hebner, K. E. Greenberg, P. D. Pochan, and B. P. Aragon, J. Res. Natl. Inst. Stand. Technol. **100**, 427 (1995).

[10] E. A. Fattah, K. Iwamoto, and H. Sugai, Proc. 5th Inter. Conf. Reactive Plasmas, Grenoble, pp. 305-306, 2002.

[11] C. M. Ferreira and J. Loureiro, J. Phys. D: Appl. Phys. **16**, 2471 (1983).

[12] U. Kortshagen, J. Phys. D: Appl. Phys. **26**, 1230 (1993).

Thermal Plasma Synthesis and Characterization of Si/Ti/N Nanoparticle Films

J. Hafiz[1], X. Wang[1], R. Mukherjee[1], A. Gidwani[1], T. Renault[1], C. Perrey[2], W. Mook[2]
P. McMurry[1], J. Heberlein[1], C. Carter[2], W. Gerberich[2], and S. Girshick[1]

[1] *Department of Mechanical Engineering, University of Minnesota, Minneapolis, USA*
[2] *Department of Chemical Engineering and Materials Science, University of Minnesota, Minneapolis, USA*

Abstract
In this paper we present recent results of synthesis and deposition of Si/Ti/N nanocomposites using hypersonic plasma particle deposition (HPPD). The study analyzes individual nanoparticles as well as nanostructured films; particularly the chemistry, phase composition and morphology. It shows that complex crystallite phases seen in the film are not present in the particles prior to deposition. Moreover, the hardness of single Si nanospheres was evaluated and found to be several times higher than its bulk counterpart.

1. Introduction

A number of studies have reported that nanostructured materials have drastically increased hardness compared to conventional material of the same composition, suggesting that nanostructured parts or coatings might offer revolutionary improvements in applications requiring friction and wear resistance [1 and references therein]. Recently Si/Ti/N nanostructured films have shown good promise as potential candidates for high hardness and friction resistant applications [2].

Thermal plasmas are well adapted to synthesize such hard coatings, and they have the added advantage of high deposition rates [3]. The HPPD process has been used previously to synthesize binary component films (i.e. SiC) of high hardness [4, 5]. This paper analyzes Si/Ti/N films synthesized and deposited by inertial impaction with the HPPD process. Moreover, the mechanical properties of individual Si nanoparticles have also been examined.

After a description of the experimental process and the different characterization tools utilized, we present and discuss the results.

2. Experimental Process

The Si/Ti/N films were synthesized using the HPPD process as shown in Fig. 1 [2, 3]. The plasma gas consisted of a mixture of Ar and H_2 with an arc current of 200 A, and a voltage of about 45 V. In order to deposit films of Si/Ti/N nanocomposites, $SiCl_4$ and $TiCl_4$ vapors were premixed and injected in the hot plasma jet (about 4000 K) at the exit of the plasma torch, into a nozzle, whereas NH_3 is injected further downstream of the nozzle. Due to rapid quenching of the flow inside the nozzle, Si and Ti vapors reach supersaturated conditions and start to nucleate. The nucleus grows [6] to a few tens of nanometers in diameter. Due to rapid expansion into a chamber at a pressure of ~350 Pa the particles are deposited by inertial impaction on a temperature-controlled substrate made of molybdenum. Under these conditions a 20 nm diameter particle is predicted to hit the substrate with a velocity of about 1700 $m.s^{-1}$.

Several techniques have been employed in order to investigate both nanoparticles prior to deposition, and films constructed from these nanoparticles. A sampling probe interfaced with a differential mobility analyzer (DMA) allowed in-situ access to particles in the hot gas jet. The probe was connected to a hypersonic impactor to allow nanoparticle deposition onto TEM grids for off-line analysis (morphology, chemistry and crystallinity). The sampling system can be operated in chamber pressures as low as 533 Pa, with variable location along the jet axis.

The films were deposited on Molybdenum substrates and investigated using various characterization tools. X-ray diffraction (XRD) spectra were obtained with a Bruker AXS microdiffractometer (CuKα). The beam was collimated to a spot size of 0.8 mm. Rutherford back scattering (RBS) experiments were conducted in a MAS 1700 pelletron tandem accelerator (5SDH) equipped with charge exchange RF plasma by National Electrostatics Corporation (NEC). For each spectrum, 35 μC of 3.4 MeV He^{++} ions were collected. An Ortec Ultra ion detector, with an energy resolution of 12 keV, was placed at 165^o from the incident beam to collect the backscattered ions. X-Ray photoelectron spectroscopy (XPS) was carried out with a Physical Electronics model PHI-5400 equipped with an Al X-ray source. Scanning electron microscopy (SEM) was performed on a JEOL 6500 field emission gun microscope equipped with an energy dispersive spectrometer.

Transmission electron microscopy (TEM) was performed on a Philips CM30 with an operating voltage range of 50 to 300 kV. The CM30 was also equipped with energy dispersive x-ray spectroscopy analysis capabilities (EDAX PV9900).
Finally, the study of the mechanical behavior of individual Si nanoparticles was carried out with a scanning probe microscope-based nanoindenter (Hysitron TriboScope, Hysitron Inc., Edina, MN) equipped with a 1 μm radius diamond tip. The process of obtaining individual nanoparticles using the HPPD system is described elsewhere [7, 8].

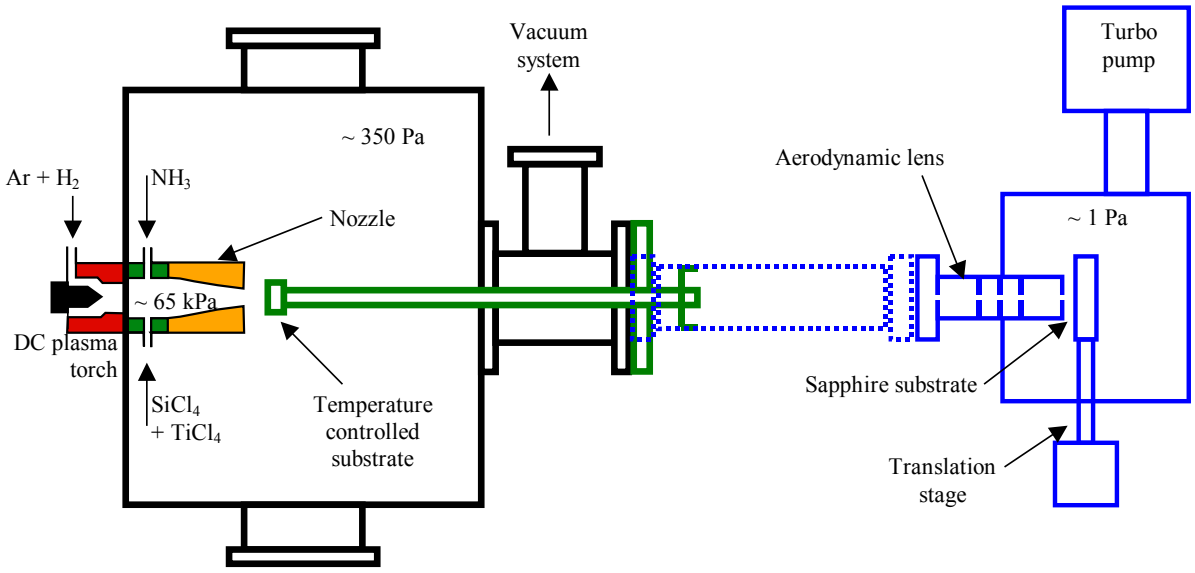

Figure 1. Schematic of the HPPD system.

3. Results and Discussion

3-1. Film Deposition

Analyses of the films for which the $SiCl_4$ and $TiCl_4$ reactant vapors were premixed show the presence of crystalline phases of Si, TiN and $TiSi_2$ and amorphous phases of Si_3N_4. Veprek et al. recently concluded that films of nanocrystalline TiN and $TiSi_2$ in an amorphous Si_3N_4 matrix can have hardness values as high as 105 GPa [2]. The ratio of the different elements, phases and morphology of the film depended on the substrate temperature, reactant flow rates, and whether reactant premixing was performed. The effects of these parameters are discussed below.

3-2. Substrate temperature

Substrate temperature was varied during deposition of the Si/Ti/N films to gauge the effect of substrate thermal conditions on film quality. Two temperature ranges were selected for the experiments. The lower range was set at 320°C, which is the lowest temperature at which films can be deposited under stable conditions. The higher range was set to be ~800°C.
The morphology of the top and cross sections of the films from SEM images (Fig. 2) shows primarily a cluster like structure at high temperatures while clusters mixed with glassy splats were observed at the low temperatures.
XRD spectra show that films deposited at higher temperature are more crystalline than films deposited at low substrate temperatures. The substrate temperature affects the quench rate of the particle after impaction thus either freezing in an amorphous phase or allowing sufficient time for the atoms to order themselves into nanocrystalline phases of TiN, $TiSi_2$ and Si.

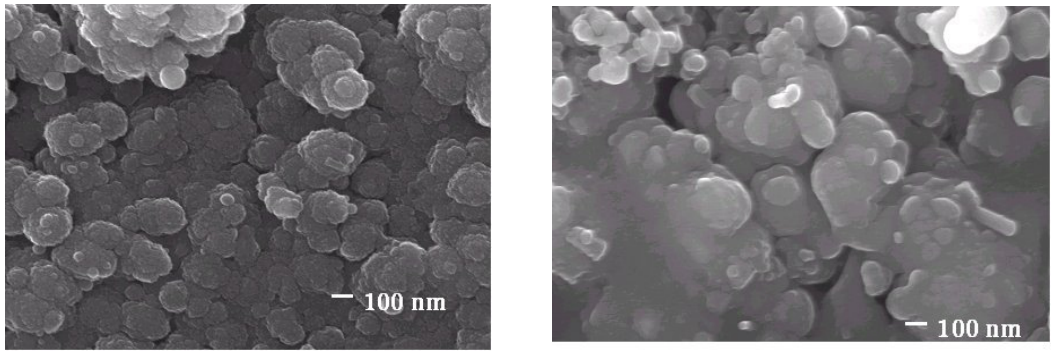

(a) (b)

Figure 2. SEM pictures of Si/Ti/N films. (a) Topography of a film deposited at 800°C. (b) Topography of a film deposited at 320°C.

3-3. Effects of Premixing

Experiments were conducted in which vapors of $SiCl_4$ and $TiCl_4$ were either premixed or unmixed before injection into the nozzle. Analysis of the films show that premixing the reactants before injection resulted in the formation of a crystalline $TiSi_2$ phase while unmixed injection was notable for the absence of crystalline $TiSi_2$ (see Fig. 3). This phenomenon is related to possible reaction chemistry between $TiCl_4$ and $SiCl_4$ before injection into the plasma jet, but the exact cause has not been determined yet.

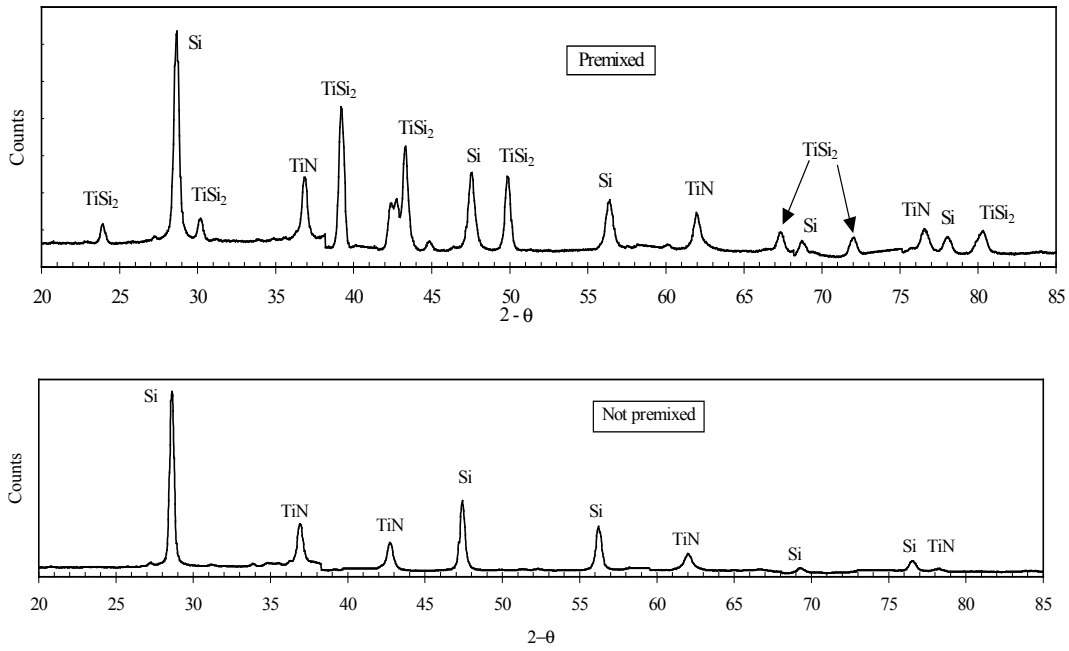

Figure 3. Micro XRD spectra of a premixed and unmixed film.

3-4. Effects of Reactant Flow Rates

Reactant flow rates were varied to determine the effect of $SiCl_4$, $TiCl_4$, NH_3 flow rates and their ratios. The atomic percentage ratios obtained from the RBS spectra (Fig. 4) show that to obtain a ratio of Si:Ti = 2 in the film the amount of $TiCl_4$ (volumetric) needs to be at least twice as that of $SiCl_4$. The presence of nitrogen was detected in RBS and XPS spectra only with ratios of $NH_3/(SiCl_4/TiCl_4) \geq 2.4$. Moreover, the high content of Si and N, the Si-N bond existence in the XPS spectra, and the weak Si_3N_4 peaks in the corresponding XRD spectra point to the presence of amorphous Si_3N_4 in the films. Interestingly, crystalline phases of Si_3N_4 were detected only when the $SiCl_4$ to $TiCl_4$ ratio was two or higher.

Also, the RBS spectra show that higher the NH_3 flow rate, lower the O contamination.

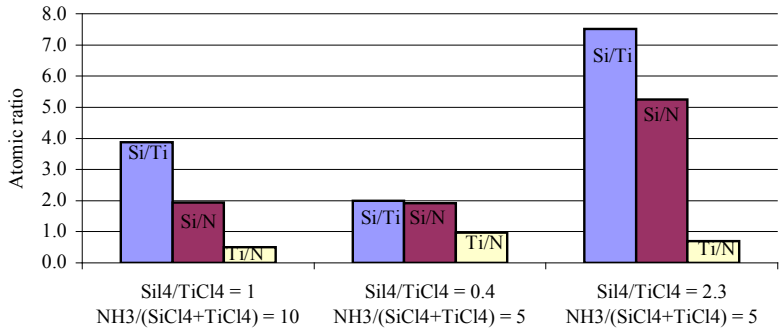

Figure 4. RBS atomic ratios of Si/Ti/N films for different reactant ratios.

3-5. Particle Size Distributions

Particle size distributions were measured using the sampling probe for chamber pressures from 533 Pa to 11 kPa. The sampling probe distance from the nozzle was 2 cm, corresponding to the substrate standoff distance for film deposition (Fig. 5). This allowed us to compare the properties of the particles prior to films produced by impaction under the same conditions (other than differences in pressure).

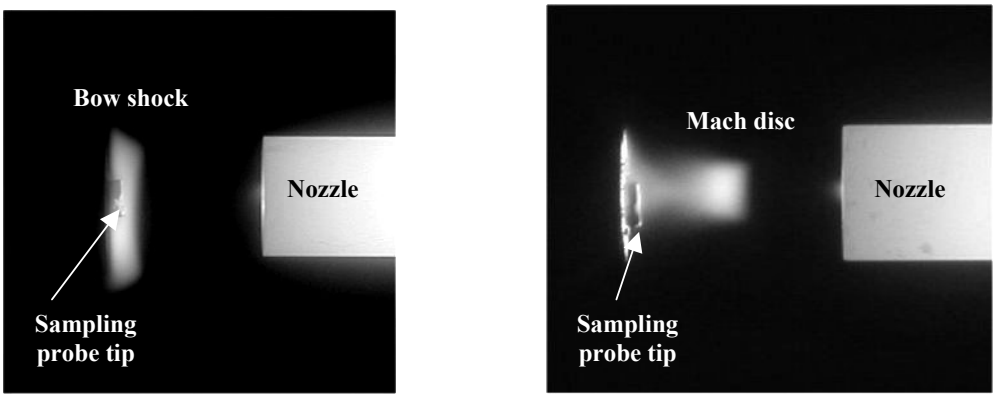

(a) (b)

Figure 5. Sampling probe during actual experiment. (a) Chamber pressure = 800 Pa. (b) Chamber pressure = 3.7 kPa.

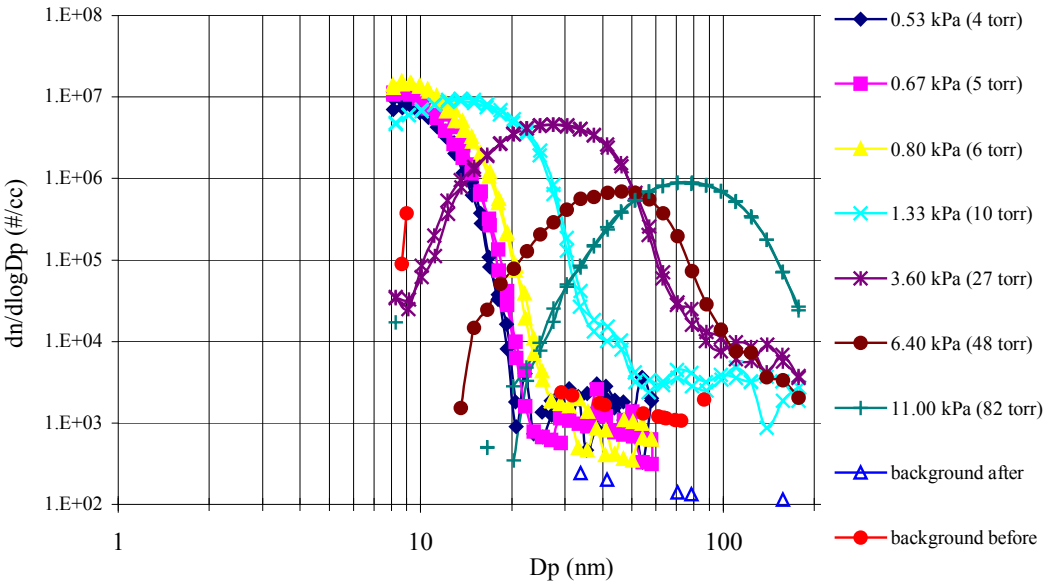

Figure 6. Pressure dependence of the particle size distribution (SiCl4: TiCl4: NH3 = 20:30:500 sccm).

The size distribution plot exhibits remarkably uniform peak behavior with respect to the chamber pressure (Fig. 6). For instance, the size distribution plot of particles sampled at 3.6 kPa (27 torr) shows a peak diameter of approximately 27 nm. Selected area diffraction patterns from a typical deposit obtained in the impactor show mainly amorphous material with isolated bright spots from polycrystalline material. EDS spectra from the same sample show the presence of both Si and Ti as expected. The EDS spectra of particles sampled from the free jet with the hypersonic impactor were consistent with the spectra obtained from the films.

TEM analysis of a randomly selected individual nanoparticle in the impactor shows a complex crystalline diffraction pattern with particle diameter of approximately 100 nm (Fig. 7 (a) and (b)).

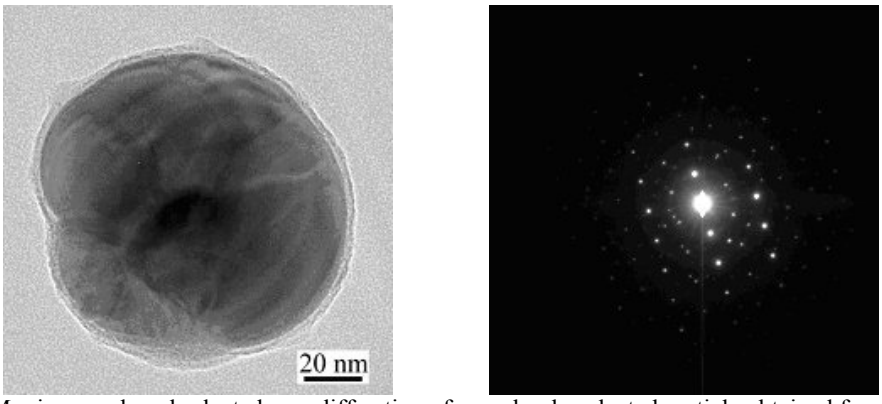

Figure 7. TEM micrograph and selected area diffraction of a randomly selected particle obtained from the impactor.

3-6. Individual Si Nanoparticle Hardness Measurements

A series of repeat loading experiments using the Hysitron Triboscope nanoindenter was performed on Si nanoparticles ranging from 20 to 70 nm in radius. The experiment started with small loads near 10 μN and was incrementally increased to a final value of 200 μN.

Hardness curves for spherical Si nanoparticles of various dimensions are given in Fig 8. The hardness values of the nanoparticles go up to 50 GPa, which is more than four times greater than the 12 GPa value for bulk silicon. It is interesting to note that the hardness increases dramatically as the particle size gets smaller. A particle with a radius of 46 nm has hardness values similar to bulk silicon while the hardness values of a 38 nm radius particle go up to 50 GPa. Extrapolation of this trend predicts hardness rivaling that of diamond for Si nanoparticles in the 5-10 nm range. The reader is referred to Gerberich et al. for detailed information on studies of superhard silicon nanoparticles synthesized in the HPPD system [8].

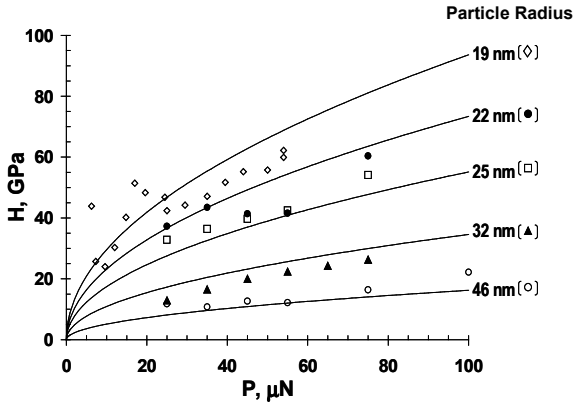

Figure 8. Hardness values of Si nanoparticles [8].

4. Conclusion

The work reported here presents preliminary results of using the HPPD process to deposit Si-Ti-N nanocomposite films. Phase distribution and stoichiometry in the films was studied as a function of process parameters. In-situ measurements of particle size distributions showed that the impacting particles were

mostly below 10 nm in diameter. It is also shown using the sampling probe that particle size distribution is well-behaved with the peak particle diameter linearly related to the sampling pressure.
The way nitrogen reacts with the nanoparticles and/or the film is not yet well understood: whether the particles contain N prior to their impaction onto the substrate or does nitrogen deposit on the film by a chemical vapor deposition route.
Nanoindentation studies of single Si nanoparticles showed that their hardness increases dramatically as particle size decreases, reaching several times the bulk material values for diameters below 40 nm. Work is in progress to determine mechanical properties of the films by nanoindentation.

Acknowledgments
This work was partially supported by the U.S. National Science Foundation (grant DMI-0103169) and by the Minnesota Supercomputing Institute.

References
[1] S. Veprek, J. Vac. Sci. Technol. A **17**, 2401 (1999).

[2] S. Veprek, A. Niederhofer, K. Moto, T. Bolom, H.-D. Männling, P. Nesladek, G. Dollinger, A. Bergmaier, Composition, nanostructured and origin of the ultrahardness in nc-TiN/a-Si_3N_4/a- and nc-$TiSi_2$ nanocomposites with Hv=80 to ≥ 105 Gpa, Surface and coatings Technology **133-134**, 152-159 (2002).

[3] J. Heberlein, O. Postel, S. Girshick, P. McMurry, W. Gerberich, D. Iordanoglou, F. Di Fonzo, D. Neumann, A. Gidwani, M. Fan and N. Tymiak, "Thermal Plasma Deposition of Nanophase Hard Coatings," *Surface and Coatings Technology* **142-144**, 265-271 (2001).

[4] N.P. Rao, N. Tymiak, J. Blum, A. Neuman, H.J. Lee, S.L. Girshick, P.H. McMurry and J. Heberlein. Journal of Aerosol Science, **29**, 707-720 (1998).

[5] J. Blum, N. Tymiak, A. Neuman, Z. Wong, N.P. Rao, S.L. Girshick, W.W. Gerberich, P.H. McMurry and J. Heberlein, J. Nanopart. Res. **1**, 31 (1999).

[6] S.L. Girshick, Plasma Sources Sci. Technol. **3,** 388-394, (1994).

[7] F. Di Fonzo, A. Gidwani, M. H. Fan, D. Neumann, D. I. Iordanoglou, J. V. R. Heberlein, P. H. McMurry, S. L. Girshick, N. Tymiak, W. W. Gerberich and N. P. Rao, "Focused Nanoparticle-Beam Deposition of Patterned Microstructures," *Applied Physics Letters* **77**, 910–912 (2000).

[8] W. Gerberich, W. Mook, C. Perrey, C. Carter, M. Baskes, R. Mukherjee, A. Gidwani, J. Heberlein, P. McMurry and S. Girshick, J. Mech. Phys. Solid., in press (2002).

Three-dimensional modeling of the long laminar plasma jet with transverse particle and carrier-gas injection

Dong-Yan Xu and Xi Chen

Department of Engineering Mechanics, Tsinghua University, Beijing 100084, China

Abstract

Modeling results are presented concerning the characteristics of a long laminar plasma jet with transverse particle and carrier gas injection. It is shown that the long laminar plasma jet has well enough stiffness to endure the impact of the laterally injected carrier gas, although the laminar jet assumes slight deflection from its geometrical axis. The three dimensional effects caused by the lateral carrier-gas injection on the jet characteristics and on the particle moving trajectories and heating histories are shown to be appreciable.

1. Introduction

In various applications of thermal plasmas (e.g. plasma spraying, plasma cladding and remelting, etc.), the plasmas are usually issued from thermal plasma torches in the form of plasma jets. Long laminar plasma jets have been successfully produced by use of elaborately designed plasma torches in recent years [1-3]. In comparison with the turbulent jet widely used in materials processing, the long laminar plasma jet has a few marked advantages including adjustable high-temperature region length, small axial gradients of temperature and velocity, low-level noise emission and weak entrainment of ambient air into the jet. Those advantages make the long laminar plasma jet very attractive from the materials processing viewpoint, since low-noise working surroundings, reduced oxidation degree of processed metallic materials and enhanced process controllability or repeatability can be achieved.

So far, our understanding on the characteristics of long laminar plasma jets is still far from completeness. Preliminary modeling results reported in Refs. [1, 4] showed that the laminar plasma jet assumed much longer high-temperature region length than that for the turbulent jet, in consistence with the experimental observation [1, 3]. Although it is expected that the entrainment of ambient air into the laminar jet is weaker than that for the case of turbulent jet, up to date there is lack of detailed information about the species diffusion in the long laminar plasma jet. On the other hand, since the mass velocity of the laminar plasma jet is relatively small compared with that for the turbulent plasma jet, there often exists a doubt about whether the laminar plasma jet can endure the impact of laterally injected carrier gas. For this reason, in experiments sometimes researchers turned to rely completely on the gravity (instead of carrier gas) to feed the material particles into the laminar plasma jet. In order to clarify the foregoing problems, modeling work is conducted in this paper to study the characteristics of the long laminar plasma jet with lateral injection of carrier gas and particles, using the laminar argon plasma jet issuing into ambient air as the calculation example.

2. Modeling approach

2.1 Modeling of the long laminar plasma jet

The assumptions employed in the jet modeling include: (i) the plasma flow is laminar and steady; (ii) the plasma is optically thin, in LTE state and with temperature- and composition-dependent properties; (iii) the pertinent Mach number is small (e.g. less than 0.3), and thus the viscous dissipation and the pressure work terms in the energy equation can be neglected; (iv) only the effect of the laterally injected cold carrier gas on the plasma jet is considered, i.e. ignoring the effect of the particle injection on the jet characteristics.

Based on the foregoing assumptions, the continuity, momentum, energy and species conservation equations in the cylindrical coordinate system (r, θ, z) can be written as follows:

$$\frac{1}{r}\frac{\partial}{\partial r}(r\rho v_r)+\frac{1}{r}\frac{\partial}{\partial \theta}(\rho v_\theta)+\frac{\partial}{\partial z}(\rho v_z)=0 \tag{1}$$

$$\frac{1}{r}\frac{\partial}{\partial r}\left(r\rho v_r^2\right)+\frac{1}{r}\frac{\partial}{\partial \theta}(\rho v_r v_\theta)+\frac{\partial}{\partial z}(\rho v_r v_z)=-\frac{\partial p}{\partial r}+\frac{\partial}{\partial r}\left(2\mu\frac{\partial v_r}{\partial r}\right)+\frac{1}{r}\frac{\partial}{\partial \theta}\left[\mu\left(\frac{1}{r}\frac{\partial v_r}{\partial \theta}+\frac{\partial v_\theta}{\partial r}-\frac{v_\theta}{r}\right)\right]$$
$$+\frac{\partial}{\partial z}\left[\mu\left(\frac{\partial v_r}{\partial z}+\frac{\partial v_z}{\partial r}\right)\right]+\frac{2\mu}{r}\left(\frac{\partial v_r}{\partial r}-\frac{1}{r}\frac{\partial v_\theta}{\partial \theta}-\frac{v_r}{r}\right)+\rho\frac{v_\theta^2}{r} \tag{2}$$

$$\frac{1}{r}\frac{\partial}{\partial r}(r\rho v_\theta v_r)+\frac{1}{r}\frac{\partial}{\partial \theta}(\rho v_\theta^2)+\frac{\partial}{\partial z}(\rho v_\theta v_z)=-\frac{1}{r}\frac{\partial p}{\partial \theta}+\frac{\partial}{\partial r}\left[\mu\left(\frac{\partial v_\theta}{\partial r}-\frac{v_\theta}{r}+\frac{1}{r}\frac{\partial v_r}{\partial \theta}\right)\right]+\frac{1}{r}\frac{\partial}{\partial \theta}\left[2\mu\left(\frac{1}{r}\frac{\partial v_\theta}{\partial \theta}+\frac{v_r}{r}\right)\right]$$
$$+\frac{\partial}{\partial z}\left[\mu\left(\frac{\partial v_\theta}{\partial z}+\frac{1}{r}\frac{\partial v_z}{\partial \theta}\right)\right]+\frac{2\mu}{r}\left(\frac{1}{r}\frac{\partial v_r}{\partial \theta}+\frac{\partial v_\theta}{\partial r}-\frac{v_\theta}{r}\right)-\rho\frac{v_r v_\theta}{r} \quad (3)$$

$$\frac{1}{r}\frac{\partial}{\partial r}(r\rho v_z v_r)+\frac{1}{r}\frac{\partial}{\partial \theta}(\rho v_z v_\theta)+\frac{\partial}{\partial z}(\rho v_z^2)=-\frac{\partial p}{\partial z}+\frac{1}{r}\frac{\partial}{\partial r}\left[\mu r\left(\frac{\partial v_z}{\partial r}+\frac{\partial v_r}{\partial z}\right)\right]+\frac{1}{r}\frac{\partial}{\partial \theta}\left[\mu\left(\frac{1}{r}\frac{\partial v_z}{\partial \theta}+\frac{\partial v_\theta}{\partial z}\right)\right]+\frac{\partial}{\partial z}\left(2\mu\frac{\partial v_z}{\partial z}\right) \quad (4)$$

$$\frac{1}{r}\frac{\partial}{\partial r}(r\rho v_r h)+\frac{1}{r}\frac{\partial}{\partial \theta}(\rho v_\theta h)+\frac{\partial}{\partial z}(\rho v_z h)=\frac{1}{r}\frac{\partial}{\partial r}\left(r\frac{k}{c_p}\frac{\partial h}{\partial r}\right)+\frac{1}{r^2}\frac{\partial}{\partial \theta}\left(\frac{k}{c_p}\frac{\partial h}{\partial \theta}\right)+\frac{\partial}{\partial z}\left(\frac{k}{c_p}\frac{\partial h}{\partial z}\right)-U_r-\frac{\partial}{\partial z}[(h_A-h_B)J_z]$$
$$-\frac{1}{r}\frac{\partial}{\partial r}[r(h_A-h_B)J_r]-\frac{1}{r}\frac{\partial}{\partial \theta}[(h_A-h_B)J_\theta]-\frac{1}{r}\frac{\partial}{\partial r}\left[r\frac{k}{c_p}(h_A-h_B)\frac{\partial f_A}{\partial r}\right]$$
$$-\frac{1}{r^2}\frac{\partial}{\partial \theta}\left[\frac{k}{c_p}(h_A-h_B)\frac{\partial f_A}{\partial \theta}\right]-\frac{\partial}{\partial z}\left(\frac{k}{c_p}(h_A-h_B)\frac{\partial f_A}{\partial z}\right) \quad (5)$$

$$\frac{1}{r}\frac{\partial}{\partial r}(r\rho v_r f_A)+\frac{1}{r}\frac{\partial}{\partial \theta}(\rho v_\theta f_A)+\frac{\partial}{\partial z}(\rho v_z f_A)=\frac{1}{r}\frac{\partial}{\partial r}\left(r\Gamma_f\frac{\partial f_A}{\partial r}\right)+\frac{1}{r^2}\frac{\partial}{\partial \theta}\left(\Gamma_f\frac{\partial f_A}{\partial \theta}\right)+\frac{\partial}{\partial z}\left(\Gamma_f\frac{\partial f_A}{\partial z}\right)+S_f \quad (6)$$

In these equations, v_r, v_θ and v_z are the velocity components in r-, θ- and z-directions, p and f_A the gas pressure and the mass fraction of argon in the argon-air mixture, whereas ρ, μ, h, k, c_p and U_r are the temperature- and composition-dependent density, viscosity, specific enthalpy, thermal conductivity, specific heat at constant pressure and radiation power per unit volume of the plasma, respectively. The combined diffusion coefficient method proposed by Murphy [5, 6] is employed in this study to treat the diffusion of argon in the argon-air mixture. Since both argon and air are involved in this study, the source terms in the energy equation (5) are much more complicated than those for the case only one gas species is involved. In equation (5), h_A and h_B are the specific enthalpy of species A (argon) and B (air). J_r, J_θ and J_z are the r-, θ- and z-component of the following diffusion flux vector of argon species [5, 6]:

$$\vec{J}_A=-(n^2/\rho)\overline{m}_A\overline{m}_B\overline{D}_{AB}^{x}\nabla X_A-\overline{D}_{AB}^{T}\nabla\ln T \quad (7)$$

where n is the total gas particle number density, $\overline{m}_A$ and $\overline{m}_B$ are the averaged gas particle mass for all the heavy particles (excluding electrons) coming from argon (i.e. species A) and from air (i.e. species B), X_A is the mole fraction of argon in the argon-air mixture, whereas $\overline{D}_{AB}^{x}$ and $\overline{D}_{AB}^{T}$ are the combined ordinary diffusion coefficient associated with the mole-fraction gradient ∇X_A and the combined thermal diffusion coefficient associated with the temperature gradient ∇T, respectively [5, 6]. The transport coefficient in equation (6) can be expressed as $\Gamma_f=\left[\overline{m}_A\overline{m}_B/(\overline{M}\overline{M}_A)\right]\rho\,\overline{D}_{AB}^{x}$, in which $\overline{M}$ and $\overline{M}_A$ are the averaged gas particle mass for all the gas particles (including electrons) of the gas mixture and that for the gas particles coming from argon, respectively. The source term S_f in equation (6) can be expressed as

$$S_f=\frac{1}{r}\frac{\partial}{\partial r}\left(r\Gamma_f\frac{f_A}{\overline{M}}\frac{\partial\overline{M}}{\partial r}\right)-\frac{1}{r}\frac{\partial}{\partial r}\left(r\Gamma_f\frac{f_A}{\overline{M}_A}\frac{\partial\overline{M}_A}{\partial r}\right)+\frac{1}{r^2}\frac{\partial}{\partial\theta}\left(\Gamma_f\frac{f_A}{\overline{M}}\frac{\partial\overline{M}}{\partial\theta}\right)-\frac{1}{r^2}\frac{\partial}{\partial\theta}\left(\Gamma_f\frac{f_A}{\overline{M}_A}\frac{\partial\overline{M}_A}{\partial\theta}\right)+\frac{\partial}{\partial z}\left(\Gamma_f\frac{f_A}{\overline{M}}\frac{\partial\overline{M}}{\partial z}\right)$$
$$-\frac{\partial}{\partial z}\left(\Gamma_f\frac{f_A}{\overline{M}_A}\frac{\partial\overline{M}_A}{\partial z}\right)+\frac{1}{r}\frac{\partial}{\partial r}\left(r\overline{D}_{AB}^{T}\frac{\partial\ln T}{\partial r}\right)+\frac{1}{r^2}\frac{\partial}{\partial\theta}\left(\overline{D}_{AB}^{T}\frac{\partial\ln T}{\partial\theta}\right)+\frac{\partial}{\partial z}\left(\overline{D}_{AB}^{T}\frac{\partial\ln T}{\partial z}\right) \quad (8)$$

The computational domain used in this study is shown in figure 1 with domain sizes as follows: $0\le z\le 450$ mm, $0\le r\le 50$ mm, $0\le\theta\le 2\pi$. The mesh on the longitudinal section (θ = constant) and that on the cross section (z = constant) are also shown in figure 1. 24 (r-) × 35 (θ-) × 60 (z-direction) grid points are employed in the computation and are arranged to be finer near the jet axis and near the jet inlet.

The following boundary conditions are used in the modeling: (i) At the jet inlet (z=0 and $r\le$4 mm), we use

$$v_z(r)=U_0\left[1-(r/R)^2\right],\quad v_r(r)=0,\quad v_\theta(r)=0,\quad T(r)=(T_0-T_W)\left[1-(r/R)^2\right]+T_W,\quad f_A=1 \quad (9)$$

It is noted that the inlet enthalpy profile can be readily calculated from the given temperature profile. In equation (9), R is the jet inlet radius (4 mm), T_0 and U_0 are the maximum temperature and axial velocity at the jet inlet. T_0 = 15835 K and U_0 = 146 m/s are taken, corresponding to the argon flow rate 120 STP cm^3 / s

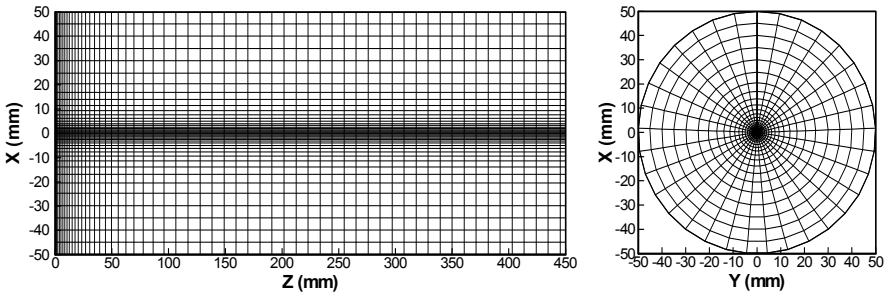

Figure 1. Computational domain and meshes on the $r-z$ section and the $r-\theta$ section.

and torch current 160 A (the measured jet power is 1.59 kW [2]). The other part of the upstream boundary (with z = 0 and 4 mm< r ≤50 mm) is assumed to be solid wall with zero velocity components, zero diffusion flux and fixed temperature (wall temperature T_W =300 K). (ii) One-way boundary conditions are adopted at the downstream boundary (with z = 450 mm), i.e. $\partial\phi/\partial z = 0$, ($\phi = v_r, v_\theta, v_z, h, f_A$). (iii) At the outer boundary of the jet (r = 50 mm), the following free-boundary conditions are used:

$$\partial(\rho r v_r)/\partial r = 0,\ \ \partial(r v_\theta)/\partial r = 0,\ \ \partial v_z/\partial r = 0,\ \ \begin{cases} T = 300\ \text{K},\quad f_A = 0 & \text{for}\quad v_r \le 0 \\ \partial T/\partial r = 0,\ \ \partial f_A/\partial r = 0 & \text{for}\quad v_r \ge 0 \end{cases} \tag{10}$$

(iv) Along the geometrical axis of the jet (r = 0), rv_θ =0 and the averaged values of ϕ_i (i = 1, 2, …, N) at all the N grid points on the small circle nearest to the axis in the mesh are employed for other variable ϕ, namely,

$$\phi|_{r=0} = \frac{1}{N}\sum_{i=1}^{N}\phi_i\ , \quad (\phi = v_z, v_r, h\ \text{or}\ \bar{f}_A) \tag{11}$$

(v) At the longitudinal section with θ = 0 or $\theta = 2\pi$, the value of variable ϕ at a boundary point is taken as the average of the ϕ values at its two neighbour grid points in θ direction. (vi) If there is radial carrier-gas (argon) injection, $v_r = V_{in}$, v_θ =0, v_z =0, T = 300 K and f_A =1 are taken at the exit of the injection tube, here V_{in} is the injection velocity of carrier gas.

2.2 Particle motion and heating in the laminar plasma jet

The following assumptions are employed in the study of particle behavior: (i) The particle is spherical. (ii) The pertinent Biot number is small (e.g. less than 0.02) so that the temperatures within the injected particle can be treated as everywhere uniform. This assumption is expected to be good for metal particles. (iii) The particle-particle interaction is negligible. (iv) The initial velocity of the particle is identical to the carrier gas velocity at the exit section of the injection tube.

Many factors may affect the motion and heating of the particle injected into the plasma jet. Drag and thermophoretic forces are expected to be the most important among the forces governing the particle motion. Hence, particle motion is described by the following equations:

$$m_p\frac{d\mathbf{V}_p}{dt} = \mathbf{F}_d + \mathbf{F}_t\,, \qquad \frac{dx_{pi}}{dt} = V_{pi}\,, \quad (i = 1,\ 2,\ 3) \tag{12}$$

where x_{pi} , m_p and t are the ith component of particle location vector, particle mass and time, whereas $\mathbf{V}_p$, $\mathbf{F}_d$ and $\mathbf{F}_t$ are particle velocity, particle drag force and thermophoretic force vectors, respectively. Using the drag coefficient and thermophoretic force expressions [7], equation (12) can be rewritten as

$$\frac{dV_{pi}}{dt} = \left(\frac{3\rho C_D}{8 r_p \rho_p}\right)\cdot\left|\mathbf{V}-\mathbf{V}_p\right|\left(V_i - V_{pi}\right) - 9\left(\frac{\mu^2}{\rho\rho_p r_p^2}\right)\cdot B\cdot\left(\frac{1}{T_\infty}\frac{\partial T_\infty}{\partial x_i}\right) \quad (i=1, 2, 3) \tag{13}$$

for a spherical particle with radius r_p . In equation (13), C_D is the drag coefficient, $\mathbf{V}$, T_∞ and $\partial T_\infty/\partial x_i$ are the plasma velocity vector, the plasma temperature and the temperature-gradient component in x_i-direction at the particle location if the particle is absent, whereas

$$B = C_s\,\frac{\left(k/k_p\right) + C_t\left(\lambda^*/r_p\right)}{\left[1+3C_m\left(\lambda^*/r_p\right)\right]\times\left[1+2\left(k/k_p\right)+2C_t\left(\lambda^*/r_p\right)\right]} \tag{14}$$

where ρ_p and k_p are the density and thermal conductivity of particle material, whereas C_s, C_t and C_m are three constants equaling to 1.17, 2.18 and 1.14, respectively. λ^* is the effective mean-free-path length of gas particles and can be calculated by $\lambda^* = \bar{k} \cdot \mathrm{Pr}_w/(2\psi_w \bar{C}_p)$ [7, 8], in which ψ_w is the gas particle flux incident upon the particle surface [8], and is calculated by $\psi_w = \rho_w \bar{v}_w /[2 \cdot (1+\sqrt{T_j/T_w})]$. Here ρ_w and $\bar{v}_w$ are the gas density and average thermal speed of gas particles evaluated at particle surface temperature T_w, whereas the average value of the gas thermal conductivity and specific heat within the Knudsen layer around the suspended particle are respectively calculated by

$$\bar{k} = \frac{1}{T_j - T_w}\int_{T_w}^{T_j} k dT = \frac{S_j - S_w}{T_j - T_w}, \qquad \bar{C}_p = \frac{1}{T_j - T_w}\int_{T_w}^{T_j} C_p dT = \frac{h_j - h_w}{T_j - T_w} \tag{15}$$

T_j is the jump temperature and is calculated by use of the relations $q_0 = (S_\infty - S_j)/r_p$, $(dS/dr)_w = q_0$ and $S_j = S_w + z^*(dS/dr)_w$ starting from a guessed value of T_j. Several iterations are enough to get a convergent value of T_j [7].

The drag coefficient C_D in equation (13) is calculated by $C_D = \alpha_1\alpha_2 f(\mathrm{Re}_\infty)(\mathrm{Re}_\infty/\mathrm{Re}_w)^{0.1} = \alpha_1\alpha_2 f(\mathrm{Re}_\infty)(\nu_w/\nu_\infty)^{0.1}$ [7, 8]. Here $f(\mathrm{Re}_\infty)$ is the standard drag coefficient of a sphere based on the Reynolds number evaluated at plasma temperature T_∞ (i.e. $\mathrm{Re}_\infty = 2\rho_\infty r_p |\mathbf{V} - \mathbf{V}_p|/\mu_\infty$) and the detailed piecewise expressions [7] are used. The factor $(\nu_w/\nu_\infty)^{0.1}$ is introduced to correct the great temperature-difference effect [8], whereas α_1 and α_2 are for the corrections due to, respectively, the Knudsen (rarefaction) effect and particle evaporation (if exists) [7] and can be calculated by

$$\alpha_1 = \left[1 + \left(z^*/r_p\right)\right]^{-0.45}, \quad \alpha_2 = \frac{L_v}{S_\infty - S_w}\int_{T_p}^{T_\infty} \frac{k dT}{h - h_w + L_v} \tag{16}$$

where $S = \int_{T_0}^{T} k dT$ is the so-called heat conduction potential, L_v is the evaporation latent heat of particle material, whereas z^* is the jump distance and is calculated by $z^* = [(2-a)/a][\gamma/(1+\gamma)](2\lambda^*/\mathrm{Pr}_w)$. Here a and γ are the thermal accommodation factor (a = 0.8 is used in this study) and specific heat ratio, whereas Pr_w ($= \mu_w C_{pw}/k_w$) is the Prandtl number evaluated at particle surface temperature.

The specific heat flux q from the plasma to the suspended particle is calculated by $q = \beta_1\beta_2 q_c$, in which q_c is the heat flux without accounting for the Knudsen (rarefaction) effect and particle evaporation and calculated using the following expression [7, 8] for the Nusselt number defined as $Nu_s = 2q_c r_p/(S_\infty - S_w)$:

$$Nu_s = 2\left[1 + 0.63\,\mathrm{Re}_\infty\,\mathrm{Pr}_\infty^{0.8}\left(\frac{\mathrm{Pr}_w}{\mathrm{Pr}_\infty}\right)^{0.42}\left(\frac{\rho_\infty\mu_\infty}{\rho_w\mu_w}\right)^{0.52} C^2\right]^{0.5} \tag{17}$$

in which factor $C = \left[1-(h_w/h_\infty)^{1.14}\right]/\left[1-(h_w/h_\infty)^2\right]$. The factors β_1 and β_2 are introduced to correct the Knudsen effect and particle evaporation (if exists) [7], and calculated by $\beta_1 = [1 + z^*/r_p]^{-1}$ and $\beta_2 = \alpha_2$.

For the case with small Biot numbers, the calculation of particle heating can be significantly simplified [7]. The temperature rising rate for the solid-phase heating of the injected particle is calculated by

$$dT_p/dt = 3(q - q_r)/(\rho_p C_{ps} r_p) \tag{18}$$

in which q_r is the radiation heat loss from the particle surface and $q_r = \varepsilon\sigma T_w^4$, whereas C_{ps} is the solid-phase specific heat of the particle material. During the melting period, the metallic particle temperature (T_m) would remain unchanged and the liquid-phase fraction (F) increment within the ith time step (Δt_i) is calculated by $\Delta F_i = 3(q - q_r)\cdot\Delta t_i/(L_m\rho_p r_p)$, in which L_m is the melting latent heat. The temperature rising rate for the liquid phase heating of the injected particle is also calculated using equation (18) but C_{ps} should be replaced by C_{pl} (the liquid-phase specific heat). As the injected particle has been heated to the period of intense evaporation, particle radius will reduce with the time as $dr_p/dt = -(q - q_r)/(\rho_p L_v)$ [7].

Sometimes, the moving particle may pass through the high-temperature core region of the plasma jet and reach the region with plasma temperatures less than the particle surface temperature. For this case, the heat flux from the plasma flow to the particle will be negative and the particle temperature will decrease gradually. The cooling of the heated particle can still be calculated using above equations.

3. Modeling results and discussions

3.1 Characteristics of the long laminar plasma jet with lateral carrier-gas injection

The carrier-gas (argon) injection tube is taken to be directed to the jet center and normal to the geometrical axis of the jet. The inner diameter of injection tube is 1.5 mm with a distance between the exit section of the carrier-gas injection tube and the geometrical axis of the plasma jet being 4 mm, whereas the distance between the carrier-gas injection tube and the jet inlet is 1.5 mm. Figure 2 presents computed isotherms within the laminar plasma jet on the plane formed by the plasma torch axis and injection tube axis (i.e. the $\theta = 0 - \pi$ section, this plane will be called injection plane hereafter) with the carrier-gas injection velocity of 5 m/s (or carrier-gas / plasma mass-flow-rate ratio being 0.074). Corresponding computed iso-contours of axial-velocity and argon mass fraction on the injection plane are shown in figure 3 and figure 4, respectively. The computed isolines of the temperature and argon mass fraction on the cross section at the axial distance z = 253 mm are shown in figures 5. In those figures, Z represents the axial distance from the plasma jet inlet, whereas X is the coordinate in radial direction with $X>0$ expressing the upper semi-plane (i.e. with $\theta = 0$) and $X<0$ denoting the lower semi-plane (i.e. with $\theta = \pi$). Examination of figures 2–5 shows that the lateral injection of carrier gas causes appreciable three-dimensional (3-D) features of the plasma jet. The carrier-gas injection induces marked deformation of the temperature, concentration and velocity fields near the carrier-gas injection port on the injection plane, and the 3-D effects of carrier-gas injection preserved in the downstream region of the plasma jet. Appreciable non-axisymmetry of the jet can be clearly seen in figure 5. The plasma jet assumes slight deflection on the injection plane due to the impact of the injected carrier gas, but the stiffness of the laminar plasma jet is still good. Namely, the long laminar plasma jet still assumes well enough stiffness to endure the impact of the laterally injected carrier gas. This predicted result implies that the particulate matter can be injected into the long laminar plasma jet with the aid of the carrier gas.

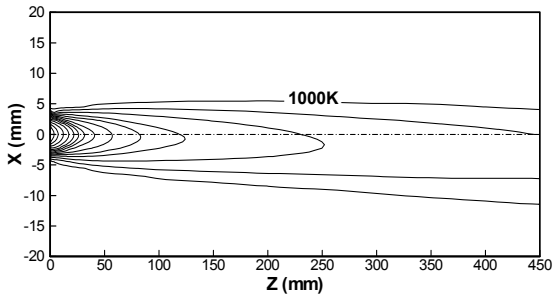

Figure 2 Computed isotherms in the laminar plasma jet on the injection plane ($\theta = 0$ -- π). Interval – 1000 K.

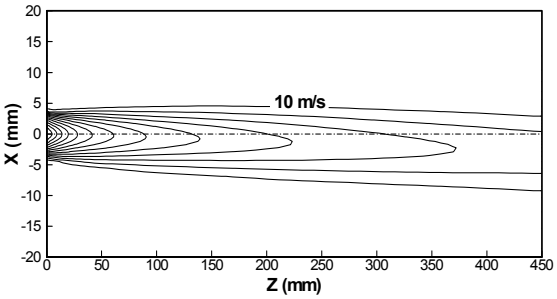

Figure 3 Contours of the axial velocity in the plasma jet on the injection plane (θ=0--π). Interval – 10 m/s.

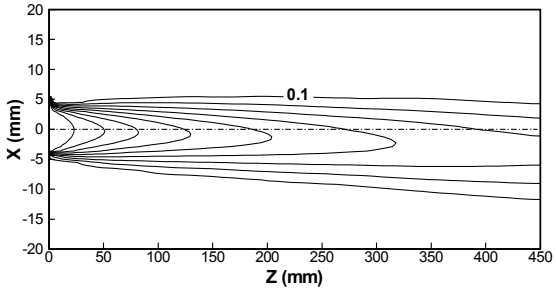

Figure 4 Computed contours of the argon mass fraction on the injection plane ($\theta = 0 - \pi$). Interval – 0.1.

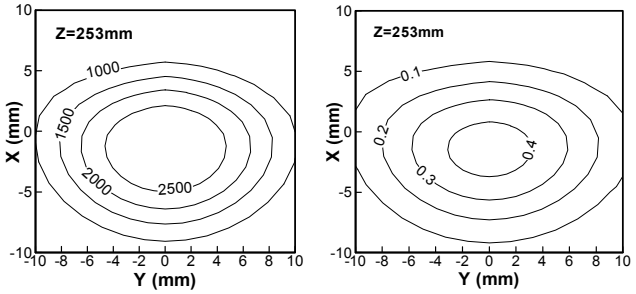

Figure 5 Computed isolines of the temperature and argon mass fraction on the cross section at z =253 mm.

3.2 Motion and heating of particles injected into the laminar plasma jet

Since the feedstock particles are injected into the plasma jet with the aid of the carrier gas, the 3-D features of the plasma jet flow caused by the lateral carrier-gas injection will cause the moving trajectories and heating histories of the particles somewhat different from those for the 2-D case ignoring the influence of the carrier gas injection. In the present study, metallic (nickel) particles have been employed and the counter-action of heated and accelerated particles on the plasma jet has been neglected for simplicity.

Figure 6 compares the moving trajectories of 10 μm and 20 μm nickel particles in the plasma jet with initial inward injection velocity of 5 m/s. Figure 7 compares the typical calculated heating histories of a 15 μm

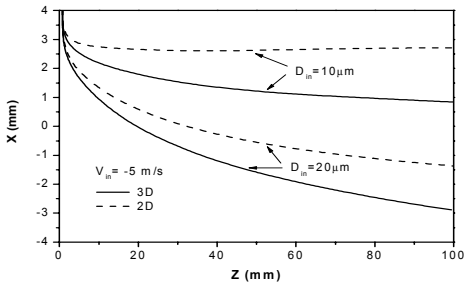

Figure 6 Comparison of the calculated trajectories of 10 μm and 20 μm particles injected into the 3-D plasma jet with their 2-D counterparts. V_{in} = – 5 m/s.

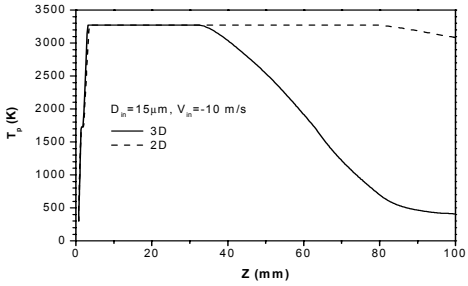

Figure 7 Comparison of the calculated heating history of a 15 μm particle moving in the 3-D plasma jet with its 2-D counterpart. V_{in} = –5 m/s.

particle. It is seen from figure 6 that the lateral injection of carrier-gas injection affects significantly the particle trajectories due to its appreciable influence on the temperature, velocity and concentration fields of the plasma jet. As expected, the particle with larger diameter will assume deeper penetration distance for both the 3-D and 2-D cases, with the 3-D penetration depth larger than its 2-D counterpart. Those calculated results can be readily understood, since the carrier gas not only makes the particle gaining an initial inward velocity, but also interacts with the plasma stream itself, resulting in the formation of an injection gas channel. The injected particles will move within the injection gas channel during the initial period of their movement, resulting in different predicted results from the 2-D case for the particle trajectories and also for the particle heating histories. For the case shown in figures 7, since the particle assumes a deeper penetration in the 3-D flow field than that for the 2-D case, the particle passes through the high temperature core region and reaches the region with lower gas temperatures in the 3-D jet. Consequently, the temperature of the injected particle is appreciably lower than that for the 2-D case at the later stage of its heating.

4. Conclusion

Main conclusions obtained from the present study are as follows.

(1) The lateral injection of the carrier gas will induce appreciable 3-D effects in the long laminar plasma jet. The jet will be deflected from its original geometrical axis, and the temperature, argon mass fraction and velocity distributions on the jet cross sections will assume appreciable non-axisymmetry. These 3-D effects also affects appreciably the moving trajectories and heating histories of the injected particles.

(2) However, the long laminar plasma jet still has well enough stiffness to endure the impact of the lateral carrier-gas injection for the carrier-gas injection velocities within a reasonable range from the viewpoint of materials processing. Hence, feedstock particles can be injected into the long laminar plasma jet with the aid of carrier gas.

Acknowledgement

This work was supported by the National Natural Science Foundation of China (grant Nos. 50176024, 59836220). The authors thank Dr. A. B. Murphy, who provided us the argon-air plasma properties.

References

[1] Wenxia Pan, Wenhua Zhang, Wenhong Zhang, Chengkang Wu – *Plasma Chem. Plasma Process*. **21**, 23 (2001).

[2] Wenxia Pan, Wenhong Zhang, Wei Ma, Chengkang Wu – *Plasma Chem. Plasma Process*. **22**, 271 (2002).

[3] K. Osaki, O. Fugumasa, A. Kokayashi – *Vacuum* **59**, 47 (2000).

[4] He-Ping Li – *Studies of heat transfer and fluid flow in a d. c. arc plasma torch and plasma jet* Ph. D. Thesis, Tsinghua University, Beijing, China (2001, in Chinese).

[5] A. B. Murphy – *Plasma Chem. Plasma Process.* **15**, 279 (1995).

[6] A B. Murphy – *J. Phys. D: Appl. Phys.* **29**, 1922 (1996).

[7] Xi Chen – *Heat Transfer and Fluid Flow under Thermal Plasma Conditions* (Beijing: Science Press) chapters 4 and 5 (1993, in Chinese).

[8] Xi Chen – *Thin Solid Films* **345**, 140 (1999).

Improved analysis of the noise emission from a turbulent plasma jet

Kai Cheng and Xi Chen

Department of Engineering Mechanics, Tsinghua University, Beijing 100084, China

Abstract

This paper improves the previous analysis concerning the turbulent plasma jet noise emission presented in Ref. [1] by using the computed temperature fluctuations from solving a second-order turbulent Reynolds heat flux equation. It is shown that the temperature fluctuation is still the dominant source of plasma jet noise emission. The predicted noise emission intensities are reasonably consistent with available experimental data.

1. Introduction

As is well known, strong noise emission is always generated in thermal spraying and has been harassing researchers since the atmospheric plasma spraying (APS) technology was employed in modern industry many years ago. However, so far our knowledge concerning the noise emission under plasma conditions is very pool. In Ref. [1], the approach originally proposed by Fortuné and Gervais [2] for predicting the noise emission from a hot non-ionized gas jet was extended to the study of the noise emission from a turbulent plasma jet with the atmospheric plasma spraying as the research background.

Pertinent two-dimensional continuity, momentum, energy, species, turbulent kinetic energy and turbulence dissipation rate equations were simultaneously solved in Ref. [1] to determine the turbulent plasma jet characteristics and then the noise emission intensity-frequency spectrums and noise levels were calculated. It was found that the noise intensity is roughly proportional to the square of the velocity at the plasma jet inlet. Among the noise emission sources due to, respectively, velocity fluctuation, temperature fluctuation and their mixed effect, the temperature fluctuation was the dominant one for the turbulent plasma jets.

In Ref. [1], however, the local temperature fluctuation in the turbulent plasma jet was simply calculated from the velocity fluctuation at the same location by assuming that there exists a directly proportional relation between the temperature fluctuation and the velocity fluctuation. Due to the extreme importance of the temperature fluctuation in determining the jet noise emission, such a simplified treatment is obviously unsatisfactory. Hence, this paper presents an improved approach to predict the plasma jet noise emission by using a more sophisticated method to calculate the temperature fluctuations in the turbulent plasma jet.

2. Modeling Approach

Main assumptions employed in the present study include (i) the turbulent plasma jet is axi-symmetrical and steady; (ii) the plasma is in the local thermodynamic equilibrium (LTE) state and is optically thin to radiation; (iii) all the current-related terms in momentum and energy equations, including the Lorentz force, Joule heating rate and electron enthalpy transport, can be ignored in the whole plasma jet region; (iv) swirling velocity component can be neglected; and (v) the argon plasma jet is issuing into ambient air.

The governing equations in a cylindrical coordinate (*x*-*r*) system concerning the continuity, momentum, energy, species, turbulent kinetic energy and its dissipation rate and the temperature fluctuation can thus be written as follows.

$$\frac{\partial}{\partial x}(\rho u)+\frac{1}{r}\frac{\partial}{\partial r}(r\rho v)=0 \tag{1}$$

$$\frac{\partial(\rho uu)}{\partial x}+\frac{1}{r}\frac{\partial(r\rho uv)}{\partial r}=-\frac{\partial p}{\partial x}+2\frac{\partial}{\partial x}\left(\Gamma_u\frac{\partial u}{\partial x}\right)+\frac{1}{r}\frac{\partial}{\partial r}\left[r\Gamma_u\left(\frac{\partial u}{\partial r}+\frac{\partial v}{\partial x}\right)\right] \tag{2}$$

$$\frac{\partial(\rho uv)}{\partial x}+\frac{1}{r}\frac{\partial(r\rho vv)}{\partial r}=-\frac{\partial p}{\partial r}+\frac{2}{r}\frac{\partial}{\partial r}\left(r\Gamma_u\frac{\partial v}{\partial r}\right)+\frac{\partial}{\partial x}\left[\Gamma_u\left(\frac{\partial v}{\partial x}+\frac{\partial u}{\partial r}\right)\right]-2\Gamma_u\frac{v}{r^2} \tag{3}$$

$$\frac{\partial(\rho uh)}{\partial x}+\frac{1}{r}\frac{\partial(r\rho vh)}{\partial r}=\frac{\partial}{\partial x}\left[\Gamma_h\frac{\partial h}{\partial x}\right]+\frac{1}{r}\frac{\partial}{\partial r}\left[r\Gamma_h\frac{\partial h}{\partial r}\right]-U_r-\frac{\partial}{\partial x}\left[(h_A-h_B)J_x\right]$$
$$-\frac{1}{r}\frac{\partial}{\partial r}\left[r(h_A-h_B)J_r\right]-\frac{\partial}{\partial x}\left[\frac{k}{C_P}(h_A-h_B)\frac{\partial f_A}{\partial x}\right]-\frac{1}{r}\frac{\partial}{\partial r}\left[r\frac{k}{C_P}(h_A-h_B)\frac{\partial f_A}{\partial r}\right] \tag{4}$$

$$\frac{\partial(\rho uf_A)}{\partial x}+\frac{1}{r}\frac{\partial(r\rho vf_A)}{\partial r}=\frac{\partial}{\partial x}\left[\Gamma_f\frac{\partial f_A}{\partial x}\right]+\frac{1}{r}\frac{\partial}{\partial r}\left[r\Gamma_f\frac{\partial f_A}{\partial r}\right]+S_f \tag{5}$$

$$\frac{\partial(\rho uK)}{\partial x}+\frac{1}{r}\frac{\partial(rv\rho K)}{\partial r}=\frac{\partial}{\partial x}\left(\Gamma_K\frac{\partial K}{\partial x}\right)+\frac{1}{r}\frac{\partial}{\partial r}\left[r\Gamma_K\left(\frac{\partial K}{\partial r}\right)\right]+G-\rho\varepsilon \tag{6}$$

$$\frac{\partial(\rho u\varepsilon)}{\partial x}+\frac{1}{r}\frac{\partial(rv\rho\varepsilon)}{\partial r}=\frac{\partial}{\partial x}\left(\Gamma_\varepsilon\frac{\partial\varepsilon}{\partial x}\right)+\frac{1}{r}\frac{\partial}{\partial r}\left[r\Gamma_\varepsilon\left(\frac{\partial\varepsilon}{\partial r}\right)\right]+\frac{\varepsilon}{K}(C_1G-C_2\rho\varepsilon) \tag{7}$$

$$\frac{\partial\left(\rho u\overline{v'T'}\right)}{\partial x}+\frac{1}{r}\frac{\partial\left(r\rho v\overline{v'T'}\right)}{\partial r}=\frac{\partial}{\partial x}\left(\Gamma_T\frac{\partial\overline{v'T'}}{\partial x}\right)+\frac{1}{r}\frac{\partial}{\partial r}\left(r\Gamma_T\frac{\partial\overline{v'T'}}{\partial r}\right)-\frac{2}{3}\rho K\frac{\partial T}{\partial r}$$
$$-C_{T1}\rho\frac{\varepsilon}{K}\overline{v'T'}+(C_{T2}-1)\rho\overline{v'T'}\frac{\partial v}{\partial r} \tag{8}$$

Here u and v are the axial (x-) and radial (r-) components of velocity vector, J_x and J_r the x- and r-components of argon diffusion flux vector, ρ, T, h and p the density, temperature, specific enthalpy and pressure, whereas f_A is the mass fraction of argon in the argon-air mixture. They are all the time-averaged values. K and ε are the turbulent kinetic energy and its dissipation rate. $\overline{v'T'}$ is the radial component of the so-called turbulent Reynolds heat flux, which represents the correlation of the radial velocity fluctuation and the temperature fluctuation. All the transport coefficients are their combinations of pertinent values for molecular and turbulent transport. For example, the transport coefficient Γ_u in momentum equations (2) and (3) is calculated by $\Gamma_u = \mu + \mu_T$, where μ and μ_T are the temperature- and composition-dependent viscosity of gas mixture and the turbulent viscosity, and $\mu_T = C_\mu\rho K^2/\varepsilon$. The empirical constants in standard two-equation turbulence model are used here, i.e. $C_\mu = 0.09$, $C_1 = 1.44$, $C_2 = 1.3$, and 1.0, 1.3, 0.9 and 0.9 are for the turbulent Prandtl numbers in the equations for turbulent kinetic energy, its dissipation rate, energy and species. In Eq. (8), $C_{T1} = 3.2$ and $C_{T2} = 0.5$ are used [3]. h_A and h_B in Eq. (4) are the specific enthalpies of pure argon and pure air, respectively, whereas U_r is the temperature- and composition-dependent radiation power per unit volume of the plasma. The combined-diffusion-coefficients method suggested by Murphy [4] has been employed here to treat the diffusion of argon in argon-air mixture, but here turbulent effect is also added. The source term in Eq. (5) is calculated by

$$S_f=\frac{\partial}{\partial x}\left(\Gamma_f\frac{f_A}{\overline{M}}\frac{\partial\overline{M}}{\partial x}\right)-\frac{\partial}{\partial x}\left(\Gamma_f\frac{f_A}{\overline{M}_A}\frac{\partial\overline{M}_A}{\partial x}\right)+\frac{1}{r}\frac{\partial}{\partial r}\left(r\Gamma_f\frac{f_A}{\overline{M}}\frac{\partial\overline{M}}{\partial r}\right)$$
$$-\frac{1}{r}\frac{\partial}{\partial r}\left(r\Gamma_f\frac{f_A}{\overline{M}_A}\frac{\partial\overline{M}_A}{\partial r}\right)+\frac{\partial}{\partial x}\left(\overline{D}_{AB}^T\frac{\partial\ln T}{\partial x}\right)+\frac{1}{r}\frac{\partial}{\partial r}\left(r\overline{D}_{AB}^T\frac{\partial\ln T}{\partial r}\right) \tag{9}$$

where $\overline{M}_A$ and $\overline{M}$ are the mean mass of the gas particles coming from argon and that of all the gas particles, whereas $\overline{D}_{AB}^T$ is the turbulence-enhanced combined thermal diffusion coefficient associated with the temperature gradient. The turbulence generation term in Eq. (6) and (7) is expressed as

$$G = \mu_t \left[2\left(\frac{\partial v}{\partial r}\right)^2 + 2\left(\frac{\partial u}{\partial x}\right)^2 + 2\left(\frac{v}{r}\right)^2 + \left(\frac{\partial u}{\partial r} + \frac{\partial v}{\partial x}\right)^2 \right] \tag{10}$$

As in Refs. [1,2], the following expression is used to calculate the noise intensity-frequency spectrums:

$$\mathbf{I}(\mathbf{x},\boldsymbol{\omega}) = \frac{1}{16\pi^2 |\mathbf{x}|^2 \rho_0 c_0} \left\{ \frac{\omega^4}{c_0^4} \iint_{VV} \hat{A}(\mathbf{y}') \hat{A}(\mathbf{y}'') \Gamma(\mathbf{y}', \xi, \omega) d\mathbf{y}' d\xi \right.$$

$$\left. - \omega^2 \iint_{VV} \hat{S}(\mathbf{y}') \hat{S}(\mathbf{y}'') \Gamma(\mathbf{y}', \xi, \omega) d\mathbf{y}' d\xi - j \frac{2\omega^3}{c_0^2} \iint_{VV} \hat{A}(\mathbf{y}') \hat{S}(\mathbf{y}'') \Gamma(\mathbf{y}', \xi, \omega) d\mathbf{y}' d\xi \right\} \tag{11}$$

where ρ_0 and c_0 are density and sound speed for the surrounding gas, ω the circular frequency, $\boldsymbol{x}$ or $\boldsymbol{y}$ ($\boldsymbol{y}'$ or $\boldsymbol{y}''$) are the distance vector from a far-field observer or a noise source position to the coordinate origin at the jet inlet center. $\boldsymbol{\xi}$ is also a position vector. $\hat{A}(\boldsymbol{y}) = \overline{\rho}(2K/3)(\boldsymbol{y})$ and $\hat{S}(\boldsymbol{y}) = \rho_0 \frac{1}{\overline{T}} \frac{\partial \overline{v'T'}}{\partial r}(\boldsymbol{y})$ are root-mean-square of the noise sources due to, respectively, velocity fluctuation and temperature fluctuation. Γ in Eq. (11) is the so-called space-frequency coherence function, which denotes the interactions between the source terms in the spectral domain, and is given by [2]

$$\Gamma(\mathbf{y}', \xi, \omega) = \pi \exp\left(\frac{-\pi \xi_x^2}{L_x^2}\right) \exp\left(\frac{-\pi \xi_r^2}{L_r^2}\right) \left[\beta \omega_t \cosh\left(\frac{\pi C \omega}{2\beta \omega_t}\right) \right]^{-1} \tag{12}$$

Here L_x, L_r, β and ω_t are all empirical constants, whereas C is a parameter linking with the observer's position and the velocity at the jet inlet [2]. The three terms in the parentheses on the right-hand side of Eq. (11) represent the contribution to the noise emission due to velocity fluctuation, temperature fluctuation and their mixed effect, respectively.

After Eqs. (1) – (8) have been simultaneously solved using the SIMPLE-like algorithm [5], the spatial distributions of the turbulent kinetic energy K and the velocity-temperature fluctuation correlation $\overline{v'T'}$ can be obtained, and thus the source terms $\hat{A}(\boldsymbol{y})$ and $\hat{S}(\boldsymbol{y})$ as well as $\mathbf{I}(\mathbf{x},\boldsymbol{\omega})$ can be calculated. The noise intensity can then be predicted from the integration of $\mathbf{I}(\mathbf{x},\boldsymbol{\omega})$ with respect to the frequency.

3. Computational Domain and Boundary Conditions

The computational domain is shown in Fig. 1. The inner radius (R_0) of the torch exit or the jet inlet (AB in Fig. 1) is 4 mm, whereas torch wall thickness BC is 15 mm. The axial length AF is 200 mm, while the radial width AD is 50 mm. In our numerical simulation, a 62 (x-direction) × 40 (r-direction) rectangular non-uniform mesh is adopted with finer spacing near the jet inlet and the axis.

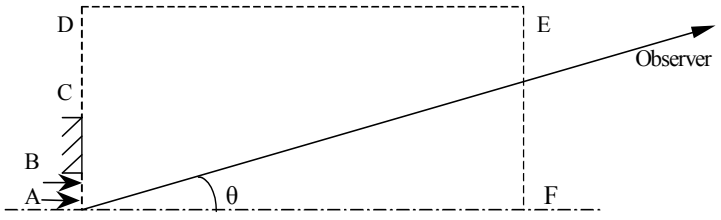

Fig. 1 Computational domain

In the modeling, the following axial velocity and temperature profiles are adopted at the jet inlet (AB):

$$u = U_0\left[1-(r/R_0)^2\right], \qquad T = (T_0 - T_w)\left[1-(r/R_0)^2\right] + T_w \tag{13}$$

where T_w=500 K is the torch wall temperature. In addition, $v = 0$, $f_A = 1.0$, $K = 0.005u^2$, $\varepsilon = 0.1K^2$, $\overline{v'T'} = -(C_\mu / P_{rt})(K^2/\varepsilon)(\partial T/\partial r)$ with $C_\mu = 0.09$ and $P_{rt} = 0.9$ are used at the jet inlet; turbulence-wall-functions used along BC, one-way conditions used at the downstream boundary (EF), free boundary conditions used along CD and the radial outer boundary DE, whereas axi-symmetrical conditions are used along the jet axis (AF).

4. Results and Discussion

For a typical case with U_0 =300 m/s and T_0=13000 K, the computed spatial distributions of the turbulent kinetic energy and temperature in the plasma jet are shown in Figs. 2(a) and 2(b), respectively. It is seen from Fig. 2 that both the turbulent kinetic energy and the temperature gradient assume their maximum values near the jet inlet, and decrease rapidly with increasing distance from the jet inlet. Hence, it is expected that the most important contribution to the jet noise will come from the region near the jet inlet or torch exit. Corresponding computed results concerning the spatial distributions of the noise sources due to velocity fluctuation and temperature fluctuation demonstrate this expectation, as shown in Figs. 3(a) and 3(b). From Figs. 3(a) and 3(b) one can find that both the noise sources are mainly distributed within a narrow region near the plasma jet inlet, and the noise emission due to the temperature fluctuation is much larger than that due to the velocity fluctuation.

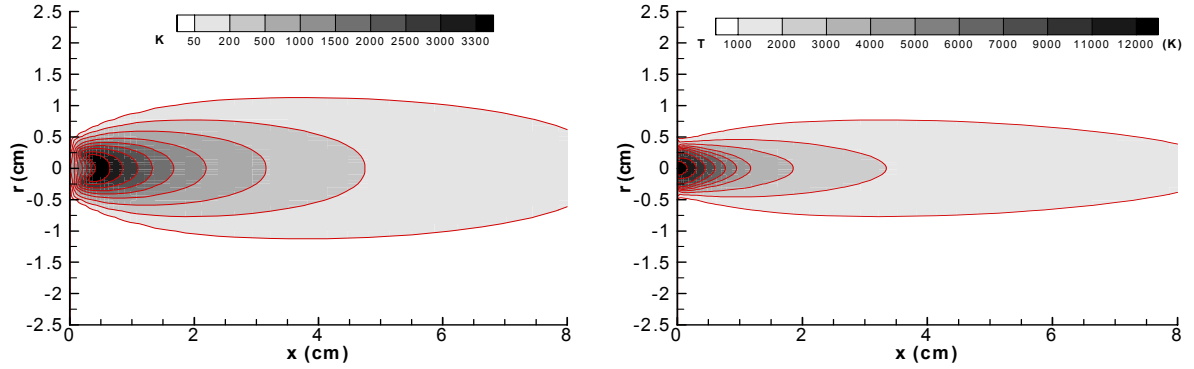

(a) (b)

Fig. 2 (a) Turbulent kinetic energy distribution, (b) Temperature distribution in the plasma jet

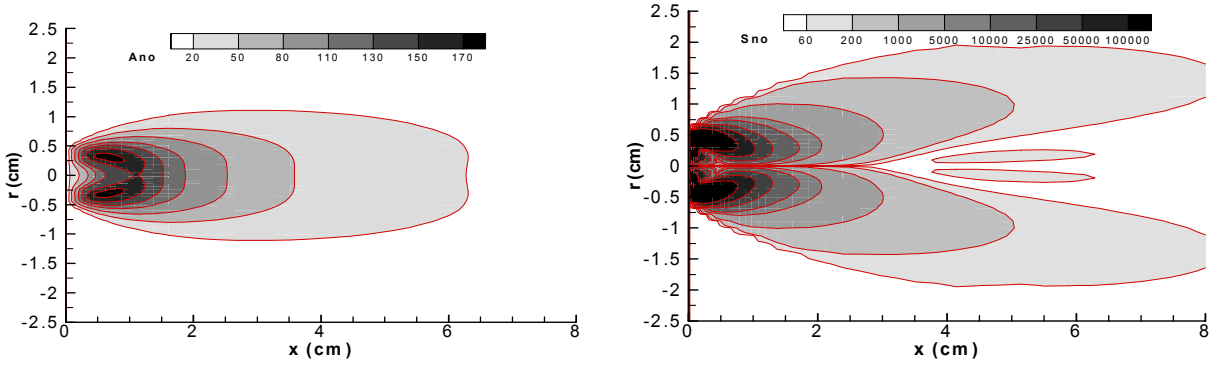

(a) (b)

Fig. 3 Noise source distributions. (a) Due to velocity fluctuation, (b) due to temperature fluctuation.

The computed noise intensity spectrums of the plasma jet are shown in Fig. 4, with the reference intensity being $I_0=10^{-12}$ W/m^2 and for an observer located at 0.4 m distance from the center of jet inlet and at observation angle of 90 deg ($\theta=90^o$) with respect to the jet axis. Here the individual contributions due to the different noise sources including velocity fluctuation, temperature fluctuation and their mixed effect are all presented besides their summation. It can be clearly seen from Fig. 4 that, similarly to that obtained in Ref. [1], the temperature fluctuation is the dominant noise source (i.e. its contribution is much greater than that due to the velocity fluctuation or due to the mixed effect of velocity and temperature fluctuations). However, we find that the computed summated noise intensities using the new modeling approach are about 10 dB higher than their counterparts given by Ref. [1]. This fact implies that the noise model employed in Ref. [1] somewhat underestimated the APS noise emission.

Fig. 5 compares the computed noise intensity spectrums for three different plasma jets with the same inlet temperature (i.e. T_0=13000 K) but different inlet velocities, i.e. U_0 =300, 600 and 900 m/s. It is found that with the increase of the jet inlet velocity, both the maximum noise intensity and the frequency corresponding to the maximum noise intensity increase. And the total noise intensity (or power, W/m^2) also increases approximately proportionally to the square of inlet velocity.

Although not shown here as separate figures due to the paper space limit, our computational results show that the noise emission increases with increasing inlet plasma temperature and decreasing observation angle.

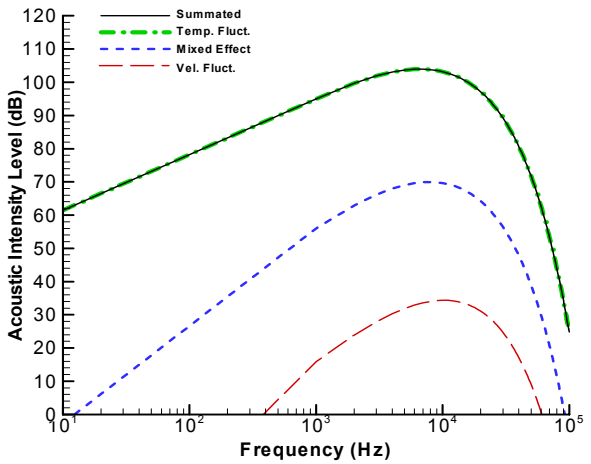

Fig. 4 Computed noise intensity spectrums of turbulent plasma jet with U_0 =300 m/s and T_0=13000 K

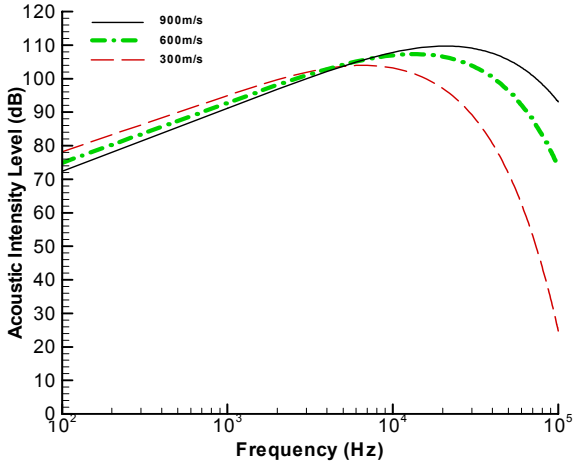

Fig. 5 Comparison of computed noise spectrums for 3 plasma jets with U_0 =300, 600 and 900 m/s. T_0=13000 K

Recently, the emitted noise intensity levels for plasma spraying were measured by Gross [6] using a real-time sound analysis meter. It was found that the cold gas flowing into the plasma torch could only produce a noise level below 80 dB, but the operating 30 kW plasma spraying torch with argon and helium as the working gas could enhance the noise levels to about 112 dB [6].

Fig. 6 presented our computed noise intensity-frequency spectrum characteristics for a turbulent plasma jet with U_0 =300 m/s and T_0=16000 K, which are roughly corresponding to the Gross' experiment. In Fig. 7, the predicted noise intensity-frequency spectrums are compared with Gross' experimental data for the 30 kW plasma torch. Totally, the agreement is reasonable. The experimental data are somewhat higher than the predicted values, partially due to that our modeling does not consider the existence of chamber which may increase the noise level. Moreover, the maximum velocity at the plasma jet inlet encountered in the Gross' experiment may be higher than 300 m/s employed in the computation.

In addition, our modeling results show that a great deal of the noise power is due to high frequency noise emission, which cannot be heard by the workers. This predicted result demonstrates that it is necessary for us

to pay more attention to the ultrasonic emission in plasma spraying.

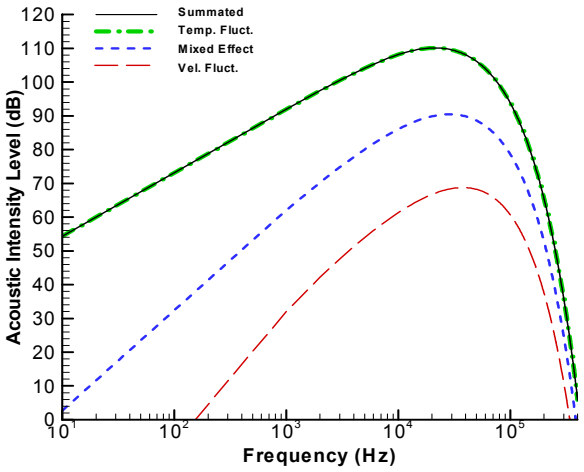

Fig. 6 Computed noise intensity spectrums of turbulent plasma jet with U_0 =900 m/s and T_0=16000 K

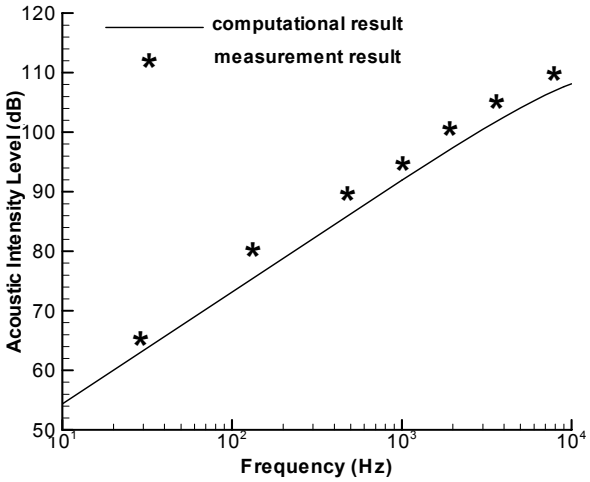

Fig. 7 Comparison between the computational noise intensity spectrums and experimental data [6]

5. Conclusions

As the improvement of the noise emission analysis, an improved modeling approach has been employed to predict the APS noise emission, in which the temperature fluctuations are computed by solving the second-order turbulent Reynolds heat flux equation. Main conclusions obtained from this study are as flows.

(1) Although the approach used in Ref. [1] somewhat underestimated the noise emission levels, the temperature fluctuation in the turbulent plasma jet is shown still to be the main source of noise emission, similarly to that obtained in Ref. [1].

(2) With the increase of the jet inlet velocity, the noise intensity increases approximately proportionally to the square of inlet velocity, and the frequency corresponding to the maximum noise emission intensity shifts towards the direction of high frequency.

(3) We should pay attention to the fact that the noise emission intensities at ultrasound frequencies may be high.

Acknowledgement

This study was supported by the National Natural Science Foundation of China (grant No. 50176024). The authors would like to thank Dr. A. B. Murphy, whose argon-air plasma properties are used in this study.

References

[1] Xi Chen, Yong-Xian Gu – *Proceedings of the 15th International Symposium on Plasma Chemistry* (July 9-13, 2001, Orleans), Vol. 3, 1045-1050.

[2] V. Fortuné, Y. Gervais – *AIAA Journal* **37**, 1055 (1999).

[3] Ching-Jen Chen, Sheng-Yuh Jaw – *Fundamentals of Turbulence Modeling*, New York: Taylor & Francis, Chap. 2-3 (1997).

[4] A. B. Murphy, C. J. Arundell – *Plasma Chemistry and Plasma Processing* **14**, 451 (1994).

[5] S. V. Patankar – *Numerical Heat Transfer and Fluid Flow*, Washington: Hemisphere (1980).

[6] K. A. Gross – *Journal of Thermal Spray Technology* **11**, 350 (2002).

The effects of the Joule heating on the DC arc plasma jet characteristics

He-Ping Li[1, 2] and Xi Chen[1]

[1] *Department of Engineering Mechanics, Tsinghua University, Beijing 100084, China*
[2] *Present Address: Department of Mechanical Engineering, University of Minnesota, Minneapolis, MN 55455, USA*

Abstract
Modeling results are presented concerning the effects of Joule heating on the characteristics of laminar plasma jet issuing from a DC arc plasma torch. It is shown that the Joule heating effect is dependent on the combination of torch operation parameters. For the case with arc root attachment near or at the anode nozzle exit of the torch, the Joule heating effect may not be ignored. On the other hand, the Joule heating rate can be neglected for the case that the anode arc root stays upstream far away from the anode nozzle exit.

1. Introduction

Thermal plasmas are widely used as the high temperature sources in many applications, such as the thermal plasma spraying, the ultra-fine powders synthesis, etc. In actual applications, usually the high-temperature partially-ionized gas is issuing from the plasma torch as the form of plasma jet. Studies of DC arc plasma jets have been conducted extensively in the past a few decades. Because of the existence of complex magneto-hydrodynamic effects inside the plasma torch and the interactions between the plasma jet and its environment, complicated physical phenomena may be involved in the studies. For example, the arc may assume unsteady behavior leading to the fluctuation of plasma jet, whereas the transverse injection of particulate matter and its carrier gas will cause appreciable three-dimensional features of the plasma jet characteristics [1]. So far our understanding on the arc plasma jet is incomplete. Many researchers studied the plasma jet characteristics by treating the jet separated from the plasma torch. They used the assumed (e.g. [1]) or computed (e.g., [2]) profiles obtained from the modeling of DC arc plasma torch as the jet-inlet boundary conditions, and solved the pertinent continuity, momentum, species and energy equations (and turbulent kinetic energy and its dissipation rate equations if turbulent flow is involved). In those studies it was assumed that no current-related effect (will be called Joule heating effect hereafter) existed in the plasma jet. Some other researchers simulated the heat and flow fields by combining the DC arc plasma torch and the plasma jet as a whole, i.e. solved the complete set of magneto-hydrodynamic (MHD) equations [3-6] for both torch and jet regions. Temperature and flow fields inside and outside the plasma torch were presented, but no clear description was given concerning whether or not the Joule heating effect is important in the plasma jet region. In addition, Ref. [6] mentioned that that electric potential equation was solved only for the plasma torch region, i.e. the Joule heating effect was not considered in the jet region. Another aspect should be pointed out is that the length of anode nozzles used in Refs. [3-5] is comparatively long (~29 *mm*), while the length of anode nozzle used in Ref. [6] is only 6.5 *mm*. So it is interesting to study the Joule heating effect on the plasma jet characteristics under different operation conditions (e.g. arc current, working-gas flow rate, etc.).

In this paper, for simplicity a two-dimensional (2-D) modeling for the DC arc plasma torch and plasma jet in laminar regime is conducted by solving the pertinent MHD equations in the computational domain including both the plasma torch and the plasma jet. By comparing the computed results with and without accounting for the current-related terms (i.e. Joule heating, electron enthalpy transport and Lorentz force) in the plasma jet region, the effect of Joule heating on the plasma jet characteristics can be revealed.

2. Mathematical models

2.1 Basic assumptions

The assumptions employed in this study are as follows:
(1) The flow is quasi-steady, laminar and with temperature-dependent properties.
(2) The plasma is in local thermodynamic equilibrium (LTE) state and optically thin to radiation.
(3) The pertinent Mach number inside and outside plasma torch is small (e.g. less than 0.3), and thus the viscous dissipation and the pressure work terms in the energy equation can be neglected.
(4) Argon is used as the working gas of plasma torch and as the ambient cold gas.

(5) The induced electric field $\vec{V} \times \vec{B}$ is negligible in comparison with the static electric field intensity $\vec{E}$.

2.2 Governing equations

Based on the foregoing assumptions, the governing equations for the 2D quasi-steady numerical simulations can be written in cylindrical coordinates (z, r) as follows:

$$\frac{\partial}{\partial z}(\rho v_z) + \frac{1}{r}\frac{\partial}{\partial r}(\rho r v_r) = 0 \tag{1}$$

$$\frac{\partial}{\partial z}(\rho v_z v_z) + \frac{1}{r}\frac{\partial}{\partial r}(r\rho v_z v_r) = -\frac{\partial p}{\partial z} + 2\frac{\partial}{\partial z}\left(\mu\frac{\partial v_z}{\partial z}\right) + \frac{1}{r}\frac{\partial}{\partial r}\left[r\mu\left(\frac{\partial v_z}{\partial r} + \frac{\partial v_r}{\partial z}\right)\right] + j_r B_\theta \tag{2}$$

$$\frac{\partial}{\partial z}(\rho v_z v_r) + \frac{1}{r}\frac{\partial}{\partial r}(r\rho v_r v_r) = -\frac{\partial p}{\partial r} + \frac{\partial}{\partial z}\left[\mu\left(\frac{\partial v_r}{\partial z} + \frac{\partial v_z}{\partial r}\right)\right] + \frac{2}{r}\frac{\partial}{\partial r}\left(r\mu\frac{\partial v_r}{\partial r}\right) - \frac{2\mu v_r}{r^2} - j_z B_\theta \tag{3}$$

$$\rho c_p v_z \frac{\partial T}{\partial z} + \rho c_p v_r \frac{\partial T}{\partial r} = \frac{\partial}{\partial z}\left(k\frac{\partial T}{\partial z}\right) + \frac{1}{r}\frac{\partial}{\partial r}\left(kr\frac{\partial T}{\partial r}\right) + \frac{j_z^2 + j_r^2}{\sigma} - S_R + \frac{5}{2}\frac{k_B}{e}\left(j_z\frac{\partial T}{\partial z} + j_r\frac{\partial T}{\partial r}\right) \tag{4}$$

$$\frac{\partial}{\partial z}(\sigma\frac{\partial \phi}{\partial z}) + \frac{1}{r}\frac{\partial}{\partial r}(r\sigma\frac{\partial \phi}{\partial r}) = 0 \tag{5}$$

where ρ, μ, c_p, k, σ and S_R are the temperature-dependent mass density, viscosity, specific heat at constant pressure, thermal conductivity, electric conductivity and radiation power per unit volume of argon plasmas. v_r and v_z are the components of the velocity vector in r-, and z-direction, while j_r and j_z are the r- and z-components of the current density vector $\vec{j}$, respectively. T, p and ϕ are the gas temperature, pressure and electrical potential, respectively. k_B is the Boltzmann constant, and e is the elementary charge. The current density components can be calculated from the electrical potential by

$$j_r = -\sigma\frac{\partial \phi}{\partial r}, \quad j_z = -\sigma\frac{\partial \phi}{\partial z} \tag{6}$$

B_θ is the circumferential component of the self-induced magnetic induction vector due to the existence of arc current, and is calculated by

$$B_\theta = \frac{\mu_0}{r}\int_0^r j_z \xi d\xi \tag{7}$$

in which μ_0 is the permeability in vacuum.

In this study, two different sets of governing equations are employed in order to reveal the effect of current-related terms on the plasma jet characteristics, namely,

G. E. I: Equations (1)~(7) are solved simultaneously in both torch and jet regions, i. e. the effects of Lorentz force, Joule heating and electron enthalpy transport on the plasma jet characteristics are taken into account.

G. E. II: Equations (1)~(7) are only solved in torch region. In the plasma jet region, the current-related terms $j_r B_\theta$, $-j_z B_\theta$, $\frac{j_z^2 + j_r^2}{\sigma}$ and $\frac{5}{2}\frac{k_B}{e}\left(j_z\frac{\partial T}{\partial z} + j_r\frac{\partial T}{\partial r}\right)$ are all not included in the momentum or energy equations, i. e. the effects of Lorentz force, Joule heating rate and electron enthalpy transport on the plasma jet characteristics are not taken into account.

2.3 Computational domain and boundary conditions

Figure 1 shows the computational domain (ABCDEFGHIA) used in this study, which includes the plasma arc, the plasma jet and the anode region. The geometrical sizes are also shown in this diagram. The inner diameter of the anode nozzle is 8 *mm*, and the length of the cylindrical nozzle part is 10 *mm*. It should be noted that the physical properties c_p, k and σ, appearing in Equations (4) and (5), should be the values of anode material (copper) instead of those of argon plasmas in the anode region.

The boundary conditions used in this 2-D modeling are listed in Table 1. At the inlet section of the torch (BC), we assume that the cold gas is admitted in axial direction uniformly, i. e.

$$v_z = Q/A, \; v_r = 0 \tag{8}$$

where Q is the volumetric flow rate of the working gas (STP m^3/s), A is the inlet cross-section area of the torch (m^2). On the cathode surface, no-slip boundary condition is employed for velocity components. The temperature (T_c) and current density ($\vec{j}_0$) distributions are specified as shown in Figure 2 according to the experimental data presented in Ref. [7]. The electric potential gradient is thus calculated by

$$\vec{j}_0(r) = -\sigma \frac{\partial \phi}{\partial n} \tag{9}$$

where $\vec{j}_0(r)$ is the local current density vector at the cathode arc root. This vector is normal to the cathode surface and is a function of the radial distance (r) and the axial distance from the cathode tip (z_c), while n is the normal at the cathode surface directed from the inner side to the outer side of the cathode.
Lines GH and HI represent the free boundaries and mass conservation should be satisfied. Line IA represents the extended outer surface of the anode region with zero electric potential and constant temperature (500 K).

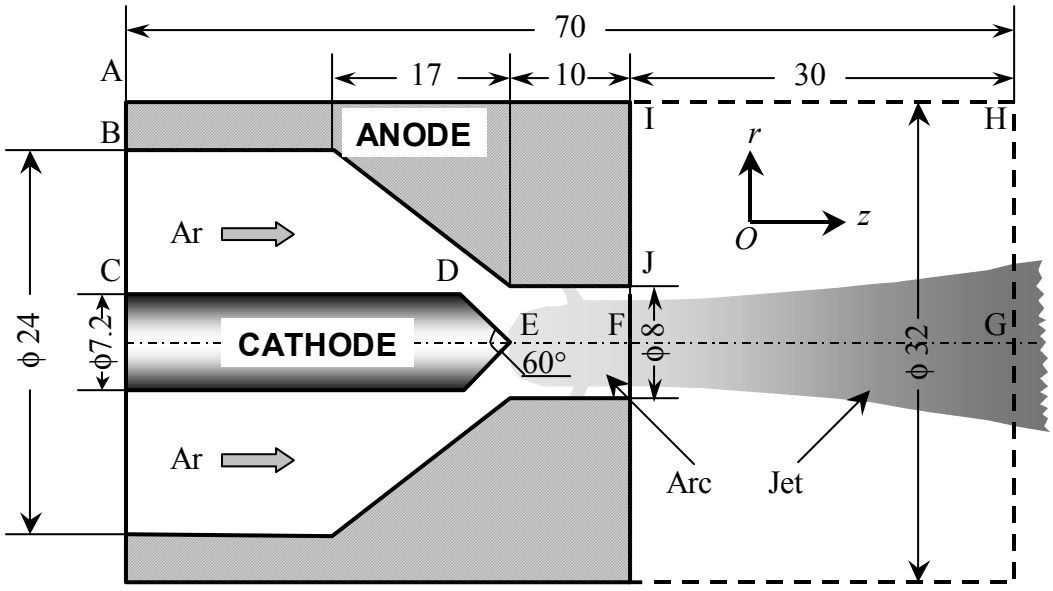

Figure 1. Schematic diagram of the computational domain.

Table 1. Boundary conditions used for the governing equations along the boundaries shown in Figure 1.

	AB	BC	CDE	EFG	GH	HI	IA
v_z (m/s)	0	Q/A	0	$\partial u/\partial r = 0$	$\partial u/\partial z = 0$	$\partial u/\partial r = 0$	0
v_r (m/s)	0	0	0	$v = 0$	$\partial v/\partial z = 0$	$\partial(\rho v r)/\partial r = 0$	0
T (K)	300	300	Fig. 2	$\partial T/\partial r = 0$	$\partial T/\partial z = 0$	$\begin{cases} v > 0, \partial T/\partial r = 0 \\ v \le 0, T = 300 \end{cases}$	500
ϕ (V)	$\partial\phi/\partial z = 0$	$\partial\phi/\partial z = 0$	$\vec{j}_0(r) = -\sigma \frac{\partial \phi}{\partial n}$	$\partial\phi/\partial r = 0$	$\partial\phi/\partial z = 0$	$\partial\phi/\partial r = 0$	$\phi = 0$

3. Modeling results and discussions

In this modeling work, the SIMPLE-like algorithm [8] has been employed to solve the non-linear equations (1)~(5) simultaneously with a new version of the non-commercial software FAST-2D (Fluid Analytical Simulation Tools—Two Dimensional) [9]. This software has been employed to simulate 2-D heat and flow patterns of plasma arc and plasma jet [10]. The detailed description of the features of this modified computer code FAST-2D was presented in Ref. [10]. A 2-D, body-fitted, non-orthogonal, non-uniform mesh $67\,(z) \times 41\,(r)$, as shown in Figure 3, is adopted for the 2-D modeling of the plasma torch and plasma jet in this paper.

In this section, the influences of current-related terms (Joule heating, electron enthalpy transport and Lorentz force) on the plasma jet characteristics with different arc currents ($I = 100\ and\ 200\ A$) and working gas flow rates ($Q = 0.35\ and\ 0.5\ \mathrm{STP}\ m^3/hr$) are studied, which are listed in Table 2.

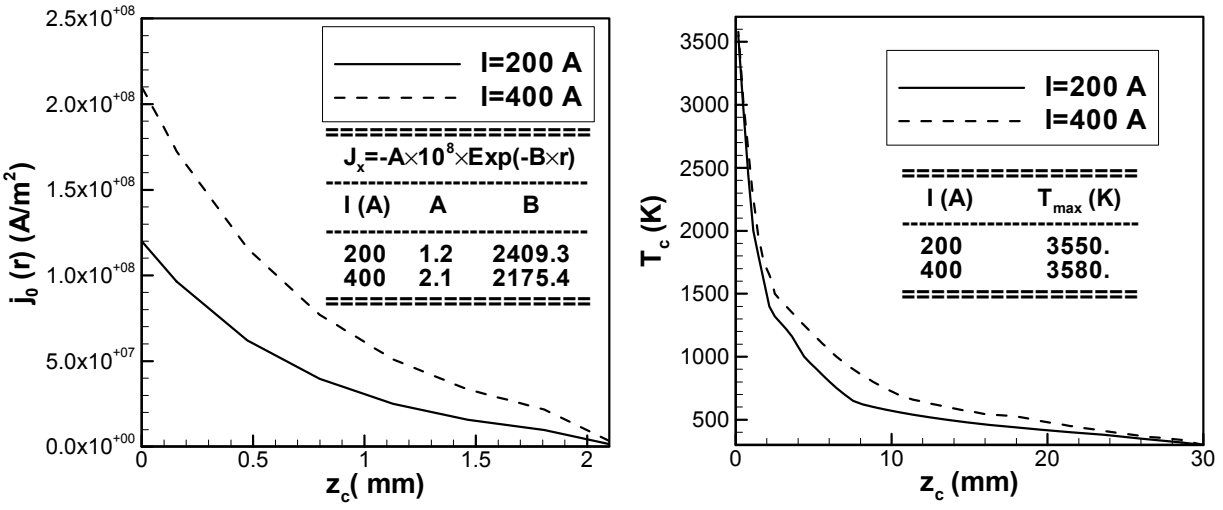

(a) (b)

Figure 2. The assumed current density (a) and temperature (b) distributions on the cathode surface.

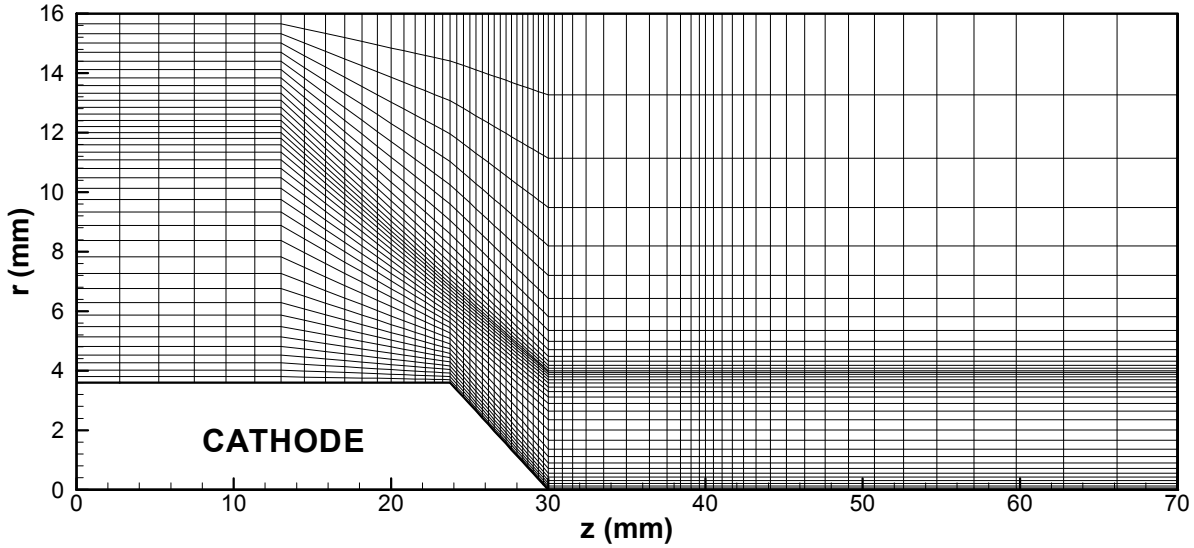

Figure 3. 2-D mesh generation.

Table 2. Different cases studied in the present paper.

Case No.	I (A)	Q (STP m^3/hr)	Governing Equations
1	200	0.35	G. E. I
2	200	0.35	G. E. II
3	400	0.35	G. E. I
4	400	0.35	G. E. II
5	200	0.50	G. E. I
6	200	0.50	G. E. II
7	400	0.50	G. E. I
8	400	0.50	G. E. II

3.1 Modeling results

The radial temperature profiles in the cross section located at 0.8 *mm* downstream of the torch exit for Case 1, 2, 5 and 6 are shown in Figure 4, respectively. It can be seen that for Cases 1 & 2, the influence of the current-related terms (Joule heating rate, electron enthalpy transport and Lorentz force) on the plasma jet temperature fields can be ignored completely. But for Cases 5 & 6, the effects of current-related terms cannot be neglected, especially for the region near the plasma jet edge. The maximum relative discrepancy at the location $r = 4\,mm$ is about 30% between Case 5 and Case 6. Additionally, comparisons of the computed results for Cases 3 & 4 and Cases 7 & 8 show that the influence of current-related terms in the jet region can be neglected for those cases.

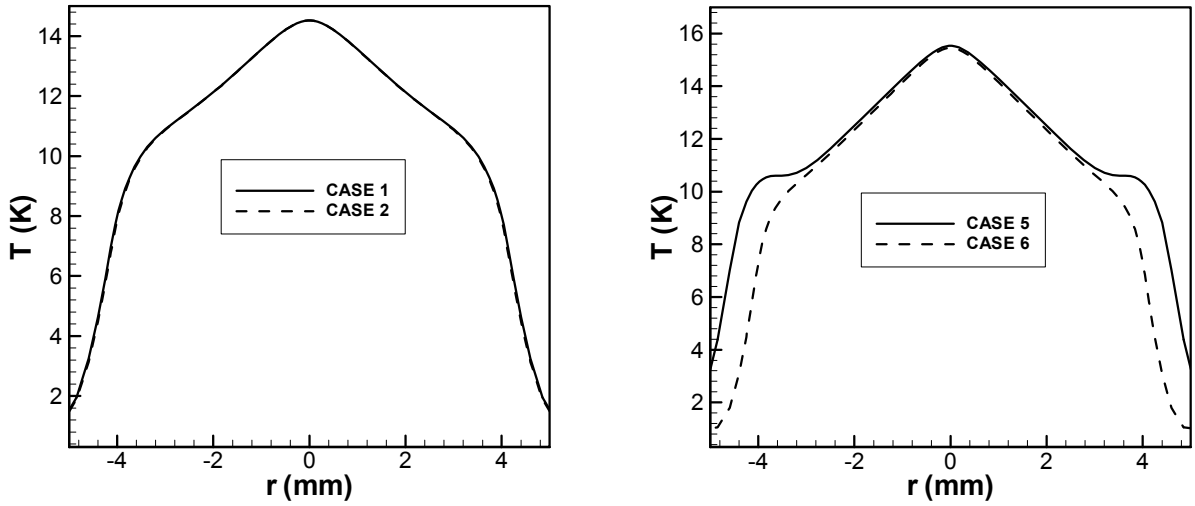

(a) (b)

Figure 4. Temperature profiles in radial direction at the section located at 0.8 *mm* downstream of the torch exit.

3.2 Discussion

Based on the foregoing computed results, we can analyze the related mechanism of the current-related effects on plasma jet characteristics as follows: As indicated in Ref. [11], the gasdynamic force acting on the anode column should be balanced by the magnetic body force in order for the anode terminus of the arc to assume a stable axial location. With an increase of the working gas flow rate, the location of anode arc-root attachment will move downstream due to the enhanced gasdynamic drag force, leading to a longer arc length; while with the increase of the arc current, the location of anode arc-root attachment will move upstream due to the enhanced magnetic body force, leading to a shorter arc length, where arc length is defined as the axial distance between the cathode tip and the point of the anode arc root (with the maximum radial current density at the inner surface of the anode). The possible current path in the partially ionized high temperature gas region is shown in Figure 5. It can be seen that for a long arc length [Figure 5 (b)], the current path possibly exists in the plasma jet region, which will influence the characteristics of the plasma jet in the pertinent region; while for a short arc length [Figure 5 (a)], the current path will dominantly appear inside the plasma torch, and thus there is almost no effect of the Joule heating on the plasma jet characteristics.

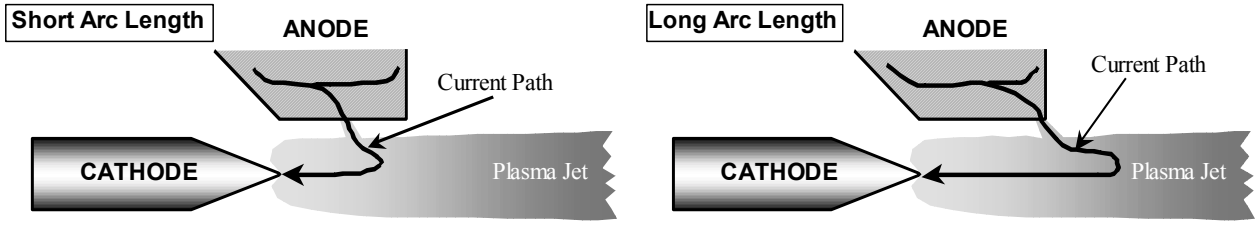

(a) (b)

Figure 5. Schematic diagram of the possible current paths in the plasmas for short (a) and long (b) arc length.

The computed temperature distributions for Case 1 and Case 5 are shown in Figures 6 (a) and (b), respectively. From Figure 6, we can see that the arc length for Case 1 is 8.2 mm, i. e., the axial distance between the anode arc root and the exit of the anode nozzle is 1.8 mm; while for Case 5, the anode arc root just stays at the exit plane of the anode nozzle. Based on our preceding analysis, Case 1 and 5 should correspond to the "short arc length" case and the "long arc length" case shown in Figures 5 (a) and (b), respectively.

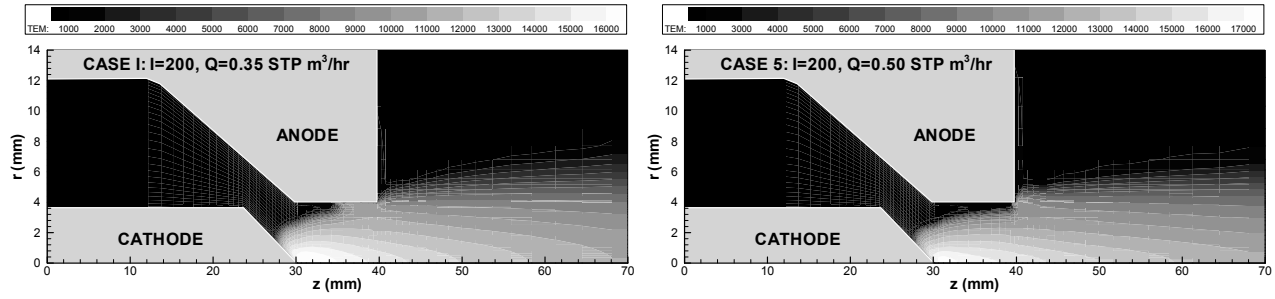

(a) (b)

Figure 6 Isotherms inside and outside of plasma torch for Case 1 (a) and Case 5 (b)

4. Conclusions

In this paper, the effects on the plasma jet characteristics are studied of current-related terms, including the Joule heating, the electron enthalpy transport and the Lorentz force. Main conclusions obtained are as follows:

(1) The extent of effects of the current-related terms on the characteristics of a plasma jet, issuing from a DC arc plasma torch, depends on the axial distance between the location of anode arc root attachment and the anode nozzle exit, i. e. on the magnitude of current density in the plasma jet region at the downstream of the anode nozzle exit.

(2) If the anode arc root stays upstream far away from the anode nozzle exit (e.g. operating at high arc current and low working-gas flow rate), i. e. the current density in the plasma jet region is very small, the influence of the current-related terms on the jet characteristics can be neglected completely.

(3) If the anode arc root stays at a location near the anode nozzle exit (e.g. operating at lower arc current and high working gas flow rate), the current density in the plasma jet region could be large enough and the influence of the current-related terms on the jet characteristics should be taken into account.

Acknowledgement

This study was supported by the National Natural Science Foundation of China (grant No. 50176024).

References

[1] He-Ping Li, Xi Chen - Plasma Chemistry and Plasma Processing **22**, 27 (2002).

[2] Peng Han, Lan Yu, Xi Chen - Proc. 13th Int. Symp. Plasma Chem. (August 18-22, 1997, Beijing, China), Peking University Press, Vol. 1, 338 (1997).

[3] D. A. Scott, P. Kovitya, G. N. Haddad - Journal of Applied Physics **66**, 5232 (1989).

[4] R. Westhoff, J. Szekely - Journal of Applied Physics **70**, 3455 (1991).

[5] A. B. Murphy, P. Kovitya - Journal of Applied Physics **73**, 4759 (1993).

[6] J. M. Bauchire, J. J. Gonzalez, A. Gleizes – Plasma Chemistry and Plasma Processing **17**, 409 (1997).

[7] Xin Zhou - Ph. D. Thesis, Department of Mechanical Engineering, University of Minnesota (1995).

[8] S. V. Patankar - *Numerical Heat Transfer and Fluid Flow*, Hemisphere Publishing, Washington (1980).

[9] J. Zhu - *FAST-2D: A Computer Program for Numerical Simulation of Two-Dimensional Incompressible Flows with Complex Boundaries,* Institute for Hydromechanics, University of Karlsruhe, Report No. 690 (1991).

[10] He-Ping Li - Ph. D. Thesis, Department of Engineering Mechanics, Tsinghua University (2001, In Chinese).

[11] S. A. Wutzke - Ph. D. Thesis, Department of Mechanical Engineering, University of Minnesota (1967).

Analysis of the laser-induced plasma plume characteristics in laser welding

Hai-Xing Wang and Xi Chen

Department of Engineering Mechanics, Tsinghua University, Beijing 100084, China

Abstract
Typical computed distributions of temperature, velocity and some other parameters within the plasma plume are presented with the CO_2 laser welding of an iron workpiece as the calculation example. The computed results show that the height of the plasma plume is dependent on the vapor / shielding-gas momentum ratio. The laterally injected assisting gas may also significantly affect the plasma plume and thus can be used to control the effect of the laser-induced plasma plume on the laser welding process.

1. Introduction

In many laser welding processes, a continuous wave (CW) CO_2 laser beam is focused on the surface of a metallic workpiece with a sufficient high power density (e.g. higher than 10^{10} W/m^2) at the light spot, causing the localized heating and evaporation of the workpiece material and the formation of a keyhole in the wrkpiece. The vapor evaporated from the keyhole wall will be partially ionized due to its interaction with the incident laser beam, resulting in the formation of laser-induced plasma. A plasma plume appearing above the workpiece surface may affect the welding process through its absorption and refraction to the laser beam.
Herziger [1] summarized some research results up to the middle of 1980's concerning the plasma plume characteristics in laser welding. The measured electron (or plasma) temperatures by various authors differ significantly. For example, the reported values of the measured plasma plume temperatures are from around 8000 K to over 14000 K. Szymański et al [2] indicated that since iron atom spectral lines usually assume their maximum intensities near the temperatures around 10000 K. The approach that employs only the relative intensity ratio of two atom spectral lines to determine the plasma plume temperature is not suitable when higher plasma plume temperatures are involved. Instead, they suggested to us the ion spectral line intensity ratio for the measurement of the plasma temperature. They showed that when the intensity ratio of two different atom lines was used in their spectroscopic temperature measurements, the plasma temperature around 8000 K was obtained (Szymański and Kurzyna [3], Szymański et al [2]). However, when the intensity ratio of an ion line to an atom line was used to determine the plasma temperature, 11000 K was obtained for the same experimental conditions (Szymański et al [3]).
In the recent work of Kim and Farson [4], the plume-beam interaction is studied by applying an axi-symmetrical, high-temperature gas-dynamic model to the plasma plume formed above an iron workpiece surface. However, due to the inherent limitation of two-dimensional model itself, they could not well treat the actual three-dimensional problem concerning the effect of laterally injected assisting gas on the laser-induced plasma, although the laterally injected assisting gas might significantly affect the heat transfer and fluid flow within the plasma plume. In addition, the radiation energy loss from the plasma plume was not included in their 2-D model.
This paper presents a more generalized 3-D modeling approach to study the plasma plume characteristics. The plasma plume parameters including the spatial temperature distribution and the flow field are investigated in some detail. Laser absorption and refraction are then evaluated based on those modeling results of plasma plume characteristics.

2. Mathematical model

2.1 Basic assumptions

In this paper, the following assumptions are employed for the plasma plume modeling:
(1) The welding process and the plasma plume are steady in the coordinates fixed with the laser beam;
(2) The gas flow is laminar;
(3) The plasma is in the local thermodynamic equilibrium (LTE) state;
(4) The plasma plume absorbs part of the incident laser energy through the inverse Bremsstrahlung and radiates energy to the surroundings;

(5) Pure iron is used as the workpiece, the coaxially injected shielding gas and the laterally injected assisting gas (if any) are pure argon, whereas the plasma plume consists of the mixture of argon and iron vapor.

2.2 Governing equations

Based on the foregoing assumptions, the governing equations used for the 3D quasi-steady numerical simulations can be written in a cylindrical coordinate system (r, θ, z) as follows:

$$\frac{1}{r}\frac{\partial}{\partial r}(r\rho v_r)+\frac{1}{r}\frac{\partial}{\partial \theta}(\rho v_\theta)+\frac{\partial}{\partial z}(\rho v_z)=0 \tag{1}$$

$$\rho\left(v_r\frac{\partial v_r}{\partial r}+\frac{v_\theta}{r}\frac{\partial v_r}{\partial \theta}+v_z\frac{\partial v_r}{\partial z}\right)=-\frac{\partial p}{\partial r}+\frac{\partial}{\partial r}\left(2\mu\frac{\partial v_r}{\partial r}\right)+\frac{1}{r}\frac{\partial}{\partial \theta}\left[\mu\left(\frac{1}{r}\frac{\partial v_r}{\partial \theta}+\frac{\partial v_\theta}{\partial r}-\frac{v_\theta}{r}\right)\right]+\frac{\partial}{\partial z}\left[\mu\left(\frac{\partial v_r}{\partial z}+\frac{\partial v_z}{\partial r}\right)\right]+\frac{2\mu}{r}\left(\frac{\partial v_r}{\partial r}-\frac{1}{r}\frac{\partial v_\theta}{\partial \theta}-\frac{v_r}{r}\right)+\rho\frac{v_\theta^2}{r} \tag{2}$$

$$\rho\left(v_r\frac{\partial v_\theta}{\partial r}+\frac{v_\theta}{r}\frac{\partial v_\theta}{\partial \theta}+v_z\frac{\partial v_\theta}{\partial z}\right)=-\frac{1}{r}\frac{\partial p}{\partial \theta}+\frac{\partial}{\partial r}\left[\mu\left(\frac{\partial v_\theta}{\partial r}-\frac{v_\theta}{r}+\frac{1}{r}\frac{\partial v_r}{\partial \theta}\right)\right]+\frac{1}{r}\frac{\partial}{\partial \theta}\left[2\mu\left(\frac{1}{r}\frac{\partial v_\theta}{\partial \theta}+\frac{v_r}{r}\right)\right]+\frac{\partial}{\partial z}\left[\mu\left(\frac{\partial v_\theta}{\partial z}+\frac{1}{r}\frac{\partial v_z}{\partial \theta}\right)\right]+\frac{2\mu}{r}\left(\frac{1}{r}\frac{\partial v_r}{\partial \theta}+\frac{\partial v_\theta}{\partial r}-\frac{v_\theta}{r}\right)-\rho\frac{v_r v_\theta}{r} \tag{3}$$

$$\rho\left(v_r\frac{\partial v_z}{\partial r}+\frac{v_\theta}{r}\frac{\partial v_z}{\partial \theta}+v_z\frac{\partial v_z}{\partial z}\right)=-\frac{\partial p}{\partial z}+\frac{1}{r}\frac{\partial}{\partial r}\left[\mu r\left(\frac{\partial v_z}{\partial r}+\frac{\partial v_r}{\partial z}\right)\right]+\frac{1}{r}\frac{\partial}{\partial \theta}\left[\mu\left(\frac{1}{r}\frac{\partial v_z}{\partial \theta}+\frac{\partial v_\theta}{\partial z}\right)\right]+\frac{\partial}{\partial z}\left(2\mu\frac{\partial v_z}{\partial z}\right) \tag{4}$$

$$\rho c_p\left(v_r\frac{\partial T}{\partial r}+\frac{v_\theta}{r}\frac{\partial T}{\partial \theta}+v_z\frac{\partial T}{\partial z}\right)=\frac{1}{r}\frac{\partial}{\partial r}\left(rk\frac{\partial T}{\partial r}\right)+\frac{1}{r^2}\frac{\partial}{\partial \theta}\left(k\frac{\partial T}{\partial \theta}\right)+\frac{\partial}{\partial z}\left(k\frac{\partial T}{\partial z}\right)+\alpha I-U_r \tag{5}$$

$$\rho\left(v_r\frac{\partial f}{\partial r}+\frac{v_\theta}{r}\frac{\partial f}{\partial \theta}+v_z\frac{\partial f}{\partial z}\right)=\frac{1}{r}\frac{\partial}{\partial r}\left(rD\frac{\partial f}{\partial r}\right)+\frac{1}{r^2}\frac{\partial}{\partial \theta}\left(D\frac{\partial f}{\partial \theta}\right)+\frac{\partial}{\partial z}\left(D\frac{\partial f}{\partial z}\right) \tag{6}$$

In the preceding equations, v_r, v_θ and v_z are the velocity components of the gas mixture in *r*-, θ- and *z*-directions, *T* and *p* the gas temperature and pressure, whereas *f* is the mass fraction of iron vapor in the gas mixture. ρ, μ, *k*, c_p and *D* are temperature- and composition-dependent gas density, viscosity, thermal conductivity, specific heat at constant pressure and iron-vapor diffusion coefficient, respectively, for the iron-argon plasma, and the property database given by Samsonov and Shambetov [5] is employed in the present modeling study. In Eq. (5), the source terms U_r is the temperature- and composion-dependent radiation power per unit volume of plasma, and the data presented by Menart and Malik [6] and Essoltani et al [7] are used for the U_r calculation. *I* is the local laser intensity, whereas α is the local laser absorption coefficient. For the case of CO_2 laser, the absorption coefficient is calculated by [8]

$$\alpha = 1.63\times10^{-42}\,\frac{N_e^2}{T_e^{1/2}}\times\left[1-\exp\left(\frac{-1.36\times10^3}{T_e}\right)\right] \qquad \left(m^{-1}\right) \tag{7}$$

2.3 Computational domain and boundary conditions

The computational domain used in the modeling is the cylindrical region shown in figure 1 with sizes $0 \le r \le 5$ mm, $0 \le \theta \le 2\pi$ and $0 \le z \le 10$ mm. Altogether 22 (r-direction) × 22 (θ-direction) × 42 (z-direction) grid points are employed in the modeling. Boundary conditions are as follows. Metal vapor with fixed temperature (T_{va}) and upward velocity (U_{va}) enters into the plasma plume from the small circular area AB (light spot) on the bottom boundary shown in fig. 1, and thus the boundary conditions at AB are $v_z = U_{va}$, $v_r = 0$, $v_\theta = 0$, $T = T_{va}$ and $f = 1.0$. For the other part of the workpice surface except for the small circular area AB (i.e. along JA and BC), $v_r = 0$, $v_\theta = 0$, $v_z = 0$, $T = T_f$ and $\partial f/\partial z = 0$ are used. At the outer boundary (r = 5 mm) of computational domain for the gas-phase region (i.e. CD or GJ in figure 1), free-boundary conditions are used, i.e. $\partial(\rho r v_r)/\partial r = 0$, $\partial(r v_\theta)/\partial r = 0$, $\partial v_z/\partial r = 0$, $\partial T/\partial r = 0$ and $\partial f/\partial r = 0$. For the case including the effect of laterally injected assisting gas on the laser-induced plasma, the argon is assumed to be injected from the region HI on the western boundary in figure 1 with a fixed velocity U_{as} and

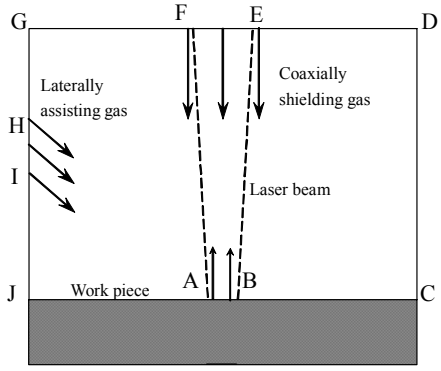

Figure 1. Computational domain.

inclination angle of 45°, and thus $v_z = -U_{as}/\sqrt{2}$, $v_r = U_{as}/\sqrt{2}$, $v_\theta = 0$, $T = T_f$ and $f = 0$ are employed, where T_f is the ambient gas temperature (i.e. 300 K). Along the geometrical axis of the computational domain ($r = 0$), $rv_\theta = 0$ and the averaged values of ϕ_i (i = 1, 2, …, N) at all the N grid points in the θ-direction and on the small circle nearest to the axis in the mesh are employed for other variable ϕ. Namely,

$$\phi|_{r=0} = \frac{1}{N}\sum_{i=1}^{N}\phi_i \qquad (\phi = v_z, v_r, T \text{ or } f) \qquad (8)$$

At the vertical section with $\theta = 0$ or $\theta = 2\pi$, the value of variable ϕ at a boundary point is taken as the average of the ϕ values at its two neighbour grid points in θ direction.

In order to protect the laser head from thermal damage by the high temperature plasma plume, the shielding gas is injected from a nozzle (i.e. EF in figure 1) coaxially placed with the laser beam. For the region EF on the top boundary where the laser beam and shielding gas enter into the computational domain, the boundary conditions $v_z = -U_{sh}$, $v_r = 0$, $v_\theta = 0$, $T = T_f$ and $f = 0$ are used, where U_{sh} is the shielding gas velocity. The boundary conditions for other part (except for EF) on the top boundary (i.e. GF and DE in figure 1) are $v_z = 0$, $v_r = 0$, $v_\theta = 0$, $T = T_f$ and $\partial f / \partial z = 0$.

3. Modeling results and discussions

One of the difficulties encountered in the modeling is how to determine the vapor temperature (T_{va}) and velocity (U_{va}) on AB region at the bottom boundary of computational domain. Although many studies have been conducted (e.g. Dowden et al [9], Tix and Simon [10], etc.), so far no reliable analysis is available concerning the vapor flow and heat transfer within the keyhole since very complex physical phenomena are involved there. Hence, as the first step to treat such a complicated problem, the vapor velocity and temperature at AB region of the bottom boundary are treated as parameters in the present modeling study, and their effects on the plasma plume characteristics are revealed by the parameter study.

3.1 Effects of the coaxially injected shielding gas velocity on plasma plume

Figures 2(a) and 2(b) show the computed flow fields (expressed using uniform vector length for clarity) on the middle vertical section for two different shielding gas velocities, i.e. 5 and 35 m/s. The metal vapor velocity (U_{va}) and temperature (T_{va}) are fixed in the computation, i.e. 100 m/s and 10000 K, whereas there is no laterally injected assisting gas. Corresponding computed isotherms are shown in Figs. 3(a) and 3(b) with isotherm range 1000 *K*~13000 K and isotherm interval of 1000 K. It is seen from the computed results that there always exist vortexes in the flow fields. In addition, the present modeling results clearly demonstrate that the coaxially injected shielding gas can significantly affect the plasma plume characteristics besides its original function to protect the laser head from thermal damage. With the increase of the shielding gas velocity, the plasma plume height (e.g. represented by the isotherm 2000 *K*) and the distance from the bottom boundary to the stagnant point at the plume axis (the location with zero axial velocity) decrease. However, it is found that the computed maximum temperature at the plasma plume core is always about 13800 K and less dependent on the shielding gas velocity.

We can compare our modeling results with some available experimental data. The conditions employed in the present modeling study are quite similar to those for the experiment of Szymański et al [2]. In their experiment, CO_2 CW laser with intensity of 3.76×10^{10} W/m^2 at the laser spot and diverging angle of 1.7 mrad were used in the welding of stainless steel and titanium. Argon was employed as the coaxially injected shielding gas with average injection velocity of 23.7 m/s. Using the intensity ratio of an ion spectral line to an atom spectral line, they measured the averaged electron temperature distribution above the stainless steel workpiece. The maximum value of the measured electron temperatures was about 11000 K with a location near the workpiece surface. Although this measured maximum temperature (~11000 K) is lower than our predicted value (~13800 K), the agreement between the modeling results and experimental data can still be considered to be reasonable. It is because that Abel inversion is not employed in the experiment of Szymański et al [2] and the ion / atom spectral intensity ratio is employed for the temperature measurements (they did not succeed in using the spectral intensity ratio of two ion lines). It is expected that if the Abel inversion was employed, the actual value of the maximum temperature in the plasma plume core region would be somewhat higher than the measured average maximum temperature 11000 K. In addition, it is also expected that if ion / ion (instead of ion / atom) spectral intensity ratio could be used to determine the plasma

temperature, somewhat higher value of the measured plasma temperature would be obtained. Our modeling results show that the plasma temperature decreases rapidly within the distance of a few millimeters from the workpiece surface. This prediction is also roughly consistent with the experimental observation of Szymański et al [2]. They showed that the measured electron temperature decreased appreciably with increasing distance from the workpiece surface within the height range of 0 – 1.25 mm. In addition, in their experiment Miller and DebRoy [11] found that the increase of the shielding-gas flow rate reduced the plasma sizes but did not affect the measured values of the electron temperature. Those results are also consistent with our modeling predictions, although their measured plasma temperatures are much lower than those predicted by the present modeling. Their measured plasma temperatures are also much lower than those reported by Szymański et al [2], although are consistent with the earlier results of Szymański and Kurzyna [3].

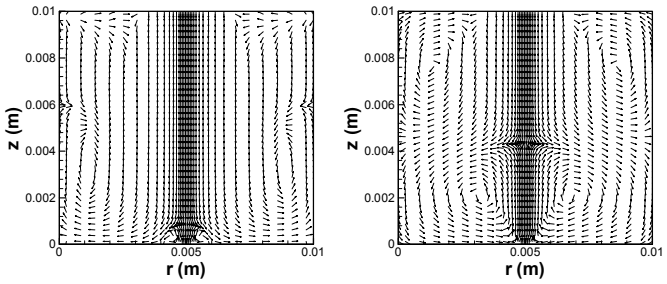

(a) U_{sh}=5 m/s (b) U_{sh}=35 m/s

Figure 2 Computed velocity vector fields on the vertical section ($\theta = 0 - \pi$) for different velocities of the axially injected shielding gas.

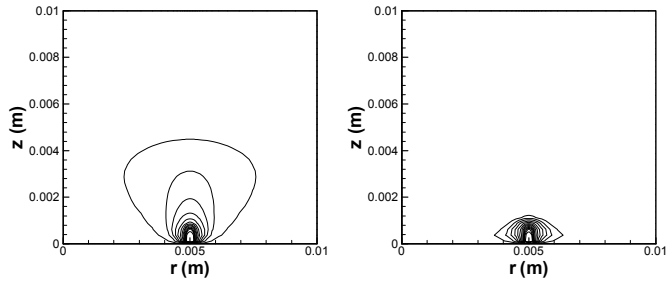

(a) U_{sh}=5 m/s (b) U_{sh}=35 m/s

Figure 3 Computed isotherms on the vertical section ($\theta = 0 - \pi$) for different velocities of the axially injected shielding gas.

3.2 Effects of the laterally injected assisting gas on plasma plume

It is expected that the laterally injected assisting gas can significantly affect the plasma plume characteristics. In fact, the laterally injected assisting gas has often been employed to suppress the unfavourable effect of the plasma plume on the laser welding process. In the present parameter study, the injection port at the left boundary is 5 mm above the bottom boundary and directed to the center of the laser spot on the workpiece surface. The injection angle of the assisting gas is thus 45^o with respect to the workpiece. In this subsection, the metal vapor velocity (U_{va}) and temperature (T_{va}) at AB on the workpiece surface are assumed to be fixed, i.e. 100 m/s and 10000 K respectively, whereas the shielding gas velocity is 5 m/s. Typical 3-D modeling results are presented in Figs. 4(a) and 4(b) and Figs. 5(a) and 5(b) for two different assisting gas velocities, i.e. U_{as}= 5 and 50 m/s. Figs. 4(a) and 4(b) show the computed flow fields (denoted with uniform vector length) on the middle vertical section (i.e. on the $\theta = 0 - \pi$ plane). Corresponding

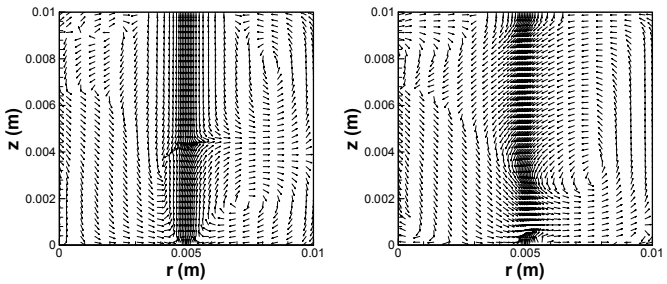

(a) U_{sh}=5 m/s (b) U_{sh}=35 m/s

Figure 4 Computed velocity vector fields on the vertical section ($\theta = 0 - \pi$) for different velocities of the laterally injected assisting gas.

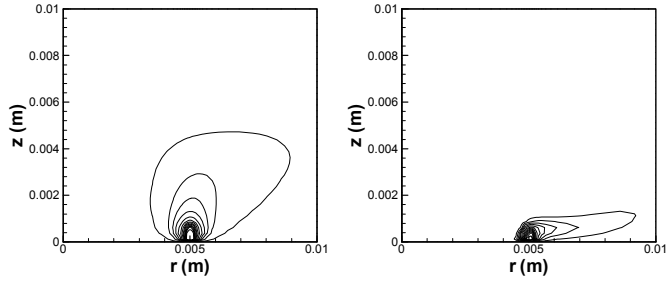

(a) U_{sh}=5 m/s (b) U_{sh}=35 m/s

Figure 5 Computed isotherms on the vertical section ($\theta = 0 - \pi$) for different velocities of the laterally injected assisting gas.

computed isotherms are shown in Figs. 5(a) – 5(b) with isotherm range 1000 K~13000 K and isotherm interval of 1000 K. It is seen from the computed results shown in Figs. 4(a) and 4(b) and in Figs. 5(a) and

5(b) that the velocity of the laterally injected assisting gas significantly modifies the temperature and flow fields of the plasma plume. The plasma plume is blown away from its original location along the geometrical axis by the laterally injected assisting gas, showing an appreciable deflection. However, the present modeling results show that the maximum temperature of the plasma plume is less influenced by the laterally injected assisting gas. The maximum temperature of plasma plume decreases only from about 13800 K for the case with U_{as} = 0 (i.e. without the laterally injected assisting gas) to about 13100 K for the case with U_{as} = 50 m/s.

Comparison of these computed results to those without including laterally injected gas (e.g. the results shown in Fig. 2 and Fig. 3) reveals that due to the cooling effect of the laterally injected assisting gas, the dimensions of plasma plume become smaller. It is expected that the laser absorption and refraction caused by the plasma plume can be appreciably suppressed if the injection velocity and angle of the assisting gas are adjusted appropriately.

3.3 Laser absorption and refraction

The local values of the absorption coefficient of plasma plume are calculated using Eq. (7), whereas the complex refraction index is calculated using the following expression (Beck et al [12])

$$\hat{n} = 1 - \frac{\omega_p^2}{\omega(\omega_p + i\omega_e)} \tag{9}$$

In Eq. (9), ω_p is the plasma frequency， ω_e the electron collision frequency whereas ω is the frequency of CO_2 laser. As an example, the calculated results are presented here for the case that the metal vapor temperature (T_{va}) and velocity (U_{va}) at AB on the bottom boundary are 10000 K and 100 m/s, respectively, and the velocity of coaxial shielding gas is 5 m/s. Laterally injected assisting gas is not considered here.

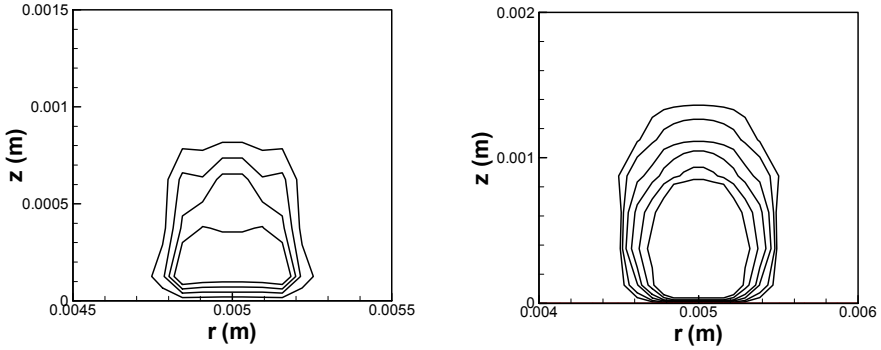

(a) Absorption coefficient (b) Real part of refraction index

Figure 6 Computed distributions of the absorption coefficient (a) and the real part of refraction index (b) at the middle vertical section (θ = 0 – π).

The computed spatial variations of the absorption coefficient and the real part of the refraction index within the plasma plume are shown in Figs. 6(a) and 6(b), respectively. Fig. 6(a) shows the computed contours of the absorption coefficient in the range of 15~75 m^{-1} with interval 20 m^{-1}, whereas Fig. 6(b) plots the computed contours of the real part of refraction index in the range of 0.999~0.989 with interval −0.002. Changing from the non-ionized gas region outside the plume to the core of the plasma plume, the absorption coefficient increases from 0 to larger than 75 m^{-1}, whereas the real part of refraction index decreases from 1.000 to less than 0.989.

Using the computed spatial variations of the absorption coefficient and the refraction index within the plasma plume, we can further calculate the absorption and refraction of the laser beam when it passes through the plasma plume. After passing through a control volume, the laser energy will be partially absorbed and the fraction of absorbed power can be calculated by

$$\frac{I_{in} - I_{out}}{I_{in}} = 1 - \exp(-\alpha \Delta x) \tag{10}$$

where I_{in} and I_{out} are the laser intensity as the laser beam enters into and departs from the control volume, respectively, Δx is the axial size of the control volume, whereas α is the local absorption coefficient. Using

Eq. (10) and repeating the calculation for all the control volumes along the laser beam path, the total fraction of absorbed laser power is easily obtained. For the case as shown in Figs.6(a) and 6(b), the evaluated fraction of the laser power absorbed by the plasma plume is about 6 %.

The variation of the laser beam radius due to refraction can be estimated by the ray-tracing method. The deflection angle increment $\Delta\theta$ for the outermost ray at the edge of the laser beam as it passes through a control volume in the plasma plume with non-uniform refraction index can be calculated by (Eckert and Goldstein [13])

$$\Delta\theta = \frac{1}{n}\frac{\partial n}{\partial y}\Delta x \tag{11}$$

where n is the local value of the refraction index, $\partial n/\partial y$ the lateral derivative of the refraction index, whereas Δx is the axial size of the control volume. Repeating the calculation for all the control volumes along the ray path, the calculated deflection angle of the outermost ray at the edge of the laser beam is $\sim 3^0$ with respect to the laser beam axis and its lateral displacement is $\sim 0.3\times 10^{-4}\, m$ as it reaches at the workpiece for the present case. Hence, considering the refraction, the laser beam radius (originally 0.15 mm) at the spot will become $1.8\times 10^{-4}\, m$, and thus the laser beam intensity at the light spot will decrease by 30 % after the laser beam passes through the plasma plume and arrives at the workpiece surface.

4. Conclusions

A 3-D variable-property modeling approach is employed in this paper to study the laser-induced plasma plume characteristics with the CO_2 laser welding of iron workpiece as the calculation example. The modeling results show that the velocity of the coaxially injected shielding gas may appreciably affect the plasma plume characteristics. The height of the plasma plume is dependent on the metal-vapor / shielding-gas flow momentum ratio. Complicated flow pattern always exists in the plasma plume, but the maximum temperature in the plume core is always 13100–13900 K for the iron-argon system. Although laser absorption is important for the maintenance of plasma plume, its effect on the laser intensity attenuation is not significant. On the other hand, refraction may appreciably affect the laser intensity at the light spot. It is also shown that the laterally injected assisting gas can significantly affect the plasma plume characteristics. In order to obtain good welding quality, the velocity of the coaxially injected shielding gas and that of the laterally injected assisting gas should be carefully adjusted. Modeling results concerning plasma plume temperatures are shown to be reasonably consistent with available experimental data.

Acknowledgement

This work was partly supported by the National Natural Science Foundation of China (grant Nos. 50176024, 59836220).

References

[1] G. Herziger – *The Industrial laser annual handbook,* PennWell Pub. Co., eds. Belforte D and Levitt M (1986).

[2] Z. Szymański, J. Kurzyna, W. Kalita – *J. Phys. D: Appl. Phys.* **30**, 3153 (1997).

[3] Z. Szymański, J. Kurzyna – *J. Appl. Phys.* **76**, 7750 (1994).

[4] K.R. Kim, D. F. Farson – *J. Appl. Phys.* **89**, 681 (2001).

[5] M. A. Samsonov, Z. S. Shambetov – *Effects of Metal Vapors on Two-Phase Plasma Flows,* Bishkek: Ilim, (1993 in Russian).

[6] J. Menart, S. Malik – *J. Phys. D: Appl. Phys.* **35**, 867 (2002).

[7] A. Essoltani, P. Proulx, M. I. Boulos, A. Glezes – *Plasma Chem. Plasma Process.* **14**, 301 (1994).

[8] J. F. Ready – *Effects of High-Power Laser Radiation,* New York, Academic (1971).

[9] J. Dowden, W. S. Chang, P. Kapadia P, C. Strange – *J. Phys. D: Appl. Phys.* **24**, 519 (1991).

[10] C. Tix, G. Simon – *Phys. Rev. E* **50**, 453 (1994).

[11] R. Miller, T. DebRoy – *J. Appl. Phys.* **68**, 2045 (1990).

[12] M. Beck, P. Berger P, H. Hügel – *J. Phys. D: Appl. Phys.* **28**, 2430 (1995).

[13] E. R. G.Eckert, R.J. Goldstein – *Measurements in Heat Transfer,* New York: McGraw-Hill, Chapter 5 (1976).

OES Study of CH_4 : H_2 Microwave Plasma During Deposition of Different Carbon Materials

N. Dzbanovsky[1], V. Dvorkin[1], A. Filippov[2], A. Pal[2], N. Suetin[1], A.Yuriev[1]

[1] *Institute of Nuclear Physics, Moscow State University, 119992, Moscow, Russia*
[2] *Troitsk Institute for Innovation and Fusion Research, 142190 Troitsk, Moscow reg., Russia*

Abstract
We have carried out the comparative study of the luminescent spectra of plasma during different carbon film deposition in MW CVD system using CH_4/H_2 gas mixture in a wide range (0.5-17%) of CH_4 concentrations. It was found out that there is abnormally high rotational temperature of carbon dimers of up to 5000 K. The model of the C_2 molecule formation process was constructed to explain the observed phenomenon.

1. Introduction

The plasma of microwave discharge in methane-hydrogen mixtures is widely used for various carbon films deposition. Increase of the methane concentration from fractions of percentage up to tens of percent results in a fundamental change in the structure and in the composition of the deposited films. In low methane concentration range of 0.5-1% there is a high quality diamond film growth (both polycrystalline and single-crystalline ones – depending on the substrate type). In the next range (2-4%), as a rule, a nanodiamond film growth is observed. In this case the film contains a great share of amorphous carbon in addition to diamond nano-crystals. When we increase the methane concentration further, the result of the deposition process basically depends on the chemical composition and morphology of the substrate surface. In particular, when the methane concentration reaches 15% and there are catalytic particles (Ni, Fe etc.), the formation and growth of carbon nanotubes or nanowhiskers occur. Thus, physical and chemical properties of substrate surface substantially determine the characteristics of the deposited carbon materials at high methane percentage. However, the substrate having "optimal" for the growth of the required structure characteristics is necessary but insufficient for this structure deposition. Another necessary condition is the "required" plasma-chemical composition of the discharge to provide the required flux of radicals and ions with the required energy upon the substrate.

The density of radicals and ions in plasma, as well as their energy, depends not on the initial gas composition only, but also on the absorbed microwave power, the gas pressure, the rate of the gas pumping, and on many other parameters. This is the reason why the control of plasma-chemical composition and temperature of plasma during the deposition process is of fundamental importance for the reproducible production of the films with the required properties. Optical emission spectroscopy is a most available and noncontact method of control, however this method is the most complicated in the view of quantitative interpretation of results.

The present work is devoted to comparative study of luminescent spectra of microwave plasma in CH_4–H_2 mixtures. These spectra were obtained during the deposition of different carbon materials, from diamond to nanotubes. To explain the revealed spectra behavior the model of C_2 molecule formation was developed.

2. Experiment

Experimental setup. The experiments were carried out using the microwave setup having a 2.45 GHz magnetron as a microwave generator with spectroscopy system connected to the reactor's view port.

Electromagnetic energy generated by magnetron capable to produce up to 6 kW of the microwave power, comes through the waveguide to the resonator-type reactor and ignites the discharge in the reactor volume over the Mo substrate holder where the maximal energy concentration is situated. The plasma position just near the substrate is provided by reactor configuration and waveguide tuners set. To enable plasma spectroscopy and substrate temperature measurements the reactor has two inspection ports. For checking the substrate temperature we used Williamson Pro 90 dual-wavelength pyrometer.

Working gas mixture is injected directly in the discharge area from the top of the reactor. Fluxes of the hydrogen and of the carbon source (methane) were controlled with flow-meters. Gas evacuation carries out near the bottom of the reactor.

For plasma diagnostics we used the specially developed home made spectroscopy system which can control the wavelength range from 350 nm to 800 nm. System resolution was 0.05 nm that was achieved with B&M Spektronik BM-100 monochromator having 100 cm focal length and 0.83 nm/mm dispersion. The light-sensitive element was a Toshiba TCD1201 CCD linear sensor. Spectroscopy system was connected to the inspection port by way of quartz optical fiber equipped with the system of focusing lens. Spectra were collected and processed by the computer having spectral data analyzer program.

Substrates preparation. For diamond film growth we used Si(100) (4.5 Ω·cm) with the suspension of nanodiamond in photoresist put upon Si surface. This nucleation method allowed us to get 10^{10}-10^{11} cm^{-2} nucleation density. In the other case, to grow the carbon nanotubes the Ti layer (100 nm thick, as a diffusion barrier) under either Ni or Co layer (20 nm, as nanotube growth catalyst) was deposited upon Si(100) (4.5 Ω·cm).

Experimental conditions. In our experiments we operate with H_2 and CH_4/H_2 gas mixtures under the pressure in a chamber within 40-80 Torr. The CH_4 concentration in the methane/hydrogen mixture was varied from 0.5% (diamond film growth regime) to 16% (carbon nanotube growth regime). Microwave power absorbed by plasma was in the range of 0.5-1.5 kW. During the deposition process the substrate temperature was 700-800 °C.

Every process began with sample annealing in hydrogen atmosphere for five minutes to eliminate any possible sign of organic contamination on the substrate's surface to improve film's uniformity and quality. After the above procedure the methane was added to the feed gas and the film deposition process began. During this step the plasma spectrum was recorded. After the deposition process was over, in case of diamond film growth, the sample was annealed in hydrogen for 5 min. to remove the sp^2 phase, inevitably formed on the surface.

Films characterization. In our experiments in the methane concentration range indicated above we obtained a wide variety of carbon materials, from diamond to nanotubes. Films' phase and morphological properties were studied with Raman spectroscopy and scanning electron microscopy. Typical SEM-images and Raman spectra of the samples grown in both low and high methane concentration conditions (diamond and nanographite growth respectively) are presented in Fig. 1(a, b) and Fig. 2(a, b).

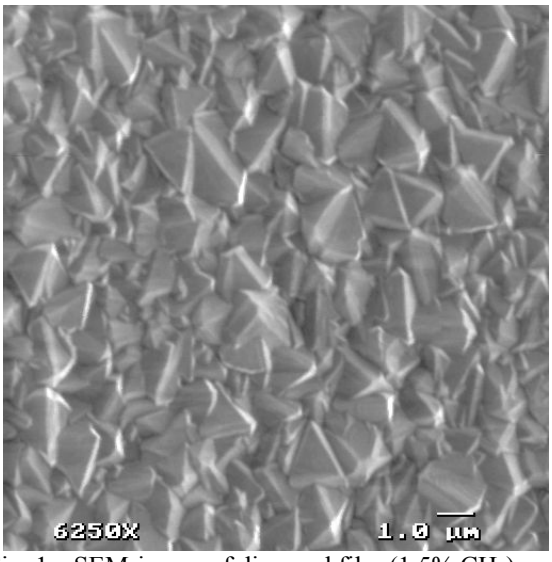

Fig. 1a. SEM-image of diamond film (1.5% CH_4)

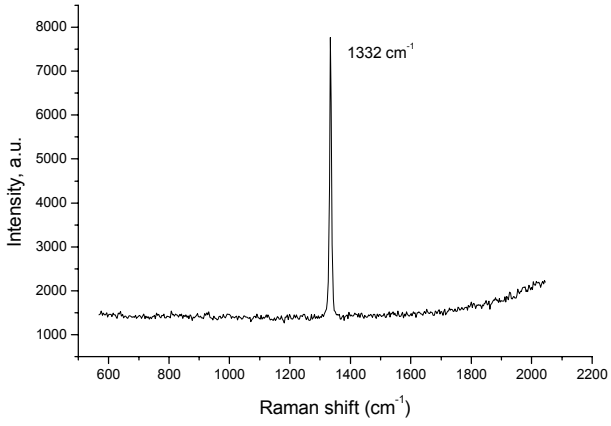

Fig. 1b. Raman spectra of diamond film (1.5% CH_4)

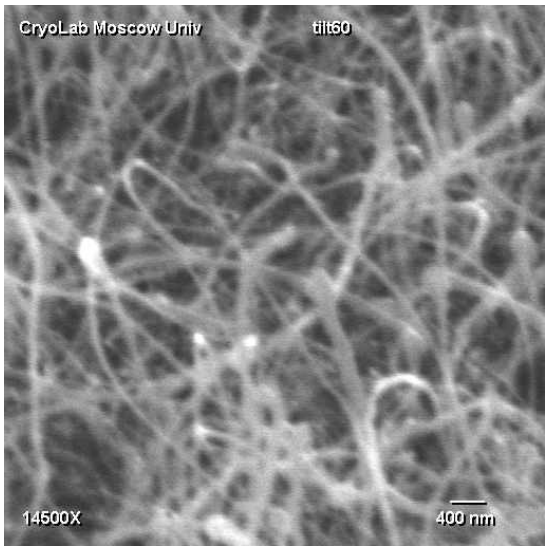

Fig. 2a. SEM-image of multiwalled carbon nanotubes (16% CH_4)

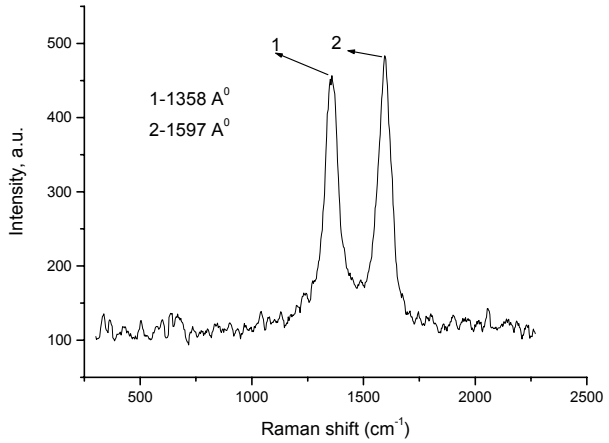

Fig. 2b. Raman spectra of multiwalled carbon nanotubes (16% CH_4)

3. Results and Discussion

For the case of methane density varied from 0.5 to 16% the behavior of the following most high intensity molecular band systems C_2 ($d^3\Pi_g \rightarrow a^3\Pi_u$, 516.5 nm) and CH ($A^2\Delta \rightarrow X^2\Pi_r$, 431.4 nm), as well as of H_α (n=3→n=2, 656.3 nm), H_β (n=4→n=2, 486.1 nm) and H_γ (n=5→n=2, 434.0 nm) hydrogen atom lines was studied.

One of the fundamental characteristics of the weakly ionized plasma is the temperature of the neutral gas, determining either expressly or by implication practically all the processes in plasma. This characteristic determines the rates of physical and chemical processes, the direction and the intensity of heat fluxes, reduced electrical field strengths and mean electron energies, line widths, etc. The method of relative intensities of electronic-vibrational-rotational lines (EVR) [1] for diatomic molecules is widely used for the evaluation of the gas temperature. To apply this method it is necessary that the distribution of molecules over the rotational levels of the excited electron state should be of Boltzmann behavior with some rotation temperature, which, it should be noted, can be different from the gas temperature. If the typical time of the rotation relaxation in the excited state τ_{rot} exceeds the radiation life time τ_{rad} of this state, that is,

$$\tau_{rot} \gg \tau_{rad}$$

if the excitation of the upper state occurs by the electron strike and there is Boltzmann rotation distribution in the basic state, then the rotation temperatures T^0_{rot} and T'_{rot} of the basic and excited states are in the following ratio:

$$T'_{rot} B' = T^0_{rot} B^0 \quad (1)$$

where B^0 and B' are the corresponding rotation coefficients. And if the opposite inequality

$$\tau_{rot} \ll \left(\tau^{-1}_{rad} + k_q n_q\right)^{-1}$$

is true, then it is possible to conclude that within the considered system the rotation relaxation has been completed and the rotation temperature of the upper excited state is equal to the gas one. Here k_q is the rate coefficient of the collision quenching, n_q is the density of quenchers.

The present work is devoted to studying the $d^3\Pi_g \rightarrow a^3\Pi_u$ Swan band system of C_2 molecule and the $A^2\Delta \rightarrow X^2\Pi$ band system of CH molecule. The spectroscopic data and the radiation lifetime of these states are shown in table 1 [2-6]. The both studied transitions are associated with low states, therefore, the assumption can be made that in the studied mixtures, where the basic component is a light hydrogen molecule having abnormally large rotation constant, the rate of collision quenching is greater than that of the rotation relaxation. Therefore, the rotation distribution in the spectra of these bands most likely depends on the

excitation mechanism. If the electron excitation from the basic state prevails, then the temperatures are connected by ratio (1).

Under the Boltzmann distribution within the rotation levels with the temperature of T'_{rot} the intensities of the spontaneous radiation of the individual EVR line are determined according to the following expression [6-8]:

$$I_{n'\upsilon'J'\to n''\upsilon''J''} = const \cdot \left(\nu_{n'\upsilon'J'\to n''\upsilon''J''}\right)^4 S_e q_{\upsilon'\upsilon''} S_{J'J''} g_{s,a} \exp\left(-\frac{hcF'(J')}{kT'_{rot}}\right), \quad (2)$$

where $\nu_{n'\upsilon'J''\to n'''\upsilon'''J'''}$ is the wave number of the EVR transition $n'\upsilon'J'\to n''\upsilon''J''$, n indicates the electron state, υ is the number of the vibration level, J is the total momentum of the rotation level, the values with one prime refer to the upper state, those with two primes to the lower state; S_e is the electron momentum of the transition, $q_{\upsilon'\upsilon''}$ is the Frank-Condon factor, $S_{J'J''}$ is the Holn-London coefficient, $F'(J')$ - is the rotation term of the upper state, $g_{s,a}$ is the parameter taking into account the statistical weights symmetrical and anti-symmetrical states of homonuclear molecules, h is the Planck's constant, c is the velocity of light, k is the Boltzmann constant.

Table 1. Spectroscopic data of the studied states [2-6].

	$C_2(d^3\Pi_g)$	$C_2(a^3\Pi_u)$	$CH(A^2\Delta)$	$CH(X^2\Pi_r)$
T_e, cm^{-1}	20022.5	716.24	23151.8	0.0
A	–16.9	–15.25	–1.02	27.95
ω_e, cm^{-1}	1788.22	1641.35	2930.61	2858.55
$\omega_e x_e$, cm^{-1}	16.440	11.67	96.65	63.03
$\omega_e y_e$, cm^{-1}	–0.5067	0.0	0.0	0.0
B_e, cm^{-1}	1.7527	1.63246	14.9145	14.4717
α_e, cm^{-1}	0.01608	0.01661	0.695	0.528
γ_e, cm^{-1}	–0.001274	0.0	0.0	0.0
D_e, cm^{-1}	6.74×10^{-6}	6.44×10^{-6}	1.493×10^{-3}	14.68×10^{-4}
β_e, cm^{-1}	-0.103×10^{-6}	0.0	5.5×10^{-5}	-1.8×10^{-5}
τ_{rad}, ns [6]	122		500	

The rotation terms of duplet and triplet states were determined according to the relationships in [7]. In fig.3 contains the schemes of the studied transitions for C_2 and CH molecules. Only the transitions of basic branches are shown. Besides the basic branches, there 6 more satellite branches for $CH(A^2\Delta)\to CH(X^2\Pi_r)$ and 18 ones for $C_2(d^3\Pi_g)\to C_2(a^3\Pi_u)$. The Honl-London factors were calculated according to [7].

In fig.4 there is comparison of the experimental spectrum with the calculation one for different rotation (the first number in the legend) and vibration (the second number) temperatures of the upper state of the $CH(A^2\Delta)\to CH(X^2\Pi_r)$ system, 0-0, 1-1, 2-2 и 3-3 bands. No agreement with the experiment was achieved under any rotation temperature. It is seen that the temperature of high rotation levels is close to 2000 K (the sizes of peaks corresponding to individual rotation levels in the calculation and in the experiment practically coincide in the value), but in the range of low rotation levels the temperature is lower. The figure also shows the emission of C_2 molecules in the Swan system, the 2-0, 3-1 and 4-2 bands of $\Delta v=2$ sequence.

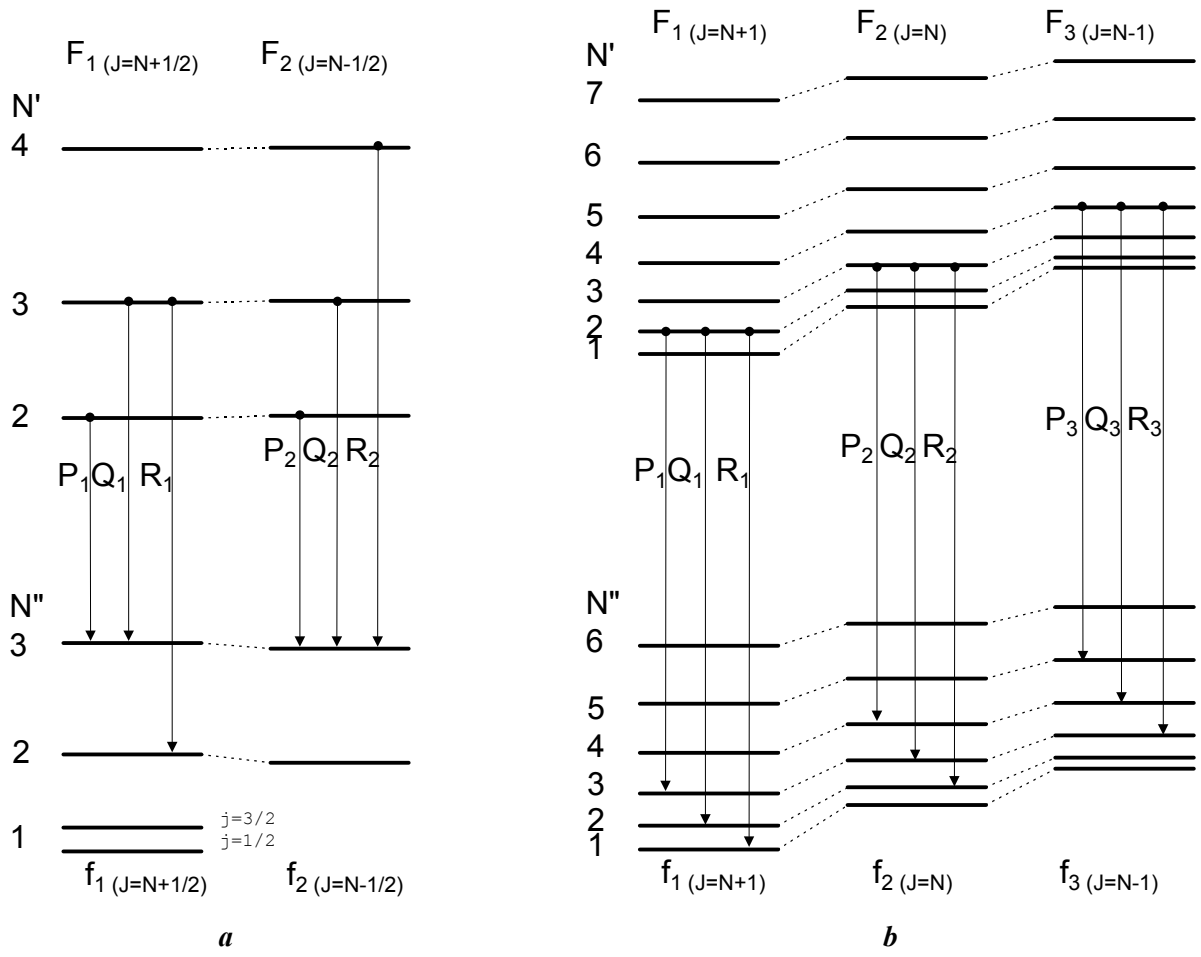

Fig.3. The rotation levels and the transition schemes of the basic branches for $CH(A^2\Delta)\rightarrow CH(X^2\Pi_r)$ and $C_2(d^3\Pi_g)\rightarrow C_2(a^3\Pi_u)$ band systems.

In fig.5 there is comparison of experimental and calculation spectra within the Swan band system for C_2 molecules, $\Delta v=0$ sequence in the mixture of H_2+C_2H_5OH with a small addition of $(CH_3O)_3B$, and also in the mixture of H_2+CH_4. The H_2 percentage in the mixtures exceeded 90%. It is seen that the rotational temperature of the upper state is close to 5000 K. Energy estimation and independent measurements result in the gas temperature, not exceeding 1000°C. Therefore, we can conclude that the rotation temperature determined by the emission within the Swan band system does not correspond to the gas temperature, but indicates the fact that the mechanism of exciting the $d^3\Pi_g$ is non-electron.

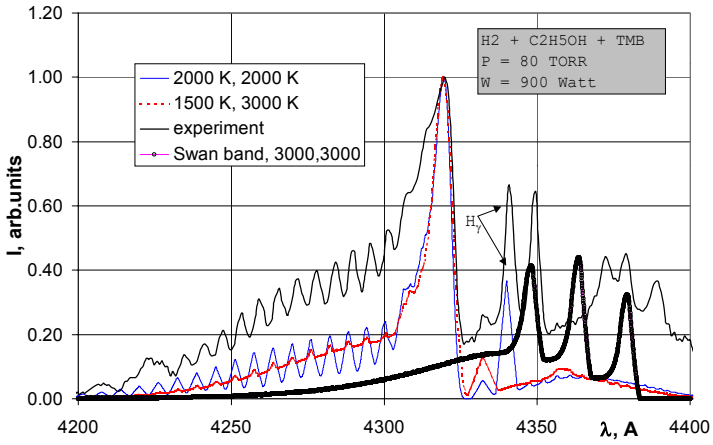

Fig.4. Experimental and calculation glow spectra of CH molecules within the $A^2\Delta\rightarrow X^2\Pi$ band system of the $\Delta v=0$ sequence.

The analysis of the processes with the participation of methane and hydrogen radicals shows that the excitation of high rotation levels can result from the following:

$$CH + CH_2 \rightarrow C_2H^*(E\approx 4.6\ eV) + H_2 \qquad (R1)$$
and/or
$$C_2H + e \rightarrow C_2H^*(E\approx 4.6\ eV) + e; \qquad (R2)$$

$$C_2H^* + H \rightarrow C_2(d^3\Pi_g) + H_2 + \Delta E\approx 1.0\ eV \qquad (R3)$$
and/or
$$C_2H^* + C_2(a^3\Pi_u) \rightarrow C_2H + C_2(d^3\Pi_g) + \Delta E\approx 2.1\ eV. \qquad (R4)$$

A share of the extra energy ΔE is spent for the excitation of rotation levels. In this case the process (R3) most likely occurs within the migration mechanism, when the hydrogen atom collides with one of the carbon atoms of the C_2H complex, and then "migrates" to the hydrogen atom, which is followed by the hydrogen molecule escape. According to [9] the migration mechanism is characterized by a high degree of rotation excitation of the reaction products. At present there occurs the creation of the complete chemical model for the discharge processes in the mixtures containing hydrogen and methane to explain the results revealed in this work.

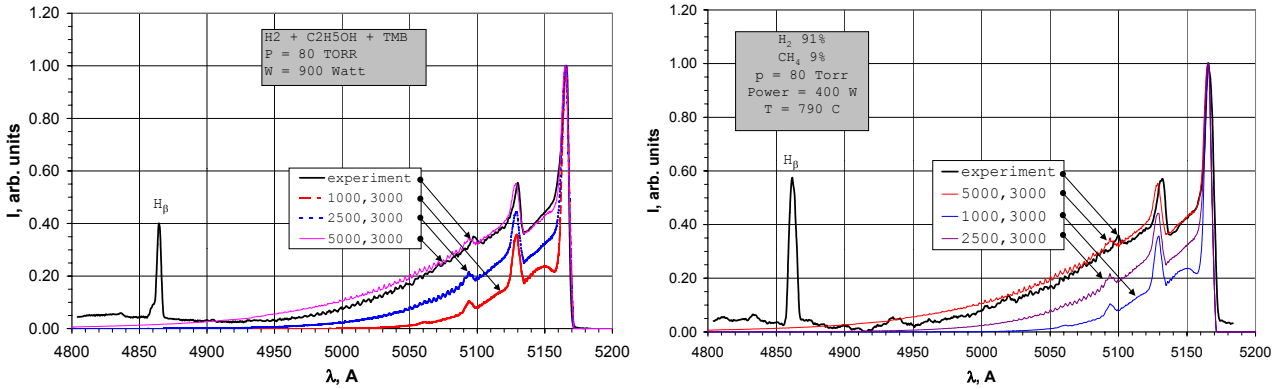

Fig.5. Experimental and calculation emission spectra of C_2 molecules within the Swan band system, the sequence is Δv=0.

Acknowledgement
The work was accomplished due to ISTC support, project No. 2484.

References

[1]. G. Herzberg - Molecular spectra and molecular structure. I. Spectra of diatomic molecules. N. Y.: D. van Nostrand, 1951.
[2]. K.F.Huber, G. Herzberg - Molecular spectra and molecular structure. IV. Constants of diatomic molecules. N. Y.: D. van Nostrand, 1979.
[3]. S. Pellerin, K. Musiol, O. Motret, B. Pokrzywka, J. Chapelle - J. Phys. D: Appl. Phys. **29,** 2850 (1996).
[4]. B.M. Krupp - The Astrophysical Journal **189,** 389 (1974).
[5]. S.W. Reeve, W.A. Weimer - J. Vac. Sci. Tech. **13**(2), 359 (1995)
[6]. L.A. Kuznetzova, N.E. Kuz'menko, Yu.Ya. Kuzyakov - Probabilities of optical transitions of diatomic molecules, Moscow, Nauka, 1980.
[7]. I. Kovacs - Rotational structure in the spectra of diatomic molecules, Budapest, Akademiai Kiada, 1969.
[8]. N.E. Kuz'menko, L.A. Kuznetzova, Yu.Ya. Kuzyakov - Frank-Condon factors of diatomic molecules, Moscow State University, 1984.
[9]. G.K. Vasil'ev, E.F. Makarov, V.L. Tal'roze - Khimiya Plazmy, Ed. by B.M. Smirnov, Moscow, Energoizdat, **9,** 3 **(**1982)

Fabrication of bioactive surfaces by plasma polymerisation techniques using a new synthesized acrylated-derived monomer

L. Francesch[1], E. Garreta[1], M. Balcells[2], S. Borrós[1]*

[1]*Materials Science Laboratory, Institut Químic de Sarrià (IQS), University Ramón Llul, Barcelona, Spain*
[2]*Harvard University-Massachusetts Institute of Technology Biomedical Engineering Department, Cambridge,USA*
*s.borros@iqs.url.edu

Abstract
A new monomer has been synthesized, a pentafluorophenyl acrylate, that has been polymerised by plasma techniques. The polymer leaves labile groups on the surface, which facilitate a fast reaction with biotinylated molecules. Other monomers, such as acrylic acid and allylic alcohol, have also been polymerised by plasma, leading to a surface with functional character that would result into a versatile platform for further linkage of biotinylated biomolecules to promote cell attachment.

1. Introduction

Our research group is involved in the development of biomaterials that facilitate new tissue in-growth for bone and cartilage restoration. To this end, improvement of surfaces is crucial, so that they become attractive to cells so that their adhesion, growth and proliferation are enhanced. Initial cell adhesion can be induced by bioactive surfaces, obtained by linkage of biological ligands, which enable control of cell-substrate interactions. The main approach to immobilize ligand motifs on biomaterial surfaces consists of creating covalent attachments to reactive polymer side chains [1]. Surface modification techniques have been shown to be suitable, because a thin film may be deposited onto substrates of complex geometry [2] with a uniform distribution of functional groups.
Our goal was set in covalently linking biotin to a polymer surface. Subsequent assembling of streptavidin with the biotin-coated surface would result into a versatile platform for further linkage of other biotinylated biomolecules of interest to promote cell attachment [3].
µcontact printing methods are attractive for micropattering of biomolecules like biotin because of their simplicity and ease of use [4]. For applying this method it is necessary to have a very reactive surface, which is achieved by having labile groups like pentafluorophenyl. In consequence, the monomers developed untill now for getting these coatings having this kind of labile groups, are complicated and have long and complex synthesis [3]. The aim of this study is to get an easy way to synthesise different kinds of small acrylate derivates to be used afterwards as monomers for plasma polymerization, leaving a functionalized surface with this labile group. In the present work pentafluorophenyl methacrylate has been synthesized. Although methacrylate derivatives of pentafluorophenol are well known [5], their use as monomers for plasma polymerisation hasn't been studied in deep.
For the implementation of other methods for biotin linkage, polymerisation other kinds of monomers have also been studied.

2. Experimental section

2.1 Pentafluorophenyl methacrylate synthesis
2.1.1 General
Florosil® (60-100 mesh, Aldrich), Methacryloyl chloride (+98%, Aldrich), 2,6-lutidine (97%, Aldrich), 2,3,4,5,6-pentafluorophenol (99%, Aldrich), THF, Pentane.
^{1}HNMR and ^{13}CNMR spectra were determined in $CDCl_3$ as solvent on a Gemini 300 Varian spectrometer at 300.1 and 75.5 MHz, respectively. Chemical shifts are reported in δ (ppm) from internal TMS. IR spectra were made on a Nicolet Magna 5600 spectrophotometer.

2.1.2 Typical procedure [5]
Methacryloyl chloride (8ml, 82mmol) is added drop wise to a stirred solution of pentafluorophenol (7.6g, 41mmol) and 2,6-lutidine (6.6g, 62mmol) in THF (100ml) at 0ºC. After 10 min stirring at the same temperature, the precipitate is filtrated and washed with THF (50ml). Then, the solvent is removed under reduced pressure and the residue was purified by chromatography on a Florosil® column (Aldrich 60-100mesh), using pentane as eluent. The pentafluorophenyl methacrylate is stored at 4ºC.

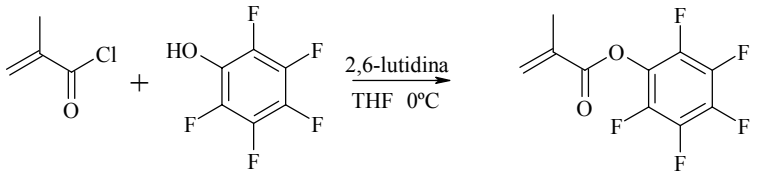

Fig.1 Monomer synthesis

2.2 Plasma reactor system
The plasma deposition apparatus consisted of a stainless steel discharge vessel (diameter 26 cm, length 24 cm) with internal electrodes which were connected to a RF power source (13,56MHz). The gases or monomers were supplied via a standard manifold with gas fluxes adjusted with needle valves. A pressure meter positioned between the reactor and the cold trap before the vacuum pump, measured the system pressure. The two stages mechanical pump (Edwards, RV12 903) evacuates de vessel. The reactor chamber was evacuated to a base pressure of 0,1mbar.
Each polymer was deposited on a square of silicon wafer (100) oriented 250-350µm thickness and on 25µm polyethylene. The RF power was around 10W. Deposition times were within two and eight hours.
Pentafluorophenyl methacrylate (PFM) was used as synthesized. It was necessary to heat the monomer to reach the desired pressure to polymerise. The monomer flow rate was set so that the pressure within the reactor was 0.3mbar.
Acrylic acid (99%, Aldrich), 1,7-octadiene (98%, Aldrich) and allyl alcohol (98,5%, Aldrich) were used as supplied. The pressure within the reactor for the DACH was typically 0.4mbar (it was also needed to heat the monomer). Acrylic acid and allyl alcohol were polymerized at a pressure of 0.4mbar and 0.8mbar each. They were also copolymerized with 1,7-octadiene, with a relationship between the monomers of $3_{Octadiene}/4_x$.

2.3 Infrared (IR) Sprectroscopy
IR spectra were collected by the transmittance mode with the plasma polymers deposited on the polyethylene by the use of an FT-IR spectrophotometer (Bormen MB-120). In the reflectance mode a microscope (IR-Plan-Spectra Tech) was attached to the spectrophotometer.

2.4 XPS
The XPS analysis were carried out using a Perkin Elmer PHI 5500 spectrometer, fitted with a monochromatic Al X-ray gun, operated with a gun of 350W. The pass energy for the acquisition of C 1s narrow scans was 23.50 eV. All XPS spectra were recorded at a take off angle of 45ºC relative to the surface normal. The pressure in the main UHV chamber was maintained below $5x10^{-9}$ Torr for all analyses. Data analyses were carried out using Multipax software (PHI) with the C1s component of the aliphatic hydrocarbon set a 285.00 eV as a reference.

3. Results

3.1 Monomer synthesis
Pentafluorophenyl methacrylate is obtained as a colourless oil (7.0g, 35%).
1H NMR: 6.454ppm (1H, dq, H_b), 5.914ppm (1H, dq, H_a), 2.093ppm (3H, dd). See figure 2.
13C NMR: 162.910ppm (1C, s, CO), ca.139.6ppm (5C, m, C-F), 133.626ppm (1C, s, H2C=C), 129.786ppm (1C, s, H2C=C), 18.272ppm (1C, s, C-CH3).

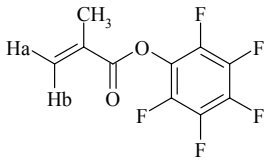

Fig.2 pentafluorophenyl methacrylate

IR spectra (figure 3):
The IR spectrum of the pure PFM shows some characteristic peaks. Around 2950 cm^{-1} there are peaks that reveal hydrocarbon activity, the peak at 1764 cm^{-1} shows a carbonyl stretch of a carboxylate ester. Between 1625 and 1475 cm^{-1} there are some peaks for the skeleton vibrations. Around 1100-1000 cm^{-1}, there are some peaks characteristics for C-F stretching.

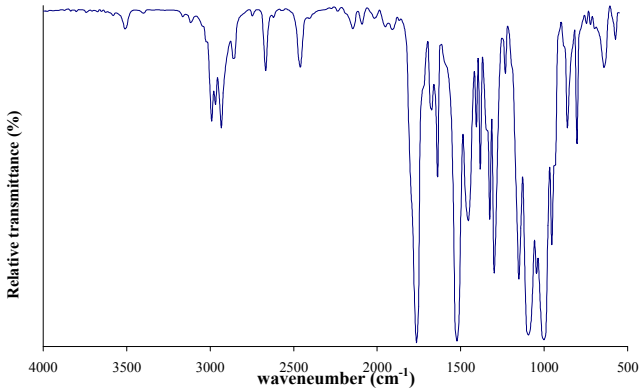

Fig.3 IR spectra of pentafluorophenyl methacrylate

3.2 Plasma polymerisation
3.2.1 FT-IR
In the FT-IR spectra of the continuous plasma acrylic acid films appeared some characteristic peaks. There is a broad absorption peak around 3200 cm^{-1}, assigned to the stretching vibration of O-H in the carboxylic acid, and around 2950 cm^{-1} there is a peak that reveals hydrocarbon activity, the peak at 1738 cm^{-1} shows a carbonyl stretch of a carboxylic acid. [6]
The FT-IR spectra of the allyl alcohol films show retention of hydroxyl functional groups. The peak around 3350 cm-1 is due to the stretching vibration of the polymeric O-H, the presence of hydrocarbon activity is also shown by the peak at 2935 cm-1, additionally there is a peak which shows C-O presence at 1050 cm-1. It is to be shown, that there is a presence of carbonyl groups with peaks around 1650 cm-1, that is created under the high energy conditions of the plasma polymerisation. [7]

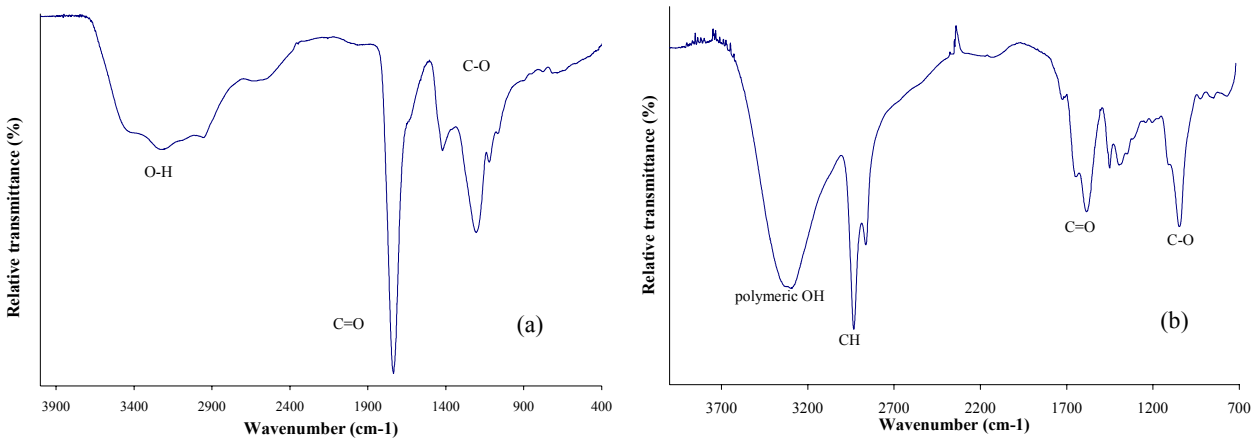

Fig.4 (a) IR spectrum of plasma polymer of acrylic acid, (b) IR spectrum of plasma polymer of allyl alcohol

3.2.2 XPS

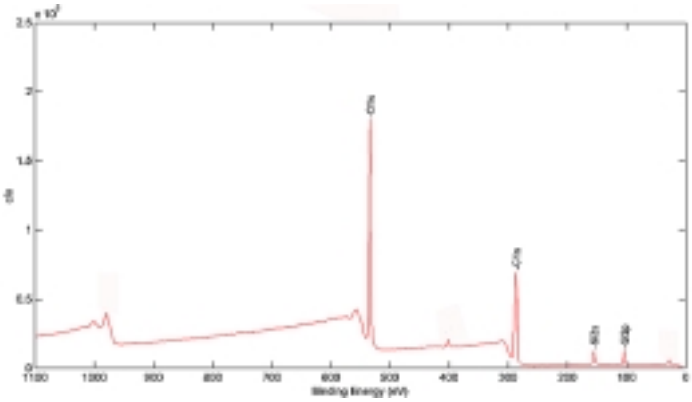

Fig.5 Survey spectrum of allyl alcohol plasma polymer

The different XPS spectra revealed the presence of silicon, oxygen and carbon. Additionally the spectrum of the PFM revealed fluorine. The presence of silicon is due to the nature of the bracket, a silicon wafer. The C 1s core level spectra were peak fitted on various oxygen-containing functionalities, except the PFM C 1s core level, that was peak fitted on oxygen-containing functionalities and also on fluorine-containing functionalities. First, spectra were corrected for sample charging, setting the hydrocarbon signal to 285 eV, and the position of the others centroids adjusted accordingly. The 1s levels of oxygen and carbon occur at 528 and 280 eV, respectively, and fluorine in the PFM occurs at 690 eV.

Figure 6 shows the C 1s core-level spectra of plasma polymerised pentafluorophenyl methacrylate and the copolymerised allyl alcohol and octadiene.

In the XPS spectrum prepared from acrylic acid and 1,7-octadiene carbon environments of the form C-R, C-O, C=O and COOR (R = C or H) are expected to be present, each exhibiting a characteristic chemical shift. This spectrum has been fitted using three peaks corresponding to hydrocarbon (C-C/H) set a 285 eV, an alcohol or ether carbon (C-O) at 286.5 eV, and carboxyl/carboxylate COOH/R at 289.2 eV [8]. The existence of carbonyl functionalities is not to be noticed, but other functionalities like alcohol/ether are present as expected.

For allyl alcohol and 1,7-octadiene samples, carbon environments of the form C-R, C-O, C=O and COOR (R = C or H) are also expected to be present, with its characteristic chemical shift. This spectrum has been fitted using four peaks corresponding to hydrocarbon (C-C/H) set a 285 eV, an alcohol or ether carbon (C-O) at 286.5 eV, carbonyl (C=O) at 288 eV, and carboxyl/carboxylate COOH/R at 289.2 eV.

The PFM spectra, it is expected, that carbon environments like C-R, COOR (R = C or H), C-F are present, each exhibiting a characteristic chemical shift. The XPS spectrum reveals the presence of fluorine. This spectrum has been fitted using three peaks corresponding to hydrocarbon (C-C/H) set at 285 eV, an ester carbon at 286.6 eV, and fluorinated carbon (C-F) at 288.9 eV.

XPS data are summarized in Table 1.

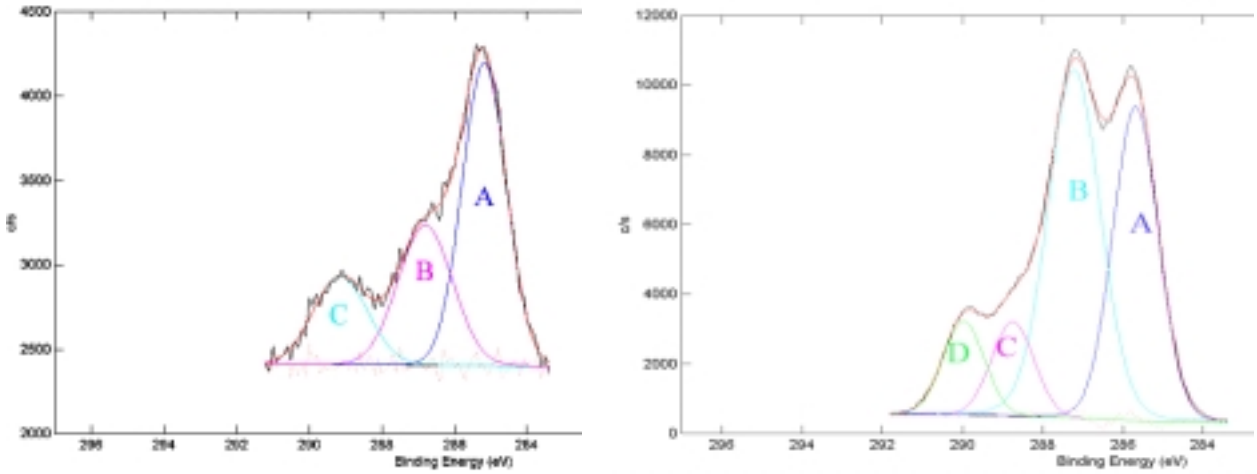

Fig.6 (a) Peak fitted C 1s core levels of pentafluorophenyl methacrylate. A: C-C/H, B: COOR, C: C-F (b) Peak fitted C 1s core levels of allyl alcohol + octadiene. A: C-C/H, B: C-O, C: C=O, D: COOR/H

Table 1. Results of quantification of the XPS spectra of plasma polymerised monomers

		percentage of functionality in the C 1s core level (%)				
	O/C ratio	C-C/H	C-O	C=O	COOH/R	C-F
PFM	0,48	51,84	-	-	29,5	18,7
Acrylic acid + Octadiene	0,49	52,95	24,85	-	22,2	-
Allyl alcohol + Octadiene	0,65	35,1	45,97	9,58	9,35	-

4. Discussion

The synthesis of the PFM is made following a general synthesis way for acrylate derivatives. The use of a hindered pyridine as proton acceptor is to limit the side Michael addition of the pyridine to the acrylate. Moreover, an excess of the base is used to prevent the addition of hydrogen chloride onto the activated double bond of the acrylate. The high basicity of he 2,6-lutidine compared to pyridine increases the extent of deprotonation of the phenol [5]. The reaction product is purified by a chromatography column filled with Florosil®, which allowed its isolation in a very pure form, as it is seen in the MNR spectra. The product has to be stored at 4ºC, to avoid its degradation.

The FT-IR analysis for the plasma polymerisation of acrylic acid and allyl alcohol already showed a retention of functional groups on the surface. But these surfaces were not stable with the contact of water. As the surfaces were desired to react in water, these monomers were let to copolymerise with 1,7-octadiene, to get a bigger cross linking of the end-polymer. The results of the FT-IR and XPS analysis showed that the retention of the functionality was also achieved.

In the plasma copolymerisation of octadiene and acrylic acid the retention of carboxylic groups is to be seen, but also the presence of other oxygen-containing functionalities like ethers or alcohols. These can arise as a result of the fragmentation of the monomer in the plasma and can be assigned to side products formed during polymerisation. Reaction between the deposit and the water desorbed from the walls of the plasma vessel (during polymerisation) and the atmospheric oxygen and the water (after polymerisation) can also contribute [9,10].

In the case of the copolymerisation of allyl alcohol and octadiene, it can be noticed that there's a big retention of the alcoholic functionality. The functionalities like carboxyl/carboxylate are less important and are the ones which can arise as a result of the fragmentation of the monomer in the plasma and, as previously, they can be assigned to side products formed during polymerisation. Once more, reaction between the deposit and the water desorbed from the walls of the plasma vessel (during polymerisation) and the atmospheric oxygen and the water (after polymerisation) can also contribute [10,11].

Regarding the polymerisation of the pentafluorophenyl methacrylate, the existence of other oxygen-containing functionalities besides to carboxylates is not to be noticed. The atomic content of fluorine reveals a relation between carbon and fluorine (C/F=3,7), higher than theoretical It could be explained if some the labile groups are supposed to fragmentise during the plasma treatment. Nevertheless, it is confirmed by the analyses that the fluorinated group on the surface is mainly retained.

5. Conclusions

Pentafluorophenyl methacrylate has been synthesized by a general derivatization method for acrylates.. It has been possible to get a simple monomer in an easy way that afterwards has been polymerised by plasma. It has been proved that labile groups are staying on the surface. These labile groups enable a fast reaction with molecules containing a primary amine groups making possible the use of microcontact printing technique.

Surface has also been activated by polymerization of other commercial monomers achieving hydroxyl and carboxylic groups that could react subsequently with molecules of interest.

These functionalities allow the covalent linkage of biotin or other biomolecules that permit substrate-cell interaction. Hence, the possibility of easy surface modification is of great interest to improve the control of cell attachment.

6. Acknowledgments

This work is partially suported (M.B.), by NIH Grant 5 RO1 HL60407

7. References

[1]F. E. Black, M. Hartshorne, M. C. Davies, C. J. Roberts, S. J. B. Tendler, P. M. Williams, K. M. Shakesheff, S. M. Cannizzaro, I. Kim and R. Langer, Langmuir **15**, 3157-3161 (1999).
[2] J. D. Whittle, N. A. Bullett, R. D. Short, C. W. Ian Douglas, A. P. Hollander and J. Davies, Journal of Materials Chemistry **12**, 2726-2732 (2002).
[3] J. Lahann, M. Balcells, T. Rodon, J. Lee, I. S. Choi, K. F. Jensen and R. Langer, Langmuir **18**, 3632-3638 (2002).
[4] Z. Yang, A.M. Belu, A. Liebmann-Vinson, H. Sugg, A. Chilkoti, Langmuir **16**, 7482-7492 (2000).
[5] J.C. Blazejewski, J.W. Hofstraat, C. Lequesne, C. Wakselman, U. E.Wiersum, Journal of Florine Chemistry **91**, 175-177 (1998).
[6] T. Hirotsu, C. Tagaki, A. Partridge, Plasmas and Polymers **4**, 353-366, (2002)
[7] C.L. Rinsch, X. Chen, V. Panchaligam, R.C. Eberhart, J.H. Wang, R.B. Timmons, Langmuir **12**, 2995-3002 (1996)
[8] S. Fraser, R.D. Short, D. Barton, J.W. Bradley, Journal of Physical Chemistry B **106**, 5596-5603 (2002)
[9] R.M. France, R.D. Short, R.A. Dawson, S. MacNeil, Journal of Materials Chemistry **8**, 37-42 (1998)
[10] N. Völcker, D. Klee, H. Höcker, S. Langefeld, Journal of Materials Science: Materials in Medicine **12**, 111-119 (2001)
[11] R. M. France, R. D. Short, E. Duval, F.R. Jones, R.A. Dawson, S. MacNeil, Chemistry of Materials **10**, 1176-1183 (1998)

Dissociation mechanisms in nitrogen discharges

V. Guerra[1], E. Galiaskarov[2] and J. Loureiro[1]

[1] *Centro de Física dos Plasmas, Instituto Superior Técnico, 1049-001 Lisboa, Portugal*
[2] *Ivanovo State University of Chemical Technology, Ivanovo, Russia*

Abstract
This work presents a theoretical and experimental investigation of the dissociation rate and N(^4S) atom concentrations in a nitrogen DC discharge operating at gas pressures p = 0.5 – 4 Torr and discharge currents I = 10 – 80 mA. It is shown that electron impact dissociation controls nitrogen dissociation only at the lower pressures considered in this study. For p > 1 Torr, dissociation proceeds essentially via reactions involving the long-lived metastable heavy-particles $N_2(X\,^1\Sigma_g^+,v)$ and $N_2(A\,^3\Sigma_u^+)$, such as $2N_2(X, 10<v<25) \rightarrow N_2(X) + 2N$ and $N_2(X, 14 \le v' \le 19) + N_2(A) \rightarrow N_2(X) + 2N$.

1. Introduction

It is well known already for a long time that the high dissociation degrees observed experimentally in nitrogen discharges at pressures above ~1 Torr and low values of the reduced electric field, E/N, typically below 8×10^{-16} V.cm^2, cannot be explained by electron impact dissociation only [1]. Several authors have then proposed dissociation to occur by a vibration-dissociation (V-D) mechanism, in which the vibration-vibration (V-V) and vibration-translation (V-T) energy exchanges would induce transitions into a pseudo-level above the last bound vibration level [2,3]. However, the vibrational distribution functions (VDFs) of ground-state N_2 molecules considered in those works were unrealistically overpopulated in the very high v-levels, since they were calculated neglecting both the deactivation of the vibrationally excited molecules at the discharge tube walls [4] and the strong quenching of vibrations in V-T N_2-N collisions [5]. Although the direct V-D mechanism cannot be effective under discharge conditions, these early works have pointed out the importance of vibrationally excited $N_2(X,v)$ molecules in nitrogen dissociation.

The problem of lack of dissociation in nitrogen discharges was recently stressed in [6-8], which have proposed, respectively, additional channels of dissociation according to reactions

$$N_2(A) + N_2(A) \rightarrow N_2(X) + 2N\,, \quad (1)$$

$$N_2(X, v>10) + N_2(X, v>10) \rightarrow N_2(X) + 2N \quad (2)$$

and

$$N_2(X, 13<v<20) + N_2(A) \rightarrow N_2(X) + 2N\,. \quad (3)$$

Reaction (1) was abandoned soon later due to difficulties in the explanation of experimental data, but anyway the need for an extra source of dissociation was clearly pointed out in [6].

In this report we present a theoretical and experimental study of nitrogen dissociation in a N_2 DC glow discharge, operating at gas pressures p = 0.5 – 4 Torr and discharge currents I = 10 – 80 mA. In order to investigate the contribution of reactions (2) and (3) to the total rate of dissociation, we have developed a kinetic model coupling in a self-consistent way the electron Boltzmann equation and the rate balance equations for the populations of the most important neutral and charged heavy-particles, in which the maintaining electric field is self-consistently calculated. The calculated densities of ground-state atomic nitrogen are then compared with absolute measurements performed using the method of electron spin resonance (ESR), for the same conditions as in the calculations.

2. Experiment

The measurements were performed in a flow system using the setup described in [9]. Briefly, the discharge was produced in a borosilicate glass molybdenum sealing cylindrical tube with inner radius R = 7.5 mm. The gas flow rate was measured by a capillary rotameter calibrated at atmospheric pressure and room temperature. The electric field sustaining the discharge was measured by the voltage of current compensation in a circuit of two cylindrical probes, each of diameter of 20 μm. The gas temperature at the positive column axis and the wall temperature were determined using a copper-constantan thermocouple. The concentration of ground-state N(^4S) atoms was determined by electron spin resonance (ESR), using a RE1301 radio spectrometer. The atomic nitrogen ESR spectrum consisted of three symmetric equidistant lines of equal

intensity and was registered for a magnetic field intensity H_0=3100 Oe. The absolute concentrations of N(^4S) were determined with an uncertainty of less than 40%. The main plasma parameters corresponding to the conditions of the present investigation can be found in [7]. The series of experiments carried out in [7] allowed to determine not only the stationary concentration of nitrogen atoms in the zone of the positive column, but also the probability for heterogeneous loss of N(^4S) atoms in the plasma zone γ and the rate of dissociation of nitrogen atoms W.

3. Kinetic model

In order to investigate the effect of reactions (2) and (3) on nitrogen dissociation, we have used a self-consistent kinetic model, that has already proved in many different conditions to be a powerful predictive tool (see ref [8] and refereces therein). This model is described in detail in [10,11], but a brief outline is given below. Essentially we solve the homogeneous electron Boltzmann equation, coupled to a system of equations describing the creation and loss of the most important neutral and ionic heavy-particles, $N_2(X\ ^1\Sigma_g^+$, v), $N_2(A\ ^3\Sigma_u^+$, $B\ ^3\Pi_g$, $C\ ^3\Pi_u$, $a'\ ^1\Sigma_u^-$, $a\ ^1\Pi_g$, $w\ ^1\Delta_u$, $a''\ ^1\Sigma_g^+$), N(^4S, ^2D, ^2P), N_2^+ and N_4^+. The electric field sustaining the discharge is determined from the requirement that the total rate of ionization must compensate exactly the total electron loss rate due to ambipolar diffusion and electron-ion recombination. The ionization rate includes both direct and stepwise electron impact ionization, as well as Penning/associative reactions involving the metastable species $N_2(A\ ^3\Sigma_u^+)$ and $N_2(a'\ ^1\Sigma_u^-)$ [10]. Reactions (2) and (3), not considered before, were added to the kinetic scheme described in [10,11].

The input parameters for the model are the ones usually controled in a real experiment, namely the gas pressure p, discharge current I, and tube radius R. The gas temperature can be calculated from the model [12], but was taken here as an input parameter as well. It is still worth to note that we have used the constant value $\gamma = 10^{-3}$ for the probability of recombination of N(^4S) atoms at the wall. This approximation is well justified by the measurements of γ reported in [7] for the conditions of this investigation, which did not exhibit any significant dependence of the recombination probability with the pressure (and thus with the wall temperature).

Looking for mechanisms that could provide additional dissociation in N_2 discharges at low reduced electric fields, we have only considered reactions (2) and (3). On one hand, these reactions had already been proposed in the literature; on the other hand, both require an important role of vibrationally excited molecules, as it was suggested in the early works [1-3]. Reaction (3) seems a natural candidate, since it is likely to occur via the excitation of the predissociative v' ≥ 13 levels of the $N_2(B\ ^3\Pi_g$, v') state [13],

$$N_2(X, 13 < v < 20) + N_2(A) \rightarrow N_2(X) + N_2(B, v' \geq 13) \rightarrow N_2(X) + 2N\ . \quad (4)$$

We note that this reaction is known to be very efficient in the excitation of the bound v' < 13 levels, in collisions involving $N_2(X, 4<v<14)$ and $N_2(A)$ states [10]. At first sight reaction (2) seems to bring more problems. However, the direct excitation of different states in similar processes is often invoked in the literature, such as [13,14]

$$2N_2(X, v > 16) \rightarrow N_2(X) + N_2(a') \quad (5)$$

and

$$2N_2(X, v > 13) \rightarrow N_2(X) + N_2(B)\ , \quad (6)$$

reported with rate coefficients of the order of 10^{-15} cm^3/s. Process (5) can be followed by a reaction very similar to (3), like

$$N_2(X, v \geq 7) + N_2(a') \rightarrow N_2(X) + N_2(a, v' \geq 6) \rightarrow N_2(X) + 2N\ . \quad (7)$$

In this case the mechanism (2) would in fact represent formally the sequence of reactions (5) and (7). Another possibility is the direct excitation of the predissociative levels $N_2(B\ ^3\Pi_g$, v' ≥ 13) and/or $N_2(a\ ^1\Pi_g$, v' ≥ 6) in reactions of type (5) and (6). At the present stage it is not possible to determine which is the actual mechanism leading to dissociation.

4. Results and discussion

All the calculations have been carried out for the conditions described above, p = 0.5 – 4 Torr, R = 0.75 cm and three values of I, 20, 50 and 80 mA. For this set of conditions, the gas temperature varies between 330 and 680 K [7].

To illustrate the effect of reaction (2) on nitrogen dissociation, figures 1 and 2 show the measured and calculated concentrations of N(^4S) atoms for I = 20 and 80 mA, respectively, when reaction (3) is neglected and reaction (2) is considered with a rate coefficient k_2 of zero (full curves, A), $k_2 = 10^{-15}$ cm^3/s (dashed

curves B), $k_2 = 5\times10^{-15}$ cm^3/s (dotted curves C) and $k_2 = 7.5\times10^{-15}$ cm^3/s (dash-dot curves D). Next, figures 3 and 4 show the effect of additional dissociation only according to reaction (3), considered with a rate coefficient k_3 of zero (full curves, A), $k_3 = 10^{-12}$ cm^3/s (dashed curves B), $k_3 = 5\times10^{-12}$ cm^3/s (dotted curves C) and $k_3 = 6.5\times10^{-11}$ exp (-1765/T_g) cm^3/s (dash-dot curves D). Finally, the conjoint effect of both reactions can be evaluated and compared to the former cases in figures 5 to 7, where we depict the results when the following situations are considered: dissociation occurs by electron impact only, $k_2 = k_3 = 0$ (full curves A); the best case considered when additional dissociation results from reaction only (2), $k_2 = 7.5\times10^{-15}$ cm^3/s and $k_3 = 0$ (dashed curves B); the best case considered when additional dissociation results from reaction only (3), $k_2 = 0$ and $k_3 = 6.5\times10^{-11}$ exp (-1765/T_g) cm^3/s (dotted curves); both reactions are considered, with rate coefficients of $k_2 = 3.5\times10^{-15}$ cm^3/s and $k_3 = 4.5\times10^{-11}$ exp (-1765/T_g) cm^3/s. From figures 1 – 6 we can immediately confirm that electron impact dissociation cannot provide a satisfactory explanation of the experimental data for pressures above ~1 Torr. Furthermore, reaction (2) can conciliate the calculations with the measurements at low discharge currents, but is unable to do so for the higher values of I. On the contrary, reaction (3) provides the correct amount of dissociation for high currents, but fails in the opposite limit. Finally, the results are quite acceptable in the full range of values of I and p considered in this investigation when both mechanisms are taken into account as extra sources of dissociation (curves D in figures 5 – 7).

The results from the previous figures can be quantified in figure 8, where we plot the relative contribution of each of the dissociation mechanisms to the total dissociation rate, for I = 20 mA (full curves) and I = 80 mA (dashed curves). Thus, curves A correspond to the contribution of electron impact dissociation on N_2 molecules, curves B to the contribution of reaction (3), and curves C to the percentage contribution of reaction (2). It can be seen that electron impact dissociation is the major channel of dissociation only at the lower pressures considered in this study. For p ≥ 1 Torr the mechanisms (2) and (3) start to be dominant, their contribution to the total dissociation reaching values as high as 90%. Figure 8 confirms as well that reaction (2) is more important at lower values of I, while reaction (3) has the opposite behavior. The reason for this is related to the effect of superelastic electron-vibration (e-V) collisions, which significantly heat the electron energy distribution function. The effect is more dramatic at low values of E/N and, therefore, for the higher pressures. We recall that the vibrational temperature of ground state N_2 molecules, T_V, increases with the discharge current, while the reduced electric field remains practically unchanged, as it has been determined experimentally in [7] and theoretically in [15].

5. Conclusions

In this work we have presented a theoretical and experimental study of the mechanisms of nitrogen dissociation in N_2 DC discharges. The calculated densities of ground-state atomic nitrogen were compared with absolute measurements performed using the method of electron spin resonance (ESR), for the same conditions as in the calculations.

It has been shown that electron impact dissociation is the dominant mechanism of dissociation only at pressures below ~1 Torr. The results of this investigation suggest that reaction (3) may control nitrogen dissociation for p≥1 Torr and I≥50 mA, whereas reaction (2) may be important at lower discharge currents. The rate coefficients for these two reactions were estimated to be of the order of 10^{-15} cm^3/s and 10^{-12} cm^3/s at T_g = 500 K, respectively for reactions (2) and (3).

References

[1] L. S. Polak, *Pure Appl. Chem.* **39** (1974) 307.

[2] L. S. Polak, P. A. Sergeev, D. I. Slovetskii and R. D. Todesaite, *Proc. 12th Intern. Conf. on Phenomena in Ionized Gases* (ICPIG), Eindhoven, The Netherlands, (1975) 65.

[3] M. Capitelli and M. Dillonardo, *Chem. Phys.* **24** (1977) 417.

[4] J. Loureiro, *Chem. Phys.* **157** (1991) 157.

[5] V. Guerra and J. Loureiro, *J. Phys. D: Appl. Phys.* **28** (1995) 1903.

[6] B. F. Gordiets, C. M. Ferreira, M. J. Pnheiro and A. Ricard, *Plasma Sources Sci. Technol.* **7** (1998) 363

[7] I. N. Brovikova and E. G. Galiaskarov, *High Temp.* **39** (2001) 809.

[8] V. Guerra, P. A. Sá and J. Loureiro, accepted for publication in *Plasma Sources Sci. Technol.*

[9] I. N. Brovikova, E. G. Galiaskarov, V. V. Rybkin and A. B. Bessarab, *High Temp.* **36** (1998) 681; *ibid*, pag 842.

[10] V. Guerra and J. Loureiro, *Plasma Sources Sci. Technol.* **6** (1997) 361.

[11] V. Guerra, E. Tatarova and C. M. Ferreira, *Vacuum* **69** (2003) 171.
[12] V. Guerra, P. A. Sá and J. Loureiro, *J. Phys. D: Appl. Phys.* **34** (2001) 1745.
[13] D. I. Slovetskii, Mechanisms of Chemical Reactions in Nonequilibrium Plasmas, Nauka 1980.
[14] B. F. Gordiets, C. M. Ferreira, V. L. Guerra, J. M. A. H. Loureiro, J. Nahorny, D. Pagnon, M. Touzeau and M. Vialle, *IEEE Trans. on Plasma Sci.* **23** (1995) 750.
[15] V. Guerra, E. Galiaskarov and J. Loureiro, *Chem. Phys. Lett.* **371** (2003) 576.

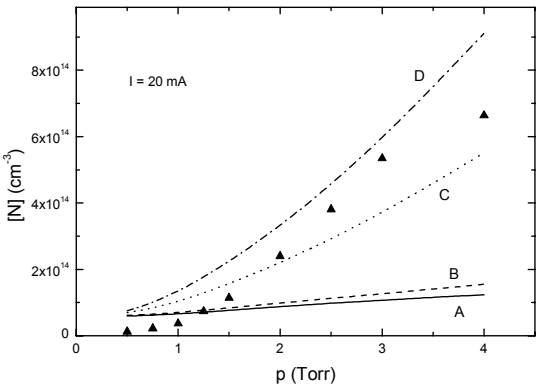

Fig.1: Measured (points) and calculated (curves) concentratrions of ground-state atoms for I = 20 mA and k_3 = 0, when k_2 = 0 (A), $k_2 = 10^{-15}$ cm^3/s (B), $k_2 = 5\times10^{-15}$ cm^3/s (C) and $k_2 = 7.5\times10^{-15}$ cm^3/s (D).

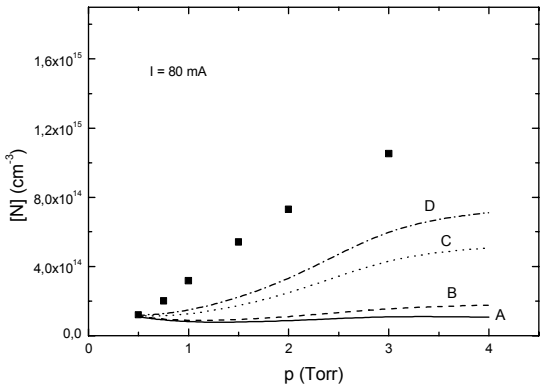

Fig. 2: The same as in figure 1, but for I = 80 mA.

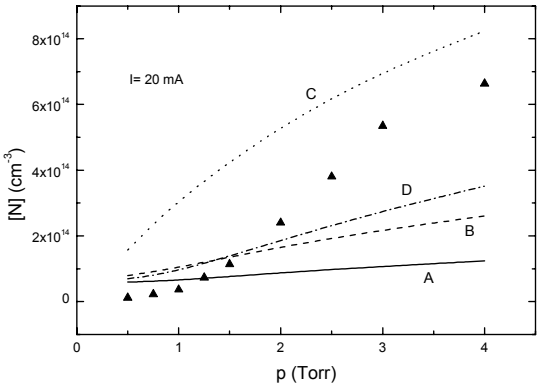

Fig.3: Measured (points) and calculated (curves) concentratrions of ground-state atoms for I = 20 mA and k_2 = 0, when k_3 = 0 (A), $k_3 = 10^{-12}$ cm^3/s (B), $k_3 = 5\times10^{-12}$ cm^3/s (C) and $k_3 = 6.5\times10^{-11}$ exp (-1765/T_g) cm^3/s (D).

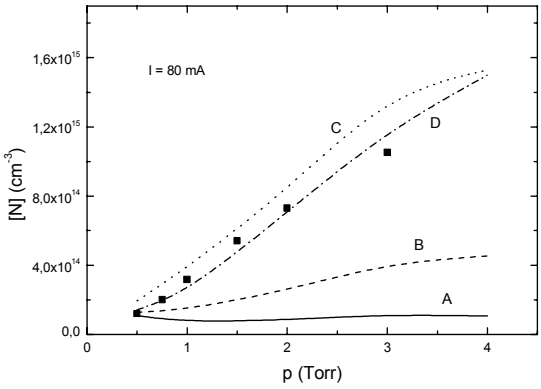

Fig. 4: The same as in figure 3, but for I = 80 mA.

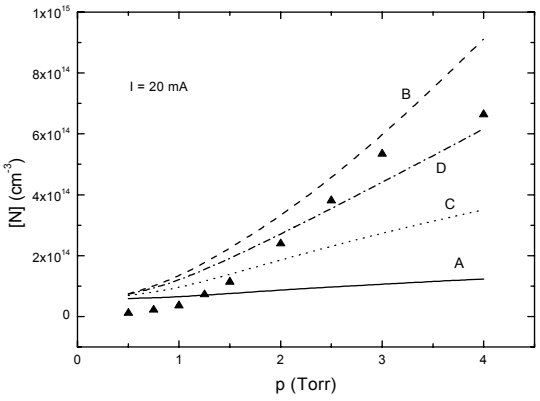

Fig.5: Measured (points) and calculated (curves) concentratrions of ground-state atoms for I = 20 mA when $k_2 = k_3 = 0$ (A), $k_2 = 7.5\times10^{-15}$ cm^3/s and $k_3 = 0$ (B), $k_3 = 0$ and $k_3 = 6.5\times10^{-11}$ exp (-1765/T_g) cm^3/s (C), and $k_2 = 3.5\times10^{-15}$ cm^3/s $k_3 = 4.5\times10^{-11}$ exp (-1765/T_g) cm^3/s (D).

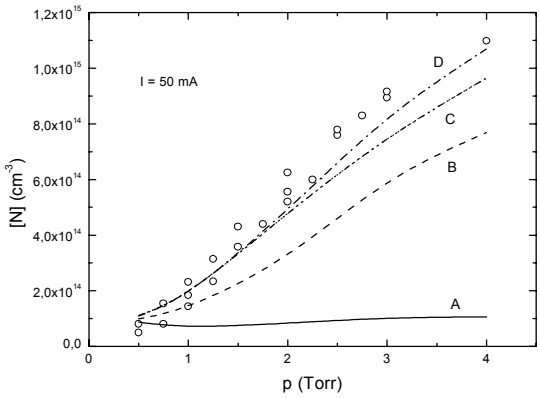

Fig. 6: The same as in figure 3, but for I = 50 mA.

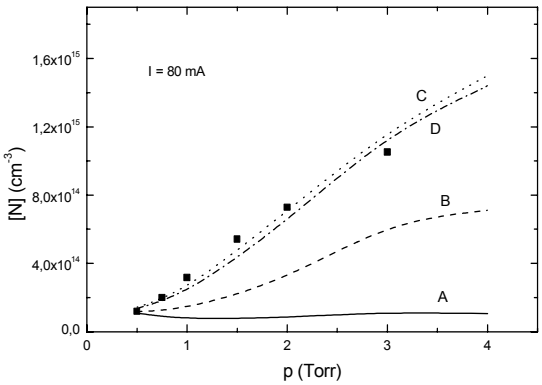

Fig.7: The same as in figure 3, but for I = 80 mA.

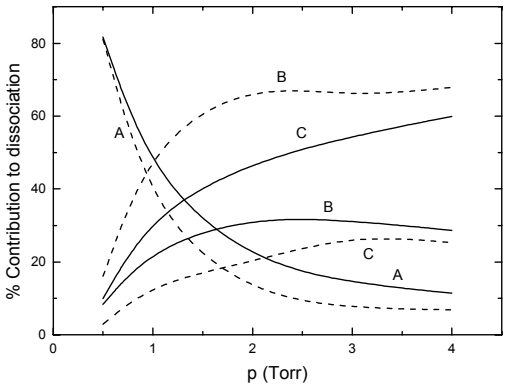

Fig. 8: Relative contribution of the different dissociation channels to the total dissociation rate, for I = 20 mA (full curves) and I = 80 mA (dashed curves): electron impact dissociation (A); dissociation according to process (3) (B); dissociation from reaction (2) (C).

Removal of NO_x from Flue Gas by Non-thermal Plasma-Catalyst System

J. Mizeraczyk and M. Dors

Centre of Plasma and Laser Engineering, Institute of Fluid Flow Machinery, Polish Academy of Sciences, Fiszera 14, 80-231 Gdańsk, Poland, e-mail: jmiz@imp.gda.pl

Abstract

The objective of this work was to investigate NO_x removal with a hybrid system consisting of a DC corona discharge and a catalyst at a room temperature (22ºC) in the presence of ammonia. In the hybrid reactor a positive DC corona discharge was generated between a hollow needle and a flat mesh. The catalyst was a layer of V_2O_5 and TiO_2 deposited on Al_2O_3 globules. The catalyst surface was either free of NH_3 or saturated with NH_3. A gas mixture of N_2(80%):O_2(5%):CO_2(15%):NO(200ppm), simulating a flue gas, flowed through the tube with a flow rate of 1 l/min. NH_3 was added to the gas mixture through the hollow needle.

The obtained results showed that the proposed hybrid reactor consisted of the corona discharge and NH_3-saturated catalyst is attractive for NO_x removal and may be an alternative to other non-thermal plasma methods used for NO_x removal.

1. Introduction

Investigations carried out in laboratories and pilot plants showed that removal of NO_x from flue gases by corona discharges may be efficient [1, 2]. However, the energy consumption in this new technology is still not acceptable for commercial use and is to be improved.

A technology competitive to the corona discharge processing is the selective catalytic reduction (SCR) which has proved its efficiency in NO_x removal [3]. In the SCR process, ammonia (NH_3) and a catalyst operating at a relatively high temperature range of 280-430ºC are used to reduce NO_x to N_2 and H_2O which are harmless products. The efficiency of NO_x removal using the SCR method is up to 90 %.

In the corona discharge processing, the dominant mechanism of NO_x removal is its oxidation to gaseous HNO_3 which then is converted to NH_4NO_3 solid particles by adding NH_3 [4-9]. Among many corona discharge types, the most efficient in NO_x removal is a corona radical shower (CRS) [6, 7]. In the CRS reactor, NH_3 is introduced through a hollow needle electrode into the corona discharge zone where NH_3 molecules dissociate to NH_2 and NH radicals. These radicals react with NO_x molecules converting them into NH_4NO_3 solids. The record NO_x removal energy yield of the CRS method is 15 g/kWh at NO_x removal efficiency of 90 % [7].

In recent years hybrid plasma-catalyst systems have been proposed because of their capability to reduce NO_x into N_2 and other harmless molecular gases [10-18]. A typical hybrid system consisted of a corona discharge and a catalyst operating at temperature over 120°C. In some hybrid systems, first the corona discharges were used for oxidizing NO into NO_2, and then the SCR processing with NH_3 was used to convert NO_2 into N_2 and H_2O [10-12]. The efficiency of NO_x removal using hybrid plasma-catalyst systems was up to 98 % at an energy yield up to 55 g/kWh [12]. In other hybrid systems, hydrocarbons were added to the flue gas polluted with NO_x to improve its removal [14-16].

This work was aimed at studying NO_x removal in a hybrid system consisted of a DC streamer corona discharge with a catalyst operating under low temperature (22ºC) in the presence of NH_3. In our reactor a catalyst typical of the SCR method, but operating at low temperature, interacted with a corona discharge. Gaseous NH_3 was introduced into the corona discharge zone either conventionally through a hollow needle electrode, similarly as in the CRS reactors, or using a novel method. In this new method, the gaseous NH_3 diffused into the discharge zone after releasing it by the corona discharge from an NH_3 phase, which has been earlier adsorbed on the catalyst surface. The performance of our hybrid corona discharge–catalyst reactor is described below.

2. Experiment

The hybrid corona discharge-catalyst reactor used in this experiment is shown in Fig. 1. The positive DC corona discharge was generated between a stainless steel hollow needle electrode and grounded flat mesh electrode (1 mm x 1 mm) made of brass. The outer and inner diameter of the hollow needle was 2 mm and 1.6 mm, respectively. The hollow needle-mesh spacing was 40 mm.

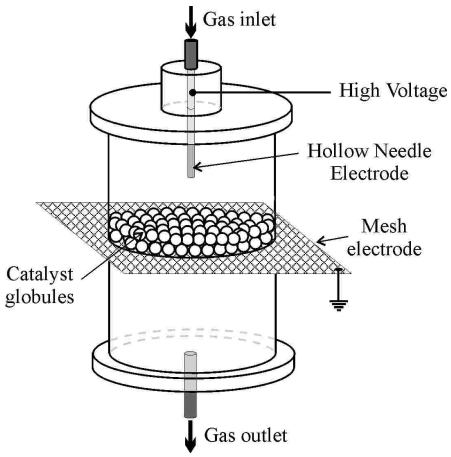

Fig. 1. The hybrid corona discharge-catalyst reactor.

The catalyst used in this investigation was a layer of V_2O_5 and TiO_2, as in the SCR processing, deposited on Al_2O_3 globules of 5-6 mm in diameter. The catalyst globules were placed on the mesh in the form of 2 layers. The hollow needle-catalyst spacing was about 30 mm.

The catalyst layer deposited on Al_2O_3 globules was used to play two roles. The first one, when a "pure" catalyst-covered globules were used, was the typical role of a catalyst. The another role, which is a new approach in this investigation, resulted from using the catalyst-covered globules as an adsorber of NH_3 before placing the globules into the reactor. We expected that the NH_3-saturated globules could become a gaseous NH_3 source in the reactor, when subjected to the corona discharge.

The positive polarity DC high voltage (15-38 kV) was applied through a 10 MΩ resistor to the hollow needle electrode. The time-averaged discharge current varied in the range of 50-200 μA.

A gas mixture of N_2(80%):O_2(5%):CO_2(15%):NO(200ppm), simulating a flue gas, was supplied through the hollow needle and then flowed through the reactor with a flow rate of 1 l/min.

When the performance of the reactor with the "pure" catalyst was investigated, gaseous NH_3 was first mixed with the N_2:O_2:CO_2:NO mixture, forming the working gas. Then the working gas was introduced through the hollow needle electrode into the reactor. The NH_3 concentration in the working gas was 400 ppm, which corresponds to a molar ratio of NH_3 to NO equal to 2:1 [7].

When the performance of the reactor with NH_3-saturated catalyst globules was tested, gaseous NH_3 (30 ppm) was introduced into the reactor, after mixing with the N_2:O_2:CO_2:NO mixture. This additional gaseous NH_3 was supposed to make up a loss of NH_3 released from the globules and sustain steady concentration of NH_3 in the reactor with a minimum slip in the outlet gas (at an NH_3 level of 1 ppm). As the concentration of NH_3 adsorbed on the globules layer was expected to decrease with elapsing time of the discharge operation, this part of the investigation had a time-dependent character.

Concentrations of NO, NO_2 and NH_3 in the working gas at the reactor inlet and outlet were measured by absorption spectroscopy method using a Perkin-Elmer 16 PC FTIR spectrophotometer.

The investigation of performance of the hybrid corona discharge-catalyst reactor for NO_x removal from the flue gas was carried out for the following cases:

a) without catalyst [without or with gaseous NH_3 (400 ppm) supply],
b) with NH_3-free catalyst [without or with gaseous NH_3 (400 ppm) supply],
c) with NH_3-saturated catalyst [without or with gaseous NH_3 (30 ppm) supply].

3. Results

Corona discharge processing without catalyst and gaseous NH_3 supply

The removal efficiency of NO from the working gas by processing it with the corona discharge without catalyst and NH_3 was no higher than 25 % (at 200 μA, 34 kV, Fig. 2). The processing was accompanied with production of NO_2 (up to 50 ppm). As a result, NO_x removal was not higher than 8 %.

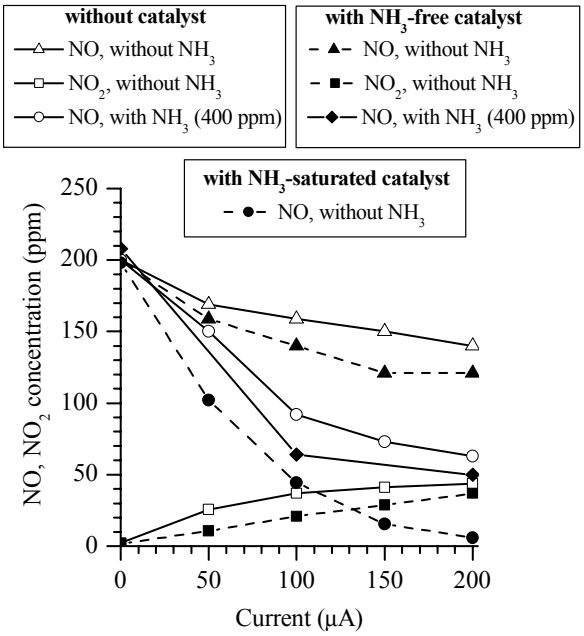

Fig. 2. Concentrations of NO and NO_2 in the working gas at the reactor outlet as a function of time-averaged corona discharge current. Cases: a) processing without catalyst [without or with gaseous NH_3 (400 ppm) supply], b) processing with NH_3-free catalyst [without or with gaseous NH_3 (400 ppm) supply], c) processing with NH_3-saturated catalyst [without gaseous NH_3 (30 ppm) supply].

Corona discharge processing without catalyst and with gaseous NH_3 (400 ppm) supply

NH_3 (400 ppm) added to the working gas increased NO removal to 66 % (at 200 μA, 31 kV) and resulted in the absence of NO_2 molecules in the outlet gas (Fig. 2). Deposits of white NH_4NO_3 solids, produced during the corona processing, could be found on the reactor wall and mesh electrode. Only a small fraction (about 15 %) of the introduced NH_3 was consumed during the corona discharge processing. This resulted in a high slip of NH_3. It seems that the initial concentration of NH_3 used in this experiment after [7] was too high.

Corona discharge processing with NH_3-free catalyst and without gaseous NH_3 supply

In the presence of the NH_3-free catalyst in the reactor, NO removal from the working gas without NH_3 was higher (about 40 % at 200 μA and 32.5 kV) than that without catalyst and NH_3 (Fig. 2). The NO removal was accompanied with NO_2 production, which is, however, lower than that without catalyst and NH_3. As a result, NO_x removal increased up to 25 %. The higher efficiency of NO removal in the presence of the catalyst seems to be caused by the lower concentration of NO_2 molecules, which easily reduce to NO.

Corona discharge processing with NH_3-free catalyst and gaseous NH_3 (400 ppm) supply

When 400 ppm of NH_3 was introduced into the reactor with NH_3-free catalyst globules, removal of NO and NO_x increased up to 75 % at 200 μA and 29 kV (Fig. 2). Like in the case without catalyst, NH_3 in the working gas caused absence of NO_2 in the outlet gas. Consumption of NH_3 in the

processing increased with increasing corona discharge current and reached 60 % at 200 μA and 29 kV.

Deposits of NH_4NO_3 solids were found on the catalyst globules and reactor wall. After 5 min. of processing, the number of NH_4NO_3 solid deposits on the catalyst surface was relatively low. The NH_4NO_3 solids had the form of irregular conglomerates (like incipient crystals), the size of which was approximately 5 μm. However, after longer time of the processing the catalyst surface became considerably deteriorated with NH_4NO_3 deposits, which resulted in a progressive decrease of NO removal. Eventually, the deteriorated catalyst surface stopped acting as a catalyst.

Corona discharge processing with NH_3-saturated catalyst without gaseous NH_3 supply

When the NH_3- saturated catalyst without any additional supply of gaseous NH_3 was used, removal of NO and NO_x increased to 96% (Fig. 2). NO_2 molecules were not present in the outlet gas, which, however, contained 2 ppm of NH_3. This NH_3 slip was formed by those NH_3 molecules, which released from the catalyst surface, were not consumed in reactions with NO, NO_2 and HNO_3.

The very high efficiency of NO (and NO_x) removal recorded in this case suggests that the surface reactions leading to NO (and NO_x) removal are very efficient when the interaction of the corona discharge with the NH_3-saturated catalyst takes place.

The NO removal efficiency of 96 % at a discharge power of 4.8 W resulted in the energy yield of 3.4 g NO/kWh. This is superior to the other cases tested in this experiment (Tab. 1). However, better results were obtained in other hybrid plasma-catalyst [12] and CRS systems [7].

Tab. 1. Parameters of NO_x removal processing in selected systems using corona discharge (CD) and ammonia.

System	Initial NO concentration	Flow rate	Specific energy	NO_x removal efficiency	Energy yield	Ref.
	[ppm]	[l/min]	[Wh/m^3]	[%]	[g NO/kWh]	
CD (wire-to-cylinder)	400	2	333	90	0.6	[4]
CD (wire-to-plate)	300	10,000	12	60	20	[5]
CD (needle-to-plate)	200	60	230	90	0.2	[9]
CRS	200	5	18	90	15	[7]
Hybrid CD-catalyst	430	2-6	8.3	75	21	[10]
Hybrid CD-catalyst	198	1314	2.5	60	55	[12]
Hybrid CD-catalyst	200	1	80	96	3.4	This work

The number and shape of NH_4NO_3 solids deposited on the catalyst surface were similar to those of the case of NH_3-free catalyst and gaseous NH_3 supply.

After some time, the NH_3-saturated catalyst started to loose its properties due to either NH_3 depletion on the catalyst surface or deterioration of the catalyst surface by NH_4NO_3 solids. This was investigated in the following experiment.

Temporal performance of the hybrid reactor

Fig. 3 illustrates temporal performance of the hybrid reactor for the cases listed in Chapter 2. In all the cases the discharge current was fixed at 100 μA.

As expected, NO concentration at the reactor outlet remained constant when the corona discharge processing was carried out either without catalyst or with NH_3-free catalyst without gaseous NH_3 supply.

When the NH_3-saturated catalyst without gaseous NH_4 supply was used, NO (and NO_x) removal efficiency was relatively high (78% at a discharge current of 100 μA) and remained constant over the

first 20 hours. After that time, the NH_3-saturated catalyst started to loose its activity and NO removal efficiency decreased. After the next 10 hours, the NO removal efficiency remained steady at a level corresponding to the corona discharge processing without catalyst but with gaseous NH_4 (400 ppm) supply.

When the corona discharge processing was performed in the presence of NH_3-saturated catalyst with gaseous NH_3 (30 ppm) supply, NO removal efficiency was equal to that without gaseous NH_4 supply (78%) but it remained constant longer (during about 30 hours). After that time the catalyst lost its activity. As a result, NO removal efficiency started to decrease and NO concentration increased during the next 20 hours until it leveled at a concentration typical of the processing without catalyst but with gaseous NH_3 (400 ppm) supply. After leveling at a time of 50 hours, the performance of the hybrid reactor became unchanged over the next 20 hours.

The significant changes of the catalyst surface due to NH_4NO_3 deposits after 67-hour corona discharge processing were revealed by scanning electron microscopy (SEM) imaging. The catalyst surface exposed to the corona discharge was almost completely covered with NH_4NO_3 solids, which formed relatively large crystals.

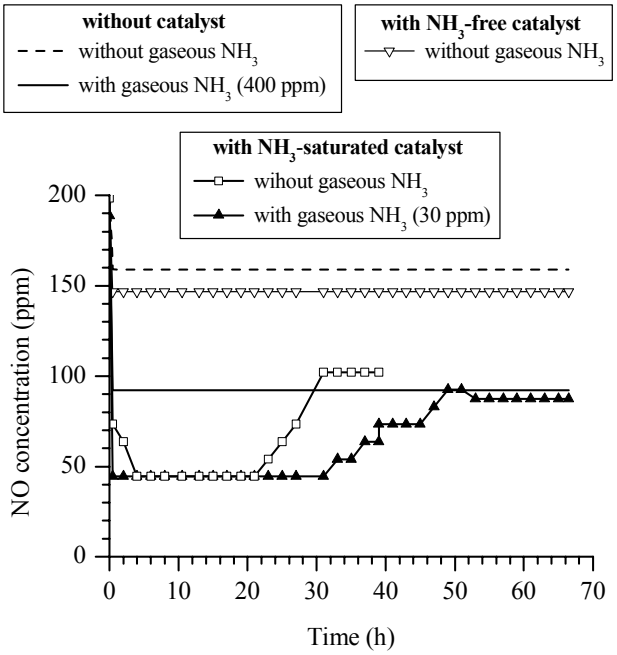

Fig. 3. Time dependence of NO concentration in the working gas at the reactor outlet. Corona discharge current 100 μA. Cases: a) processing without catalyst [without or with gaseous NH_3 (400 ppm) supply], b) processing with NH_3-free catalyst [without gaseous NH_3 (400 ppm) supply], c) processing with NH_3-saturated catalyst [without or with gaseous NH_3 (30 ppm) supply].

Taking the above into consideration, we conclude that the NH_3-saturated catalyst (without or with gaseous NH_4 supply) lost its activity not due to releasing NH_4 from its surface but due to NH_4NO_3 deposits. The surface-deteriorated catalyst still was able to release NH_3 molecules enough to remove NO molecules on a level typical of processing with gaseous NH_3 (400 ppm) supply.

From the weight balance analysis of the NH_3 and NH_4NO_3, we found that only a small fraction of NO and NO_2 was transformed into NH_4NO_3. This may mean that considerable part of NO and NO_2 molecules was decomposed to N_2 and H_2O, which is mostly desired.

4. Summary and conclusions

In this paper results of investigation of the performance of a hybrid corona discharge-catalyst reactor to be used for NO_x removal from the flue gases are presented. The catalyst was a layer of V_2O_5 and TiO_2 deposited on Al_2O_3 globules. The gas mixture, which simulated a flue gas, was

N_2(80%):O_2(5%):CO_2(15%):NO(200ppm). The corona discharge processing of the gas mixture was carried out: without catalyst, with NH_3-free catalyst, and with NH_3-saturated catalyst, all either without or with gaseous NH_3 supply.

The investigation showed that:

- The catalyst increased significantly NO_x removal efficiency. The highest NO_x removal efficiency (96 % at a corona discharge current of 200 μA and operating voltage of 24 kV) was observed when NH_3-saturated catalyst was used [without or with gaseous NH_3 (30 ppm) supply];
- In the presence of NH_3, the corona discharge produced solid particles of NH_4NO_3 which depositing on the catalyst surface shortened the active life of the catalyst (due to poisoning of the catalyst). The life-time of the catalyst due to its poisoning was about 30 hours;
- NO_x removal energy yield in the presented hybrid reactor with NH_3-saturated catalyst without or with gaseous NH_3 (30 ppm) supply was up to 3.4 g/kWh (at 96 % of NO_x removal) compared to 1.8 g/kWh in the "pure" corona discharge processing with gaseous NH_3 (400 ppm) supply;
- The hybrid reactor with NH_3-saturated catalyst operated efficiently over 30 hours without additional gaseous NH_3 supply.

The obtained results showed that the proposed hybrid reactor consisted of the corona discharge and NH_3-saturated catalyst is attractive for NO_x removal and may be alternative to other non-thermal plasma methods used for NO_x removal. The processes which occur when the corona discharge interacts with NH_3-saturated catalyst are not known and need further investigation to improve the performance of the reactor.

References

[1] J.S. Chang, in: Non-thermal Plasma Techniques for Pollution Control, Eds. B.M. Penetrante and S.E. Schultheis, Springer-Verlag Berlin Heidelberg, NATO ASI Series, 1993, vol. G 34 (A), pp. 1-32

[2] E. M. Van Veldhuizen, Electrical Discharges for Environmental Purposes, Nova Science Publishers, New York, 2000

[3] A.K. Hjalmarsson, Int. J. of Ener. Res. **14** (1990) 813-820

[4] A. Mizuno, K. Shimizu, T. Matsuoka, S. Furuta, IEEE Trans. Ind. Appl. **31** (1995) 1463-1467

[5] G. Dinelli, L. Civitano, M. Rea, IEEE Trans. Ind. Appl. **26** (1990) 535-541

[6] T. Ohkubo, S. Kanazawa, Y. Nomoto, J.S. Chang, T. Adachi, IEEE Trans. Ind. Appl. **30** (1994) 856-860

[7] J.Y. Park, I. Tomicic, G.F. Round, J.S. Chang, J. Phys. D: Appl. Phys. **32** (1999) 1006-1011

[8] J.S. Chang, J. Aerosol. Sci. **20** (1989) 1087-1090

[9] K. Onda, K. Kato, Y. Kasuga, JSME International Journal, Series B, **39** (1996) 202-210

[10] H.H. Kim, K. Takashima, S. Katsura, A. Mizuno, J. Phys. D: Appl. Phys. **34** (2001) 604-613

[11] T. Hammer, S. Broer, Plasma Enhanced Selective Catalytic Reduction of NO_x for Diesel Cars (1998), Society of Automotive Engineers Technical Paper Series, No. 982428

[12] T. Hammer, S. Broer, Plasma Enhanced Selective Catalytic Reduction of NO_x in Diesel Exhaust: Test Bench Measurements, Society of Automotive Engineers Technical Paper Series, No. 1999-01-3633

[13] H. Suhr, G. Weddigen, Combust. Sci. Technol. **72** (1990) 101-115

[14] K. Shimizu, T. Oda, IEEE Trans. Ind. Appl. **35** (1999) 1311-1318

[15] T. Oda, T. Kato, T. Takahashi, K. Shimizu, J. Electrostatics **42** (1997) 151-157

[16] T. Yamamoto, C.-L. Yang, M. R. Beltran, Z. Kravets, (1997) IEEE Ind. Appl. Society Annual Meeting, New Orleans, USA, pp. 1956-1960

[17] T. Kawasaki, S. Kanazawa, T. Ohkubo, J. Mizeraczyk, Y. Nomoto, Thin Solid Films **386** (2001) 177-182

[18] B.S. Rajanikanth, S. Rout, Fuel Processing Technology, **74** (2001) 177-195

A novel approach to interpret enthalpy probe measurements in low pressure supersonic plasma jets

J.-L. Dorier[1], B. Jodoin[2], M. Gindrat[1], A. Blais[2], C. Hollenstein[1], and G. Barbezat[3]

[1]*Plasma Physics Research Centre, Swiss Federal Institute of Technology, Lausanne, Switzerland*
[2] *Department of Mechanical Engineering, University of Ottawa, Ottawa, Canada*
[3] *Sulzer Metco Switzerland AG, Wohlen, Switzerland*

Abstract

The first steps in the development of a new method to interpret enthalpy probe measurements in supersonic plasma jets is presented. This method relies on a special post-shock probe which allows measurement of the (unknown) static pressure downstream of the shock induced by the probe. Conservation equations are used to infer the jet parameters in two steps: backwards from stagnation to post-shock, and then to free stream. The assumptions of this new method are less restrictive than previous ones. The new method will also allow for inclusion of non-LTE effects. Comparison with previous approaches shows the improved accuracy of the described technique.

1. Introduction

Low Pressure Plasma Spraying (LPPS) processes, using plasma torches operated at reduced pressure, have emerged as reliable technologies with broad industrial successes for the deposition of numerous coatings [1]. However, the majority of advances in LPPS have been made by empirical means and have reached their limit [2]. To further improve the control and quality of the processes, and to develop new applications, a more quantitative approach is required in which the fundamental physics of the process should be investigated. In particular, the phenomena controlling the expanding plasma jet should be studied both experimentally and by numerical simulations. This requires the knowledge of key parameters such as the temperature, pressure, chemical composition, velocity or local heat flux.

To measure these parameters, the enthalpy probe measurement technique has been extensively applied in Atmospheric Plasma Spraying (APS) jets assuming Local Thermodynamic Equilibrium (LTE) and incompressible flow [3]. However, the latter is not valid in low-pressure plasma jets and the formation of a normal shock wave (NSW) in front of the probe must be accounted for. Although specific technological constraints (low gas density) have been recently overcome [4], there are still severe conceptual complications in the use of enthalpy probes for low-pressure plasma jets.

First, the Pitot tube technique commonly used for the determination of the flow velocity cannot be directly applied because these jets are usually not in aerodynamic equilibrium with the surrounding atmosphere [5]. This means that the free stream local static pressure (P_1) can differ strongly from the chamber pressure. Erroneous results are obtained if the latter is used to approximate P_1 [4, 6], which is not directly accessible by measurement. A second complication comes from the required assumptions about the stagnation process that have been made in order to infer the free-stream jet properties from the quantities measured downstream of the shock [7]. Third, the low collisionality and high velocity of these flows can lead to deviations from LTE, which cannot be accounted for with the usual approaches [4, 6, 7].

In a previous attempt to solve the aerodynamic non-equilibrium problem, P_1 has been determined from numerical simulations of the plasma flow, which were then back-validated by the enthalpy probe results [8]. This approach, although valid, is complex and inconvenient to use.

The new enthalpy probe measurement approach presented here improves the accuracy of the technique by introducing a new way to deal with and interpret the data provided by the probe. It does not require the knowledge of the jet static pressure P_1, which is a major advantage over existing methods. It is also less restrictive in the assumptions used and can be modified to include non-LTE effects. As before, the stagnation pressure and enthalpy (P_{02} and h_{02}) behind the NSW induced by the probe are measured and used to compute the flow properties of the free plasma jet in front of the NSW (P_1, T_1, M_1, V_1). To achieve that,

the jet static pressure behind the NSW (P_2) is required and a special post-shock static pressure probe (PSSPP) is developed and used as presented in the next section.
The experimental technique is described in section 3. In section 4, our new approach is demonstrated for the interpretation of enthalpy probe measurements performed on an argon plasma jet at 10 mbar. These results are discussed and compared with those obtained by previous approaches [4, 6 - 8].

2. Description of the method

The deceleration of the free supersonic plasma jet towards the enthalpy probe can be seen as two separate evolutions (figure 1). The first evolution, from state (1) to state (2), represents the strong deceleration from the free stream conditions (1) to the post-shock conditions (2) through the NSW present in front of the enthalpy probe. The second evolution, from state (2) to state (02), represents the deceleration of the flow after the NSW to the stagnation condition in the probe. The proposed method consists of solving the governing flow equations for the two evolutions, starting backward from (02) to (2) and then from (2) to (1). The required data are obtained from the enthalpy probe (P_{02} *and* h_{02}) and the post-shock static pressure probe (P_2) described below.

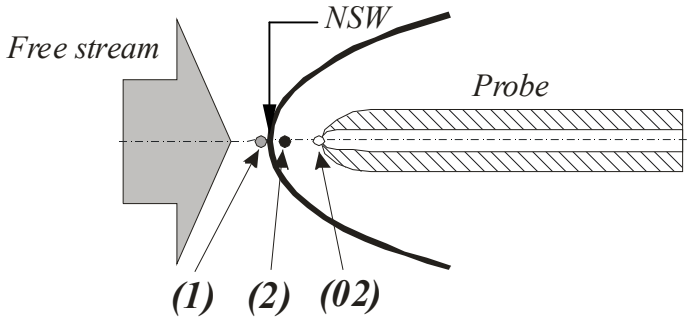

Figure 1 : Schematic representation of the free plasma jet deceleration by the probe.

Evolution (02) to (2)

Knowing from the enthalpy probe P_{02} and h_{02} and assuming that at stagnation the plasma is in local thermodynamic equilibrium (LTE), it is possible to find the plasma stagnation composition (ω_{Ar02}, ω_{Ar+02}, ω_{e02}), temperature (T_{02}) and entropy (s_{02}). Assuming that the flow is steady and reversible, the mass and energy conservation can be combined to give:

$$h_{02} = h_2 + \frac{V_2^2}{2}$$

In the same way the mass conservation and the second law can be combined to give:

$$s_{02} = s_2.$$

Assuming that the plasma is in LTE at location (2), and since s_2 (from the second law) and P_2 (from the post-shock static probe) are known, it is possible to find the plasma composition (ω_{ar2}, ω_{ar+2}, ω_{e2}), temperature (T_2) and enthalpy (h_2) behind the NSW [9, 10]. Using the energy equation, one can then find the velocity (V_2) behind the NSW. The flow properties are then all known at location (2).

Evolution (2) to (1)

The fundamental governing laws are again applied for this evolution and are expressed as:

$$\rho_1 V_1 = \rho_2 V_2 \quad \text{(mass conservation)}$$

$$p_1 + \rho_1 V_1^2 = p_2 + \rho_2 V_2^2 \quad \text{(momentum conservation)}$$

$$h_1 + \frac{V_1^2}{2} = h_2 + \frac{V_2^2}{2} \quad \text{(energy conservation)}$$

$$s_2 > s_1 \quad \text{(2nd law of Thermodynamics)}$$

This system of equation is closed with a state equation, $s=s(P,T)$. Due to strong non-linearity, a graphical Fanno-Rayleigh line solution method [11] was preferred to a classical iterative one. A general representation of the Fanno and Rayleigh lines is presented in figure 2. The Fanno line represents solutions to the mass, energy and state equations on a Mollier (enthalpy *vs* entropy) diagram. The Rayleigh line represents solutions to the mass, momentum and state equation on the same diagram. The flow going through the NSW must obey all three mass, momentum and energy conservation equations as well as the state equation. Therefore, the solutions ((1) and (2)) of the system must lie on the intersections of the Fanno and the Rayleigh lines.

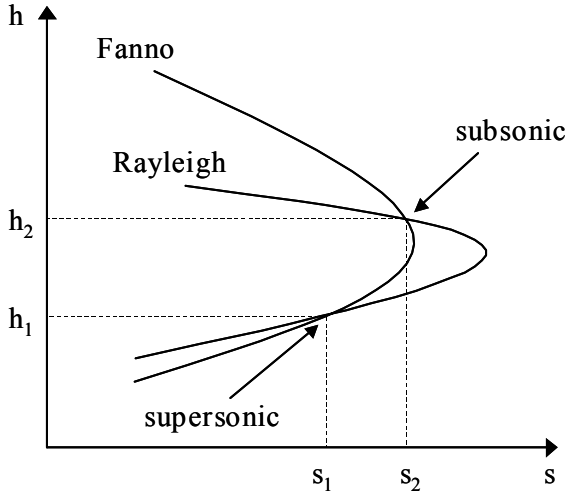

Figure 2 : General representation of the Fanno and Rayleigh lines on a Mollier diagram.

As shown, two (*h,s*) combinations lie on both lines. To determine which is condition (1) and which is condition (2), the second law of Thermodynamics is used : s_2 should be larger than s_1. Therefore it becomes clear that the intersection of the Fanno and Rayleigh lines at the smallest entropy value represents the flow at location (1). The flow properties at location (1) are then found by reading the Mollier diagram.

3. Experimental

The plasma jet under investigation is produced by a Sulzer Metco F4-VB gun operated in a vacuum chamber. The operation conditions are 40 SLPM of pure argon flow with a 400 A current. For the 10 mbar chamber pressure used here the plasma jet flow is under-expanded, as shown in figure 3. Further details about the experimental set-up and phenomenology of under-expanded plasma flows are described elsewhere [5, 8]. The enthalpy probe system, described in more detail in [4], is a specially designed version [12], which allows measurements down to a pressure of 2 mbar. Two different types of probe tips are used in the present study. The first type is a usual, water-cooled, stainless steel Pitot tube (3.2/0.8 mm external/internal diameter, see Fig. 4a). The second type is a specially designed graphite appendice, the Post-shock static pressure probe (PSSPP), which is plugged in the orifice of a probe (Fig 4b). The first probe allows measurement of the stagnation quantities P_{02} and h_{02}. The second one is equipped with a 0.5 mm diameter static pressure tap that allows measurement of the static pressure behind the NSW (P_2) using the enthalpy probe system (Fig 4c).

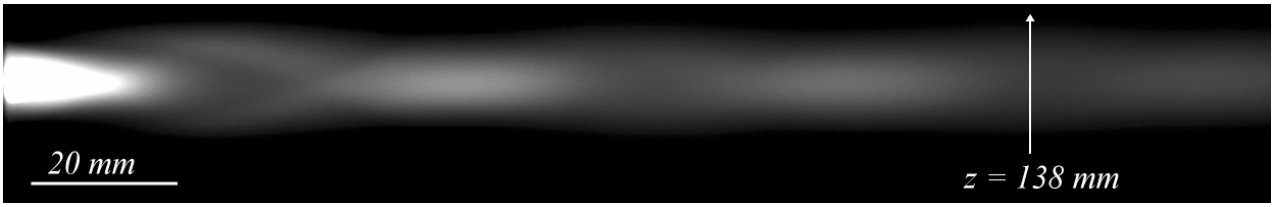

Figure 3 : Image of the investigated plasma jet (400A, 40 SLPM Ar, 10 mbar). "z =138 mm" indicates the axial position of the probe measurements presented below.

The design of the PSSPP is made as follows: First the profile and angle of the graphite probe have been determined in order to insure that the NSW-probe distance and the stagnation pressure are similar to those obtained with the enthalpy probe. This ensures that the PSSPP induces the same shock strength as the enthalpy probe. Second, numerical simulations of the flow around the PSSPP were conducted to get a mapping of the static pressure after the NSW. These simulations show that the static pressure behind the NSW (P_2), is recovered at a given location on the PSSPP surface, due to the flow re-acceleration. The pressure tap was then tuned to this location, obtained from the numerical simulations. Finally it was checked that P_2 obeys the condition : $0.6\ P_{02} < P_2 < P_{02}$, ensuring that the flow has undergone a NSW [11].

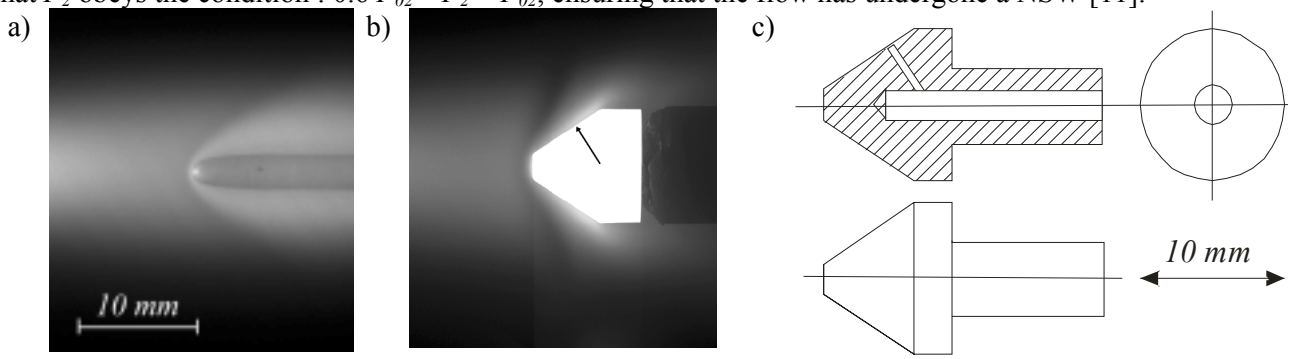

Figure 4 : Images of (a) the enthalpy probe tip and (b) one of the PSSPP developed for the p_2 measurement, both located on jet axis at 138 mm from nozzle exit. (c) shows a drawing of the PSSPP geometry with the pressure tap.

Measurements have been made at different locations in the plasma jet, and tuning of the PSSPP has been made with various shapes and pressure tap positions. The experimental error on the measured pressure is estimated to be within 2% of the measured value. For every measurement location an image of the probes has been acquired with a CCD camera equipped with a band-pass filter to reduce the bright emission from the heated PSSPP in favor of the emission from the plasma jet.

4. Results and discussion

The new approach is tested in the supersonic plasma jet described in the previous section and shown in Figure 3. Measurements are taken at the location z = 138 mm, shown on figure 3, for 5 radial positions, (r = 0, 2, 4 and 8 mm). The choice of this location is justified as follows: It is desired to test the new approach in a zone where the jet is not in aerodynamic equilibrium and where the static pressure changes radially. Such a region would allow testing of the sensitivity of the new probe. By looking at Figure 3, it is possible to deduce that the location z = 138 mm corresponds to the beginning of an expansion zone (where the pressure near the axis of the jet is higher than the chamber pressure) and that it well suits the requirements to test the method. Table 1 presents the raw data *(h_{02}, p_{02}* and *P_2)* as measured.

Table 1 : Raw data as measured, used in the new method

r (mm)	h_{o2} (kJ/kg)	p_{o2} (Pa)	p_2 (Pa)
0	9556	5941	3943
2	10982	5905	3731
4	8009	5752	3519
8	3236	4471	3085

The results of the new approach are then compared with the results obtained using the classic approach [4, 6, 7, 8]. Figure 5 presents a comparison of the static pressure (P_1), temperature (T_1) and velocity (V_1) profiles across the plasma jet as computed using both methods.

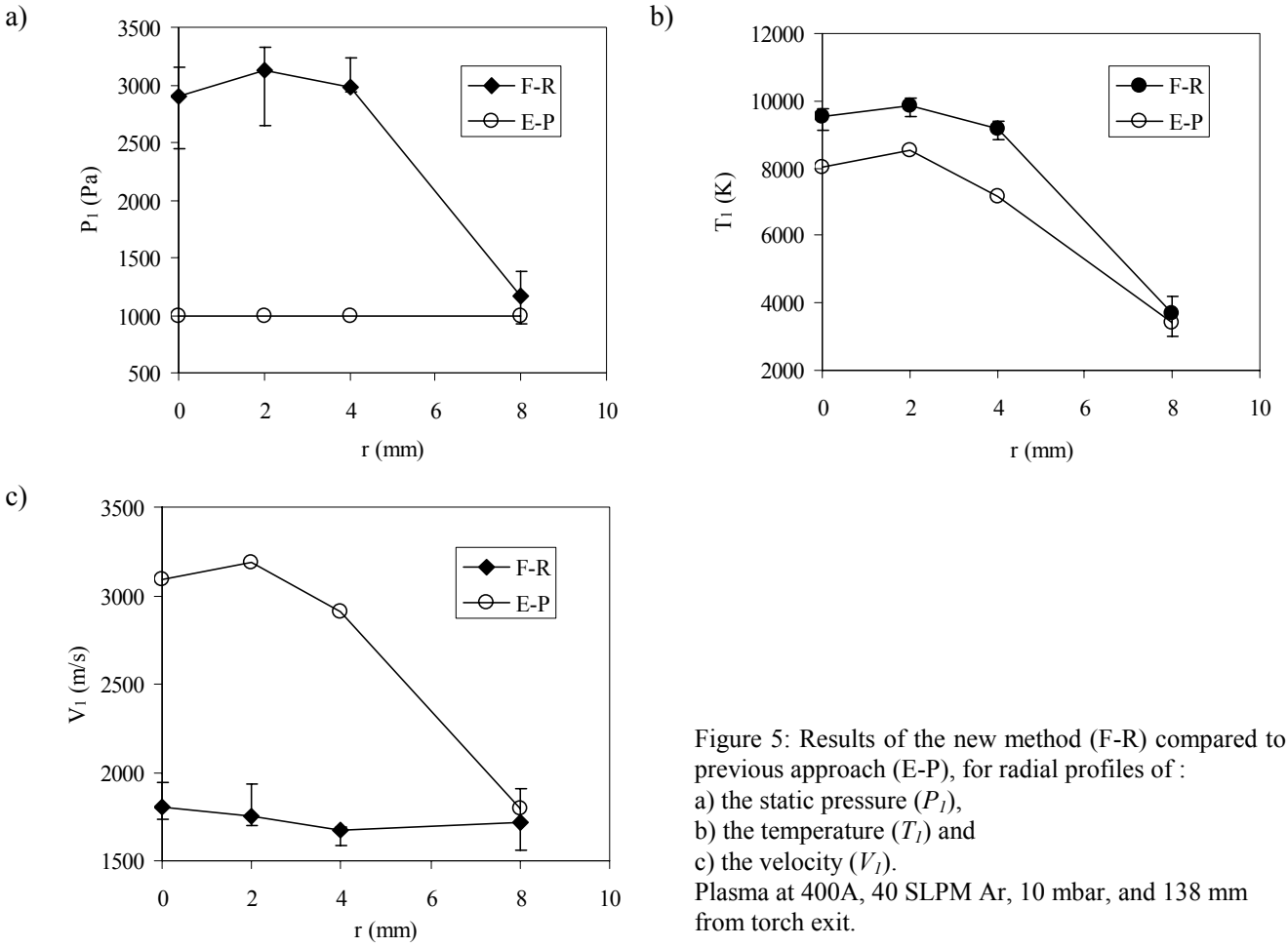

Figure 5: Results of the new method (F-R) compared to previous approach (E-P), for radial profiles of :
a) the static pressure (P_1),
b) the temperature (T_1) and
c) the velocity (V_1).
Plasma at 400A, 40 SLPM Ar, 10 mbar, and 138 mm from torch exit.

In figure 5a, the pressure distribution given by the new approach differs strongly from the one assumed by the classic method (chamber pressure). The new method predicts a higher static pressure than the chamber pressure on the axis, which was foreseen since this axial location is before full expansion (see Fig 3). It is well known that in an expansion zone, expansion waves reduce the jet static pressure radially from a maximum on the axis down to the level of the chamber pressure in the fringe of the jet. This behaviour is captured by the new approach since it predicts a pressure very close to the chamber pressure used in the classic method at the jet fringe where it is close to aerodynamic equilibrium.
The two temperature distributions have the same general trend (Fig 5b), showing a radial temperature drop. An important feature is that both methods predict the same temperature at r = 8mm, where both static pressures are identical. However, the new method gives a higher temperature in the core of the jet.
The two velocity profiles are very different as shown in figure 5c. The new method presents a relatively flat profile compared to the classic method which significantly overestimates the jet velocity on axis (a factor of 1.7 higher). This is due to the fact that the classic method underestimates the core jet static pressure. The flatter profile given by the new approach follows better the free jet boundary layer behaviour predicted by the jet boundary layer theory [13]. Again, the two methods give the same velocity at r = 8mm, due to the aerodynamic equilibrium at this location and provides a validation test case for the new method.

5. Conclusions

The first steps of a new approach have been presented to interpret enthalpy probe measurements performed in supersonic plasma jets which are not in aerodynamic equilibrium. This technique is based on the resolution of the fundamental governing flow equations throughout the NSW induced by the probe and towards stagnation. It uses the second law of Thermodynamics to include non-isentropic effects and relies on the measurement of the post shock static pressure using a specially developed probe. The advantages of

this new approach over previous ones are the less restrictive assumptions and the possibility to include non-LTE effects. In addition, the unknown static pressure of the free jet (usually wrongly approximated by the chamber pressure) is not required as an input, but is obtained as a result of the method.
This new technique has been tested and compared with previous approaches for the case of an under-expanded argon plasma jet produced by a DC plasma torch operated at 10 mbar. The results obtained, in terms of static pressure, temperature and velocity profiles, are consistent with the jet flow phenomenology. Moreover, agreement is found with previous methods at the fringe of the jet where non-aerodynamic equilibrium effects are negligible.
Work is underway to further improve the post-shock static pressure probe developed here, and will allow to extensively characterize the plasma jet flow topology. Inclusion of non-LTE is also foreseen.

Acknowledgments

This work was partially funded by a CTI Swiss Federal Research Projet No. KTI 4403.1KTS. The authors are grateful to Sulzer Metco Switzerland AG for their interest in this work, and for technical support.

References

[1] P. Fauchais and M. Vardelle, "Plasma Spraying: Present and Future", Pure and Appl. Chem., Vol. 66, No. 6, p. 1247-1258, (1994).
[2] M. Loch, and G. Barbezat, "Characteristics and Potential Application of Thermally Sprayed Thin Film Coatings", "Thermal Spray: Surface Engineering via Applied Research", Ed. C. C. Berndt, Pub. ASM International, Material Park, OH, USA, 1141, (2000).
[3] M. Rhamane, G. Soucy, and M. I. Boulos, "Analysis of the enthalpy probe technique for thermal plasma diagnostics", Rev. Sci. Instrum. **66** (6), 3424, (1995).
[4] J.-L. Dorier, M. Gindrat, Ch. Hollenstein, M. Loch, A. Refke, A. Salito, and G. Barbezat, "Plasma jet properties in a new spraying process at low pressure for large are thin film deposition", in Thermal Spray 2001 : New Surfaces for a New Millenium, Pub. ASM International, Materials Park, OH, USA, 2001, p.759-764
[5] B. Jodoin, M. Gindrat, J.L. Dorier, Ch. Hollenstein, M. Loch and G. Barbezat, "Modelling and Diagnostics of a Supersonic DC Plasma Jet Expanding at Low Pressure", Proceedings of the 3rd International Thermal Spray Conference, Essen, Germany, p. 716 – 720, (2002).
[6] M. Hollenstein, M. Rahmane, and M. I. Boulos, "Aerodynamic study of the supersonic induction plasma jet", Proc. of the 14th Int. Symposium on Plasma Chemistry, Prague, Czech Republic, p.257, (1999).
[7] J. R. Fincke, W. D. Swank, S. C. Snider, and D. C. Haggard, "Enthalpy probe performance in compressible thermal plasma jets", Rev. Sci. Instrum. **64** (12), 3585, (1993).
[8] M. Gindrat, J.L. Dorier, Ch. Hollenstein, M. Loch, A. Refke, A. Salito and G. Barbezat, "Effect of Specific Operating Conditions on the Properties of LPPS plasma Jets Expanding at Low Pressure", Proceedings of the 3rd International Thermal Spray Conference, Essen, Germany, p. 459 – 464, (2002).
[9] M. I. Hoffert and H. Lien, "Quasi-One-Dimensional, Nonequilibrium Gas Dynamics of Partially Ionized Two-Temperature Argon", Physics of Fluids, vol. 10 (8), p. 1769-1776, 1967.
[10] A. B. Murphy and C. J. Arundell, "Transport Coefficients of Argon, Nitrogen, Oxygen, Argon-Nitrogen, and Argon-Oxygen Plasmas", Plasma Chemistry and Plasma Processing, vol. 14 (4), p.451-490, 1994.
[11] A.H. Shapiro, "The Dynamics and Thermodynamics of Compressible Fluid Flow Volume I", The Ronald Press Company, New York, 647 p., 1953.
[12] Tekna Plasma Systems Inc., 3535 Boul. Industriel, Sherbrooke, Québec, Canada.
[13] H. Schlichting, "Boundary-Layer Theory 7th Edition", McGraw-Hill Book Company, New York, 817 p., 1987.

The treatment of incineration wastes in a pilot-scale plasma reactor

A. Huczko, H. Lange, J. Golimowski

Department of Chemistry, University of Warsaw, Warsaw, Poland

Abstract
Different solid residues resulting from the incineration of municipal solid wastes (MSW) were processed in a pilot-scale /100 kW/ arc plasma reactor. Depending upon the specific energy of the processed material (within 0.8 ÷ 10.7 kWh / kg) the melting degree varied between 9.7 and 97.4 %

1. Introduction

Current regulations impose the stabilization of much of the wastes before dumping [1]. Containing significant amount of leachable heavy metals (i.e., Cd, Pb, Zn and Cr) and chlorine, the solid residues from MSW incineration are classified as toxic (fly ash) and noxious (bottom ash and slag) wastes [2]. Thus, many techniques hare been tried to neutralize them. Since the incineration has been commonly accepted as the only basic safe and reliable technique to process various wastes, the problem of further utilization, remediation, recycling and management of incineration residues is currently of high interest. One of a proposed solution is plasma processing [3] which profoundly changes the physical and chemical nature of these "wastes resulting which from wastes". As a matter of fact, there has been growing interest in the application of plasma techniques in environmental engineering recently [3]. While non-thermal plasmas (mostly corona discharge) have been tried to process gaseous reactants [4], the thermal plasmas (DC and RF) have been widely applied to process various solid and liquid wastes [5].
Earlier we reported [6,7] the results of a low-power thermal plasma processing of different solid residues resulting from the incineration of domestic waste. A DC plasma jet, RF plasma and a rotating arc ware tested and the highest melting degree was achieved using a high-volume, low-velocity conical and rotating plasma. Thus, in the present study a higher power rotating plasma was used to assess the economical validity of the process.

2. Experimental

A 100 kW plasma reactor, in which solid matter was caused to interact with a thermal plasma comprised spaced stationary electrode (graphite rods, 60 mm dia) structures. (Fig.1). An arc was established by a power supply between annular cathode and anodes (5) in a star-like configuration. The arc was caused to orbit at high angular velocity (15000 rpm) round the anode structure to form a conical plasma zone between the cathode and the anodes. It is worth mentioning that the thermal efficiency of this plasma system is very high since only the anode holders are water-cooled. Thus, practically all arc power is transformed into plasma enthalpy. Particulate solids were introduced through the feeding probe to enter the interelectrode zone and interact with the plasma therein. The arc could be circulated by electromagnetic force with the help of coils fitted outside the anode structure. Downstream of the plasma head is a reacting chamber and a bottom collector. The tests were carried out under atmospheric pressure and the flow of plasma gas (Ar) was equal to 1800 dcm^3/h.
The starting material to be plasma processed was the post-incineration solid waste from the Municipal Incinerator in Warsaw (Table 1).

Table 1. Particulate size characteristic of processed wastes

Origin	Granulation
Crushed slug	below 3 mm[a]
Bottom ash	below 1 mm[b]
Fly ash	below 0.060 mm[c]

[a]49 per cent of total [b]87 per cent of total [c]100 per cent of total

The solid products were collected and analyzed using different techniques: SEM, XRD, ICP-MS, and sieve analysis. The melting degree was evaluated, too.

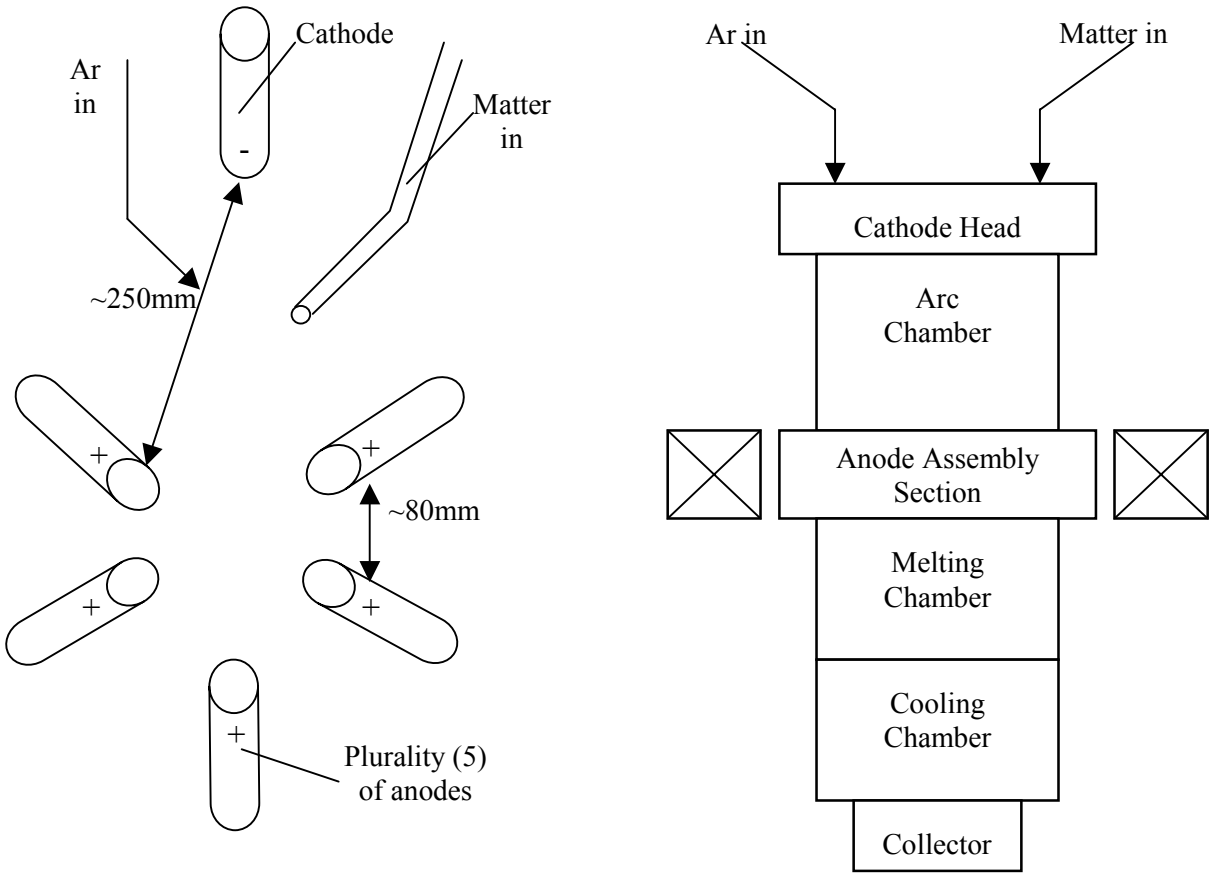

Fig.1. The scheme of the plasma reactor

3. Results and discussion

The operational parameters and the results of a plasma melting of different wastes shown are in Table 2.

Table 2. Operational parameters and results of plasma processing of incineration wastes

Run No	Processed Waste	Feeding Rate [kg/h]	I [A]	U [V]	Power [kW]	Energy Consumption [kWh / kg]	Melting Degree[a] [%]
1	Crushed slug	17.1	300	270	81	4.7	83.2
2	Crushed slug	51.6	320	300	96	1.9	38.2
3	Bottom ash	32.5	300	300	90	2.8	51.0
4	Bottom ash	94.7	250	300	75	0.8	9.7
5	Fly ash	13.6	450	325	145	10.7	97.4

[a]calculated from the mass and the sieve analysis of solid products

A high power of an arc plasma and a very low flow of plasma gas resulted in a high plasma temperature and a long reaction time. Consequently, the high melting degree of processed solids , close to 100 %, was obtained. Fig.2 shows the plasma melted incineration waste (fly ash).

Fig.2. Starting fly ash (left) and the plasma melted product (right)

Surprisingly, the size of the processed solid particulates does not seem to influence the melting efficiency. As it can seen from Fig.3 the specific energy of the processed matter defined as the arc power divided per feeding rate (see the energy consumption in Table 2.) is clearly the operational parameter characterizing the process efficiency.

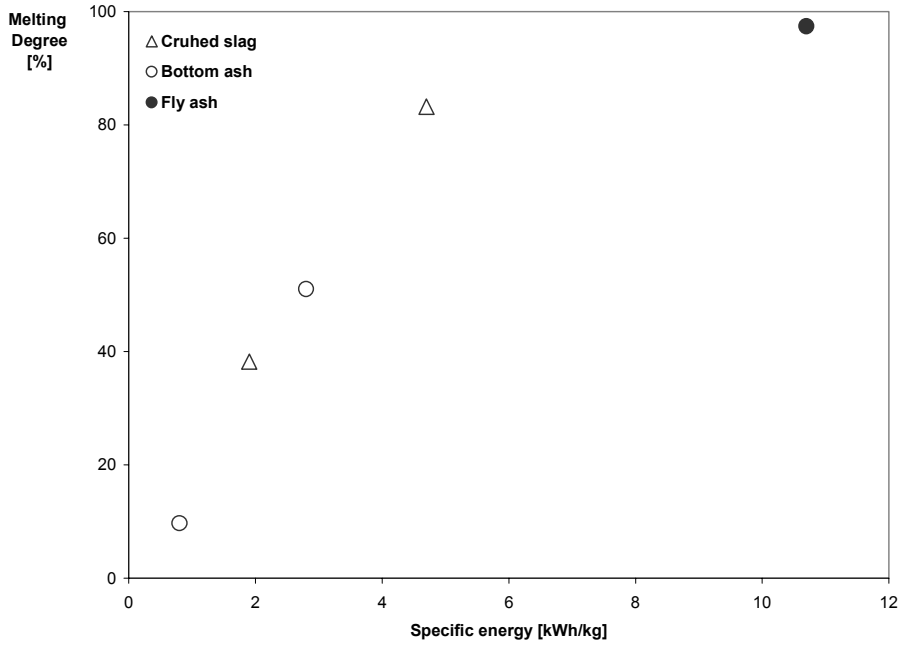

Fig.3. Melting efficiency of incineration residues vs. specific energy

It is also worth mentioning the relatively low energy consumption for the melting of wastes, much lower comparing to the tests in a laboratory-scale plasma systems [6,7].
The analysis are under way to evaluate the chemical transformation of wastes during plasma processing and, above all, the change in the leachability of heavy metals.

Acknowledgment
The work was supported by the Committee for Scientific Research (KBN) through the Department of Chemistry, Warsaw University, under Grant No. 7 T09C 130 20.

References
[1] F. Lebrun, C. Oberlin, P. Pasquini, R. Fante, High Temp. Mat. Proc., **5**, 291 (2001).
[2] J.M. Badie, X. Chen, G. Flamant, D. Gauthier, High Temp. Mat. Proc., **1**, 441 (1997).
[3] A. Huczko, Chemical News, (in Polish), **48,** 567 (1994).
[4] R. Benoci, G. Bonizzioni, E. Sidoni, Thermal Plasmas for Hazardous Waste Treatment, World Scientific, London (1996).
[5] A. Huczko, J. Jurewicz, Chemical Industry (in Polish), **76**, 3 (1997).
[6] A. Huczko, G. Chojecki, J. Golimowski, J. Kowalska, D. Dziadko, H. Tanaka, T. Ishigaki, Ecological Chemistry and Engineering, **9**, 9 (2002).
[7] H. Lange, A. Huczko, G. Chojecki, J. Golimowski, W. W. Płotczyk, B. Krasnodębska-Ostręga, D. Dziadko, J. Pacheco, T. Ishigaki, H. Tanaka, Acta Agrophysica, **80**, 327 (2002).

Plasma polymer adhesion and interfacial hydrolytic stability

R. Prikryl, V. Cech, L. Kripal, and J. Vanek

Institute of Materials Chemistry, Brno University of Technology
Purkynova 118, CZ-612 00 Brno, Czech Republic

Abstract

Adhesion of plasma-polymerized films on planar glass substrates has been tested using a micro-scratch tester and an optical polarizing microscopy. Plasma-polymerized films of vinyltriethoxysilane were deposited by helical coupling pulsed plasma system. Adhesion tests has revealed that the interfacial hydrolytic stability of plasma-polymerized films has been much better with respect to polycondensed films prepared from the same monomer by wet chemical process.

1. Introduction

Thin films are deposited on surface of various materials to change (increase or decrease) wettability, surface roughness, chemical functionality, and mechanical or electrical properties, which could be utilized for adhesive bonding, corrosion and scratch protection, and electronic applications. Films prepared from organosilicon monomers by wet-chemical processes (sol-gel) (e.g. silane coupling agents) are of good adhesion to glass substrates due to forming of siloxane bonds at the glass/film interface. However, the siloxane bond is hydrolytically unstable [1] and the film adhesion therefore decreases if water molecules diffuse to the interface, which results in splitting of chemical bonds. The siloxane bonds are only partially reformed upon removal of the water during the drying process. In industry, silane coupling agents are applied for surface modification of glass reinforcements (fibers, particles) in order to form a thin interlayer. Modified glass fibers or particles are used as reinforcements for polymer composites. The interlayer has to provide a strong and simultaneously tough bonding between the reinforcement and the polymer matrix. Degradation of a composite material due to the interfacial hydrolytic instability may result in worsening of its mechanical properties or even collapse of composite if it is used in humid or aqueous environment [2]. An improvement of interfacial hydrolytic stability in polymer composites enables an expansion of composite applications.

Plasma polymerization has been utilized for surface modification of fibers mainly since 1980s. Most studies were aimed at an improvement of surface properties of carbon, aramid and polyethylene fibers for advanced composites [3]. Thin layers of plasma polymer deposited on fibers result in an increase of composite strength and modulus [4,5]. The world market is dominated by glass reinforcements with appropriate mechanical properties and low costs. Organosilicones are potential compounds for successful surface modification of glass fibers and particles. Plasma polymer films prepared form organosilicon monomers may be of good adhesion to glass substrates due to strong siloxane bonds at the glass/film interface, which was formed in vacuum and so without occurrence of water molecules. Organosilicon monomers are very popular and often utilized for thin film deposition [6,7].

Of all the properties of a thin-film system, adhesion is one of the most important but difficult to measure. We can describe fundamental adhesion in terms of the energy per unit area needed to separate a thin film from its substrate. This energy is known as the work of adhesion. Practical adhesion refers to a thin film's ability to resist delamination in a practical setting, under stresses appropriate to the application [8]. Although there are no ways to directly measure the work of adhesion, there are a number of tests, which characterize adhesion practically. Three basic types of tests can be distinguished as follows: tensile-type adhesion tests, shear-type tests, and scratch tests [9]. Practically, hard films and coatings are easily characterized, as measured responses and delamination are more evident. Thin films deposited from organosilicon monomers belong among softer materials and adhesion measurements and their evaluations are more complicated [6]. Adhesion measurements of such softer films are the aim of this paper. Interfacial adhesion and its stability is compared for films prepared by plasma polymerization and wet-chemical process using the same monomer.

2. Experimental

2.1. Materials

Monomer for thin-film deposition was vinyltriethoxysilane $CH_2{=}CH{-}Si\ (-O-CH_2-CH_3)_3$ (VTES, ≥ 98% purity, Fluka). Glass substrates were special microscope slides without flaws (1.0×26×76 mm^3, refractive index n = 1.518, Knittel Glaser, Germany).

2.2. Plasma process

Plasma polymerized films of VTES were deposited on glass substrates using helical coupling plasma system (13.56 MHz); details on the apparatus have been described in Ref. 10. The deposition process is very important to control interfacial adhesion with high reproducibility. Vacuum system was evacuated to a pressure of 5×10^{-3} Pa and then flushed by argon gas (10 sccm) for 10 min. Glass substrate was placed into a side vacuum chamber and the chamber was evacuated by an independent vacuum system. Basic pressure of 2×10^{-3} Pa was established in the deposition chamber after flushing. Argon gas was again introduced (10 sccm) into deposition system. The glass substrate was placed into the deposition chamber using a manipulator and was cleaned by Ar plasma (continuous or pulsed plasma) for a given treatment time. Then the substrate was saved in the side chamber, the plasma was switched off, and argon gas was evacuated. Monomer vapor at a given mass flow rate was introduced into deposition chamber using a dose valve and then the plasma was ignited at a chosen power (pulsed plasma). When the pressure in deposition chamber was stabilized, the fresh substrate was placed into the chamber and thin film was deposited on its surface during a given time. Finally, the deposited specimen was saved in the side vacuum chamber, the deposition process was finished and all the apparatus was flushed by argon gas. After 30 min the side chamber was flooded by air up to the atmospheric pressure and the prepared specimen was conveyed from the side chamber into a desiccator to avoid contamination before measurements.

Pulsed plasma: The plasma was switched on (switched off) during the time denoted as t_{on} (t_{off}). Sum of them represents a period $P = t_{on} + t_{off}$. The effective power used for thin film deposition may be evaluated as follows: $W_{eff} = W_{total} \times (t_{on}/P)$, where W_{total} = 50 W.

2.3. Wet-chemical process

VTES monomer belongs among organofunctional silane coupling agents recommended for surface modification of glass fibers applied as reinforcements for unsaturated polyester resin. The silane molecule is a multifunctional one, which reacts at one end with the glass surface and at the other end with the polymer matrix. The ethoxy group ($-O-CH_2-CH_3$) represents a hydrolysable unit and so the silane is hydrolyzed to the corresponding silanol in the aqueous solution to which the glass substrate is exposed. These silanol molecules compete with water molecules to form hydrogen bonds with the hydroxyl groups bound to the glass surface. When the glass substrate is dried, the free water is driven off and condensation reactions then occur, both at the silanol/glass interface and between neighboring silanol molecules. The result is a polysiloxane layer bonded to the glass surface, presenting an array of vinyl groups ($CH_2{=}CH-$) to the environment.

Glass substrates were twice rinsed by fresh acetone in an ultrasonic bath for 10 min and dried at room temperature (cleaning procedure). 3 ml of VTES was hydrolyzed for 60 min in 100 ml of deionized water using a magnetic stirrer. The initial VTES concentration was about 3% by weight. The pH value of the solution was adjusted to about 4 by adding acetic acid. Aqueous solution was poured into a Petri dish where the cleaned substrates were placed. The dish was brought to a vacuum oven and the solution was concentrated at room temperature for 6 hr so that free water molecules were eliminated during the condensation process. Glass substrates coated by the polycondensed film (pc-VTES film) were removed from the Petri dish and were dried in a vacuum oven at 60 ^{o}C for next 20 min. Prepared samples were saved in a desiccator to avoid contamination before measurements.

2.4. Scratch test

Scratch testing is widely used to evaluate film adhesion since it can provide fast qualitative, semi quantitative, or quantitative information. The test consists of drawing a stylus (Rockwell ball or diamond tip) with known radius of curvature over a film under increasing normal (vertical) loads and the value of the load, at which adhesion failure (delamination between the film and the substrate) is detected, is known as the critical load, L_C. The acoustic emission signal and the tangential (friction) force are monitored as a function

of the progressively increased load. Scratch lines are also investigated by means of optical and scanning electron microscope to determine the critical load (normal force).

Soft polymeric films produce negligible acoustic emission during scratching and so the signal cannot be utilized for evaluation of the critical load. Special low-load micro-scratch tester has to be used for adhesion measurements of soft films. Such a micro-scratch tester was developed at the Institute of Materials Chemistry. A description of the instrument has been reported in Ref. 11. Three Rockwell diamond tips with an apex radius of 50, 90 and 120 μm worked with the apparatus. A special instrument arrangement enabled the normal load ranging from 20 mN to 10 N at the scratching speed ranging from 1 to 20 mm/min. Scratch lines were observed by an optical polarizing microscope (BX-P 50, Olympus) using a digital video camera.

3. Results and discussion

Aqueous solution of VTES monomer is frequently used for surface modification of glass fibers by glass manufactures. It is known that the silanol molecules tend towards self-condensation, forming siloxane oligomers, rather than complete bonding with the glass surface and so, there is only a low density of siloxane bonds at the glass/film interface [12]. Plasma treatment and plasma polymerization are processes that could improve interfacial adhesion in the examined system.

Plasma-polymerized vinyltriethoxysilane (pp-VTES) was deposited by a mass flow rate of 0.5 sccm and a corresponding pressure of 1 Pa. Pulsed plasma was maintained at a constant t_{on} = 1 ms. The effective power used was ranging from 0.05 to 25 W. So, a relatively low power was used in order to prepare tenacious material with low modulus (10^9 Pa), which is appropriate as the interlayer for polymer composites.

Thin polymer films deposited by plasma polymerization and wet-chemical process were characterized by scratch test under a loading rate of 500 mN/min and a scratch length of 5 mm. Every specimen was tested using four scratch lines and the critical load was determined as the mean value with standard deviation. All measured scratch lines are characteristic of the stylus reaching the substrate and then recovering due to pile-up of material, which is typical for soft materials and in contrast to hard films.

Typical scratch recordings and a corresponding microphoto of scratch lines in pp-VTES film are depicted in Fig. 1. The critical load, L_C, is marked out in the graph. We can distinguish three important levels of critical loading; L_{C0} corresponds to the beginning of visible path, L_{C1} denotes a level of the first local failure, and L_{C2} corresponds to the beginning of permanent failure.

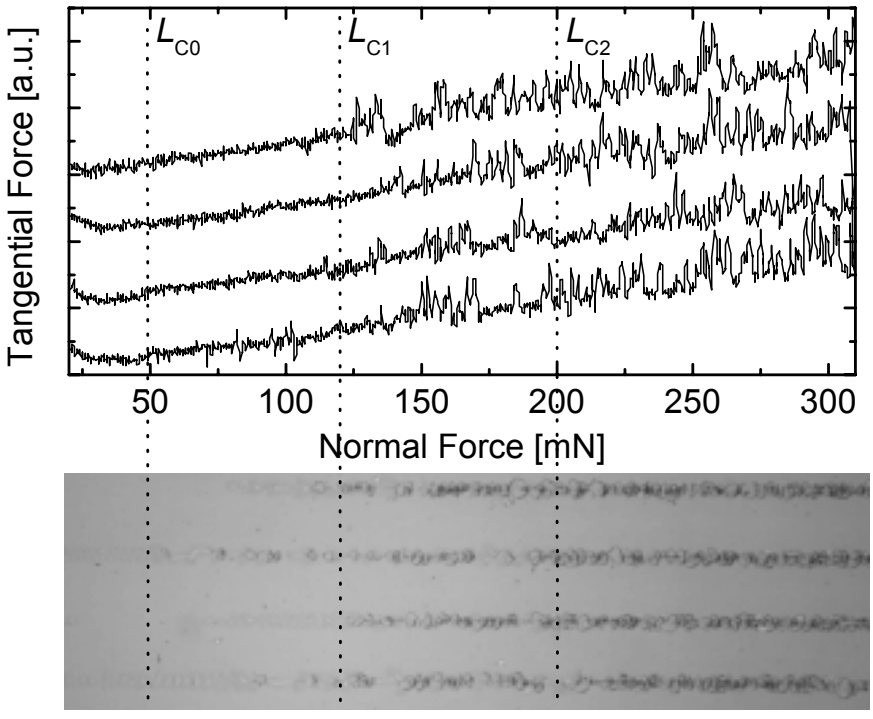

Fig. 1. Typical scratch recordings and a corresponding microphoto for pp-VTES film on glass substrate. Critical loads, L_c, are marked out in graph.

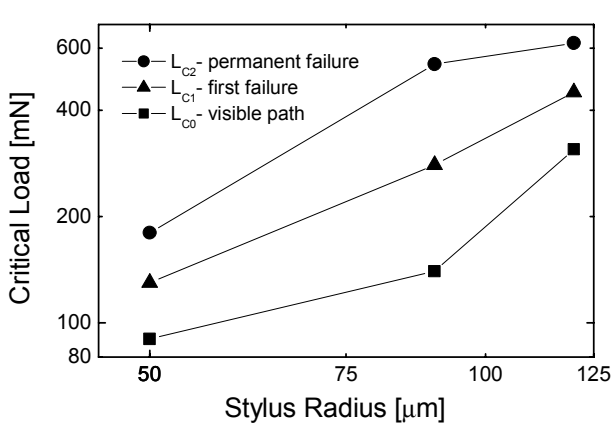

Fig. 2. Critical load versus stylus radius for three levels of film failure.

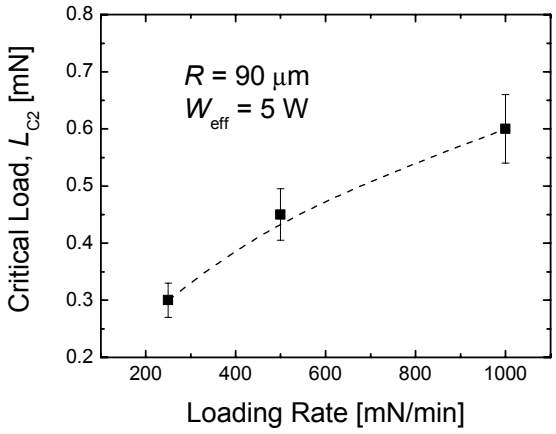

Fig. 3. An influence of the loading rate on critical load for pp-VTES film.

The glass/film interface was subjected to an impact of the stylus changing the stylus radius, R (50, 90 and 120 μm). The critical loads (L_{C0}, L_{C1}, and L_{C2}) versus the stylus radius for the same plasma-polymerized film are depicted in Fig. 2. A value of the critical load L_{C2} (permanent failure) is more reproducible than that of the first failure (L_{C1}) and therefore, we use L_{C2} as a measure of adhesion in next text. According to Ohring [9], theoretical analyses relating the critical load, stylus geometry and material parameters of the film lead to a relation $L_C \sim R^n$, where $n = 2$. Martinu found out that $1 < n < 2$ for hard films on polymer substrates [13]. The log-log scale in Fig. 2 enables to determine the degree $n = 1.48$ for the L_{C2} dependence. All our measurements confirmed results obtained by Martinu and $1 < n < 2$ is valid for the soft films (pp-VTES) on the glass substrates as well.

The critical load is intensely dependent on the loading rate as evidenced from the dependence in Fig. 3. The critical load increased twice with the loading rate ranging from 250 to 1000 mN/min. Changes in the critical load are a consequence of different response in visco-elastic behavior of the material. Obviously, we use a loading rate of 500 mN/min in our measurements.

Thin films of different thickness were deposited at the same deposition conditions using an effective power of 5 W. Critical loads evaluated from scratch recordings and scratch lines are plotted as a function of the film thickness in Fig. 4. The critical load corresponding to the film of thickness 190 nm is much higher than the remaining data, likely due to a lower internal stress in the film of lower thickness. Therefore, the critical load decreases with the increasing film thickness of pp-VTES films. This trend of the dependence was observed for oxide thin films by Ottermann *et al.* [14] as well. They found out that increasing the film stress the critical load decreased.

A set of pp-VTES films was prepared at different effective power using a constant t_{on} = 1 ms and changing t_{off} (1, 9, 99, 999 ms). Remaining process conditions (flow rate, pressure) were the same and all prepared films were of similar thickness about 1 μm. The critical load versus the effective power is shown in Fig. 5. One can see that adhesion slightly increases with the power. However, the reason of adhesion enhancement is not quite clear, as many film properties could be different (internal stress, film density and related Young's modulus and hardness) due to different growth conditions. For example, Ottermann *et al.* [14] observed that the critical load increased with increasing Young's modulus of the film.

Pp-VTES and pc-VTES films on glass substrates were subjected to scratch tests under dry and wet conditions to investigate hydrolytic stability of adhesion bonding at the glass/film interface. Pp-VTES films were deposited on untreated and Ar-plasma treated (10 min) glass substrates and pc-VTES films were prepared on acetone pretreated glass substrates, see Chapter 2. The film thickness of pp-films was about 1.2 μm and that of pc-films was about 7 μm. Thinner pc-films were inhomogeneous and not appropriate for scratch measurements, which gave results of bad reproducibility. Specimens stored in a desiccator were tested under dry (as prepared) and wet conditions. Wet conditions mean that specimens were dipped into distilled water at a temperature of 22 or 100 ^{o}C for a given time and after removing them they were dried at a temperature of 60 ^{o}C for 2 hr. Critical loads corresponding to specimens tested under dry and wet conditions are depicted in Fig. 6. All pp-VTES films on untreated glass substrates started to delaminate and were completely separated from the substrate during the wet test and so the critical load is assigned to be zero.

Adhesion of pc-VTES films did not change if the film was immersed into water (22 ^{o}C) for 1 hr but decreased by 45% after 21 hr (22 ^{o}C water) and 60% after 2 hr (100 ^{o}C water). The decrease of film adhesion is connected with a scission of siloxane bonds [1] at the glass/film interface. The diffusion of water molecules to the interface can be enhanced increasing the temperature and so the degradation process was accelerated using boiling water. Pp-VTES films on Ar-plasma pretreated glass substrates exhibited a higher adhesion with respect to the pc-VTES films and the interfacial hydrolytic stability of plasma-polymerized films was much better. Critical loads of pp-VTES films immersed in cold and boiling water did not change towards that obtained for dry conditions. The reasons could be a higher density of siloxane bonds at the glass/film interface and/or a higher crosslinking of plasma polymer and resulting lower diffusion rate of water molecules.

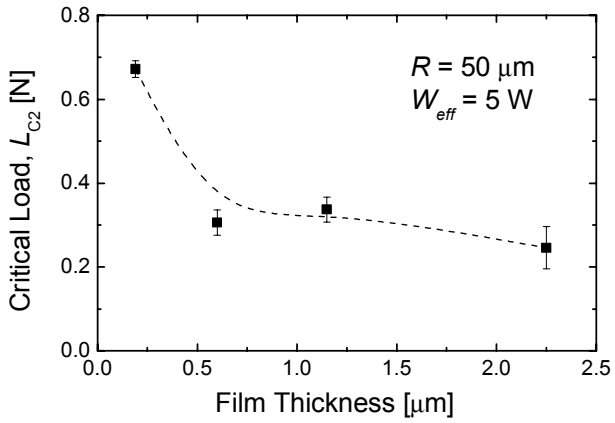

Fig. 4. Critical load as a function of film thickness for pp-VTES films.

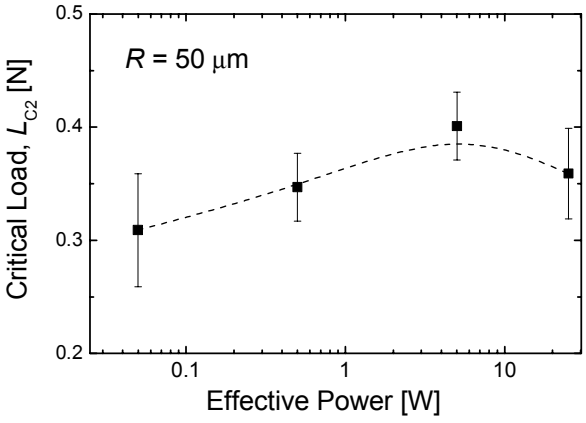

Fig. 5. Dependence of critical load on effective power for pp-VTES films.

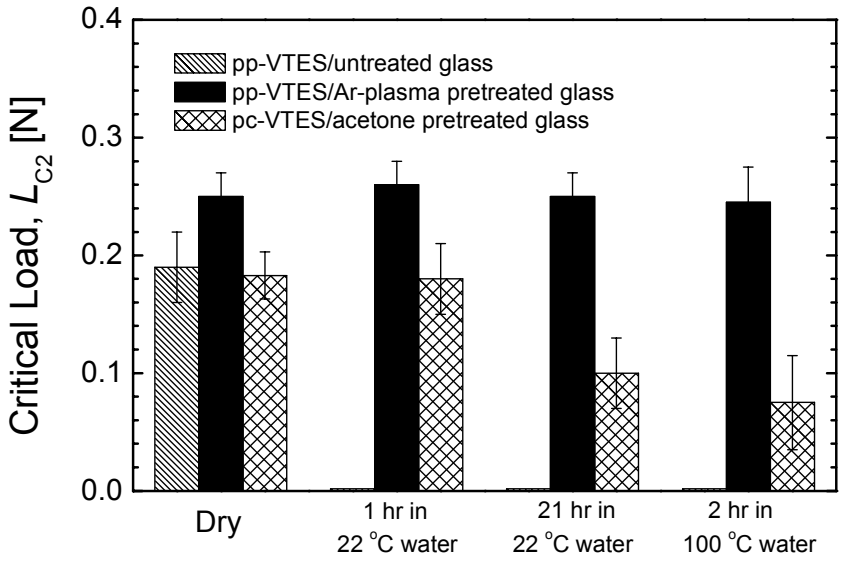

Fig. 6. Interfacial adhesion of plasma-polymerized and polycondensed films under dry and wet conditions.

4. Conclusion

Plasma-polymerized films of vinyltriethoxysilane were deposited on planar glass substrates using RF pulsed plasma. Polycondensed films were prepared on glass substrates using the same monomer. A micro-scratch tester and an optical polarizing microscopy enabled to analyze a scratch path together with normal and lateral force recordings. Our study has pointed out to an influence of the stylus radius and the loading rate on measured data. The critical load, L_C, increased with the increasing stylus radius according to a relation $L_C \sim R^n$ with the degree $1 < n < 2$. The loading rate has to be maintained constant so that we could compare scratch data, as the critical load is intensely dependent on the loading rate. Our results has confirmed that adhesion of thin films could be improved depositing films of lower thickness, probably due to a lower film stress. Plasma-polymerized and polycondensed films were tested under dry and wet conditions. While interfacial adhesion of polycondensed films immersed into cold and boiling water decreased with time, the adhesion of plasma-polymerized films was unvarying. Therefore, interfacial hydrolytic stability of plasma-polymerized films was very good, probably due to a higher density of siloxane bonds at the glass/film interface and/or a higher crosslinking of plasma polymer.

Acknowledgements

This work was supported in part by the Ministry of Education, contracts ME 597, COST 527.110, and the Grant Agency of Czech Republic, contract No. 104/03/0236.

References

[1] E.P. Plueddemann, Silane Coupling Agents, Plenum Press, New York, 1991.
[2] J.G. Marsden, in Handbook of Adhesives (I. Skeist, Ed.), Chapman & Hall, New York, 1990, pp. 536.
[3] R. Li, L. Ye, Y-W Mai, Composites Part A 28 (1997) 73.
[4] W. Weisweiler and K. Schlitter, Thin Solid Films 207 (1992) 158.
[5] E. Eber and W. Weisweiler, in Interfacial Interactions in Polymeric Composites (G. Akovali, Ed.), Kluwer Academic Publishers, Dordrecht, 1993, pp. 287.
[6] A.M. Wrobel and M.R. Wertheimer in Plasma Deposition, Treatment, and Etching of Polymers (R.d'Agostino, Ed.), Academic Press, New York, 1990, pp.163.
[7] Y. Segui, in Plasma Processing of Polymers (R.D. Agostino, P. Favia, F. Fracassi, Eds), Kluwer Academic Publ., Dordrecht, 1997, pp.305.
[8] R. J. Stokes and D. F. Evans, Fundamentals of Interfacial Engineering, J. Wiley, New York 1997, pp. 606.
[9] M. Ohring, Materials Science of Thin Films, Academic Press, San Diego, 2002, pp. 764.
[10] R. Prikryl, O. Salyk, J. Vanek, and V. Cech, Czech J Phys. 52 (2002) D816.
[11] R. Prikryl, O. Salyk, L. Kripal, and V. Cech, Czech J Phys. 52 (2002) D824.
[12] W. Wang and A.T. DiBenedetto, J Adhesion 68 (1998) 183.
[13] L. Martinu, in Plasma Processing of Polymers (R.D. Agostino, P. Favia, F. Fracassi, Eds), Kluwer Academic Publ., Dordrecht, 1997, pp. 247.
[14] C.R. Ottermann, K. Bange, A. Braband, H. Haefke, and W. Gutmannsbauer, Mat. Res. Soc. Symp. Proc. Vol. 436 (1997) 109.

Mechanical properties of pulsed-plasma polymerized vinyltriethoxysilane

V. Cech[1], A.A. Goruppa[2], J. Vanek[1], and F.R. Jones[2]

[1]*Institute of Materials Chemistry, Brno University of Technology*
Purkynova 118, CZ-612 00 Brno, Czech Republic
[2]*Department of Engineering Materials, University of Sheffield*
Sir Robert Hadfield Building, Mappin Street, Sheffield S1 3JD, UK

Abstract

Plasma-polymerized thin films of vinyltriethoxysilane have been prepared by plasma-enhanced chemical vapor deposition using an RF (13.56 MHz) helical coupling pulsed-plasma system. Thin films of the thickness ranging from 80 nm to 1.5 μm were subjected to nanoindentation measurements. The Young's modulus determined from the indentation load-displacement curve has increased with the effective power used from 4 GPa to 11 GPa. Thin films have exhibited an abrupt increase of the hardness at the film surface.

1. Introduction

Silane coupling agents (e.g. vinyltriethoxysilane) are utilized for surface modification of glass fibers, which are embedded in polymer matrix forming the fiber-reinforced polymer composite. The fibers are coated by thin film during a wet-chemical process (sol-gel) in order to prepare the interlayer (thin film) that forms a strong but tough link between the fiber and the polymer matrix. Recently, it has been found out that the interlayer seems to be the most important part in composite materials [1]. The interlayer properties (elastic modulus) can influence or even control performance of composite material, i.e. the composite strength and the composite toughness [2]. However, thin films of various moduli cannot be prepared from a given monomer using the wet-chemical process. What are the possibilities of plasma-enhanced chemical vapor deposition (PE CVD) using RF plasma?

In an effort to determine mechanical properties (elastic modulus, strength, hardness, internal stress, adhesion) of thin films a number of methods has been evolved [3]. However, different methods resulted in different values of mechanical parameters. For example, the elastic modulus of plasma-polymerized hexamethyldisiloxane (pp-HMDSO), calculated from internal stress measurements, was found to be of order 10^6 Pa, as it was published in 1980s. At present we know that such a value is unreal low. A rough estimation of the film modulus can be done using a two-layer or three-layer sandwich structure [4]. This simple method enabled an estimation of the elastic modulus to be 1 GPa for pp-HMDSO [5]. Similar values were obtained for pp-tetramethylsilane (2 GPa) [6], pp-tetraethylsilane (3 GPa) [6] and pp-dichloro- (methyl) phenylsilane (6 GPa) [4].

Nanoindentation is a modern technique, which is able to estimate modulus and hardness at the nano scale and so it is helpful for probing of sub-micron films. The aim of our study was to deposit plasma polymer films of vinyltriethoxysilane (VTES) under different RF power and to find out if the elastic modulus of film differs.

2. Experimental

Plasma-polymerized films were prepared by plasma-enhanced chemical vapor deposition (PE CVD) employing an RF (13.56 MHz) helical coupling pulsed-plasma system [7]. Vinyltriethoxysilane (VTES, purity ≥ 98%, Fluka) was used as a precursor with a vapor flow rate of 0.45 sccm, which corresponds to a process pressure of 2 Pa. Thin films were deposited on silicon (100) wafers pretreated by Ar plasma (10 sccm, 10 Pa, 25 W) for 10 min so that the activated surface could improve interfacial adhesion between the wafer and the film. Plasma-polymerized VTES (pp-VTES) was prepared at different effective power in a form of thin film of a thickness ranging form 80 nm to 1.5 μm. The effective power (W_{eff}) of pulsed plasma can be controlled by changing the ratio of the time when plasma is switched on (t_{on}) to the time when plasma

is switched off (t_{off}), $W_{eff} = W_{total} \times t_{on}/(t_{on} + t_{off})$, where W_{total} = 50 W. Plasma polymers were prepared at three (effective power) values of 0.05, 5.0 and 25 W with t_{on} = 1 ms. Employing a mechanical manipulator the pretreated silicon wafer was placed into the plasma zone after plasma reached the steady state monitored by mass spectroscopy. The film thickness was measured by a Profiler Talystep (Taylor-Hobson) and the mean deposition rate was determined as the film thickness divided by the deposition time.

The mechanical properties of the films were determined from load-displacements curves obtained using a Nanoscope III A (Veeco Instruments Inc). A three-sided pyramid Berkivich indenter was employed in our study. Measured data were obtained from one complete cycle of loading and unloading. The unloading data were then analyzed according to the equation

$$S = \frac{2}{\sqrt{\pi}} E_r \sqrt{A}, \tag{1}$$

where the experimentally measured stiffness (S) was determined as a slope ($S = dP/dh$, P is the applied force, h is the displacement) of the upper portion of the unloading curve. A is the projected area of the elastic contact and E_r is the reduced modulus defined through the equation

$$\frac{1}{E_r} = \frac{(1-\nu^2)}{E} + \frac{(1-\nu_i^2)}{E_i}, \tag{2}$$

where E and ν are Young's modulus and Poisson's ratio for the specimen and E_i and ν_i are the same parameters for the indenter with E_i = 1141 GPa and ν_i = 0.07 for the diamond indenter used. A description of the indentation procedure and the apparatus is reported in Ref. 8. The hardness is determined from measured data using the equation

$$H = \frac{P_{max}}{A}, \tag{3}$$

where P_{max} is a maximum of the applied force. Nine up to fifteen indentations were made on each sample into a penetration depth of 30% of the film thickness. The elastic modulus was estimated by averaging the values measured up to 10% of the film thickness, where the measurements are not influenced by substrate properties [9]. The Poisson's ratio, ν, used in (2) for all samples was 0.3.

3. Results and discussion

Deposition conditions and mechanical properties of pp-VTES films are summarized in Table 1. H_{max} denotes the maximum value of the hardness at the film surface and H_{bulk} is a bulk value of the hardness estimated as an average one of data obtained down from 20 nm of the film thickness.

Table 1. Deposition conditions and mechanical properties of pp-VTES films.

Effective power	Film thickness	Mean deposition rate	Young's modulus	Hardness [GPa]	
[W]	[nm]	[nm/min]	[GPa]	H_{max}	H_{bulk}
0.05	112	5	4.9	1.7	1.2
0.05	240	6	3.7	1.2	0.7
5.0	180	180	7.4	2.0	1.1
5.0	390	181	6.8	2.2	1.0
5.0	1480	148	6.6	2.1	1.1
25	80	107	11.3	2.5	2.1

Plasma polymers behaved almost as the true elastic material as it is evidenced from the load-displacement recording, see Fig. 1. Deformation of the film material induced by the indenter at the loading part of measured cycle is almost completely removed after unloading. So, there is practically no visual footprint of the indenter in the film after measuring cycle.

The only deposition parameter, the effective power, was changed at preparation of a set of samples. The Young's modulus of pp-VTES as a function of the effective power is depicted in Fig. 2. In spite of different

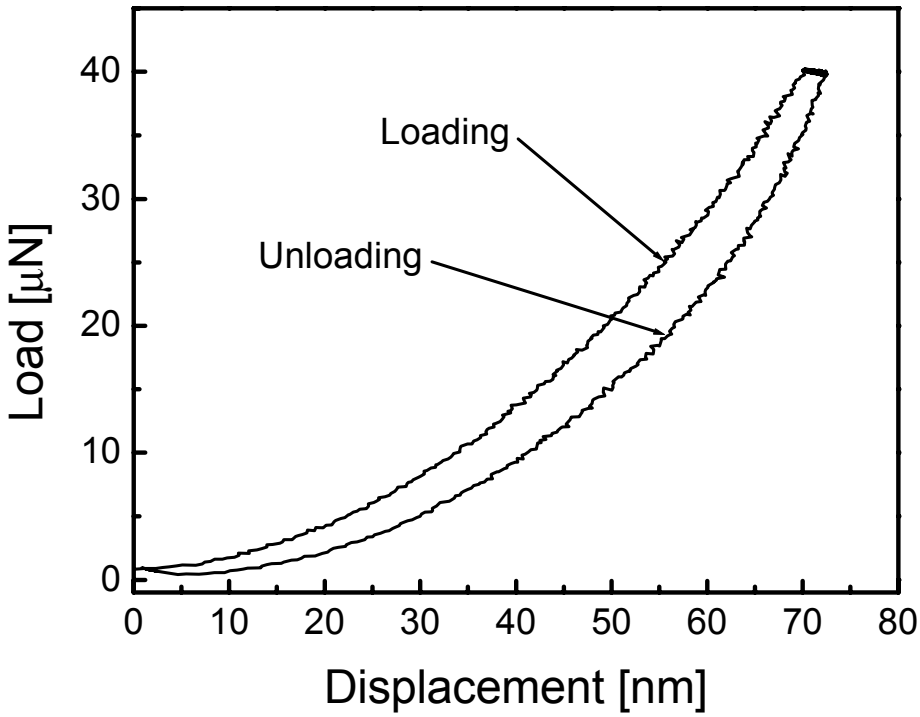

Fig. 1. Load (unload) versus indenter displacement for plasma-polymerized vinyltriethoxysilane (pp-VTES).

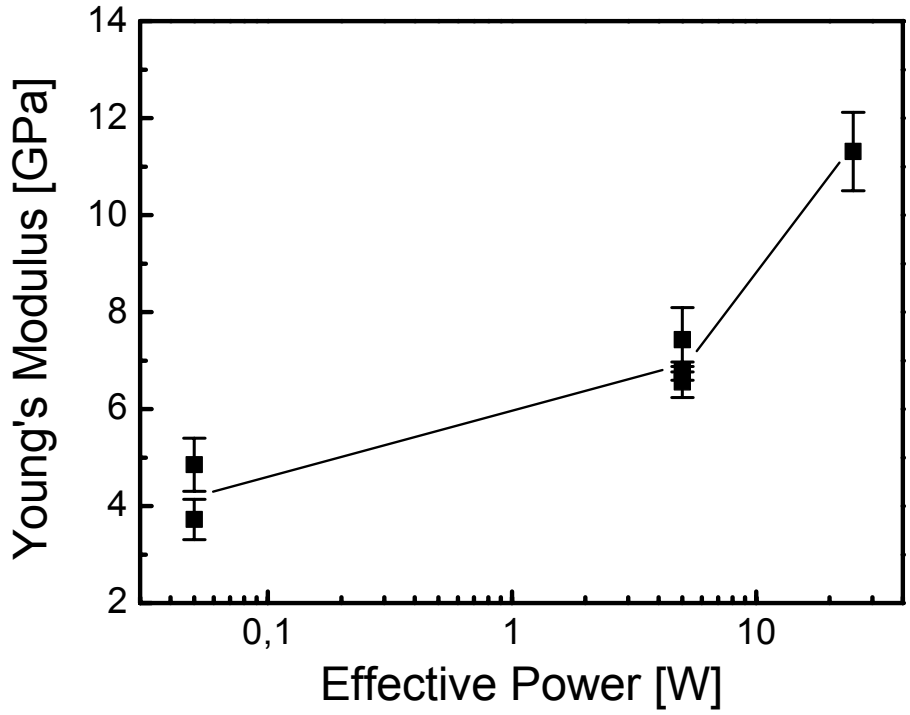

Fig. 2. Young's modulus of pp-VTES as a function of the effective power.

film thickness, it is evident that the modulus increases with the increasing power from about 4 GPa to 11 GPa. This change represents an enlargement of the modulus by 175%. It means that we are able to control film modulus very simply changing the effective power. Values of the modulus (pp-VTES) are relatively small with respect to those estimated for other amorphous hydrogenated films prepared by plasma techniques, i.e. hydrogenated silicon (a-Si:H, 60-100 GPa [10]), hydrogenated carbon (a-C:H, 40-145 GPa [10,11]), hydrogenated silicon carbide (a-SiC:H, 130-160 GPa [12]) hydrogenated silicon nitride (a-SiN:H, 140 GPa [13]) and hydrogenated silicon oxide (a-SiO_2:H, 85 GPa [13]). For a comparison, the modulus of silicon wafer is 170 GPa. Our films were prepared at relatively low power and the low plasma energy seems to be the reason of reduced modulus. Monomer molecules are more activated and fragmented forming higher density of free radicals if the plasma energy increases, and the reactive species result in a highly cross-linked polymer. A cross-linking of material may be supported by ion bombardment as well. It has been shown that the ion energy effectively enhances the film packing density [14].

We prepared thin films of different thickness purposely to investigate a variation of elastic modulus. There is the modulus dependent on the film thickness in Fig. 3. The Young's modulus slightly decreases with the film thickness for both sets of samples prepared at the different power. It is known that the kinetics of film growth changes during thin film deposition [6]. At the beginning of deposition process the film growth is very fast and decelerates with an increasing film thickness as a result of competition between the plasma polymerization and ablation processes. Therefore, a value of the mean deposition rate (determined as film thickness/deposition time ratio) is lower for thicker film as it is evident for the sample (1480 nm) in Table 1. A modulus descent with the film thickness could be a consequence of lower material compaction.

A dependence of the mean deposition rate on the effective power is not a trivial function, see Fig. 4. The kinetics of film growth changes with the effective power and can be faster for an optimal t_{on}/t_{off} ratio. The infrared spectroscopy did not reveal differences in chemical structure of films prepared at different power [15]. However, differences could be expected in microstructure of film material and the plasma polymer deposited at high deposition rate could be more porous. Porosity of films will be investigated in our next research.

Figure 5 shows a development of the hardness along the contact depth [8], which is the distance (from film surface) along which contact between the indenter and the film is made. Simply, there is the depth profile of the hardness in Fig. 5. One can see that the hardness decreases from the film surface (H_{max}) to the bulk value (H_{bulk}) within the range of 20-30 nm for most of samples. This phenomenon could be a consequence of post-deposition oxidation at the film surface. The surface layer of films stored in the open air can react with atmospheric humidity and the reaction results in oxygen incorporation into the polymer network. The oxygen is able to diffuse into the film material increasing the cross-linking of plasma polymer [16].

4. Conclusion

Plasma-enhanced chemical vapor deposition was used to prepare thin and ultrathin films of vinyltriethoxysilane employing an RF helical coupling pulsed-plasma system. Plasma-polymerized films of the thickness ranging from 80 nm to 1.5 μm were deposited on silicon substrates at a flow rate of 0.45 sccm, a process pressure of 2 Pa and an effective power ranging form 0.05 to 25 W. Prepared films were subjected to an investigation of mechanical properties using nanoindentation. It means that the elastic modulus and the hardness of plasma polymers were evaluated from the indentation load-displacement behavior of materials tested with a Berkovich indenter. Plasma polymers behaved almost as the true elastic material and the Young's modulus increased with the effective power from 4 GPa to 11 GPa. The relatively low values compared to similar material data published by other authors were explained as a result of low power used. The modulus of VTES films slightly decreased with the film thickness for the films prepared at the same deposition conditions. Nanoindentation measurements revealed an abrupt increase of the hardness at the film surface form about 1 GPa in bulk to 2 GPa at the film surface. Investigation of mechanical properties in context with preparation of thin film of controlled properties could enable progress in performance of composite materials.

Acknowledgements

This work was supported in part by the Ministry of Education, contracts ME 597, COST 527.110, and the Grant Agency of Czech Republic, contract No. 104/03/0236.

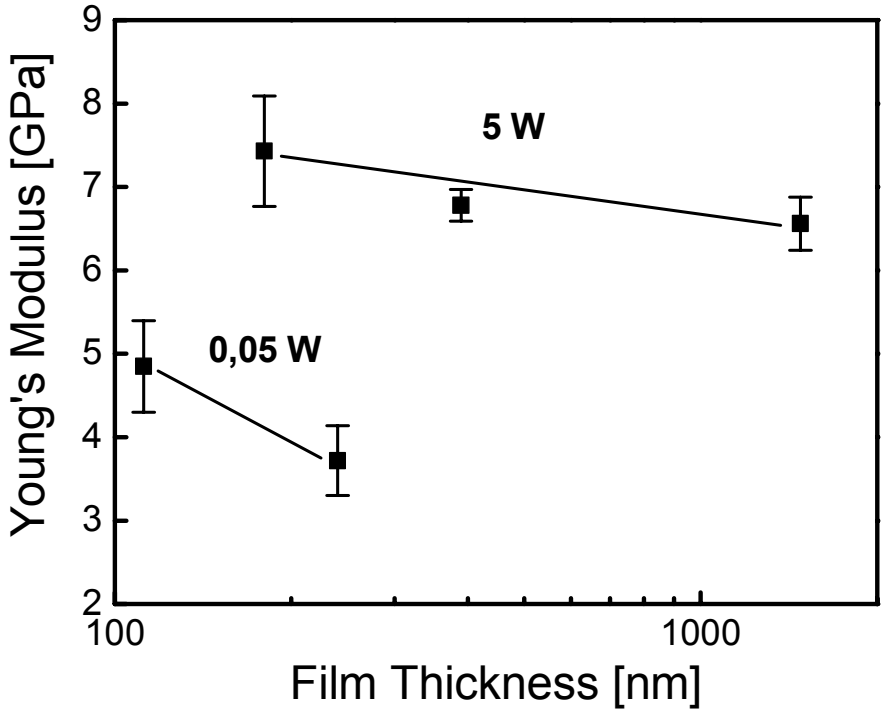

Fig. 3. Thickness dependence of the Young's modulus for two sets of films prepared at an effective power of 0.05 W and 5 W.

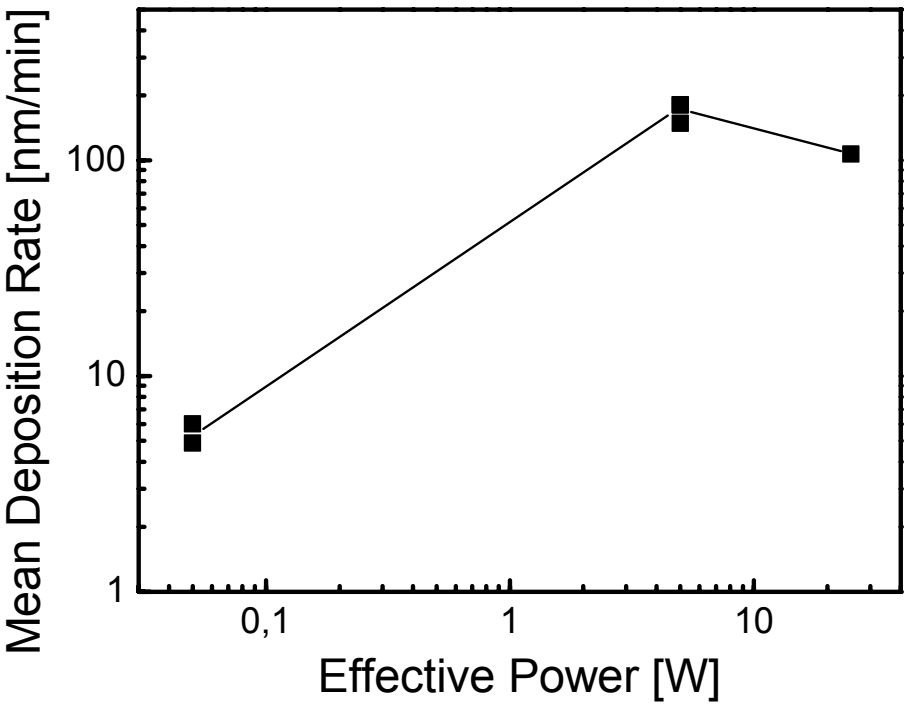

Fig. 4. Variations of the mean deposition rate of pp-VTES with the effective power.

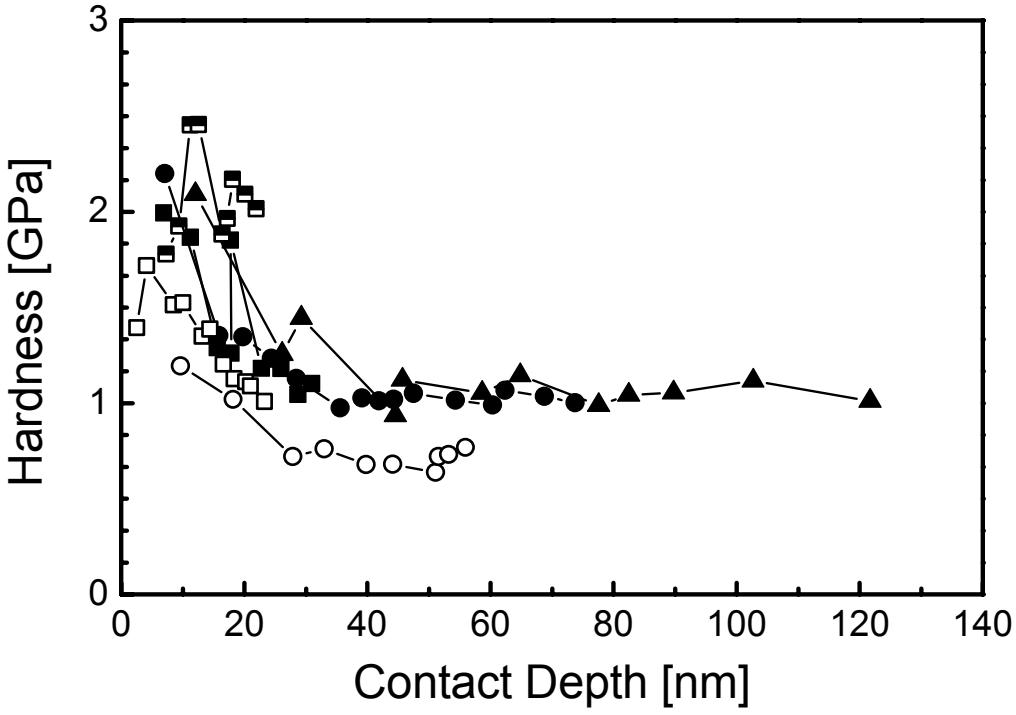

Fig. 5. Distribution of the hardness along the contact depth (depth profile) for thin films of pp-VTES. Empty symbols denote data corresponding to films deposited at 0.05 W, similarly full symbols – 5 W, half-full symbols – 25 W.

References

[1] Conclusion from the 7th Int. Conf. on Interfacial Phenomena in Composite Materials, September 11-14, 2001, Arcachon, France.
[2] M. Labronici, H. Ishida, Comp. Interfaces **2**, 199 (1994).
[3] M. Ohring, Materials Science of Thin Films. Academic Press, New York 2002.
[4] V. Cech, P. Horvath, J. Jancar, F. Schauer, and S. Nespurek, Macromolecular Symposia **148 (**1999) 321.
[5] R. Balkova, R. Prikryl, V. Cech, and O. Salyk, Proc. 15th Int. Symposium on Plasma Chemistry, Orleans 2001, Vol. 5, pp.1747.
[6] N. Inagaki, Plasma Surface Modification and Plasma Polymerization. Technomic Publ., Lancaster 1996.
[7] R. Prikryl, O. Salyk, J. Vanek, and V. Cech, Czech. J. Phys. **52** (2002) D816.
[8] W.C. Oliver, G.M. Pharr, J. Mater. Res. **7** (1992) 1564.
[9] B.N. Lucas, C.T. Rosenmayer, and W.C. Oliver, Mat. Res. Soc. Proc. Vol. 505 (1998) 97.
[10] X. Jiang, K. Reichelt, B. Stritzker, J. Appl. Phys. **66** (1989) 5805.
[11] J.C. Sanchez-Lopez, C. Donnet, J.L. Loubet, M. Belin, A. Grill, V. Patel, and C. Jahnes, Diam. Rel. Mater. **10** (2001) 1063.
[12] J.F. Zhao, P. Lemoine, Z.H. Liu, J.P. Quinn, P. Maguire, and J.A. McLaughlin, Diam. Rel. Mater. **10** (2001) 1070.
[13] D. Rats, V. Hajek, and L. Martinu, Thin Solid Films **340** (1999) 33.
[14] L. Martinu, J.E. Klemberg-Sapieha, O.M. Kuttel, A. Raveh, M.R. Wertheimer, J. Vac. Sci. Technol. A **2** (1994) 1360.
[15] R. Balkova, R. Prikryl, A. Grycova, J. Vanek, and V. Cech, Czech. J. Phys. **52** (2002) D807.
[16] T.R. Gegenbach and H.J. Griesser, J. Polym. Sci. Part A, Polym. Chem. **36** (1998) 985.

Recent Development of Waste Treatment by Reactive Thermal Plasmas in Japan

Takayuki Watanabe

Research Laboratory for Nuclear Reactors, Tokyo Institute of Technology, Tokyo, Japan

Abstract
Attractive waste treatments by plasmas under atmospheric pressure have been proposed, because atmospheric pressure plasmas offer unique advantages. In this paper, the application for destruction of hazardous and waste materials, such as low-level radioactive waste, ion-exchange resin waste, and ozone-depleting substances, will be reviewed. Also selective separation mechanism by reactive thermal plasmas will be discussed for waste treatment.

1. Introduction

Attractive material processes by thermal plasmas have been proposed especially for waste treatments, because thermal plasmas offer unique advantages; these advantages include high enthalpy to enhance reaction kinetics, high chemical reactivity, oxidation and reduction atmospheres in accordance with required chemical reactions, and rapid quenching (10^6 K/s) to produce chemical non-equilibrium materials. However, thermal plasmas have been simply used as high temperature source. This indicates that thermal plasmas may have more capability for waste treatment, if thermal plasmas are utilized effectively as chemically reactive gas. In this paper, the application for destruction of hazardous and waste materials will be discussed. Melting and solidification of incineration ash by thermal plasmas will not be discussed in this paper, because these systems have been already commercially operated at several sites.

2. Low-Level Radioactive Waste Treatment

Low-level radioactive wastes (LLW) are generated from nuclear power plants and will be generated from decommissioning of nuclear power plants in future. In Japan, there are three facilities for volume reduction of LLW by thermal plasmas. Thermal plasma process offers attractive advantages for treatment of LLW because of high heat transfer rate from plasmas to wastes.

Two facilities of LLW treatment by thermal plasmas are being conducted at Tokai Research Establishment of Japan Atomic Energy Research Institute (JAERI). One is twin torch transferred arc system with the capacity of 4 tons/day, and another is induction thermal plasmas with induction melting furnace [1]. The melting furnace with induction thermal plasma torch is presented in Fig. 1. Three torches of induction plasmas (200 kW x 3) with an induction furnace up to 800 kW are used for melting and volume reduction for LLW. Capacity of LLW treatment is 4 tons/day. Compared with DC transferred and non-transferred arc, air and oxygen can be used as the plasma gas of induction thermal plasmas. Therefore, complete combustion of the waste can be achieved, resulting in stabilization of radionuclide.

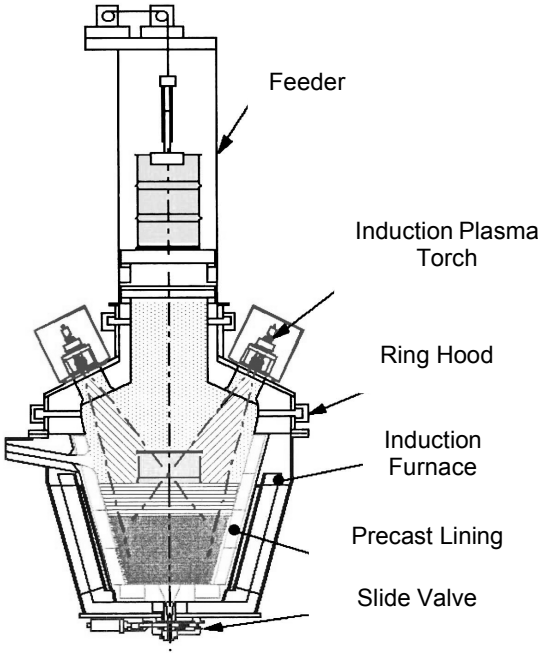

Fig. 1 Plasma – induction melting furnace [1].

The Japan Atomic Power Company (JAPC) has decided to construct LLW treatment facility by the Plasma Arc Centrifugal Treatment (PACT) system at the Tsuruga Power Station [2]. The PACT system with an 8 ft rotating hearth and 1.2 MW transferred arc torch was developed by Retech, Inc., USA. The treatment capacity for LLW is 600 kg/hr.

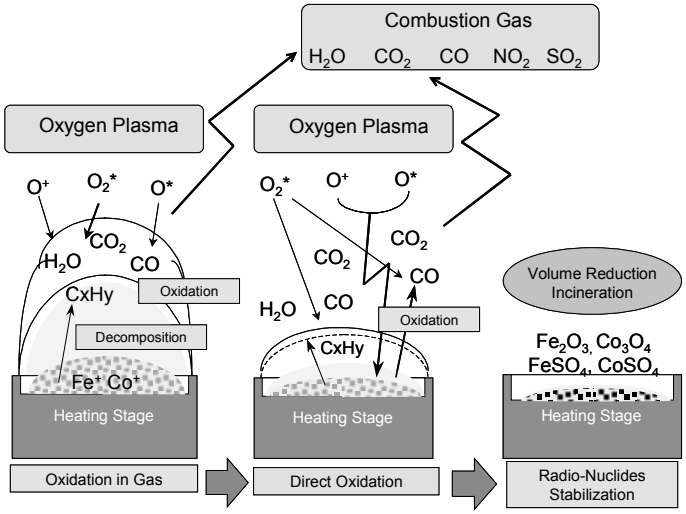

Fig. 2 Ion-exchange resin treatment mechanism by induction oxygen plasma generated at low pressure [4].

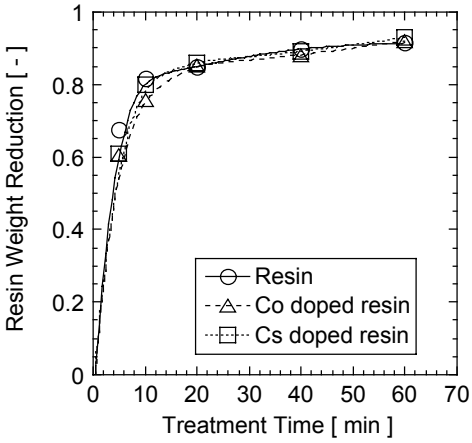

Fig. 3 Weight reduction of ion-exchange resin by thermal plasma treatment.

Radionuclide can be stabilized in the slag generated from the melted LLW by the thermal plasma treatment. Especially cesium entrapment in slag layer is important for LLW treatment. The effect of waste components on the vaporization behavior of Cs was investigated using simulated waste materials [3]. The vaporization rate of cesium increases with an increase in the slag basicities defined as (CaO+FeO+MgO) / (SiO_2+Al_2O_3). Entrapment of Cs into the slag can be enhanced by an increase in the content of Al_2O_3 or SiO_2 in the waste.

3. Treatment of Waste Ion-Exchange Resin

The amount of the waste ion-exchange resins adsorbing of radionuclide is increasing, therefore the effective method to reduce the volume of the waste is required. Fuji Electric Co. Ltd. developed volume reduction system for resin waste using low pressure plasma [4]. The concept of ion-exchange resin by an oxygen plasma is shown in Fig. 2. The process consists of two stages; the first stage is the low volume-reduction (1/4-1/5) by gas-phase plasma oxidation, and the second stage is the high volume-reduction (1/10-1/20) by direct oxidation on the ion-exchange resin. The reduction ratio achieved is 1/20 of the original volume at the treatment rate of 2 L/hr. The migration ratio of radionuclide in the exhaust gas generated in the process is below 10^{-6} under the pressure of 1-10 kPa..

The reactive thermal plasmas were also used to reduce the weight and volume of ion-exchange resins [5]. In the experiment, cation exchange resins (SKN-1) doped with Co and Cs were used as simulated waste resins. Oxygen or air used as reaction gas was injected in the downstream of the anode under atmospheric pressure. Figure 3 shows the weight reduction of waste resins by thermal plasma treatment. The weight was reduced to 80 % after 10 min treatment. After 40 min treatment, the weight was reduced to 95 %. Small difference in the weight reduction was found among the undoped resins and Co and Cs doped resins. XRD analysis indicates that Co in resins remains as CoO and Co_3O_4, while Cs in resins remains as Cs_2SO_4. Retention of Co after the treatment was approximately 100 %. Retention of Cs was approximately 100 % except for large flow rate of oxygen injection. Thermal plasma treatment provides the effective and rapid reduction in weight and volume of ion-exchange resins. The treatment has also good advantages for the stabilization of radionuclide.

4. Plasma Direct Melting Furnace

Waste treatment requires dioxin destruction, landfill-site life extension, material recycling and effective use of waste heat from high-temperature off-gas. A system of gasification of waste with ash melting should meet those requirements. A plasma direct melting furnace for waste gasification was developed by Hitachi Metals, Ltd [6]. Figure 4 shows the pilot-scale of 24 tons/day for municipal solid waste by thermal decomposition and melting using a vertical shaft furnace. This system meets environmental requirements for slag recycling and dioxin destruction. The advantage of this system is smooth and continuous extraction of melted waste with quick starting-up. In this system, crushing, drying and other waste pretreatment are not

necessary. The melting section of the furnace maintains at 1,500-1,700°C through the injection of a flame from a plasma torch. The condition of the plasma torch can be controlled to respond the fluctuations in the waste quality, and the coke bed maintains a high temperature in the melting section, enabling stable operation.

The plasma torch consists of a closely spaced pair of tubular water-cooled electrodes. The generated arc discharge is magnetically rotated at extremely high speeds. During operation, a process gas is injected into the heater through a space between the electrodes.

5. Selective Separation by Reactive Plasmas for Waste Treatment

Plasma enhanced vaporization is well-known method for production of ultrafine particles of metal. The plasma-enhanced vaporization can be applied to the selective separation for waste treatment. Hydrogen in arc plasmas enhances the vaporization of particular metals on the anode. In Si-Ti system, the vaporization rate of Ti is enhanced selectively by hydrogen in the arc [7]. An increase in H_2 concentration in the arc leads to an increase in Ti fraction in the prepared particles.

The dissociated hydrogen in arc plasmas enables the dissolution of a large amount of hydrogen into molten metals as well as the generation of metal vapor from the molten metals. The vaporization enhancement is attributed to the following four factors; recombination of hydrogen atoms in molten metals; high thermal conductivity of hydrogen; formation of intermediate products such as hydride; activity modification by hydrogen in molten metals. The first and second factors have small effect on the vaporization enhancement, therefore the third and/or fourth factors were considered to be the main factors. However hydride produced from molten metals with hydrogen arcs has not been identified yet. Instability and unknown properties of hydride give rise to difficulty in the quantitative examination.

Investigation of reaction mechanism of molten metals with chlorine or fluorine in arc plasmas would lead to the alternative solution, because chloride and fluoride are more stable and their properties have been known compared with hydride. Arc plasma reactions with chlorine was investigated for the separation of particular elements from alloys since chlorine atoms react with particular elements to form chlorides that have high vapor pressures and are especially separated from alloys [8,9]. The components of the fumes produced by changing O_2 flow rate are shown in Fig. 5. The component using Ar plasmas is almost identical to the initial KOVAR alloy (Fe=53, Co=17, Ni=29 mass %). The concentration of Fe in the fumes is highest by Ar-Cl_2 and Ar-Cl_2-O_2 (0.25 NL/min) plasma treatments. The concentration of

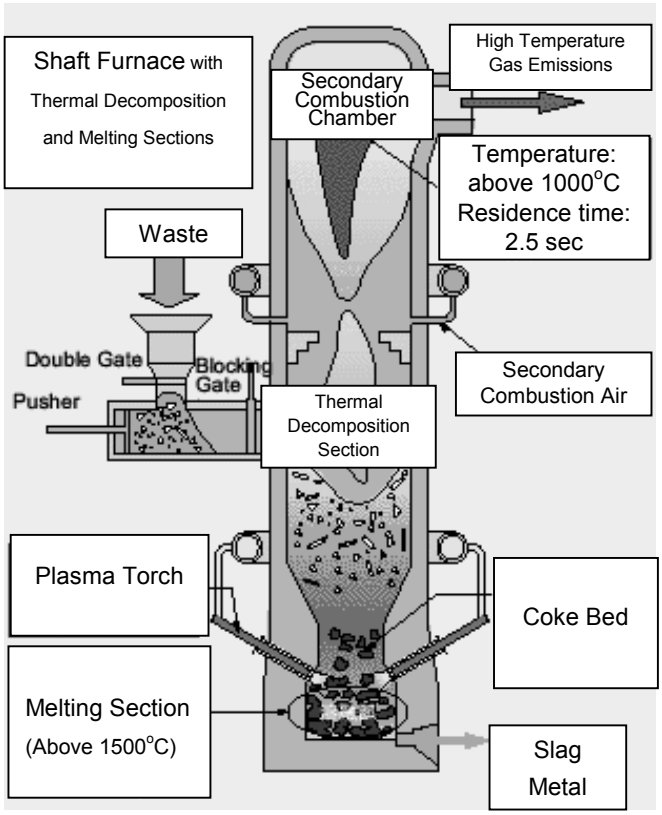

Fig. 4 Schematic diagram of plasma direct melting furnace for waste gasification [6].

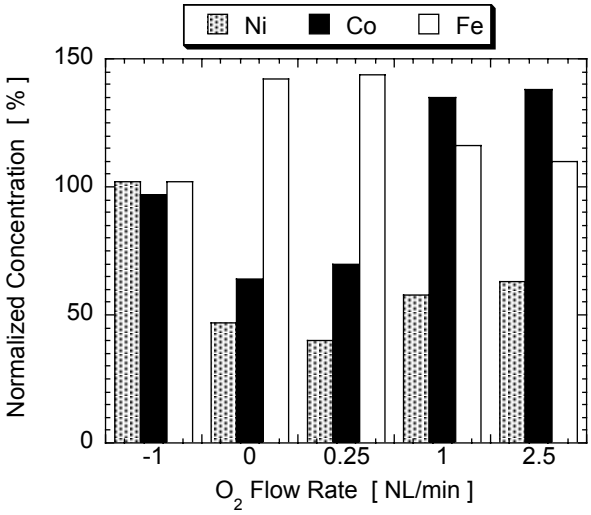

Fig. 5 Selective separation of particular elements from alloy by chlorine thermal plasma with oxygen addition.

Co increases with O_2 flow rate of the plasma gases, while the concentration of Ni using Ar-Cl_2 and Ar-Cl_2-O_2 plasmas is low since Ni compounds are difficult to vaporize. The reaction mechanism using these plasmas with Cl_2 and O_2 can be correlated to Gibbs free energy changes of chlorination and oxidation.

6. Plasma Decontamination

The highly effective decontamination process is required for the treatment of material generated from a decommissioned nuclear reactor as well as from the nuclear reprocessing plant and nuclear waste processing plant. Many wet processes for the decontamination have been proposed, but the wet process has the drawbacks due to the large volume production of secondary waste such as the contaminated solvent and ion-exchange resin. Therefore the plasma methods were proposed owing to the small secondary waste production. The decontamination researches have been carried out under the low pressure plasma conditions, however the low pressure condition is not favorable considering the practical application.

Decontamination process by microwave plasma under atmospheric pressure was developed for the removal of deposition of radionuclide on the surface of stainless steel [10]. The decontamination reaction is based on the formation of volatile compound such as fluoride produced by CF_4/O_2 plasma. Using the stainless steel sample prepared in water in autoclave simulated BWR condition, the surface oxide film was removed by irradiation of CF_4/O_2 plasma, resulting from the fluorination of the oxide.

7. Fly Ash Detoxification

Incineration of municipal waste generates incineration ash and fly ash. Induction thermal plasma system for fly ash treatment was proposed to recover the useful metals and materials from fly ash generating from melting furnace [11,12]. Fly ash fed into the induction thermal plasma was completely vaporized and decomposed during thermal plasma process.

After thermal plasma treatment of fly ash, the components were recovered separately owing to the difference of each condensation temperature. The H_2 injection into the induction thermal plasma strongly influences the difference of each condensation temperature, especially Zn compounds. The atomic fractions of the heavy metals of Zn and Pb included in the recovered materials increase under 800°C with Ar-H_2 plasma treatment, as shown in Fig. 6. More amounts of heavy metals than initial fly ash are included in the materials recovered at lower temperature. On the other hand, the materials recovered at higher temperature are detoxified because they contain extremely less heavy metal components than in initial fly ash.

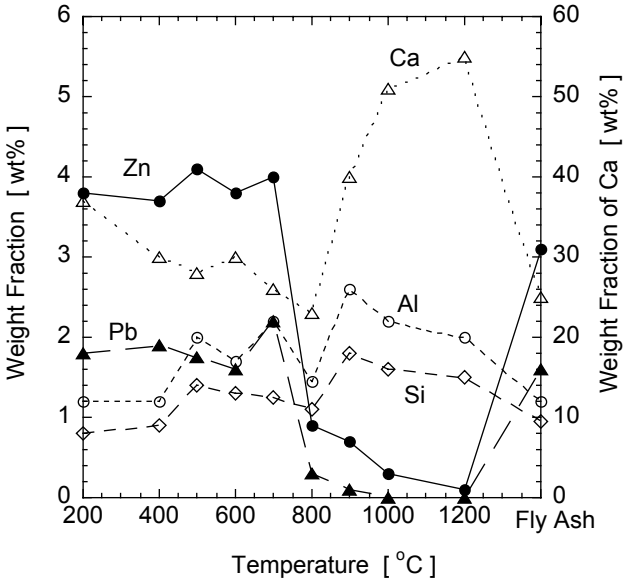

Fig. 6 Recovered materials with changing of the temperature after induction Ar-H_2 plasma treatment.

8. CFC and Halon Destruction

The destruction of ozone-depleting substances (ODS) such as chlorofluorocarbons (CFCs) and halons was developed by using steam thermal plasmas. The use of steam as oxidizing gas has the advantage for the destruction of CFCs and halons. Steam plasmas are successfully utilized to decompose ODS. In Japan, there are two commercial facilities for ODS decomposition by induction thermal plasmas with 100%-steam. The total system for ODS decomposition is shown in Fig. 7. In the first facility, a 200 kW plant under reduced pressure is operated by the Clean Japan Center [13]. ODS fed into a 100%-steam plasma are completely decomposed and converted to CO_2 and hydrogen halides. The feeding rate for CFC-12 and halon 1301 is more than 50 kg/hr under the pressure at 26 kPa. The second facility in Japan, ODS has been decomposed by atmospheric pressure induction plasmas. The second system has important technology for waste treatment;

generation of 100%-steam plasma under atmospheric pressure at 70-90 kW with the steam feeding rate at 14-20 kg/hr. The treatment capacity for CFCs is 30-40 kg/hr.

The small commercial facilities for CFCs decomposition were developed by Mitsubishi Heavy Industries [14]. The CFCs are decomposed by a 100%-stream microwave plasma. In the plasma, The CFCs are injected into the plasma at the concentration of 23-33 vol% under atmospheric pressure. The treatment capacity is 2 kg/hr at the power of 1.8 kW for CFC-12, 1.4 kg/hr at 2.0 kW for HCFC22, 1.5 kg/hr at 2.0 kW for HFC134a. Besides, the destruction of ODS by DC plasmas have been already operated at several sites in Japan. An Ar plasma jet is generated with the injection of oxidizing gas such as steam and oxygen to suppress the formation of soot [15,16]

Treatment of exhaust gas after the decomposition of CFCs and halons is the major concern, because the exhaust gas contains toxic and corrosive gas such as fluorine, chlorine, bromine, fluorohydride, chlorohydride and bromohydryde. In the above-mentioned process, hydrogen halides are quenched and neutralized in a scrubber to convert into calcium halides. Recently, dry process to recover these corrosive gases was developed [17]. Solid alkaline carbonate and hydrate made from dolomite were used as the reactant to adsorb these gases. This dry process of hydrogen halides into calcium halides would be applied to ordinary exhaust gas treatment for combustion.

9. Medical Waste Treatment

Medical waste treatment system for volume reduction and detoxification was developed by several companies in Japan. Figure 8 shows the schematic diagram of the medical waste treatment system by non-transferred arc developed by Chubu Electric Power Co. Inc [18]. This system can treat medical wastes containing a large volume of polyvinyl chlorides, which may cause production of dioxins. This system heats waste without oxygen until the waste breaks down. Then thermal plasma (50 kW) is applied to remaining injection needles, bottles, and other unburned substances to melt and solidify them into stable slag. The volume reduction ratio is 1/250 for treatment capacity of 100 kg/day. The field test has been conducted at Nagoya Daini Red Cross Hospital for a year to check the operability, durability, economy, and other properties of the product.

Another field test of medical waste treatment was conducted at The University of Tokyo Hospital by Koike Sanso Kogyo Co. Ltd. Twin Torch system, which uses two electrodes of opposite polarity connected in series to form a single circuit, was adopted in this system.

10. Conclusions

Thermal plasmas have been simply used as high temperature source. If thermal plasmas are utilized effectively as chemically reactive gas, thermal plasmas would provide more capability for waste treatments. The advantages of thermal plasmas, such as high enthalpy to enhance reaction kinetics, high chemical reactivity, oxidation and reduction atmospheres in accordance with required chemical reactions, and rapid quenching rate, should be utilized effectively for waste treatment. The researches about the reaction mechanism in the plasmas as well as sophisticated numerical analysis of reactive plasmas are important for the development of attractive waste treatment.

References

[1] M. Murata, *Abs. 16th Symp. Plasma Sci. Mater.*, p.65 (2001).
[2] Y. Akagawa, *J. Plasma Fusion Res.*, **73** (9), p.946 (1997).
[3] T. Amakawa and S. Yasui, *Nuclear Technology*, **141** (2), p.167 (2003).
[4] G. Katagiri, *57th Meeting Record of JSPS 153rd Committee on Plasma Material Science*, p.6 (2002).
[5] A. Nezu, T. Morishima and T. Watanabe, *Thin Solid Films,* to be published.
[6] K. Nagata, *et al.*, *Hitachi Metals Technical Review*, **17**, p.99 (2001).
[7] T. Watanabe, H. Itoh and Y. Ishii, *Thin Solid Films,* **390** (1-2), p.44 (2001).
[8] A. Takeuchi and T. Watanabe, *J. Japan Inst. Metals*, **63** (1), p.28 (1999).
[9] A. Takeuchi, *et al.*, *Thin Solid Films*, **407** (1-2), p.179 (2002).
[10] H. Windarto, *et al.*, *J. Nuclear Sci. Tech.*, **37** (10), p.913 (2000)
[11] M. Sakano, T. Watanabe and M. Tanaka, *J. Chem. Eng. Japan*, **32**, p.619 (1999).
[12] M. Sakano, M. Tanaka and T. Watanabe, *Thin Solid Films*, **386** (2), p.189 (2001).
[13] J. Takeuchi, *J. Plasma Fusion Res.*, **73** (9), p.941 (1997).
[14] M, Bessho, *et al.*, *Mitsubishi Heavy Industries Technical Review*, **37** (2), p.90 (2000).

[15] H. Sekiguchi, T. Honda and A. Kanzawa, *Plasma Chem. Plasma Processing*, **13** (3), p.463 (1993).
[16] A. B. Murphy, *et al*., *Plasma Chem. Plasma Processing*, **22** (3), p.371 (2002).
[17] A. Takeuchi, S. Kato, T. Watanabe and Y. Akatsuka, *J. Chem. Eng. Japan*, **35** (3), p.234 (2002).
[18] K. Tanaka, *et al*., *J. Japan Medical Waste Research Association*, **13** (1,2) p.41 (2000).
[19] K. Tanaka, *57th Meeting Record of JSPS 153rd Committee on Plasma Material Science*, p.21 (2002).

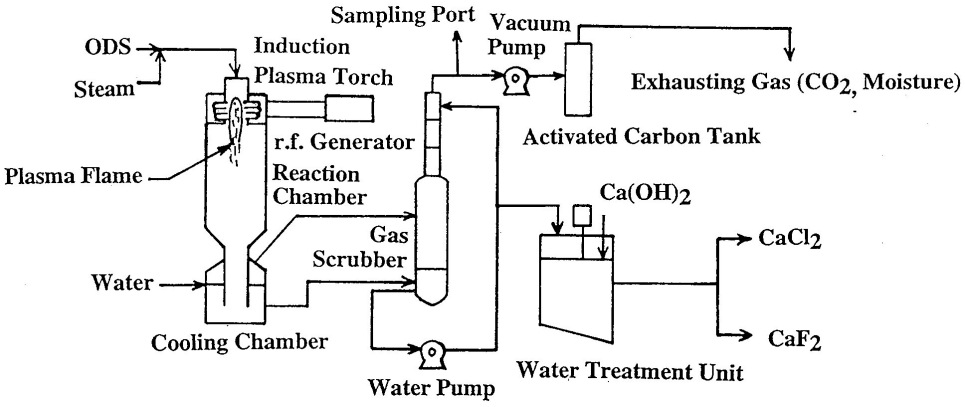

Fig. 7 The total system for ODS decomposition by induction steam plasma [13].

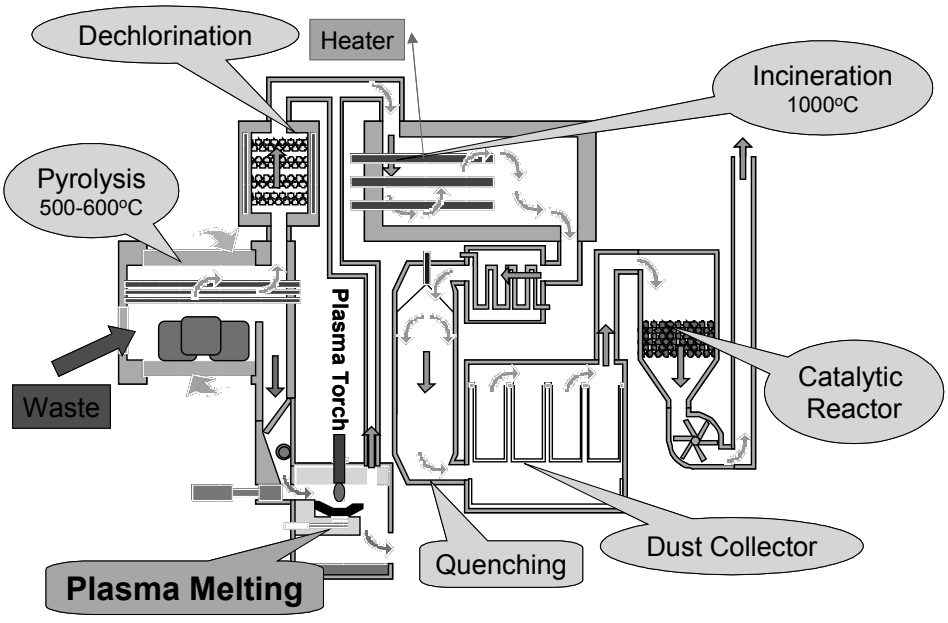

Fig. 8 Medical waste treatment system for volume reduction and detoxification [19].

DNA adsorption on NH_2-functionalized plasma polymer films

R. Förch[1], Z. Zhang[1], Q. Chen[1], W. Knoll[1], Rob Holcomb[2], Daniel Roitman[2]
Max Planck Institut für Polymerforschung, Ackermannweg 10, 55128 Mainz
Agilent Technologies, Palo Alto, California, USA

Abstract

Surface Plasmon Resonance techniques were used to study the properties of NH_2-functionalized plasma polymer coatings and their applicability for oligonucleotide/ DNA binding as a function of molecular architectures and amine group density. Low duty cycle films with a relatively high $–NH_2$ group density, low contact angle and low degree of cross-linking showed optimal properties for DNA probe attachment.

1.Introduction

The controlled attachment of biological molecules on plasma polymerized thin organic films has received increased attention over the past years. In the past, we have described the use of impedance spectroscopy (1) and optical methods such as Surface Plasmon Resonance spectroscopy (SPR) (2) and waveguide mode spectroscopy (WaMS) (3) to study the properties of plasma films in solution. These electrochemical and optical measurements of plasma films in solution have shown that plasma polymer films deposited at low DC swell considerably and exhibit hydrogel-like character when submersed in aqueous solution. This property decreased with increasing DC and was not observed for high power plasma deposits. If the plasma polymer contains ionizable groups such as amines or anhydrides the films show polyeletrolyte behaviour in aq. solution (1, 4) and the reactivity of the functional groups can be influenced by the pH of the solution used.(5, 6) These unique properties of functional plasma polymer films makes them particuarly attractive for use as supports for biological material.

The present work describes the fabrication, characterization and optimization of NH_2-derivatized polymer coatings prepared by pulsed plasma polymerization for applications as adhesion layers in DNA immobilization. In situ Surface Plasmon Resonance (SPR) (2, 7) measurements were used to study the behaviour of the pulsed plasma polymerized allylamine films in solution and to correlate DNA adsorption to the chemical nature of the plasma films as observed by FTIR and contact angle goniometry.

2.Experimental

The substrates used throughout the work were LaSFN9 optical glass slides coated with approximately 50 nm gold. A monolayer of octadecanethiol was allowed to self assemble on the gold surface and used as an adhesion layer between the plasma polymer and the gold surface. The plasma polymers were prepared in a cylindrical (300mm long, ∅ 100mm) 13.56 MHz rf plasma reactor under pulsed plasma conditions. The samples were placed half way between the electrodes, which consisted of two concentric rings wrapped around the outside of the chamber and separated by 12 cm.(3)

The plasma polymers were prepared either using a high duty cycle (DC= t_{on}/ t_{on}+ t_{off}) of 10/50 using a P_{peak} of 100 W or a low DC of 10/200 at a P_{peak} of 50 W. The equivalent power (P_{eq}=P_{peak} x DC)

during the pulsed experiments were thus 20 W and 2.5 W respectively. The process pressures used were 0.06 mbar and 0.1 respectively. Deposition times ranged between 30 seconds and 15 minutes.

The adsorption of single stranded DNA (25 mer) was monitored using a SPR spectrometer equipped with a wet cell made of teflon and sealed with a viton O-ring. Measurements were made using a continuous flow of buffer or buffer/DNA mixtures over the polymer surface. The DNA solutions were made up using phosphate buffer solutions consisting of (A) 0.2 mol/L NaH_2PO_4 (27g in 1L H_2O) and (B) 0.2 mol/L Na_2HPO_4 (53.65 g $Na_2HPO_4 \cdot 7H_2O$, or 71.7g $Na_2HPO_4 \cdot 12H_2O$ in 1L H_2O. Depending on the pH required these were mixed as follows: (i) dilute (A) to give 0.1 mol/L buffer at pH 4.5, (ii) 93.5 ml of (A) and 6.5 ml (B) plus 100ml H_2O give 200ml of 0.1 mol/L buffer of pH 5.7, (iii) 39.0 ml of (A) and 61.0 ml (B) plus 100ml H_2O give 200ml of 0.1 mol/L buffer of pH7, (iv) dilute (B) to give 0.1 mol/L buffer at pH 9.

For comparative experiments, poly-L-lysine (500 WG, Dg16, MW 3400) was self assembled onto the gold coated glass substrates from a solution of 5mg/L in PBS. This typically lead to a PL- film thickness of approximately 2 nm.

3.Results and Discussion

The chemical structure of plasma polymerized allylamine in air and in solution has previously been discussed in the literature.(3, 5) With decreasing duty cycle the deposited films show increased retention of the amine functionality within the film, as can be seen in Table 1 for two different preparation conditions.

Table 1 FTIR and contact angle data for different pulsed plasma polymerized allylamine films

Duty cycle	**Pressure / mbar**	**P_{peak} / W**	**P_{eq} / W**	**Rel. area from 3100-3500 cm^{-1} (NH_2 – band) ± 1%**	**θ_A / ° ± 3°**
10/50	0.06	100	20	16%	60°
10/200	0.13	50	2.5	26%	33°

After equilibration of the polymer films in PBS buffer, the kinetics of DNA probe attachment were studied using a probe concentration of 100 nMol. After adsorption appeared to be complete the surfaces were rinsed with four cell volumes of buffer to remove any unspecifically bonded DNA from the surface. The kinetic scans of DNA adsorption as measured by the SPR techniques, Figure 1, show that adsorption was more efficient for the low DC films with the high -NH2-group density, than for the high DC (high P_{eq}) films which characteristically have a lower –NH2 functional group density. The data was compared to the immobilization of DNA on poly-L-lysine keeping all other conditions constant. As is evident from the data in Figure 1, the high DC plasma polymer appears to exhibits similar binding properties as the polylysine film, both showing an optical thickness increase of approximately 3 nm. The thickness of the DNA layer measured for the low DC film, however, showed a 6-fold improvement and a typical DNA thickness of approximately 17 nm.

Figure 1 SPR kinetic measurements of DNA binding on low DC (d ≈ 18 nm), and a high DC (d ≈ 10 nm) plasma polymerized allylamine compared to that on a polylysine film (d ≈ 2 nm), C_{DNA} 100nMol, PBS buffer at pH 7.4

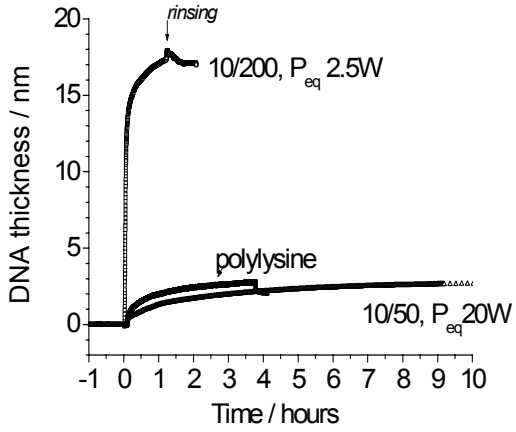

DNA adsorption was found to be depend not only on the DC, but also on the polymer film thickness, Figure 2. With increasing polymer thickness, the low DC films indicated a much higher affinity for DNA probe attachment. For films with d > 20 nm the measured DNA thickness was approximately 4-5 times greater for the low DC, low cross linked films than for the highly cross linked films, high DC films.

Figure 2 Dependence of the DNA optical thickness on the plasma polymer thickness for DNA adsorption on high and low duty cycle plasma films, C_{DNA} 100nMol, pH 7.4

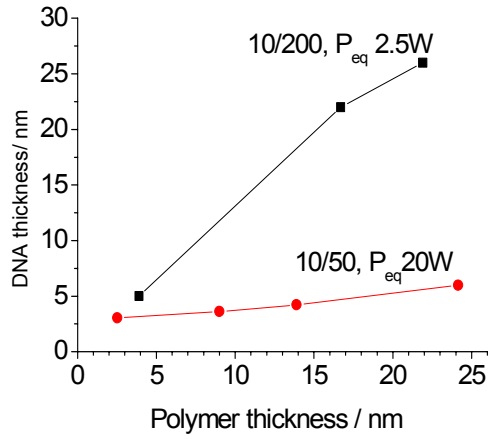

The increase in the probe sensitivity is believed to be related to the cross link density and thus the swelling characteristics of the low P_{eq} films. Since the low P_{eq} polymers are less cross linked and the chains have a greater freedom of mobility, the network can expand in solution making the functional groups within the bulk of the swollen polymer network more accessible to the DNA molecules possibly allowing the DNA molecules to penetrate into the bulk of the film.

In solutions of low pH the amine functional groups exist predominantly in the protonated form ($-NH_3^+$) following the reversible reaction:

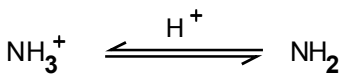

Figure 3 Effect of pH on the DNA adsorption on plasma polymerized allylamine films using P_{eq} of 20 W and 5W.

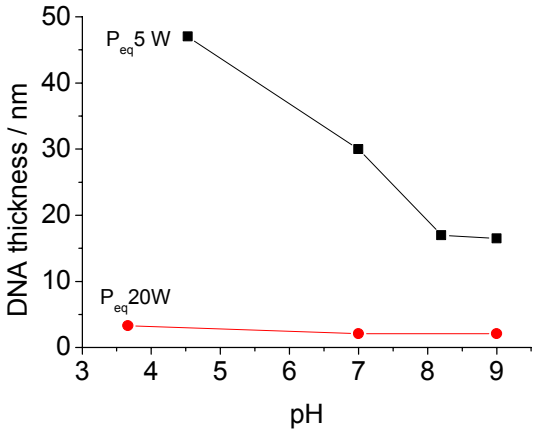

An increase in positive charge on the plasma polymer will lead to improved binding of the negatively charged DNA to plasma polymer film. Keeping all other conditions constant and only changing the buffer pH, the thickness of DNA probe measured on low DC plasma polymers was found to increased significantly, Figure 3. In contrast, the pH effect was significantly less on the highly cross-linked, high DC films even though the general trend was the same. This appears to be in agreement with the relative, estimated functional group densities and the accessibility of the groups within the two types of films as discussed above.

4.Summary

Plasma polymerized, amine functionalized films appear to exhibit properties, which render them suitable for DNA adsorption. DNA probe immobilization was found to be optimal for low duty cycle films with a relatively high density of $-NH_2$ groups, low contact angles and a low cross link density. When in solution, polyelectrolytic and hydrogel characteristics of low DC films seem to enhance DNA probe adsorption. Probe thicknesses observed on these films were up to 6 times greater than on the highly cross linked films and on polylysine.

References

1. Jenkins, A. T. A., Hu, J., Wang, Y. Z., Schiller, S., Foerch, R., Knoll, W. *Langmuir* **16**, 6381 (2000)
2. Knoll, W. *Annual Review of Physical Chemistry*. 49: 569 (1998)
3. van Os, M. T., Menges, B., Foerch, R., Vancso, G. J., Knoll, W. *Chemistry of Materials*. **11**, 3252 (1999)
4. Z. Zhang, B. M., R.B. Timmons, W. Knoll, R. Förch, *Langmuir*. in press, (2003)
5. Schonherr, H., van Os, M. T., Forch, R., Timmons, R. B., Knoll, W., Vancso, G. J. *Chemistry of Materials*. **12**, 3689 (2000)
6. H. Schönherr, M. T. v. O., Z. Hruska, J. Kurdi, R. Förch, F. Arefi-Khonsari, W. Knoll, G.J. Vansco *Chem. Comm.* 1303 (2000)
7. Aust E.F., I. S., Sawodny M., Knoll W. 1994. *Trends in Polymer Science*. **2**, 313 (1994)

PROTECTIVE PROPERTIES OF ORGANIC COATINGS ON PLASMA TREATED COLD ROLLED ALUMINIUM

Tullio Monetta and Francesco Bellucci

Department of Materials and Production Engineering, Piazzale Tecchio 80142 Napoli Italy

Abstract

The adhesion and protective properties of organic coatings on cold rolled aluminium alloy, treated by NH_3 radio frequency plasmas, were tested using the Electrochemical Impedance Spectroscopy (EIS) technique. Epoxyphenolic, and epoxypolyester solvent based, and water based epoxyphenolic resins deposited on 8011 aluminium alloy were investigated in presence and in absence of plasma treatments. Plasma treatments were carried out in a parallel plate reactor using pure NH_3 as a gas feed and three treatment time (i.e. 3-30-300 s) were used. Results obtained suggest that plasma treatment produce significant modification onto the metallic surface enhancing or decreasing adhesion.

1. Introduction

Aluminium alloys exhibit a large number of interesting properties such as (i) high thermal conductivity, (ii) light weight, (iii) mechanical strength (iv) moderate production costs and so on. Such properties make Al alloys suitable for its use in a large number of applications. Indeed, aluminium alloy foils are largely employed in both the automotive and home commodity industry (refrigerators and air conditioners) [1]. Currently, in order to withstand the large plastic deformation occurring during the lamination process high ductility alloys (containing high amount of Fe, Cu, Mn, Mg and Si), 8000 series, are employed [1, 2]. The relatively high concentration of alloying elements, however, reduces the corrosion resistance of these alloys. To improve corrosion resistance of this series an on-line chemical conversion process and a subsequent coil coating treatment is necessary [3,4].

Conventional treatments used for aluminium alloys as those mentioned above, are very polluting requiring large area for the storage of liquids used in the conversion treatment. In this work an attempt is made to use cold plasma treatments to modify the surface chemical structure of aluminium alloys in order to enhance adhesion in the coil coating treatment. In this investigation, plasma treatments were carried out on samples that were neither cleaned nor washed (as received samples).

Cold plasma treatments are widely used in a large number of industrial applications and an enormous number of papers appeared in the scientific and technological literature dealing with such applications. In the field of corrosion protection plasma treatment was addressed mainly to investigate the effect of treatment on cold rolled steel [5-9]. Specific issues investigated were (i) the cleaning of the metallic surface, and (ii) the application of a protective layer via plasma polymerisation [10].

2. Materials and methods

The plasma reactor used in this work to treat the metallic surface, was an internal parallel plate electrode type in which the plasma was generated at 13.56 MHz. During the treatments the pressure chamber was held at 200 mTorr, the flow rate was 20 sccm using pure NH_3 and power was set at 20 W. Treatment time were 3, 30 and 300 s, respectively. Cold rolled aluminium (8011 alloy) was used as the metallic substrate in the form of square panels of 100 cm^2.

The following three types of commercial resin (kindly furnished by Eco-Polifix) were used in this work: (i) a waterborne epoxyphenolic system, (ii) and epoxyphenolic solvent-based coating, and (iii) an epoxypolyester solvent-based system (see Tab. 1). Coated aluminium samples were prepared, immediately

after the plasma treatment, by adopting the following procedure. Samples were first dipped in the liquid resin, dried in air and cured in an oven at the cured temperature as determined via Differential Scanning Calorimetry (DSC) analysis. (see Table 2 for details). The average thickness of the coating was 10 μm. Three samples were prepared for each system, and experimental data reported in this work are the "best performance" observed for each system. It is important to stress that the resins used in this work were commercial grade and their formulation is proprietary.

Tab. 1 Acronyms used to individuate resins used in this work.

	Epoxyphenolic	Epoxypolyester
Organic solvent based	SEPH	SEPO
Water based	WEPH	

Tab. 2 Time and temperature used in samples preparation.

	Contact time, min	Drying time , min	Cure time, min	Temperature of cure, °C
WEPH	15	6	15	240
SEPO	30	3	10	220
SEPH	30	5	10	220

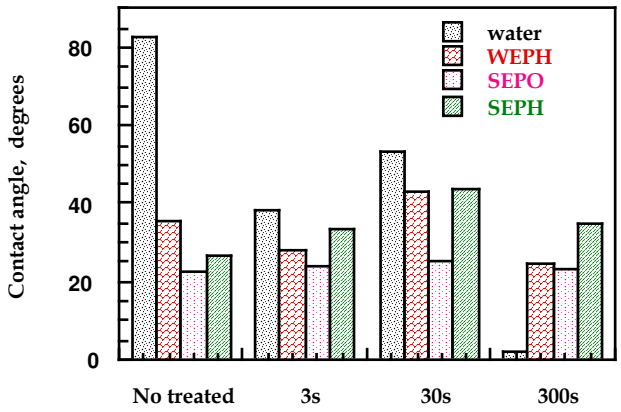

Fig. 1 Contact angle values obtained using water, WEPH, SEPO, SEPH resins on treated and untreated aluminium substrate.

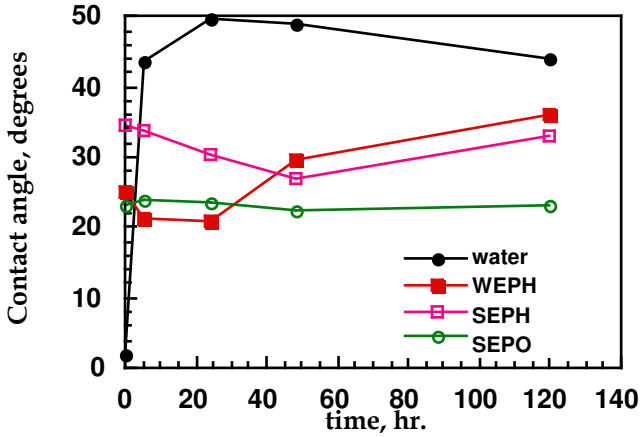

Fig. 2 Ageing of plasma treatments evaluated using contact angle.

The experimental apparatus for the electrochemical investigation is described in ref. [13] Contact angle measurements were performed using Imass Inc. contact angle analyser. The data reported is an average of five measurements on five different samples. DSC measurements were performed using a Mettler Toledo DSC12E calorimeter.

3. Results and discussion

One of the main problems in the characterisation of organic coatings is related to the structural properties of the cured materials. DSC measurements and permittivity data were used in this work for evaluating the initial properties of the coating and their reproducibility for all the samples investigated.

The effect of plasma treatment on the aluminium surface was evaluated by measuring the contact angle for both water and resins used in this study. Measurements were performed on both treated and untreated substrates. As shown in Fig. 1, NH_3 plasma significantly affect the water contact angle; in fact it decreases from 83° for

the untreated sample, to 3° for the sample treated for 300 s. Opposite behaviour was exhibited by the SEPH sample. The value for the untreated sample was 26°, while a maximum value of 42° was observed after 30 s of treatment. On the other hand, this treatment does not modify the contact angle (a constant value of (22-24°) for both the treated and untreated sample) when the SEPO resin is employed. The WEPH contact angle reveals an initial value of 35° reaching a maximum value of 44° for the sample treated for 30 s. The ageing of the plasma treatment was addressed by measuring the contact angle as a function of time of exposure to laboratory atmosphere. Results are reported in Fig. 2 for sample after 300 s of treatment. As can be seen from this figure, a sharp increase of water contact angle is observed after few hours of exposure to the test atmosphere, and a maximum value is reached after about 20 hours. The subsequent decrease observed at late exposure is of minor significance. In this case, however, the maximum value reached (50°) is far from that of the untreated sample (83°) as shown in Fig. 1. No ageing was observed for the SEPO resin. The SEPH contact angle returns to the value of the untreated material (26°) after 50 hours of exposure, before a subsequent increase observed at late exposure. Finally, the contact angle for the WEPH resin comes to the value of the untreated sample after 120 hours of exposure.

In this work, an attempt is made to estimate the ratio of delaminated area between the treated and untreated coated samples. If C_t and C_{coat}^{t} are the total (interface and coating) and coating capacitance at time t, respectively, one has:

$$C_{t=t'} = C_{coat}^{t=t'}(1-x) + xC_{dl}^{t=t'} \qquad (1)$$

Where $x = A_{dl}^{t}/A_t$; $C_{t=0} = C_{coat}^{t=0}$; C_{dl}^{t} is the double layer capacitance, while A_t and A_{dl}^{t} are the total and delaminated area, respectively.

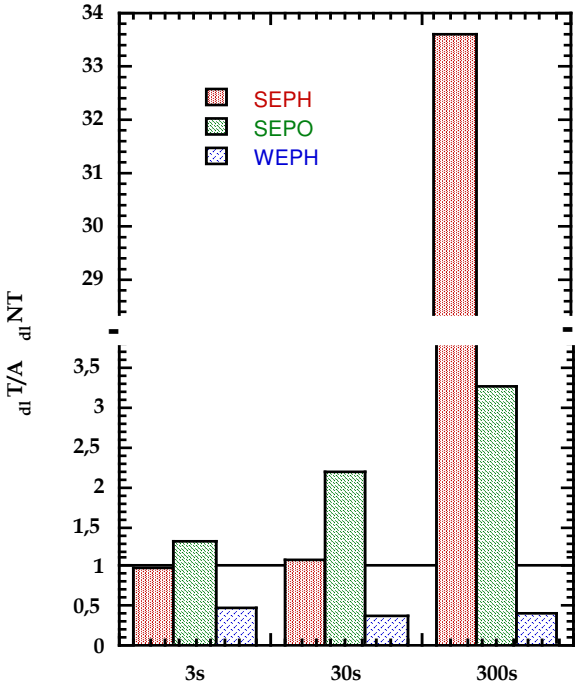

Fig. 3 Ratio between the delaminated area of the treated and the untreated samples as a function of treatment time.

$$\%\Delta C = \frac{C_{t=t'} - C_{t=0}}{C_{t=0}} \times 100$$

$$\%\Delta C = \frac{C_{coat}^{t=t'}(1-x) + xC_{dl}^{t=t'} - C_{coat}^{t=0}}{C_{coat}^{t=0}} \times 100$$

If the delaminated area is small (1-x) ≈ 1 and the coating and the double layer capacitance variation with ageing can be neglected, one has:

$$\%\Delta C = \frac{xC_{dl}^{t}}{C_{coat}^{t=0}} \times 100 = \frac{C_{dl}^{t}}{C_{coat}^{t=0}} \frac{A_{dl}^{t}}{A_t} \times 100$$

If A_{dl}^{t} NT and A_{dl}^{t} T are the delaminated area of he untreated and treated coated sample, respectively; and %ΔCT and %ΔCNT are the values assumed by the previous equation at time t, then:

$$\frac{\%\Delta CT}{\%\Delta CNT} = \frac{A_{dl}^{t}T}{A_{dl}^{t}NT} \qquad (2)$$

Equation 2 indicates that if the ratio %ΔCT/%ΔCNT is less than 1, the delaminated area of the treated samples is smaller than that of the untreated one.

Fig. 3 shows the ratio $A_{dl}T/A_{dl}NT$ evaluated for samples investigated in this paper at the same ageing time. The frequency at which C was evaluated is in the range 10-60 Hz depending on the type of resin employed. As can be seen from Fig. 3, SEPO resin exhibits a ratio $A_{dl}T/A_{dl}NT$ is >1 for all treatments time.

Thus, the delaminated area is always larger than for the untreated sample. Plasma treatment does not improve adhesion of this resin to the aluminium metallic substrate. For the system SEPH, with the exception of the sample of the 300s of treatment in which a complete cracking of the coating occurred, the delaminated area for both treated and untreated samples is approximately the same. It is interesting to observe that for the water borne coating the above ratio is less than 1 indicating an effectiveness of the plasma treatment.

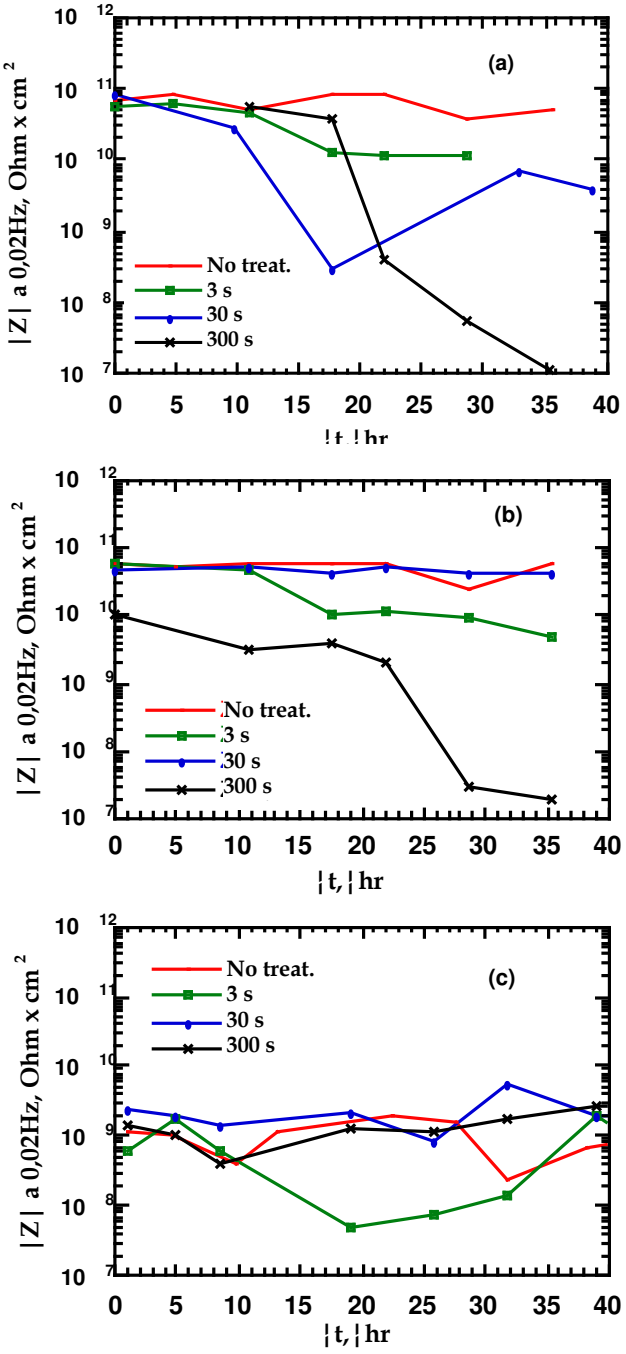

Fig. 4 Modulus of impedance, |Z|, as a function of time evaluated at 0.02 Hz for the system SEPO (a), SEPH (b), WEPH (c).

The value of modulus of impedance, |Z|, calculated at 0.02 Hz, is reported in Fig. 4, as a function of time of exposure to the test solution (aerated synthetic seawater). As can be seen from this figure, the untreated SEPO system exhibits better performance when compared to the treated one. It is worth to mention, however, that the sharp decrease of |Z| after about 16 days of exposure, for the 300s treated sample, is in good agreement with the time required t o Cl^- ions to reach the metallic substrate by diffusion [13]. Similar conclusions can be drawn by analysing the behaviour of the SEPH system as represented in Fig. 4b. Finally, no major differences were observed between the treated and untreated WEPH samples (see Fig. 4c).

It is often reported in the literature that contact angle values furnish an indication of the extent of adhesion. Experimental data reported in this investigation do not support such evidence. In fact, while contact angle measurements suggest that the SEPO system is not affected by the NH_3 plasma treatments (see Fig. 1), impedance data (see Fig. 4) show that an effect is observed. In addition, the worst performance for the SEPH system should be expected after 30 s of treatment, while data in Fig. 4 show an excellent behaviour for such system. Finally, data for WEPH system furthers support the view that low values of contact angle are not predictive of good adhesion. At the same time, however, these data seem to be promising as far as the use of friendly coatings is concerned. It is, thus, possible to conclude that: (i) "total" contact angle value does not allow us to forecast the adhesion strength, and (ii) a plasma treatment may improve adhesion between coating and substrate when a water based resin is used. Then, for some applications, it could be of interest to choose a low cost and less pollutant resin together with a plasma treatment to increasing paint/substrate adhesion and thus performance of the system.

4. Conclusions

In this paper the effect of NH_3 plasma treatment on "as received" aluminium alloy sample has been evaluated. Results obtained in this investigation further support the view that contact angle does not correlate to adhesion strength.

Cold plasma could be an effective *clean* technology to improve adhesion for painted aluminium systems for water based resins. However further experimental data must be collected to optimise the process.

References

[1]. M. Leoni, R. Zocchi, C. Sinagra, Alluminio Magazine, **7/8**, 6, (1990).

[2] L. De Rosa, T. Monetta, F. Bellucci, R. Zocchi, A. Atienza, C.Sinagra "Atti del IV Congresso nazionale AIMAT", Ed. by U. Sanna, **309**. PTM, Cagliari (1998).

[3]. G.S. Chen, M. Gao, R.P. Wei, Corrosion , **52**, 8 (1996).

[4] R. Zocchi, C. Sinagra, A. Atienza, A. Vignati, Alluminio Magazine, **3/4**, 20, (1991).

[5] H. K. Yasuda, Plasma Processing of Polymers, Ed. by R. d'Agostino, P. Favia, F. Fracassi, **298**, (1997), Kluwer Academic Pub.

[6] W. J. Van Ooij, K. D. Conners, Organic Coatings for Corrosion Control, Ed. G. P. Bierwagen, **323**, (1998), ACS.

[7] W. J. Van Ooij, N. Tang, S.E. Hornsstrom, J. Karlsson, Organic Coatings for Corrosion Control, Ed. G. P. Bierwagen, **335**, (1998), ACS.

[8] K.D. Conners, W.J. Van Ooij, S.J. Clarson, A. Sabata, J. Of Applied Polymer Science, 54.(1994) 167-184.

[9] T. F. Wang, T.J. Lin, D.J. Yang, J.A. Antonelli, H.K. Yasuda, Progress in organic coatings, **291**, 28, (1996).

[10] W.J. Van Ooij, A. Sabata,, Ih-Houng Loh, in Modifications of Passive Films, (1994) 253-259.

[11] Y. Matsuda, H. Yasuda, Thin solid films, 118(1984) 211-224.

[12] H. P. Schreiber, M.R. Wertheimer, A.M. Wrobel, Thin solid films , 72 (1980) 487-493.

[13] T. Monetta, F. Bellucci, L. Nicodemo, L. Nicolais, Progress in Organic Coatings, 21 (1993) 353-369.

RF Plasma Surface Modification of Potatoe Starch

Mariusz Kaczmarek[1], Maciej Gazicki-Lipman[1], Hieronim Szymanowski[1], Leszek Klimek[1]
Dariusz Bieliński[2]

[1]*Institute for Materials Science and Engineering, Technical University of Łódź, Łódź, POLAND*
[2]*Institute of Polymers, Technical University of Łódź, Łódź, POLAND*

Abstract

Potatoe starch was hydrophobized in a rotating reactor, using a capacitively coupled RF glow discharge. Two working media were used, one was tetramethylsilane(TMS)/argon mixture, and the other was methane. Water capillary elevation measurements showed that the best results were obtained for TMS/Ar system at relatively mild RF power of 20 W. FTIR studies revealed an absence of Si bonding. Instead, an increasing (CH)/(CH_2) ratio strongly suggests a crosslinking of starch surface.

1. Introduction

One possible approach to the manufacture of biodegradable polymer materials concerns a use of starch as a biodegradable filler in composites with typical thermoplastic polymers, such as polyethylene or polypropylene. In these materials, degradation of the filler should be subsequently followed by a disintegration of the entire piece into environmentally harmless polyolefine powder. However, the main problem with a manufacture of composite materials, comprising a polyolefine as a matrix and starch as a filler, is a mixing difficulty. A polyolefine, such as polyethylene, with a very low polar component of its surface energy [1], does not sufficiently wet the surface of starch grains, characterized by a relatively high polar component. As a result, agglomerates of starch in polymer are easily formed in the extrusion process. An obvious solution to this problem is a minimization of the surface energy of the interface polymer/starch [2]. One way to realize this process is through such a modification of the surface energy of starch, which will significantly lower the polar component of this energy and, consequently, improve the conditions of matrix-filler interactions. Plasma processes are well known to be effective in hydrophobization of polymer surfaces [3-5]. The principal difficulty with a modification of materials remaining in a fine particulate form, such as starch, is comprised of the fact that the surface of each particular grain has to be modified with similar efficiency. One technological solution to this problem consists in a use of a fluidized bed reactor [6]. An approach of this work comprises an application of a rotating RF plasma reactor for that purpose, and particularly for the purpose of hydrophobizing potatoe starch.

2. Experimental

The rotating RF plasma reactor is schematically represented in **Figure 1** below. The main part of this

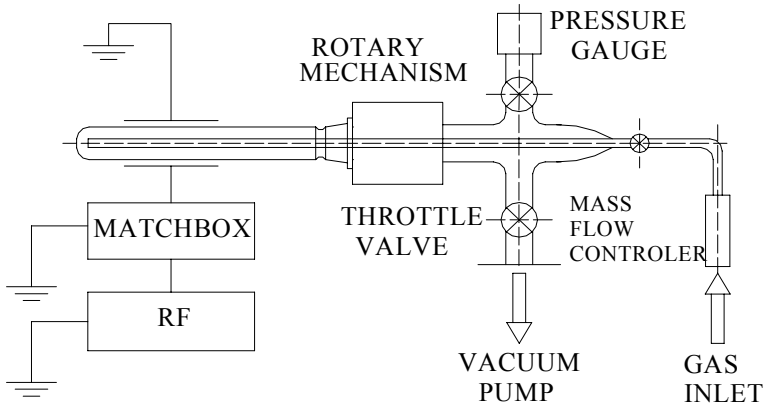

Figure 1. Schematic representation of the rotating RF plasma reactor

reactor is a 450 mm long tubular element, that may be rotated with frequency ranging from 0 RPM to 60 RPM. The reactor is equipped with a set of external electrodes, to which the RF power is supplied from the

Plasma Products RF5S power generator through a self-designed matching circuit. MKS 1179 AX mass flow controllers are used to control the flow rates of gaseous media. The flow rate of a vapour of liquid medium (TMS) is controlled by both the temperature and the pressure of a liquid container, and the *rate-of-rise* technique is used to measure its magnitude. A starch modification cycle starts with setting the flows of working media, then the rotation of the tubular element with a selected RPM value is introduced, and finally radio frequency plasma is generated in the reactor. Powdered starch contained in this reactor is stirred very efficiently, thus enabling an effective plasma deposition or modification of the surface of each grain.

As working media, two different systems were used: a) saturated hydrocarbon such as methane and b) TMS/Ar mixture. Methane plasma modification was performed at two different magnitudes of flow rate, namely at 2 sccm and 6 sccm, while TMS/Ar plasma modification was carried out at the total flow rate of 7 sccm, with the TMS to Ar ratio amounting to 1:6. In each case the RF power was used as an operational parameter in the process optimization. Process pressure was maintained at the 400-420 mTorr level.

An assessment of the modification process efficiency is comprised of measurements of capillary rise of water in glass tubes filled with starch. Since the principal aim of the modification process has been a surface hydrophobization of starch, i.e. a substantial decrease of its water contact angle (a direct measurement of which is impossible) the above method, although very simple, is thought to be a sufficiently good assessment tool. In practice, the measurement was realized in the following way. Into a glass tube of an ID of 1.8 mm, starch was compressed in such a way that its weighted amount of 0.2 g always corresponded to 55 mm of height. The tube was then immersed in a beaker filled with water and water capillary elevation was measured, using a cathetometer, as a function of time. A result that did not exhibit any changes within 100 minutes was taken as a maximum capillary elevation of water.

FTIR studies of selected starch samples (both native and modified) were performed with the help of a BioRad, model 175C, FTIR spectrometer, equipped with a Harric Sci. split-pea attachment and a silicon crystal. Such an experimental configuration allows one to record IR absorption spectra from the surface layer of starch grains, down to the depth of approximately 200 - 1800 nm, depending on the radiation wavelength. Each spectrum was constructed by collecting 64 consecutive scans, with a resolution of a single scan amounting to 4 cm^{-1}. Finally, SEM imaging of starch particles was carried out, using a Hitachi F 3000 N scanning electron microscope.

3. Results

Subjected to capillary water elevation measurements described above, a sample of native starch exhibit a maximum water elevation of 62 mm. **Figure 2** presents a set of water elevation results for starch modified with methane plasma, for the methane flow rate of 2 sccm. Since they all remain within the range of 16- 20 mm, the water capillary elevation results shown in this figure indicate much higher hydrophobicity than those obtained for an unmodified starch.

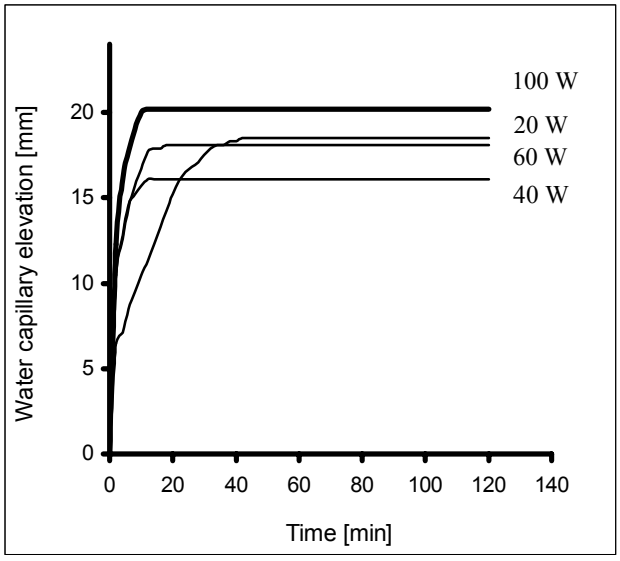

Figure 2. Results of water capillary elevation for starch modified with methane plasma at the flow rate of methane of 2 sccm and different values of RF power.

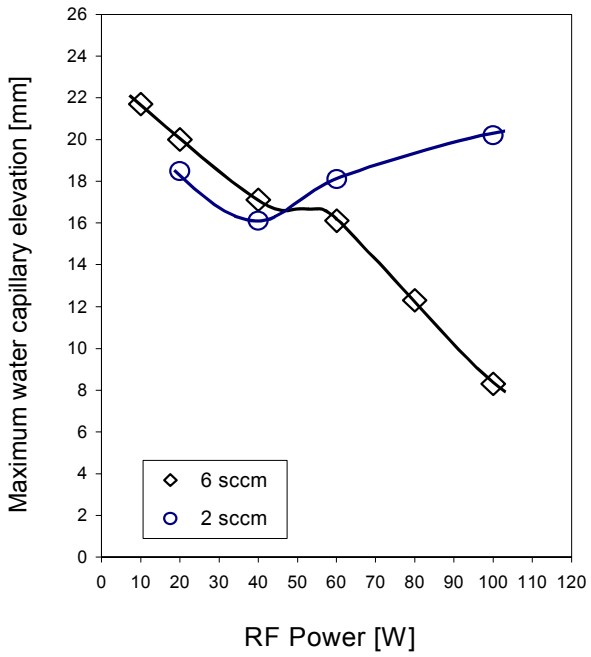

Figure 3. Maximum water capillary elevation for starch modified with methane plasma as a function of the RF power of modification

In **Figure 3**, the maximum values of water capillary elevation from **Figure 2** are plotted against the RF power. Data collected for the methane flow rate of 6 sccm are also presented in the same plot. As seen in the figure, the results obtained at the lower value of flow rate pass a minimum, while those obtained for the higher one exhibit a decreasing tendency within the entire range of power values used. The course of this line very likely constitutes a left wing of another minimum reaching dependence, which cannot be tracked along higher RF power values due to starch degradation. In other words, under these conditions the RF power of 100 Watt is the highest power level at which no visible signs of degradation take place.

The dependence of maximum water capillary elevation for starch modified using the TMS/Ar plasma on the RF power of modification is presented in **Figure 4**.

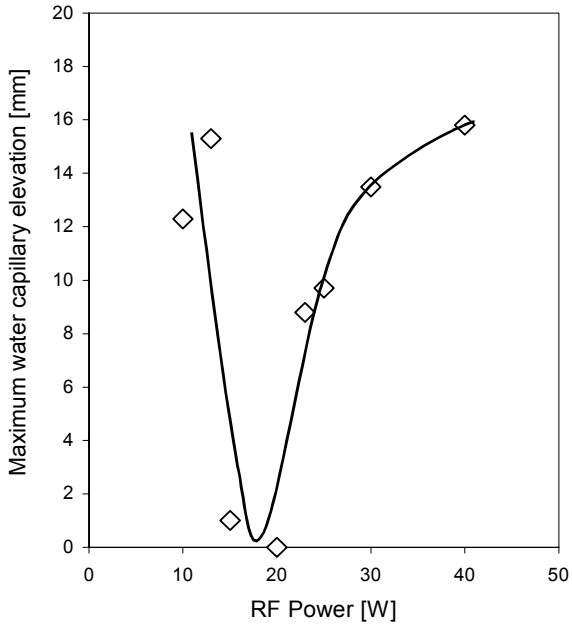

Figure 4. Maximum water capillary elevation for starch modified with TMS/Ar plasma as a function of the RF power of modification

In the above relationship, there is evident and sharp minimum at approximately 20 Watt of RF power, for which the practical value of water capillary elevation, under the measurements conditions, amounts to zero. It is the best result of this work and, indeed, the macroscopic tendency to agglomerate for TMS/Ar plasma modified starch is much lower than that observed for the native material. What this tendency looks like at the microscopic level, is presented in **Figure 5** in the form of SEM micrographs.

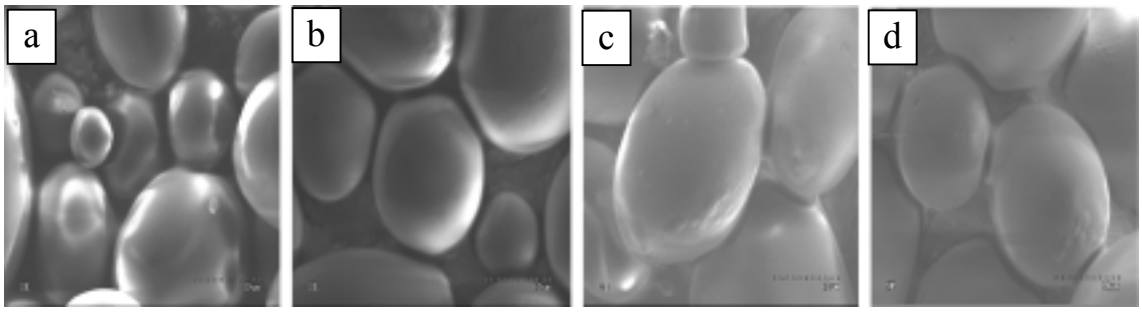

Figure 5. SEM micrographs of starch grains modified with TMS/Ar plasma at different RF power values: 10 Watt (a), 20 Watt (b), 25 Watt (c) and 30 Watt (d)

As seen in the above micrographs, it is only the starch sample modified with TMS/Ar plasma at RF power of 20 Watt (sample b), that exhibits a clear separation of its grains. It is the same sample that shows practically no water capillary elevation in the hydrophobicity measurements.

In order to look for structural changes responsible for the presented increase of starch hydrophobicity, IR absorption spectra have been recorded for selected samples. Principal structural features that constituted a subject of interest were: 1) potential changes in the carbonous network of starch (in both cases: methane and TMS/Ar plasma modification) and 2) grafting of any silicon containing surface functions, reflected in the presence of such bonds as Si-C, Si-O or Si-H bonds (in the case of TMS/Ar plasma modification).

First of all, it has to be stated that no silicon bonding was observed in TMS/Ar plasma modified starch. Fingerprint region of IR absorption (where Si-C stretching, Si-O stretching and Si-H bending vibrations should be observed) for these samples was identical with that of native starch. In addition, no traces of Si-H stretching band were observed in the vicinity of 2000 cm^{-1}.

The main changes take place in the C-H bond stretching IR absorption region, shown in **Figure 6**.

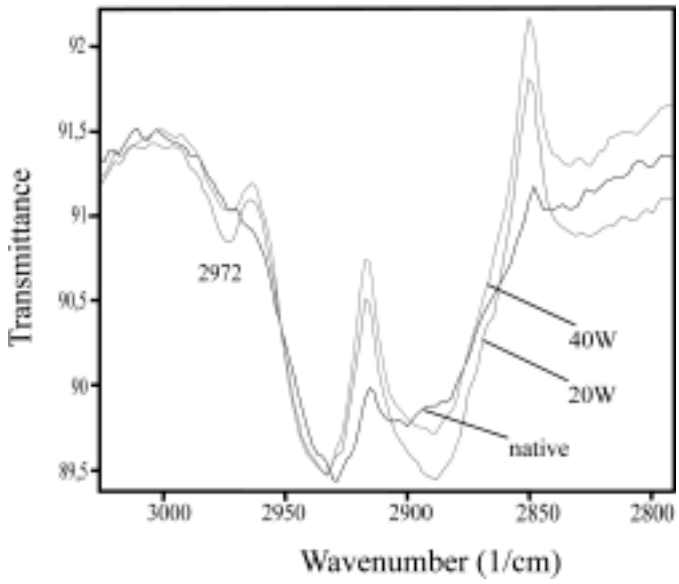

Figure 6. C-H bond stretching IR absorption region for native and TMS/Ar plasma modified starch

As seen in **Figure 6**, the main changes in C-H bond stretching region comprise a rise of the 2972 cm^{-1} band, corresponding to C-H asymmetric stretching vibrations in methyl groups, and an even stronger increase of the intensity of 2883 - 2906 cm^{-1} band, corresponding to C-H stretching vibrations in isolated carbon-hydrogen bonds. Both these features strongly suggest that it is the hydrocarbon part of a tetramethylsilane molecule that is responsible for the surface modification in this case. Indeed, similar to the changes observed for TMS/Ar plasma modification of starch, are those presented in **Figure 7**and recorded for starch samples modified with methane plasma.

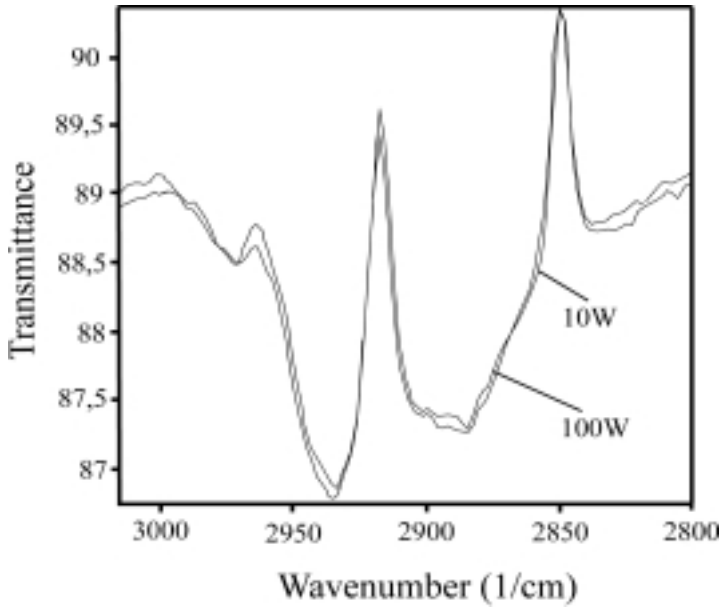

Figure 7. C-H bond stretching IR absorption region for starch modified with methane plasma.

A brief comparison of the presented spectra reveals extended similarities between the results of plasma modification of starch with both types of working media. These results are predominantly present in the structure of carbon bonding, reflected in the proportions between integrated absorption of stretching vibrations of C-H bonds in different environment. Other absorption ranges remain to a large extent unaltered and, in particular, no silicon containing bonding has been found in the IR spectra of TMS/Ar plasma modified samples. Since a molecule of tetramethylsilicon contains four methyl groups, splitting these groups off the silicon atom should have similar effect as breaking a C-H bond in methane. The fact that silicon carbon bond has a lower bond energy (301 kJ/mole) than hydrogen-carbon bond (416 kJ/mole) [7] explains why the respective magnitudes of RF power necessary to introduce required changes in the starch structure are substantially lower for TMS than for methane.

In **Figures 6** and **7**, the band at 2972 cm^{-1} is assigned to asymmetric stretching vibrations of C-H bond in methyl groups, the bands at 2940 cm^{-1} and at 2927 cm^{-1} to asymmetric stretching vibrations of the same bond in methylene groups, and those at 2906 cm^{-1} and at 2883 cm^{-1} to the stretching vibrations of this bond in methine systems. In a first approximation, symmetric vibrations of both methyl and methylene group originating C-H bonds have been disregarded. As mentioned above the particular changes taking place within the scope of C-H bonding as a result of plasma modification consist in an increasing number of both methyl groups and trifunctional methine moieties, as compared to the concentration of methylene groups. While grafting methyl groups should directly lead to an increased hydrophobicity of the surface, an increase of methine/methylene ratio suggests a process of surface cross-linking. Table 1 presents the values of ratio of integrated absorption of methyl group and methine group originating C-H bonds to that of integrated absorption of these bonds vibrations (asymm.) in methylene groups, for native starch as well as for starch samples modified with TMS/Ar and with methane plasmas.

Table 1. A ratio of integrated absorption of C-H bonds in methyl group and methine groups to that of integrated absorption of C-H bonds (asymmetric vibrations) in methylene groups, for native starch as well as for starch samples modified with TMS/Ar and with methane plasmas.

	CH_3/ CH_2	CH/ CH_2	Maximum water capillary elevation [mm]
Unmodified starch	0.121	0.87	62
Modified (CH_4 10 W)	0.082	1.15	22
Modified (CH_4 100 W)	0.313	1.31	7
Modified (TMS 40 W)	0.276	1.57	16
Modified (TMS 20 W)	0.293	1.87	0

In **Table 1**, results of surface hydrophobicity for respective samples, obtained with water capillary elevation measurements, are also presented. There is a sound correlation between the values of maximum water capillary elevation of starch, and the CH/CH_2 ratio in the samples. It appears that an increase of this ratio, most likely connected with an enhancement of surface cross-linking of starch, has an effect of lowering its water capillary elevation potential, i.e. of increasing its hydrophobicity.

4. Conclusions

Out of the experimental results the following conclusions may be drawn:

1. RF plasma modification of particulate materials may be effectively carried out in a rotating plasma reactor, presented in this work.
2. The described process is well suited for the purpose of hydrophobization of potatoe starch.
3. The best hydrophobizing effect has been achieved in the case of tetramethylsilicon/argon plasma modification of starch under relatively mild conditions of RF power (20 Watt).
4. An alteration of starch structure responsible for its hydrophobization appears to be a surface cross-linking combined with grafting with non-polar methyl groups.

Acknowledgement

This work has been entirely supported by the Polish Committee for Scientific Studies (Komitet Badań Naukowych), under the project code of 4 T08E 049 23.

References

[1] D. K. Owens, R. C. Wendt, J. Appl. Polym. Sci. **13,** 1741 (1969).
[2] A. W. Adamson, Physical Chemistry of Surfaces, Interscience Publishers Inc., New York 1960.
[3] C. Bamford, K. Al-Lamee, Polymer **37**, 4885 (1996).
[4] A. Nihlstrand, T.Hjertberg, K.Johanson, Polymer **38,** 3581 (1997).
[5] J. Gancarz, G. Poźniak, M. Bryjak, Europ. Polym. J. **35**, 1419 (1999).
[6] W.J. van Ooij, A. Chityala, in: Polymer Surface Modification; Relevance to Adhesion, vol. **2**, (K.L.Mittal, ed.), 234, VSP Utrecht, 2000.
[7] J. Bullot, M.P. Schmidt, Phys. Stat. Sol.(b) **143**, 345 (1987)

RF Plasma Synthesis and Deposition of SOFC Materials

G. Schiller, M. Müller, E. Bouyer, M. v. Bradke

German Aerospace Center (DLR), Institute of Technical Thermodynamics, Stuttgart, Germany

Abstract
Thermal spray technology is considered to be a suitable mass production method for solid oxide fuel cells. A thermal plasma chemical vapour deposition process (TPCVD) using inductively coupled RF plasma was applied to synthesise and deposit porous perovskite-type SOFC cathode coatings from liquid precursors such as aqueous solutions of the nitrates of the relevant elements. Results on the phase purity, the microstructure and the growth rates of perovskite-type cathode coatings $La_xSr_{1-x}MO_3$ and $Pr_xSr_{1-x}MO_3$ (M = Mn, Fe, Co) are presented that prove the suitability of this method for the preparation of highly efficient SOFC cathodes.

1. Introduction

Solid oxide fuel cells (SOFC) are electrochemical converters that convert chemical energy of fuel gases (hydrogen, natural gas, other hydrocarbons) with oxygen directly into electrical energy in an environmentally friendly way, thereby also exhibiting higher overall efficiency than conventional combustion processes for power generation. Thermal spray technology is considered to be a suitable mass production process for SOFC as an alternative method to conventionally used sintering processes. These processes such as tape casting of the electrolyte layer and screen printing or wet powder spraying of the electrodes and subsequent sintering are widely used for SOFC fabrication [1, 2], but they are time-consuming and they require high sintering temperatures partly far above 1000 °C which can give rise to undesired solid state reactions. Thermal spray techniques, on the other hand, such as atmospheric or vacuum plasma spraying are very rapid processes with a moderate temperature regime at the substrate surface and needing no further thermal post-treatment after deposition. Additionally, these processes can be fully automated to a production line. DLR pursues a planar SOFC concept for a metallic substrate-supported thin-film SOFC which is based on vacuum plasma spray technology as manufacturing process for the entire membrane-electrode assembly (MEA), the core element of SOFC stacks. Specially further developed and adapted DC and RF plasma deposition processes are applied for the manufacture of SOFC cells to be integrated in a stack assembly [3].

Conventional thermal spray techniques require particular powder conditioning being a considerable cost factor that should be reduced or even avoided. A promising approach for the preparation of SOFC components such as dense electrolyte and in particular porous cathode layers is given by the in situ synthesis and deposition in an inductively coupled RF plasma from liquid precursors. Perovskite coatings from aqueous solutions were deposited in a thermal radio-frequency (RF) plasma with a "plasma expanded through a nozzle" (PETN) technique achieving a growth rate of about 1 µm/min [4]. Similar precursors were injected into a plasma generated by a triple direct current (DC) torch reactor with growth rates of about 7 µm/min [5]. Using suspensions as well as aqueous solutions of suitable salts, two methods – suspension plasma spraying (SPS) [6] and thermal plasma chemical vapour deposition (TPCVD) [7] – have recently been developed for the deposition of SOFC components. Deposition rates of 30 – 100 µm/min were achieved but the phase purity of the cathode coatings was not sufficient for SOFC application. This paper focuses on the preparation of highly porous and pure perovskite-type cathode coatings by applying the TPCVD method.

2. Experimental

2.1 Set-up and Process Conditions

The experiments were performed using a vacuum reactor and a PL50 induction plasma torch from TEKNA Plasma Systems, Sherbrooke/Canada which is operated with a radio frequency generator from Himmelwerk, Germany, at 500 kHz (Fig. 1). The RF power was varied in the range from 20 to 30 kW, the chamber pressure was between 12 and 38 kPa and spraying distance between 150 and 600 mm. The plasma gas composition was varied over a wide range from argon/hydrogen mixtures to plasma mainly consisting of oxygen. The precursors were fed with a rate between 1.5 and 3 ml/min by a peristaltic pump using two channels to avoid pulsing. The material was directly injected into the hot plasma core by means of a gas-

assisted atomiser. Argon flow rates in the range of 2-10 slpm were used to atomise the precursors. Slabs of the SOFC bipolar plate material 94Cr5Fe1Y_2O_3 were used as substrates in order to match the thermal expansion coefficient of the ceramic SOFC components.

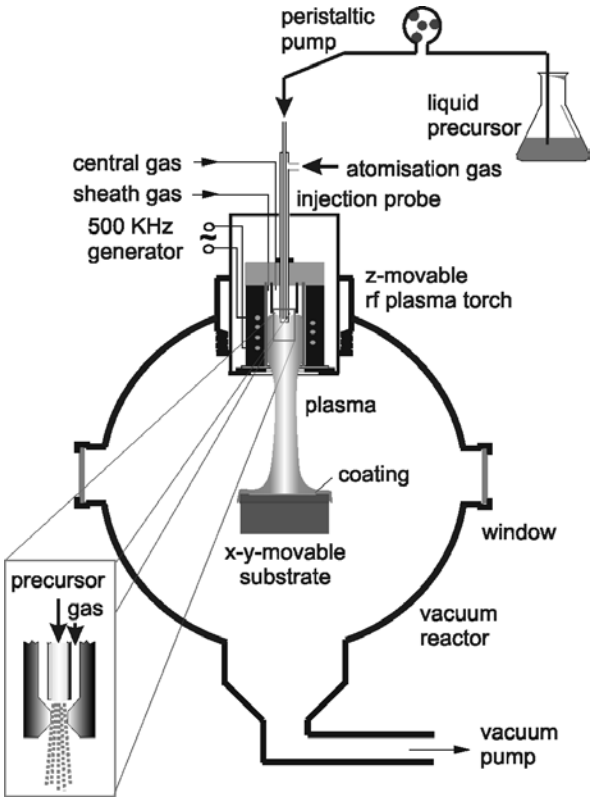

Fig. 1: Experimental set-up, detail in left corner: principle of gas-assisted atomisation

2.2 Precursors

Aqueous solutions of metal nitrates of different concentrations were used as precursors for the preparation of perovskite-type cathode coatings by means of TPCVD. A summary of the main precursor solutions applied and the desired synthesis products is given in Table 1.

Table 1: Summary of the precursor solutions applied and the desired synthesis products

	Synthesis product	Precursor	Concentration
A	$La_{0.9}Sr_{0.1}MnO_3$ (LSM)	$La(NO_3)_3 \cdot 6\ H_2O$ $Sr(NO_3)_2$ $Mn(NO_3)_2 \cdot 4\ H_2O$	0,9 M 0,1 M 1,0 M
B	$La_{0.5}Sr_{0.5}MnO_3$ (LSM)	$La(NO_3)_3 \cdot 6\ H_2O$ $Sr(NO_3)_2$ $Mn(NO_3)_2 \cdot 4\ H_2O$	0,5 M 0,5 M 1,0 M
C	$La_{0.65}Sr_{0.3}MnO_3$ (ULSM)	$La(NO_3)_3 \cdot 6\ H_2O$ $Sr(NO_3)_2$ $Mn(NO_3)_2 \cdot 4\ H_2O$	0,65 M 0,3 M 1,0 M
D	$Pr_{0.65}Sr_{0.3}MnO_3$ (UPSM)	$Pr(NO_3)_3 \cdot 5\ H_2O$ $Sr(NO_3)_2$ $Mn(NO_3)_2 \cdot 4\ H_2O$	0,65 M 0,3 M 1,0 M
E	$La_{0.8}Sr_{0.2}FeO_3$ (LSF)	$La(NO_3)_3 \cdot 6\ H_2O$ $Sr(NO_3)_2$ $Fe(NO_3)_3 \cdot 9\ H_2O$	0,8 M 0,2 M 1,0 M

	Synthesis product	Precursor	Concentration
F	$La_{0.8}Sr_{0.2}Co_{0.5}Fe_{0.5}O_3$ (LSCF)	$La(NO_3)_3 \cdot 6\ H_2O$ $Sr(NO_3)_2$ $Co(NO_3)_2 \cdot 6\ H_2O$ $Fe(NO_3)_3 \cdot 9\ H_2O$	0,8 M 0,2 M 0,5 M 0,5 M
G	$La_{0.58}Sr_{0.4}\ Co_{0.2}Fe_{0.8}O_3$ (LSCF)	$La(NO_3)_3 \cdot 6\ H_2O$ $Sr(NO_3)_2$ $Fe(NO_3)_3 \cdot 9\ H_2O$ $Co(NO_3)_2 \cdot 6\ H_2O$	0,58 M 0,4 M 0,8 M 0,2 M
H	$Pr_{0.58}Sr_{0.4}Co_{0.2}Fe_{0.8}O_3$ (PSCF)	$Pr(NO_3)_3 \cdot 5\ H_2O$ $Sr(NO_3)_2$ $Fe(NO_3)_3 \cdot 9\ H_2O$ $Co(NO_3)_2 \cdot 6\ H_2O$	0,58 M 0,4 M 0,8 M 0,2 M

2.3 Coating Evaluation

The phase content of the coatings was determined by XRD using a STOE Stadi P diffractometer and MoKα radiation. Polished cross sections and fracture surfaces were prepared by standard metallographic procedures to study the coating microstructure by optical and scanning electron microscopy (SEM) as well as EDX mapping.

3. Results and Discussion

Lanthanum manganite doped with 20 % Sr ($La_{0.8}Sr_{0.2}MnO_3$, LSM) is the preferred cathode material for high operating temperatures with SOFCs. It has reasonably good electronic conductivity but the oxide ion conductivity is very low even at 1000 °C. Therefore, mixing of LSM with yttria-stabilised zirconia (YSZ) which is used as electrolyte material is a common approach to overcome the oxygen transport limitation. But at temperatures below 800 °C which is a general goal in present SOFC development such two-phase cathodes cannot support high current densities. Ferrites, cobaltites and nickelites have better oxide ion conductivities than manganites [8], hence these perovskite phases promise high electrochemical performance at reduced SOFC operating temperature. Particularly strontium doped lanthanum ferrite (LSF) and cobaltite ferrite (LSCF) achieve low areal resistances and stable performance probably due to the higher ionic conductivity compared to LSM.

In previous investigations suspension plasma spraying was applied for LSM preparation by using suspensions of MnO_2 particles in saturated aqueous and ethanolic solutions of La salts [6]. The perovskite phase was formed as the main phase but also La_2O_3 was observed as an additional phase in significant extent in the coating. Post-treatment with an 80 % oxygen plasma improved the coating purity but the occurrence of detrimental La_2O_3 which reacts to $La(OH)_3$ causing severe volume change and destruction of the coating could not completely be suppressed. Furthermore, the coatings exhibit a layered microstructure resulting from impinging molten particles which is known from conventional thermal spraying processes. Although porosity can be affected by the solid content of the suspension SPS coatings showed a porosity which is too poor for gas migration in SOFC cathodes. Much more porous microstructures of LSM coatings were observed when using the TPCVD process, but phase purity remained still a problem to be solved [7]. The development of perovskite-type cathode coatings by using TPCVD is reported in more detail in the following chapters.

3.1 Phase composition

A key parameter governing the purity of the coatings appears to be the radial temperature gradient within the plasma jet. When using lanthanum and manganese nitrates (precursors A, B, C), the high temperature along the axis of the jet combined with the high volatility of Mn results in a non-stoichiometric composition with regard to La and Mn in the central part of the coating on a stationary substrate. The deviations from stoichiometry are larger than the perovskite structure con tolerate, thus, the presence of surplus La causes La_2O_3 to appear in the coating beside the desired LSM phase. The cooler outer regions of stationary substrates were always covered with pure or almost pure perovskite phase. Fig. 2 shows an extreme example of the different phase content obtained in the centre and in the outer region of a stationary substrate.

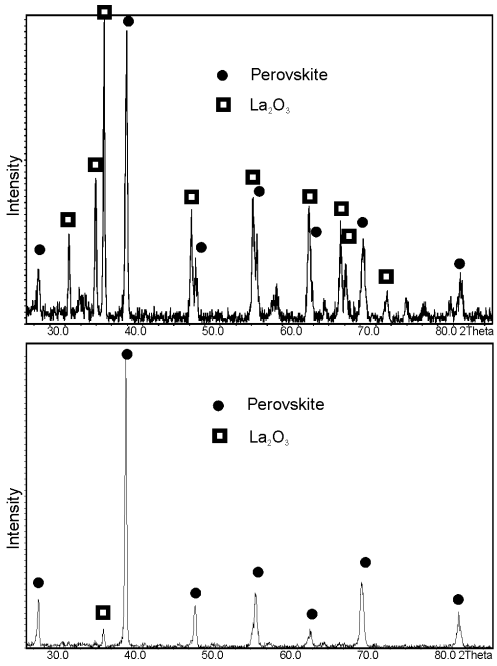

Fig. 2: XRD patterns of a TPCVD coating of LSM (precursor A) top: centre, bottom: margin of the sample

Scanning of the substrate results in the simultaneous deposition of the two main phases La_2O_3 and LSM. The homogeneity of the perovskite phase could be substantially improved by using precursors with lower lanthanum content, e.g. $La_{0.5}Sr_{0.5}MnO_3$ (precursors B and C) or by replacing lanthanum by praseodymium (precursor D), but a completely single-phase, large area perovskite coating could not be achieved. The synthesis of LSM, LSF (precursor E) and LSCF (precursor F) showed the same tendency concerning the formation of La_2O_3 but to a different extent. A semi-quantitative method was applied to compare the phase purity of different compounds by calculating the percentage of pure perovskite phase from the intensities of the main XRD peaks of the perovskite and La_2O_3. Table 2 depicts the phase composition of different perovskite layers.

Table 2: Phase purity of different TPCVD perovskite coatings

Precursor	ULSM		UPSM		LSCF		PSCF	
Position	centre	margin	centre	margin	centre	margin	centre	margin
Phase purity	85 %	100 %	92 %	100 %	65 %	100 %	100 %	100 %

It is concluded that the volatility of the manganese cannot be the only reason for the non-stoichiometric incorporation of the elements into the central part of the perovskite coating. Regarding the melting points of the simple oxides of the considered elements, La_2O_3 and SrO show far higher values than the other oxides of Mn, Fe and Co. This leads to the consideration that clusters of La_2O_3 or La-Sr-oxide might form in the hot zone along the plasma jet by homogeneous nucleation similar to the observation made in the system with yttria-stabilised zirconia [7]. These clusters might then be deposited and cannot completely be transformed to the perovskite phase due to the limited interdiffusion of Mn, Fe and Co. A break-through concerning phase purity was achieved when using precursors where La is substituted by Pr (precursor H). With the slightly non-stoichiometric composition $Pr_{0.58}Sr_{0.4}Co_{0.2}Fe_{0.8}O_3$ (PSCF) absolutely pure perovskite phase could be observed by XRD measurement both in the centre and on the margin of the layer as can be seen from Fig. 3. An explanation of this behaviour cannot be given at present and needs further investigation.

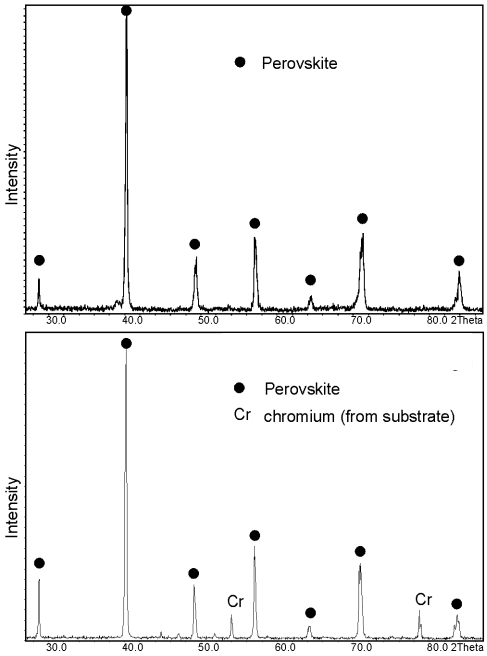

Fig. 3: XRD patterns of a TPCVD coating of PSCF (precursor H), top: centre, bottom: margin of the sample

Microstructure of TPCVD coatings

The coatings prepared from the precursor solutions A to H show a columnar or cauliflower-like microstructure as it is shown in SEM images of fracture surfaces in Fig. 4. Obviously they are a result of heterogeneous nucleation of the material on the substrate surface as it is well known from conventional CVD. During growth of the perovskite layer needle-shaped single crystals are initially formed. The substrate is in a temperature range that provides enough surface diffusion of the impinging species. Therefore the needles can coalesce resulting in a columnar growth. The resulting microstructure is of high open porosity offering efficient vertical as well as horizontal gas migration paths. This is an ideal microstructure for application as SOFC cathode enabling excellent gas permeability and creating a lot of reaction zones. Improved electrochemical performance is expected with this cathodes compared to conventionally DC plasma sprayed ones which suffer from a limited porosity due to their splat-shaped microstructure [3]. By depositing such TPCVD cathode coatings on half cells consisting of DC plasma sprayed anode and electrolyte layers on porous metallic substrates, full cells will be prepared and electrochemically characterised in the near future to prove their electrochemical performance.

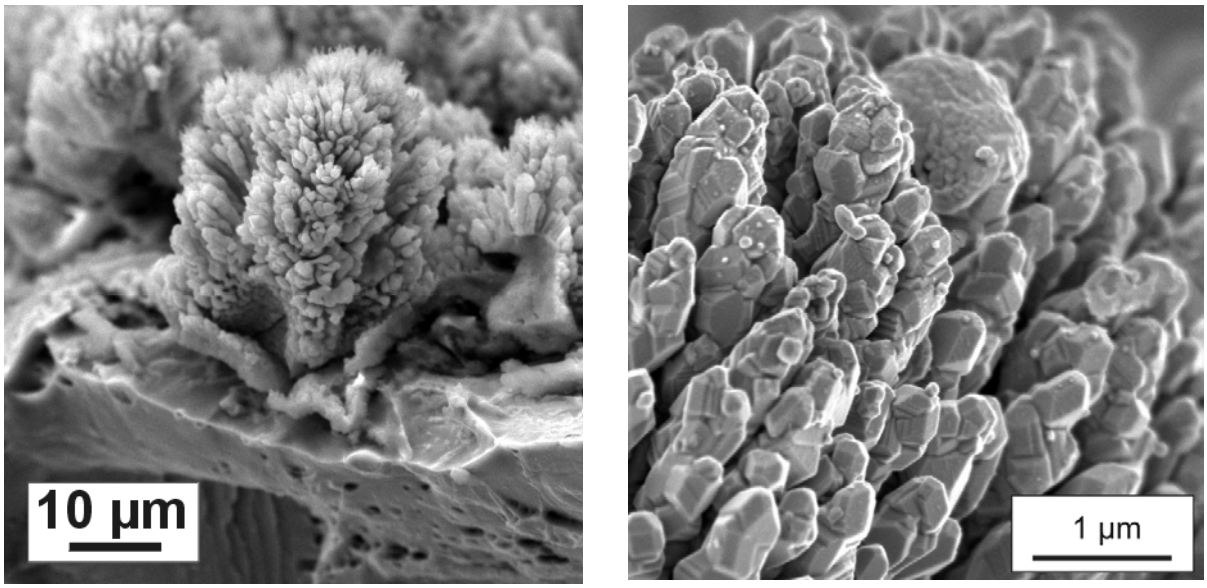

Fig. 4: SEM images of a fracture surface of a TPCVD perovskite coating

3.2 Growth Rate and Deposition Efficiency

The deposition of perovskite coatings by means of the TPCVD process from aqueous solutions resulted in growth rates of up to 25 µm/min on substrates with a size of 25 cm² that were scanned with the plasma jet. Depending on the process conditions and the precursor composition approximately 10 to 40 % of the theoretical oxide content of the precursors contributed to the coating growth. With optimisation of the plasma parameters and application of larger substrates the deposition efficiency of the TPCVD process may achieve the range of about 100 µm/min which is typical for plasma sprayed ceramic coatings.

4. Conclusion

Thermal plasma-assisted chemical vapour deposition (TPCVD) was applied to produce perovskite-type cathode coatings for solid oxide fuel cells from liquid precursors such as aqueous solutions of the relevant metal nitrates. The solutions completely vaporise in the plasma and condense through heterogeneous nucleation on the substrate surface forming a columnar structure. This microstructure provides an open porosity that is very advantageous for gas migration in SOFC cathodes. Deposition rates of up to 25 µm/min were achieved which is orders of magnitude higher than most of the comparable values found in the literature for TPCVD of oxide layers. Phase purity of the perovskite coatings is not easy to be achieved but we succeeded in preparing pure perovskite phase PSCF, checked by XRD, by replacing La by Pr in the perovskite structure. The expected improvement in electrochemical performance by applying these TPCVD cathodes in comparison to conventional DC plasma sprayed ones remains to be proven.

5. Acknowledgement
Financial support for this work through the Federal Ministry of Education, Science, Research and Technology (BMBF) is gratefully acknowledged.

References

[1] G. M. Christie, P. N. Nammensma, J. J. P. Huijsmans, Proc. Fourth European SOFC Forum, Vol. 1, 3-11 (2000)
[2] D. Stöver, U. Diekmann, U. Flesch, H. Kabs, W. J. Quadakkers, F. Tietz, I. C. Vinke, The Electrochemical Society, Proc. Vol. 99-19, 812-821 (1999)
[3] G. Schiller, R. Henne, M. Lang, R. Ruckdäschel, S. Schaper, Fuel Cells Bulletin – An International Newsletter, No. 21, 7-12 (2000)
[4] S. F. Miralai, D. Morvan, J. Amouroux, A. Naoumidis, H. Nickel, R. Avni, ISPC-12, Vol. 4, 199-204 (1995)
[5] H. C. Chen, J. Heberlein, R. Henne, J. Thermal Spray Techn., 9 (3), 348-353 (2000)
[6] G. Schiller, M. Müller, F. Gitzhofer, J. Thermal Spray Techn. 8 (3), 389-392 (1999)
[7] M. Müller, E. Bouyer, M. v. Bradke, D. W. Branston, R. B. Heimann, R. Henne, G. Lins, G. Schiller, Materialwissenschaft und Werkstoffkunde, 33 (6), 322-330 (2002)
[8] M. Krumpelt, J. Ralph, T. Cruse, J.-M. Bae, Proc. Fifth European SOFC Forum, Vol. 1, 215-224 (2002)

Attenuated total reflection infrared spectroscopic study of hydrogenated amorphous and microcrystalline silicon film evolution

P.J. van den Oever, I.J. Houston, M.C.M. van de Sanden, W.M.M. Kessels
Dept. of Applied Physics, Eindhoven University of Technology,
P.O. Box 513, 5600 MB Eindhoven, The Netherlands

Abstract
The highly sensitive attenuated total reflection Fourier transform infrared spectroscopy technique (ATR-FTIR) has been used for *in-situ* measurements of amorphous (a-Si:H) and microcrystalline silicon
(μc-Si:H) film growth. A data analysis procedure for the ATR-FTIR measurements has been developed to obtain quantitative information on the hydrogen (H) concentration and bonding in the films. Contrary to
a-Si:H films, μc-Si:H films shows a non-homogeneous distribution of the hydrogen throughout the film, which suggests columnar growth of the μc-Si:H.

Introduction
Hydrogenated amorphous (a-Si:H) and microcrystalline silicon (μc-Si:H) thin films have important applications in semi-conductor devices and solar cell fabrication. In particular, a-Si:H and μc-Si:H are used in thin film transistors (TFTs) and the next generation thin film solar cells. Over the last few years, μc-Si:H has gained a lot of interest, because it exhibits important advantages compared to a-Si:H. Hydrogenated microcrystalline silicon has a lower bandgap (1.1 eV) than a-Si:H (1.7 eV), which enables a better use of the solar spectrum in tandem solar cell configurations [1]. Furthermore, it shows less light induced degradation [2] and a higher electron mobility. Future industrial applications of a-Si:H and μc-Si:H require deposition processes with a high growth rate (> 1 nm/s) and high film quality. High growth rate deposition of a-Si:H and μc-Si:H films is possible with the expanding thermal plasma (ETP) deposition technique.
The H concentration and bonding in a-Si:H and μc-Si:H films plays a key role in determining the film properties such as defect density, film structure and optical absorption. In this work, attenuated total reflection Fourier transform infrared (ATR-FTIR) spectroscopy [3] is used to measure the H concentration and bonding in very thin films (< 200 nm). For the quantification of the ATR-FTIR measurements, a data analysis method that includes interference effects has been developed.
The evolution of the H concentration and bonding as a function of the film thickness is measured for a-Si:H and μc-Si:H films. These experiments provide more insight in the growth mechanism of the film, especially for μc-Si:H that is not isotropic and grows in a non-uniform way [4,5]. The evolution of the H concentration and bonding in a-Si:H and μc-Si:H film growth has been studied.

Experimental setup, procedures and results
The expanding thermal plasma (ETP) setup consists of a thermal plasma source and a low pressure deposition chamber (~ 20 Pa). The plasma source is a DC cascaded arc discharge operated on a mixture of argon and hydrogen at a sub atmospheric pressure (~ 400 kPa). After creation, the plasma expands into the low pressure deposition chamber, where it dissociates the injected silane (SiH_4) gas. The deposition setup and the cascaded arc plasma source have been described in detail elsewhere [6].
The plasma species cause the deposition of a film on a substrate holder whereon an internal reflection element (IRE) is placed. The substrate holder is actively temperature controlled at 250 °C and a helium back flow ensures a proper thermal contact between substrate holder and IRE. During the starting of the plasma, deposition on the substrate holder and IRE was prevented by a shutter that was situated approximately 5 cm from the substrate holder.
The films are deposited on a GaAs IRE, which is a trapezoidal substrate with the dimensions 50 x 20 x 0.7 mm^3 and edges beveled at 60 °. Furthermore, the refractive index of GaAs is almost equal

to that of a-Si:H and μc-Si:H films, which has advantages in the analysis of the data. Infrared light from a Bruker Vector 22 FTIR spectrometer is focused onto the beveled edge of the IRE. In the IRE, the light undergoes 21 total internal reflections on both sides of the IRE, enhancing the sensitivity of the measurement technique. The light exiting the IRE passes a polarizer and falls on a MCT detector that detects the intensity of the light.

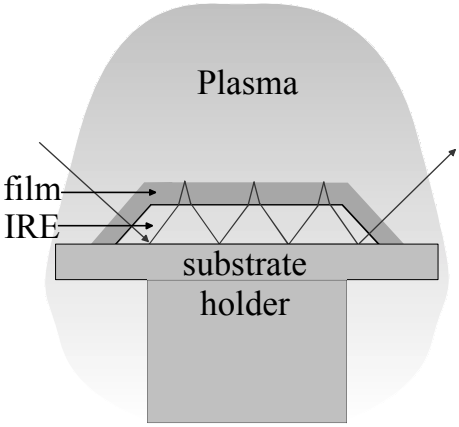

Figure 1: An IRE on the substrate holder.The film is probed by infrared light in the MTIR mode.

To obtain spectra with a good resolution 1000 scans of the FTIR spectrometer are integrated, which takes approximately 7 minutes. The combination of the long integration time and the fast deposition rate (3 – 10 nm/s) prevent real time measurements of the spectra during film growth. Therefore, the evolution of the H concentration and bonding as a function of the film thickness is obtained in a step-by-step deposition scheme.

The refractive index of the film on the IRE determines the way (mode) in which the film is probed. Two modes of probing are distinguished, the attenuated total reflection mode (ATR-mode) and the multiple total internal reflection mode (MTIR-mode). The MTIR mode, which is depicted in Fig. 1, occurs when the condition for total internal reflection (TIR) is not fulfilled at the interface IRE-film. Now the electromagnetic wave traverses into the film and TIR occurs at the film vacuum interface (if the condition for TIR is fulfilled there). In this work, all the films are probed in the MTIR mode.

In order to quantitatively analyze the ATR-FTIR measurements, an optical model has been constructed. The model takes into account several effects, including interference in the film, the influence of a deposited film on the bevels and the influence of multiple passes in the IRE that can occur when a part of the infrared beam is reflected back into the IRE at the bevels. Absorption in the film is taken into account by the introduction of a complex refractive index of the film: $\tilde{n}_f = n_f + ik$. Here n_f is the real part of the refractive index and k is the extinction coefficient that is related to the absorption coefficient $\alpha = 4\pi k/\lambda$, with λ the wavelength of the infrared light.

The transmission through the IRE can be described with the following equation:

$$T_{IRE}(d,\alpha) = \frac{T_{in} R_{ATR}^{M} T_{out}}{1 - R_{out}^{2} R_{ATR}^{2M}} \tag{1}$$

In this equation T_{in} is an expression for the transittance of the input bevel, T_{out} for the transmittance at the output bevel and R_{out} for the reflectance at the both bevels when the beam is incident from the inside of the IRE. R_{ATR} is an expression for the reflectance at the top surface of the IRE and includes possible interference effects and the absorption in the film on top of the IRE (dependent on absorption coefficient of the film and film thickness). M is the number of reflections at the top surface of the IRE. Because all the transmittances and reflectances are based on the Fresnel equations that are polarization dependent, also T_{IRE} is polarization dependent. Therefore, it is essential for a quantitative data analysis to use polarized light in the measurements. More information on the measurement technique and data analysis method is given elsewhere [7]

As a measure for the amount of absorption in the film on the IRE the quantity absorbance is used. Absorbance is defined as:

$$A(d) = -\log \frac{T_{IRE}(d,\alpha)}{T_{IRE}(0)} \tag{2}$$

Because of the complexity of the expressions in Eq. 1 a mathematical inversion is required to obtain the absorption coefficient from Eq. 2. In this work an iterative numerical procedure has been used to extract the absorption coefficient from the measurement.

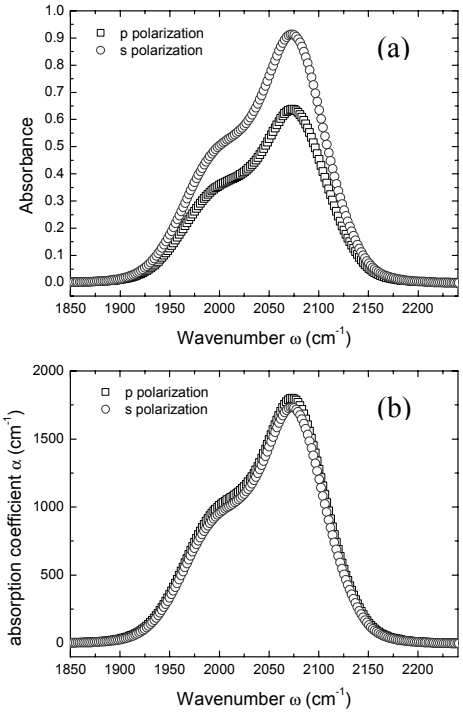

Figure 2: (a) The absorbance spectra for measurements with s and p polarized light of a 200 nm thick a-Si:H film. (b) The calculated absorption coefficient for the same film.

In Fig. 2(a) the absorbance for measurements with *s* and *p* polarized light of a 200 nm thick a-Si:H film is given. Clearly a large difference between the measurements observed. By the application of the optical model, the resulting absorption coefficient can be calculated. In Fig. 2(b) the calculated absorption coefficient is shown, also for measurements with *s* and *p* polarized light. The calculated absorption coefficients are equal for *s* and *p* polarized measurements. This is expected for an isotropic material like a-Si:H, which verifies the validity of the used model.

Absorption in a film depends linear on the density of absorbing species, which means that the total density in a specific infrared bonding mode N_i can be expressed in terms of the absorption coefficient α:

$$N_x = P_x \int \frac{\alpha}{\omega} d\omega \approx \frac{P_x}{\omega} \int \alpha d\omega \qquad (3)$$

where P_x is the proportionality constant for the silicon hydride bonding mode *x*. The proportionality constant has been set to 9.0 x 10^{19} cm^{-2} for all bonding modes [8]. Now the H concentration $C_{H,x}$ in atomic percent can be calculated for the bonding mode *x* according:

$$C_{H,x} = \frac{N_x}{N_{tot}} \times 100\% = \frac{P_x}{\omega N_{tot}} \int \alpha d\omega \times 100\% \qquad (4)$$

where N_{tot} is the total atomic density of the film (5.0 x 10^{22} cm^{-3} for c-Si). The hydrogen concentrations determined from the ATR-FTIR measurements are in good agreement with *ex-situ* FTIR measurements of similar films.

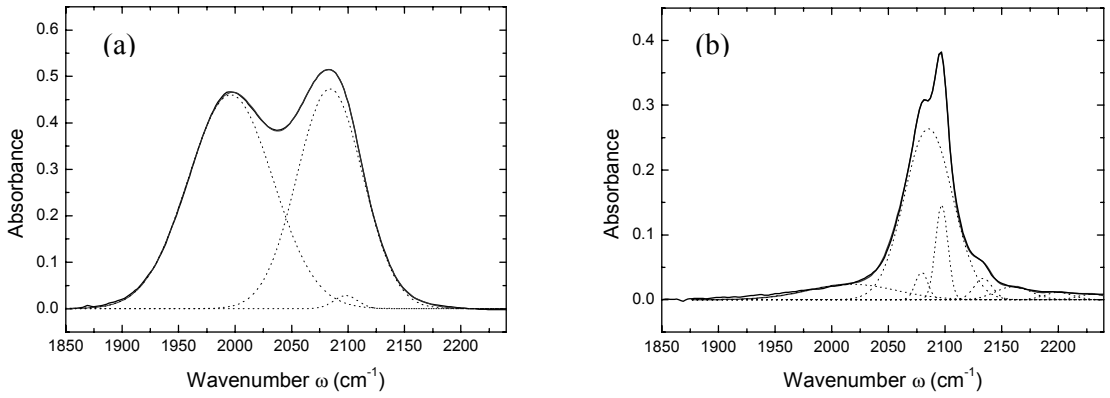

Figure 3: (a) The ATR-FTIR spectrum of a 200 nm thick a-Si:H film. Three peaks can be distinguished, the LSM, HSM and a small peak corresponding to surface-like modes. (b) The ATR-FTIR spectrum of a 200 nm thick μc-Si:H film.

In Fig. 3 (a) the ATR-FTIR spectrum of a 200 nm thick a-Si:H film is shown. In the spectra two main peaks are present, the lower stretching mode (LSM) and the higher stretching mode (HSM). The LSM is assigned solely to SiH bonds in the material and the HSM to SiH_2 bonds and SiH bonds on internal surfaces. Furthermore, a small peak is present that is assigned to surface-like modes of SiH bonds. In Fig. 3 (b) ATR-FTIR spectrum for a 200 nm thick μc-Si:H film is shown.

Apart from the LSM and HSM that are also present in the spectrum of the a-Si:H film, several well-defined surface-like peaks can be seen that are essential for fitting the spectrum properly.

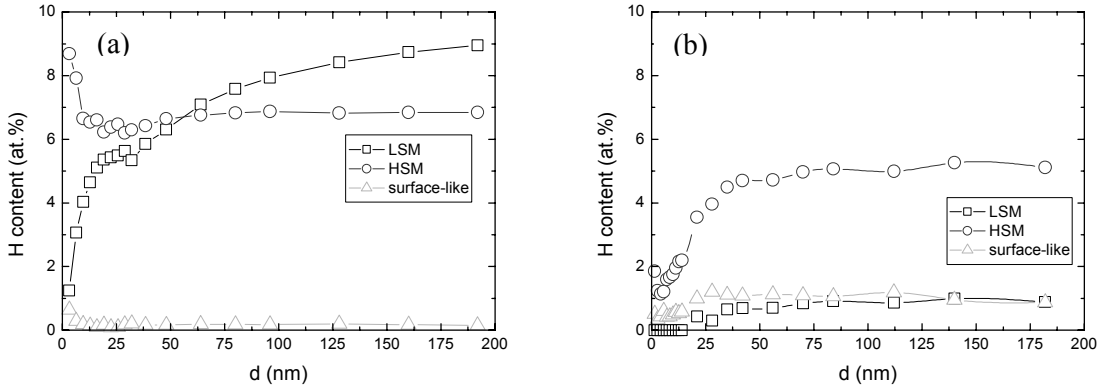

Figure 4: (a) The ATR-FTIR spectrum of a 200 nm thick μc-Si:H film. Apart from the LSM and HSM that were also present in the spectrum of the a-Si:H film, several surface like peaks are necessary to fit the spectrum properly. (b) The evolution of the H concentration and bonding in a μc-Si:H film as a function of the film thickness.

In Fig. 4 (a) the evolution of the H concentration and bonding as a function of the film thickness is shown for the a-Si:H film. The initial phase of the a-Si:H growth is characterized by a high H concentration in the HSM. When the film thickness increases, the H concentration in the HSM decreases sharply and becomes constant, while the H concentration in the LSM gradually increases. Eventually the LSM becomes dominant over the HSM and the total H concentration is ~ 16 at. %.
Fig. 4 (b) shows the evolution of the H concentration and bonding for the μc-Si:H film growth. Initially the H concentration in the HSM and surface-like modes increases, while the H concentration in the LSM remains zero. Eventually the LSM increases slightly. After 25 nm the film growth reaches a steady state and the HSM is dominant in the film. The total H concentration in the μc-Si:H film is ~ 7 at. %.
The well defined surface-like modes in the μc-Si:H film have been assigned to hydrogen on the boundaries of crystallites in the material. These measurements, combined with spectroscopic ellipsometry measurements of the μc-Si:H film growth [9,10], suggest the following growth mechanism. Initially small crystallites are formed in the material. The crystallites grow in size, which corresponds to the increase in surface-like modes. After approximately 25 nm, the crystallites make contact and from there columnar growth of the μc-Si:H is observed. This columnar growth is characterized by a constant H concentration in the surface-like modes (on grain boundaries).

The authors would like to acknowledge the technical assistance of Ries van de Sande, Jo Jansen, Herman de Jong and Bertus Hüsken.

References

[1] J. Meier, S. Dubail, J. Cuperus, U. Kroll, R. Platz, P. Torres, J. A. A. Selvan, P. Pernet, N. Beck, N. P. Vaucher, et al., J. Non-Cryst. Solids **227-230**, 1250 (1998).
[2] B. Rezek, J. Stuchlík, A. Fejfar, and J. Kočka, J. Appl. Phys. **92**, 587 (2002).
[3] N. Harrick, *Internal Reflection Spectroscopy* (John Wiley & Sons Inc., New York, 1967).
[4] D. Franz, F. Grangeon, T. Delachaux, A. Howling, C. Hollenstein, and J. Karner, Thin Solid Films **383**, 11 (2001).
[5] H. Fujiwara, M. Kondo, and A.Matsuda, J. Appl. Phys. **91**, 4181 (2002).
[6] W. Kessels, R. Severens, A. Smets, B. Korevaar, G. Adriaenssens, D. Schram, and M. van de Sanden, J. Appl. Phys. **89**, 2404 (2001).
[7] P. van den Oever, I. Houston, M. van de Sanden, and W. Kessels, *to be published*

[8] A. Smets, Ph.D. thesis, Eindhoven University of Technology (2002).
[9] I. Houston, E. Hamers, W. Kessels, and M. van de Sanden, *to be published*
[10] W. Kessels, P. van den Oever, J. Hoefnagels, I. Houston, and M. van de Sanden, Mater. Res. Soc. Symp. Proc. **715**, A25.6 (2002).

PLASMA TECHNOLOGY AND TECHNIQUE IN NUCLEAR FUEL CYCLE

I.N.Toumanov

Russian Research Centre "Kurchatov Institute"-HEPTI, Moscow, Russia

1. Traditional nuclear fuel cycle includes the next stages: opening up and enrichment ores, leaching and purification of uranium, producing of uranium and uranium compounds designed for synthesis of uranium hexafluorides, uranium enrichment, producing ceramic nuclear fuel, generation of power in a nuclear reactor, regeneration of uranium, recovery of plutonium, processing and burial of nuclear waste. Plasma, direct inductive heating and laser technology in combination with new purification technologies (sorption, liquid extraction, counter flow distillation) enable to reconstruct the nuclear fuel cycle efficiently and to solve a lot of specific economic and social problems of nuclear power engineering.
2. Technical basis include: DC plasmatrons generating air, nitrogen, steam, hydrogen plasma streams; high frequency plasmatrons supplied with slotted water – cooled discharge chamber made of non-magnetic metal; all metal microwave plasmatrons; combined plasmatrons supplied with reinforcement of coupling a basic power supply with plasma. Laser technique used for uranium enrichment includes technological and auxiliary lasers equipped in AVLIS and MLIS technologies.
3. Large scale plasma processes realized on the level of plasma plants, at least, are following:

- plasma processing of ores for destruction of crystallic lattice of resistive ores for more efficient hydrochemical opening up and leaching of valuable components;
- plasma conversion of disintegrated liquid nitric raw materials (predominantly re-extracts or melts) to disperse oxide materials and nitric acid solutions;
- producing of the MOX – fuel;
- plasma steam conversion of low enriched uranium hexafluorides to uranium oxides for following making of oxide nuclear fuel and hydrofluoric acid solution;
- plasma steam conversion of depleted uranium hexafluorides to uranium oxides and anhydrous hydrogen fluoride in combination with counter flow distillation;
- high frequency technology for reactant free reduction of uranium from uranium hexafluorides in combination with processes of separation of uranium and fluoride;
- plasma reduction of metallic uranium from oxide raw material accompanied with plasma - electronic refining;
- plasma conversion of gas exhausts of hydrogen fluoride production;
- high frequency synthesis of ceramic materials used in the nuclear fuel cycle: carbides, borides, nitrides, solid solutions etc.;
- low frequency reduction of rare metals (zirconium, hafnium, scandium etc.);
- calcination of aqueous nitric radioactive waste;
- plasma processing of condensed nuclear waste.

4. There are several approaches for reconstruction of the nuclear fuel cycle both based on plasma and frequency technique and on combination of the technique aforesaid with laser technology used for uranium enrichment:

- plasma technology of producing of nuclear materials in combination with high frequency and low frequency direct inductive heating;
- plasma technology of producing of nuclear materials in combination with AVLIS technology for uranium enrichment and with frequency direct inductive heating;
- plasma technology of producing of nuclear materials in combination with MLIS technology for uranium enrichment and with frequency direct inductive heating.

SIMPLIFIED MODEL FOR GENERATION OF ARC COLUMN IN A PLASMA SPRAYING TORCH.

E. Meillot, D. Guénadou

C.E.A. LE RIPAULT, B.P. 16, 37260 MONTS, France
Erick.Meillot@cea.fr

Symposium topic number 3 : Modeling in plasma chemistry.

In the plasma spraying process, the influence of the gas flow dominates to determine the state of the particles at impact onto the substrate. To better comprehend this influence, 2 D. numerical simulations are carried out with the C.F.D. ESTET code using the k-? turbulent model.
A simple model generating the plasma in the anode is proposed and analyzed. The model leads to simulate the arc generation in a simplified way : it mainly depends on the macroscopic operating parameters of the plasma torch and so allows the numerical simulations of the process for industrial applications without expecting high level measurement diagnostics such as velocity or temperature of the flow at the nozzle exit.
The plasma is simulated by a volume energy source inside the nozzle. Several designs of torch are investigated. The main parameters are discussed and comparisons with experiments are done in the steady state of the plasma flow.

The discussed model of plasma column permits the correct simulation of the plasma spraying process with only operating conditions and design parameters of the torch.

Relationships between induction plasma spraying parameters and TiO_2 particle characteristics at impact.

N. Branland[1], E. Meillot[1], P. Fauchais[2], A. Vardelle[2], M. Boulos[3], F. Gitzhofer[3] , D. Drouin[4], P. Magny[4]

[1] *C.E.A. LE RIPAULT, B.P. 16, 37260 MONTS, FRANCE,*
[2] *Sciences des Procédés Céramiques et Traitements de Surface, Université de LIMOGES, 123, av. A. Thomas, 87060 LIMOGES, FRANCE.*
[3] *Centre de Recherche en Technologie des Plasmas , Université de SHERBROOKE, SHERBROOKE (Qc) J1K 2R1, CANADA*
[4] *Faculté de Génie, Université de SHERBROOKE, SHERBROOKE (Qc) J1K 2R1, CANADA*

Abstract
Many studies have been devoted to the effect of the plasma spray process parameters on the in-flight particle velocity and temperature because of the recognized relationships between the latter and the quality of the coating. The objective of this work is to link the main operating parameters of the induction plasma spray process with the impact parameters of titania particles. The use of inductive plasma torches working under subsonic or supersonic conditions makes it possible to get particles with velocity ranging between 40 and 730 m/s and temperature between 2000 and 2150°C.

1. Introduction

Over the past 15 years, the **I**nductive **P**lasma **S**praying (IPS) technology has gained important credibility for the manufacturing of plasma-sprayed coatings of metals and ceramics. Its main advantages are the low velocity and large volume of the plasma plume that result in an increase of the particle residence time compared with the particle residence time in d.c. plasma spraying and, therefore, in an improvement in their melting state before impact. Moreover, the absence of electrodes involves the possibility to operate under a wide range of conditions at atmospheric and low pressure, with inert, reducing or oxidizing gases [**1**].

At the end of the eighties, a specific effort was made to measure the velocity of particles before impact onto the substrate under typical IPS conditions [**2-3**]. Measurements were carried out using Laser Doppler Anemometry that is a well established diagnostic tool under plasma conditions. Also, Coulombe et al [**4**] examined the correlations between the morphology of the splats obtained by IPS and particle characteristics thanks to the simultaneous measurement of particle velocity by a time-of-flight technique and surface temperature by two-color pyrometry. They showed that the uniform radial distributions of particle temperature and velocity gave rise to a high deposition efficiency (up to 90 %) and homogeneous quality of coatings.

The objective of this work is to correlate the operating conditions of an IPS spray process with the particle parameters that are measured using a commercial diagnostic system (DPV-2000, Tecnar-Canada) [**5**]. Two operating modes of the inductive plasma spray torch are investigated: subsonic and supersonic. The latter results from the use of a "de Laval" nozzle. This convergent-divergent nozzle presents a critical throat diameter that brings about particle velocity equal or higher than the velocity reached under d.c. plasma spray conditions [**6-7**].

This study deals with titania coatings that are mainly used in photo-electric energy applications [**8**] and wear-resistance applications [**9**]. The first part of the paper gives a description of the plasma-sprayed materials and experimental procedure. The second part refers to the effect of the main parameters of the IPS process on the in-flight particle characteristics. A special section examines the relationships between particle velocity and coating stoichiometry.

2. Materials and experimental procedure

Materials

The commercially available powders (H.C. Starck) had a particle size distribution ranging between 22 and 45 µm when working with subsonic IPS conditions and between 5 and 20 µm with the supersonic conditions. In order to obtain the pure rutile phase, the powders were heat-treated in air for a period of three hours at 1000°C before plasma processing. After this treatment, the Magneli phases (Ti_nO_{2n-1} with n = 4-10), present in the original powders, were eliminated.

Plasma conditions

Plasma spraying was performed with a 3-MHz induction plasma unit (Figure 1). An inductive plasma torch (Model PL 35 - Tekna Plasma Systems Inc., Canada) with a ceramic plasma-confinement tube of 35 mm in internal diameter, was used to study the effect of the subsonic IPS parameters on the in-flight particle characteristics. In supersonic IPS, a convergent-divergent nozzle with a critical throat diameter of 10 mm was used as a substitute for the convergent nozzle of the standard PL-35 plasma torch.

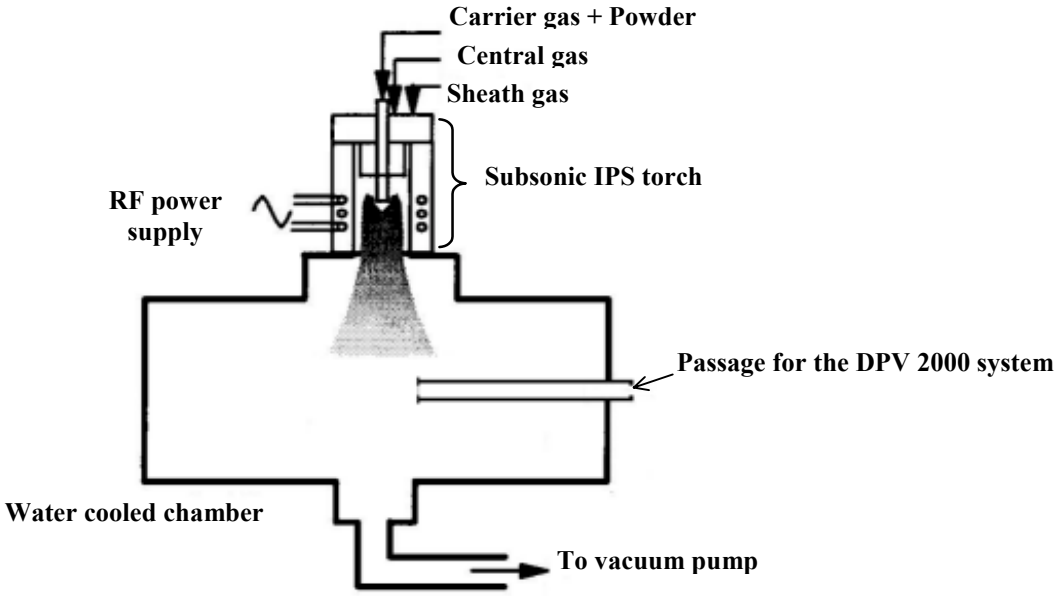

Figure 1 : Schematic illustration of the IPS setup.

In subsonic IPS, the powder was injected axially into the plasma flow through a water-cooled stainless steel probe with an exit tip located at 40 mm upstream of the exit plane of the torch nozzle. The external and internal diameters of the powder-feeding probe were 4.8 mm and 2.5 mm, respectively. The powder feed rate was 11 g/min. In supersonic IPS, the powder feed rate was 3.5 g/min and the probe was located 90 mm upstream of the exit plane of the torch nozzle.

In both modes, oxygen, at 70 NL/min, was used as sheath gas in order to limit the reduction of titania particles in the plasma flow while argon was used as plasma and powder carrier gases at flow rates of 40 and 4 NL/min, respectively.

The torch power, the spraying distance and the expansion chamber pressure were varied as shown in Table 1. These parameters were expected to affect the residence time of the particles in the plasma flow and, consequently, the momentum and heat transfer between the plasma gas and particles. It must be noted that in subsonic IPS, the pressures were the same in the expansion chamber and coil region while in supersonic IPS, the pressure was higher in the coil region and varied between 40 and 60 kPa.

In order to study the effect of oxygen and particle velocity on the decomposition of titania particles during plasma processing, coatings were deposited on stainless steel substrates (X13M), 25 mm in diameter and 5 mm in thickness, prepared by grit blasting and degreasing before spraying. The coatings were subjected to metallographic preparation before observation by cathodoluminescence.

Table 1 : Variation range of the induction plasma spraying parameters.

Process	Powder size range	Spraying Parameters	Variation range
Subsonic mode	22-45 µm	Torch power	35 to 50 kW
		Spraying distance	150 to 200 mm.
		Expansion chamber pressure	33.3 to 79.9 kPa
		Coil chamber pressure	33.3 to 79.9 kPa
Supersonic mode		Powder granulometry	[5 –20 µm] and [22-45 µm]
	5-20 µm	Expansion chamber pressure	3.3 to 13.3 kPa
		Coil chamber pressure	40 – 60 kPa

In-flight particle velocity and temperature

Particle temperature and velocity were measured using a DPV-2000 diagnostic system. The measurements were carried out on the torch axis at 100 mm from the DPV-2000 sensor head. The accuracy of measurements was estimated to be about 5 % for particle velocity and 20 % for particle temperature [**5**]. However, it can be noticed that temperature measurements give a correct trend of the effect of spray parameters on particle behaviour.

3. Results and discussion

3.1 Subsonic IPS

Spraying distance

The spraying distance is defined as the distance between the torch exit and substrate surface. As the total distance covered by the particles is the distance between the tip of the powder feeding probe and the substrate, 40 mm for the subsonic torch and 90 mm for the supersonic one must be added to the spraying distance.

The study of the effect of the spraying distance on particle parameters was carried out at a torch electric power of 40 kW and a pressure of 53.3 kPa.

An increase in spraying distance results in a longer residence time in cooler zones outside the plasma plume. Therefore, the particles decelerate and cool down gradually in this part of their trajectory. It was observed a decrease in particle velocity by 15 % (from 48 to 40 m/s) for an increase in spraying distance of 70 mm while the particle temperature difference was only 20°C (from 2120°C to 2100°C). It should be noticed that, first, the particle temperature was higher than the melting point of titania (Tm = 1850°C) and, second, the accuracy of the DPV 2000 for temperature measurement is not high enough to observe any effect of the spraying distance on particle temperature.

The spraying distance also affects the flattening behaviour of the particles impinging onto the substrate : a short spraying distance (150 mm) limits the cooling of the particles and results in thinner splats (about 3 µm instead of 10 µm for a spraying distance of 200 mm).

Torch power

The spraying distance was fixed at 150 mm and the chamber pressure at 53.3 kPa.

The electric power input to the torch has an effect on the plasma discharge volume and enthalpy. An increase in the plasma power causes a slight rise in the degree of ionisation of the gas and results in a higher plasma enthalpy and a larger discharge volume. Consequently, the heat transfer between plasma and particles is enhanced. However, it was found that an increase in torch power by 29 % resulted in an increase in particle temperature by 100°C while, as generally observed, the particle velocity was, by far, more sensitive to the gas enthalpy (Figure2).

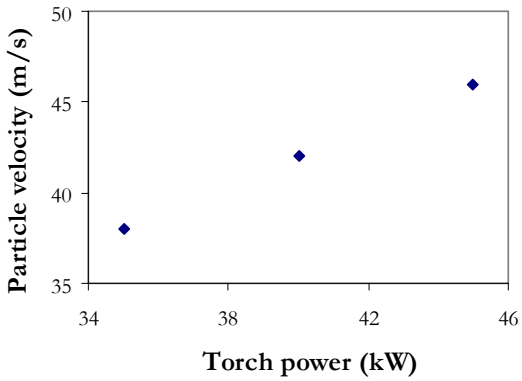

Figure 2 : Variation of the mean particle velocity with the torch power.

Chamber pressure

The study of the effect of the pressure in the expansion chamber on particle acceleration and heating was carried out at a spraying distance of 150 mm and a torch power of 40 kW.

The expansion chamber pressure affects the plasma discharge volume and length. Indeed, an increase in the chamber pressure causes a decrease in the length and velocity of the plasma plume as a result of the mixing with the denser environment gas. The higher the expansion chamber pressure, the lower the velocities of particles at impact as shown in Figure 3.

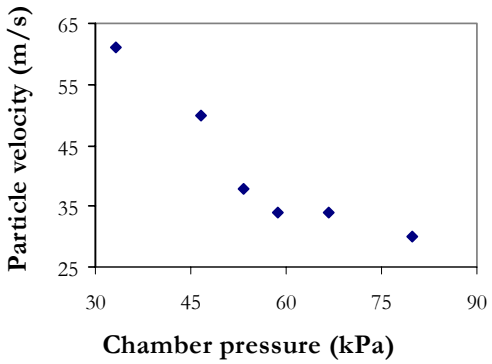

Figure 3 : Variation of the mean particle velocity with the chamber pressure under subsonic IPS conditions.

However, when the chamber pressure decreases, the heating of particles is less efficient because of shorter particle residence time in the gas flow and Knudsen effect. As seen in Figure 4, the particles collected in the chamber at 13.3 kPa, had an irregular shape similar to that of the titania powder feedstock. Whereas, at a chamber pressure around 53.3 kPa, particles exhibited a spherical shape highlighting a good melting state.

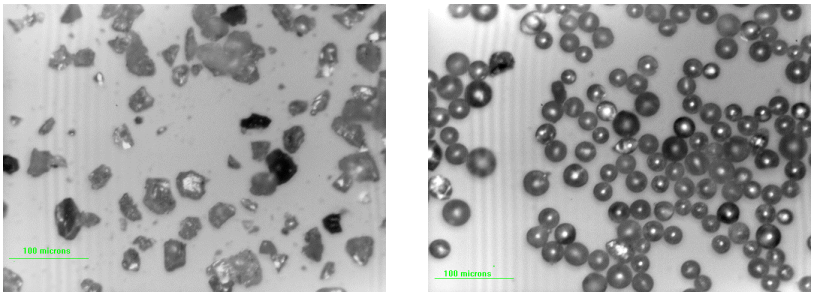

p = 13.3 kPa **p = 53.3 kPa**

Figure 4 : Optical micrographs of titania particles collected in the spraying chamber at two different pressures.

3.2 Supersonic IPS

Powder granulometry

The effect of the powder granulometry on the particle characteristics is shown in Table 2. The pressure in the expansion chamber was kept constant at 13.3 kPa and the spray distance at 200 mm whereas the torch power was varied between 35 and 50 kW resulting in a coil chamber pressure between 40 and 60 kPa.

Table 2 : Effect of the powder granulometry on the in-flight particle characteristics at different torch powers.

	Particle size range : 22-45 µm		Particle size range : 5-20 µm	
Torch power (kW)	Mean particle temperature (°C)	Mean particle velocity (m/s)	Mean particle temperature (°C)	Mean particle velocity (m/s)
35	1690	330	2020	440
40	1720	355	2040	435
45	1710	350	2050	485
49	1715	380	2100	495

Because of the high plasma and particle velocity compared to that in subsonic IPS, finer particles are generally used in supersonic induction plasma spraying as the heat required to melt the particles is proportional to the cube of the particle diameter. Under the conditions of this study, the heat transfer to the powder with particle size ranging between 22 and 45 µm was not sufficient to melt them and particle surface temperature at impact was less than the titania melting point (T_m = 1850°C) against more than 2140°C in subsonic IPS.

Chamber pressure

The effect of the expansion chamber pressure was studied at a spraying distance of 200 mm and a torch power of 35 kW.

In supersonic IPS, the effect of the expansion chamber pressure on the in-flight particle behaviour was similar to the effect observed in subsonic IPS : an increase in the chamber pressure results in a decrease in the length and velocity of the plasma plume as a result of the mixing with the denser environment gas. Consequently, the increase in the expansion chamber pressure brings about a decrease in particle velocity.

In addition, the decrease in the expansion chamber pressure enhances the supersonic conditions because of a larger difference between the pressure in the coil region (about 60 kPa) and the pressure behind the torch, i.e. in the expansion chamber. Consequently, the lower the expansion chamber pressure, the higher the velocity of the particles. The latter ranged between 440 and 730 m/s for an expansion chamber pressure varying from 13.3 to 3.3 kPa

3.3 Effect of particle velocity on coating stoichiometry

As previously shown, the use of a supersonic nozzle leads to particle velocities ranging between 330 m/s and 730 m/s whereas under subsonic IPS conditions, particle velocities were in the order of 40-60 m/s.

The distinctive characteristic of titania is that the plasma-sprayed coatings exhibit large variations in stoichiometric composition depending on the operating conditions of the deposition process. The coating stoichiometry affects its electrical properties [**7**]. When titania is plasma-treated, the insulating rutile is changed in a n-type semiconductor because of some oxygen loss during the spray process. To quantify this effect, the coatings were observed by a cathodoluminescence (CL) technique [**10**] that is often used to study semiconductor materials.

Figure 5 shows that the subsonic IPS coatings present a less luminous response because of a less marked presence of semiconductor zones contrary to the supersonic IPS coatings. In both IPS processes, oxygen was used as sheath gas to limit the de-oxidation of the in-flight particles. However, in the case of subsonic IPS, the lower particle velocity favours the chemical equilibrium between the particles and plasma environment. Consequently, the oxygen loss is compensated explaining why there are less semiconductor zones.

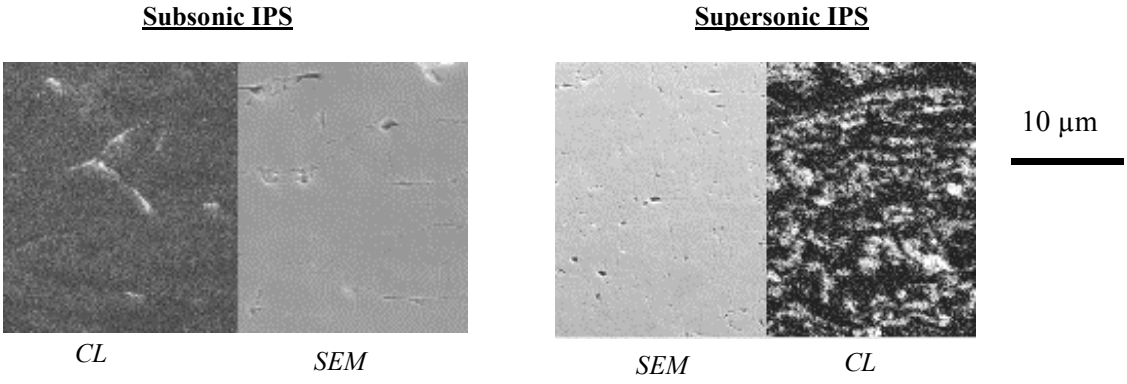

Figure 5 : CL and SEM micrographs of titania coatings prepared by subsonic IPS and supersonic IPS.

4. Conclusion

This work deals with the study of the heating and acceleration of titania particles in Inductive Plasma Spraying. The objective was to limit the decomposition of titania particles by using oxygen as sheath gas and a convergent-divergent "de Laval" nozzle to increase particle velocity.

The measurement of particle velocity and temperature made it possible to link the plasma spraying parameters and in-flight particle characteristics prior to impact on the substrate. For the powder with particle size between 22 and 45 µm, the particle temperatures ranged between 2100 and 2240°C and velocities between 30 and 60 m/s under IPS subsonic conditions, while they ranged between 1690 to 1715°C and between 330 to 380 m/s, respectively, under IPS supersonic conditions. For the powder with particle size between 5 and 20 µm, the measurements showed that the particle velocity was comprised between 440 and 730 m/s and the particle temperature between 2050 and 2150°C. The pressure in the chamber was found to be the factor that affects the most particle velocity whatever the inductive plasma spraying process was.

Moreover, thanks to the analysis of the titania plasma-sprayed coatings by a cathodoluminescence method, it was observed that the use of oxygen is not the only necessary condition to limit the decomposition of titania. The oxygen gas must be combined with a low particle velocity, obtained under subsonic IPS conditions, to favour the chemical equilibrium between the particles and plasma environment.

5. References

[1] M.I. Boulos, J. of Thermal Spray Technology, **1**(1), p.33-40 (1992)
[2] M. S. Bronet, M.I. Boulos, Plasma Chem. & Plasma Process., **9**, p.343-353 (1989)
[3] J. Lesinski, M.I. Boulos, Plasma Chem. & Plasma Process., **8**, p.133-139 (1988)
[4] S. Coulombe, X.L. Jiang, F. Gitzhofer, M.I. Boulos, Thermal Spray : Industrial Applications, (Ed.) C.C. Berndt, (Pub.) ASM Int., OH, USA, p.563-568 (1994)
[5] C. Moreau, P. Gougeon, M. Lamontagne, V. Lacasse, G. Vaudreuil, P. Cielo, Thermal Spray : Industrial Applications, (Ed.) C.C. Berndt, S. Sampath, (Pub.) ASM Int., OH, USA, p.431-437 (1994)
[6] R. Henne R., V. Borck, M. Muller, R. Ruckdaschel, G. Schiller, Proc. of the United Thermal Spray Conference 99, (Ed.) E. Lugscheider, P.A. Kammer, (Pub.) DVS Publishing House, Düsseldorf, Allemagne, p.598-599 (1999)
[7] N. Branland, Ph.D. University of Limoges (France) – University of Sherbrooke (Canada) (2002)
[8] L. Parent, J.P. Dodelet, G.G. Ross, B. Terreault, S. Dallaire, J. Electrochem. Soc., **132**, p.2590-2593 (1985)
[9] O. Storz, H. Gasthuber, M. Woydt, Surface and Coatings Technology, **140**, p.76-81 (2001)
[10] V.I. Petrov, Phys. Stat. Sol. (a), **133**, p.189-230 (1992)

MEASUREMENTS OF COOLING AND HEAT FLUXES IN A CRYOGENIC ATOMIZATION AND PLASMA SPRAYING PROCESS

E. Meillot
C.E.A. LE RIPAULT, B.P. 16, 37260 MONTS, France
Erick.Meillot@cea.fr

Abstract. This paper is devoted to heat flux measurements in a plasma spraying process to which a cooling system by liquid cryogenic atomization is added. The heat fluxes are measured for both systems and the interactions between the two jets are investigated via these fluxes. The goal of this study is to analyze the heat received by the substrate to determine the cooling, avoiding an increase in the local substrate temperature and therefore the damage of the substrate.

Key words : Plasma spraying, cooling, heat flux, cryogenic atomization.

Introduction. Plasma Spraying heats and accelerates sub-micron particles which crash onto a substrate. This results in a coating by the piling up of particles which improves the performance of the substrate. Generally, the substrate temperature grows due to the heating by the melted particles and by the enthalpy plasma gas which reach the substrate. The coating properties depend on the thermocinetic state of the particles impacting onto the substrate, but also on the cooling speed of the particles spreading out on the substrate while spraying /1/. The increase in temperature has high importance due to the consequences in the coating properties. The residual stress distribution within coatings depends mainly on the temperature distribution within coatings during spraying /2/ /3/. At the end, this increase could lead to the destruction of the substrate, or the piece to be coated, by thermal dilatations (for example) or by chemical behavior, if the temperature over grows the changing phase temperature. So several methods were followed to cool the substrate while spraying : high velocity cold gas cooling /4/, cryogenic spray cooling /5/…
At the beginning of the 80's, the CEA patented this last cooling : argon liquid at low temperature (≈ 84 K) pulverized by spraying nozzles onto the substrate /6/. This process is called Atmosphere and Temperature Control (A.T.C.) Plasma Spraying. This involves a high cooling by low temperature droplets impacting the substrate simultaneously with the deposition formation. So high melting temperature particles can be deposited onto low destruction temperature substrates (less than 100°C).
This paper is devoted to the heat and cooling flux measurements from both plasma spraying torch and cryogenic cooling device. The goal of this work is to compare the fluxes obtained by different operation parameters of the cooling nozzles and to quantify the interactions of the cooling droplet jet with the plasma flow near the substrate.

I – Experimental System.

Plasma operating parameters. An F100 CONNEX SULZER METCO plasma torch is equipped with a 6 mm diameter anode and stands on a 6 axis robot arm. The operating parameters, summarized in table 1, were determined to spray ceramics or metals such as TIO_2 /7/ for example. These conditions lead to an effective power at the torch exit of about 9.5 kW resulting in gas enthalpy of 13.8 MJ/kg. In the L.T.E. assumption, the average off-gas temperature is more than 10000 K.
Cooling operating system. The robot arm is also equipped with the cooling system. In case of important heat to evacuate, several cooling devices stand around the plasma torch (cf. figure 1).
The first one concerns the cooling with high speed argon gas flow rate through two rods each side of the torch at 18 mm from the torch axis. The argon flow rate is typically 15 sm^3h. These two rods are copper tubes with an inside diameter of 4 mm and a length of 80 mm. Five holes of 2 mm diameter are spaced 10 mm from each other. The 3rd hole is at the same centerline as the torch axis. This configuration produces a vertical barrier of cold gas in each part of the torch.

The second one is composed of two atomizers 40 mm from the axis of the torch. These atomizers are SPRAYING SYSTEMS referenced 100150. They are assisted atomizers because of the injection of high speed gas around the liquid jet.

Table 1 : Plasma operating conditions

Parameter	Value
Argon flow rate (slm)	20
Helium flow rate (slm)	30
Intensity (A)	50
Spraying distance (mm)	120
Electric power (kW)	15.75

The front face of the global apparatus (torch, nozzles, rods) stands in the same plan at 120 mm from the substrate.
Let us closer describe the nozzles with their two feed networks. The liquid flows in a central pipe. With the 100150 nozzle, the exit diameter is 2 mm but it has been drilled at 2.9 mm for a higher flow rate.
To feed the nozzles in liquid, the pressure is regulated from 1.2 10^5 to 1.8 10^5 Pa in the feedstock. The liquid flows in vacuum isolated pipes from the feedstock to the nozzles.
Around this network exit, the first circuit of the assistance gas takes place. It has a smaller diameter of 3.9 mm and an upper one of 4.9 mm. The goal of the assistance gas is to destroy the liquid jet in small droplets due to the high speed difference between the two jets. In this kind of nozzle , the goal of the second gas network is to put in shape the droplet jet: so two lateral holes take places in each part of the jet at some millimeters after the exit (3 mm). With this configuration, the droplet jet is in shape as a vertical plan, normally avoiding the interactions with the plasma or the sprayed particles. The two gas networks are in connection: so it is impossible to determine the gas flow rate passing in each part. We only know the global gas flow rate, around 22 sm^3h in nominal operating conditions. A remark : the central assistance gas network can be closed. In this case, the gas passes through the second circuit by the two lateral holes. This configuration is a particular motivation for this study.

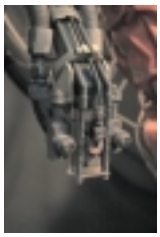

Figure 1 : Torch and cooling systems.

Figure 2 : Flux measurement device.

Heat flux measurement device. To quantify the plasma and atomized cooling fluxes, a heat flux measurement has been developed. First measurements have shown the opportunity to quantify the fluxes but also to determine the fluctuations of the plasma /8/ impacting the substrate due to the movement of the arc foot in the anode.
Eleven sensors are attached to a copper support (figure 2), and linked to a data acquisition computer. These sensors are copper/constantin multi-layers. The small sensor size (10 mm x 10 mm x 70 µm) gives them a high sensitivity (about 0.50 $\mu V/W/m^2$) and a short reaction time (less than 1 ms). The signal is directly proportional to the heat flux, positive for heating and negative for cooling. Moreover, three thermocouples measure the surface temperature of the copper sheet. The system drawback, due to the varnish protecting the probes, is the operating temperature, which must range between -200 and +200 °C.
Operating procedure tests have shown that the results are reproducible with an acquisition data frequency less than 350 Hz. In fact, for each sensor, an average of five consecutive measurements is

made: this averaged value is recorded in a file and corresponds to one measurement point. The error is around 10% in steady state.

II – Experimental Conditions.

The plasma conditions of table 1 remained constant in surrounding air. The stand off distance between the torch exit and the substrate was 120 mm. This distance was also kept for the cooling devices.
The translation movement of the robot arm, equipped with the global apparatus, was regulated at 1000 mm/s which is a usual velocity for this kind of applications.
Let us have a look of the cooling conditions. First, the atomizers were analyzed alone without the two gas rods. Four liquid pressures were investigated to feed the atomizers : 0.12 ; 0.14 ; 0.16 ; 0.18 MPa. According to the exit diameter of the atomizers and the BERNOUILLI law, neglecting the charge looses in the pipes, the liquid flow rates were respectively 7.24, 7.82, 8.36 and 8.87 kg/mn. Three gas pressures (0.4 ; 0.6 ; 0.8 Mpa) were also used to destroy the liquid jet; they lead respectively to 18, 22, 25 sm^3h gas flow rates.
All these conditions were explored in two designs of the atomizers : firstly in normal configuration with the two opened gas networks (It will be called case I in the following paragraphs). Secondly, with the central assistance gas network closed (It will be called case II in the following paragraphs). After that the gas rods were under pressure. The experiments were carried out with the highest gas pressure (0.8 MPa) and with the four liquid flow rates.

III – Results And Discussion.

For all the investigations, references are necessary. So, the single plasma heat flux received by the substrate will be analyzed first. Then the plasma flux will be investigated with the substrate cooling by the two ways, firstly with the single atomizers, secondly with the addition of the gas rods. At the end, the interactions between the two different kinds of jet will be analyzed to conclude this work.

The plasma flux.

The plasma flux without cooling. First of all, let us have a look at the heat generated by the plasma and received by the substrate without any cooling. Figure 3 shows the heat flux recorded by one captor during time. The maximal average flux is around 15 W/cm². In figure 4, the space distribution of the maximum flux is rather extensive : the half-height width gets a surface with a radius of 25 mm. This result will be kept as reference for the following comparisons.

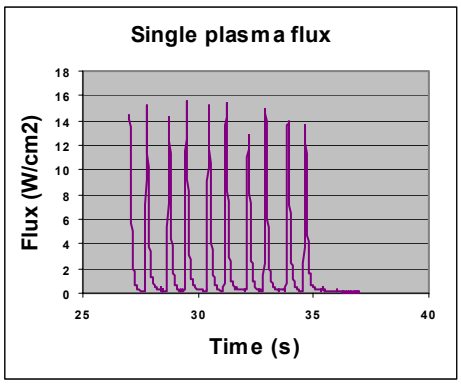

Figure 3 : Plasma flux measured by the central captor versus time.

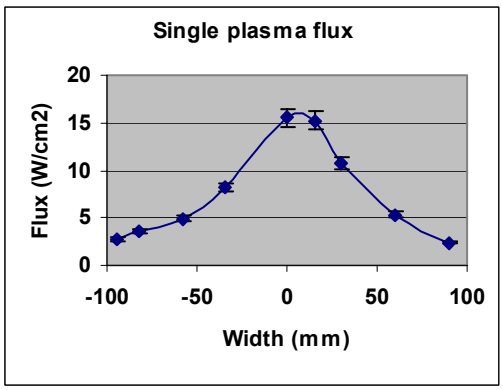

Figure 4 : Plasma flux spatial distribution.

The plasma flux with cryogenic atomization. After measurements of the single plasma flux, the cooling of the substrate is introduced by cryogenic atomization. The liquid flow rate (7.24 kg/mn) and the gas pressure (0.4 Mpa) lead to a decrease in the plasma flux to around 9 W/cm² (figure 5).

The plasma flux decreases with an increase in the assistance gas of atomization (figures 5 and 6). When the central assistance gas network is closed, it brings about a strong decrease in the flux (figure 6). Similar behaviors are noticed for every liquid flow rate.

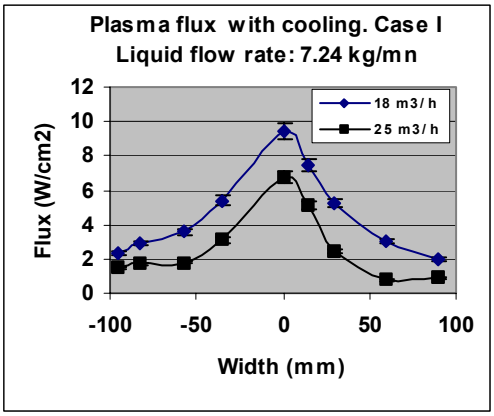

Figure 5 : Plasma flux with cooling in case I (Liquid flow rate: 7.24 kg/mn; Gas flow rate: 18 and 25 sm^3h)

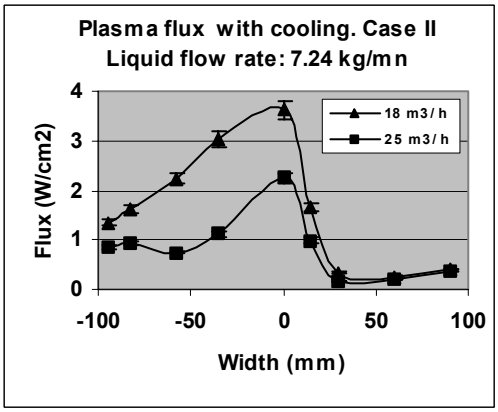

Figure 6 : Plasma flux with cooling in case II (Liquid flow rate: 7.24 kg/mn; Gas flow rate: 18 and 25 sm^3h)

In figure 6 (case II), the two curves show a asymmetry of the flux which is present for every experiment. We assume this is due to a bad position of the lateral holes on either side of the liquid centerline. In fact, the first goal of these lateral holes is to put in shape the liquid jet, not to destroy it.

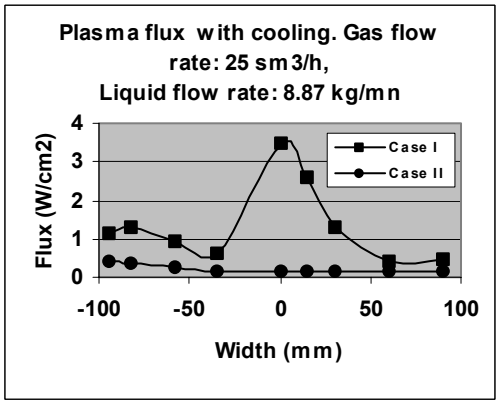

Figure 7 : Plasma flux with cooling by single nozzles in cases I and II (Liquid flow rate: 8.87 kg/mn; Gas flow rate: 25 sm^3h)

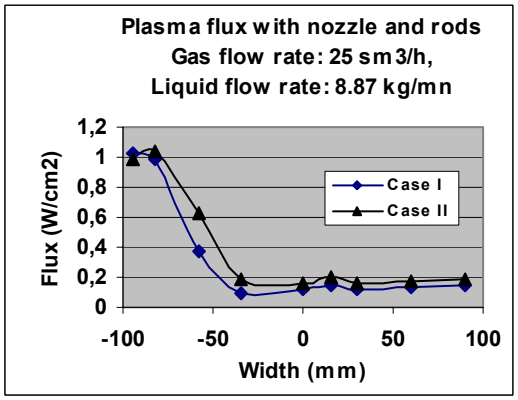

Figure 8 : Plasma flux with cooling by nozzles and rods in cases I and II (Liquid flow rate: 8.87 kg/mn; Gas flow rate: 25 sm^3h)

These experiments show strong interactions between the plasma and the cooling flows as if the cooling jet acts as a screen between the plasma and the substrate. The interactions could be due to the low distance (40 mm) between the plasma and the two atomizers. These interactions increase strongly with the liquid flow rate (figure 7): the flux reduces to less than 4 W/cm² in case I and less than 1 W/cm^2 in case II. This has a high consequence on the substrate temperature increase and certainly on the deposition efficiency by the elimination of the finest particles before impacting the substrate. This cannot be investigated in this study.

The plasma flux with cryogenic atomization and the gas rods. To conclude the measurements of the plasma flux, the second device with the gas rods is active with an argon gas flow rate of 15 sm^3h for both rods (figure 8). The previous conclusion about the interactions between the plasma and the cooling gas flows is strongly amplified : the plasma flux impacting the substrate is less than 1 W/cm² and presents a strong asymmetry.

The cooling flux. Let us consider different argon liquid flow rates.
The first one is called case A for low liquid flow rate (7.24 kg/mn) and for the three gas flow rates. Comparisons are made with the central atomization gas network opened (case I) or closed (case II).

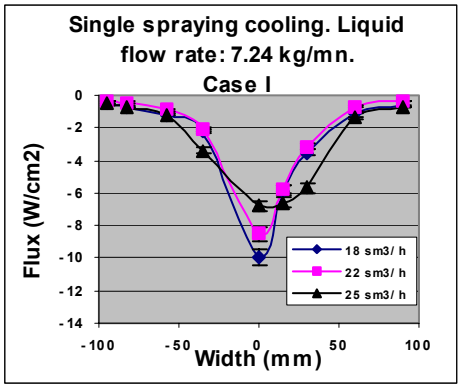

Figure 9: Single spraying cooling case I
(Liquid flow rate: 7.24 kg/mn)

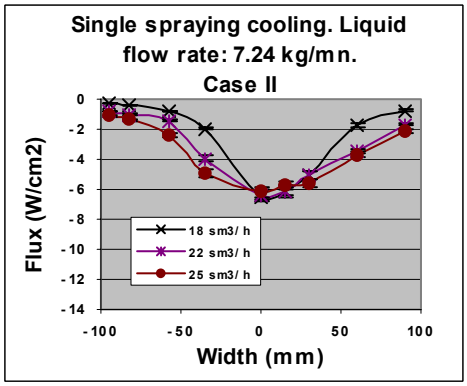

Figure 10: Single spraying cooling case II
(Liquid flow rate: 7.24 kg/mn)

Figures 9 and 10 show the space flux distributions for both cases I and II. In figure 9, the two higher fluxes (around –9 W/cm2) are due to the lower gas flow rates passing through the central atomization gas network. The decrease in the flux is due to the increase in the gas flow rate : over 22 m^3/h, the gas flow is too important and breaks the liquid sheet in very small droplets which can evaporate before impacting the substrate. This trend is a standard: the flux always decreases with an increase in the gas flow rate for every condition but this evolution is more or less important depending on the liquid flow rate. In case II (figure 10), the flux intensities are in the some order independent of the gas flow rate but with a tendency to spread. The half-height width leads to a 40 mm radius. This spreading is observed each time the central atomization gas network is closed.

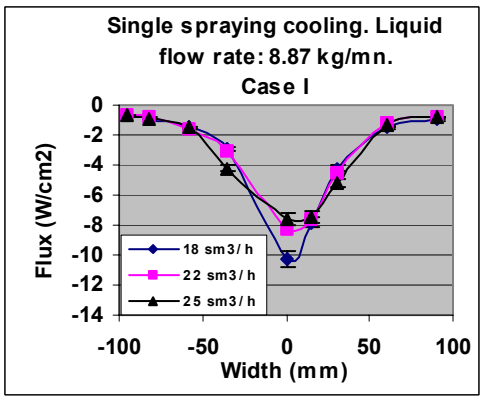

Figure 11: Single spraying cooling case I
(Liquid flow rate: 8.87 kg/mn)

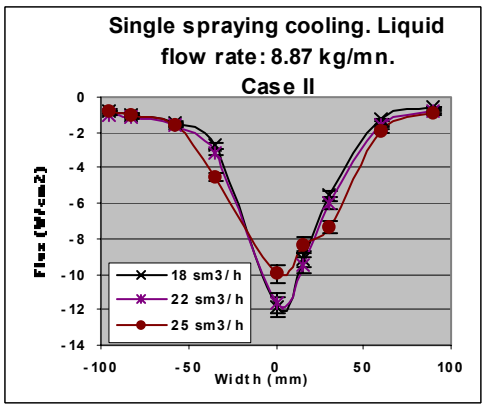

Figure 12: Single spraying cooling case II
(Liquid flow rate: 8.87 kg/mn)

Let us consider case B with the highest liquid flow rate (8.87 kg/mn) and for the different gas flow rates. Figures 11 and 12 present the comparisons with the central atomization gas network opened or closed. Of course, the maximum flux increases (around –12 W/cm²) but the droplet jet spreads less than in the previous case for any parameters. Moreover, the higher fluxes are obtained when the central atomization gas network is closed: there is an inversion of the cooling efficiency in comparison with the case A. The asymmetry is weaker and does not depend on the introduction way of gas flow rate : We only notice it with the highest gas flow rate (figure 12).
Different conclusions can be extracted from these experiments :

- The maximum flux diminishes with an increase in the gas flow rate.
- This flux increases with the liquid flow rate, but with the lowest flow rates (7.24 kg/mn and 7.82 kg/mn) the measured flux leads to an asymptote around – 8 W/cm².
- The central atomization gas network must be closed or not, depending on the liquid flow rate. For the low liquid flow rate, the closing is not approved : it leads to a liquid spreading and to lower cooling flux. For the high liquid flow rate, the closing is approved : there is no significant step of spreading by comparison with and without closing, but the cooling flux is higher when the network is closed.

Plasma-Cooling flux interactions. In this part, the interactions between the two sources of heat and cooling are further investigated. The following assumption is set down: the devices are in steady state so that the flux measurements are still correct at the same point independent of time. So the way to identify these interactions uses the difference between fluxes from the plasma and the cryogenic atomization without and with the gas rods.
In the general way, the main conclusions are :

- The difference is positive for nearly every case and less than 1 W/cm² on the edges.
- This difference becomes negative in the center of the measurement area: the higher liquid flow rate, the higher difference. This is amplified when the central atomization gas network is closed. So the plasma produces less calories than the pulverization can extract (but the sprayed particles have to give their energy to the substrate too).

The minimum of the difference is slightly displaced for the low liquid flow rate as seen in figure 13. This gap is also noticed, but in less of a way, without closing the central atomization gas network. An increase in the liquid flow rate in both configuration (closing or opening the central atomization gas network) leads to a complete reduction of the displacement (figure 14). This could be explained by the difference in momentum between the plasma and the liquid argon jets. This last one becomes stronger with the increase in the mass flow rate and so less sensitive to hydrodynamic forces of the plasma jet.

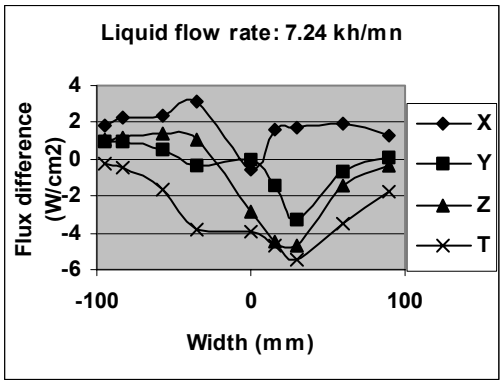

Figure 13 : Flux difference. Liquid flow rate : 7.24 kg/mn for different configurations :
X : case I and 18 sm^3h gas flow rate
Y : case I and 25 sm^3h gas flow rate
Z : case II and 18 sm^3h gas flow rate
T : case II and 25 sm^3h gas flow rate

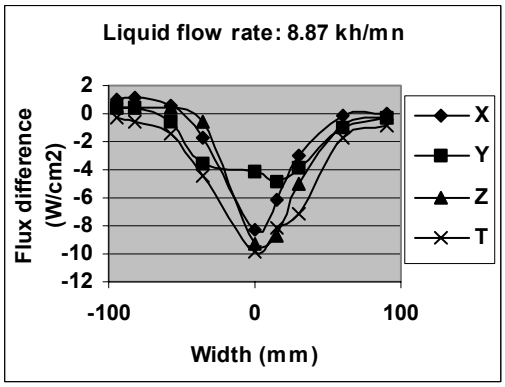

Figure 14 : Flux difference. Liquid flow rate : 7.24 kg/mn for different configurations :
X : case I and 18 sm^3h gas flow rate
Y : case I and 25 sm^3h gas flow rate
Z : case II and 18 sm^3h gas flow rate
T : case II and 25 sm^3h gas flow rate

Now, let us introduce the gas rods in the experiments. The presence of the argon gas flow replaces the maximum in the difference in the center of the measurement area. This trend is always true for every experiment (comparison between Y and X or Z and T in figures 15 or 16). So the first consequence of the argon gas rod is to separate well the two heat and cooling sources. The second one concerns the cooling efficiency. The cooling flux changes from –4 W/cm² to –6 W/cm² without and with the argon gas rods. This efficiency trends to slightly diminish with an increase in the liquid flow rate.

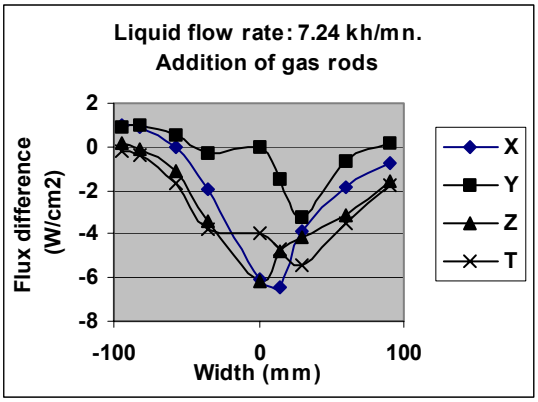

Figure 15 : Flux difference. Liquid flow rate : 7.24 kg/mn and addition of gas rods for different configurations :
X : case I and 18 sm^3h gas flow rate
Y : case I and 25 sm^3h gas flow rate
Z : case II and 18 sm^3h gas flow rate
T : case II and 25 sm^3h gas flow rate

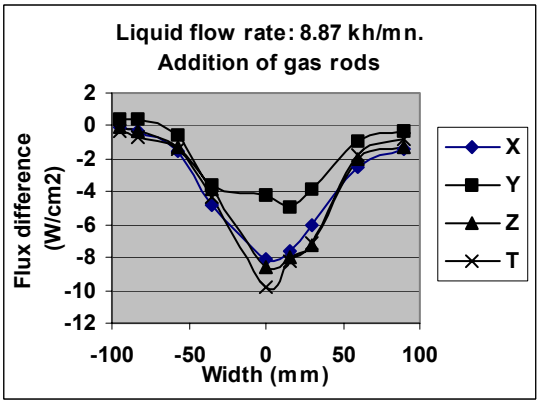

Figure 16 : Flux difference. Liquid flow rate : 8.87 kg/mn and addition of gas rods for different configurations :
X : case I and 18 sm^3h gas flow rate
Y : case I and 25 sm^3h gas flow rate
Z : case II and 18 sm^3h gas flow rate
T : case II and 25 sm^3h gas flow rate

When the central atomization gas network is opened (case I), the cooling flux increases strongly from 0 W/cm² to –6 W/cm² (figure 15) when the liquid flow rate is rather low (comparison Y and Z in figure 15). The same conclusions can be extracted from figure 16 for higher liquid flow rate (comparison Y and Z in figure 15).

Conclusion. Measurements of plasma heat and pulverized argon liquid cooling fluxes impacting a substrate have been carried out in several configurations. For the plasma, the maximum heat flux is up to 15 W/cm² but with cryogenic atomization cooling, it goes down to 9 W/cm² and the adding of argon gas rods on both side leads to less than 6 W/cm². These first measurements show strong interactions between the plasma and the cooling jets.
For the cryogenic atomization cooling, two ways were investigated :

- firstly in standard configuration, with the central atomization gas network opened (case I)
- secondly this one closed (case II).

The best configuration in term of cooling fluxes received by the substrate depends on the argon liquid flow rate. For low argon liquid flow rate, the standard configuration leads to higher cooling fluxes. For high argon liquid flow rate, the closing of the central atomization gas network shows a better efficiency of cooling.
The addition of two argon gas injection rods in each part of the torch and between it and the spraying system leads to well separate the plasma and the droplet jets and so diminishes the interactions between the two jets. In this case, the cooling efficiency is upper.

/1/ D. BERNARD et al., Influence of the Torch-Substrate Relative Movements and Cooling of the Coatings During Spraying on the Technical Properties of TBCs, Thermal Spray Research and Applications, Proc of 3rd National Thermal Spray Conference, Long Beach, CA, USA, 20-25 May 1990.

/2/ F. GITZHOFER et al., Influence of Plasma Torch to Substrate Speed and Overlap on Deposit Temperatures during Spraying and on Residual Stresses : Theoretical Study and Preliminary Experiments, 1989.

/3/ N. BARADEL, Etude de la génération des contraintes au sein de revêtements de zircone triée réalisées par projection plasma sur substrats métalliques, Ph. D. Thesis, Ecole Nationale Supérieure des Mines de Paris, 26 mai 1999.

/4/ B. SIWON , Comparisons of Heat Transfer from a Warm Flat Surface Cooled by Impinging a Liquid Jet and a Gas Liquid Spray Jet, Int. Comm. Heat Mass Transfer, Vol. 18, pp 229-238, 1991.

/5/ A. FRESLON, E. MEILLOT, Plasma Spraying at Controlled Temperature by Cryogenic Cooling : Pulverizing of Liquefied Gas, Proceeding of 9th N.T.S.C., Atlanta, USA, oct. 96.

/6/ B. HANSZ, M. BONCOEUR, Process and Apparatus for Cooling a Material and Application to the Manufacture of Refractory Materials by Tempering, European Patent EP0125964, nov. 1984.

/7/ N. BRANLAND at al., Relationships between Microstructure and Electrical Properties of Plasma Sprayed Tio_2 Coatings, Proceeding of CIMTEC 2002, FIRENZE, ITALIA, 2002.

/8/ E. MEILLOT at al., Measurements of Heat Flux in an Atmosphere and Temperature Controlled Plasma Spraying Process, Heat and Mass Transfer under Plasma Conditions, Annals of the New York Academy of Sciences, Vol. 891, pp 90-97 , Dec. 1999

Simulation of gas-phase chemistry and hydrogenated silicon cluster time-evolution during corpuscular deposition

A.F. Stekolnikov[1], D.V. Feshchenko[1], O.N. Petrovich[2],
T.A. Metelskiy[1], P.G.Makshov[1], A.G.Galkevich[1]

[1]*Belarus State University of Informatics and Radioelectronics, Minsk, Belarus*
[2]*Polotsk State University, Novopolotsk, Belarus*

Abstract

New gas-phase model of silane decomposition during plasma enhanced chemical vapor deposition with formation of stable negative hydrogenated silicon ion clusters is suggested. The kinetics equations describing time dependent cluster formation are computed.

Introduction

The simulation of particle growth kinetics requires a time-dependent modeling of the gas-phase plasma chemistry. Currently negative ions are believed to be the precursors of silicon dust in a SiH_4 plasma. Mass spectroscopy reveals that negative ions can grow up to 60 Si atoms. We have suggested a generalized model of gas-phase reactions of silane decomposition initiated by the electron impact with formation negative, containing up to 30 silicon atoms, and positive, containing 5 silicon atoms, hydrogenated ion clusters following [1-2].

In the kinetics scheme of silane decomposition 219 reactions were included.

The mathematical model of the task comes to a set of stiff ordinary first-order-differential equations with the given initial conditions, which describe in time the processes of the production of both stable products and fast-reacting species:

$$\frac{dN_i}{dt} = \sum n_e K_{ij} N_j + \sum_{jl} K_{ijl} N_j N_l - N_i \left(\sum n_e K_{ji} + \sum_{jl} K_{ijl} N_l \right)$$

Results and discussions

The computed kinetic curves of the negative hydrogenated silicon ion clusters behaviour for the silane density $N=10^{15}$ cm^{-3}, the electron density $Ne=10^9$ cm^{-3} and electron temperature Te=1.0 eV are presented on fig. 1-4. The cluster growth mechanism considered involves initiating, growth and suppressing spices.

Numerical results on negative hydrogenated silicon ion clusters point out forming of stable negative molecular cluster groups: $Si_6H_{13}^-$, $Si_7H_{15}^-$, $Si_8H_{17}^-$, $Si_9H_{19}^-$, $Si_{10}H_{21}^-$, $Si_{11}H_{23}^-$, $Si_{12}H_{25}^-$, $Si_{13}H_{27}^-$, $Si_{14}H_{29}^-$, $Si_{15}H_{31}^-$, $Si_{16}H_{33}^-$, $Si_{17}H_{35}^-$, $Si_{18}H_{37}^-$, $Si_{19}H_{39}^-$, $Si_{20}H_{41}^-$, $Si_{21}H_{43}^-$, $Si_{22}H_{45}^-$, $Si_{23}H_{47}^-$, $Si_{24}H_{49}^-$, $Si_{25}H_{51}^-$, $Si_{26}H_{53}^-$, $Si_{27}H_{55}^-$, $Si_{28}H_{57}^-$, $Si_{29}H_{59}^-$, $Si_{30}H_{61}^-$. The threshold of the appearance of main stable group of high-mass negative ions $Si_{15}H_{31}^-$ up to $Si_{30}H_{61}^-$ is in time limit $1.5 \cdot 10^{-5}$ s and $1.1 \cdot 10^{-4}$ s. Their concentration ranges from $7 \cdot 10^7$ cm^{-3} up to $8 \cdot 10^3$ cm^{-3} for the time $5 \cdot 10^{-4}$ s.

In conclusion we have simulated plasma enhanced silane decomposition on base of the generalized model of gas-phase reactions. The calculation performed with the account for recent experimental result indicate formation of study negative hydrogenated silicon ion clusters at high concentrations. They have masses bigger than those of positive ion clusters. It allows us to state confidently that the formation of a silicon dust with the particle more than 10 nm is connected with a continuum of negative clusters in a silane plasma.

Finally, we have developed theory of the negative hydrogenated silicon ion clustering in corpuscle deposition processes.

References

[1] C. Hollenstein et al., J. Phys. D 31, (1998) 74.
[2] A.F. Stekolnikov, D.V. Feshchenko et al., Proc. *XV ESCAMPIG* (Lillafured, Miskolc, Hungary, 2000).

Scheme of reaction	Rate reaction constant
1. $SiH_4 + e = SiH_3 + H + e^*$	1.59(-10)
2. $SiH_4 + e = SiH_2 + 2H + e^*$	1.87(-11)
3. $SiH_4 + e = SiH + 3H + e^*$	6.20(-09)
4. $SiH_4 + e = SiH_2 + H_2 + e^*$	2.53(-10)
5. $SiH_4 + e = SiH + H_2 + H + e^*$	9.34(-12)
6. $SiH_4 + e = SiH_3^+ + H + 2e^*$	5.64(-12)
7. $SiH_4 + e = SiH_2^+ + H_2 + 2e^*$	7.19(-12)
8. $SiH_4 + e = SiH^+ + H_2 + H + 2e^*$	1.39(-12)
9. $SiH_4 + e = Si^+ + 2H_2 + 2e^*$	1.19(-12)
10. $SiH + e = Si + H + e^*$	3.97(-09)
11. $SiH_3^+ + e^* = SiH_3$	5.00(-07)
12. $SiH_2^+ + e^* = SiH_2$	5.00(-07)
13. $SiH^+ + e^* = SiH$	5.00(-07)
14. $Si^+ + e^* = Si$	5.00(-07)
15. $e + e^* = 2e$	3.25(-09)
16. $SiH_4 + e = SiH_3^- + H$	2.50(-13)
17. $SiH_4 + e = SiH_2^- + H_2$	1.50(-13)
18. $SiH_3^- + SiH_3^+ = 2SiH_3$	5.00(-12)
19. $SiH_2^- + SiH_2^+ = 2SiH_2$	5.00(-12)
20. $SiH_2 + SiH_2 = Si_2H_4$	1.00(-07)
21. $SiH_3 + SiH_3 = Si_2H_6$	1.00(-10)
22. $Si_2H_6 + e = SiH_4 + SiH_2 + e^*$	2.86(-10)
23. $Si_2H_6 + e = Si_2H_4 + H_2 + e^*$	1.23(-10)
24. $Si_2H_6 + e = Si_2H_4^+ + H_2 + 2e^*$	2.45(-11)
25. $Si_2H_6 + e = SiH_3^+ + SiH_3 + 2e^*$	1.75(-11)
26. $Si_2H_6 + e = Si_2H_5^+ + H + 2e^*$	1.75(-11)
27. $Si_2H_6 + e = Si_2H_2^+ + 2H_2 + 2e^*$	1.15(-11)
28. $Si_2H_6 + e = SiH_3^- + SiH_3$	9.45(-14)
29. $Si_2H_6 + e = SiH_2^- + SiH_4$	9.45(-14)
30. $Si_2H_2^+ + e^* = Si_2H_2$	5.00(-07)
31. $Si_2H_4^+ + e^* = Si_2H_4$	5.00(-07)
32. $Si_2H_5^+ + e^* = Si_2H_5$	5.00(-07)
33. $SiH_4 + H = SiH_3 + H_2$	2.86(-12)
34. $SiH_4 + SiH_2 = Si_2H_6$	1.00(-10)
35. $SiH_4 + SiH_3 = Si_2H_3 + 2H_2$	1.78(-15)
36. $SiH_4 + Si_2H_4 = Si_3H_8$	1.00(-11)
37. $SiH_4 + Si_2H_5 = Si_2H_6 + SiH_3$	5.00(-13)
38. $Si_2H_6 + SiH_3 = SiH_4 + Si_2H_5$	1.00(-12)
39. $Si_2H_6 + SiH_2 = Si_3H_8$	1..20(-10)
40. $Si_2H_6 + H = SiH_3 + SiH_4$	1.11(-12)
41. $Si_2H_6 + H = H_2 + Si_2H_5$	2.16(-12)
42. $SiH_3 + H = SiH_2 + H_2$	1.00(-10)
43. $SiH_3 + SiH_3 = SiH_2 + SiH_4$	7.00(-12)
44. $SiH_3 + Si_2H_5 = Si_3H_8$	1.00(-11)
45. $SiH_2 + H = SiH_3$	1.11(-12)
46. $SiH + H_2 = SiH_3$	1.98(-12)
47. $SiH^+ + SiH_4 = Si_2H_3^+ + H_2$	1.36(-09)
48. $SiH^+ + SiH_4 = Si_2H^+ + 2H_2$	8.10(-11)
49. $SiH^+ + Si_2H_6 = Si_2H_3^+ + SiH_4$	1.90(-09)
50. $SiH_2^+ + SiH_4 = SiH_3^+ + SiH_3$	1.13(-09)
51. $SiH_2^+ + SiH_4 = Si_2H_4^+ + H_2$	8.20(-10)
52. $SiH_2^+ + SiH_4 = Si_2H_2^+ + 2H_2$	1.50(-10)
53. $SiH_2^+ + SiH_4 = Si_2H_6^+$	2.00(-11)
54. $SiH_2^+ + Si_2H_6 = SiH_3^+ + Si_2H_5$	1.52(-09)
55. $SiH_2^+ + Si_2H_6 = Si_2H_4^+ + SiH_4$	1.28(-09)
56. $SiH_2^+ + Si_2H_6 = Si_2H_5^+ + SiH_3$	8.80(-10)
57. $SiH_2^+ + Si_2H_6 = Si_2H_2^+ + SiH_4 + H_2$	3.20(-10)
58. $SiH_3^+ + SiH_4 = SiH_3^+ + SiH_4$	1.10(-09)
59. $SiH_3^+ + SiH_4 = Si_2H_5^+ + H_2$	2.80(-11)
60. $SiH_3^+ + SiH_4 = Si_2H_3^+ + 2H_2$	8.00(-12)
61. $SiH_3^+ + Si_2H_6 = Si_2H_5^+ + SiH_4$	6.00(-10)
62. $Si_2H^+ + Si_2H_6 = Si_3H^+ + SiH_4 + H_2$	5.70(-10)
63. $Si_2H^+ + Si_2H_6 = Si_3H_3^+ + SiH_4$	2.70(-10)
64. $Si_2H^+ + Si_2H_6 = Si_4H_3^+ + 2H_2$	1.60(-10)
65. $Si_2H_2^+ + SiH_4 = Si_3H_4^+ + H_2$	3.20(-11)
66. $Si_2H_2^+ + Si_2H_6 = Si_3H_4^+ + SiH_4$	4.60(-10)
67. $Si_2H_3^+ + SiH_4 = Si_3H_5^+ + H_2$	7.90(-10)
68. $Si_2H_3^+ + Si_2H_6 = Si_3H_5^+ + SiH_4$	4.60(-10)
69. $Si_2H_3^+ + Si_2H_6 = Si_4H_5^+ + 2H_2$	8.70(-11)
70. $Si_2H_3^+ + Si_2H_6 = Si_4H_7^+ + H_2$	3.50(-11)
71. $Si_2H_4^+ + SiH_4 = Si_3H_6^+ + H_2$	5.00(-13)
72. $Si_2H_4^+ + Si_2H_6 = Si_3H_6^+ + SiH_4$	3.60(-10)
73. $Si_2H_5^+ + SiH_4 = Si_3H_7^+ + H_2$	2.10(-11)
74. $Si_2H_5^+ + SiH_4 = Si_3H_9^+$	1.40(-12)
75. $Si_2H_5^+ + Si_2H_6 = Si_3H_7^+ + SiH_4$	7.00(-10)
76. $Si_2H_6^+ + Si_2H_6 = Si_2H_5^+ + Si_2H_5 + H_2$	4.80(-11)
77. $Si_2H_6^+ + Si_2H_6 = Si_3H_8^+ + SiH_4$	9.50(-11)
78. $Si_2H_6^+ + Si_2H_6 = Si_3H_9^+ + SiH_3$	8.10(-10)
79. $Si_3H^+ + Si_2H_6 = Si_4H_3^+ + SiH_4$	1.40(-09)
80. $Si_3H_2^+ + SiH_4 = Si_4H_6^+$	1.00(-12)
81. $Si_3H_2^+ + Si_2H_6 = Si_4H_4^+ + SiH_4$	2.00(-12)
82. $Si_3H_3^+ + Si_2H_6 = Si_4H_5^+ + SiH_4$	2.70(-10)
83. $Si_3H_4^+ + SiH_4 = Si_4H_6^+ + H_2$	1.74(-10)
84. $Si_3H_4^+ + Si_2H_6 = Si_4H_4^+ + SiH_4 + H_2$	4.70(-10)
85. $Si_3H_4^+ + Si_2H_6 = Si_4H_6^+ + SiH_4$	4.70(-10)
86. $Si_3H_5^+ + SiH_4 = Si_4H_7^+ + H_2$	9.80(-10)
87. $Si_3H_5^+ + Si_2H_6 = Si_4H_5^+ + SiH_4 + H_2$	2.90(-10)
88. $Si_3H_5^+ + Si_2H_6 = Si_4H_7^+ + SiH_4$	5.10(-10)
89. $Si_3H_6^+ + Si_2H_6 = Si_4H_8^+ + SiH_4$	3.90(-10)
90. $Si_3H_7^+ + SiH_4 = Si_4H_9^+ + H_2$	5.00(-14)
91. $Si_3H_7^+ + SiH_4 = Si_4H_{11}^+$	1.20(-13)
92. $Si_3H_7^+ + Si_2H_6 = Si_4H_9^+ + SiH_4$	3.10(-11)
93. $Si_3H_7^+ + Si_2H_6 = Si_5H_{11}^+ + H_2$	1.00(-12)
94. $Si_3H_7^+ + Si_2H_6 = Si_5H_{13}^+$	2.00(-12)
95. $Si_3H_8^+ + Si_2H_6 = Si_4H_{10}^+ + SiH_4$	6.40(-11)
96. $Si_3H_9^+ + Si_2H_6 = Si_4H_{11}^+ + SiH_4$	3.50(-10)
97. $Si_4H_2^+ + SiH_4 = Si_5H_4^+ + H_2$	1.80(-10)
98. $Si_4H_4^+ + Si_2H_6 = Si_5H_6^+ + SiH_4$	2.00(-10)
99. $Si_4H_5^+ + Si_2H_6 = Si_5H_7^+ + SiH_4$	1.30(-11)
100. $Si_4H_6^+ + Si_2H_6 = Si_5H_8^+ + SiH_4$	5.50(-11)
101. $Si_4H_7^+ + SiH_4 = Si_5H_{11}^+$	1.00(-10)
102. $Si_4H_7^+ + Si_2H_6 = Si_5H_9^+ + SiH_4$	2.70(-10)
103. $Si_4H_8^+ + Si_2H_6 = Si_5H_{10}^+ + SiH_4$	8.40(-11)

104. $Si_4H_{11}^+ + Si_2H_6 = Si_5H_{13}^+ + SiH_4$ 7.00(-12)
105. $Si^- + SiH_4 = H_2SiSi^- + H_2$ 1.29(-09)
106. $Si^- + SiH_4 = H_2SiSiH_2 + e^*$ 1.29(-09)
110. $SiH^- + SiH_4 = Si_2H_5 + e^*$ 1.28(-09)
111. $SiH^- + Si_2H_6 = H_3SiSi^- + SiH_4$ 1.53(-09)
112. $SiH^- + Si_2H_6 = Si_3H_7 + e^*$ 1.53(-09)
113. $SiH_2^- + SiH_4 = H_3SiSiH^- + H_2$ 1.27(-09)
114. $SiH_2^- + SiH_4 = Si_2H_6 + e^*$ 1.27(-09)
115. $SiH_2^- + Si_2H_6 = H_3SiSiH^- + SiH_4$ 1.51(-09)
116. $SiH_2^- + Si_2H_6 = Si_3H_8 + e^*$ 1.51(-09)
117. $SiH_3^- + SiH_4 = Si_2H_5^- + H_2$ 1.26(-09)
118. $SiH_3^- + Si_2H_6 = Si_2H_5^- + SiH_4$ 1.50(-09)
119. $Si_2^- + SiH_4 = Si_3H_2^- + H_2$ 1.11(-09)
120. $Si_2H^- + SiH_4 = Si_3H_3^- + H_2$ 1.10(-09)
121. $H_2SiSi^- + SiH_4 = Si_3H_4^- + H_2$ 1.10(-09)
122. $H_3SiSi^- + SiH_4 = Si_3H_5^- + H_2$ 1.10(-09)
123. $H_3SiSiH^- + SiH_4 = Si_3H_6^- + H_2$ 1.10(-09)
124. $Si_2H_5^- + SiH_4 = Si_3H_7^- + H_2$ 1.09(-09)
125. $Si^- + SiH_3 = Si + SiH_3$ 1.40(-09)
126. $Si^- + SiH_3 = Si_2H^- + H_2$ 1.40(-09)
127. $Si^- + SiH_2 = Si_2^- + H_2$ 1.40(-09)
128. $SiH^- + H = Si^- + H_2$ 1.93(-09)
129. $SiH^- + SiH_3 = SiH + SiH_3^-$ 1.40(-09)
130. $SiH^- + SiH_3 = H_2SiSi^- + H_2$ 1.40(-09)
131. $SiH^- + SiH_3 = Si_2^- + 2H_2$ 1.40(-09)
132. $SiH^- + SiH_2 = Si_2H^- + H_2$ 1.40(-09)
133. $SiH^- + SiH = Si_2^- + H_2$ 1.40(-09)
134. $SiH^- + Si = SiH + Si^-$ 1.40(-09)
135. $SiH_2^- + H = SiH^- + H_2$ 1.93(-09)
136. $SiH_2^- + SiH_3 = SiH_2 + SiH_3^-$ 1.40(-09)
137. $SiH_2^- + SiH_3 = H_3SiSi^- + H_2$ 1.40(-09)
138. $SiH_2^- + SiH_3 = Si_2H^- + 2H_2$ 1.40(-09)
139. $SiH_2^- + SiH_2 = H_2SiSi^- + H_2$ 1.40(-09)
140. $SiH_2^- + SiH_2 = Si_2^- + 2H_2$ 1.40(-09)
141. $SiH_2^- + SiH = SiH_2 + SiH^-$ 1.40(-09)
142. $SiH_2^- + SiH = Si_2H^- + H_2$ 1.40(-09)
143. $SiH_2^- + Si = SiH_2 + Si^-$ 1.40(-09)
144. $SiH_2^- + Si = Si_2^- + H_2$ 1.40(-09)
145. $SiH_3^- + H = SiH_2^- + H_2$ 1.93(-09)
146. $SiH_3^- + SiH_3 = H_3SiSiH^- + H_2$ 1.40(-09)
147. $SiH_3^- + SiH_3 = H_2SiSi^- + 2H_2$ 1.40(-09)
148. $SiH_3^- + SiH_2 = H_3SiSi^- + H_2$ 1.40(-09)
149. $SiH_3^- + SiH_2 = Si_2H^- + 2H_2$ 1.40(-09)
150. $SiH_3^- + SiH = H_2SiSi^- + H_2$ 1.40(-09)
151. $SiH_3^- + SiH = Si_2^- + 2H_2$ 1.40(-09)
152. $SiH_3^- + Si = Si_2H^- + H_2$ 1.40(-09)
153. $Si_2^- + SiH_3 = Si_3H^- + H_2$ 1.20(-09)
154. $Si_2^- + SiH_2 = Si_3^- + H_2$ 1.20(-09)
155. $Si_2H^- + H = Si_2^- + H_2$ 1.92(-09)
156. $Si_2H^- + SiH_3 = Si_2^- + SiH_4$ 1.20(-09)
157. $Si_2H^- + SiH_3 = Si_3H_2^- + H_2$ 1.20(-09)
158. $Si_2H^- + SiH_2 = Si_3H^- + H_2$ 1.20(-09)
159. $Si_2H^- + SiH = Si_3^- + H_2$ 1.20(-09)
160. $H_2SiSi^- + H = Si_2H^- + H_2$ 1.92(-09)
107. $Si^- + Si_2H_6 = H_2SiSi^- + SiH_4$ 1.55(-09)
108. $Si^- + Si_2H_6 = Si_3H_6 + e^*$ 1.55(-09)
109. $SiH^- + SiH_4 = H_3SiSi^- + H_2$ 1.28(-09)
161. $H_2SiSi^- + SiH_3 = Si_2H^- + SiH_4$ 1.20(-09)
162. $H_2SiSi^- + SiH_3 = Si_3H_3^- + H_2$ 1.20(-09)
163. $H_2SiSi^- + SiH_2 = Si_2^- + SiH_4$ 1.20(-09)
164. $H_2SiSi^- + SiH_2 = Si_3H_2^- + H_2$ 1.20(-09)
165. $H_2SiSi^- + SiH = Si_3H^- + H_2$ 1.20(-09)
166. $H_2SiSi^- + Si = Si_3^- + H_2$ 1.20(-09)
167. $H_3SiSi^- + H = H_2SiSi^- + H_2$ 1.92(-09)
168. $H_3SiSi^- + SiH_3 = H_2SiSi^- + SiH_4$ 1.20(-09)
169. $H_3SiSi^- + SiH_3 = Si_3H_4^- + H_2$ 1.20(-09)
170. $H_3SiSi^- + SiH_2 = Si_2H^- + SiH_4$ 1.20(-09)
171. $H_3SiSi^- + SiH_2 = Si_3H_3^- + H_2$ 1.20(-09)
172. $H_3SiSi^- + SiH = Si_2^- + SiH_4$ 1.20(-09)
173. $H_3SiSi^- + SiH = Si_3H_2^- + H_2$ 1.20(-09)
174. $H_3SiSi^- + Si = Si_3H^- + H_2$ 1.20(-09)
175. $H_3SiSiH^- + H = H_3SiSi^- + H_2$ 1.92(-09)
176. $H_3SiSiH^- + SiH_3 = H_3SiSi^- + SiH_4$ 1.20(-09)
177. $H_3SiSiH^- + SiH_3 = Si_3H_5^- + H_2$ 1.20(-09)
178. $H_3SiSiH^- + SiH_2 = H_2SiSi^- + SiH_4$ 1.20(-09)
179. $H_3SiSiH^- + SiH_2 = Si_3H_4^- + H_2$ 1.20(-09)
180. $H_3SiSiH^- + SiH = Si_2H^- + SiH_4$ 1.20(-09)
181. $H_3SiSiH^- + SiH = Si_3H_3^- + H_2$ 1.20(-09)
182. $H_3SiSiH^- + Si = Si_2^- + SiH_4$ 1.20(-09)
183. $H_3SiSiH^- + Si = Si_3H_2^- + H_2$ 1.20(-09)
184. $Si_2H_5^- + H = H_3SiSiH^- + H_2$ 1.92(-09)
185. $Si_2H_5^- + SiH_3 = H_3SiSiH^- + SiH_4$ 1.20(-09)
186. $Si_2H_5^- + SiH_3 = Si_3H_6^- + H_2$ 1.20(-09)
187. $Si_2H_5^- + SiH_2 = H_3SiSi^- + SiH_4$ 1.20(-09)
188. $Si_2H_5^- + SiH_2 = Si_3H_5^- + H_2$ 1.20(-09)
189. $Si_2H_5^- + SiH = H_2SiSi^- + SiH_4$ 1.20(-09)
190. $Si_2H_5^- + SiH = Si_3H_4^- + H_2$ 1.20(-09)
191. $Si_2H_5^- + Si = Si_2H^- + SiH_4$ 1.20(-09)
192. $Si_2H_5^- + Si = Si_3H_3^- + H_2$ 1.20(-09)
193. $Si_3H_7^- + SiH_4 = Si_4H_9^- + H_2$ 1.00(-10)
194. $Si_4H_9^- + SiH_4 = Si_5H_{11}^- + H_2$ 1.00(-10)
195. $Si_5H_{11}^- + SiH_4 = Si_6H_{13}^- + H_2$ 1.00(-10)
196. $Si_6H_{13}^- + SiH_4 = Si_7H_{15}^- + H_2$ 1.00(-10)
197. $Si_7H_{15}^- + SiH_4 = Si_8H_{17}^- + H_2$ 1.00(-10)
198. $Si_8H_{17}^- + SiH_4 = Si_9H_{19}^- + H_2$ 1.00(-10)
199. $Si_9H_{19}^- + SiH_4 = Si_{10}H_{21}^- + H_2$ 1.00(-10)
200. $Si_{10}H_{21}^- + SiH_4 = Si_{11}H_{23}^- + H_2$ 1.00(-10)
201. $Si_{11}H_{23}^- + SiH_4 = Si_{12}H_{25}^- + H_2$ 1.00(-10)
202. $Si_{12}H_{25}^- + SiH_4 = Si_{13}H_{27}^- + H_2$ 1.00(-10)
203. $Si_{13}H_{27}^- + SiH_4 = Si_{14}H_{29}^- + H_2$ 1.00(-10)
204. $Si_{14}H_{29}^- + SiH_4 = Si_{15}H_{31}^- + H_2$ 1.00(-10)
205. $Si_{15}H_{31}^- + SiH_4 = Si_{16}H_{33}^- + H_2$ 1.00(-10)
206. $Si_{16}H_{33}^- + SiH_4 = Si_{17}H_{35}^- + H_2$ 1.00(-10)
207. $Si_{17}H_{35}^- + SiH_4 = Si_{18}H_{37}^- + H_2$ 1.00(-10)
208. $Si_{18}H_{37}^- + SiH_4 = Si_{19}H_{39}^- + H_2$ 1.00(-10)
209. $Si_{19}H_{39}^- + SiH_4 = Si_{20}H_{41}^- + H_2$ 1.00(-10)
210. $Si_{20}H_{41}^- + SiH_4 = Si_{21}H_{43}^- + H_2$ 1.00(-10)
211. $Si_{21}H_{43}^- + SiH_4 = Si_{22}H_{45}^- + H_2$ 1.00(-10)

212. $Si_{22}H_{45}^- + SiH_4 = Si_{23}H_{47}^- + H_2$ 1.00(-10)
213. $Si_{23}H_{47}^- + SiH_4 = Si_{24}H_{49}^- + H_2$ 1.00(-10)
214. $Si_{24}H_{49}^- + SiH_4 = Si_{25}H_{51}^- + H_2$ 1.00(-10)
215. $Si_{25}H_{51}^- + SiH_4 = Si_{26}H_{53}^- + H_2$ 1.00(-10)
216. $Si_{26}H_{53}^- + SiH_4 = Si_{27}H_{55}^- + H_2$ 1.00(-10)
217. $Si_{27}H_{55}^- + SiH_4 = Si_{28}H_{57}^- + H_2$ 1.00(-10)
218. $Si_{28}H_{57}^- + SiH_4 = Si_{29}H_{59}^- + H_2$ 1.00(-10)
219. $Si_{29}H_{59}^- + SiH_4 = Si_{30}H_{61}^- + H_2$ 1.00(-10)

where - 7.00(-12) =$7.0*10^{-12}$ rate constants have units cm^3s^{-1}, e* - slow electron

.

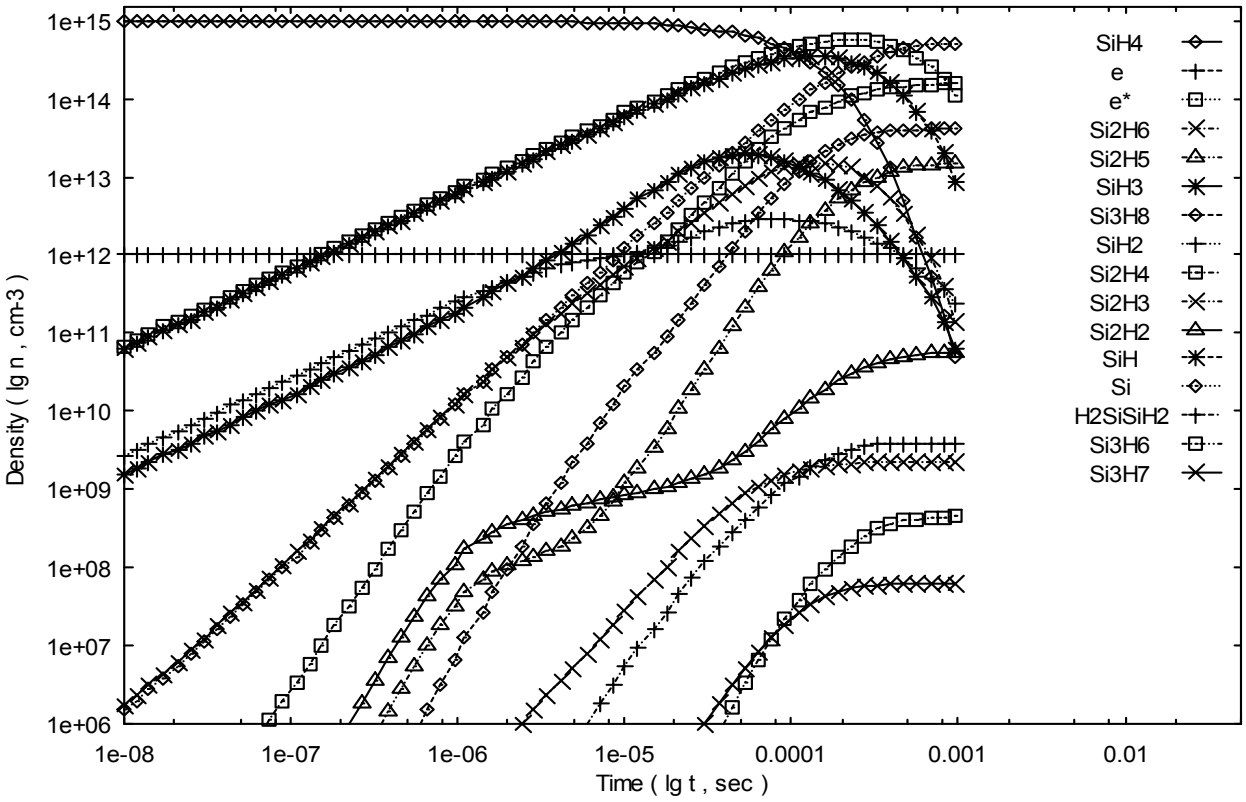

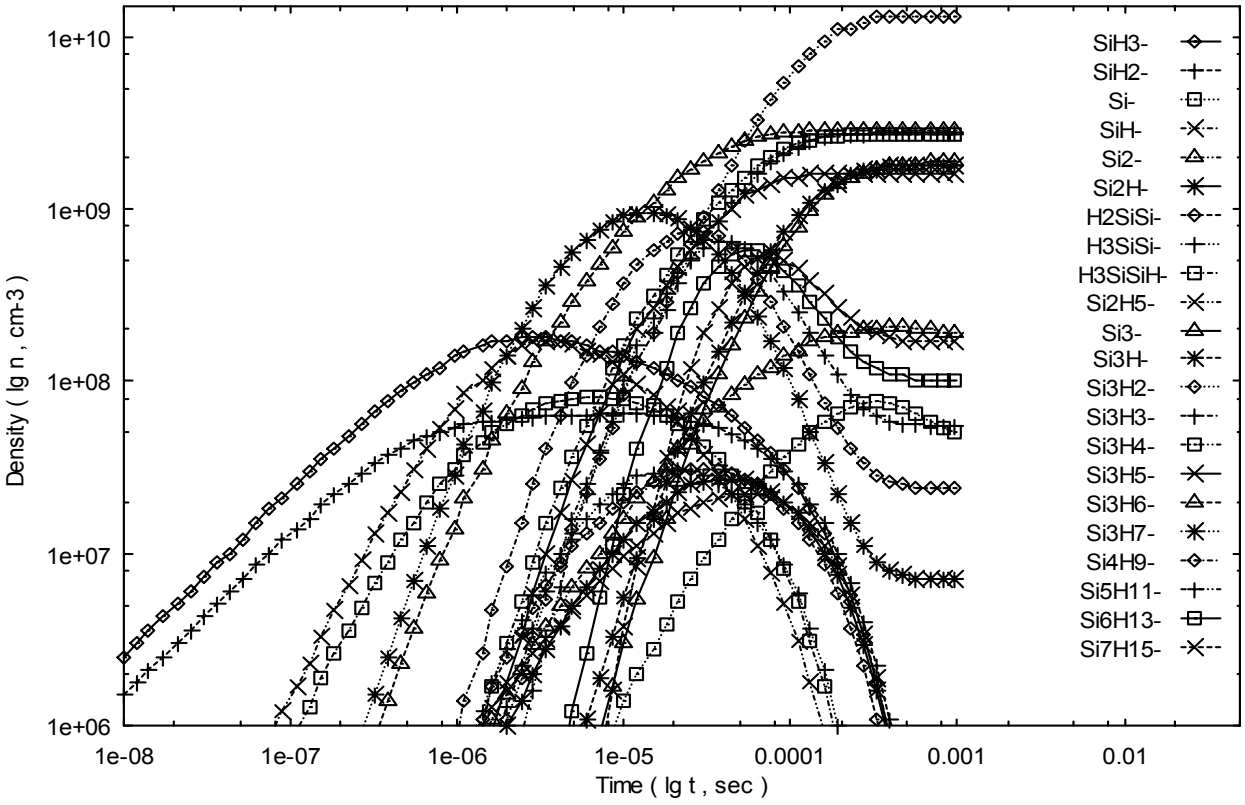

Figure 1 - 2. Time-evolution of neutral and negative charge spicies in silane plasma.

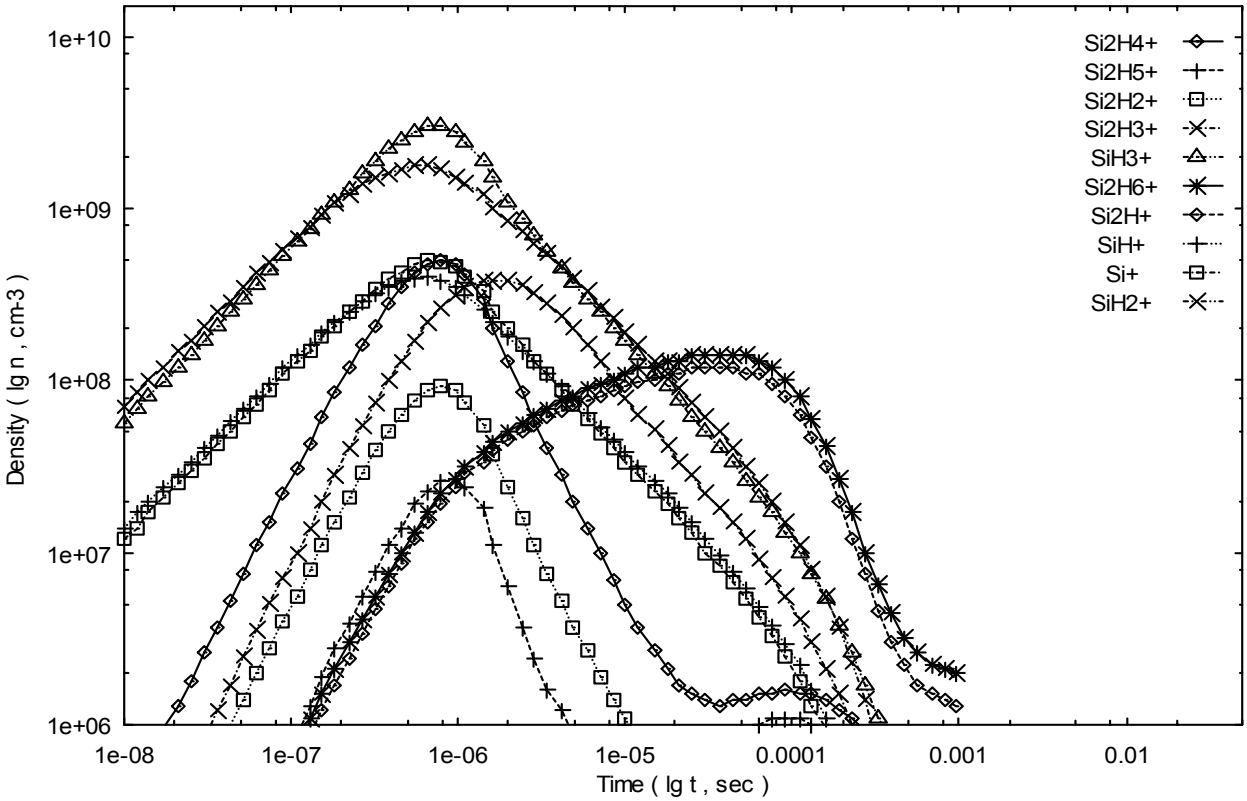

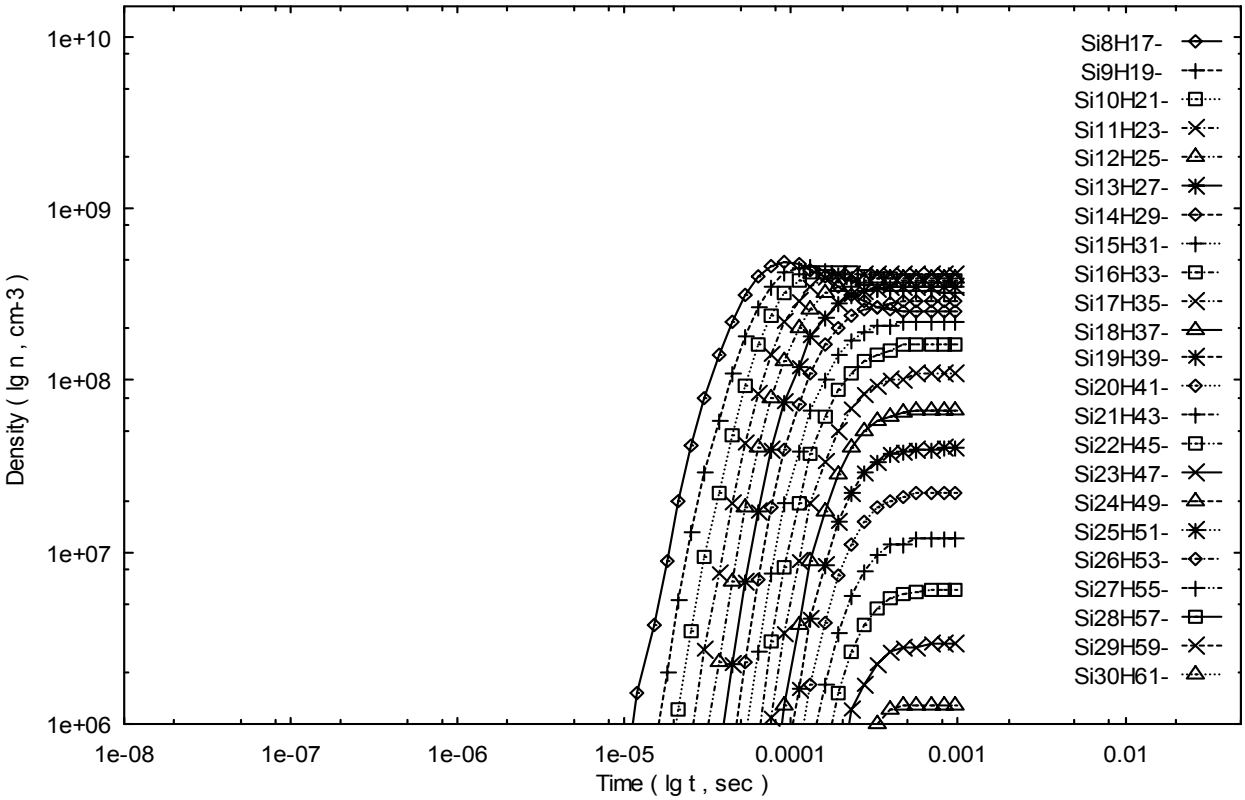

Figure 3 - 4. Time-evolution of negative charge spicies in silane plasma.

Etching of organic compounds by oxygen plasma

M. Mozetič[1], U. Cvelbar[1], A. Zalar[1], D. Babič[2]

[1] *Plasma laboratory, Institute of Surface Engineering and Optoelectronics, Ljubljana, Slovenia*
[2] *Department of Physics, University of Ljubljana, Ljubljana, Slovenia*

The etching rates of different polymers versus the dose of neutral oxygen atoms was measured in an oxygen plasma postglow reactor. The source of neutral oxygen atoms was an inductively coupled RF oxygen plasma with the electron temperature of 5 eV and the density of about 10^{16} m^{-3}. The density of oxygen atoms in the postglow reactor was measured with a catalytic probe. The O density was up to $4x10^{21}$ m^{-3}. It was found that the activation of a polymer was completed after the O dose of $6x10^{21}$ m^{-3}. Further exposure to O atoms caused continuous etching of polymers. The combination of rather precise measurements of both the oxygen atom density and the thickness of polymers allowed for the determination of the etching rate. It was found that the oxidation probability did not depend on the density of the O atoms in the vicinity of samples but rather on the dose of oxygen atoms. The etching rate was found to be of the order of $1nm/10^{20}$ cm^{-2}. The etching rate depended on the type of polymer. The highest etching rate was measured for alkyd resin, a polymer often used as the basis of different paints. The lowest etching rate was detected for polyether sulphone – a pretty stable plastic that is widely used in electronic industry.

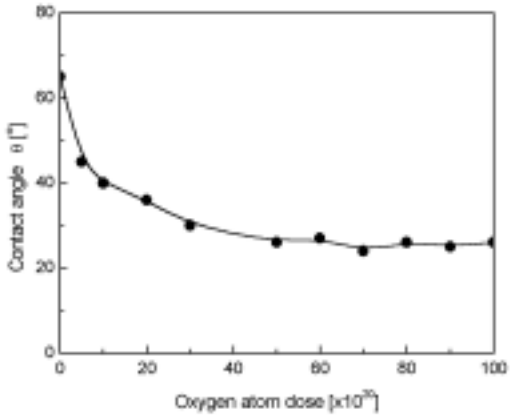

Fig. 1. Contact angle of a water drop versus oxygen atom dose.

Table 1. Etching rates of different materials

Type of material	Etching rate ($nm/10^{20}atoms/cm^2$)
alkyd resin	20
nitrocellulose	1.6
mylar	1.2
polyether sulphone	0.6

Plasma treated polymers as supports for structured antibacterical materials

T. Yuranova, A. Bozzi, J. Kiwi

Laboratory of Photonics and Interfaces, Institute of Molecular Chemistry and Biology, EPFL, Lausanne, Switzerland

Abstract.

The bacterial inactivation efficiencies of silver metal and oxides and their combinations on textile plasma treated fabric was investigated to evaluate the disinfectant action on airborne bacteria. The inactivation performance was seen to depend on the amount of silver on the textile surface and RF plasma treatment conditions.

1. Introduction

Silver has been known as a disinfectant for many years and is being used in many forms in the treatment of infectious diseases [1-3] and has a broad spectrum antibacterial activity while exhibiting low toxicity towards mammalian cells. In a very low concentration silver-ions are effective against bacteria in water systems [4-5].

This investigation is directed towards the fixation and catalytic performance of Ag-clusters on polyamide-polystyrene textile fabrics. After a long series of preliminary experiments the most suitable experimental conditions for the RF-plasma activation of the fabric surface were found. Then the chemical deposition of Ag-clusters was carried out on these activated surfaces checking subsequently each Ag-deposit against the antibacterial activity observed. Once the optimization of the Ag-clusters was completed the latter clusters were characterized by complementary surface techniques like: elemental analysis, X-ray photo-electron spectroscopy (XPS) and transmission electron microscopy (TEM).

2. Experimental section

2.1. Materials

Reagents like $AgNO_3$, ammonia, isopropanol, Ag_2CO_3 were Fluka p.a. and used without further purification. De-ionized water was employed throughout this work. Industrial textile fabric consists of polyamide blended polyester was received from Tissupor AG, St.Gallen, Swiss.

2.2. Functionalization of textile fabrics by RF-plasma

The textile polymer fabric surface was treated in a RF-plasma cavity (Harrick Corp, 13.56 MHz, 100 W) at an air pressure of 0.1 torr. RF plasma was created in a quartz reactor where textile samples

were placed. A variety of oxygen functional groups: >C-O, >C=O, -O-C=O, -COH, -COOH, were produced on the fabric through the reaction between the active species induced by the plasma in the gas phase and the C-surface atoms [2-5]. These oxygen functionalities obtained by oxygen plasma are located are in the topmost layers and increase with longer treatment time, but remain constant with treatment time > 30 minutes. This is why the latter time has been chosen for RF-plasma treatment.

2.3. Loading of silver on activated textile fabrics

After functionalizing the textile surfaces by RF-plasma or vacuum-UV the fabrics are immersed in solutions with different concentrations of $AgNO_3$. Afterwards the silver is reduced at a suitable pH with mild reducing agent [6] and the final fabric presenting a dark yellow color is dried in air at room temperature.

2.4. Bacterial growth testing

Textiles with silver attached and textiles without silver that have not been previously sterilized are incubated for 24 hours at 37 °C in Luria Bertani media (LB) plates under controlled conditions. After the latter time period the assessment of partial or total bacterial inhibition by the Ag-loaded fabric is observed and compared with the non-loaded fabric. To determine bacterial survival in water, *E coli* K-12 was used as a bacterial model. Cultures in the exponential phase of growth were obtained using an aliquot part of the inoculum grown overnight in 20 ml of Luria Bertani media at 37°C. After centrifugation, the cells were re-suspended in tryptone (Merck AG) solution. Finally the cell suspensions were diluted with Milli-Q de-ionized water to the required cell density corresponding to 10^4 (CFU/ml) colony forming units (CFU/ml).

In a typical experiment bacterial suspensions were contacted with the textile fabric for 24 hours in the dark and samples were plated on agar PCA (plate count Agar Merck AG, Germany). The plates were incubated at 37°C for 24 hours before counting and the reported results were the media of 3 experimental runs.

Additional tests were carried out using *Pseudomonas Aeruginosa* following Swiss EMPA Norms 2003 and for *Bacillus subtilis* and *Aspergillus niger* according to Swiss EMPA Norms 510. The bacterial growth inhibition followed the same pattern as observed for the case of *E coli* K-12.

2.5. X-ray electron spectroscopy (XPS)

Measurements were carried out in a Leybold-Heraeus instrument calibrating the binding energies (BE) to the Au $f_{7/2}$ level taken as 84.0 eV. The evaluation of the binding energies of the Ag-clusters was carried out following the DIN norms [7] and after taking into consideration the sensitivity factors allowed a reproducibility of ±5% in the measurements. The spectra were analyzed in a DS 100 data set after X-ray satellite subtraction and smoothing of the polynomial fit. The relative sensitivity factors used were: O1s 0.78; Cls 0.78: S2p 0.84; Ag3d5/2 3.23. The quantitative evaluation of the

experimental data was carried out with a Shirley type background correction due to the electrostatic charging of the particles during the measurements [8]. Electrostatic charging effects were referenced calibrating to the C1s signal.

2.6. Transmission electron microscopy (TEM)

Electron microscopy was carried out with at the Philips CM 120 microscope to observe the Ag-clusters on the textile surface. The instrument used for electron microscopy (120 kV, 0.35 nm point resolution) was equipped with energy dispersive X-ray analysis EDAX to identify the deposition of Ag-clusters on the textile fabric.

3. Results and discussion

3.1. Biological testing of the Ag-loaded textile prepared by RF-plasma activation

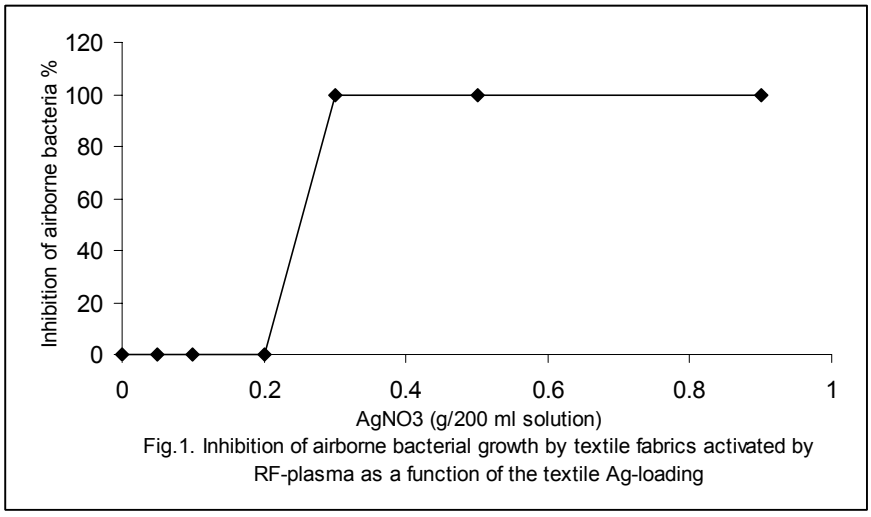

Fig.1. Inhibition of airborne bacterial growth by textile fabrics activated by RF-plasma as a function of the textile Ag-loading

Figure 1 shows the effect of Ag-loaded textiles surfaces activated by RF-plasma on the airborne bacteria after 24 hours. The antibacterial effect reported in Figure 1 was carried out in the dark. Adsorption of bacteria on the textile was observed on the unloaded fabric and as well as on the Ag-loaded fabric. The abscissa refers to the $AgNO_3$ grams in 200 ml solution used in the silver loading after the RF-plasma treatment. After the relative index of 0.3g Ag/200 ml solution (Figure 1), the inhibition of bacterial activity at 24 hour seems to be complete. This suggests that a direct contact between the bacteria and the textile having an adequate density of silver clusters is necessary for the bacterial abatement process to proceed. The latter observation is consistent with some recent work on the mechanism of bacterial abatement due to metal/oxides and ions [1,2,9]. Lower levels of silver loading in the textile do not allow the formation of a sufficient number of Ag-clusters necessary for the total inhibition of bacterial growth.

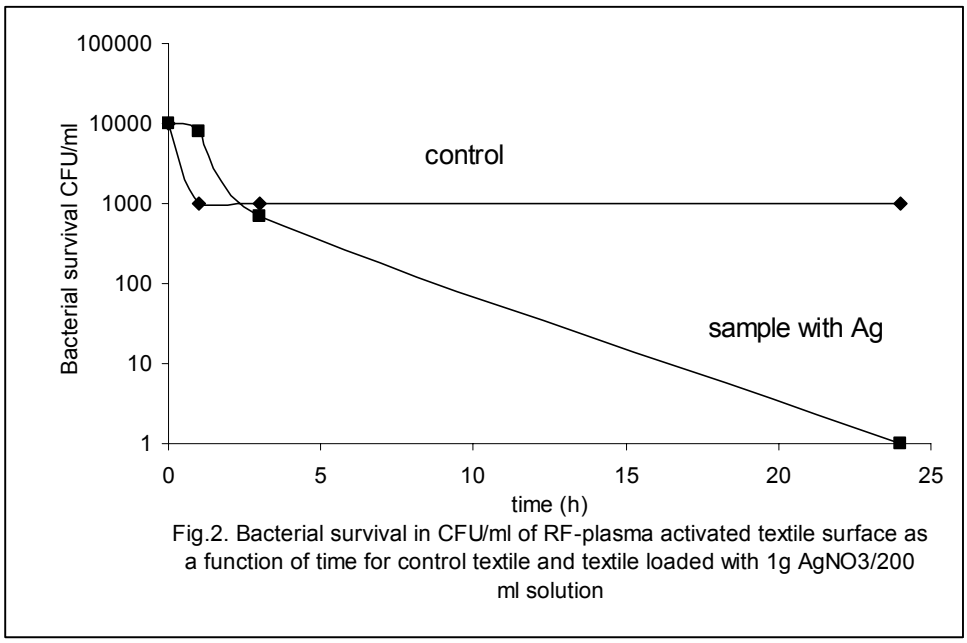

Fig.2. Bacterial survival in CFU/ml of RF-plasma activated textile surface as a function of time for control textile and textile loaded with 1g AgNO3/200 ml solution

Figure 2 shows the decrease in the number of *E coli* K-12 colonies suspended in Milli-Q water as a function of time in contact with a textile sample activated by RF-plasma with ($AgNO_3$ 1g/200 ml) and for a second control fabric without silver loading. It is readily seen from Figure 2, that during 24 hours the Ag-loaded fabric inhibits any bacterial growth. Moreover, a bacterial decrease from 10^4 CFU/ml to a non-detectable level below 10 CFU/ml was detected within 24 hours. The control fabric shows only a modest reduction of one order of magnitude due to adsorption of *E coli* K-12 on the textile fabric surface.

3.2. X-ray photoelectron spectroscopy (XPS) of RF-plasma activated surfaces loaded with silver.

The percentage surface composition of RF-plasma loaded silver textiles by XPS spectroscopy is presented in Table 1. The silver content of topmost layer surface of the textile increases with the concentration of the silver solution used to react this metal with the functional groups introduced on the textile by RF-plasma. The reference for the values obtained has been carried out according to reference [8] comparing the spectra obtained with related spectra of silver found in the scientific literature. The background correction for the obtained signals was carried out according to reference [7]. The values reported in Table 1 do not represent bulk or deeper layer content of silver that can be treated as integral value for the attached silver. This observation will be discussed with the right perspective in relation to the Ag found by elemental analysis in the last section below.

The binding energies (BE) of the silver were quantified for the silver species deposited on the textiles for the different concentrations of silver used. For 0.05, 0.3 and 1g $AgNO_3$ / 200 ml, the BE was close to 368.2 eV which is the reference value for metallic Ag[10]. The reference values for the BE of Ag_2O were 367.8 eV and AgO 367.4 eV.

Table 1. Percentage surface composition of RF-plasma loaded silver textiles.

	0.05 g $AgNO_3$/200 ml	**0.3 g $AgNO_3$/200 ml**	**1 g $AgNO_3$/200 ml**
C1s	63.2	63.3	69.7
N 1s	1.13	0.82	0.92
O 1s	33.0	33.6	26.7
Na 1s			0.59
Si 2p	2.70	1.85	1.45
Cl 2p			
Ag $3d_{5/2}$	0.06	0.40	0.62

3.4. Transmission electron microscopy (TEM) of Ag-loaded fabrics activated by RF-plasma

The data of the TEM for the thick polyamide fiber component of the textile fabric allow to estimate the size of Ag-clusters varied between 50 and 500 nm. The spacing between the fibers was observed to be highly irregular. The heterogeneous deposition of the Ag-clusters on the textiles is probably due to the numerous oxygen gas species produced during RF-plasma leading subsequently to different anchoring groups on the textile surface. The analysis of Ag-clusters on thinner poylester fibers demonstrates a more regular spacing on the fiber surface. The size of the clusters was seen also to vary widely between 8 and 40 nm counting around 100 Ag-clusters.

4. Conclusions

This study has shown the beneficial antibacterial activity of silver grafted on textile fabrics by RF-plasma followed by chemical treatment of the silver salt on the fabric surface. A minimum loading of silver was seen to be necessary to inhibit the airborne bacterial growth depending on the method used to activate the textile surface. This effect was also investigated and reported for aqueous suspensions of *E coli* K-12 taken as a bacterial model. The electron microscopy carried out shows different clusters of silver in size and distribution depending on the type of surface activation of the textile surface.

References

[1] G. Zhao and E. Stevens, Biometals, 11 (1998) 27.

[2] F. Fu-Ren, A. Bard, J. Phys. Chem. B., 106 (2002) 279.

[3] R. Demling, L. deSanti, Wounds, 13, (2001), 11.

[4] J. Kusnestov, N. Elomaa, P. Martikainen, Wat Res., 35 (2001) 4127.

[5] J. Keheler, J. Bashant, L. Johnson, Y. Li, World J. Microb. Biotech., 18 (2002) 133.

[6] H. Hada, A. Yoshida, A. Kurakake, J. Phys. Chem., 80 (1976) 2728.

[7] National Physics Laboratory, Teddington UK, 1982.

[8] A. Shirley, Phys. Rev., B5 (1979) 4709.

[9] Q. Feng, J. Biomed. Mater. Res., 52 (2000) 668.

[10] C. Wagner, W. Riggs, L. Davis, J. Moulder, G. Mullenberg (Eds). Handbook of X-ray Photo-electron Spectroscopy. Perkin Elmer Corp. Eden Prairie, Min. 55344, USA

Decomposition of isooctane using a Dielectric Barrier Discharge reactor

K.Bouamra, N. Blin-Simiand, F. Jorand, S. Pasquiers, C. Postel

Laboratoire de Physique des Gaz et des Plasmas, Bat.210, Université Paris-Sud, 91405 Orsay Cedex, France

Abstract:
Decomposition of isooctane is investigated in a nonthermal plasma reactor under atmospheric pressure. The highest isooctane consumption, obtained at an electrical power of 12 W, is around 93 % in wet air and 85 % in dry air. Identification of reaction products is done by a GC/MS. Acetone, dimethoxypropane and dimethoxyethane are identified.

1. Introduction

Non-thermal atmospheric plasmas are under study since the beginning of the eighties for decomposition of Volatile Organic Compounds with different chemical structures, for application in pollution control [1,2]. Some experiments [3], as well as kinetic modelling [4], have been performed on conversion of hydrocarbon molecules.
The aim of this study is to investigate the decomposition of isooctane (iC_8H_{18}), a primary reference fuel with n-heptane, using a Dielectric Barrier Discharge reactor (DBD).

2. Experimental description

The experimental setup was schematically illustrated in Figure 1. The plasma-chemical reactions took place in a cylindrical DBD reactor, which was made of a quartz tube (14 mm inner diameter and 2 mm wall thickness) surrounded by a copper tape as the outer electrode. The outer electrode connected to the earth was 14.5 cm length. On the inner electrode, which consisted of a central stainless-steel rod (e.d. 5 mm), was applied a high voltage pulse (up to 40 kV) with a repetition frequency value up to 120 Hz. The discharge volume was about 19.5 cm^3.
The isooctane liquid was injected with a syringe through a vaporizer producing gaseous isooctane. The hydrocarbon streamed along a glass rod located at the center of a heated tube through which air, either dry or with water vapor, flowed. At the outlet of the vaporizer, the homogeneous gas mixture was continuously carried through the DBD reactor at different frequencies. The gases resulting from these discharges passed through a U-tube cooled to –40°C, where condensable products were trapped during 20 min. All these experiments were carried out at ambient temperature and atmospheric pressure.

Chemicals

In the experiments reported here, about 1000 ppm of iC_8H_{18} balanced with air N_2/O_2 (80/20) was introduced into the reactor. Air flow rate was adjusted with a flowmeter at 1 L/min and the residence time in the reactor was about 1.2 s. Moisture was added to the mixture by bubbling the sample gas through a small volume water bath. The water vapor concentration was 3 %.

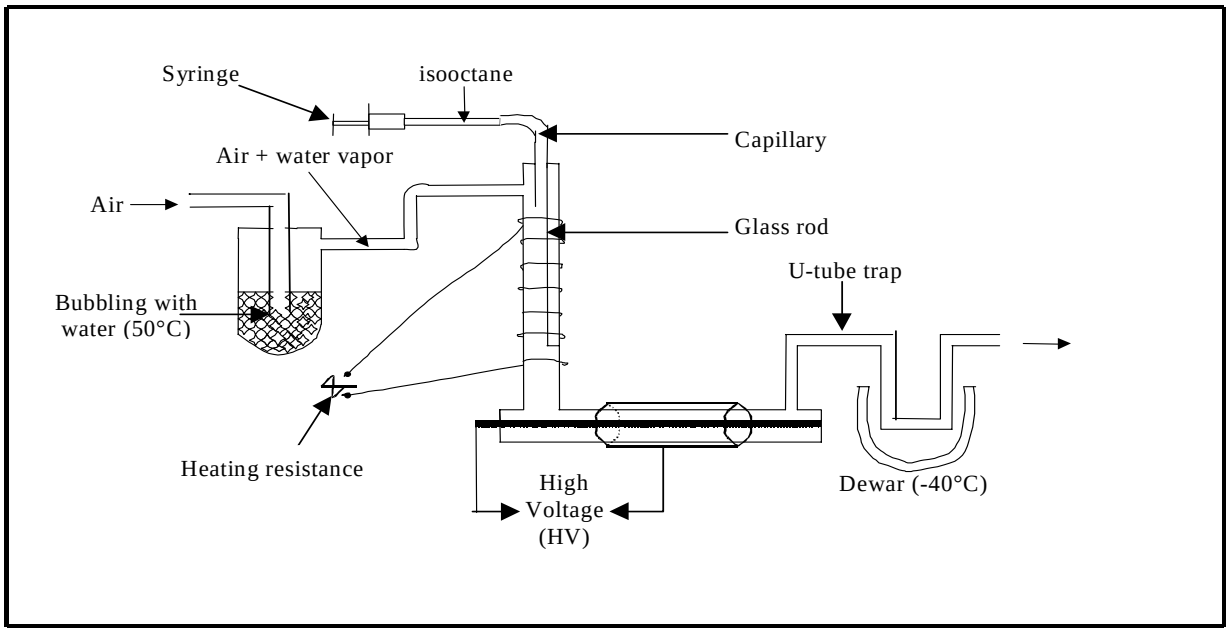

Figure 1: Schematic representation of experimental setup.

Techniques used for the identification

Analysis by GC/MS was performed using a Varian 3800 gas chromatograph, coupled to an ion trap mass detector Varian Saturn 2000. The mass spectrometer operated in the *m*/*z* range of 20–350, and it was used either with Electron Impact (EI), with an ionisation energy of 70 eV, or with Chemical ionisation methanol (CI) mode. The separation was performed on a fused silica column (VARIAN CP-SIL 5 CB, 30 m×0.25 mm I.D., 0.39 mm O.D. and 0.25 μ m film thickness, 1 ml/min). The carrier gas was helium with flow-rate of 1.0±0.1 ml/min. The gas chromatograph was equipped with a split/splitness injection port operating in the split mode with a split ratio equals to 60. The column temperature program was: 45°C for 6 min, 45–160°C at 30°C/min, and 10 min at 160°C. Injector, transfer line and ion trap were at 100°C, 170°C and 150°C.

3. Results and discussion

3.1 Effect of frequencies on decomposition efficiency

As shown in table 1 and figure 2, consumption of isooctane increased with frequency. The highest isooctane decomposition, was obtained at 120 Hz, which corresponds to a maximum electrical power consumption in the discharge circuit of about 12 W. Many products issued from the discharge were observed on chromatograms. These products were analysed by GC/MS.

Frequencies (Hz)	1	20	50	70	120
% of consumption (mixture air/isooctane)	26	62	67	74	**85**
% of consumption (mixture air/isooctane/ water vapor 3 %)	20	45	71	70	**93**

Table 1 : Effect of frequencies and moisture on consumption rate.

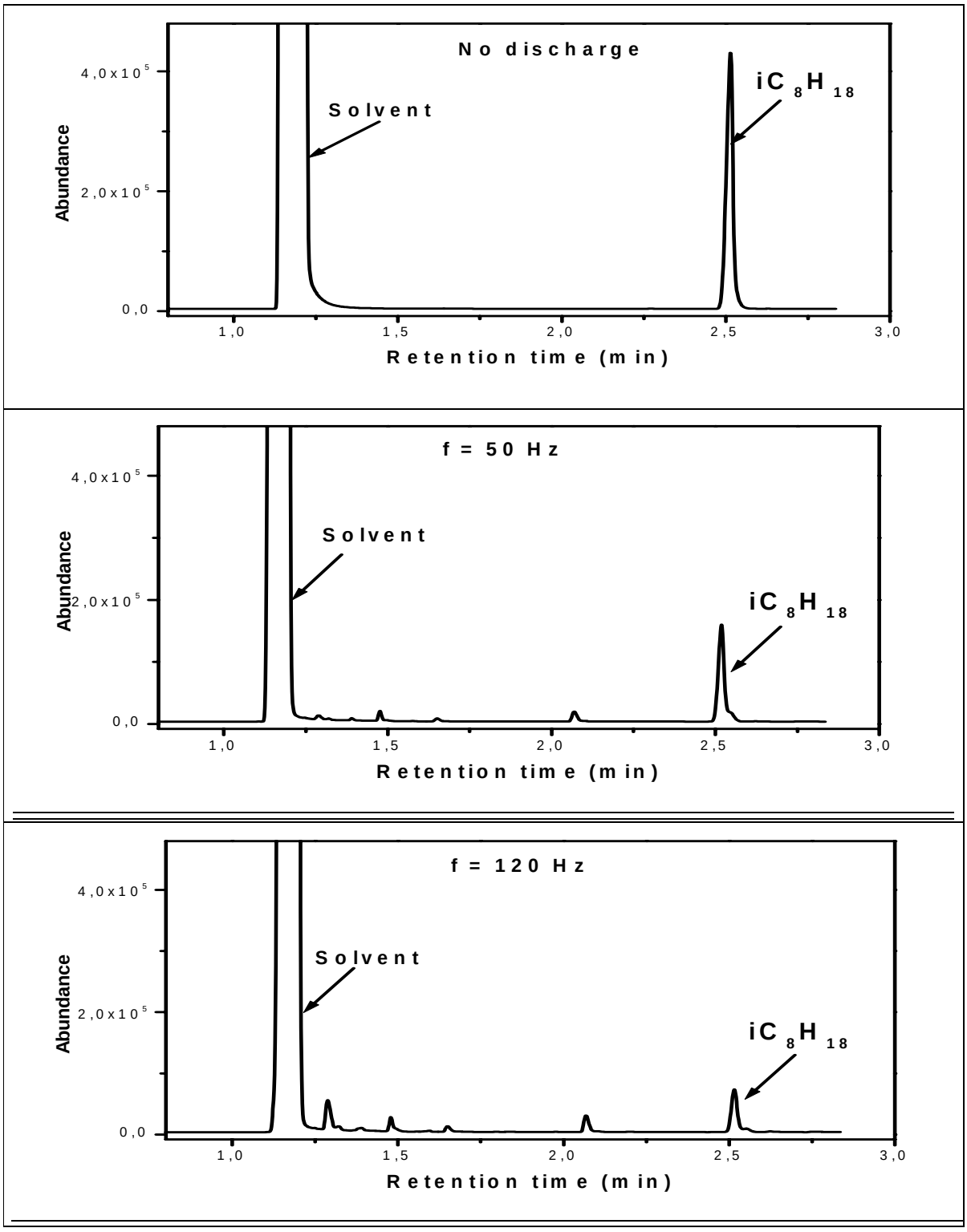

Figure 2: Chromatograms of isooctane consumption at different discharge frequencies.

3.2 Effect of water vapor on consumption of iC_8H_{18}

The highest isooctane decomposition was around 93 % in wet air and 85 % in dry air. Decomposition seems to be easier in wet air than in dry air (Figure 3, table 1).

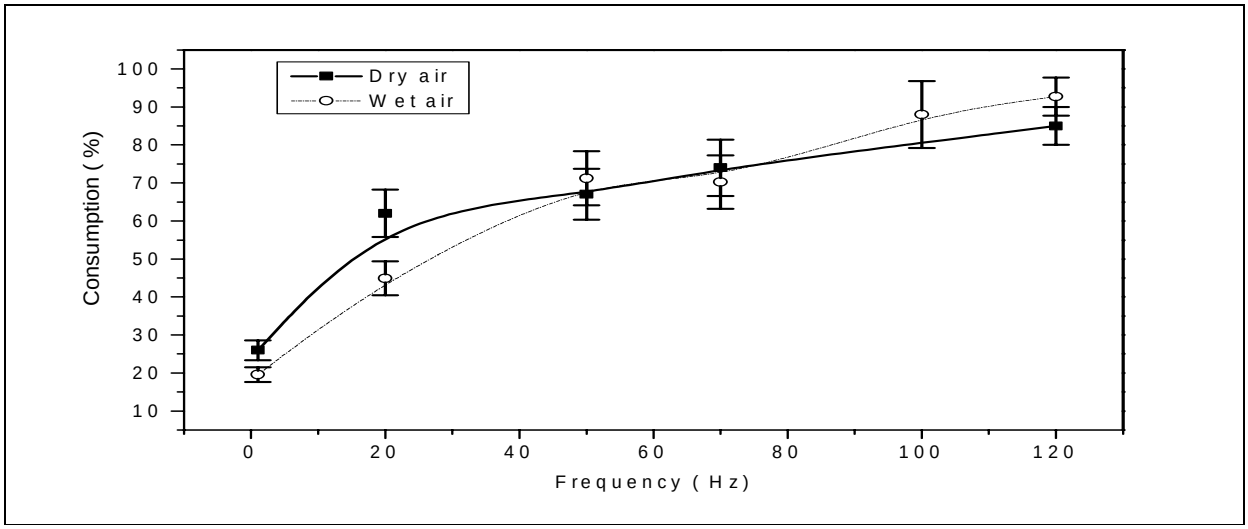

Figure 3 : Effect of frequency and water vapor (3 %) on consumption of 1000 ppm of isooctane in 1L/min air

However, wet air had negative effect on isooctane decomposition under low frequencies. These observations suggested that isooctane can decompose in a DBD reactor, at atmospheric pressure and ambient temperature without initiation by active oxygen species issued from water at high frequencies.

Products identified by GC/MS

Products obtained during the isooctane decomposition in dry air and at 120 Hz were analyzed by GC/MS. The chromatogram shown in figure 4 includes many peaks. They correspond to molecules issued either from decomposition of iC_8H_{18}, or from recombination processes between the various products. Molecules were analyzed both with EI and CI modes.

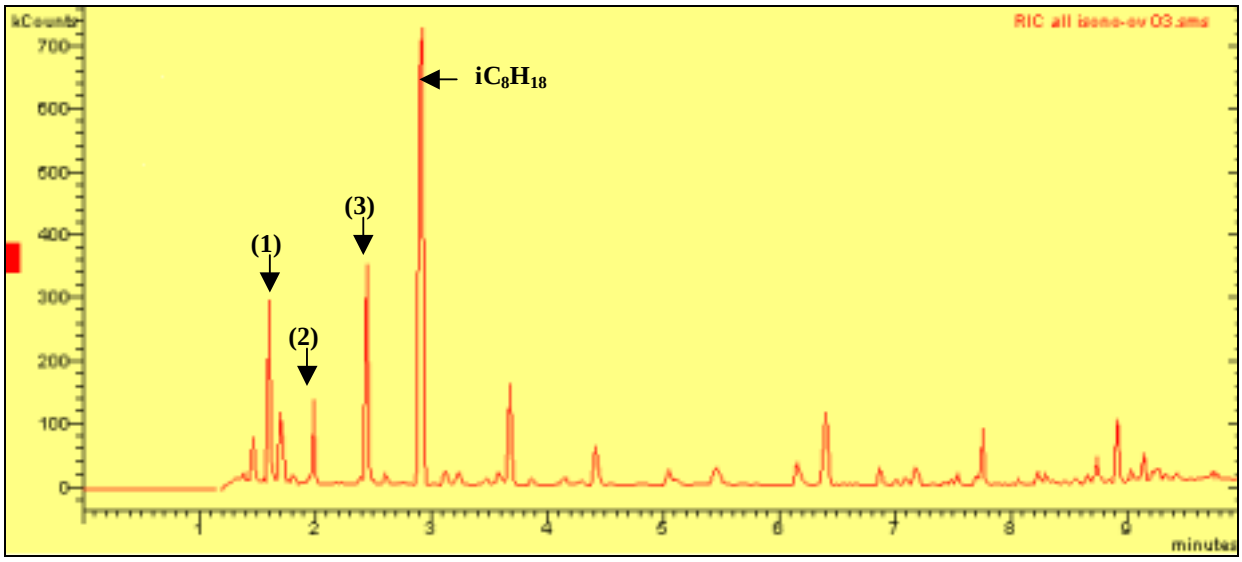

Figure 4 : GC/MS chromatogram of products obtained in dry air (1L/min) and 1000 ppm of isooctane at 120 Hz.

Three molecules, with a weak retention time (Figure 4), were identified:
- Acetone C_3H_6O (Molecular Weight (MW) = 58)
- Dimethoxyethane $C_4H_{10}O_2$ (MW = 90)
- Propane 2,2 dimethoxy $C_5H_{12}O_2$ (MW = 104)

3.3 Effect of temperature

The temperature effect on isooctane decomposition without discharge was investigated at 200, 400 and 600°C. Gases CO, CO_2, O_2 and N_2 were analyzed by gas chromatography VARIAN CP-4900 Micro-GC, using molecular sieves (10 m × 0.32 mm I.D) and a PoraPlot U column. Hydrocarbon was analyzed by a GC/MS. It was found that isooctane consumption was near zero at 200 and 400°C. However, experiments shown a weak decomposition at 600°C. CO and CO_2 were only detected at this temperature.

4. Conclusion

The experiment showed that DBD plasma reactor can lead to a high decomposition of iC_8H_{18} in dry or wet air. The conversion of the hydrocarbon molecule led to production of various species. GC/MS spectra enabled to identify some of them.

At atmospheric pressure, no conversion was observed for isooctane under temperatures of 200 to 400°C without plasma. Effect of plasma, under high temperature, on hydrocarbon conversion will be treated in next works. Identification of more species will allow us to understand isooctane degradation kinetic mechanism.

References

[1] - L. Rosocha, R. Korzekwa, J. Adv. Oxid. Technol. **4,** 247 (1999).
[2] - Th. Hammer, Contrib. Plasma Phys. **39,** 441 (1999).
[3] - S. Futumura, A. Zhang, G. Prieto, T. Yamamoto, IEEE Trans. Ind. Appl. **34,** 967 (1998).
[4] - E. Filimonova, R. Amirov, Plasma Phys. Rep. **27,** 708 (2001).

Reduction of oxides and chlorides of metals in low pressure plasma-beam discharge.

V.M. Atamanov, L.I. Elizarov, A.A. Ivanov, A.V. Pereslavtsev, G.V. Povolotskaya

Russian Research Centre "Kurchatov Institute", Moscow, Russia

Abstract
Low pressure beam–plasma discharge in hydrogen and deuterium was used to obtain the pure metals from the pure oxides or chlorides: Fe_2O_3, $FeCl_3$, $CuCl_2$, $LaCl_3$, Sc_2O_3. The series of the experiments on the reduction of oxides and chlorides in low pressure beam-plasma discharge were carried out in the "Oratoria-10" installation. The decreasing of purity degree of the metal reduced in the comparison with initial oxide (or chloride) was not observed.

1. Introduction

The beam-plasma discharge was proposed for plasma chemistry in 1975 [1-3]. The discharge is initiated in a gas of low density in the magnetic trap known as mirror machine when electron beam of moderate energy penetrates gas along the magnetic force lines. Due to the collisions with neutral atoms or molecules the electrons of the beam produced ions and the secondary electrons. Then the plasma of very low density due to beam-plasma instability brings about the non-collision losses of beam energy in plasma thus heating the plasma and increasing essentially the degree of ionisation. The density of plasmas achieved 10^{13} cm^{-3} the neutral pressure of the order of several tenths of millitorr. The discharges of various configurations were studied when various type of the cathode of electron guns were used. The plasma produced was suitable for processing however the optimisation of equipment was not done. As known, the beam-plasma discharge can be successfully used in plasma chemical studies [1-3]. Recently the attention was drawn again to this problem [4, 5]. According to the analysis done in the papers cited electron beams can generate processing plasmas with greater process control and larger areas than present plasma generation techniques such as capacitive or inductive discharges, electron cyclotron resonance (ECR), surface wave or helicon reactors.
In the cited papers a plasma configuration early known as "ribbon" beam configuration [1-3] is described. This beam has been shown to generate 60x60 cm^2 sheets of high density (10^{12} cm^{-3}), cold (<1eV) plasma this system is called Large Area Plasma Processing System (LAPPS). Study of those configurations earlier has given us the criterion of plasma-beam discharge ignition, however the main factor for this discharge to be so interesting is the second study of the discharge, viz. the development of Langmuir waves and their role in plasma heating. Nevertheless the fact of development of technique of beam plasma discharge is very important despite of different interpretation of experiments. We have used the beam plasma discharge for direct reduction of metals from oxides and chlorides. The chemistry of the process of metal reduction from the oxides or chlorides by hydrogen is well known. There are the hydrogen atoms and ions besides the molecular hydrogen in the beam-plasma discharge. At the presence of hydrogen atoms and ions the process of metal reduction from oxide can take place at the room temperature. The hydrogen was injected in the working chamber; the reaction products were removed with the rest of hydrogen by the pumping-out system. The process of metal reduction from oxide or chloride by hydrogen in beam-plasma discharge is non-equilibrium. It means, that the fixation of the reaction products can be simplified. When the process of treatment is over the neutral gas such as argon or nitrogen is introduce into the working chamber up to the atmospheric pressure and the products can be taken from the system.

2. Experimental Device

The experiments are performed on the device "Oratoria10", the scheme being shown at Fig.1. The installation «Oratoria-10» is intended for the plasma chemical researches. The working vacuum chamber (1) of radius 252,5 mm and the length of 1m is made of stainless steel. All the chamber was immersed in magnetic field created by the coils (2), the voltage 100 V and the current 200A. The constant magnetic field in the centre of chamber can be varied from 300Gs up to 600Gs. The magnetic system of a "mirror-like magnetic trap" type produces magnetic field of maximum strength 800 Gs and magnetic mirror (max/min) ratio R~3.5. The electron beam of a cylindrical geometry of maximum diameter up to 4 cm is formed by means of an electron gun (3) with a beam current of up to 2 A and of its energy up to 6 keV. The electron

beam penetrates chamber via small orifices that lead to the electron gun (3) from one side and to the electron beam receiver (4) on the other side. To provide the necessary high vacuum conditions for the electron gun to operate the system of differential pumping (5) was used. Differential pumping system consists of three groups of thin diaphragms with the intermediate pumping out between the two ending diaphragm groups and through the middle group. The holes in the diaphragms are equal to a diameter of the electron beam. The necessary vacuum conditions in the electron gun chamber are provided by the oil vapour high vacuum diffusion pump (6) with liquid nitrogen-cooled trap. The working chamber (1), the differential pumping system (5) and the volume of electron beam receiver (4) are pumping out by the oil vapour booster vacuum pumps (7) with liquid nitrogen-cooled traps. The residual gas pressure is not more than 1.10^{-5} Torr in the working chamber and not more than 5.10^{-7} Torr in the electron gun chamber with the using of nitrogen cooled traps. The maximum working pressure in working chamber is about ~ 10^{-1} Torr and is about 10^{-5} Torr in the electron gun chamber. The "Oratoria -10" installation enables to carry out the researches of non equilibrium plasma with the density of $10^{10} – 10^{13}$ cm^{-3} produced in a beam-plasma discharge.

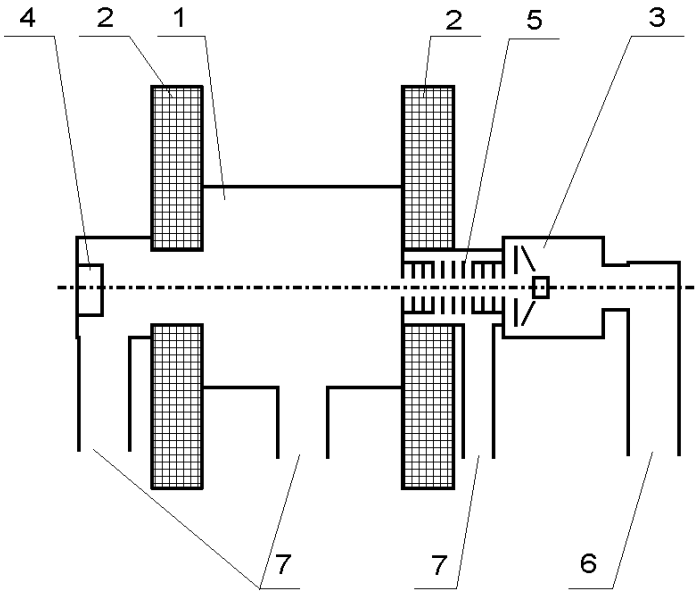

Fig. 1. The scheme of «Oratoria - 10» device.
1 - vacuum chamber; 2 - magnet coils; 3 - electron gun; 4 - electron beam receiver; 5 – the diaphragms of differential vacuum pumping out system; 6 – oil vapour high vacuum diffusion pump; 7 – oil vapour booster vacuum pump.

3. Experiments

The scheme of the experiments on the reduction of metals from oxides or chlorides is shown on the fig.2. The electron gun produces the electron beam (1) of power W=2-4 kW, the voltage being up to 2kV and the current up to 2 A. The electron beam penetrates the working chamber from one side another side (from the electron gun to the electron beam receiver) through the cylinder tube (2). There is the working table (3) with the small volumes (4) with powder metal oxide (or chloride) on it in the tube (2). The internal diameter of the tube (2) is 95 mm. The hydrogen is supplied into the reaction zone through the inlet nozzle (5). The temperature of the small volume (4) walls was measured by the thermocouple (6) that had the diapason of measurement from 100C up to 1000C. The small volumes (4) have the shape of a parallelepiped with the area 10x30 mm and height of walls 3 mm. Volume is made of a tantalum. The surface of a reduced metal oxide (or chloride) powder was at the distance 18-25 mm from the boundary of the electron beam. The bottom of volume is made corrugated with the corrugations along the long side. Powder of metal oxide studied is filled in small volume (4) up to height of 1 mm. The intermixing of a powder can be carried out by the rotational displacement of the tube (2) around of a long axis in limits of angle ±90°. The experiments on the reduction of metals were executed in non-equilibrium hydrogen or deuterium plasma produced by the beam-plasma discharge in plasma chemical installation “Oratoria-10”. The study the process of metal reduction from oxides or chlorides was executed with the compounds in powder form.

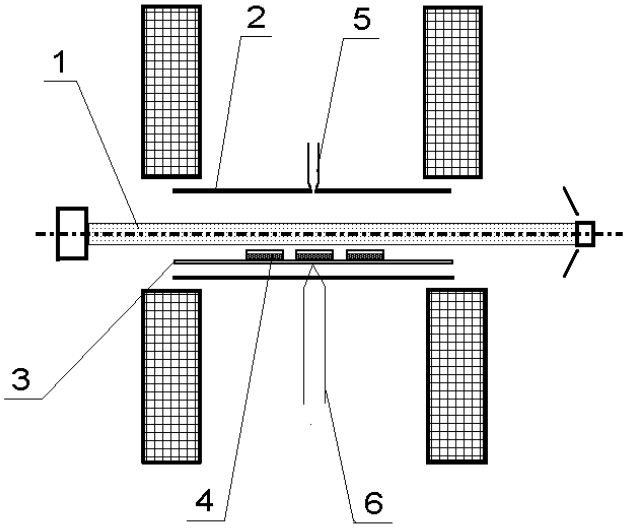

Fig. 2. The scheme of the experiment on the reduction of oxides and chlorides of metals.
1 – electron beam; 2 – tube; 3 – working table; 4 – small volume with powder oxide; 5 – inlet gas nozzle; 6 – thermocouple.

The studied powders were filled in small volume (4) that was fixed on the table (3) and was positioned in the tube (2) in the working chamber (1) of the installation (Fig.1). Then the pumping-out up to the minimal pressure of residual gas was executed. The working chamber was pumped out first up to 10^{-5} Torr and then the hydrogen or the mixture of argon and hydrogen were delivered into the chamber by a nozzle up to the pressure 4.10^{-2} - 6.10^{-2} Torr. The initial gas pressure was supported at stationary value; at that there was the equilibrium of the inlet gas supply and the pumping-out. The pressure of hydrogen (or the intermixture of hydrogen and argon) in the working chamber (or in the reaction zone) was controlled by the quantity of inlet gas flow through the nozzle. After the achieving of the working pressure the discharge was ignited. The exposition time of the hydrogen plasma interaction with studied materials was from two up two and one half hours. The powder was stirred up by a special mechanism for the interaction of hydrogen with treated material to improve. Moreover to improve stirring the walls of volumes were corrugated. The studied substance in small volumes was heated by the effect of beam-plasma discharge up to the temperature 400C – 500C. In several experiments the addition of argon to the hydrogen was used to increase the plasma electron density. The mixture argon and hydrogen was fifty-fifty. The deuterium was used to decrease the plasma losses thus increasing of the electron density as well. In the experiments with the argon addition the total gas pressure before the discharge ignition was ~(6.10^{-2} - 9.10^{-2}) Torr. The argon was used for the discharge in the electron gun to evade for relative high pressure of the order of 10^{-3} Torr. For lower pressures of the order of 10^{-4} Torr the addition of argon was not necessary. The initial compounds to be treated were Fe_2O_3, $FeCl_3$, $CuCl_2$, $LaCl_3$, and Sc2O3. The treatment time was from two up to two and a half hours and treatment was repeated four times. On having finished treatment we supplied the chamber by a nozzle with dry nitrogen to evade the oxidation processes of reduced metal powder obtained. The dry nitrogen was supplied into the "Oratoria-10" vacuum volume up to the pressure equalled to one atmosphere. Thus the dry nitrogen permitted to open the chamber having isolated the product (reduced metals) from air. The product obtained was studied by optical spectral method and by the X- ray analysis.

A typical experiment with iron oxide was as follows. All the small volumes were filled with Fe_2O_3. The initial pressure of residual gas in chamber corresponds to 10^{-5} Torr. Then the hydrogen in chamber was delivered up to the pressure 4.10^{-2} Torr. Argon was added up to the total pressure 9.10^{-2} Torr. The beam power was 1,9 kW. The total time of exposition was eight hours (four times for two hours). The temperature of powder during the experiment was 225C. The X-ray structure analysis showed: 10% of Fe_2O_3; 10% of Fe_3O_4; 10%; the rest 70% was pure iron represented in two forms, viz., 60% of α - Fe modification and 10% of β - Fe modification.

The second experiment was executed with the powder of $CuCl_2$. The sequence of the operations in the experiment was the similar to the above. The initial pressure and the pressure of hydrogen were the same. The adding gas was the mixture of Ar and He up to the total pressure $8.2 \cdot 10^{-2}$ Torr. The electron beam power

was 3,5 kW. The time of exposition was two hours and ten minutes. The temperature of powder was 470C. The obtained powder was consisted of 10% $CuCl_2$, 20% CuCl and 60% pure Cu.
The third experiment was the reduction of Sc from Sc_2O_3. The experiment was carried out by the analogy the experiments on the reduction of iron and copper. The adding gas was argon. The total pressure was the same as in the experiment with iron. The electron beam power was 2.2 kW. The time of exposition was one hour and forty-seven minutes. As a result we had the reduction of one half from the initial scandium oxide (50% of Sc and 50% of Sc_2O_3).
The fourth experiment was executed with the powder of $LaCl_3$. The experiment was the similar to the three above. The adding gas was helium. The total pressure of gas mixture was $7.4 \cdot 10^{-2}$ Torr. Two expositions were executed. In the first one the electron beam power was 2.25 kW during the time of one hour and forty-seven minutes. In the second one the electron beam power was 2.25 kW during the time of two hours. The product result contained 20% of $LaCl_3$, 15% of LaCl and 65% of pure La.
The last fifth experiment was the reduction of scandium from $ScCl_3$. This experiment was the similar to the above too. The adding gas was helium and the total pressure was same as in the fourth one. The electron beam power was 2kW. The total time of the exposition was one hour and forty minutes (five times for twenty minutes). As in the experiment on the reduction of scandium from the scandium oxide we had in a result the reduction of one half scandium chloride (50% of pure scandium, 20% of $ScCl_3$ and 30% of Sc_2Cl_3).

4. Results

It was shown, that the reduction of metals (iron, copper, scandium, lanthanum) from its oxides and chlorides in hydrogen plasma of the beam - plasma discharge was good enough, not less than 50 %. As a rule the reduced metals were obtained in the powder form, the special attention was being to be drawn to the problem of transportation of the obtained metal samples to avoid their oxidation. Usually the total gas pressure was 10^{-2} Torr, the hydrogen pressure being 10%, argon pressure being 90%. The other mixtures were used as well. The transition to the lower pressure when the soft X-ray emission appeared was performed and the comparison of results for high pressure (10^{-2} Torr) and low pressure (10^{-4} Torr) was done. The low pressure permits to dispense with argon and deuterium. The processing studied can be of interest for the direct reduction of the oxides of the rare earth metals.

5. Discussion

The obtained result confirms the opportunity to use the method of direct reduction of metals from oxides and chlorides in hydrogen plasma for the production high pure metals from high pure oxides (chlorides). We have not achieved the complete reduction of metals oxides (and chlorides). The possible reason could be the excessive thickness of the sheet of an initial powder and poor intermixing. Because of it is difficult to speak about reaction rate and the productivity of the process. In any case the obtained results confirm the opportunity to create the technology of direct reduction of high pure metals from oxides (or chlorides). There are two main ways of the further researches: to extract the reduced metal from oxide (or chloride) and to achieve the complete reduction of metal oxide (chloride) up to metal. The solution of a problem of complete reduction of metal oxide up to metal is possible by the increasing density of hydrogen ions in plasma for example by the decreasing of argon addition and the using of only hydrogen plasma. Now, the reconstruction of device is in progress. The minimal residual gas pressure in the working chamber is 10^{-6} Torr. Beam-plasma discharge is stable ignited and burns in wide pressure range of hydrogen from 5.10^{-5} Torr up to 10^{-3} Torr and higher at the energy of beam electrons from 2 keV up to 6 keV and current of the beam from 0,5 A up to 2 A. In this regime there is the X-ray generation with the energy up to 250 keV is observed. The presence of X-ray generation testifies the existence of a group of "hot" electrons with energy much more than energy of beam electrons in the discharge. The hot electrons appear in the beam - plasma discharge at equality of plasma oscillations frequency to doubled Larmor oscillations frequency. The existence of such mode also is the confirmation that the process of reduction of metal from oxide is carried out with the most efficiency in the beam-plasma discharge. It is necessary to take into account the opportunity of X-rays generation in the experiments with beam-plasma discharge from the view point of a safety of the operative personnel. It is of interest to carry out the experiments at more thin layers of studied compounds at smaller pressures of initial gas and without the use of argon additions. With this respect it should be pointed out that the beam-plasma discharge is rather turbulent heating phenomenon rather than support of discharge only due to pair collisions [3]. The outcome of X- ray radiation from the beam plasma discharge is well known in the physics of hot plasma since 1963. It should be noted that the appearance of the hot electron and of X-ray

emission should be taken into account very seriously. From one side it demonstrates the possibility of this type of discharge from the other side it calls for certain accuracy.

References

[1] A. A. Ivanov, G. B Levadny, et al. Investigation of Dissociation and Synthesis in Plasma Chemical Reactors Based on Plasma-Beam Discharge. 4-th International Symposium on Plasma Chemistry (ISPC-4). Zurich, August 1979, 427–232.

[2] A. A Ivanov, G. B. Levadny, S. Klagge, The Investigation of Dry Etching Process of Refractory Materials in Beam-Plasma Discharge. 5-th International. Symposium on Plasma Chemistry (ISPC-5) Contributed Papers, p. 336–339, Edinburgh, 1981.

[3] A. A. Ivanov. The present state and development trends of discharges. Physics and chemistry of plasmas. Phenomena in Ionized Gases (XXII ICPIG) Hoboken, NJ July-August 1995, p.41 – 74.

[4] R. A. Meger, D. D. Blackwell, R. F. Fernsler, M. Lampe, D. Leohardt, W. M. Manheimer, D. P. Murphy, and S. G. Walton. Beam-generated plasmas for processing applications. Paper V12, Bull. Am. Phys. Soc. **45**, 323 (2000).

[5] R. A. Meger, D. D.; Blackwell, R. F. Fernsler, M. Lampe, D. Leonhardt, W. M. Manheimer, D. P. Murphy, and S. G. Walton Phys. Plasmas **8**, 2558 (2001).

Formation Mechanism of Boride Nanoparticles by Induction Thermal Plasmas

Takayuki Watanabe[1], Tsuyoshi Ibe[1], Yoshiyuki Abe[2], Yoshiro Ishii[2], Kenji Adachi[2]

[1] *Research Laboratory for Nuclear Reactors, Tokyo Institute of Technology, Tokyo, Japan*
[2] *Central Research Laboratory, Sumitomo Metal Mining Co., Ltd., Chiba, Japan*

Abstract
The condensation mechanism of rare-earth boride in thermal plasmas was investigated experimentally. In the thermal plasma, the premixed powder of rare-earth boride with boron was evaporated immediately and nanoparticles were produced through the cooling process. The nucleation temperature of boron, lanthanum and cerium have wide liquid range between the nucleation and melting temperature, resulting in better preparation of boride.

1. Introduction

Induction thermal plasmas have been used for production of high-quality and high-performance materials, such as synthesis of nanoparticles, deposition of thin films, plasma spraying and treatments of powders. Induction thermal plasmas have been also applied for treatment of harmful waste materials and recovery of useful material from wastes [1, 2]. These attractive material processes with induction thermal plasmas result from unique advantages; these advantages include high enthalpy to enhance reaction kinetics, high chemical reactivity, large volume with low velocity, oxidation and reduction atmospheres in accordance with required chemical reactions, and rapid quenching (10^6 K/s) to produce chemical non-equilibrium materials. These advantages increase the advances and demands in plasma chemistry and plasma processing, such as preparation of various kinds of nanoparticles in metallic and ceramic systems.

The purpose of this paper is to prepare rare-earth boride nanoparticles by induction thermal plasmas. Rare-earth boride is attractive materials because of their high melting temperature, high electrical conductivity and low work function. Therefore these nanoparticles would be applied for the electromagnetic shielding, and solar control windows with interaction with IR and UV light. Some reports about the preparation of boride nanoparticles were published previously; YB_{66} nanoparticles were prepared by plasma chemical process using starting powders of YB_4 and B [3]. TiB_2 nanoparticles were synthesized in the vapor-phase reaction of sodium with $TiCl_4$ and BCl_3 [4].

Another purpose is to investigate the condensation mechanism of mixture vapor of rare-earth metal and boron in thermal plasmas. Investigation of physical and chemical processes in thermal plasma processing is indispensable for production of nanoparticles. Co-condensation process of metal vapors was investigated for Nb-Al and Nb-Si systems [5], Nb-Si and V-Si systems [6]. Formation mechanism was investigated for silicide nanoparticles [7,8]. Vaporization process for Ti-Si, V-Si and Mo-Si systems were also investigated [9]. For nanoparticle preparation with stoichiometric composition, the vaporization and condensation rates of the constituent metals should be controlled in the case of large difference in the vapor pressure.

2. Experimental Set-ups

Figure 1 shows a schematic illustration of experimental set-ups for the production of nanoparticle preparation. Induction thermal plasmas were used for preparation of rare-earth bride nanoparticles. The set-ups consist of a plasma torch, a reaction chamber, a

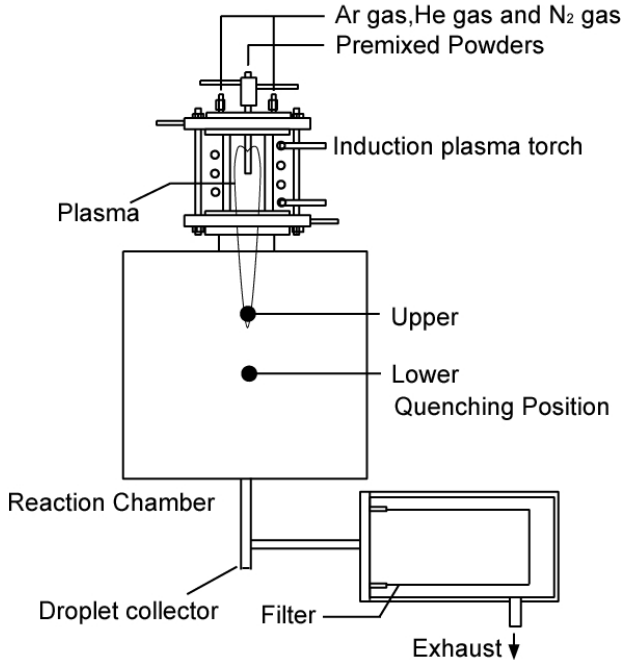

Fig. 1 Experimental set-up for nanoparticle preparation.

prepared particle collection filter and a power supply (4 MHz) at 25 kW. The plasma torch (45 mm i.d., 128 mm length) consists of a water-cooled quartz tube and a working induction coil (3 turn). The reaction chamber was set below the torch. Total system was evacuated and then Ar was introduced up to a pressure of 101 kPa. Premixed powders of La_2O_3, B and C were introduced into the thermal plasma from the top of plasma torch at the feed rate of 0.1 g/min. Premixed powders of $La(OH)_3$, B and C were also used for the preparation of LaB_6. For the preparation of CeB_6, premixed powders of CeO_2, B and C were used. Raw material powders used in this study are La_2O_3 (average: 14.4 μm), $La(OH)_3$ (average: 1.34 μm), CeO_2 (average: 20.2 μm), B (average: 15.0 μm), and C (average: 1.34 μm). In the thermal plasma, injected powders were evaporated and reacted with boron. After the evaporation and reaction, the vapor was rapidly cooled after the plasma flame. Through the cooling process, metal vapor condensed and boride nanoparticles were produced. The prepared nanoparticles were collected at quenching condition by the water-cooled coil.

The structures of the prepared nanoparticles were determined by X-Ray Diffractometry (XRD, Mac Science MXP3TA). Concentrations of La and B in the prepared particles were determined by Inductively Coupled Plasma Spectrometry (ICP, Seiko Instruments SPS4000), while that of C were measured by Carbon Determinator (LECO EC12). The size distribution of the particles was measured from the photographs of Transmission Electron Microscopy (TEM) for about 1000 particles. TEM observations as well as Electron Diffractometry (ED) were performed on JEOL JEM-2010 operated at an accelerating voltage of 200 kV.

3. Experimental Results

a) La-B-C system

The TEM photograph of the prepared nanoparticles for La_2O_3-B-C system was shown in Fig. 2. The particle size distribution shown in Fig. 3 presents the average particles size of 15.0 nm with the geometrical standard distribution of 1.58. The XRD spectrum charts of the prepared nanoparticles for La_2O_3-B-C system with the Ar plasma are demonstrated in Fig. 4. LaB_6 and La_2O_3 were identified from the XRD spectrum peak of the as-prepared particles. The as-prepared particles were separated to nanoparticles in suspension and agglomerated particles in precipitate by ultrasonic dispersion. Nanoparticles are mainly composed of LaB_6 with small fraction of $La(OH)_3$ made from La_2O_3 at ultrasonic dispersion. The agglomerated particles are identified as LaB_6, $La(OH)_3$, $LaBO_3$ with unreacted B from XRD and ED analysis. Induction thermal plasmas provide a powerful tool for the preparation of functional nanoparticles because the phase and composition in nanoparticles can be well controlled.

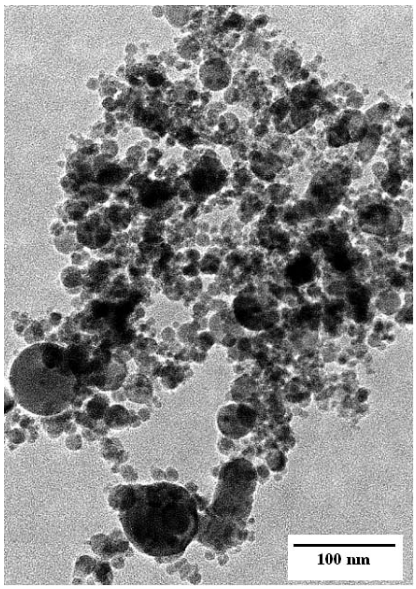

Fig. 2 TEM photograph of nanoparticles for La_2O_3-B-C system; La_2O_3:B:C = 1:12:3; powder feed rate: 0.1 g/min.

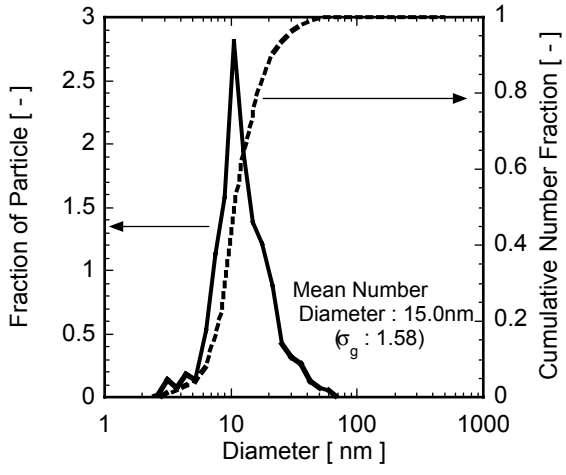

Fig. 3 Particle size distribution for La_2O_3-B-C system; La_2O_3:B:C = 1:12:3; powder feed rate: 0.1 g/min.

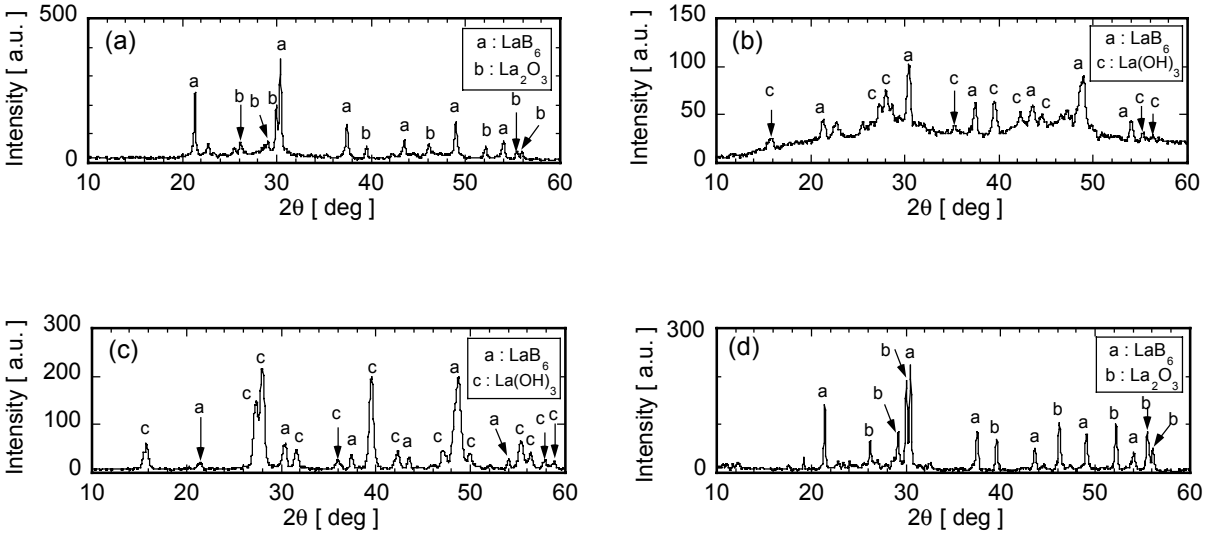

Fig. 4 XRD spectrum charts of nanoparticles for La_2O_3-B-C system; La_2O_3:B:C = 1:12:3; powder feed rate: 0.1 g/min. (a) as-prepared particles, (b) nanoparticles in suspension, (c) particles in precipitation, (d) unvaporized particles.

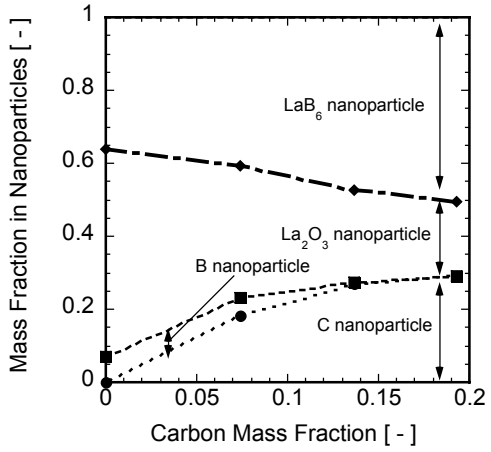

Fig. 5 Effect of carbon mass fraction in the injected powders on the nanoparticle composition for La_2O_3-B-C system.

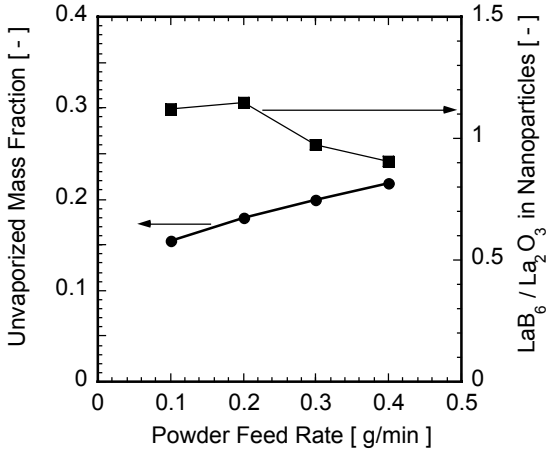

Fig. 6 Effect of powder feed rate on the unvaporized fraction and on the nanoparticle composition for La_2O_3-B-C system.

Figure 5 shows effect of carbon mass fraction in the raw powders on the nanoparticle composition. The prepared amount of LaB_6 increases with the carbon content, because the injected La_2O_3 is easily reduced by carbon in the plasma. Increasing in the carbon content in the feed powder also causes the increase in the carbon content in the prepared nanoparticles. However the carbon in the nanoparticles can be separated by hydrochloric acid treatment; 3 N hydrochloric acid during 20 min at room temperature.

Effect of powder feed rate on the unvaporized fraction of the particles was shown in Fig. 6. The composition of the nanoparticles was also shown in this figure. The unvaporized fraction deceases with a decrease in the powder feed rate, resulting in the enhanced vaporization of boron powders. Therefore the prepared amount of LaB_6 nanoparticles are larger at smaller powder feed rate.

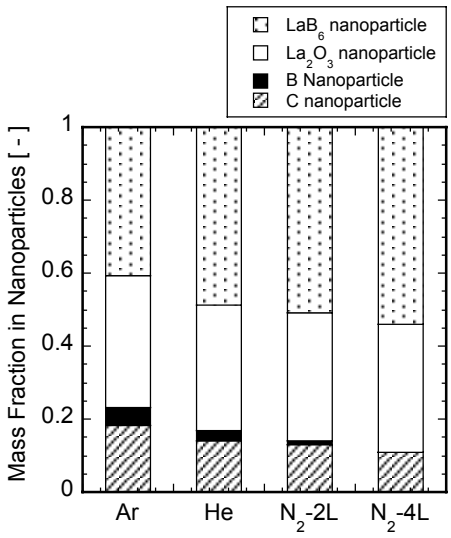

Fig. 7 Effect of plasma gas composition on the nanoparticle composition for La_2O_3-B-C system.

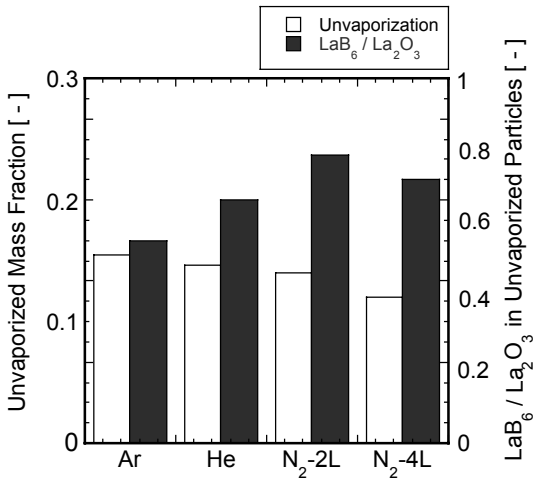

Fig. 8 Effect of plasma gas composition on the unvaporized fraction and on the composition of unvaporized particles for La_2O_3-B-C system.

Plasma gas composition has important role on the nanoparticle composition, because the heat transfer rate as well as the reaction mechanism are influenced by the plasma gas composition. Nitrogen (2 or 4 NL/min) or helium (3 NL/min) was added to argon induction plasmas. From the XRD analysis, no peaks due to BN and LaN were not found because ΔG of La nitridation is higher than that of boridation. Effect of plasma gas composition on the nanoparticle composition was shown in Fig.7. Prepared amount of LaB_6 nanoparticles were increased by helium or nitrogen plasmas. Addition of helium or nitrogen enhances the heat transfer rate to the injected powders as shown in Fig. 8. The unvaporized fraction of the injected powders is reduced by helium or nitrogen plasma.

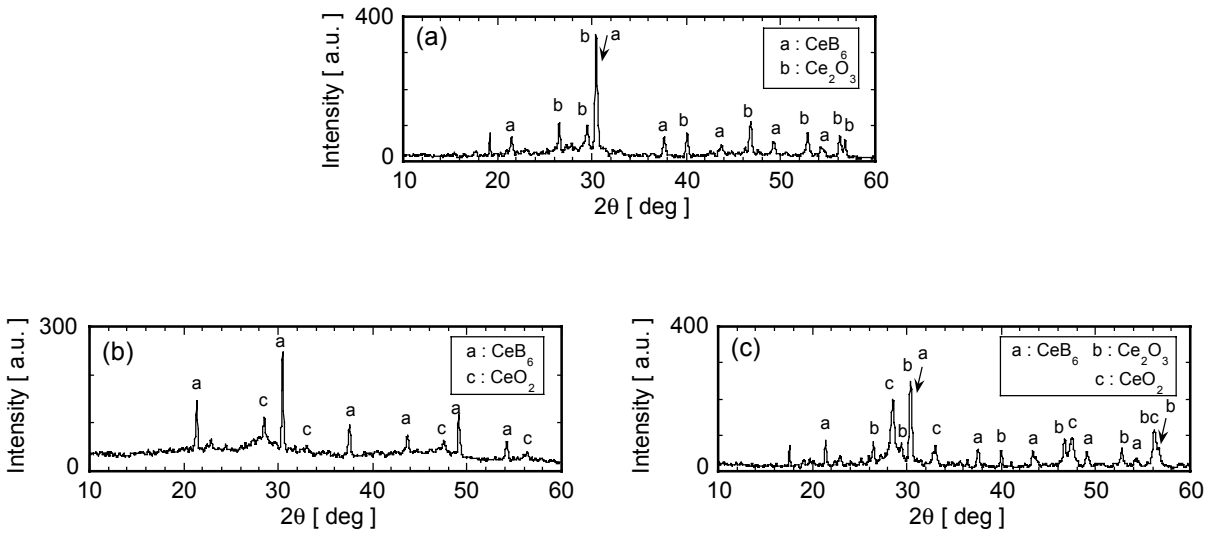

Fig. 9 XRD spectrum charts of nanoparticles for CeO_2-B-C system; CeO_2:B:C = 1:12:3; powder feed rate: 0.1 g/min. (a) as-prepared particles, (b) nanoparticles in suspension, (c) unvaporized particles.

b) Ce-B-C system

The XRD spectrum charts of the prepared nanoparticles for CeO_2-B-C system with the Ar plasma are demonstrated in Fig. 9. CeB_6 and Ce_2O_3 were identified from the XRD spectrum peak of the as-prepared particles. The as-prepared particles were separated to nanoparticles in suspension and agglomerated particles in precipitate by ultrasonic dispersion. Nanoparticles are mainly composed of CeB_6 with small fraction of CeO_2 made from oxidation of Ce_2O_3 at drying.

Figure 10 shows the comparison of nanoparticles composition for La_2O_3-B-C and CeO_2-B-C systems. The ratio of LaB_6 to La_2O_3 is larger than the ratio of CeB_6 to Ce_2O_3 in the as-prepared particles. The better preparation of LaB_6 than that of CeB_6 is attributed to lower ΔG of lanthanum boridation than that of cerium boridation.

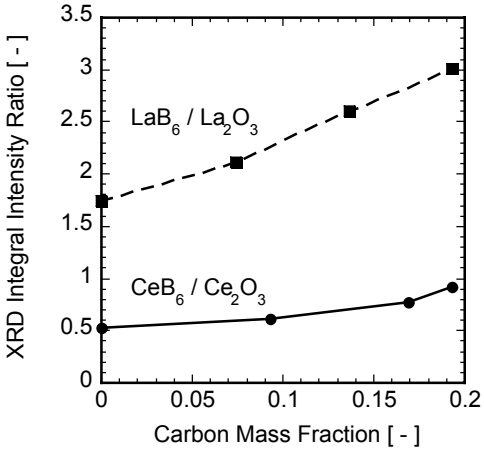

Fig. 10 Comparison of nanoparticle composition for La_2O_3-B-C and CeO_2-B-C systems.

4. Discussions

a) Vapor pressure

Vapor pressure difference of boron and rare-earth is the important factor for the controlled composition of the prepared rare-earth boride nanoparticles. The vapor pressure ratio of lanthanum to boron is 13, while that of cerium to boron is 18 at the melting point of born. Small difference in vapor pressure of the constituent components leads to better preparation of boride nanoparticles.

b) Nucleation Temperature

Homogeneous nucleation rate has been proposed by Girshick et al. [10]. They derived the expression as an extension of kinetic nucleation theory. The proposed expression can be used over a wide range of physical conditions. Furthermore, the expression for homogenous nucleation, J, was consistent with experimental data. Therefore Eq. (1) was used for the estimation of critical saturation ratio.

$$J = \frac{\beta_{ij}\, n_s\, S}{12}\sqrt{\frac{\Theta}{2\pi}}\exp\left[\Theta - \frac{4\Theta^3}{27(\ln S)^2}\right] \tag{1}$$

where n_s is the equilibrium saturation monomer concentration at temperature T, β_{11} the collision frequency function between monomers, and S the saturation ratio. The dimensionless surface tension Θ is given by

$$\Theta = \frac{\sigma s_1}{kT} \tag{2}$$

where σ is the surface tension, and s_1 the monomer surface area. The collision frequency function β_{11} can be estimated by Eq. (3) when the Knudsen number is more than 10 [11].

$$\beta_{ij} = \left(\frac{3v_1}{4\pi}\right)^{1/6}\sqrt{\frac{6kT}{\rho_p}\left(\frac{1}{i}+\frac{1}{j}\right)}\times\left(i^{1/3}+j^{1/3}\right)^2 \tag{3}$$

where ρ_p is the particle mass density and v_1 the monomer volume. In this model, the particle nucleation is due to the monomer collision, therefore $i = j = 1$.

Relationship between the nucleation rate and saturation ratio is shown in Fig. 11. The nucleation rate is strongly dependent on the surface tension and saturation ratio. When the nucleation rate is over 1.0 cm^{-3} s^{-1}, particle formation can be conveniently observed experimentally. Therefore the corresponding value of saturation ratio is defined as the critical saturation ratio [11]. The critical saturation ratio of boron was estimated to be 2, while lanthanum and cerium have the critical saturation ratio of 14 and 16, respectively. Carbon has the highest critical saturation ratio of 42.

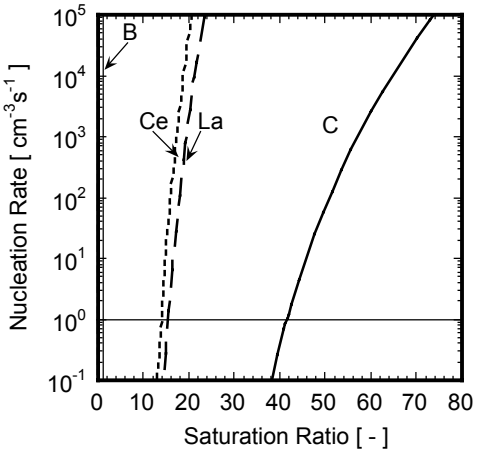

Fig. 11 Relationship between homogenous nucleation rate and saturation ratio for La, Ce, B and C.

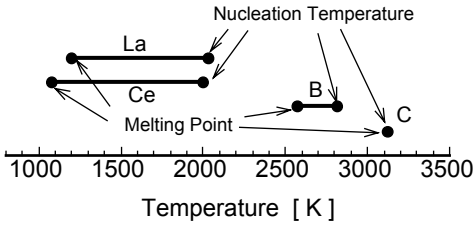

Fig. 12 Nucleation and melting temperature of La, Ce, B and C.

The nucleation temperature at the critical saturation ratio is presented in Fig. 12 for constituent components of boride. The nucleation temperature of carbon corresponds to the melting temperature, while boron, lanthanum and cerium have wide liquid range between the nucleation and melting temperature. The wide liquid range combination of boron with rare-earth metals leads to better preparation of rare-earth boride nanoparticles.

5. CONCLUSIONS

Experiments were performed to investigate the condensation of mixture of rare-earth metal with boron in thermal plasmas for the preparation of LaB_6 and CeB_6 nanoparticles. The nucleation temperature of boron, lanthanum and cerium have wide liquid range between the nucleation and melting temperature, resulting in better preparation of boride. Induction thermal plasmas provide a powerful tool for the preparation of functional nanoparticles because the phase and composition in nanoparticles can be well controlled.

References

[1] M. Sakano, T. Watanabe and M. Tanaka, *J. Chem. Eng. Japan*, **32**, p.619 (1999).
[2] M. Sakano, M. Tanaka and T. Watanabe, *Thin Solid Films*, **386**, p.189 (2001).
[3] J. Y. Huang, T. Ishigaki, T. Tanaka, S. Horiuchi, *J. Mater. Sci.*, **33**, p.4141 (1998).
[4] R. L. Axelbaum, D. P. Dufaux, and C. A. Frey, *J. Mater. Res.*, **11**, p.948 (1996).
[5] T. Harada, T. Yoshida, T. Kozeki and K. Akashi, *J. Japan Inst. Metals*, **45**, p.1138 (1981).
[6] Y. Anekawa, T. Koseki, T. Yoshida and K. Akashi, *J. Japan Inst. Metals*, **49**, p.451 (1985).
[7] K. Katsuda, T. Watanabe, Y. Abe and Y. Ishii, *Trans. Mater. Res. Soc. Japan*, **27**, p.137 (2002).
[8] T. Watanabe, A. Nezu, Y. Abe and Y. Ishii, *Thin Solid Films, to be published*.
[9] T. Watanabe, H. Itoh and Y. Ishii, *Thin Solid Films,* **390**, p.44 (2001).
[10] S. L. Girshick, C. P. Chiu and P. H. McMurry, *Aerosol Sci. Tech*., **13**, p.465 (1990).
[11] S. K. Friedlander, Smoke, Dust and Haze, John Wiley and Sons (1977).

Plasma sputtering technique for problems to solve by making use of environment at the outdoor conditions

V.S. Blokhin[2], A.A. Ivanov[1], A.V. Pereslavtsev[1]

[1] *Russian Research Centre "Kurchatov Institute", Moscow, Russia*
[2] *Center of Ecological Technologies – "Intellect of Creation", Moscow, Russia*

Abstract
The plasma sputtering technology of decorative and moisture-proof coatings on the base of natural sand is developed. The direct current arc plasmatron is applied for the sputtering of coatings. The air is used in plasmatron as the plasma forming gas. The plasma equipment complex for the coating producing may be made as in stationary or in the mobile variant for the using at the outdoor conditions. The technology can be applied for the producing of corrosion resisting and wear-resistant chemically proof coatings.

1. Introduction

One of the perspective trends in the modern technologies development is the wide using of various types of coatings such as decorative coatings, moisture-proof coatings, anticorrosive coatings, wear-proof coatings, chemically resistant coatings, and also various multipurpose coatings. Rather complicated stationary equipment required for the application of plasma sputtering techniques is the main problem for its wide application. The modern materials in plasma equipment make it possible to develop new advanced techniques for the production of protecting coatings based on natural materials. The using of air, water aerosols or natural gas in plasma sputtering techniques simplifies the plasma equipment and increases its mobility. The application of natural sands as the base component of plasma ceramic coatings in sputtering process decreases the cost of the technological process and the cost of coatings simultaneously. The development of the new approach to the interaction of powder particles with the flow of high temperature plasma allows to increase the efficiency of the powder heating in plasma flow in 2.5 - 3 times. This approach makes it possible to decrease the power consumption of the plasmatron sputtering equipment about two times.

2. Technology

The scheme of plasmatron for the producing of protective coatings on the base of natural materials is shown on the fig.1.

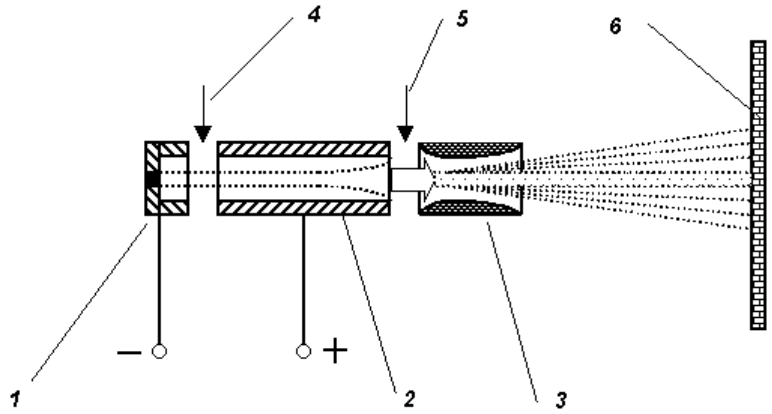

Fig. 1. Special plasmatron for plasma sputtering deposition on the base of natural materials. 1 – cathode; 2 – anode; 3 – sputtering nozzle; 4 – plasma forming gas; 5 – working intermixture; 6 – handled surface.

The direct current arc plasmatron is applied as the source of low temperature plasma for the plasma sputtering process. The plasma forming gas is being supplied to the inter-electrode space, between the cathode (1) and anode (2). The air is used as the plasma forming gas in the presented technology. The gas heating and the plasma flow formation take place in the plasma filament of arc discharge of plasmatron. The

heat content (enthalpy) of gas flow is determined by the parameters of arc discharge (arc current and arc voltage) and gas flow. The spraying nozzle (3) is set at the outlet of the plasmatron anode. The working intermixture being the base for the coating is supplied to the space between the anode (2) and the spraying nozzle (3).
The heating of the working intermixture particles up to the required temperatures and their transportation up to a handled surface is carried out by the high temperature gas-plasma flow. The temperature of the working intermixture particles depositing on a handled surface, their phase state and their velocity are determined by the following parameters:

- the heat content (enthalpy) of gas-plasma flow,
- the relation of the plasma forming gas flow and working intermixture flow,
- the composition of the working intermixture,
- the configuration of the spraying nozzle.

The main problem in the development of presented technology is the choice of the working intermixture composition, the temperature and the velocity of the particles at the interaction with the handled surface [1,2]. The characteristics of the coating obtained (the composition and the structure of the coating, the adhesion with the handled surface) depend on the above parameters of the working intermixture and the gas-plasma flow produced by plasmatron.
The above approach allows us to form the coatings of the required composition and structure on the base of rather various materials. It makes it possible to obtain the composite coatings [3,4,5].

3. Application

The above principle of the interaction of working mixture particles with the gas-plasma flow is applied in the plasma sputtering technology for the producing of decorative protective coatings. The developed technology is based on the using of natural sands and it is intended for the application in the building construction. The gas for the plasma formation is the air. The features of the produced coatings and their characteristics depend on the composition of the working mixture. One can obtain the coatings of different colours mixing natural sand with the different inorganic dyes. The use of widely accessible natural materials and the rather low requirements to their preparation allow us to realise the technology not only in the stationary variant, but as the mobile complex of equipment, too. The scheme of the mobile complex of plasma sputtering equipment for the application in the building construction is shown on the fig.2. The process of the plasma sputtering deposition is realised by the specially designed plasmatron. One can use the air, water vapour, and the natural gas as the plasma forming gas in the plasmatron. The composite materials are used in the construction of plasmatron [6,7]. The spraying nozzle is manufactured with the using of composite materials. The durability and the lifetime of plasmatron and spraying nozzle are determined first of all by the application of these composite materials. The complex of equipment is intended for the producing of coatings of any types, including the decorative and moisture-resistant coatings by the method of plasma sputtering on the surfaces of concerts and on the other constructional materials.
The complex of plasma equipment consists of:

- the power supply system (autonomous electric generator and voltage transformation unit);
- compressor;
- the system of working intermix supply (receiving bunker with disintegrator and the dispensing mechanism of the mix supply: sand + admixture);
- water-cooling system;
- plasmatron;
- control system.

The plasma equipment complex can be transported by the automobile or may be installed on the automobile chassis or auto trailer.
At the use of computer control and monitoring system two operators can serve the plasma equipment complex.
Some technical parameters of the plasma equipment are as follows:

- the power of plasmatron is 30 kVA;
- the productivity of process per square unit is about 3 - 6 m^2/hour;
- the productivity of plasmatron is about ~ 1.5 kg/h;
- small dimensions of the plasma device.

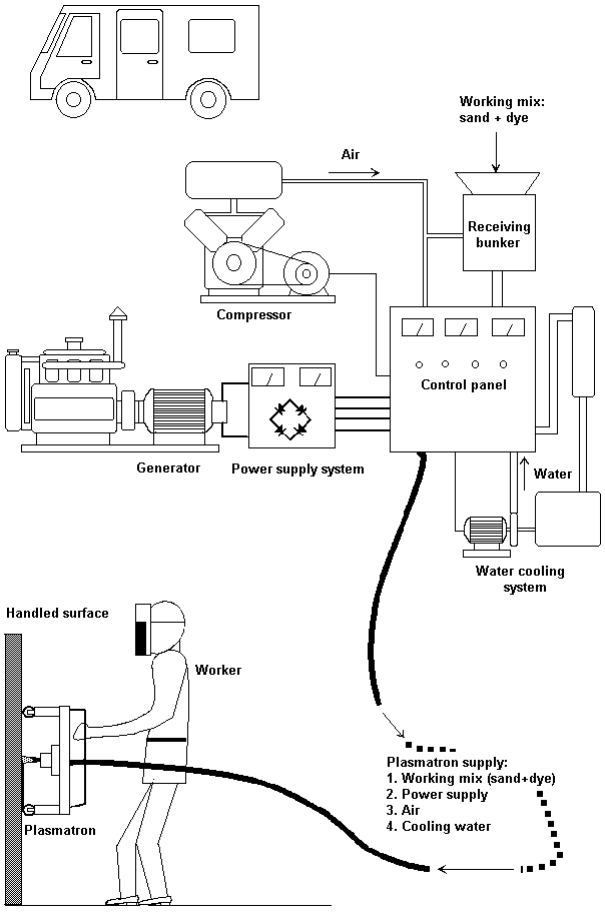

Fig. 2. Structure of the mobile complex of plasmatron equipment for the plasma sputtering of coatings on the base of nature sands in the buildings construction.

The presented technology allows to produce the ceramic coatings of the thickness 0.15 – 0.3 mm with waterproof glassy (fused) structure. Also the presented technology allows to create the facing details with any thickness.

The process of preparation of working intermixture for plasma sputtering technology is not very complicated and there is no need to organise the special industrial productions.

The manufacturing equipment intended for the preparation of the working intermixture can be mobile. One can use the equipment as in industrial variant or in the variant for outdoor conditions. One can see the possible variant of the scheme of manufacturing equipment for the preparation of working intermixture on the base of natural sand on the fig.3.

The technology of the working sand mixture preparation includes the following operations:

- sand drying;
- sizing, and the grinding up to the size of 50 - 150 microns;
- the mixing with the admixtures (inorganic colour dye and some others).

One preparation equipment complex can be utilised to serve several plasma sputtering equipment installations for the coating producing. This example of use of the above-stated approaches to the application of plasma sputtering technologies demonstrates us the new opportunities of plasma methods to improve and to get the new qualities of large-sized products.

4. Discussion

The technology of the deposition of coatings by plasma sputtering method based on the using of air, water aerosols, and natural sand allows us to obtain the "ceramic" or “cermets” coatings. Ceramic or cermets coatings have high durability and the resistance to external actions in outdoor conditions. The approach based on the above principles may be used for the creating of the techniques for the sputtering of protective

chemically resistant and corrosion-proof coatings for trunk pipelines, for the sea ship bottoms exposed to action of aggressive environment and for other objects and the directions of technique.

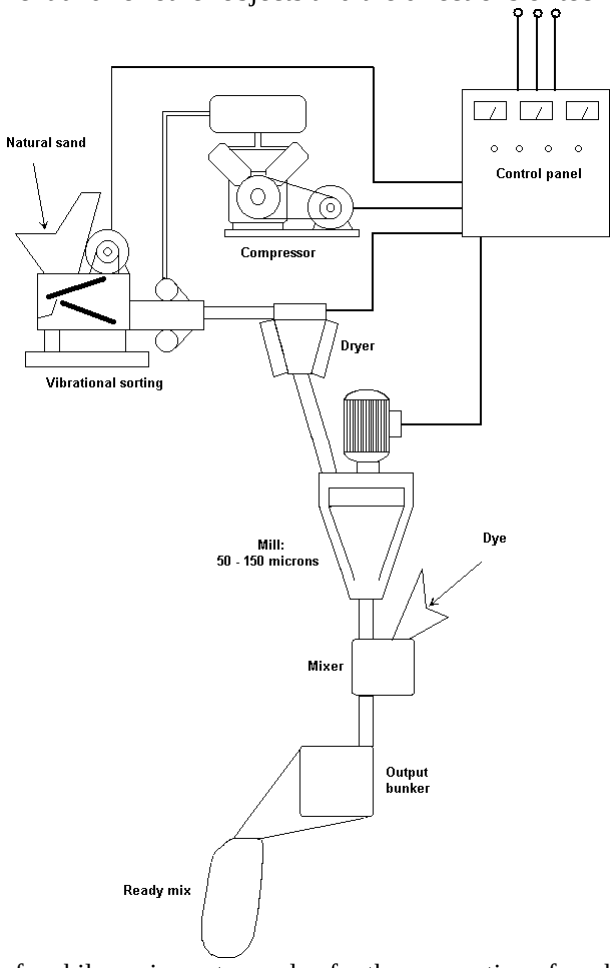

Fig. 3. The structure of mobile equipment complex for the preparation of working intermixture for the deposition of coatings by plasma sputtering method on the base of using of natural sand.

The presented technology accords to the modern ecological requirements and makes it possible to decrease the man-caused influence on the environment.

One can successfully apply the plasma sputtering technique for the producing of more complicated ceramic coatings on the metal surfaces with required characteristics. So, for example, the new approach to the formation of plasma jet containing the depositing material can be applied for the development of wider spectrum of products and to increase the operation resource of these products.

The simplicity and the cheapness of this technology make us hope on its wide application.

References

[1] V.S. Blokhin et al. Decoding of a phase composition of plasma deposited coatings on the base of niobium carbide with the use of a micro X-ray and colour structure analysis. Proceedings of 6-th all-Union conference on heat-resistant coatings. Nauka, 1976, p. 122 – 127. [In Russian].

[2] V.S. Blokhin et al. Study of behaviour of niobium carbide in low-temperature plasma jet and properties of the formed coating. Proceedings of 6-th all-Union conference on heat-resistant coatings. Nauka, 1976, p. 128 – 130. [In Russian].

[3] V.S. Blokhin et al. Some features of composite materials depositing having different thermal-physics properties. Proceedings of 7-th all-Union conference on heat-resistant coatings. Nauka, 1977, p. 154 – 157. [In Russian].

[4] V.S. Blokhin et al. Looses of powder materials at plasma sputtering deposition. Proceedings of 7-th all-Union conference on heat-resistant coatings. Nauka, 1977, p. 158 – 160. [In Russian].

[5] V.S. Blokhin et al. Evaluation of effectiveness of plasma deposition process of composite materials. Theses of reports of 7-th all-Union conference “Theory and practice of gas-thermal producing of coatings“. MHTS, 1978, p. 88. [In Russian].
[6] V.S. Blokhin et al. “Plasma burner” Certificate of authorship No 1092847 on 15.01.1984. [In Russian].
[7] V.S. Blokhin et al. “Plasmatron” Certificate of authorship No 727369 on 21. 21.1979. [In Russian].

OES CHARACTERISATION OF A PARTICULATE PLASMA FLOW FOR NANOTUBES SYNTHESIS FROM POWDERS

Badie J.M.[1], Fabry F.[2], Fulcheri L[3], Gruenberger T.M.[3], Gonzalez-Aguilar J.[3], Flamant G.[1]

1- IMP-CNRS, BP 5, 66125 Font-Romeu Cedex, France

2- ERACHEM COMILOG, Av. Louise 534, 1050 Bruxelles, Belgique

3- CENERG-EMP, BP 207, 06904 Sophia Antipolis, France

Abstract

This paper presents results about time evolution of OE spectra in a pilot 3-phase AC plasma reactor for nanotubes synthesis. Experiments are related to the injection of powder mixtures of carbon black with nickel or cobalt (or both metals). The following is commented: (1) He, Ni, Co, CN atomic lines and spectrum are observed when carbon, nickel and cobalt are injected together in the He plasma; (2) The mean plasma temperature is about 5200 K; (3) There is a strong influence of Ni on Co emission.

Introduction

In-situ diagnostics of high temperature processes for nanotubes synthesis is a critical issue addressing process monitoring and control in the view of the increase of selectivity. Nevertheless available data are very poor in the literature. Scott et al. [1] and Puretsky et al. [2] have published data about the laser ablation method. Concerning the arc and the solar methods data were given in the fullerene synthesis configuration, i.e. without catalysts, in [3] and [4] respectively. The C_2 emission is generally used as a temperature probe. Very recently results were obtained at CPAT (Toulouse, France) in conditions of single wall nanotubes (SWNT) synthesis by the arc method [5], Ni and Co lines were observed and analysed.
The data presented in this paper are related to an original plasma process in which carbon vapors are obtained from the evaporation of carbon powder in plasma whereas they are produced by electrode erosion in the standard electric arc process. Time evolution of the emission spectra is emphasized.

Experimental

The Reactor. The principle of this process consisted in introducing carbon particles, with or without metallic powders (Ni, Co), in a reactor equipped with 3-phase AC plasma torches. Both gas and solid were carried away in a filtration device where the carbon products were separated from gases. The gas was again injected at the bottom of the reactor. Inert or reducing plasma gas was used.
The complete system shown in Figure 1 was mainly composed of:

- A 200 kW 3-phase AC plasma source with consumable graphite electrodes, located at the top of the reactor;
- A high temperature reaction zone in which the carbon particles were injected. This top zone was separated from the rest by a graphite nozzle
- An insulated hot wall reacting chamber with graphite walls placed downstream the nozzle
- A circulation loop equipped with a bag-filter (PTFE bags) where carbon and gas were separated and collected
- An external vessel double-walled and water-cooled.

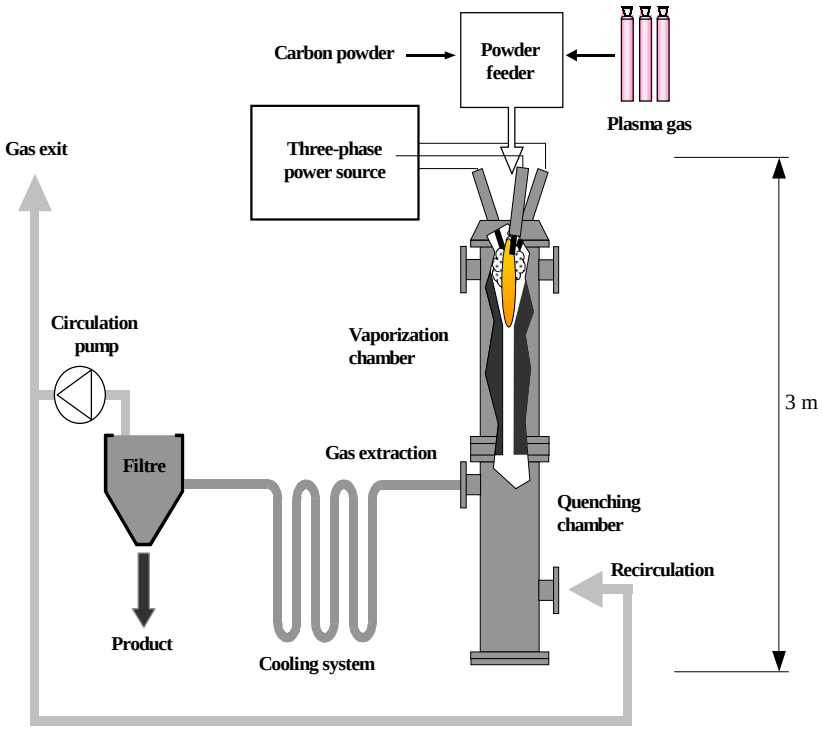

Figure 1: Scheme of the experimental system

Spectroscopic equipment:

The light emitted from the plasma was analysed by a monochromator (320 mm focal distance, with a 1200 lines/mm grating and 50 µm inlet slit). The detector was a 1024 x 128 photodiodes matrix. This device permitted a quasi-instantaneous analysis in a spectral range of about 60 nm. The duration time for the acquisition of an entire spectrum was 1 second. The spectral resolution was about 0.12 nm. An axial exploration of the plasma was performed using an optical device composed of:

- A lens: focal distance; 19 mm, diameter; 12.7 mm,
- An optical fiber: silica-silica, core diameter: 200 µm, length: 20 m,
- A measurement bench allowing 25 mm x and y displacement, and 1 meter z displacement.

The volume integrated by the fiber was perpendicular to the z-axis and centered on this axis. It was considered as a cylinder (4 mm diameter and 280 mm length).
The plasma gas was helium with a flow rate of 3 Nm^3/h. OES diagnostics of such plasma, seeded with cobalt and nickel powders, were performed in the arc zone through a window located at Z_1 = 15 cm. The mass flow rates of graphite powder and of metal (single or mixture of Ni + Co) were 100 g/h and the 10 g/h respectively. Standard electric characteristics were: U=80 V, I=250 A.

In this paper the comments will be focused on the time evolution of the emission spectra observed just underneath the arc zone during a injection sequence where pure carbon is first injected, then carbon plus cobalt powder and finally carbon plus nickel powder without cobalt.

Results

The walls of the reactor were first heated using nitrogen plasma. The nitrogen was then replaced by helium to perform the OES experiments. The Ni and Co powders were injected using Helium as carrier gas. Figure 2 shows a typical spectrum recorded in the arc zone during experiments without metallic powder injection. This Figure shows that the main lines are due to the bands of the violet system $B^2\Sigma$-$X^2\Sigma$ of CN. This species is produced from carbon and residual nitrogen coming from the preheating phase of the reactor.

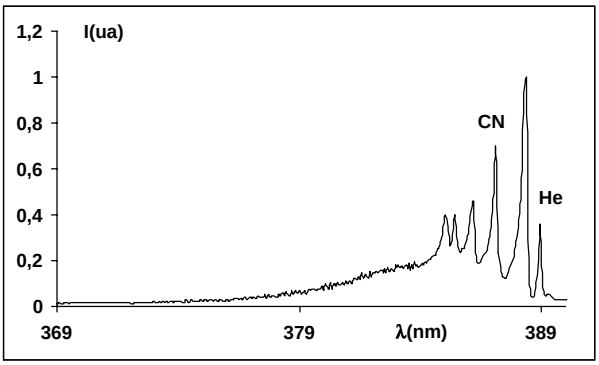

Figure 2: Typical OES spectrum without metallic powder injection

The head of the CN most intense band (0,0) for this system lies at 388.34 nm. The molecular spectrum of CN was observed for all our experiments. An atomic line of helium can also be observed at 388.86 nm, close to the CN band head.
Of course when pure cobalt powder is introduced in the plasma one can detect the emission of some atomic lines of this element mainly evidenced by the line at 389.4 nm (see Figure 3). But at the same time the intensity of the He line decreases.

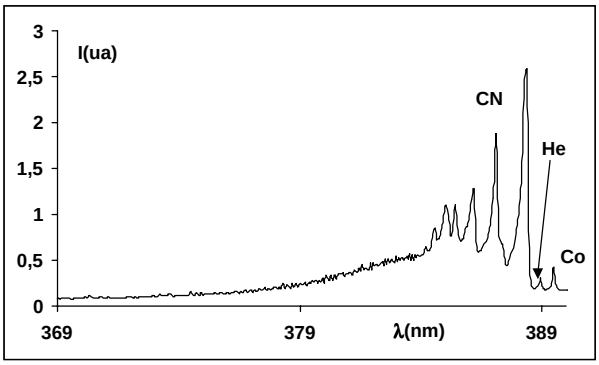

Figure 3: Typical OES spectrum with pure Co injection

Figure 4 shows the spectra obtained when the feeding of pure cobalt was stopped and replaced by pure nickel at the same flow rate. The spectrum shown in Figure 4 was obtained ten minutes after the spectrum in Figure 3. The feeding of Co was stopped five minutes before the introduction of pure nickel. Considering the time of nickel introduction as t= 0 one can deduce that the spectra on Figure 4 was recorded at t=2 mn.

In Figure 4 an emission of Ni atomic lines is clearly evidenced by the Ni line at 372.25 nm and three lines respectively at 377.56nm, 378.35 nm and 380.71 nm. More surprisingly is the important increase of the cobalt line intensities while there is no Co feeding.

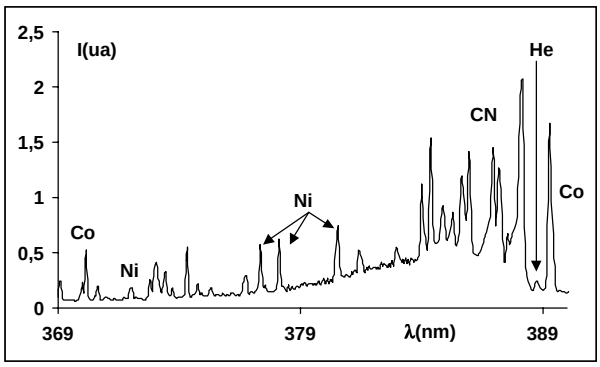

Figure 4: Typical OES spectrum with pure Ni injection at t=2 mn (Co injection stopped)

Moreover this Figure indicates an enhancement of the intensity of the 389.4 nm cobalt line with respect to the intensity of the helium line. Otherwise two atomic cobalt lines, respectively at 370.22 nm and 370.41 nm, can be observed in this Figure while they are almost undetectable for the experimental conditions of Figure 3.

A temperature can be derived from the relative intensities of these two lines assuming that the population of the upper level of the corresponding transition obeys a Boltzmann distribution (Local Thermodynamic equilibrium assumption). The temperature determined from the ratio intensities of the Co lines lead to a mean value of about 5200K ±200 K. This result agrees with data from [5].

Figure 5 shows the spectra recorded one minute after the experiment corresponding to the Figure 4. It is very surprising to observe a relative decrease of the same time of the Co and Ni lines intensities with respect to the helium line intensity.

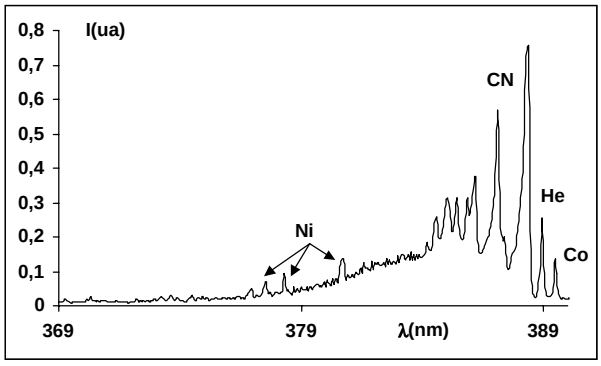

Figure 5: Typical OES spectrum with pure Ni injection at t=3 mn (Co injection stopped)

Figure 6 summarizes the intensity evolution of the Co, Ni, and He atomic lines for the three situations corresponding to the time sequence from Figures 3 to 5. The relative density of gaseous species Ni and Co in the arc zone is calculated assuming LTE, i.e. a same temperature for Co and Ni species.

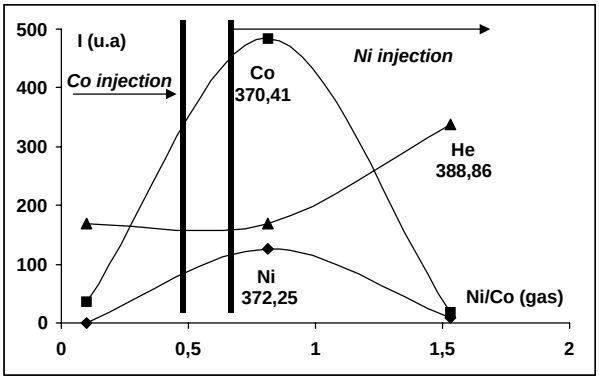

Figure 6**:** Line intensities evolution vs density ratio Ni/Co in the arc zone

The abscissa axis of Figure 6 gives the calculated Ni/Co ratio from the measured intensities and the calculated temperature. The obtained results are consistent: it is obvious that the ratio Ni/Co in the plasma (deduced from the intensity analysis) increases when pure Ni is introduced while the Co feeding is stopped.

When pure Co is injected the Ni/Co ratio is obviously small, the lines emission is weak meaning that the partial pressures of gaseous Co and Ni are low in the plasma. On the contrary it is difficult to explain the peak intensity mainly for the Co line while the helium intensity remains constant (constant temperature) and there is no Co injection inside the reactor, the only source of cobalt may be due to residual powder in the feeding pipes.
We have no satisfactory explanation for such behaviour and more experiments would be necessary for a better understanding of this phenomenon.

Conclusion

The main conclusions of this study are:

- He, Ni, Co, CN atomic lines and molecular spectrum are observed in the plasma flow during injection of powders.
- The derived plasma temperature assuming LTE is about 5200 K.
- An enhancement of Co emission is observed if Ni is present, this point is not explained but is perhaps related to the good performance of nanotubes synthesis observed when both catalysts are used.

Acknowledgement. This work was supported by the EC “PLASMACARB” Project under contract GRD1-1999-10617

References

[1] Scott C.D., Arepalli S., Nikolaev P., Smalley R.E. Appl. Phys. A, 72, 573 (2001).
[2] Puretsky A.A., Schiltenhelm H., Fan X., Lance M.J., Allard L.F., Geohegan D.B. Physical Review B, 65, 245425 (2002).
[3] Lange H., Saidane K., Razafinimanana M., Gleizes A. J. Phys: Appl. Phys., 32, 1024 (1999).
[4] Badie J.M., Flamant G., Guillard T., Laplaze D. Chemical Physics Letters 258, 199-206 (2002).
[5] Pacheco Pacheco M. Ph D thesis, Université Paul sabatier, France, January 30, 2003.

Plasma thermal synthesis of ozone

V.S. Blokhin[2], A.A. Ivanov[1], A.V. Pereslavtsev[1]

[1] *Russian Research Centre "Kurchatov Institute", Moscow, Russia*
[2] *Center of Ecological Technologies – Intellect of Creation, Moscow, Russia*

Abstract
The experimental technology of the thermal synthesis of ozone is developed. The technique can be applied in the systems of drinking water conditioning on the base of the ozonization and for the utilisation of different kinds of industry waste and domestic waste. The water vapour is supplied in plasmatron as the plasma-forming gas. It results in the thermal dissociation and ionisation water molecules with subsequent recombination and formation of atomic oxygen. The synthesis of ozone occurs in the freezing plasma jet.

1. Introduction

The ecological problems are the essential problems of our civilisation. The problem of drinking water conditioning is one of them today. The ozonization process, which is applied in drinking water conditioning, requires certain amount of ozone. The main modern method of ozone production is based on the oxygenation air passing through the barrier discharge. The plasma thermal synthesis of ozone is the essentially new method of ozone producing. The ozone synthesis is based on the use of water vapour dissociation in thermal plasma onto the atoms of hydrogen and oxygen with the subsequent partial ionisation up to the ions of oxygen and hydrogen. The system of ozone thermal synthesis is equipped by the reactor that provides the recombination of oxygen ions into ozone molecules with simultaneous freezing of plasma jet to the temperature 10 - 12°C. The obtained ozone may be used in the processes of water ozonization and in the technologies of utilisation of different kinds of waste.

2. Technology

The scheme of process of the ozone thermal synthesis is shown on the fig.1. The water vapour is chosen as the parent material for the ozone synthesis. The water vapour is the plasma-forming gas in the plasmatron. The arc discharge burns in the direct current arc plasmatron. The water vapour decomposes at the heating in the arc discharge:

$$H_2O \rightarrow OH + H \rightarrow O + H + H.$$

There is the partial ionisation of atomic oxygen and atomic hydrogen in the plasma filament of arc discharge. The equilibrium between the charge carriers is established: between positively ionised atoms of hydrogen, electrons and negatively ionised atoms of oxygen. Heat content (enthalpy) and the freezing rate of plasma jet determine the output of reaction products.

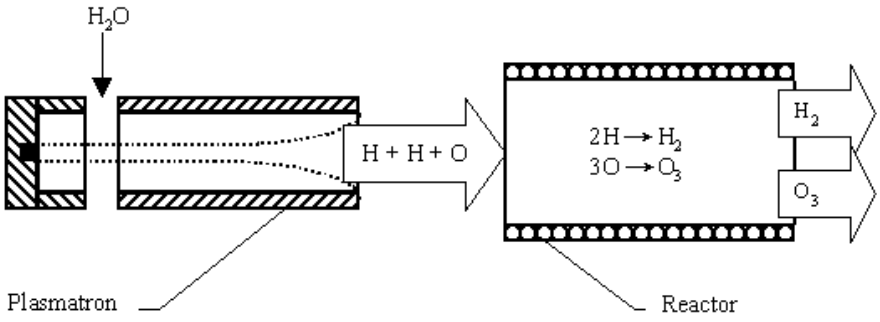

Fig.1. The scheme of the ozone thermal synthesis.

One can see the ideal scheme of ozone thermal synthesis on fig.1. There is the possibility of the opposite process to the initial process:

$$O + H + H \rightarrow OH + H \rightarrow H_2O.$$

It takes place with the heat evolution. There is the possibility of formation of molecular hydrogen and molecular oxygen. Only the existence of the atomic oxygen and its interaction with oxygen molecules results in the ozone formation in the process. As known, the interval of ozone thermal stability corresponds to the temperatures below the 16 - 18°C. To fix ozone it is required "to freeze" the plasma jet coming out of a plasmatron. The process is realised in the reactor that has a form providing to the cooling of gas flow. The cold walls carry off the heat from the reaction zone. At the same time the molecular hydrogen is formed simultaneously with the molecular oxygen and ozone in such process too. It requires to solve the problem of the selection of reaction products. The choice of water vapour as the plasma-forming gas is explained by that the alternative to it is the atmospheric air. The choice of air as the parent material for the ozone producing results in the necessity to remove the nitric oxides nascent in the freezing plasma jet. It results in more complexities, than in the case of water vapour.

The unstable burning of arc discharge is the other essential problem when the water is used in plasmatron as plasma-forming gas. This problem is caused first of all by the phase change of water that takes away the considerable amount of heat in the discharge thereby the temperature of plasma filament of arc iss decreased. To solve this problem it is necessary to supply the plasmatron by water vapour instead of the water. On the other hand the using of water vapour in plasmatron as plasma-forming gas requires to design the special plasmatron. Namely, it is necessary to provide the stable plasmatron operation at the temperature higher than 100°C on its internal parts to avoid the water condensation on the cold details. The problem becomes complicated by the presence of rather aggressive oxidising atmosphere containing atomic oxygen in the plasmatron. To solve these problems the special plasmatron is designed on the base of the application of high temperature constructional materials such as cermets and metal-composites [1,2]. It operates at the temperatures of internal surfaces about 140 - 150°C.

The preparation of water vapour for the supply of plasmatron (evaporation and vapour heating up to the temperatures 140 - 150°C) is carried out in gas generator.

As it was mentioned above one can see the ideal scheme of ozone thermal synthesis on fig. 1. In reality the plasma jet contains H, O, H^+, O^-, OH^- at the plasmatron outcome. There is the displacement of thermal equilibrium in the association – dissociation reactions with the formation of water vapour, molecular hydrogen, molecular oxygen and ozone at the cooling of plasma jet. The process of plasma jet cooling is realised in the refrigerator-cooler where the heat of plasma jet is taken away and it is utilised in a gas generator for the preparation plasma forming gas. Then the cooled gas flow comes in a reactor, where the necessary requirements for synthesis of ozone are provided at constant temperature about 15 - 18°C. The main requirement to the process is to provide the stationary temperature and required conditions for the interaction of atomic and molecular oxygen with the formation of ozone in a gas phase. The gas-water intermixture coming out of the ozone reactor-synthesizer is secondary cooled in the refrigerator-cooler, where there is a final ozone fixing. The heat taken away in the refrigerator-cooler is utilised in the first step of a gas generator for water preheating. Further, the cooled gas-water intermixture is moved in the gas-water separator, where molecular hydrogen, molecular oxygen, and ozone are selected from the intermixture. The hydrogen is removed from gas mixture at last stage of the technological process of ozone production by the method of thermal synthesis. The problem of hydrogen removal is solved on the base of use of hydrogen catalytic oxidizing with the addition of atmospheric air.

The scheme of technological process of ozone producing by the method of thermal synthesis is shown on the fig.2.

The experimental study of the ozone thermal synthesis from the water vapour was executed on the experimental plasma installation with the plasmatron by power 50 kVA. The stable output of ozone was obtained in the experiments. It was planned to carry out the work on the creating of complete cycle of ozonization of drinking water on the base of the executed experimental studies. One can use special small dimensional plasmatron by power from 50 up to 250 kVA designed on the assumption of the above-stated requirements for the ozone thermal synthesis in the systems of water conditioning.

Thus, the following equipment is required to produce ozone by the method of thermal synthesis:

- gas generator (It prepares the water vapour with the temperature 140 - 150°C),
- the special plasmatron (It carries out the thermal dissociation of water vapour and ionisation of hydrogen and oxygen atoms),
- refrigerator-cooler I (It cools gas-plasma jet),
- the reactor for ozone thermal synthesis,
- refrigerator-cooler II (It cools gas-water mixture and fixes the ozone obtained),

- gas-water separator (It separates gas mixture from water),
- gas separator (It separates oxygen and ozone from hydrogen).

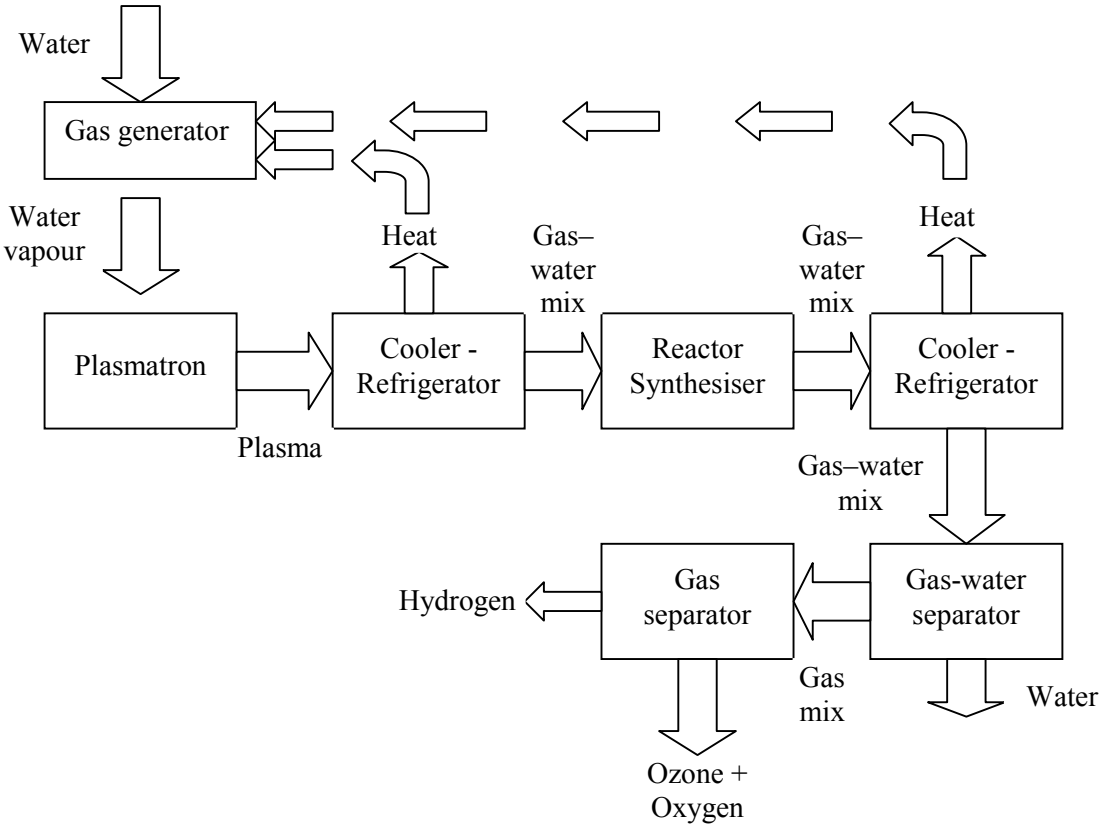

Fig.2. Scheme of technological process of the ozone obtaining by the method of thermal synthesis.

3. Discussion

The method of ozone thermal synthesis with the use of special plasmatron has some advantages before a widely used method based on barrier discharge. The ionisation degree of the arc plasma discharge is about 2 - 3 times higher than in the barrier discharge. It allows to increase the concentration of oxygen ions in plasma and to increase the probability to get ozone as the reaction product consequently. The feature of plasma thermal synthesis of ozone is that this method of the ozone producing does not require the special preparation of plasma-forming gas, namely, drying, compression and refinement off oil vapours being in air as a result of compression. The equipment for the ozone producing by the thermal synthesis method has no lengthy details with precision gaps, as it takes place in the case of the barrier discharge. All this gives in the essential decrease of metal consumption and energy consumption. It gives also, both the decrease of equipment cost, and the decrease of operating costs.

The perspective direction in the application of presented method of ozone production is its using in the technological processes of treatment of various types of waste. As known the oxidising processes are basic for the treatment of various types of waste excepting radioactive waste. Ozone is the second strongest natural oxidising agent after fluorine. Ozone oxidises other chemical agents and decays, thus it superimposes the minimal damage of the environment. It means that the ozone using in the technologies of waste treatment is safe for the environment.

Ozone has strong bactericidal activity and it can be successfully applied in the treatment of domestic and industrial wastewater. It can be used in the technologies of treatment of toxic agents and dangerous medical drugs and waste. It is possibility to use ozone in the technologies of the treatment of bacteriological and chemical weapons.

Other perspective application of the method of plasma thermal synthesis of ozone is use of ozone in technological processes of waste treatment in chemical industry, pulp and paper industry, timber industry, and petrochemical industry.

It is necessary to note the opportunity to create the mobile devices of plasma thermal synthesis of ozone for the treatment of oil spills on water and land by means of disintegration of lengthy hydro carbonaceous chains (–CH–CH–) with the formation of carbon oxide (CO) and water (H_2O).
The plasma thermal synthesis of ozone is extremely perspective to use it for the desalination of seawater and producing of drinking water by an oxidising of the dissolved salts with their subsequent deposition.
The plasma thermal synthesis of ozone in XX1 century will define the ecological face of our planet.
The compactness of the plasma thermal sources of ozone gives the unique opportunity to make the mobile ozonization devices for the application in the places of ecological distresses, number of which continuously grows on a planet.

References

[1] V.S. Blokhin et al. Decoding of a phase composition of plasma deposited coatings on the base of niobium carbide with the use of a micro X-ray and colour structure analysis. Proceedings of 6-th all-Union conference on heat-resistant coatings. Nauka, 1976, p. 122 – 127. [In Russian].
[2] V.S. Blokhin et al. Study of behaviour of niobium carbide in low-temperature plasma jet and properties of the formed coating. Proceedings of 6-th all-Union conference on heat-resistant coatings. Nauka, 1976, p. 128 – 130. [In Russian].

Gas Temperature Effects on CF_x Kinetics in a CF_4 Inductively Coupled Plasma

J.P.Booth[1], H.Abada[1], P.Chabert[1] and D.B. Graves[2]

[1] *Laboratoire de Physique et Technologie des Plasmas, Ecole Polytechnique, Palaiseau, France*
[2] *Department of Chemical Engineering, UC Berkeley, USA*

Abstract
CF and CF_2 absolute number density profiles have been determined in steady-state and pulse-modulated inductively-coupled plasmas in pure CF_4, allowing their production and destruction mechanisms to be investigated. In the steady state plasma there is net production of the CF radical in the gas phase (probably by electron impact dissociation of CF_x species), and CF is destroyed at the reactor surfaces with a probability of about 4%. In the afterglow CF stops reacting at the walls, but is destroyed by a rapid gas phase reaction. The CF_2 radical is produced in large quantities at the reactor walls, probably by conversion of incident CF_x^+ ions, and is destroyed in the gas phase (probably electron-impact dissociation). The emission of CF_2 continues for a few milliseconds into the afterglow, indicating the existence of a long-lived intermediate, possibly CF_2 physisorbed in a polymer layer. This mechanism is largely responsible for the observed sharp rise in CF_2 density in the initial afterglow, when gas-phase CF_2 destruction mechanisms have stopped. The central plasma volume is significantly above ambient temperature in the steady state (about 900 K), and gas temperature and density gradients must be taken into account in transport calculations. In the afterglow the gas cools (and contracts) in a few milliseconds, causing gas to flow back towards the central region, also contributing to transient increases in the CF and CF_2 number densities.

1. Introduction

Radio-frequency discharges in low-pressure fluorocarbon gases are widely used for the etching of SiO_2 layers in microelectronics circuit fabrication. By careful adjustment of the gas composition (using mixtures of CF_4, H_2, CHF_3, C_2F_6, C_4F_8, Ar, O_2 etc.) and external plasma parameters it is possible to etch sub-micron features in SiO_2 with vertical side-walls and without etching the underlying silicon. This etch selectivity occurs due to the selective formation of a protective fluorocarbon polymer film on the Si surface. Polymer film formation has been found to be well correlated to high concentrations of CF and CF_2 radicals, motivating studies of the kinetics of these species in plasmas.

Previously [1, 2] time and space resolved LIF has been used to investigate CF and CF_2 production and destruction mechanisms in capacitively-coupled radio-frequency plasmas in pure CF_4. Although industrial processes use more complex gas mixtures, pure CF_4 was used as it is the most "simple" fluorocarbon gas, allowing the basic reaction pathways producing and destroying CF and CF_2 radicals to be elucidated. These studies showed the power of comparing steady-state to afterglow number density profiles in separating electron and ion induced processes from neutral chemistry. One of the major findings of these studies was that, under many conditions CF and CF_2 radicals are produced predominantly by neutralisation and backscattering of CF_x^+ ions (either instantaneously or via deposition and sputtering of a fluorocarbon film) at the strongly-biased RF electrode, rather than by direct electron-impact dissociation of feedstock.

In this study[3] the same methodology has been applied to an inductively-coupled plasma in pure CF_4. This system differs from the capacitively-coupled case in that the plasma density is higher (as are the associated electron-impact dissociation and ionisation rates) and the gas pressure is somewhat lower. In addition, there is no intentional RF biasing, so the ion flux to all the walls is large in magnitude but everywhere low in energy. Furthermore, a number of studies [4] have shown that significant gas heating occurs in these systems, leading to strong gas temperature and number density gradients in the reactor. One of the aims of this paper is to elucidate the effect this has on radical transport and kinetics. As before, we have used the comparison of density profiles in the steady state to those in the afterglow to separate electron- and ion-induced processes from neutral chemistry. However, in this case it is essential to take into account the gas cooling before drawing conclusions: indeed it was necessary to simultaneously model the heat and mass transfer and chemistry, as presented elsewhere [5].

2. Experimental

The experimental set-up is shown schematically in Fig. 1. The inductive plasma is created in a cylindrical aluminium chamber which is 5.3 cm high and 30 cm in diameter. Pure CF_4 is flowed at 25 sccm through the reactor and pumped by a turbo-molecular pump via a throttle valve. In all experiments presented here the pressure was maintained at 33 mTorr. At the bottom of the reactor there is a 25 cm diameter aluminium grounded electrode. At the top is a 1.5 cm thick alumina window, cooled by forced air. The plasma was excited with a 3 turn flat spiral copper coil, placed on this window. Radio-frequency power at 13.56 MHz (up to 400 W) was supplied via a classical L-Type matching network, which could be switched on and off in 5 μs. Before data was taken the reactor was run for 30 minutes in order to reach thermal equilibrium and for any wall passivation processes to reach steady state.

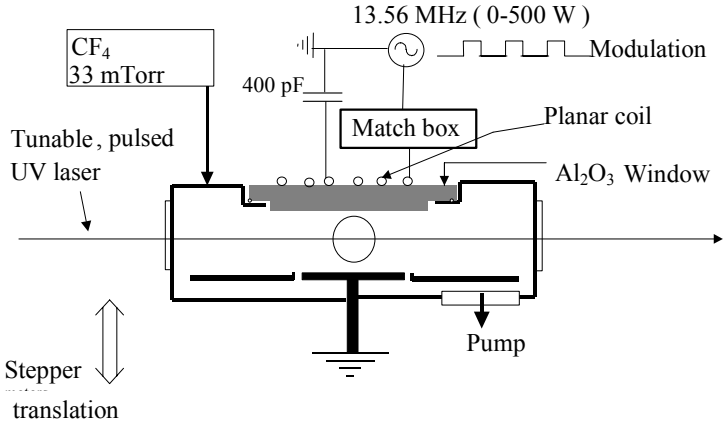

Fig. 1. Experimental Layout

The CF and CF_2 radicals were detected by Laser Induced Fluorescence using a frequency-doubled dye laser pumped by a XeCl excimer laser. Three fused silica windows allow the passage of the probe laser beam at any position between the grounded electrode and the alumina window, and detection of the induced fluorescence perpendicular to it. The fluorescence was focused onto the entrance slit of a 60 cm monochromator and detected with a photo-multiplier. Axial temperature and radical density profiles between the alumina window and the grounded electrode were obtained by translating the reactor relative to the laser beam and the detection optics. To achieve this, the whole reactor and pumping system was mounted on three stepper-motor driven lead-screws. Measurements in the afterglow were obtained by stopping the RF power for 20 ms at a repetition rate of 10 Hz, and triggering the laser shot accordingly.

Relative CF radical densities were determined by exciting the P_{11} band-head of the A-X (1,0) transition at 223.89 nm, with detection of the (1,1) fluorescence at 230.6 nm. The profiles were corrected, as before [6], for variations in the solid angle by normalising to the signal profile obtained from LIF of NO molecules introduced at known static pressure into the reactor. The gas temperature was determined as a function of position and time from the relative intensities of the CF P_{12} bands in the spectral region 224.20 nm to 224.25 nm [4] allowing for partial optical saturation of the transitions [7].

The relative CF_2 number densities were obtained by exciting at the peak of the A(0,5,0)←X(0,0,0) transition at 251.989 nm, with detection of the A(0,5,0)→X(0,3,0) fluorescence at 264.9 nm. Previously[1] CF_2 density profiles were determined by exciting the A(0,11,0) level at 234 nm, using the same laser dye as for CF. However, here it was necessary to use a band that has been characterised spectroscopically, so that the temperature correction factors could be calculated. A further complication of using this (longer wavelength) band was that the solid angle normalisation could no longer be accomplished with NO LIF. Instead we filled the reactor with a static pressure of benzene vapour: this molecule can be laser excited at 252.94 nm, with observation of the fluorescence at 264.9 nm.

For the sake of experimental convenience, number density profiles are generally determined from the LIF signal, I(λ), taken at a *single* wavelength, λ. If the gas temperature is constant in time and space then this signal is representative of the variations in the *total* ground state density, n_{tot}. However, if the temperature is not constant then it is necessary to add a correction factor that accounts for the change of the relative fraction of the molecules that are in the particular ground state rotational quantum level that is excited by the laser. We calculated these correction factors by simulating the spectra (for both CF and CF_2) over a range of rotational temperatures and comparing the intensity of the relevant peak to the integrated band intensity. The

spectroscopic constants for CF_2 were taken from Mathews [8], and for CF they were taken from Porter et al. [9]. As the temperature is increased, more population is transferred from the probed lower level into higher rotational states, lowering the overall detection sensitivity; therefore the correction factors C increase with temperature. Finally, the corrected profiles were put on an absolute scale by broad-band UV absorption measurements[10, 11]. This technique gives absolute line-integrated radical densities. Combined with the radial density profiles determined by LIF we could then determine the absolute radical number density at the reactor centre.

3. Gas temperatures

The measured gas temperature axial profiles, along with model results [4] are shown in Fig. 2. The steady state gas temperature in the centre of the reactor is of the order of 900 K, dropping sharply towards the walls. At constant gas pressure this implies, from the ideal gas law, that the total gas number density at the reactor centre is about one half of that close to the walls. In the afterglow the gas cools quickly, dropping to within 100 K of the wall temperature after 1 ms. The reactor walls are somewhat above ambient temperature (measured by thermocouple, 370 K at the bottom and 340K at the top (alumina) surface), due to the significant power dissipated.

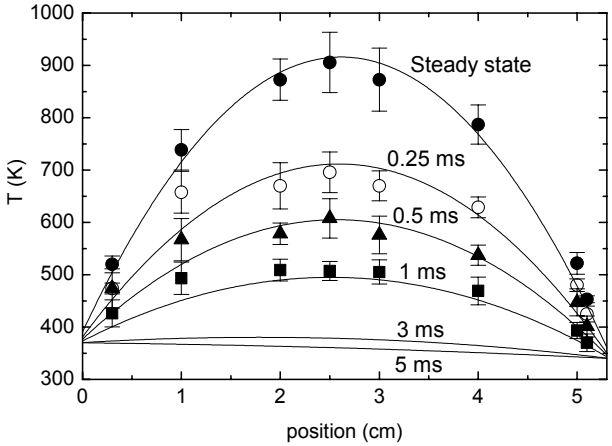

Fig. 2. Measured and modelled axial gas temperature profiles in the steady state and in the afterglow. 250W nominal RF power, 33 mTorr total gas pressure. Zero corresponds to the lower surface, the alumina window is at 5.3 cm.

4. CF number density

Fig. 3 shows the raw LIF signal profiles in the steady state and in the afterglow; also shown is the effect of correcting for the temperature coefficient. Even after correction, the steady-state number density profiles are markedly concave, suggesting that there is a flux of CF radicals produced at the surface and destroyed in the gas phase (but see below). In the afterglow the profile becomes flat, and the number density drops rapidly.

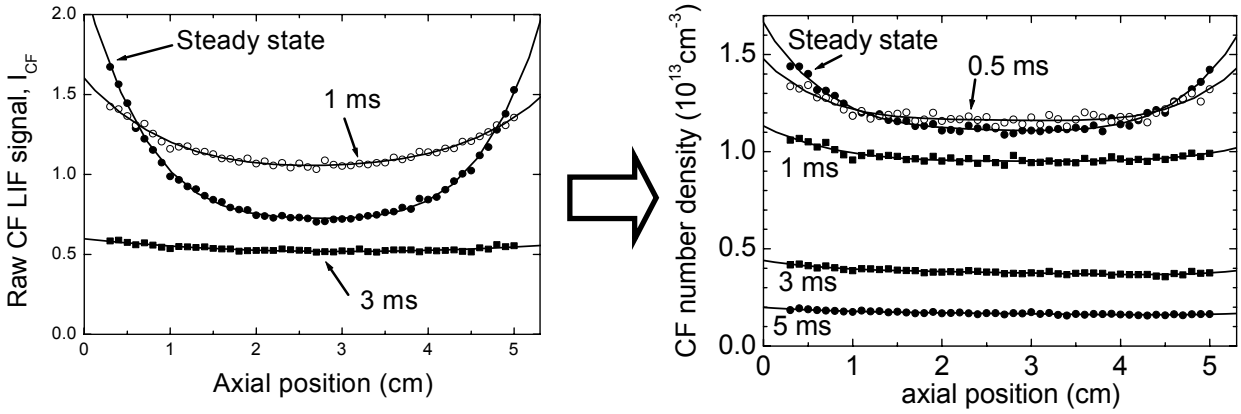

Fig. 3. Raw LIF signal and corrected absolute axial density profiles for CF in the steady state and afterglow.

The absence of significant number density gradients in the afterglow indicates that *surface production or loss* of CF are negligible in the afterglow. The diffusive flux, *Ji* (molecules.m^{-2}s^{-1}) of a radical *i*, (diluted in a bath gas) is related to the gradient of the number density, n_i, by Fick's law:

$$J_i = -D\nabla n_i \quad , \tag{2}$$

where D is the diffusion coefficient. However, in the presence of a temperature gradient the flux must be calculated from the *mole-fraction* gradient, y_i. For a binary mixture the flux can be estimated from [12]:

$$J_i \approx -\frac{P}{kT} D\left(\nabla y_i + \alpha_T y_i (1 - y_i) \frac{\nabla T}{T} \right), \tag{3}$$

where P is the total gas pressure. The mole-fraction gradient can be calculated from :

$$y_i = n_i \frac{kT}{P} \quad . \tag{4}$$

The second term in equation (3) is the thermo-diffusion term, with α_T being the (dimensionless) thermo-diffusion factor. For a light molecule in a heavier carrier gas α_T is negative: assuming that the majority gas is (un-dissociated) CF_4, the thermo-diffusion effect will cause a flux of CF from cold regions (edges) to hotter regions (the reactor centre). The CF mole-fraction profile in the steady state is shown in Fig. 4. The CF mole-fraction is maximal at the reactor centre, suggesting that there is a net flux of CF *from* the reactor centre *towards* the reactor walls: however, this component is opposed by the thermo-diffusion term. For CF in CF_4 we estimated a thermo-diffusion factor of -0.18.

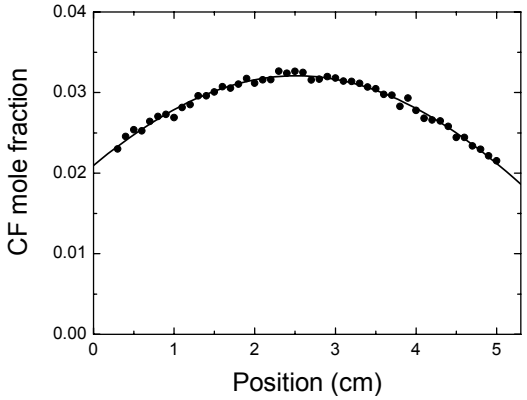

Fig. 4. CF mole fraction axial profiles in the steady state and in the afterglow.

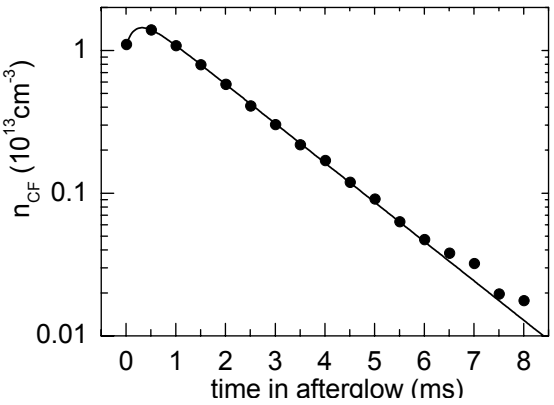

Fig. 5. CF number density decay in the afterglow at the reactor centre.

The relative importance of the two terms in equation (3) can be evaluated by comparing $\nabla y_i / y_i$ to $\alpha_T . \nabla T/T$. We find that the thermo-diffusion term is about one half of the mole-fraction gradient term, but opposite in sign: there is still a net flux of CF to the walls. We estimate a diffusion coefficient of 4400 $cm^2 s^{-1}$ for CF in CF_4 at 33 mTorr and 370 K (based on the value for N_2 in CF_4 at this temperature[13], corrected for the reduced mass and for the slightly smaller collision cross-section). This gives a flux of CF destroyed at the surface, Φ_{loss}, of $1.6 \times 10^{16} cm^{-2} s^{-1}$. We can estimate the reaction probability, β, from:

$$\Phi_{loss} = \frac{1}{4} n \bar{v} \beta , \tag{6}$$

where $\bar{v}$ is the kinetic mean velocity, giving a value $\beta_{CF} = 3.7\%$. Interestingly, in the afterglow this reaction probability appears to drop to near zero, as noted above. It may be that the CF radical can only become chemisorbed at the polymer surface at sites that have been previously activated by ion impact; in the afterglow these sites rapidly become saturated.

These observations are very different to the findings in a capacitively-coupled plasma in CF_4[1], where there was strong production of CF at the powered electrode, and strong destruction of CF (β_{CF} close to unity) at the grounded reactor surfaces (and, in the afterglow, also at the powered electrode). However, the energy of ions hitting the surfaces is much lower in the present case (= plasma potential = a few tens of eV), and is inadequate to dissociate CF_3^+ ions into CF radicals: the majority of the incident CF_x^+ ions are either incorporated into C/F film on the surface, or are returned to the gas phase as CF_3 or CF_2. Indeed, in the present experiments the central top and bottom surfaces of the reactor were coated with a black polymer layer. This polymer surface appears to have a much lower reactivity to CF than the clean Al surfaces in the capacitive reactor (kept clean by high energy ion bombardment).

In the steady state there is therefore a net production of CF in the plasma centre, which flows to the walls where it is destroyed. This net production, however, is the difference between simultaneous production and destruction processes. Fig. 5 shows the CF number density variation at the centre of the reactor as a function of time in the afterglow. There is a small initial rise for the first half millisecond, followed by a rapid exponential decay (rate 640 s^{-1}). One possible explanation for the initial rise is an influx of CF-rich gas

towards the reactor centre as the gas cools and contracts in the first millisecond [5]. The rapid subsequent decay of the CF number density in the afterglow must be due to a gas-phase reactions: the axial number density profiles show that the flux to the reactor top and bottom is negligible. At this point we can only speculate as to the identity of this process. The only processes that are sufficiently rapid are (exothermic) bimolecular exchange reactions of the type:

$$CF + F_2 \rightarrow CF_2 + F. \quad (8)$$

or

$$CF + CF_3 \rightarrow 2CF_2, \quad (9)$$

The rate constant for reaction (9) has been measured[14] to be $3.9\text{x}10^{-12}\text{cm}^3\text{molecule}^{-1}\text{s}^{-1}$. An F_2 density of $1.6\text{x}10^{-14}\text{cm}^{-3}$ would be necessary to account for this observed CF loss rate, or some 15% of the total gas composition: this seems unlikely. The rate constant for reaction (10) is not known; however, exothermic exchange reactions typically have rate constants of the order $10^{-11}\text{cm}^3\text{molecule}^{-1}\text{s}^{-1}$. Singh et al. [15] found a density of $4\text{x}10^{13}\text{cm}^{-3}$ under similar conditions, which would give a CF loss rate of the correct order of magnitude. One consequence of these reactions is the production of a significant quantity of CF_2 in the afterglow. This CF loss process indeed occurs in the steady state, but is exceeded by rapid production of CF (for example, electron-impact dissociation of higher CF_x species). This production process stops immediately in the afterglow, leaving the gas-phase reaction process to destroy the remaining CF.

4. CF_2 number density

The CF_2 steady state axial number density profile is seen in Fig 6. This profile is more strongly concave than was observed for CF. When this is converted to mole-fraction, we observe a profile that is essentially flat, with CF_2 representing about 6 % of the total gas composition. However, when the thermo-diffusion term is included in equation (3), we see that there is a strong net flux of CF_2 emitted by both the top and bottom surfaces of the reactor, and that there is net destruction of CF_2 in the plasma centre. Taking a value of 0.076 for the thermo-diffusion factor, α_T, and a diffusion coefficient of 3060 cm^2s^{-1} (from the experimental value of $65\text{cm}^2\text{s}^{-1}\text{Torr}$[16] for CF_2 in CF_4, corrected for the pressure and assuming a $T^{1.823}$ temperature dependence[12]) and using equation (3), the value obtained for the flux of CF_2 emitted by the surfaces is of the order of $1\text{x}10^{16}\text{cm}^{-2}\text{s}^{-1}$.

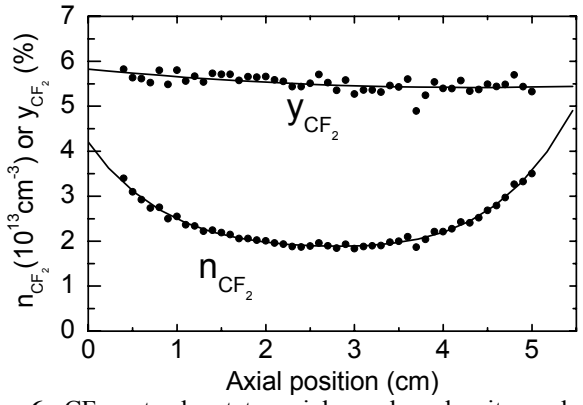

Fig. 6. CF_2 steady state axial number density and mole-fraction profiles

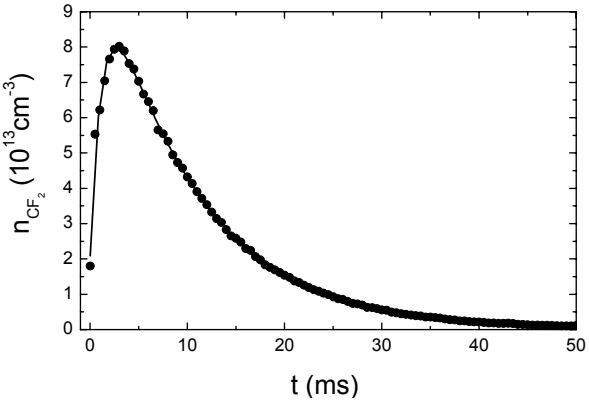

Fig. 7. CF_2 number density decay in the afterglow at the reactor centre.

We measured an ion flux density at the reactor centre of about 1.1 mAcm^{-2}, or $7\text{x}10^{15}\text{cm}^{-2}\text{s}^{-1}$. Considering the uncertainties involved, it is reasonable to postulate that the major source of CF_2 produced at the surface is neutralised ions, and that the majority of the ions return as CF_2 . It is also possible that the CF which is destroyed at the surfaces returns as CF_2 after recombining with a fluorine atom.

The afterglow behaviour of the CF_2 number density at the reactor centre is shown in Fig. 7. A very marked initial *increase* in the CF_2 density is observed, peaking at four-times the steady state density after three milliseconds. Subsequently the CF_2 density decays away exponentially at a rate of about 100 s^{-1}. A number of mechanisms can be advanced to explain this "initial rise" phenomenon. Firstly, it should be stressed that our data are corrected for the partition function dependence on gas temperature, so that Fig. 7 indeed shows the variation of the total ground state CF_2 density. One possible mechanism is the return of CF_2 –rich gas into the central region as the gas cools and contracts in the afterglow. However, the gas temperature changes from 915 to 360 K, a factor of only 2.6 in temperature and gas density, so it would appear that this phenomenon cannot account for all of the initial rise. A quantitative evaluation of the relative importance of

this contribution can only be made from a full model of the gas transport [5]. Further information can be obtained from the CF_2 number density profiles in the afterglow (shown in Fig. 8).

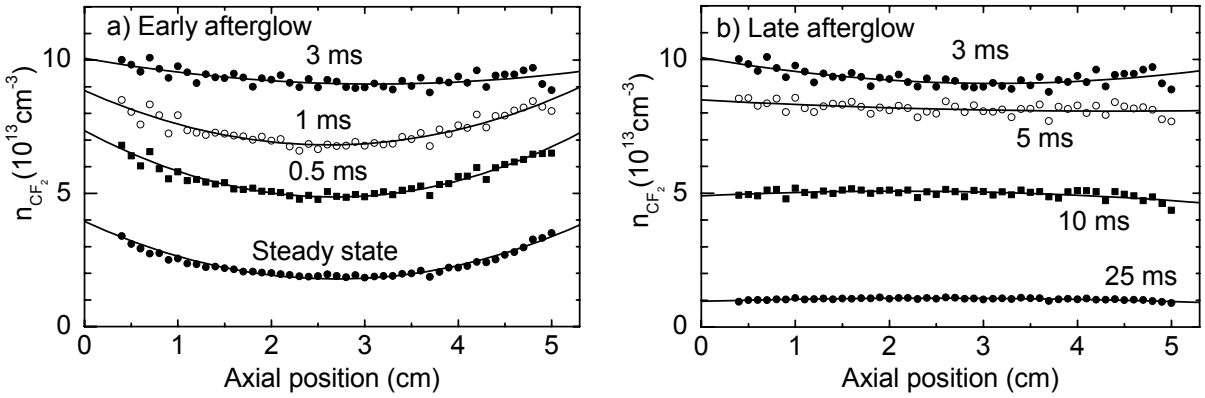

Fig. 8. CF_2 axial number density profiles, a) steady state and early afterglow, b) late afterglow

It can be seen that the CF_2 density profiles remain *concave* until about 3 ms. After 1 ms the gas temperature (and density) has almost fully relaxed, so the radical diffusive flux can be deduced directly from the number density gradient: the data shown in Fig 8 (a) gives clear evidence that the surface emission of CF_2 *persists for a few milliseconds after the incident ion flux has ceased*. This mechanism therefore makes a strong contribution to the CF_2 "initial rise" phenomenon. This result is similar to that observed in capacitive discharges in fluorine-poor gases[2], where it was concluded that there was formation of a porous fluorocarbon layer containing sub-surface physisorbed CF_2 that takes a few milliseconds to diffuse to the surface.

In the late afterglow (after 3 ms, Fig. 8 (b)) the CF_2 density decays, and relaxes to a convex profile, indicating diffusion of CF_2 to the reactor top and bottom surfaces, where it is destroyed by (an unidentified) chemical reaction. The gradient adjacent to the surface allows the effective reaction coefficient to be estimated (equations 2 and 6), giving a value of 2.7%. With this reaction coefficient we estimate[17] a value of 100 s^{-1} for the CF_2 loss rate due to diffusion and loss at the reactor top and bottom surfaces, in excellent agreement with the observed late afterglow CF_2 decay rate. From this we can conclude that CF_2 is lost by principally by reaction at the surfaces in this period, gas phase reactions being negligible (the gas flow rate is slow, accounting for only about 3 s^{-1}).

References

[1] J. P. Booth, G. Cunge, P. Chabert, and N. Sadeghi, *J. Appl. Phys.*, **85**, 3097, (1999).
[2] G. Cunge and J. P. Booth, *J. Appl. Phys.*, **85**, 3952, (1999).
[3] J. P. Booth, H. Abada, P. Chabert, and D. B. Graves, *J. Appl. Phys.*, **submitted**, (2003).
[4] H. Abada, P. Chabert, J. P. Booth, J. Robiche, and G. Cartry, *J. Appl. Phys.*, **92**, 4223, (2002).
[5] D. B. Graves and J. P. Booth, *J. Appl. Phys.*, **submitted**, (2003).
[6] G. Cunge, P. Chabert, and J. P. Booth, *Plasma Sources, Sci. Technol.*, **6**, 349, (1997).
[7] G. Cunge, J. P. Booth, and J. Derouard, *Chem. Phys. Lett.*, **263**, 645, (1996).
[8] C. W. Mathews, *Can. J. Phys.*, **45**, 2355, (1967).
[9] T. L. Porter, D. E. Mann, and N. Acquista, *J. Molec. Spectrosc.*, **16**, 228, (1965).
[10] J. P. Booth, G. Cunge, F. Neuilly, and N. Sadeghi, *Plasma Sources, Sci. Technol.*, **7**, 423, (1998).
[11] J. Luque, E. A. Hudson, and J. P. Booth, *J. Chem. Phys.*, **118**, 622, (2003).
[12] R. B. Bird, W. E. Stewart, and E. N. Lightfoot, *Transport Phenomena*: Wiley, 2002.
[13] J. Bzowski, J. Kestin, E. A. Mason, and F. J. Uribe, *J. Phys. Chem. Ref. Data*, **19**, 1179, (1990).
[14] J. Peeters, J. Van Hoeymissen, S. Vanhaelermeersch, and D. Vermeylen, *J. Phys. Chem.*, **96**, 1257, (1992).
[15] H. Singh, J. W. Coburn, and D. B. Graves, *J. Vac. Sci. Technol.*, **A19**, 718, (2001).
[16] T. Arai, M. Goto, Y. Asoh, D. Takayama, and T. Shimuzu, *Jpn. J. Appl. Phys.*, **32L**, 1469, (1993).
[17] P. J. Chantry, *J. Appl. Phys.*, **62**, 1141, (1987).

From pore to microscopic porosity to improve the low k PECVD dielectric film

A. Zenasni[1], D. Escaich[1], P. Raynaud[1], S. Sahli[2], S. Rebiai[2], and Y. Segui[1]

[1] *Laboratoire de Génie Electrique de Toulouse, UPS, 118 route de Narbonne 31062 Toulouse, cedex, France*
[2] *Laboratoire d'Instrumentation et Microsystème, Université Mentouri, Constantine, Algeria*

Abstract
Bonding characteristics of low dielectric constant (low k) cyclic organosilicon films ($Si_xC_yH_w$) prepared by Plasma Enhanced Chemical Vapor Deposition technique were investigated. Reducing film density study, by incorporating more void in the bulk, has been developed to overcome negative effect caused by macroscopic porosity in spin-on film. A cyclic structure and deposition conditions appear as important parameters to reduce the dielectric constant of the material.

1. Introduction

With the miniaturization of silicon ultra-large-scale integrated circuits (ULSI), the increase in interconnect delay time exceeds the delay of the transistors. Therefore, the interconnect delay begins to control the performance of the entire ULSI chip [1]. One way to overcome this problem is the dielectric constant reduction of the material between the interconnected layers. Current technologies in low k dielectric materials propose intermetal dielectric (IMD) below k=3,0. Including porosity in the bulk open a large perspective in ULSI future circuit, and, is expected to reach integrable films permittivity lower than 2,0. However, the pore structure of these low-k dielectric materials strongly affects some material properties other than the dielectric constant such as mechanical strength, moisture uptake, coefficient of thermal expansion, and adhesion to different substrates [2]. All this problems prevent any integration in manufacturing processes.

In previous study, we highlighted a polar kind effect in the dielectric constant evolution [3]. A best control of Si-O and Si-C densities in a bulk appear as interesting parameters to reduce the permittivity. Hence, reducing films density was emerged as a determinant factor to improve our films quality and decrease the dielectric constant.

This work is devoted to elaborate, via PECVD technique, a low k film from a new cyclic organosilicon precursor. PECVD technique is proposed as substitute solution than spin-on process to grow low k film ($k \leq 2,5$). Film properties such as chemical bonding structure, density and refractive index, are investigated. The new cyclic organosilicon behavior is observed to look into the deposition conditions and their effect on the dielectric properties.

2. Experiment

The plasma is generated in Multipolar Microwave Plasma (MMP) (2,45 GHz) reactor excited by Distributed Electron Cyclotron Resonance (DECR). A Diphenylmethylsilane (DPMS) precursor is used to deposit the $Si_xC_yH_w$ films on intrinsic silicon Si (100) substrates.
In the deposition chamber, the total pressure was maintained at 1 mTorr of DPMS. The microwave power was varied from 50 to 400 watts. The chemical bonding states of the $Si_xC_yH_w$ films were characterized by Fourier Transform Infrared spectroscopy (FTIR) in the absorbance mode using a Bio-Rad (FTS60A) spectrometer. The thickness (d) was estimated by profilometer (TENCOR). The density of the films were measured by ellipsometry. The films composition was determined by XPS analysis. Metal-insulator-metal (MIM) structures (the insulator is constituted by the deposited film) and a HP4280A LCZ-meter have been used to measure the films capacitance C. The total dielectric constant was evaluated from the equation (1):

$$\varepsilon = \frac{C.d}{\varepsilon_0.S} \qquad (1)$$

Where ε_0 is the vacuum permittivity ($\varepsilon_0 = 8,854.10^{-12}$ F.m^{-1}) and S the electrode surface area.

Diphenylmethylsilane monomer ($SiC_{13}H_{14}$) contains two aromatic structures bonded on central silicon. One hydrogen and methyl group (CH_3) are also connected to the silicon atom. The molecular weight is 198,34 g/mol.

The boiling temperature of DPMS is 366 °C at 760 Torr. Therefore, the organosilicon is putting on bottle heated (Mary's bath) at about 130°C, to obtain a sufficient pressure to correctly injected the vapour inside the plasma chamber.

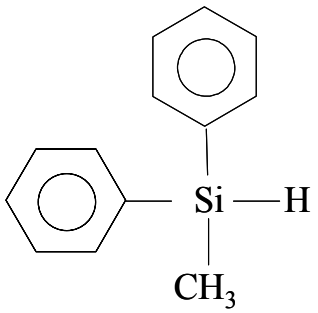

Figure.1 Diphenylmethylsilane monomer structure (DPMS).

The organosilicon vapour was injected close the substrate, while the oxygen or argon were used to initiate the plasma in mixture condition. The film thickness are maintained in the range of 2000 Å and 2500 Å.

3. Results and discussion

The semiconductor industry is aggressively investigated electrical insulators with dielectric constant less than that SiO_2 (k<3,9). Material which includes porosity can achieve k values below 2,2, these are the so called "ultra low k" dielectrics. The ultra low dielectric constant results from the incorporation of pores. Such materials are more fragile than non-porous dielectrics, and suffer from several integration problems. Porous structure is very sensitive to air exposure and includes moisture inside the material structure, which causes an increase of the dielectric constant. The idea is to include high rate of microscopic void without making any macroscopic porosity.

Figure 1 shows the growth rate evolution of films deposited from DPMS/ Ar (3:1) and DPMS/ O_2 (3:1) mixtures as function of injected power. We can distinguish two growth modes separated at 200 watts. At low injected power, the deposition rate increases linearly for the both cases. This means that the deposition process is activated mainly by monomer reaction in plasma and no difference can be noticed between the two mixtures. The growth rate increases from 155 Å/min at 50 watts to 905 Å/min at 200 watts.

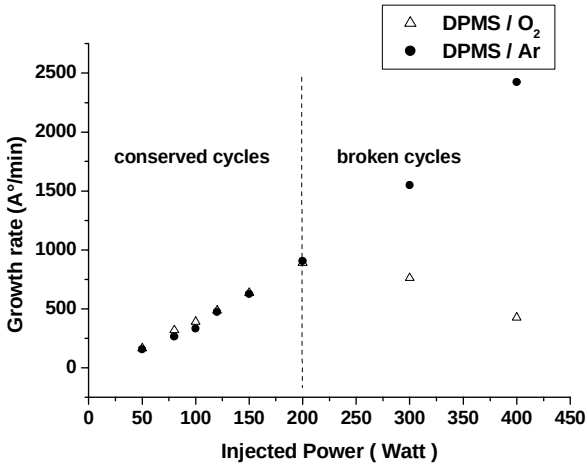

Figure 2 : Growth rate evolution for DPMS/O_2 and DPMS/Ar mixtures vs. injected power.

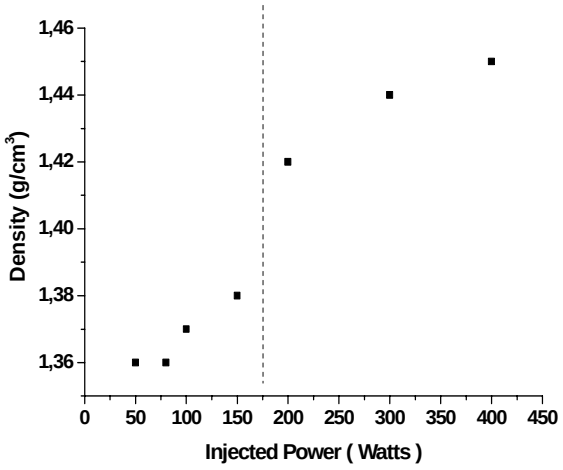

Figure 3: Density evolution of pure DPMS films vs. injected power

Beyond that, the deposition rate increases for DPMS/Ar films. This later go up from 905 Å /min to 2400 Å /min. This suggests the increase of the monomer fragmentation. Indeed, as the injected power increases, the Ar addition involves the increase of the electronic density as can be seen in equation (1) [4]:

$$Ar + e \rightarrow Ar^{+} + e + e \quad (1)$$

The precursor dissociation is improved with the electronic density. This is in agreement with the increase of the deposition rate [5].

In the DPMS/O_2 case, the decrease of the growth rate traduces a stronger effect of the etching process. The oxygen molecules dissociation produces more atomic oxygen in the plasma which affects the surface as described below. The interaction of the atomic oxygen with the surface produces volatile species as O-H and C=O [6]. Beside the dissociation and the etching phenomena, the deposition rate change beyond 200 watts can be also attributed to the break of cycle structures into the films.

We have studied the density evolution as function of power input. The shape is similar to the deposition rate evolution with the change at 200 watts. This suggests that the cycle structure conservation is governed by the input power. As the input power increases, the monomer dissociation increases and the cycle density decrease. So more smaller fragments are deposited on the surface and then the density increases.

Electrical analysis reveals that the films deposited at low power have a lower dielectric constant. In fact, the permittivity tends to increase as a function of the power input (figure 4). In previous study, we have shown the density change induces a permittivity evolution in our film and, the dielectric constant of the structure is a function of different polarization kind [3].

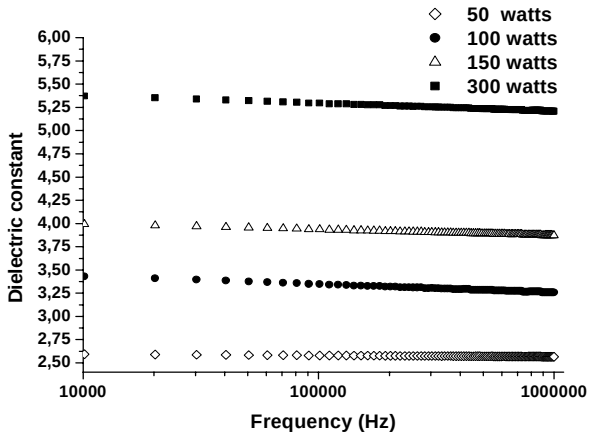

Figure .4 Dielectric constant evolution vs. injected power
for films deposited from pure DPMS

X-ray photoelectrons spectroscopy was used to determine the relative amounts of C, and Si at the film surface. The atomic ratios of carbon and silicon are evaluated from the relative peaks areas of C (1s), and Si (2p) peaks of the XPS spectrum. It is found that pure DPMS film possesses oxygen in addition to constituent elements of the monomer.

Figure 5 shows the composition evolution of pure DPMS films elaborated at different microwave power. The carbon percentage decreases slightly with the injected power, while the silicon and oxygen increase. This tendency results from the etching effect of oxygen by removing some carbon and hydrogen atom from the surface. Nevertheless, these little changes do not affect the carbon, silicon and hydrogen relative amount in the film. This composition stability suggests that the atomic ratio at the film surface was the same for each injected power condition. Hence, the dielectric constant change can not arise from polar group kind modification. We can clearly show this effect on the infrared spectrum made on the films from pure DPMS. The IR spectrum of pure DPMS films shows the main absorption bands features of diphenyl monomer [6] (figure 6).

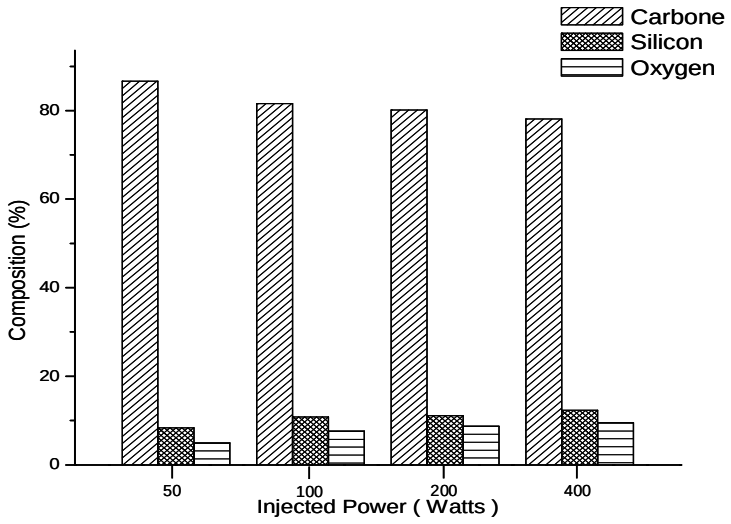

Figure.5 Evolution of pure DPMS films composition for different power condition.

FTIR spectrum shows at 689, 734, 787, 832 and 875 cm^{-1} peaks corresponding to the =C-H out-of-plane phenyl ring bending vibrations. We can also observe the peaks at 3050 cm^{-1} (aromatic C-H), at 1595 cm^{-1} (aromatic C=C) and at 1118 cm^{-1} (Phenyl group), which constitute a serious proofs of aromatic cycles integrity in the film. Absorption bands correlated to vibration of aromatic $Si-CH_2$ are also observed at 1429 cm^{-1}. The symmetric bending of cyclic $Si-CH_3$ appears at 1262 cm^{-1}, and the stretching mode of cyclic dimmers of carboxylic (C=O) group at 1720 cm^{-1}. The Si-H peak intensity at 2140 cm^{-1} decreases at high power input. The OH band can be seen in the range of 3200 to 3700 cm^{-1}.

By following the evolution of these spectra as function of injected power we can notice a reduction in intensity from peaks associated to the presence of DPMS cycle structure. Figure 6 shows a comparison between spectra of films elaborated at different power. We can observe that the aromatic structure intensity of C-H at 3050 cm^{-1} decreases with injected power, while the $C-H_x$ intensity increases. This fall is also observed for the phenyl group at 1118 cm^{-1} and the remainders peaks which reveal the cycle structure presence. These evolutions are serious indications which inform us about cycle structure destruction.

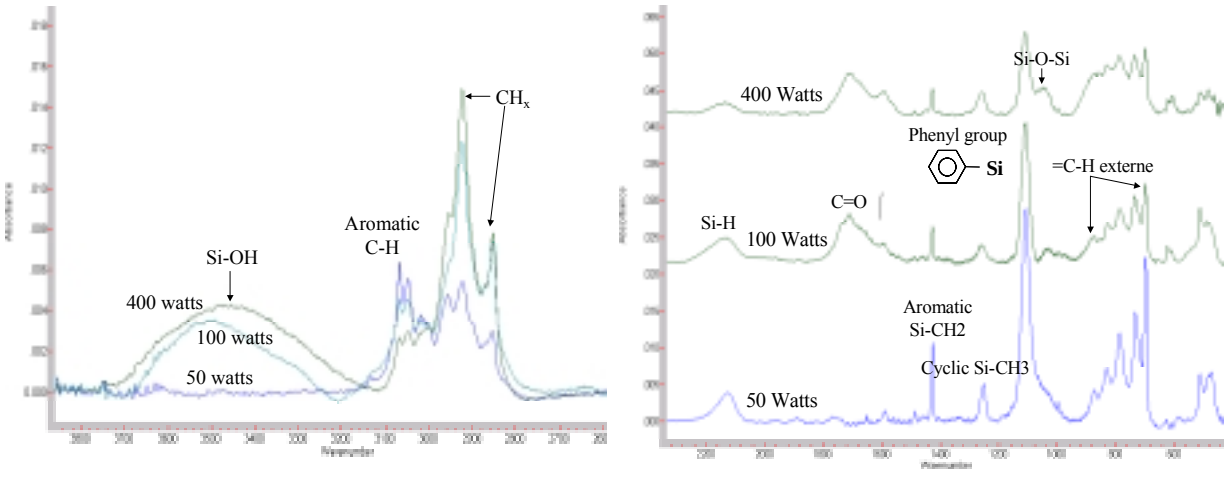

Figure .6 Spectra evolution of DPMS pure films as function of injected power.

At high power we can observe Si-O-Si stretching peak vibration, probably due to more interaction of oxygen in plasma and/or in the deposited film. The origin of the oxygen incorporated into the pure DPMS film, which is not a constituent element of the starting material used, may either be from the reaction chamber and/or due to exposure in air. At low power (50 watts) the film exhibits a good resistance to moisture absorption. This can explain the low permittivity that we have obtained. Besides this, the cycle conservation at low power improves the low dielectric value of the elaborated films.

Figure 7 shows the dielectric evolution vs. exposed to air time for film deposited from pure DPMS and pure HDMSO (hexamethyldisiloxane). HMDSO films have bad ageing, due to the moisture uptake. We can observe a slight increase of the dielectric constant for pure DPMS films, which indicates that the permittivity do not shows a big change on its values. These results reveal that the film has a good barrier properties to moisture absorption.

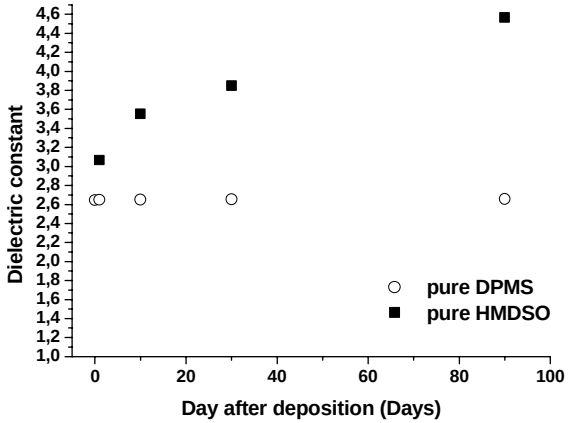

Figure 7. Ageing effect on the dielectric constant

4. Conclusions

This work demonstrated the ability of our PECVD technique to propose stable film with low dielectric constant ($k \approx 2.5$). For that reason, Plasma process could be an interesting alternative solution to overcome problems met with instable pores in spin-on process.

The pure DPMS films deposited at low power and high pressure can offer permittivity as low as 2.5.

Decrease films density without making any macroscopic porosity appears as a real answer to improve the dielectric properties of our films.

References

[1] T. Kikkawa, Electronics and Communications in Japan, Vol 84, N°4, 26, 2001.

[2] M. E. Clarke "Introducing low k Dielectric into Semiconductor Processing", Applications Note MAL123, Mykrolis, 2000.

[3] A.Zenasni, P.Raynaud, S. Sahli, S. Rebiai, and Y. Segui, published soon in Surf. Coat. Technol.

[4] M. Latreche, Ph.D Thesis of Toulouse University, 1991.

[5] K. Aumaille, C.Vallée, A.Granier, A.Goullet, F.Gaboriau, G. Turban, Thin solid films, 359, 247, 2000

[6] F. -U. -Z. Chowdhury , A. B. M. O. Islam and A. H. Bhuiyan, Vacuum, Vol 57, 1, p 43, 2000.

A RF low-pressure pulsed discharge as OH source for LIF field instruments calibration

G. Dilecce, P.F. Ambrico and S. De Benedictis

Istituto di Metodologie Inorganiche e dei Plasmi – CNR
Sez. territoriale di Bari, via Orabona 4, 70126, Bari Italy

Abstract
An on-line reference OH source based on a pulsed N_2-H_2O RF discharge is described. Its operation principles are demonstrated together with its stability with respect to variations of discharge conditions and laser energy. Such stability is the basis for the operation of the source at less controlled conditions, i.e. with simple ambient air gas feed that greatly simplifies the source apparatus. This is an important requisite for operation in field instruments.

1. Introduction

The detection of OH is a difficult issue in atmospheric research, due to the low OH concentration found in the troposphere. The Laser Induced Fluorescence (LIF) has been employed to this end [1], but it suffers of the not easily solvable problem of its calibration, and, in particular, of the disposal of a simple and robust calibration method available in field and airborne instruments. We have recently proposed [2] a N_2-H_2O low-pressure, low-power pulsed RF discharge as a calibrated source of OH, based on:

a. the observation that the $OH(A^2\Sigma^+)$ and $NO(A^2\Sigma^+)$ states have the same excitation precursor, $N_2(A^3\Sigma_u^+)$, in this kind of discharges [3].

$$N_2(A^3\Sigma_u^+)+OH(X^2\Sigma) \xrightarrow{k_{OH}} N_2(X^1\Sigma^+)+OH(A^2\Sigma^+) \qquad (1)$$

$$N_2(A^3\Sigma_u^+)+NO(X^2\Sigma) \xrightarrow{k_{NO}} N_2(X^1\Sigma^+)+NO(A^2\Sigma^+) \qquad (2)$$

Therefore the OH density can be quantitatively correlated to the NO density through the intensity ratio of $OH(A^2\Sigma^+)$ and $NO(A^2\Sigma^+)$ emissions. The OH density can then be brought back to the NO density.

b. a novel LIF scheme by which OH and NO can be detected simultaneously by the use of one laser only, in which OH and NO are detected by the second and third harmonic respectively of the same dye laser output [4].

The simultaneous detection of the LIF from OH and NO in the post-discharge, the LIF from NO in a static cell, the post-discharge emission from the (0,0) band of the OH 3064 Å system and from one of the NO γ-system bands, provides a reliable real-time calibration that is intrinsically stable with respect to variations of the production of OH and NO in the discharge and laser energy and wavelength drifts.
The stability of such OH source allows its use without a strict control of the discharge conditions. In this contribution we demonstrate the operation of the source obtained by a discharge gas feed of ambient air through a needle valve, in which the water vapor is supplied by the natural air humidity. This greatly simplifies the apparatus, avoiding the need of a gas bottle and a water vapor generator. Furthermore the source is operated at a discharge pulse frequency in the kHz range, i.e. close to the laser repetition rate in use in FAGE field instruments, thus matching the FAGE operation conditions and increasing the measurement statistics.

2. Experimental

The scheme of the OH reference cell apparatus is shown in fig.1. The discharge is a cylindrical external electrodes discharge in a 4 cm dia. quartz tube. The discharge is operated in a N_2-H_2O mixture by a 13.56 MHz RF supply pulsed at controlled T_{ON} and T_{OFF}. The NO cell is filled with a 300-ppm N_2-NO mixture from a bottle with a certified NO concentration uncertainty < 3%.
The laser is a pulsed dye laser pumped by a Nd-YAG at 10 Hz. The laser wavelength in the region 303 - 311 nm, that is the initial part of the OH(A--X) (0,0) band, is obtained by the R640 dye output doubled by a BBO crystal. The third harmonic of the dye is obtained by a second BBO crystal, and falls in the region 204-207 nm that corresponds to the spectral region of the (2,0) band of NO γ system. In particular for our purposes we have

used OH LIF excitation by both $R_{11}(1.5)$ at 3072.01 Å or $R_{11}(2.5)$ at 3070.32 Å lines [4]. The fluorescence light is revealed by photomultipliers preceded by interferential filters.

The self-calibration on-line procedure is based on the formula:

$$[OH]_{source} = \frac{I_E(OH(A))}{I_E(NO(A))} \frac{k_{NO}}{k_{OH}} \frac{I_{LIF}^{disch}(NO)}{I_{LIF}^{cell}(NO)} [NO]_{cell} \quad (3)$$

and requireres the simultaneous measurement of:

1. the LIF from OH and NO in the post-discharge;
2. the LIF from NO in the cell;
3. the post-discharge plasma emission from the (0,0) band of the OH 3064 Å system and from one of the NO γ-system band, $I_E(OH(A))$ and $I_E(NO(A))$ respectively; these quantities are measured by the photon counter by the same photomultipliers used for the LIF, in a gate opened for 10 μs immediately before the laser pulse.

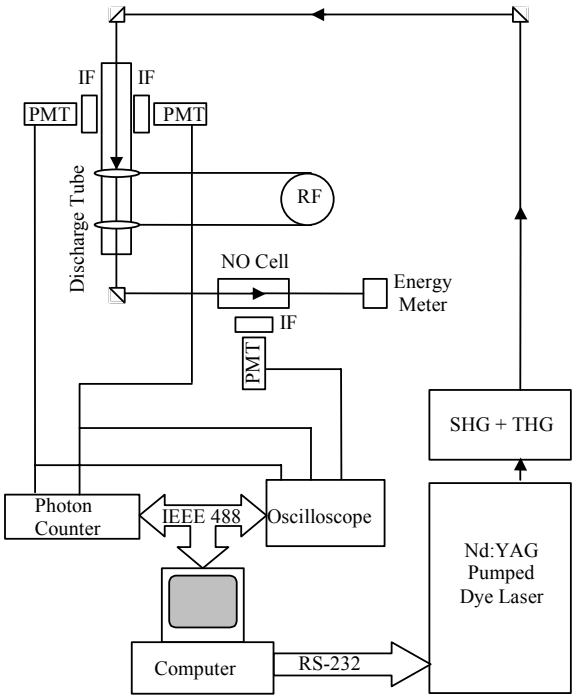

Fig. 1 Scheme of the OH reference source apparatus. IF: interferential filter; PMT: pulsed photomultiplier

The measurements are made in the post-discharge since the (0,0) band of the OH 3064 Å system is overlapped by the strong Δv=1 sequence of the N_2 SPS emission. Such SPS emission is dominant in the discharge while, being mainly due to electron impact excitation, it rapidly falls down to a negligible intensity in the post-discharge, leaving a clean OH emission after few hundreds of microseconds [3].

As a whole, then, [OH] in the source is continuously measured by formula (3) and monitored by LIF. In other words, the OH LIF signal in the source is always correlated to a measured OH density. Placing the sample (the FAGE [1], for example) in the laser beam path, the OH LIF signal from the source then constitutes a reference signal for the sample OH LIF, always tied to a measured OH density.

This scheme is intrinsically robust with respect to:

a) variations of the production of OH and NO in the discharge reference source;
b) laser energy drifts, i.e. it is not necessary to monitor the laser energy and to correct for its fluctuations according to *ad hoc* saturation curves;
c) small wavelength drifts of the laser.

Such a robustness was demonstrated in [2], in a N_2-H_2O discharge, in which the water vapor was supplied by an *ad hoc* generator. It was shown in practice that the scheme is valid whatever the discharge conditions, and in particular the gas composition, provided the OH(A) and NO(A) excitation by $N_2(A)$ is still the dominant mechanism.

3. Validation of the source with ambient air gas feed

The discharge in this new configuration is fed with ambient air through a needle valve that regulates the air flux. No bottles and flux meters/regulators are needed. In order to verify that processes (1) and (2) are still the dominant ones in the post-discharge, we have investigated the new discharge by the same method as that applied in [3]. That is to look for a correlation between the decay of the OH(A) and NO(A) emissions in the post-discharge. To this end we have measured:

1. the time-resolved emission by the digitizing oscilloscope, through a monochromator with wavelength at 308 nm for OH(A) and at 227 nm for NO, and 1 nm bandwidth;
2. the time-resolved LIF on OH(X) and NO(X). The NO(X) practically does not change in the post-discharge, so we will not report NO(X) LIF results.

In Fig 2 we report some such measurements, taken at 0.1 Torr, 1W average discharge power, and at different T_{ON} and T_{OFF} values, all with $T_{ON} << T_{OFF}$. The combination low power – small duty cycle ensures that the gas temperature in the discharge does not exceed the ambient one.

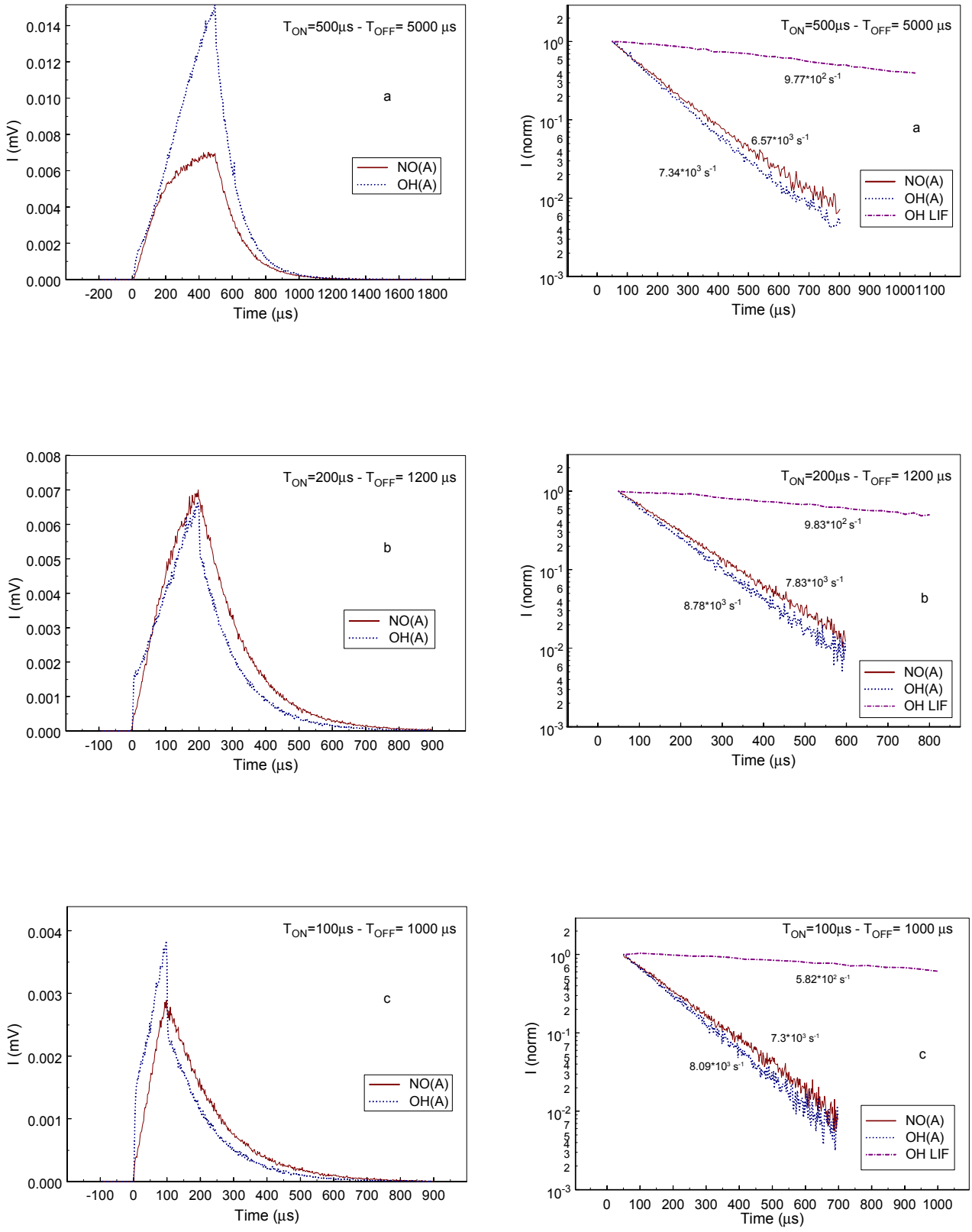

Fig. 2 Time resolved emissions and OH LIF at 0.1 Torr, various T_{ON}, T_{OFF} times. In the right figures the measurements are restricted to the post-discharge and plotted in log scale.

It is shown that in all the cases presented, the decays are single-exponential, and that the following relationship is satisfied, within the experimental error:

$$K_{OH(A)} = K_{NO(A)} + K_{OH(X)}$$

where K is the post-discharge decay time constant. This means that both OH(A) and NO(A) have the same excitation precursor, and that this is the nitrogen triplet metastable (see the discussion in [3] and also [5]).

In the figures containing the emission in the discharge pulse, it is worth noting that, on decreasing the discharge time both OH(A) and NO(A) emission intensity decrease. In the OH(A) emission a fast component, both at discharge ON and at discharge OFF, is increasingly recognizable on decreasing T_{ON}, due to the superimposed SPS emission and an eventual OH(A) excitation by electron impact, that becomes relatively more important when the long-time-constant component decreases. It is clear, then, that, increasing T_{ON}, the $N_2(A)$ density increases, with a corresponding rise of the OH(A) and NO(A) emission.

The next step is to test the source principle robustness with respect to variations of the discharge conditions and laser operating conditions. To this end we have artificially caused such variations. Discharge conditions are varied by detuning the matching network or increasing the applied RF voltage. The laser energy output is instead varied by detuning the TH generator: this causes both a large variation of the TH energy and a smaller variation, of the order of 30%, of the SH, since a low TH conversion results in an increase of SH energy passing through the TH BBO crystal. The results of the test at T_{ON}=100μs, T_{OFF}=1000 μs, are shown in Fig.3. The test is made of 100 runs, each of which is the result of 256 laser shots statistics for the LIF, and 5000 openings of a 10μs photon counter gate for the emissions. The measurements are made at 700 μs in the post-discharge. In Fig. 3a it is reported the OH LIF signal, corrected for the SH energy according to a measured saturation curve. The SH energy is measured by a pyroelectric energy meter simultaneously to the LIF measurements.

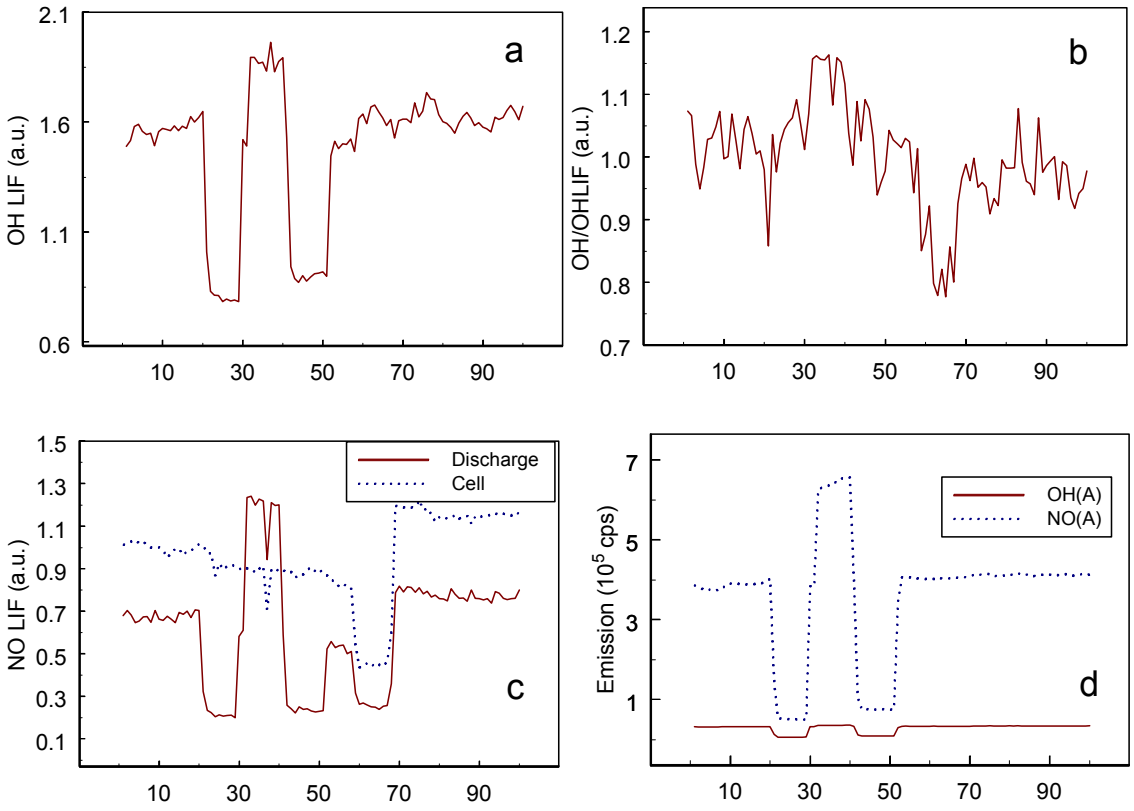

Fig. 3 Test runs of the source scheme robustness with respect to discharge and laser operating conditions variations. On the x-axis the run number is reported. For the details of each figure see the text.

In Fig. 3c it is reported the NO LIF in the post-discharge and in the reference cell. The LIF variations induced by the TH generator detuning are of the order of a factor 6. Roughly the same factor six, or more, is the range of variation of the emission intensities, reported in Fig. 3d, induced by discharge power changes. Finally the result of the test is shown in Fig. 3b, in which the ratio of the OH density calculated by formula (3) and the OH LIF (Fig. 3a) is plotted against the run number, after normalization to the mean value of the ensemble. The standard deviation of the ensemble of Fig 3b is about 8%. A large contribution to the standard deviation comes from the measurements between runs 30-40 and runs 60-70, corresponding to the large TH energy variations and is due to an identified cause. The LIF on NO is made in partial saturation conditions, in spite of the quite low laser energy (about 200 μJ per pulse). This is due to the spatial non-homogeneity of the laser beam, characterized by the presence of a "hot spot". The TH energy in the discharge vessel is not the same as that in the NO cell, since the beam passes through two windows and one prism before reaching the NO cell. This means that the LIF in the discharge and in the cell are made at different points, with different slopes, of the saturation curve. On reducing the TH energy the "relative slopes" of the two LIF measurements slightly change. This is a very small effect, about 10% when changing the LIF signal by a factor 3, but it is visible in Fig. 3b. The way out of this problem is to reduce as much as possible the windows number by an appropriate design of the discharge-NO cell system, to use very high optical quality windows, and to work with a TH that does not change as much as in our tests.

As a whole, the result of Fig. 3b is very satisfactory. It is the combination of six measurements, each of which changes very much in the ensemble. Furthermore the measurements statistics is not high. We are using a 10 Hz repetition rate laser, while in actual FAGE systems the laser operates at repetition rates in the kHz range. This means that, in the same measurement time the LIF statistics can be increased by a factor 100. Furthermore, as already pointed out, the problem of the NO LIF saturation can be drastically reduced by an appropriate design of the apparatus. It is then reasonable to estimate that the source can operate at a statistical precision of 1-2%, whichever the discharge and gas feed conditions are.

4. Discussion and conclusions

The data shown in the preceding paragraph are a striking evidence of the correctness of the method. Furthermore the scheme we have proposed is only apparently complex: it in fact opens the possibility for a simple, robust and small reference cell. A key role in the miniaturization of the source is played by the LIF spectroscopic scheme, detailed in [4], that allows solution of the laser scattered light elimination from the OH LIF signal by the use of a precision multi-cavity interference filter. This eliminates the need of long arms with baffles on the laser beam path. With the aid of up-to-date miniature photomultipliers, one can envisage a source apparatus 10-20 cm long, and supplied by a very low power (< 1W) pulsed RF generator. The other key for miniaturization and portability of the apparatus is the fact that it uses ambient air as gas feed. This is the field where our scheme shows the major advantage with respect to the other method actually available for the generation of a known OH density. This latter is based on the well known reaction[6], [7]:

$$H + NO_2 \rightarrow OH + NO \qquad (4)$$

H atoms are generated in an Ar/H_2 microwave discharge and NO_2 is added downstream the discharge in a flow tube. The OH density is classically obtained by a volumetric measurement of NO_2, provided the H density is well known in the flow tube. Alternatively, and perhaps more easily, the measurement of OH can be reduced to the measurement of NO, since equal amounts of OH and NO are produced by reaction (4), provided the ratio of OH and NO density remains constant in the measurement region. The big practical drawback of this method compared to our scheme is the need for hydrogen and nitrogen dioxide bottles, i.e. hazardous/harmful gases, in the apparatus, that is not desirable in an on-line reference source for a portable field instrument.

A further development of our scheme could be a "local" application of the pulsed discharge in the same region as the sample one, with an time alternation of the "sample" and "reference cell" measurements instead of a simultaneous "sample" and "reference" measurements, but with the reference cell physically located in a different space position. In the FAGE case this could be done by switching-on a small confined pulsed discharge close to the nozzle of the sample air expansion. Two important advantages of such a "local reference cell" would be:

1. the “reference” measurements are made in the same pressure and temperature conditions as the sample ones;
2. the “reference” signals are measured by the same optical collection-measurement system as the sample signals.

Acknowledgements
The invaluable technical assistance of Mr. Agostino Parodi is gratefully acknowledged

References

[1] M.R. Heal, D.E. Heard, M.J. Pilling and B.J. Whitaker - J. Atmos. Sci. **52** 428 (1995).
[2] G. Dilecce, P.F. Ambrico and S. De Benedictis - contr. pap. FLTPD-V, Specchia - Italy , april 3-7 2003, p. 218-221, available on-line at http://fltpd-5.ba.cnr.it/.
[3] G. Dilecce, M. Simek and S. De Benedictis - J. Phys. D: Appl. Phys., **34** 1 (2001).
[4] G. Dilecce, P.F. Ambrico, M. Simek and S. De Benedictis - Appl. Phys. B, **75**, 131 (2002).
[5] S. De Benedictis, G. Dilecce and M. Simek - J. Phys. D: Appl. Phys., **30** 2887 (1997).
[6] S.J. Wategaonkar and D.W. Setser, J. Phys. Chem. **94** 7200 (1990).
[7] G.H. Ho and M.F. Golde, J. Chem. Phys. **95** 8866 (1991).

MAGNETIC PROPERTIES AND CORROSION RESISTANCE OF PLASMA POLYMER STABILIZED COBALT NANOPARTICLES

Hrishikesh Manian [1], W.J.VanOoij [1], Y.Huang [2]

[1] *Department of Chemical and Materials Engineering, University of Cincinnati, Cincinnati, USA*
[2] *Chemat Technology Inc, USA*

Abstract
In the present work, cobalt nanoparticles have been stabilized by coating RF plasma polymerized C_6F_{14}.SEM and Transmission Electron Microscopy and have been used to study the morphology and thickness of the coating. The protective property of the coating was studied by TOFSIMS. The degradation over time in magnetic behavior of the coated cobalt nanoparticles at room temperature were studied using Vibrating sample Magnetometry

Introduction
There has been an increased interest in ferromagnetic nanoparticles of Cobalt because of their potential use in magnetic data storage as well as in sensors. Co nanoparticles have been synthesized by colloidal chemistry [1], and by a modified arc discharge method [2]. The stability of nanoparticles has long been a concern for useful applications. Some advances have been made towards this end by encapsulating them in graphitic layers [3, 4]. Specifically for cobalt nanoparticles, the sensitivity of the magnetic properties to oxidation [5] points towards the necessity for stabilization of the nanoparticles. One method of achieving this has been to form and coat the nanoparticles insitu in microwave plasma [6, 7].
In the present work we have synthesized Co nanoparticles from Cobalt carbonyl and coated with a stabilizer plasma polymer layer of C_6F_{14}.

Experimental
Chemicals Cobalt carbonyl (1-5% hexane as a stabilizer) and perfluorohexane were purchased from alfa-aesar.
Apparatus The reactor consists of a 2 piece Pyrex glass set consisting of a flask at the bottom of diameter 7.5 cm, a vertical tube of 25 cm length and 2.5 cm diameter. Two inlets are provided in the top portion for monomer and carrier gas if required. The inductively coupled plasma was excited by means of an RF generator operating at 13.56 MHz. The reactor was subjected to oxygen plasma cleaning to ash any organic matter from previous depositions, followed by argon plasma treatment for 15 minutes.

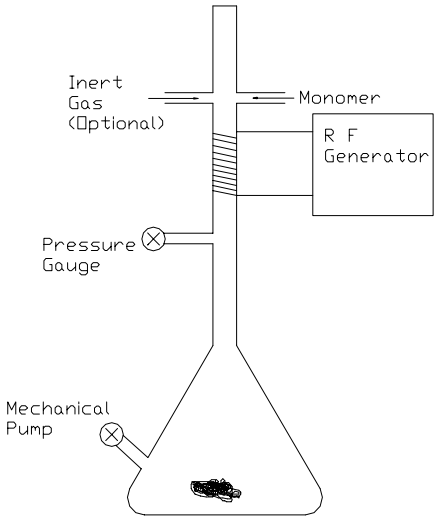

Figure 1 The RF plasma reactor used to make and coat cobalt nanoparticles

The cobalt carbonyl, in the form of crystals, is introduced in the bottom flask of the reactor in a vial. Typically, 0.2-0.3 g is taken so that the yield may be at least 10-20 mg. The reactor is pumped to a base vacuum of 80 mtorr. The cobalt carbonyl is then heated so as to decompose it to form metallic cobalt. This is followed by introduction of the perfluorohexane monomer at a pressure of 200 mtorr over base pressure in the reaction chamber where it is polymerized by the plasma. The plasma power was between 115 and 120 W. The deposition time of the polymer was 30 minutes.

Scanning Electron Microscopy The coated samples were studied for the aggregation in a Hitachi 3200 N variable pressure SEM.

Transmission electron microscopy Transmission electron microscopy was done in a Phillips CM-20 TEM. The samples were suspended in methanol and ultrasonically shaken to concentrate the particles. The solution was then placed on a Ni grid and evaporated under a nitrogen atmosphere. The operating voltage was 20 KV.

Time of Flight Secondary Ion Mass Spectrometry (TOFSIMS) The particles where characterized in an ION-TOF IV Time of flight SIMS system. The primary ion source consists of 25 KV Ga^{3+}. The typical raster area is 75 µm * 75µm. The pressure in the analysis chamber is kept below 10^{-8} mbarr.

Vibrating sample Magnetometry (VSM) The magnetic property studies were carried out in an EG & G PAR model 4500, Vibrating Sample Magnetometer system equipped with a 1 Tesla Electromagnet.

Results

The synthesized nanoparticles were found to have an average size of 60 nm in the agglomerated form as seen from the SEM micrograph in figure 2.

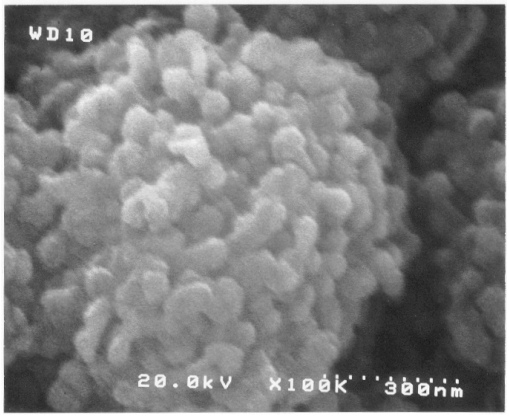

Figure 2 The agglomerated cobalt nanoparticles

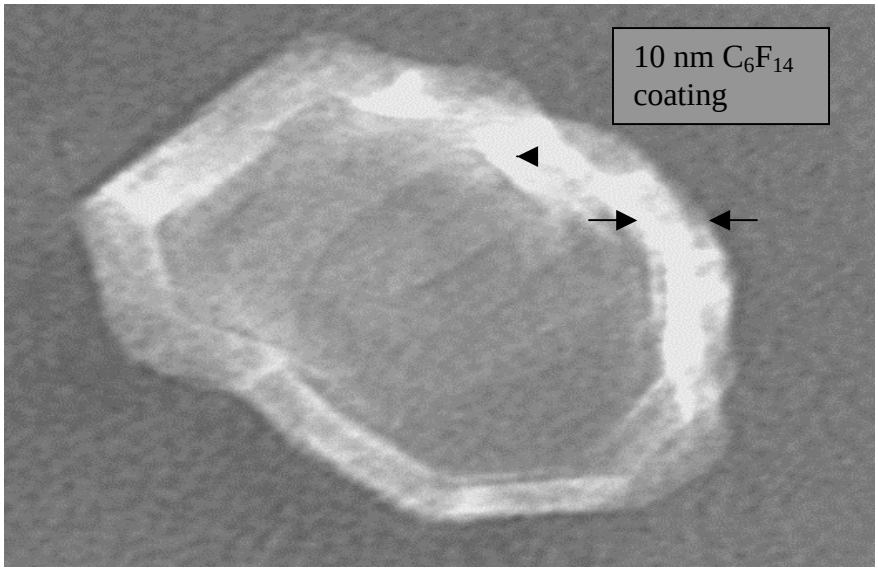

Figure 3 TEM micrograph of C_6F_{14} coated cobalt particle

The TEM micrograph shown in figure 3 clearly shows the coating of C_6F_{14} of 10nm thickness on a cobalt particle of about 100 nm thickness.
Time of Flight-Secondary Ion Mass Spectroscopy (SIMS) was done to determine the protective property of the stabilizer coating. The intensity ratio of Co and various oxides of cobalt to that of the total ion intensity is a tool which can quantify the amount present. SIMS was done in the same sample under two different conditions:
a) As prepared condition
b) Exposed to moisture for 3 months.

Table 1 The intensities of Co and various Co oxides as compared to the total ion intensity for SIMS

Condition	Co	CoO	Co_2O_3	Total Ion Intensity
As prepared	446657	748	0	1451160
Exposed to moisture	135422	1436	111	814380

Table 2 The Intensity ratios of Co, CoO and Co_2O_3

	Intensity ratio in as Prepared Sample	Intensity ratio in sample exposed to moisture
Co	0.31	0.17
CoO	0.0005	0.0010
Co_2O_3	0	0.00007

It is observed that there is a significant decrease in the Co content but not much of an increase in the oxide content. The increase may be attributed to the formation of hydrated cobalt oxides because of the reaction with moisture.

The magnetic property of Cobalt was measured using Vibrational Sample Magnetometry (VSM) and also after exposure to moisture after 3 weeks.

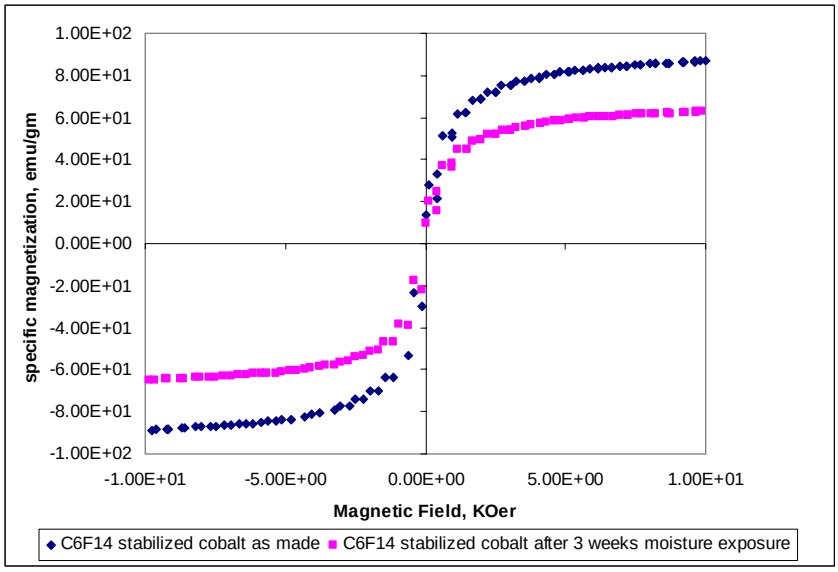

Figure 4 The Magnetic Hysteresis curves of C_6F_{14} stabilized Cobalt

Table 3 The various magnetic properties of the 2 samples under consideration

	As made Sample	3 weeks moisture exposed Sample
Retentivity, M_r (emu/g)	18.80	18.74
Coercivity	192.5	191.01
Saturation Magnetization, M_s, (emu/g)	88.73	87.34
Mass (gm)	0.0158	0.0213

The retentivity value of the C_6F_{14} stabilized Co is 18.80 in as prepared condition and reduces to 18.74 after a 3 week exposure to moisture which is not a very significant reduction. This comapares well with that of Sun etal [2]. The Saturation Magnetization, M_s is rising in the as made case even on application of 10 KOer field. This may be due to super- paramagnetic property. This will be verified further with Mossbauer spectroscopy studies. However, after exposure to moisture for 3 weeks there is a slight decrease indicated by the less sharp slope in the curve. This may be due to the nonmagnetic nature of moisture and also some increase in oxide content as discussed in SIMS analysis.

Conclusion

It has been shown that nanoparticles of the order of 100 nm have been formed and coated insitu with a 10 nm coating in RF plasma. The protective nature of the perfluorohexane plasma polymer has been shown by the SIMS analysis. The magnetic properties of the stabilized particle are comparable to that of only cobalt nanoparticle. There is also not much of a change in these properties in the time period considered. This further indicates the protective nature of the coating.

References

1. C. Petit etal, J. Phys. Chem. B, **103**, 1805 (1999).
2. Xiangchen Sun, A. Guttierez, M. Jose Yacaman, Xinglong Dong, Shouri Jin, Materials Science and Engineering, **A286**, 157 (2000).
3. Y. Saito etal, J. Phys. Chem., **98**, 6696 (1994).
4. S.A. Majitech etal, Phys. Rev. B, **48**, 16485 (1993).
5. M. Rutnakornpituk etal, Polymer, **43**, 2337, (2002).
6. D. Vollath, D.V.Szabo, J. Nanoparticle Research, **1**, 235 (1999).
7. D. Vollath, D.V. Szabo, J. O. Willis, Materials Letters, **29**, 271 (1996)

Experimental study of electron heating in beam-plasma discharge

V.M. Atamanov[1], T.A. Biman[2], L.I. Elizarov[1], A.A. Ivanov[1], Al.A. Ivanov[1], A.O. Livadniy[2], M.V. Paltov[2], A.V. Pereslavtsev[1]

[1] *Russian Research Centre "Kurchatov Institute", Moscow, Russia*
[2] *People Friendship University of Russia, Moscow, Russia*

Abstract
It is shown; there are the conditions of heating of electrons in a beam - plasma discharge up to high energies. The experimental studies of electrons heating in beam-plasma discharge in mirror magnetic trap are executed. The experimental spectra of X-rays quanta energy from the discharge plasma are given. The maximum of X-ray quanta energy distribution is in the area of energies 200 - 250 keV. The results may be used for the creating of X-ray source on the base of beam -plasma discharge.

1. Introduction

There is the interest to the advantages of beam-plasma discharge in recent years [1]. There are the conditions in beam-plasma discharge when there is the group of hot electrons with energies much higher, than the energy of beam electrons. These high-energy electrons may produce high energy X-rays. The possibility of X-ray generation by the electrons heating in plasma discharge and to create the X-ray sources on this basis for the practical application in the technology and medicine was been demonstrated by the series of experiments that were executed at 60-th - 70-th. First off all we should mark the experimental work by Alexeff and others [2]. An electron temperature of 32 keV and an electron density of $4 \cdot 10^{11}$ cm^{-3} was obtained in beam-plasma discharge in mirror magnetic trap in the stationary mode. The electron beam current was 0.5 A, the energy of beam electrons was 5 keV. It was shown in work [3] that the high-energy electrons are generated in a mirror magnetic trap with high mirror ratio at the interaction of pulse electron beam with the plasma density $2 \cdot 10^{10} cm^{-3}$ in volume of 20 litres. The energy of electrons was 200 keV at the magnetic field 1.65 kOe in the centre of the trap and the electron energy was 40 keV when the magnetic field was 0.5 kOe [3]. The plasma with electron temperature 550 keV and density of 10^{11} cm^{-3} in volume of 4.2 litres was produced in installation PN-2 by means of adiabatic plasma compression [4]. The intensive X-ray radiation in the experiments was up to 1 MeV. The hot plasma was confined by mirror magnetic field without decay for a few seconds in the experiment. The powerful beam-plasma amplifier is described in work [5]. The amplifier is manufactured as a separate vacuum device. In the amplifier the accelerating voltage of electron beam was U_0=15 - 25 kV, the beam current was I= 3 - 5 A, the strength of magnetic field of a solenoid was 2 - 3 kOe, the pressure range of working gas (hydrogen) in the interaction space was $10^{-6} \div 10^{-3}$ Torr. This experiment confirms the possibility of hot electron generation in the separate device. The actual selection of method to get X-ray generation by beam-plasma discharge in a mirror trap is based on its energy-economical capability, simplicity for realisation, possibility to create a compact device for generating hot electrons which can be used as a source of X-ray without the using of high energy power supply (5 ÷ 6 keV, but not 100 keV). Meanwhile, for the tropical countries, due to humidity, high voltages occur such accident like fire. Replacing X-ray tubes (feeding voltage ≅ 100 kV) by our experimental device (feeding voltage≅ 6 kV) can consider this loss. The series of experiments are going on the plasma chemical installation "Oratoria-10" to generate X-ray from the non-equilibrium plasma by beam-plasma discharge [6]. The experiments are carried out in the stationary mode with continues electron beam injection. The X-ray generation was obtained in argon and in hydrogen plasma. During the stationary process some parameters (like magnetic field, electric beam energy, pressure of working gases, Type of gases) were changed to get the optimal results on the X-ray generation. The outcome of X-ray was formed through the aluminium diaphragm with the thickness of 1.4 mm. The dose rate of X-ray was measured by the using of the sandwich of two thermo-luminescence tablets *LiF* with the thickness of 1 mm. The first one absorbed the doze and it's the filter for the second tablet at the same time. The measurements showed that the doze rate measured was 1.7 R/h in the experiments with argon plasma and 3.7 R/h in the experiments with hydrogen plasma. The doze rate measured by the second tablet of the sandwich was 82-84% of the doze rate measured by the first tablet. In the assumption of the mono energy distribution the energy of X-ray quanta was about 20 keV. In the assumption of the Maxwell distribution for the fluid of hot electrons the obtained energy of thermal

electrons was about 30 keV. One can obtain more reliable results with the measurements of X-ray spectra from plasma by using of scintillation detector.

2. Mechanism of electron heating

The analysis of the experimental and theoretical researches of the beam heating of electrons in mirror magnetic trap is resulted in work [7]. When the electron beam is injected in a mirror magnetic trap [7] the strong beam-plasma interaction takes place and it results in the growth of the cross size of plasma and in the strong heating of the hot electrons confined by the trap. The electron beam excites the Langmuir oscillation at the interaction with plasma [8]. The heating of hot electrons takes place because of its interaction with the electron Langmuir oscillations $\omega_{pe} > \omega_{He}$. The width of the beam in the space of velocities Δv becomes to the initial velocity of the beam u at the distance of 20 ÷ 30 cm from the beam input in the system. The characteristic increment of instability is $\gamma \sim \omega_{pe} n_{0b}/n_0$. The electron beam excites the oscillations mainly with the wave vectors parallel to its axes. The spectrum of Langmuir oscillations is essentially non-isotropic. If the electrons at interaction with noise will not get in a cone of losses in the space of velocities, they will diffuse in usual space to the periphery of installation and its energy will slowly increase. The cone of losses in the space of velocities is the function of mirror ratio R. Thus to obtain hot electrons it is necessary to satisfy the series of conditions for the confinement of electrons in mirror magnetic trap and for their heating up to high energies, namely:

$\omega_{pe} > \omega_{He}$,

$\gamma \sim \omega_{pe} n_{0b}/n_0$,

$R > 1/\cos^2\theta_0$,

where $arctg\theta = k_\perp / k_{//}$, and θ_0 is some limiting angle.

If to take into account, that the radius of a beam $a \sim 1$, and characteristic wave vector of raised oscillations $\boldsymbol{k} \sim \omega_{pe}/u \approx 5$ cm^{-1}, that $k_a >> 1$. It means, that for estimations it is possible to use outcomes of the theory of a boundless beam.

Energy of oscillations in a transverse direction is transferred with formation speed

$$\frac{\partial \omega}{\partial k} \sim \left(\frac{\omega_{He}^2}{\omega_{pe}^2} \right) v_\phi .$$

The time of propagation of oscillations up to diaphragms limiting plasma is much less then decay time on hot particles. At on frequency, wave number k and the speed of hot electrons v is superimposed a condition

$$\omega_{pe} = kv\cos\varphi ,$$

where φ is an angle between k and v. The vigorous electron will be effective to interact only with those oscillations, which wave numbers are almost perpendicular to their velocities.

On the base of the above one can observe the dependence of the energy of hot electrons on the strength of the magnetic field. The electrons involved in process of acceleration increase the energy and diffuse from a beam to an exterior wall of the trap. The energy of electrons is determined by the time of its life in the trap τ, that it is possible to write as:

$$\tau \sim \left(\tau_D^{-1} + \tau_S^{-1} \right)^{-1} ,$$

where τ_S is the time of dispersion in a cone of losses, and τ_D is the time of a diffusion of an electron up to the external boundary of plasma. Thus, the time of leaving of an electron in a cone of losses is defined by the configuration of magnetic field (mirror ratio) and does not depend on its strength. The time of electron diffusion across the magnetic field is proportional to a quadrate of plasma radius and it is in inverse proportion to an effective diffusion constant or proportionally to quadrate of the magnetic field strength. Thus, in the area of "small" magnetic fields, while $\tau_D < \tau_S$, the lifetime is determined by the time of diffusion and increases proportionally to quadrate of a magnetic field strength. At some value of a magnetic field strength the diffusion time is compared to the dispersion. At the further magnification of a magnetic field the lifetime ceases to depend on a magnetic field strength and it is defined only by the leaving of "hot" electrons in a cone of losses.

3. Experimental device

The experiments on plasma producing and electron heating in beam-plasma discharge were executed on plasma chemical device “Oratoria-10”, the scheme being shown at Fig.1. The "Oratoria -10" device enables

to carry out the researches of non-equilibrium plasma with the density of $10^{10} \div 10^{13}$ cm^{-3} produced in a beam-plasma discharge. The working vacuum chamber (1) of diameter 0.5 m and the length of 1m is made of stainless steel. All the chamber is immersed in magnetic field created by the coils (2). The magnetic system of a "mirror-like magnetic trap" type produces magnetic field of strength 600 Oe in the centre of the magnetic mirror trap and accordingly in the centre of the working chamber (1) and magnetic mirror (max/min) ratio R~3.5. The strength of magnetic field can be varied from 300 Oe up to 600Oe. The maximum magnetic field strength is about 800 – 900 Oe in short time regime (10 – 15 minutes). The electron beam of a cylindrical geometry of maximum diameter up to 4 cm is formed by means of an electron gun (3) with a beam current of up to 2 A and of its energy up to 6 keV. The electron beam formed by the electron gun is injected into the working chamber (1) along the axis of the magnetic field and through the system of diaphragms (5) with the small orifices. The electron beam penetrates the chamber from one side to the electron beam receiver (4) on the other side. The system of differential pumping is used to provide the necessary high vacuum conditions for the electron gun operating. Differential pumping system consists of three groups of thin diaphragms with the intermediate pumping out between the two ending diaphragm groups and through the middle group. The orifices in the diaphragms are equal to a diameter of the electron beam. The necessary vacuum conditions in the "Oratoria-10" chambers are provided by the oil vapour high vacuum diffusion pump (6) with liquid nitrogen-cooled trap. The residual gas pressure is not more than $3 \cdot 10^{-7}$ Torr with the using of nitrogen-cooled traps and not more than 5.10^{-6} Torr without the using of nitrogen cooled traps. The maximum working pressure in working chamber is about ~ 10^{-3} Torr. High-energy electrons heated by beam-plasma interaction in the discharge produce the X-ray quanta at Coulomb scattering in plasma and at the electron - wall collisions. X-ray quanta attain the scintillation detector (7) passing through the thin beryllium diaphragm and the orifice in the lead collimator. X-ray quanta are registered by the detector (7) on the base potassium-iodine crystal. Photo multiplier tube enables us to measure the signal and determine the X-ray spectrum. 1024 channel amplitude analyser is used to measure X-ray spectrum. The plasma density was measured by the using of Langmuir probe (8). The working plasma forming gas is supplied into the working chamber through the piezoelectric inlet valve (9).

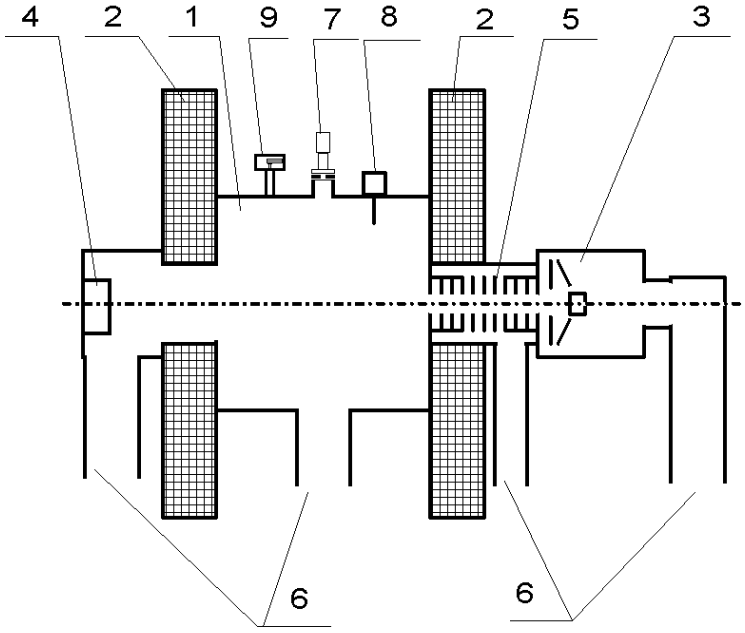

Fig. 1. The scheme of «Oratoria - 10» installation.
1 - vacuum chamber: 2 - magnet coils; 3-electron gun; 4 - electron beam receiver; 5 - diaphragms;
6 - vacuum pump; 7 - X-ray diagnostic; 8 - Langmuire probe; 9 – piezoelectric inlet valve.

4. Experimental results

The experiments were carried out for two aims – to measure integral intensity of X-ray radiation and to find out the dependence of spectral distribution of X-ray energy on the strength of magnetic field, electron beam parameters, initial gas pressure in the working chamber and the composition of plasma forming gas. In our

researches we used two gases for the plasma forming: argon and hydrogen. One can explain our choice to study the X-ray generation in the plasma of gas with minimum excite states of the molecules and to study the plasma of more complicated composition with plenty of excite states of atoms.
A typical experiment to study the X-ray generation in plasma beam-plasma discharge in "Oratoria-10" device was as follows. The initial pressure of residual gas in working chamber is about $5 \cdot 10^{-6}$ Torr. The magnetic field is switch on. Nominal current in magnet coils is about 200 A corresponds to the strength of magnetic field about 600 Oe in the centre of magnetic trap. The electron beam is injected into the working chamber along the axis of magnetic field. The electron beam current is about 1 A, the energy of beam electrons is about 3 – 4 keV. The hydrogen is being supplied through the piezoelectric inlet valve into the working chamber. The hydrogen inlet flow is adjusted concerning to the maximum of integral intensity of the X-ray radiation. The inlet hydrogen gas flow corresponds to the total gas pressure in the working chamber about $(7 – 9) \cdot 10^{-5}$ Torr. Then the spectrum of the X-ray radiation is measured by the using of scintillation detector, photo multiplier tube and amplitude spectrum analyser. The experiments on the study of X-ray generation was carried out in the accordance with the above operation sequence at the variable parameters of the discharge: the strength of magnetic field, the electron energy and the current of electron beam, the plasma forming gas pressure. The typical experimental spectrum of the X-ray generation in hydrogen plasma of beam-plasma discharge is shown on fig.2 and fig.3.

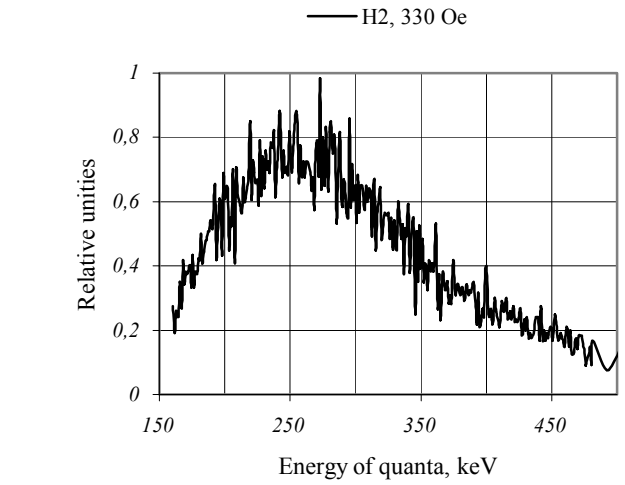

a)

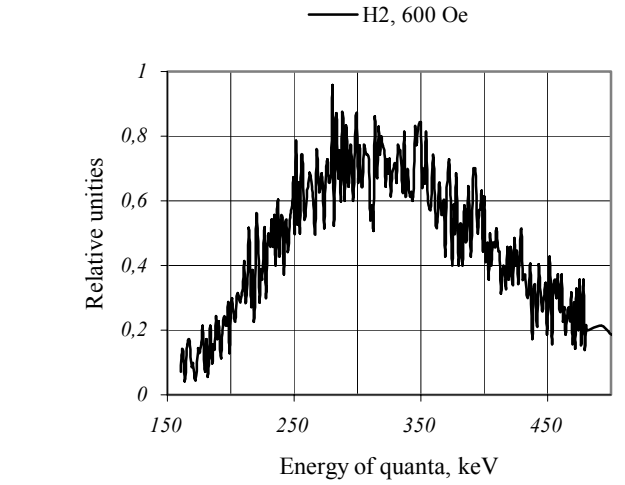

b)

Fig. 2. X-ray spectrum in hydrogen plasma. Initial pressure $\sim 8.5 \cdot 10^{-5}$ Torr, beam current ~0.75A, electron beam energy 3 keV : a) H=330 Oe; b) H=600 Oe

One can see the maximum of X-ray energy distribution in the experiments with hydrogen plasma is about 230 - 250 keV at the strength of magnetic field *H=330 Oe* and about 270 - 300 keV at *H=600 Oe*.

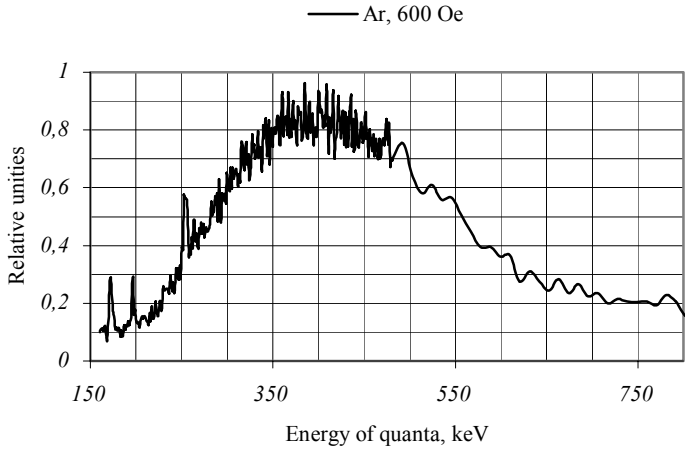

Fig. 3. X-ray spectrum in argon plasma
H=600 Oe, initial pressure ~$8.5 \cdot 10^{-5}$ Torr, beam current ~0.75A, electron beam energy 3 keV

The typical experimental spectrum of the X-ray generation in argon plasma of beam-plasma discharge in the "Oratoria-10" device one can see on fig. 3.
In the case of argon plasma maximum of X-ray energy distribution is about 350 keV.
The X-ray registration system (scintillation crystal, photo multiplier tube and amplitude spectrum analyser) was calibrated against the isotopes ^{241}Am, ^{60}Co and ^{137}Cs.
We carry out the series of experiments with argon and hydrogen plasma. All these curves were Maxwell-like. Our experiments demonstrate some interesting dependence: integral intensity is the highest in the experiments with hydrogen plasma and maximum energy of quanta is reached when argon was used as plasma forming gas.

5. Discussion

First of all we must mark some new physical results of our experiments.

- In our experiments we obtained rather high energy of hot electrons that is about 250 – 350 keV in the maximum of the energy distribution.
- There is the X-ray emission in hydrogen plasma at the strength of magnetic field about 300 – 330 Oe.
- The energy of hot electrons and its quantity depends on the kind of plasma forming gas.

One can explain the increasing of X-ray energy distribution maximum at the higher magnetic field in the experiments with hydrogen plasma by the dependence of hot electrons transverse velocity on the strength of magnetic field.
If it is possible to explain the smaller intensity of X-rays in the experiments with argon plasma from the point of view of a lot of excitation levels of argon atoms and accordingly more losses of energy, this mechanism does not explain the increasing of "temperature" of hot electrons in argon plasma. Thus it is necessary to assume the presence of other mechanism responsible for this phenomenon. It is possible to assume the existence of dependence of transverse diffusion velocity of hot electrons on the kind of ions in the plasma (the relation of mass to a charge). In the case of heavier ions in plasma the velocity of transverse electron diffusion is less, the time of the transverse diffusion is accordingly more, the lifetime in a trap is more too. It results in the decrease of amount of hot electrons i.e. more part of electrons leaves in a cone of losses and simultaneously to the increasing of hot electrons energy in a trap.
On the other hand the executed experiments demonstrate the opportunity to obtain hot electrons in plasma of beam - plasma discharge. The temperature of hot electrons in plasma is much higher than the temperature of electrons in a beam. To compare the obtained experimental results with the earlier experiments on installations working in the pulse mode it is interesting to continue the study of electron heating in beam - plasma discharge and to find the time of formation of electron acceleration mode at the pulsing injection of electron beam in the same conditions as at the continuos injection of the beam. The other direction of the researches is the obtaining of high temperature relativistic electrons at the adiabatic compression of plasma of the beam - plasma discharge containing hot electrons. The existing of hot electrons in the experiments with hydrogen plasma at the strength of magnetic field about 300 Oe enables us to assume the possibility to

obtain rather high-energy electrons by the adiabatic plasma compression. One more perspective direction in the study of heating of electrons in the beam-plasma discharge is the researching of plasma decay after the termination of electron beam injection into the mirror magnetic trap and first of all the study of hot electrons that leave the magnetic trap through the magnetic mirror.
All these results will be very useful for the application in the science, technology and medicine.
There is the possibility to create X-ray source with the variation of X- ray quanta energy and the intensity of the X-ray generation. Such X-ray source may be used in medicine for the X-ray therapy. The hot electrons produced in beam-plasma discharge may be used to obtain the multi charged ions. The sources of multi charged ions are applied in science and industrial technology.
The electron bunch leaving the hydrogen plasma through the magnetic mirror of the trap in the processes of plasma decay can carry away the hydrogen ions. Taking into account the high velocity of hot electrons and the relation of proton mass to the electron mass (equal to 1840) one can assume the possibility to accelerate the protons by the electron bunch in the process of collective acceleration. It opens the perspective to create the collective proton accelerator on the base of the obtained results and above-mentioned processes.
It is necessary to take into account the presence of X-ray generations in beam plasma discharge devices is the indicator of the existence of beam-plasma instability in the discharge.
The opportunity to heat electrons in beam - plasma discharge has also the own back, namely, practically in any device with the beam - plasma discharge exists a mode, at that the X-rays radiation may be intensive enough. It is the problem of operation personal safety.

6. Acknowledgement

The generation of high energy X-rays in beam-plasma discharge in mirror magnetic trap was studied by our team with the support of INTAS (grant 97-0094) and Federal Programme “Integration of Science and High Education” (grant И0602/1378 and Я0068/2137).

References

[1] A.A. Ivanov. The present state and development trends of discharges. Physics and chemistry of plasmas. Phenomena in Ionized Gases (XXII ICPIG) Hoboken, NJ July-August 1995, p.41 – 74.
[2] I. Alexeff, R. V. Neidigh, W. F. Peed, E.D. Shipley and E. G. Harris. Hot-electron plasma by beam-plasma interaction. Phys. Rev. Letters, **10**, (1963) No 7, p.273-276.
[3] L.P.Zakatov, A.G.Plakhov, D.D.R’utov, V.V.Shapkin. The research of a high-temperature electron component of plasma formed in the system a plasma-beam. JETPh, 54 (1968), No. 4, P 1088-1098 [In Russian].
[4] L.P.Zakatov, A.A.Ivanov, A.G.Plakhov, V.V.Shapkin. The obtaining of relativistic plasma by adiabatic compression in the system plasma-beam. Pisma v JETPh, **15** (1972) No 1, P 16-20 [In Russian].
[5] L.A.Mitin, V.I.Perevodchikov, M.A.Zav’alov, V.N.Tskhay, A.L.Shapiro. Powerful microwaves wide band beam-plasma amplifiers and generators. Physics of plasma, **20** (1994) No 7-8, P 733 - 746 [In Russian].
[6] V.M. Atamanov, L.I. Elizarov, et al. X-ray generation in plasma by beam-plasma discharge in the stationary mode. Probl. Atomic Sci. and Techn. Series Nucl. Synth., No 3, 2001, p. 30–36 [In Russian].
[7] A.A.Ivanov. Physics of strongly non-equilibrium plasma. M. Atomizdat, 1977, 350 p [in Russian].
[8] J.B.Fainberg. Interaction of charged particles with plasma. Atomic Energy, **11** (1961), P 313 [In Russian].

Measurements of Local Plasma Parameters for an Ionized Inert Gas Flowing in a Magnetic Field

E.D.Roach, R.V.Vasil'eva, A.V.Erofeev, T.A.Lapushkina, S.A.Poniaev

Gasdynamic Laboratory, Ioffe Physico-Technical Institute RAS, St.Petersburg, Russia

Abstract
Method of measuring electron temperature and concentration in fluctuations of ionization unstable inert gas plasma in presence of regular plasma structures is presented. Experiment was made in a disk magnetohydrodynamic channel in Xe. Maximum magnetic induction value was 1.4T. Local electron temperature and concentration are measured. Evolution of plasma inhomogeneities is analyzed. Average values of plasma parameters are estimated.

1. Introduction

It is known that ionization (electrothermal) instability is the type of instabilities that earlier than others occurs in closed-cycled magnetohydrodynamic (MHD) generators [1-3]. Therefore, such type of instability has more influence on MHD channel characteristics and generator performance. Traditionally, pure inert gases with alkali seed use as a working substance for closed-cycled MHD generators. Effective conductivity decreases in the MHD channel with developing ionization instability at using traditional working substance. There is an opposite result when using pure inert gas without alkali seed as a working gas. The development of ionization instability in plasma of pure inert gases without alkali seed leads to increasing effective conductivity and, therefore, to growing extracted power, as it was discovered in our previous studies [4-6]. The major purpose of this work is to study ionization instability in great detail for deeper understanding this phenomenon, which will lead us to presenting the accurate physical model of increasing effective conductivity in unstable plasma flow when there are regular plasma structures. Our main goal of this study is to determine electron temperature and concentration in plasma fluctuations for determination of the relationship between the structures of inhomogeneities, distributions of plasma parameters, and integral characteristics of MHD channel.

2. Experimental setup

The experiment was performed in a disk MHD channel 0.32 m in diameter and 0.01 m high. Ionized gas flow was produced in a shock tube. Xenon was used as a working gas. The experiment was made at a Mach number of the incident shock wave of 6.9 and under initial pressure of 26 Torr. The maximum value of magnetic induction was 1.4T. The channel is shown in fig.1.

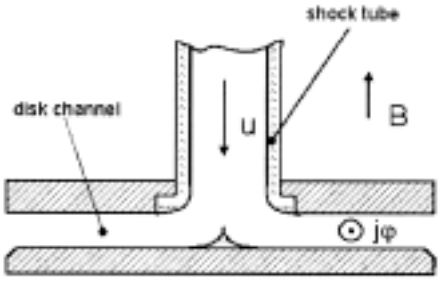

Fig.1 Scheme of disk MHD channel with shock tube.
j_φ – azimuthal Faraday current , B – magnetic field, u – velocity of gas flow.

In a disk MHD channel, MHD interaction gives rise to an azimuthal Faraday current (j_φ) and a radial Hall field. The more detailed descriptions of setup and measuring methods are contained in the Refs. [4-6]. In our terminology, instabilities or strata are names for regular structures with high electron temperature and concentration, which occur in the plasma flow at ionization instability at magnetic induction greater than 0.57 T for this experiment. Plasma parameters at the inlet of the disk MHD channel (at r=0.04 m) are: u_0 $=1.27 \cdot 10^3$ m/s, ρ_0 =0.45 kg/m^3, T_{ao} =2600 K, T_{eo} =3100 K, α_o $=2.6 \cdot 10^{-4}$, M=2.45.

3. Plasma state

Presence of MHD interaction leads to a temperature separation between electrons (T_e) and heavy component (T_h). This separation can be presented by an expression similar to the Kerrebrock formula (1):

$$(T_e-T_h)/T_h=\gamma k_\sigma \beta^2 M^2 (1-k)^2 (3\delta)^{-1} \qquad (1)$$

where $\gamma=c_p/c_v$; M – the Mach number of the flow; k_σ – correction multiplier used in conductivity calculations [7]; δ - inelastic loss factor which is mainly associated with the energy spent on gas ionization; β - Hall parameter; T_e and.T_h – temperature of electrons and heavy component, respectively. The temperature separation was $T_e/T_h=4$. At B=0, the gas ionization degree (α) in the recombining plasma proves to be higher than the equilibrium value (α_0) because of slow recombination. In the presence of a magnetic field, the process of ionization began to dominate due to selective electron heating. The ratio between the nonequilibrium and equilibrium ionization degrees became less than 1, $\alpha / \alpha_0<1$. The electron velocity distribution can be considered as Maxwellian for the gas ionization degrees in our MHD channel, $2\cdot10^{-4}<\alpha<2\cdot10^{-3}$. The increase of ionization degree due to selective heating leads a change of ratio between collision frequencies with atoms and ions. In the experiment, the ratio is between 0.2 and 1. According to ionization kinetic theory [8] of inert gases, the basic ionization mechanism is the following: ionization rate is determined by the rate of excitation of lower energy levels by an electron impact. The reverse process determines the recombination rate. For example, at T_e=8000K the three-particle recombination coefficient in Xe is $Kr=5\cdot10^{-41}$ m^6/s. If $n_e=10^{21}$ m^{-3}, the characteristic recombination time under these condition is $2\cdot10^{-2}$ s. In the experiment, the flight time was the order of 10^{-4} s.

4. Theoretical basis

The method of determination of electron concentration and electron temperature in an inert gas is based on continuum radiation peculiarities of the inert gas. There is a wide range of wavelengths for Xe, where radiation intensity drop is as an exponential function. The measurements of electron concentration (n_e) and electron temperature (T_e) are based on recording the absolute and relative intensities of the continuous radiation. A.Unsold and Kramers [9] established the general mechanism of the continuous emission. Corrections due to the nonhydrogen-like nature of the complex atoms were taken into account in the Biberman-Norman theory [10]. The energy distribution in continuous spectrum of Xe was studied in work [11]. It was shown that there is dependence on the intensity of the continuum radiation (I_ν) from frequency in some areas of xenon continuous spectrum:

$$I_\nu = \begin{cases} 4.3\xi(\nu)\frac{2h}{c^2}\cdot\frac{N_e N_i}{(kT_e)^{1/2}} = A & \nu \leqslant \nu_I \\ A\cdot\alpha\cdot\exp(-h\nu/kT_e) & \nu_I < \nu < \nu_{II} \\ A\,(1-\beta\cdot\exp(-h\nu/kT_e)) & \nu > \nu_{III} \end{cases}$$

$$\alpha = \exp(h\nu_I/kT_e), \qquad \beta = \exp(h\nu_{II}/kT_e) - \exp(h\nu_I/kT_e),$$

$$\gamma = \exp(h\nu_I/kT_e) - \exp(h\nu_{II}/kT_e) + \exp(h\nu_{III}/kT_e);$$

$$\nu_I = 3\cdot10^{14}\,s^{-1}, \quad \nu_{II} = 4.5\cdot10^{14}\,s^{-1}, \quad \nu_{III} = 6\cdot10^{14}\,s^{-1}. \qquad (2)$$

The radiation intensity drop is as an exponential function for wide range of wavelengths (470-300 nm) in xenon radiation at $\nu>10^{14}$ s^{-1}. Therefore, as shown in work [11], electron temperature can be determined based on the results of comparison of I_ν for two frequencies as following:

$$T_e=h \bullet (\nu_1-\nu_2) \bullet [k \bullet \ln(I_1/I_2)]^{-1} \qquad (3)$$

The major question with using this method is what is reasonable to use as standard values for intensity of radiation, electron temperature and electron concentration in MHD channel. Studies of other authors, for instance work [12], show that at M≥10, the measured parameters of a shock-compressed gas plug in shock tubes match well with their computed values. The part of shock-compressed gas plug with thermodynamic equilibrium (Mach number of shock front M_1=10.5 and p=7.7 mm Hg) served as the standard for the intensity of radiation I_ν, electron temperature T_e and electron concentration n_e. In the experiment it was area

with maximum radiation of shock-compressed plug, close to the shock wave front. Under these conditions, radiation intensity, electron concentration and electron temperature are close to calculated equilibrium values of these parameters. Standard electron temperature is determined to within 2%. This accuracy determines the absolute accuracy of measurements. The relative value of electron temperature is obtained with the ratio of a noise to a signal and is 1.5%.

Electron concentration was determined with radiation intensity and electron temperature. For this purpose, the area with wavelength 566 nm was extracted with an interferential filter. In this wavelength range the correct formula is the following:

$$I_\nu = 8.6 \bullet (h/c^2) \bullet \xi(\nu) \bullet n_e^2 \bullet (kT_e)^{-0.5} \qquad (4)$$

where $\xi(\nu)$ is a multiplier taking into account non-hydrogen nature of atoms [10].

Radiation of a shock-compressed gas plug from the volume with thermodynamic equilibrium was taken as a standard value of radiation. All plasma parameters are calculated with good accuracy for this part of shock-compressed gas. If we are taking absolute electron temperature values to within 2%, then absolute values of electron concentration are within 25% using this method of determination.

5. Optical scheme of measurements

The optical scheme of continuum radiation registration for two wavelengths from the disk MHD channel and shock tube was designed. Ultra-violet (UV) monochromator was designed with a concave diffraction grating (R=1m) as shown in fig.2.

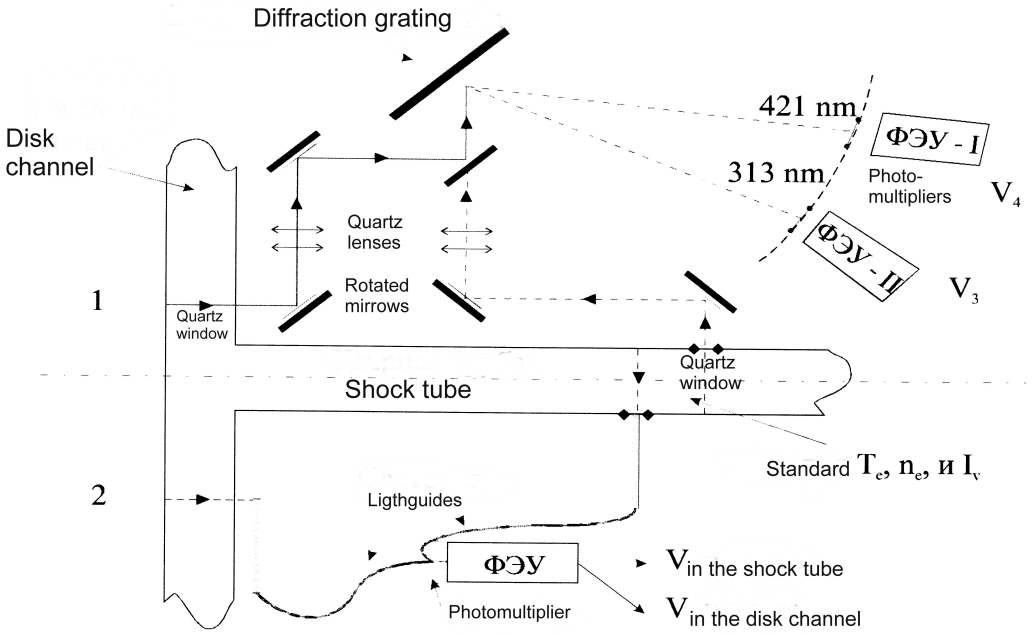

Fig.2 Schemes for measuring electron temperature (1) and absolute intensity of radiation (2)

The solving ability of the monochromator was 0.8 nm/mm and was determined with the distance between mercury lines using standard mercury lamp. Two quartz windows with diameter 0.01 m were installed in plexiglass disks in MHD channel at radii r_1=0.07 m and r_2=0.096 m. Plasma radiation from the disk channel was directed on a diffraction grating with rotated mirrors and quartz lenses. Two areas of xenon spectrum λ_1=423±1.5 nm and λ_2=313±1.5 nm were extracted at the same time. Radiation from these two areas was registered with two identical photomultipliers. Signals from photomultipliers were transferred to a digital oscilloscope. Computer analysis was used for obtaining data.

6. Fluctuations of electron concentration and temperature

Our previous study [13] shows that luminous inhomogeneities (magnetic strata) are shaped as spokes, oriented at 20-30^o with an azimuthal direction, placed in the distance of 0.03m from each other in the azimuthal direction. At the same time there are 3 strata in the length of the channel. In the channel, they appeared with the same time interval ($2\cdot10^{-5}$ s – $3\cdot10^{-5}$ s), their propagation velocity was close to flow velocity, i.e. it was as if the strata were frozen to the flow. While strata were moving in the channel, they become more luminous, wider and more oriented with the initial current direction. Once formed, the strata do not decay. They have a lifetime longer than a flow time. It is possible to follow the strata evolution in more detail by detecting temporal variations in electron concentration at different fixed locations in the channel. To this end, photomultypliers were used to measure plasma luminousity through windows in the disk channel wall. Fig.3 demonstrates how the electron concentration changes at distances r_1 and r_2 as different volumes of plasma move past the measurement window. It can be seen that the time interval between the first electron concentration maxima is close to the time difference between the shock wave arrivals at r_1 and r_2, which suggests that the same strata are observed at r_1 and r_2. The electron concentration in the strata grows as they propagate downstream. The electron concentration distribution shown in Fig.6 is seen to have large-scale inhomogeneities with duration of 20-50 μs. During a flow time of 400 μs, about eight large-scale strata pass through the channel. On their background, small-scale inhomogeneities, which are more pronounced at larger radii, are present. We find a certain analogy with the development of classical turbulence [14] when small-scale pulsations are regarded as a fine structure superimposed on large-scale inhomogeneity.

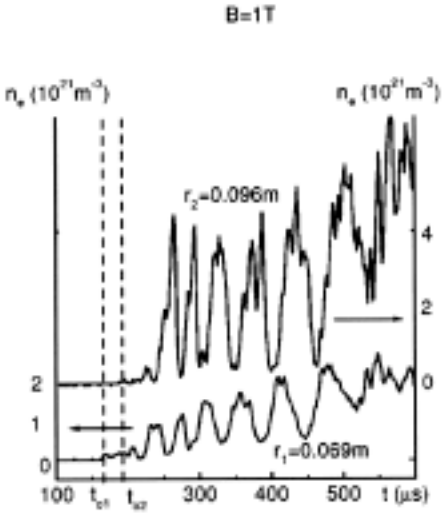

Fig.3 Electron concentration for two radii along the channel radius at B=1T.
t_{01} and t_{02} are times of the shock wave arrives into the first and second measuring locations.

Fig.4 shows electron concentrations and temperatures in the inhomogeneities that move past the measurement window at r=0.096 m for B=1T. It can be seen that, in general, large-scale regions with higher temperatures (strata) have higher electron concentrations and, conversely, that lower-temperature regions are characterized by lower electron concentrations, although the positions of the n_e and T_e maxima and minima are somewhat shifted. In the large-scale inhomogeneities, the highest and lowest electron concentrations differ by approximately a factor of 3-3.5, the electron temperature varies from 8500 to 7000K. In the small-scale inhomogeneiteies, variations in the electron concentration are weaker by about 50%, while the temperature may rise as high as 10000-11000K. The average value of T_e over fluctuations $<T_e>$is 7800K. Measurements of electron temperature T_e at radii r_1 and r_2 revealed that average temperatures at these radii were nearly equal.

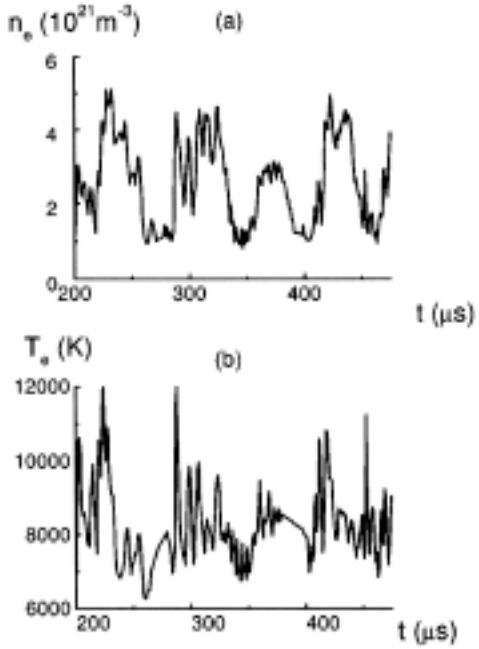

Fig. 4 Fluctuations in luminous inhomogeneities of electron concentration and electron temperature at B=1T, r_2=0.096m.

7. Average values of T_e and n_e

The average value of electron temperature over fluctuations in the region (r_2-r_2) was obtained by averaging the results of several experiments, fig.5a. The picture also shows calculated values of electron temperature for magnetic induction lower than critical magnetic induction value, i.e. for stable plasma. The measured values of T_e in ionizational unstable plasma proved to be lower than those calculated on the assumption of stable plasma. Fig.5b presents electron concentration values, which were averaged over fluctuations for different magnetic fields at two radii. Each point was determined by processing several measurements.

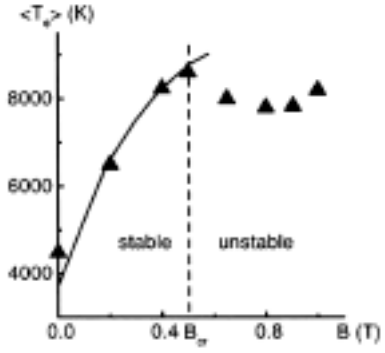

(a)

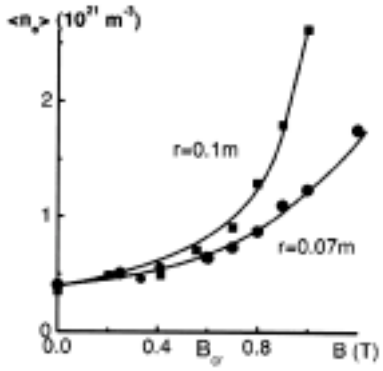

(b)

Fig. 5 (a) - Average electron temperature for different magnetic induction values. Curve is the temperature calculated on the stable plasma assumption. Points are experimental data. (b) - Average electron concentration for different values of magnetic induction at two radii.

8. Conclusions

The lifetime of plasma strata is longer than their flight time in the MHD channel and the strata are "frozen" in the flow. Therefore, plasma flow consists of volumes with lower and higher electron temperatures and electron concentrations. Among the plasma parameters considered, the most significant changes were observed in electron concentration. Average values of electron concentration and their modulation depth increase with increasing magnetic induction values.

References

[1] J.L. Kerrebrock - AIAA J. **2** No.6, 1072 (1964)
[2] R.J. Rosa – Magnetohydrodynamic Energy Conversion (McGraw-Hill, New York, 1968)
[3] E.P. Velikov and A.M. Dykhne – Proc. Compt. Rend. Conf. Int. Phenomenes Ionieat. Gas. Paris **4**, 511 (1963)
[4] R.V. Vasil'eva et al. – Low Temperature Plasma of Inert Gases with Non-Equilibrium Ionization and MHD Generators (Ioffe PTI RAS, St.Petersburg, Russia, 1991), p.206.
[5] R.V. Vasil'eva, E.A. D'yakonova (E.D. Roach), A.V. Erofeev, A.D. Zuev, T.A. Lapushkina, A.A. Markhotok – Tech. Phys.**42**, 1376 (1997)
[6] R.V. Vasil'eva, E.A. D'yakonova (E.D. Roach), A.V. Erofeev, T.A. Lapushkina – Tech. Phys.**44**, 1312 (1999)
[7] V.A. Brzhezitskii – High Temp.**10**, 6 (1972)
[8] L.M. Biberman, L.M. Vorob'ev, and V.S. Yakubov – Kinetics of Non-Equilibrium Low-Temperature Plasma (Nauka, Moscow, 1982), p.376.
[9] A. Únsold – Physik der Sternatomspharen, Springer-Verlag, Berlin, 1955 (Russian translation, Inost.lit., Moscow, 1949), p.630.
[10] L.M. Biberman and G.E. Norman - Sov.Phys.Usp. **10**, 52 (1967)
[11] A.P. Dronov, A.G. Sviridov, and N.N. Sobolev – Opt. Spectrosc. **12**, 383 (1962)
[12] G.K. Tumakaev and V.R. Lazovskaya – Aerophysical Inverstigations of Supersonic Flows [in Russian], Nauka, Moscow, 1967, p.304
[13] R.V.Vasil'eva, A.V.Erofeev, D.N.Mirshanov, T.A.Alexeeva - Journal of Tech. Phys. 59,N7, 27 (1989)
[14] L.D. Landau, E.M. Lifshits – Mechanics of Continuous Medium (State Publishing House of Technico-Theoretical Literature, Moscow, 1954).

Analysis of the motion of a three-phase plasma arc

J. Gonzalez-Aguilar[1], T. M. Gruenberger[1], L. Fulcheri[1], F. Fabry[2], B. Ravary[3], G. Flamant[4] and W. Xia[5]

[1] *Centre for Energy Studies, Ecole des Mines de Paris, Sophia Antipolis, France*
[2] *Erachem Comilog S.A., Brussels, Belgium*
[3] *SINTEF Materials Technology, Trondheim, Norway*
[4] *IMP – CNRS, Odeillo, France*
[5] *University of Science and Technology of China, Hefei, China*

Abstract
In this paper, a model is presented describing the dynamics and motion of the electric arcs in a three-phase AC configuration without neutral point. The model considers that the arcs are conducting filamentary wires that carry a given current. Incorporated into a conventional computational fluid dynamics (CFD) simulation of the entire plasma system in the form of an arc sub-model, this new approach will allow a more detailed definition of the reactor inlet conditions.

1. Introduction

An original three-phase AC plasma arc technology has been developed over the last 10 years for the production of carbon nanostructures such as carbon black, nanotubes or fullerenes [1]. In this technology, the discharges do not transit via a star neutral point as commonly found in metallurgical applications but the arcs change in time between delta and star configurations showing complex motions caused by interactions between arcs themselves and the crossing gas flow. As the arc region plays a crucial role in the transfer of energy and momentum to the plasma gas inside the plasma reactor, a better understanding of the phenomena occurring in the arc zone is needed in order to improve the control of the process as well as the CFD modelling of the plasma system.

In an earlier approach by Ravary and co-workers [2, 3], analytical expressions describing the Lorentz forces were presented. Ravary assumes small arc displacements with respect to an initial (star or triangle-type) arc configuration. For that reason the geometry is mainly fixed even if the current in the electrodes and the arcs change in time. Finally, a model of the arc is described which is used in the CFD simulation. The model assumes that time-averaged Lorentz forces are distributed homogenously inside a torus whose radius is set to be equal to the radial position of the electrode tips. The value of the Lorentz force is derived from the average in the space of the analytical expressions determined previously. Although the essential characteristics of the arc forces are given by this model, that means the presence of a positive radial force and the S-shape arc observed by high-speed camera analysis, the films also show that the arc deflection displacements are as large as the distance between the electrode tips. Moreover, in the previous approaches the location of the momentum and energy sources is only justified within the small volume of the arc region compared to the reactor volume.

To overcome these inconveniences, a more sophisticated model of the electric arc is proposed in this work. The force distribution used in the CFD calculation is obtained after direct calculation of the arc positions in time.

2. Theoretical model

Figure 1 shows the electrode configuration. Three cylindrical electrodes of length L and radius r_c are arranged with a 120° symmetry around the vertical z-axis in such way that their tips are on a circumference of diameter D and their axis form an angle α with respect to the z-axis.

The arcs are established between the electrode tips and they are assumed to be conducting wires with uniform properties along their length and having constant cross section S. No constraint is imposed on the arc shape whereas its maximum length is limited. This assumption is justified by energy balance considerations: the electric power dissipated in the arc must achieve a certain value to sustain the discharge and simultaneously it must be lower than the maximum electric power supplied by the electric source.

The arc deformation is governed by the dynamic equation that takes into account the magnetic interaction of the arc with itself, the other arcs and the electrodes or Lorentz force $\mathbf{F}_L$ and the drag force $\mathbf{F}_D$ due to the

relative motion of the arc with respect to the gas surrounding it. Thus, the forces applied on an element of the arc with length *dl* is written as:

$$\rho\, dlS\ddot{\mathbf{x}}=\mathbf{F}_L+\mathbf{F}_D\,, \tag{1}$$

where the Lorentz force is given by

$$\mathbf{F}_L=I\,(\mathbf{dl}\times\mathbf{B}) \tag{2}$$

with *I*, the electrical current across the arc and **B** is the magnetic field.
The drag force $\mathbf{F}_D$ is expressed as

$$\mathbf{F}_D=-C_D\frac{1}{2}\rho_g\,\dot{\mathbf{x}}_2\,A\mathbf{n}\,. \tag{3}$$

In this formula, C_D is the drag coefficient, ρ_g is the density of the cold gas surrounding the arc, *A* is the cross-sectional area of the element of the arc and **n** is a unitary vector in the direction of the element motion. An explicit scheme of equation (1) is used to calculate the evolution in time of the arc motion.
The algorithm is described as follow: At a given initial time t_0, the arc configurations (positions and velocities) are defined and a cold gas velocity distribution is fixed as well as the thermodynamical properties of the fluid and the arcs. In each time step, the intensities are estimated, the Lorentz and Drag forces along the arcs are calculated and the arc position is updated by solving equation 1.
Once the new position and velocities are known, the extinction condition is verified using the arc power which is expressed in terms of the product of the current intensity and the arc length. If the extinction conditions are satisfied, the position and velocity of the arc are restarted setting the arc geometry as a straight segment joining the corresponding electrode tips and the velocity distribution from the corresponding one of the cold gas.
After each time step, the points composing the arc are rearranged equidistantly along the arc improving the accuracy of the algorithm.
In order to obtain a Lorenz force field, the volume which contains the arc region is discretised in small cells $\Delta r\Delta\theta\Delta\phi$. In each time step, the Lorentz force along the wire is mapped on this discretised space and stored as a function of the index (*i*, *j*, *k*) of the cell. Once the time evolution is finished, the spatial distribution of density of the Lorentz forces is obtained by time averaging of the storage data and dividing by the cell volume. The field is expressed in terms of spherical harmonics to better show the angular dependence:

$$\langle\mathbf{F}_L\rangle=\frac{1}{T}\int_0^T\mathbf{F}_L(\mathbf{r},t)dt=\sum_{l=0}^{\infty}\sum_{m=-l}^{l}\mathbf{f}_{lm}(r)Y_{lm}(\theta,\phi) \tag{4}$$

where the coefficients $\mathbf{f}_{lm}$ are calculated by the expression:

$$\mathbf{f}_{lm}=\int_{4\pi}d\Omega\langle\mathbf{F}_L\rangle Y_{lm}^{*}(\theta,\phi) \tag{5}$$

At present stage, experimental values have been used to close the model. The maximum arc length and the arc density was determined after examination of the ultrahigh-speed camera films [3].
A previous sensibility study has been made with the aim to establish the dependence of the final Lorentz force distribution with the initial conditions, with the number of points that compose the arcs and electrodes and with the number of cells used to obtain the distribution.

3. Results

Figure 2 (left) shows a typical arc picture seen from the bottom of the reactor (plane *XY*) obtained by an ultrahigh-speed cine-camera 'NAC' (7000 frames/s) in argon plasma. The theoretical calculation obtained assuming that the gas involving the arcs remains stationary is plotted in figure 2 (right). In the case of argon, the calculation compares very well with the experimental data in spite of the simplicity of the model.

Moreover, theoretical results allow to take a tri-dimensional outlook of the motion of the arcs which is impossible to obtain under experimental conditions due to the inaccessibility to the plasma region. This idea appears clearly illustrated in figure 4 which contains two projections of the same calculation than in figure 3 on the planes *XZ* and *YZ*. We have observed that the elongation of the arcs in the vertical direction is at least as important as the radial displacement originating very complex forms whose XY projection shows S-shapes and occasionally the presence of boucles justified by a helicoidal pattern. Another characteristic is the strong curvature of the arc around the electrodes due to the strong magnetic interaction in the vicinity of the electrode tips.

The series in spherical harmonics show the angular dependence of the force distribution. As example, figures 5 and 6 show the series at l = 0, 1, 2 and 3 for the radial and axial Lorentz forces obtained as explained above versus the radial distance divided by the parameter *D*. The figures correspond to high (10^3 kg/m^3) and low (10^{-1} kg/m^3) arc mass densities, respectively. Hence, the first one represents an ideal case with a quasi-stationary triangle-type arc configuration and it should be compared with the results published by Ravary *et al* [2].

In the quasi-stationary case (fig. 5), the functions take non-zero values for radial values between 1/4 and $3^{1/2}/4$. The radial force distribution is mainly positive with a maximum centered around 0.29 whereas the axial force distribution is negative showing a minimum at the same position. When the density decreases, the arc deflection is increased and the distribution is spread to a larger radius. Simultaneously, the sign of the terms f_{lm} oscillate with the parameter *l* being positive when *l* is even for the radial force and negative for the axial component distribution.

4. Conclusions

An improved model describing the motion of the arcs has been reported which allows to generate a time-averaged Lorentz forces field. The results derived let us described more accurately the momentum transfer in the arc region. The model shows good agreement with the experimental data, however some improvements are needed in terms of energy balance. So far, the model does not take into account the temperature description along the arcs and the radiative emission. In a next step, this arc submodel will be implemented in a CFD code in order to better describe the momentum sources due to the arc presence in the arc zone.

The authors wish to thank the European Commission for the support in the frame of the following projects : NanoComp HPRN-CT-2000-0037 and PlasmaCarb G5RD-CT-1999-00173

References

[1] T. M. Gruenberger, J. Gonzalez-Aguilar, L. Fulcheri, F. Fabry, E. Grivei, N. Probst, G. Flamant and J.-C. Charlier, “Continuous production of fullerenes and other carbon nanomaterials on a semi-industrial scale using plasma technology” in *Structural and Electronic Properties of Molecular Nanostructures*, edited by Kuzmany et al., AIP Conference Proceedings (2002).

[2] B. Ravary, L. Fulcheri, G. Flamant, F. Fabry - Journal of High Temperature Material Processes, **2**, 245 (1998).

[3] B. Ravary, L. Fulcheri, J. A. Bakken, G. Flamant, F. Fabry – Plasma Chem. Plasma Process. **19**, 1 (1999).

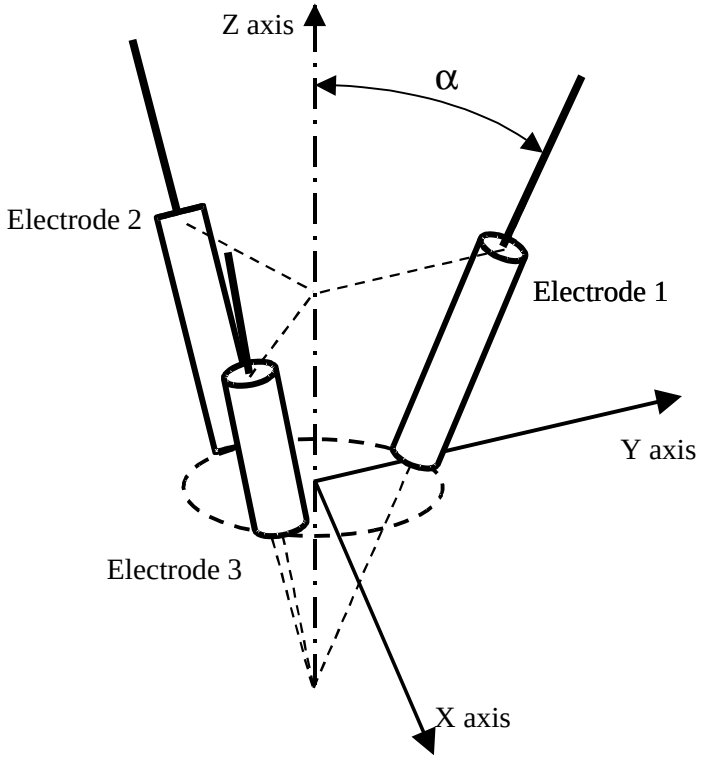

Figure 1. Schematic configuration of the electrodes and the arcs.

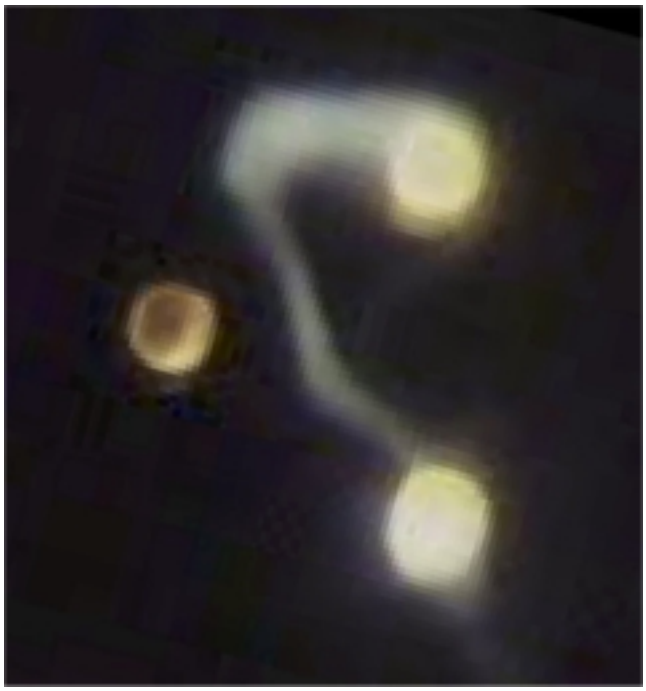

Figure 2. Arc view from the bottom of the reactor (plane *XY*) obtained by ultrahigh-speed cine-camera in argon plasma.

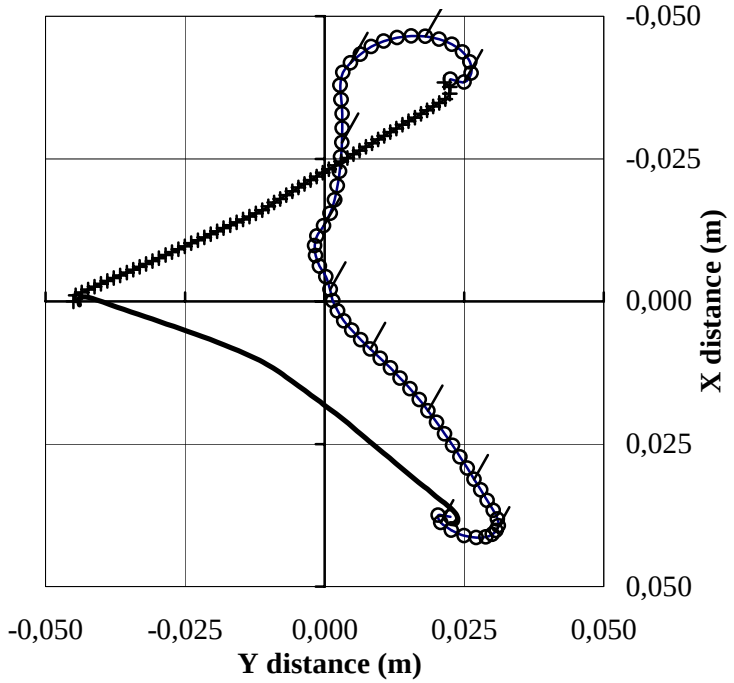

Figure 3. Theoretical calculation obtained assuming that the gas surrounding the arcs remains stationary. The arrows indicate the velocity distribution.

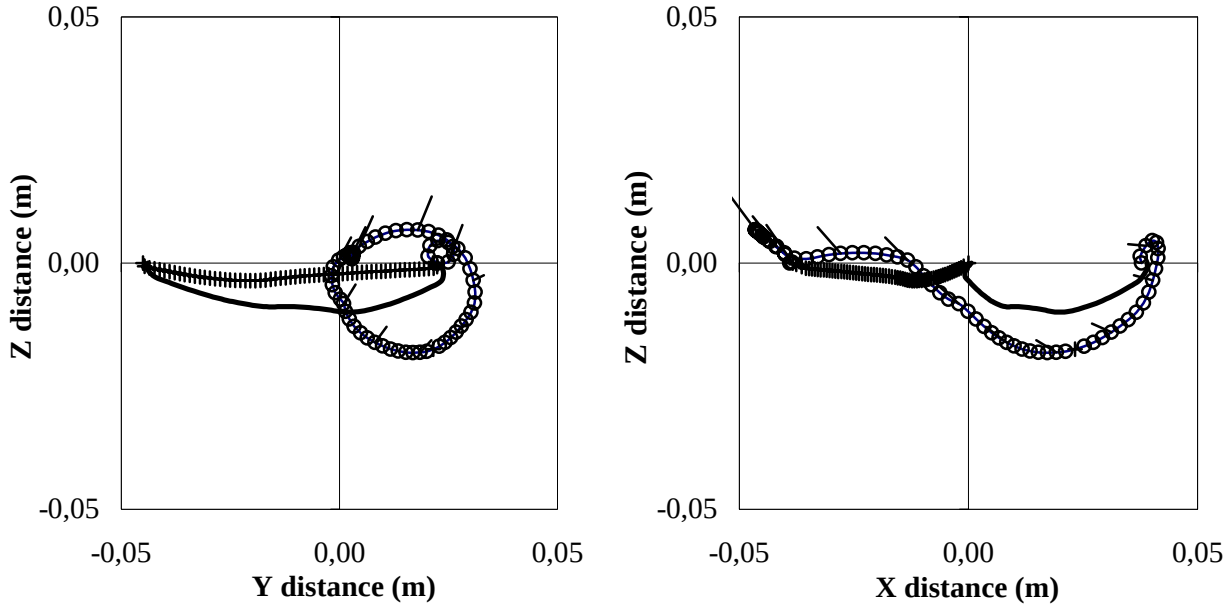

Figure 4. Projections of the same calculation than in figure 3 on the planes *XZ* (left) and *YZ* (right).

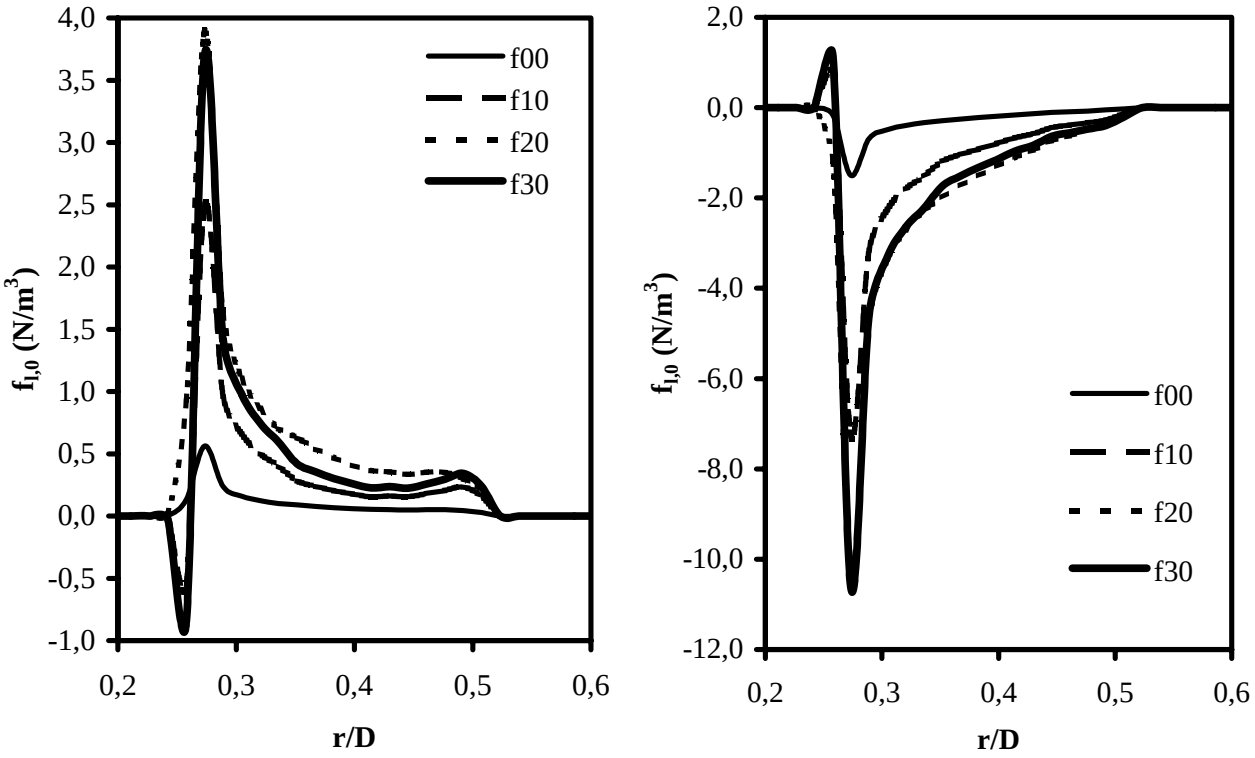

Figure 5. Series f_{l0} with l = 0, 1, 2 and 3 for the radial (right) and axial (left) Lorentz forces obtained as explained in the text versus the radial distance divided by the parameter D in the quasi-stationary triangle-type arc configuration.

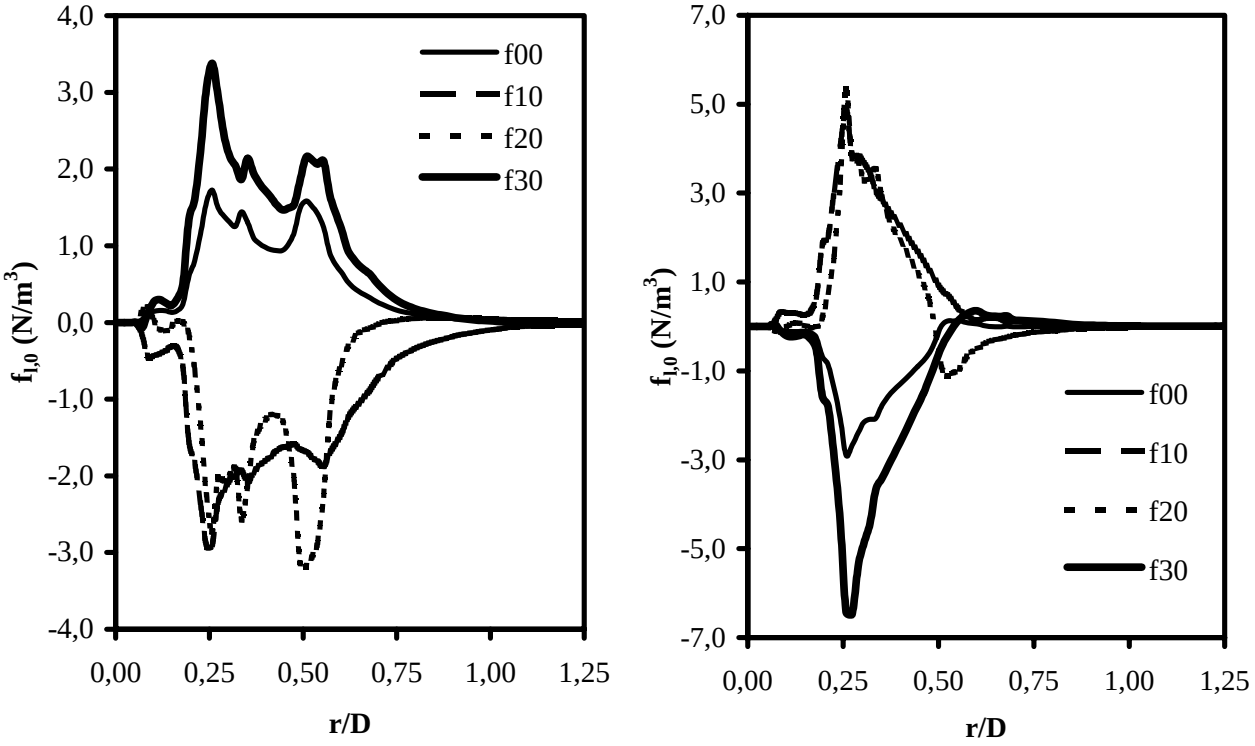

Figure 6. Series f_{l0} with l = 0, 1, 2 and 3 for the radial (right) and axial (left) Lorentz forces obtained as explained in the text versus the radial distance divided by the parameter D to low (10^{-1} kg/m^3) arc mass densities.

Large Area Plasma Processing System Based on Electron Beam Ionization

D. Leonhardt[1,*], C. Muratore[†], S. G. Walton[1], D. D. Blackwell[2], R. F. Fernsler[1] and R. A. Meger[1]

[1] *Naval Research Laboratory, Plasma Physics Division, Washington, DC 20375*
[2] *SFA, Inc., Largo, MD 20774*

Abstract
NRL has developed a number of hollow cathodes to generate sheets of high energy electrons, culminating in a 'Large Area Plasma Processing System' (LAPPS) based on the electron beam ionization process. In this work, we discuss (1) a large area (0.5 m x 1 m) plasma with a comparably large substrate stage and (2) various materials modification tests on smaller (20 cm x 30 cm) systems, both complemented by time-resolved, *in situ* plasma diagnostics (mass spectrometry, Langmuir probes, cathode currents). The materials' modification tests consist of polymeric material (photoresist) and silicon removal, and also nitriding of stainless steel. Results of *ex situ* materials analysis are used to qualify the processing capability and plasma source.

1. Introduction

Conventional discharges (such as dc/rf glows, capacitive, ECR, ICP) directly heat electrons with externally applied fields to ionize the gas, which results in a significant loss of input power to low-energy gas excitation processes rather than plasma production (ionization or dissociation). Hence, plasma electron temperatures are typically multiple electron volts, which translates to an environment of high plasma potentials (> 10 V), sheath drops and ion isotropy at surfaces. Plasmas produced by electron beams (e-beams) are quite different than conventional discharges. When a high energy beam of electrons passes through a gas, its dominant energy loss process is ionization of the gas followed by dissociation and finally inelastic excitations. Secondary electrons are created over a wide energy spectrum but cool rapidly through collisions with the background gas and thus the plasma electron temperature is low. Moreover, the direct ionization mechanism makes this plasma production process extremely efficient when compared to conventional plasma discharges. These attributes coupled with the independence of plasma gas composition and uniform scalability make e-beam produced plasmas well suited for materials applications, from surface activation of fragile polymer substrates to high energy reactive ion etching of hard semiconductor materials.

Electron beam ionization has been shown to be both efficient at producing plasma and scalable to large area (square meters). Fernsler [1] and Manheimer [2] *et al.* have discussed the detailed physics behind the plasma production mechanisms, which agree with *in situ* experimental measurements [3,4]. More recently, a broader view of e-beam produced plasmas was presented [5] to illustrate both the fundamental aspects and the range of plasma source configurations being investigated for various applications. This work reports on the recent experimental progress of some of the applications that are being pursued for materials' surface modification, and the development of a large area plasma processing system (LAPPS).

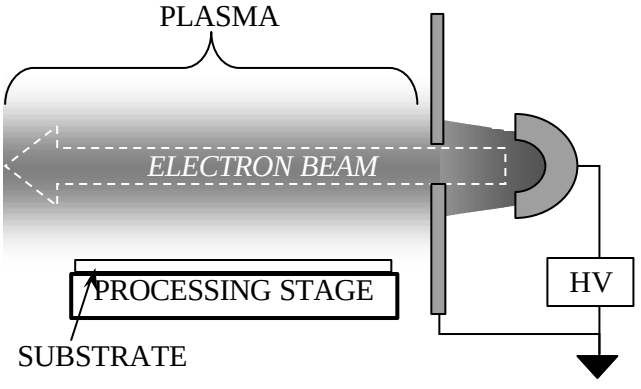

Figure 1 Electron-beam generated plasma in materials' processing arrangement.

2. Experimental Details

Generally, these systems consist of a pulsed, planar plasma generated by a magnetically collimated sheet of 2-3 kV, < 1 mA/cm^2 electrons injected into a neutral gas background (oxygen, nitrogen, sulfur hexafluoride, argon) with typical operating pressures in the range of 20 to 150 mtorr. The arrangement of the planar plasma processing

* Email: darrin@ccs.nrl.navy.mil
† ONR/ASEE Postdoctoral Research Fellow

system is shown in Fig 1. The processing stage (or substrate holder) was introduced laterally, to the 'face' of the plasma sheet. In the application tests, the stage was introduced at the middle of the 25 cm x 50 cm plasma sheets. Stage construction consisted of a 13 cm diameter electrode with grounded support structures, rf-bias and temperature control capabilities. All construction materials were stainless steel and machinable ceramic. Linear hollow cathodes operating at –2 kV with 0.5-10 ms pulse lengths and various duty cycles generated the electron beam, as described previously [6]. External magnetic fields of 150-165 Gauss collimated the e-beam to maintain a localized ionization region. All chambers were metal in construction and had base pressures below $2x10^{-6}$ Torr.

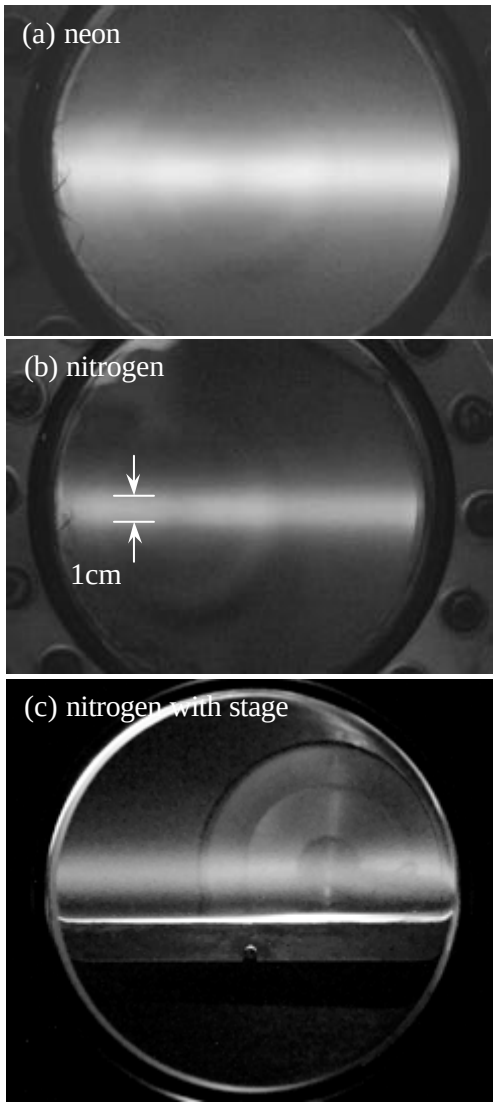

Figure 2 Large area plasma without stage (a) neon (b) nitrogen and with stage in (c).

The LAPPS hollow cathode was 50 cm long, providing a 50x1 cm^2 electron beam source which traveled the length of the chamber (~ 100 cm). Figure 2 shows a portion of this plasma source, photographed through a 20 cm viewport. In these photos, the 50 cm dimension goes into the page surface while the 100 cm dimension was along the page. The 1 cm beam thickness is marked in (b). Figure 2 shows a (a) 75 mT neon plasma, (b) 55 mT nitrogen plasma, and a (c) 55 mT nitrogen plasma with the large processing stage introduced. The processing stage was slightly wider than the plasma surface (~60x90 cm^2), and made similar to the smaller stages previously discussed. The stage is grounded in Fig 2c. With a cathode operating current of <100 mA/pulse, these plasmas had densities of $2\text{-}6x10^{11}$ cm^{-3} in the beam channel.

Applications

Polymeric and semiconductor samples were cut into ~ 1cm^2 pieces and mounted on the processing stage, which was positioned 1 cm from the e-beam edge. The processing stage was water cooled to keep the temperature at 20±4°C. In the etching tests, an rf-induced dc bias level (bias voltage) was applied to the processing stage to vary the incident ion energies during the plasma pulse. Etch rates (ER) were determined through stylus profilometry (Tencor P-10) or scanning electron microscopy (SEM) analysis and are calculated from the total plasma exposure time and not the actual laboratory time. The polymeric materials were industry standard negative or i-line photoresists, etched in O_2/Ar gases. Figure 3a shows the ER dependence for a negative resist as the bias voltage was varied. In these tests, plasmas were formed in 55 mTorr of pure oxygen (80 sccm). A moderately linear relationship between bias voltage and ER was seen, which increased strongly at higher voltages. Diluting the working gas with argon (keeping a fixed bias voltage of –50 V) resulted in the ER behavior shown in Fig 3b. From this data, the ER remained fairly constant until the oxygen percentage dropped below 20%. The total pressure of the mixtures was 65 mT, increasing to 70 mT for pure Ar.

Figure 4 shows the results from a feature cleaning test carried out in a pure O_2 plasma with a –50 V bias on the processing stage. The samples came from a commercial ashing process for Cu vias on i-line resist, shown by the SEM photo in Fig 4a. This photo shows residual spires coming from around the edges of a 300 nm via, left behind after the [cleaning] ash process. The SEM photo in Fig 4b shows removal of the residual spires after the 3-minute e-beam plasma exposure.

Mixtures of Ar or O_2 with SF_6 gas were used to etch crystalline <100> silicon. Figure 5 shows the measured etch rates with respect to the bias voltage for O_2/SF_6 mixtures (55/8 sccm) and Ar/SF_6 mixtures (35/15 sccm). Operating pressures were 60 and 70 mT, respectively. The O_2 plasma shows an increase in ER at V_{bias} > -100 V, but was generally an order of magnitude smaller than the Ar plasma for lower energies.

The Ar plasma ER varies strongly with the applied bias level, starting out slowly before rapidly increasing to ~ 1 micron/min at V_{bias} = -125 V.

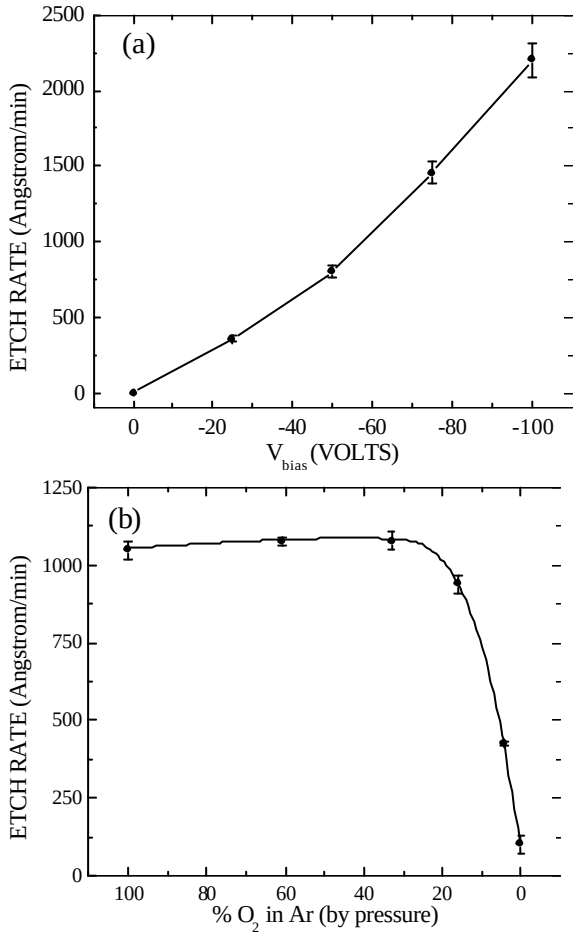

Figure 3 Etch rates of resist material with respect to (a) V_{bias} and (b) % O_2.

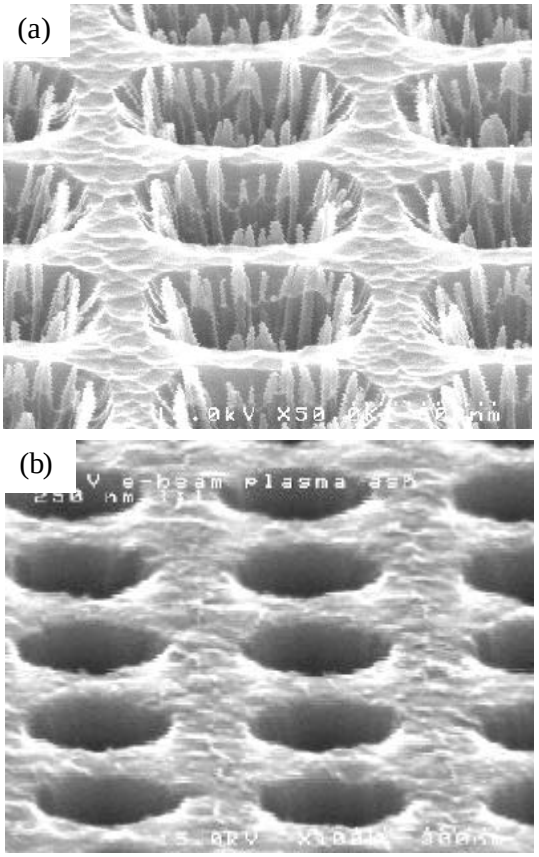

Figure 4 300nm via structures after standard ash process (a) before and (b) after a –50V_{bias} etch in O_2 plasma.

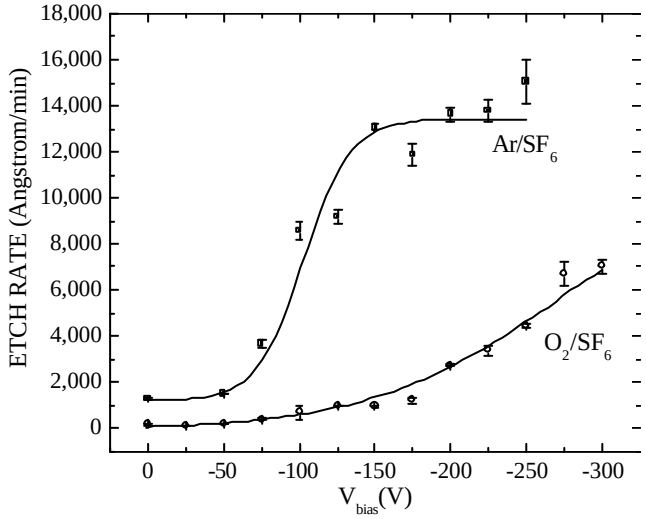

Figure 5 Silicon etch rate with respect ot bias voltage for O2/SF6 (55:8) and Ar/SF6 (35:15) mixtures.

Plasma nitriding experiments were carried out on 316 stainless steel substrates. Sample tiles, approximately 5x5 cm^2 were cut from a 02 cm thick plate and polished to a surface roughness of 7 nm. Samples were then heated to 340-440°C and cleaned in an Ar/H_2 plasma for 30 minutes before being exposed to a 60 mTorr N_2 plasma for 1.4 hours of plasma exposure. A constant –100 Vdc signal was applied to the processing stage for the cleaning and nitriding periods. Samples were allowed to cool, removed from vacuum and analyzed in the SEM to determine the surface nitride thickness. At 340°C, a 0.75 micron thick layer was observed, increasing to 1.3 microns at 400°C and 2.1 microns at 440°C. An Arrhenius plot of these growth rates and temperatures, gives a surface activation energy of 85 kJ/mole (0.90 eV) for this process.

The plasma diagnostics presented here consist of Langmuir probe and ion mass spectrometry measurements as discussed in References [3] and [4], respectively. The ion mass spectrometry provides information of the relative ion fluxes and their energies at the substrate, while the Langmuir probe data, taken at the center of the e-beam, provides plasma density, electron temperature and plasma potential. For the nitrogen plasma discussed previously, the temporally resolved plasma characteristics from these measurements are shown in Fig 6 for a 3 ms e-beam pulse with the grounded sampling stage (mass spectrometer in this case) located 1 cm away from the e-beam. The data shown in Fig 6 illustrates: (a) a rapid ion flux build up, particularly for the more energetic ions; (b) low energy atomic ions with a long decay after the e-beam was turned off but a rapid decay of molecular ion flux; and (c) a steady-state plasma electron densities of $2x10^{11}$ cm^{-3} and temperatures of 0.4 eV. The variation in ion flux with gas composition was also measured and is shown in Fig 7 for mixtures of argon and nitrogen. This data was time averaged and integrated over the entire ion energy distribution before normalized to the total ion flux. The dominant ion fluxes (N^+ and Ar^+) show a linear relationship with the concentration of their parent gas pressure.

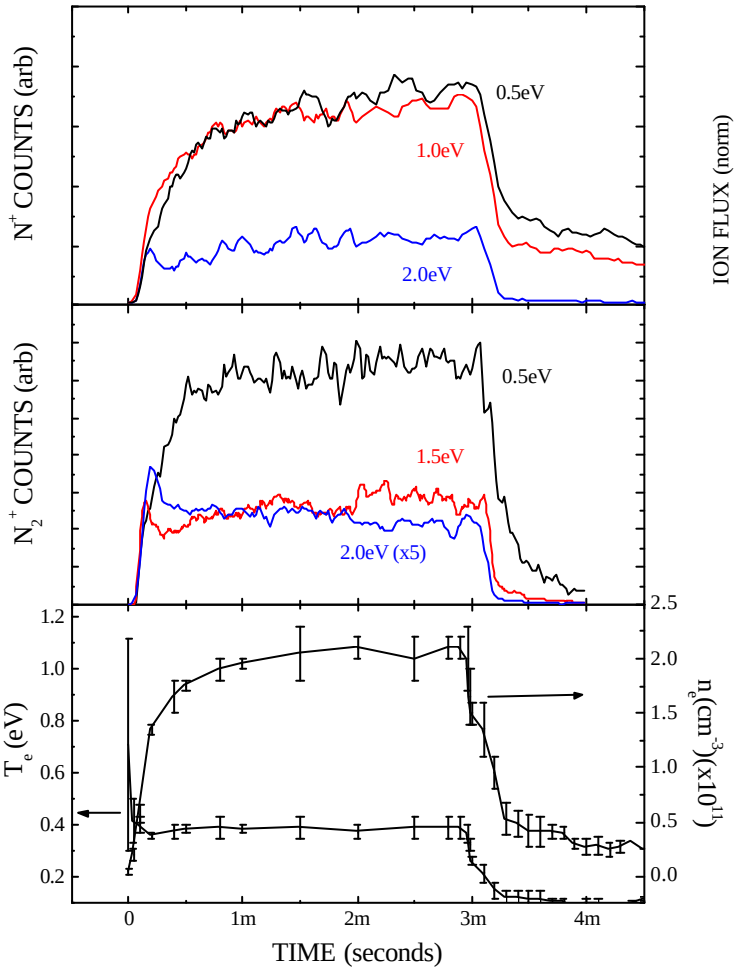

Figure 6 Temporally resolved ion fluxes and bulk plasma characteristics. Flux measurements are made at fixed energy analyser settings. The plasma pulse length was 3 ms.

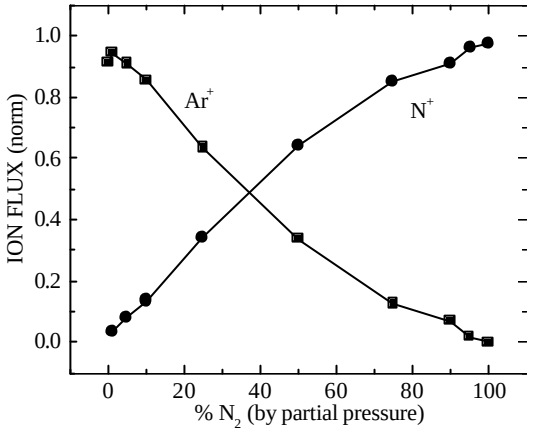

Figure 7 Normalized fluxes of dominant ions to a grounded stage for mixtures of Ar and N_2.

3. Results and Discussion

The photographs in Fig 2 illustrate the plasma localization, differences due to gas composition and the independence of the processing stage location in e-beam produced plasmas. Since the e-beam is the ionization source, the plasma is independent of the chamber and stage design (as long as the e-beam isn't intercepted). The visible light emission from the Ne plasma shows a diffusive nature of the emission while the N_2 plasma is strongly confined to the e-beam channel. Uniformity tests on this LAPPS are presently underway. The additional plasma characterizations shown in Fig 6 illustrate the plasma characteristics of very low electron temperatures, which result in a high density plasma with low plasma potentials and ion energies. From Fig 6, an abrupt peak in the electron temperature and the higher energy ion fluxes characterizes the ignition of the plasma, before the steady-state condition is reached.

The demonstrated reactive ion etching of polymer materials shows strong promise in terms of precise control of a typically isotropic, uncontrollable process that relies strongly on the desorption of carbon monoxide (CO) from the surface. From the data shown in Figs 3 and 4, etching of the resist material was an ion-driven process in an environment that contained an abundance of atomic oxygen neutrals. The direct

correlation between ion energy and material removal in Fig 3 shows that some ion energy was in fact necessary to remove material and the removal was not automatic (exothermic) in the presence of atomic oxygen (especially since the ER drops to nearly zero with no bias energy). In other plasma sources, organic material removal is considered a chemical process dependent only on the atomic oxygen flux to the surface. Thus, ion energy is not considered important in sources where the plasma potential exceeds 10 V. However, plasma potentials in e-beam produced plasmas are only 1-5 V, so initial ion energies are greatly reduced. Without some sort of additional activation (ion energy, temperature) the desorption of volatile etch species does not progress at measurable rates. This control of ion energy down to extremely low values provides additional benefits, as shown by the via residue removal in Figure 4. These test structures provided a much more rigorous test for process anisotropy and showed submicron feature evolution in an otherwise isotropic process. With only very fine (~ 50 nm) residues within small features, any process isotropy would quickly destroy the feature profile. Instead, a clean removal of the residuals left behind was seen, leaving the via structure intact. The results of Figure 3b suggest the plasma source produced a large reactive neutral flux, as the ER remained constant while the feedstock gas source of atomic oxygen was reduced. The ER was therefore not neutral-limited, until the molecular gas percentage fell below 20%.

The reactive ion etching of silicon also showed promising results in terms of material removal rates. At a moderate bias voltage of –125 V, the ER of ~ 1 micron/min for the Ar/SF_6 mixtures is comparable to other high density plasma etchers, although the ER for the O_2/SF_6 mixtures was much remarkably lower. Although the amount of SF_6 was lower in the O_2/SF_6 plasmas, the order of magnitude difference in ER at low energies was surprising, since a strong chemical etch component was expected. This lower ER is more indicative of a SiO_2 sputter yield at these energies, which is reasonable for the more dilute SF_6 plasmas. In this case, the flux of etchants was dominated by oxidizing species, which caused the surface to become more like SiO_2 prior to etching. In addition, the selectivity of SiO_2 over Si using SF_6 at these ion energies should be appreciable, although preliminary tests using an SiO_2 mask showed no selectivity in this plasma chemistry further suggesting SiO_x removal as the limiting step. The Ar/SF_6 plasma chemistry conversely showed a strong chemical and reactive ion etch components from 0-50 V and 50-150V, respectively, and then leveled out at the –275 V energy threshold.

While the present plasma nitriding experiments require further composition analysis, the results are impressive for an non-optimized plasma process. These growth rates are comparable with standard techniques[7] using rf and dc discharges, but the activation energy is low, making this process attractive from the thermal management standpoint. This low activation energy is believed to be due to the large fluxes of atomic nitrogen ions and neutrals produced in these plasmas. With the additional kinetic energy from the applied dc voltage, the atomic ions are the likely critical species for this process, considering that it is atomic nitrogen that adsorbs and diffuses into the bulk. These preliminary results along with the ion specie control demonstrated in Fig 7 makes the development of this process very lucrative from a materials standpoint.

Summary and Conclusion

Electron-beam produced plasmas were readily produced and used in various materials processing applications. The etching of photoresist in O_2/Ar chemistries demonstrated a high degree of control over a predominantly chemical process. This control is attributed to the low incident ion energy from the plasma source, which resulted in better ion energy control with an externally applied rf bias. Similarly, the silicon etching in O_2/SF_6 and Ar/SF_6 mixtures showed a stronger ion-driven component than expected. The limiting step in the O_2/SF_6 mixtures was the removal of an SiO_x layer, due to the large amounts of atomic oxygen generated by the plasma. The use of Ar/SF_6 mixtures eliminated the SiO_x layer as a limiting step and dramatically increased the Si etch rate, at both low and high ion energies. Further tests will focus on feature evolution and anisotropy of these etching conditions. The stainless steel nitriding experiments were encouraging, resulting in both high growth rates (~ 1 micron/hr) and low activation energy (85 kJ/mole), for a large area process. The fact that e-beam produced plasmas in diatomic gases supply predominantly atomic ions to the workpiece makes it an attractive system for plasma nitriding of materials.

The reactive ion etching and nitriding experiments discussed here were proof-of-concept tests for the practicality of applying e-beam produced plasmas to more widespread applications. In order to take full advantage of the versatility of these plasma sources, a more comprehensive design-of-experiments is necessary to optimize the processes. The fact that modulated plasmas offer additional process space not always accessible with continuous plasma sources is another area to be further explored. These plasma sources offer considerable flexibility for modifying materials, although only a few of the attributes have been

investigated thus far. The absence of high plasma electron temperatures (and therefore large plasma potentials) allows a variety of processing conditions without sacrificing flux of reactive charged or neutral species. This work demonstrated important attributes of ion energy control and damage-free etching possibilities, versatility of ion flux through gas composition, competitive nitriding rates and scalability within an actual plasma processing environment.

Acknowledgements

The authors gratefully appreciate the assistance of Dr. John Hallock (formerly of Axcelis Technologies, Rockville, MD) with the via structures. The technical assistance of Anthony Noll (NRL) and Robert Lanham (SFA, Inc., Lanham, MD) was also greatly appreciated. The Office of Naval Research supported this work.

References

[1] R. F. Fernsler, W. M. Manheimer, R. A. Meger, J. Mathew, D. P. Murphy, R. E. Pechacek and J. A. Gregor, *Phys. Plasmas* **5**, 2137 (1998).

[2] W. M. Manheimer, R. F. Fernsler, M. Lampe and R. A. Meger, *Plasma Sources Sci. Technol.* **9**, 370 (2000).

[3] D. Leonhardt, S. G. Walton, D. D. Blackwell, W. E. Amatucci, D. P. Murphy, R. F. Fernsler and R.A. Meger, *J. Vac. Sci. Technol. A* **19**, 1367 (2001).

[4] S. G. Walton, D. Leonhardt, D. D. Blackwell, D. P. Murphy, R. F. Fernsler and R. A. Meger, *J. Vac. Sci. Technol. A* **19**, 1325 (2001).

[5] D. Leonhardt, *Vacuum Technology and Coating* 24 (November 2001).

[6] D. Leonhardt, C. Muratore, S. G. Walton, D. D. Blackwell, R. F. Fernsler and R.A. Meger, submitted to *Surface Coatings and Technology*.

[7] D. L. Williamson, et al. *Surf. Coat. Technol.* **65**, 15 (1994); E. Menthe, K.-T. Rie, *Surf. Coat. Technol.* **116/119**, 199 (1999); M.P. Fewell, J. M. Priest, M. J. Baldwin, G. A. Collins, K. T. Short, *Surf. Coat. Technol.* **131**, 284 (2000).

Plasma-solid interaction in electronegative plasma: comparison of self-consistent particle modelling and experiments

R. Hrach, V. Hrachová, M. Vicher, J. Šimek

Department of Electronics and Vacuum Physics, Faculty of Mathematics and Physics
Charles University, Prague, Czech Republic

Abstract
The contribution presents results of the computer experiment describing the interaction of electronegative plasma with immersed substrates. The simulation was performed under several approximations; the most important was the simplified geometry of substrates. The results of simulation were compared with experimental data obtained in mixtures of oxygen with rare gases.

1. Introduction

The inert gas plasma-solid interaction is of fundamental importance for the understanding of plasma properties and also of a great interest in plasma diagnostics. Especially the electrostatic probes are indispensable diagnostic tools in low-pressure weakly ionised plasma. On the other hand, the interaction of chemically active plasmas with immersed substrates takes part in many plasma technological applications such as plasma processing of materials or plasma-assisted deposition processes. The resulting influence of the both inert gas and chemically active plasmas on immersed materials depends not only on plasma properties but also on properties of processed solid substrates.

In various plasma chemical technologies electronegative gases are widely used. The presence of negative particles, i.e. the application of three-component plasma containing electrons and both positive and negative ions, significantly alter the formation of sheath and in this way modifies the fluxes of charged species to the substrate. However, the detailed description of physical and chemical processes taking part during plasma-solid interaction in such kind of plasma is very difficult. The same holds for the interpretation of results of probe diagnostics in plasmas containing negative ions, especially for higher pressures and/or for dynamic measurements.

For these purposes the computational approach seems to be very convenient. Typical method of modelling used in such studies is the fluid simulation technique (e.g. [1]-[4]), however more detailed results can be obtained with the help of various particle simulation codes (e.g. [5]-[7]). In our laboratory the combination of two types of particle simulation codes, i.e. the molecular dynamics and Monte Carlo methods, PIC-MC, was used for the modelling of the spatial and energy distributions of charged particles during the plasma-solid interaction. Results of the modelling were compared with experimental data obtained in our laboratory, too. The present contribution is devoted to the discussion of these problems.

2. Experimental technique

The structure and properties of the discharges in oxygen are intensively studied for a very long period. In our laboratory the measurements were performed in a positive column of the dc glow discharge, as this part of discharge is often used in various plasma technologies as oxidation, etc. The plasma consisted of oxygen both pure and in the mixtures in rare gases – argon, neon and helium. Main parameters of our experiments were the total pressure of the mixture, the composition of mixtures and the discharge current. In recent measurements an attention was devoted to the properties of substrates/walls, as it was found that they influence the plasma properties profoundly. For the study of plasma properties various diagnostics were used – optical, microwave and probe diagnostic. Some experimental results obtained in our laboratory can be found e.g. in [8]-[11].

It is well known that in the positive column of glow discharge in oxygen there exist at higher pressures two forms of discharges – so-called T and H forms. These two forms differ in the axial electric field (H-form with higher value of this parameter and T-form with the lower one), in the plasma parameters, in the instabilities and in the emitted spectrum. In order to simplify further computer analysis only such experimental data were used, where due to the discharge parameters the transition between these two forms was not observed.

3. Experimental results

In our experiments the positive column of dc glow discharge was studied in the mixtures of rare gases containing oxygen in the pressure range 67 to 800 Pa. All plasma parameters were measured in the dependence on the discharge current 5-30 mA (for discharge tube with diameter 0,02 m).

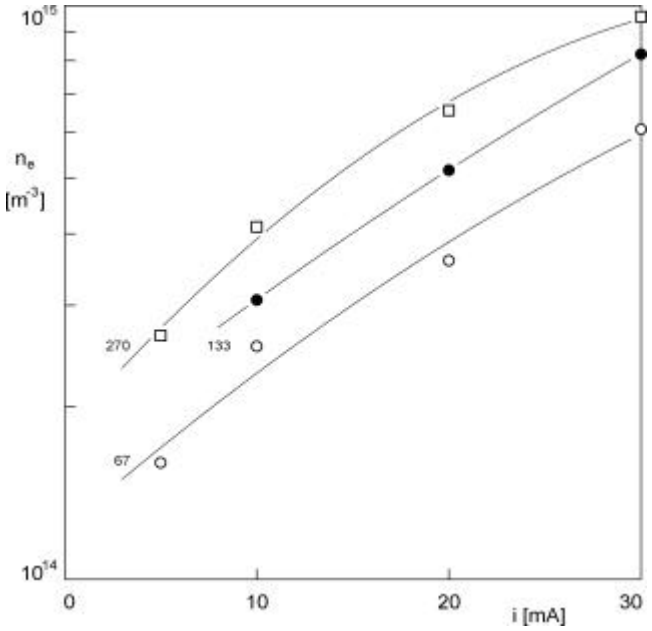

Fig. 1: Measured electron density n_e in the pure oxygen plasma in the dependence on the discharge current. Parameter: pressure of oxygen in limits 67-270 Pa.

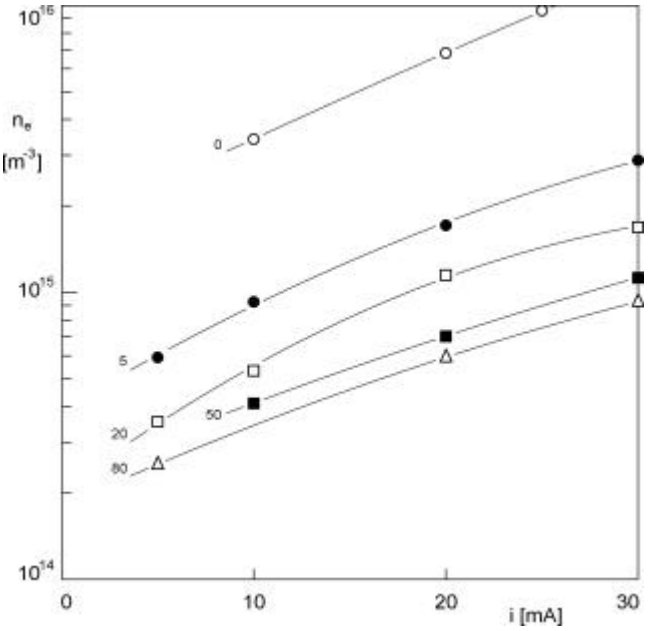

Fig. 2: Measured electron density n_e in the O_2-Ne plasma in the dependence on the discharge current i. Pressure 800 Pa. Parameter: concentration of neon in the mixture (0-80 %).

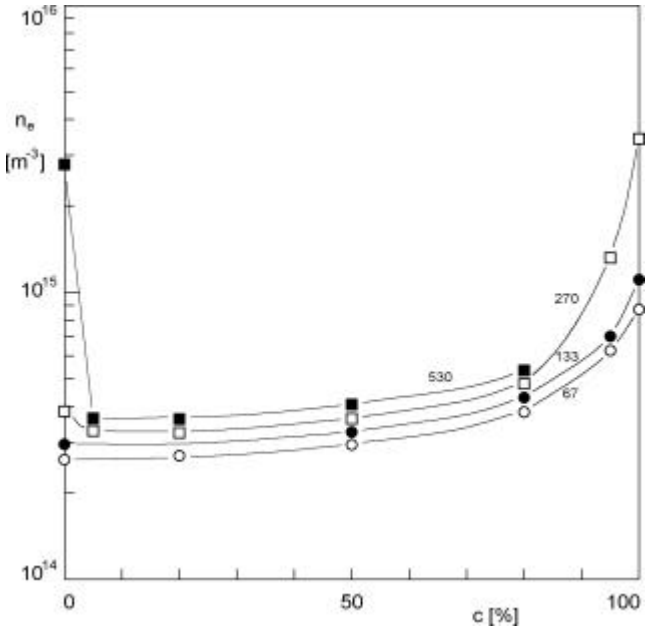

Fig. 3: Measured electron density n_e in the O_2-Ne plasma in the dependence on the concentration of neon in the mixture c. Discharge current 10 mA. Parameter: pressure of the mixture in limits 67-530 Pa.

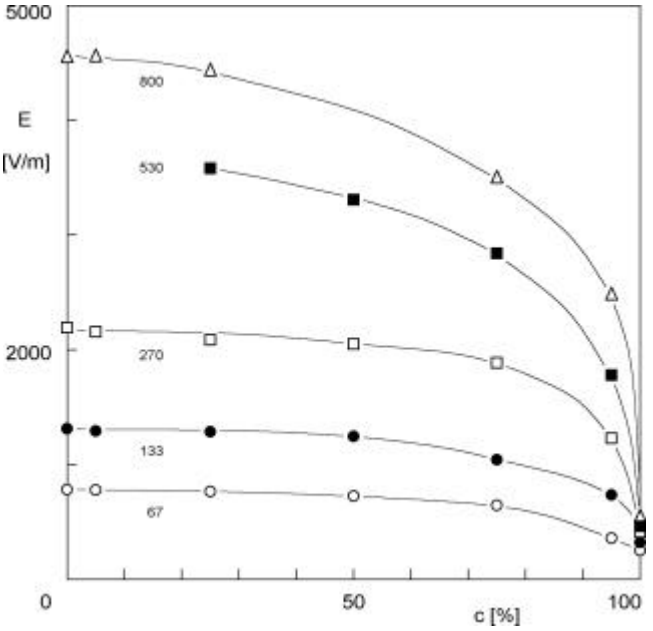

Fig. 4: Measured intensity of axial electric field E in the O_2-Ar plasma in the dependence on the concentration of argon in the mixture c. Discharge current 20 mA. Parameter: pressure of the mixture in limits 67-800 Pa.

In Figs. 1-3 the dependences of electron densities n_e determined by microwave toroidal resonator method on various experimental parameters are shown. The measurements were performed both in the pure oxygen and in the mixtures of oxygen with rare gases, the composition of the mixture being one of experimental parameters.

In Fig. 3 (characteristics for 530 Pa and partially for 270 Pa) it can be seen the starting transition between the T and H forms. Influence of this transition can be observed in the change of axial electric field and collision frequency. Except of the mentioned curves in Fig. 3 all other characteristics in Figs. 1-4 correspond to the H form of the oxygen discharge.

In Fig. 4 the dependence of the intensity of electric field in the positive column of discharge is presented in the dependence on the pressure and composition of oxygen-argon mixture.

The experimental results shown in this section as well as some other characteristics were used as input data and data for testing of results of our computer experiment described in the following section.

4. Computer experiment

In our computer experiment the main attention was devoted to the role of negative ions in the formation of sheath region in the vicinity of metal substrate immersed into plasma. For this purpose several models were prepared. All models are based on the particle simulation approach, i.e. on the combination of deterministic molecular dynamics simulation (for the determination of movement of charged particles in both external and local electric fields) and stochastic Monte Carlo simulation (for the description of interactions between charged and neutral particles). The models differ in the geometry and in the techniques of calculation of self-consistent local forces.

The standard model (see e.g. [12] and [13]) is limited to very simplified geometries of studied problems. There exist three modifications of this model: all modifications are one-dimensional in space and differ in geometries – planar, cylindrical or spherical – corresponding to various forms of probes or substrates. The coordinates used in these modifications are either *1d2v* (planar geometry) or *1d3v* (cylindrical and spherical geometry), where *d* denotes the number of spatial and *v* the number of velocity coordinates. The coordinate system consists of the *x*-axis, perpendicular to the surface of metal substrate (zero being on the surface of substrate), and two or three velocities – v_x and either v_r (i.e. $[v_y^2 + v_y^2]^{1/2}$) or v_y and v_z.

The simulation technique used in this standard model was PIC-MC. The simulations were performed for O_2-Ar plasma in the positive column of dc glow discharge. The model consists of following parts:

Source of particles:

Undisturbed plasma consisting of individual species with concentrations obtained from the macroscopic kinetics model of plasma chemistry of the mixture oxygen-argon. Present simulations were performed for the Maxwell distribution of charged particles with different temperatures of electrons and ions, T_e and T_i.

Interactions:

For electrons elastic collisions in the plasma were supposed, charge transfer interactions for Ar^+ ions and inelastic interactions for all other particles. The interactions were characterised by mean free paths $?_j$, different for various species *j*, the data were taken from [14].

Trajectories of particles:

The trajectories of particles between scattering events were simulated by the molecular dynamics technique, i.e. the Newton´s equations of motion were solved by means of a leap-frog scheme. The scattering of particles was simulated by the Monte Carlo technique – random free paths were derived from the mean free paths $?_j$ with the help of null-collision method and the types of individual interactions were generated statistically, too.

Force calculations:

The most time consuming part of molecular dynamics simulations is the self-consistent calculation of the force $\boldsymbol{F}_i$ acting on the *i*-th particle. This force generally consists of two parts, $\boldsymbol{F}_i^{ext} + \boldsymbol{F}_i^{loc}$. The external force $\boldsymbol{F}_i^{ext}$ is given by voltage bias of the probe/substrate, the local force $\boldsymbol{F}_i^{loc}$ is a sum of Coulomb forces of all interacting particles. The direct summation depends on the number of particles *N* as $O(N^2)$, therefore in our standard model the PIC method was applied with the linear interpolation of resulting space charge. The distribution of electric potential was derived by solving the Poisson equation with boundary values equal to plasma potential (undisturbed plasma) and probe potential (metal electrode).

Time steps:

The leap-frog method handles the problem discretely in time with constant time step $?t$. In order to speed-up calculations, in static regime different time steps for electrons and heavier particles were used, 10^{-11} to

10^{-12} s and 10^{-8} s. However, in dynamic regime this technique cannot be used and all calculations ought to be performed with the electron time step and thus the simulation was extremely time consuming.

Advanced computational techniques:

In order to obtain more efficient code some rather complicated techniques were used – variable numbers of particles increasing during the simulation (especially in dynamic regime) and variable statistical weights of particles depending on their positions (for cylindrical and spherical geometries).

The model was written in FORTRAN 90 programming language and processed by the PC computer. The total number of particles in the model treated simultaneously was $1 \cdot 10^5$ to $6 \cdot 10^6$ (in some special cases even more than $1 \cdot 10^7$) and the number of time steps was about $1 \cdot 10^5$.

5. Results of modelling

The simulations were performed both in static and dynamic regimes. As a result of simulation the spatial and temporal evolutions of velocity and angular distributions of basic types of charged species in the plasma were derived. The studied questions were: the influence of negative ions, the influence of gas pressure and the influence of probe form in the discharge tube versus the properties of sheath region.

Influence of negative ions:

In order to study the influence of negative ions on the plasma properties in the vicinity of the substrate various relative concentrations of oxygen negative ions were introduced – ranging from 0 to 100 %. The steady-state potential distribution in the sheath is shown in Fig. 5. The spatial distributions of basic charged species in the discharge (electrons, Ar^+ and O^-) are demonstrated in Fig. 6. It can be seen, first, that the presence of negative ions influence profoundly the sheath thickness, and second, that the electrons and negative ions behave diversely in the sheath region

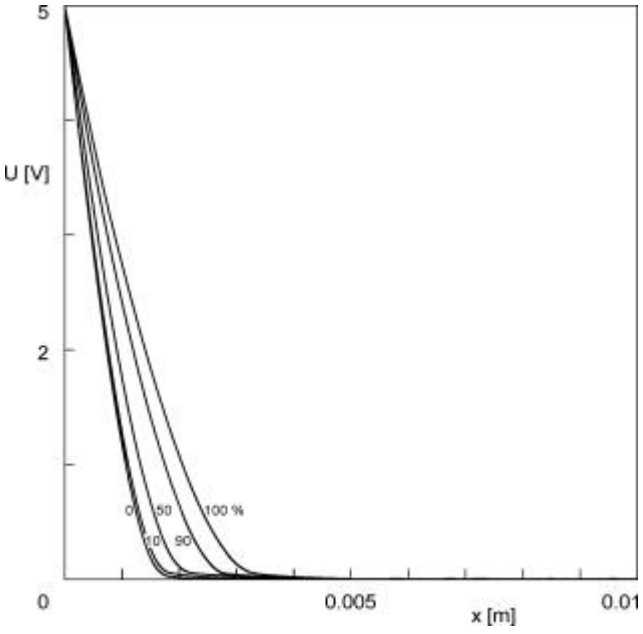

Fig. 5: Distribution of electric potential U(x) in the distance *x* from the substrate. Relative concentrations of negative species Γ^-/e: from 0 % (only electrons) to 100 % (only oxygen ions).

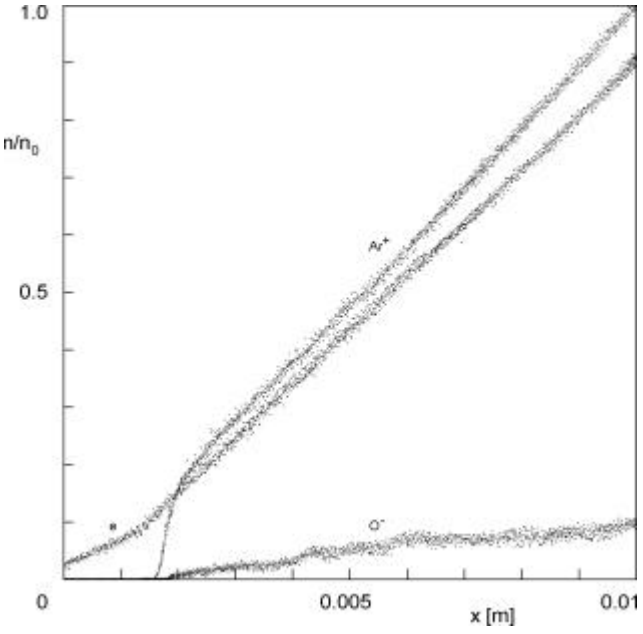

Fig. 6: Distributions of normalised concentrations of individual charged species *n(x)* in the distance *x* from the substrate. Relative concentration of negative particles Γ^-/e: 10 %.

Dynamic properties:

Further studied problem was the dynamics of processes in the sheath, i.e. the temporal evolution of the sheath region after the application of step voltage, both without and with the presence of negative ions in the mixture. Some preliminary results are shown in Fig. 7. When changing from negative to positive bias, as a response the positive ions are ejected from the vicinity of the substrate and the negative charge is attracted.

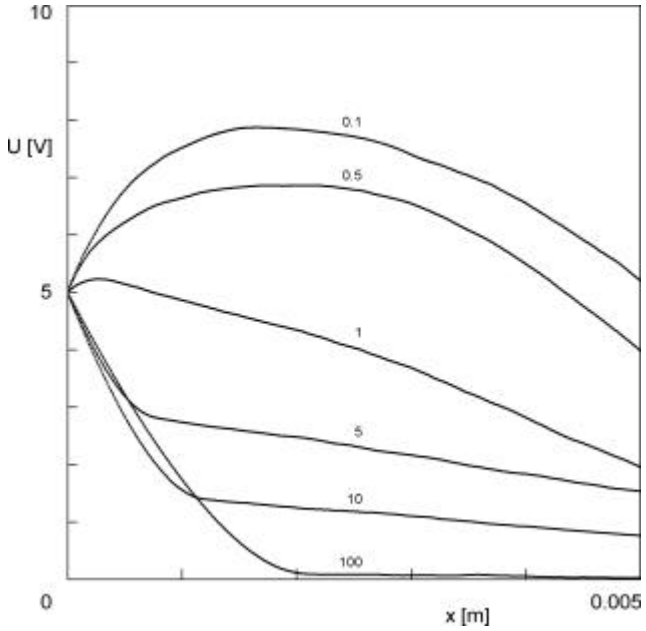

Fig. 7: Dynamics of the potential distribution near the substrate *U(x)* for positive bias. Parameter: time of simulation in microseconds – in limits 0.1 to 100 μs. Relative concentration of negative species 50 %. Total number of charged particles $2 \cdot 10^7$.

Dynamical simulations were performed for various composition of plasma. It was found that the sheath dynamics is extremely sensitive to the concentration of negative ions. For electropositive plasma the typical switching time was found to be in the order of nanoseconds, while in the case of electronegative plasma the process is slowed down – see the time scale in Fig. 7. It was observed that due to strong electrostatic interaction, even the electrons in electronegative plasma reach their stable positions in several tens of microseconds, the switching process being dependent on the relative concentration of negative ions.

Pressure dependence:

Most simulations were performed at 133 Pa. Beside them some results were obtained at higher or lower pressures. It was found that both the composition of the mixture and its total pressure influence the sheath region and the fluxes and distributions of particles striking the substrate. The computer experiment enabled us to discuss the importance of various physical mechanisms and processes influencing the plasma-solid interactions by means of the macroscopic characteristics of plasma.

6. Discussion

The main part of simulations was performed with the help of standard one-dimensional models in three geometrical modifications. However, due to the basic physical restrictions only the simulation of plasma-solid interactions with spherical geometry of substrate enables us to obtain quantitative results, for another two geometries only qualitative results can be derived and the relative changes of plasma parameters can be discussed.

For this purpose an attempt was made to extend the simulation of plasma-substrate interaction to more complex systems. Two new models with geometries both spatially two-dimensional (*2d2v* and *2d3v*) and fully three-dimensional both in space and velocities (*3d3v*) were prepared. These models differ from the previous one-dimensional models only in their geometries, other parameters of the models were standard ones: Maxwell distribution of charged particles in undisturbed plasma with superimposed drift, movement of charged particles influenced by self-consistent electric field created by these particles and by bias of metal substrate, limited set of interactions for electrons, positive ions and negative ions consisting of elastic scattering, inelastic scattering, charge transfer interactions and Coulomb interactions. The simulation was performed again for the O_2-Ar plasma with changing concentration of oxygen and changing total pressure of the mixture.

Besides the particle simulation methods another simulation technique is tested in our laboratory – the hybrid modelling combining the particle techniques with fluid modelling. We hope that this approach can help to create more efficient computer codes without significant loss of their preciseness.

During the modelling it was observed that the pressure of the gas mixture influences the sheath region in two opposite ways (see Fig. 8):

?? due to the increase of the pressure the mean free paths of all particles are reduced and their concentrations are increased, the change in mean free paths becoming more significant – approx. linear compared to slower dependence of charged particle concentrations observed experimentally and demonstrated in Figs. 1-3

?? the decrease of mean free paths enlarges the region of disturbed plasma (1), while the increase of particle concentrations reduces it (2).

However, in accordance with known experimental data it was found that the sheath thickness is decreasing with increasing pressure of the gas mixture in the discharge (3). From it follows that the sheath region is more sensitive to changes of particle concentrations than to other parameters.

In similar way the dependence of other characteristics of the sheath region on the parameters of simulation can be found. Although the basic results can be obtained with the help of 1D models, the more precise analysis can be performed on the basis of models in more dimensions only.

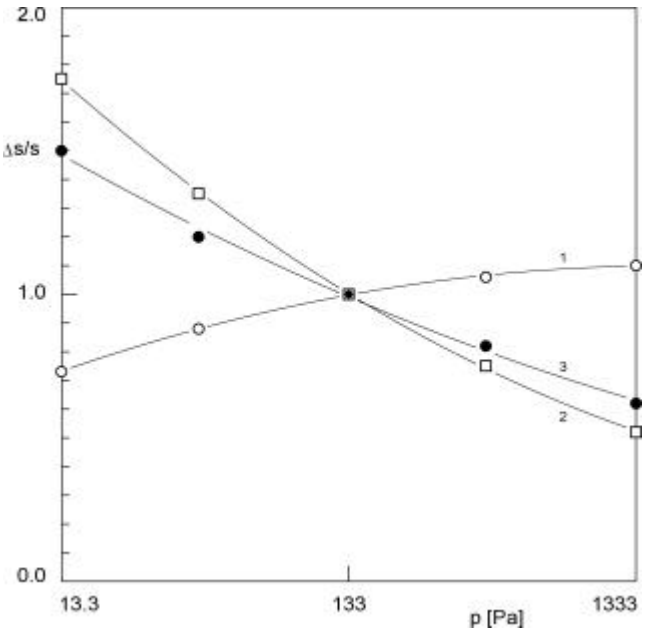

Fig. 8: Dependence of the relative sheath thickness *?s/s* on some plasma parameters – mean free paths (1) and concentrations of charged particles (2).

Acknowledgement

This work is a part of the research program MSM113200002 that is financed by the Ministry of Education of Czech Republic. The support of Charles University Prague, Grant No.GAUK-174/2003 is gratefully acknowledged. The author J. Š. acknowledge the support of the Czech Ministry of Education, Grant No. FR-2737/2003.

References

[1] E. Stoffels, W.W. Stoffels, D. Vender, M. Haverlag, G.M.W. Kroesen, F.J. De Hoog - Contrib. Plasma Phys. **35**, 331 (1995).
[2] T.H. Chung, L. Meng, H.J. Yoon, J.K. Lee - Jpn. J. Appl. Phys. **36**, 2874 (1997).
[3] I.G. Kouznetsov, A.J. Lichtenberg, M.A. Lieberman - J. Appl. Phys. **86**, 4142 (1999).
[4] S. Mukherjee - Physics of Plasmas **8**, 364 (2001).
[5] R.T.Farouki, S. Hamaguchi, M. Surendra, M. Dalvie - Phys. Rev. A **46**, 7815 (1992).
[6] R. Hrach - Czech. J. Phys. **49**, 155 (1999).
[7] P. Chabert, T.E. Sheridan - J. Phys. D: Appl. Phys. **33**, 1854 (2000).
[8] V. Hrachová - Proc. XVII ICPIG, Budapest 1985, 688.
[9] V. Hrachová, A. Langr - Proc. XVIII ICPIG, Swansea 1987, 776.
[10] V. Hrachová, A.-M. Diamy, O. Kylián, A. Kanka, J.-C. Legrand - Behaviour of Glow and Microwave Discharges of Oxygen, in *Advances in Plasma Physics Research*, Volume II, NOVA, Science Publishers Inc., Hunhington, NY, USA 2003.
[11] A. Kanka, V. Hrachová, O. Kylián - Proc. 15th Intern. Symp. on Plasma Chemistry "ISPC-15", Orléans 2001, France, Vol. IV, 1405.
[12] R. Hrach, V. Hrachová - Vacuum **60**, 229 (2001).
[13] R. Hrach, V. Hrachová, M. Vicher - Computer Physics Comm. **147**, 505 (2002).
[14] S.C. Brown - in *Basic Data of Plasma Physics: The Fundamental Data on Electrical Discharges in Gases*, AIP Press, New York 1994.

Etching and Post Etch Processing of Porous and Conventional SiO_2 in Fluorocarbon Based Chemistries

Arvind Sankaran[1] and Mark J. Kushner[2]

[1]*Dept. of Chemical and Biomolecular Engineering, University of Illinois, Urbana, IL 61801 USA, asankara@uiuc.edu*
[2]*Dept. of Electrical and Computer Engineering, University of Illinois, Urbana, IL 61801 USA, mjk@uiuc.edu*

Abstract: Porous SiO_2 (PS) is being investigated as a low dielectric constant material for the insulator in interconnect wiring due to its inherent low mass density. In this paper, the results from a computational investigation of the fluorocarbon plasma etching and post etch processing (polymer stripping and seed layer deposition) of PS and non-porous SiO_2 will be discussed. We found that mass normalized etch rates of PS depend on L/r_0 (the ratio of polymer thickness to pore size). Polymer removal is less efficient for materials having larger pores due to the shadowing of ion fluxes.

Introduction

As microelectronics device sizes continue to shrink, there is a propensity for increased delay in signal propagation in interconnect wiring due to higher resistances in the lines and larger capacitance between the lines.[1] In this regard, low dielectric constant (low-k) materials are being investigated as the insulator in interconnect wiring. Low-k dielectrics can be broadly classified as organic and inorganic.[2] Organic materials such as polytetrafluoroethylene (PTFE) and parylene are etched in oxygen based high plasma density systems (O_2/Ar and O_2/N_2).[3,4] Inorganic dielectrics typically use SiO_2 based materials which are etched in fluorocarbon plasmas. Porous SiO_2 (PS) is one such inorganic low-k material. PS typically has pore sizes of 2-20 nm and porosities of 20-70%.[5] The dielectric constant is reduced in proportion to the mass density, which in turn is proportional to the porosity.[1,5] The residual polymer layer which remains after etching in fluorocarbon plasmas results in high contact resistance and defects at the metal-silicon interface and so needs to be removed.[6] Oxygen containing plasmas are extensively used for such post-etch cleaning and for photoresist stripping.[7,8]

In this work the etching of PS will be discussed using results from a two-phase algorithm incorporated into the Monte Carlo Feature Profile Model (MCFPM).[9,10] The MCFPM was integrated with the reactor scale Hybrid Plasma Equipment Model (HPEM), which provides the energy and angular distributions of the neutral and charged species incident on the wafer.[11] A surface reaction mechanism was developed for fluorocarbon etching of SiO_2 and was applied to the investigation of etching of PS in fluorocarbon plasmas. Dielectric etching is the first step of process integration, which includes polymer and resist removal, and metal deposition. In this regard, surface reaction mechanisms for etching of organic polymers in oxygen plasmas were developed and applied to the stripping of the residual fluorocarbon polymer. Copper ionized metal physical vapor deposition (IMPVD) was then investigated as a surrogate to deposition of a barrier coating or seed layer.

Reaction Mechanism

A schematic of the reaction mechanism for etching of SiO_2 in fluorocarbon plasmas is shown in Fig. 1. Etching of SiO_2 proceeds through the formation of an overlying fluorocarbon polymer layer [nominally $(C_2F_4)_n$)] on the SiO_2.[12] C_xF_y radicals are the precursors to polymer formation following low energy ion activation of surface sites.[13] Upon delivery of activation energy to the polymer-SiO_2 interface the SiO_2 reacts with the fluorocarbon species in the polymer to release etch products such as COF_x. In

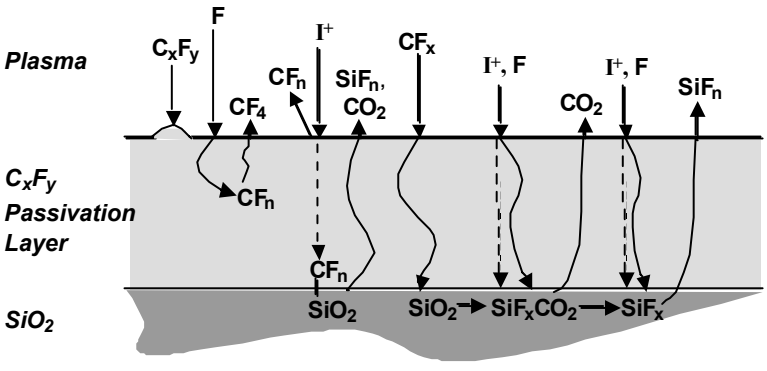

Figure 1 – Schematic of the surface mechanism for etching of Si and SiO_2 in a fluorocarbon plasmas.

this process, the polymer is consumed.[14] The polymer layer is also consumed by energetic ion sputtering and F atom etching.[15] The polymer layer is the main inhibitor for the transport of species and activation energy to the SiO_2 interface. As such the etch rate generally scales inversely with the polymer thickness.[16] A very thin polymer layer also produces low etch rates due to the lack of reactants in the overlying layer. Si is less reactive with the polymer, being unable to consume the carbon, and so produces thicker films and lower etch rates.

The removal of organic materials using oxygen plasmas has widespread applications in semiconductor processing.[3,17,18] The primary etching specie in oxygen plasmas is the O radical. Molecular oxygen has little effect on the etch characteristics at low temperatures.[8] The primary etch products are CO_2, CO, COF_x in the case of fluorocarbons and CO_2 and H_2O in the case of hydrocarbons. [7] Little etching of fluorocarbon polymers occurs in the absence of ion bombardment even with plentiful oxygen radicals.[3] This suggests an ion-activated pathway for the etching of these materials.[8,19] For example, the etching of photoresist by an oxygen ion beam is limited by the availability of oxygen radicals at low pressures and by ions at higher pressures.[17] Generally etch rates increase with increasing oxygen mole fraction in mixtures and substrate bias. Joubert *et al* suggested a reaction pathway whereby oxygen radicals first adsorb on the polymer interface. The etch reaction on the surface is then initiated by the impact of energetic ions.[7] The etch mechanism was modeled here as a multi-step ion-assisted process. When the polymer is passivated by oxygen radicals, ion activation produces volatile etch products,

$$P(s) + O(g) \rightarrow P^*(s) \quad (1)$$
$$P^*(s) + I(g) \rightarrow COF_x(g), \quad (2)$$

where P is the polymer, P* is the activated polymer complex, I is the ion, O is the etchant and COF_x is the volatile gas product.

Calibration and validation of the fluorocarbon surface reaction mechanism was performed for three fluorocarbon chemistries; C_2F_6, C_4F_8 and CHF_3. The logic is that the reaction mechanism is an intrinsic property of incident gas phase reactant species and surface resident species, and so should not depend on the source of gas phase fluxes. The choice of the fluorocarbon plasma (e.g., CHF_3 vs. C_4F_8) may determine the magnitude and energies of individual species fluxes but the reaction mechanism should be the same. The reaction mechanism was validated by comparison to experiments by Oehrlein *et al* using an inductively coupled plasma, with an rf substrate bias.[5] Validation for the oxygen reaction mechanism was performed varying compositions Ar/O_2 gas chemistries. The reaction mechanism was validated by comparison to experiments by Standaert *et al* using an inductively coupled plasma, with an rf substrate bias and is discussed elsewhere.[3]

PS is modeled as stoichiometric SiO_2 having vacuum pores, characterized by an average pore radius and porosity. The pore locations were randomly distributed in the numerical mesh used by the MCFPM with a Gaussian distribution of radii having probability $p(r) \sim \exp(-((r-r_0) / \Delta r)^2)$, where r is the radius of the pore in, r_0 is the average pore radius and Δr is the standard deviation. Algorithms were developed to distribute the pores so that the network of pores was independent until the desired porosity was achieved. We acknowledge that many PS films incorporate some organic groups and may have interconnecting pores. We intend to address these issues in future work. For brevity only CHF_3 plasma etching will be further discussed here.

Etch, Clean and Fill of Solid and Porous SiO_2

Process conditions for the ICP reactor used for the cases discussed here are 10 mTorr CHF_3 at 50 sccm flow rate, and 1400 W ICP power at 13.56 MHz with a substrate bias at 3.4 MHz, producing a self-bias from 0-150 V. Fluxes to the center of the wafer obtained from the HPEM were used as input to the MCFPM. The ions included in the mechanism are CF_3^+, CF_2^+, F^+, F_2^+, $C_2F_4^+$, $C_2F_5^+$ and CHF_2^+, H^+ and H_2^+. The polymerizing radicals are CF_2, CF, C_2F_3 and C_2F_4. Typical reactor properties (power deposition, and density of CHF_3 and CF radicals) as obtained from the HPEM are shown in Fig. 2. Power deposition is restricted to the top of the reactor to within the skin depth of the electromagnetic field, a few cm. The large electron density (10^{11} cm^{-3}) highly dissociates the CHF_3 feedstock, which is injected through an annular nozzle and is pumped at the bottom of the reactor. As a result of the high degree of dissociation, the major fluorocarbon radicals are CF and CF_2.

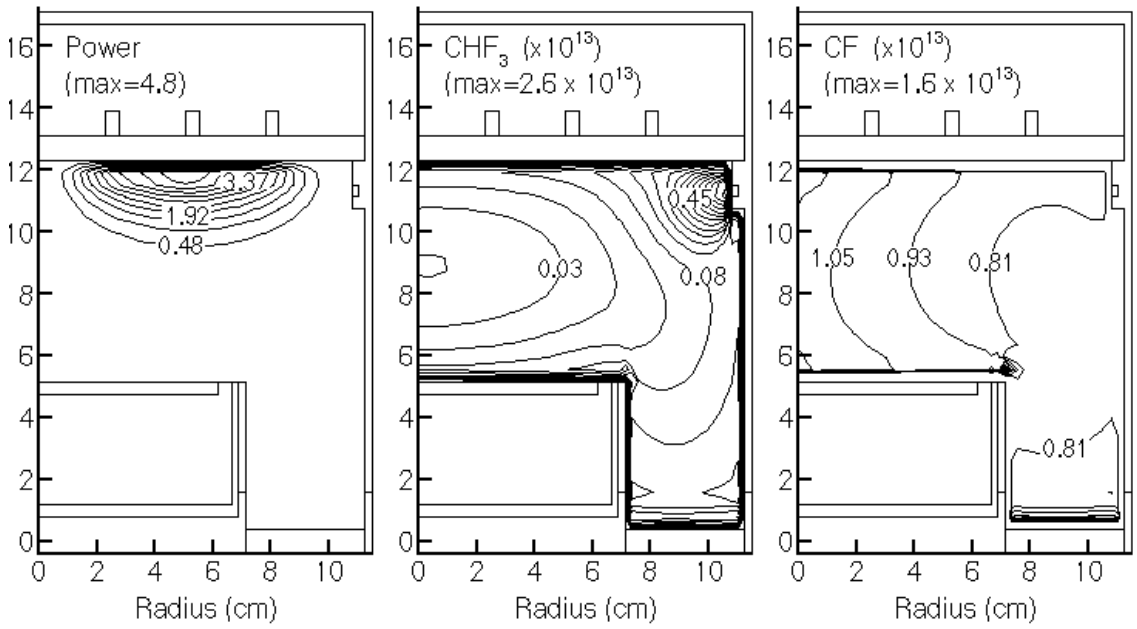

Figure 2 – Power deposition (W/cm^3); and density (cm^{-3}) of CHF_3 and CF radicals for base case operating conditions. (10 mTorr CHF_3, 10 mTorr, 50 sccm, 1400 W).

Etch rates as a function of self-bias for PS and solid SiO_2 are compared to experiments in Fig. 3. Three materials are examined: solid SiO_2; PS having 2 nm pores and 30% porosity; and PS having 10 nm pores and 58% porosity. The solid SiO_2 etch rates were used to validate the reaction mechanism. The etch rates generally increase with increasing self-bias voltage as the incident ion energy increases. The onset of etching at around 40 eV for both solid SiO_2 and PS occurs as the polymer thins and energy is delivered more efficiently through the polymer to the SiO_2 interface. At low biases and low ion energy the polymer thickness is large as there is insufficient ion energy to sputter the polymer and low energy ion activated polymer deposition is rapid. The polymer thickness is large and etching is negligible. At large biases the polymer thickness is sub-monolayer and there is insufficient passivation to etch the SiO_2 layer and hence the increase in etch rate flattens out. The etch rates for the PS are typically higher than that of conventional SiO_2 due to the inherent lower mass densities of the porous materials. The threshold bias is similar for both solid and porous materials, an indication that the fundamental reaction chemistries are the same.

To. isolate the effect of pores on etch rates, a corrected etch rate is defined as C = ER(1-p), where p is the porosity of the substrate and ER is the gross etch rate. C is, effectively, the etch rate per unit mass. If pores had no kinetic effect on etching, the C of PS should be the same as the ER of solid SiO_2. Corrected etch rates as a function of self-bias are shown in Fig. 3(c). For a pore radius of 2 nm and porosity of 30%, the C of PS is greater than the ER of solid SiO_2, which implies that the presence of pores enhances the etch rate. In contrast, for 10 nm pores and 58% porosity, C of PS is less than the ER of solid SiO_2, which implies that the

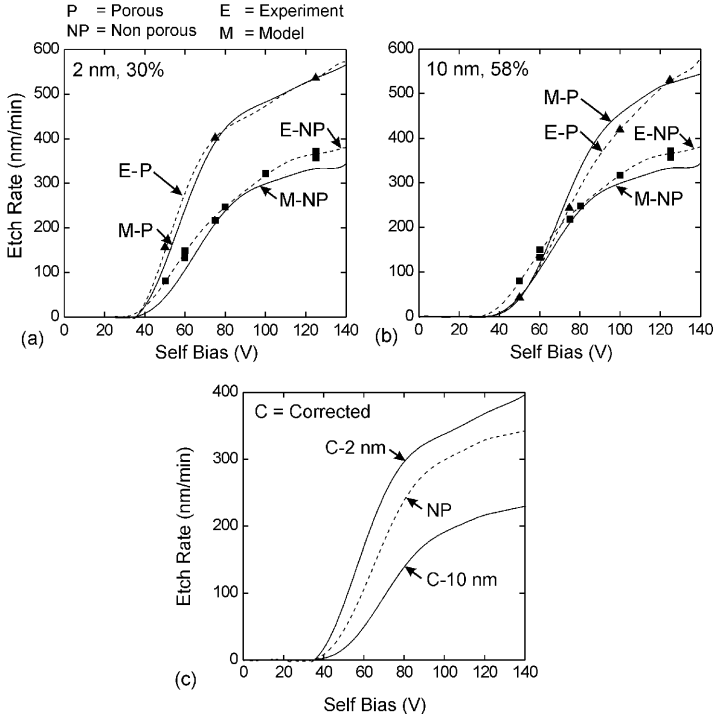

Figure 3 – Etch rates as a function of self-bias voltage for 2 nm and 10 nm porous SiO_2 compared to the solid material. C denotes the mass corrected etch rate.

presence of pores decreases the mass removal rate. Similar dependencies were obtained in the experiments.[5]

In highly polymerizing environments, such as fluorocarbon plasmas of this type, the steady state polymer thickness, L, can be many nm. As the PS is etched, pores are exposed and are filled with polymer. If $(L/r_0) > 1$, as in the 2 nm case, then the increase in local polymer thickness due to pore filling is fractionally small. The end result is that C is not significantly different from the ER of solid SiO_2. The increase of C above ER is likely due to the angle of incidence for chemically enhanced sputtering, on the average, being closer to the optimum at $\approx 60^{\circ}$ due to the non-planar surfaces of the exposed pores. If $(L/r_0) < 1$, as is the case for the 10 nm pores, pore filling produces significantly thicker polymer at local sites. This effect is more pronounced for larger pores and larger porosities. The increased polymer layer thickness decreases delivery of activation energy to the SiO_2 interface and hence reduces the etch rates. The larger pores also have SiO_2 – polymer interfaces at shallow angles to the ion-flux or which do not have line-of-sight to the incident ions. These locations therefore rely on reflected species for activation, which typically have lower energies. The end result is a reduced etch rate per unit mass and C is less than the ER of solid SiO_2.

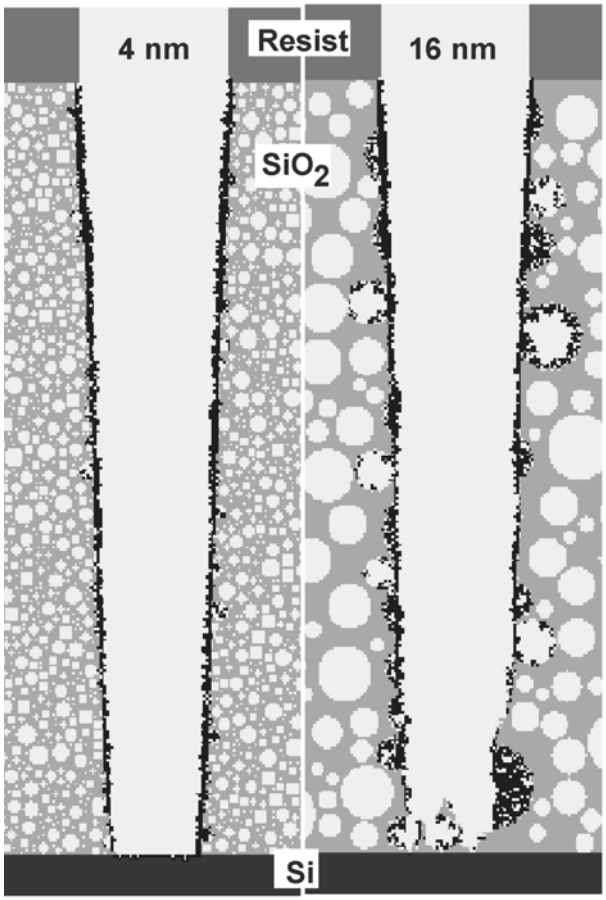

Figure 4 – High Aspect Ratio features (0.1 μm width) etched through 4 nm and 16 nm PS to a Si layer below. The dark material on the SiO_2 is polymer. The larger pores fill with polymer as they are exposed.

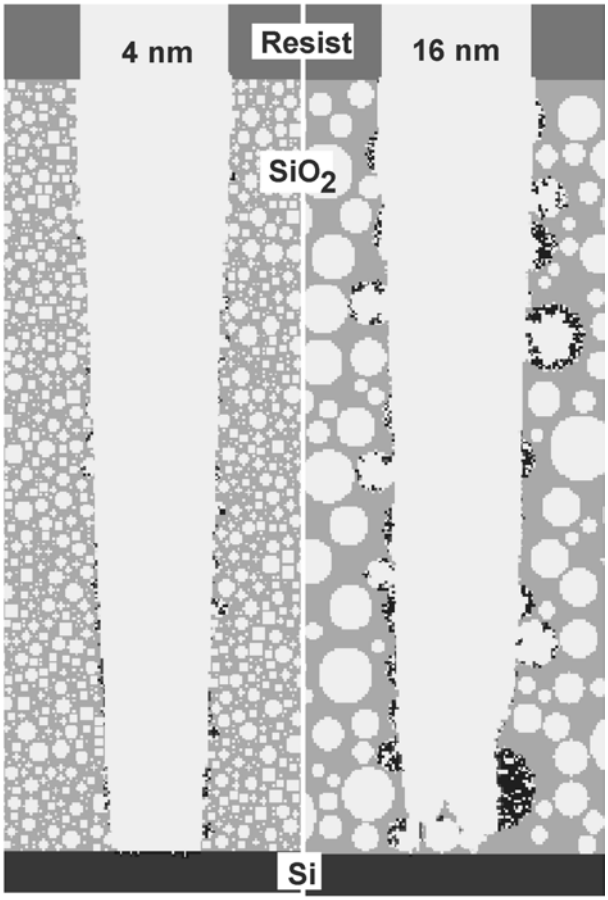

Figure 5 – High Aspect Ratio features (0.1 μm width) in 4 nm and 16 nm PS following stripping of post-etch polymer using an Ar/O_2 plasma. The dark material on the SiO_2 is polymer. The larger pores are more difficult to clean due to unfavorable view angles to the ion flux.

These trends are shown in Fig. 4 where high aspect ratio trenches (0.1 μm width) of SiO_2 having a hard-mask and Si underlayer are shown for 4 nm and 16 nm PS having 50% porosity. The large pores exposed at the surface by the etch fill with polymer, producing, on the average, a thicker overall polymer layer. These scalings depend both on the pore size and the porosity and are discussed elsewhere.[20] Note that a few marginally opened pores are lined with polymer, providing additional challenges to later removal of the polymer.

Stripping of the fluorocarbon polymer was investigated for Ar/O_2 plasmas in an ICP reactor having a substrate bias. Process conditions for the case discussed here are 4 mTorr, Ar/O_2=99/1 at 40 sccm, and 600 W ICP power at 13.56 MHz with a 20 W substrate bias at 3.4 MHz. The stripping was performed long enough for the cleaning process to reach asymptotic limits. The profiles from Fig. 4 after cleaning are shown in Fig. 5. The stripping was more efficient with the smaller pores, whereas significant polymer remained with the larger pores where ≈24% of the residual polymer remained. The cleaning was ineffective with the larger pores at the bottom of the trench due to the lack of view angles for the incident ions. This results in poor activation of the polymer preventing subsequent removal of the polymer. On the other hand, the formation of polymer at these sites during fluorocarbon etching results from low ion energy activation and is more dependent on the neutral fluxes. The neutral flux being more isotropic in nature is less sensitive to the pore morphology. The complex pore morphologies are easily filled with polymer but the cleaning of PS using traditional dry etching techniques is less efficient.

To complete the interconnect wiring, following cleaning, vias are lined with a barrier coating, deposited with a seed layer and finally, in the case of copper, filled by electrodeposition. Copper IMPVD onto the cleaned vias was modeled as a surrogate to deposition of a barrier coating. Surface reaction mechanisms developed by Lu *et al* were adapted to address filling of PS materials.[21] Process conditions for the case discussed here are 1.0 kW ICP power, 0.3 kW magnetron power, 40 mTorr Ar buffer gas and 150 sccm flow rate.[21] The coated vias for solid SiO_2 and PS with 16 nm average pore radius are shown in Fig 6 for equal deposition times. The process conditions were maintained such that a void-less uniform coating is obtained for the solid SiO_2. In the case of PS, there was no conformal coverage leading to the creation of gaps and voids in the barrier coating. This effect was more pronounced for PS with larger pores. Non-uniform coverage, similar to inefficient stripping, was due to the unfavorable view angles of the incident reactant fluxes caused by the complex pore morphologies.

Figure 6 – High Aspect Ratio features (solid SiO_2 and 16 nm PS) lined with copper following IMPVD. The dark material on SiO_2 is copper. Presence of pores creates or initiates voids. This effect is pronounced for larger pores.

Concluding Remarks

Etching mechanisms for solid and porous SiO_2 were discussed based on results from a computational investigation using reactor and feature scale models. Predictions for etch rates as a function of self-bias were validated by comparison to experiments for porous and solid SiO_2. The functional dependence of etch rate on porosity in large part depends on the ratio of L/r_0, polymer thickness/pore radius. Kinetically inhibited etch rates result when this ratio is small as pore filling increases the average polymer thickness. The limiting value of L/r_0 is a function of both porosity and average pore radius. Stripping of residual fluorocarbon polymer for solid SiO_2 and PS was studied in Ar/O_2 plasmas. Unfavorable view angles for incident ions in complex porous structures lead to inefficient cleaning. Copper IMPVD inside vias was investigated following cleaning as a surrogate for deposition of barrier coatings or seed layers. The presence of pores created or initiated gaps or voids in the barrier coating.

Acknowledgements: This work was supported by the Semiconductor Research Corp., National Science Foundation (CTS99-74962) and SEMATECH.

References

[1] T. E. F. M. Standaert, P. J. Matsuo, S. D. Allen, G. S. Oehrlein, and T. J. Dalton, J. Vac. Sci. Technol. A **17,** 741 (1999).

[2] G. S. Oehrlein, T. E. F. M. Standaert, and P. J. Matsuo, in *Solid State Technology*; *Vol. May 2000* (2000), p. 125.

[3] T. E. F. M. Standaert, P. J. Matsuo, X. Li, G. S. Oehrlein, T. M. Lu, R. Gutmann, C. T. Rosenmayer, J. W. Bartz, J. G. Langan, and W. R. Entley, J. Vac. Sci. Technol. A **19,** 435 (2001).

[4] D. Fuard, O. Joubert, L. Vallier, and M. Bonvalot, J. Vac. Sci. Technol. B **19,** 447 (2001).

[5] T. E. F. M. Standaert, E. A. Joseph, G. S. Oehrlein, A. Jain, W. N. Gill, P. C. J. Wayner, and J. L. Plawsky, J. Vac. Sci. Technol. A **18,** 2742 (2000).

[6] S. J. Fonash, J. Electrochem. Soc. **137,** 3885 (1990).

[7] O. Joubert, J. Pelletier, and Y. Arnal, J. Appl. Phys. **65,** 5096 (1989).

[8] C. Steinbruchel, B. J. Curtis, H. W. Lehmann, and R. Widmer, Trans. Plasma Sci. **14,** 137 (1986).

[9] R. J. Hoekstra and M. J. Kushner, J. Vac. Sci. Technol. B **16,** 2102 (1998).

[10] R. J. Hoekstra, M. J. Grapperhaus, and M. J. Kushner, J. Vac. Sci. Technol. A **15,** 1913 (1997).

[11] R. L. Kinder and M. J. Kushner, J. Appl. Phys. **90,** 3699 (2001).

[12] M. Schaephens, R. C. M. Bosch, T. E. F. M. Standaert, G. S. Dehrlein, and J. M. Cook, J. Vac. Sci. Technol. A **16,** 2099 (1998).

[13] T. E. F. M. Standaert, M. Schaepkens, N. R. Rueger, P. G. M. Sebel, G. S. Oehrlein, and J. M. Cook, J. Vac. Sci. Technol. A **16,** 239 (1998).

[14] M. Matsui, T. Tatsumi, and M. Sekine, J. Vac. Sci. Technol. A **19,** 2089 (2001).

[15] K. Miyata, M. Hori, and T. Goto, J. Vac. Sci. Technol. A **14,** 2083 (1996).

[16] N. R. Rueger, J. J. Beulens, M. Schaepkens, M. F. Doemling, J. M. Mirza, T. E. F. M. Standaert, and G. S. Oehrlein, J. Vac. Sci. Technol. A **15,** 1881 (1997).

[17] F. Greer, L. Van, D. Fraser, J. W. Coburn, and D. B. Graves, J. Vac. Sci. Technol. B **20,** 1901 (2002).

[18] D. Shamiryan, M. R. Baklanov, S. Vanhaelemeersch, and K. Maex, J. Vac. Sci. Technol. B **20,** 1923 (2002).

[19] J. A. G. Baggerman, R. J. Visser, and E. J. H. Collart, J. Appl. Phys. **75,** 758 (1994).

[20] A. Sankaran and M. J. Kushner, Appl. Phys. Lett. **82,** 1824 (2003).

[21] J. Lu and M. J. Kushner, J. Vac. Sci. Technol. A **19,** 2652 (2001).

Cathode Erosion in a Plasma Cutting System

John Peters[1], Joachim Heberlein[1] and Charles Hackett[2]

1. Department of Mechanical Engineering, University of Minnesota, Minneapolis, MN
2. Centricut LLC, West Lebanon, NH

Abstract:

Cathode erosion in a plasma arc cutting system using oxygen as the plasma gas was investigated. Ejection of molten cathode material was the major erosion source. Proposed erosion mechanisms are high ion flux during ignition and aerodynamic drag forces during arc shutdown. Copper and silver were both used as cathode sleeve materials and had very similar erosion characteristics, however, silver sleeved cathodes had a much longer lifetime. The long lifetime appears to be due to different cathode failure mechanisms.

Introduction:

Cathode lifetime in plasma arc cutting, especially oxygen cutting, is limited because of erosion of the cathode material [1,2]. This limited lifetime increases cutting costs due to part replacement, maintenance, and potential damage to the processed material. Experiments were conducted in an attempt to identify major erosion sources as well as their causes. Several parameters of the cutting system were varied and effects on the erosion were determined qualitatively with high-speed video imaging and quantitatively by collecting eroded material. Once the cathode erosion sources and their physical causes have been identified, steps can be made to reduce the erosion rate and extend the overall lifetime of the cathode.

Experimental setup:

The cutting system used for this investigation is a Hypertherm HT2000 system. Major components of this system are a 200 amp power supply, a high frequency arc starter, a gas flow control console, and the torch. The cutting torch cathode consists of a 1.8-mm diameter hafnium cylinder set in a water-cooled copper sleeve. Plasma gas is introduced into the torch through a ceramic swirl ring at the base of the electrode. A copper nozzle directs the gas flow and shield gas cap completes the cutting torch. These standard cutting components are run with a rotating anode that is water-cooled to allow operation without the cost or byproducts from cutting material. Measurement of the arc voltage and current during operation is recorded. This setup is very similar to that used by Yin [1]. All of the major components and the electrical diagnostics are shown in Figure 1.

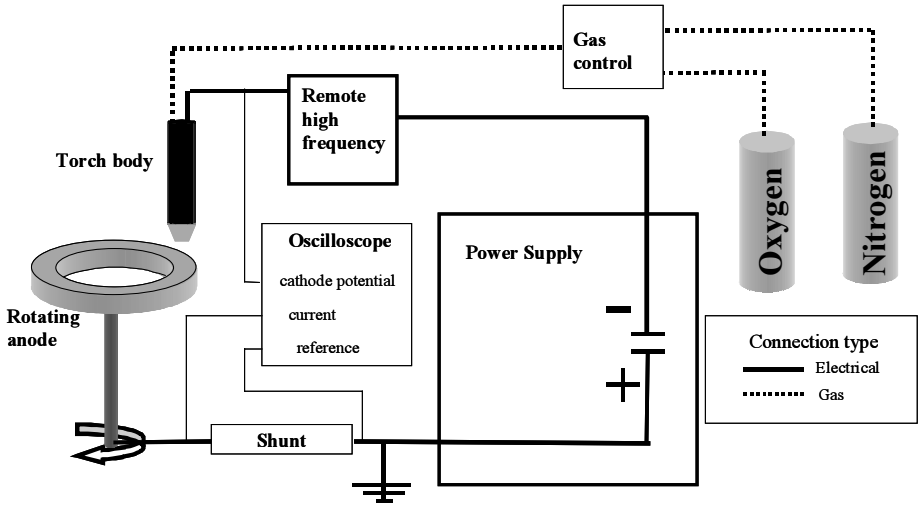

Figure 1. General experimental setup.

Modifications were made to the standard nozzle design to aid in the study of the cathode during arc operation. The first modification allows optical access to the cathode. In this modification scheme the shield gas cap is removed and 2 small holes are drilled into the nozzle. Sapphire windows are then cemented into the nozzle holes. These windows are placed nearly flush to the nozzle wall to minimize the effect on the gas flow through the nozzle. The windows have a diameter of 2.5 mm and are angled at 45 degrees to show the entire cathode surface [1]. A standard nozzle is shown next to this nozzle modification in Figure 2.

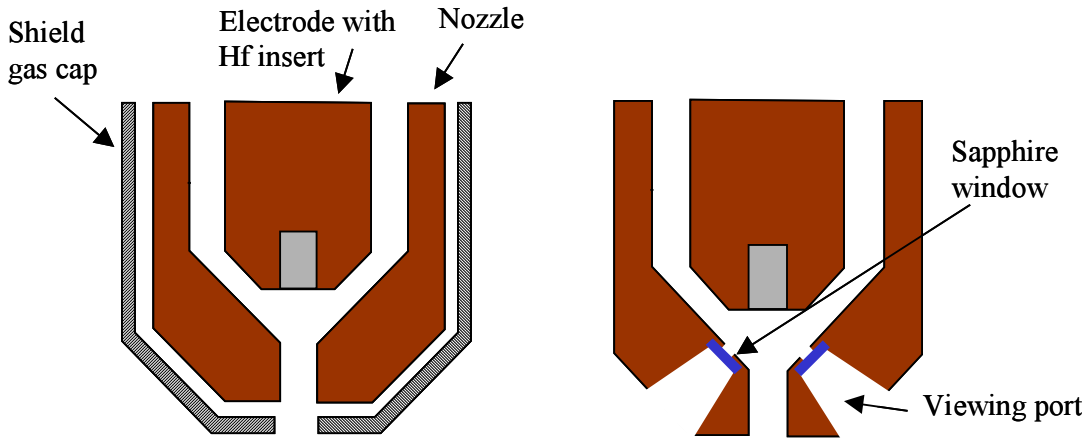

Figure 2. Nozzle modification for optical access to cathode.

Using this imaging system, pictures of the cathode during operation were obtained using a high framing rate system as well as a short exposure time system. A typical image of the cathode is shown in Figure 3. The round hafnium insert appears as an ellipse under the viewing angle. In the figure the hafnium surface is the bright ellipse, the extinguishing arc is visible and the round viewing window is highlighted.

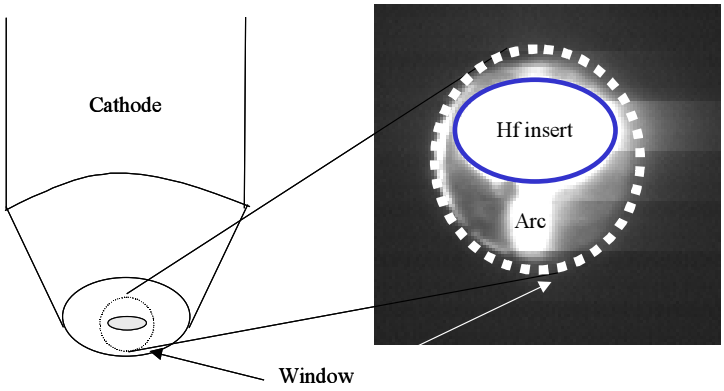

Figure 3. Typical cathode image during operation.

The qualitative erosion information from the cathode images was quantified using another nozzle modification to allow collection of eroded material. This modification has one window in the side of the nozzle. This window leads to a collection surface. Material eroded from the cathode should deposit on the collection surface if the ejected droplet has a radial velocity and hits the window. The collection surface is a segmented stainless steel tube that is moved during torch operation to allow time-resolved measurements of the erosion. The nozzle modification for mass collection and the collection surface are shown in Figure 4.

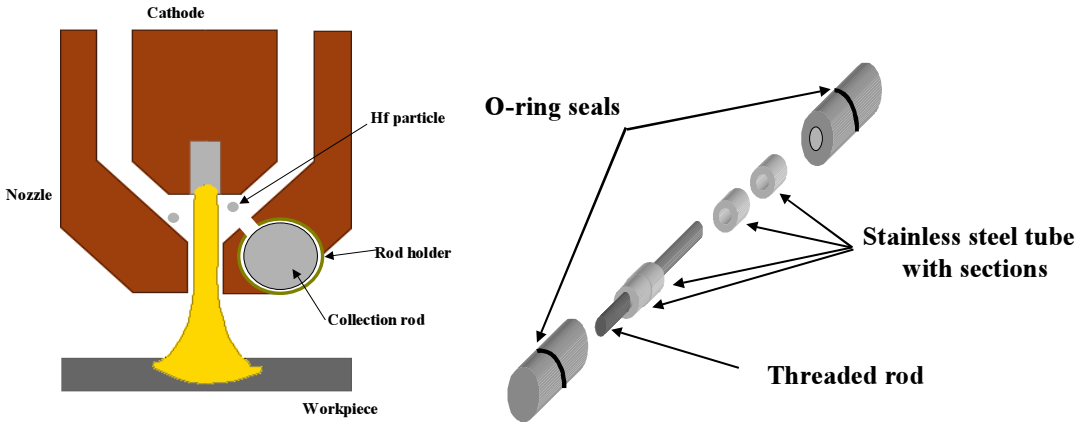

Figure 4. Mass collection system

This setup requires many starts of the torch to obtain a measurable amount of eroded material on the collection surface. We used 4 sections on the collection surface so we could look at 4 discrete time intervals. Once the deposit was collected for 400 torch starts, the mass of each section was determined with the deposit, then the deposit was removed and the mass of the cleaned collection section was measured. The difference was the mass of eroded cathode material.

The total cathode pit depth and the total mass lost from the cathode were also recorded as a means of measuring the erosion rate. Pit depth is the distance the hafnium insert has receded into the copper. It is measured as the distance from the lowest point on the hafnium surface to the top surface of the copper. Pit depth is similar to the cavity depth used by Nemchinsky [2].

The cathode imaging system was used to investigate the sources of the cathode erosion during arc operation. This system was used to study the effect of transients in the cutting cycle, such as arc start, arc shutdown and gas flow changes, on erosion. For the imaging experiments the arc was started, run for 2.5 seconds then shut down. This time was long enough for the voltage, current and nozzle pressure to reach steady values. Parameters that were investigated using this experimental technique were the current ramp-down during arc shutdown and the pre-flow gas type and flow rate. There were 2 available shutdown methods. The normal shutdown procedure for the cutting system has a current ramp down over a few hundred ms before the arc is completely extinguished. The other shutdown method is a fast current stop where the current decay occurs over the course of a ms. Standard torch operation begins with a pre-flow gas mixture of nitrogen and oxygen. The pre-flow mix is then switched to pure oxygen after 0.65 seconds. The pure oxygen is the cut flow gas. Mixtures of the pre-flow gas have been varied from pure oxygen to pure nitrogen; the total flow rate of the gases was also changed.

For the mass collection experiments, effects of specific operating parameters were considered and were based in part on observations of the cathode with the imaging system. The pre-flow gas configurations tested were the standard N2 and O2 mix and a low flow rate of O2 that showed the minimal number of ejections during the second and third time intervals. Normal and fast current shutdowns were compared using this characterization method and different cathode sleeve materials were investigated because of field observations that silver sleeved cathodes have extended life characteristics when compared to copper cathode sleeves.

Results:

A sequence of images from the high-framing rate camera is shown in Figure 5. These images have been taken immediately after the arc was extinguished using the fast current shutdown with a camera frame rate of 9000 frames per second. The frame when the arc is first completely extinguished was labeled as time zero. The first frame in the sequence shows the arc as it is extinguishing. As the pool cools, the bright spot representing the molten hafnium shrinks. There are three distinct droplet ejection events from the molten pool at 2.3 ms, 5.8 ms and 7.5 ms after arc extinction. This image sequence shows a typical erosion event. The erosion event shows distinct bright flares caused by the ejected molten particle.

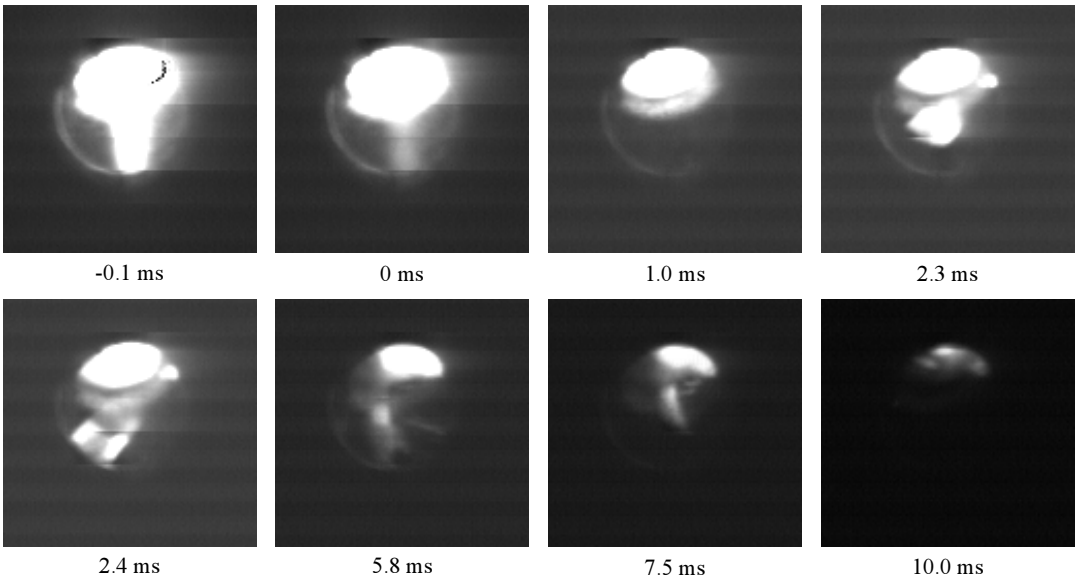

Figure 5. Cathode erosion after arc shutdown using 9000 fps.
Eroded droplets appear at times 2.3, 2.4, 5.8 and 7.5 ms.

These ejection events occurred at specific times during arc operation. For any arcing sequence, four specific ejection events have been identified. The first ejection occurs during the arc ignition within the first 0.2 seconds of operation. This ejection occurs when the arc root is very small and the current is being increased and the cathode just begins to melt. The second ejection occurs about 0.35 seconds after the arc is ignited. At this time the molten pool under the arc root is nearing the end of its expansion. The third ejection occurs at 0.65 seconds after the arc start and corresponds to the change in gas flow from the pre-flow to the cut-flow. The final ejection event occurs during the arc shutdown immediately after the arc has been extinguished. There were no observed ejections during the steady operation of the torch [1].

A significant difference was observed in the size and number of droplets that were ejected depending on the current shutdown method. The fast current shutdown produced many large particles while the normal shutdown was very clean. There was also an effect of the gas flow on the second and third ejections. As the pre-flow composition approached pure nitrogen the second ejection was no longer observed and the third ejection increased. When the composition was pure oxygen, the second ejection increased and the third ejection decreased. A pre-flow of pure oxygen at a flow rate of less than 19 slm led to the fewest number of particle ejections. There was no observed effect on the start up erosion events from the pre-flow gas that was chosen.

Mass collection experiments were performed based on the observed droplet ejection times from the imaging results. The collection surface was divided into four sections. The corresponding time intervals were 0.0 to 0.2 seconds which included the ignition ejection, 0.2 to 0.6 seconds which included the second observed ejection event, 0.6 to 1.0 seconds which would include the ejection during the gas flow change and 1.0 to 2.5 seconds which captured the steady state operation and arc extinction ejections. The results are shown in Figure 6 and are labeled according to pre-flow gas – shutdown type – sleeve material. The fast current shutdown is the dominant erosion source. If the controlled shutdown is used the arc ignition becomes the most important source.

Another interesting observation is shown in Figure 6. The collected particle sizes from the start and the stop erosion events are quite different. The particles collected during shutdown are much larger while the particles eroded during the arc start are more numerous and smaller.

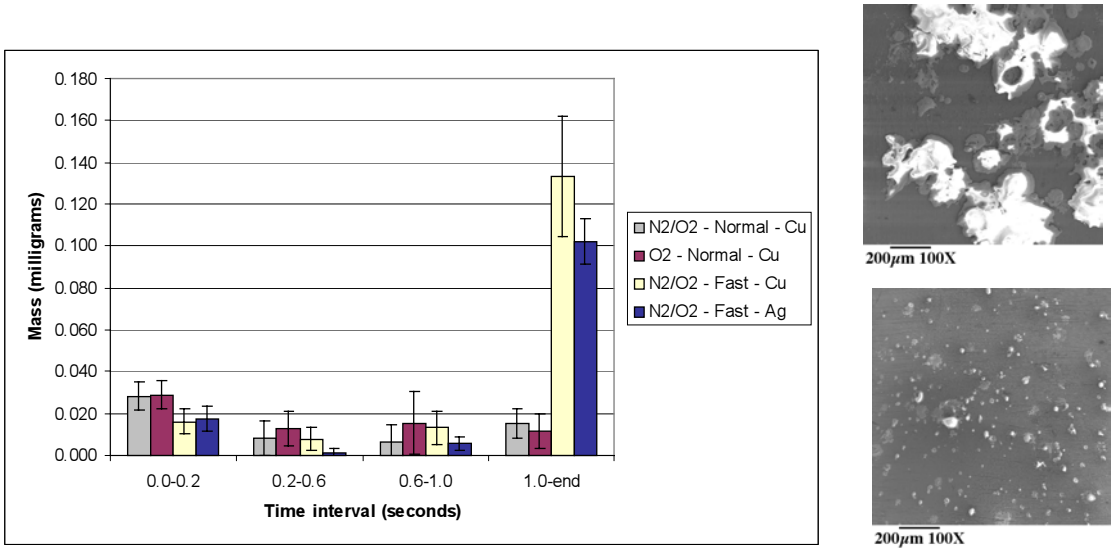

Figure 6. Mass collection results. Graph of cathode erosion using mass collection system (left). Legend shows pre-flow gas type – shutdown type – cathode sleeve material. Pictures of the large particles collected during arc shutdown (top – right) and the small particles collected during arc start (bottom - right)

For the silver and copper sleeved cathodes with fast current shutdown the pit depth erosion rate was very similar up to about 500 starts. At this point the copper sleeved cathode experienced rapid copper erosion that destroyed the cathode and the nozzle, erosion measurements were stopped at this point. Silver sleeved cathodes did not experience this rapid destructive erosion and the pit depth increased steadily for many more starts. In fact the rapid erosion of silver was never observed with this experimental method. The erosion rate determined from the pit depth is shown in Figure 7.

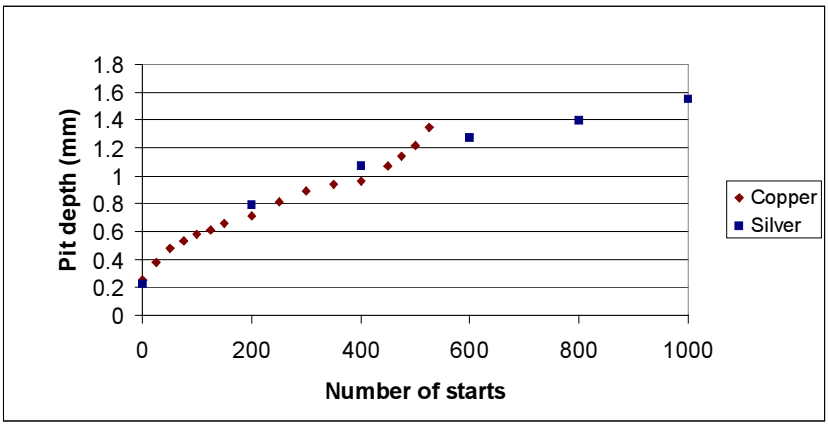

Figure 7. Silver and copper sleeved cathode erosion comparison

Discussion:

Ejection of droplets from the molten cathode surface is a major component of the total cathode erosion. From the visual observations there appear to be four important times during arc operation at which these ejections are occurring. Quantitative measurements show that the dominant erosion periods are the arc start and fast current shutdown. There were no measured effects of the pre-flow gas on the middle two ejection events as was observed with the imaging system. It may be that the total size of the ejection event is too small to be detected or the ejected particle trajectory may not lead to deposition on the nozzle wall.

The varied size and trajectory of the ejected droplets, as well as the arc conditions present during the various ejection times, point to different mechanisms causing the different ejection events. Yin proposed hypothesis for the two major sources of erosion [1,3]. During fast current shutdown the erosion is a result of aerodynamic forces and during the arc ignition the erosion is a result of high ion backpressure.

During the arc shutdown the primary difference between the normal and fast current ramp-down is the pressure in the nozzle. Aerodynamic drag forces from residual gas flow in the nozzle after current shutdown cause motion of the molten pool and droplet ejection from the cathode pool surface. When a controlled current ramp-down is used, the gas flow is reduced simultaneously with the current, as indicated by a comparison of the pressure decay in the nozzle with the current decay. The molten pool is not affected by the gas flow when the arc is present due to the arc's high viscosity and low density.

The second most important erosion interval is the arc start. A static force balance applied to the region of the cathode arc attachment has been used to formulate a hypothesis for this ejection [3]. Major forces acting on the molten cathode pool are the surface tension, ion flux pressure and electromagnetic force. Surface tension acts on the edges of the molten cathode material to keep the material together. The ion flux pressure acts on the surface of the molten pool and works to spread the material out. Electromagnetic or j x B forces also act on the molten pool. During arc ignition the arc root is very small leading to a very high current density. This high current density can lead to a very high ion flux pressure and will push particles out from the edge of the small molten pool. When the arc is in steady operation the pressure acting to push particles out from the edge is reduced because of the reduced current density and a reduction in the fraction of the current carried by the ions.

The observed reduction in the first erosion event using the fast current shutdown is most likely caused by the deep pit that rapidly develops and keeps the molten droplets that would normally be ejected from the edge of the pool during arc ignition in the hafnium pit.

Although there is slightly less mass eroded during the fast current shutdown for the silver sleeved cathode, this difference was not significant for the available sample size, and the erosion mechanisms at the start and shutdown appear to be the same for both cathode sleeve materials. Even though the erosion of hafnium from both of the sleeve materials is similar, there is a significant difference between the lifetime of the cathodes. Rapid erosion of the cathode sleeve material indicates cathode failure. For the copper sleeved cathodes the critical parameter for failure was a pit depth of 1.3 mm. As seen in Figure 7, this depth was usually reached around 600 starts. Silver sleeved cathodes could be operated to pit depths greater than the critical value for those with copper sleeves. This greater operational pit depth translated into an additional 400 starts for the experimental operating conditions. There appears to be a difference in the failure mechanism between the two cathode sleeve materials.

Conclusion:

In order to identify means to extend cutting torch life, the cathode erosion mechanisms and torch failure have been studied. Erosion occurs as the ejection of droplets of cathode material and is strongest during the transients of the cutting process. Causes of droplet ejection appear to be aerodynamic drag forces during shut down and high ion pressure during the start-up. Reduction of erosion may be achieved by different current ramp up methods and controlling the gas flow during arc shutdown. Because the erosion rate is so dependent on the transients of arc operation, design of the cutting process to avoid arc starts and stops may be beneficial in cathode life extension. Erosion leads to cathode failure when a certain pit depth is reached. Failure of the cathode is significantly postponed when silver is used as the cathode sleeve material because of a different failure mechanism, or a deeper value of pit depth necessary for failure to occur.

Acknowledgement: We gratefully acknowledge the support of Hypertherm Inc.

References:

[1] F.Yin, J. Schein, C. Hackett, J. Heberlein. ISPC 14 1999, vol. 1 49-54

[2] V. Nemchinsky. IEEE Trans. on Plasma Sci. **30** (6) (2002) 2113-2116

[3] F. Yin. MS Thesis, University of Minnesota. 1999

The Chemistry of SiO_2 Deposition from Novel Alkoxysilane Systems

J. Zhang[1], D. S. Wavhal[1], K. L. Williams[2], Ellen R. Fisher[1]

[1] *Department of Chemistry, Colorado State University, Fort Collins, Colorado, USA,*
[2] *Agilent Technologies, Fort Collins, Colorado, USA*

Abstract

We have investigated the deposition of SiO_2 films from alkoxysilane/O_2 and alkoxysilane/N_2O plasmas using a number of novel precursors, i.e., 1,3,5,7-tetramethylcyclotetrasiloxane (TMCTS), dimethyldimethoxysilane (DMDMOS), trimethylsilane (TMS), and hexamethyldisiloxane (HMDSO). Plasma parametric effects on film characteristics, gas phase, and gas-surface interface were examined. The combination of these studies leads to a better overall understanding of the molecular-level chemistry occurring in these plasma systems.

1. Introduction

SiO_2 is ubiquitous in manufacturing semiconductor devices, primarily as gate oxides, interlayer dielectrics, or passivation layer over devices.[1] Plasma-enhanced chemical vapor deposition (PECVD) of SiO_2 films using organosilane precursors, such as tetraethoxysilane (TEOS), is commonly used. Other organosilane precursors such as 1,3,5,7-tetramethylcyclotetrasiloxane (TMCTS), dimethyldimethoxysilane (DMDMOS), trimethylsilane (TMS), and hexamethyldisiloxane (HMDSO) have also drawn much attention.[2,3] Similar to TEOS, these novel precursors are noncorrosive and non-pyrophoric. Moreover, they all have much higher vapor pressures than TEOS, making controlled source delivery easier.

Plasma parameters that affect deposition of SiO_2 films using organosilane-based plasmas include oxidant addition, applied rf power, and substrate temperature. Here, we explored PECVD of SiO_2 films using TMCTS, DMDMOS, TMS, and HMDSO precursors. O_2 or N_2O was used as the oxidant. The effects of oxidant addition, applied rf power, substrate temperature, and substrate position in the reactor were studied. The films were analyzed with FTIR, x-ray photoelectron spectroscopy (XPS), spectroscopic ellipsometry, and scanning electron microscopy (SEM). The gas phase species were examined with optical emission spectroscopy (OES) and mass spectrometry (MS), and correlated with film deposition and characteristics. In addition, the surface interactions of small molecules in the plasma, such as OH, during film deposition were also studied with our Imaging of Radicals Interacting with Surfaces (IRIS) technique.[4,5] The overall deposition processes in these plasma systems were explored by correlating film characterization, gas-phase composition, and gas-surface interactions.

2. Experiments

The inductively coupled rf plasma reactor used in these experiments was described in detail previously.[6] The pressures of TMCTS, DMDMOS, and HMDSO in the reactor were controlled with a Nupro bellows-sealed metering valve and TMS was introduced into the reactor through an MKS mass flow controller. In all systems (except for 100% precursors), O_2 or N_2O was also introduced into the reactor through an MKS mass flow controller and allowed to stabilize prior to the addition of the precursors. The total pressure in the reactor was maintained at 100 mtorr (± 2%) and the ratios of precursor to O_2 or N_2O were calculated from partial pressures.

Substrates of Si wafers (p-type, ⟨100⟩) with ~25 Å of native oxide (scribed to ~20 mm × 15 mm) and KBr pellets were placed on glass slides oriented parallel to the gas flow. Unless otherwise noted, the distance of the substrates from the plasma discharge region was 5 cm. The following plasma parameters were varied: ratio of precursor to oxidant (from 1:0 to 1:30), applied rf power (P = 20–150 W), substrate temperature (T_s = 373–573 K). To distinguish the ambient T_s from elevated T_s, the ambient T_s is defined as the temperature the substrate achieves simply through plasma heating, without specifically heating the substrate with a substrate heater. The deposited films were analyzed *ex situ* using FTIR spectroscopy and XPS for film composition, spectroscopic ellipsometry for film thickness, and SEM for film morphology. Gas phase species were studied with OES and MS.

The surface reactivity of OH was measured with our IRIS apparatus.[4,5] In the IRIS experiment, the plasma is expanded into a differentially pumped high vacuum chamber through a 10-mm orifice of the tubular glass reactor and two collimating slits, creating a near-effusive molecular beam containing virtually

all the species present in the bulk plasma. A laser beam tuned at 307.853 nm intersected the plasma molecular beam downstream at a 45° angle and excited the ground-state OH. Spatially resolved laser induced fluorescence (LIF) images of OH $A^2\Sigma^+ - X^2\Pi$ (0,0) transition were collected with a gated intensified charge-coupled device (ICCD) camera located perpendicular to both the laser beam and the plasma molecular beam. An Si substrate oriented parallel to the laser beam was rotated into the path of the plasma molecular beam and the LIF images were again collected. The difference between LIF images collected with the substrate in and out of the path of the molecular beam was attributable to the OH scattered off the substrate surface. Comparisons between the spatial distribution of scattered and incident molecules were used to determine the surface reactivity of OH. To quantify the spatially-resolved LIF data, one-dimensional cross-sections were created by averaging 15 pixel columns along the laser axis and plotting signal intensity as a function of distance along the laser path. A numerical simulation[4,5] was used to obtain the surface reactivity. It is based on known experimental geometry and calculates the spatial distribution of molecule number density along the laser beam in the molecular beam at the interaction region as well as those for molecules scattered from the substrate surface. The scattering coefficient, *S*, defined as the ratio of the flux of scattered molecules to that of incident beam, is adjusted to best fit the experimental data. The surface reactivity, *R*, is defined as $1 - S$.

3. Results

3.1 Film Characterization. The composition and properties of SiO_2 films deposited from TMCTS, DMDMOS, TMS, and HMDSO with the addition of O_2 or N_2O, are very similar. All precursors can produce high quality SiO_2 films provided that sufficient oxidants are added to the systems. The general trends observed are similar for these precursors. In addition, the two oxidants, O_2 and N_2O, yield nearly identical results.

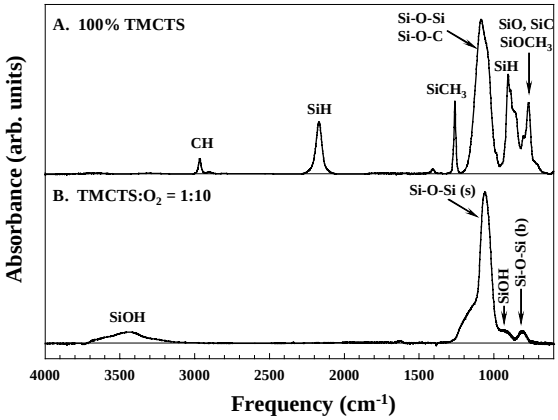

Figure 1. FTIR transmission spectra of films deposited from plasmas of (A) 100% TMCTS and (B) TMCTS:O_2 = 1:10 at P = 50 W.

The addition of oxidants to alkoxysilane plasmas reduces the hydrocarbon incorporation in SiO_2 films. Figure 1 shows representative transmission FTIR spectra for SiO_2 films deposited from TMCTS-based plasmas at P = 50 W and ambient T_s. The amount of hydrocarbon and SiH decreases with increasing O_2 addition. At a 1:10 ratio of TMCTS:O_2, only the Si–O–Si and silanol species were observed. The reduction of carbon and hydrogen demonstrates that a more stoichiometric and higher quality SiO_2 film is produced. Similar trends were observed for N_2O as the oxidant and for other precursors.

The XPS composition results correlate with the FTIR results. The Si concentration appears insensitive to the addition of oxidant, while the O concentration increases and the C concentration decreases with addition of oxidant. The Si bonding environment also changes with oxidant addition. High-resolution XPS analyses show that Si_{2p} peak position increases with addition of oxidant. The Si_{2p} peak width also narrows with increasing oxidant. These trends indicate that with different oxidant addition to the precursor, the structure of SiO_2 network of the deposited films also changes. Alexander *et al.*[3] proposed that the number of O atoms bonded to Si varies from 1 to 4, denoted by $Si(-O)_1$, $Si(-O)_2$, $Si(-O)_3$, and $Si(-O)_4$ with the binding energies of 101.5, 102.1, 102.8, and 103.4 eV, respectively. Figure 2 shows representative fitting of Si_{2p} peak for films deposited from plasmas of 100% TMCTS and TMCTS:O_2 of 1:10. For film deposited from

100% TMCTS, the distribution of Si_{2p} peak is: 40% $Si(-O)_1$, 35% $Si(-O)_2$, 25% $Si(-O)_3$, and 0% $Si(-O)_4$. As oxidant concentration increases in the plasma, the contribution of higher binding energy Si environments increases. For films deposited from TMCTS:O_2 of 1:10, the distribution is simply 34% $Si(-O)_3$ and 66% $Si(-O)_4$.

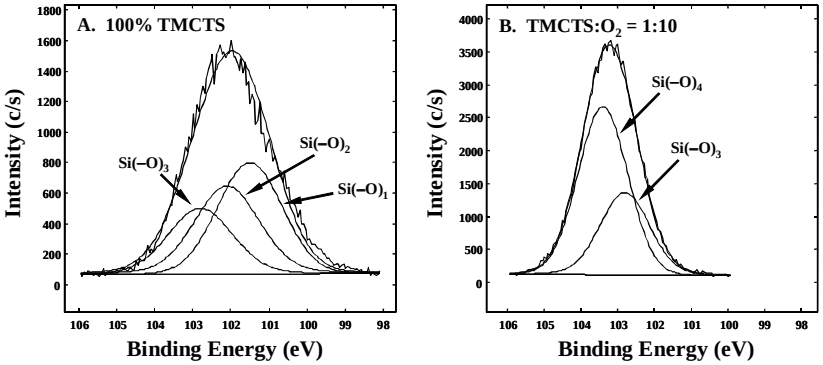

Figure 2. Curve fit of the Si_{2p} high resolution XPS peak for films deposited from plasmas of (A) 100% TMCTS and (B) TMCTS:O_2 = 1:10 at P = 50 W.

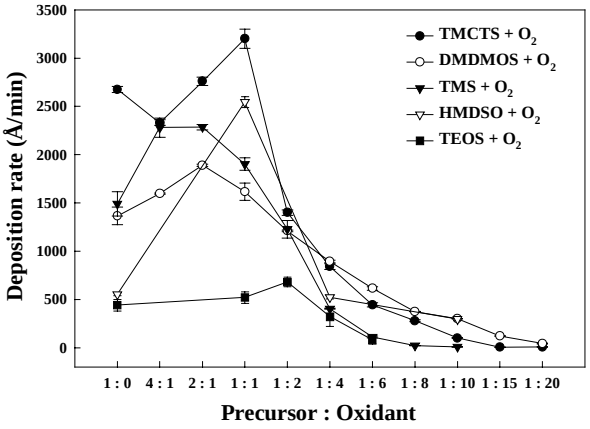

Figure 3. Dependence of deposition rate on oxidant addition for films deposited from plasmas of TMCTS + O_2 (closed circles), DMDMOS + O_2 (open circles), TMS + O_2 (closed triangles), HMDSO + O_2 (open triangles) at P = 50 W, and TEOS + O_2 (closed squares) at P = 85 W.

Deposition rate is another important factor in film deposition. Figure 3 shows the deposition rate of the SiO_2 films as a function of oxidant addition at P = 50 W for TMCTS-, DMDMOS-, TMS-, and HMDSO-based plasmas. The results from TEOS/O_2 plasmas at P = 85 W[7] are also plotted as a comparison. With increasing amount of oxidant, the film deposition rate initially increases to a maximum and then declines sharply, ultimately approaching zero. The position of the maximum varies with different systems. The deposition rate for TMCTS-based plasmas is significantly higher than those for other precursors when the ratio of precursor to oxidant is higher than 1:1. Deposition rate is also strongly affected by substrate temperature. The deposition rates were found to decrease with increasing T_s. From the Arrhenius plots of the logarithm of deposition rate as a function of $1/T_s$, the apparent activation energy, E_a, can be calculated. The values of E_a for TMCTS- and DMDMOS-based plasmas at P = 50 W and for TEOS/O_2 and other alkoxysilane/O_2 plasmas[7] are listed in Table I. All the E_a values are negative. For TMCTS- and DMDMOS-based plasmas, the E_a values for films deposited from plasmas of 1:1 ratios are generally more negative than those for the ratios of 1:10. For the other alkoxysilane/O_2 plasmas, the E_a values for P = 22 W are generally more negative than those for P = 85 W. Furthermore, the E_a values for films deposited from the other alkoxysilane/O_2 plasmas are significantly more negative than TMCTS- and DMDMOS-based plasmas.

Table I. Apparent activation energies (eV) for deposition of SiO_2 films from TMCTS-, DMDMOS-, TEOS-, and other alkoxysilane-based plasmas. [a]

***P* = 50 W**	**1:10**	**1:1**
TMCTS:O_2	–0.0938 ± 0.0099 (0.96)	– 0.0804 ± 0.0074 (0.97)
TMCTS:N_2O	– 0.0758 ± 0.0118 (0.91)	– 0.0785 ± 0.0190 (0.85)
DMDMOS:O_2	– 0.0511 ± 0.0076 (0.94)	– 0.0547 ± 0.0034 (0.99)
DMDMOS:N_2O	– 0.0566 ± 0.0091 (0.91)	– 0.0715 ± 0.0059 (0.97)
Precursor:O_2 = 1:4	***P* = 22 W**	***P* = 85 W**
TEOS:O_2 [b]	– 0.278 ± 0.017 (0.87)	– 0.295 ± 0.009 (0.96)
Triethoxysilane:O_2 [b]	– 0.209 ± 0.005 (0.98)	– 0.059 ± 0.008 (0.69)
Tetramethoxysilane:O_2 [b]	– 0.224 ± 0.009 (0.94)	– 0.122 ± 0.011 (0.80)
Trimethoxysilane:O_2 [b]	– 0.204 ± 0.114 (0.94)	– 0.102 ± 0.007 (0.89)

[a]Errors represent the standard deviation, as determined by linear regression analysis. The linear correlation coefficients are listed in parenthesis.
[b]Values from ref.[7]

The effects of other plasmas parameters on film deposition are summarized as follows. Increasing applied rf power decreases the hydrocarbon incorporation in the film and the deposition rate. The amount of silanol species decreases with increasing T_s and disappears at $T_s \geq 473$ K. The film deposition rate decreases and silanol species increases with increasing distance from the plasma discharge region. It also should be noted that all the deposited SiO_2 films are very smooth.

3.2 Gas-phase Composition. Our OES results indicate the presence of CO, CO_2, OH, O, O_2, and H species in the gas phase. This is also confirmed by the mass spectrometry results. In addition, larger molecules of fragments of the precursor molecules were also observed. From the MS data, we observed that the dissociation percentage of the precursor molecules increases with increasing *P* and oxidant addition. In addition, smaller fragments and molecules of OH, H_2O, CO, and CO_2 also increase with increasing *P* and oxidant addition. Moreover, the relative LIF intensity of OH molecules also has the same trend.

3.3 OH Surface Reactivity. As mentioned in Section 2, the surface reactivity *R* is measured by comparison of the ICCD images obtained with the substrate surface in and out of the path of the plasma molecular beam. Figure 4 shows a typical set of cross sections (solid curves) of the OH LIF images along

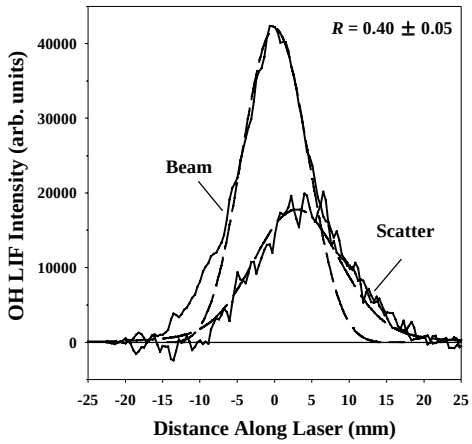

Figure 4. Cross-sectional (solid curves) data for the LIF of OH in the incident plasma molecular beam and scattered from the Si substrate for plasma of TMCTS:O_2 = 1:10 at *P* = 100 W. The laser-surface distance is 3 mm. Dashed curves represent the simulation results assuming *S* = 0.60, which gives *R* = 0.40.

the laser axis for a 1:10 TMCTS/O_2 plasma at P = 100 W and T_s = 300 K. The simulation results (dashed curves) yield a scattering coefficient, S = 0.60 ± 0.05, which gives a surface reactivity R = 0.40 ± 0.05. Averaging 3 sets of data gives R = 0.40 ± 0.03 for OH from 1:10 TMCTS/O_2 plasma at P = 100 W at the surface of a depositing SiO_2 film. The effects of P and the precursor-to-oxidant ratio on OH surface reactivity have been studied and the R values are about the same: R = 0.40 ± 0.10 at T_s = 300 K under all conditions, for TMCTS- and DMDMOS-based plasmas. This value is identical to the surface reactivity of OH for TEOS/O_2 plasmas.[5,8] However, the reactivity of OH decreases with increasing T_s. For 1:10 TMCTS/O_2 plasma at P = 100 W, R = 0.21 ± 0.03 at T_s > 350 K. For 1:10 DMDMOS/O_2 plasma at P = 100 W, R = 0.33 ± 0.07 at T_s > 350 K. Similar results were observed for TEOS/O_2 plasmas, in which R decreases to 0.15 ± 0.05 at T_s > 350 K.[5]

4. Discussion

The deposition of SiO_2 films from these precursors have similar dependencies on oxidant addition, P, T_s, and substrate position in the reactor. Among these parameters, the effect of T_s on deposition kinetics provides insight into the deposition mechanism. The deposition rate decreases with increasing T_s. The negative apparent activation energies of deposition indicate that the adsorption of precursor and its fragments on the substrate surface is the rate-determining step.[9] Increasing oxidant addition and P improves the quality of the SiO_2 films through a better precursor dissociation in the gas phase and oxidation on the gas-surface interface. With increase in oxidant addition and P, the gas-phase homogeneous reactions with O atoms improve the precursor fragmentation. In addition, the heterogeneous reactions between O atoms and adsorbed precursor fragments also increase, and thus reduce hydrocarbon incorporation into the deposited SiO_2 films. OH is an important oxidation product and reactant of the reactions of oxygen with hydrocarbon species. In both gas phase and gas-surface reactions, O atoms react with hydrocarbons typically through H-atom abstraction to form OH.[10] In TEOS/O_2 plasmas, using isotopically labeled $^{18}O_2$ as the oxidant, we have previously identified that the oxygen source of OH is from the O_2 gas, not from the oxygen in the TEOS precursor.[5] For the plasma systems studied in this work, we believe that the oxygen source of the OH is also from the oxidants, O_2 and N_2O. This is supported by the observation that no OH LIF signals were detected for 100% precursor plasmas and the direct correlation of the OH LIF intensities with oxidant addition.

The OH surface reactivity of ~0.40 at T_s = 300 K during SiO_2 film deposition indicates that 40% of the incident OH molecules in the plasma react with the surface and 60% scatter or desorb from the surface. As the IRIS experiment does not track individual molecules, the reactivity value could be the result of combinations of gas-surface interactions that consume and generate OH. The OH molecules may adsorb on the surface and the adsorbed OH may desorb subsequently. OH may also react with other surface species such as H atom to form H_2O or Si to form –SiOH. Reactions that produce OH include surface H-atom abstraction by gas-phase and/or surface O atoms. This process will be enhanced by increasing oxidant addition or P, which increases the O-atom concentration in the gas phase. Therefore, the apparent OH surface reactivity will decrease with increasing oxidant addition or P. However, the R-values are unaffected by changes in oxidant addition or P. This suggests that the overall OH surface reactivity is mainly governed by the chemistry of OH alone and the O-atom reaction with surface to produce OH is not significant compared to overall interactions of OH with the surface. However, the OH surface reactivity could be dramatically different for different systems due to difference in the surfaces. On the other hand, the reactivity of OH during SiO_2 film formation in the plasma systems of TMCTS/O_2(N_2O) and DMDMOS/O_2(N_2O) is identical to that in TEOS/O_2 plasma system,[5] i.e., R = 0.40. This is not surprising as these systems are all depositing systems with similar deposition processes that can deposit high-quality SiO_2 films. Therefore, the surfaces that OH molecules interact with during film formation are very similar. However, at elevated substrate temperature, these systems show slightly different OH surface reactivity: R = 0.15 ± 0.05, 0.21 ± 0.03, and 0.33 ± 0.07 at T_s > 350 K for TEOS/O_2, TMCTS/O_2, and DMDMOS/O_2, respectively. This indicates that the concentrations of active species on the surface that react with OH have different T_s dependence. At elevated T_s, the concentrations of surface-active species decrease, (but not to zero even at 573 K), which leads to decreased R-values. During SiO_2 deposition, reactions of OH with surface Si atom produce undesirable –SiOH species. Increasing T_s leads to a decrease in the surface reactivity of OH, thus a

decrease of the possibility of the reaction to form surface –SiOH. This is consistent with the observation that increasing T_s decreases or eliminates silanol species in the SiO_2 films.

5. Conclusion

We have deposited SiO_2 films from TMCTS-, DMDMOS-, TMS-, and HMDSO-based plasmas. Addition of O_2 or N_2O to the feed gas is essential to deposition of high quality SiO_2 films. Parametric studies have shown that the film quality is improved with increasing oxidant addition, P, T_s, and distance from discharge region. Negative apparent activation energies for film deposition have been observed, suggesting a deposition mechanism dominated by adsorption/desorption processes. Gas phase studies have shown that the dissociation percentage of the precursor molecules, the fragments, and oxidation products such as OH, H_2O, CO, and CO_2 increase with increasing oxidant addition and P. We have also measured the surface reactivity of OH during film deposition, which is ~0.40 at T_s = 300 K and is independent on changes in the precursor-to-oxidant ratio or P. The OH surface reactivity decreases to 0.21 ± 0.03 for TMCTS/O_2 system and to 0.33 ± 0.07 for DMDMOS/O_2 system at elevated T_s (from 350 to 573 K). Comparisons with previous results for TEOS/O_2 plasma systems suggested that OH participates in SiO_2 film deposition and contributes to hydrocarbon removal, precursor fragmentation, and surface silanol formation.

Acknowledgment

This work is supported by the National Science Foundation (NSF 0137664).

References

[1] D. A. DeCrosta, J. J. Hackenberg, and J. H. Linn, J. Electrochem. Soc. **143**, 1079 (1996); S. C. Deshmukh and E. S. Aydil, Appl. Phys. Lett. **65** (25), 3185 (1994); S. C. Deshmukh and E. S. Aydil, J. Vac. Sci. Technol. A **13** (5), 2355 (1995).

[2] C. S. Pai, Materials Chemistry and Physics **44**, 1 (1996); K. Fujino, Y. Nishimoto, N. Tokumasu, and K. Maeda, Jpn. J. Appl. Phys. **33**, 2019 (1994); M. J. Loboda, Microelectronic Engineering **50**, 15 (2000); Y. Inoue and O. Takai, Plasma Sources Sci. Technol. **5**, 339 (1995).

[3] M. R. Alexander, R. D. Short, F. R. Jones, M. Stollenwerk, J. Zabold, and W. Michaeli, J. Mater. Sci. **31**, 1879 (1996); M. R. Alexander, R. D. Short, F. R. Jones, W. Michaeli, and C. J. Blomfield, Appl. Surf. Sci. **137**, 179 (1999).

[4] P. R. McCurdy, K. H. A. Bogart, N. F. Dalleska, and E. R. Fisher, Rev. Sci. Instrum. **68** (4), 1684 (1997).

[5] K. H. A. Bogart, J. P. Cushing, and E. R. Fisher, J. Phys. Chem. B **101**, 10016 (1997).

[6] K. H. A. Bogart, N. F. Dalleska, G. R. Bogart, and E. R. Fisher, J. Vac. Sci. Technol. A **13** (2), 476 (1995).

[7] K. H. A. Bogart, S. K. Ramirez, L. A. Gonzales, G. R. Bogart, and E. R. Fisher, J. Vac. Sci. Technol. A **16**, 3175 (1998).

[8] K. H. A. Bogart, J. P. Cushing, and E. R. Fisher, Chem. Phys. Lett. **267**, 377 (1997).

[9] C. S. Pai and C. P. Chang, J. Appl. Phys. **68**, 793 (1990); C. P. Chang, C. S. Pai, and J. J. Hsieh, J. Appl. Phys. **67**, 2119 (1990).

[10] P. Andresen and A. C. Luntz, J. Chem. Phys. **72**, 5842 (1980); J. Zhang, D. J. Garton, and T. K. Minton, J. Chem. Phys. **117**, 6239 (2002).

Low Dielectric Constant Porous Organosilicate Glass Films via Plasma Enhanced Chemical Vapor Deposition

Qingguo Wu, Daniel D.Burkey, April Ross, and Karen K. Gleason

Department of Chemical Engineering, Massachusetts Institute of Technology
Cambridge, MA 02139, USA

Abstract

Chemical vapor deposition (CVD) of nanoporous dielectric films was achieved using multilayer assemblies of polystyrene spheres as the template for creating the pore structure. The polymer beads were dispersed from aqueous suspension onto a silicon wafer and then dried to remove the water. Next, the CVD dielectric matrix was grown in the interstitial spaces between the beads using a dimethylsilane/oxygen mixture. Subsequent annealing at 300 to 500 ºC resulted in depolymerization of the labile polystyrene phase, leaving spherical pores behind in the more thermally stable CVD matrix. The lowest dielectric constant achieved was 1.4. The refractive index of this film was 1.067.

Introduction

As semiconductor feature sizes decrease, ultra low-k interlayer dielectric materials are needed to minimize transmission delays[1]. Presently, the standard manufacturing methods for interlayer dielectrics include the chemical vapor deposition (CVD) of SiO_2 and organosilicate glass (OSG, Si:O:C:H). The dielectric constant, k, of fully dense SiO_2 layer is 4.0 while for OSG, k values are typically 2.7. The inclusion of pores is an evolutionary pathway for reducing k. Indeed, a variety of porous materials have achieved dielectric constants in the ultra low-k region (2.5-1.5)[2-4]

In this work, a nanoporous CVD matrix is created having extremely low values of dielectric constant, 1.4, and refractive index, 1.067. Assemblies of polymer nanospheres 15 hm. to 96 nm. in diameter serve as templates for the pores. The precursor for the CVD matrix are dimethylsilane and oxygen.

The CVD step fills the interstices of the colloidal crystal to form the OSG matrix. The CVD process for OSG matrix must satisfy three simultaneous criteria. First, the fully dense OSG films must be hard as soft films collapse when the template is removed. A CVD matrix material that is mechanically robust will leave behind spherical pores. Second, the OSG layer should be chemically stable. In particular, incorporation of Si-H bond is undesirable as these bonds are susceptible to attack by water[5]. Finally, the CVD process must exhibit excellent gap fill in order to deposit OSG material into the void spaces within the multiple layers of the polystyrene beads. Thus, the CVD feed gases and conditions selected must generate reactive species having low sticking coefficients. Conditions that enhance the sticking probability of the film forming species and promote deposition on the top surface of the colloidal crystal are undesirable, as channels needed to fill the interstices within the template structure become blocked.

With subsequent annealing at 300 to 500 ºC the labile polymer beads depolymerize, resulting in a nanoporous thin film. To enable three-dimensional crystal templates to form on substrate areas larger than 10 cm^2, a rapid evaporation-induced self-assembly of labile polystyrene (PS) nanospheres was developed. Colloidal crystallization can yield either two or three dimensional crystals of polymeric beads onto a substrate[6-8].

Results and Discussions

First, an aqueous suspension of the polymer nanospheres was diluted to 0.1-0.5 w/v % and dispensed over the surface of a rectangular silicon piece by a syringe. Two opposing edges of the rectangular substrate were heated to 60-70 ºC. The polymer suspension of nanospheres at the two heated edges dried and crystallized first. Then, the two crystal domains propagated towards the cooler center of the wafer. Arrays as large as 10 cm^2 containing multiple layers of polymer beads were obtained in less than 60 minutes. Figure 1 shows scanning electron micrograph (SEM) of a three-dimensional crystal of monodisperse polystyrene beads of 96 ± 4 nm diameter assembled using this rapid, large-area process.

The top down view (Fig. 1a) reveals well-ordered hexagonal arrays of the polymer beads. Five layers of beads can be seen in the cross sectional view (Fig. 1b). Varying the concentration of the polymer microspheres in the suspension provides precise control over the number of layers formed, from two to over 15.

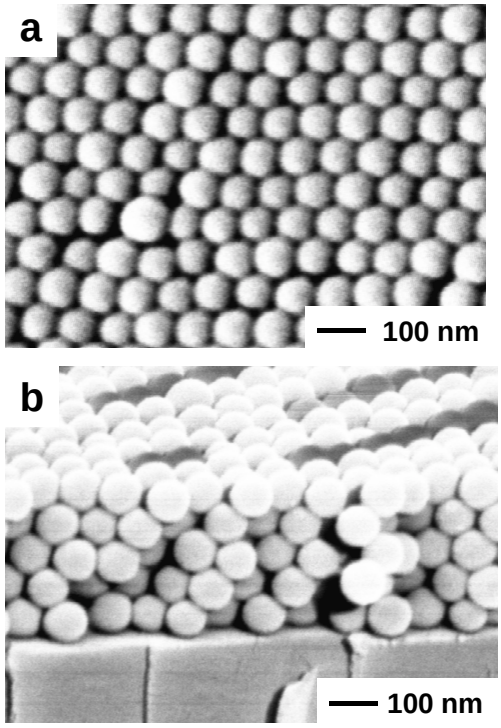

Fig 1. SEM images of a five-layer polystyrene template assembled on Si wafer from 96 nm polystyrene nanospheres : (a) Top view; (b) Oblique view.

This approach is remarkable for simplicity, speed, and effectiveness in producing large area crystalline templates of well-defined thickness. The degree to which the OSG matrix infiltrated the voids between the template beads was inferred from ellipsometric measurements of refractive index of the composite film.

The substrate temperature, vapor pressure, and peak RF power of the CVD OSG process were varied 25°C to 100°C, 200 to 110 mTorr and 200 to 120 W, respectively, resulting in composite films with degrees of infiltration ranging from 0% to 100%. The degree of infiltration was observed to increase with increasing substrate temperature, decreasing vapor pressure, and decreasing plasma power.

The highest degree of infiltration was achieved using pulsed plasma enhanced CVD from dimethylsilane (2MS) at 4 sccm mixed with argon at 15 sccm and oxygen at 2.5 sccm at a total pressure of 110 mTorr. For excitation cycle, the plasma was pulsed on at a peak rf power of 120 W for 10 ms followed by an off time of 600 ms.

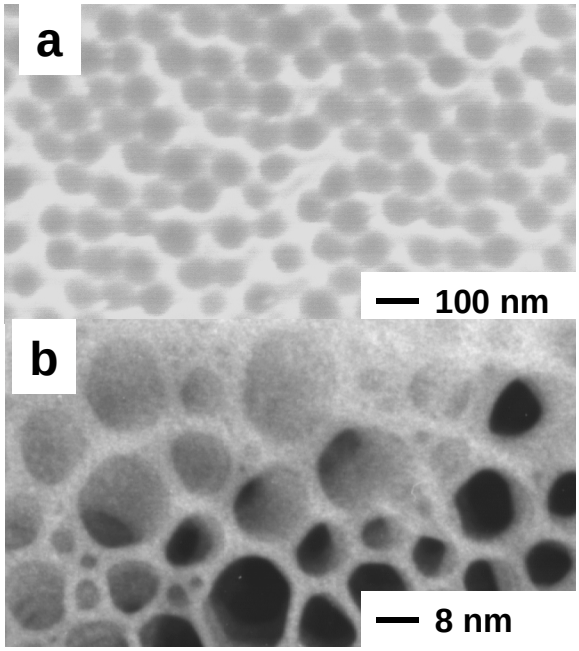

Fig 2 (a). SEM images of the nanoporous OSG film using the template beads of 96 nm mean diameter. (b) TEM image of nanoporous OSG film using the template beads of 15 nm mean diameter.

The filling of the OSG matrix at a substrate temperature of 95 ºC is superior to that for 20 ºC substrate temperature This observation is consistent with the expected decrease in the sticking coefficient with increasing temperature for an adsorption limited process. A lower sticking coefficient increases the probability that the OSG precursor is able to traverse the small channels within the template of polymer beads prior to reacting to form film.

The generation of the nanoporous organosilicate glass was accomplished by thermal treatment to remove the template of polymer beads from the composite film. The polystyrene is expected to decompose at temperatures above 280 ºC[9]. Annealing was accomplished under N_2, ramping the temperature at approximately 8°C/min. A ramp to 500°C followed by isothermal anneal at 500 °C for one hour resulted in complete removal of the polymer. A ramp up to 300 °C, an 1 hour isothermal anneal at 300 °C for 1 hour.

The C-H stretch region of the FTIR associated with the polystyrene appears from 2844-3091 cm^{-1}. Additionally, the CH_3 stretching bands from OSG are centered at 2960 cm^{-1}. After annealing, only the 2960 cm^{-1} band remains, clearly demonstrating the complete removal of the polystyrene template and retention of the OSG matrix material and porous structure.

Control over the pore size is critical for obtaining materials with suitable properties for different insulator feature sizes in microelectronic devices[10]. To obtain different pore sizes in the nanoporous organosilicate glass, templates were assembled using polystyrene beads of 96 nm, 19 nm and 15 nm mean diameter. Figure 2c shows cross-

sectional SEM image of resultant nanoporous OSG film produced using 96 nm polystyrene beads while Figure 2(b) shows transmission electron micrograph (TEM) image of resultant nanoporous OSG film produced using 15 nm polystyrene beads. Spherical ordered pores created by the decomposition of the 96 nm beads are clearly visible in Fig. 2(a) and spherical pores created by decomposition of the 15 nm beads can be also seen in Fig. 2(b) although pore sizes are very different due to high standard deviation of diameter for 15 nm beads. The porosity is also attested by the extremely low values measured for the refractive index, 1.067, and dielectric constant, 1.4.

Conclusions

Nanoporous organosilicate via CVD onto a colloidal template is a new approach to the synthesis of extremely low-k dielectric materials. The technological steps of CVD and annealing are standard semiconductor manufacturing techniques. Control over the template area for polymer bead assembly and control over bead shape and size are key issues remaining for the development of this material for practical application.

References

1. Miller, R. D. , *Science* **286**, 421-423 (1999).
2. Hedrick, J. L., Miller, R. D., Hawker, C. J., Carter, K. R., Volksen, W., Yoon, D. Y. & Trollsåo, M., *Adv. Mater*. **10**, 1049-1053 (1998).
3. Leung, R., Fan, W., Silkonia, J. & Wu, H.-J., *US Patent* **6214746** (April, 2001).
4. Baklanov, M. R. et al., *Proceeding of the IEEE*, 189-191 (2001).
5. Wang, B. K., Loboda, M. J., Cerny, G. A., Schneider, R. F., Seifferly, J. A., and Washer, T., *Proceedings of the IEEE 2000 IITC*, Piscatawy, NJ, USA, 277, pg52-4 (2000).
6. Denkov, N. D., Velev, O. D., Kralchevsky, P. A., Ivanov, I. B., Yoshimura, H. & Nagayama, K., *Nature* **361**, 26 (1993).
7. Park, S. H., Qin, D. & Xia, Y., *Adv. Mater*. **10**, 1028-1032 (1998).
8. Van Blaaderen, A., Ruel, R. & Wiltzius, P., *Nature* **385**, 321-324 (1999).
9. Kelen, T. *Polymer* (Van Nostrand Reinhold, New York, 1983).
10. Peters, L., *Semiconductor International*, May, pg 55 (2002).

Acknowledgements

We gratefully acknowledge the MRSEC for using shared facilities supported by National Science Foundation under Award Number DMR-9400334.

Microwave Plasma Barrier Coating Technology for PET Beverage Containers

Christopher Weikart, Todd Smith

The Dow Chemical Company
Chemical Sciences, 1776 Bldg
Midland, MI 48674

The PET packaging environment remains competitive in the development of commercial barrier solutions for extending the shelf-life of beverages and ensuring the quality of products such as beer, carbonated soft drinks and juice. Among the many different technologies that exist today, plasma-based barrier coating technology is an attractive solution due to the high performance properties, ease of recyclability and competitive cost compared to other technologies. Research and development work conducted at The Dow Chemical Company has demonstrated high barrier coatings on PET containers with a microwave PECVD device. The device deposits thin (10-30nm) barrier coatings on plastic containers to provide enhanced barrier performance to small gaseous permeants such as oxygen and carbon dioxide. A bi-layer coating, composed of a patented organosiloxane layer and a SiOx layer, was deposited uniformly over the interior surface of the container. The organosiloxane layer acts as a flexible interfacial layer before depositing the brittle SiOx barrier layer. The nature of the microwave deposition process, the challenges of coating a complex-shaped container and the barrier performance properties as they relate to the coating properties will be addressed.

Thermodynamic and Kinetic Study of Black Liquor Treatment by the Submerged Plasma Technology

V. Yargeau, B. Marcos and G. Soucy

Department of Chemical Engineering, Université de Sherbrooke, Québec, Canada, J1K 2R1

Abstract

A novel technology, the submerged plasma reactor, is used to study the kinetic and thermodynamic model of thermal treatment of black liquor. An innovative kinetic approach is proposed and validated: the severity factor, a phenomenological kinetic approach developed for lignocellulosic fractionation. Thermodynamic modeling of plasma treatment is improved by the use of Pitzer's parameters. Key characteristics of this use of submerged plasma technology are identified as the influence of the catalyst on organics decomposition and the lignin decomposition.

1. Introduction

Several industries, such as the Pulp and Paper industry, experience problems with the treatment of caustic solutions used in their processes. Better kinetic and thermodynamic predictions would be beneficial in the optimization of the actual treatment and in the development of new treatment technologies such as the submerged plasma system that could address the need of incremental solution treatment capacity.

The global kinetic approach, the simplest model of kinetic behavior [1], gives poor results for complex systems having kinetic parameters varying with the operating conditions. On the other hand, a detailed model can be developed by a mechanistic approach [2] but the complete reaction mechanism must be known, which is not the case for the complex black liquor system. Between those two approaches lies the phenomenological approach that has given rise to the severity factor kinetic model for the complex system of the decomposition of the lignocellulosics fractionation [3], [4]. This study evaluates the suitability of this kinetic model for thermal treatment of black liquor. The ideal solution model is often used in the thermodynamic analysis of solutions thermal treatment. This approach is not adequate however for concentrated electrolyte solutions such as black liquor. This present study evaluates the potential gain in using a real solution model, based on Pitzer's parameters. The last objective of this study is to identify key characteristics of the submerged plasma for the treatment of black liquor.

2. Thermodynamic study

The relevance of the real solution model in thermodynamic prediction was verified by the introduction of available Pitzer's parameters as reported in the following Tables, in a new version of FactSage program.

TABLE 1 Binary Pitzer's parameters [6]

	BINARY PARAMETERS			BINARY PARAMETERS DERIVATIVE[1]		
ION PAIR	β_o	β_1	C^ϕ	β_o	β_1	C^ϕ
Na[+] HCOO[-]	0,0820	0,2872	-0,00523			
Na[+] CH_3COO[-]	0,1426	0,3237	-0,00629			
Na[+] HCO_3[-]	0,028	0,044				
Na[+] HS[-][2]	0,1396	0,0	-0,0127			
Na[+] OH[-]	0,0864	0,253	0,0044	7,00E-04	1,34E-04	-18,9E-05
Na[+] CO_3[2-]	0,0362	1,5098	0,0026			
Na[+] SO_4[2-]	0,0187	1,0995	0,0027	2,36E-03	5,63E-03	-1,72E-04

[1] Others derivatives are estimated by the method proposed in FactSage.

[2] Park et coll., 1999.

TABLE 2 Mixing Pitzer's parameters [6]

ION PAIR	MIXING PARAMETERS $\theta_{aa'}$	$\psi_{aa'A}$
OH[-] CO_3[2-]	0,1	-0,017
OH[-] SO_4[2-]	-0,013	-0,009
CO_3[2-] SO_4[2-]	0,02	-0,005
HCO_3[-] SO_4[2-]	0,01	-0,005
HCO_3[-] CO_3[2-]	-0,04	0,002

3. Kinetic study

SEVERITY FACTOR KINETIC MODEL

The severity factor kinetic model, as applied to the lignocellulosics fractionation, demonstrates that it is possible to predict the kinetic behavior of a complex system by the use of a severity factor; a descriptor of the importance of operating conditions on the extent of conversion of the input material as products. This severity factor *(Ro)* is a parametric combination of temperature *(T)*, time *(t)* and catalyst concentration *(C)*.

The phenomenological approach was first introduced in 1930 by Geniesse and Reuter [7], followed by Brash and Free [8] and Whitehurst [9]. In 1990, Montané, Overend and Chornet revised this literature and proposed the use of the severity factor combining temperature and residence time. In 1992, Abatzoglou et al. [3], unified these two approaches and introduced the catalyst effect to the severity factor. From the hypotheses set out below and the mathematical development presented in [4], the severity factor is defined as follow:

$$R_0 = \exp\left(\frac{1}{\omega_0}\left(1-\frac{T_{ref}}{T}\right)\right)\frac{t^{\gamma}}{\gamma} \quad \text{.....(1)}$$

The conversion, *f*, is then expressed as a function of the severity factor means of the following equation, where *m* is the reaction order for the catalyst:

$$\ln(1-f) = -k_{Tref,Cref}\left(\frac{C}{C_{ref}}\right)^{m} R_0 \quad \text{.....(2)}$$

Parameters γ, $k_{Tref,Cref}$

To determine the parameters γ, $k_{Tref,Cref}$ of the model from experimental data, equation (1) and (2) are combined, the catalyst concentration is fixed at the reference and $\omega_0 T$ is replaced by ω to obtain the linearized equation:

$$\ln(-\ln(1-f)) = \ln\left(\frac{k_{Tref,Cref}}{\gamma}\exp\left(\frac{T-T_{ref}}{\omega}\right)\right) + \gamma \ln t \quad \text{.....(3)}$$

From which the least square function indicates gamma as the slope and the rate constant as a function of the y-intercept, *b* :

$$k_{Tref,Cref} = \gamma \exp\left[b - \frac{T-T_{ref}}{\omega}\right] \quad \text{.....(4)}$$

Parameter m

To determine the parameter m of the model from experimental data, the catalyst contribution term is linearized through a series expansion around C_{ref}, truncated to the first term to obtain:

$$\ln(-\ln(1-f)) = \ln(\frac{k_{Tref,Cref}}{\gamma}\exp\left(\frac{T-T_{ref}}{\omega}\right)\exp\left(\frac{m(C-C_{ref})}{C_{ref}}\right)) + +\gamma\ln(t) \quad \text{.....(5)}$$

from which the least squares function indicates that the parameter *m* can be estimated from y-intercept, *b* and the following equation:

$$m = \frac{C_{ref}\left[\omega(\ln\gamma - \ln k_{CrefTref}) + \omega * b + T_{ref} - T\right]}{\omega(C - C_{ref})} \quad \text{.....(6)}$$

HYPOTHESES OF THE MODEL

§ Reaction rate doubles for a specified temperature increment.
§ Temperature dependence of reaction rate follows the Arrhenius equation.
§ Process is isothermal and irreversible.
§ Catalyst concentration is constant with time.
§ Reaction rate is independent of the conversion.

REFERENCE CONDITIONS

The model is based on a reference temperature and a reference catalyst concentration. The reference temperature chosen is 25^0C since no significant reaction occurs at this temperature. The catalyst concentration is chosen to lie midway in the interval of catalyst concentrations studied, 0.033 ml/L.

4. Experimental set-up and procedures

SUBMERGED PLASMA TECHNOLOGY

The technology used during this study, shown in Figure 1, is based on a submerged plasma system designed for fluids treatment (*US Patent* 6187 206 B1: February 13, 2001 and *Patent Cooperation Treaty* (PCT) WO9722556: December 20, 1996) adapted for this study as described in [5]. The solution to be treated **(1)** is pumped **(2)** into the reactor **(3)** prior to plasma ignition. To place energy in direct contact with the solution to be treated, thermal plasma generated by a 45 kW DC plasma torch **(4)** is submerged in the solution, at the bottom of the reactor. The torch, fed with plasma gas **(5),** is cooled by tap water **(6)**. To control both the liquid and gases flow patterns in the reactor and to obtain adequate contact between the gas and liquid phase, a draft tube **(7)** is placed above the torch. Visual observations of the treatment are possible through the porthole **(8)**. During the reactor operation, make-up water is added, using the reservoir **(1)** or a tap water line **(9),** at a flow rate known to keep the solution volume constant at 15 L. The volume level is verified by the magnetic indicator located in a side tube **(10)**. Treatment is carried out under pressure (445 kPa) to reduce foaming problems and to increase the boiling temperature of the system. Liquid samples are taken by the sampling line at the half-height level of the reactor **(11)**, the reactor being drained by a line at the bottom **(12)** while the gases leaving the reactor at the top are cooled by heat exchangers **(13)**. The condensate from the gases is recuperated in a reservoir **(14)** and the cooled gases are sampled and sent to a scrubber **(15)** before exhaustion.

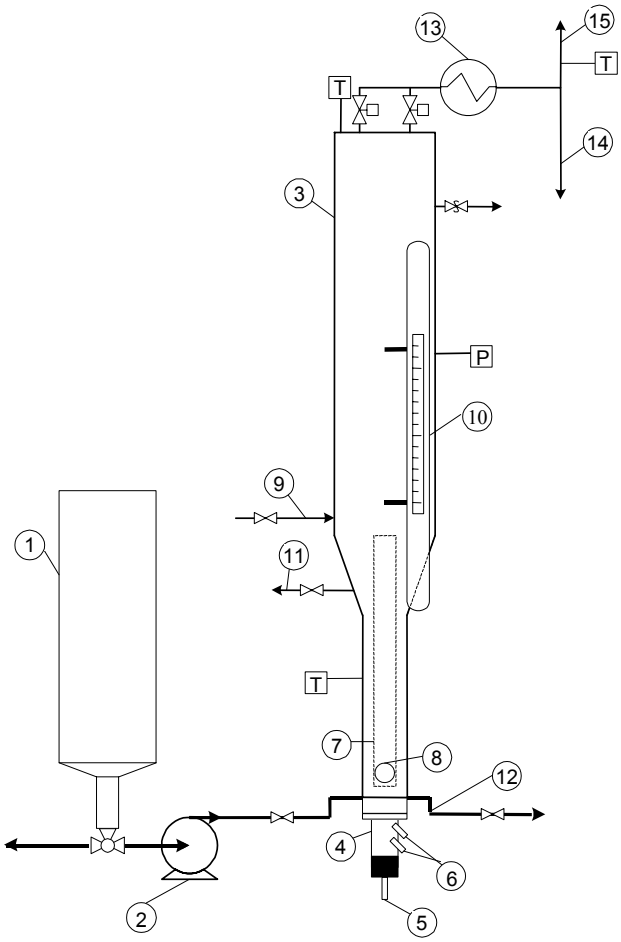

Figure 1 Experimental set-up

BLACK LIQUOR SOLUTION

To streamline the chemical analysis and to focus the analysis on major compounds, a synthetic solution is used as a surrogate for the black liquor for most of the experimental runs. The compounds introduced into the test solution are summarized in Table **Errore. L'origine riferimento non è stata trovata.** along with the concentration interval studied. Fifteen liters of solution are prepared and treated for each experiment.

TABLE 3 Solution concentration

SPECIES	CONCENTRATION
NaOH	0.23 mol/L
Na_2CO_3	0.13 mol/L
Lignin	[0.0 , 15.0] g/L
HCOOH	[0.14 , 0.28] mol/L
CH_3COOH	[0.07 , 0.14] mol/L
Na_2S	[0.07 , 0.14] mol/L

EXPERIMENTS

The main set of experiments, structured by a partial factorial analysis 2^{4-1}, are described in Table 4.

TABLE 4 Experiments from a Factorial 2^{4-1} to evaluate the parameters $k_{Tref,Cref}$ and γ

TEST #	PLASMA GAS	Na_2S (mol/L)	ORGANIC ACIDS (mol/L)	CATALYST (ml/L)
01	Air	0.07	0.21	0
02	O_2	0.07	0.21	0.033
03	Air	0.07	0.42	0.033
04	Air	0.14	0.21	0.033
05	O_2	0.14	0.21	0
06	O_2	0.07	0.42	0
07	Air	0.14	0.42	0
08	O_2	0.14	0.42	0.033

To determine the value of the third parameter of the severity factor, *m*, the reaction order for the catalyst, additional experiments, as described in Table 5, are undertaken. Knowing the parameters $k_{Tref,Cref}$ and γ, it is then possible to calculate the reaction order for the catalyst by means of equations (5) and (6).

TABLE 5 Experiments to evaluate the reaction order for the catalyst

TEST #	PLASMA GAS	Na_2S (mol/L)	ORGANIC ACIDS (mol/L)	CATALYST (ml/L)	PRESSURE (kPa)
03cat1	Air	0.07	0.42	0.017	445
03cat2				0.067	

SAMPLES ANALYSIS

Liquids

During each 20 minute treatment, samples are taken from the reactor just over the reactor elbow (see #11 on Figure 1) at various times: 0, 3, 8, 13, and 20 minutes. Samples are analyzed, for the anions; SO_3^{2-}, SO_4^{2-}, $S_2O_3^{2-}$, $HCOO^-$ and CH_3COO^- by ionic chromatography, using method based on TAPPI standard methods, T699 om-87.

Gases

During each 20 minute treatment, gas samples are drawn off in front of the scrubber entrance (see #15 on Figure 1) at various times: 7 and 20 minutes. The analysis performed is limited to the qualitative identification of the most probable "sulphurated" gases products: SO_2(g) and H_2S(g). Analysis are conducted with the aid of a CP-3800 Varian chromatograph equipped with a Porapack QS Teflon column and a TCD detector.

5. Results and Discussion

EVALUATION OF PARAMETER $K_{TREF,CREF}$ AND γ

Kinetic parameters $k_{Tref,Cref}$ and γ are calculated for each test through the use of equations (3) and (4). The mean parameter $k_{Tref,Cref}$, obtained for formic acid decomposition, is 1.5E-05 min^{-1} and is 3.32E-05 min^{-1} for sulfur oxidation. The parameter γ for formic acid decomposition seems to be quite variable with respect to the operating conditions. It has been statistically verified by factorial analysis that the plasma gas type influences the parameter γ for acid decomposition. The dependence of this variation with operating conditions is not

statistically significant for sulfur oxidation, for which and the mean value obtained is γ = 0.44 [10]. The variation of these γ parameters with temperature is analyzed in the following section.

Variability of γ with temperature

To verify the variability of the parameter γ with temperature, test 03 is replicated and another test is performed under higher pressure condition (Test 03Pd: 585 kPa) to increase the treatment temperature. The results obtained at different temperatures indicate that the variation of parameter γ with operating conditions is significant, as is shown on Figure 2, for both formic acid decomposition and sulfur oxidation.

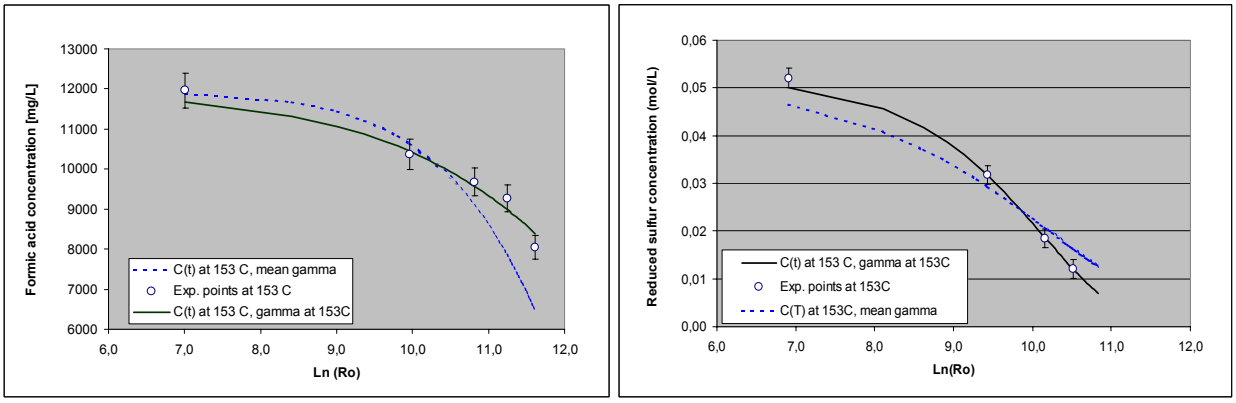

Figure 2 Significance of variability of γ with temperature

EVALUATION OF PARAMETER *m*

The calculation of the reaction order for the catalyst, using equations (5) and (6), indicates that the reaction order for the catalyst, in the formic acid decomposition, is 0.85 and almost 0 for the sulfur oxidation. The conclusion that the oxidation of sulfur is not catalyzed is also statistically validated by the results of factorial analysis [10].

VALIDATION OF THE KINETIC MODEL

Figure 3 demonstrates that the model is adequate for the prediction of formic acid decomposition and also for sulfur oxidation in the plasma treatment of black liquor. The information so obtained can be used to optimize the conventional thermal treatment or to design new ways of treatment.

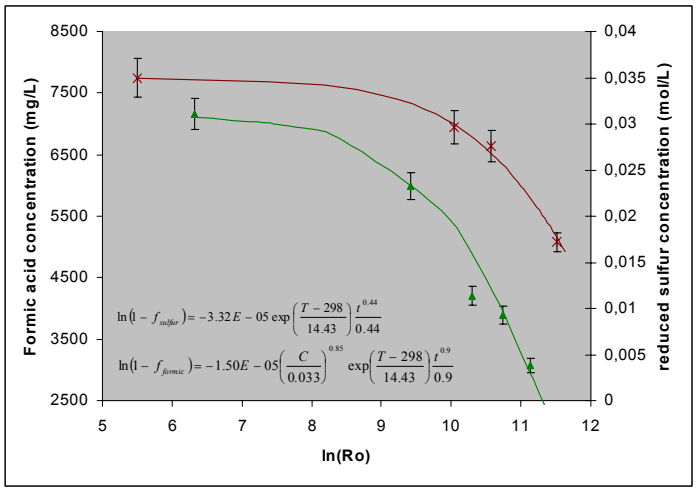

Figure 3 Kinetic model validation

KEY CHARACTERISTICS OF THE TECHNOLOGY

The factorial analysis demonstrates that the influence of a catalyst is significant on the decomposition of black liquor organics. It also reveals that it is possible to decompose the lignin content even if it remains in a bulk solution at a mean temperature lower than the lignin decomposition temperature, 220^{0}C [11]. No "sulphurated" gases were analyzed from these tests.

VALIDATION OF THE THERMODYNAMIC MODEL

The comparison of the models' predictions (ideal and real solution) to the experimental observations, as summarized in Table 6, indicates that the real solution model provides improved results.

TABLE 6 Comparative results between models' predictions and experimental observations

CRITERIA	PREDICTION IDEAL SOLUTION	PREDICTION REAL SOLUTION	EXPERIMENTAL OBSERVATION
Precipitation temperature for Na_2CO_3	143^0C	155^0C	No precipitate observed at 153^0C
Solution pH	7,5	6,9	6,0
Oxidized sulfur after solution preparation	none	none	15% of initial sulfur
Formic acid residual percentage	0%	0%	42% à 74%
Acetic acid residual percentage	0%	0%	51% à 110%
Carbonates	0,7 g/L	8,9 g/L	3,3 à 6,4 g/L
Oxalates	0 mol/L	0 mol/L	50 à 350 mg/L

6. Concluding remarks

The submerged plasma technology, described above, offers considerable advantages for practical lignin decomposition and kinetics. The real solution model improves thermodynamic predictions. The phenomenological severity factor kinetic model, developed for the decomposition of cellulose, is adequate to predict the kinetic behavior of complex systems such as those formed during the thermal treatment of black liquor and to optimize the submerged plasma treatment operating conditions. However, the results obtained in this work indicate that the severity factor kinetic model might be more efficient through the optimization of the gamma parameter to adapt the model to the more homogeneous molecular composition of black liquor. This optimization will be evaluated in further work.

7. Acknowledgements

Grateful acknowledgements are made to Domtar Inc. of Windsor (Québec) for their samples analysis support and to the Natural Sciences and Engineering Research Council of Canada (NSERC) and the Fonds pour la formation de chercheurs et l'aide à la recherche (FCAR Funds) for their financial support.

8. Nomenclature

R_o	:	Severity factor	(dimensionless)
$k_{Tref,Cref}$	:	Rate constant at T_{ref} and C_{ref}	(min^{-1})
γ	:	Parameter defining the shape of the Kohlrausch relaxation function and which also defines the shape of the activation energies distribution	(dimensionless)
ω	:	Parameter expressing the averaged influence of temperature on the reaction rate	(K)
ω_0	:	Parameter expressing the energetics of the process respect to a reference reaction temperature	

9. References

[1] Cusack, R.W., Chemical Engineering, 134-146 (1999).
[2] WESTBROOK, C.K. and F.L. DRYER, Prog. Energy Combustion Science, **10**, 1-57 (1984).
[3] Abatzoglou, N., E. Chornet, K. Belkacemi and R.P. Overend, Chem. Eng. Sc., **47**, 5, 1109-1122 (1992).
[4] Montané, D., R.P. Overend and E. Chornet, The Canadian Journal of Chem. Eng., **76**, 58-68 (1998).
[5] Yargeau, V., B. Marcos and G. Soucy, "Proc. ISPC15", Orléans, France, July 9-13, (2001), 2987-2992.
[6] Pitzer, K.S. (1991), 2nd edition, CRC Press, Boca Raton, 1991.
[7] Geniesse, J.C. and R. Reuter, Ind. Eng. Chem. **22**, 1274-1279 (1930).
[8] Brasch, D.J. and K.W. Free, Tappi J. **48**, 4, 245-248 (1965).
[9] Whitehurst, D.D., T.O. Mitchell and M. Farcasiu, Academic Press, NewYork, NY (1980).
[10] Yargeau, V, Ph.D. thesis, Université de Sherbrooke, 2002.
[11] Beckwith, W.F., D.L. Kasbohm and J.C. Hassler, The American Inst. of Chem. Eng., **77**, # 207, 68-71 (1981).

Molecular Dynamics Calculations of Carbon/Hydrocarbon Reflection Coefficients on Hydrogenated Graphite Surfaces

D.A. Alman, J.P. Allain, D.N. Ruzic

Department of Nuclear, Plasma, and Radiological Engineering, University of Illinois, Urbana, Illinois, USA

Abstract

Reflection coefficients for carbon and hydrocarbon atoms/molecules on carbon-based surfaces are critically needed for plasma-surface interaction analysis in fusion devices, as carbon will continue to be used in next step devices like ITER. These have been calculated at different energies and angles with a molecular dynamics code using the Brenner hydrocarbon potential [1]. Hydrogen saturated graphite was prepared by bombarding a pure graphite lattice with energetic hydrogen, until a saturation at ~0.42 H:C. Carbon at 45° has a reflection coefficient (*R*) of 0.64 +/- 0.01 at thermal energy, decreasing to 0.19 +/- 0.01 at 10 eV. Hydrocarbons reflect as molecules at thermal energies and break up at higher energies. The total reflection via these fragments decreases with energy, and increases with hydrogen content. The results compare reasonably well with trend in VFTRIM-3D [2] modeling and experimental sticking data of A. von Keudell [3]. A second surface, representing a "soft" redeposited carbon layer formed by the deposition of hydrocarbons onto a graphite surface, is also analyzed. In general, reflection is lower from the "soft" surface (0.2 vs. 0.4 at 1 eV). These reflection coefficients, together with the energy and angular distribution of reflected particles, can be incorporated in erosion/redeposition codes to allow improved modeling of chemically eroded carbon transport in fusion devices.

[1] D.W. Brenner, Phys. Rev. B, **42,** 9458-9471 (1990).
[2] D.N. Ruzic, Nucl. Instr. Meth. Phys. Res. **B47**, 118-125 (1990).
[3] A. von Keudell, T. Schwarz-Selinger, M. Meier, W. Jacob, Appl. Phys. Letters **76**, 676 (2000).

1. Introduction

The use of carbon-based surfaces, structures, and materials has led a wide range of scientific development and technological applications, in particular the use of hydrocarbons [1]. Examples include the application of nanotubes, diamond-like amorphous carbon films [2], and nanocrystalline diamond films and their production from low-temperature hydrocarbon plasmas [3]. An understanding of the chemical processes and physical mechanisms governing the interaction of carbon-based surfaces and hydrogenic/hydrocarbon environments is necessary to further advance hydrocarbon technology applications. One particular application of carbon-based materials is their use as plasma facing surfaces in magnetic confinement fusion reactors [4-6]. The uptake and release of hydrogen species at the plasma boundary in fusion devices is an important issue that requires vast knowledge of the nature of chemical and physical phenomena in hydrocarbons [7]. In a fusion device an understanding of how hydrocarbon surfaces erode and how impinging hydrocarbon and hydrogenic species reflect is vital to assess fusion plasma performance.

Carbon has been a leading candidate for use as a plasma-facing component for some time. As such, carbon-based materials, in such forms as graphite or CFC (carbon fiber composites), have been widely used in fusion devices. This typically means covering the surface of the walls with carbon tiles, especially in regions where a large flux of heat or particles to the wall is expected, e.g. on the *divertor*. The divertor is a place where the magnetic field lines that confine the plasma ions intentionally intersect a material surface. Carbon based materials are attractive because carbon has a low atomic number (Z=6), which is critical to keeping radiation power losses from the core to a minimum. Additionally, they have good thermomechanical properties [8]. Most notably, carbon materials can withstand the large heat fluxes of a tokamak without their structure being degraded. Carbon will not melt, and seems to be the material best suited to dealing with the required heat load, especially during off-normal events (e.g. disruptions) characterized by unusually large heat and particle loads.

However, carbon is not a perfect choice. Carbon is more susceptible to *physical sputtering* (defined as the release of one or more target atoms due to an incident particle) than higher Z materials (e.g. tungsten, molybdenum) and has a lower energy threshold for physical sputtering. The major problem with carbon comes from the special chemical relationship between carbon and hydrogen, the main component of a fusion plasma. The chemical affinity between the two causes carbon-based materials to be susceptible to chemical sputtering in the presence of a hydrogen plasma. The result is the release of hydrocarbon impurities into the plasma. These hydrocarbons are dominated by methane, but have been shown to contain significant amounts of heavier hydrocarbons, i.e. C_2H_x and C_3H_x species, which can account for up to 50% of the total chemical erosion of graphite under hydrogen impact [9].

Another important issue related to the erosion of hydrocarbons is the sticking of impinging hydrocarbon or hydrogenic species on the carbon-based surface. An eroded particle released into the plasma boundary of a fusion device will undergo a number of reactions, in some cases leading to ionized states. Due to the sheath potential in the plasma boundary and collisions with the background plasma these ionized species (atomic and/or molecular) are drawn back to the carbon-based surface[10]. This process has been successfully modeled by erosion/redeposition codes such as WBC and REDEP[11,12]. The energetic incident particles/molecules will either be implanted (stick) or reflected. This outcome will be dependent on a variety of parameters including: the incident energy, angle, mass and the surface chemical and thermodynamic state. Therefore, a critical improvement to erosion/redeposition codes (e.g. WBC, REDEP) would be the inclusion of realistic carbon/hydrocarbon reflection/sticking coefficients. The work presented here attempts to provide such reflection/sticking data using a molecular dynamics code to provide a realistic model for carbon/hydrocarbon interaction with carbon-based surfaces.

2. Modeling description

2.1. Description of computational models

A molecular dynamics (MD) code, MolDyn [13], was modified to study reflection of carbon and hydrocarbon molecules on a hydrogenated carbon (C:H) film. The code uses parameter set II of the Brenner hydrocarbon potential [14], an empirical many-body potential based on the Abell-Tersoff covalent bonding formalism [15,16]. This potential describes reasonably well the chemical bonding in graphite and diamond lattices, as well as hydrocarbon molecules. The second parameter set was chosen because it gives more accurate C-C bond stretching force constants. Temperature is controlled in the simulations with the velocity scaling method of Berendsen [17]. The simulation cell begins as a pure graphite lattice that is 39.1 Å by 40.2 Å and 20.1 Å deep, containing 4032 carbon atoms, and is modified as described below. Boundary conditions were chosen to simulate a small region of a much larger bulk material. The atoms within 2 Å of the bottom surface are held fixed, the top surface is free, and the sides of the cell have periodic boundary conditions.

VFTRIM-3D is used to compute the reflection coefficient as a function of incident particle energy [18]. In this paper the cohesion energy calculated from molecular dynamics is applied to the surface binding energy (SBE) in VFTRIM-3D. The bond energy is taken as 10% of the surface binding energy. Two layers are used in the VFTRIM-3D simulation with input data from the molecular dynamics code. The first layer has a SBE equal to 6.98 eV, the mass density as 1191 kg/m^3 and a 0.2 H-C composition. The second layer has a SBE equal to 7.04 eV, mass density of 1286 kg/m^3 and a 0.3 H-C composition.

2.2. Surface preparations

The MolDyn code was originally able to generate a carbon lattice in either graphite, diamond, or zinc-blende configuration. In order to study a surface more relevant to fusion devices, the original pure graphite surface was modified in one of two ways. Because a carbon surface in a fusion reactor will be bombarded by large fluxes of hydrogen, graphite will quickly become saturated with hydrogen. Therefore, the original pure graphite surface was bombarded with hydrogen atoms incident at at 20 eV and 45°, roughly what may be expected to occur in a tokamak. This process was carried out for over 4000 individual atom impacts, during which hydrogen is primarily implanted in the lattice but may also reflect or later be evolved

from the surface. The process leads to the evolution of the surface's hydrogen content as shown in Figure 1. The resulting surface is a hydrogenated graphite surface with 0.42 H:C, near what is typically found in experiments. The surface is near steady-state, as the H:C ratio is not completely constant at the end of the process shown in Figure 1. The CPU time requirements were the limiting factor in how long the preparation of the surface could be carried out.

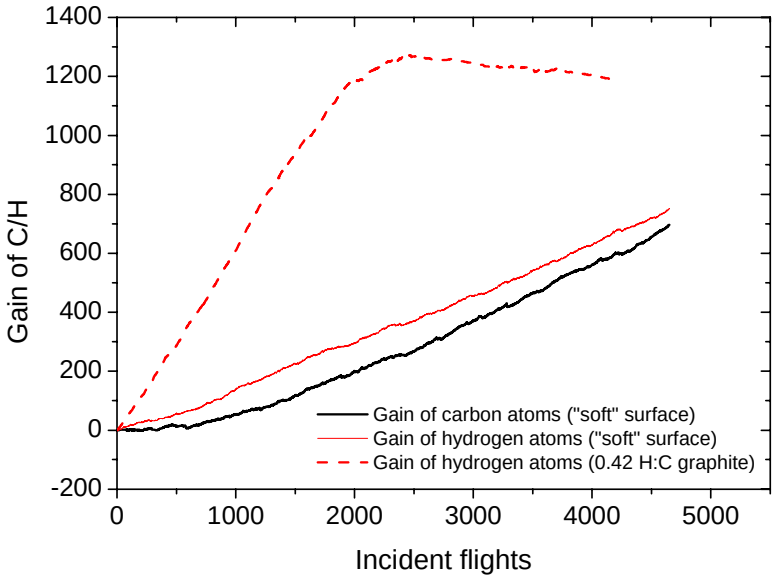

Figure 1. The gain of carbon and hydrogen atoms during surface preperation to get (1) a hydrogen saturated graphite surface [dashed line] and (2) a "soft" redeposited layer [solid lines]. For the 0.42 H:C graphite, saturation is reached as the line levels off. The "soft" layer, however, continually grows.

The second surface that has been developed is meant to go a step further to replicate real carbon PFCs. It also began as pure graphite, but instead of bombarding it with hydrogen only, as in the first process, both hydrogen and hydrocarbon molecules were launched at the surface. This emulates the redeposition of chemically sputtered hydrocarbons on the surface of PFCs in fusion devices. As in the prior case there were over 4000 flights run, with the effects of each being cumulative. Unlike the first case, however, the surface did not reach a steady-state. Instead, the number of carbon and hydrogen atoms comprising the surface both continued to grow, as shown in Figure 1. As such, the thickness of the surface grew from the original 20.1 Å to 47 Å – representing the deposition of a redeposited carbon layer almost 27 Å thick. This matches what occurs in experiments, as do some of the qualities of the layer; namely a lower density, higher H:C ratio, and less strongly bound carbon atoms in the "soft" layer.

2.3. Reflection calculations

The pre-prepared surfaces described above were used as input to all of the following reflection calculations. Carbon at 45° and 60°, and some hydrocarbon molecules (CH, CH_2, CH_3, and CH_4) at 45° were incident on the surface at 300 Kelvin. Incident energies ranged from thermal to ~10s of eV, coinciding with the upper end of the energy range where the potential is valid. Molecules were rotated randomly so that they struck the surface in a different 3D orientation each time. Thousands of separate flights were run for each incident species and energy to develop good statistics, giving reasonably small errors in the reflection coefficient of generally under 5%.

3. Results and Discussion

Molecular Dynamics simulations of carbon and hydrocarbon reflection were initally performed using the first (0.42 H:C graphite) surface, and were reported in detail in [19]. To summarize the results, carbon was found to reflect nearly 70% of the time at thermal energies, with the reflection coefficient decreasing to only 0.2 at 10 eV. It was found that the reflection coefficient was slightly higher at 60° incidence (from normal) than at 45°. The angular dependence on reflection probability was more pronounced at the upper end of the energy range. Reflected carbon atoms at 45° incidence came away with ~32% of their original energy. Also, they tended to reflect with a distribution of elevation angles peaked at 45°, and tending to continue in their original direction parallel to the surface. Carbon atoms at 60° incidence showed some evidence of a specular component in the reflected elevation angle distribution, and a more definite tendency to continue in their original azimuthal direction.

The reflection behavior of hydrocarbon molecules was more complicated, as the molecules tend to break up upon hitting the surface at significant energy. The result is that various fragments can be reflected from the surface. For example, an incident methane molecule can come back as CH_4, CH_3, CH_2, CH, C, H_2, or H. In order to effectively summarize these type of results, the total carbon recycling was calculated as the sum of all carbon atoms reflected in various fragments, divided by the number of incident carbon atoms. Comparison of such a calculation for carbon and all of the methane family of hydrocarbons (CH_x) is shown in Figure 2 and demonstrates that the reflection coefficient tends to increase with the hydrogen content of the molecule. Methane, a saturated molecule, shows almost no sticking over most of this energy range. However, at higher energies the molecule breaks up, allowing the fragments to stick. As one goes from CH_4 to CH_3 to CH_2 to CH the reflection coefficient decreases. The behavior of molecules, in terms of reflected energy and angle, was similar to that of carbon atoms, although this is complicated by their tendency to break apart upon impact.

An attempt was made to compare these results to those of a Monte Carlo BCA-based code, such as VFTRIM-3D. This data is shown in Figure 2, and seems to agree reasonably well with the results of the MD code. It is somewhat difficult to directly compare the two, mainly because they are valid at different energy ranges. A similar comparison was made between the MD code and some experimental data on hydrocarbon sticking/reflection at thermal energy for CH_2 (reflection coefficient $R \approx 0.972$-0.975) [20] and CH_3 ($R \approx 0.986$-0.999) [21-24]. The data presented here shows good agreement to these reflection coefficients.

The second type of surface analyzed is a “soft” redeposited carbon layer, formed by the process described in Section 2.1. As mentioned briefly above, this surface is characterized by a lower density, higher H:C ratio, and less strongly bound carbon atoms. Figure 3 shows some of these characteristics. First, the ratio of hydrogen atoms to carbon atoms reaches over 0.6 in the redeposited layer, increasing toward the very top of the layer. It is possible that this ratio would continue to increase if the redeposited layer was allowed to continue to grow. Second, there is a dramatic decrease in density (proportional to the number of atoms in each slice of volume) as one approaches the surface. Additionally, carbon atoms very near the surface have an average potential energy of -6.0 eV, compared to -7.4 eV on a pure graphite surface. It has been theorized that the existance of such layers on plasma facing components, which would cause them to erode more easily[25], may help to better explain some experimental findings[26].

Reflection measurements on this “soft” surface were performed for CH_3, CH_2, CH, and C at 1 eV and 45° incidence. The resuling data points are shown in Figure 2, allowing for comparison to the data on the previous surface. In each case, reflection was less likely on the “soft” layer. This effect was the largest for carbon atoms, for which the reflection coefficient decreased from 0.42 to 0.18 (a 57% decrease). CH went from the previous value of 0.37 to 0.21, CH_2 declined from 0.63 to 0.42, and finally CH_3 decreased from 0.86 to 0.63. Simulations at a full range of incident energies, as well as for other incident hydrocarbon molecules, are currently underway.

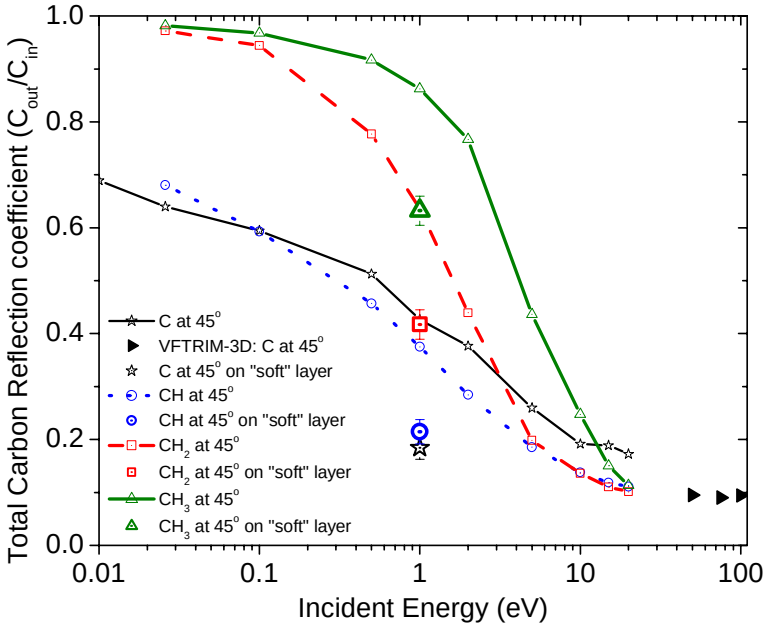

Figure 2. The total carbon reflection coefficient for C, CH, CH_2, CH_3 at various energies on the 0.42 H:C graphite surface (lines) and at 1 eV on the new "soft" redeposited layer (data points at 1 eV). For comparison, VFTRIM-3D data for carbon incident at 45 degrees is also shown.

4. Conclusions

A molecular dynamics code has been optimized for studying surface interactions between carbon and hydrocarbon molecules and carbon-based surfaces. Reflection data for carbon and several hydrocarbon molecules (CH, CH_2, CH_3, and CH_4) has been calculated. There appears to be a definite trend in the data, i.e. molecules with a higher hydrogen content are more likely to reflect. The data is compares relatively well with VFTRIM-3D modeling at the higher energies and with experimental hydrocarbon sticking data at thermal energy.

The information gained from these simulations, namely reflection coefficients and reflected energy and angular distributions, have been included in erosion/redeposition codes to improve the capability of modeling chemically sputtered carbon transport in fusion devices [26]. One remaining unknown is the chemical erosion yield, which is thought to vary depending on the type of surface in question. For example, the "soft" redeposited layers that are thought to erode more easily. Additional modeling and experimental work is required to resolve certain discrepancies between modeling and experiment, e.g. the codeposition problem in JET [26]. In terms of the MD modeling presented here, future work includes studying more hydrocarbon molecules (including C_2H_y and C_3H_y species) and looking a larger range of incident energies.

Acknowledgements

The authors would like to thank Jeffrey Brooks, whose work with erosion/redeposition modeling provided the motivation for this work, and Robert Averback for providing the MolDyn code used as a starting point for the modeling discussed herein. This work was supported by the United States Department of Energy, under a subcontract from Argonne National Laboratory.

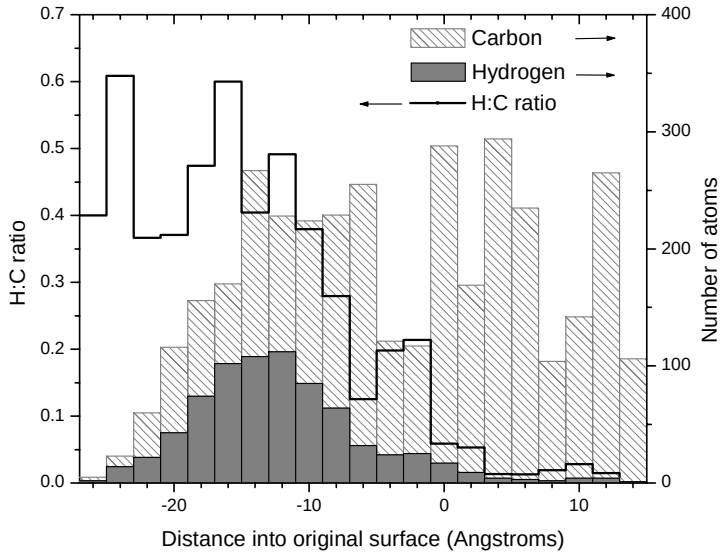

Figure 3. Properties of the "soft" redeposited carbon surface showing the hydrogen to carbon ratio (line) and the concentration of carbon (cross-hatched) and hydrogen (gray) atoms versus depth. A depth of zero represents the original surface, and the deposited layer extends in the negative direction.

References

[1] W. Jacob, Thin Solid Films **326**, 1 (1998).
[2] J. Robertson, Materials Science and Engineering: R: Reports **37** (4-6), 129 (2002).
[3] Dieter M. Gruen, Annual Reviews of Materials Science **29**, 211 (1999).
[4] W. Moller, P. Borgesen, B.M.U. Scherzer, Nuclear Instruments & Methods in Physics Research **B19/20**, 826 (1987).
[5] V. Phillips, M. Stamp, A. Pospieszczyk *, et al.*, J. Nucl. Mater. **313-316**, 354 (2003).
[6] J. Roth, J. Nucl. Mater. **266-269**, 51 (1999).
[7] A. A. Haasz, J. W. Davis, J. Nucl. Mater. **232**, 219 (1996).
[8] S. K. Ray, S. Das, C. K. Maiti *, et al.*, Applied Physics Letters **58** (22), 2476 (1991).
[9] B. V. Mech, A. A. Haasz, J. W. Davis, J. Nucl. Mater. **241-243**, 1147 (1997).
[10] J. N. Brooks, Phys. Fluids B **2** (8), 1858 (1990).
[11] J.N. Brooks, D.A. Alman, G. Federici *, et al.*, J. Nucl. Mater. **266-69**, 58 (1999).
[12] J.N. Brooks, D.G. Whyte, Nuclear Fusion **39** (4), 525 (1999).
[13] K. Beardmore, MolDyn (Loughborough University,UK).
[14] D.W. Brenner, Phys. Rev. B **42** (15), 9458 (1990).
[15] G.C. Abell, Phys. Rev. B **31** (10), 6184 (1985).
[16] J. Tersoff, Phys. Rev. B **37** (12), 6991 (1988).
[17] H.J.C. Berendsen, J.P.M. Postma, W.F. van Gunsteren *, et al.*, J. Chem. Phys. **81** (8), 3684 (1984).
[18] D. N. Ruzic, Nuclear Instruments and Methods in Physics Research **B47**, 118 (1990).
[19] D.A. Alman, D.N. Ruzic, J. Nucl. Mater. **313-316**, 182 (2003).
[20] H. Toyoda, H. Kojima, H. Sugai, Applied Physics Letters **54** (16), 1507 (1989).
[21] H. Kojima, H. Toyoda, H. Sugai, Applied Physics Letters **55** (13), 1292 (1989).
[22] M. Shiratani, J. Jolly, H. Videlot, J. Perrin, Japanese Journal of Applied Physics **36**, 4752 (1997).
[23] P. Kaenune, J. Perrin, J. Guillon, J. Jolly, Plasma Sources Science & Technology **4** (2), 250 (1995).
[24] A. von Keudell, T. Schwarz-Selinger, M. Meier, W. Jacob, Applied Physics Letters **76**, 676 (2000).
[25] E. Vietzke, A.A. Haasz, in *Physical Processes of the Interaction of Fusion Plasmas with Solids* (1996), pp. 135.
[26] J.N. Brooks, A. Kirschner, D.G. Whyte *, et al.*, J. Nucl. Mater. **313-316**, 424 (2003).

Global Model of High/Low Frequency Decoupling in Dual Frequency Capacitive Discharges

M.A. Lieberman and Jisoo Kim

Department of Electrical Engineering and Computer Science, University of California, Berkeley, CA 94720

Abstract

Large area capacitive discharges driven at two frequencies, one of which is is higher than the usual industrial frequency of 13.56 MHz, have attracted recent interest for dielectric etching on large area substrates. In the ideal case, the high frequency controls the plasma density n (ion flux) and the low frequency controls the ion bombarding energy $\mathcal{E}_i$. A global (volume averaged) model of dual frequency discharge operation is described, and the conditions for the decoupling of the high and low frequencies are obtained.

1. Introduction

Large area plasma processing systems capacitively driven at frequencies higher than the conventional industrial frequency of 13.56 MHz, and dual frequency capacitive reactors with one high and one low frequency drive, have attracted much recent interest from researchers and equipment manufacturers for silicon wafer and flat panel display processing [1–14]. Larger areas are required as semiconductor manufacturers increase wafer sizes from 200 mm to 300 mm, and also for processing large (1 meter $\times$ 1 meter) glass panels for active matrix LCD flat panel computer and TV screens. Higher frequency produces a reduced ion bombarding energy for a given ion flux to the substrate [1, 3, 6, 15–17]. A reduced bombarding energy is required in the near future, to process integrated circuits with smaller critical dimensions (gate widths) and to increase reactor throughput. Higher frequency also permits the addition of a second, low frequency bias voltage, for additional flexibility. With both a high frequency and a low frequency drive, independent control of *both* the ion flux and ion bombarding energy can be achieved in capacitive reactors [8, 9, 11–14, 18].

2. Dual Frequency Discharges

Dual frequency capacitive reactors can have desirable properties for dielectric etch: low cost, robust uniformity over large areas, and control of dissociation (F-atoms). In the ideal case, the high frequency controls the plasma density n (ion flux) and the low frequency controls the ion bombarding energy $\mathcal{E}_i$. Typical operating conditions are: discharge radius $R \sim$ 15–30 cm, length $L \sim$ 1–3 cm, pressure $p \sim$ 50–300 mTorr, high frequency $f_1 \sim$ 27.1–160 MHz, low frequency $f_2 \sim$ 2–13.6 MHz, high frequency voltage amplitude $V_{\rm rf} \sim$ 250–1000 V, low frequency voltage amplitude $V_B \sim$ 500–2000 V, and powers of 500–3000 W for both low and high frequency sources.

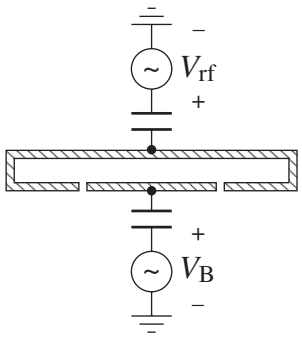

Figure 1. Diode model (two electrodes).

The two main types of dual frequency discharges are shown in Figs. 1 and 2. The diode configuration has the high frequency voltage applied to the larger area electrode and the low frequency voltage applied to the smaller area electrode. However, components of both high and low frequency voltages appear across the sheaths at both electrodes. The triode configuration has an added ground electrode.

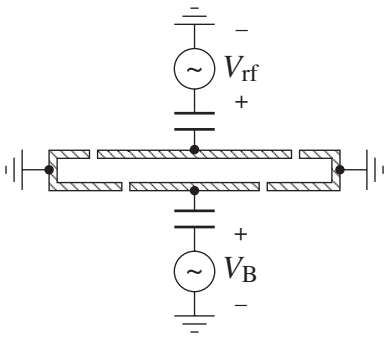

Figure 2. Triode model (three electrodes).

If the area of this ground electrode is large compared to the areas of the two driven electrodes, then the high frequency can mainly appear across the upper electrode sheath, and the low frequency across the lower electrode sheath. However, for both diodes and triodes, it is possible to achieve a good decoupling of the effects of the high and low frequencies, such that the high frequency mainly controls the plasma density (ion flux) and the low frequency mainly controls the ion energy at the lower electrode.

To understand the decoupling, let us consider a cylindrical (radius $R >>$ length L) discharge model in a simple gas (argon). We use a global (volume-averaged) model. In the steady state, the production of electron-ion pairs in the volume by electron-neutral ionization must be balanced by the loss of pairs to the walls. It is well known [19, Sec. 10.1] that this particle (ion) balance relation sets the electron temperature T_e of the plasma, independent of the plasma density n. Typically $T_e \sim$ 2–5 eV, depending weakly on the pressure. The corresponding electron power balance relation is

$$P_e = enu_B\, 2A\, \mathcal{E}_e \tag{1}$$

where P_e is the electron power absorbed, $u_B = (eT_e/M)^{1/2}$ is the ion loss (Bohm) velocity, $A = \pi R^2$ is the discharge plate area, and $\mathcal{E}_e$ is the total electron energy loss per electron-ion pair created (typically $\mathcal{E}_e \sim$ 30–100 eV for argon, depending on the pressure). We see that the density is simply proportional to the electron power absorbed P_e.

To understand why the high frequency controls the density, let us consider the ohmic heating of the plasma $P_e = \frac{1}{2} I_{rf}^2 R$ for the usual "sandwich" structure of a capacitive discharge carrying an rf current I_{rf}, with sheaths of thickness s each having capacitance C, and with a plasma resistance R, as shown in Fig. 3.

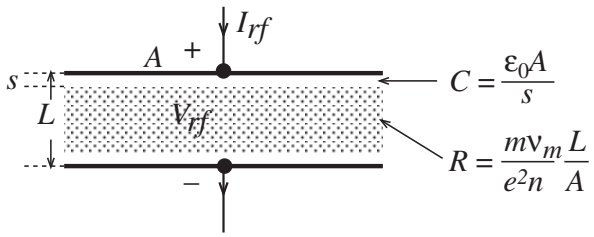

Figure 3. Sandwich structure of a capacitive discharge.

Since the current $I_{rf} \propto \omega C V_{rf} \propto \omega V_{rf}/s$ and the resistance $R \propto n^{-1}$, we have the scaling for ohmic power

$$P_e \propto \frac{\omega^2 V_{rf}^2}{s^2 n} \tag{2}$$

On the other hand, the Child law scaling for the sheath thickness is

$$n \propto \frac{V_{rf}^{3/2}}{s^2} \tag{3}$$

Eliminating s from (2) and (3) yields

$$P_e \propto \omega^2 V_{rf}^{1/2} \tag{4}$$

Since $n \propto P_e$ from electron power balance, a high frequency source at moderate voltage yields a high density, while a low frequency source even at fairly high voltage has almost no effect on density. *Hence, the high frequency power controls the density.*

For a diode (Fig. 1), the ion energy is controlled by the amplitude of the *total* voltage (high + low frequency) across the lower electrode:

$$\mathcal{E}_i \sim 2\,|V_{\rm rf} + V_B| \tag{5}$$

If the low frequency is at a high voltage V_B compared to the high frequency voltage $V_{\rm rf}$, *then the low frequency voltage controls the ion energy.* For a triode (Fig. 2), one can make the ground area large for additional control of ion energy by V_B. Hence the two conditions for good decoupling of high and low frequencies are:

$$\omega^2 V_{\rm rf}^{1/2} \gg \omega_B^2 V_B^{1/2} \tag{6}$$

$$V_B \gg V_{\rm rf} \tag{7}$$

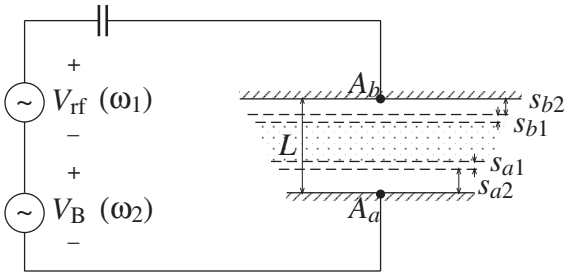

Figure 4. Global model of dual frequency diode discharge.

Let us examine a typical global model result for the dual frequency asymmetric diode model shown in Fig. 4. The discharge conditions are plate areas A_a = 544 cm^2, A_b = 707 cm^2, length L = 1.6 cm, high frequency f_1 = 27.1 MHz, low frequency f_2 = 2 MHz, and pressure p = 190 mTorr in argon. The physics incorporates Child law sheaths at the low frequency (thicknesses s_{a2} and s_{b2}) and homogeneous sheaths at the high frequency (thicknesses s_{a1} and s_{b1}).

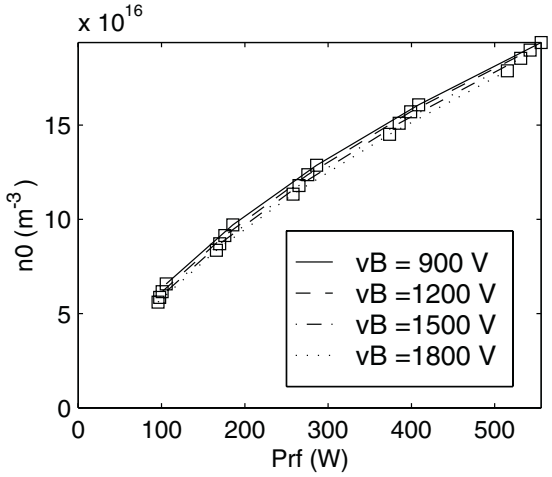

Figure 5. Central density versus high frequency power.

Homogeneous sheaths are used at high frequencies because the low frequency sheath thicknesses are generally larger than the high frequency sheath thicknesses. The low frequency sheaths act like capacitors that vary on the low frequency timescale, limiting the flow of high frequency current through the discharge. The model physics incorporates all ohmic and stochastic heating terms for both high and low frequencies, as well as the usual particle balance relation for ions.

The results for the central density n_0 versus the high frequency power absorbed $P_{\rm rf}$ are shown in Fig. 5 for four different low frequency voltages V_B. We see a good decoupling of low and high frequencies, with almost

the same central density n_0 at the same high frequency power $P_{\rm rf}$ over the range of low frequency voltages V_B = 900–1800 V.

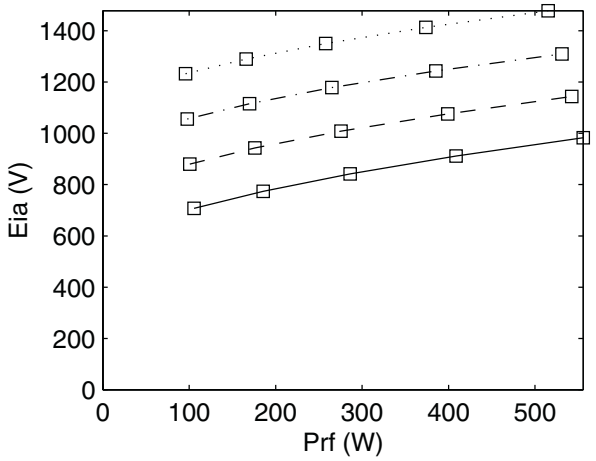

Figure 6. Ion bombarding energy versus high frequency power at electrode a.

The results for the ion bombarding energy $\mathcal{E}_i$ at electrode a are shown in Fig. 6. We see a reasonably good decoupling, with reasonably flat curves for $\mathcal{E}_i$ versus $P_{\rm rf}$ for each value of V_B. There is some slope to each curve, showing the influence of $P_{\rm rf}$ on $\mathcal{E}_i$. Ideally, for perfect decoupling, the curves would have zero slope everywhere.

3. Conclusions

We have described work in progress aimed at understanding and modeling dual frequency capacitive discharges for dielectric etch applications. A global (volume-averaged) model has been developed to determine the discharge parameters and to investigate the influence of the high and low frequency drives on the plasma density (ion flux) and ion bombarding energy. The conditions for decouping the effects of the high and low frequencies were examined.

We have previously examined the standing wave and skin effects due to the high frequency drive [20]. We showed that the discharge is excited at the high frequency by the propagation of surface and evanescent waves from the discharge periphery into the center. We showed examples of discharges where skin effects and standing wave effects could be important, and we found the conditions for which standing surface wave effects, surface wave skin effects, and evanescent wave effects can be neglected.

Acknowledgements

One of the authors (MAL) gratefully acknowledges valuable discussions of this work with A.J. Lichtenberg, and the support provided by the Lam Research Corporation, National Science Foundation Grant ECS-0139956, California industries, and the State of California UC-SMART Program under Contract SM99-10051.

References

1. V. Vahedi, C.K. Birdsall, M.A. Lieberman, G. DiPeso and T.D. Rognlien, *Phys. Fluids B* **5** 2719 (1993).
2. A.A. Howling, J.L. Dorier, C. Hollenstein and U. Kroll, *J. Vac. Sci. Technol. A* **10** 1080 (1992).
3. K.K. Kalpakjian, M.A. Lieberman and W.G. Oldham, *J. Vac. Sci. Technol. B* **12** 1351 (1994).
4. L. Sansonnens, A. Pletzer, D. Magni, A.A. Howling, C. Hollenstein, and J.P.M. Schmitt, *Plasma Sources Sci. Technol.* **6** 170 (1997).
5. G.J. Nienhuis and W. Goedheer, *Plasma Sources Sci. Technol.* **8** 295 (1999).
6. M.J. Colgan, M. Meyyappan and D.E. Murnick, *Plasma Sources Sci. Technol.* **3** 181 (1994).
7. M. Meyyappan and M.J. Colgan, *J. Vac. Sci. Technol. A* **14** 2790 (1996).
8. H.H. Goto, H.D. Lowe and T. Ohmi, *IEEE Trans. Semicond. Manuf.* **6** 58 (1993).
9. W. Tsai, G. Mueller, R. Lindquist, B. Frazier and V. Vahedi, *J. Vac. Sci. Technol. B* **14** 3276 (1996).
10. A.A. Howling, J.L. Dorier, C. Hollenstein, U. Kroll and F. Finger, *J. Vac. Sci. Technol. A* **10** 1080 (1992).
11. H.H. Goto, H.D. Lowe and T. Ohmi, *J. Vac. Sci. Technol. A* **10** 3048 (1992).

12. T. Kitajima, Y. Takeo, Z.L. Petrovic and T. Makabe, *Appl. Phys. Lett.* **77** 489 (2000).
13. T. Kitajima, Y. Takeo and T. Makabe, *J. Vac. Sci. Technol. A* **17** 2510 (1999).
14. S. Rauf and M.J. Kushner, *IEEE Trans. Plasma Sci.* **27** 1329 (1999).
15. V.A. Godyak, *Sov. J. Plasma Phys.* **2** 78 (1975).
16. V.A. Godyak and O.A. Popov, *Sov. J. Plasma Phys.* **5** 227 (1979).
17. M. Surendra and D.B. Graves, *Appl. Phys. Lett.* **59** 2091 (1991).
18. V. Vahedi and G. DiPeso, *J. Comp. Phys.* **131** 149 (1997).
19. M.A. Lieberman and A.J. Lichtenberg, *Principles of Plasma Discharges and Materials Processing,* (Wiley, New York, 1994) .
20. M.A. Lieberman, J.P. Booth, P. Chabert, J.M. Rax, and M.M. Turner, *Plasma Sources Sci. Technol.* **11** 283 (2002).

Scaling up the Synthesis of Nano Size Aluminum Particles

F. Aristizabal[1,2], R. J. Munz[1,3], and D. Berk[1]

[1] *Department of Chemical Engineering, McGill University, Montreal, Canada*
[2] *Department of Physiology, McGill University, Montreal, Canada*
[3] *CRTP, Plasma Technology Research Center, Montreal, Canada*

Abstract
A convenient way to synthesize aluminum nano particles is to evaporate the metal, direct this vapor into a tubular reactor and quench it with a radial flow of cold gas. The supersaturated vapors nucleate and grow into the desired nano particles. For small scale operations, because of the high temperatures and relatively low flow rates involved, the conditions of operation are usually laminar. As the units are scaled up to higher production rates, the flows become transitional or even fully turbulent. This work reports on the use of a Low Reynolds Number (LRN) turbulent model to simulate this system and its scale up for the synthesis of pure aluminum powders. The dynamic behavior of the particulate system was modeled in terms of the leading moments of a log-normal particle size distribution.

1. Introduction

The unique properties associated to nano size metal particles, thanks to the high fraction of atoms that reside at the grain boundaries, make them very attractive for different applications such as super alloys, thick film conductors, catalysis for the chemical industry, coatings, and others. A common method of production of metal powders is the Inert Gas Condensation (IGC). Pure product due to the inert atmosphere, relative ease to control by adjusting operation parameters, and possible continuous operation are the main features that make the IGC method appropriate for the production of aluminum nano particles.

The objective of this work was to develop a model to study the growth and transport of nano size metal particles inside a tubular reactor with radial injection of a quenching gas. The model is used to study the effect of the different operation parameters on the particle properties and to assist the scale up of the system. In this paper two cases are studied, the effect of the injection flow rate and the scale up of the process.

2. Mathematical model

Figure 1 shows a schematic drawing of the process, the plasma chamber and the particle generator. The particles are collected at the end of the particle generator by a filter. It is assumed that the particles are only formed inside the particle generator. This permits the separation of the model for the particle generator from

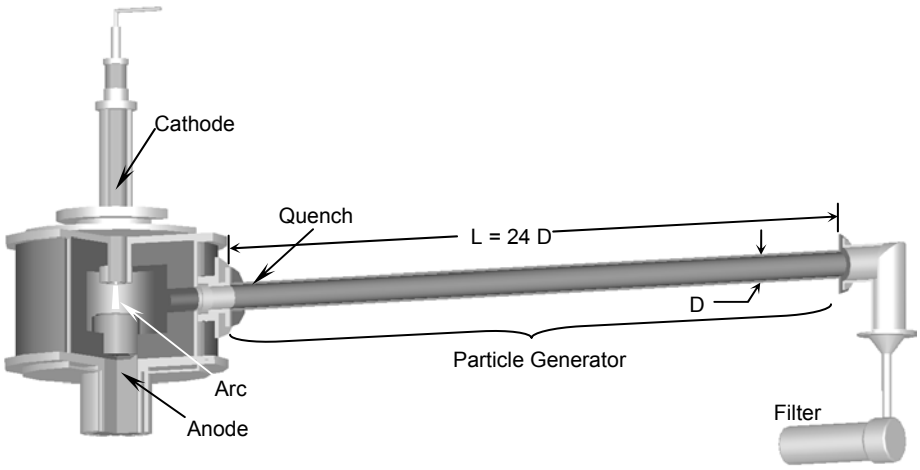

Figure 1: Schematic of the process of generation of nano size particles from the quench of a superheated vapor. The plasma chamber uses a transferred arc to evaporate the metal placed as the anode.

that for the heat source [1]. The particle generator is 60 cm in length and 5 cm in diameter. The quenching gas is injected through a slot 2.5 mm wide, located 5 cm from the entrance. The model has been developed for dilute systems, where the concentration of metal vapor in the gas phase is small (~ 10^{-3} kg Al/kg gas). The properties of the metal vapor and carrier gas mixture are assumed those of the carrier gas [2].

The Jones-Launder LRN $\kappa-\varepsilon$ turbulence model [3] was selected for its simplicity and low computational expense. This model also can be integrated to solid walls without fixing an artificial point below which a laminar sublayer is expected to exist. It uses a series of damping functions to force the desired behavior near the wall. It can also be used for both, laminar and turbulent flows as well as transitional flows [2, 4].

The metal vapor concentration is modified by convection, diffusion, nucleation and condensation and therefore it is coupled to the moment equations. The form of the conservation of metal vapor is presented in Eq. (1). The last two terms of this equation represent the amount of vapor being condensed by nucleation and by condensation, respectively.

$$\nabla\cdot\left(\rho\,\vec{u}\,w_{Al}\right)=\nabla\cdot\left[\left(\rho D_{Al,Ar}+\frac{\mu_t}{\sigma_w}\right)\nabla w_{Al}\right]-I\,\rho_p v^{*}-\rho_p^{1/3}B_1\left(S-1\right)\hat{M}_{2/3} \tag{1}$$

The moment equations are derived from the General Dynamic Equation (GDE) for turbulent flow [5]. The fluctuating sources of growth, coagulation, and nucleation rate are neglected (Eq. 2). The turbulent diffusion term is taken to be proportional to the gradient of the mean value of the transported quantity, by analogy with turbulent transport of momentum, since both phenomena are due to the same mechanism, eddy mixing [6].

$$\begin{aligned}\underbrace{\nabla\cdot\rho\,n_m\,\vec{v}}_{Convection}=&\underbrace{\nabla\cdot\left(\rho\left(D_p+\frac{\mu_t}{\sigma_t}\right)\nabla n_m\right)}_{Diffusion}-\underbrace{\nabla\cdot\rho\,n_m\,\vec{v}_{ther}}_{Thermophoresis}+\underbrace{I\left(v^{*}\right)\delta\left(v-v^{*}\right)}_{Nucleation}-\underbrace{\frac{\partial\left(G\,\rho\,n_m\right)}{\partial\,v}}_{Condensation}\\&\underbrace{+\frac{1}{2}\rho^2\int_0^{v}\beta\left(\tilde{v},v-\tilde{v}\right)n_m\left(\tilde{v}\right)n_m\left(v-\tilde{v}\right)d\tilde{v}-\rho^2\,n_m\left(v\right)\int_0^{\infty}\beta\left(\tilde{v},v\right)n_m\left(\tilde{v}\right)d\tilde{v}}_{Coagulation}\end{aligned} \tag{2}$$

The first step in deriving the moment equations is to define the moments of the particle size distribution. The particle size distribution is normalized by a constant n_0 [2], which represents the number of monomers at a certain location in the reactor, as presented in Eq. (3). Using this definition of the moments, a conservation equation for the k^{th} moment can be obtained by multiplying Eq. (2) by m^k and integrating over the entire particle size. The result of this procedure is presented in Eq. (4)

$$\hat{M}_k=\int_0^{\infty}m^k\,\frac{n_m\left(v,t\right)}{n_0}dv \tag{3}$$

$$\begin{aligned}\underbrace{\nabla\cdot\rho\vec{u}\hat{M}_k}_{Convection}=&\underbrace{\nabla\cdot\left(\rho\left(D_k+D_{turb}\right)\nabla\hat{M}_k\right)}_{Diffusion}-\underbrace{\nabla\cdot\rho\,\vec{u}_{ther}\hat{M}_k}_{Thermophoresis}\\&\underbrace{+I\left(v^{*}\right)\delta\left(v-v^{*}\right)v^{*k}\rho_p^k}_{Nucleation}+\left[\dot{\hat{M}}_k\right]_{Condensation}+\left[\dot{\hat{M}}_k\right]_{Coagulation}\end{aligned} \tag{4}$$

D_k represents the Brownian diffusion coefficient for the k^{th} moment, and D_{turb} is the diffusivity due to the turbulent motion. The Brownian diffusion coefficient is calculated using the simplified expression presented by Chiu [7]. The thermophoretic coefficient K_{Th} can be assumed to be independent of particle size for large Knudsen numbers, since it approximate an asymptotic value of 0.55. The nucleation term can be easily integrated since it is independent of the particle size distribution. I is calculated from the expression for the self-consistent nucleation rate [8]. The condensation [9] and coagulation [9, 10] terms in the Free Molecular Regime (FMR) are used in this work [5].

The integration of some of the terms in Eq. (4) requires the assumption of a particle size distribution function. In this work the distribution is approximated by a lognormal function which fits the observed size distributions reasonably well and its mathematical form is convenient for dealing with weighted distributions

[11]. Any moment of the size distribution is related to the zero moment, the geometric mean volume, and the geometric standard deviation. These parameters can be calculated from the first three moments of the distribution, Eq. (5) [9].

$$v_g = \frac{\hat{M}_1^2}{\hat{M}_0^{3/2}\hat{M}_2^{1/2}} \cdot \frac{1}{\rho_p}; \qquad \ln^2 \sigma_g = \frac{1}{9}\ln\left(\frac{\hat{M}_0\hat{M}_2}{\hat{M}_1^2}\right) \tag{5}$$

The equations are discretized using the Finite Volume Finite Difference Method (FVFDM). The set of algebraic equations is solved using the Gauss-Seidel line-by-line iteration scheme using a Tri-Diagonal-Matrix-Algorithm (TDMA of Thomas algorithm) to solve for each line. Moreover, the SIMPLER algorithm (Semi-Implicit Method for Pressure-Linked-Equations Revised) was used to solve the fluid flow field coupled to the continuity equation [12]. Here, the Power Law scheme for the diffusion-convection problem was used. The thermophoretic term also needs an interpolation function to calculate consistent fluxes at the interfaces; in this case, the Upwind scheme was implemented [6]. The solution of the equations is an iterative procedure that is manipulated in two different forms, relaxation factors or the method of false transients.

The equations are solved in a two dimensional axi-symmetric domain. The boundary conditions of the model are presented below; otherwise they are set to zero. At the entrance of the reactor the axial velocity, the temperature (2000 K), and the metal vapor concentration are specified (10^{-3} kg/kg). At the injection only the radial velocity and the temperature are specified. The turbulent quantities at these two positions are calculated from the relationships presented by Launder and Spalding [6] and a turbulent intensity parameter of 6%. The wall temperature is set to 1000 K. The different moments are set to zero at the entrance, the wall and the injection, indicating that no particles exist at these locations. At the outlet straight out boundary conditions are used, the axial gradients are zero. At the centerline standard symmetry boundary conditions are used.

3. Results and discussion

The model is used to predict the number density, the geometric mean diameter and the geometric standard deviation of the particles inside the generator. Figure 2 presents the spatial distribution of the geometric mean diameter. The main flow rate is 100 slpm and the injection is 60 slpm. The formation of particles is at two different positions, near the entrance and at the injection. At the entrance nucleation takes place near the cold wall, and a boundary layer, similar to a thermal one, is formed. The high injection rate penetrates the boundary layer and decreases the temperature of the gas inside the reactor. The injection also induces recirculation of cold gas near the wall. The low temperature in this zone prevents coalescence of the particles; therefore the mean diameter does not increase here. The high concentration of particles nucleated at the injection increase the coagulation rate. Since no new particles are formed, besides the two nucleation spots, the concentration of particles decreases along the reactor due to coagulation, thus slowly decreasing the coagulation rate.

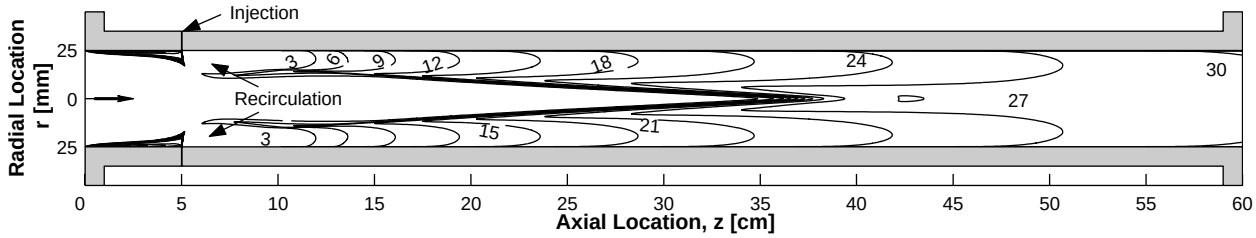

Figure 2: Spatial distribution of the geometric mean diameter (d_{pg} [nm]). Main flow rate 100 slpm and Injection rate 60 slpm

Injection

One of the main advantages of gas aerosol processes is that the characteristics of the product are relatively easy to control by adjusting key operating parameters. The easiest to change and control is the quenching flow rate. However, increasing the injection rate introduces turbulence in the reactor. At low injection rates, the flow rate should be laminar. Studying the effect of operating parameters, such as injection rate, will assist in the selection of optimum conditions for the synthesis of aluminum powder with the desired characteristics.

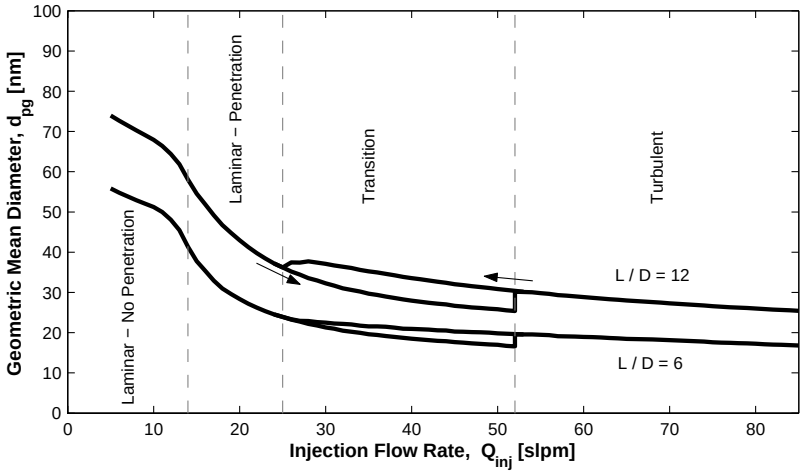

Figure 3: Mixing cup geometric mean diameter as a function of the flow rate of quenching gas. The figure shows the size of the particles at tow different positions in the reactor.

The effect of the injection flow rate on the particle characteristics was studied. The quenching gas flow rate was changed from 5 to 85 slpm, while the main flow rate was kept constant at 100 slpm. Figure 3 shows the effect of the injection rate on the geometric mean diameter. This figure presents mixing cup results at two different positions in the reactor. As the injection rate was increased four different flow regimes were found. At low flow rates, there is a laminar zone (<14 slpm) where the jet cannot penetrate the concentration boundary layer. Then there is a laminar zone (14 – 25 slpm) where the jet penetrates and a second nucleation zone occurs. This is followed by a transition zone (25 – 52 slpm) where either the turbulent or the laminar characteristics may prevail, and finally, there is a turbulent zone (>52 slpm).

Increasing the injection rate increases the number density, decreases the size and slightly increases the polydispersity of the particles. One of the important features of Figure 3 is that the particle geometric mean diameter is almost constant for high injection rates. This is important because it shows that at high injection rates the particle characteristics are less sensitive to changes in the injection than for low flow rates.

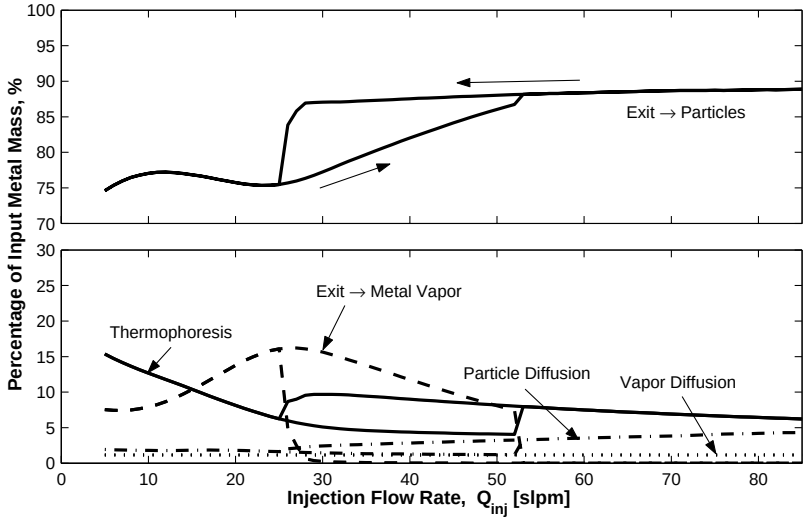

Figure 4: Mass balances and percentage of metal removed by different mechanisms as a function of the flow rate of quenching gas. The figure shows the results at the end of the reactor (L/D = 12).

It is also important to quantify the amount of material that has been condensed and that can be collected as product at the end of the reactor. Figure 4 shows the percentage of metal removed by different mechanisms and the percentage of metal at the exit of the reactor in either condensed or vapor phase. As the injection rate is increased, more material can be recuperated as particles at the end of the reactor since turbulence

increases. Thermophoresis is the main mechanism for deposition of particles on the wall of the reactor. For small injection rates it is responsible for depositing up to 16% of the metal.

Scale up

Two cases are presented here; the first case is scale up with dynamic similitude, where the geometry and the Reynolds number are held constant. Figure 5 shows the effect of increasing the scale factor on the particle size. An almost linear increase in the geometric mean diameter with increasing the reactor diameter can be observed from this figure. The increase in the particle size is accompanied with a decrease in the particle number concentration and slight increase in the geometric standard deviation. The main reason for these changes with increasing reactor size is the increase in the mean residence time, allowing particles to coagulate for longer periods of time.

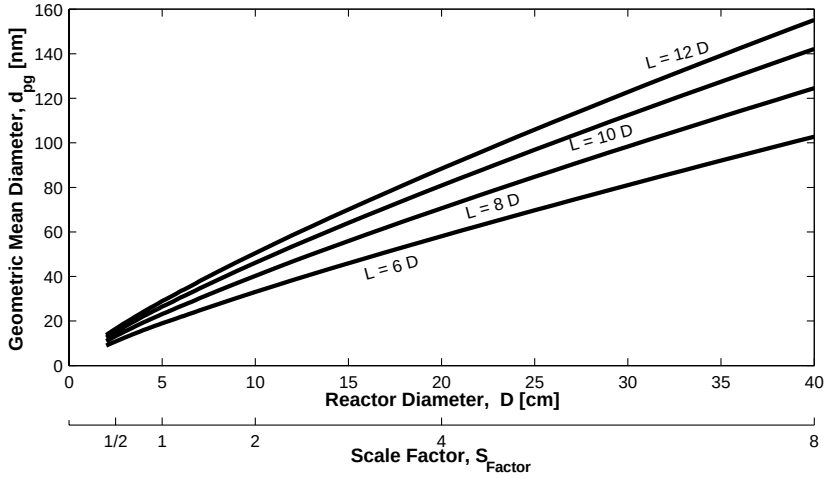

Figure 5: Mixing cup geometric mean diameter as a function of the scale factor for different length to diameter ratios. Scale up with dynamic similitude and 60 % injection.

The second case studied is scale up maintaining geometric similitude and constant mean residence time. When this type of scale up is performed, dynamic similitude no longer holds, and changes in the flow regime are likely to occur as the size of the reactor increases.

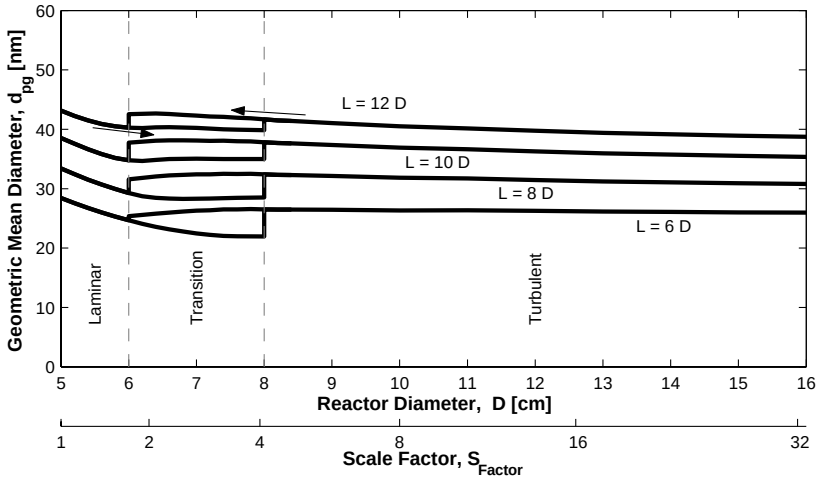

Figure 6: Mixing cup geometric mean diameter as a function of the scale factor for different length to diameter ratios. Scale up with constant mean residence time and 20 % injection.

Figure 6 shows the mixing cup geometric mean diameter for different length to diameter ratios. Although the mean residence time is constant, this figure shows that the particle characteristics are affected by the flow regime. For small length to diameter ratios the effect is significant while for longer reactor the effect

vanishes. By increasing the reactor diameter holding the mean residence time constant, the particle number concentration increases, while the geometric mean diameter and standard deviation decrease.

The question of what would be the best way to scale up this process has not been answered. In fact, there are many ways of increasing the product mass flow rate for the system. For example, pushing higher flow rates through the same reactor, or increasing the concentration of the metal vapor at the inlet, amongst others which can also be analyzed using the present model [2].

4. Conclusions

A two dimensional axi-symmetric model was used to study the phenomena taking place inside the particle generator. It was found that as the quenching rate is increased, the flow regime changes from laminar to turbulent, and four different regimes have been identified. Particles nucleate near the walls at the entrance of the reactor and at the injection; they then grow either by condensation and/or coagulation, being coagulation the dominant mechanism. The characteristics of the particles can be easily controlled by adjusting the quenching gas flow rate. Increasing this parameter increases the number of particles produced, and decreases the mean geometric diameter.

The study of process scale up examined two cases. The first was scale up at constant Reynolds number with geometric similitude, to have dynamic similitude between the small and large scale. Here, scale up increases the mean residence time and decreases the particle number concentration due to nucleation suppression. The particle geometric mean diameter increases almost linearly with the size of the reactor while the geometric standard deviation is almost constant. The second case maintained geometrical similitude and constant mean residence time. Here the flow field regime changes from laminar to turbulent in the scale up process. These changes in the flow regime affect the particle characteristics significantly for reactors of small length to diameter ratio (L/D = 6), but are almost insignificant for large length to diameter ratios (L/D = 12). Turbulent reactors showed small changes in the particle characteristics, plus a better percentage of mass recuperated at the end of the reactor.

Acknowledgements

The present work was supported by NSERC (Natural Sciences and Engineering Research Council of Canada).

References

[1] A. C. da Cruz, Ph.D Thesis, Chemical Engineering, McGill University, Montreal (1997).
[2] F. Aristizabal, M.Eng Thesis, Chemical Engineering, McGill University, Montreal (2002).
[3] W. P. Jones; B. E. Launder, *Int. J. Heat Mass Transfer*, ***16*** (1973).
[4] W. P. Jones; B. E. Launder, *Int. J. Heat Mass Transfer*, ***15*** (1972).
[5] S. K. Friedlander, *Smoke, Dust, and Haze: Fundamentals of Aerosol Dynamics*, 2nd ed.; Oxford University Press, Oxford (2000).
[6] H. K. Versteeg; W. Malalasekera, *An Introduction to Computational Fluid Dynamics. The Finite Volume Method*; Longman Scientific & Technical, England (1995).
[7] C. P. Chiu, Ph.D., Univ. Minnesota, Minneapolis (1992).
[8] S. L. Girshick; C. P. Chiu; R. Muno; C. Y. Wu; L. Yang; S. K. Singh; P. H. McMurry, *J. Aerosol Sci.*, ***24***, 3 (1993).
[9] S. E. Pratsinis, *J. Colloid Interface Sci.*, ***124***, 2 (1988).
[10] K. W. Lee; H. Chen, *Aerosol Sci. Technol.*, ***3***, 3 (1984).
[11] W. C. Hinds, *Aerosol technology*; John Wiley & Sons, New York (1982).
[12] S. V. Patankar, *Numerical Heat Transfer and Fluid Flow*; Hemisphere Publishing Corporation, New York (1980).

Experimental Study on Propagation Characteristics of Microwave in GlidArc Discharge Plasma

LIN Lie, WU Bin, WU Cheng-kang, PAN Wen-xia
Institute of Mechanics, Chinese Academy of Sciences
Beijing 100080, China

Abstract

The GlidArc discharge plasma at atmospheric pressure is a type of non-thermal plasma, and has many applications in chemical industry and environment engineering. In this paper we study the propagation characteristics of the microwave in GlidArc discharge plasma. And then according to the power absorption coefficient we calculated the electron density in plasma.

1. Introduction

Research on the propagation of electromagnetic wave in plasmas has been sustained many years as a result of applications, such as broadcast communication, radio astronomy and plasma diagnostics with microwave [1-5]. The propagation properties of electromagnetic wave in plasma are related to many factors, such as the frequency of electromagnetic wave, electron density, electron temperature, collision frequency and size of the plasma slab.

The GlidArc discharge is a type of production technologies for non-equilibrium plasma at atmospheric pressure. The electron density is a very important parameter for his application. By the Research on the propagation of electromagnetic wave in plasmas, we can calculate the electron density in plasma. But the GlidArc discharge plasma is a type of pulse discharge plasma, so the measurement of electron density is more difficult. In this paper we measure the power absorption coefficient with a microwave transmission system and then calculated the electron density in plasma.

2. Measurement of the power absorption coefficient

In this paper, we assume:

(1) The electromagnetic wave is a plane wave and has single frequency.
(2) The plasma slab is a uniform medium.
(3) The incident wave travels vertically on the plasma slab.
(4) The effects of electromagnetic wave on plasma can be neglected for the low-power electromagnetic wave.

In this case, we can calculate the electron density with the propagation properties of electromagnetic wave (power absorption coefficient) in a plasma slab.

Fig. 1 shows the model for calculation of propagation characteristics of electromagnetic wave in plasma slab.

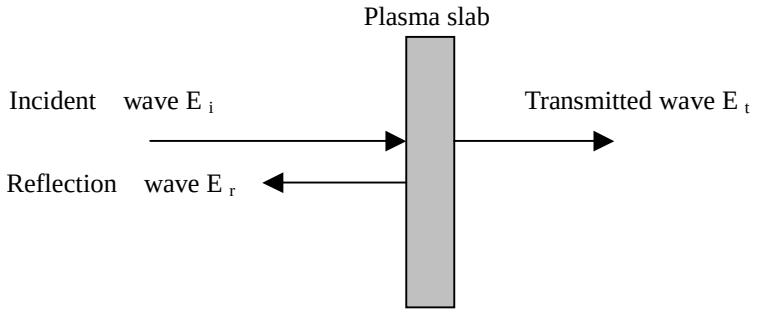

Fig.1. One dimension model for calculation.

In this condition, the refractive index μ and attenuation index χ are [5]

$$\mu = \{\frac{1}{2}(1-\frac{\omega_p{}^2}{\omega^2+\nu^2}) + \frac{1}{2}[(1-\frac{\omega_p{}^2}{\omega^2+\nu^2})^2 + (\frac{\omega^2}{\omega^2+\nu^2}\frac{\nu}{\omega})^2]^{\frac{1}{2}}\}^{\frac{1}{2}} \qquad (1)$$

$$\chi = \{-\frac{1}{2}(1-\frac{\omega_p{}^2}{\omega^2+\nu^2}) + \frac{1}{2}[(1-\frac{\omega_p{}^2}{\omega^2+\nu^2})^2 + (\frac{\omega_p{}^2}{\omega^2+\nu^2}\frac{\nu}{\omega})^2]^{\frac{1}{2}}\}^{\frac{1}{2}} \qquad (2)$$

Where ω is the circular frequency of the electromagnetic wave, ω_p is the plasma frequency, ν is the collision frequency.

The attenuation coefficient α is

$$\alpha = \chi\frac{c}{\omega} \qquad (3)$$

Where c is the velocity of light in vacuum.

The collision frequency is

$$\nu = \sqrt{\frac{8kT_e}{\pi m_e}}(N_i Q_{ei} + N_n Q_{en}) \qquad (4)$$

Where k is the Boltzmann constant, T_e is the electron temperature, m_e is the electron mass, N_i is the number density of the positive ions, Q_{ei} is the collision cross section of electron to ions, N_n is the neutral particle number density, Q_{en} is the collision cross section of electron to neutral particle.

According to the above equations, we can calculate the electron density when the attenuation coefficient is measured.

3. Experimental setup

In the following we will describe the experimental setup for the measurement of the power absorption coefficient. The setup includes: a GlidArc non-equilibrium plasma generator, a microwave measurement system and a data treatment system. Fig. 2 shows the sketch diagram of the experimental setup.

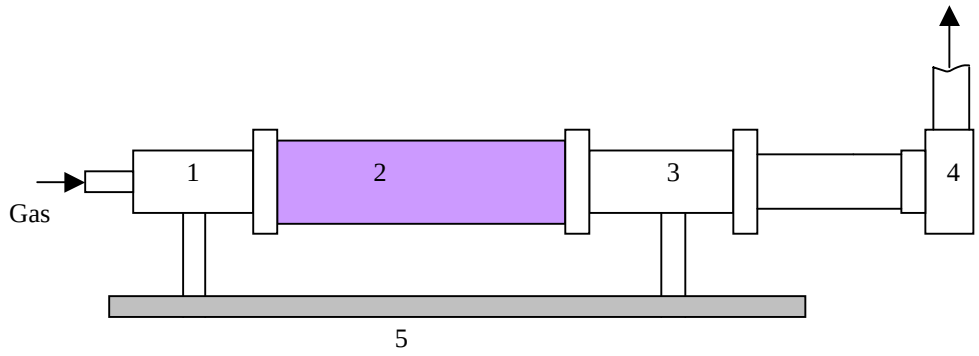

Fig. 2. Setup of the non-equilibrium plasma production
(1) GlidArc discharge plasma generator (2) Test section
(3) Cooling jacked (4) Exhaust blower (5) Seat of the equipment

The plasma generator is a rotating GlidArc discharge setup; the power of the plasma generator is 200-400Watts. The gas flow rate of the generator is 2.5-4.0m^3/h. The test section has a 30mm×60mm square uniform cross section. The test section is made of quartz glass. The transmitting antenna and receiving antenna are set the two lengthways sides of the test section.

Fig. 3 shows the block diagrams of the microwave measurement setup for the power absorption coefficient.

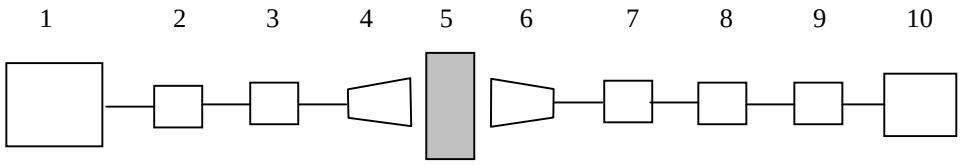

Fig.3. Experimental setup for measurement of power
absorption coefficient in GlidArc discharge plasma
（1）Signal source (2) Ferrite isolator (3) Coupler (4) Transmitting antenna
(5) Plasma region (6) Receiving antenna (7) Coupler (8) Crystal detector
(9) Amplifier (10) Digital oscilloscope

The signal source produces an electromagnetic wave with 9.6GHz frequency, and then the wave travels into the isolator, the coupler and transmitting antenna. The transmitted wave is received by the receiving antenna. The received electromagnetic wave can be detected by the crystal detector. The detected signals will be amplify by the amplifier, and treat with a digital oscilloscope. So we can obtain a curve with time about the measured signal of the transmitted electromagnetic wave. And then we can calculate the absorption coefficient and the electron density.

4.Results

Fig. 4 shows the curve of measured signal with time by the crystal detector in GlidArc discharge plasma.

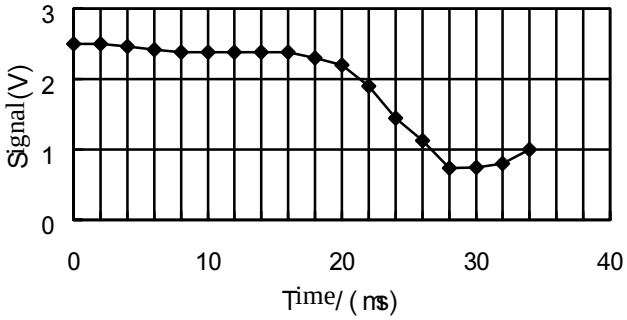

Fig. 4. Curve of measured signal by the crystal detector

According to the curve of the measured signal, we can calculate the power absorption coefficient and the electron density in GlidArc discharge plasma. The calculation results show that the peak electron density in the plasma is about $1\times10^{12}/cm^3$.

This work is supported by National Nature Science Foundation of China №. 90205026.

References

[1] H Nowakowska, Z Zakrzewski and M Moison, “Propagation Characteristics of Electromagnetic Waves Along a Dense Plasma Filament”, Journal of Physics D: Applied Physics, 34(2001) P. 1474-1478

[2] Fabien Huot, et al., “Study of Propagation of Ultraintense Electromagnetic Wave Through Plasma Using Semi-Lagrangian Vlasov Codes”, IEEE Transaction on plasma Science, Vol.28, No.4, 2000, P.1209-1223

[3] Mounir Laroussi and J. Reece Roth, “Back-Scattering Cross-section of a Cylindrical Uniform Plasma Column”, International Journal of Infrared and Millimeter Waves”, Vol.14, No.8, 1993, P.1601-1617

[4] B.L.Ginzburg,“The Propagation of Electromagnetic Waves in Plasmas”，pergamen，1970

[5] M. A. Heald, C.B. Wharton, “Plasma diagnostics with microwaves”, John Wiley & Sons Inc. New York, (1972)

Investigations of CF and CF_2 in C_4F_8 Plasmas

Ina T. Martin, Ellen R. Fisher

Department of Chemistry, Colorado State University, Fort Collins, CO 80523

Abstract

C_4F_8 plasmas are used in both fluorocarbon film depositions and the etching of Si-based materials. To better understand the chemistry that occurs during these processes we have used our laser induced fluorescence (LIF) based imaging of radicals interacting with surfaces (IRIS) method to characterize the relative densities of CF and CF_2 in C_4F_8 plasmas and explore the surface interactions of CF_2 during plasma processing of Si.

1. Introduction

Fluorocarbon (FC) plasmas are widely used in the deposition of thin films and the etching of silicon based materials [1]. The predominant behavior of the plasma largely depends on the concentration and energetics of the different plasma species. Studying the behavior of a specific molecule in the plasma can yield information on its role in the chemistry that occurs at the plasma surface interface. CF_2 is a particularly interesting species in FC plasmas because its role differs under various plasma conditions and systems. Both CF_x (including CF_2) and C_xF_y radicals are cited as FC polymer deposition precursors [1,2]. Conversely, other work has shown cases where CF_2 is not a deposition precursor. For example, Kadota and coworkers have used LIF spectroscopy and quadrupole MS measurements to show that CF_2 was not a FC film deposition precursor in their C_4F_8 plasmas systems [3]. To date, we have explored the role of CF_2 molecules in both etching and depositing FC and HFC plasma systems: CF_4, C_2F_6, C_2F_6/H_2, and CHF_3 [4, 5, 6]. These results show that the CF_2 reactivity can be correlated to the overall plasma regime: etching or deposition. This work furthers these studies by exploring the role of CF_2 in C_4F_8 plasma processing of silicon. The processed Si was analyzed by XPS for additional insight into the overall plasma process.

The IRIS apparatus has been described in detail previously [7]. Briefly, it combines molecular beam and laser induced fluorescence (LIF) measurements to thoroughly characterize specific fluorescing species in a variety of plasmas. Ground state species are identified through the collection of excitation spectra, which are also used to measure their rotational temperatures (Θ_R). The relative gas phase density of these species can then be measured as a function of changing plasma parameters (input power, pressure etc.), and we are also capable of measuring the surface reactivity of gas-phase species during plasma processing of a substrate.

2. Experimental Details

In a typical IRIS experiment, the feed gas enters the rear of the reactor, 13.56 MHz rf power is applied and a plasma is produced. Expansion of the plasma into a differentially pumped vacuum chamber, and ultimately into a high-vacuum region, generates a nearly effusive molecular beam consisting of virtually all species present in the plasma, including the species of interest. An excimer-pumped (XeCl, 150 mJ, 70 Hz, 308 nm) tunable dye laser beam intersects the molecular beam downstream from the plasma source and excites the species of interest. Spatially resolved LIF signals are collected by an electronically gated, intensified charge coupled device (ICCD) located perpendicular to both the molecular beam and the laser beam, directly

above the interaction region (Figure 1a). For a reactivity experiment, a substrate is rotated directly into the path of the molecular beam and LIF signals are collected again (Figure 1b). Differences between the spatial distributions with the surface in and out of the path of the molecular beam (Figure 1c) are used to measure the ratio of incident radicals in the molecular beam with respect to those scattering from the surface (denoted as *S*).

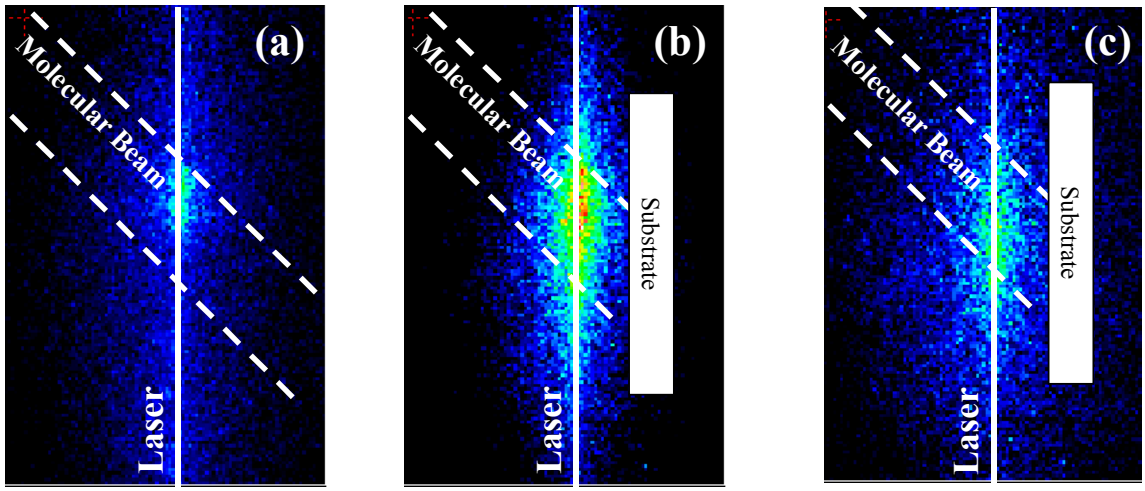

Figure 1. Spatially resolved 2D ICCD images of the LIF signal for the CF_2 (0,11,0) state (a) in the 50 W 100% C_4F_8 molecular beam (no substrate) and (b) with a 300 K Si substrate rotated into the path of the molecular beam. (c) Difference between the images shown in (a) and (b) which shows only the CF_2 molecules scattering from the surface.

In this work, tunable laser light in the 229-240 nm range was produced by frequency doubling the output of an excimer pumped dye laser (Coumarin 47, 0.6-1.3 mJ/pulse). Substrates were 25 x 40 mm p-type silicon (100) wafers with ~20 Å of native oxide; these were placed 2-5 mm from the laser beam. For CF_2 reactivity experiments, the laser was tuned to 234.323 nm, corresponding to the (0,11,0)-(0,0,0) vibronic band of the A^1B_1-X^1A_1 transition. For CF density measurements, the laser was tuned to 223.840 nm corresponding to the P_{11} bandhead of the $A^2\Sigma^+$–$X^2\Pi$ (1,0) transition. The molecular beam sources were plasmas created with 100% C_4F_8 (Matheson, 99.99%). The source pressure was maintained at ~ 40 mTorr and the applied rf power, *P*, ranged from 0 – 150 W. The effects of ions on *S* measurements were investigated by placing a grounded mesh in the path of the molecular beam. Previous work shows that the grounded mesh removes ~90% of the charged species from 50 W C_4F_8 plasmas [8].

XPS analyses were performed on a Physical Electronics PE5800 ESCA/AES system. Spectra were collected using a 2 mm monochromatic Al Kα X-ray source (1486.6 eV), hemispherical analyzer, and multichannel detector. A low energy (~1 eV) electron neutralizer was used for charge neutralization, and survey spectra were collected with a pass energy of 93.90 eV.

3. Results and Discussion

Figures 2a and b show excitation spectra collected from 228.000 – 240.000 nm in a 50 W C_4F_8 plasma and from 223.750 – 224.000 nm in a 100 W C_4F_8 plasma. Comparison to the literature confirms the presence of CF_2 and CF in 2a and 2b respectively [9, 10, 11].

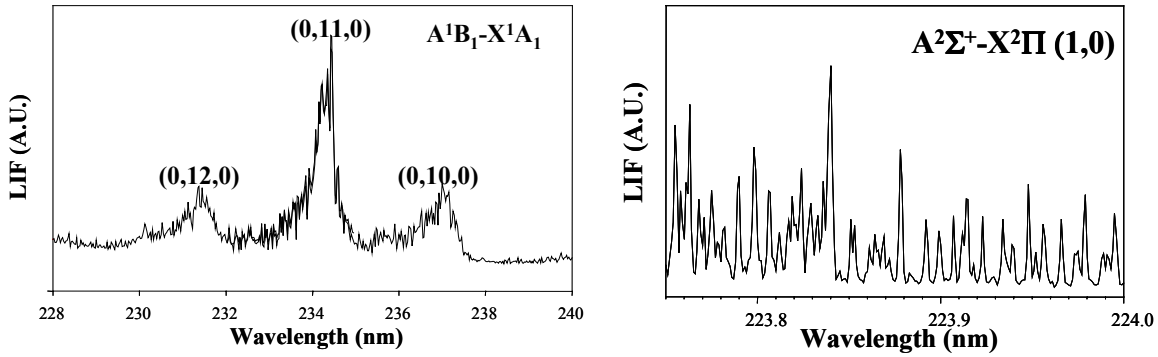

Figure 2. Experimental fluorescence excitation spectrum of (a) CF_2 and (b) CF in 100% C_4F_8 plasmas.

Figure 3 shows the relative densities of CF and CF_2 in C_3F_8 plasmas as a function of the applied plasma power (*P*). Increasing *P* results in an increase in the formation of both CF and CF_2 molecules, most likely a result of increased fragmentation of the monomer gas. Since the relative CF_2 density does not decrease, it appears that further fragmentation of CF_2 does not significantly contribute to CF formation in this *P* range.

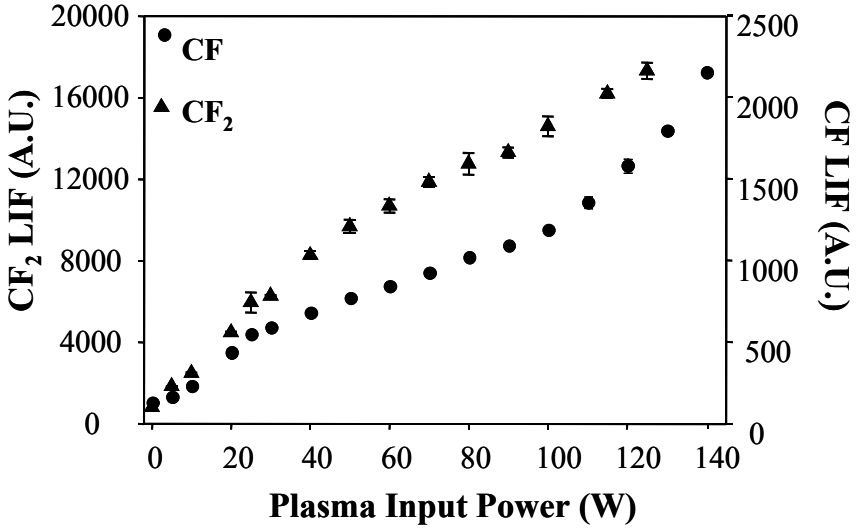

Figure 3. Relative LIF intensities of CF_2 and CF radicals in C_4F_8 plasmas as a function of applied rf power.

Table I lists *S* values measured for CF_2 from C_4F_8 plasmas during processing of a silicon substrate with and without a grounded mesh in the path of the molecular beam. Previous data taken for other plasma systems is included for discussion purposes.

Table I. CF_2 scatter coefficients for FC processing of Si.

Plasma	25 W	35 W	50 W	200 W	Regime
C_2F_6 [6]	----	----	1.44 ± 0.03	----	Etching
50/50 C_2F_6/H_2 [6]	----	----	0.84 ± 0.02	----	Fast depositor
HFPO [6]	----	0.97± 0.03	----	1.29 ± 0.05	Slow depositor
C_4F_8	1.29 ± 0.03	----	1.67 ± 0.03[b]	----	**?**
C_4F_8 (ion free)	0.97 ± 0.05	----	1.08 ± 0.04[b]	----	**?**

[b] Values from reference [8]

Previous work in our group has shown that CF_2 reactivity can be generally used to gauge the overall behavior of a plasma system. $S < 1$ is characteristic of a fast depositing system, such as 50 W 50:50 C_2F_6/H_2 plasmas. $S \geq 1$ (35 and 200 W HFPO) is characteristic of a slowly depositing system, while $S >> 1$ is characteristic of an etching system (50 W C_2F_6). CF_2 S values measured for C_4F_8 plasmas suggest that it too is an etching system. XPS results do show that materials processed with C_4F_8 plasmas in the IRIS chamber have significantly lower F/C ratios than materials deposited under ion-limited conditions in 50 W C_4F_8 plasmas in similar reactors (F/C = 1.1 – 1.4) [12]. Indeed, the materials deposited in the IRIS chamber have F/C ratios ~0.2 which are even lower than that measured for 100 % C_2F_6 (F/C = 0.72) [6]. To further investigate this, ongoing work in our laboratory involves variable angle spectroscopic ellipsometry measurements of treated and untreated Si to determine if the overall regime is indeed etching.

Additional information can be garnered from the trends apparent in S values measured for the C_4F_8 system. For the unperturbed system, CF_2 is produced at the surface (i.e. $S > 1$) at all P studied, and S increases concomitantly with P. When a grounded mesh was placed in the path of the molecular beam, S decreases to ~1, and the power dependence is eliminated. This suggests that charged species significantly contribute to the surface production of CF_2, a trend that has been seen in several other FC systems [6]. Ions can contribute to CF_2 formation simply through ion bombardment of CF_2 from the surface. Increasing the applied rf power is known to increase the ion density in the plasma. This would result in increased ion bombardment of the surface, which could explain the increase of S with P. Previous work in our laboratory used plasma ion mass spectrometry (PI-MS) to identify nascent ions in C_4F_8 plasma molecular beams. Results showed that CF^+ is the predominant ion in this system, and, unlike other ions detected in the system, the relative concentration of CF^+ increased significantly with P [8]. This allows for the possibility of the following surface reaction:

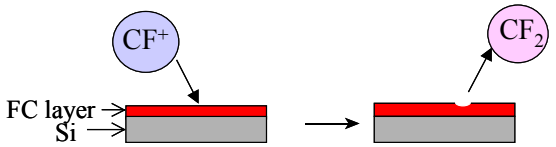

For this to be possible, F would have to be present on the surface. Preliminary XPS data for Si processed in the IRIS chamber with a 50 W C_4F_8 plasma for 60 minutes showed that the surface composition was ~20% F, allowing for the above reaction. Even in a virtually "ion-free" system, the S values measured for CF_2 are ~1. This could be the result of several mechanisms, the simplest one being the adsorption/desorption of CF_2 from the surface. Another possible mechanism is the abstraction of surface F atoms by gas-phase CF molecules. To test this possibility, we will measure the surface reactivity of CF in these systems.

4. Conclusions

Whether or not CF_2 is a deposition precursor depends on the nature of the other species in the plasma systems. Discerning the role of a specific species in a plasma becomes more complicated as we move to larger chain molecules because the number of fragmentation products increases. This work has shown that CF_2 is not a deposition precursor in the unperturbed C_4F_8 system. S values measured for CF_2 in C_4F_8 plasmas suggest that this system falls into an etching regime. However since ions contribute significantly to the surface production of CF_2, further film deposition studies in the IRIS chamber will help us determine if this is still the case under "ion-free" conditions.

Acknowledgments

Financial support for this work was provided by the National Science Foundation (NSF-0137664).

References

(1) R. d'Agostino, F. Cramarossa, and F. Fracassi, in *Plasma Deposition, Treatment, and Etching of Fluorocarbons*, edited by R. d'Agostino (Academic Press, Inc., San Diego, 1990), p. 95-143.

(2) S. Samukawa, AIP Conference Proceedings **636**, 95-107 (2002).
(3) K. Sasaki, K. Takizawa, N. Takada, K. Kadota, Thin Solid Films **374(2)**, 249-255 (2000)
(4) N. M. Mackie, V. A. Venturo, and E. R. Fisher, J. Phys. Chem. B **101,** 9425-9428 (1997).
(5) N. E. Capps, N. M. Mackie, and E. R. Fisher, Journal of Applied Physics **84,** 4736-4743 (1998).
(6) C. I. Butoi, N. M. Mackie, K. L. Williams, N. E. Capps, and E. R. Fisher, Journal of Vacuum Science & Technology, A: Vacuum, Surfaces, and Films **18,** 2685-2698 (2000**).**
(7) P. R. McCurdy, K. H. A. Bogart, N. F. Dalleska, and E. R. Fisher, Rev. Sci. Instrum. **68,** 1684-1693 (1997).
(8) K. L. Williams, I. T. Martin, and E. R. Fisher, J. Am. Soc. Mass. Spectrom. **13,** 518-529 (2002).
(9) D.S. King, P. K. Schenck, J.C. Stephenson, J. Mol. Spectrosc. **78**, 1–15 (1979).
(10) N. M. Matthews, Can. J. Phys. **45**, 2355-2374 (1967).
(11) E. B. Andrews, R. F. Barrow, Proc. Phys. Soc. **64**, 481 (1950).
(12) I. T. Martin, G. Sh. Malkov, C. I. Butoi, and E. R. Fisher; J. Vac. Sci. Technol. A, submitted for publication.

Relationship between the electron temperature and the spatial profile of the microwave power absorption in ECR plasma

N. Itagaki[1], K. Muta[1], N. Ishii[2] and Y. Kawai[1]

[1]*Interdisciplinary Graduate School of Engineering Sciences, Kyushu University, Fukuoka 816-8580, Japan*
[2]*Tokyo Electron Co. Ltd., Osaka 532-0003, Japan*

Abstract
The electron temperature in an ECR plasma is clarified to depend on the spatial profiles of the microwave-power absorption by both the electromagnetic-waves measurement and the simulation of microwave power absorption. It is also found from the experimental and numerical results that the electron temperature in an ECR plasma can be controlled by varying the magnetic field configuration and/or the microwave frequency since the power absorption profile is influenced by the effective resonance zone width.

1. Introduction

Electron cyclotron resonance (ECR) discharges have attracted considerable attention due to their advantages which allow their use in several industrial processes such as submicron etching, thin-film deposition, etc [1,2]. A significant feature of ECR plasma sources is the high electron density which can be achieved at low gas pressures. Specifically, as devices and features decrease in size, an ECR plasma becomes indispensable for the etching process. Recently, great interest has been directed toward the electron-temperature control in order to realize the less-damage processing, because high electron temperature plasma sources have shown to cause serious problems such as substrate damage due to ion bombardment from plasma [3,4]. Moreover, in the case of plasma etching, charge build-up damage, low etching selectivity and local side etching are caused by the high degree of dissociation and charge accumulation on the substrate by high-energy electrons in the plasma [5,6]. Since the production of reactive species including plasma production or the decomposition of source gas molecules are triggered by the electron collisions, the electron temperature control is also essential to find out the best conditions necessary for qualified material processing. However, the electron temperature in an conventional ECR plasma produced by 2.45 GHz microwave is relatively high, and it is quite hard to control the electron temperature in a wide range.

Up to now, several attempts for producing an ECR plasma with variable electron temperature have been reported. In our previous experiment, the mean electron temperature was decreased by pulse modulation of the incident microwave power, and high-quality amorphous Si thin films were obtained at room temperature using such control [7]. Okugi et al. observed that applying the magnetic filter, which is the localized transverse magnetic field of sheet type geometry and has an ability to reflect preferentially the high energy electrons and pass through low energy ones, leads to reduction of the electron temperature [8,9]. Tanaka et al. controlled the electron temperature by inserting a mesh grid into plasma [10]. However, the electron-temperature control with keeping the high electron density, which is earnestly required from industry, has not been achieved with those methods.

Recently, the effects of the electromagnetic-wave frequency on the plasma parameters have been giving some attention and it has been reported that in the plasma produced by the microwaves of the frequency below 2.45 GHz the electron temperature and the density of high energetic electrons that contributes to ionization are low [11]. We also observed that a low-electron-temperature ECR plasma with high electron density was produced by using 915 MHz microwaves [12]. Furthermore, it was found from our experimental results that the electron temperature in a 915MHz ECR plasma can be controlled by adjusting the external conditions such as incident microwave power, gas pressure and magnetic field configuration. The numerical simulation of the microwave-power absorption suggested that the electron temperature in an ECR plasma changes with changing the spatial profile of the power absorption [13], however, the mechanism of low-electron-temperature plasma production by using the microwaves of lower frequency has not still

been clarified. In this report, we firstly tried to experimentally clarify the relationship between the electron temperature and the power-absorption profile by measuring the spatial profiles of the plasma parameters and wave patterns of the electromagnetic waves at the different values of the electron temperature. The results were also compared with 2.45 GHz ECR plasma in order to investigate the effect of the microwave frequency on the electron temperature. In addition, based on the experimental and numerical results, a new simple method of the electron-temperature control for an ECR plasma was proposed.

2. Experiment

A schematic diagram of the experimental apparatus is shown in Fig. 1(a). The cylindrical chamber was made of stainless steel with an inner diameter of 290 mm and a length of 1200 mm. The chamber wall was grounded. The microwave was introduced through a quartz window and a substrate holder was placed approximately 550 mm from the window. The chamber was evacuated using a rotary pump and a 2000 l/sec turbomolecular pump to a base pressure of less than 2×10^{-6} Torr. N_2 gas was introduced into the chamber at a total flow rate of 50 sccm and the operating pressure was selected to be 5×10^{-3} Torr. Six magnetic coils with a thickness of 100 mm and an inner diameter of 320 mm were placed adjacent to the chamber to control the magnetic field distribution. The resonant magnetic field for a frequency of 915 MHz and 2.45GHz were 0.0327 T and 0.0875 T, respectively, and the position was set at 120 mm or 300 mm from the window, which is shown in Fig. 1(b). Microwaves were converted from the rectangular TE_{10} mode to the circular TM_{01} or TE_{11} mode by a mode converter and were launched into the chamber through a waveguide uptaper [14]. The microwave power could be up to 5 kW. The plasma parameters were measured with a three-dimensional movable cylindrical Langmuir probe whose radius and length were 0.5 mm and 1 mm, respectively. The used loop antenna was made of a coaxial cable with heat-resistance (<1000 ℃) and the wave patterns were obtained by the interferometric method. A reference signal of electromagnetic waves from a directional coupler and signal of waves in a plasma are introduced into an balanced mixer, whose output shows the phase difference of these waves depending on the positions of a loop antenna. The amplitudes of wave patterns are given with arbitrary units because the loop antenna was not calibrated.

3. Results and Discussion

In order to clarify the actual relationship between the electron temperature and the power-absorption profile in an ECR plasma, the spatial wave patterns were firstly measured for different electron temperatures. Figures 2(a) and 2(b) show the spatial distributions of the amplitude of radial electric field at the electron temperature of 2 eV and 7 eV, respectively, where the magnetic field configuration was (A) and the electron density was about 2×10^{17} m^{-3}. The contour diagrams corresponding to the electric field strength were made using interferometer traces, and those waves were confirmed to be the R waves by calculating their dispersion relations. As seen in Fig. 2(a), the microwaves injected in TM_{01} mode, which has an electric field profile peaked near the waveguide wall, propagated not only in the vicinity of the chamber wall but also toward the centre of the chamber, consequently, the microwave diverged along the z-axis at the electron temperature of 2 eV. On the other hand, it was observed that the microwave gradually refracted toward the chamber wall along z-axis at the electron temperature of 7 eV, which is shown in Fig 2(b). These interferometer traces suggest that the spatial profile of the microwave power absorption at the electron temperature of 2 eV was different from that at the electron temperature of 7 eV, but do not show which way the power is really transported. Therefore, the spatial distribution of microwave electric fields and the power absorption corresponding to the interferometer traces were calculated to investigate the correlation between the electron temperature and the power-absorption profile, which was performed by using a simulation code 'TASK/WF' [15]. This is a code that uses the finite-element method to solve boundary value problems of the Maxwell equation for stationary oscillation of electromagnetic waves, and makes two-dimensional analysis of wave propagation in a partially filled plasma chamber possible. Figures 4 and 5 show the spatial

distributions of the amplitude of the radial electric field and the power absorption numerically obtained by assuming that the plasma profiles were similar to the experimental results shown in Fig. 3. The contour diagrams correspond to the strength of the electric field and the power absorption. As seen in Figs. 4(a) and 5(a), the microwave diverged along the z-axis when the electron temperature was low, and the ones refracted toward the chamber wall when the electron temperature was high, which was consistent with the experimental results. In the former case, the positions where the power absorption took place spread out in both of r and z directions, on the other hand, the power absorption profile peaked strongly near the window in the vicinity of the chamber wall in the latter case, which was seen in Figs. 4(b) and 5(b). It was clarified from these experimental and numerical results that the electron temperature in an ECR plasma depends on the spatial profiles of the power absorption, that is, the electron temperature is low when the power absorption takes place in a wide area and the electron temperature increases when the power absorption is concentrated.

As mentioned in Sec. 1, the electron temperature in a 2.45 GHz ECR plasma is higher than that in a 915 MHz ECR plasma, whose reason is considered as follows. Since the effective resonance zone width is in inverse proportion to $\sqrt{\omega}$, where ω is the microwave angular frequency, the width becomes narrower as the frequency becomes higher [16]. Therefore, the power absorption profiles at higher microwave frequency are expected to peak strongly and to be changed little with changing the external conditions. consequently, the electron temperature becomes high and cannot be controlled in a wide range in a 2.45 GHz ECR plasma. Figure 6 shows the measured spatial profiles of the electric-field amplitude and the contour plot at the microwave frequency of (a) 915 MHz and (b) 2.45 GHz, respectively. The resonance point was set at z = 300 mm and the gradient in the magnetic field strength was about 0.2 G/mm for each cases, whose configuration is similar to the magnetic field configuration (A) in Fig. 1(b). Here, the pressure of N_2 gas and the incident power were 5 mTorr and 0.5 kW, respectively. As seen in Fig. 6, the microwaves gradually damped along the z-axis in the case of 915 MHz, on the other hand, the waves abruptly damped in the 2.45 GHz ECR plasma, which suggests that the area where the power absorption takes place in a 915 MHz ECR plasma is much larger than that in a 2.45 GHz ECR plasma.

In addition, the electron temperature in the magnetic field configuration (B) was observed to be higher than that in the configuration (A) and could not be controlled efficiently. The reason is also considered in the same way. In case of the configurations (B), the gradient in the magnetic field strength near the resonant zone was steep, so that the effective resonance zone width was narrow compared with that of the configuration (A) [16]. Therefore, the power absorption profiles in these configurations are expected to peak strongly and to be changed little with changing the external conditions, consequently, the electron temperature becomes high and cannot be controlled in a wide range. In fact, it was observed that the microwaves gradually damped along the z-axis and propagated for several wavelengths up to the ECR point in the case of magnetic field (A), on the other hand, the microwaves abruptly damped in the case of magnetic field (B), which is shown in Fig. 7.

Thus, our experimental and numerical results suggest that the electrton temperature in an ECR plasma can be controlled by changing the microwave frequency and/or the gradient in the magnetic field strength near the resonant zone because the power absorption profile is controlled by changing the effective resonance zone width. Furthermore, N_2 gas was used to investigate the electron-temperature control in our experiments, however, many kinds of reactive gases such as CF_4, C_4F_8, Cl_2 and SF_6 are used in the plasma processing and the plasma parameters depend on the gas species. It is necessary to clarify the electron-temperature control not only in nitrogen plasma but also in the reactive plasmas, which will be future work.

4. Conclusions

In order to investigate the production mechanism of a low-electron-temperature ECR plasma, the relationship between the electron temperature and the power-absorption profile was studied. The spatial profiles of the electromagnetic wave patterns were firstly measured for different electron temperatures, which suggested that the electron temperature changes with changing the spatial profiles of the power absorption.

This dependence of the electron temperature on the power absorption profile was examined by numerical simulation, and it was confirmed that the spatial profile of the microwave absorption by plasma has an effect on the electron temperature in an ECR plasma, that is, the electron temperature is low when the power absorption takes place in a wide area and the electron temperature increases when the power absorption is concentrated. Furthermore, our experimental and numerical results suggest that the electron temperature in an ECR plasma is controlled by changing the gradient in the magnetic field strength near the resonant zone and/or the microwave frequency because the power absorption profile is changed with changing the effective resonance zone width.

References

[1] N. Fujiwara, S. Ogino, T. Maruyama and M. Yoneda, Plasma Sources Sci. Technol. **5**, 126 (1996).
[2] O. A. Popov, Phys. Thin Films **18**, 121 (1994).
[3] M. Kondo, Y. Toyoshima, A. Mathuda - J. Appl. Phys. **80**, 6061 (1996).
[4] G. Ganguly, A. Matsuda - Mater. Res. Soc. Proc. **336**, 7 (1994).
[5] S. Samukawa, Y. Nakagawa, T. Tsukada, H. Ueyama - Jpn. J. Appl. Phys. **34**, 6805 (1995).
[6] Y. Hukumoto, T. Kinoshita - Proc. 10th Symp. Plasma Electronics, 1999, p.99. [in Japanese].
[7] N. Itagaki, A. Fukuda, T. Yoshizawa, M. Shindo, Y. Ueda, Y. Kawai, Surf. Coat. Technol. **131**, 54 (2000).
[8] T. Okugi, K. Horiuchi, S. Iizuka, N. Sato, Extended Abstract (47th Spring Meet. 2000) Japan Society of Applied Physics and Related Societies, 30a-C19.
[9] O. Fukumasa, H. Naitou, S. Sakiyama, J. Appl. Phys. **74**, 848 (1993).
[10] T. Tanaka, K. Kato, S. Iizuka, N. Sato, Proceedings of the 1994 Asia-Pacific Conference on Plasma Science and Technology, p. 337
[11] K. Yokogawa, N. Itabashi, K. Suzuki and S. Tachi, Proc. 43th National Symp. of American Vacuum Society, 1996, PS2-WeA5.
[12] N. Itagaki, S. Kawakami, N. Ishii, Y. Kawai, Vacuum **66**, 323 (2002).
[13] N. Itagaki, S. Kawakami, N. Ishii, Y. Kawai, J. Vac. Sci. Technol. **A20**, 1967 (2002).
[14] S. Samukawa, J. Vac. Sci. Technol. **A11**, 2572 (1993).
[15] Y. Yasaka, A. Fukuyama, A. Hatta, R. Itatani, J. Appl. Phys. **72**, 2652 (1992).
[16] M. A. Lieberman, A. J. Lichtenberg, Principles of Plasma Discharges and Materials Processing (John Wiley & Sons, Inc., New York, 1994) Chapter 13.

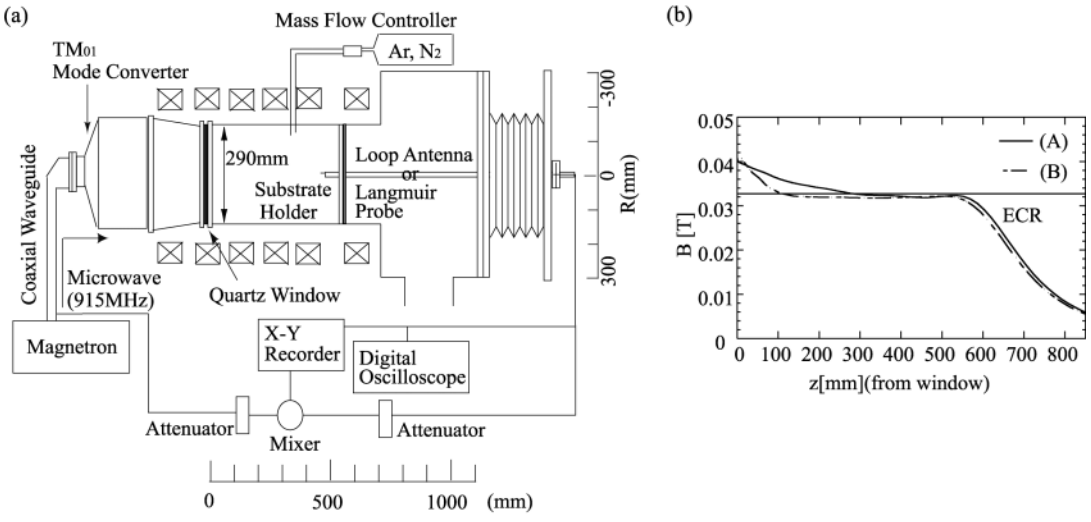

Fig. 1. Experimental apparatus: (a) the experimental setup, (b) the axial profiles of magnetic field at the center.

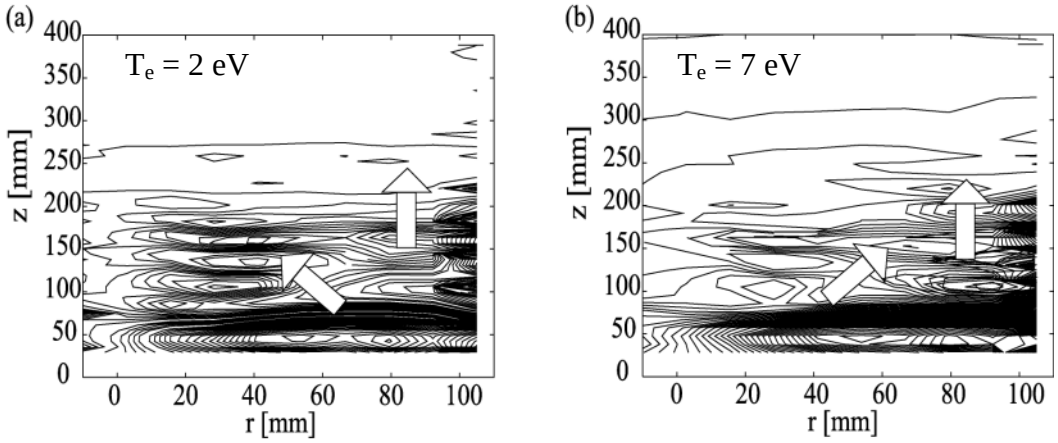

Fig. 2. The contour diagrams corresponding to the electric field strength made out of interferometer traces for the electron temperature of (a) 2 eV and (b) 7 eV. Here the magnetic field configuration was (A) and the electron density was about 2×10^{17} m^{-3}.

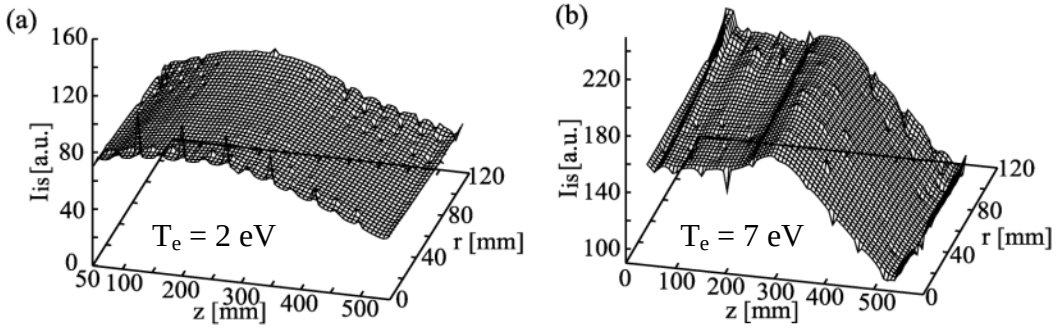

Fig. 3. The spatial profiles of the ion saturation current density in the magnetic field configuration (A) at the electron temperature of (a) 2 eV and (b) 7 eV.

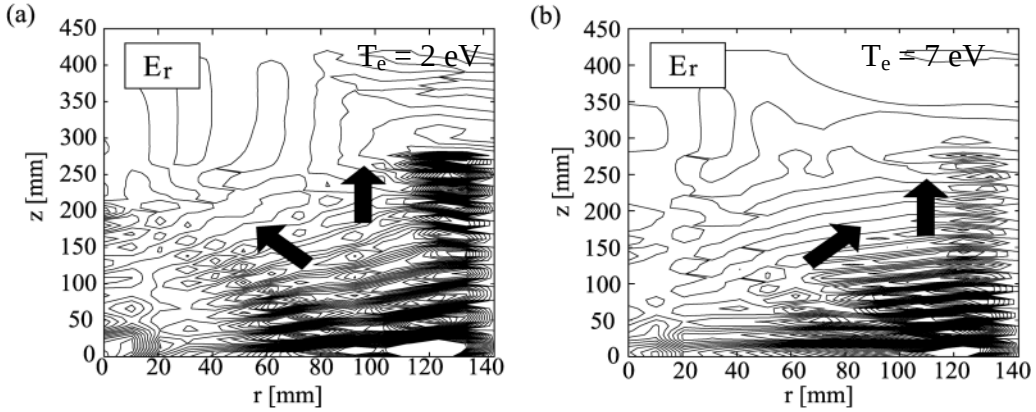

Fig. 4. The spatial profiles of the amplitude of radial electric fields numerically obtained by assuming that the plasma profiles were similar to the experimental results at the electron temperature of (a) 2 eV and (b) 7 eV.

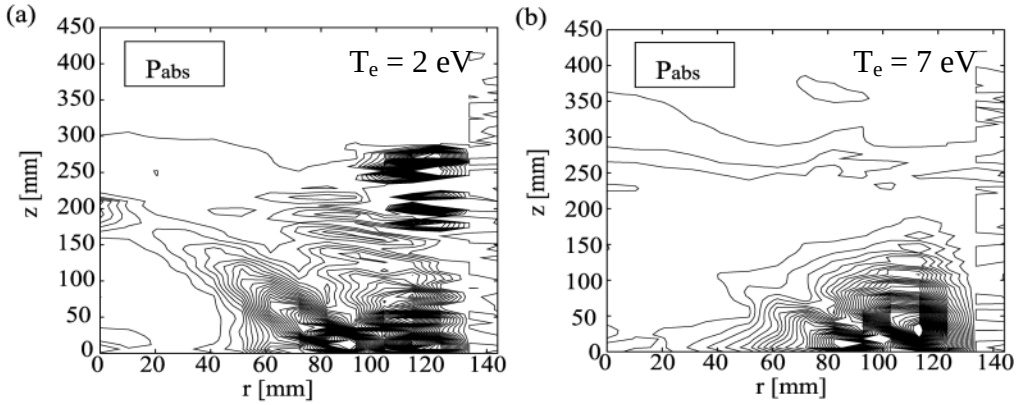

Fig. 5. The spatial distributions of the power absorption numerically obtained by assuming that the plasma profiles were similar to the experimental results at the electron temperature of (a) 2 eV and (b) 7 eV.

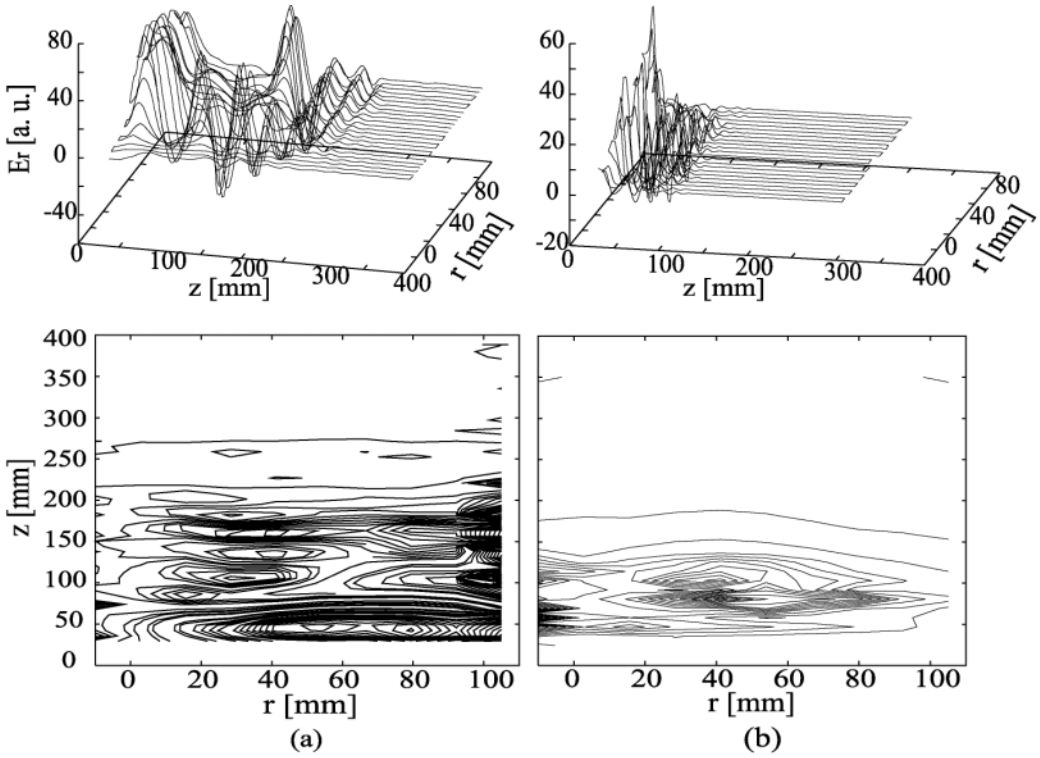

Fig. 6. Measured spatial profiles of the amplitude of the electric field and the contour plot at the microwave frequency of (a) 915 MHz and (b) 2.45 GHz, where, the pressure of N2 gas and the incident power were 5 mTorr and 0.5 kW, respectively.

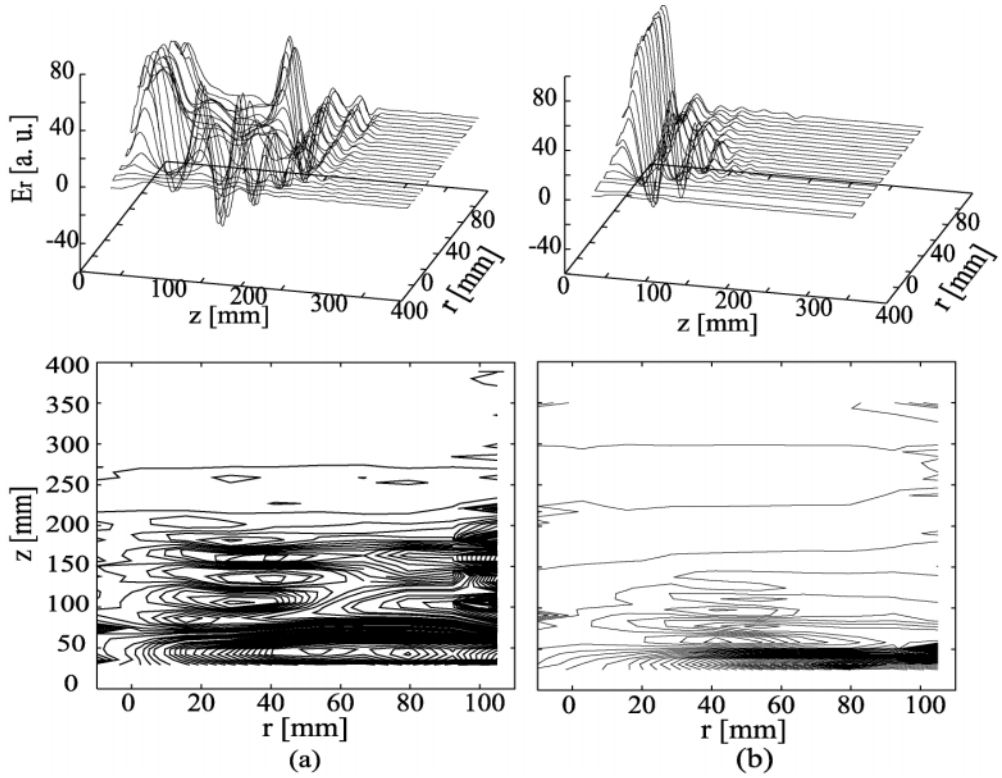

Fig. 7. Measured spatial profiles of the amplitude of the electric field and the contour plot in the magnetic field configuration (a) A and (b) B , where the incident power was 0.5 kW

Scaling up of a Magnetic Pole Enhanced Inductively Coupled Plasma Source (MaPE-ICP)

T. Meziani, P. Colpo, and F. Rossi

Joint Research Centre of the European Commission, Ispra, Italy

Abstract

The principles of a Magnetic Pole Enhanced Inductively Coupled Plasma are presented. Plasma characterization made on a 200 mm source show that the electrical coupling efficiency is increased by a factor 4 as compared to a conventional coil configuration. Scaling up of the reactor to the dimension of 800×800 mm poses several technological problems that have been solved and are presented. Results of plasma diagnostic are presented. Characterization of the large scale source show that a plasma density of 2 to 4.10^{11} cm^{-3} in *Ar* plasma at 2 MHz is obtained with a homogeneity of the ion current density better than 20 % over 800 mm. Application of the source to the etching of SiO_2 layers is presented. Etching rates of the order of 100 nm/mn are obtained over the whole area.

I Introduction

Inductively coupled plasma (ICP) sources are now recognized to be major processing tools for dry etching thanks to their very good performances in terms of etch rates and uniformity, and to their ability to work under low pressure conditions. Nevertheless, the size of the available ICP sources remains limited mainly because of the uniformity problems appearing above 200 mm diameter. The scale up to a large, uniform, high density plasma source poses a few technological problems that need to be addressed: uniform electromagnetic heating profile with a large antenna, careful scale up of the dielectric window to ensure both an efficient electromagnetic coupling and vacuum sealing, loss of coupling efficiency, correct impedance matching, and standing wave effects. Part of these major issues was not completely solved up to now even if several large area plasma sources have been reported in the literature [1-4]. The magnetic pole enhanced inductively coupled plasma source was developed in our lab in order to solve the aforementioned problems [5]. In this paper is presented the development of this source with a study of a 200 mm reactor in a first part, followed by the main results of the scale up study to a 1 m^2 reactor.

II Principle

The main improvement in our ICP source consisted in embedding the coil antenna in a magnetic core. This magnetic core is a low loss material having a high magnetic permeability. Due to its large magnetic permeability, the magnetic field tends to zero within the core. Thus, it concentrates the magnetic flux on the load (i.e. the plasma) and reduces the losses in the back path (figure 1). Furthermore, it provides higher process flexibility since the magnetic field may be concentrated in specific zones. As soon as the power density value and its distribution can be controlled, the plasma uniformity can also be expanded.

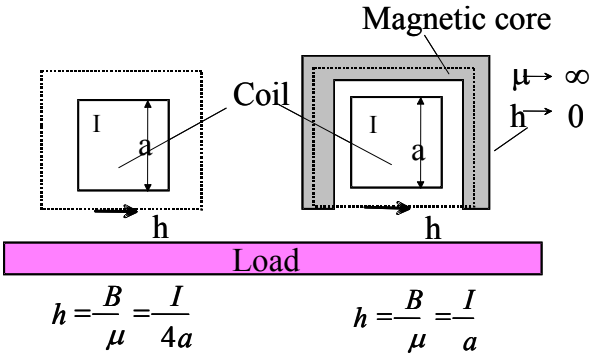

figure 1. Illustration of the magnetic core effect applying Ampere's theorem.

Scaling up an ICP source to a large, uniform, high-density plasma source requires a careful scale up of the two following components:

- the coil antenna that generates the electromagnetic energy
- the dielectric window to ensure the electromagnetic coupling and the vacuum sealing

To achieve a good uniformity over large areas, the usual spiral antenna is not efficient because of the inherent non-uniformity of the electromagnetic field profile that peaks at the semi-radius. Alternative antenna geometries showing much better uniformity are available (like the serpentine, the ladder-shaped antenna, etc.) but they suffer from a low coupling efficiency.
The loss in the electromagnetic coupling efficiency when scaling up the coil antenna can be partly compensated by the concentration of the magnetic flux. But, the increase in the antenna diameter is done together with an increase in the dielectric window diameter. The thickness of this element (that should withstand the pressure difference between the atmosphere and the vacuum chamber) has thus to be increased in order to maintain its the mechanical strength. Then, the mutual inductance decreases with the higher plasma to coil distance [6] and this results in a drastic decrease of the power transfer efficiency.
This problem can be solved by using the magnetic core, which is a rigid material, as a vacuum seal, or by integrating the inductive source (antenna + magnetic core) in a stainless steel cover flange leading to an easier scaling up of the system. The dielectric window doesn't have a mechanical function anymore and only acts as an insulating barrier between coil and plasma. Its thickness can then be reduced thus improving the magnetic coupling between coil and plasma.

III 200-mm diameter MaPE-ICP source

In a first part, we developed a 200-mm diameter source in order to assess the effect of the magnetic core addition and of the dielectric window thickness reduction on plasma density and uniformity at reduced scale.

III.1 Experimental setup

A schematic diagram of the 200 mm diameter MaPE-ICP reactor is shown in figure 2. The stainless steel plasma chamber has a square geometry with a 300 mm characteristic dimension and a 150 mm height.
The 2-turn water-cooled coil is powered by a 13.56 MHz RF generator via a 'Γ' layout matching network composed of two driven air capacitors (Advanced Energy RFX II generator 1.25 kW, matching network AZ90). The gas is injected through a single tube placed at the top of a chamber wall, in the center. The gas feed uniformity is of particular importance for achieving good plasma uniformity and care has been taken to optimize it in the large-scale reactor that will be described in the second part. The magnetic core used in this study is a 200-mm diameter disc, having a 45 mm thickness.

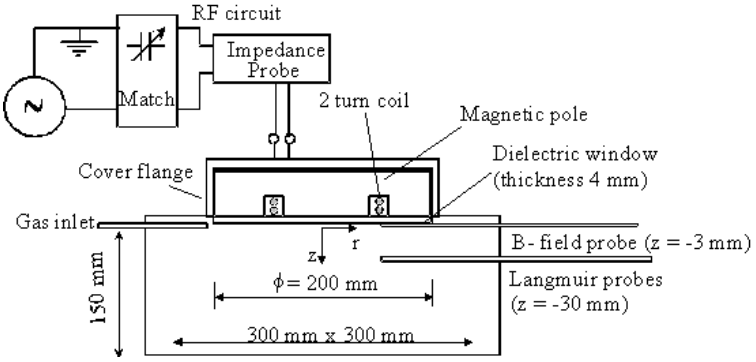

figure 2. Schematic diagram of the experimental setup of the 200-mm diameter MaPE-ICP reactor

To determine the effect of the magnetic core on plasma characteristics, a set of different inductor configurations has been tested:
C1: a two turn cylindrical coil (ϕ=120 mm) with a thick dielectric window (thickness = 25 mm)
C2: a two turn cylindrical coil (ϕ=120 mm) embedded in the magnetic core with a thick dielectric window
C3: a two turn cylindrical coil (ϕ= 120 mm) embedded in the magnetic core with a thin dielectric window (4 mm). This device is arranged within a cover flange for vacuum sealing. This configuration is the so-called MaPE-ICP configuration.
C4: a four-turn spiral coil made from 20-mm large copper strap has been used. This geometry is used in planar ICP processing and acted as a reference for comparative purposes (diameter = 200 mm).
The electrical parameters of the discharge were measured with a RF impedance probe (Advance Energy Z-scan). This device allows the measurements of the r.m.s. RF voltage applied to the coil, the r.m.s. coil current, the phase angle between voltage and current, and the impedance of the circuit load (coil and plasma).

The radial component B_r of the magnetic induction field has been measured with a magnetic induction probe [7]. All the measurements were carried out at approximately 3-mm from the dielectric window.
Plasma characteristics have been measured in a pure argon discharge by means of two different Langmuir probes. A planar probe has been used to measure the radial profile of the ion current density in the chamber whereas the electron temperature has been measured by a compensated cylindrical probe. Both probes were placed at a distance of 3 cm below the dielectric window. This distance ensures an absence of perturbation to the measurements since the magnetic induction field is low in such systems (< 10 G) and decreases exponentially with the axial distance from the window.

III.2 Results and discussion

At constant net power, the magnetic core induces a reduction of the coil current by a factor 2 whereas the coil voltage is only slightly modified. Thus, the ohmic losses in the matching network circuitry are reduced resulting in an increase in power transfer efficiency.

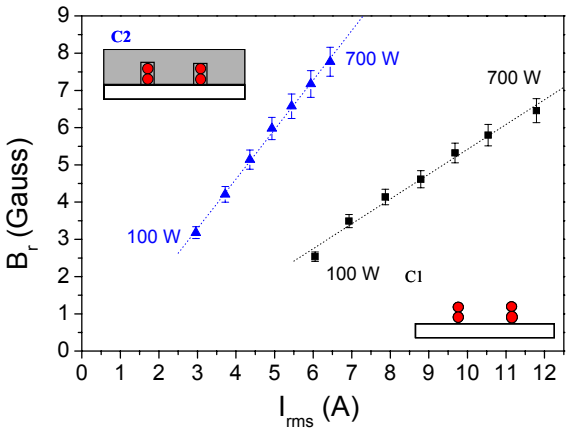

figure 3. Radial component of the magnetic field vs coil current with (▲) and without (■) magnetic core.

Ion current density measurements have been performed on C1 and C2 configurations to assess the magnetic core efficiency in a classical configuration (with a thick dielectric window). The results show that at constant RF power, the ion current density is increased by nearly 50 % with the use of a magnetic core, which corresponds to the 24 % increase observed on the radial component of the magnetic induction.
The ion current density measurements on the MaPE configuration (C3) as compared to the C1 configuration (with a thick window and without magnetic core) and C4 configuration (spiral coil) is represented in figure 4. In the final configuration (MaPE) the ion current density is increased drastically as compared to other configurations due to the combined effect of the magnetic core addition and the dielectric window thickness reduction. The

The time-varying radial magnetic field magnitude B_r has been measured with (▲) and without (■) magnetic pole to assess the flux concentration efficiency. Figure 3 shows that the magnetic field intensity is increased by the presence of the flux concentrator at constant RF power. But, the magnetic induction value should be compared at constant coil current and we observe then that a significant increase takes place thanks to the magnetic core. The gain achieved also indicates a net increase of the power absorbed by the plasma since it is directly proportional to the square of the magnetic field ($P_{abs} \approx n_e^{1/2} B_r^2$) [8]. This figure shows also that the magnetic induction B_r presents a linear dependence with the coil current, demonstrating that the magnetic core does not saturate when the power increases in the range of parameters studied. Saturation is unwanted since losses, and especially eddy current losses, increase when saturation is reached.

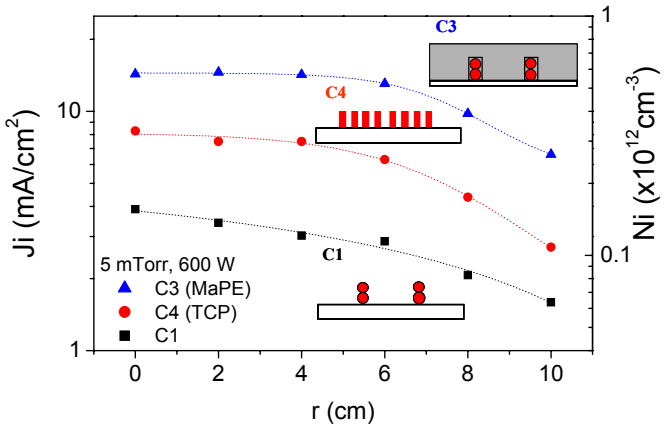

figure 4. Ion current density radial profiles for the MaPE configuration as compared to the spiral coil source (C4) and to the 2-turn helicoidal coil source (C1).

ion current density is increased as compared to the cylindrical coil antenna C1 by a factor of 3 and a factor 2 as compared to the spiral coil.
The plasma uniformity is also improved with a deviation from ion current density uniformity going from 16 % with the single 2-turn coil to approximately 5 % within the area of the coil radius in the MaPE configuration.

IV Scale-up to a Large Area MaPE-ICP source

Based on the previous study, a large area plasma semi industrial reactor was constructed using the same technology. The antenna geometry was modified though in order to provide for a uniform electromagnetic heating profile over such a large area. Following previous studies [9], experiments on the 200 mm diameter MaPE-ICP reactor and numerical simulations, a serpentine coil antenna appeared to be the best solution.

IV.1 Experimental setup

A schematic diagram of the experimental setup is presented in figure 5. The reactor is a squared chamber of 1000 × 1000 mm for 300 mm in height. The 13.56 MHz RF power is supplied by a 5.5 kW Advanced Energy APEX generator via a 'Γ' matching network (Advanced Energy AZX 90) composed of two driven vacuum capacitors.
The tested antennas were embedded within a magnetic core as shown in figure 5. The inductive source arrangement is included in the vacuum part of the chamber in order to use a thin dielectric window (5 mm). The gas is uniformly injected in the reactor through the magnetic core through small pipes equally distributed along the inductive source area.

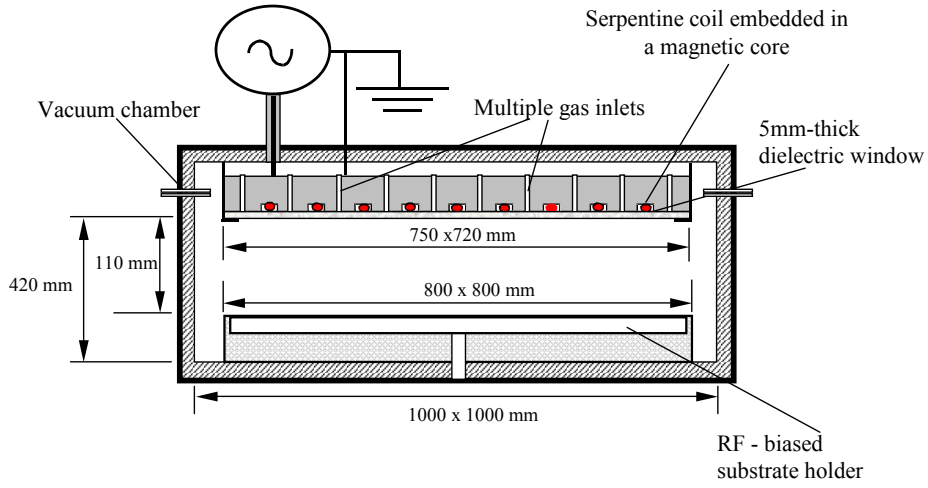

figure 5. Schematic representation of the experimental setup.

For the diagnostic of the plasma in this source, a multiple Langmuir probe system was used. This system is composed of 9 probes placed in line so that we can measure the electron density every 10 cm along the whole substrate-holder length on the *X* direction. The multiple probe system is then translated in the *Y* direction to get a bidimensional profile.

IV.2 Results and discussion

First tests have been made using two serpentine coils connected in series and arranged in order to form current loops keeping the same current direction in each magnetic core groove and an opposite direction between neighbouring grooves. The normalized ion density profile measured at 3 cm from the dielectric window across the coil (along the *X* direction, at *Y = 0*) is presented in figure 6. The first results showed that the profile is

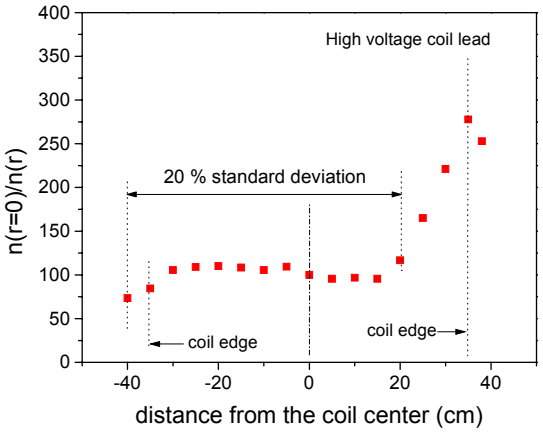

figure 6. Normalized ion density profile in a 5mtorr Ar discharge.

MHz than at 13.56 MHz. This is mainly due to the different electric behavior of the inductive source. Indeed, the magnetic core specifications show that its characteristics are much better at 2MHz with in particular a 5 times higher magnetic permeability and lower losses.

Following numerical simulations and experimental investigations, the antenna geometry was optimized and a special arrangement was used in order to improve the plasma uniformity.

The ion current density profile measured along the *X* axis (at *Y = 40* cm from the edge) shows a much higher uniformity (figure 8) than was previously obtained (figure 6). The uniformity as defined by the ratio (standard deviation/average) reaches 7 % over 60 cm and 14 % over the inductive source length. The

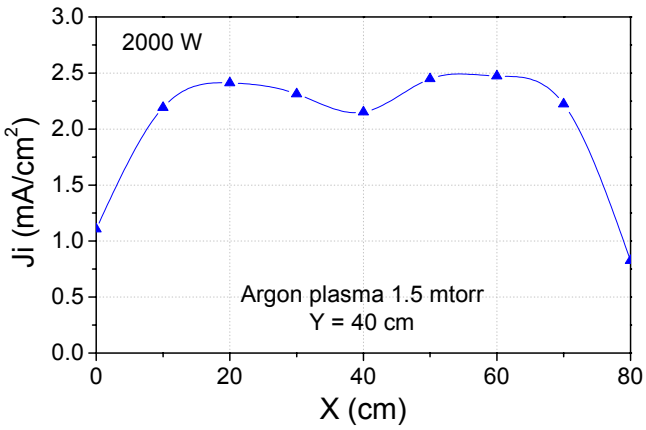

figure 8. Longitudinal profile of the ion current density measured in an Ar plasma at 1.5 mtorr and 2 kW.

relatively flat except at the edge close to the coil leads. Considering the coil length, this strong non-uniformity was likely to be due to standing wave effects resulting in non-uniform dissipation.

To get rid of these standing wave effects, we decided to decrease the coil length/wavelength ratio by using a 2MHz RF excitation frequency. The 13.56 MHz RF power supply was thus substituted by an Advanced Energy 2 MHz RF generator delivering 8 kW maximum power.

With a shorter antenna, the first noticeable difference between the two-excitation frequency operations was observed on the ion density values. As shown in figure 7, the ion current density is 4 to 5 times higher at 2

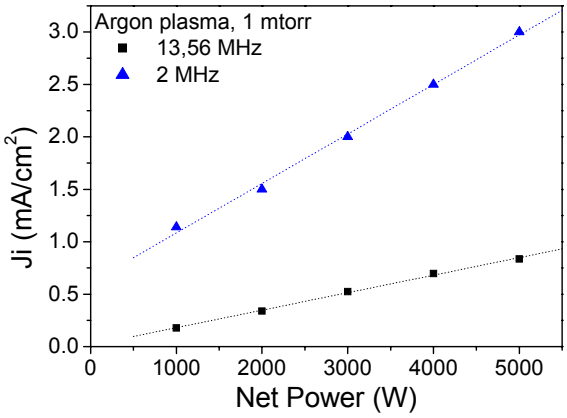

figure 7. Ion current density vs RF power in an Ar plasma excited at 13.56 MHz and 2MHz.

profile suffers from the vicinity of the walls that are only at 10 cm away from the substrate holder on each side.

The uniformity achieved over the whole area is relatively good with approximately 30 % over 80×80 cm^2 and less than 15 % over 60×60 cm^2.

The ion density is around 3.10^{11} cm^{-3} for 5 kW, which is quite high considering the source size and the relatively low pressure (1.5 mtorr).

The same kind of measurements was carried out in CHF_3, which has been used for the etching of SiO_2 layers. The results were similar with the ones obtained in *Ar* in terms of uniformity, while the ion density was 30 % lower.

SiO_2 etching tests were carried out in this reactor with CHF_3 and latter with CF_4 gas. The etching rate reaches about 100 nm/min at 3 kW input power applied to the inductive source and 1 kW RF bias power applied to the substrate holder. Preliminary SiO_2 etching results are presented in figure 9. The normalized profile shows that the overall uniformity is around 9 % on 60×60 cm^2. Further improvement is expected to be achieved by a correct tuning or process parameters such as substrate holder temperature uniformity and gas flow control.

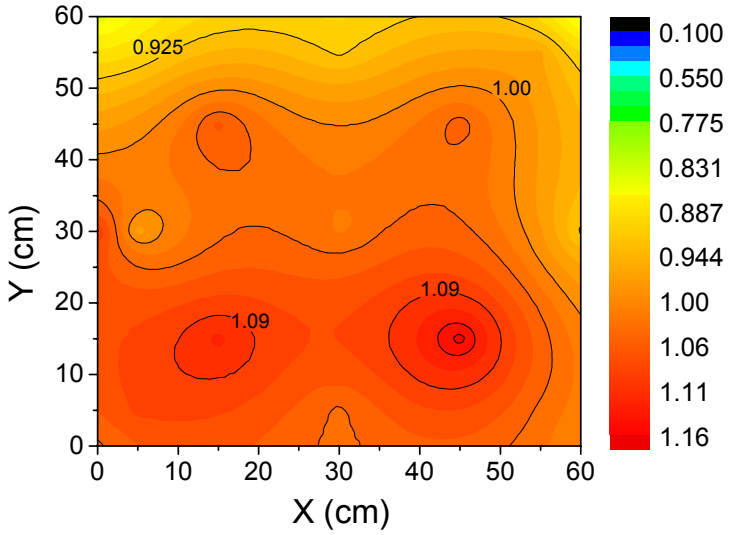

figure 9. Normalized SiO_2 etching rate profile in CF_4 atmosphere at 1.5 mtorr and 2 kW.

V Conclusion

The development of a novel reactor using an improved inductive source opened the way to the design of a large area ICP source. The key issues of impedance matching, standing wave effects, capacitive coupling, and plasma uniformity were addressed and solved. Plasma density is of the order of 10^{11} cm^{-3} at argon pressures as low as 1 mtorr and the uniformity was better than 15 % on 60×60 cm^2. Preliminary etching SiO_2 etching experiments showed very promising results in terms of etching rates and uniformity with less than 9 % on 60×60 cm^2.

[1] F. Heinrich, U. Bänziger, A. Jentzsch, G. Neumann, C. Huth, J. Vac. Sci. Technol. B 14 (1996) 2000.
[2] Y. Kawai, M. Yoshioka, T. Yamane, Y. Takeuchi, M. Murata, Surface and Coatings Technology 116-119 (1999) 662.
[3] Y. Setsuhara, S. Miyak, Y. Sakawa, T. Shoji, Jpn. J. Appl. Phys. 38 (1999) 4263.
[4] Y. Wu, M.A. Lieberman, Plasma Sources Sci. Technol. 9 (2000) 210.
[5] T. Meziani, P. Colpo, F. Rossi, Plasma Sources Sci. Technol. 10 (2001) 276.
[6] J. Hopwood, Plasma Sources Sci. Technol. 3 (1994) 460.
[7] J. Hopwood, C.R. Guarnieri, S.J. Whitehair, J.J. Cuomo, J. Vac. Sci. Technol. A 11(1) (1993) 147.
[8] N. Forgotson, V. Khemka, J. Hopwood, J. Vac. Sci. Technol. B 14(2) (1996) 732.
[9] M.M. Patterson, A.E. Wendt, in AVS Fall Conf., Unpublished, Seattle, 1999.

DCM Production in a Dusty Plasma Trap

A. Ivanov[1], V. Mitin[2], A. Pal[3], A. Ryabinkin[3], A. Serov[3], E. Skryleva[4], A. Starostin[1], V. Fortov[4], Yu. Shulga[4]

[1] *RCC "Kurchatov Institute", Kurchatov Square, 123182, Moscow, Russia*
[2]*Institute of Inorganic Material, Moscow, Russia*
[3]*Moscow State University, Institute of Nuclear Physics, Moscow, Russia*
[4]*Institute of Problem of Chemical Physics, Chernogolovka, Russia*

Abstract
Diamond-nickel disperse composite materials (DCM) representing diamond powder consisting of particles with mean size of 5 μm, covered by nickel metal was obtained using dusty plasma technique. Amount of DCM obtained is quite enough for physical and technologic studies. The coating is shown to be a solid nickel layer of 10 nm in thickness with characteristic roughness of 3 nm.

1. Introduction

Disperse composite materials (DCM) consist of small particles having the size of $10^2 \div 10^4$ nm and covered with a coating. These materials can be used both in the processes of fabricating structural and special materials with unusual properties and in the production of highly efficient catalysts. This report presents some results of studying DCM produced in a dusty plasma trap by means of the technology which is similar to [1,2]. Disperse particles in such a trap are charged with electrical charges of $10^3 \div 10^4 e$ where e is the charge of electron. The Coulomb repulsion results in suppressing of the coagulation processes forming long-lived quasi-liquid state in our case.

2. The setup for DCM production

The experimental setup for dusty plasma trap creation includes the vacuum chamber with electrode system inside where the RF discharge plasma is available. The electrode system is powered by the RF generator at fundamental frequency of 5.28 MHz. The discharge power was up to 30 W. The argon gas was used at pressure of 0.1÷0.3 Pa and 1÷5 sccm flow rate. The disperser of the accelerative type was used to inject a cloud of powder particles into discharge chamber. The cloud levitated in the plasma trap and exposed it to the atom beam from magnetron sputtering system (fig.1).

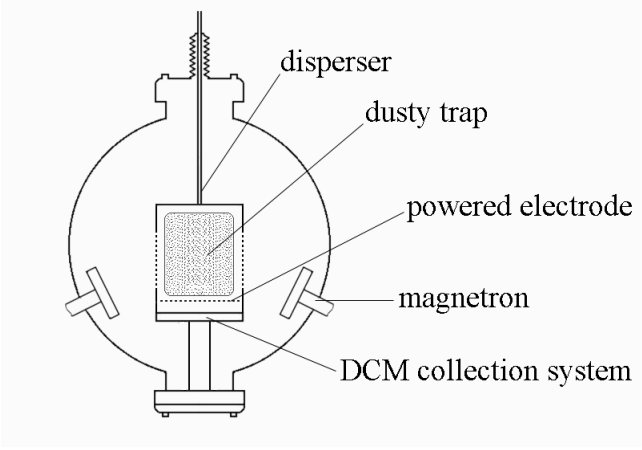

Fig. 1. Scheme of the reactor.

We used two ion-plasma sputtering magnetron systems with the cylindrical cathodes. The ring magnetic balanced system is inside the water cooled cathode frame. The magnetic system is pieced together from permanent Nd-Fe-B magnets with residual induction of 0.45÷0.55 T. The sputtering target is placed over the magnetic system. Nickel is a magnetic material, so the target is of special construction providing the effective sputtering of magnetic materials at the magnetron mode of operation where strong arc magnetic field (0.03 T) is present above the target surface. The latter is necessary for trapping of the electrons above

the intensive sputtering zone. The construction provides the nickel sputtering in a high-speed mode at the power density of 45÷50 W/cm^2 (intensive sputtering zone takes the ring-shape with the external diameter of 52 mm and with the square of 19 cm^2). The magnetron sputtering systems are located close to the RF-electrode and its magnetic fields influence significantly to the discharge properties and the dusty trap location.

3. Results and discussion

Analysing the fabricated product was accomplished with the use of a number of methods including electron-microscopic research, X-ray analysis, cathode-luminescent analysis, X-ray photo-electron spectroscopy, precision chemical analysis, and some others.

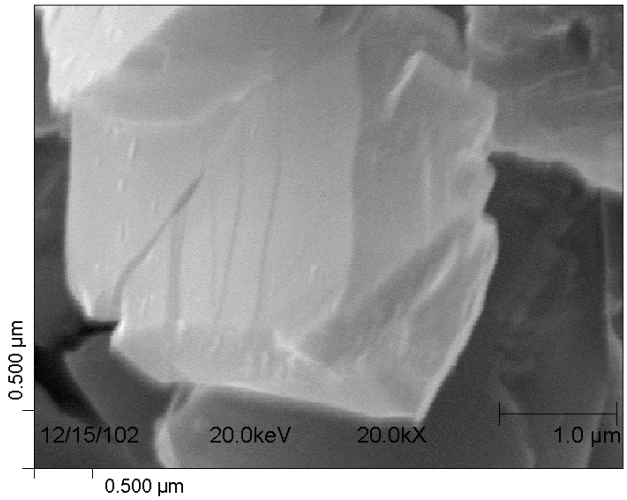

Fig. 2. SEM photo of the diamond particle covered by nickel metal

Electron-microscopic research of diamond particles coated with Ni was performed with using the high-resolution (~30 nm) scanning electron microscope. Electron-microscopic pictures show that the coated particles, unlike the particles of the initial diamond powder, are quite sharply defined (fig. 2). This indicates high electro-conductivity of the coating. Within the mentioned resolution the formed coating is quite smooth, follows the substrate relief, and does not contain fractured structures of "cauliflower" type.

Besides that, we obtain the micrographs of the specimens by means of the transmission electron microscope at accelerating voltage of 50 kV. The specimens were spotted on the copper mesh coated preliminarily by collodion and reinforced by carbon. The micrographs of the coated powder particle edge are given in Fig.3. The edges of the main part of the investigated particles seem to be quite uniform, similar to the edges of the initial diamond. The coating characteristic roughness size is about 3 nm. There are no signs which would be evidence of the nickel coating exfoliation from the diamond substrate.

Measurement of the mean nickel content

To analyze the nickel content C_{Ni} in the powder we used the method of specimen combustion in oxygen at the temperature of 1673 K. The initial powder burns completely in this process. The rest of DCM combustion seems to be consisting of the nickel oxide NiO. The mass of nickel in the rest to the initial mass of processed specimen is the quota of the metal in the composite material. Three samples from each specimen were combusted, the obtained data were averaged. Calculated from the averaged data, the concentration of the metal in one of investigated specimens is given in Table 1.

Measurement of the specific surface

The method of the argon adsorption at the liquid nitrogen temperature was used for measuring of the powder specific surface. The characterization of specific surface S from the adsorption measuring is reduced to the measuring of quantity of matter which is necessary to cover the surface by the monomolecular layer. This quantity was measured according to the method using the linear form of the adsorption isotherm equation. The specimen was degassed at the temperature of

150°C. The special argon (5%) – helium mixture was used as the working gas. The relative error in the specific surface measured is 5%. The results are given in Table 1.

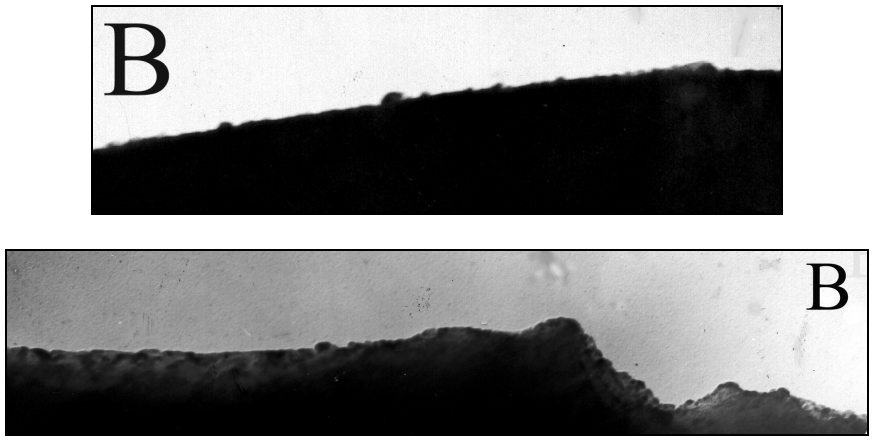

Fig. 3. The micrographs of the edges of the diamond particles covered by nickel metal. The vertical size of "B" is of 57 nm.

Table 1. The results of analysis.

specimen	C_{Ni}, mass.%	S, m^2/g	H_c, Oe	M_1, emu/g (H =10^4 Oe)	C_{fNi}, mass.%
The original diamond powder	0	0.76	0	0	0
Diamond covered by nickel	7.5	1.14	131	0.85	1.55

X-ray diffraction investigations

The X-ray diffractograms were obtained using monochromatic Cr K_α radiation. The original diamond diffractograms exhibit the alone peak due to the diamond (111) lattice reflection (Fig. 4).

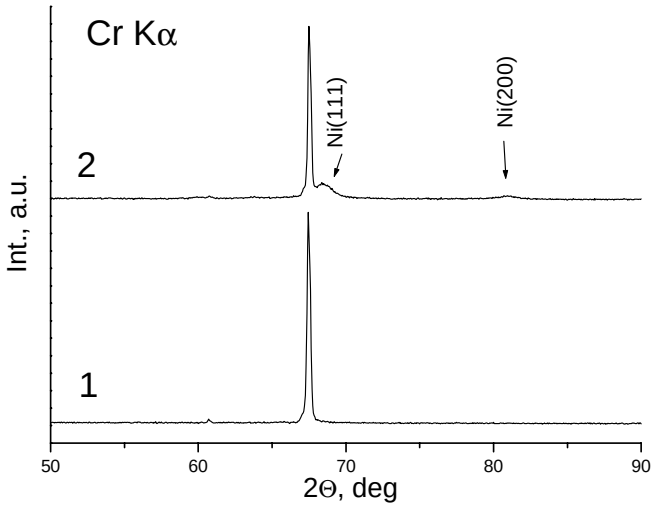

Fig. 4. The X-ray diffractograms of the original diamond powder (1) and of the processed specimen (2)

Nickel is seen in the diffractogram of the processed specimen as two peaks corresponding to the reflections of (111) and (200) face-centered cubic lattice. The lattice parameter value calculated using these peaks data is of 0.3529 nm and exceeds one of a bulk nickel (0.3524 nm [7]). The size estimation of the nickel coherent scattering domain corresponding to the coating thickness in the direction which is perpendicular to the plane (200) was carried out. The estimation formula was $D_{200} = \lambda/\beta\cos\Theta$, where λ is the X-ray length, β is the half-width of the Ni (200) diffraction peak. The lower peak was chosen because it is noticeably easer to size its half-width compared to the Ni (111) peak, which is overlapped by the diamond (111) peak. The D_{200} value seems to be of 12 nm according to the mean thickness value, obtained as result of the specific surface and the mean nickel content measurements.

Magnetic properties of the processed powder

We studied the magnetic properties of the specimens by means of vibration magnetometer EG&G PARC M4500. The specimens under investigation were placed into a thin diamagnetic ampoule whose own signal may be allowed in the course of analysis of observations. The magnetization curves of the processed specimens are the hysteresis loops with $H_c = 130$ Oe, where H_c is the coercive force (Fig.5).

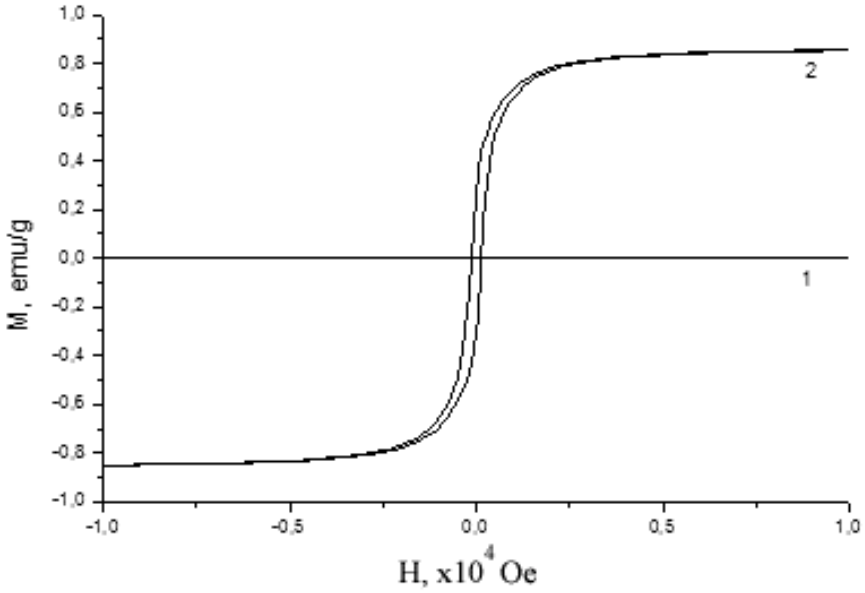

Fig. 5. The magnetization curves of the initial diamond (1) and of the processed specimen (2)
M is the specific magnetic moment, *H* is the magnetic strength.

One may see that the saturation state is not achieved even at $H = 10^4$ Oe. Therefore there are superparamagnetic nickel particles in the specimen. One may estimate the relative content of ferromagnetic nickel $C_{f\,Ni}$ in the specimen by formula $C_{f\,Ni} = M_1 / M_s^0$ where M_1 is the experimental value of M at $H = 10^4$ Oe, M_s^0 is the saturation specific magnetic moment for a bulk nickel ($M_s^0 = 55$ emu/g [8]). The $C_{f\,Ni}$ value is appreciably smaller than C_{Ni} value which was sized using the method of specimen combustion (Table 1). So nickel in the form of nickel oxide is thought to be present in the specimen besides the super-paramagnetic nickel particles. Nickel oxide is known to be antiferromagnet [9].

X-ray photoelectron spectroscopy

The X-ray photoelectron spectra were taken with the spectrometer PHI-5500 *(Physical Electronics Industries*) equipped by the precision analyzer of spherical type. The spot diameter where analysis is carried out was of 0.8 mm. The specimens were embedded into the indium substrates as permanent layer. The base gas pressure in the spectrometer chamber did not exceed $7 \cdot 10^{-8}$ Pa. The ion gun built in the spectrometer chamber makes it possible to clean the specimen surface from the adsorbed admixtures and to carry out the ion etching of the specimen to the hundreds of nanometers in depth.

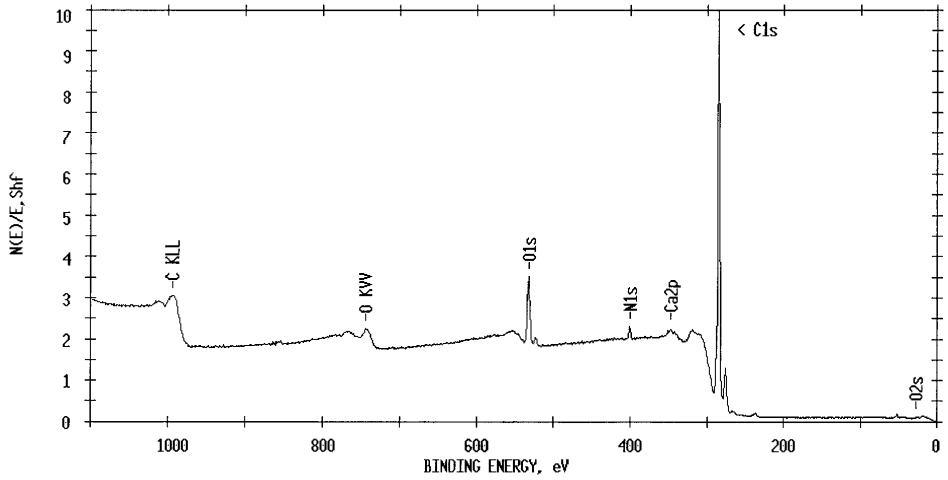

Fig. 6. The general X-ray photoelectron spectra of the initial diamond powder

The general X-ray photoelectron spectra of the diamond powder before and after the sputtering process realization are given in Figs. 6 and 7 correspondingly.

The carbon is seen to be the main element of the initial specimen surface. After the sputtering process performed, the nickel becomes the main one. Nickel is in the specimen surface layer in two forms: as the metal and as the nickel oxide over the metal surface. The Ni 2p (Fig.7) line is the complicate curve consisting of three peaks, the two of which appear due to nickel oxide (861.2 and 855.6 eV), and the rest (852.8 eV) – due to metal nickel. The correspondence of the peaks was taken from [10]. Cleaning of the smooth surface region of the specimen by Ar^+ ions leads to vanishing of nickel oxide peaks and to only metallic nickel practically remaining in the surface layer. It means that the coating is quite uniform and even if there are large aggregations on the particle surfaces, their relative part is not great.

So, according to X-ray photo-electron spectra the coating thickness was not less than 10 nm. The short-time etching of the specimen by an ion beam in the chamber of X-ray photo-electron spectrometer made it possible to practically completely remove the NiO film from the specimen surface. That indicates abnormally low oxidation of the produced composite material in spite of the fact that this material had been kept for quite a long period (about 10 days) in the air medium before it was placed in the chamber of the X-ray photo-electron spectrometer.

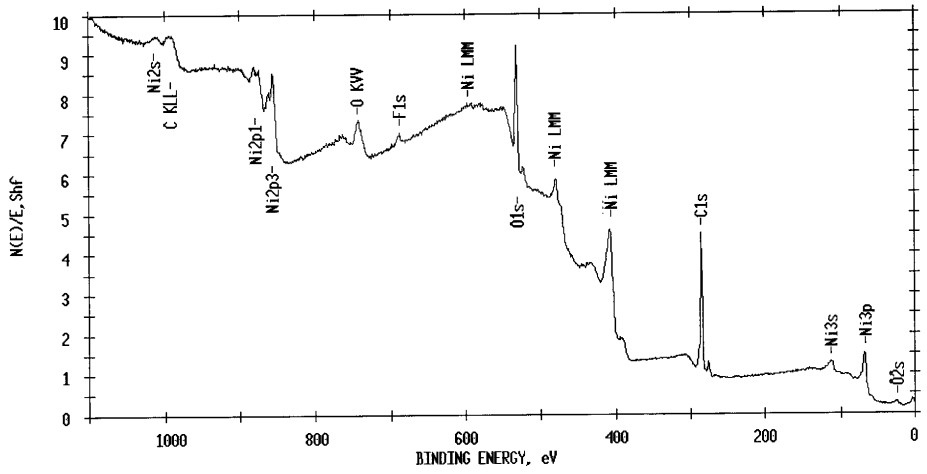

Fig. 7. The general X-ray photoelectron spectra of the processed powder

4. Conclusion

The performed investigation showed that the dusty plasma technology made it possible to obtain the diamond-nickel composition material in such amount which was enough for physical and technologic studies. The coating is a solid nickel layer of 10 nm in thickness with characteristic roughness of 3 nm.

Dendrite fragments and coatings with fractal structure are practically absent in the metal layer and the nickel film is strongly bound up with the diamond surface.

Acknowledgment
This study was supported by the Russian Foundation for Basic Research (project nos. 01-02-17726).

References

[1] V.E. Fortov, A.N. Starostin, A.S. Ivanov et al. Method and equipment for manufacturing disperse composite materials. German Patent Application, No 19832908.3 of (July 1998).
[2] H. Kersten, P. Schmetz, G.M.W. Kroesen, Surf. Coat. Technol., **108-109,** 507 (1998).
[3] I.A. Belov, A.S. Ivanov, A.F. Pal, A.N. Ryabinkin, A.O. Serov, Phys. Letters A, **306**, 52-56 (2002).
[4] D. P. Sheehah, M. Carillo, W. Heidbrink, «Device for Dispersal of Micrometer- and Submicrometer-sized Particles in Vacuum», Rev. Sci. Instrum., **61**, 12, (December 1990).
[5] Hiroharu Kawasaki at al., Study on Growth Progresses of Particles in Germane Radio Frequency Discharge Using Laser Light Scattering and Scanning Electron Microscopic Methods, J. of Appl. Phys., **83**, 11 (1998).
[6] H.M. Anderson, S.B. Radovanov, Dusty Plasma Studies in the Gaseous Electronics Conference Cell, J. Res. Natl. Stand. Technol., **100**, (1995).
[7] Card-File of JCPDS – International Centre for Diffraction Data, 04-0850 (1995).
[8] Ch. Kittel, Introduction to a Solid-State Physics, Moscow, Science, (1978).
[9] N. Ashkroft. N. Mermin, Solid-State Physics, **2**, Moscow, World, (1978).
[10] Handbook of X-Ray Photoelectron Spectroscopy (Eds by C.D. Wagner, W.M. Rigg**)**

Treatment of Incineration Ash and Sludge using Thermal Plasma

Hak In Kim and Dong-Wha Park

Department of Chemical Engineering, Inha University, Incheon, 402-751, Korea

Abstract

The application of thermal plasma to waste treatment may be a possible method for treating various kinds of hazardous waste through volume reduction and detoxification. The vitrified slag's safety test was performed. The leaching tests of the solution in pH 2, 4, 6 were examined. At pH 4, the leaching limit was satisfactory. The concentration of non-organic material in sludge was not enough to vitrify. Properties of slag were affected by differences in cooling rates. A fast cooling rate showed good elution proof.

1. Introduction

Recently, the products of hazardous waste have increased with the increase of population, improvement of living quality, etc. Waste treatment involves disposal cost, environmental pollution and social problems. One waste treatment is landfill. However, this method causes many problems--for example, groundwater pollution from landfill leachate, shortage of landfill site, and soil contamination. Another type of waste treatment is incineration. However, fly ash contains many inorganic compounds of hardly decomposable heavy metals such as Pb, Cr, Zn. So even though they are buried, they could strike a lethal blow if the heavy metal is exposed and accumulates to excess [1]. Therefore, incinerated ash needs a proper treatment method that excludes the possibility of leaching heavy metal [2].

Sludge forms after wastewater treatment. Most sludge is buried underground or dumped into the sea. But direct disposal is prohibited by law. So after partial incineration the sludge is buried underground. However, incinerated ash needs proper treatment. With incinerated ash treatment, there is cementation or solidification of plastic, which results in economic problems and increased volume. Therefore, the vitrification process is more efficient; with this process, the temperature is higher than the melting point of the fly ash, which turns into slag. Thus, thermal plasma arc vitrification is one possible solution, since plasma arc systems can reach high temperatures regardless of the maximum temperature of fossil fuel. With the plasma arc system, it has been expected that the ashes can be converted to high-quality slag, thereby reducing the volume.

Treated slag can be used as construction materials such as interlocking blocks and roadbed material because the hazardous substances are fixed in the slag without leach [3]. This research studied volume reduction, detoxification (removal of hazardous elements) of fly ash, conversion to stable slag, and behavior of hazardous material by elution tests with ashes. Then, through testing the physical properties of the slag, we confirmed that it could be reused.

2. Experiment

2. 1 Experimental equipment and process

Figure 1 shows a schematic diagram of the experimental apparatus for plasma vitrification. The apparatus consisted of a plasma torch, a reaction chamber and an off-gas system. The non-transferred type of plasma jet was used, with a tungsten cathode and a copper anode. Both electrodes were water-cooled and the plasma torch was made to rotate 360°. The chamber was made with a double wall of water-cooled stainless steel and had a view port. The sludge and fly ash were put inside the chamber where they were melted. The fly ash, consisting of very fine particles, would be blown away by the plasma jet; therefore, it could not be placed on the crucible as it was. So we prepared pellets for samples. The samples were put on a water-cooled Cu holder to control the height between pellet and torch. The arc length was kept to thirty mm, and the output power of plasma was about six to nine kW. The exhaust gas was treated and led through a scrubber and duct. The sludge and fly ash were melted for ten to fifteen minutes, respectively, and then the slag was analyzed by a leaching test. Table 1 shows the experimental conditions. The leaching solution was analyzed by a ICP-MS and a conductivity meter. Vickers hardness of slag was measured with a micro hardness tester.

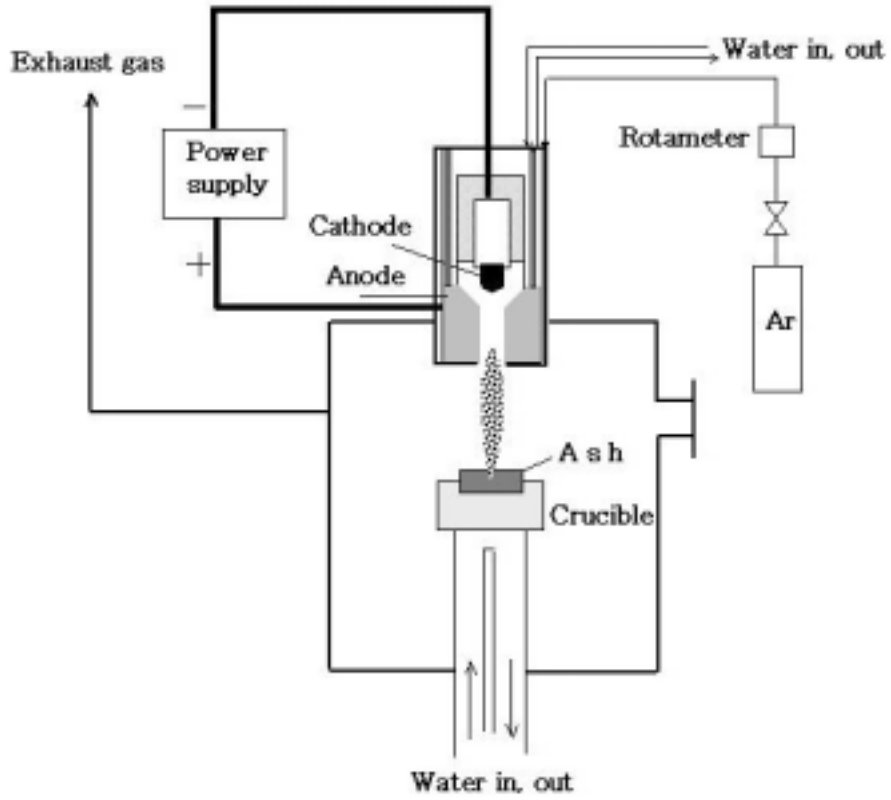

Fig. 1. Schematic diagram of set-up

Table. 1. Experimental condition

Plasma torch	Input power : 6 - 9 kW (40V)
Plasma gas flow rate (Ar)	15 l/min
Distance (from torch to waste)	30 mm
Ash weight	25 g
Operating time	10-15 min

2. 2 Leaching Test

2. 2. 1 Standard leaching test

The leaching test was used to estimate the elution of hazardous waste. A criterion of the leaching test is given in Table 2. The standard leaching test was carried out using acid solutions (pH 5.8-6.3) with a liquid-to-solid ratio of one hundred ml of solution for ten g of solids. The solution was stirred by the shaker with an amplitude of four to five cm at two hundred rpm for six hours in the atmospheric temperature, pressured and filtered on one μm filter paper to separate the solid and liquid phases.

Table 2. Criterion of leaching test [ppm]

Item	Cd	Pb	Zn	As	Se	Pb	Cr	Hg
Leaching limit	0.3	3	-	1.5	-	3	1.5	0.005

The leaching solution was analyzed concerning As, Cr, Cu, Cd, Hg, Se, Pb, Zn, following the Korea Standard Leaching Procedure [4]. Zn, Se is not a standard elution test material but is included for reference in this research because it is plentiful in the environment and toxicity is a concern.

2. 2. 2 Leaching test by different conditions

The pH condition and the slag diameter have the most influence on leaching of the heavy metal [5]. So we conducted a leaching test of plasma molten slag by changing the pH 2, 4, 6 of the solution and changing the slag diameter to pH 4. Other leaching terms are equal to that of the standard leaching test.

2. 3 Contrast of the cooling rate

After ash and sludge are melted, the property of molten slag is influenced by different cooling rates. So we conducted differences of cooling rates. The Vickers hardness of molten slag was measured. The leaching solution, slag, was analyzed by ICP-MS, KEM conductivity.

3. Result and discussion

3. 1 Fly ash and sludge

Fly ash contains amounts of heavy metal, so if buried in the ground it would be exposed to acid rain in the future. Therefore, it should be treated before being buried. Before and after vitrification, we conducted leaching tests of fly ash and sludge. The Korean Standard Leaching Procedure stipulates that the leachate for the test should be pH 5.8-6.3. In this experiment, we performed leaching tests in pH 6. Tables 3 and 4 show the results of the leaching test before and after vitrification. Zn, Se is not in the standard leaching test materials but it is included for reference in this research. After vitrification, more heavy metals flowed from the sludge. The concentration of non-organic material in sludge was not enough to vitrify. So we mixed sludge and fly ash to increase non-organic material in the sludge. In the mixture the fly ash-to-sludge ratio was 1 : 1 in wt %. In the mixture, each heavy metal had a value below the leaching limit after vitrification.

Table 3. Leaching test results of fly ash and sludge [ppm]

	Cd	Cu	Zn	As	Se	Pb	Cr	Hg
Leaching limit	0.3	3	-	1.5	-	3	1.5	0.005
Fly ash	142.8	3640.5	2869.3	0.334	1.330	11.19	1.170	ND
Mixed	62.39	843.6	1228.5	0.206	0.619	0.490	0.106	ND
Sludge	0.004	0.123	0.125	0.017	0.006	0.001	0.016	ND

Table 4. Leaching test results of its slag [ppm]

	Cd	Cu	Zn	As	Se	Pb	Cr	Hg
Leaching limit	0.3	3	-	1.5	-	3	1.5	0.005
Fly ash	0.021	0.332	0.431	0.032	0.222	1.198	0.004	ND
Mixed	0.081	0.379	0.234	0.415	0.617	0.152	0.014	ND
Sludge	0.144	12.47	2.955	0.044	0.022	1.904	0.182	ND

3.2 Heavy metal leaching according to changing conditions

The pH has the most influence on leaching of heavy metal. So a leaching test of the molten slag by changing pH was performed. Other leaching conditions are equal to that of standard leaching procedure. Tables 5 and 6 show the results of leaching tests by changing pH. The slag was safe in pH 4 compared to the standard leaching limit. As the pH becomes more acid, more heavy metals leach out. Table 7 shows the results of the leaching test by changing the slag's diameter. If the slag is buried underground, it breaks easily, so the surface area increases. If the particle diameter decreases, more heavy metal leaches out. The slag's

diameter is classified to 1~5mm, 5~10mm and over 10mm. The leaching test was performed in pH 4. The result shows that more heavy metals leached out as the slag's diameter decreased.

Table 5. Leaching test of the fly ash slag by changing pH [ppm]

	Cd	Cu	Zn	As	Se	Pb	Cr	Hg
Leaching limit	0.3	3	-	1.5	-	3	1.5	0.005
pH 4	0.145	1.836	1.096	0.005	0.007	0.093	0.0004	ND
pH 2	0.213	20.449	3.337	0.060	0.010	0.083	0.0002	ND

Table 6. Leaching test of the mixed slag by changing pH [ppm]

	Cd	Cu	Zn	As	Se	Pb	Cr	Hg
Leaching limit	0.3	3	-	1.5	-	3	1.5	0.005
pH 4	0.014	0.153	0.075	0.079	0.095	0.021	0.001	ND
pH 2	0.107	0.461	1.597	0.415	0.185	0.010	0.0005	ND

Table 7.The result of leaching test by changing the slag's diameter at pH 4 [ppm]

	Cd	Cu	Zn	As	Se	Pb	Cr	Hg
Leaching limit	0.3	3	-	1.5	-	3	1.5	0.005
X > 10 mm	0.128	1.512	1.043	0.006	0.007	0.04	0.001	ND
5 ~ 10 mm	0.25	1.692	1.779	0.006	0.012	0.118	0.0002	ND
X < 5 mm	0.335	3.163	2.647	0.012	0.014	0.176	0.0007	ND

3.3 Comparison of cooling rates

The property of molten slag is influenced by different cooling rates. If the cooling rate is fast, slag becomes amorphous, and the slag's hardness increases. An experiment with different cooling rates was performed. A leaching test was performed, and the slag's hardness was measured. The leaching solution was analyzed by ICP-MS. The electric conductivity for the leaching solution was measured using the KEM conductivity meter. Tables 8 and 9 show the results of the ICP-MS and the conductivity meter. The cooling rate was classified as fast, medium and slow. Fast is water-cooled; medium is air-cooled; slow is natural convection.

.

Table 8. The results of leaching tests by different cooling rates (sludge + bottom ash) [ppm]

	Cd	Cu	Zn	As	Se	Pb	Cr	Hg
Leaching limit	0.3	3	-	1.5	-	3	1.5	0.005
Slow	0.0042	0.7444	0.1619	0.0149	ND	0.0184	0.0263	ND
Medium	0.0046	0.4675	0.1311	0.0183	ND	0.0198	0.0074	ND
Fast	0.0006	0.1954	0.0211	0.0043	ND	0.0017	0.0058	ND

Table 9. Electric Conductivity of mixed slag by different cooling rates [μs/cm]

	Slow	Medium	Fast
Electric Conductivity	53	35.3	28

Vickers hardness of mixed slag and mixed slag after leaching tests by different cooling rates is shown in Table 10. All slags have a strong physical property like ceramics. The amount of heavy metal and Vickers hardness decreased if the cooling rate was fast. This fact indicated that the amorphous structure enhanced the problem of heavy metals flowing out. With a faster cooling rate, the physical hardness decreased but had more Vickers hardness than the ceramic. This slag was found to exhibit sufficient strength to be utilized as construction material such as interlocking blocks or road-bed material.

Table 10. Vickers Hardness of mixed slag by different cooling rates [Hv]

	Slow	Medium	Fast
Before leaching test	1983.4	1669.7	1243.7
After leaching test	1585.7	1600.4	1238

4. Conclusion

The fly ash and sludge were treated by a DC non-transferred type of thermal plasma. It was concluded that the heavy metal in slag leached a value below the standard level by plasma vitrification. The leaching test by changing conditions was conducted. An experiment with different cooling rates was also performed. The results are as follows:

1. The results of leaching tests showed that such heavy metals as Cu, Zn, Pb in fly ash leached over the standard. Fly ash must be detoxified by plasma vitrification before its final disposal.
2. By plasma vitrification of fly ash, the heavy metal in fly slag leached a value below the standard.
3. After vitrification, more heavy metals flowed from the sludge. The concentration of non-organic material in sludge was not enough to vitrify.
4. The sludge and fly ash for increasing non-organic material in sludge was mixed. In the mixed, each heavy metal had a value below the leaching limit after vitrification.
5. As the pH becomes more acidic, more heavy metals leach out. And as the particle diameter decreases, more heavy metals leach out.
6. The results of differing cooling rates show a lower leaching from rapidly cooled slag than from the slowly cooled slag. This is due to the structure of the slag.

Acknowledgement

This work was supported by the Regional Research Center for Coastal Environments of Yellow Sea (CCEYS) at Inha University designated by MOST and KOSEF(2003).

Reference

[1] E. A. Korzun,, H. H. Heck - J. Air Waste Manage. Assoc. 40, 9 (1990).
[2] W. K. Lee, J.B. Kim, E.M. Kim - J. Korea Solid Wastes Engineering Society. 14, 3 (1997).
[3] T. Inaba, M. Nagano, M. Endo - Electrical Engineering in Japan. 126, 3 (1999).
[4] The Ministry of Environment Republic of Korea, Article 11, Amended by Law No. 5865 (1999).
[5] N. Furuta, T. Hosoi, M. Ohata and T, Inaba - Workshop on Use of Incinerator Ash (2000).

Plasma Deposition of Nano-Structured and Nano-Layered Thin Films for Biomedical Applications

P. Colpo, G. Ceccone, F. Rossi

European Commission, Joint Research Centre, Italy

The present work concerns the deposition of multi-component nano-structured thin films to control the adhesive surface properties under conditions of contact with the bio-medium. Nano-structured thin films based on the system Ti-X-Y (X=Al,Si,V,Zr,Nb, and Ca; Y=C,O, and N) are deposited using ionised PVD (I-PVD) of composite targets.

Plasma diagnostics is performed by means of optical emission spectroscopy, and mass spectrometry including ion detection. The relative ionised fraction of metal atoms for different PVD parameters is measured. Influence process parameters (power, pressure…) on the structure and mechanical properties of the layers was studied and related to the diagnostics results.

The Study on Plasma Pyrolysis of Biomass and Plastic

Zeng-li Zhao[1], Hai-bin Li[1], Chuang-zhi Wu[1] , Yong Chen[1], You-san Fan[2]

[1]*Guangzhou Institute of Energy Conversion，CAS, Guangzhou ,China*
[2]*Tsinghua University, Beijing, China*

With the rapid urbanization and industrialization in China, the amount of municipal solid waste (MSW) produced is increasing at a rate of 8~10% each year. The calorific value and composition of MSW are also changing due to increasing waste plastic and paper. Now many landfill sites are full beyond capacity. Other traditional disposal technologies caused serious environmental pollution that deserves public concern. There are two principal combustible wastes in MSW: cellulose (paper, wood, etc) and polymer (plastic, textile and tire). These wastes constitute about 20~30% by weight and only a small amount can be recycled as material. Thermal process is one kind of effective technologies to reduce the volume and mass, while the energy can be recovered in an environmentally friendly and safe way.

There are many thermal treatment processes of converting these complex mixtures into valuable products, such as pyrolysis, gasification, etc. Because of their high calorific and volatile, currently there is considerable interest in the efficient use of combustible composition in MSW as a fuel source or a possible chemical feedstock. But it is very difficult for the complete and ecologically safe disposal of unsorted, unpurified mixed plastic waste. Thermal plasma technology can offer a new way to convert the mixtures [(1,2)]. Plasma pyrolysis process uses extremely high temperature to completely decompose waste material into very simple molecules and the byproduct is an energy-rich gas used for power generation or methanol synthesis.

A DC plasma pyrolysis device with a maximum power input of 50KVA was used in the experiments. The mixtures of biomass and plastic were feed continuously into the reactor using nitrogen as the operating gas and carrier gas. The feeding rate varied from 1.0kg/h to 3.6kg/h. Polyethylene（PE）and Polypropylene (PP) are chosen as the plastic materials in pyrolysis experiments for that they are the principal components contributing to the plastics in MSW. The results indicated that product gas is rich in hydrogen, carbon monoxide and acetylene. The influences of the feeding rate and steam partial pressure on the products distribution and gas composition were investigated. Appropriate synthesis gas for difference industry uses may be obtained by adjusting those key process parameters. It indicates that synergetic effects happen in the co-pyrolysis process. By using instruments analysis (TG, XRD, ICP and SEM/TEM), the characteristics of the pyrolysis char, the transfer mechanism of heavy metals and acid gases emission from the pyrolysis process were obtained.

ACKNOWLEDGEMENTS

The authors are pleased to acknowledge the financial support of Nation Nature Science Foundation of China (Contract No. 59906013) and Guangdong Nature Science Foundation (Contract No.990036 and No.003045).

REFERENCES

[1] A.K. Gupta, “Thermal Destruction of solid waste”, Journal of Energy Resources Technology, Vol. 118, pp187~192 (1996)

[2] R.R. Guddeti, R.Knight, and E.D. Grossmann, “Depolymerization of Polyethylene using Induction-Coupled Plasma Technology”, Plasma Chemistry and Plasma Processing, Vol.20, No.1, pp37~64 (2000)

CONTRIBUTION OF CU VAPOUR TO RADIATION TRANSFER IN SF_6 AND PTFE ARC PLASMAS

V. Aubrecht[1] and M. Bartlova[2]

[1] *Department of Power Electrical and Electronic Engineering, Brno University of Technology, Brno, Czech Republic*
[2] *Department of Physics, Brno University of Technology, Brno, Czech Republic*

Abstract
An approximate method of partial characteristics (MPC) was used to evaluate radiation properties of SF_6 and PTFE arc plasmas with various admixtures of Cu (1%, 5% and 10%, respectively). Radiation flux and net emission were calculated using MPC for various temperature distributions in the arc plasmas. Our calculations have proved that admixture of Cu vapour in a plasma contributes to the both radiation flux and the net emission increasing.

1. Introduction

An electric (switching) arc between separated contacts is an integral part of a switching process. For any kind of high power circuit breakers, the basic mechanism is the extinguishing of the switching arc at the natural current zero by gas convection. The switching arc is responsible for proper disconnecting of a circuit. In the mid and high voltage region, SF_6 self-blast circuit breakers are widely used. Radiation transfer is dominant energy exchange mechanism during the high current period of the switching operation. Detailed information about the local arc structure can only be given by mathematical models, which allow the calculation of the distribution of emission and absorption throughout the entire arc plasma volume. Recently, we have used an approximate method of partial characteristics (MPC) to evaluate the radiation properties of pure SF_6 and various mixtures of SF_6 with PTFE (material of ablation nozzle) [1, 2]. In this paper, the method of partial characteristics has been used to extend previous data for Cu vapour contribution with various Cu admixture ratios. Resulting data could be used for a modeling of the radiation transfer in the switching arc, including vaporization from Cu contacts.

2. Plasma composition.

Radiation in arc plasmas depends, besides others physical quantities, also on concentrations of all chemical species occurring in the plasma. In mixture of SF_6 and Cu plasma, we assume the following species: SF_6 molecules, S, F, Cu neutral atoms, S^+, S^{++}, S^{+++}, F^+, F^{++}, Cu^+ ions and electrons. In case of PTFE (C_2F_4) plasmas, there are also C, C^+, C^{++}, C^{+++} atoms and ions taken into consideration. In Figs. 1 and 2, we plot the particle densities for 99% SF_6 + 1% Cu and 90% PTFE + 10% Cu plasmas, respectively as a function of the plasma temperature. Concentrations of each species were calculated at RWTH Aachen, Institute for High Voltage Technology [3]. Molecules and highly ionized atoms were neglected since up to know we have not found simple appropriate mathematical model for description of molecule dissociation. We have only taken into account SF_6 molecules with their experimentally measured absorption cross sections [4].

2. Theory – Method of Partial Characteristics

The basic quantity in radiation transport of energy is intensity of radiation I ($\mathbf{n}$, X) which is the radiation power per solid angle per unit area perpendicular to the direction $\mathbf{n}$ at a point X. An exact calculation of the radiation intensity is based on the knowledge of the plasma composition and subsequently absorption coefficients. Prediction of the later is a very difficult task since one must usually deal with complex structure of atomic spectra [5, 6] which is a very time consuming for any kind of computation. One must deal both with continuous radiation made by photo-recombination and “bremsstrahlung” processes and discrete radiation which consists of hundreds of spectral lines. Spectral lines broadening and their complex shapes have to be carefully considered. Due to the very fine structure of the lines, very fine integrations step has to be chosen in all considered computations which leads to the enormous computation times.
The approximate method of partial characteristics consists of "pre-computing" the most time consuming calculations in the form of data tables which can be then easily used for the prediction of radiation quantities. Details of the method of partial characteristics have been described in our previous paper [1].

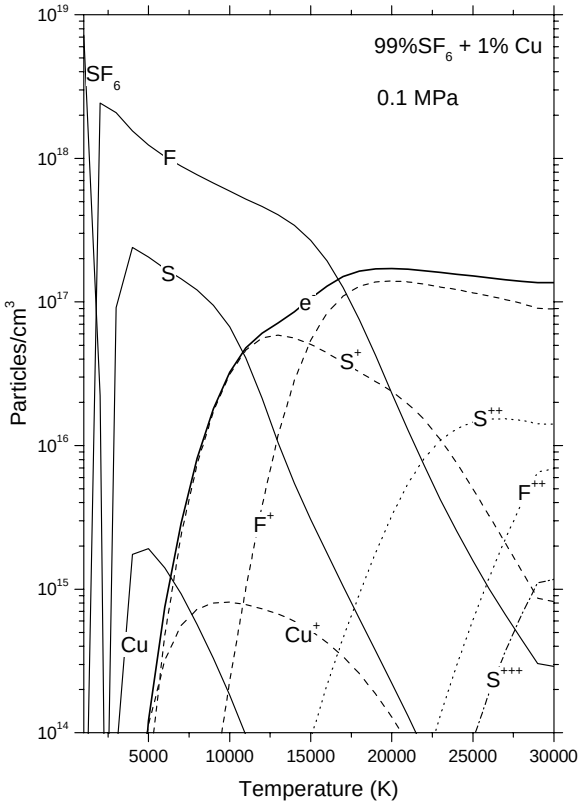

Fig. 1: Composition of 99% SF_6 + 1% Cu plasma as a function of temperature at a pressure of 0.1 MPa.

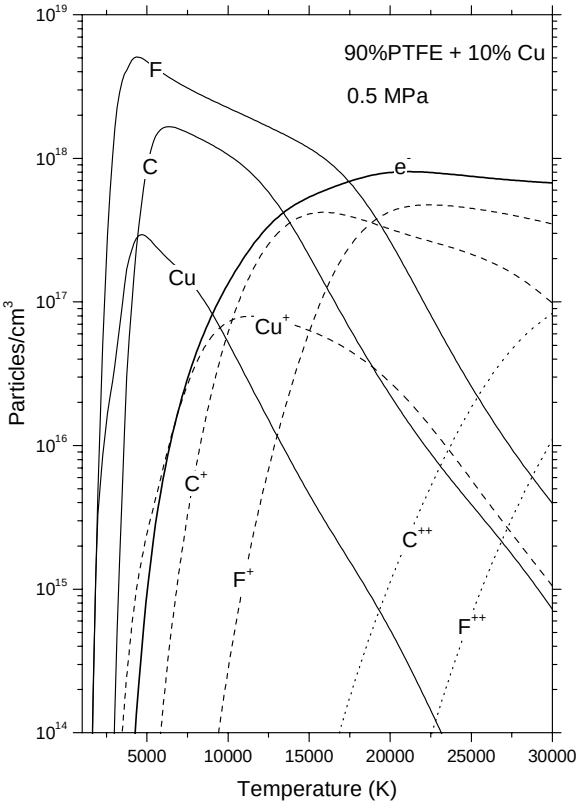

Fig. 2: Composition of 90% PTFE + 10% Cu plasma as a function of temperature at a pressure of 0.5 MPa.

Total radiation intensity at point X can be calculated by summation of all partial intensities between point X and plasma boundary R

$$I(X) = \int_X^R \Delta I\left(T_X, T_\xi, |X-\xi|\right) d\xi \tag{1}$$

Explanation of the meaning and symbols of partial intensities is in Fig. 3. Signs "+" and "-" denote radiation intensity in direction $R \rightarrow X$ and $X \leftarrow R$, respectively.

Net emission of radiation $\nabla I(X)$ along a line segment $\overline{XR}$ can be evaluated as

$$\nabla I(X) = \Delta I\left(T_R, T_X, \overline{XR}\right) - \int_X^R \Delta Sim\left(T_X, T_R, \overline{X\xi}\right) d\xi \tag{2}$$

where the functions ΔI and ΔSim are the partial characteristics defined in [1]. These two functions are pre-calculated in advance with parameters T_X, T_ξ, $\overline{XR} = |X-R|$ and they are used in the form of tables for prediction of radiation intensities, fluxes and their divergences (net emission). Equations (1) and (2) have to be integrated over all angles to obtain complete radiation emission or absorption from all directions.

With a simple one dimensional plasma of length $2R$ the formulas for radiative flux and its divergence in terms of the partial characteristics are given by:

$$\mathbf{F}^{1D}(X) = \int_{-R}^{X} \Delta I\left(T_\xi, T_X, \overline{X\xi}\right) dx - \int_X^R \Delta I\left(T_\xi, T_X, \overline{\xi X}\right) dx \tag{3}$$

and

$$\nabla \mathbf{F}^{1D}(X) = \Delta I\left(T_{-R}, T_X, \overline{-RX}\right) + \Delta I\left(T_R, T_X, \overline{XR}\right) - \int_{-R}^{R} \Delta Sim\left(T_X, T_\xi, \overline{X\xi}\right) d\xi \tag{4}$$

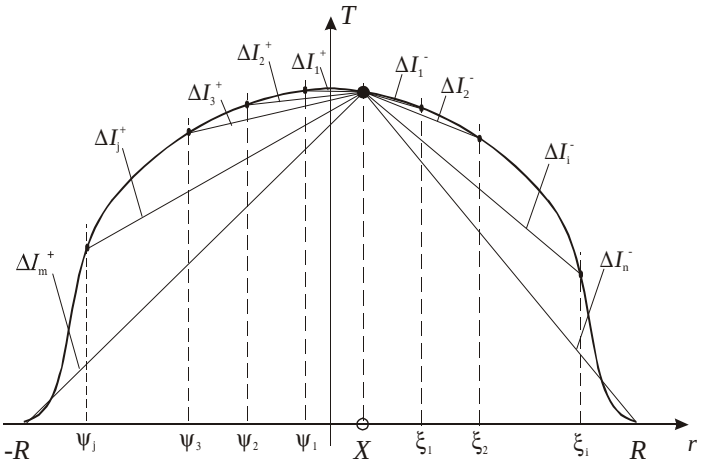

Fig. 3: Schematic drawing with symbols explaining principle of the method of partial characteristics.

The radiation quantities in three-dimensional plasma – the radiation flux $\mathbf{F}^{3D}$ and divergence of radiation flux $\nabla\mathbf{F}^{3D}$ - are predicted according formulas (5 - 8), where the intensity of radiation I and the net emission ∇I along a particular directions (angles) are evaluated using tables of pre-calculated partial characteristics ΔI and ΔSim.

In spherical coordinates, the individual components of vector $\mathbf{F}^{3D}(X)$ are given as follows:

$$F_x^{3D}(X) = \int_0^{\pi}\int_0^{2\pi} I(X,\theta,\phi)\sin^2\theta\cos\phi\, d\phi\, d\theta \tag{5}$$

$$F_y^{3D}(X) = \int_0^{\pi}\int_0^{2\pi} I(X,\theta,\phi)\sin^2\theta\sin\phi\, d\phi\, d\theta \tag{6}$$

$$F_z^{3D}(X) = \int_0^{\pi}\int_0^{2\pi} I(X,\theta,\phi)\sin\theta\cos\theta\, d\phi\, d\theta \tag{7}$$

and the divergence of radiative flux

$$\nabla\mathbf{F}^{3D}(X) = \int_0^{\pi}\int_0^{2\pi} \nabla I(X,\theta,\phi)\sin\theta\, d\phi\, d\theta \tag{8}$$

Meaning of symbols in the previous formulas is given in schematic diagram of the integration over angles in Fig. 4.

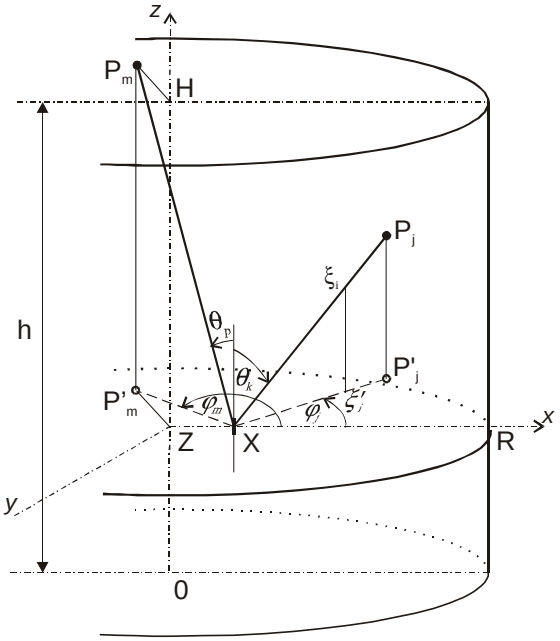

Fig. 4: Schematic diagram of the integration over angles.

3. Results

We have calculated tables of partial characteristics for mixtures of SF_6 and Cu and PTFE + Cu plasmas, respectively at temperatures between 2 000 K and 30 000 K and pressures of 0.1 and 0.5 MPa. Our tables cover admixture ratios of Cu of 1%, 5% and 10%, respectively. In the following figures we show some results of net emission (divergence of radiation flux) calculations, using the tables of partial characteristics.
In Figs. 5 and 6, we compare our results with ones published by Raynal et al. [7]. Fig. 5 represents a variation of function Sim (one of the partial characteristics) as a function of end-temperature for given temperature with the second end-temperature as a parameter. Agreement between our calculations and ones of [7] is quit well. Discrepancies are given fairly by various sources of atomic data and different approach to prediction of absorption coefficients. In Fig. 6, we plot calculated radial distribution of divergence of radiation flux (net emission) using MPC at the cross section of SF_6 + Cu plasma cylinder with height of 8 cm at a pressure of 0.1 MPa. Given radial temperature profile is the same as for [7].

Contribution of Cu vapour to the net emission in SF_6 and PTFE arc plasmas at a pressure of 0.5 MPa is illustrated in Figs. 7 and 8. Radial temperature distribution for these plots has been chosen according to experimental predictions [3]. The resulting divergences of radiation flux are related again to the plasma cylinder with height of 8 cm with radial distributions of net emission given at the central cross section of the cylinder. From the figures it can be seen that copper admixtures contributes mainly to the radiation emission in the hot central regions whereas the absorption in the cold regions is not much influenced. Furthermore, as can be seen from the Figs. 7 and 8, the influence of copper is significant for relative higher admixture ratios, more then a few percent.
In real applications copper concentrations varies both in radial and axial directions. In our calculations we assumed the constant Cu admixture ratio as well as the constant plasma pressure within the arc column. It is very rough approximation, but in spite of this we are convinced of a benefit of the method of partial characteristics which can be used at least for the first estimation of radiative heat transfer in the arc plasmas.

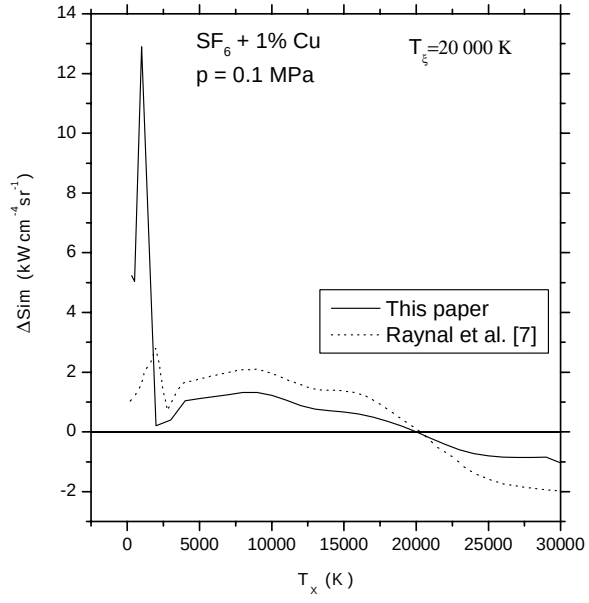

Fig. 5: Partial function ΔSim as a function of end-point temperature T_X for source temperatures T_ξ of 20 000 K in gaseous plasma of 99% SF_6 + 1% Cu at a pressure of 0.1 MPa.

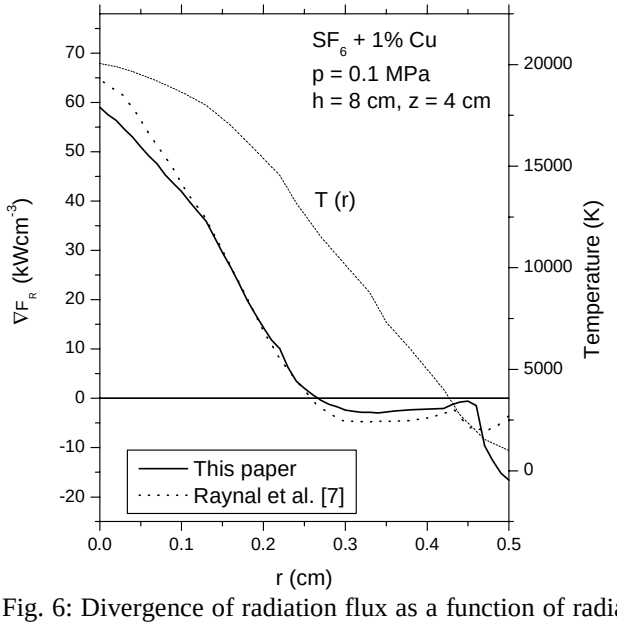

Fig. 6: Divergence of radiation flux as a function of radial distance in a cylindrical plasma of 99% SF_6 + 1% Cu at a pressure of 0.1 MPa.

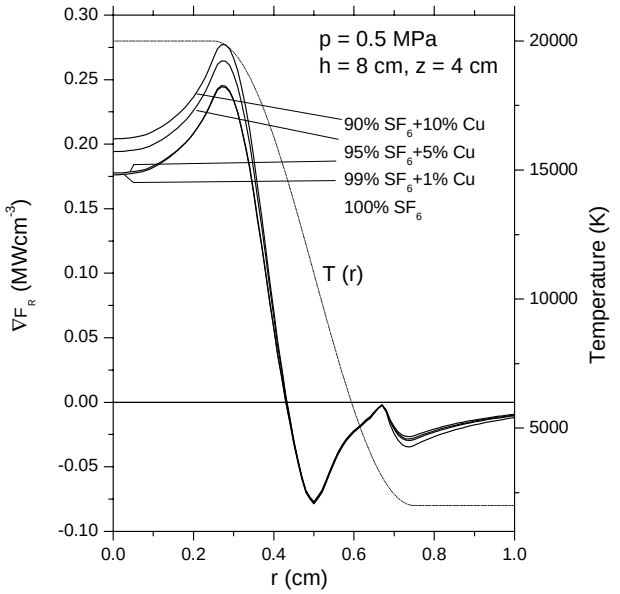

Fig. 7: Influence of copper admixture on the divergence of radiation flux as a function of radial distance in a cylindrical plasma of SF_6 at a pressure of 0.5 MPa

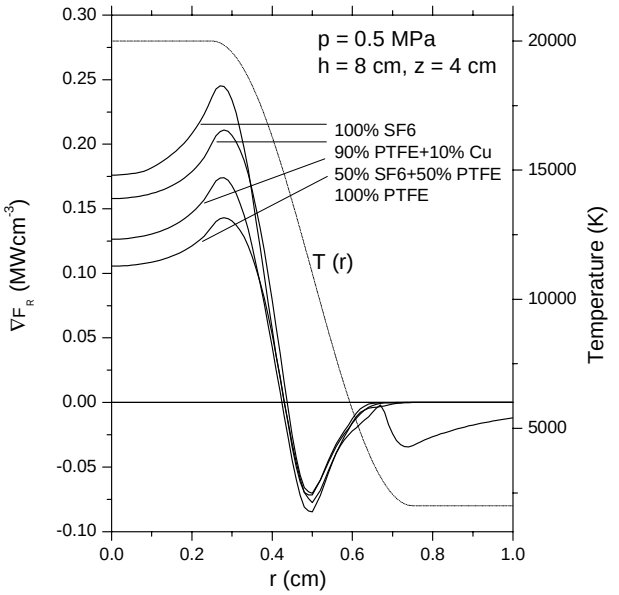

Fig. 8: Influence of copper admixture on the divergence of radiation flux as a function of radial distance in a cylindrical plasma of SF_6 and PTFE at a pressure of 0.5 MPa.

Acknowledgement:
Authors gratefully acknowledge financial support from Grant Agency of Czech Republic under projects Nos. 202/02/1027/A 102/03/0813 and Ministry of Education under project No. CEZ:J22/98:262200010.

References

[1] V. Aubrecht and J. J. Lowke, J. Phys. D: Appl. Phys., Vol. 27, pp. 2066-2073, 1994
[2] V. Aubrecht and M. Bartlova, In Proceedings of the XIV International Conference on Gas Discharges and their Applications, pp. 47 – 50, Liverpool, 2002
[3] C. Lüders, private communication
[4] M. Sasanuma, E. Ishiguro, T. Hayaisha, H. Masuko, Y. Morioka, T. Nakajima, M. Nakanuta, J. Phys. B: Atom. Molec. Phys., Vol. 12, p. 4057, 1979
[5] R.W. Liebermann, J.J. Lowke, Quant. Spectrosc. Radiat. Transfer, Vol. 16, p. 253, 1967
[6] V. Aubrecht, B. Gross, J. Phys. D: Appl. Phys., Vol. 27, p. 95, 1994
[7] G. Raynal, P.J. Vergne, A. Gleizes, J. Phys. D: Appl. Phys., Vol. 28, pp. 508-515, 1995

Production and reduction of higher silanes in modulated silane plasmas

A. Suzuki

Energy Electronics Institute, National Institute of Advanced Industrial Science and Technology, Tsukuba, Japan

Abstract
Higher silane production and reduction processes in modulated silane plasmas are investigated by measuring time-dependent densities using photoionization mass spectroscopy. With a discharge is turned on, higher silanes increase and saturate with several seconds, and decrease with the rate of diffusion after a discharge-off. These results indicate that the higher silanes are not trapped around plasma/sheath boundary, different from silicon particles.

1. Introduction

Plasma enhanced chemical vapor deposition (PECVD) process by a radio frequency (13.56 MHz) silane (SiH_4) discharge is the most favorable method to prepare hydrogenated amorphous silicon (a-Si:H), which is important material for solar cells and thin film transistors [1, 2]. Higher silanes are hydrogenated silicon molecules such as disilane (Si_2H_6), trisilane (Si_3H_8) tetrasilane (Si_4H_{10}) and pentasilane (Si_5H_{12}), and produced by gas-phase reactions in the silane plasmas.

Among the silane plasmas, it is well known that modulated silane plasmas are effective to suppress silicon particles, which degrade photoelectric properties of a-Si:H films [3]. The silicon particles can be contamination in the silane plasma process as is seen in semiconductor process, therefore, should be reduced from the gas-phase in the silane discharge to improve quality of a-Si:H films. A couple of works reported that the silicon particles start to grow from small radicals, ions, atoms, and molecules through gas-phase reactions [4]. The higher silanes are also one of products by these gas-phase reactions. With increasing in the size of higher silanes, they are electronegative because of their larger electron affinity. Such negatively charged hydrogenated silicon clusters are trapped by the sheath potentials between the parallel electrodes. This concentration enhances growth of the clusters via condensation reactions with the positive ions generated by ionization of neutral radicals and molecules in the plasma [4]. Rates of the condensation reactions between positive and negative ions are several times higher than that of the other reactions between ions and neutral species, and between neutral species [5]. The modulated plasma reduces the silicon particles by terminating the condensation reactions. Intermission of the plasma by the modulation breaks the concentration of the negatively charged clusters by collapsing the sheath potential between the electrodes. It is reported that several microsecond terminations are enough to break the sheath potential and suppress the silicon particles [3].

Since the silicon particles grow from small chemical species through gas-phase reactions, higher silanes can be intermediate to the silicon particles. Suppression of the higher silanes might be effective to reduce the silicon particles in the process for a-Si:H more drastically. From this point of view, it is important to identify the time evolution of the higher silanes in the modulated plasmas and compare with that of the silicon particles. Few works reported the temporal change of chemical species in the modulated plasma including higher silanes. This information should be helpful not only to understand the kinetics of higher silanes but also to reduce the silicon particles in the modulated silane plasmas.

In addition, the higher silanes need to be reduced to improve the a-Si:H film properties because it is suggested that they are responsible to photodegradation of the photoelectric properties of a-Si:H [6]. Higher silanes may induce the deviated structure of a-Si:H because they are difficult to diffuse the surface during the a-Si:H film growth due to their heavier mass than those of monosilicon radicals such as sylil (SiH_3) radicals.

As above, it is worth investigating the time evolution of the higher silanes in the modulated silane plasmas to improve the properties of a-Si:H films. In this work, the time-dependent higher silane densities in the gas-phase of the modulated silane plasmas are measured by photoionization mass spectroscopy (PIMS). From saturation and decay time after discharge-on and –off, the production and reduction of the higher silanes in the modulated silane plasmas are discussed and compared with that of the silicon particles.

2. Experimental

Experimental setup is shown in Fig. 1. A power-modulated silane rf (13.56 MHz) glow discharge plasmas, which is controlled by a pulse/function generator, were generated between parallel-plate electrodes in a conventional PECVD chamber. The electrically neutral higher silanes in the gas-phase of the modulated silane plasmas were detected by PIMS using a reflection type time-of flight mass spectrometer (RETOF). Details are described elsewhere, briefly, the higher silanes from the gas-phase of the silane plasma are introduced in to the RETOF, and photoionized by an ArF excimer laser (193 nm, 6.4 eV, 10 mJ/pulse, 30 ns). Positively ionized higher silanes are mass separated in the RETOF. The ion signals from a high mass detector (HMD) are processed by a digital storage oscilloscope and a personal computer [7].

The discharge-on and –off time in one period of the modulation are 10 and 20-50 seconds, depending on the initial silane pressure of 4.0 – 13.0 Pa. A flow rate of a silane gas, an anode temperature, and a rf power density is 5 SCCM, 250 ˚C and 100 mW/cm^2, respectively.

To identify the time-dependent higher silane densities in one period of the modulation, the PIMS measurement must be synchronized with the modulation temporally. Here, the optical emission from the plasma is used to trigger the PIMS measurement against the modulation. There are many emissive species in silane plasmas such as Si* (288 nm), SiH* (413 nm), H* (656 nm), and H_2 (602 nm) [8]. The emission is the probe for rf power introduction into the electrodes because the rate of the emission is on the order of femtoseconds. The steep decrease in the emission detected by a photomultiplier (PMT) triggered a delay generator that gives a delay time to a laser beam from the ArF laser. By varying the delay time by the delay generator, the time dependent higher silane densities over one cycle of the modulated plasma can be obtained. Under the conditions above, the production and reduction of higher silanes over one period of the modulation were investigated.

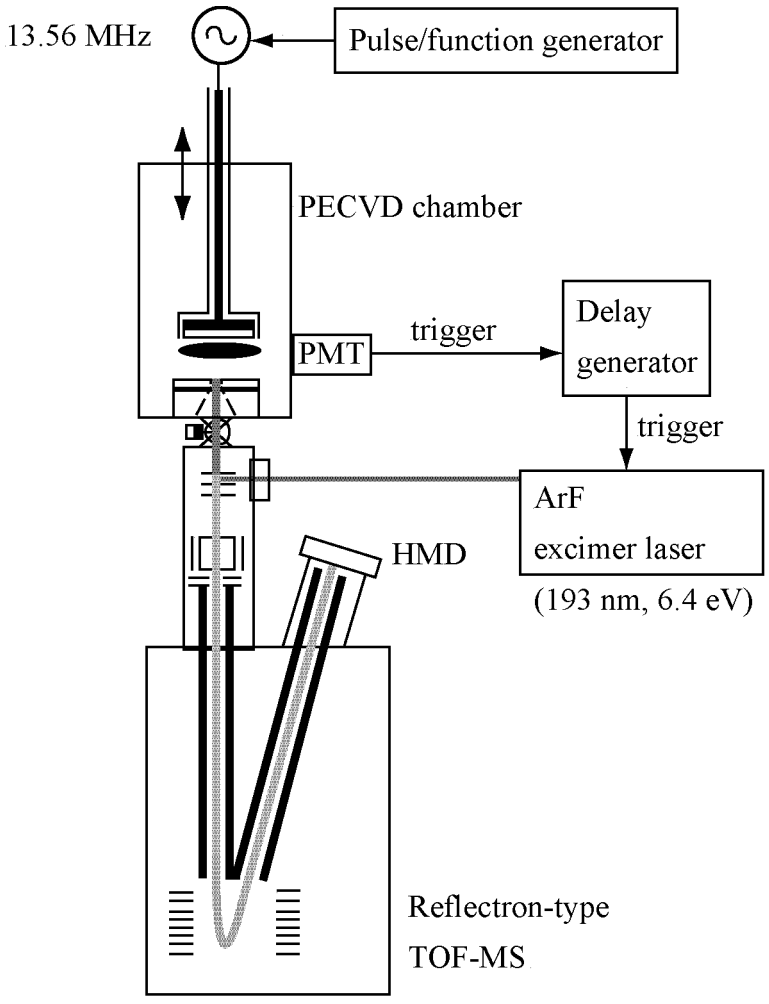

Fig. 1 Experimental setup used in this study.

3. Results and discussion

Figure 2 shows the time-dependent densities of higher silanes in one cycle of the modulation plotted against the time after a discharge starts at the total pressure of 13 Pa. The saturated higher silane densities at the discharge time of 10 s are corresponds to the densities observed in the continuous silane discharge at 13 Pa. It is suggested that the higher silanes in figure 2 are produced by the gas-phase reactions as follows [9];

$$SiH_4 + SiH_2 \rightarrow Si_2H_6$$
$$Si_2H_6 + SiH_2 \rightarrow Si_3H_8$$
$$Si_3H_8 + SiH_2 \rightarrow Si_4H_{10}$$

These reactions are the radical-molecule reactions, which rate is on the order of microsecond [10]. The higher silanes generated during the discharge-on period decay after the discharge is turned off until a next discharge starts. At 60 seconds after a discharge starts, which is 50 seconds after the discharge is turned off, the ion signals from all higher silanes by PIMS are below detection limit. Each higher silane increases with comparable rate; that is, the relative densities between disilane, trisilane, and tetrasilane are almost constant. No results are obtained that higher silanes are sequentially grown in this study, because the time-resolution of the present experimental condition is on the order of sub seconds, which is mainly limited by the fluctuation in the modulation of the plasma. Since the reaction time of higher silane generation is of the order on microseconds, it is impossible to investigate each generation reaction with sufficient temporal resolution.

Disilane production at 4 and 13 Pa is shown in fig. 3. The time evolution of disilane can be fitted by a following formula;

$$\text{Ion signal from the disilane} = C(1-\exp(-t/t_{SAT})) \quad (1)$$

Where t_{SAT} is the time for the saturation. The equation (1) is the solution to the mass diffusion by the simple Fick's model, which expresses one-dimensional mass diffusion [10]. This indicates that disilane production follows the one-dimensional mass diffusion. This result shows that the higher silanes are generated at the narrow area that is probably the sheath region, and not uniformly filled in the PECVD chamber before the saturation. The t_{SAT} is derived to be 4 - 8 s at 4 - 13 Pa, respectively, from the fitting by the equation (1).

Since the stable state disilane density at 13 Pa is higher than that at 4 Pa as shown in fig. 2 and 3, the higher silane production at 13 Pa should be higher than that at 4 Pa. However, it takes much time to saturate at 13

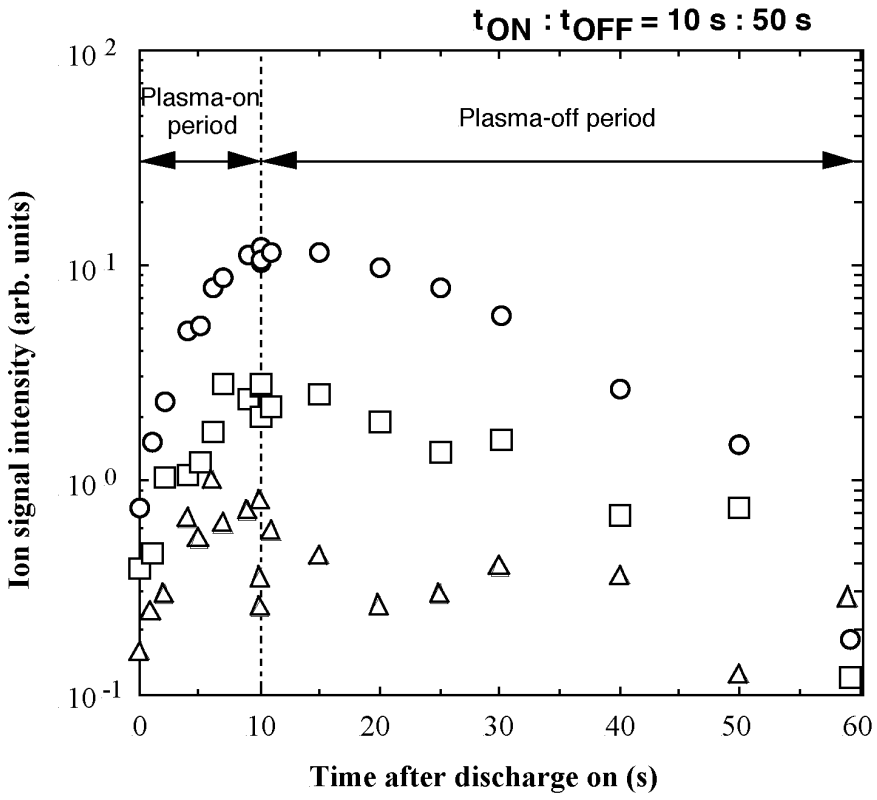

Fig. 2 Time evolution of disilane (○), trisilane (□), and tetrasilane (△) in one cycle of the modulation.

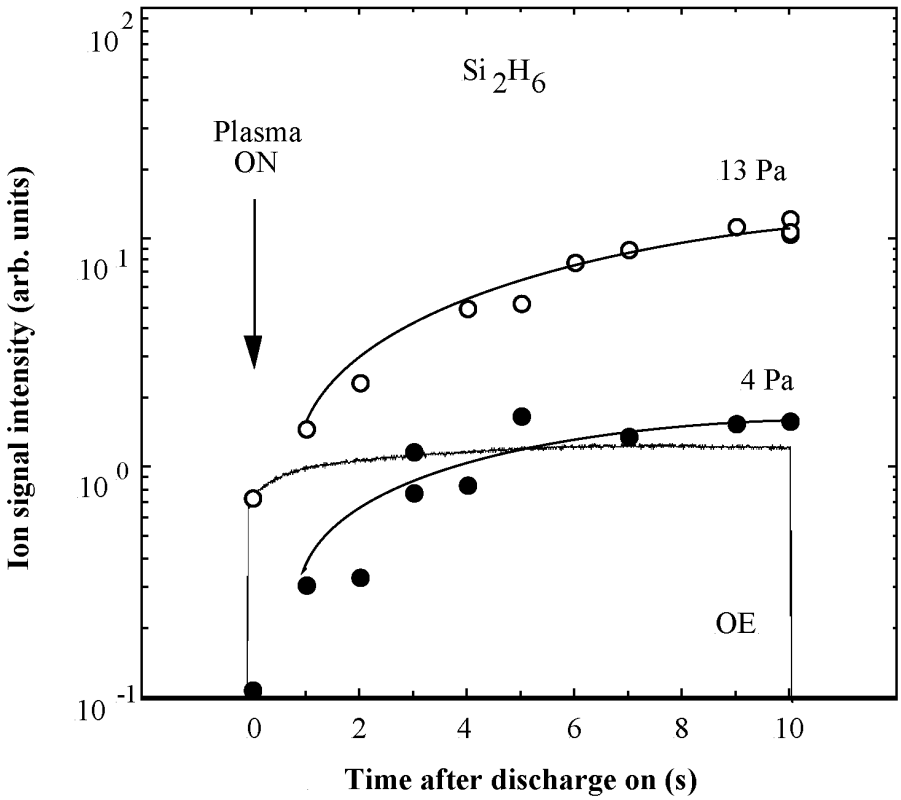

Fig. 3 Time evolution of disilane in the plasma-on period at pressure of 4 Pa (●), and 13 Pa (○). Fittings are by one-dimensional mass difussion (*see in the text*). Time evolution of optical emission (OE) at 4 Pa is also plotted.

Pa than at 4 Pa. This means that the present slow saturation of higher silane density is not attributed to the rate of the production reactions.

The optical emission from a PMT at 4 Pa is also plotted in fig. 3. Clearly, the t_{SAT} for disilane is more slowly than the saturation time of the optical emission. Although the optical emission is mainly from SiH*, its time evolution should be the same as those of other reactive species such as atoms, ions, and radicals. These reactive species can be the reactants for the higher silanes and the silicon particles, thereby, the time evolution of the disilane should follow that of the optical emission from the plasma.

One explanation for this discrepancy is difference in the measured area between optical emission spectroscopy (OES) and PIMS. A photomultiplier detects the emission at the close position to the emissive area that is near the cathode electrode. On the other hand, the ion signal from the PIMS is a trace of the averaged density because PIMS measures the sampled gas from the PECVD chamber.

From this point of view, it is supposed that the slow saturation of the higher silanes results from the slow diffusion to fill the PECVD chamber. If the diffusion of higher silane is the rate determination step for the time evolution, the t_{SAT} of the higher silanes can be of the order on several seconds even if the rate of higher silane production reactions is on the order of microseconds. This also explains the reason for that the saturation at 13 Pa is slower than that at 4 Pa because the rate of diffusion is proportional to the total pressure as is confirmed in the proceeding section.

After a discharge is turned off, disilane decreases with an exponential decay until a next discharge starts as shown in fig. 4. Diffusion lifetime (t_{DIF}) depends on pressure, and is obtained to be 7 – 20 s at 4.0 - 13 Pa, respectively, by exponential fitting. They are consistent with a residence time of a gas in the PECVD chamber in the present experimental conditions, implying that the higher silane reduction is attributed to a diffusion loss. This means that the higher silanes are uniformly filled in the PECVD chamber after the saturation. Since the decay rates of disilane, trisilane, and tetrasilane are mostly comparable, it is concluded that all higher silanes are reduced by a diffusion loss.

As expressed previously, it is reported that silicon particles can be drastically suppressed by the termination of silane plasma. Several microseconds intermission of a discharge can reduce silicon particles drastically [3].

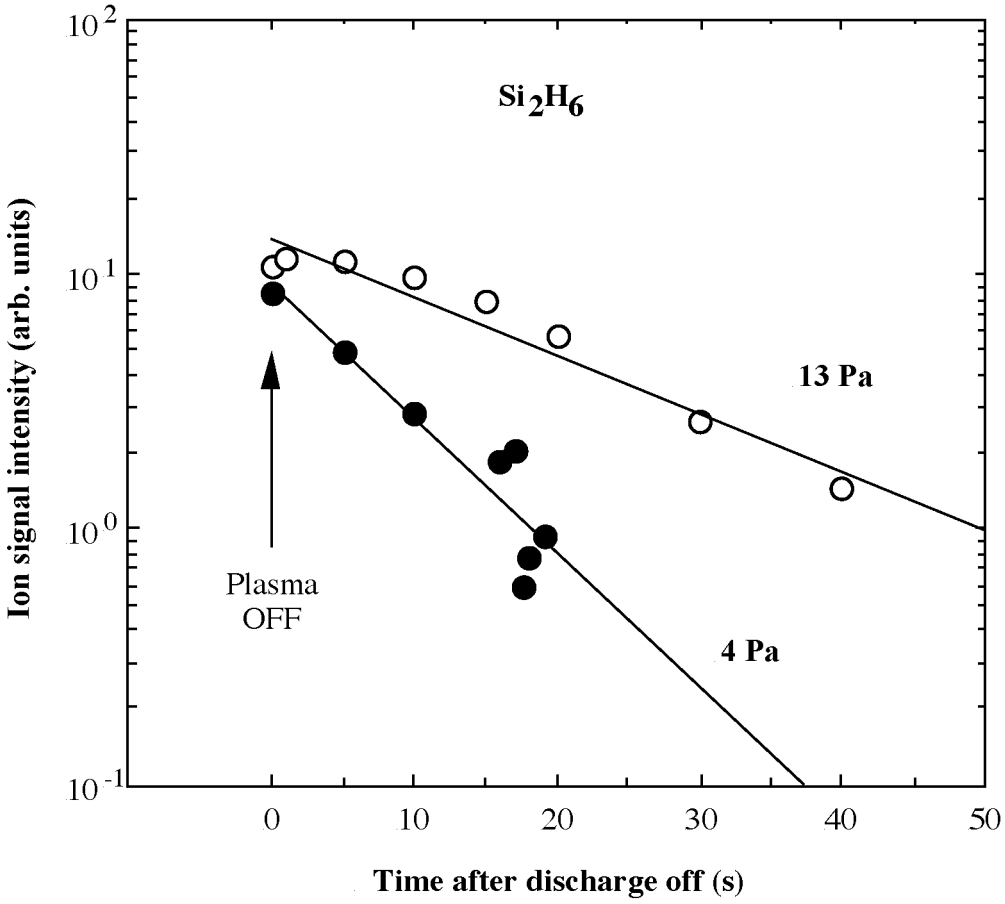

Fig. 4 Time evolution of disilane in the plasma-off period at pressures of 4 Pa (●) and 13 Pa (○). Lines are by exponentioal fitting.

Result in figure 4 indicates that the decay of higher silane is different from that of silicon particles. This difference can be explained by the difference of the measurement between PIMS and laser scattering (LS), which measure silicon particles. As well as OES, LS is optical measurement. Since LS only measures an area where a laser beam is passed, it is easy to concentrate the laser beam to the position which the silicon particles concentrate such as the plasma/sheath boundary. That is, LS and OES measurement is more spatially sensitive than PIMS. The sudden decrease of silicon particles in the modulated silane plasmas measured by LS indicates that the population of silicon particles is spatially concentrated. Since the higher silane is measured by PIMS in the present experiment, the spatially insensitive measurement can not detect the spatial distribution of the higher silanes even if they are concentrated. The higher silane densities should be also relatively high near the plasma/sheath boundary because the radical reactions which generates higher silanes occur near the cathode electrode. However, for the case of higher silanes, its t_{DIF} is comparable to the residence time of a gas, thereby, the higher silanes are filled uniformly in the PECVD chamber except the sheath region at the end of the discharge-on period. This is different from the silicon particles, which are trapped near the sheath/plasma boundary and difficult to escape from the sheath region under the discharge.
Diffusion coefficient (D) of the disilane is calculated from t_{DIF} using following formula based on the Fick's model [11].

$$D = L^2/2\, t_{DIF} \quad (2)$$

Where L is a characteristic length of the diffusion and assumed to be 32 cm, which is the maximum length of the axis of the PECVD chamber. From the results of t_{DIF} from fig. 4, D of disilane is estimated to be 25 – 60 cm^2/s at 4.0 - 13 Pa, respectively, in the present experiment conditions. The D is mostly identical to that of trisilane and tetrasilane because the decay rate is comparable to all higher silanes.
In general, lifetimes of high reactivity reactants such as radicals are short to be on the orders of millisecond [9]. Longer t_{DIF} indicates that the higher silane molecules measured by PIMS is non-reactive, and are not terminated by a reaction with a chamber wall or other reactants. Because of their non-reactivity, the role of

higher silanes for the a-Si:H deposition is small, however, contributes to the deposition through the source of higher silane radicals (Si_nH_x, $x<2n+2$), which probably one of the precursors to the a-Si:H films. For the silicon particle formation, the electrically neutral higher silanes are not only the direct intermediates but also the source of the positive higher silane ions which contributes to the condensation reactions at the plasma/sheath boundary where the negative cluster ions are trapped.
The pressure dependence of t_{SAT} is also explained by the slow diffusion of higher silanes. Since it takes time for higher silane to diffuse in the gas-phase in the PECVD chamber, the t_{SAT} is on the orders of several seconds even if the rate of the higher silane production reactions is on that of microseconds. Consequently, t_{SAT} is proportional to t_{DIF}, and to the total pressure in the PECVD chamber as well.
As above, there are many different characteristics between higher silanes and silicon particles. First of all, the spatial distribution of higher silanes and silicon particles is not identical. Higher silanes are almost spatially uniform in the PECVD chamber during the discharge, on the other hand, silicon particles concentrate around the plasma/sheath boundary. Second, higher silanes are not reduced by the modulated plasmas, different from silicon particles. To suppress higher silanes drastically, each production reaction should be suppressed. The longer lifetime of higher silanes might be advantage to exclude them from the gas-phase in the PECVD chamber.

4. Conclusions

The time-dependent densities of higher silanes in the modulated silane plasmas are investigated by PIMS for the first time. It is seen that the saturation of higher silanes in the PECVD chamber takes several seconds and does not follow that of the optical emission. The slow saturation of higher silanes is explained by the slow diffusion, as seen in the discharge-off period. Even if the generation reactions for higher silanes are fast, it takes time to saturate a chamber because the saturation is limited by the slow diffusion.
The reduction process of higher silanes after a discharge-off is dominated by the diffusion, not by the reaction with a wall, molecules, and a deposition. It is found that the modulation is not effective to suppress higher silanes, indicating that they are not concentrated at the sheath region, different from silicon particles. The slow decrease in higher silanes after the discharge-off is also not observed for the silicon particles, which rapidly decrease by the intermission of a discharge. D of higher silane was estimated to be comparable to a residence time of a gas from the decay lifetime in the discharge-off period.
As above, the behavior of higher silanes is different from that of the silicon particles in the PECVD chamber. Higher silane contributes to the a-Si:H deposition as a source of the higher silane radicals. To reduce the higher silane gases in the gas-phase of the plasma to improve the photoelectric properties of a-Si:H, their production reactions need to be controlled.

References

[1] D. E. Carlson and C. R. Wronski - Appl. Phys. Lett. **28**, 671 (1976).
[2] P. G. LeComber, W. E. Spear and A. Ghaith - Electro. Lett. **15**, 179 (1979).
[3] Y. Watanabe, M. Shiratani, Y. Kubo, I. Ogawa and S. Ogi - Appl. Phys. Lett. **53**, 1263 (1988).
[4] A. A. Howling, L. Sansonnens, J.-L. Dorier, and Ch. Hollenstein - J. Appl. Phys. **75,** 1340 (1994).
[5] D. Smith, M. J. Church, and T. M. Miller - J. Chem. Phys. **68,** 1224 (1978).
[6] A. Suzuki - Jpn. J. Appl. Phys. part 2 **38,** L1315 (1999).
[7] A. Suzuki - Trans. Mater. Res. Soc. Jpn. **20**, 400 (1996).
[8] A. Matsuda and K. Tanaka - Thin Solid Films, **92,** 171 (1982).
[9] J. R. Doyle, D. A. Doughty and A. Gallagher - J. Appl. Phys. **68,** 4375 (1990).
[10] G. Inoue and M. Suzuki - Chem. Phys. Lett., **122,** 361 (1985).
[11] J. Crank - *The Mathematics of Diffusion* (Clarendon, Oxford, 1975).

TPCVD of Si-[X-]C-N from Liquid Organometallic Precursors

E. Bouyer, M. Müller, G. Schiller

German Aerospace Center (DLR), Institute of Technical Thermodynamics, Stuttgart, Germany

Abstract
Coatings of Si-B-C-N from *1,1,3,3,5,5hexamethylcyclotrisilazaneborane* were deposited by means of thermal plasma chemical vapour deposition (TPCVD). The elemental composition of the deposited materials was dependent on the precursor and the plasma gas composition. Silicon carbide is the only crystalline phase formed during the process while silicon nitride was not formed even in a nitrogen containing plasma. The boron is integrated in an amorphous boron nitride compound.

1. Introduction

Several phases in the system Si-C-N are forming a group belonging to high performance ceramics with outstanding properties concerning thermomechanical strength. The addition of a fourth element X with X = B, Ti, Zr giving a quaternary phase Si-X-C-N will permit to even improve many of the properties. As an example addition of boron (Si-B-C-N) enhances the stability of the silicoboron carbonitrides in the range between 1400 and 2000°C. The origin of the enhanced thermal stability is not yet understood. It is assumed that boron plays a major role in stabilising the metastable amorphous phase and in suppressing the thermal degradation of the silicon carbonitride matrix [1]. The presence of a turbostratic non-stoichiometric B-C-N phase that inhibits diffusion processes and decreases the activity of free carbon was also mentioned [2]. These turbostratic layers probably consist of a mixed phase of boron nitride and carbon with various amounts of B, C and N. Multielement ceramic materials are difficult to synthesise by traditional high-temperature synthesis methods such as solid-state reactions, owing to the thermodynamic instability of their solid solutions, especially of those in the ternary and quaternary systems considered in this work. The Si-B-C-N system exhibits an increased thermal stability with respect to pure Si_3N_4 even in nitrogen-free atmospheres. The high onset temperature of crystallisation and/or the high thermal stability are properties required for the development of novel high temperature resistant ceramics with sufficient mechanical properties to withstand service temperatures exceeding 1500°C.
The goal of the study is the thermal plasma deposition of coatings in the system Si-X-C-N with X = B, Zr, Ti from X-bearing silazane precursors. Since so far the most intense part of the study was dedicated to the Si-B-C-N system our contribution will focus only on this material.

2. Experimental

2.1 Materials

The precursor used is a silazane borane (*1,1,3,3,5,5hexamethylcyclotrisilazaneborane*) obtained from the boration of 1,1,3,3,5,5hexamethylcyclotrisilazane by borane with tetrahydrofurane. The precursor is a monomer/oligomer with n = 1 to 3. The stoichiometric ratios of the organometallic precursor are the following: Si/N = 1 ; Si/C = 0.5 ; Si/B = 3. Thus the theoretical formula is $SiB_{0.33}C_2N$.
Plates of molybdenum 40 x 40 x 3 mm³ in size were used as substrates. The Mo plates were either non-cooled or maintained at a low temperature by means of a water cooling system.

2.2 Plasma Processing

The experimental set-up for the synthesis experiments was basically built of an rf plasma torch connected to a vacuum reactor. The liquid precursors were directly injected into the hot plasma core by means of a gas-assisted atomiser (Fig. 1) as previously described more detailed [3]. The process might be understood as a thermolysis process but with the reverse temperature characteristics. Figure 2 describes schematically the steps involved in the synthesis process by high temperature thermolysis of the oligomer Si-B-C-N precursor. Most of the fundamental plasma parameters were kept constant at previously optimised conditions: (i) reactor pressure 20 kPa, (ii) spray distance 200 mm, (iii) plasma central gas 15 slm argon, (iv) atomisation gas 8 slm argon, (v) precursor feed rate 1,3 ml/min, and (vi) rf power about 25 kW. One parameter was varied to study its influence on the synthesis: (vii) plasma sheath gas composition either 60 slm Ar + 3 slm H_2 or 50 slm Ar + 10 slm N_2.

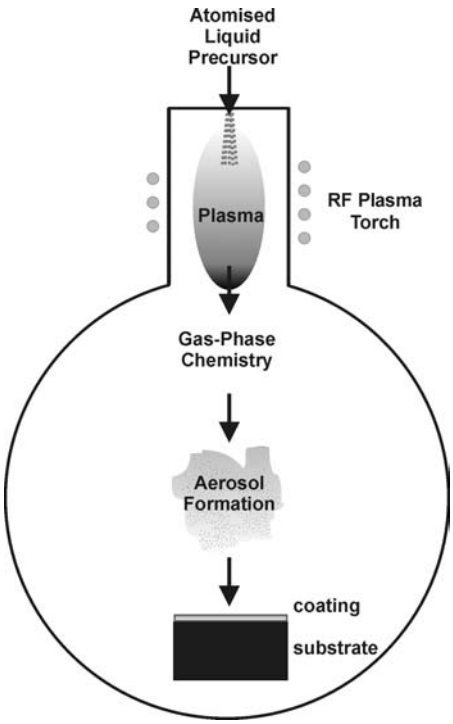

Fig. 1: RF plasma synthesis

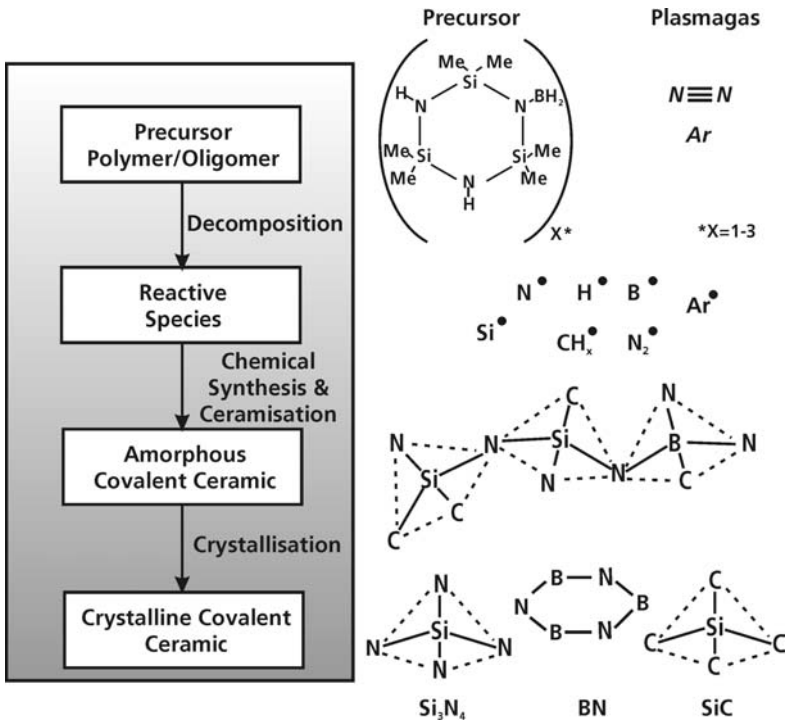

Fig. 2: Thermolysis process under thermal plasma conditions

2.3. Characterisation

Several techniques were used for the characterisation of the synthesised materials. First of all, the composition of the product is determined by elemental analysis in order to derive the stoichiometry of the material. The study of the crystalline phase was performed by means of X-ray diffraction. The structural evaluation of the product is also performed by using multinuclear solid-state nuclear magnetic resonance spectroscopy (NMR) and Fourier transform infrared spectroscopy (FT-IR). The morphology as well as the elemental distribution were investigated by means of transmission electron microscopy associated with an electron energy loss spectrometry imaging detector (TEM-EELS).

3. Results and Discussion

The coatings obtained so far revealed usually poor cohesion and adhesion properties. Therefore the material to be characterised was scratched from the substrates to be investigated as powders.

3.1 Elemental Content and Distribution

Table 1 shows the molar composition and the derived empirical formula of two samples synthesised under two different plasma conditions, basically differing in the plasma gas composition. While in the first case H_2 was added to the sheath gas, the second run plasma contained N_2.

Table 1 – Molar composition of the synthesised powder, ratio of the elements and empirical formula

Run	Si	B	C	N	O	H	Si/B	Si/C	Si/N	Empir. formula
Ar-H-plasma	34.7	10.8	39	9.9	5.6	<0.1	3.2	0.9	3.5	$SiB_{0.31}C_{1.1}N_{0.29}$
Ar-N-plasma	35.6	10.7	36.4	13.9	3.4	<0.1	3.3	1.0	2.6	$SiB_{0.30}C_{1.0}N_{0.39}$

From these results one can observe that the second sample synthesised under slightly nitrogenated conditions contains more nitrogen than the one synthesised in an Ar/H_2 plasma. It is worth noting that in both samples Si and C have almost a 1 to 1 ratio as well as B and N. In comparison to the liquid precursor's theoretical formula, i.e. $SiB_{0.33}C_2N$, the silicon and boron remain with the same amount while a loss of carbon and nitrogen is observed during the plasma treatment. It is probably due to a loss of the elements which possess the greater ability to recombine with hydrogen to form a gas phase like CH_x and NH_x. The loss of nitrogen was partly suppressed by the addition of elemental nitrogen to the plasma gas.

The elemental distribution can be illustrated with TEM-EELS maps that were established using the three window technique [2,4]. Figure 3 shows both the TEM image with the corresponding EELS maps obtained from material synthesised under Ar/H_2 (left) and Ar/N_2 (right) plasma conditions. The EELS elemental maps confirm that carbon as well as silicon are the two main components in the resulting synthesised products. In contrast to silicon and carbon, boron and nitrogen are less present corresponding to the stoichiometry of the precursors and the products. It is worth noting that the elemental distribution of the elements through the particles considered is relatively homogeneous. One has to be careful with the interpretation of the EELS results. Indeed, the intensity of the signal measured, namely the electron current transmitted through the sample to be investigated, strongly depends on the probe thickness. The thinner the sample the higher is the transmitted electron signal. A dark area on the map shows either a zone with a low element content or can also signify that the zone is too thick to permit the electrons to go through the sample. To overcome this possible misinterpretation, one has to compare the different EELS maps with the original bright-field TEM image. The intensity of a classic TEM image is principally a function of the sample thickness crossed by the electron beam and therefore does not depend, in first approximation, on the elements contained in the sample. Even with respect to this preconditions the higher nitrogen content of the sample obtained in an Ar-N-plasma can be observed. Furthermore in some regions rich zones of both B and N show the presence of BN either in the hexagonal form or as turbostratic structure.

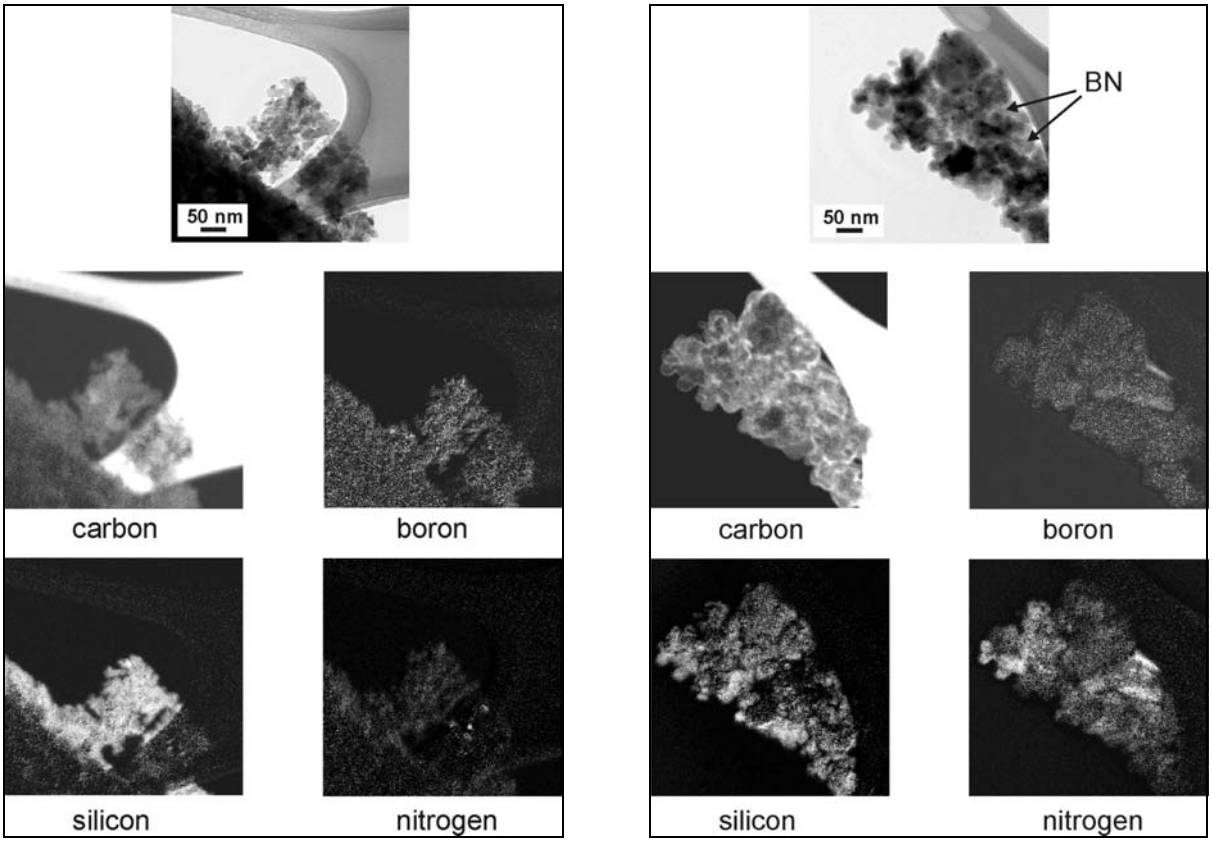

Fig. 3: TEM-EELS maps of Si-B-C-N synthesised in an Ar-H-plasma (left) resp. in an Ar-N-plasma (right).

3.2 Chemical Structure

Fourier transform infrared spectroscopy is used as analytical technique to investigate the chemical structure of the product. The absorption band in the mid infrared (2.5-25 μm) gives the richest information. Figure 4 shows the FTIR spectra which contain only two broad absorption peaks. The absorption peak at ~850 cm^{-1} corresponding to the Si-C bond fundamental stretching vibration is observed [5]. The weak absorption peak at about 1400 cm^{-1} is interpreted as the in-plane B-N stretching vibration of sp^2 bonded BN, which is a typical peak for hexagonal boron nitride (h-BN) [6]. The broadness of the peak shows the low crystallinity of the synthesised material. The spectrum on the right hand side of Fig. 4 corresponds to the material synthesised

using a slightly nitrogenated plasma. The intensity of the peaks is lower than the one of the spectrum of the material derived from the argon-hydrogen plasma.
A signal of Si-N bond could not be detected in any sample indicating no significant formation of silicon nitride. In addition, neither signals of Si-H nor of C-H bonds are detected as a consequence of a complete dehydrogenation of the precursor during thermolysis under plasma condition.

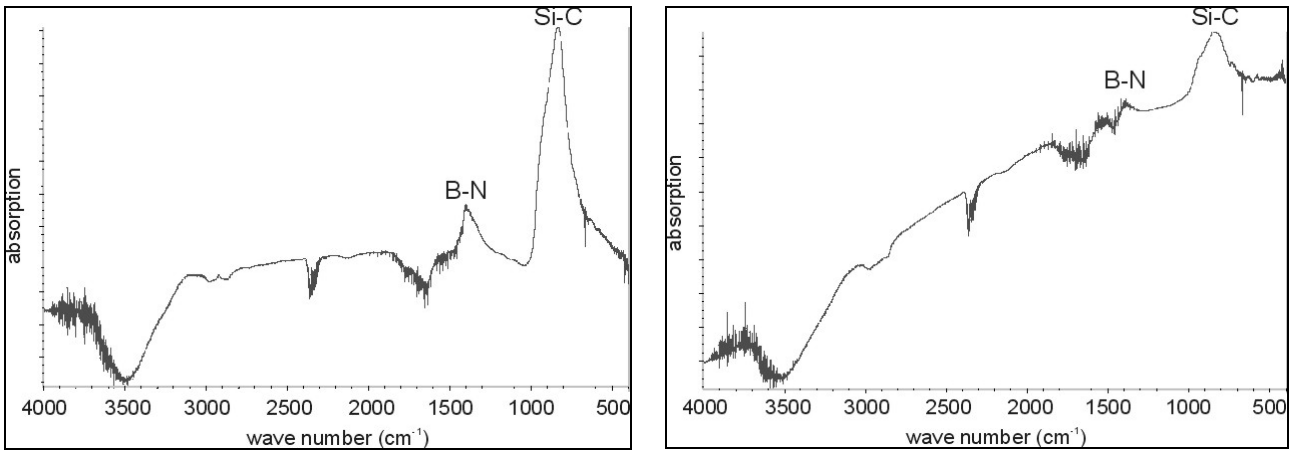

Fig. 4: FTIR spectra of Si-B-C-N synthesised in an Ar-H-plasma (left) resp. in an Ar-N-plasma (right).

To characterise the low range chemical structure of the as-synthesised materials, magic angle spinning nuclear magnetic resonance (MAS-NMR) was employed, both ^{29}Si and ^{11}B MAS NMR were used. Figure 5 shows the results of the sample obtained from an argon-hydrogen plasma. The signal at –15,7 ppm chemical shift (Fig. 5 left) is typical for a beginning or a poor crystallisation of β-SiC. The ^{11}B MAS NMR spectrum (Fig. 5 right) indicates the existence of boron in a B^3 but amorphous environment.
The results of the argon-nitrogen plasma were quite similar but even less precise: A peak at –17 ppm indicates the existence of Si in an SiC_4 environment (any SiC polytype), and the boron content is confirmed but no structural information can be assigned.

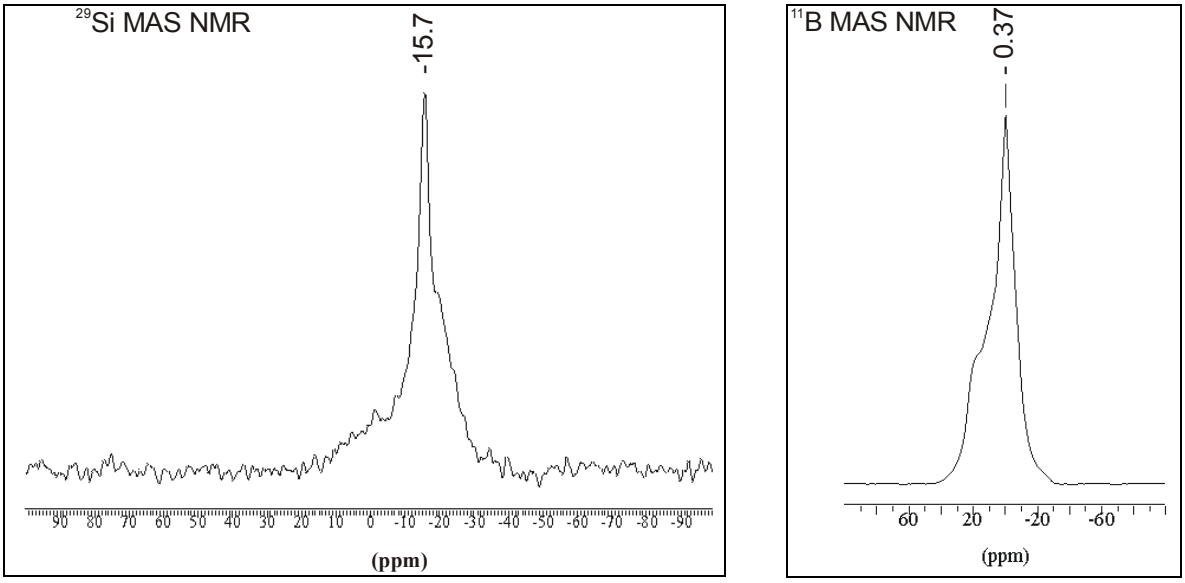

Fig. 5: MAS NMR spectra of Si-B-C-N synthesised in an Ar-H-plasma, ^{29}Si spectrum (left) ^{11}B spectrum (right).

3.3 Phase Content

The X-ray diffraction investigations made on the as-synthesised samples gave the following results: only relatively poor crystallised SiC material without presence of crystalline silicon nitride, boron nitride, boron silicide nor boron carbide has been detected, Fig. 6 (left). The absence of silicon nitride is probably due to the relatively low nitrogen content in the precursor as well as in the plasma even for the attempt made with 10 slm nitrogen in the plasma sheath gas. From the empirical formulas of the products it becomes obvious that a large amount of amorphous phases is present in the product. In some XRD patterns one can notice a broad peak/dome centred at 21° (two theta) which represents the appearance of amorphous phases (C or Si-B-C-N) in the sample.

The XRD pattern of the sample synthesised in a slightly nitrogenated plasma (Fig. 6 right) shows a lower intensity of the diffraction peaks compared to the sample synthesised under similar conditions except no addition of nitrogen but hydrogen to the plasma. This confirms the results of a former study namely that nitrogen impedes the crystallisation of SiC [3].

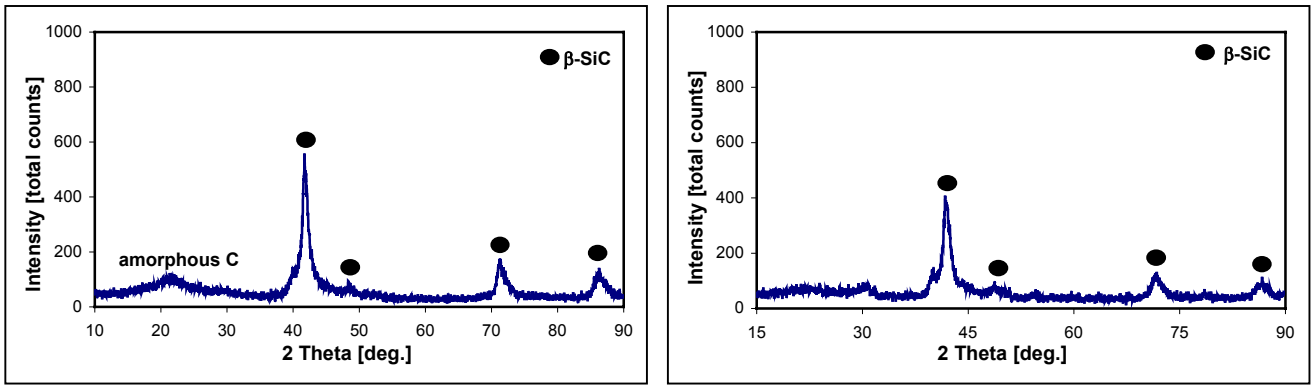

Fig. 6: XRD patterns of Si-B-C-N synthesised in an Ar-H-plasma (left) resp. in an Ar-N-plasma (right).

3.4 Discussion

With the small amount of nitrogen in the plasma gas chosen in our experiments the formation of Si_3N_4 is not observed. The precursors contain an excess of carbon, and according to the following equation the formation of silicon nitride is suppressed:

$$Si_3N_4 + 3C \xrightarrow{T>1440°C} 3SiC + 2N_2$$

In the experiments described above it is more likely that most of the silicon is caught by carbon to form SiC as a result of the higher affinity.

The thermal stability of nitride-based ceramics is strongly dependent on the nitrogen partial pressure. The decomposition reaction of the binary compound Si_3N_4 according to the equation

$$Si_3N_4(s) \leftrightarrow 3Si(l) + 2N_2(g)$$

has an equilibrium vapour pressure of 0.1 MPa at 1775 °C [7]. The volatility of silicon nitride ceramics limits their use to about 1,500°C. Therefore, according to Le Chatelier's principle, an increase of the nitrogen partial pressure permits the stabilisation of the silicon nitride phase at high temperature. This was observed previously with chlorocarbodisilane precursors: a small amount of nitrogen does not permit to synthesise silicon nitride while with a plasma containing 60 % nitrogen only silicon nitride was formed [8].

As recently published, boron stabilises the amorphous state in the Si-B-C-N ceramics. In other words boron hinders crystallisation and forms a turbostratic BN phase built at elevated temperature [9].

The observation of poor crystallisation of both silicon carbide and silicon nitride as a result of the addition of nitrogen to the process as reported previously for plasma conditions [3] was confirmed more generally in another study [10].

4. Conclusions

The experiments performed with this new precursor, i.e. *1,1,3,3,5,5 hexamethyl-cyclotrisilazaneborane*, have shown that the phases synthesised under plasma conditions are mainly constituted of poor crystallised SiC mixed with amorphous BN and probably amorphous carbon. Despite of the nitrogen content in the precursor and in the plasma presence of Si_3N_4 has not been detected neither crystalline nor amorphous, by means of the different characterisation methods employed. However, the results of the different investigation methods show a logical mutual correlation.

Since the microstructural and mechanical properties of the coatings as well as the phase composition are still far away from our project goal the understanding of the process and the process itself must be improved mainly in terms of (i) the formation and the homogeneity of the spray, (ii) the composition of the plasma, and (iii) the vaporisation, condensation, and deposition processes.

5. Acknowledgement

The project is supported by the Deutsche Forschungsgemeinschaft under contract number Schi 539/1-2. The precursors were prepared by the research group of Prof. Röwer at the Institute of Inorganic Chemistry of Freiberg University of Mining and Technology, Germany.

References

[1] R. Riedel, A. Kienzle, W. Dressler, L. Ruwisch, J. Bill and T. Aldinger - Nature **382,** 796-798 (1996).

[2] A. Jalowiecki, A. Bill, F. Aldinger and J. Mayer - Composites part A: Applied Science and Manufacturing **A27**, 717-721 (1996).

[3] E. Bouyer, G. Schiller, M. Müller, R. Henne - Plasma Chem. and Plasma Processing **21**, 523-546 (2001)

[4] J.-P. Eberhart - Structural and chemical analysis of materials, X-ray, electron and neutron diffraction, X-ray, electron and ionspectrometry, electron microscopy, Wiley, Chichester (1994).

[5] H.-P. Martin, E. Müller, R. Richter, G. Roewer and E. Brendler - Journal of Materials Science **32,** 1381-1387 (1997).

[6] H. Lüthje, K. Bewilogua, S. Daaud, M. Johansson and L. Hultman - Thin Solid Films **257,** 40-45 (1995).

[7] H.-J. Seifert, H.-L. Lukas and F. Aldinger – Berichte der Bunsengesellschaft für Physikalische Chemie **102**, 1309-1313 (1998).

[8] E. Bouyer, G. Schiller, M. Müller and R.H. Henne - Applied Organometallic Chemistry **15**, 833-840 (2001).

[9] A. Müller, P. Gerstel, M. Weinmann, J. Bill and F. Aldinger - Journal of European Ceramic Society **20,** 2655-2659 (2000).

[10] D. Kurtenbach, H.-P. Martin, E. Müller, G. Roewer and A. Hoell - Journal of the European Ceramic Society **18**, 1885-1891 (1998).

Comparison of low pressure plasma and eximer laser treatments of PET before Al deposition

P. Laurens[1], S. Petit [1], F. Arefi-Khonsari[2]

[1] *CLFA-CNRS, 16 bis av. Prieur de la Côte d'Or, 94114 Arcueil Cedex - France*

[2] *Laboratoire des Réacteurs Plasmas et des Traitements de Surface, E.N.S.C.P., 11 rue Pierre et Marie Curie, 75231 Paris Cedex 05 – France*

Abstract

The modifications induced on PET surface by an excimer laser radiation performed below the ablation threshold, and by a low pressure plasma were investigated, as well as their ability to improve Al-PET adhesion. The results indicated that, if very significant and similar improvements of the Al-PET adhesion were obtained after both laser and plasma treatments, the mechanisms responsible for the adhesion gain were different for the two types of pretreatments.

1. Introduction

Al/PET adhesion has been extensively studied and it is widely known that a strong adhesion is obtained at the interface due to the formation of C-O-Al bonds from C=O and ether groups of PET. Despite the natural affinity of PET to create bonds with Al atoms, the strength of the Al/PET interface can be further enhanced using surface pretreatment of PET. Improvement of Al/PET interface strength after plasma treatment was observed and attributed either to surface crosslinking or increase of the oxygen and /or nitrogen concentrations. Laser surface treatment can also enhance adhesion at the metal/polymer interface. This was observed for metal electroless deposition or evaporation [1,2]. Improvements of the adhesion at PET/Co alloys [3] or PI/Al [4] interfaces were reported for treatments performed below the PET ablation threshold whereas in similar conditions PBT/Al [5] adhesion was degraded. Despite this literature, the respective contribution of the observed surface changes under UV photons to the mechanism of the adhesion improvement (or degradation) is still to be investigated. In this work, the modifications of PET resulting from laser and plasma treatments were studied as well as the consequences of such treatments on the strength of the Al-PET interface.

2. Experiments

100 μm thick films of PET (Melinex) were used. The laser treatment was carried out using a pulsed excimer laser emitting at 193 nm (20 ns pulse duration) or, at 248 nm (pulse duration : 30 ns). A beam homogenizing system was used in order to perform a uniform treatment of the whole surface of the polymer and X-Y motorized tables were used to scan the polymer under the laser beam. Treatments were carried out at atmospheric pressure. A gas shielding device around the interaction zone permitted to perform the treatment under different gaseous atmospheres : air, helium (or He-O_2 mixtures). Laser treatments were always performed below the ablation threshold of PET, i.e. below 17 mJ/cm^2 at 193 nm and 22 mJ/cm^2 at λ = 248 nm. The pulse repetition rate was 10 Hz and the number of pulses varied from 1 to 2000.

Plasma treatment were realized in a glass reactor with a non-symmetrical configuration of electrodes. RF power (70 kHz) was capacitively coupled to a blade type electrode. The polymer films were enrolled on the grounded cylinder. Plasma power was 2.2 watts (plasma power density was 3.5 W/cm^3) and gas pressure was 100 Pa. Treatments were carried out in a He-O2 (5%) optimized gas mixture [8, 9]. Treatment time was ranging between 1 and 20 s.

Al film was then deposited by thermal evaporation in a vacuum chamber (P = 10^{-3} Pa).

The surface roughness of the PET film surfaces was investigated using AFM. The polymer surfaces were analyzed by XPS. Contact angle measurements were performed using the sessile drop technique using methylene iodine and double-distilled water. The strength of Al/PET interface was investigated using a 180° peel test technique using an EAA (Ethylene-Acrylic Acid) adhesive as detailed in [6]. The peeling occurred at the Al/PET interface and the peel force was recorded (N/cm).

3. Results

3.1 Chemical modifications

After laser treatment in air (or He-5% O_2 mixture), the evolution of the O_{1s}/C_{1s} ratio of treated PET versus the number of pulses was sensitive to the laser fluence i.e. : at low fluences, a global surface oxidation took place while at high fluences (> 10 mJ/cm^2), oxygen depletion was observed (Table 1). This fluence dependent behavior was a consequence of a competition between decarboxylation under UV photons (which is the predominant phenomenon detected under He gas) and oxidation of the UV activated surface in presence of a reactive atmosphere [7]. Plasma treatments always gave rise to an increase of the O_{1s}/C_{1s} ratio. The O_{1s}/C_{1s} ratio was 0.44 after 0.1s and 0.46 after 1s (plasma power : 2.2 watts). As a general feature, a higher level of surface oxidation was observed after plasma compared to laser (only laser treatments at low fluence and high number of shots allowed to reach an oxidation level similar to that reached after plasma treatment). The specific decarboxylation of PET under UV laser may be responsible for the rather moderate level of oxygen incorporation.

Table 1 : O/C after excimer laser (λ = 248 mn) and plasma treatments

Laser (pulses)	0	50	100	200	500
Air,5 mJ/cm^2	0.39	0.37	0.41	0.43	0.48
Air,10 mJ/cm^2	0.39	0.42	0.37	0.37	0.42
Air,20 mJ/cm^2	0.39	0.38	0.39	0.37	0.31
He,10 mJ/cm^2	0.39	0.31	0.29	-	0.26
He,20 mJ/cm^2	0.39	0.32	0.28	0.20	0.16

Plasma	0.1 s	1 s
2.2 W	0.45	0.46
[8] 3.3 W	0.53	0.54

After decomposition of the C_{1s} spectra, some differences were noticed concerning the nature of the chemical bondings detected on the surface after plasma or laser treatment. In the case of plasma treatment, surface oxidation was responsible for the increase of both O-C=O/C and C-O/C ratios and no other peak could be identified. In the case of laser treatment in air**,** besides the presence of the two oxygen components corresponding to C-O and O=C-O groups, a third peak was identified probably corresponding to C=O groups (287.3 eV). This peak was detected for all the laser treatments in air, in oxidizing (low fluence) and deoxidizing (high fluence) conditions but was not identified for laser treatments in helium. Therefore the formation of the C=O groups on PET is specific to the reaction of the UV activated layer with oxygen. It should not be ruled out that plasma treatment also led to the formation of new chemical bondings (carboxilic acid, alcohol, ...) . However, XPS analyses did not allow to identify them. Even for a similar O_{1s}/C_{1s} ratio of the laser and plasma treated PET, differences in the chemical bondings were thus reported as the result of XPS analyses.

3.2. Surface Wettability

The contact angle on untreated PET surface was 77° ($\pm$3°) with water and 26°($\pm$3°) with methylene iodide.For laser or plasma treatments (in air or He-O_2 (5%) mixture), the water wettability (measured just after the treatment) was enhanced (methylene iodine wettability remained almost unchanged). The lower the laser fluence was, the higher the surface wettability (Table 2). Increasing the plasma treatment time improved the water wettability that stayed stable after a 1s treatment. The evolution of wettability, when liquids with different pH values were used, also indicated that acidic sites were created on the surface after plasma and laser treatments.

Table 2 : Water contact angle wettability of PET after laser and plasma treatments (λ = 248 nm ; *: λ *=193 nm*).

Laser (pulses)	10	50	100	500	1000
Air,5 mJ/cm^2	77	78	77	52	41
Air,10 mJ/cm^2	77	72	64	53	55
Air,20 mJ/cm^2	72	63	61	61	60
**Air,5 mJ/cm^2*	77	66	65	56	38
**Air,10 mJ/cm^2*	76	63	60	55	52
**He,10 mJ/cm^2*	68	-	64	68	70

Plasma	0	0.1 s	1 s	5 s
2.2 W	77	68	36	36

The stability with time of the water wettability of treated PET after plasma and laser treatments were compared. For both treatments, the surface stability was good and the increase of the water contact angle with time stayed rather moderate. For plasma treatment, it has already been shown that PET treated with He-O_2 plasmas containing less than 5% O_2 had a very good stability (about 10 % variation of the water contact angle after 60 days) and that increasing the percentage of O_2 in the gas mixture degraded the stability [6]. For a He-O_2 (5%) gas mixture, the water contact angle increased from 28° just after treatment up to 35° after 60 days (20 % variation of the water contact angle). Even if a considerable variation the water wettability with time was observed, it stayed very low compared to the untreated PET. The stability with time of laser treated PET was slightly lower than that observed for plasma treated PET. Variations of 9 % to 30 % were obtained after 60 days (compared to the water wettability just after the treatment). Smaller variations were observed for treatments at high fluences compared to lower ones.

The wettability of the PET surface treated in oxidative conditions (5 mJ/cm^2, 1000 pulses) was changed after surface washing. After water rinsing, the hydrophilicity of the surface was lowered (water contact angle increased from 40° before rinsing to 48° after rinsing) but stayed higher than that of the untreated surface; after rinsing in acetone, the wettability was almost equal to that of the untreated surface (water contact angle : 70°). This shows that fragments, that could be removed after surface rinsing, were created on the laser treated surface.

3.3. Surface Topography

The changes of the surface roughness after the treatment under air, probed by AFM. For a low number of laser pulses (10 pulses), the surface was not significantly modified after treatment at low fluences. When increasing the fluence to 20 mJ/cm^2, very fine cone-like structures (often reported after treatment near the ablation threshold fluence) started to be visible. For a high number of pulses (> 50 pulses), the surface roughness increased with the number of pulses and micrometer size nodules appeared after the treatment. No quantitative data concerning the change of the roughness was obtained from the present results but rougher surfaces were obtained after treatments in air compared to helium. The surface topography of laser treated PET in oxidizing conditions before and after acetone rinsing was compared and the elimination of the degraded layer after washing was clearly evidenced. Washed treated surfaces showed grooves. Surfaces treated by plasma with a low treatment time (0.1s and 1s) were not significantly modified compared to the untreated surface.

3.4. Adhesion Properties

The efficiency of the laser and plasma treatments to improve Al-PET adhesion was demonstrated (Fig.1). Without treatment, the peel force was negligible and visual observation of the peeled surfaces showed that the failure took place at the Al-PET interface. It is generally assumed that, due to the strong affinity between Al and PET, the failure occurred in the skin layer (which represents a weak boundary layer on the PET film surface due to the manufacturing process of stretched films). After an optimized laser treatment, a considerable improvement in the Al-PET adhesion was obtained : the peel force reached 6N/cm and the failure occurred in the EAA adhesive. The Al/PET interface strength was dependent on the laser treatment conditions. The results

obviously emphasized the influence of the laser fluence : as a matter of fact, the peeling force was maximum after a treatment at 20 mJ/cm^2 and a failure occurred within the EAA adhesive even after a single laser pulse. On the contrary, after a low fluence treatment (5 mJ/cm^2), limited improvement of the Al-PET strength was obtained (failure at the metal-polymer interface). Degradation of the Al-PET interface strength always occurred when increasing the treatment time irrespective of the laser fluence. Same trends were observed for Cu/PET interface strength after laser treatment. A comparison of Cu/PET adhesion on treated PET with and without rinsing before copper deposition indicated that Cu-PET adhesion is much higher on rinsed PET. (Table 3).

Al-PET adhesion was also enhanced after a plasma treatment . In the investigated range of time (0.1 s to 5 s), no degradation of Al/PET adhesion due to over-treatment was noticed.

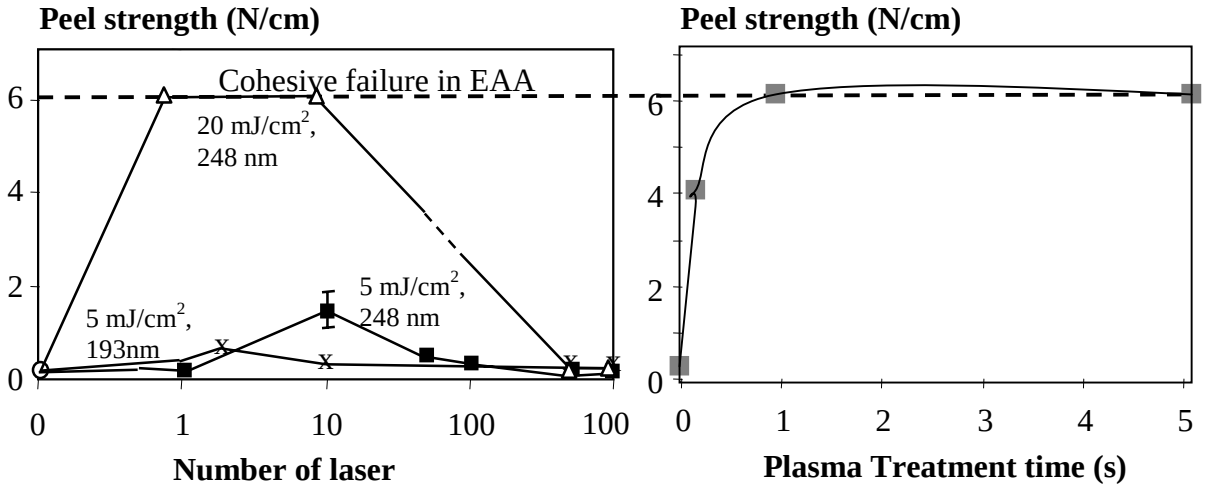

Figure 1 : Al-PET peel strength after laser (a) and plasma (b) treatments.

Number of laser pulses	0	100	1000
Cu-PET peel strength before rinsing (N/cm)	0.2	0.15	0.02
Cu-PET peel strength after rinsing (N/cm)	0.2	0.47	0.40

Table 3 : Role of the surface rinsing of PET on Cu-PET adhesion after laser treatment : Cu-PET peel strength for different number of pulses with and without PET rinsing before Cu deposition.
(Laser treatment : air, 5 mJ/cm^2)

4. Discussion

The efficiency of the laser and plasma treatments to improve the strength of the Al-PET interface has been undoubtedly demonstrated. Now the evolutions of the Al-PET strength, and the surface properties with the laser or plasma parameters will be discussed.

In the case of laser treatment, it was found that the number of pulses and the fluence had a major influence on Al-PET adhesion. For moderate number of pulses (1 to 100 pulses), the adhesion was enhanced and the role of the laser fluence was crucial : the higher the fluence was, the better the Al-PET adhesion. At 20 mJ/cm^2, the highest adhesion (failure in the EAA adhesive) was obtained ; at 5

mJ/cm^2, an improvement of the adherence compared to the untreated surface is also detected but to a much lower level. For a high number of pulses (> 100 pulses), surface degradation and poor Al-PET adhesion were always the major consequences of long laser treatments whatever were the conditions. This is attributed to an extended photolysis and/or photo-oxidation.

For plasma treatments, an increase of the Al-PET adhesion was always obtained. No sign of surface degradation was ever noticed.

Comparison of the effects of plasma and laser treatments on Al-PET adhesion showed that, for each treatment, the highest adhesion level was obtained for surfaces presenting very different surface properties. As a matter of fact, for a similar improvement of the water wettability after plasma or laser treatment, the Al-PET adhesion was completely the opposite : good adhesion resulted from plasma treatment but laser treatment did not significantly enhance the adhesion. In the case of plasma treatment, the improvement of Al-PET adhesion possibly depended on the enhancement of the surface wettability resulting from surface oxidation (as detected by XPS). On the opposite, for laser treatment, oxidation and high water wettability degraded the adhesion (Fig. 2).

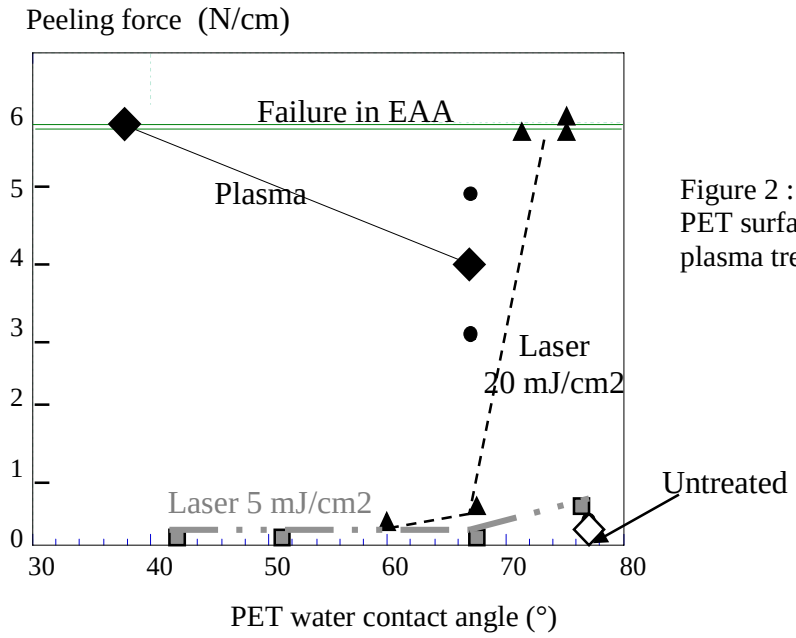

Figure 2 : Al-PET peel strength versus the PET surface water wettability after laser or plasma treatments.

The difference in the chemistry of treated surfaces, induced by laser or plasma treatment for an identical oxidation level could be responsible for differences in their adhesive properties. However the lack of adhesive properties after laser treatment was rather attributed to the surface degradation and to the formation of low molecular fragments due to photolytic or pyrolytic mechanisms under UV.

Consequently, for an "identical oxygen uptake", less damages were induced after plasma treatment. It can also be postulated that surface degradation under excessive oxidation was not reached in our treatment conditions due to the optimized gas mixture and plasma conditions. As a matter of fact, the He-O_2 plasma favoring surface crosslinking prevented the surface degradation [9, 10]. In addition, for plasma treated surfaces, the removal of a degraded layer (if any) in the gas flow rate during the treatment could be possible. Surface etching was detected by mass spectrometry and weight loss measurements [9].

For laser treatment, the highest enhancements of the adhesion were obtained for PET surfaces showing no (or very little) change of the surface wettability and identical Al-PET strengths were obtained after treatment under He and air (manual peeling).

For both fluences, the maximum Al-PET adherence obtained for a given fluence was always reached after a few pulses (between 1 and 10 pulses). The nature of the physical and/or chemical effects responsible for this enhancement remained unclear because for such short treatments, PET surface

modifications were hardly detected. Only AFM analyses indicated some visible modifications of the surface topography after a single laser pulse at high fluences. If changes of the surface topography may play a role in improving Al adhesion by providing anchoring points, a possible oxidation of the first atomic layers of the surface (not detected by XPS) and its participation to the adhesion improvement should not be ruled out. However, oxidation is not expected to be the major effect involved in the adhesion enhancement since at high fluences the carboxylic and ether groups (sites for Al atoms binding) removal rate was maximum and re-oxidation rate was not increased. Consequently, the excellent efficiency of a high fluence treatment with a very low number of pulses should possibly depend on the morphological modifications of PET under an intense flux of photons. Among possible changes, the removal (or modifications) of the initial skin layer (due to thermal and/or photolytic effect), changes of the surface cristallinity, increased surface mobility after chain scission could significantly participate to the adhesion improvement. At low fluences, the degree of surface morphological transformation would not be sufficient due to the low temperature increase and/or limited photolytic transformation. Surface adequate transformation would be fully achieved at higher fluences. Since surface amorphization after surface melting has been found to take place around 10 mJ/cm^2 (7 mJ/cm^2 at 193 nm and 17 mJ/cm^2 at 248 nm), it could be postulated that surface morphological transformations after surface melting obtained above that threshold were responsible for the high adherence.

5. Conclusion

Modifications induced on PET after an excimer laser irradiation or a low pressure plasma treatment performed below the polymer ablation threshold were characterized and the efficiency of such treatments on the Al-PET adhesion of thermally evaporated aluminum was investigated. The results clearly indicated that very significant improvement of the adhesion can be obtained after very short treatment times both with laser and plasma. However, the present observations support the idea that the mechanisms responsible for the adhesion gain were different for the two types of pretreatments. In the case of plasma treatment, surface oxidation and increased wettability associated with surface crosslinking were probably responsible for the reinforcement of the Al-PET strength In the case of laser treatment, surface oxidation had a deleterious effect on the adhesion. An accelerated degradation of the surface by UV photons irradiation is probably responsible for such a behavior. The improvement of the Al-PET adhesion after laser treatment was particularly evident at high fluences after a single or a few laser pulses. Consequently, the effects of a single high dose of photons to on the enhancement of the Al-PET adhesion, could probably be either initial skin layer removal or change of the surface morphology.

References

[1] H. Niino, A. Yabe, Proceed of LAMP'92, Nagoaka-japan ,Vol.2 (1992) 1093.

[2] D.A. Wesner, H. Horn, E.W. Kreutz, J. Adhesion Sci; and Technol.,**11**(9) (1997) 1229.

[3] E. Arenlotz, J. Heitz, M. Wagner, D. Bauerle, Appl. Surf. Sci., **69** (1993) 16.

[4] D.A. Wesner, R. Weichenhain, W. Pfleging, Fresenius J. Anal. Chem., **358** (1997) 248.

[5] E. Kreutz, H. Frerichs,D.A. Wesner, Nucl. Instrum. Meth. Phys. Res. B, **105** 245 (1995).

[6] Q. T. Le, PHD Thesis, "Modifications of PET surface by plasma treatment – The Al-plasma modified interface study"., University of Namur (Belgium) Presse Universitaire de Namur (1996).

[7] S. Petit, P. Laurens, M. G Barthes-Labrousse, J. Amouroux, F. Arefi-Khonsari, J. Adhesion Sc. Technol. (to be published).

[8] Q. T. Le, J.J. Pireaux, R. Caudano, P. Leclere, J. Adhesion Sc. and Technol., **2** (9) 999 (1998).

[9] G.Placinta, PhD Thesis « Caractérisation des plasmas hors-équilibre en milieu He-O_2 appliqués aux traitements physico-chimiques des films polymère PET »,University of Paris IX (Orsay-France), (1997).

[10] F. Arefi-Khonsari, G. Placinta, J. Amouroux, G. Popa, Eur. Phys. J. ,**4** (1998) 193.

Plasma conversion of fluorocarbon waste materials to useful products

A.A. Ponelis and I.J. van der Walt

PELDEV, The Fluorochemical Technology Division of of NECSA, PO Box 582, Pretoria 0001, South Africa

1. Introduction

NECSA (South African Nuclear Energy Corporation), and its subdivision PELDEV have been involved since the early 1990's developing technology to manufacture tetrafluoroethylene (TFE or C_2F_4) and associated useful products from alternative fluorocarbon feedstock. The experimental results of the plasma conversion of typical fluorocarbon waste materials such as industrial off gas, liquid effluent, solid fluoropolymer and others are reported. It is shown that typically a yield of 40% TFE (w/w) is achieved.

2. Process description and operation

The process basis for the conversion is that the fluorocarbon material is subjected to very high temperatures (5000 to 10000 K). This results in radicals such as CF_2 and C_2F_2 being formed. These are then quenched and during the simultaneously occurring reactions, olefinic fluorocarbons form. Else, if the plasma product mixture is cooled slowly, the initial feed composition would essentially form, predicted by thermodynamics.

The plasma conversion system consists of the DC power supply, the plasma torch, decomposition zone, dry quenching zone and product collection. In some cases the torch can be turned into an upside down configuration with the tail flame flowing upwards into a spouted bed reactor, which is filled with carbon particles.

The plasma torch is the central part of the equipment and the 30 kW unit is shown in figure 1.

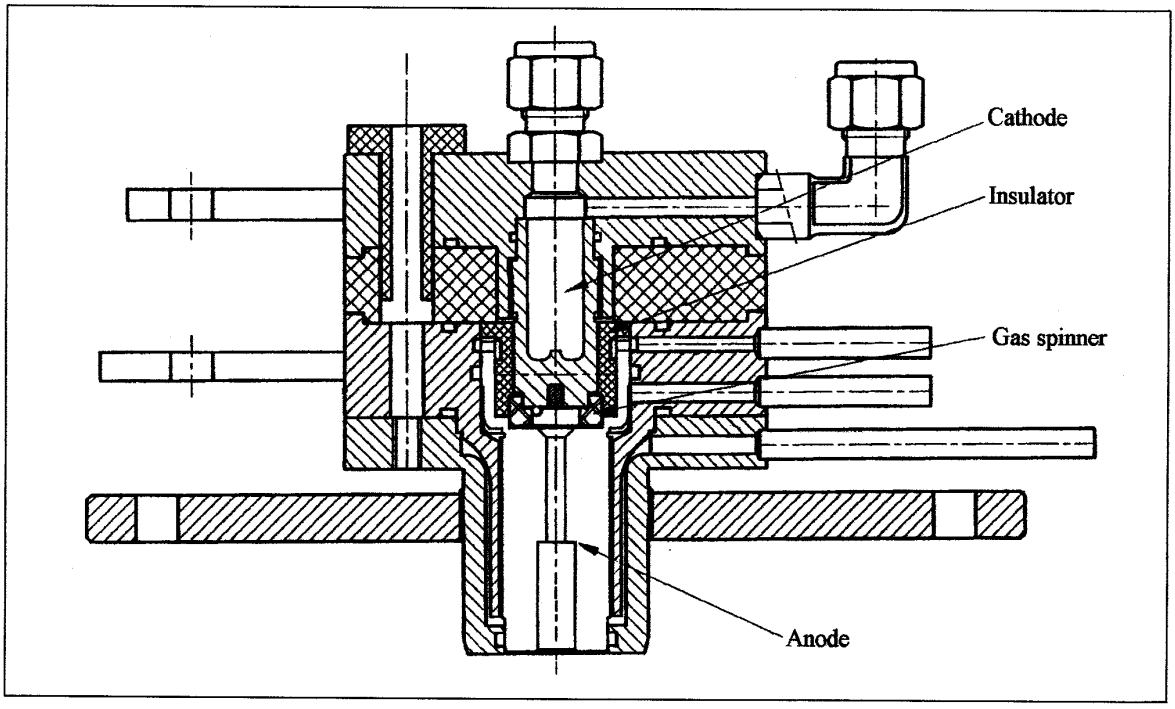

Figure 1: AEC designed plasma torch

The toch consists of a hollow copper cathode (for cooling water) with a graphite insert and a concentric copper anode. The arc chamber is inside the tubular anode. The arc length is kept as near as possible at a constant value by using a stepped anode as indicated. The upper inner diameter is 4mm diameter and the bottom section has an 8mm inner diameter. The lengths of the two sections are 24 and 24 mm for the 24/24 anode or 33mm and 15 mm for the 33/15 system. The linear direct current plasma arc is established between

the graphite insert in the cathode and the "step" in the anode. The DC power supply is current controlled and the resulting voltage of the arc is determined by its length. The cathode and anode are separated by an insulator made from polycarbonate. This piece fits inside on the top of the anode and a gas spinner made from pyrophyllite which fits into the bottom of the insulator. The plasma gas enters the torch through four small holes in the top of the anode, moves downward between the anode and the insulator and is fed into the plasma arc through four 2 mm holes in the gas spinner. The plasma is vortex stabilised. Both the anode and cathode are water cooled during operation.

The fluorocarbon feed material is fed (in the case of the 30 kW) just below the anode into the tailflame, but it can also be co-fed at the top with the plasma gas (Ar, CF_4, N_2, etc). In the case of the 150 kW or 450 kW plasma torches the feed position can be also between the first and second anodes. (Anode inner diameter and lengths: 16mm x 124mm + 30mm x 67mm = 191mm length for the 150 kW; for the 450 kW: 18mm x 375mm + 46mm x 160mm = 535mm). The decomposition zone is a graphite lined cylindrical section where the temperature is maintained at about 3500 K with sufficient residence time 10 to 20 ms, so that the fluorcarbon material can be dissociated into precursor radicals like CF_2, C_2F_2, C(g), F, etc.

Just downstream of the high temperature decomposition zone is the quenching zone where the radicals react chemically to form the required products. The quenching is achieved on a dry water cooled surface. The quench section is like an annular heat exchanger, consisting of an inner water cooled finger made of copper enclosed in a water cooled stainless steel cylinder. The diameter is about 20mm and length about 500 mm (80mm en 770mm for the 150 kW; 244mm and 850mm for the 450 kW). The gas flowing from the hot decomposition zone flows in the annulus between the copper finger and the stainless steel cylinder. The quenching of the gas mainly takes place in the first few centimetres of the quench exchanger. The rest of the surface serves as a heat exchanger to cool the gas to temperatures lower than 400 K. It is essential that the quenching rate exceeds 10^5 K/s to obtain the desired products.

The process schematic for the 30 kW torch is shown in figure 2. The layout for the 150 kW demonstration system and 450 kW semi-technical plant is similar to this, except that the semi-technical plant has a plasma gas handling system downstream of the vacuum pump, where the gas is compressed and fed into a four column distillation train to separate the TFE from the other product gases, mainly CF_4 and C_3F_8.

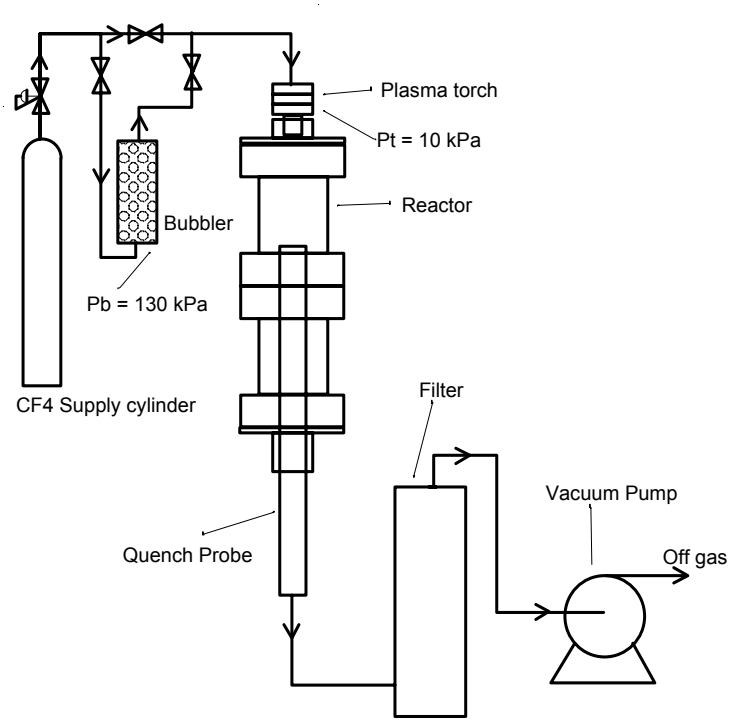

Figure 2: Process schematic of 30 kW experimental system

The arrangement in figure 2 shows how liquid fluorocarbons are first evaporated and fed as vapour into the torch, together with a carrier gas, which is typically CF_4. In the case of R23 (CHF_3), large amounts of HF is generated by the plasma and this is removed from the product gas with a condenser (150 kW) followed by a NaF trap. For the smaller 30 kW test rig a NaF trap is sufficient to remove the bulk of HF.

The startup and operational procedure is typically as follows. The entire process system, which is vacuum tight, is evacuated to about 1,0 kPa with the vacuum pump. Plasma gas is now fed into the torch (Ar, CF_4, N_2, etc). The spark is now initiated across the cathode anode gap. The values of the plasma gas mass flow rate and the power supply current are set to the required set points. The voltage of the torch is then obtained. For the 30 kW torch with an anode of 48mm the voltage is about 125V (CF_4). After the plasma arc has been established the fluorocarbon can be fed. In some cases the pure fluorocarbon gas is fed or the gas might be co-fed with CF_4 as carrier gas. Samples of the product gas are taken periodically and analysed with a GC (and in case of HF a Infra Red spectrum is also taken.) In the case of the 150 and 450 kW systems, there are inline GC analysis.

3. Experimental results and interpretation

The conversion of five types of fluorcarbon materials are reported here. The compositions are given in table 1 below. It can be seen that liquid (low boiling amines), industrial off gas, a pure vapour, solid carbon particles and a solid polymer (THV – tetrafluorethylene hexafluoropropylene vinylidene fluoride) were converted.

Table 1: Fluorocarbon feed material composition

Feed fc Material	**Composition**	**% (v/v)**	**C/F**	**Formula**
Liquid fc Effluent	$C_6F_{14}N$ $C_7F_{17}N$ $C_8F_{19}N$ $C_9F_{21}N$	15 24 17 44	0,42	$C_8F_{19}N$
Industrial Off Gas #2	CHF_2Cl CCl_2F_2 c-C_4F_8 C_3F_6 C_3F_5H C_2F_4H C_3F_7H	3 5 9 22 43 9 8	0,53	$C_{20}F_{38}H_5Cl$
R23 vapour	CHF_3	100	0,33	N/A
CF4 + C)s	CF_4 C	10% (w/w) 90%(w/w)	16	N/A [C particles:106-150Φm]
THV solid Spouted bed	-$(CF_2$-$CF_2)_x$-(CF-CF_3-$CF_2)_y$-(CF_2-$CH_2)_z$-	100	~0,50	N/A

Table 2 give the operational conditions, where some parameters were varied to indicate effects if some typical controlling parameters are varied. The parameters being varied, while keeping the other parameters constant, were: reactor pressure (8 to 50 kPa), plasma gas type (CF_4, N_2, Ar) fluorocarbon feed rate (3.62 and 8.63 kg/h).

Table 3 show the converted fluorocarbon's product gas composition and the calculated value of the yield of TFE from the fluorocarbon on a weight basis. The conversion of the fluorocarbon in all cases is 100% except for the case where the carbon particles are fed in vast excess.

The following observations can be made. **Pressure:** The lower the pressure, the higher the yield of TFE (ref's 1, 2, 3 & 6, 7 & 8, 9). The **liquid effluent** (low boiling amine), gives a 40%(w/w) of TFE on the larger plasma system at 20 kPa, rather than the 64% expected value. This is still an economic yield though. The **industrial off gas** gives a 87% yield of TFE at 10 kPa reactor pressure, with N_2 as plasma gas. The yields with CF4 is higher, but this is due to CF_4 also being converted. The typical freon off gas **R23** gives a 20%

yield of TFE. Solid carbon particles together with CF_4 of 106-150Φm are converted to TFE. Conversion of the solid polymer THV results in a yield of about 60% TFE.

In addition, it can be seen from table 2 that the Specific Energy Requirement (SER) to convert the fluorocarbons vary approximately between 3,0 and 7,0 kWh/kg, except for the THV which is only 1,8 kWh/kg. This is due to Argon being used as plasma gas which requires a low voltage to generate the plasma, in contrast to CF_4. From table 1 it can be seen that the voltage (30 kW) for Ar is 25V, for N_2 it is about 90V and for CF_4 it is about 125V.

The wide operational window of the DC plasma is shown for the 150 kW plasma conversion of liquid effluent at either 3,62 or 8,63 kg/h, Both these feed rates give a yield of about 40% (w/w) – References 4&5.

4. Practical aspects of the DC plasma process

The following aspects are of importance of the process and must be taken into account during design and operations.

* Clogging and deposit formation in the quench due to incorrect positioning of feed point
* Low molecular weight PTFE type materials deposition in downstream equipment
* Electrode erosion due to oxygen inleakage
* Arc instability due to acoustic resonance, feed gas flow variations
* Safety due to toxic gases generation (PFIB) and explosive gases (TFE)
* Plasma gas selection depends on the downstream capabilities, e.g. CF_4 separation
* The liquid fc effluent generates CF4, this excess must be converted with $C)_s$
* There is no nett effluent stream from the plasma, unwanted products are recycled (e.g. C_2F_6).

5. Conclusions

The DC plasma is a powerful process unit with wide potential to convert fluorocarbon materials whether it be solids, liquids or gases. The basic plasma torch can be used in a number of configurations to suit the physical requirements of the of the materials, i.e. a downward flow for gases, vapours and solid small particles flowing towards the quench or the torch facing upwards in a spouted bed to convert the solids in the bed.

Typical yields of TFE is 40% (w/w) for a variety of fluorocarbons. The conversions are in the order of 100%.

6. Acknowledgements

The authors wish to thank the South African Nuclear Energy Corporation for permission to publish the results and attending the ISPC 16. We are also indebted to Dyneon GmbH for their support and assistance during some of these investigations.

Table 2: DC Plasma experimental conditions

Ref	Feed fc Material	Reactor size	Reactor P kPa (a)	Voltage Volts	Current Amperes	Plasma gas (type)	Plasma gas kg/h	fc Feed rate kg/h	Energy in kW	SER kWh/kg
1	**Liquid fc Effluent**	30 kW	8	127	140	CF_4	3.0	0.50	18	4.7
2	**Liquid fc Effluent**	30 kW	20	124	141	CF_4	3.0	0.17	17	4.7
3	**Liquid fc Effluent**	30 kW	40	125	141	CF_4	3.0	0.17	18	4.6
4	**Liquid fc Effluent**	150 kW	20	255	446	CF_4	9.0	3.62	91	7.2
5	**Liquid fc Effluent**	150 kW	20	270	460	CF_4	9.0	8.63	99	5.6
6	**Industrial Off Gas #2**	30 kW	10	88	200	N_2	1.6	0.50	18	6.7
7	**Industrial Off Gas #2**	30 kW	50	88	200	N_2	1.6	0.50	18	6.7
8	**Industrial Off Gas #2**	30 kW	9	132	200	CF_4	3.0	0.22	26	6.6
9	**Industrial Off Gas #2**	30 kW	50	125	200	CF_4	3.0	0.22	25	6.2
10	**R23 vapour**	30 kW	8	85	200	N_2	1.0	1.00	17	6.8
11	**CF_4 + C)s**	30 kW	6	118	240	CF_4	2.7	4.00	23	3.1
12	**THV solid Spouted bed**	30 kW	10	25	241	Ar	3.0	0.30	6	1.8

Table 3: Plasma gas product composition

Ref	Feed fc Material	Reactor size	CF_4 % (v/v)	C_2F_6 % (v/v)	C_2F_4 % (v/v)	C_3F_6 % (v/v)	C_3F_8 % (v/v)	Other % (v/v)	Yield TFE TFE/fc (w/w)
1	**Liquid fc Effluent**	30 kW	80	5	12	0			85
2	**Liquid fc Effluent**	30 kW	91	1	3	0			64
3	**Liquid fc Effluent**	30 kW	96	0	2	0			39
4	**Liquid fc Effluent**	150 kW	79	4	16	1	0		40
5	**Liquid fc Effluent**	150 kW	68	5	24	1	1		41
6	**Industrial Off Gas #2**	30 kW	5	2	89	3	1		87
7	**Industrial Off Gas #2**	30 kW	26	14	55	5	1		52
8	**Industrial Off Gas #2**	30 kW	76	7	15	1	1		232
9	**Industrial Off Gas #2**	30 kW	89	3	7	1	0		112
10	**R23 vapour**	30 kW	8	5	44	1	3	39	20
11	**CF4 + C)s**	30 kW	56	7	37	0	0		39
12	**THV solid Spouted bed**	30 kW	4	20	69	4	2		59

Chemical and physical properties of hydrophobic coatings obtained in a dielectric barrier discharge

S. Paulussen, O. Goossens, D. Vangeneugden

Materials Department, Flemish Institute for Technological Research (VITO), Mol, Belgium

Abstract
The presented work reports on the formation of hydrophobic plasmapolymer coatings in a dielectric barrier discharge at atmospheric pressure. Coatings characterized by a low surface energy were produced in N_2 and Ar plasma starting from a variety of both gaseous and liquid precursors, including pure organic compounds, fluorinated hydrocarbons and organically modified silicon compounds.

1. Introduction

Over the last decade, several applications of low pressure plasma assisted treatments for surface modification have reached the point of industrialization and are currently being used in production. However, for many applications the use of low pressure plasmas is too expensive, mainly due to the high equipment and exploitation cost and the inability to work in-line.
In recent years, a lot of effort has been put into the development of plasma treatments at intermediate and atmospheric pressure. In this new field of technology, dielectric barrier discharges (DBD) have proven successful in a number of applications including tailoring of the surface wettability properties, improving adhesion properties, cleaning and sterilization [1-4]. Currently, research focus is shifting towards the deposition of thin films.
The configuration used to obtain a DBD consists of two parallel electrodes of which at least one is covered with a dielectric material. When an AC-field in the range of 250 Hz - 250 kHz and 1 - 30 kV is applied to the electrodes a transient, spatially uniform glow can be observed [5]. The space between the electrodes may range between 1 and 10 mm. Reactive species or polymer precursors can be administered to the plasma in order to enhance surface activation or to achieve thin film deposition. The main advantage of this technique is that it allows environmental-friendly (solvent-free), in-line processing of heat-sensitive materials like plastic foil and textiles. The latter is due to the fact that the gas temperature of the plasma varies between room temperature and 100 °C, while the mean electron temperature can amount up to 10 eV (1 eV ≈ 11600 K).
This paper deals with the formation of hydrophobic plasmapolymer coatings in a dielectric barrier discharge at atmospheric pressure. Such coatings are of great industrial relevance as they can, among other things, optimize printing properties and introduce water and dirt repellent properties to surfaces of a wide range of materials. The chemical and physical properties of hydrophobic coatings obtained in N_2 and Ar plasma starting from a pure organic precursor, a fluorinated hydrocarbon and an organically modified silicon compound will be compared.

2. Experimental set-up

The experimental configuration of the dielectric barrier glow discharge (DBD) consists of two parallel electrodes (160x180 mm), both covered with an insulating Al_2O_3 plate of 2 mm thickness (figure 1). In order to perform tests in a controlled atmosphere, the electrode configuration is mounted in a closed chamber which is evacuated and subsequently filled with the carrier gas before deposition is started. To ensure stable plasma operation, the gap between the electrodes was limited to a few millimeters. Plasma discharges were generated by a 20 kV/200 mA AC power supply with variable frequency, in this case ranging between 1 and 10 kHz. In this set-up, the bottom electrode is connected to a high voltage AC power source while the top electrode is grounded.
Coatings were produced in N_2 and Ar plasma starting from both gaseous and liquid precursors. The flow rate of the carrier gas was controlled by mass flow controllers and set at 15 l/min. Liquid precursors were added to the inert carrier gas by means of an atomizer which generates a polydisperse submicron aerosol. Gaseous plasmapolymer precursors were simply mixed with the carrier gas at 1 l/min. The precursor molecules under investigation include butane (C_4H_{10}, Air Products), perfluorohexane (C_6F_{14}, 99 %, Aldrich) and

hexamethyldisiloxane (HMDSO) ($C_6H_{18}Si_2O$, 98+%, Aldrich). The deposition time was set at 10 minutes for deposition experiments with butane and at 2 minutes for the other precursors.

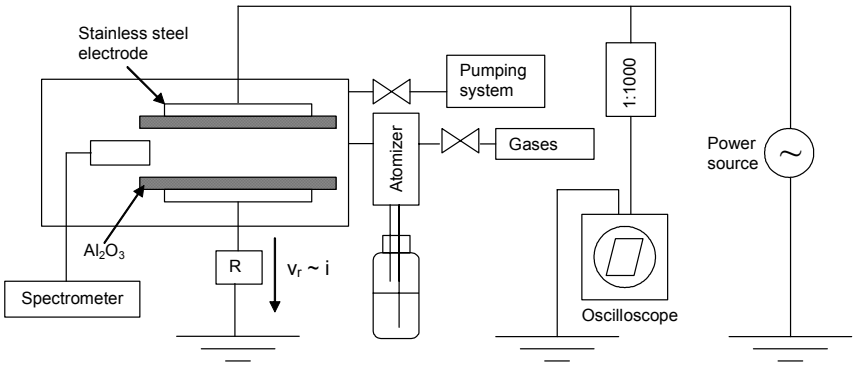

Figure 1: Configuration of the dielectric barrier discharge.

Double polished silicon substrates (12 x 12 mm) were used as substrates for plasmapolymer deposition and placed on the lower (high voltage) electrode. Contact angle measurements of the coatings were carried out using the sessile drop technique (OCA 15 Plus, Dataphysics Instruments GmbH, Germany). In addition, the samples were analyzed by FESEM (JSM-6340F, JEOL, USA), XPS (Fisons Instruments, USA) and FTIR-spectroscopy (Avatar 360 ESP, Nicolet, USA). The plasmapolymers used for NMR measurements (Varian Inova, USA) were recovered from deposits on polished glass substrates. Coatings obtained from perfluorohexane could not be removed from the glass surface.

3. Results and Discussion

Surface Energy Measurements

According to the Owens-Wendt (OW) method, the surface energy of a material (γ) equals the sum of a dispersive (γ^D) and a polar component (γ^p) [6]. The latter two can be determined from the measurement of the contact angles of the surface under investigation with two different liquids of which the dispersive and the polar components of the surface energy are known. The OW-method is commonly used in the studies of the surface energy of polymer films. In this work, surface energy calculations are based on the contact angles of water (CA_{H2O}) and diiodomethane (CA_{CH2I2}) with the coated surface. The values obtained are summarized in table 1.

Table 1: Contact angle of the coated surfaces with water (CA_{H2O}) and diiodomethane (CA_{CH2I2}), surface energy (γ) and polar (γ^P) and dispersive component (γ^D) of surface energy for coatings obtained after plasmapolymerization of butane, perfluorohexane and HMDSO in Ar and N_2 plasma.

Precursor / Carrier Gas	CA_{H2O} [°]	CA_{CH2I2} [°]	γ [mJ/m^2]	γ^P [mJ/m^2]	γ^D [mJ/m^2]
Blanco substrate (Si)	60.7	49.7	46.5	15.7	30.8
Butane / Ar	85.8	45.3	37.9	2.5	35.4
Butane / N_2	83.5	47.8	37.3	3.5	33.8
Perfluorohexane / Ar	102.6	88.2	15.3	2.7	12.6
Perfluorohexane / N_2	94.9	76.9	21.4	3.6	17.8
HMDSO / Ar	99.8	71.8	22.6	1.5	21.1
HMDSO / N_2	105.6	67.7	24.2	0.3	23.9

The lowest surface energies and thus the most hydrophobic coatings are obtained with the fluorinated hydrocarbon precursor. Values as low as about 15 mJ/m^2 could be obtained after plasmapolymerization of perfluorohexane in argon, while plasmapolymerization in a nitrogen discharge resulted in a somewhat higher surface energy. The latter phenomenon was also observed for other precursors and can be attributed to the incorporation of polar N-based functional groups into the coating as expressed by a higher value for γ^P. In

addition, the interactions responsible for the dispersive share of the surface tension, like van der Waals forces, may be influenced by the presence of stable radicals in the coating.
Apart from the fluorinated hydrocarbon precursor, also plasmapolymerization of the hybrid organic-inorganic precursor HMDSO resulted in the formation of hydrophobic plasmapolymer coatings. Although the total surface energy of these coatings is slightly higher compared to the values obtained with the perfluorohexane-based coatings, γ^P is even lower and the contact angle of the coating obtained in N_2 plasma with water is the highest value achieved in this set of experiments.
The plasmapolymer coatings obtained from butane are characterized by significantly higher surface energies than those obtained from the other two precursors.

SEM-analysis
Figure 2 shows some FESEM pictures taken from cross-sections of coatings deposited on polished silicon. From these pictures, the thickness of the coatings and hence the deposition rates could be determined. The values obtained are summarized in table 2.

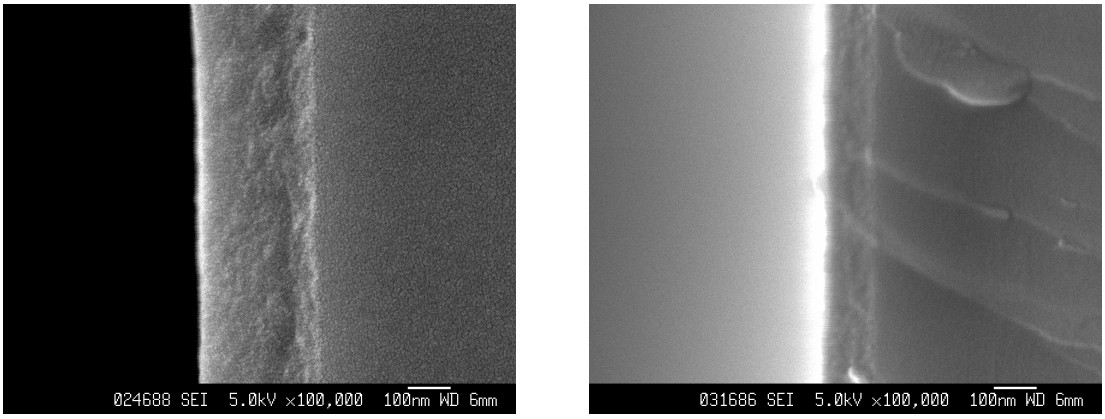

(a) (b)

Figure 2: FESEM pictures of plasmapolymer coatings obtained from HMDSO (a) and perfluorohexane (b) in N_2 plasma.

Table 2: Coating thickness and deposition rate of plasmapolymer coatings obtained from butane, perfluorohexane and HMDSO in Ar and N_2 plasma.

Precursor / Carrier Gas	Coating Thickness [nm]	Deposition Time [min]	Deposition rate [nm/min]
Butane / Ar	150	10	15
Butane / N_2	200	10	20
Perfluorohexane / Ar	80	2	40
Perfluorohexane / N_2	120	2	60
HMDSO / Ar	160	2	80
HMDSO / N_2	250	2	125

Coatings obtained in both argon an nitrogen discharges appear homogeneous and without pinholes or structural defects. Deposition rates were however between 25 and 35 % lower in argon discharges than in nitrogen discharges, probably due a different polymerization mechanism. The highest deposition rates were obtained with the atomized precursors perfluorohexane and HMDSO. Plasmapolymers of the latter precursor grew about twice as fast as those of perfluorohexane and 5 times as fast as the ones obtained from the gaseous precursor butane. This is due to the fact that the amount of precursor administered to the plasma was higher in the case of the liquid precursors.

FTIR

Although it is quite difficult to obtain adequate information about the hydrocarbon or silicon backbone of coatings using FTIR analysis, some information concerning the presence of functional groups in the coatings could be gathered this way. Figure 3a shows the FTIR spectrum of the plasmapolymer obtained from HMDSO in a N_2 discharge. Obviously, the functionalities present in de monomer are retained after plasmapolymerization ($Si-(CH_3)_n$ at 1260 and 840 cm^{-1}, $R_3Si-O-SiR_3$ at 1030 cm^{-1}, C-H stretching at 2960 and 1460 cm^{-1}). Additional signals include a broad peak around 3300 cm^{-1}, which can be attributed to O-H or N-H stretching, and two peaks at 1700 and 1750 cm^{-1}, which are typical for C-O stretching in ketones and aldehydes. These signals are not found in the spectrum of the coating obtained after polymerization of HMDSO in argon plasma and they probably result from the incorporation of nitrogen and oxygen in the coating, either from the carrier gas or from exposure to air after deposition. The latter assumption will be verified by XPS and NMR-measurements. The spectrum of the plasmapolymer coating obtained from perfluorohexane in a N_2 discharge (fig. 3b) contains a large peak around 1220 cm^{-1} and a small peak near 740 cm^{-1}. Both signals are attributed to the presence of C-F bonds. As could be expected from the chemical nature of the precursor, no hydrocarbon signals are observed. The weak signal near 3200 cm^{-1} is only found after plasmapolymerization in N_2 and can be rationalized in the same way as for figure 3a. The spectra obtained form the plasmapolymer coatings based on butane are not shown but merely contain hydrocarbon signals.

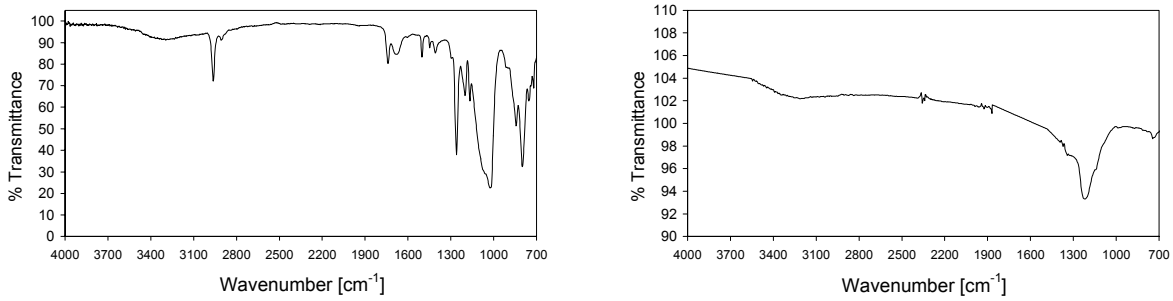

(a) (b)

Figure 3: FTIR spectra of plasmapolymer coatings obtained from HMDSO (a) and perfluorohexane (b) in N_2-discharges.

XPS

X-ray photoelectron analysis was carried out in order to determine the relative amounts of C, O, N, F and Si at the plasmapolymer surfaces (table 3).

Table 3: XPS-data (surface mole fraction of elements excluding hydrogen in %) obtained from butane, perfluorohexane and HMDSO plasmapolymer coatings prepared in N_2 and Ar DBD glow discharges.

Precursor / Carrier Gas	C [%]	O [%]	N [%]	F [%]	Si [%]
Butane / Ar	82.5	16.9	-	-	0.6
Butane / N_2	77.7	17.3	4.6	-	0.4
Perfluorohexane / Ar	47.5	8.8	0.1	43.0	0.6
Perfluorohexane / N_2	42.3	7.9	7.0	42.3	0.5
HMDSO / Ar	51.9	22.2	-	-	25.9
HMDSO / N_2	50.3	24.0	2.0	-	23.7

While perfluorohexane and butane do not contain any oxygen, relatively large amounts of oxygen were found at the surface of their plasmapolymers. Moreover, when N_2 was used as the carrier gas, also some nitrogen could be detected, which may be incorporated in the coating during polymerization. However, after exposure of the plasmapolymer coatings to air, stable radicals of organic origin that remain present in the coating after deposition may react with oxygen and/or nitrogen and thus give rise to the formation of nitrogen or oxygen containing functional groups at or near the surface as well. Such functionalities were

found in some of the FTIR spectra and may be the cause of the higher surface energies found after plasmapolymerization in N_2.
Another striking fact in table 3 is the C/F-ratio of the plasmapolymers obtained from perfluorohexane. While the C/F-ratio of perfluorohexane equals 0.42, the C/F-ratio of its plasmapolymers is about 1. Apparently, some fluor is split of during plasmapolymerization and although some oxygen (and nitrogen) is incorporated in the coating, this indicates that a cross-linked carbon network is formed.
A similar effect is observed in the case of HMDSO. While the C/Si-ratio of HMDSO equals 3, the C/Si-ratio of its plasmapolymers is only about 2 which may indicate that cross-linking of silicon occurs.

NMR-measurements
Nuclear magnetic resonance (NMR), and in particular ^{13}C-NMR, has proven to be a powerful technique to perform detailed investigations of the hydrocarbon backbone of polymers [7]. It also seemed an interesting technique to gain some more insight in the chemical structure of the plasmapolymers obtained. In principle, one should be able to evaluate for instance the retention of the chemical structure of the monomers in the plasmapolymers and the degree of cross-linking. Therefore, ^{13}C-NMR measurements were performed on plasmapolymers of butane and HMDSO recovered from depositions on large glass plates. The plasmapolymers obtained from perfluorohexane could not be isolated from the substrate and hence no spectra of these compounds are available.
However, the recorded ^{13}C-NMR spectra only showed very weak signals that were strongly broadened and hence not very informative. This could be due to the presence of strong paramagnetic sites, such as remaining stable radicals.
In contrast to the ^{13}C-NMR measurements, ^{1}H-NMR analysis of the plasmapolymers resulted in more useful spectra (figure 4). Although the line broadening in these spectra is also considerably higher than usual for polymers, some qualitative information can be extracted.

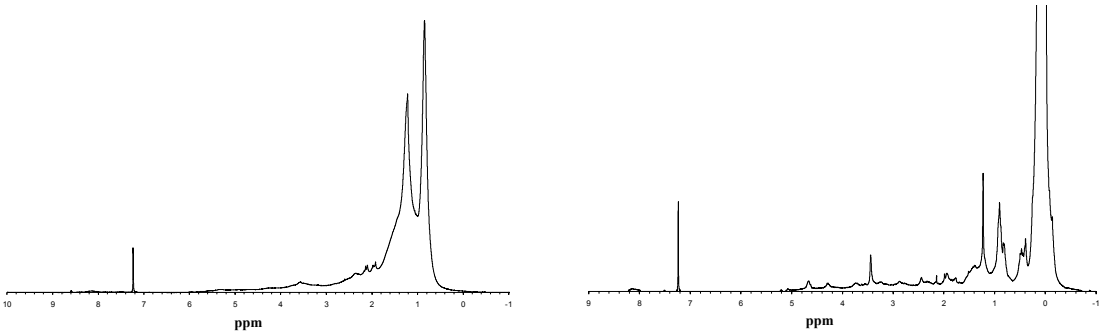

(a) (b)

Figure 4: ^{1}H-NMR spectra of plasmapolymers obtained from butane (a) and HMDSO (b) in N_2 discharges.

The spectrum obtained from the plasmapolymers of butane (fig 4a) is dominated by the signals of $–CH_3$ (at 0.8 ppm) and $–CH_2$ (at 1.3 ppm).The latter peak has a shoulder at about 1.6 ppm, which can be attributed to the presence of CH-groups. The relatively low intensity of the CH_3-peak compared to the proportion of CH3-groups in butane and the presence of a CH-signal indicate that cross-linking of C-atoms has occured in the plasma.
The origin of the weak signals between 2 and 3.5 ppm is difficult to determine but they probably originate from the presence of hetero-atoms like O and N in the plasmapolymers.
The strong signal near 0 ppm in figure 4b is typical for CH_x-Si bonds. The signals at 0.8 and 1.2 ppm can be attributed to-CH_3 and -CH_2 groups bound to other carbon atoms, which indicates that new C-C bonds are formed in the plasma. Also in this case, the small peaks between 2 and 3.5 ppm probably result from the incorporation of O and N. More information on the plasmapolymers obtained from HMDSO will be available after ^{29}Si-NMR-measurements.

4. Conclusions

Hydrophobic films characterized by surface energies as low as 15 mJ/m^2 were obtained by plasmapolymerization of perfluorohexane in a dielectric barrier discharge at atmospheric pressure. While also HMDSO proved to be a suitable precursor for the deposition of hydrophobic coatings with surface

energies between 20 and 25 mJ/m^2, a pure hydrocarbon precursor like butane gave rise to significantly higher surface energies. In general, lower surface energies are achieved when argon is used as a carrier gas. This is due to the fact that in a DBD discharges with nitrogen as carrier gas, more oxygen and nitrogen-containing functionalities are incorporated at the surface of the coating, which in turn results in slightly higher surface energies. However, higher deposition rates are obtained in nitrogen discharges. In addition, XPS and NMR-measurements indicate that a cross-linked network of carbon (and silicon when HMDSO is used as a precursor) is formed through plasmapolymerization of hydrocarbons, fluorinated hydrocarbons and organically modified silicon compounds.

Acknowledgements

The authors wish to thank Prof. P. Adriaensens from the Limburg University Centre (LUC) for the NMR-measurements.

References

[1] T.O. See You, N. Ext June, I.N. Taormina - We. Hope. You. Enjoy. **22**, 6 (2003).
[1] O. Goossens, E. Dekempeneer, D. Vangeneugden, R. Van de Leest, C. Leys – Surf. Coat. Technol. **142-144** (2001).
[2] Y. Tsuchiya, K. Akutu, A. Iwata – Prog. Organ. Coat. **34**, 1-4 (1998).
[3] F. Massines, R. Messaoudi, C. Mayoux – Plasmas Polym. **3**, 1 (1998).
[4] R. Ben Gadri, J.R. Roth, T.C. Montie, K. Kelly-Wintenberg, P.P. Tsai, D.J. Helfritch, P. Feldman, D.M. Sherman, F. Karakaya, Z.Y.Chen – Surf. Coat. Technol. **131**, 1-3 (2000).
[5] F. Massines, A. Rabehi, P. Decomps, R. Ben Gadri., P. Segur., C. Mayoux – J. Appl. Phys. **83**, 6 (1998).
[6] D.K. Owens, R.C. Wendt – J. Appl. Polym. Sci. **13** (1969).
[7] J. Prasad – J. Polym. Sci.: Part A: Polym. Chem. **30** (1992).

The device and algorithm for estimation of the chaos on mechanical activated plasma in blood of patients with gastric cancer

V.E. Orel, Yu.I. Mel'nik, A.V. Romanov, N.N. Dzyatkovskaya

Physics-Technical Laboratory, Institute of oncology, 33/43 Lomonosova Str., Kiev, 03022, Ukraine

Abstract

The mechanoemission (ME) of blood is developed as a result of mechanical activation of plasma in a sample which is layered onto chromatographic paper. This paper describes computer-controlled device, aimed for generation, detection and analysis of ME data in blood of investigated persons. The original algorithm for estimation of ME chaos in blood is developed. For gastric cancer patients an increase of ME chaos is observed in comparison with healthy individuals and patients with inflammatory of gastric mucosa.

Introduction

The idea that in living structures plasma physico-chemical mechanisms can occur was first expressed more than 30 years ago. Subsequently Sedlak published qualitative considerations of the plasma state in living systems leading him to suggest the existence of a fifth state of matter he termed “bioplasma”. Inushin and his group focused on applications of the bioplasma concept to clinical practice. Fröhlich alluded to possible plasma oscillations in cells in the context of Böse condensation within biological structures [1].

Yet none of the work cited above was devoted to detailed consideration of whether plasma physical mechanisms are compatible with biological structures. But we don’t know about non equilibrium effects in the plasma for cancer patients.

ME or triboemission – is the property of non-equilibrim discharges in nitrogen plasmas during mechanical stresses, deformation, or friction in biological objects. The mechanism of ME excitation is based on the processes of conversion of the mechanical energy of a substance into other forms: electronic excitation and ionization, chemical bond energy and the kinetic energy of atoms, etc. The dissipation of mechanical energy results in the emergence of polar electric charges, between which, in the presence of gas and liquid, there appear weakly luminescent aggregates of ionized particles in the form of Lichtenberg figures [2]. Accompanying this process are mechanochemical reactions of free radical oxidation, chemisorption and other events influencing ME. The relaxation of mechanical tension is also accompanied by pulse electromagnetic emission due to fluctuation in the electrical dipole moment [3–5].

This mechanism may be represented by the following equations

$$\sigma = \frac{\varepsilon_0 \varepsilon}{H}\left(\Delta\Phi - \frac{kT}{e}\ln n_i \pm HE \right), \tag{1}$$

$$\frac{\mathrm{d}\Phi}{\mathrm{d}t} = \sum_i W_i\, n_i, \tag{2}$$

where: σ – the surface density of the charge; ε_0 – an electric constant; ε – a relative dielectric penetrability; $\Delta\Phi$ – work function; k – Boltzman constant; T – thermodynamic temperature; e – electron charge; n_i – particle concentration; H – distance between electrization surfaces; E – electrostatic field strength. Equation (2) describes the process of microdischarge between dielectric barriers, where W_i – drift velocity of electrons, ions, photons, neutral atoms and molecules.

The present work use physical principles described above for the device and algorithm for estimation of the ME chaos in blood of patients with gastric cancer.

Materials and methods

Device description. The principal element of the analyser of ME is a tribogenerator unit (Fig. 1). An electret fluoroplastic probe is used as a roll measuring 30 mm in diameter. The rolling unit is installed on axis and is rotated with an electric motor. The sample in frame is moved to the electret probe using a pressing device. The measuring electrode for recording of electrical component of electromagnetic ME generated by electret probe and sample friction is located directly in the vicinity of the sample contact and rotating probe. Electrical signals enter the input of the aerial amplifier and after amplification in the frequency range of 1 Hz

to 100 kHz, they are transmitted to the input of the analogue-digital converter (ADC). A grounded cleaning brush wetted with 25 % ethanol solution removes electrostatic charge from the probe surface after each measuring cycle. The tribogenerator chamber is continuously flushed with nitrogen gas.

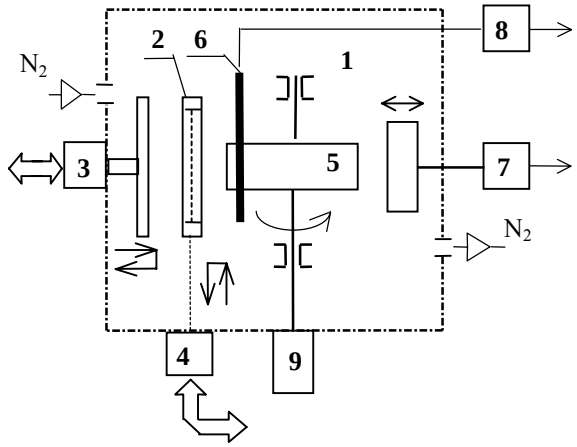

Fig. 1. Tribogenerator unit with electric channel of ME detector: 1. chamber; 2. frame with the investigated sample; 3. device of the frame pressing to the electret probe; 4. device of the frame passing to the chamber; 5. electret probe; 6. the measuring electrode; 7. device of the working surface clearance; 8. operational amplifier; 9. electric motor.

Description of the algorithm. The phase space method was used for the analysis of ME chaos in blood [6]. Let I_0, I_1, …, I_N be the ME value being measured at discrete time moments t_0, t_1, …, t_N, $t_i = t_0 + i\tau$, $i = 1, 2, \ldots, N$. In order to build a continuous phase trajectory, values I_0, I_1, …, I_N were interpolated with a cubic spline $f(t)$, $t_0 \le t \le t_N$

The phase trajectory is defined as the multitude $\{(x, y) | \, x = f(t+\tau), \; y = f(t), \; t_0 \le t \le t_{N+1}\}$. Let $\Phi = \{(x, y) | \, x = \varphi(t), \, y = \psi(t), \, t \in [\theta_1, \theta_2]\}$ be the phase diagram of a certain process, functions φ and ψ being continuously differentiable on segment $[\theta_1, \theta_2]$. Let $x_{\min} = \min\limits_{t \in [\theta_1, \theta_2]} \varphi(t)$, $x_{\max} = \max\limits_{t \in [\theta_1, \theta_2]} \varphi(t)$, $y_{\min}(x) = \min\limits_{t \in \varphi^{-1}(x) \cap [\theta_1, \theta_2]} \psi(t)$, $y_{\max}(x) = \max\limits_{t \in \varphi^{-1}(x) \cap [\theta_1, \theta_2]} \psi(t)$. Let us define spread parameter $S(\Phi)$ of phase diagram Φ as

$$S(\Phi) = \int_{x_{\min}}^{x_{\max}} (y_{\max}(x) - y_{\min}(x)) dx. \tag{3}$$

The physico-mathematical interpretation of statistical parameter S is approximately the area of the figure outlined with the envelope of the phase trajectory.

To approximately calculate the integral on the right in the formula (3), let us use the quadrature rectangles formula:

$$S(\Phi) \approx S_\varepsilon(\Phi) = \sum_{i=0}^{n-1} (y_{\max}(x_i) - y_{\min}(x_i)) \cdot \varepsilon, \tag{4}$$

where $n = [(x_{\max} - x_{\min})/\varepsilon]$, $x_i = x_{\min} + i\varepsilon$, $i = 0, 1, \ldots, n$.

A special algorithm is developed for calculation of the blood ME phase trajectory spread parameter S [7]. The flowchart of the algorithm of estimation of the phase trajectory spread parameter is shown in Fig. 2.

Patient population. We studied ME in three groups of patients. Group 1 included patients with gastric cancer (22 persons), group 2 – patients with inflammation of gastric mucosa, chronic gastritis (20 persons) and group 3 – healthy subjects (21 persons). Cancer patients were evaluated at Stage II-IV with morphologic and histologic confirmation of diagnoses. All groups consisted of male aged 45–60.

Mechanoemission studies. 0.02 ml of blood (3 samples from every patient) was layered onto FN-2 chromatographic paper (Filtrak, Germany) which was placed in the slide frame. A sample of whole blood dried to 45 % relative humidity was triboelectrified using a rotating electret probe at 1400 ± 50 rpm with

enhanced mode of 1.2 N in the atmosphere of highly purified gaseous nitrogen under excessive pressure of 1 kPa at 37 ± 0.5 °C.

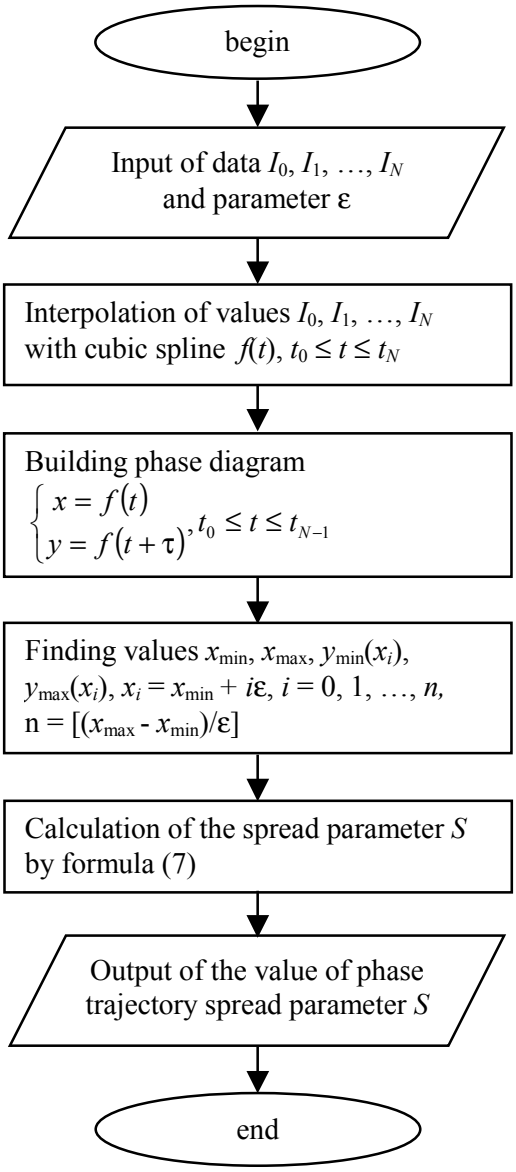

Fig. 2. The flowchart of algorithm for calculation of phase trajectory spread parameter.

Results and discussion

Fig. 3 shows a signal time series ME from blood of patients with gastric cancer, patients with inflammation disease, apparently healthy volunteer patients, and technological control (bidistilled deionized water). The time duration $[\theta_1, \theta_2]$ taken for experimental results is from 0 to 12.5 msec. Measurements were taken every 25 μsec. Fig. 3.2. shows phase diagrams of blood ME. We can see that cancer patients have greater spread parameter *S* than healthy individuals. At the same time, the mechanical activation of a chromatography paper with the bidistilled deionised water showed a different pattern of ME. The spread parameter *S* for technologic control was the least. Our findings allow to view oncogenesis as an expression of impairments of determined chaos of homeostasis.

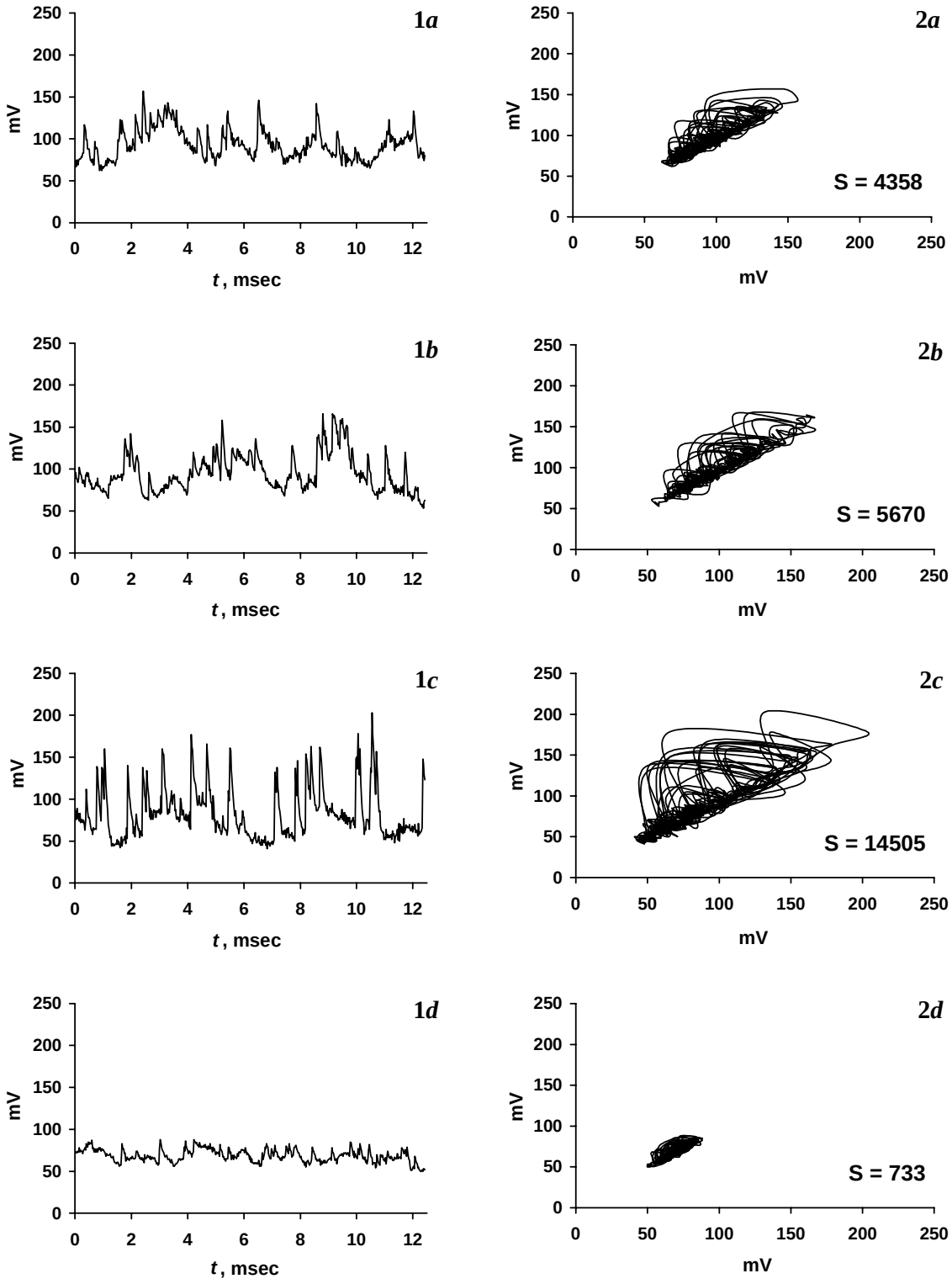

Fig. 3. Time evolution (1) and phase diagram (2) of ME. Blood of patients: *a* – healthy individuals; *b* – inflammatory conditions of gastric mucosa; *c* – gastric cancer. Technologic control: *d* – bidistilled deionized water.

Thus, during a malignant tumor process blood ME dynamics is characterized by higher chaotics. In normal subjects and in inflammations the ME kinetics has an intermediate stable unbalanced nature. One might suggest that manifestation of ME chaos effects the processes of host self-organization for activating determined fluctuations as defensive reactions in inflammatory processes [8] and initiation of self-disorganization in accidental imbalanced fluctuations in oncogenesis [9].

What is the interrelation between the physical and biomedical process? The chaotic structure of blood flow is typical for cancer [10]. Gastric cancer is usually accompanied by disseminated intravascular coagulation. In our early papers we found the effect anticoagulant influence additionally influencing on the autocorrelation function of ME in blood [11]. We suggest that the coagulation has an influence on chaotic topological properties of structural elements of blood and stipulate ME chaos. These results allows to consider oncogenesis as a kind of impairment of a homeostatic deterministic chaos at the molecular level [12].
It seems likely that nature uses such self-disorganization principles not only in blood, but also in other biological systems. The concept of deterministic chaos is biohierarchical for host in contemporary ideas about role of chaos for potential applications in oncology [13–15].

Conclusion

A formalized description utilizing the algorithm for estimation ME chaos in blood parameters can be used in future for estimation and prognosis of treatment efficiency of patients with gastric cancer.

References

[1] Zon J. The living cells as a plasma physical systems. Physiol. Chem. & Physics. **12** (1980), p.357–364.
[2] Femia N., Lupo' G., Tucci V. Fractal characterization of Lichtenberg figures: a numerical approach. 20th International Conference on Phenomena in Ionized gases. Barga, (July 1991), p.4.
[3] Nakayama K., Hashimoto H. Triboemission from various materials in atmosphere. Wear. **147**, (1991), p.335–343.
[4] Heinike G. Tribochemistry. Akademia-Verlag, Berlin, (1984), p.584.
[5] Orel V.E., Kadyuk I.N., Mel`nik Yu.I., Dzyatkovskaya N.N. Physical and engineering principles in the study of mechanically-induced emission of blood. Medical Engineering. **28**, 6 (1995), p.335–341.
[6] Moon F. Chaotic fluctuation. John Wiley & Sons Inc. (1987), 312p.
[7] Orel V.E., Romanov A.V., Dzyatkovskaya N.N., Mel`nik Yu.I. The device and algorithm for estimation of the mechanoemisson chaos in blood of patients with gastric cancer. Medical Engineering and Physics. **24**, 5 (2002), p.365-371
[8] Daams J.H., Westerholf H.V. The possible of chaos in chronic inflammation. Clin. Rheumatol. **15** (1996), Suppl 1, p.34–39.
[9] Waliszewski P, Molski M, Konarski J. On the holistic approach in cellular and cancer biology: nonlinearity, complexity, and quasi-determinism of the dynamic cellular network. J Surg Oncol. **68**, 2 (1998), p.70–78.
[10] Jain R.K. Transport of molecules, particles, and cells in solid tumors. Annu. Rev. Biomed. Eng. **1** (1999), p.241–263.
[11] Orel V.E., Ganul V.L., Dzyatkovskaya N.N., Kadyuk I.N., Melnik Yu.I. Electromagnetic mechanoemission of whole blood from cancer patients. Dopovidi National academiy nauk Ukraine. **11 (**1995), p.134–136.
[12] Cross SS, Cotton D WK. Chaos and antichaos in pathology. Hum Pathol, 1994, 25, p.630–637.
[13] Sedivy R. Fractal tumours: their real and virtual images. Wien Klin Wochenschr. **108**, 17 (1996) p.547–551.
[14] Shwab E.D., Pienta K.I. Cancer as a complex adaptive system. Med Hypotheses. **47**, 3 (1996), p.235–241.
[15] Andrey L. Chaos in cancer. Med Hypotheses. **28**, 3 (1989), p.143–144.

Decomposition Behaviors of Gaseous Cyanides in Non-thermal Plasma and Plasma-Catalyst Hybrid Reactor

S. G. Ryu, M. K. Park, H. W. Lee, and H. B. Park

Agency for Defense Development, Yuseong P.O. Box 35-1, Yuseong, Daejeon, 305-600, Korea

Abstract

The decomposition behaviors of gaseous cyanides in non-thermal plasma and plasma-catalyst hybrid reactor have been investigated with the variation of discharge power, influent concentration of cyanide, humidity of air carrier and packed materials in the reactor. Destruction of cyanides by plasma only process was very difficult compared to that of trichloroethylene. But the destruction efficiencies of cyanides were dramatically improved through packing Pt/alumina bead in the plasma discharge region.

1. Introduction

Because of the strong toxicities of cyanides (ex. hydrogen cyanide and cyanogen chloride), methods for destruction of them are of considerable interest in both industrial and military environments. Currently used systems for military air purification are carbon-based. But the service lives of the carbon-based air purification systems are limited especially for gaseous cyanides, and shortened by degradation of carbon under some environmental conditions such as high humidity and high temperature. Recently catalytic oxidation of gaseous cyanides was studied some extents [1, 2] for the purpose of offering some advantages over the carbon-based systems. Some limited results were reported [3] about the destruction of hydrogen cyanide in a non-thermal plasma reactor. But the detailed results of gaseous cyanides destruction in non-thermal plasma/catalyst hybrid systems are not reported yet.

In this research, the decomposition behaviors of gaseous cyanides (mainly methyl cyanide, CH_3CN) in non-thermal plasma and plasma-catalyst hybrid reactor are investigated with the variation of discharge power, influent concentration of cyanide, humidity of air carrier and packed materials in the reactor. And the reaction kinetic of cyanides in non-thermal plasma condition and the synergic effect of plasma-catalyst in cyanides decomposition are discussed with some experimental evidences.

2. Experimental

A laboratory scale packed-bed-plasma-reactor(PBPR) is adopted for the experiments of gaseous cyanides decomposition in non-thermal plasma conditions. The schematic diagram of the experimental system is illustrated in Fig.1.

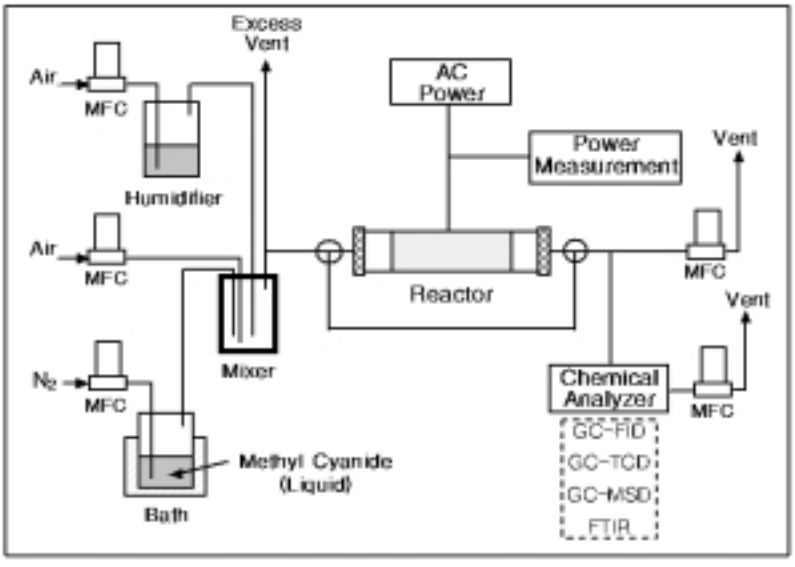

Fig.1. Schematic diagram of the non-thermal plasma apparatus for cyanides decomposition

The system is consisted of a continuous flow gas generation apparatus, a laboratory scale PBPR, a high voltage alternative current power supply, discharge power measuring system, and gas sampling and detection system. The PBPR is made of a quartz tube with the inner diameter of 26 mm and wall thickness of 2 mm. The inside electrode, made of a stainless steel rod with a diameter 1 mm, is aligned horizontally along the centerline of the reactor. The outside of the quartz tube is wrapped by copper foil, which is served as the outside electrode. The reactor is packed with spherical $BaTiO_3$ (diameter, 3-4mm) for smoothing the plasma discharge, and is packed with γ–Al_2O_3 or 0.25 wt% Pt/γ- Al_2O_3 for investigation of the catalytic effect in the non-thermal plasma reaction. The packing volume is 53 cm^3 in the reactor with 10cm length of discharge and 106 cm^3 in the reactor with a 20cm length of discharge. The bed porosity is about 0.4 for all packing. All experiments are performed at atmospheric pressure and relative humidity 8% or 75% condition at 25^{o}C of air carrier. The discharge power in the reactor is measured by a digital oscilloscope (Tektronix TDS 460) and voltage dividers. Gas flows of the system are controlled by mass flow controllers (MFC, Brooks 5850E). The analysis of cyanides concentration in the feed and the effluent of the reactor is performed with a on-line GC(HP 5890 FID), and other byproducts such as O_3 and N_xO_y are monitored with a FTIR or a GC-MSD.

3. Results

In Fig.2, decomposition efficiency of methyl cyanide (acetonitrile) in a $BaTiO_3$ packed bed plasma reactor is illustrated as a function of discharge power with the variation of influent methyl cyanide concentration from 500 to 3000ppm at 2 L/min of dry air carrier.

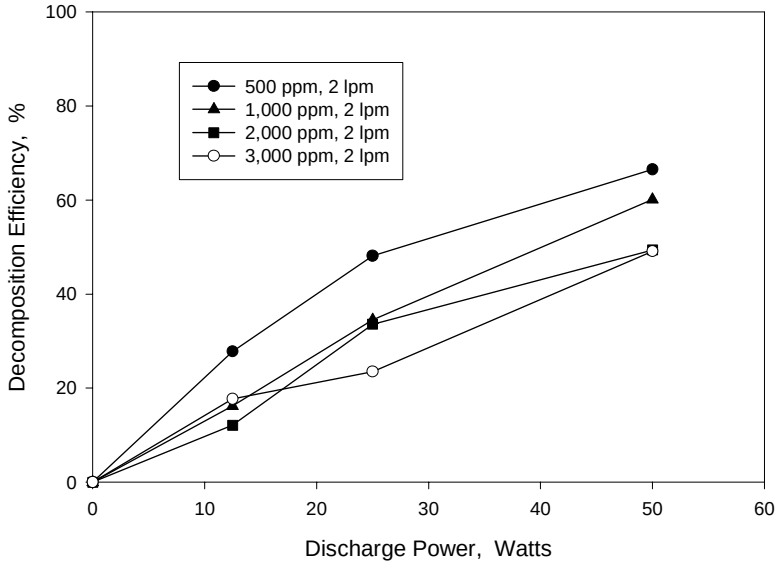

Fig.2. Decomposition efficiency of methyl cyanide as a function of discharge power
Humidity of supplied air flow: RH 8% at 25^{o}C, Length of discharge: 20cm

Because the gas adsorption capacity of $BaTiO_3$ bead could be neglected, the results in Fig.2 represent the only effect of non-thermal plasma discharge. The figure shows that the decomposition efficiency of methyl cyanide is increased when the discharge power is moved to higher energy as expected. And the decomposition efficiencies are slightly higher when influent concentration is lower than the cases of high influent concentration at a given discharge power. Some discrepancies or uncertainties of the data in Fig.2 are seemingly caused by fluctuation of discharge in the reactor. The decomposition efficiencies are slightly above 60% and 40% at 50 watts of discharge power when the influent concentrations are 500ppm and 3000ppm respectively. The differences of decomposition efficiencies of methyl cyanide with the variation of influent concentrations are not significant. Namely, the difference of decomposition efficiencies is only 20% between 500ppm and 3000ppm at the discharge power of 50 watts, but the difference of concentrations between them is six times.

The detected noxious products at the effluent of $BaTiO_3$ packed PBPR are hydrogen cyanide (HCN), O_3,

N_2O, NO_2 and remaining (not decomposed) methyl cyanide. Ozone is detected at the conditions of lower discharge power, N_2O and NO_2 are produced at the conditions of higher discharge power, but the quantitative analyses of them are not attempted. The concentration of produced hydrogen cyanide and remaining methyl cyanide at the effluent of $BaTiO_3$ packed PBPR versus discharge power are shown in Fig.3.

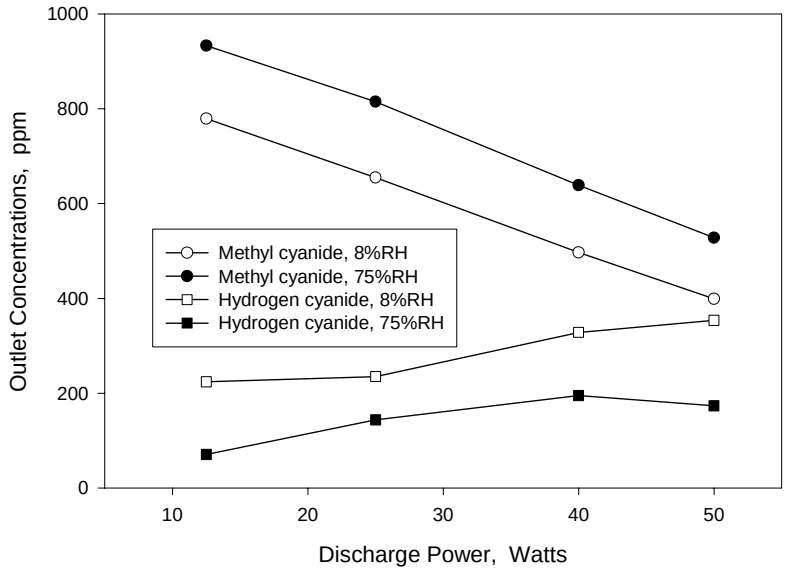

Fig.3. Outlet concentrations of remaining CH_3CN and produced HCN as a function of discharge power
Reactor: $BaTiO_3$ packed PBPR, Length of discharge: 20cm, Inlet concentration of CH_3CN: 1000ppm
Humidity of supplied airflow: RH 8 and 75% each at 25^oC,

The effects of airflow humidity (RH 8 and 75%) on the product distribution and the efficiency of methyl cyanide decomposition are also presented in Fig.3. The results show that the humidity in the airflow affects negatively to the decomposition of methyl cyanide in $BaTiO_3$ packed PBPR; at the higher relative humidity condition, the higher outlet concentration of remaining methyl cyanide is detected. The produced HCN concentration is over 200ppm and below 400ppm at the condition of RH 8% of air carrier, and the concentration of HCN is increasing with the discharge power. But the produced HCN concentration is below 180ppm through the entire range of discharge power at the humidified condition of RH 75%.

The concentration of produced HCN and remaining methyl cyanide at the effluent of Al_2O_3 packed and Pt/Al_2O_3 packed PBPR versus discharge power are shown in Fig.4 and Fig.5 each. In Fig. 4, the concentrations of produced HCN and remaining methyl cyanide at the effluent of Al_2O_3 packed PBPR are reduced to some extent compared to the results of $BaTiO_3$ packed PBPR (Fig.3), but the humidity effect to the decomposition of methyl cyanide is still existed. And the increasing trend of HCN concentration with the increasing of discharge power that is shown at the $BaTiO_3$ packed PBPR is existed only at low discharge powers. On the other hand, the HCN concentration is slightly diminished at the discharge power of 30 and 40 watts than the concentration at the discharge power of 20 watts. Especially, the concentration of remaining methyl cyanide is below 80ppm and the concentration of HCN is only 15ppm at the condition of discharge power 40 watts and RH 8%.

In the case of Pt/Al_2O_3 packed PBPR as shown in Fig.5, the concentration of produced HCN and remaining methyl cyanide are quite low compared to that of $BaTiO_3$ or Al_2O_3 packed PBPR even at the low discharge powers 10 and 20 watts. The outlet concentrations of remaining methyl cyanide are under 50ppm at above 30 watts of the discharge power. Especially, HCN concentration is zero (not detectable with GC-FID at the effluent of the reactor when the discharge power is over 30 watts).

The humidity effect on methyl cyanide decomposition exists evidently below 30 watts in the case of Pt/Al_2O_3 packed PBPR also. But the gap between dried and humidified air carrier is diminished evidently above 30 watts as shown in Fig.5.

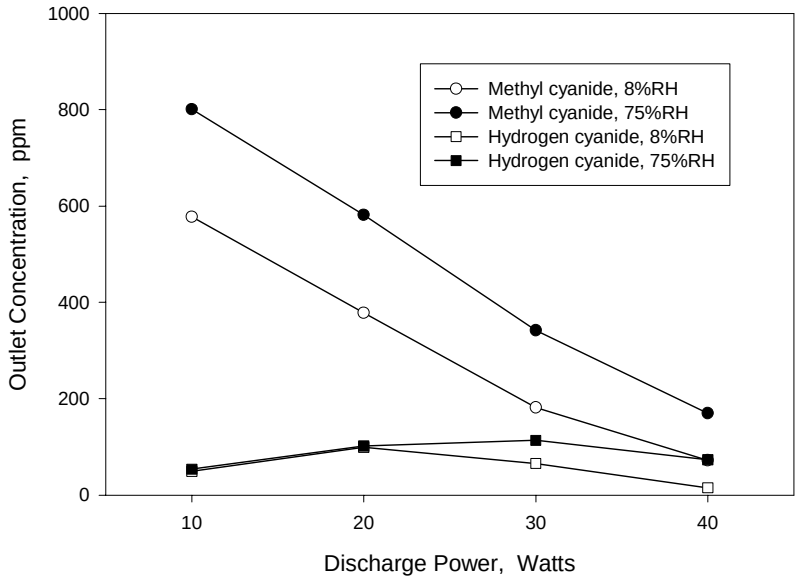

Fig.4. Outlet concentrations of remaining CH_3CN and produced HCN as a function of discharge power
Reactor: Al_2O_3 packed PBPR, Length of discharge: 10cm, Inlet concentration of CH_3CN: 1000ppm
Humidity of supplied airflow: RH 8 and 75% each at 25°C,

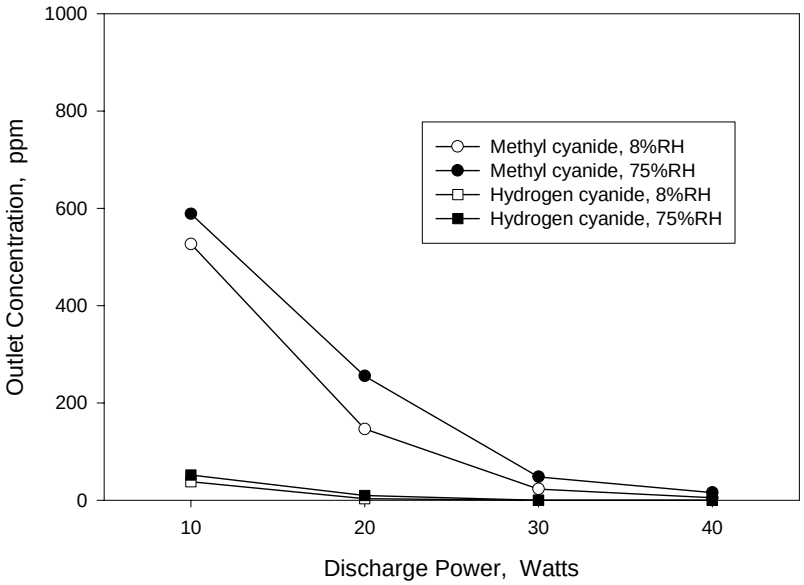

Fig.5. Outlet concentrations of remaining CH_3CN and produced HCN as a function of discharge power
Reactor: Pt/Al_2O_3 packed PBPR, Length of discharge: 10cm, Inlet concentration of CH_3CN: 1000ppm
Humidity of supplied airflow: RH 8 and 75% each at 25°C,

4. Discussions

From the result of Fig.2, it is known that the differences of decomposition efficiencies of methyl cyanide with the variation of influent concentrations are not significant. So, it reflects that the energy efficiency namely, the total numbers of decomposed molecules at a given supplied energy (discharge power) increase with increasing the influent concentration.

To show the difference of decomposition behaviors of cyanides and general VOC materal (here we select trichloroethylene, TCE), the degrees of removal ($[X]/[X]_o$, [X] : outlet concentration of cyanides or trichloroethylene, $[X]_o$: inlet concentration of them) versus specific energy density (SED) are presented in Fig.6.

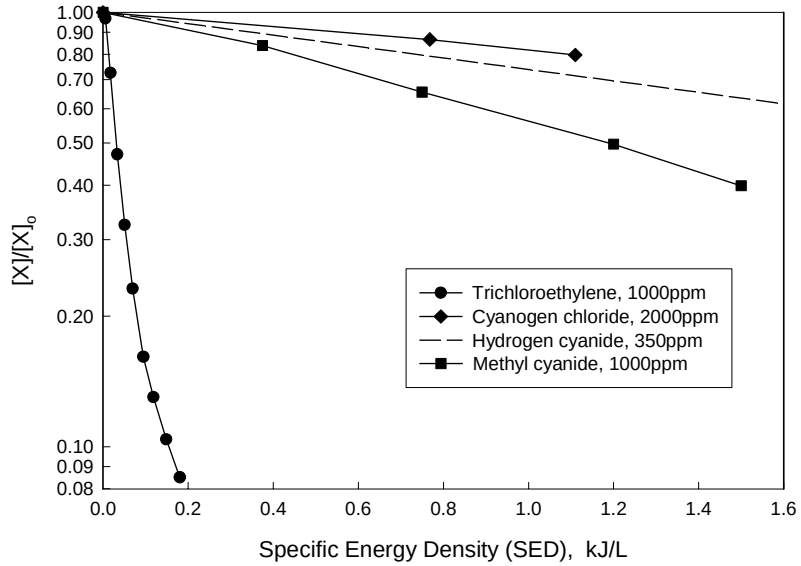

Fig.6. Degrees of removal for cyanides and trichloroethylene in non-thermal plasma reactor
Humidity of supplied airflow: RH 8 % at 25°C

The data for trichloroethylene and cyanogen chloride in Fig.6 are from the previous results of this laboratory [4, 5]. And, the data for hydrogen cyanide are extrapolated from the results of Fraser et. al. [3]. It is confirmed from the data of Fig.6 that trichloroethylene is one of the easily decomposed VOC compound [6] in non-thermal plasma reactor, but cyanides are considerably hard to decompose in non-thermal plasma condition. The question is still remained what makes the big difference in degrees of removal between trichloroethylene and cyanides. Krasnoperov et. al. [7] suggested that the decomposition of molecules on non-thermal plasma condition in air is closely related to the ionization energy of molecular oxygen (12.06 eV). If Krasnoperov's suggestion is effective, the decomposition of a molecule that the ionization energy is lower than that of oxygen molecule will be easy in a non-thermal plasma condition, but the ionization energy of a molecule is higher than that of molecular oxygen the opposite phenomenon will be appeared. The ionization energies of cyanides (cyanogens chloride: 12.49, hydrogen cyanide: 13.8, and methyl cyanide: 12.2eV respectively) are higher than that of molecular oxygen. But the ionization energy of trichloroethylene is 9.45eV that is lower than that of oxygen molecule. So the data of Fig.6 could be explained somewhat with the relation of ionization energy of molecular oxygen. But more data will be needed for the detailed discussion about the reaction kinetic of cyanides in non-thermal plasma condition.

From the results of Fig.3 to Fig.5, it is found that packing materials in the discharge region affect significantly on the decomposition of cyanides. Degree of removal for methyl cyanide versus SED is illustrated in Fig.7 for detailed comparison. In the case of $BaTiO_3$ packed, the destruction of methyl cyanide has linear relation to the supplied energy density, so the reaction order is pseudo-first. It reflects that the decomposition of methyl cyanide in $BaTiO_3$ packed PBPR is the only function of supplied energy density.

Enhancement of the decomposition in alumina and Pt/alumina packed reactor is more significant at the higher energy densities. The relation between degree of removal and supplied energy density is not leaner, therefore it means the order of reaction is changed and is not first anymore. Similar result was observed in the case of the decomposition of cyanogen chloride in PBPR [5] also. The alumina and Pt/alumina packed in the reactor have high specific surface area of around 250 m^2/g.

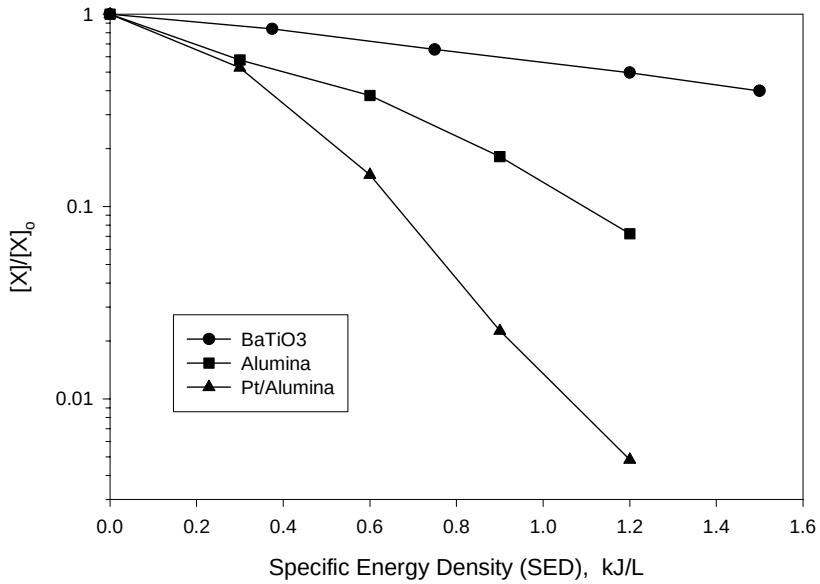

Fig.7. Effects of packing materials on the decomposition of methyl cyanide
Humidity of supplied airflow: RH 8 % at 25^{o}C, Inlet concentration of CH_3CN: 1000ppm

So we could assume that adsorption or (and) thermal catalytic effect in addition to the plasma effect is involved in the destruction of methyl cyanide (and cyanogens chloride) on the alumina or Pt/alumina packed PBPR. From the lower effluent consideration of HCN in Fig.4 and Fig.5, it could be assumed also that the HCN produced by plasma discharge is further decomposed by thermal catalytic effect on alumina or Pt/alumina.

5. Conclusions

The decomposition of methyl cyanide in a non-thermal plasma and plasma-catalyst hybrid reactor is conducted with the variation of discharge power, humidity of air carrier, and packed materials. HCN is produced by the decomposition of methyl cyanide, and the humidity of air carrier affects negatively to the decomposition of methyl cyanide. In comparison with the decomposition of trichloroethylene, cyanides are considerably hard to decompose in non-thermal plasma condition. The reason is explained somewhat in connection with the ionization energy of molecular oxygen. And, thermal catalytic effect in addition to plasma effect appears when alumina and Pt/alumina is packed in the PBPR.

References

[1] S.K. Agarwal, J.J.Spivey, D.E. Tevault, J. Chem. Soc., Chem. Commun., 911 (1993) and Appl. Catal. B: Environmental, **5**. 389 (1995).
[2] A.A. Klinghoffer, J.A. Rossin, Ind. Eng. Chem. Res., **31**, 481 (1992)
[3] M.E. Fraser, R.S. Sheinson, Plasma Chem. Plasma Process., **6**, 27 (1986)
[4] H.W. Lee, S.G. Ryu, M.K. Park, H.B. Park, K.C. Hwang, J. Korean. Inst. Chem. Eng., in press (2003).
[5] M.K. Park, S.G. Ryu, H.B. Park, H.W. Lee, C.H. Lee, Plasma Chem. Plasma Process., submitted.
[6] K. Yan, E.J.M. van Heesch, A.J.M. Pemen, P.A.H.J. Huijbrechts, Plasma Chem. Plasma Process., **21**, 107 (2001).
[7] L.N. Krasnoperov, L.G. Kristopa, J.W.Bozzelli, J. Adv. Oxid. Technol., **2**, 223 (1997).

Rational tools for data obtaining and processing in local plasma spectroscopy.

L. Luizova, A. Khakhaev, K. Ekimov and A. Soloviev

Petrozavodsk State University, Russia

Abstract

The software for data acquisition and processing in spatial resolved optical emission spectroscopy is developed. The experimental set up is controlled by LabView and compatible instrument interfaces . The algorithm of joint data processing is based on principal components method and allows to increase the stability of results of the radial transform and the instrument distortion elimination in the presence of noises. The method is applied to diagnostics of the arc discharge in mercury vapors with addition of thallium.

Introduction

For determination of inhomogeneous plasma local parameters, such as ground state and excited atom and electron densities, atomic and electronic temperatures, the great array of experimental data is to be collected, which contains spatial, spectral and temporary distribution of a source surface radiance. Some image spectrometers can be used for this purpose [1], but they, as a rule, have the software unauthorized for the user. The set up and software for local plasma spectroscopy based on LabView and compatible instrument interfaces is described here. It is built of separated modules and can be easily adapted for any set of the spectral equipment and any modern operational environment. In the given case the concrete variant of an installation includes scanning diffraction spectrometer and spatial scanning block, it allows to choose the certain moments of time for radiation measurement, if a source characteristics are periodically varying. The received experimental data array is processed by rational joint algorithm, which allows to decrease the processing time as well as the noise influence to results.

Experimental set up and software

The set up for local plasma spectroscopy is based on large aperture diffraction spectrometer with dispersion 0.05nm/mm in the range 300-800 nm. Spectral scanning is carried out by step motor, one step corresponds to $\delta\lambda$=0.015nm. Special spatial scanning device with step motor and mirror system allows to receive the source surface radiance distribution in direction perpendicular to system optical axis. The step of spatial scanning is δx= 0.0076 mm in the range ±3cm. Light intensity is measured by photomultiplier, amplifier with time resolution less than 10^{-3} c and analog- digital converter (ADC). As an instrument interfaces in automated experiment the CAMAC crate is used. It contains two modules for stepper motors control, modules for scanning begin - end control and two analog- digital converters: one for light intensity measurement and the other for discharge voltage measurement. It allows to carry out the intensity measurements in chosen phases of current period.

The software of the experiment is based on LabVIEW system and connected with CAMAC by special program driver. In our case it runs under the control of the IBM-compatible computer with OS Windows-98 but it is known that virtual instruments, developed by LabVIEW may be easily adapted to other modern operational environment (e.g. Macintosh, Linux [2]). The software for data acquisition in local plasma spectroscopy consists from separate modules mounted as virtual instruments (VI) The software includes:

a) VI for spectral device calibration on wave lengths by a source with a known spectrum ("Spectrum calibration").

b) VI for the photodetector sensitivity calibration by the registration of a certificated temperature lamp spectrum. ("Sensitivity calibration").

c) VI for spectrum scanning in the given spectral range with the given step ("Spectrum scanning"). It is used on the preliminary stage of experiment for choosing spectral lines for further analysis and then for measurement of the spectral device spread function. The example of the module control panel one can see in Fig. 1.

d) VI for spatial gating at a given wave length ("Spatial scanning"). It is used for measurement of surface radiance values. First of all the spatial point, corresponding to the maximum of radiance is found. This point is accepted as the center of discharge (x=0). The measurement of radiance are carried out for the center and other points x_k (k=1, 2...m-1), corresponding to m equidistant positions of the spatial gating system.

e) VI for automated spatial and spectral scanning in the given spectral and spatial intervals and the definite phase of current period. ("Spectrum -spatial scanning").
f) Module of data loading for subsequent analysis ("Spectrum load/Analysis"). This module allows to load any data, received by other modules and to derive various information from a spectrum (e.g. maximum positions and values, line widths) by LabVIEW tools for graphic processing (scaling and cursor positioning). If the photodetector sensitivity calibration have been done this module transforms photodetector readings $F(\lambda, x)$ to spectral surface radiance values $b(\lambda,x)$. It allows also to join some arrays, corresponding to different spectral ranges and different time moments (but spatial points must be the same), in common array for joint processing , calculate the covariance matrix of this array, find its eigenvalues and eigenvectors (there is the standard LabVIEW module for this purpose "EigenValues & Vectors.vi"), and calculate the projections of each spectral point to all eigenvectors. It is the essential part of the joint processing algorithm, which will be described in detail in the next section.
This module is also used for calculation of estimator S^2 of experimental random error by using data corresponding the same spectral, spatial and phase points received in several recurring experiments. In this estimator not only instrumental noises but also light source possible instability are taken into account.
g) Module of the remote access server. It is used for remote control of experiment (mainly in student laboratory training).

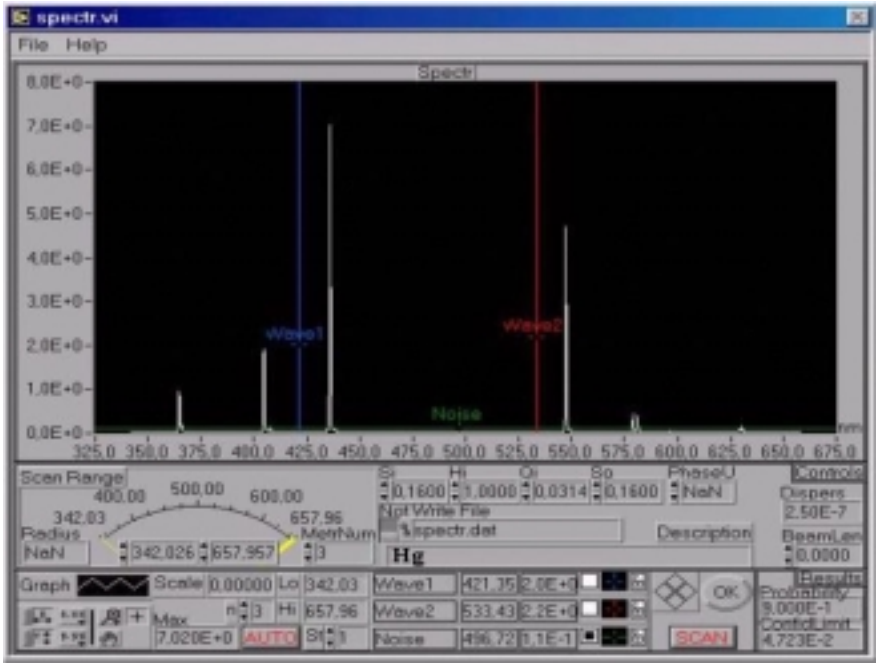

Fig.1 Control panel of VI "Spectrum scanning".

3. The data processing algorithm

For investigation of one section of cilindrically symmetric plasma the two-dimensional array of reading $F(\lambda_i,x_j)$ corresponding to spectral surface radiance spectral $b(\lambda_i,x_j)$ have to be measured along a series of chords, perpendicular to plasma axis (x_j- the displacement of chord from plasma centerline, λ_i - wavelength of spectral point inside the profile). From the array $b(\lambda_i,x_j)$ the array of spectral emissivities $\varepsilon(\lambda_i,r_j)$ has to be reconstructed and spectral line profiles $\varepsilon_j(\lambda_i,)$ for distance r_j from the section center have to be found. These profiles may be used for the determination of plasma parameters in this spatial point. The reconstruction of emissivity $\varepsilon(r)$ from measured intensity $b(x)$ is known as Abel's inversion

$$\varepsilon_\lambda(r) = -\frac{1}{\pi}\int_r^L \frac{db_\lambda(x)}{dx}\frac{dx}{\sqrt{(x^2-r^2)}}. \qquad (1)$$

Here L is the discharge tube radius.
It is so called improperly posed problem and the solution is impossible without using of *a priory* information about function $\varepsilon(r)$. The quantity of this information is to be in accordance with the level of

experimental noise. The rational algorithm of Abel's inversion, when a big data array is collected, was proposed in the paper [3]. But it was not taken into account there that measured line profiles $F(\lambda_i,x_j)$ may be distorted by the spectrometer spread function.

$$F_{out}(\lambda) = \int F_{int}(\lambda') \cdot g(\lambda - \lambda') d\lambda' . \quad (2)$$

$g(\lambda)$ is the spectrometer spread function , F_{out} is the observed line profile, F_{int} is the true line shape, it is proportional to $b(\lambda)$. The elimination of instrument distortion is possible, for example, by use of the convolution theorem:

$$\Phi\{F_{out}(\lambda)\} = \sqrt{2\pi}\Phi\{F_{int}(\lambda)\} \cdot \Phi\{g(\lambda)\} , \quad (3)$$

where Φ is Fourier transform operator. If $g(\lambda)$ is known we simply have to divide Fourier transform of F_{out} by Fourier transform of g and restore F_{int} by the inverse Fourier transform of the result. But it is also an improperly stated problem, its solving is very sensitive to experimental data noises. The algorithm proposed here significantly increases the result stability in the presence of experimental data noises, when it is necessary to solve at once both improperly stated problems. The algorithm is based on collective processing of large data arrays of readings $F(\lambda_i,x_k)$, measured along a series of chords, perpendicular to plasma axis. (If we are interested only in line shapes but not in the intensities we may use the array $F(\lambda_i,x_k)$ instead of $b(\lambda_i,x_j)$. We only have to be sure that the photodetector system is linear. If it is necessary, the coefficient of proportionality of readings to intensities may be introduced at the final step of calculation because all the following data transformations are linear.)

For the first step of algorithm one has to calculate the covariance matrix A of the array of profiles $F(\lambda_i,x_k)=F_{ik}$, corresponding to one or , perhaps , several spectral lines and time points.

$$A_{k,j} = \frac{1}{n}\sum_{i=1}^{n}(F_{i,k} - \overline{F}_k)(F_{i,j} - \overline{F}_j) , \quad (4)$$

where n is a number of spectral points, $\overline{F_k} = \frac{1}{n}\sum_{i=1}^{n} F_{i,k}$ is the average spatial vector .

Then the array F_{ik} may be described by a model:

$$F_{i,k} = \overline{F}_k + \sum_{p=1}^{q} M_{i,p} U_{p,k} \quad (5)$$

where U_p are eigenvectors of the covariance matrix A. and $M_{i,p}$ are the projections of i-th spectral point to eigenvector U_p

$$M_{i,p} = \sum_{k=1}^{m}(F_{i,k} - \overline{F}_k) U_{p,k} \quad (6)$$

As a consequence of mutual dependence of elements of F the number q of significant eigenvectors of A is less than m. The eigenvector is significant if corresponding eigenvalue is no less than S^2. Before further processing one has to prove that model (5) with m(q+1)+qn coefficients is adequate. For this purpose the Fisher criterion has to be used [4].

Let us note that vectors $\overline{F}$ and $\mathbf{U}_p$ depend only on spatial coordinates and projections $M_{i,p}$ depend only on spectral points. The operations of radial transform (let us denote the corresponding operator $\boldsymbol{R}$) and elimination of instrument distortion (let us denote the corresponding operator $\boldsymbol{C}$) are linear and applied to different variables. So instead of the instrument distortion elimination from each profile $F_k(\lambda)$, and then Abel inversion for each wave length λ_i for the next steps of algorithm one can eliminate the instrument distortions from projection $M_{i,p}$, then fulfill the radial transform for $\overline{F}$ and $\mathbf{U}_p$ and restore the required profiles $\varepsilon(\lambda_i,r_j)$ in various plasma points r as:

$$\varepsilon(\lambda, r) = \boldsymbol{R}\{\overline{F}\} + \sum_{p=1}^{q} L_p(\lambda)\, \boldsymbol{R}\{U_p\}, \quad (7)$$

where $L_{ip} = \boldsymbol{C}\{M_{i,p}\}$ are the results of instrument distortion elimination from parts of projections $M_{i,p}$, corresponding to the each spectral line.

4. The example of application of experimental technique and data processing algorithm

The application of described experimental technique and data processing algorithm is illustrated in the case of diagnostics of high pressure arc discharge in mercury vapors with the addition of thallium iodide. The observed array F contains 558 rows and 10 columns. The rows from i=0 to i=198 correspond to thallium line 553 nm ($9^2P_{3/2} \rightarrow 7^2S_{1/2}$) and first phase of current period, i=199 - 397 correspond to the same line and second current phase, i=398 - 477 correspond to mercury line 577 nm ($6^3D_2 \rightarrow 6P_1$) in first phase of current period, i=478 - 557 correspond to the same line and second current phase. Each column corresponds to one spatial position (m=10).

The comparison of eigenvalues of A with estimator S^2 shows that in our case only q=2 eigenvectors are significant and model (4) with this two eigenvectors is adequate. In Fig.2 one can see the average vector $\overline{F}$ and eigenvectors of covariance matrix U_1 , U_2 before and after radial transform. (relative units corresponds to units in which the ADC readings were expressed).

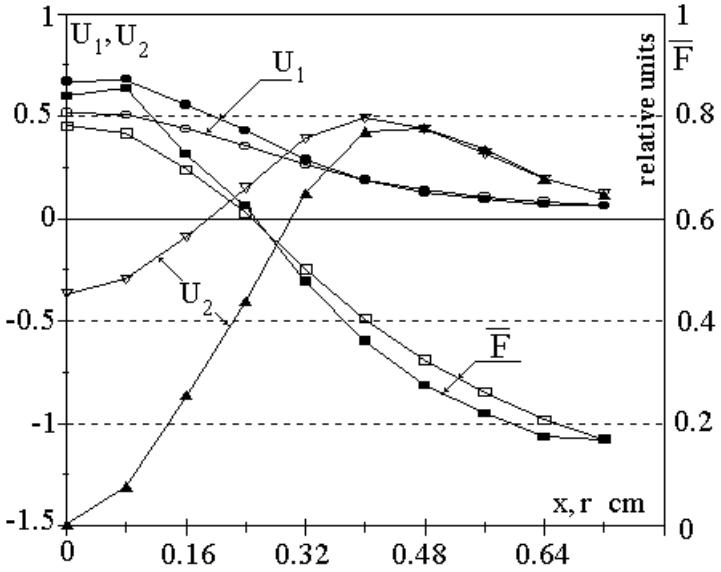

Fig.2 Average vector $\overline{F}$ and eigenvectors of covariance matrix U_1 , U_2 before (light markers) and after (black markers) radial transform

The spread function was received in experiment with the cadmium spectral lamp. The line widths in this lamp are less than 0.001nm. The computer program for elimination of instrument distortion was described in [5]. It was shown that the algorithm is very sensible to experimental noises, even to limited accuracy of computer calculation. The stability of the results may be reached by multiplying Fourier transform of restored distribution by special function, which is equal to 1 inside specified part Q of full spectral range Ω ($\Omega = 2\pi/\delta\lambda$, $\delta\lambda$ is the step of spectral scanning) and exponentially decreases to the range ends.

Q depends on noise level and ratio of output and spread function widths. Very small Q leads to additional distortion of the restored function.

In each case the appropriate value Q may be selected by simulating experiment. In Fig.3 the results L_{ip} of instrument distortion elimination from parts of projections $M_{i,p}$, corresponding to the each spectral line, are presented.

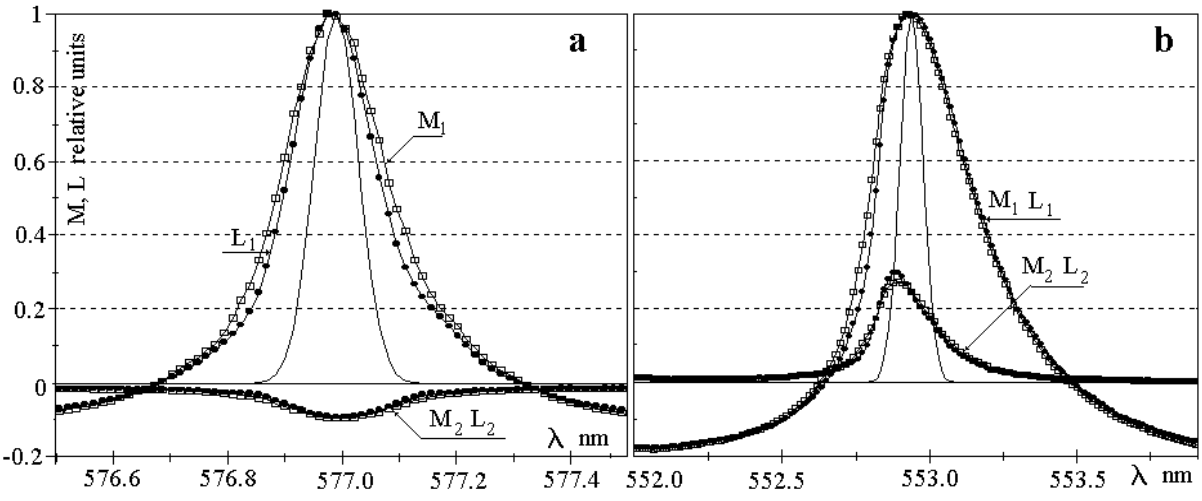

Fig.3. The projections to eigenvectors for mercury (a) and thallium (b) spectral lines before (light markers) and after (black markers) elimination of instrument distortions. Thin line without markers is the spread function.

For the wider thallium line the instrument distortion is small and L_{ip} practically coincides with $M_{i,p}$. The restored line profiles for one current phase are presented in fig 4.

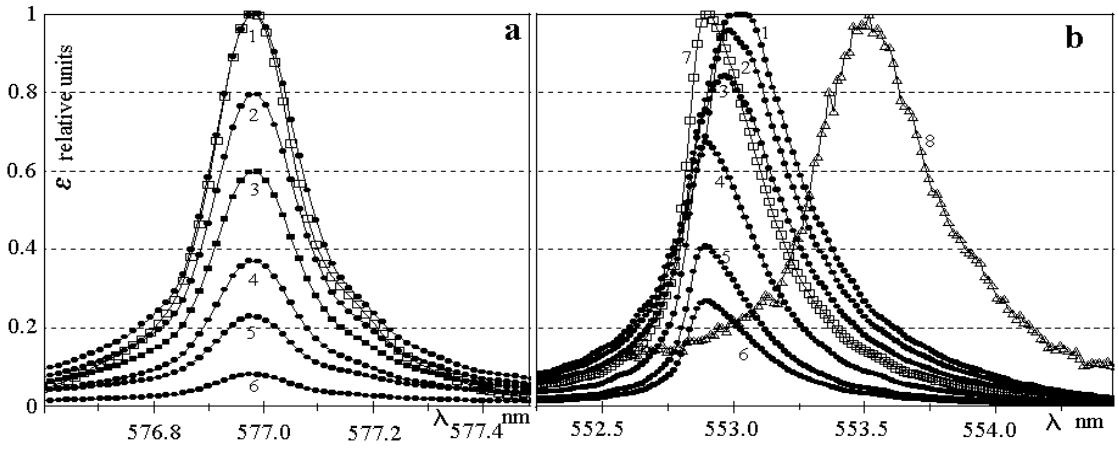

Fig 4. Restored line profiles of mercury (a) and thallium (b) spectral lines for different spatial points 1-r=0, 2-r=0.16cm, 3- r=0.32cm, 4- r=0.48cm, 5-r=0.64cm, 6-r=0.72 cm. Light markers (curve 7 in "b") denote the profile for r=0.72 cm, these curves are standadized to 1 in maximum to demonstrate visually the line shift in comparison with the case r=0. Curve 8 in "b" -the result for r=0 of "individual" processing of experimental array of thallium line profiles: elimination of instrument distortion from each of 10 profiles and radial transform from each of 199 spectral points by using the same programs as for joint processing. (for clearness the maximum of this curve is shifted from true position).

The mercury line 577 nm broadening is resonance [6]. So there are no shifts in profiles corresponding to different spatial points and different time moments. Line width is almost constant for different spatial points. It is in accordance with our previous work, where by the analysis of plasma interference data it was shown that in such sources mercury atoms density is almost constant over the most part of the arc section and changes sharply only near the source wall [7]. By this line width we can estimate mercury atoms density in the first current phase as $N_{Hg}=(6.8\pm0.2)\cdot10^{18}cm^{-3}$.

The thallium line 553 nm is broadened mainly by Stark-effect, it leads to appreciable shifts of profiles in different spatial points and different current phases. The broadening by Van-der-Waals interaction with Hg atoms , estimated with above-mentioned N_{Hg} value, is less then 10% from full line width. It is within of accuracy of the known Stark- broadening constant [8], therefore we attributed the experimental line width and shift to Stark- broadening and estimated electron density in the arc center in the first current phase as $N_e(r=0)=(1.0\pm0.1)\cdot10^{16}cm^{-3}$ and $N_e(r=0.72cm)=(7.5\pm0.5)\cdot10^{15}cm^{-3}$ (The radius of the source L=1cm).

Acknowledgments

Authors wish to acknowledge the support of the Russian Ministry of Science and Technology and the U.S. Civilian Research & Development Foundation for the Independent States of the Former Soviet Union (CRDF) (Award No. PZ-013-02);

References

[1] http://www.jyinc.com/oem3/spectros.htm
[2] http://www.ni.com/
[3] L.A. Luizova - JQRST. **66**. 277 (2000)
[4] J. E. Jackson A -User's Guide To Principal Component. New York : John Willey &Sons , 1991.
[3] L.A. Luizova., A. V. Soloviev - Proc. SPIE. **4588**, 440 (2002)
[6] H. R. Griem -Plasma Spectroscopy. New York: MCGraw-Hill (1964).
[7] V.I..Borodin. L.A. Luizova, A.D. Khakhaev - Plasma Physics. **12**, 887 (1986).
[8] G.A. Kasabov, V.V.Eliseev- Spectr. Tables for Low Temp. Plasma. Moscow: Atomizdat (1973)

Comparative characteristics of the ordered dusty structures in plasma with various physical conditions.

A. Khakhaev, L. Luizova, S Podryadchikov, A.Scherbina and A. Bulba

Petrozavodsk State University, Russia

Abstract

The experimental installation and software for studying the ordered dusty plasma structures in the direct current glow discharge were developed, which provide the simultaneous control of the electrical and spectroscopic parameters of plasma and dusty cloud images registration. The area of ordered structure existence has been found. The dependence of interparticle distance on the gas pressure and current and the influence of particles on spectral line intensities and spatial distribution have been investigated.

1. Introduction

The ordered dust structures in the plasma, formed by the interaction charged macro particles with each other, components of plasma and an environment, represent significant interest for fundamental physics and its applications. Problems of their synthesis, controlled modification and destruction are far from decision. The effects of "crystallisation", melting of "crystals" and "evaporation" are accepted to connect with Coulomb parameter [1].

$$\Gamma_p = \frac{Z^2 e^2}{akT_g} \exp(-a/r_D) \qquad (1)$$

Here e is the electron charge, Ze is the particle charge, a is the interparticle distance, k is the Boltzmann constant, $T_g$is the particle temperature, r_D is the Debye length.

The condition of "crystallisation" Γ_p>170 and more precise condition Γ_p>54/(a/ r_D) $^{1.38}$ were received by theoretical calculation and simulating experiments [2,3]. However, one cannot use these conditions for prognostication of plasma crystal forming, because even if the plasma parameters, determining r_D, are known, Z may be estimated from particle size ant electron temperature [4] and T_g is accepted to be equal to plasma atom temperature, the interparticle distance cannot be predicted before experiment. So one can say that in spite of a lot of papers devoted to dusty plasma the relations between plasma parameters, dust particle substance and properties of ordered dusty structure have not been investigated in detail. Therefore the experimental research of dusty ordered structure characteristics remains the problem of today.

2. The experimental set up and software

The scheme of experimental set up is presented in Fig.1

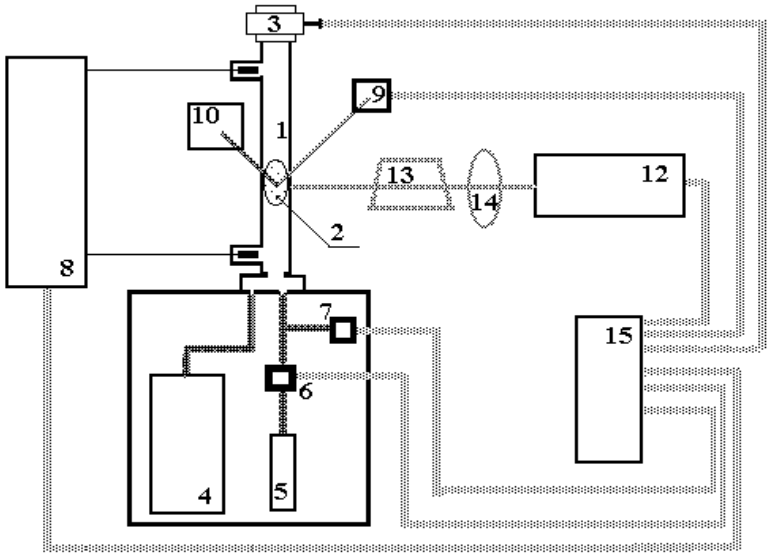

Fig. 1 Experimental set up for researches of dusty structure in the glow discharge

Here (1) denotes the discharge tube with dusty cloud (2), (3) is the system for injection of particles, (4)is the vacuum pump , (5) is the gas cylinder with the system of gas injection control (6) and pressure control (7). (8) is the system of power supply and discharge electrical parameters control. (9) is CD camera for dusty cloud image registration when the structure is illuminated by "laser knife" or other light source (10) (we use also flash lamp and mercury high pressure lamp with addition of thallium iodide). (12) is the spectral system based on diffraction spectrometer with resolution of 0.015nm in the range 300-800 nm. The photo-electric registration of spectrum is possible in two variants: single channel - with photomultiplier and multichannel - with CCD matrix. The lens (14) draws the discharge image to the spectrometer input slit, the direction of the slit is parallel to the direction of discharge tube axis, the Dovet prism (13) is used for turning of the tube image perpendicularly to slit direction when the spatial distribution of spectral line intensities along the tube diameter are investigated.

All experimental devices are controlled by personal computer (15) with instrument interfaces based on LabPC board, CAMAC equipment and LabView graphical enviroment, which provides the simultaneous control of optical and electrical parameters of the plasma, synchronized with the moment of particles injection. (In Fig.1 black lines are electrical channels, thin grey lines are optical channels and thick grey lines are information channels). In Fig.2 the panel of the virtual instruments for control of discharge electrical parameters is presented. One can see a leap of voltage and current at the moment of particle injection.

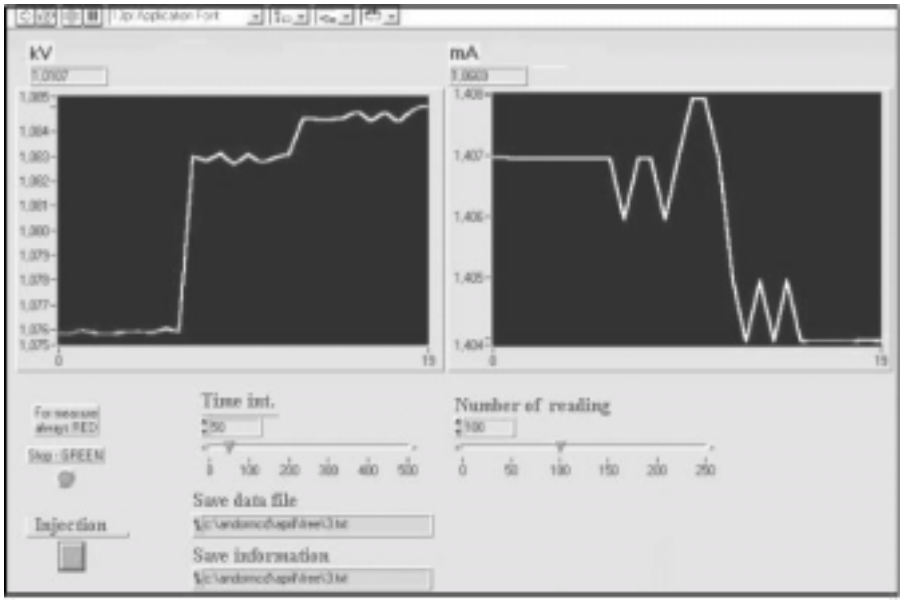

Fig. 2. The virtual instruments for control of discharge electrical parameters.

CCD matrix allowed to register simultaneously the spectral interval of 20 nm before and just after injection of particles. The same interval was registered also in several seconds after injection when all plasma parameters have been stabilized. In Fig.3 virtual instruments for control of the spatial distribution of the spectral line radiance is presented.

For registration of structure images digital photo and video cameras were used. Some observed dusty structures are shown in Fig. 4.

The software for the analysis of the 2D and 3D structure images in plasma has been developed. The program builds the histogram of distances between particles (i.e. experimental analogue of the binary correlation function) if the image of structure is a black-and-white graphic file. The program allows to delete some noise of the image, and in a case of a very "bad" picture (for example, the glass spheres are poorly appreciable on the background of plasma radiation), when the computer processing is impossible, one can "mark" particle images manually.

The program window for menu item "2D image processing" is shown in Fig.5. The number of peaks of binary correlation function is the criterion of structure classification as "crystal", "liquid" or "gas"

The program also allows to restore 3D distribution of particles, if not less than three projections are received.(But this function of software is tested now only in simulating experiment).

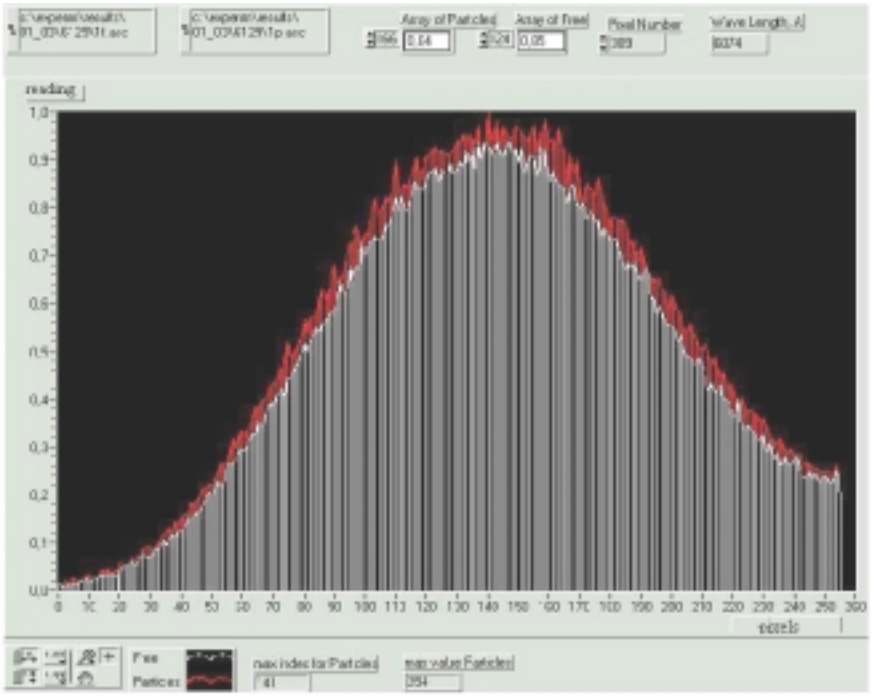

Fig 2. Spatial distribution of neon spectral line (674 nm) before (white) and after (red) particle injection

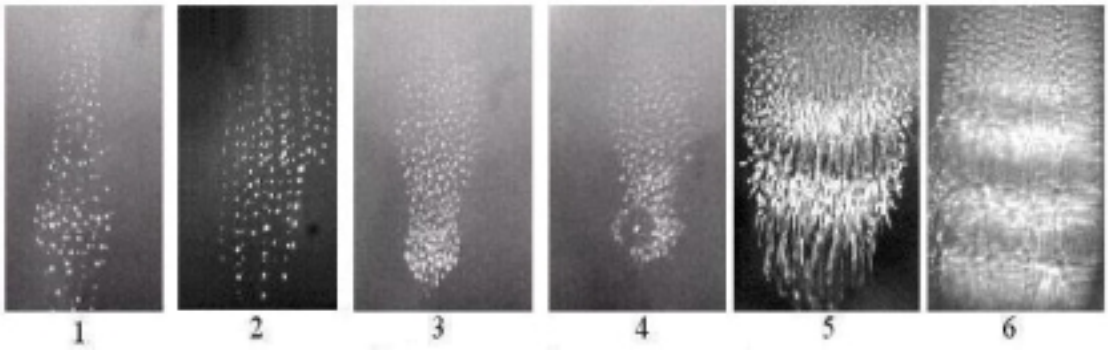

Fig. 4. The examples of observed dusty cloud images in striated glow discharge: 1-5 Al_20_3 in neon (1-P=0.4 Torr, I=0.3mA; 2-P=0.5 Torr, I=0.4 mA; 3- P=0.7 Torr , I=0.5 mA; 4- the unique picture , the condition is the same as in the case 3; 5- dusty-acoustic waves, P=0.7 Torr, I=2.3 mA). 6- dusty-acoustic waves in the cloud of Zn particles in neon, P=1.3 Torr, I=1.5 mA.

3. Experimental conditions and results

The direct current striated glow discharge, was initiated in Ne, Ar, N_2. Discharge tube was established vertically, had an internal diameter 2.6 cm and space gap between electrodes 45 sm. Dust macro particles with diameter from 5 up to 60 microns were injected from the top end of the discharge tube.

Different substances were used: metal (Zn), semiconductor (VN), dielectric (Al_2O_3 and glass micro spheres)

The aforementioned experimental set up has allowed us to establish the areas of existence of various dusty ordered structures. For example, in neon for Al_2O_3 particles with the size up to 5 microns the structure was observed in a range of currents (I) 0.4-3 mA and pressures (P) 0.26-1.4 Torr.(Fig.6).

In nitrogen the range of currents for structure existence is wider than in neon (0.1-8 mA), and the range of pressure is narrower (0.2-0.5 Torr). The same range of conditions for structure existence in neon, as for Al_2O_3 , was defined for VN particles , zinc and for glass spheres. It has been revealed, that the vacuum conditions and the gas purity are very important for ordered dusty structures properties. Therefore careful gas

and particles cleaning is necessary, as well as continuous control of pressure in discharge volume and spectral control of gas clearness during the experiment.

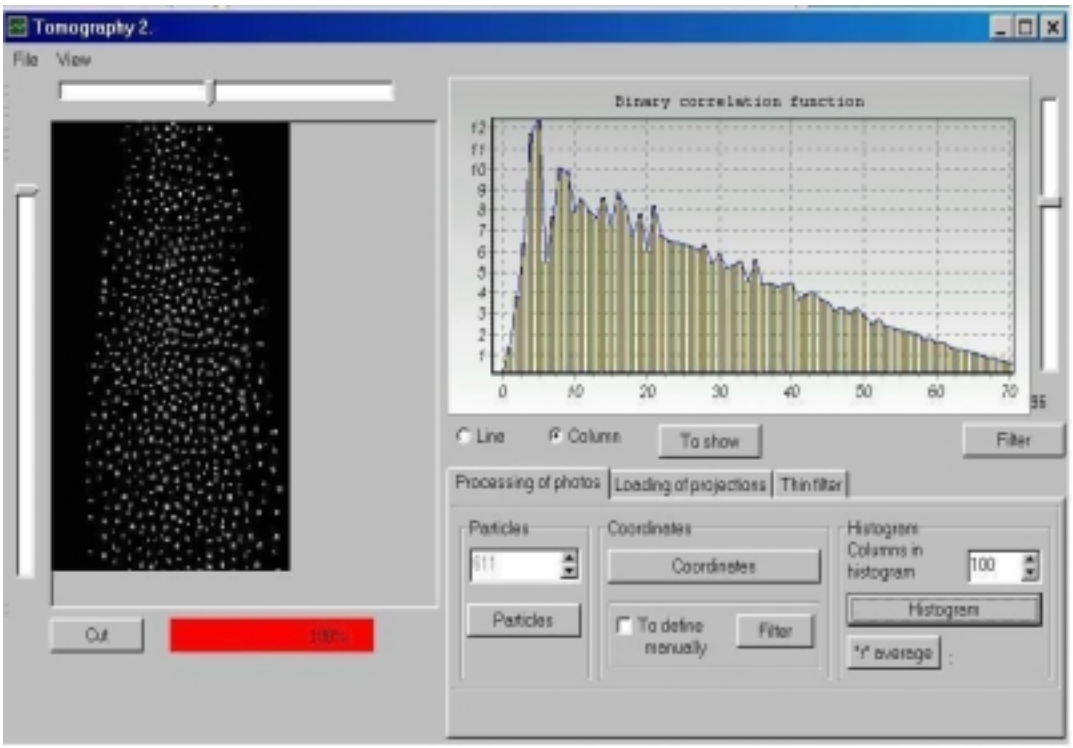

Fig.5. Main window of 2D dusty cloud image processing

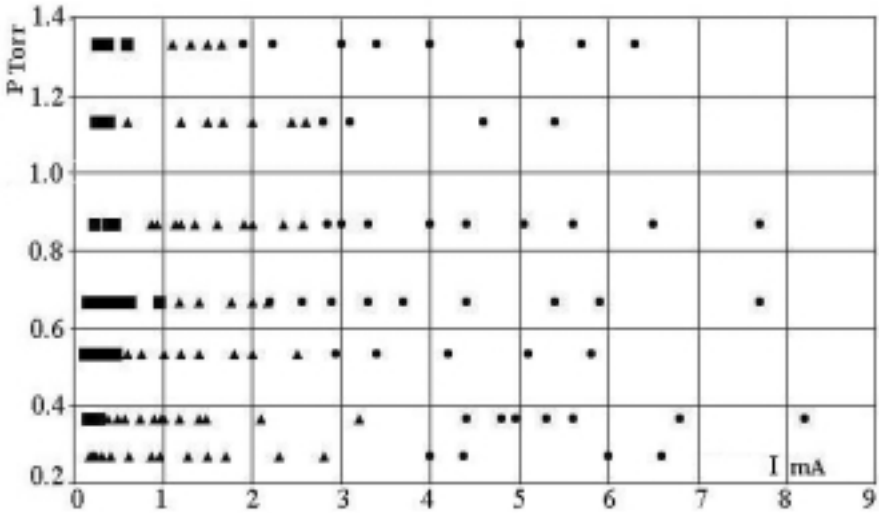

Fig. 6. The area of dusty structure of Al_2O_3 particles in neon: rectangles-"crystal", triangles -"liquid", circles-"gas".

It have been shown that mean distance between particles increases as a rule with the discharge current. The dependence of mean interparticle distance (R) on discharge current (I) was investigated in detail for Al_2O_3 particles in neon. It was shown that for definite pressure this dependence may be approximated by linear function

$$R=bI+c, \qquad (3)$$

where b noticeably depends on pressure.(Fig.7)

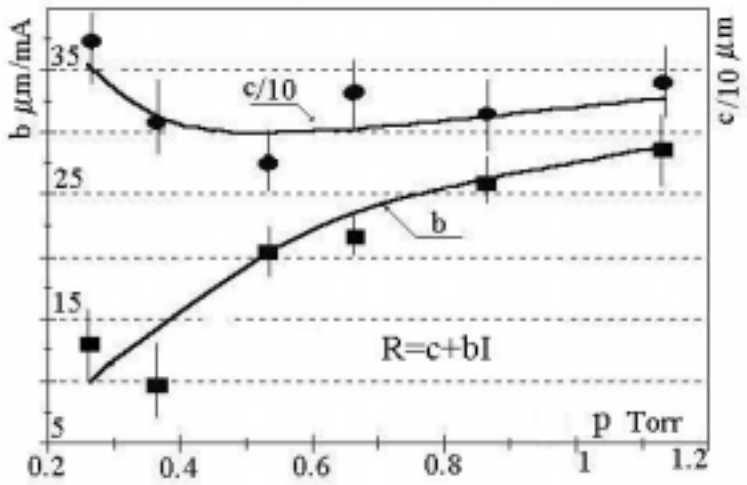

Fig. 7 The dependence of interparticle distance on current (I) and pressure (p) for Al_2O_3 in neon

We have investigated also the dependence of plasma spectroscopic characteristics on dust particle presence. Whereas the changes of discharge electrical parameters after particle injection are less the 1%, the changes of spectral line intensities are above the noise level [5]. The dependence of line intensity change after the injection of Al_2O_3 particles on the discharge current in neon discharge with pressure 0.4 Torr is presented in Fig. 8. Here $\Delta F = F_p - F$, where F_p is the photodetector reading for given spectral line in the presence of particles and F is the reading for the same line without particles in the discharge. Values $\Delta F/F$ are averaged over 10 spectral lines corresponding to transitions $2p^53p$-$2p^53s$ in neon atom. The change of the intensity of lines may be explained by influence of dust particles on the electron energy distribution function. The spatial distribution of spectral line intensity also depends on the presence of particles. The statistic processing of array of spatial radiance distributions has showed that the spatial distribution width becomes wider by 3% after the injection of particles. These results shows that in spite of a very low particle density (about 10^4 cm^{-3}, when electron density in our condition is about 10^8 cm^{-3}, and atom density is about 10^{16} cm^{-3}) not only dusty structure properties depends on plasma conditions but plasma characteristics also depends on dust presence.

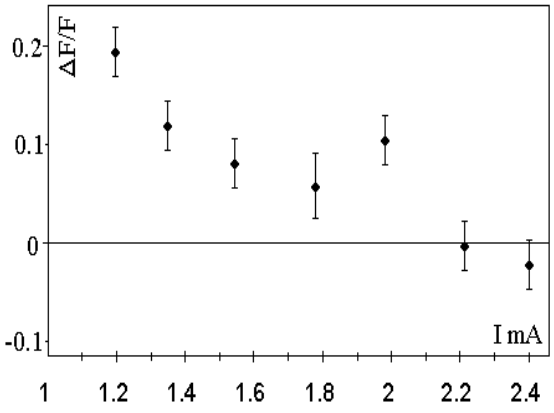

Fig. 8 The dependence of relative intensity change on the discharge current

So the complex investigations of such objects have to be continued.

Acknowledgements

Authors wish to acknowledge the support of the Russian Ministry of Science and Technology and the U.S. Civilian Research & Development Foundation for the Independent States of the Former Soviet Union (CRDF) (Award No. PZ-013-02) and INTAS (grant 2000 0522)

References

[1] H. Ikezi -Phys. Fluids. **29**,1764 (1986)
[2] Ch. Hollenstein -Plasma Phys. Control. Fusion. 42, R93 (2000)
[3] A.F. Pal, D. V.Sivochin, A.N. Starostin, A.V. Fillipov, V.E .Fortov - Plasma Physics. **28,** 32 (2002)
[4] V.N. Tsytovich -Physics- Uspekhi. **167**, 57 (1997)
[5]. D.V.Vlasov, L.V.Deputatova, L.A.Luizova, S.F.Podryadchicov, V.M.Torchinsky, A.D.Khakhaev. Proc. PLTP-2001, Petrozavodsk, part 2, 124 (2001)

PLASMA ENHANCED THIN FILM DEPOSITION ON POLYCARBONATES

B. Ulejczyk[1], T. Opalińska[2], L. Karpiński[3], K. Schmidt-Szałowski[1]

[1] *Warsaw University of Technology, Faculty of Chemistry, Noakowskiego 3, 00 664 Warszawa, POLAND*
[2] *Industrial Chemistry Research Institute, Rydygiera 8, 01 793 Warszawa, POLAND*
[3] *Institute of Plasma Physics and Laser Microfusion, Hery 23, 01 497 Warszawa, POLAND*

Abstract
The subject of the investigations was the process of deposition of thin organo-silicon films on polycarbonates in the pulsed dielectric barrier discharge. Thin films were deposited from gas mixture of helium, oxygen and tetraethoxysilane at the atmospheric pressure. The deposition rate decreased with increase of O_2 concentration was observed Two separately sets of the deposition rate was obtaining for two different ranges of discharge gap, 0.2-0.5 and 0.75-1.5 mm.

1. Introduction

Polycarbonates (PC) are found in number of products from essential medical devices (3%), electronics equipments (22%), cars (9%), building and construction applications (32%) as well as consumer goods. PC is extensively used in optical data storage applications, safety equipment and lightweight, transparent roofing in building and construction. The global market for PC was 1,800,000 tons in 2000 and growth with an average growth rate of approximate 10% with new applications developed [1]. PC is a high quality, engineering plastic with a unique combination of properties including strength, lightness, durability, high transparency, and heat resistance. However, PC must be coated with a protective, thin film against scratching and action of solvents, oxygen, humidity or solar radiation.

An interesting technique to improve of the surface properties seems to be the plasma enhanced/assisted chemical vapor deposition (PECVD/PACVD). The thin film is formed directly in the electric discharge volume (PECVD) or out of it (PACVD). The process of depositing protective film from the gas phase is initiated by electric discharge. The reactive species, like excited molecules, radicals and ions, are formed as the result of collisions of high-energetic electrons with gas molecules of precursors. These reactive species take part in the formation of the thin film on the surface. Various gases were used, as the precursors, like tetraethoxysilane, hexamethoxydisilazane or tetramethylosilane for deposition of organo-silicon film and methane or acetylene for deposition of diamond-like film.

The processes of thin film deposition usually run in glow discharges at low pressure (1-1000 Pa) [2-4], but the low-pressure apparatus and it operation is expensive. On the other hand, it was found, that the thin films might be deposited on solid surfaces using filament barrier discharges at the atmospheric pressure. However, the film was usually not uniform [5,6]. In order to increase the homogeneity of the barrier discharge, we have developed a new process run under conditions of pulsed dielectric barrier electric discharges (PDBD).

In this study were investigated:

1) influence of the position of PC in reactor on the deposition rate;
2) influence of the width of discharge gap on the deposition rate;
3) influence of the oxygen concentration on the deposition rate.

2. Experimental

The process of thin films deposition was carried out in the apparatus consisted of plasma reactor, gas supply system, and electric supply system. These elements are described in our former work [7,8]. The PC plates were placed on both, high-voltage and grounded electrodes. The PC plates were characterized by the relative electric permittivity 2.3 (measured by a Precision LCR Meter HP 4284A). The PC plates formed double dielectric barrier. The discharge gap, where discharge was developed and plasma was generated, was between the PC plates. In the discharge zone chemical reactions were initiated.

The thin films were deposited from mixture of helium, oxygen and vapor of tetraethoxysilane (TEOS). The experimental parameters are shown in **Table I**.

Table I. Experimental parameters

Total gas flow rate [l (s.t.p.)/h]	100
Pressure [atm]	1
He concentration [% by vol.]	50-95
O_2 concentration [% by vol.]	5-50
Vapor of TEOS concentration [ppm]	220-320
Discharge gap [mm]	0.2-1.5
Thickness of PC plates [mm]	0.5-0.75
Frequency of pulse repetition [Hz]	400

The mass of deposited film was determined gravimetrically using Sartorius BP 221S balance. On the basis of on these measurement the deposition rate was evaluated.
Morphology and topography of thin film were investigated using atomic force microscopy (AFM – Nanoscope 1030) and scanning electron microscopy (SEM – LEO1530).
The chemical composition was studied using Fourier transform infrared spectroscopy and X-ray energy disperse detector attached to LEO1530.
The electric parameters (voltage pulse, current pulse and frequency of pulse repetition) were recorded using Tektronix TDS 3054 oscilloscope.

3. Results and Discussion

FTIR spectra exhibited Si-OH, Si-$(CH_3)_x$, Si-O-Si, Si-O-C and EDX spectra exhibited Si, C, O elements as component of thin films [7,8].
The AFM and SEM microimages, as presented in our former work [7,8], showed, that thin film coated uniformly PC. The surfaces of deposited films were similar to the surfaces of original PC plates. The surfaces of films was very smooth and any holes were observed on the surfaces after thin film deposition.
PDBD, which was used in our study, was a special form of dielectric barrier discharge. PDBD was characterized by very short time of voltage pulses (50ns) and current pulses (20 ns) [7,8].
The masses of deposited film referred to unit of covered PC area ($\Delta\mathbf{m}$) versus time of plasma treatment ($\boldsymbol{\tau}$) are shown in **Fig. 1-4**. It was linear dependence, but the regression lines did not cross the origin. It demonstrated that the deposition process was not started in the same time as plasma treatment started. This behavior was different than the thin film deposition on inorganic material, because plastics are lesser resistant on plasma action than metals or silicon wafers. Probably before the process of deposition some other processes, like etching or activation, take place in the first period of plasma treatment of polymer material. This problem was discussed in other work [9-11].
The linear dependencies were described by equation:

$$\Delta\mathbf{m} = \boldsymbol{r} \bullet \boldsymbol{\tau} + \boldsymbol{b} \qquad (1)$$

The value of ***r*** parameter in this equation correspond to the deposition rate, which is shown in **Table II** and **Table III** for various discharge gap and oxygen concentration respectively. The results in these tables showed, that PC position on the electrodes have an influence on the deposition rate. There was found, that the deposition rate on PC placed on high-voltage electrode was usually higher, than the deposition rate on PC placed on grounded electrode.

Table II. The deposition rate of thin film on PC placed on grounded and high-voltage electrodes for various discharge gaps (thickness of PC – 0.75 mm, TEOS concentration – 330-320 ppm, O_2 concentration – 5%)

Discharge gap [mm]	Deposition rate of thin film on PC placed on grounded electrode [μg cm^{-2} min^{-1}]	Deposition rate of thin film on PC placed on high-voltage electrode [μg cm^{-2} min^{-1}]
0.2	4.6±0.1	4.1±0.3
0.5	6.1±1.1	6.8±0.8
0.75	2.5±0.4	3.4±0.2
1.0	6.0±0.4	7.3±0.4
1.5	10.1±0.5	10.4±0.4

Table III. The deposition rate of thin film on PC placed on grounded and high-voltage electrodes for various O_2 concentration (thickness of PC – 0.75 mm, discharge gap – 0.2 mm, TEOS concentration – 330-320 ppm)

Discharge gap [mm]	Deposition rate of thin film on PC placed on grounded electrode [μg cm^{-2} min^{-1}]	Deposition rate of thin film on PC placed on high-voltage electrode [μg cm^{-2} min^{-1}]
5	5.6±0.4	7.8±0.5
25	2.3±0.3	2.6±0.1
50	0.6±0.1	0.7±0.1

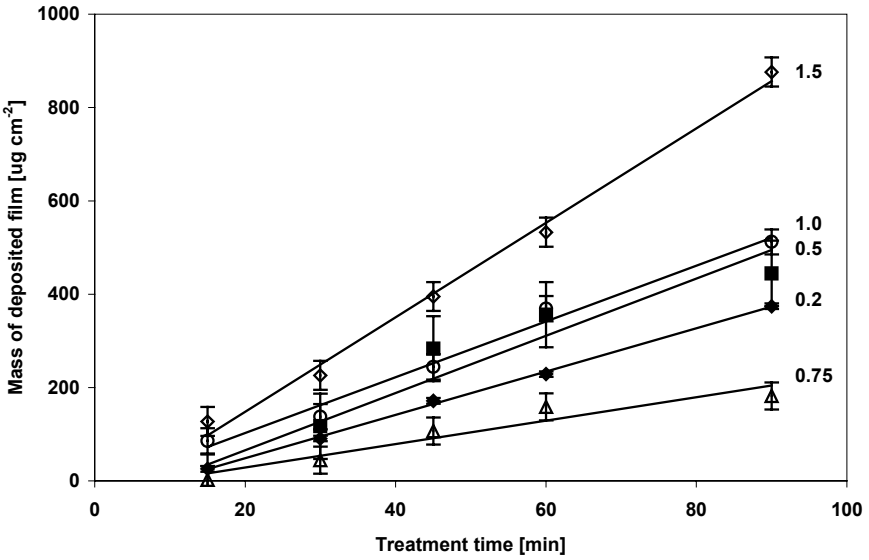

Fig. 1. Variation of the mass of deposited film on PC placed on the grounded electrode versus time of plasma treatment for discharge gap in range of 0.2-1.5 mm (thickness of PC – 0.75 mm, TEOS concentration – 220-320 ppm, O_2 concentration – 5%)

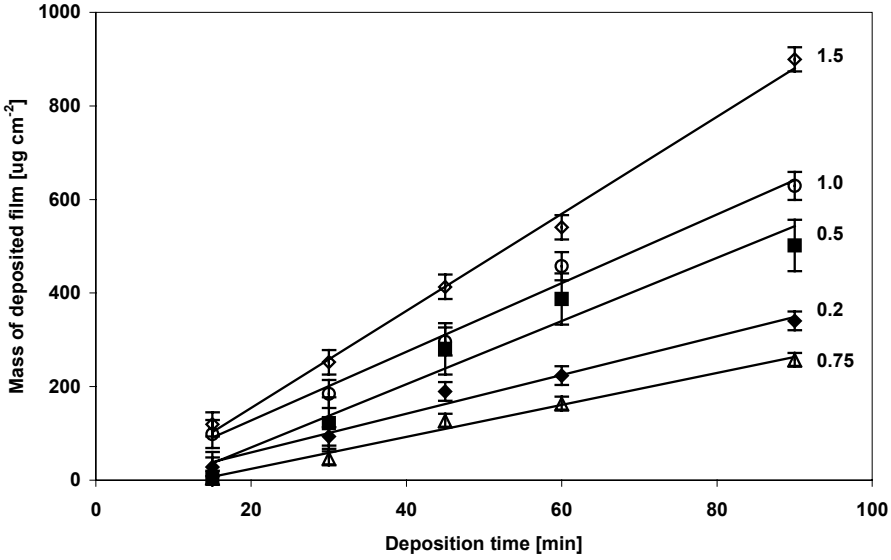

Fig. 2. Variation of the mass of deposited film on PC placed on the high-voltage electrode versus time of plasma treatment for discharge gap in range from of 0.2-1.5 mm (thickness of PC – 0.75 mm, TEOS concentration – 220-320 ppm, O_2 concentration – 5%)

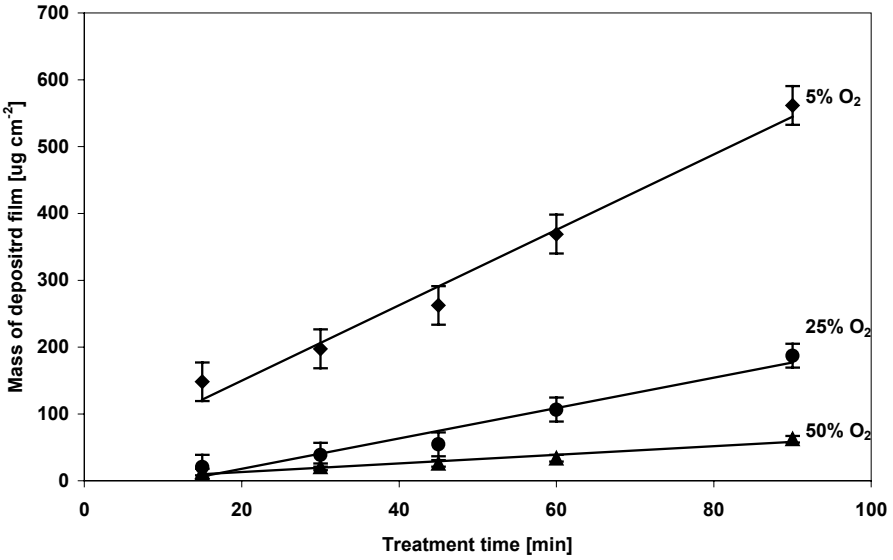

Fig. 3. Variation of the mass of deposited film on PC placed on the grounded electrode versus time of plasma treatment for O_2 concentration in range of 5-50% (thickness of PC – 0.75 mm, TEOS concentration – 230-250 ppm, discharge gap – 0.2 mm)

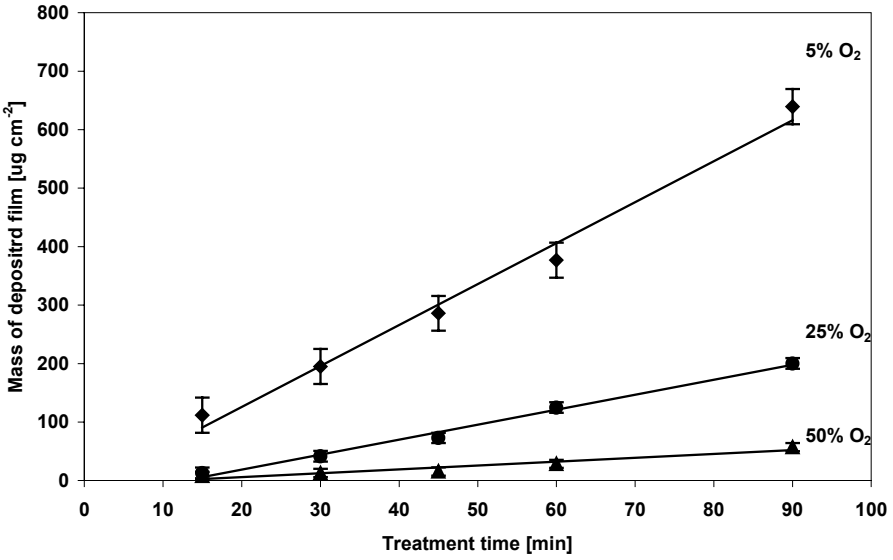

Fig. 4. Variation of the mass of deposited film on PC placed on the high-voltage electrode versus time of plasma treatment for O_2 concentration in range of 5-50 (thickness of PC – 0.75 mm, TEOS concentration – 230-250 ppm, discharge gap – 0.2 mm)

The deposition rates versus discharge gap are shown in **Fig. 5**. It was found, that two separately sets of the deposition rate was obtaining for two different ranges of discharge gap. The first set was form for the discharge gap in range of 0.2-0.5 mm and the second set was form for the discharge gap in range of 0.75-1.5 mm. This behavior was the same for PC placed on high-voltage electrode and PC placed on grounded electrode. The deposition rate increased from 4.6 to 6.1 μg cm^{-2} min^{-1} (grounded electrode) with increasing of discharge gap from 0.2 to 0.5 mm. Next the deposition rate decreased to 2.5 μg cm^{-2} min^{-1} (grounded electrode) when the discharge gap increased to 0.75 mm and the deposition rate again increased to 10.1 μg cm^{-2} min^{-1} (grounded electrode) with increasing of discharge gap to 1.5 mm (**Table II**). It was obvious, that the characteristics were similar for both sets of the deposition rate points and they regressions were almost parallel (**Fig. 5**).

This behavior could be possible to explain by change of character of PDBD. It was possible, that homogeneity of PDBD decreased while discharge gap changed from 0.2-0.5 to 0.75-1.5 mm. This problem has not been fully researches yet and it will be studied, but similar result was obtained in former work [8] while were compared the deposition rate obtained for different configuration of reactor. When the deposition process was carried out in reactor with single dielectric barrier (PC of 0.75 mm of thickness, discharge gap 0.75 mm) placed on grounded electrode the deposition rate was 40.8 nm min^{-1} and was much higher that the deposition rate (3.4 nm min^{-1}) obtained for reactor with double dielectric barriers (two PC, each of 0.75 mm of thickness placed on high-voltage and grounded electrodes, discharge gap 0.75 mm) [8].

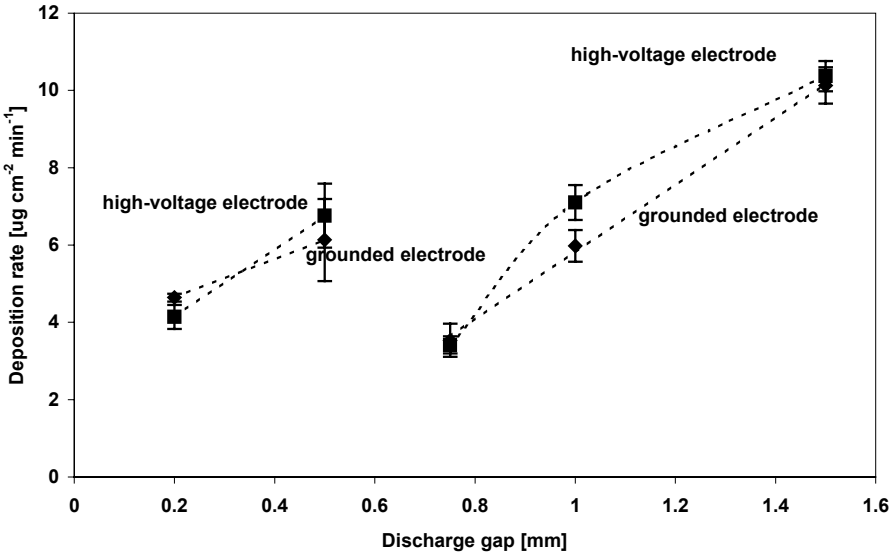

Fig. 5. The effect of the discharge gap on the deposition rate (thickness of PC plates – 0.75 mm, TEOS concentration – 220-320 ppm, O_2 concentration – 5%)

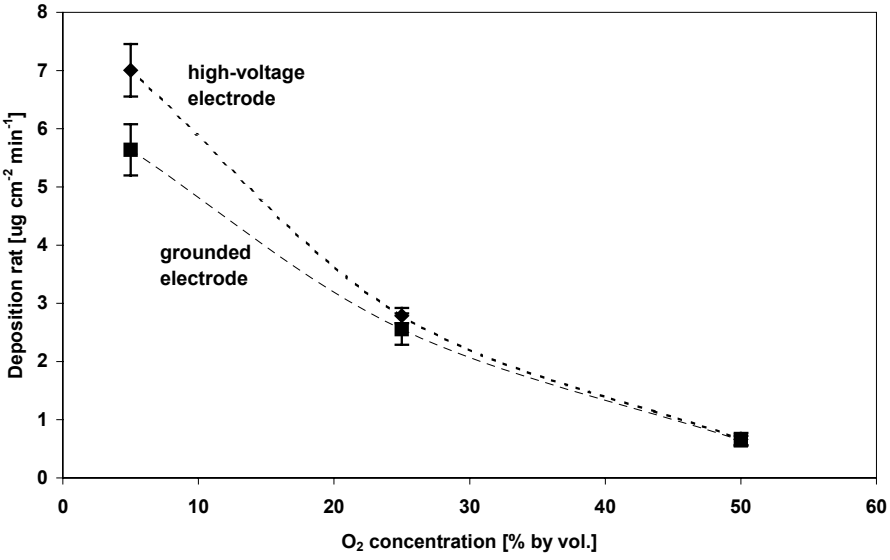

Fig. 6. The effect of the O_2 concentration on the deposition rate (thickness of PC plates – 0.75 mm, discharge gap – 0.2 mm, TEOS concentration – 230-250 ppm)

The deposition rates versus oxygen concentration were shown in **Fig. 6**. Oxygen and TEOS participated in the reaction of thin film forming [12], but the results demonstrated that high concentration of oxygen have negative effect on the deposition rate. The influence of O_2 concentration on the deposition rate was simple, the deposition rate decreased with increase the oxygen concentration in plasma-generating gas. This was in agreement with the results obtained under different conditions [7,13-15] and could be explained by increase

of the etching rate with increase of O_2 concentration in plasma-generating gas. For this reason, the gas composition, especially O_2 concentration, must be choose with care.

4. Conclusions

Pulsed dielectric barrier discharge (PDBD) is useful technique for thin organo-silicon film deposition on polycarbonate (PC) at the atmospheric pressure. The obtained results showed that:

1. The process of thin film deposition did not started immediately with plasma treatment of polymer material. Probably, before that process some, in the first period of plasma treatment, other processes, like etching or activation, take place.
2. The deposition rate of thin film on PC placed on high-voltage electrode, was faster than the deposition rate on PC placed on grounded electrode.
3. The deposition rate decreased with increase of the oxygen concentration in plasma-generating gas.
4. Two separately sets of the deposition rate was obtaining for two different ranges of discharge gap, 0.2-0.5 and 0.75-1.5 mm and the regressions of the two sets were almost parallel:
   - 4.1. The deposition rate increased from 4.6 to 6.1 $\mu g\ cm^{-2}\ min^{-1}$ (grounded electrode) with increasing the discharge gap from 0.2 to 0.5 mm.
   - 4.2. The deposition rate decreased from 6.1 to 2.5 $\mu g\ cm^{-2}\ min^{-1}$ (grounded electrode) with increasing the discharge gap from 0.5 to 0.75 mm.
   - 4.3. The deposition rate increased from 2.5 to 10.1 $\mu g\ cm^{-2}\ min^{-1}$ (grounded electrode) with increasing the discharge gap from 0.75 to 1.5 mm.

References

1. Special: Plastics Market; Plast Europe **10**, 110 (2001).
2. M. Wróbel, M. R. Wertheimer, Plasma Deposition, Treatment, and Ething of Polymers, edt. R. d'Agostino, Chapter 3, Academic Press Inc., San Diego, (1990).
3. Y. Hatanaka, K. Sano, T. Aoki, A. M. Wróbel, Thin Solid Films, **368**, 287 (2000).
4. J. Behnisch, J. Tyczkowski, M. Gazicki, I. Pela, A. Holländer, R. Ledzion, Surf. Coat. Technol., **98**, 872 (1998).
5. K. Schmidt-Szałowski, Z. Rżanek-Boroch, J. Sentek, Z. Rymuza, Z. Kusznierewicz, M. Misiak, Plasmas and Polymers, **5,** 173 (2000).
6. K. Schmidt-Szałowski, W. Fabianowska, Z. Rżanek-Boroch, J. Sentek, , J. Chem. Vap. Deposition, **6,** 183 (1998).
7. T. Opalińska, B. Ulejczyk, L. Karpiński, K. Schmidt-Szałowski, Pol. J. Chem. Technol., **4**, 30 (2002).
8. T. Opalińska, B. Ulejczyk, L. Karpiński, K. Schmidt-Szałowski, Proceedings Int. Symp. High Pressure Low Temperature Plasma Chemistry (HAKONE VIII), Puhajarve, Estonia, 425 (2000).
9. B. Ulejczyk, T. Opalińska, L. Karpiński, K. Schmidt-Szałowski, Acta Agrophysica, **80** 275 (2002).
10. C. Vallée, A. Goullet, A. Granier, A. van der Lee, J. Durand, C. Marlière, J. Non-Crys. Sol., **272,** 163 (2000).
11. R. Delsol, P Raynaud, Y. Segui, M. Latreche, L. Agres, L. Mage, Thin Solid Films, **289,** 170 (1996).
12. M. Wróbel, A. Walkiewicz-Pietrzykowska, S. Wickramanayaka, Y. Hatanaka, J. Electrochem. Soc., **145,** 2866 (1998).
13. A. M. Wróbel, M. Kryszewski, G. Czeremuszkin, Thin Solid Films, **289,** 112 (1996).
14. M.-R. Yang, K.-S. Chen, S.-T. Hsu, T.-Z. Wu, Surf. Coat. Technol., **123,** 204 (2000).
15. M. Shirai, S. Umeda, M. Tsunooka, T. Matsuo, Eur. Polym. J., **9,** 1295 (1998).

Effect of rf plasma treatment on polyethersulphone films for improvement of silicon films adhesion

M. Gheorghiu[1], I. Rusu[1], J.L. Sullivan[2], S.O.Sayed[2], G. Popa[1]

[1]*Plasma Physics Department, "A.I.Cuza" University, Iasi – 6600, ROMANIA*
[2]*Surface Science, Electronic Engineering, Aston University, Birmingham B4 7ET, UK*

Abstract
In this paper we report the results of the surface modifications of PES films induced by treatments in argon rf discharge, modifications which could improve the properties of adhesion. Our results of XPS analysis and contact angle measurements stood out the introduction of oxygen functionality in the PES surface by argon rf treatment. An increasing of the surface roughness with treatment time increasing, was found.

1. Introduction

Polyethersulphone (PES) has many properties that make it suitable for many applications as resists for microelectronics, heat-resistant materials in aerospace applications, polymeric membranes, matrices for composites, etc., More precisely polyethersulphone (PES) has many issues that are suitable for electronics, but not a very good adhesion with Si [1]. Hence, surface treatment of PES is expected to achieve good adhesion. Modification by exposure to cold plasmas (which only affect the uppermost layers) has been found to be one of the most reliable methods of improving adhesion.
In this paper we report the results of the surface modifications of PES films induced by treatments in argon rf discharge, modifications which could improve the properties of adhesion. The polymer surface modifications were investigated using X-ray photoelectron spectroscopy, contact angle methods and AFM measurements.

2. Experimental

Low pressure plasma surface modification experiments were carried out in an asymmetrical industrial OPT (Oxford Plasma Technology) Plasmalab 100 capacitively coupled system with the grounded electrode (including the chamber walls) area much larger than the driven electrode [2]. A matching network was used to match the impedance in order to maximise the energy transfer from the power supply to the plasma. The pressure was achieved automatically by measurement of the pressure via a capacitance manometer (CM) gauge and a pumping throttle valve.
The PES samples Good fellow 200 μ foils, were washed with methanol and dried with hot air before the treatment.
Argon of 99.095 % was used without further purification. No effort was made to dry the gas, because of the amount of residual water adsorbed on the surfaces of the reactor vessel, which could not be readily removed. The reactor was flooded with argon to a pressure of 1 Torr, for 5 min. prior to plasma treatment.
Typical treatment parameters were: Ar gas pressure between 100 mTorr and 400 mTorr, rf power 100 W, gas flow rate 10 sccm, treatment times between 1 min and 30 min. XPS and contact angle measurements were employed to characterise PES surface modifications.
XPS was performed in a VG ESCALAB 200D spectrometer with non-monochromatized MgKα radiation. The binding energy is determined by setting the aromatic carbon at 284.7 eV and shifting the complete spectrum accordingly. This is necessary due to charging of the non-conducting polymer samples. Survey spectra and high resolution spectra were taken with 50 eV and with 20 eV pass energy, respectively, in the constant analyser energy mode. The XPS peaks were analysed by means of a computer program incorporated in the VG Eclipes data system. Elements concentration was evaluated from peak area after Shirley background subtraction using the theoretical cross sections [3]. The XPS investigations were realised at two photoelectron take-off angles, about 0° and 70°, measured with respect to the sample normal. If the mean free path (λ) for the C 1s electrons is taken approximately 14 Å, the sampling depths ($3\lambda\cos\theta$, where θ is the take-off angle) for 0° and 70° are found to be 42 and 14.3 Å, respectively.
In terms of the Lifshitz-van der Waals-acid/base (LW-AB) model, Young's equation for the work of adhesion of a liquid to a solid surface W_a can be written [4]:

$$W_a = \gamma_l(1+\cos\theta) = 2\left[\left(\gamma_s^{LW}\gamma_l^{LW}\right)^{1/2} + \left(\gamma_s^{+}\gamma_l^{-}\right)^{1/2} + \left(\gamma_s^{-}\gamma_l^{+}\right)^{1/2}\right]$$

where γ^+ and γ^- note the contribution due to the electron acceptor (Lewis acid) and donor (Lewis base) part respectively, for solid (s) or liquid (l). The Lifshitz-van der Waals contribution to the solid surface energy γ_s^{LW} is obtained using a non-self-associating liquid with no acidic or basic character (i.e. a "neutral liquid") with the relation:

$$\gamma_s^{LW} = \left(\frac{\gamma_{probe}}{4}\right)\cdot\left(1+\cos\theta_{probe}\right)$$

where θ_{probe} and γ_{probe} are the contact angle and surface tension respectively for neutral liquid.

The AFM images were obtained using a Topometrix scanning probe microscope. Contact mode topographic images were recorded with a scan rate of 0.5 Hz.

3. Results and discussions

The XPS analysis for the untreated PES – sum formula $(C_{12}H_{12}O_3S)_n$ - showed three main peaks: O1s, C1s and S2p. In particular, the O1s peak can be resolved into a component at lower binding energy (531.31 eV) assigned to the oxygen present in SO_2 groups and a component at 532.89 eV assigned to the other type of oxygen binding (O-C). The ratio of the two components is slightly different from that expected (1.67:1 instead of 2:1). The C/S ratio (12.05:1) is in very good agreement with the theoretical composition of PES (12:1).

Untreated PES has an acidic component of the surface energy, $\gamma_l^+ = 10.2$ mN/m, much greater that the basic one $\gamma_l^- = 0.3$ mN/m and also a great dispersive or Lifshitz-van der Waals component $\gamma_l^{LW} = 43.1$ mN/m.

XPS analysis

In the literature one of the most striking feature for the PES treated in Ar-plasma is the reduction of the oxygen content, mainly by the reduction of the sulphonic ($-SO_2-$) to sulphide (-S-) groups [5]. Such reduction is very important especially at very low pressure ($<10^{-3}$ Torr). Treatment of PES with keV Ar atoms also stood out a strongly decreasing in oxygen content [6]. In both mentioned studies, the XPS surface analyses of the treated samples were performed without contamination from the atmospheric contact.

Both exposure to the laboratory atmosphere and some oxygen-containing plasma species are thought to be responsible for oxygen functionalisation in our experiments.

Results about XPS analysis made one day after the treatment are presented in this section. Both types of treatment, at 100 mTorr and at 400 mTorr, show the diminishing of C%, increasing of O% and slightly diminishing of S% (Figs. 1 and 2). The most important changes in the total atomic percentages of carbon, oxygen and sulphur are realized in the first 10 minutes of treatment. A saturation trend is stood out for longer exposure times for both treatment pressures.

Generally, the total oxygen content is similar in the outermost and in the deep surface layers, which shows that the thickness of the oxide surface layer is greater that the XPS analysis depth.

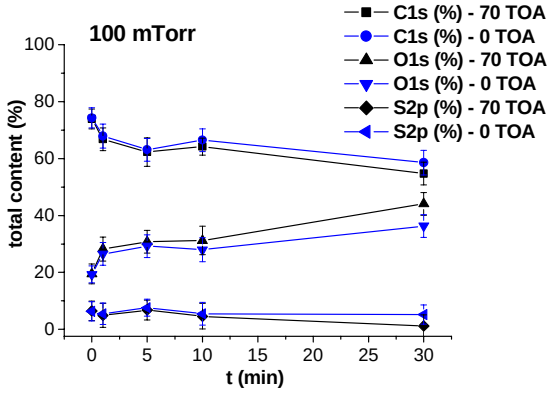

Fig. 1

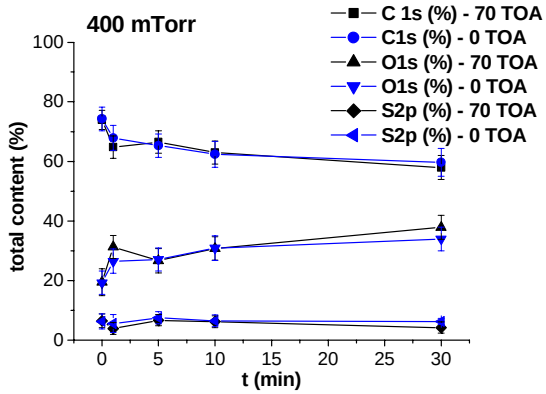

Fig. 2

For all investigated plasma conditions the C1s trend vs. time is guided by the ArC (284.7 eV) peak decreasing. At 100 mTorr, on the polymer surface (TOA = 70º) the C-S (285.0 eV) peak is increasing with the treatment time, and the C-O peak (286.3 eV) is slightly decreasing. In the polymer depth (TOA = 0º), both C-S and C-O peaks are decreasing (Figs 3 and 5). At 400 mTorr and 70º TOA the contribution of C-S and C-O peaks trend to be equal for longer exposure times. The XPS analysis at 0º TOA show that the C-O peak is more important than C-S (Fig.5).

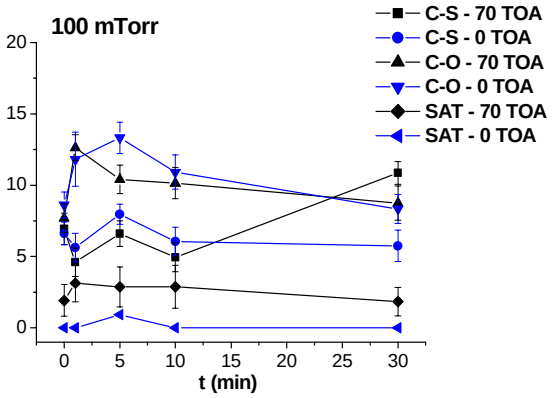

Fig. 3

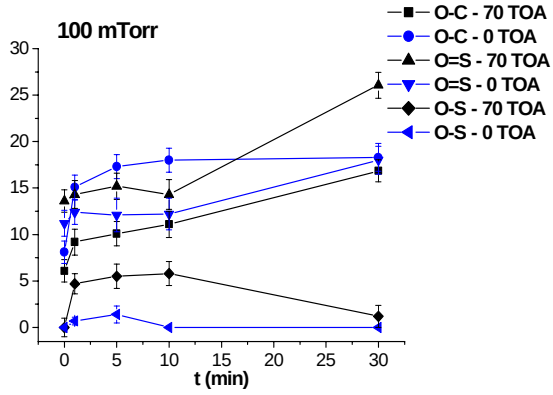

Fig. 4

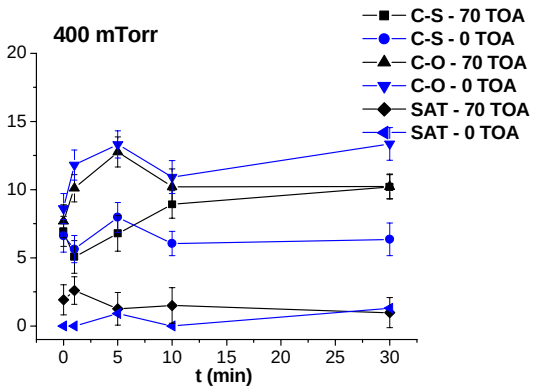

Fig. 5

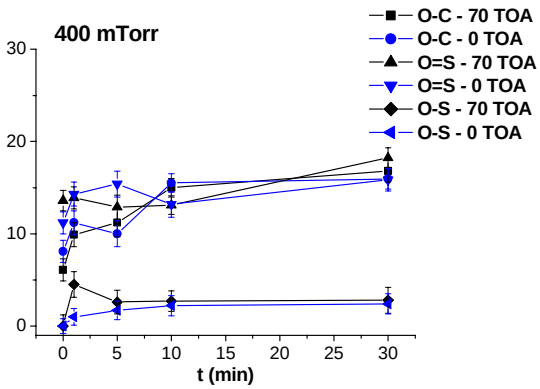

Fig. 6

The total O1s peak is increasing for all investigated plasma conditions (Fig. 1 and 2). At 100 mTorr, we found an increasing of the O=S and O-C peaks for longer exposure time. On the surface (TOA = 70º) the O=S is the most important peak, whilst in polymer depth (TOA = 0º) the contribution of the O-C is bigger (Fig.4). Increasing the treatment time, at 400 mTorr, the O=S peak is almost constant and O-C peak is slightly increasing (Fig. 6).

Surface energy data

The surface free energy components were determined by sessile drop technique. The reported values are the average over at least ten measurements performed in different areas of the sample surface, the typical dispersity of the values being ±2°. The values for the surface energy components of the liquids used in this study, in mN/m, are given in Table 1.

	γ_l^{LW}	γ_l^+	γ_l^-	γ_l
water	21.7	25.5	25.5	72.8
formamide	32.0	3.0	22.4	57.4
α-bromonaphthalene	44.8	0		44.8

Table 1

Surface energy data collected one day after the treatment will be presented in order to compare with XPS data.

Treatments in Ar discharges do not appreciable modify γ_s^{LW} component, a medium value of 44.5 mN/m being obtained for treated PES.

Acid/base component $\gamma_s^{ab} = \gamma_s^+ + \gamma_s^-$ versus treatment time and type is presented in Fig. 7. There is a very good concordance between the change the O_{total} component (Figs. 1 and 2) with treatment time and γ_s^{ab}, for both investigated pressures. The direct correlation between oxygen component and γ_s^{ab} means that the few outermost layers, which directly influence the γ_s^{ab} value, have the same oxygen component as the depth layers. These results confirm the depth dependence of oxygen functionality, obvious from XPS data.

Acid γ_s^+ and base γ_s^- components increase for both pressures and treatment types (as comparing with values for untreated PES), but more important is the increase in γ_s^+ (Fig. 8). Only one minute of treatment is necessary to increase γ_s^+ from 10.2 mN/m to 30-38 mN/m and γ_s^- from 0.3 mN/m to 5-6 mN/m. For longer exposure times either γ_s^+ and γ_s^- do not appreciable change or they decrease slightly.

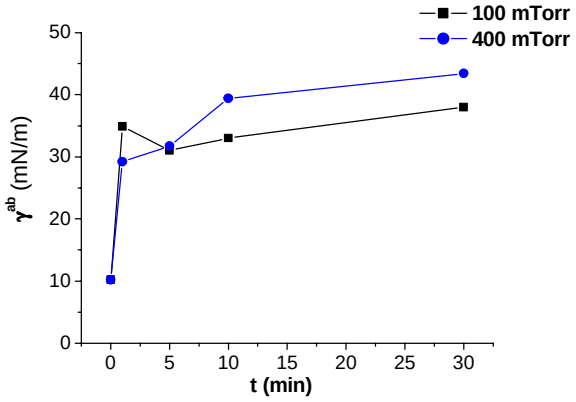

Fig. 7

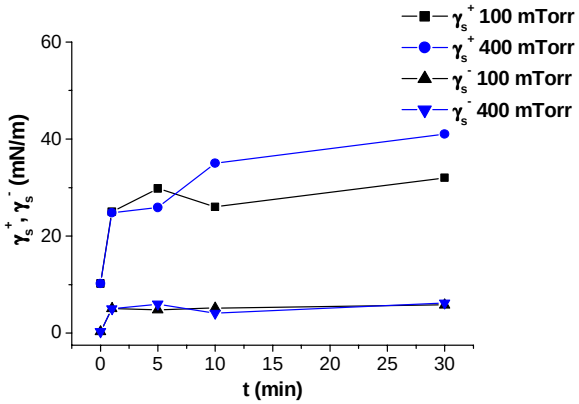

Fig.8

Ageing effects

Surface energy measurements, for all treated PES samples were collected immediately and after 1 day, 3 days, 5 days and 7 days from the treatment. The γ_s^{LW} component remains almost unchanged during the investigated ageing period.

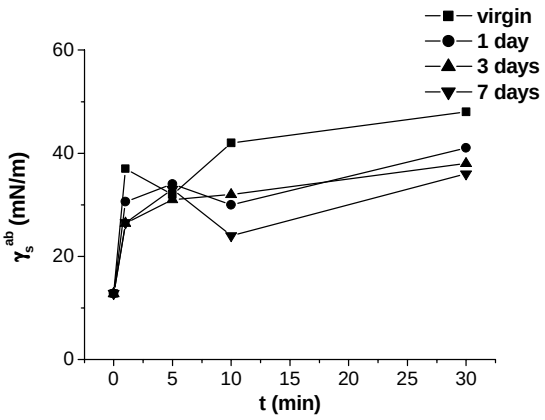

Fig.9

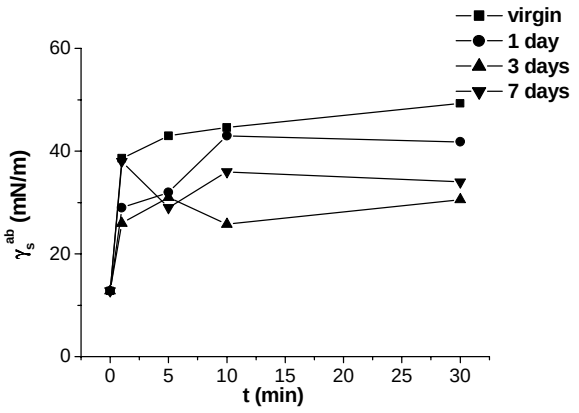

Fig. 10

The change in γ_s^{ab} with the ageing time, for PES samples treated at 100 mTorr and 400 mTorr are illustrated in Figs. 9 and 10 respectively. Besides the expected behaviour, namely a more or less decreasing of γ_s^{ab} with the ageing time, an unexpected feature is also evident, especially for PES samples treated at 400 mTorr. After an initial decrease, γ_s^{ab} increases at various ageing times, this increase being appreciable for some samples. The transient increase in γ_s^{ab} could be also present for the other Ar-treated PES samples, but for longer ageing times.

Behaviour such as this has also been observed for other polymers PET treated with low energy oxygen ions [7]. Generally γ_s^+ decreases and γ_s^- increases with the ageing time, as comparing with values measured immediately after the treatment. More information about the contribution of each process in the ageing effects were obtained from XPS data. The obvious similarity of the development with the ageing time of γ_S^{ab} and O_{total} (%) for these samples (Fig. 11) sustain the fact that migration of the small fragments from the surface is the main process involved in the surface reorganisation.

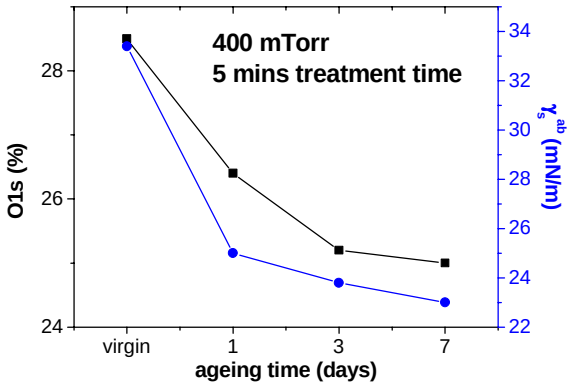

Fig. 11

AFM results

Increasing the treatment time, we found an increasing of the surface roughness, especially for 100 mTorr (Figs. 12, 13, 14.)

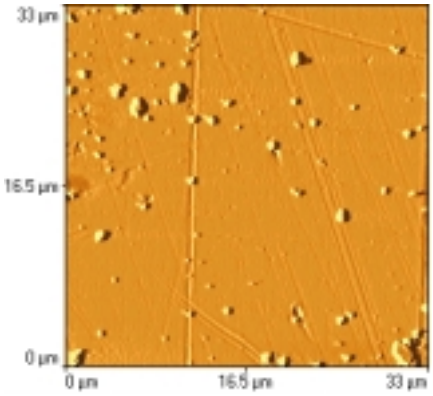

Fig. 12 AFM image for untreated PES

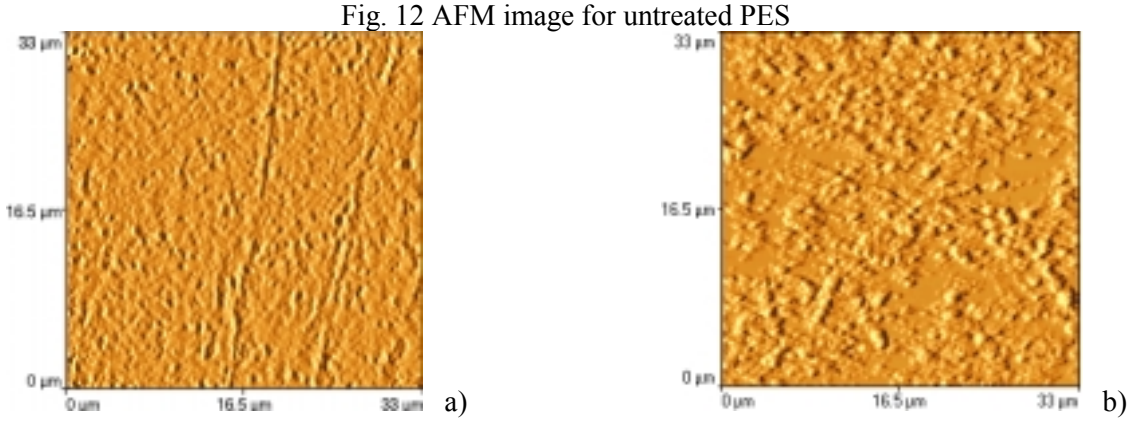

a) b)

Fig. 13. AFM images for PES at 100 mtorr and 10 min(a) and 30 min (b) treatment time

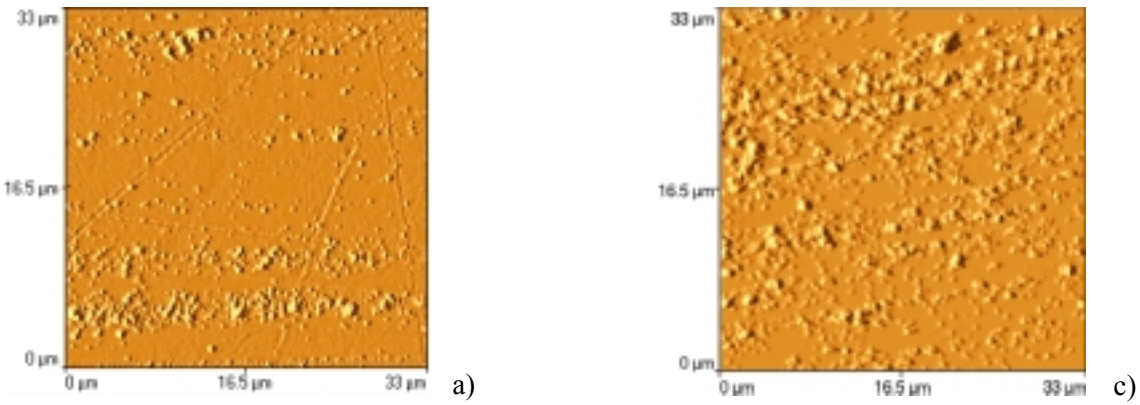

a) c)

Fig. 14. AFM images for PES at 400 mtorr and 10 min(a) and 30 min (b) treatment time

Conclusions

We found in the literature that at very low pressure (<10^{-3} Torr) one of the most important feature for the PES treated in Ar-plasma is the reduction of the oxygen content, mainly by the reduction of the sulphonic (-SO_2-) to sulphide (-S-) groups [5]. Treatment of PES with keV Ar atoms also stood out a dramatically decreasing in oxygen content [6]. In both mentioned studies, the XPS surface analyses of the treated samples were performed without contamination from the atmospheric contact.

Our results of XPS analysis stood out the introduction of oxygen functionalities in the PES surface by argon rf treatment. The oxygen component is higher, higher the pressure.

More oxygen functionalities are introduced in PES film treated at the same treatment time, at 400 mTorr, for all investigated treatment times.

The oxidation rate is increasing more quikly in the first minute of the treatment for both work pressures. For the treatments at 100 mTorr, the oxidation rate is increasing especially due to the O=S=O group increasing. At 400 mTorr both oxygen peaks, O=S=O and O-C, are increasing in the same manner.

The total C content is decreasing for all investigated plasma conditions, especially due to the ArC peak decreasing.

Surface energy data collected one day after the treatment were compared with the XPS results.

Treatments in Ar discharges do not appreciable modify γ_s^{LW} component, a medium value of 44.5 mN/m being obtained for treated PES. Direct correlation between oxygen component and γ_S^{ab} is obvious for both investigated pressures. he direct correlation between oxygen component and γ_s^{ab} means that the few outermost layers, which directly influence the γ_s^{ab} value, have the same oxygen component as the depth layers. These results confirm the depth dependence of oxygen functionality, obvious from XPS data.

Both acid and base components are increased whatever the pressure and treatment type, but the increase in γ_S^+ is more important. The more or less decreasing of γ_S^{ab} with the ageing time is evidentiated for most of treated PES samples; for some of them a transient increase in γ_S^{ab}, at different ageing time, is observed.

Acknowledgements

The experiments were performed in Surface Science Laboratory, Aston University, Birmingham, UK. The authors would like to thank Mr. A. Abbot and all members of the laboratory for their collaboration during experiments.

References (Times 11, bold)

[1] N.D. Young, G. Harkin, R.M. Bunn, D.J. McCulloch, – IEEE Trans. Electron. Dev. **11**, 1930 (1996)
[2] I.A.Rusu, G. Popa, J.L.Sullivan – J. of Phys. D: Appl. Phys. **35**, 2808 - 2814 (2002)
[3] G. Beamson and D. Briggs, - in "High Resolution XPS of Organic Polymers", John Wiley, New York, 1992.
[4] D. T. Clark and H. R. Thomas, *J. Polym. Sci., Polym. Chem. Ed.* **15**, 2843 (1977)
[5] P. Gröning, M. Collaud, O. M. Küttel and L. Schlapbach, *Appl. Surf. Sci*. **103**, 79 (1996)
[6] G. Marletta and F. Iacoma, *Nucl. Instr. And Meth*. **B 116**, 246(1996)
[7] M. Gheorghiu, M. Pascu, G.Popa and C. Vasile, *Inter. J. Polymeric Mater*. **40** (1998) 257

Deposition of thick diamond-like nanostructured coatings by Plasma Enhanced CVD

S. Thollon, M. Plissonier, N. Scheer, C. Cayron, A. Ruchier [1]

[1] *CEA Grenoble, Département des Technologies des Energies Nouvelles, 17 rue des Martyrs, 38054 GRENOBLE cedex, France*

Abstract
Thick multilayer coatings consisting of a stack of Diamond Like Carbon nanolayers alternated with Hydrogenated Silicon doped carbon nanolayers were developped by a Low Frequency PECVD computer-controlled technology (50-100 kHz), which can be easily scaled up from the laboratory to the industrial scale. Comparing to traditionnally high compressive stressed DLC coatings, this specific architecture consisting of dense and amorphous stacked nanolayers with a total thickness up to 10 µm leads to lower internal stresses, better adhesion and very good mechanical and tribological properties in dry and humid conditions, enabling promising industrial applications in various fields.

1. Introduction

Hydrogenated or non-Hydrogenated Diamond-like carbon (DLC) films have been the subject of intensive technological research since they exhibit many attractive properties : high hardness and wear resistance, low friction coefficient (<0.15 in air), chemical interness, IR optical transparency, high thermal and low electrical conductivities [1-4]. Owing to these properties, DLC films are suitable for a wide range of applications such as protective coatings for mechanical, optical, biomedical or electronic applications. However, DLC coatings exhibit drawbacks. Some applications may be limited by the high internal compressive stress (usually several GPa) [5-7] mainly induced by the ionic bombardment during deposition process and by the significant increase of the friction coefficient as the environmental humidity increases.
Consequently, alternative coatings for widening technical application fields have been developed. It was commonly assumed that alloying element such as Si improves tribological properties (friction and wear) under humid atmosphere and reduces internal stresses, enhancing better coating adhesion strength [8,9]. Still with the aim to enhance adhesion and reduce the level of compressive stress in these films, there has been recently interest in the development of amorphous diamond-like nanocomposites coatings (DLN), consisting of atomic-scale composite random networks of carbon (a-C:H) and silicon (a-Si:O) with mininal bonding between them [10, 11] and in the deposition of thick multilayer coatings being an alternation of wear resistant DLC layers and stress relieving DLN films [12]. Such Diamond-like carbon based structures have been synthesized through RF or DC Plasma Enhanded CVD combined with a heated filament [10**,** 12] and PVD (ion-beam assisted deposition) [13].
These developments have shown very promising applicability of such materials where abrasive wear mechanisms become predominants. For such specific industrial applications, thick coatings (up to 12 µm) combining high hardness and low friction coefficient in dry and humid conditions have been developed. In this paper, first results concerning the deposition and characterization of the as-deposited multilayer coatings consisting of a stack of Diamond Like Carbon nanolayers alternated with Hydrogenated Silicon doped carbon nanolayers obtained by Low Frequency Plasma Enhanced CVD technique in a pilot scale reactor are reported.

2. Experimental details

The experimental apparatus used is schematically reported in figure 1. The deposition process was carried out in a stainless steel reactor with a capacitively coupled electrode configuration and a 5 cm inter electrode gap. The lower electrode serving as substrate holder is powered via a 100kHz LF transmitter. The pressure was monitored using a capacitance manometer (MKS Baratron) and the deposition chamber was pumped down with a rotary pump and a roots with volume flow rates of 80

and 1200 $m^3.h^{-1}$, respectively. A base pressure of 0,1 Pa is reached with the reactor set-up used. Cyclohexane in hydrogen and tetra methylsilane in argon were respectively used for C:H and SiC:H deposition. Both monomers were evaporated at 30°C under reduced pressure, supplied through mass flow controllers into the upper electrode and diffused downward from nozzles onto the lower electrode. A thin bond layer of SiC:H was deposited between the thick multilayer coatings and the substrate in order to promote adhesion. The multilayer deposition was performed with Diamond Like carbon nanolayers alternated with hydrogenated silicon carbide nanolayers and a final Diamond like carbon coating approximately 1 µm thick. Thickness and periodicity of nanolayers were modified in order to keep a total thickness constant at about 12µm. During processing, reactor's devices were automatically controlled with a computer.

Diamond-like nanostructured coatings were deposited on <110> oriented silicon to perform the microstructural characterization and on steel substrate (HS 6.5.4.2) in order to investigate mechanical and tribological behaviour. Cross sections of the multilayer structure were examined by Transmission Electron Microscopy (TEM) on a Jeol 2000FX microscope (200 kV). The elementary depth profiles in the multilayered structure were investigated by means of Dynamic Secondary Ion Mass Spectrometry (DSIMS) using a radio frequency quadrapole detector and a liquid metal source Ga^+. The samples were depth profiled under ultra high vacuum with positive ions for Silicon, Carbon, Hydrogen elements. The erosion speed was fixed quite low in order to achieve an excellent depth resolution.

Wear and friction properties were evaluated using a conventional ball-on-disk apparatus with control of the relative humidity. The unlubrificated sliding experiments were performed at room temperature, applying a normal load of 5 N on a 1.58mm alumina bearing ball and a sliding speed of 0.17 $m.s^{-1}$. The wear volume of the wear track was then evaluated from profilometry measurements.

A Nanoindenter CSEM apparatus with a Vickers diamond tip was used to measure hardness (H) and Elastic modulus (E) values. The continuous stiffness option was used, the maximun depth was fixed at 200 nm, the loading and unloading rates at 10 mN/min. The H and E values were calculated from the indentation load-displacement data [14].

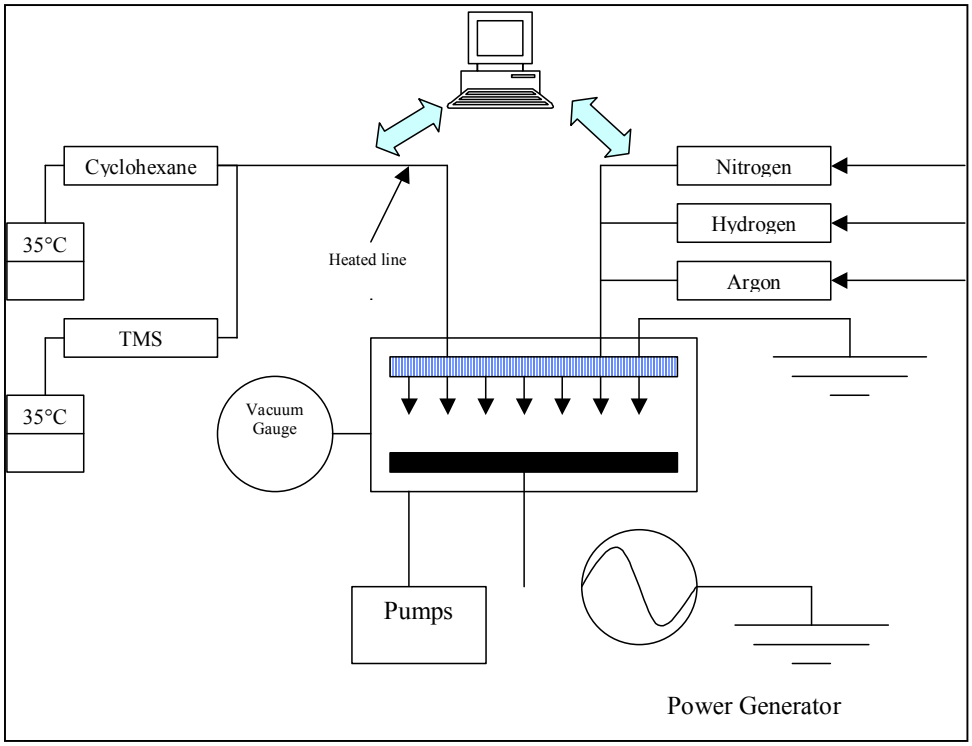

Figure 1 : schematic representation of the LF-PECVD computer-controlled reactor

3. Results

	SiC:H Base layer	**Multilayer Structure** (number of layers, elementary thicknesses)	DLC top layer
Sample A	225 nm	**240 layers** (120 periods): $e_{SiC:H}$= 45nm, e_{DLC}=110nm	1 µm
Sample B	195 nm	**980 layers** (490 periods): $e_{SiC:H}$= 5nm, e_{DLC}=15nm	1 µm

Table 1 : Experimental details on the multilayer coating architecture.

In table 1 are reported details on the diamond-like nanostructured coating architecture.
Cross sectional Transmission Electron Microscopy images of two PECVD diamond-like nanostructured coatings, samples A and B (see table 1) clearly revealed the multilayer microstructure of the films (figures 2 and 3) : *i.e.* the stack of Diamond Like Carbon (DLC) nanolayers alternated with Hydrogenated Silicon doped carbon (SiC:H) nanolayers, with a glassy underlying layer of SiC:H. Selected Area Diffraction patterns showed the amorphous nature of the stacked DLC and SiC:H nanolayers. Nanolayers elementary thicknesses were estimated within 5 to 50 nm and 10 to 150 nm for SiC:H and DLC respectively, depending on the process conditions.

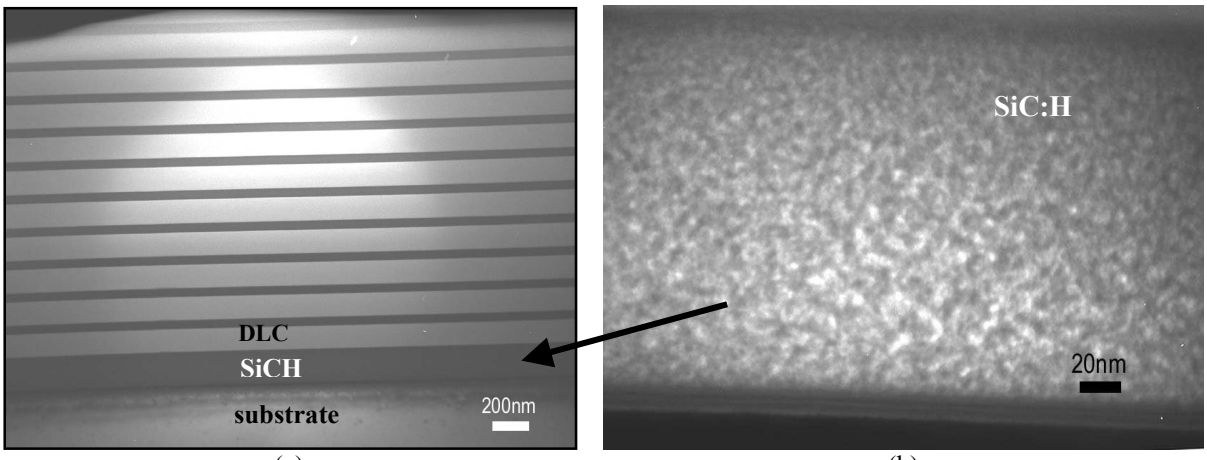

(a) (b)

Figure 2 : Cross-sectional TEM images of sample A near the substrate interface (a) global view of the first SiC:H and DLC nanolayers, (b) SiC:H base layer.

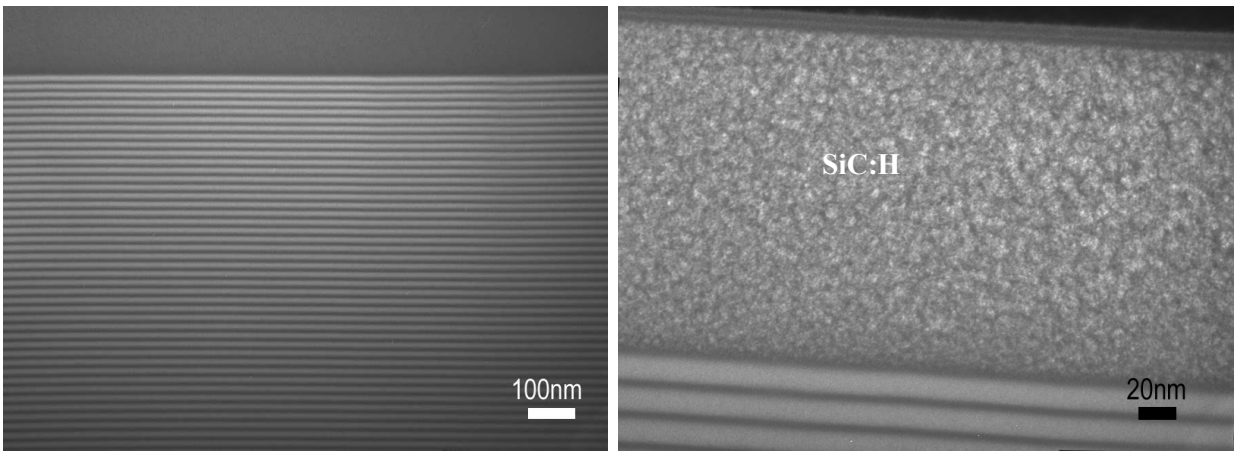

Figure 3 : Cross-sectional TEM images of sample B near the substrate interface (a) global view of the first SiCH and DLC nanolayers, (b) SiCH base layer.

The microstructural integrity of this structure was demonstrated since no defects were observed within nanolayers and at interfaces. Furthermore, the nanolayers appeared to be very dense, homogeneous and well bonded to the substrate and to each other. The observed microstructure and the sharpness of the interfaces clearly tends to point out that this process is readily controlled by surface reaction

kinetics, *i.e.* the rate limiting step is strongly dependent on the amout of reactant gases available. This point is very significant since, by proper manipulation of the process parameters, it is possible to control the reaction and deposition rate to a great degree, insuring very good step-coverage characteristics even on complex shaped pieces.

The repeatability of the investigated LF-PECVD process within time was confirmed by SIMS investigations. On figure 4 is presented the SIMS depth profiles of sample B in positive ions ($^{1}H^{+}$, $^{12}C^{+}$, $^{16}O^{+}$, $^{28}SiC+$) from the top layer surface up to the hundredth layer of the multilayer structure obtained with a slow erosion speed. This profile presents a depth resolution not even shaded off after the 80th layer. This analysis confirms the TEM observations that the stacking of the nanolayers is reliable and perfectly repeatable in time.

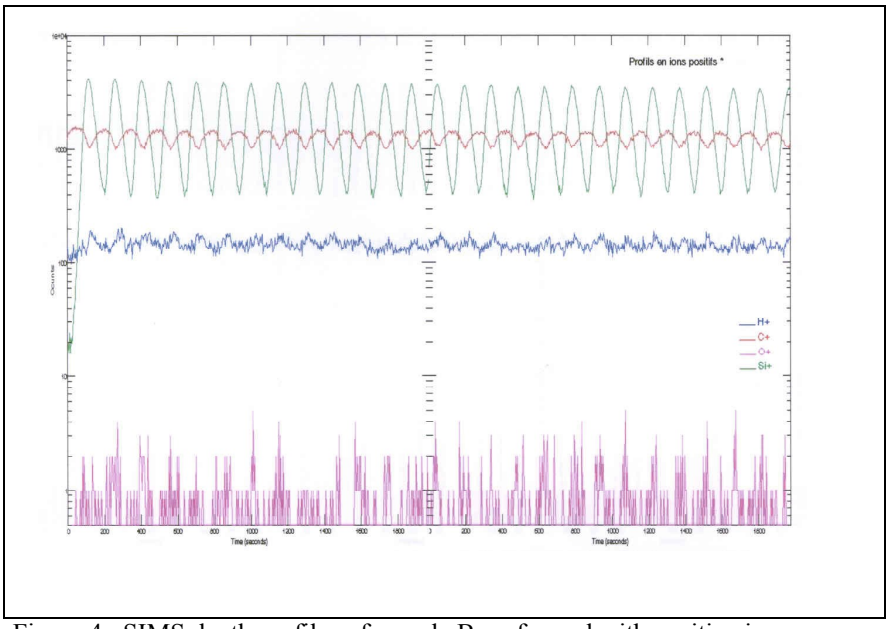

Figure 4 : SIMS depth profiles of sample B performed with positive ions

The results of the different mechanical tests performed on the diamond-like nanostructured coatings (samples A and B) are summarized in the following table, where μ is the friction coefficient and V_w the wear volume.

	Tribological test		Nanoindentation test	
Atmosphere	**Dry**	**Wet**	**H (MPa)**	**E (GPa)**
DLC : reference	μ=0.063 V_w= 4.10^{-8} mm^3.N^{-1}.m^{-1}	μ=0.122 V_w= 2.10^{-5} mm^3.N^{-1}.m^{-1}	21000	190
Sample A	μ=0.053 V_w= 2.10^{-6} mm^3.N^{-1}.m^{-1}	μ=0.094 V_w= 7.10^{-7} mm^3.N^{-1}.m^{-1}	20000	180
Sample B	μ=0.038 V_w= 8.10^{-6} mm^3.N^{-1}.m^{-1}	μ=0.088 V_w= 5.10^{-7} mm^3.N^{-1}.m^{-1}	18000	140

Table 2 : mechanical and tribological properties of the as-deposited multilayer coatings

As shown in figure 5, even with the incorporation of silicon into the stacking network within the SiC:H nanolayers, the multilayer structure exhibit a linear friction behaviour, consistent with that of DLC coatings deposited in a RF-PECVD coating system [15]. An improvement of the tribological properties under humidity was clearly achieved with the silicon doping in the nanolayered structure (table 2) : the friction coefficient of the multilayer structure has been shown to remain below 0.1 even at relative humidity levels of 99%. In the case of the DLC film, the friction coefficient increased significantly under water, up to 0.122. In the case of tribological tests performed under high humidity rate, large fluctuations of the friction coefficient values were recorded. These variations may be due to

the debris trapped and recycled in and out of the transfer layer formed during sliding contact. This mechanism has been already pointed out with silicon containing coatings [16].
The wear volumes obtained by profilometry measurements of the cross-sectional areas of the wear tracks are listed in table 2. The hardness values of the as-deposited multilayer coatings were found to range from 18000 to 20000 MPa and elastic moduli values from 140 to 180 GPa from Nanoindentation test. The general trend is that wear volume decreases as hardness value increases ; similar behaviour was noticed by Kester *et al.* in sliding wear behaviour tests of diamond-like nanocomposites coatings worn by WC balls [10]. Thus, the hardness of the as-deposited LF-PECVD multilayer structure is lower than the standard hardness of DLC but the mechanical properties of these stackings combine good microhardness with elasticity and low friction under dry and wet atmopheres. The lower hardness level could be explained by the "dilution"effect of diamond-like properties in the carbon network with the presence of the Silicon element.

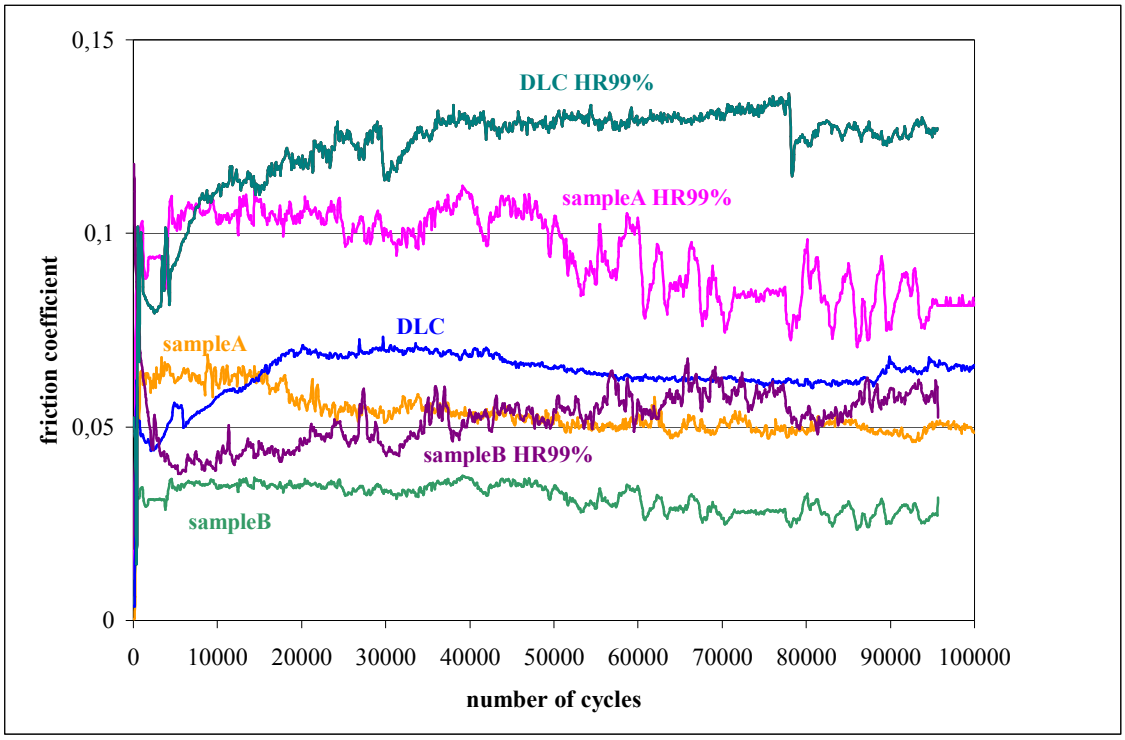

Figure 5 : evolution of the friction coefficient of the as-deposited materials (see table 2) as a function of cycles number : under dry atmosphere and with humidity rate (HR) of 99%.

3. Conclusion

Thick multilayer film consisting of several hundreds of Diamond-Like carbon nanolayers alternated with hydrogenated silicon carbide nanolayers were deposited in a LF-PECVD computer controlled reactor. Thickness and periodicity of nanolayers have been sucessfully controlled by proper manipulation of the process parameters and, thus, we demonstrated that this process is reliable and repeatable. Furthermore; this study performed in a Low Frequency pilot-scale reactor can be scaled up relatively easily from the laboratory to the industrial scale, enabling promising industrial applications.
It has been shown that silicon incorporation is favourable to the tribological properties in humid atmosphere : in fact, the friction coefficient of the multilayer structure remains below 0.1 even at relative humidity levels of 99%.
Further work with these nanostructured coating is in progress, especially with respect to the mechanical and tribological behaviour.

References

[1] H. Dimiden, H. Hübsch, R. Memming, Appl. Phys. Lett., 50 (1987) 1056.
[2] J. Robertson, Surf. Coat. Technol., 50 (1992) 185
[3] J.W. Zou, K. Schmidt, K. Reichelt, B. Dischler, J. Appl. Phys., 67 (1990) 487
[4] A. Grill, Surf. Coat. Technol., 94/95 (1997) 507
[5] D. Nir, Thin Solid Films, 146 (1987) 27
[6] E. Enke, Thin Solid Films, 80 (1981) 227
[7] X.L. Peng, T.W. Clyne, Diamond and Related Materials, 7 (1998) 944-950
[8] K.R. Lee, M.G. Kim, S.J. Cho, K.Y. Eun, T.Y. Seong, Thin Solid Films, 308-309 (1997) 263
[9] C. Donnet, Surf. Coat. Technol., 100-101 (1998) 180
[10] D.J. Kester, C.L. Brodbeck, I.L. Singer, A. Kyriakopoulos, Surf. Coat. Technol., 113 (1999) 268
[11] V.F. Dorfman, Thin Solid Films, 212 (1992) 267
[12] E. Dekempeneer, K. Van Acker, K. Vercammen, J. Meneve, D. Neerinck, S. Eufinger, W. Pappaert, M. Sercu, J. Smeets, Surf. Coat. Technol., 142-144 (2001) 669
[13] X.Z. Ding, F.M. Zhang, X.H. Liu, P.W. Wang, W.G. Durrer, W.Y. Cheung, S.P. Wong, I.H. Wilson, Thin Solid Films, 346 (1999) 82
[14] W.C. Oliver, G.M. Pharr, J. Mater. Res., 7 (1992) 1564
[15] R.S. Bonetti, M. Tobler, Matériaux techniques, Printemps 1992, 41
[16] K. Oguri, T. Arai, J. Mater. Res., 7 (1992) 1313

Particle-in-cell/Monte Carlo simulation of cc rf $Ar/CF_4/N_2$ discharges

V. Georgieva, A. Bogaerts and R. Gijbels

Department of Chemistry, University of Antwerp (UIA), B-2610 Antwerp, Belgium

Abstract
A one-dimensional particle-in-cell/Monte Carlo model is developed to study capacitively coupled radio-frequency discharges in a gas mixture of Ar, CF_4, and N_2. The calculation is performed for a 0.8/0.1/0.1 ratio of $Ar/CF_4/N_2$ mixture at a pressure of 30 mTorr in a dual frequency (2+27 MHz) reactor. Results show that the structure of the discharge is electronegative and CF_3^- ions are the main negative carriers. The IEDF is wide and bimodal. The EEPF has a bi-Maxwellian profile with a high energy tail.

1. Introduction

Radio-frequency (rf) plasma etching is well recognized for its anisotropy, which is a critical process parameter in integrated circuit (IC) manufacture. Conventional capacitively coupled (cc) reactors powered by 13.56 MHz rf sources meet many plasma processing requirements. However, the scaling evolution of semiconductor devices needs more and more accurate transfer patterns with minimum damages on the substrate, which can be achieved by precise control of both the ion bombardment energy and the ion flux. Single frequency systems face difficulties providing an independent control of ion energy. For that reason dual-frequency systems have been introduced and studied [1-3]. The dual rf excitation scheme allows the plasma density to be determined by one high-frequency (HF) source, while the substrate self-bias voltage can be controlled by the secondary low-frequency (LF) source. In addition, the LF-HF scheme provides a significantly wider ion bombardment energy range in comparison with a single HF configuration.

Plasma chemical issues are as much important in further optimization of etching processes as plasma processing units. Feedgas mixes are usually complex because of the conflicting requirements on the etch rate, selectivity to mask, and anisotropy. Carbon tetrafluoride CF_4 is a basic component in gas mixtures for plasma etching of silicon and silicon dioxide, and therefore is the most well-studied etch system [4-6]. While the investigation of pure CF_4 discharges gives the pattern for describing plasma etching, the study of discharges in a mixture of Ar and CF_4, which is a representative feedstock gas, provides insight into the process. In our previous paper we presented a one-dimensional particle-in-cell/Monte Carlo (PIC/MC) model and clarified the plasma structure and parameters in electropositive Ar, in electronegative CF_4, and in Ar/CF_4 discharges at different ratios [7]. A rapid decrease in electron density is observed with the addition of even a small amount of CF_4 to Ar, i.e. the dominant negative carriers are the negative ions, which profoundly influence the sheath dynamics. In the present paper the model is extended to examine the discharge structure in a mixture of Ar, CF_4 and N_2, which is a feedstock gas for etching in a cc dual-frequency rf reactor.

A PIC simulation treats the charged particles in a kinetic way. It is attractive because the fields and the energy distributions are obtained self-consistently from first principles. The collisions between the charged particles are added by combining the PIC model with a MC procedure. In case of modeling of electronegative discharges the major disadvantage of this method is that it requires a long computational time to reach convergence. The negative charges are confined in the bulk plasma and the only loss mechanism, i.e., ion-ion recombination, has a relatively low reaction frequency. Kawamura *et al*. point out many physical and numerical methods of speeding up the PIC calculations [8]. Some of the methods, such as longer ion time steps, different weights for electrons and ions and improved initial density profiles, are applied in this simulation. In Sec. 2 the input parameters, the outline of the model, and the collisions included in the simulation are given. In Sec. 3 the results of the simulation, such as the electric field, charged particle densities, and energy distributions, are presented and discussed. Finally, in Sec. 4 a summary is given.

2. Description of the model

A schematic diagram of the cc rf reactor considered in this study is shown in Fig.1. The plasma is sustained between two parallel plates, each 20 cm in diameter and separated from the other by 2 cm. One of the electrodes is driven by a dual frequency (2+27 MHz) power supply. The amplitude of the applied voltage is 700V. The other electrode is grounded. The simulation is carried out at a pressure of 30 mTorr. It should, however, be mentioned that the model presented here can be applied to other operating conditions. The

computation is based on a one-dimensional coordinate space and three-dimensional velocity space PIC/MC algorithm. The motion of the charged particles is simulated by the PIC method using the standard explicit 'leap frog' finite difference scheme. A detailed description of the PIC technique can be found in Birdsall and Langdon [9]. Electrons are absorbed and ions are neutralized on the electrodes. Secondary electron emission is included here because the rf discharge is assumed to be in the γ-regime at the conditions under study [10]. The initial densities of the charged species in the model are based on experimental and simulation data [4-7]. The initial velocities are calculated from the Maxwellian distribution at an average electron temperature of 2 eV and an average ion temperature of 0.043 eV (500K).

The charged species, which are followed in the model, are: electrons, Ar^+, CF_3^+, N_2^+, F^-, and CF_3^- ions.

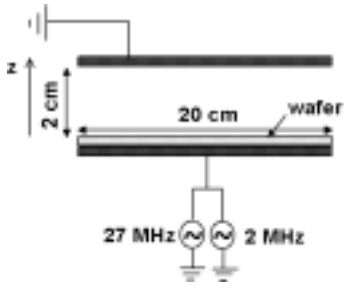

FIG. 1. Schematic diagram of the reactor

Simulation results in a pure cc rf CF_4 discharge show that the dominant positive ions are CF_3^+, with a density exceeding those of CF_2^+, CF^+, C^+ and F^+ by more than 2 to 3 orders of magnitude, and $N_{CF_3^+} \cong N_{F^-} + N_{CF_3^-} + N_e$, where N denotes the number densities in the bulk plasma [6]. For that reason CF_3^+ is the only type of positive ions of CF_4 followed in the model.

The interactions between the particles are treated by a Monte Carlo method, which is basically a probabilistic approach. To calculate collision probabilities, it is necessary to have the corresponding collision cross section data, which are not always available. Hence, the present model uses several techniques to define the collision probabilities even when the collision cross sections are unknown. The electron - neutral collision probability is determined by the null collision method based on cross section data [11]. In the present model, however, the expression for determining the electron scattering angle differs from the one proposed in Ref. 11, as it is explained in Ref. 12. The Ar^+ - Ar, Ar^+ - N_2, N_2^+ - N_2 and N_2^+ - Ar collision probabilities are calculated in the same way. The other ion – neutral elastic and reactive collisions, included in the model, are calculated by an ion-molecule collision model for endothermic reactions [6]. The probability for positive-negative ion recombination is determined from a recombination rate constant [13]. The outlines of all techniques are given in our previous paper [7]. In this paper the electron – positive ion (CF_3^+ and N_2^+) recombination is newly included and details for the method are given later in this section.

The electron-neutral collisions considered in this simulation, along with the corresponding threshold energies and references are presented in Table I.

The Ar^+ - Ar and N_2^+ - N_2 elastic isotropic and backward scattering (to simulate charge transfer) cross sections are taken from Phelps [18]. The cross section data for non-resonant charge transfer between Ar^+ and N_2 and between N_2^+ and Ar are adopted from Spalburg and Gislason [19]. The collision probabilities for these reactions are calculated by the null-collision method [11].

TABLE I. Electron-neutral (Ar, CF_4, N_2) collisions.

Reaction	ε_{th} (eV)	Ref.	Reaction	ε_{th} (eV)	Ref.
$e + Ar \rightarrow e + Ar$	-	14	$e + CF_4 \rightarrow e + CF_4$ (v4)	0.077	16
$e + Ar \rightarrow e + Ar^*$	11.5	14	$e + CF_4 \rightarrow e + CF_4^*$	7.54	16
$e + Ar \rightarrow 2e + Ar^+$	15.8	14	$e + CF_4 \rightarrow F^- + CF_3$	6.4	16
$e + N_2 \rightarrow e + N_2^*$ (Y) [a]		15	$e + CF_4 \rightarrow F + CF_3^-$	5	17
$e + N_2 \rightarrow 2e + N_2^+$ (Y) [b]	15.6	15	$e + CF_4 \rightarrow e + F^- + CF_3^+$	12	17
$e + N_2 \rightarrow 2e + N_2^+ (B\ ^2\Sigma)$	18.8	15	$e + CF_4 \rightarrow 2e + F + CF_3^+$	16	16
$e + CF_4 \rightarrow e + CF_4$	-	16	$e + CF_4 \rightarrow e + F + CF_3$	12	16
$e + CF_4 \rightarrow e + CF_4$ (v1)	0.108	16	$e + CF_4 \rightarrow e + 2F + CF_2$	17	16
$e + CF_4 \rightarrow e + CF_4$ (v3)	0.168	16	$e + CF_4 \rightarrow e + 3F + CF$	18	16

[a] N_2^* (Y) = N_2 (υ = 0-8, A $^3\Sigma$, B $^3\Pi$, W $^3\Delta$, B′ $^3\Sigma$, a′ $^1\Sigma$, a $^1\Pi$, w $^1\Delta$, C $^3\Pi$, E $^3\Sigma$, a″ $^1\Sigma$, and "sum of singlets", including dissociation)

[b] N_2^+ (Y) = N_2^+ (X $^2\Sigma$ and A $^2\Pi$)

The CF_3^+ - CF_4, F^- - CF_4 and CF_3^- - CF_4 elastic and reactive collisions are simulated using the ion-molecule collision model for endothermic reactions developed by Nanbu and Denpoh [6]. All ion - CF_4 reactions considered in the model and the corresponding thermodynamic threshold energies, are given in Ref. 7. The Ar^+ - CF_4, CF_3^+ - Ar, F^- - Ar, and CF_3^- - Ar elastic collisions are treated by means of the same technique [7].
The positive-negative ion and electron – ion recombination and the corresponding rate constants, along with the references are presented in Table II.

TABLE II. Positive-negative ion and electron – positive ion recombination reactions considered in the model and the corresponding recombination rate coefficients.

Reaction	Rate constant (m^3/s)	Ref.	Reaction	Rate constant (m^3/s)	Ref.
$F^- + Ar^+ \rightarrow F + Ar$	1×10^{-13}	20			
$F^- + CF_3^+ \rightarrow F + CF_3$	1×10^{-13}	20	$e + CF_3^+ \rightarrow CF_3$	$3.95\times10^{-15}/\sqrt{T_e}T_i$	21
$CF_3^- + Ar^+ \rightarrow CF_3 + Ar$	1×10^{-13}	20			
$CF_3^- + CF_3^+ \rightarrow CF_3 + CF_3$	1×10^{-13}	20	$e + N_2^+ \rightarrow 2N(^4S)$	$7.72\times10^{-14}/\sqrt{T_e}$	22

The ion-ion and electron-ion recombination cross sections and hence the probabilities are determined from a given expression for the corresponding rate constant, as proposed by Nanbu and Denpoh [13, 21]. We have already explained the collision model for ion – ion recombination [7]. The dependence of the electron - ion rate constants on the electron temperature T_e and ion temperature T_i makes the model more complicated. The electron – ion recombination is treated using the null-collision technique [21]. Let us express the electron – ion rate constants as $k_{e\text{-}i} = a / (T_e)^{1/2}$, where a is equal to 3.95 x 10^{-15} / T_i and 7.72 x 10^{-14} for electron – CF_3^+ and electron – N_2^+ recombination, respectively. The electron temperature is calculated from $T_e = m_e v_e^2 / 3e$, where m_e and v_e are the mass and velocity of the electron, respectively, and e is the electron charge. The probability that an electron with velocity v_e recombines with a positive ion in time step Δt is given by [21]

$$P_{r_{e-i}} = W_i \frac{N_i}{V_c} \frac{a}{\sqrt{m_e/3e}} \frac{\Delta t}{v_e}, \quad (1)$$

where W_i and N_i are the ion weight (representing the real ions in one simulated super-particle) and the number of the simulated ions, respectively, in a cell with a volume V_c. Since eq. (1) has a singularity at v_e = 0, a cutoff parameter $(v_e)_{\min}$ is introduced to obtain the maximum recombination probability [21]. The cutoff parameter is chosen to be 1/5 of the mean electron velocity in each cell so that the probability that a randomly sampled electron has a velocity less than $(v_e)_{\min}$ is only 1.1 % in equilibrium [21]. If the number of the simulated electrons in a cell is N_e, the maximum number of the simulated electrons N_{re} that can recombine is calculated from

$$(N_{re})_{\max} = W_i \frac{N_e N_i}{V_c} \frac{a}{\sqrt{m_e/3e}} \frac{\Delta t}{(v_e)_{\min}}. \quad (2)$$

The colliding electrons $(N_{re})_{\max}$ are chosen randomly. Then call a random number R and check each electron with velocity v_e if it recombines with an ion, i.e., if R is less than $(v_e)_{\min}/ v_e$. If $R \geq (v_e)_{\min}/ v_e$ the recombination is null.
It should be kept in mind that in case of different weights for ions W_i and electrons W_e, as in the present simulation, the maximum number of simulated ions that can recombine $(N_{ri})_{\max}$ is not equal to $(N_{re})_{\max}$ and is given by $(N_{ri})_{\max} = (N_{re})_{\max} W_e/W_i$.
For the electron – CF_3^+ recombination model the ion temperature is determined as the mean energy in each cell, i.e. $T_i = m_i \langle v_i^2 \rangle / 3e$, where m_i and v_i are the mass and velocity of the ion, respectively [21].
In the simulation the recombination time step is taken to be 10^5 times longer than the electron time step; the probability for recombination is, indeed, low because of the much lower ion densities in comparison with the neutral gas density.

3. Results and discussion

The calculation is performed for an $Ar/CF_4/N_2$ mixture at a ratio of 0.8/0.1/0.1. In Figs. 2 - 4 the rf powered electrode is at position 0 and the grounded electrode is at position 2cm. The gas temperature is set to 300 K. The choice of the grid spacing and the time steps is defined by the accuracy criteria for PIC/MC codes with explicit mover [8]. Typical results of this model are electron and ion densities, fluxes and energy distributions, collision rates and electric field and potential distributions.

Fig. 2 presents the simulation results of the electric field distribution (a) and (b), and the electron density distribution (c) in 2 LF cycles. A close look at the electric field in the bulk plasma [Fig. 2(b)] shows the appearance of double-layer structures and field reversal near the bulk – sheath interface, i.e. the discharge structure is electronegative (cf. with the results for a pure CF_4 discharge, presented in Ref. 7). The electron density has maxima at the bulk – sheath interface [Fig. 2(c)]. Moreover, the main negative carriers are CF_3^- ions and their density in the bulk exceeds the electron density by 1 order of magnitude [cf. Figs. 2(c) and 3(c)]. The average electron energy in the bulk plasma is calculated to be around 7 eV, which is comparatively high due to the substantial electric field in the center (on the order of 5000 V/m). The electron density and consequently the sheath width oscillate with the applied double frequency.

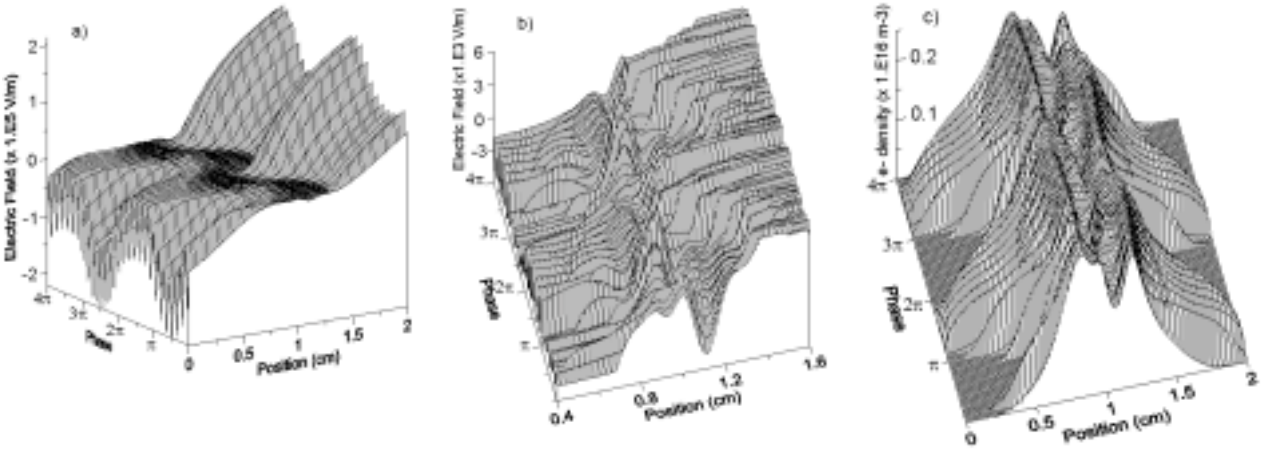

FIG. 2. Electric field in the simulated (a) and in the bulk region (b), and electron density (c) in 2 LF cycles.

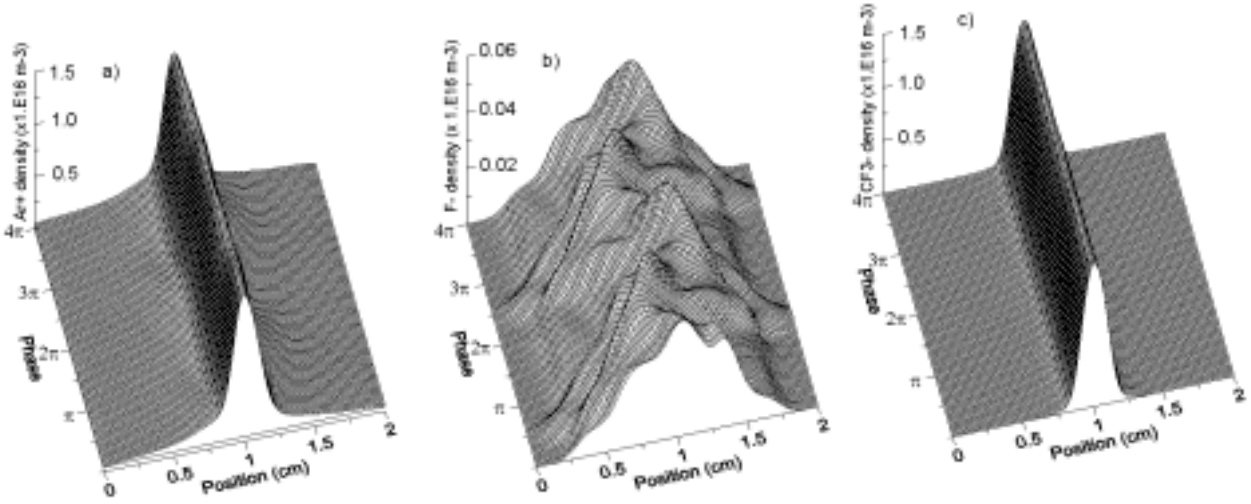

FIG. 3. Ar^+ (a), F^- (b), and CF_3^- (c) ion densities in 2 LF cycles.

The Ar^+ (a), F^- (b) and CF_3^- (c) ion densities in 2 LF cycles are shown in Fig. 3. The density distributions of the other positive ions CF_3^+ and N_2^+ are not given because their profiles are similar to that of Ar^+ ions. The major positive ion is Ar^+ and its density in the bulk center has a value of 1.5×10^{16} m^{-3}, whereas CF_3^+ and N_2^+ densities have values of only 1.2×10^{15} m^{-3} and 6.0×10^{14} m^{-3}, respectively (not shown). Contrary to other investigations of cc single HF pure CF_4 and Ar/ CF_4 discharges, CF_3^- ions are the dominant negatively

charged species and the density of the F^- ions is rather small [4-7]. In the presence of LF (2MHz) and the strong electric field the light F^- ions are not confined in the bulk plasma as in one-frequency discharges. They have enough time to move towards the electrodes. The much heavier CF_3^- ions cannot respond to the LF and they remain in the bulk plasma [cf. Fig. 3 (b) and (c)]. The F^- density profile is greatly modulated by the LF and F^- ions are detected at the powered electrode at phase $\pi/2$ of the LF cycle. From the electric field distribution one could expect that F^- ions are able to reach the powered electrode at phase $3\pi/2$, when the electric field is almost 0, like the electrons [Fig. 2]. However, at that time F^- ions are detected at the grounded electrode [Fig. 3(b)]. A possible explanation is that F^- ions are inert in comparison with the electrons and 2 MHz is not low enough for F^- to respond instantaneously to the electric field. Our simulation results for a dual frequency (1+27 MHz), which are not presented here, show that F^- ions reach the electrodes at phase shifted with $\pi/2$ (cf. with π in the present simulation) in comparison with the phase when the electric field is almost 0. In addition, the higher electron density [cf. Figs. 2(c) and 3(b)] and the movement of electrons with 2 frequencies make the detailed analysis very complicated.

The Ar^+ (a), CF_3^+ and N_2^+ (b) ion energy distribution functions (IEDF) at the powered electrode, averaged for 2 LF cycles is presented in Fig. 4. The IEDF is broad and bimodal as it is expected in the presence of the LF [23, 24]. In LF regime the ion transit time τ_{ion} is less than the rf period $\tau_{rf} = 2\pi/\omega_{rf}$, i.e., the ions cross the sheath in a small fraction of the rf cycle and they reach the electrode with an energy equal to the instantaneous sheath potential drop. The two outstanding peaks in the profile correspond to the minimum and maximum sheath potential drop. In this simulation τ_{ion}/τ_{lf}, where τ_{lf} is the LF period (f = 2MHz), is calculated to be 0.6, 0.8 and 0.5 for Ar^+, CF_3^+, and N_2^+ ions, respectively. Analytical calculations and experiments show that the IEDF width $\Delta E = E_2 - E_1$, where E_1 and E_2 are the energies at which the peaks are observed, depends on the ion mass ($\sim m_i^{-1/2}$) [23]. The simulation verifies that as m_i is increased, ΔE is reduced [cf. the IEDF width for the 3 positive ions in Fig. 4 (a) and (b), considering that $m_{N2+} < m_{Ar+} < m_{CF3+}$].

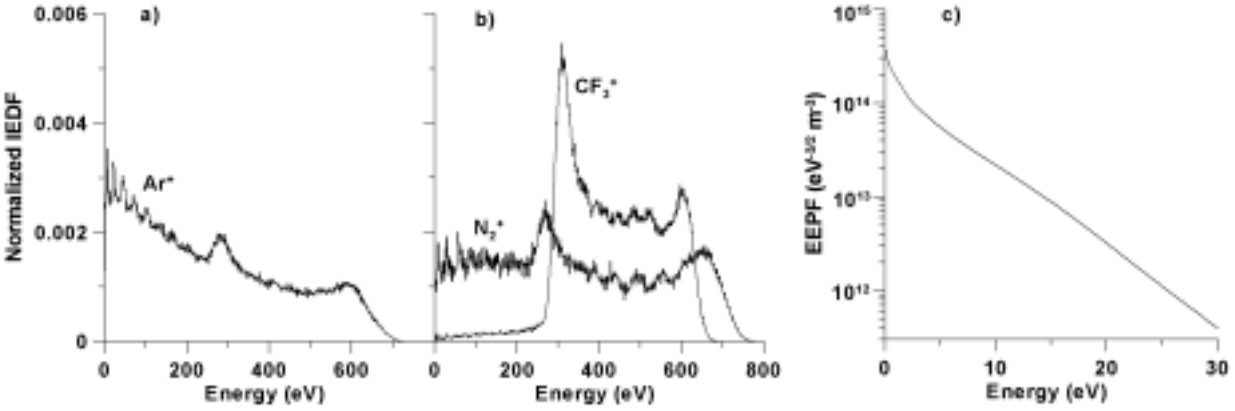

FIG. 4. Ar^+ (a), CF_3^+ and N_2^+ (b) IEDF at the powered electrode, and the EEPF at the bulk center (c), averaged for 2 LF cycles.

The number of secondary peaks in the Ar^+ and N_2^+ IEDF are due to the frequent resonant and non-resonant charge transfer between Ar^+ or N_2^+ and Ar or N_2 [24]. The charge transfer CF_3^+ - CF_3 is not considered in the model since the density of the CF_3 radicals is much lower in comparison with the CF_4 density, with a value in the order of 10^{17} m^{-3} [5]. Elastic collisions lead to the tail of lower energies in the IEDF of the 3 ions [24]. The IEDF profile dependence on the applied frequency and ion mass will be described in detail in another article.

Fig. 4 (c) shows the electron energy probability function (EEPF) $f_e(\varepsilon)$ (= $F_e(\varepsilon)\varepsilon^{-1/2}$, where $F_e(\varepsilon)$ is the electron energy distribution function and ε is the electron energy) at the center of the discharge and averaged for 2 LF cycles. The profile is a bi-Maxwellian distribution. The high energy tail is due to the comparatively strong electric field in the bulk, which is a characteristic feature of electronegative discharges.

4. Summary

A one-dimensional PIC/MC model has been developed to describe the structure of a cc rf discharge in a gas mixture of Ar, CF_4 and N_2. The model follows electrons, Ar^+, CF_3^+, F^-, CF_3^-, and N_2^+ ions. The collisions

treated by the Monte Carlo method include electron – neutral (Ar, CF_4, and N_2) collisions, various kinds of collisions of Ar^+, CF_3^+, F^-, CF_3^- or N_2^+ with neutrals, positive - negative ion recombination, and electron – ion recombination.

The simulation is performed for 0.8/0.1/0.1 ratios of $Ar/CF_4/N_2$ mixture in a dual frequency (2+27 MHz) reactor at a pressure of 30 mTorr. This model yields results for the electron and various ion densities, their fluxes and energy distributions, the collision rates and the electric field and potential distributions.

The results show that the structure of the discharge is electronegative, i.e. double layer structure and electron density maxima at the bulk – sheath interface are observed. Contrary to other investigations of pure CF_4 or mixes of CF_4 discharges in single frequency reactors, in the present simulation CF_3^- ions are the dominant negatively charged species and the density of the F^- ions is rather small. In the presence of LF (2MHz) and the strong electric field F^- ions are not confined in the bulk plasma as in single HF discharges and they have enough time to move towards the electrodes. The much heavier CF_3^- ions cannot respond to the LF and they remain in the bulk plasma. The electron density and the sheath width oscillate with the applied double frequency.

The IEDF is broad with two outstanding peaks, which correspond to the minimum and maximum sheath potential drop. The EEPF has a bi-Maxwellian profile with a high energy tail.

Acknowledgments

V. Georgieva would like to thank W. Goedheer for the helpful discussions. This research is sponsored by the Flemish Fund for Scientific research (FWO) and the Federal Services for Scientific, Cultural and Technical Affairs of the Prime Minister's Office through IUAP – V.

References

[1] H. H. Goto, H.-D. Löwe and T. Ohmi, J. Vac. Sci. Technol. A **10**, 3048 (1992).
[2] T. Kitajima, Y. Takeo and T. Makabe, J. Vac. Sci. Technol. A **17**, 2510 (1999).
[3] K. Maeshige, G. Washio, T. Yagisawa and T. Makabe, J. Appl. Phys. **91**, 9494 (2002).
[4] M. Haverlag, A. Kono, D. Passchier, G. M.W. Kroesen, W. J. Goedheer and F. J. de Hoog, J. Appl. Phys. **70**, 3472 (1991).
[5] N. V. Mantzaris, A. Boudouvis and E. Gogolides, J. Appl. Phys. **77**, 6169 (1995).
[6] K. Denpoh and K. Nanbu, J. Vac. Sci. Technol. A 16, 1201 (1998).
[7] V. Georgieva, A. Bogaerts and R. Gijbels, J. Appl. Phys. **93**, 2369 (2003).
[8] E. Kawamura, C. K. Birdsall and V. Vahedi, Plasma Sources Sci. Technol. **9**, 413 (2000).
[9] C. K. Birdsall and A. B. Langdon, *Plasma Physics via Computer Simulation* (McGraw- Hill, New York, 1985).
[10] Ph. Belenguer and J. P. Boeuf, Phys. Rev. A **41**, 4447 (1990).
[11] V. Vahedi and M. Surendra, Comput. Phys. Commun. **87**, 179 (1995).
[12] A. Okhrimovskyy, A. Bogaerts, R. Gijbels, Phys. Rev. E **65**, 037402 (2002).
[13] K. Nanbu and K. Denpoh, J. of the Phys. Society of Japan **67**, 1288 (1998).
[14] A. V. Phelps, J. Appl. Phys. **76**, 747 (1994).
[15] A.V. Phelps and L. C. Pitchford, Phys. Rev. A **31**, 2932 (1985). A.V. Phelps et al., Joint Institute for Laboratory Astrophysics (JILA) Information Center Report No.26 (1985), (to be found on ftp://jila.colorado.edu/collision_data/).
[16] M. Kurihara, Z. Lj. Petrovic and T. Makabe, J. Phys. D **33**, 2146 (2000).
[17] R. A. Bonham, Jpn. J. Appl. Phys., Part1 **33**, 4157 (1994).
[18] A. V. Phelps, J. Phys. Chem. Ref. Data **20**, 557 (1991).
[19] M. R. Spalburg and E. A. Gislason, Chem. Phys. **94**, 339 (1985).
[20] S. Rauf and M. J. Kushner, J. Appl. Phys. **82**, 2805 (1997).
[21] K. Denpoh and K. Nanbu, , Jpn. J. Appl. Phys., Part1 **39**, 2804 (2000).
[22] J. Henriques, E. Tatarova, V. Guerra and C. M. Ferreira, J. Appl. Phys. **91**, 5622 (2002).
[23] E. Kawamura, V. Vahedi, M. A. Lieberman and C. K. Birdsall, Plasma Sources Sci. Technol. **8**, R45 (1999).
[24] W. J. Goedheer, Plasma Sources Sci. Technol. **9**, 507 (2000).

Developing a Particle Detection System in a Capacitively Coupled GEC Cell

S. Hong[1], J.-C. Schauer, J. Berndt, J. Winter

Institute for Experimental Physics II, Applied Plasma Physics, Faculty for Physics and Astronomy, Ruhr-University Bochum, Universitätsstr. 150, 44780 Bochum, Germany

Abstract

The behavior of the harmonics at different conditions including Ar/CH_4 dusty plasma is studied. It is found that the presence of the 7th harmonic is strongly correlated with the plasma sheath thickness. This may be due to a series resonance. A simple explanation for the increase of the 2nd and 3rd harmonics during the dust particle formation is given.

1. Introduction

The dust particle formation in reactive plasmas is now well known. Since the growth of the particles in reactive plasmas, especially so called "killer particles", causes major defects of the semiconductor productions in industry, detecting, monitoring, and controlling methods for the particle formations are highly desired. Known particle diagnostic methods are 1) laser light scattering for presence and density [1], 2) Mie-ellipsometry for particle density, size, size distribution, and shape of particles [2], 3) *in situ/ex situ* infrared absorption, Raman spectroscopy, mass spectrometry for chemical compositions [3], 4) mass spectrometry, photodetachment for particle charge and electronegativity [4], 5) phosphoresence, black body radiation for particle temperature and velocity distribution [5, 6] 6) SEM/TEM, X-ray diffraction, photoluminescence for morphology and structure of the particles [1, 7], and 7) optical spectroscopy, electrical probe measurements, mass spectrometry, and microwave diagnostics for the influence of particles on the plasmas [7, 8, 9].

In this paper, we have investigated the influence of particles on the plasmas by means of electrical voltage/current probe measurements in a capacitively coupled plasma. It is well known that the presence of dust particles in a rf excited plasma has a dramatic effect on the plasma impedance [8, 9]. Consequently, the Fourier analyzed voltage/current harmonic signals of both electrodes are strongly influenced by the formation of particles. A possibility to use the change of the plasma impedance monitored by a spectrum analyzer as a particle detecting system is suggested by Boufendi et al [8]. Recently the use of the 7th harmonic voltage signal as a particle size indicator was suggested by Hong et al [7]. However, care must be taken, since voltage/current measurements show the global change from the whole reactor. Also, particle density and spatial distribution of the particles can not be measured or determined directly. Despite of those disadvantages, it is shown that a strong correlation exists between two completely independent "global" and "local" measurement methods, e.g. between Fourier analyzed signal of the powered electrode and Mie-ellipsometric measurements [10]. These results support the basic idea of using the harmonic signals as a particle detector and size indicator. As a first step, we have investigated the change of plasma impedance, i.e., the behavior of the harmonics at different conditions.

2. Experimental Setup

Figure 1 shows a simple sketch of the experimental setup. A standard GEC cell is pumped by a rotary vane vacuum pump (Pfeiffer DUO 10 C) resulting in a pressure of about 10^{-4} mbar. Flow rates of the gases are controlled by MKS Mass-Flow controller. Gases are introduced through the showerhead of the upper electrode. A 13.56 MHz rf generator (Dressler Cesar 133) is capacitively coupled to one of the electrodes through an impedance matching network. To be sure that external circuit elements do not affect the measurements, we have carefully tested the measurements using three different types of matching networks. The other electrode is grounded. The electrodes are 10.2 cm in diameter and are separated by 3.1 cm. Homemade voltage/current probes are attached to the end of each electrode. The voltage/current signals are then measured *in situ* by a digital oscilloscope (Tektronix TDS 784A). For the Fourier analyzed signal measurements, the digital oscilloscope is removed and one of the voltage measurement nodes of the probes is connected to a spectrum analyzer (Rohde & Schwarz FSEM 30) directly and the harmonic signals are measured.

3. Parasitics of the GEC Cell

In general, care must be taken during the interpretation of measured voltage/current signals, since higher harmonics can be caused by resonances with external circuit components used in the matching network or probe itself. Such resonances caused by the admittance of driven Langmuir probe systems have already been reported

[1]e-mail address: hong@plas.ep2.rub.de

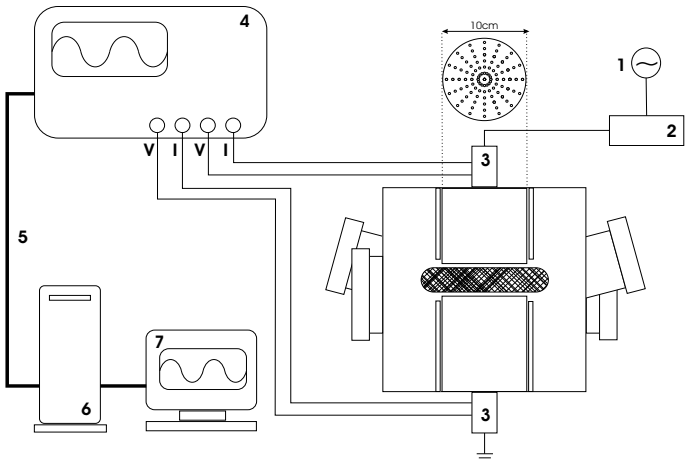

Figure 1: Experimental Setup. (1) 13.56 MHz rf power generator, (2) Matching Network, (3) Voltage/Current probe, (4) Oscilloscope, (5) GPIB cable, (6) PC, (7) Monitor

[11]. In order to clarify that the external circuit connected to the upstream of the voltage/current probes does not influence the measurements, we have tested the harmonics of the voltage signal using 6 different combinations of three different types of matching networks and two different types of voltage probes. The "empty cell" measurements (no gas flow, 20 Watt input power only) show the fundamental frequency of 13.56 MHz only. Despite the different configurations of the matching networks, even when we have replaced the matching network by a blocking capacitor, we have confirmed the same characteristic behavior of the harmonic signals up to the 8th harmonic measured by two different types of voltage probes in an Ar plasma. Furthermore, we have simulated plasma impedance using a "well-matched" 2nd matching network placed at the position of the reaction chamber, while the setting of the primary matching network for the Ar plasma is maintained. The term "well-matched" means that the 2nd matching network is adjusted for the primary one in order to get maximum power transfer. In this case, however, we have different harmonic signals, i.e. the fundamental, the 2nd, and a very small amplitude of the 3rd harmonic. These results reveal that the higher harmonic signals are mainly generated by the impedance from the downstream of the voltage/current probe. The sources of the resonance might be nonlinear behavior of the sheath and/or parasitic impedance of the electrodes resonating with plasma sheath capacity. Since parasitic impedance of the electrodes is an important factor which can make systematic errors for both measurements and interpretations of the harmonic measurements, the effects should be carefully considered [12, 13]. Direct measurements of the impedance of the electrodes in the range of 1-200 MHz by a network analyzer (HP4195A) show that main resonance frequencies for the parasitic impedances of both electrodes are 28.5 MHz (lower) and 37 MHz (upper) respectively. These resonance frequencies are consistent with the results performed using 5 different GEC cells, reported by Hargis et al [12]. Together with the "empty cell" measurements and the harmonic measurements using the "well-matched" 2nd matching network, these results indicate that the higher harmonics might be generated by the nonlinear behavior of the sheath. These will be discussed in the next section in detail.

4. Presence of Harmonics

Figure 2(a) and 2(b) show the Fourier analyzed harmonic signals present in an Ar plasma at different pressures. The input power is coupled to the upper electrode at a constant level of 20 Watts. The voltage signals are measured by the voltage probe placed at both upper and lower electrodes and the measured waveforms are Fourier analyzed by fast Fourier transformation. At a high pressure of 5.6×10^{-1} mbar, the fundamental, the 2nd, the 3rd, the 4th and a small amplitude of the 7th harmonic are present at the upper electrode (solid). As the pressure decreases, other higher harmonics are present. At a pressure of 8.2×10^{-2} mbar, the 5th harmonic signal is present. At this pressure the 4th and the 7th harmonic signals have higher amplitudes than other harmonic signals. At a pressure lower than 3.8×10^{-4} mbar, the Ar plasma can not be maintained with 20 Watts input power. At this pressure the "empty cell" measurement is performed. It is clear that only the fundamental frequency is present (dash-dot). In the case of the grounded lower electrode, the fundamental, the 2nd, the 3rd, and the 5th harmonics are present at a high pressure of 5.6×10^{-1} mbar. At a pressure of 8.2×10^{-2} mbar, the harmonics up to the 8th are present. As the pressure decreases further, the 2nd harmonic signal is the most dominant harmonic (dot in the figure 2(b)) at a pressure of 4.4×10^{-4} mbar.

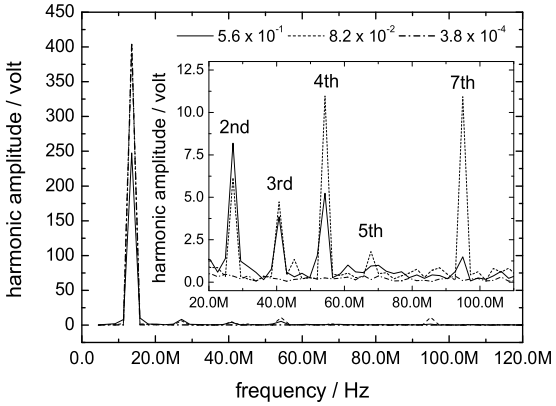

(a) at the powered upper electrode

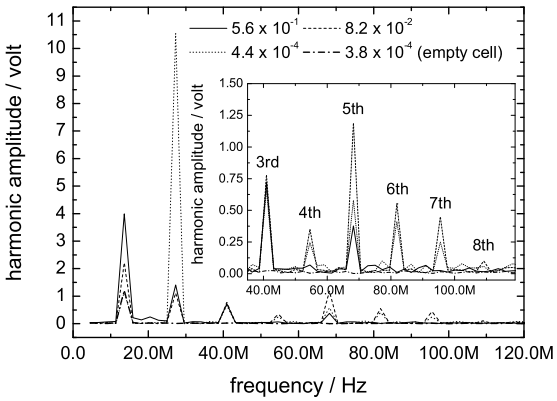

(b) at the grounded lower electrode

Figure 2: Fourier analyzed harmonic signals from the fundamental up to the 8th frequency measured as a function of pressure (solid: 5.6×10^{-1} mbar, dash: 8.2×10^{-2} mbar, dot: 4.4×10^{-4} mbar, dash-dot: 3.8×10^{-4} mbar: empty cell).

Figure 3 shows the harmonic amplitudes from the 2nd up to the 8th harmonic signals and both plasma sheath thicknesses at both electrodes as a function of pressure. At a pressure higher than 1×10^{-1} mbar, the amplitudes of the harmonics are slightly changed at the powered upper electrode, and they are independent of the plasma sheath thickness of the upper electrode except for the 7th harmonic (figure 3(a)). Instead, it seems that they depend on the plasma sheath thickness of the lower electrode as shown in figure 3(b). At a pressure lower than 1×10^{-1} mbar, the plasma sheath thickness at the upper electrode increases rapidly, the 7th harmonic behaves the same as the plasma sheath thickness (figure 3(a)). The strong correlation between the 7th harmonic and the plasma sheath thickness indicates that the resonance might be a series resonance. A series resonance occurs when a cold plasma behaves inductively and resonates with two sheath simultaneously at a frequency below the electron plasma frequency, $\epsilon = 1 - (\omega_{ep}^2/\omega_R^2) < 0$. It depends on the plasma and sheath thickness and the plasma density. Figure 3(c) and Figure 3(d) show that the harmonics measured at the grounded lower electrode behave the same as the plasma sheath thickness of the upper electrode except for the 3rd harmonic at a high pressure. At a pressure lower than 1×10^{-1} mbar, the 3rd harmonic shows the same behavior. Ku et al. have reported [14] that, 1) the plasma-sheath resonates at a lower pressure than 1 Pa (1×10^{-2} mbar), 2) the resonance regime at a higher pressure than 1 Pa has been identified as the sheath capacity of the driven electrode resonating with the inductance of the external rf circuitry. However, it should be pointed out that the plasma sheath resonance can be tuned by altering excitation voltage [14]. The excitation voltage V_{pp} is over 700 V, which is much higher than in their experiments (V_{pp}=400 V), the harmonics present in the plasma - in our case - cannot be interpreted simply as a resonance with external rf circuits.

5. Response of the Plasma to the Formation of Dust Particles

As long as the plasma is dust free, the harmonics remain almost constant. As soon as dust particles are present in the plasma, all measured harmonics show certain characteristic features indicating the particle formation and their growth as a function of time: the evolution of the signals measured in an Ar/CH_4 plasma is divided into 4 time periods as labelled in figure 4(a). To initiate the particle formation in the Ar/CH_4 plasma, it is necessary - in our experiment - to apply transiently high power (ignition power > 60W, 15∼30 sec; maintenance power 20 W) to the plasma [7]. The first time period of the evolution (label 1 in figure 4(a)) consists of two physical situations: 1) the initiation of the particle formation. The critical concentration of proto-particles is generated as long as high input power is applied, and the particle formation is initiated. 2) the coagulation process takes place [8]. As the coagulation takes place, the particle size grows up while the particle number density in the plasma decreases rapidly. The emission light intensity starts to increase indicating that the $\alpha \rightarrow \gamma'$ transition takes place. The plasma resistance increases and the plasma sheath thickness decreases resulting the decrease of resonance amplitudes. Especially the 7th harmonic amplitude decreases rapidly. The 8th harmonic signal is completely disappeared. However, the 2nd and the 3rd harmonics increase slightly. These results reveal that

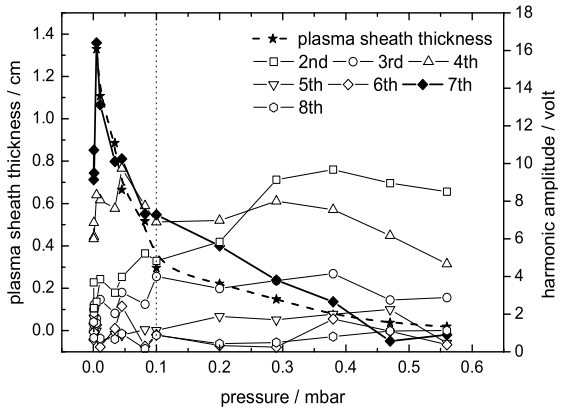

(a) harmonics at the powered upper electrode with the plasma sheath thickness at the upper electrode

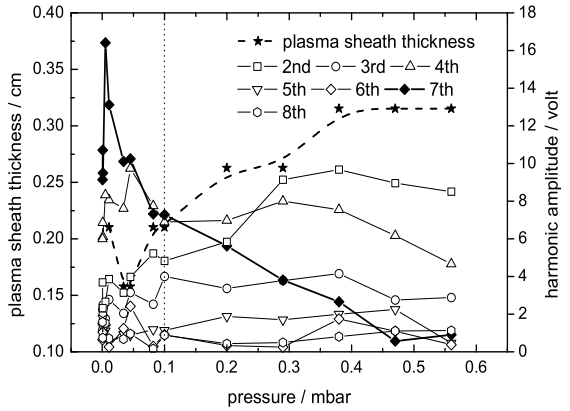

(b) harmonics at the powered upper electrode with the plasma sheath thickness at the lower electrode

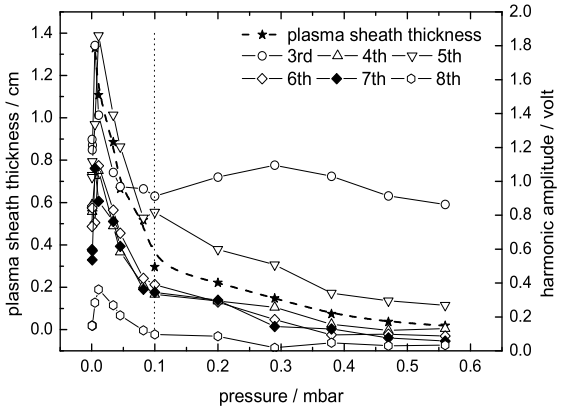

(c) harmonics at the grounded lower electrode with the plasma sheath thickness at the upper electrode

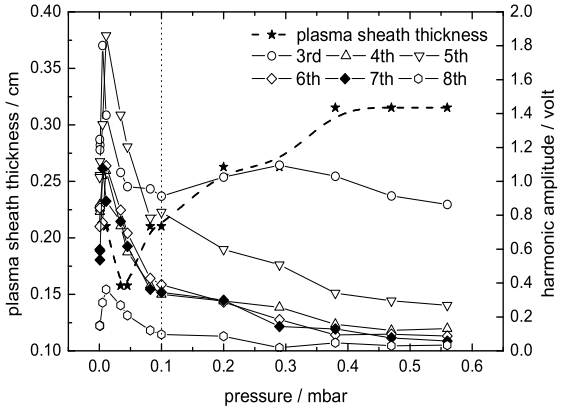

(d) harmonics at the grounded lower electrode with the plasma sheath thickness at the lower electrode

Figure 3: Amplitude of Fourier analyzed harmonics from the 3rd up to the 8th harmonic frequency and plasma sheath thicknesses as a function of pressure [closed star: plasma sheath thickness, open square: the 2nd (27.12 MHz), open circle: the 3rd (40.68 MHz), open triangle: the 4th (54.24 MHz), open inverted triangle: the 5th (67.8 MHz), open diamond: the 6th (81.36 MHz), closed diamond: the 7th (94.92 MHz), open hexagon: the 8th (108.48 MHz)]

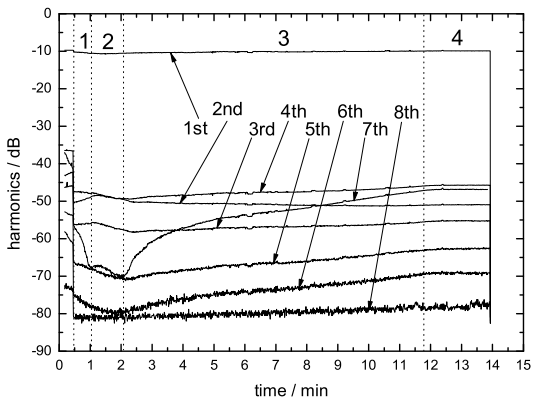

(a) harmonics at the powered upper electrode

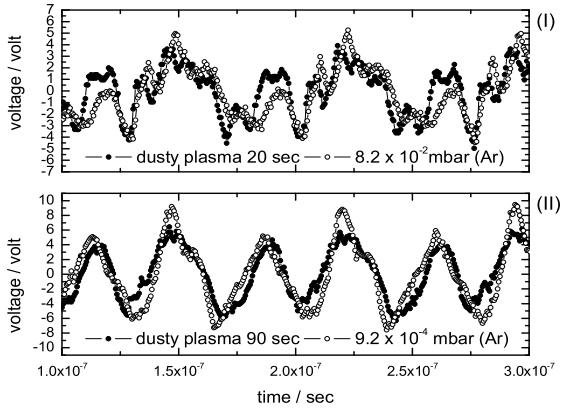

(b) waveform at the grounded lower electrode (closed circle: dusty plasma - 20 second (I), 90 second (II) operation time in an Ar/CH_4 plasma, open circle: 8.2×10^{-2} mbar (I), 9.2×10^{-4} mbar (II) in an Ar plasma)

Figure 4: Amplitude of Fourier analyzed harmonic signals at the powered upper electrode and waveforms at the grounded lower electrode in two different situations of the particle formation comparing with situations in an Ar plasma

the plasma characteristic at the upper electrode region might be shifted towards that of the high pressure region in figure 3, because the plasma sheath thickness decreases as a function of time. Therefore the 2nd and the 3rd harmonics might be increased slightly. If the plasma at the lower electrode region behaves the same way as that of the upper electrode region, i.e. the plasma sheath thickness decreases as a function of time, the 2nd harmonic should be the dominant frequency as shown in figure 2(b) and the plasma characteristics shold be shifted towards that of the lower pressure region. During this phase, as expected, the 2nd harmonic is found as the dominant frequency at the lower electrode. Figure 4(b) shows waveforms at the lower electrode at two different situations for the particle formation compared with situations in an Ar plasma: closed circles show the waveform measured at 20 seconds (I) and 90 seconds (II) after the particle formation is initiated in an Ar/CH_4 plasma. The open circles represent the waveform measured at pressures of 8.2×10^{-2} mbar (I) and 9.2×10^{-4} mbar (II) in an Ar plasma. Shortly after the particle formation is initiated, the two waveforms in both plasmas are similar as shown in figure 4(b)-(I). Since the pressures are at the same range, there are only small effects of the dust particles. As the dust particles grow up, measured waveforms show completely different patterns. The 2nd harmonic is the dominant one as shown in figure 4(b)-(II). A similar situation is observed in the Ar plasma at a low pressure of 9.2×10^{-2} mbar (see figure 2(b)). This similarity can be explained in following way. A strong correlation between mass spectra (i.e. partial pressure) and the 7th harmonics has been found [7, 15]. Because the dust particles behave as a sink for the small particles, they absorb the particles in the plasma resulting a high growth rate of about 100nm/min. As a result, the partial pressure starts to decrease the same as the 7th harmonic does. Then, the plasma at the lower electrode region might react as if the pressure is decreased: the plasma sheath thickness decreases. The 3rd harmonic shows similar behavior.

The decrease of the harmonic signals in the 2nd time period (label 2 in figure 4(a)) indicates - in our case - the development of the void. The presence of the void is strongly correlated with the particle size in the plasma, since the neutral drag force acting on the particles plays an important role. When the void starts to develop the 7th harmonic shows a small shoulder. The particle diameters before and after the void development are about 150±15 nm and about 318±30 nm, respectively. This means that particles that have a size greater than approximately 150-200 nm in diameter will be pushed away from the center region by the neutral drag force.

After the void is developed, the dust particles are continuously grown up at the outside of the electrodes where the electric field is relatively weak (label 3, the 3rd time period in the figure 4(a)). The emission light intensity decreases as the electron temperature decreases. The plasma becomes slowly capacitive again, the amplitudes of the harmonics begin to return to their initial values. At the last stage of the 3rd time period, the particle diameter is about 673±65 nm. In the 4th time period when the particles that have a size lager than 800 nm $\sim$

1 μm are lost due to the gravitational force, harmonic signals show a steady state.

6. Summary and Discussion

We have investigated behaviors of the harmonic signals at different conditions as a first step of developing a particle detection system in a capacitively coupled plasma. As a result we have found that the presence of the 7th harmonic is strongly correlated with the plasma sheath thickness, it might be due to a series resonance. We have described the correlation between particle formation, the plasma sheath and the behavior of the harmonics. The change of plasma impedance and sheath thickness may cause the small increase of the 2nd and 3rd harmonics during the particle formation in the 2nd time period in figure 4(a). Further investigation is under way to analyze these phenomena.

Acknowledgement

This study is partially supported by BMBF (FKZ: 13N8049) and MSWF NRW (FKZ: 315 108 0302)

References

[1] A. Bouchoule and L. Boufendi, Plasma Sources Sci. Technol. **2** (1993) 204-213

[2] G. Gebauer, PhD Thesis, Ruhr-Universität Bochum, Germany, 2002

[3] Ch. Deschenaux, A. Affolter, D. Magni, Ch. Hollenstein and P. Fayet, J. Phys. D:Appl. Phys. **32**, (1999) 1876

[4] E. Stoffels and W. W. Stoffels, PhD Thesis, Eindhoven University of Technology, Netherland, 1994

[5] J. E. Daugherty and D. B. Graves, J. Vac. Sci. Technol. A **11**(4), (1993) 1126-1131

[6] A. Melzer, V. A. Schweigert, A. Schweigert, A. Homann, S. Peters and A. Piel, Phys. Rev. E, **54**(1) (1996) R46-R49

[7] S. Hong, J. Berndt, J. Winter, Plasma Sources Sci. Technol. **12**, 46-52 (2003)

[8] L. Boufendi, J. Gaudin, S. Huet, G. Viera, and M. Dudemaine, App. Phys. Lett. **79**, (2001) 4301

[9] L. Boufendi, A. Bouchoule and T. Hbid, J. Vac. Sci. Technol. A **14**(2), (1996) 572-576

[10] G. Gebauer, S. Hong, T. Galka, J. Berndt, J. Winter, Proceedings of the 29th EPS Conference on Plasma Physics and Controlled Fusion (EPS29), Montreux, 2002, Vol. **26B**, O5.24

[11] T. H. Y. Yeung and J. Sayers, Proc. Phys. Soc. London, Sect. **B 70**, (1957) 663

[12] P. J. Hargis, Jr., K. E. Greenberg, P. A. Miller, J. B. Gerardo, J. Ft. Torczynski, M. E. Riley, G. A. Hebner, J. R. Roberts, J. K. Olthoff, J. R. Whetstone, R. J. Van Brunt, M. A. Sobolewski H. M. Anderson, M. P. Splichal, J. L. Mock, P. Bletzinger, A. Garscadden, R. A. Gottscho, G. Selwyn, M. Dalvie, J. E. Heidenreich, Jeffery W. Butterbaugh, M. L. Brake, M. L. Passow, J. Pender, A. Lujan, M. E. Elta, D. B. Graves, H. H. Sawin, M. J. Kushner, J. T. Verdeyen, R. Horwath, T. R. Turner, Rev. Sci. Instrum., **vol. 65**, (1994) 140

[13] M. A. Sobolowski, IEEE Trans. plasma Sci., **vol. 23**, (1995) 1006

[14] V. P. T. Ku, B. M. Annaratone, and J. E. Allen, J. App. Phys. **84** (1998) 6536

[15] S. Hong, J. Berndt, J. Winter, The 3rd International Conference on the Physics of Dusty Plasmas. (ICPDP3), 20-24 May 2002, Durban, Southafrica, AIP Conference proceedings, "Dusty Plasmas in the New Millenium", ISBN 0-7354-0106-3, 305-308 (2002)

Acetylene carbon black production in plasma process

Tomasz Zieliński, Teresa Opalińska, Jacek Kijeński

Industrial Chemistry Research Institute, Rydygiera 8, 01-793 Warsaw, Poland

Abstract
Carbon black is an important raw material for plastics and rubber industries all over the world. The efficient, economical, and environmental friendly process for acetylene carbon black manufacturing was the goal of our investigations. The new method and the apparatus for preparation of high quality carbon black from acetylene and plasma mediums, argon and helium, using gliding discharge was proposed.

1. Introduction

The increase of using and application of plastics and rubber products in various branches of industry all over the world, creates the needs of finding new and safe methods of making carbon black. The competition on rubber market forces the carbon black industry to improve, modernize and develop. That is why there is ceaseless necessity of the elaboration the high efficient, economical and environment friendly process and finding new technologies of carbon black production of the best quality and purity. Besides rubber industry, carbon black is used in plastics industry (as a filler) and in production of paints, lacquers and inks.
Carbon black is generic name, which describes wide group of industrial carbon products with systematic nanostructures of elementary carbon [1,2]. The conventional processes for carbon black making under industrial conditions are based on an incomplete combustion of high-boiling aromatic oils or natural gas (furnace and channel processes). These processes are hardly operable and fails to meet the environmental requirements, because of the emission to the atmosphere of CO, CO_2, NO_x volatile hydrocarbons, carbon black and aromatic hydrocarbons seated on carbon black particles [3]. There is also known number of methods of carbon black making from acetylene, but with using mostly equilibrium plasma. Up till now, some investigations have been performed where a new process and apparatus were developed for hydrocarbon processing into carbon black by gliding discharge under non-equilibrium plasma conditions.
The present paper shows the results of our investigations relating to some physical and chemical properties and surface development of carbon black received in non-equilibrium plasma from acetylene, as feedstock, and argon and helium, as plasma mediums.

2. Experimental

In our study, acetylene, as a source gas, was used under argon or helium, as plasma mediums, using gliding discharge process to produce carbon black.

2.1. Apparatus

The gliding discharge was fed by a special three-phase 50 Hz high voltage power system. The plasma reactor consisted of three stainless steel main bar electrodes of special shape and one ignition electrode. The main bar electrodes were situated symmetrically around the ignition electrode at an angle of 120º. The reactor was connected to the water cooler and cyclone where all the post-reaction dust was precipitated from gas. Carbon black was accumulated in a tank situated under the cyclone. Next to the cyclone, the filtering system was located for final remove of the dust from gas. The cleaned gas was taken to the gas burettes for analysis using g. c. method. The chromatograph was supplied by the flame ionization detector (FID). B/5% Fluorocol™ Packed Column was put into use with length of 4m and diameter of 3mm. The helium was used, as a carrier gas, in the chromatograph, with flow rate of 25ml/min. the temperature of the detector was contained between 30°C and 50°C with heatup rate of 4°C/min. The equipment allowed to realize the process continuously. The schema of the apparatus is shown in Fig. 1.

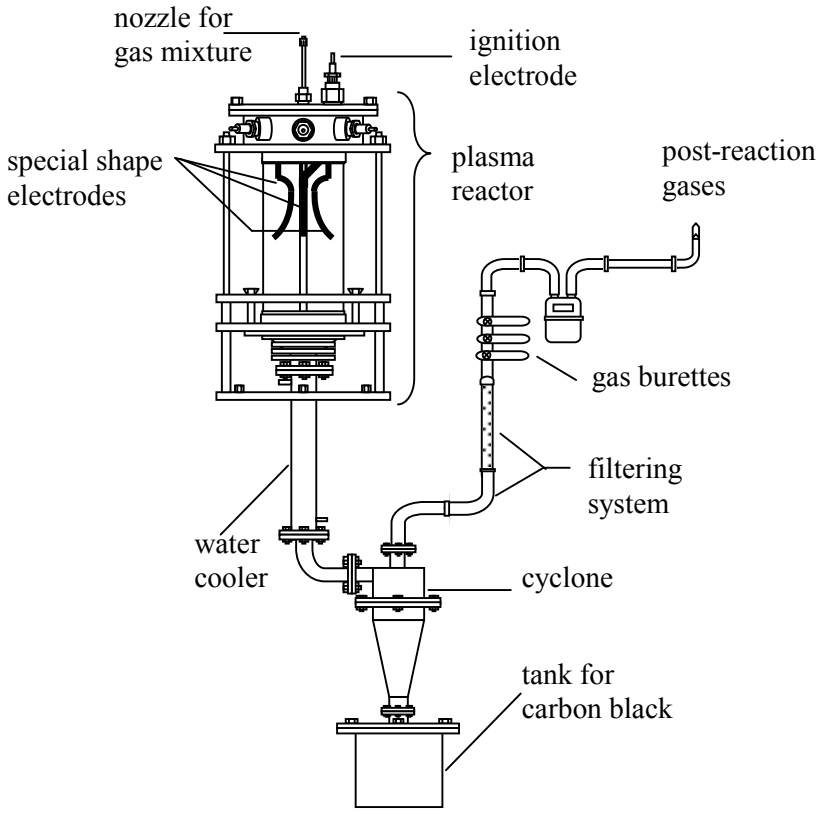

Fig. 1. The schema of acetylene carbon black making apparatus in gliding discharge.

2.2. Procedure

Gas stream of suitable composition and flow rate was injected into the reactor by a nozzle, which was situated above the electrodes. The plasma reactor and installation parameters were optimized to form the most effective field of reactions in gliding discharge. This field of reactions was situated in the whole plasma flame area, which included the maximum volume of gas mixture during the discharge in the reactor. The optimal setting of the main electrodes, besides the maximum field of reactions, allowed to get the conversion of gas reactants to 77%. Scanning electron microscopy (SEM) was used to characterize shape and size of carbon black particles formed in plasma process from various reactants. The carbon black structure properties, like interplanar distance (d_i), diameter of areas of the aromatic layers (L_a), the average thickness of layers packets (L_c), were established with using X-ray diffraction (XRD) method. The flow rate of gas mixture was changeable form 0.5 to 1.25 m^3/h and the source gas content was also changeable from 2 to 10 vol.% in the gas mixture. The compositions of the studied gas mixtures are listed in Table 1.

Table 1. The gas mixtures composition in carbon black making process.

Gas composition [plasma medium and gas reactant in gas mixture]	**Content of reactant in gas mixture** [vol.%]
Ar – C_2H_2	5
He – C_2H_2	10

3. Results and discussion

The efficiency of the process and energy consumption depend on kind of carrier gas in the mixture content of the hydrocarbon in the gas mixture. The process efficiency in acetylene carbon black production in different plasma mediums is shown in Table 2. For example, conversion of C_2H_2 and conversion of C_2H_2 to carbon black in Ar-plasma are similar and they grow up with increasing of the source gas content in the mixture, the same like process leaded in He-plasma (Fig. 2, Fig. 3). Fig. 2 shows the process conditions of Ar-C_2H_2 gas mixture composition with changeable source gas content from 2vol.% to 5vol.% of C_2H_2 in the mixture with

1.0 m^3/h flow rate of the gas mixture. Fig. 3 shows the process conditions of He-C_2H_2 gas mixture composition with changeable source gas content from 2vol.% to 10vol.% of C_2H_2 in the mixture with 1.0 m^3/h flow rate of the gas mixture.

Table 2. Process efficiency in acetylene carbon black production.

Gas composition [source gas and plasma medium mixture]	**Process efficiency**	
	[% of conversion of source gas]	[% of conversion of source gas to carbon black]
Ar – C_2H_2	37-48	35-48
He – C_2H_2	42-60	41-60

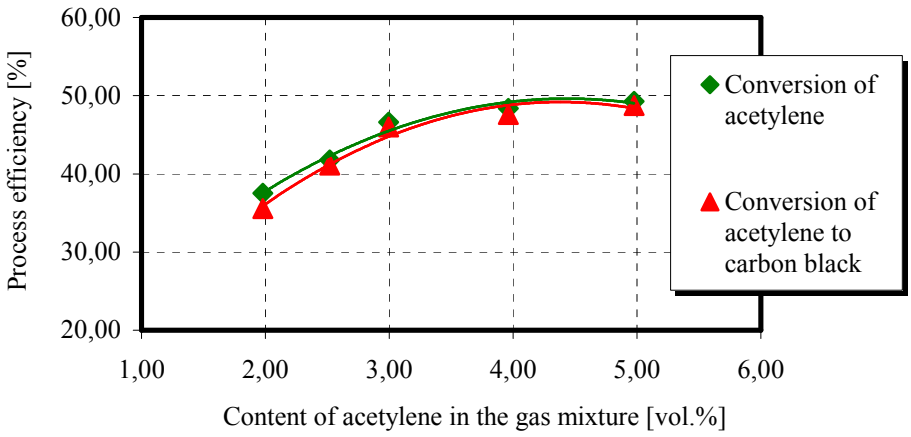

Fig. 2. Process efficiency of carbon black making process depended on content of acetylene in Ar-plasma

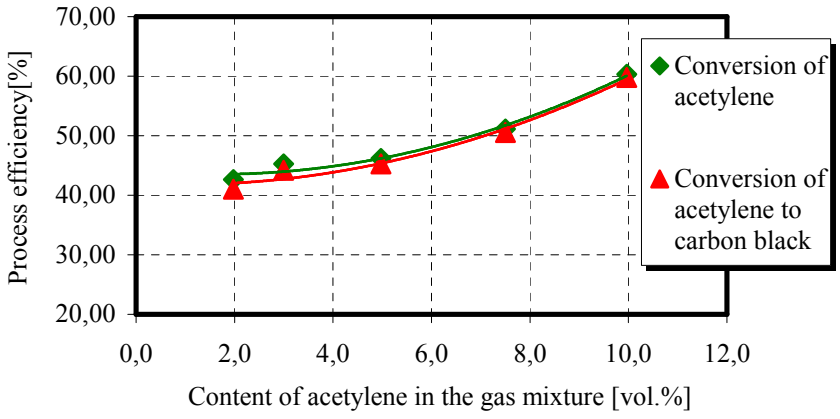

Fig. 3. Process efficiency of carbon black making process depended on content of acetylene in He-plasma

The first group of carbon blacks was obtained from acetylene and in argon as plasma medium. The results of the investigations indicated that changes of the amount of acetylene in reacting gas and its flow rate do not remarkably influence the properties of carbon black surface and its physical-chemical properties. At the different contents of gas reactants in gas mixture carbon black was synthesized of the same structure of the surface. The application of argon as plasma medium led to the formation of carbon black of more interesting properties. The optimal content of reactant in gas mixture was 5vol.% of C_2H_2 in argon plasma and with 1.0 m^3/h of gas mixture flow rate under the atmospheric pressure. SEM pictures indicated that the shapes of particles of obtained carbon black were similar independing on reaction conditions. They look like fuzzy flakes

connected together very closely. The morphology of carbon black made from acetylene in argon plasma is shown on Fig. 4.

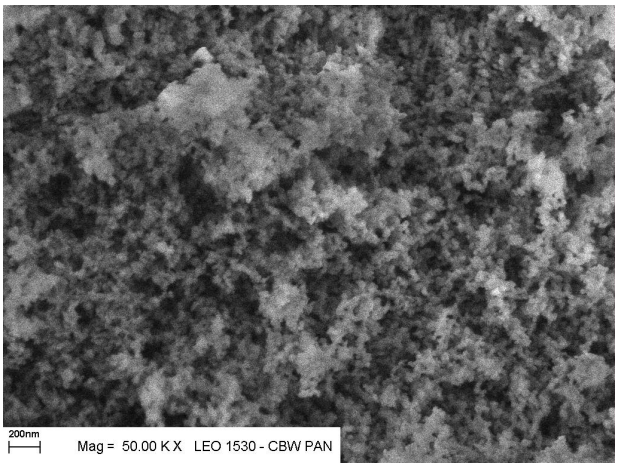

Fig. 4. The surface morphology of carbon black made from acetylene in argon plasma

The SEM picture of carbon black, prepared from C_2H_2 both in Ar plasma, showed that the particles possessed large area. Fuzzy flakes indicated on very good surface development, what was strictly connected with the high adsorption capacities. The X-ray diffraction results have shown that interplanar distance (d_i) measured for carbon black obtained from gas mixture with 5vol.% of C_2H_2 in Ar-plasma was large (Fig. 5). The large distance between layers can be considered as large as graphite layers interplanar distance (c.a. 3.4Å). The diameter of agglomerates of the aromatic layers (L_a), (Table 2) was also large and the layers did not have a bearing point. The aromatic layers could easily deflect and were mobile. The average thickness of layers packets (L_c) (Table 2) resulted in good properties and behavior of large agglomerates. The physico-chemical properties, mostly the interplanar distance closed to graphite (close to 3.4Å of d_i) and the results of BET adsorption – the specific surface area over 80 m^2/g, the iodine adsorption capacity (IA) – over 80 mg/g and dibutyl phthalate adsorption capacity (DBP) – over 100cm^3/100g, in comparison with the commercial furnance carbon black, confirmed the significant development of the surface. The produced carbon blacks exhibited high absorbability, which could facilitate the drive of molecules of various substances into their internal structure and the subsequent deposition. This was reflected by the results of adsorption like BET, adsorption of iodine (IA) and adsorption of DBP (Table 3).

Table 3. The results of XRD and adsorption measurements of carbon black made in gliding discharge

Gas mixture composition	**d_i** [Å]	**L_a** [Å]	**L_c** [Å]	**BET** [m^2/g]	**IA** [mg/g]	**DBP** [cm^3/100g]
Ar – C_2H_2	3.8	7.8	32	156	95	125
He – C_2H_2	3.7	10	38	164	127	128

The carbon black prepared from acetylene in He, as plasma medium, exhibited similar properties to the carbon black obtained from acetylene in Ar-plasma. SEM picture of C_2H_2 carbon black from He-plasma have shown the similar surface structure as in the case of C_2H_2 derived carbon black from Ar-plasma. The shape and size of particles were very borne resemblance and look like fuzzy flakes too. Nevertheless, the structure of C_2H_{42} carbon black generated in helium plasma was more agglomerated and less fluffy than C_2H_2 carbon black obtained in Ar-plasma. The particles had similar sizes like these of C_2H_2 carbon black from Ar-plasma. The morphology of carbon black surface from acetylene in He-plasma is shown on Fig. 6.

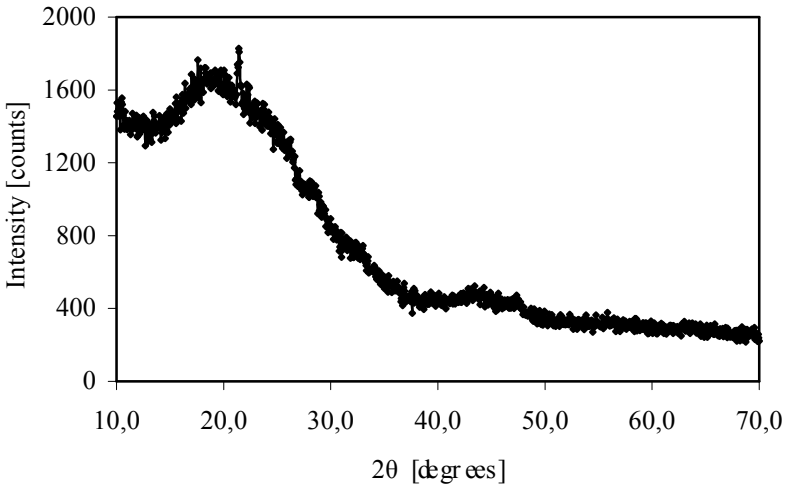

Fig. 5. The XRD pattern of carbon black surface (5vol.% of C_2H_2 in Ar)

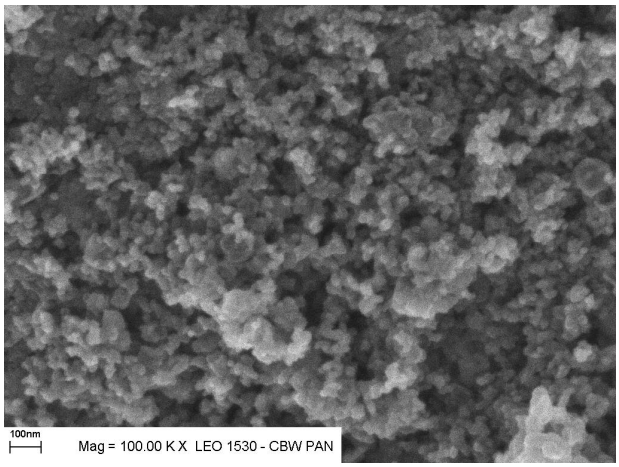

Fig. 6. The surface morphology of acetylene carbon black made in helium plasma

The structure of C_2H_2 carbon black formed in helium plasma was also similar to the one of C_2H_2 carbon black in argon plasma, however, it was more densely packed and little less fluffy. The particles had smaller diameter and were little more minute, but they were more compact.
The interplanar distance (d_i=3.7Å) established for carbon black obtained from 10vol.% of C_2H_2 in He-plasma was little lower (Fig. 7) than the interplanar distance measured for carbon black produced from gas mixture with 5vol.% of C_2H_2 in Ar-plasma (Fig. 5) (Table 3). The diameter of agglomerates of the aromatic layers (Table 3) of C_2H_2 carbon black prepared from gas mixture in He-plasma equaled to 10Å and was significantly higher than the diameter of agglomerates of C_2H_2 carbon black obtained from gas mixture in Ar-plasma, which equaled to 7.8Å. The average thickness of layers packets was higher for C_2H_2-He carbon black (38Å) than for C_2H_2-Ar carbon black (32Å). The high values of XRD parameters (L_a and L_c), calculated for Ar-C_2H_2 carbon black (Fig. 5) and for C_2H_2-He carbon black (Fig. 7.), showed their influence on upgrading the carbon black physicochemical properties. The large dimension of the agglomerates of the aromatic layers and the large average thickness of layer packets together with small interplanar distance (more densely packed particles, more stable and regular strusture) resulted in good commercial properties of carbon black surface.

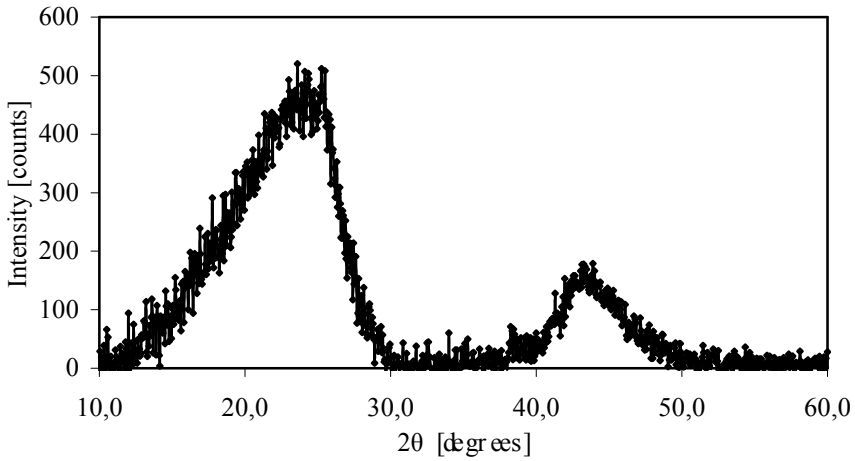

Fig. 5. The XRD pattern of carbon black surface (10vol.% of C_2H_2 in He)

The carbon black obtained in helium as plasma medium possessed the largest specific surface area and adsorption capacity (Table 3), independing on the content of gas reactant used for synthesis. From XRD results one could ascertain that C_2H_2-He carbon black had the best surface properties (facility of drive into and deposition of introduced alien molecules) of all studied carbon blacks.

4. Conclusions

The task of the study was to investigate the surface development of carbon black made in gliding discharge plasma treatment of acetylene in argon or helium. The results of the studies indicated the high increase of the carbon black surface area, especially measured by BET adsorption of nitrogen. The application of gliding discharge for the preparation of carbon black from acetylene allowed to produce material of stable and regular structures. The high adsorption capacity of the prepared carbon black in respect to nitrogen (BET), iodine and dibutyl phthalate indicated a good absorbability, allowing molecules of various substances easily drive into and settle on carbon black surface. This makes possible to use these kinds of carbon black as fillers in rubbers or plastics. There existed the relationship between the values of XRD parameters, like average interplanar distance, diameter of agglomerates of the aromatic layers, the average thickness of layers packets and studied physicochemical properties. E.g. the increase of interplanar distance was reflected in a rise in adsorption capacity. The process efficiency depends on and grows with the increase of source gas content in the mixture, but it has no influence on properties of produced carbon black. Therefore the C_2H_2 in Ar-plasma derived carbon black seemed to be more useful than the one produced from C_2H_2 in He-plasma, because of the economy of the process and the much lower commercial price of argon, than helium, as plasma medium.

Acknowledgement

This work has been supported by the State Committee for Science Researches (KBN, Grant No. PBZ/KBN/018/T09/99).

References

[1] L. Fulcheri, Y. Schwob, B. Variot, G. Flamant, J.M. Badie, G. Vallbona, F. Kassabji, J. Saint Just, A 3-Phase A.C., VDI Berichte, **1166,** 525-532 (2003)
[2] L. Fulcheri, Y. Schwob, Int. Workshop on Nanostructured Materials, NANOS 94, Odeilo, France, (1994)
[3] Ullmann's Encycl. of Ind. Chem., vol. A5. Weinheim: VCH Verlags Gesellschaft, 140 (1986)

SPECTROSCOPIC CHARACTERIZATION OF PLASMA DURING PULSED LASER ABLATION OF GRAPHITE FOR THE SYNTHESIS OF CARBON NANOSTRUCTURES

V.S. Burakov, N.V. Tarasenko, A.F. Bokhonov and M.I.Nedel'ko

Institute of Molecular and Atomic Physics National Academy of Sciences of Belarus, 70 Scaryna Ave., 220072 Minsk, Belarus

During recent years laser ablation of carbon containing targets has been an attractive subject of studies because of promising technological applications, in particular, carbon clusters and nanotubes fabrication [1,2]. For optimization of these applications the detailed understanding the basic physical and chemical processes governing the ablation plume composition and reliable methods for controlling of the relative amounts of plume species are required. The physical properties of plasma plume, such as species concentrations and temperature, directly affect the properties of the material being formed. Different laser-induced effects through mechanisms of laser-surface and laser-plasma interactions may be useful for the management of ablation plume characteristics. In this context, the double-pulse laser ablation technique leading to better coupling of laser pulse energy to the target and ablated matter is of great interest.

This paper presents diagnostic data obtained for the laser ablated plume of a graphite composite samples during the synthesis of carbon nanostructures.

The Nd-YAG (1064 nm, 10 ns, $5 \cdot 10^8$ W/cm^2) laser radiation in combination with the second harmonic (532 nm, $5 \cdot 10^7$ W/cm^2) radiation of another Nd-YAG laser at different temporal delays between pulses were employed for ablation. The laser beams were focused on the surface of the graphite sample (with 1% nickel catalyst) placed in the chamber under helium environments.

Spectroscopic characterization of the ablated plume was performed by the time resolved emission spectroscopy and laser-induced fluorescence methods. The details of these diagnostic techniques were described in [3].

The plasma emission spectra (300-700nm) were recorded and compared for different ablation regimes (single pulse and double pulse in coincidence and in sequence at various delays between pulses and laser fluences). The major species including CI, CII, and C_2, C_3 radicals within the plume have been identified. The spectra were dominated by the C_2 Swan bands ($d^3\Pi_g$ - $a^3\Pi_u$). The emission in the wavelength range 390 - 410 nm was identified as the C_3 (Comet Head System: $A^1\Pi_u$ - -$X^1\Sigma_u^+$). The C_2 high-pressure bands in the spectra were also recorded including the (6 - 7) band at 543.4 nm and (6 - 8) band at 589.9 nm. From emission spectrum of C_2 molecules the vibrational temperatures at various experimental conditions were determined. The vibrational temperatures were found to be much higher than the carbon sublimation temperature (≈4100K for 100 Torr helium atmosphere).

The experiments demonstrated increased plasma emission, higher degree of particle atomization and a higher proportion of ions in dual-pulse ablation regime compared to the plasma produced by one laser. The optimal pulse separations were found both for atomic and ionic lines. The coupling of the second laser beam into the laser-ablated plume caused both significant ionic excitation as well as changes of molecular plume dynamics.

The C_3 band intensity in plasma produced by the sequence of two laser pulses was larger in comparison to the single pulse mode. In contrast to the ionic lines the enhancement of molecular emission was observed in a rather small interval of pulse separations (0-5 μs for C_3 molecules). The dependence of C_2 band intensities on the time delay between laser pulses was similar to that for C_3 molecules, but the enhancements were smaller. When two pulses were fired simultaneously the effect was more than just additive both for the C_3 and C_2 band intensities.

So, the double-pulse laser ablation enables the plasma to be further affected in a controlled way. By proper selection of the pulse separations and wavelengths in the sequence of two laser pulses the parameters of the near-surface plasma can be adjusted to optimize the synthesis of carbon nanostructures.

[1] C.D.Scott, S.Arepalli, P.Nikolaev, R.E.Smalley - Applied Physics. **A72,** 573 (2001)
[2] A.A. Puretzky, D.B. Geohegan, X. Fan, S.J. Pennycook - Applied Physics. **A70**, 153, (2000).
[3] V.S. Burakov, N.V. Tarasenko, N.A. Savastenko - Spectrochimica. Acta. **B 56**, 961 (2001).

Modeling the plasma etching process of SiO_2 substrates: from the equipment setting to the profile morphology

Antonino La Magna[1] and Giuseppe Garozzo[2]

[1] *Istituto per la Microelettronica e Microsistemi CNR-IMM Sez. Catania Stradale Primosole I-95121 Catania*
[2] *STMicroelectronics Stradale Primosole 50, I-95121 Catania*

Abstract
In this paper a complete modeling methodology is applied to the simulation of the dry-etching process of SiO_2 substrates in fluoride-carbon plasmas. The model, implemented in a profile solver based on the level-set method for evolving surfaces, considers the concurrent ion enhanced chemical etching of the adsorbed film and the deposition of an inhibitor compound (polymer) film. The simulation results are compared with experimental etched profiles in different conditions in order to demonstrate the approach reliability.

1. Introduction

The control of the plasma-etched profile geometry in term of the profile Aspect Ratio (AR) and topography is a stringent requirement for the front-end and back-end manufacturing process for microelectronics devices [1]. The complexity of the surfaces phenomena occurring during the erosion process makes strongly inefficient an empirical process development procedure, since a simple extrapolation of the needed machine parameters from known process recipes leads frequently to erroneous predictions of the etching results. In the case of fluoride-carbon plasma etching the situation is even more critical since dry-etch proceeds by means of concurrent Ion-enhanced Chemical Etching (IeChE) of the exposed surface and the deposition of an inhibitor compound [2,3]. Consequently, the need for reliable simulation codes, supporting the process development, is urgent.
Recent theoretical works have been dedicated to investigate different aspects related to the modeling of the plasma etching process, addressing e.g.: the plasma status [4] the surface erosion mechanism [5], the profile evolution [6]. However a comprehensive approach to the plasma etching problematic in view of the application to the process development is still in evolution. Aim of this work is presenting a complete formulation and the implementation of a computational tool for the dry-etching simulation, which should able to support the experimental work on this field.

2. The etching modeling

We implemented our model for the dry-etching process using the level-set scheme for the simulation of an evolving front proposed by Sethian and co-workers [7]. In the level-set method the evolution of the moving front is ruled by a master equation for a function having the moving surface as zero level. Assuming that the initial position of the interface can be represented by the curve Φ in R^d, we can define a function $\phi(r, t=0)$ from R^d to R having the following property $\Phi(t=0) \equiv \{r \in R^d: \phi(r, t=0) = 0\}$. The evolution equation for ϕ is

$$\phi_t + F\,|\nabla\phi| = 0 \qquad (1)$$

where F is the speed of the front in its normal direction (i.e. the etch rate or the deposition rate). The profile curve at a given time $\Phi(t=t^*)$ can be interpolated as the zero level of the evolving function $\phi(t^*)$ since $\Phi(t=t^*) \equiv \{r \in R^d: \phi(r, t=t^*) = 0\}$.
Dry etch in medium/high density fluoride-carbon plasmas is believed to be the result of a concurrent etching (of the SiO_2 substrate) and deposition (of a fluorocarbon film) phenomena. In our model we consider a single active specie (namely the reagent), a single inhibitor specie (namely the polymer) and a single ion specie. Three surface coverages (i.e. the fraction of surface covered by given specie) are considered in the model Θ_e, Θ_P and $\Theta_{e/P}$ relative to the dielectric-reagent, polymer and polymer-reagent. The coverages satisfy to the following sites balance equations:

$$\frac{d\Theta_e}{dt} = J_e S_e (1 - \Theta_e - \Theta_P) - k_{ei}^e J_i Y_{ei}^e \Theta_e - k_{ev} J_{ev} \Theta_e \cong 0 \qquad (2)$$

$$\frac{d\Theta_P}{dt} = J_P S_P - J_i Y_{ei}^P \Theta_P \Theta_{e/P} \cong 0 \qquad (3)$$

$$\frac{d\Theta_{e/P}}{dt} = J_e S_{e/P}(1-\Theta_{e/P}) - J_i Y_{ei}^P \Theta_{e/P} \cong 0 \qquad (4)$$

We assume a simple sticking model for the dielectric-reagent, polymer and polymer-reagent adsorption and the relative sticking coefficient are S_e, S_P and $S_{e/P}$ respectively. These latter are the probabilities to obtain a reactive event form an impinging (surface encounter) event. We note that the reagent can cover the nude dielectric surface or the polymer coverage. Therefore, while polymer coverage growth-rate is proportional to the relative flux J_P; both dielectric-reagent and polymer reagent growth-rate is proportional to the global neutral fluxes J_e. Ion enhanced chemical etching is assumed to occur for the three species (negative terms in Eqs (2-4) proportional to the ion flux J_i) whilst evaporation is considered only for the dielectric-reagent (term in Eq. 2 proportional to the evaporation flux J_{ev}). Note that J_{ev} is proportional to J_e, and in the following we $J_{ev} = 2.71^{-3}\ exp(-0.168/kT)\ J_e$. The other parameters are the k factor relative to the stochiometry of the reactions and the chemical sputter yields Y_{ei} (normalised to the local ion fluxes).

The etched surface speed in eq. (1) depends on the materials (reagent or polymer) covering the surface element taken into account, and it can be positive (etch case) or negative (deposition case). Let us consider first the polymer case. Assuming a polymer erosion by chemical sputtering we have that polymer etch rate is

$$ER_P = \rho_P^{-1} Y_{ei}^P J_i \Theta_{e/P} \qquad (5)$$

where ρ_P is the polymer density. The polymer deposition rate is

$$DR_P = \rho_P^{-1} S_P J_P \qquad (6)$$

If $DR_P > ER_P$ (i.e. if $\Theta_P>1$) the inhibitor polymer film will soon cover the whole surface elements. Therefore we can neglect Eq.2 and the normal profile speed will be

$$F = \rho_P^{-1}(Y_{ei}^P J_i \Theta_{e/P} - S_P J_P)\,. \qquad (7)$$

Where ρ_P is the polymer density. Else if $DR_P \le ER_P$ the film etches can occur. We can derive the coverage Θ_e from the equations (2-4) and the etch rate is

$$F = \rho_{SiO2}^{-1}\left[J_i Y_{ie}^e \Theta_e + J_i Y_s (1-\Theta_e) + J_{ev}\Theta_e\right] \qquad (8)$$

here ρ_{SiO_2} is the dielectric density. In this case we consider also the possibility of physical sputtering of the SiO_2 substrate and Y_s are the sputtering yield.

Yields, fluxes and, consequently, coverages in Eqs. (2-8) depends self-consistently on the profile evolution and they should be explicitly determined at each profile point *P* when the instantaneous global geometry of the front itself is given. Neutral and polymer fluxes J_e and J_P are isotropic; therefore the component of the flux normal to the surface element located at a given front point *P* is

$$J_{iso} = J_0 / 4\pi \int_\Omega \cos[\alpha(\hat{n}(P),\hat{\omega})]d\hat{\omega} \qquad (9)$$

where J_{iso} is J_e *or* J_P, while J_0 is J_{e0} or J_{P0}, i.e. the incoming fluxes on the wafer (flat) surface. $\alpha(\hat{n}(P),\hat{\omega})$ is the angle between the normal at the profile point *P* and the direction ω of the incoming molecular specie, while the integral is performed over the whole visibility solid angle Ω. Ion flux is directional and its value is the summation over the ionic distribution exiting from the sheath potential zone. If the sheath is collisionless, we can reasonably assume that the ion distribution is a shifted maxwellian [7] and for the ion flux we obtain

$$J_i = (J_{i0}/2\pi)\iint_\Omega \cos[\alpha(\hat{n}(P),\hat{\omega})]G(\theta)d\hat{\omega} \qquad (10)$$

where

$$J_{i0} = n_{i0}\left(2kT_+ / M\pi\right)^{1/2} \qquad (11)$$

is the ionic flux over a flat surface, $3kT_+/2$ is the average kinetic energy of the ions when they reach the sheath edge, while the $G(\theta)$ function depends only on the angle θ which the ions form with the electric field

$$G(\theta) = \exp(R)\exp(-R\sec^2\theta)(1 + R\sec^2\theta) \qquad (12)$$

with $R=eV_s/kT_+$. In the following we assume that T_+ is equal to the electron temperature T_e.

Using analogous considerations and assuming an univeral dependecnce of the yeild efficiency on the ion energy [5]: $Y(E) \propto E^{1/2}-E_{th}^{1/2}$; we can derive the local yield functions:

$$Y(P) = \widetilde{Y} / 2\pi \int_{\Omega} Y(\alpha[\hat{n}(P), \hat{\omega}]) G_Y(\theta) d\hat{\omega}; \qquad \widetilde{Y} = A / \eta \left(kT_+ / \pi\right)^{1/2}, \qquad (13)$$

here η is the rate between of the ion density at the substrate n_s and ion density in the plasma region

$$\eta = n_s / n_{i0} = 0.5\exp(R)erfc(\sqrt{R}). \qquad (14)$$

The expression of $G_Y(\theta)$ depends on the sheath potential value. In particular, if $eV_s \geq E_{th}$

$$G_Y(\theta) = \exp(R)\left[\exp\left(-R\sec^2\theta\right)\left[1 + R\sec^2\theta - \sqrt{RR_{th}}\sec\theta\right] - \sqrt{\frac{\pi}{2}}\sqrt{RR_{th}}erfc\left(R\sec\theta\right)\right] \qquad (15)$$

with $R_{th} = E_{th} / kT$. Once the actual profile geometry is given, we can calculate the front speed at each profile point, using the fluxes and yields expressions (Eqs. 9-18) in the equations of the deposition/etch model (Eqs. 2-8).

We note that the etching features related self-consistently with the profile geometry during the etching evolution could be analysed only using the profile solver. Simulation results relative to dry-etching processes ($t_{tot}=80s$ and $\Delta t=2s$) at different values of reagent and polymer fluxes ($J_{i0}=5.6\times10^{16}$ at/cm^2s) are shown in the fig. 1. We consider a 300nm thick ideal resist film ($F=0$ in the resist region) and different window sizes: 300nm, 200 nm, 400 nm (only the final profile is shown for these last two cases). The profile shape is the result of the interplay between geometrical constrains and the relative weight of the active/passive adsorbed species. Of course the increase of the active component improves the vertical speed of the etch; however it also causes a further shrinking of the profile bottom (see Figs 1 a,b,c) which does not allows to change substantially the verticality of the wall. In turn the decrease of the polymer component (fig. 1 b,c) , while it does not affects so much the vertical speed, results in a less tailored profile. The entity of the RIE-lag effect is more pronounced for low polymer fluxes when the visibility constrain reduces mainly the role of the active component. Finally the effect of the window size on the overall profile shape is typical of the single processes.

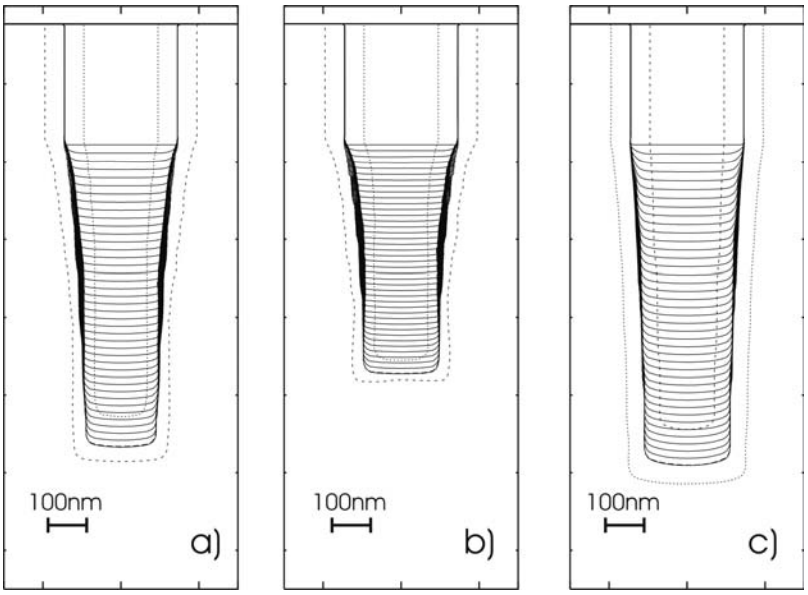

Fig. 1 Simulated profile evolution as consequnce of different dry-etching processes in a trench geometry. The initial profiles are a 300nm (solid lines), 200nm (points), 400nm (dashed lines) wide vertical windows opended in a 300 thick nm ideal resist mask. The flux values are a) $J_{i0}=5.6\times10^{16}$, $J_{e0}=3\times10^{17}$ and $J_{P0}=1\times10^{17}\,at/cm^2s$; b) $J_{i0}=5.6\times10^{16}$, $J_{e0}=1\times10^{17}$, $J_{P0}=1\times10^{17}\,at/cm^2s$ c) $J_{i0}=5.6\times10^{16}$, $J_{e0}=3\times10^{17}$ $J_{P0}=3\times10^{16}\,at/cm^2s$. The total etching time is $t_{tot}=80s$. In the 300nm cases profiles simulated after time interval of $\Delta t=2s$ are also shown.

4. Experimental conditions and model parameters estimate

The application of the model to the simulation of experimental dry-etching processes requires the estimate of model parameter in relation to the equipment parameters, which can be tuned by the process engineers (electrode powers, gas fluxes, etc.). In the experiments, the equipment used is a dual frequency Diode Reactor Etcher (see ref. [9] for details on the equipment characteristics). The plasma formation is controlled by the top electrode at the frequency of *27 MHz*, whilst the ion acceleration by the bottom electrode at *2 MHz*. The equipment parameters that we can handle are: the electrode watt top (*Wt* in watt), the electrode watt bottom (*Wb*), the gas fluxes (Q_X in standard cubic centimeter *sccm, 1sccm = 2.689 · 10^19 molecules/min* at standard condition, i.e. at *Pressure=1Atm* and *T =273.15°K*), the chamber pressure (*P* in *mT*). In the process, analysed with the simulation code in the following section, we choose this set of machine parameters: *Wt=1000W*, *Wb=2000W*, *P=30 mT*. The used chemistry is based on C_4F_8 and more precisely we have used this following gases mixing $Ar/C_4F_8/N_2/O_2$ with fluxes $Q_{Ar}=120sccm$, $Q_{C4F8}=10sccm$, $Q_{O2}=3sccm$, $Q_{N2}=70sccm$, therefore the correspondent total flux (Q) is $Q=203\ sccm$.

In order to test the reliability of the simulation code we considered different geometries for the etching, therefore a ~80nm thick anti-reflecting film and ~320nm thick resist film (formed by different moistures of organic polymers) were deposited on the SiO_2 substrate and different windows was opened in the film, considering: 1D flat zone (18μm wide), 2D trenches (340 nm wide) and 3D hole (radius 100nm). The etching time was $t_{tot} = 40s$. In fig. 6 we show an analysis of the etched profile in the case of the 2D trench, performed by means of Scanning Electron Microscopy (SEM). The resist film, the anti-reflective film and the substrate zones are well visible in the image, as well as the residual polymer film deposited mainly on the walls in the substrate zone.

In the derivation of the model parameters (see Ref [10] for details] we should distinguish the chemical-physical (fixed) parameters from the parameter related to the plasma characteristics, which can be modified, is means of the equipment setting. In the first set we can include the quantities related to the interactions between ions, etchant, polymer and material, i.e. IeChE and sputtering yield efficiencies, sticking coefficients, stoichiometry factors, threshold energies, material properties. We extracted these parameters from literature data (see Refs.[5,8]) and their are reported in Table 1. The second set table2 includes fluxes and sheath potential (in particular $R_s=eV_s/kT_e$, J_{i0}, J_{n0}, J_{p0} or equivalently R_s, n_{i0}, n_{n0}, n_{p0}) which can be relied to W_t,W_b,P,Q_X.

S_e	$S_{e/P}$	S_P	A^e_{ei}	A^P_{ei}	A^e_{sp}	B^e_{sp}	k^e_{ei}	E^e_{th}	E^P_{th}	E^e_{thsp}
0.9	0.6	0.26	0.036	$4A^e_{ei}$	0.014	9.3	2	4	4	18

Table 1 Model parameters related to the interaction between plasma and substrate. Their values are extracted by the references [9] and [15].

eV_s [eV]	kT_n [eV]	kT_e [eV]	$n_{i0}[cm^{-3}]$	$n_{e0}[cm^{-3}]$	$n_{p0}[cm^{-3}]$
500 (P=30mT)	0.2	5 (P=30mT)	$1\times10^{11} \div 3\times10^{11}$	$1\times10^{13} \div 2\times10^{13}$	$10^{12} \div .10^{13}$

Table 2 Estimates of the model parameters related to the plasma status in our experimental conditions.

5. Comparison between experiments and simulation results

In order to demonstrate the simulation reliability we should achieve a reasonable agreement between the morphology of simulated profiles and the real profile for different geometric constrains. In fact, as we verified by means of simulations performed in a wide range of condition, the profile topography is a fingerprint of the assumed plasma related parameters.

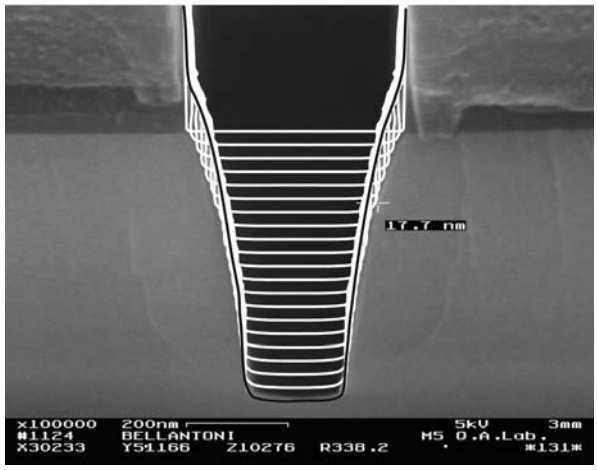

Fig. 2 Comparison between eroded profile and simulated profile evolution in the 2D trench geometry. The density values are $n_{i0} = 2.3\times10^{11}$, $n_{e0}=1.6\times10^{13}$, $n_{p0} = 6.4\times10^{12}$ cm^{-3}. Simulation parameters are reported in Tables I and II. The final simulated profile is evidenced by the black line.

In fig 2 we show a SEM image of the etched profile obtained by means of the process described in the previous section in the case of large stripes. The eroded depth in a flat zone is $z_{1D} \cong 490$nm (i.e. an etch rate of $F_{1D} \cong 12.25$ nm/sec), where the depth measurement was performed away from the edge zone. Of course the measured etch rate in a flat zone can be predicted only for a further restricted range of parameters, with respect of the range reported in Table II. However, using the same parameter set, we should be able to recover the profile evolution and morphology in the 2D and 3D geometries (trench and hole).

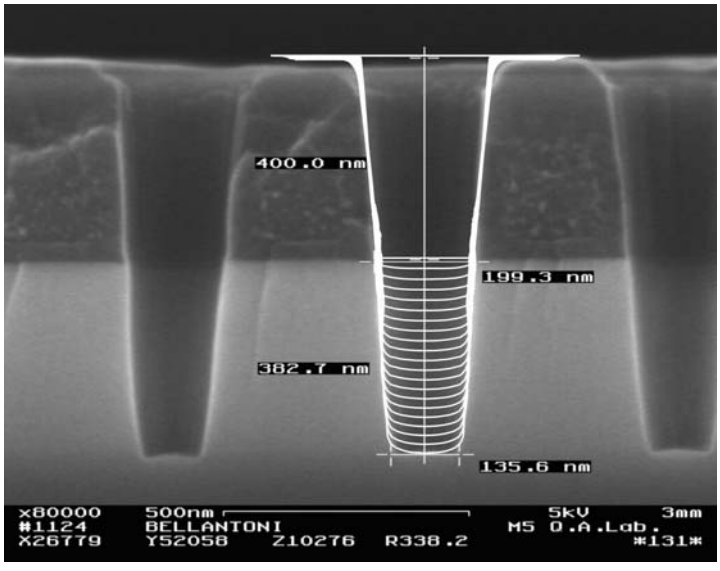

Fig.3 Comparison between eroded profile end the simulated profile evolution in the 3D hole geometry The density values are $n_{i0} = 2.3\times10^{11}$, $n_{e0}=1.6\times10^{13}$, $n_{p0} = 6.4\times10^{12}$ cm^{-3}. Simulation parameters are reported in Tables I and II.

In fig. 3 the simulation of the etched profile evolution in the trench case is compared with the SEM analysis of the process. In this case also the evolution in the resist zone (resist + antireflective film) is simulated using the same model used in the case of the SiO_2 substrate. The different resist behaviour is recovered considering low IeChE yield ($A^e_{ei}(Resist) / A^e_{ei}(SiO_2) = 10^{-3}$) and sticking coefficients ($S_e(Resist)=0.1$,

$S_P(Resist)=0.01$) so that the physical sputtering mainly causes the resist erosion ($A^e_{sp}(Resist)/A^e_{sp}(SiO_2)=1.5$). Moreover, we assume that $S_P=0.6$ in the antireflective organic film (see the darker zone over the SiO_2 substrate). We note that a reliable simulation of the erosion evolution in the resist zone is necessary since, in general, it could affect considerably the visibility angle seen by the profile points in the substrate. The following parameter are used $n_{i0} = 2.3\times10^{11}$, $n_{e0}=1.6\times10^{13}$, $n_{p0} = 6.4\times10^{12}$ cm^{-3} (which give the flat etch rate value F_{1D}=12.25 nm/s). Note in the optimisation of the model parameters we used valued in the range reported in the Table II, moreover practically only n_{p0} was changed considerably (within one order of magnitude wide range) in order to obtain a good estimate of the polymer deposited thickness on the walls.
A noteworthy agreement between simulation and experimental analysis of the profile can be observed. Simulation reproduces correctly the small *inverse RIE-lag* evidenced by the erosion process in the 2D trench (520 nm eroded depth with respect of 490nm eroded depth of the flat zone). Moreover, both the profile shape than the amount of polymer deposited on the wall evidenced by the SEM analysis are recovered by the simulation within the grid resolution (10 nm).
Finally, in fig.9 we show the comparison between simulations results and SEM analysis of the etching process in the 3D-hole geometry (a section passing on the hole axes is reported). In this case the geometric constrain causes the *RIE-lag*. All the flux components are strongly reduced and the small polymer deposition on the wall cannot be experimentally evidenced. The comparison demonstrates further the reliability of the numerical simulations: a good agreement between the simulated and eroded profile can be observed in term of depth and shape.

6. Discussion

The methodology presented in this work deals with all the steps needed in order to build up a simulation code which should lead to useful prediction on profiles resulting after a plasma-etching process. These steps are: the implementation of a robust profile solver, the formulation of a surface etching model including all the relevant microscopic phenomena, the derivation of the relationships between local parameter to plasma parameters and between plasma parameters and machine parameters and, finally, the application on real processes by means a comparison between simulations and eroded profile microscopes. Our aim is implementing a code which is able to predict the resulting profile shape in various geometry constrain. Achieving this target should provide to the process engineers a useful tool in the scaling-down of the microelectronic device technology. The method looks like promising: Indeed the code is robust and highly versatile; moreover is able to capture the features commonly observed in the development of dry-etching processes varying the machine parameters and the gas moisture. The capabilities of the simulator has been demonstrated comparing simulated profile evolution and the SEM analysis of the profile resulting in plasma-etching processes specifically designed in different geometries in order to test the code. After a suitable paramerization the simulations quantitatively estimate the profiles depth and shape in really different geometrical constrains where inverse-RIE, lag, RIE-lag and profile tailoring occur changing the opened window.

References

[1] International Technology Roadmap for Semiconductor, 1999 edition, see the site http://public.itrs.net.
[2] R. A. Gottscho, C.W.Jugensen e D.J.Vitkavage, J. Vac. Sci. Technol. B **10**, 2133 (1992)
[3] G.S. Oehrlein, Y. Zhang, D. Vender, and M. Havelang, J. Vac. Sci. Technol B **12** 323 (1994)
[4] H. Hayashi, S. Morishita, T. Tatsumi, Y. Hikosaka, S. Noda, H. Kakagawa, S. Kobayashi, M. Inoue, T. Hoshino, J. Vac Sci Technola **A17**, 2577 (1999).
[5] E. Gogolides, P. Vauvert, G. Kokkoris, G. Turban, A. Boudouvis J. Appl. Phys, **88,** 5570 (2000).
[6] M. Tuda, K. Nishikawa, K. Ono J. Appl. Phys. **81**, 960 (1997).
[7] S. Osher and J.A. Sethian, Jour. Comp. Phys, **79**, 12 (1988).
[8] V. Vahedi, D.J. Cooperberg, J.M. Cook and R.A. Gottscho (unpubblished)
[9] M.A. Lieberman, A.J. Lichtenberg ‘’Principles of Plasma Discharges and Material Processing’’ (Wiley, New York 1994).
[10] A. La Magna and G. Garozzo, submitted to J. Chem. Soc.

RF electrode sheath formation near non-flat substrates

K.E. Orlov, A.S. Smirnov, T.V. Chernoiziumskaya, D.A. Malik

Plasma Physics Department, St.-Petersburg State Polytechnical University, Politechnicheskaya 29, St.-Petersburg, 195251, Russia

Abstract

In this work we present experimental results concerning electrode sheath and ion flux formation near non-flat electrode with dimension of a cavity comparable to the electrode sheath length. It is shown that the secondary electron emission can play a crucial role in plasma molding over electrode surface. It is also observed that plasma has a tendency to "self-leakage" in electrode cavities. In this case, separate discharges sustained by enhanced secondary electrons ionization are formed in cavities.

1. Introduction

The interaction of plasma with a surface containing topographical features is critical for coating of curved objects, etching of surfaces of complex form and plasma immersion ion implantation. The flux, energy, and angular distributions of ions incident on the target are of primary importance. These quantities depend critically on the shape of the meniscus plasma–sheath boundary formed over the surface topography. Electrode sheath formation near surface topography is governed by ratio between electrode sheath length (L) and characteristic dimension of surface structure (d). In limiting cases L>>d (thick sheath) and L<<d (thin sheath) two dimensional perturbation of a sheath structure is minimal and the sheath can be considered as a locally flat one [1]. In this work we present experimental results concerning sheath structure formation in an intermediate case of cavity dimension comparable with electrode sheath length.

2. Experimental setup

Experiments were carried out using a setup schematically drafted on Fig.1. 13.56 MHz driven discharge was burned between two parallel plane electrodes. The upper electrode 22 cm in diameter was connected through a blocking capacitor to RF generator, the lower electrode was connected to the grounded discharge chamber walls. The chamber was equipped by standard electrical diagnostics, thus, the applied voltage amplitude, self-bias, RF current and loaded power were controlled during experiments. The discharge was operating in Ar with background pressure 4?30 mTorr. Due to low operating pressures and the difference in electrodes area, the discharge was operating in asymmetrical regime and the voltage drop in the grounded electrode sheath was typically 10 times lower than on powered electrode. An energy distribution of ions impinging the grounded electrode surface was controlled by means of a multi-grid energy analyzer [2-3]. The analyzer was placed in differentially pumped high vacuum chamber and connected with discharge region by 1 mm diameter orifice. Ion energy distribution functions (IEDF) were obtained by differentiation of the retarding characteristics. The overall energy resolution in obtained ion spectra was about 3 eV.

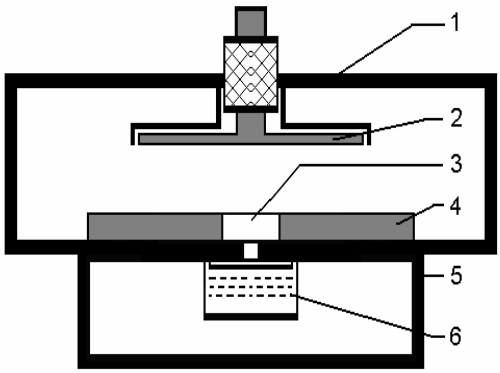

Fig. 1 Schematic draw of the experimental system. 1 – discharge chamber, 2 – powered electrode with ground shield, 3 – cavity on the grounded electrode, 4 – grounded electrode, 5 – high vacuum chamber, 6 - multi-grid energy analyzer

Experiments were carried out in two regimes; flat and holed electrode surface. In the first set of experiments, IEDF was measured for usual capacitive discharge configuration with flat, parallel electrodes. In the second series, the grounded electrode was equipped by a flat cover plate with a cylindrical cavity (15 mm. diameter, 10 mm. height). The axis of the cavity was alignment with 1 mm inlet orifice of the energy analyzer. In this series the IEDF was measured for ions flowing to the down faceplate of the cavity.

3. Experimental results

Experimentally observed ions spectra are presented in Fig.2,3. For the flat electrode regime, the IEDF always has a clearly pronounced peak at high energy part with a semi-exponential tail towards low energy part. The maximal ions energy rises with increasing loaded power. Such ions spectra are typical for low-pressure RF discharges and were previously observed by many authors [3,4].

The main features of the ions flux formation in the cavity are represented in Fig.3. As the discharge loaded power increases the IEDF experiences two realignments of the shape. In the low power regime (Fig.3a), the IEDF stepwise switches from single peaked shape to two-peaked one. The low energy peak is observed around energies 8-9 eV. With increasing of loaded power the height of low energy peak increases while the energy remains approximately constant. The high energy peak is also observed and its energy increases with increasing loaded power. With further increasing of loaded power (Fig3.b) the IEDF switches back from two-peaked shape to single peaked one.

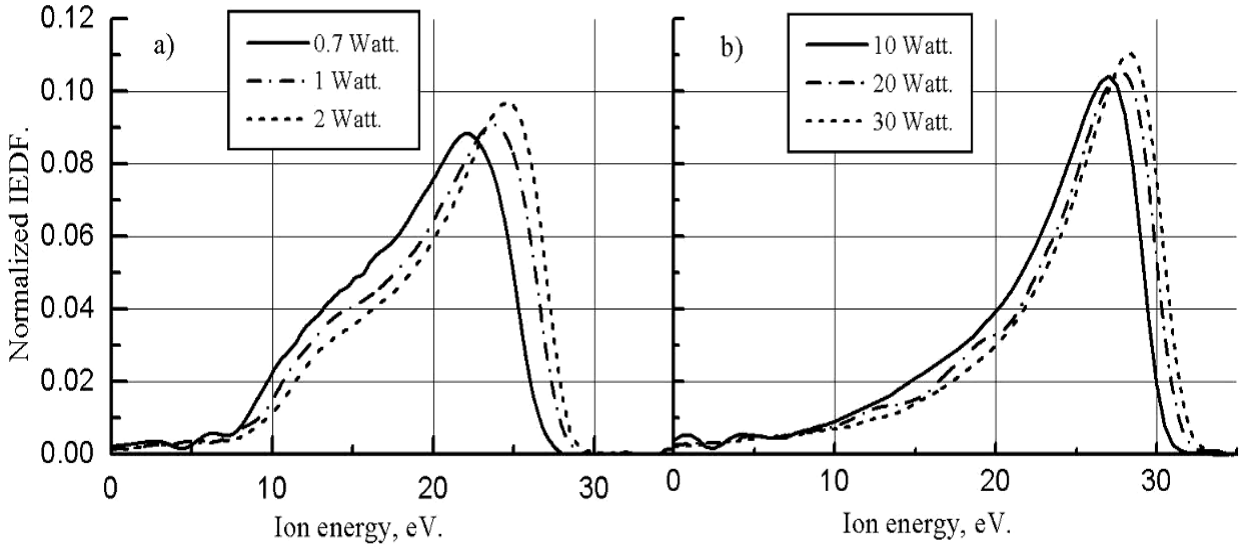

Fig. 2 Energy distribution function of ions bombarding the flat electrode surface at different values of discharge loaded power. Ar, p=5mTorr

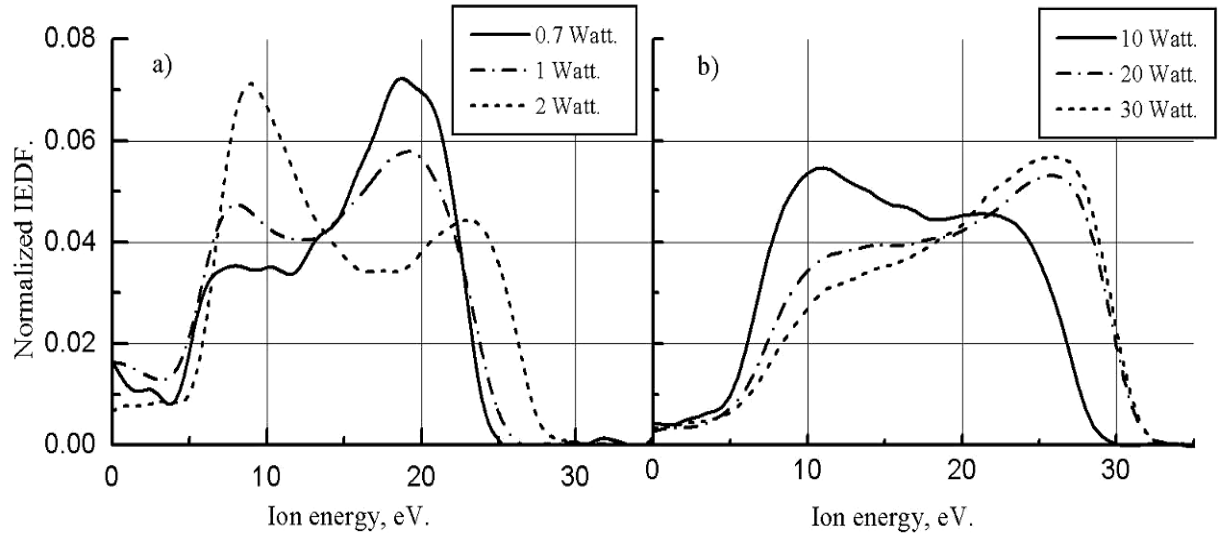

Fig. 3 Energy distribution function of ions bombarding the down faceplate of cylindrical cavity at different values of discharge loaded power. Ar, p=5mTorr

4. Discussion

To analyze obtained data let us consider general features of electrode sheaths formation in a RF driven discharges. The condition $?_i << ? << ?_e$ ($?_i$, $?_e$ are ions and electrons plasma frequencies respectively, $?$ is driven frequency) is typically satisfied for RF discharge operation regimes. In this case, ions form a steady-state density profile and positive charged sheaths are formed near electrode surfaces. The boundary between the quasi-neutral plasma and space charge sheath oscillates between maximum distance from electrode L (typically called "sheath length") and electrode surface. Consequently, voltage in the sheath changes from a maximum value U_{max} to zero. Ion movement toward electrode surface is governed by an averaged over many RF periods electric field in the sheath. Ions energy distribution near electrode surface critically depends on ratio between ions mean free path ($?_i$) respect to charge-exchange collisions and electrode sheath length (L).

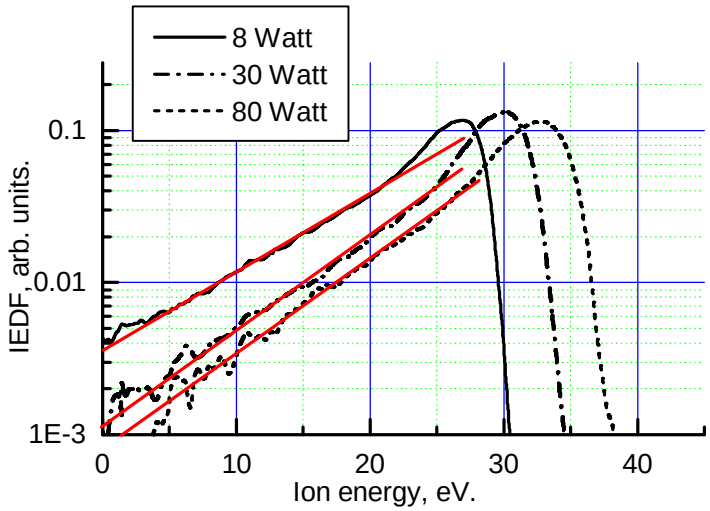

Fig. 4 Exponential fitting of IEDF slope, obtained for the flat electrode case. Ar, p=5mTorr.

In a collisionless regime ($?_i >> L$), ions are continuously accelerated during their traveling to the electrode surface and IEDF has a strong maximum around energies corresponded to an averaged potential drop in the sheath <U>. The IEDF tail towards lower energies is formed due to a non-zero collision probability for ions traveling in the sheath. For a linear regime, then a probability to experience only one collision in the sheath is much higher than probability of two collisions, the IEDF slope can be roughly fitted by exponential dependence which is proportional to $\exp(-?_i/L)$. By this way, the sheath thickness can be extracted directly from experimentally measured IEDF (Fig.4). For presented experimental conditions, $?_i/L$ can be estimated in the range of 4?5. Combining above data with the charge-exchange cross-section value for Ar ions [5] we can estimate the sheath length as L~4?5 mm.

In the regime with holed electrode, the sheath formed far away from the cavity should be identical to sheath formed in regimes with the perfectly flat electrode. Consequently, the cavity diameter is in the same order of magnitude as doubled unperturbed sheath length (d~2L). The sheath structure is essentially two-dimensional as it is illustrated on Fig.5. The plasma-sheath boundary oscillates by the same way as in unperturbed regions and periodically touches the internal surface of the cavity. However, a stationary quasi-neutral plasma can not be sustained inside the cavity until 2L>d.

The observed features of IEDF (Fig.3) can be explained be secondary electron emission from electrode surface and extension of the secondary electron trajectories in the cavity. Electrons are emitted from electrode surface mainly due to ion bombardment. These electrons are accelerated by a momentary value of voltage drop in the sheath (since $? << ?_e$) toward plasma body. A sufficient fraction of secondary electrons is accelerated up to energies equal to a maximal potential drop in the sheath (U_{max}) [6]. As U_{max} becomes larger than ionization potential secondary electrons could produce a sufficient ionization. However, in the low pressure case considered here, an electrons mean free path respect to ionization collisions ($?^i_e$) exceeds the sheath length ($?^i_e >> L$). Consequently, in the flat region, ionization by secondary electrons in the sheath is negligible. The situation in the cavity is sufficiently different. The potential structure in the cavity is radial-symmetric, so that, the secondary electrons emitted from side walls of the cavity are trapped in a potential well. The bouncing between the potential walls leads to an increasing of the electrons path in the cavity region. The total electron path in the cavity is now $?_{eff} \sim nd$ (n is a number electron flight across the cavity) and can be comparable with ionization length ($?_{eff} \sim ?^i_e$). The similar mechanism of electron trapping and extension of the secondary electron trajectories in the cavity is observed in so called "hollow cathode" discharges and leads to increasing of ionization rate in DC sheath [7,8].

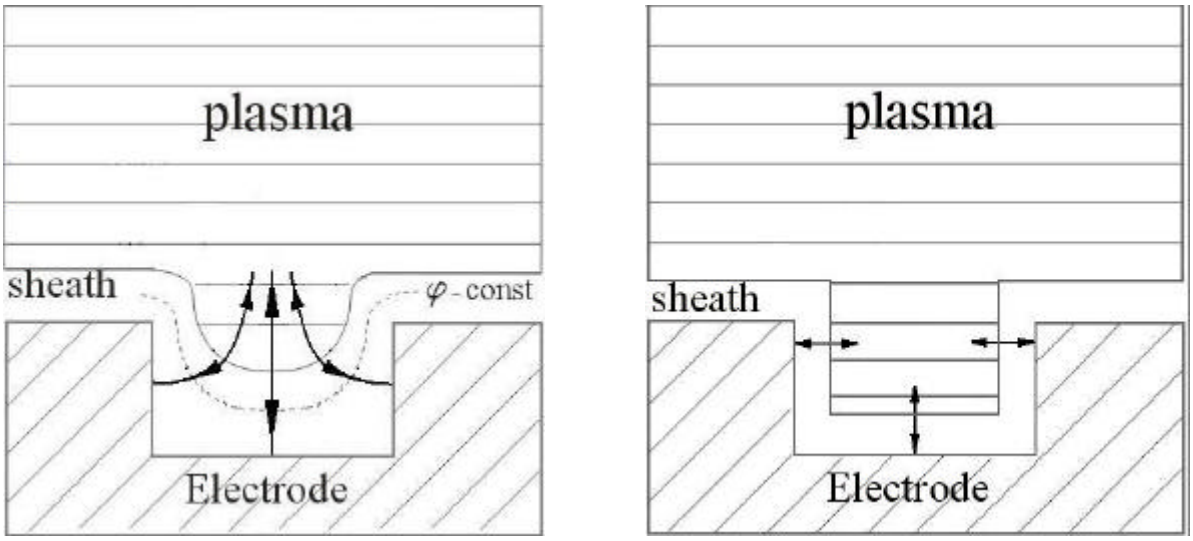

Fig. 6 Illustration of a sheath structure near cylindrical cavity for different ratio of cavity diameter (d) and sheath length (L). Left picture corresponds to the case 2L>d, right – 2L<d. Lines with arrows schematically show plasma-space charge boundary oscillations during RF period.

Now the observed IEDF features can be explained by the following way. First transition in the IEDF shape (Fig.3a) appears when the voltage drop in the cavity becomes enough to accelerate electrons emitted from cavity wall up to an ionization potential. Consequently, low energy fraction of IEDF is formed by ions produced inside the cavity while the high-energy fraction consists of ions travelling from a plasma edge lying in outside the cavity. The high energy group of ions is accelerated up to total averaged sheath potential <U>, while low energy group is formed in a region where averaged potential is about 8?9 volts. As it was discussed above, secondary electrons are accelerated by a momentum value of the sheath voltage. The ratio between averaged and maximum momentum potential value can by roughly taken as ? . Above consideration now can be confirmed by comparing Ar ionization potential (*?i=15.8* eV) and doubled ions energy in the low energy peak.

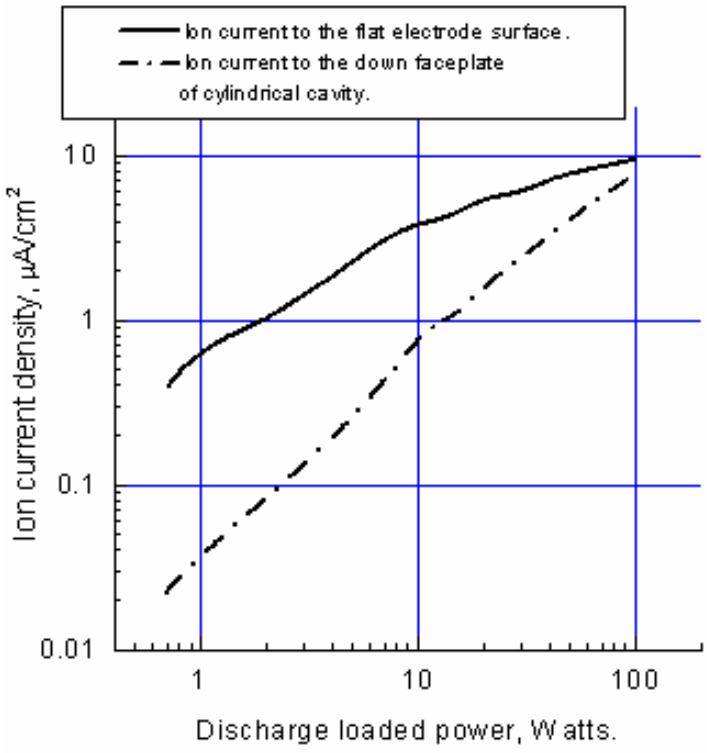

Fig. 5 Ion current density to the flat electrode and down faceplate of the cavity. Ar, p=5mTorr.

With increasing the power loaded in the discharge, the sheath potential, ions energy, ions flux and secondary electrons emission rate increase. Simultaneously, the ionization ratio and ions density in the cavity grow up. The sheath length is related to ion density and voltage amplitude by rough estimate $L\sim(U_{max}/en_i)^{1/2}$ [9]. While potentials of electrode surface and plasma body are fixed, the voltage drop in the unperturbed sheath should be similar to one in the cavity region. The increasing of ions density in the cavity now leads to local decreasing of the sheath length. The second evolution of IEDF shape (Fig.3b) appears when the ionization inside the cavity becomes high enough to locally decrease the sheath length to satisfy a condition 2L<d. At this stage, the cavity

is filled up by stationary quasi-neutral plasma and a thin electrode sheath is faced parallel to the cavity surface as it is schematically illustrated on Fig.5. The ions born inside the cavity are accelerated by a total potential drop in the sheath and low energy fraction of IEDF disappears.
An existence of a sufficient ionization in the cavity by secondary electrons is also confirmed by absolute measurements of ion currents flowing to the down faceplate of the cavity. On Fig.6 ion current densities are compared for flat electrode and electrode with cavity. It is easily seen that ion current from cavity grows faster than ion current to flat electrode. Consequently, we can conclude that in a high power regime, separated secondary electron sustained plasma is formed inside the cavity.

Concluding remarks

The presented investigation can be drafty resumed by following conclusions:

Secondary electron emission plays a significant role in plasma molding over non-flat electrode surface.

In the case of symmetrical cavities on electrode surface secondary electrons are trapped by potential well inside the cavity, this leads to extension of secondary electron trajectories and high ionization by secondary electrons in the cavity.

Additional ionization in the cavity leads to local decreasing of the space-charge sheath length and provoke plasma leakage inside the cavity.

An isotropic ion bombardment of the cavity surface can be obtained only in the regime of thin sheath (d>2L), however, due to additional ionization in the cavity, ion flux intensity in the cavity may be higher than in flat electrode region.

Acknowledgments

This work was supported by NATO SfP grant N 974354 and RBRF grant N 01-02-16874.

References

[1] Chang-Koo Kim, Demetre J. Economou, Journal of Applied Physics, **91**, 5. p. 2594 (2002).
[2] Bohm C., Perrin J. J. Rev. Sci. Instr. **64**. 1. p. 31 (1993).
[3] A.S. Smirnov, K.S. Frolov. A.Yu. Ustavschikov Sov. Phys.: Techn. Phys., **40**, p. 624 (1995).
[4] Kohler K., Coburn J.W., Horne D.E. et al. J. Appl. Phys. **57**. 1. p. 59 (1985).
[5] Earl W. McDaniel. "Collision Phenomena in Ionized Gases" John Wiley and Sons, New-York (1964)
[6] K.E.Orlov, A.S.Smirnov. IEEE Trans. Plasma Sci., **27.** p. 1348 (1999)
[7] Moskalev B.I. "Hollow Cathode Discharges" Energoizdat, Moscow (1969) (in Russian)
[8] V.I. Kolobov, L.D. Tsendin. Plasma Souces Sci. Technol. **4** p. 551 (1995)
[9] K.E. Orlov, A.S. Smirnov Plasma Sources Science and Technology. **8**, p. 37 (1999)

Low temperature RF PECVD of hard carbon films: preparation and material characterization.

A.Ya. Vinogradov[1], A.S. Abramov[1], A.S. Smirnov[2], K.E. Orlov[2], V.S. Kostylev[3]

[1]*A.F. Ioffe Physical-Technical Institute, Russian Academy of Sciences, St.-Petersburg, Russia*
[2]*State Technical University, St.-Petersburg, Russia*
[3]*Central Research Institute for Materials, St.-Petersburg, Russia*

Abstract

The main features of carbon films low temperature (250^0C) radio frequency plasma enhanced chemical vapor deposition (RF PECVD) process, structure and properties of diamond like carbon films were studied. Obtained films properties were found to depend on substrate material, film thickness, RF power and DC bias. Regime of ion bombardment of growing film surface was found to be the key factor controlling carbon (including diamond like) films deposition.

Introduction

In the present time, carbon and particularly diamond-like carbon (DLC) films are widely studied materials because of its attractive visible and infrared optical, electrical, chemical and tribological properties. The films have been fabricated by a variety of methods including single low-energy beams of carbon ions, dual ion beams of carbon and argon, ion plating, sputtering from graphite target, vacuum-arc discharges, laser ablation and different modifications of plasma-enhanced chemical vapor deposition. The details of the films deposition techniques and specific references can be found in [1].

PECVD possessing has such advantages as possibility of uniform coating of large area, simplicity of impurities incorporation, absence of uncontrolled heating of the substrate, flexibility and controllability of the process, possibility of charged particles flows control by applying of magnetic field or (and) DC electrical fields and low cost. It makes PECVD an attractive technique for thin carbon films fabrication under low temperature processes required to obtain technological compatibility in complicated technological lines. For example - coating of substrates with low melting temperature, semiconductor device structures fabricated at low temperatures (e.g. those on base of hydrogenated amorphous silicon layers), metal details “afraid” of thermal annealing and other similar tasks.

Since then a first successful DLC films deposition was achieved [2], all the researchers noted importance of a continuous ions bombardment of the growing film for DLC preparation by different deposition technique including RF PECVD [3, 4, 5]. The goal of this work is to develop the technology of the DLC films growth on low temperature substrates in capacitively coupled discharge reactor and to understand the influence of ion bombardment on film growth rate and film properties.

Experiment

The films were prepared by RF (40 Ì Hz) PECVD in the flat capacitive diode system. Both RF power and positive DC bias were applied to the upper 220 mm diameter electrode. The substrates were mounted on the lower electrode (230?230 mm^2) which was grounded. Ion flux characteristics were investigated by a flat four-grid retarding field energy analyzer mounted close to the substrate. Pure methane was used as carbon film precursors source.

Glass covered by titanium and/or molybdenum, crystalline silicon and Ti, Mo, Ni, Ta and stainless steel foils were used as substrates. The deposition was performed within a variety of parameter sets. Variation parameters were: final film thickness (d=0.3-2?m), positive DC bias applied to the powered electrode (U=50–300V) and RF power (W=100–700W). The values of these parameters for used deposition regimes are summarized in Table 1.

Methane flow rate and substrate temperature were kept constant during the films deposition: 16 sccm and 250^0 C correspondingly. Low operating pressure (10^{-2} Torr) was chosen in order to minimize scattering of ions accelerated by DC bias of the powered electrode towards the substrate.

The values of ions energy and ion flux onto the substrate were estimated from retarding characteristics of the energy analyzer. The energy analyzer construction and key points of the measurement procedure have been described earlier [6, 7]. The input aperture of the energy analyzer was 2 mm in diameter. All parts of

the analyzer, except the stainless steel casing, were made of nickel. The grids had a 140?140 ?m^2 mesh size and 80 % transmission. The energy scanning time was approximately 5 s.

Raman scattering spectroscopy of the samples was used for chemical and structural characterization of the films.

Table 1: Carbon films deposition conditions and properties.

Sample #	W, W	U_b, V	R, A/c	d, ?m	E_i, eV	J_i, ?A/cm^2	[sp^3] fraction
262-3	100	300	5.9	0.3	~300	~1	0.60
262-4	700	300	11.8	0.4	~300	~20	0.67
262-6	700	200	11.1	0.4	~200	~20	0.59
262-5	100	200	5.1	0.4	~200	~1	0.55
262-7	100	200	5.1	1.0	~200	~1	0.59
262-8	100	200	5.1	2.0	~200	~1	0.64

Results and discussion

Retarding curves measured at different RF power and applied DC bias values are presented in Fig. 1. Because of fundamental difficulties to adequate detect high ion energies by retarding field analyzer, ion flux parameters were extrapolated for some deposition regimes with high loaded power and high positive bias. Scaling laws describing a dependence of ion flux parameters from RF power and DC bias were found earlier in [8]. Such scaling generally states that an increasing of RF power leads to increasing of ions flux value with negligible changes in ion energies, increasing of positive DC bias strongly increases ions energy and slightly affect ions flux value. These scaling are generally valid until RF power loaded in the discharge is larger that DC power. For some regimes with extremely high DC bias the above condition may not be satisfied, consequently, the corresponded ion flux characteristics should be considered only as a rough estimate. The summarized data concerned ion bombardment characteristics are presented in Table 1.

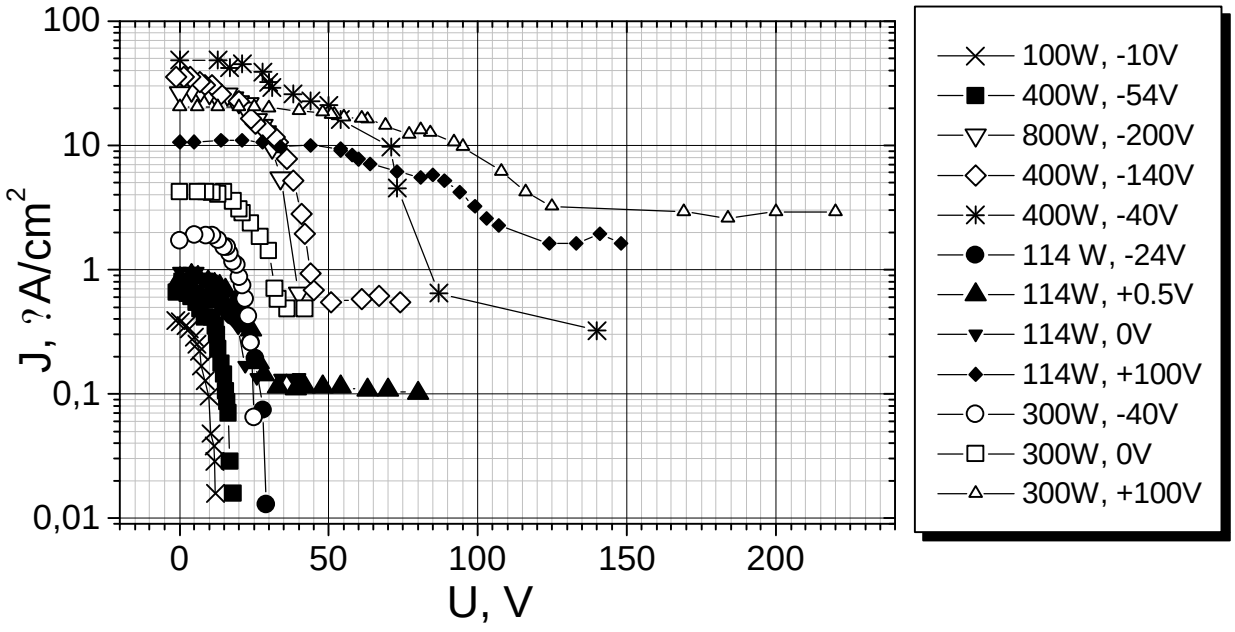

Fig. 1: Retarding characteristics obtained with the energy analyzer for different deposition regimes

From the Table 1 one can see that the films deposition rate increases with RF power and DC bias. More obvious it is demonstrated in the diagram presented in Fig. 2. This observation confirms that ion

bombardment is stupendous in the deposition process in spite of the low ion concentration in gas phase compared with neutral particles once.

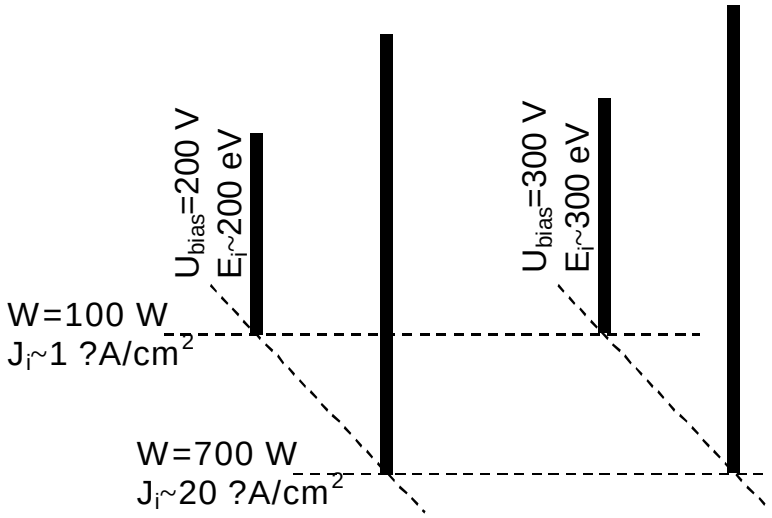

Fig. 2: Diagram of the films deposition rate values
vs. RF power and DC bias (ions energy and flux).

All the films deposited were transparent and demonstrated room temperature conductivity less than 10^{-14} $Ohm^{-1}cm^{-1}$. It was found that all the films deposited at RF power less than 100 W and/or DC bias less than +50 V were soft. All the films deposited under heavy ion bombardment (RF power more than 100 W and applied DC bias more than +100 V) were hard and demonstrated good adhesion to crystalline silicon and foil substrates. The film adhesion to the metal covered glass substrate was very poor. Adhesion of the films deposited on silicon and metal substrate was satisfactory.

Raman spectra of the films studied are presented in Fig.3.

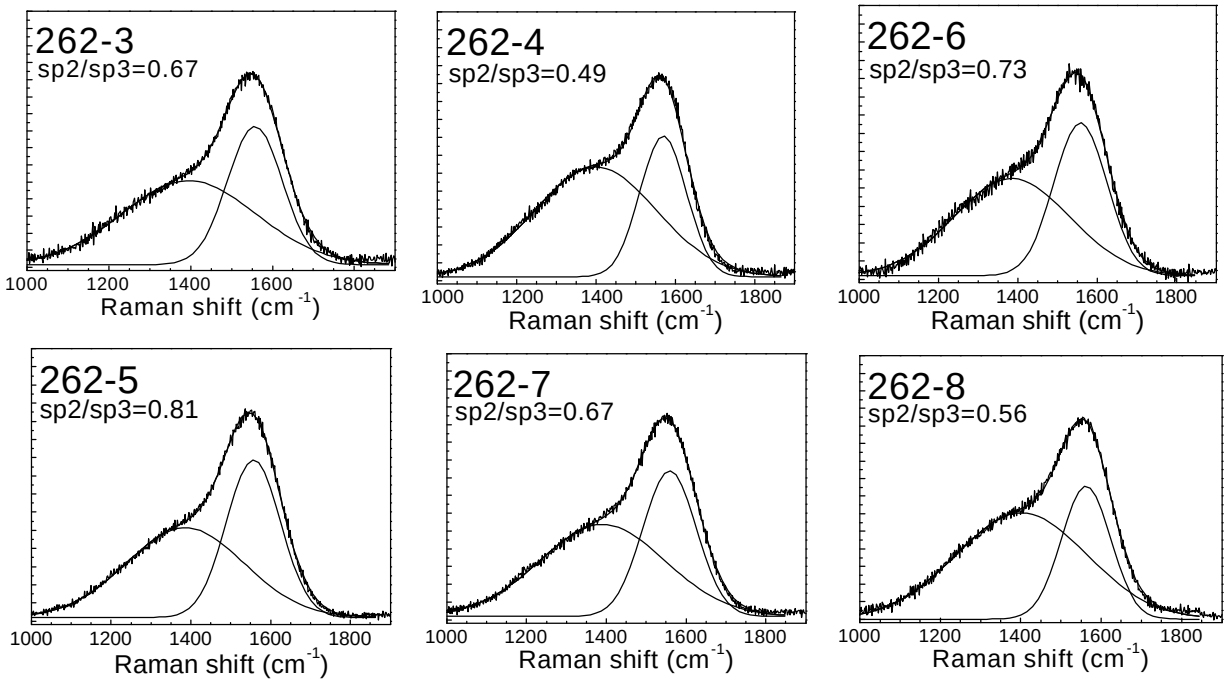

Fig.3: Raman spectra of the films studied.

Deconvolution of the spectra by Gaussians at about 1580 cm^{-1} (G - peak) and 1350 cm^{-1} (D – peak) in correspondence with [9, 10] showed that all the films deposited consisted of two phases: sp^3- and sp^2-hybridized carbon. We supposed that sp^3-hybridized carbon is diamond-like carbon and sp^2-hybridized carbon is polymer-like carbon rather than graphite-like carbon. Optical transparency and very low conductivity of the films corroborate this.

The ratios of sp^2 to sp^3 peak area are presented in Fig.3. Determined from these ratios sp^3-hybridized carbon fraction, which supposed to be proportional to the peak area, are presented in Table 1. From the table one can see that both: increase of ion flux, which increases with discharge power, and increase of ion energy, which increases with bias voltage, results in increase of sp^3-hybridized carbon fraction. Maximal sp^3 fraction content 67% was found in the film deposited under the heaviest ion bombardment (W=700W, U_{ab}=300V).

Typical 0.63 ?m wave length laser beam interference patterns plotted in reflection mode during the films deposition is presented in Fig.4. This trace demonstrates a change of the film growth at the point 2, which usually corresponds to the film thickness about 0.5 ?m. At this point light amplitude sharply falls due to the strong light absorption or scattering. Really, the thicker films were found to be hard but the films surface roughness was evident by sight. Optical microscope image of thick film (sample 262-8) is shown in Fig. 5b in comparison with surface of the thinner film presented in Fig. 5a.

Approximately linear dependence of sp^3-hybridized carbon fraction on film thickness was found. It is presented in Fig. 6. This feature of the film growth and dependence of sp^3-hybridized carbon fraction on film thickness can be explained by formation of negative floating potential on highly resistive carbon film and ion bombardment enhancement due to charging of film surface. Another possible reason is increasing of the film surface temperature due to the ion bombardment and suppressing of the heat transmission through thick film.

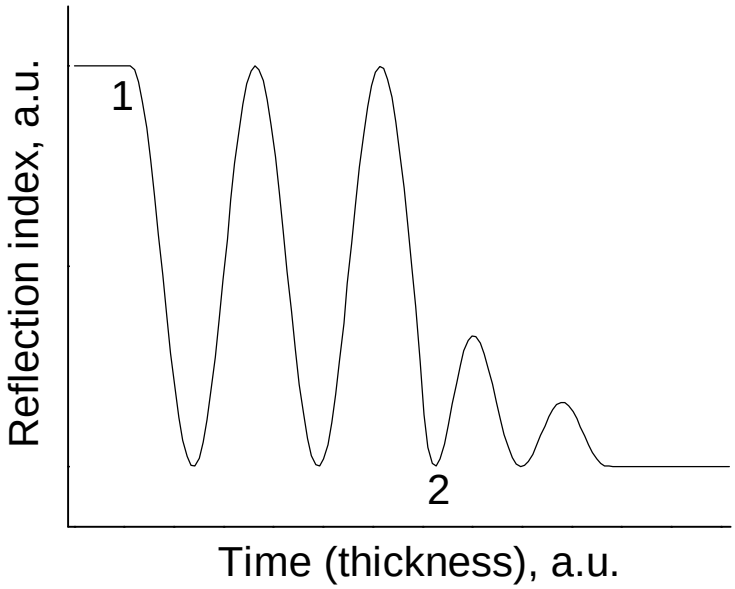

Fig. 4: View of the interferogram:
point 1 – beginning of the film deposition,
point 2 – beginning of the signal damping.

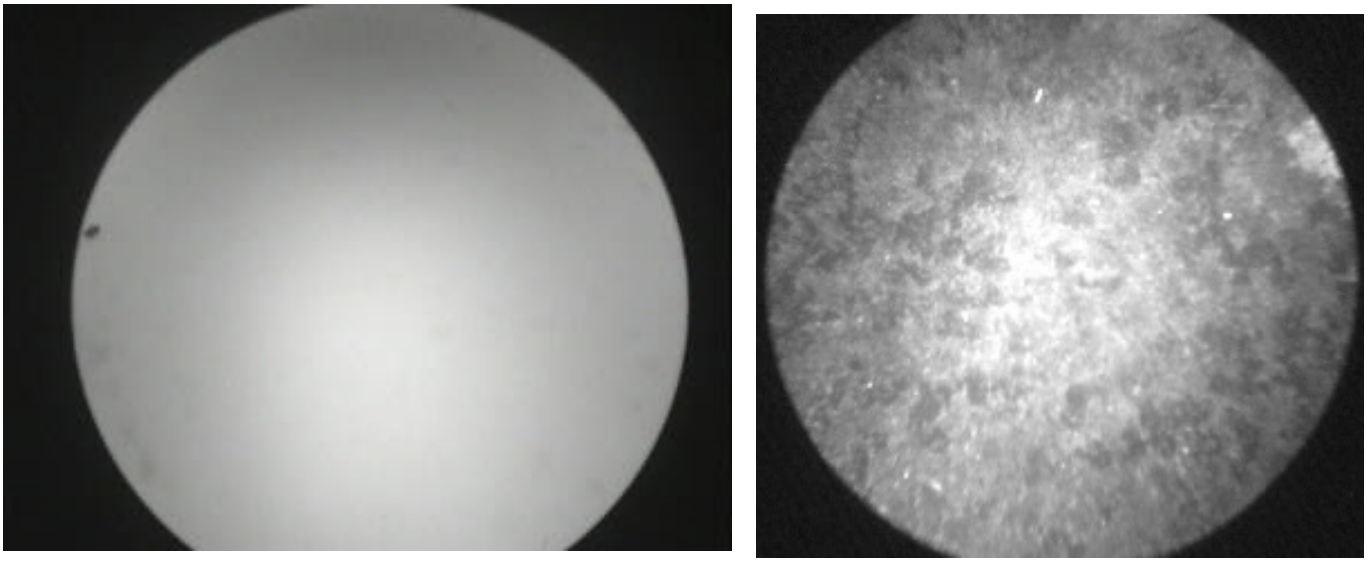

a b

Fig. 5: Optical microscope image of the films of 0.3 (a) and 2 ?m (b) thickness.
Images diameter is 1 mm.

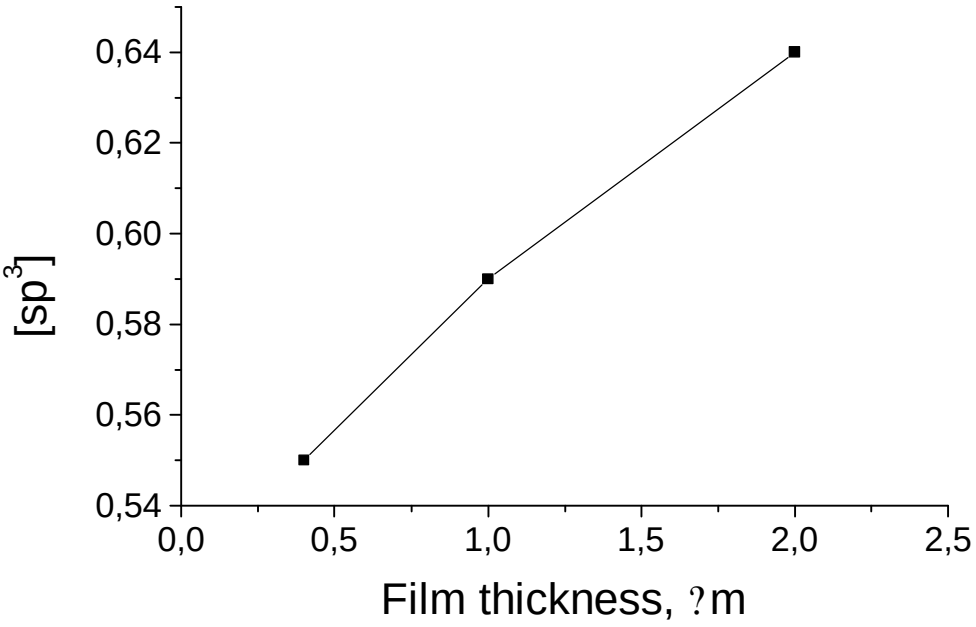

Fig. 6: Dependence of sp^3-hybridized carbon fraction on film thickness.

Summary and conclusions

1. The samples of hard carbon films with good adhesion to substrate were deposited at controllably varied regime of ion bombardment of the growing film surface.
2. Growth rate and sp^3-hybridized carbon fraction increase with the flux and energy of the ions impinging on the substrate.
3. Film smoothness and sp^3-hybridized carbon fraction changes with the increasing of the film thickness. This effect can be connected with film surface heating or charging.

4. Substrate material, film thickness and ion bombardment of growing film surface (controlled by RF power and DC bias) were found to be the key parameters providing hard carbon films deposition.

Acknowledgements
This work was supported by NATO SfP grant N 974354 and RBRF grant N 01-02-16874.

References
[1]. A. Grill and B. Meyerson, in Synthetic Diamond: Emerging CVD Science and Technology, K. E. Spear and J. P. Dismukes, Eds., John Wiley & Sons, Inc., New York, 1994, p. 91
[2]. S. Aisenberg and R. Chabot, J. Appl. Phys. **42** (1971) 2953
[3]. A. Grill and V. Patel, Diamond Films & Technol. **1** (1992) 219
[4]. A. Grill and V. Patel, in Applications of Diamond Films and Related Materials, Third International Conference, A. Feldman, Y. Tzeng, W. A. Yarbrough, M. Yoshikawa, and M. Murakawa, Eds., NIST Special Publication 885, Washington, DC, 1995, p. 771
[5]. A.Ya. Vinogradov, A.N. Andronov, A.I. Kosarev, A.S. Abramov, Semiconductors, 35, 6 (2001) 669
[6]. C. Bohm, J. Perrin, Rev. Sci. Instrum. 64 (1993) 31
[7] A.S. Smirnov, K.S. Frolov, A.Yu. Ustavshchikov, J. Tech. Phys. **40** (1995) 768
[8]. A.S.Smirnov, A.S.Abramov, A.J.Vinogradov, A.I.Kosarev, K.S.Frolov, A.Yu.Ustavschikov, Inst. Electr. Eng. Japan, 1 (1995) 526
[9]. J. Shwan, S. Ulrich, V.Batori, H.Ehrhardt, S.R.P Silva, J. Appl. Phys, 80, 1 (1996) 440
[10]. M. Tarmor, W. Vassel, J. Appl. Phys. 76 (1994) 3823

COMPARATIVE MODELLING OF ENDOTHERMIC REACTIONS LEVEL RATE CONSTANTS

B.F. Gordiets [1], S.A.Losev [2] , M Capitelli.[3], A.L Sergievskaya.[2], E.A.Kovach [2]

1. *Physical Institute of Russian Academy of Science, Russia*
2. *Institute of Mechanics, M.V.Lomonosov Moscow State University, Russia*
3. *Dipartimento di Chimica Universita di Bari, Italy*

Abstract

The simple method is proposed to calculate the vibrational level rate constants of endothermic reactions with the vibrationally excited reactants. The method is based on using of some empirical and semi-empirical models for calculation of level rate constants and information about the energy fraction ξ_v – total energy part going into vibrations of the molecule-product of reverse exothermic reaction. The comparative analysis of three known models for level rate constants of chemical reactions is carried out with use of this method.

1. Introduction

The intensive development of the non-equilibrium plasma chemistry and laser chemistry excites the great interest to investigation of kinetics for chemical reactions, which are proceeded in the non-equilibrium conditions for vibrations of molecules – reactants. For study such reactions it is necessary to know the values of its level rate constants that are the reaction rate constants for molecules–reactants on the individual vibrational levels. The some analytical models exist for these rate constants. There are the information theoretical approach (ITA) [1–3], intuition empirical α–model [4,5], and CVCV–model [6]. The level rate constants $k(m,T)$ for diatomic molecules – reactants are calculated in the framework of these models with use of simple formulas as a function of vibration energy for level "*m*" of molecule – reactant and one or two parameters. These parameters determine the efficiency for vibrational energy to get over of the activation barrier of endothermic reaction. The values of these parameters are, for many cases, not known and must be determined.

One of simple method for determining of these parameters is the use of information about the reverse exothermic reaction – it is exactly about the energy fraction ξ_v – total energy part which goes into vibrations of the molecule-product of reverse exothermic reaction, that is the molecule – reactant of direct endothermic reaction. Now, many experimental and computational data are existed for values ξ_v of different exothermic reactions [7].

The purpose of present work is to obtain the relatively simple equations and its solutions as well as the universal figures-diagrams, which can be easy used to determine the level rate constants $k(m,T)$ of the direct endothermic exchange reactions of molecules-reactant AB(*m*) on the vibration level *m*:

$$\mathrm{AB}(m) + \mathrm{C} \rightarrow \mathrm{AC} + \mathrm{B} \qquad (1)$$

2. The basic equation and used model rate constants

To solve the task we will use the principle of detailed balance for the level rate constant $k(m,T)$ of a direct (from the level *m* of AB molecule) and $k(\rightarrow m,T)$ of a reverse (to the level *m* of AB) reaction (1):

$$K(T)P(m,T)k(m,T) = k(\rightarrow m,T) \qquad (2)$$

Here $K(T)$ is the equilibrium rate constant for direct and reverse reaction; $P(m,T) = \exp(-E_m/kT)/Q_{vib}$ is the equilibrium (at the gas temperature *T*) normalized vibrational distribution of AB(*m*) molecules; Q_{vib} is the vibrational partition function; E_m is the energy of vibration level *m*. Taking into account (2) we have for fraction ξ_v:

$$\xi_v = \frac{1}{E_a}\frac{\sum_m E_m k(\to m,T)}{\sum_m k(\to m,T)} = \frac{1}{E_a}\frac{\sum_m E_m e^{-E_m/kT} k(m,T)}{\sum_m e^{-E_m/kT} k(m,T)}, \qquad (3)$$

where T is gas temperature, E_a is the total energy realized in the reverse exothermic reaction (1). It will be assumed here that this reverse reaction has not the activation energy barrier. Therefore E_a is the activation energy for direct endothermic reaction. The summing in (3) is carried up to level "m" with energy $E_m \le E_a$. Three different models will be used to describe the level rate constant $k(m,T)$ in eq. (3).

We have for information theoretical approach (ITA) model [2]:

$$k(m,T) = A(T)\frac{1}{1-\lambda}\left\{\left[12+\frac{6}{1-\lambda}+\frac{2}{(1-\lambda)^2}\right]-\left(6+\frac{2}{1-\lambda}\right)\Delta_m+\Delta_m{}^2\right\}\exp\{(1-\lambda)\Delta_m\}$$

for $\Delta_m \le 0$, (4a)

$$k(m,T) = A(T)\left\{12\left(\frac{1}{1-\lambda}-\frac{1}{|\lambda|}\right)+6\left(\frac{1}{(1-\lambda)^2}+\frac{1}{\lambda^2}\right)-\frac{2}{|\lambda|^3}+\frac{2}{(1-\lambda)^3}\right\}-$$

$$-A(T)\frac{1}{|\lambda|}\left\{12+\frac{6}{|\lambda|}+\frac{2}{\lambda^2}+\left[6+\frac{2}{|\lambda|}\right]\Delta_m+\Delta_m{}^2\right\}\exp(-\Delta_m|\lambda|)$$

for $\Delta_m > 0$ (4b)

$$\Delta_m = (E_m - E_a)/kT, \qquad (5)$$

where $A(T)$ is the normalization multiplier; $\lambda(T)$ is the searched parameter of "vibrational surprise"[8]. It determines the difference of the real rate constants from the "prior" rate coefficients $k^0(m,T)$, which are depended only on density of states and full (internal and translational) energy of colliding particles. The values $k^0(m,T)$ are determined by formulas (4) with $\lambda(T)$=0.

Well known α- and CVCV- models [4-6] have been modified in the present work to obtain more correct description of rate constants $k(m,T)$ and $k(\to m,T)$ on upper levels *m,* such that $E_m > E_a$. The one parametric dependence has been also used for description of rate constants in the CVCV- model.

For modified α -model the following formulas have been used:

$$k(m,T) = k_0(T)\exp\left[-\frac{E_a - \alpha E_m}{kT}\right] \quad \text{if } \alpha E_m \le E_a \text{ (for } \alpha \le 1\text{) or if } E_m \le E_a \text{ (for } \alpha > 1\text{)} \quad (6a)$$

$$k(m,T) = k_0(T) \quad \text{if } \alpha E_m > E_a \text{ (for } \alpha \le 1\text{)} \quad (6b)$$

$$k(m,T) = k_0(T)\exp\left[-\frac{E_a}{kT}(1-\alpha)\right] \quad \text{if } E_m > E_a \text{ (for } \alpha > 1\text{)} \quad (6c)$$

For modified and already one parametric CVCV−model the following level rate coefficients have been used:

$$k(m,T)=\begin{cases} k_0'(T)\exp\left(-\dfrac{E_a-E_m}{kT}+\dfrac{E_m}{U}\right) & \text{for } E_m \le E_a \quad \text{(a)} \\ k_0'(T)\exp\left(\dfrac{E_a}{U}\right) & \text{for } E_m > E_a \quad \text{(b)} \end{cases} \tag{7}$$

Notice, that dependence of level rate constants (7) on vibrational energy E_m of molecules-reactants for modified CVCV-model is identical with CVDEV model, suggested in [9].

For case $E_a/kT >>1$ all investigated models give the similar dependencies $k(m,T)$ on E_m for low vibrational levels (where $E_m << E_a$). It takes place, if the parameters $\lambda(T)$, α and U are connected by relationship

$$\lambda(T) \approx 1-\alpha \approx -T/U\,. \tag{8}$$

The correlation (8) can be easy obtained if to compare the models formulas for $|\Delta_m| >>1$. It is necessary to emphasize that the λ parameter in ITA–model can be both positive and negative. It is confirmed by numerical calculations and experiments. Therefore, it is logically (in according with (8)) considered that the parameter α in α –model can be both less and more than 1 and parameter U in CVCV–model can be positive or negative. It can be in our modified formulas (6), (7).

3. The finding of parameters for level rate constants

Let's find the parameters λ, α and U. If to insert (4)–(7) in (3) we have the equation for λ, α or U as a function of ξ_v and dimensionless input parameters $a = kT/E_a$, $b_m = kT/E_m$. The results are also depended on view of function E_m (that is on vibrational model: harmonic or anharmonic model of molecular vibrations). However, the simplification of analysis can be obtained if to use for function E_m the model of harmonic oscillator $E_m = mE_1 \equiv mE_{10}$, where E_{10} is the energy of vibrational quanta of molecule-reactant AB in reaction (1).

More clear view of the nonlinear equation for α, U and λ, which are depended on ξ_v and $a \equiv kT/E_a$, $b_1 \equiv kT/E_{10}$ for each of model, can be obtained with additional condition

$$E_{10} \ll E_a\,, \quad \text{that is } a << b_1\,,\ m_a >> 1 \tag{9}$$

In this case, the integration can be carried out in eq.(3). As a result, the following nonlinear equation have been obtained to determine α and U parameters:

$$\xi_v \approx \frac{1}{x_a}\cdot\frac{1+(x_a-1)\exp(x_a)}{\exp(x_a)-1} \tag{10}$$

Here $$x_a = (\alpha-1)E_a/kT \quad \text{for modified } \alpha\text{–model} \tag{11a}$$

$$x_a = E_a/U \quad \text{for modified CVCV–model} \tag{11b}$$

For ITA–model with condition (9), the obtained equation is more complicated and has the following view:

$$\xi_v = -\frac{1}{x_a}\cdot\frac{A+\dfrac{2B}{x_a}+\dfrac{6}{x_a^{\,2}}+x_a\left(A-B+1-\dfrac{A-2B+3}{x_a}+\dfrac{6-2B}{x_a^{\,2}}-\dfrac{6}{x_a^{\,3}}\right)\exp(x_a)}{A+\dfrac{B}{x_a}+\dfrac{2}{x_a^{\,2}}-\left(A-B+1-\dfrac{2-B}{x_a}+\dfrac{2}{x_a^{\,2}}\right)\exp(x_a)} \tag{12}$$

Here
$$x_a = -\frac{\lambda}{a} \equiv -\frac{E_a}{kT}\lambda \tag{13}$$

$$A = 1 + Ca + Da^2\,; \quad B = 2 + Ca\,;\; C = 6 + \frac{2}{1-\lambda}\,; \quad D = \frac{2}{1-\lambda}\left[6 + \frac{3}{1-\lambda} + \frac{1}{(1-\lambda)^2}\right] \tag{14}$$

The approximate solution of eq. (10) for modified α– and CVCV–models is

$$x_a \approx -\frac{1}{\xi_v} + 0.928 \qquad \text{for} \quad \xi_v < 0.289 \tag{15a}$$

$$x_a \approx 12\left(\xi_v - \frac{1}{2}\right) \qquad \text{for} \quad 0.289 < \xi_v < 0.711 \tag{15b}$$

$$x_a \approx \frac{1}{1-\xi_v} - 0.928 \qquad \text{for} \quad \xi_v > 0.711 \tag{15c}$$

Here the parameter x_a is connected with α and U by relationships (11).

We also obtain the approximate solution of eq.(12) for ITA-model:

$$x_a \approx -\frac{1}{\xi_v} + x_1 \qquad \text{for} \quad \xi_v < \xi_1\,, \tag{16a}$$

$$x_a \approx \frac{\xi_v - \xi_v^o}{(R - \xi_v^0)\xi_v^0} \qquad \text{for} \quad \xi_1 \le \xi_v \le 1 - \xi_1\,, \tag{16b}$$

$$x_a \approx \frac{1}{1-\xi_v^0} + x_2 \qquad \text{for} \quad \xi_v > 1 - \xi_1\,, \tag{16c}$$

$$\xi_1 = \sqrt{(R - \xi_v^0)\xi_v^0}\,, \quad x_1 = \frac{2\xi_1 - \xi_v^0}{\xi_1^2}\,, \quad x_2 = \frac{1 - 2\xi_1 - \xi_v^0}{\xi_1^2}\,, \quad R = \frac{2.4 + 4A - 3B}{3 + 6A - 4B} \tag{17}$$

Here the parameter x_a is connected with λ by formula (13); ξ_v^0 is the value ξ_v for $\lambda = 0$, that is the total energy part which goes into vibrations of the molecule AB in the reverse exothermic reaction (1) with assumption that the level rate coefficients $k(\to m, T)$ for such reaction are the "prior" rate coefficients. The value ξ_v^0 is calculated from (3) with use of (2), (4a), (5), (9) and is following:

$$\xi_v^0 = 0.25\left(1 + 16a + 120a^2\right)\Big/\left(1 + 12a + 60a^2\right) \tag{18}$$

The solutions (15b), (16b) are corrected in the range of ξ_v which gives $x_a << 1$. However, the numerical calculations show that this range can be extended without marked loss of precision. It is made in (15b), (16b). At this, the range boundaries are chosen so that the values x_a and derivatives $dx_a / d\xi_v$ (which are calculated from (15b), (16b)) must be equal to the values x_a, $dx_a / d\xi_v$ calculated from (15a), (16a) and (15c), (16c). The accuracy of these formulas increases with growth of $|x_a|$ for respectively $x_a \ll -1$ and $x_a \gg 1$. Thus, the searched parameters α, U and λ for α–, CVCV– and ITA–models can be easy estimated form (10), (12), (15), (16) if the activation energy E_a and part of energy ξ_v are known for direct and reverse reaction (1) and the condition (9) are fulfilled. The more exact calculation of α, λ and U parameters can be carried out if to solve the eq.(3) by the numerical method. Such solution has been obtained for both harmonic and anharmonic (Morse oscillator) vibrational models. It is found that the anharmonicity has weak influence on the values α, λ and U.

Some results of numerical solution of the equation (3) are given on Figs. 1,2. Here the dependence of the dimensionless parameter x_a on the energy part ξ_v is presented for different values of the dimensionless parameters $a = kT/E_a$, $b_1 = kT/E_{10}$. These figures can be as diagrams for the fast determination of λ, α, U.

The analytical dependencies $x_a(\xi_v)$ (formulas (15)) are also given on Fig.1 for α-model and CVCV-model. The approximate analytical solutions (16) for ITA-model are presented on Fig.2.

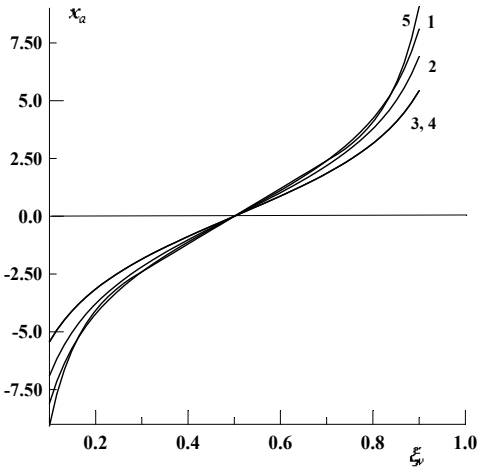

Fig. 1. Dependence of the dimensionless parameter x_a on the energy part ξ_v for α- and CVCV-models. Different lines are for different parameters E_{10}/T and m: 1 – E_{10}/T = 0.5, m = 20; 2 – E_{10}/T = 1.0, m=10, 3 – E_{10}/T = 25, m = 5; 4 – E_{10}/T = 0.5, m = 5. 5 is the results of approximate solutions

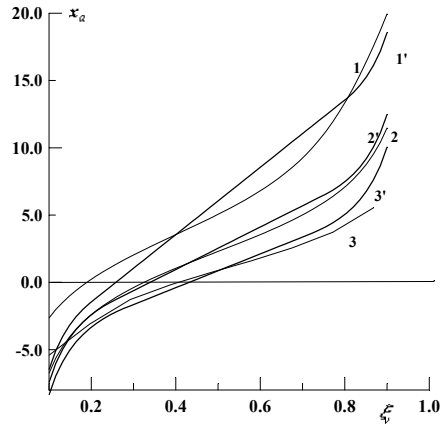

Fig. 2. Dependence of the dimensionless parameter x_a on the energy part ξ_v for ITA-model. Different lines are for different parameters E_{10}/T and m: 1, 1′ – E_{10}/T=25.0, m=5; 2, 2′ – E_{10}/T =0.5, m=20; 3, 3′ – E_{10}/T =0.5, m=5. 1,2,3 are the results of numerical calculations; 1′, 2′, 3′ are the results of approximate solutions.

The dependencies λ, α and U on the gas temperature T calculated from numerical solution of eq.(3) are given on Figs.3, 4 for some specific reactions. The dependencies of relative level rate constants $k(m,T)/k(0,T)$ and $k(m,T)/k(1,T)$ on vibrational level m are presented on Fig.5, 6 for reactions O + $N_2(m) \rightarrow$ NO + N at T = 10000 K and HCl(m)+I→Cl+HI at 850 K. Calculation is carried out for anharmonic Morse oscillator and ITA–, α– and CVCV–models with obtained from eq. (3) parameters λ, α and U. It is seen that all models gives the similar results for low levels.

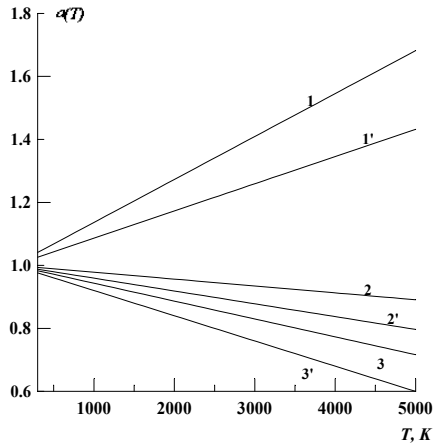

Fig. 3 The dependence of parameter α on the gas temperature T in α-model with taking into account experimental errors of measurement of ξ_v.

1, (1') HCl(m)+I→Cl+HI , ξ_v = 0.67 (ξ_v = 0.75)

2, (2') HCl(m)+Cl→H+Cl_2 , ξ_v = 0.39 (ξ_v = 0.44)

3, (3') N_2(m)+O→N+NO, ξ_v =0.25 (ξ_v = 0.31)

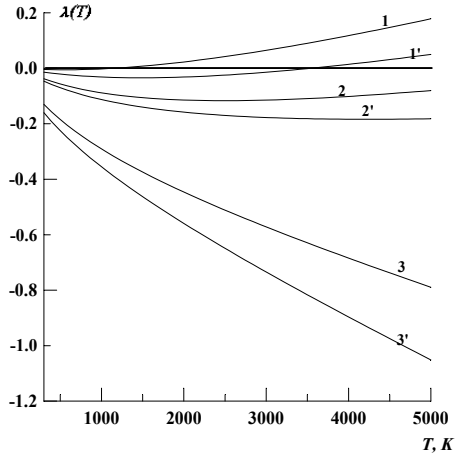

Fig. 4 The dependence of parameter λ on the gas temperature T in ITA-model with taking into account experimental errors of measurement of ξ_v.

1, (1') N_2(m)+O→N+NO, ξ_v =0.25 (ξ_v = 0.31)

2, (2') HCl(m)+Cl→H+Cl_2 , ξ_v = 0.39 (ξ_v = 0.44)

3, (3') HCl(m)+I→Cl+HI , ξ_v = 0.67 (ξ_v = 0.75)

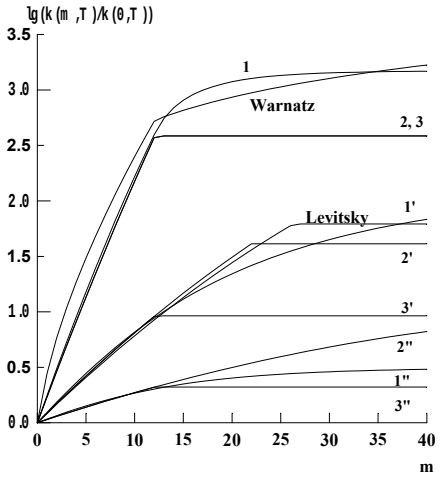

Fig. 5. The dependence of relative rate constant *k(m,T)/k(0,T)* on number of vibrational level *m* for reaction $N_2(m)+O \rightarrow NO+N$ at $T = 10000$ K. Lines shows results which were obtained by Warnatz [10] and Levitsky [11], and by investigated models with various values of ξ_v: 1, 1′, 1″ – ITA-model; 2, 2′ ,2″ – α-model; 3,3′,3″ – CVCV-model; 1, 2, 3 – $\xi_v = 0.7$; 1′, 2′, 3′ – $\xi_v = 0.36$; 1″, 2″, 3″ – $\xi_v = 0.25$.

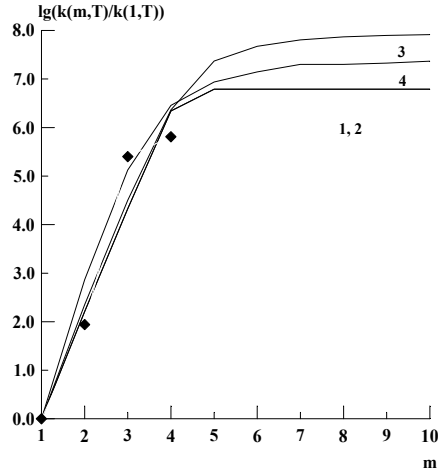

Fig. 6.The dependence of relative rate constant *k(m,T)/k(1,T)* on number of vibrational level *m* for reaction $I+HCl(m) \rightarrow Cl+HI$ at $T = 850$ K. Lines shows following models: 1 – α-model; 2 – CVCV-model; 3 – ITA-model; 4 – results of trajectory calculations [2]; points are values obtained by way recalculation of experimental data of reverse reaction $Cl+HI \rightarrow I+HCl(m)$ [7].

3. Conclusion

Thus, the simple and reliable method for calculation of the relative level rate constants $k(m,T)$ of endothermic exchange reaction (1) is given in the present work. The method uses three simple intuitive empiric models for description of these rate constants (ITA–, α– and CVCV–models) and only one parameter: energy part ξ_v, which goes into vibration in the reverse exothermic reaction. The modification of literature α– and CVCV–models is made to correct description of the level rate constant for cases $\alpha > 1$ and $0 < U < T$ on the levels with energy $E_m > E_a$. It is found that the proposed method for calculation of $k(m,T)$ can good describe both experiment and difficult trajectory computational calculations.

Acknowledgements

This work is fulfilled in the framework of the INTAS grant No 99-00464.

References

[1] Levine R.D. and Manz J. – J.Chem.Phys., **63**, 10, P.4280 (1975)

[2] Pollak E. – Chem.Phys., **22**, P.151 (1977)

[3] Levine R.D. – Ann.Sci.Phys.Chem., **29**, P.59 (1978)

[4] Physical and Chemical Processes in Gas Dynamics. Vol. I, Ed. by G.G. Chernyi, S.A. Losev, S.O. Macheret, and B.V. Potapkin. Progress in Astronautics and Aeronautics, **196** (2002)

[5] Capitelli M., Ferreira C.M., Gordiets B.F. and Osipov A.I.- Plasma Kinetics in Atmospheric Gases, Springer, Berlin, N.-Y., London, Paris, Tokyo (2000)

[6] Knab O., Fruhanf H.N. and Jonas S. – AIAA Paper, N 92-2947 (1992)

[7] Vasil'ev G.K., Makarov E.F., Tal'rose B.L. - Energy Distribution in Exothermic Chemical Reaction Products. Khimiya Plasmy. V.9 (Ed. By Smirnov B.M.), Moscow, Energoatomizdat, , p.3-79 (1982)

[8] Dmitrieva I.K., Zhdanok S.A. and Zenevich V.A. - Preprint ITMO, N24, Minsk (1985).

[9] Seror S., Drugulet M.-C., Schall E. and Zeitoum D.E. – AIAA Paper, N 97-2556 (1997).

[10]. Warnatz J., Riedel U., Schmidt R. In: Advanced in Hypersonic Flows. Vol.2: Modeling Hypersonic Flows. Birhauser, Boston (1992)

[11] Levitsky A.A. Mathematical simulation of plasma chemical processes. Thesis, Inst. Oil-Chemistry Synthesis, Acad. Sci. USSR, Moscow (1986)

Solid softwood treated by plasma jet

W. L. E. Magalhães[1], and M. F. de Souza[2]

[1] *Embrapa Florestas, Colombo-PR, Brasil*
[2] *Interunidades em Ciência e Engenharia de Materiais, IFSC, USP, São Carlos-SP, Brasil*

Abstract
Cold plasma jet was produced by electrical glow discharge in a gas jet under reduced pressure and at a low frequency. The precursor gases used were 1-butene and a mixture of oxygen (O_2) and vapor of tetraethyl-orthosilicate (TEOS). Although the surface plasma treatment with 1-butene resulted in water repellence, permeability to water vapor remained unaltered. A mixture of TEOS and O_2 allowed us to investigate the ability of the glow discharge to coat the internal surface of slits made in wood.

1. Introduction

Solid wood is a natural polymer composite in which lignin plays the role of the continuum matrix phase and the cellulose acts as the reinforcement fibers. Hemicelluloses are the coupling agents between the matrix (lignin) and fibers (elementary cellulose fibrils), and the extractives are the additives [1].
The use of cold plasmas is common in treatments of polymer surfaces for multiple applications; it stands to reason, therefore, that wooden surfaces should also be treatable.
Two of the characteristics of solid wood are hydrophilicity and hygroscopicity. Moist wood, which is vulnerable to attack by fungi and termites, loses its dimensional stability. Solid wood can be subjected to a wide variety of treatments to make it suitable for specific technical applications. The most widely used treatments for solid wood are impregnation [2] and coating with paints and varnishes [3]. Film-forming finishes slow both the absorption of water vapor and drying out of the wood. This retardation of drying, in cyclic high and low relative humidities, causes the moisture content of the wood to increase over time. Thus, the moisture content of the wood can approach the range wherein decaying fungi may become active. Plasma coating can overcome this drawback, rendering the outermost surface highly hydrophobic without altering either the natural appearance or the water vapor permeability of wood.
Solid wood permeability can be altered along the grain with cold radiofrequency plasma [7]. Several gases (CH_4, C_2F_2, vapor of hexamethyldisiloxane, O_2, vapor of acrylic acid) have been used to control the hydrophobicity of solid wood surfaces and to improve paint adhesion [8]. Vapor of hexamethyldisiloxane – plasma has also been used to produce water repellent characteristics [9]. Plasma treatment can be used to improve the weathering resistance of wooden surfaces [10,11]. Cold plasmas capacitively arranged and operated at low frequencies, such as 60 Hz, though efficient to alter wooden surfaces chemically, cannot be used to treat orifices smaller than 3 mm wide [4,11].
The apparent contact angle is a useful and cheap technique to identify the penetration of liquids into rough wooden surfaces [5]. The apparent contact angle depends on both the roughness and the chemical nature of the surface [6]. This technique is also used in the present study to characterize plasma-treated wooden surfaces.
A new technique for finishing wood - called plasma jet - was tested in this study. This technique appears promising in view of the low vacuum level and low 60 Hz power supply required, the lack of pollutants, and the use of industrial chemicals.

2. Materials and methods

Defect-free pine (*Pinus caribaea hondurensis*) was sawn into blocks with a 2.0x2.0x1.0 cm nominal size in the radial, tangential and longitudinal directions, respectively. Flat-grained boards with a nominal dimension of 0.5x2.0x2.0 cm were sawn and sanded with 220-grit sandpaper. The blocks and boards were oven-dried at 100^{o}C for 24 h, plasma treated, and then used for water absorption measurements in a controlled environment. After being plasma treated, the boards were used for contact angle measurements along the grain.
The 1-butene, argon (Ar) and O_2 gases were supplied by Air Liquid do Brasil and the tetraethyl orthosilicate (TEOS) came from DATIQUIM Produtos Químicos Ltda (Brasil). The rest of the chemicals were supplied by Aldrich Chemical Company Inc.

Scanning electron microscopy (SEM) micrographs and Si mappings were made using a Zeiss 980 microscope equipped with an EDS Analytical Link QX 2000 analyser.
Static advancing water contact angle measurements were taken at room temperature by the sessile drop method, using optical microscopy (MM Optics, Inc. Brazil) and digitizing the image obtained with a CCD (LG Honeywell) camera. The photographs were enlarged on a computer screen, providing a clear picture of the contact between the droplet (2 μl) and the substrate surface. About 9 contact angle measurements were measured at different points of one wood sample for each reported average value of the angle in the parallel and perpendicular directions of the wood's surface grains. The standard deviation of the contact angle was less than 2 degrees for glass substrates and less than 8 degrees for wood substrates.
The 1-butene deposition rate was measured on 1 mm thick B270 optical glass substrate. The film growth rates were calculated after measuring the film thickness on glass substrate using a Tyle Step Hudson stylus profilometer. The glasses were immersed for 1 h in a sulfuric acid/hydrogen peroxide 70/30 volume solution, after which they were washed with pure water and dried with dry nitrogen. After they were cleaned and rendered hydrophilic, these glasses were used as substrate for the plasma treatments.
For deposition of the plasma jet, an ion beam was built (fig 1) and operated attached to a homemade plasma chamber window that has been described elsewhere [4]. The plasma jet consists of a cylindrical aluminum tube (2.0 cm inner diameter) into which the gas or the mixture of gases is admitted at one end, while three metallic grids with different electric potentials are mounted at the other end to generate and accelerate the plasma through the substrate. The first grid operates at 260 VAC, 60 Hz, the second one at minus 5 kVDC, and the third at 15 kVAC, 60 Hz. Permanent ring magnets are fixed around the external aluminum cylinder. Thus, the magnetic field (1,200 Gauss) is applied parallel to the cylinder's axis. Electrons repelled from the cathodes are attracted to the anode but the magnetic field constrains the electrons to follow helical trajectories, increasing their path length and enhancing the ionization efficiency.

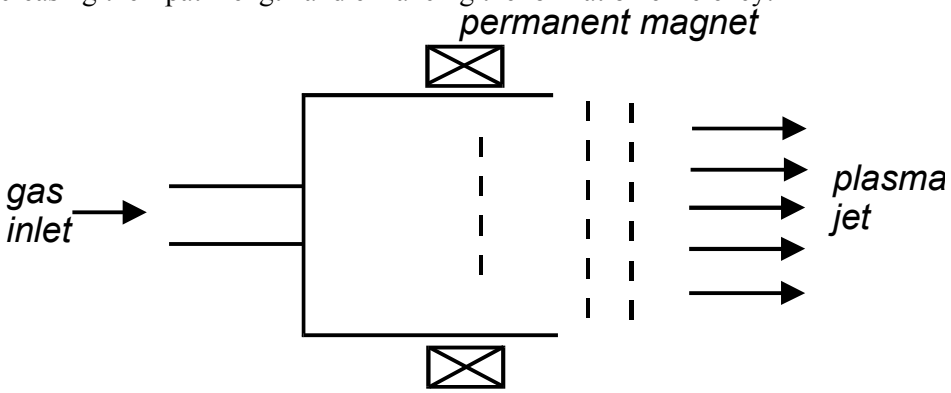

Figure 1- Diagram of the plasma jet.

Before deposition of the plasma-polymerized film, the reactor chamber was evacuated to a base pressure of 9.33 Pa and flushed three times with argon. A glow discharge with Ar at 30 mTorr and 50 sccm was then applied for 5 min to clean the surfaces, after which the reactor was again evacuated to the base pressure. The next step was the admission of the reactive gas, with the control valve adjusted to set the pressure and the flow in the chamber at pre--established levels before the glow discharge was switched on. A four factor (pressure, gas flow, substrate distance from the third grid, and deposition time), two level experiment design was followed. Two levels of pressure and gas flow were tested for 1-butene plasma jet experiments, 30 or 10 mTorr and 50 or 25 sccm, respectively. The substrate distance was 2.0 or 1.0 cm apart from the third grid, and the deposition time was 10 or 1 min.
TEOS was vaporized into the interior of the reactor using an appropriate apparatus with heating. The partial pressure of the TEOS vapor was 25 mTorr, and that of the O_2 was 75 mTorr. TEOS/O_2 mixture plasma jet deposition time was 20 min and the total flow was 50 sccm.

3. Results

Table 1 shows the values of the film growth rate, which was evaluated using optical glass substrates at a distance of 2.0 and 5.0 cm from the third metallic grid of the ion beam. It can be noted that the deposition rate was greater for the substrate closest to the third grid. The substrate's distance from the grid is an important factor owing to the low level of vacuum in the chamber, since the mean free path of the ions is very short. Thus, if the distance is great, the ions collide with the gas species along the way rather than with

the substrate's surface. The film growth rate reported in table 1 does not depend on the deposition time, which ranged from 1 to 15 minutes in this experiment. Moreover, the film deposition rate does not depend on substrate thickness, contrary to the capacitive coupled plasma operated at low frequencies. Thus, the plasma jet technique is highly efficient for thickly coating solid wood surfaces.

Table 1- Film growth rate of 1-butene plasma jet deposition. The thickness of the film was measured at two glass substrate distances from the third metallic grid of the ion beam.

	Substrate distance from the third grid	
	2 cm	5 cm
film growth rate (nm/min)	33.0	25.0

A TEOS/O_2 mixture was used as reactive gas in the plasma jet in order to deposit SiO_x films on the solid wood surface. The deposited film was characterized by Si EDX mapping. Figures 2 and 3 show SEM micrographs of solid wood surfaces exposed to the TEOS/O_2 plasma jet. Figure 2A illustrates the morphology of the SiO_x deposited film, showing that the deposit is as rough as the woody substrate. However, the coating concealed the ultrastructure of the solid wood surface. Figure 2B shows the Si mapping, revealing white dots spread over the entire surface, which confirms the complete coating of the wooden surface.

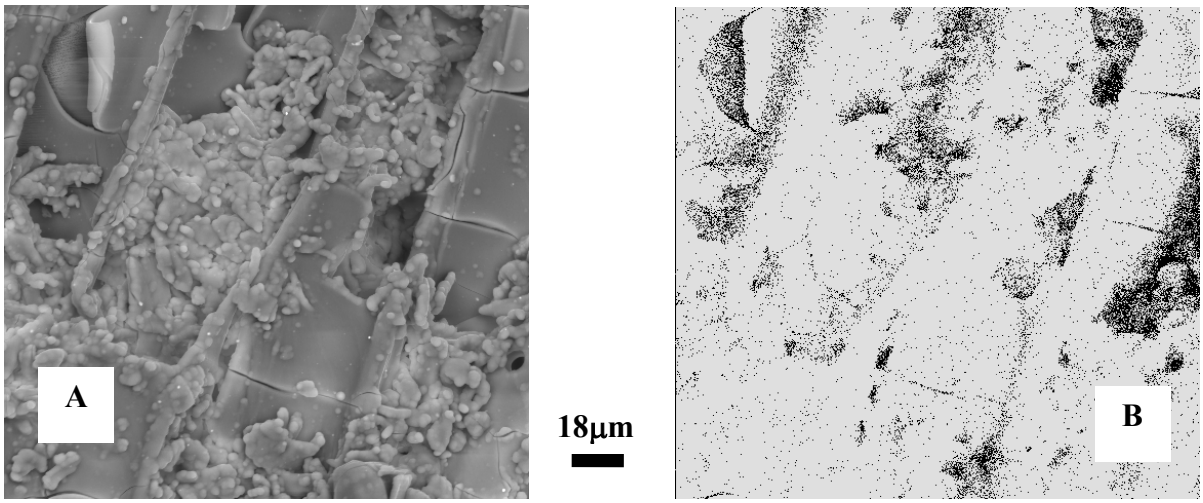

Figure 2- Solid wood surface along the grain coated with SiO_x by plasma jet. A) SEM using secondary electrons, and B) Si mapping of the same region. Magnification: 500X.

Figures 3A and 3B show, respectively, SEM micrographs and Si mapping of the surface of the 1.0-mm wide, 3.0-mm deep slit cut into the solid wood. These micrographs reveal that the plasma jet coated orifices which capacitively-coupled plasma was barely able to coat.

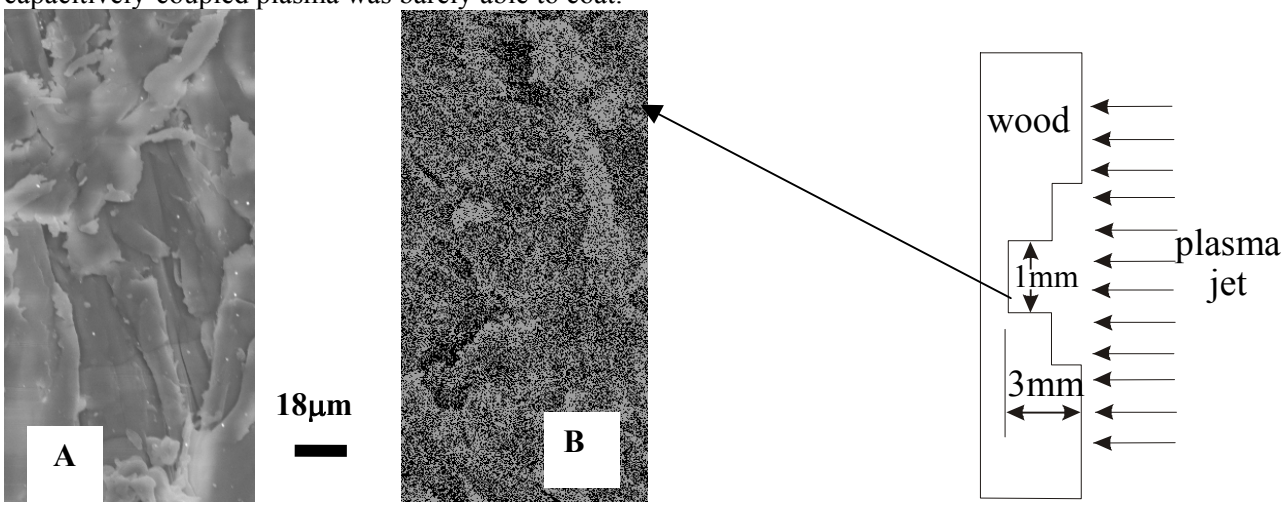

Figure 3- Surface of the slit cut into the solid wood and exposed to TEOS/O_2 plasma jet. A) SEM, and B) Si mapping of the same region.

Table2 shows the contact angle of a water droplet on a plasma jet-treated flat grained wooden surface with 1-butene gas for a 2^4 factorial design experiment. It was interesting to find that the contact angle was different and depended on the direction of the measurement. The contact angle values were found to be higher in the direction perpendicular to the grains and lower in the direction parallel to the grains. The distinct contact angle values in both cases were attributed to uneven roughness or porosity and chemical heterogeneity of the surface. It is a well known fact [6] that the roughness or porosity of the substrate alters the apparent contact angle (Wenzel's law). If the true contact angle is large and the surface is porous or sufficiently rough, the apparent angle shows higher values than the true angle. The plasma jet treatment changed the hydrophilic character of the solid wood surface to a hydrophobic one, with contact angles of up to 144 and 137 degrees in the directions perpendicular and parallel to the grain, respectively.

Table 2- 2^4 factorial design for the plasma jet experiment.

experiment	Pressure -=10 mTorr +=30 mTorr	Gas flow -=25 sccm +=50 sccm	Substrate distance -=1 cm +=2 cm	Deposition time -=1 min +=10 min	Contact angle (degrees) //	Contact angle (degrees) ⊥
1	+	+	+	+	108.9	128.1
2	-	+	+	+	123.7	132.7
3	+	-	+	+	130.0	135.3
4	-	-	+	+	130.6	134.9
5	+	+	-	+	136.7	142.1
6	-	+	-	+	113.7	124.6
7	+	-	-	+	129.7	125.5
8	-	-	-	+	117.8	124.1
9	+	+	+	-	130.5	138.0
10	-	+	+	-	135.2	144.5
11	+	-	+	-	137.4	136.5
12	-	-	+	-	117.3	132.8
13	+	+	-	-	129.5	140.7
14	-	+	-	-	128.6	138.5
15	+	-	-	-	132.0	126.8
16	-	-	-	-	117.4	122.5

An analysis of table 2 revealed the effects that remained over the statistical noise. These effects, for a contact angle parallel to the grain, were the pressure of the chamber and the crossed effects of second order- pressure/distance, gas flow/deposition time – and the crossed effect of the third order – pressure/distance/deposition time. Increasing the pressure from 10 to 30 mTorr caused a 6 degree increment of the contact angle. The angle parallel to the grain contact angle did not depend on gas flow or on the substrate's distance from the third grid of the ion beam. As the deposition time increased from 1 to 10 min, the angle parallel to the grain contact angle decreased by 4.5 degrees.

For the angle perpendicular to the grain contact angle, the effects that remained over the statistical noise were different from the effects responsible for alterations in the angles parallel to the grain. The second order cross effects of gas flow/substrate distance and gas flow/ deposition time were the ones that most strongly influenced the angle perpendicular to the grain contact angles.

The same change in the operating parameters of the plasma jet caused different statistical increments between contact angles perpendicular and parallel to the grain. This important difference indicated that the roughness of the wooden surface after treatment was the main reason for uneven contact angles. In fact, the deposition rate was too low to alter the more widely spaced irregularities in the direction perpendicular to the grain because of the wood's cellular structure. Along the grain, inside exposed semi-cylindrical wood fibers, the plasma jet was able to alter the roughness (fig 4).

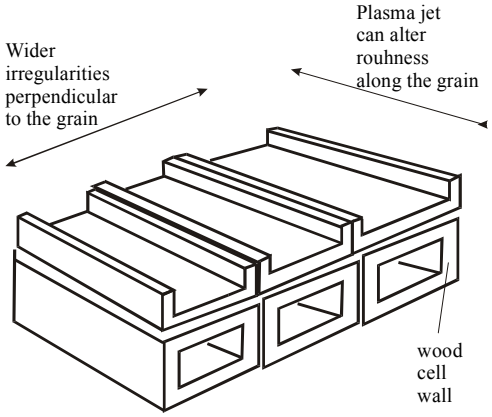

Figure 4- Schematic of wood surface showing semicylinder fibers exposed to the plasma.

Since the plasma jet penetrates solid wood orifices more efficiently than does the capacitively-coupled plasma, new experiments with 1-butene as precursor were conducted to evaluate water vapor exclusion. Wooden blocks and boards were used as substrates, with both the cross section and the flat-grained surface exposed to the plasma jet. Each wood surface was exposed to the plasma twice owing to the plasma jet's small (2 cm) diameter. Only the two largest surfaces of the wooden samples were directed coated by the plasma jet; the other four faces were treated indirectly.

The untreated and treated samples were cyclically exposed to a humid and dry environment and their weight monitored at regular intervals. Figure 5 shows graphs of the water vapor absorption of the 1-butene treated and the untreated solid wood. Although the plasma jet treatment provided efficient protection from liquid water, it proved ineffective against humid air.

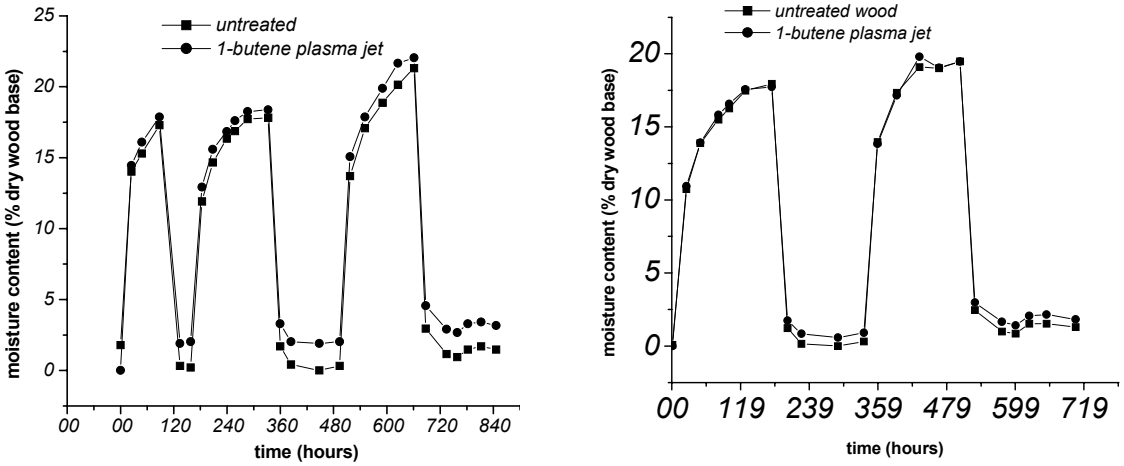

Figure 5- Change in moisture content of Caribbean pine finished with 1-butene plasma jet coat and exposed to alternating cycles of 95 and 22 percent relative humidity at room temperature, compared with untreated wood. Left: boards with nominal dimensions of 0.5 (R) x2.0 (T) x2.0 (L) cm. Right: blocks with nominal dimensions of 2.0 (R) x2.0 (T) x0.5 (L) cm

Although the plasma jet easily penetrates 1-mm size slits and fibers exposed lengthwise, deposition inside the cell lumen of the cross section wood plane (diameter smaller than 40 μm and length longer than 1 mm) is very difficult. When the jet's incidence was not aligned with the longitudinal cell axis, internal coating of the cell wall was very difficult to achieve. Moreover, wood powder and debris adhered to the surface after the wood was sanded and machined, serving as a shield that prevented the capillaries from being coated.

4. Conclusions

A thin solid film deposited by 1-butene-cold plasma jet successfully coated solid pine wood. Plasma jet treatment is more effective for coating wooden surfaces than capacitive coupled plasma treatment. The plasma jet is a promising technique owing to its low cost and its ability to coat orifices up to 1 mm wide and 3 mm deep. Moreover, the technique can be successfully used to coat solid wood with SiO_x films.

The wooden surface became highly hydrophobic after the plasma treatment. The plasma-deposited film was unsuccessful in preventing water vapor absorption and desorption because the technique proved inadequate to coat wood capillaries. By allowing the wood to breathe, plasma jet coating does not trap moisture that might otherwise lead to decay.
The contact angle showed different values depending on the direction of the measurement, being highest and lowest, respectively, in the direction perpendicular and parallel to the grain. The contact angle value was affected by the chemistry and roughness of the surface, which were both altered by the plasma jet treatment.

Acknowledgment
Financial support for this work was provided by FAPESP, a Brazilian research funding institution.

References
[1] Monties, B. 1991. Plant cell walls as fibrous lignocellulocic composites: relations with lignin structure and function. Animal Feed Science and Technology, v. 32, p.159-75.
[2] Rowell, R. M. and Konkol, P. 1987. Treatments that enhance physical properties of wood. Gen. Tech. Rep. FPL-GTR-55, Madison, WI: U.S.D.A., Forest Service, Forest Products Laboratory.
[3] Williams, R. S.; Knaeb, M. T. and Feist, W. C. 1996. Finishes for exterior wood. U.S.D.A., Forest Service, Forest Products Laboratory, Madison, Wisconsin.
[4] Magalhães, W. L. E. and de Souza, M. F. 2002. Solid softwood coated with plasma-polymer for water repellence. Surface and Coatings Technology, v.155(1), p. 11-15.
[5] Scheikl, M. and Dunky, M. 1998. Measurement of dynamic and static contact angles on wood for the determination of its surface tension and the penetration of liquids into the wood surface. Holzforschung, v.52(1), p.89-94.
[6] Adamson, A. W. 1990. Physical chemistry of surfaces. 5th edition. John Wiley & Sons, Inc.
[7] Chen Hy and Zavarin, E. 1990.Interactions of cold radiofrequency plasma with solid wood. 1. Nitrogen permeability along the grain. Journal of wood chemistry and technology, v. 10(3), p. 387-400.
[8] Cho, D. L. and Sjöblom, E. 1990. Plasma treatment of wood. Journal of Applied Polymer Symposium, v.46, p.461-472.
[9] Denes, A. R.; Tshabalala, M. A.; Rowell, R. and Young, R. A. 1999. Hexamethyldisiloxane-plasma coating of wood surfaces for creating water repellent characteristics. Holzforschung, v. 53(3), p. 318-326.
[10] Denes, A. R. and Young, R. A. 1999. Reduction of weathering degradation of wood through plasma-polymer coating. Holzforschung, v.53(6), p. 632-640.
[11] Magalhães, W. L. E. and de Souza, M. F. 2000. 1-butene –cold plasma coating of solid softwood. 2nd Woodcoatings Congress, Challenges and solutions in the 21st Century.23-25 October, The Hague, The Netherlands, paper 32.

Temperature measurements in absorbing inhomogeneous plasmas by relative intensity of spectral lines

E. Ershov-Pavlov[1], K. Catsalap[1], K. Stepanov[2]

[1]*Institute of Molecular and Atomic Physics, National Academy of Sciences, Minsk, Belarus*
[2]*Heat and Mass Transfer Institute, National Academy of Sciences, Minsk, Belarus*

Recently temperature measurements have been considered by relative intensity of spectral lines in emission spectra of inhomogeneous plasmas [1]. The plasmas have been supposed to be optically thin, close to thermal equilibrium and to have temperature distributions along the observation direction y, which could be approached by the formula: $T(y)=T_0[1+(y/y_0)^{\alpha}]^{-1}$, where y_0 is an effective dimension of the volume, α determines a rate of the plasma inhomogeneity ($\alpha=\infty$ for homogeneous plasmas). It has been in particular shown, that maximum temperature T_0 can be measured using an intensity I ratio of two (or more for Boltzmann plot) spectral lines of the same atom:

$$kT_0 \approx (E_a-E_b)[\ln(C_a/C_b)-\ln(I_a/I_b)-\alpha^{-1}\ln(E_a/E_b)]^{-1}, \quad (1)$$

where E is energy of the upper level of the transition under consideration and C is a common parameters combination for every (a, b) line. The equation differs from the conventional Boltzmann relation by the member $\alpha^{-1}\ln(E_a/E_b)]^{-1}$ depending on the plasma inhomogeneity and on the lines used. Also, emission intensity of the plasma volume is here instead of plasma emissivity, which normally must be taken for inhomogeneous plasmas.

Eq. (1) cannot be directly used for the measurements in absorbing plasmas, as far as emission intensity for optically thin plasmas must be taken in it. One can overcome the problem using an additional information. It has been shown [2], that emission intensity I_0 of an optically thin plasma volume identical to the absorbing one under consideration (having the same properties and temperature distribution) can be found from the following relation:

$$\frac{I_0}{I_1} \approx \frac{1}{2}\left(1+\frac{I_1}{I_2}\right), \quad (2)$$

where I_1 and I_2 are emission intensity of the absorbing plasma measured directly and after it re-passes the same volume in the observation direction. The value I_2 can be measured, e.g., with a mirror placed at the volume backside, as a difference between intensity measured with the mirror (I^*) and without it (I_1), i.e. $I_2=I^*-I_1$ (the intensity loses are not taken into account). The relation works at moderate optical density ($D\leq 1$, $I_1/I_2\leq 1.5$). For strongly absorbing plasmas ($D\leq 5$) a parametrical approximation of eq. (2) was found [2].

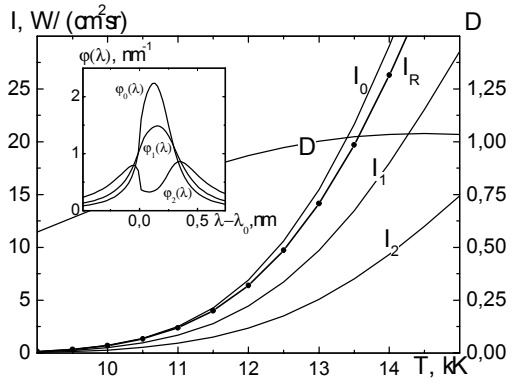

Spectral line Ar I 696.5 nm intensity and profiles in the emission of the argon plasma volume at 5 bars, y_0=5 cm, α=2 and temperature T_0=9-15 kK. The line profiles for T_0=13 kK are shown.

A numerical simulation of different plasma volume emission has been performed to study the possibility and errors of determination of I_0 and T_0 using eqs (2) and (1) at absorbing plasma diagnostics. Calculations of I_0, I_1 and I_2 have been performed with a numerical code reported elsewhere [3]. Argon plasma and atomic lines has been used for the modelling. Plasma volumes with different temperature distributions and optical thickness have been simulated by changing α, T_0 and y_0 at the program entrance. Also, atmospheric and higher plasma pressure has been taken to widen the volume absorption interval. One of the simulation results is shown in the figure. Here, with I_R the results are shown of our I_0 "measurements" using simulated values of I_1 and I_2 and eq. (2).

[1] E. Ershov-Pavlov, K. Stepanov - Proc. ISPC-15, Orleans, **3**, 1057 (2001).
[2] A. Kurskov, E. Ershov-Pavlov, L. Chvyaleva - J. Appl. Spectr. (in Russ.). **49**, 393 (1988).
[3] E. Ershov-Pavlov, K. Stepanov - J. Appl. Spectr. (in Rus.). **68**, 264 (2001).

Complex (dusty) plasmas: trends in applications and diagnostics

H.Kersten[1], R.Wiese[1], G.Thieme[1], H.Deutsch[1], E.Stoffels[2], W.W.Stoffels[2], G.M.W.Kroesen[2]

[1]*E.-M.-Arndt-University Greifswald, Institute for Physics, Domstr.10a, D-17487 Greifswald*

[2]*Department of Physics, TU Eindhoven, P.O.Box 513, NL-5600MB Eindhoven*

The research effort in the area of complex (dusty) plasmas initially aimed at avoiding particle formation and controlling the contamination level in industrial reactors. Nowadays, dusty plasmas have grown into a vast field and new applications of plasma-processed dust particles are emerging. There is demand for particles with special properties, and for particle-seeded composite materials. Low-pressure plasmas offer a unique possibility of confinement, control and fine tailoring of particle properties.

An approach for coating of externally injected particles will be demonstrated, where an argon rf-plasma was employed to charge and confine particles, while a metal coating has been performed by means of a separate dc-magnetron sputter source. Also, we perform the synthesis of small carbon particles as well as the deposition of thin amorphous carbon (a-C:H) films onto SiO_2 grains (~1μm) in an acetylene process plasma. Already after a very short process duration, the laser light scattering increases remarkably due to the simultaneous formation of dust in the course of a-C:H deposition. After examination of the collected particles by electron microscopy (SEM) the carbon dust particles show almost the same size.

The interaction between plasma and injected micro-disperse powder particles can be used as a diagnostic tool for the study of plasma surface processes, too. Examples for determining the electric fields in front of electrodes, substrates or beam sources by dust particles are given as well as for obtaining information on the energy fluxes in the plasma. As examples, the additional electrostatic forces are supplied by inserting floating substrates which are placed perpendicular to the rf-electrode, by an external ion beam source, or by a dc-magnetron.

Etching of SiO_2 rods by a DC plasma torch

R. Benocci, P. Esena, A. Galassi, M. Piselli, M. Sciascia, N. Spinicchia°

Università degli Studi di Milano-Bicocca, Dipartimento di Fisica, P.zza della Scienza 3, 20126 Milano, Italy.

° *Istituto di Fisica del Plasma ENEA-CNR-EURATOM, Via Cozzi 53, 20125 Milano, Italy.*

Abstract

Etching of SiO_2 rods has been obtained with a DC torch with argon as process gas; the high temperature of the plasma jet causes vaporisation of the area exposed. Apparatus and torch operative parameters have been set up to obtain a depth etch rate of 0.6 mm/min corresponding to 0.826 g/min. An enthalpy probe has been employed to monitor plasma condition before thermal plasma etching (TPE) process and from experimental values of etch rate a surface temperature of T_{sur}=2057 K has been derived. Etching has been obtained with uniformity over the entire area exposed with peak to peak differences below 1%.

1. Introduction

Thermal plasmas appeared in the sixties, either produced by arc plasmas by the interaction between an electric arc (DC) [1] or inductively coupled plasma discharges (ICP) [2] and a gas which ionises and becomes a plasma near the condition of local thermodynamic equilibrium (LTE).

Since then, a number of industrial applications were developed. Among these some examples can be given as: welding, cutting, spraying in ambient air and under soft vacuum, surface treatment with plasma transferred arcs, heating of air in blast furnaces or cupolas, purification of metals, ICP analysis, extractive metallurgy and steel dust recovery, optical fibers production [3].

SiO_2 rods, usually preforms, from which optical fibers are drawn, need surface treatments due to OH radical contamination, external pollution or surface imperfections. OH ions contamination is generally due to optical fibers conventional manufacture method which utilises hydrogen or methane burners as thermal source. These burners produce water causing OH ions contamination on silica rod surface. The external polluted layer reaches depths of about 0.3-1 mm and can be removed by chemical (HF) or plasma etching. Faster etch rate than conventional anisotropic plasma-chemical etching used in micro-electronics industry [4-11] (typical etch rate of about 0.5-1 μm/min) is needed, due to the tick layer to remove.

Mechanical removal (grinding) is not suitable because it can cause mechanical stress and can lead to SiO_2 rods structural failure, e. g., formation of cracks propagating through the rod.

Chemical etching is obtained by HF attack: the rod is plunged in a H_2O-HF solution allowing an isotropic corrosion but with poor etch rate. In this paper thermal plasma etching (TPE) is employed exposing the rod surface to a substantial portion of the electrically conducting plasma region (the plasma core) extending from a DC plasma torch with argon as process gas. Significantly, the surface material is substantially removed by vaporisation, due to the extremely high plasma temperature of the plasma torch.

Though the temperatures in the tail of the plasma jet are lower than at the plasma core, the temperatures are generally still several hundreds degrees centigrade. These tail temperatures typically are sufficiently high to cause vaporisation of most refractory dielectrics.

Even if a portion of the refractory dielectric body surface changes from a solid phase to a vapor phase, the remainder substantially maintains its pre-etch shape.

2. TPE experimental set-up

The experimental set-up employed for TPE is showed in figures 1 and 2.

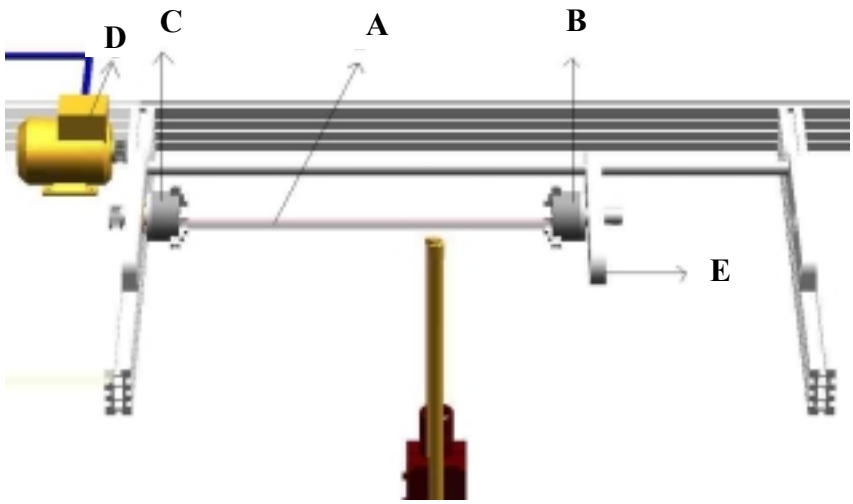

Figure 1: TPE experimental set-up: rod assembly.

SiO_2 rod ends (A) have been placed between two mandrels; the first (C) is connected to an engine (D) through a transmission system, whereas the second (B) can be moved on a guide (E). The engine allows a rotating speed ranging between 27 and 1200 r.p.m.

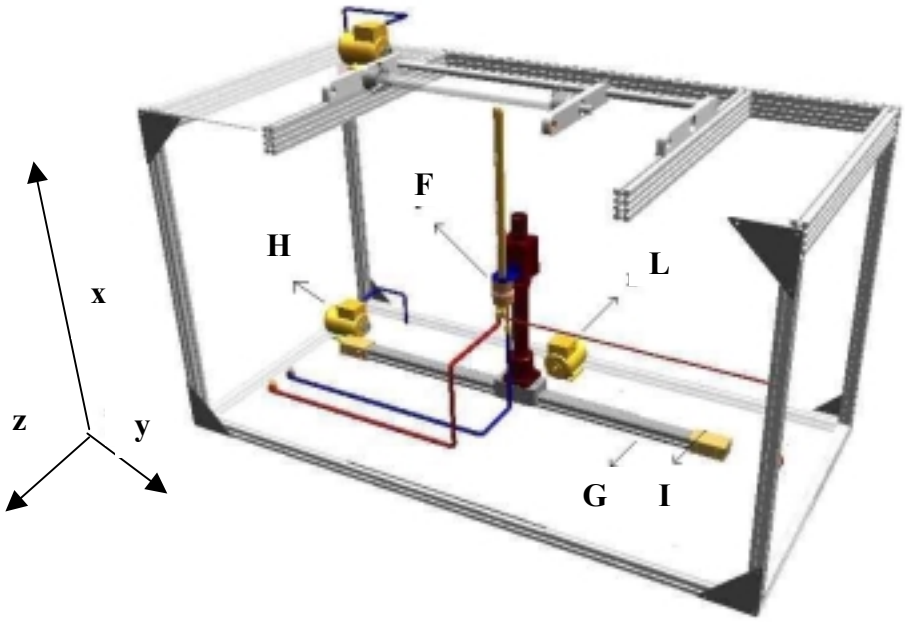

Figure 2: TPE experimental set-up: torch assembly.

The DC torch (F) is mounted on a 2D-displacement system. The engine (H) supplies a speed between 0.034 cm/s and 3 cm/s, whereas the engine (L) allows the torch to be moved along z-axis.
Rotating the cylindrical silica rod uniformly, with proper movement of the plasma torch along the rod, allows material to be removed from substantially the entire surface such that the rod retains its cross-sectional shape. The plasma jet, as it moves across the rotating rod, contacts and etches the rod. The etch rate is a function of plasma transverse speed and, among other factors, to the extent the transverse speed influences the silica rod surface temperature.

Apparatus parameters
Apparatus and torch operative parameters employed are summarized below.

- torch to rod distance: 1-4 mm
- rod revolving speed: 30-900 r.p.m.
- torch transverse speed: 0.04-1 cm/s
- torch to rod orientation: axial

Torch operative parameters

The reactor used (F) is a non-transferred plasma torch, connected to a power supply of 16 kW maximum power.
Operative conditions employed for plasma etching are the following:

- Process gas: argon
- Gas flow rate: 20 slm
- Power supplied: 5.4 kW
- Thermal efficiency: 27%

The choice of argon as process gas has been dictated by the potential less electrode erosion that reduces the risk of metal contamination on the silica rod surface as a consequence of the low thermal local heat flux on the electrodes compared with other molecular gases such as N_2 or H_2.
Gas flow rate has been taken as low as 20 slm to avoid instantaneous cracks due to the excessive kinetic impact and for increasing the mean temperature, making vaporisation easier.

Discussion and results

An enthalpy probe [12-18] has been used to monitor plasma condition in order to obtain plasma temperature, velocity and air entrainment maps [19] before TPE process. In figure 3 the air entrainment distribution in the plasma jet is shown, whereas in figures 4 and 5 radial and axial temperature and velocity profiles at the nozzle exit are presented for a 5 mm torch nozzle operating at 200 A with 20 slm of argon.

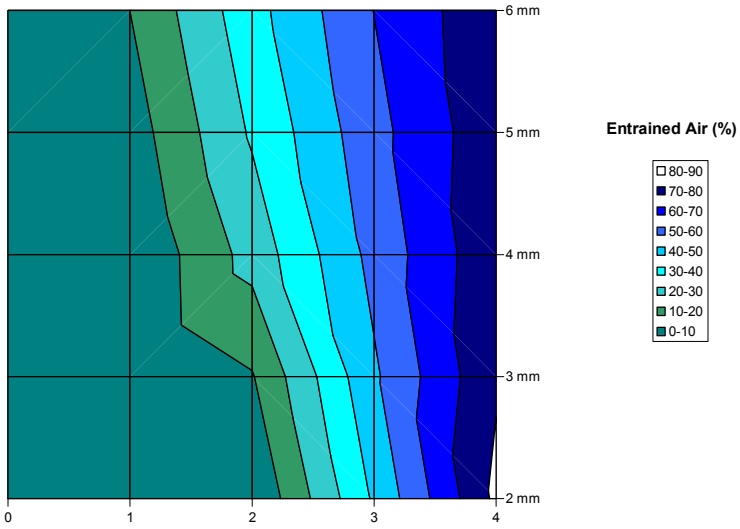

Figure 3: Air entrainment map of an argon plasma jet at 200 A, 20 slm.

In figure 3 the core region is clearly recognized inside the zero percentage contour. This zone is characterized by high temperature 3000-4000 K (figure 4) and high velocity 400-500 m/s (figure 5) whereas in the outer region the presence of air tends to chill and slow the argon region.

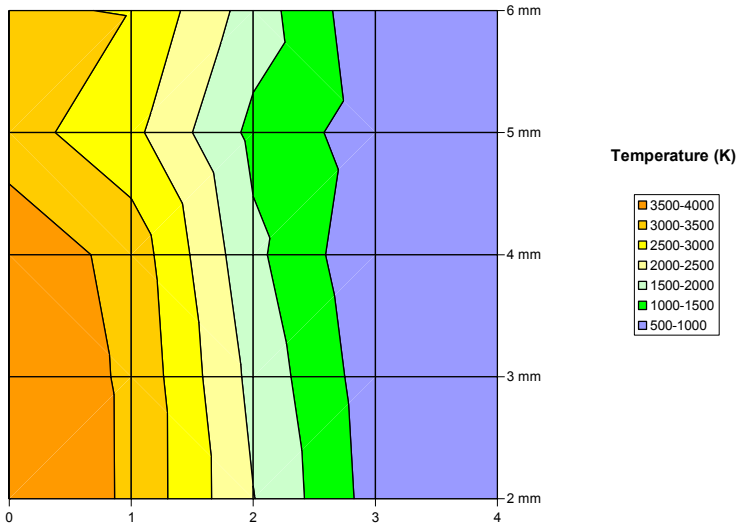

Figure 4: Temperature map of an argon plasma jet at 200 A, 20 slm.

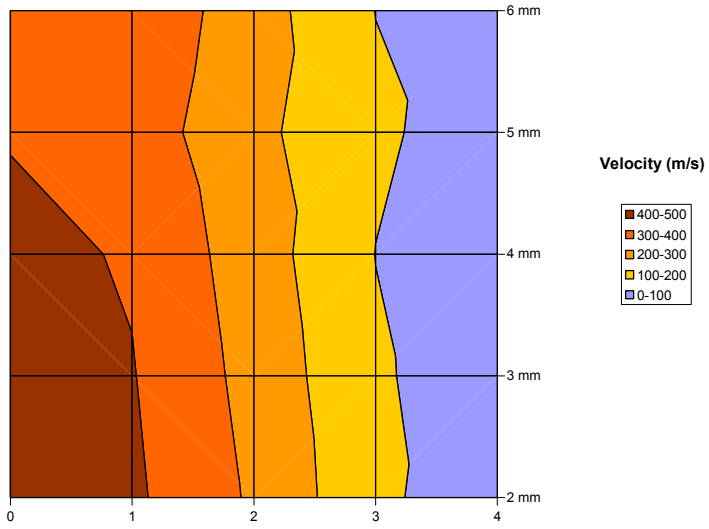

Figure 5: Velocity map of an argon plasma jet at 200 A, 20 slm.

Torch to rod distance, rod rotating speed, torch transverse speed have been optimized on a number of silica sample rods in order to reduce surface etch non uniformities and cracks formation. Such tests lead to the definition of the following apparatus working parameters:

- Torch to rod distance: 2 mm
- Rod rotating speed: 42.96 r.p.m.
- Torch transverse speed: 0.056 cm/s

With the previous parameters three silica rods (length 1 m, diameter 10 mm) have been treated at a distance of 2 mm from the anode exit. Table 1 reports the volume removed from each rod, the time interval of treatment, the total mass removed (SiO_2 density = 2.2 gr/cm^3) and the mass loss rate (M_c).

	rod 1	rod 2	rod 3
Total volume removed [mm^3]	9660	7725	19295
Total time of treatment [min]	28.9	36	52
Total mass loss [g]	26	20.85	52.1
M_c [g/h]	53.9	34.75	60.11

Table 1: TPE experimental data.

A mean vaporisation value of M_c = 49.58 g/h ± 7.47 g/h has been obtained with the described set of operative condition. The lower rod 2 vaporisation rate compared to rod 1 and rod 3 has been ascribed to initial non uniform diameter of rod 2 causing different longitudinal torch to rod distances. The result is a lower mean vaporisation rate.
Assuming that the main cause, in stationary conditions, for the rod erosion is due to material evaporation, ignoring redeposition of materials as whiskers, the mass loss can be calculated through the number of atoms leaving the cathode per unit time and surface area (vapour density flux). According to the kinetic theory of gases the vapour pressure $p_{ev}(T_c)$ can be described as a process in which the particles leaving the surface transfer their momentum per unit surface area and time to the surroundings. The maximum vapour density flux J_n^{max} will be given by:

$$J_n^{max} = \frac{p_{ev}(T_c)}{\bar{p}} \qquad (1)$$

where

$$\bar{p} = m_c \sqrt{\overline{v^2}} = \sqrt{3 m_c k_B T_c} \qquad (2)$$

$m_c = 1.0049 \cdot 10^{-25} kg$ being the silica atomic mass and T_c the surface temperature. Thus the mass loss rate M_c^{max} is given by:

$$M_c^{max} = J_n^{max} \pi r_s^2 m_c \qquad (3)$$

where r_s is the jet radius, taken as 2.5 mm (see figure 4).
From equations (1-3) and the experimental mass loss rate M_c, a surface temperature T_c=2057 K during the TPE process has been calculated (see figure 6).

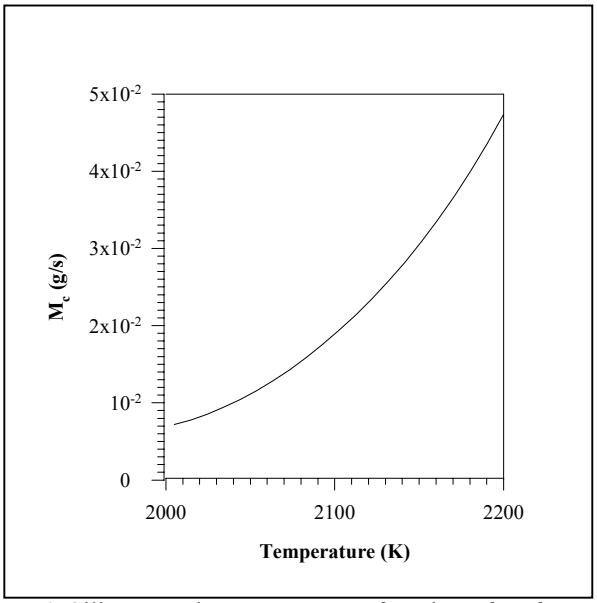

Figure 6: Silica mass loss rate M_c as a function of surface temperature.

TPE rate has been compared with chemical etching rate carried out on two silica rods.
The reaction exploits HF (40% solution for RPE analysis in watery solution at 20° C temperature) as etch agent to give:

$$SiO_2+4HF\rightarrow SiF_4+2H_2O$$

Silica rods have been plunged in a cylindrical box containing 4 l of HF and connected to a peristaltic pump.
Time of treatment has been based on calibration measurements previously obtained with periodic check of rod diameter.
Before rod inspection and at the end of silica etching treatment, rods have been washed with distilled water in order to stop the acid corrosion.
The two silica rods have been step treated lengthwise in order to estimate chemical etching rate for increasing level of removing.
The four segments, illustrated in figure 7, correspond to different levels of silica removed depth, that is to say 0.1, 0.2 ,0.4 and 0.8 mm.

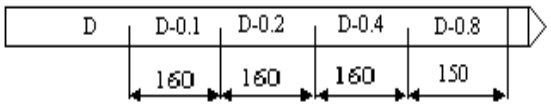

Figure 7: Treatment outline of chemical etching.

A mean chemical etch rate of 0.1 ± 0.01 mm/ h has been measured.
Despite the high uniformity achievable through chemical etching, the presence of surface defects tend to amplify their dimensions due to the isotropic features of chemical action. On the other hand TPE is an anisotropic process being directed essentially as the plasma jet. The coupled displacement of the torch and the rod rotation can give rise to grove formation. However the described choice of parameters have been found to minimise the difference between the maximum and minimum rod diameter $\frac{d_{\max} - d_{\min}}{d_{rod}}$. This value has been evaluated to be less than 1 %.

3. Conclusion.
TPE through the use of a DC plasma torch has been employed to remove surface impurities from silica rods. The process allows etching rate up to about 50 g/h (36 mm/h) to be obtained.
This etching rate is very high compared to both chemical and RF or MW plasma etching at low pressure. Though uniformity is the key issue to be pursued, a correct choice of plasma and relative displacement parameters allows acceptable surface non uniformities (below 1%) together with limited surface thermal stress.

4. Bibliografy
[1] E. Pfender: *Gaseous Electronic*, N. H. Hirsh and H. J. Oskam, Vol. 1, Academic Press, N. Y., 1978.
[2] H.U. Eckert: High Temperature Sci. 1974, **6**, 99.
[3] P. Fauchais, J. F. Coudert, B. Pateyron: Proceedings of Workshop on *Thermal Plasmas for Hazardous Waste Treatment*, Varenna (Italy), 1995, Word Scientific.
[4] J. Pelletier and M.J. Cooke: *Journal of Vacuum Science & Technology*, **7**, 1, 59.
[5] A.J.Perry and R. W. Boswell: *Appl. Phys. Lett*. **55** (2), 148.
[6] Eichelberg, Friedrich et alt.: *Review of Scientific Instruments*, **6**, 4, 2394.
[7] M.V. Bazylenko and M. Gross: *Journal of Vacuum Science & Technology*, **14**, 6, 2994.

[8] James E.Stevens, ISPP Proceedings of Workshop on *Industrial Application of Plasma Physics*, Varenna (Italy), 1992, p 95**,** Editrice Compositori Bologna.
[9] R. D'Agostino and F. Fracassi: , ISPP Proceedings of Workshop on *Industrial Application of Plasma Physics*, Varenna (Italy), 1992, p 309**,** Editrice Compositori Bologna.
[10] M.Bobbio: , ISPP Proceedings of Workshop on *Industrial Application of Plasma Physics*, Varenna (Italy), 1992, p 327**,** Editrice Compositori Bologna.
[11] N.Mutsukura, Y. Fukazawa et al: , ISPP Proceedings of Workshop on *Industrial Application of Plasma Physics*, Varenna (Italy), 1992, p 509**,** Editrice Compositori Bologna.
[12] J. Gray: ISA Transactions, **4**, 1965, 102.
[13] J. Grey, P.S. Jacobs and M.P. Scherman: Rev. Sci. Instr., **33**, 1962, 738.
[14] S. Katta, J. Lewis and W.H. Galvin: Rev. Sci. Instr. **44**, 1973, 1519.
[15] T. J. O'Connor, E. H. Comfort, L. A. Cass: AIAA J. **4**, 1966, 2026.
[16] L. A. Anderson, R.E. Sheldahl: AIAA J. **9**, 1971, 1804.
[17] W.D. Swank, J. R. Fincke, D.C. Haggard: Rev. Sci. Instrum., **64**, 1993, 56.
[18] W. L. T. Chen, J. Heberlain, E. Pfender: Plasma Chem. Plasma Process., **14**, 1991, 317.
[19] R. Benocci: PhD Thesis, UMIST, Manchester, 2000.

Effect of reactive gas partial pressure on plasma chemistry during magnetron sputtering

S. Mráz, J. M. Schneider

Materials Chemistry, RWTH-Aachen, Aachen, Germany

The plasma composition of sputtered aluminium in an oxygen background has been investigated by mass energy analysis. As the oxygen partial pressure is increased during reactive magnetron sputtering a sharp decrease in deposition rate is commonly observed. This can be explained by the formation of a compound layer at the target surface. Here we report initial plasma chemistry data of an aluminium – argon – oxygen system. Changes in plasma chemistry are measured versus the oxygen partial pressure while the total pressure was kept constant. A strong dependence of the plasma chemistry with respect to the oxygen partial pressure was found. Besides the identification of the expected aluminium, argon and oxygen based ionic species and their dependence on the oxygen partial pressure, we present initial data supporting the formation of aluminium based clusters.

Experimental validation of a model predicting the evaporation of zinc in an argon transferred arc

L. Aguilera, R.J. Munz, and D. Berk

Plasma Technology Research Center (CRTP), Dept. of Chemical Engineering, McGill University

Abstract

Experimental work was carried out on a transferred arc evaporator to validate and calibrate a simple numerical model which predicts metal evaporation rates as a function of crucible temperature, arc current, arc length and plasma gas flow rate. The model gave good qualitative predictions of the effects of all parameters but arc length. The model underpredicted the evaporation rates because of the assumption that the evaporation rate was heat transfer controlled at the boiling point of the metal. The low thermal gradients in the metal result in considerable evaporation at lower temperatures. It is recommended that the model be modified to take this into account

1. Introduction

A transferred arc system, in which an arc is struck from a thoriated tungsten cathode to a metal bath anode, is a convenient way of producing a superheated stream of metal vapour which may be quenched externally to produce ultrafine metal powders or reacted further to produce ultrafine ceramic powders. The scaleup and optimization of the overall system requires knowledge of the operational characteristics and efficiency of the plasma metal evaporator. A simple model has been developed [1,2] which predicts the temperature and velocity fields in the plasma arc and the molten metal bath and also the evaporation rate of metal as a function of arc current, gas flow rate and composition, and arc length. In the present work, experimental data are presented for the validation and calibration of this model using an argon plasma to evaporate zinc. Zinc was chosen because its relatively low melting and boiling points allow more precise experimental measurements to be made.

2. Experimental Set-up

The experimental equipment (Figure 1) consisted of a transferred arc torch set in a cylindrical, water-cooled stainless steel vessel (I.D. = 25 cm; h= 43 cm) a side outlet (I.D.=3.5 cm). The cathode assembly consisted of a water-cooled conical thoriated tungsten tip surrounded by a water-cooled copper nozzle which acted as auxiliary anode. The anode (Figure 2) was a graphite crucible (O.D.= 13.0, h=3.1 cm) with a truncated cone internal cavity (depth=2.1 cm, I.D= 10 cm at the top and I.D.= 5.0 cm). The cathode assembly could be moved vertically to adjust the torch-crucible distance. The crucible was mounted on a hollow graphite cylinder (16.2 cm in length with O.D.=1.3 cm and I.D.= 0.95 cm) inserted in a graphite base. The purpose of the cylinder was to provide an electrically conductive path while minimizing heat losses from the crucible.

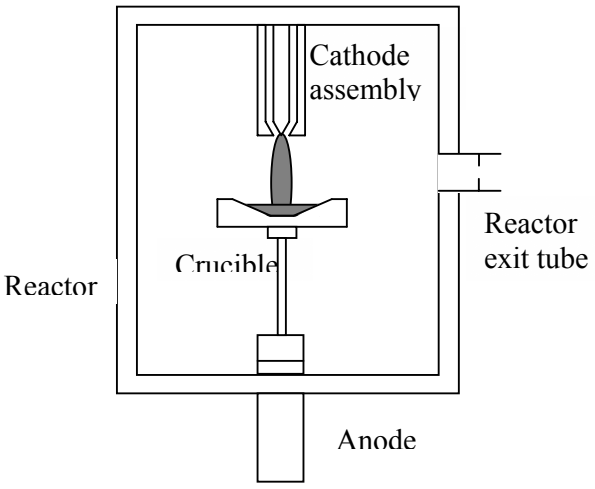

Figure 2:Equipment

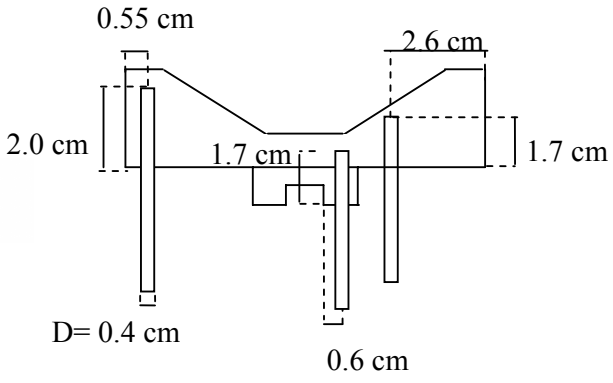

Figure 1: Details of Crucible

Eight DC rectifiers connected in series supplied power to the transferred arc torch with a maximum current of 275 A and an open circuit voltage of 600 V. The outputs of the rectifiers were connected to a high frequency generator used for igniting the arc.

The current and voltage of the arc were monitored using an analog ammeter and voltmeter located in the control console. The current was measured across a shunt (500 A, 50 mV) placed in series with the anode. The voltage was measured between the cathode output of the high frequency generator and the anode of the reactor. The variation of temperature at three different points in the crucible was measured using ungrounded type K thermocouples (see Figure 2). The values of temperature, current and voltage were recorded with the a data acquisition system starting 60 s after arc ignition. The pressure inside the chamber was monitored using a pressure gauge

3. Experimental Procedures

The metal used was zinc with a purity of 99.97 % supplied by Noranda Inc (Quebec, Canada). Before each experiment, a sample of zinc weighing about 400 g was loaded into the crucible and the reactor was purged with argon to remove any residual oxygen. The cathode assembly was positioned to within a few millimeters of the zinc and the arc ignited. The arc was then adjusted to the appropriate length, current and gas flow rate and operated for the required time. After the experiment, the reactor was cooled under argon purge, and the metal remaining in the crucible was weighed.

4. Results and Discussion

a. Temporal variation of crucible temperature and calculation of evaporation rate

The model being tested is a steady state model but the experiments are necessarily batch. Figure 3 shows the temperature variation at the centre of the crucible for several experiments performed under the same conditions with different operating times. The results show a rapid increase in temperature over approximately the first 720 seconds after arc ignition. During that time the zinc melts and is heated to a pseudo steady state temperature. Following that time the temperature of the crucible increases slowly by 0.12°C/s. Long runs were inappropriate because the temperature increases were higher due to appreciable changes in the level of metal in the crucible and arc length. After arc extinction, the metal and crucible cooled, exhibiting a freezing plateau about 19 degrees below the freezing point of zinc. This temperature difference allowed the true wall temperature at the zinc-crucible interface to be estimated for the simulations.

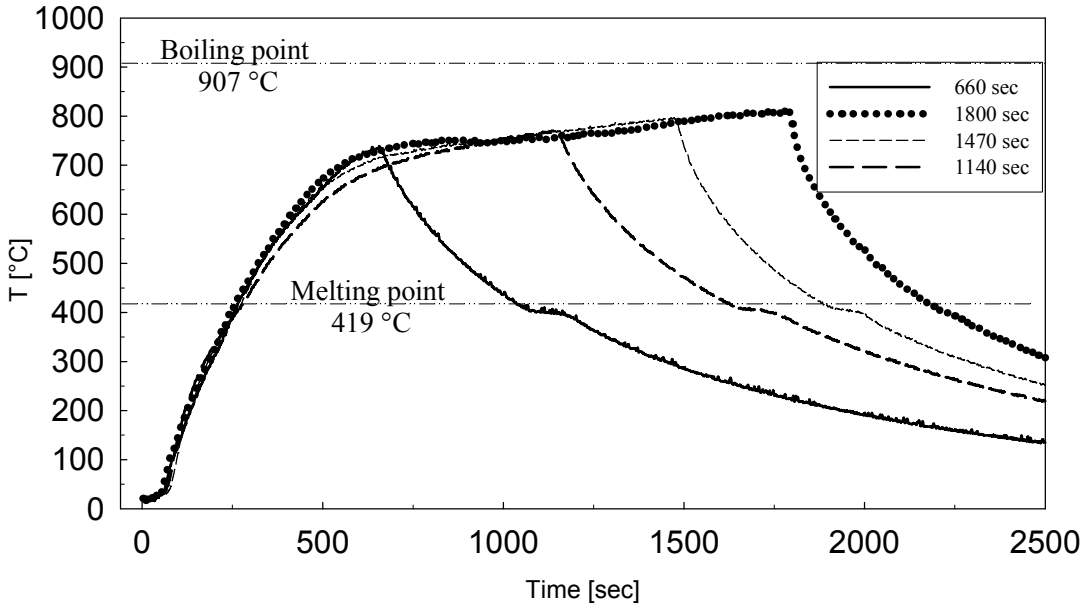

Figure 3. Temperature variation at the center of the crucible under the same conditions of operation: plasma gas: argon, I=104 A, arc length = 3 cm, gas flow rate = 11.5 lpm at 21°C and 1 atm.

The slight differences between crucible temperatures in runs performed at identical operating conditions are attributed to variations in the thermal contact resistance in the crucible-anode assembly and were unavoidable. In the subsequent discussion, the evaporation rate during an experiment was based only on the time from 720 s to arc extinction, and the metal evaporated during the heat up period was subtracted from the weight lost during the entire experiment.

b. Spatial variation of temperature in crucible.

Figure 4 shows the temperature variation at three different points in the crucible during a typical experiment as well as the arc current and voltage. Thermocouple 1, which is located far from the metal is lower than thermocouple 2 by a maximum of 50^{o}C during the pseudo steady state while thermocouples 2 and 3 showed a difference of no more than 10^{o}C during the pseudo steady state.

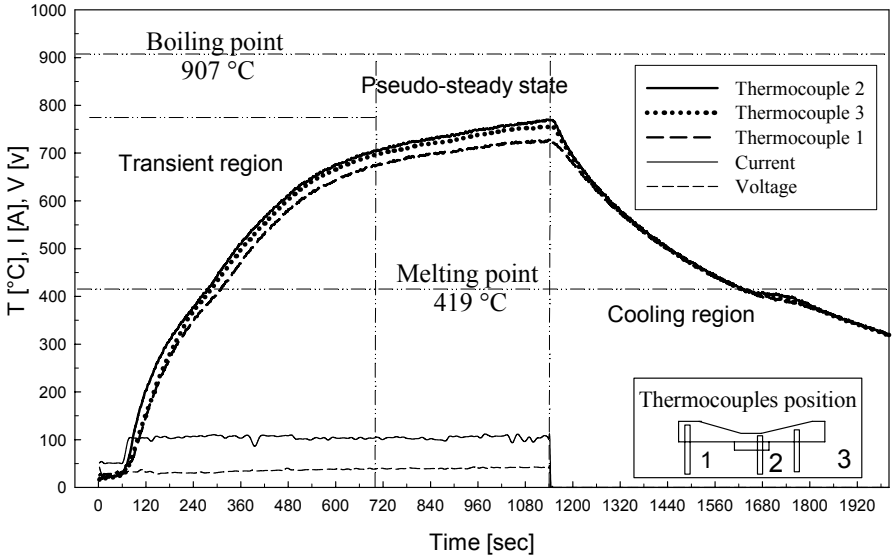

Figure 4. Temperature variation of the crucible, operation conditions: I=104 A, arc length = 3 cm, gas flow rate = 11.5 lpm at 21°C and 1 atm.

c. Evaporation rate at base conditions as a function of crucible wall temperature

Figure 5 shows the experimental and predicted values of the evaporation rate as function of the mean wall crucible temperature at a single set of operating conditions. Although the maximum variation in mean temperature is only 45^{o}C, the experimental and predicted evaporation rates are quite sensitive to the crucible wall temperature. The model predicts a positive linear increase of evaporation rate with temperature. If it is accepted that the experimental evaporation rates are also linear with temperature, the experimental rates are an average of 2.3 times higher. A major assumption of the model is that the evaporation of metal is heat transfer controlled and limited to the area immediately below the arc where the metal reaches its boiling point. The experimentally observed higher evaporation rates may be attributed primarily to the evaporation of metal by a mass transfer mechanism from areas of the surface which are below the boiling point.

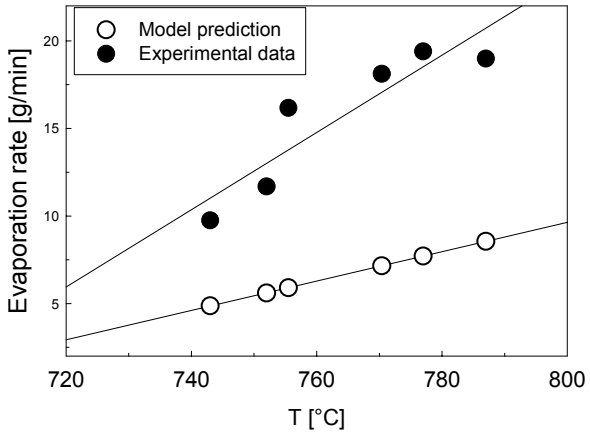

Figure 5. Experimental and predicted values of evaporation rate as function of the crucible wall temperature: Operation conditions: plasma gas: argon, I=104 A, arc length= 3.0 cm, gas flow rate=11.5 lpm at 21°C and 1 atm

d. Effect of the current on the evaporation rate

The effect of the current on the evaporation rate was studied by melting the zinc and heating it at the standard conditions shown in Figure 5 for 720 s, followed by an adjustment of current to the test value for the remainder of the experiment. The experimental and model results showed that an increment in the current led to higher evaporation rates (figure 6 and 7). Figure 6 shows the raw values with the unavoidable changes in crucible temperature. Figure 7 is a plot of the results at a constant temperature of 780^{o}C. In this plot, the effect of current is seen to be linear for both the experimental results and the predictions. Again, the model underpredicted the evaporation rates.

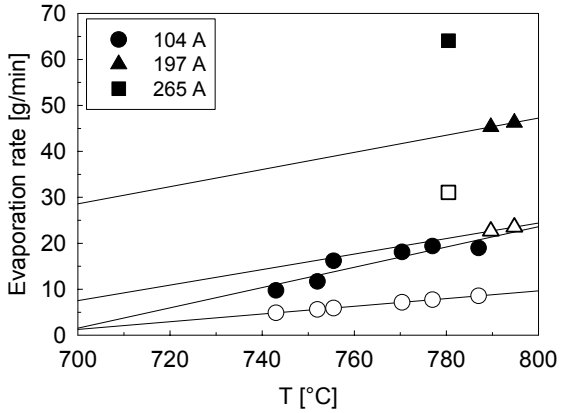

Figure 6. Experimental and predicted values of evaporation rate as function of the crucible wall temperature. Current effect, plasma gas: argon, arc length= 3.0 cm, gas flow rate=11.5 lpm at 21°C and 1 atm, Dark symbols are experimental, open symbols are predictions.

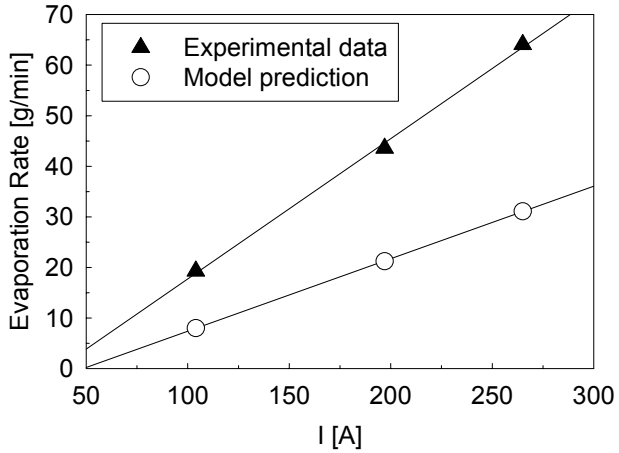

Figure 7. Experimental and predicted values of evaporation rate as function of the current at a crucible wall temperature of 780^{o}C; operation conditions: plasma gas: argon, arc length= 3.0 cm, gas flow rate=11.5 lpm at 21°C and 1 atm.

e. Effect of the gas flow rate on the evaporation rate

To examine the effect of plasma gas flow rate, the system was again operated at the base conditions for 720 s after which the plasma gas flow rate was increased from 11.5 to 30 lpm. Experimentally, increasing the plasma gas flow rate decreased the crucible temperature as is shown in Figure 8. The experimental evaporation rate increased with increasing gas flow rate. The model predicted that increasing the gas flow rate would slightly increase the evaporation rate of metal. The model does not predict the crucible temperature since this is a boundary condition. The effect of gas flow rate on the evaporation rate at the arc root is very complex. The model assumes a heat transfer limited process for evaporation at the boiling point of the metal. Increasing the gas flow rate increases convective heat transfer to the surface by increasing the gas velocity but also modifies the arc power through voltage. The arc voltage was predicted to increase from 16.8 to 20.8 V or by 24% as the gas flow rate increased from 11.5 to 13 slpm. The measured voltage increased from 19.8 to 23.6 which is very similar. Experimentally, increasing the plasma gas flow rate modifies the arc and also increases mass transfer at the surface leading to higher than predicted evaporation rates. For this reason, the experimental results are more sensitive to plasma gas flow rate than the modeling results.

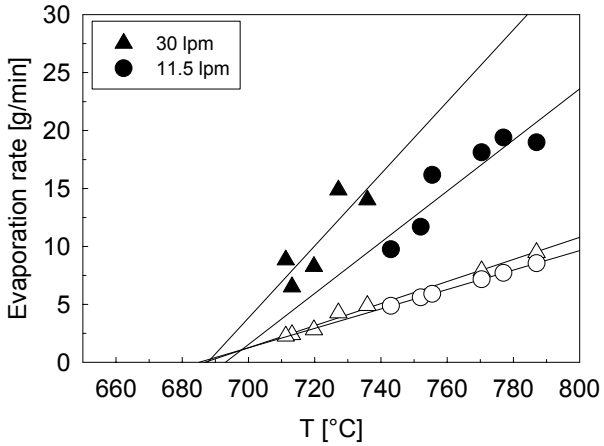

Figure 8. Experimental and predicted values of evaporation rate as function of crucible wall temperature, Plasma gas flow rate effect, plasma gas: argon, I=104 A, Arc length=3.0 cm. Dark symbols are experimental, open symbols are predictions.

f. Effect of the arc length on the evaporation rate

To examine the effect of arc length on evaporation rate, the arc length was increased from 3 cm to 5,2 cm after 720 s. The results are summarized in Figure 9. As was always the case, the experimental evaporation rates were higher than those predicted by the model. The effect of arc length on the experimental results is less clear. The model predicts an increase of evaporation rate with shorter arcs. However there appears to be a crossover in the experimental results with higher evaporation rates observed for longer arcs at higher crucible temperatures. The arc voltage was predicted to increase from 16.8 to 19.4 V as the arc length increased from 3.0 to 5.2 cm, an increase in power of 16%. The reason for the predicted higher evaporation rates for shorter arcs is due to the higher rates of convective heat transfer due to higher jet velocities. Experimentally, the arc voltage increased from 19.8 to 32 V as the arc length was increased. This 62% increase in power may explain the higher evaporation rates observed for these arcs. The reasons for the poorer prediction of the model voltage in this case are still unclear.

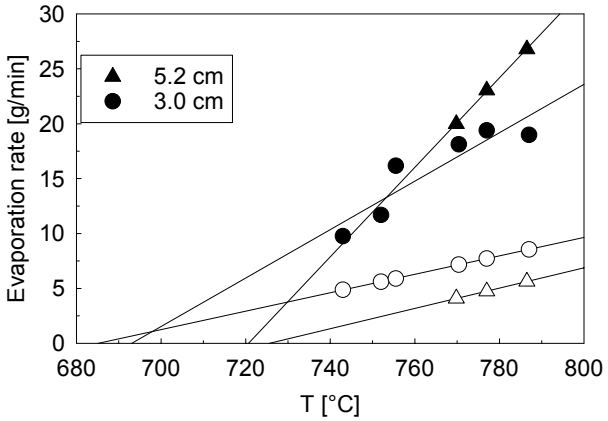

Figure 9. Experimental and predicted values of evaporation rate as function crucible wall temperature, Arc length effect, plasma gas: argon, I=104 A, gas flow rate=11.5 lpm at 21°C and 1 atm. Dark symbols are experimental, open symbols are predictions.

5. Conclusions

Experimental work was carried out on a transferred arc evaporator to validate and calibrate a simple numerical model which predicts metal evaporation rates as a function of crucible temperature, arc current, arc length and plasma gas flow rate. Argon gas and zinc metal were used as the test system. The model gave good qualitative predictions the effects of all operating parameters except the effect of arc length. The model consistently underpredicted the evaporation rates by a factor of about two and this is attributed to the assumption that the evaporation rate of liquid metals in this system is a heat transfer controlled process at the boiling point of the metal. The low viscosity and high thermal conductivity of the metal result in considerable evaporation of metal outside the region immediately below the arc. It is recommended that the model be modified to take this into account.

References

[1] Addona, T. P. Proulx, and R.J. Munz, 'Mathematical modelling of silica anode decomposition', Plasma Chem. Plasma Processing, 20 (4), pp 521-553, 2000

[2] Munz, R.J. , Jun Yu, and Ian Castillo, 'Modeling of a transferred- arc metal evaporator' 15th International Symposium on Plasma Chemistry, Orleans, July 9-13, 2001, Symposium Proceedings, Vol II, pp 385-390, 2001.

Acknowledgement

The financial support of the Natural Sciences and Engineering Research Council of Canada is gratefully acknowledged.

Modification of PVDF properties by microwave plasma treatment

M. Pascu[1], F. Poncin-Epaillard[2], D. Debarnot[2], S. Durand[3]

[1]*Department of Physics, "Gr. T. Popa" University, Iasi, Romania*
[2]*Laboratoire Polymères, Colloïdes, Interfaces, UMR 6120, Université du Maine, Le Mans, France*
[3]*Laboratoire d'Acoustique, UMR 6613, Université du Maine, Le Mans, France*

Abstract
Films of polyvinylidene fluoride (PVDF) have been treated in a microwave nitrogen plasma, for different conditions, in order to establish the treatment parameters which constitute a good compromise between an optimum functionalization and a minimum degradation. Surface properties of PVDF have been modified in a controlled manner, allowing its metallization, necessary in a wide range of applications.

1. Introduction

In order to be used in acoustic sensors, a polymeric material have to fulfill two essential conditions, that is to present a piezoelectric character and to be covered with an homogeneous metal layer, with a good adherence to the polymer surface.

It is well known that fluoropolymers are characterized by a small surface energy, which does not allow an adequate adhesion with a metal layer. That is why, activation of polymer surfaces prior to metallization is absolutely necessary. Before metallization of fluoropolymer, the respective surface must be modified to become hydrophilic, in order to be well-wet by an electrolessplating solution [1]. Gas plasma treatment under various glow discharge conditions was extensively used for this type of surface modification of fluoropolymers [2]. Polar groups introduced by plasma treatment on the film surface favor the reaction of copper (for eg.) to form a copper-nitrogen-carbon complex in the interface region [3]. It was proved that Cu binds preferentially to oxygen and nitrogen functional groups. It is thus expected that, by treating the polymer surface with nitrogen or oxygen plasmas, the reactivity of the polymer with the copper may increase [4].

The introduction in abundance of functional groups or polymer chains is not always a good surface modification for the electrical insulators. That is why, the choice of the remote plasma as a pretreatment method for obtaining a Cu/fluoropolymer composite is often used [1].

In this study, polyvinylidene fluoride (PVDF) films have been treated in a nitrogen microwave plasma, for different treatment conditions, in order to appropriate modify its surface properties, without significantly changing the bulk ones (in this way, the piezoelectric character being not influenced by the treatment). After applying the plasma treatment, the PVDF surfaces have been covered with a copper layer, by means of an electrolessplating procedure.

2. Materials and methods

Films of polyvinylidene fluoride (PVDF) (0.25 mm in thickness), obtained from Goodfellow, England, have been used in this study. This is a semi-crystalline, semi-opaque and white fluorinated polymer. Its density is 1.76 g/cm^3 and its upper working temperature ranges between 135 and 150 ºC.

In order to prepare a polymer surface with a good adhesion to the metal (condition which has to be fulfilled for being used in acoustic sensors), pretreatment of the PVDF film prior to metallization is necessary. In this purpose, PVDF films have been treated in a microwave nitrogen plasma (the gas flow: D=10 sccm), for different conditions, in order to establish the treatment parameters which constitute a good compromise between an optimum functionalization and a minimum degradation. Treatment power

varied between 20 and 80 W, the distance between the sample and the surfatron was comprised between 2.5 and 30 cm, and the exposure time between 30 and 300 s.

Modification of the surface and bulk properties of PVDF has been followed by contact angle and weight loss measurements, XPS, UV spectroscopy, wide angle X-ray diffraction. Subsequent surface metallization was realized by an electrolessplating procedure.

3. Results and discussion

3.1. Contact angle and weight loss measurements

Whatever the applied treatment power and the exposure time, an important increase in the hydrophilicity of the PVDF surfaces was obtained. This behaviour is evidenced by the significant decrease of the advancing and receding water contact angles in respect with the untreated sample (Figure 1) and it was also evidenced by other authors [5].

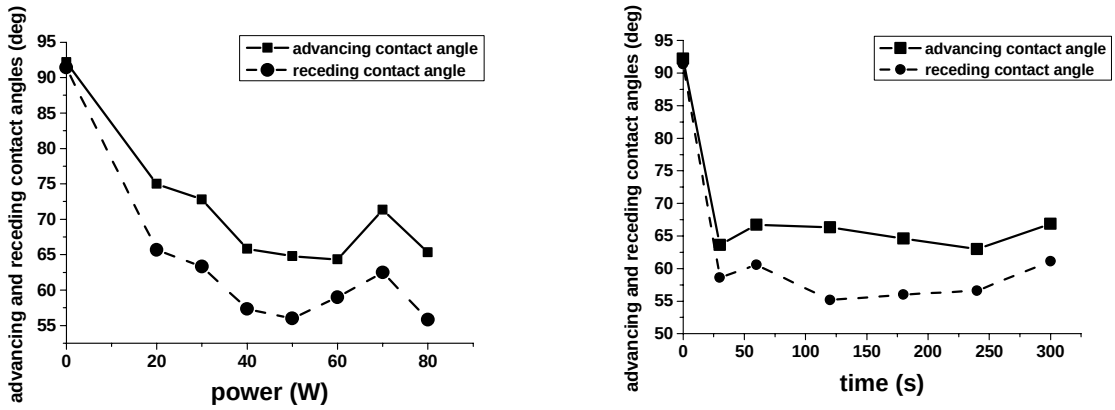

Figure 1. Water advancing and receding contact angles vs the discharge power and the treatment time for PVDF, N_2 plasma treated.

After plasma exposure, water contact angle hysteresis increases when compared with the pristine PVDF (Figure 2), indicating the obtainment of a significant roughness for the treated surface [6, 7]. The important hysteresis of the water contact angle in the case of PTFE ammonia plasma treated was explained by Badey et al. [8] by the fact that, in contact with water, nitrogen and oxygen containing groups reorient to minimize the interfacial energy, a very low receding water contact angle being measured. An increase in the micro-roughness could be a sign for the obtainment of a better adherence of the respective surface with a metal layer [9].

It is well known [6] that N_2 or NH_3 plasma treatments give rise to N–containing functionalities, such as: amine ($–NH_2$), imine (–CH=NH), cyano (–C=N) on polymer surfaces, as well as oxygen–containing groups, such as amide ($–CONH_2$), due to post-discharge atmospheric oxidation. This fact is also evidenced in our case, the increase of the acid-base component of the free surface energy with the discharge power and the treatment time being obvious (Figure 3. a, b).

As the polymer surface functionalization under plasma exposure is a very rapid phenomenon which, generally, occurs during a period inferior to 1 min [10], the acid-base component of the free surface energy significantly increases during the first 30 s, after this period, its value remaining almost constant for the entire period of plasma exposure (Figure 3.b).

For a given power, treatment time and gaseous flow, the acid-base component decreases with the distance sample-surfatron (Figure 3.c). This behaviour evidences that, in the case of a polymer sample treated far enough from the direct plasma, the influence of the charged particles (electrons, ions) is

cancelled [8] and radicals alone should be predominantly as active species for the surface modification [11].

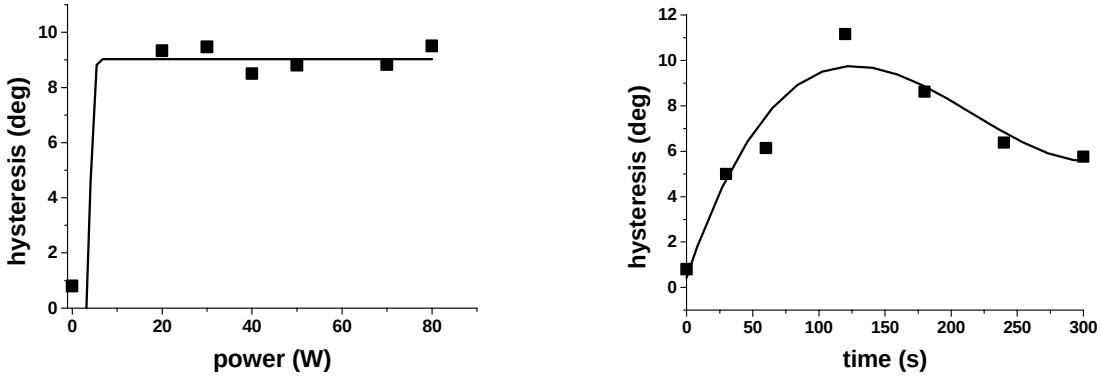

Figure 2. Water contact angle hysteresis vs the discharge power and the treatment time for PVDF, N_2 plasma treated.

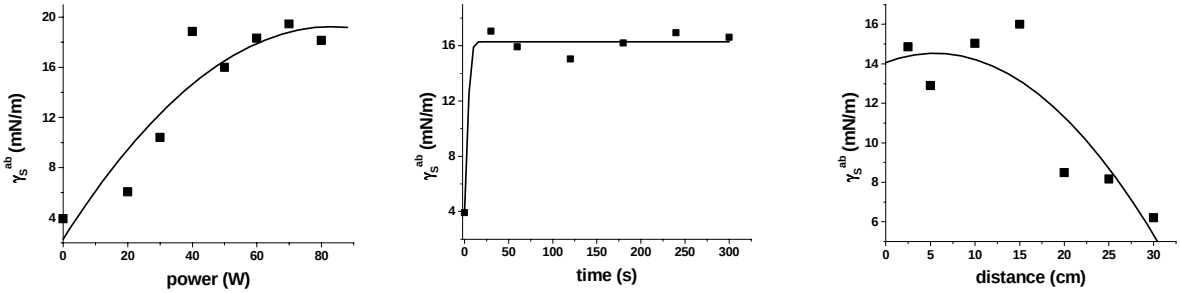

a **b** **c**

Figure 3. Acid-base component of the free surface energy for PVDF, N_2 plasma treated, vs: (a) the discharge power, (b) the treatment time, (c) the distance between the polymer sample and the surfatron.

Taking into account also the weight losses results (Figure 4), it could be concluded that the optimum treatment conditions which constitute a good compromise between an optimum functionalization and a minimum degradation for PVDF, N_2 plasma treated, are: P = 50 W, t = 1 min, d = 10 cm.

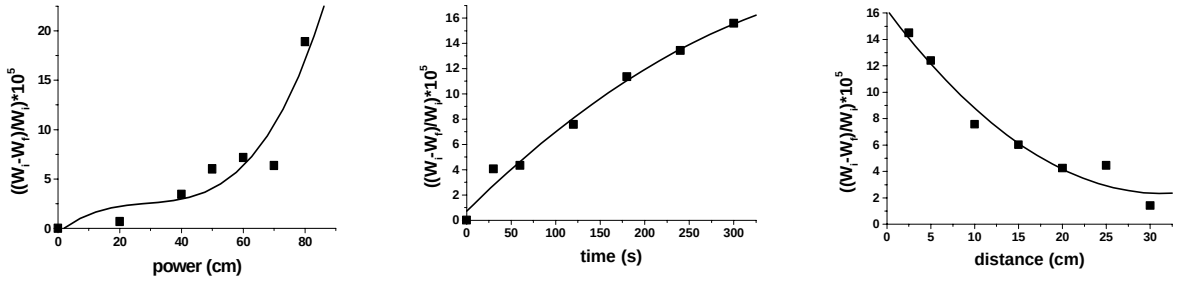

a **b** **c**

Figure 4. Weight losses for PVDF, N_2 plasma treated, vs: (a) the discharge power, (b) the treatment time, (c) the distance between the polymer sample and the surfatron.

3.2. XPS results

In order to obtain information on the type of functional groups introduced on PVDF surface under plasma treatment, XPS analysis has been realized. As it was expected, N-containing groups were detected on the polymer surface after the applied treatment (Table 1).

Table 1. Results of XPS analysis for untreated and N_2 plasma treated PVDF surface.

Sample	Spectrum	Position of the pics (eV)	Attributed groups
untreated PVDF	C1s	280.4 284.8	carbide carbon
	F1s	685	
	O1s	531.1	carbonates
PVDF / N_2	C1s	280.1 284.7	carbide carbon
	F1s	685.1	
	O1s	531 532.6	metal oxides nitrates
	N1s	397.9	nitride

As it was also pointed out by other authors [12], atomic composition on PVDF surfaces evidence a surface defluorination under plasma exposure (a decrease in fluorine atom concentration from 41.5 % for the untreated PVDF to 28 % for the N_2 plasma treated surface). In the meantime, an increase in oxygen atom concentration (from 3.2 % to 9 %) is obvious after the applied treatment.

3.3. Titration of the surface amino groups

Titration of the surface amino groups, followed by UV spectroscopy [13], was in a good agreement with surface energetic results, the variation of the amino groups concentration with the treatment parameters following almost the same behaviour as the polar component of the free surface energy (Figure 5 a, b, c).

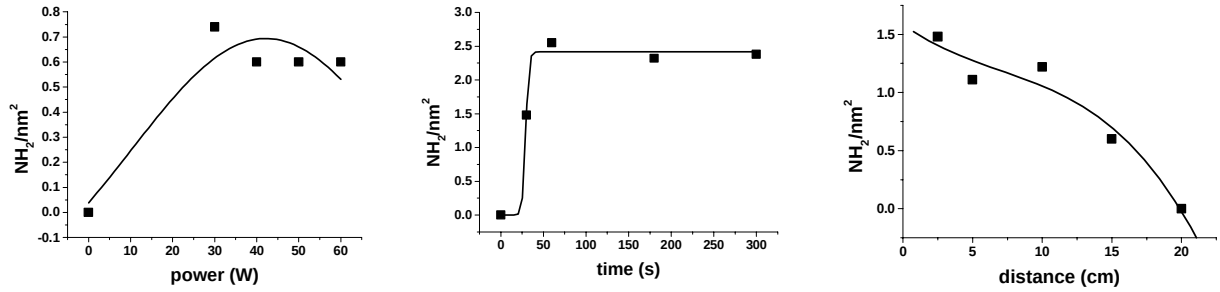

a **b** **c**

Figure 5. Concentration of the amino groups on PVDF surface, N_2 plasma treated, vs: (a) the discharge power, (b) the treatment time, (c) the distance between the polymer sample and the surfatron.

3.4. Wide angle X ray diffraction

No significant change in the diffraction pattern for N_2 plasma treated PVDF has been observed, whatever the discharge power, the treatment time and the distance between the polymer sample and the core of the discharge (Figure 6). In the meantime, the crystallinity degree for PVDF does not change significantly under plasma treatment (Table 2).

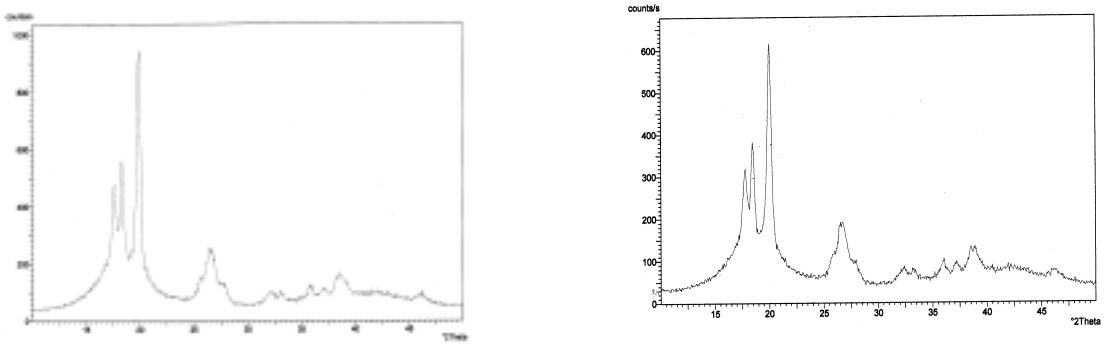

Figure 6. X-ray diffraction patterns for: (a) untreated PVDF and (b) N_2 plasma treated PVDF (50 W, 1 min, 10 cm).

Table 2. Crystallinity degree evaluated from X-ray spectra for untreated and plasma exposed PVDF, in different treatment conditions.

Treatment conditions	X_C
Untreated	0.870
50 W, 30s, 10 cm	0.870
50 W, 2 min, 10 cm	0.880
50 W, 5 min, 10 cm	0.876
70 W, 2 min, 15 cm	0.880
50 W, 2 min, 2.5 cm	0.876

The fact that bulk properties of PVDF seem to not change under plasma exposure could be a good sign for the maintenance of the piezoelectric character of polymer samples treated in these conditions.

3.5. Preliminary results on PVDF metallization

Samples of PVDF, plasma pretreated, were metallized by chemical way, using a two step procedure [14], consisting in the substrate activation using a mixed solution of $PdCl_2$ and $SnCl_2.2H_2O$ (realized at two different temperatures, 25 and, respectively, 40°C), followed by acceleration in HCl 1M, and, finally, the metallization in a solution based on $CuSO_4$ [4]. All the pretreated samples were covered with an homogeneous layer of copper, with an improved adhesion at the PVDF surface, in respect with the pristine sample (Table 3).

Table 3. Results obtained by the normalized scotch test for PVDF surface, untreated and N_2 plasma exposed (P = 50 W, t = 1 min, d = 10 cm).

Sample	Adherence (%)	
	t = 25 °C	t = 40 °C
untreated PVDF	0	0
PVDF / N_2	72	93

4. Conclusions

Choosing appropriate treatment conditions, surface properties of PVDF can be modified in a controlled manner, allowing its metallization, necessary in a wide range of applications. The fact that no significant changes appear in bulk properties of the polymer could be a good sign in the possibility of maintaining the piezoelectric character of some plasma exposed polymers, condition necessary in order to be used in acoustic sensor.

References

[1] N. Inagaki, S. Tasaka, T. Umehara - J. of Appl. Polym. Sci. **71**, 2191 (1999).
[2] S. Wu, E.T. Kang, K.G. Neoh, H.S. Han, K.L. Tan - Macromolecules **32**, 186 (1999).
[3] T.P. Nguyen, A. Lahmar, P. Jonnard - J. Adhesion **66**, 303 (1998).
[4] G. H. Yang, E. T. Kang, K. G. Neoh, Y. Zhang, K. L. Tan - Langmuir **17**, 211 (2001).
[5] N. Inagaki, S. Tasaka, K. Narushima, K. Mochizuki, Macromolecules **32**, 8566 (1999).
[6] P. Favia, M. V. Stendardo, R. d'Agostino - Plasmas and Polymers **1**, 91 (1996).
[7] J. Tsibouklis, P. Graham, P. J. Eaton, J. R. Smith, T. G. Nevell, J. D. Smart, R. J. Ewen - Macromolecules **33**, 8460 (2000).
[8] J. P. Badey, E. Espuche, D. Sage, B. Chabert, Y. Jugnet, C. Batier, Tran Minh Duc - Polymer **37**, 1377 (1996).
[9] E. Sacher, L. Martinu, M. Meunier - Journal de Physique, Colloque **C6**, C6.239 (1997).
[10] D. A. Biro, G. Pleizier, Y. Deslandes - J. Appl. Polym. Sci. **47**, 883 (1993).
[11] N. Inagaki, « Remote plasma and pulsed plasma modification of polymeric materials for adhesion », 5-th Europeean Adhesion Conference, 2000, Sept. 18 – 21, Lyon, France, pp. 227 – 236.
[12] E. T. Kang, Y. Zhang - Adv. Mater. **12**, 1481 (2000).
[13] F. Poncin-Epaillard, N. Medard, J. C. Soutif – Macromol. Chem. Phys. **201**, 212 (2000).
[14] D. Debarnot, PhD Thesis, l'Ecole Centrale de Lyon, France, 1997, July, 9.

The plasma synthesis of ultrahydrophobic surface : the study of its 'hydrophilic behavior' !

J. Fresnais[1], L. Benyahia[1], J.P. Chapel[2], F. Poncin-Epaillard[1]

[1]Laboratoire Polymères, Colloïdes et Interfaces, U.M.R. 6120, Université du Maine
Avenue Olivier Messiaen 72085 Le Mans, France
[2]Laboratoire des Matériaux Polymères et des Biomatériaux UMR CNRS 5627
"Ingénierie des Matériaux Polymères" Université Claude Bernard - Lyon I
ISTIL , 43, Bd du 11 Nov. 1918 69622 Villeurbanne Cedex France

The synthesis of low density polyethylene (LDPE) ultrahydrophobic surfaces with controlled roughness is described in a two steps O_2 and CF_4 plasmas treatment. Water contact angle as high as 171°, contact angle hysteresis less than 2 °, and sliding angle as 2 ° are obtained on those surfaces. Beside dynamic dewetting experiments show a particular behavior. While it is wet by water, the surface seems to loose its ultrahydrophobic properties.

While natural ultrahydrophobic materials are observed for a long time [1], synthetic ultrahydrophobic surfaces are of great interest for few years[2-6]. The definition of an ultrahydrophobic surface is now clear[2] : this surface must present very high contact angles with water (more than 150°), small contact angle hysteresis (less than 10°) and small sliding angle (less than 10°). The sliding angle is the angle needed from which the droplet is removed from the surface. A smooth hydrophobic surface[7] does not show those properties. With rough hydrophobic surface, ultrahydrophobic behavior appears. However the applications of such surfaces[8] are still limited because of their non transparency and their fragility.

We present, here, the synthesis in a two steps microwave plasmas treatment (O_2 then CF_4 plasmas) of low density polyethylene ultrahydrophobic surface with controlled roughness.

First an O_2 plasma treatment is used to increase LDPE roughness by etching the amorphous phase. O_2 plasma parameters are optimized by mass spectrometry. Figure 1 shows partial pressure of oxygen atoms in O_2 plasma versus the power delivered by the microwave generator. Too high O concentration in the plasma will induce the etching of both amorphous and crystalline phases. In order to only degrade the amorphous phase and to limit the ablation of the crystalline phase, we choose an intermediary situation : 15 sccm (standard cm^3 per minute) rate and a power of 50 W (see figure 1). In this case roughness will increase as the amorphous phase is etched.

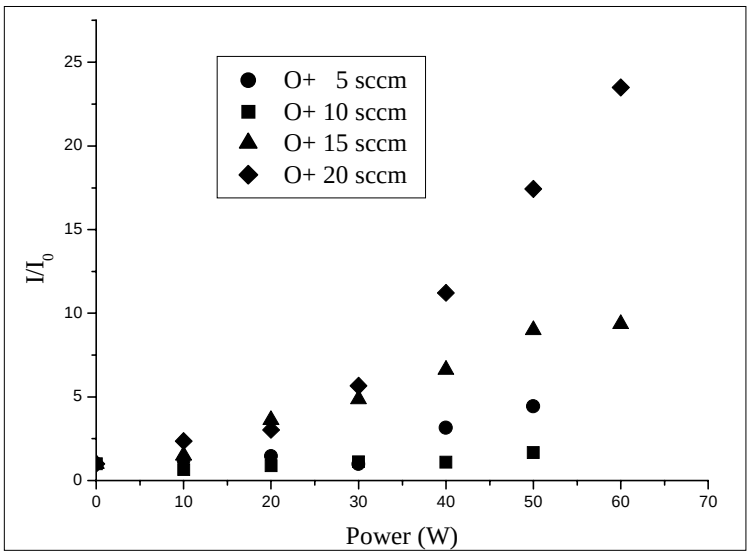

Figure 1 : normalized partial pressure of oxygen atoms in O_2 plasma versus the microwave discharge power (rates from 5 sccm to 20 sccm)

These conditions (50 W and 15 sccm) of plasma treatment are applied to LDPE surfaces. A 3 minutes O_2 plasma treatment allows the maximum increase of contact angle hysteresis (figure 2). As the chemical nature of the surface should be homogeneous, the increase of contact angle hysteresis is due to the increase of roughness. This roughness will be characterized later in this article. So that plasma treatment at 50 W corresponds to the optimized treatment in terms of roughness.

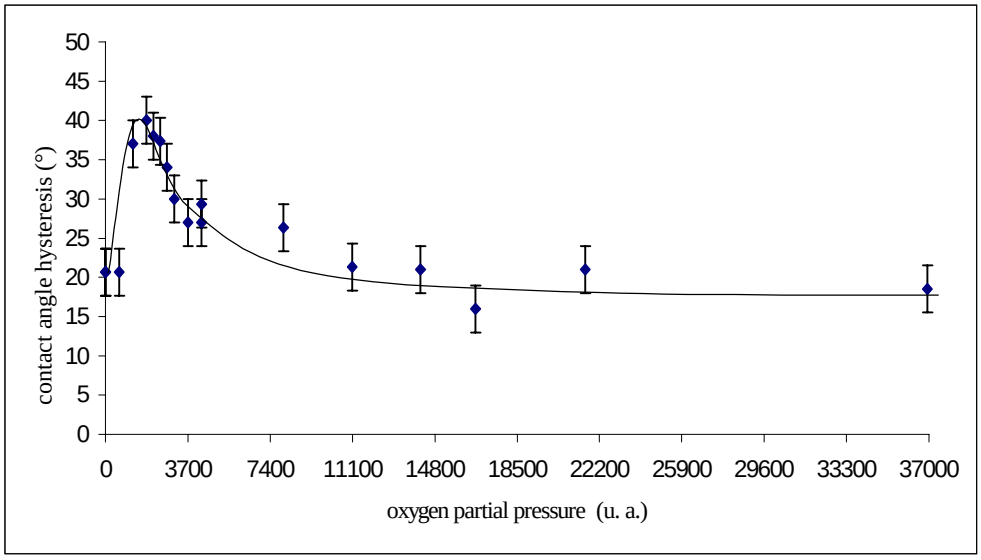

Figure 2 : contact angle hysteresis of O_2 plasma treated films versus the partial pressure of O atoms (time multiplied by the partial pressure of O per second determined by mass spectrometry) (P=50 W ; D=15 sccm ; d=15 cm)

The plasma etching is confirmed by weight loss measurements (figure 3). Those results show that an O_2 plasma treatment can divide the film weight by a factor 2 after one hour treatment with a rate of 43 $\mu g.cm^{-2}.mn^{-1}$.

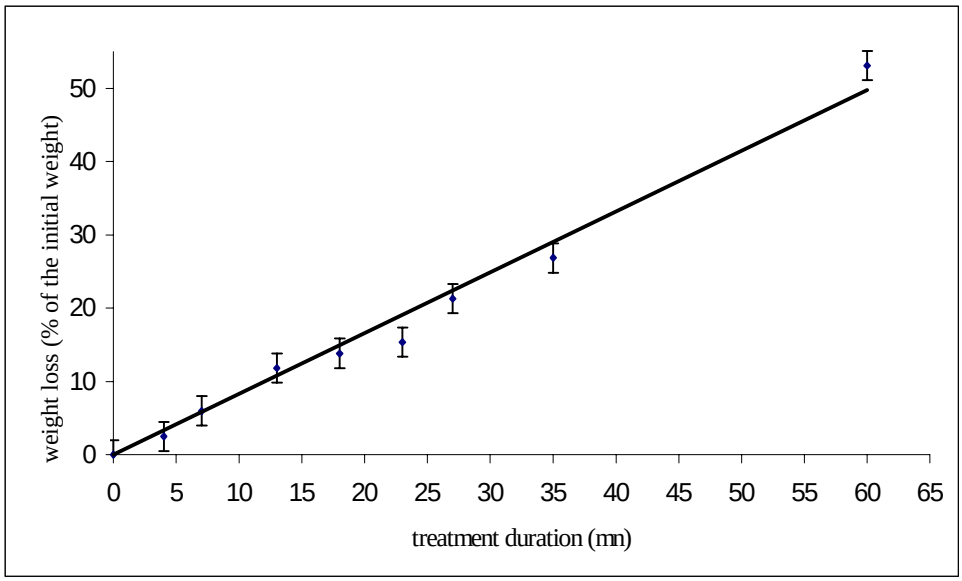

Figure 3: weight loss (the difference between treated and untreated films weight divided by the untreated film weight) versus the treatment duration (P=50 W ; D=15 sccm ; d=15 cm)

Then, the following CF_4 plasma treatment increases both hydrophobic behavior and roughness of the surface. The figure 4 shows the dependence of water contact angle versus plasma parameters. Several sets of durations and discharge powers lead to an ultrahydrophobic surface. For example, with contact angle of 171°, contact angle hysteresis of less than 2° and sliding angle of 2° is obtained at P=40 W for 15 minutes of

duration. The water droplet looks like a pearl (in this case : figure 5). Longer treatments give also ultrahydrophobic surfaces, however with too long durations the modified films become opaque.

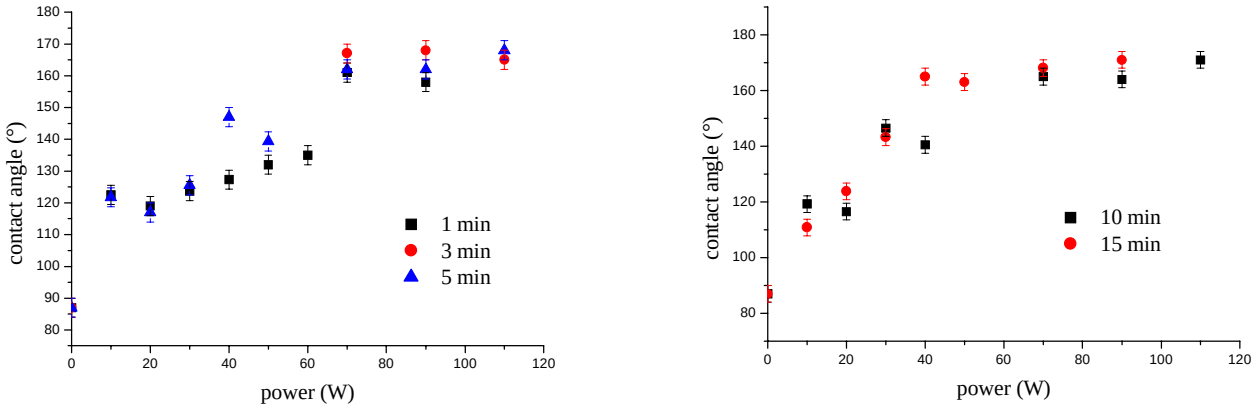

Figure 4 : optimization of the CF_4 plasma treatment : contact angle measurement for different powers and treatment durations (d=5 cm)

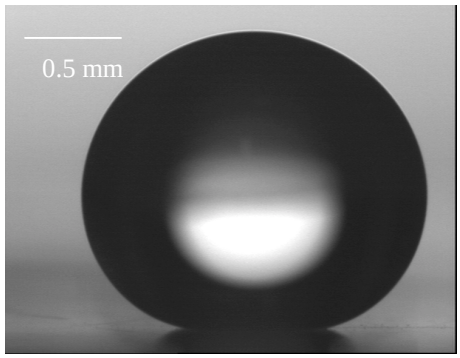

Figure 5 : water droplet on an ultrahydrophobic LDPE surface (θ= 171 °)

The contact angle hysteresis of these ultrahydrophobic surfaces falls to less than 3° (figure 6).

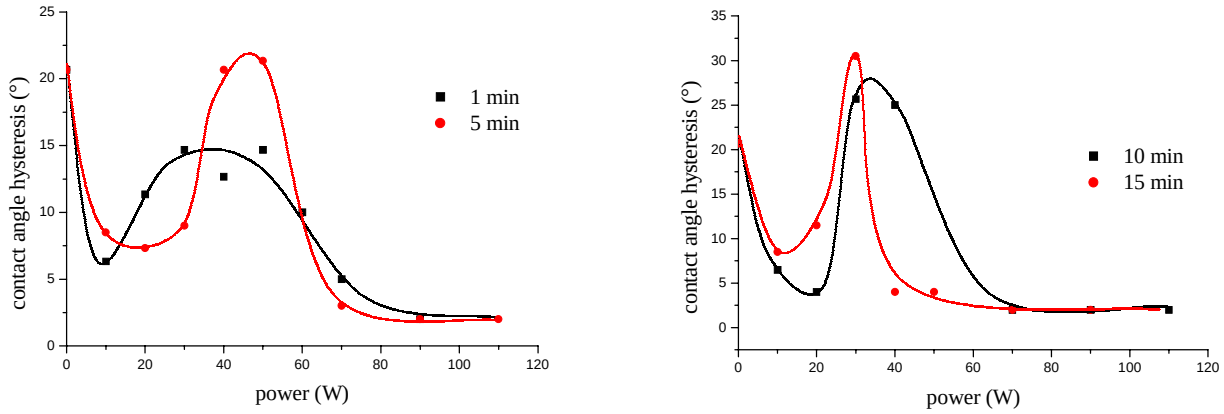

Figure 6: contact angle hysteresis versus power of treatment for different treatment durations (d=5 cm)

The ultrahydrophobic surface topography is analyzed by Atomic Force Microscopy. Rms roughness (eq 1) of ultrahydrophobic surfaces increases when the power and the treatment duration increase (table 1). Because their roughnesses are lower than 200 nm, some ultrahydrophobic surfaces are transparent.

$$R_{ms}=\sqrt{\sum(z_i-z_{ave})^2/N}\ , \qquad (1)$$

Z_{ave} is the average of the z values within the given area, z_i is the z value for a given point, and N is the number of points within the given area.

Table 1 : Rms roughness and contact angle for ultrahydrophobic surfaces treated with O_2 plasma (3 minutes at 50 W) and then with CF_4 plasma

sample	Rms roughness (nm) 10*10µm / 1*1µm	Contact angle (°)
Untreated LDPE	5.3 / 2.2	87
15 minutes at 40 W	34.9 / 26.4	169
10 minutes at 90 W	94 / 14	171
15 minutes at 90 W	248 / 135	171

X-ray photoelectron spectroscopy characterizes the surface fonctionnalization. Whatever the plasma parameters are, the fluorine amount (figure 7) is constant and closed to 60%.

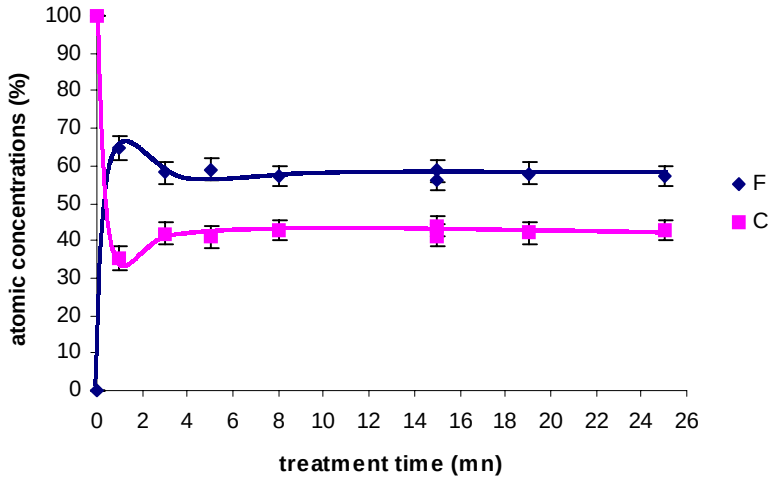

Figure 7 : fluorine and carbon proportions versus treatment duration for different LDPE plasma treated samples (P= 40 W; d= 5 cm)

The C_{1s} spectra of an ultrahydrophobic surface (figure 8) shows the C-C bond peak at 285 eV[9]. 5 other peaks corresponding to $*CH_2$-CF_2, CHF, CF, CF_2 , CF_3 respectively are found on this C_{1s} spectra. This result may confirm the fact that the LDPE surface is only fonctionalized and that no deposition process is taken place.

Then dynamic dewetting properties of ultrahydrophobic films are studied. Depositing a water droplet on a such surface gives information about the surface repellency, but what will be its behavior when a water film is deposited on it ?

A water film with controlled thickness is deposited on an ultrahydrophobic film. When the dewetting is initialized by creating a dry patch in the middle of the surface, the dry patch diameter increases until the complete dewetting of water from the surface. The speed of the water front is about 5 to 10 cm/s. A rim[10] is created and goes from the center of the film to the border.

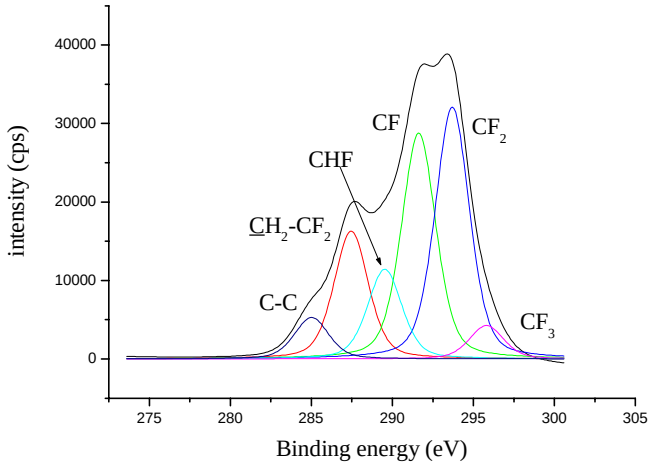

Figure 8 : C_{1s} spectra of LDPE ultrahydrophobic surface (P= 90 W, d= 5 cm, D= 15 sccm, t= 15 min)

If ultrahydrophobic film is wetted by water vapor then dried under vacuum, the surface behavior changes. The water film deposited in the same conditions will dewett the surface more slowly.

To describe more precisely this phenomenon, other experiments are run. The ultrahydrophobic film is placed in contact of water surface and the force needed to break the water / LDPE interface is measured with an ARES type rheometer (Rheometrix Scientific). If the film shift is disrupted just after dewetting begins, the untreated LDPE film (figure 9a) dewett very rapidly while an ultrahydrophobic surface dewets slowly in the same conditions (see figure 9b).

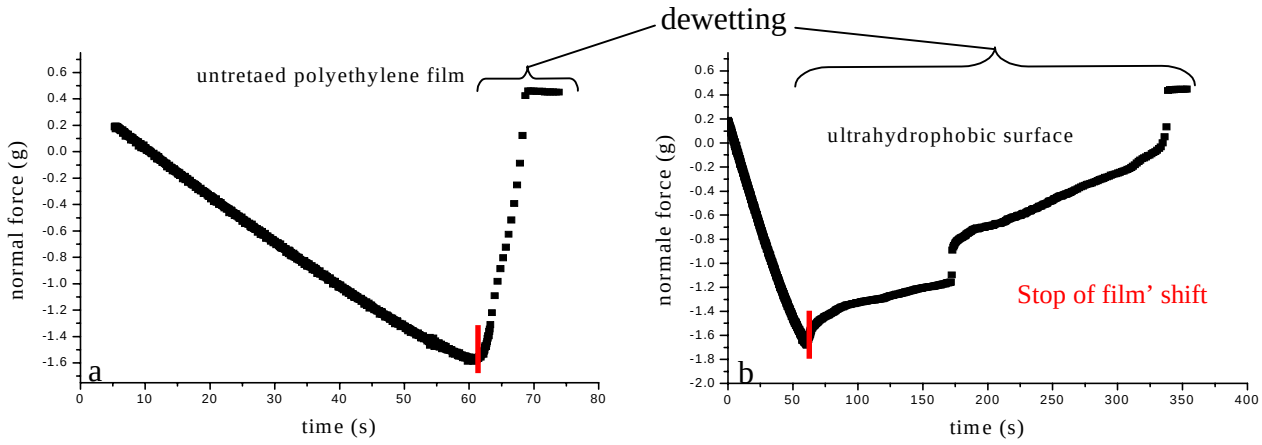

Figure 9 : normal force versus time : (a) untreated PE film; (b) Ultrahydrophobic film (rms roughness : 35 nm; P= 50 W, d= 5 cm, D= 15 sccm, t= 15 min)

The two different methods of the dewetting observation show both that ultrahydrophobic surfaces loose their properties when several times dipped in water (fig 10) or in contact with water vapor. If only a droplet is deposited, this phenomenon is absent. Moreover, the behavior is not dependent of the roughness. Same results are obtained with larger roughnesses. These experiments confirm the fact that the more the surface is wetted, the more the normal force needed to dewett the film surface is high.

Another experiment confirms the total wetting of the holes in the roughness of the ultrahydrophobic surfaces (figure 11) showing water contact angles varies from 171° to 142° after 10 minutes of immersion.

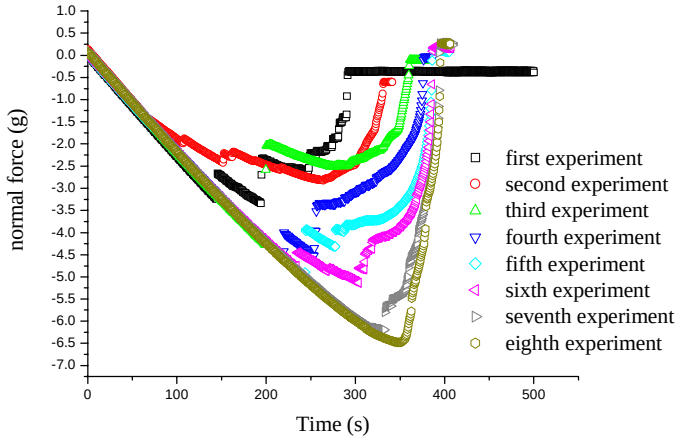

Figure 10 : normal force versus time : multiple experiments with the same experimental conditions (P= 90 W, d= 5 cm, D= 15 sccm, t= 15 min)

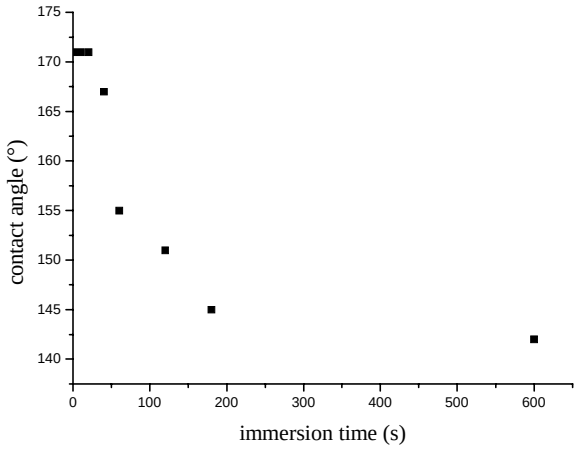

Figure 11 : contact angle versus immersion time

To conclude, we synthesize LDPE ultrahydrophobic surfaces with controlled roughness. We also show that those ultrahydrophobic surfaces have different behavior when they are totally wetted. This behavior differs strongly in the case of partial wetting (water droplet deposition). Ultrahydrophobic roughed surfaces loose their properties and contact angle decreases strongly.

[1] Neinhuis, C.; Barthlott, W. *Annals of Botany* **1997**, *79*, 667-677.
[2] Chen, W.; Fadeev, A. Y.; Hsieh, M. C.; Öner, D.; Youngblood, J.; McCarthy, T. J. *Langmuir* **1999**, *15*, 3395-3399.
[3] Genzer, J.; Efimenko, K. *Science* **2000**, *290*, 2130-2133.
[4] Miwa, M.; Nakajima, A.; Fujishima, A.; Hashimoto, K.; Watanabe, T. *Langmuir* **2000**, *16*, 5754-5760.
[5] Öner, D.; McCarthy, T. J. *Langmuir* **2000**, *16*, 7777-7782.
[6] Youngblood, J.; McCarthy, T. J. *Macromolecules* **1999**, *32*, 6800-6806.
[7] Nishino, T.; Meguro, M.; Nakamae, K.; Matsushita, M.; Ueda, Y. *Langmuir* **1999**, *15*, 4321-4323.
[8] Tadanaga, K.; Katata, N.; Minami, T. *J. Am. Cer. Soc.* **1997**, *80*, 3213-3216.
[9] Langeron, J. P. *Le Vide* **1989**, *249*, 479-488.
[10] Andrieu, C.; Sykes, C.; Brochard, F. *J. Adhesion* **1996**, *58*, 15-24.

Influence of vibrational kinetics in a low pressure radio frequency hydrogen discharge

L. Marques[1], A. Salabas[1], G. Gousset[2], L. L. Alves[1]

[1]*Centro de Física dos Plasmas, Instituto Superior Técnico, 1049-001, Portugal*
[2]*Lab. de Physique des Gaz et des Plasmas, Université Paris-Sud, 91405 Orsay Cedex, France*

Abstract

This paper presents the self-consistent coupling of a two-dimensional charged particle transport model, for a parallel plate radio frequency discharge in pure hydrogen, with a homogeneous kinetic model including $H_2(X^1\Sigma_g^+,v=0..14)$ molecules and H(n=1-5) atoms. It is shown that the inclusion of vibrational kinetics increases both the H_3^+ ion density and the electrical coupled power by 40% .

1. Introduction

Parallel plate capacitively coupled radio frequency (RF) discharges are of great interest in plasma assisted material processing applications, as in the plasma enhanced chemical vapour deposition (PECVD) of silicon and diamond thin films using hydrogen based mixtures. The correct optimisation and scale-up of such reactors, requires the development of complete transport plasma models including the gas phase description of charged particle transport and multicomponent diffusion of neutral species, to be coupled to a kinetic description of reactor surface.

The present work is part of an effort to model and optimise an existing PECVD reactor for quality μ-Si:H deposition, using SiH_4-H_2 mixtures under high dilution conditions for silane. The RF reactor is similar to the GEC reference cell, with 6.2 cm radius and 3 cm inter-electrode distance [1], operating at pressures between 0.1 – 1 Torr, frequencies in the 13.56 - 80 MHz range and RF voltages 50 – 250 V. The translational gas temperature is assumed to be 323 K.

We have started by studying a 13.56 MHz capacitively coupled RF discharge in pure hydrogen, using a two-dimensional (2D) time dependent fluid model that describes the production, transport and destruction of electrons, H^+, H_2^+ ,H_3^+ and H^- ions in the reactor under study [2]. In a previous work [3], it was shown that this model predicts the correct trends of the plasma density and self-bias voltage variations with changes in the driving frequency or the RF voltage. However, model predictions were found to be systematically underestimated with respect to measurements, which was attributed to both experimental uncertainties and the simple hydrogen kinetics considered.

A realistic hydrogen chemistry must include the kinetics of vibrationally excited molecules and electronically excited atomic species. In particular, the hydrogen vibrational excited species can have an important role in RF discharges, as a significant part of the electrical coupled power is lost in low energy vibrational excitations. Moreover, these species are also important channels of atomic hydrogen and charged particle production. In order to clarify the role of these species, we have self-consistently coupled the previously developed charged particle transport model to a homogeneous kinetic model for hydrogen, including $H_2(X^1\Sigma_g^+,v=0..14)$ molecules and H(n=1-5) atoms.This paper analyses the effect of the improved hydrogen kinetic model in reactor operation.

2. Model

A rigorous description of low temperature non-equilibrium plasmas, must couple the electron transport to the gas phase chemistry, because the electron rate coeficients strongly depend on the gas chemical composition. The correct modelling of this problem involves the calculation of the non-equilibrium electron energy distribution function (EEDF) and the vibrational distribution function (VDF) of hydrogen molecules.

2.1 Hydrogen Kinetics

The very complete hydrogen kinetics adopted here was based in the work of several authors [4-14]. It describes the dynamics of vibrationally excited molecules in ground state $H_2(X^1\Sigma_g^+, v=0..14)$, hydrogen atoms in different electronic states H(n=1-5), positive ions H_3^+, H_2^+, H^+, and negative ion H^-. The kinetic processes considered are datailed in table 1.

Table 1

	Process	Reference
Vibrational species		
e - V	$e + H_2(v) \leftrightarrow e + H_2(v\pm i)$, i=1..3	[4,5]
E - V	$e + H_2(v) \rightarrow e + H_2(B^1\Sigma_u^+, C^1\Pi_u) \rightarrow e + H_2(v')$	[4,5]
V - V	$H_2(v) + H_2(w) \leftrightarrow H_2(v\text{-}1) + H_2(w+1)$	[5]
V - T	$H_2(v) + H_2 \leftrightarrow H_2(v\pm 1) + H_2$	[5]
V - T	$H_2(v) + H \leftrightarrow H_2(v\pm i) + H$, i=1..5	[5,6]
Dissociation	$e + H_2(v) \rightarrow e + H_2(a^3\Sigma_g^+, b^3\Sigma_u^+, c^3\Pi_u, e^3\Sigma_u^+) \rightarrow e + 2H(1s)$	[4,5]
	$e + H_2(v) \rightarrow e + H(1s) + H(n=2,3)$	[4]
Ionisation	$e + H_2(v) \rightarrow e + e + H_2^+$	[4,15]
	$\rightarrow e + e + H^+ + H$	
Diss. Attachment	$e + H_2(v) \rightarrow e + H_2^- \rightarrow H + H^-$	[8]
Wall	$H_2(v>0) \rightarrow H_2(v=0)$	[7]
Dissociation by Vib. Pumping	$H_2(v=14) + H_2 \leftrightarrow 2H(1s) + H_2$	[9]
	$H_2(v=14) + H \leftrightarrow 3H(1s)$	
Atomic species		
Exc/De-exc.	$e + H(n) \leftrightarrow e + H(m)$, n,m=1..5	[13]
Ionisation	$e + H(n) \rightarrow e + H^+$	[13]
Rad. De-exc.	$H(n) \rightarrow H(m) + h\nu$	[13]
Deactivation	$H(2s) + H_2 \rightarrow H(2p) + H_2$	[11]
	$H(2p) + H_2 \rightarrow H(2s) + H_2$	[13]
Ass. Ionisation	$H(2s) + H_2 \rightarrow H_3^+ + H$	[11]
	$H(2s) + H_2 \rightarrow 3H(1s)$	[13]
Wall	$H(1s) \rightarrow \frac{1}{2}H_2(v=0)$	[12]
	$H(n>1) \rightarrow H(1s)$	[13]
Aditional Processes		
Electron – ion recombination	$e + H_3^+ \rightarrow 3\ H$	[10]
	$e + H_2^+ \rightarrow H(1s) + H(n)$, n>1	[10]
	$e + H^+ \rightarrow H(n) + h\nu$	[10]
	$2e + H_3^+ \rightarrow H_2 + H + e$	[9]
	$2e + H_2^+ \rightarrow 2H(1s) + e$	[9]
	$2e + H^+ \rightarrow H(n) + e$	[9]
	$e + H_3^+ + wall \rightarrow H_2 + H$	
	$e + H_2^+ + wall \rightarrow H_2$	
	$e + H^+ + wall \rightarrow H$	
Ion – ion neutralization	$H^- + H_3^+ \rightarrow 2\ H_2$	[9]
	$H^- + H_2^+ \rightarrow H_2 + H(n>2)$	[14]
	$H^- + H^+ \rightarrow H(n=3) + H$	[9]
Ass. detachment	$H + H^- \rightarrow H_2 + e$	[9]
Ion conversion	$H_2^+ + H_2 \rightarrow H_3^+ + H$	[9]
	$H_2^+ + H \rightarrow H^+ + H_2$	[9]
	$H^+ + 2H_2 \rightarrow H_3^+ + H_2$	[9]
	$H^+ + H_2(v>3) \rightarrow H_2^+ + H$	[9]

2.2 Charged particle model

A 2D time-dependent fluid model was developed to describe the transport of electrons, H^-, H^+, H_2^+ and H_3^+ ions in the reactor under study [2], by solving the corresponding continuity, momentum transfer and mean energy equations (the latter for electrons only), coupled with Poisson's equation.
Electron transport parameters are calculated adopting the local electron mean energy approximation [2], which assumes that the space-time dependence of the EEDF and its related transport parameters proceeds via the electron mean energy. The latter has space-time profile given from the solution to the fluid code, being related to the EEDF by solving the electron Boltzmann equation (EBE) (in a homogeneous and stationary, two-term approximation) using the electron cross-sections compiled in reference [4,5,13]. The ion mobilities are those of reference [15].
The system of equations is discretized in a grid of 16x32 points using finite differences, and is solved subject to appropriated boundary conditions. Typically, 1000 time steps are used within each RF period, and a few hundred RF cycles are needed to reach the convergence criterion: relative changes of particle densities, mean electron energy, plasma potential and self-bias voltage, between two consecutive periods, less than 0.05%.

2.3 Kinetic model

The kinetic model solves the set of coupled rate balance equations for the different neutral species considered here. To limit calculation times (due to the considerable number of species and kinetic processes involved), we have adopted zero dimensional versions of the continuity equation for each species, by averaging them in space as follows

$$\frac{\partial \overline{n}_i}{\partial t} = \left(\frac{\partial \overline{n}_i}{\partial t}\right)_{coll} - \left(\frac{\partial \overline{n}_i}{\partial t}\right)_{wall} . \qquad (1)$$

In equation (1), $\left(\frac{\partial \overline{n}_i}{\partial t}\right)_{coll}$ is the average net gain rate of species i in the volume, $\left(\frac{\partial \overline{n}_i}{\partial t}\right)_{wall}$ is the net loss rate of species i at the wall, and $\overline{n}_i$ represents the averaged density defined as

$$\overline{n}_i = \iint n_i r dr dz \Big/ \iint r dr dz . \qquad (2)$$

The integration in equation (2) distinguishes between two regions in the plasma: a spatially homogeneous one, corresponding to the plasma bulk; and a boundary layer with size equal to the plasma sheath thickness, where the densities of neutral species are assumed to vary linearly. This assumption is accurate enough as to allow an analysis of the neutral chemistry influence, in reactor operation. The resulting set of non-linear equations was couply solved using a semi-implicitly Gauss-Seidel relaxation technique. The procedure converges after several thousand iterations, for relative variations of 10^{-12} in the densities of any neutral species.

The coupling between the above models is made by calculating the average (in space and time) electron collision frequencies as obtained from the charged particle model, and by using them as input data to the kinetic model. The kinetic model is solved every 5 RF periods, until steady-state convergence is achieved. The densities of neutral species, obtained after each run of the kinetic model, is used to update the electron transport parameters and rate coeficients by solving the homogeneous and stationary EBE (under the two-term approximation), before running the plasma transport model. Note that this kind of self-consistent coupling between plasma transport and chemical kinetics was sucessfully used in other works [16].

3. Results

The problem was firstly solved by negleting the presence of both atomic hydrogen excited species and negative ions, for an applied RF voltage of 100V, pressure of 300 mTorr and excitation frequency of

13.56MHz. Figure 1 represents the calculated axial profiles (at discharge axis) of the time averaged H_3^+ density, obtained in this work and using our previous model with a simplified hydrogen kinetics [2,3]. From this figure we conclude that the adoption of more complete hydrogen kinetics increases the H_3^+ ion density by 40 %, which can be atributed to the enhancement of the global ionisation coeficient when vibrationally excited species are considered. Figure 2 shows the calculated VDF of hydrogen molecules.

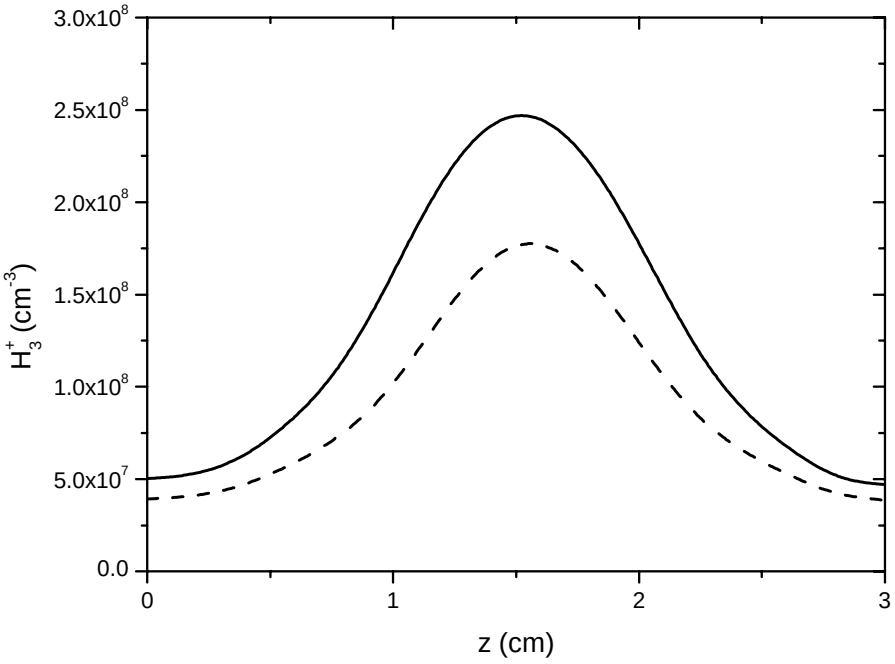

Figure 1 Axial profile of H_3^+ ion density.
Present (——) and previous (-----) model estimates.

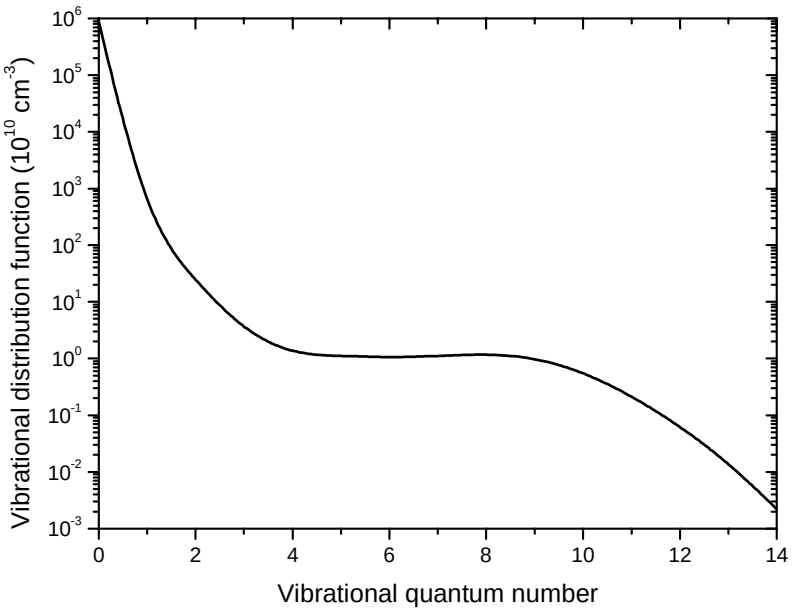

Figure 2 Vibrational distribution function of hydrogen molecules.

Simulations show that the electrical power coupled to the discharge also increases by 40 % when vibrational kinetics is considered, because more energy is lost in the vibrational excitation, ionisation and dissociation of hydrogen. Note that the self-bias voltage is only slightly affected by the improved kinetics.
Introduction of negative ions in the kinetics results in a significant slow down of model convergence. The H^- ion concentrates at discharge centre, where the plasma potential is higher, and its density is comparable to that of H_2^+ and H^+, while the main plasma parameters are only marginally affected.
When atomic excited species are considered the associative ionisation mechanism (see table 1) becomes the most important production channel of electrons and H_3^+ ions, contributing to a significant increase of their densities. Unfortunately, the introduction of this mechanism deteriorates the convergence of the global model, as the absence of a spatial profile for the atomic species leads to an overestimation of the ionisation rate near reactor boundaries. Studies are in progress to correctly solve this problem, in particular by taking into account more realistic de-excitation probabilities for atomic species.

4. Conclusion

We have self-consistently coupled the vibrational kinetics of hydrogen to a charged particle transport model in capacitively coupled RF discharges. The inclusion of low energy vibrational excitations allows to correct previously model predictions, which were underestimated when compared to experimental measurements. We have shown that associative ionisation involving atomic excited hydrogen species is a fundamental mechanism to consider.

References

[1] O. Leroy et al, Plasma Sources Sci. Technol. **7,** 348 (1998).
[2] A. Salabas, G. Gousset and L. L. Alves, Plasma Sources Sci. Technol. **11,** 448 (2002).
[3] L. Marques et al, Proceedings of Escampig **XVI**, Vol 2, 69 (2002).
[4] H. Tawara et al, J. Phys. Chem. Ref. Data **19,** 617 (1990).
[5] J. Loureiro et al, J. Phys. D: Appl. Phys. **22,** 1680 (1989).
[6] Gorse et al, J. Chem. Phys. **117,** 177 (1987).
[7] Gorse et al, Chem. Phys. **93,** 1 (1985).
[8] Hickman, Phys. Rev. A **43,** 3495 (1991).
[9] Matveyev A., V. Silakov, Plasma Sources Sci. Technol. **4,** 606 (1995).
[10] R. Janev et al, Elementary processes in Hydrogen –Helium plasmas
ed G. Ecker, P. Lambropolous, and H Wlather (Berlin Springer) (1987).
[11] M Glass - Maujean, Phys. Rev. Lett. **62,** 144 (1989).
[12] P Kae-Nune, J Perrin, J Jolly, Surf. Sci. Lett, L495 (1996).
[13] G. Gousset, Private comunication.
[14] M Eerden et al, Phys. Rev. A **51,** 3362 (1995).
[15] T. Simko et al, Phys. Rev. E **56,** 5908 (1997).
[16] S Longo, I Boyd, Chem. Phys. **238,** 445 (1998).

Relation between the recombination coefficient of atomic oxygen and surface properties of materials

C. Guyon, G. Hermosilla-Lara, I. Mabille, M. Moscosa-Santillian,
S. Cavadias and J. Amouroux
LGPPTS,Université Pierre et Marie Curie, ENSCP, 11 rue Pierre et Marie Curie, 75005 Paris, France

Abstract

Our goal is to qualify the recombination coefficients gamma of the atomic oxygen on the target, to measure the correlation between gamma and the gap of the semiconductor and finally to determine the activation energy of recombination for the n and p semiconductor surface. These results point out the correlation between the activation energy of recombination and the electronic gap of the semiconductor targets which demonstrate that catalytic phenomena and excited states of oxygen atoms depend of specific properties of the semiconductor oxide surface.

1. Introduction

Under the condition of a hot shock wave or a plasma discharge, oxygen and nitrogen molecule will be dissociate into oxygen and nitrogen atoms. This atom will diffuse in the boundary layer of surface of a material and they may be recombined to form molecules. The formed molecules can transfer part or all of their heat of formation to the surface. The number of the recombined atoms and the energy transferred depend on the nature of the surface and the process is referred to be a catalytic atom recombination. The recombination reaction can be quantified by the recombination coefficient (γ) and the accommodation coefficient (β) representing respectively the mass and the heat transfer to the surface. When the recombination species are oxygen atoms, the process leads to the formation of an oxide layer on the surface, resulting in a modification of the nature of the surface and its properties[2-9].

The aim of this work is to underline the influence of the electronic properties of the material on its catalytic activity by measurements performed on n and p-type semiconductors having different band gap energies, in a pulsed plasma reactor, using an actinometrical method. In result of these experiment we can observe a correlation between the activation energy of recombination and the electronic gap of the semiconductor targets. The interest of these phenomena is great toward the conception of catalytic materials and the qualification of materials submitted to high thermal constraints[1]. Furthermore for SiO2/SiC, the surface oxidation is followed by ESCA, SEM and dynamic SIMS analyses.

2. Experimental Set-Up

2.1 Experimental Device

The experimental set-up includes a plasma tubular reactor, the controlling and acquisition device. Tests are performed at 110 Pa pressure, with 400 sccm flow for the air gas flow, and 25 sccm flow for the Argon (about 5% of the total gas flow). The plasma is created by a 13.56 MHz generator. The time discharge “on” is of 2s for each measurement and the time discharge “off” is of 5s. The emission spectroscopy signal was transmitted via a fibre optics, analysed by a monochromator and detected by an Optical Multichannel Analyser (O.M.A.).

2.2 The Actinometric Method Applied to Recombination Coefficient Measurement

The recombination coefficients are calculated using the actinometry spectroscopic method[10]. Actinometry involves using of optical emission intensity ratios to provide an estimation of ground state species concentrations. The intensity emitted from the species is divided by the emission intensity from actinometer (Argon) which is added to the plasma in small quantity, without any modification of discharge properties in comparison with other one . In our case the O atom concentration has been monitored with optical emission from O (844.6 nm) and Ar (811.5 nm). The ratio I_O/I_{Ar} obtained by actinometry is related to the concentrations ratio by the following relation[11]:

$$I_O / I_{Ar} = k\,(O) / (Ar)$$

and it can be used as a tracer for atomic oxygen concentration. The validity of the actinometry method has been previously verified by titration of the atomic oxygen with nitric oxide.

The movement of oxygen atoms in the boundary layer near the sample is controlled by diffusion and described by the general diffusion equation. The recombination coefficient (γ) can be deduced from this equation and can be calculated from the atomic oxygen concentration profile along the reactor:

$$\gamma = \frac{-4D\nabla(I_O/I_A)_x}{c(-\nabla(I_O/I_A)_x L + (I_O/I_A)_o)}$$

D: binary diffusion coefficient ($m^2.s^{-1}$)
c: atomic velocity ($m.s^{-1}$)
L: width of the boundary layer (m)
$\nabla(I_O/I_{Ar})_x$: axial concentration gradient
$(I_O/I_{Ar})_o$: steady state concentration

3. Results and interpretation

3.1. Determination of the Recombination coefficient (γ) and the activation energy (Ea) from the recombination on oxide semiconductors and ceramics materials.

The targets consist in discs of pure oxides semiconductors. The recombination coefficient of atomic oxygen on each sample have been measured in a temperature range of 300 K- 923 K. The energy gap of the materials has been measured by optical reflection measurements[13] (Table 1).

For all the samples, it can be noted an increasing of the recombination coefficient with its surface temperature.

From the Maxwell-Boltzmann statistic, we can link the recombination coefficient to the surface temperature (T) by the following relation (1):

$$\gamma = \frac{T_o}{T}\exp\left(-\frac{E_a}{RT}\right) \quad (1)$$

Where $T_o = \frac{Cah^2}{2\pi m_o k}$

Ea= activation energy of the surface reaction ($J.mol^{-1}$)
Ca= number of active sites ($atoms.m^{-2}$)
m_O= mass of an oxygen atom (kg)

The activation energy of the process and the number of the active sites can be deduced by plotting Ln(γT) versus 1/T (Table 1 and figure 1).

Figure 1 Evolution of the recombination coefficient with the surface temperature. Determination of the activation energies

The results for p type semiconductors show an increase of the activation energy with the energy gap increase. The lowest is the energy gap of the oxide, the highest is the recombination coefficient. The electronic properties of the material influences strongly the heterogeneous recombination of the oxygen atoms. In the case of n type semiconductors the activation energy can be correlated to the number of active sites[16] (Table 1).

In a previous work it was showed that the behaviour of p type or n type oxide semiconductors is due to the absorbed oxygen on the material[15-17].

Moreover for some samples we can observe that it appears a break in the slope that means a modification of the recombination mechanism (figure 1). For a SiC sample, the reaction process is clearly different and we can distinguish two scales of temperature. First of all, at low temperature (300 K - 900 K) the activation energy of the reaction can be estimated at (7±1) $kJ.mol^{-1}$. At 900 K, it appears a break in the slope which means a modification of the recombination mechanism. From 900 K to 1123 K the activation energy is now equal to (74±11) $kJ.mol^{-1}$. The strong difference between the activation energies shows clearly a change in the reactional process when the temperature increases. Indeed, at low temperature, the reactional mechanism is compared to an Eley-Rideal mechanism whereas at high temperature, the recombination reaction is controlled by a Langmuir-Hinshelwood mechanism. As we show in Table 1 this mechanism is available for other samples as WO_3, $BaTiO_3$ and $CaTiO_3$.

	Gap energy E_{gap}(eV) (semiconductor type)	*Recombination Coefficient γ (± 20%) 300 K*	*Recombination Coefficient γ (± 20%)*	*Activation Energy E_a (kJ.mol^{-1}) (± 15%) 300 K*	*Active Sites C_a (atoms.m^{-2}) (± 15%) 300 K*	*Activation Energy E_a (kJ.mol^{-1}) (± 15%) 773 K*	*Active Sites C_a (atoms.m^{-2}) (± 15%) 773 K*
CoO	***0.8 (p)***	***29 10^{-3}***	***34 10^{-3}*** *(473 K)*	***4.1***	***2.3 10^{20}***	***4.1***	***2.3 10^{20}***
MnO	***1.3 (p)***	***17 10^{-3}***	***25 10^{-3}*** *(473 K)*	***5.9***	***2.8 10^{20}***	***5.9***	***2.8 10^{20}***
PbO	***2.3 (p)***	***13 10^{-3}***	***18 10^{-3}*** *(473 K)*	***6.4***	***3.0 10^{20}***	***6.4***	***3.0 10^{20}***
Sb_2O_3	***4.2 (p)***	***8.210^{-3}***	***21 10^{-3}*** *(473 K)*	***9.9***	***6.3 10^{20}***	***9.9***	***6.3 10^{20}***
Fe_3O_4	***0.4 (n)***	***15.10^{-3}***	***28.10^{-3}*** *(873 K)*	***6.9***	***3.3 10^{20}***	***6.9***	***3.3 10^{20}***
WO_3	***2.8 (n)***	***11.10^{-3}***	***24.10^{-3}*** *(773 K)*	***4.3***	***1.1 10^{20}***	***12.9***	***7.3 10^{20}***
$BaTiO_3$	***3.1 (n)***	***12.10^{-3}***	***78.10^{-3}*** *(773 K)*	***5.2***	***1.6 10^{20}***	***23.4***	***79 10^{20}***
TiO_2	***3.1 (n)***	***14.10^{-3}***	***31.10^{-3}*** *(773 K)*	***5.4***	***2.5 10^{20}***	***5.4***	***2.5 10^{20}***
$CaTiO_3$	***3.5 (n)***	***13.10^{-3}***	***28.10^{-3}*** *(773 K)*	***5.8***	***2.0 10^{20}***	***19.6***	***25 10^{20}***
Al_2O_3	***7.3 (n)***	***9.7.10^{-3}***	***61.10^{-3}*** *(773 K)*	***10.3***	***8.1 10^{20}***	***10.3***	***8.1 10^{20}***
CVD-SiC	***11 (n)***	***3 10^{-3}***	***30 10^{-3}*** *(773 K)*	***11.8***	***3.4 10^{20}***	***29,6***	***78.8 10^{20}***
SiC/SiO_2	***11 (n)***	***4.10^{-3}***	***9.3.10^{-3}*** *(773 K)*	***7***	***1.1 10^{20}***	***74 (973 K)***	*-*

Table 1 : Determination of the recombination coefficients of atomic oxygen on semiconductors and ceramics materials. Evolution with the surface temperature. Recombination activation energy of semiconductors.

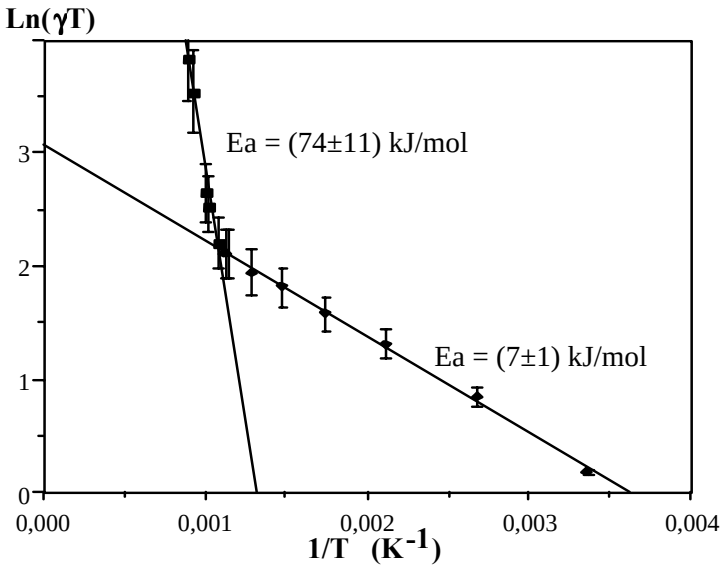

Figure 1 : Evolution of the recombination coefficient with the surface temperature. Determination of the activation energies for a SiC sample. D(O_2)=50 sccm.min^{-1}, D(N_2)=200 sccm.min^{-1}, D(Ar)=15 sccm.min^{-1}, Pressure=110 Pa, Power of the RF=240 W, discharge time of 2000 ms.

3.2 Surface Characterization : Chemical evolution of the material

The plasma-surface interaction, and particularly the specific surface recombination reaction of atomic oxygen, depends strongly on the chemical state of the surface material. In fact, the reactive flow interaction should be different if the material is already oxidised or not. Moreover, this surface "passivation" can occur in the very first milliseconds of the discharge.

3.2.a. Oxidation of the surface

The chemical structure of SiC surfaces has been followed by XPS analyses. Figure 3 relates the quantitative evolution of the O, C and Si species on the material surface when the sample is exposed to the plasma and heated. Figure 2 compares the silicon carbon bond and the silicon oxygen bond peaks for an untreated sample and for a sample exposed to the plasma at 300 K and at 1073 K.

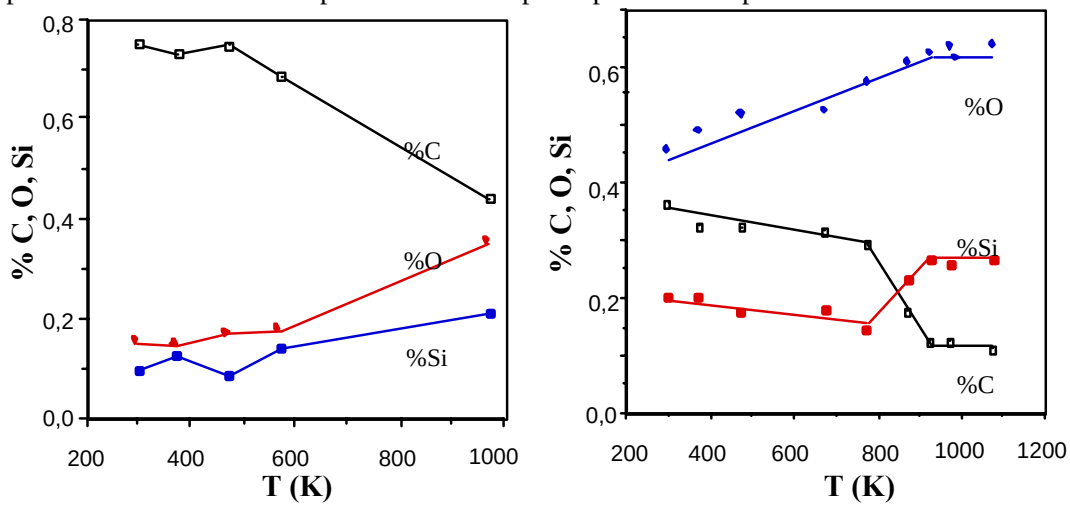

a) Air/SiC interaction (no plasma)
Heating time: 45 minutes

b) Air plasma/SiC interaction
Heating time: 45 minutes

Figure 2 XPS analysis. Evolution of oxygen, carbon and silicon mass fractions on the surface with the temperature for treated and untreated SiC.

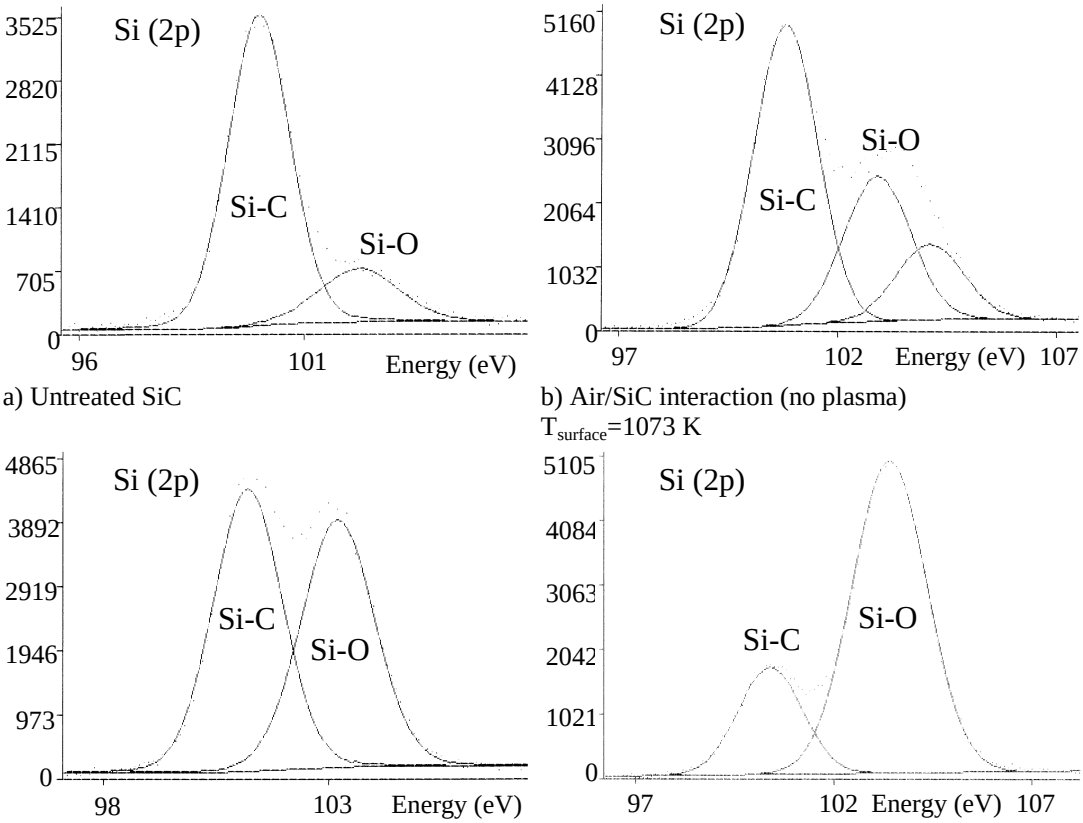

a) Untreated SiC

b) Air/SiC interaction (no plasma)
$T_{surface}$=1073 K

c) Air plasma/SiC interaction
$T_{surface}$=300 K

d) Air plasma/SiC interaction
$T_{surface}$=1073 K

Figure 3 XPS analysis. Evolution of the silicon carbon bond and the silicon oxygen bond peaks for treated and untreated SiC at different temperatures.

The whole results shows the progressive evolution of the SiC structure towards an oxidized silicon structure as SiO_2. Carbon atoms are substituted by oxygen atoms and the recombination reaction does not occur on the SiC surface but on the SiO_2 layer formed since the first exposure times to the oxygen plasma. This layer presents semiconductive properties; the SiC material is also covered by a -n type semiconductor of SiO_2. The recombination mechanisms are still controlled by the electronic conduction of the semiconductor. The low reactivity of the material in respect with atomic oxygen is in agreement with the previous study carried out on semiconductors[17,18].

3. 2.b. Diffusion of oxygen in the bulk material

In order to control the diffusion of oxygen into the bulk material, Secondary Ions Mass Spectrometry (SIMS) analyses have been performed on an untreated SiC, SiC exposed 60 s to oxygen plasma at 300 K and SiC exposed 60 s to oxygen plasma at 1000 K.

Concerning the untreated sample, the oxygen content decreases rapidly under 100 nm depth and is stabilized. One can note a few oxidation of the surface in that case. As expected, when the material is exposed to the oxygen plasma at 300 and 1000 K, the decrease of the oxygen content in the bulk material is slower than previously. Some oxygen atoms have diffused into the SiC matrix. On figure 4, one can compare the oxygen content in the material for different treatments to the oxygen plasma.

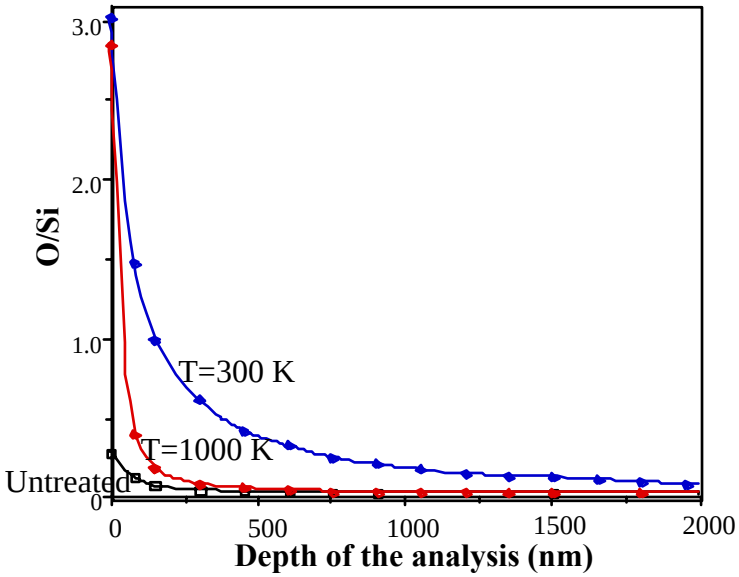

Figure 4: Evolution of oxygen content in the material bulk for untreated SiC, Air plasma/SiC interaction at 300 K and Air plasma/SiC interaction at 1000 K.

First of all, the concentration of oxygen is really important near the surface of the material when it is exposed to the oxygen plasma. However, when the material is heated at 300 K, the oxygen content is higher than for a surface treatment at 1000 K. So, the diffusion of oxygen is less important at high temperature. This result seems to eliminate the hypothesis of a predominant diffusion mechanism in this temperature range (T>900 K). So, the change in the reactional mechanism is not due to the diffusion of oxygen. The hypotheses of a change in the recombination mechanism (Eley-Rideal/Langmuir-Hinshelwood) or more complex mechanisms of oxidation/ablation are more probable.

Moreover Scanning Electronic Microscopy (SEM) have been performed on treated and untreated SiC surfaces. Comparing to the surface oxidation pointed out by ESCA analyses, SEM analyses show a macroscopic change of the surface structure after exposition to the plasma gas. These structure modifications can also be due to the surface oxidation[19].

Conclusion

The determination of gamma coefficient on metallic oxide semiconductors, leads to the determination of the role of the electronic properties of material. The p-type semiconductors are more efficient to recombine the oxygen atoms than the n-type semiconductors. The electronic conduction of

the material seems to have a great importance in the recombination efficiency. There is a correlation for p type semiconductors between the activation energy and the gap energy. The lowest is the gap energy of the oxide, the highest is the recombination coefficient. Moreover for the n type semiconductors the activation energy can be correlated to the number of active sites. The evolution of the activation energy of silicon carbide in a large field of temperature has demonstrated a real change in the reactional mechanism around 900 K. The recombination reaction occurs according to an Eley-Rideal mechanism at low temperature and to a Langmuir-Hinshelwood mechanism at high temperature. Moreover, the surface analyses by ESCA show clearly an important evolution of the SiC surface when it is exposed to the oxygen plasma. The SiC structure is oxidised to a SiO_2 structure and then the recombination reaction occurs on the SiO_2 layer formed since the first exposure times. The SIMS analyses show the diffusion of oxygen into the bulk material when silicon carbide is under oxygen plasma conditions, but this diffusion mechanism is not so dramatic even for high surface temperatures. So, the change in the recombination mechanism does not depends at all on the diffusion reaction. In complement of this work, a modelling of the recombination of oxygen atoms and transfer of the energy to a metallic or ceramic material by using the Chemkin® code was made[20]. The results shows a good agreement for at least silica.

Acknowledgments
This work was financially supported by CNES and ESA under Dassault aviation contract.

References

[1] J. Warnatz, 24th Symposium Intern. on Combustion, Pittsburgh, 1992, 553-579.

[2] F. Nguyen-Xuan, O. Mallard, S. Cavadias, J. Amouroux, A. Le Bozec and M. Rapuc, Proceedings of the 2nd European Symposium on Aerothermo-dynamics for Space Vehicles, Noordwijk, The Nederlands, 1994, 457-461.

[3] G.A. Melin and R.J. Madix, Trans. Far. Soc. 67 (1971), 198-211.

[4] A.L. Myerson, J. Chem. Phys. 50 (1969), 1228-1234.

[5] K. Nakada, Bulletin Chem. Soc. of Japan 32 (1959), 1072-1078.

[6] J.C. Greaves and J.W. Linnett, Trans. Far. Soc.54 (1958), 1323-1330.

[7] C.D. Scott, AIAA Paper 80-1477, Snowmass, CO, 1980.

[8] E.V. Zoby, R.N. Gupta and A.L. Simmonds, AIAA Paper 84-0224, Reno, Nevada, 1984.

[9] R.H. Krech, J. Spacecraft and Rockets 30 (1993), 509-513.

[10] D.Pagnon J. Phys .D; Appl. Phys .2B (1995) 1856-1868 .

[11] Nguyen-Xuan, F., Thesis of Pierre and Marie Curie University, (1997).

[12] C. Guyon, P. Cauquot, S. Cavadias, J. Amouroux, Progress in plasma processing of materials 2001, p101-108

[13] J.I.Pankove, Optical process in semiconductors (1975)

[14] P.B. Weisz, J. Chem. Phys. 21 (1953), 1531-1538.

[15] P.B. Weisz, J. Chem. Phys. 20 (1952), 1483-1484.,

[16] C. Guyon, S. Cavadias and J. Amouroux, Surface and Coatings Technology (Elsevier), 142-144 (2001) pp. 959-963

[17] Kaufman, F., « The Air Afterglow and its Use in the Study of some Reactions of Atomic Oxygen, » Proceedings of the Royal Society of London, A247, 1958, pp. 123-139.

[18] Laidler, K.J., Glasstone, and Eyring, J., « Application of the Theory of Absolute Reaction Rates to Heterogeneous Processes, » Journal of Chemical Physics, Vol. 8, 1940, pp. 659-676.

[19] P.Cauquot, S Cavadias, J Amouroux, High Temp. Material Processes 4 (2000), 365-378.

[20] C. Guyon, I. Mabille, M. Moscosa-Santillan, S. Cavadias and J. Amouroux,, Catal. Today (Elsevier), , in press 2003

Alternative Routes of Thermal Plasma Synthesis of Composite Oxide Nanopowders

Jerzy W. Jurewicz, Glen Lemoine, Alexandre Fortier

CRTP – Plasma Technology Research Centre
Chemical Engineering Department, Faculté de génie
Université de Sherbrooke

The extensive use of solid oxide fuel cells (SOFC) as an electrical energy source requires among others the use of very efficient electrodes especially the fuel electrode (anode). The anode is characterized by such parameters as the low overvoltage, the thermal expansion coefficient comparable to the electrolyte material, the chemical resistance to reduction by a combustible as well as to some sulfur presence in the fuel, controlled porosity etc. The choice of materials for such electrode is very limited and some composite oxides have been identified as possible candidates.

The induction plasma system has been used for the synthesis of nanosized composite oxides. The process is based on the high temperature oxidation of either solid or liquid (water soluble) precursors followed by rapid quenching of products by the water spray. The powdered feed was composed either of metallic powders or of chlorides. The liquid (water based) feed was in the form of saturated solution of chlorides. The metallic feed of identical elemental composition (Ni-Cr ratio) was fed in three different form: pure mixture of metals, mechanically agglomerated powders or the intermetallics synthesised prior to the combustion. The obtained very fine (d_p< 100 nm) products were subjected to extensive physico-chemical analysis including that by SEM, EDX and XRD methods. The particle size analysis was done by Zeta potential analyser. The results of the influence of the processing parameters including the plasma power, powder feedrate, processing pressure and oxygen partial pressure in a plasma gas as well as particle size of the raw materials on the final products particle size distribution and their chemical composition will be presented.

Solution Plasma Spraying of NiO/YSZ Cermet Anode for SOFC Preparation. Influence of Plasma Processing Parameters on the Porosity of Deposits.

Glen Lemoine, Hugues Ménard and Jerzy W. Jurewicz

CRTP, GRAPES,
Université de Sherbrooke, Qué. J1K 2R1

The objective of the present study is to determine the influence of plasma processing parameters on the porosity of NiO/YSZ deposits obtained by solution plasma spraying (SolPS). The SolPS technology is based on injection of atomized concentrated solution of chlorides into the RF thermal plasma discharge where droplets are thermally treated resulting in solvent evaporation, evaporite consolidation, melting of the formed solid followed by its deposition on a preheated target. Oxygen rich argon plasma was used in this work as the processing atmosphere. The thin (30 – 60 μm) layers of NiO/YSZ anodes so obtained were analysed by X-ray diffraction (XRD), scanning electron microscopy (SEM) and image analyses. The porosity of the deposits as a function of the plasma power, the deposition angle and the rotation speed of the target, was also studied.

Powder densification and spheroidization using induction plasma technology

X. Fan, J. Guo, N. Dignard, and C. Normand

Tekna Plasma Systems Inc., 2935 Boul. Industriel, Sherbrooke, Quebec, Canada, J1L 1X7

Abstract

Spheroidization of powder particles is one of the successful commercial applications of induction plasma technology. A review is presented of case studies in which powder densification and spheroidization using induction plasma technology has played a key role in substantial improvement of powder quality and fluidity. Results are given for both metallic and ceramic powders at the pilot and industrial scale production.

1. Introduction

The last decades has seen a vivid technology transfer from laboratory to industrial scale application of induction plasma processing [1, 2]. While a number of the subjects of induction plasma process, such as plasma-particulate interaction, heat and mass transfer, plasma reactor mixing pattern mode, and particulate nucleation and growth mechanism etc. have been widely studied in laboratory, the successful industrial application of induction plasma process depends largely on many fundamental engineering support. For example, the industrial plasma torch design, which allows high power level (50 to 600 kW) and long duration (24 hours) of plasma process. Another example is the powder feeders that convey large quantity of solid precursor (1 to 100 kg/h) with reliable and precise delivery performance.

Tekna Plasma Systems, inc., one company bridging the gap between academic laboratory and industry, has developed many induction plasma processes in various industrial applications. Powder particles spheroidization/densification is one of the successful example in commercial application of induction plasma process. The requirement of powders spheroidization comes from very different industrial fields, e.g., from powder metallurgy to the electronic packaging. Generally speaking, the pressing need for an industrial process turns to the spherical powders, is to seek at least one of the following benefits, the spheroidization process would bring in:

Figure 1: A 200 kW industrial unit of powder spheroidization, manufactured in Tekna Plasma Systems. This system produces spheroidized cemented powders at the productivity of 30 kg/h.

- Improve the powders flow-ability ;
- Increase the powders packing density ;
- Eliminate powder internal cavities and fractures ;
- Change the surface morphology of the particles ;
- Other unique motive, such as optical reflection, chemical purity etc.

For instance, in the field of thermal spraying, the quality of coatings (density, microstructure etc.) can be dramatically improved by using spherical and dense powder particles as the starting material for spray.

The specific advantages of induction plasmas have been well defined in earlier researches[3,4]. Owing to its large volume, axial materials feeding, and long residence time of precursor, induction plasma process is an ideal process for the spheroidization of powders. In recent years, Tekna has provided clients a number of integrated units of powder spheroidization at the industrial scale. The particular features of these industrial systems of induction plasma process are their easy operation, automatic control, real-time data acquisition, and the facilitating collection of the treated powders on the basis of continuous operation mode. One typical system is shown in Figure 1.

A great variety of ceramics, metals and metal alloys have been successfully spheroidized/densified using Tekna's integrated systems. The following table lists some typical materials spheroidized in commercial scale by Tekna integrated systems.

Table 1: Typical powder materials spheroidized in industrial scale by Tekna integrated system.

Powder category		Powder name
Ceramics	Oxide	SiO_2, ZrO_2, YSZ, Al_2TiO_5, glass
	Non-oxide	WC, WC-Co, CaF_2, TiN
Pure metals		Re, Ta , Mo, W
Alloys		Cr/Fe/C, Re/Mo, Re/W,

2. Spheroidization Process Case Studies

CEMENTED ALLOY POWDERS

Cast Tungsten Carbide is powder materials of WC-W_2C alloy. This material is harder than most steels, has greater mechanical strength, transfers heat quickly, and resists wear and abrasion better than other metals. The service life of many kinds of machinery can be greatly prolonged by the surface coating of wear-prone materials with cemented alloy. It has wide applications in construction, coal mining, cement production, rock crushing and agricultural industries, The powder metallurgical products of this material are used primarily and extensively for making drilling tips tunneling, mining and quarrying purposes, i.e. for most geological activities.

Table 2: Mechanical properties of cemented alloy before and after spheroidization

	Angular	Spheroidized
Tap density (g/cm^3)	7.5	10
Micro-hardness (kg/mm^2)	2000	4000

Besides the powder metallurgical method, the laser cladding, PTA (Plasma transferred arc) overlaying, plasma spraying etc. are widely used as the vehicle of hard-surfacing of cemented alloy[5]. The latest practice revealed that using spheroidized cemented alloy powders significantly increase the quality of cemented coating layers, overcoming the notorious "corner effect", in associated with the usage of angular shape of WC powder particles in a hard Ni-Cr or Co matrix. While there is no apparent improvement in powder flow rate, a significant change in powders tap density is obtained after Tekna's spheroidization processing. The materials hardness of the cemented alloy components could be

doubled. This is no-doubt relevant to the dense, flaw-free microstructure obtained in Tekna's spheroidization processing. The common existence of fissures, pores etc. in angular cemented powders, inherited from the WC powders manufacture processing, could be eliminated.

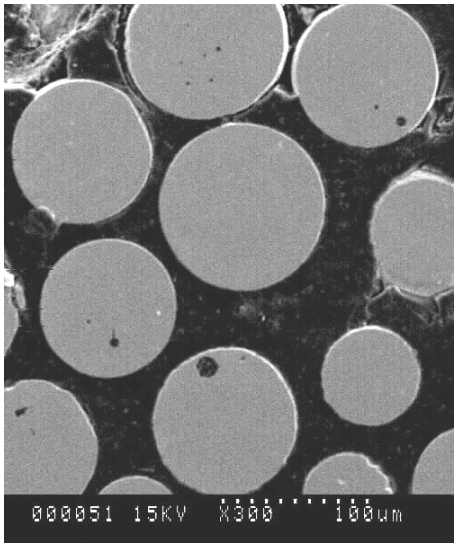

Figure 2: The dense, flaw-free microstructure of the spheroidized WC powders.

REFRACTORY METALS

In modern high-tech filed, some refractory metals play key role.

Tantalum: Tantalum is used to make electrolytic capacitors and vacuum furnace parts, which account for about 60% of its use. The metal is also widely used to fabricate chemical process equipment, nuclear reactors, aircraft, and missile parts. A tantalum carbide graphite composite material is said to be one of the hardest materials ever made. Tantalum also found wide use in making surgical appliances. The growth in demand Ta material has been due largely to the use of tantalum capacitors in small portable electronic components such as laptop computers, video cameras, games consoles and, most importantly, mobile phones.

Rhenium: Rhenium is extremely attractive for high temperature structural and energy system applications, such as space and missile propulsion systems. Used either as a pure structural material or as a liner in conjunction with graphite or carbon-carbon structural materials in high temperature rocket engine and hot gas valves. Rhenium is the only material to date that exhibits near-zero erosion in the high temperature (2000 – 4000 °C) high-pressure rocket throat and nozzle and is virtually inert to thermal shock . Using as a coating on carbon materials, rhenium does not form carbide, yet it has an excellent bond strength between the two materials. Rhenium has repeatedly outperformed all other coating candidates on solid rocket hot section components in tests.

The apparent motive to spheroidized these powder materials is to increase their packaging density and to impart the fluidity to the flaky powders, so that the further engineering manufacture with these materials becomes easier or feasible. Figure 3 shows the Re powders before and after the induction plasma spheroidization processing. The spheroidization efficiency is 100 %, despite the high melting point of rhenium (3180 °C). It is worth mentioning here, that there is no electrode contamination problem in induction plasma processing, on the other hand, the processing with Ar-H_2 plasma may further purify the precursor materials. This is a strong attraction for those clients seeking high purity, to turn to the induction plasma spheroidization processing.

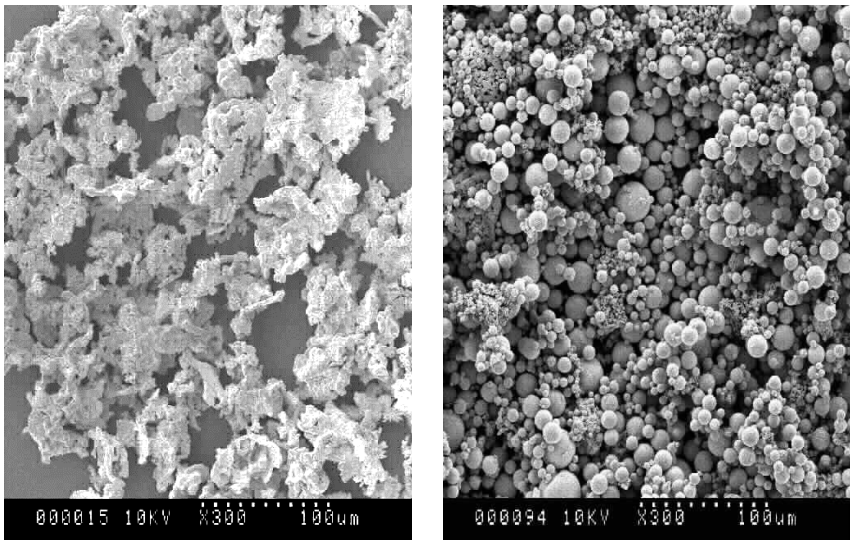

Figure 3: The flaky, sticky Re powder (left) become dense and spherical (right) after the induction plasma spheroidization processing.

OXIDES CERAMICS

As the mainstay of the oxide ceramics material market, Al_2O_3 and ZrO_2 powders, are widely used as the structural material. Lately, the demand of spheroidized oxide ceramic powders are increasing. Though, some powders of them are spray-formed and originally assume the spherical shape, further densification or phase transformation via plasma processing is requested for some special applications.

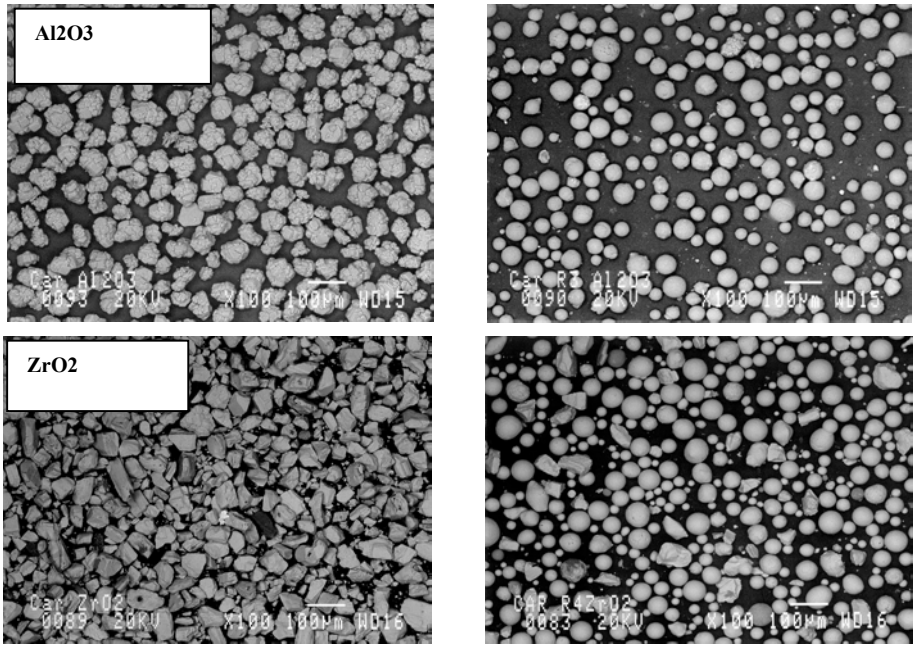

Figure 4: Oxide ceramic powders before and after the induction plasma spheroidization processing.

The challenge for induction plasma spheroidization processing to spheroidize/densify these materials are (1) the poor thermal conductivity, and (2) the relatively high melting point of the material. Although, the spheroidization of these powders in laboratory scale has produced many interesting results, see Fig. 4. The further scale-up to a commercial production (20 kg/hr) is hindered by the fact that the power intensity of induction plasma is relatively "thin" , despite its large volume and the longer residence time of precursors.

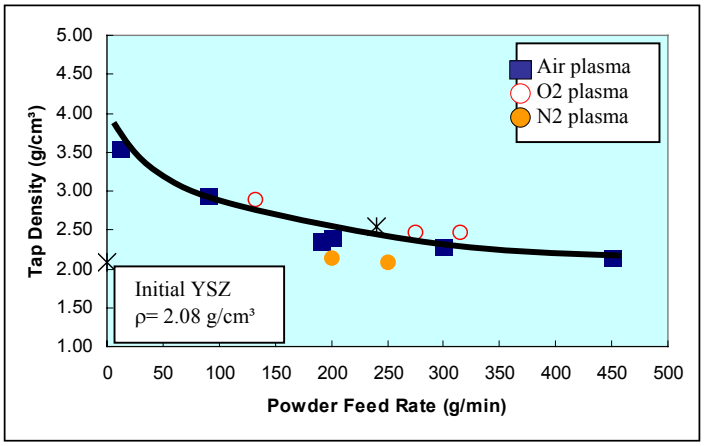

Figure 5: The relationship between tap density and the precursor (YSZ) feed rate in different induction plasma spheroidization/densification processing.

QUARTZ POWDERS AND OTHERS

"Semiconductor packaging material" is one of the key-technologies for the electronic industry. The material encapsulates integrated circuit and other discrete components (resister, capacitor etc.) to disconnect electrically, and reinforce mechanically as well as chemically. It use a resin polymer composite filled with silica (SiO_2) filler-powder. The material necessitates a high thermal conductivity, a low thermal expansion and good mold-ability. Spherical SiO_2 filler-powder is highly desired in this field, as the good fluidity of the filler and the high packing density impart more reliable insulation function to the packaging process, which is more critical issue when the electronic devices become smaller and smaller.

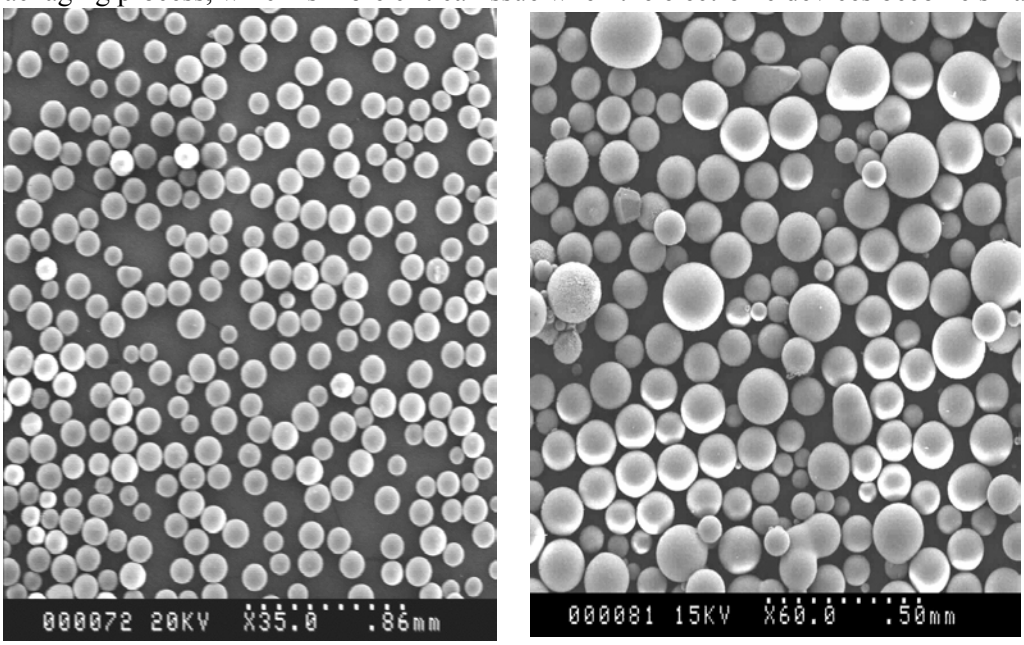

Figure 6: (left) SiO_2 powder spheroidized by air plasma, output 10 kg/h. (right) silicate glass beans, output 15~20 kg/h.

The spheroidization demand also come from the traffic sign board manufactures. Spherical glass beans are superior to the convenient glass powders in the uniformity and intensity of the reflexion, that widely used in the reflective paints. Owing to its low glass transition temperature, spherical glass beans could be obtained via induction plasma process in very high throughput, provide that there are high efficient precursor feeding and product collection capacity.

3. Process cost analysis

With the fact that induction plasma processing could spheroidize almost any kind of powder material, the only determinant factors for its successful application in commercial scale are the operation cost and the price/quality ratio, especially where there is another competing industrial processing, such as combustion processing; *d.c*. plasma processing etc.

An industrial systems of induction plasma process should have the throughput as high as possible. Theoretically and technically, this capacity is limited by (1) the maximum power level (energy density) the induction plasma torch can achieve; and (2) the maximum precursor feed rate determined by the "loading effect"[6]. These issues remain the subjects in the research and development work of induction plasma science. Tekna is to present 500 kW industrial unit in the near future and turn to the solid-state inverter as the radio frequency power source, in order to increase the electric coupling efficiency, and so the energy density of the induction plasma.

In aspect of industrial engineering, Tekna has designed many unique mechanisms to decrease the operation cost. For example, the cooling water and the heat energy are recycled. The plasma gases(argon, hydrogen etc.) are also recycled during operation to lower down the operating cost of the process.

Another important cost reduction advantage of the integrated systems manufactured by Tekna Plasma Systems is the ability to treat the powders in a 24 hours continuous operation mode. The continuous production of powder will greatly reduce the overall cost of the powder by allowing depreciation of the investment costs on a more important number of hours and powder production.

4. Summary

The late decade has seen the induction plasma technology reached a level of maturity. Induction plasma processing has been successfully applied in many materials' commercial scale production. Tekna Plasma Systems, inc. promotes and pioneers this laboratory-industry technology transfer. In our commercial practice and expertise, we have recognized many opportunities to apply induction plasma processing to spheroidize the powder material, in responding the challenging and demanding of different industrial fields.

5. References:

[1] M. I. Boulos, Radio frequency plasma developments, scale-up and industrial applications, *High. Temp.Chem. Processes*, 1(1992)401-411.

[2] M. I. Boulos, The inductively coupled radio frequency plasma, High. Temp. Material Processes, 1(1997)17-39.

[3] X. Fan, F. Gitzhofer, and M.I. Boulos, Statistical Design of Experiments for the Spheroidization of Powdered Alumina by Induction Plasma Processing, *Journal of Thermal Spray Technology*, 7 (2)(1998)247-253.

[4] N.M Dignard, M.I. Boulos, Powder spheroidization using induction plasma technology, in Thermal Spray: Surface Engineering via Applied Research, ed. Berndt, ASM international, 2000, pp887.

[5] D. Harper, M. Gill, K.W.D. Hart, and M. Anderson, Plasma transferred arc overlays reduce operating costs in oil sand processing, in Thermally Sprayed Metallic Deposits Using Scattering Techniques, ed. Berndt, ASM international, (2000)

[6] P. Proulx, J. Mostaghimi, and M. I. Boulos, Heating of powder in an r.f. inductively coupled plasma under dense loading conditions, *Plasma Chem. Plasma Process*., 7-1 (1987) 29-52.

Main defects occurring in a cryogenic and deep silicon etching under a SF_6/O_2 plasma mixture studied by a Monte Carlo simulator

G. Marcos[1,2], A. Rhallabi[1], P.Ranson[2]

1. *Laboratoire des Plasmas et des Couches Minces, IMN, UMR 6502, CNRS-Université de Nantes,2 rue de la Houssinière, BP 32 229, 44 322 Nantes Cedex 3, France. E-mail :gregory.marcos@polytech.univ-nantes.fr ;Tel : 02 40 68 32 03 ; Fax : 02 40 68 30 66*

2.*GREMI,CNRS-Université d'Orléans ,UMR 6606, 14 rue d'Issoudun, BP 6744, 45 067 Orléans Cedex 2, France*

Abstract

In this paper, we describe and show the main results performed by an etching simulator based on a Monte Carlo method. It allows to calculate the temporal evolution of a Si substrate under a SF_6/O_2 plasma chemistry. One collisioneless sheath model is connected to the surface model to introduce accuracy incident energetic and angular ion distribution function. Surface parameters such as fluorine and oxygen sticking coefficients were estimated by comparing simulation results with experiments. Our study mainly concerns the defects encountered during one etching process: undercut, bowing and roughness. For their understanding, it appears that the ion bombardment plays an important role in particularly for the bowing and trenching formation, whereas chemical reactions are the key to explain the undercut intensity and roughness growth.

I Introduction

The realisation of new power components needs a strong control of the different manufacturing steps. In particular, the emergence of the microelectro mechanical systems (MEMS) requires the development of rigorous, reliable and reproducible technological processes. In this context, the research to improve the techniques of dry plasma etching is an essential stake. The studies are focused on profiles properties, as well topographic as kinetic ones.

Our work deals with the understanding of silicon etching mechanisms in an ICP Alcatel reactor with a SF_6/O_2 plasma chemistry. The objective is the realisation of very deep trenches with high aspect ratio (AR). For these properties, the mean etching rate and anisotropy are the essential parameters. The process is cryogenic (a drop in the chuck temperature around – 100°C), allowing to reduce the chemical etching mechanisms by the growth of an oxide layer on the trench sidewalls. To complement our experimental study [1], we have developed a silicon etching simulator, which takes into account the main plasma-surface mechanisms involved in this type of process.

In our ICP reactor, we obtain thin and deep trenches (AR>50) with a high mean etching rate (> 5µm/mn) and good anisotropy. Nevertheless, as it is shown in Figure 1, the profile is still deformed by two main lateral defects: an undercut, just under the mask, and the bowing phenomenon whose consequences are very dramatic during the post etching steps (a void appears during trench refilling).To reduce these defects and improve the process, it is necessary to understand their growth mechanisms. This research implies a detailed study of plasma-surface interaction mechanisms.

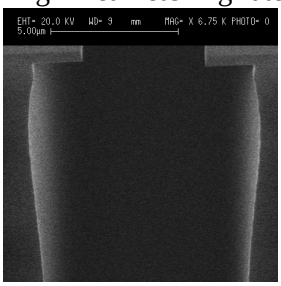

Fig 1 : High part of an experimental trench. This area is marked by the growth of undercut and bowing.

In this article, we present and discuss numerical results performed by the 2-D silicon etching model. Based on Monte Carlo techniques, this simulator has been already described in a previous paper [2]. After a brief recalling of its main characteristics in the following part, we will show profiles obtained according to specified parameters.

II The Monte Carlo simulator

II.1 Initial structure

The first step is the definition of the material submitted to the etching plasma. It is composed by a silicon substrate and a mask for which we specify physical and geometrical parameters (thickness, width and side slope). The method consists in a two dimensional cellular discretization. Each cell has the same size which really defines a number of sites inside. With this approach, we can follow at any moment a specific photography of physical state of the silicon etched surface through the mask.

II.2 The chemical precursors

The main reactive species in the gas phase plasma are fluorine and oxygen radicals. Provided by SF_6 dissociation, the fluorine atoms react with silicon sites to form Si-F bonds. The final step of surface fluorination is the creation of SiF_4 species which are spontaneously volatile, producing the isotropic chemical etching. These reactions of adsorption are defined according to a fluorine-silicon reactivity parameter which is introduced into the simulator by an adsorption probability (P_{aF}). We have studied its effect on the profile isotropy degree. Figure 2 shows experimental results realised in these following conditions: a pure SF_6 plasma, no bias to limit the ionic bombardment effects and a pressure of 22 mTorr. Two temperatures were tested: + 30 °C (Fig. 2.a) and – 110 °C (Fig. 2.b). The trenches are characterised by the same etching rate of about 1.4 µm/min, with an isotropic profile. In a first approximation, these results allowed to consider a constant adsorption parameter with temperature. To define P_{aF}, a series of simulations were calculating. Some results are shown in Fig. 2.c and Fig. 2.d. The profiles were obtained by considering a pure fluorine flux and different values of P_{aF}: 0.9 and 0.1. One notes that undercut is all the more developed that P_{aF} is small. The many random reflections of fluorine atoms inside the trench before being adsorbed explain this trend. These reflection processes lead to the increase of the flux of the reactive chemical species in the totally shadowed areas, like that located just under the mask. A comparison between experiments and simulation results allowed to estimate P_{aF} at 0.1 [2].

A work concerning the reactivity between oxygen atoms and silicon (parameter P_{aO}) is given in Fig 2. e, f, g and h. The experiments were realised in the same conditions mentioned previously, with an oxygen addition of about 10%. For a chuck temperature of + 30 °C, no significant differences are noted with precedent results: topography is still isotropic and the etching rate is the same. In contrary, a drop of substrate temperature modifies seriously the surface kinetics: the profile becomes more anisotropic and the etching rate increases. At –110 °C, the passivation processes are also activated. In simulation, we show results for two values of P_{aO}: 0.1 and 0.9. For a low P_{aO}, the profile

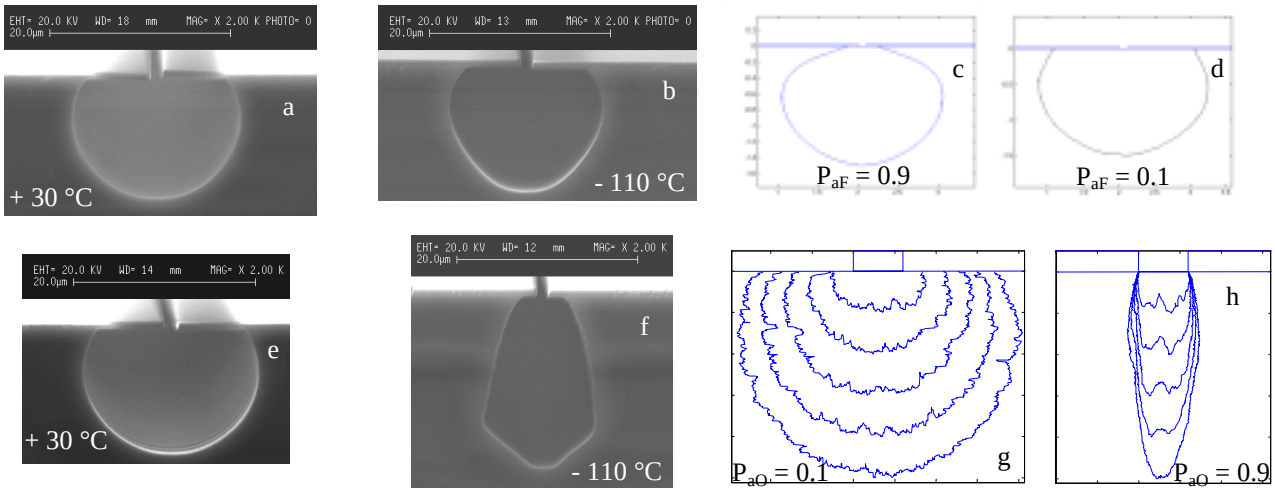

Figure 2 : Study of surface parameters by comparison between experiments and simulation results. a and b : etching with a pure SF_6 chemistry for two temperatures. c and d : simulation results for high and low P_{aF}. e and f: etching with a SF_6/O_2 plasma mixture at + 20 and – 110°C. g and h: corresponding simulations obtained with two levels of P_{aO}.

is still isotropic, with a strong roughness due to micromasking effects. When this parameter increases, the trench becomes anisotropic and the roughness is lower on the sidewalls. The simulator predicts also a rise of the etching rate. So, to model a cryogenic etching process using a based-oxygen chemistry, it is necessary to introduce an high value of the oxygen-silicon adsorption probability.

II. 3 Plasma ions

Ion distribution function are determined by a transport model in the sheath [3] which is connected to the surface model. Based on Monte Carlo technique, it takes into account sheath characteristics that are controlled by pressure, bias tension voltage and injected power in the reactor. Two reactions are considered: elastic and charge exchange collisions.

When one ion strikes the surface, a preferential sputtering yield is determined in accordance with ion energy [4], local angular incidence and the nature of impacted sites. A sputtering process is automatically followed by a redeposition study of the etched species. The level of this mechanism is defined by an homogeneous surface parameter which allows to consider etchings with low or high redeposition. Even if the experiments show a strong selectivity between the mask etching and the silicon substrate, the simulator can introduce processes of mask erosion caused by the ionic bombardment in the case of an used soft-mask. For high ion energy, specular reflexions from the trench sidewalls are considered.

II. 4 Surface displacement

In the model, etching is symbolized by a cellular transition between a full state to an empty state. Etched surface displacement is also realised by site disappearance, produced by spontaneous chemical etching or preferential sputtering. For a given depth, an average etching rate is calculated by comparing the total number of introduced species with the real experimental fluxes.

III Results and discussion

We have studied final trench topographies by varying independently relevant parameters: effect of an oxygen addition, mask geometry and angular dependence of the sputtering yield.

III. 1 Role of the SF_6/O_2 rate

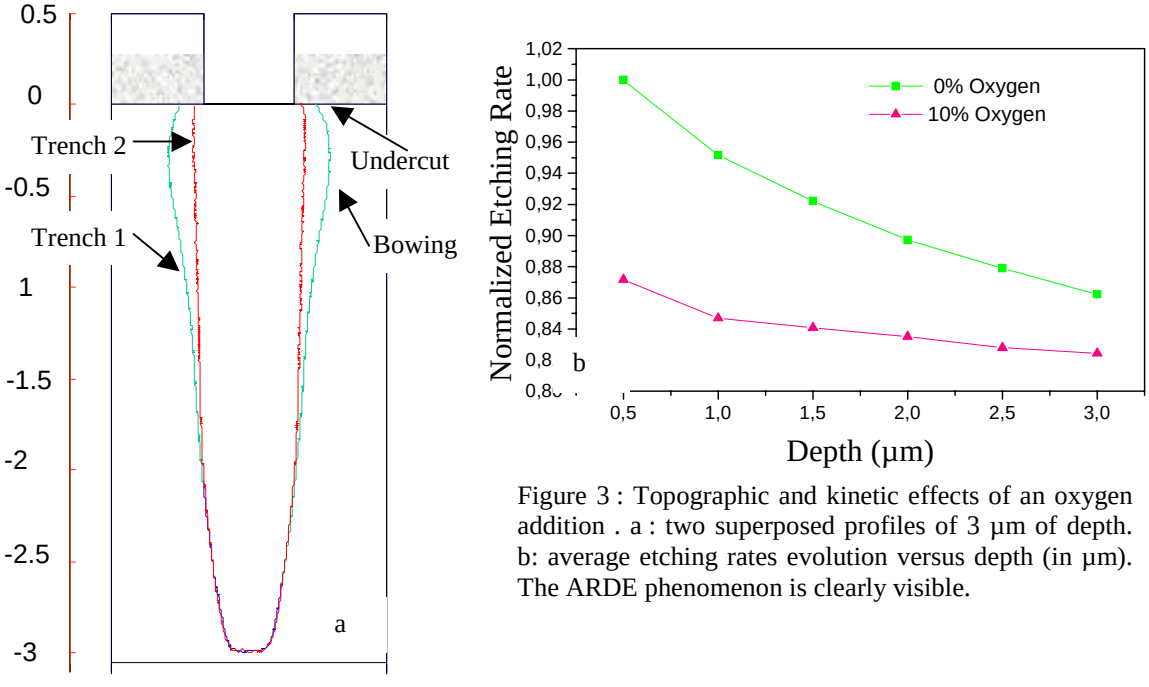

Figure 3 : Topographic and kinetic effects of an oxygen addition . a : two superposed profiles of 3 µm of depth. b: average etching rates evolution versus depth (in µm). The ARDE phenomenon is clearly visible.

Figure 3.a presents two simulated profiles of 3 µm of depth obtained with these initial conditions: a pressure of 22 mTorr, a bias of –30 V, an ion flux of 0.1 %. The mask has the following geometry: a thickness and aperture of 0.5 µm, vertical slopes. The trench 1 was realised without oxygen flux, whereas trench 2 was calculated with 10 % of oxygen in the total neutral flux.

The trench 1 is characterised by a good general anisotropy, with, in the upper part, a large undercut and bowing. These defects are completely removed in the trench 2, for which oxygen produces a passivation layer on the sidewalls. Figure 3.b shows the corresponding etching rates variation versus depth, so with time processing. The data are normalised with the higher one. The ARDE (Aspect Ratio Dependent Etching) phenomenon is obviously visible. This progressive vertical etching rate reduction is due to the transport mechanisms of the introduced species in the trench. The shadowing effect becomes all the more important that the etched depth increases. The surface kinetic lowers and so the etching rate falls. We can observe that this trend is a quiet different for the two simulations, with a more marked decrease for the trench 1. We have shown [5] that this kinetic comportment is caused by a more significant fluorine flux at the trench 2 bottom when the silicon sites are saturated with oxygen on the upper sidewalls.

III. 2 Mask geometry

It is well known by experimental results that mask aperture and thickness can have great consequences for the final trench properties. However, the role of the mask slopes orientation is not usually investigated, this geometrical parameter being not easily modifiable. On this point, the simulation can give complementary and new information. In Figure 4.a, we present two superposed profiles obtained with the same conditions as Trench 1 but with two different masks: one with vertical sides (Trench 3) and one other with inclined sides (Trench 4). Compared with Trench 3, Trench 4 is more deformed, with a greater undercut and bowing. Moreover, one can remark a second lateral overetch in the middle of the structure.

To understand these modifications, we have calculated the neutral angular distribution function after their mask crossing. The results are shown in Figure 4.b. Two differences are observed in relation with the mask sides inclination: when the sides are sloped, the total neutral flux is more important and spreader. In consequences, the surface kinetics are motivated, increasing the etching processes. Undercut and bowing are also more developed. Thanks to the cellular discretization, we have studied the nature of the surface corresponding to the area where the second lateral overetch occurs. It appears that this zone is less fluorinated, the ion bombardment being very important. This elevated sputtering process is due to impacts of the reflected ions which come from the inclined sides

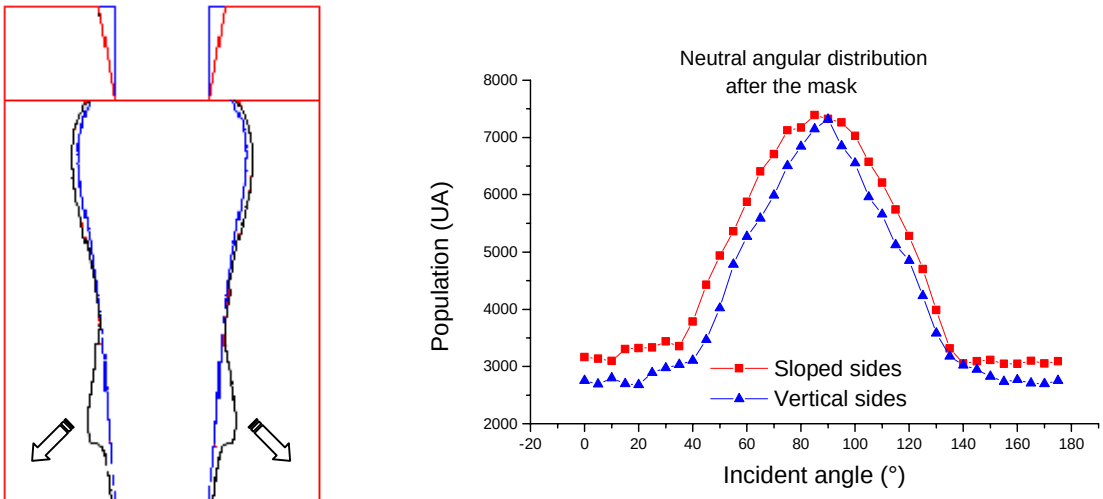

Figure 4 : role of the mask sides. Their inclination plays a great role on the incident flux received on the sidewalls. Undercut and bowing are strong dependent on this geometrical parameter.

of the mask. If we consider this defect as a part of the bowing, this study allows to define one cause of it.

III. 3 Angular dependence of the sputtering yield

Figure 5 shows the sputtering yield evolution calculated by using TRIM [6] for a pure silicon wafer versus ion incident angle and for three different input energies. The shapes are strongly different and we observe one peak structure around 60° for higher energy. For this work, we have assumed an uniform angular distribution for any input energies and we have studied the impact on feature profiles of various angular dependence laws. An example is given in Figure 5 (law-2).

Figure 6 presents two simulation results with the following input parameters: an aspect ratio of 20 for an ion to neutral flux ratio of 0.3. No oxygen was added. In figure 6-a, angular dependence of sputtering yield is not introduced, while in figure 6-b a constant value between 0 and 60° was imposed, followed by a linear decrease of sputtering yield until 90°. For very low incident ion energy, this shape is usually met on silicon substrate. One can observe for (b) a strong trench contracting, with a very narrowed bottom. The sidewalls are also more inclined. This typical feature profile has been obtained in our ICP reactor by using a grid system placed above the wafer to reduce all incident charged species.

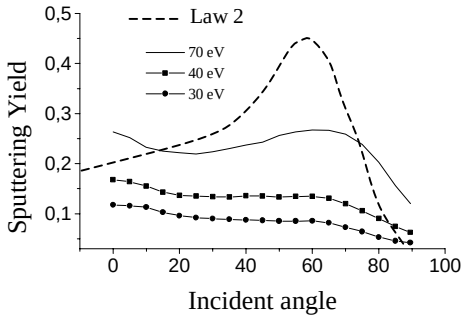

Figure 5 : Sputtering Yield evolution versus incident angle for three ion energies.

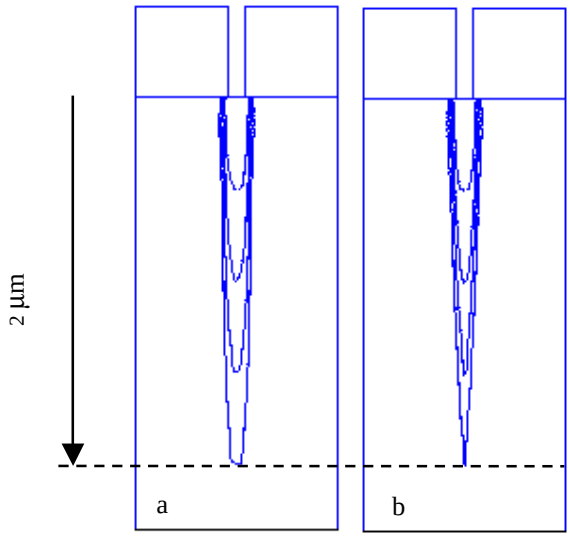

Figure 6 : Two simulations obtained by the etching simulator for two different laws of sputtering yields versus incident angle. The mask has vertical sides with 0.1 µm of opening and 0.5 µm of thickness.

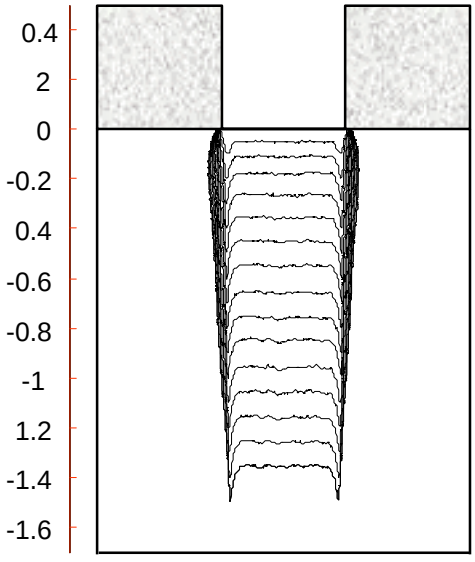

Figure 7 : Formation of microtrenches at the trench bottom.

In the Figure 7, we have used the Law 2 to calculate the sputtering yields. The corresponding trench was calculated without oxygen, a pressure of 22 mTorr and a high ion flux of 5 % in the total

incident flux. We observe the growth of two microtrenches at the trench bottom. This defect has been already expected by other authors [7] and their investigations have shown a strongly dependence of microtrenches evolution with plasma parameters. Moreover, simulation results obtained by Vyvoda et *al* [8] present a prominent role of ion scattering behaviour for microtrenches appearance. In this context, our results appear as a new mean of study and understanding of this defect which induces damage for the post etching steps.

IV Conclusion and perspectives

We have described and illustrated our silicon etching simulator. This work, which is developed in strong collaboration with experiments, introduces coherent kinetic parameters and reactional scheme. The results permit to show the implications of certain parameters such as nature of incident fluxes, mask geometry and angular dependence of the sputtering yield.

Improvements of the model to simulate the etching profiles with a good accuracy are in hand. In the next step, we will develop a kinetic model allowing to quantify the fluxes of different reactive species of SF_6/O_2 plasma. A such model will be coupled to the present etching surface model. With this approach, we can thus describe self consistently the etching process directly with the reactor parameters.

Moreover, a special study concerning the surface kinetic to understand the growth of the passivation layer has started [9].

V References

[1] S. Aachboun and P. Ranson, “Deep anisotropic etching of silicon”, J. Vac. Sci. Technol. A, 17 (4), 2270 (1999)

[2] G. Marcos, A. Rhallabi and P. Ranson, “Monte Carlo simulation method for etching of deep trenches in Si by a SF_6/O_2 plasma mixture”, J. Vac. Sci. Technol. A, 21 (1), 87 (2003)

[3] A. Rhallabi, thesis, University of Nantes (1992)

[4] T. Chevolleau, P. Y. Tesier, C. Cardinaud and G. Turban, “Etching of Si at low temperature using a SF_6 reactive ion beam-effect on the ion energy and current density”, J. Vac. Sci. Technol. A 15(5), 1997.

[5] G. Marcos, , thesis, University of Orleans (France) (2002)

[6] J. F. Ziegler, TRIM (the Transport of Ions in Matter) IBM-Research, 28-0 Yorktown, NY 10598

[7] J. M. Lane, F. P. Klemens, K. H. A. Bogart, M. V. Malyshev and J. T. C. Lee, “ J. Vac. Sci. Technol. A 18(1), 2000.

[8] M. A. Vyvoda, M. Li, D. B. Graves, H. Lee, M. V. Malyshev, F. P. Klemens, J. T. C. Lee, and V. M. Donnelly, J. Vac. Sci. Technol. B 18(2), 2000.

[9] R. Dussart, M. Boufnichel, G. Marcos, P. Lefaucheux, R. benoit, H. Estrade-Szwarckopf and P. Ranson, “Passivation mechanisms in cryogenic SF_6/O_2 etching process”, submitted to J .vac. Sci. Technol.

Plasma based ionic implantation of titanium and titanium alloy : Ti6Al4V.

V.Fouquet, L.Pichon, M.Drouet, A.Straboni
Laboratoire de Métallurgie Physique, université de Poitiers, Chasseneuil France

Abstract

Plasma co-implantations of N_2 and H_2 in titanium and Ti6Al4V were shown to introduce high doses of nitrogen below the surface leading to the growth of δ-TiN nitride layer. Moreover the high density of defects created by the high energy ion fluxes in the subsurface region enhance its diffusivity ; then the δ-TiN layer didn't act as a diffusion barrier any more and a long range diffusion mechanism can occur at moderate temperature.

1. Introduction

Titanium and titanium alloys, especially Ti6Al4V, are attractive materials with low density, very good resistance to corrosion and high strength. Nevertheless, their resistance to frictional wear is poor. Surface nitridation has been proposed to improve surface properties. However the conventional thermo-chemical processes require high temperatures [1], which may induce structural modifications and thus degradation of the mechanical properties. Plasma Based Ion Implantation (PBII) is a novel process [2] that enables the lowering of temperature by increasing the nitrogen incorporation efficiency. Compared to conventional in-line implantation, the advantage of PBII is that the process is non-directional and that all surface are simultaneously treated. Samples are immersed in a plasma and a pulsed high voltage is applied. Large fluxes of ions are available and high doses are incorporated in the near surface of the sample. Together with the ions impinging the surface, a substantial amount of thermal energy is transferred.

2. Experiment

2.1 Samples

Commercial Ti6Al4V and Ti plates were cut into circular shapes with dimensions of 16 mm in diameter. Work pieces were mechanically ground with abrasive papers and polished with diamond spray (1μm) then degreased ultrasonically in acetone and in ethanol and finally dried with nitrogen. The nitrogen and hydrogen plasma co-implantations were carried out using our PBII equipment.[3-4] The cold and homogeneous down-stream plasma is generated in the entire silica tubular chamber using r.f excitation. A three-zone furnace around the tube allows to control the temperature and the voltage is pulsed in order to reduce the thermal energy deposited. The operating pressure in the chamber was fixed at 1 Pa, and the flow rates of the N_2-H_2 (90%-10%) gas mixture was fixed at 25 sccm. The nitriding temperatures were taken between 200°C and 800°C and implantation were performed for 120 minutes to 360 minutes. Applied voltage varied between 10 kV and 35 kV. Pulse duration, repetition rate were fixed at 10 μs and 200 Hz respectively.
Phase identification was conducted by X-Ray diffraction (XRD) and carried out on a Siemens diffractometer D5005 with monochromatic CuKα radiation in a glancing geometry (5°) with a scan step of 0.02°. Surface analysis by X-Ray photoelectron spectroscopy (XPS) was conducted in the Leybold AG LHS12 spectrometer with a MgKα (1253.6 eV) X-Ray source of the LPCM de Nantes. Detailed spectra of the O1s, Ti2p, N1s and C1s lines were recorded in 0.1 eV steps for all samples. Quantification and chemical-state determination were conducted by using a Shirley-type background. The Nuclear Reaction Analysis (NRA) measurements were carried out with the Van de Graaff accelerator of the Université de Paris VI et VII, by using an incident deuteron energy of 3 MeV. Vickers micro-hardness tests were made using SHIMAZU HMV 2000 micro-hardness tester with 0.10N 0.25N 1N 2N and 3N loads for micro hardness measurements on surface and 0.25N load for

micro hardness measurements on cross section.

2.2 X-Ray measurements

The figure 1 shows the effect of temperature on the diffraction patterns for 25 kV implanted Ti6Al4V samples for 240 minutes. At 200°C, the presence of surface nitride compound is revealed by the disappearance of the β-Ti phase. According to the N-Ti phase diagram this phase is destabilized by nitrogen incorporation. A phase identification shows the presence of δ-TiN for temperatures over 200°C and ϵ-Ti_2N for temperatures over 500°C. The δ-TiN peaks are growing as the treatment temperature increases. The main nitride phase are respectively δ-TiN up to 500°C and ϵ-Ti_2N at 800°C, whereas α-Ti grains disappear in the probed depth with the nitriding temperature. A slight shift with increasing temperature of the α-Ti(100) peak to the high 2θ values and α-Ti(002)peak to the low 2θ values can be noticed. It indicates a lower a cell parameter and a bigger c cell parameter. Moreover the δ-TiN peaks have slightly shifted towards the low 2θ values, indicating a larger cell parameter.
The figure 2 illustrates the effect of nitriding time for 25 kV implanted samples at 500C. The δ-TiN peaks appears as soon as 120 minutes of treatment and grows with the treatment time. After 360 minutes of implantation the peaks relative to ϵ-Ti_2N are evidenced. Whatever the treatment time, a line shifts of the α-Ti peaks is observed compared to the α-Ti initial. Moreover a shift of δ-TiN peaks to the high 2θ values evidences that the probed inter reticular distance increases with treatment duration.
The figure 3 illustrates the effect of the applied high voltage for treatment at 500°C and for 240 minutes. At 10 kV δ-TiN phase is not clearly observed whereas it appears at 25 kV and its intensity keeps constant with increasing applied voltage. Nevertheless the presence of surface nitride compound is revealed by the disappearance of the β-Ti phase. The ϵ-Ti_2N phase is only evidenced for treatment performed at 35 kV.

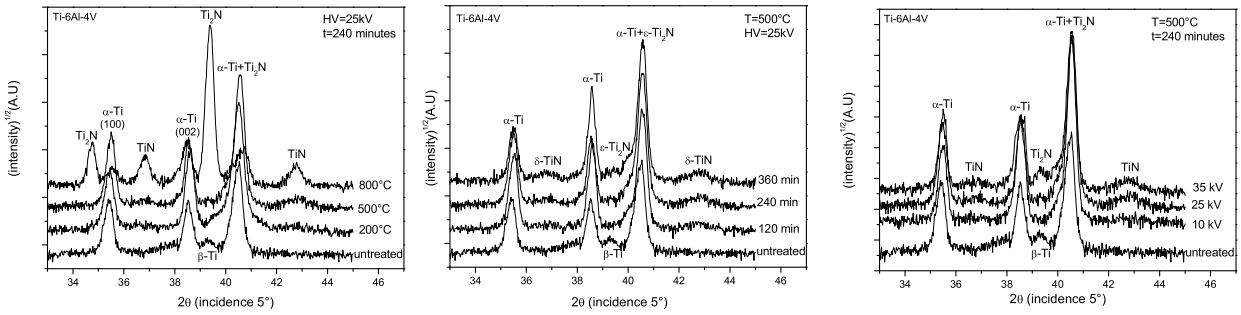

Fig 1a Fig 1b Fig 1c

Fig 1 : Effect of the temperature (Fig 1a), the nitriding time (Fig 1b) and the applied voltage (Fig 1c), on XRD pattern of Ti6Al4V samples

2.3 XPS measurments

In order to counteract charge effect, impurity carbon (C-C and C-H bounds) was set at 284.7 eV binding energy (BE). Results of chemical-state determination are presented in table 1. The Ti2p envelope of a nitrogen plasma implanted sample is composed of 3 synthetic components (T_1 T_2 T_3). The measured binding energies of the $Ti2p_{3/2}$ for the various identified or assigned chemical states were compiled and are listed in Table 1 together with data from our experiments. As shown, the position of $Ti2p_{3/2}$ for nearly stoichiometric TiN_x (x=1) falls in the range of 454.8-455.5 eV (T_1)and the T_3 peak found between 458.0 and 458.2 eV is unambiguously identified as Ti in a TiO_2 environment. The T_2 peak appearing in the 456.4-457.0 eV range is assigned to TiN_xO_y or TiN_xO_{1-x} type oxynitrides together with the super-stoichiometric TiN_{1+x} nitride.

Table 1 : Chemical state and binding energies of our samples and literature values of $Ti2p_{3/2}$ line positions

Line	Name	State	Position	State	Position	Reference
Ti2p	T_1	Ti in $TiN_{x=1}$	454.8-455.5	Ti^0	453.8 ± 0.2	[5]
	T_2	Ti in TiN_{1+x}orTiN_xO_y	456.4-457.0	TiN	454.5-455.3	[5-8]in[5]
	T_3	Ti in TiO_2	458.0-458.2		454.7 ± 0.1	[5]
N1s	N_1	N in TiN_{1+x} or TiN_xO_y	395.7-396.0	TiN_xO_{1-x}	455.4	[22]in[5]
	N_2	N in $TiN_{x=1}$	396.7-397.0		456.4	[14]in[5]
	N_3	N in contaminant	398.2-398.8	TiN_xO_y	456.9-457.3	[22]in[5]
O1s	O_1	O in TiO_2	529.6-529.8		456.7	[9]in[5]
	O_2	O in TiO_xN_y	531.2-531.5	TiN_{1+x}	456.9	[7]in[5]
	O_3	O in contaminant	532.6-532.9	TiO	454.9	[6]in[5]
C1s	C_1	C in TiC_x	281.7-282.9		455.2	[22]in[5]
	C_2	C in contaminant	284.7	Ti_2O_3	457.0	[22]in[5]
	C_3	C in contaminant	286.1-286.4	TiO_2	458.9	[22]in[5]
	C_4	C in contaminant	288.3-288.6		458.9	[5]

The N1s envelope of our samples is composed of 3 synthetic components (N_1 N_2 N_3). Considering the literature [5], the N_2 component is representative of N in stoichiometric TiN. The origin of the N_1 component found between 395.7 and 396.0 eV can be correlated with the Ti2p component for TiN_xO_y compounds or to a super-stoichiometric nitride. The peak N_3 is related to the N-O bound of the surface contaminants.

Oxygen and carbon are common bulk surface contaminants. The O1s envelope is composed of 3 synthetic components (O_1 O_2 O_3). A major part of oxygen belongs to adsorbed water and C-O type adsorbed impurity corresponds to the peak O_3. The two peaks O_1 and O_2 are related to oxygen chemically bound to Ti. The C1s enveloppe is composed of 4 synthetic components (C_1 C_2 C_3 C_4). All the peak are related to surface contaminant. Quantification was recalculated, according to equation (1), by removing the contaminants contributions ; the results are presented in table 2.

Table 2 :Recalculated elements concentration

$[Xi] = \frac{Xi}{\sum Ti}$ (1)	25kV		10kV		35kV		2h		6h		200C		800C	
	Ti	alloy	Ti	alloy	Ti	alloy	Ti	alloy	Ti	alloy	Ti	alloy	Ti	alloy
$[T_1]$	0.23	0.27	0.27	0.29	0.24	0.24	0.28	0.30	0.23	0.26	0.23	0.24	0.41	0.39
$[T_2]$	0.28	0.27	0.27	0.26	0.26	0.25	0.29	0.28	0.25	0.25	0.33	0.33	0.21	0.22
$[T_3]$	0.49	0.47	0.46	0.45	0.50	0.51	0.43	0.41	0.52	0.49	0.44	0.43	0.38	0.39
$[N_1]$	0.39	0.38	0.39	0.43	0.39	0.44	0.39	0.39	0.40	0.40	0.60	0.75	0.19	0.21
$[N_2]$	0.62	0.50	0.69	0.73	0.66	0.72	0.60	0.67	0.56	0.56	0.42	0.38	0.63	0.66
$[O_1]$	1.38	1.31	0.98	1.07	1.39	1.57	1.07	1.13	1.23	1.48	1.02	1.10	0.84	0.81
$[O_2]$	0.56	0.62	0.36	0.35	0.61	0.85	0.39	0.55	0.54	0.71	0.39	0.48	0.38	0.35

Relationships between the different contribution are obtained by plotting the obtained concentrations versus the different $Ti2p_{3/2}$ contributions. Results indicate that $[O_1]$ and $[O_2]$ grow as $[T_3]$ and $[T_2]$ increases. $[N_1]$ grows as $[T_2]$ increases. On the other hand $[N_2]$ increases as $[T_1]$. These results are in agreement with peak attribution. The oxyde contribution $[T_3]$ increases as increasing treatment time and applied voltage but decreases with increasing temperature contrary to δ-TiN contribution $[T_1]$ which behave in the opposite way. $[T_2]$ decreases with increasing treatment time and temperature but doesn't seem to have a linear behavior according to the applied voltage.

2.4 NRA measurements

Few samples were characterized by NRA. Nitrogen and oxygen concentrations are presented in table 3. Calculated implanted dose were obtained using equation (2)

$$IonicDose = \frac{f * t * \tau * I}{(1+\gamma) * S * e} \quad (2)$$

with f the repetition rate (Hz), t the implantation time (s), τ the pulse duration (s), I the sample current (A), S the electrode surface (cm^2), γ the secondary electron emission coefficient. In order to obtain atomic dose the ionic dose is multiply by a factor 2 by considering that that nitrogen ions are 100% N_2^+ type. Nitrogen fixed rate (ρ) is deduced from the ratio of the concentration obtained by NRA over the calculated implanted dose. The δ-TiN layer thickness equivalent to the detected N concentration was calculated using the cell parameter obtained by XRD (a= 0.423nm). The same kinds of calculus was realized by considering that nitrogen is fully present within ϵ-Ti_2N phase (a= 0.492nm, c= 0.303nm JCPDS). Projected ranges were calculated using SRIM.

table 3 NRA results

Sample	240min 500°C 10kV	240min 500°C 25kV	240min 500°C 35kV	240min 500°C 25kV	360min 500°C 25kV	240min 500°C 25kV	240min 500°C 25kV
$N_{calculated}$: calculated implanted N (10^{15}at.cm^2)	225	1050	1800	1050	1800	1800	1800
Projected Range(Rp)(nm) (SRIM)	10.7	22.9	31.6	22.9	22.9	31.6	31.6
ΔRp (nm) (SRIM)	$\pm$8.9	$\pm$16.6	$\pm$21.5	$\pm$16.6	$\pm$16.6	$\pm$21.5	$\pm$21.5
N_{byNRA} : N concentration(10^{15}at.cm^2)	101	180	245	180	218	245	359
ρ Nitrogen fixed rate ($N_{byNRA}/N_{calculated}$)	0.45	0.17	0.14	0.17	0.12	0.14	0.20
Equivalent δ-TiN thickness (nm)	19	34	47	34	41	47	68
Equivalent ϵ-Ti_2N thickness (nm)	37	66	90	66	80	90	130
oxygen concentration (10^{15}at.cm^2)	145	162	145	162	175	145	110

Effective nitrogen concentration is more than twice lower than calculated dose and slightly increases with increasing applied voltage and increasing treatment duration. The effective oxygen concentration is not negligible but seems to be independent from treatment parameter. As no oxide phases has been detected, the major part of the oxygen is thought to be dispersed within the nitride or the titanium grains. In the case of 10kV applied voltage the amount of oxygen is upper than the amount of implanted nitrogen. Effective nitrogen concentration seems to be higher in the case of titanium samples, but whatever the treatment performed the equivalent thicknesses obtained are lower than one micrometer and remain in the range of Rp $\pm$ δRp.

2.5 Vickers micro hardness measurements

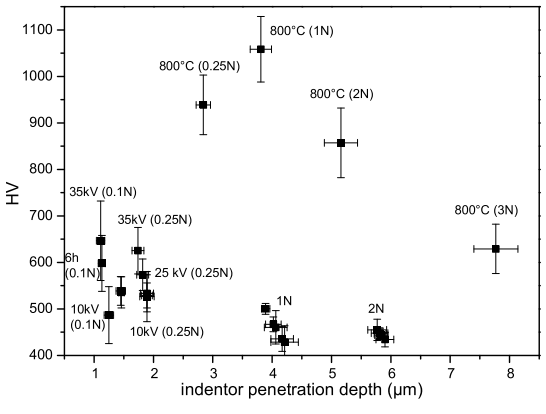

Fig 4 surface micro-hardness of samples treated by PBII

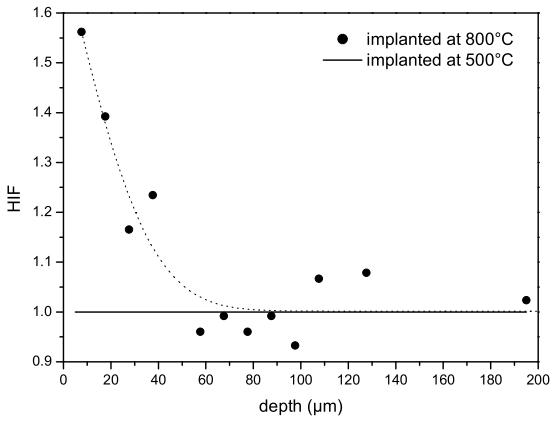

Fig 5 micro-hardness profiles of samples treated by PBII

The hardness of implanted samples were measured at various loads (Fig.4). With the exception of treatment performed at 800°C the values obtained are similar whatever the treatment. Although the data are scattered, it can be seen that the hardness improvement is more pronounced at low loads ; with increasing load it approaches the hardness of the unimplanted samples. Micro-hardness profiles

were realized with 0.25N load on the cross section of the samples treated at 800°C and 500°C for 240 minutes and an applied voltage of 25kV. The figure 5 presents the hardness improvement factor (HIF) calculated as the hardness ratio of an implanted sample to the hardness of the bulk. Flat profile is obtain for the sample treated at 500C. Concerning the 800°C the inward modification of the hardness is effective up to a depth of about 50 ± 10 μm. The curve can be fitted by a erfc function. The diffusion coefficient obtained is 2.7 10^{-10} $\pm$ 1 10^{-10} $cm^2.s{-}1$. According to literature nitrogen diffusion coefficients obtained by conventional plasma nitriding are in the range of 10^{11} $cm^2.s{-}1$ [6].

3. Results ans discussion

The plasma implantation nitriding reaction has been shown to lead to the formation of a surface δ-TiN layer with α-Ti grains underneath. The ϵ-Ti_2N phase is only detected on sample treated for a long time or at a high temperature. Micro hardness profiles performed on cross section may be related with nitrogen diffusion. The flat profile obtained on sample treated at moderate temperature ($\leq$500°C) evidence the slow diffusion process in bulk titanium at this temperature.
For low temperature ($\leq$500°C) stoichiometric nitride layers are obtain by PBII process whereas their formation is not possible using conventional process such as thermo chemical treatments or plasma reactor. Nitride layers formation is then related to the nitrogen implantation in the titanium subsurface. Ions impinging on the surface transfers a substantial amount of energy to the material and leads to the formation of the nitride by activating the chemical reaction. Consequently the thickness of the detected δ-TiN layer is of the order of the projected range. Moreover the fixed nitrogen rate is much lower than 1. In fact, only nitrogen necessary to the nitride formation on the implanted depth is remaining. Surplus nitrogen exo-diffuses or is eliminated by sputtering. At low or moderate temperature the deep nitrogen diffusion process, governed by the presence of impurity [7], remains very slow.
For long treatment time, enough nitrogen may however diffuse to the titanium bulk. It leads to the formation of ϵ-Ti_2N compound under the δ-TiN layer. However, in spite of an increase of treatment time, the δ-TiN layer almost doesn't grow and remains of the order of the projected range. A saturation-like phenomenon is then occurring, as shown by the decrease of the fixed nitrogen rate (ρ)with the implanted dose.
The nitride layer grows with ions energy. This is mainly linked with the longer projected range. Moreover defects created and energy transferred by impinging ions leads to a local activation of the deep nitrogen diffusion process. The detected ϵ-Ti_2N compound on sample treated with high applied voltage (35 kV) may be induced by this last phenomenon. Moreover the surface sputtering yield depends on applied voltage. SRIM calculations show the decrease of the sputtering yield with the applied voltage within the studied range. However nitrogen fixed rate is found to decrease with the applied voltage. Indeed the nitrogen implanted dose is higher and higher compared to the nitrogen quantity necessary to form a δ-TiN layer which thickness remaining of the order of the projected range. The saturation phenomenon is one again evidenced.
At higher temperature (800°C) PBII treatment coupled implantation effects and an efficient deep diffusion process. Mode of diffusion through the δ-TiN layer changes to a lacunar mechanism [7] leading to : a thicker nitride layer, the formation of ϵ-Ti_2N phase and of a few tens of micrometers long zone with nitrogen in solid solution in α-Ti bulk. The presence of ϵ-Ti_2N compound is also favored by the long period of the sample cooling : time consuming diffusion processes of nitrogen coming from δ-TiN layer to the α-Ti bulk can then occur, leading to a flatness of the nitrogen profile. Compared with a conventional plasma treatment, the apparent diffusion coefficient is higher. Indeed, in case of conventional treatment, the presence of a thick nitrogen-rich compounds layer induces a limitation of the inward nitrogen diffusion. The diffusion coefficient in the nitride being significantly lower than in the titanium. Plasma implantation allows the direct incorporation of high concentration of nitrogen in the subsurface. The first step of conventional nitriding plasma treatment, consisting in transforming nitrogen adsorbed on surface to nitrogen in solid solution in δ-TiN, is then skipping over. Moreover the surface nitride becomes super-stoichiometric and acts as an unstable nitrogen storage, which supplies and activates the nitrogen diffusion through the δ-TiN layer. Finally the high

defect density created by nitrogen implantation contributes to an increase of the nitrogen diffusion coefficient through the δ-TiN layer.
The internal compressive stress of the δ-TiN layer induce a cell distorsion of the α-Ti phase. The lower a and the bigger c cell parameters may imply that nitridation of the grains depends on their orientation. It is effective on the grains with (100) plans parallel to the surface : N diffuse in between the basal plane leading to an higher c cell parameter and, by consequence, to a lower a cell parameter. On the other hand nitridation of grains with their plans (001) parallel to the surface is less efficient and these grains sustain the compressive stress due to the δ-TiN growth.
In order to find an optimal treatment, the nitride oxidation should remain low. High applied voltage and long treatment induce a slight increase of the surface temperature. As in this moderate temperature range the oxidation is thermodynamically favored reaction, it is found to increased as shown by XPS. However at temperature high enough to promote the nitride formation, oxydation is reduce to the benefit of nitride formation as it can be concluded for the XPS results on the samples treated at 800°C.

4. Conclusion

Plasma implantations of N_2 were performed in titanium and Ti6Al4V samples. High doses of nitrogen were implanted in a depth of the order of the projected range leading to the formation of a δ-TiN layer. At moderate temperature a saturation-like phenomenon occurs. At high temperature the high defect density created by nitrogen implantation and the high nitrogen concentration in the subsurface contribute to an increase of the nitrogen diffusion coefficient.

Acknowledgments

Thanks are due to Professor J.Perrière (GPS-Université Paris VI et VII) for NRA analysis. XPS experiments has been supported by the GDR "carbone amorphe et nanostructuré".

References

[1] J-P. Bars, E. Etchessahar, J. Debuigne, CNRS RCP n°244 (1976)
[2] J. Conrad, J.L. Radkte, R.A. Dodd, F.J. Worzala, N.C. Tran, J. Appl. Phys. 62 (1987) 4591.
[3] L. Marot, A. Straboni, M. Drouet, Surf. Coat. Technol 142-144 (2001) 384.
[4] L. Marot, M. Drouet, F. Berneau, A. Straboni, Surf. Coat. Technol 156 (2002) 155-158.
[5] I. Bertoti, M. Mohai, J.L. Sullivan, S.O. Saied. Appl Surf. Science 84(1995) 357-371
[6] E. Metin, O. T.Inal, Metal Trans A 20A (1819-1832) 1989
[7] F. Anglezio-Abautret thèse Université de Paris Sud Centre d'Orsay (1990)

Local plasma diagnostics using H_β-profile features

L. Krat'ko, K. Catsalap, E. Ershov-Pavlov

Institute of Molecular and Atomic Physics, National Academy of Sciences, Minsk, Belarus

Balmer lines are widely used at low-temperature plasma diagnostics. Especially H_β line is very popular at electronic density measurements by the line half-width. It is because the line profile can be easy recorded, and good theoretical approximations exist to account for the profile and its principal parameters. However, in emission spectra of plasmas at high electron density the line is very large, and it is rather difficult to select it at the plasma background continuum, which intensity also strongly increases. In these conditions, measurements of the line halfwidth are not practical, and one usually uses the profile approximations by existing models. For inhomogeneous plasmas, the line profiles in the plasma emissivity spectra have to be measured demanding solution of the inversion problem. Measurements of the H_β-profile features in the plasma emission spectra can be a good alternative. This paper is devoted to the problem.

First, H_β-profile characteristics in plasma emissivity spectra have been studied depending on electron density N_e for the region of N_e high (up to 10^{18} cm^{-3}) values poor studied before. A special arc in hydrogen and argon has been used to produce the plasma at pressure up to 30 bars [1]. The arc column is a highly stable plasma volume of axial symmetry, and common Abel inversion procedure has been used to find plasma emissivity. The following H_β-profile characteristics have been studied versus N_e: a distance between its maxima Δ (nm) (peak separation), a dip in the profile centre $D=(\bar{I}_{\max} - I_{\min})/\bar{I}_{\max}$ ($\bar{I}_{\max}=(I^B_{\max}+I^R_{\max})/2$, $I^B_{\max}$ and $I^R_{\max}$ are the profile blue and red maxima, respectively), as well as the profile asymmetry $\delta I=(I^B_{\max} - I^R_{\max})/I^B_{\max}$. Some of the study results are shown in the figure in comparison with the calculation [2, 3] and experiment [4] data. It is seen from the figure, that our results agree with the measurement data [5] in an optical discharge. At $N_e<10^{17}$ cm^{-3} our data are closer to [3] and increase faster at high electron density. General view, the experimental $\Delta(N_e)$ dependence corresponds to that calculated in [2], but measured Δ values are lower.The measured data confirm that a ratio of the peak separation Δ to the H_β halfwidth depends little on N_e up to 10^{18} cm^{-3}. But we have obtained a bit lower ratio values (~0.3). The profile asymmetry δI measured here agrees with other experiment data till $N_e<7\cdot10^{17}$ cm^{-3}. At higher density our δI values increase with N_e stronger. We have also observed different dip D behavior in emission spectra of Ar and H_2 plasmas having reduced masses of the perturbing particles $\mu\approx1$ and $\mu=0.5$, respectively.

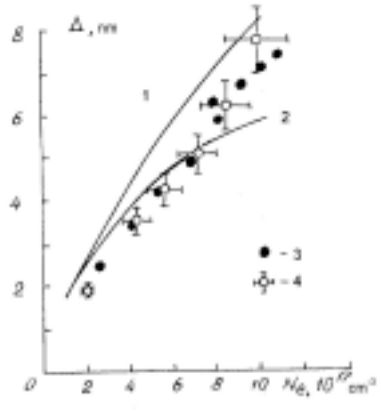

Peak separation Δ (nm) in H_β-profile vs N_e calculated [2] (1), [3] (2), and measured [4] (3). Points 4 - our data.

Generally, we have found Δ value to be the most promising for the plasma diagnostics at high electron density, where H_β is very broad. First, because of this value is much more measurable in this conditions in comparison with other profile characteristics. So, one can easily measure Δ, and determine N_e, e.g., using Δ ratio to the line halfwidth. Secondly, due to a weak dependence on N_e of the ratio, one can suppose it will be applicable also at diagnostics by emission spectra of inhomogeneous plasmas. We have made a numerical simulation of the H_β emission by inhomogeneous plasmas having different temperature distributions. A numerical code for the radiation transfer has been presented earlier together with the temperature distribution approach [5]. The results show the H_β peak separation in the directly measured plasma emission spectra can be used for the plasma diagnostics.

[1] E. Ershov-Pavlov, L. Krat'ko, N. Chubrik, V. Shimanovich – Contrib. Plasma Phys. **29**, 299 (1989).
[2] J. Seidel - Z. Naturforschung. **32a**, 1195 (1977).
[3] H. Griem. "Spectral Line Broadening by Plasmas". Academic Press, N-Y, London (1974).
[4] C. Carlhoff, E. Krametz, J. Schäfer et al. - Proc. ICPIG XVII. Budapest (1985).
[5] E. Ershov-Pavlov, K. Catsalap, K. Stepanov – J. High Temp. Mat. Process. **6**, 239 (2002).

Plasma Surface Modified Polystyrene Biochip for Enhanced Biological Coupling

Xin Gao[1], Ch. Hollenstein[2], Manfred Schawaller[3], and Hans-Jörg Mathieu[1,*]

[1] *LMCH, Swiss Federal Institute of Technology Lausanne (EPFL), CH-1015 Lausanne, Switzerland*
[2] *CRPP, Swiss Federal Institute of Technology Lausanne (EPFL), CH-1015 Lausanne, Switzerland*
[3] *DiaMed, Applied Diagnostic Systems AG, 1785 Cressier, Switzerland*
[*] *email: hansjoerg.mathieu@EPFLch*

Abstract

N_2/H_2 and NH_3/H_2 RF plasmas are used to activate the polystyrene (PS) surface. The capacitively coupled RF plasmas applied for the surface modifications have been characterised by commercial plasma diagnostic methods including ion flux probe, RF power sensor, and mass spectrometer. In particular the ion species and the ion energy have been measured as well as the ion dose impinging onto the polymer surface. The surface modifications are characterized with surface sensitive X-ray Photoelectron Spectroscopy (XPS).

Introduction

Polystyrene (PS) is a popular substrate for disposable ware in medical diagnostic, primarily due to its optical transparency, durability, low cost, and good mouldability.[1] Non-modified polystyrene may cause non-specific adsorption. Therefore it is customary to modify it with hydrophilic polymers.[2] Many polymers such as poly(ethylene glycol) and dextran have been studied for their usefulness in producing pharmacologically active complexes with proteins or drugs. PS surfaces have been successfully modified by high-energy irradiation: γ and UV radiation,[3, 4] plasma treatment[1, 5] and glow discharge plasma.[6]

Plasma surface treatments are potentially very useful for the covalent incorporation into polymer surfaces of extraneous reactive groups suitable for participation in further, conventional chemical reactions at the surface.[7] It is possible to change continuously the chemical composition and properties such as wettability, metal adhesion, dryability, lubricity and biocompatibility of materials surfaces.[8] The plasma modification can be carried out in the presence of specific gases, such as O_2, Ar, He, NH_3, N_2, and H_2. This results in the generation of active species, which can activate and modify the material depending on the nature of the gaseous medium.

The aim of this work is to prepare chemically reactive yet specific PS surfaces for subsequent high-density bio-immobilization such as protein molecules. These modified surfaces are potentially efficient substrates of medical diagnostic tools for use in a proprietary ADS fluorescence reader.[9] The surface modification strategy is shown in Figure 1. In this paper we present the plasma activation and correlated to XPS surface characterization with XPS. Subsequent functionalizations with proteins such as Streptavidin and Neutravidin, and the application study by optical fluorescence measurements will be reported later.

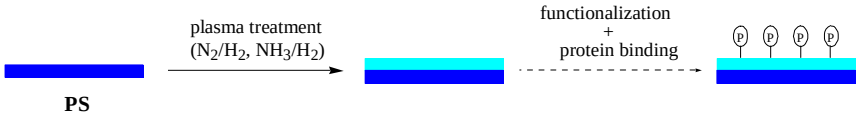

Fig.1 Functionalization (schematic) of a polystyrene chip

Experimental

Polystyrene chips were obtained by injection molding of Polystyrol (BASF). Plasma treatment of PS chips was carried out in a capacitively coupled rf reactor operating at 13.6 MHz. The reactor consisted of two cylindrical electrodes of 13 cm diameter and 4.3 cm apart in a cubic vacuum vessel. The upper electrode and the reactor walls were grounded. The PS chip was placed on the grounded electrode and the system was evacuated to 10^{-6} mbar. The needed gas mixture was introduced into the chamber at a flow rate of 60 sccm and the plasma was operated at a gas pressure of 0.4 mbar at a power of 60 W. The sample exposure time was 3 minutes. The PS chip was directly transferred after exposure for XPS analysis.

For plasma diagnostics only commercial equipment has been used in order to demonstrate that basic plasma diagnostics is now commercially available and to show its necessity for an advanced understanding of the surface modification by plasmas and the industrialisation of the processes. A Scientific System ion flux probe (IFT) has been applied to measure the ion flux on the grounded electrode. A Balzers PPM 422 mass spectrometer system has been used to measure the ion composition and the energy of the impinging ions. Both measuring systems have been incorporated into the grounded electrode. This experimental arrangement permits to measure the characteristics of the ion bombardment at the same place as the treated substrate. Therefore correlations and comparison between plasma parameters and the results from surface analysis can be made.

XPS analysis was performed using an imaging Kratos Axis Ultra X-ray photoelectron spectrometer equipped with a conventional hemispherical analyser. The X-ray source employed was a monochromatized Al Kα (1486.6 eV) source operated at 150 W. Data acquisition was performed under UHV (10^{-9} mbar) conditions. Analysis area was 0.21 mm^2 (300 μm × 700 μm) using a take-off angle of 70° relative to the surface normal. The pass energies were 80 eV and 20 eV for wide scan and high-resolution elemental scans, respectively. The operating software, Vision2, corrects for the transmission function. Charge compensation was performed with a self-compensating device (Kratos patent) using field emitted low energy electrons (0.1 eV) to adjust the main C-C component to 285 eV.[10] The data reduction (atomic concentration, shifting, curve fitting, etc) was performed with CasaXPS Version 2.1.9 software.

Results and Discussion

The electrical asymmetry of the plasma reactor leads to maximum ion energies in the order of 15-20 eV. Under these conditions the ion energy does change only weakly with RF power and other process parameters. Therefore the maximum energy of the bombarding ions for all the cases studied here was below 20 eV (data not shown). However, the energy spectrum depends on the properties of the considered ion. In the case of ions undergoing charge exchange reaction a broad energy spectrum was measured whereas for ions without these reactions the ion energy was peak around the maximum energy.

Table 1 shows the influence of gas mixtures on ion flux and ion doses for various N_2/H_2 and NH_3/H_2 plasmas.

Table 1. Parameters for plasma activations[a]

Prim. Gas / Sec. Gas (% / %)	Ion Flux (mA/cm^2)	Ion dose ($Ions/cm^2$)
100 NH_3 / --	26	2.9E+19
92 NH_3 / 8 H_2	26	3.0E+19
95 N_2 / 5 H_2	87	9.8E+19
90 N_2 / 10 H_2	95	1.1E+20
70 N_2 / 30 H_2	101	1.1E+20

[a] Activation conditions: 60 W, 0.4 mbar, exposure of 3 minutes.

Figure 2 shows the effect of hydrogen dilution on ion compositions when nitrogen is used as a primary gas. In the dilution range from 0-25 % N_2^+, N_2H^+, and H_x^+ are the dominating ions. For higher hydrogen dilutions the measured ion composition is not significantly affected.

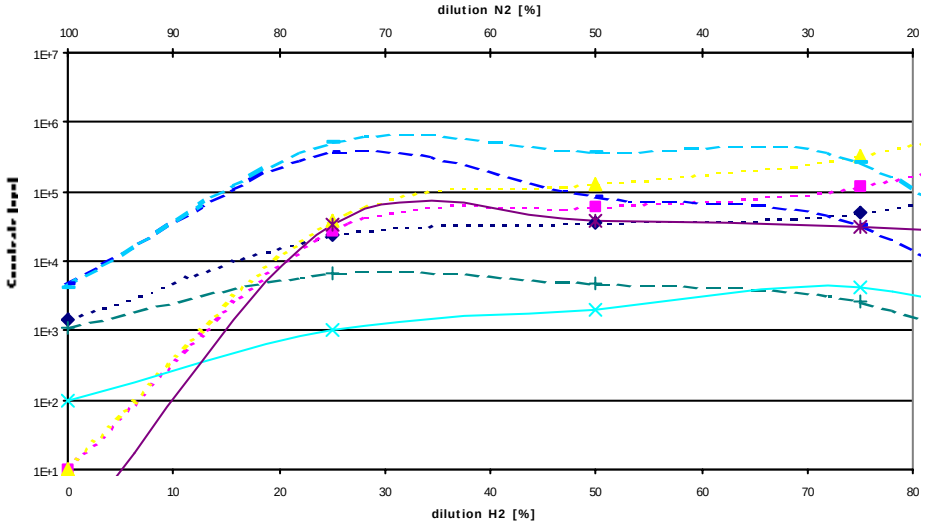

Figure 2. Effect of H_2 admixture on the ion compositions for N_2/H_2 plasmas.
H^+, H_2^+, H_3^+; N^+, N_2^+, N_2H^+; NH_3^+, NH_4^+.

The effect of hydrogen dilution on ion compositions was also studied for ammonium used as a primary gas. The result is shown in Figure 3. One observes that the admixture of hydrogen doesn't affect the ion composition: NH_x^+ ions are always by far the most abounded ion in these plasmas.

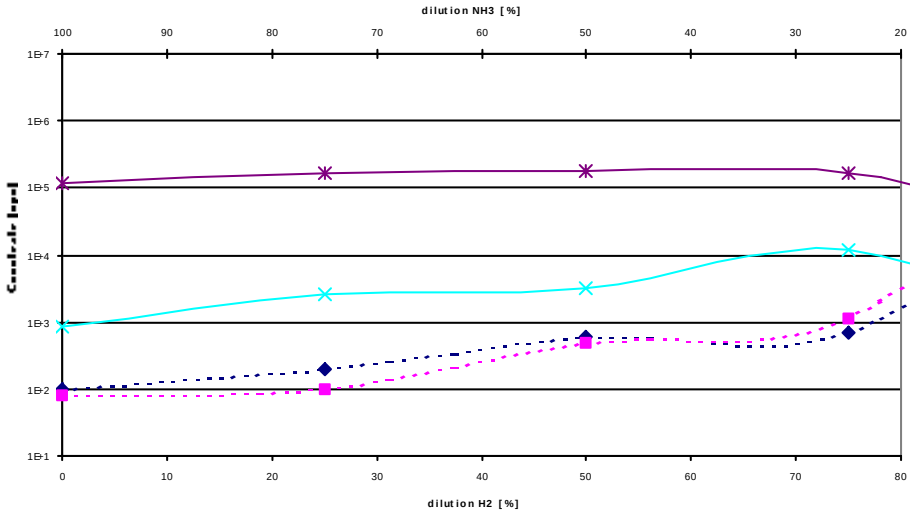

Figure 3. Effect of H_2 admixture on the ion compositions for NH_3 plasma.
H^+, H_2^+; NH_3^+, NH_4^+.

PS samples are treated with N_2/H_2 (95/5, 90/10, and 70/30 respectively), NH_3/H_2 (92/8) and pure NH_3 plasmas. The efficiency of the plasma activation on PS is checked by nitrogen concentration from XPS analysis. These results are summarized in Table 2. Inspection reveals that hydrogen dilution into a nitrogen plasma has no direct effect on the modification efficiency. According to the results concerning the plasma composition as a function of the hydrogen dilution in N_2 plasma (Figure 2), N_2H^+ ions are the most abundant ion. In the case of hydrogen diluted ammonia plasma NH_x^+ ions are dominating. XPS analysis showed that in these three considered N_2/H_2 plasma cases, similar surface modification efficiencies are observed. Under the present plasma conditions, NH_3 or NH_3/H_2 plasmas are more efficient than N_2/H_2 plasma in providing a nitrogen-amino surface. C1s narrow scan spectrum of PS treated with a NH_3 plasma is shown in Figure 4. Spectra for other samples listed in Table 2 give similar results. Aromatic and aliphatic carbons from PS are observed between 284.7-285.3 eV. As expected, C-N is observed at 286±0.1 eV. The detected oxygen results from the exposure of PS surface to the air when the plasma chamber is opened after the plasma treatment.

Table 2. Nitrogen concentrations of plasma activated PS[a]

Prim. Gas / Sec. Gas (% / %)	at % N
95 N_2 / 5 H_2	11
90 N_2 / 10 H_2	14
70 N_2 / 30 H_2	11
100 NH_3 / --	19
92 NH_3 / 8 H_2	19

[a] Activation conditions: 60 W, 0.4 mbar, exposure of 3 minutes.
error: ± 3 at %

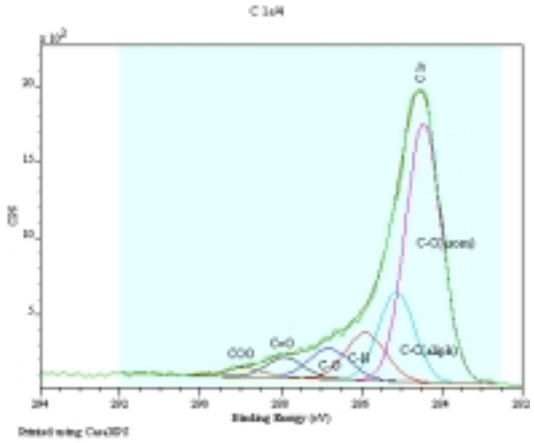

Figure 4. XPS narrow scan spectrum of PS treated with plasma by using pure NH_3.
(Take-off angle 70 degree from surface normal)

Although the ion doses of N_2/H_2 plasmas are higher than for the NH_3/H_2 plasma (Table 1), their efficiency to produce nitrogen-containing functional groups at the surface is lower, i.e. that the NH_3 plasma treatment is more effective. Comparing Figure 2 with Table 2 for N_2/H_2 plasmas one notices that the influence of the variation of H_2 is small: although the admixture of H_2 influences strongly the plasma composition in the range from 5-30 %; the nitrogen concentration found at the PS surface remains constant within experimental precision as shown in Table 2. A monolayer of PS contains approximately 10^{15} molecules/cm^2. Compared to the doses values given in Table 2 this means that 10^4-10^5 ions/molecule are needed for nitrogen activation on the PS surface.[11]

Conclusions

The ion energy of the bombarding species is found to be 15-20 eV and the necessary ion density for PS surface activation is 10^4-10^5 ions/molecule per cm^2. H_2 admixture to N_2 or to NH_3 has only small influences on ion composition and nitrogen concentrations at the surface. However a NH_3 plasma is almost two times more efficient than a N_2/H_2 plasma to create active nitrogen-containing sites.

Acknowledgements

The authors would like to acknowledge Nicolas Xanthopoulos for assistance with the XPS analysis. The project was financed on a grant no 6142.MTS of the Commission for Technology and Innovation CTI, Bern Switzerland.

Reference

[1] S. B. Idage, S. Badrinarayanan. Langmuir **14** (1998) 2780-2785.
[2] L. Bromberg, L. Salvati, Jr. Bioconjugate Chem **10** (1999) 678-686.
[3] EC. Onyiriuka. *J Appl Polym Sci*. **47** (1993) 2187.
[4] EC Onyiriuka, LS Hersh, W. Hertl. *J Colloid Interface*. **144** (1991) 98.
[5] D. Keller, K. Schroder, B. Husen, A. Ohl. *Polym Prepr Am Chem Soc Div Polym Chem*. **38** (1997) 1043.
[6] Y. Tamada, Y. Ikada. *Polymer*. **34** (1993) 2208.
[7] T. R. Gengenbach, X. M. Xie, R. C. Chatelier, H. J. Griesser. J. Adhesion Sci. Technol **8** (1994) 305-328.
[8] P. K. Chu, J. Y. Chen, L. P. Wang, N. Huang. Materials Science and Engineering R **36** (2002) 143-206.
[9] patent no. WO 01/14859 A1, EP 1 079 226 A1.
[10] G. Beamson, D. Briggs. *High Resolution XPS of Organic Polymers. The Scienta ESCA300 Database*. John Wiley & Sons Ltd, England, 1992.
[11] X. Gao, Ch. Hollenstein, M. Schawaller, H. J. Mathieu, to be submitted.

Modeling of non-equilibrium DC and surface-wave discharges in atmospheric-pressure air and its mixtures with hydrocarbons

M. S. Benilov[1], G. V. Naidis[1,2]

[1] *Departamento de Física, Universidade da Madeira, Largo do Municipio, 9000 Funchal, Portugal*
[2] *Institute for High Temperatures, Russian Academy of Sciences, Moscow 127412, Russia*

Abstract
Models of stationary direct-current and surface-wave discharges in atmospheric-pressure air and its mixtures with hydrocarbons are developed that account for deviation of plasma state from the local thermodynamic equilibrium. Results of discharge simulation are presented for a wide range of external conditions. Calculated plasma parameters agree with available experimental data.

1. Introduction

Simulation of discharges in molecular gases at pressures of the order of one atmosphere is usually based on the approximation of local thermodynamic equilibrium (LTE). This approach is justified if the gas temperature in the discharge core is high enough (typically higher than 4000 K), which is the case in DC discharges in atmospheric-pressure air if the electric current is higher than approximately 0.1 A. Recently, considerable attention has been paid in the literature to experimental investigation of atmospheric-pressure DC discharges in the current range 0.01-0.1 A (e.g., [1-6]), in which non-equilibrium effects become important. In this work, a model of a low-current DC and surface-wave discharges in air and its mixtures with hydrocarbon fuels is developed on the basis of a solution of kinetic equations for the densities of plasma species. (Note that discharges in fuel-air mixtures are considered as a perspective tool for production of hydrogen.) Calculation results are presented for the case of a wall-stabilized discharge in a cylindrical tube.

2. The model

Among various non-equilibrium effects that come into play at decrease of the gas temperature inside the discharge core, the most essential is the deviation of the electron number density n_e from its LTE value, caused by the change of dominating ionization mechanism. While at high gas temperatures the major source of electrons is ionization in collisions between heavy particles (in air, the associative ionization in collisions of N and O atoms), at low gas temperatures the direct ionization of molecules by electron impact dominates. The rate constant of the latter process is governed by the value of the electron temperature T_e, depending both on T and on the reduced electric field E/n (here E is the electric field and n is the gas number density).
The distribution of the gas temperature along the radial coordinate r is governed by the Elenbaas-Heller equation

$$\frac{1}{r}\frac{d}{dr}\left(\chi r \frac{dT}{dr}\right) + \sigma E^2 = 0, \qquad (1)$$

where χ and σ are the thermal and electrical conductivity coefficients. Since the plasma temperature does not exceed 6000 K under the conditions considered, radiation effects are minor and can be neglected. The boundary conditions for equation (1) are as follows:

$$\frac{dT}{dr} = 0 \text{ at } r = 0, \quad T = T_W \text{ at } r = R. \qquad (2)$$

Here T_W is the wall temperature, R is the tube radius.
Knowledge of the thermal and electrical conductivity coefficients χ and σ is required for a solution of equation (1). The thermal conductivity coefficient is not affected strongly by non-LTE effects, therefore the LTE χ values are used in the present calculations. An effect of deviations from LTE on the electrical conductivity coefficient σ is much more substantial, because the value of σ is proportional to the electron number density n_e. In a wide range of discharge conditions the radial distribution of n_e may be calculated,

with high enough accuracy, using the local approximation (neglecting diffusion term). The local balance equation for electrons with account of both ionization channels mentioned above is

$$K_i n_e n + \beta_{ei}(n_{e0}^2 - n_e^2) = 0 \,, \tag{3}$$

where K_i and β_{ei} are the rate constants of direct ionization and electron-ion recombination, n_{e0} is the LTE value of n_e. The rate constant K_i, depending on E/n, T, and on the mixture composition, is obtained by solution of the Boltzmann equation for the electron energy distribution function.
The system of equations for DC discharge includes also the Ohm's law

$$I = 2\pi E \int_0^R \sigma(r) r dr \,, \tag{4}$$

where I is the electric current.
Calculation of discharges sustained by travelling electromagnetic waves is based on a simplified approach in the framework of which the wave equation (for axially and radially uniform plasma with given parameters) and discharge equations (at a given value of the maintenance electric field) are treated separately with a subsequent matching of results. In this approach the plasma parameters in any plane z are determined by the local value of the power loss per unit length, $L(z)$. The latter is related with the flux of electromagnetic power $P(z)$ by the equation of electromagnetic energy balance, $L(z) = - dP/dz$. The distribution of the power flux along z axis is described by the equation

$$\frac{dP}{dz} = -2\alpha P(z) \,, \tag{5}$$

where α is the attenuation coefficient. The value of α is obtained by solution of the system of equations describing propagation of the electromagnetic wave along a plasma filament. For weakly non-uniform plasma, this system may be solved in the local uniformity approximation (e.g., [7]). That is, the value of α is related to a given position z through the plasma parameters in z plane and, hence, through the local value of $L(z)$. The distribution $P(z)$ is governed by equation (5) with the initial condition of a given power flux, $P = P_0$ at $z = 0$ (at the beginning of the discharge). The value of P decreases with z, due to absorption of the electromagnetic energy by the discharge plasma, and vanishes at some point $z = l$ (at the discharge end). The discharge model, that includes equations (1)-(3), is the same as for DC discharges. Conditions are considered when skin effect is small, and the electric field inside the plasma filament is nearly independent on the radial position. The value of E in equation (1) is related with the power losses per unit length L as

$$L = 2\pi E^2 \int_0^R \sigma(r) r dr \,. \tag{6}$$

The discharge model allows one to calculate radial distributions of plasma parameters in the cross section z as functions of the local value $L(z)$. At known radial distribution of n_e, the attenuation coefficient α can be expressed as a function of L.

3. Results of simulation

Modelling has been performed of DC discharges in cooled tubes (at T_w = 300 K) with radii R = 1-10 mm, for the current range 0.005-1 A. Figure 1 shows axial values of the gas temperature T versus the discharge current in atmospheric-pressure air. The gas temperature at low currents is nearly independent of the tube radius. In figure 2 the relation is shown between the axial values of n_e and of the gas temperature (the latter being dependent on the current, as shown in figure 1). The equilibrium, at the gas temperature, values of n_e are also shown. Deviations from equilibrium manifest themselves at low enough gas temperatures at the axis. The larger is the tube radius, the smaller is the value of $T(0)$ corresponding to the boundary between the LTE and non-LTE discharge regimes.

The model described above has been developed for discharges in tubes. In experiments [1-6], DC discharges have been studied in atmospheric-pressure air with free boundaries (without walls): low-current arc discharges between parallel electrodes, with liquid [1,6], plasma [3] or metal [5] cathodes, and gliding arcs [2,4]. The heat losses were due to convection under conditions of these experiments. Therefore, a direct comparison of the simulation results with the experimental data is not possible. Still, some common features exist between discharges stabilised by walls and those stabilised by convection. In both cases the discharge volume includes two regions: a central conducting zone (a core) and an outer region. In both cases the heat transfer from the discharge core to the outer region is due to thermal conduction, and the central part of the discharge may be described by means of the above model. Thus, with a proper choice of the radius of conducting zone, the model is applicable to discharges stabilised by convection. The measured and calculated values of the electric field versus the current are given in figure 3. Simulation results obtained using the equilibrium values of the electrical conductivity are also shown. It is seen that the measured values of E agree with the results of non-LTE calculations.

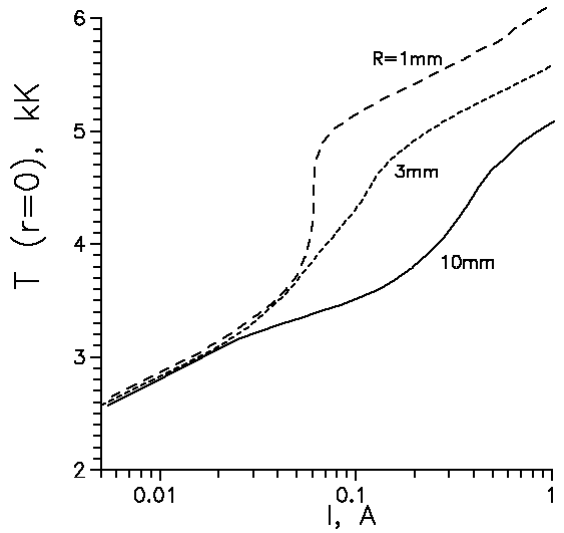

Figure 1. The gas temperature at the axis versus the current in DC discharges in air.

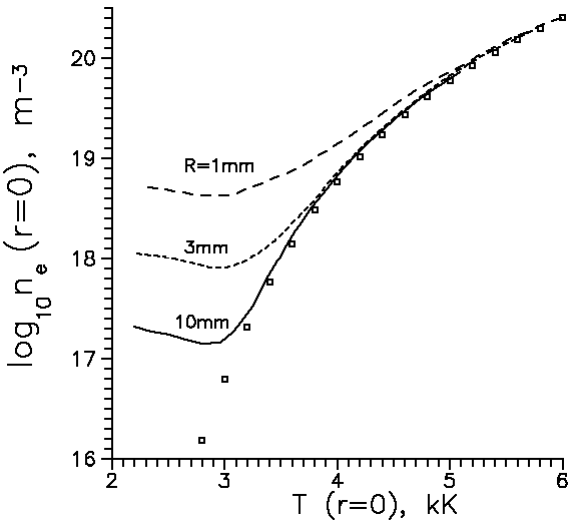

Figure 2. The electron number density at the axis versus the gas temperature at the axis of DC discharges in air. Points: equilibrium n_e values.

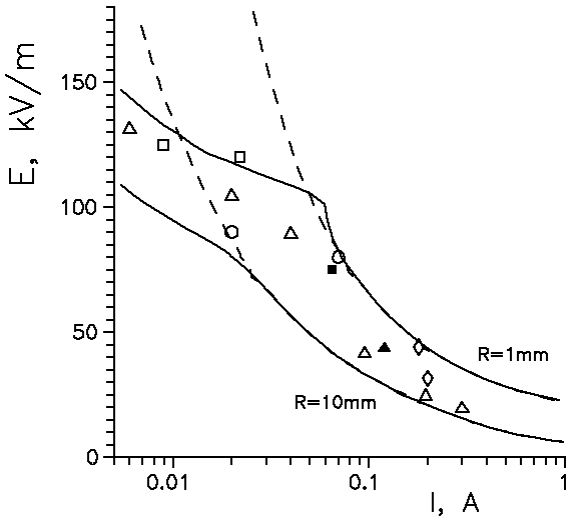

Figure 3. The electric field versus the current in DC discharges in air.
Experimental data: ○ [1], ◊ [2], □ [3], Δ [4], ▲ [5], ■ [6];
simulations: solid lines – non-LTE, dashed lines – LTE.

In figure 4 the electric field is given versus the current in discharges in atmospheric-pressure mixture of octane with air C_8H_{18}:O_2:N_2=1:4:15 (the mixture composition close to optimal for production of hydrogen), for two values of the tube radius R. Results obtained using both non-LTE (solid lines) and LTE (dashed lines) σ values are shown. It is seen that non-LTE effects become substantial at currents lower than 0.1 A. In comparison with air (figure 3), in fuel-air mixtures the transition between LTE and non-LTE regimes is sharper.

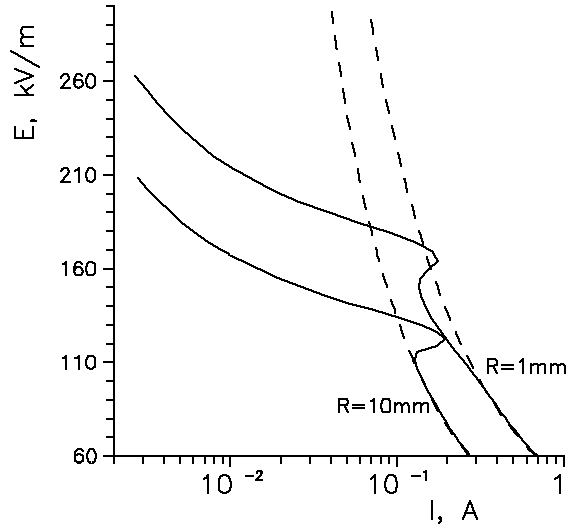

Figure 4. The electric field in arc discharge in the mixture C_8H_{18}:O_2:N_2=1:4:15 versus the current

Distributions of the axial value of the gas temperature $T_{ax} = T$ (r=0) along the surface-wave discharge in air in a tube with radius 10 mm are given in figure 5. The axial coordinate $x = l - z$ is counted from the discharge end, that is, the wave propagates from the right to the left. (Note that the increase of the total absorbed power P_0 results only in elongation of the discharge and does not influence the distributions of plasma parameters

along the discharge axis, as functions of x.) The temperature has a minimum at the discharge end and increases monotonously with x. The values of T_{ax} grow with increase of the wave frequency.

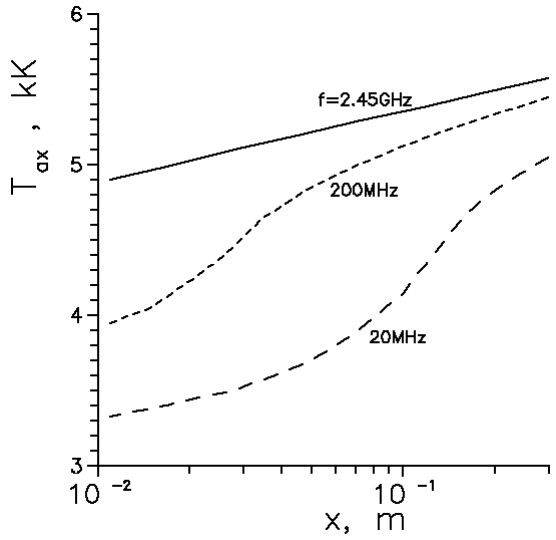

Figure 5. The distribution of the gas temperature at the axis along the surface-wave discharge in air at the tube radius R = 10 mm.

In figure 6 the values are given of the surface-wave discharge length l versus the total power P_0 absorbed by the discharge in a tube with radius R = 10 mm, in atmospheric-pressure air, nitrogen and mixture C_8H_{18}:O_2:N_2=1:4:15. In the same figure experimental data [8] are shown. It is seen that, at given P_0, the discharge length in fuel-air mixture is about three times smaller than in air.

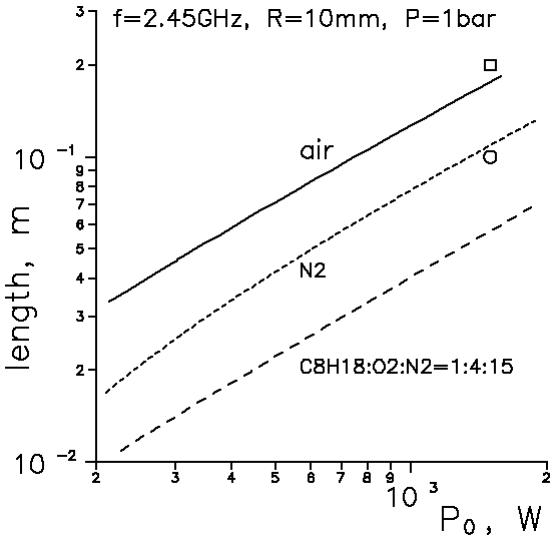

Figure 6. The surface-wave discharge length versus the power.
Points – experimental data [8] for air (square) and N_2 (circle)

Distributions of the axial value of the gas temperature along the discharge are given in figure 7, for the same conditions as in figure 6. The temperature has a minimum at the discharge end and increases monotonously with *x*. The temperature in fuel-air mixture is about 1000 K higher than in air. Calculated decrease of temperature in nitrogen-oxygen mixture (air) in comparison with pure nitrogen agrees with measurements [9].

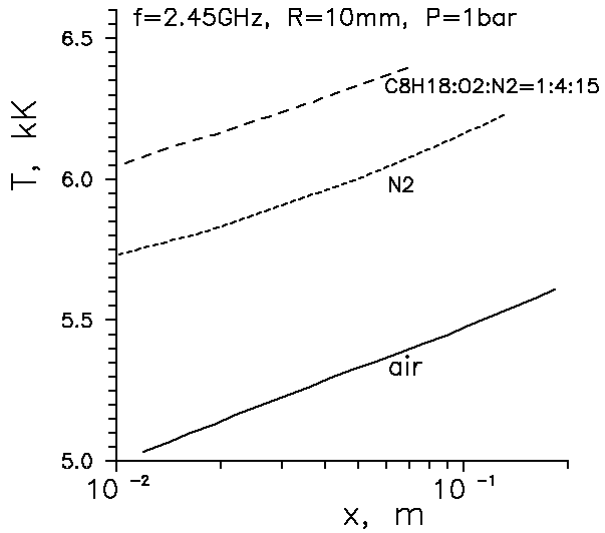

Figure 7. The gas temperature at the axis of surface-wave discharge versus *x*.

4. Conclusion

Departures of the electron density from the LTE take place at gas temperatures in the discharge core lower than 3000-4000 K. In DC discharges in atmospheric-pressure air and its mixtures with hydrocarbons such low temperatures correspond to currents lower than about 0.1 A. In surface-wave discharges the non-LTE effects may be substantial at wave frequencies lower than several tens of MHz. In microwave frequency range the discharge parameters may be calculated in the framework of LTE approximation.

Acknowledgment

The work was supported by the EC through the project N° ENK5-CT-2000-00346.

References

[1] T. Cserfalvi, P. Mezei, P. Apai - J. Phys .D: Appl. Phys. **26**, 2184 (1993).
[2] V. Dalaine, J.M. Cormier, S. Pellerin, P. Lefaucheux - J. Appl. Phys. **84**, 1215 (1998).
[3] R.H. Stark, K.H. Schoenbach - Appl. Phys. Lett. **74**, 3770 (1999).
[4] O. Mutaf-Yardimci, A.V. Saveliev, A.A. Fridman, L.A. Kennedy - J. Appl. Phys. **87**, 1632 (2000).
[5] P. Mezei, T. Cserfalvi, M. Janossy - J. Phys. D: Appl. Phys. **34**, 1914 (2001).
[6] P. Andre, Yu. Barinov, G. Faure, V. Kaplan, A. Lefort, S. Shkol′nik, D. Vacher - J. Phys. D: Appl. Phys. **34**, 3456 (2001).
[7] Z. Zakrzewski, M. Moisan - Plasma Sources Sci. Technol. **4**, 379 (1995).
[8] P.P. Woskov, K. Hadidi - IEEE Trans. Plasma Sci. **30**, 156 (2002).
[9] K. Hadidi, P.P. Woskov, G.J. Flores, K. Green, P. Thomas - Jpn. J. Appl. Phys. **38**, 4595 (1999).

Absolute total electron impact ionization cross sections of CCl_xF_{4-x} (x=1-4). Experimental versus theoretical determinations.

Roberto Martínez[1], Borja Sierra[2], Fernando Castaño[2]

[1]*Department of Physical Chemistry. Facultad de Farmacia. University of the Basque Country. Vitoria. Spain*

[2]*Department of PhysicalChemistry. Facultad de Ciencias. University of the Basque Country. Bilbao. Spain*

Abstract

A set of experimental electron-impact total ionization cross sections (TICSs, ICSs) of CCl_4, CCl_3F, CCl_2F_2 and $CClF_3$ chlorofluoromethanes obtained with a linear double focusing time-of-flight mass spectrometer, have been compared with the *ab initio* and (semi)empirical based ICS available methods: binary-encounter-Bethe method (BEB), the Deutsch-Märk formalism (DM) and the modified additivity rule (MAR).

1. Introduction

The knowledge of the electron-impact ionization cross sections (ICS) of chlorofluoromethanes in the energy range 0-100 eV is crucial for the modelling and optimization of industrial plasmas [1]. Chlorofluoromethane molecules are widely employed to create reactive etching species in semiconductor processing plamas and in other plasmas.

In the studied energy range of electron energies most of the precursor excited electronic states and dissociative ionization channels are accessible, and the cross section curves reach their maxima. The production of highly reactive fragments and ions create efficient systems able to produce chemical attack on low reactive surfaces.

Electron impact dissociative ionization of halogen containing molecules is of importance in many applications, inasmuch as such interactions are fundamentals in low-temperature non-equilibrium production plasmas [2]. Release of halogen atoms and/or halogenated ions and radicals from these molecules make them useful in plasma vapour deposition, high quality thin films, etching of semiconductor structures, etc. Precise knowledge of ICS and other related parameters are required in the modelling of these plasma processes. The efforts to develop efficient and easily applicable theories to calculate ICS of molecules have grown considerably during the last years. However theoretical progresses are more evident in the low energy region of the electron-molecule interaction, where rotational and/or vibrational excitation are produced.

This work presents computational ICS carried out by a variety of methods and the results are compared with our experimental measurements on chlorofluoromethanes: $CClF_3$, CCl_2F_2, CCl_3F and CCl_4.

2. Experimental

Experimental ICS measurements were carried out in a time-of-flight mass spectrometer. A pulsed supersonic molecular beam of the selected chlorofluoromethane collides at a right angle with a pulsed electron beam (0.5 eV full width at half maximum, at 10 μA electron intensity and energy up to 100 eV) in the ionization region. 300 ns after the collisions are over, a negative voltage pulse is applied to the extraction grid, creating and electric field that drives the ions onto the 86.5 cm long flight tube, perpendicular to both molecular and electron beams, where a set of *x-y* plates focuses the ions onto a three-stage microchannel plate (MCP).

Reference and/or target gases were stored in a stainless steel cylinder at a pressure of about 3 bar (1% accuracy). The supersonic expansion beam was skimmed and further crossed with a well-characterized energy electron beam. Ions resulting from the collisions were converted to absolute scale by comparison with the ICS of close-in-mass reference gases (Ar or He). The absolute partial ICS for the CF^+ ion, chosen as an illustration of the method is given by:

$$\sigma_{CF^+}(E) = \frac{I_{CF^+} . n_{Ar}}{I_{Ar^+} . n_{CCl_xF_{4-x}}} . \sigma_{Ar^+}(E) \qquad (1)$$

where I_{CF^+} and I_{Ar^+} are the detector currents for CF^+ and Ar^+ ions, and n_{Ar}, $n_{CCl_xF_{4-x}}$ the gas density of the reference and precursor gas.
Total ionization cross sections (counting) were determined by adding up the partial ICS of all ions observed [3].

3. Total ionization cross sections

Electron-impact ICS have been computed by the binary-encounter-Bethe method (BEB) [4], the Deutsch-Märk (DM) formalism [5] and the modified additivity rule (MAR) [6]. Strictly speaking these methods are the most accepted in ICS determinations. However theoretical and experimental ICS agreement depends on the atom or molecule, and measurements on different molecule families are useful to clarify these disagreements.

BEB method

This method requires molecular orbital energies (B), and average kinetic energy (U) knowledge, and the ICS as a function of the kinetic energy of the incident electron (T) is computed as

$$\sigma_{MO}(T) = \frac{S}{t + \frac{(u+1)}{n}}\left[\frac{\ln t}{2}\left(1-\frac{1}{t^2}\right)+1-\frac{1}{t}-\frac{\ln t}{t+1}\right] \qquad (2)$$

with t=T/B; u=U/B and $S=4\pi a_o^2 N(R/B)^2$; a_o is the Bohr radius, R the Rydberg energy, N the occupation number, and n is an empirical parameter to be applied for molecules that contain atomic like orbitals with quantum number n≥3.

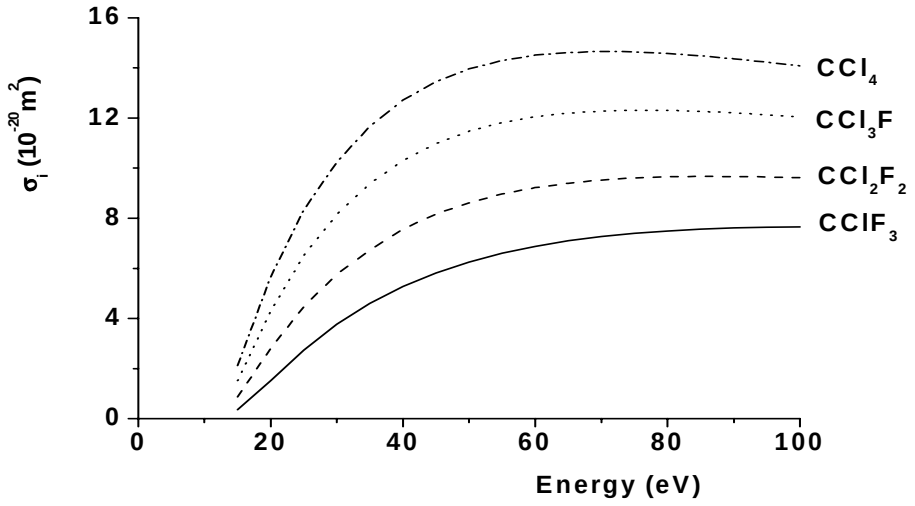

Figure 1. Total ICS computed by the BEB method for CCl_xF_{4-x} molecules

DM formalism

The Deutsch-Märk formalism is an extension to molecular species of earlier models for the electron-impact ionization of ground state atoms. This method computes ICS as:

$$\sigma_{MO}(T) = \sum_j g_j \pi r_j^2 \xi_j f(u) \qquad (3)$$

where g_j are weighting factors which value is atomic orbital dependent, r_j the mean atomic radius of each atomic orbital and ξ_j the atomic orbital contribution determined by a population analysis (for example by the Mulliken method). The function f(u) describes the energy dependence of the ionisation cross section and is related with both electron kinetic energy and ionization energy, its explicit form has different values for s-, p-d-, and f-electrons.

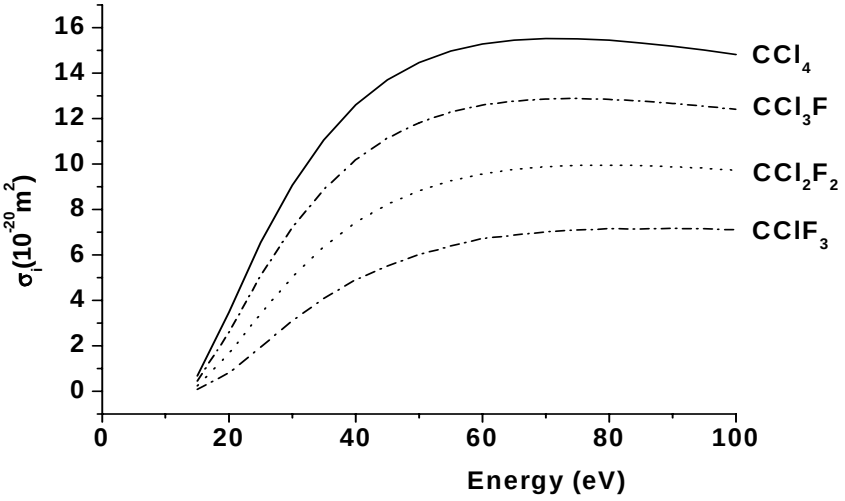

Figure 2. Total ICS computed by the DM method for CCl_xF_{4-x} molecules

MAR approach

The molecular additivity rule is a semiempirical method. Total ICS is given by the sum of weighted ionization cross sections of the different atoms of the molecule:

$$\sigma(CCl_xF_y) = f_C\sigma_C^+ + xf_{Cl}\sigma_{Cl}^+ + yf_F\sigma_F^+ \quad (4)$$

where f_C, f_{Cl} and f_F are parameters related to the number of atoms, the atomic radii and the number of electrons.

Molecule	$\mathbf{f_C}$	$\mathbf{f_F}$	$\mathbf{f_{Cl}}$
CCl_4	0.12	-	3.89
CCl_3F	0.16	0.26	5.17
CCl_2F_2	0.16	1.32	1.77
$CClF_3$	0.16	4.43	0.42

Table 1. MAR coefficients for ICS determination of chlorofluoromethanes

Experimental results

Figure 3 shows experimental results of total ICS for CCl_2F_2, $CClF_3$ and CCl_4 molecules.

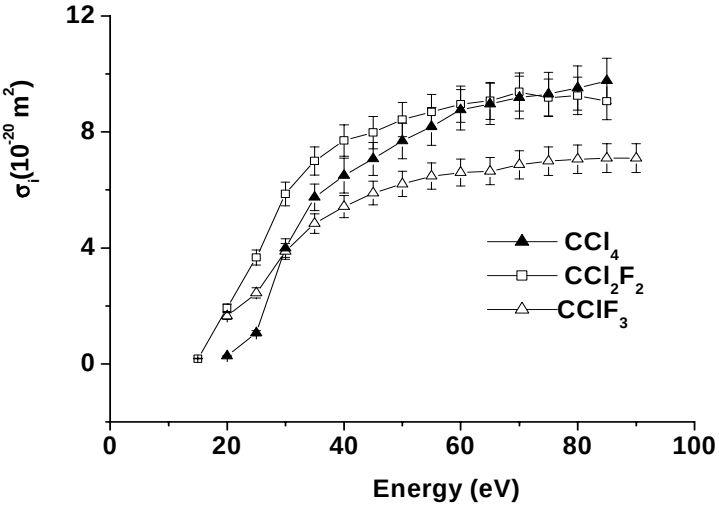

Figure 3. Experimental total ICS for CCl_2F_2 and $CClF_3$ molecules

A discussion on the theoretical and experimental ICS agreement, along this chlorofluoromethane family, will be presented.

References

[1] L.G. Christophorou, J.K. Olthoff – J. Phys. Chem. Ref. Data **27**, 1 (1998).
[2] K.H. Becker – Electron Collisions with Molecules, Clusters, and Surfaces ed. H.Ehrhardt, L.A. Morgan. 1993.
[3] I.Torres, R.Martínez, M.N.Sánchez Rayo, F.Castaño – J. Phys. B: At. Mol. & Opt. Phys. **33**, 3615 (2000).
[4] Y.K. Kim, M.E. Rudd – Phys. Rev. A **50**, 3954 (1994).
[5] H. Deutsch, T.D. Märk – Int. J. Mass Spectrom. Ion Processes **79**, R1 (1987).
[6] H. Deustch, K. Becker, T.D. Märk – Int. J. Mass Spectrom. Ion Processes **167/168**, 503 (1997).

Influence of DC voltage field on ion and O_3 formation in a high frequency surface discharge

M.V.Kozlov[1], M.V.Sokolova[2], A.G.Temnikov[2], V.V.Timatkov[2], I.P.Vereshchagin[2]

[1] Now at Export Dept. of Russian Joint Stock Company "Unified Energy System of Russia", Russia
[2] Dept. of Electro Physics and High Voltage Technique, Moscow Power Engineering Institute (Technical University), Moscow, Russia

Possibility of intensification of plasma chemical processes that go on in a high frequency surface discharge is analyzed. The HF discharge is generated on a surface of a ceramic plate with metallic stripes on its surface and a metallic layer on its other side. Such element is used generally as an ozone generator. The frequencies of the applied voltage are in the range 500-6000 Hz.

When a DC high voltage is applied to a metallic plate placed 5 – 15 mm above the ceramic plate surface (the DC electric field being in the range 3 – 12 kV/cm) a DC current appears connected with ion movement in the gas gap between the surface discharge layer and the metallic surface.

As the DC current is defined by the intensity of the ion formation in the HF surface discharge, it depends on the surface discharge conditions such as the frequency and amplitude of the applied HF voltage and on the field intensity of the DC voltage. In addition to this fact an influence of the type of the ceramic material of the dielectric barrier on the ion and ozone formation intensity has been registered.

Theoretical equations for current characteristics and ion concentration are derived. Calculations based on these equations show good coincidence with experimental current values. An analyze of the results for a wide range of the frequency and amplitude of the applied HF voltage shows that there is a significant increase of ozone formation with an increase of the DC voltage. The investigations have shown also that for high values of the frequency and amplitude of the HF applied field the concentration of ions near the surface of the barrier increases with an increase of the DC field and this fact is explained by an increase of the thickness of the ionized gas layer near the barrier.

At the same time it has been found that this increase can be only for a certain range of surface discharge conditions. More of it such range depends on the material of the dielectric barrier.

PEG/PMAA patterned structures performed by plasma treatments; stabilisation and etching

A. Valsesia*, M. Manso*, D. Gilliland, G Ceccone, F. Rossi

Institute for Health and Consumer Protection, Joint Research Center, 21020 Ispra (Va) Italy
**Authors with equal contributions*

Abstract
In this work we report the processing of micropatterned templates based on the non fouling Polyethylene glycol (PEG) and the functional surfaces of polymethacrylic acid (PMAA). Two Ar plasma treatments were optimised to: a) stabilise the inherently soluble spin casted PEG and b) to expose the underlying PMAA through a masked etching treatment. Both spectroscopic and surface morphology techniques have been used to characterise these devices.

1. Introduction

Patterned polymer surfaces present ideal properties for performing biomedical assays at molecular and cellular level. On one side, a polymer with high affinity towards the target biomolecule can be prepared while the negative part is formed by depositing a non-fouling film. With this configuration a biomolecule can be constrained to certain regions of a surface (f.i. in order to detect it [1]) or a group of cells can be forced to follow a desired distribution (f.i. for cell physiology and cellular engineering [2]).
Polyethylene glycol (PEG) is a reputed non-fouling polymer. However, it forms unstable films that dissolve in water [3] so that a stabilization treatment is required for the processing of a device. Stable PEG films can be performed in different ways. PEG silanes can be grafted to a glass or silicon surface after an intense acid treatment [4,5]. Gold surfaces can be also coated by using an oligo(ethylene glycol) associated to a thiol group which leads to self assembled monolayes of great fundamental interest.
However, these chemical techniques present a main drawback since they are not universal (not every substrate can be used). Thus, physical methods applied to spin casted PEO films can give an added value if they prove their non-fouling reliability. In this frame, photo and ionizing irradiation inducing random cross linking can be expected to have a favourable effect towards stabilization [6].
On the other hand, Polymethacrylic acid (PMAA) contains carboxylic groups which can be activated to functionalise its surface. PMAA combines the stability of polymethylmethacrilate with the biofunctional properties of polyacrylic acid. These polymers frequently used in the biomedical field, ensure a high quality response of this polymer in biomolecular assays.

2. Materials and Methods

The polymers PMAA (in practice methacrylic acid-methylmathacrylate copolymer, Mw 500000, Fluka) and PEG (Mw 6000, Fluka) were dissolved in methanol and trichloroethylene respectively. The solutions were used to form films onto Si (100) substrates for analytic purposes and finally PEG/PMAA/Si structures were also grown for device processing. The device preparation scheme is presented in figure 1.Firstly, a plasma treatment in a distributed electron cyclotron resonance (DECR) reactor is applied to the PEG surface in order to stabilize it. A microwave power of 1400 W (2.45 GHz) was supplied to the Ar plasma (10 sccm, 1 mTorr) for 30 s. Ar ion energy was further increased by applying a –50 V RF bias (13.54 MHz) to the substrate holder. After covering with a mask, a second plasma treatment is applied in order to etch the non fouling polymer reaching the PMAA surface and rendering its carboxylic groups active. In this case MW power was 1000 W and the RF bias reduced to –25 V increasing the treatment time to 120 s.
Plasma diagnostic techniques (Langmuir probe and mass spectrometry) were used to monitor relevant plasma parameters such as ion densities and temperatures. The film characterisation was performed by using Fourier transformed infrared spectroscopy (FTIR, Bruker Vector 22, 4 cm^{-1} res.), X-ray photoelectron spectroscopy (XPS, Ultra photoelectron spectrometer, KRATOS UK, monochromatic Al Kα 150 W, high resolution pass energy 20 eV, operating pressure, 2.10^{-9} mTorr), atomic force microscopy (AFM, NT-MDT Solver-Smena head, silicon cantilevers k= 5 N/m and first harmonic frequency of 158 KHz), scanning electron microscopy (SEM, LEO) and contact angle measurements (CA, DGD Fast/60, GBX technologies).

Finally the device processing parameters were obtained with the help of a quartz crystal monitor (QCM, LH Inficon deposition monitor).

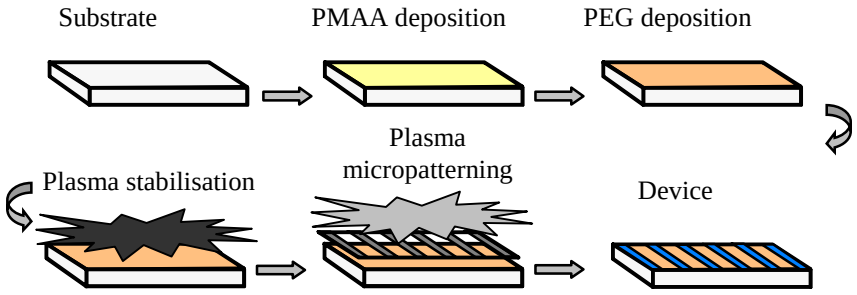

Figure 1. Scheme of the procedure followed for the processing of the PEG/PMAA biomedical micropatterns by using a double step plasma treatment.

3. Results and Discussion

The stabilisation treatment of the spin casted PEG was monitored by studying the changes induced by the plasma treatment on the molecular configuration of the polymer. Figure 2 depicts the FTIR spectrum of the PEG film after modification in the DECR reactor in comparison with an as spin casted film. The bands detected in both samples are in accordance with those reported for high quality PEG crystals [7]. Two main differences between the etched and the as deposited samples are worth to note. First, the notable decrease in the film absorption (the thickness of both PEG films was identical before the plasma treatment), which indicates that the plasma treated PEG experiences an intense etching process. Remarkably, this decrease is not homogeneously distributed being more acute in the case of bands oriented in parallel to the polymer backbone (indicated with ▲ in figure 2). This preferential decrease can be clearly evidenced by comparing the changes in relative intensities between the following pairs of perpendicular-parallel bands: 1358-1342 cm^{-1}, 1278-1240 cm^{-1}, 947-958 cm^{-1}. These features indicate a drastic modification of the molecular structure. The originally linear polymer chains are broken by the Ar ions and reorganise giving a branched-crosslinked structure.

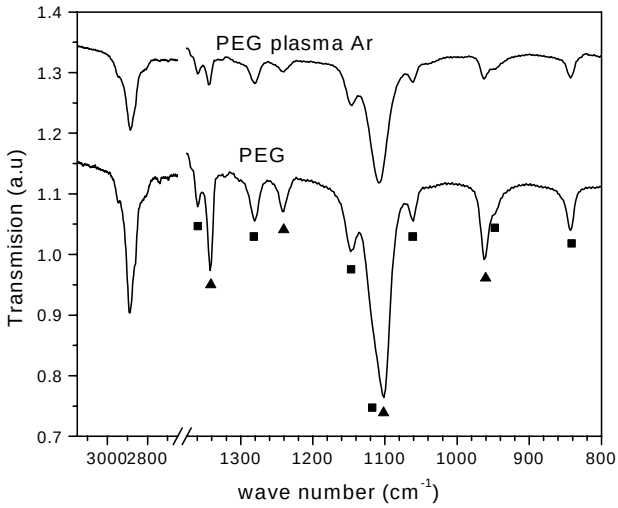

Figure 2. FTIR spectra corresponding to as deposited (bottom) and plasma treated (top) PEG films. (▲, ■) Modes parallel and perpendicular to the polymer backbone, respectively.

As derived from the evidences of the intense etching process, the plasma treatment was selected as to be energetic enough to produce crosslinking, but short enough as to avoid excessive sputtering. In order to optimise the treatment, plasma diagnostic techniques allowed us to derive that, the mean energy of the Ar+ ions followed a linear behaviour with respect to plasma power, reaching a value of 18 eV for 1400 W. The extra energy and directionality supplied by the bias RF voltage was found to increase the PEG film stability at any plasma power tested. However, films stabilised at plasma powers lower than 1400 W could not be satisfactorily processed requiring too long plasma exposure which made etching processes dominant.
A first evaluation of PEG film stability was performed by water CA. A clear change in the wettability dynamics was observed between the as deposited and the plasma modified film. Water droplets on the as spin casted films presented an initial CA of $14^{o}6$. In the following seconds the droplet retracted and stabilising at $24^{o}3$ after 5 s. This tendency, attributed to a modification of the water surface tension as a result of the polymer solubility, was not observed in the plasma treated samples. A stable CA of $20^{o}4$ was measured in this case, evidencing a certain decrease in the PEG film hydrophilicity.

The surface of the functional PMAA were characterised by XPS in order to evaluate the content of the carboxyl functional group. Figure 3 presents the XPS spectrum corresponding to the as spin casted films. The raw spectrum (dots) could be deconvoluted on the basis of four components which stand for the four main C 1s interactions in the polymer [8]. From lower to higher binding energies the peaks were assigned to: C-C, CH-COOH, CO-COOH and -COOH. In such films the carboxyl content (peak 4) was estimated to be at around 15 % of the C surface composition.
The plasma treatment was observed to modify the polymer carboxyl content. In order to minimise the loss of carboxyl groups when performing the device, the plasma power was reduced to 1000 W for the etching of the overlaying stabilised PEG film. In this conditions the carboxyl content remained over the 10% of the C surface composition.
CA measurements also confirmed that the plasma treatment induces a modification of the PMAA surface composition. Water CA's were observed to reduce from $62^{o}4$ to $58^{o}2$ after the plasma etching treatment. The total formamide wettability of as deposited and plasma etched PMAA surfaces confirmed that surface tension of this polymer presents in both cases a preferential acid polar component. However, the reduction of the water CA after the Ar plasma treatment indicates a slight increase of the base polar component.

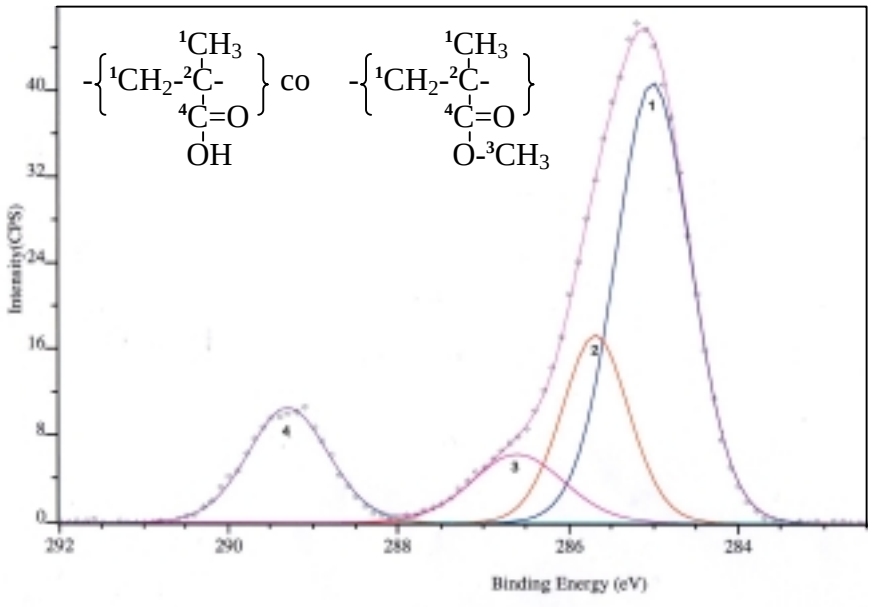

Figure 3. XPS C1s spectrum of PMAA as casted from 2% methanol solution. The peak is de-convoluted in four components.

This behaviour of the CA on PMAA surfaces is in agreement with the loss of carboxylic groups detected by XPS. In any case, the difference in water CA's between the stabilised PEG and exposed PMAA ($20^{o}4$ against $58^{o}2$) evidences the relevant contrast in the wettability properties.

A QCM was used in order to help in the determination of the device processing parameters. The curve presented in figure 4 stands for a two step plasma process inducing two major mass reduction slopes. The first step produced a very intense mass decay as a result of the high energy input (MW plasma and RF bias). The lower slope of the mass decay in the second step confirms the milder plasma conditions during the final etching of the PEG film to expose the PMAA film. In the early stages of the second step the curve clearly shows a non constant derivative. As long as the time passes the derivative becomes almost constant and not so steep as a result of the etching of a denser material. Polymers present non uniform etching yields that induce non constant derivatives while dense homogeneous materials (i.e. gold underlying contact) present an almost linear mass decay. Devices performed on Si confirmed that limiting the second plasma treatment time to 120 s (i.e. non constant derivative region) the etching process was stopped at the PEG/PMAA interface. The samples were subsequently observed by AFM to confirm these features.

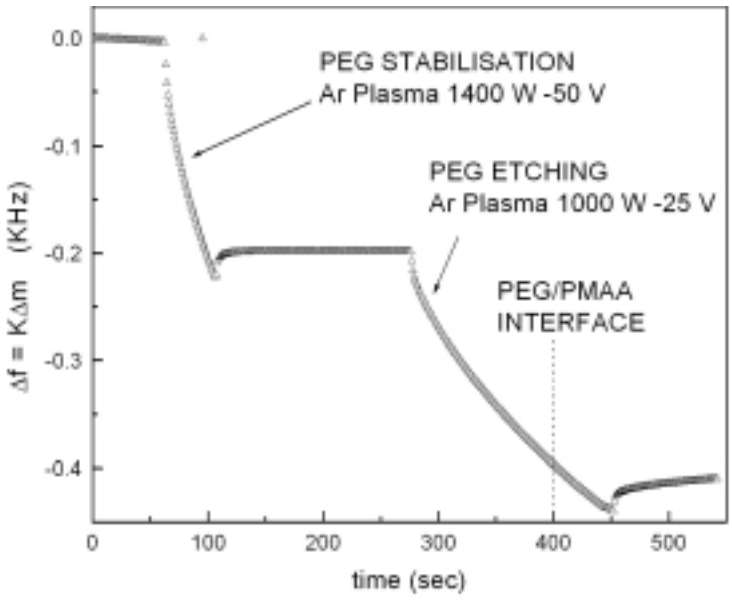

Figure 4. Quartz crystal monitor profile of a PEG/PMAA device.

SEM and AFM images were used to show the morphological changes induced by the plasma treatments on the PEG/PMAA device. The SEM image presented in figure 5a shows a general overview of the device with 500 μm homogeneous stabilised PEG regions separated by 50 μm wide PMAA stripes. Higher magnification images were obtained by AFM. The as deposited PEG is characterized by a polycrystalline organization [9] with grains with the typical size of hundreds of micrometers. Inside these micro-grains there are long parallel chains of flake-like elements with well defined shape and typical lateral size of 300 nm.
The AFM image presented in figure 5b evidences that the Ar plasma induces a redistribution of these long chains, mainly as a result of the intense sputtering process co-induced during stabilisation. The crystalline structure is modified and a new morphological organization occurs. The modified film is characterized by deep wrinkle–like structures. The lateral size of the hills and the grooves is 5 μm and the typical peak-to-valley height is 150 nm. Figure 5c shows a detail of the PMAA stripe with the neighbouring PEG. It can be outlined that the particular morphology of the stabilised PEG is transferred to the PMAA surface after the plasma etching treatment. In this case the typical peak-to-valley height is reduced to 40 nm. The transfer of the PEG treated morphology to the PMAA surface is due to the high directional character of the Ar ions in the plasma discharge induced by the RF bias applied to the sample. The thickness profile presented in figure 5.d clearly illustrate these features.

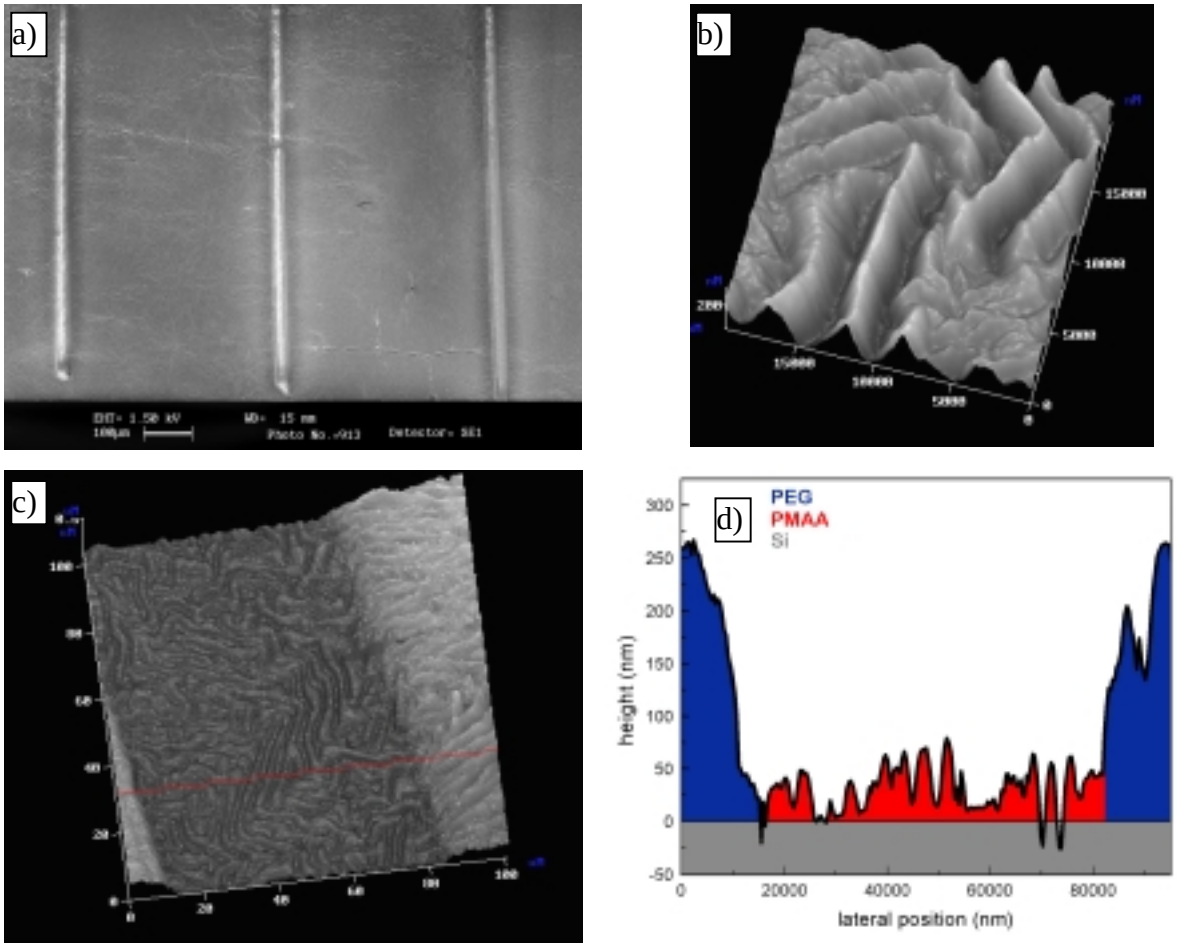

Figure 5. (a) SEM image of the device surface with three 50 μm PMAA stripes spaced out by 500 μm PEG regions. (b) 20x20 μm AFM image of the PEG surface. (c) 100x100 μm AFM image of one etched stripe of the device. The darker region corresponds to PMAA exposed after plasma etching while the clearer one corresponds to stabilised PEG protected by the nickel mask. (d) Cross section from the horizontal line in (c). The etched film thickness is approximately 200 nm setting the height zero at the PMAA/Silicon interface.

4.Conclusions

A procedure for the processing of micropatterned PEG/PMAA structures has been described. Before device processing, the plasma treated films of both PEG and PMAA were analysed independently by surface characterisation techniques. FTIR measurements showed the presence of crosslinking on PEG films as deduced from the changes in the relative absorption of bands assigned to parallel and perpendicular modes. XPS was used to follow the behaviour of the PMAA carboxylic group along with different plasma treatments. Furthermore, PEG water CA's were observed to increase after the plasma treatment as a result of the reduction of the dissolving interactions. In the case of the PMAA surface, the XPS results were correlated with CA measurements, which allowed to explain the changes induced in the polymer surfaces after the plasma treatment in terms of evolution of the surface tension components. A topographic evaluation of the film was performed by atomic force microscopy. Near contact images revealed that the surface roughness of the films was increased during the treatment but remained in any case below 150 nm for both polymers after the final plasma treatments selected for device processing.

The first assays in biomolecular media are in progress in order to prove the functionality of the PEG/PMAA micropatterns. From the biomolecular point of view, protein attachment tests will be performed in order to illustrate whether the Carboxylic groups in PMAA retain their functionality and the stabilised PEG behaves efficiently as a non fouling film. From the cellular point of view, these structures are of significant interest because of the competitive chemical and topographical mechanisms towards cell attachment [10].

References

[1] A.S. Blawas, W.M. Reichert. Biomaterials. 19, 595 (1998).
[2] Y. Ito. Biomaterials. 20, 2333 (1999).
[3] E.W. Merrill, E.W. Salzman, K.A. Dennison, S.W. Tay, R.W. Pekala. Progr. Artif. Org. 1985. ISAO Press, Cleveland 1986. 909-912.
[4] H. Sorribas, C. Padeste, L. Tiefenauer, Biomaterials, 893, 23 (2002).
[5] A. Papra, N. Gadegaard, N.B. Larsen. Langmuir 1457, 17 (2001).
[6] L.G. Griffith. Acta Mater. 263, 48 (2000).
[7] V.M. Da Costa, T.G. Fiske, L.B. Coleman. J. Chem. Phys. 2746, 101 (1994).
[8] G. Beamson, D. Brigs. High resolution XPS of organic polymers. John Wiley & Sons, Chichester (1992).
[9] G.Magonov, A.Godowsky, Amer. Lab. 51 (1999)
[10] A. Curtis, C. Wilkinson. Biomaterials. 18, 1573 (1997).

Structure and current characteristics of surface discharge for different kinds of barrier materials

M.V.Sokolova, A.G.Temnikov, V.V.Timatkov

Dept. Of Electro Physics and High Voltage Technique, Moscow Power Engineering Institute Technical University), Moscow, Russia

Recent publications show that surface discharge can be effectively used for modification of the surface of dielectric materials, especially of polymers. The intensity of the treatment depends on the discharge structure and on the kind of the high voltage applied. Our previous studies [1] have shown that the electrical and structure characteristics of the discharge in its turn depend on the applied impulse voltage amplitude and its duration and on the ceramic material used as the dielectric barrier. As a result the intensity of the ozone formation can change as well if the surface discharge element is used for ozone production.

The above investigation has been extended on a more wide range of the dielectric barrier materials including not only ceramics, but polymer material as well.

To analyze the influence of the polymer material several polymers have been used such as Plexiglas, Polytetraftorethylene, Polyvynylchloride, Polyethylene that have very near values of surface and volume resistance and ε values. The electrode system consists of a metallic stripe (1 mm wide and 50 μm thick) on the surface of a dielectric barrier (its thickness being in the range 1-2 mm) with a wide metallic layer on the other side of the dielectric plate. To analyze the discharge structure voltage pulses of nanosecond duration (350 ns) and different polarity and dust technique have been used. The dust figures permit to see the charge distribution on the barrier surface after the discharge.

In all cases of positive discharge a distinct discrete structure is seen but for negative polarity much depends on the amplitude of the applied voltage and polymer material. Current pulses of the discharge are analyzed and show a certain dependence on the material as well.

[1] M.V. Kozlov, M.V. Sokolova, A.G. Temnikov, V.V. Timatkov, I.P. Vereshchagin. Surface discharge characteristics for different types of applied voltage and different dielectric materials. Proceedings, HAKONE VIII, Inter. Symp. on High Pressure Low Temperature Plasma Chemistry, Tartu, Estonia, 2002, Vol. 1, pp. 43-47.

Molecular dynamics simulations of radical-surface interactions: Growth of amorphous carbon films

D. Humbird[1] and D. B. Graves[1]

[1] *Department of Chemical Engineering, University of California, Berkeley, USA*

Radical-surface interactions are often crucial in plasma and beam technologies. While molecular dynamics (MD) simulations have proved useful for modeling ion impacts on surfaces, they have been less successful in simulating the reactions of radicals on surfaces, mainly because these occur on larger time scales than are tractable with MD.

Using the REBO interatomic potentials for carbon and hydrogen developed by Brenner and coworkers [1], we have considered the growth of amorphous hydrogenated carbon films from beams of H· and CH_3· radicals. The experimental beam studies of von Keudell and coworkers suggested that the rate-limiting step in film growth is abstraction of a surface H by an incident H· to create a dangling bond where an incoming CH_3· can attach [2,3]. Initial simulations confirmed this to be case. By treating the abstraction process with a pseudo-steady-state approximation, we greatly accelerated our simulations of carbon film growth, e.g. the one shown in Fig. 1, which was deposited with 1eV CH_3·. We feel the high kinetic energy helped to bring the reaction probability to observable levels without changing the mechanisms significantly.

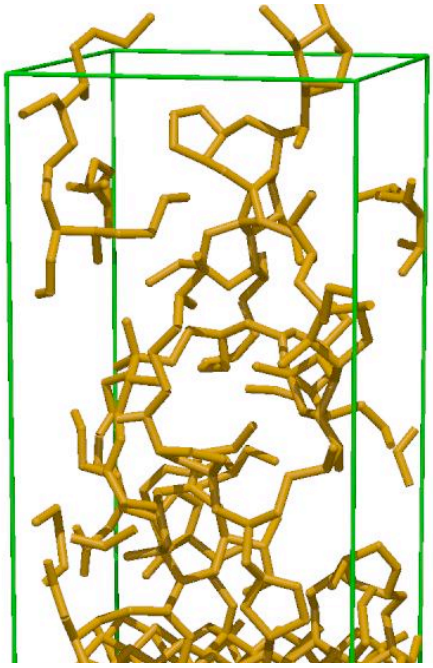

Fig 1. Complex structure of hydrogenated carbon film grown on diamond (100) surface. Hydrogens are not shown.

The film growth mechanisms from the simulations are in good qualitative agreement with the beam experiments: H· abstracts H to create a dangling bond and CH_3· saturates it. At first, growth occurs in chains originating from the surface. As the film grows larger, the chains branch into complex tree structures. As the structure becomes more complex, dangling bonds appear near each other and cross-links and rings are formed. The formation of these new C—C bonds in the film reduces the H/C ratio. The density of our film is the same as in the experiments (1 g/cm^3), but the H/C ratio is higher—about 1.7, compared to 1 in the experiment.

[1] D.W. Brenner, O.A. Shenderova, J.A. Harrison, S.J. Stuart, B. Ni, S. Sinnott - J. Phys. Cond. Mat. **14** (2002) 783.

[2] A. von Keudell, T. Schwarz-Selinger, and W. Jacob - J. Appl. Phys. **89** (2001) 2979.

[3] A. von Keudell, M. Meier, C. Hopf - Diamond Rel. Mat. **11** (2002) 969.

Deep silicon etching by cryogenic process applied to via drilling

R. Dussart[1], X. Mellhaoui[1], A. Basillais[1], P. Lefaucheux[1], T. Tillocher[1],
M. Boufnichel[2], G. Marcos[3], P. Ranson[1]

[1)] *GREMI/ESPEO, Université d'Orléans, 14, rue d'Issoudun, BP 6744, 45067 Orléans, France*
[2)] *STMicroelectronics, 16, rue Pierre et Marie Curie, BP 7155, 37071 Tours Cedex , France*
[3)] *LPCM/IMN, 2, rue de la Houssinière, BP 3222, 944322 Nantes Cedex , France*

Abstract

A cryogenic process is used to etch high aspect ratio silicon structures. An inductively coupled plasma of SF_6/O_2 is created and expands through the diffusion chamber to a biased silicon wafer. This configuration was used to study silicon drilling by plasma for via production from one side to the other side of the wafer. Etching rates as high as 7 µm.min^{-1} were reached with 12 µm diameter vias using this process. A parametric study of the process performances is presented.

1. Introduction

Deep silicon dry etching processes are used for the elaboration of integrated components in power microelectronics and for MEMS and MOEMS fabrication (see for example references [1,2]). For example, deep trench isolation is necessary to separate active components on chips and requires etching of high aspect ratio silicon structures. In this paper, we present the etching of high aspect ratio via structures. As integrated circuits require a high level of integration, electrical connexions can be reported to the backside of the wafer increasing the integration level. Connexions are made by means of resistive vias, which cross the wafer from one side to the other side (400 µm thick wafers). Via etching is performed using an ICP plasma reactor and the so-called cryogenic process for deep silicon etching.

Deep silicon dry etching can actually be achieved by different processes. The Bosch process, which is intensively studied and used for industrial production and especially for MEMS fabrication [1,2], operates at ambient temperature [3]. It consists of alternative steps of etching (SF_6 plasma) and deposition (C_4F_8 polymerizing plasma). In this process, a passivating layer is obtained on the sidewalls during the deposition step. The passivating layer deposited on the trench bottom is sputtered during the etching step by incident ions accelerated in the plasma sheath. Even if it is currently used, some particular characteristics due to the Bosch process itself (scalloping, deposition on the reactor walls, long dead times necessary for gas changes…) can appear as a drawback for some component elaboration. When such drawbacks have to be avoided, the so-called cryogenic etching process can be a good alternative, if it is perfectly controlled.

The cryogenic etching process requires a low chuck temperature of about –100 °C to form a passivating layer on the sidewalls while silicon is etched on the trench bottom. The plasma is composed of a SF_6/O_2 mixture. Cryogenic etching was first studied by Tachi et al. in 1988 [4] and by other teams (see for example reference [5]). Trench slopes can be adjusted by changing the wafer temperature [6], which could be of interest for designing special MEMS. A high etch rate (ER > 5 µm.min^{-1} for a 5 µm aperture trench) and very large selectivity Si:SiO_2 (~1000) were obtained using this process [7,8]. However, the passivating layer seems to be much more fragile than in the Bosch process [9].

In this paper, we will present our last results on silicon via drilling. Some experiments have been carried out to decrease local bowing effect and improve the passivation layer efficiency present on sidewalls. Since Aspect Ratio Dependent Etching is an important phenomenon in this kind of structure, vias were first etched on one side and etched on the other side. Endpoint detection was carried out when vias join at about the middle of the wafer. Drilling is faster by using this technique. At lower temperature, crystal orientation dependent etching can appear [10,11]. This phenomenon can be responsible for negative slope observed when temperature is lower than in the working point. We will discuss this aspect as well.

2. Experimental setup

Via drilling is performed in an Alcatel 601 etcher. A schematic of the machine is given in reference [8]. A mixture of SF_6 and O_2 gas is introduced in the reactor. The plasma is created inductively with an antenna excited at 13.56 MHz, placed around an Al_2O_3 tube. The maximum incident power is 3000 W. Plasma confinement is supposed to be enhanced by a magnetic field produced by a coil surrounding the tube. The plasma expands towards the diffusion chamber where an electron density as high as 10^{10} cm^{-3} is obtained for a total pressure of about 3.10^{-2} mbar. The silicon wafer to be etched is located in the lower part of the diffusion chamber. We use (100) wafers with 35 Ω.cm resistivity. The wafer is independently self biased using an RF capacitive coupling. The ion energy on the wafer can be varied from 10-15 eV (plasma potential) to several hundreds eV. The wafer is mechanically clamped on a cryogenic chuck cooled by liquid N_2. A good thermal conductivity is ensured by 10 mbar of helium gas flowing at the backside of the substrate. The wafer temperature (~ -110°C) is maintained by ohmic heating of resistances placed at different positions of the chuck. After etching, the wafer is cleaved with a clivage machine equipped with a binocular system to cut along a line of vias and in the middle to study the profile on the cross section. Via patterns (aperture, depth, slope, and defects) are measured by Scanning Electron Microscopy (SEM) with a Leica Cambridge Ltd. S360 microscope.

3. Optimization of cryogenic process for via drilling

The cryogenic process has been previously used to etch trenches with a high aspect ratio (depth up to 100 µm) [7, 8]. As mentioned in the introduction, the aim of this work is to drill 400 µm thick silicon wafers and to form 20 µm diameter vias. To optimize the process, etching is carried out in two steps on each side of the wafer. To efficiently etch a silicon thickness of 200 µm without defect, a previous process we used for trench patterns is actually modified. Indeed, a constant ratio O_2/SF_6 can induce defects on via sidewalls in the end of the process, because oxygen is not sufficient to maintain the passivation layer during the whole process. In order to prevent those defects, passivation mechanisms must be activated and increased during the process. Hence, oxygen concentration must be increased while the total area of the via sidewalls increases. With a linear increase of oxygen content in the plasma, via profile can be preserved as shown in Figure **1**.

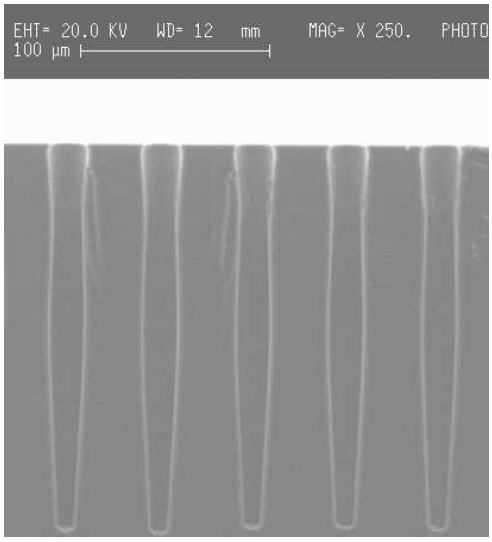

Figure 1 : SEM picture of 12 µm diameter etched vias. (Depth : 210 µm ; final diameter < 19 µm)

Via drilling has been studied for various via diameters: from 9 to 30 µm, some process parameters (SF_6/O_2 ratio and bias voltage) are optimised in each case to obtain a depth between 130 to 200 µm depending on the via aperture.

Industrial specifications concern not only the etching depth but also the final via diameter, which must remain below 20 µm (with an initial diameter of 12 µm). To achieve this specification, it is necessary to

reduce etching defects such as bowing and undercut. The next section is dedicated to the reduction of bowing [12].

4. Reduction of bowing

In via etching, bowing appears during the first minutes of the process. As mentioned in a previous study [12], the bowing origin can be due to ions, which can sputter the passivation layer present on the sidewalls. In that case, oxygen content in the plasma seems not sufficient to form an efficient passivating layer. To limit the bowing effect, etching rate is reduced during the first minute of the process using a lower SF_6 flux and an O_2 flux varying linearly. After this step called "soft etching", the process is continued with the standard process parameters. Results on bowing are presented in **Figure 2**. The bowing evaluation in standard conditions is indicated on this figure. As appearing on the figure, an increase of O_2/SF_6 ratio reduces bowing effect. But for a O_2/SF_6 ratio higher than 13.5 %, black silicon appears, which indicates an over-passivating regime.

27 µm diameter vias dedicated to this particular study were etched to facilitate the cleavage before analysis. Nevertheless, this technique to reduce bowing effect has been successfully applied to 12 µm vias, leading to a significant reduction of bowing and undercut.

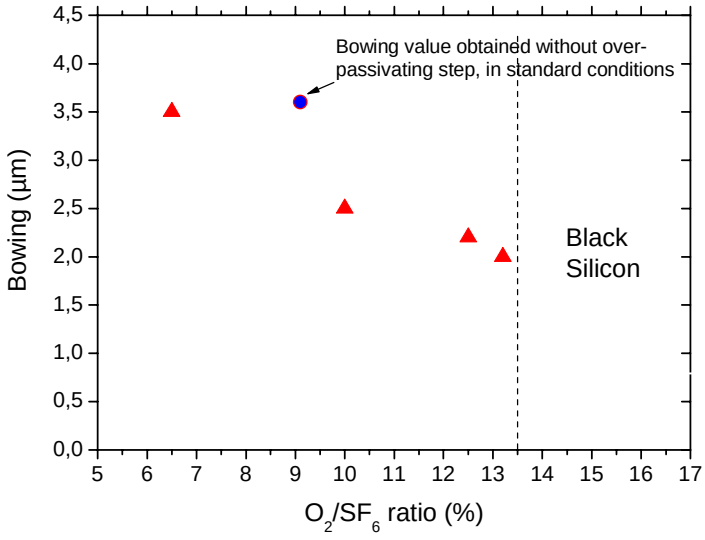

Figure 2 : Bowing evolution versus O2/SF6 ratio during the first step of etching

(a)

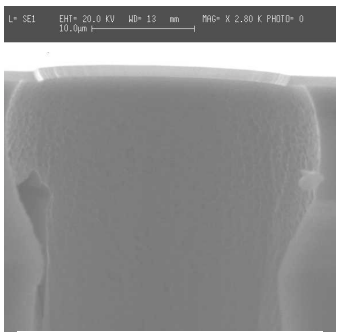

Bowing: 3,6 µm

(b)

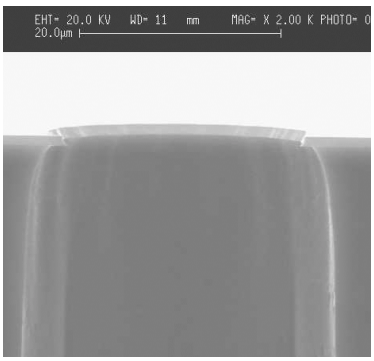

Bowing: 2 µm

Figure 3 : Top of etching vias : (a) standard point process,
(b) insertion of a passivation step at the beginning of the process

In optimal conditions, bowing can be reduced by a factor of about 50% without affecting the etching rate as this passivation is only done during a very short time (1 minute). Scanning electron microscopy images of the top of the via are presented in **Figure 3**.

5. End point detection

As illustrated in Figure 4, vias of each side join in less than one hour corresponding to an average etching rate as high as 7 µm.min^{-1}. The etching of the upper part of the wafer was first performed. During the 10 first minutes, the etch rate is greater than 10 µm.min^{-1}. The profile is quite vertical on the first 100 µm. Then, the profile slope becomes positive. Up to 230 µm depth silicon was etched during this first step. The backside etching was performed in the same conditions.

(a) (b)

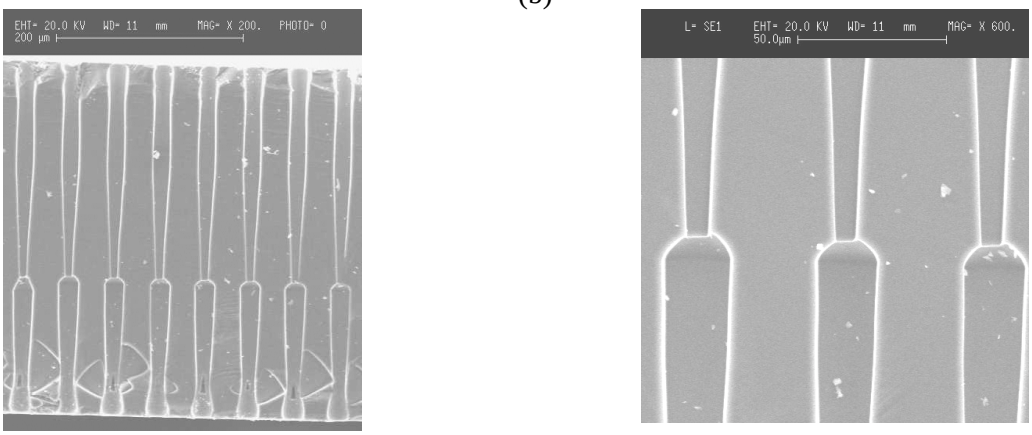

Figure 4 : SEM pictures of vias drilled in both sides of a wafer. The upper part was first etched (30 minutes process). The wafer is then returned to etch the backside. (b) is a zoom of (a)

As appearing in Figure 4, via profiles are different for each side of the wafer, whereas the same process is used for both sides. The profile slope of the backside vias is negative. This different profile shape could be due to the fact that temperature was not exactly the same for both sides during the proces. When the temperature is too low, profile slope is usually negative [10]. When the wafer is returned in order to etch the backside, we have to take into account the fact that vias which we observe were not etched exactly at the same position as the ones appearing on top side, excepted if the vias are exactly in the middle of the wafer (see Figure 5). In the case of figure 4, we were not able to cleave the wafer exactly at the center of the wafer to observe via profiles. Since the vias which were etched were not exactly at the same position on the chuck, there might be a difference in temperature. The cryogenic process is very sensitive to temperature variations. One degree difference is sufficient to modify the profile shape. We plan to use an electrostatic chuck equipped with a cooling system achieving a very high uniformity in temperature on the wafer.

But another mechanism can explain this profile difference. Due to the presence of the etched vias on the first side, temperature regulation can be perturbed.

The process duration of the front side must be reduced to make vias join in the middle of the wafer. End point detection is obtained by the helium leakage occurring at via junction. Plasma is maintained few minutes after the junction to make sure that all vias are joined.

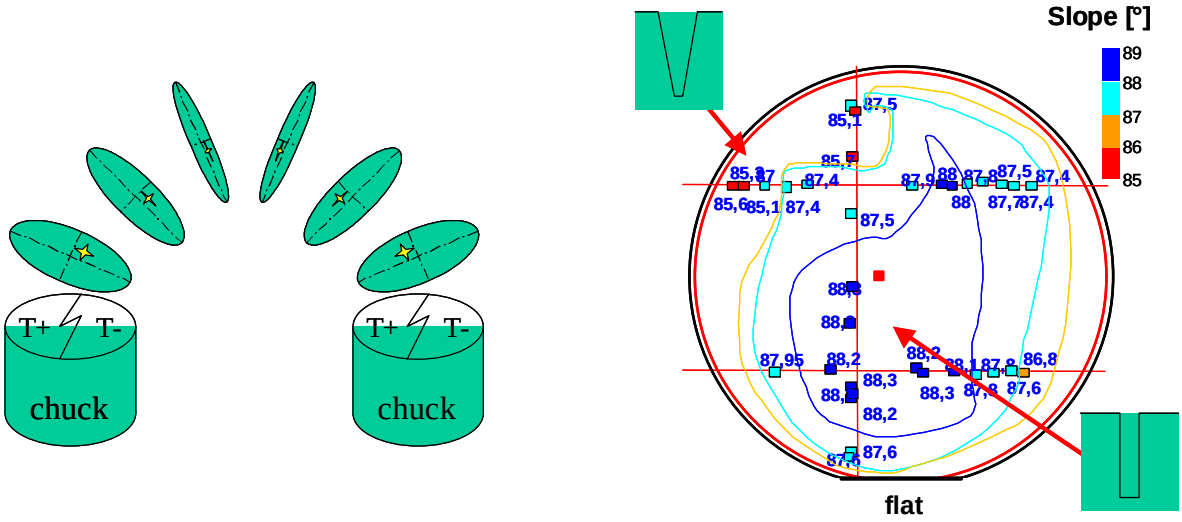

Figure 5 : (left) Schematic diagram, which shows that analyzed vias from both sides are not etched at the same position on the chuck. Wafer temperature is not highly uniform on the wafer surface and can induce some difference in the profile slope.

(right) : wafer mapping showing the trench slope value obtained on a wafer, which is directly connected to temperature non uniformity.

6. Crystal orientation dependent etching

As mentioned in some other papers, crystal orientation dependent etching can appear at very low temperature [10, 11, 13]. We have also observed this mechanism. Etching rate is enhanced in the <111> crystal direction. This effect can be responsible for the negative slopes, which are observed when the wafer temperature is lowered. As shown in figure 6-a, in this case of very low temperature, the etching rate is composed of two components: one high vertical component (V_G) and another one (V_C) in the <111> direction. The total etch rate leads to a negative slope as appearing in figure 6-a and -b.

(a) (b)

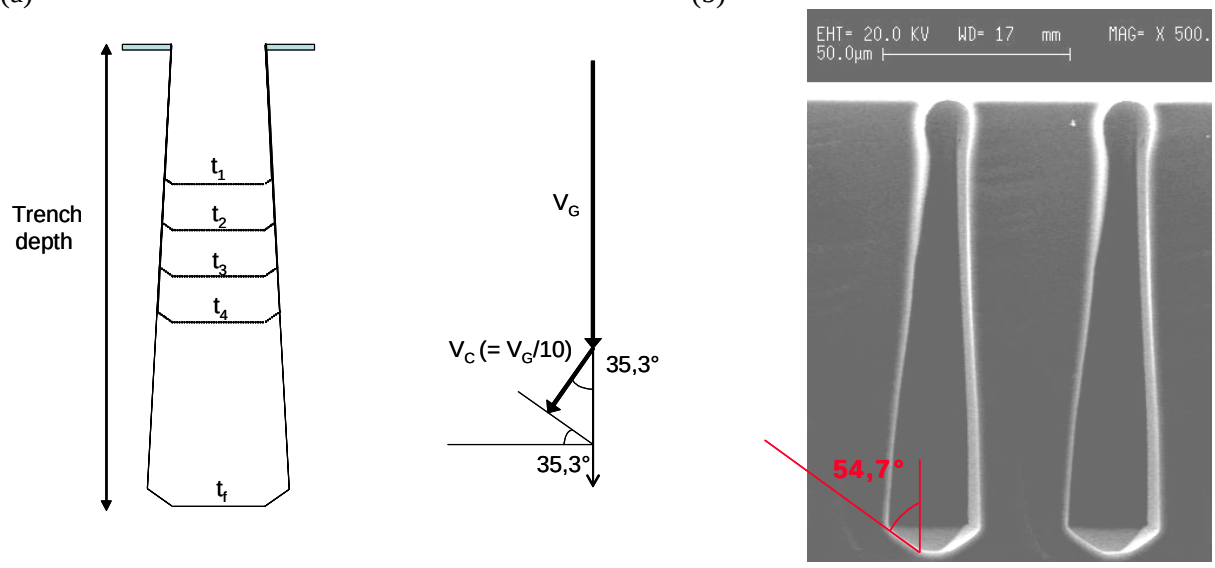

Figure 6 : Crystal orientation dependent etching :

(a) Schematic diagram of the crystal orientation dependent etching. As shown on the profile, the crystallographic component of the etch rate induces a negative slope. On this example of principle, the crystallographic component VC is one order of magnitude smaller than the averaged etching rate vertical component VG

(b) Experimental result obtained for vias. The crystal orientation etching appears clearly at the bottom of the structure

7. Conclusion and perspectives

Via structures were etched using the cryogenic process. Average etch rates as high as 7 µm.min^{-1} were obtained for 12 µm diameter and about 200 µm deep vias. Etching is performed in two steps to drill faster the wafer. Bowing effect can be reduced significantly by introducing a fast overpassivating step at the beginning of the process. Endpoint detection is obtained with the He leakage. The backside etching might require a modified process compared to the front side treatment. Crystal orientation dependent etching was observed for lower temperatures. This mechanism can be responsible for the negative slope, which is obtained in this case of very low temperature. Via profiles of the middle of the wafer were characterized in this study. The uniformity of profile shape on the wafer will be improved by using a new electrostatic cryogenic chuck supplying a high uniformity of temperature ($\Delta T<0.5$ °C).

7. Acknowledgments

This work is supported by STMicroelectronics (Tours, France) and by the French ministry of economy, finance and industry. The authors would like to thank R&D service of Alcatel Vacuum Technology - MMS (Annecy, France) for its strong technical support.

8. References

[1] I.W. Rangelow « Dry etching-based silicon micro-machining for MEMS », Vacuum, 62, 279 (2001)
[2] S. A. McAuley, H. Ashraf, L. Atabo, A. Chambers, S. Hall, J. Hopkins, G. Nicholls, « Silicon micromachining using a high-density plasma source », J. Phys. D : Appl. Phys. 34, 2769 (2001)
[3] F. Lärmer, A. Schilp, German patent n°DE4241045
[4] Tachi, K. Tsujimoto, and S. Okudaira, « Low temperature reactive ion etching and microwave plasma etching of silicon » Appl. Phys. Lett. 52 (8) 616 (1988)
[5] T. Chevolleau, P.Y. Tessier, C. Cardinaud, G. Turban, « Etching of Si at low temperatures using SF6 reactive ion beam : effect of the ion energy and current density », J. Vac. Sci. Technol. A, **15**(5), 2661 (1997)
[6] H. Jansen, M. de Boer, H. Wensink, B. Kloeck, M. Elwenspoek, « The black silicon method. VIII. A study of the performance of etching silicon using SF_6/O_2-based chemistry with cryogenical wafer cooling and a high density ICP source», Microelectronics Journal, 32, 769 (2001)
[7] M. Boufnichel, S. Aachboun, F. Grangeon, P. Lefaucheux, P. Ranson, « Profile control of high aspect ratio trenches of silicon. I. Effect of process parameters on local bowing », J. Vac. Sci. Technol. B, 20 (4), 1508 (2002)
[8] S. Aachboun and P. Ranson, « Deep anisotropic etching of silicon », J. Vac. Sci. Technol. A, 17 (4), 2270 (1999)
[9] R. Dussart, M. Boufnichel, G. Marcos, P. Lefaucheux, R.Benoit, H. Estrade-Szwarckopf, P. Ranson, « Passivation mechanisms in cryogenic SF_6/O_2 etching process », submitted to J. Vac. Sci. Technol.
[10] M.J. de Boer, J.G.E. Gardeniers, H.V. Jansen, E. Smulders, M.J. Gilde, G. Roelofs, J.N. Sasserath, M. Elwenspoek, « Guidelines for etching silicon MEMS structures using fluorine high-density plasmas at cryogenic temperatures » Journ. Microelectromechanical Systems, 11(4), 385 (2002)
[11] M. A. Blauw, T. Zijlstra, R. A. Bakker, E. Van der Drift, « Kinetics and crystal orientation dependence in high aspect ratio silicon dry etching », J. Vac. Sci. Technol. B, 18 (6), 3453 (2000)
[12] M. Boufnichel, S. Aachboun, P. Lefaucheux, P. Ranson, « Profile control of high aspect ratio trenches of silicon. II. Study of the mechanisms responsible for local bowing formation and elimination of this effect », J. Vac. Sci. Technol. B, 21(1), 267, (2003)
[13] G. Craciun, M. A. Blauw, E. van der Drift, P. M. Sarro, P. J. French « Temperature influence on etching deep holes with SF_6/O_2 cryogenic plasma », J. Micromech. : Microeng, 12, 390 (2002)

Copper phthalocyanine films grown by glow discharge-induced sublimation for gas sensing applications

G. Maggioni[1,2], A. Quaranta[2], S. Carturan[3], E. Negro[2], A. Patelli[4], M. Tonezzer[2] And G. Della Mea[2]

[1] *INFN - Legnaro National Laboratories, Legnaro, Padua, Italy*
[2] *Department of Materials Engineering, University of Trento, Povo, Trento, Italy*
[3] *Department of Physics, University of Trento, Povo, Trento, Italy*
[4] *Department of Electronics and Informatics, University of Padua, Padua, Italy*

Abstract
The deposition of copper phthalocyanine (CuPc) thin films for gas sensing applications by using a plasma-based method i.e. glow discharge-induced sublimation (GDS) is studied. Deposition rate of the CuPc molecules was measured by a quartz thickness sensor. The properties of the deposited films were studied by FT-IR spectroscopy, RBS, ERDA, SEM and AFM. Preliminary measurements of the gas-sensing properties of the films were performed by measuring the electrical conductivity in N_2+NO_2 10 ppm gas mixture.

References
[1] C.C. Leznoff, A.B.P. Lever - Phthalocyanines: properties and applications, VCH Publishers, Inc. (1996).
[2] C.-G. Choi, S. Lee, W.-J. Lee - Sens. Actuators B **32**, 77 (1996).
[3] G. Maggioni, S. Carturan, V. Rigato, G. Della Mea, Surf. Coat. Technol. **142-144**, 156 (2001).
[4] G. Maggioni, S. Carturan, A. Quaranta, A. Patelli, G. Della Mea, Chem. Mater. **14**, 4790 (2002).
[5] G. Maggioni, S. Carturan, D. Boscarino, G. Della Mea, U. Pieri, Mater. Lett. **32**, 147 (1997).
[6] A.K. Hassan, R.D. Gould, Phys. Status Solidi A **132**, 91 (1992).
[7] Y. Sadaoka, W. Goepel, B. Suhr, A. Rager, J. Mater. Sci. Lett. **9**, 1481 (1990).
[8] O. Berger, W.-J. Fischer, B. Adolphi, S. Tierbach, V. Melev, J. Schreiber, J. Mater. Sci.: Mater. In Electronics **11**, 331 (2000).
[9] M.I. Newton, T.K.H. Starke, M.R. Willis, G. McHale, Sensors and Actuators B **67**, 307 (2000).

1. Introduction
The unique properties of metal phthalocyanines (MPcs), such as thermal stability, chemical inertness and biocompatibility make these organic semiconductors very interesting for several applications, including chemical sensing, photoconducting agents, photovoltaic cell elements, non-linear optics and electrocatalysis [1]. As far as the gas sensing applications are concerned, it is well known that the electrical conductivity of thin MPc films changes owing to the adsorption of oxidizing or reducing gases such as NO, NO_2 and CO.
The classical deposition methods of thin organic films such as spin coating, dip coating and the sol-gel method cannot be easily applied to the production of MPc coatings owing to the low solubility of these compounds in organic solvents, inaccurate thickness homogeneity control and solvent retention. These drawbacks are avoided by using high vacuum evaporation which has become the most widely used technique for the deposition of MPc films over the last decades. In particular, plasma-activated evaporation has been reported to be very effective in improving the mechanical properties and chemical resistance of copper phthalocyanine (CuPc) films without compromising their gas-sensing features [2].
Recently a plasma-based technique has been developed for the deposition of thin organic coatings [3,4]. This method is based on the use of a weakly ionized glow discharge produced in a standard radio frequency magnetron sputtering equipment. Low energy (E<1 keV) noble gas (He, Ar, ..) ions impinge on the solid organic precursors (e.g. pyromellitic dianhydride, PMDA, and 4,4'-oxydianiline, ODA, for the PMDA-ODA polyimide deposition [3] or 3-hydroxyflavone [4]), leading to the sublimation of the organic molecules and to their condensation onto the substrate. In the case of polyimide coating deposition, the as-deposited films mainly consist of a mixture of polyamic acid and nonreacted monomers, as revealed by Fourier transform infrared spectroscopy (FT-IR). The polymerization of the deposited coatings is completed only after a thermal treatment (typically 250°C, 1 hour, in air or argon). As compared to the well known chemical synthesis methods the main advantage of this physical technique is the absence of any solvent.

In this work is tested the deposition of CuPc films by means of this novel technique, named Glow Discharge induced Sublimation (GDS). The sublimation of the CuPc molecules is studied by measuring the deposition rate using a quartz crystal microbalance. In order to compare the properties of the GDS films with standard samples, CuPc films are also deposited by vacuum evaporation (VE). The chemical structure of the deposited films is studied by FT-IR analysis. Rutherford Backscattering Spectrometry (RBS) and Elastic Recoil Detection Analysis (ERDA) are used to determine the film composition. Scanning Electron Microscopy (SEM) and Atomic Force Microscopy (AFM) are performed in order to investigate the film morphology.
Preliminary measurements of the gas response of the VE and GDS deposited films have been also performed by exposure to a N_2+NO_2 10 ppm mixture.

2. Experimental

The experimental setup used for the deposition of CuPc films consisted of a vacuum chamber evacuated by a turbomolecular pump to a base pressure of 10^{-4} Pa. The device used to sustain the glow discharge was a 1-inch cylindrical magnetron sputtering source connected to a radio frequency power generator (600 W, 13.56 MHz) through a matching box. The CuPc powder (99.5% purity, Acros Organics) was put on the surface of an aluminum target, placed on the sputtering source. The amount of powder used in every deposition was 750 mg. The glow discharge feed gas was argon (99.9999%). The pressure inside the chamber was measured through a capacitance gauge. Typical values of rf power, target DC self-bias and working pressure were in the ranges 10 to 20 W, -20 to –300 V and 5.00±0.05 Pa, respectively.
CuPc coatings were deposited on two types of substrates: 350-μm thick silicon wafer (Atomergic Chemetals Inc.) for FT-IR, RBS/ERDA and SEM analyses and quartz glass (Heraeus Quarzglas GmbH & Co) for the electrical measurement. The substrates were mounted on a rotating sample holder placed 6 cm above the source. The thickness of the organic layer and the deposition rate were measured in real time by a quartz crystal microbalance.
The experimental setup used for the evaporation of CuPc coatings has been described elsewhere [5]. The substrates were placed on a sample holder placed 7.5 cm above the crucible. The deposition rate was measured by a quartz microbalance.
FT-IR spectra of the samples were recorded using a Jasco FT-IR 660 Plus spectrometer with a resolution of 4 cm^{-1}. During the measurements, the sample cell and the interferometer were evacuated so as to remove from the spectra the absorption peaks coming from the atmospheric gases, therefore obtaining a cleaner signal.
The measurement of the film composition was performed by Ion Beam Analysis (IBA) using a Van de Graaf accelerator at the Laboratori Nazionali di Legnaro. Copper, nitrogen and carbon concentration was determined by Rutherford Back-scattering Spectrometry (RBS) using a 2.2 MeV $^4He^+$ beam, at normal incidence and at the scattering angle of 160°. Hydrogen concentration was measured by Elastic Recoil Detection Analysis (ERDA) using a 2.2 MeV $^4He^+$ beam at a recoil angle of 30° and at grazing incidence of 15°.
The surface morphology of the samples was investigated by using a Scanning Electron Microscope (SEM, Philips XL-30) and an atomic force microscope (AFM, Danish Micro Engineering model C-21, mounting a DualScopeTM Probe Scanner 95-50).
The electrical measurements were performed with an electrometer (Keithley Instruments, model 237). Twenty gold parallel rectangular electrodes (0.57 mm far apart) were evaporated on the quartz glass and then the CuPc film was deposited on the sample. The CuPc sample was put inside the measurement chamber and a background pressure of 1 atm of flowing N_2 was fixed. A ceramic heater was used to increase the sample temperature up to 150°C and then the electrodes were biased at 10 V and the current was measured. In order to avoid humidity contribution to the measured values, the conductivity in N_2 atmosphere vs 1/T was measured after the starting heating during the temperature decrease. For the test of the gas sensitive behaviour the sample was kept at 150°C and the flowing N_2 was replaced by N_2+NO_2 10 ppm mixture and the conductivity changes were recorded. All the measurements were performed without light irradiation (dark measurements).

3. Results and discussion

In Figure 1 is reported the deposition rate and the total thickness of films deposited by GDS as a function of deposition time: as can be seen, the deposition rate is relatively unstable during the first 150 seconds, being quickly increasing at the beginning and then abruptly decreasing, while it becomes nearly constant during the

last part of the deposition. However the mean value of the deposition rate is very high as compared to the evaporation one (up to ten times) and it gives rise to films which are some microns thick in few minutes.

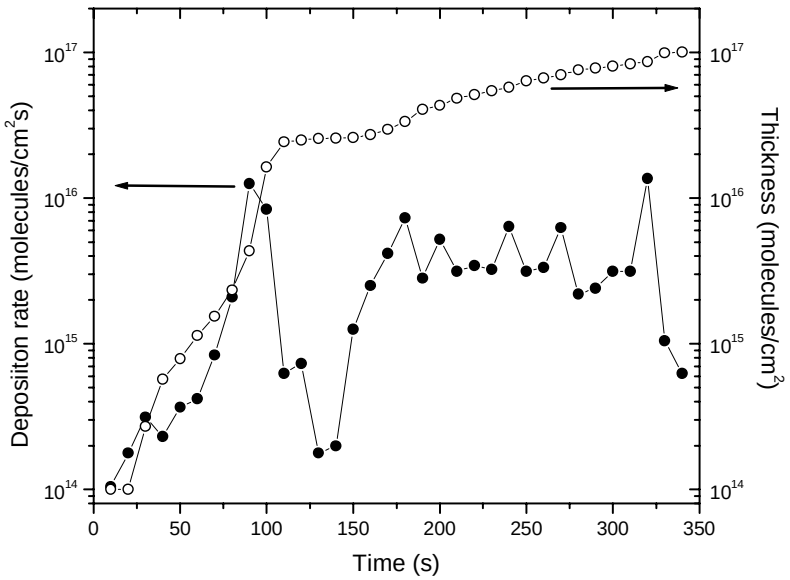

Figure 1. Deposition rate (•) and thickness (o) of CuPc films deposited by GDS as a function of time

FT-IR spectra of a vacuum evaporated film (VE) and of a GDS film in the range 3800 to 500 cm^{-1} are compared in Figure 2: the spectra appear very similar and all the main peaks of CuPc molecule can be identified in the GDS film, showing that a significant incorporation of integer CuPc molecules in the deposited film takes place.

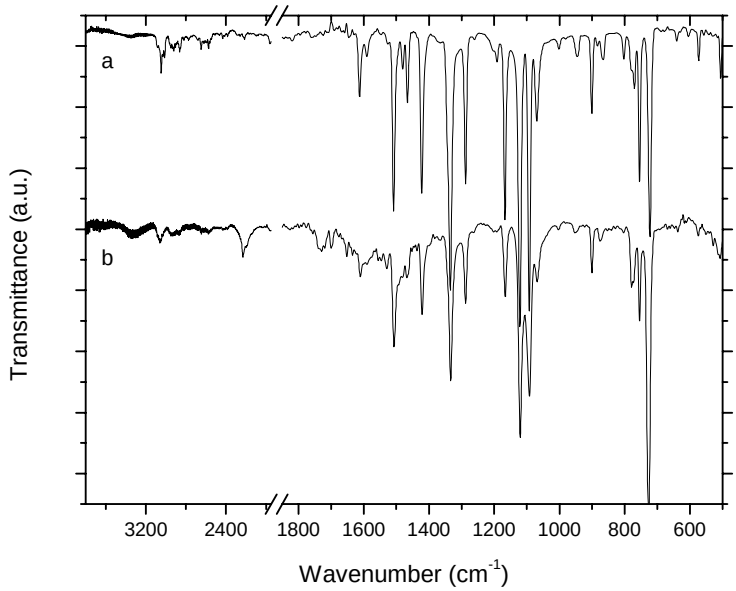

Figure 2. FT-IR spectra of evaporated film (a, upper curve) and GDS film (b, lower curve)

However some differences between the reported spectra can be found: a peak centred at 2230 cm^{-1}, which is ascribed to the C≡N stretching, a small band at 3350 cm^{-1}, due to the N-H stretching, and a broad, small band between 1700 and 1250 cm^{-1}. All these features suggest a non negligible incorporation of CuPc molecular

fragments during the GDS deposition, as due to the ion bombardment of the target CuPc powder. The molecular damage is thought to involve mainly the N atom bonds in the central region of the CuPc molecule as also shown by the low ratio between the intensity of the peaks at 900 and 573 cm^{-1} (metal-ligand Cu-N vibration [2]) and the peak at 724 cm^{-1} (C-H out-of-plane vibration) in the GDS film as compared to the VE one.

FT-IR analysis has been also used to study the film structure since it is well known that the MPcs crystal form is detectable by infrared spectroscopy [6,7]. In particular have been considered the position of the peak between 730 and 720 cm^{-1} and the intensity ratio between the peak at 780 cm^{-1} and the peak at 770 cm^{-1}. Figure 3 shows the infrared spectra of the starting CuPc powder, VE film and GDS film in the range from 820 to 680 cm^{-1}. In the spectrum of the CuPc powder, which is mainly β-phase as shown by several authors [6,8], the first peak is centered at 729 cm^{-1} and the peak at 780 cm^{-1} is more intense than the peak at 770 cm^{-1}. On the contrary, the spectrum of the VE film shows a peak centered at 722 cm^{-1} and the peak at 780 cm^{-1} is less intense than the peak at 770 cm^{-1}: these features characterize the α-phase as it could be expected for CuPc films evaporated on substrates kept at room temperature [8]. The spectrum of GDS film is different from both the previous samples: the first peak is centered at 727 cm^{-1} and the peak at 780 cm^{-1} is only slightly intense than the peak at 770 cm^{-1}. These features can be explained by assuming that the structure of the GDS film consists of a mixture of α- and β-phase.

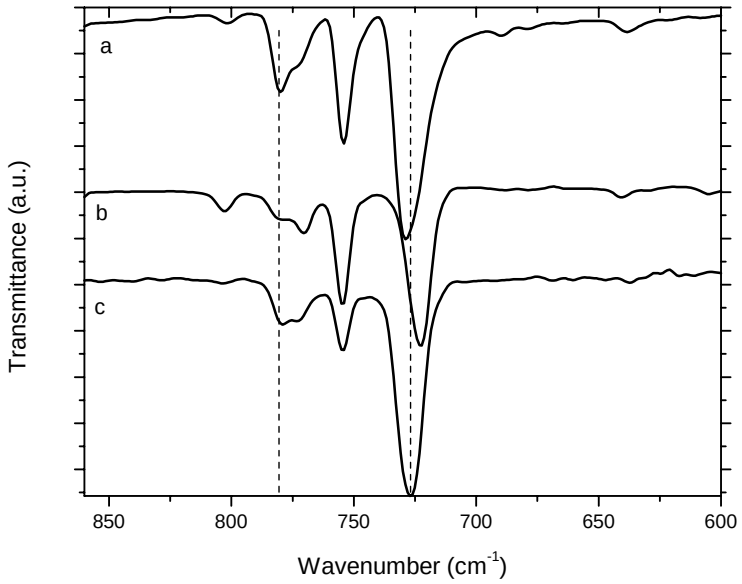

Figure 3. FT-IR spectra of CuPc powder (a, upper curve), VE film (b, middle curve) and GDS film (c, lower curve)

Table 1 shows the atomic ratios between the main elements of the GDS film (Cu, N and H) and carbon as determined by RBS/ERDA analyses. Taking into account that the experimental error on the hydrogen determination is relatively high, the average molecular formula of GDS film well corresponds to the expected CuPc molecular formula. This result confirms that the GDS film mainly consists of integer CuPc molecules as already shown by FT-IR analysis.

Table 1. Atomic ratios between the elements of the GDS film as determined by RBS/ERDA

Cu/C	N/C	H/C	Molecular formula
0.031 ± 0.002	0.25 ± 0.02	0.50 ± 0.07	$C_{32}H_{16}N_8Cu$

SEM micrographs of the deposited films (Fig. 4) together with the AFM analysis point out their very different morphology: the VE film is relatively flat (the mean roughness is about 40 nm) and small grains (0.5-1 μm wide) appear on a smoother background. On the contrary a rough structure with big grains (up to 5

μm wide) characterizes the GDS film, whose roughness is too high to be measured by AFM. The morphology of the GDS film suggests a more porous structure than the VE one, which can be particularly suitable for gas sensing applications, since the interaction surface between gas and sensor and the gas diffusion into the film are enhanced.

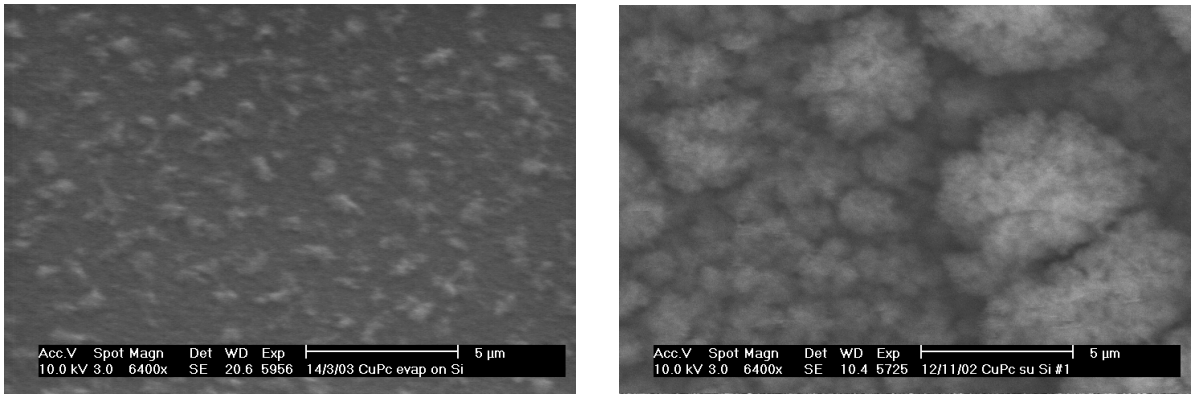

Figure 4. SEM micrographs of VE film (left) and GDS film (right)

The results of the electrical conductivity measurements of GDS film are reported in Figure 5: the temperature ranged from 313 to 423 K. The linear trend of LnI points out the semiconductor nature of the deposited film: the activation energy is calculated to be 0.23 eV.

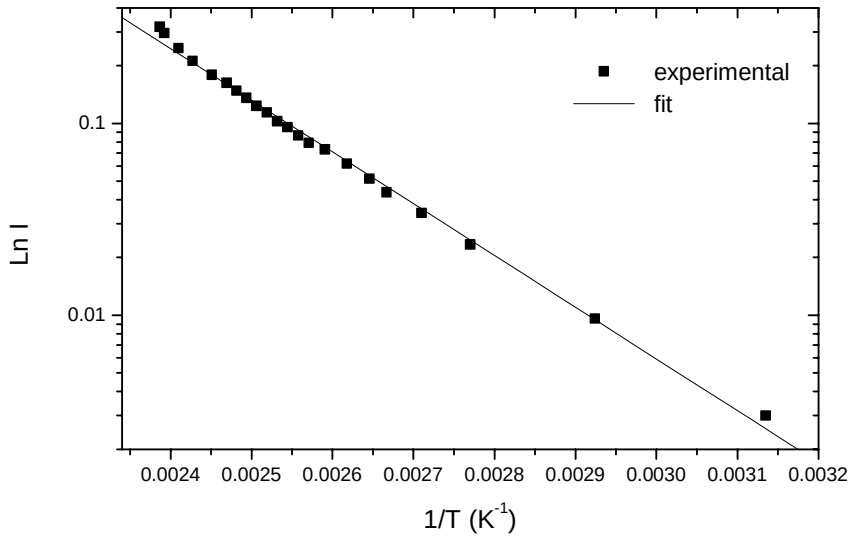

Figure 5. LnI vs 1/T for the GDS film

Preliminary measurements of the gas sensing properties of the VE and GDS films in N_2+NO_2 10 ppm mixture are compared in Figure 6: the gas mixture was admitted at the beginning of the measurement and it was removed after 20 minutes. Some interesting features can be observed: before the gas admittance the conductivity of the GDS film is slightly higher than the VE one, showing that the electrical properties of CuPc are preserved during the GDS deposition process. Moreover both films are very sensitive to NO_2: when the gas is removed the current has increased three orders of magnitude for the VE film and two orders for the GDS one. The conductivity increase is steeper for the VE film than for the GDS one, suggesting a higher sensitivity of the former film. However both films are characterized by high response and recovery times. On the other hand, the most important feature for the final gas sensing application concerns the reversibility of the electrical behaviour of the tested films: 160 minutes after the gas removal the conductivity of the VE film is nine times the starting value and an asintotic trend can be also assumed, pointing out the electrical

irreversibility which characterizes the evaporated CuPc films [9]. On the contrary the conductivity of the GDS film decreases down to 1.4 times the starting value, indicating that the gas/film interaction gives rise to reversible effects. This different behaviour is thought to be mainly due to the different structure of the films: the GDS film is more porous and the gas adsorption and release are promoted, while for VE the higher compactness appears to inhibit the gas release. However since these measurements are only preliminary, further work shall be done to confirm this difference.

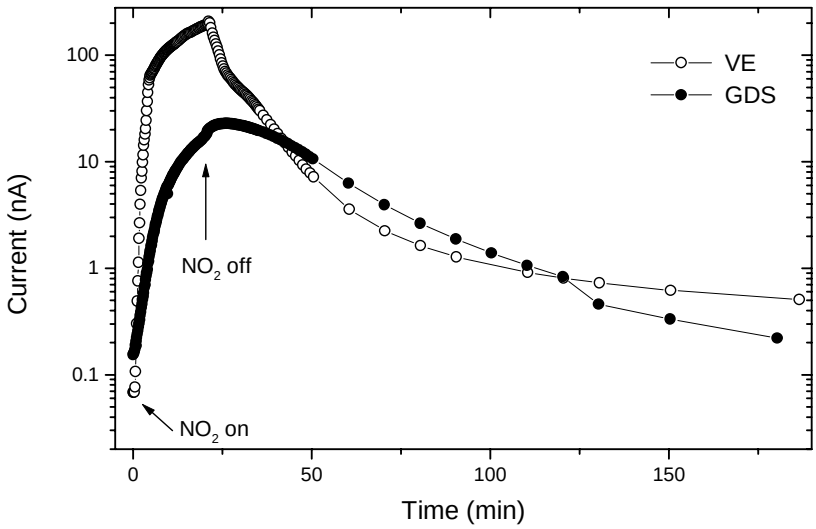

Figure 6. Electrical response of VE film (o) and GDS film (•) to NO_2 10 ppm exposure

4. Conclusions

The deposition of gas sensitive coatings by using plasma-based method has been shown. Glow Discharge induced Sublimation (GDS) has been used to grow thin coatings of copper phthalocyanine (CuPc).

The deposited films mainly consist of integer CuPc molecules as shown by FT-IR and RBS/ERDA analyses. However the incorporation of a non negligible amount of molecular fragments in the GDS film is found.

The film structure is different from the powder and from the evaporated film one and consists of a mixture of α- and β-phase. The porous and rough morphology of GDS films as compared to the VE ones makes these coatings particularly interesting for gas sensing applications.

The gas sensitivity of the deposited films has been shown by preliminary measurements of the electrical response to a N_2+NO_2 10 ppm mixture: both VE and GDS films are particularly sensitive to NO_2, but long response and recovery times are found. As far as the reversibility of the gas response the GDS films show a reversible behaviour maybe due to their less dense structure as compared to the VE films which, on the contrary, are characterized by irreversibility.

Comparative study of energy deposition estimation in Dielectric Barrier Discharge reactor

O. Martinie, J. M. Cormier and A. Khacef

GREMI, Université d'Orléans, 14 rue d'Issoudun, B.P. 6744, 45067 Orléans Cedex 2, France

Abstract

The aim of this paper is to present NO reduction experimental results obtained in non-thermal plasma (dielectric barrier discharge). Because of very fast transient discharges, energy deposition measurements are quite difficult in such reactors. This determination is a key factor to estimate the process efficiency. Various energy measurement techniques are presented. We operated with a N_2/NO mixture and we particularly interest to the chemical reduction of NO by the N radical. Finally we determined the yield for this process by measuring the NO destruction rate as a function of the power deposited into the reactor.

1. Introduction

Plasma processing and particularly non-thermal plasmas are subjected to a new interest for pollution control. The research in this field gained considerable interest and a number of researchers are working on it. Number of various devices had been developed in laboratories and proposed for. The already well known industrial applications processes are:

- Radio frequencies and microwaves discharges,
- Electrons-beam reactor,
- Corona discharge,
- Dielectric barrier discharge (DBD),
- Gliding discharge.

The energy cost involved on treating a given volume of polluted gas in normal conditions and the pollutant rate conversion are the main parameters in view of industrial applications are.

DBD is a well known transient discharge applied to pollutant control [1-6]. A dielectric layer covers one or two of the electrodes in the discharge gap. At a sufficiently high voltage, the discharge starts in the gas volume between the electrodes. Afterwards, it spreads out until it reaches the electrodes but at the dielectric it builds up a space charge that cancels the electric field. At that moment the discharge stops. The dielectric barrier discharge is supplied by a high voltage generator and the energy is transferred to the discharge with energy losses. One of the main problems is to know the real energy deposed in the plasma mixture. The aim of the paper is to measure this energy by various methods.

2. Experimental arrangement

The DBD reactor consists of a cylindrical pyrex tube. The 1.5 mm diameter electrode is arranged on the axis. A 10 μm thick external electrode is rolled up on the tube. The efficient inner volume of the reactor is about 6.8 cm^3.

The inlet gas consists of a 1000 ppm NO in N_2 as balance at atmospheric pressure. The gas flow rate is fixed at about 8.1 $cm^3.s^{-1}$.

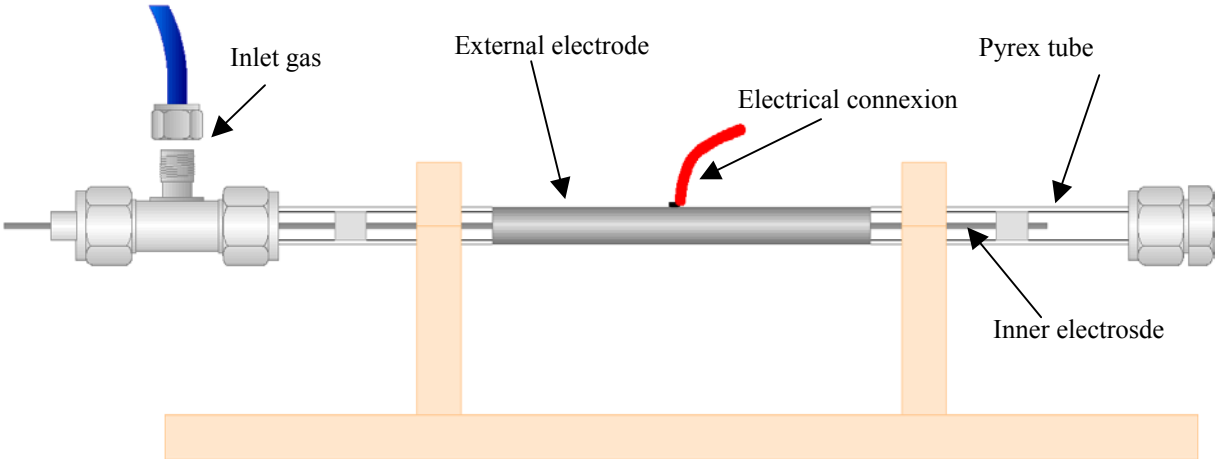

Figure 1: The DBD reactor.

The DBD reactor can be described using a series capacitance circuits as shown in figure 2. Details of capacitances effects are given in details by Z. Falkenstein and J. J. Coogan in reference [7]. The first capacitance C_g is corresponding to the gas capacitance and the second C_d is corresponding to the dielectric capacitance. These well-known capacitances are given by:

$$C_g = \frac{2\pi\varepsilon_0 l}{\ln\left(\frac{d}{r_0}\right)} \qquad \text{and} \qquad C_d = \frac{2\pi\varepsilon_0\varepsilon_r l}{\ln\left(\frac{d+x}{d}\right)}$$

Values are respectively: C_g = 3.7 pF and C_d = 91 pF.

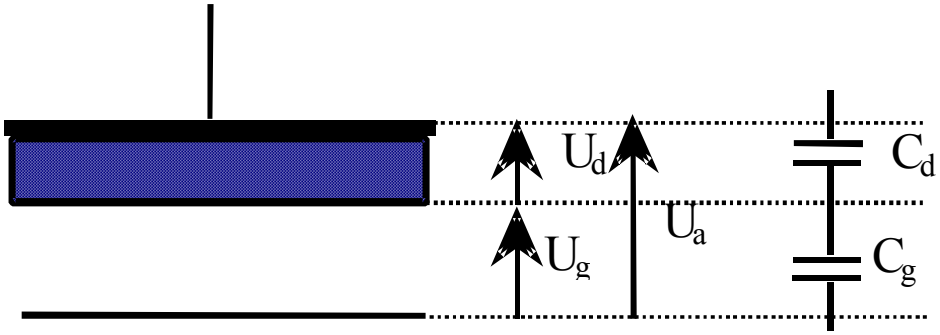

Figure 2: Equivalent circuit of a dielectric barrier discharge.
The generator voltage is: $U_a = U_g + U_d$

The power supply is a 50 Hz sinusoidal generator which deliver a 10 kV RMS voltage. No limitation of current is needed because of the dielectric effect. The corresponding voltage and current are showed in figures 3 and 4.

During the breakdown phase a number of discharges are generating in gap. In order to determine the corresponding number of elementary discharges a specific electronic counter has been designed. The elementary discharges number for positive voltage is written n_+ and the number in negative ones is written n_-. Experimental and model ($\exp(-t/\tau)$) of a typical current peak for an elementary discharge is plotted on figure 4. Time constant of positive peaks are written τ_+ and negative ones τ_-.n_+

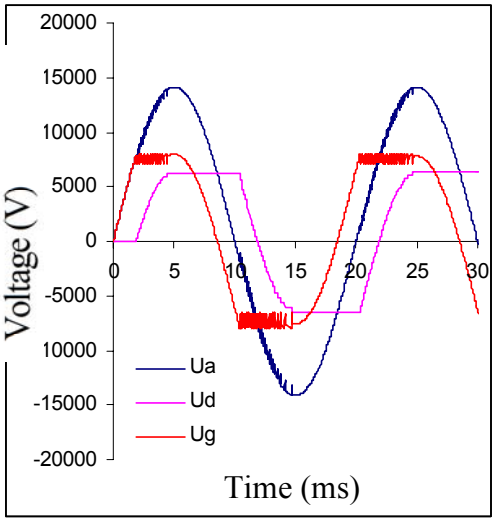

Figure 3: Voltage waveforms

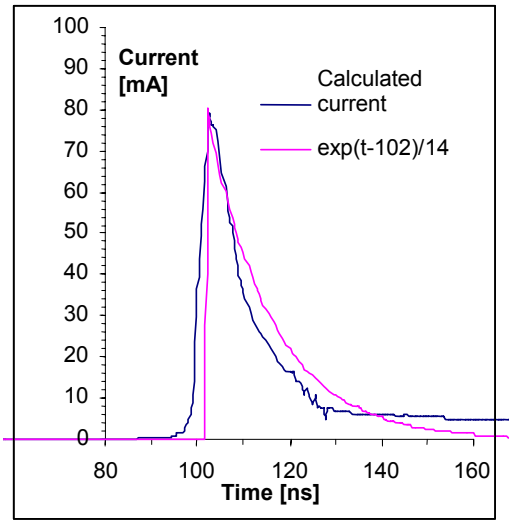

Figure 4: Current waveforms

3. Energy Measurements using voltage and current recording

A special probe is used for current variation measurements, both voltage and current can be recorded using an oscilloscope.

Energy exchange for an elementary discharge is written:

$$W_c = \int_\tau U_g i_{pic} dt$$

We have to notice that the corresponding voltage is the gap voltage which is generally quite different of the generator voltage

As it is shown above the discharges current variations are exponentials and have to be extracted from a more complex signal with a 50 Hz component. Extraction of the useful signal is performed using a high frequency pass filter. We make the assumption that the gas voltage has approximately the breakdown value. In this case the mean power can be written as:

$< P >= U_{bd} \times 0.63 \times (n_+ i_+ \tau_+ + n\_i\_\tau\_) f$ where U_{bd} and f are the breakdown and frequency voltage respectively.

The experimental results for N_2-NO mixture and air respectively are shown in the table 1.

	U_{bd} [kV]	i_+ [mA]	n_+	τ_+ [ns]	i_- [mA]	n_-	τ_- [ns]
N_2/NO	9.2	800	32	40	430	20	120
Air	8.6	900	78	18	450	39	45

Table 1: Experimental parameters for NO-N_2 and air plasma.

From the above formula we obtain <P> = 0.57 W for the N_2/NO mixture and <P>=0.53 W in the case of discharge in air.

4. The "Manley method"

This method wad proposed by Manley [8] in 1943. This is a simple way to determine the energy of the discharge in the case of a sinusoidal powering system. Parameters involved are the breakdown voltage U_{bd} and the two capacities C_g and C_d. Results are deduced by analysis of voltage versus charge plot (Lissajous figure). An auxiliary condenser (C_m = 2 nF) is series connected with the reactor in order to determined the electric charge Q. Typical Lissajous figures are shown below.

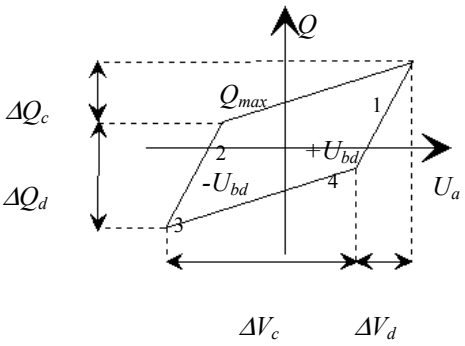

Figure 5: Theoretical Lissajous figure

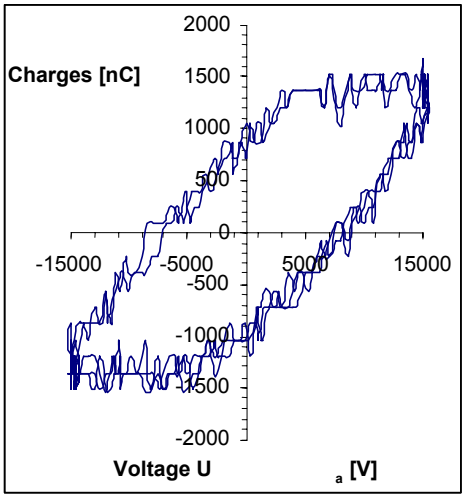

Figure 6: Experimental Lissajous figure

The power of the discharge can be calculated from the following relation :

$$P = 4U_{bd}C_d\left(U_{a,max} - \left(C_d + C_g\right)/C_d U_{bd}\right)f$$

For $U_{a,max}$ = 14.1 kV, C_g = 3.7 pF and C_d = 91 pF, we found that the calculated power is in the range 0.773 W and 0.743 W.

5. Energy deposition obtained from chemical reaction N + NO → N_2 + O

Plasma process efficiency is often characterized by the G-Value defined as the number of molecules removed by 100 eV of input energy.

$$G_{100eV} = \frac{100\,k_{ion/diss}}{v_e E/n}$$

The quantity $k_{ion/diss}\, n_e n$ is the number of reactions in a unit volume per unit time where n_e is the electron density. The quantity $n_e E v_e$ represents the amounts of energy expended by the electrons in a unit volume per unit time.

Because of variations in electric field an average value of the G factor must be used:

$$\left\langle G_{100eV}\right\rangle = \frac{1}{\tau}\int_0^{\tau} G_{100eV}(t)\,dt$$

where τ is the time duration of the discharge.

The $<G_{100eV}>$ factor had been calculated as a function of the reduced field, using a code described in reference [9] for pure N_2 and air. Results are presented below.

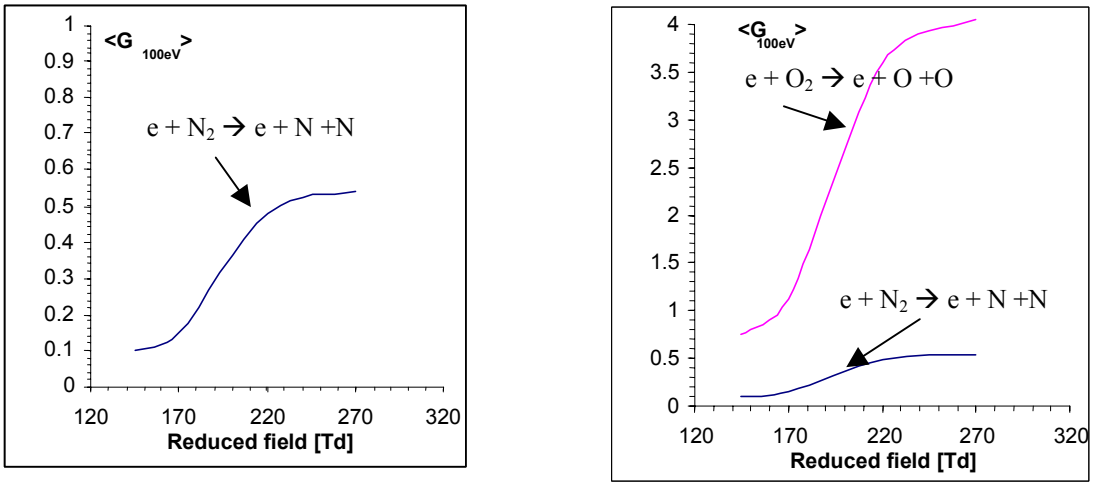

Figure 7: G_{100eV} as a function of the reduced field in nitrogen (a) and air (b).

From the destruction rate for a well chosen species it is possible to determine an electron production rate. Using the streamer simulation and breakdown voltage the input energy can be calculated.

We operated with a N_2/NO mixture and we particularly consider the chemical reduction of NO by the N radical [3]:

$NO + N \rightarrow N_2 + O$

This 2-body reaction predominates on the 3-body reactions:

$N + N + M \rightarrow N_2 + M$

and

$NO + O + M \rightarrow NO_2 + M$

N radicals are produced by electronic impact on N_2 molecule. The number of dissociations can be obtained from the $<G_{100eV}>$ factor.

For plasma processing of N_2-NO (1000 ppm) mixture, we measured at the output of the reactor 843 ppm NO and 75 ppm NO_2. This means that 75 ppm NO are oxidised in NO_2, and 82 ppm NO reduced in N_2. In that case, the residence time in the reactor is τ_s = 0.6 s, the reacting volume V = 4.85 cm^3 and the flow rate Q = V/τ_s = 8.1 $cm^3.s^{-1}$. Then, it is possible to calculate the number of nitrogen dissociations (8.13 10^{15} in that case). Using the G value for a reduced field of 170 Td, we determined the corresponding power of 0.62W.

Conclusion

The average value of the energy deposition into the gas in DBD reactor was determined by three methods: current-voltage characteristics, Manley's method and chemical transformation. The three techniques give a similar magnitude order (0.6 W) but accuracy (15%) is not sufficient to extend the results for large gas flow treatment devices. It should be necessary to performed accurate losses measurements in order to obtain a detailed balance of Joule effect heating and dielectric losses. Such a work is in progress to study.

References

[1] H. Masuda, Adv. Chem. Phys. **80,** (1991).

[2] S. Masuda, Pure Appl. Chem. **60**, (1988).
[3] B. M. Penetrante, M. C. Hsiao, B. T. Merritt, G. Vogtlin and P. H. Wallman, IEEE Transactions on Plasma Sc. **4**, Vol. 23 (1995).
[4] M. B. Chang, M. J. Kushner and M. J. Rood: Environ. Sci. Technol. **26,** (1992).
[5] Non-thermal Plasma Techniques for Pollution Control, part A and B, ed B. M. Penetrante and S. E. Schultheis (New York: Springer-Verlag), (1993)
[6] F. Westley, D. H. Frizzell, J. T. Herron, R. F. Hampson, W. G. Mallard, NIST Standard Reference Database 17, Gaithersburg, MD 20899 USA
[7] Z. Falkenstein and J. J. Coogan, J. Phys. D: Appl. Phys. 30, (1997)
[8] T. C. Manley, Trans. Electrochem. Soc. 84, 83 (1943).
[9] O. Martinie, Ph D thesis, Orleans, December 2000

Possibilities of VOC Treatment in Cylindrical Foaming Reactor

J. Pawlat[1], K. Hensel[2], C. Yamabe[1] and A. Mizuno[2]

[1]*Department of Electrical and Electronic Engineering, Saga University, Saga, Japan*
[2] *Department of Ecological Engineering, Toyohashi University of Technology, Toyohashi, Japan*

Abstract
The possibility of the treatment of VOC in the cylindrical foaming reactor is presented. About 55 mg/l of H_2O_2 and 20 ppm of O_3 were formed within the foam as an effect of the electrical discharges in oxygen. The experiments evaluating the absorption range of acetaldehyde within foam formed with pure water and additionally with the solution of surfactant in pure water were performed. The influence of the electrical discharge on the absorption and on the decomposition of acetaldehyde was observed.

1. Introduction of the foaming system

The problems of accretive devastation of natural environment and the increasing emissions of pollutants gain recently much attention of the authorities and local communities. It is necessary to develop new, environmentally safe techniques of production of goods, and also of recycling and utilization of wastes.

In this paper a foaming system is proposed. Despite of the small amount of required liquid, foaming column could be applied not only for polluted gas treatment but also for specific type of water and wastewater purification. The electrical discharge might be applied directly in foam, partly consisted of pollutant. Foaming column became the generator of various oxidants and the reaction vessel in the same time. The losses of oxidants in the providing system could be reduced.

Foam belongs to the special colloids group [1,2]. It can be generated in various ways in dependence of the required structure. On the base of those qualities foams are categorized as homogenous, (standing) and pneumatic (dynamic) foams [3], which both ensure the significant expansion of the contact surface between gaseous and liquid phases.

The most of foams are produced using the surface active compounds. However, foams created without any surfactants were very desirable from the environmental point of view. The experiments using this kind of foam, generated from gas and pure water only were performed as well as with the addition of the surface active substance to improve the absorption, to lower the gas flow limits and to avoid the pressure losses.

Pneumatic foam in presented experiments was formed without the addition of any foaming agents using only the gas kinetic energy, keeping the strict conditions of the medium flow and using the diffusers. Co-current flow, when gas and liquid flow through the same diffuser's hole, allowed for the appropriate inside-area usage [4]. The linear velocity of substrate gas for whole apparatus cross-section for dynamic foam should range 0.1-4.0 m/s, the gas velocity in the diffuser hole - 10-20 m/s, and 5-20% perforation of whole shelf area of the diffuser is advised.

2. Acetaldehyde as a substrate for technology and as an undesired pollutant in environment.

The treatment methods of ethanal

Acetaldehyde was first produced commercially in the United States in 1916. Nowadays, it is manufactured by the oxidation of ethylene with a palladium catalyst and by the catalytic hydration of acetylene.

Acetaldehyde is used in various branches of the industry as a chemical intermediate and basic substance for the production of acetic acid, pyridine and pyridine bases, peracetic acid, butylene glycol, esters, flavor and fragrance acetals, paraldehyde, metaldehyde, phenolic and urea resins, antioxidants, polymers, and various halogenated derivatives. It is also a common compound in manufacturing of aniline dyes, synthetic rubber, silver mirrors, fuel compositions, disinfectants, drugs, perfumes, explosives, pesticides, and room air deodorizers. Acetaldehyde is used as a fungicide, substrate of food flavorings, preservatives, lacquers and varnishes, photographic chemicals as well [5, 6].

Properties of acetaldehyde are presented in Table 1 and its molecular structure is depicted in Fig.1A.

Tab.1. Properties of acetaldehyde.

Name/Formula:	Acetaldehyde, Ethanal, acetic aldehyde, ethyl aldehyde, CH_3CHO, NCI-C56326
Physical Properties	Volatile, flammable, clear, colorless liquid, miscible in water, alcohol, ether, benzene, gasoline, solvent naphtha, toluene, xylene, turpentine, acetone, and other common organic solvents
Odor	Pungent, suffocating (in low concentration- fruity) odor, detectable at 0.0068 to 1000 ppm
Molar Weight	44.05
Specific Gravity	0.78 - 0.79
Vapour Density	1.52 (air = 1.0)
Vapour Pressure	740 mmHg at 20 °C
Melting Point	of -123.5°C
Boiling Point	20.2 to 20.8°C
Flash Point	-38 °C
Autoignition Temperature	185 °C
Stability	A highly reactive compound that undergoes numerous condensation, addition, and polymerization reactions (autopolymerization with metals (iron) or acids (concentrated sulfuric acid)). It oxidizes readily to form corrosive acetic acid.
Toxicity Data	LD_{50} oral (rat) 661 mg/kg
Major Hazards	Highly flammable liquid, its vapor is explosive in the concentration range 4 to 66% in air. Irritating to the eyes and respiratory system.

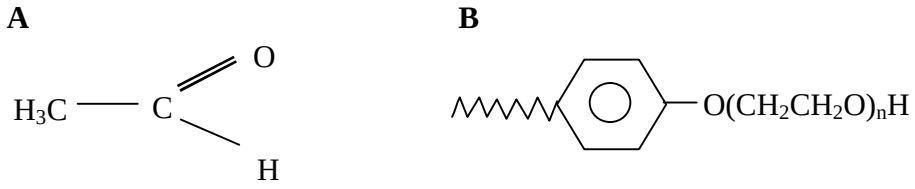

Fig.1. The structure of acetaldehyde (A) and Tritron X-100, n=9,10 (B).

Acetaldehyde is considered as a mutagen and possible human carcinogen [5-7]. Exposure to acetaldehyde by inhalation is irritating to the respiratory tract and mucous membranes; this substance is a narcotic and the chronic exposure can produce symptoms similar to alcoholism. Ingestion of acetaldehyde may cause severe irritation of the digestive tract. Ethanal causes irritation upon skin contact and eye burns.

Above premises gave an additional propulsion for research centers to study on the removal of acetaldehyde from exhaust gases and wastewaters.

Acetaldehyde decomposes above 400°C to form mainly methane and carbon monoxide, however thermal methods with large volumes seemed to be quite costly.

Various attempts of immobilization and treatment of acetaldehyde have been done. The amorphous silica [8], activated carbon with about 13% adsorption efficiency [9] and the polymer filters [10] were used to limit the concentration of acetaldehyde in the outlet fluid. Interesting solution based on biodegradation of ethanal in packed column with immobilized activated sludge gel was presented by Ibrahim et al. [11].

Other direction was the photodecomposition using surfactants and organic solvents, which amplified the overall decay rate [12]. The photon dissociation of acetaldehyde was described by [13, 14] with indicating

formaldehyde, metylhydroperoxide, CO as the products generated mainly via free radical channel. Those results were partly confirmed by the report based on acetaldehyde reactions with hydroxyl radicals [15].

In this paper a new method of absorption of acetaldehyde within foam is introduced. Additionally, the oxidants were formed in foam as an effect of electrical discharge [16] and the results of combination of electrical discharge and absorption in foaming apparatus were analyzed. The ideal treatment process of acetaldehyde using generated oxidants could be described by the equations (1-4) :

$$3CH_3CHO + O_3 \rightarrow 3CH_3COOH \quad (1)$$
$$3CH_3COOH + 4O_3 \rightarrow 6CO_2 + 6H_2O \quad (2)$$
$$2CH_3CHO + H_2O_2 \rightarrow 2CH_3COOH + H_2 \quad (3)$$
$$CH_3COOH + 4H_2O_2 \rightarrow 2CO_2 + 6H_2O \quad (4)$$

3. Experimental apparatus

The experimental set-up consisted of the foaming sub-system (gas and liquid providing), the electrical discharge sub-system and the chemical analysis sub-system.

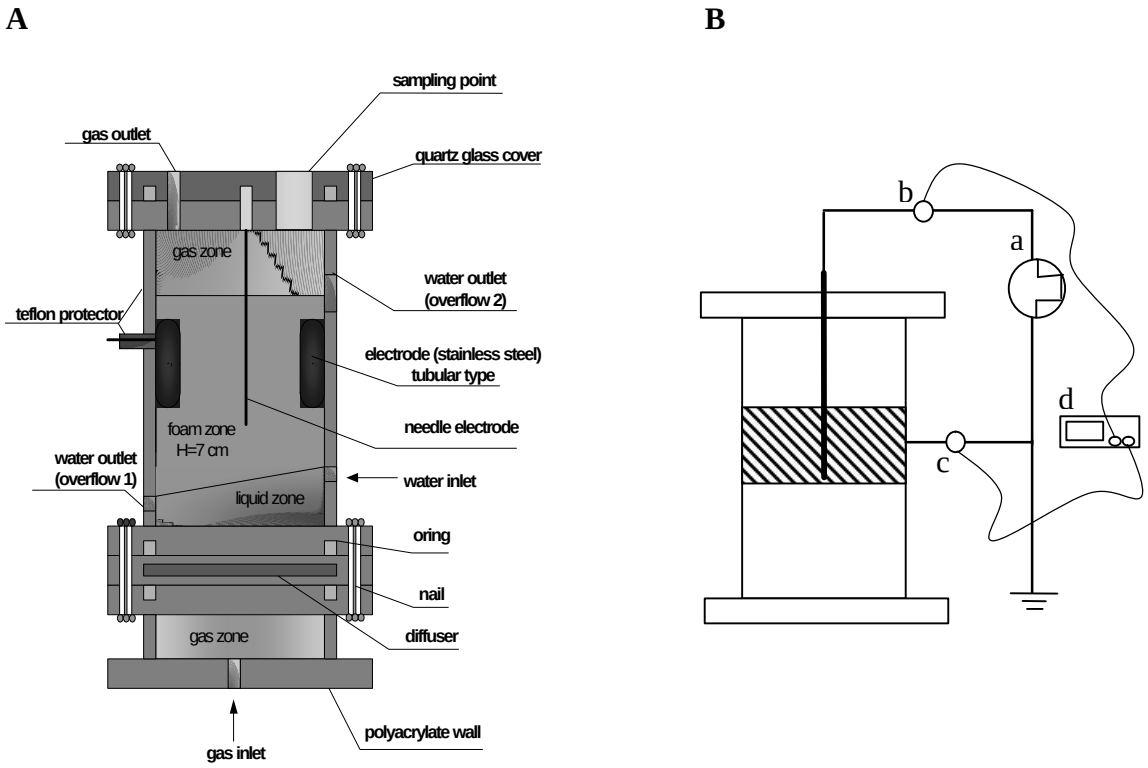

Fig. 2. Cylindrical foaming column (A) and the electrical circuit (B),
(a- pulse power source, b- high voltage probe, c-current probe, d-oscilloscope).

Main reactor, depicted in Fig. 2A was a cylindrical column (D_{in}=50 mm, L=200 mm). The ceramic diffuser type IA-500 was placed inside the apparatus. Stainless steel electrodes were located in the homogenous foam zone, above the diffuser. The inner electrode (d_{out}= 1.5 mm) was placed inside the outer electrode (d_{in}=40 mm, l= 30 mm).

The column was connected to the liquid and gas providing system. In the performed investigations pure water or pure water with addition of common surfactant (1 ml/500 ml H_2O) and Tritron X-100 (1ml/300ml H_2O)

was used as a substrate liquid. Substrate gases were air, oxygen and acetaldehyde with nitrogen as a carrying gas.

The electrical circuit is presented in Fig.2B. The pulse power source was operated at 250 Hz. The discharge voltage and current were measured using the high voltage probe (Tektronix, model P6015A) and the current probe (Tektronix, model P6021) with an oscilloscope (Tektronix, model TDS 644A), respectively.
The discharge pictures were taken using the digital camera Olympus Camedia X-2.

The hydrogen peroxide concentration was determined using Hydrogen Peroxide Test Kit (HACH, Model HYP-1). Thiosulfate titration of the sample (liquid after discharge application, mixed with specially formulated starch-iodide reagent used in hydrogen peroxide tests and with ammonium molybdate reagent) was performed in a low pH (pH=3.5) condition.

The ozone concentration in the outlet gas was measured using the GASTEC and KITAGAWA ozone gas probes. Outlet gas was collected in the gasbags and sampled.

The acetaldehyde concentration was measured using GASTEC and KITAGAWA acetaldehyde gas probes and gas chromatography (SHIMADZU GC-14B).

3. Results and discussion

Dynamic foam was formed in the reactor. Average diameter of the single bubble in foam ranged from 1 mm to 5 mm. The diameters of the bubbles tended to be bigger in the case of the lack of the surfactant, with increasing the distance from the diffuser and with increasing the substrate gas flow as well. Dosing of the additional amount of water caused the bubble diameter to decrease. Foam with surfactant was stable. Natural decay of foam formed with Tritron X-100 took more than 5 minutes whereas decay of dynamic foam without surface active compound took place immediately after the gas flow was shut down.

Several types of non- uniform discharges were obtained within dynamic foam. The typical electrical characteristics of the discharge and its photo taken from the top- side of the reactor in oxygen and pure water are shown in Fig.3.

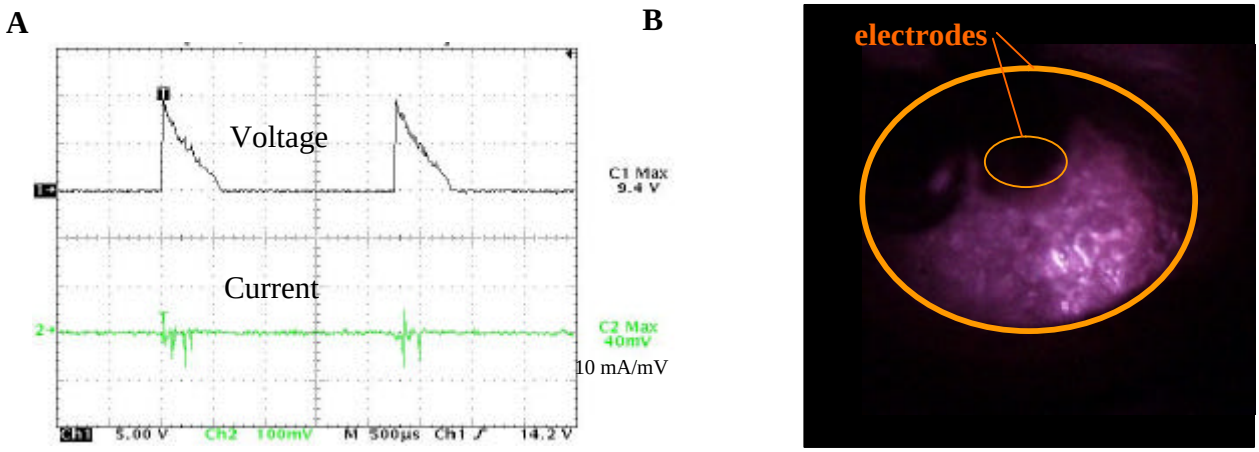

Fig. 3. Typical applied voltage and current waveforms of the electrical discharge in foam (A), and the photograph of the discharge (B). Oxygen flow rate 5 l/min, total power (including losses) 40 W.

The measurements were performed to confirm the presence of hydrogen peroxide and gaseous ozone generated by the electrical discharge. The concentrations of hydrogen peroxide in cylindrical column in the case of air without and with the addition of the common surfactant are depicted in Fig. 4. The small amount of gaseous ozone was also detected.

Generally, with the higher applied voltage, the concentration of oxidants increased as expected. For the relatively low gas flow rate for the formation of foam in the column, only low concentration of hydrogen peroxide was achieved. In the case of addition of surfactant the oxidants concentration decreased within the

same flow limits as without the addition of surface active compound. In the case of long term experiment added surfactant was gradually decomposed by formed oxidants and foam stability decreased.

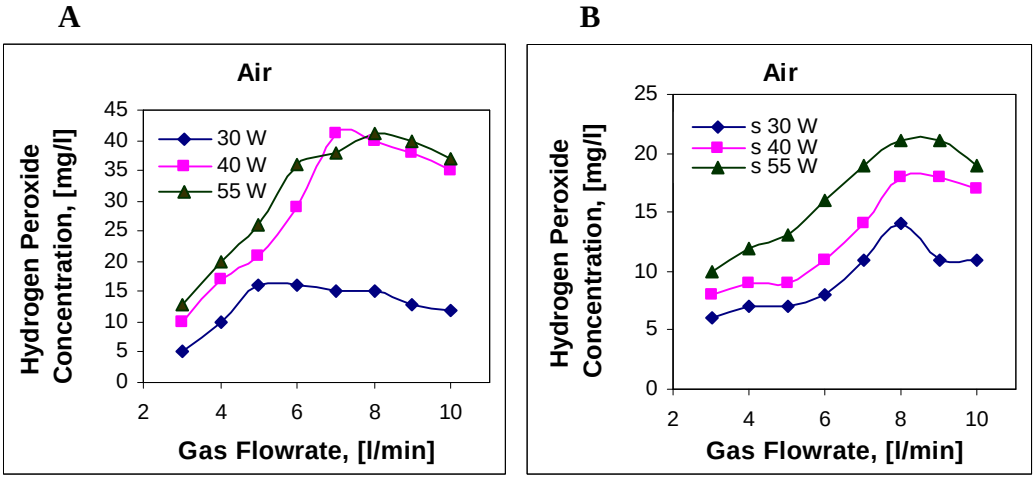

Fig.4. The hydrogen peroxide concentration in dependence on the gas flow without (A) and with the common surfactant (B), (power losses included).

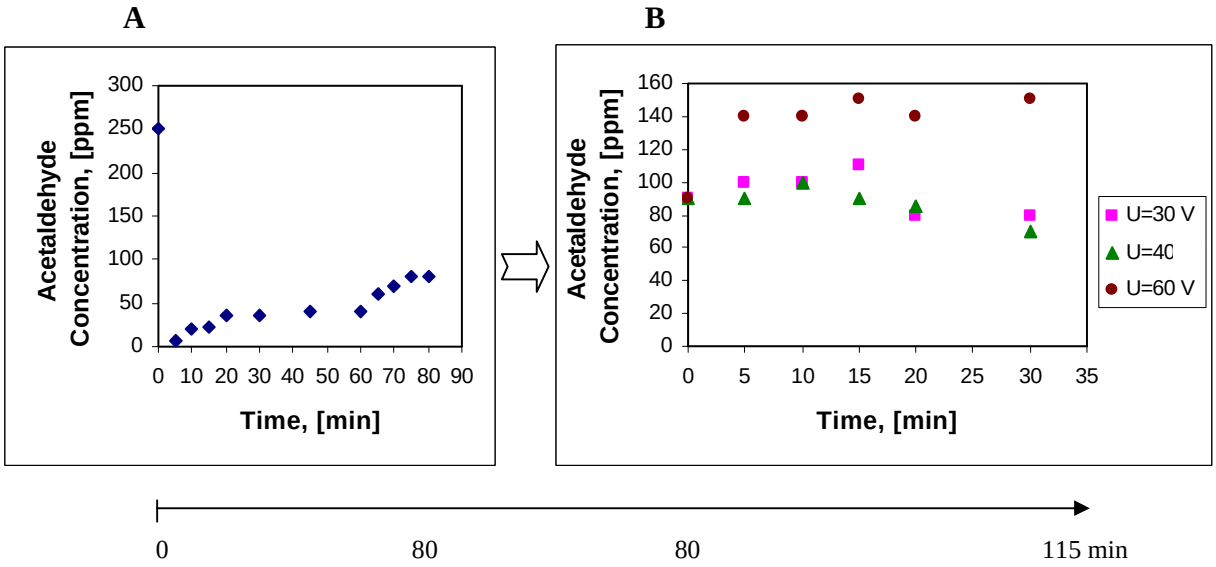

Fig.5. The absorption of acetaldehyde within foam with addition of Tritron X-100 versus time (A) and change in acetaldehyde concentration after application of electrical discharge to the saturated solution (B), (power losses included).

The process of absorption of acetaldehyde within foam without and with addition of Tritron 100 X was studied. The example of the one absorption cycle with 5 ml of the solution of surfactant in pure water is presented in Fig.5. In that case air-acetaldehyde in nitrogen gas flow rate was 1,2 l/min and initial concentration of ethanal was 250 ppm. After the 80 minutes of saturation time, the electrical discharge was applied. The proceeding of electrical discharge caused the releasing of acetaldehyde absorbed before and decomposition of the surfactant then gradually concentration of CH_3CHO decreased. The absorption process in presence of

Tritron was much more efficient than in the case of pure water only because of hydrophobic nature of acetaldehyde molecule.

4. Conclusions

An apparatus based on the discharge in the foam was designed.

Foam was obtained without the dosing of the surface-active substances, keeping the strict conditions of the gas flow rate and with the addition of common surfactant and Tritron X-100.

The high amount of hydrogen peroxide and low amount of gaseous ozone were formed within foam. The combination of various kinds of oxidants makes foam belong to the Advanced Oxidation Processes.

The acetaldehyde could be absorbed within the foam. The superposition effect of combining the absorption process with the electrical discharge was not fully confirmed. The absorption was improved when the surfactant was dosed to the substrate liquid.

The foaming system allows obtaining various species in one compact apparatus, potentially even directly in the polluted medium and it connects in one body the advantages of oxidants' generator and the reaction vessel.

Acknowledgments

A part of this work was supported by the Grant of Japanese Society for Promotion of Sciences.

References

[1] E. Dickenson, Introduction to Food Colloids, Oxford University, Press (1992).
[2] J. Patino, M. Delgado and J. Fernandez, Colloids and Surfaces: A, **99**, 65-78, (1995).
[3] S. Bistron, P. Sarre, and B. Szymonik, Chemik, **3**, 81-83, (1978).
[4] J. Pawlat, C. Yamabe, I. Pollo, Proc.2000 National Convention I.E.E. of Japan, Tokyo, Japan, vol.**1**, 232, (2000).
[5] International Agency for Research on Cancer. IARC Monographs on the Evaluation of the Carcinogenic Risk of Chemicals to Humans. Allyl Compounds, Aldehydes, Epoxides, and Peroxides. Vol. **36**, Lyon, France: IARC, (1985).
[6] International Agency for Research on Cancer. IARC Monographs on the Evaluation of Carcinogenic Risks to Humans. Re-evaluation of Some Organic Chemicals, Hydrazine, and Hydrogen Peroxide. Vol. **71,** Lyon, France: IARC, (1999).
[7] International Agency for Research on Cancer. IARC Monographs on the Evaluation of Carcinogenic Risks to Humans. Overall Evaluations of Carcinogenicity. Supplement **7**, Lyon, France: IARC, (1987).
[8] M.A. Natal-Santiago, Josephine M. Hill, J.A. Dumesic, Journal of Molecular Catalysis A: Chemical **140,** 199–214, (1999)
[9] Y. El-Sayed and T. Bandosz, Journal of Colloid and Interface Science **242**, 44–51 (2001).
[10] S. Shiratori, Y. Inami, M. Kikuchi, Thin Solid Films **393,** 243-248, (2001).
[11] M. Ibrahim, H. Mizuno, Y. Yasuda, K. Fukunaga, K. Nakao, Biochemical Engineering Journal **8**, 9–18, (2001).
[12] W. Chu, C.Y. Kwan, Water Research **36**, 2187–2194, (2002).
[13] S. Shin, S. Kim,H. Kim, C. Park, Journal of Photochemistry and Photobiology A: Chemistry **143,** 11–16, (2001).
[14] K. Wirtz , US/German Environmental Chamber Workshop Riverside, (1999).
[15] S. Vandenberk, J. Peeters, Journal of Photochemistry and Photobiology A: Chemistry **6272,** 1–6, (2003).
[16] J. Pawlat, A. Mizuno, C. Yamabe, Proc. Conference of Institute Electrostatics Japan, Tokyo, Japan, (2003).

On the use of a magnetic blow out glidarc reactor for the syngas production by steam reforming

J.M. Cormier[1], I. Rusu[2] and A. Khacef[1]

[1]*GREMI, Université d'Orléans, 14 rue d'Issoudun, BP 6744, 45067 Orléans Cedex 2, France,*
[2]*Technical University "Gh. Asachi", Faculty of Industrial Chemistry, Bd. Dimitrie Mangeron 71, Iasi 6600, Romania*

Abstract

This work is dedicated to the experimental study of methane steam reforming using a magnetic blow out discharge at atmospheric pressure. Results obtained from a new three-phase reactor using a rotating effect produced by a magnetic field on the ionised gases, are presented. Experiments clearly demonstrated the ability of magnetic blowing discharges to increase the conversion efficiency of chemical reactions at low temperature.

A simple model is deduced from the chemical and physical analysis. According to this model we have calculated the gas fraction that passes through the discharge and discussed the efficiency.

On the other hand, we notice the possibility of using this kind of device to feed fuel cells with hydrogen. Therefore, due to its compactness and small dimensions the glidarc reactor may have potential automotive applications.

1. Introduction

There are several methods to produce syngas but most of it (40%) is obtained by steam reforming (SR) [1]. The conventional catalytic technology presents several shortcomings as: large size of the equipment, high investments and exploitation costs, limitations on rapid response, catalyst sensitivity to poisons, and extreme operating conditions that limit the lifetime of reactors [2, 3].

Plasma is known to be a very high energy density media and gives an attractive alternative for the production of hydrogen and synthesis gas. In this approach, the plasma replaces catalysts and accelerates chemical reactions due to both temperature and active species effect. Plasma reactors represent an incisive approach by their simplicity, compactness and low price.

Gliding arc reactors are the subjects of multiple possible applications to a variety of chemical processes. The gliding discharges allow high specific throughputs in the reaction zone, which generally largely exceed other chemical methods, including electrochemical and thermal ones. However, previous studies on the methane steam reforming indicated that these types of reactors must be improved in order to obtain better conversions [2-5].

The aim of this paper is to present a new three-phase reactor which has been proposed with good results, the conversion increasing up to 50% [6]. The reactor uses a rotating effect, produced by a magnetic field, on the ionised gases.

2. Experimental

1.1. Magnetic blowing arc reactor

The new reactor design is shown in Figure 1. The plasma reactor consists of three anodes that are arranged around of a single cathode. The cathode is a 6 mm diameter tungsten rod. The anodes are fixed at the output of the inlet tube, which is made in ceramic. A magnet is surrounding the inlet tube. Discharges are ignited at the outlet of this tube and then pushed by the flow. The discharge column is a plasma string with a visible diameter less that one millimetre that slides in the gas flow and the magnetic field. At the same time the

voltage increases and the length of the discharge grows up. Due to the magnetic field a rotating effect of the plasma strings is produced.

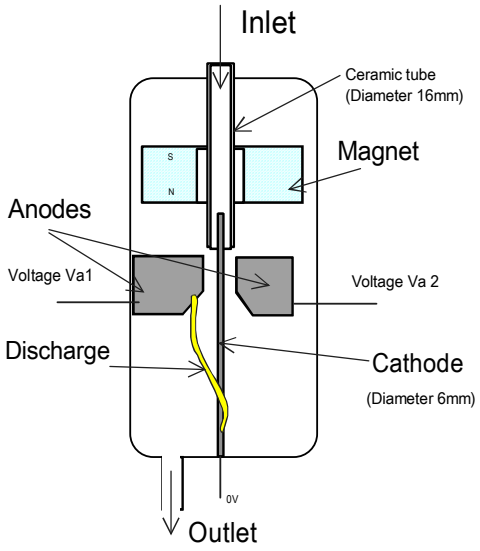

Figure 1: Photo and scheme of the new reactor

The discharge behaviour in a magnetic field is quite different than the usual gliding discharges. The first effect is the increase of the mixing properties of the reactor [6]. The plasma string performs a helix movement and looks like a wrapped wire around the cathode. As a result the plasma can sweep a large part of the inlet gas. The second effect is the maintaining of the non-equilibrium behaviour of the discharge. For usual gliding discharges, the transition to the arc must be avoided using external current limitation (resistors, reactors, etc). In the case of magnetic blow out, the force acting on the lengthening discharge column is proportional to the product between the current and the magnetic-field strength. This force produces a very rapid lengthening of the discharge column (Figure 2). The de-ionisation occurs much faster, leading to the mixing of the discharge gases with the cold gas through which the core is forced to pass in its rapid motion. Due to the magnetic field, a self-limitation of the current intensity is produced.

The electrical supply is a three channels one, which is used to power up the three cascading discharges. One channel consists of two transformers with rectifiers that allow two running phases: the ignition at high voltage and low current intensity and a complementary energy supply with higher current [7]. Due to the magnetic field there is no need of additional resistance for current limitation.

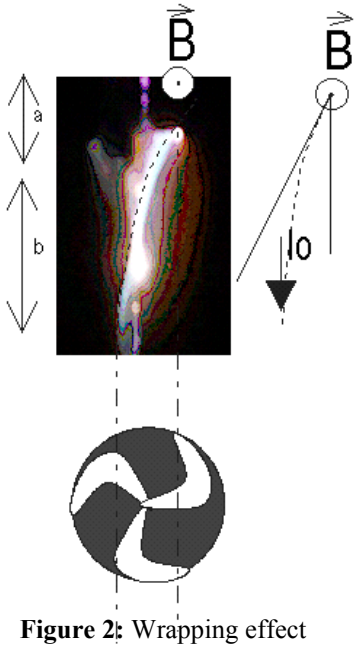

Figure 2: Wrapping effect

Figure 3 shows the variation of voltage current and power for one of the three discharges as a function of time. In order to clarify the diagram from Figure 3 we have to mention that the voltage is plotted as a negative signal. As can be seen on this figure, the discharge behaviour is not definitely periodic due to the instabilities in the growing discharge. The electrical power is obtained by averaging results over a large number of periods.

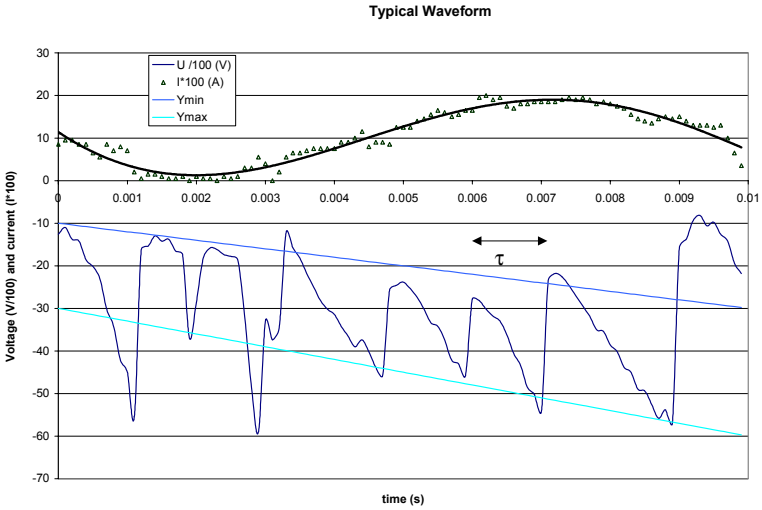

Figure 3: Voltage and current waveforms

1.2. Chemical tests

All experiments were conducted at atmospheric pressure. The water and methane are mixed before injection in a heating line. The inlet temperature was fixed at about 150°C for all the experiments. The exhaust gas from the reactor was passed through a condenser and then through a desiccant column. The major gaseous components were analysed on-line and quantified using gas chromatography (TCD detector - HP5890 for H_2, FID detector - Varian 3400CX for CO, CO_2, CH_4 and C_2).

2. The magnetic wrapping effect and sweeping effect.

Let us consider the orthogonal component of the magnetic field B (figure 2). The plasma wire is lengthening in the flow and the wrapping effect is produced around the cathode.

The first zone corresponds to the magnetic disturbed region (a) and the second is the lengthening region (b). From a very simple point of view the reactor efficiency is directly related to the plasma volume in comparison of the gas volume.

Below the opposite photo, the covered discharge area is pictured in white. And from experimental determinations we can consider that only 35-45 % of the gas is swap by the discharge

3. Temperature of the plasma string

One of the most important features of gliding discharge is the so called "*back-breakdown phenomenon*". The plasma string is stretched in the flow and its length is increasing till the back-breakdown time. At this time, the electrical charges take a short cut resulting from the spark breakdown between two parts of the plasma column. Then the new shortened plasma string is stretched in the flow till a new back-breakdown.

The saw-tooth variation of voltage is corresponding to the extension of the plasma string which is followed by the fast back-breakdown, the corresponding duration is written τ. The voltage drop along the positive column is approximately proportional to the discharge length. Then the minimum of voltage is corresponding to a minimum of length and the maximum voltage to a maximum of length.

Then from a previous paper [8], it is possible to express the discharge power as a function of the discharge parameters. We consider a classical discharge string surrounded by an excited region which is few

millimetres wide. We make the assumption that the electrical charges drift in the core of a cylindrical discharge of radius r_o. This surface is supposed to represent the boundary between the high temperature conduction core and the excited region.

The ambient temperature is T_a and the temperature at $r=r_o$ is $T_b \# T_m$. The mean power exchange for a plasma column with an average length <L> during the extension duration τ is given by:

$$EI = 4\sqrt{\pi}\ \frac{\lambda}{\sqrt{D}}\ T_m\left(1-\frac{T_a}{T_m}\right)\ \frac{r_o}{\sqrt{\tau}}$$

E: Electric field strength
I: Electric current
D: diffusion coefficient in the temperature range [T_a, T_m].
λ: Thermal conductivity at the temperature T_m
r_o: discharge core radius
T_m: axial gas temperature

From the above relation the temperature can be evaluated using the experimental values of EI, r_o, and τ. The values of $\lambda/\sqrt{D}$ are taken from the literature and are fitted as a function of the temperature.
Then we find that the T_m temperature range is 2000-4000 K.

Taking account these results and the sweeping efficiency it can be assumed that, approximately 50% of the gas, can be treated. This value indicated a significant improvement of the results in comparison with the previous ones.

4. Experimental results

Concentrations of the outlet products are shown in figure (4) as a function of the power. The CO_2 and C_2 concentrations are not significant (less than 1%).

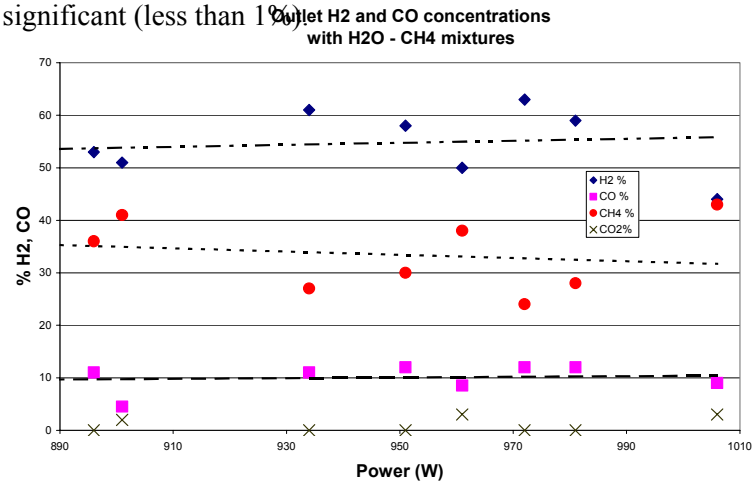

Figure 4: Outlet H_2 and CO concentrations with H_2O-CH_4 mixtures

5. Discussion

5.1. Thermodynamic model

We have tried to model the chemical processes occurring in the glidarc reactor starting from conclusions drawn in our previous studies [4]. Firstly, we considered that the reactions occur mainly in the discharge string. As is shown above 35-45% of the inlet gases penetrates the discharge [6]. Therefore, in our model we have considered that the inlet gas stream is divided in two parts: the main part that remains at 400 K and a smaller percent that is heated up in the discharge. We also have considered that both streams arrive at thermodynamic equilibrium. According to the above measurements, the temperature on the outer surface of the discharge string ranges between 2000 and 4000 K. The fact that the mean temperature in the reactor is increasing during the experiments from one end to another with only 100 K [8], is leading to the conclusion that the glidarc zone has to be treated as an almost adiabatic zone. In this kind of model, the gas penetrating the discharge is almost instantly heated up to more than 2000 K. Afterwards, its temperature follows the

temperature profile of the arc and when it leaves the string, sharply cools down to ambient temperature almost without heat exchange.

5.2. Comparison between model and experiment

An example of thermodynamic calculation results for the composition of gases quenched out from the arc discharge is shown in Figure 5. The calculations suggest that the temperature is usually not higher than 2700K, but in some cases the possibility of having higher temperatures (up to 3000K) on the outer surface of the arc could explain the presence of acetylene in some of the samples collected from the reactor outlet.

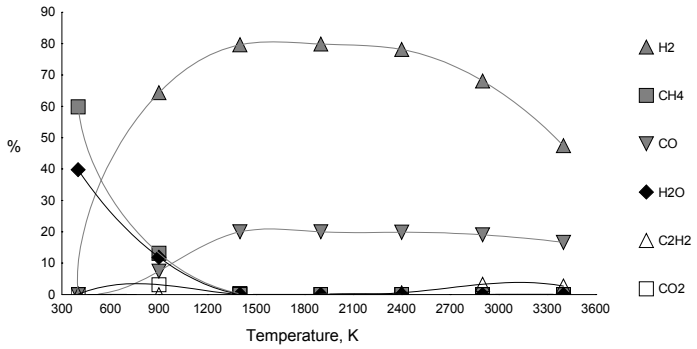

Figure 5: Concentration of different reaction products at the outlet of the discharge string calculated by means of the Chemical Workbench code for the molar ratio $CH_4/H_2O = 1.5$.

If we consider a large heat exchange between the discharge and the gas stream, the outlet temperature from the reactor has to rise up to about 800 K. However, this is not true, because neither the chemical analysis (i.e. the lack of CO_2) nor the temperature measurements indicate this behaviour. Therefore, the model implies mass transfer but no heat transfer between the arc and the rest of the gas stream.

According to this model we have calculated the gas fraction that passes through the arc as a function of chemical analyses. On our calculation, we also have taken into account the volume modification due to the chemical reactions occurring in the glidarc. As expected, the values are in the range 50-45% explaining the methane conversions.

Conclusions

The new magnetic blow out glidarc reactor has reached its main aim – the increase of the methane rate conversion. The back- breakdown model leads to the temperature range operating conditions. A simplified model then can be used. On the other hand the system is well suited for plasma catalytic reactions. Further tests must to be performed, in order to determine the best feeding parameters of the reactor and the effect of plasma catalysis and/or classic catalysis on hydrogen production.

Acknowledgments

The authors would like to acknowledge the support of the European Community - Access to Research Infrastructure action of the Improving Human Potential Programme.

References

[1] C. Liu C, R. Mallison and L. Lobban, J. Catal., 179, (1998)
[2] J. M. Cormier, I. Rusu. and N. Apostolescu, Proc. ISPC 15, ed. A. Bouchoule, J.M. Pouvesle, A.L. Thomann, J.M. Bauchire & E. Robert, International Plasma Chemistry Society, (2001)
[3] J. M. Cormier and I. Rusu, J. Phys. D: Appl. Phys., 34, (2001)
[4] J. M. Cormier, I. Rusu, and A. Kaminska, J.High Temp.Mat.Proc, Vol6, N°4, 2002, pp.421-429
[5] I. Rusu and J. M. Cormier, Chem. Eng. J., 91 (2003) 23-31)..
[6] J. M. Cormier, I. Rusu I., M. Dudemaine and D. Sibiescu, Proc. OPTIM 2002, Brasov, 2002.

[7] N. Reveau N, M. Nikravech., O. Martinie, P. Lefaucheux, and J. M. Cormier, Proc. HAKONE VII, ed. H.E. Wagner, J.F. Behnke and G. Babucke, Greifswald, (2000)
[8] S. Pellerin, O.Martinie, J. M. Cormier, J. Chapelle, and P. Lefaucheux, J.High Temp. Mat. Proc 3-2&3 (1999).

Surface Changes of Atmospheric Glow Discharge Treated PTFE Films

Aubrecht L., Koller J.

Department of Physics, Faculty of Electrical Engineering, Czech Technical University, Technická 2, 166 27 Prague 6, Czech Republic

Both atmospheric and low-pressure electrical discharges are used for enhancing properties of polymer substrates. The deposition and modification of thin films is mostly performed by high frequency or microwave discharges under vacuum conditions in the range between 0.001 and 1 mbar. Due to the requirement of a vacuum system, these processes are very expensive, particularly for large substrates. Therefore, the plasma-enhanced deposition and modification of various films at atmospheric pressure is a promising approach to perform the modification of large-sized low-cost products such as polymer foils, metal bands, textiles or papers.

The state of the art of this new technology is discussed. The influence of various process parameters on the discharge properties is shown. The various surface modification plasma technologies are also discussed.

This paper deals with phenomena observed during the study of plasma deposition and modification of polymer surfaces – effects of corona discharge treatment on PTFE surfaces and the influence of treatments on the physical properties of these surfaces.

Positive ion and neutral radical measurements in $Ar/C_4F_8/O_2$ capacitive discharges

Nicolas Bulcourt[1], Jean-Paul Booth[1], Jacques Jolly[1], Eric A. Hudson[2], Jorge Luque[2]

[1] *Laboratoire de Physique et Technologie des Plasmas (LPTP), Ecole Polytechnique, France.*
[2] *Lam Research Corp., Fremont, USA*

Introduction

Capacitive discharges in gas mixtures such as $Ar/C_4F_8/O_2$ are widely used in the microelectronic industry for integrated circuit fabrication. This plasma chemistry allows selective etching of SiO_2 over Si, while depositing polymer films to control the feature profiles and dimensions. Nevertheless, small changes in the gas composition can cause drastic changes in the etch behavior, giving a narrow process window. It is therefore necessary to obtain a better understanding of the processes governing the fluxes of reactive ionic and neutral species to the etched substrate.

1. Ions in a single frequency discharge

Experimental Setup

The $Ar/O_2/C_4F_8$ capacitive discharge is generated in a confined parallel plate reactor at a pressure of 50 mTorr. The diameter of the electrodes is 12 cm and the gap distance is 3 cm. A grid connected to ground confines the plasma. Consequently the area ratio, defined as area of the ground electrode (and grid) to the powered electrode is equal to 2. A Hiden quadrupole mass spectrometer (QMS) is implanted under the ground electrode. The species are collected through a hole with a diameter of 100 microns in the center of the ground electrode. A differential pumping system maintains a pressure inside the mass spectrometer lower than 10^{-6} Torr. The figure 1 shows a schematic diagram of the experimental apparatus.

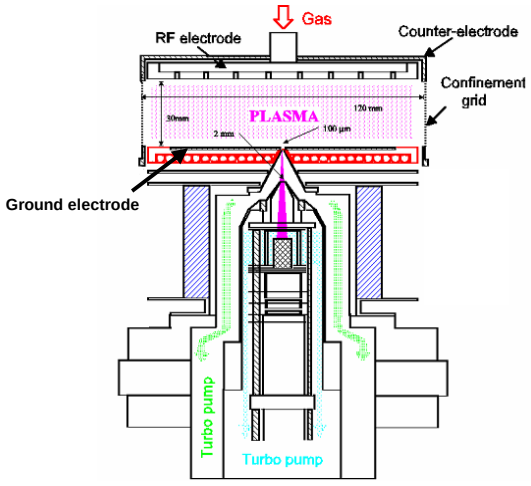

Figure 1: *Experimental Setup for the mass spectrometry.*

Results

We determined the composition and energy distribution functions of the positive ions (figure 2 and figure 3) for different conditions of discharge. We especially investigated the effect of the RF power (20 and 50 Watts), the addition of oxygen gas to the mixture and the excitation frequency (13.56 to 40.68 MHz).

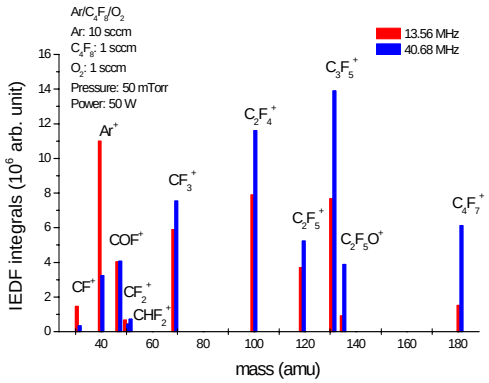

Figure 2: *Effect of the frequency on the positive ionic composition.*

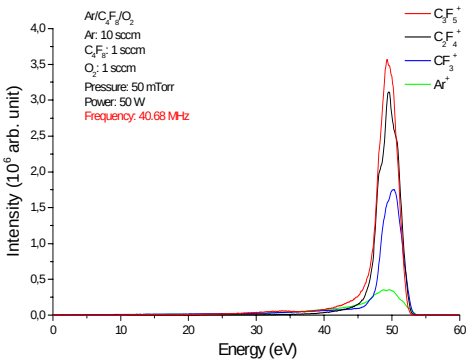

Figure 3: *Ion energy distribution functions for some positive ions.*

The major positive ions observed were Ar^+, COF^+, CF_3^+, $C_2F_4^+$, $C_2F_5^+$, $C_3F_5^+$ and $C_4F_7^+$. This mass distribution is in broad agreement with the measurements of Jiao et al. [1] of the dissociative ionization cross-sections of C_4F_8. Increasing the oxygen flow-rate favors the ions CF_3^+ and COF^+ and decreases the flux of the heavier fluorocarbon ions.

Figure 4 shows an example of the ion energy distribution functions observed at the grounded electrode. At the lowest excitation frequency the ions have a high average energy due the high plasma potential in this nearly symmetrical system, and the saddle structure can be seen, caused by the large RF modulation of the plasma potential [2,3,4]. As the excitation frequency is increased, the average ion energy decreases, as does the width of the saddle: at 40.68 MHz the ions are nearly mono-energetic.

Figure 5 shows the IEDF's of certain ions that show low energy structure. As expected, the Ar^+ ion is strongly affected by the rapid symmetric charge exchange occurring with neutral Ar, present in large concentration [5, 6 and 7]. More surprising is the low-energy structure observed for CF_2^+, CF_3^+ and CF^+. We attribute this again to symmetric charge exchange, this time with the appropriate neutral free radicals, present in significant concentration. This technique can therefore also give information about the presence of neutral free radicals in the plasma.

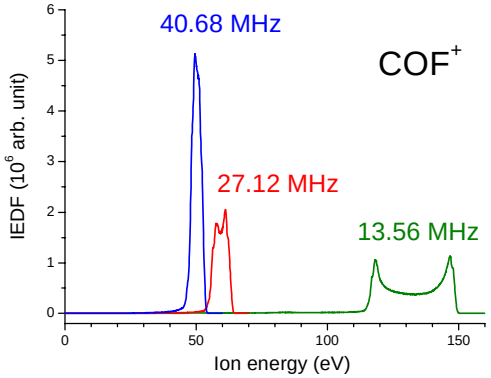

Figure 4: *IEDF of the ion COF^+ as a function of excitation frequency: 50 mTorr, 50 W RF power.*

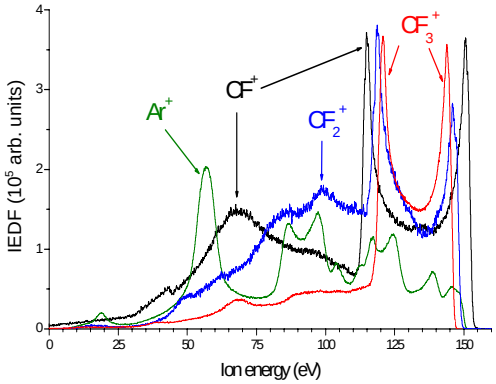

Figure 5: *IEDF's showing low energy structure. 13.56 MHz, 50 W, 50 mTorr.*

Mass spectrometry allows measurement of the mass distribution of the discharge and the energy distribution functions of the different species that are present in the plasma. We were able to study the major positive ions that are present in this discharge and to demonstrate the importance of complex mechanisms such as charge exchange.

2. CF_2 study in a Dual frequency capacitive discharge

Experimental Setup

The CF_2 radicals were created in an $Ar/C_4F_8/O_2$ dual frequency (27 MHz + 2 MHz) capacitive discharge. The discharge was generated in a commercial dielectric etch system (Lam Research) that was modified to permit optical measurements (figure 6). We measured the UV absorption spectra of CF_2 A-X band using the broad band UV spectroscopy technique [8] using a commercial broad band Xenon lamp and a commercial 0.75 m spectrograph with multi-channel photodiode array detector (PDA).

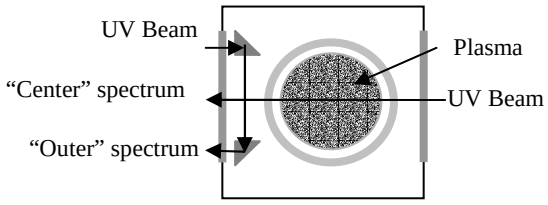

Figure 6: *Experimental Setup for the measurements of the UV absorption spectra.*

The plasma is radially confined by quartz rings. The CF_2 radical is relatively unreactive and therefore is present in significant number density outside the confined plasma volume. Consequently, to measure the CF_2 density in the plasma we need to measure two spectra. The "center" spectrum (measured across the chamber (figure 6)), and an "outer spectrum" measured in the chamber but outside the confinement quartz rings (figure 6) using quartz prisms to direct the beam. From these two spectra we were able to determine the CF_2 density in the plasma. Figure 2 shows examples of the UV absorption spectra obtained.

These results show that the CF_2 spectra in the plasma and outside the confinement rings have a very different shape. The "center" spectrum is more intense and hotter (the vibrational hot bands are more visible) than the "outer spectrum". Moreover we can see that the radical CF is present inside the confinement rings but not outside the rings. This is due to its shorter lifetime compared to CF_2 (the surface reaction coefficient of CF is higher,).

A more detailed analysis of the "center" spectrum indicates that CF_2 is not only hot but has vibrational energy distributions that deviate from a Boltzmann distribution (figure 8).

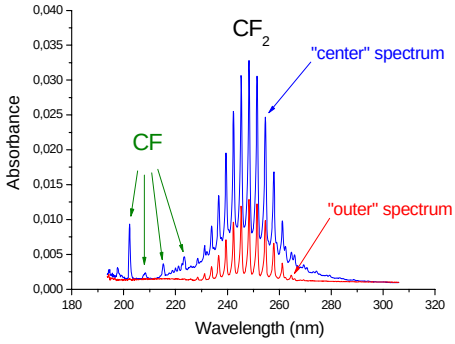

Figure 7: *UV absorption spectra of the radical CF_2.*

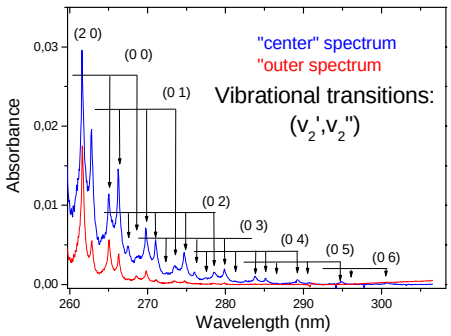

Figure 8: *Assignment of the vibrational hot bands for the CF_2 spectra.*

This suggests that the CF_2 molecules are initially produced in highly-excited vibrational states and are only partially relaxed by collisions. The presence of these highly-vibrationally-excited molecules can explain the apparent continuum absorption that we can see in figure 7. However, even for the "hot" spectra it should be possible to deduce the CF_2 density from the *integrated* band intensity, independent of the vibrational level distribution.

Determination of the CF_2 density

A fitting routine was written to determine the density and the temperature of CF_2 from the UV absorption spectrum. We simulated the different spectra using a program that takes into account the spectroscopic constants, the wavelengths and the Franck-Condon factors (FCF's) of the different transitions we considered. The spectroscopic constants and the wavelengths were taken from the literature [9, 10]. When the constants were not known they were estimated by linear extrapolation.

The formula used to fit the different spectra is:

$$Y = Baseline + \sum_{\nu'\nu''} P_{\nu''} * FCF_{\nu'\nu''} * \lambda_{\nu'\nu''} * S_{\nu'\nu''}(Trot) \quad (1)\ [11]$$

where:

$P_{\nu''}$ is proportional to the relative number density of the different vibrational levels in the ground state.

$FCF_{\nu'\nu''}$ is the Franck-Condon factor of the transition $A(0,\nu',0) \leftarrow X(0,\nu'',0)$.

$\lambda_{\nu'\nu''}$ is the wavelength in nanometers of the transition.

$S_{\nu'\nu''}(Trot)$ is the rotational envelope for each vibronic transition, calculated from the rotational temperature and the spectroscopic constants. Each integrated band intensity is normalized to unity.

Results

Figure 9 shows the agreement between the simulated and experimental spectra. The Franck-Condon factors were deduced using the following formula:

$$Y = Baseline + \sum_{\nu'\nu''} P_{\nu'\nu''} * S_{\nu'\nu''}(Trot) \quad (2)$$

where $P_{\nu'\nu''}$ is equals to $P_{\nu''} * FCF_{\nu'\nu''} * \lambda_{\nu'\nu''}$.

Consequently, the ratios of the different parameters $P_{\nu'\nu''}$ for the same ground state level and the relation $\sum_{\nu'} FCF_{\nu'\nu''} = 1$ allows the FCF's to be deduced, as shown in Table 1:

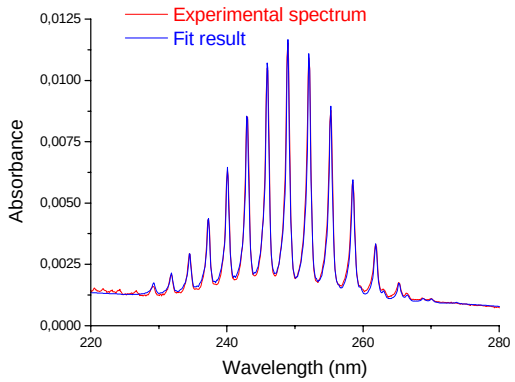

Figure 9: *Result of the fit of a CF_2 spectrum.*

	X(0 0 0)	X(0 1 0)
A(0 0 0)	0.0020236824	0.0232531383
A(0 1 0)	0.0103882846	0.0664486564
A(0 2 0)	0.0330011722	0.1220384103
A(0 3 0)	0.0727253050	0.1587078136
A(0 4 0)	0.1167213999	0.1604230967
A(0 5 0)	0.1516350890	0.0993654566
A(0 6 0)	0.1606418524	0.0731734228
A(0 7 0)	0.1512419930	0.0045126062
A(0 8 0)	0.1167430562	0.0542213390
A(0 9 0)	0.0828107036	0.0630409260
A(0 10 0)	0.0510448127	0.0691059530
A(0 11 0)	0.0276570779	0.0588132872
A(0 12 0)	0.0147738121	0.0421578833
A(0 13 0)	0.0085917590	0.0047380105

Table 1: *Experimental Franck-Condon Factors*

The FCF's are normalized to unity for the same ground state level.

Fitting of the spectra allows the line-integrated CF_2 number density to be determined as a function of process parameters including pressure, total gas flow, residence time etc. Figure 10 is an example of results for this study.

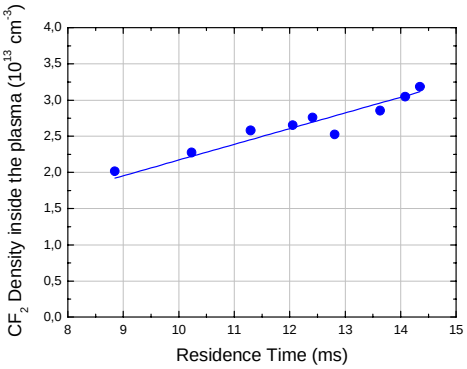

Figure 10: *CF_2 density versus the residence time.*

Ultraviolet absorption spectroscopy is a simple technique for measuring the density and the temperature of the radical CF_2. The measurements of the "outer" and "center" spectra have different band shapes that can be explained in terms of the different cooling, production and destruction mechanisms.

3. Conclusion

The chemistry of the Ar/O2/C4F8 capacitive discharges brings into play complex mechanisms where the positive ions and the neutral species play an important part. Indeed, this kind of discharge contains a large range of species. The major positive ions are Ar^+, COF^+, CF_3^+, $C_2F_4^+$, $C_2F_5^+$, $C_3F_5^+$ and $C_4F_7^+$ with quite different energy distribution functions due to charge exchange processes. Concerning the study of CF_2 , we deduced from the experimental results a set of Franck-Condon factors that permitted us to simulate with a good agreement the UV absorption spectra and to determine the absolute density and the rotational temperature of this radical which plays an important part for etching SiO_2 during processes applied in microelectronics industry.

4. Acknowledgements

The authors wish to acknowledge the Lam Research Corp. for supporting this research.

References

[1] C. Q. Jiao, A. Garscadden, P. D. Haaland, Chem. Phys. Lett., **297**, 121 (1998).
[2] C. Wild and P. Koidl, Appl. Phys. Lett., **54**, 6 (1989).
[3] A. Manenschijn, G. C. A. M. Janssen, E. van der Drift and S. Radelaar, J. Appl. Phys., **69**, 3 (1991).
[4] C. Wild and P. Koidl, J. Appl. Phys., **69**, 2909 (1991).
[5] A. Manenschijn, W. J. Goedheer, J. Appl. Phys., **69**, 2923 (1991).
[6] H. H. Goto, H-D. Löwe, T. Ohmi, J. Vac Sci. Technol. A, **10**, 5 (1992).
[7] W. J. Goedheer, Plasma Sources Sci.Technol., **9**, 507 (2000).
[8] J.P. Booth et al., Plasma Sources Sci. Technol., **7** (1998).
[9] C. W. Mathews, Canadian Journal of Physics, **45** (1967).
[10] Hai-Bo Qian and P. B. Davies, Journal of Molecular Spectroscopy, **169** (1995).
[11] Jorge Luque and al., J. Chem. Phys. **118**, 622, (2003).

PFCS ABATEMENT SYSTEM BY THE ATMOSPHERIC PRESSURE ICP PLASMA

Masuhiro Kogoma [1], Toshiya Abe [1], Kunihito Tanaka [1] and Tsuyoshi Naitou [2]

[1] *Department of Chemistry, Faculty of Science and Technology, Sophia University*
7-1 Kioicho, Chiyoda-ku, Tokyo 102-8554, Japan
[2] *TechBridge International Co.*
2100-99 Kusabana, Akiruno-shi, Tokyo 197-0802, Japan

Abstract

An atmospheric pressure plasma abatement system of PFC in a capacitive-coupled plasma (CCP) reactor is proposed. CF_4 abatement attained 96 % decomposition efficiency of CF_4(flow rate, 20 sccm) at 2.4 kW of discharge power in the H_2/O_2/He plasma. We also proposed an atmospheric pressure plasma abatement system of PFC using 27.12 MHz inductive-coupled plasma (ICP) reactor. In case of ICP plasma, CF_4 abatement attained almost 100 % decomposition efficiency for 100 sccm at 2.5 kW of discharge power in the H_2O/Ar plasma. We found only CO_2 and HF as the reaction products in the composition of exhaust gas.

1. Introduction

In the semiconductor fabrication industry, fluorocarbons (FC) such as CF_4, C_2F_6, and CHF_3 are used as the etching gases. They have been identified as global warming gases. For example, CF_4 has a long lifetime of more than 50000 years and the global warming potential (GWP) of CF_4 is 65000 times higher than CO_2. From the point of view of the protection of the environment as required in the Kyoto protocol, scientists had been requested to remove perfluorocompounds (PFCs) from the exhaust gases. The large combustion system had been used to achieve the abatement of PFCs. But such a combustion system is unable to decompose all of the fluorinated compounds and needs great running cost. Therefore, a compact and effective abatement system was required, such as a point-of-use (POU) reactor in the exhaust gas line. Recently, a plasma abatement system that was inserted between a primary process turbo pump and a secondary dry pump was introduced as the POU abatement system for exhaust gas [1]. However, the inner surface of the secondary dry pump must be protected from the erosion of HF or F atoms, which were exhausted from the abatement system. When the abatement system needs repairing or cleaning inside, the main etching chamber that is kept in very clean condition must also stop and one must spend longer than 2days for interruption and rebuilding, because the etching chamber needs hard baking out for out - gassing of the chamber walls exposed in atmosphere. If we could destroy the PFC just after the dry pump at atmospheric pressure, this problem should be solved. We need not open the etching chamber for repairs and we need not clean the inside of the atmospheric abatement system. So we propose new atmospheric pressure plasma abatement systems. The first system uses 13.56MHz capacitive-coupled plasma (CCP) as low temperature plasma system and the second one uses 27.12 MHz inductive-coupled plasma (ICP) reactor as high temperature plasma system.

2. Experimental

Figure 1 shows the schematic diagram of capacitive-coupled (CCP) abatement system (reactor No. 1). The inner electrode is a stainless steel tube cooled by water. The outer tube is an alumina tube that is covered by a stainless mesh outer electrode, to which is applied 13.56 MHz RF high voltage. The outer tube was cooled by blown air. We used He as a carrier gas and O_2 and H_2 as abatement gases in CCP system.

Figures 2 and 3 show the schematic diagram of ICP abatement system (reactors No. 2 and 3). We used a

Table 1 The discharge conditions of CCP and ICP

	No. 1	Nos. 2 and 3
Discharge frequency / MHz	13.56	27.12
Discharge power / kW	0.4 - 2.4	0.5 - 2.8
He / slm	2 - 10	0
Ar / slm	0	0.5 - 11
CHF_3, CF_4 / sccm	10, 20	20 - 100
H_2 / sccm	0 - 100	0
O_2 / sccm	20	0
H_2O	0	0 - 200

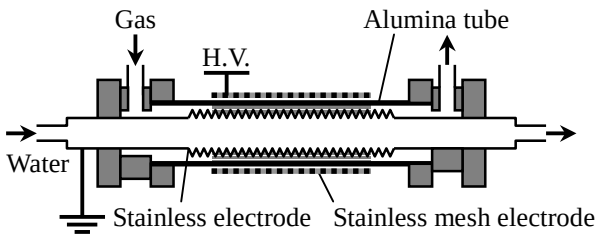

Fig. 1 Reactor No. 1

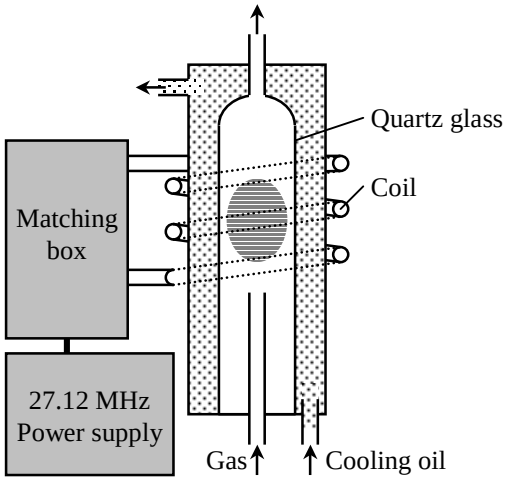

Fig. 2 Reactor No. 2.

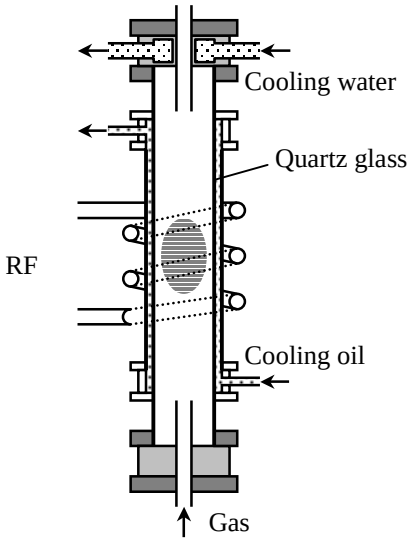

Fig. 3 Reactor No. 3.

cylindrical quartz reactor (reactor diameter: 30mm ϕ for No.2 and 28mm ϕ for No.3). The outer side of the reactor cylinder was cooled by a silicone oil flow. A three-turn water-cooled coil is wound on the reactor and 27.12 MHz RF high voltage is applied; then ICP discharge is generated in the reactor. Ar is a carrier gas to sustain the ICP discharge at atmospheric pressure. For the apparatus in Figure 3 (reactor No. 3), the configuration is not different from reactor No.2 except for a smaller coil diameter than in reactor No.2. In ICP system, we used H_2O vapor as abatement gas supplied from Ar-water bubbling system and mixed with main flow. CHF_3 and CF_4 were used as fluorocarbon sample gases mixed with Ar carrier. The discharge conditions of CCP and ICP (reactors No. 2 and No. 3) are shown in Table 1.

The chemical products in the exhaust gas were analyzed by means of GC-MS (Shimazu, QP-5050) and FTIR (Nihon Bunko, Ltd; FT2000).

3. Results and Discussion

3.1 CHF_3 decomposition using CCP

First, we used the CCP system for CHF_3 abatement. We found CHF_3, CF_4, H_2O, CO_2 and SiF_4 in the FTIR

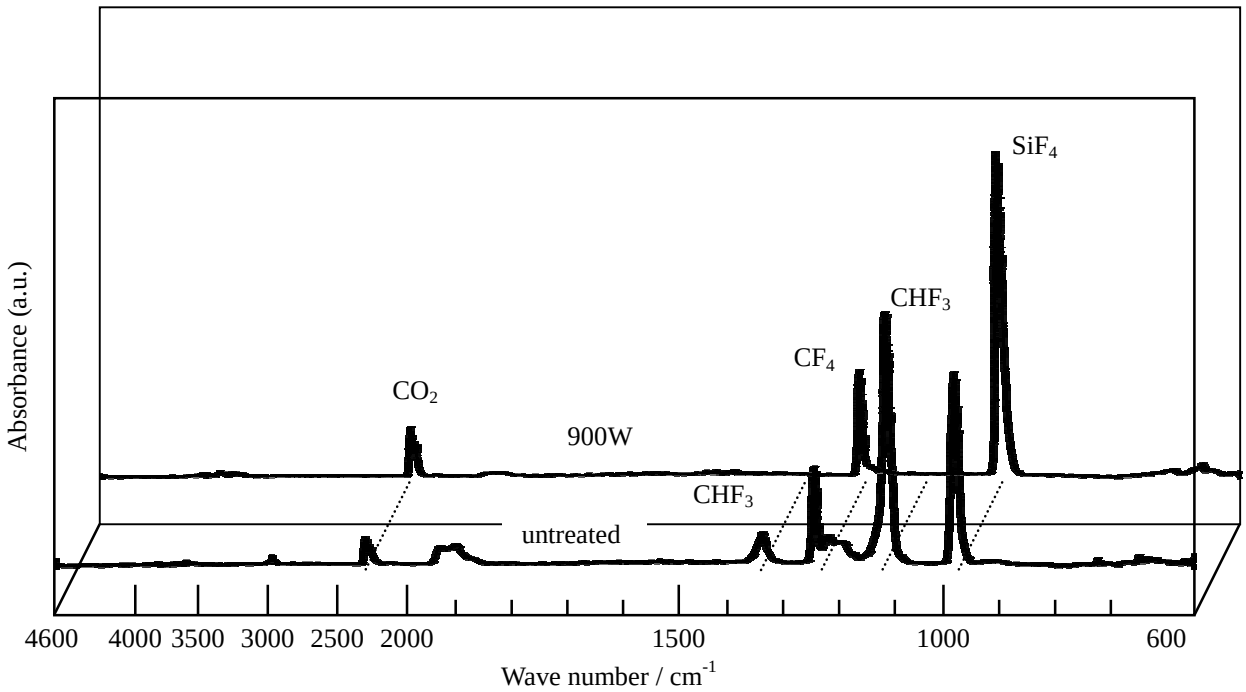

Fig. 4 The FTIR spectrum of CHF_3 decomposed by H_2/O_2/He system

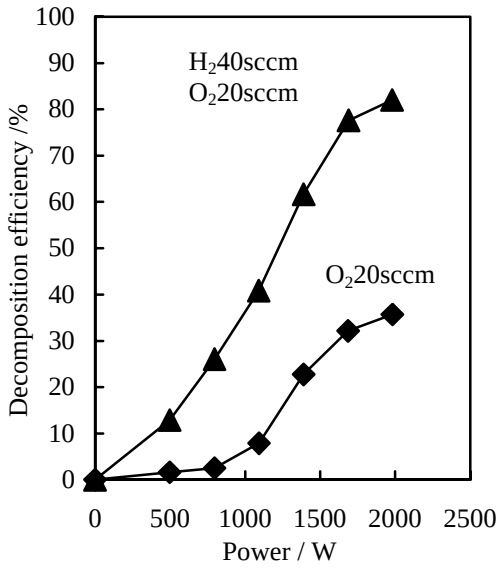

Fig. 5 Decomposition efficiency vs. discharge power

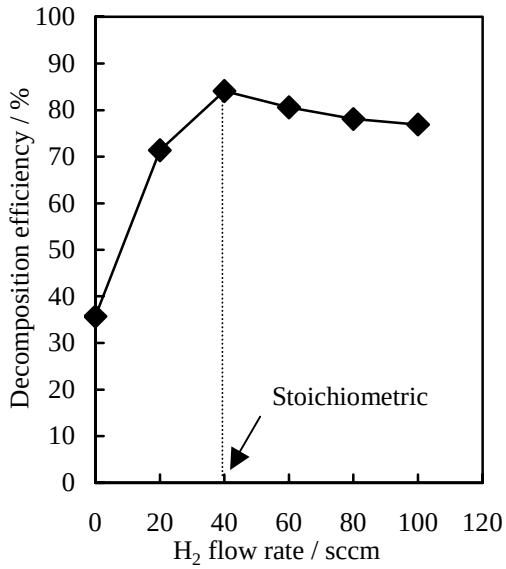

Fig. 6 The efficiency vs. H_2 flow rates in conditions of CF_4: 20sccm, O_2: 20sccm, He: 2slm

spectrum of CHF_3 decomposed by H_2/O_2/He system, as shown in Figure 4. The system line was partly made of Pyrex glass. The HF gas generated in plasma zone reacted with SiO_2 and produced SiF_4. The amount of CHF_3 decreased rapidly with increasing of the RF power and then disappeared at 700 W [2-3]. On the other hand, CF_4 that was one of the products increased with increasing of the CHF_3 decomposition, because CF_4 is one of the most stable FC molecules. CHF_3 produces CF_4 that has higher GWP than CHF_3 in the reactor. It is frequently reported that CF_4 is a kind of final product obtained by decomposing of other HFCs [1] not only for CHF_3. It seems that if CF_4 is decomposed completely, the abatement system will be effective enough in other FC decompositions. This means CF_4 is the next important target of FC abatement.

3.2 CF_4 decomposition using CCP

We tried to abate CF_4 by H_2/O_2/He using CCP system. Figure 5 shows decomposition efficiency vs. discharge power. In the figure, the parameters are abatement gas mixing conditions. When we put H_2/O_2 as (H_2: 40 sccm and O_2: 20 sccm) abatement gas in the reactor, the decomposition efficiency of CF_4 attained about 80% in 2kW, but if we put only O_2 (with out H_2) in the mixture, only 35% of CF_4 is dissociated at the same power. We suppose that produced F atoms immediately reacted with H_2 to produce stable molecules such as HF in H_2/O_2 system. But, due to the lack of H_2, F atoms reacted with CF_x radicals to produce CF_4 in the reactor. In the latter condition, when we increased O_2 concentration higher than 20sccm, we could not have higher efficiency than in Figure 5, because the reaction rate of F and H_2 is some orders higher than with F and O_2.

Figure 6 shows the efficiency vs. H_2 flow rates in conditions of CF_4: 20sccm, O_2: 20sccm, He: 2slm. We attained maximum efficiency at 40sccm of H_2. This means the stoichiometric concentration of H_2, O_2 and CF_4 gives a maximum for the CF_4 abatement, as in the total reaction scheme (1):

$$CF_4 + 2H_2 + O_2 = CO_2 + 4HF \qquad (1)$$

The efficiency decreased with increasing of the concentration of H_2 for higher stoichiometric flow rates. When we put more hydrogen than stoichiometric, hydrogen consumes the power to produce hydrogen atoms. On the other hand, the hydrogen atoms can not take part in abstraction reactions of fluorine atoms from CF_4. Therefore the efficiency decreases in the concentration region higher than stoichiometric.

Figure 7 shows the effect of carrier gas flow rate or residence time vs. efficiency in the reactor in the stoichiometric condition of H_2, O_2 and CF_4. In the Figure, there is almost no change of the efficiency for the He flow rate changing from 2slm to 10slm. In the plasma, the starting reaction is He excitation by electron impact. Then, He in excited state reacts with all molecules as sample gases to produce many kinds of radicals. All reaction rates containing fluorine abstraction reaction must be very fast compared with the

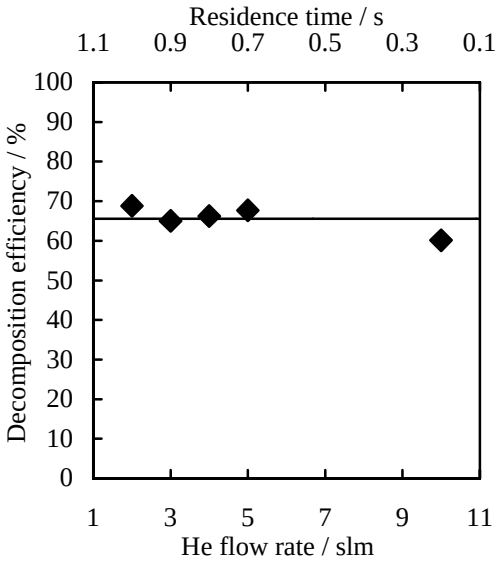

Fig. 7 The effect of carrier gas flow rate or residence time vs. efficiency in the reactor with the stoichiometric condition of H_2, O_2 and CF_4

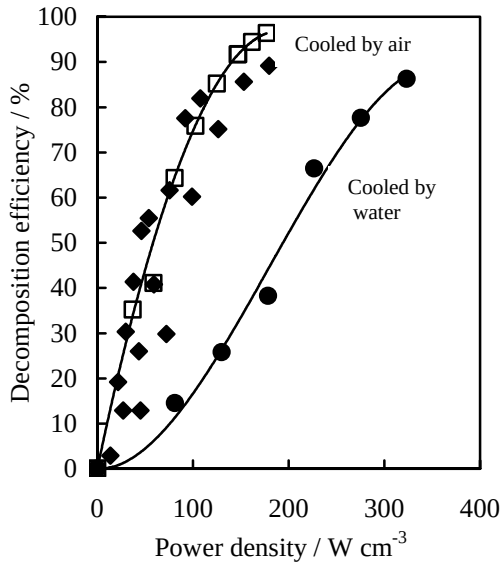

Fig. 8 Decomposition efficiency of CF4 vs. discharge power density in H2O/He CCP system

residence time in the reactor.

Figure 8 shows the decomposition efficiency vs. discharge power density; parameter is cooling situation of outer electrode of the reactor tube. As shown in Figure 8, the results were separated into two groups. One was using an outer electrode cooled by blown air and the other was using the outer electrode cooled by water. When we used blown air-cooled outer electrode, the maximum dissociation efficiency attained 99.6% with 20sccm of CF4, but in the case of using water-cooled outer electrode, the efficiency decreased to 85%. The decomposition efficiency is dependent on the temperature in the reaction zone as shown in the Figure 8. Because the temperature in the discharge zone will be changed by cooling conditions of outer electrode. It seemed that the plasma decomposition mechanism might include part of the thermal dissociation even in CCP. But in the CCP system, the temperature of reaction zone was somewhat higher than 1200 K measured by thermal crayon method. So it wasn't high enough to abate CF_4 completely because the thermal dissociation of CF4 will begin at about 1500 K resulting from the higher bond energy of C-F.

In the CCP discharge, primary electrons to start the glow discharge will be exhausted from the reactor wall then accelerated by the field and will ionise the molecules to maintain the discharge. The main part of the source power is not consumed to heat gases but to accelerate electrons. We conclude that, if we wish to dissociate more than 20 sccm of CF4, we need higher than 3kW of the power in the CCP. So CCP system cannot accomplish the perfect dissociation of concentrations higher than 20 sccm of CF4 at reasonable source power.

3.3 CF_4 decomposition using ICP

In the ICP system, it is easier to obtain high temperature than in the CCP system. In the ICP, after the discharge starts, the electron will be produced from molecules or atoms by thermal ionisation in high temperature condition (higher than a few thousand K). Thus, electron energy is consumed only for heating the gas molecules. So we used the ICP system for FC abatement to obtain higher power density and higher temperature in the reactor. We tried to abate the CF_4 in H_2O/Ar system as shown in

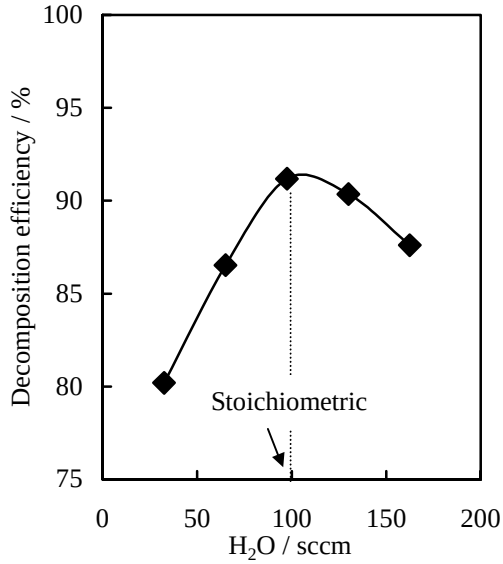

Fig. 9 The decomposition efficiency as a function of flow rate of H_2O vapour

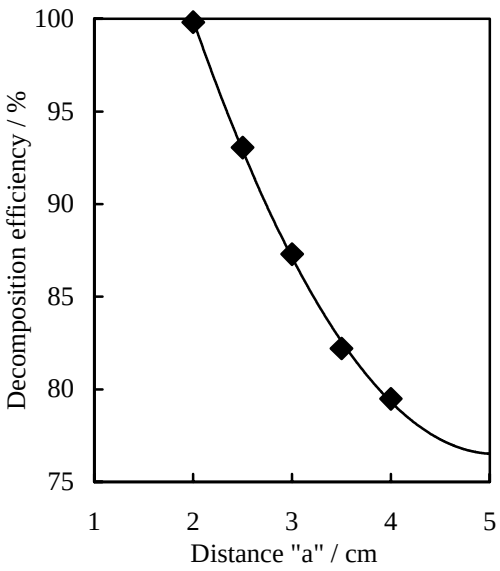

Fig. 11 The decomposition efficiency vs. the position of an inlet tube with fixed coil

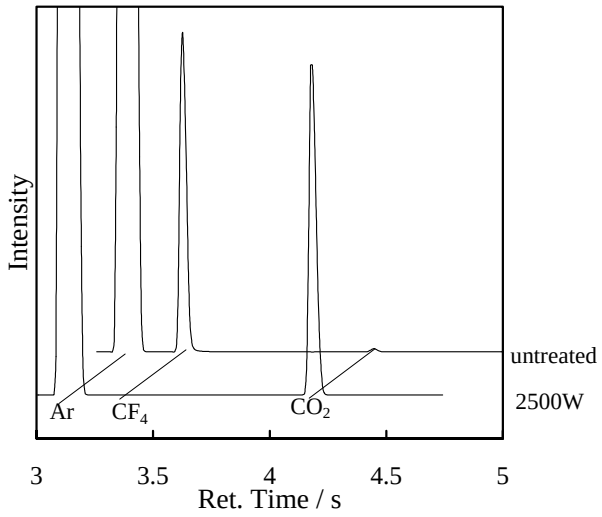

Fig. 12 GC-MS spectra of untreated gas containing CF_4 100sccm and treated gas

Figure 2 (reactor No.2). Figure 9 shows the decomposition efficiency as a function of flow rate of H_2O vapour. The maximum efficiency is always attained at stoichiometric concentration of H_2O with CF_4 added as in the CCP system. We fixed the concentrations of CF_4 and H_2O at stoichiometric ratios. Figure 10 shows the decomposition efficiency vs. Ar flow rates obtained in the reactor No.2. The maximum decomposition efficiency of 50 sccm CF_4 was 100 %, attained at 2.4kW discharge. By using ICP, we attained much higher decomposition efficiency than in CCP system even at about the same discharge power.

Figure 11 shows the decomposition efficiency vs. the position of an inlet tube with fixed coil. The distance (a) means the distance to inlet top measured from the centre of the coil. The centre of a hot plasma bowl is almost in the coil centre. The efficiency is strongly dependent on the distance (a). When we introduce the sample flow in the plasma centre or near the coil centre (1-2cm), we have maximum efficiency, but at longer than 2.5 cm, the efficiency is going to decrease. The space of the reactor was cooled through the wall by the silicone flow. When the inlet is far from the plasma bowl, a part of the sample flow will pass through the cooled crevice between the wall and the edge of the hot plasma bowl. The decreasing of the efficiency in

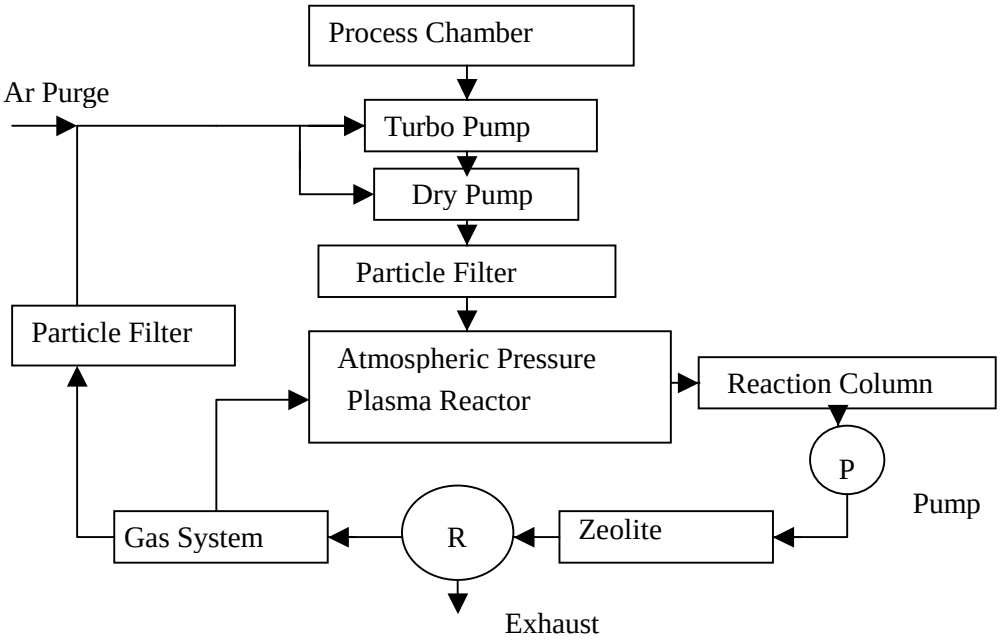

Fig. 13 Schematic of carrier gas recycling system for the atmospheric CF_4 abatement

Figure 11 can be explained by the presence of a of low temperature region at the side of the crevice flow. Because CF_4 molecules will not dissociate enough in the low temperature zone, the sample flow must be placed as close as possible to the centre. We found only CO_2, H_2O and HF as the products by using GC-MS and IR measurements of the exhaust gas. HF and other fluorine components were trapped with a solid alkaline absorber. The maximum dissociation ability for CF_4 flow rate was 50sccm at Ar flow rate of 3.25slm in reactor No.2.

Trying to realize the dissociation of a certain amount of CF_4 (100 sccm) and to find optimum conditions by H_2O/Ar ICP, we used smaller diameter of the induction coil to have higher plasma density in the reactor. The coil diameter of reactor No.3 is 45mm ϕ instead of 58.5 mm ϕ in reactor No.2. By using the small size coil, the field strength in the reactor will become stronger than that of large one.

Figure 12 shows GC-MS spectra of untreated gas containing CF_4 100sccm and treated gas. In the treated gas, CF_4 peak is lost and CO_2 peak is increasing. The system that can dissociate 100sccm of CF_4 is able to correspond to the total exhaust amount of a few normal-sized etching apparatuses.

We will finally propose the **NO EMISSION SYSTEM** using Ar carrier gas recycling circuit and solid absorber such as soda-lime for HF and CO_2 absorption, as shown in Figure 13.

4. References

[1] SEMATECH report, International SEMATECH, Inc. USA. (1998).

[2] M. Kogoma, Proceedings of the Second Polish-Japanese HAKONE Group Symposium at Nagoya, pp. 49(2001).

[3] T. Abe, K. Tanaka, M. Kogoma and T. Naito, The Proceedings of The 20th Symposium on Plasma Processing, BI-4, (2002) Nagaoka, Japan.

Passivation layer in a deep Si plasma etching cryogenic process

X. Mellhaoui[1], R. Dussart[1], A. Basillais[1], P. Lefaucheux[1],
M. Boufnichel[2], G. Marcos[3], P. Ranson[1]

[1)] *GREMI/ESPEO,Université d'Orléans,14, rue d'Issoudun, 45067 Orléans, France*
[2)] *STMicroelectronics, 16, rue Pierre et Marie Curie, BP 7155, 37071 Tours Cedex , France*
[3)] *LPCM/IMN, Université de Nantes, 2 rue de la Houssinière, 44322 Nantes, France*

Abstract

A cryogenic SF_6/O_2 plasma process is used to etch silicon trenches with a high aspect ratio (depth/width>10). Test experiments have been carried out to characterize the passivating layer, which forms on the structure sidewalls. These tests revealed that the layer doesn't need sulfur to be rebuilt. In certain process conditions (high O_2 flow), black silicon phenomena appears in trench bottom. A statistical study of its apparition will be also presented.

1. Introduction

Power microelectronics and microsystems industries intensively utilize silicon deep etching processes to elaborate high aspect ratio structures. At least two different kinds of dry etching process are used to realize such structures.

First, the so-called Bosch process [1] is probably the most used in industry. It operates at ambient temperature and consists of a succession of etching and deposition steps. Etching is performed with SF_6 plasma and deposition with C_4F_8 plasma. The etching step is isotropic. The passivation layer, which is deposited on the bottom of the structure during the C_4F_8 plasma, is then sputtered by energetic incident ions produced during the etching step. Sidewalls remain protected by the passivating layer since ions don't sputter this part of the structure. After many steps of etching and deposition, a high aspect ratio structure forms. This process can be very well controlled and can be applied to many different types of structure. Although it is often used, the Bosch process presents many drawbacks. First, a scalloping effect appears on sidewalls. This issue can be important especially when structures have to be filled with specific materials. During this filling step, some unwanted voids can be obtained due to the scalloping effect. Moreover, the reactor has to be frequently cleaned since deposition on reactor walls can induce some process parameter shifts.

An other process can be used for anisotropic etching of silicon: the cryogenic process. Cryogenic process consists of cooling the wafer during etching. A mixture of SF_6 and O_2 gas is introduced into the reactor. A passivation layer is formed on sidewalls while silicon is continuously etched at the bottom of the structure. This passivation layer forms only at very low temperature and in presence of oxygen. This phenomenon was first observed by Tachi et al.[2] in the end of the 80's. The etching rate can be as high as 4 $\mu m.min^{-1}$ for a 80 µm deep, 4 µm wide Si trenches [3]. In this process, the reactor remains quite clean and doesn't need any step of cleaning. Moreover, structure sidewalls are particularly smooth and no scalloping effect appears, which is quite convenient for filling steps. In spite of these significant advantages, the cryogenic process is not yet very much used because it is a very sensitive process. For example, a shift of one degree at the surface of the wafer is sufficient to modify the profile shape.

The passivation layer, which forms at low temperature, is not yet very well characterized. It seems to be composed of $SiO_xF_yS_z$. Some previous XPS analyses have shown that the passivation layer is removed when the wafer is warmed up to the ambient temperature [4]. This passivating layer is not mainly composed of SiO_2. Some characterization tests were realized to rebuild this passivation layer when it is destroyed [4]. We present in this paper new results, which indicate that the passivation layer doesn't need the presence of sulphur to efficiently protect sidewalls from etching.

In some process conditions (high O_2 content and low temperature), black silicon forms in the bottom of structures. This black silicon is considered as a significant defect since it can definitely stop etching. The black silicon origin is not very well defined. It seems to come from roughness, which dramatically amplifies in such processes [5,6]. We performed a parametrical study of the black silicon apparition versus O_2 content, bias and temperature. A statistical study will be presented as well.

2. Materials and methods

2.1 ICP reactor

Etching experiments are carried out in an ICP (Inductively Coupled Plasma) reactor (601E Alcatel) (Figure 1). On the top of plasma source, up to 1000 sccm SF_6 flow and 200 sccm O_2 flow can be injected. Up to 3000W power can be applied to the plasma source. Si wafer is mechanically clamped on the wafer holder. Chuck is cooled by liquid nitrogen and heated by a set of resistors to control the temperature between +40°C to – 150°C. Thermal contact is assured by helium at pressure of 10 mbar. The wafer is self-biased by applying independently an RF voltage (capacitive coupling). A constant magnetic field is applied to the plasma source part to confine the plasma. Permanent magnets are placed around the diffusion chamber.

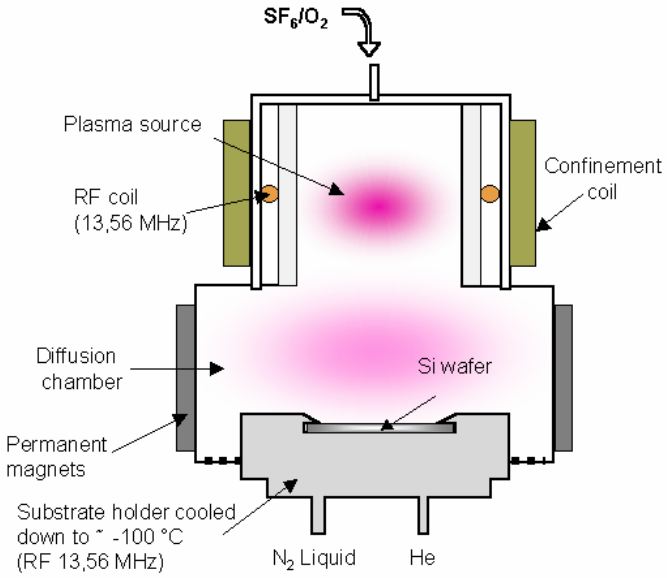

Figure 1 : Schematic diagram of the ICP reactor

Profiles are characterized using a Scanning Electron Microscope after cleavage. We worked with (100) silicon wafers (P doped). For passivation test experiments, we used trench patterned wafers with a 1 µm thick SiO_2 mask, which offers a very high selectivity (>300:1) [3].

2.2 Statistical method for black-silicon analysis

Top views of black silicon are observed by SEM and recorded. Images are then treated using imaging software. An example, which does not correspond to a real SEM image, is given in figure 2. We made a test picture (figure 2.a) to validate the image analysis method.

The first treatment consists of applying a threshold to detect areas in relief (figure 2.b). The different areas are then numbered and their surface is measured (figure 2.c). A table is made gathering all the detected areas. An histogram can be drawn giving the number of objects versus area ranges.

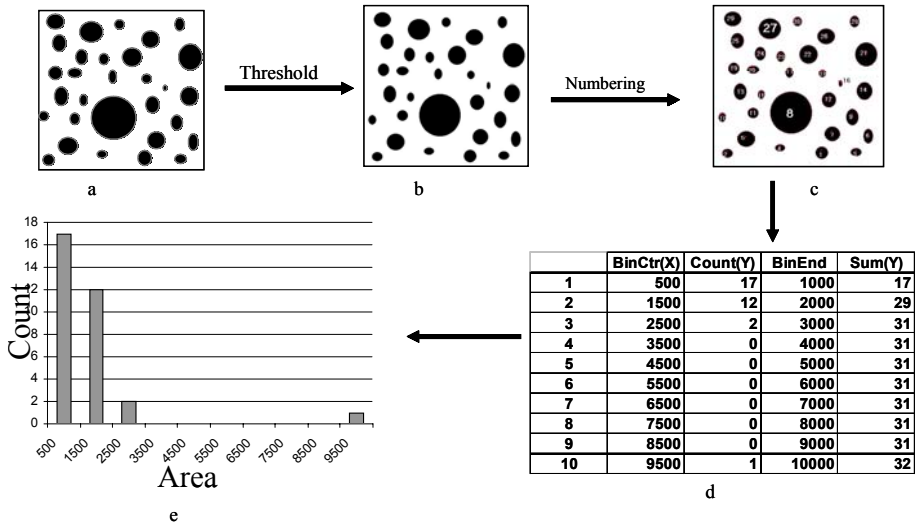

	BinCtr(X)	Count(Y)	BinEnd	Sum(Y)
1	500	17	1000	17
2	1500	12	2000	29
3	2500	2	3000	31
4	3500	0	4000	31
5	4500	0	5000	31
6	5500	0	6000	31
7	6500	0	7000	31
8	7500	0	8000	31
9	8500	0	9000	31
10	9500	1	10000	32

Figure 2 : Image analysis method for the black silicon statistical study

3. Passivation layer

As described in a previous paper, the passivating layer is not mainly composed of SiO_2 [4]. This was shown by XPS analysis. The passivating layer is actually removed when the wafer is warmed to ambient temperature. We have made some new test experiments to better understand what the passivation layer is composed of. As mentioned in reference [4], the passivation layer can be rebuilt when it is destroyed. It requires the insertion of a so-called "over-passivating" step. We reported that a plasma with oxygen only (without SF_6) was not able to reform an efficient passivating layer. The passivation layer was successfully rebuilt by linearly increasing the SF_6 flow during 1 min so that O_2/SF_6 ratio varied from 86 % down to 6.5 % at constant O_2 flow. This result showed that SF_6 was necessary to properly rebuild the passivation layer when destroyed.

In figure 3, we present some new experiments, which indicate with more accuracy the necessary SF_6 content for a good passivation layer reconstruction. In figure 3.a, we remind the reference profile, which corresponds to a 10 minute process in standard etching conditions. The profile slope is slightly negative. With this particular process, usual defects are significantly reduced (very low bowing, weak undercut). It is important to notice that this process was very reproducible. Hence, it is used as a reference for this set of test experiments.

As explained in [4], after this 10 min etching step, the wafer is warmed up to remove the passivation layer. The wafer is then cooled again down to -110°C. The experiments corresponding to 3.b, 3.c, and 3.d figures were dedicated to the passivation layer reconstruction. On each profile, the reference profile was added in dotted line for comparison. One can notice that this reference process is very reproducible since the obtained profiles fit perfectly with other profiles. The 3.b profile was obtained after a 30 second step of "over-passivating" regime. In this regime, SF_6 flow is reduced and O_2 is maintained at the standard etching condition value. In figure 3.b, an O_2/SF_6 ratio as high as 1.3 was settled. After the over-passivating step, a 3 min standard etching process is applied to check if the passivation layer was well rebuilt. The profile is partially destroyed during the 3 min additional etching step. Damages appear on top of the trench, which indicate that the passivating layer was not completely rebuilt.

In the next experiment (figure 3.c), the same experimental procedure was performed except that the over-passivating step was modified : O_2/SF_6 ratio was reduced to 0.65 instead of 1.3. In this case, we see on figure 3.c that the 3 min additional etching step didn't induce any defect. We can conclude that this over-passivating process successfully rebuilt an efficient passivation layer. Other experiments showed that the upper O_2/SF_6 ratio limit must be lower than 0.85 to make the passivation layer grow in our experimental conditions. The lower O_2/SF_6 ratio limit is not yet defined. We just know that a ratio of 0.065 is too low to properly rebuild the passivation layer [4].

Finally, an experiment was carried out to check if sulphur is a necessary element in the passivation layer. The over-passivating step was modified in order to check this point. SF_6 was replaced by SiF_4 gas during the over-passivating step to rebuild the passivating layer. As shown on figure 3.d, SiF_4 was injected

with O_2 (O_2/SiF_4 = 0.65) during 30 seconds before the 3 min etching in standard conditions. The profile shows that the passivating layer was successfully rebuilt with SiF_4. This result indicates that sulphur is not a necessary element in the passivation mechanisms involved in the cryogenic process.

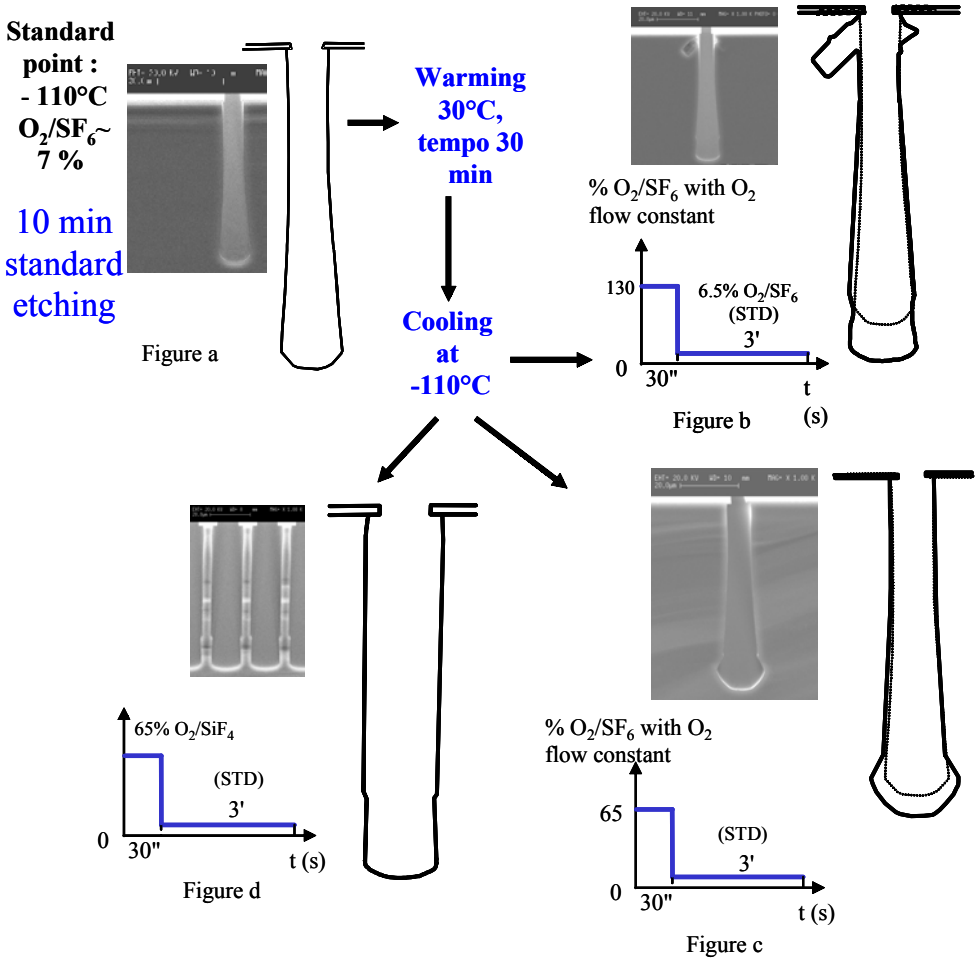

Figure 3 : Test experiments to rebuild the passivation layer after destruction

a)- Reference profile, 10 min etching in standard conditions

b)- After passivation layer destruction (warming step) and cooling back down to -110, insertion of a 30 sec long over-passivation step with O2/SF6 = 1.3, followed by a 3 min etching in std conditions.

c)- Reduction of the O_2/SF_6 ratio to 0.65 during the over-passivating step

d)- SF6 is replaced by SiF4 during the over-passivating step

3. Black silicon

Black silicon can appear in the bottom of trenches. It consists of a sort of "grass" in the micrometric scale, which appears black when enlightened. This phenomenon can be significant and can stop the etching process. Black silicon can be produced on wafers without mask. Experiments were carried out to investigate black silicon apparition mechanisms. 4 cm² silicon samples without mask were used for this experiment. They were cooled by the same system as the one used for regular wafers.

Black silicon appears only when O_2 flux is sufficient and at very low temperature. In figure 4, profile (a) and a top view (b) SEM images of black silicon are shown. On the top view, the black parts are in depth and white parts are in relief. This particular black silicon was obtained after a 40 min long process in over-passivating regime. Black silicon dimensions can reach several tens of micrometers (figure 4.a). Quite circular patterns are naturally generated. Their diameter is of the order of 1 µm in these process conditions.

A study of black silicon apparition was performed versus bias applied to the wafer in order to investigate the role of ion energy on its apparition. Other parameters (wafer temperature, pressure, source power, and process duration) were kept constant. We just varied the wafer bias, and the O_2/SF_6 ratio. On the graph of figure 5, squares are drawn when black silicon appeared and circles were used to indicate that no

black silicon was obtained. Between squares and circles, a boundary can be defined between the two regions of presence and absence of black silicon. It is clear that black silicon only appears whenever oxygen content is sufficient. A bias increase can be used to avoid black silicon apparition since the boundary shifts to the higher O_2/SF_6 values for higher bias. Some additional experimental points have to be added to draw the boundary of the two regions with accuracy.

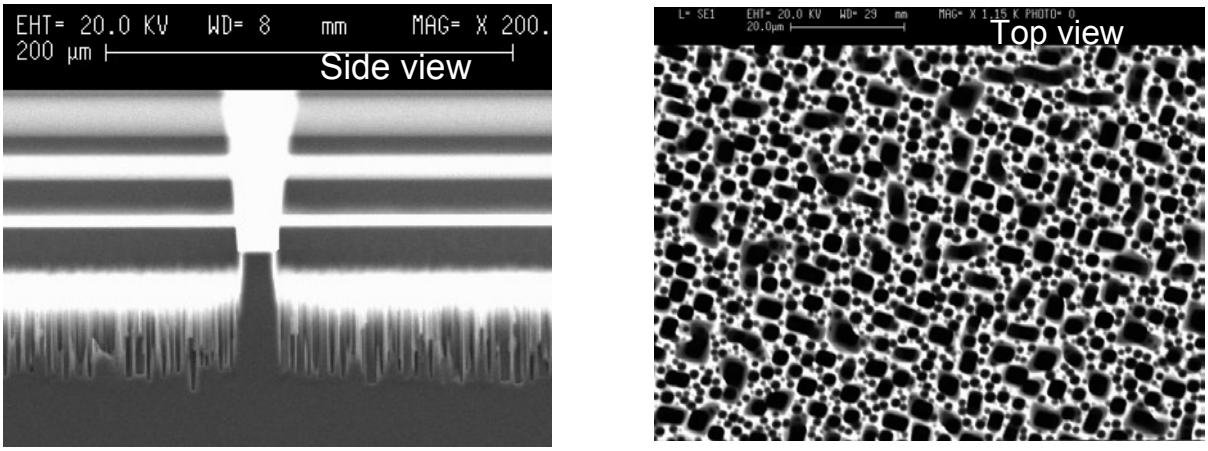

Figure 4 : Side view (left) and top view (right) of black silicon obtained after 40 min process in over-passivating regime

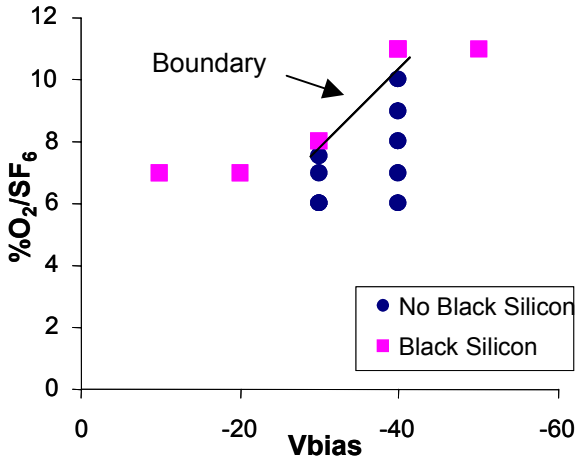

Figure 5 : Black silicon apparition versus Vbias and O2 content (SF6 flow was kept constant)

A statistical study on patterns created in the black silicon region is under progress in our laboratory. The method was described in paragraph 2.2. An example of such a statistics is given in figure 6 where a SEM picture (left) and the corresponding histogram (right) are presented. A characteristic dimension of 0.25 µm is obtained in the experimental conditions (T :-110 °C, O_2/SF_6 = 0.07, Pressure : ~3 Pa, Bias = -20 V). When temperature is increased up to –105°C, we observed that characteristic pattern dimensions increased (figure 6). Characteristic height of the black silicon can also be determined. We observed that this value increases with bias. Typically, in the same conditions, a typical height of 5 µm was obtained for a -20 V bias whereas it reaches up to 40 µm with a -50 V bias.

Black silicon formation seems to be linked to the surface roughness [5,6]. In the cryogenic process, this roughness amplifies dramatically due to passivation and shadowing effects [5]. Some additional experiments are planned to better understand the kinetic formation of black silicon.

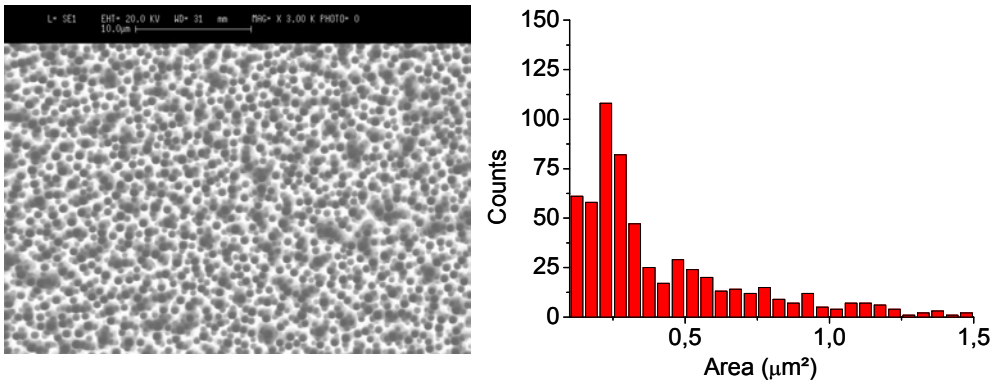

Figure 6 : SEM image (left) and its histogram (right) giving the number of detected holes vs. their area

4. Conclusion

Passivation layer and black silicon formation were investigated in order to better understand the mechanisms involved in the cryogenic process. Moreover, these experiments can help for defining special processes for which the passivation layer has to be rebuilt. They can also give hints to avoid black silicon apparition.

After destruction, the passivation layer can be rebuilt. It requires not only the presence of oxygen, but also the presence of SF_6 in a right concentration (typically of the order of 0.6 for the O_2/SF_6 ratio in our experimental conditions). Another experiment showed that sulphur is not necessary to rebuild an efficient passivating layer.

Concerning black silicon, we have seen that it forms when temperature is sufficiently low and O_2 content high enough. A characteristic dimension can be determined by statistical analysis. This characteristic dimension increases with temperature. The average height increases with bias voltage. At constant O_2 content, black silicon can be avoided by increasing bias.

Other experiments are planned to refine this first study. The lower O_2/SF_6 ratio limit to rebuild the passivating layer has to be determined. We will investigate the necessary process duration, which should be smaller than 30 seconds, to reform this layer. Black silicon apparition will be modelized using the Langevin diffusion equation [5,6]. Other experiments will also be carried out to complete the charts. In situ ellipsometry experiments will be performed to study the passivation layer growth.

5. Acknowledgments

This work is supported by STMicroelectronics (Tours, France) and by the French ministry of economy, finance and industry. The authors would like to thank Julien Steelandt (ESPEO-Orleans) for his help during the passivation characterization experiments.

6. References

[1] F. Lärmer, A. Schilp, German patent n°DE4241045
[2] Tachi, K. Tsujimoto, and S. Okudaira, « Low temperature reactive ion etching and microwave plasma etching of silicon » Appl. Phys. Lett. 52 (8) 616 (1988)
[3] M. Boufnichel, S. Aachboun, P. Lefaucheux, P. Ranson, « Profile control of high aspect ratio trenches of silicon. II. Study of the mechanisms responsible for local bowing formation and elimination of this effect », J. Vac. Sci. Technol. B 21(1), 267, 2003.
[4] R. Dussart, M. Boufnichel, G. Marcos, P. Lefaucheux, R. Benoit, H. Estrade-Szwarckopf, P. Ranson, « Passivation mechanisms in cryogenic SF_6/O_2 etching process », submitted to J. Vac. Sci. Technol.
[5] P. Brault, P. Dumas, F. Salvan, « Roughness scaling of plasma-etched silicon surfaces », J. Phys. : Condens. Matter 10 , 27 (1998)
[6] J. T. Drotar, Y.-P. Zhao, T.-M. Lu and G.-C. Wang, « Mechanisms for plasma and reactive ion etch-front roughening », Phys. Rev. B 61(4), 3012 (1999)

Physical characteristics of a non-thermal plasma arc applied to NO reduction

O. Martinie, J. M. Cormier and A. Khacef

GREMI, Université d'Orléans, 14 rue d'Issoudun, B.P. 6744, 45067 Orléans Cedex 2, France
e-mail : jean-marie.cormier@univ-orleans.fr

Abstract

The aim of this paper is to present experimental results using a non-thermal plasma arc in order to reduce nitrogen monoxide (NO). We operated with a N_2/NO mixture and we particularly interest to the chemical reduction of NO by the N radical ($N + NO \rightarrow N_2 + O$). The yield for this process was determined by measuring the NO destruction rate as a function of the power deposited into the reactor.

1. Introduction

Plasma processing and particularly non-thermal plasmas (discharges) are subjected to a new interest for pollution control. The research in this field gained considerable interest and number of researchers is working about it. The reduction of the nitrogen oxides (NO, NO_2, N_20_5, N_2O) from industrial systems and exhausts is one of the critical and urgent topics in environmental and pollution control researches. Among the systems proposed for the NOx reduction are those based on atmospheric non-thermal plasma (NTP) discharges.

A new generation of technologies based of non-thermal plasma (NTP) has been developed since 1960. NTP can be produced by large variety of processes: electron beam or electric discharge methods. The plasma is non-thermal in the sense that the electron temperature is different from that of gas which remains at room temperature. The great part of the input electrical energy goes into electron production rather into gas heating. In these methods, energetic electrons (up to 5 eV for electric discharges and up to a few MeV for electron beam processes) are produced. Then, these electrons create free radicals, secondary electrons and ions which react with the pollutants. Therefore, non-equilibrium plasmas can be used for a selective destruction of dilute concentration of pollutant molecules, typically from 1 to 10 000 ppm.

In order to choose the best operating conditions for the NOx removal it is necessary to compare different non-thermal plasma sources. The two principal characteristics of a plasma process are the destruction rate and the energy cost. Plasma process efficiency is often characterized by the G-Value defined as the number of pollutant molecules removed by 100 eV of input energy.

$$G_{eV} = \frac{\text{Number of pollutant molecules destroyed}}{\text{Deposite energy [eV]}} * 100$$

Many types of sources have been studied as dielectric barrier discharges (DBD), corona discharge or surface discharge (1-5). These methods proved their efficiency to destroy a great variety of pollutants.

Results obtained from a transient arc-glow discharge called "NTP Arc" are presented in this paper. Dilute amounts of NO in N_2 were chosen as mixture test. NO was described to be destroyed by

the N radical [3]. To avoid NO reformation by reaction between nitrogen and oxygen which complicated the removal mechanisms identification, we used N_2 rather than air.

2. Electron and Chemical Kinetic

In non-equilibrium plasma discharge, the main part on the input energy is used for producing high-energy primary electrons. If the pollutant molecules are very dilute, these electrons principally collide with the gas background molecules. Then these electrons produce secondary electrons, free radicals and ions which react with the pollutant molecules. In N_2 background electrons have two ways for reacting.

- Electron impact dissociation produces the fundamental atomic nitrogen N(4S) and excited nitrogen $N(^1D)$

$$e + N_2 \rightarrow e + N(^4S) + N(^4S)$$

$$e + N_2 \rightarrow e + N(^4S) + N(^1D)$$

- Electron impact ionization produces the N_2^+ and N^+ ions and secondary electrons.

$$e + N_2 \rightarrow N_2^+ + 2e$$

$$e + N \rightarrow N^+ + 2e$$

The reaction rates for above reactions are strongly dependent of the electron mean energy. The electron energy function is difficult to obtain due to the complexity of non-elastic energy transfer mechanisms. Furthermore, all the equations required to calculate this function are time dependent.

For few energetic electrons (< 8 eV) only a few part of the initial input electrical energy is used for dissociation or ionization because the main part of this energy is used for exciting N_2 vibrationnal states.

All the following reaction rates are taken from the NIST database [6]. In the following, T is the local plasma temperature (in Kelvin), and k is the reaction rate (in cm^3/molecule.s). The main mechanism for NO removal is the reaction with the N radical by the reaction:

$$N + NO \rightarrow N_2 + O$$

$$k = 7.12\ 10^{-11} \exp(-787/T)$$

One must consider the NO oxidation by the O radical following the three body reaction (X is a third body, principally N_2 in our case)

$$NO + O + X \rightarrow NO_2 + X$$

$$k = 9.1\ 10^{-28}\ T^{-1.6}$$

The NO_2 molecules product by this reaction are reduced by O radical

$$O + NO_2 \rightarrow NO + O_2$$

$$k = 6.5\ 10^{-12} \exp(120/T)$$

NO can be reformed too by the reaction

$$N + O_2 \rightarrow NO + O$$

$$k = 1.5\ 10^{-11} \exp(-3573/T)$$

3. Experimental set-up

For the results presented in this work, we operated with an atmospheric-pressure flow-through configuration. The gas flow was controlled using two mass-flow controllers. The first one was connected to a pure N_2 bottle whereas the second one was connected to a mixture bottle containing

3600 ppm of NO diluted in N_2. This allows us to control the NO concentration in the gas. We fixed it to about 100 ppm with a flow rate of 10 Nl/min.

The reactor is shown on figure 1. Two parallel Pyrex plates and two divergent copper electrodes form it. The arc ignites where the electrodes are the nearest, then it glides upwards where it remains caught. When the arc extinguishes, a new one starts immediately. The gas flow must not be too important otherwise the arc cannot remain caught at the electrode top.

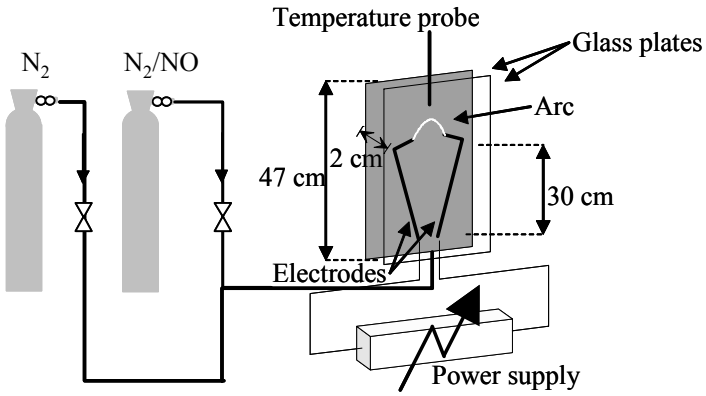

Figure 1: Experimental setup

The power supply was a leakage transformer able to deliver a 50 Hz sinusoidal current of typically 100 mA intensity. The voltage delivered by this system adjusts itself between 1 kV and 10 kV according to the gas nature and the input voltage transformer. The power into the discharge could adjusted by varying the input voltage. The arc current I and voltage U variations were directly registered using a numeric oscilloscope [Tektronix TDS 460 A] equipped with voltage and current probes. The average power (over a period of time) consumed by the arc was calculated by meaning the product "U_xI". Figures 2 and 3 show an example of the time-behaviors of the voltage and the current.

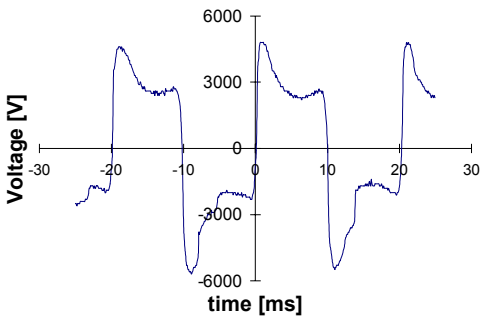

Figure 2: Voltage curve. N_2/NO (100 ppm), Primary power 390 W, Flow rate 10 Nl/min.

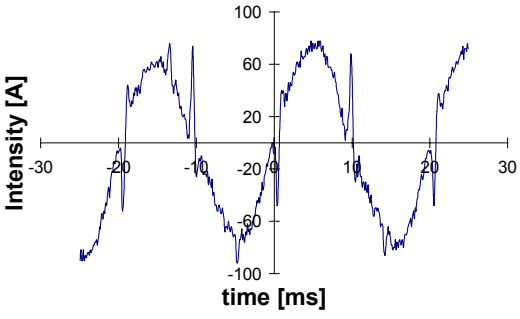

Figure 3: Current curve. N_2/NO (100 ppm), Primary power 390 W, Flow rate 10 Nl/min.

The chemical analyzes were performed in line using a Fourier Transform Infrared (FTIR) spectrometer (Nicolet MAGNA IR 550 Series II). The FTIR was used for by-product identification. For monitoring the NO evolution we used a combustion analyzer (Quintox) which works by chemiluminescent. This device was also used for output gas temperature measurement (T_{output}) at 10 cm above the discharge.

We used a fast CCD camera (Sony) for arc radius and length measurement. It allowed us to take two consecutive pictures in 100 ms with a variable exposure time.

4. Plasma Characteristics

First the plasma aspect is rather that of a flame. But this results from the retinal persistence. Indeed if we took a short time exposure (10 µs) picture of the arc we can see distinctly two zones appearing (figure 4). The first zone corresponds to a very bright thin wire of plasma. Its apparent diameter is about 0.1 mm and its mean length increase linearly with the flow rate as shown on figure 5. We can consider that the electrical current is confined in this area, supposed to be quasi cylindrical. This kind of representation is often used in arc modeling [7-8]. Inside it, the gas temperature T_{gas} was measured by spectroscopic method using the UV $OH(A^2\Sigma, v=0) \rightarrow OH(X^2\Pi, v'=0)$ band spectrum [9]. We found values between 1600 and 2000 K. The plasma wire is cooled by convection.

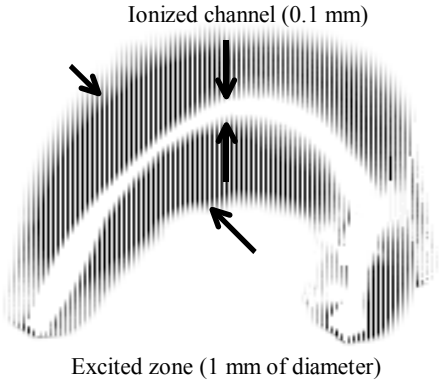

Figure 4: Short time exposure picture of the arc (10 µs).

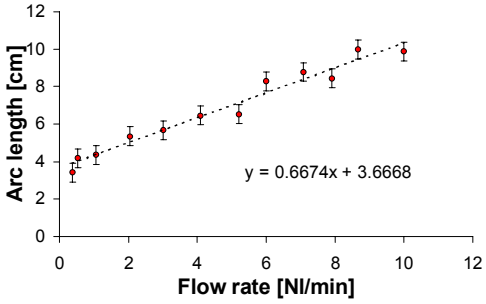

Figure 5: Arc length as a function of the flow rate

Due to the action of the anodic and cathodic arc spots, Cu atoms are extracted from electrodes. Assuming that the energy levels of Cu atoms are populated by electronic collisions following a Maxwell distribution, we can determine the electron temperature. A typically value of 12 000 K was obtained. This quantity is almost independent of the radial position.

When the number of electrons in the discharge increase beyond 10^{18} electrons per cm^3, the plasma becomes very ionized. In this case the electrons cannot reach a high energy value because the main part of the electrical power obtained from the electric field is lost by collision with ions. This kinetic energy transfer mechanism is very efficient due to the Colombian interaction. Then, the ions transfer a fraction of their energy to gas molecules by elastic collisions. The energy is well distributed between all the plasma species ($T_{gas} \approx T_{ions} \approx T_{electrons}$). Such a discharge is called electric arc or thermal arc. But in our case the electrical generator limits the current value and consequently the electron and ion densities are not very high. In that case the electrons collide principally with the gas molecules, and in this case the Colombian interaction stays negligible. The elastic collision are not able to heat the gas molecules (the electron mass is 10^4 lower than N atoms mass). That is why our plasma is non-thermal.

The second zone presents like a weakly luminous halo. Its diameter is about 1 mm. We suppose that the chemical reactions occur principally in this area. The ionized canal produces primary electrons and excited species that diffuse outside it and react with the pollutant molecules.

5. Experimental results

Using FTIR spectroscopy we observed that the only by-products formed in the discharge are NO_2. None of the other nitrogen oxides, like N_2O or N_2O_5, has been detected. Figure 6 show the concentrations of NO (residual) and NO_2, and the output reactor gas temperature (T_{Output}) as a function of the electrical energy density deposition.

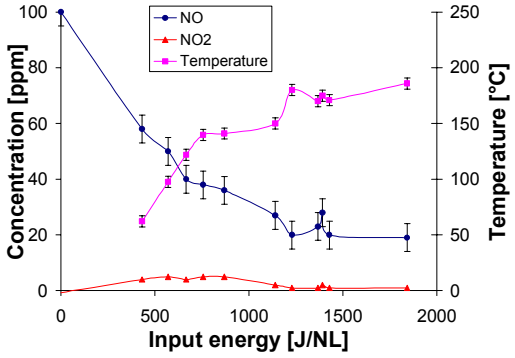

Figure 6: Output NOx concentration - 100 ppm NO in N_2 - Flow rate 10 Normal liter/min.

The destruction process efficiency increases with the input energy until the value reaches 880 J/Nl. In this area the only reaction that occurs is $N + NO \rightarrow N_2 + O$. Thus, the number of NO molecules destroyed is equal to the number of N atoms produced. In that case, the energy cost for NO removal (G_{eV} value) varied between 0.034 and 0.020.

Above 1000 J/NL the NO concentration is constant. We suppose that the main reason of such a behavior is the NO production according the reaction $N + O_2 \rightarrow NO + O$. This reaction becomes more and more significant due to gas heating. These NO produced are called "thermal NO". The additional electrical energy deposit into the reactor is simply lost.

For both previous cases the NO_2 production is not higher than 5 ppm. All the destroyed NO molecules are chemical reduced to N_2 and O_2.

The yield obtained for this non thermal plasma arc is ten times smaller than this obtained by Penetrante et al [3] using DBD or corona discharge. In these experiments, the input gas was heated and the energy cost for this operation was not taken into account.

Conclusion

In this work we have shown the efficiency of non-thermal plasma arc used for dilute NO removal in N_2. We could determinate the chemical efficiency of this process by measuring the number of pollutant molecules destroyed per 100 eV of input energy. We have observed that it is not useful to inject more than 1000 joules per liter of gas. Furthermore the only undesirable by-product formed is NO_2 and its production is not higher than 5 ppm.

Results obtained from discharge in air are not similar because of oxidation processes. So, there is no direct application of this process but such experiments can help us to understand plasma physical processes. The subject of electrical discharges for environmental purpose is still in its infancy, the above results shows the interest to keep up and develop research in this field

References

[1] H. Masuda, Adv. Chem. Phys. **80,** (1991).
[2] S. Masuda, Pure Appl. Chem. **60**, (1988).
[3] B. M. Penetrante, M. C. Hsiao, B. T. Merritt, G. Vogtlin and P. H. Wallman, IEEE Transactions on Plasma Sc. **4**, Vol. 23 (1995).
[4] M. B. Chang, M. J. Kushner and M. Jc. Rood: Environ. Sci. Technol. **26,** (1992).
[5] Non-thermal Plasma Techniques for Pollution Control, part A and B, ed B. M. Penetrante and S. E. Schultheis (New York: Springer-Verlag), (1993)

[6] F. Westley, D. H. Frizzell, J. T. Herron, R. F. Hampson, W. G. Mallard, NIST Standard Reference Database 17, Gaithersburg, MD 20899 USA
[7] Y. P. Raizer, Physical Fundamentals of Gas Discharge Processes, Moscow: Nauka (1980).
[8] H. Maecker, Z. Phys., **156**, No 1 (1959).
[9] S. Pellerin, J. M. Cormier, F. Richard, K. Musiol and J. Chapelle, J. Appl. Phys. **29**, (1996)

Deposition of diamond-like carbon film on three-dimensional objects using glow plasma CVD method

S. Takada, Y. Ohgoe, T. Saito and K. Hirakuri

Department of Electronic & Computer Engineering, Tokyo Denki University, Ishizaka, Hatoyama, Saitama, 350-0394, Japan

Deposition of a functional thin film, surface modification and fine pattern etching are available by the plasma chemical vapor deposition (CVD) method at low temperature. Since it is popular to form and control uniform plasma on the flat surface of the objects, flat parallel electrodes are generally used to plasma CVD process. However, there are big restrictions of the application of this system because it is difficult to generate the uniform plasma on the objects with 3-dimensional structure. N. Mutsukura et al reported the relationship between the structure of objects and the property of deposited carbon films; i.e. position dependence between bulk-plasma and ion-sheath region.[1)] The properties of carbon films deposited in each region were quite different. In the bulk-plasma region, the film was transparent in visible wavelength and mechanically soft. In contrast, the film formed in the ion-sheath region was chromatic and extremely hard. The kinetic energy of the ion bombardment at the substrate surface can be estimated from the mechanical hardness of the deposited carbon film. The reason is that the hardness is strongly depended on the cathode dc self-bias voltage in the rf plasma CVD. And the authors also indicated that hard carbon film deposition to insulator objects, such as glass plate, at the across the sheath-plasma boundary are available by metal step on the cathode electrode. It enables to develop an obvious sheath formation around the metal step. Therefore, ion bombardment always occurs during deposition at spatial position.

In order to realize uniform deposition of the diamond-like carbon (DLC) film to the 3-diminsional insulator objects, the electrode adjusted to the objects (improved electrode) was utilized. Improved electrode was set on the cathode electrode and generates the uniform plasma to the surface of the object. Then the availability of improved electrode was discussed by evaluating uniformity of DLC film properties. Since the characteristics of DLC film is remarkably depended on the plasma condition, it is effective to analyze the process by evaluation of the film characteristics. If deposition of uniform DLC film to the 3-dimensional objects using plasma CVD method is attained, an application are expected to the other thin film deposition techniques.

In this experiment, two kind of 3-dimensional structures, the hemispheric surface and the cylindrical inner wall surface, were used as the object of DLC film deposition. Hemispheric object was made of polyurethane, and cylindrical one consisted of polycarbonate. Improved electrodes were set on the cathode electrode with the dc self-bias voltage, and objects were fully covered by them from backside. In order to estimate the uniformity of DLC film properties, small pieces of silicon substrates were located on each point of the objects on the improved electrodes. Deposition uniformity was measured on thickness and hardness, and properties of DLC film was investigated from infrared spectroscopy and Raman spectroscopy.

In case of hemispheric object without improved electrode, film thickness and hardness was dispersed within 60.4nm ~ 511.7 nm and 8.3GPa ~ 14.8GPa, respectively.

On the other hand, in our proposal process, thickness and hardness were quite uniformized. Film thickness was within 492.6nm ~ 618.7nm, and film hardness was within 12.0GPa ~ 13.4GPa. Furthermore, similar result was indicated by the properties of DLC film. Standard DLC film has two typical Raman peaks, around 1390cm^{-1} from D-band and 1530cm^{-1} from G-band. Raman spectra of deposited films without improved electrode were broad and had no carbon peak because substrates were in the bulk-plasma region and the object was attacked by ion bombardment with low energy. In contrast, each Raman spectrum of DLC films deposited by the improved electrodes was similar and had two typical peaks of DLC film. These experimental results are based on the ion-sheath formation around the object's surface by improved electrodes. Finally, the use of improved electrodes was enabled to deposit uniform DLC film on 3-dimensional objects.

References

[1] N. Mutsukura et al, Journal of Applied Physics, Vol.72, No.1 (1991) 43-53

Separation of Zr-Nb alloy by Reactive Thermal Plasma

M. Suzuki[1], T. Ichihashi[1] A. Jote[1] and S. Nishio[2]

[1] *Department of Chemical Engineering, Tokyo Institute of Technology, Japan*
[2] *The Wakasa Wan Energy Research Center, Japan*

Abstract

In order to remove niobium (Nb) from Zirconium-Niobium alloy, some experiments which uses thermal fluorine plasma has been carried out. When processing around the melting point of this alloy, Zr is extracted in the evaporated fine particles and Nb enriches in the bulk alloy. This phenomenon can be explained well by using Gibbs free energy of fluorinate reactions. For the better separation the higher temperature of the sample is kept and the more effective mass transfer of Nb in the melting alloy is required.

1. Introduction

The plasma technology, which is used widely for producing many valuable materials[1], can be also an effective technology in nuclear engineering fields. In downstream and backend of fuel cycle, several researchers have suggested various applications[2,3], for example, the direct melting method of spent fuel assembly, the treatment of spent fuel separation, vitrification of HLW, the volume reduction of LLW and the stabilization of radio nuclides and the decommissioning of reactors.

Objective of this study is to remove niobium (Nb) from Zirconium-Niobium alloy, which has been used for pressure tubes of the Japanese advanced thermal nuclear reactor "Fugen". This alloy has small cross section of thermal neutron absorption and is very convenience for reactor material. Although Nb in this alloy is stable isotope "Nb-93" before neutron irradiation, but it converts to radioactive "Nb-94" after absorbing thermal neutrons. "Nb-94" has a very long half-life and emits high-energy gamma ray. This is the reason why we have to separate this alloy, remove "Nb-94" and recycle zirconium.

Some research works concerning with metal separation by using reactive plasma have been done already. Mimura[4] reported the refining of zirconium by using hydrogen plasma and Takeuchi et.al.[5] reported the separation of Fe and Ni from Fe-Co-Ni alloy by using chlorine/oxygen mixture plasma.

In this paper, we report some results of experiments to separate Zr and Nb from Zr-Nb alloy by using reactive fluorine thermal plasma and we make mechanism of separation and optimum conditions clear. And we also discuss about possibility of removing "Nb-94".

2. Experimental

Figure 1 shows the experimental set up. Experiments were carried out in a water-cooled plasma chamber where an thermal plasma generator and a sample holder are set inside. A DC plasma jet and an DC arc were used as a thermal plasma generator. Processing gas is argon/CF_4 (carbon tetrafluoride) mixture or argon/F_2 mixture which were prepared properly and fed at the constant flow rate. Experimental conditions are arc current 100-250A and operation pressure 760Torr. The waste gas which is toxic is introduced into a scrubber and processed befor releasing into the atmosphere. A sample holder is a water-cooled hearth or a graphite cruisible with the coil for high frequency (420kHz) induction heating. Figure 2 shows the typical configuration of experiments, which uses plasma jet and inductiuon heating.

Samples of fine particles generated by the plasma processing were collected by sampling tube and membrane filter and by scraping from the chamber wall. The samples were analyzed by using WDS (Wave Dispersive Spectrometer) of X-ray fluorescence, whose data were calculated by fundamental parameter method for highl accurate quantitative analysis.

Sample surface temperature was measured by an pyrometer. This pyrometer is connected to personal computer for data transfer and processing. Although it is impossible to measure accurate temperature according to the plasma emission during plasma processing, the surface temperature was estimated by recording transition data before and after plasma irradiation sampled every 0.06sec and taking this sampling time into account.

Sample metal, Nb-Zr alloy, which has not been installed and radioactivated in the nuclear plant was used in this experiments. This sample was cut to small size (about 6g) for experiments. Components of this metal sample are listed in Table.1.

Table 1. Components of Nb-Zr alloy used in this experiments.

Elemnts	Zr	Nb	O	Fe	C	Ta	Co
wt%	97.1	2.67	0.125	0.0065	0.001	0.01	0.001

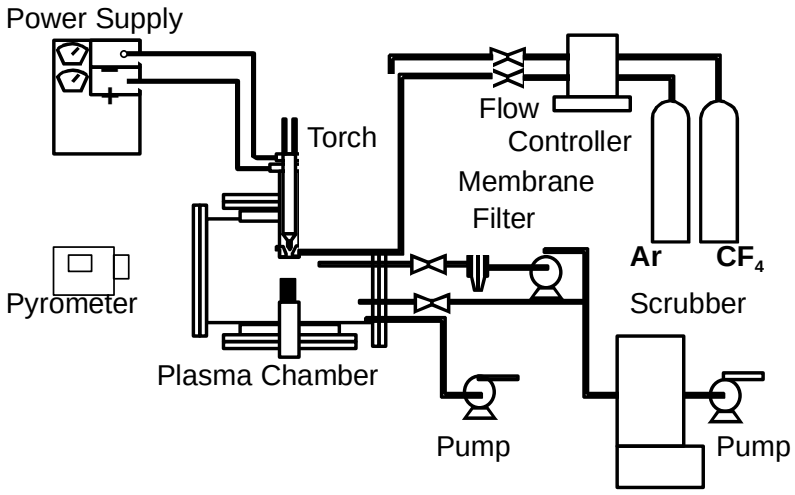

Fig.1 Schematics of experimental setup.

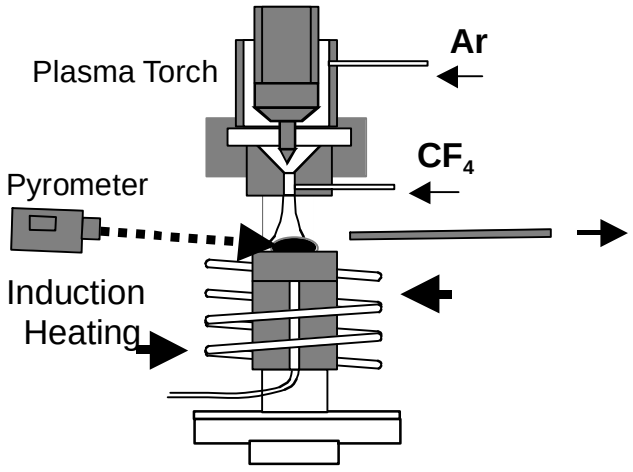

Fig,2 Detailed configuration of heating, gas feeding and sampling systems.

3. Results and Discussions

3.1 Definition of separation factor.

In order to express separation effect, we use the separation factor defined by the following equation.

$$\alpha = \frac{C_{Nb}/C_{Zr}}{C_{Nb0}/C_{Zr0}}$$

Here C_{Nb} and C_{Zr} mean the concentration (weight fraction) of each components after plasma processing and C_{Nb0} and C_{Zr0} mean those before plasma processing. Therefore, α=1 and α=0 mean no separation and perfect separation of zirconium, respectively.

3.2 Plasma jet experiments and themodynamics.

At first we show the results in the plasma jet experiment. In these experiments only argon gas was used for discharge gas and CF_4 gas was introduced into its tail plasma. It is convenient for the tungsten cathode when using such eroded gas as fluorine, the erosion of cathode can not be avoided in the case of arc discharge. In order to compensate low heat flux caused by using plasma jet installation, the induction heating was used for these experiments. In this situation, we have two important parameters to control the separation effect. One is the sample temperature and another is CF_4 concentration in plasma gas.

In the fluorination reaction of alloy, it is guessed that products are NbF_5 and ZrF_4 according to following reactions.

$$Zr + 4F(g) \rightarrow ZrF_4 \qquad Nb + 5F(g) \rightarrow NbF_5$$

Their boiling point at atmospheric pressure is 229 ^{0}C and 580 ^{0}C, respectively. Although according to this information it can be expected that Nb fluoride evaporates prior to Zr fluoride, experiments bring the opposite result. However, it is clear from the temperature dependence of Gibbs energy of fluorination reaction for Zr and Nb, as shown in Fig.3. The fluorination reaction of Zr is dominated over 1000K, which is the high temperature range expected in the plasma processing

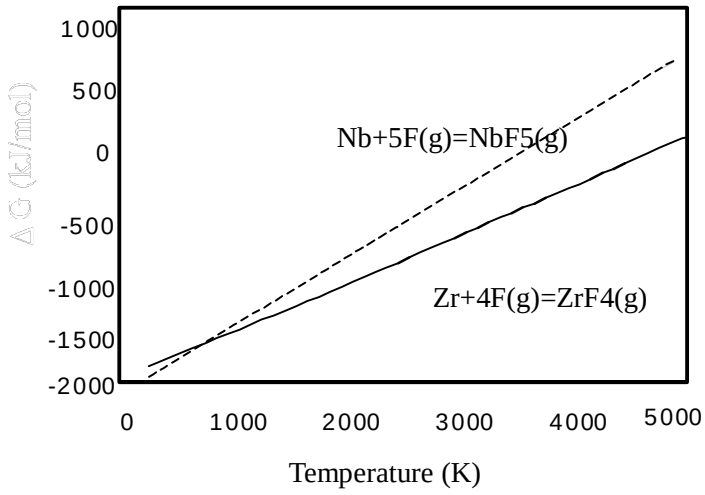

Fig.3 Temperature dependence of Gibbs energy of fluorination reactions.

3.3 Separation factor and evaporation factor.

Figure 4 shows the dependence of the sample temperature and the CF_4 concentration on the separation factor, simultaneously. Also Fig.5 shows the dependence of those parameters on the evaporation rate (weight reduction rate). All of key marks imply the various discharge and heating conditions. In these data the processing continues during several minutes and data are the time averaged ones, unless a special notice is stated. In Fig.4 it is clear that the higher temperature gives the better separation of zirconium and the complete separation (α=0) can be obtained over 2000 ^{0}C. Also it seems that the separation factor depends slightly on the CF_4 concentration. On the other hand there appears no effect of temperature in the evaporation rate and it depends on the CF_4 concentration as shown in Fig.5. From other experiments, we obtain some information that the reactive fluorine atom concentration increases with the CF_4 concentration, although it is not linear according to the temperature lowering by dissociation reaction. We can not explain its slight dependence on the separation factor, although it is nature that the evaporation rate depends on fluorine concentration.

Here, we consider about two additional reasons why the temperature and the CF_4 concentration depend on the separation factor. One is that the melting point is around 1800 ^{0}C and another is the existence of carbon atoms deriving from CF_4 in the reaction system. Carbon atoms react with Zr and Nb to form metal carbides, whose melting point is so high. In fact, we observed the carbide formation on the sample surface. When carbide formation is going on, the surface changes to black color and it prevents from evaporation. The reason why separation becomes bad around 1800 ^{0}C seems similar to that, although it is not carbide formation. The common point in these two facts can be fluidity of sample alloy. When the sample temperature is enough to melt the sample alloy, it has enough convection and gives the proper mass transfer inside the bulk. Also when the carbide forms on the sample surface, it disturbs convection and the proper mass transfer.

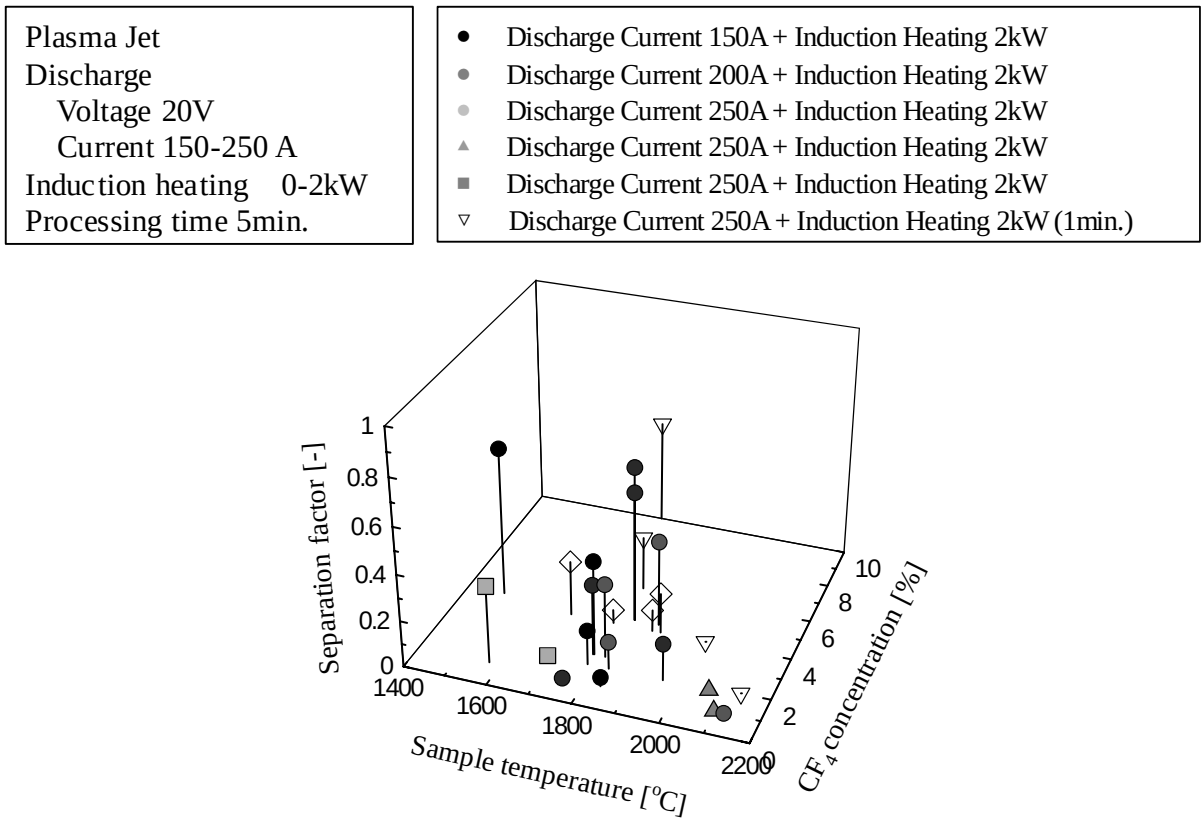

Fig. 4 Dependences of sample temperature and CF_4 concentration on separation factor.

Plasma Jet Discharge Voltage 20V Current 150-250 A Induction heating 0-2kW Processing time 5min.	● Discharge Current 150A + Induction Heating 2kW ● Discharge Current 200A + Induction Heating 2kW ● Discharge Current 250A + Induction Heating 2kW ▲ Discharge Current 250A + Induction Heating 2kW ■ Discharge Current 250A + Induction Heating 2kW ▽ Discharge Current 250A + Induction Heating 2kW (1min.)

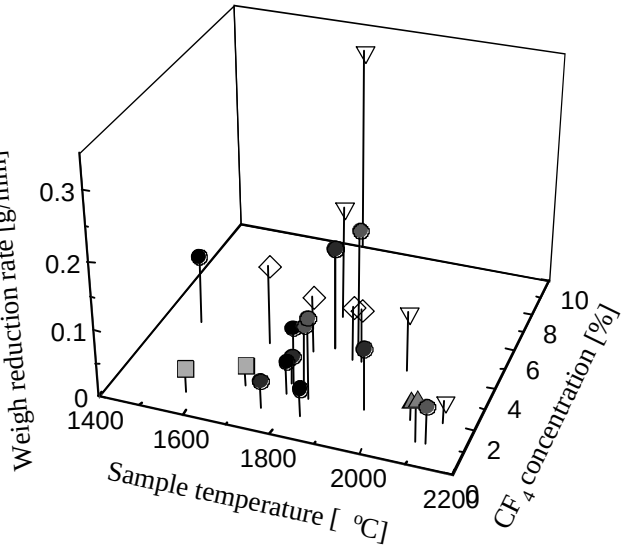

Fig. 5 Dependences of sample temperature and CF_4 concentration on weight reduction rate.

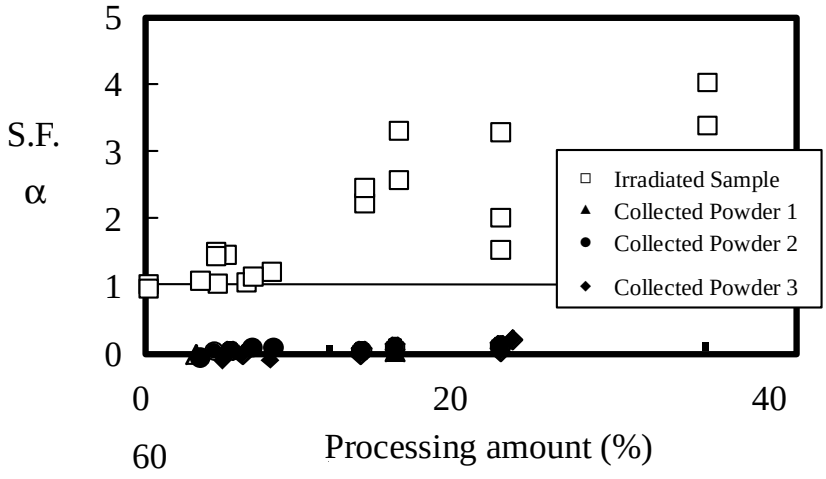

Fig.6 Dependence of processing amount on separation factor. As products shown by black keys evaporating, Nb enriches in the bulk alloy shown by white key implies Nb enrichment.

3.4 Separation experiments by arc discharge.

The plasma processing by arc discharge drawn between tungsten cathode and metal sample anode has advantage to obtain higher temperature than the plasma jet processing, although arc discharge has disadvantage of cathode erosion by reaction with plasma gas. Especially, fluorination reaction with tungsten anode takes place easily to erode it rapidly. In order to verify the conclusion obtained by the plasma jet processing, however, we dare to try some high temperature experiments by using arc discharge at the sacrifice of cathode erosion. Figure 6 shows the results. Here, the product Zr contains no Nb and also Nb enriches gradually in the bulk alloy as the Zr extraction proceeds. From these results it can be verified that the high temperature processing leads to good separation. Practically, we suggest that the transferred arc system is the best one for this purpose and it should be chosen.

From the above-mentioned results we conclude that Zr can be extracted from Nb-Zr alloy, effectively. Although extraction of a large amount of Zr instead of Nb is not economy, it can be favorable at the viewpoint of safety aspect. The most important issue is safety, when adopting this method to the separation process of radioactive “Nb-94”. Especially, this process generates the fine particle by fluorination reaction and it will be required to estimate the release of radioactive aerosol into the environment. However, the radioactive nuclide “Nb-94” enriches in the bulk alloy fortunately and it will minimize the release of radioactive aerosol. Of course, an amount of radioactive elements entrained by zirconium should be estimated for safety assessment.

4. Conclusion

In order to remove niobium from Zirconium-Niobium alloy, we carried out some experiments which uses thermal fluorine plasma and obtained the following conclusions.

(1). When processing around the melting point of Nb-Zr alloy, Zr is extracted in the evaporated fine particles and Nb enriches in the bulk alloy.

(2). This separation phenomenon can be explained well by using Gibbs free energy of fluorinate reactions.

(3). For the better separation the higher temperature of the sample is kept and the more effective mass transfer in the melting alloy is required.

(4). For the separation process a transferred arc system should be used to avoid the cathode erosion and to heat sample effectivelly.

(5). This process can be effective to separate the radioactive Nb-94, also.

References

[1] Dembovsky, V. :Plasma Metalurgy, Material Science Monographs 23, Elsevier (1995)

[2] Mitsuda, Y., et al. : *Rev. Sci. Instrum*, **60**, 249 (1986)

[3] Suzuki. M. et al : *J. Nucl. Sci. Tech.* , 34[12], 1159(1997)

[4] Mimura, K. and S. W. Lee : Journal of Alloys and Compounds 221(1995) p.267-273

[5] Takeuchi, A. et al : J.Japan Inst. Metals Vol. 63 , No. 1 (1999) pp. 28-33

Boron carbide synthesis by plasma spray process

P.Ctibor[1], V. Brozek[1], R. Hofman[2]

[1]*Institute of Plasma Physics, Academy of Sciences of the Czech Republic, Praha, Czech Republic*
[2]*Institute of Chemical Technology, Praha, Czech Republic*

Abstract
Boron carbide was synthesized from precursors in a classical plasma spray process. Layers deposited as coatings on metallic substrates were studied to resolve the degree of boron carbide formation in the layer and its character. The chemical composition and structural characteristics of free-flight particles were studied as well to establish support for a determination which stage of the plasma spray process is critical for reactions leading to boron carbide formation.

1. Introduction

1. 1 Boron carbide in research and technology

Boron carbide with its hardness between 39 and 45 GPa is the third hardest industrially produced material with only diamond (H = 75 - 100 GPa) and cubic boron nitride (H = 50 - 76 GPa) being harder. Until today boron carbide was used as free abrasive in applications for which the hardness of silicon carbide (H = 38 - 41 GPa) is not satisfactory and the price of natural or synthetic diamond is unacceptably high. Machining of silicate glass is an example of such a process. High effective absorption profile for neutrons, excellent chemical stability of boron carbide in oxidizing, reducing, acidic, or alkaline environment and high thermal decomposition point (2990 K) are properties favorable for using this material in nuclear energy-related applications.

1. 2 Water stabilized plasma and its features

At the Institute of Plasma Physics, a plasma generator WSP® with water-stabilized plasma has been developed, in which the temperature range is entirely suitable for most endothermic chemical reactions and makes it possible to melt not only the incoming precursors but also the products of the thermally and plasma-activated synthesis.
Comparing the gases commonly used for gas-stabilized plasma (GSP) generation (Ar, N_2…) with water-stabilized plasma, it is evident that the sonic velocity and enthalpy of water-stabilized plasma are higher, while the electrical conductivity at higher temperatures is similar to gases. Consequently, the enthalpy flow rate, or, in other words, the power dissipated in the arc column per unit length is higher for the water plasma. Water stabilized plasma gun takes the advantage of combining stabilizing system and cooling system in one.
To summarize the effect of material properties of water-stabilized plasma, we can conclude that WSP provides the possibility to achieve very high power outputs and higher flow velocities and temperatures of generated plasma. One of the probable reasons behind the limited use of WSP is the widely accepted beliefs that the oxidation power of WSP spraying is intolerably high and that the quality of the coatings made by WSP is generally insufficient. Therefore, for a long time there has been a general belief that WSP must be used for oxide ceramics spraying only.
It is important to note, that for each atom of oxygen in the plasma jet there are two atoms of hydrogen. Therefore oxidizing power of oxygen from the water plasma is balanced by reducing power of hydrogen and overall chemical influence of the stabilizing water in the flame is rather neutral. However, oxides were found in the non-oxide coatings. They are of similar origin as for GSP – i.e., oxidation due to the entrainment of surrounding atmosphere (air) into a highly turbulent plasma jet and from the carrier gas used for the powder feeding.
Comparing GSP and WSP, the main advantages of the WSP® deposition system are: i) lower operational costs; ii) higher production rates with a possible use of less expensive feedstocks (higher throughput); iii) higher attainable temperature allowing spraying of materials with higher melting

points. The operational costs are reduced because water is used instead of expensive stabilizing gases and also because the cooling and stabilizing systems are combined, thus simplifying maintenance. In addition to that, larger and wider cuts of feedstock powders can be used which are less expensive.
Also the temperatures in the plasma jet are significantly higher: maximum temperature is around 30 000 K, compared to about 15 000 K maximum for GSP. Even when the velocity of plasma jet is from 5 000 to 7 000 ms^{-1} at the nozzle [1], compared to 1 000 to 1 500 ms^{-1} for GSP, the impact velocities of deposited particles however are about the same or slightly lower than for GSP spraying. This is caused by a lower acceleration of injected particles due to the lower density of plasma.
Higher plasma temperature and higher available thermal energy can be used to spray materials with high melting points (e.g. MgO or W) [2, 3], and for a whole spectrum of less-common processes, such as solid feedstock based synthesis by plasma spraying.

1. 3 Synthesis by plasma spraying utilizing WSP system

Feedstock powder is introduced into the water plasma jet outside of the gun using one or several injectors. The goal of all thermal spray processes is to deliver a powder particle to the substrate in such a state that after impacting the substrate, the particle will flatten as one piece. To achieve that the particle (droplet) must be either slightly above liquidus, between the liquidus and solidus curves or, at worst, in a plastic state just below the solidus line. During melting of a high-melting point component of multi-component powder a low-melting point component could be released from the droplet in gaseous state.
Even from the short description of the WSP system, the main processing parameters for spraying can be derived:
- spraying distance (or stand-off distance) SD, which is the distance between the gun's nozzle and a substrate (same as for GSP);
- feeding distance FD, which is the position of an injector downstream from the nozzle;
The actual state of a droplet on impact is given mainly by SD. FD, on the other hand, decides on melting/evaporation state of an injected particle. The right melting for a given chemistry results from a proper combination of the power, feedstock's size and feed rate (dwell time at a high temperature). Taking into account the enormous amount of available heat in WSP, larger powder sizes are needed to avoid evaporation or bouncing-off of the injected particles from the plasma jet. This condition is important even in the case of solid precursors for synthesis plasma spraying. Similarly, the melting point of a given feedstock generally suggest the FD value – a low melting point materials cannot be fed into high temperature regions of the plasma jet.
Boron carbide synthesis from both solid and liquid precursors in water-stabilized plasma and also injection and formation of coating and free standing parts of B_4C powder were subject of previous research carried out by the authors [4]. Utilization of high-velocity plasma systems for synthesis by plasma spraying of precursors fed-in as solid feedstock is less common process and it represents serious challenge for the above-described water-stabilized system. Direct deposition of boron carbide from non-carbide solid precursors on metallic substrates is the main topic of the present paper.

2. Experimental

2. 1 Precursor and critical aspects of its use

Boric acid creates only 5-percentual solution in the water at room temperature. It was shown in the previous set of experiments [5], where water solution of the precursor was used, that it was very difficult to ensure parameters of plasma system suitable for stable plasma flow and for precursor melting at once. At majority of suitable plasma system settings with current between 300 A and 500 A, the water evaporation was enormous. Fine particles of solid precursor, and also the entire precursor dissolved in water solution, were evaporated. Only coarse-grained fraction was captured as a product, but it contained large amount of impurities, first of all from the water and industrial purity boric acid.
The authors' attention in the next series of experiments turned to preparation of BUS precursor (Boric acid - Urea - Sucrose) in the form of powder sprayable by classical plasma spray procedure. The nature of the precursor makes it difficult to obtain powder with proper size distribution and with good flow properties. BUS precursor is not inert to water at all because sucrose content. Problems with its

moistening and in contrary softening under ambient conditions – powder is not hard enough to be successfully fed – were serious. Despite such problems pure precursor (size 90-180 μm) was used as a feedstock.
Better yield – powder amount captured after passing through the plasma – was achived when the precursor was mixed with a mild amount of inert ceramic powder. The fact was utilized, that alumina is a material commonly used in thermal spray, especially by WSP. Moreover, alumina is described [6] as a material enhancing mechanical properties of B_4C, if the alumina content in the mixture is around 10 vol. percent. This amount was not high enough to create powder with acceptable flow behavior, therefore the authors decided to increase the alumina content to 40 – 50 vol. percent.

2. 2 Plasma spray procedure

The feedstock was composed from BUS precursor (size 75-224 μm) and alumina (size 50-63 μm) and plasma sprayed. Previous tests ensured that alumina helped to feed the properly mixed powder into the plasma flow whereas size distribution of BUS was not critically important.

Table 1
Experiment 1 - Spray round with precursor BUS only
Experiment 2 - Spray round with precursor BUS with Al_2O_3

Parameter	Unit	Experiment 1	Experiment 2
FD	mm	20	20
SD	mm	280	280
Torch power	kW	114	114
Theoretical temperature at the feeding point	K	18 000	18 000
Feeding medium	-	Compressed air	Compressed air
Throughput	kg/hour	6	12 at all, BUS cca 6

Purity of the feedstock was measured by XRF analysis. The sum of major impurities (Si, Ca, Fe) does not exceed 0.5 percent. XRF is not able to detect boron; therefore boron analysis was carried out by the Atomic Absorption Spectroscopy method after burning up the substance in the air (boron transfer to B_2O_3) and its dissolution (Varian Spectr AA 880).

2. 3 Samples of free-flight particles (FFP) and deposits

Free-flight particles were obtained as feedstock particles conventionally fed into the plasma, but caught into a vessel placed in the distance high enough from the plasma gun. In such a way, the particle state is “frozen” and the influence of the substrate on solidification is eliminated. In the studied case the distance was 900 mm. FD was set as 22 mm, for other parameters see Tab. 1.
Plasma deposited samples were prepared by the process described in the paragraph 1.3, where at SD = 280 mm, a substrate from carbon steel (dimensions 120x40x8mm) was placed.

3. Results and discussion

3. 1 Free-flight particles (FFPs)

The feedstock was amorphous in all cases. FFPs contain everywhere large carbon content (identified by XRD in the product) in crystalline form, see Fig. 1. This fact is interesting – extremely short dwell time in the plasma leads at the majority of substances to amorphization of the originally crystalline feedstock, but rarely to the opposite process. Shape of FFPs signalizes reaching of the melting point of all feedstock components in the plasma flow. Originally irregular and porous precursor particles (Fig. 2, left) were spheroidized in the plasma (Fig. 2, right).
The size of single FFPs implies remelting and densification of originally larger precursor particles. Standard deviation of mean size (equivalent diameter) measured by image analysis is two times lower for the FFPs compare to the feedstock. This fact signalizes that only certain size fraction of particles could be caught as FFPs. The smaller ones were evaporated or bounced-off at the feeding into the

plasma. Too large particles dwell only in colder parts of the plasma flow and remain unmelted, out of the main particle stream caught.
X-ray diffraction shows that monocomponent FFPs are amorphous; several extracts from FFPs exhibit presence of graphite in addition to the amorphous phase. The FFPs crystallize upon annealing in protective atmosphere at 1600°C for 1 hour. Indication of boron carbide presence in FFPs was indirect: comparison of infrared spectra of crystalline B_4C (or $B_{12}C_3$) of the annealed precursor with IR spectra as-caught FFPs. In both the spectra, antisymmetrical vibrations of B-C bonds at 650 cm^{-1} and 1150 cm^{-1} as well as symmetrical vibrations between 850 and 750 cm^{-1}, typical for crystalline B_4C, were detected. Other vibrations detected at 1627 cm^{-1} and 1385 cm^{-1} by IR measurement were not the subject of deeper investigation.

3. 2 Deposits

For the observation by scanning electron microscope, single particles were deposited on steel substrates. Such a particle, or better, particle conglomerate, is shown on Fig. 3, left.
Fig. 3, right picture, demonstrates that particle conglomerate passed through the plasma and embedded on the substrate consists of elements with lower atomic number Z compared to surrounding surface. Energy-dispersive microanalysis shows that the elements found in the particles have lower Z than what is possible to detect by used apparatus. This serves as an indirect proof of boric compound. Therefore, those particles were stripped from the substrate and studied by IR, XRD and AAS. The same results as in the case of FFPs were obtained – i.e. XRD shows amorphous structure and IR confirms the B_4C pattern. AAS analysis found lower boron content in the product, which documents higher content of free carbon, embedded in the precursor particles to create CO/CO_2 protective atmosphere around individual particle at spray process. It is reported [7] that free carbon in B_4C decreases the melting point at the B_4C-C interface to the eutectic point and thereby enhances the material transport. Optimization of the carbon content in the precursor to fulfill the above-mentioned roles is rather complex task, in this moment not well solved. Free carbon removal from the carbide product doesn't represent insoluble chemical problem.
When spraying the mixture BUS-Al_2O_3, first of all, interlayer of pure Al_2O_3 0.4 mm thick was sprayed to enhance removal of the deposits from the substrate, which was helpful for certain measurements. Figure 4, left, shows substrates covered by plasma deposits. The deposit of the mixture BUS-Al_2O_3 is partly removed to show individual layers. Right picture shows the detail of the deposit surface. Here it is visible that the structure is "columnar" with individual globular particles bonded together dominantly perpendicularly to the substrate. As a result of imperfect contact between the "columns", the structure is extremely porous. This is valid also for the alumina component, whereas spray conditions were in the frames of common alumina spraying. Alumina normally builds layers with lamellar structure and good cohesion. Here (Fig. 4) the resulting structure is related more to those of plasma deposits of B_4C, which were sprayed from B_4C powder as the subject of former projects [8, 9]. Absence of typical splats Al_2O_3 is interesting, spheroidal particles of boron carbide are the consequence of higher melting point. Infrared spectroscopy again indicated presence of B-C bonds in the product. X-ray diffraction recorded in the deposits the α phase of Al_2O_3, AlB_{10} phase and amorphous fraction in all cases. Presence of AlB_{10} documents boronizing ability of the used precursor. This ability is thereby present also at an extremely short reaction time represented by heating in thermal plasma. Absence of δ phase of Al_2O_3, normally present in alumina plasma-sprayed layers, could indicate inhibitive action of the boride phase.

4. Conclusions

Described experiments document that at the conditions of thermal plasma, creation of amorphous product, having reactions typical for boron carbide, is possible. Precursors were invented and synthesized to contain over-stoichiometric carbon content whose aim was to create protective atmosphere for boron carbide production in the plasma and subsequent deposition. This protection is crucial because water-stabilized plasma system has very narrow redox-zone of the plasma. Other measures to limit losses of bonded boron should be tested in future research (system gas-tight sealing, shrowding). The first stage of the plasma spray process – i.e., before solidification of the particles – was resolved as a critical period, which decides the boron carbide formation and the product nature at all.

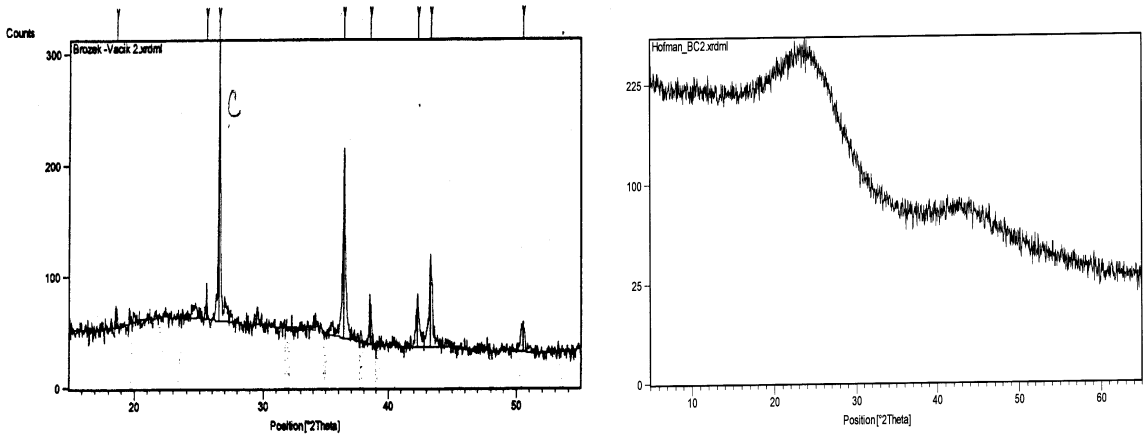

Fig. 1 – XRD patterns of FFPs prepared using BUS precursor (left) and of the deposit (right)

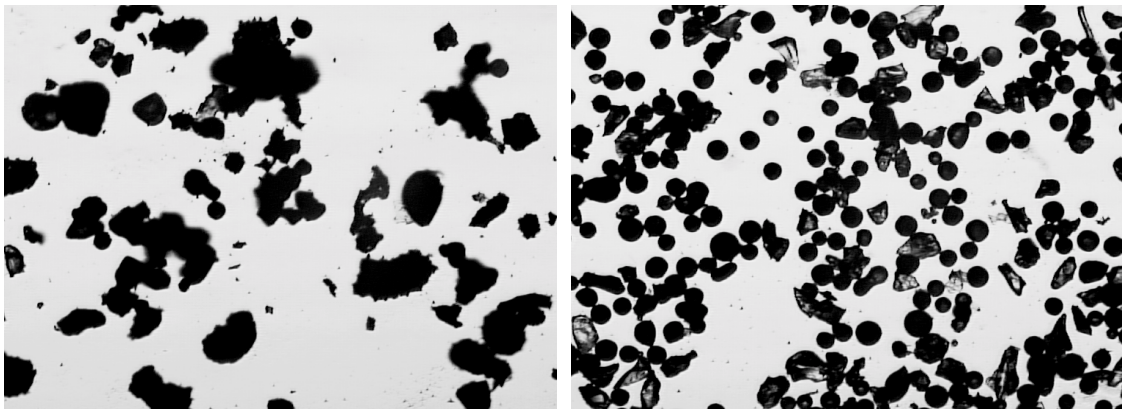

Fig. 2 – Precursor BUS as a feedstock (left) and as free-flight particles (right).
Light microscopy. Image width corresponds to 1.45 mm.

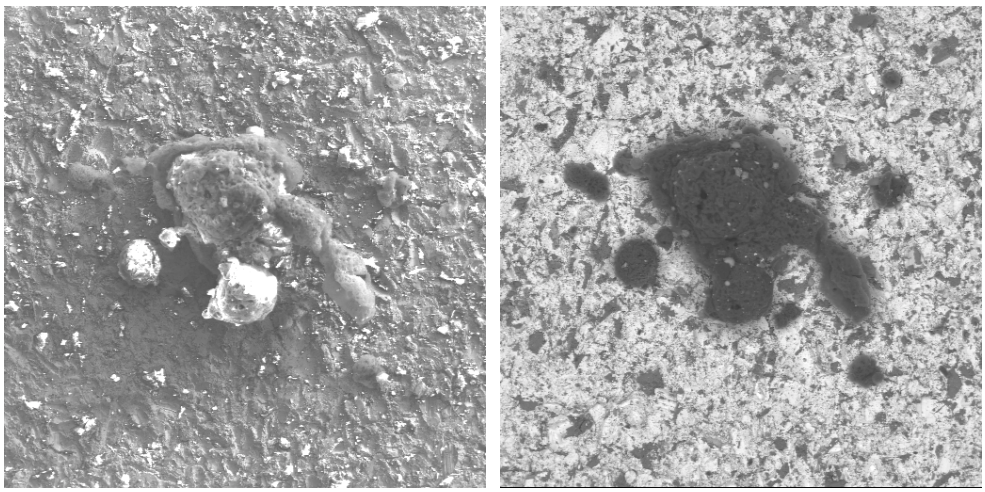

Fig. 3 – Conglomerate of single particles of plasma-deposited BUS. SEM-SE (left) and SEM-BE (right). Image width corresponds to 1.4 mm.

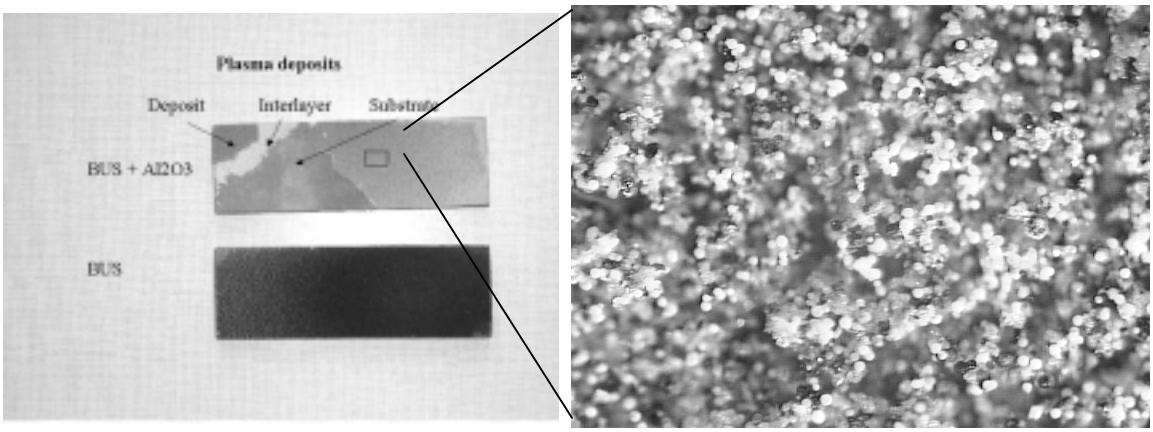

Fig. 4 – Plasma deposits (left) and detail of the surface (right) – light microscopy. Image width corresponds to 375 μm.

Acknowledgment

The work has been supported by Grant Agency of the Czech Republic, project No. 104/01/0149.

References

[1] Chraska, P., Hrabovsky, M.: An overview of water stabilized plasma guns and their applications, Proceedings of the International Thermal Spray Conference, Orlando, FL, USA, 81-85 (1992)

[2] Brožek, V., Bohac, P., Gauckler, L., Paul, W., Chráska, P.: Sealing of MgO and CeO_2 Plasma Sprayed Substrates, Proceedings of the Conference Metal 1999, Ostrava, Czech Rep. Vol.III, p.266-272 (1999)

[3] Brožek, V., Dufek, V., Neufuss, K., Šarman, L.: Spheroidisation of Tungsten Metal Particles by Plasma Spraying Process. Materials Week & Exhibition MATERIALICA, October 2001 Munich, CD-G5-918 (2001)

[4] Brožek, V., Hofman, R., Ctibor, P., Hrabovsky, M.: Plasma spray deposition of boron carbide, Abstracts of the 12th Joint Seminar „Development of Materials Science in Research and Education“, Ostravice, Czech Rep., p.11-12 (2002)

[5] Brožek, V., Hofman, R., Ctibor, P.: Plazmochemical synthesis of boron carbide, Journal “Chemické listy” 96, 364 (2002) (in Czech)

[6] Hae-Won, K., Young-Hag, K., Hyoun-Ee, K.: Densification and mechanical properties of B_4C with Al_2O_3 as sintering aid, *J. of Am. Ceram. Soc.*, **83** [11] 2863 65 (2000)

[7] Sinha, A., Mahata, T., Sharma, B. P.: Carbothermal route for preparation of boron carbide powder from boric acid-citric acid gel precursor, *J. of Nuclear Materials,* **301,** 165-169 (2002)

[8] Matějíček, J., Nanobashvili, S., Ctibor, P., Neufuss, K., Brožek, V., Chráska, P.: Properties of Boron Carbide Coatings and Free-Standing Parts Prepared by WSP, Proceedings of Materials Week 2001, Munich, Germany, 2001, Paper. No. 914 (2001)

[9] Matějíček, J., Neufuss, K., Ctibor, P., Rohan, P., Dubský, J., Chráska, P., Brožek, V.: WSP-Sprayed Boron Carbide Coatings for Fusion Applications, Proceedings of International Thermal Spray Conference 2002, Ed. C. Berndt, Essen , Germany, pp. 1-5 (2002),

Powder Treatments at Atmospheric Pressure

Masuhiro Kogoma, Katsunori Suzuki, and Kunihito Tanaka

Department of Chemistry, Faculty of Science and Technology, Sophia University
7-1 Kioicho, Chiyoda-ku, Tokyo 102-8554, Japan

Abstract

We examined the silica coating methods on the surface of TiO_2 powder by means of atmospheric pressure glow discharge using TEOS adsorbing and plasma oxidation. XPS analysis and TEM photography were performed to determine whether the powders were covered by silica. The attained silica protection layer could prevent the oxidation of squalene oil with TiO_2 in the UV irradiation.

1. Introduction

Some kinds of pigments that are used for cosmetics give rise to a skin irritation problem when they contact the skin directly. In this study, we used TiO_2, a UV-reflective white pigment powder that is frequently used for cosmetics. TiO_2 is a kind of photosensitive catalyst. So the photosensitised powder may oxidize oil in the sweat as a squalene. Such oxidized oil can easily attack a human skin surface. An oxidized squalene molecule produces many kinds of per-oxy-organic compounds that arouse allergies or sometimes a cancer. Our previous studies reported the possibility of powder handling with atmospheric pressure glow discharge [1-4]. We thus tried to develop the SiO_2 coating methods on the TiO_2 powder pigments by means of atmospheric pressure glow discharge using TEOS adsorbing and plasma oxidation to prevent the oxidation of squalene oil in the UV irradiation.

2. Experiment

The diameter of TiO_2 (anatase 80%, rutile 20%; $15 m^2/g$ in adsorption area; Toho Titanium Corporation) particles is a few hundred nm. In this study, we employed the Adsorb and Dry method using He-O_2 system [5]. We used squalene oil (2,6,10,15,19,23-hexamethyl-2,6,10,14,18,22-tetracosahexaene; Maruha Co,Ltd) to examine the surface activity of TiO_2 powder. First, the TiO_2 powder was pre-treated with TEOS (tetraethoxysilane) - ethanol mixture aero - sol to adsorb TEOS on the surface of particles. After the ethanol dried (about 2 days) in air ambience, the powder was treated in He-O_2 plasma to produce SiO_2 as an inorganic super - fine layer on the TiO_2 surface. The amount of deposited SiO_2 can be controlled by the concentration of TEOS in the solvent ethanol during the adsorbing process. Figure 1 shows a schematic of the discharge reactor. It consists of a quartz glass tube and a stainless steel centre electrode, which is

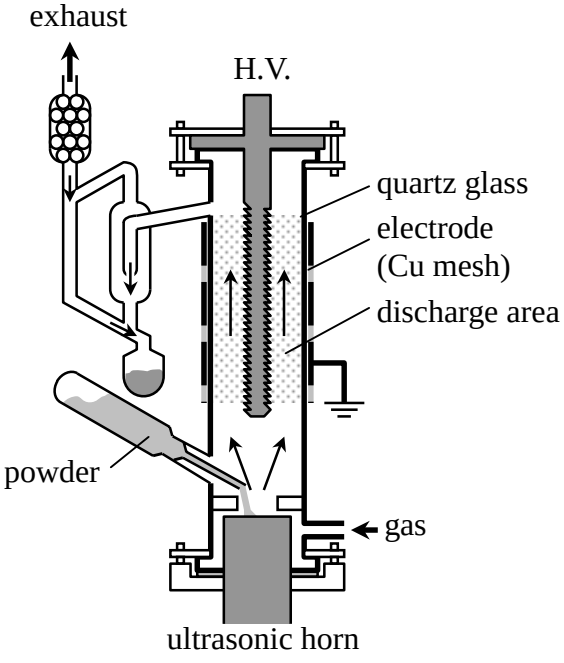

Fig.1 Schematic of discharge apparatus

Discharge Conditions	
Powder / g	10
Discharge Time / min	5
He Flow Rate / cm^3min^{-1}	10000
O_2 Flow Rate / cm^3min^{-1}	100
Discharge Power / W	2500
Discharge Frequency / MHz	13.56

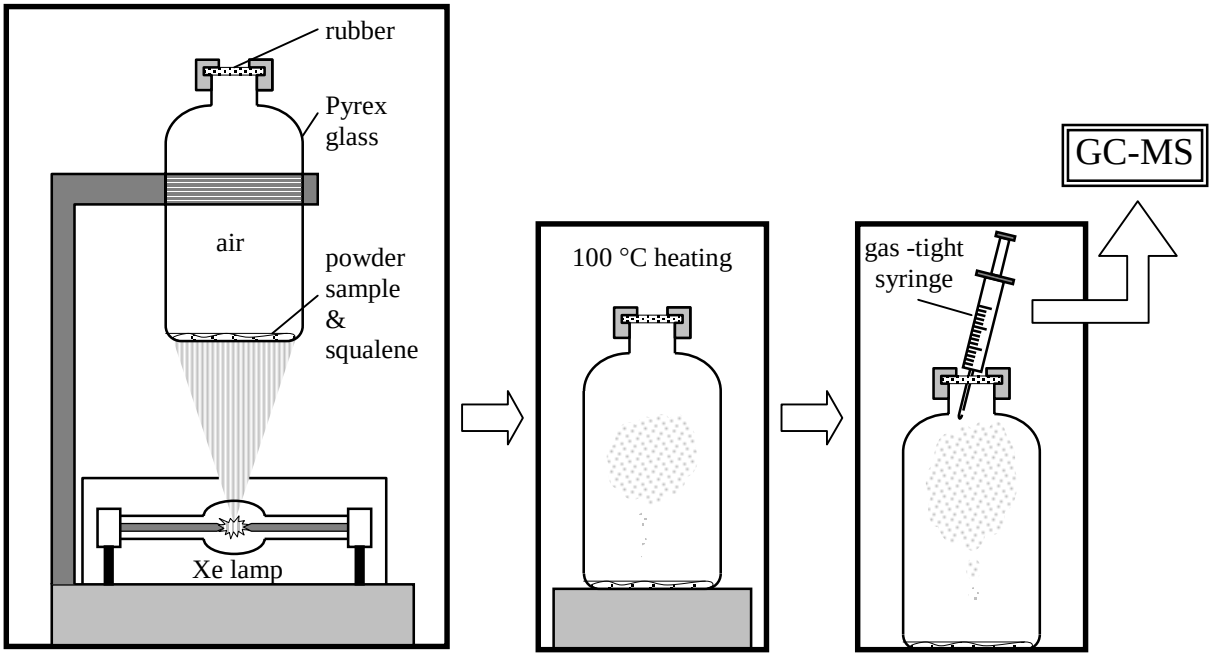

Fig.2 Schematic of the apparatus to measure the gas reaction products from UV-irradiated mixtures of powder and oil.

connected with a matching network and a radio frequency generator (13.56MHz); a Cu mesh outer electrode is connected with the earth. The apparatus was also equipped with an ultrasonic homogeniser to flocculate the aggregated powder into the single particles. RF power applied to the reactor was 2500W . Reaction gases were He and O_2. Gas flow rates were 10 l and 100 ml per minute, respectively. In the reaction device, fine particles were introduced on an ultrasonic horn and were flicked strongly. Then they were carried in the gas and went through the plasma area and were carried into the separation trap, and finally they were collected into the collecting bottle. Treating rate is about 100gr/50min for the powder.

The surface of treated TiO_2 that was coated with SiO_2 was analysed by XPS. Besides, we irradiated UV squalene oil with treated TiO_2 in a Pyrex glass bottle, which contained air. Then the composition of the gas that arose from UV-irradiated squalene oil by heating of the bottle was measured by GCMS (Shimazu QP5050).

3. Results and Discussion

3.1 XPS specta

In Figure 3, we measured Si2p spectra on TiO_2 (a) and that had adsorbed TEOS on TiO_2 (b), and that had

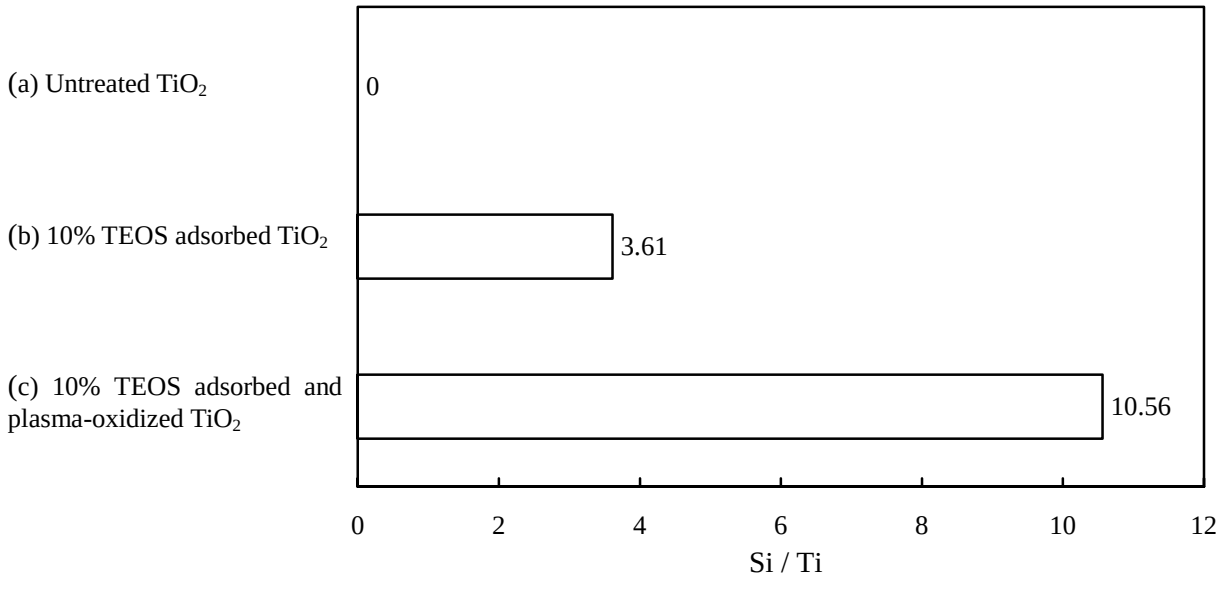

Fig.3 Atomic concentration ratios of Si /Ti on the treated TiO_2 powder surfaces.

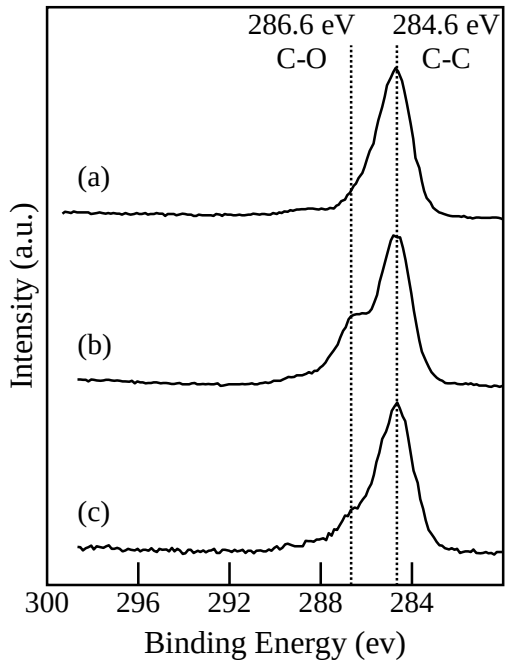

Fig. 4 C_{1s} spectra of XPS.
(a) untreated TiO2,
(b) 10wt%TEOS adsorbed TiO_2,
(c) 10wt%TEOS adsorbed TiO_2, and plasma oxidation.

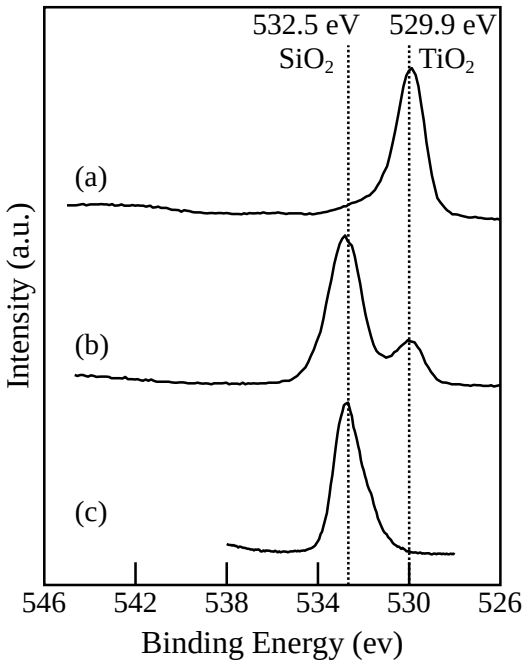

Fig.5 O_{1s} spectra of XPS.
Marks (a), (b), and (c) are the same as the marks in Fig. 4.

adsorbed TEOS and then was oxidized in the He-O_2 plasma (c). After the plasma oxidation(c), atomic concentration is increased because naked TiO_2 surfaces are lost and inorganic SiO_2 thin layer arose on the surface.

Figures 4 and 5 show C1s spectra and O1s of TiO_2 by XPS of untreated TiO_2 (a), 10% TEOS adsorbed TiO_2 (b), 10% TEOS adsorbed and plasma oxidized TiO_2 (c) respectively. In Figure 4, peak (a) shows

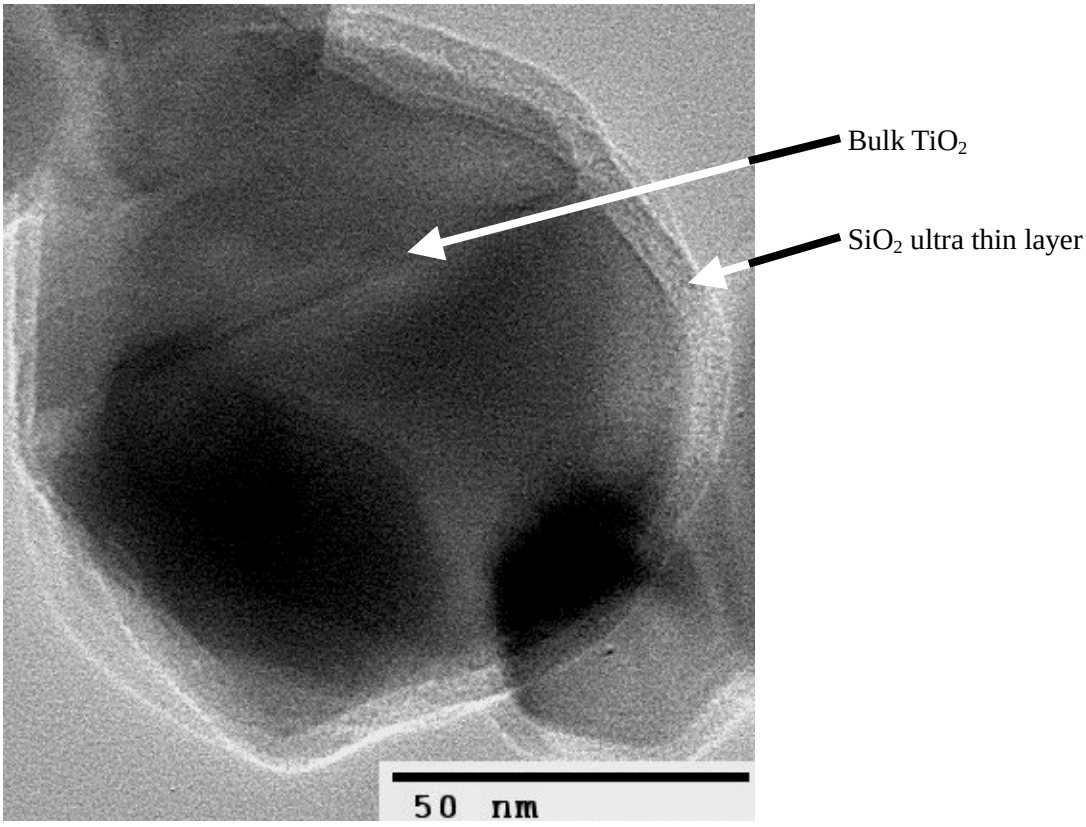

Photo 1 TEM photography of TiO_2 treated by SiO_2 in plasma oxidation.

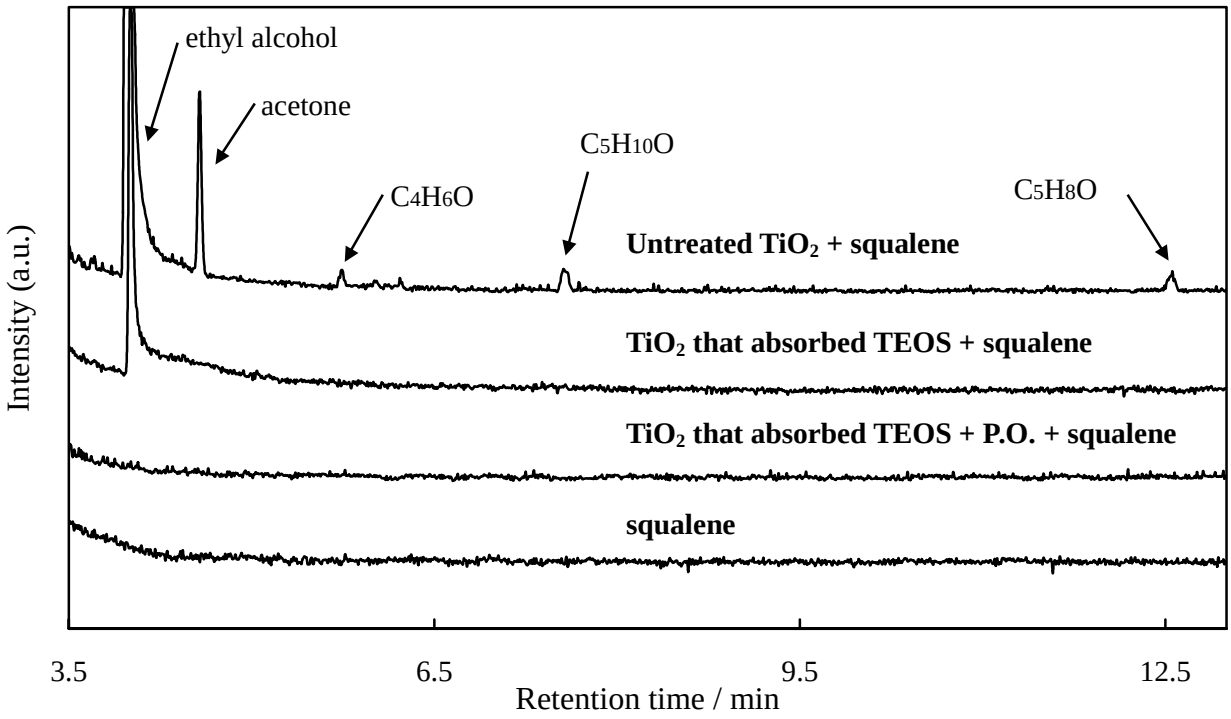

Fig. 6 GCMS spectra of vapor that arose from UV - irradiated mixture of the squalene oil and treated powders.

untreated TiO_2 powder that contains small amounts of carbon impurity that came from as-received TiO_2. After TEOS was adsorbed on the powder surfaces, another peak arose on the shoulder of the main peak; this should be assigned to the carboxyl groups in adsorbed TEOS molecule. In peak (c), carbon contamination peak is decreased by plasma oxidation and coating of SiO_2.

In Figure 5, sharp peaks of O_{1s} were obtained in the spectra of (a), (b) and (c). In the spectrum of (a) only one peak (529.9eV) assigned to TiO_2 existed. On the other hand, in the spectrum of (b) the peak (532.5eV) assigned to SiO_2 newly appeared, while the peak assigned to TiO_2 decreased. Therefore, it was found that the surface of (b) was coated with SiO_2 but the coating was not complete. In other words, the surface of TiO_2 is still partly covered by half - dissociated TEOS molecules. That is supported by the result of Figure 4. In the spectrum of (c) the peak assigned to TiO_2 almost disappeared and the shape of the peak looked like that of pure SiO_2. So, we could confirm that the surface of (c) was coated completely with inorganic SiO_2 layer without any organic contamination.

3.2 TEM photograph of powder

In the TEM photographs of treated particles, we can see an ultra thin layer covering the TiO_2 bulk powder surfaces. The thickness is about 5nm. It seems that the homogeneous inorganic layer interrupts the penetration of large - sized molecules such as squalene. The layer should be an amorphous SiO_2 because inside of the layer we can see no crystal lattice. Hence, as for the particles which adsorbed TEOS and were dried in air without plasma oxidation, their surfaces were covered by a thick porous layer.

3.3 GCMS spectrum of a vapour from UV - irradiated squalene oil mixed with the powders

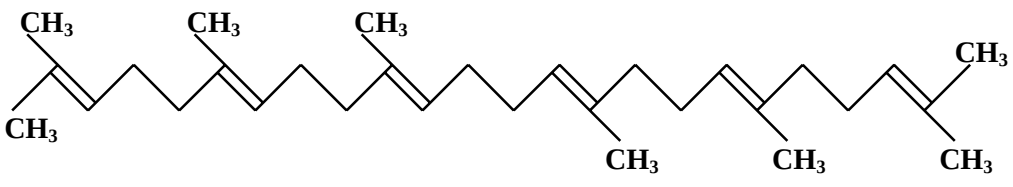

Fig. 7 Molecular structure of squalene ($C_{30}H_{50}$).

Figure 6 shows the GCMS spectrum of UV - irradiated squalene with TiO_2 and without TiO_2 in the atmosphere. The marks of (a), (b), and (c) are the same as the marks above. The spectrum of UV-irradiated squalene with (a) has peaks of ethyl alcohol and acetone and so on. These compounds are being generated in the squalene. The spectrum of UV-irradiated squalene with (b) has only one peak of ethyl alcohol; the small peak of acetone and those of other materials disappeared. The peak of ethyl alcohol decreased drastically but the quantity of the detected ethyl alcohol is still harmful to human skin. The spectrum of UV-irradiated squalene of sample (c) has no signal, so it was found that (c) could form a SiO_2 protection film that will prevent the oxidation of squalene oil even in the UV irradiation.

The squalene molecule has 8 methyl groups in the sides of the structure. The naked TiO_2 surface has strong oxidation reactivity. Thus, untreated TiO_2 will react with squalene and cut the main chain of the molecule, producing many kinds of organic oxide products such as $C_5H_{10}O$ shown in Figure 6. On the other hand, sample (b) has only a few low molecular number oxides such as acetone or ethanol. Probably, the surface of the sample (b) has been partly covered with SiO_2 caused by hydrated TEOS molecules that reacted with adsorbed water on the TiO_2, as shown in reaction (1).

$$Si(CH_3CH_2O)_4 + 2H_2O = SiO_2 + 4C_2H_5OH \qquad (1)$$

We confirm that ethanol found in spectrum(c) in Figure 6 should not be attributed to the solvent ethanol used for C_2D_5OH and GC-MS analysis. So, the surface of the sample (b) should have many small pits whose sizes are smaller than nm. A large molecule such as squalene cannot fully penetrate inside of the SiO_2 layer through the pits. Only the small size parts of ends of the main chain such as methyl groups can creep into the inside layer, and can react with TiO_2 surfaces to produce low molecular number oxides. But the sample (c) is completely covered by a tight quartz layer. No hydrocarbon molecules can penetrate the hard layer. This is the reason why we have no signals in the line of sample (c) in GCMS spectra.

4. Conclusion

We attained the ultra - thin silica layer by means of atmospheric pressure glow plasma using TEOS adsorbing and plasma oxidation method. The attained silica protection layer interrupted perfectly the oxidation of squalene oil mixed with treated TiO_2 powder under the UV irradiation. The ‘Adsorbing and Plasma Oxidation Process’ can be applied not only for TiO_2 but also for many kinds of powders that should have complete protection from the penetration of gases or molecules. The powder treatment system shown in Figure 1 has many advantages compared with the low pressure glow plasma powder treatment system, for example, very simple apparatus and easy cleaning of inside of the reactor without breaking any complicated vacuum seals. Moreover, because only radical reactions will only take place in the reactor without any ion-damaging effect in such high pressure–non thermal plasma reactors, one can treat very soft materials such as biomedical powders or organic pigments [4][5].

5. Reference

[1] S. Kanazawa, M. Kogoma. T. Moriwaki, S. Okazaki, J. Phys. D: Appl. Phys. 21 (1988) 838.
[2] T. Yokoyama, M. Kogoma, S. Kanazawa, T. Moriwaki, S. Okazaki, J. Phys. D: Appl. Phys. 23 (1990) 374.
[3] T. Yokoyama, M. Kogoma. T. Moriwaki, S. Okazaki, J. Phys. D: Appl. Phys. 23 (1990) 1125.
[4] T. Mori, K. Tanaka, T. Inomata, A. Takeda, M. Kogoma, Thin Solid Films 316 (1998) 89.
[5] S. Ogawa, K. Kiuchi, K. Tanaka, M. Kogoma, Proc. 18th Symp. Plasma Process. (2001) 449.

Surface functionalization in ammonia microwave plasmas for biomedical applications

K. Schröder, R. Ihrke, A.A. Meyer-Plath[1], B. Finke, A. Diener*, B. Nebe*, A. Ohl

Institut für Niedertemperatur-Plasmaphysik, Greifswald, Germany
** University of Rostock, Department of Internal Medicine, Rostock, Germany*

Abstract
Highly selective plasma-assisted amino-functionalization of polystyrene (PS) and polyetheretherketone (PEEK) was developed with regard to a controllable density of nitrogen-containing functional groups in general and of amino groups, specifically. The results were tested for polymer utilization as biomaterials, either direct in cell culture or after immobilization of collagen I (COLL I). Cell culture experiments were performed to check the plasma treatment and immobilization strategy.

1. Introduction

Low pressure gas-discharge plasmas are widely used for polymer surface functionalization on industrial scale. For biomaterial applications, functionalization density and selectivity are of particular importance, since functional groups are needed to control the conformation of biomolecules during adhesion and coupling reactions for immobilization [1], [2]. The idea is, that amino groups itself or in combination with a biofunctionality are very well suited for these purposes. In this context, nitrogen-containing plasmas are widely used to equip biomaterials surfaces with amino groups [3], although the plasma technology is not perfect regarding a controlled and selective generation of amino groups on polymer surfaces.
Here, we describe results of experiments of microwave (MW) - excited plasmas in continuous wave (cw) and pulsed mode (pp) in NH_3 in respect of PS and PEEK surface functionalization to check the above mentioned ideas in detail. Initially, a well-defined functionalization was acquired in a clean, ultra high vacuum (UHV) - compatible plasma environment. The results were tested for utilization, either direct in cell culture or indirect by transfer of the processes to a biologization of PEEK surfaces. In the latter case, collagen I (COLL I) was immobilized via different spacer molecules and osteoblast cells were cultivated to check the plasma treatment and immobilization strategy.

2. Experimental

Plasma experiments on PS were performed in 15 sccm ammonia (0,1 mbar) at 600 W in the afterglow (distance 9 cm) in a UHV-compatible reactor. The base pressure of the reactor is better than 10^{-6} mbar. It is part of a cluster tool, which comprises reactors, analysis and storage chambers (for details see ref. [4]). This cluster tool allowed to perform experiments under very well-defined conditions and including quasi *in situ* X-ray photoelectron spectroscopy (XPS) surface analysis of plasma-functionalized samples via a transfer in UHV from the reactor to the analysis chamber.
PEEK (25 µm thick foils for minimized fluorescence) was treated in an ammonia plasma in 40 sccm ammonia (0,2 mbar) at 550 W in the afterglow (distance 5 cm) in a commercially available reactor (V55GM, Plasma Finish, Germany), i.e. under conditions typical for application.
Amino groups were quantified via the fluorine surface density (XPS) after a derivation reaction with trifluoromethylbenzaldehyde (TFBA) within two hours after leaving the vacuum system (for details see [4]).
The reactors are installed in clean room areas for direct transfer of samples to the biological work space, subsequent processing steps, and sample transfer to cooperating cell-biological research groups.
The immobilization of COLL I was performed either with glutardialdehyde (GDA, 2 % in H_2O) for 2 h or a polyethylene glycol (PEG) spacer containing diacid (HOOC-PEG_{10}-COOH in PBS) by the carbodiimide (EDC) method over night.
Nasopharyngeal epithelial cells (KB) were cultivated on PS for 24 h, whereas MG-63 osteoblast cells were seeded on differently modified PEEK surfaces for 1 h. In both cases, temperature and CO_2 concentration were kept constant at 37 °C and 5 % CO_2, respectively. For staining of the actin-cytoskeleton of MG-63 cells, the samples were rinsed with PBS and fixed with 4 % paraformaldehyde and permeabilised with 0,1 %

[1] Present address: Bundesanstalt für Materialprüfung und -forschung, Berlin, Germany

TritonX-100 (in PBS) for 10 min at room temperature. After washing with PBS, cells were incubated for 30 min with BODIPY®FL phallacidin (diluted 1:40 with PBS) at room temperature and washed with PBS. The samples were embedded and analysed with a 63× oil immersion objective by confocal laser scanning microscopy (LSM 410, Carl Zeiss, Jena, Germany, excitation 488 nm, emission bandpass 510-525 nm).

3. Results and discussions

Highly selective functionalization of polymer surfaces represents the principal prerequisite for a successful subsequent improvement of surface biocompatibility, because it is the origin of the exploitation by materials of the proteins and cells of the body, independent of the subsequent manner of interaction. Amino groups carry a positive charge in aqueous solution at physiological pH values and possess a good chemical reactivity. On these accounts, amino groups are especially well-suited for the improvement of biocompatibility of usual polymers, which do not possess functional groups.

Consequently, plasma-enhanced selective generation of amino groups is an essential research topic. Until now, plasma processes in nitrogen and ammonia equip surfaces with multiple nitrogen- and oxygen-containing functional groups. Here, we will present some experiments aimed at an improved functionalization.

For oxygen-containing plasmas, it is well known, that optimum plasma functionalization is only possible for short treatment duration not exceeding a few seconds. Longer treatments cause undesired surface decompositions accompanied by deterioration of the desired functionalization [5].

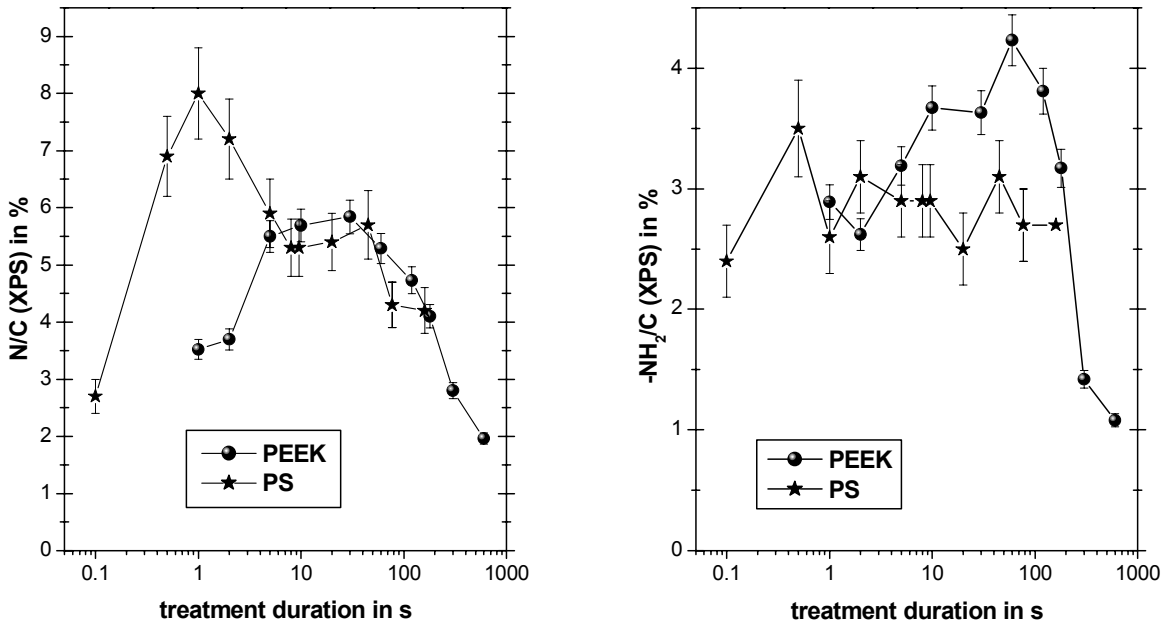

Fig. 1: Nitrogen (left) and amino group (right) density in dependence of treatment duration in a cw ammonia plasma for PEEK and PS.

Indeed, this effect was also seen in our case for ammonia plasma treatment both for PS and PEEK and similarly in UHV- and HV- environment. A cw MW plasma in ammonia lasting for 100 ms generated a PS surface with a N/C ratio and -NH_2/C ratio smaller than after a treatment duration of 300 ms and more. Interestingly, these short treatment times yielded the maximum selectivity of -NH_2/N (100 %) [6]. A similar situation was found for PEEK at elongated treatment duration. A maximum of N/C and –NH_2/C at still short treatment duration of 1-60 s is clearly visible for both polymers. This way, the polymer surfaces can be equipped with N/C of 5-8 % densities by considering the treatment time dependence. Optimized amino group densities reach more than 3 % -NH_2/C, i.e. 50 % of the implemented nitrogen (50 % -NH_2/N). Note, that plasma treatment in an environment with normal purity yielded similar levels of –NH_2 concentrations like in the ultra-clean reactor.

As expected, these changes in surface chemistry affect the water contact angle, shown in Fig.2.

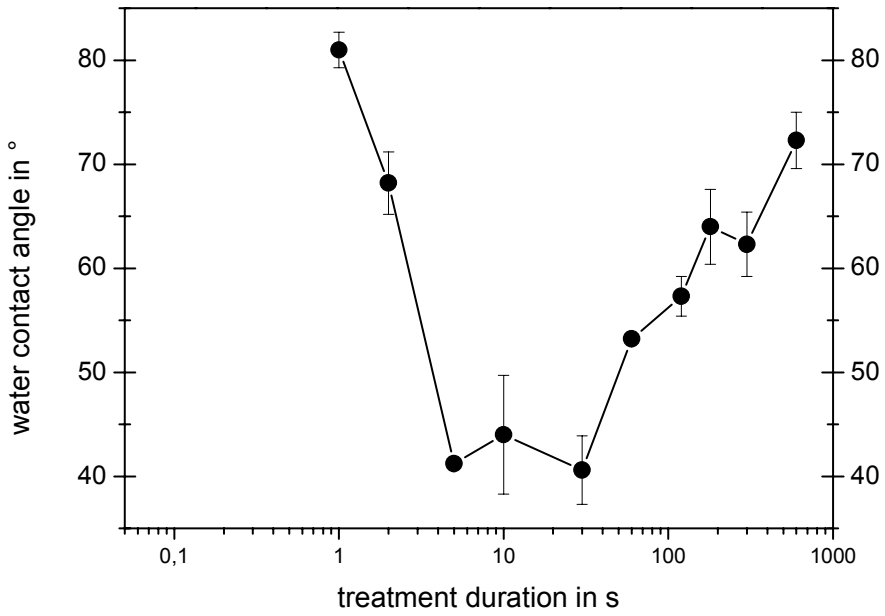

Fig. 2: Water contact angle of PEEK in dependence of the treatment duration in cw MW ammonia plasma.

This figure demonstrates the enormous dynamic of plasma-induced surface alterations. Obviously, wettability is related to the nitrogen content of the surface.

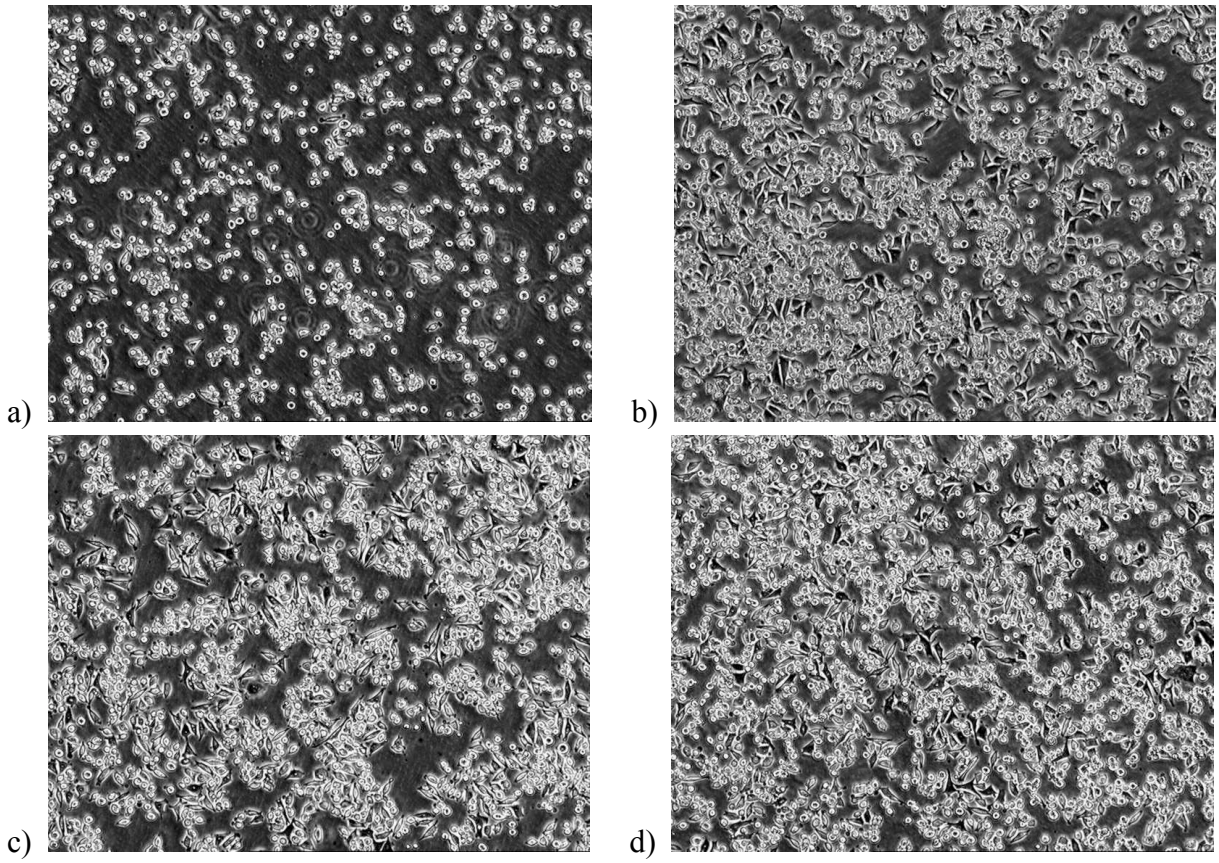

Fig. 3: Nasopharyngeal epithelial cells grown on different plasma treated PS substrates for 24 h: a) untreated PS, b) tissue culture treated PS (TCPS), c) 80 s cw MW NH_3 plasma treated, d) 10 s pp MW NH_3 plasma treated.

PS dishes treated in these short cw NH_3 plasmas are superior cell culture substrates, compared to PS and TCPS [3] (Fig. 3c). Additionally, the diversification of functionalization could be used to tune cell culture results. Extremely high densities of nitrogen were obtained after pp MW NH_3 plasma with a treatment duration of 10 s and more [7]. In this case, an exceptionally high cell density could be achieved (Fig. 3d). Here, cell behaviour must be understood as a result of self-organized attachment of biomolecules on chemically functionalized polymer surfaces.

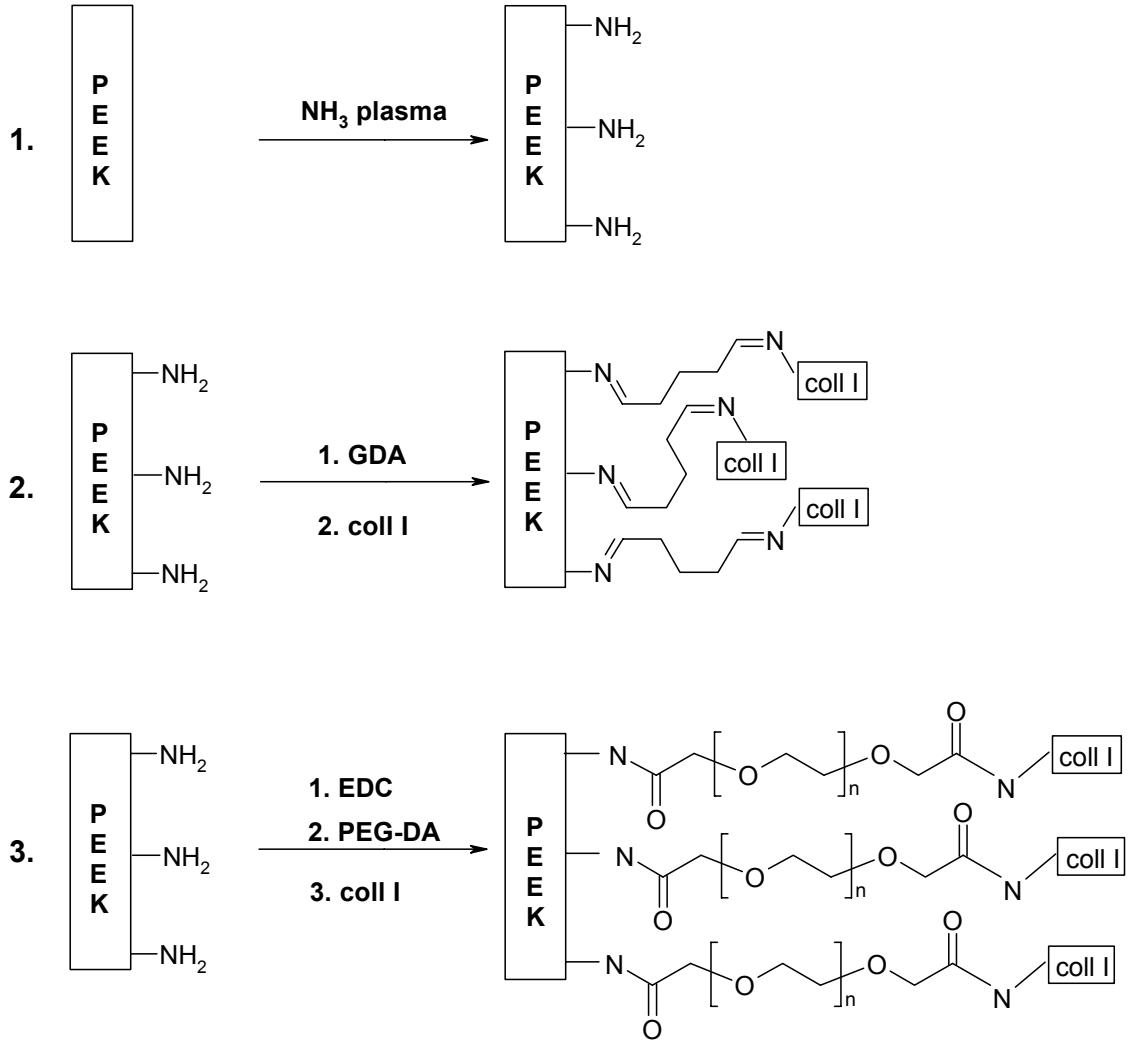

Fig. 4: Scheme of plasma induced PEEK surface activation in ammonia plasma (1) and collagen I (COLL I) immobilization via glutardialdehyde GDA (2) or carbodiimide (EDC) with a polyethylene glycol (PEG) spacer molecule PEG-diacid (PEG-DA) (3), respectively.

Instead of self-organization, immobilization of selected biomolecules can be performed by a directed covalent chemical coupling strategy. This necessitates:
- assembly of different well-defined layers, which bridge the inert polymer surface to the signal-guided cell environment and
- establishment of defined and durable connections between the single layers, i.e. covalent bonding and
- adequate characterization of every single layer or reaction step to ensure the reproducible success.

This strategy was tested for COLL I coating of PEEK. The fundamental step again is surface functionalization (scheme 1 in Fig. 4). The cw ammonia plasma lasted for 5 s in order to realize a very high amino group density ($–NH_2/C$) of about 3,5 % and a high wettability, i.e. contact angle of 40-50 ° (see Fig. 2). A short distance covalent link of COLL I to these surfaces could cause conformational hindrances reducing its bioactivity (scheme 2 in Fig. 4). More extended spacer molecules should facilitate an improved sterical constitution. Additionally, PEG should maintain functionality by optimized chain length and prevent

unspecific adsorption of proteins (scheme 3 in Fig. 4). These ideas were tested by means of GDA versus PEG/EDC bifunctional linker molecules (Fig. 5).

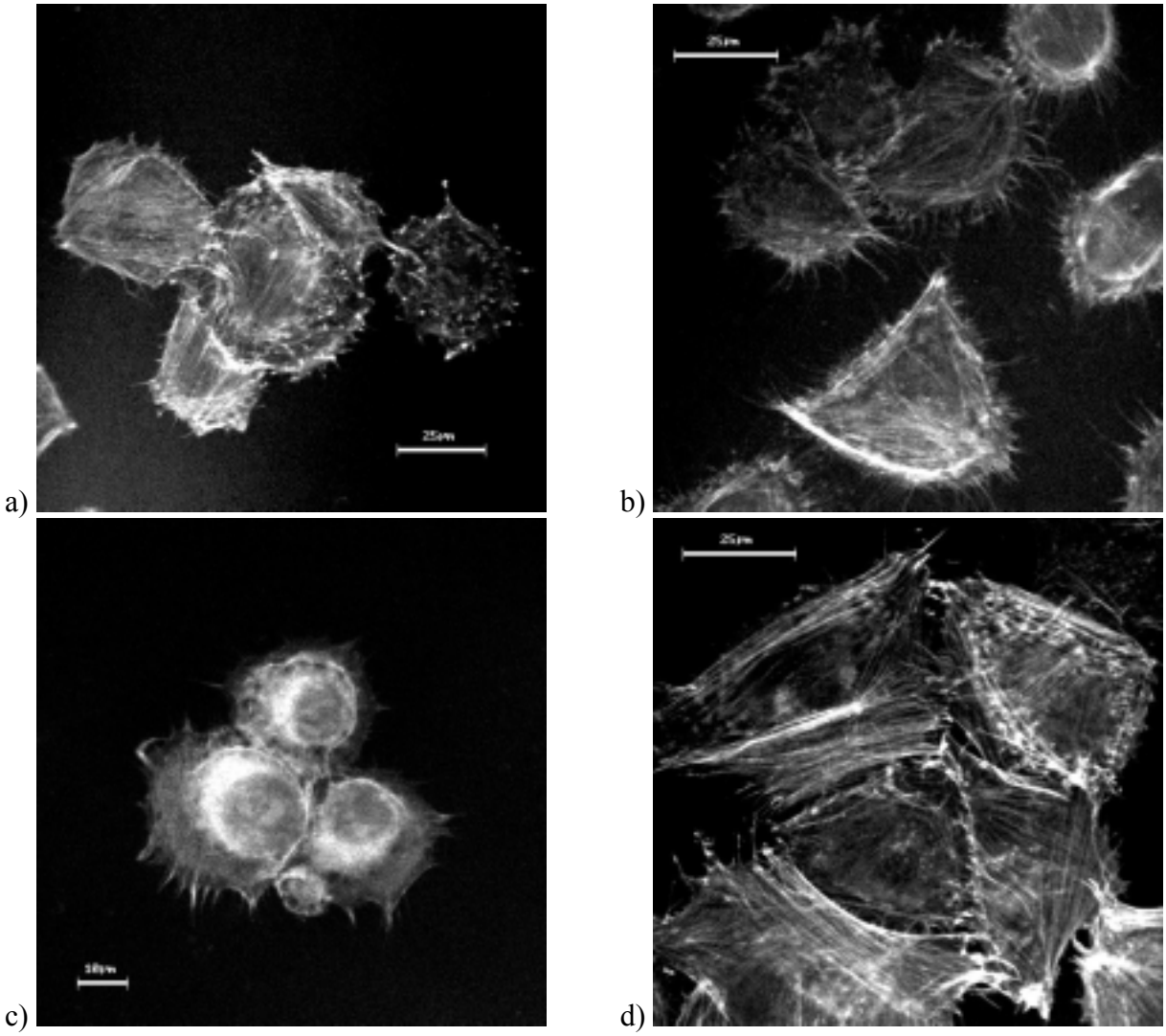

Fig. 5: MG-63 osteoblastic cells grown on differently treated PEEK surfaces, Fluorescence staining of F-actin (component of the cytoskeleton): a) untreated, b) 5 s NH_3 plasma, c) COLL I coupled via GDA after 5 s NH_3 plasma, d) COLL I coupled via EDC after 5 s NH_3 plasma. For the abbreviations see Fig 4.

MG-63 osteoblastic cells were seeded for 1 h in order to investigate the formation of the cytoskeleton. MG-63 cells on non-treated PEEK were still round, but contained a distinct cytoskeleton visible even through the strong fluorescence of PEEK (Fig. 5a). This behaviour was different from "normal" *in vitro* behaviour, namely COLL I adsorbed on cover glass (not shown). There, slightly spread and polygonal cells were obtained with a strongly developed actin-cytoskeleton. If the cells were cultivated on ammonia-plasma treated PEEK, they appeared much more spread in comparison to non-treated PEEK (Fig 5b). Cells on PEEK with covalently bound COLL I showed a different appearance when cultivated either on COLL I bound with glutardialdehyde (GDA, Fig 5c) or with carbodiimide (EDC) and polyethylene glycol (PEG, Fig 5d) spacer molecule. The cells on PEEK with COLL I bound with the PEG spacer (Fig 5d) were more spread than on PEEK with COLL I bound via GDA (Fig. 5c). In comparison to ammonia plasma treated PEEK(Fig 5b), the cells on COLL I coupled with PEG spacer (Fig. 5d) showed a more uniform appearance starting to form a meshwork of F-actin fibres.

These results correspond to the time dependence of MG-63 osteoblast adhesion (Fig. 6). Once more, clear differences between untreated and ammonia plasma treated PEEK could be demonstrated. Additionally, cell adhesion on COLL I immobilized by a GDA spacer is inferior to an immobilization via PEG spacer. Note, that only minor differences could be measured between ammonia plasma treated surfaces and surfaces with immobilized COLL I via PEG spacer. This indeed correlates with the results given in Fig. 5.

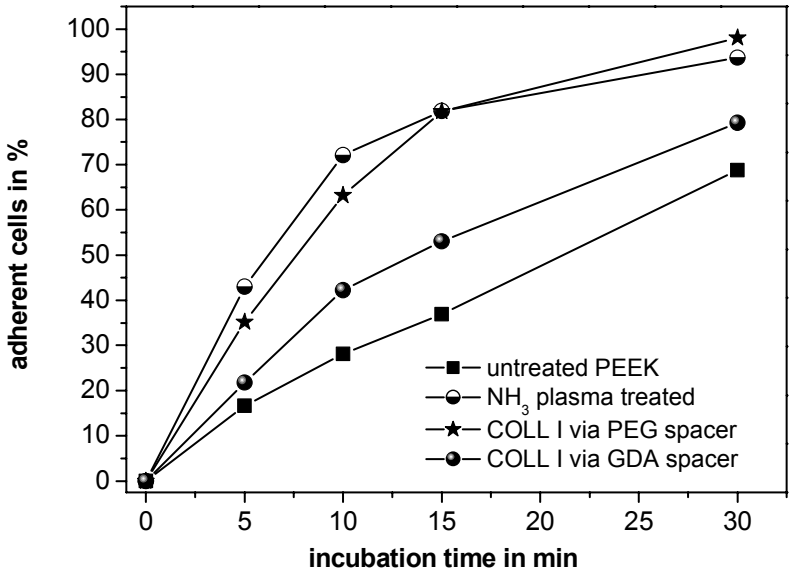

Fig. 6: Time-dependent adhesion of MG-63 osteoblastic cells on differently treated PEEK surfaces. Note, that the coupling of COLL I was carried out on NH_3 plasma treated surfaces.

Summary

Functionalization of PS and PEEK surfaces was performed in MW-excited ammonia plasmas. Short treatment durations enabled reproducible amino group and nitrogen densities of more than 3 % -NH_2/C and 35 % N/C, respectively. Hence, the wettability of the surfaces was increased reaching a medium hydrophilic character. These surfaces were either directly applied for cell culture or after using a directed immobilization strategy based on plasma chemically generated amino groups. Both approaches demonstrated significantly improved cell behaviour compared to untreated polymers. The successful covalent immobilization of COLL I depended on the applied spacer molecule and chemistry. A very promising result was obtained if a PEG-based spacer was utilized. The cell density after cultivation on solely plasma functionalised polymers was exceedingly high and of similar quality as for PEG/EDC based immobilization of COLL I. The result indicates, that further considerations and investigations are necessary to refine the design strategy of biomaterials surfaces.

Acknowledgements

The authors would like to thank Urte Kellner in plasma treatment and culture of KB cells. The financial support of the "Stifterverband für die deutsche Wissenschaft", Grant No. H 150 5503 5010 00386 is gratefully acknowledged.

References

[1] J.G. Steele, B. Ann Dalton, G. Johnson, P.A. Underwood, Biomaterials, 16 (1995), 1057-1067.
[2] P. Favia, R. d'Agostino, F.Palumbo, J. Phys. IV France 7 (1997), C4, 199-208.
[3] K. Schröder, A. Ohl, In vitro News (2001), 1, 3.
[4] K. Schröder, A. Meyer-Plath, D. Keller, W. Besch, G. Babucke, A. Ohl, Contrib. Plasma Phys., 41 (2001) 6, 562-572.
[5] J. Friedrich, P. Rohrer, W. Sauer, T. Gross, A. Lippitz, W. Unger, Surf. Coat. Technol. 59 (1993), 371-378.
[6] A.A. Meyer-Plath, K. Schröder, B. Finke, A. Ohl, "Current trends in biomaterial surface functionalization - nitrogen-containing plasma assisted processes with enhanced selectivity",Vacuum, in print.
[7] K. Schröder, A. Meyer-Plath, A. Ohl, 9. Neues Dresdner Vakuumtechnisches Kolloquium, 18. – 19.10.2001, Dresden, Tagungsband S. 154-158.

Effect of Microwave Oxygen Plasma on Elements Behavior in Melting Glass

T.Osugi[1], S.Kusumo[1], M. Hiraoka[1], H.Kobayashi[2], M.Suzuki[1]

[1] *Department of Chemical engineering, Tokyo Institute of Technology, Tokyo, Japan*
[2] *Waste Management and Fuel Cycle Research Center, Tokai Works, Japan Nuclear Cycle Development Institute, Ibaragi, Japan*

Abstract

Microwave oxygen plasma is irradiated on glass melt which contains mixed metal chlorides. The chlorine in glass melt is removed and large amount of oxygen dissolved into melt by using oxygen plasma. An advanced experiment is done to investigate the dissolution behaviour of oxygen into glass in detail. As a result, it is found that oxygen dissolved in surface of glass melt and the solubility of oxygen into glass melt increase with increasing applied power.

1. Introduction

In the field of nuclear industry, it is one of main problem to solidify high-level radioactivity waste into safety form, and dispose it. Especially, the waste from the pyrochemical reprocessing of future is discharged as metal chloride. Then, the problem of safety appears, when these chloride wastes vitrified into glass as same as now going on. As one solution of this problem, we have suggested and developed the methods to oxidize chloride into oxide directly by using oxygen plasma.

In this method, we use the plasma torch by heating microwave. This plasma torch can generate the plasma of 100% oxygen easily at atmospheric pressure. We reported that many kind of metal chlorides could be oxidized by its strong oxidation power.[1] Then, for using a heat from plasma, we suggest the application to direct vitrification of chloride waste by using this oxygen plasma. And we study its feasibility. Some experiments are carried out to investigate the effect appeared on glass when the glass melt was irradiated by plasma, especially, the influence of amounts of chlorine in glass. In this paper, we will report some experimental results, including the result from experiment that for study the effect of plasma to dissolving phenomena of oxygen.

2. Investigation of chlorine removal in glass melts

2.1 Experimental

Figure1 shows a diagram of experimental setup. This setup consists of an electric furnace part for glass melting and a plasma torch part for oxygen plasma generation. Furnace has a shutter board made from heat insulating material. In a process to melt glass, torch part is isolated from furnace by shutter board to prevent to escape the heat from furnace and to overheat the torch.

In this study, microwave plasma torch is used to generate pure oxygen plasma at atmospheric pressure. Figure 2 shows the diagrams of plasma torch. Torch is made from stainless steel and is a coaxial cavity resonator. Microwave power is introduced to plasma torch through wave guides. Plasma gas is introduced into torch cavity and then flow downwards to discharge around nozzle by impedance matching. The discharge starts with spark at nozzle part, then the bell shaped plasma generate to flow towards down stream. The net power that consumed by plasma is defined as difference of supplied power and reflects power measured by power monitor placed on wave-guide.

Glass sample is the mixture of 100g borosilicate glass and 5.0g metal chlorides. Composition of glass is 56.1wt% SiO2, 17.1wt% B_2O_3, 6.0 wt% Al_2O_3, 3.6 wt% CaO, 3.6 wt% ZnO, 3.6 wt% Li_2O, and 10.0 wt% Na_2O. Glass transition temperature and soften point are 500 and 618 ^oC, respectively. Here, bead formed glass is used to avoid gas babble mixing into melt and to make homogenous melt easily.[2] Sr chloride and Ni chloride are used as metal chloride to be mixed with glass. Used chlorides are divalence and hexahydrete each other mixed 5.0g as hydrate.

At first, mixture sample was put into alumina crucible to be heated in furnace. To make homogeneous glass melt without gas babble, sample was heated slowly to 1000 ^oC with taking one and a quarter hours, and kept at same temperature during 1 hour for Sr mixed sample and 2 hours for Ni mixed one. Then oxygen plasma is irradiated to a homogeneous glass melt that prepared by above procedure. Applied power is 1.9kW or 1.5kW and gas flow rate is 19.0L/min. or 13.1L/min, respectively. An spacing for irradiation between plasma torch and the surface of glass melt was 65mm. Irradiation time was changed up to 60min. However,

in the case of 60min. irradiation, the irradiation period was divided into 2 time irradiations to avoid overheating the plasma torch.

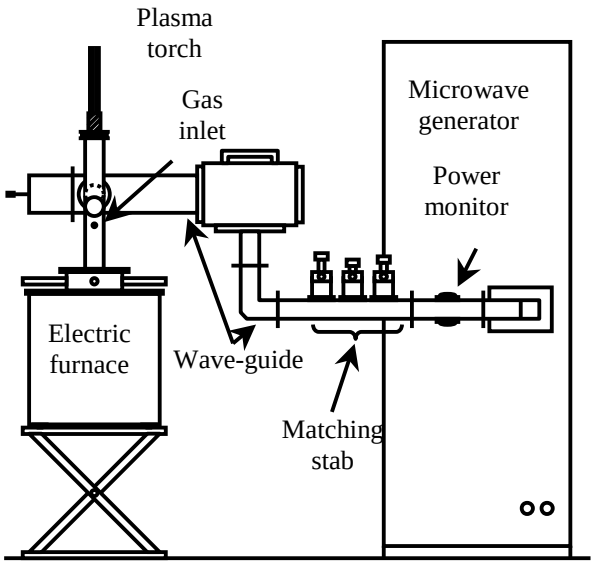

Fig.1 Schematic diagram of experimental setup

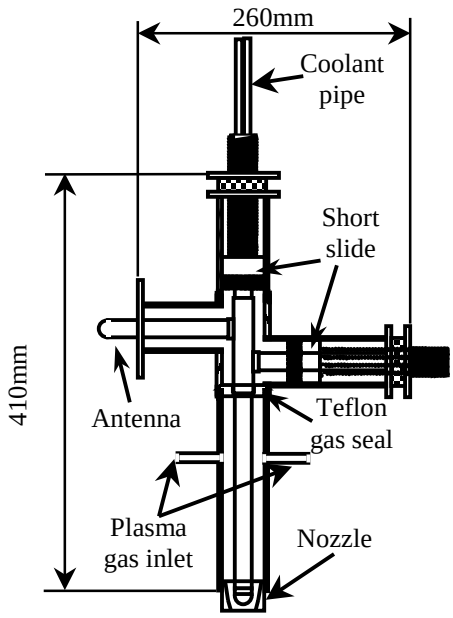

Fig.2 Schematic diagram of microwave plasma torch

2.2 Results and discussion

Solidified glass sample after cool down coloured by metal dissolution into glass melt. The colour of glass which contains Sr was transparent. And Ni one was purple. No change of colour was observed during plasma irradiation. We observed sometimes a mall amount of precipitation on surface of glass product after irradiation. In the glasses containing Sr, the layer of precipitation was observed on all samples whether plasma irradiate or not. On the other hand, in the glasses contained Ni, the layer was observed on samples irradiated by plasma, except samples irradiated on 1.5kW for 60min and no irradiation samples. A composition of precipitation was analyzed on wavelength-dispersed XRF. It was found from result of analysis that this precipitation consists of mainly Sodium, Chlorine (Na: Cl=52:45) and small amount of Si.

The composition of glass product was analyzed by WDXRF, to investigate the change of amount of chlorine contained in glass. Data were converted into the ratio to whole weight of glass product. The ratio of chlorine is shown in Fig.3. In this figure, ratio measured before experiment is also shown.

The figure indicates that the ratio of chlorine in glass decreases by plasma irradiation. Focusing on its detail; same tendency appears in the case of applying same power. The ratio of chlorine decreases simply with increasing irradiation time, when plasma irradiated on 1.9kW. While, in the case of irradiated on 1.5kW, the ratio decreases until 15 min. and increases slowly. This increasing tendency causes to decrease other components. There is clearly difference between the change of ratio during plasma irradiation and during heating. When plasma irradiating, there appears no difference between tendency of glass which contain Sr and one which contains Ni. However, the change of ratio during heating was affected on metal, which was mixed into melt. Judging from the above, it is found that we can remove chlorine from glass by using plasma treatment.

The change of sample weight during plasma irradiation is shown in Fig.4. The weight of sample which contains Sr increases with increasing plasma irradiating time. The rate of change in weight is calculated to investigate in detail. This rate is shown in Fig.5. Since a mixed chloride is hexahydrate, the weight of sample decreased due to thermal decomposition of hydrate during heating. Because water releasing occurs up to 200^{o}C and the glass melting takes place above 900^{o}C. Therefore, the interaction between water and melt can be ignored consequently. The weight of water which is contained as hydrate is subtracted in calculation of rate during heating. In the case of irradiating on 1.9kW to melt which contains Sr, the rate is calculated in

two parts. one part is increasing part until 15min. and the other is decreasing part after 15min.The rate of change in weight during plasma irradiation decreases in comparison to the rate on heating in the glass which contains Ni, the weight of sample dose not increase. However, the rate of change in weight increases against the rate on heating.

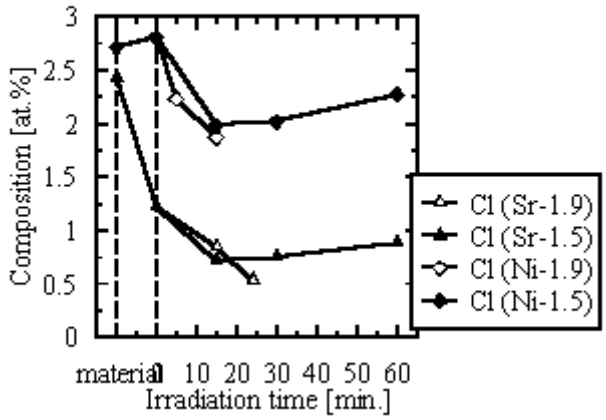

Fig.3 The effect of plasma irradiation on Cl composition in glass

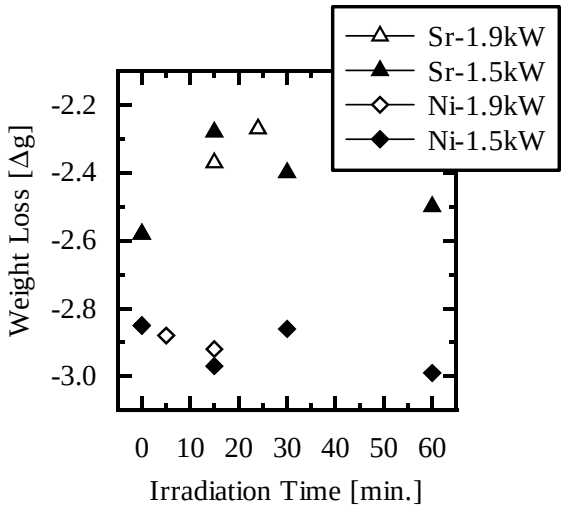

Fig.4 The effect of plasma irradiation time on glass weight loss

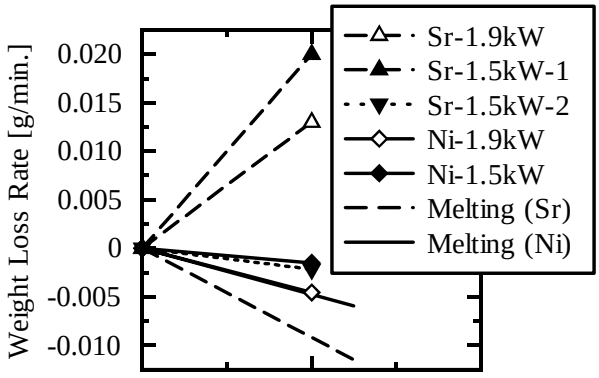

Fig.5 Competition of weight loss rate

It is well known that the components that have high vapour pressure such as alkali metal volatilizes easily from glass melt. The volatilization is affected on a composition of glass melt and on a temperature of melt. It is reported that borosilicate glass which contains B_2O_3, and phosphate glass which contains P_2O_5 have large change in weight on volatilization. The volatile rate per unit area is constant until 10 hour[3][4][5] and the weight of melting glass decreases. Therefore, it seems reasonable to conclude that the positive change of weight, which is seen in this experiments is cause to the dissolution of plasma gas into melts by irradiating plasma. It is found that plasma irradiation can dissolve more gases into glass melt in comparison to using normal gases.

It is supposed that the dissolution of large amount of gas into inorganic melt affects to so many properties of melt. For example, it is known that the activity of glass melt is affected on the non-bridging oxygen. In

addition, argon gas is babbled into ferric melt to remove gases in field of making steel. Then it may be truth that the remove of chlorine from melt is related to dissolution of oxygen. More investigation is needed to discuss this relationship.

3. Investigation of dissolution of oxygen into melts

3.1 Experimental

It is found that the amount of dissolved oxygen increases by irradiating plasma to glass melts. Experiment to investigate the behaviour of dissolving in detail is done. Setup, which is used in this experiment, is shown on Fig.6. Sample glass is melted in silica tube. The change of gas composition is measured. A coaxial-type dielectric barrier discharge is used. Pt electrodes place on centre of tube and on outer wall of tube. Phosphate glass, which have low melting point, is used as sample glass, because of temperature limit of seal material. The composition of glass is 3.4Wt% B_2O_3, 18.2 Wt% Na_2O, 15.9 Wt% ZnO and 62.5 Wt% P_2O_5. The glass transition temperature is 315 ^oC. The glass sample was put on SiO_2 tube to heating with pumping out for preparing the glass melt. Glass was heating up to 900C to avoid gas mixing into melt. Kr was added 500 Torr to tube, and then the melt kept at 700^oC for 5 hours. After addition of 300 Torr of O_2 , melt kept at same temperature for more 1 hour. Then glass melt is irradiated plasma. The ratio of O_2/Kr is measured continuously on gas chromatography after irradiating plasma for constant times. Plasma turned off during sampling gases. It is assumed that the ratio of O_2/Kr is reflected the behaviour of O_2 directly, with ignoring the behaviour of Kr. Because atomic size of Kr is enough too large than that of O_2 in dissolution phenomena.

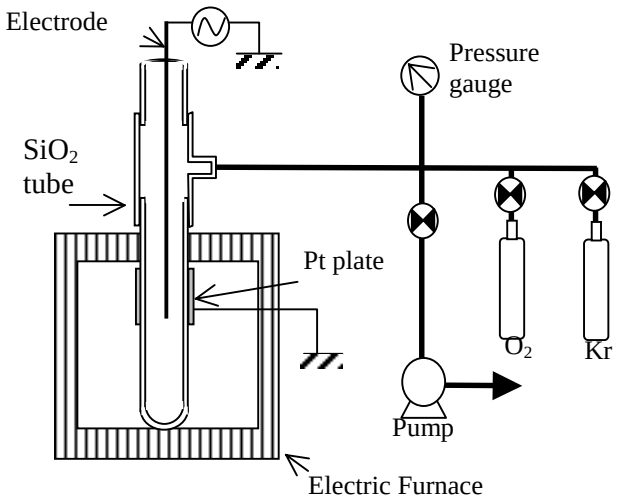

Fig.6 Schematic diagram of experimental setup

3.2 Results and discussion

The result of experiment on various applied power is shown on Fig.7. Amount of glass is 0.3g. O_2/Kr ratio increased until 1 hour in experiment. The cause of this increasing is mixing of O_2 and Kr in gas phase. Therefore, the difference O_2/Kr ratio from maximum value of O_2/Kr ratio is shown in this figure.

The tendency changes at the point of 4 hour. Until 4 hour, the oxygen ratio increases with linear relationship. The degree of change increases with increasing applied power. On the other hand, over 4 hours, fluctuation and the discontinuous points appears in the series of data. However, tendency that O_2/Kr ratio increases with increasing applied power appears.

Next, plasma irradiated to sample with various volume. Applied power is fixed on 40W.This result is shown in Fig.8. In this figure, the gradient changes at the point of 4 hours. Until 4 hour, the change of O2/Kr ratio is not affected on the volume of sample. In addition, also over 4 hour, the behaviour of O2/Kr ratio on 0.3g corresponds to the behaviour on 1.0g. In the series of 3.0g, it is seen that the dissolution occurs continuously over 4 hours, too. However, there is the discontinuous point between 3 and 4 hour. In this experiment, the same sample is measured continuously. Therefore, a possibility that this discontinuous point

comes from any mistake on operation cannot deny. It is shown from discussed above that the amount of dissolved oxygen is not affected on glass weight. Therefore, the dissolution of oxygen is occurring on near the surface.

Plasma can supply active gas species such as some ions or atomic gas. It is mainly difference between neutral gas and plasma, and merit of using plasma for treatment of material. The oxygen which is supplied to glass melt from plasma contained a large amount of atomic oxygen in this experiment.

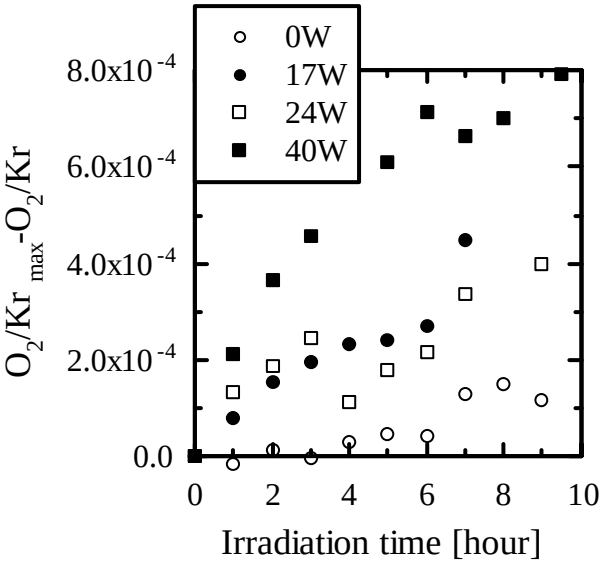

Fig.7 The oxygen behavior by plasma irradiation in various powers

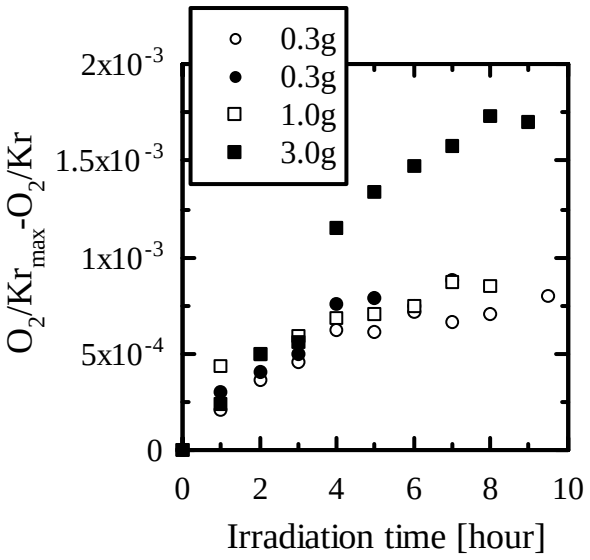

Fig.8 The oxygen behavior by plasma irradiation in various volume of glass.

It is known that a solubility of gases to liquid is depended on the size of solute, the polarity between solute and solvent and the viscosity of solvent. The size effect in the case of dissolving inert gases into inorganic melt is reported by Lax[7]. The solubility decreases with increasing the size of solute gases. As stated above, the solubility on surface of melts increases, since the atomic oxygen that has half size of molecular oxygen supplied from plasma. It is known that the volume of dissolved gases into glass melt obey the Henry's low. When amount of dissolving gases increase, the behaviour cannot obey the Henry's low exactly. However, it is reasonable to suppose that the volume of dissolved gases proportionate the amount of gases existing on surface. The change in applied power causes to change the amount of atomic oxygen supplying to surface of melt. This is a reason to increase dissolved oxygen with increasing applied power. In the data of 17W and 25W, the difference between both series is not clear. Further research is needed to understand this problem. Oxygen dissolution into whole glass melts con be promoted effectively by such as convective mass trasnsfer.

4. Conclusion

Firstly, we carried out some experiments that microwave oxygen plasma was irradiated on glass melt which contains mixed metal chlorides and obtained the following results

- Oxygen plasma irradiation enhances to remove chlorine from glass melt
- Oxygen plasma affects on behavior of oxygen gas dissolution in comparison with the case that used neutral oxygen.
- Plasma irradiation promotes gas dissolution.

Secondly , we carried out experiment to investigate the dissolving behavior of oxygen into glass melt and obtained the results, which are shown below.

- The amount of dissolved oxygen increases as the applied power increases.
- Plasma irradiation promotes oxygen dissolution on melt surface.

From above results, following conclusions are lead. It is found that oxygen plasma irradiation enhances oxygen dissolution and it plays a role to remove chlorine from glass melt. It is concluded that plasma can be strong tool to give new state for melt in field of material processing .

References

[1] M. Suzuki, M.Komatsubara, et al Journal of Nuclear Science and Technology. **34**, 12 (1997).
[2] J.C.Potts, G.Brookover et al., Journal of the American Ceramic Society, **27**, 8(1944)
[3] M.Yamane Handbook of glass industry , Asakura, (1999)
[4] L.F.Oldfield and R.D.Wright: Glass Technology, **3,** 2(1962)
[5] R.Terai, E. Uesaka Osakakogyogijutukihou, **27**, 3(1976)
[6] G.Lax Geochim. Cosmochim.Acta, **54**, (1990)

Investigations of the Dissociation of NH_3 in Pulsed and Quasistationary Microwave-generated Plasmas

J. Krueger, T. Kubach, M. Walker, U. Schumacher

Institute of Plasma Research, University of Stuttgart, Faffenwaldring31, D-70569 Stuttgart, Germany

Abstract

The process of the dissociation of ammonia in pulsed and quasistationary microwave-generated plasmas is investigated by means of optical emission spectroscopy and Langmuir probe measurements. The results of the determined spatially and temporally resolved plasma properties as electron density, electron temperature, optical emission and rotational temperature of N_2 are discussed and correlated with the reaction rate constants of the dissociation of NH_3.

1. Introduction

Pulsed microwave-generated plasmas are of increasing importance for low temperature plasma applications. Detailed knowledge of the spatial and temporal dependence of the plasma parameters and of the species distributions is indispensable for the understanding of the plasma technological process and for optimising the surface property of the treated substrates as well. The investigations are performed applying the microwave generated plasma source Plasmodul®[1], a modular plasma reactor with a diameter of 35 cm, provided from two sides with microwaves at 2.45 GHz with a maximum power of 2x2 kW, for discharges in ammonia NH3. The plasma is analysed by a Langmuir probe system and, moreover, by emission spectroscopy in the spectral range from 300 to 900 nm. With a spectral resolution of 40 pm of the emission spectra it is possible to determine the rotational temperature from the shape of the vibrational bands of N_2 and N_2^+. In the observed spectra the temperature values are between 600 and 900 K, showing a strong dependence on the distance to the plasma source as well as on the applied parameters of the plasma pulses. In the plasma of ammonia the emission lines of 9 different molecules and atoms such as NH_3, NH_2, NH, NH^+, N_2, N_2^+, N, H_2 and H are identified. In the temporal evolution of the plasma these different species show a different behaviour: In the beginning of the discharge all lines show a clear increase of their intensities and further on a decrease to a value of 50-90% of the initial intensity, according to the observed atoms or molecules. While most of the lines reach a quasistationary value after about 50 µs, the emission of NH starts a strong increase and reaches its quasistationary final value after 700-800 µs. Also, compared to most of the observed lines, NH shows a different decay time after switching off the microwaves. Assuming that the intensity of the emitted lines corresponds to the density of the respective species, a well directed tuning of the pulse parameters is a way to adjust the composition of the species in the plasma in order to optimise the deposition process of Si_3N_4 layers in pulsed silane-ammonia plasmas. The temporal and spatial behaviour of the emissions will be discussed by means of reaction rate constants of the dissociation of NH_3.

These investigations are part of a German BMBF project (13N8048) to examine the influence of pulsed plasmas on surfaces.

2. Experimental Setup

The experiments are performed in the Plasmodul®, based on the principle of the Duo Plasmaline, which is schematically shown in Fig. 1. The device consists of an array of four Duo Plasmalines, each of them has a copper rod centred in a quartz tube, being fed from each end by microwaves at 2,45 GHz from two magnetrons with a maximum power of 2000 W each. The vacuum chamber can be pumped down by rotary and turbo molecular pumps to a pressure of less than about 0.1 Pa. The chamber wall has large windows for diagnostic

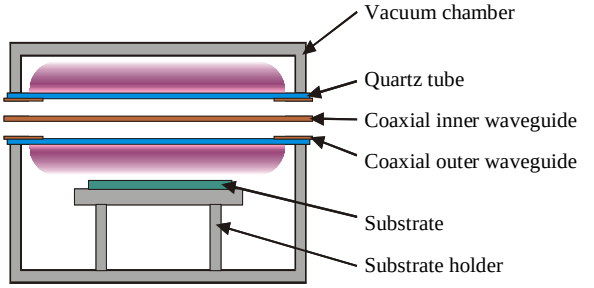

Fig. 1 Experimental setup, schematic description of the Duo Plasmaline®.

access for the Langmuir probe as well as for the optical spectroscopy. The Langmuir probe system is a Smart Probe manufactured by Scientific Systems, Dublin, Ireland, and the spectroscopic measurements are performed with the 750 mm Acton spectrometer and the MicroMAX ICCD camera.

3. Probe measurements

Results for the radial distribution of the electron density perpendicular to the plasma source for different microwave powers are given in Fig. 2. The measurements were performed at a total pressure of 20 Pa in the temporal afterglow of an ammonia plasma, 50 µs after the pulse power was switched off with a temporal resolution of 1 µs. The discharge was pulsed with a frequency of 1 kHz and a pulse to pause ratio of 1:1, The electron density distribution shows a clear maximum at a distance of about 15 mm from the quartz tube. The position of this maximum strongly depends on the total ammonia pressure, i.e. with decreasing pressure the density increases and the discharge expands. With variation of the deposited microwave power this expansion cannot be observed, the shape of the radial distribution is preserved but only the density increases linearly with the applied microwave power.

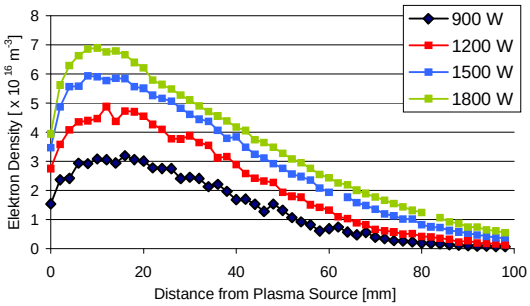

Fig.2: Radial distribution of the electron density for different applied pressures.

4. Spectroscopic Diagnostics

Fig. 3 shows an overview spectrum of an ammonia plasma at a gas pressure of 20 Pa, pulsed with 1 kHz at an aspect ratio of 1:1 and an injected average microwave power of 500 W (1 kW peak power) in the spectral range from 330 nm to 410 nm with a resolution of 40 pm. In this range the spectrum is dominated by the emission of N_2 and N_2^+ but also NH and the atomic hydrogen Balmer lines H_ε and H_δ, fragments at the dissociation of ammonia, are clearly visible. In the spectra of ammonia plasmas spectral lines of nine

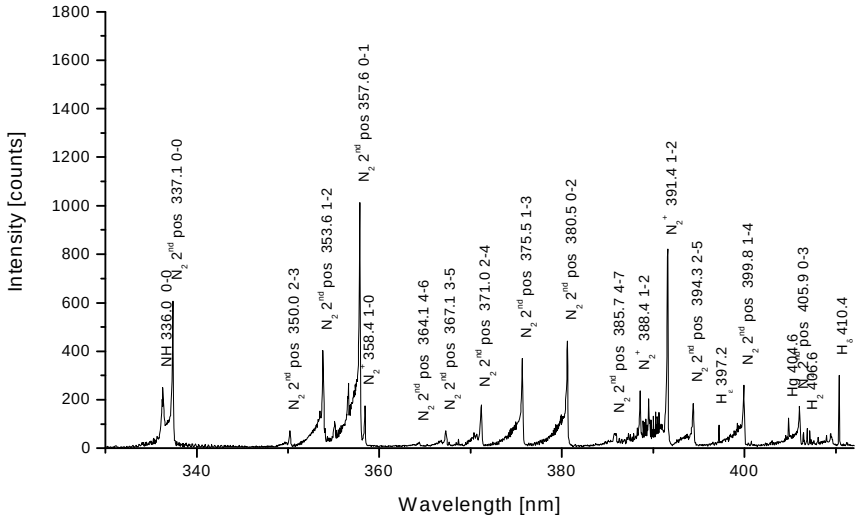

Fig. 3: Overview spectrum of an ammonia plasma at 20 Pa, pulsed at 1 kHz temporally averaged.

different species of atoms and molecules such as N_2, N_2^+, H_2, N, H, NH, NH^+, NH_2 and NH_3 could be identified. To point out the difference between a pulsed and a quasistationary plasma the spectra of two bands in NH and N_2 are compared with decreasing gas pressure in Fig. 4. On the left side the spectrum in a pulsed plasma (1 kHz, 1:1) is seen and on the right side the same spectrum in a quasistationary plasma at the same applied microwave peak power, averaged in time is shown. Both band heads show a uniform increase with decreasing pressure. This decrease is notably stronger in the emission of NH, an intermediate product at

the dissociation of ammonia, leading to the assumption that the dissociation process is slower at lower pressure due to less chemical reactive impacts.

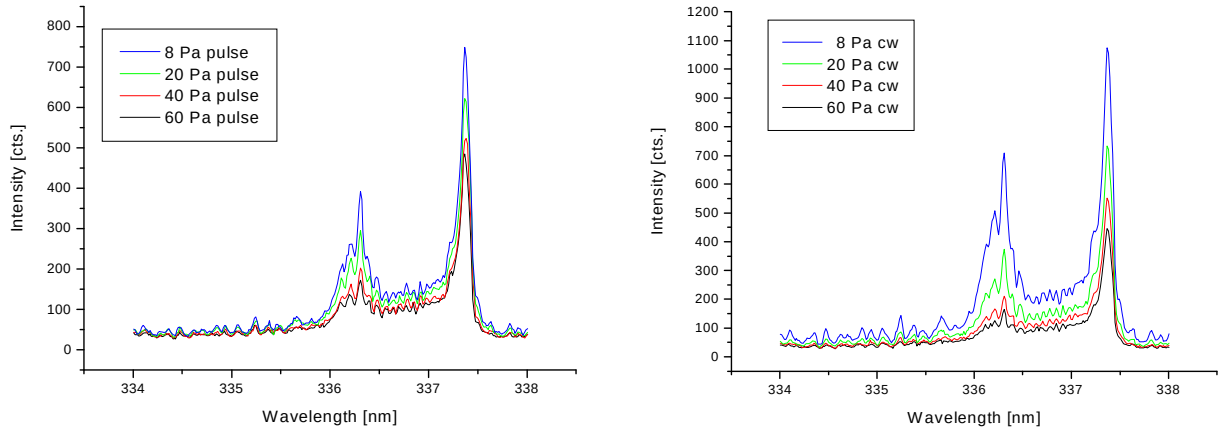

Fig. 4: Comparison of the emission of NH and N_2, left side in a pulsed plasma, right side in a quasistationary plasma of NH_3. In the continuous plasma the emission of NH increases stronger compared to the emission of N_2, and also compared to the pulsed plasma.

Comparing a quasistationary and a pulsed plasma directly, Fig. 5 shows the difference of the two spectra in the range from 330 nm to 460 nm. The spectra were obtained at a total gas pressure of 8 Pa and an average absorbed microwave power of 400 W. In pulsed mode the emission was registered averaged over 2000 complete pulse cycles and thus the exposure time was equal in both cases (1 second). To work out the

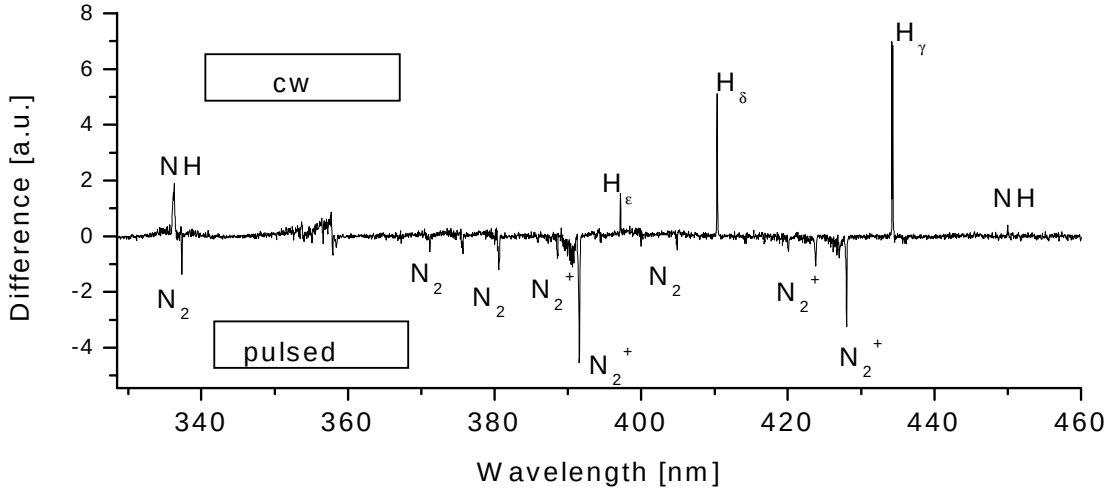

Fig. 5: Difference between a pulsed and a quasistationary plasma with constant average microwave power, normalised to H_2-emission.

difference, both spectra were normalised to the emission strength of molecular hydrogen. Thus positive values show a stronger emission in the stationary plasma and negative values show a stronger emission in the pulsed case. It is evident that the emissions of NH and atomic hydrogen are stronger in the continuous mode while in the pulsed plasma the bands of molecular nitrogen, especially N_2^+ appear stronger.

4.1 Rotational temperature

In the spectra of ammonia the molecular bands of N_2 and N_2^+ are well resolved such that the rotational temperature of nitrogen could be determined from the rotational band structure. Based on an algorithm of K. Behringer [2] for simulations of the rotational bands in the first negative system of N_2 and the second positive system of N_2^+, a computer code was developed to match the simulated rotational bands to the measured spectra by variation of simulation parameters, in particular the rotational temperature, and minimisation of the mean square errors given in the difference between measured and simulated spectra. The program is automated in order to analyse a large amount of data, i.e. several spectra from a sequence of temporal succeeding measurements.

The parameters for the simulation were the offset of the measurement, the intensity of the band, an offset for the wavelength (for a possible misadjustment of the spectrometer), the spectral resolution for the linewidth of the single transitions and finally the rotational temperature. Fig. 6 shows a comparison of a measured and a simulated spectrum of the $1 \rightarrow 4$ transition in the second positive system of N_2. The fit in the upper example results in a rotational temperature of 811 ± 25 K.

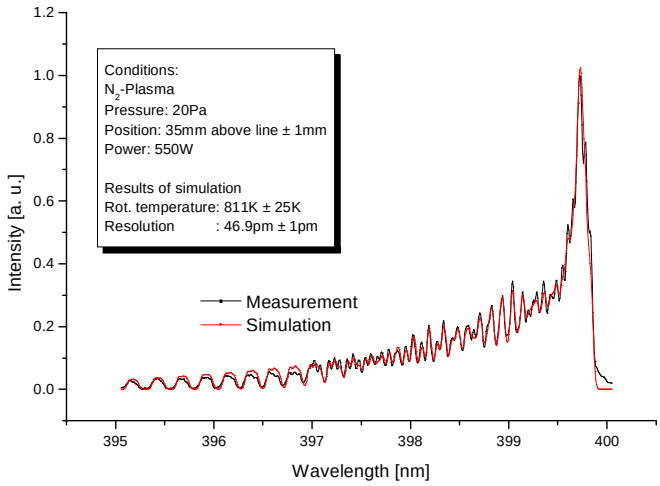

Fig. 6: Measured and simulated spectrum of the 1à 4 transition in the 2nd pos. system of N_2.

The dependence of the rotational temperature from the pulse frequency shows an interesting correlation (Fig. 7): with increasing frequency the rotational temperature initially decreases exponentially until a minimum is reached at about 7 kHz. With higher frequencies the temperature raises again. The only variable parameter was the pulse frequency besides the constant conditions like microwave power and pulse-pause proportion. For each measuring point an own spectrum was registered and the rotational temperature was respectively determined, thereby the emission intensity was integrated over the whole pulse leading to an average temperature.

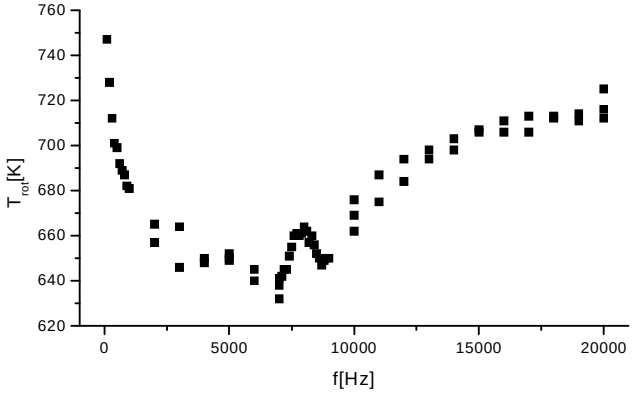

Fig. 7: The dependence of the N_2 rotational temperature from the pulse frequency shows a clear minimum at 7 kHz.

The minimum in the rotational temperature is due to the fact that the rise time of the temperature during the pulse phase is different to the decay time in the (temporal) afterglow. The rise time mostly depends on the applied microwave power, while the cooling of the gas depends on the geometry of the reactor and the gasflow and thus from the removal of the heated gas. With the given geometry and plasma parameters and the interaction of heating and cooling of the gas, a minimum of the rotational temperature appears at a pulse frequency of 7 kHz. This effect can be used to prevent thermally sensitive substrates from damages.

The small but clear peak appearing at the frequency of 8 kHz, could be identified as a resonance of a standing sonic wave in the reactor.

4.2 Time-dependent Investigations

By means of the gated ICCD camera and the spectrometer the temporal behaviour of the emission during the pulses could be registered with a temporal resolution of 300 ns. The emission of some selected species at

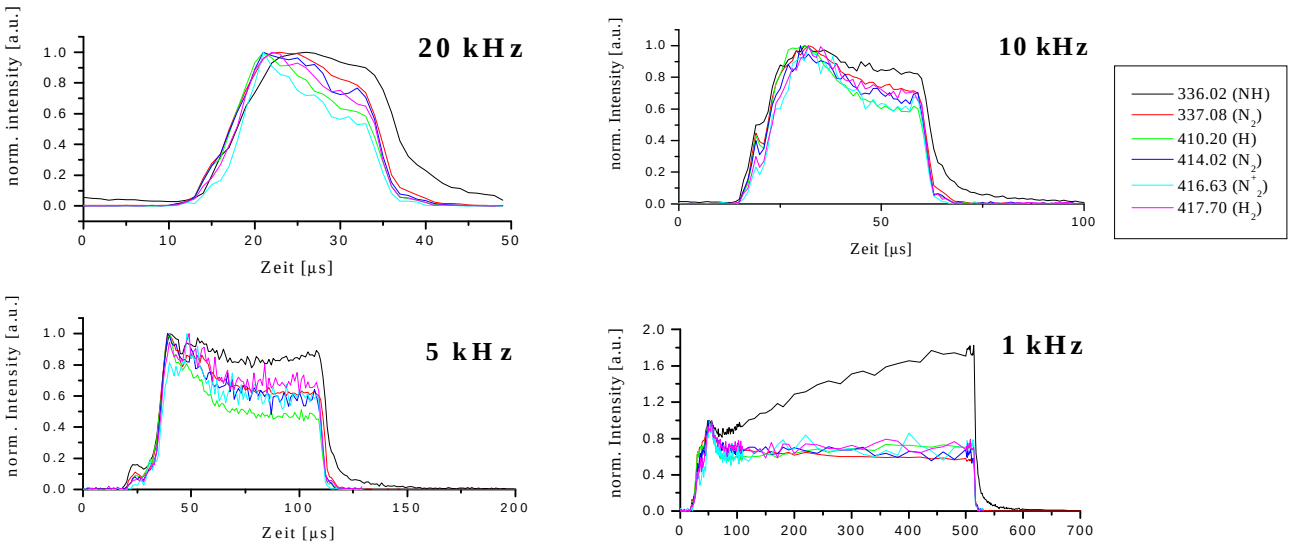

Fig.8: Temporal behaviour of some selected lines in the spectrum of ammonia.

different pulse frequencies is shown in Fig. 8. All lines indicate a distinctive overshoot in the emission at the beginning of the pulses. This region is featured by excitation and dissociation with fast electrons during the ignition of the plasma. After this overshoot the emission decreases down to a value of about 50 % to 90 % of this maximum value, according to the kind of molecule or atom. Most of the line emissions reach a quasistationary value in about 100 µs after the overshoot. An impressive exception in this behaviour is given by the NH molecule at 336.0 nm: though this emission shows the same characteristic at the beginning of the pulse, it starts raising strongly after 50 µs and finally reaches its quasistationary value after 700-800 µs. In the next section possible reaction channels in the dissociation of ammonia are discussed. Here a hint is given for the late appearance of NH in the plasma. Also the continuous plasma showed a stronger emission of NH compared to the pulsed mode. By a suitable choice of the pulse parameters the mean concentration of NH in the plasma could be influenced directly.

Further on, the emission of NH distinguishes by an explicitly longer decay time at the end of the pulses. Observing even shorter pulses, also a different behaviour in the overshoot can be seen (Fig.9). Here the pulse frequency was kept constant at 1 kHz and the temporal behaviour of the emissions of NH and N_2 is compared at different pulse lengths. With increasing pulse length also the overshoot of N_2 increases,

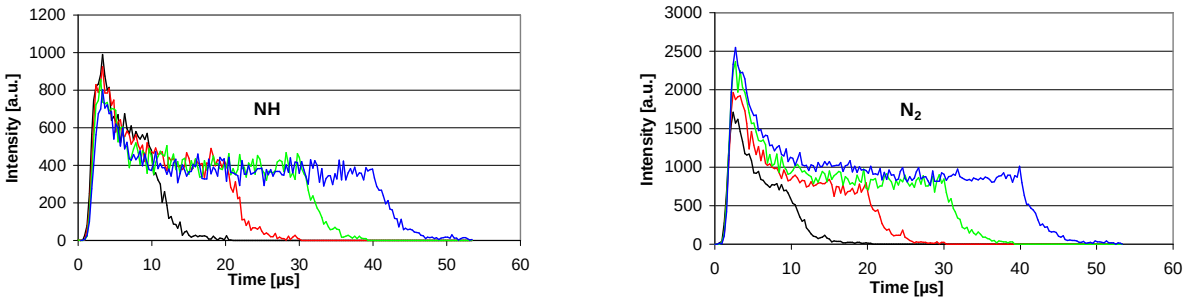

Fig. 9: The emissions of NH (336.0 nm) and N_2 (337.1 nm) at constant pulse frequency (1 kHz) and variable pulse duration between 10 µs and 40 µs.

indicating that with a short pulse duration the dissociation of ammonia is less advanced, i.e. that the stable end products of the dissociation are not yet formed completely. In the emission of NH, an intermediate step of the dissociation of NH_3, this effect is rather slightly reverse.

5. Discussion of the reaction channels during the dissociation of ammonia

The dissociation of ammonia is accompanied by an outstanding phenomenon: The acceleration of the dissociation by reactions with radical dissociation products. There is a large number of possible reactions at the dissociation of ammonia, some of the most important reaction rate constants are compiled from different sources [3,4,5]
In the first step the dissociation is dominated by collisions of molecules with electrons and leads to neutral or excited products via excitation of unstable electronic states. Reaction products by electron collisions are produced such as

$NH_3 + e$	$\rightarrow$	$NH_2 + H + e$	
	$\rightarrow$	$NH + H_2$ (2H) +e	10%-30% of all processes
	$\rightarrow$	NH_2- + H	in stationary plasmas
	$\rightarrow$	$NH_2 + H^-$	
		etc.	

This type of reactions is responsible that in the beginning of a plasma pulse all investigated species are existent and emitting. This points to the overshoot in the time resolved spectra which occurs in all species similarly. This overshoot was also predicted theoretically for the behaviour of the electron temperature in pulsed plasmas [6]. After some time in the pulse these reactions amount only to 10% - 30% of all processes [7].
Mainly chemical reactions are now contributing to the dissociation process like reactions of ammonia with excited nitrogen atoms or imidogen:

$NH_3 + NH$	$\rightarrow$	$2NH_2$	$k_0 = 1.32 \cdot 10^{-10}$ cm3/s
$NH_3 + N^*$	$\rightarrow$	$NH + NH_2$	$k_0 = 1.1 \cdot 10^{-10}$ cm3/s
		etc.	

These secondary reactions provide a different distribution of concentrations until a stationary state is reached.
NH_2 and NH are unstable intermediate products and are reacting rapidly:

NH_2	+ H	$\rightarrow$	H_2 +NH	$k_0 = 6.6 \cdot 10^{-11}$ cm^3/s
NH_2	+ N	$\rightarrow$	N_2 + 2 H	$k_0 = 1.2 \cdot 10^{-10}$ cm^3/s
NH	+ N	$\rightarrow$	H + N_2	$k_0 = 5.0 \cdot 10^{-11}$ cm^3/s
NH	+ H	$\rightarrow$	N + H_2	$k_0 = 4.4 \cdot 10^{-11}$ cm^3/s
NH	+ NH	$\rightarrow$	N_2 + 2H	$k_0 = 8.5 \cdot 10^{-11}$ cm^3/s
			etc.	

Molecular nitrogen N_2 and hydrogen H_2 are the stable end products of the dissociation of ammonia.

6. Summary

The measurements in ammonia plasmas increased our knowledge of the correlations and dependencies of plasma parameters in pulsed plasmas in ammonia. A suitable set of plasma parameters can now be chosen in order to adjust the concentration of radical molecules like NH or to control the gas temperature to prevent thermal sensitive substrates from damage. These results can now be applied to the treatment of substrates like the deposition of silicon nitride layers in ammonia-silane plasmas.

References

[1] M. Walker, K.-M. Baumgärtner, A. Schulz, E. Räuchle: ISPC 14, Prague, (1999).
[2] K. Behringer: Plasma Physics and Controlled Fusion, UK, **33**, 3990, (1991).
[3] B Gordiets, C M Ferreira, M J Pinheiro and A Ricard: Plasma Sources Sci. Technol. 7, 363–378, (1998).
[4] T. Ko, P. Marshall, A. Fontijn: J. Phys. Chem, 94, 1401-4,(1990).
[5] A.A. Mayer-Plath: Dissertation U. Greifswald, (2002).
[6] Ashida, Lieberman: J. Vac. Sci. Technol. A, Vol 13, No.5, 2498-2507, (1995).
[7] R. d'Agostino, F. Cramarossa, S. de Benedictis, G. Ferraro: Plasma Chem Plasma Proc., Vol.1, No. 1, 19-35, (1981).

Diagnostics of N_2/He pulsed purely inductive Rf discharges

P. Ambrico[1] , S. De Benedictis [1]and G. Dilecce[1]

[1] *Istituto di Metodologie Inorganiche e dei Plasmi, CNR*
c/o Department of Chemistry, University of Bari
Via Orabona 4, Bari Italy

Abstract
A planar coil inductive rf pulsed discharge in N_2-He mixtures has been investigated by optical spectroscopy. The kinetic analysis of vibrational excitation of $N_2(C)$ state reveals a high vibrational excitation of ground state nitrogen. The atomic nitrogen has been monitored by TALIF. The decay of N-atoms in post discharge at different pressure, and duty cycle has been investigated.

1. Introduction

A planar coil inductive *rf* pulsed discharge generated in N_2-He mixtures has been investigated by optical spectroscopy. The planar coil faced to a quartz window has been used to produce a plasma inside a cylindrical stainless steel chamber. We have investigated two different ignition of the inductive regimes. One (type-A) is operated by a pre-short pulsed capacitive discharge produced inside the chamber with an internal electrode faced to the inductive one [1]. The planar coil is screened using a Faraday shield between the coil and the quartz window. The electrostatic shield of the type described in [2] completely cancels any capacitive coupling. Since a purely inductive discharge is not self-ignited, a secondary capacitive discharge is produced by a plate electrode by another pulsed low power rf supply. The second one (type-B) operated without Faraday shield is spontaneously ignited by the capacitive coupling formed by the planar coil and the grounded plasma chamber. The main 500 watt inductive discharge can be driven under pulsed or continuous *rf* regime. In our previous study [1] carried out by Langmuir probes in He-N_2 ICP discharge type-A with large planar coil (12 cm diameter) and Faraday shield evidenced a pure inductive pulsed regime characterized by electron density close to 10^{12} cm^{-3} and electron mean energy of about 1-2 eV at 0.2 Torr. The decay of N_e in post discharge was in a millisecond time scale. T_e of about 0.5-1 eV, depending on the experimental conditions (pressure and mixture composition), was maintained in the post-discharge at 1 ms. This slow electron relaxation was considered as due to molecular collisions with long lived species. This issue is of great relevance because of the present widespread use of planar ICP reactors as alternative way to dense plasma commonly realized by microwave discharges, and calls for further diagnostic investigations.

Here an analysis of vibrational excitation of $N_2(C^3\Pi u)$ state at different duty cycles, mixture compositions and pressures has been carried out by time and space resolved emission spectroscopy, running ICP discharge under regime type-A as in [1], and regime type-B with a coil of 6 cm diameter. The measurements have been done at the end of the discharge pulse after transition from capacitive to inductive regime for different duty cycles. Since a relevance of long lived species processes is expected, laser diagnostics have been set in order to measure atoms, vibrationally excited molecules and metastable. In the present contribution we describe only preliminary results on N-Atoms TALIF detection.

2. Experimental and Results

The experimental apparatus supports Langmuir probes, LIF and CARS diagnostics. The sketch of the experiment in ICP type-B is shown in Fig. 1. In the figure it is also sketched the laser configuration. It allows production of VIS -UV photons with narrow line width through the Second and Third Harmonic generation of the dye. The laser set-up can be switched from LIF configuration to a CARS one for collinear or box-CARS narrow band measurements. A planar coil faced to a quartz window ignites a plasma inside a cylindrical stainless steel chamber with axial and radial glow inhomogeneity.

a) Time resolved Langmuir probe

In tab 1 we have reported the values of the electron temperature and the electron density measured at the end of the discharge pulse [1] in ICP type-A discharge. The measurements have been done at 0.2 Torr with the Langmuir probe tip set on the axis of the discharge at two distances form the discharge window (p_1= 1 cm

and p_2= 2.5 cm) for three nitrogen contents (m_1=5% N_2 , m_2=25% N_2 m_3=100% N_2) and for three duty cycles $d=T_{ON}/(T_{ON}+T_{OFF})$ (d_1=1/15, d_2= 5/15, and d_3=15/15 for T_{OFF}= 15 ms). Total flow rate is 40 sccm.

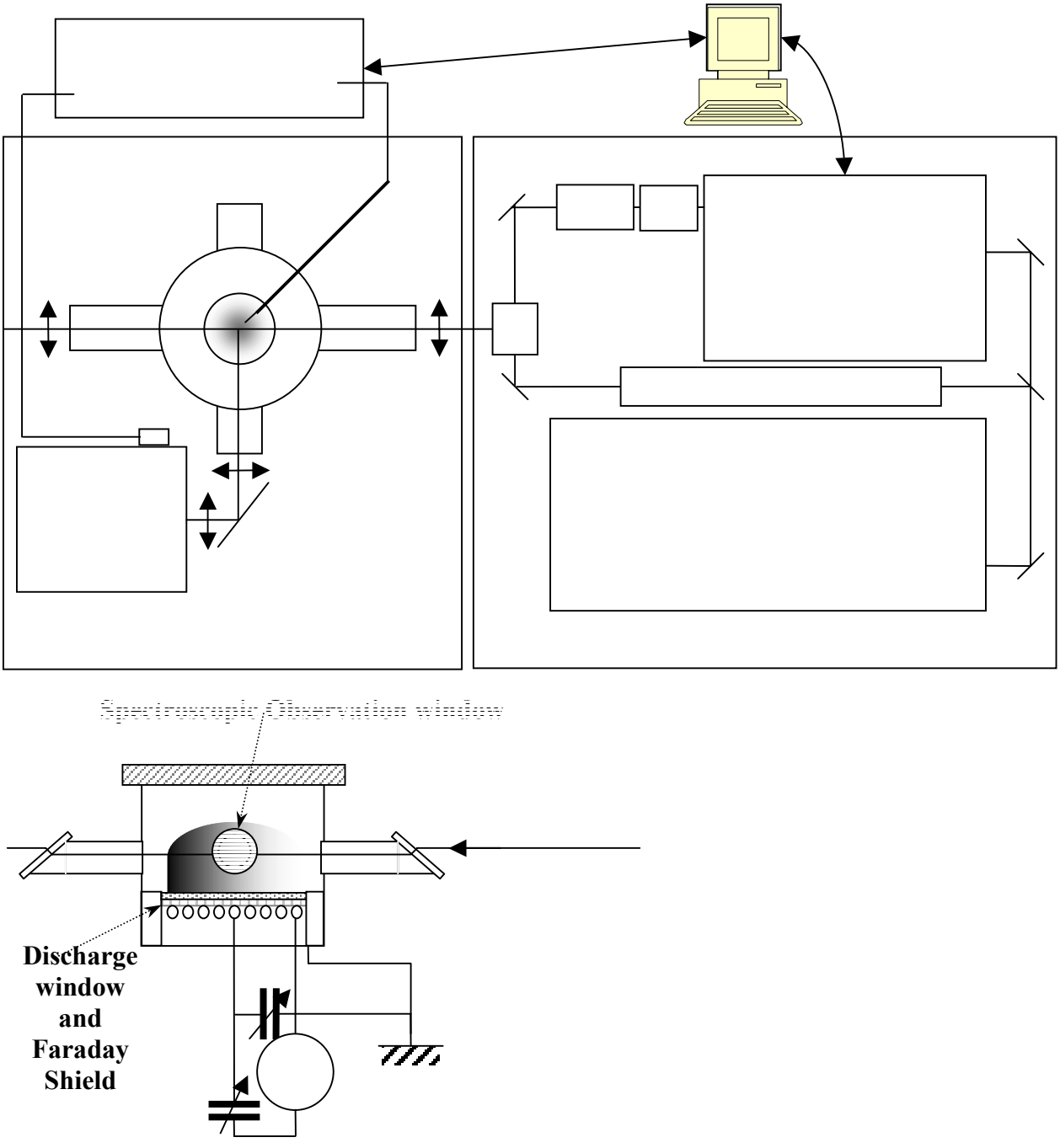

Fig. 1 Experimental setup. Top and side view of the reactor of ICP type B discharge with laser facilities (Quanta System)

Table 1 Electron parameters in ICP type- A, at P= 0.2 Torr for various axial positions (p_1= 1 cm and p_2=2.5 cm), duty cycles d=$T_{ON}/(T_{ON}+T_{OFF})$ (d_1=1/16, d_2= 5/20, and d_3=15/30 for T_{OFF}= 15 ms), mixture compositions (m_1=5% N_2 , m_2=25% N_2 m_3=100% N_2).

Experimental conditions	p_1 d_2 m_1	p_2 d_2 m_1	p_1 d_2 m_2	p_1 d_3 m_2	p_2 d_2 m_2	p_2 d_3 m_2	p_1 d_2 m_3	p_2 d_2 m_3
Te (eV)	2.9	1.4	2.45	2.55	1.11	1.29	2.10	0.95
Ne ($10^{11}cm^{-3}$)	3.5	6.1	2.5	2.0	0.42	0.43	1.0	0.26

b) Time resolved emission spectroscopy

The spectroscopic measurements have been done at p_2 distance in the ICP type-A and at p_3= 0.7 cm in the ICP type-B. The $N_2(C,v)$ vibrational distributions inferred from Δv =-2 sequence of nitrogen Second Positive spectra are shown in fig. 2.

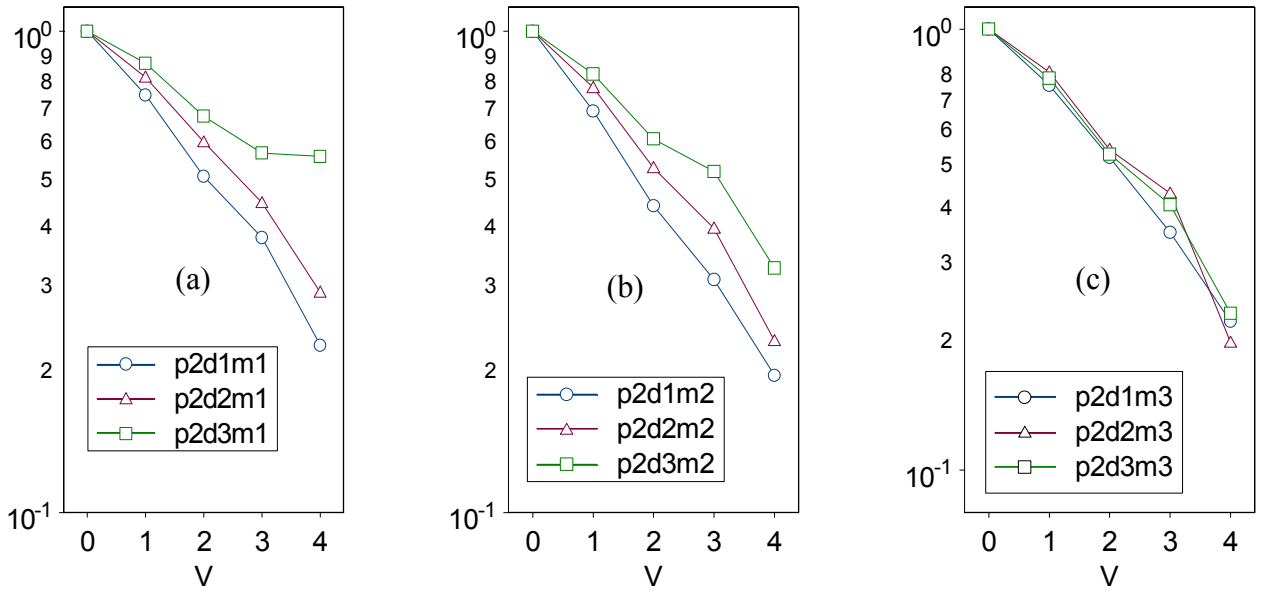

Fig. 2 $N_2(C,v)$ vibrational distributions in ICP type-A measured at p_2=2.5 cm, P= 0.2 Torr for various mixtures(m_x), duty cycle (d_x) (see table 1).

c) TALIF measurements

TALIF measurements of $N(^4S)$ have been carried out using the two-photon excitation pathway

$$N(\,2p^3\,{}^4S^0 + 2h\nu_L \rightarrow 3p\,{}^4S^0_{J=3/2} \rightarrow 3s\,{}^4P + h\nu_E) \qquad (1)$$

In this pathway the laser excitation occurs with two photons at λ_L =206.718 nm while fluorescence is detected at λ_E = 746.83 nm. The excitation wavelength is obtained by Third Harmonic Generation (THG) of the dye output by means of a BBO crystal. In this laser set-up the line width of the R610 dye fundamental is quite narrow (0.04 cm^{-1}). This allows a quite high LIF signal with typical TH energy of about 300 μJ. The N-TALIF signals measured at 5 mm from the discharge window in P=2.0 Torr pure nitrogen for various times in post-discharge and for different duty cycle (T_{ON}+T_{OFF} = 30 ms) are shown in figures 3 and 4. The decays are significantly non-exponential and look similar at 0.5 and 1.0 Torr.

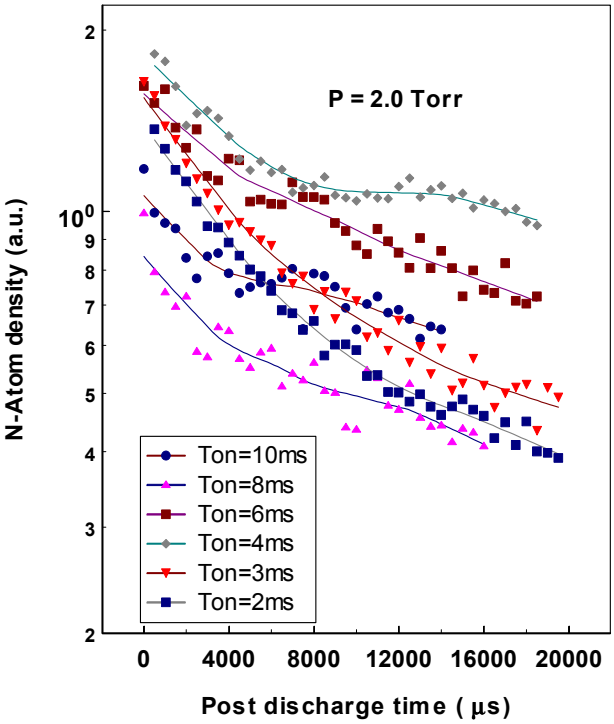

Fig. 3 N-atom TALIF signal decay in post discharges at various T_{ON} (*2D lowess plot*)

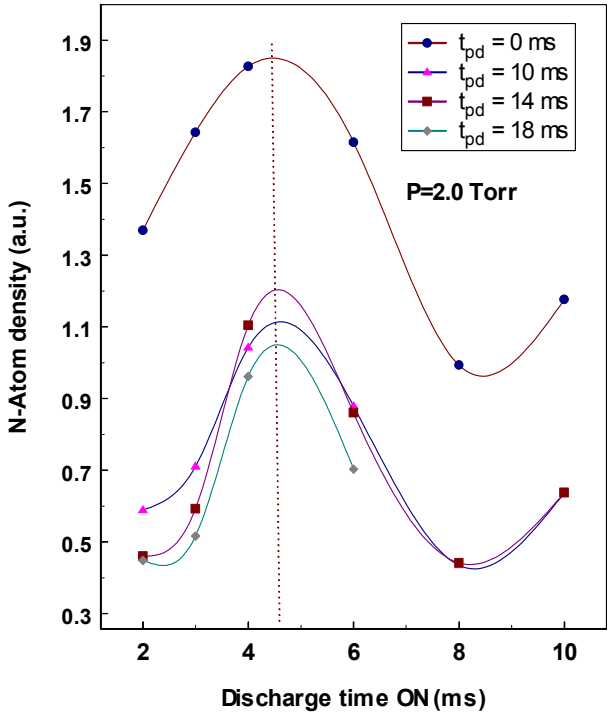

Fig. 4 N-atom TALIF signal vs. T_{ON} at various post discharge times (*2D lowess plot)*

3. Analysis of the discharge

The analysis of the electron data evidences that, at any mixture and position, the increase of the discharge T_{ON} leads to an increase of the electron temperature in discharge and post-discharge. The electron temperature and the density decreases as moving far from the discharge windows, while increases as the nitrogen content mixture is decreased.

Having in mind this view, we have applied the kinetic analysis of $N_2(C,v)$ formation described in [3,4] using the electron data measured in the present conditions and synthetic $N_2(X,v)$ and $N_2(A,v)$ distributions. The simulation of the distribution $<p_2d_2m_2>$ are shown in Fig. 3. The best fit is achieved with a Boltzmann like (X,v) distribution at 7000-8000 K and $N_2(A)/N_2(X)=3.7x10^{-4}$ together with a low vibrational excitation of $N_2(A)$ metastable. $N_2(A,v)$ distribution has been approximated by a Boltzmann one at about 2000K. The main point of (C,v) distribution analysis is that the best fit is achieved only when electron impact excitation from $N_2(X,v)$ and $N_2(A,v)$ manifolds have almost similar rates, then the structures depend on $N_2(X, v)$ and $N_2(A, v)$ shapes. The contribution by pooling A+A process is about one order lower and affects only the high vibrational levels. Fits by individual processes like (in the legend: NVCEX <e+X>, NVCEA <e+A>, NVCP <A+A> calculated with Piper rate coefficients (see in [3]), NVCPGAP <A+A> calculated with energy gap state–to-state rate coefficients [3, 4], NVC is the complete distribution) were not adequate. The relevant fact is that $N_2(X,v)$ vibrational excitation must be high, but fits using Treanor-Gordietz distribution with various lengths of plateau are not adequate.

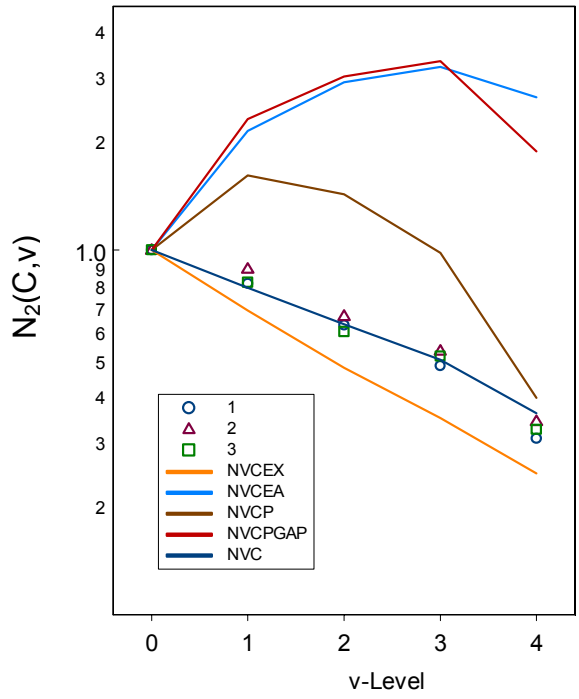

Fig. 5 Measured and calculated $N_2(C,v)$ vibrational distribution. ICP type A: (1) $<p_2d_2m_2>$ at 0.2 Torr; ICP type B: (2) at 4 Torr and (3) at 0.2 Torr. Calculations (continuous line) of single processes and complete distribution (see text). Best fitting rates: ReX≈(4xReA)≈ (10xRAA)

For ICP discharges, a high vibrational pumping of $N_2(X,v)$ low vibrational level would be expected because of the high electron density and the Maxwell character of the EEDF, but the absence of the plateau typical of the vibrational pumping is not established, likely because of the low pressure as well as because of a significant nitrogen atom quenching effect that could be also responsible of the deactivation of the whole vibrational manifold of the A state.

It should be noted that the distribution $<p_2d_2m_2>$ measured in ICP type-A is practically coincident with that measured in the reactor ICP type-B under similar conditions (0.2 Torr, and 25% N_2) even though measured at a shorter distance from the discharge windows (p_3=0.7 cm). So the previous analysis is still valid under this discharge configuration. The present experiments, hence, do not evidence significant differences due to the presence of a Faraday shield once the inductive regime is established. The (C,v) distribution at 4 Torr measured at a distance of about 0.5 cm close to discharge window, shown in Fig. 3), indicates a significant vibrational (even higher) excitation of C and X states. It should also be noted that the glow is contracted towards the discharge window on increasing the pressure.

For what concerns the N-atoms the decay of TALIF signal in post-discharge is non exponential. Under some cases it reveals quasi double-exponential character. The slow part of the decay seems to depend on the time of discharge ON as can be seen in figure 4 where the TALIF signal is reported as a function of T_{ON}. The N–atoms production apparently presents a maximum in the discharge for T_{ON} of about 4 ms.

4. Concluding Remarks

The excitation of $N_2(C,v)$ molecules of the present ICP discharge differs from that we observed in a capacitively coupled discharge, where it was dominated by electron impact excitation from a Treanor-Gordietz $N_2(X,v)$ like distribution, typically characterized by a 3000-4000K first level temperature and a plateau extending up to 15-16 levels. Here, the shape of $N_2(C,v)$ distributions measured at 5 and 15 ms (end of discharge time) is very similar to that measured in the afterglow of capacitively coupled pulsed *rf*

discharge [3] or in plasma jet [4] in millisecond time scale. The peculiarity of electron properties in ICP excitation appears also on the vibrational excitation of the $N_2^+(B,v)$ state. The distributions measured in He-(2-10%) N_2 at 0.2 Torr in the reactor ICP type-A through the analysis of the $\Delta v=-2$ sequence of First Negative spectra have been shown in Fig. 4 of ref. [5]. The vibrational distributions (v=0-6 levels) evidence structures and 0-1 population inversion. Instead in typical parallel plate capacitive coupled discharges the distributions measured in similar mixtures [6] declined regularly covering more than one order of magnitude. The excitation was mainly due to $He(2^3S)$ Penning ionisation and/or to electron impact (see ref. [6]). In the present ICP experiments we expect a predominant electron impact excitation.

Actually we have examined only the TALIF signal behaviour with the discharge parameters. The effective measurement of N-atom density by TALIF does require a calibration procedure. It is in due course according to [7,8]. However considering our previous detection experiments, the high TALIF signal indicate that the N density could be significant, thus in agreement with the deactivation of $N_2(X,v)$ tails. Further work in progress concerns preliminary investigations of the vibrational excitation of ground state by CARS.

Acknowledgments
Work supported by the Italian Space Agency (ASI). A. Parodi is acknowledged for his valuable technical assistance.

References
[1] G. Dilecce, P. Ambrico, R. Bektursunova and S. De Benedictis, *Proc.s of ESCAMPIG-XVI-ICRP5*, Grenoble 2001, Vol.1, p.211.
[2] V.A. Godyak, R.B. Piejak and B.M. Alexandrovic, *J. Appl. Phys*. **85** (199) 703
[3] S. De Benedictis, G. Dilecce, M. Simek, *Chem. Phys.*, **192** (1995) 149
[4] S. De Benedictis G. Dilecce, M. Simek, M. Vigliotti, *Plasma Source Sci. & Technol*., **7** (1998) 557.
[5] P. Ambrico, S. De Benedictis and G. Dilecce Proc.s of FLTPD-V workshop, 2003, Villaggio Cardigliano, Specchia (LE) Italy, (Ed.s S. De Benedictis and G. Dilecce), available on-line at http://fltpd-5.ba.cnr.it/
[6] S. De Benedictis G. Dilecce and M. Simek, *J Phys. B : At. Mol. Opt. Phys*., **27** (1994) 615.
[7] A. Broc, G. Dilecce, R.G. Sharafutdinov, P.A. Skovorodko and S. De Benedictis, *Proc.s ISPC-XV*, Orleans 2001, Vol. IV, pp.1285-1291.
[8] K. Niemi, V Schultz von der Gathen, H. F. Dobele, *J. Phys. D: Appl. Phys*., **34** (2001) 2330.

Calculations for a global model of the plasma of a pulsed microwave discharge in nitrogen at atmospheric pressure

J. Stańco, H. Nowakowska, Z. Zakrzewski

Institute of Fluid-Flow Machinery, Polish Academy of Sciences, Gdańsk, Poland

Abstract
A global numerical model of the plasma of a pulsed microwave discharge in nitrogen has been developed. The aim was to determine the temporal variation of the densities of various species present in the discharge. The object modeled is the plasma of a microwave torch operating at atmospheric pressure. The ultimate goal is to adopt the methods developed for these calculations for studying properties of discharges in polluted air.

1. Introduction

Non-thermal discharges offer a promising way of pollutant abatement in air or flue gases. The primary role of a gas discharge in the process of pollutant elimination is to provide free electrons which, colliding with the gas molecules, give rise to production of chemically active species that can favor decomposition of pollutants. Adjusting the discharge to that purpose is an important issue. Especially worth studying seem to be pulsed discharges. A pulsed microwave discharge with a properly chosen pulse power, length and repetition rate may prove more energetically efficient in pollutant abatement than a continuous wave discharge. Also the thermal loading of the plasma reactor materials can be reduced.
This paper is concerned with modeling the plasma of a microwave discharge in polluted air or flue gas. For preliminary evaluations of the modeling procedures a discharge in N_2 is considered. The object modeled is the atmospheric pressure plasma of microwave torches, known and investigated for the last decades (e.g. [1], [2], [3]). More recently a device of simple design, capable of sustaining multiple torches, has been disclosed [4]. Such a torch system is well suited for large-volume treatment of pollutants.

2. The model

We consider a 2.45 GHz microwave plasma generated in a torch as described above, operating in nitrogen at a low flow rate of the gas. The discharge is fed with microwave power pulses at a kilohertz repetition rate, superimposed on a continuous power background.
A global, that is a spatially averaged model is formulated. Although such a model can not provide spatial distributions of the plasma parameters, it is useful for establishing their scaling with the operating parameters of the discharge. For a discussion of the model see [5]. The following assumptions are adopted:

- densities and temperatures of all species are averaged over the plasma volume;
- the electric field is regarded as uniform within the plasma volume and the effective field approximation is applicable;
- the non-equilibrium plasma of the microwave torch is characterized by two temperatures: the heavy particle temperature T and the electron temperature T_e. The vibrational temperature T_v is assumed to be equal to T;
- radiation is neglected.

The set of equations describing the global model consists of particle balance equations and energy balance equations. The latter provide species densities n_i, while the particle balance decides on the value of the electron temperature T_e.

2.1. Electron kinetics

For preliminary calculations we limited the number of species and primary reactions considered in the balance equations for the model to those which really matter. We adopted for the global model the following set of reactions between the plasma species of the discharge in nitrogen:

- electronic excitation

$$N_2 + e \rightarrow N_2^* + e \qquad (k_1) \qquad (1)$$

- quenching of electronically excited molecule states by N atoms

$$N_2^* + N \rightarrow N_2 + N \qquad (k_2) \qquad (2)$$

- ionization by electron impact

$$N_2 + e \rightarrow N_2^+ + e + e \qquad (k_3) \qquad (3)$$

- dissociation

$$N_2 + e \rightarrow N + N + e \qquad (k_4) \qquad (4)$$

- neutral recombination

$$N + N + N_2 \rightarrow N_2 + N_2 \qquad (k_5) \qquad (5)$$

- dissociative recombination

$$N_2^+ + e \rightarrow N + N \qquad (k_6) \qquad (6)$$

The following species are taken into account: nitrogen molecules in the electronic ground state, their concentration assumed to be almost equal to the overall concentration of N_2 molecules (n); electronically excited nitrogen molecules N_2* (n_x); nitrogen atoms N (n_a); electrons e (n_e); molecular nitrogen ions N_2^+ (owing to the plasma quasi-neutrality their concentration is equal to n_e).

The rate coefficients for the processes involving collisions with electrons depend on the form of the electron energy distribution function f_e for the discharge plasma. They are determined by solving the Boltzmann equation for the electrons and calculating the rates as cross section averages over f_e. For that purpose the ELENDIF code [6] is used. The rate coefficients k_5 and k_6 are taken from [7] and [8], respectively.

2.2. Particle balance equations

The particle balance equations according to reactions (1)-(6) read

$$dn_x/dt = k_1\, n\, n_e - k_2\, n_x\, n_a \qquad (7)$$

$$dn_a/dt = 2k_4\, n\, n_e + 2k_6\, n_e\, n_e - 2k_5\, n\, n_a\, n_a \qquad (8)$$

$$dn_e/dt = k_3\, n\, n_e - k_6\, n_e\, n_e \qquad (9)$$

In the first approximation we neglect the flow. This is justifiable for calculations covering time intervals no longer than 100-200 μs, as the characteristic time of particle residence in the torch under consideration is of the order of 10 ms.

2.3. Energy balance equations

The electron energy balance equation is written as

$$\frac{3}{2} k_B n_e \frac{dT_e}{dt} = P_v - n_e \nu_{iz} \varepsilon_L \qquad (10)$$

where k_B is the Boltzmann constant, $\nu_{iz}\, \varepsilon_L$ is the plasma energy loss per electron-ion pair created due to all electron-neutral collision processes and

$$P_v = \sigma E^2 \qquad (11)$$

is the density of the microwave power absorbed by the plasma. Here E is the effective electric field intensity and σ is the plasma conductivity

$$\sigma = (e^2 n_e \nu/m_e)/(\omega^2 + \nu^2) \qquad (12)$$

where m_e is the electron mass, ν is the electron collision frequency for momentum transfer and ω is the microwave field circular frequency.

The energy balance equation for the heavy particles has the form

$$\left[\frac{7}{2} kn + \frac{5}{2} kn_a\right] \frac{dT}{dt} = \frac{3}{2} \delta_e \nu n_e k (T_e - T) - \frac{2\lambda}{3R^2} T \qquad (13)$$

where δ_e is the fraction of energy lost by an electron in a collision with a heavy particle, and λ is the thermal conductivity. The value of λ is taken from[8], and ν is calculated by ELENDIF, as is $\nu_{iz}\, \varepsilon_L$ in equation (10). For preliminary calculations the heavy particle temperature was assumed constant, as the characteristic time for temperature changes due to heat conduction is on the order of several milliseconds.

Equations (7)-(10) and (13) for 4 unknowns n_x, n_a, n_e and T_e form the set to be solved for given microwave power density values P_{v1} (background) and P_{v2} (pulse), the repetition rate and duty cycle of the pulse waveform and the heavy particle temperature T.

3. Calculation method

To solve the set of ordinary differential equations describing the global model one must determine first the initial values of the unknowns for given discharge conditions corresponding to the cw microwave background. This is done by putting

$$dn_i/dt = 0 \qquad dT_e/dt = 0 \qquad dT/dt = 0 \tag{14}$$

in the respective equations, where $i = x, a, e$, and solving the resultant set of nonlinear algebraic equations. Actually, in the presented model some equations may be solved independently of the others, which simplifies the solving procedure.

The reduced electric field intensity E/n and electron concentration n_e are calculated by simultaneously solving the steady-state balance equation for ionization and dissociative recombination and the energy balance equation for the heavy particles. Calculations are performed by iteration, with the Boltzmann equation for the electrons solved in each step in order to update the values of the electron temperature, rate coefficients, collision frequencies and electron energy losses.

Next, particle balance equations for the stationary initial state are solved, providing the initial values for populations of the electronically excited nitrogen molecules N_2^* (n_x) and nitrogen atoms N (n_a). The rate coefficients are again determined based on the solution to the Boltzmann equation for the electrons.

For solving the set of stiff differential equations (7)-(10) the Gear's method is used. The instantaneous value of E/n is determined in each step of integration by iteration, based on a transformed formula (11) $P_v = \sigma (E/n)^2 n^2$. This is done on assumption that the efficiency of power transfer from the microwave field to the plasma is constant and independent of the input power density level. Any rise of P_v must result in an instantaneous rise of E/n, as the electron concentration can not change instantaneously. The rise of E/n causes an increase of the ionization rate. That results in an increase of the electron concentration and plasma conductivity, and a decrease of E/n. In the numerical code each change of E/n triggers solving the Boltzmann equation for the electrons and updating the rate coefficients.

4. Calculation results

The example of calculation results presented in this paper concerns the following initial data: continuous wave background with a power density $P_{v0} = 1300$ Wcm^{-3}, gas flow rate of 2 l/min, gas temperature $T = 2200$ K, rectangular pulses 15 μs long, with a peak power $P_{v1} = 3250$ Wcm^{-3}, repeated at a rate of 15.4 kHz.

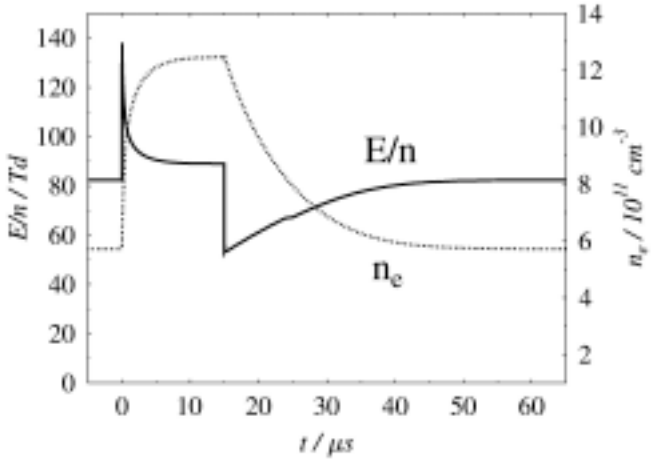

Fig. 1. Variation of the reduced electric field intensity E/n and electron concentration n_e for the first pulse; $t_{pulse} = 15$ μs, $t_{period} = 65$ μs, peak power density $P_{v1} = 3250$ Wcm^{-3}.

Figure 1 shows the variation of the reduced electric field intensity E/n and electron concentration n_e for the first period of the pulse waveform at the very beginning of pulsed operation. The stepwise rise of the power density input to the plasma causes a rapid rise of the electric field, as the electron concentration can not change instantaneously. The resulting rise of the ionization rate causes the electron concentration increase, which in turn allows E/n to decrease gradually.

Figure 2 shows changes of the electron temperature T_e and electron concentration n_e for the same period. Temporal changes of populations for all plasma species considered in the model are shown in Figure 3. The number density of N atoms remains almost unaffected by the pulse, while those of electrons (and, on the strength of plasma quasi-neutrality, of N_2^+ ions) as well as electronically excited nitrogen molecules N_2* increase rapidly during the pulse, to decrease behind it to the initial level in about 50 μs. It is interesting to note the difference in the rise and fall times of the electron concentration, reflecting the different plasma behaviors in the ionizing and recombining regimes.

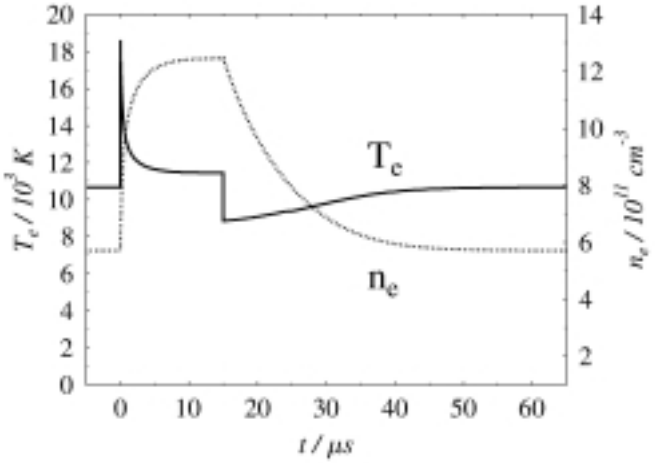

Fig. 2. Variation of the electron temperature T_e and concentration n_e for the first pulse; conditions as for Fig. 1.

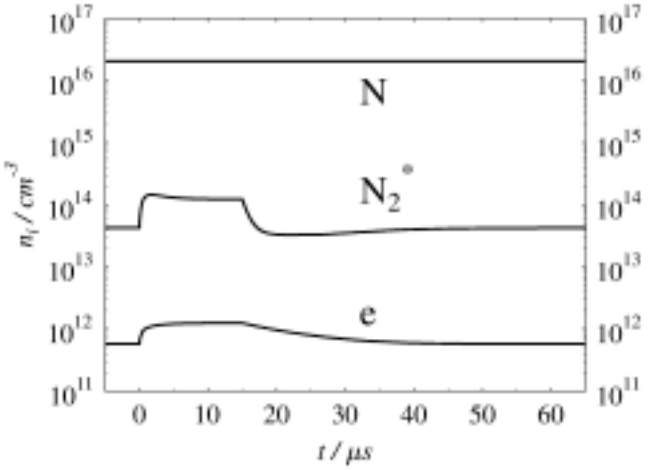

Fig. 3. Variation of the plasma species concentrations during the first cycle of pulsed operation; conditions as for Fig. 1.

5. Conclusions

It should be emphasized that the results presented are correct only within the limits imposed by the adopted model. For more precise calculations a more consistent model is needed. Unfortunately, the nature of the microwave plasma torch makes formulation of a sound global model difficult. Nonetheless, the model described in this paper provides relatively easily insight into temporal variations of plasma parameters in the microwave torch.

Research work supported partly by the Polish State Committee for Scientific Research in the years 2003-2004.

References

[1] Q. Jin, C. Zhu, M.W. Borer, G.M. Hieftje, Spectrochim. Acta **46B**, 417 (1991).
[2] M. Moisan, G. Sauvé, Z. Zakrzewski, J. Hubert, Plasma Sources Sci. Technol. **3,** 584 (1994).
[3] http://www-ph.postech.ac.kr/~mhcho/psl/publication/poster/article/2002/kps_2002_s_ysbae_torch.pdf.
[4] M. Moisan, Z. Zakrzewski, J.C. Rostaing, Plasma Sources Sci. Technol. **10,** 387 (2001).
[5] J. Stańco, in: Proc. 15th International Symp. on Plasma Chemistry, Orléans, France, 2001, p. 1577.
[6] W.L. Morgan, ELENDIF for Windows 95, Kinema Research & Software, 1999.
[7] A.A. Matveyev, V.P. Silakov, Plasma Sources Sci. Technol. **8,** 162 (1999).
[8] J. Hugill, T. Saktioto, Plasma Sources Sci. Technol. **10**, 38 (2001).

A high-frequency plasma discharge effect on polymeric films irradiated by heavy ions

Lyubov I. Kravets[1], Serguei N. Dmitriev[1], Vladimir V. Sleptsov[2], Vyacheslav V. Potryasai[2]

[1] *Joint Institute for Nuclear Research, Flerov Laboratory of Nuclear Reactions, 141980 Dubna, Russia; Tel., Fax: (7-09621) 65955, E-mail: kravets@lnr.jinr.ru*

[2] *Tsiolkovsky Moscow State Aviation Technological University, 121552 Moscow, Russia Tel., Fax: (7-095) 9155719, E-mail: ntr@akkt.mati.ru*

An effect of plasma RF-discharge on the chemical etching rate of heavy energy ion tracks in poly(ethylene) terephthalate (PET) and polypropylene (PP) films has been studied. Investigated was also an influence of the plasma treatment conditions on the structure and the properties of the track membranes produced in the course of etching. Polymeric films of a thickness of 10 μm exposed to 1 MeV/nucleon xenon ions and 3 MeV/nucleon krypton ions accelerated at the cyclotron (FLNR, JINR) were used at the experiments. The plasma treatment was performed by the method described in [1] at a plasma-chemical device (MSTAU) providing RF-discharge of 13.56 MHz frequency. Only one side of the films was exposed to plasma. Nitrogen and a mixture of nitrogen and cyclohexane in the ratio of 3:1 were used as plasma-forming gas. Discharge parameters (gas pressure, discharge power) and duration of plasma effect were varied. Chemical etching is performed in a conductometrical cell by method [2]. A water solution of 3 mol/l sodium hydroxide was used as an etchant for the samples of PET films and a water solution of chromic anhydride with concentration of 1000 g/l for the samples of PP films.

It has been shown that the character of the changes in etching the ion tracks in a polymer and a polymeric matrix at plasma effect is specified, mainly, by the nature of the polymer. So, the effect of the non-polymerizing gas plasma on the PET films exposed to heavy ion causes a decrease in the etching of both the tracks and the source polymeric matrix. The rate of these processes depends upon the discharge parameters, i.e. increasing the discharge parameters leads to decreasing the etch rate. The changes in the track etching and the polymeric matrix caused by coupling the polymer surface layer lead to appearing an asymmetry in the PET track membrane structure. As electron microscopic investigations have shown, the pore diameter on the side exposed the plasma treatment is less than the pore diameter on the opposite side not treated by plasma. The effect of the non-polymerizing gas plasma on the PP films exposed to heavy ion causes as against an increasing in the etching of tracks, i.e. lead to their sensitization. This effect can be explained by a thermal effect of the plasma discharge on the tracks in PP. The rate of these processes also depends upon the discharge parameters – increasing the discharge parameters leads to more essential increasing the etch rate. The character of etching the polymer in this case does not change. This means that the effect of plasma of under investigation gas does not result in appearing an asymmetry in the shape of the pores formed at the chemical etching of PP track membranes.

It has been found that the polymerizing gas plasma effect on the PET films exposed to heavy ions also causes decreasing the track etching effect. This result from the formation of a thin polymeric chemically stable diamond-like carbon (DLC) film on the surface exposed to plasma. The chemical etching of the PET films exposed to ions with the deposited DLC layer leads to formation of composite semipenetrable membranes. Changing the time of etching in organic compound plasma and the composition of the plasma-forming gas allows one to vary a thickness of the deposited polymeric layer and the selective properties of the formed composite membranes.

[1] S.N. Dmitriev, L.I. Kravets, V.V. Sleptsov - Nucl. Instrum. and Meth. **142 B**, 43 (1998).
[2] P.Yu. Apel, S.P. Tretyakova - Devices and Experimental Techniques. **3**, 58 (1980).

Linearly Extended Plasma Source Based on Bifocal Microwave Concentration

M. Kaiser*, M. Graf, R. Emmerich, H. Urban, E. Räuchle

Fraunhofer Institute For Chemical Technology, Pfinztal, Germany

Plasma chemistry is used in a wide field of application, especially for PECVD-deposition, activation and etching. Many plasma sources are constructed with high electrical field and therefore the highest plasma density close to the antenna, with a divergent (usually 1/r) decay outwards. Such a set-up is accompanied by some disadvantages. The recombination process of the plasma is accelerated through plasma wall interactions with highest plasma activity at the antenna or the place of power input. There highest deposition rates, plasma activity, light emission and heating occurs. Usually this phenomena is a parasitic effect, that is only desired, when the substrate itself is the interface to the plasma generating power source. To separate the power input from the plasma zone, usually the ECR-effect, typically used in the sputter technology, or any kind of high frequency resonator is used. The disadvantage of these systems is the requirement of low pressure or the punctiform plasma generation.

A new solution for this problem will be introduced in this contribution. The key point is the microwave concentration, used to generate the plasma and performed by a linearly extended bifocal plasma device. With this device a linear extended plasma up to atmospheric pressure has been tested successfully.

The prototype of the device was built up from a cylindrical barrel with elliptical cross-section. The dimensions of the ellipse was 30cm and 50cm for the respective semi–axes. The linear extension was 1m.

This bifocal shape has two focus lines where a linearly extended microwave antenna is placed in one focus line and the sector of plasma generation is placed in the second focus line. The divergent emitted microwave radiation is reflected by the metallic walls of the barrel and concentrated in the second focus line apart from the antenna.

In the sector of plasma treatment a quartz tube of 3 cm diameter was used for simple pressure and gas flow control. With the assumption of geometrical optics for the reflection and concentration of microwaves, the shape and set-up was simulated with a numerical simulation program (flex pde). Changes and limits of the microwave concentration in dependence on geometry and simulated power consuming load (plasma) was investigated.

The following picture shows an argon plasma at atmospheric pressure:

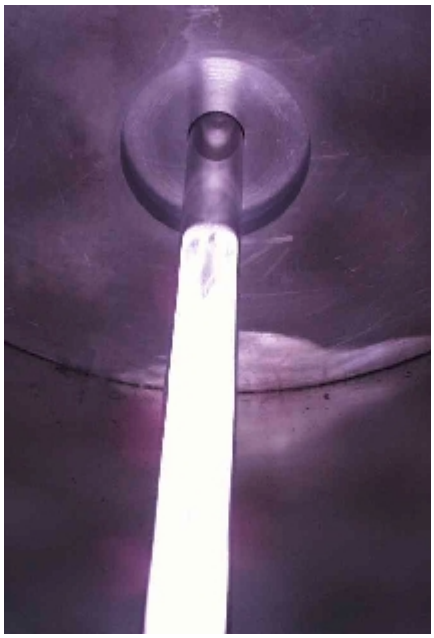

Laminar plasma jets: generation, characterization and applications for material surface processing

W.X.Pan, G.Li, X.Meng, W.Ma, C.K.Wu

Institute of Mechanics, Chinese Academy of Sciences, Beijing 100080, China

Non-transferred DC plasma jets under turbulent flow condition at atmospheric pressure have been widely used and much discussed. The laminar flow plasma jet, although seldom studied and used, has stable flow, low noise and favorable temperature and velocity distributions for materials processing usage [1, 2]. The reasons that handicapped its development could be the insufficient understanding which emphasized its shortcoming of low thermal efficiency [3], relatively complicated torch structure [1, 3], narrow range of generating parameters, and delicate state that can be easily disturbed by additional operating parameters such as powder feeding in plasma spraying.

In the present work, DC laminar plasma jets of pure argon were generated at atmospheric pressure with a generator having an inter-electrode insert between the cathode and the anode. The fluctuation of arc voltage, light intensity and stagnation pressure of the jet flow were measured simultaneously to examine the flow stability and response of its characteristics to the change of generating parameters. Thermal efficiency, jet power and jet length were measured, and the mean gas temperature at the anode exit was calculated. Combined with the experimental results, similarity theory [4] was adopted to establish formulas for examining the arc voltage character, thermal efficiency and jet length of the laminar plasma. The application of laminar plasma jets for materials surface processing, such as ceramics coating spray and remelt strengthening of metals surface, were attempted.

The arc column seems to be stable and almost fully developed in the torch channel. Thermal conductivity feature of the plasma working gas could play an important role in affecting thermal efficiency character of the laminar-plasma generator having relatively long arc channel. The mean flow temperature at the torch nozzle exit could be over 14000 K at arc current of 200 A. The stable high-energy intensity and relatively low flow velocity make the laminar plasma jet suitable for remelt hardening of metal surface. When used for spraying, the long laminar jet flow can't be easily disturbed by the powder feeding gas injection, and the long stable jet could improve the heating effect on powder particles.

Acknowledgements: This work is financially supported by the National Natural Science Foundation of China with Project Nos. 59836220 and 19975064. And authors give their heartfelt thanks to professor X.Chen, Tsinghua University, for his many useful discussions and help.

[1] V. I. Kuz'min, O. P. Solonenko and M. F. Zhukov - Proceedings of the 8th National Thermal Spray Conference, Houston, Texas, Materials Park, OH, ASM International, 83 (1995).
[2] W. X. Pan, W. H. Zhang, W. Ma and C. K. Wu - Plasma Chem. Plasma Process. **22 (2)**, 271 (2002).
[3] K.Osaki, O.Fukumasa, A.Kobayashi, Vacuum, **59**, 47 (2000).
[4] O. I. Yas'ko - J. Phys. D: Appl. Phys. **2**, 733 (1969).

METHANE-OXYGEN MIXTURE COMBUSTION INITIATED BY HIGH-CURRENT GLIDING SURFACE DISCHARGE

I.A.Kossyi, V.P.Silakov and N.M.Tarasova

General Physics Institute of Russian Academy of Sciences,
19991, Vavilov Street 38, Moscow, Russia

Results of experimental investigation of combustion of $CH_4 + O_2$ mixtures ignited by high-current pulse gliding surface discharge are presented.

It has been demonstrated [1-3] that the process of combustion initiated by gliding surface discharge exhibit certain characteristic features such that the propagation of combustion.

Application of high-current initiator changes significantly the process of ignition of the gaseous volume remote from the initiator (as compared with standard low-power two-electrode spark ignition or ignition with a heated metal filament). The standard dynamics of combustion described by thermal or detonation waves propagated from a point of local heating (or a breakdown) of gas medium is replaced – in initiating by a high-current gliding discharge – by a complicated sequence of phenomena. Such a sequence consists in exciting a glow wave that lifts off the initiator and halts in the sufficient vicinity of the initiator with the subsequent homogeneous combustion in the whole volume of the reactor. In this case the glow wave can not be identified neither with a combustion wave, nor with a detonation wave.

It has been found that the burning time of $CH_4 + O_2$ mixture significantly depend on the energy released in the slipping surface discharge decreasing with its increasing.

New experimental results concerning to the nonidentified wave preceding the combustion have been received. Analysis of these results is presented. According it a new form of long-lived plasmoid in a chemical active gaseous medium is predicted. The role of such a plasmoids in combustion ignition is discussed. New optical spectroscopic diagnostics intended to the gas temperature determination are described. Dependence of gas temperature on the energy release in the gliding surface discharge and on the content of flammable gaseous mixture has been received.

References

[1] I.A.Kossyi, V.P.Silakov, N.M.Tarasova. Combustion of Methane-Oxygen and Methane-Oxygen-CFC Mixtures Initiated by a High-Current Slipping Surface Discharge. – Plasma Physics Reports, v. 27, No 8, (2001), pp.715-725.

[2] S.I.Gritsinin, I.A.Kossyi, Yu.F.Kolesnichenko, M.A.Misakyan, V.P.Silakov, N.M.Tarasova and S.M.Temchin. The Features of Gaseous Mixtures Combustion Initiated by High Current Slipping Surface Discharge. - 32nd A–AA Plasmadynamics and Laser Conference, 2001, Anaheim, USA, Report AIAA 2001-2947.

[3] S.I.Gritsinin, E.G.Korchagina, I.A.Kossyi, M.A.Misakyan, V.P.Silakov, N.M.Tarasova and S.M.Temchin. Decomposition of Chlorine and (or) Fluorine-Bearing Substances in a Gas Mixture Ignited by a Slipping Surface Discharge. – Plasma Sources. Sci. Technol., v. 10, No 2, (2001), pp. 125-133.

Thermal-Plasma Jet Oxidation of Organic Compounds in Aqueous Solutions.

N.V.Alexeev, A.V.Samokhin, E.V.Troitskaya, Y.N.Mamontov, A.N.Belivtsev, and V.I.Zhavoronkova.

State Research Institute of Organic Chemistry and Technology, Moscow, Russia

Abstract

Chemical transformations occurring in distilled water and aqueous phenol solutions during treatment with an oxygen plasma jet were experimentally studied. The phenol conversion by plasma treatment of its aqueous solutions was found to be mainly due to reactions involving free radicals.

1.Introduction

In the last decade, a great interest of researchers was focused on studying processes resulting in complete oxidation to carbon dioxide and water of organic compounds initially dissolved in water. Despite fundamental differences in their conduction, these processes are based on chemical reactions of oxidation of organic molecules by highly reactive OH radicals [1]. The OH radical is a highly reactive species whose reaction rate with organic components in aqueous solutions is of the order of 10^6-10^9 mol 1^{-1} s^{-1} [2]. In the aqueous medium OH radicals can be generated in various chemical and physicochemical processes such as Fenton reactions, photolysis of ozone or hydrogen peroxide, and the actions of ultrasound or pulsed electric discharge.

On ultrasonication of aqueous solutions, as well as during a pulsed electric breakdown in a liquid, the primary generation of reactive species (atoms and radicals) takes place in the gas phase as a result of thermal dissociation of water molecules in the volume of gas bubbles at the expense of ultrasonic or electric field energy, respectively.

Reactive species in gas phase can be generated outside the bulk of water in thermal-plasma generators in which the dissociation of starting molecules is induced by passing a gas through an arc, radiofrequency, or microwave electric discharge. The treatment of an aqueous solution of organic compounds with a highly dissociated gas stream under certain conditions must lead to oxidation of these compounds in reactions involving atoms and radicals.

The fundamental difference of such a process from the aforementioned ultrasonic or pulsed electric discharge-induced processes is that an aqueous solution can be treated not only with water dissociation products but with virtually any reactive species (e.g., atomic oxygen), thus allowing oxidation reactions to be induced in a liquid by various reactive particles.

It is clear that the mass transfer intensity in gas phase will be the rate-determining step of oxidation of components in solution since atoms and radicals are unstable particles within the temperature range of existence of water in the liquid state and that recombination of atoms and radicals upon their gas-phase transfer in a temperature gradient Held is inevitable at a low intensity of mass transfer processes.

In this work, the processes of oxidation of organic compounds in aqueous solution are furnished by an outflow of a stationary high-velocity (about 10^3 m/s) jet of a dissociated gas into the bulk of a liquid. Under these conditions, the gas-liquid system has an intense turbulence resulting in a rapid degradation of the jet into small-sized gaseous inclusions. This ensures high rates of mass transfer processes [3] and, hence, the possibility of transport of dissociated entities to the gas-liquid interface and their subsequent participation in chemical reactions with the liquid-phase components.

Despite a wealth of studies concerned with chemical reactions in a thermal plasma, attempts at using stationary flows of thermal plasma to conduct oxidation reactions of organic compounds in aqueous solutions under conditions of plasma efflux into the bulk of a liquid have not been reported.

2.Theoretical

Thermal Dissociation of Molecules in Gas Phase. For accomplishing oxidation reactions of organic compounds, the most interesting are oxygen and water vapor dissociation products. As follows from calculations of equilibrium dissociation constants for oxygen and water molecules, a noticeable dissociation of the initial molecules at a pressure of the order of atmospheric begins at a temperature above 2000 K, and, at a temperature above 4500 K, the atoms (O from O_2 or O and H from H_2O) become dominating components (Fig. 1).

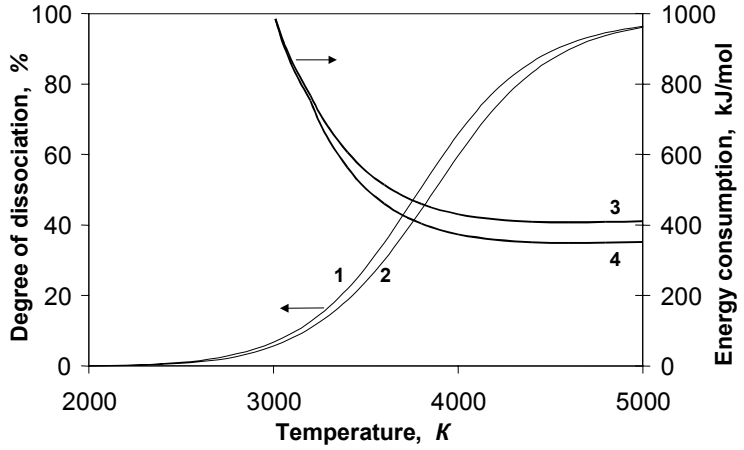

Fig.1. Temperature dependence of the degree of dissociation and the energy consumption for generation of atoms and radicals from H_2O (/, *3)* and O_2 (2, *4)* molecules (a pressure of O.I MPa).

For the equilibrium dissociation of oxygen and water molecules in the gas phase, the minimum energy consumption for generating O atoms (from molecular oxygen as a process gas) and the set of species O + H + OH (from water vapor) corresponds to a temperature in the vicinity of 4500 K (Fig. 1), about 70% of the energy being consumed directly to the breaking of chemical bonds, thus suggesting a quite high energy efficiency of generation of atoms by thermal dissociation.

Thus, these calculations show that the generation of "reactive species" by equilibrium thermal dissociation of molecular oxygen and water vapor is characterized by close values of both yield and energy consumption.

Plasma Jet Outflow into Liquid. Although the mechanics of gas-liquid systems formed upon gas efflux into a liquid are rather extensively studied (e.g., see the review [3]), the problems of interaction mechanics in such systems are far from being resolved. This is due to difficulties in describing and experimental studying such systems since they are generally nonequilibrium, unstable, and nonstationary systems. In the case of plasma efflux, the problem is additionally complicated by strong initial nonisothermicity. Experimental studies on the structure of the gas-liquid system formed upon high-velocity (subsonic) discharge of a plasma jet into a water bath [4] showed that the character of plasma jet discharge in general corresponds to phenomena in weakly nonisothermic systems.

For horizontal outflow, two regimes of gas efflux into a liquid are observed depending on the dynamic action of a plasma jet on the liquid (according to the classification [5]): the transient and the jet regimes. The intensity of the dynamic action of a gas jet can be evaluated with the modified Froude number Fr_0 ($Fr_0 = \rho_0 w_0^2 / \rho_l d g$, where ρ_0 and w_0 are density and the velocity of gas outflow, respectively; ρ_l is the density of the liquid; d is the diameter of a gas flow nozzle; and g is the acceleration of gravity).

The jet regime is realized at high values of the Froude number ($Fr_0 > 500$), a short region of stable jet flow of the gas existing near the nozzle so that the gas flow breaks to form a system of small bubbles at the end of this region. This regime is characterized by the most intense breaking of the gas flow and by the highest rates of mass transfer processes in the system gas-liquid.

As shown experimentally, the penetration depth of a plasma jet into a liquid is significantly smaller than that of an isothermal gas jet, which is explained by an additional decrease in the dynamic head along the plasma jet length as a result of cooling.

The results of investigation of heat transfer in the system plasma jet-liquid in the case of horizontal outflow show that virtually complete heat transfer from the plasma to liquid phase is provided at a nozzle immersion $Hid > 15$ and an Fr_0 value greater than 20, the central role upon thermal interaction of plasma jet with the liquid being played by the jet breaking rather than bubbling region.

3. Experimental

An experimental apparatus (Fig. 2) comprised a direct-current arc plasma torch of 5 kW power, a barrel reactor having a system for thermostat ting (cooling) a treated solution, and a droplet entrainment trap. The cooling system provided the maintenance of a constant temperature in the reactor during outflow of a high-temperature gas jet. Two reactor modes, the one with the lateral and the other with the bottom feed of the. plasma jet were used, the volume of treated liquid in these modes being 3 or 0.71, respectively.

Plasma gases were oxygen-argon mixtures (an oxygen concentration of 10-35 vol. %) which were heated in the torch up to a mass-average temperature of 3300-3700 K. In some experiments, nitrogen-argon mixtures were used. The total flow rate of a plasma gas was 0.5-0.6 m^3/h.

The mass-average temperature was determined by calorimetric measurements and thermodynamic calculations of equilibrium compositions.

The plasma jet discharged into a solution through the lateral hole in the reactor body had a velocity of 300-400 m/s. The pressure in the reactor was close to atmospheric.

Subjected to treatment were phenol (C_6H_5OH) solutions and distilled water. The concentrations of phenol and its oxidation products were determined by the conventional procedures, photometrically with 4-aminoantipyrine and by gas-liquid chromatography [6]. The concentration of hydrogen peroxide was measured by titration with a $KMnO_4$ solution.

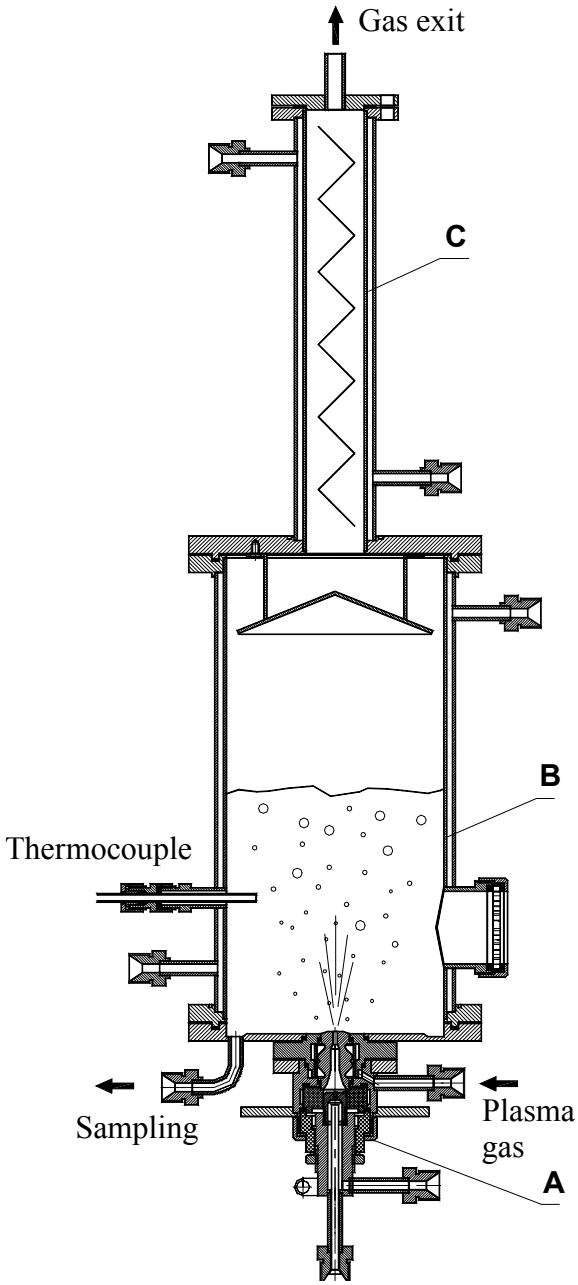

Fig. 2. Schematic of experimental apparatus: (A) plasma torch, (B) reactor, and (C) droplet entrainment trap.

4. Results and discussion

The experiments on the thermal-plasma jet treatment of aqueous phenol solutions were preceded by the set of experiments on the treatment of distilled water in the bottom feed plasma-jet reactor. The conditions of the experiments are given in the Table 1.

As seen from the data presented in Fig. 3, the formation of hydrogen peroxide takes place when the plasma jet is discharged into the bulk of distilled water.

Hydrogen peroxide formation in water is characteristic of such a water treatment process as sonolysis [7] or pulsed electric discharge treatment [8].

According to the current concepts, dissociation of water molecules

$$H2O \rightarrow H + OH \quad (1)$$

and dissolved oxygen O_2

$$O2 \rightarrow O + O \quad (2)$$

in produced vapor bubbles takes place under these conditions.

The resulting atoms and radicals react to yield H_2O_2 molecules:

$$O + H2O \rightarrow OH + OH, \quad (3)$$

$$OH + OH \rightarrow H_2O_2 \quad (4)$$

$$H + O2 \rightarrow HO2 \quad (5)$$

$$Ho2 + HO2 \rightarrow H_2O_2 + 0_2 \quad (6)$$

A similar mechanism can be used to describe chemical reactions in the gas-liquid system formed by plasma jet outflow into the bulk of water.

From the experimental results, it follows that the amount of H_2O_2 produced in water by plasma jet treatment is much greater in the case of an oxygen-containing rather than argon-nitrogen plasma (Fig. 3). This difference suggests that the major role in chemical reactions is played by oxygen atoms generated in the plasma torch and the role of water vapor dissociation products ejected by the plasma jet is relatively small. The dissociation of process oxygen in the plasma torch occurs by passing the gas through an electric discharge in which the arc zone temperature is higher than 10^4 K, whereas the dissociation of water vapor takes place upon degradation of the plasma jet in the liquid; i.e., under conditions of rapid cooling of the gas.

Table 1. The conditions of experiments.

No.	Plasma gas composition, volume fraction			Enthalpy of plasma, MJ/m^3	Temperature of water, C
	N_2	0_2	Ar		
1	0.19	0.00	0.81	4.80	45
2	0.48	0.00	0.52	8.42	50
3	0.00	0.19	0.81	6.66	45
4	0.00	0.19	0.81	4.57	70
5	0.00	0.19	0.81	6.01	45
6	0.30	0.04	0.66	6.34	45

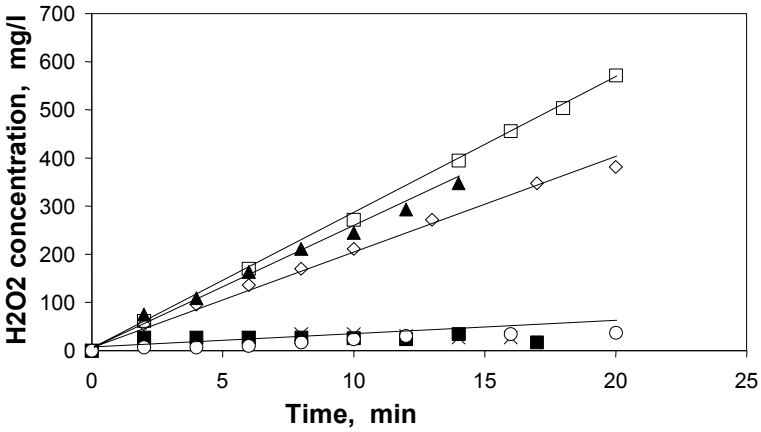

Fig. 3. Change in time for H_2O_2 concentration in distilled water upon thermal-plasma jet treatment: (1) x , (2) ■ , (3) ▲ , (4) ◇, (5) □ , and (6) O. Curve numbers correspond to numbering the experiments in the table.

The dissociation energy of water molecules by reaction (1) is 105 kcal/mol [9]; therefore, the reaction rate does not provide a noticeable yield of atoms and radicals within a short time of plasma jet degradation.

The oxidation of phenol was studied with the oxygen-argon plasma jet. The concentration of oxygen in the initial mixture was 35 vol. % and the equilibrium mass-average gas temperature at the plasma torch outlet was 3600 K. The experiments were carried out in the lateral feed plasma-jet reactor, the initial phenol concentration in water was 15 or 145 mg/1, and the temperature of solution during the treatment was 55°C. It was found that the plasma jet treatment decreases the phenol concentration in solution (Fig. 4). The phenol conversion rate depends on the pH of the starting solution. The maximum conversion rates were attained in experiments at a low pH (5.45). The conversion of phenol is accompanied by the formation of hydrogen peroxide (Fig. 5) whose concentration monotonically increases with time in an almost identical manner at any pH value.

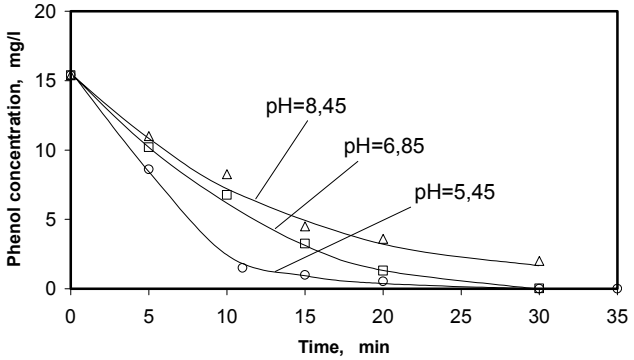

Fig. 4. Change in time for phenol concentration in water solution at different initial pH values.

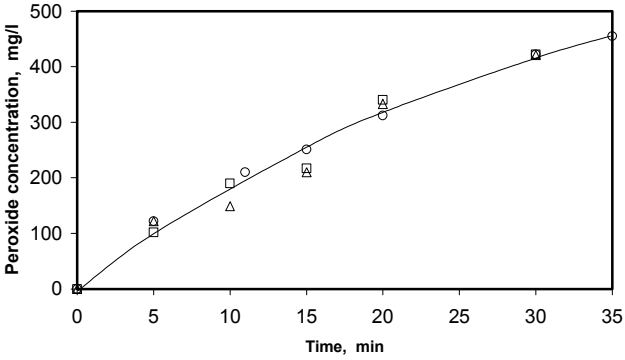

Fig. 5. Change in time for H_2O_2 concentration in water solution at initial pH of 5.45, 6.85, and 8.45.

The oxidation of phenol upon plasma treatment of its aqueous solution seems to be due to reactions involving free radicals, as in the case of ultrasonic treatment [10,11].

The identification of phenol oxidation products showed that, after the 115-min plasma jet treatment of a solution having an initial phenol concentration of 145 mg/1, the final solution contained phenol (7.5 mg/1), pyrocatechol (8.1 mg/1), pyrogallol (10 mg/1), formaldehyde (0.26 mg/1), and acids (67 mg/1).

This set of products indicates that phenol conversion by plasma jet treatment may occur via two routes (reactions (7) and (8)) which should not be considered elementary steps. By the first route, successive oxidation of phenol yielding polyhydric phenols (pyrocatechol, pyrogallol, hydroquinone) takes place:

$C_6H_3OH + 20H — C_6H_4(OH)_2 + H_2O$, (7)

$C_6H_3OH + 30H — C_6H_4(OH)_3 + H_20$. (8)

The polyhydric phenols are further oxidized to quinonoid compounds, which, in turn, are oxidized to cleave the quinone ring yielding unsaturated acids and, ultimately, carbon dioxide and water.

On the other hand, the conversion of initial phenol can proceed directly by cleaving its molecules to yield formaldehyde which, under certain conditions, forms phenol-formaldehyde resins via condensation with phenol. This reaction route is qualitatively confirmed by appearance of a transient brown color of solution during the treatment, although this color further disappears.

It may be assumed that the presence of H_2O_2 in solution plays a minor role in phenol oxidation reactions, as in the case of ultrasonic treatment.

4. Conclusion

The experiments have shown that the treatment of aqueous solutions by oxygenated thermal plasma jet can induce chemical reactions initiated by free radicals. The major role in generating these radicals seems to be played by oxygen atoms that are present in thermal plasma, whereas the effect of dissociation of water molecules ejected by plasma jet is insignificant.

The plasma jet treatment of aqueous phenol solutions results in chemical reactions with participation of phenol, its chemical transformations being qualitatively consistent with the mechanism involving OH radicals.

The obtained results open up new possibilities for using a thermal plasma jet as a means of accomplishing gas-liquid oxidation reactions of organic compounds in aqueous solutions.

Acknowledgments

This work was supported by the Russian Foundation for Basic Research (project no.03-03-32818) and International Science and Technology Center (project no.1338).

References

[1] Andreozzi, R., Caprio, V., Insola, A., and Marott, R.t *Catal Today,* 1999, vol. 53, p. 51.
[2] Farhataziz, R. and Ross, A.B., *Natl. Stand. Ref. Data Ser.t* 1977, p 59.
[3] Surin, V.A. and Nazarov, Yu.N., *Massd- i tephobmen, gidrogazodinamika metallurgicheskoi vanny* (Mass and Heat Transfer, Hydraulic Gas Dynamics of Metallurgical Baths), Moscow: Metallurgiya, 1993.
[4] Alekseev, N.V., Pozdnyakov, O.E., and Shorin, S.N., *Inzh.-Fiz. Zh.,* 1983, vol. 44, no. 4, p. 537.
[5] Ginzburg, I.R, Surin, V.A., Bagautdinov, A.A., and Grigor'yants, A.S., *lnzh.-Fiz. 2h.%* 1977, vol. 33, no. 2, p. 213.
[6] *Unifitsirovannye melody analiza vody* (Unified Methods for Water Analysis), Lur'e, Yu.Yu., Ed., Moscow: Khimiya, 1971.
[7] *Ultrasound—Its Chemical, Physical and Biological , Effects,* Suslick, R.S., Ed., New York: VCR, 1988.
[8] Ooryachev, V.I., Rutberg, F.G., and Fedyakovich, V.N., *Teplofiz. Vys. Temp.,* 1996, vol. 36, no. 5, p. 767.
[9] Kondrat'ev, V.N., *Konstanty skorosti gazofaznykh naktsii* (Gas-Phase Reaction Constants). Moscow: Nauka, 1970.
[10] Kandzas, P.P., A Study on the Applicability of Ultrasonic , Vibration to Industrial Wastewater Purification, *Abstract ' of Cand. Sci. Dissertation,* Moscow: VNIIVODGEO, 1963.
[11] Khenokh, M. and Lapinskaya, E.M., Z/i. *Org. Khim.,* 1956, vol. 26, no. 8, p. 2439.

Structure and bonding studies of a-C:H films produced by plasma enhanced CVD using CH_4-CO_2 mixtures.

G. Gottardi[1], N. Laidani[1], M. Anderle[1], R. S. Brusa[2] and M. Spagolla[2]

[1] *ITC-Irst (Centro per la Ricerca Scientifica e Tecnologica), Divisione Chimica Fisica delle Superfici e Interfacce, 38050 Povo (Trento), Italy*
[2] *INFM, Dipartimento di Fisica, Università degli Studi di Trento, 38050 Povo, Trento, Italy*

Abstract
Hydrogenated carbon films have been deposited on Si substrates in a RF plasma-enhanced chemical vapor deposition (PECVD) system, using CH_4-CO_2 mixtures as gas precursor. A multi-technique approach has been used for a thorough characterization of the deposited films. Aim of this work has been the optimization of the deposition process for obtaining dense and hard films, by studying the effects of parameters such as the gas composition, the cathode self-bias (V_{RF}) and the sample negative biasing level.

Keywords: PECVD, carbon films, CH_4-CO_2 plasma, characterization.

---

1. Introduction

Increasing interest in the deposition and characterization of amorphous hydrogenated carbon (a-C:H) films stems from their outstanding attractive properties that offer a wide range of commercial applications. Various plasma-assisted deposition techniques and carbon bearing source materials have been investigated and can be used for the synthesis of a-C:H films. In particular, radio frequency (RF) plasma-enhanced chemical vapor deposition (PECVD) systems are the most common type employed, over a broad range of deposition voltages, gas pressures, gas composition and substrate temperatures [1,2,3].

Nevertheless deposition of coatings by PECVD is one of the most complex of all plasma surface treatment techniques. In-depth understanding is still limited and the development of new deposition processes is mostly empirical. A large number of process parameters have to be controlled such as power, total pressure, flow rates of the different gases, substrate temperature, electrode spacing and ion bombardment of the growing film. Their effects are interdependent and it is generally accepted the existence of a strict relationship between film properties and process conditions [1,3,4]. The deposition temperature and the degree of ion bombardment during growth, in particular, mostly determine several material features. Moreover ion bombardment during deposition at low temperatures can yield film properties similar to those of films deposited at higher temperatures without ion bombardment [5]. Dense and hard materials can be deposited at high values of impact ion energy. Bombardment can be controlled by varying the RF power, the pressure and the substrate bias voltage [1,4].

The main purpose of the present work has been the optimization of the deposition process to obtain dense and hard carbon films at room temperature in a RF-PACVD reactor, using a mixture of methane and carbon dioxide. We examined process parameters such as the gas precursor composition, the cathode self-bias (V_{RF}) and the sample negative biasing level. In order to study their effects on the material chemical structure, composition and mechanical behavior, a systematic characterization of the films was performed. Specifically, the chemical composition and structure were investigated by means of X-ray photoelectron spectroscopy (XPS) and Fourier-transform infrared spectroscopy (FT-IR). Positron annihilation spectroscopy (PAS) was used for the detection of nano-scale open volume defects. Finally, mechanical tests using indentation and profilometric techniques were made to evaluate the hardness and the internal residual stress.

The first results indicate an evolution of the film structure from a mainly polymer-like one to that of a more rigid amorphous carbon phase when increasing the impact ion energy on the film surface during the deposition.

2. Experimental procedure

Hydrogenated carbon films were deposited on (100) Si wafers, previously organically degreased in ultrasonic bath and then etched in dilute HF. The deposition was carry out in a capacitively coupled RF-PECVD system (13.56 MHz) using a mixture of CH_4-CO_2 as gas precursor. The samples were mounted on a moveable electrode which acts as anode. The distance between cathode and anode was set at 6.8 cm. The base pressure (p) in the reactor was in the 10^{-8} Torr range while the deposition was operated at pressure values varying from 0.09 to 0.2 Torr. A total gas flow of 70 sccm was always used in the deposition process. A series of samples was prepared ranging the content of carbon dioxide in the feed gas from 0 to 50 at.%, while a constant concentration of carbon dioxide (50%) was used in all the other experiments. In addition, the substrates were polarized by applying a DC negative bias voltage (V_{BIAS}), which was changed in a range depending on the V_{RF} and on the film adhesion.

The application of high values of bias voltages to the anode resulted in poor adhesion of the films on the substrate. In order to enhance adhesion and allow the study of ion bombarding effect on the film quality, a pre-treatment of the Si wafer had then to be performed before deposition. This point will be discussed in the next section where the details of the treatment will be given.

Spectroscopic techniques were used to evaluate the chemical composition and the structural features of the films. X-ray photoelectron spectroscopy (XPS) spectra were recorded with a Scienta ESCA 200 instrument equipped with a hemispherical analyser and a monochromatic Al Kα (1486.6eV) X-ray source. The core lines were acquired at a pass energy of 150 eV, which leads to an energy resolution of about 0.4 eV. After a Shirley-type background subtraction, the spectra were fitted using a non-linear least squares fitting program adopting a Gaussian-Lorentzian peak shape. Detailed scans were acquired for the C1s and O1s regions.

The FT-IR spectra were collected by a Bio-Rad FTS 185 spectrometer equipped with a DTGS detector and a KBr beamsplitter. The spectra were then fitted using Gaussian line-shape and a linear baseline subtraction. For semi-quantitative analysis purposes, the areas under the bands were normalized to the film thickness. The normalization was necessary to relate the different signal intensity variations to real differences in the concentration of a given group.

The film thickness was measured with a Kla Tencor P15 profilometer. The deposition rate of the films was then calculated from the film thickness and the deposition time. The films were also characterized from the mechanical point of view using nanoindentation and profilometric techniques to evaluate their hardness, Young's modulus and internal stress. Determination of the stress in particular was based on measuring radii of curvature of the wafers [6], after and before deposition, by means of the profilometer.

Finally, for the detection of the film nano-scale open volume defects, positron annihilation spectroscopy (PAS) analysis was performed. The positron trapping by defects was detected by the Doppler broadening technique. The shape of the positron annihilation line, sensitive to the momentum distribution of electrons, was characterized by the so-called S parameter. The last is the ratio of the counts in a central region of the annihilation line and the total counts in the line. The data were normalized to the bulk value S of silicon. The mean positron penetration depth was calculated on the basis of the positron implantation energy and the film density. For the latter we used a mean value of 2.1 g/cm^3, as obtained from gravimetric measurements.

3. Results and discussion

This work has been a systematic investigation on the chemical and structural evolution, with regard to the process conditions, of carbon films deposited via RF-PACVD technique at room temperature. We tried to optimize the plasma parameters, such as the gas precursor composition, the cathode self-bias (V_{RF}) and the sample negative bias level (V_{BIAS}), in order to produce carbon thin films as much as possible approaching a diamond-like structure. This means that we explored different experimental conditions to obtain films with good mechanical properties (e.g. high hardness) and a structure evolving towards a three-dimensional interlinked array of carbon atoms, which may be achieved by enhancing sp^3 carbon hybridization. In this paper we'll present the first results of the work.

As a first step a series of samples was deposited on a grounded substrate (V_{RF} = –300V ; p= 0.2Torr) at different CO_2 concentrations ranging from 0 to 50 at. %. The composition of the gas precursor affects the deposition rate of the films, so strongly that 50% of CO_2 is the maximum fraction allowing the formation of a carbon film, as can be seen from Table 1. This parameter has an influence also on the mechanical properties of the material. Relatively harder films can be deposited at the highest CO_2 content. Even though the values obtained are typical of polymeric carbon films, the doubled hardness values and the increase in the

Young's modulus lead us to choose a mixture with 50% of CO_2 as gas precursor for any further deposition experiment.

Table 1. Deposition rate, nano hardness H, Young's modulus E of films deposited at different concentration of CO_2 in the feed gas mixture and at two sample bias values.

% CO_2	Sample Bias [V]	Deposition rate [nm/h]	Nano Hardness, H [GPa]	Young's modulus, E [GPa]
10	0	786.54	0.747	7.043
50	0	90.86	1.482	11.185
50	-60	74.46	2.257	22.993
66	0	0	-	-

The influence of the self-bias V_{RF} was then examined. The RF power applied to the cathode was such to have V_{RF} changed in the range –200V to –500V. The deposited films were probed with positron annihilation spectroscopy (PAS) to obtain information about nano-scale open volume defects. The PAS measurements (S parameter versus depth) on the carbon films obtained with different V_{RF} values are reported in Fig. 1. Let's recall that S increases if more open volume defects are present in the material. Apart the initial surface values, the S parameter is here almost constant throughout the films, which indicates that the coatings are homogeneous in their bulk. At the film-silicon interface, S increases to reach the bulk value of silicon at a depth that depends on the film thickness. In spite of the similarity in shape, the S parameter profiles give a relatively lower mean value of S for V_{RF}=-300V than for all the other conditions, showing that films grown at –300V of V_{RF} contain less open-volume defects.

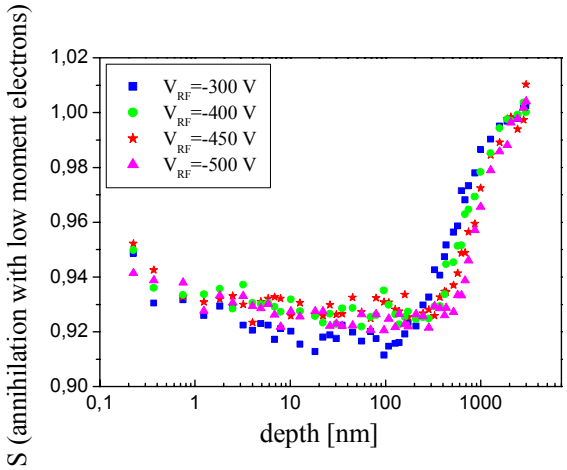

Fig.1 S parameter versus positron mean implantation depth in carbon films deposited at various V_{RF}. (p=0,2Torr; [CO2] = 50%, V_{BIAS} = 0V).

Such a result indicates that samples deposited at low V_{RF} are denser. This might correlate with a peculiar structure of the films, characterized by a higher sp^3 sites content. Such hypothesis is borne out by the outcomes of the FT-IR analyses described in what follows.

IR spectroscopy has been often used for characterizing C-H bonds in hard carbon films, for its capability to give information on the vibration modes of the interconnected sp^3 carbon sites (provided the latter were hydrogenated) and on a semi-quantitative determination of the hydrogen content of the films [8,9,10,11].

In the spectra acquired on the films deposited for different RF powers (not shown here), prominent absorption bands occur at approximately 2875, 2890, 2930, 2960 and 3020 cm^{-1} which can be assigned to the sp^3-CH_3 (symm.), sp^3-CH, sp^3-CH_2 (asymm.), sp^3-CH_3 (asymm.) and sp^2-CH_2 stretching modes, respectively [9]. Another absorption band emerges at approximately 1613 cm^{-1} (sp^2 C=C stretching). These spectra are typical of polymer-like carbon films [9] with large bonded-hydrogen content that, in the present case, decreases at higher RF powers (data not shown here). In Fig.2 we plotted the area ratio sp^3/sp^2 between the hydrogenated sp^3 C and the sp^2 C versus the V_{RF} voltage. This parameter is calculated as the ratio of the sum

of the areas of the Gaussian components fitting the sp^3-CH_x bands (x= 1-3) to the area of the sp^2 C=C band. The rise in the sp^3/sp^2 ratio, which we observe when decreasing the RF power, is consistent with the PAS analysis results. This means that deposition at the lowest V_{RF} (-300V) yields films with the lowest defect-content in correlation with the highest bounded hydrogen amount and an increase of the sp^3 character of the polymeric component of the film structure. For this reason, such plasma condition was kept as a starting point for a further optimization of the process parameters aiming to the increase of the film density.

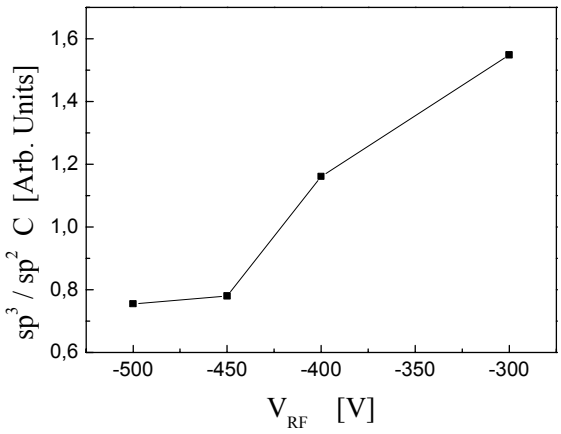

Fig. 2. Dependence of the C sp^3/sp^2 ratio on the V_{RF}. (Values obtained from the fitting of the normalized C-H_x stretching range of the FT-IR spectra.)

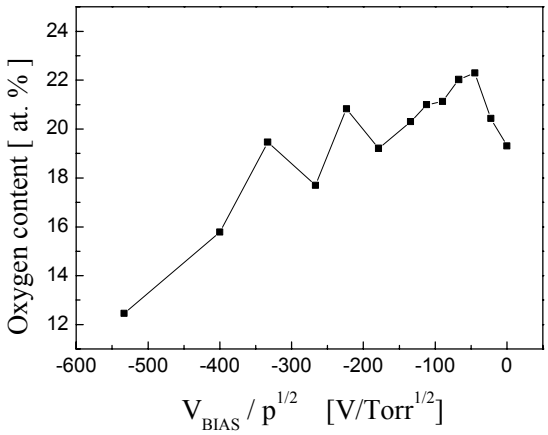

Fig. 3. Trend of the oxygen content in the carbon films with the $V_{BIAS} / p^{1/2}$ parameter, as measured by XPS.

Regarding the densification of films by ion-assistance during the film growth, experimental evidence in literature is abundant [1,2,7,12]. In order to promote the formation of dense films, some activation of surface diffusion of the atoms which impinge and stick to the substrate must be provided. Energetic particle bombardment, prior and during the initial stages of film formation, may enhance the surface mobility of ad-atoms by the introduction of thermal energy directly into the surface region, thus decreasing interfacial voids. Besides, the bombardment of the growing film surface with energetic ions is believed to be a key step in layer formation and film densification [12]. Within a collision cascade, impinging and penetrating ions displace atoms, mainly bonded hydrogen, in the film: these can desorb producing surface dandling bonds or can be recoil-implanted below the surface. The process results in an activation of the growing surface and in an inward packing of the atoms, which favours the deposition of a densely packed structure.

In the present work, ion assistance of the film growth was carried out in the deposition of a series of samples at V_{RF} =-300V, by biasing negatively the substrates. The average impact energy of ions bombarding the growing film depends on both the negative bias applied to the substrate (V_{BIAS}) and on the inelastic collisions between ions and the neutrals in the sheath surroundings the substrate, in other words on the pressure. Bubenzer et al. [13] found the relation

$$E \propto \frac{V_{BIAS}}{p^{1/2}}.$$

From now on, the data obtained from the analyses of films deposited at different impact ion energy will be presented in terms of $V_{BIAS}/ p^{1/2}$. Such a choice stems from the necessity of joining together and correlating data regarding films grown at different energetic conditions by tuning either the pressure or the negative bias.

In order to fulfil the ion-assistance effect study, a pre-treatment of the substrate surface was necessary, as already mentioned in section 2. Due to the ion bombardment, carbon films suffer from extremely high intrinsic compressive stress, which limits the thickness of adhesive films [3]. The basic problem is that the stress and the diamond-like character of the carbon films are strongly linked. This means that any attempt towards a densification of the film will result also in an increase of the stress level. We encountered such kind of problem during the deposition of the films on polarized substrates (measured stress values not shown

here). When applying to the sample a bias voltage higher than –60V, spontaneous adhesion failure occurred if the substrates were not previously treated.

In order to enlarge the bias value range to be applied and allow the study of the ion bombardment effect, various strategies were used to enhance the adhesion even at higher bias voltages. The substrates were first sputter-cleaned for 30' using an Ar DC glow discharge (p=0.3Torr, V_{RF}=-360V). Then followed a treatment of 10' in a RF glow discharge (p=0.2Torr, V_{RF}=-300V, V_{BIAS}=-80V) from a mixture of Ar (5sccm) and CH_4 (35sccm). The former step was used for completely removing any residual contaminants and oxide from the wafer, the latter to cause ion beam mixing between film and substrate in order to ensure a mixed interface [14, 15]. For high sample bias conditions a further step was finally introduced to improve the ion mixing, which consisted in the use of high ion energy (V_{BIAS}=-200V) for the very first stage of the deposition (5'). This allowed to reach bias values up to –160V without undergoing adhesion failure of the films.

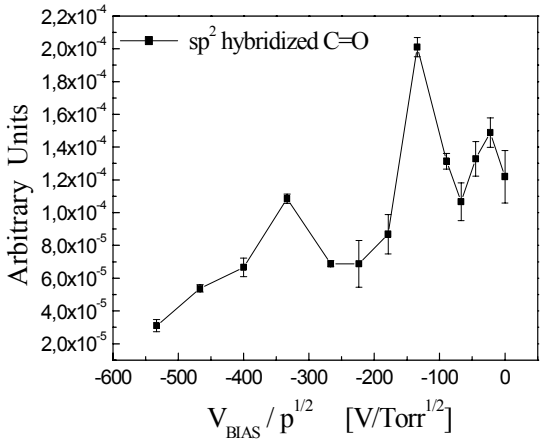

Fig. 4. Dependence of the sp^2 hybridized C=O band area on the V_{BIAS} / $p^{1/2}$ parameter. (Values obtained from the fitting of the normalized FT-IR spectra.)

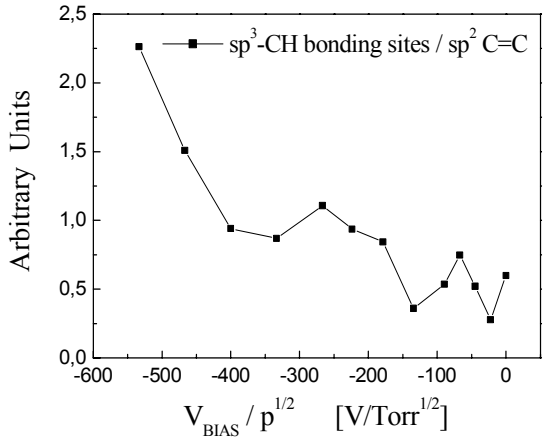

Fig. 5. Dependence of the sp^3-CH /sp^2-C=C ratio on the V_{BIAS} / $p^{1/2}$ parameter. (Values obtained from the fitting of the normalized FT-IR spectra.)

As far as the correlation between film chemical and structural properties and impact ion energy is concerned, XPS and FT-IR analyses provided us with some information. As we can see from the data reported in Fig. 3, the chemical composition of the films, in particular the oxygen content, was found to be dependent on the level of ion bombarding during the deposition. The intensity of the O1s peak in the XPS spectra was observed to significantly decrease with increasing impact ion energy on the surface of the growing film. This result was confirmed by the IR absorption analysis, which revealed a reduction in the oxygen bonding sites amount when raising the ion bombardment energy. In Fig. 4 we can see the evolution of the sp^2-C=O stretching band area (peak occurring at 1710 cm^{-1}) as a function of the ratio $V_{BIAS}/p^{1/2}$, as evaluated from the curve fitting.

The IR spectra of the samples deposited with different impact ion energy still contain the broad band due to CH_x bonding and that due to C=C. As in the case of films grown without bias, the sp^3-CH_3, sp^3-CH_2 and sp^3-CH bands were identified. In order to clarify the effect of the bias on the film structure, the sp^3-CH and the C=C peaks in particular were followed. In Fig. 5 the area ratio between these two peaks is presented. The plotted results indicate a clear trend of the number of sp^3 hybridized C-H sites to get higher, at the expense of the sp^2 C=C ones, with increasing impact ion energy. What is interesting is that we didn't observe a similar trend in the total amount of hydrogenated carbon sites, which would otherwise indicate an increase in the bounded-hydrogen content. On the contrary, the total bounded hydrogen content (as it can be estimated from the area under the whole CH_x band) was found to remain constant when varying V_{BIAS} (data not shown here). This means that the increase in the sp^3-CH/sp^2-C=C ratio shown in Fig. 5 for the films prepared at higher energetic conditions could be attributed to a real evolution of the film structure.

Regardless of the sp^3-CH_3 end groups, which cannot contribute to the structure rigidity, it's worth noting that a trend like the one shown in Fig.5 is more pronounced for the sp^3-CH groups (where the C atom is linked to other three C atoms) rather than for the sp^3-CH_2 ones. The evolution of the sp^3-CH/ sp^3-CH_2 area

ratio in fact is found to increase with the average impact ion energy (plot not shown here). This therefore implies that high ion bombardment energies during the film growth are useful to enhance the formation of a three-dimensional interlinked structure.

The first mechanical tests performed by nano indentation technique on films deposited on polarized substrates gave a confirmation of our hypothesis. Applying a –60V bias to the substrate in fact produced an increase in the Young's modulus and in the hardness, with respect to the values obtained from the unbiased samples (data displayed in Table 1). The change in the bonding configuration, as inferred from the FT-IR spectra, so results in a denser material which may indicate an evolution of the film structure from a mainly polymer-like one towards that of a more rigid amorphous carbon phase.

4. Conclusions

Hydrogenated carbon films were deposited at room temperature by RF PACVD using a mixture of CH_4-CO_2 as gas precursor. Different plasma conditions were explored and the effect of the physical parameters of the glow discharge on the chemical, structural and mechanical features of the coatings were investigated.

It was found that the composition of the gas precursor affects the deposition rate and the mechanical properties of the material. In particular the higher the CO_2 content the harder the film obtained. PAS and FT-IR analyses indicate that samples deposited at low V_{RF} have a denser structure, with less open volumes. Finally, depositions carried out at low energetic conditions result in essentially polymeric films, as revealed by the FT-IR spectra. On the contrary ion bombardment during the film growth enhances the formation of a more rigid and dense structure, composed by carbon sites involved in three-dimensional sp^3-C-C bonding.

We believe this route to be promising for the production of diamond like carbon films, for both the mixture chosen as gas precursor and the energetic activation of the deposition process.

Acknowledgments

The authors are thankful to "Fondo Progetti – Provincia Autonoma di Trento" who financed the project. Many thanks also to CNR- Istituto di Biofisica (Laboratorio Biomolecole e Membrane Biologiche, Trento) for making available the FT-IR spectrometer and to G. Favaro from CSM Instruments (Neuchatel, Switzerland) for the nanoindentation measurements.

References

[1] A. Grill in "Cold Plasma in Materials Fabrication", IEEE Press Ed., New York, 1993.
[2] J. Robertson - Adv. Phys. **35**, 4 (1986) 317.
[3] J. Robertson - Mater. Sci. Eng. R **37** (2002) 129.
[4] F. Jansen in "Plasma-Enhanced Chemical Vapor Deposition", H.G. Tompkins Monograph Ed., New York, 1997.
[5] K.A. Buckle, J. Rodgers, K. Pastor – Appl. Phys. Lett. **50** (1992) 2601.
[6] N.Laidani, L.Calliari, G.Speranza, V.Micheli, E.Galvanetto – Surf. Coating Technol. **100-101** (1998) 116.
[7] J.-W. Chung, D.-H. Ko, K. Y. Eun, K.-R. Lee – Diamond Rel. Mater. **11** (2002) 1441.
[8] A. Grill, V. Patel – Appl. Phys. Lett. **60** (1992) 2089.
[9] M. Veres, M. Koos, I. Pocsik - Diamond Rel. Mater. **11** (2002) 1110.
[10] W. Zhang, A. Tanaka, K. Wazumi, Y. Koga - Diamond Rel. Mater. **11** (2002) 1837.
[11] S. Neuville - Diamond Rel. Mater. **11** (2002) 1721.
[12] A. von Keudell, M. Meier, C. Hopf - Diamond Rel. Mater. **11** (2002) 969.
[13] A. Bubenzer, B. Dischler, G. Brandt, P. Koidl – J. Appl. Phys. **54** (1983) 4590.
[14] J.H. Hsieh, L.H. Fong, S. Yi, G. Metha - Surf. Coating Technol. **112** (1999) 245.
[15] B.H. Lung, M.J. Chiang, M.H. Hon – Mater. Chem. Phys. **72** (2001) 163.

A DC Diaphragm Discharge in Water Solution

Z. Stara, F. Krcma, Z. Raskova

Faculty of Chemistry, Brno University of Technology, Purkynova 118, 612 00 Brno, Czech Republic

Abstract

In this contribution, the DC diaphragm discharge in water solutions is described. The batch reactor was used in experiments. The discharge configuration was „electrode-less". The dependence of the light intensity of hydroxyl radicals on the discharge conditions (applied voltage, initial conductivity of the liquid, salt in water solution) was studied by optical emission spectroscopy. The influence of these conditions on the generation of hydrogen peroxide by the discharge was also investigated.

1. Introduction

The discharges generated in liquids have been subject of intense research during a few last yaers [1-4]. The processes taking place in such discharges are applied in fields of water treatment, destruction of various organic pollutants dissolved in water and in specific reactions in liquid phase. The common discharge configurations are point-to plane [1, 2] and coaxial [3], several experiments were done in diaphragm (electrode-less) configuration [4]. During almost all of these experiments, a pulsed high voltage in range from about 10 to 20 kV was used to create the discharge. The present contribution focuses on the diaphragm discharge created using the non-pulsed DC high voltage, which could be lower than in case of the pulsed high voltage (only about 2 kV) [5]. Various active species are produced by such discharge (hydroxyl radicals, hydrogen ans oxygen radicals, hydrogen peroxide etc.) [2].

2. Experimental

A simplfied scheme of the discharge reactor is shown in Fig. 1. It consists of two parts – a negative part with a cathode and positive part with an anode. The stainless steel electrodes were planary and the distance between them was 4 cm. The parts of the reactor were divided by the PTFE diaphragm (0,25 mm) with a pinhole in the centre. To generate high voltage and to create the discharge, a non-pulsed DC high voltage source was used. The range of voltage was from 1,4 kV to 2,8 kV. Due to considerable heating of the reactor by the discharge and to prevent the destruction of the hydrogen peroxide, two cooling boxes with ice were installed in both parts of the reactor. This system kept the temperature under 15˚C. To ensure the homogeneous conditions in the whole volume of the liquid, a mixing system was used. The demineralised water containing NaCl and Na_2HPO_4 salts were used to obtain the defined initial conductivity [5].

The optical emission spectroscopy was used for investigating the emission intensity of hydroxyl radicals.

Hydrogen peroxide was determined spectrophotometrically using the specific reaction with titanyl ions in presence of the sulphuric acid (the titanium reagent) [6]. The created peroxotitanyl complex gave a yellow color with the maximum absorbance at 407 nm. The absorbance intensity was depended on the amount of the hydrogen peroxide according to the equation [7]:

$$y = 0{,}4596 \cdot x, \tag{2.1}$$

were y means absorbance intensity and x is the concentration of the hydrogen peroxide.

The samples were taken from both parts of the reactor (negative and positive) and the sampling time was estimated on 5 minutes.

The metallic traces (Fe, Cr) involved from the electrodes during the discharge were determined by the ICP method [5].

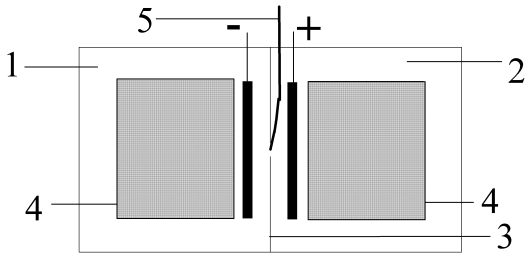

Fig. 1: Scheme of the reactor: 1 – negative part, 2 – positive part, 3 – dielectrical diaphragm with a pinhole, 4 – cooling boxes, 5 – optical fiber.

3. Results and discussion

During the experiments the emission spectra of the diaphragm discharge were observed. Especially hydroxyl radical and some elements contained in used salts (Na) were determined in the spectra. The relative OH integral intensity from the range 306.5 – 318 nm, a quantitative parameter of the diaphragm discharge, was counted from each measurement and plotted as a function of the discharge conditions. The spectroscopic observations were done in both salts (NaCl and Na_2HPO_4), the high voltage varied from 1,4 to 2,8 kV and two different initial conductivities (400 and 550 $\mu S \cdot cm^{-1}$) were used. The same feature in evolution of the light intensity in both salts was its decreasing magnitude in time (Fig. 2). In case of NaCl, the decrease was slower than in the hydrogenphosphate. Comparing the relative OH intensity as a function of the initial conductivity, the difference in NaCl salt was more evident than in Na_2HPO_4, where the evolution in time was similar. In NaCl, the decrease in intensity was much higher at the higher initial conductivity (550 $\mu S \cdot cm^{-1}$).

The dependence of the relative OH intensity on the magnitude of the applied high voltage is shown in Fig. 3. The emitted light increases with increasing voltage for both types of salts. The evolution of this dependence is more or less linear and it is similar to the dependence of H_2O_2 concentration on the applied voltage (Fig. 10). In the case of NaCl and higher initial conductivity, the increase in relative OH intensity was lower than in Na_2HPO_4 salt at the same initial conductivity. There was no obvious difference between the two initial conductivities in Na_2HPO_4 solution. The increase in relative OH intensity in the case of NaCl at a lower conductivity (400 $\mu S \cdot cm^{-1}$) was much higher than at another conditions.

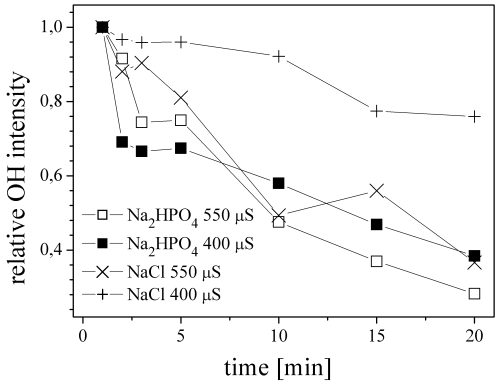

Fig. 2: The time evolution of the relative OH intensity (for various salts and initial conductivity).

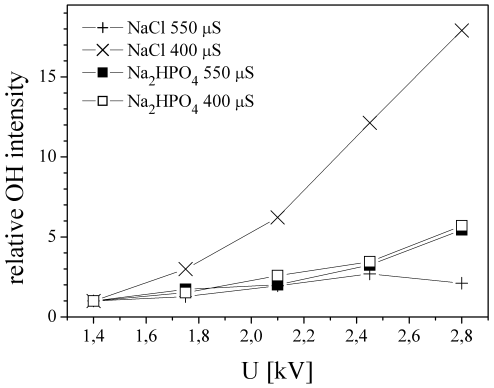

Fig. 3: The relative OH intensity as a function of the applied voltage.

The production of the hydrogen peroxide generated by the discharge was not the same in both parts of the reactor (Fig. 4). The produced amount of hydrogen peroxide was much higher in the negative polarity than in the positive part of the discharge reactor. Due to this phenomenon, next measurements were focused on the negative part of the discharge reactor. The evolution of H_2O_2 concentration in time was during the experiment (60 minutes) approximately linear (Fig. 4). In the case of longer measurement (over 60 minutes), the production of hydrogen peroxide reached the point of saturation (Fig. 5). The concentration of H_2O_2 could be described as a function of time by the following equation:

$$c_{H2O2,\,t} = k_{H2O2} \,.\, t, \tag{3.1}$$

where $c_{H2O2,\,t}$ means concentration of hydrogen peroxide, k_{H2O2} is the rate constant of the H_2O_2 production and t is time of the discharge.

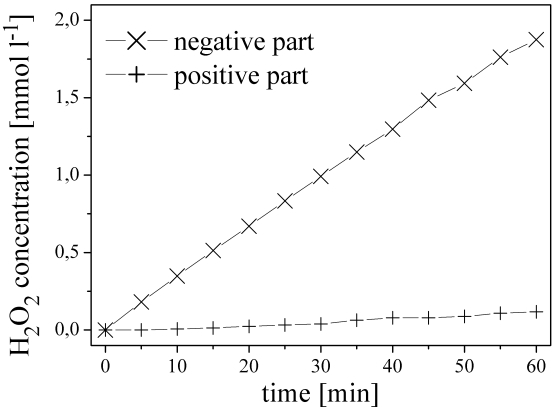

Fig. 4: Hydrogen peroxide generation in time (2,4 mM Na_2HPO_4, 2,1 kV, 500 μS·cm^{-1}).

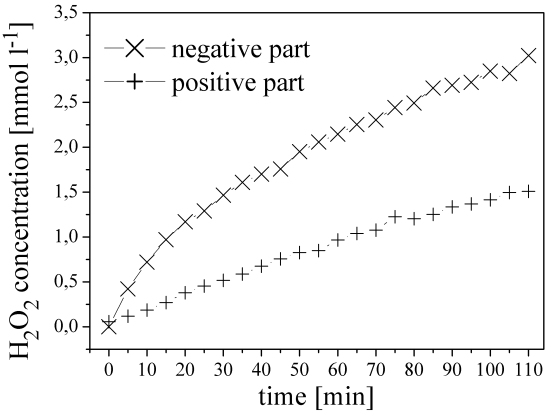

Fig. 5: Hydrogen peroxide generation in time (5 mM NaCl, 2,8 kV, 500 μS·cm^{-1}).

The rate constant of the generation of hydrogen peroxide was different for various discharge conditions. Table 1 shows the comparison of the rate constants in case of NaCl and Na_2HPO_4 salt at different initial conductivity. The dependence of the rate constant on the applied voltage, in the NaCl solution, is given in Table 2. The highest rate constant was achieved in the case of NaCl salt at the initial conductivity 600 μS·cm^{-1} and applied voltage 2,8 kV.

Table 1: The rate constants of H_2O_2 production in NaCl and Na_2HPO_4 solutions at different initial conductivity (2,8 kV, 2,1 kV respectively).

	Rate constant (·10^{-7} mol·l^{-1}·s^{-1})								
Initial conductivity (μS·cm^{-1})	100	200	300	400	500	600	700	800	900
NaCl	1,43	5,35	5,68	6,20	5,13	6,70	4,63	2,75	
Na_2HPO_4			3,10		5,67		6,20		6,43

Table 2: The rate constants of H_2O_2 production in NaCl solutions at different applied voltage (300 μS·cm^{-1}).

	Rate constant (·10^{-7} mol·l^{-1}·s^{-1})			
High voltage (kV)	1,75	2,10	2,45	2,80
NaCl	1,32	3,55	4,35	6,00

The estimated concentration of H_2O_2 in the positive part of the reactor was slightly increased by diffusion from the other part of the reactor and by metallic traces (Fe, Cr). They were involved from the stainless electrodes by the electrolysis. This phenomenon was confirmed by the ICP method. The involved amount of metals depended on the initial conductivity of the solution as given in Fig. 6.

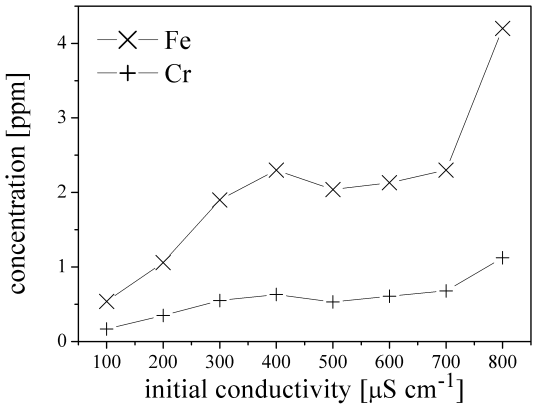

Fig. 6: Concentration of Fe and Cr traces as a function of the initial solution conductivity.

The conductivity of the solution was not constant during the discharge. It significantly increased in time and in each part of the reactor it had a different growth (Fig. 7). The increasing conductivity was caused by the involved metallic traces (Fe and Cr ions).

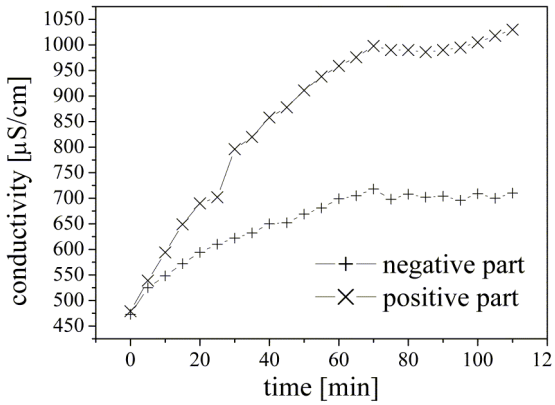

Fig. 7: Time evolution of solution conductivity (5 mM NaCl, 2,8 kV, 500 $\mu S \cdot cm^{-1}$).

The hydrogen peroxide dependence on the initial conductivity was more complicated. The experiments were done in both salts (NaCl and Na_2HPO_4) with initial conductivity in the range 100 – 900 $\mu S \cdot cm^{-1}$. In the case of Na_2HPO_4, the production of H_2O_2 increased with increasing initial conductivity (Fig. 8). In the case of NaCl, the dependence was also increasing but at the initial conductivity of 400 $\mu S \cdot cm^{-1}$ it achieved its maximum and then the dependence became descended. This is shown in Fig. 9. The small amount of hydrogen peroxide produced by the discharge in the solution with very small conductivity (until 300 $\mu S \cdot cm^{-1}$) was caused by a very unstable discharge under these conditions. The discharge at the initial conductivity of 100 $\mu S \cdot cm^{-1}$ burnt very irregularly so the generation of hydroxyl radicals and consequently hydrogen peroxide was discontinuous.

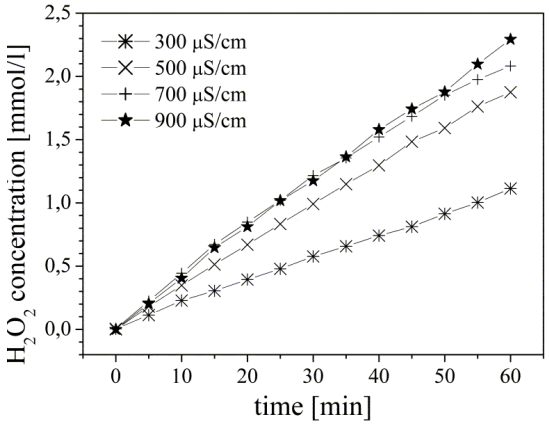

Fig. 8: Hydrogen peroxide generation in time as a function of the initial conductivity (Na_2HPO_4, 2,1 kV).

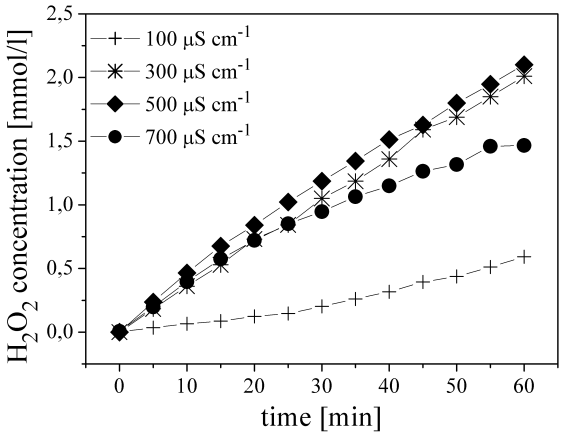

Fig. 9: Hydrogen peroxide generation in time as a function of the initial conductivity (NaCl, 2,8 kV).

The production of H_2O_2 was influenced by the used electrolyte. But this influence also depended on the initial conductivity. In the case of lower initial conductivity (about 300 µS·cm^{-1}), the hydrogen peroxide generation was higher in the NaCl solution. At about 500 µS·cm^{-1}, the H_2O_2 production was similar in both salts and at the higher initial conductivity (700 µS·cm^{-1}), higher production overweighed in Na_2HPO_4 solution. The reduced amount of H_2O_2 at the higher initial conductivity is caused by the chloride anions, which destructed hydrogen peroxide in several reactions.

The hydrogen peroxide generation also depended on the applied high voltage. The lowest limit at the configuration used was about 1,4 kV and the generation increased with the increase in the applied voltage as shown in Fig. 10.

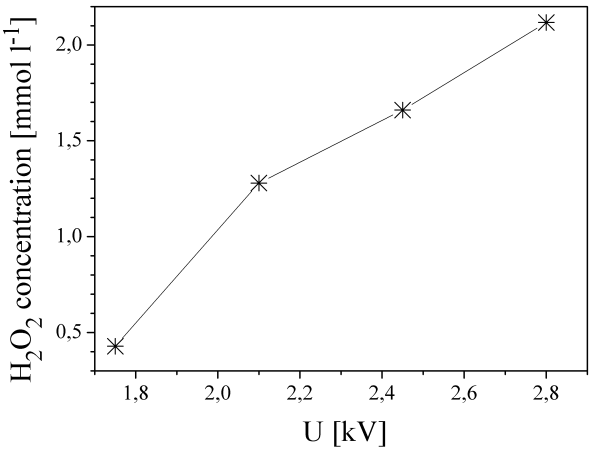

Fig. 10: Hydrogen peroxide concentration after 60 minutes of the discharge treatment as a function of the applied voltage (3 mM NaCl, 300 µS·cm^{-1}).

4. Conclusion

The results of optical and chemical observations of the DC diaphragm discharge in water solutions are presented in this contribution. The dependence of the emission spectra of hydroxyl radicals on the initial discharge conditions for two salts was studied. The relative OH integral intensity in the range 306.5 – 318 nm was calculated. The light intensity of OH radicals increases with increasing voltage in both types

of used salts. But the light intensity decreased with increasing initial conductivity. This phenomenon was more remarkable in NaCl solution. The relative OH integral intensity rapidly decreases in time for both types of the solution. In the case of NaCl, the decrease was the lowest at lower initial conductivity.

The hydrogen peroxide generation as a function of the initial discharge conditions (applied voltage – its magnitude and polarity, initial solution conductivity and used salt) was studied. The rate constants of the H_2O_2 production were calculated. The production of H_2O_2 is higher in the negative part of the discharge reactor in the both salts (NaCl and Na_2HPO_4). It increases with the increasing applied high voltage. The dependencies of H_2O_2 concentration and OH intensity on the applied voltage had an analogous development. In the case of Na_2HPO_4, the hydrogen peroxide concentration grows with increasing initial conductivity. In the case of NaCl, this dependence is growing at the lower initial conductivity, it reaches a maximum at about 400 $\mu S \cdot cm^{-1}$ and the next generation of H_2O_2 is decreasing with increasing conductivity. The production of hydrogen peroxide is higher in NaCl solution than in Na_2HPO_4 at lower initial conductivity. At the initial conductivity above 500 $\mu S \cdot cm^{-1}$, the situation is opposite.

The estimation of H_2O_2 concentration was influenced by metallic traces (Fe, Cr) involved by the electrolysis during the discharge. The amount of involved metals was proportional to the initial conductivity. This phenomenon is one of the reasons of increasing conductivity of the solution during the discharge.

5. Acknowledgements

This work was supported by the Czech Ministery of Education Research layout CD MSM 263100019 and by the Grant of the Czech Ministery of Education number 2003/0894.

References

[1] J. S. Clements, M. Sato, R. H. Davis – IEEE Trans. Ind. Appl. IA **23**, 224 (1987).

[2] A. A. Joshi, B. R. Locke, P. Arce, W. C. Finney – J. Hazard. Mater. **41**, 6 (1995).

[3] P. Sunka, V. Babicky, M. Clupek, P. Lukes, M. Simek, J. Schmidt, M. Cernak – Plasma Source Sci. Tech. **8**, 258 (1999).

[4] I. P. Kuzhekin – Proc. 9th Int. Symp. High Voltage Eng., Graz, 8073-1 (1995).

[5] F. Krcma, Z. Stara – Chemical Papers **96**, 82 (2002).

[6] P. Lukes – Water Treatment by Pulsed Streamer Corona Discharge, Ph.D. Thesis, Prague (2001).

[7] Z. Stara – The Diaphragm Discharge in Liquids, Thesis, Brno (2002).

Flow Field and Heat Transfer Characteristics of a Laminar Plasma Jet

Xian Meng, Wenxia Pan, Chengkang Wu

Institute of Mechanics, Chinese Academy of Sciences, Beijing, 100080, China `

Abstract

Spectrometric method was applied to measure the temperature distribution of a DC argon laminar plasma jet. A stick-shaped transient probe of 1 mm outer diameter was designed to measure the heat flux distribution. A water-cooled pitot tube was used to measure the impact pressure and the flow velocity was calculated according to the measured pressure and temperature. The dependence of heat transfer coefficient from jet flow to the transient probe on flow temperature and velocity was derived.

1. Introduction

Non-transferred DC laminar plasma jet has the stable flow, low entrainment of the surrounding atmosphere, and thus low temperature and velocity gradient along its axis. Pure argon laminar jet can be 550 mm in length with little change in diameter under suitable generating conditions [1], and the jet length changes appreciably with good repeatability with the change of arc current and gas flow rate. These characters could be favorable for systematic experimental characterization of the jet flow field, compared with turbulent jets of serious fluctuating parameters and complex boundary condition at the interface with the surroundings [2-4]. It could also be advantageous for the comparison study between experiment and numerical simulation work.

Experimental characterization and simple simulation of the free laminar plasma jet and a jet impinging on a copper plate were carried out recently [1, 5, 6]. Due to the lack of experimental data of the laminar jet temperature and velocity, the simulation and analytic work of the laminar plasma jet were usually based on assumed values. Therefore, it is necessary to characterize the flow field of laminar plasma jet systematically for its better understanding and application.

In this study, the jet temperature, maximum heat flux to probe surface and impact pressure were measured by using spectrometric method, small transient heat flux probe of the stick type and a pitot-tube separately, with the argon laminar plasma jet issuing into air atmosphere. The relationship between heat transfer coefficient and gas flow velocity or gas temperature were derived through the measurement data.

2. Experiment

The laminar plasma generator is the same as used in former work [1, 5]. Plasma jet was generated with pure argon as the working gas at a feeding rate of 1.57×10^{-4}kg/s to 2.47×10^{-4}kg/s at arc currents of 110-180 A. The plasma jet was injected into the atmosphere after leaving the torch nozzle.

Relative-intensity method [7] was used to measure the jet temperature. The spectrometric system consisted of a lens with focal length of 120mm, an optical fiber of 0.4mm in diameter, and an Optical Spectra Analyzer (OSA) through which the light signals of spectral lines could be detected. The image of the plasma jet was formed on one side of the optical fiber through the lens, and was transferred to the slit of the OSA by the fiber. The light intensities along the radial direction of the jet were detected point by point at a step of 0.5mm. The spectral lines of argon atom, 750.4nm and 751.5nm were used, and the jet temperature could be obtained according to the LTE assumption and the Abel inversion [8].

Impact pressures along the jet axis were measured by using a water-cooled pitot tube with the spherical tip facing the jet to reduce disturbance to the flow. The probe is 13mm in diameter with a Φ0.8mm hole in its center, the small hole was connected to an U-tube manometer. The measured pressure is the impact gage pressure. Then, the flow velocity at the measuring point can be calculated by using the Bernoulli's equation at the stagnation point $P=1/2\rho v^2$, where P, ρ, v are the impact pressure, gas density and jet flow velocity respectively, while ρ is a function of gas temperature.

A stick-type, 1mm-diameter transient heat-flux probe was used to measure the heat flux to the probe surface. Fig. 1 shows the schematic diagram of the sweeping probe method. A 0.8mm -diameter and 0.8mm-length copper slug was fixed at one end inside a 1mm-diameter glass tube, ensuring just the front surface exposed as the heat flux response surface. The rear surface of the copper slug was attached with a pair of

Nickel/Chromium -Nickel/Aluminium thermocouple. Two thermocouple wires of 0.1 mm diameter are insulated from each other with Teflon and then connected to a data collecting system. The heat flux probe was fixed in the center of a cone-typed water-cooled support, and the 1mm-diameter probe stretched 20mm out of the support to ensure minimum disturbance to the laminar jet flow. The temperature-response curve could be obtained by sweeping the probe across the laminar jet perpendicularly at a speed from 130mm/s to 260mm/s to prevent the probe from melting. The heat flux distribution can be obtained by differentiating the temperature with respect to time according to the response curve [6, 9]. The maximum heat flux corresponds to the heat flux at the jet center.

The heat transfer coefficient h_i from the jet flow to probe surface can be obtained by using the heat transfer equation $q = h_i(i_e - i_w)$ [10], where q is the heat flux to the probe surface, i_e is the stagnation enthalpy of the gas outside the boundary layer, and i_w is the enthalpy at the wall surface. Besides the temperature change, effect of jet flow velocity on heat transfer was also considered.

The mean temperature of the jet flow at the torch exit was estimated by measuring the jet power. The setup is the same as the former work [1], which ensures a complete cooling of the jet flow to the room temperature with little disturbance of the jet condition. The enthalpy change of the cooling water caused by the temperature rising is considered to be equal to the jet power, and then the specific enthalpy of the argon jet is the ratio of the jet power to the gas flow rate. Thus, the mean temperature of the jet flow at the torch exit can be obtained by referring to [11].

3. Results and discussion

Fig. 2 shows that the maximum heat flux of the laminar plasma jet changes as a function of the sweeping speed from 130mm/s to 260mm/s at different axial distance of 0.5mm to 80mm from torch nozzle to probe surface. It is evident that the maximum heat flux increases as the sweeping speed decreases. This phenomenon is consistent with the results in Ref. [12, 13], which could infer that the frozen boundary layer existed during the heat transfer process, because the heat from the jet flow had more time to reach the probe surface as the sweeping speed decreases. It is also found that the effect of sweeping speed on the detected maximum heat flux appreciably increased as the probe was close to the torch nozzle. This means that increasing the probe sweeping speed will increase the measured heat flux error from its real value, especially when flow temperature and velocity increased. However, in the following experiments, the sweeping speed was chosen as 260mm/s to prevent the probe from melting, because the main measurement region is close to the torch nozzle, though it is better to choose low sweeping speed for accurate measurement.

Fig. 3 shows the axial distributions of maximum heat flux and flow temperature of the laminar plasma jet at the arc current of 170A and gas flow rate of 1.57×10^{-4}kg/s, measured by the heat flux probe and the spectra analyzer separately. The temperature along the jet axis changes smoothly with the temperature gradient of about 55K/mm within the distance of 10mm from the torch nozzle, and about 50K/mm from the distance about 10mm to 80mm. This measured value of the axial temperature gradient has the similar trend as the numerical simulation work [5], and it is much lower than that of a turbulent plasma jet flow [14] which is generally over 200K/mm at the position near the torch nozzle. Though the maximum heat flux changes smoothly along the distance from 20mm to 80mm, it varies significantly within the distance of 20mm, especially within the distance of 5mm from the torch nozzle. This significant variation of the maximum heat flux is difficult to be explained clearly now, because of the possible complex affecting factors, such as the surrounding atmosphere mixing with the jet flow, the catalytic effect on the probe, etc. In order to get exact results, much careful work should be carried out to eliminate the effect of disturbance factors.

Fig. 4 shows the dependence of jet flow temperature on the gas flow rate. The arc current was fixed at 170A and the gas flow rates changed from 1.57×10^{-4}kg/s to 2.47×10^{-4}kg/s. The center temperature is the jet axial temperature 0.5mm away from the nozzle exit; and the mean temperatures at the nozzle exit were obtained by measuring the jet power. The results show that the jet center temperature and mean temperature at the nozzle exit are almost constant with the change of gas flow rate. That is, the change of gas flow rate could change the power (total enthalpy) of the plasma jet, but the gas temperature at the torch nozzle will keep unchanged, when the arc current is kept at a constant within the range of this experiment.

Fig. 5 shows the variations of the maximum heat flux and gas temperature on arc current at gas flow rate of 1.57×10^{-4}kg/s. The measuring point for the probe and spectra analyzer is all 0.5mm from the torch nozzle. Temperatures and maximum heat fluxes increase almost linearly with the increasing arc current. The points

at the bottom of the graph stand for the mean temperatures at the exit of the torch nozzle estimated by measuring the jet power. It has the same trend as the measured center temperature by using spectrometric method.

The distributions of impact pressure and calculated jet velocity along the jet axis are shown in Fig. 6. The working conditions are the same as for Fig. 3. Since the diameter of the pressure probe is somewhat large, it could influence the gas flow field when put very close to the torch nozzle. Thus, the impact pressures within the distance of 5mm from the torch nozzle were not used for the calculating of the corresponding flow velocity. In this range, the pressure value was corrected as the dash line by extrapolating the measured data at 10mm and 5 mm from the torch nozzle. As a result, the velocity distribution along the jet flow axis is obtained through the corrected pressure and the temperature data by using Bernoulli's Equation. The flow velocity along the jet axis decreases, as the distance from torch nozzle increases. The axial variation trend of the velocity is similar to the simulation result [15], with large gradient at close distances. The maximum velocity of the jet flow at the torch nozzle exit is about 840m/s under the generating condition with the arc current of 170A and gas flow rate of 1.57×10^{-4}kg/s. The estimated velocities of the laminar plasma jet flow are almost the same order as a turbulent jet, which is much higher than the generally considered values for the laminar plasma jet. Reynolds number of the jet flow is calculated to be about 340, which is reasonable for laminar jet flow [16].

The results in figures 3 and 6 also indicate that the laminar plasma jet keeps high temperature and kinetic energy along the axis for a large distance. These characteristics of the laminar plasma jet could result in high reliability and controllability for materials surface processing [5].

According to the experiment results shown in Fig. 4, the jet center temperature at the nozzle exit is almost independent of the gas flow rate when arc current is a constant, but the corresponding velocity increased as the increasing gas flow rate. On the other hand, i_w could be neglected in the heat transfer equation, for its small value compared to the gas enthalpy outside the boundary layer. Then the relationship between the heat transfer coefficient and the flow velocity is obtained as show in Fig.7, at a constant arc current of 170 A and gas flow rates from 1.57×10^{-4}kg/s to 2.45×10^{-4}kg/s, because the exit center temperature of the jet flow is about a constant of 16500K, and the change of heat flux can be considered only caused by the velocity change, under this condition. The heat transfer coefficient increases simply as the increasing of flow velocity when the flow temperature kept constant.

Fig. 7 also shows the relationship between the heat transfer coefficient and gas temperature. The relationship was obtained by measuring the center temperature and the heat flux at the same point of the laminar plasma jet at constant gas flow rate of 1.57×10^{-4}kg/s and changed arc current from 110A to 180A. The effect of gas velocity on heat transfer coefficient was also implied in this curve, the flow velocity generally increases too as the increase of flow temperature at a certain gas flow rate. The variation trend of heat transfer coefficient here is a result of the simutaneous changing of the flow velocity and temperature.

4. Conclusion

The sweeping speed can affect appreciably the measuring results of maximum heat flux from laminar plasma flow to the probe surface, which could infer that frozen or non-equilibrium boundary layer existed during the heat transfer process; The mean temperature and jet center temperature at the torch exit are independent of the gas flow rate, while the temperature increase as the increase of the arc current, within the working range; And the heat transfer coefficient was derived through the experimental data of gas temperature, heat flux and flow velocity, both the gas temperature and jet flow velocity could affect the heat transfer coefficient.

Acknowledgement:

This work was supported by the National Natural Science Foundation of China under the grant Nos. 59836220 and 50276065. The authors would like to thank Professor X. Chen of Tsinghua University for his helpful discussions.

References

[1] W. X. Pan, W. H. Zhang, W. Ma, C. K. Wu - Plasma Chem. Plasma Process. **22 (2)**, 271 (2002).
[2] R. Spores, E. Pfender - Surf. Coating Technol. **37**, 251 (1989).
[3] E. Pfender, J. Fincke, R. Spores - Plasma Chem. Plasma Process. **11 (4)**, 529 (1991).
[4] M. E. Vinayo, F. Kassabji, J. Guyonnet, P. Fauchais - J. Vac. Sci. Technol. **6**, 2483 (1985).

[5] W. X. Pan, W. H. Zhang, W. H. Zhang, C. K. Wu - Plasma Chem. Plasma Process. **21 (1)**, 23 (2001).
[6] X. Meng, W. X. Pan, W. H. Zhang, C. K. Wu – Plasma Sci. Tech. **3**, 953 (2001).
[7] S. Semenov, B. Cetegen – J. Thermal Spray Technol. **10 (2)**, 326 (2001).
[8] W. L. Barr - J. Opt. Soc. Am. **52**, 885 (1962).
[9] X. Chen, P. Han, H. P. Li – Proc. ISPC **14 (1)**, 61 (1999).
[10] E. R. G. Eckert, R. M. Drake, Jr. –Heat and Mass Transfer, 2nd Ed. McGrawhill, New York, (1959).
[11] M. I. Boulos, P. Fauchais, E. Pfender – Thermal Plasmas **1**, Plenum Press, New York (1994).
[12] E. Pfender – Pure Appl. Chem. **48**, 199 (197).
[13] T. W. Petrie, E. Pfender – Warme- u. Stoffubertragung, **5**, 85 (1972).
[14] E. Pfender, R. Spores, W. L. T. Chen - Int. J. Mater. Product Technol. **10 (3-6)**, 548 (1995).
[15] P. Han, X. Chen – J. Engineering Thermophysics. **19(5)**, 590 (1998). (in Chinese)
[16] V. I. Kuamin, O. P. Solonenko, M. F. Zhukov – Proceed. 8th National Thermal Spray Conference, 83 (1999).

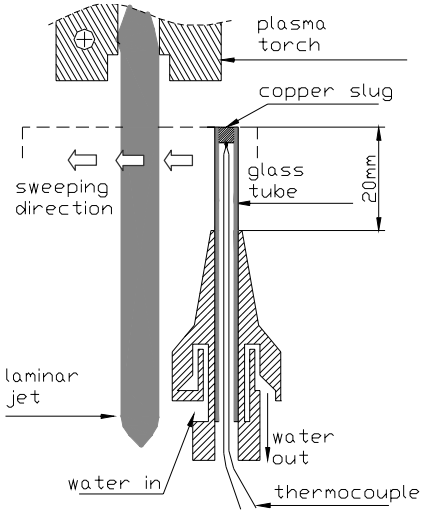

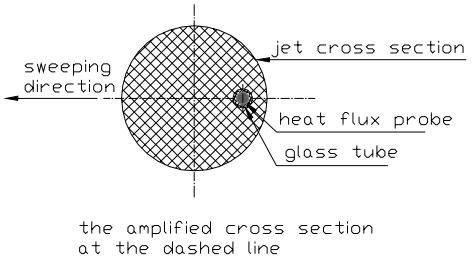

Fig. 1. schematic diagram of the sweeping probe method.

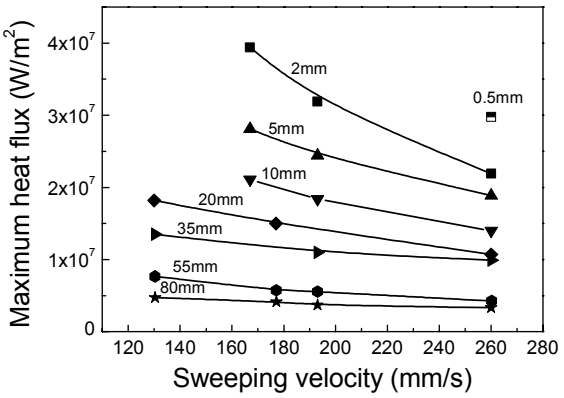

Fig. 2. effect of sweeping velocity on maximum heat flux at the arc current of 170A, gas flow rate of 1.57×10^{-4}kg/s and the numbers from o.5 to 80 represent the distance between torch nozzle and probe surface.

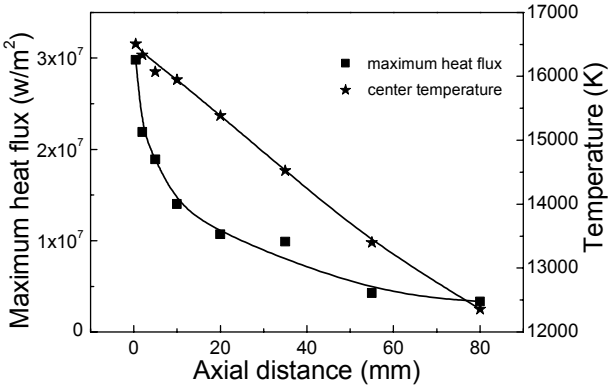

Fig. 3. the distributions of maximum heat flux and jet temperature along the jet axis. arc current: 170A, gas flow rate: 1.57×10^{-4}kg/s.

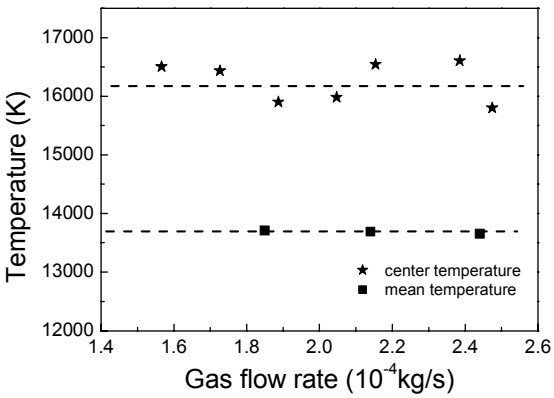

Fig. 4. dependence on gas flow rate of jet temperature at arc current of 170A.

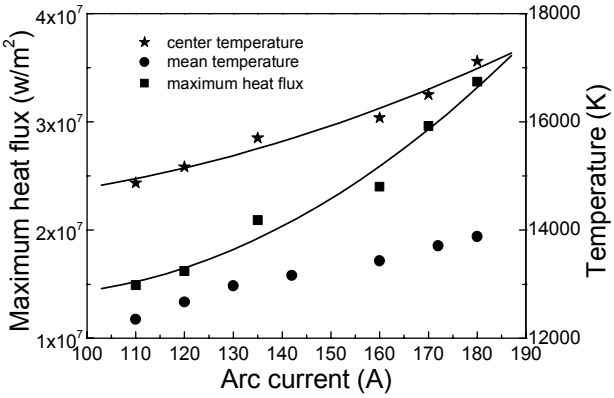

Fig. 5. dependence on arc current of the maximum heat flux and jet temperature at the distance of 0.5mm from the torch nozzle.

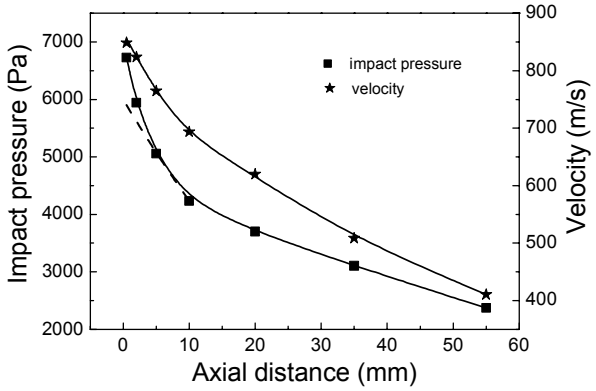

Fig. 6. the distributions of impact pressure and jet velocity along the jet axis at the arc current of 170A and gas flow rate of 1.57 $\times 10^{-4}$kg/s.

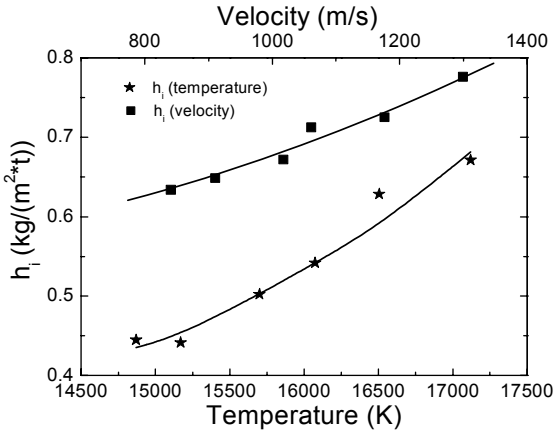

Fig. 7. dependence of heat transfer coefficient on jet velocity and temperature at the distance of 0.5mm from the torch nozzle

Hydrogen atom formation in the magnetically enhanced RF discharge in Ar-CH_4 mixtures

S.V. Avtaeva, D.K. Otorbaev

Kyrgyz-Russian Slavic University, Bishkek, Kyrgyzstan

Abstract
Effect of argon on production of atomic hydrogen in the magnetically enhanced RF discharge in argon-methane mixtures is studied by optical actinometry method. It is shown that in the experimental condition formation of hydrogen atoms is realised by Penning dissociation of methane molecules by collisions with metastable argon atoms: $Ar + e \to Ar^* + e;\ \ Ar^* + CH_4 \to CH_3 + H + Ar$.

1. Introduction

At present time low-temperature plasma in mixtures of hydrocarbon containing gases with noble gases and hydrogen is an object of greeting interest. This is cased with applications of the plasma for plasma deposition of amorphous hydrogenated carbon films. In the plasma deposition methods, the structure and properties of deposited carbon films can be varied widely by changing deposition parameters. It has been found that the atomic hydrogen radicals play a key role in the formation of properties of the layers in all kinds of carbon deposition schemes. Their presence is very essential for the stabilization of the carbon bonds and for the selective etching of the dangling bonds during the deposition processes [1, 2]. This paper is devoted to study effect of argon on production of atomic hydrogen in the magnetically enhanced RF discharge in argon-methane mixtures.

2. Experiment

A magnetically enhanced asymmetric capacitive coupling RF reactor was used in the experiments [3]. The reactor chamber consists of the stainless steel cylindrical vessel with a diameter of 30 cm and a height of *25* cm and has the ports to allow optical and contact diagnostics. The chamber walls were grounded. RF power (frequency is 13.56 MHz) from the RF generator has been applied to the stainless steel plane square electrode (*10×10 cm)* arranged in a middle of the chamber. The power supply was connected to the electrode through the special matching device (L-type matching circuit). Two magnetic coils induced in the chamber a homogeneous magnetic field in respect to the vertical symmetry axis.
The basic vacuum was produced and maintained by two pumps connected to the discharge chamber via a magnetic valve. The system can be evacuated to a base pressure of 10^{-3} *Pa*. Reactive gas was injected into the plasma region through a hole at the bottom of the chamber after passing a mass flow controller. The mixtures of methane and argon have been used as working gases. The partial methane pressure in the discharge chamber was maintained equal to *0.1 Pa*. The volume content of methane in the gas mixtures was varied from *1* to *10%*, while a gas pressure was adjusted in the range of *1÷10 Pa.* A magnetic field can be adjusted in the range of 25 - *200 G* and a discharge power was *80 W*.
The gas temperature measurements in the plasma have been carried out by a thermocouple, which could be moved along the radial direction of the chamber, perpendicularly to the powered electrode. For the determination of electron density and the electron temperature a double Langmuir probe has been employed. The probe was made from tantalum wire with the diameter of *0.1 mm*, and has free tip length of *8 mm*. The probe was immersed in the plasma region at the distance of *1 cm* from powered electrode. The optical system, based on the high resolution monochromator and the photomultiplier has been used to measure the spectral line intensities. An Intel 8088 microprocessor has been used to digital recording of the measured data.

3. Results and discussion

In the low pressure glow discharge plasma in the gas mixtures of hydrocarbons with the noble gases it is possible, in principle, to measure the absolute density of atomic hydrogen by optical actinometry method. For measuring atomic hydrogen density by this method it has been proposed to use a spectral line of hydrogen HI 656.2 nm (H_α of Balmer's series) and a spectral line of argon ArI 696.5 nm [4, 5]. However, in

the conditions of glow discharges plasma in the gas mixture of hydrocarbon-argon not only the direct electron excitation from the ground state, but also the process of stepwise excitation of the radiative states of argon Ar($4p^3P_1$) and hydrogen H(3S,3P,3D) through the metastable states Ar($^3P_{0,2}$) and H($2^2S_{1/2}$) respectively, becomes important. Therefore it is essential to make a detailed analysis of the excitation kinetics of the radiative states Ar($4p^3P_1$) and H(3S,3P,3D) for the particular experimental situation. The following excitation and de-excitation reactions for radiative A^* and metastable A_m atomic states should in principle be discussed [3]:

$$A + e \xrightarrow{k_1} A^* + e, \quad (1) \qquad A + e \xrightarrow{k_2} A_m + e, \quad (2)$$

$$A_m + e \xrightarrow{k_3} A^* + e, \quad (3) \qquad A_m + e \xrightarrow{k_4} A + e, \quad (4)$$

$$A_m + M \xrightarrow{k_5} A + M, \quad (5) \qquad A^* + M \xrightarrow{k_6} A_k + M, \quad (6)$$

$$A^* \xrightarrow{k_7} A_k + h\nu, \quad (7) \qquad A_m + wall \xrightarrow{k_8} A \quad (8)$$

Where e means the electrons and M the heavy particles (atoms and molecules) (Ar, CH_4, H_2, etc..) in the ground and in the excited states, A_k is the atoms in the excited state k.

Combining (1) -(8) the stationary density of the ground state A can be derived:

$$[A] = [A^*] \cdot \frac{k_7 + [M]k_6}{[e]k_1 + [e]^2 k_2 k_3/([e](k_3+k_4) + [M]k_5 + k_8)} \qquad (9)$$

Finally the absolute population density of atomic hydrogen in the ground electronic state $[H]$ can be derived from known absolute density of argon atoms $[Ar]$, relative population densities of hydrogen $[H^*]$ and argon $[Ar^*]$ in the excited states, and the rate coefficients of elementary collisional and radiative processes:

$$\frac{[H]}{[Ar]} = \frac{[H^*]}{[Ar^*]} \cdot \frac{\{k_1+[e]k_2k_3/([e](k_3+k_4)+[M]k_5+k_8)\}_{Ar}\{k_7+[M]k_6\}_H}{\{k_1+[e]k_2k_3/([e](k_3+k_4)+[M]k_5+k_8)\}_H\{k_7+[M]k_6\}_{Ar}} \qquad (10)$$

In the equation (10) for density ratio $[H]/[Ar]$ it is assumed that the excitation of the radiative states of Ar($4p^3P_1$) and H(3S,3P,3D), were realized directly from the corresponding ground states of Ar and H, as well as stepwise via metastable levels of Ar($^3P_{0,2}$) and H($2^2S_{1/2}$), respectively. The de-excitation of Ar($4p^3P_1$) and H(3S,3P,3D) levels were assumed to be a result of the radiative decay and their depletion by collisions with the heavy particles (atoms and molecules in the ground states).

Quantitative analysis of importance of the various kinetic processes of formation of stationary population densities of the radiative Ar($4p^3P_1$) and H(3S,3P,3D) states in the case of magnetically-enhanced RF discharge under our experimental conditions allow us to get the following conclusions :

1. Let the excited state of Ar($4p^3P_1$) are depleted by the Ar atoms in the ground state. Then under conditions of our experiments the quenching time τ for the excited state of Ar($4p^3P_1$) is ~ 10^{-4} - 10^{-5} s that is much larger in comparison with the radiative decay time ($\tau_{rad} \sim 1.5 \cdot 10^{-7}$ s) [6]. Therefore, it is possible to exclude the equation (6) from our consideration. There is a valid reason to apply the same approach to $3^2S_{1/2}$, $3^2P_{3/2}$, $3^2P_{1/2}$, $3^2D_{5/2}$, $3^2D_{3/2}$ states of H, which are responsible for the emission of the Balmer's H_α line.

2. Quenching of the metastable states of argon Ar($^3P_{0,2}$) and atomic hydrogen H($2^2S_{1/2}$) are taken place predominantly under collisions with the methane molecules CH_4. Flux of the direct excitation remarkable exceeds flux of the stepwise excitation of the radiative states of Ar($4p^3P_1$) and H(3S,3P,3D), if the metastable states of Ar($^3P_{0,2}$) and H($2^2S_{1/2}$) are effectively depleted by collisions with the methane molecules. Under condition of small methane concentration in the initial gas mixture of CH_4-Ar the picture presented above is not valid any more since the stepwise excitation mechanism via the corresponding metastable states will play more significant role. Especially it should be taken into account by the examination of the population mechanism of Ar($4p^3P_1$) state.

In particular experimental conditions, in according with the evaluations, excitation of the radiative state of $Ar(4p^3P_1)$ was realized stepwise via the metastable level of $Ar(4s^3P_{0,2})$ and excitation of the radiative state of H(3S, 3P, 3D) was realized directly from the ground state of hydrogen atoms. The de-excitation of both radiative states is the result of radiative decay. In this case relationship of densities of hydrogen atoms [H] and argon atoms [Ar] is related to relationship of of H_α(λ=656.2 nm) and Ar (λ=696.5 nm) spectral line intensities with the expression

$$\frac{[H]}{[Ar]} = \frac{I_H (A_{ki}/\lambda_{ki})_H}{I_{Ar} (A_{ki}/\lambda_{ki})_{Ar}} \left(\frac{1}{k_{1H}}\right) \times \left(\frac{k_2 k_3 [e]}{(k_3 + k_4)[e] + k_5[CH_4] + k_8}\right)_{Ar} \frac{\tau_{Ar}}{\tau_H} \quad , (11)$$

where k_{1H} is excitation rate constant of H(3S, 3P, 3D) level, $k_2k_3[e]$ is proportional to excitation velocity of $Ar(4p^3P_1)$ level, k_4, k_5, k_8 are collisional quenching coefficients for the metastable state $Ar(4s^3P_{0,2})$, A_{ki} is the absolute transition probability at the wave length λ_{ki}, τ is the lifetime of the radiative state.
The more simple expression may be taken for the relationship of the rate constants k_{2Ar} and k_{1H}:

$$\frac{k_{2Ar}}{k_{1H}} = \frac{\sigma_{2Ar}(\varepsilon) f(\varepsilon)_{|\varepsilon=\varepsilon t+1}}{\sigma_{1H}(\varepsilon) f(\varepsilon)_{|\varepsilon=\varepsilon t+1}} \quad , \qquad (12)$$

where $\sigma(\varepsilon)$ is the electron impact cross-section for the corresponding reactions of excitation, $f(\varepsilon)$ is the electron energy distribution function (EEDF), ε is the energy of free electrons, εt is the threshold energy of the excitation. So evaluation of hydrogen atom density from the relationship of the spectral line intensities calls for knowing electron densities, which were measured independently with the double probe.
The rate constants k_1 and k_2 have been calculated using excitation cross sections of the reactions (1) and (2), respectively. The excitation cross section for the transition H(1S →3S,3P,3D) has been taken from work [7], for the transition H(1S $\rightarrow 2^2S_{1/2}$) from work [8]. In case of argon the excitation cross section σ_1 and σ_2 were taken from work [9].
The transition probabilities and the radiative lifetimes (constants k_7) were taken from [6,10].
Intensities of spectral lines ArI (696.5nm) and H_α(656.2nm) as functions of gas pressure and magnetic field are shown in figure 1 (a, b). Intensities of both spectral lines increase with increasing magnetic field, that is caused by increase in excitation velocity of radiative states due to magnetic confinement of electrons. The decreasing intensities of both spectral lines ArI (696.5nm) and H_α(656.2nm) with increasing gas pressure is probably because of the reduced magnetic confinement with pressure (the Hall parameter for the electrons becomes smaller). The effect of collisional de-excitation of the radiative and metastable states in particular experimental conditions should be small.
The dependencies of electron density on argon pressure measured in RF discharge plasma in pure argon are

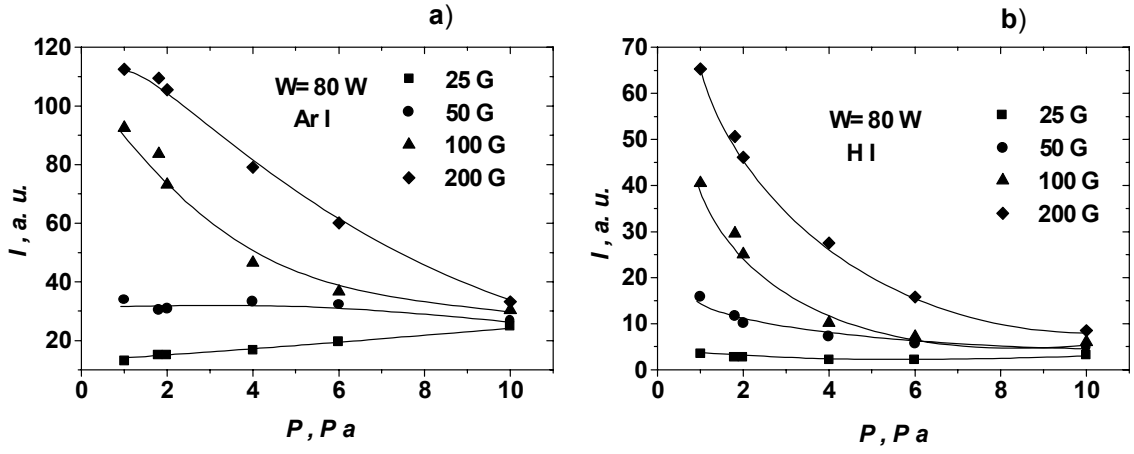

Figure 1. Intensities of emission lines of ArI (696.5nm) –(a) and H_α(656.2nm)-(b) with increasing argon pressure in CH_4/Ar RF discharge.

shown in figure 2(a). In magnetically enhanced discharges magnetic field has a high effect on velocities of charged particles generation and loss processes. Due to magnetic confinement the electron losses on the chamber walls decrease but frequency of electron collision with atoms increases, caused to increase in ionization frequency and, consequently, in electron density. For magnetized electrons Holl's factor decreases with increasing gas pressure, that caused to increase in electron losses on walls, therefore electron density decreases with increasing gas pressure. Electron temperature was in the range of 6÷8 eV in particular experimental conditions.

The dependencies of the charged particle density on argon pressure and magnetic field well correlate with similar dependencies of intensity of argon spectral line ArI (696.5 nm). Addition of small methane content to argon not changes the behavior of electron density dependencies on gas pressure. One can see it in figure 1 (a).

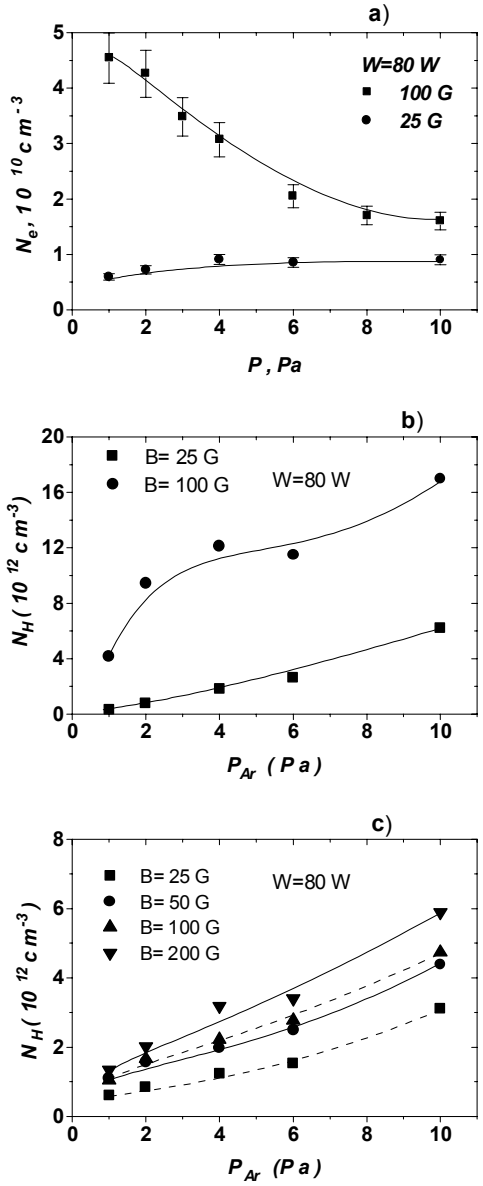

Figure 2. Electron density (a) and absolute density of hydrogen atoms (b, c) as a function of gas pressure; b) the stepwise excitation of the radiative state of $Ar(4p^3P_1)$ via the metastable level of $Ar(4s^3P_{0,2})$; c) the direct excitation of the radiative state of $Ar(4p^3P_1)$ from the ground state.

The atomic hydrogen densities in the RF discharge in argon-methane mixtures as a function of gas pressure, calculated without and with account of stepwise excitation of the radiative state of argon $Ar(4p^3P_1)$ via the metastable level of $Ar(^3P_{0,2})$ are shown in figure 2(b, c). It was assumed EEDF is maxwellian with electron temperature ~6 eV. The account of stepwise excitation of the radiative state of argon $Ar(4p^3P_1)$ via the metastable level of $Ar(^3P_{0,2})$ caused to variation of calculated density of hydrogen atoms approximately from 1 to 5 time.

As it can be seen in figure 2, the atomic hydrogen density increases with increasing argon pressure and magnetic field. At the same time methane density remains constant and electron density decreases (100 G) or increases weekly (25 G) with argon pressure.

Let us to analyze mechanisms of formation of atomic hydrogen in magnetized plasma of the RF discharge in argon-methane mixtures. The formation of the hydrogen atoms in the RF discharge in argon-methane mixtures under separation of electron temperature from gas temperature can proceed by electron impact methane dissociation:

$$CH_4 + e \rightarrow CH_3 + H + e \qquad (13)$$

$$CH_4 + e \rightarrow CH_3^+ + H + 2e \qquad (14)$$

$$CH_4 + e \rightarrow CH + H_2 + H + e \qquad (15)$$

and by following electron impact dissociation of methane radicals. Velocity constants of the processes (3)- (5) depend on form of EEDF and in a case of the maxwellian EEDF this constants are functions of electron temperature. The velocity constant values of reactions (3)-(5) were used from work [11], where capacitive RF discharge (f=2MGz) in methane at pressure ~40 Pa and power 15 W was investigated. There are following values of velocity constants $45 \cdot 10^{-15} m^3 s^{-1}$, $32 \cdot 10^{-15} m^3 s^{-1}$ and $3.7 \cdot 10^{-15} m^3 s^{-1}$ for reactions (3), (4) and (5), accordingly. However, under predominant

formation of hydrogen atoms in reactions (3)- (5) the dependence of hydrogen atom density on gas pressure should to agree with analogic dependence of charged particle density. As it can be seen in figure 1, 2(b), 3 opposite dependencies are observed at magnetic field values >25 G.

The methane thermal decomposition is small at the characteristic gas temperature (more than 1000K) in the magnetically enhanced RF discharge [3]. Methane radicals interaction causes to formation of more heavy hydrocarbons and their radicals and also no promotes to increase in hydrogen atom density.

The dissociative ionization of methane molecules in the process of charge exchange on argon ions [12] causes to formation of hydrogen atoms also. However, the velocity constant of resonance charge exchange ($\sim 1 \cdot 10^{-15} m^3 s^{-1}$ (T=1000K) [12]) is substantially less than the velocity constant of electron impact methane dissociation (3), (4). So phenomenon of charge exchange of methane molecules on argon ions can not compete with processes (3) and (4) as long as approximate equilibrium of electrons and ions density exists.

In review [13] is remarked, that in the glow discharges in argon methane- mixtures at pressure ~10 Pa, when density of metastable argon atoms reaches a value about $10^{11} cm^{-3}$, quench of metastable argon atoms in the Penning dissociation of methane molecules produces basic contribution into methane dissociation

$$Ar^* + CH_4 \rightarrow CH_3 + H + Ar \qquad \left(3 \times 10^{-16}\ м^3 c^{-1}\right). \qquad (16)$$

The metastable argon atoms Ar* are formed by electron impact excitation

$$Ar + e \rightarrow Ar^* + e; \qquad (\sigma_{max} = 4.8 \times 10^{-21}\ м^2) \qquad (17)$$

and its density N_{Ar^*} is proportional to product of $N_{Ar} N_e$. At that formed by Penning dissociation hydrogen atom density is ~ $N_{Ar^*} N_{CH_4} \sim N_{Ar} N_e N_{CH_4}$. While gas pressure increases from 1Pa to 10 Pa argon density N_{Ar} increases into 10 times, at that electron density decreases about in 2.5 times (Fig. 2(c)). In so far as methane pressure was maintained constant, hydrogen atom density must increase in about 4 times with increasing gas pressure from 1 Pa to 10 Pa as long as hydrogen atoms are predominantly formed by Penning dissociation (16). As one can see in figure 2, experimentally observed increase in hydrogen atom density with increasing argon pressure is close to the evaluated value.

4. Conclusion

Formation of hydrogen atoms in the magnetically enhanced RF discharge in argon-methane mixtures (1÷10% CH_4+Ar) in pressure range of 1-10 Pa can not be responsible for electron impact methane dissociation and following methane radicals dissociation also by electron impact. Increase in hydrogen atom density with increasing argon pressure as long as charged particle density decreases (figure 2) is possible when hydrogen atoms are formed in processes of the Penning dissociation of methane molecules by collisions with metastable argon atoms: $Ar + e \rightarrow Ar^* + e;$ $Ar^* + CH_4 \rightarrow CH_3 + H + Ar$.

References

[1] J.W.A.M. Gielen, W.M.M. Kessels , M.C.M. van de Sanden and D.C. Schram - J. Appl. Phys**. 82,** 2643 (1997).

[2] J. C. Angus, P. Koidl and S. Domitz - In Plasma deposited thin films, edited by Mort J. and Jansen F. CRC Press. Boca Raton. Florida. 89 (1986).

[3] S. V. Avtaeva, D. K. Otorbaev and M.Z. Mamytbekov - J. Phys. D: Appl. Phys. **30,** 3000 (1997).

[4] V.E. Galtsev, Yu.I. Ivanov , D.I. Slovetsky, N.M. Rytova and L.S. Polak -High Temp.Chemistry. **17** , 164 (1983).

[5] Yu.I. Ivanov, N.M. Rytova, I.V. Soldatova and V.N. Timakin - In book: Physical and Chemical Processes in Low-Temperature Plasmas. Moscow . 140 (1985).

[6] P.F. Gruzdev - Transition Probabilities and Radiative Lifetimes of Atom and Ion Levels. Moscow: Energoatomizdat. (1990).

[7] J. Callaway - Phys.Rev. **A. 37,** 3692 (1988).

[8] D. Hills, H. Kleinpoppen and H. Koschmieder - Proc. Phys.Soc. **89,** 35 (1966).

[9] A. Chutjan and D.C. Cartwright - Phys.Rev.**A. 23,** 2178 (1981).

[10] Ya.F. Verolainen and A.A. Osherovich - Opt.Spectrosc. **25,** 466 (1968).

[11] L.E. Kline, W.D. Partlow and W.E. Bies - J. Appl. Phys.**65,** 73 (1989).

[12] A. de Graaf - Deposition of CNH materials: plasma and film characterization. Thesis. Eindhoven.: Eindhoven University of Technology. 59 (2000).
[13] Yu.A. Ivanov - In book: Encyclopedia of low-temperature plasma. Edited by V.E. Fortov. Moscow: Nauka. **3,** 330 (2000).

Study to improve the absorbing coating in bolometric loads for high power microwave nuclear fusion applications

N.Spinicchia[1], R.Benocci[2], A.Bruschi[1], V.Muzzini[1], A.Simonetto[1]

[1] *Istituto di Fisica del Plasma ENEA-CNR-EURATOM, via Cozzi 53, 20125 Milano.*
[2] *Università di Milano-Bicocca, Dip.di Fisica, P.zza della Scienza 3, 20126 Milano.*

Introduction

In the framework of thermonuclear fusion research**,** increasing interest is focussed on high power high frequency millimeter-wave generators like gyrotrons. Measurements of gyrotron power and energy allow an accurate energy balance in ECRH (Electron Cyclotron Resonance Heating) to be carried out during plasma heating. The ongoing improvements in generator power and pulse duration ask for uninterrupted development of matched calorimetric loads in terms of design and technological solutions.

The expected increase of the power, until 2 MW, and time, until 10 s (or continuous wave), calls for new technological solutions in manufacturing bolometric loads, particularly in making use of absorbing layer ceramics better resistant to thermal shocks. In this particular case, the use of high thermal shock resistance ceramic coating is requested as well as a good absorption capability at 140 GHz.

The present work is devoted to studying and selecting an absorbing ceramic coating to be deposited on the inner surface of the load. The aim is to characterize the material with respect to absorbing capability at a frequency of 140 GHz and thermal shock and fatigue resistance caused by long-term exposure to high power mm-wave radiation. Bolometric loads are planned to resist to 1-2 MW power continuously.

To this purpose APS (Air Plasma Spray) ceramic deposits have been studied to search for a convenient substitute to the actual Alumina-Titania coating (Al_2O_3-$13TiO_2$) [1].

A number of physical parameters such as thermal conductivity, thermal expansion coefficient (TEC), coating porosity and melting point were also considered to select among the candidate materials.

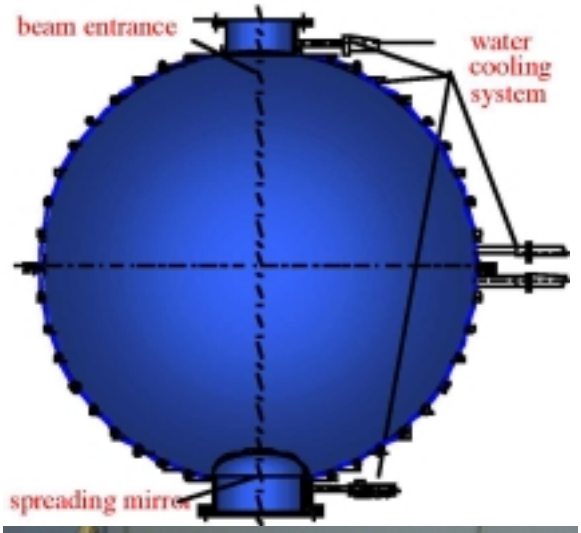

Fig. 1: Matched load. Cross sectional view.

Fig. 2: Matched load. View lower hemisphere.

The bolometric spherical load

The load consists basically of a hollow copper sphere having the inner wall covered with a plasma-sprayed lossy ceramic, a spreading mirror in front of the beam entrance and an external cooling circuit (Fig.1). Its high absorbition capability allows fast calorimetric measurement of the millimeter-wave power also at long pulse duration.The low total reflectivity, measured in the order of 5%, is obtained with multiple reflections on the inner walls, characterized by an average reflectivity of 40%, and with a proper design of the mirror (visible in fig.2), whose surface profile was computed assuming an input beam with gaussian distribution of power and correct phase front curvature radius [2]. Four loads like that described are installed on the ECRH (Electron Cyclotron Resonance Heating) plant of the FTU (Frascati Tokamak Upgrade) in Frascati at present. They are used at a frequency of 140 GHz, power of 0.5 MW and pulse duration of 0.5 s.
The same load is being tested at higher power and longer pulse (0.7 MW and 1 s) on the ASDEX Upgrade ECRH plant in Garching (Germany).

Thermal diffusivity measurements

The thermal diffusivity of the coating was investigated using bolometric loads like the one described by measuring the absorber temperature during and after the pulse**,** both on the inner wall of the sphere, during a real full-power pulse (Fig.3) and on samples of different coatings, placed on the edge of the main beam.
In the first case the measurements were performed with an infrared detector directed into the load from the entrance, imaging a small spot (<1cm diameter) near the mirror. The temperature of the coating in real working conditions was measured; the pulse shape was fitted with the waveform resulting from a thermal model of the coating over the copper substrate, in slab geometry.
The code solves the partial differential equation for heat transport with given deposition profile in the coating layer: the spatial and temporal evolution of the coating temperature depends mostly on its diffusivity. A good agreement with experimental data was obtained for a 0.5 s. shot, provided the substrate diffusivity is taken around 2.73 10^{-7} m^2 s^{-1}, less than half the values found in literature [3,4].This is explained as either due to a greater porosity obtained in the plasma spray process or a weakened contact between the small drops constituting the plasma sprayed ceramics or with the copper layer, due to repeated thermal cycling.

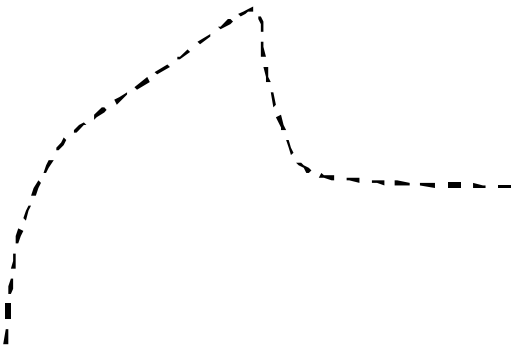

Fig. 3: IR temperatures of the coating during shots.

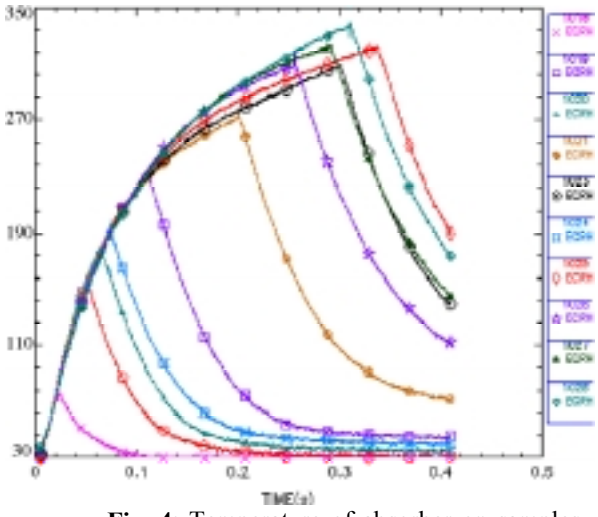

Fig. 4: Temperature of absorber on samples.

The effect of higher power densities on samples placed near the edge of the beam has been investigated. At higher temperatures than observed in the sphere, a new effect appears: above a certain threshold the temperature of the coating increases faster, pulse after pulse, as one can see from fig 4, where pulses of the same power, but different length, were overlapped. The slope of the curves can be clearly seen to vary after 100ms, showing a larger power absorption. Analysis of the temperature recovery time constant also shows that cooling becomes slower when the anomalously high absorption appears, indicating a permanent change in the thermal diffusivity that leads to the runaway process. The thermal conductivity of the samples can be inferred, knowing the incident power density on the measured area of the substrate, even if the presence of steep gradients in the power density (and as a consequence in the local temperature) at the beam edge makes the analysis with the slab code less accurate.

Measurements of electromagnetic properties

The electromagnetic properties of any candidate material (table 1) must be measured to allow the proper choice of thickness for achieving the required absorption level with a sufficiently thin deposit.

The complex dielectric constant of the sample material deposited on a thick metal substrate can be inferred from free-space reflection measurements.

The material reflectivity was estimated by the ratio of power reflected from the metallic side of the target and the one reflected from the deposit side. The target support allows reproducible positioning. The measured on-axis power was used in computing the ratio, which is correct as long as the substrate is flat.

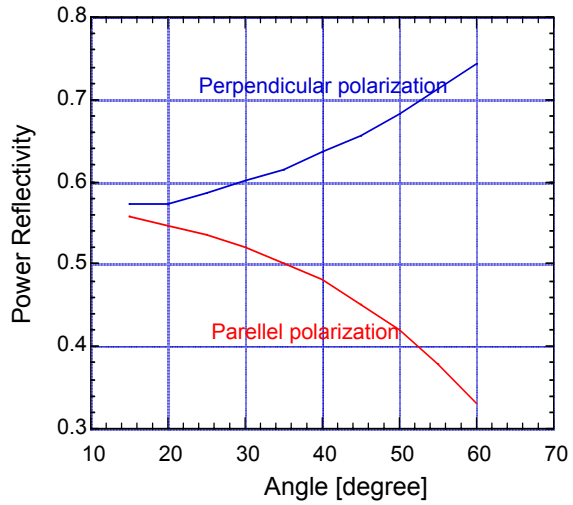

Fig. 5: Reflectivity at fixed frequency

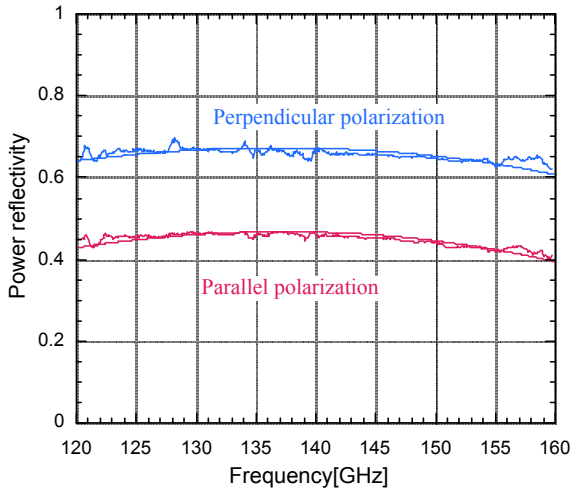

Fig. 6: Reflectivity at fixed angle

The reflectivity was measured at first for all samples at fixed angle of incidence (15°) and fixed frequency (140 Ghz) only for the polarization perpendicular to the plane of incidence. Then, only for suitable samples, varying the angle of incidence between *15* and *60 deg*, for both polarizations, parallel and perpendicular to the plane of incidence, and for the largest range of frequency easily achievable *(120–160 GHz)* with the vector network analyzer we used. Only the amplitude information was used in the analysis, though (fig. 5).

The dielectric constant was found with a least-squares fit between experimental data and the predictions of a model. The model assumes that the incident wave is plane, the metal substrate is a perfect conductor, the sample deposit is an infinite homogeneous slab and the dielectric-metal interface is abrupt and perfectly smooth. The model used for wave propagation inside the dielectric is general for arbitrary lossy, homogeneous, isotropic, linear materials.
When the deposit thickness is precisely known, the reflection measurements allow the estimate of the dielectric constant**.** Fig. 6 shows the comparison between experimental data and model predictions in a sample case, as a function of frequency at fixed angle.

Table 1: Reflectivity measurements for all samples. Polarization perpendicular to the plane of incidence.

Material	**Thickness**	**Power Refl. vert. polar. 15°**	**Thickness**	**Power Refl. vert. polar. 15°**
	µm	**%**	**µm**	**%**
NiCoCrAlY alloy	250	0.94	470	0.97
ZnO	224	0.95	376	0.94
ZrO2-Y2O3	350	0.98	900	0.69
ZrO2-Y2O3 black	360	0.76	750	0.68
ZrO2-8Y2O3	233	0.99	353	0.69
ZrO2-10%Y2O3-18%TiO2	290	0.98	580	0.76
Al2O3-3%TiO2	224	0.67	346	0.87
Al2O3-13%TiO2	350	0.90	950	0.27
Al2O3-13%TiO2	155	0.98	309	0.96
Al2O3-13%TiO2	302	0.88		
Al2O3-40%TiO2	270	0.43	560	0.09
TiO2	260	0.89	570	0.85
Al2O3-30%SiO2	157	0.98	221	0.88
Cr2O3	270	0.79	590	0.49
Cr2O3	179	0.69	325	0.59
Cr2O3	352	0.60		

The choice of coating
The choice of the candidate coating for an optimum use, according to the operative conditions of bolometric loads (1MW-CW power capability), mainly regards some physical features such as: good absorption capability to microwave in the range 120-160 GHz, high thermal conductivity, high melting temperature and thermal shock resistance. Among the considered deposits, alumina based coatings have been rejected, even in presence of low reflectivity to microwaves. As a matter of fact, in depth analysis with various techniques - ESEM (Environmental Scanning Electron Microscopy), micro-analysis with X-ray EDS, Differential Scanning Calorimeter (DSC), X-ray diffraction analysis (XRD) - showed that repeated exposure to high energy flux causes the degradation of the absorber. The main constituents of such coating, γ-Al_2O_3 is subject to a phase transition for temperatures above 950 °C turning into α-Al_2O_3 (Corundum). The associated density change thus may cause the coating deterioration and detachment from the substrate [5]. Other investigated deposits such as: NiCoCrAlY alloy, ZnO, ZrO_2-Y_2O_3, ZrO_2-10Y_2O_3-18TiO_2, TiO_2 have not been considered because of the high reflectivity (>90%) at low power measurements at 140 GHz (table 1).

Two ceramic coatings (Cr_2O_3 e la ZrO_2-$8Y_2O_3$) revealed good structural and electromagnetic characteristics to be elected as valid substitute of Al_2O_3-$13TiO_2$. Table 2 shows the relatively high thermal diffusivity and melting temperature of Cr_2O_3 as well as the high melting point for ZrO_2-$8Y_2O_3$. This latter is known to have its chief application as Thermal Barrier Coating (TBC) in gas turbines for its good TEC (Thermal Expansion Coefficient) and low thermal conductivity. For this reason thick deposits of about 1.5 mm against state of the art 0.5 mm have been recently procured with a porosity up to 20 % [6].
The present application requires the thermal conductivity to be as high as possible in order to rapidly transfer heat to the cooling system. As a reference the actual ZrO_2-$8Y_2O_3$ specimens have been obtained using standard spraying parameters as those employed for TBC applications. Moreover the resistance at thermal shock is better of Cr_2O_3 because his TEC is near that of copper.
The coatings we examined for this preliminary survey tests in order to identify suitable ceramic materials, have been obtained with APS technique using a Sultzer Metco F4 plasma gun.

Table 2: Comparison between physical features of some coating with respect to the copper. (The Science and Engineering of Thermal Spray Coatings – L. Pawlowski) . The last column contains information about the powders really employed (*).

	Thermal	**Thermal**	**Adhesion**	**Thermal exp.**	**Melting**	**Porosity**	**Particle**
	diffusivity	**conduct.**		**coeff. (TEC)**	**Points**		**size (*)**
	(m^2/s)	(W/m*°C)	(Mpa)	(1/°K)	°C	%	μm
	x10 $^{-6}$			x10 $^{-6}$			
Al2O3-13TiO2	1 (300 °K)	2	30	8.0	2050	4÷9	-53+15
Cr2O3	1.3 (900 °K)		20	7.5	2330	2÷5	-45+22
ZrO2-8Y2O3	0.2	0.6		10.9	2400	10÷14	-90 +15
Bond Coat (NiAl)	4 (900 °K)	10		14.9		<1	-106 +45
Copper		390		17.0	1083		

Conclusions
Two coating materials have been selected among a number of ceramic and non-ceramic deposits**.** They have absorption capabilities to microwave radiation in the range of 120-160 GHz as good as those of Al_2O_3-$13TiO_2$, but with better characteristics in terms of TEC (ZrO_2-$8Y_2O_3$ as discussed above), melting temperature and thermal diffusivity (Cr_2O_3).
The coating deposits obtained using APS technique are prone to further improvements in terms of thermal conductivity using VPS (Vacuum Plasma Spray). This technique should reduce open porosities thus providing better adhesion and density which are the key issues to rise the maximum thermal flux to the deposit for fixed surface temperature.
Another perspective is to employ a bond coat between the top coat and the copper support, with an intermediate TEC (see table 2 for NiAl), thus allowing thermal shock resistance to be further improved.

References

[1] L.Argenti et al., A Proposal for a Calorimetric Load at 140 GHz for High Power HE11 Transmission Lines, Proc. of 18th Int. Conf. on Infrared and Millimeter Waves, Colchester (UK) 1993, J.R.Birch, T.J. Parker, Ed. Proc. SPIE 2104.

[2] A.Bruschi et.al., Calorimetric loads for high power transmission lines at millimeter wavelengths, Fusion Engineering and Design 56-57 (2001) 649-654.

[3] L. Pawlowski , The Science and e Engineering of Thermal Spray Coatings, J. Wiley & sons Ltd (1995), pp 286.

[4] Chuanxian Ding, et al., Properties and applications of plasma sprayed ceramic coatings, in Suryanarayanan (ed.), Plasma Spraying, Theory and Applications, World Scientific Publ (1993), pp.163 ff.

[5] N. Spinicchia et al., Studio del rivestimento assorbente di un carico bolometrico per microonde ad alta potenza per applicazioni fusionistiche, Proc. of 16th Congress Italian Association of Vacuum, Catania (I) 2002, pp 259-265

[6] G. C. Gualco et al. : Proc. ITSC 2002, Essen, 4-6 March 2002.

ATMOSPHERIC PRESSURE PLASMA LIQUID DEPOSITION – A NEW ROUTE TO HIGH PERFORMANCE COATINGS

Stuart Leadley, Liam O'Neill, Andy Goodwin

Dow Corning (Ireland) Ltd., Owenacurra Business Park, Midleton, Co.Cork, Republic of Ireland.

Plasma enhanced coating processes are well known as a route to well adhered, conformal, high performance coatings. These processes deliver industrial coatings without the need for solvent, surfactant and drying ovens. However, application has often been restricted to high value opportunities as plasma processes typical operate at reduced pressure, with high capital cost and batch wise operation.

By combining Atmospheric Pressure Glow Discharge (APGD) technology with a unique precursor delivery system Dow Corning Plasma has developed a new coatings approach – Atmospheric Pressure Plasma Liquid Deposition. Operating at atmospheric pressure and ambient temperature this process allows the use of a wide range of liquid precursors delivering high coating rates onto flexible substrates. Patented APGD equipment enables the treatment of wide area substrates in true reel-to-reel conditions. Substrates can be both insulating and conducting. The apparatus and process will be described, with a summary of unique coating chemistry that is achieved.

Deposition of protective hydrophobic thin films in surface discharge at atmospheric pressure

P. Sťahel[1], V. Buršíková[1], Z. Navrátil[1], A. Záhoranová[2] , J.Janča[1] and J. Buršík[3]

[1] *Department of Physical Electronics, Masaryk University, Kotlářská 2, 611 37 Brno, Czech Republic*
[2] *Department of Physics,FMPI, Comenius University, Mlynská dolina, 842 48 Bratislava, Slovak Republic*
[3] *Institute of Physics of Materials, Academy of Sciences of the Czech Republic, Žižkova 22, 616 62 Brno, Czech Republic*

Abstract
In the present paper an atmospheric pressure deposition technique has been introduced enabling to protect the paper or pulp board surface with thin films with desired surface properties, permeability and wear resistance. The protective hydrophobic films were deposited by means of surface barrier discharge using different mixtures of organosilicon monomers with nitrogen. The water permeability of thin film substrate system decreased more then 5000 times. The surface free energy decreased from 53 mJ/m^2 (uncoated paper) to 9-20 mJ/m^2 due to protection with plasma deposited thin polymer organosilicon film.

1. Introduction

Even in our electronic age the paper remains the most common information carrier. In 19th century, the technology of the paper fabrication changed in order to decrease the manufacturing costs. However, this fact caused succesive decrease in quality, mainly in resistance against the air pollution, humidity and UV radiation [1]. One way to suppress the above mentioned degradation processes and improve the paper strength may be the deposition of thin protective transparent coating on the paper surface. The film can protect the paper not only against the aggressive environmental conditions but also against natural disasters as floods etc.
Plasma enhanced chemical vapor deposition (PECVD) techniques enable to prepare coatings with well-defined wetting and sticking behavior. The disadvantage of the low-pressure PECVD techniques is that they demand expensive vacuum pumping systems [2]. Moreover, there are difficulties to arrange the deposition system for large area depositions. Recently plasma deposition at atmospheric pressure becomes a promising technology due to its economical and ecological advantages [3].

The objective of the present work is to develop technique for deposition of thin films with desired surface properties, permeability and wear resistance on paper by means of atmospheric pressure surface barrier discharge. The decrease in surface energy and permeability may enable protection of wettable materials against deterioration due to soaking of liquids. Thanks to good mechanical properties of the deposited films the covered paper is reinforced. Moreover, the films deposited from organosilicons have high absorption down to 200 nm that is why this coating protects paper against the UV radiation.

2. Experimental

The deposition of thin films was carried out by barrier surface discharge at atmospheric pressure with the operation frequency of 5 kHz. The surface discharge was created on the surface of the insulating glass plate, which was from one side fully covered with metal electrode. On the other side of the glass plate the metal electrode consisted of 9 connected rotating rods with 9 mm of spacing. The rods were 6 cm long. The whole arrangement was placed in deposition chamber. The paper strips

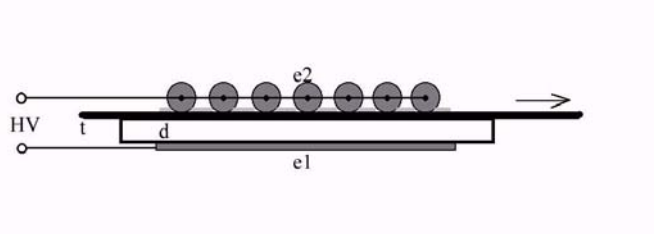

Fig. 1 Configuration of the deposition reactor. The bottom metal electrode is marked as e1, the upper rotating electrodes are marked as e2, d is the insulating glass plate, t is the paper strip and the arrow indicates its movement.

were drawn with controlled speed through the chamber between the metal electrodes and the glass insulator plate. The discharge appeared along the insulator and the substrate surface in the decreasing initial electric field from the side of the thin metal electrodes. The surface power density was kept at 0.4 W/cm^2 in all cases. Configuration of the reactor is shown in Fig. 1.

The films were deposited from different mixtures of organosilicon monomers (hexamethyldisilazane - $C_6H_{19}Si_2N$ - HMDSZ, hexamethyldisiloxane - $C_6H_{18}Si_2O$ - HMDSO) with nitrogen. The nitrogen was bubbled through liquid HMDSZN or HMDSO monomers. The flow rate of nitrogen Q_{N2} was kept at 6 l/min. The organosilicon to nitrogen flow rate ratio Q_{org}/Q_{N2} was varied between 0.01 and 0.2 in order to optimize the coating properties.

Filter paper was used as a substrate because of its similar properties to pulp. The film total surface energy was investigated by means of the sessile drop technique using the Surface Energy Evaluation System (SEE System) developed by our research team [4]. The contact angles were measured directly from the images of the solid-liquid meniscus of a liquid drop set on a solid, taken with CCD camera. The liquids used for the testing and their surface parameters are listed in Table I.

The surface free energy of the deposited films was calculated according Lifshitz-Van der Waals/acid-base approach proposed by van Oss, Good and Chaudury [5]. This method enables to determine the electron-acceptor and electron-donor parameters of the surface tension.

The total surface tension is a sum of its apolar and polar components

$$\gamma = \gamma^{LW} + \gamma^{AB}, \tag{1}$$

where LW indicates the total apolar (dispersive) Lifshitz-Van der Walls interaction and AB refers to the acid-base or electron-acceptor/ electron-donor interaction according to Lewis.

The surface energy can be calculated according to Young-Dupré equation expressed by terms as acid component γ^+ (acceptor effect) and basic component γ^- (donor effect)

$$(1+\cos\theta_i)\gamma_i = 2\left(\sqrt{\gamma_i^{LW}\gamma_j^{LW}} + \sqrt{\gamma_i^+\gamma_j^-} + \sqrt{\gamma_i^-\gamma_j^+}\right), \tag{2}$$

where i refers to liquid and j refers to solid material. The values can be determined from contact angle measurement with three liquids of which two must have polar component. The polar component is given by

$$\gamma^{AB} = 2\sqrt{\gamma^+\gamma^-}\ . \tag{3}$$

Testing liquid	γ [mJ·m^{-2}]	γ^{AB} [mJ·m^{-2}]	γ^+ [mJ·m^{-2}]	γ^- [mJ·m^{-2}]	γ^{LW} [mJ·m^{-2}]
Water	72,8	51,0	25,50	25,5	21,8
Glycerol	64,0	30,0	3,92	57,4	34,0
Ethylene glycol	48,0	19,0	3,00	30,1	29,0
Diiodomethane	50,8	0	0	0	50,8

Table. 1 Surface tension parameters of the testing liquids used for the contact angle measurement.

The wetting properties were studied by means of industrial permeability tests. The permeability was measured as time necessary for penetration of 5 ml of testing liquid through the sample to special wettable paper ERT FF3. This measurement is consistent with the norm ISO 9073-8:1995.

The composition of the film was studied by means of Fourier Transform Infrared Spectroscopy (FTIR). The refractive n and absorption k indices were determined by means of the optical transmission measurement (OT) obtained by spectrophotometer LAMBDA4. The mechanical properties were studied by means of the depth sensing indentation technique using a Fischerscope H100 tester. In the case of the mechanical tests polycarbonate plates were used as the substrate. The morphology of the paper surface before and after deposition was observed using a Philips SEM 505 scanning electron microscope.

The discharge was studied by means of the optical emission spectroscopy. The spectra emitted by the discharge were recorded by the Jobin – Yvon TRIAX 550 monochromator, equipped with CCD detector cooled by liquid nitrogen.

3. Results and discussion

In the first part of the presented study, the discharge properties are investigated by optical emission spectroscopy. The free surface energy of the coated papers and wettability are studied in second part. Optical parameters are investigated in next subsection, morphology and mechanical properties of the systems are presented in last part.

3.1. Optical emission spectroscopy

Emission spectra of the discharge in nitrogen were recorded in the range 300 – 800 nm. A typical spectrum of the discharge created in mixture of nitrogen and HMDSZ vapours is shown in Fig. 2. The spectra recorded for HMDSO/N_2 mixture are very similar to the spectra of HMDSZ/N_2 mixture.
The spectrum is plotted in the range 300 - 500 nm, because above 500 nm only the second spectral order was registered.

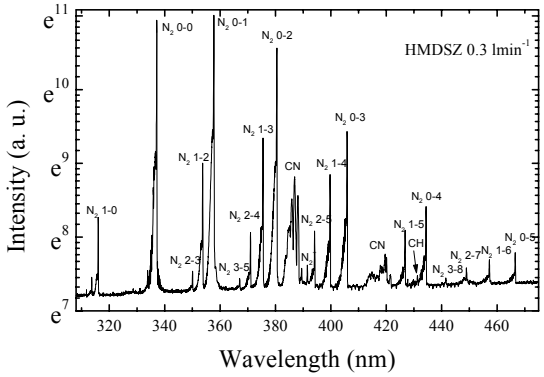

Fig. 2 Emission spectrum of the surface discharge in nitrogen with admixture of HMDSZ

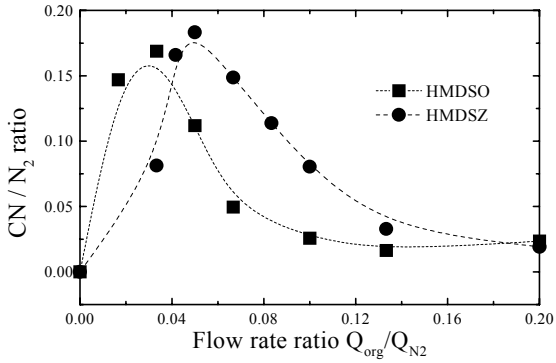

Fig. 3 Ratio of integrated intensities of CN and N_2 bands for different flow HMDSO to N_2 and HMDSZ to N_2 flow rate ratio.

The spectra consist of the molecular bands of second positive system of nitrogen ($C\ ^3\Pi_u \rightarrow B\ ^3\Pi_g$). When organosilicon monomer was mixed into nitrogen, intensive bands of CN violet system ($^2\Pi \rightarrow\ ^2\Sigma$) at 388 nm and 422 nm were observed. The weak band at 431 nm belongs probably to CH system ($^2\Delta \rightarrow\ ^2\Pi$).
Intensity of N_2 and CN system depends on the organosilicon to nitrogen flow rate ratio Q_{org}/Q_{N2}. Therefore integrated intensity of the CN band at 388 nm and integrated intensity of N_2 system was calculated. The ratio of integrated intensities of CN and N_2 bands as a function of organosilicon to nitrogen flow rate ratio Q_{org}/Q_{N2} is shown in the Fig. 3. The CN/N_2 ratio at the beginning increases with increasing flow rate of organosilicon, than it decreases. The maximum decomposition of monomer is at Q_{org}/Q_{N2} = 0.03 for HMDSO, however in the case of HMDSZ the maximum is shifted to Q_{org}/Q_{N2} = 0.05.
The vibrational temperature was calculated from the bands of second positive system of nitrogen N_2 0-2, N_2 1-3 and N_2 2-4. The value of the vibrational temperature varied only slightly with flow rate of organosilicon admixed to pure nitrogen, and its value was at about 1800 K in all cases.

3.2.Surface energy and wettability

Highly hydrophobic thin polymer-like layers were deposited on the filter paper surface in order to protect it against the water penetration. Because of well known hydrophobation effect of silicon [6], organosilicon monomers mixed with nitrogen were used to create protective layers. The deposition time was 90 s. We

tested the wetting properties of the prepared coatings by permeability tests. All tested coatings were well resistant and thick enough to protect the whole paper surface against the penetration of water. As the water of testing volume 5 ml dropped on the coated filter paper did not soak even after 10 hours, the permeability test was stopped after achieving this time.

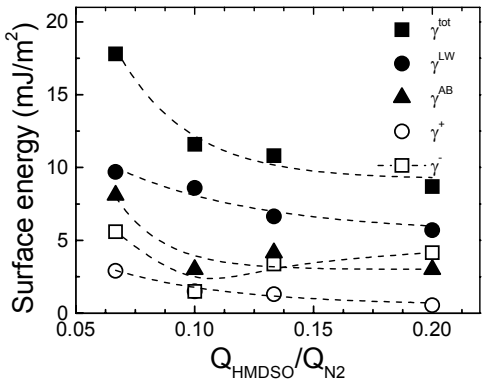

Fig. 4 Dependence of the coating total surface energy γ^{tot} and its apolar γ^{LW}, polar γ^{AB}, acid γ^+ and base γ^- components on the HMDSO to N_2 flow rate ratio.

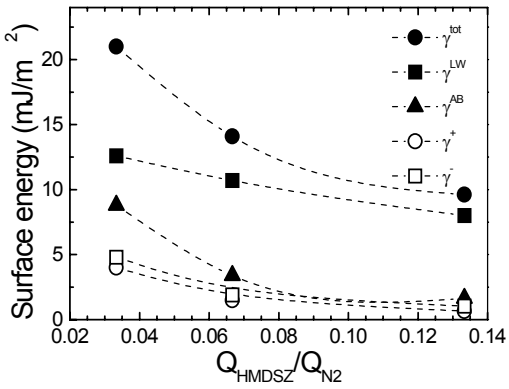

Fig. 5 Dependence of the coating total surface energy γ^{tot} and its apolar γ^{LW}, polar γ^{AB}, acid γ^+ and base γ^- components on the HMDSZ to N_2 flow rate ratio.

Figs 4 and 5 show free surface energy and its polar and apolar parts as a function of monomer (HMDSZ or HMDSO) to N_2 flow rate ratios. Similar behavior was observed for both types of films i.e. the total free surface energy exponentially decreases with increasing monomer to N_2 flow rate ratio. While the apolar part of surface energy changes only slightly, the polar part of free surface energy exhibits more significant changes. The acidic and basic components of polar part of free surface energy are plotted too. However, these values are only informative, due to high experimental error in this case.

3.3 Chemical composition

The chemical composition was investigated by means of FTIR spectroscopy. The characteristic spectra of the film deposited from HMDSO and HMDSZ are shown in Figs 6 and 7. Most dominant are absorption peaks at

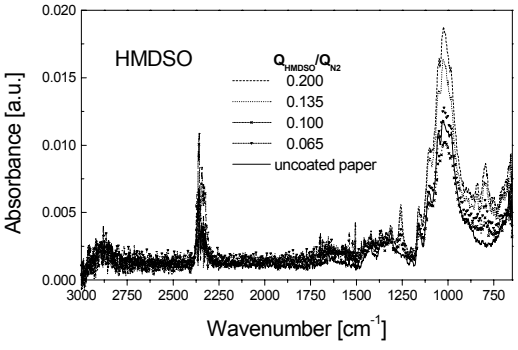

Fig. 6 FTIR spectrum for coatings prepared from HMDSO/N_2 mixtures.

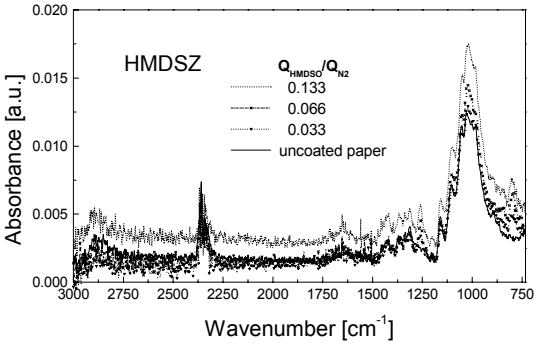

Fig. 7 FTIR spectrum for coatings prepared from HMDSZ/N_2 mixtures.

760-860cm^{-1} corresponding to Si-C stretching bonds. The increase at 1000 - 1130 cm^{-1} can be correlated with Si-O-Si or Si-O-C stretching bonds. The CH_3 bonds represent small absorption peaks at 1255 -1280 cm^{-1}

3. 4. Structure, morphology and mechanical properties

An important result is, that the plasma deposition of the hydrophobic films did not affect the appearance of the paper surface, i.e. we did not observe any yellowing of the substrate material. Moreover the morphology of the filter paper did not change during the plasma deposition (see SEM micrographs illustrating the surface morphology of the paper before and after plasma deposition on the Fig. 9). The coatings exhibited good abrasion resistance and the microhardness of the films deposited from organosilicon/nitrogen mixtures (measured on films deposited on polycarbonate plate) was about 0.1 -0.2 GPa. This value is comparable with the microhardness of wide range of polymer materials.

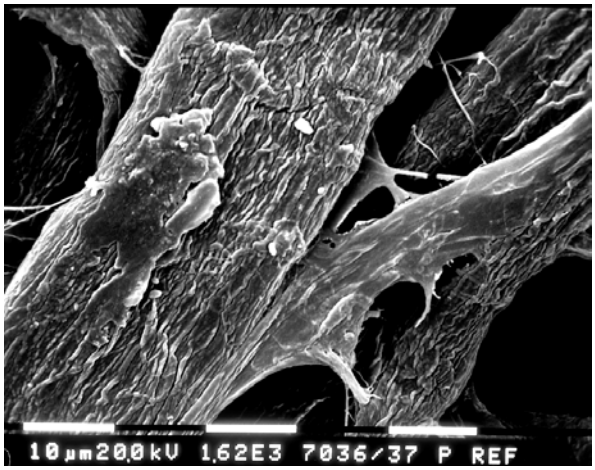

Fig. 8 SEM micrograph of the uncoated paper surface

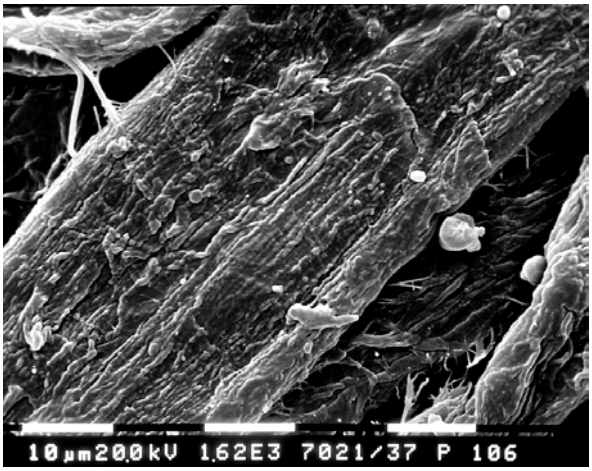

Fig. 9 SEM micrograph of paper surface coated by hydrophobic protective film

4. Conclusion

A new deposition technique based on atmospheric pressure barrier surface discharge was developed in order to protect the paper surface against air pollutant, humidity and UV radiation. Highly hydrophobic plasma polymer coatings were deposited on the filter paper substrate from mixtures of organosilicon monomers with nitrogen. The free surface energy decreased from 53 mJ/m^2 for the uncoated paper to about 9 -17 mJ/m^2 (HMDSZ/N_2, 11-22 mJ/m^2 and (HMDSO/N_2). A substantial decrease of the water permeability was achieved in all cases. The water permeability decreased in the case of the organosilicone/nitrogen mixtures at least 5000 times already after one minute of deposition. This deposition technique may enable for example the utilisation of the pulp board made of waste paper as ecological containers.

Acknowledgement

This work has been supported by Grant Agency of Czech Republic, contract No. 202/02/0880 and 202/02/D097 and by the Grant Agency of Academy of Sciences of the Czech Republic under project S2041105.

References

[1] M. Ďurovič, Restaurování a konzervování archiválií a knih, Paseka (2002)
[2] M. Kogoma, R. Prat, T. Sowa, at al, Plasma Processing of Polymers,R.d'Agostino et al. Plasma Processing of polymers, NATO ASI Series E **346,** 379 (1996)
[3] A. Sonnenfeld, T.M. Tun, L. Zajíčková, K.V. Kozlov, H.-E. Wagner, J.F. Behnke, R. Hippler, Plasma and Polymers, **6,**4, 266-295 (2001).
[4] www.seesystem.vz.cz
[5] R.J. Good: Contact Angle, Wettability and Adhesion ed. K.L. Mittal 3 (1993)
[6] J.Benish, Plasmachemical modification of natural polymers, R. d'Agostino et al. Plasma Processing of polymers,NATO ASI Series E **346,** 345-363 (1996)

Plasma deposited acrylic acid: film characterisation and human endothelial fibroblast cell response

P. Rossini[1,2], I. Malerba[1], G. Ceccone[1], L. Gribaldo[1], and F. Rossi[1]

[1]*European Commission, Joint Research Centre, IHCP, TP 203 21020 Ispra (VA) Italy*
[2]*Univ. of Bristol, Faculty of Medicine, Dep. of Oral and Dental Science, Lower Maudlin Street, Bristol, BS12LY, UK*

Abstract
The present study deals with the deposition of acrylic acid thin films by RF PACVD. This kind of surface modification is suitable for biomedical application to control proteins adsorption and to surface immobilization of bioactive molecules. Plasma diagnostics, surface analysis and physical-chemical characterisation have been performed in order to relate the deposition processes to the film properties. The protein attachment kinetics, as well as the cells growth are presented and discussed.

1. Introduction

Low-pressure plasma processes have been widely recognised as technology of choice for the functionalisation of the material surfaces to control the biological response of the host (human body) to improve the biocompatibility. One of the advantages that plasma techniques offer is the possibility to modify very first layers of the surface, keeping the bulk material properties unchanged [1, 2]. Plasma treatments and plasma deposition of films are easily controllable by choosing suitable precursors and appropriate plasma conditions. Moreover, in case of polymers, the selectivity (or density) and the mobility of the functional groups on the surface can be varied to some extent by changing the degree of crosslinking. Thus, biomedical materials can be engineered with different surface properties in order to improve and control their compatibility with the biological fluids. Among the wide spectrum of possible treatments, plasma polymerisation of acrylic acid (PPAA) has proven to provide highly functionalised surfaces, with a high retention of the monomer structure and high density of –COOH groups. This kind of surface modification is suitable either to promote and control cellular growth [3] and for immobilisation of bioactive molecules [4]. Therefore one of the key issue in this deposition process is the stability of the films in liquid environments. In the present article, we report results on the PPAA films by rf-plasma assisted chemical vapour deposition (PACVD). The plasma parameters were investigated by means of plasma diagnostics, while surface analysis and physico-chemical characterisation of the coatings have been performed in order to explore possible relation between the deposition processes and the film properties.

2. Materials and method

The source used for the deposition is a Capacitively Coupled Plasma source described in detail elsewhere [5]. The plasma chamber consists in a cylindrical stainless steel vessel (Φ = 210 mm, h = 350 mm) in which the part to be processed is placed and the process gases introduced at reduced pressure (10^{-3} to 1 torr). The plasma discharge between the two internal SS parallel plate electrodes is sustained by a RF unit operating at 13.56 MHz. Samples are placed on the powered electrode, while the upper one is grounded. The electrodes are located at the half height of the plasma chamber and the distance between them is of 5 cm. The liquid precursor (Acrylic Acid of > 99% purity from Aldrich Chemical Co) is vaporised from a heated vessel connected to the reactor. The monomer is injected through the upper electrode at a constant flow rate (ϕ) of 5 sccm, and it The working pressure is fixed at 50 mTorr, whilst the RF power range explored is between 5 and 60 Watts. Finally, the deposition time is fixed to 15min.

Plasma phase diagnostics are performed both with mass spectrometry (MS) and with optical emission spectroscopy. Mass Spectral analyses are realised with a Hiden HAL PSM spectrometer interfaced to the deposition chamber. The sampling aperture (30 μm) is at the geometric centre, in the middle of the electrodes. The signals are collected in Residual Gas Analysis (RGA) and in Secondary Ion Mass Spectrometry (SIMS) mode. Optical Emission Spectroscopy (OES) is performed with a Chromex 500IS/SM spectrometer having a 50 cm focal length for a theoretical resolution of 0.08 nm. The associate detector is an air-cooled CCD camera (DV401-UV CCD2477 Andor Technology). A 600 μm diameter fused silica optical fibre is used to transmit the signal to the spectrometer. The optical detection is made through a quartz window. A semi-quantitative evaluation of the species present in the different conditions is obtained by using the actinometric approach [6, 7]. Argon is used as actinometer in concentration of 5% of the total flux.

The chemical characterisation of the deposited films is performed by X-ray Photoemission Spectroscopy (XPS) and Fourier Transformed Infrared Spectroscopy (FTIR). The XPS analyses are performed with a Nanoscan 50 (Cameca, France) instrument with non-monochromatic MgK_α radiation (12 KV, 20 mA) X-ray source. Spectra are acquired at a take-off angle of 45°, with an energy resolution of 1 and 0.5 (CAE mode), and 0.1 eV of step width. On each sample, a survey scan (0-1100eV) is recorded together with high-resolution scans for the C1s and O1s regions. Sample charging was between 3 and 6 eV and has been corrected for by setting hydrocarbon to 285 eV. All fittings were performed using a commercial software package (XI-SDP, XPS Int., USA). Curve fitting of C1s peaks was carried out using the same initial conditions and inter-peak constrain, with a G/L mix of 0.7-1, and a total intensity of β-shifted carbon constrained to be equal to that of the carboxylic acid component [8].
The FTIR Spectra of the coatings are acquired in transmission mode using a Perkin Elmer 1600 spectrometer with 8 cm^{-1} of resolution.
The protein adhesion experiments were studied with the QCM-D technique (from Q-Sense AB, Göteborg, Sweden) is used in order to study the protein adsorption kinetics. The detection principle of this technique is described by Rodhal et al. [9]. Briefly the Quartz Crystal Microbalance sensor is an AT-cut piezoelectric-crystal usually coated with thin metal film electrodes deposited on its faces. The crystal is induced to oscillate in the thickness share mode at its fundamental (or an overtone) resonant frequency by applying a RF voltage across the electrodes. A mass added to the electrodes induces a decrease in the resonant frequency; the relationship between Δm and the relative Δf is given by the Sauerbrey's equation [10]:

$$\Delta f = -\Delta m/nC \qquad (1)$$

where C is the mass sensitive constant and n is the overtone number. Usually a mass load introduces dissipative losses in the oscillating systems; in such cases also the dissipation factor (D) has to be considered. When the voltage is switched off, the voltage over the crystal decays as an exponentially damped sinusoidal. By recording the decay voltage and by numerically fitting the relative curve, both the resonant frequency and the dissipation factor of the crystal are obtained simultaneously in real time. Therefore the frequency and the dissipation shifts caused by the adsorption of the proteins to the crystal surface can be measured as a function of the time. The frequency and the dissipation shifts caused by the adsorption of the proteins to the crystal surface are measured as a function of the time. Human Serum Albumin in water (1 μg/ml) was used in order to test the first biological response to PPAA obtained in different conditions and with different surface properties. The measurements were performed at 37 °C.
Scanning probe experiments were performed with a commercial Atomic Force Microscope, AFM, (SMENA head, Solver electronics, NT-MDT Zelenograd, Moscow, Russia). All measurements were done directly on QCM crystals after experiments in the Q-Sense, positioning the scanning probe in the crystal active zone using the optical microscope integrated with the AFM. Measurements were done in Milli-Q water using standard Si_3N_4 cantilever (NT-MDT) in resonating mode (ν_{res} = 65 KHz) in order to prevent possible surface damages..
CRL-1999 cells, human endothelial fibroblast from smooth muscle of aorta, were cultured in Ham's F12K medium with 2mM L-glutamine, 1.5 g/L sodium bicarbonate (Gibco Life Technologies Italia S.r.l) supplemented with 10% of Fetal Bovine Serum (Gibco Life Technologies Italia S.r.l), 10 mg/ml insulin, 10 mg/ml transferin, 10 ng/ml sodium selenite and 20 mg/ml endothelial cell growth supplement (Sigma-Aldrich S.r.l.). CRL-1999 cells were counted in a hemocytometer and resuspended in medium (Sigma-Aldrich S.r.l.). $30x10^5$ cells per chamber were then plated onto the coated 4-chambers slide and $60x10^5$ cells per well onto coated 6-well plates and incubated at 37°C, 5% CO_2 and 100% of humidity. The cells growth was controlled with an inverted optical microscope after 2h, 24h, 48h, 96h and 1 week of incubation.

3. Results and discussion

The plasma phase is first characterised with MS and OES. Characteristic Electron Impact (EI) mass spectrum peaks of neutrals for an acrylic acid plasma are observed at m/z 72 $M^{\cdot+}$, 26 ($C_2H_2^{\cdot+}$), 27 ($C_2H_3^{\cdot+}$), 28 ($CO^{\cdot+}$), 44 ($CO_2^{\cdot+}$), 45 (CO_2H^+), 55 (CH_2CHCO^+) (Fig.1). The MS peaks can be divided in 2 categories based on their origin, following the fragmentation scheme proposed by Candan et al. [11]. In fact the 72 and 55 peaks are due to the mass spectrometer ionisation of the "intact" acrylic acid; whilst the 26, 28 and 44 peaks are predominantly formed during the production of precursor fragments in the plasma phase, which are subsequently ionised in the mass spectrometer. In particular the peaks at m/z=17 (OH) and 28 (CO) are

followed because they are strictly linked to the monomer functionality fragmentation (-COOH) in the discharge.

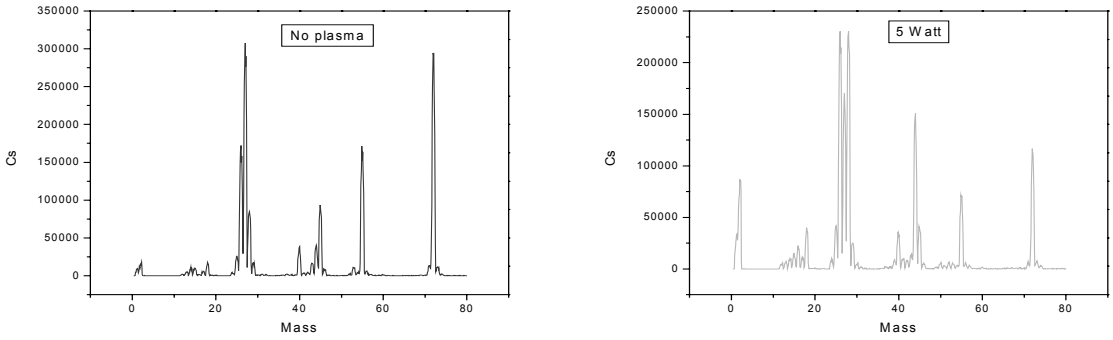

(a) (b)

Figure 1: Typical Mass Spectrum of Acrylic Acid (a) without and (b) with plasma.

Even in the Optical emission Spectroscopy (OES) the OH and the CO emission systems are analysed in order to link these results to those of the MS and to the monomer functionality retention. Either Mass spectral analyses or OES measurements show that in the plasma region, the precursor fragmentation (CO and OH products) increases with the RF power injected in the plasma. Both the OH and the CO fragments have an initial fast increase and then they suddenly reach a plateau at 50 Watt of RF Power. It could mean that only at low RF Power the fragmentation degree is minimum and the COOH retention on the coatings could be high.

Furthermore the discrimination of dissociative ionisation products can be inferred from the examination of radical species of the plasma by using the Appearance Potential MS (APMS) in RGA mode [12].

Briefly, the selective ionisation of a radical (X) can be obtained from APMS measurements through the energy difference (typically grater than 2 eV) between the ionisation threshold of the radical ($E_i^{X\rightarrow X^+}$) and the dissociative ionisation threshold of the parent molecule XY ($E_a^{XY\rightarrow X^+}$). For electron energies $E_i^{X\rightarrow X^+}<E<E_a^{XY\rightarrow X^+}$, the signal measured is only due to the direct ionisation of the radical, and thus the radicals density can be estimated together with their dissociation paths. Our APMS experiments have been carried out by following the most significant MS ion peaks, i.e. m/z=72, 55, 44, 28, 26, whilst the electron energy scale has been calibrated by following the process: $Ar + e \rightarrow Ar^+ + 2e$ at 14.75 eV(EI) [13].

Figure 2a) shows the APMS data obtained for m/z=26, corresponding to the $C_2H_2^+$ ions. It can be seen that additional ions are produced for electron energies of 11.5 <E< 15 eV when the plasma is turned on. The plasma off curve corresponds to the fragmentation of the acrylic acid starting monomer in the MS, whilst when the plasma is turned on, additional ions are produced by the direct EI reaction: $C_2H_2 + e \rightarrow C_2H_2^+ + 2e$. The ionisation energy of the $C_2H_2^+$ is 11.41 eV (EI) [13]. The same behaviour is observed when analysing peaks at m/z=28 ($C_2H_4^+$ and CO^+ ions)

In Figure 2b) APMS data for m/z= 72 (AA^+) are illustrated; a strong decrease of signal, due to the depletion of acrylic acid is observed when the plasma is turned on. Similar results are obtained for the peak at m/z=55 ($C_3H_2O^+$).

A different situation is observed for the peak at m/z= 44 (CO_2^+) (Figure 2c). In plasma on condition, the contribution of CO_2^+ fragments originating from EI in the plasma phase (13.78 eV) increases, like in the case of the m/z=26 and 28 ions. However in the plasma off condition, additional radical contributions are observed due to other fragmentation processes that could occur in the mass spectrometer. This can come from contamination products or acrylic acid dimers or trimers that the mass spectrometer can detect (for instance the formation of $C_2H_4O^+$ ions: EI= 10.14 eV [13]). However further investigations are on going to clarify this point.

The APMS results are in agreement with the considerations derived from the analysis of the neutral spectra (Figure 1) confirming the different origin of fragments and the acrylic acid fragmentation path published [11]. By following the positive ions spectra coming from the fragmentation and the ionisation of acrylic acid at different power in SIMS mode, it can be pointed out the presence of fragments above m/z 72. The ion at m/z145 corresponds to $2(M+H)^+$, and peaks in the cluster around corresponding to the addition or loss of H, the m/z 127 corresponds to $145\text{-}H_2O$. The oligomerisation in the plasma phase could be evaluated by

dividing these peaks to that of acrylic acid monomer. The Figure 3 shows that the RF power has a strong influence in the retention of the oligomers in the plasma phase. It can be observed a transient region between 5-10 and 20 Watt; at very low power there is a strong contribution from oligomers created in the plasma region taking part in the polymerisation process by falling down and being incorporated in the plasma coating structure. This could be a reason of the low stability of the film growth at very low power, as has been discussed elsewhere [5].

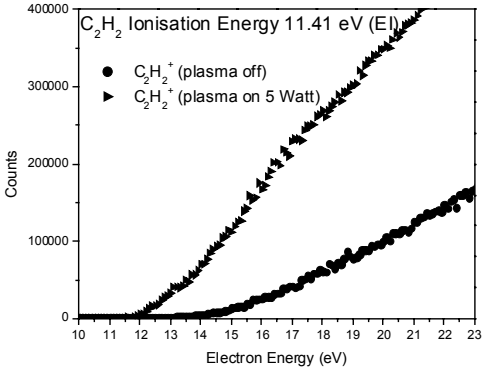

(a)

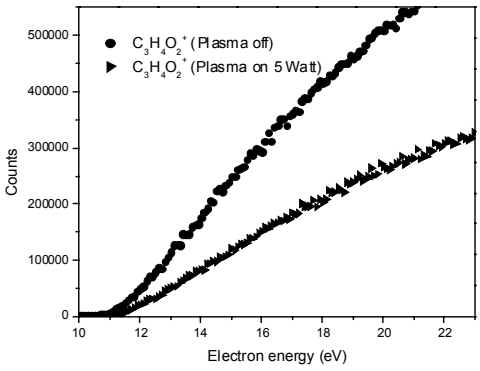

b)

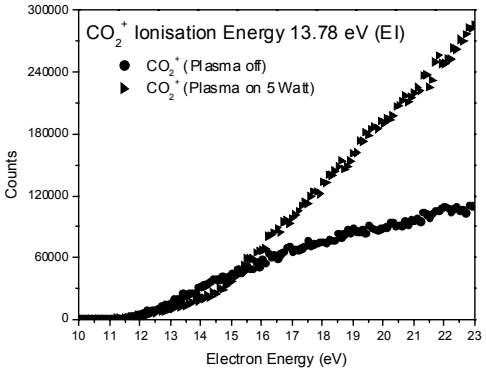

(c)

Figure 2: Measured beam signal for different radicals with Plasma Off and Plasma On (at 5 Watt of RF power) respectively: (a) $C_2H_2^+$, (b) $C_3H_4O_2^+$ and (c) CO_2^+

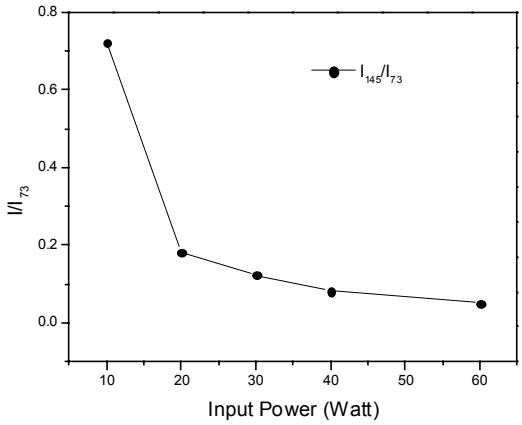

Figure 3: Intensity ratio measured at m/z 145 and m/z 73 in the positive-ion plasma mode mass spectra of acrylic acid vs power

In order to study the RF power influence on the PPAA deposited films structures, different films have been deposited at different powers 30, 40, 60 Watts respectively. From a typical XPS survey spectrum obtained for a PDAA film, only carbon and oxygen are detected. The C1s core level spectrum obtained for each sample has been peak-fitted based on chemical basis [11], starting with the hydrocarbon signal at 285 eV. Other four components are identified: C-CO_2H/R (+0.5 eV); C-O (+1.9 eV); C=O (+2.9 eV); CO_2H/R (+4.35

eV) (the values in brackets correspond to the shifts relative to the hydrocarbon positions). The C1s core level spectra analysis shows that the percentage of the peak due to COOH/R carbon in the spectra decrease as the power increases [14]. Cross-linked results are found between surface analysis (XPS) and plasma diagnostics (MS/OES): the COOH concentration in the films decreases with the CO molecules increase in the plasma phase. The next step consists in the assessment of the plasma parameters influence on the proteins and cells response. Figure 4 shows different responses to different coatings in the QCM experiments. It is clear that films with the highest retention of the carboxylic groups (deposited at low RF-power) have the highest amount of BSA adsorbed. Analysis of the morphology of the films after the protein adsorption with the AFM, reveals a different organization of the protein films onto different surfaces. The films deposited at 30 watts (Figure (5a)) permit the adsorption of the proteins in different multi-layers, showing the highest affinity versus the biomolecules adhesion; by increasing the RF power, the proteins adhere in minor extension (Figure 5(b)). For the films obtained at very high power we can observe from figure 5(c) that only few proteins are attached to the surface.

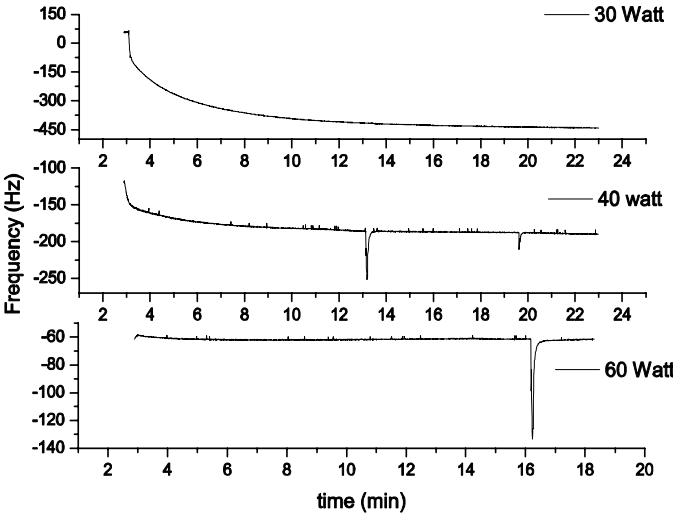

Figure 4 QCM-D results on PPAA films deposited at 30, 40 and 60 Watts

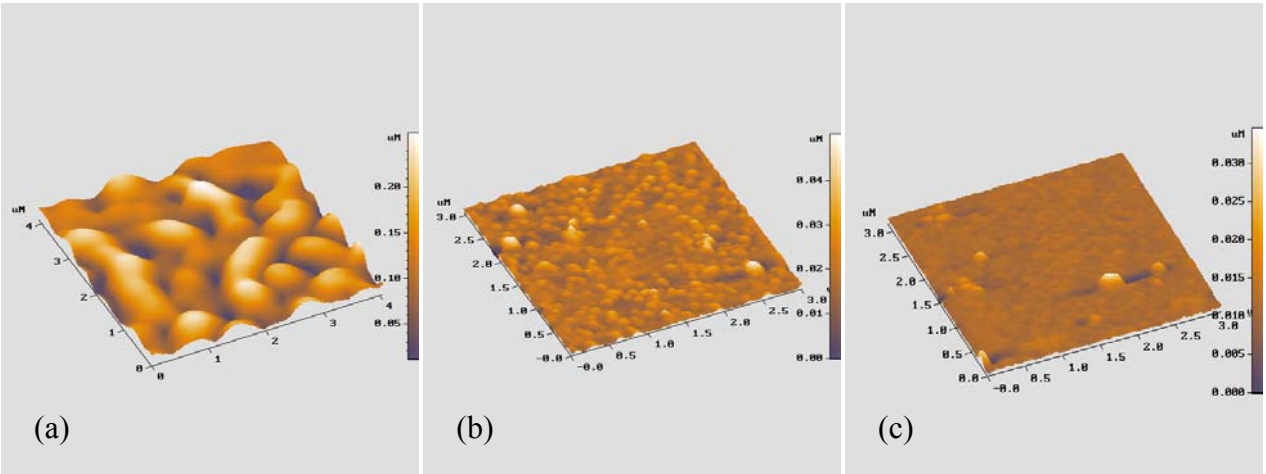

Figure 5: AFM images of BSA on PPAA films deposited at (a) 30 Watts (b) 40 Watts (c) 60 Watts.

Optical microscopy studies of fibroblast cells growth show that cells adhered well to the coated support, showing the typical morphology of fibroblast growth in monolayer, reaching the confluence after 96h of culture. In particular as shown in figure 6, for the coating deposited at low RF power conditions, the cells

reach the cellular confluence symptomatic of good cells adhesion. On the other hand a remarkable decrease of the cell adhesion is observed on the films deposited at high RF power (figure 6 (b)).

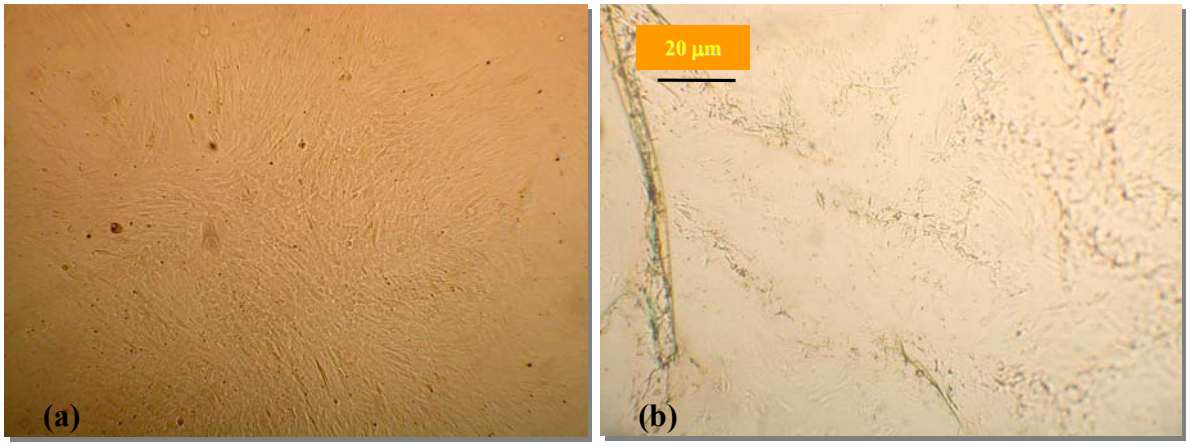

Figure 6 Human endothelial fibroblast from smooth muscle of aorta growth on PDAA at (a) 30 Watt and (b) 60 Watts

4. Conclusion

The combination of the plasma phase diagnostics and the PPAA films surface analysis is a powerful tool for drawing important conclusion concerning the plasma polymerisation processes.
It can be observed a clear distinction between conditions of low and high power. The process can be rationalised by using the Yasuda concept about an "energy- deficient region" at low power and a "monomer-deficient region" at high power [15]. By increasing the RF power the acrylic acid content in the plasma phase is depleted, and the COOH functionality retention on the deposited films decreases. On the other hand, in low power region there is a strong contribution of the oligomers formed in the plasma phase to the plasma deposition, this could be linked to the highest retention of the acrylic acid structure, but also the cause of a bad stability of the obtained films. By tailoring the deposition conditions it is possible to prepare films with different surface properties leading to diverse biological responses.

Acknowledgements
The authors would like to thank Dr. P. Colpo, Dr. T. Meziani and Dr. A. Valsesia for their collaboration during the experiments and for the useful discussions about the results.

References

[1] H. Yasuda, M. Gazicky, Biomaterials **3**, 68, (1982).
[2] D. G. Castner and B. D. Ratner, Surface Science, **500**, 28-60, (2002)
[3] B. Gupta, C. Plummer, I. Bisson, P. Frey, J. Hilborn, Biomaterials **23**, 863-871, (2002).
[4] P. Favia, F. Palumbo, R. d'Agostino, S. Lamponi, A. Magnani, R. Barbucci, Plasma and Polymers **3**, N° 2, (1998).
[5] P. Rossini, P. Colpo, G. Ceccone, F. Rossi and K.D. Jandt, Plasma and Polymers, (submitted).
[6] J. W. Coburn, M. J. Chen, J. Appl. Phys. **51**, 3134-3136, (1980).
[7] R. d'Agostino, F. Cramarossa, S. De Benedictis, G. Ferraro, J. Appl. Phys. **52**, 1259-1265, (1981).
[8] M. R. Alexander, and T. M. Duc, J. Chem. Mat., **8**(4), 937-43, (1998).
[9] M. Rodhal, F. Höök and B. Kasemo, Anal. Chem. **68**(13), 2219, (1996).
[10] G. Suerbrey, Z. Phys.**155**, 206, (1959).
[11] S. Candan, A. J. Beck, L. O'Toole, R. D. Short, J. Vac. Sci. Technol. *A*, **16**(3), 1702, (1998).
[12] Harmeet Singh, J. W. Coburn, David B. Graves, J. Vac. Sci. Technol. *A* **18**(2), (2000)
[13] NIST Chemistry Web Book: http://webbook.nist.gov/chemistry/
[14] P. Rossini, P. Colpo, G. Ceccone, K. D. Jandt and F. Rossi, Mat. Sci. Engin., **C23**, 353-58, (2003).
[15] H.K. Yasuda, Plasma Polymerization, Academic Press, London, 1985

Combination of Plasma and Catalyst for Removal of Formaldehyde

K. Hensel[1], J. Pawlat[2], A. Mizuno[2]

[1] *Department of Plasma Physics, Comenius University, Bratislava, Slovakia*
[2] *Department of Ecological Engineering, Toyohashi University of Technology, Toyohashi, Japan*

Abstract
Removal of formaldehyde by streamer corona discharge was studied. Efficiency of the removal and by-products formation in the non-thermal plasma of the discharge depending on the initial concentration, gas flow rate, carrier gas and discharge polarity was evaluated. The combined effect of plasma and catalytic pellets of various materials placed in the discharge reactor was investigated via by-products formation. Adsorption abilities of catalyst pellets combined with discharge affected the chemical process and formed by-products. An improvement compared with using plasma or catalyst only was observed for TiO_2, γ-Al_2O_3 and 13X pellets at higher input energies and long operating times.

1. Introduction

Formaldehyde is one of the most common volatile organic compounds (VOC), used mainly for the production of urea-formaldehyde resins, phenol-formaldehyde resins, plastics and intermediates. It is also used in building materials such as plywood, chipboard and panelling, released by gas cookers, found in tobacco smoke and emissions from gasoline powered motor vehicles. Numerous adverse health problems have been ascribed to formaldehyde exposure, such as eye, nose and throat irritation, to more controversial claims including asthma, cancer, chronic respiratory diseases and neuropsychological problems [1].

A number of studies have been directed to formaldehyde removal, most of them related to its removal by adsorbents, e.g. activated carbon, ceramic porous materials and composite oxidized catalyst [2, 3]. Recently a promising method of non-thermal plasma is used to control VOCs. The plasma is highly effective producing active radicals, enhancing molecular dissociation and promoting oxidation. In addition, its combination with the catalyst was found to effect the formation of active radicals, control their distribution and therefore process of treatment [4, 5].

The authors performed the research to investigate the possibilities of formaldehyde reduction from dry air and nitrogen using DC streamer corona discharge. Evaluation of removal efficiency in different conditions was made. In addition, a combination of discharge plasma with catalyst was investigated too. Pellets of various catalytic materials were placed in the discharge reactor and their effect on the decomposition and by-products formation was studied.

2. Experimental Apparatus

The used experimental reactor is depicted in the fig. 1. Discharge reactor of multi-point-to-mesh geometry was used and set inside Pyrex glass tube 35 mm diameter. The distance between electrodes was set to 16 mm. The tube was closed with silicon stoppers at the both ends. A layer of 8mm thickness composed of catalytic pellets (average diameter 2-3 mm) was placed on the mesh electrode. The investigated materials were TiO_2, Pt/Al_2O_3, γ-Al_2O_3, zeolites 13X and LZ-Y54. The formaldehyde vapours were produced by bubbling 36% liquid solution of formaldehyde by dry air or nitrogen. The total gas flow rate 0.25, 0.5 or 1.0 l/min was controlled by mass flow meters. DC high voltage power supply was used to generate streamer corona discharge. Evaluation of efficiency of the removal

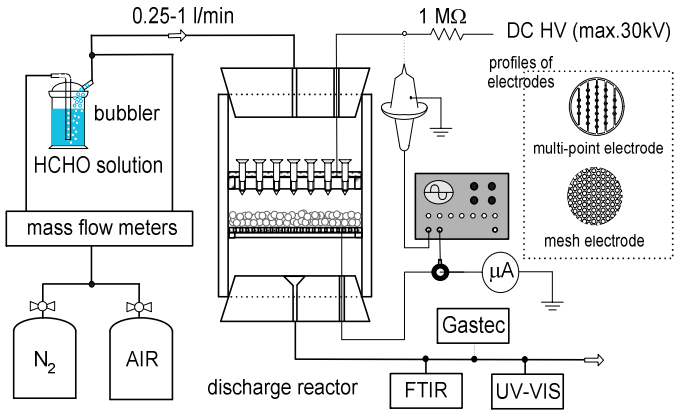

Figure 1: *Experimental setup.*

process the term of specific input energy (SIE), defined as discharge energy dissipated per unit volume of the gas, was used. The analysis of gas composition was performed using infrared spectrometry (Bio-Rad FTS-3000), ultraviolet spectrometry (Shimadzu UV-1200) and gas analyzing tubes (Gastec).

3. Experimental Results

Formaldehyde is an organic compound, which can be comfortably detected by infrared absorption spectrometry. Typical aldehydic absorption characteristics are stretching vibration of carbonyl group C=O in the region 1740-1720 cm^{-1} and aldehydic C-H stretching vibration in the 2830-2695 cm^{-1} region (fig. 2). The formaldehyde solution used for the experiment contained methanol as a stabilizer. The infrared spectrometry is effective for the quantitative and qualitative analysis of products of formaldehyde decomposition, and therefore was utilized in the experiment.

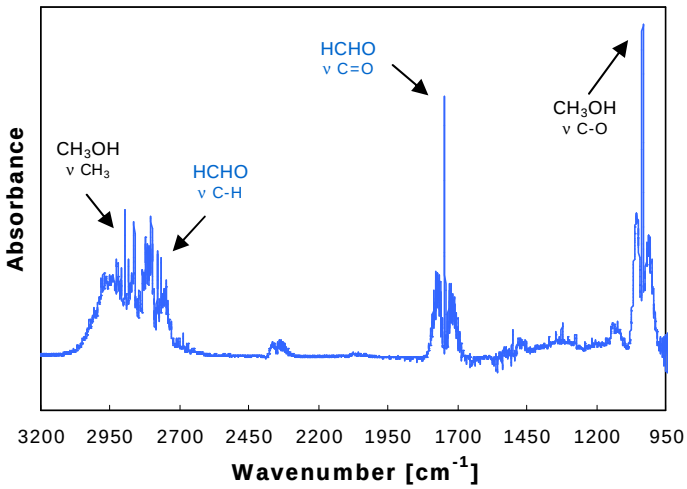

Figure 2: *IR spectrum of used formaldehyde vapours.*

3.1 Chemical Processes and By-Products

Formaldehyde decomposition results mostly into formation of carbon oxide CO and formic acid HCOOH. The formation of CO occurs most probably by photolytic reactions ($HCHO + h\nu \rightarrow HO_2 + CO$ or $HCHO + h\nu \rightarrow CO + H_2$) by light produced by streamer discharge. In dry air, where oxygen is present, CO can also be formed by reaction ($HCHO + h\nu \rightarrow H + HCO$), followed by ($HCO + O_2 \rightarrow CO + HO_2$). Oxygen in the gas mixtures also supports formaldehyde oxidation to formic acid by oxygen radicals, produced through dissociation of molecular ozone by the discharge ($HCHO + O \rightarrow HCO + OH \rightarrow HCOOH$). The reaction with ozone ($HCHO + O_3 \rightarrow HCOOH + O_2$) appeared not to be much effective. Oxidation of formaldehyde mixed with the gas containing high concentration of ozone (up to 1000 ppm) was negligible. Carbon oxide formed is expected to be further oxidized in carbon dioxide, either by ozone but rather OH radicals ($CO + OH \rightarrow CO_2 + H$, $CO + O_3 \rightarrow CO_2 + O_2$). Due to the existing oxidation process the removal is slightly better in dry air mixtures. The process of formaldehyde removal leads also to formation of many other minor products (e.g. CH_3O, CH_3OCO and CH_4).

3.2 Removal by Plasma

Removal efficiency of formaldehyde depended on its *initial concentration*. For smaller initial concentrations, higher removal efficiency was achieved. An increase of initial concentration of formaldehyde resulted in the increased formation of CO and HCOOH. Increasing SIE resulted in decrease of relative production of HCOOH and increase of relative production of CO. As follows from the carbon balance, part of CO is also produced from methanol contained in the formaldehyde solution. Increasing the *gas flow rate* from 0.25 to 1.0 l/min at the constant SIE caused more formaldehyde was removed with relatively smaller production of HCOOH and CO. As follows also from carbon balance, it can be explained by smaller decomposition of methanol at higher gas flow and better utilization of energy for HCHO removal. The effect of *discharge polarity* was examined too. Achieving the same production of oxygen radicals/ozone in both polarities (although at different SIE) resulted in approximately the same amount of formaldehyde removed.

Finally the removal efficiency of formaldehyde depends also on the *carrier gas*. At the same SIE, the removal is better in dry air mixtures, rather than nitrogen. It is because of existing oxidation processes driven by oxygen radicals. The reaction of formaldehyde with oxygen radicals can either lead to formation of HCOOH or production of CO. Generally, the production of CO is higher in dry air, while formation of formic acid was found negligible in nitrogen mixtures. Removal of formaldehyde in nitrogen mixtures is less effective, however, compared with dry air it produces less CO_2, NO_2 and N_2O.

3.3 Removal by Plasma and Catalyst

The presence of catalyst pellets in the discharge volume has been investigated for effect on removal of formaldehyde and formed by-products. A layer of catalyst pellets with the thickness of 8 mm was placed

onto mesh electrode. Catalysts were expected to affect the formaldehyde decomposition, either due to their activation by discharge (TiO_2), and utilizing their oxidative properties (Pt/Al_2O_3) both resulting in improvement of oxidative removal of small amounts of VOCs and/or to their adsorption abilities (especially zeolites).

Effects of Catalyst

The effect of catalytic material without discharge was examined from differential spectra of gas composition at inlet and outlet of reactor. The presence of the catalytic material in the discharge reactor caused concentration of formaldehyde at the outlet of the reactor decreased, due to adsorption to the surface of pellets or oxidation properties. Thus prior to the every experiment a certain time was needed (several hours) until concentration of formaldehyde at the reactor outlet saturated. The outlet concentration either almost reached the level of input concentration (e.g. TiO_2) or saturated at the value down bellow the inlet concentration, e.g. Pt/Al_2O_3 or zeolites (fig.3). Comparing the absorption spectra of the input and output gas composition, generally observed effect was specific removal of formaldehyde and methanol, without formation of by-products. Formation of CO, CO_2 and HCOOH was not observed. It can be explained by adsorption properties of the used pellets.

The effect of adsorption without by-products formation was the most evident in the cases of γ-Al_2O_3 and LZ-Y54. Using 13X, also the effective removal of water vapours was observed. Adsorption effect of TiO_2 pellets after was minimal among the used catalyst. The best result for formaldehyde removal was obtained using Pt/Al_2O_3 catalyst, which can be explained by both adsorption and effective oxidative removal of formaldehyde by catalyst. Different to all other catalysts, the removal here was accompanied by formation of CO_2 (2360 cm^{-1}) and CH_3OCO (1755 cm^{-1}).

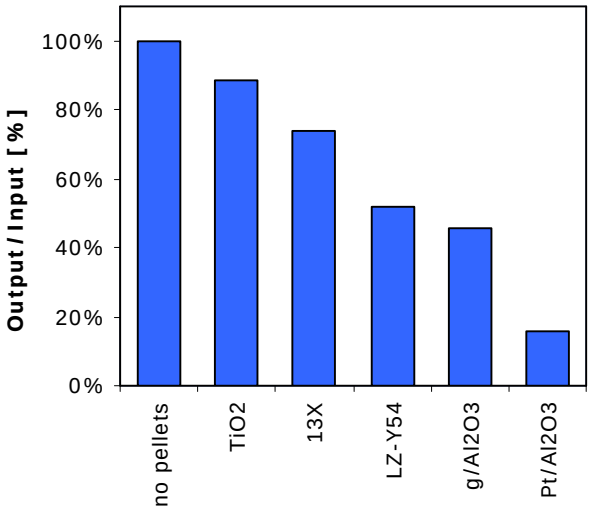

Figure 3: *Formaldehyde removal by pellets without discharge (230 ppm in air; after 12-14 hours).*

Effects of Discharge and Catalyst

The layer of catalyst pellets between electrodes resulted in smaller onset and operating voltage for a given current. The streamers generated by discharge with pellets had faster rise time and their distribution appeared to be more uniform. The discharge was more stable with minimum of random spark breakdowns (fig. 4).

Formaldehyde treatment using discharge with catalyst pellets and its development in time and depended on SIE in the case of TiO_2 pellets is reported here as an example (fig. 5). Concentration of formaldehyde was 200 ppm. An application of the discharge resulted in sudden increase of formaldehyde concentration (exceeding the initial value). Within 240 minutes during which SIE of the discharge was kept almost

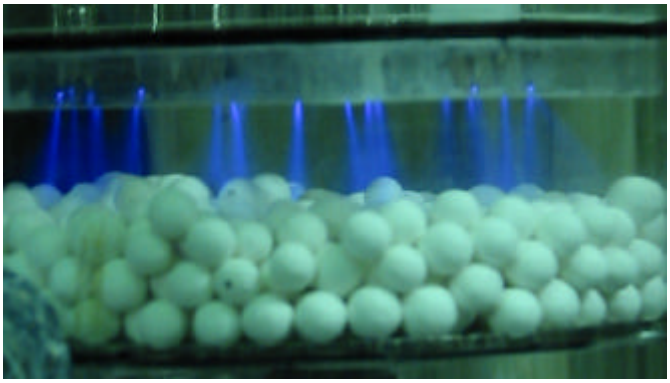

Figure 4: *Streamer corona discharge with TiO_2 catalyst placed on the grounded electrode.*

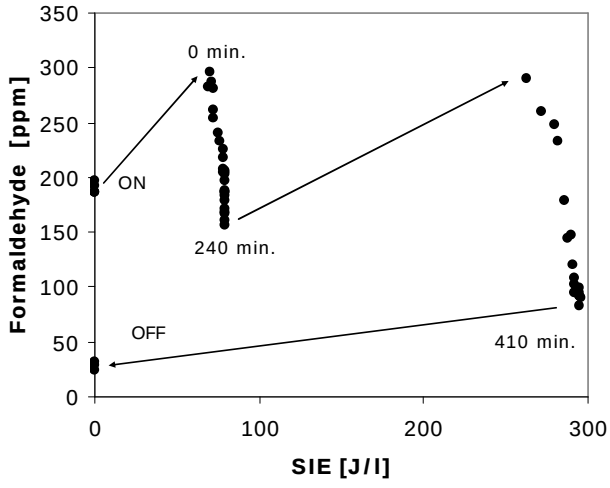

Figure 5: *Formaldehyde decomposition using TiO_2 pellets in the discharge volume (200 ppm in air).*

constant (approx. 75 J/l) the concentration decreased bellow the input concentration. Increasing SIE further (265-294 J/l) and waiting for additional 170 minutes, the amount of formaldehyde removed increased to 60% (294 J/l) slowly saturating in time. After switching the discharge off, the concentration of formaldehyde decreased a little further and then gradually started to recover toward the initial value.

The increase of the concentration of formaldehyde during the discharge with catalytic pellets can result from *desorption* of formaldehyde molecules adsorbed before the discharge. It is suggested that desorption from the surface occurs during the contact of the streamers with the surface of pellets, which increase the local temperature. In a similar way a possibility of discharge formation between catalyst pellets must be considered as another source of formaldehyde increase. Assuming TiO_2 catalyst, the concentration of formaldehyde may also increase due to its formation from adsorbed molecules of methanol $CH_3OH \rightarrow CH_3O(ad) \rightarrow HCHO(g) + H(ad)$ at higher temperatures [6], eventually formic acid $HCOOH(ad) \rightarrow HCHO(g) + ½O2$ and $2HCOOH(ad) \rightarrow HCHO(g) + CO_2 + H_2O$ [7]. The effect of desorption is the most evident after the discharge application or during sudden increase of the discharge power. In such moment desorption effect prevails the removal caused by discharge for a limited period giving a negative result of the treatment. The negative result is however recovered during long operation times and using higher SIE and is also dependent on the used catalyst material.

Comparing the results of formaldehyde removal using *different catalysts*, the relative improvement of removal efficiency was observed especially at higher SIE (> 200 J/l). The effect of treatment time was important as the concentration of formaldehyde decreased slowly and at the constant SIE more than three hours were needed for data saturation. Tendency similar to that of TiO_2 was observed in the cases of 13X, LZ-Y54 and γ-Al_2O_3. Small SIE (less than 100 J/l) gave negative result of formaldehyde removal. However increasing SIE to 300 J/l the treatment efficiency was improved, while achieved efficiency was better than using either catalyst or plasma alone (e.g. TiO_2, 13X, γ-Al_2O_3). The case of Pt/Al_2O_3 appeared to be a little different compared with the other catalyst. Although similar to other catalyst, the discharge caused concentration of formaldehyde at the reactor output increased, however further increase of SIE had negative impact on the removal efficiency. Using discharge and catalyst affects also the type and amount of by-products formed both without and with discharge (fig. 6).

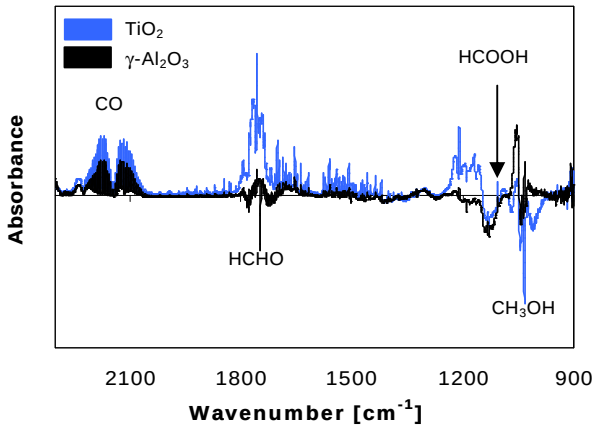

Figure 6: *Part of differential spectra for discharge with TiO_2 and g-Al_2O_3 catalyst (250 ppm HCHO, 250 J/l).*

Conclusions

The possibility of formaldehyde removal by streamer corona from the dry air and nitrogen was investigated. For a given SIE, removal efficiency increased when initial concentration of formaldehyde and decreased with the gas flow rate. Removal was more effective in dry air mixtures, due to the existing oxidation process. A combination of plasma and catalyst was investigated and improvement was observed when TiO_2, γ-Al_2O_3 and 13X pellets were used at higher SIE. Presence of catalyst affected also formation of by-products

References

[1] http://www.nsc.org/library/chemical/formalde.htm
[2] D. Gesser, S. Fu - Environ. Sci. Technol. **24** (4), 495–497 (1990).
[3] J.M. Saleh, S.M. Hussian - J. Chem. Soc. - Faraday Trans. 1 **82**, 2221–2234 (1986).
[4] S. Futamura, A. Zhang, H. Einaga, H. Kabashima - Catal. Today **71**, 259-265 (2002).
[5] M. Kang, B. J. Kim, S. M. Cho, C. H. Chung, B. W. Kim et al. - J. Mol. Catal. **180**, 125-132 (2002).
[6] Q. Wang and R.J. Madix - Surf. Sci. **496**, 51-63 (2002).
[7] R.E. Tanner - Surf. Sci. **506**, 251-271 (2002).
[8] G.S. Wong, D.D. Kragten, J.M. Vohs - Surf. Sci. **432**, L293-297 (2000).

Problems of Gas Discharge Processing of Medical Instruments

A.G.Shishkin[1] and G.G.Shishkin[2]

[1] *Department of Computational Mathematics & Cybernetics, Moscow State University, Moscow, Russia*
[2] *Moscow Aviation Institute, Moscow, Russia*

Abstract
The use of gas discharge plasma for sterilization of different types of articles is considered. The main processes of plasma sterilization and requirements to gas discharges are discussed. The role of each process is estimated. The results obtained in plasma sterilization for the last several years are analyzed. The advantages and problems of plasma sterilization technique are shown.

1. Introduction and background of plasma sterilization
Various methods have been used for the sterilization of different types of articles including disposable and reusable medical equipment, materials and foods [1]. But all of them suffer from different great shortcomings. For example, sterilization by steam or by dry heat is not useful to sterilize materials that are adversely affected by such heat or steam. Ethylene oxide gas has also been used but suffers from residues on the articles to be sterilized, which may have adverse effects, particularly on patients and demands long-time period of detoxication. Radiation sterilization has been limited to large industrial applications because of the large investment to build gamma irradiation facilities, the stringent technical controls for safe operation and change of bulk properties of some nonmetallic materials.
Gas discharge plasma sterilization has been considered for several years [2] as an alternative to heat sterilization and as a method close to an ideal sterilization. The ideal sterilization system can be summarized as follows: quick turnaround time, low temperature, versatility, low toxicity. The ideal sterilization should at least have instrument turnaround time less than one hour as modern hospital steam sterilizers have; an operating temperature should be between 45-55$^{\circ}C$ as in ethylene oxide sterilizers; the technology of ideal sterilization should be adaptable for a wide range of applications and give a good safety with respect to both operators and patients as well as to the environment in general. From a fundamental point of view glow discharge plasmas approach the features desired for an ideal sterilization systems and realize the above demands [1, 3].
In present paper we discuss the main problems of the plasma sterilization and give estimations of the main underlying processes.

2. Physical and chemical sterilization agents
Viruses and bacterial spores are the most resistant microorganisms to various sterilization methods [4]. Bacterial spores are complex structural entities (Fig.1).

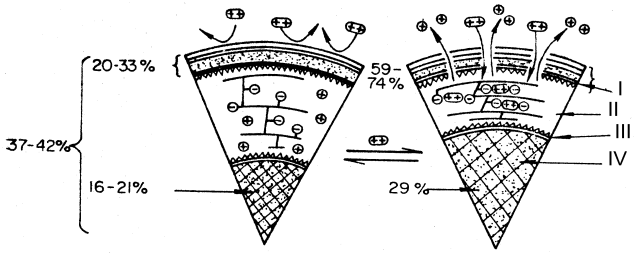

Fig.1 The surface structure of endospores. Here I is a coat, II is a cortex, III is a cytoplasmic membrane, IV is a core. The left part of the figure is a thermal stable anabiotic spore form, the right one is a thermal sensitive spore form. "+" denotes mono- and polyvalent ions, "-" denotes peptidoglycan ions, % denotes regional water content.
Bacterial endospores, that are spores formed within cells, are peculiar species of anabiotic cells. The structure of endospores includes multilayer albumen coats, outer and inner membranes, cortex and core (Fig.1). From the cytological point of view spores differ from vegetative cells primarily by its surface

structures that lie outside the cytoplasmic membrane and differ from each other drastically by chemical content:

- ?? by cortex that includes layer of mucopolymers lying between inner and outer membranes;
- ?? by covers that are the layers of protein nature covering the outer membrane;
- ?? by exosporium that is a structure lying outside the covers and having a form of wide coat (often with many layers) where the spore lies.

The cortex consists largely of peptidoglycan, and a dense inner layer (cortical membrane) develops into the cell wall of the emergent cell the cortex is degraded during germination. The inner and outer forespore membranes become the cytoplasmic membranes of the germinating spore or persist in the spore integuments, respectively. The spore coats consist mainly of protein. The RNA, DNA and most of the calcium, potassium, manganese and phosphorus are present in the spore and are located in the protoplast (spore core) [4].

The main factor that determines the ametabolic (anabiosis) state of spore protoplast is its relative dehydration. The obtained data show that dehydration of spore is of regional nature. The water content in the protoplast of intact spores is only about 16-21% (Fig.1) whereas in cytoplasm of vegetative cells it exceeds 80%. Spores have a perfect mechanism of stabilization of structures and cell macromolecules, of their defenses from the influence of both external and internal media.

Bacillus subtilis spores are very often used as a test objects. The thickness of the cell wall is 30-40 nm, the cell wall is a spongy structure with pore diameters (1-6) nm. The coat is adjoined to cytoplasmic membrane very tightly by fibralate bridges. Inner osmotic pressure of *B. subtilis* is 25-30 atmosphere. Optimal conditions of spore germination are: 7 days in peace, then heating at 60 C in 5 minutes. The sterilization conditions: vegetative cells perish in 5-10 minutes; 90% spores perish in 28 s for T=100 C and in 0.5 s for T=160 C [5].To sterilize the spores the chemical, physical and plasma physical processes are used.

Chemical agents - biocides

The comparatively high resistance of spores to many biocides is related to the presence of the spore coats and cortex [4]. Ethylene oxide (ETO) is effected by alkylation of amino groups in the proteinaceous structure of any microorganism. ETO sterilization requires the attachment of the entire ETO molecule, a polyatomic structure containing seven atoms to the protein. This is accompanied by the requirement of hydrogen atom rearrangement on the protein to enable the attachment of ETO. Because of the space factors governing the attachment of such a bulky molecule, the process needs to be carried out at high pressure and be extended over a long period of time [1]. There are two ways of chemical sterilization: gas (ETO) sterilization and with the help of aldehydes (glutaraldehyde and formaldehyde).

Physical agents

Effects of physical processes are connected with inactivation of bacterial spores by high temperatures, high doses of ionizing, ultraviolet or electromagnetic radiations, gas discharge plasma, vacuum and often by combinations of mentioned physical factors.

Temperature.

Thermal sterilization can be realized by moist and dry heat. Moist heat resistance depends upon several factors, in particular, on sporulation, heating and recovery conditions. The exact mechanism of heat resistance remains unclear, but the main reasons are associated with partial dehydration of coat and general molecular stabilization of core components (stabilization results from molecular rearrangements in the core).

The heat sensitive site and resistance to dry heat depends mainly on the location of water in the spore and on its association with other molecules [4].

Ionizing radiation. Ionizing radiation (IR) is highly lethal to most organisms. IR induces single strand and dirible strand breaks in microbial DNA that can be repaired and likely to inhibit DNA synthesis or cause some error in protein synthesis, leading to cell death [4]. Ionizations occur principally in water, resulting in the formation of short-lived, but highly reactive hydroxyl radicals and protons. Damage to DNA is brought about by OH radicals which are responsible for inducing strand breakage.

Ultraviolet radiation. Ultraviolet radiation (UV) is a less effective process than ionizing radiation since UV radiation does not possess energy to eject an electron to produce ion. UV spores resistance is associated with the ability and UV sensitivity with failure, to remove the spore photoproduct TDHT (5 thyminyl - 5,6 dihydrothymine). TDHT is identical to a product that accumulates in DNA exposed dry to UV radiation.

Vacuum. Vacuum influence on different micro-organisms have been investigated to understand panspermia problems connected with technical and ethical evolution of seeding nearby the solar systems [6]. There are

several mechanisms of vacuum destruction of microorganisms such as dehydration, diffusion osmotic pressure, biochemical effects, cell destruction connected with large inner pressure in vacuum condition etc.

Gas discharge plasma effects. The efficiency of plasma chemical processes is due to small sizes of the active plasma entities (usually monoatomic or diatomic) and therefore exhibit an enhanced ability to attach themselves to a proteinaceons structure and abstract hydrogen atom from it. Another specific types of interaction is rupturing ring structures, particularly those including nitrogen, or carbon-carbon bond cleavage.

Thus analysis of physical and chemical processes in existing sterilization methods shows that the main mechanisms leading to microorganisms perishing are the following ones:

- ?? dehydration of various elements of microorganism structure (thermal sterilization);
- ?? chemical reactions of sterilizing agent with chemical elements of microorganisms (gas sterilization);
- ?? energy damage and excitation of atom and molecule structures of microorganisms resulting in sporicidal compound formations (ultraviolet and radiation sterilization);
- ?? mechanical damage of microorganism structures (vacuum, particle bombardment etc.).

All these processes are relevant to the gas discharge plasma generated for the certain degree of rarefaction.

3. Discharges suitable for sterilization

All sporicidal processes in plasma can be divided into two large groups: physical and plasma-chemical ones. It should be noted that in any case these two groups cause the interaction of particles with the surfaces of medical instruments. This is especially important for metal, dielectric (polymer) instruments and some other products that can change their physical properties under the influence of plasma processes such as sputtering and vaporization of surface material, adsorption of surface atoms etc.

The intensity of these processes strongly depends on particle energy distribution. In Fig.2 the dependences of ions and neutral particles energy distribution are shown for different plasma-vacuum processes. Curve 1 corresponds to theoretical material vaporization. Thermal heating is due to the surface heating by particle fluxes from the plasma to the surfaces of instruments. Curves 2 show the energy distribution of vaporized particles near the electrodes, one of which can be the processed instrument. It should be noted that in principle the instrument can be not only sputtered because of plasma action but also can be covered by thin film formed by sputtering of other elements of gas discharge (sterilizing) chamber. The particle distribution function for different shift potentials between the discharge and electrodes that create the plasma is illustrated by curves 3 and 4.

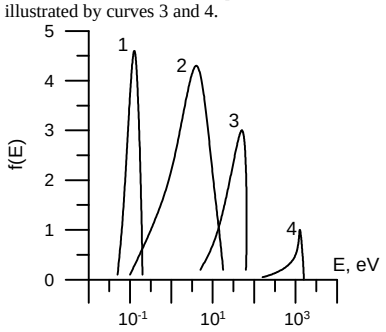

Fig.2 Ion and neutral particles distribution function in arbitrary units for different plasma-vacuum processes.

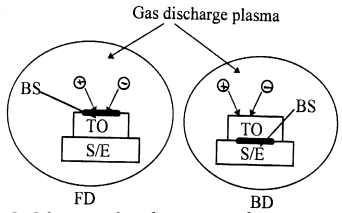

Fig.3: Schematic plot of two types of experiments to study the effect of particle bombardment. Here BS denotes *B.subtilis*, TO - test-object, S/E - substrate or electrode. FD: *B.subtilis* are bombarded by particles. BD: bombardment is absent.

In most cases the plasma ion bombardment of surfaces prevails over other processes during material sputtering. The impulse transfer in elastic collisions resulting in direct knocking-out of atoms from equilibrium states is the main way of interaction between bombarding ions and material atoms.

The ion sputtering of material starts when the ion energy E_i exceeds the threshold value E_{thr}. The energy E_{thr} depends weakly on the masses of colliding particles and lies in the range 10-30 eV [7]. For plasma

sterilization of medical instruments the ion energy must be less than E_{thr}. In that case ions do not sputter the material. During the intensive ion bombardment the surface layers of monocrystals first are transformed into polycrystal layers and then into amorphous ones. In most cases it is inadmissible for medical instruments.
The average distance the intruded ion covers before being stopped depends on ion energy and atom number both the intruded ion and bombarded material. For example, the average depth of Ar^+ intrusion into aluminum equals to ~1.5 nm/keV (this value is significantly greater for dielectrics). 70-90% of ion energy is dissipated into the material in the heat form, less than 5% is expended on the sputtering and the rest part of the energy is expended on the radiation damage of material, ion intrusion and secondary electron emission and electromagnetic radiation in a wide frequency range [7].
Thus to approach the features desired for an ideal sterilization systems it is necessary to create a plasma with definite values of parameters such as:

1. The energy of falling-down on the electrodes particles must be as low as possible to exclude the sputtering and damage of dielectric and metallic products;
2. The operating gas of the discharge must allow to create sporicidal agents;
3. To prevent the intensive heating of sterilized products the particle fluxes to their surfaces must be small that is the plasma current density must be insignificant;
4. Discharge plasma must provide the complex physical and chemical actions on microorganisms for greater efficiency and reliability of sterilization. Among these actions are thermovacuum actions, radiation treatment of products by electromagnetic fields and some other effects [8].

Among the large number of gas discharges studied to the moment the discharges in alternative fields especially high-frequency (HF) and microwave (MW) ones meet the above requirements. In alternative fields discharges the electrodes can be absent and this is an advantage for the sterilization. Such discharges can be divided in low frequency (LF) and impulse ones with a long duration of a pulse, HF (radio frequency) and MW discharges. Low-frequency fields ($f < 10^5$ Hz) do not result in any additional effects that differ drastically from the direct electric field discharges. The typical frequency for HF discharges is ~10^5-10^8 Hz, for MW ones – 10^9-10^{11} Hz.

4. Plasma sterilization action

To determine the role of particle bombardment we used LF and HF capacitive and inductive air gas discharges. The test-objects with *B.subtilis* were located inside plasma in two different manners: they were (FD) and were not (BD) subject to particle bombardment action (Fig.3). The results are in Table 1.

Table 1. Influence of particle bombardment on *B.subtilis* survival (*N*). N_0 is initial number of organisms.

τ_{st}, min	Test-object (TO)	Substrate material	*N*
f=27 MHz, *p*=1 Torr, P_{RF} =65-70 W, $N_0 = 10^4$			
1	*Al* foil BD	Teflon	10^2 - 10^3
1	*Al* foil FD	Teflon	0
20	glass BD	Teflon	10^0
20	glass FD	Teflon	0
20	rubber BD	Teflon	10^2
20	rubber FD	Teflon	0

Plasma chemical processes

Operating gas selected for plasma sterilization determines not only the antimicrobial species but also toxicity-related factors such as chemical residues and products from the process. It is very desirable to have active species with high sporicidal activity such as OH, H_2O, O and H in plasma and to select precursors gases with nontoxic compounds such as O_2, H_2O and H_2. In order to evaluate their relative sporicidal activity, oxygen, hydrogen, nitrous oxide, nitrogen dioxide and others in various combinations as precursor gases were used for microwave and RF discharges (Fig.4) [9]. The mechanism for the generation of the highly reactive mixture in a hydrogen peroxide plasma can be simplified as illustrated below [3]:

$$H_2O_2 \text{ - H-O-O-H} \xrightarrow[1 < 10eV]{e} HO^{\cdot} + {}^{\cdot}OH; \qquad HO^{\cdot} + \text{H-O-O-H} \rightarrow HOH + {}^{\cdot}\text{O-O-H}$$

$$\text{H-O-O-H} \xrightarrow{e,\ h\nu} \text{H-O-O-H}^{\cdot}; \qquad \text{H-O-O-H}^{\cdot} \rightarrow \text{H-O-O-H + optical radiation including UV radiation.}$$

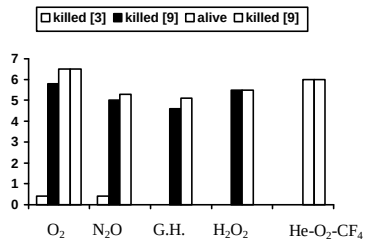

Fig.4: Sporicidal activity of various plasmas against *B. Subtilis*. Here *N* is the number of microorganisms, *G.H.* stands for glutaraldehyde.

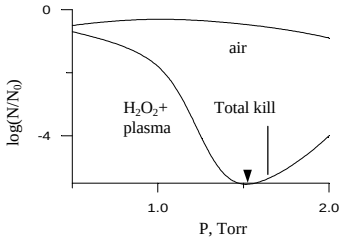

Fig.5: Effects of gas pressure on sporicidal activity of plasma. N and N_0 are the surviving and initial numbers of microorganisms.

The efficacy of these processes depends on hydrogen peroxide concentration, gas pressure and RF power [3] (Fig.4,5) and is connected with the fact that active plasma species are small in comparison with ethylene oxide. The space restriction for these species is at least one thousand time lower than that for ETO alkylation and so they penetrate into bacteria through pores (diameter 1-6 nm for *B.Subtilis*) in outer covers and attach themselves to a proteinaceous structure and abstract hydrogen atoms from it. Another specific type of interaction is rupturing ring structures with nitrogen or carbon-carbon bond cleavage. These processes produce only gaseous effluents (for example H_2O and O_2). There are many oxygen atoms in hydrogen peroxide and air plasmas, so negative oxygen ions are produced very effectively. In the patent [9] examples of sporicidal activity of different gases (O_2, N_2, *He*) and gas mixtures such as O_2-CF_4, (O_2-*He*)-CF_4, (O_2-CF_4)-*He*, air are given for sterilization temperature about 60°C. The most sporicidal activities are inherent in O_2 and oxidizing gas mixture (Fig.4). A predominance of oxygen in the above mixture is preferred but not mandatory [9]. The inert gas fraction can be varied in the range 10 to 95%; the higher the fraction the lower the processing temperature for a given pressure and power density, but sterilization exposure time increases the higher the inert gas fraction in the mixture.

Thermovacuum effects

Analysis of microorganism stability in vacuum for various temperatures is the most informative one for understanding high vacuum action on microorganisms. Investigations show that microorganisms destruction does not change for residual pressure $10^{?1}$-$10^{?9}$ Torr. The total temperature range for these pressures can be divided on three ranges: from cryogenic till room ones, 20-70°C and higher than 70°C.

Table 2. Thermal-vacuum processing of test objects for p~1 Torr, $N_0=10^5$ *B.subtilis*. Figures in table denote the total (sterilized) number of test-objects.

Type of test-object	$?_{st}$, min	Sterilization temperature, °C		
		110	130-135	120-125
metal	15		7(7)	7(7)
glass	15		6(6)	1(1)
metal	60	6(6)	3(3)	6(6)
glass	60	4(4)		4(4)

Table 3. Survival of *B.subtilis* on different materials. Here f=40 MHz, P_{RF}=100 W, p=0.1-1 Torr, $N_0=10^5$, TO is test-object.

Material of TO	$?_{st}$, min	N
rubber	(1-5)/10	$10^4/10^3$
glass	(1-5)/10	10^3-$10^4/10^2$
Al foil	(1-5)/10	0/0
rubber	10	10^3-10^4
glass	10	10^2
Al foil	10	0

For high temperatures (T>70°C) irreversible injures of bacteria membranes and outer covers are predominant ones. These injuries are provoked by cell water vaporization, complex biochemical processes connected with protein denaturation etc. Results of our investigation for pressure 0.1-1 Torr in 110-135°C range are given in Table 2 where 7(7), 6(6) are control (sterilized) number of test-objects. Heating of test-objects have been carried out by inductive RF coil without gas discharge. *B. Subtilis* spores can be killed by

thermal-vacuum effects for temperature below 120 C. These results agree with Silverman's and Beecher's findings for survival of cocci after exposure to ultra high vacuum and different temperatures [10].

Ultraviolet radiation and elecromagnetic field

Bacterial spores are inactivated by high doses of ultraviolet (UV) radiation. UV light is only slowly lethal to spores and thus is not considered to be a sterilization. As for the electromagnetic field action our estimations and experiments show that it can change inner processes in cells.

Influence of medical instruments material

Medical instruments are substrates for microorganisms. Our microbiological testing of an efficacy of sterilization on test-objects from different materials including rubber, stainless steel, aluminum, glass etc. showed that spores were injured more effectively on metal test-objects than on dielectric ones (Table 3).

Physical contact between a microorganism and solid state determines charge distributions and influence on ion transport of cell [11]. Contact parameters cell-metal and cell-dielectric are considerably different. Possible reasons of bacteria injury on metal and dielectric are connected with charge transition between bacteria and different solid states and with thermal conditions of the material.

5. Discussion. Plasma sterilizers

Our analysis of experimental data show that there are no special difficulties for the sterilization of medical products having direct contact with a plasma. Under the influence of all considered above processes microorganisms perish in several seconds or minutes at worst. The particle bombardment, thermovacuum conditions and the dynamics of change of parameters that determine these conditions play the main role. The problems of microorganisms killing in hollows, channels and hidden surfaces of medical instruments made from metal, ceramic, glass, plastic and other solid materials are quite difficult. In such cases the sterilization is due to plasma-chemical, thermal and vacuum processes. As a confirmation of that is an only industrial plasma sterilizer STERRAD by Johnson & Johnson Medical Ltd.

STERRAD-100 is a sterilizer for the processing of thermo-sensitive medical products that uses low temperature gas discharge hydrogen peroxide plasma [12]. Plasma generated is by its nature a plasma-chemical reactor that creates sporicidal factors described above. Sterilization time is about 75 min. It is necessary to use special adapters for long narrow products. Closed from one end channels are hardly processed due to weak penetration properties of H_2O_2 and its fractions since there is no gas movement. Beside some materials adsorb H_2O_2 resulting in decrease of its concentration and in negative consequences.

Thus in our opinion the main problems to be solved are the following ones:

1. To eliminate the use of special operating gases such as H_2O_2 since it leads to the complication of plasma system constructions and their service. The best solution is a use of air.
2. To find the optimal combination of plasma-chemical and plasma-physical processes.
3. To study the influence of dynamics of parameters change on the sterilization efficiency.
4. To sterilize the narrow channels especially closed from one end, hollows, hidden surfaces etc.
5. To sterilize the cotton, woven, other organic materials and some polymer and synthetic products.

References

[1] J.A.Lindsey, W.G.Murell, A.D.Warth, in *Sterilization of Medical Products*, edited by L.E.Harris and A.J.Skopek (Johnson & Johnson, North Ryde, v.III, p. 162-186, 1986).

[2] G.G.Shishkin, A.G.Shishkin, *Proc. 12 Int. Conf. Gas Disch.&Their Appl.* (Greifswald, II, p.783, 1997).

[3] T.O.Addy, in *Sterilization of Medical Products - Proc. Int. Kilmer Conf. On Steriliz. Med. Prod.*, edited by R.F.Morrissey and Yu.I.Prokopenko (Johnson & Johnson, Canada, p. 81-95, 1986).

[4] A.D.Russel, Ibid, p.22-42, 1981.

[5] B.V.Gromov, *Bacterial Structure* , 1985 (in Russian).

[6] M.D.Nusinov, *Influence and Modelling of Space Vacuum* (Mashinostroenije, Moscow, 1982).

[7] B.S.Danilin, Low temperature plasma applications for thin films deposition,(Enorgoizdat, Moscow, 1989)

[8] A.G.Shishkin, G.G.Shishkin, *Proc.11th Int. Conf. Gas Disch. & Their Appl.* (Tokyo, v.1, p.462, 1995).

[9] A.Jacob, Int. Patent WO 88/06459 (1988).

[10] G.S.Silverman, N.Beecher, Appl.Microbiology, **15**, 665 (1967).

[11] *Electrical Regulation System of Vital Functions*, ed. by G.Zatsepina (MSU Publ., Moscow, p.28,1992).

[12] M.S.Kyi, J.Holton and G.L.Ridgeway, J.Hosp.Inf., **31**, 275 (1995).

The recombination of D_3^+ and D_5^+ with electrons - Dependence on partial pressure of D_2 and on temperature

J. Glosík, A. Pysanenko, O. Novotný, P. Zakouřil, R. Plašil, V. Poterya

Charles University Prague, Mathematics and Physics Faculty, Department of Electronics and Vacuum Physics, V Holešovičkách 2, 180 00 Prague 8, Czech Republic, juraj.glosik@mff.cuni.cz

Abstract

The flowing afterglow and stationary afterglow experiments were used to study recombination of D_3^+ and D_5^+ ions with electrons in afterglow in He-Ar-D_2 mixtures. Two experiments were used to cover large extend of pressures of He buffer gas (2-10 Torr) and large extend of partial number densities of D_2 (10^{10}-10^{16} cm^{-3}). It was observed that the rate of the decay of D_3^+ and D_5^+ containing afterglow plasma is dependent on partial pressure of D_2 and on temperature.

Introduction

The ions H_3^+ and D_3^+ have been the subject of a number of studies because of their important roles in the astrophysical and laboratory research. Recent discovery of interstellar H_3^+ in molecular clouds has opened a problem of observed high column density, which critically depends on the rate of recombination of H_3^+ with electrons. The kinetics of the formation of H_3^+ and D_3^+ ions and their reactions with neutrals are well understood. However, despite enormous efforts the results of studies determining the rate of recombination of H_3^+ and D_3^+ ions with electrons are very controversial [1]. In the late nineties, it was generally accepted that recombination coefficient for H_3^+ ions $\alpha \sim 2\times10^{-7}$ cm^3 s^{-1}. This finding was in agreement with results of many beam studies and several afterglow experiments. Studies of D_3^+ recombination reported smaller rate coefficient values, generally by a factor about 1-4. Among the recent measurements on D_3^+ recombination, we wish to mention explicitly flowing afterglow (FALP) studies of the recombination of D_3^+. Smith and Španěl obtained in FALP studies $\alpha \sim 2\times10^{-8}$ cm^3 s^{-1} [2]. In 1995, Gougousi *et al.* [3] obtained in the FALP study $\alpha \sim (0.7\text{-}1.3)\times10^{-7}$ cm^3 s^{-1} dependent on deuterium partial pressure. Laubé *et al.* [4] obtained in FALP-MS a value of $\alpha \sim 0.7\times10^{-7}$ cm^3 s^{-1}. All experimental recombination rate coefficients obtained at thermal energies for both H_3^+ and D_3^+ are significantly larger than the values predicted by theory [5,6]. In our recent study of recombination of D_3^+ ions with electrons we have observed strong dependence of recombination rate coefficient of recombination of D_3^+ ions on partial pressure of D_2 [7]. In present study we further increased partial pressures of D_2 and buffer gas pressure to enhance formation of D_5^+ and to measure recombination in afterglow plasma containing mixture of D_3^+ and D_5^+.

Experiment

The Flowing Afterglow with Langmuir Probe (FALP) is based on simple principle: the buffer gas flowing along the flow tube is carrying decaying plasma created upstream in the plasma source. In the different positions along the tube there is plasma in different degree of decay. The cardinal condition is to adjust parameters in the flow tube in such a way that the process under study is the dominant process during the afterglow. In present experiment it is the recombination of D_3^+ and the formation and destruction of D_5^+. High pressure and low temperature is required to form D_5^+. These conditions are fulfilled in our High Pressure Flowing Afterglow – HPFA. In the present UHV version of HPFA the differential pumping of mass spectrometer chamber is used to increase the operational pressure of the buffer gas. The HPFA has been described in detail previously [8,9], so only short description will be given. The schematic diagram in Figure 1 outlines the essential parts of the used HPFA. The axially movable Langmuir probe (tungsten wire 14 μm in diameter and 7 mm long) is used to determine the electron number densities along the flow tube. A region of the saturated electron current of probe characteristics is used to calculate electron number densities. **Formation of $D_3^+/D_5^+/e^-$ plasma**: The pure He is flowing through the microwave discharge and He^+, He^m and electrons are formed. Downstream from the discharge region (position corresponding to ~ 1 ms of the decay time) Ar is added to the flow and the plasma is converted to the Ar^+ dominated plasma.

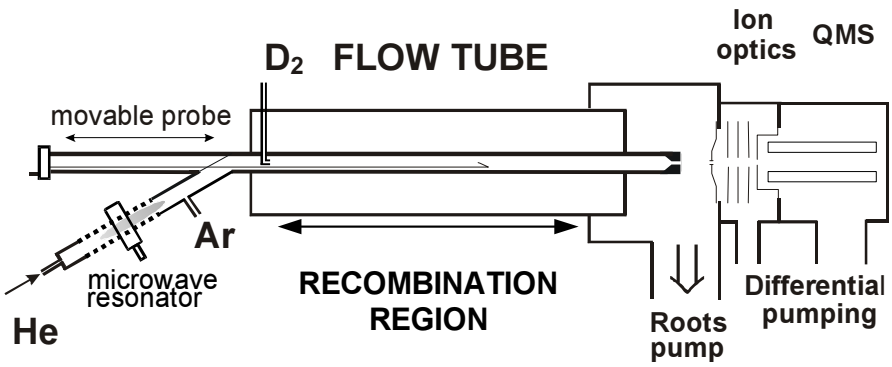

Figure 1: The schema of High Pressure Flowing Afterglow. QMS indicates the downstream mass spectrometer with a detector.

Further downstream (~ 2 ms of the decay) deuterium is added to the already relaxed Ar^+/electron plasma and D_3^+/D_5^+/electron plasma is formed in a sequence of ion-molecule reactions. The kinetics of these processes is well understood and the rate coefficients are known. The rate coefficients of the reactions important in the formation of D_3^+ and D_5^+ ions are given in Table 1 [10]. Briefly, deuterium reacts with Ar^+ ions to form ArD^+ (major channel) and some D_2^+. Both ions react further with D_2 and D_3^+ ions are formed. In the present experiment the high pressure and lower temperature of the buffer gas is essential to enhance formation of D_5^+. We are not discussing eventual vibrational excitation of recombining ions, because of high probability of deexcitation in multiple collisions with He and D_2 We assume that few cm downstream from deuterium entry port the plasma is fully thermalised and the temperature of the ions and of the electrons is equal to the temperature of the buffer gas, this assumption is confirmed by the probe measurements of the electron temperature in the decaying plasma. Relaxation of kinetic and rotational temperature of H_3^+ ions in similar conditions is discussed in accompanying paper [11].

TABLE 1: Rate coefficients of the reactions are participating in the formation of D_3^+ and D_5^+ ions. The reaction rate coefficients are given for 300 K. The typical reaction times were calculated for decay at 9 Torr of He and for $[D_2] = 4\times10^{14}$ cm^{-3} and $[Ar] = 3\times10^{13}$ cm^{-3}. (*) Rate coefficients were deduced from equivalent reactions with hydrogen.

Reaction	Rate coefficient [cm^3 s^{-1}] or [cm^6 s^{-1}]	Reaction time [ms]
$He^+ + 2He \rightarrow He_2^+ + He$	1×10^{-31}	1.1×10^{-1}
$He^m + Ar \rightarrow Ar^+ + He + e$	7×10^{-11}	4.8×10^{-1}
$He_2^+ + Ar \rightarrow Ar^+ + 2He$	2×10^{-10}	1.7×10^{-1}
$Ar^+ + D_2 \rightarrow ArD^+ + D$ $\rightarrow D_2^+ + Ar$	7.5×10^{-10} ArD^+ is dominated	3.3×10^{-3}
$D_2^+ + Ar \rightarrow ArD^+ + D$	1.5×10^{-9}	2.2×10^{-2}
$D_2^+ + D_2 \rightarrow D_3^+ + D$	1.6×10^{-9}	1.6×10^{-3}
$ArD^+ + D_2 \rightarrow D_3^+ + Ar$	4.6×10^{-10}	5.4×10^{-3}
$D_3^+ + D_2 + He \rightarrow D_5^+ + He$	$<1 \times 10^{-29}$ *	8.4×10^{-1}
$D^+ + He + He \rightarrow DHe^+ + He$	0.9×10^{-31} *	1.2×10^{-1}

The axially movable Langmuir probe enables the measurement of the electron number density n_e along the flow tube. In the Figure 2 examples of probe characteristics measured along the flow tube in the D_3^+/D_5^+/electron plasma are plotted. Because of the semilogarithmic plot the absolute values of the probe current are used in the plot (the branches corresponding to electron and ion current are plotted both with

positive sign). The values of n_e(t) are obtained from the slope of the plot of I_e^2 versus probe potential, U. The examples of such plots are given in Figure 3.

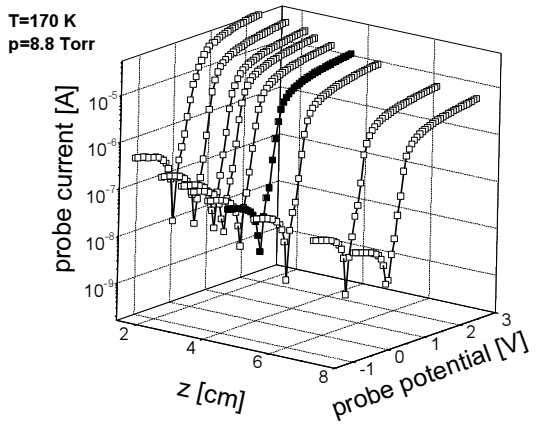

Figure 2: The evolution of the probe characteristics along the flow tube. Decay time is correlated with position along the flow tube, $z = \upsilon_p \cdot t$. The probe potential U_p is measured against the potential of the metal body of the flow tube.
P_{He} = 8.8 Torr, Ar flow 1.1 sccm (corresponding to 1.4 mTorr), $[D_2] = 2.4\times10^{14}$ cm^{-3}, T = 170 K.

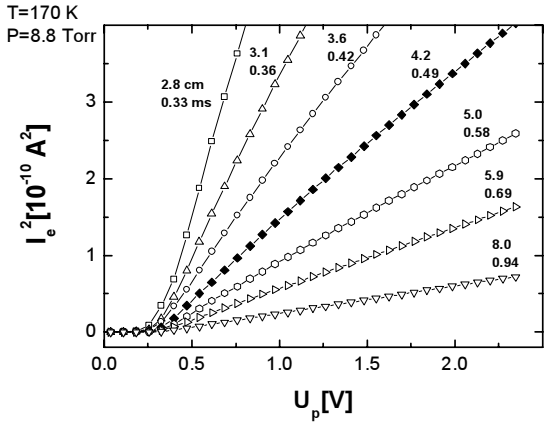

Figure 3: The examples of plots of I_e^2 versus probe potential. The data were measured at different positions (decay times) along the flow tube. The slopes of linear portions of the plots provide the electron number densities. The data from Figure 2 are used in the plot. The numbers indicate position in the flow tube (z) and corresponding decay time in cm and ms, respectively.

Data analysis

If D_3^+ ions are the dominant ions in decaying plasma and the diffusion can be neglected then the determination of the rate coefficient (α_3) is straightforward. The balance equation for electrons is:

$$\upsilon_p \frac{dn_e(z)}{dz} = \frac{dn_e(t)}{dt} = -\alpha_3[D_3^+]n_e = -\alpha_3 n_e^2 \tag{1}$$

Where z, υ_p and t are a position in the flow tube, plasma velocity and decay time, respectively. These parameters are coupled by equation: $z = \upsilon_p \cdot t$. $[D_3^+]$ indicates number density of D_3^+, and α_3 is the recombination rate coefficient. Last equality is given by quasineutrality of the plasma, $n_e = [D_3^+]$. The solution of the balance equation is:

$$\frac{1}{n_e(t)} = \frac{1}{n_e(0)} + \alpha_3 t \tag{2}$$

Thus a plot of $1/n_e$ against t should be linear if the recombination rate coefficient is constant along the flow tube.

In HPFA at a relatively low temperature and at high pressures of He and D_2 a formation of cluster ions D_5^+ in three-body association reaction and their destruction by a collision induced dissociation (CID) in collisions with He atoms [12,13] can play essential role. On such case we have to consider reaction scheme:

$$D_3^+ + D_2 + He \underset{k_{-3}}{\overset{k_3}{\leftrightarrow}} D_5^+ + He \tag{3}$$

Where k_3 is the rate coefficient of the three-body association (the forward process) and k_{-3} is the binary rate coefficient of the CID (the reverse process). In the same time both ions recombine with electrons:

$$D_3^+ + e \xrightarrow{\alpha_3} products \tag{4}$$

$$D_5^+ + e \xrightarrow{\alpha_5} products \tag{5}$$

Where α_3 and α_5 are respective recombination rate coefficients. We are not considering diffusion losses at this moment. In actual data analysis we are taking diffusion into account. When considering processes (3), (4) and (5), the balance equation for electrons is:

$$\frac{dn_e(t)}{dt} = -\alpha_3[D_3^+]n_e - \alpha_5[D_5^+]n_e = -\left(\alpha_3 + R\alpha_5\right)\frac{n_e^2}{1+R} = -\alpha_{eff}n_e^2 \tag{6}$$

Where $R = [D_5^+]/[D_3^+]$, $n_e = [D_3^+] + [D_5^+]$. We introduced here effective recombination rate coefficient α_{eff} by equation:

$$\alpha_{eff} = \left(\alpha_3 + R\alpha_5\right)\frac{1}{1+R} \tag{7}$$

If the ratio R is constant during the decay of the plasma (along the flow tube) then α_{eff} is constant and we can observe decay typical for plasma governed by recombination. Such situation occurs e.g. if the ions are during the decay of the plasma in the equilibrium described by the scheme (3). For ions in equilibrium we can write:

$$R = [D_5^+]/[D_3^+] = k_3[D_2]/k_{-3} = K_C[D_2] \tag{8}$$

Where K_C is the equilibrium constant, given by an entropy and an enthalpy change (van't Hoff equation) [14,15]. Using K_C and $[D_2]$ the equation (7) can be written in the form:

$$\alpha_{eff} = \left(\alpha_3 + \alpha_5 K_C[D_2]\right)\frac{1}{1+K_C[D_2]} \tag{9}$$

This equation describes the influence of a deuterium partial pressure on the overall (apparent) rate of the recombination in $D_3^+/D_5^+/e^-$ plasma. From equation (9) follows: for a very small $[D_2]$ $\alpha_{eff} = \alpha_3$, for a medium $[D_2]$ value $\alpha_{eff} = \alpha_3 + \alpha_5 K_c [D_2]$ and for very high deuterium pressure $\alpha_{eff} = \alpha_5$. This conclusion is obvious; for very small $[D_2]$ formation of D_5^+ is negligible and the recombination of D_3^+ is dominant, for a medium $[D_2]$ both ions recombine and for very high deuterium pressure formation of D_5^+ is very fast and its recombination is the dominant loss process. If α_{eff} is constant then the solution of the equation (6) is given by formula (2).

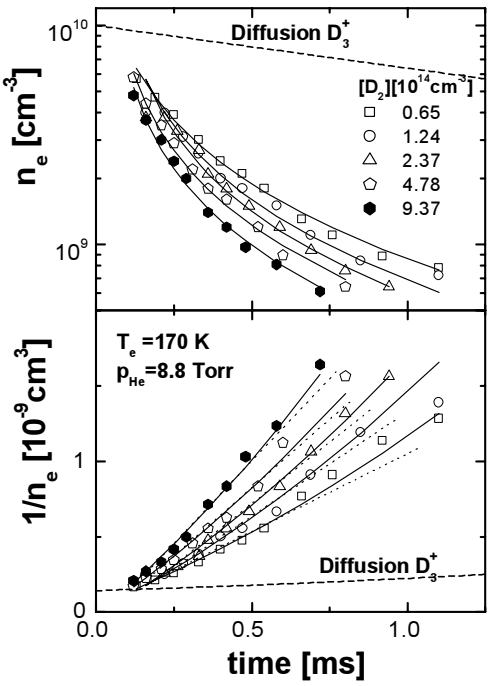

Figure 4: The decay of the plasma containing a mixture of D_3^+ and D_5^+ ions at 170 K and P_{He} = 8.8 Torr.
Upper panel: The decay of the electron number density measured at several number densities of deuterium.
Lower panel: The corresponding plots of $1/n_e$ versus decay time.

Results and Discussion

We have measured decay of the plasma in He/Ar/D_2 mixture at several temperatures ranging from 170 K up to 260 K. The deuterium number density was changed from $[D_2] = 2\times10^{13}$ cm^{-3} up to $[D_2] = 10^{16}$ cm^{-3}. This

large variation makes it possible to cover plasmas dominated: by the recombination of D_3^+ ions, by the recombination in the mixture of D_3^+ and D_5^+ ions and also by the recombination of D_5^+ ions only. In Figure 4 there is example of several decay curves measured in one set of measurements at 170 K, 8.8 Torr, Ar flow 1.1 sccm (corresponding to 1.4 mTorr). In the lower panel there are reciprocal plots. The dashed line indicates decay dominated by the diffusion; the dotted lines indicate the fit by the simple formula (2) considering only the recombination losses. From the data plotted in Figure 4 it is obvious that the decay of plasma at 170 K is dependent on a deuterium number density.

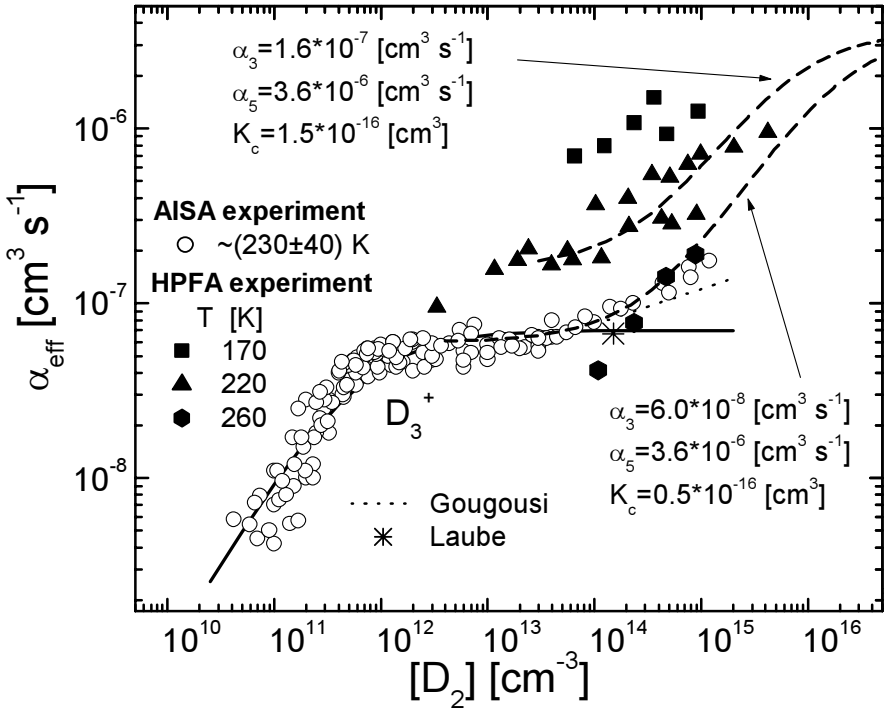

Figure 5: The effective recombination rate coefficients α_{eff} measured over very broad range of deuterium number densities on AISA (open symbols) and on HPFA (closed symbols).

We will not discuss here data obtained on AISA at very small deuterium number densities, $[D_2] < 10^{12}$ cm^{-3} where is D_5^+ not formed in time scale of experiment and cannot play role [7] in variation of α_{eff} with $[D_2]$. Lets consider at this moment data obtained on HPFA at 260 K and data from AISA obtained at 230 K as data corresponding to one temperature. Increase of α_{eff} at $[D_2] > 5\times10^{13}$ cm^{-3} observed in both experiments can be explained by formation of D_5^+ ions. We assume that α_3 is given by value of α_{eff} at $[D_2] \sim 10^{13}$ cm^{-3} , which gives $\alpha_3(260\text{ K}) = 7\times10^{-8}$ cm^3 s^{-1}, and we also assume that H_5^+ and D_5^+ have similar recombination rate coefficients and $\alpha_5(D_5^+, 260\text{ K}) \sim \alpha_5(H_5^+, 260\text{ K}) = 3.6\times10^{-6}$ cm^3 s^{-1} [16]. Using these values we can fit the data with function (9) to obtain K_C, see dashed line in Figure 5. It is evident that observed increase of α_{eff} can be explained by formation and consequent recombination of D_5^+.

By assuming that $\alpha_5(D_5^+)$ is not changing substantially with temperature we have used value $\alpha_5(D_5^+) = 3.6\times10^{-6}$ cm^3 s^{-1} to fit the data obtained at 195 K (not plotted in Figure 5) and 220 K and we obtained $K_C(195) = (1.5\pm0.7)\times10^{-16}$cm^3 and $K_C(220) = (1.1\pm0.4)\times10^{-16}$cm^3, respectively. The obtained K_C are in excellent agreement with thermodynamic data obtained by Hiraoka and Mori [17] in their high-pressure mass spectrometer. We have studied also pressure and temperature dependence of recombination in $H_3^+/H_5^+/e^-$ plasma [18,19] and we obtained similar results.

The aim of the present work was to study influence of formation of D_5^+ in $D_3^+/D_5^+/e^-$ plasma and to define regions of partial pressures and temperatures where formation of D_5^+ cannot be neglected in deionisation of deuterium containing plasma. The study confirms that pressure dependence of α_{eff} at $[D_2] < 5\times10^{13}$ cm^{-3} observed in AISA experiment is not due to formation of D_5^+.

Acknowledgement
Thanks for financial support are due to GACR (205/02/0610, 202/02/0948). The experiments were carried out with support from EC's RTN under contract HPRN-CT-2000-0142, ETR and with support from Euroatom.

References

[1] R. Plašil, J. Glosík, V. Poterya, P. Kudrna, J. Rusz, M. Tichý, A. Pysanenko - *Int. J. Mass Spectr.* **218**, 105 (2002).
[2] D. Smith, P.·Španěl - *Int. J. Mass Spectrom. Ion Proc.* **129**, 163 (1993).
[3] T. Gougousi, R. Johnsen, M.F. Golde - *Int. J. Mass Spectr. Ion Proc.* **149/150**, 131 (1995).
[4] S. Laubé et. al - *J. Phys. B.* **31**, 2111 (1998).
[5] I. F. Schneider, A. E. Orel, A. Suzor-Weiner - *Phys. Rev. Lett.* **85**, 3785 (2000).
[6] V. Kokoouline, C.H. Greene, B.D. Esry - *Nature* **412**, 891 (2001).
[7] V. Poterya, J. Glosík, R. Plašil, M. Tichý, P. Kudrna, and A. Pysanenko - *Phys. Rev. Lett.* **88**, 044802 (2002).
[8] J. Glosík P. Zakouřil, V. Hanzal, V. Skalský - *Int. J. Mass Spectr. Ion Proc.* **149/150,** 187 (1995).
[9] J. Glosík, G. Bánó, R. Plašil, A. Luca, P. Zakouřil - *Int. J. Mass Spectrom.* **189,** 103 (1999).
[10] V.G. Anicich - *J. Phys. Chem. Ref. Data* **22** (1993).
[11] R. Plašil, G. Bánó, J. Glosík, P. Macko, P. Hlavenka, A. Pysanenko, P. Kudrna, V. Poterya, in present volume, ISPC 2003.
[12] J. Glosík, V. Skalský and W. Lindinger - *Int. J. Mass Spectr. Ion Proc.* **134**, 67, (1994).
[13] J. Glosík, V. Skalský, C. Praxmarer, D. Smith, W. Freysinger and W. Lindinger - *J. Chem. Phys.* **101**, 3792, (1994).
[14] P.W. Atkins, Physical Chemistry - *Oxford University Press, Oxford* (1988).
[15] K. Hiraoka, P. Gebarle – *J. Chem. Phys*. **62**, 2267 (1975).
[16] M.T. Leu, M.A. Biondi, R. Johnsen - *Phys. Rev. A.* **8**, 413 (1973).
[17] K. Hiraoka and T. Mori - *J. Chem. Phys.* **91,** 4821 (1989).
[18] J. Glosík, O. Novotný, A. Pysanenko, P. Zakouřil, R. Plašil, P. Kudrna, V. Poterya, K. Dryahina - Submitted for publication in, Plasma Source Science & Technology (2003).
[19] A. Pysanenko, O. Novotný, P. Zakouřil, R. Plašil, V. Poterya, J. Glosík - *Czech. J. Phys.* **52,** D681 (2002).

Low-pressure arc discharge plasma sources

P.M. Schanin, N.N. Koval, S.V. Grigoriev

Institute of High Current Electronics, RAS, Tomsk, Russia

The low voltage and low pressure at which the high - current arc discharge is initiated and steadily burns allow one to consider this discharge promising for the production of gas plasmas of high density in large volumes. The high plasma density with reasonable homogeneity at low pressures makes it possible to realize the different technological processes of surface modification with high energetic efficiency: ion nitriding, plasma - assisted deposition and ion implantation [1, 2, 3, 4].

Two types of stationary arc discharge sources with a hollow cathode are presented. In the first type of source a non self-sustained arc is initiated by the electrons emitted by a hot W-filament inserted into hollow cathode. The cylindrical hollow cathode of diameter 100 mm and length 150 mm is immersed in the axial magnetic field created by a magnetic coil. The electrons emitted by the filament in the magnetic field efficiently ionize the working gas that is leaked in the hollow cathode and produces gas plasma. The non magnetized ions accelerated in the cathode potential fall knock secondary electrons and enhance ionization processes in discharge gap between the hollow cathode and working chamber which serve as a hollow anode in this discharge system. A low pressure arc discharge with a low burning voltage is thus established. The discharge current can be controlled over a range without a cathode spot by varying the filament current and the gas flow rate in hollow cathode. Discharge currents of 30 A to160 A have been obtained with the filament current varied in the range from 90 to 130A and discharge voltage of 50 V and flow rate of 96 sccm and magnetic field of 0.02 T. The plasma with density of $n_e = 1\times10^{11}$ cm^{-3} and temperature Te = 5 eV was generated in the vacuum chamber volume of 0.3 m^3 at an Ar-gas pressure of 3×10^{-1} Pa and a discharge current of 50 A.

The plasma source with a cold hollow cathode was developed to produce plasmas of chemically active gas such as O_2, CH_4, and the like. The design and the power supply circuit of discharge system are similar to these considered above, but the initiation of an arc is performed by a trigger system based on a dielectric flashover, placed inside the hollow cathode. The cathode spot develops on the internal surface of the hollow cathode and produces primary plasma. In traversed electric and axial magnetic fields, the cathode spot executes a rotational motion over the internal surface of cathode at a maximum of magnetic field. The electrons emitted by the cathode spot and accelerated in the cathode potential fall ionize the gas in the hollow cathode and in the discharge gap. In these conditions, the ions, atoms, and droplets of the cathode material deposit on opposite, relative to the spot, side of the hollow cathode and this increases the cathode lifetime. Experiments have shown that there is practically no cathode material in the plasma of the working chamber and the erosion rate of this cathode is about ten times smaller then that of a conventional arc.

In similar discharge condition the first type plasma source produces oxygen plasma with density $n_e = 5\times10^{10}$ cm^{-3} and temperature Te = 2.5 eV.

References

[1] F.Sanchette, E.Demonde, M. Burvorin, et.al. Surf. Coat. Technol., **94-95**, 1-3,261, (1997).

[2] P.M. Schanin, N.N. Koval, I.M. Goncharenko and S.V. Grigoriev, Fiz. Khim. Obrobotki Materialov, No.3, pp.16-19, (2001).

[3] D.P. Borisov, I.M. Goncharenko, N.N. Koval and P.M. Schanin, IEEE Trans. Plasma Sci.. **26**, No.6, pp.1680-1684, (1998)

[4] J.R. Conrad, J. Appl. Phys. **62**, p.777, (1987).

Synthesis of AlN nano powder by transferred type arc plasma

Mikimasa Iwata*, Kazuo Adachi, Shizue Furukawa and Tadashi Amakawa

Central Research Institute of Electric Power Industry (CRIEPI), Yokosuka, JAPAN
(*m-iwata@criepi.denken.or.jp)

Abstract
Nano powder of aluminum nitride (AlN) is one of the necessary materials in order to develop solid insulating materials with high thermal conductivity. This paper describes calculation results of chemical equilibrium composition and the results of experiments in synthesizing AlN nano powder using transferred type arc plasma. In order to increase the AlN content in synthesized powder, ammonia was recommended as a reacting/quenching gas, to be blown into aluminum gas in a temperature region of between 2100 and 2300 K.

1. Introduction

Downsizing of electrical equipment has meant that such equipment have required high thermal conductivity. In order to develop solid insulating materials with high thermal conductivity, it is necessary to add large quantities of ceramic powder with high thermal conductivity to organic insulating materials. Mixing small powder with large powder is considered a good way to achieve a high ceramic powder content. Aluminum nitride (AlN) is a ceramic with high thermal conductivity. Commercially available AlN powder is sized at a few microns, therefore AlN nano powder is required. However the low production capacity of nano powder makes it extremely expensive. There are many methods of producing nano powder, however methods that utilize arc plasma are a good choice in terms of raising the production rate, because they allow plasma power to be upgraded with ease. There are many reports on synthesis of AlN nano powder using the arc plasma [1-8]. The production rate will increase if the raw materials are injected into the high power arc plasma continuously. Transferred type arc plasma has a long high temperature zone and the advantage of making it easy to upgrade plasma power, and therefore the potential to reduce production costs [9]. A report exists on the subject of AlN nano powder production by injecting aluminum powders into the transferred type arc plasma [3]. The report however does not discuss the AlN content and diameter of the synthesized powder in sufficient detail. This paper describes the synthesis of AlN nano powder from aluminum (Al) powder using transferred type arc plasma. Calculations of chemical equilibrium composition and experiments in the synthesis of AlN nano powder were carried out. Nitrogen (N_2) – ammonia (NH_3) mixed gas was used as the reacting/quenching gas, and the AlN content and average diameter of the synthesized powder were investigated.

2. Equilibrium modeling of the synthesis

Chemical equilibrium composition was calculated to predict the optimal conditions for AlN synthesis. The calculation was carried out using the "HSC Chemistry (Outokumpu)" program based on the minimization of Gibbs free energy of the system. Calculation conditions (molar rate, pressure) were similar to the experimental conditions described later in chapter 3.

2.1 Conversion of Al into AlN

Figure 1 shows the calculation result for an Al/NH_3 system. Al gas was converted into AlN solid at around 2300K. Figure 2 shows the conversion temperatures for Al/NH_3 and Al/N_2 systems. In the Al/NH_3 system, conversion of Al gas into AlN solid started at approx. 2300K and finished at approx. 1900K. On the other hand, in the Al/N_2 system, conversion started at approx. 2400K and finished at approx. 2000K.

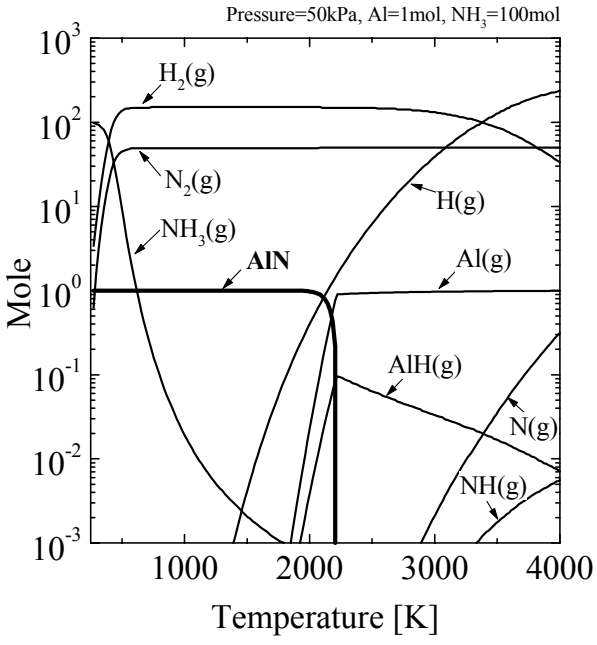

Figure 1. Equilibrium composition of Al/NH_3 system.

2.2 Condensation of non-reacted Al

In order to predict the conditions under which non-reacted Al gas would condense and convert to Al solid, equilibrium composition was calculated assuming that AlN solid was not synthesized. The condensation temperature that the Al solid started to appear was calculated when the non-reacted rate of Al gas of 1mol was varied 0.1-100%. Figure 3 shows the condensation temperature of Al gas. As the non-reacted rate of Al gas decreased, the condensation temperature of Al fell, due to a decline in the partial pressure of Al gas in the system. The condensation temperature of Al/N_2 system was higher than that of the Al/NH_3 system by approx. 100K. The condensation temperature was 2000-2100K when the non-reacted rate of Al gas was 100%.

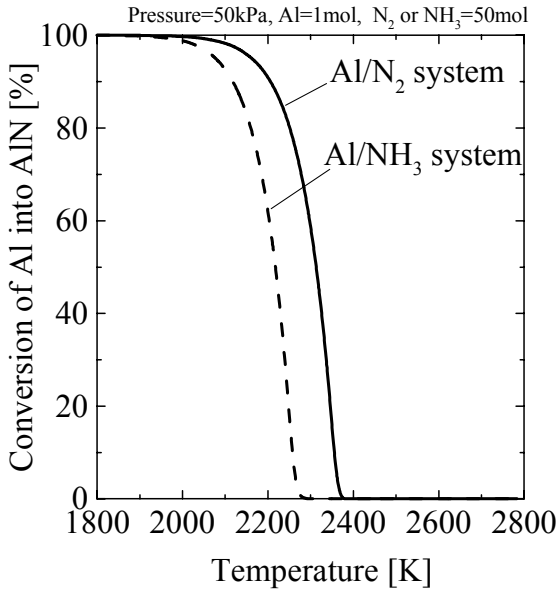

Figure 2. Characteristics of AlN synthesis for different systems.

2.3 Optimal conditions for AlN synthesis

In order to increase AlN content in the synthesized powder, it was recommended that a reacting gas be blown into the Al gas in a temperature region between the conversion temperature and the condensation temperature mentioned above. The optimal temperature region was between 2100 and 2300 K.

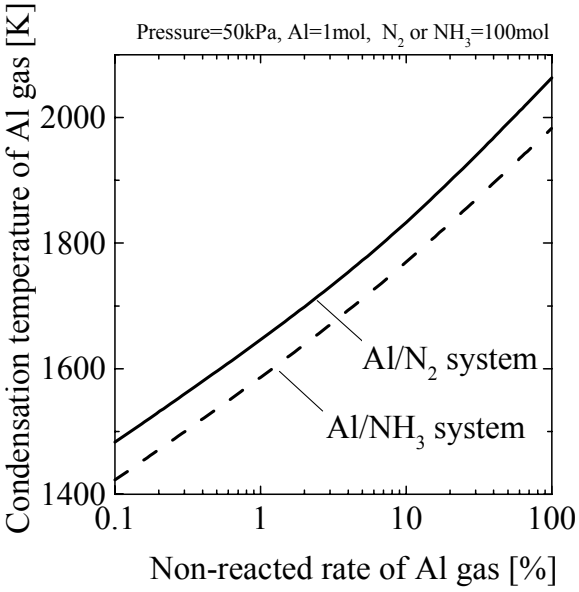

Figure 3. Condensation temperature of Al gas.

3. Experimental setup and conditions

Figure 4 shows the experimental setup. A transferred type arc plasma was generated between a tungsten cathode of plasma torch and a graphite anode in a chamber. The distance between the two electrodes was 75mm. The cathode consisted of a tube-shaped electrode, and the anode a rod-shaped electrode, and the two electrodes were water-cooled. Al powders were injected into the arc plasma through the cathode using a plasma gas (N_2). Diameter of the Al powder was 20-25μm with a feed rate of 0.5g/min and a feed time of 1-2 minutes, and DC arc current was 140A. A suction pipe was positioned downstream from the anode. The distance between the anode and the tip of the suction pipe was 75mm. A reacting/quenching gas was blown into the suction pipe. N_2-NH_3 mixed gas was used as the reacting/quenching gas. The Al powder melted and evaporated in the arc plasma, then the Al gas reacted with and was quenched by the reacting/quenching gas. The synthesized powder was collected on the wall of the suction pipe. The flow rates of plasma gas and reacting/quenching gas were 20 liters/min and 10-50 liters/min respectively. The off-gas was exhausted through the suction pipe and a filter using a vacuum pump. The pressure in the chamber was 30-50kPa. The temperature of the space near the powder-collection area in the suction pipe was measured by an R-type thermocouple with a cap of alumina at the tip. In order to determine the flight velocity of the Al powder in

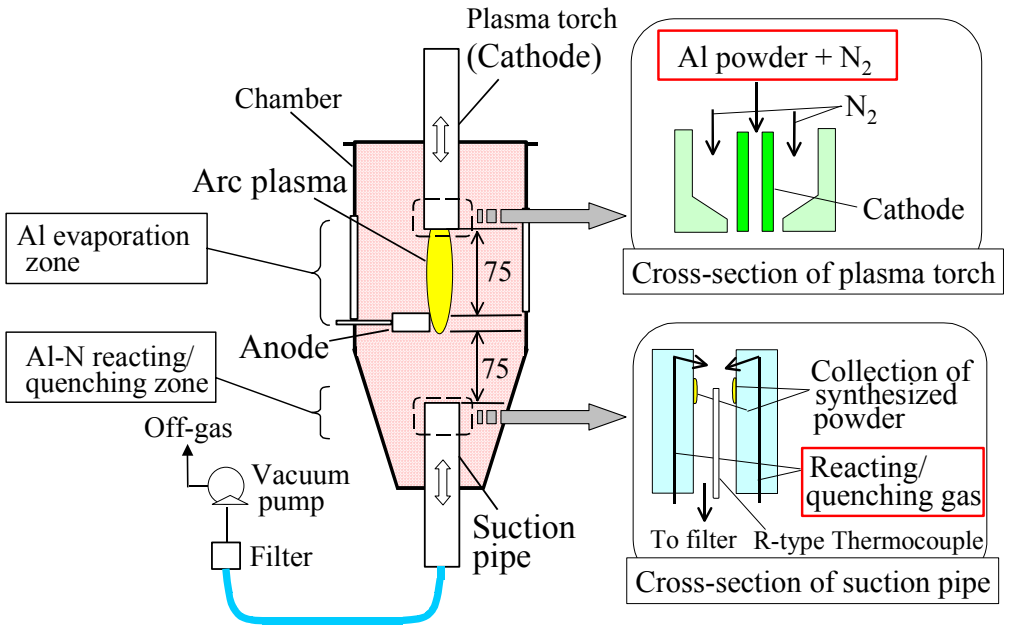

Figure 4. Experimental setup.

arc plasma, the emission of Al atomic line (396.1nm) owing to evaporation of Al powder was recorded using a high-speed ICCD camera with a band-pass filter (central wavelength: 394nm, half-width wavelength: 13nm). The interval time and exposure time of the observation were 100μs and 3μs respectively. The AlN content in the synthesized powder was analyzed by X-ray diffraction (XRD). The diameter of the powder was analyzed by the BET method and TEM observation.

4. Experiment results

4.1 Evaporation of Al powder in arc plasma

The flight velocity of the Al powder in arc plasma was determined from the movement of the emission from the powder using the same method as ref [9]. The flight velocity was 10-20m/s. Calculations of the melting and evaporation behavior of Al powder injected into arc plasma were performed using the heat transfer coefficient based on the Ranz-Marshall equation. The calculation method is described in detail in ref [10]. As a result, an Al powder (25μm) evaporated completely in approx. 2ms even when the powder passed through the plasma outskirts (5000K). Therefore the required plasma length was 40mm. Since the plasma length was set at 75mm, the Al powder injected into arc plasma would evaporate completely.

4.2 Effect of NH_3 content of the reacting/quenching gas

Figure 5 shows an XRD profile of the synthesized powder. Both AlN and Al peaks were observed. AlN content in the synthesized powder was determined by comparing the observed intensities of two lines, i.e. AlN(100) and Al(200). These lines were selected because the intensities were strong and not subject to interference by another lines. The ratio of intensities of AlN(100)/Al(200) was calibrated using the data of pre-mixed AlN/Al powder. Figure 6 shows the AlN content in the synthesized powder at a reacting/quenching gas flow rate of 20 liters/min. As NH_3 content of the reacting/quenching gas increased from 0% to 100%, the AlN content in the synthesized powder increased from approx. 20%wt to approx. 90%wt. Temperature of the space near the powder-collection area was 1500-1600K, irrespective of the NH_3 content of the reacting/quenching gas. Since the temperature was near the condensation temperature of Al gas mentioned in section 2.2, the non-reacted Al gas could be expected to condense and convert to Al solid. Therefore the results exhibited in figure 6 were considered to be due to the increase in the NH_3 content of the reacting/quenching gas causing the generation of a reacting N-source due to the ease of NH_3 decomposition.

Figure 7 shows the average diameter of the synthesized powder. The average diameter was 30-40nm irrespective of the NH_3 content of the reacting/quenching gas. TEM observation of the synthesized powder

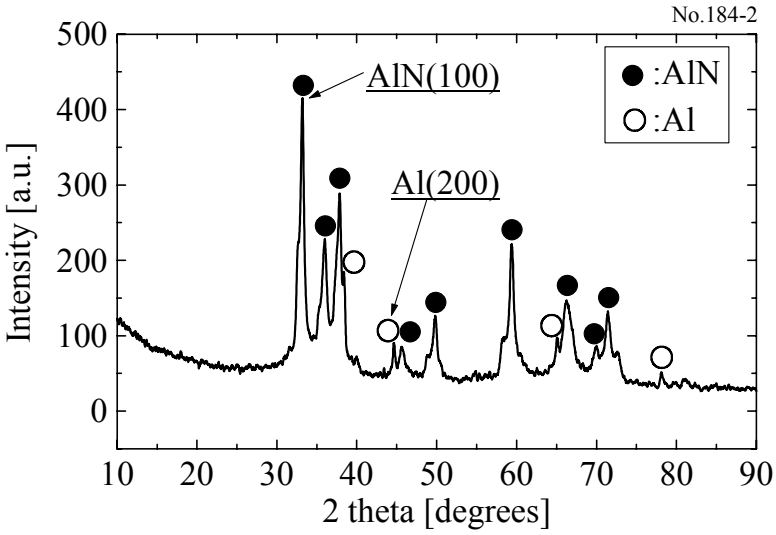

Figure 5. X-ray diffraction profile of synthesized powder.

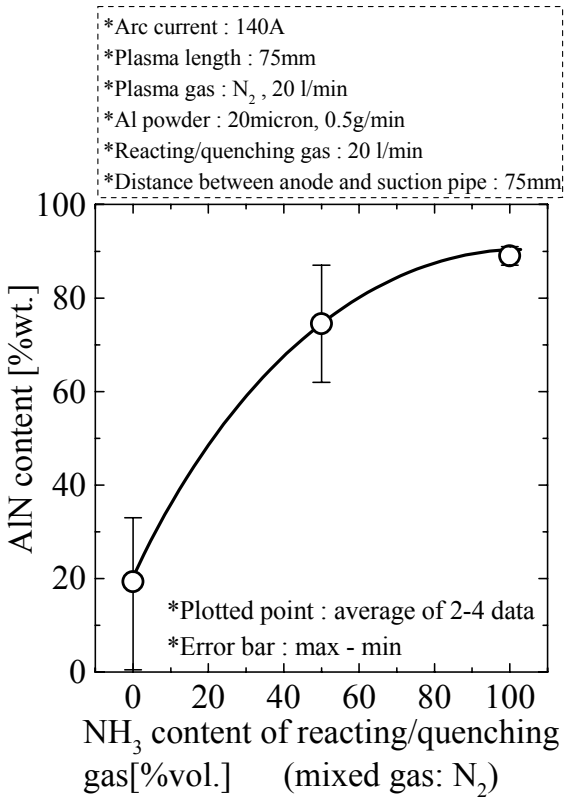

Figure 6. Dependence of AlN content in synthesized Powder upon NH_3 content of reacting/quenching gas.

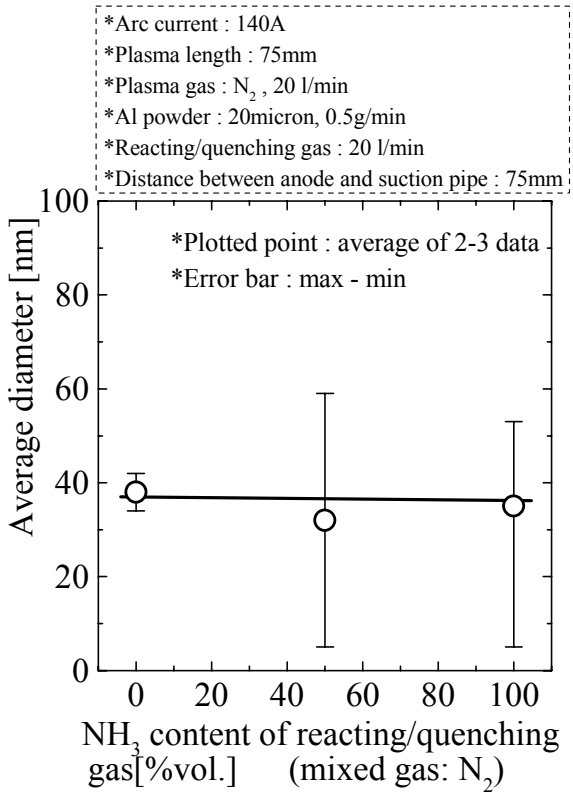

Figure 7. Dependence of average diameter of synthesized powder upon NH_3 content of reacting/quenching gas.

was carried out. Many spherical particles of 20-50nm and a few cubic/hexagonal particles of approx. 50nm were observed when the reacting/quenching gas was N_2. On the other hand, a few spherical particles of approx. 10nm and many cubic/hexagonal particles of 30-70nm were observed when the reacting/quenching gas was NH_3. The spherical particles were non-reacted Al, and the cubic/hexagonal particles AlN [1, 4]. The results of TEM observation coincided with the tendency observed in the results for AlN content in the synthesized powder as shown in figure 6.

4.3 Effect of flow rate of the reacting/quenching gas

The circular and triangular plots in figure 8 show AlN content in the synthesized powder and temperature of the space near the powder-collection area respectively when the reacting/quenching gas used was NH_3. As the flow rate of the reacting/quenching gas increased from 10 to 50 liters/min, the AlN content increased from approx. 70%wt to approx. 90%wt and decreased to approx. 70%wt, while the temperature decreased from approx. 1700K to approx. 1400K. These results suggest that with the increasing flow rate of NH_3 gas the reacting N-source and the AlN content would increase and the condensation of non-reacted Al gas would increase owing to the decline in temperature.

The average diameter of the synthesized powder was measured by the BET method supposing that density of the synthesized powder would be that of AlN because the AlN content in the synthesized powder was relatively high as shown in figure 8. Figure 9 shows the average diameter of the synthesized powder. As the flow rate of the reacting/quenching gas increased from 10 to 50 liters/min, the average diameter decreased from approx. 90nm to approx. 20nm. A reason for this decrease in diameter was considered to be that the temperature of the powder-synthesized space decreased [11, 12] and the AlN density and time spent in the space decreased [11]. TEM observation of the synthesized powder clarified the presence of a few spherical particles of approx. 10nm and many cubic/hexagonal particles when the flow rate of the NH_3 gas was 10 and 20 liters/min. The size of the cubic/hexagonal particles was 100nm and 30-70nm when the flow rate of the NH_3 gas was 10 and 20 liters/min respectively.

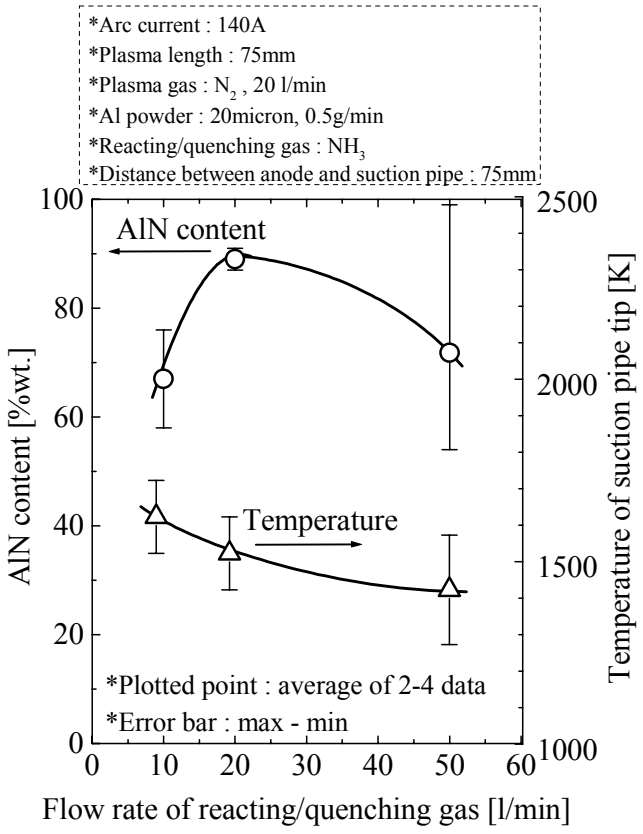

Figure 8. Dependence of AlN content in synthesized powder and temperature of the space near the powder-collection area upon flow rate of reacting/quenching gas.

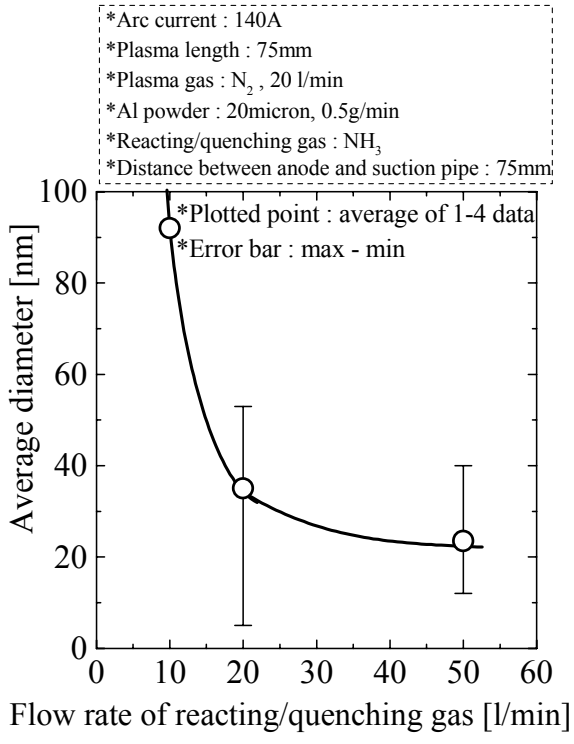

Figure 9. Dependence of average diameter of synthesized powder upon flow rate of reacting/quenching gas.

5. Conclusions

Calculations of chemical equilibrium composition and experiments in the synthesis of AlN nano powder by a transferred type arc plasma were carried out. The calculations clarified that the reacting/quenching gas was recommended to be blown into Al gas in a temperature region of between 2100 and 2300 K, in order to increase AlN content in the synthesized powder. Parameters in the experiment were the NH_3 content and the flow rate of reacting/quenching N_2-NH_3 mixed gas blown into Al gas. As the NH_3 content of the reacting/quenching gas increased from 0% to 100%, the AlN content in the synthesized powder increased from approx. 20%wt to approx. 90%wt, however the average diameter of the synthesized powder did not change greatly (30-40nm). As the flow rate of the reacting/quenching gas increased from 10 to 50 liters/min, the AlN content increased from approx. 70%wt to approx. 90%wt and decreased to approx. 70%wt, while the average diameter decreased from approx. 90nm to approx. 20nm.

Acknowledgements

The authors wish to thank Dr. S. Ito of CRIEPI for his helpful discussions.

References

[1] M. Uda, K. Ohsaki and Y. Morita: *Phys. Chem. Powders Metals Production and Processing*, 261 (1989)
[2] Z. P. Lu and E. Pfender: *Mat. Res. Soc. Symp.*, **180**, 857 (1990)
[3] N. Kikukawa and M. Makino, *NRIPR Report*, **20**, 19 (1990) [in Japanese]
[4] A. Inoue, B. G. Kim, K. Nosaki, T. Yamaguchi and T. Masumoto: *J. Appl. Phys.*, **71**, 4025 (1992)
[5] H. Ageorges, S. Megy, K. Chang, J. M. Baronnet, J. K. Williams and C. Chapman: *Plasma Chem. and Plasma Processing*, **13**, 613 (1993)
[6] S. M. Oh and D. W. Park: *Thin Solid Films*, **316**, 189 (1998)
[7] R. J. Munz, T. Addona and A. C. da Cruz: *Pure Appl. Chem.*, **71**, 1889 (1999)
[8] A. C. da Cruz, O. W. Bender, O. Thomaz, H. N. Yoshimura and P. K. Kiyohara: *Proc. of 15th ISPC*, 2729 (2001)
[9] M. Iwata and K. Adachi: *Proc. of 15th ISPC*, 2769 (2001)
[10] K. Adachi, M. Iwata and T. Amakawa: *Proc. of 15th ISPC*, 2505 (2001)
[11] G. D. Ulrich: *Combus. Sci. Technol.*, **4**, 47 (1971)
[12] J-F. Biodeau and P. Proulx: *Proc. of 12th ISPC*, 1201 (1995)

Recombination of H_3^+(v=0) ions with electrons. Cavity Ring-down Spectroscopy in pulsed microwave discharge.

R. Plašil, G. Bánó[1], J. Glosík, P. Macko[2], P. Hlavenka, A. Pysanenko, P. Kudrna, V. Poterya

Charles University Prague, Mathematics and Physics Faculty, Department of Electronics and Vacuum Physics, V Holešovičkách 2, 180 00 Prague 8, Czech Republic,radek.plasil@mff.cuni.cz
[1]Research Institute for Solid State Physics and Optics, HAS, Konkoly-Thege út 29-33, 1121 Budapest, Hungary
[2]Comenius University, Faculty of Mathematics, Physics and Informatics, Department of Plasma Physics, Mlynska dolina F2, Bratislava, Slovak republic

Abstract

The recombination of $H_3^+(v=0)$ ions with electrons was studied in stationary afterglow apparatus equipped with infrared Cavity Ring-down absorption spectrometer. From the decay of $H_3^+(v=0)$ density during the afterglow in He/Ar/H_2 mixture the recombination rate coefficient was measured. The recombination rate coefficient obtained at hydrogen density $[H_2] = 1\times10^{14}$ cm^{-3} is $\alpha = 1.2\times10^{-7}$ cm^3 s^{-1}. The kinetic and rotational temperature of recombining $H_3^+(v=0)$ ions was determined from absorption spectrum.

Introduction

H_3^+ ions play very often the dominant role in laboratory and astrophysical hydrogen containing plasmas. $H_3^+(v=0)$ ions were many times detected in interstellar molecular clouds and in atmospheres of large planets (Jupiter, Saturn, Uranus, and Neptune). The knowledge of the reaction kinetics of $H_3^+(v=0)$ ions with molecules and with electrons is required to understand formation, evolution and destruction of those environments. Kinetic of ion – molecule reactions of $H_3^+(v=0)$ ions was subject of numerous studies and is well understood. There are also many experimental and theoretical studies dealing with recombination of H_3^+ ions. The corresponding rate was measured by means of different beam and swarm techniques, however the discrepancy between the most recent data is still very large. Despite the fact that in interstellar medium $H_3^+(v=0)$ ions are present, only very exceptionally internal state of recombining ions was directly determined in experimental studies.

In our very recent stationary afterglow studies of H_3^+ recombination we observed dependence of the recombination rate coefficient on partial pressure of hydrogen molecules [1,2,3]. The density of the ions was measured using a Langmuir probe thus the internal excitation of recombining ions was not directly determined. In the present study infrared Cavity Ring-down absorption spectrometer is used to measure number density of $H_3^+(v=0)$ ions, their kinetic and rotational temperature during the afterglow. From these data recombination rate coefficient for $H_3^+(v=0)$ at 320 K was obtained.

Apparatus

A new cavity ring-down spectrometer was built in our laboratory recently (see description inref. [4]). This absorption technique allows us to detect $H_3^+(v=0)$ ions in a given rotational state. The spectrometer is equipped with an infrared tuneable diode laser in a continuous mode. The high sensitivity of the method is due to the enhancement of the effective optical path-length when laser light is reflected back and forth between the mirrors of an optical cavity. The cavity is inside the discharge chamber and plasma is created between the mirrors of the cavity. A presence of absorbing medium, $H_3^+(v=0)$ ions in our case, is influencing the decay rate of the energy stored in the cavity. The absorption signal is obtained from the characteristic time of the light intensity decay. The characteristic decay time of empty cavity is ~43 μs. The experimental set-up is described in Figure 1. Pulsed microwave plasma is created in the central part of the optical cavity. The discharge operates in a mixture of He and Ar with small amount of H_2. Because the decay of the plasma is very fast it is essential to have very fast operating switch to stop microwave generator (2.45 GHz).

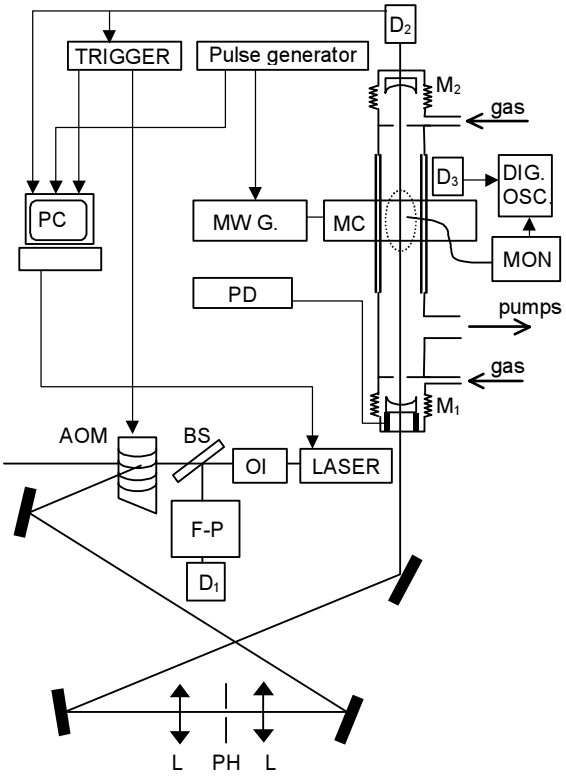

Figure 1: The experimental setup:
OI - optical isolator,
BS - beam-splitter,
F-P - Fabry-Perot interferometer,
AOM - acousto-optical modulator,
D_1 - InGaAs photodiode,
D_2 - avalanche photodiode,
L - lenses, PH - pinhole,
$M_{1,2}$ - dielectric mirrors,
D_3 - high-frequency diode,
MON - monochromator equipped with photomultiplier tube,
MW G. - microwave generator,
PD - piezo-element driver,
MC - microwave cavity.

We have measured microwave signal inside the microwave cavity and in addition also emission of light generated by plasma (see Figure 2). The light emission can be considered as information about electron temperature. From the plots in Figure 2 it is clear that microwaves are cut down within <20 μs and similar it is with light emission.

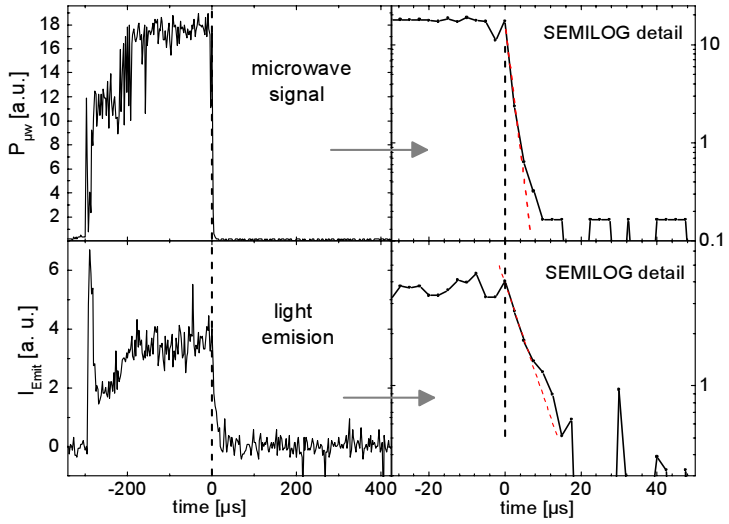

Figure 2: The fall off in the microwave signal and light emission after the discharge switch off. The emission line was not identified. Note that after 20 μs s microwave signal and light intensity can be considered to be zero.

At this moment we are not interested in processes taking place during the microwave discharge. To obtain information about recombination of $H_3^+(v=0)$ ions it is enough to monitor decay of the afterglow plasma in the moment when $H_3^+(v=0)$ ions are dominant ions and when electron temperature is close to buffer gas temperature. We calculated from the kinetic model [1] that in the used mixture of gases the majority of ions and metastables formed during the discharge are converted to $H_3^+(v=0)$ ions within less than 50 μs. In this sense we can skip first 50 μs of the afterglow – early afterglow and use only decay after 50 μs

to determine recombination rate coefficient. The spectrometer was calibrated with water vapor. In Figure 3 there is scan used for calibration

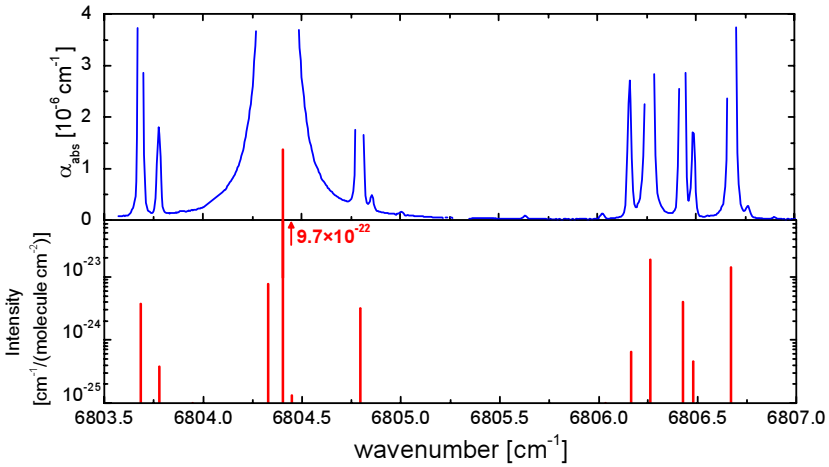

Figure 3: The scan in water vapours, which is used to calibrate the spectrometer. Upper panel: The signal obtained from water vapours. Lower panel: Intensities of the absorption lines from HITRAN 96 database.

Results and discussion

When wavelength were calibrated we introduced mixture of He, Ar and H_2 and we measured absorption spectrum in range 6807 to 6808 cm^{-1}. The composition of the mixture was calculated from kinetic model to obtain maximum absorption. The spectrum was measured in continuous and pulsed discharge. Example of the obtained spectra is plotted in Figure 4.

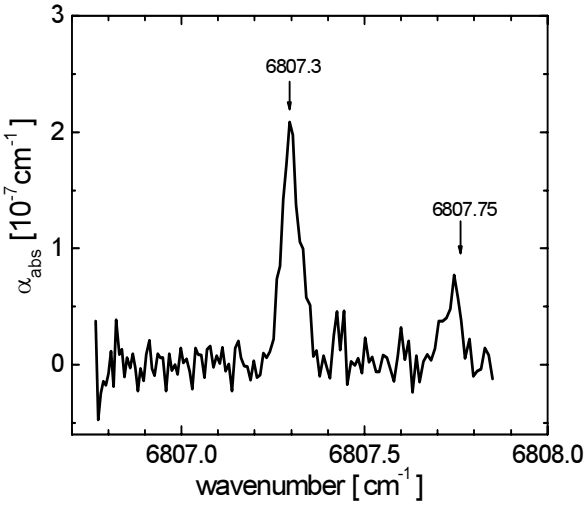

Figure 4: The absorption spectrum of H_3^+(v=0) for ν_2 = 3←0. The line 6807.3 cm^{-1} was used for further evaluation. Conditions in the experiment: the overall pressure p_{He} = 7 Torr, [Ar] = 6×10^{-14} cm^{-1}, and [H_2] = 1.5×10^{-14} cm^{-1}.

The absorption signal corresponding to number density of H_3^+(ν=0) ions was detected on the 6807.3 cm^{-1} (ν_2=3←0) transition. The resonance of the cavity is achieved by sweeping the length of resonator through the resonance position. Once the light intensity becomes high enough the laser beam is switched off and the decay of the light intensity (leaking through one of the mirrors) is detected. Assuming linear absorption the decay is exponential with decay time $\tau(\nu)$, given by:

$$\frac{1}{\tau(\nu)} = \frac{1}{\tau_0} + \frac{d}{L} c\alpha(\nu) \quad . \tag{1}$$

ν is the frequency of the laser light, τ_0 is the decay time in the absence of absorption, d and $\alpha(\nu)$ are the length and absorption coefficient of the absorbing medium, respectively. L is the length of the cavity.

In the Figure 5 the measured time evolution of $H_3^+(v=0)$ density is plotted. The simple evaluation procedure with assumption that the ion density is constant during the ring-down was used to obtain the data were obtained using.

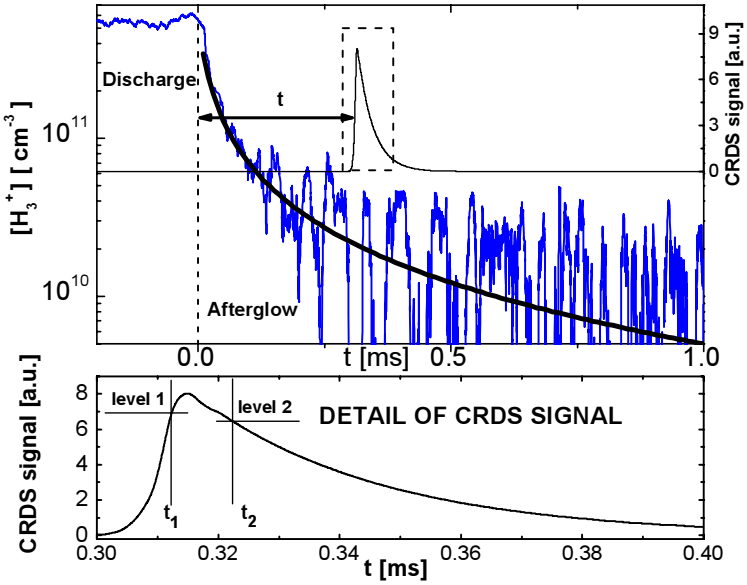

Figure 5: Upper panel: Schematic data showing time dependence of $[H_3^+]$ during the discharge and the afterglow period. Simulated CRDS signal obtained with time delay of t is also shown. Lower panel: detailed view of the CRDS signal. The laser is switched off at the moment t_1, when the signal reaches "level 1". Data acquisition starts at t_2, when the signal drops below "level 2".

As can be seen from the plot, the ion density drops very rapidly in the early stages of the afterglow, this can influence ring-downs started during this fats decay. The ring-down signal cannot be any more described with a single exponential decay and variation of ion density during ring down has to be considered. We decided to use an iterative correction method to improve the density evaluation. The example of obtained decay of $H_3^+(v=0)$ ion density during the afterglow is plotted in Figure 6. The decay curves were fitted by function in which both recombination and diffusion were considered. The obtained recombination rate coefficient is given by the decay in early stages of the afterglow, first ~250 μs. As was already mentioned first 50 μs are influenced by transition from active discharge to afterglow and by formation of $H_3^+(v=0)$. The data from this interval are not considered in evaluation of recombination rate coefficient. The ion number density decrease by one order in magnitude during interval 50-250 μs and this decay is sufficient to obtain reliable recombination rate coefficient.

Absorption spectra during active discharge and during afterglow were also measured. From the shape of spectra rotational temperature of $H_3^+(v=0)$ ions was calculated. From the Doppler broadening the kinetic temperature of $H_3^+(v=0)$ ions was also calculated. Because the decay of $H_3^+(v=0)$ density is very fast signal to noise ratio drops down during early stages of afterglow. That is why kinetic temperature was measured only during the active discharge and during early afterglow period.

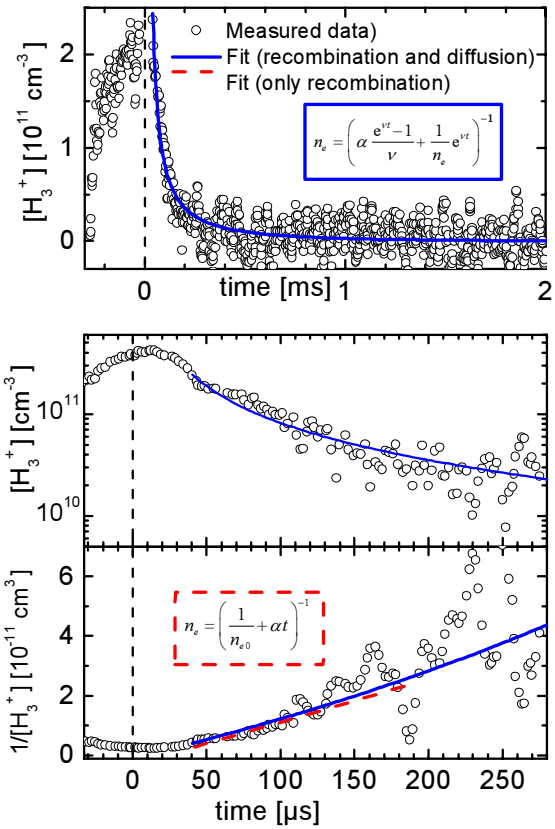

Figure 6: Time dependence of the $H_3^+(v=0)$ density during the afterglow. Upper panel: A decay of $H_3^+(v=0)$ during afterglow. Data are obtained by iteration method. Central panel: The detail of the decay of recombination dominated plasma in log scale. Lower panel: The detail of data in central panel in reciprocal scale. The slope of the linear part of plot is given by rate coefficient of recombination.

In Figure 7 is plotted evolution of kinetic temperature obtained from Doppler broadening. Note that in the active discharge kinetic temperature is ~350 K and within 50 μs after shutdown of microwaves it drops down to ~320 K. The actual temperature of the discharge tube was also ~320 K. We can conclude, that kinetic temperature of the recombining $H_3^+(v=0)$ ions is equilibrated with buffer gas temperature. Similar result was obtained for rotation temperature of recombining $H_3^+(v=0)$ ions. In used experimental conditions pressure broadening can be neglected in comparison with Doppler broadening.

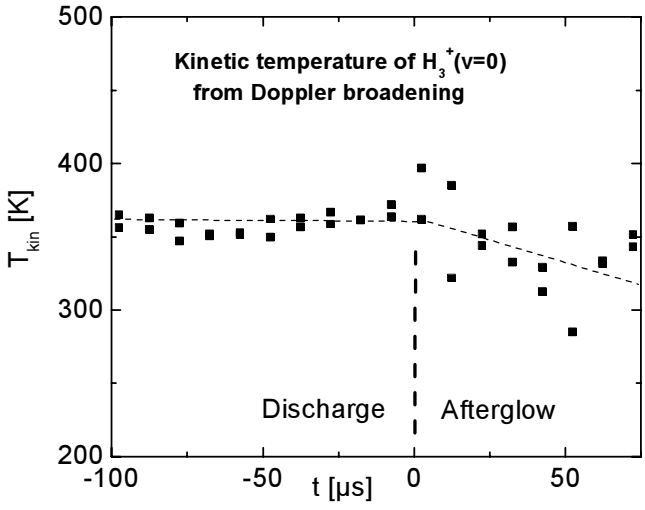

Figure 7: Kinetic temperature of $H_3^+(v=0)$ as obtained from Doppler broadening of the spectral line.

As an average result of many different data sets the rate-coefficient for recombination of $H_3^+(v=0)$ ions with electrons was derived to be $(1.2 \pm 0.7) \times 10^{-7}$ cm^3 s^{-1}, this value belongs to hydrogen density of about 4×10^{14} cm^{-3} and to temperature 320 K. We stress here once again that kinetic temperature and rotational temperature of recombining ions was measured in present experiment. The obtained recombination rate coefficients are plotted in Figure 8 together with our earlier results. In the figure are included data obtained in three different experiments: AISA – Advanced Integrated Stationary Afterglow [1,2,3]; HPFA – High Pressure Flowing Afterglow with Langmuir probe [5,6]; and present SA - CRDS – Stationary afterglow with infrared cw-diode cavity ring-down spectrometer (see also refs. [4]). Because of dependence of recombination rate coefficient on hydrogen number density symbol α_{eff} is used to stress the fact that observed recombination is a three-body process. Data obtained on HPFA at high pressures and lower temperature shows influence of formation of H_5^+ ions and their recombination to the overall loss process in hydrogen plasma [5,7]. This recombination channel is not playing role at lower pressure in AISA and at higher temperature in SA – CRDS. Note that independent on differences in temperature and buffer gas pressures the recombination rate coefficients obtained in different experiments for similar hydrogen number densities are in very good agreement.

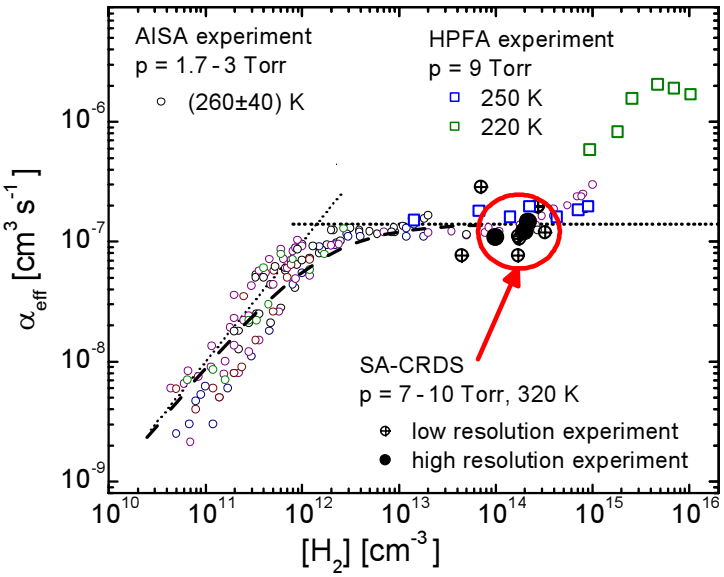

Figure 8: Dependence of observed α_{eff} on hydrogen number density. The FALP and AISA data are also included.

Acknowledgement: Thanks for financial support are due to GACR (205/02/0610, 202/02/0948). The experiments were carried out with support from EC's RTN under contract HPRN-CT-2000-0142, ETR and with support from Euroatom.

References

[1] R. Plašil, J. Glosík, V. Poterya, P. Kudrna, J. Rusz, M. Tichý, A. Pysanenko - *Int. J. Mass Spectr.* **218**, 105 (2002).
[2] J. Glosík, R. Plašil, V. Poterya, P. Kudrna, M. Tichý - *Chem. Phys. Letters* **331** (2000) 209
[3] J. Glosík, R. Plašil, V. Poterya, P. Kudrna, M. Tichý, A. Pysanenko - *J. Phys. B: At. Mol. Opt. Phys.* **34,** L485 (2001).
[4] P. Macko, R. Plašil, P. Kudrna, P. Hlavenka, V. Poterya, A. Pysanenko, G. Bánó, J. Glosík - *Czechoslovak J. Phys.,* **52** Suppl. D, D695 (2002).
[5] J. Glosík, O. Novotný, A. Pysanenko, P. Zakouřil, R. Plašil, P. Kudrna, V. Poterya, K. Dryahina - Submitted for publication in, Plasma Source Science & Technology 2003.
[6] J. Glosík, G. Bánó, R. Plašil, A. Luca, P. Zakouřil – *Inter. J. Mass Spectrom.*, **189**, 103-113 (1999).
[7] A. Pysanenko, O. Novotný, P. Zakouřil, R. Plašil, V. Poterya, J. Glosík - *Czechoslovak J. Phys.* **52,** D681 (2002).

Laser plasma soft x-ray and EUV source based on a laser-irradiated double- stream gas puff target

R. Rakowski[1], A. Bartnik[1], H. Fiedorowicz[1], R. Jarocki[1],
J. Kostecki[1], J. Krzywiński[2], J. Mikołajczyk[1], A. Szczurek[1], M. Szczurek[1]

[1] *Institute of Optoelectronics, Military University of Technology, Warsaw, Poland*
[2] *Institute of Physics, Polish Academy of Sciences, Warsaw, Poland*

Abstract
In this paper a laser-plasma source of soft x-rays and extreme ultraviolet (EUV) is presented. The source is based on a recently developed double-stream gas puff target, irradiated with a Nd:YAG laser. The characterization and optimization of the source measurements have been made using the grating spectrographs and the absolutely calibrated silicon photodiodes.

1. Introduction

A laser plasma can be produced in result of interaction of a high power laser pulse with a gas puff target, created by pulsed injection of gas through the nozzle of the electromagnetic valve. The use of the gas puff target eliminates production of target debris associated with solid targets [1]. The gas puff laser plasma can be an efficient source of soft x-rays and extreme ultraviolet in the wavelength range from about 1nm to 20 nm. The radiation characteristics of the source have been improved by using a new double-stream gas puff target approach, developed at the Institute of Optoelectronics, Warsaw, Poland [2]. In this approach the gas puff target is formed by injection of high-Z gas (xenon, krypton, argon) from the circular nozzle into a hollow stream of low Z gas (hydrogen or helium) from the outer nozzle in a form of a ring. The target design assures high density of gas in the interaction area, what leads to efficient absorption of the laser energy and high production of x-rays and EUV. Strong x-ray and EUV production from the double-stream gas puff target irradiated with nanosecond laser pulses from Nd:glass and Nd:YAG, approaching production from solid targets irradiated in the same conditions, has been demonstrated [3, 4].

In this paper a compact laser plasma soft x-ray and EUV source based on a double-stream gas puff target is presented. The target is irradiated using a Nd: YAG laser producing pulses with time duration of 4 ns and energy about 0.5 J. The spectral characteristics of x-ray and EUV emissions have been studied with the use of the transmission grating spectrograph (TGS) and the grazing incidence spectrograph (GIS). Additionally, the absolutely calibrated photodiodes (AXUV-100 Si/Zr and AXUV HS1, IRD Inc.) were used to measure the EUV yield at 13.5 nm. The source has been developed under the European MEDEA + programme (project T 405).

2. Experimental arrangement

2.1. Laser plasma x-ray and EUV source

The laser plasma x-ray and EUV source consists of a vacuum chamber equipped with the gas puff target system and a Nd:YAG laser to irradiate the target. The gas puff target system is made of two electromagnetic valves combined in a common body and a double-nozzle setup. The nozzle setup is schematically shown in Fig. 1. Both valves are separately driven by the current pulse from the power supply. The power supply is synchronized with the laser pulse. The diameter of the inner nozzle was 0.4 mm and the diameters of the outer nozzle 0.8 mm and 1.5 mm, respectively. The outer stream from low-Z gas confines the high-Z gas stream along the nozzle axis and prevents from its decompression. By changing the time delay Δt between the laser pulse and the opening of the valve one can change the parameters of the target. An example view of the shadowgram of the target is presented in Fig. 2. The valve system allows to produce the gas puff targets with the repetition rate up to 100 Hz, but only a single laser shot operation was used in this study.

The schematic diagram of the laboratory model of the laser plasma x-ray and EUV source with diagnostics is shown in Fig. 3. The experimental setup consists of a vacuum chamber with the electromagnetic valve system, an aspherical lens to focus the laser beam, a compact Nd: YAG laser system, which generates 4ns pulses with repetition rate up to 10 Hz and energy up to 550 mJ, and an oil-free vacuum pump (Varian) enabled to evacuate the chamber up to pressure of about $2 \cdot 10^{-2}$ mbar. The laser beam is

focused onto the gas puff target perpendicularly to the gas flow. The laser focus was about 100 μm in diameter giving the radiation power density of about 10^{12} W/ cm^2.

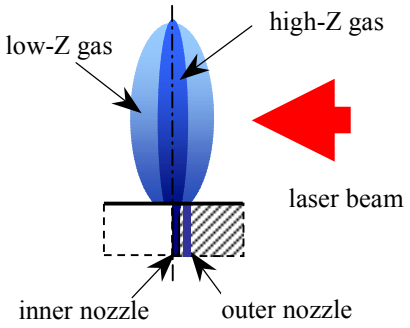

Fig. 2. Schematic of the double nozzle setup.

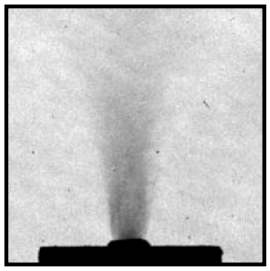

Fig. 1. View of the shadowgram (Δt_{Ar} = 600 μs, Δt_{He}= 600 μs).

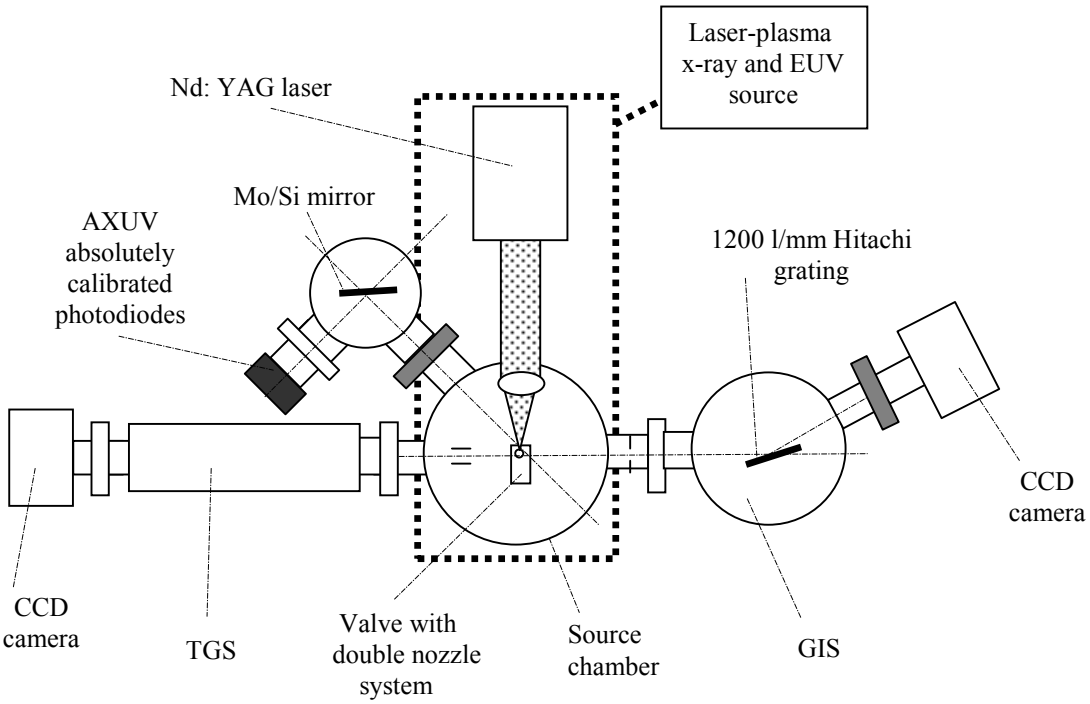

Fig. 3. Schematic of the source with diagnostic.

2.2. Transmission grating spectrograph (TGS)

Spectral studies of the x-ray and EUV emissions from the source for different spatial position of the laser beam focus to the gas puff target using the transmission grating spectrograph were carried out. The spectrograph was equipped with the free-standing grating of 1000 lines/mm inside the 50 μm in diameter pinhole (Heidenhain GmbH) and enabled use a slit and was coupled to back-thinned array CCD camera, 1340 x 400 pixels, 20 μm square shape each (Roper Scientific, SX-400). The chip of the camera was placed at the distance of 70 cm from the grating, giving the magnification of about 10 and could cover the spectral range up to 20 nm. Although the spectral resolution of the used transmission grating was smaller as compared with the reflection grating, however location the grating in a pinhole with known diameter makes it possible to estimate absolute energy of the source at specific wavelength.

2.3. Grazing-incidence spectrograph (GIS)

For spectral measurements of the source in the soft x-ray and EUV region a spectrograph with a gold reflection grating Hitachi 1200 lines/mm was used. The spectrograph may be used to measure x-ray wavelength between the 5 nm and 15 nm region. The spectrograph was equipped with a back illuminated

CCD camera (Roper). Experimentally the spectral resolution of the spectrograph about 0.2 Å on basis the oxygen spectra was estimated.

2.4. Photodiode detectors

The photodiode detectors were set beyond a selective multilayer Mo/Si mirror (IOF, Jena). The selective Mo/Si multilayer mirror was located inside the separate chamber between the source and the spectrograph. The mirror has a shape of a 1 cm^2 square and was optimized at 13.5 nm in the EUV region for an incidence radiation angle of 45°. Two absolutely calibrated photodiodes AXUV-100Si/Zr (pass band 11 nm – 17 nm) with a filter made from 200 μm thick Zr onto a 100 μm Si plate, sensitive especially at 13.5 nm and AXUV-HS1 photodiode with a filter made from a 0.2 μm thick Si_3N_4 membrane onto a 1 μm thick Mo layer were used to register energy signals of EUV pulses. Detector HS1 was placed at the distance of 485 mm from the plasma and photodiode with Zr filter at 610 mm distance.

The signals from the AXUV-100Si/Zr were registered with the use of the monitoring system. The signals from fast HS1 detector exceeding the time resolution of 0.25 ns were detected by the 500 MHz digital oscilloscope, thus time shape of the EUV signal could be stored.

3. Results of experiments

3.1. Transmission grating spectrograph measurements

Four distances Δh between the laser focus and the nozzle output were chosen: 0.8; 1; 1.5 and 2 mm for which investigations were carried out. For this distances various locations of the laser beam in relation to the axis of the nozzle were set. Depending on the laser focus position different spectral distributions were observed. The change of the focus position perpendicularly to the axis beam strongly affected on the emission measurements, while the change towards the axis beam weakly depends on the results. Because the grating was placed inside the pinhole, perpendicular distribution to spectral distributions in the spectra are spatial sizes of the source at specific wavelength. An example of the Soft x-ray and EUV spectra corresponding to the laser focus position, where the focus was set 2 mm beyond the target and 1.5 mm above the nozzle output is shown in Fig. 4. The x-ray and EUV emissions from the spectra can be distinguish. In the soft x-ray region a dominant spectral feature is laid near 6 nm, in the EUV region near 10.7 nm. From the spectra the x-ray yield 4.1 mJ/sr at the wavelength 6 nm ± 1 nm and EUV yield 4.3 mJ/sr at the wavelength 13.5 nm ± 1 nm was evaluated.

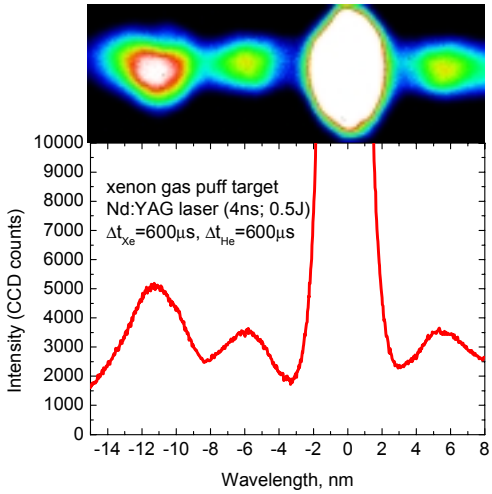

Fig. 4. Spectral image and distribution of the Xe/He source for no slit case (Δ t_{Xe}= 600 μs Δ t_{He}= 600 μs).

3.2. Grazing-incidence spectrograph measurements

Although the source covers x-ray and EUV emission ranges the most interesting for us spectral region was laid near 13.5 nm. This region is strongly important for EUV metrology and lithography application, because advanced optics in this range was developed. Thus was put emphasis on diagnostic at 13.5 nm. A dependence of the emission of the source at 13.5 nm from the time delay between the laser pulse and the triggering pulses of the valves was investigated. Measurements for the time delay in the range from 500 μs to 900 μs with the step 100 μs were carried out. For each time delay settings mentioned above time delay for

helium or hydrogen valve in the range from 200 µs to 800 µs, 100 µs step were set. In Fig. 5 the typical spectra and calculated from images spectral distributions for Δt_{Xe}=800µs, $\Delta t_{He,H}$=350µs in the Xe/He and Xe/H cases are shown. For fixed time parameters four measurements for statistics in single laser shot regime were done. The maximum emission at 10.7 nm (4d - 4f) from created in those condition laser plasma was observed. The strongest emission at interesting us 13.5 nm was registered for Δt_{Xe}= 800 µs and $\Delta t_{He,H}$ in the range 300 µs to 400 µs. These results are presented in Fig. 6. This range of the time delay for auxiliary gas was investigated with the step 25 µs what is presented in Fig. 7. From this picture is clearly seen that for fixed other parameters the optimum conditions are Δt_{Xe}= 800 µs, $\Delta t_{He,H}$= 350 µs, where the EUV yield was the highest, moreover emission ratio of the radiation at 13.5 nm to radiation at 10.7 nm was as 1:2. Generally for various time delays higher emissions at 13.5 nm were registered for hydrogen as a auxiliary gas as compared with helium. Proper results are presented in Fig. 8.

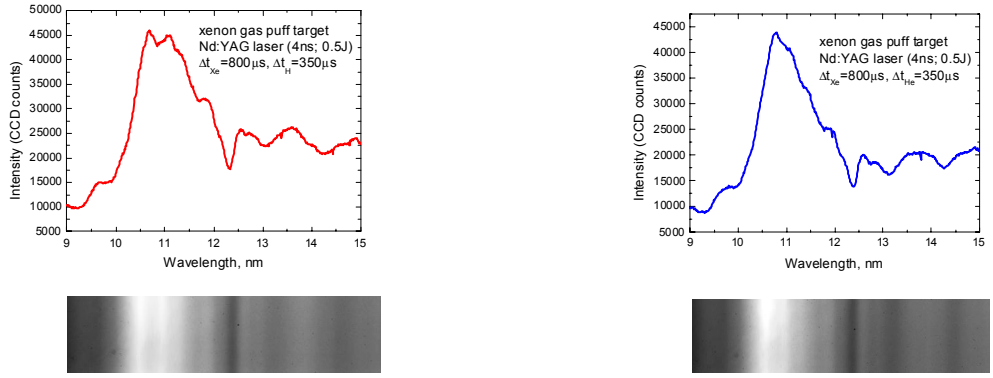

Fig. 5. Spectral images and spectral distributions obtained from GIS for Δt_{Xe}=800µs, $\Delta t_{He,H}$=350µs. (a) Xe/H, (b) Xe/He

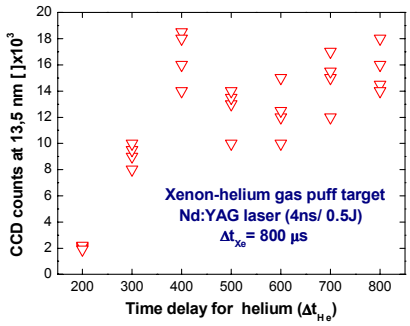

Fig. 6. CCD counts at 13.5 nm. Δt_{Xe}=800µs, Δt_{He}=200-800µs

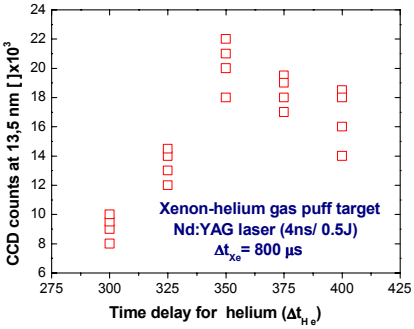

Fig. 7. CCD counts at 13.5 nm. Δt_{Xe}=800µs, Δt_{He}=200-800µs

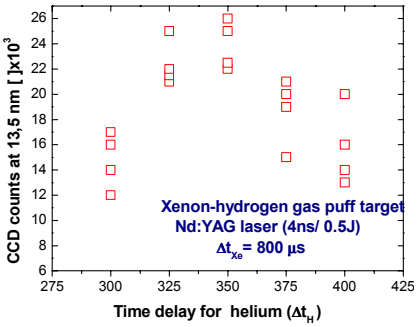

Fig. 8. CCD counts at 13.5 nm. Δt_{Xe}=800µs, Δt_{H}=200-800µs

3.3. Silicon photodiodes measurements

The detectors beyond the selective multilayer Mo/Si mirror were installed. The signals from the absolutely calibrated AXUV-100Si/Zr photodiode for various locations of the laser beam in relation to the axis of the nozzle were measured. A proper geometry is shown in Fig. 9

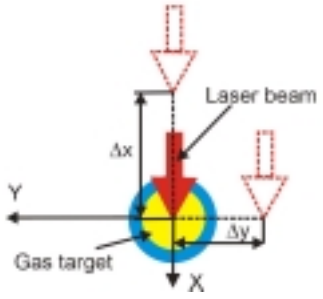

Fig. 9. Settings geometry for fixed distance between the laser focus and the nozzle output.

In Fig. 10 the results from the AXUV-100Si/Zr detector are presented. From these pictures is seen that the position of the laser focus above the nozzle output and along the axis of the beam as well are not critical.

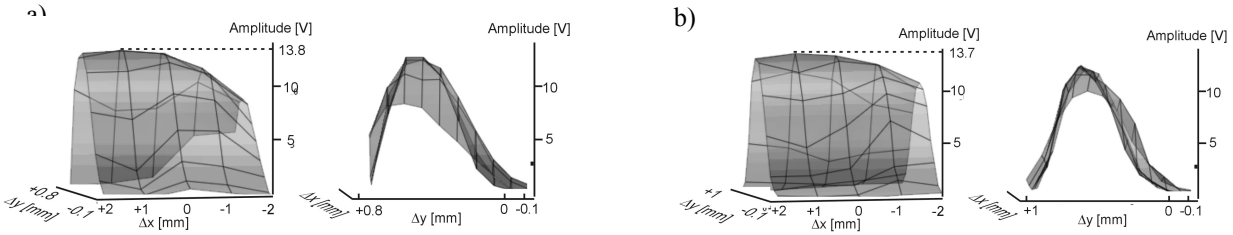

Fig. 10. Dependence of EUV production at 13.5 nm on the position of the laser focus to the nozzle output from AXUV-100 Si/ Zr. (a) 1.5mm, (b) 2 mm distances between the laser focus and the nozzle output of the valve.

The use AXUV-HS1 photodiode with a time resolution of 0.25 ns made it possible to measure time shape of the EUV pulse out of the selective mirror. The typical signal from HS1 diode is presented in Fig.11.

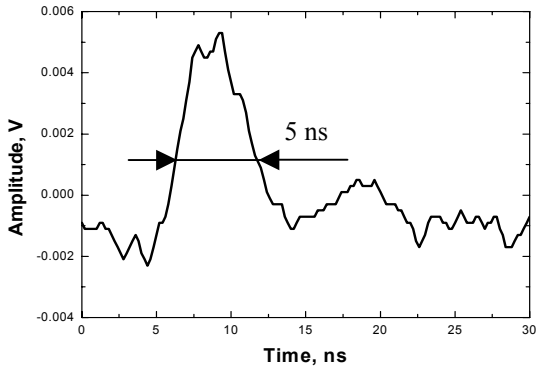

Fig. 11. Typical pulse shape from AXUV-HS1 detector.

The highest emission of the source for $\Delta x = 0$ and $\Delta y = 0.5$ mm settings was observed, however size of the plasma in this case was bigger compared with focusing the laser beam on the axis of the valve nozzle ($\Delta x = 0$, $\Delta y = 0$). Although the emission in those condition was the biggest the plasma size was big too. Considering the EUV source application for metrology one ought to optimize position of the laser focus in order to obtain high emission at 13.5 nm behaving the spatial sizes of the plasma as small as possible.

4. Conclusions

Recently carried out research of the laser plasma EUV source were presented. In the source a commercial Nd: YAG laser (4 ns, 0.5 J, 10 Hz) and developed at the Institute of Optoelectronics double nozzle valve system to create double stream gas puff target were used. The measurements of the source emission near 13.5 nm were made. Thus an emission of about 4.3 mJ/sr from TGS, 1.45 mJ/sr for AXUV-HS1 diode and 2 mJ/sr for AXUV-100Si/Zr at the wavelength 13.5 nm was estimated. Next step should be the measurements with the repetition rate regime of the work source with the use a differential gas pumping, each chamber separately method.

Acknowledgements – This work was supported by the State Committee for Scientific Research (KBN), Poland, under the grant No. 217/E-284/SPUB-M/EUREKA/0-13/DZ 214/2001-2003

References

[1] H. Fiedorowicz, A. Bartnik, Z. Patron, P. Parys, Appl.Phys.Lett. **62**, 2778 (1993)
[2] H. Fiedorowicz, A. Bartnik, R. Jarocki, R. Rakowski, M. Szczurek, Appl. Phys. B 70, 305 (2000)
[3] H. Fiedorowicz, A. Bartnik, H. Daido, I. W. Choi, M. Suzuki, S. Yamagami, Optics Communications 184 (2000) 161
[4] H. Fiedorowicz, A. Bartnik, R. Jarocki, J. Kostecki, J. Krzywiński, R. Rakowski, M. Szczurek, in Proc. Spie vol. 4504, Applications of X-Rays Generated from lasers and Other Bright Sources II,eds. G. A. Kyrala and J. C. Gauthier (SPIE Press Bellingham, 2001)

Expanding thermal plasma deposition and etching of textured zinc oxide

R. Groenen[1], M. Creatore[1], J.L. Linden[2], M.C.M. van de Sanden[1]
[1] *Department of Applied Physics, Eindhoven University of Technology, Eindhoven, The Netherlands*
[2] *Division Models and Processes, TNO TPD, Eindhoven, The Netherlands*

Abstract
Initial insight into the plasma chemistry taking place during deposition of textured ZnO is obtained from mass spectrometry. A new method for fast dry ZnO etching using a remote argon - hydrogen plasma is demonstrated, including competitive film modification. Atomic hydrogen is considered to be the reactive species, the excess of molecular hydrogen in the gas phase does not contribute to the etching.

1. Introduction

Zinc oxide (ZnO) is a transparent conducting oxide (TCO) of considerable technological interest for amongst others application in thin film solar cells. Recently, a new method has been presented for low temperature deposition of surface textured ZnO utilizing an expanding thermal argon plasma created by a cascaded arc [1]. It has been shown that high quality material is obtained, showing excellent performance in thin film a-Si:H solar cells [1,2,3]. Initial plasma chemistry aspects obtained from mass spectrometry are presented. Considering the recently recognized role of hydrogen in ZnO film modification [4,5,6], a new method for fast dry etching is demonstrated using a remote argon - hydrogen plasma implying the absence of significant ion bombardment. Contrary to numerous wet etching chemistries for ZnO [7,8,9], just a few attempts on dry ZnO etching have been reported [10,11,12] all involving ion-assisted halogen- or carbon-based chemistries.

2. Experimental

Undoped substoichiometric ZnO films are deposited on Corning 1737F glass substrates (100x50 mm^2) by the expanding thermal plasma (ETP) chemical vapor deposition process as described in detail elsewhere [1]. Oxygen and diethylzinc (DEZ) are used as the (co)precursors for deposition. In order to gain initial insight into the chemistry taking place, a Balzers QMS 200 Prisma mass spectrometer operating at an ionization energy of 70 eV is mounted in the reactor pump line. This way, only stable reaction products can be detected. All recorded m/Z signals are normalized to argon to compensate for fluctuations of pressure and temperature, and corrected for the background contribution of this specific m/Z value.
Etching experiments are performed in a similar ETP set up. A subatmospheric thermal argon plasma (typically 0.3 - $0.4 \cdot 10^5$ Pa) is generated in a dc arc discharge and expands supersonically into the low pressure (100 Pa) reactor chamber. At 5 cm from the arc outlet, the hydrogen is injected in the plasma by means of a ring. No power is coupled in downstream leading to a low electron temperature (0.2 - 0.3 eV) in the expanding beam [13,14]. Electron-induced molecular dissociation is unlikely to occur, the chemistry is dominantly controlled by (Ar^+, e^-) emanating from the arc [15],

$$Ar^+ + H_2 \rightarrow ArH^+ + H \qquad 1.2\ 10^{-9}\ cm^3/s \qquad (1a)$$
$$ArH^+ + e^- \rightarrow Ar + H^* \qquad 10^{-7}\ cm^3/s \qquad (1b)$$

The mixture of reactive particles flows at subsonic velocities to the substrate placed at 60 cm from the nozzle where, without any significant ion bombardment [16], etching takes place. *In-situ* real time spectroscopic ellipsometry is applied to evaluate the etching process in terms of structural and compositional modification. Ellipsometric Ψ and Δ data were acquired at an angle of incidence of 68° over the spectral range of 245 – 1000 nm with a resolution of 1.6 nm using a Woollam M-2000F rotating compensator ellipsometer.

3. Results and Discussion

Spontaneous decomposition of DEZ, $Zn(C_2H_5)_2$, in absence of either oxygen or plasma exposure is very low. A strong signal at m/Z values related to the monomer is visible, there appear to be no reaction products other then belonging to the monomer cracking pattern visible in the spectrum. Decomposition of DEZ can occur either thermally, directly stimulated by the plasma, or through reaction with oxygen due to its pyrophoric

nature. Under plasma exposure DEZ is completely decomposed, even in the absence of oxygen. In all conditions no Zn related fragments are detected, indicating the relatively low density of $Zn(C_2H_5)_2$, $Zn(C_2H_3)_2$, ZnH_2, $Zn(OC_2H_5)_2$, $Zn(OCH_3)_2$, $Zn(OH)_2$ and ZnO in the gas phase. Main products detected in the plasma induced decomposition are C_2H_6, C_2H_4, C_2H_2, and H_2, see Figure 1, in the plasma induced oxidative decomposition CO, CO_2, H_2O and H_2. The presence of these product suggests a rich plasma induced hydrocarbon chemistry.

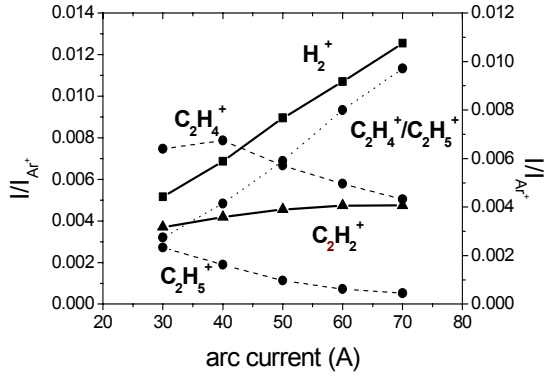

Figure 1: Different reaction product related fragments detected with mass spectrometry in the plasma induced decomposition of DEZ. Notice that the fragment $C_2H_4^+$ can be attributed to both C_2H_4 and C_2H_6. To distinguish its contribution to these species, the ratio $C_2H_4^+/C_2H_5^+$ has been plotted as the fragment $C_2H_5^+$ is solely attributed to C_2H_6.

The initial decomposition of DEZ is stimulated by (Ar^+, e^-) emanating from the cascaded arc favorably breaking the Zn-C bond (Figure 2), although in presence of oxygen (Ar^+, e^-) will be partly consumed to produce atomic oxygen, which also directly might attribute to the decomposition of DEZ.

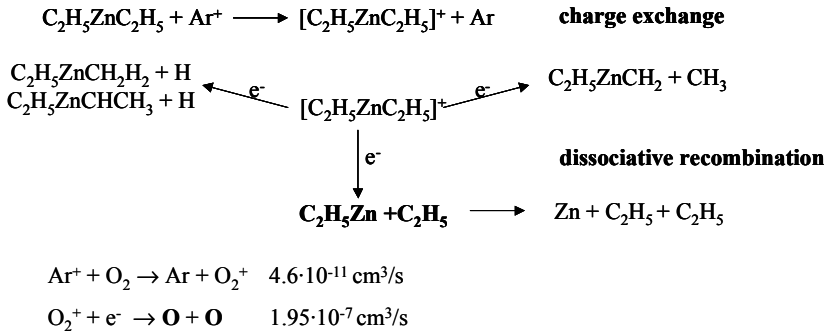

Figure 2: (Ar^+, e^-) dominated plasma induced decomposition pathways of DEZ and oxygen.

Dry etching of textured ZnO is demonstrated using a remote argon - hydrogen plasma. In absence of plasma exposure, i.e. in an argon / hydrogen gas mixture, as well as under plasma exposure without any hydrogen dosing, no etching is observed at all. From 2 sccs hydrogen, saturation occurs, indicative for a limitation of the reactive etching species present, see Figure 3. This is confirmed by the lowering of the effective etch rate at a lower amount of (Ar^+, e^-) emanating from the arc at a lower arc current or total argon flow, indicating atomic hydrogen is the reactive species whereas the excess of molecular hydrogen in the gas phase does not contribute to the etching.

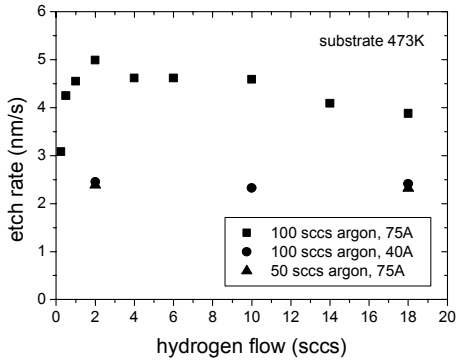

Figure 3: ZnO etch rate versus hydrogen flow for different amounts of (Ar^+, e^-) emanating from the arc.

With a variation of substrate temperature in the range 323 – 573K, visualised in Figure 4, an *overall* apparent activation energy of 0.23 ± 0.01 eV (22.3 ± 1.0 kJ $mole^{-1}$) is determined, which is indicative for a limitation of formation and removal of reaction products from the substrate surface (surface kinetics control). It's likely the etching occurs due to removal of O bij H, followed by vaporisation of free Zn [12]. Removal of the latter might be the limiting step due its rather low vapor pressure (10^{-3} mbar at 573K) [17].

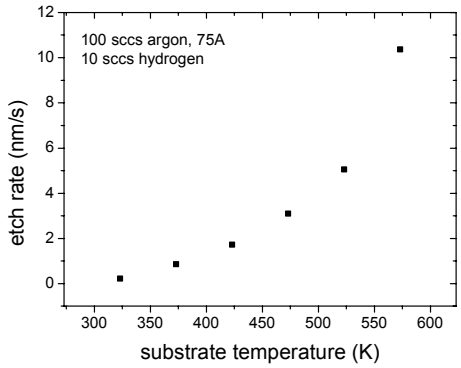

Figure 4: ZnO etch rate versus substrate surface temperature.

Evaluation of the etching process in terms of structural and compositional modification is obtained from *in-situ* real time spectroscopic ellipsometry. A simple but appropriate optical model for the visible wavelength range is the Cauchy model, an approximated polynomial form of the Sellmeier relation commonly used for ZnO [18]. The optical constants of the silicon substrate with native oxide are determined separately for each different temperature. The model is used to determine film thickness and roughness, the optical constants of the surface layer being described as a mixture of ZnO and void (ambient) using the Bruggeman Effective Medium Approximation (BEMA). The presence of any voids in the bulk layer is neglected, and the optical properties are considered to be homogeneous in depth initially. The optical constants of the film are calculated subsequently 'point by point', that is, without assuming any dispersion model.

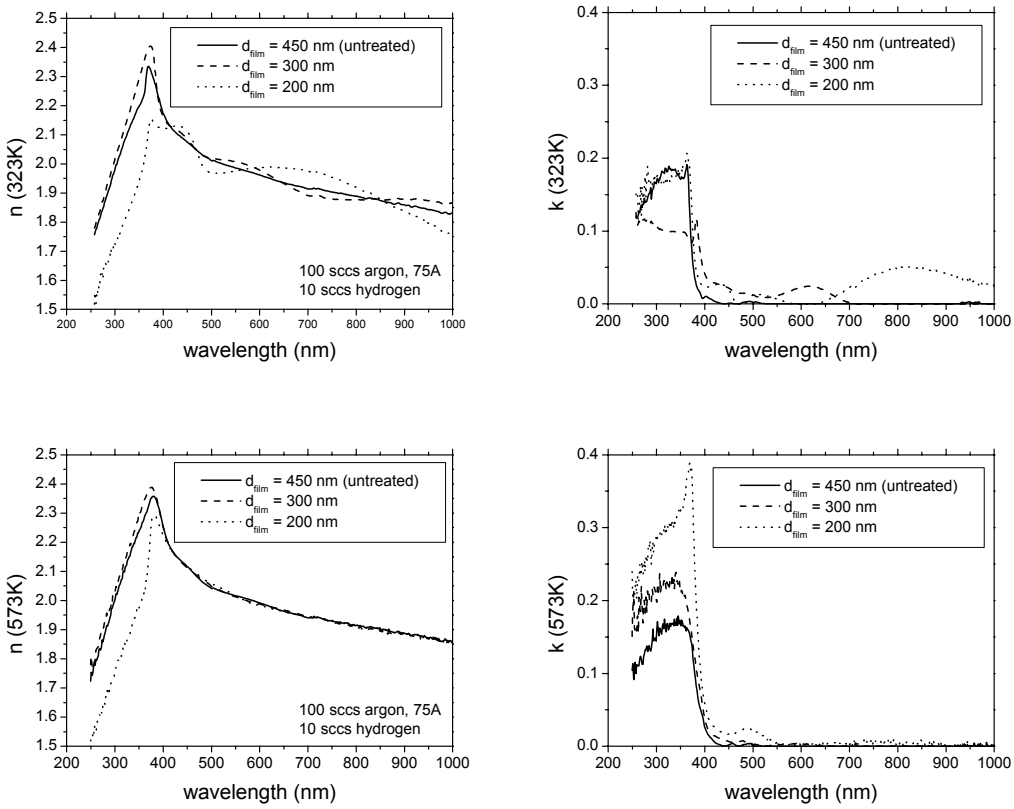

Figure 5: Ellipsometric film composition (optical constants n and k) for untreated and hydrogen treated ZnO films at different substrate surface temperature.

At a high substrate temperature, etching appears to be homogeneous, moderate surface roughening e.g. increasing top layer thickness and void fraction is observed, indicating a merely confined hydrogen film penetration. On the contrary, with lowering the substrate temperature it is assumed the formation and / or reaction product removal is becoming slow compared to hydrogen film penetration, resulting in both significant roughening and a changing film composition as deduced from the optical constants, see Figure 5. Hardly any change in film composition in comparison to the untreated material is observed at a high substrate temperature. Film etching and modification therefore become competitive processes, possibly in combination with a faster removal of the modified material.

4. Conclusions

Initial insight into the plasma chemistry taking place during deposition of textured ZnO is obtained from mass spectrometry. Main products detected in the plasma induced decomposition of $Zn(C_2H_5)_2$ are C_2H_6, C_2H_4, C_2H_2 and H_2, in the plasma induced oxidative decomposition CO, CO_2, H_2O and H_2. A new method for fast dry etching of textured ZnO using a remote argon - hydrogen plasma is demonstrated, including competitive film modification in terms of surface roughness and composition. Etch rates up to over 10 nm/s have been obtained. Atomic hydrogen is considered to be the reactive species, the excess of molecular hydrogen in the gas phase does not contribute to the etching. A more detailed study with respect to film properties is in progress.

Acknowledgements

The authors gratefully acknowledge Hans van Hemmen, Bas Kniknie and Guido Schiffelers for their contribution to the measurements, Jochen Löffler and Ruud Schropp (UU) for the fruitful discussions, and Ries van de Sande, Jo Jansen (TU/e), Gerwin Kirchner and Leo Toonen (TNO TPD) for their skilful technical assistance. This research has been financially supported by the Netherlands Agency for Energy and Environment (NOVEM).

References

[1] R. Groenen, J.L. Linden, H.R.M. van Lierop, D.C. Schram, A.D. Kuypers, M.C.M. van de Sanden - Appl. Surf. Sci. **173**, 40 (2001).
[2] R. Groenen, J. Löffler, P.M. Sommeling, J.L. Linden, E.A.G. Hamers, R.E.I. Schropp, M.C.M. van de Sanden – Thin Solid Films **392**, 226 (2001).
[3] J. Löffler, R. Groenen, J.L. Linden, M.C.M. van de Sanden, R.E.I. Schropp – Thin Solid Films **392**, 315 (2001).
[4] S.J. Baik, J.H. Jang, C.H. Lee, W.Y. Cho, K.S.Lim - Appl. Phys. Lett. **70**, 3516 (1997).
[5] C.G. van de Walle - Phys. Rev. Lett. **85**, 1012 (2000).
[6] J.-M. Lee, K.-K. Kim, S.-J. Park, W.-K. Choi - Appl. Phys. Lett. **78**, 3842 (2001).
[7] O. Kluth, A. Löffl, S. Wieder, C. Beneking, W. Appenzeller, L. Houben, B. Rech, H. Wagner, S. Hoffmann, R. Waser, J.A. Anna Selvan, H. Keppner - Proc. 26th IEEE-PVSC, Anaheim 715 (1997).
[8] Y. Li, G.S. Tompa, S. Liang, C. Gorla, Y. Lu, J. Doyle - J. Vac. Sci. Technol. A **15**, 1063 (1997).
[9] J.G.E. Gardeniers, Z.M. Rittersma, G.J. Burger - J. Appl. Phys. **83**, 7844 (1998).
[10] G.D. Swanson, T. Tamagawa, D.L. Polla - J. Electrochem. Soc. **137**, 2982 (1990).
[11] J.-M. Lee, K.-M. Chang, K.-K. Kim, W.-K. Choi, S.-J. Park - J. Electrochem. Soc. **148**, G1 (2001).
[12] K. Ip, H. Baik, M.E. Overberg, E.S. Lambers, Y.W. Heo, D.P. Norton, S.J. Pearton - Appl. Phys. Lett. **81**(19), 3546 (2002).
[13] M.C.M. van de Sanden, J.M. de Regt, D.C. Schram - Phys. Rev. E **47**, 2792 (1993).
[14] M.C.M. van de Sanden, J.A. Tobin - Plasma Sources Sci. Technol. **7**, 28 (1998).
[15] S. Mazouffre, M.G.H. Bogaarts, I.S.J. Bakker, P. Vankan, R. Engeln, D.C. Schram - Phys. Rev. E **64**, 016401 (2001).
[16] W.M.M. Kessels, C.M. Leeuwis, M.C.M. van de Sanden, D.C. Schram - J. Appl. Phys. **86**, 4029 (1999).
[17] J.D. McKinley, J.E. Vance - J. Chem. Phys. **22,** 1120 (1954).
[18] X.W. Sun, H.S. Kwok - J. Appl. Phys. **86**, 408 (1999).

LOW PRESSURE NITROGEN GLOW DISCHARGE WITH GRAPHITE ELECTRODES

M.J. Pinheiro[1], B. F. Gordiets[2] and N. Pinhão[3]

[1] *Department of Physics, Centro de Física de Plasmas, Instituto Superior Técnico, Lisboa, Portugal*
[2] *Lebedev Physical Institute of the Russian Academy of Sciences, Moscow, Russia*
[3] *Instituto Tecnológico e Nuclear, Estrada Nacional 10, 2685 Sacavém, Portugal*

Abstract
We present a model describing the main trends of the principal processes occurring in nitrogen DC glow discharge plasma with two parallel graphite electrodes. The computational model describes the axial structure as composed by the bulk plasma in the positive column of the gas discharge tube. Due to the surface processes occurring at both electrodes, the gas phase species C, CN are generated in the discharge. These particles together with N atoms are deposited on discharge tube surface. The sputtering efficiency for production of CN molecules from cathode due to ion bombardment and the probability of wall losses of CN are determined from comparison with the experiment.

1. Introduction

The study of CN molecules has attracted much interested in the last decades due to the prominent role played in astrophysical processes. Much research effort has recently been also directed to the use of plasma-enhanced chemical vapour deposition (PECVD) to produce thin-films which consist of components C and N.
Here we present a model describing the main trends of the principal processes occurring in the positive column of a nitrogen DC glow discharge with graphite electrodes. This device is a source of gas phase C and N atoms and CN molecules and can be used for deposition of C and N and thin film production.

2. Kinetic model for bulk plasma processes

Only the positive column is described. The cathode sheath extends through a small region l_{cathode} (l_{cathode} (cm) ~ 0.45/p, with p the gas pressure in Torr). Electron current and electron density are small in this region, the plasma is not quasineutral and the main current is formed of positive ions to cathode. These ions have a big average kinetic energy, bombard graphite cathode cause the sputtering of C atoms and CN molecules. The calculation of C atom and CN molecule densities in the discharge is carried out in our model. The negative glow region is not investigated in the present work. In the positive column, electron transport parameters are obtained by solving the homogeneous Boltzmann equation, as derived from the classical two-term expansion in spherical harmonics; quasi-neutrality is assumed and ambipolar diffusion control the behavior of electrons and ions in the bulk plasma.
The kinetics in nitrogen considered in this model is the same as used in previous model [1]. Spectroscopic measurements done on this kind of discharge [2], have indicated that the most important carbonated species are CN(X) and CN(B). That is why, additionally to C, CN the calculations of CN(B) and CN^+ densities are also included in model. To simplify, we assume that all C atoms are in the fundamental state and the chemical reactions take place both in volume and at the surfaces. The CN(B) kinetics are the same as used in [3]. The most important reactions pertaining to the kinetics of carbonated species are listed in [4].

3. Surface model

The wall tube losses for all species can be described in the framework of one dimension by the formula [5]

$$K_w\,(\text{s}^{-1}) \approx [R^2/(5.8D) + 2R/(\gamma_i < c >)]^{-1} \qquad (1)$$

Here, D is the diffusion coefficient, $< c >$ is the particle mean velocity near the wall and γ_i is the probability of wall deactivation for the *ith* species. For ions γ_{ion}=1; this gives losses by ambipolar diffusion.

We introduce in our kinetic model the production of C atom and CN molecules at the graphite electrodes. At the cathode, it occurs the well-known process of sputtering of C atom due to bombardment of the cathode by energetic positive ions, which are accelerated in the cathode fall region:

$$N_2^+ \text{ (or } N_4^+) + \text{C(surface)} \rightarrow \text{C(gas)} \qquad (2)$$

However, experiments show that the source of C and CN can be also at anode. That is why we have assumed that the surface process for production of C atoms is the process of collision with graphite surface of metastable molecules $N_2(a')$:

$$N_2^* + C(surface) \rightarrow C(gas) \quad (3)$$

Here N_2^* is $N_2(a')$. The energy of these metastables is enough to break the chemical bond C-C on graphite surface

We have also assumed that similar processes can produce gas phase CN molecules:

$$N_2^+ \text{ (or } N_4^+) + CN(surface) \rightarrow CN(gas) \quad (4)$$

$$N_2^* + CN(surface) \rightarrow CN(gas) \quad (5)$$

The surface molecules CN(surface) on graphite electrodes can be produced due to chemical adsorption of gas phase N atoms. We have introduced the processes (4), (5) in our kinetic model because the calculation of [CN] with taking into consideration only volume processes gives the very small CN density which is not in agreement with experiment.

4. Calculation of carbonated species

If we accept these mechanisms for surface production of C atoms and CN molecules, the fluxes $G_{cathode}$ and G_{anode} of gas phase C or CN from cathode and anode, respectively, are equal:

$$G_{cathode} = B\,[N_2(a')]_{cathode} + F\,J, \quad (6)$$

and

$$G_{anode} = B\,[N_2(a')]_{anode} \quad (7)$$

Here J is the current density (in A cm^{-2}) and the metastable densities $[N_2(a')]$ (in cm^{-3}) are the densities nearby the cathode or anode. The dimension of coefficients B is cm s^{-1} and it is, in fact, a value of the type $b\langle c \rangle$, where $\langle c \rangle$ is thermal average velocity of N_2 molecules near the surface and $b < 0.25$. The dimension of F is 1/e (e=1.6 10^{-19} is electron charge in Coulomb). The parameter F is differ from 1/e by some coefficient *d*. The coefficients *b* and *d* have been estimated in the present work using experimental data for relative intensities of CN(B->X) and N_2^+(B->X) bands near the cathode and in the positive column, respectively. The mechanism for generation of these bands is the same (see below, process (12) and [1]) and connects the relative intensities I(CN(B->X))/I(N_2^+(B->X)) with relative densities [CN(X)]/[N_2^+]. The concentration of N_2^+ have been calculated from our kinetic model (see Table 1) and [CN(X)] was obtained considering the flux $G_{cathode}$ as well as both coefficients *b* and *d*. If we neglect the volume production of C atoms and CN molecules, the approximate analytical solution is searched for the transport of C and CN from cathode and anode inside of the discharge tube. Taking into account axial diffusion with the diffusion coefficient D (in $cm^2\ s^{-1}$) and gas flow velocity **v** (from cathode to anode) we have the following equation:

$$dG(A)/dz = -L_C[A]; \qquad L_C = k_w. \quad (8)$$

Here, A=C or CN; k_w is the probability (in s^{-1}) for wall losses of C or CN (see Eq. (1)); G is the flux of "A" along the gas discharge tube:

$$G = \{v - (D/[A])\, d[A]/dz\}\,[A] \quad (9)$$

Here, z is distance from the point of gas inlet (cathode) into discharge. The transport equation for the "A" particle has the analytical solution

$$[A] = B_1 \exp\{z/L_1\} + B_2 \exp\{z/L_2\}, \quad (10)$$

where $L_1 = 2D/[v + \sqrt{(v^2 + 4\,k_w\,D)}]$ and $L_2 = 2D/[v - \sqrt{(v^2 + 4\,k_w\,D)}]$ are a kind of "relaxation lengths" for "A" particles. The values B_1 and B_2 depend on anode and cathode fluxes due to surface production of "A" particles which are the flux boundary values of G..

Note that the comparison of relative value of the [CN(X)] along the discharge tube with the experimental measurements gives the possibility to estimate k_w and, as a result, the probability γ_{CN}.

The calculation of electronically exited species CN(B) is interesting because the violet CN(B) bands are recorded experimentally. Those radicals are assumed to be created and deactivated according to the following reactions

$$CN(X) + N_2(A) \rightarrow CN(B) + N_2(X, v=0) \quad (11)$$

$$CN(X) + N_2(X, v \geq 12) \rightarrow CN(B) + N_2(X, v-12) \quad (12)$$

$$C + N + N_2 \rightarrow CN(B) + N_2 \quad (13)$$

$$CN(B)+N_2 \rightarrow CN(X)+N_2 \quad (14)$$
$$CN(B) \rightarrow CN(X) + h\nu \quad (15)$$

The diffusion coefficients were calculated using a known expression and we present results for probability for losses of C and CN to the wall: $\gamma_C = \gamma_{CN} = 0.05$. The value of γ_{CN} have been obtained by fitting of theoretical value of relative intensities $I(CN(B->X))_{z=1\ cm}/ I(CN(B->X))_{z=7\ cm}$ to the experimental ones.

As carbonated species diffuse to the wall, a thin film is building up. Its properties depend on the ratio [N]/[C].

5. Partial results

The calculations were done for conditions similar to the experiment [2] for conditions: p=0.451 Torr, I=2.5 mA,. The tube diameter is 2.17 cm and the tube length is 25 cm.

As the gas velocity is small (at p=0.451 Torr, v=0.7 cm/s), the magnitude of the gas and vibrational temperatures, as well electronic temperature and densities remain constant along the positive column, as shown in Table 1.

Table 1 - Relevant discharge output at two different pressures at the positive column

	p=0.451 Torr		P=1 Torr	
	2.5 mA	10 mA	2.5 mA	10 mA
$N_2(A)$	6.95×10^{11}	1.10×10^{12}	9.72×10^{11}	1.61×10^{12}
$N_2(a')$	4.07×10^{11}	1.70×10^{12}	2.66×10^{11}	1.23×10^{12}
N	1.15×10^{14}	3.84×10^{14}	1.14×10^{14}	3.65×10^{14}
N_e	3.46×10^{8}	1.21×10^{9}	3.35×10^{8}	1.42×10^{9}
N_2^+	2.34×10^{8}	9.89×10^{8}	9.95×10^{8}	5.11×10^{8}
N_4^+	5.38×10^{7}	2.19×10^{8}	2.35×10^{8}	9.07×10^{8}
T_g (K)	308	335	317	363
T_{vib} (K)	3230	4270	3120	3980
E/N(10^{-16} V cm^2)	14.3	13.2	11.4	10.5
T_e (eV)	2.41	2.45	1.98	2.06

Figs.1,2 show the concentrations of C atoms along the discharge tube for p=0.451 Torr and 1 Torr. The same values of parameters γ_C, b and d were used to obtain [CN] (see below) as well for the C concentration.

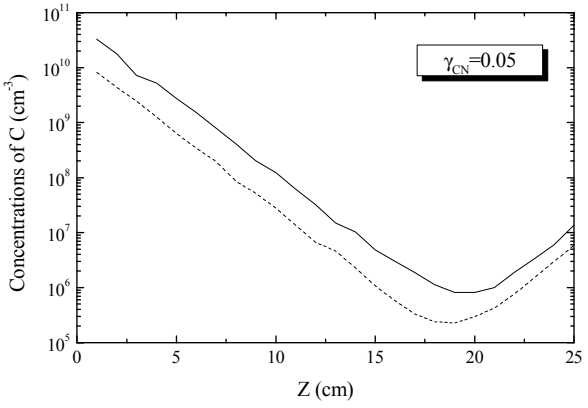

Fig. 1 - Concentrations of C along the discharge tube at p=0.451 Torr. Solid curve I=10 mA; dashed curve I=3 mA.

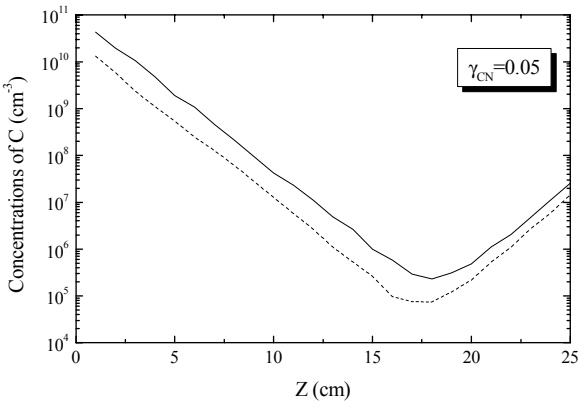

Fig. 2 - Concentrations of C along the discharge tube at p=1 Torr. Curves as in Fig.1.

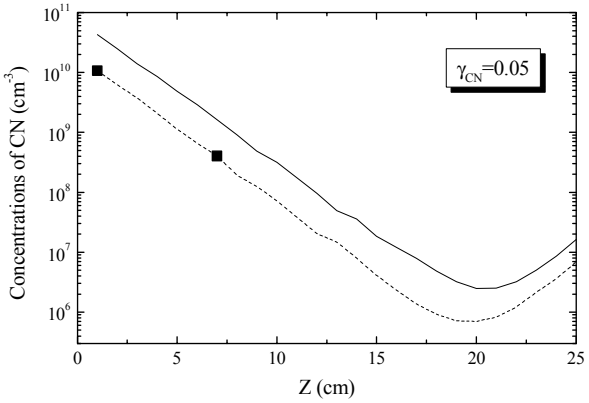

Fig. 3 - Concentrations of CN vs. position for p=0.451 Torr. Solid curves, I=10 mA and dashed curves, I=3 mA. ▫ - Values extracted from experimental data [6].

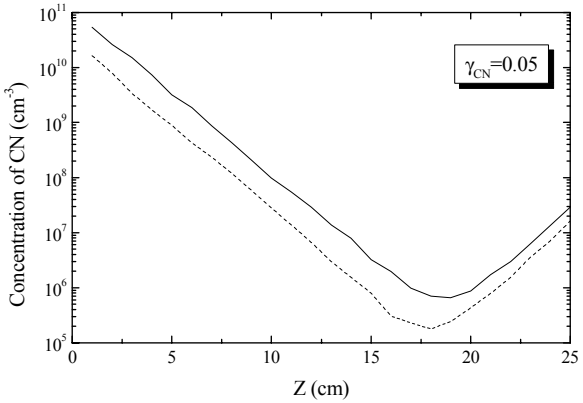

Fig. 4 - Concentrations of CN vs. position for p=1 Torr. Curves as in Fig.3.

As can be seen through Figs.3-4, the CN species concentration decreases from cathode to anode and increases with current. The agreement with experiment at p=0.451 Torr is good for the following values of parameters: $\gamma_{CN} = 0.05$; d=6.7 10^{-3}; b=6 10^{-6}. Figs.5-6 show the relative intensities of CN(B→X) band. The best agreement with experiment is attained when using the above given values for γ_{CN}, d and b.
To conclude, we believe that the electrode graphite surface source for gas phase production of CN molecules is more effective than the volume production. However, to obtain more accurate calculations and to compare with experiment, it is necessary to include in the present model the negative glow region of the discharge, which has in our operating conditions a relative big length in the discharge tube. In this region, additional interesting experimental results have been obtained. This topic will be investigated in the near future.

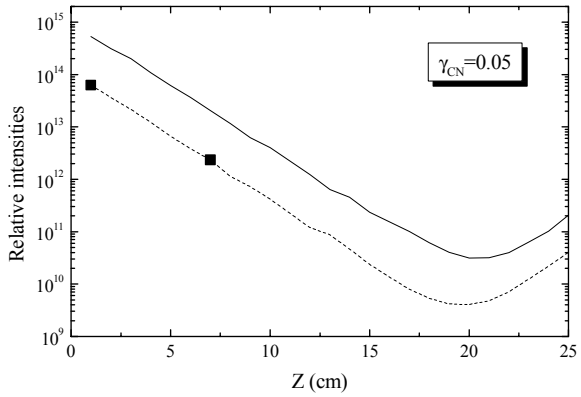

Fig.5 - Relative intensities of CN(B→X) at p=0.451 Torr. Curves as in Fig. 1. ▫ - Experimental data [6].

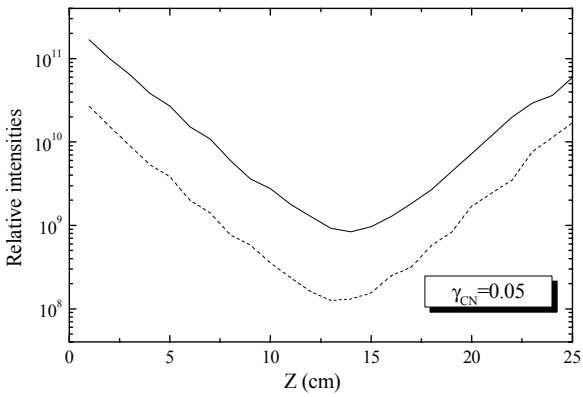

Fig. 6 - Same representation as in Fig. 5, but at p=1 Torr.

Acknowledgments
We thank Zoltán Donkó and Kinga Kutasi for providing us with experimental data.

References

1 B. Gordiets, C. M. Ferreira, M. J. Pinheiro and A. Ricard, Plasma Sources Sci. Technol. **7**, 363 (1998)
2 K. Kutasi, Z. Donkó, M. Mohai, L. Nemes, G. Marosi, Vacuum **68**, 311 (2003)
3 C.D.Pintassilgo, J. Loureiro, G. Cernogora and M. Touzeau, Plasma Sources Sci. Technol. **8**, 436 (1999)
4 T.J. Millar, J. M. C. Rawlings, A. Benett, P. D. Brown and S. B. Charnley, A & AS **87**, 585 (1991)
5 M.Capitelli, C. M. Ferreira, B. F. Gordiets, A. I. Osipov – "Plasma Kinetics in Atmospheric Plasma", Springer, Berlin, N.Y., London, Paris, Tokyo, 2000
6 Zoltán Donkó and Kinga Kutasi, private communication

Influence of plasma source on atmospheric pressure PE-CVD process characteristics

I. Dani[1], V. Hopfe[1], D. Rogler[1], G. Mäder[1], C. Schreuders[1], K. Landes[2], E. Theophile[2], M. Dzulko[2], R. Spitzl[3]

[1] *Fraunhofer Institut Werkstoff- und Strahltechnik, Dresden, Germany*
[2] *Universität der Bundeswehr, Neubiberg, Germany*
[3] *IPLAS GmbH, Troisdorf, Germany*

Atmospheric pressure CVD processes are promising for the development of cost effective technologies for wide area coating. Two distinctly different plasma sources have been studied for continuous CVD: (i) CYRRANUS®, a non-thermal volume source with microwave activation, developed at (3) and, (ii) LARGE, a thermal line plasma source based on an extended DC arc, developed at (2). Both plasma sources have been used to deposit oxide and non-oxide layers on temperature sensitive substrates. Comparative source evaluation was based on obtained layer properties. Different methods including optical emission and *in-situ* FTIR spectroscopy have been used for process/source characterisation. Temperature distributions have been measured within the plasma downstream region using spectroscopic and conventional tools. Depending on plasma gases applied a range of atomic and molecular intermediates, TEOS precursor fragments, and reaction products have been identified. Several gaseous key species have been found indicating e.g. the degree of precursor conversion and/or its tendency for powder formation. The plasma chemical reactions involved result in a complete conversion of the element-organic precursor into an inorganic layer without any organic residues. Extensive fluid dynamic calculations have been applied targeting on both the optimisation of reactor design and the kinetics of the rate determining step. Comparing the calculated layer profile with the experimental obtained ones the conclusion has been drawn that the deposition process is transport controlled.
It was demonstrated, both the CYRANNUS, and the LARGE plasma source, are well suited for plasma enhanced CVD at atmospheric pressure.

Humidity sensitivity of hydroxyapatite films by r.f. plasma sputtering method

K. Shimizu[1], T. Ishikawa[2], K.Ozeki[3], K.K. Hirakuri[2] and H. Aoki[4]

[1] *Applied Electronic Engineering, Tokyo Denki University, Saitama, Japan*
[2] *Department of Electronic and Computer Engineering, Tokyo Denki University, Saitama, Japan*
[3] *Applied Systems Engineering, Tokyo Denki University, Saitama, Japan*
[4] *Frontier Research and Development Center, Tokyo Denki University, Saitama, Japan*

Hydroxyapatite (HAp:$Ca_{10}(PO_4)_6(OH)_2$), a crystallographical analogue to calcified tissues of vertebrates, has been well developed as an implant material because of its outstanding biocompatibility. Recent studies are spreading its application to such fields as liquid chromatographic column for the separation of proteins and nucleic acids, a catalyst for dehydration or dehydrogenation of some alcohols, powder carries for removing heavy metal ions, and chemical sensors for various gases [1]. The characteristics of HAp are strongly depended on their stoichiometry, crystallinity and particle size [2]. The stoichiometry of ratio between calcium and phosphorus of a HAp is 1.67.

A common ceramic sensor with humidity sensitivity was used adsorption of the moisture. However, it has big problem to use for humidity sensor because the moisture is adsorped on the surface and it reacts to make hydroxyl group. Furthermore, the resistivity was increased with time of use. However, HAp has be expected that this degradation can be prevented, because it has the hydroxyl group during the crystal. Although the humidity sensor using the HAp of sintered compact have already been put in practical use, the thin film of HAp is developed for trial.

In this study, we have been investigated the humidity-sensitive characteristics of the HAp thin film deposited by the sputtering method and the validity as a humidity sensor material. The aim of this study is to apply a HAp to sensing material, and develop a new type of humidity sensor.

Using r.f. plasma sputtering method, Ar was utilized for the deposition of the HAp films on a silica glass substrate. Target of disc shape consist of the HAp powder, which is made of Ube Material Industries, LTD. Discharge power of plasma was kept at 100W. Frequency of th r.f. generator was 13.56 MHz. Gas pressure and gas flow rate were 5 Pa and 10 sccm, respectively. HAp was deposited with thickness of 0.2 μm at room temperature.

Furthermore, hydrothermal process was carried out to enhance crystallization of the deposited films. Hydrothermal process is a water solution reaction which raises a crystallinity of the films at high temperature and high-pressure conditions. The films were treated in the reaction chamber at 200 ℃ and 1.5 MPa. The time of reaction is 24 hours.

The humidity-sensitive characteristics of the samples was measured before and after the hydrothermal process. The characteristic is the relationship between electrical resistivity and relative humidity (30～90%).

Structure morphology of the deposited films was observed by scanning electron microscopy (SEM). The crystalline phase and the Ca/P ratio of the deposited films were estimated by X-ray diffraction (XRD) and energy dispersive spectroscopy (EDS). The analysis of adsorption of hydroxyl group in before and after measurement of humidity-sensitive characteristics was measured by FT-infrared (IR) spectroscopy.

As the result of the analysis, it seems that the composition deviance of the films before the hydrothermal process has been caused by the heat of the plasma.

However, the composition deviance has been improved by the hydrothermal process. The excellent humidity-sensitive characteristics of the HAp films after the process is confirmed as compared with those of other ceramic humidity sensors.

[1]K.Yamashita, K.kitagaki, and T.Umegai, Journal of the American Ceramic Society, 78 [5] 1191-1197(1995)

[2]T.Kanazawa, Inorganic Phosphate Materials, in Materials Science Monographs, vol.52, Kodanska Elsevier, Tokyo 1989.

Characterization of oxygen plasma with a catalytic probe

U. Cvelbar[1], M. Mozetič[1], I. Poberaj[2]

[1] *Plasma laboratory, Institute of Surface Engineering and Optoelectronics, Ljubljana, Slovenia*
[2] *Department of Physics, University of Ljubljana, Ljubljana, Slovenia*

Reactive oxygen plasmas are used in several advanced technologies including the unisotropic plasma etching, plasma drilling, plasma oxidation, plasma cleaning, plasma ashing and plasma surface activation [1-6]. Different technologies require application of plasma with different parameters. For unisotropic etching and drilling, a plasma with a high degree of ionization is needed, while for some other technologies, an oxygen plasma with a low density of charged particles performs better. For very delicate treatments of samples, for instance during plasma ashing and selective plasma etching, a state of a gas with a negligible concentration of charged particles should be used. In such cases, it is much better to treat samples in post - discharges rather than in plasmas themselves. In systems used for delicate plasma treatments, the most important parameter is the density of neutral oxygen atoms.
The density of neutral oxygen atoms can be measured by different means including a variety of optical emission and absorption spectroscopy methods, NO titration, and catalytic probes. Recently, it was shown that catalytic probes have some advantages over the other methods[10,11]. The main advantage is a low cost and the ability for real time measurement of the O density.
A catalytic probe was used to measure the O density in a plasma reactor. An integral part of the reactor was a movable recombinator that allowed for adjusting the O density without changing other plasma parameters. The O density was measured at different pressure between 10 and 100 Pa and different recombinator position. The result is plotted in Figure 1.

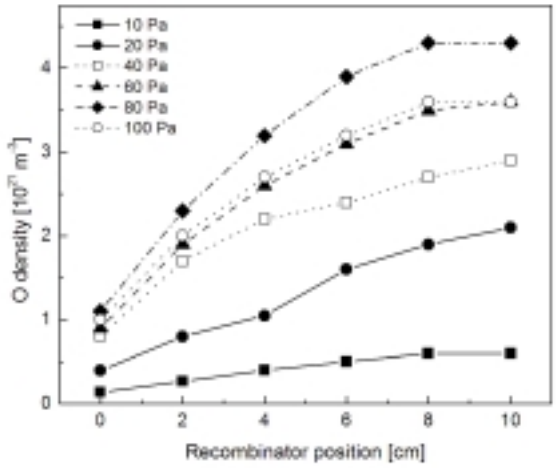

Fig. 1. Density of neutral oxygen atoms versus the distance between the probe and recombinator tip.

[1] B. Chapman, Glow Discharge Processes (Willey, New York, 1980).
[2] H. Boeing, Plasma Science and technology (Cornell Univerity Press, London, 1982).
[3] A. Ricard , Reactive plasmas (Societe Francaise du Vide, Paris, 1996).
[4] L. A. Simpson, Australian OCCA Proc. and News 16, 1 (1979).
[5] B. Figler, W. Sahle, S. Krantz and U. Ulfvarson, Sci. Tot. Envir. 20, 77 (1996).
[6] M. Schmeling and D. Klockow, Anal. Chim. Acta 30, 121 (1997).
[7] D. Babič, I. Poberaj and M. Mozetič, Rev. Sci. Instr. 72 (2001), 4110.
[8] I. Poberaj D. Babič and M. Mozetič, J. Vac. Sci. Technol. A 20 (2002), 189.

Degradation and decolourization of textile dyes (Orange I, Indigo Carmine, Eriochrome black T) by non thermal plasma process

F. Abdelmalek[1]; M.R.Ghezzar[1]; M. Belhadj[1]; A. Addou[1]; J.L. Brisset[2]

[1]*Laboratoire des Sciences et Techniques de l'Environnement et de la Valorisation. Faculté des Sciences de l'Ingénieur, Université de Mostaganem . Algérie*
[2]*Laboratoire d'Electrochimie Interfaciale et de Chimie Analytique. Faculté des Sciences Université de Rouen. France.*

Abstract:
The glidarc degradation of various dyes (Orange I, Indigo Carmine, Eriochrome black T) has been studied, using non thermal plasma. All dyes solutions underwent a decolourization. The kinetics of reaction have been studied and were found to be zero or first order with respect to the dyes. A hight decolourization degree was however accompanied by an important reduction of chemical oxygen demand (COD), a correlation between decolourization and degradation has been established.

Introduction
Dyes makes our world beautiful, but it brings us pollution; colored water is unattractive and generates more and more complaints.
Environmental pollution by organic dye sets a sever ecological problem, which is increased by the fact that most of them are difficult to degrade by traditional techniques. In this process, hydroxyl radicals (OH°) are generated when a discharge is applied in the presence of air and water. The reactives species generated are able to degrade the organic pollutants like dyes, because the treatment consists of oxidative destruction [1,2,3,4].
Azo dyes constitue the largest class of dyes in industry, in the present work, we examine the degradation of Orange I and Eriochrome black T. The destruction of the azo bond –N=N– of this dyes, in the chromophore of azo dyes led to decolourization of dyes solutions. The Indigo Carmine is an indigoid dye, acid blue 74 (AB74), it's a carbonyl dye[5].

Material and methodes:
The tested azo dyes: Orange I, Carmine indigo, Eriochrome black T (EBT) were purchased from Aldrich. Purified water was obtained from a Millipore equipment. COD of samples from various treatment times was mesured by the potassium dichromate standard methods
The gliding arc system was described previously [6]. An electric is created between two metallic electrodes raised a convenient voltage difference (10 kV). The arc is blown away by a gas flow air the axis of the system and glides towards the end of the electrode before it breaks and a new arc forms. A plasma is generated by the arc in a volume located at the tips of the electrodes . Aqueous solutions are exposed to the plasma flux. The degradation was followed for different treatment times.

Results and discussion:
The color of solutions was studied from the comparaison of UV-VIS spectra. Each dye solution was scanned and its maximum absorbency visible wavelength determined.
The color of water polluted with organic colorants reduces when the cleavage of the –C=C- bonds, the –N=N- bonds and the aromatic rings occurs. The absorption of light by the associated molecules shifts from the visible to the UV or IR region of the electromagnetic spectrum, it is means that the dye is degraded into smaller products [7]. The UV-VIS spectra obtained for all the dyes shown a reduction in the absorbance at the maximum wavelenght. We can see on the spectra UV-VIS the decrease of the absorbance for the Orange I (475 nm), Indigo Carmine (288 and 612 nm) and Eriochrome Black T (525 nm) respectively (fig 1,2,3).

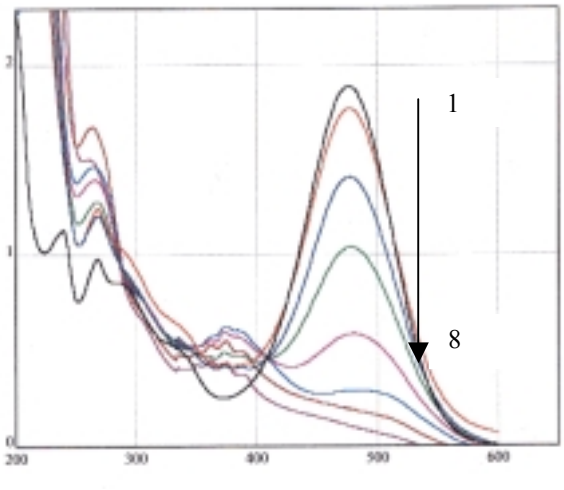

Fig 1: Variation of the spectral absorbance with time of OrangeI
1 : 0 min ; 2 : 1,5 min ; 3 : 2min ; 4 : 2,5min ;
5 : 3min ; 6 : 3,5min ; 7 : 8min ; 8 : 13min.

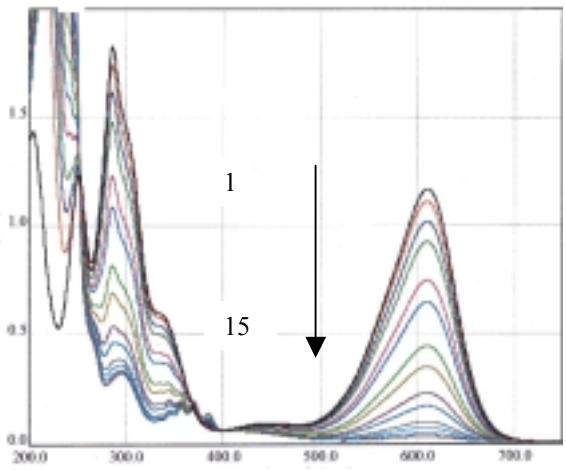

Fig 2: Variation of the spectral absorbance with time of Carmine Indïgo
1 : 0min ; 2 : 1min ; 3 : 2min ; 4 : 3min ;
5 : 4min ; 6 : 5min ; 7 : 6min ; 8 : 7min ; 9
8min ; 10 :9min ; 11 :10min; 12 : 11min ;
13 : 12min; 14 : 15min .

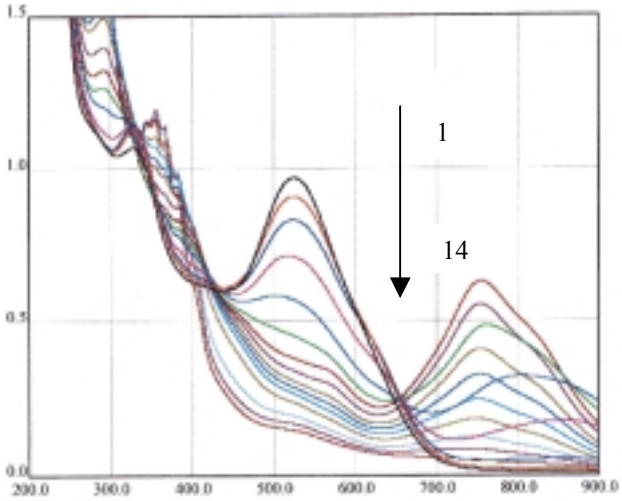

Figure 3 : Variation of the spectral absorbance with time of Eriochrome black T
1 : 0min ; 2 : ,1,5min ; 3 : 1,75min ; 4 : 2min ; 5 : 42,5min ; 6 : 3,25min ; 7 : 4min ; 8 : 5,5min ;
9 : 9min ; 10 :15min ; 11 :20min; 12 : 30min ; 13 : 40min ; 14 : 50min ; 60: min .

The decrease of absorbance means the decolourization of dyes solutions [8]. The table 1 shows the kinetics constants of decolourization and degradation of the three dyes.

Table 1: the kinetic constants of decolourization and degradation

Dyes	Orange I	Indigo Carmine	Eriochrome Black T
Kinetic constants of decolourization (min^{-1})	0,886	0,311	0,1
Kinetic constants of degradation (min^{-1})	0,0173	0,0237	0,0296

The decreased of apparent colour was accompanied by an reduction of COD (fig 4,5,6). The removal of the color and COD were 94,6% and 41,7% for the Orange I, at 30 min of treatment, while it was 97,9% and 8,8% for the Indigo Carmine for 15 min of treatment, we noticed that the decolourization is

easier than COD removal. The removal of color and COD of Eriochrome black T solution was equal to 64,2% and 51,4% respectively after 50 min .

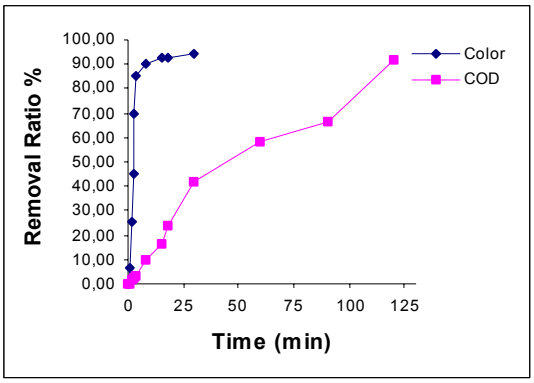

Fig 4: The decolorization and COD removal of Orange I

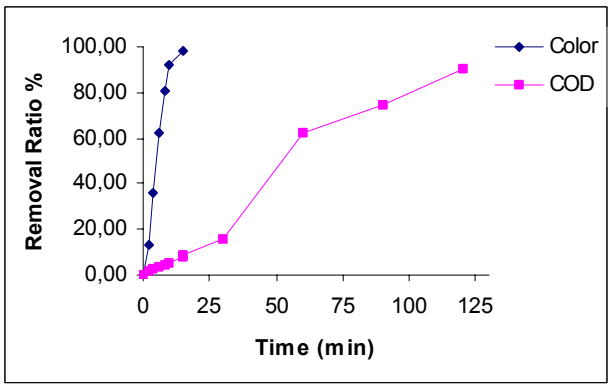

Fig 5: The decolorization and COD removal of Carmine Indigo

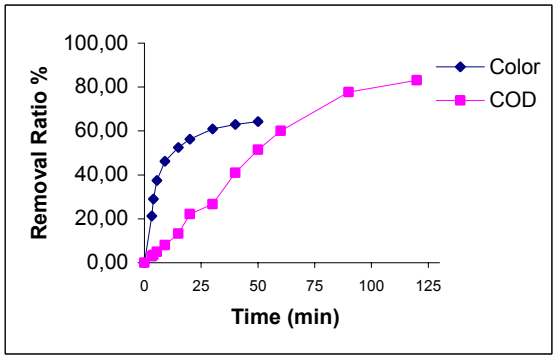

Fig 6: The decolorization and COD removal of Eriochrome black T

The degradation of dyes has been followed using the COD. The disappearance of the COD expresses the detoxification level of water and mineralization of organic compounds according to the equations of the dye total oxidation (1, 2, 3) .

Orange I

$$C_{16}H_{11}N_2O_4S^- + \frac{42}{2} \rightarrow 16CO_2 + 2NO_3^- + SO_4^{2-} + 3H^+ + 4H_2O \qquad (1)$$

EBT

$$C_{20}H_{12}N_3O_7S^- + \frac{50}{2} \rightarrow 20CO_2 + 3NO_3^- + SO_4^{2-} + 4H^+ + 4H_2O \qquad (2)$$

Carmine

$$C_{16}H_8N_2O_8S_2^{2-} + \frac{79}{4} \rightarrow 16CO_2 + 2NO_3^- + 2SO_4^{2-} + 5H^+ + \frac{3}{2}H_2O \qquad (3)$$

The COD values decreased as the treatment time increased as we can see on figures (7,8,9). The COD removal of Orange I, Indigo Carmine, and Eriochrome Black T are 92%, 90,6%, 83%, respectively after 120 min of treatment.

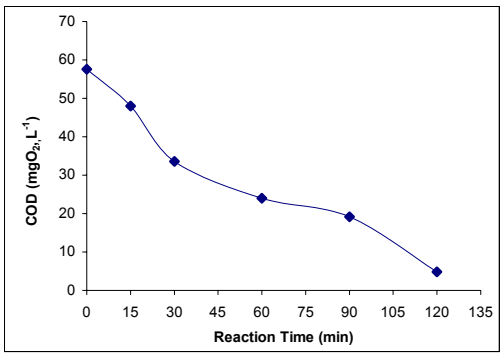

Fig 7: Variation of COD of Orange I dye

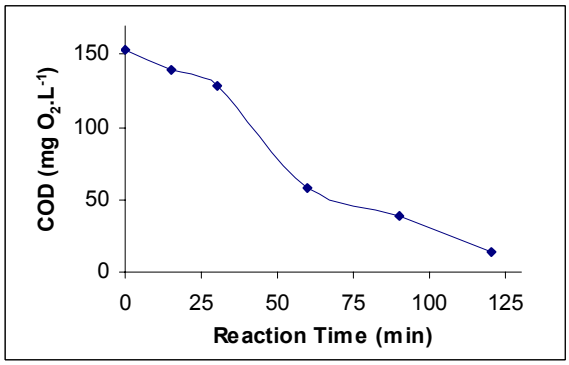

Fig 8: Variation of COD of Carmine Indigo dye

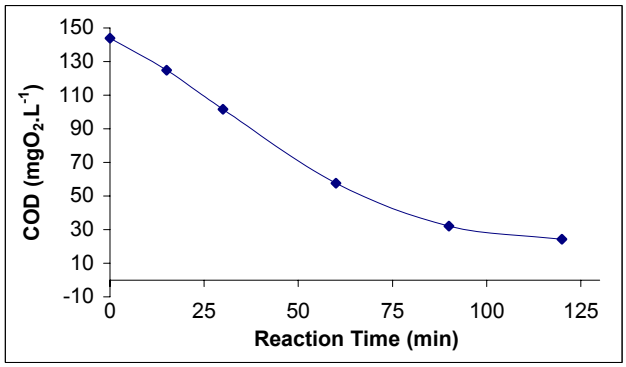

Fig 9: Variation of COD of Eriochrome black T dye

Formation and disappearance of Eriochrome Black T intermediate were evaluated by monitoring the evolution of absorbance at 764 nm during the treatment, as we can see on fig 10.

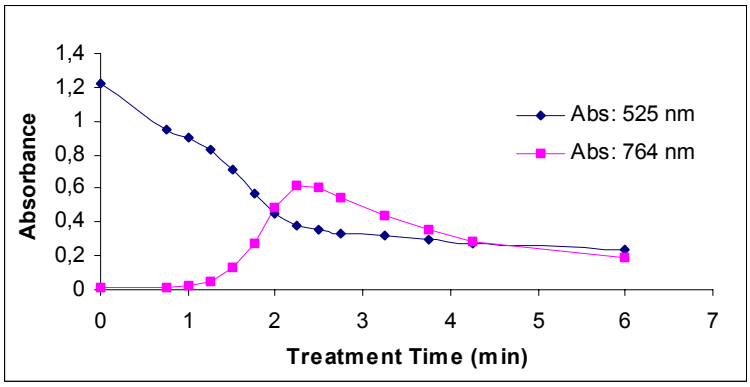

Figure 10: Formation and disappearance of intermediate at 764 nm

Conclusion:

The gliding arc treatment proved to be powerful in destroying the three dyes. The following conclusions can be drawn:

- Complete color removal needed 15, 30 and 50 min for Indigo Carmine, Orange I and Eriochrome black T respectively.
- Complete COD removal can be obtained after 120 min of treatment.
- Relationship between decolorization and degradability of dyeing solutions, the complete decolourization is achieved for about 15, 30, 50 min. At the same time, the COD conversion was 8,8 %, 41,7 % and 51,4 % respectively.
- Relationship between the rates removal of color/COD and kinetic constants of decoloration/degradation.

References:

1- B. Benstaali, B.G. Chéron, A. Addou, and J.L. Brisset, Proc. ISPC-14, Praga, Czech Rep. H. Hrabovski, M. Konrad, V. Kopecki Eds.; 939-944, (1999).

2- F. Abdelmalek; S. Gharbi; B. Benstaali; A. Addou; J.L Brisset. Dégradation du jaune supranol YS 4GL par plasma d'air humide. European Congress on Molecular Spectroscopy, Villeneuve d'Ascq. France 1-6 Septemer 2002.

3- F. Abdelmalek; S. Gharbi; B. Benstaali; A. Addou; J.L Brisset. Plasmachemical degradation of Azo Dyes: Scarlet Red Nylosan F3GL and Industrial waste Water Research , article submitted in 2002.

4- F. Abdelmalek; A.Addou; A.Semmoud; JL.Brisset. Gliding arc degradation of dyes (OrangeII, Methylene Blue, Malachite Green and Methyle Red). 3rd European Meeting on Environmental Chemistry, Geneva.Switzerland; 11-14-December 2002.

5- Galindo, P.Jacques, A. Kalte. Photochemical and photocatalytic degradation of an indigoid dye : a case study of acid blue 74 (AB74). Journal of Photochemistry and photobiology A : Chemistry 141 47-56, (2001).

6- H. Lesieur, A. Czernichowski, J. Chapelle, Brev.Fr. 2639172 (1988).C. A.F.

7- Strickland, W.S. Perkins. Decoloration of continuous dyeing wastewater by ozonation. Textile Chemist and Colorist; 27 (5): 11-15, (1995).

8- J.Cao, L. Wei, Q. Huang, S. Han. Reducing degradation of azo dye by zero-valent iron in aqueous solution. Chemosphere, Vol. 38, N°. 3, pp. 565-571, (1999).

Distribution and Sources of the Contaminated Minerals of Industrial Effluents in Water from Oued Cheliff and their Treatment by Plasma in Humid Air

M. Belhadj[1]; M.R. Ghezzar[1]; F. Abdelmalek[1]; B. Benstaali[1]; A. Addou[1]; J.L. Brisset[2]

[1] *Laboratoire des Sciences et Techniques de l'Environnement et de la Valorisation (STEVA), Faculté des Sciences de l'Ingénieur, Université de Mostaganem. 27000 Mostaganem, ALGERIA*
[2] *Laboratoire d'Electrochimie Interfaciale et de Chimie Analytique (LEICA), Faculté des Sciences, Université de Rouen, 76821 Mont-Saint-Aignan, France*

Abstract.
Liquid wastes of several manufactures in west Algeria, are poured in the country's longest "Oued Cheliff" river bed, polluting its mountain born water. It is reused by neighbouring agricultural farmers for cultures and crops irrigation. The actual report shows that the water is strongly contaminated by heavy metals and non-biodegradable organic compounds due to the high toxicity level of the liquid wastes. We propose, here, a method of their degradation by plasma of humid air.

1. Introduction.

The Oued cheliff river is the longest river in Algeria tributary to the Mediterranean sea. Several industries (tannery, cutlery) use enormous amount of water for their running and pour it afterwards in the river, filled with excess of toxic dyes, organic and mineral compounds, causing water pollution which in turn affect cultures, harm fish reproduction in ponds alongside the river and cause health problems, etc. The aim of this work is to evaluate the Oued Cheliff contamination level caused by industries. Some physico-chemical parameters such as: the chemical oxygen demand (COD), the amount of nitrites, chlorides as well as the metallic traces of elements were measured for various water samples. They were exposed afterwards to the plasma particles flux where the treatment parameters are set constant throughout the investigation. The application of the plasma to these water samples is carried out in order to investigate the effect of the interaction of the simultaneously present highly neutral reactive species OH° (as an oxidant agent) and NO° (as an acidic agent) obtained in the plasma with the solution [1]. We expose here the sampling procedure, the measurements of the toxic level and the results of the plasma treatments.

2. Experimental set-up and methods.

Sampling procedure has been realised in various sites localised in adjacent industrial sectors to the river which pour into the Mediterranean sea during different periods of the year. Various samples collection sites were chosen such that:

- site X(0) is situated at the exit of the factory and corresponds to the raw industrial effluent
- site X(1) corresponds to the first contact of industrial effluent with the river, or the impact of the industrial wastes with the river
- site X(2) is chosen upstream before the site effluent impact X(1)
- site X(3) is situated downstream the point X(1). This will furnish precious information on the origin of the pollution along the river.

Waste samples taken at the waste contact with the river X(1)) are analysed first of all in order to evaluate the mineral compounds. Various specific analytical techniques are used:

- inductively coupled plasma-atomic emission spectrometry (ICP-AES) for the determination of Zn, Cr, Cu, and Fe concentrations [2];
- BOD-meter BSB-Controller 1020T type, pH-meter Multiline P4 type, UV-Vis ANTELLI Spectrometer for the nitrites
- volumetric methods with AFNOR norms to evaluate Cl^{-}, COD and PIS (particles in suspension) [3].

The experimental procedure is described in detail elsewhere and shown in figure. 1.

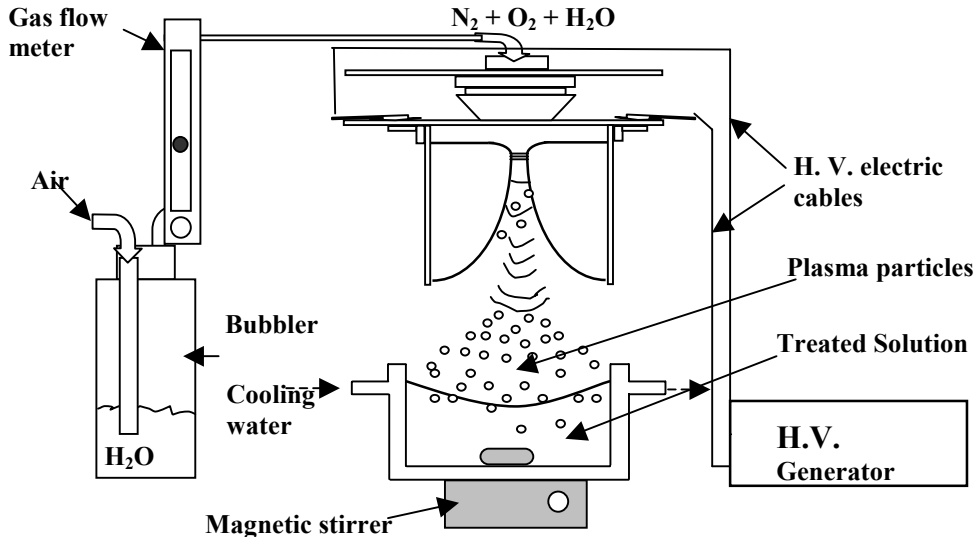

Figure 1 : Experimental set-up of the glidarc.

Pressurised humid air gets though a gliding electric arc obtained between two diverging electrodes where a high voltage is applied [4]. The electronic collisions between energetic electrons and humid air compounds provoke chemical interactions which lead to the formation of highly reactive neutral radicals OH° and NO°. The simultaneous presence is already confirmed in previous emission spectroscopy investigation [4]. The oxidant radical OH° abundance over the acidic NO° confers to the humid air plasma a major oxidant role
The manufactures wastes are exposed afterwards to the humid air plasma with a constant air flow rate, at a fixed distance and different exposure time: 5, 10, 15, 30, 60 and 90 minutes. COD measurements are taken before and after plasma treatments in order to evaluate the rate of degradation of the waste samples.

3. Results and discussion

3. 1 Analytical results.

The tannery uses, in its fabrication processes, products of organic (leather, dye) and mineral (oxidants of $K_2Cr_2O_7$ type) nature. On the other hand, cutlery products are made of metals but industrial oil, some mineral acids for cleaning and inhibitive products of corrosion are also encountered. This information clearly shows organic and mineral pollutions generated by their products.
The existence of maroon alga level within the Oued Cheliff river, on the tannery side near site X(1), is confirmed by a higher concentration of particles in suspension of the order of 2930 mg/L which goes far beyond the fixed norm 30 mg/L of approximately 100 times [5]. Besides, we remark that the concentration of nitrites (0.75 mg/L) is seven times higher than the standard norm (0.1 mg/L), where it is only twice more in the stream. The value of chrome (≈18 mg/L at X(0) point), is too much higher than the current norm (0.5 mg/L). The site of collection is also contaminated by iron.
Concerning the cutlery manufacture results, the values of registered nitrites in this part of the Oued Cheliff are eight times superior to the standards norm, where it is only twice more in the stream. Values of metals concentrations: chrome, copper, zinc and iron revealed in the sample are, in all cases, far beyond the required norms. In fact, the analysis has given 9.5 mg/L of chrome at the point of the impact of effluent with the river X(1), which may be due to the dilution in the Oued Cheliff river. Sampling points are also contaminated by iron and zinc, which are used in the cutlery. The registered COD value of 1600 mg d'O_2/L which goes beyond all admissible values, is in fact 39 times more than the norm in the point of effluent. The high values of COD during all sampling campaigns show high level pollution.
Around the cutlery manufacture pouring sites, the high values COD measured during all campaigns, show a quiet important organic pollution. Thus we have noticed the presence of inhibitive organic corrosion. A summary of the results of wastes analysis concerning both cutlery and tannery manufactures at sites X(1) and X(2) are shown in the table 1.

Table 1: Results of physico-chemical analysis and humid air plasma treatment of tannery and cutlery wastes samples.

	Tannery		Cutlery		Standard (mg/L)
Elements (mg/L)	X(1)	X(2)	X(1)	X(2)	
NO_2^-	0.75	0.75	1.24	0.32	0.1
Cl^-	6000	5700	3036	600	200
Cr	17.85	14.02	9.52	4.05	0.5
Fe	12.63	10.01	3.43	11.18	5
Zn	0.37	0.29	3.01	15.14	5
Cu	0.08	0.03	19.56	10.44	3
PIS	2930	2910	5445	900	30
BOD_5	233	250	850	270	40
COD	4000	2000	16000	1344	120
Treatment by plasma COD (mg of O_2/L)					
After 90 minutes	Before	After	Before	After	Standard (mg/L)
	2000	150	1344	80	120
	93 %		94 %		

3. 2 Plasma treatment

We record that the pollution in the Oued Cheliff river presents mineral and more important organic pollution characteristics. This pollution which will eventually cause too many problems, must be taken rapidly into account in order to preserve the river and its ecosystem. We take advantage of the oxidant phenomenon of the glidarc reactor which can be used to degrade non-biodegradable organic products as potential pollutants. Previous work was undertaken to treat aqueous solutions and organic products by plasma of humid air of gliding arc type [6]. In the aim of investigating the oxidation properties of OH° radicals produced by plasma, we have studied their degrading power on the tannery and cutlery industrial wastes poured in the river. We mention that the effluents collected at point X(0) are those treated by the gliding arc plasma of humid air.

The analysis of the tannery and cutlery industrial wastes which follow the plasma treatment, have revealed that the COD measured values increase with the treatment time. In fact, we expected a decrease in the values since the plasma is endowed of a high oxidant power and consequently degradation should follow. The results obtained are illustrated in figures 2 and 3.

A possible explanation to the COD behaviour could be attributed to the presence of nitriding entities NO° generated by the plasma. They transform to nitrites in aqueous media which may probably hinder oxidation to proceed and become then, due their reduction properties, cumbersome in the COD measurement [7]. So, the presence of radical species of type NO° slows down the degradation of the industrial wastes by the plasma of humid air. The reduction properties of nitrites have been minimised if not achieved by the addition of quantities of sodium azide (NaN_3) or sulfamic acid (H_3NO_3S) [7].

After the elimination of nitrites, the effluent samples are treated, with the same conditions as previous established, at different exposure times. The tannery and cutlery treated liquid effluents show that the COD values decrease considerably with the treatment time (figure 2 and 3).

The results of degradation show that the plasma treatment in the presence of sodium azide produced, after 90 minutes, a COD decrease from 2000 mg/L to 150 mg/L, which corresponds to a rate of elimination of 93% of the COD initial value. The corresponding results are presented in the table 2 and illustrated on figure 2.

Table 2: COD values of tannery waste samples treated by humid air plasma.

Time (min)	COD (mg d'O_2/L)			
	Tannery		Cutlery	
	700L/h	900 L/h	700 L/h	900 L/h
0	2000	2000	1344	1344
5	1732	1560	1050	1020
10	1376	1252	860	757
15	981	916	630	500
20	983	873	400	249.6
30	586	543	280	158.4
60	331.6	285	230	134.4
90	195.5	150	190	80

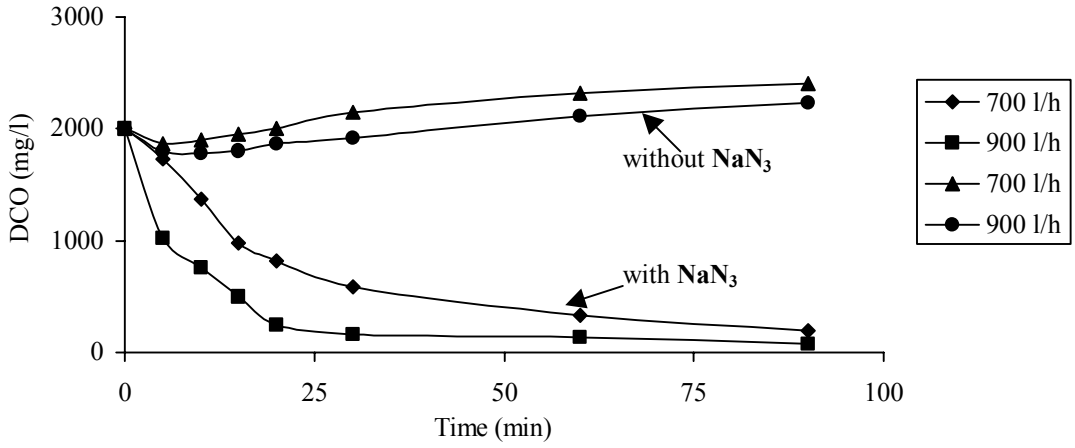

Figure 2. Tannery effluents behaviour with plasma treatment time with or without NaN_3

The COD measured after 90 minutes of treatment of the cutlery effluent samples is 80 mg/L against 1344 mg/L initially, a decrease which corresponds to a rate of elimination of 94%. The results obtained are gathered in the table 2 and presented on figure 3.

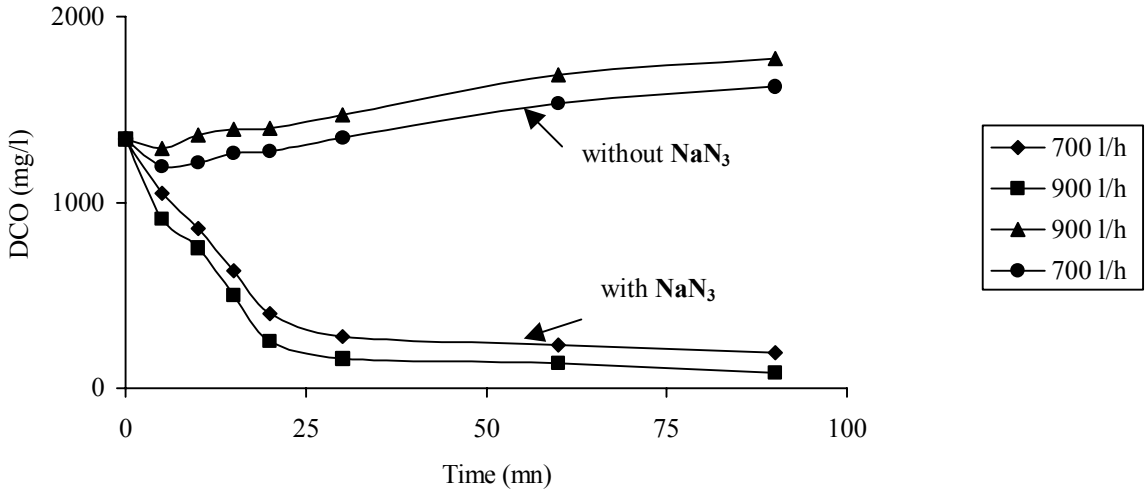

Figure 3. Cutlery effluents behaviour with plasma treatment time with or without NaN_3

The knowledge of the ratio COD/BOD_5 enables to appreciate the quality of the mineral pollution (BOD_5 ≈80% COD) [1]. After that, proportions of $COD/BOD_5>12$ for the tannery and $COD/BOD_5>11$ for cutlery were obtained. They indicate that the contamination was due to heavy effluents rich in organic materials content owing to COD values, as well as heavy metals presence preventing the evolution of the BOD_5. This indicates that the detected pollution was mainly due to uncontrolled wastes pouring of neighbouring manufactures located alongside the river. Previous remarks suggest that metallurgy manufactures such as cutleries and tanneries using leather for skin treatment, are the main sources of all kinds of pollution.
The treatment of the industrial wastes by the gliding arc plasma in humid air, evaluated by the measurement of the COD, proved to be efficient for both the cutlery and tannery cases only in the presence of sodium azide.
We have noticed as well a high resistance to the plasma treatment from the tannery effluents. This resistance is mainly due to the existence of organic charges in this type of effluents compared to the cutlery ones. That is translated by a final COD value 93.5 % which is nearly similar for both the tannery and the unity of cutlery.

4. Conclusion

The investigation carried out at different sites of the polluting industrial manufactures pouring their effluents in the Oued Cheliff coastal river, revealed two main sources of mineral and organic pollution of the water. All the concentrations values obtained for this mineral and organic pollution, or both for some sites, are alarming and far beyond the minimum standards.
The sampling sites alongside the river expose a real image of marine environment. The results show clearly that the plasma treatment changes the effluent character as well as of its general chemical composition. This is evidently in favour of an attack by high reactive oxidant species generated by the plasma of humid air .
The use of plasma enables us to degrade both manufacture wastes for a period of 90 minutes treatment by an attack of OH°, NO°, O_3 , H_2O_2 species, at a speed of which depends the chemical nature of the effluent [8]. All treatment resulted in a pollution abatement of 93.5 % of the COD independently on the nature of the effluent composition which confirms the reliability of the technique for such a domain. The plasma efficiency is also proved for the treatment of effluents containing toxic dyes such Yellow Supranol 4 GL and Scarlet Red Nylosan F3GL [7] where the degradation results in a decrease of dyes in the effluents. The different steps of oxidation could be determined by the use of CPG/MS, HPLC or more powerful techniques in order to make in evidence the chemical reaction mechanisms undergone for a better exploitation in the future.

References

[1] Benstaali B.,Moussa D., Addou A., Brisset J.L., Euro Phys. J. AP: 4, 171-179 (1998).
[2] Martin T.D., Kopp J.F., Determination of Metals and Trace Elements in Water and Wastes by Inductively Coupled Plasma-Atomic Emission Spectrometry, Environnemental Monitoring Systems Laboratory Office of Research and Developpement, Ohio, (1995).
[3] AFNOR, La Qualité de l'Eau 'Tome 1, 2, 3 et 4, (1999).
[4] Benstaali B, Boulet P, Chéron BG, Addou A, Brisset JL (2002) Density and rotational temperature measurement of th OH° and NO° radicals produced by a gliding arc in humid air. Plasma Chem. Plasma proc 22(4): 553-571.
[5] Journal Offciel de la République Algérienne N°146, Décret Exécutif N°93-160 Réglementant les Rejets d'Effluents Liquides Industriels, .5-7, 10-14 Juillet 1993
[6] N. Bellakhal; F. Moras; S. Boulay; C. Desanaux; JL. Brisset, The use of the gliding arc discharge for pollution abatement of industrial waste waters. Water Waste&Environmental Res:2; 59-68; 2002
[7]. Abdelmalek F., Gharbi S., Benstaali B., Addou A., Brisset J.L., Plasmachemical Degradation of Azo Dyes: Yellow Supranol 4 GL, Scarlet Red Nylosan F3 GL and industrial waste, Submitted to Water Research.
[8] Moussa D., Destruction du Tributylphosphate par Effluvage Electrique. Utilisation d'un Réacteur à Décharges Glisantes. Université de Rouen, France, 1998.

Dust particles in the dc glow discharge plasma: self-organization and peculiarities of behavior

V.E. Fortov, A.G. Khrapak, V.I. Molotkov, O.F. Petrov, M.Y. Poustylnik, V.M.Torchinsky

Institute for High Energy Densities, Russian Academy of Sciences, Moscow, 125412 Russia

Abstract

The review of the investigations of strongly coupled dusty plasma in the dc glow discharge striations is presented. The formation of plasma crystals, liquids and plasma liquid crystals is considered. Results of the experiments on different external influences on dusty plasma structures are discussed. It is demonstrated that external influences can be used to measure the grain charge and field of forces acting on a dust grain levitating in the plasma.

1. Introduction

The work is devoted to investigations of dusty-plasma formations in the dc glow discharge striations. Striations in the neon gas discharge have been studied in [1,2].

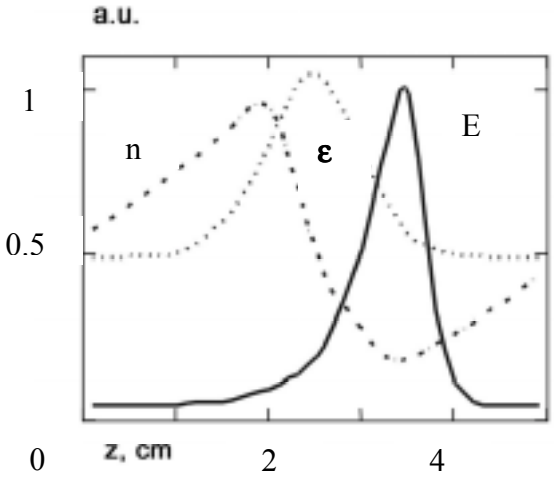

Fig.1. Relative distributions of plasma density n, mean electron energy ε and electric field E in the neon glow discharge

Fig.1 presents relative distributions of the electric field, plasma density and mean electron energy in a striation of the glow discharge in neon. It is seen that there is a region where the electric field increases in the direction of the cathode. If the discharge is vertically oriented and the lower electrode is a cathode stable levitation of dust grains in the striation is possible. Plasma parameters in striations may reach the following values: electric field up to 10 –15 v/cm, plasma density 10^7 – 10^8 cm^{-3}. These values just correspond to conditions of the strongly coupled dusty plasma [3].

The plasma nonuniformity in striations, a presence of the longitudinal electric field gradients lead to an appearance in the dusty plasma structures some peculiarities such as convective motions of dust grains, dust-acoustic instability and others.

In section 2 we present the experimental set-up for the dc glow discharge dusty plasma studies. In section 3 different kinds of dusty plasma structures formed in the neon glow discharge striations are given.

Section 4 is devoted to wave phenomena of the dust component including self-excited waves and waves excited by the gas dynamic impact. In section 5 we present methods to measure a charge of dust grains and a field of forces acting to the dust particle levitating in the plasma.

2. Experimental set-up

The experimental set-up for studies of the dusty plasma in the dc glow discharge is shown in Fig.2. It is a vertically positioned glass tube in which the glow discharge with cold electrodes is created.

The upper electrode is the anode and the lower one is the cathode. The tube is filled with neon or with a mixture of neon with hydrogen up to the pressure 0.1-2 Torr.

The discharge current varies from 0.1 to 4 mA. The standing striations exist in these regimes. The plasma parameters are as given in Section 1.

The dust particles were held above the discharge area in a container with the grid bottom. When shaking the container the dust grains fell down through the grid and levitate in striations forming the ordered structures.

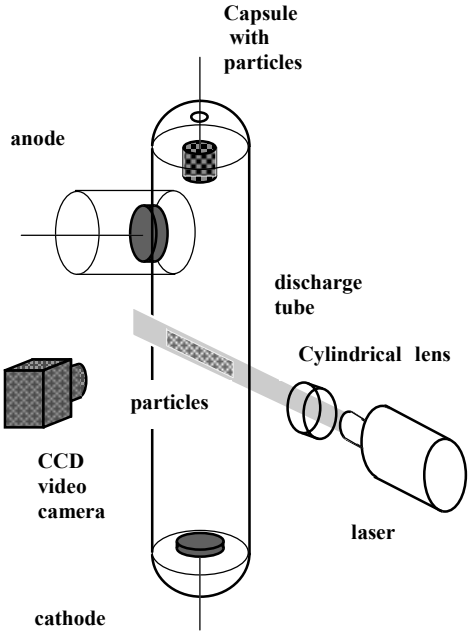

Fig.2. Experimental set-up

The dust grains are visualized with a diode laser sheet. The sheet thickness is 150 μm and the width is 1.5 cm. The laser sheet may be positioned both vertically and horizontally that allowed us to obtain the vertical section of the structure as well as the horizontal one. The light scattered by dust grains was imaged by a video camera.

To register fast processes the video camera Phantom 5 with a frame frequency up to 1000 frames per second was used. The video frames were later digitized for computer processing.

The glow discharge with cold electrodes is characterized by discharge oscillations connected with the cathode spot movements. This leads to fluctuations of dusty plasma structures. To damp out these fluctuations the additional insert with a constriction was placed in the lower part of the discharge tube above the cathode [4].

3. Plasma crystals and liquids

3.1 Structures of spherical grains

The formation of structures in the dc glow discharge striations proceeds in the following way: after the container shaking dust particles fell down and are captured in a trap created by the longitudinal and radial electric forces of a striation. The charged dust grains form the ordered structure preserved for as long as the discharge exists at constant parameters.

We used spherical particles of different materials: borosilicate glass (ρ= 2.3 g/cm^3) in the form of thin-walled, hollow spheres of diameter 50 – 60 μm with wall thickness 1 – 5 μm, Al_2O_3 particles (ρ= 4 g/cm^3) with diameter 3 –5 μm, melaminformaldehyde spheres (ρ= 1.5 g/cm^3) with diameters 1.87, 4.82, 10.24, 13.57 μm. The mass of the particles lies in the range from 10^{-12} to 10^{-7} g.

Fig.3. Horizontal section of plasma crystal

The particles formed in striations ordered structures with a different degree of ordering.

Fig.3 shows a video image of the plasma crystal. The structure was obtained in the discharge in a mixture of neon with hydrogen when the ratio of the length of the visible part of the striation to its total length decreases and the electric field acting on grains increases. The interparticle distance of the plasma crystal presented is about 700 μkm. In the case when the discharge current increases the plasma crystal is being melted firstly in the peripheral region and then in the center. This is connected with an increase of the plasma density, a decrease of the screening length of the dust grains, a weakening of an interaction between dust particles and an increase of the dust particles kinetic temperature.

In our experiments we observed levitation of separate particles as well as chains of several particles arranged along the axis of the discharge [5]. The formation of structures with a coexistence of different regions has been revealed. It is possible to study complicated formations with the regions of strong ordering (plasma crystal) and the regions with convective and oscillatory motion of grains (dusty plasma liquid) [5]. The complicated structures are associated with the peculiar distribution of forces acting on the dust particles: the ion drag force, the electrical force and distribution of plasma parameters along the striation.

3.2. Plasma liquid crystal

Besides spherical grains we used extended cylindrical grains.

To provide the levitation of nylon (ρ= 1,1 g/cm^3) microcylinders of diameter 10 μm and length 600 μm a neon-hydrogen mixture was used. These dust grains formed the structures consisting of 3-4 horizontal layers. Lighter particles (diameter 7.5 and 10 μm, length 300 μm) levitated in neon striations and formed much more axially prolonged structures. The structures formed of microcylinders indicated a pronounced short-range order [6]. All the particles lied in the horizontal plane and all aligned in the certain direction.

The preferential direction of the particle orientation seems to originate from the slight constructional asymmetry of the discharge tube. To verify this supposition an asymmetrical distortion was introduced into the discharge. A dielectric plate with a hole placed several centimetres above the cathode induced it.

The plate overlapped the discharge section so that the formation of the column started through the hole with the diameter of 1 cm. The visually observed distortion of the standing striation indicated the presence of the axially asymmetric part of the electric field. The turning of the plate resulted in the change of the orientation of particles.

The charge on the dust particles estimated from the levitation conditions is assumed to be about $8 \cdot 10^5$ electrons.

The structures formed of the highly charged elongated cylindrical grains exhibit the properties similar to those of nematic liquid-crystal structures, namely, that the positions of the centers of gravity of the grains show the short range ordering; the grains are oriented strictly in parallel with a certain common axis. The experiments with microcylinders of diameter 10 μm and length 300 and 600 μm with a thin layer of a conducting polymer revealed that these particles behaved in the same way and formed structures of the same shape as dielectric micro-rods of the same size.

4. Wave phenomena

Wave phenomena in the dust component are at present of great interest for researchers. The presence of the dust component in a plasma leads to the appearance of new modes in the wave spectrum in comparison to the plasma without dust grains. It has been demonstrated [7] that the dc glow discharge dusty plasma is a very useful instrument to study self-excited waves of the dust component density. It has been revealed that under certain conditions the self-excited dust-acoustic waves could appear in the dc glow discharge striations.

It was shown [7] that the instability is caused by the joint effect of the ion drift and fluctuations of the dust grain charge.

To excite instabilities of the dust component we proposed a gas-dynamic impact. The experimental set up was similar to that shown in Fig.2. But the lower electrode was made as the hollow cylindrical cathode.

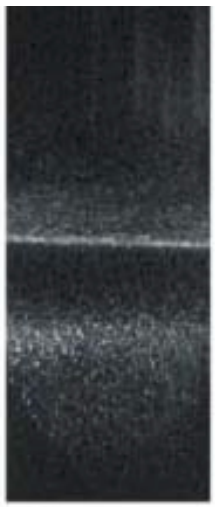

Fig.4. Video image of the disturbance

The electrodes were separated by 26 cm. In some experiments a grid was inserted into the tube 7 cm above the upper cut of the cathode. The grid was kept under the floating potential.

For the excitation of the waves a plunger was set below the cathode. The plunger was a hollow thin-walled nickel cylinder of 26 mm diameter and height with the bottom made of a polymeric pellicle.

It was freely installed at the bottom of the tube and moved with the help of a permanent magnet manually approached to the plunger from outside the tube. The plunger could be moved upward and downward with a speed of 30-40 cm/s and 4-5 cm space, creating a gas flow with a duration of 0.1 s which displaced the dust grains with respect to the striation. Current of 0.1-1 mA could be driven through this system at neon pressure of 0.3 Torr. Melamineformaldehyde dust grains 1.03 μm diameter were used to form dusty plasma structures in striations.

In the case of experiments without the grid it was possible to generate waves of dust density component. The properties of these waves are similar to the properties of the self-exited waves obtained in [7].

In the case of experiments with the grid quite a new type of instability was obtained. This occurred at the current value of 0.1 mA. The dusty plasma structure was very close to the grid (at a distance of 4 mm). After moving the plunger downward the structure was again for some time streaming downward, then it stopped and began moving towards its initial equilibrium position and when it returned to the stable position a disturbance propagating through it appeared (Fig.4).

Fig.5 presents the shape of the compression factor ξ, which is the ratio of the distribution of brightness in the initial structure, at different moments of time. The disturbance consists of two humps (A,C) separated by a

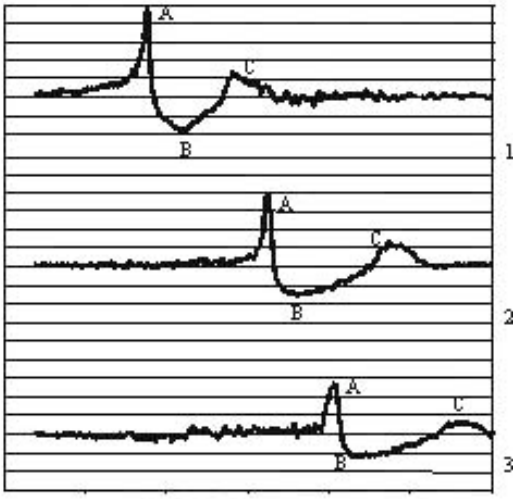

Fig.5. Compression factor in the wave at different moments of time. Time interval between curves 1and 2 – 120 ms, between 2 and 3 –60 ms.

dip(B). It is seen that the amplitudes for zones A and C reach to the values of 2.1 and 1.2 and 0.65 for the rarefaction.

All three structures move approximately with the same speed of 2-2.5 cm/s. These velocities of the wave lie in the range of the dust acoustic velocity C_{da} estimated from the plasma parameters, dust density and the grain charge. According to this C_{da}=1.8-5.2 cm/s.

The gas pressure in our experiments is rather high and the character time of the wave damping, estimated on pressure, mass of the dust grain and thermal velocity of neon atoms is about 15 ms. But the observed time of the wave propagation is 500 ms. It means that the wave must have an energy source other than the initial impulse. The dust acoustic instability could serve as a mechanism by means of which the energy is supplied to the wave.

5. Diagnostics of the dc glow discharge plasma

5.1. Measurement of the grain charge

Measurements of the charge were conducted in the following way. The light beam from an Ar^+ laser was focused onto a single particle in the structure. The beam power was up to 200 mW, the waist thickness was about 60 μm and the corresponding power density of the order of 10^3 W/cm^2. Under the effect of the light pressure the particle moves 1.5 – 3 mm out of the structure, then comes out of the beam and returns back to the structure. When returning back to the structure a dust particle is the subject mainly to the radial electric force and the neutral drag force. The radial electric field is found from the ambipolar diffusion condition. Since the deflection of the particle is small compared to the tube radius R = 18 mm the linear approximation of the radial electric field can be used:

As follows from the observation, the particle performs the aperiodical motion. Starting its way back with the zero radial velocity the particle is first accelerated by the electric force and then, while its velocity increases and the electric field decreases towards the tube center, neutral drag starts to prevail and the particle is slowed down. Thus there must be a maximum of velocity on the returning trajectory of the particle. In the point of this maximum the radial electric force must be balanced by the neutral drag:

$$E_r q = \frac{16\pi}{3} p a^2 \frac{v}{v_{th}} \qquad (1)$$

where E_r is the radial electric field, q is the charge, a is the grain radius, ν is the particle velocity, v_{th} is the thermal velocity of gas atoms. This equation gives the possibility to determine the charge. Estimated accuracy of the εq product measurements is 40%.

5.2. Application of thermophoresis for diagnostics of dust particle's confinement

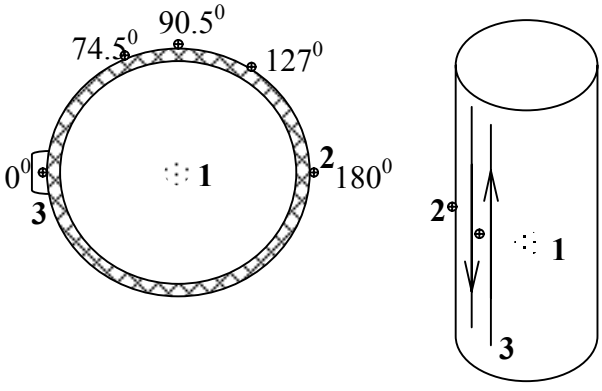

Fig.6. Scheme of the experiment on the thermophoretic influence on the dusty plasma structures. 1 – dust particles, 2 – thermocouples, 3 – heater.

Thermophoretic force is the force acting on a body in a rarefied medium, in which the temperature gradient exists.

To create the temperature gradient a heater was maintained on a discharge tube. The heated was made as a double-wound wire in order to exclude the influence of the magnetic field. The distance between single wires was 7 mm. The heater was (Fig.1) installed parallel to the discharge axis. Its length was 16 cm, whereas the tube diameter was 3 cm. So, the temperature distribution produced by the heater could be treated as two-dimensional.

Temperatures were measured in a certain section of the tube close to the area of levitation of the dust grains. Chromel-alumel thermocouples were employed for temperature measurements. Their sensitivity is of the order of 65 μV/K. Thermocouples were placed in 5 points of the tube semicircle as shown in Fig.1. The other semicircle is left free to allow the observation of the dust grains. The measured temperature profile is symmetrically depicted onto the free semicircle and in this way the temperature profile on the whole circumference is determined.

To reconstruct the temperature distribution inside the tube we have to solve the following equation

$$\Delta T = 0$$

$$\frac{T_w(\phi) - T(R,\phi)}{d} \lambda_{glass} = \lambda_{gas} \frac{dT}{d\rho}\Big|_{R,\phi} \tag{2}$$

where ρ, ϕ are polar coordinates, T(R, ϕ) is the temperature distribution inside the tube, $T_w(\phi)$ is the interpolation of the measured temperatures over the tube circumference, R is the tube radius, d is the tube wall thickness, λ_{glass} and λ_{gas} are heat conductivities of glass and gas in the tube respectively. Equation (2) is considered linear since the dependence of the gas heat conductivity on the temperature is negligible due to small temperature variations. The boundary condition accounts for the continuity of the heat flux on the internal surface of the tube.

The experiment proceeds as follows. First a chain of dust particles is formed on the axis of the discharge tube and initial positions of the dust grains are recorded. Then the heater is turned on. It takes about 15 minutes for the temperature to reach steady-state distribution. Dust particles acquire new equilibrium positions. Their positions are again recorded and indications of the thermocouples are taken. Then the heater power is increased and the procedure is repeated.

Measured temperatures are interpolated along the circumference and equation (1) is solved. In this way the distribution of temperatures for each equilibrium position of dust grains is obtained. In an equilibrium position the thermophoretic force acting on a dust particle is balanced with a confining force of the discharge. The thermophoretic force is expressed as follows:

$$F_{th} = \frac{8}{45} \sqrt{\pi}\, p a^2 l \frac{\nabla T}{T}, \tag{3}$$

where p is the neutral gas pressure, l is the mean free path of neon atoms, a is the dust grain radius. F_{th} can be easily calculated if the temperature distribution and the particle position is known. Calculating thermophoresis for a set of equilibrium positions of the dust grains we acquire the distribution of the confining force.

Conclusion

In this work we have presented the results of the investigations of the behavior of the dust grains in the dc glow discharge striations. It has been shown that dust particles can form structures with short-range as well as long-range order. The experiments were performed with spherical and elongated cylindrical grains. In the case of microcylinders structures with strong orientational order were obtained. These structures were called plasma liquid crystals. It has been demonstrated that the gas-dynamic impact is a useful tool for excitation of high-amplitude waves of dust density. A method for measuring the charge on the dust grains levitating in plasma was suggested. Influence of thermophoresis on the dust grains was used to measure the field of confining forces.

Acknowledgements

This work was partially supported by the Russian Foundation for Basic Research, project 03-02-16316.

References

[1] Y. Golubovsky, S. Nisimov – Journal of Tech. Phys. (in Russian) **64**, 54 (1994).
[2] Y. Golubovsky, S. Nisimov – Journal of Tech. Phys. (in Russian) **65**, 46 (1995).
[3] H. Ikezi – Phys. Fluids **29**, 1764 (1986)
[4] A.M. Lipaev, V.I. Molotkov, A.P. Nefedov et.al. – JETP **85**, 1110 (1997)

[5] V.E. Fortov, A.P. Nefedov, V.I. Molotkov et.al. – in *Dusty Plasmas in the New Millenium,*ed. by R. Bharuthram, M. Hellberg, P.K. Shukla, F. Verheest, AIP Conf. Proc. **649**, 394 (2002)
[6] V.I. Molotkov, A.P. Nefedov, M.Y. Poustylnik et.al. – JETP Lett. **71**, 102 (2000)
[7] V.E. Fortov, A.G. Khrapak, S.A. Khrapak et.al. – Phys. Plasmas **7**, 1374 (2000)
[8] V.E. Fortov, A.P. Nefedov, V.I. Molotkov et.al. – Phys. Rev. Lett. **87**, 205002 (2001)

Temporal development of a charge state resolved Zr plasma stream in a N_2 environment.

J. Rosén[1], A. Anders[2], J. M. Schneider[3]

[1] *Department of Physics, Linköping University, Linköping SE-58183, Sweden*
[2] *Lawrence Berkeley National Laboratory, Berkeley, California 94720, USA*
[3] *LTH, RWTH-Aachen, D-52056 Aachen, Germany*

The temporal development of the plasma composition in a pulsed cathodic arc has been investigated. Charge state resolved data has been evaluated for a Zr cathode used at various nitrogen pressures. The plasma composition was measured by time-of-flight charge-to-mass spectrometry and showed a strong time as well as pressure dependence. Large nitrogen concentrations were detected in the beginning of the arc pulse. These results may be explained by the formation and erosion of a compound layer at the cathode surface, and a varying interaction between the expanding plasma and the surrounding gas. The time dependence of the metal charge states was most pronounced at lower pressures, with as much as 40 % and 20 % of Zr^{3+} and Zr^{4+} respectively. As the pressure increased the concentrations of Zr^{1+} and Zr^{2+} increased at the expense of the former concentrations, which may be due to an increased probability of charge exchange collisions. These findings are of importance for reactive plasma processing, through an increased understanding of the film composition and via the ion energy the film microstructure.

Measurement of N(^{2}D) density in nitrogen afterglow

V. Kiohara[1], J. Levaton[1,2] and J. Amorim[1,2]

[1]*Departamento de Física, Instituto Tecnológico de Aeronaútica, Centro Técnico Aeroespacial, 12228-900 São José dos Campos, Brazil*
[2]*Laboratório Interdisciplinar de Materiais (LABMAT), Universidade Federal de Santa Catarina, 88040-900, Florianópolis, Brazil*

Abstract

Post-discharges were created from direct current (dc) discharges operating at pressures varying from 3.0 to 9.0 Torr, current between 20 and 50 mA and flux from 300 to 950 sccm. Densities of N(^{4}S) and N(^{2}D) were measured along the post-discharge respectively by emissions of the first and second positive systems of N_2. These measurements reveal that N(^{2}D) may reach densities of about 5 % [N(^{4}S)].

1. Introduction

Nitrogen afterglow has been studied along the last years due to technological applications of these post-discharges in nitriding [i], sterilization [ii] and study of atmospheric chemistry [iii]. Another importance of afterglow studies is the understand of the complex non-equilibrium kinetics of this medium that involves transport of vibrationally excited molecules, molecular and atomic metastable states. One important active specie is the nitrogen atom, so the comprehension of its transport along the flux is very important. Nitrogen atom in their first excited state N(^{2}D) is a very important radical in atmospheric chemistry and in materials processing, because it has 2.38 eV of energy above the ground state N(^{4}S), radiate lifetime of 26 hours and is a key specie in the transport of N(^{4}S) atoms along the post-discharge afterglow through reactions with $N_2(A\ ^3\Sigma^+_u)$. In this work we propose a novel method to determine the N(^{2}D) density along the pink and Lewis-Rayleigh afterglow. The densities of N(^{4}S) and N(^{2}D) were measured along the post-discharge respectively by emissions of the first and second positive systems of N_2. These measurements reveal that N(^{2}D) may reach densities of about 5 % [N(^{4}S)].

2. Experimental set-up and methods

The experimental apparatus consisted of a 14-mm i.d. Pyrex tube, 1m long with a post-discharge length of 600 mm. A direct current (dc) discharge is operated at pressures varying from 3.0 to 9.0 Torr, current between 20 and 50 mA and flux from 300 to 950 sccm. Two electric probes, 10 cm apart, were inserted into the positive column in order to measure the electric field. The pressure was measured in the central region of the post-discharge tube by means of a capacitive transducer Baratron. A mechanical pump maintains the flow of the gas. The nitrogen employed in the experiments was of ultra-high purity 99.999%. The gas flow was controlled by a flowmeter connected to the discharge tube. The light emitted by the discharge and post-discharge was sent, by an optical fiber, into the entrance slit of a 1 m monochromator (THR 1000) equipped with a grating of 1800 lines mm^{-1} and blazed in the region 450 – 850 nm. The light collimated at the exit slit was converted to electric current by a R928 Hamamatsu photomultiplier tube. This current was sent to a data acquisition electronics Spectralink and the signal processed by a Spectramax software. The whole optical system was calibrated in intensity with aid of a tungsten lamp and in frequency with a pure argon discharge.

3. Inverse predissociation kinetics in the afterglow

Büttenbender and Herzberg [iv] observed predissociations in the $N_2(C\ ^3\Pi_u)$ state at v = 2, 3 and 4. Carroll and Mulliken [v] attributed these predissociations to an $N_2(^5\Pi_u)$ state. Carroll and Mulliken also identified another predissociation channel through the $N_2(C'\ ^3\Pi_u)$ state. Tanaka et. al. [vi], working in a nitrogen cooled afterglow, observed abnormal strong emission line intensity from the v'=4 level in the Second Positive System (transition $N_2(C\ ^3\Pi_u) \rightarrow N_2(B\ ^3\Pi_g)$) and proposed inverse homogeneous predissociation involving $N(^4S)$ and $N(^2D)$, forming the $N_2(C\ ^3\Pi_u$, v = 4) state, to explain this strong emission. They suggested that the cooled discharge tube wall produced conditions favorable for preventing decay of the metastable atoms thus enabling the observation of the Second

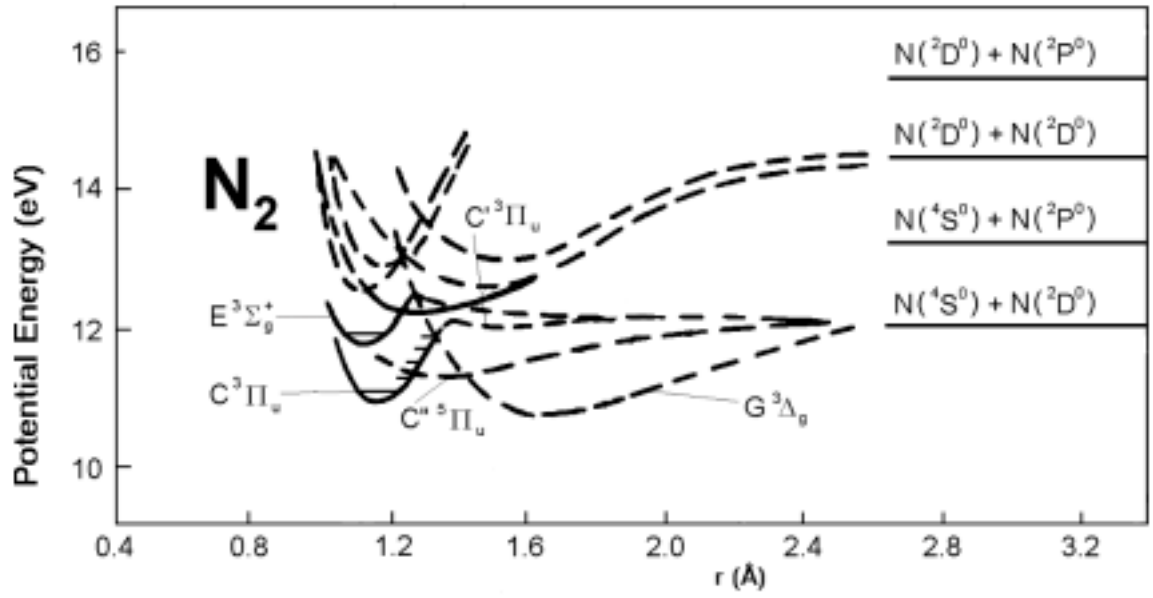

Figure 1 : Potential energy curves of N_2

Positive System. As can be seen in Fig. 1, inverse homogenous predissociation involving $N(^4S)$ and $N(^2D)$ may induce the formation of N_2 ($C'\ ^3\Pi_u$, $C''\ ^5\Pi_u$, $G\ ^3\Delta$) states.

The potential energy curve of the N_2 ($C''\ ^5\Pi_u$) state crosses the potential energy curve of the N_2 ($C\ ^3\Pi_u$) state near v =2 while the potential energy curves of N_2 ($C'\ ^3\Pi_u$, $G\ ^3\Delta$) states intersects the potential energy curve of the N_2 ($C\ ^3\Pi_u$) state at v =4.

In the conditions found in nitrogen afterglow, *i.e.* temperatures lower than those found in the discharge, inverse predissociation reaction may induce overpopulation on the N_2 ($C\ ^3\Pi_u$, v=4) state by:

$$N_2(A\ ^3\Sigma^+_u) + N(^4S) \rightarrow N_2 + N(^2D) \quad (1)$$

$$N(^2D) + N(^4S) + N_2 \rightarrow N_2\ (C'\ ^3\Pi_u) + N_2 \rightarrow N_2\ (C\ ^3\Pi_u, v=4) + N_2 \quad (2)$$

$$N(^2D) + N(^4S) + N_2 \rightarrow N_2\ (C''\ ^5\Pi_u) + N_2 \rightarrow N_2\ (C\ ^3\Pi_u, v=2) + N_2 \quad (3)$$

This overpopulation leads to an increase in the intensity of the Second Positive System of nitrogen, transition $N_2(C\ ^3\Pi_u$, v=4 $\rightarrow$ B $^3\Pi_g$, v=6). However, pooling reactions due to $N_2(A\ ^3\Sigma^+_u)$ state may populate N_2 (C' $^3\Pi_u$, C'' $^5\Pi_u$) states :

$$N_2(A\ ^3\Sigma^+_u) + N_2(A\ ^3\Sigma^+_u) \rightarrow N_2(X\ ^1\Sigma^+_u) + N_2\ (C'\ ^3\Pi_u) \qquad (4)$$

$$N_2(A\ ^3\Sigma^+_u) + N_2(A\ ^3\Sigma^+_u) \rightarrow N_2(X\ ^1\Sigma^+_u) + N_2\ (C''\ ^5\Pi_u) \qquad (5)$$

In the Lewis-Rayleigh post-discharge, the density of the $N_2(A\ ^3\Sigma^+_u)$ state is about ten times lower than in the pink afterglow [vii]. Simple estimation of rate of formation of the $N_2(C\ ^3\Pi_u$, v=4) state by N_2 (C' $^3\Pi_u$) and N_2 (C'' $^5\Pi_u$), taking into account rate coefficients for reactions (4) and (5) [viii,ix], give values that are negligible if compared with formation by reactions (2) and (3). This is not the case in the pink afterglow were pooling reactions are more efficient in the formation of the $N_2(C\ ^3\Pi_u$, v=4) state.

In this work we studied the variation of the vibrational distribution (VDF) of the Second Positive System of nitrogen as a function of post-discharge parameters.

4. Results

The vibrational distribution of N_2 (B $^3\Pi_g$,v) and N_2 (C $^3\Pi_u$, v) states have been determined in the early, pink and late afterglow from the First and Second Positive systems:

$$I_{B,C} = K(\lambda_i)\, hc/\lambda_i\, A_i\, [B/C, v] \qquad (6)$$

where $K(\lambda_i)$ is the system spectral optical response at λ_i , A_i is the Einstein transition probability of spontaneous emission and [B/C, v] is the N_2 (B $^3\Pi_g$ *v*) or N_2 (C $^3\Pi_u$, *v*) density. The normalized VDF can be obtained from:

$$r_{C,v'} = N_2(C\ ^3\Pi_u, v) / \Sigma\, N_2(C\ ^3\Pi_u, 0 \le v \le 4) \qquad (7)$$

Typical normalized VDF of the N_2 (C $^3\Pi_u$, v) state can be seen in Figure 2. The normalized VDF in the late afterglow is overpopulated for v = 4. Vibrational levels *v* =2,3 are less populated in the late afterglow than in the early and pink afterglow. This figure illustrate the population inversion for v = 4 due to homogeneous inverse predissociation. The same procedure was applied to the N_2 (B $^3\Pi_g$,*v*) levels in order to obtain its VDF.

From normalized VDF for the N_2 (B $^3\Pi_g$,*v*) state, we determined the N(^{4}S) density along the post-discharge following the method described in [x]. This method is based on abacus constructed from the normalized VDF's of the N_2(B $^3\Pi_g$) state. It revealed an increase in the population of the N_2(B $^3\Pi_g$, v =11) level, which is due to inverse predissociation of two recombining N(^{4}S) atoms, through the N_2 (A' $^5\Sigma_g$) intermediate state.

The same procedure was applied in this work for the VDF of the N_2 (C $^3\Pi_u$, v) state. Briefly, in the late afterglow, the most important mechanism responsible for populating the level N_2 (C $^3\Pi_u$, *v* = 4) is homogenous inverse predissociation.

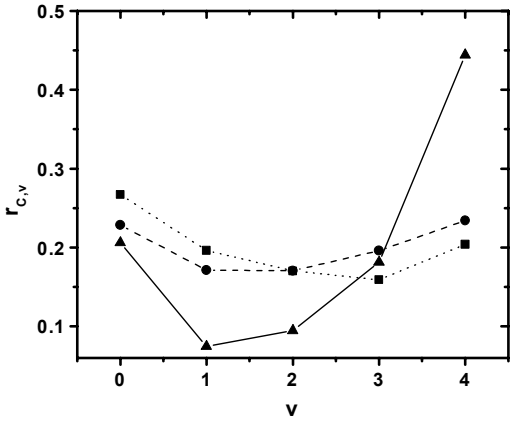

Figure 2 : Normalized vibrational distribution of N_2 (C, v') for v' = 0-4 in a dc post-discharge, 5 Torr, 300 sccm, 30 mA. early (square); pink (circle); Lewis-Rayleigh afterglow (triangle).

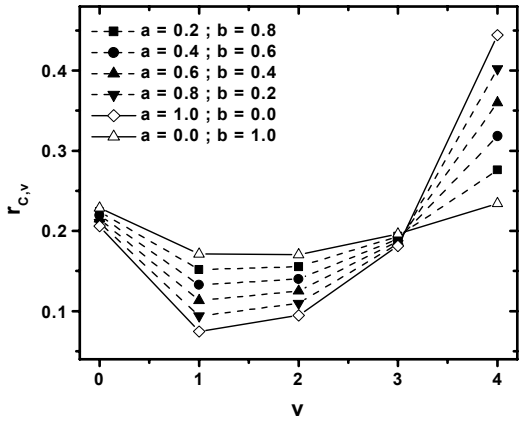

Figure 3: Normalized vibrational distribution of N_2 (C, v') for v' = 0-4 calculated (dash lines) by adding the $r_{C, v'}$ [$N(^4S)$ + $N(^2D)$] (a) and $r_{C, v'}$ [pooling](b) contributions.

In early and pink afterglow the pooling involving $N_2(A\ ^3\Sigma^+_u)$ states is the predominant mechanism in populating level N_2 ($C\ ^3\Pi_u$, v = 4). Along the post-discharge, both mechanisms are presented in the formation of the N_2 ($C\ ^3\Pi_u$, v = 4) state. As we are interested in the part of the emission coming from inverse predissociation, normalized VDF's were constructed, see Figure 3, where a combination of the two process were taken into account. In Figure 3, are presented the $r_{C,v'}$ = $a\ r_{C,v'}$ ($N(^2D)$ + $N(^4S)$) + $b\ r_{C,v'}$ (pink) in the v' = 0 - 4 range for a = 0, 0.2, 0.4, 0.4, 0.6, 0.8 and 1.0. Given a specific experimental condition, the value of a is determined and the density of the $N(^2D)$ state is obtained from :

$$\frac{a\ I_{N2\ (C\ 3\Pi u,\ v=4)}}{b\ I_{N2\ (B\ 3\Pi g,\ v=11\ )}} \quad \alpha \quad \frac{hc/\lambda_i\ A_i\ [N(^2D)]\ \ [N(^4S)]\ [N_2\ ]\ k_2}{hc/\lambda_j\ A_j\ [N(^4S)]\ \ [N(^4S)]\ [N_2\ ]\ k_1} \qquad (8)$$

where b is the fraction of the First Positive emission that comes from ground state $N(^4S)$ atoms recombination, k_1 is the rate coefficient for $N(^4S)$ atoms recombination. Due to the lack of knowledge of rate coefficient for reaction (2), we supposed in this work to be equal to, k_1 = 2.4 x 10^{-33} $cm^6\ s^{-1}$ [xi]. The density of the $N(^2D)$ was determined along the afterglow as a function of [$N(^4S)$].

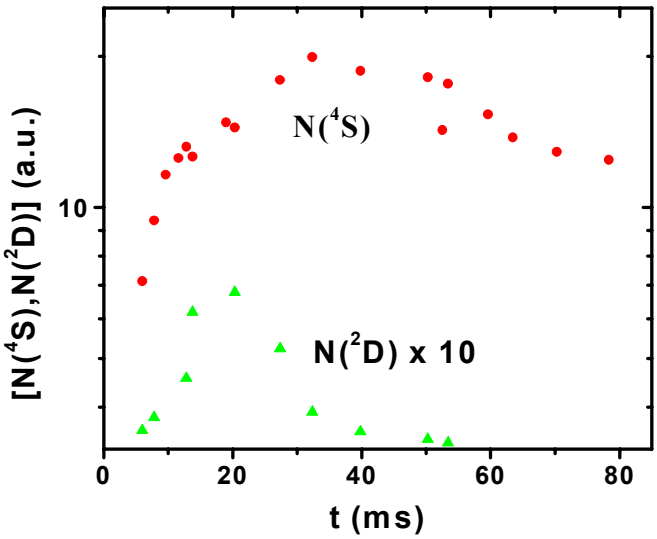

Figure 4: N(^{4}S) and N(^{2}D) atoms as a function of time. Pressure of 5.0 Torr, Id = 30 mA and flux of 300 sccm.

As can be seen in the figure 4, the N(^{4}S) atoms density is maximum at t ~ 32 ms while the N(^{2}D) density is maximum at t ~ 20 ms. Another important result is that the maximum density of N(^{2}D) state measured is ~ 5% of the N(^{4}S) density.

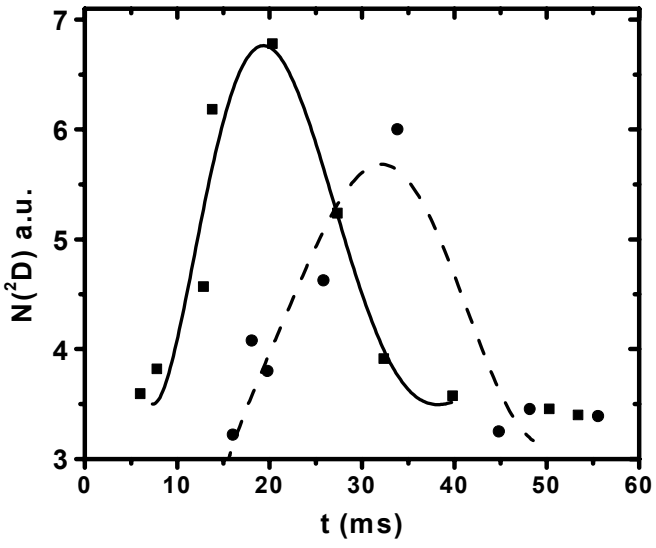

Figure 5: [N(^{2}D)] as a function of time. Pressure of 5.0 Torr, Id = 30 mA (square) and 20 mA (dashed) for a flux of 300 sccm.

Figure 5 shows the variation of N(^{2}D) density as a function of time when the discharge current is varied between 20 mA and 30 mA. The time for maximum of [N(^{2}D)] changes from 20 ms to 32

ms. This displacement is due to changes in the density of $N_2(A\ ^3\Sigma^+_u)$ and $N(^4S)$ specie, that are precursors for $N(^2D)$ formation when discharge current is changed.

5. Conclusion

The study of homogenous inverse predissociation of $N(^4S)$ and $N(^2D)$ atoms was accomplished in order to measure the $N(^4S)$ and $N(^2D)$ densities along the post-discharge. The density of $N(^4S)$ was initially determined using an abacus constructed from the VDF of the N_2 ($B\ ^3\Pi_g$,v) state. From the measured VDF of the N_2 ($C\ ^3\Pi_u$, v) state, a second abacus was done in order to obtain the fraction of emission of the Second Positive System due to inverse predissociation. From the ratio of First and Second Positive Systems, due to inverse predissociation reaction, the density of $N(^2D)$ could be obtained along the afterglow. For discharge pressure of 5.0 Torr, current of 30 mA and flux of 300 sccm, the density of $N(^2D)$ atom was found to be 5%[$N(^4S)$] at t ~ 20 ms.

References

[i] A. Ricard, B. F. Gordiets, M. J. Pinheiro, C. M. Ferreira, G. Baravian, J. Amorim, S. Bockel, and H. Michel, *Eur. Phys. J. Appl. Phys.* **4**, 87 (1998).
[ii] A. Ricard M. Moisan, S. Moreau, *J. Appl. Phys.D : Appl. Phys.* **34**, 1203 (2001).
[iii] C. D. Pintassilgo, J. Loureiro, G. Cernogora, and M. Touzeau, *Plasma Sources Sci. Technol.* **8** 463 (1999).
[iv] G. Herzberg, *Molecular Spectra and Molecular Structure vol. I* 2nd ed.1989.
[v] P.K. Carroll, and R.S. Mulliken, *J. Chem. Phys.* **43**, 2170 (1965).
[vi] Y. Tanaka, F.J. Le Blanc, and A. S. Jursa *J. Chem. Phys.* **30**, 1624 (1959).
[vii] J. Levaton, J. Amorim, A . R. Souza, D. Franco and A . Ricard, , *J. Appl. Phys.D : Appl. Phys.* **35**, 689 (2002).
[viii] L. G. Piper, *J. Chem. Phys.* **88**, 231 (1988).
[ix] J. S. Moril, W. M. Benesch, *J. Chem. Phys.* **92**, 104 (1990).
[x] S. Bockel, A. M. Diamy and A. Ricard, *Surf. Coating Tech.* **74**, 474 (1999).
[xi] C. Gorse, and M. Capitelli, *J. Appl. Phys.* **62** 4072 (1987).

A MODEL OF THE SHORT-LIVED AFTERGLOW INCLUDING THE N(^{2}D) AND N(^{2}P) STATES

J. Levaton[1,2,3], V. Kiohara[2], J.Amorim[1,2]

[1] *Laboratório Interdisciplinar de Materiais (LABMAT) - Universidade Federal de Santa Catarina - 88040-900 - Florianópolis – Brazil*

[2] *Departamento de Física - Instituto Tecnológico de Aeronáutica, Centro Técnico Aeroespacial - 12228-900 - São José dos Campos – Brazil*

[3] *Centre de Physique des Plasmas et leurs Applications (CPAT) - Université Paul Sabatier - 31062 Toulouse Cedex, France*

ABSTRACT

A numerical model was implemented to describe the behaviour of many N_2 molecular states and also the N(^{4}S), N(^{2}D) and N(^{2}P) atomic ones in the N_2 short-lived afterglow. We have assumed the reactions N(^{4}S) + N_2(A $^3\Sigma^+_g$) $\rightarrow$ N(^{2}D, ^{2}P) + N_2(X $^1\Sigma_g^+$) to account for the N(^{2}D, ^{2}P) generation in the post-discharge. The atomic species densities, as a function of residence time, present the same behaviour observed experimentally for the excited molecular states since they are strongly coupled to N_2(A $^3\Sigma^+_g$) by the quenching mechanisms.

INTRODUCTION

The short-lived afterglow has been recently studied both theoretically and experimentally **[1-3]**. In our last work **[3]**, we developed a numerical model to describe the short-lived afterglow (SLA). The model described qualitatively well the behavior of many experimentally studied species, as the N_2(A $^3\Sigma^+_g$) and n_e (electron density) **[2]**, the N_2^+, N_3^+ and N_4^+ ground state-ions **[4]**, the N_2($B^3\Pi_g$), N_2($C^3\Pi_u$) and N_2^+($B^2\Sigma^+_u$) radiative states **[5]** and the N(^{4}S) fundamental state atom **[6]**. Nowadays, it is a common idea the fact that the short-lived afterglow results from the relaxation of the N_2(X $^1\Sigma_g^+$) vibrational distribution function (VDF) in the post-discharge, which tends to populate the intermediate **[3]** and high **[1]** vibrational levels of the N_2 electronic fundamental state. These energetic species are capable to initiate all

the reactive pathways responsible for the phenomenon. Loureiro *et al.* **[1]** attribute to the formation of the molecular metastables $N_2(A\ ^3\Sigma^+_g)$ and $N_2(a'^1\Sigma^-_u)$ the following mechanisms:

$$N_2(X\ ^1\Sigma^+_g, v>24) + N(^4S) \rightarrow N_2(A\ ^3\Sigma^+_g) + N(^4S) \quad \text{and} \quad \textbf{(01)}$$

$$N_2(X\ ^1\Sigma^+_g, v>37) + N(^4S) \rightarrow N_2(a'^1\Sigma^-_u) + N(^4S) \quad . \quad \textbf{(02)}$$

Levaton *et al.* **[3]** suggest other pathways:

$$N_2(X\ ^1\Sigma^+_g, v>15) + N_2(X\ ^1\Sigma^+_g, v>15) \rightarrow N_2(a'^1\Sigma^-_u) + N_2(X\ ^1\Sigma_g^+, v)\ , \quad \textbf{(03)}$$

$$N_2(a'^1\Sigma^-_u) + N_2(X\ ^1\Sigma_g^+) \rightarrow N_2(B^3\Pi_g) + N_2(X\ ^1\Sigma_g^+) \quad \text{and} \quad \textbf{(04)}$$

$$N_2(B^3\Pi_g) + N_2(X\ ^1\Sigma_g^+) \rightarrow N_2(A\ ^3\Sigma^+_g) + N_2(X\ ^1\Sigma_g^+) \quad . \quad \textbf{(05)}$$

This local creation of molecular metastables, in a region with a large density of $N(^4S)$ atoms **[6]**, seems to be a helpful environment to the $N(^2P)$ generation via reaction:

$$N(^4S) + N_2(A\ ^3\Sigma^+_g) \rightarrow N(^2P) + N_2(X\ ^1\Sigma_g^+)\ . \quad \textbf{(06)}$$

The rate constant of this reaction was measured by Piper **[7]** as being $4x10^{-11}$ cm^3s^{-1}. Moreover, he also observed the presence of the $N(^2D)$ state in an environment rich in $N_2(A\ ^3\Sigma^+_g)$ and $N(^4S)$ species **[8]**. Its density was of the same order of magnitude of the $N(^2P)$ one. Recent experiments **[9]** indicate the existence of $N(^2D)$ atoms in the N_2 flowing post-discharge when the SLA is observed. The $N(^2D)/ N(^4S)$ ratio is estimated to be on the order of 1 – 5 %.

The purpose of the present work is to introduce the relevant kinetics concerning the excited atomic states $N(^2D)$ and $N(^2P)$ in the model and to study the behaviour of them in the SLA. The local generation of the $N(^2D)$ is discussed on the basis of the introduction or not of reaction:

$$N(^4S) + N_2(A\ ^3\Sigma^+_g) \rightarrow N(^2D) + N_2(X\ ^1\Sigma_g^+)\ , \quad \textbf{(07)}$$

whose rate constant is considered the same as that one of reaction (06).

NUMERICAL MODEL PRESENTATION

The model main features are exhaustively depicted in ref.**[3]**. A new set of reactions was included to describe the atomic metastables kinetics and to complete the former set of reactions. Altogether, the diffusion constant of the $N_2(A\ ^3\Sigma^+_g)$ metastable was changed. The V-V and V-T rate coefficients were calculated following the formalism presented in ref.**[10]**.

DISCUSSION

The SLA has been recently analysed **[1,3]**, but no attention has been devoted to the metastable atomic states. As discussed in the introduction, both of works predict the formation of $N_2(A\ ^3\Sigma^+_g)$ species in the afterglow region. In fact, Sadegui *et al*.**[2]** have experimentally demonstrated that $N_2(A\ ^3\Sigma^+_g)$ density increases from 4 x 10^9 cm^{-3}, at the SLA minimum, to 5.5 x 10^{10} cm^{-3}, at SLA maximum. Such a high metastable density, along with the high $N(^4S)$ density (10^{14} – 10^{15} cm^{-3} **[6]**), develop a strong source term for the $N(^2P)$ state via reaction (06). In this way, we have included this mechanism and the other relevant mechanisms (reactions R1, R4, R6-R14) in the main block of reactions of the model **[3]**.

In figure 1 are presented the atomic and the $N_2(A\ ^3\Sigma^+_g)$ and $N_2^+(X\ ^2\Sigma^+_g)$ molecular densities as a function of time. We have considered the initial vibrational temperature as 6000 K and the same initial concentrations assumed in ref.**[3]**, which implies in initial concentrations of 7.5 x 10^{12} cm^{-3} for $N(^2D)$ and 3 x 10^{12} cm^{-3} for $N(^2P)$. We are considering the ratio $N(^2D)/N(^4S)$ as 1% in the discharge and the ratio $N(^2D)/N(^2P)$ being 2.5:1, as determined by Piper in the Ar-N_2 post-discharge **[8]**. Also, in addition to the metastable $N_2(A\ ^3\Sigma^+_g)$ generation mechanisms assumed before, we have included reaction (R1) (see table I), as proposed by Loureiro **[1]**. The constant of this reaction was obtained from the fit of numerical data to our experimental results. As shown, the $N(^2P)$ density follows the $N_2(A^3\Sigma^+_g)$ one, presenting the same behaviour of the molecular species in the SLA. The $N(^2D)$ density also presents an increase in the afterglow that is caused by the quenching of $N(^2P)$ (see reaction R13 in table 1). In this simulation, the product of reaction (R12) was $N(^4S)$, but it should be equally considered as $N(^2D)$. To our knowledge, there is not clear information about the branching ratio of reaction (R12) or about its rate constant (see table I), whose value is widely spread. We have studied the contribution of reaction (R12) in the $N(^2D)$ density when the product of this reaction is $N(^2D)$. A drastic change is observed in the density profiles (see figure 2) only for the rate constant proposed by Lin and Kaufmann **[11]**. In this case, the $N(^2D)$ density becomes greater than the $N(^2P)$ one, being in qualitative agreement with experimental results. As

discussed above, Piper found a N(^{2}D) density 2.5 times greater than the N(^{2}P) one in the post-discharge, even though he worked with an Ar-N_2 discharge

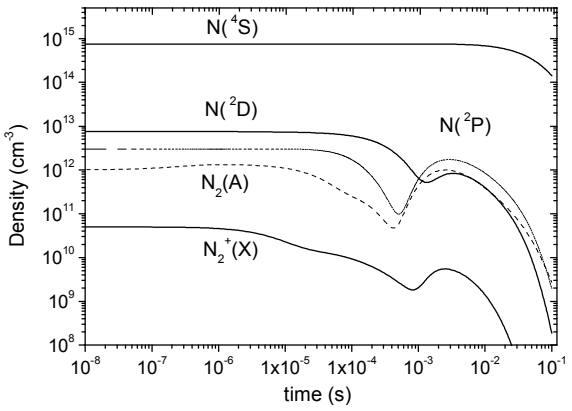

Figure 1 – Post-discharge temporal profiles for the $N_2(A\ ^3\Sigma^+_g)$, $N_2^+(X^2\Sigma^+_g)$, N(^{4}S), N(^{2}D) and N(^{2}P) densities with the product of reaction (R12) being N(^{4}S) and the rate constant 6x10^{-14} cm^{3}s^{-1}.

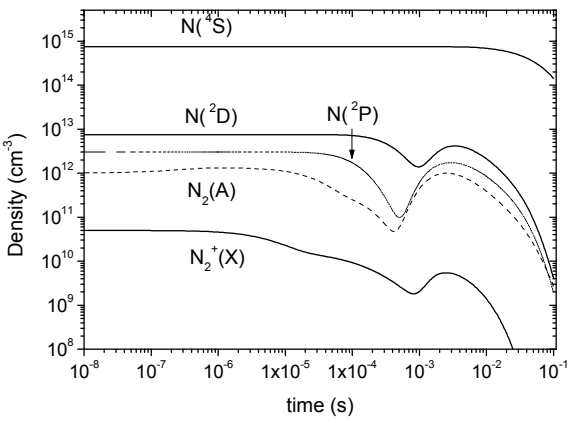

Figure 2 – Post-discharge temporal profiles for the $N_2(A\ ^3\Sigma^+_g)$, $N_2^+(X^2\Sigma^+_g)$, N(^{4}S), N(^{2}D) and N(^{2}P) densities with the product of reaction (R12) being N(^{2}D) and the rate constant 6x10^{-14} cm^{3}s^{-1}.

A similar result was obtained by Foner and Hudson **[12]** working in a pure N_2 discharge. They found N(^{2}D)/N(^{4}S) = 7 x 10^{-3} and N(^{2}P)/N(^{4}S) = 2.5 x 10^{-3}. However, the calculated N(^{2}D)/N(^{4}S) ratio at t = 10 - 50 ms, which varies from 3 x 10^{-3} to 3 x 10^{-4}, is too low. Kiohara *et al.* **[9]** worked in a N_2 post-discharge, in the presence of the SLA, and have found a N(^{2}D)/N(^{4}S) ratio on the order of 10^{-2} for the same range of residence time. Moreover, if the rate constant for reaction (R12) is that one proposed by Lee *et al.* **[13]**, or by Slovetskii and Smirnoff **[in 14]** or, if N(^{4}S) is generated in the N(^{2}P) quenching, the N(^{2}P) density overcomes the N(^{2}D) one (see figure 1) and even the qualitative behaviour with the experimental observations is not achieved. Thus, the numerical results point to the lack of mechanisms to account for N(^{2}D) generation in the post-discharge. Given that the energies of N(^{2}D) and N(^{2}P) are close, 2.38 eV and 3.58 eV, we propose the inclusion of reaction (R3) (see table I), with a rate constant of the same order of that one estimated

for reaction (R2). Figure 3 presents the densities temporal profiles, with the addition of reaction (R3). When reactions (R3) and (R4) are included in the model, it is observed that the $N(^2D)$ density is greater than the $N(^2P)$ one, for times longer than 1 ms (compare with the profile presented in figure 1), no matter what is the product of reaction (R12) or its rate constant. Although the qualitative behaviour of $N(^2D)/N(^2P)$ ratio is observed, reaction (R3) is not capable to promote the ratio $N(^2D)/N(^4S)$ to values on the order of those ones observed experimentally.

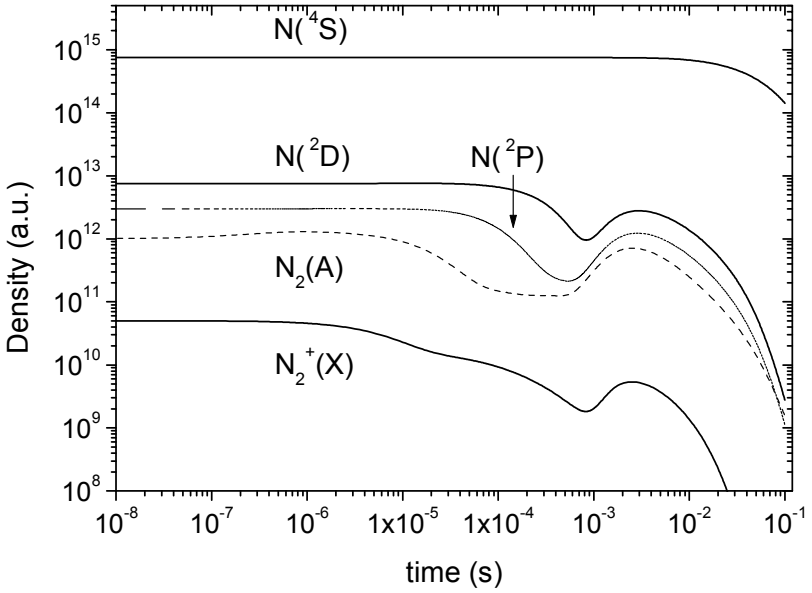

Figure 3 – Post-discharge temporal profiles as in figure 1 with the inclusion of reaction (R3).

CONCLUSION

A numerical model developed to study the N_2 short-lived afterglow was upgraded to include the atomic metastables $N(^2D)$ and $N(^2P)$. The densities of these metastables have shown the same temporal behaviour of the already studied molecular species in the SLA. A not usual mechanism (reaction R3) is required to reproduce qualitatively the $N(^2D)/N(^2P)$ ratio behaviour observed in N_2 flowing post-discharge experiments. The $N(^2D)/N(^4S)$ ratio obtained by the model is, at least, one order of magnitude lower than that one observed experimentally in a N_2 post-discharge with the presence of the SLA. Other possible $N(^2D,^2P)$ formation pathways have to be analysed to cover this issue.

Table I – Supplementary set of reactions in the N_2 afterglow.

Process :	**2-body reaction** **3-body reaction** **diffusion**	**k (cm^3s^{-1})** **k (cm^6s^{-1})** **cm^2s^{-1}**	**Ref.**
R1	$N_2(X\ ^1\Sigma^+_g, v>24) + N(^4S) \rightarrow N_2(A\ ^3\Sigma^+_g) + N(^4S)$	5×10^{-14}	**p.w.**
R2	$N_2(A\ ^3\Sigma^+_g) + N(^4S) \rightarrow N_2(X\ ^1\Sigma^+_g, v<9) + N(^2P)$	4×10^{-11}	**[7]**
R3	$N_2(A\ ^3\Sigma^+_g) + N(^4S) \rightarrow N_2(X\ ^1\Sigma^+_g, v<14) + N(^2D)$	4×10^{-11}	**p.w.**
R4	$N_2(X\ ^1\Sigma^+_g, v>8) + N(^2P) \rightarrow N_2(A\ ^3\Sigma^+_g) + N(^4S)$	$0.86 \times 10^{-10} \times (1-e^{-2062/T})/(1-e^{-3353/T}) \times e^{-1398/T}$	**[14]**
R5	$N_2(X\ ^1\Sigma^+_g, v>13) + N(^2D) \rightarrow N_2(A\ ^3\Sigma^+_g) + N(^4S)$	$0.86 \times 10^{-10} \times (1-e^{-2062/T})/(1-e^{-3353/T}) \times e^{-1398/T}$	**p.w.**
R6	$N_2^+(X^2\Sigma^+_g) + e \rightarrow N(^4S) + N(^4S)$ $\rightarrow N(^2D) + N(^4S)$ $\rightarrow N(^2P) + N(^4S)$	$1.62 \times 10^{-7} \times (300/Te)^{0.39} \times 0.143$ $1.62 \times 10^{-7} \times (300/Te)^{0.39} \times 0.771$ $1.62 \times 10^{-7} \times (300/Te)^{0.39} \times 0.086$	**[14]**
R7	$N(^4S) + N(^4S) + N_2(X\ ^1\Sigma^+_g) \rightarrow N_2(A\ ^3\Sigma^+_g) + N_2(X\ ^1\Sigma^+_g)$	$0.75 \times 8.3 \times 10^{-34} \exp(500/T)$	**[14]**
R8	$N(^4S) + N(^4S) + N_2(X\ ^1\Sigma^+_g) \rightarrow N_2(B^3\Pi_g) + N_2(X\ ^1\Sigma^+_g)$	$0.25 \times 8.3 \times 10^{-34} \exp(500/T)$	**[14]**
R9	$N(^4S) + N(^4S) + N(^4S) \rightarrow N_2(A\ ^3\Sigma^+_g) + N(^4S)$	$0.75 \times 3.35 \times 10^{-31} / T^{0.5}$	**[14]**
R10	$N(^4S) + N(^4S) + N(^4S) \rightarrow N_2(B^3\Pi_g) + N(^4S)$	$0.25 \times 3.35 \times 10^{-31} / T^{0.5}$	**[14]**
R11	$N(^2D) + N_2(X\ ^1\Sigma^+_g) \rightarrow N(^4S) + N_2(X\ ^1\Sigma^+_g)$	2×10^{-14}	**[11]**
R12	$N(^2P) + N_2(X\ ^1\Sigma^+_g) \rightarrow N(^4S,^2D) + N_2(X\ ^1\Sigma^+_g)$	6×10^{-14} **[11]**, 10^{-16} **[13]**, 2×10^{-18} **[14]**	
R13	$N(^2P) + N(^4S) \rightarrow N(^2D) + N(^4S)$	1.8×10^{-12}	**[14]**
R14	$N_2(A\ ^3\Sigma^+_g)$ diffusion	$0.179 \times (760/p) \times (T/273)^{\wedge}1.9$	**[15]**

BIBLIOGRAPHY

[1] Loureiro J, Sa P A and Guerra V 2001 J. Phys. D: Appl. Phys. **34** 1769
[2] Sadegui N, Foissac C and Supiot P 2001 J. Phys. D: Appl. Phys. **34** 1779
[3] Levaton J, Amorim J, Souza A R, Franco D and Ricard A 2002 J.Phys.D: Applied Physics **35** 689
[4] Bromer H H and Hesse J 1969 Z. Physik **219** 269
[5] Levaton J, Amorim J, Souza A R and Ricard A 2001 Proceedings of the 13th CIP **1** 218
[6] Moritts A 1997 PhD. Thesis Université de Paris-Sud, Orsay
[7] Piper, L G 1989 J. Chem. Phys. **90** (12) 7087
[8] Piper, L G 1987 J. Phys. Chem. **91** 3883
[9] Kiohara V, Levaton J and Amorim J, 16th ISPC Taormina - Italy, June 2003
[10] Loureiro, J., Ferreira, C.M., J.Phys.D: Appl.Phys. **19** (1986) 17.
[11] Lin C L and Kaufman F 1971 J. Chem. Phys. **55** 3760
[12] Foner S N, and Hudson R L 1962 J. Chem. Phys. **37** 1662
[13] Lee J H, Michael J V, Payne W A and Stief L J 1978 J. Chem. Phys. **69** 3069
[14] Matveyev A A and Silakov V P 1999 Plasmas Sources Sci. Technol. **8** 162
[15] Capitelli M, Ferreira C M, Gordiets B F and Osipov A I 2000 *Plasmas Kinetics in Atmospheric Gases*, Springer-Verlag, 1st ed., Berlin Heidelberg

Handling of fine, cohesive particles in a circulating riser reactor

B. Borer[1], Ph. Rudolf von Rohr[1]

[1] *Institute of Process Engineering, ETH Zurich, Zurich, Switzerland*

In this study three different approaches have been evaluated to improve the handling of fine, cohesive particles in a circulating riser reactor. Mixing the fine particles with large glass beads was the most suitable way to process the cohesive powder. The influence of the large particle ratio on separation efficiency of the cyclone was negligible. The deposited barrier coating showed several defects, caused by dust particles.

1. Introduction

Most solid materials used in industrial or chemical processes are processed as particles with sizes below 1 mm. Advantages are the easy handling and the high specific surface area allowing high-rate reactions with liquids and gases.

With advanced products, there is a demand for specified particle materials with controlled properties. Particle properties are strongly influenced by the surface. The deposition of thin films is a convenient way to adjust particle properties over a wide range. The broad spectrum of applications includes corrosion protection, diffusion reduction, wettability and catalytic properties.

Plasma enhanced chemical vapor deposition (PECVD) techniques are widely used for deposition of thin films at low temperature and dry environment. The circulating fluidized bed (CFB) plasma reactor provides uniform and efficient coating of particles at high deposition rates. Both, diffusion barrier and catalytic layer were successfully deposited on particles with mean diameter of 100 – 200 μm [1, 2].

However, in industry there is an increasing demand to treat even smaller particles. In the future, particle sizes of 1 μm and smaller should be possible to be processed. But the small particle size causes several problems, because cohesive forces between particles, like Van-der-Waals- or electrostatic forces become dominant compared to gravitational forces. Consequently small particles stick together and form stable agglomerates.

The cohesive behavior of the particles caused plugging and instable fluid dynamic conditions in the CFB system. Due to strong fluctuations of the solid ratio in the reactor it was not possible to ignite the plasma, and therefore the deposition process could not be performed. By introducing the circulating riser reactor design, the process conditions could be dramatically improved. However, on the cyclone wall an extensive particle layer was formed, because of the strong cohesive inter-particle forces (see Fig.3a). As a result the separation efficiency of the cyclone was decreased, and half of the valuable product was lost on the cyclone wall.

The objective of this study was to avoid a layer formation in the cyclone. Device-dependent, as well as a product-specific approaches have been investigated. Here the results of these investigations are presented.

2. Experimental

The main parts of the circulating riser reactor are a riser tube (ID 40 mm, length 900 mm) with integrated microwave plasma source, a cyclone and a re-feed section, as shown in Fig. 1. The particles are stored in the re-feed section, consisting of a PE-tube and a siphon. Introducing a small argon gas flow at the bottom of the siphon fluidizes the particle bed. By fluidizing the particle bed, the particles are fed into the riser tube, and subsequently are transported upward by the process gas flow (2570 sccm), which is distributed by a porous plate at the bottom of the riser tube. As process gas a mixture of argon, oxygen and precursor (Hexamethyldisiloxane, HMDSO) is used. In the riser tube a plasma source (μ-SLAN, *JE Plasma Consult GmbH*) is integrated, where the microwave power (2.46 GHz) is coupled into a quartz glass tube to ignite and sustain a low temperature plasma. In the plasma zone the coating process is performed at a reduced pressure of about 3 mbar. Downstream the plasma reactor the gas solid flow is separated by a cyclone, and the particles are collected in the re-feed section. The cyclone diameter is 100 mm and the height 260 mm.

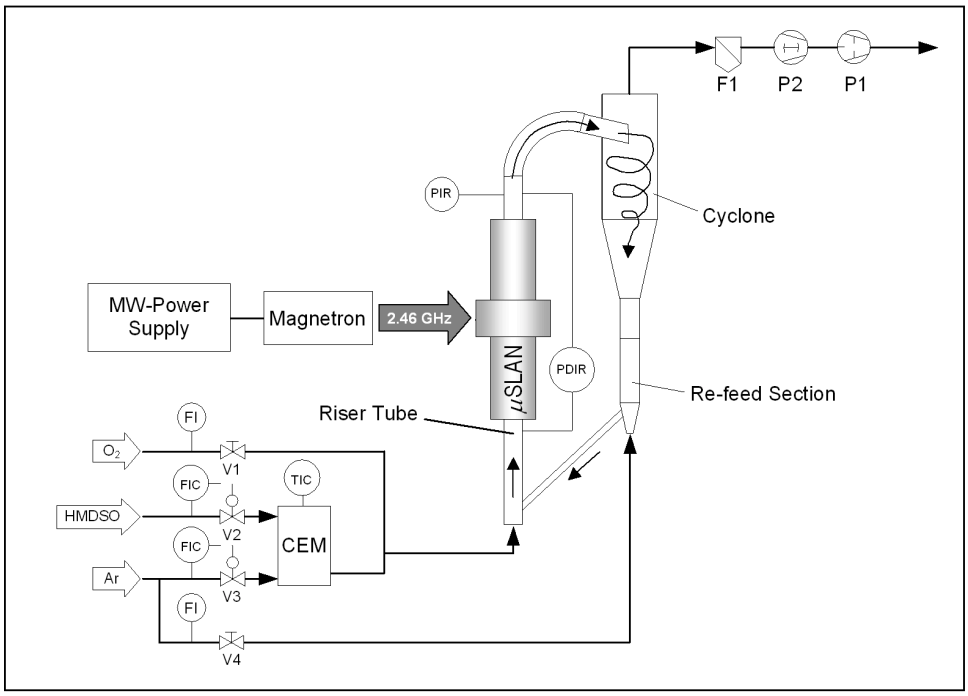

Figure 1: Scheme of the experimental setup, including the riser tube, the cyclone and the re-feed section

The gas inlet is inclined by an angle of 20° to improve the separation efficiency. The diameter of the outlet tube (vortex finder) is 35 mm, and its length 110 mm.

During a typical deposition procedure of 3.5 hours the particle batch is circulated several hundred times. This high number of circulations provides a narrow residence time distribution, thus a uniform coating thickness of the whole batch. However, the cyclone separation efficiency must be very high.

The liquid precursor (Hexamethyldisiloxane) is evaporated and subsequently mixed with the argon gas in the Controlled Evaporator Mixer (CEM, *Bronkhorst High-Tech B.V.*) device. The flow rates and the mixing temperature are controlled. The oxygen gas flow is regulated by a rotameter (V100*, Vögtlin Instruments AG*) and mixed with the argon / HMDSO gas flow downstream the CEM. The argon gas flow for fluidizing the particle bed in the re-feed section is also regulated by a rotameter (V100, *Vögtlin Instruments AG*).

The vacuum pump system (*LEYBOLD VAKUUM GmbH*) consists of a two-stage rotary vane backing pump (P1) and a Roots vacuum pump (P2). Between the cyclone and the vacuum pump system an inlet dust filter (ITM800, *BOC Edwards AG*) is installed to collect fine particles in order to protect the pumps.

The pressure is measured right above the plasma reactor by a Pirani cold cathode pressure sensor (*Balzers*). Between the reactor in- and outlet the differential pressure is measured by a low pressure differential sensor (*Honeywell*).

Non-spherical particles (ρ = 4.1 g/cm^3) were used as fine, cohesive material. The mean diameter was 15.97 µm. Further size distribution parameters were: d_{10} = 2.62 µm, d_{90} = 26.19 µm.

3. Results and discussion

3.1. Device dependent approaches

The first device-dependent approach was to decrease the electrostatic forces between the particles by reducing the electrostatic charges on the particles, because of strongly increased layer formation after igniting the plasma. Due to the higher mobility of the electrons, particles are charged negatively in the plasma at the given conditions [3, 4]. After entering the cyclone the particles repelled one another to the grounded cyclone wall, where they lost the charges and formed a stable layer.

In the outlet of the plasma reactor a honeycomb structure was installed to discharge the particles, in order to reduce the layer formation. However, shortly after starting the deposition process, the honeycomb structure was coated itself with a SiO_x layer, in spite of the attrition effect of the particles. The particles were not discharged anymore, because the SiO_x layer electrically insulated the honeycomb.

Another device-dependent approach was a mechanical cleaning system of the cyclone wall. For that purpose an elastomer liner (0.5 mm thickness) was attached to the cyclone wall. By pumping gas between the wall and the liner, the elastomer liner was inflated and the dense, stable particle layer was detached from the elastomer. Subsequently the gas was exhausted, and the elastomer liner was sucked tightly on the cyclone wall (Figure 2 & 3). This cleaning process was typically repeated every 60 seconds. Since the elastomer liner was inflated only for 0.5 seconds the flow conditions in the cyclone were not interfered remarkably, which was an important requirement for a mechanical cleaning system.

Although the cleaning system was an effective way to prevent the particle layer formation on the cyclone wall, it caused a new problem. Due to the electrical insulation of the cyclone wall by the elastomer liner, the behavior of the charged particles was dramatically changed. Again the predominantly negative charged particles repelled one another to a grounded surface. Since the gas outlet tube of the cyclone was the only grounded surface, particles formed a layer up to a thickness of 2 cm on that tube. Therefore this system was not suitable either.

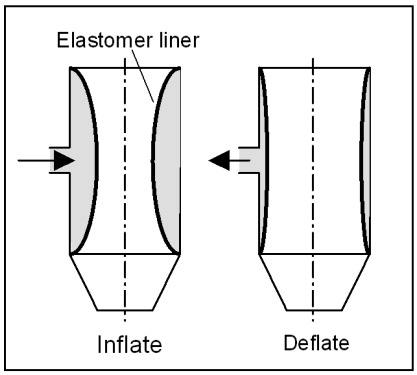

Figure 2: cleaning system principle

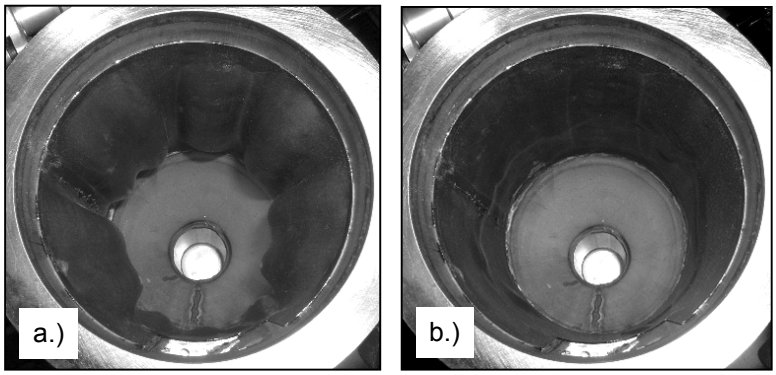

Figure 3: elastomer liner on the cyclone wall (top view): a.) inflated and b.) deflated

3.2. Product specific approach

Another approach to solve the problem of particle layer formation in the cyclone was to change the properties of the product. Mixing larger particles with the fine, cohesive powder significantly improves the handling [5]. This approach offered two advantages. First, the fluidization of the mixture was facilitated, and therefore the dosing in the re-feed section was improved. Second, the larger particles cleaned the cyclone wall, colliding with fine particles forming a layer.

However, the following drawbacks have to be considered. After the deposition process, an extra separation step is necessary to remove the large particles from the product batch. Second, by adding cleaning particles, the surface area, which has to be coated, is increased. Hence the deposition process is prolonged. Considering typical mixture parameters (diameter of fine particles: 16 µm, diameter of cleaning particles: 100 µm, mass ratio 1:1), the deposition time is increased by 25 %.

The objective of the following experiment was to investigate the influence of the "large" cleaning particles in the mixture on particle layer formation in the cyclone and the separation efficiency of the cyclone during a deposition procedure. Glass beads (d_{50} = 100 µm), used as cleaning particles, were mixed with the fine particles (d_{50} = 16 µm). Mixtures of mass ratios of 1, 2 and 4 were investigated. The mass ratio is given by the mass of large particles divided by the mass of fine particles. For each experiment 600 g of mixture were treated. The process gas flow consisted of 2250 sccm Argon, 300 sccm Oxygen, and 20 sccm HMDSO, respectively. Further process parameters are listed in Table 1.

Table 1: Process Parameters and Results

Mass ratio m_{large} / m_{fine}	**1 : 1**	**2 : 1**	**4 : 1**
Fine particles d_{50} = 16 µm	300 g	200 g	120 g
Large particles d_{50} = 100 µm	300 g	400 g	480 g
Deposition time	102.5 minutes	82.0 minutes	65.5 minutes
Specific deposition time	20.5 s/g	24.6 s/g	32.7 s/g
Reactor pressure	2.75 mbar	3.01 mbar	2.81 mbar
Solid volume concentration	0.46 %	0.46 %	0.61 %
Total loss of fine fraction d < 50 µm	31 %	30 %	39 %
Total loss of large fraction d > 50 µm	2 %	1 %	2 %
Particle layer in the cyclone	13.1 g	11.9 g	6.1 g

The deposition time was determined in order to achieve a SiO_2-layer thickness of 100 nm on the particle batch. In terms of comparison of the different deposition times, it is reasonable to consider the specific deposition time, which is the ratio of deposition time and mass of fine particles. Obviously, the specific deposition time is increased by additional amount of cleaning particles.

After each experiment the cleaning particles were separated from the fine particles using a sieve (mesh size 50 µm). Each fraction was weighted and compared with the initial amount. Thus the size dependent loss by the cyclone could be determined (Table 1). The loss of the fine particles was high in each experiment, but the experiment with 4:1 particle mixture revealed the highest loss. An explanation of this behavior is the solid volume concentration in the riser tube. It is proportional to the circulation rate of the particles. Assuming that at every circulation the same amount of fine particles is not separated by the cyclone, the circulating rate is proportional to the loss rate. The comparison of the results of particle loss and solid volume concentration confirms this statement. Thus the loss rate is independent of the mass ratio of large particles.

The particle layer on the cyclone wall was investigated by weighting. The particle layer consisted only of fine particles. Compared with previous experiments without cleaning particles a significant reduction of the particle layer has been reported, as shown in Figure 3. Considering the mixtures with 1:1 and 2:1 cleaning particle ratio the reduction was 95 %. The 4:1-mixture reduced the layer formation by 98 %.

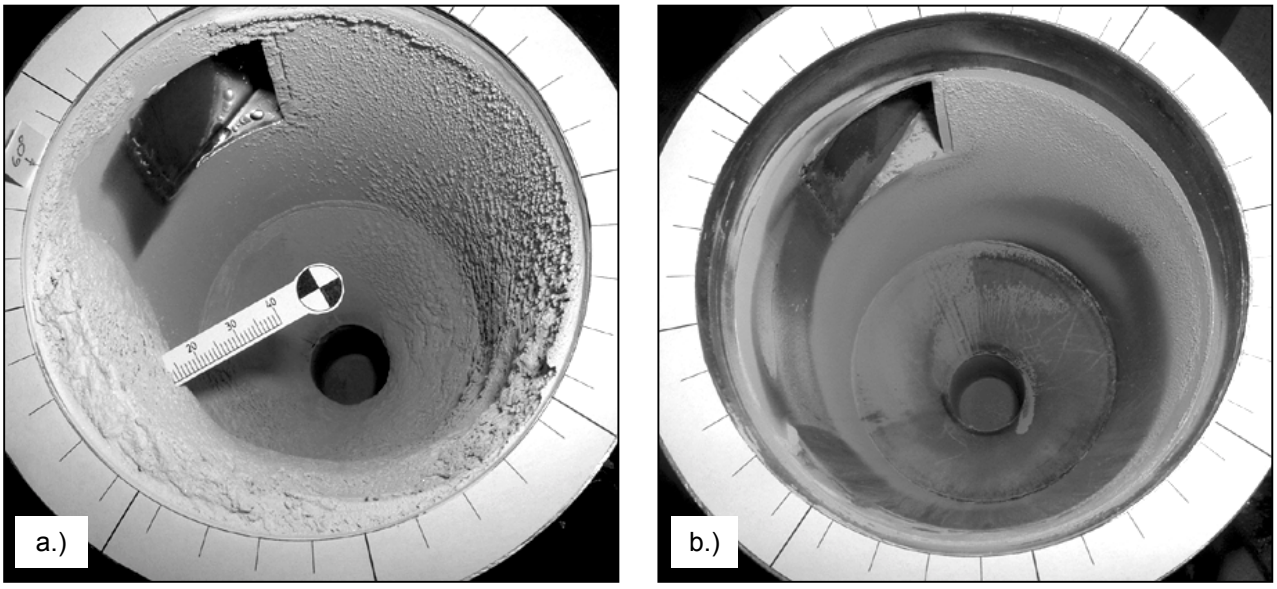

Figure 3: Particle layer on cyclone wall (top view) after circulation: a.) Without cleaning particles the layer thickness was up to 15 mm; b.) With cleaning particles only a light dust layer was deposited.

3.3 Coating structure

In this preliminary test 750 g particle mixture with a large particle mass ratio of 2:1 were coated with a 200 nm SiO_x-layer. The deposition time was 3.5 hours. The process gas flow consisted of 2250 sccm Argon, 300 sccm Oxygen and 20 sccm HMDSO, respectively. The reactor pressure was 3.17 mbar and the solid volume concentration 0.46 %.

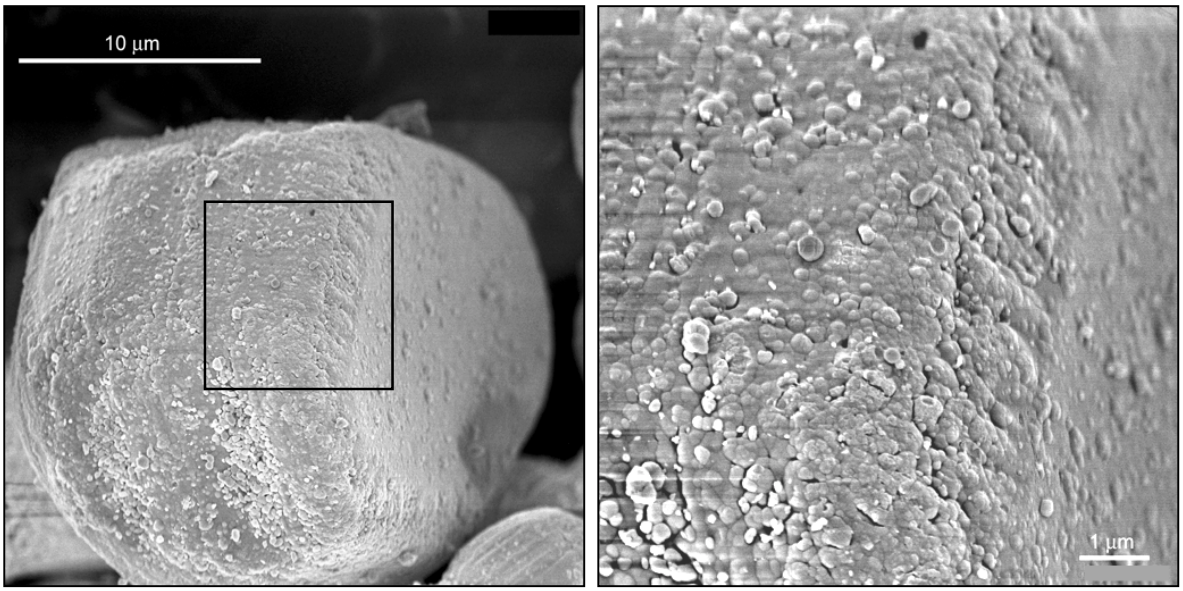

Figure 4: SEM micrographs of a coated particle; left: overview, right: enlarged section

The coating structure was qualitatively investigated by SEM micrographs (Fig.4). The SiO_x layer structure can be divided into three different categories. The first category is a smooth and dense layer. The second is a cauliflower like layer, consisting of fine, agglomerated SiO_x primary particles, which also form a dense film. Finally the third represents relatively large SiO_x particles (up to 350 nm), which loosely stick to the SiO_x layer. The first two structure categories are expected to provide good diffusion barrier properties, because they form a dense layer. But due to the large SiO_x particles sticking to the surface some pores were not coated, which could decrease the diffusion barrier properties. Future measurements of the diffusion barrier property of such coating will reveal quantitative results.

4. Conclusions

The handling of fine, cohesive particles in a circulating riser reactor is improved by mixing the batch with large 100 µm glass beads. The fluidization of the particles is facilitated and the formation of a particle layer in the cyclone is reduced. The ratio of large particles does not influence the separation efficiency of the cyclone in the investigated range. Increasing the ratio of large particles reduces the layer formation in the cyclone, but increases the specific deposition time.

The structure of the diffusion barrier coating shows several defects caused by large SiO_x dust particles. Quantitative measurements will be performed next to determine the influence of these defects on the barrier properties.

5. References

[1] M. Karches, Ch. Bayer, Ph.R. von Rohr, *Surf. Coat. Tech*. **119**, (1999) 879-885
[2] M. Karches, M.Morstein et al., *Catal. Today* **72**, (2002) 267-279
[3] Ch. Hollenstein, *Plasma Phys. Contr. Fusion* **42,** (2000) R93-R104
[4] M. Kakati, B. K. Saikia, *Phys Plasmas* **7** (12), (2000) 5263-5266
[5] Y. -D. Lui, S. Kimura, *Powder Technol.* **75** (2), (1993) 189 - 196

The F.I.R.L.I.P.A.D.: the Far InfraRed Laser Interferometer with PhotoAcoustic Detection to investigate electron density time variations

C. de Izarra and M. Pennaneac'h

LASEP: *Laboratoire d'Analyses Spectroscopiques et d'Energétique des Plasmas*
Faculté des Sciences, Site de Bourges Université d'Orléans, rue Gaston Berger BP 4043 18028 Bourges Cedex France

Abstract
Laser interferometry using the cavity of a gas laser as a reference arm (Ashby and Jephcott's interferometer [1, 2, 3]) is often employed to determine the time evolution of the electron density in unsteady plasmas. As the refractivity of free electrons varies as the square of the wavelength of the interferometer, we use a CO_2 laser (wavelength: 10.6 μm) and the recording of temporal fringes appearing at a frequency of a few kHz is carried out with a photoacoustic effect.

1. The Ashby and Jephcott interferometer

In contrast to classical interferometers (Michelson, Mach-Zehnder...), the Ashby and Jephcott interferometer is a true laser interferometer [1, 2, 3] that uses the cavity of a gas laser as the reference arm of the interferometer. However, it is limited to the study of transitory interference fringes obtained by recording the instantaneous laser intensity as a function of time.

The Ashby and Jephcott interferometer, currently employed in plasma diagnostics is based on an observation from King et Steward in 1963 [1]. These authors had noticed that the intensity of a He-Ne laser could be modulated by injecting back a low percentage of the laser beam into the laser cavity. This modulation is a function of the phase or of the optical path of the laser beam back injected in the laser cavity [4].

Let us consider the mounting presented in figure 1. Mirrors M_1 and M_2 are the mirrors of the laser cavity, a distance L apart. The mirror M_2 is semitransparent. The mirror M_3 is put outside of the laser cavity, and can be moved of a distance d. The semitransparent mirror placed between the mirrors M_2 and M_3 allows to record the laser intensity as a function of time with a photovoltaic sensor.

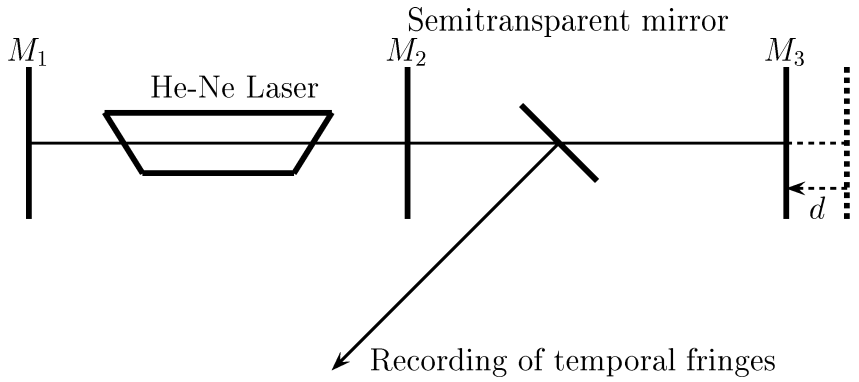

Figure 1: Principle of the Ashby and Jephcott interferometer

In the following, we suppose that the refraction index of ambient air is close to unity.

Resonance is obtained for the beam moving between M_2 and M_3 when the time necessary for a double path is equal to a whole number of time periods:

$$\frac{2D}{c} = \frac{q}{\nu}$$

where q is the order of the considered mode, c the velocity of the light and ν the wave frequency.

In the case when the mirror M_3 is moved a length d, the propagation time is:

$$\frac{2}{c}(D+d) = \frac{2}{c}D + \frac{2}{c}d.$$

The excitation frequency ν of the laser in constant, and to obtain resonance after a displacement d, it is necessary to check the relation:

$$\frac{2}{c}D + \frac{2}{c}d = \frac{q'}{\nu}.$$

The smallest detectable length d_{min} corresponds to an evolution from a mode to an adjacent mode, so

$$q' = q + 1.$$

For the shortest detectable length, we obtain:

$$\frac{2}{c}D + \frac{2}{c}d_{min} = \frac{q+1}{\nu} \implies \frac{2}{c}d_{min} = \frac{1}{\nu}$$

or, by introducing the laser wavelength λ ($\lambda = c/\nu$):

$$d_{min} = \frac{\lambda}{2}. \tag{1}$$

Experimentally, the effect described higher produces an evolution of the laser intensity that may be interpreted as a "temporal fringe".

Let us now consider that the mirror M_3 is moved at a constant speed v, and let us call f the frequency of the temporal fringes. If δt is the time between two adjacent fringes, we have $v = d_{min}/\delta t$. Since $f = 1/\delta t$, the frequency f of the temporal fringes as a function of the laser wavelength is:

$$f = \frac{2v}{\lambda}. \tag{2}$$

In plasma physics experiments, the variation of the optical path of the beam back injected in the laser cavity is given by an unsteady plasma produced in a cell (figure 2) ; the variation of the plasma refraction index as a function of time produces a variation of the optical path and consequently, apparition of time fringes which interpretation allows to measure the electron density as a function of time.

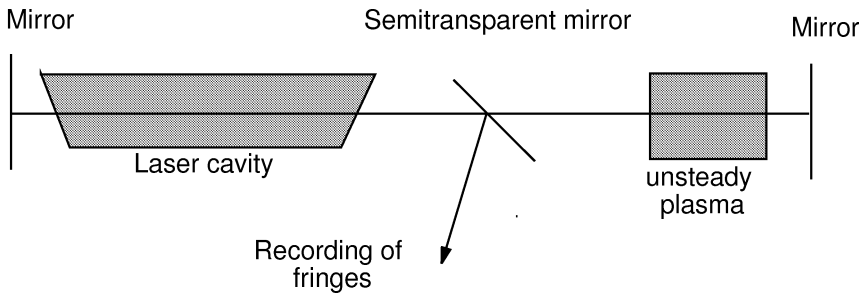

Figure 2: The Ashby and Jephcott interferometer to study the time evolution of electron density in unsteady plasmas.

It is important to underline that it is necessary to have a signal giving a rough idea of the time evolution of the electron density, because the interferometric method is not sensitive to the way of evolution (increase or decrease) of the electron density; very often, the integrated radiation of the plasma is used to fix this indetermination.

2. Plasma refractivity

The refractivity $(n-1)$ of plasmas, where n is the real part of the refraction index is given by the sum of the refractivities of particules of the plasma: neutral particules (atoms or molecules) in their fundamental state and in their excited states, ions and electrons.

The contribution of excited states in the refractivity of the plasma is negligible in front of other contributions [5]. The optical refractivities of neutral particles and of ions in their fundamental state are given by a Cauchy formula as a function of the wavelength λ. The refractivity $(n-1)_e$ of free electrons is given by

$$(n-1)_e = -C\lambda^2 N_e \tag{3}$$

where C is a constant and N_e the electron density number. Equation (3) explains the choice of laser radiations in infrared instead of in the visible part of the electromagnetic spectrum, because of the quadratic variation of the refractivity wavelength λ. This remark was employed by Ashby et Jephcott [1] with the use of the line at $3,39\ \mu$m of a He-Ne laser to probe the plasma, and the red line at $0,63\ \mu$m to detect the laser intensity variations, knowing that these two laser lines have the same upper level.

3. Elaboration of an infrared laser interferometer

In order to increase the sensitivity of the laser interferometer in the determination of electron density in unsteady arc plasmas, (see equation (3)), we employ a CO_2 laser at the wavelength $10,6\ \mu$m. The laser intensity variations are recorded with a photoacoustic effect which time response is better than the time response of common infrared sensors. The experimental results given in this communication demonstrate that an infrared interferometer is easily feasible.

The experimental set up is presented in figure 3. We use a SYNRAD Trade Mark CO_2 laser with a maximum power of 10 W.

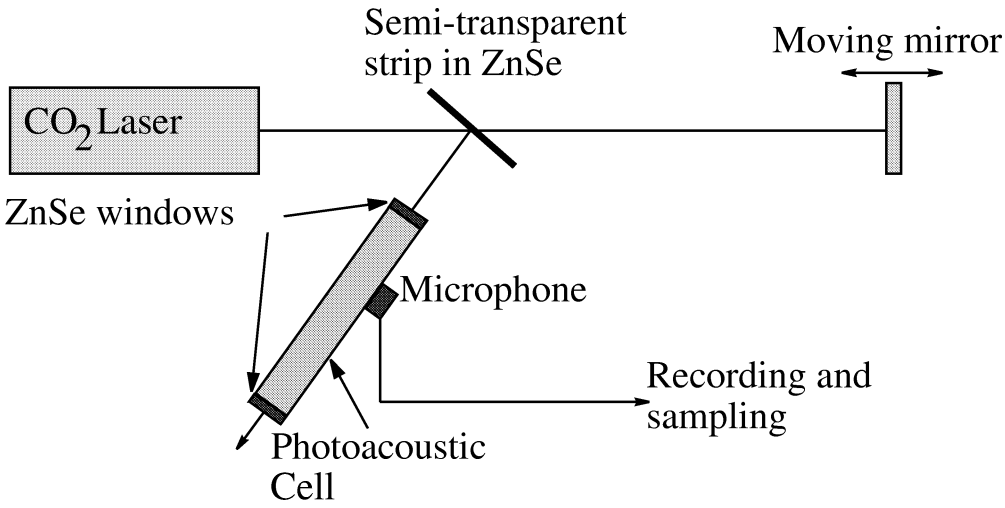

Figure 3: Experimental set up

The infrared beam is back injected in the laser cavity with a mirror fixed on a device allowing to move it along the axis of the laser beam. The motion of the mirror is sinusoïdal, with a period T and an amplitude x_0 experimentally determined with a relative precision lower than 5% with an optical sensor (KEYRENCE Trade Mark, model LB-72). The speed of the mirror is given by

$$v(t) = \frac{2\pi}{T} x_0 \sin 2\pi t/T,$$

and by applying (2), we obtain the expression of the frequency $f(t)$ of the temporal fringes as a function of

time. We have:

$$f(t) = f_0 |\sin 2\pi t/T| \tag{4}$$

with

$$f_0 = \frac{4\pi}{\lambda T} x_0,$$

the absolute value being introduced in expression (4) because the interferometric method in not sensitive to the sign of the speed v.

A semi-transparent mirror in ZnSe (see figure 3) sends a fraction of the laser intensity in a cylindrical photoacoustic cavity (diameter: 30 mm and length: 30 cm) filled with CO_2 gas at atmospheric pressure. Other absorbing systems were tested: carbon black, CH_4 ..., but the best results were obtained with CO_2 gas.

The absorption of the laser beam which intensity varies with time by the gas contained in the photoacoustic cell produces a cylindrical acoustical wave [6] with a frequency given by expression (4). The sound is recorded with a microphone and sampled at 44100 Hz with a desk computer.

With T=1 s and x_0=0, 15 mm, figure 4 presents the speed of the mirror M_3 as a function of time, and the expected acoustical frequency. One notices that the period of the signal giving the frequency f against time is half the period of the speed, because interferometry is not sensitive on an the sign of the evolution of the optical path.

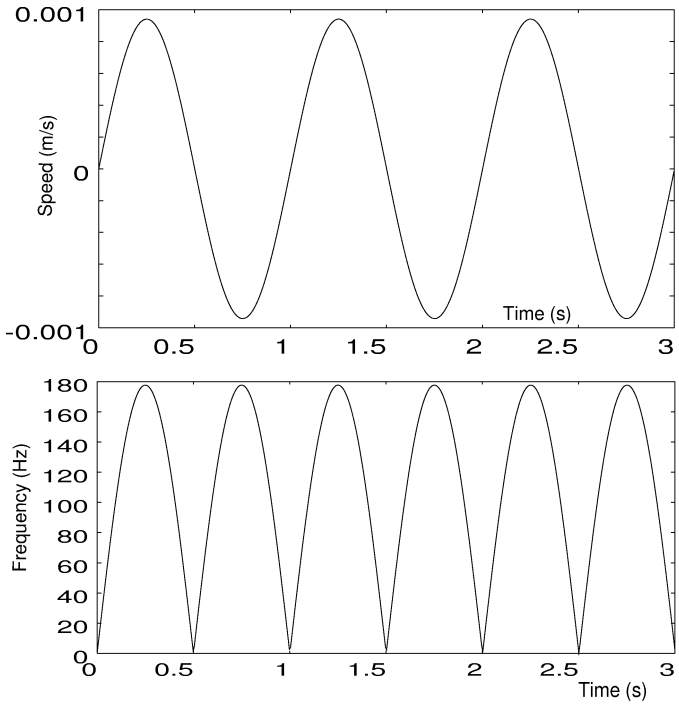

Figure 4: Plots giving the speed of the mirror M_3 against time (top) and the frequency f obtained with equation (4) (bottom).

Data processing essentially consists in the determination of the fundamental frequency as a function of time. This operation is easily realized with a speech analysis software where one deals with acoustical frequencies close to the frequencies obtained in the acoustical cell with the parameters T and x_0 chosen above.

Figure 5 gives a typical experimental result. In agreement with equation (4), one notices that the signal amplitude increases twice every period of the mirror M_3 motion.

The plot given in the bottom of figure 5 is the fundamental frequency against time. It is in agreement with theory (equation (4)), and a maximum f_0 at 166 Hz $\pm$ 10 Hz close to the theoretical predictions:

$$f_0 = \frac{4\pi}{\lambda T} x_0 = 4\pi\, 0,15\, 10^{-3}/(10,6\, 10^{-6}) = 178\,\text{Hz at 5 \%}.$$

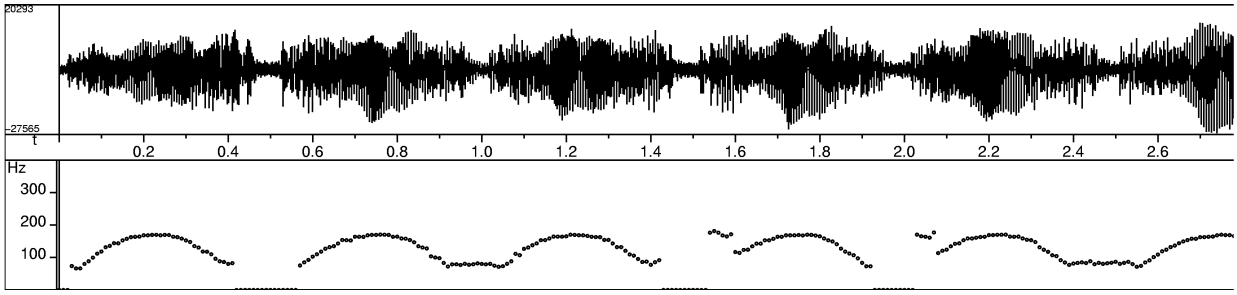

Figure 5: Example of sound signal obtained (top), and plot of the fundamental frequency as a function of time (bottom) obtained after data processing.

4. Conclusion

In this communication, we have presented an innovative infrared laser interferometer with a photoacoustic detection of temporal fringes. This interferometer has been call "F.I.R.L.I.P.A.D." (**F**ar **I**nfra**R**ed **L**aser **I**nterferometer with **P**hoto**A**coustic **D**etection).

Before to apply it in plasma diagnostics, it is necessary to consider the optimization of the photoacoustic detection chain (design of the cell, choice of an medium for absorption, ...).

References

[1] D. E. T. F. Ashby and D. F. Jephcott, Measurement of plasma density using a gas laser and an infrared interferometer, Applied Physics Letters **3** number 1 (1963) 13-16.

[2] D. E. T. F. Ashby, D. F. Jephcott, A. Malein and F. A. Raynor, Performance of the He-Ne gas laser as an interferometer for measuring plasma density, Journal of Applied Physics **36** number 1 (1965) 29-34.

[3] C. de Izarra, The Ashby and Jephcott interferometer, Eur. J. Phys. **22** (2001) 429-432.

[4] F. Rostas, Les méthodes de disgnostic des plasmas utilisant des lasers, Le Journal de Physique **27** (1966) 367-384.

[5] K. Musiol, A. Czernichowski, J. Chapelle and C. de Izarra, An interferometric and spectroscopic argon arc plasma diagnostic, J. Phys. B : At. Mol. Opt. Phys. **22** (1989) 2649-58.

[6] A. Rosencwaig, Photoacoustics and photoacoustics spectroscopy, Wiley (Interscience), New York 1980.

Chamber Size Effect on ICP discharges and Comparison with Global Model

Jie Ma[1], Yikang Pu[2]

[1]*Department of Electrical Engineering, Tsinghua University, Beijing, 100084, China*
[2]*Department of Engineering Physics, Tsinghua University, Beijing, 100084, China*

Plasma discharge chamber size is considered to be a very important factor in determining parameters such as electron temperature(Te) and electron density(Ne) in the Global Model, in which an effective area A_{eff} is introduced to evaluate this effect on plasma. In this work, the influence of different diameter sizes of the chamber on ICP discharge characteristics is investigated experimentally. A Langmuir probe and emission spectroscopy are used to measure electron temperature, electron density, plasma potential, and electron energy distribution function in different gases (and their mixture) discharges. Results will be compared with that predicted by the Global Model.

Particle formation in capacitively coupled hydrocarbon plasmas

J. Berndt, E. Kovacevic, I. Stefanovic, J. Winter

Institute of Experimental Physics II, Ruhr-University Bochum, Germany

Abstract

This paper deals with the formation of hydrocarbon dust particles in capacitively coupled discharges in argon/acetylene mixtures. First experiments performed in acetylene/nitrogen discharges are also presented, showing the existence of carbon nitride particles polymerized in the plasma. The formation of dust particles in the plasma is studied by means of in-situ-Fourier transform infrared spectroscopy (FTIR). The response of the plasma to the formation of the particles has been analyzed by plasma-ion-mass spectroscopy.

1. Introduction

Since Langmuir and his co-workers have discovered the existence of dust particles in glow discharges [1], the formation of particulates in plasmas is a well-known phenomenon. The formation of dust can be observed in several plasma processes such as etching, sputtering or thin film deposition. In semiconductor manufacturing dust particles were recognized as "killer particulates" responsible for the malfunction of integrated circuits. [2]. On the other hand a controlled growth of particles is desired for applications in catalysis and pharmacy and for the fabrication of nano-crystalline materials. In the latter case nanoparticles are incorporated into the growing film for a controlled modification of film properties [3].

This contribution deals with the formation of carbon containing dust particles in capacitively coupled hydrocarbon discharges. Although reports on powder formation in hydrocarbon plasmas together with proposed models of nucleation [4,5] have already been made in the seventies the process of particle formation in such plasmas is still not fully understood. To gain more accurate insight in the chemical nature of dust particles and the growth mechanism of powder formation for various discharge conditions and gas mixtures we used a reactor, especially suitable for multipass in-situ FTIR spectroscopy. In contrast to ex-situ FTIR-spectroscopy the corresponding in-situ observation allows to monitor the properties of the particles directly during their formation. The measurements presented in this paper are performed in discharges containing mixtures of acetylene and argon and acetylene and nitrogen respectively. Acetylene as monomer was chosen because of its important role in powder formation in hydrocarbon plasmas [4,6,7,8]. It was shown that in saturated and unsaturated hydrocarbons plasma polymerization follows after acetylene compound was formed. Also, acetylene undergoes polymerization process instantaneously, especially at low flow rate. First experiments performed with nitrogen as a carrier gas have been stimulated by the growing interest in carbon nitride materials especially in the field of thin film deposition.

Independent of the actual choice of the carrier gas it is a well known fact that the presence of particles is strongly influencing the properties of discharges [9]. This response of the plasma to the formation of particles has been analyzed in the present paper by measuring the fluxes of ions escaping from the discharge.

2. Experimental set up

The investigations were performed in a radio-frequency (RF) capacitively-coupled parallel plate reactor working at 13.56 MHz (Fig.1). The power is coupled symmetrically to both electrodes, which have a diameter of 30 cm and are separated by 8 cm. The gas flow rates are controlled and monitored by MKS mass-flow controllers. The typical flow rates are 8 sccm argon and 0.5 sccm acetylene resulting in a pressure of about 0.1 mbar. The applied RF power was 10-20 W measured before the match-box.

For diagnostic purposes we have used in this experiment a FTIR-spectrometer. The infrared (IR) absorption spectroscopy was performed in situ using a commercial Bruker FTIR (Fourier Transformed Infrared) apparatus Equinox 55. The IR beam from the spectrometer was directed through KBr windows in the plasma chamber and was focused with an off-axis gold mirror onto a liquid-nitrogen-cooled mercury-cadmium-telluride detector (MCT). By means of a multi-pass technique we were able to change the optical path length in the plasma from 0.6 meters (2 passes through plasma reactor) to 7.2 meters (24 passes) accordingly increasing the sensitivity of our system. Absorption spectra in the range 500-6500 cm^{-1} were recorded with a spectral resolution 0.5 to 3 cm^{-1}. The spectral resolution of 3 cm^{-1} was used to increase the recording speed. A plasma monitor (PPM 422, Balzers) was mounted at a side port of the reaction chamber in order to measure ion fluxes escaping from the plasma bulk. A bellows assembly allowed us to vary the distance between the sampling orifice (100 microns diameter) of the plasma monitor and the edge of the electrodes. For the measurements presented here the orifice was placed 5 cm outside the electrodes (outside the bulk of the plasma) on the mid-plane between the electrodes.

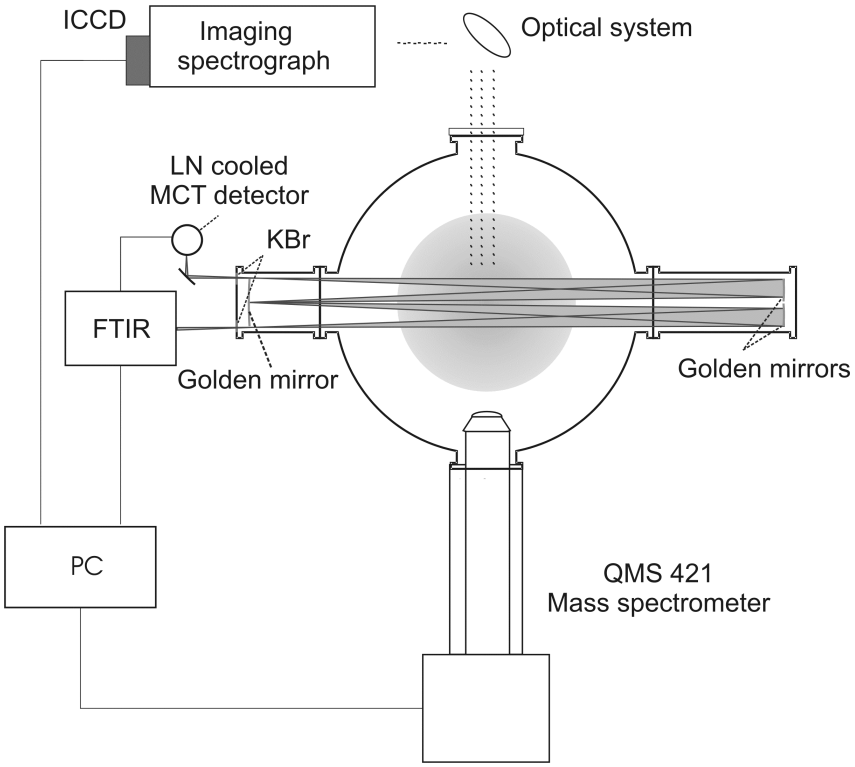

Fig. 1: Experimental set up

3. Experimental results

In this section we will present two different kinds of experimental results. In the first subsection we will focus on the in-situ-FTIR-spectroscopy, which delivers information about the temporal development of the dust formation and about the chemical nature of the dust particles formed in the discharge. In the second subsection we will discuss the response of the plasma to the formation of these particles. Here we focussed mainly on the measurement of the ion fluxes escaping from the discharge.

3.1 In-situ investigation of particle formation by means of FTIR spectroscopy

Fig. 2a shows the absorption spectrum of dust particles measured in an argon/acetylene mixture. The most striking feature of this spectrum is the strong increase of the absorbance towards higher wavenumbers. This effect is caused by Rayleigh or Mie scattering respectively and is a direct indication for the presence of dust particles in the reaction chamber. Beside this effect the spectrum exhibits several absorption peaks, which are not present in the spectrum of pure acetylene. The complicated signature of this spectrum becomes more obvious after a baseline correction. Although a unique identification of the whole spectrum is difficult to perform, some characteristic peaks can be attributed to specific, most abundant, compounds (Fig.2b).
As the formation of nanoparticles is a dynamical process the shape of the recorded FTIR spectra is strongly time dependent. An overview over the temporal development of the dust formation is given in fig.3 a and b. This figures shows the absorbance at different wavenumbers as a function of time. Depending on the

wavelength the absorbance exhibits either a damped (fig. 3a) or an undamped (fig 3b) oscillating behavior. The undamped periodic behavior can be explained in the frame of a simple model. Negatively charged particles are confined in the plasma potential as long as the different forces acting on the single particle are balanced. Since theses forces – as the electric the force, the ion drag force, the neutral drag force, the force caused by thermophoresis and the gravitational force scale with different powers of the particle radius the confinement of the particles strongly depends on their size. As soon as the particles reach a critical size they are dragged out of the plasma bulk and a new growth cycle starts. The damped oscillations observed for the absorbances at 1700 $cm^{-1}$and 3300 cm^{-1} are probably an effect induced by impurities as oxygen or water. The peak at 1700 cm^{-1} can be attributed to carbonyl C=O stretching vibrations, which results from the oxidation of carbon caused either by water or oxygen.The absorption band around 3300 cm^{-1}, which is also decreasing in time, is most likely an indication for the presence of trapped water/ OH stretching vibrations [10,11]. The temporal decrease of these peaks can be explained, if we assume, that the concentration of residual water or oxygen molecules is also decreasing in time which is indeed confirmed by mass spectrometric measurements [9]. A possible mechanism, which could enhance the removal of water is: Oxygen containing contaminations are released from the surface of electrodes and walls during their exposure to the plasma. Once these impurities arrive at the bulk plasma they can chemically react with the dust particles. In this way the dust grains itself serve as a kind of a "getter" for water molecules that are released from the chamber walls. Consequently the concentration of oxygen/water is decreasing from cycle to cycle.

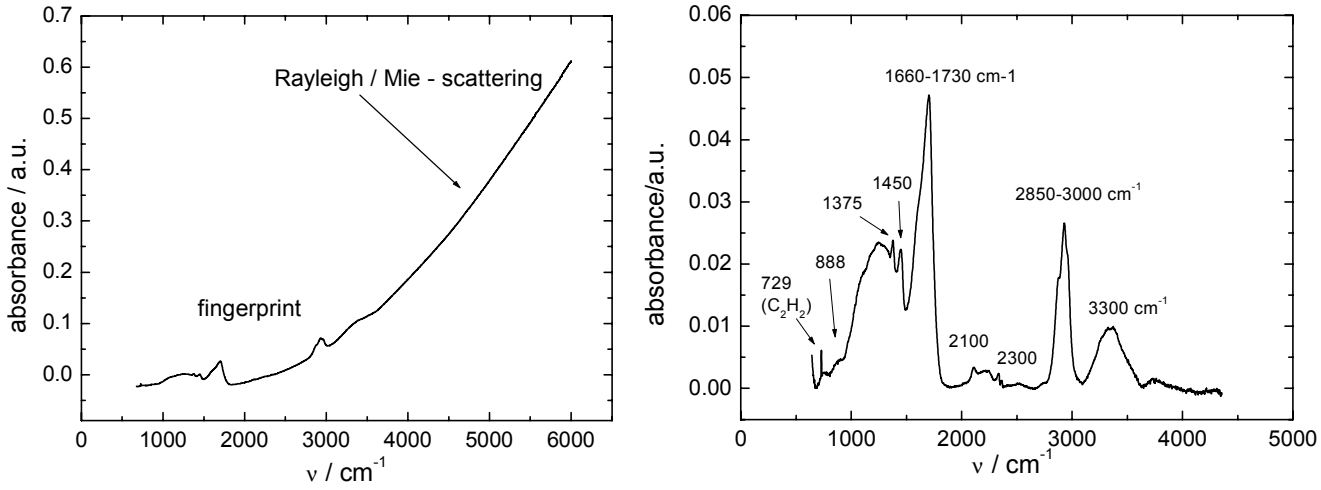

Fig. 2 a,b: Figure a shows a FTIR-spectrum measured in an argon/acetylene mixture 35 minutes after the discharge was switched on. Figure b shows the same spectrum after a baseline correction, which allows the identification of the most important absorption structures: 1375±5 cm^{-1}:CH_3 symmetric bending; 1450±20 cm^{-1}: CH_3 asymmetric bending ; 2850 – 3000 cm^{-1}: -CH_3 symmetric stretching at 2870 cm-1, antisymmetric at 2960 cm^{-1} and antisymmetric -CH_2 stretching at 2926 cm^{-1}. 1604 cm^{-1} (appearing as a shoulder within the broad peak between 1660 and 1730 cm^{-1}): aromatic C=C stretching vibrations. (The presence of aromatic compounds is confirmed by weaker peaks around 888 cm^{-1} which originate from C-H deformation vibrations of aromatic hydrocarbons [11, 12].) The strong peak between 1660 and 1730 cm^{-1} comes from carbonyl C=O stretching vibrations [9, 10, 11, 12].

Due to this effect the shape of the FTIR spectrum is changing from period to period. In the first cycle the dominating peak is that at 1700 cm^{-1}. In the next cycles the height of this peak is continuously decreasing until it is much smaller than the height of the peak at 2900 cm^{-1}. The fingerprint of the spectrum is thus changing although the absorbance at higher wavenumbers, which results from Rayleigh/Mie-scattering, is the same. This clearly demonstrates the advantages of the in-situ broadband FTIR-diagnostic. Simple scattering or absorption techniques using monochromatic laser light are not suitable for the detection of changes in the chemical composition of the particles.

A comparison between nanoparticles polymerized in an argon/acetylene discharge and particles polymerized in a mixture of nitrogen and acetylene is shown in figure 4. The infrared spectrum of the particles from the

nitrogen/acetylene discharge exhibits a strong broad absorption peak centered at about 1625 cm^{-1}. According to Gonzalez et al.[13] this peak could be attributed to N–sp^2 C vibrations which would indicate the presence of nitrogen atoms within the dust particles. The presence of C≡N bonds is indicated by the peak centered at about 2200 cm^{-1}. Although a unique identification of the whole spectrum is a difficult and somewhat tentative task a comparison of our spectra with spectra from amorphous CN_x-films shows great similarities [14,15,16]. This supports the assumption that nitrogen atoms are incorporated into the particles. Further investigations of these carbon nitride nanoparticles will include Micro-Raman and TEM measurements.

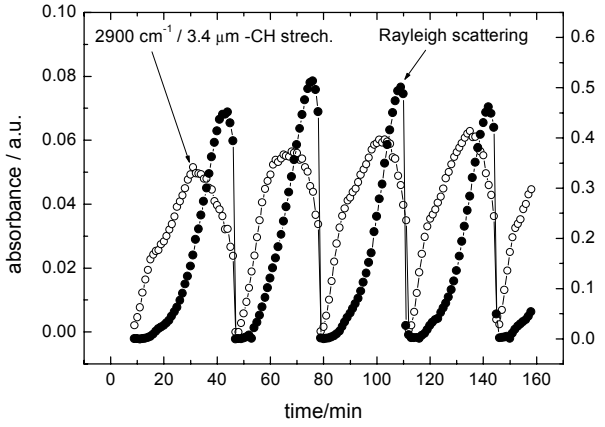

Fig.3a: Absorbance at 5000 cm^{-1} and 2900 cm^{-1} as a function of time.

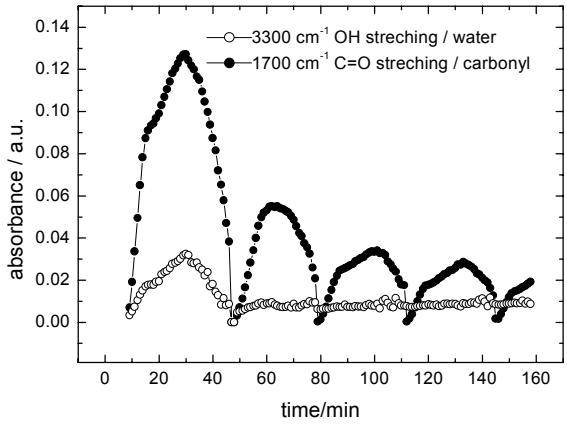

Fig.3b: Absorbance at 1700 cm^{-1} and 3300 cm^{-1} as a function of time.

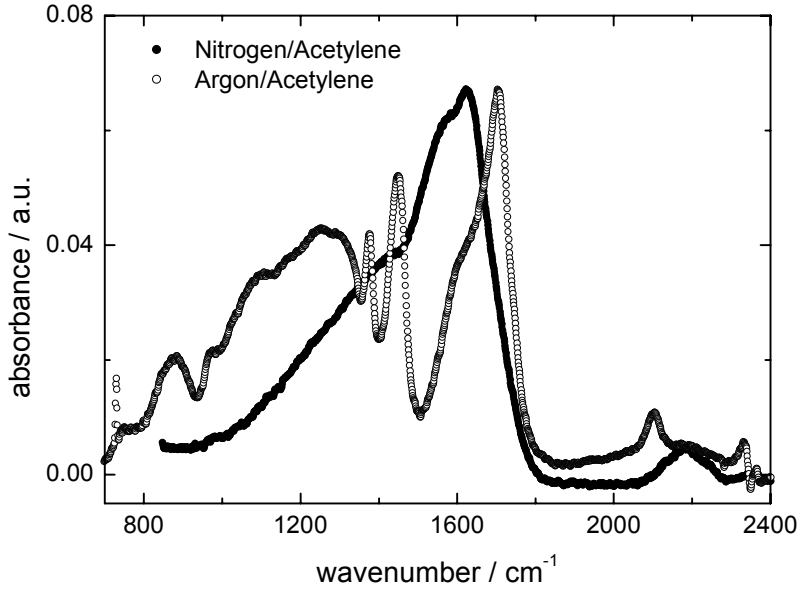

Fig. 4 Comparison between FTIR spectra polymerized in argon/acetylene and argon/nitrogen discharges.

3.2 The response of the plasma to the formation of particles

Independent of the actual choice of the carrier gas or the chemical composition of the dust particles the presence of such particles is strongly influencing discharge properties such as electron temperature, electron density, plasma composition or plasma impedance. In this paper we will mainly focus on the question how do the dust particles influence the fluxes of ions escaping from the bulk plasma. For this purpose a plasma monitor (Balzers PPM 422) was mounted at a side port of the reaction chamber. For the measurements presented here the orifice of the plasma monitor was placed 5 cm outside the electrodes (i.e. outside the plasma bulk) on the mid-plane between the electrodes. The time resolution for these measurements was 25 seconds.

Energy scans of argon ions for four different times are shown in figure 5. These times correspond to the positions also marked in figure 7 (number 1 for 33 minutes , 2 for 42 minutes, 3 for 43 minutes, and 4 for 48 minutes after the discharge ignition). The results show that the signal height as well as the position of the maximum of the distribution function is changing in time.

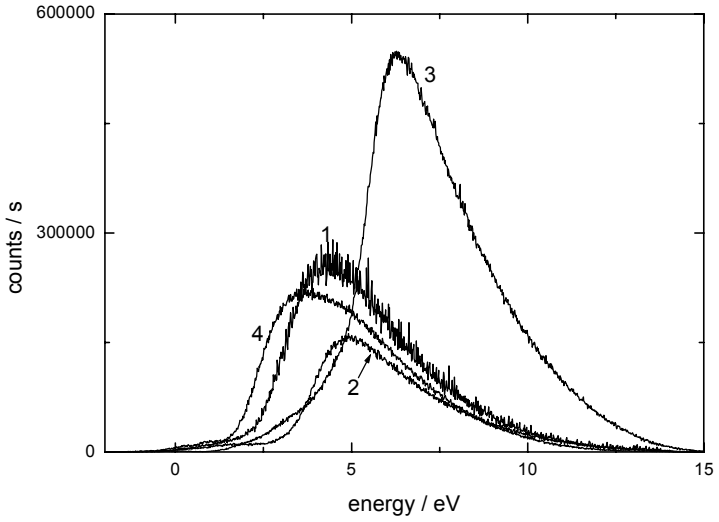

Fig. 5 : Ion energy distribution functions. The different curves correspond to different times.

The total flux of argon ions in arbitrary units, obtained by summing the count rates over the whole energy range, is shown in figure 6. The ion fluxes escaping from the bulk plasma exhibits a periodical behavior that corresponds to the periodical behavior of the dust formation observed in the FTIR measurements. The corresponding mean energy is depicted in figure 7.

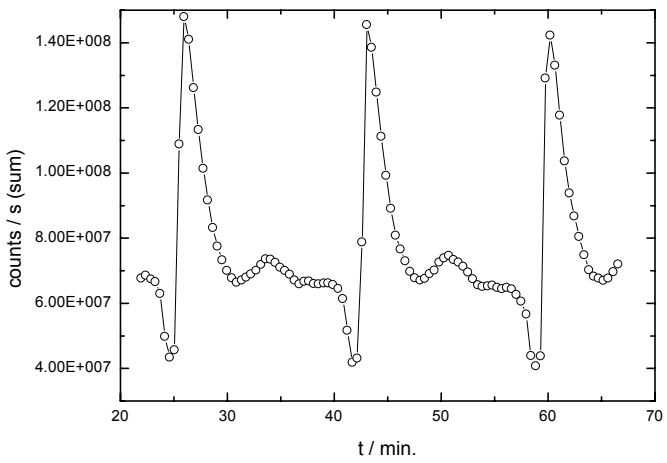

Fig. 6: Total argon ion fluxes escaping from the plasma bulk as a function of time (in arbitrary units).

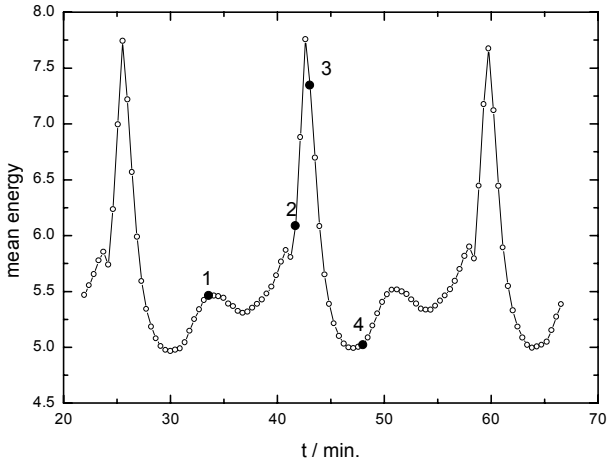

Fig 7: Mean energy of argon ions escaping from the plasma bulk as a function of time.

Both pictures exhibit complicated structures which are far from being fully understood. FTIR-measurements performed simultaneously with the plasma monitor measurements show that the period length observed in the infrared signal is the same as that observed for the signal of the ion fluxes. This fact at least proves that the complicated temporal behavior of the ion fluxes is strongly correlated to the formation of dust particles. To what extend the structures visible in figures 6 and 7 correspond to some stages in the particle formation (e.g. nucleation, agglomeration etc.) is not yet fully clear [9].

4. Conclusion and outlook

In-situ FTIR-spectroscopy in combination with a multipass arrangement was proved to be a powerful tool for the diagnostic of plasma-synthesized nanoparticles. The temporal development of the dust formation as well as the chemical composition of the dust particles can be analyzed. The latter feature is especially useful for the generation of particles in different gas mixtures. First experiments performed in acetylene/nitrogen discharges showed the existence of carbon nitride particles formed spontaneously in the plasma. Further analysis using Micro-Raman-Spectroscopy and Transmission-Electron-Microscopy has to be done to get a better insight in chemical structure and morphology of these particles.

The response of the plasma to the formation of the particles has been analyzed by measuring the energy distribution function of argon ions escaping from the plasma bulk. The measurements show a strong correlation between the ion energy distribution function and the formation of dust particles. To what extend the ion fluxes are correlated to different stages of the particle growth has to be clarified in further studies.

Literature

[1] Langmuir I, Found G and Dittmer A F, Science NewYork, **60,** 392 (1924)
[2] Semiconductor Inductry Association, National Technology Roadmap for Semiconductors (NTRS), 1997
[3] D. M. Tanenbaum, A. L. Laracuente, and A. Gallagher, Appl. Phys. Lett. **68**, 1705 (1996)
[4] H. Kobayashi, A.T. Bell, and M. Shen, *Macromolecules*, **7**, No.3,(1974), 277.
[5] J.M. Tibbitt, R. Jensen, A.T. Bell, and M. Shen, *Macromolecules*, **10**, No.3, (1977), 647.
[6] Ch. Deschaneux, A. Affolter, D. Magni, Ch. Hollenstein, and P. Fayet, *J.Phys. D: Appl.Phys.* **32** (1999), 1876.
[7] S. Stoykov, C. Eggs, and U. Kortshagen, *J.Phys. D: Appl.Phys.* **34** (2001), 2160
[8] S.H. Hong, J. Berndt, J. Winter, Plasma Sources Sci.Technol. **12** (2003) 46
[9] E. Kovačević, I. Stefanović, J. Berndt and J. Winter, *J. Appl. Phys.* **93** (2004), 2924
[10] Y.J.Pendleton and L.J. Allamandola, *The Astrophysical Journal Supplement Series*, 138,(2002), 75.
[11] H. Grünzler, H.M. Heise, "IR-Spektroskopie", VCH, Weinheim (1996)
[12] M.A. Elyshevich "Atomnay i molekulyrnay spektroskopiy",Editorial USSR, Moskau, 2000
[13] P. Gonzalez, R. Soto, E. G. Parada, X. Redondas, S. Chiussi, J. Serra, J. Pou, B. Leon, and M. Perez-Amor, Appl. Surf. Sci. **109/110**,380~1997.
[14] Jin Yong Kim, Hun Jae Chung, Hyeong Joon Kim, Hyun Min Cho, Hyung Kook Yang, and Jong Chul Park J.Vac.Sci.Technol.A,Vol.18, No4 (2000)
[15] I. H. Shin and T. D. Lee J.Vac.Sci.Technol. B 18 (2) (2000)
[16]Yoshifumi Aoi, Kojiro Ono and Eiji Kamijo , J. Appl. Phys. 86, 4

Acknolowgedment

This work is partially supported by BMBF (FKZ: 13N8049) and by SFB 591 Teilprojekt B1 and B5. The support in plasma ion mass spectroscopy by Dr. G. Peter from Inficon is gratefully acknowledged.

The Plasma Destruction of Odorous Molecules: Organosulphur Compounds

Imtiaz K. Ahmad*, Anna E. Wallis and J. Christopher Whitehead

Department of Chemistry, University of Manchester, Oxford Road, Manchester, M13 9PL, UK

Abstract

The plasma destruction of methyl mercaptan and dimethyl sulphide has been studied in nitrogen or air gas streams by a non-thermal, atmospheric pressure discharge using a packed bed of $BaTiO_3$ beads. Destructions in excess of 85% can be achieved for pollutant concentrations of 30 -100 ppm with energy costs in the order of 75 – 200 kW h / kg. The end-products of the processing are H_2S, HCN, NH_3 in a N_2 stream and SO_2, CH_2O, CO and CO_2 in air. The implications for odour control are discussed

1. Introduction

Non-thermal, atmospheric pressure plasma technology has considerable advantages to offer in the field of odour control over the existing technologies of catalytic oxidation and of chemisorption on substances such as activated charcoal. Olfactory detection thresholds for methyl mercaptan and dimethyl sulphide are approximately 0.002 ppm and 0.001 ppm respectively, much more odorous than other sulphides such as CS_2 (0.121 ppm), SO_2 (0.47 ppm) and H_2S (0.005 ppm) [1]. It is well known that plasma destruction becomes significantly more efficient as the concentration of the pollutant decreases making plasma destruction a potentially effective remediation technique for odours.

We have studied the destruction of methyl mercaptan (CH_3SH) and dimethyl sulphide ($(CH_3)_2S$) diluted in gas streams of both nitrogen and air using an AC, packed-bed plasma reactor loaded with $BaTiO_3$ beads. The principal products obtained from the plasma processing are identified using FTIR spectroscopy and chemical mechanisms are proposed for the destruction processes. The only previous plasma studies of the destruction of these compounds of which we are aware all relate to experiments at reduced pressures using RF plasmas. Nicholas *et al*.[2] studied the decomposition of both dimethyl sulphide and methyl mercaptan using a pulsed RF source in the pressure range 0.1 – 2 Torr. Tsai et al. [1] have examined the decomposition of methyl mercaptan in a non-thermal RF plasma at 30 Torr. Czernichowski [3] has review the field of plasma destruction of mercaptans concentrating on the technique of gliding arcs. To our knowledge, this paper is the first reported study of the plasma destruction of dimethyl sulphide and methyl mercaptan at atmospheric pressure using a non-thermal plasma.

2. Experimental

The experimental arrangement was essentially that employed previously [4,5]. The plasma source was a dielectric pellet-bed reactor consisting of a glass tube of 24 mm internal diameter with two electrodes ~25 mm apart through which the gas passes. The space between the electrodes was packed with 3.5 mm diameter barium titanate beads. The diameter of the beads was chosen to allow for as large a number of beads as possible (~ 315), thereby maximising the number of contact points for the formation of discharges whilst not restricting the porosity of the reactor significantly. This balances the requirements of gas flow and having as uniform a discharge as possible. An AC voltage ($V_{pk\text{-}pk} \approx 15$ kV) at a frequency between 10.25 and 13.25 kHz was applied between the electrodes. Using a digital storage oscilloscope (Tektronix TDS 3012), we recorded the current and voltage waveforms for the discharge by using a calibrated high voltage probe and measuring the current across a 1 kΩ resistor in the return earth path from the reactor. The average power of the discharge is then obtained by integrating the product of voltage and current as a function of time.

* Present Address: Department of Forensic Science and Chemistry, School of Applied Sciences, Anglia Polytechnic University, East Road, Cambridge CB1 1PT

A flow (0.1 - 1 litre min^{-1}) of pure air or nitrogen at room temperature controlled by flow controllers (MKS Mass Flo) was either blended with a small flow of gaseous methyl mercaptan or bubbled through liquid dimethyl sulphide at room temperature giving a concentration of ~ 30 – 140 ppm of methyl mercaptan or ~ 25 – 50 ppm of $(CH_3)_2S$ entering the plasma reactor. The gas mixture was maintained at a pressure of ~ 1 bar. For a gas flow of 1 litre min^{-1}, the residence time in the reactor is 0.25 s. Methyl mercaptan (Aldrich, 99.5+ % purity) and dimethyl sulphide (Fluka, ≥ 99% purity) were used as supplied. No attempt was made to further purify or dry the gases. The end-products of the plasma processing were monitored on-line by infrared spectroscopy using a long-path gas cell (4.8 m, Venus Series) and a Fourier Transform Infrared (FTIR) spectrometer (Shimadzu 8300) with a resolution of 1 cm^{-1}. Stainless steel, nylon and PTFE tubing, valves and fittings of 1/4" external diameter were used to handle the gases as appropriate. No attempt was made to bake or otherwise condition the surfaces of the system.

3. Results

Figure 1 shows a comparison of the FTIR spectrum obtained for dimethyl sulphide without plasma processing and with plasma processing in nitrogen and air. The degree of destruction for dimethyl sulphide (at initial concentrations of ~ 30 ppm) in pure nitrogen was measured as ~ 35% and the major end-products as detected by FTIR spectroscopy were found to be HCN and NH_3. No sulphur-containing end-products could be detected using infrared spectroscopy where our minimum detection limits for the likely end-product H_2S represents a concentration of ~ 1000 ppm. Using a qualitative analysis method (Draeger tube sampling), we can confirm the presence of H_2S in the processed gas stream and it is most likely that all the sulphur is converted into H_2S although alternative detection methods must be employed to confirm and quantify this. Correspondingly higher degrees of dissociation (up to 72%) were obtained when 30 ppm of dimethyl sulphide was passed through the plasma reactor in a gas stream of air. In this case, the major end-products of the destruction of dimethyl sulphide as detected by FTIR were CO, CH_2O, SO_2 and a trace amount of CO_2. The carbon balance indicates that 50% of the destroyed carbon becomes CO, 45% CH_2O and

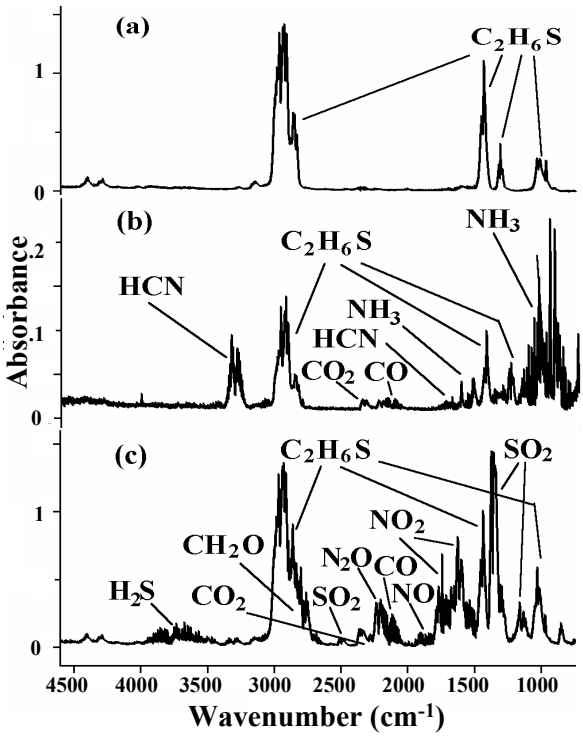

Figure 1 Plasma processing of dimethyl sulphide. (a) plasma off; (b) in nitrogen; (c) in air.

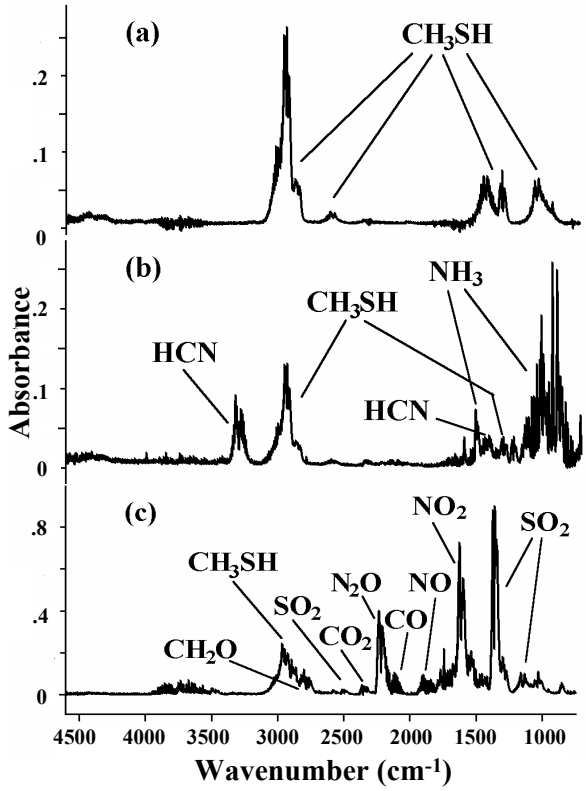

Figure 2 Plasma processing of methyl mercaptan. (a) plasma off; (b) in nitrogen; (c) in air.

balance becomes H_2S but this needs to be confirmed. Significant amounts (~ 200 ppm) of nitrogen oxides (NO, N_2O and NO_2) were also produced under these conditions, mainly N_2O and NO_2.

Figure 2 shows the corresponding spectra for the plasma processing of methyl mercaptan in both air and nitrogen. The degree of destruction for methyl mercaptan in pure nitrogen was measured as ~ 15% for an initial concentration of ~ 390 ppm and as ~ 20% at a concentration of 550 ppm in air. As with dimethyl sulphide, the major products of the plasma processing in a stream of pure nitrogen were HCN and NH_3. Qualitative sampling again indicates the production of H_2S. In the presence of air, the major detected, carbon-containing, end-product are CO (55%), CH_2O (35%) and a small amount of CO_2 (10%). The production of SO_2 accounts for ~ 30% of the sulphur removed. Again, there is significant formation of the oxides of nitrogen for processing in an air stream with ~ 170 ppm of NO, NO_2 and N_2O being formed with 50% being in the form of NO_2.

In addition to the compounds detected by FTIR as end-products of the plasma processing, we were able to eliminate the formation of any of the following compounds within our detection limits: ozone, hydrogen peroxide, acetaldehyde, any C_2 or higher hydrocarbons, OCS and CS_2.

The degree of destruction for dimethyl sulphide in air as a function of the concentration of dimethyl sulphide is shown in Figure 3. It can be seen that the destruction rises rapidly as the concentration decreases implying that essentially complete destruction will be achieved at the sub-ppm levels where odour levels are a concern. Limited studies were performed for the destruction of ~ 100 ppm of dimethyl sulphide in nitrogen where the flow rate was reduced from 1 litre min^{-1} to 0.1 litre min^{-1} causing the percentage destruction to increase from 6% to 86% as a result of the ten-fold increase in plasma residence time.

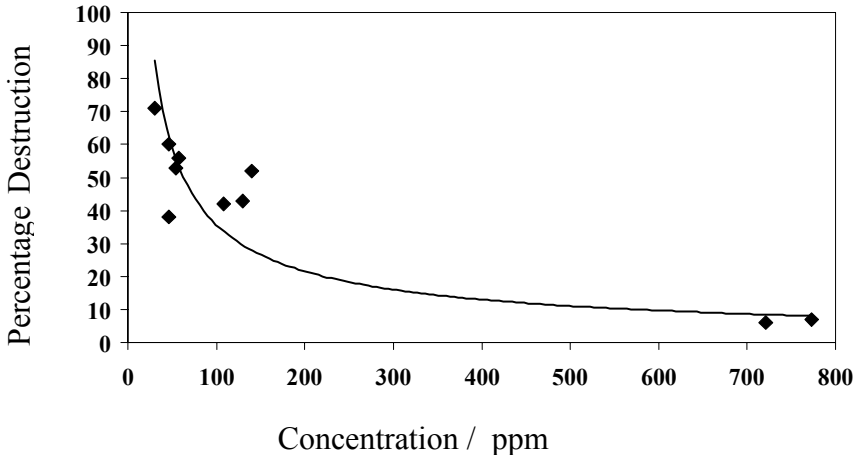

Figure 3 The percentage destruction of dimethyl sulphide in air as a function of concentration for an atmospheric pressure, non-thermal plasma discharge at a flow rate of 1 litre min^{-1}. The solid curve is to aid the eye.

The average electrical power deposited into the plasma is ~ 0.98 W, giving a reduced energy of 59 J / litre for a flow of 1 litre min^{-1}. These figures can be translated into the minimum energy required to destroy a single molecule which becomes 175 eV and 455 eV for dimethyl sulphide in air and nitrogen, respectively, and 140 and 255 eV for methyl mercaptan in air and nitrogen, respectively. For the destruction of dimethyl sulphide in nitrogen at a flow rate of 0.1 litre min^{-1}, this reduces to 175 eV per molecule destroyed.

4. Discussion

Products

We can compare the products that we find with the results from previous studies. The study of Nicholas *et al.* [2] concentrated on a spectroscopic investigation of the intermediates involved in the decomposition together with mass spectrometric and GLC analysis of the stable end-products. For methyl mercaptan, they found CS, SH and S_2 were formed as transient species and that the end-products were CS_2, CH_4, various C_2 hydrocarbons and some possible sulphur-containing hydrocarbons. The results for dimethyl sulphur showed CS and S_2 as transient species but no SH and a similar range of end-products. Tsai et al. [1] studied the destruction of methyl mercaptan in an Ar gas stream with and without the addition of molecular oxygen. In the absence of oxygen, the products that they observed included CS_2, H_2S, $(CH_3)_2S$, $(CH_3)_2S_2$, CH_4, C_2H_4 and C_2H_2. For an oxygen rich CH_3SH / O_2/ Ar mixture, the major products were found to be SO_2, CO_2, CO and H_2O which is in close agreement with our findings except that we also detect formaldehyde, CH_2O. However, in none of our systems do we detect CS_2 as an end-product even though we have a sensitivity of 3 ppm for its detection.

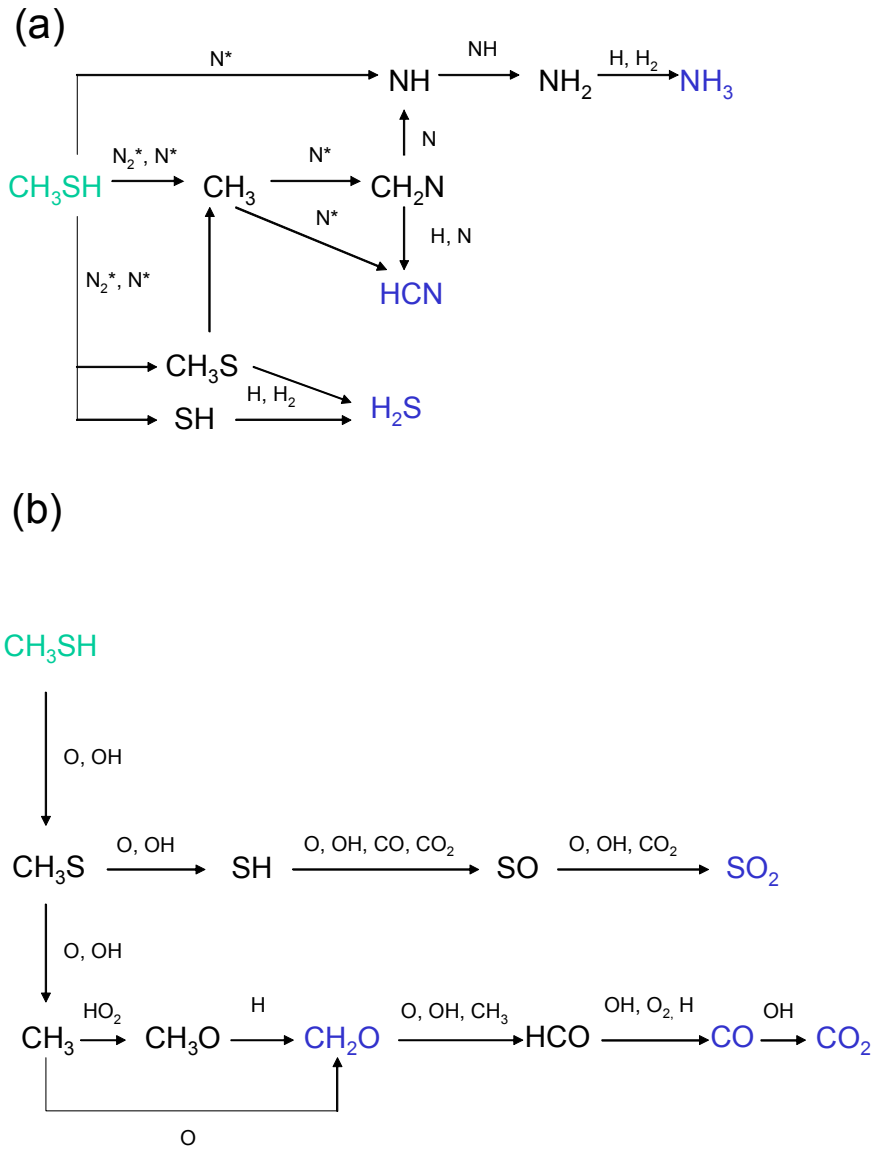

Figure 4 Schematic mechanisms for the plasma destruction of methyl mercaptan in (a) nitrogen and (b) air.

It is difficult to extrapolate from chemical mechanisms appropriate at low pressure to those at atmospheric pressure where three-body recombination processes become more important and the concentration of peroxy radicals, RO_2, becomes significant. Figure 4 shows our suggestion for the mechanism by which methyl mercaptan is destroyed in an atmospheric pressure, non-thermal plasma. This mechanism is based on our experience with modelling the plasma destruction of methane [6] and dichloromethane [5].

For both dimethyl sulphide and methyl mercaptan, the main products in pure nitrogen are HCN and NH_3 whilst in the presence of oxygen these products are not formed and CH_2O, CO and CO_2 are the oxidation end-products. In pure nitrogen the important species created in the discharge are electronically-excited nitrogen atoms, $N(^2D)$, and metastable triplet molecular nitrogen, N_2 ($A^3\Sigma_u^+$). Reaction of $N(^2D)$ with CH_3SH can give CH_3S and NH. Collision-induced dissociation of CH_3SH by $N_2(A^3\Sigma_u^+)$ is likely to break the weaker bonds to give CH_3 and SH and to a lesser extent CH_3S and H. These two processes require energies of 3.17 and 3.73 eV, respectively, considerably less than the 6.23 eV possessed by the metastable $N_2(A^3\Sigma_u^+)$. CH_3S and SH are then the precursors of H_2S, our presumed sulphur-containing end product, and CH_3 and NH provide the route (Figure 4a) to ammonia and HCN as we observed for methane and dichloromethane.

In the presence of oxygen, we observe a change in the mechanism and there is no further production of HCN and NH_3. This arises because the excited state nitrogen atoms now react with molecular oxygen to form NO which is further oxidised to NO_2

$$N^*(^2D) + O_2 \rightarrow NO + O \qquad (6)$$

The metastable *A* state of nitrogen also reacts much more rapidly with molecular oxygen than with methyl mercaptan because of the much larger concentration of O_2. The chemistry involving the nitrogen species formed in the discharge is the source of the NOx that is produced in the air discharges and is largely decoupled from the oxidative chemistry responsible for the destruction of the methyl mercaptan.

The major reactive species in the air discharges that is responsible for the destruction of CH_3S is atomic oxygen. This initially reacts with the mercaptan by abstraction of a hydrogen atom generating CH_3S which is the source of the sulphur-containing end products and OH radicals which being more reactive than O atoms rapidly take over the oxidation process and are regenerated. Oxidation of CH_3S to methyl radicals, CH_3, allows the well established pathways that yield CO_2 and CO *via* CH_2O to proceed (Figure 4b). Complete oxidation to CO_2 is not achieved under our conditions. It is possible that some of the SH formed in the oxidation of CH_3S may also yield H_2S which we speculate may be present as a sulphur-containing end-product. However, this requires additional experimental validation.

We are less certain about the chemistry involved in the decomposition of dimethyl sulphide because of a paucity of electron impact and reaction kinetic data for the sulphur containing species involved. The production of NH_3 and HCN in pure nitrogen suggests a mechanism that involves methyl and NH radicals as in Figure 4a. Methyl radicals can be formed by collisional energy transfer from metastable nitrogen, $N_2(A^3\Sigma_u^+)$, formed in the discharge through a range of dissociation channels

$$N_2(A^3\Sigma_u^+) + C_2H_6S \rightarrow C_2H_6S^* + N_2(X^1\Sigma_g^+)$$

$$C_2H_6S^* \rightarrow CH_3 + CH_3S$$

$$\rightarrow 2CH_3 + S$$

$$\rightarrow CH_3 + CS + H + H_2$$

NH radical chemistry can be initiated by abstraction of a hydrogen atom from dimethyl sulphide by $N^*(^2D)$ in an analogous manner to the reactions outlined in Figure 4a. As with methyl mercaptan, in the presence of air, NOx will be formed by the reaction of $N(^2D)$ with O_2. The reactions of O atoms, and subsequently OH radicals, with dimethyl sulphide will produce simple hydrocarbon and sulphur-containing radicals. Hynes *et al.* [7] have shown that the reaction of OH with dimethyl sulphide gives CH_3S and CH_2O under atmospheric conditions. The hydrocarbon radicals will then be oxidised to give CO, CO_2 and CH_2O in the usual manner.

The sulphur-containing end-products will be determined largely by the subsequent reactions of the free sulphur and sulphur-containing radicals formed in the initial decomposition steps. In the pure nitrogen gas flow, we conjecture that the likely end-product is H_2S which will be formed by reaction of the sulphur species with the hydrogen as in Figure 4a. With the oxygen component of the air discharge, the sulphur radicals will be oxidised to SO_2 *via* SO in reactions with O, O_2 and OH.

Energy Costs

We can compare the energy costs of the destruction of methyl mercaptan and dimethyl sulphide in our non-thermal, atmospheric pressure plasma with the work of others. Tsai *et al.* [1] find values between 30 and 90 kW h / kg for the destruction of dimethyl sulphide in a RF plasma and Czernichowski [3] quotes values between 10 and 1000 kW h /kg for the gliding arc plasma destruction of H_2S under differing conditions stating that similar energies were required for methyl mercaptan / air mixtures. In our experiments, we find comparable values of 80 – 140 kW h / kg for methyl mercaptan and 75 – 195 kW h / kg for dimethyl sulphide depending on the carrier gas and the experimental conditions.

5. Conclusions

We have demonstrated that non-thermal, atmospheric pressure plasma can be used to destroy methyl mercaptan and dimethyl sulphide in an energy efficient manner. The products are H_2S, HCN and NH_3 in an inert nitrogen gas stream and SO_2, CH_2O, CO and CO_2 in an air stream. Both of these destruction routes offer the potential for recovery of the sulphur by scrubbing of the processed gas stream. In terms of odour control, we have shown that the destruction efficiencies for these compounds at the sub ppm level where odour becomes noticeable will be complete with conversion into SO_2 or H_2S which are less odourous.

Acknowledgement Support of this work by the UK Engineering and Physical Sciences Research Council is gratefully acknowledged.

References

[1] C.-H. Tsai, W.-J. Lee, C.-Y. Chen, W.-T. Liao, Ind. Eng, Chem. Res. **40** 2384 (2001).
[2] J.E. Nicholas, C.A. Amodio, M.J. Baker, J. Chem. Soc. Far. Trans. 1 **75** 1868 (1979).
[3] A. Czernichowski, Oil & Gas Sci. Tech. **54** 337 (1999).
[4] C. Fitzsimmons, J.T. Shawcross, J.C. Whitehead, J. Phys. D: Appl. Phys. **32** 1136 (1999).
[5] C. Fitzsimmons, F. Ismail, J.C. Whitehead, J.J. Wilman, J. Phys. Chem. A. **104** 6032 (2000).
[6] K.J. Pringle, J.C. Whitehead, J.J. Wilman, J. Wu, to be submitted
[7] A.J. Hynes, P.H. Wine, D.H. Semmes, J. Phys. Chem. A. **90** 4148 (1986).

Large–Area Surface Wave Excited N_2-Ar Overdense Plasma

E. Tatarova, F.M. Dias, J. Henriques and C.M. Ferreira
Instituto Superior Tecnico, Centro de Fisica dos Plasmas, 1049-001 Lisboa Codex

Abstract
A large-scale, slot-antenna excited surface wave plasma source operating in N_2-Ar mixtures is investigated. Surface waves propagating radially and axially along the interface between the plasma and a dielectric plate are the energy source for the plasma. The overdense plasma, close to the wave energy source, sustained by a pure TM_{33} surface mode, is analyzed. Maxwell's equations and the rate balance equations for the most important excited species – vibrationally and electronically excited states, ions and nitrogen atoms N(^{4}S) - are consistently solved and the species spatial distributions are calculated and analyzed, in correlation with the total electric field spatial variation.

1. Introduction

Microwave plasma sources based on surface wave propagation without applied magnetic field are of interest for forthcoming large-scale plasma processing technologies. Recent microwave discharge experiments [1] revealed that a slot antenna is a simple and useful launcher of microwaves to obtain large volume stable plasma.

In the present work, a slot antenna excited large area surface wave plasma source operating in N_2-Ar mixtures is investigated. Surface waves propagating radially and azimuthally along the interface between the plasma and a dielectric plate located at the top wall of a large diameter cylindrical metal camera are the energy source of the plasma (see Fig. 1). The waves form a resonant eigenmode satisfying the boundary conditions and the plasma takes discrete density values which ensure that the resonant eigenmodes exactly appear at the excitation frequency (2.45 GHz). A discrete pure TM_{33} surface mode excitation is considered. The energy of the propagating surface waves close to the interface sustains an overdense plasma. As the distance from the interface increases the wave electric field exponentially decreases and vanishes at some critical distance z_{cr}. Consequently, due to the diffusion an afterglow (electric field free) plasma appears at $z > z_{cr}$.

A theoretical model for the source discharge is developed. The plasma density at which a given mode appears and the electric field 3D (r-φ-z) pattern are calculated from the Maxwell´s equations and the wave dispersion equation in complex algebra. The electrodynamical part of the analysis is coupled to the particle kinetics through the value of the electron density at which a given mode appears. The rate coefficients for electron impact processes are obtained by solving the electron Boltzmann equation. By taking into account the principal collisional and radiative processes which determine the populations in the $N_2(A^3\Sigma_u^+, B^3\Pi_g, C^3\Pi_u, a'^1\Sigma_u^-, a^1\Pi_g, w'\Delta u)$, $N_2(X^1\Sigma_g^+, v)$, and Ar($3p^5 4s$), Ar($3p^5 4p$) excited levels of molecules and atoms and the concentration of positive ($N_2^+, N_4^+, Ar^+, Ar_2^+$) ions and ground state N(^{4}S) atoms, the rate balance equations are solved and the 3D (r-φ-z) distribution of the species is obtained.

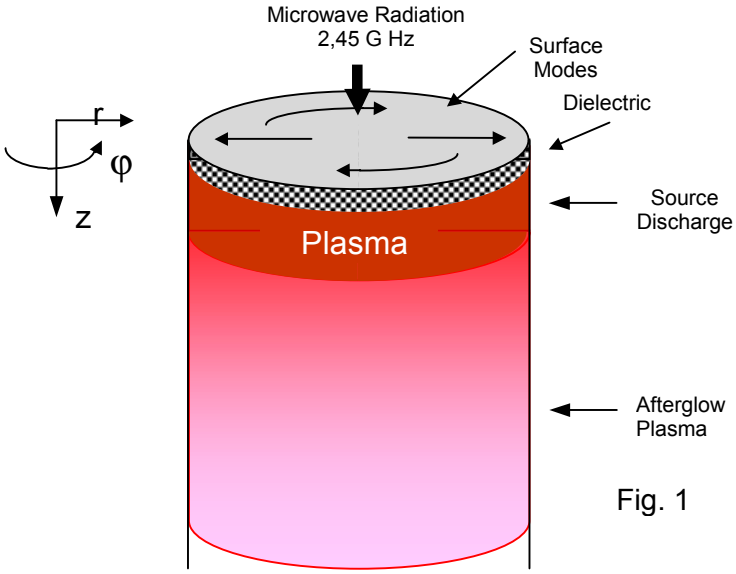

Fig. 1

2. Theoretical model.

The system under analysis is a vertical wave-guide of arbitrary cross-section (radius R) short-circuited at the top by a metal wall (Fig. 1). A dielectric plate of thickness d and permittivitty ε_d completely fills the upper region of the wave-guide. The discharge plasma (where the surface wave propagates) underneath is supposed to be homogeneous with electron density N_e. Such a structure can support transverse magnetic TM and transverse electric TE modes. Here, "pure" TM surface modes, i.e, evanescent waves along z, are considered. Weakly damped free oscillations of the type $\propto\exp(-i\omega t)$ with a complex frequency $\omega=\omega' - i\omega''$ are considered. At fixed geometry and plasma parameters, such oscillations can exist only for some discrete values of the complex frequency corresponding to the various eigenmodes.

Assuming that the surface wave propagates on the r-φ plane and is evanescent along z, the dispersion equation is obtained, as usual, from the continuity of the transverse electric and magnetic field components at the plasma dielectric interface

$$(\gamma_d/\varepsilon_d)\tanh(\gamma_d d) = \gamma_{pl}/\varepsilon_{pl}$$

Here, $\gamma_d = -\left[k^2 - \varepsilon_d \omega^2/c^2\right]^{1/2}$ and $\gamma_{pl} = -\left[k^2 - \varepsilon_{pl}\omega^2/c^2\right]^{1/2}$ are the axial propagation constants in the corresponding medium, i.e., dielectric and plasma. The relative plasma permittivity is $\varepsilon_{pl} = 1 - \dfrac{\omega_{pl}^2}{\omega(\omega + i\nu_{en})}$, where $\omega_{pl} = e(N_e/\varepsilon_o m_e)^{1/2}$ is the electron plasma frequency (m_e and e being the electron mass and charge, respectively). The transverse wave number k_τ depends only on the camera geometry and the mode; for a TM_{mn} mode, $k_\tau = U_{mn}/R$, where U_{mn} is the n-th root of the m-th Bessel function J_{mn}, i.e., $J_{mn}(U_{mn}) = 0$.

The discharge part of the model is coupled to the discharge electrodynamics through the electron density (in the discharge zone) at which the TM_{33} mode appears. The electron energy distribution function (EEDF) is determined by solving the homogeneous electron Boltzamnn equation in the local approximation [2]. The wave frequency is supposed to be much larger than the characteristic frequency of electron energy relaxation, so that the isotropic part of the distribution function may be regarded as time-independent. Momentum transfer collisions of electrons with heavy particles [N_2, N(^{4}S), Ar], electron impact excitation of electronic levels of molecules (N_2) and atoms [N(^{4}S), Ar], ionisation, step-wise processes, inelastic and superelastic collisions of electrons with vibrationally excited N_2 molecules, and electron-electron and electron-ion collisions are taken into consideration in the collision integral. The inelastic and superelastic processes taken into account and the sources used for the corresponding cross-sections are the same as in [2,3]. The electron transport parameters and the rate coefficients calculated from the EEDF are functions of the reduced electric field E/N (N is the total density of the neutrals) and of the vibrational distribution function (VDF) of the electronic ground state $N_2(X^1\Sigma_g^+, v)$, since vibrationally excited N_2 molecules constitute an appreciable fraction of the total molecular population.

Due to the significant populations in the vibrationally excited levels of the electronic ground state, the Boltzmann equation and its moment equations are coupled to the system of non-linear rate balance equations for these populations through both inelastic and superelastic collisions. The rate balance equations describing the kinetics of $N_2(X^1\Sigma_g^+, v)$ molecules take into account the processes of excitation and de-excitation of vibrational levels by electron impact (e–V processes), vibration–vibration (V–V) and vibration–translation (V–T) energy exchange processes, de-activation of $N_2(X^1\Sigma_g^+, v)$ molecules on the wall and the dissociation and re-association mechanisms of N_2. The V–T reactions concern N_2–N_2, N_2–N and N_2–Ar collisions. Due to the lack of data, the same rates are assumed for the exchanges associated with N_2–Ar and N_2– N_2 collisions [2,3]. The equations and mechanisms accounted for are described in detail in previous articles [2,3] to which the reader should refer for further information.

In addition to the above electron and vibrational kinetic processes, the model includes a large number of physical-chemical reactions which determine the populations of the electronically excited molecular states $N_2(A^3\Sigma_u^+, B^3\Pi_g, C^3\Pi_u, a'^1\Sigma_u^-, a^1\Pi_g, w'\Delta u)$ and atomic states $Ar(^1P_1, ^3P_0, ^3P_1, ^3P_2)$ as well as the concentration of positive ($N_2^+, N_4^+, Ar^+, Ar_2^+$) ions. The radial profile of excited metastable particles is assumed to be a zeroth-order Bessel function. The axial diffusion losses are taken into account in an approximative way, i.e. by introducing an effective axial diffusion coefficient. In the present model, four

types of positive ions ($N_2^+, N_4^+, Ar^+, Ar_2^+$) have been considered. The nitrogen N_2^+ ions are created by electron impact ionisation of N_2 molecules, step-wise ionisation, associative ionisation and charge transfer reactions between Ar^+ and nitrogen molecules [2,3]. N_4^+ ions are created by associative ionisation involving $N_2(A^3\Sigma_u^+)$ and $N_2(a'^1\Sigma_u^-)$ metastable molecules. Argon ions are created by direct and step-wise electron impact, charge transfer and pooling reactions [2]. The main process for the removal of charged particles is bulk dissociative recombination (N_2^+, N_4^+).

Numerous volume and wall processes involving atoms influence strongly the discharge operation. In the present model, the kinetics of nitrogen atoms in the ground $N(^4S)$ and metastable $N(^2D,^2P)$ states is taken into account by considering a number of source and loss channels. Electron impact dissociation ($e + N_2(X^1\Sigma_g^+, v = 0) \rightarrow e + N(^4S) + N(^4S)$ and dissociative recombination $e + N_2^+ \rightarrow e + N(^4S) + N(^4S)$ are important source channels for the present conditions. For the determination of the electric field maintaining the discharge ($E_t = \sqrt{E_z^2 + E_r^2 + E_\varphi^2}$) the continuity equations for the electrons and the positive ions [$N_2^+, N_4^+, Ar^+, Ar_2^+$] together with the quasineutrality condition [$n_e = N_2^+ + N_4^+ + Ar^+ + Ar_2^+$] are solved consistently. In fact, the balance between the total, volume averaged, rate of ionization {including direct, associative ionization [involving collisions between the metastable $N_2(A^3\Sigma_u^+)$ and $N_2(a'^1\Sigma_u^-)$ species], pooling ionization [involving $Ar(^1P_1, ^3P_0, ^3P_1, ^3P_2)$ species] and step-wise ionization processes [from $N_2(A^3\Sigma_u^+, a'^1\Sigma_u^-, B^3\Pi_g)$ states]} and the total rate of electronic losses due to diffusion and electron-ion bulk recombination is used to obtain the absolute values of the electric field components. In order to account for axial and radial diffusion losses of electrons an effective diffusion length is introduced. The equations are solved altogether in a self-consistent manner.

3. Results and Discussion

The 2D distribution of the total electric field ($E_t = \sqrt{E_z^2 + E_r^2 + E_\varphi^2}$) at z = 0.1 cm for the N_2 –Ar discharge (N_2(50%) –Ar(50%); p = 2 Torr) is depicted in Fig. 2. As seen, a well pronounced TM_{33} mode structure is observed. The intensity of the total electric field reaches about 5000 V/m at the maximum of the standing wave pattern. In the axial direction the electric field decays exponentially (Fig. 3) and vanishes at a distance z = 1 cm from the interface. For microwave radiation of 2.45 GHz a TM_{33} mode is satisfied when $N_e = 9\times10^{11}$ cm^{-3}. The attenuation coefficient is 2 cm^{-1}. A deep minimum of the electric field intensity in the discharge center is formed. The corresponding variation of the population density of the radiative state $N_2(C^3\Pi_u)$ closely follows the electric field distribution. Due to the fast radiative decay to $N_2(B^3\Pi_g)$, diffusion is negligible and sharp maxima corresponding to the electric field intensity maxima appear in the 2D $N_2(C^3\Pi_u)$ population density distribution. N_2^+ ions are the main positive charged particles for the conditions considered. Their principal source channel appears to be charge transfer ($Ar^+ + N_2 \rightarrow N_2^+ + Ar$) between argon ions and nitrogen molecules. The contribution of this channel at low electric field intensity is more than 90 %. As a result, the N_2^+ ion density has a maximum when the electric field intensity is minimum. The 2D distribution of ground state $N(^4S)$ atoms shows some peculiarity as demonstrated in Fig. 6. The ground state atom distribution clearly does not follow the electric field intensity distributions as the comparison shows. As seen from Fig. 6, additional maxima to those corresponding to the electric field intensity also appear. These maxima are found to be a result of dissociative recombination processes $e + N_2^+ \rightarrow N(^4S) + N(^4S)$. The correlation between the 2D distributions of the total electric field intensity, N_2^+ ion distribution and ground $N(^4S)$ state atom distribution shows that electron impact dissociation and dissociative recombination are the main source channels for ground state $N(^4S)$ atoms for the present conditions.

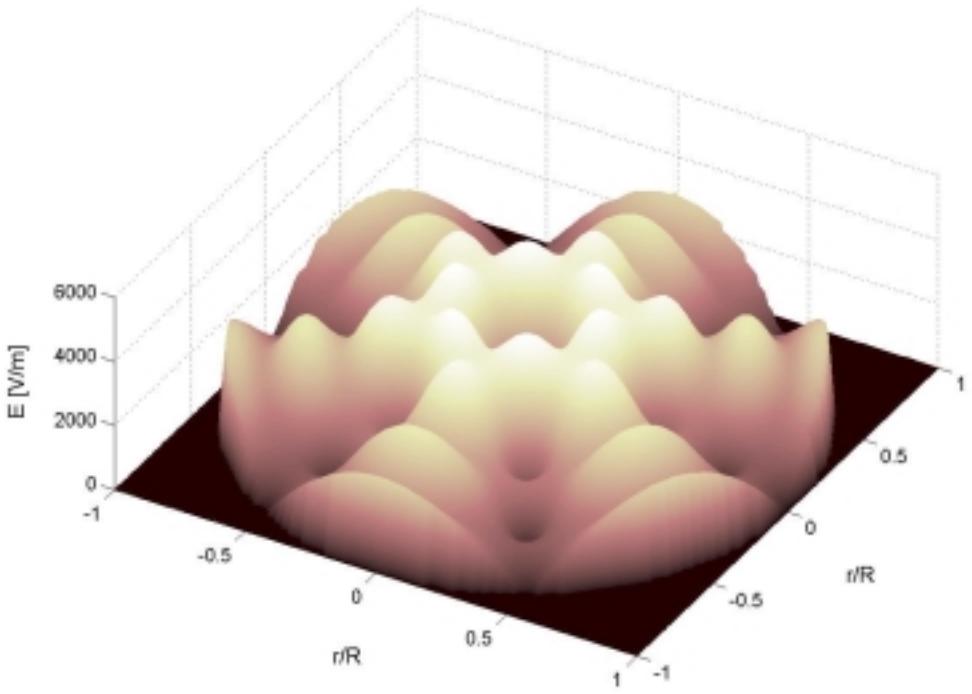

Fig. 2: (r – φ) Distribution of the total electric field intensity

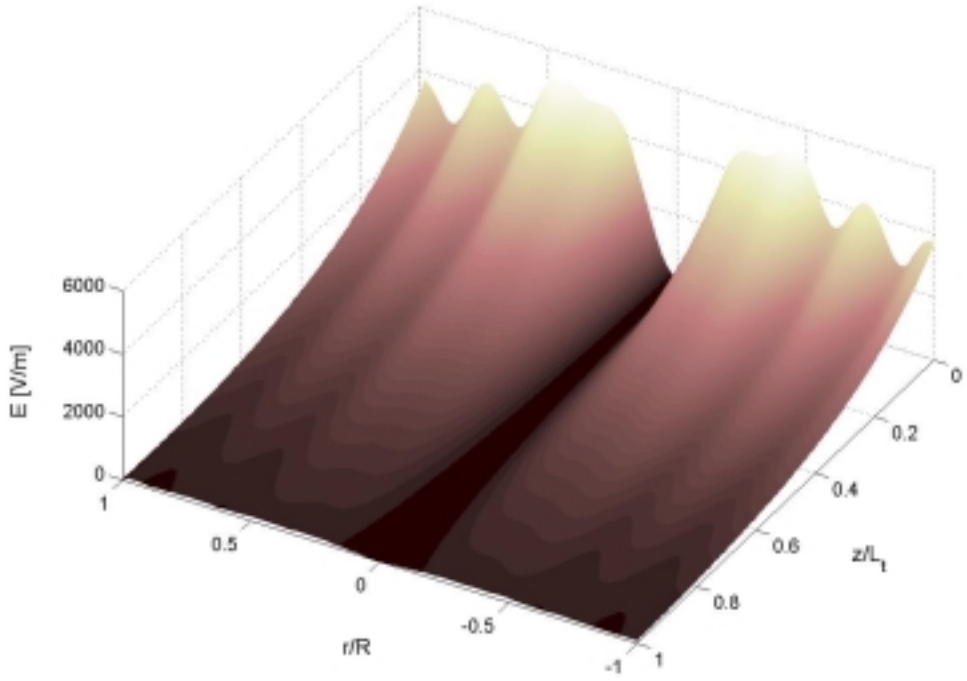

Fig. 3: (r – z) distribution of the total electric field intensity

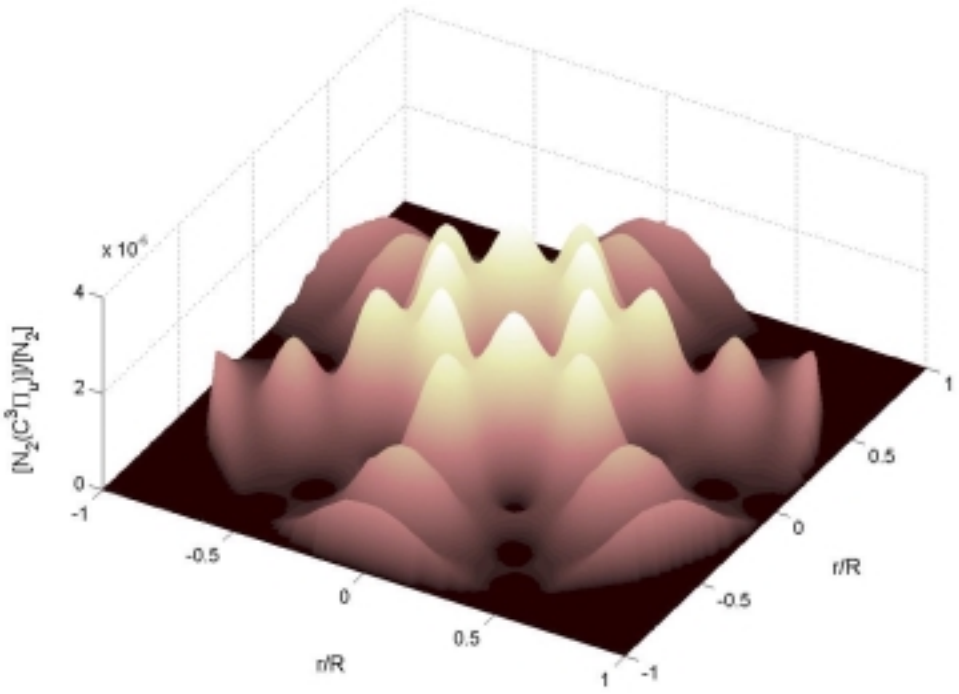

Fig. 4: (r – φ) distribution of the $N_2(C^3\Pi_u)$ state population density

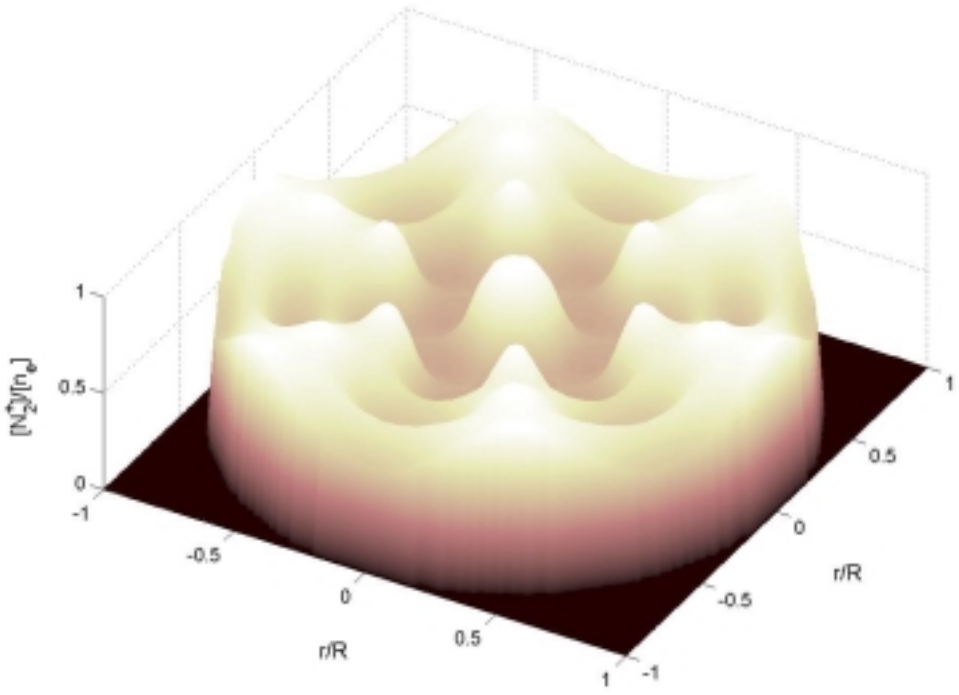

Fig. 5: (r – φ) density distribution of N_2^+

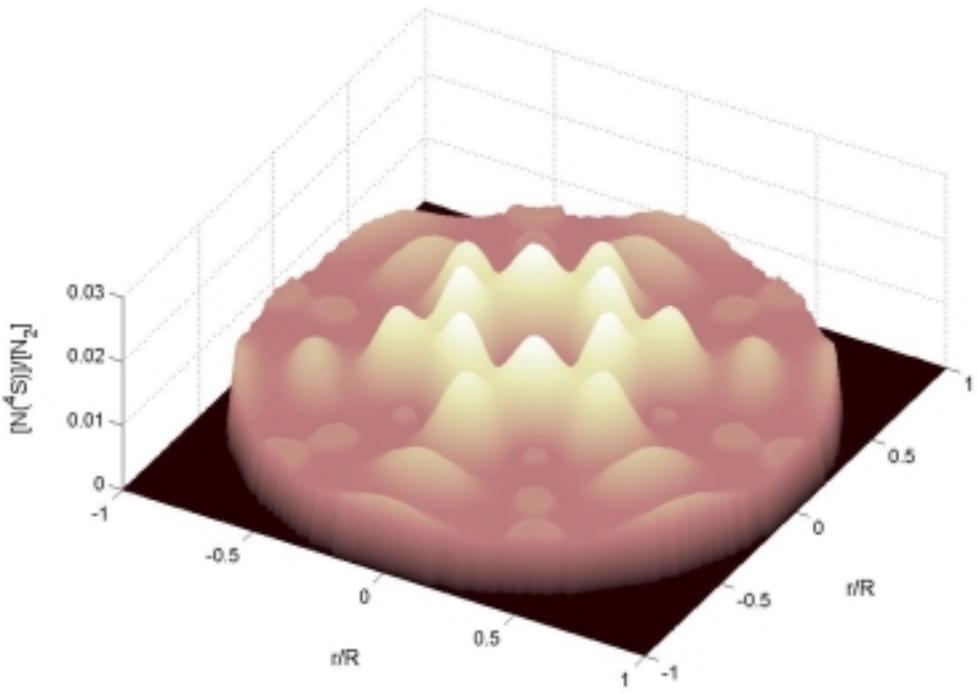

Fig. 6: (r – φ) $N(^4S)$ population density distribution

3. Conclusions

The electric field intensity distribution is strongly correlated to the density distribution of the $N_2(C^3\Pi_u)$ radiative state. Due to the contribution of charge transfer processes between argon ions and N_2 molecules, N_2^+ are the dominant positive ions for the conditions considered. The dissociative recombination processses determine the appearance of additional maxima in the 2D ground state $N(^4S)$ atom distribution with respect to those of the electric field.

References

[1] H. Sugai, I. Ghanashev, M. Nagatsu – Plasma Sources Sci. Technol. **7**, 192 (1998).
[2] J. Henriques, E. Tatarova, V. Guerra, C.M. Ferreira – J. Appl. Phys. **91**, 5622 (2002).
[3] J. Henriques, E. Tatarova, V. Guerra, C.M. Ferreira – Vacuum **69**, 177 (2003).

Simulation of double layer existence in the fullerene-ion plasma

I. Spassovska[1], P.H. Sakanaka[1], P.K. Shukla[2]

[1]Instituto de Física "Gleb Wataghin", Universidade Estadual de Campinas, Campinas, SP, Brazil.
[2]*Institute für Theoretische Physik IV, Ruhr-Universität Bochum, Bochum, Germany*

Abstract
Since the discovery of the dust acoustic wave, there has been a great interest in investigating numerous collective processes in dusty plasmas. Positively and negatively charged dust grains can co-exist both in the space and in the laboratory plasmas. As it was shown [1] the presence of a positive dust component in a multi-component dusty plasma gives rise to such novel features of the nonlinear structures as the monotonic double-layers, which otherwise are absent. In this work the finite amplitude localized electrostatic solutions in multi-component unmagnetized dusty plasma [1] was applied to the laboratory plasma reported by Oohara et al. [2]. Fullerene-ion plasma of the same mass (C_{60}) was produced in the process of a hollow electron-beam impact ionisation. Authors [2] observed two low-frequency electrostatic waves. The constituents of fullurene-ion plasma are warm electrons and negatively C_{60}^- and positively C_{60}^+ charged cold dust grains, which are simultaneously present. We introduce small quantity of positive ions so as to ion temperature did not exceed 10% of the electron temperature. Applying the conditions of the existence of double layer [1] to that experimental situation it was obtained that a double layer might be possible to be launched. The constituents of fullurene-ion plasma are warm electrons and negatively C_{60}^- and positively C_{60}^+ charged cold dust grains, which are simultaneously present. We introduce small quantity of positive ions so as to ion temperature did not exceed 10% of the electron temperature. Applying the conditions of the existence of double layer [1] to that experimental situation it was obtained that a double layer might be possible to be launched.

1. Introduction

Since the discovery of the dust acoustic wave (DAW) [3], there been a great interest in investigating numerous collective processes in dusty plasmas. In their paper, Rao, Shukla, and Yu [3], discovered the dust-acoustic wave (DAW), and introduced a theory for dust-acoustic solitons in three-component dusty plasma with negatively charged dust grains. Recently, it has been suggested that positively and negatively charged dust grains can co-exist in space [4]-[6] and laboratory [7] plasmas. Therefore, it is desirable to investigate the linear and nonlinear properties of dust-acoustic waves in four-component plasma that consists electrons, ions and positively and negatively charged dust grains.

Here we present the governing equations for the DAW when both the negative and positive dust components are simultaneously present (see [8]). We discuss the properties of the DAW in the presence of positive and negative dust components, and define parameters that are relevant for the analysis of the nonlinear DAW. Stationary solutions of the governing non-linear equations for arbitrary large amplitudes are discussed. Here, we derive the energy integral with a modified Sagdeev potential. The latter is analysed both analytically and numerically to obtain the parameter regimes where DA double-layers are possible. It turns out that the presence of a positive dust component in a multi-component dusty plasma gives rise to such novel features of the non-linear structures as the compressional DA potential distribution and the monotonic double-layers, which otherwise are absent. Finally, a possible application of our investigation in laboratory plasmas is given.

2. Governing equations

We consider unmagnetized dusty plasma consisting of the electrons, the ions, negatively and positively charged massive dust particles, with similar masses.

The quasi-neutrality at equilibrium is written

$$N_{e0} + Z_n N_{n0} = N_{i0} + Z_p N_{p0}\,, \tag{1}$$

where, N_{e0} and N_{i0} are the average electron and average ion number densities, Z_n and Z_p are the negative and positive dust particle charge, N_{n0} and N_{p0} are the average dust particles number density, respectively.

The dust particles are assumed to be point charges and their sizes are much smaller than the effective Debye length. For low phase velocity (compared to the electron and ion thermal velocities) dust-acoustic

waves, both the electrons and ions can be considered inertialess fluid and their number densities can be given by the Boltzmann distribution, respectively,

$$N_e = N_{e0} e^{e\Phi/T_e} \quad \text{and} \quad N_i = N_{i0} e^{-e\Phi/T_i}, \tag{2}$$

where, Φ is the electrostatic potential and e is the magnitude of the electron charge.

The dynamics of charged dust grains are governed by the equations of the continuity and the momentum, which are, respectively,

$$\frac{\partial N_p}{\partial t} + \frac{\partial \left(N_p V_p \right)}{\partial x} = 0 \quad \text{and} \quad \frac{\partial N_n}{\partial t} + \frac{\partial \left(N_n V_n \right)}{\partial x} = 0 \tag{3}$$

and

$$\frac{\partial V_p}{\partial t} + V_p \frac{\partial V_p}{\partial x} = -\frac{Z_p e}{M_p} \frac{\partial \Phi}{\partial x} \quad \text{and} \quad \frac{\partial V_n}{\partial t} + V_n \frac{\partial V_n}{\partial x} = +\frac{Z_n e}{M_n} \frac{\partial \Phi}{\partial x} \tag{4}$$

for positively and negatively charged dust grain. Here V_p, V_n, M_p, M_n are the fluid velocities and mass of the positively and negatively charged dust grains, respectively. We are assuming cold dust particles, so no pressure term is present. The system of equations is closed with the Poisson's equation

$$\frac{\partial^2 \Phi}{\partial x^2} = 4\pi e \left(N_e - N_i + Z_n N_n - Z_p N_p \right). \tag{5}$$

3. Finite amplitude non-linear dust acoustic waves

We can get a plane wave solution for the set of linearized equations of (1) to (5) for small amplitude disturbances with angular frequency ω and wave number k, with the dispersion relation:

$$\frac{\omega}{k} = \frac{C_{da}}{\sqrt{1 + \lambda_{Dd}^2 k^2}}, \quad \text{where} \quad C_{da}^2 = \frac{T_0}{M_0} \quad \text{and} \quad \lambda_{Da} = \frac{C_{da}}{\omega_{pd}}. \tag{6}$$

We have introduced the symbols ω_{pd}, N_0, T_0 and M_0 as

$$\omega_{pd}^2 = \frac{4\pi e^2 N_0}{M_0}, \quad N_0 = N_{e0} + N_{i0}, \; \frac{N_0}{T_0} = \frac{N_{e0}}{T_e} + \frac{N_{i0}}{T_i}, \quad \frac{N_0}{M_0} = \frac{Z_n^2 N_{n0}}{M_n} + \frac{Z_p^2 N_{p0}}{M_p}. \tag{7}$$

Here, C_{da} is the dust-acoustic velocity, λ_{Dd} the effective Debye length, ω_{pd} the dust plasma frequency, N_0, M_0, and T_0 are the effective number density, the mass and the temperature, respectively.

With the purpose of understanding the parametric space, which limits the existence of double-layers, we are normalizing all the parameters. The natural quantities for the normalization are T_0, N_0 and M_0, the effective temperature (in unit of energy), the plasma particle number density and the mass, respectively. From these we get the normalizing quantities for the time, $t \rightarrow t\omega_{pd}$, the space, $x \rightarrow x/\lambda_{Da}$, and the mass, $M_j \rightarrow M_j/M_0$. The normalized velocities are expressed as the Mach number, $M = V_0/C_{da}$.

We define, then

$$\phi = \frac{e\Phi}{T_0} \quad \text{and} \quad u(\phi) = \frac{U(\Phi)}{4\pi N_0 T_0}, \tag{8}$$

where $U(\Phi)$ is the potential energy density, and which will appear in the later context,

$$n_{e0} = \frac{N_{e0}}{N_0}, \quad n_{i0} = \frac{N_{i0}}{N_0}, \quad a_e = \frac{T_0}{T_e}, \quad a_i = \frac{T_0}{T_i} \tag{9}$$

for the electron and ion number densities and the temperatures,

$$n_n = \frac{Z_n N_{n0}}{N_0}, \quad n_p = \frac{Z_p N_{p0}}{N_0}, \quad a_n = \frac{Z_n T_0}{M_n V_0^2}, \quad a_p = \frac{Z_p T_0}{M_p V_0^2} \tag{10}$$

for the dust particle number density.

From equation (1), (7) and (8) – (10) for the non-linear dust acoustic wave parameters we have

$$n_{e0} + n_n = n_{i0} + n_p \tag{11}$$

$$n_{e0} + n_{i0} = 1 \tag{12}$$

$$n_{e0} a_e + n_{i0} a_i = 1 \tag{13}$$

$$n_n a_n + n_p a_p = \frac{1}{M^2} \tag{14}$$

These last four equations are very important because they show the relation between the four component dusty plasma parameters. We will use them for our calculations to define the regions of existence of the double layer.

For weakly non-linear perturbations we can use a higher order perturbation method and get a soliton solution or a double layer. Taking up to the second order perturbation and using the reductive perturbation technique we get Korteweg - De Vries (KdV) equation with soliton solutions. For the third order perturbation we get the modified KdV equation with a double layer solution (see [8]).

Our main thrust for this work is to find the parametric limits for the existence of double layers using equations (7) and (8) of reference [8], which we reproduce here

$$\frac{1}{2}\left(\frac{\partial\phi}{\partial\zeta}\right)^2 + u(\phi) = 0\,, \tag{15}$$

where the modified Sagdeev potential [?] for our purposes is

$$u(\phi) = -\left\{\frac{n_{e0}}{a_e}\left(e^{a_e\phi}-1\right)+\frac{n_{i0}}{a_i}\left(e^{-a_i\phi}-1\right)+\frac{n_n}{a_n}\left(\sqrt{1+2a_n\phi}-1\right)+\frac{n_p}{a_p}\left(\sqrt{1-2a_p\phi}-1\right)\right\}, \tag{16}$$

with the conditions for the existence of double layers:

$$\begin{aligned} &(i) \quad u(\phi) = u'(\phi) = 0 \text{ at } \phi = 0, \\ &(ii) \quad u(\phi) = u'(\phi) = 0 \text{ at } \phi = \phi_1 \neq 0, \\ &(iii) \quad u(\phi) < 0 \text{ for } 0 < |\phi| < |\phi_1|. \end{aligned} \tag{17}$$

Now the conditions in the item (*ii*) provide two relations:

$$n_{e0}a_e + n_{i0}a_i - n_n a_n - n_p a_p = 0 \quad \text{and} \tag{18}$$

$$n_{e0}a_e^2 - n_{i0}a_i^2 + 3n_n a_n^2 - 3n_p a_p^2 = 0\,, \tag{19}$$

which are conditions under which double-layers exist.

4. Numerical results

We proceed to obtain the parametric regions where conditions (17) are satisfied. Starting with 9 parameters defined in (9) – (10) with the inclusion of 4 equations (11) – (11), we have a 5-parameter region. We introduce parameters α and β in substitution of a_i and a_n, $\alpha = a_e/a_i = T_i/T_e$ and $\beta = a_p/a_n = Z_pM_n/Z_nM_p$. So, we have to deal which a function $f(n_{e0}, n_p, M, \alpha, \beta)$ which satisfies relations given in (17).

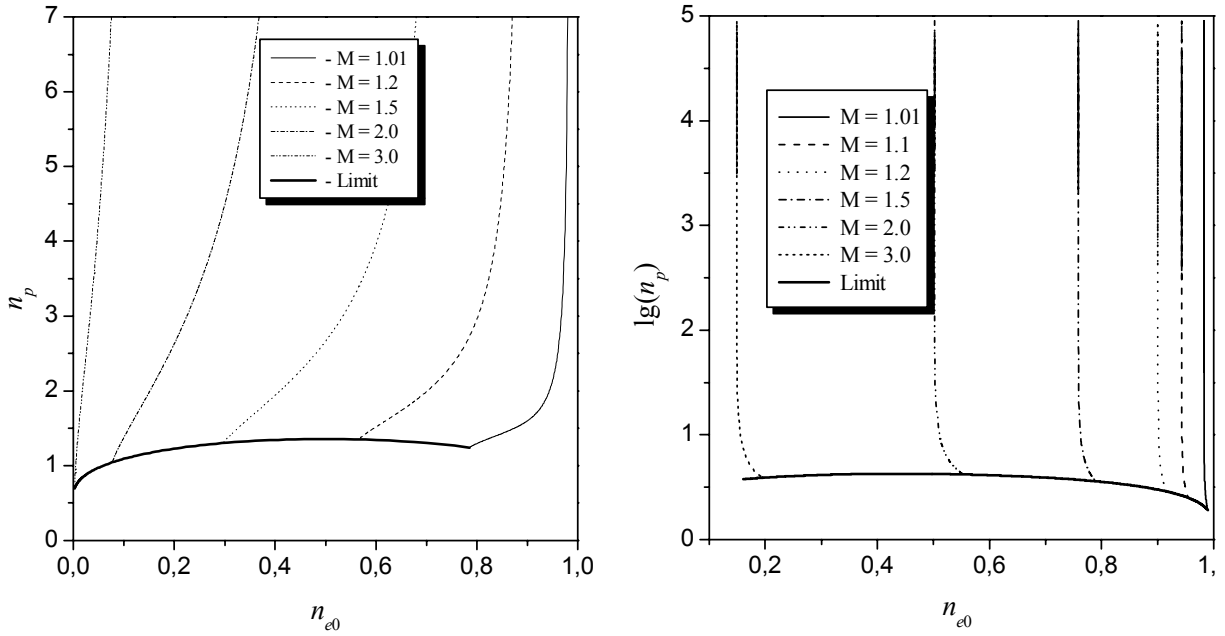

Figure 1. Relations between the parameters n_p and n_e for different values of Mach number M and parameter α = 0.09: a) β = 0.10; b) β=1.0.

Furthermore we reduce the 5 parameters to a even smaller number by taking a reasonable physical values for α, β and M, resulting in a two parametric space: $g(n_{e0}, n_p)$. In Figure 1a, we show the curves where the double layer solutions are found. We have chosen $\alpha = 0.09$ and $\beta = 0.10$. For each given value of M, from 1.01 to 3.0, a curve is drawn on $n_{e0} \times n_p$ space where DL exists.

The same treatment was applied for the particular case of laboratory plasma reported by Oohara et al [2], where a fullerene-ion plasma of the same mass (C_{60}) was produced in the process of a hollow electron-beam impact ionisation. Authors observed two low-frequency electrostatic waves. For calculations we used main characteristics of the dusty plasma, i.e. $n_e / n_p \sim 10^{-6}$, $n_e = 1.0$, $n_p = n_n \sim 10^{6}$ and $M_p = M_n$. Moreover, we introduce, on their experimental conditions, a small quantity of ions to fulfill conditions of the four component dusty plasma. Thus we have parameter $\alpha = 0.09$ and $\beta = 1.0$ that is different from the case discussed above.

In the Figure1b the result of the double layer conditions for different M values is shown. As we can see, the authors [2] have possibility to obtain a double layer in laboratory plasma. It is interesting to observe the different comportment of the curves for small values of the n_p. In contrast to the case of low β, for the DL exist it is necessary increasing both n_e and n_p for some constant M. Furthermore, the limit of the double layer existence decrease with increasing β.

5. Summary

The linear and non-linear properties of dust-acoustic waves (DAW) were studied. We used the model of multi-component dusty plasma with inertialess electrons and ions as well as positively and negatively charged inertial dust grains. We found that in four component dusty plasma there are remarkable changes in the non-linear properties of the DAW. The presence of positively charged dust grains produces double-layers in those parameter regimes. The theory was applied to the laboratory plasma reported by Oohara et al. We predict that a double-layer might be possible to be launched in their experiment if a trace ions component is added. The results of the investigation can be useful for designing laboratory experiments dealing with the demonstration of DAW in multi-component dusty plasma with the positive and negative dust grains. Our parametric studies and double-layers should be useful in identifying coherent non-linear structures in the Earth's mesosphere. Furthermore, non-stationary double-layers could be potential accelerators for dust particulates in space plasmas..

Acknowledgments

We acknowledge for the financial support of CAPES (Fundação Coordenação de Aperfeiçoamento de Pessoal de Nível Superior) and FAPESP (Fundação de Amparo à Pesquisa do Estado de São Paulo) under Proc. 98/14711-4.

References

[1] I. Spassovska, P.H. Sakanaka and P.K. Shukla – Proceedings of the 2002 International Congress on Plasma Physics, Sydney, Australia, July, 2002, (in press).

[2] W. Oohara, N. Tomioka, T. Hirata, R. Hatakeyama, and N. Sato, – Proceedings of the 2000 International Congress on Plasma Physics, Quebec, October, 2000, **1**, (2000).

[3] Rao, N. N., Shukla, P. K., and Yu, M. Y. – Planet. Space Sci. **38**, (1990).

[4] Nakamura, Y., Odagiri, T., and Tsukabayashi, I. – Plasma Phys. Control. Fusion **39**, (1997), Nakamura, Y., and Tsukabayashi, I.– Phys. Rev. Lett. **52** (1984).

[5] Watanabe, S. – J. Phys. Soc. Japan **53**, (1984), Tajiri, M., and Tilda, M., ibid. **54**, (1985).

[6] Sheridan, T. E. – J. Plasma Phys. **60**, (1998).

[7] Shukla, P. K. – Phys. Plasmas **1**, (1994).

[8] Sakanaka, P.H., and Shukla, P.K.– Phys. Scripta, **84**, (2000)

Activated carbon fiber modification by hydrocarbon-nitrogen RF discharges

T. Orfanoudaki[1,2], G. Skodras[2,3], I. Dolios[1,2] And G.P Sakellaropoulos[1,2]

[1] *Chemical Process Engineering Laboratory, Dept of Chemical Engineering, Aristotle University of Thessaloniki, Thessaloniki, Greece*
[2] *Laboratory of Solid Fuels and Environment, Chemical Process Engineering Research Institute, Thessaloniki, Greece*
[3] *Centre for Solid Fuels Technology and Applications, Ptolemais, Greece*

Abstract.
In this work, carbon films were deposited on activated carbon fibers (ACF), by using RF discharges of hydrocarbon-nitrogen mixtures. Raman and XPS spectroscopy were used to evaluate the modifications on the fiber surface after plasma treatment. The molecular sieve properties of raw and plasma treated ACF were studied by CO_2 and CH_4 adsorption measurements. Depending on hydrocarbon and plasma power used, the ideal selectivity of CO_2/CH_4 for adsorption, improved significantly after plasma treatment.

1. Introduction.

Carbon molecular sieves (CMS) are widely used in separation and purification processes. They are porous materials having the ability to discriminate between molecules of different size and shape [1,2]. Their unique pore structure is achieved either by controlled activation using oxidizing media [3] or by carbon deposition on an inherent pore structure in order to obtain homogenous pores with dimensions in the range of molecular size [4-6]. Both of these methods are associated with difficulties concerning the control of gasification in the first case and of deposition in the second [7].
An attractive alternative for CMS production is the deposition of a carbon thin film, possessing molecular sieve properties, on a suitable substrate [8,9]. Plasma polymerization processes, using various gas monomers, are quite suitable for the deposition of thin films [10,11]. Such thin films, deposited on porous supports have been tested as separation membranes [12,13], but they often cannot withstand the separation process environment [14].
ACF have the unique characteristic of possessing micropores directly connected to the surface of the fiber, thus permitting fast adsorption kinetics [15]. This feature of ACF, in addition to their relatively homogeneous pore size distribution, renders the material suitable precursor for carbon molecular sieve (CMS) production.
In this work, CMS production was attempted by depositing a carbonaceous film, on ACF surface. The molecular sieve properties of the raw and plasma treated fibers were evaluated by carbon dioxide and methane adsorption experiments. Raman and XPS spectroscopy was used in order to evaluate the film chemical structure, which probably affects the gas adsorption rates of CO_2 and CH_4, thereby improving the ideal selectivity of CO_2/CH_4 separation. SEM was used to examine the film thickness and surface.

2. Experimental.

The deposition apparatus used in this study consisted of a quartz reactor, an RF generator with an impedance matching network and a mechanical pump. The reactor was a quartz cylinder 1 m long, 65 mm diameter placed coaxially through a working coil. The coil was made of 9 turns of ¼ in diameter copper tube. RF power was supplied from a 1 KW, 13.56 MHz generator. The system was also equipped with a water circulation unit, necessary for cooling the various RF plasma components.
About 35-40 mg of activated carbon fibers (FR-10, Kuraray Chemical Co.) were introduced in the reactor in the middle of the coil and sealed therein by vacuum flanges. After system evacuation, a gas mixture, of 20% hydrocarbon and 80% nitrogen was introduced in the reactor, and plasma was ignited. Hydrocarbons used were ethane, ethylene, propane and propylene. The sample was always treated for 15 min at an 80 or 120W plasma power. Since no additional heating was employed, the temperature of the activated carbon fibers (ACF) rose only by inductive heating and energy transfer from the plasma.
Raman spectroscopy was employed to characterize the type of carbon-carbon bonds before and after plasma treatment. The 514 nm line spectra of an Ar^+ laser was used for excitation. XPS analysis was also employed to characterize the functional groups on the ACF surface before and after plasma treatment. The ionizing radiation, MgKa, was provided by a non-monochromatic X-ray source with characteristic energy 1253.6 eV.

The range of kinetic energies of the analyzer was calibrated according to the ASTM-E 902-88 standard method. Scanning electron microscopy (SEM) was also used for surface examination of the initial and the plasma treated ACF. The molecular sieving properties of samples were evaluated by measuring the adsorption of CO_2 and CH_4, volumetrically under ambient conditions.

3. Results and discussion.

3.1 Raman spectra.

The Raman spectrum of the untreated carbon fibers, shown in Figure 1(a), consists of two peaks at 1580 and 1350 cm^{-1}, and is similar to those of disordered carbons [16]. The plasma treated fibers, however, gave excessive luminescence, Figure 1(b), which is probably related to high levels of impurities, such as hydrogen [17].

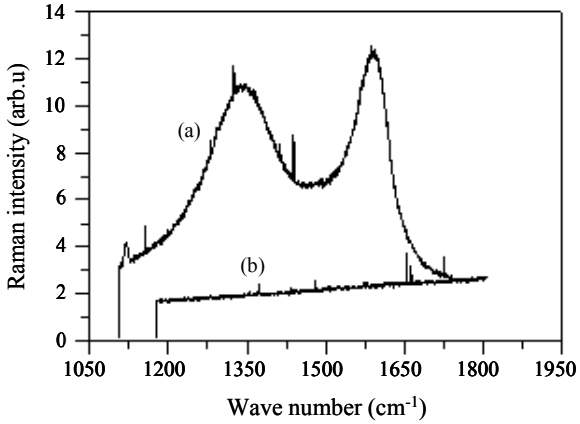

Figure 1. Raman spectrum of commercial activated carbon fibers (FR-10)
(a) before plasma treatment (b) after plasma treatment

3.2 XPS analysis.

The surface chemistry of activated carbon fibers before and after plasma treatment was characterized by XPS analysis. The main C1s peak of the raw carbon fibers was deconvoluted to three components at around 284.6, 286 and 288eV, Figure 2, which probably correspond to C–C (sp^2 or sp^3), C–OH or bridged –C=O–H–O=C–, and COOH or COOR [18-20]. A fourth peak, at the highest binding energy, is attributed to the filter used as substrate for the XPS analysis. The C1s XPS spectra of samples after plasma treatment are similar. However, C-N bonds show quite similar binding energies at 286-288eV [19]; hence, the assignment of peaks at 286 and 288eV to C-O bonds, based on C1s spectra alone, is ambiguous. For this reason, N1s spectra of raw and plasma treated samples were also obtained. Raw fibers before plasma treatment showed no N1s spectra, therefore, the peaks observed from 286 to 288eV in the C1s spectra, Figure 2, can be assigned to C-O groups as discussed above. Nitrogen is detected in plasma treated samples, analysed by XPS, Figures 3-6. The main N1s peak of plasma treated samples was deconvoluted to different components at binding energies shown in Table 1. The N1s spectra of ACF treated by alkene-nitrogen discharges are similar, Figures 3 and 5. N1s peaks at around 399eV are attributed to pyridine or amino groups [21,22], while N1s peaks at around 400eV could be attributed to pyrole or primary amine [21,23,24]. The N1s peaks at high binding energies (eg. 402eV) are probably attributed to oxidized nitrogen forms (NO), possibly embodied on the fibers surface after its exposure to atmosphere [21,25]. However, oxygen incorporation in plasma polymers is also possible during plasma treatment, even when oxygen is not introduced in the reactor intentionally. At higher plasma power (120W), with C_2H_4-N_2, the deconvoluted N1s peaks are shifted to higher binding energies, than those at 80W, probably because of intense hydrocarbon fragmentation. The peak appearing at 401.9 could probably be attributed to a free protonated amine [24], while the peak at 404.3 to pyridine-N-oxide type nitrogen [16]. With a C_3H_8-N_2 plasma at low (80W) power, peaks also shift to higher values, compared to C_3H_6-N_2, probably due to variations in the polymerization mechanism. Thus, in addition to the peak at around 400eV, a peak at 401.3eV was detected. The latter can probably be attributed to quaternary nitrogen [26].

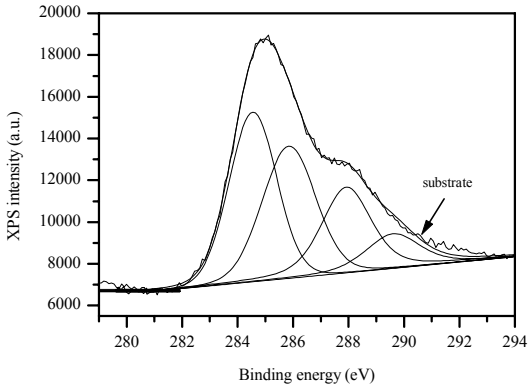

Figure 2. XPS C1s spectrum of raw (untreated) commercial activated carbon fibers (FR-10).

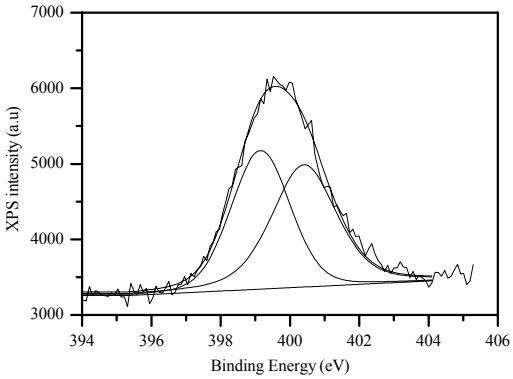

Figure 3. XPS N1s spectrum of commercial activated carbon fibers treated by propylene-nitrogen plasma at 80W.

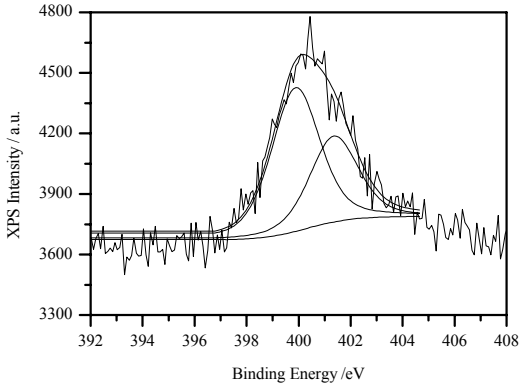

Figure 4. XPS N1s spectrum of commercial activated carbon fibers treated by propane-nitrogen plasma at 80W.

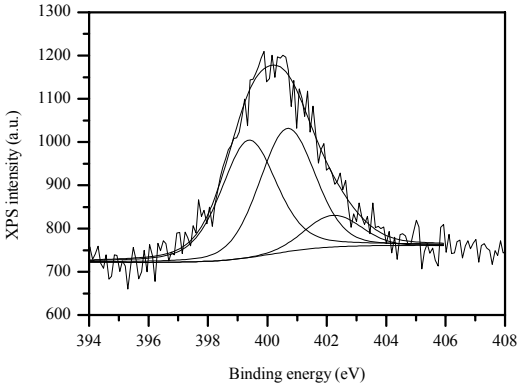

Figure 5. XPS N1s spectrum of commercial activated carbon fibers treated by ethylene-nitrogen plasma at 80W.

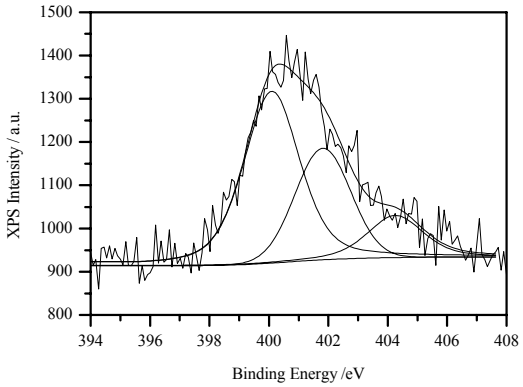

Figure 6. XPS N1s spectrum of commercial activated carbon fibers treated by ethylene-nitrogen plasma at 120W.

Table1. XPS binding energies of N1s peaks on plasma treated ACF.

Treatment	Binding energy, eV		
20% C_3H_6-80%N_2, 80W	399.2	400.4	-
20% C_3H_8-80%N_2, 80W	399.9	401.3	-
20% C_2H_4-80%N_2, 80W	399.4	400.7	402.2
20% C_2H_4-80%N_2, 120W	400.0	401.9	404.3

3.3 SEM examination.

Figure 6, shows the surface of the activated carbon fibers, as observed by SEM. In Figure 6(a) the pore structure of ACF surface can be identified, while Figure 6(b) demonstrates that the fiber surface is rough and contains defects. Figure 6(c) shows the film deposited on the activated carbon surface after propylene-nitrogen plasma treatment. The film thickness along the fiber varies between 150 and 300 nm.

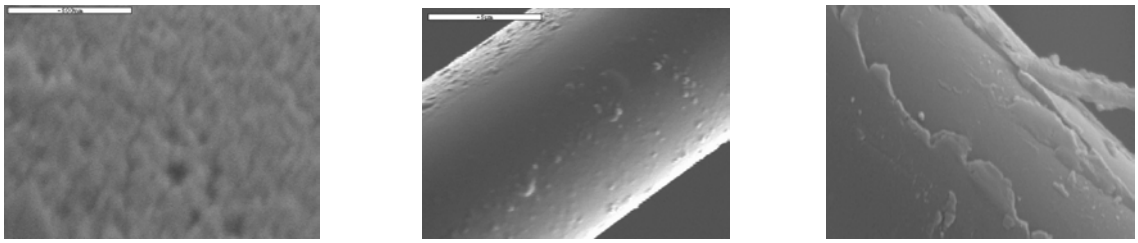

(a) (b) (c)

Figure 7. SEM characterisation of ACF
(a,b) before plasma treatment, (c) after propylene-nitrogen plasma treatment.

3.4 Molecular sieving properties.

The molecular sieving properties of the raw and plasma treated activated carbon fibers were evaluated by CO_2 and CH_4 adsorption measurements, Figures 8-9. In all cases, adsorption capacity decreased for both gases (CO_2 and CH_4), after plasma treatment, because the film formed on the ACF surface causes restriction to gas diffusion and adsorption. However, the adsorption rate decline is greater for CH_4 than for CO_2, as anticipated from the different size and shape of the two molecules. The planar CO_2 molecule diffuses faster through the film, compared to the bigger in size and spherical CH_4 molecule. In addition, CO_2 adsorption could be enhanced due to an acid-base interaction between the CO_2 molecules and the basic pyridine or amino groups [27].

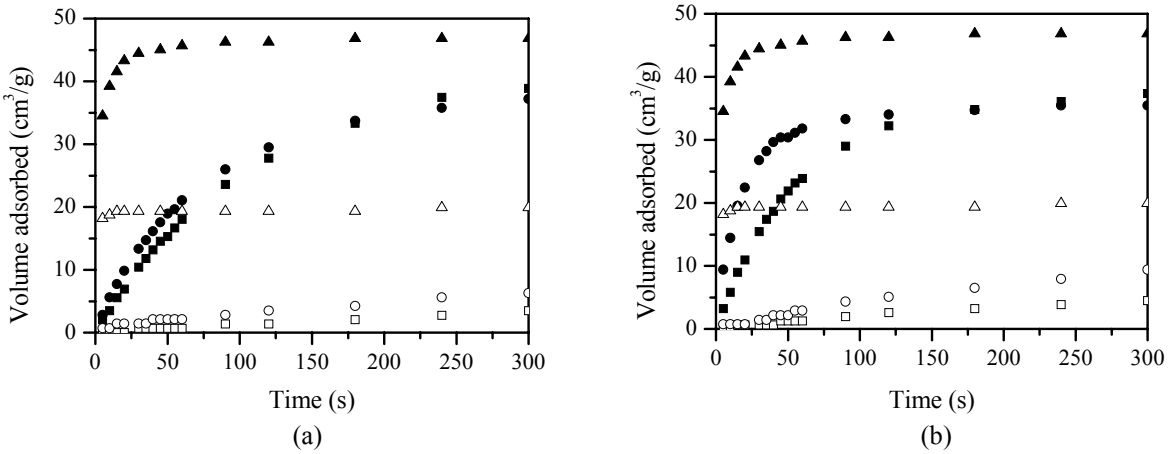

(a) (b)

Figure 8. CO_2 and CH_4 uptake curves of commercial activated carbon fibers treated by hydrocarbon-nitrogen plasma at 80W (closed symbols: CO_2 open symbols: CH_4).
(a) (▲△ FR-10, ■□ C_2H_4/N_2, ●○ C_2H_6/N_2) (b) (▲△ FR-10, ■□ C_3H_6/N_2, ●○ C_3H_8/N_2)

Adsorbed volumes of CO_2 and CH_4, especially in the first two minutes, also differ, depending on hydrocarbon used for plasma deposition. Such differences could be attributed to film chemistry and/or to film structure (thickness, tightness). Thus, films deposited on ACF by C_2H_4 and C_3H_6 plasma at 80W, contain the same nitrogen functional groups, as shown by XPS analysis. However, adsorbed volumes of CO_2 and CH_4 in the first two minutes of the adsorption process differ. Considering that film structure is related to film thickness [14], it is reasonable to correlate the variation in CO_2 and CH_4 adsorbed volume with the film thickness obtained in each case. Since, the deposition time is kept constant in all experiments, differences in film thickness, at constant plasma power, could result from different deposition rates for each gas. This is possible because the rate of deposition depends on the energy input per gram of hydrocarbon used, which in turn depends on the molecular weight of the hydrocarbon and plasma power employed. One should note that the minimum wattage necessary for plasma polymerization differs significantly among the hydrocarbons [28]. Therefore, for the same energy supplied to the hydrocarbons tested (C_2H_4, C_2H_6, C_3H_6 and C_3H_8) at a specific plasma power (80W), the energy input per gram is higher for C_2H_4 than for C_2H_6, C_3H_6 or C_3H_8 at the same flow rate. The same reasoning seems to apply also on CO_2 and CH_4 adsorbed volumes of ACF treated in C_2H_4, C_2H_6 and C_3H_6 plasma at 120W, Figure 9. Compared to results at 80W, adsorbed volumes of

CO_2 and CH_4, during the first two minutes of adsorption, increase at 120W for C_2H_4, C_2H_6, C_3H_6 sources. This implies that the deposition rate obtained at the higher plasma power (120W) resulted in a film structure which permitted easier gas transport, compared to the one obtained at 80W. However, polymers deposited at elevated plasma energies should possess a tighter network structure than those obtained at low energy input [29]. Since, gas transport depends on film thickness and structure tightness [30], it is reasonable to assume that films deposited on ACF at 120W are thinner than those obtained at 80W. This could imply that ablation takes place simultaneously with film deposition [31]. Film ablation is expected to be stronger at 120W, resulting in a lower overall deposition rate, compared to that at 80W plasma power. In contrast to C_2H_4, C_2H_6 and C_3H_6 treated ACF, adsorption of CO_2 and CH_4 decreases with plasma power for a C_3H_8-N_2 discharge. This probably indicates that for C_3H_8 polymerization, deposition prevails at 120W in the competitive plasma deposition-ablation process.

Ideal selectivities (expressed as the ratio of the amount of CO_2 adsorbed to that of CH_4) were calculated for all samples at various times of adsorption, Table 2. The best results were obtained for the C_2H_4-N_2 plasma treated activated carbon fibers at 80W. The CO_2/CH_4 ideal selectivity, measured at 60s of adsorption, improves from 2.4, for the raw ACF, to 26 for C_2H_4-N_2 plasma treated fibers. As noted earlier, C_2H_4-N_2 plasma probably gives the thickest film on ACF. The selectivity decrease, observed at longer adsorption times, e.g. ≥120s, is in agreement with the kinetic separation rules [32]. Similar behavior is also observed at plasma power of 120W, with the exception of C_3H_8 source. The low adsorption measured on ACF treated by C_3H_8-N_2 plasma, discussed previously and attributed to thicker film deposition, is accompanied by improved CO_2/CH_4 selectivity, Table 2. Further characterization of the physical and chemical structure of the plasma deposited films should provide better understanding of possible surface group interactions with the adsorbing gases and of selectivity modification.

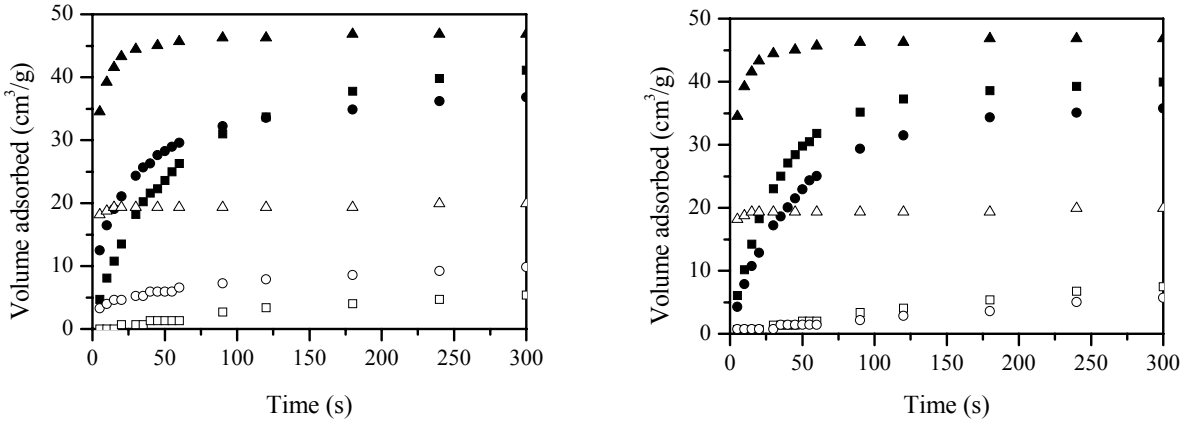

Figure 9. CO_2 and CH_4 uptake curves of commercial activated carbon fibers treated by hydrocarbon-nitrogen plasma at 120W (closed symbols: CO_2 open symbols: CH_4).
(a) (▲△ FR-10, ■□ C_2H_4/N_2, ●○ C_2H_6/N_2) (b) (▲△ FR-10, ■□ C_3H_6/N_2, ●○ C_3H_8/N_2)

Table2. Ideal selectivity (CO_2/CH_4) of raw and plasma treated ACF (FR-10) at 60 and 120s of adsorption.

Gas feed	Ideal selectivity (CO_2/CH_4)-60s		Ideal selectivity (CO_2/CH_4)-120s	
	80W	120W	80W	120W
C_2H_4/N_2	26	19.5	20	10
C_3H_6/N_2	18.5	15.6	12.5	9.2
C_2H_6/N_2	10	4.5	8.4	4.2
C_3H_8/N_2	11	17.5	6.7	11
Raw ACF	2.4		2.4	

4. Conclusions.

Carbon films were deposited on ACF by C_2H_4/N_2, C_2H_6/N_2, C_3H_6/N_2 and C_3H_8/N_2 RF discharges. XPS analysis revealed that nitrogen reacted and remained on ACF surface during plasma treatment. Films of similar chemical structure were obtained by C_2H_4/N_2 and C_3H_6/N_2 discharges, while films formed by C_2H_6-N_2 and C_3H_8-N_2 gave different N1s peak binding energies. All plasma trated ACF gave improved molecular sieve properties, as indicated by a 5 to 10 fold increase in CO_2/CH_4 ideal selectivity for adsorption. The enhanced adsorption rate of CO_2 against CH_4 can be attributed to the deposited film structure and/or to possible acid-base interactions between CO_2 and basic nitrogen groups. Selectivity variations with hydrocarbon and plasma power employed are probably caused by differences in the thickness of the deposited films.

5. Acknowledgments.

We thank the European Coal and Steel Community for financial support of this work. We also thank the Physics Division, School of Engineering of Aristotle University of Thessaloniki for Raman measurements, and the Institute of Chemical Engineering and High Temperature Processes of Patra for XPS measurements.

References.

[1] S.W. Rutherford, J.E. Coons - Carbon 41, 405 (2003).
[2] G. Bello, R. Garcia, R. Arriagada, A. Sepulveda-Escribano, F. Rodriguez-Reinoso - Micropor. Mesopor. Mat. 56, 139 (2002).
[3] Z. Hu, E. Vansant - Carbon 33, 561 (1995).
[4] M.A. de la Casa-Lillo, B.C. Moore, D. Cazorla-Amoros, A. Linares-Solano - Carbon 40, 2489 (2002).
[5] I. Praseyto, D.D. Do - Carbon 37, 1909 (1999).
[6] Y. Kawabuchi, S. Kawano, I. Mochida - Carbon 34, 711 (1996).
[7] M.M.A. Freitas, Figueiredo - Fuel 80, 1 (2001).
[8] J. Koresh, A. Soffer - J. Chem. Soc. Faraday I. 76, 2472 [1980].
[9] H. Hatori, Y. Yamada, M. Shiraishi, H. Nakata, S. Yoshitomi - Carbon 30, 305 (1192).
[10] S. Roualdes, J. Sanchez, J. Durand - J. Membr. Sci. 198, 299 (2002).
[11] W. Sohn, D. Ryu, S. Oh, J. Koo - J. Membr. Sci. 175, 163 (2000).
[12] M. Yamamoto, J. Sakata, M. Hirai - J. Appl. Polym. Sci. 29, 2981 (1984).
[13] H. Matsuyama, K. Hirai, M. Teramoto - J. Membr. Sci. 92, 257 (1994).
[14] P. Kramer, Y. Yeh, H. Yasuda - J. Membr. Sci. 46, 1 (1989).
[15] M. Inagaki - New Carbons; Control of Structure and Functions. Elsevier, Oxford (2000).
[16] M. Koh, T. Nakajima - Carbon 38, 1947 (2000).
[17] S.M. Smith, S.A. Voigt, H. Tompkins, A. Hooper, A.A. Talin, J. Vella -Thin Solid Films 398-399, 163 (2001).
[18] R. Zeng, Z. Pang, H. Zhu - J. Electrochem. Soc. 490, 102 (2000).
[19] S. Biniak, G. Szymanski, J. Siedlewski, A. Swiatkowski - Carbon 35, 1799 (1997).
[20] P.M.A. Shewood - J. Electron Spectrosc. Relat. Phenom. 81, 319 (1996).
[21] R. Pels, F. Kapteijon, A. Moulijin, Q. Zhu, M. Thomas - Carbon 33, 1641 (1995).
[22] R. Zeng, Z. Pang, H. Zhu - J. of Electrochem. Soc. 490, 102 (2000).
[23] S. Biniak, G. Szymanski, J. Siedlewski, A. Swiatkowski - Carbon 35, 1799 (1997).
[24] T. Strother, R. Hamers, L. Smith - Nucleic Acids Res. 28, 3535 (2000).
[25] T. Nakajima, M. Koh. - Carbon 35, 203 (1997).
[26] S. Kelemen, M. Gorbaty, P. Kwiateck - Energeia 6, 1 (1995).
[27] M. Yoshikawa, T. Ezaki, K. Sanui, N. Ogata - J. Appl. Polym. Sci. 35, 145 (1988).
[28] H. Yasuda - Plasma Polymerization. Academic Press, INC., London (1985).
[29] C. Ho, H. Yasuda - J. Appl. Polym. Sci. 39, 1541 (1990).
[30] P. Kramer, Y. Yeh, H. Yasuda - J. of Membr. Sci. 46, 1 (1989).
[31] K. Li, J. Meichsner - Surf. Coat. Technol. 116-119, 841 (1999).
[32] H.C. Foley - Microporous Mater. 4, 407 (1995).

Molecular Dissociation in N_2-H_2 Wave Driven Microwave Discharges

E. Tatarova[1], F.M. Dias[1], B. Gordiets[2] and C. M. Ferreira[1]

[1]*Centro de Fisica dos Plasmas, Instituto Superior Técnico, 1049-001 Lisboa*
[2]*Lebedev Physical Institute of the Russian Academy of Sciences, Russia*

Abstract
A microwave N_2-H_2 discharge driven by traveling surface waves is investigated as a source of ground state $N(^4S)$ and H(1s) atoms. The dissociation kinetics is discussed in the framework of experimental results and the a theoretical model based on a self-consistent treatment of the main discharge balances, wave electrodynamics and plasma-wall interactions.

1. Introduction

The kinetics of microwave discharges driven by a propagating wave is a complex subject due to the highly non-linear collisional reaction processes occurring simultaneously that strongly affect the non-equilibrium discharge kinetics. For this reason, it is essential to combine theoretical and experimental investigations in order to reveal the main kinetics mechanisms, in particular those of dissociation kinetics. Moreover, the whole discharge physics is strongly influenced by the degree of molecular dissociation. Keeping in mind applications, the investigation of discharges operating in N_2-H_2 mixtures presents an interest because nitrogen atoms $N(^4S)$ are the most important precursors in a number of surface treatment processes, while hydrogen atoms H(1s) are efficient etching species [1].

In this work we present experimental and theoretical results from the investigation of molecular dissociation in a traveling surface wave sustained discharge operating in N_2-H_2 mixtures. Experimental investigations have been carried in a plasma source operating at 2.45 GHz at low-pressure conditions (p = 0.5 – 2 Torr). By means of optical emission spectroscopy and probe diagnostic techniques the population densities of ground state atoms [$N(^4S)$ and H(1s)] have been detected. Since the relation between the intensity of the emission lines and the density of the corresponding species is not straightforward, the experimental results have been analyzed in the framework of a theoretical model based on a self-consistent treatment of particles kinetics, gas dynamics, wave electrodynamics and plasma-wall interactions. The dependence of the discharge properties, in particular of molecular dissociation, on the mixture composition is discussed.

2. Experimental conditions and procedures

The experiments have been performed in a microwave discharge sustained by an azimuthally symmetric surface wave of frequency $\omega/2\pi$ = 2.45 GHz excited by a waveguide-surfatron device. The plasma column, which extends outside the launcher, is created in an N_2-H_2 gas mixture at pressure p = (0.5 – 2 Torr) in a quartz glass tube with inner radius R = 0.75 cm (see Fig. 1). The gas components (N_2, H_2, Ar) are introduced in the discharge tube by means of mass flow controllers with a flow rate in the range Q = 2 – 100 sccm. The power delivered to the launcher is between 200 and 770 W. Photons emitted by the plasma are collected by a collimator and transferred via an optical fiber into the entrance slit of a SPEX 1250 M spectrometer (2400 g/mm grating) equipped with a Hamamatsu R928 photomultiplier. The current generated by the photomultiplier is sent to a data acquisition electronic device Data Scan2, and processed by Spectramax software. The whole optical system is calibrated with a tungsten lamp.

For electron temperature measurements, a probe diagnostic technique has been applied. The gas temperature has been determined, as usual for nitrogen, by measuring the rotational distribution of the 2nd positive system of N_2 in the 375.5 – 379 nm wavelength range assuming that the rotational and the translational modes are in equilibrium.

The intensity ratios $I(744)/I(750)$ and $I(746)/I(750)$ of the two nitrogen atomic lines λ = 744.23 nm and λ = 746.83 nm (transition $3p^4S^o \rightarrow 3s^4P$) to the λ = 750.39 nm argon line (transition $2p_1 \rightarrow 1s_2$) have been detected as a measure of the dissociation degree $[N(^4S)]/[N_2]$ of nitrogen molecules in the mixture. For this reason, a small amount of inert Ar gas has been added to the mixture.

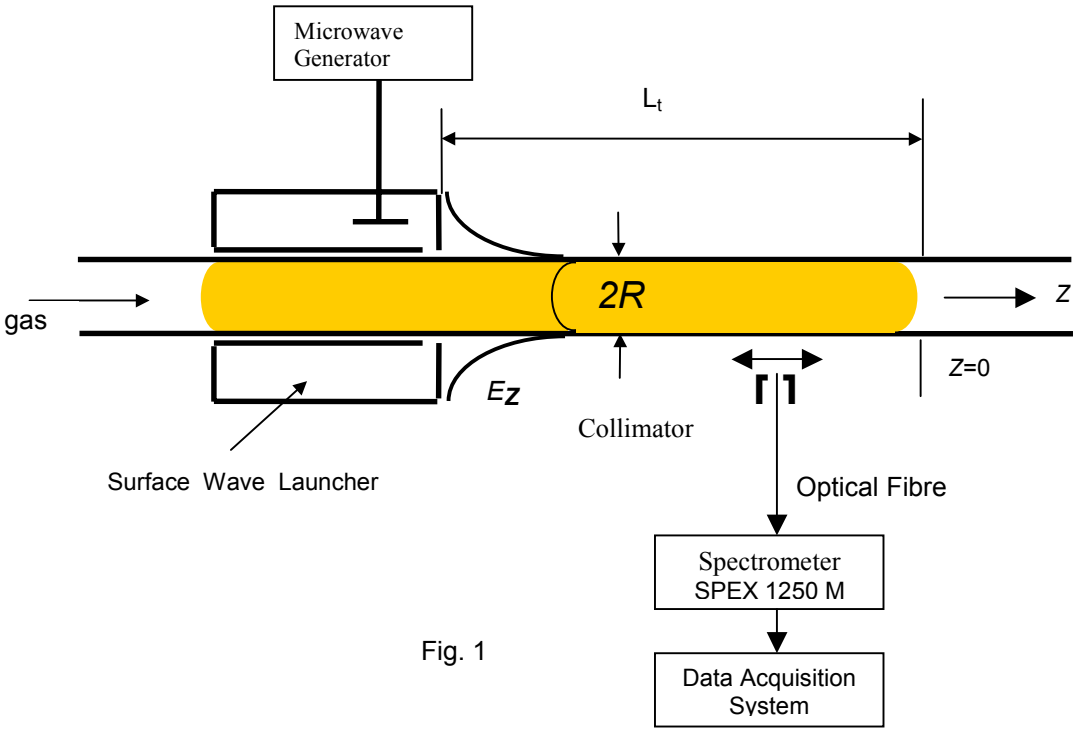

Fig. 1

Taking, for example, the λ = 744.23 nm atomic line, the relative concentration of ground state N(^{4}S) atoms can be calculated using the relation:

$$\frac{[N(^4S)]}{[N_2]} = \frac{R_{750}}{R_{744}} \frac{h\nu_{750}}{h\nu_{744}} \frac{A_{750}}{A_{744}} \frac{k_{Ar}}{k_N} \frac{\left\{\sum A_{ij}^N + K_M^N[M]\right\}}{\left\{\sum A_{ij}^{Ar} + K_M^{Ar}[M]\right\}} \frac{[Ar]}{[N_2]} \frac{I(744)}{I(750)} \qquad \text{M} = (N_2, H_2, Ar)$$

Here, $\sum A_{ij}^N$, $\sum A_{ij}^{Ar}$ are the sum of the transition probabilities for all radiative de-excitation processes from the considered excited levels (A_{744} = 1.06 × 10^7 s^{-1} and A_{750} = 4.72 × 10^7 s^{-1}), K_M^N, K_M^{Ar} are the quenching coefficients for the N(3p^{4}S^o) and Ar(2p$_1$) states by the M species and R_{744}, R_{744} are the spectral response of the system at 744 and 750 nm, respectively. The total nitrogen [N_2], hydrogen [H_2], and argon [Ar] concentrations, and the ratio [Ar]/ [N_2] can be calculated using the measured gas temperatures (applying the ideal gas law $p = NkT_g$ under nearly isobaric conditions) and the flow rates of the gas components.

3. **Theoretical model**

A nitrogen-hydrogen discharge sustained by the field of a HF, azimuthally symmetric (TM mode), traveling surface wave is under investigation. In the present work, molecular dissociation is studied on the basis of a self-consistent model including coupled equations for the plasma bulk describing the kinetics of free electrons, the vibrational kinetics of electronic ground state molecules $[N_2(X^1\Sigma_g^+, v), H_2(X^1\Sigma_g^+, v)]$, the kinetics of excited electronic states of molecules $[H_2(a^3\Sigma_g^+, c^3\Pi_u, e^3\Sigma_u^+, d^3\Pi_u^-, B^1\Sigma_u^+, c^1\Pi_u)]$, $[N_2(A^3\Sigma_u^+, a'^1\Sigma_u^-, B^3\Pi_g, C^3\Pi_u, a^1\Pi_g, w^1\Delta_u)]$ and atoms [H(1s), N(^{4}S)], the chemical kinetics of ions $[N_2^+, N_4^+, H^+, H^-]$ and the gas thermal balance. The equations for wave dispersion and wave power balance are further incorporated in the system of equations. The elementary processes taken into account to describe the electron and the heavy particles kinetics are described in previous articles [2,3] and the reader should refer to these works for details. The populations of $N_2(X^1\Sigma_g^+, v)$ and $H_2(X^1\Sigma_g^+, v)$ vibrational levels are derived from a coupled system of master equations taking into account vibrational excitation and de-excitation by electron collisions, vibration-vibration exchange between molecules, vibration-translation

single-quantum energy exchanges between molecules and molecules and atoms, (V-T) multiquantum energy exchanges between molecules and atoms, energy exchange in collisions with the wall and chemical reactions involving vibrationally excited H_2 molecules. For hydrogen, there exists an efficient vibrational excitation mechanism through electron impact excitation of the $H_2(B^1\Sigma_u^+)$ and $H_2(C^1\Pi_u)$ electronic states followed by fast decay to excited vibrational levels of the ground state $H_2(X^1\Sigma_g^+, v)$. Interaction with the discharge tube wall which strongly influences the population of some species in low-pressure discharges is taken into account by using radially averaged rates of wall losses [1] depending on the diffusion to the wall and the probability for wall deactivation γ [2,3]. For the calculation of the diffusion coefficients, the same expressions and approximations as in [2] are used. The loss of N and H atoms in low-pressure discharges is mainly due to wall reactions. The values of γ_N and γ_H substantially change in gas mixtures and have been determined on the basis of a kinetic model of surface processes involving N and H atoms which enables the calculation of γ_N and γ_H in N_2-N-H_2-H mixtures [3]. The radially averaged gas temperature has been calculated from the gas thermal balance equation together with the vibrational and chemical kinetics equations. The most important gas heating sources are V-T relaxation of N_2 and H_2 molecules and dissociation of N_2 and H_2 with production of "hot" N and H atoms. Thermal conduction to the tube wall is the main cooling mechanism. A parabolic gas temperature profile has been assumed for the calculation of the radially averaged gas temperature. The wall temperature T_W is also an important parameter because its value influences not only the gas temperature but also the probabilities for atomic wall reassociation, and, thereby, the surface kinetics of both types of atoms. The value T_W has been calculated approximately. It was assumed that T_W changes linearly along the tube and takes the value 295 K at the discharge end.

The theoretical treatment of wave-to-plasma power coupling is based as in [4] on a simultaneous solution of the wave power balance equation and the electron power balance equation, as obtained from the Boltzmann equation. The latter expresses the balance between the power gained by the electrons from the wave field and the electron collisional power losses in the plasma. Under steady-state conditions, the spatial rate of power change is due to the power absorbed by the electrons per unit discharge length. The sole input parameters of the model are the externally controlled parameters in the real experiment: operating frequency, ω; total absorbed power, P; discharge tube radius, R; pressure, p; and gas flow rate Q. As a result of the self-consistent treatment, the model determines the axial discharge structure (i.e. the axial variation of the discharge and wave quantities), and the population densities of the species of interest as a function of the mixture composition.

3. Results and discussions

The predicted and experimental discharge lengths are compared in Fig. 2 and Fig.3 as a function of the H_2 percentage. It is seen that the predicted and experimental discharge lengths are in good agreement. The observrd discrepancies can be attributed to the difference between the power delivered to the launcher (which is measured in the experiment) and the power absorbed in the discharge (which is an input parameter of the model). Another reason of discrepancy is the sensitivity of the calculated discharge length to electron ionization rate coefficients used. The large uncertainties of these coefficients should be pointed out.

When hydrogen is introduced into the mixture, the discharge length decreases because the discharge impedance changes. The reasons of this decrease are the following.

First, the role of N_2 associative ionization processes

$$N_2(A^3\Sigma_u^+) + N_2(a'^1\Sigma_u^-) \rightarrow N_4^+ + e$$

$$N_2(a'^1\Sigma_u^-) + N_2(a'^1\Sigma_u^-) \rightarrow N_4^+ + e$$

decreases since the populations of $N_2(A^3\Sigma_u^+)$ and $_2(a'^1\Sigma_u^-)$ metastables decreases due to deactivation in collisions with H_2 and H.

Second, the ionization potential of hydrogen molecules is higher than for nitrogen and more power is needed to maintain an electron-ion pair. Thus, the discharge length decreases when the H_2 percentage increases at constant power delivered to the discharge.

The axial distribution of the amount of power transferred into gas heating for 10% hydrogen percentage in the mixture is illustrated in Fig. 4. The gas temperature decreases non-linearly towards the plasma column end, scaling the non-uniform wave power dissipation.

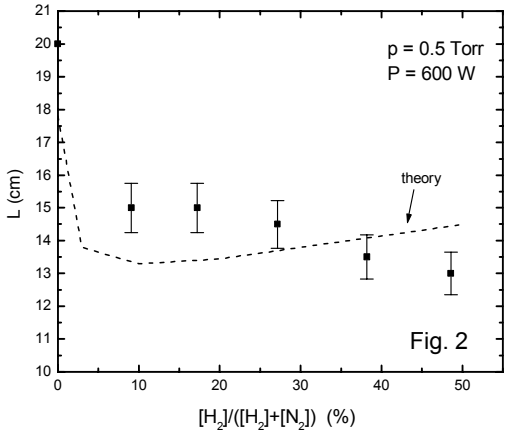

Fig. 2

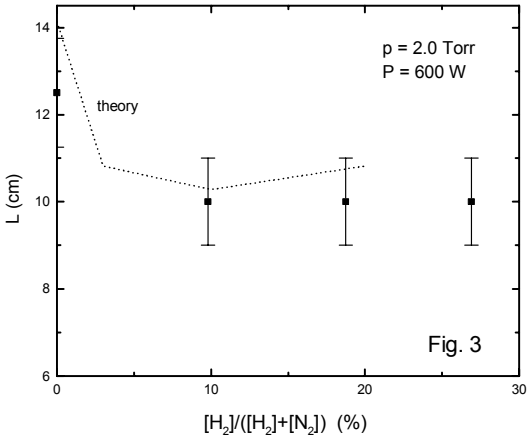

Fig. 3

The experimental gas temperatures were determined by measuring the rotational distribution of the second positive system of nitrogen $N_2(C^3\Pi_u, v') \rightarrow N_2(B^3\Pi_g, v'')$ in the 375.5- 379 nm wavelength range (i.e. 0-2 vibrational transition). Under nearly isobaric conditions as in the present experiment, the decrease in T_g results in a change of the neutral density along the discharge.

The experimental and the theoretical variation of the relative number $[N(^4S)]/[N_2]$ of ground state nitrogen atoms versus the H_2 percentage in the discharge is shown in Fig. 5. As can be seen, increasing the amount of H_2 in the discharge up to 50% causes an increase in the degree of molecular dissociation (up to about 10%) for the conditions considered. A good agreement between experimental and theoretical results should be pointed out. Besides electron impact dissociation, the important source channels of ground state atoms for the present conditions are the surface electron-ion recombination reactions

$$N_2^+ + e + \text{surface} \rightarrow N(^4S) + N(^4S)\ \text{(gas phase)}$$

$$HN_2^+ + e + \text{surface} \rightarrow NH + N(^4S)\ \text{(gas phase)}$$

The ions N_2^+ and HN_2^+ and the electrons reach the tube surface due to ambipolar diffusion. The ion HN_2^+ becomes the main positive ion with a small admixture of H_2 due to the fast ion-molecular reactions with parent ions N_2^+, H_2^+:

$$N_2^+ + H_2 \rightarrow HN_2^+ + H$$

$$H_2^+ + N_2 \rightarrow HN_2^+ + N$$

The intensity ratio of the Hα (λ = 656.2 nm) hydrogen atomic line to the λ = 750.39 nm argon line multiplied by the ratio of the fractional concentrations of Ar and H_2 in the discharge $[Ar]/[H_2]$ has been taken as a measure of the degree of hydrogen dissociation. As seen from Fig. 6 no changes have been experimentally observed when the H_2 percentage varies in the range 10-50%, i.e. the degree of molecular dissociation keeps approximatively constant for the present conditions. This behavior appears to be a net result of the competitive interplay of two important source channels of ground state hydrogen atoms, namely:

(1) electron impact dissociation;
(2) dissociation of H_2 upon quenching of nitrogen metastables [2]

$$N_2(A^3\Sigma_u^+) + H_2 \rightarrow N_2(X^1\Sigma_g^+) + H + H$$

$$N_2(a'^1\Sigma_u^-) + H_2 \rightarrow N_2(X^1\Sigma_g^+) + H + H$$

Figure 7 shows a comparison between the calculated and the measured axial profiles of the relative number density of hydrogen ground state atoms.

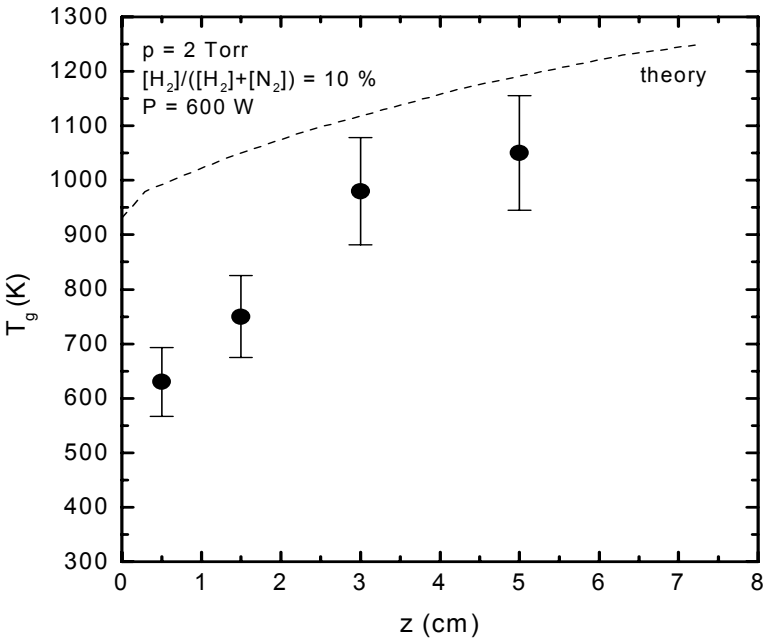
p = 2 Torr
[H2]/([H2]+[N2]) = 10 %
P = 600 W
theory
Tg (K)
z (cm)

Fig. 4

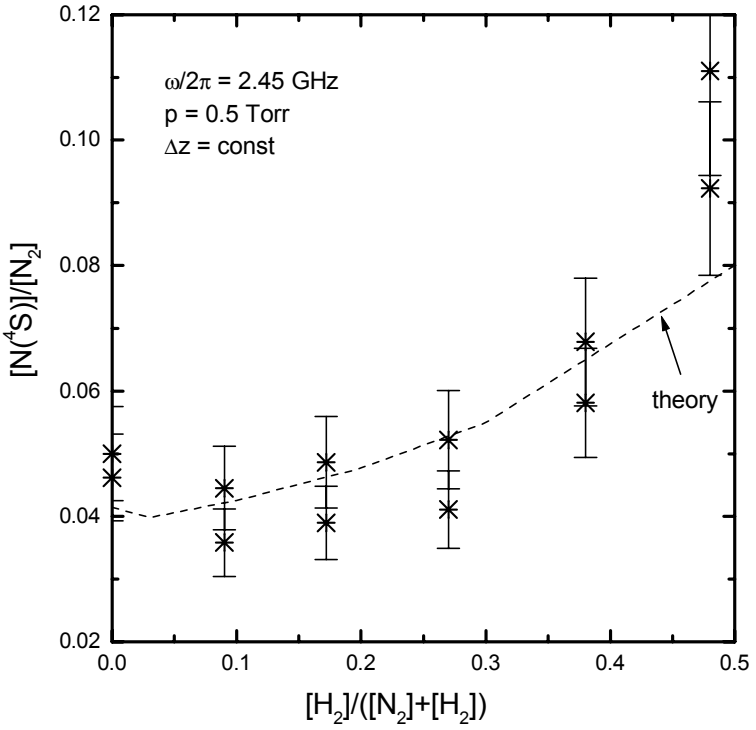
ω/2π = 2.45 GHz
p = 0.5 Torr
Δz = const
theory
[N(4S)]/[N2]
[H2]/([N2]+[H2])

Fig. 5

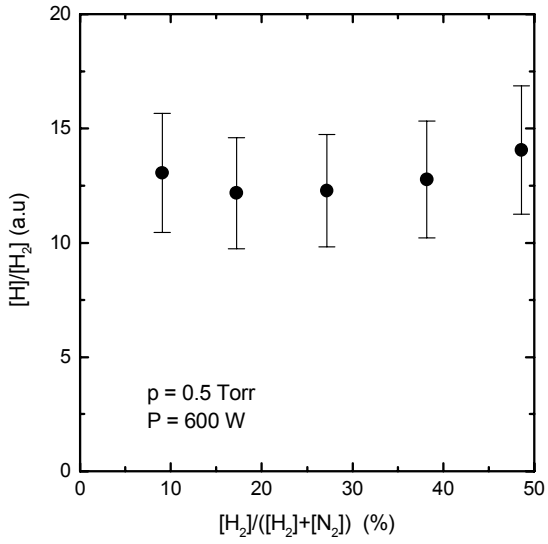

Fig. 6

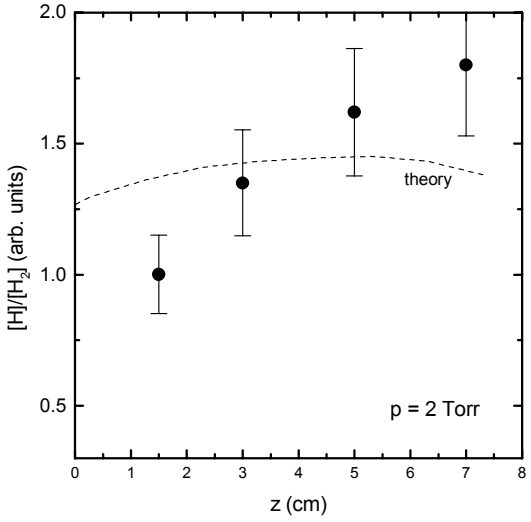

Fig. 7

4. Conclusions

The experimental investigations and the modeling of kinetic processes in N_2-H_2 surface wave discharge discusses in this paper enable one to understand the main processes of production of $N(^4S)$ and H(1s) atoms in this type of discharges. It was found that surface electron-ion recombination involving HN_2^+ ions is an important source of $N(^4S)$ gas phase atoms.

References:

[1] E. Tatarova, F. M. Dias, H. Van Kuijk, C. M. Ferreira – Vacuum **69**, 189 (2003).
[2] B. Gordiets, C. M. Ferreira, M. J. Pinheiro and A. Ricard – Plasma Sources Sci. Technol. **7**, 363 (1998).
[3] B. Gordiets, C. M. Ferreira, M. J. Pinheiro and A. Ricard – Plasma Sources Sci. Technol. **7**, 379 (1998).
[4] B. Gordiets, M. Pinheiro, E. Tatarova, F. M. Dias, C. M. Ferreira and A. Ricard – Plasma Sources Sci. Technol. **9**, 295 (2000).

Dust grains in a nuclear-induced plasma

[2]V.E. Fortov, [2]L.V. Deputatova, [2]V.I. Vladimirov, [1]V.A. Rykov, [1]A.V. Khudyakov, [2]V. S. Filinov

[1] *Leipunskii Research Institute for Physics and Power Engineering, Russian State Scientific Center, Obninsk, Russia*
[2] *Institute for High Energy Densities, Russian Academy of Sciences, Moscow, Russia*

Abstract
Results are presented from Monte Carlo calculations of the electric charge of dust grains in a plasma produced during the slowing down of the radioactive decay products of californium nuclei in neon. The dust grain charging is explained as being due to the drift of electrons and ions in an external electric field. It is shown that the charges of the grains depend on their coordinates. The time-averaged dust grain charges are used to carry out computer modeling of the formation of dynamic vortex structures observed in experiments.

1. Introduction

The objective of this paper is to produce dynamic ordered dust structures in a nuclear-track plasma created by nuclear-reaction products in inert gases and to carry out computer modeling of the processes that lead to their formation.

We apply the Monte Carlo (MC) method to calculate the time dependence of the charge of dust grains in a nuclear-track plasma that decays under the action of an external electric field into the flows of electrons and ions drifting toward the oppositely charged electrodes. We show that, since the grain charge is alternately affected by electron and ion flows, it fluctuates strongly about a value smaller than that typical of a quasineutral plasma. The mean values of the grain charge agree with those measured experimentally.

We theoretically explain the formation of the experimentally observed dynamic vortex dust structures in a nuclear-track plasma in neon in the presence of an external electric field and experimentally test our theoretical model for describing such a plasma. Numerical investigations carried out using the method of molecular dynamics make it possible to explain the characteristic features of the formation of vortex dust structures. The numerical results presented here agree qualitatively with the experimental data. Evidence is obtained of the potential character of the electrostatic forces experienced by the dust grains.

2. Calculation of the dust grain charge

Investigations of the behavior of dust grains in a plasma created by nuclear-reaction products provide new information on the self-organizing abilities of the dust in the plasma. The nuclear-track plasma differs considerably in properties from other plasmas, the primary difference being that it is strongly inhomogeneous in space and highly unsteady in time. In a nuclear-track plasma, a dust grain is affected by the flows of drifting electrons and ions that are cylindrically symmetric in structure (the symmetry axis being parallel to the propagation direction of an ionizing particle). Because of diffusion, the electron and ion flows spread out in the radial direction; simultaneously, because of a difference in the electron and ion diffusion coefficients, the radii of the electron and ion cylindrical flows increase to a far greater extent. As a rule, the dust grains acquire a negative electric charge, because the electrons are much more mobile than the ions. The ion flows efficiently discharge the grains. The external electric fields of both the dielectric walls of an experimental device and its electrodes can substantially redirect the drift flows of plasma particles.

The experimental device in which we observed the formation of levitated dust structures consists of an ionization chamber with horizontally oriented parallel electrodes. The chamber was filled with neon at a certain pressure. Dust grains were injected through a hole in the upper electrode into the interelectrode space, in which the external electric field was created. The role of the radioactive source was played by a 7-mm-diameter plane layer of ^{252}Cf at the lower electrode. The numerical results presented below were obtained for the experiments condition under which we observed liquidlike dust structures (see table 1 and Fig. 1).

Table 1. Conditions of our experiments on the formation of dynamic dust structures

Grain diameter, μm	Interelectrode distance, mm	Chamber radius, mm	Neon pressure, torr	High-voltage electrode potential, V	^{252}Cf source intensity, fission/s
1.87	17	15	380	162	10^5
2.1	35	25	557	152	$4 \cdot 10^6$

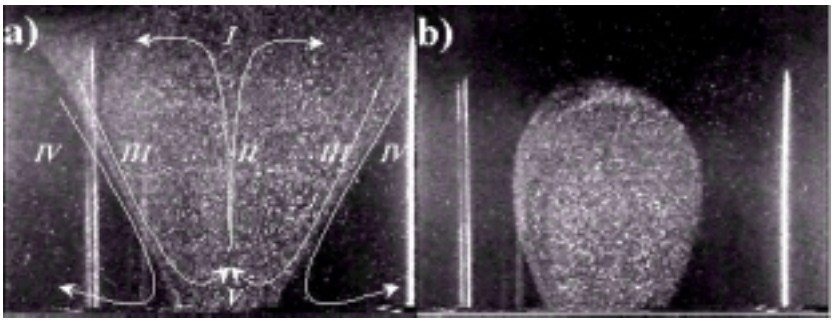

Fig. 1. Evolution of a cloud of Zn dust grains referring to conditions presented in last row of table 1. Each photograph corresponds to an observational area of 4.2x3.1 cm^2.

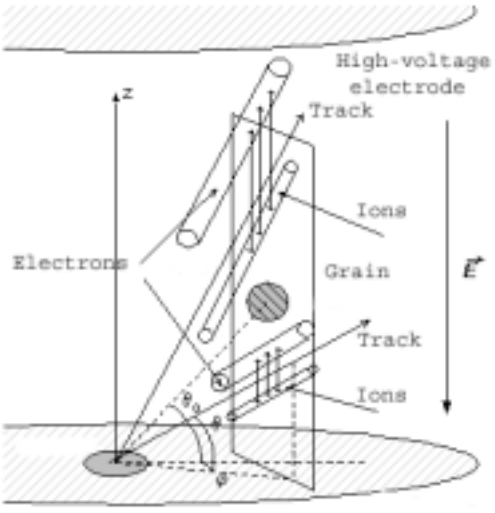

Fig. 2. Schematic of electron and ion motions in the vicinity of a dust grain in an electric field and geometry for MC simulations.

The physical model of dust grain charging consists in the following. The ionizing particles emitted from the source are stopped in the gas over a time of several nanoseconds. In turn, the primary electrons ionize neon atoms and thus produce a plasma cloud, which is called the track of an ionizing particle. The length of the track is much larger than the diameter of its cross section. As time elapses, the diameter of the track increases and, correspondingly, the electron and ion densities within the track decrease. The electric field generated in the track hinders charge separation [1] and delays this process in the presence of an external electric field. However, since the electron density gradient is large, the electron diffusion eventually reduces the electric field inside the track, so that the charges begin to be separated by the external field. Hence, the process of the formation of a track plasma and the charging of dust grains proceeds in the following two stages. The first, extremely short (~100 ns [1]), stage of the track evolution is far from being studied completely. In the second, much longer (several microseconds), stage (electron drift in the interelectrode space), the dust grain charge changes after the track plasma decays into two flows, namely, the flows of electrons and ions drifting toward the oppositely charged electrodes and toward the charged dielectric walls of the device.

Let us discuss the main physical assumptions underlying the mathematical description of the dynamic processes in a nuclear-track plasma. We start by considering the second stage of the formation of dust structures and charging of the dust grains, because the processes occurring in this stage have been studied in great detail. Since the electric field strength in our experiments was such that the measured current reached the saturation stage, we neglect the recombination of charged particles. When a dust grain is affected by an electron flow from the track toward the positively charged electrode (anode), it collects some of the electrons and thus acquires a negative charge. When an ion flux meets this grain, it decreases the grain's negative charge and may even charge the

grain positively (Fig. 2). A statistical treatment of these charging processes in time constitutes the essence of the mathematical model for calculating the grain charge. The main constants for these processes were chosen from the published data so as to satisfy the conditions of our particular experiments on the formation of ordered dust structures in neon. The energy losses were normalized to the energy cost of the production of one electron–ion pair (for neon, this cost is 35 eV). As usual, we assumed that the energy cost does not change as the energy of the ionizing particles decreases. The mathematical expression for this current is governed to a large extent by the ratio of the grain diameter to the mean free paths of the plasma particles. Thus, a grain diameter of 1μm is four times smaller than the electron mean free path, but six times larger than the ion mean free path. That is why we used two different approaches to calculating the electron and ion currents to the grain surface. The electron current, which is determined by the absorption cross section for plasma electrons, was calculated from the formula [2]

$$I_{-} = 2\sqrt{2\pi} \cdot n_{-} \cdot v_T \cdot a^2 \cdot \exp(-\frac{e\varphi}{T_{-}}), \qquad (1)$$

where a is the grain radius, n_- is the electron density, T_e is electron temperature, v_T is the electron thermal velocity, and φ is the potential acquired by the grain during the charging process. The charge acquired by a negatively charged grain in ion flows is determined by the currents of positive and negative ions to its surface. These currents are described by the following analytic formulas, which were obtained in the diffusion approximation:

$$I_{\pm} = \mp \frac{4\pi D_{\pm} N_{\pm} qe^2}{T_{\pm}\left[\exp(\mp qe^2 / r_0 T_{\pm}) - 1\right]} \qquad (2)$$

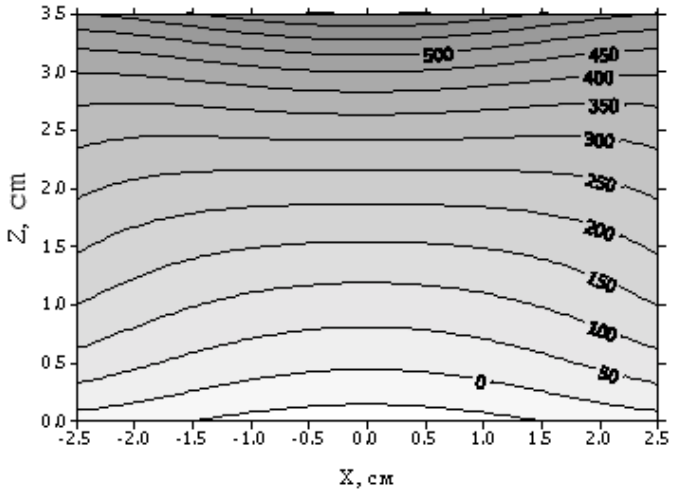

Fig.3. Dependence of the dust grain charge (in units of e) on the spatial coordinates under the conditions given in the table for a grain diameter of 2.1μm. The x-axis lies in the plane of the source, which is located at the point (0, 0).

The charge of the grain affected simultaneously by the electron and ion flows is determined by the total current of the electrons and ions. If the electron mean free path is much larger than the grain diameter, the electron current is calculated from formula (1); otherwise, it is calculated from the first of formulas (2). For electron mean free paths comparable with the grain diameter, the electron current is calculated by matching formula (1) with the first of formulas (2). The ion current to the grain surface is calculated from the second of formulas (2). As a result, the dynamics of the grain charge is described by the equation

$$\frac{dq}{dt} = I_{-} - I_{+} \qquad (3)$$

In a nuclear-track plasma with a low degree of ionization and a low electron temperature, the dust grains acquire small charges. Calculation results of time-average dust grain charge distribution are presented in fig.3.

3. Computer modeling of the dynamics of the formation of liquidlike dust structures

Since this is the first paper in which an attempt is made to model the formation of vortex structures from dust grains in a nuclear-track plasma, our theoretical approach does not pretend to completely describe the dust behavior under the experimental conditions in question. Our main objective here is to develop a reasonable model for describing the most characteristic features of the grain behavior in a plasma and to reveal the main physical mechanisms for the formation of a potential trap that ensures the levitation of the dust grains. That is why it is expedient to carry out numerical modeling for the experimental conditions under which vortex structures were stable. In this context, it is most reasonable to model the structures like that shown in Fig. 1, which were observed to form in a nuclear-track neon plasma at pressures from $2.5 \cdot 10^4$ to $7.5 \cdot 10^4$ Pa.

In order to investigate the levitation of dust grains and their mutual interactions, it is necessary not only to establish the mechanism for their charging but also to reveal the nature of the forces acting upon them. At present, several different mechanisms are being discussed in the literature that affect both the balance between the gravity and electrostatic forces experienced by the levitated dust grains and the interactions between them (see [3, 4] for details). Here, we investigate the complex dynamic problem under consideration by a simplified approach that makes it possible to trace the formation of dynamic vortex structures and their evolution using a reasonable amount of computer time. First, because of the comparatively small charges of dust grains and comparatively large mean distances between them, we neglect their mutual interactions. Second, because of the low intensity of the radioactive source and low degree of ionization of the nuclear-track plasma created by it, we ignore the drag forces exerted on dust grains by drift ion flows, which are directed primarily downward, i.e., toward the grounded electrode (with the radioactive source) and the dielectric wall of the device. In future studies, we are going to consider how the drag forces influence the formation of dynamic vortex structures. In the model developed here, we take into account the interaction of grains with the electrostatic fields of both the electrodes of the device and its walls, the weight of the grains, and the effect of their friction with the buffer gas. The levitation of dust grains results from the balance between the gravity force associated with the mass of the grain and the electrostatic forces of the device, in which case the electrostatic fields are governed equally by the internal plasma processes and by the processes of recombination and adsorption of the charges on the walls. In our experiments, the electrostatic trap was created by the electrostatic fields of both a negative surface charge on the walls of the device and a positive charge of the electrode with a hole. The effect of the steady state positive space charge induced in the plasma near the radioactive source is insignificant because the electron mobility is much higher than the ion mobility. This effect will be taken into account in ongoing studies. Numerical modeling of the vortex structures of charged dust grains in the electrostatic trap of the device requires the use of convenient analytic expressions for the electrostatic potential that should correctly reflect its physical nature. The numerical results presented in this paper were obtained from the expressions derived in [3].

Dynamic vortex dust structures in a nuclear-track plasma were simulated using the standard method of molecular dynamics. This method usually assumes calculations for a finite number N of particles in a cell of size L. In order for the computations to take a reasonable amount of time on available computers, we restricted our simulations to $N = 200$–1000. Accordingly, in order for an MC cell to capture the characteristic dust structure, the linear cell size was chosen to be equal to $L = 100 r_D \approx 3$ cm, which approximately corresponds to our experimental conditions. Note that such a small cell size, as well as a smaller number of dust grains in comparison with that in the experiments, substantially relaxed the requirements on computational resources and made it possible to reduce the run time of the code to about ten hours. We modeled levitated dust grains in an electrostatic trap with the potential derived in [3]. The characteristic potential at the chamber wall was varied in the range from 0.5 to 3 V. The z-axis was directed downward, i.e., along the direction of the gravity force. The initial spatial distribution of dust grains and their initial velocities were specified with the help of computer-generated random numbers, distributed uniformly within the interval from zero to unity.

4. Discussion of the calculated results

Here, we present the results of numerical simulations carried out by the standard method of molecular dynamics

for a cylindrical volume in space. Figure 4a shows parts of the grain trajectories inside a planar vertical axial layer of small radial thickness. The trajectories were calculated at three successive times. The arrows indicate the direction of the grain motion. The physical cause of the onset of dynamic vortex structures is the dependence of the charges of both dust grains and the device walls on the distance from the source. In fact, let us consider a grain located near the upper electrode, in which case the grain's negative charge is small because its distance from the source is large. Under the action of the gravity force, which exceeds the electrostatic force of attraction toward the upper electrode, the grain starts falling downward, i.e., toward the lower electrode. In such motion, the grain charge, first, decreases and, then, begins to increase. A downward moving grain experiences increasingly strong radial fields of the dielectric walls, whose charge, in turn, increases near the radioactive source. The radial forces bend the grain trajectory and cause the grain to move toward the device axis and toward the radioactive source at the axis. On the other hand, as the charge of the grain increases, it is affected by the increasingly strong upward-directed electrostatic force of the positively charged upper electrode. Because of inertia, the grain passes the equilibrium position and its charge continues to increase until the electrostatic force becomes larger than the gravity force. The grain begins to move upward, keeping its radial velocity component unchanged, until the gravity force becomes larger than the electrostatic force. Then, this cycle of the grain's motion repeats itself. As a consequence, most of the grain trajectories are very similar in shape to the infinity symbol. In the axial region of the device, the grains move predominantly upward, while, in the peripheral region near the walls, the grains fall downward. As a result, a dynamic vortex structure forms that consists of dust grains rotating in the same direction as the vortex structures observed in our experiments.

We stress the following important feature of the results obtained here. In our study, the main attention is focused on energy transfer from the radioactive source, which creates the plasma, to the disperse grains. The energy-transfer mechanism is associated with the variation in the charge of a moving dust grain. The charge of the grain is a function of its spatial coordinates and also depends on the energy parameters of the inhomogeneous plasma closely around it. Hence, the above system of levitated dust grains is an open system, which exchanges energy with its surrounding. Following [4], we assume that the electrostatic forces acting upon the grains are potential in character. As a result, these forces (which are defined as minus the spatial gradient of the potential energy) are described by two types of terms. The terms of the first type are formally similar in structure to those describing the Coulomb forces of particles with coordinate-dependent charges. The terms of the second type (non-Coulomb correction) account for the dependence of the charges on the spatial coordinates and are represented in terms of the gradients of the grain charges and the gradient of the surface charge on the dielectric walls of the device. Note that the effect of the surface charge is equivalent to that of an effective macroparticle. Non-Coulomb forces are directed opposite to the gradient of the absolute value of the grain charge and displace a dust cloud toward the region where the grain charges and, accordingly, the Coulomb repulsion energy in the device are both minimum.

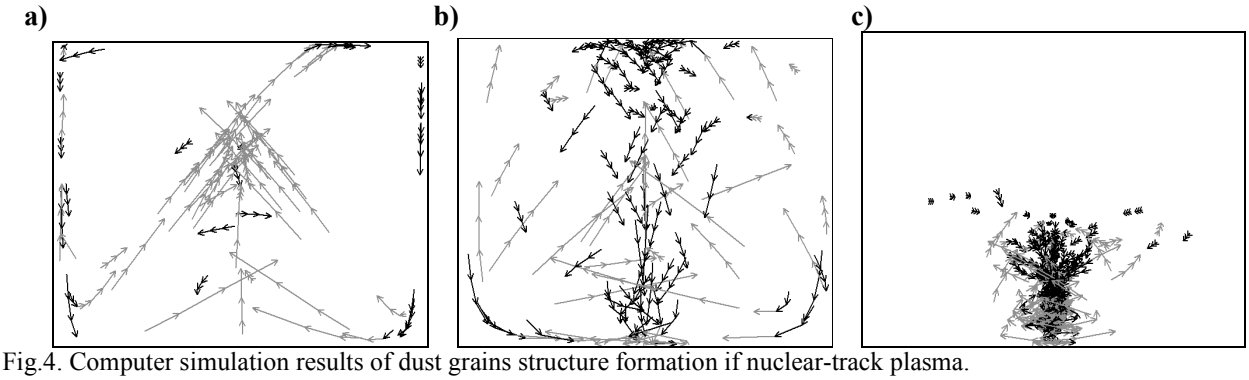

Fig.4. Computer simulation results of dust grains structure formation if nuclear-track plasma.

In the alternative approach [5], the electrostatic forces acting upon the dust grains in a plasma are assumed to be Coulomb forces $|F| \sim q(r_1)q(r_2)/| r_1 - r_2 |$ with coordinate-dependent grain charges. However, as was noted in [5], these forces cannot be represented in terms of the gradient of a certain effective potential. Consequently, the

terms describing these forces do not contain the charge gradient, as is the case with the terms of the second type. The results obtained from the alternative approach [5] for the same parameters and the same model device as in Fig. 4a are illustrated in Fig. 4b, which again shows parts of the grain trajectories inside a thin planar vertical axial layer, calculated at three successive times. We can see the formation of a vortex structure in which the grains rotate in two opposite directions, which, however, contradicts our experimental observations. Hence, a comparison of the results of numerical modeling with experimental data clearly indicates the potential character of the forces acting upon the grains in a nuclear-track dusty plasma.

The effect of the frictional forces exerted by the buffer gas on the dust grains is illustrated in Figs. 4c, which shows parts of the grain trajectories inside a vertical axial layer of small radial thickness in the model device, calculated at three successive times. The frictional forces were calculated from Stokes' law. The computations were carried out using the above two approaches. We can see that, under the action of the frictional forces, the linear dimensions of the dynamic vortex structures of dust grains become several times smaller than in the initial stage and the structures themselves evolve to a nearly steady stable state analogous to that simulated by the MC method in [5]. The calculated time evolution of the vortex structures agrees qualitatively with the experimental observations illustrated in Fig. 1. The supplemented video clip shows the simulated 3D motion of the dusty particles in the chamber of our experimental device. Red particles are moving upwards, while yellow particles are moving down. With the time evolution the size of the vertexes becomes smaller due to the friction energy losses. Detailed analysis of this motion is discussed above and the schemes of the trajectory in the thin axis layers are presented on Fig.4a and 4c.

References

[1] Budnik A. P., Sokolov Yu. V., and Vakulovskiy A. S. – Hyperfine Interact. **88**, 185 (1994)
[2] Tsytovich V. N. – Usp. Fiz. Nauk **167**, 57 (1997)
[3] Vladimirov V. I., Deputatova L. V., Molotkov V. I. *et al.*– Plasma Phys. Rep. **27**, 36 (2001)
[4] Zobnin A. V., Nefedov A. P., Sinel'shchikov V. A. *et al.*– Plasma Phys. Rep. **26**, 415 (2001)
[5] Zhakovski V. V., Molotkov V. I., Nefedov A. P. *et al.* – JETP Lett. **66**, 419 (1997)

The Oxidation of Carbon Soot in a Non-thermal, Atmospheric Pressure Plasma: Experiment and Modelling

Anthony R. Martin[1], James T. Shawcross[1] and J. Christopher Whitehead[2]

[1] *Accentus plc, F4 Culham Science Centre, Abingdon, Oxfordshire, OX14 3ED, UK*
[2] *Department of Chemistry, University of Manchester, Oxford Road, Manchester, M13 9PL, UK*

Abstract

The erosion of soot in a non-thermal, atmospheric pressure plasma has been modelled using a simplified, two layer, kinetic scheme for the surface reactions coupled with a gas-phase reaction mechanism that is appropriate to diesel exhaust gas. Experimental measurements of the rate for carbon erosion and the evolution of CO and CO_2 have been used to validate the model which has been extended to investigate the role of NOx, OH radicals and ozone in the plasma oxidation of the soot.

1. Introduction

Future legislative limits mean that it is necessary to substantially reduce the levels of pollutants such as oxides of nitrogen (NOx) and particulates in the exhausts from diesel engines. One approach is to use a non-thermal plasma or a hybrid plasma-catalyst system which has the potential for the removal of both NOx and particulates.

The work at Accentus on plasma aftertreatment has been reported previously [1,2] and it has been shown that it is possible to remove up to 99.9% of particulate matter of diameter around 60 nm. In support of this, a programme of chemical kinetic modelling of diesel exhaust aftertreatment has been undertaken. This has the objectives of aiding the understanding of the underlying principles behind the remediation processes, the improvement of these processes, and the prediction of aftertreatment performance under conditions not investigated by experiment. This paper describes the study of the heterogeneous oxidation of carbonaceous soot representative of particulate matter in diesel exhaust.

2. Experimental

The plasma reactor used for the experimental calibration tests was a single Dielectric Barrier Discharge (DBD) reactor. This consists of two concentric cylindrical electrodes; the inner electrode being the dielectric barrier in the form of a metal electrode in intimate contact with a surrounding alumina dielectric tube. The design is however flexible so that single or double dielectric barrier configurations can be evaluated. The reactor has the option of being packed with a filter material such as ceramic pellets *e.g.* 3-4mm diameter alumina spheres, fibres or monolithic type structures. The DBD reactor was powered by a 1-5 kHz AC power supply with typical applied voltages ranging from 3-15 kV resulting in plasma energy densities controlled up to ~100 J/L.

Gaseous analysis was performed using a Signal MaxSys 900 series emissions rack measuring NO_x, NO, CO_2, CO, O_2 and total hydrocarbon (THC). Hydrocarbon was measured using Flame Ionisation Detection (FID), NO / NOx using chemiluminescent analysis (CLA), CO & CO_2 using an Infra Red analyser and O_2 via a paramagnetic analyser. An FTIR (Bowmen Work*ir* / 2m gas cell pathlength; resolution $1cm^{-1}$) was used to crosscheck the THC and NOx emissions from the FID and CLA.

Experiments were performed using a pre-loaded, packed bed reactor in which the ceramic pellets were coated with carbon black (Degussa) to give a loading of about 500 mg of carbon. Soot oxidation runs were carried out at 200 °C and 300 °C with an atmospheric pressure gas stream for a fixed plasma energy density. The evolution of CO and CO_2 was recorded for varying deposited energy densities and the effect of added NOx upon the CO and CO_2 levels was also investigated.

3. Modelling

The modelling of the surface reaction chemistry is based on the mechanism detailed in Table 1. This was developed in a step-wise and systematic manner to explain the experimental results. The model represents the soot as two distinct layers. The chemistry and erosion takes place in an outer surface layer (C_s). The second layer is an inner or bulk layer which contains most of the mass of the soot (C_b). Site vacancies in the outer layer (X_s) are immediately replaced by carbon from the inner bulk layer (Reaction 5). Soot that is deposited from the gas phase as elemental carbon is absorbed into the sub-surface bulk layer (Reaction 6). The oxidation or erosion rate of the soot is given by the change in mass of the bulk layer as a function of time. The model reproduces the surface to volume ratio of the experimental reactor. This simplified two layer model derives from the work of Wicke *et al.*[3] and Mitchell *et al.*[4] It is assumed that the first step is the rapid adsorption of atomic and molecular oxygen onto the carbon surface followed by reaction to form surface adsorbed CO (Reactions 1 and 2) which can either react in a Langmuir-Hinshelwood type of mechanism to give CO_2 (Reaction 4) or desorb into the gas phase (Reaction 3). This last process is relatively slow. The rate constants are derived from the work of Wright [5], Laurendeau [6], Mitchell *et al.* [4], Backreedy *et al.*[7] and Bews *et al.*[8] The surface density of the outer layer, C_s, is taken to be 15 $m^2\ g^{-1}$. In practice, this value may be considerably larger depending on the carbonaceous material being studied [9] and its porosity which may also change during oxidation. We use the model to investigate the effect of surface density upon erosion rate.

	Reaction	A	E_a / cal $mole^{-1}$
1	$C_s + O \rightarrow CO_s$	5.00×10^7	1000.0
2	$C_s + C_s + O_2 \rightarrow CO_s + CO_s$	1.15×10^{15}	15000.0
3	$CO_s \rightarrow CO + X_s$	1.00×10^2	0.0
4	$CO_s + CO_s \rightarrow CO_2 + C_s + X_s$	4.00×10^{13}	0.0
5	$C_b + X_s \rightarrow C_s$	1.00×10^{40}	0.0
6	$C \rightarrow C_b$	1.00×10^5	0.0
7	$C_s + OH \rightarrow CO_s + H$	5.00×10^7	1000.0
8	$C_s + NO_2 \rightarrow CO_s + NO$	7.30×10^{16}	7000.0
9	$C_s + O_3 \rightarrow CO_s + O_2$	1.25×10^7	1000.0

Table 1 The surface reaction mechanism for the plasma oxidation of carbon soot. The subscript –s represents surface bound species and the subscript – b, the bulk sub-layer. Rate constants are in the form $k = A \exp(- E_a / RT)$, where A is in the units of cm^3, mol, s, as appropriate to the reaction order.

In the final stages of the modelling, gas-phase chemistry was also included in the model to simulate the presence of diesel exhaust gas mixtures. Typically, this included 10% O_2, 400 ppm propene, 500 ppm NO, 50 ppm NO_2, balance N_2. This enabled us to investigate the competition between homogeneous and heterogeneous reactions for important species such as NOx, OH radicals and atomic oxygen. The gas-phase hydrocarbon mechanism which has been extensively validated by experimental plasma measurements is outlined in Figure 1 and is detailed elsewhere [10].

The chemistry involved in the plasma processing is modelled using a FORTRAN program, PELLSOOT, which is based on the chemical kinetics package, SURFACE CHEMKIN-II [11]. Following the method of Gentile and Kushner [12,13], we assume that there is uniform processing of the gas as it passes through the reactor. During each half-cycle, the microdischarge current pulses create active species which then go on to initiate or continue the chemistry. In our model, a fresh supply of the active species is injected into the reaction mixture at each pulse and the chemistry is allowed to continue until the next pulse. The modelling continues until the experimental residence time (determined by the gas flow rate and the reactor volume) when the processing ceases and the final concentrations are output. We calculate the densities of the species produced in the discharge using the program ELENDIF [14] which indicates that atomic oxygen is the only

significant reagent produced at the plasma energy densities used in this work. Other reactive radicals such as OH may be produced by secondary gas-phase reactions.

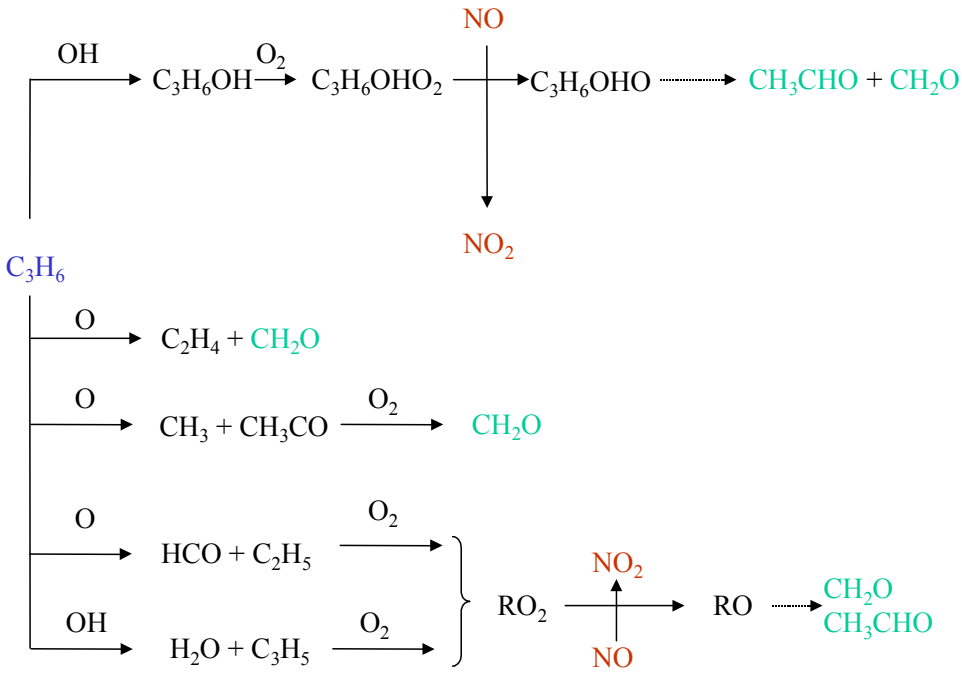

Figure 1 A schematic representation of the gas-phase reaction mechanism for propene oxidation in the presence of NOx

4. Results and Discussion

Figure 2 shows the measured evolution of CO and CO_2 resulting from the plasma oxidation of a packed bed of carbon black at 200 °C using a gas flow of 10% O_2, 90% N_2. It can be seen that the gases are evolved almost immediately upon switching on the plasma, reach a steady-state concentration and then decrease when all the soot has been removed by oxidation. The ratio of CO_2 to CO remains constant at about 2.5. Wicke et al. [3] found a value of between 1.6 and 2 for the same ratio when studying the oxidation of paraffin soot by atomic oxygen at room temperature. The oxygen atoms were produced by microwave dissociation of molecular oxygen at a pressure of 1 Torr in their experiment.

Figure 3 shows the results of the modelling of the soot erosion and the consequent evolution of CO and CO_2 using reactions 1 – 6 in Table 1. The time scale is limited by computational restrictions but it can be seen that it successfully models the form of the experimental measurements shown in Figure 2 and accurately reproduces the concentrations of the evolved CO and CO_2 and their measured ratio. Figure 4 shows the comparison of the modelling with the experimental measurements of the evolution of CO and CO_2 studied as a function of the energy deposited into the plasma (in J / litre). This deposited energy effectively controls the amount of atomic oxygen produced in the discharge. Again the agreement is good, although the curvature observed experimentally for the CO_2 evolution is not reproduced in the modelling. The modelling shows that the soot erosion rate is linear with the concentration of atomic oxygen supplied by the plasma discharge and that it is non-linear in temperature. The calculated erosion rates range between $1 - 20 \times 10^{-5}$ g s^{-1} at 200 °C. Another parameter that determines the calculated erosion rate is the surface density of the soot in the surface layer that is being eroded. A change in the surface density from 10 to 50×10^{-8} mol cm^{-2} increases the erosion rate by a factor of about 3.

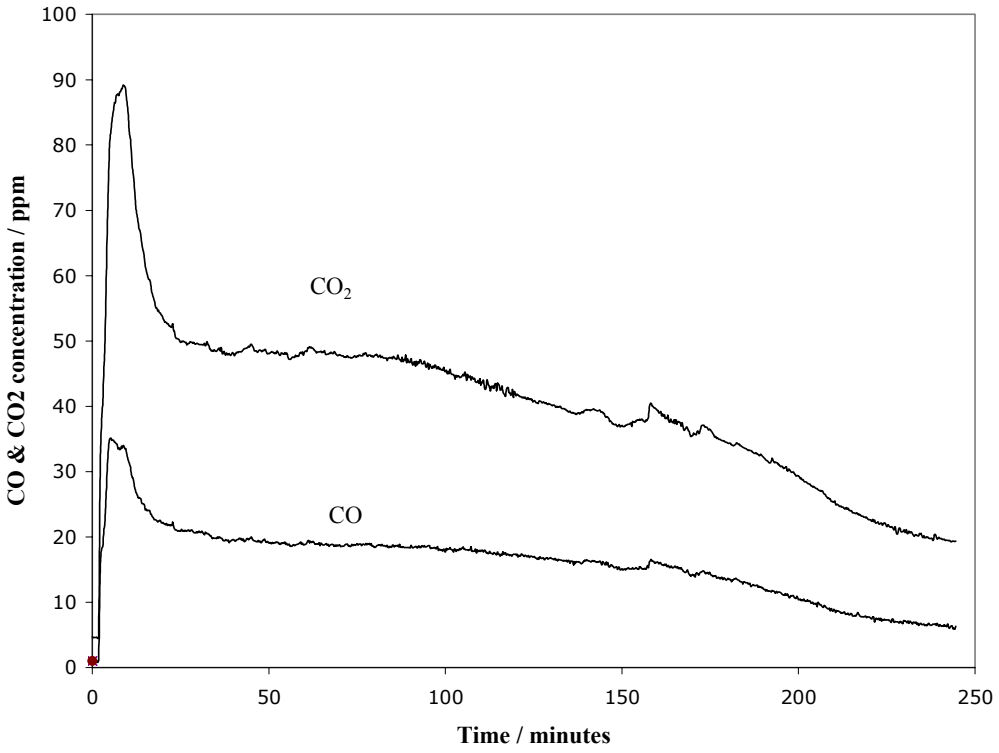

Figure 2 The time evolution of gaseous CO and CO_2 resulting from plasma oxidation of a packed bed of soot at 200 °C..

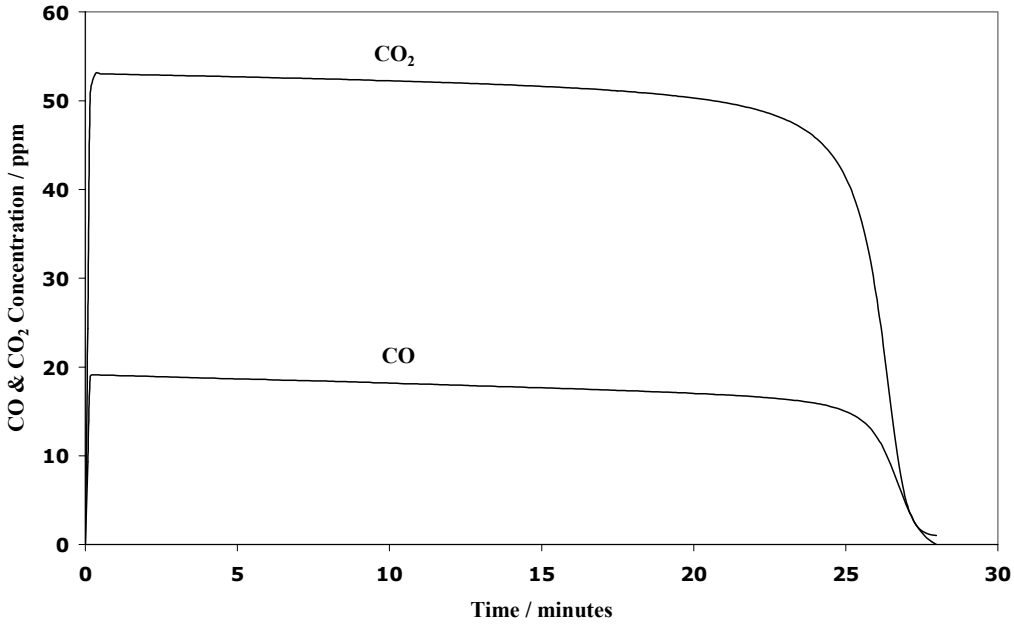

Figure 3. The modelling of the evolution of CO and CO_2 for the plasma oxidation of soot at 200 °C in 10% O_2, 90% N_2.

When the gas-phase chemistry appropriate to diesel exhaust gas is included in the plasma discharge in addition to the surface chemistry, reactions of additional species need to be considered. These include the oxides of nitrogen (NOx), ozone (O_3) and the hydroxyl radical (OH). In the absence of the simulated diesel exhaust gas with its hydrocarbon component, we find that the addition of NO (the major component of NOx in the diesel exhaust) to the reactor inhibits the formation of CO and CO_2 and decreases the oxidation rate. A similar observation has been made by Wicke and Grady [15] who attribute the reduction to the absorption of NO onto the soot surface blocking potential sites for the oxidation by the adsorption of atomic oxygen.

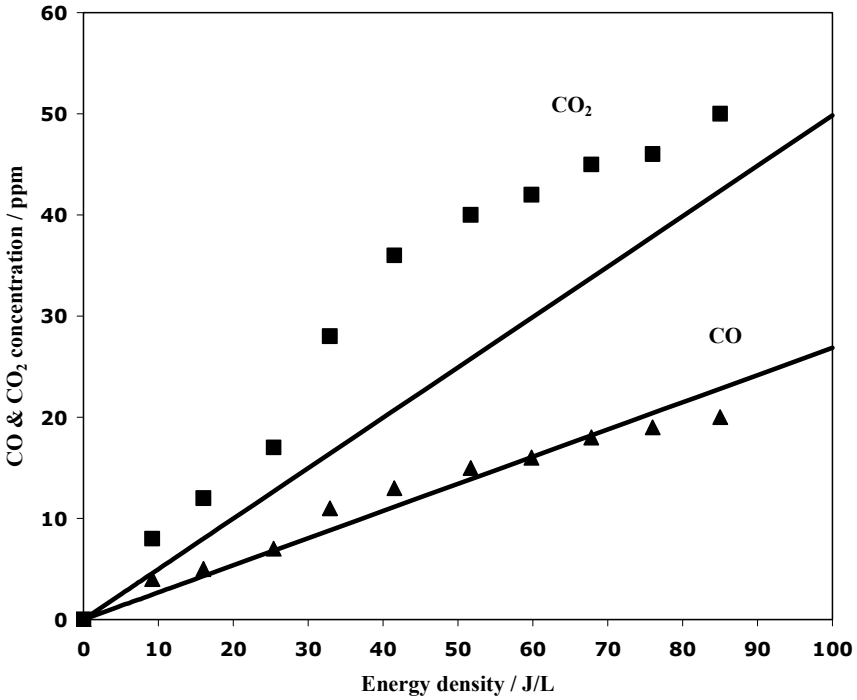

Figure 4. The variation of gas evolution as a function of the plasma deposited energy. The experimental measurements are represented by points (■ CO_2; ▲ CO) and the modelling results are the solid curves.

However, when propene is added to the system rapid gas-phase reactions convert the NO to NO_2. These reactions mainly involve HO_2 and peroxy radicals, RO_2, and are indicated in Figure 1

$$NO + HO_2, RO_2 \rightarrow NO_2 + OH, RO.$$

This conversion is the first stage of plasma remediation of NOx and the use of catalytic converters downstream of the plasma to reduce the generated NO_2 into N_2 and O_2 is the subject of much current research. However, it is known that NO_2 participates in the oxidation of soot via reaction 8 in Table 1 resulting in a heterogeneous conversion of the plasma generated NO_2 back to NO. Dorai and Kushner [16,17] have shown that the extent of this back conversion depends on the amount of soot present. We find that in the presence of 400 ppm of propene, the soot oxidation rate increases markedly for the addition of 50 ppm of NO and then becomes constant for NO concentrations above about 100 ppm.

It is known that OH radicals are more reactive than O atoms towards the oxidation of graphite at 298 K [18]. It might be expected then that in the presence of the hydrocarbon component of the simulated diesel exhaust where OH radicals are produced and play an important part in the gas-phase mechanism, there would be considerable enhancement in the soot oxidation rate via reaction 7. However, the model shows only a very modest increase in the oxidation rate of less than 10% when reaction 7 is included. This can be rationalised

when it is realised that OH radicals are very reactive in the gas-phase and participate in a chain reaction in which the hydrocarbon is oxidised. This means that the steady state concentration of OH radicals is very small and there are very few available to oxidise the soot.

In gas flows that do not contain hydrocarbon or NOx, it is possible to generate ozone when oxygen atoms are in excess. This will reduce the oxidation rate unless the mechanism correctly accounts for the oxidation of carbon by ozone (Reaction 9). It was found that a rate that is about 25% that for oxidation by atomic oxygen (Reaction 1) is required. When the simulated gas stream containing hydrocarbon and NOx representing diesel exhaust is used, it is possible that ozone is an important transient intermediate in the gas-phase chemistry. However, no net ozone is produced in the gas phase and surface oxidation *via* Reaction 9 does not take place.

5. Conclusions

We present a simplified model for the oxidation of soot by the products of a plasma discharge that considers two distinct surface layers or regions. We find that this is able to account for the measured rate of carbon erosion and the evolution of CO and CO_2 in plasma discharges of O_2 / N_2 gas streams. The model has been used to examine the effect of soot erosion when the gas stream is chosen to be representative of diesel exhaust gas using a simplified gas-phase mechanism that has been previously validated under a range of experimental conditions. In this way, the role of NOx, OH radicals and ozone has been investigated. The versatility and simplicity of the model will allow it to be used to examine a range of experimental conditions in a time-efficient manner. It is our aim to continue to support this modelling activity with a range of experiments that can be used to further validate and extend the model.

References

[1] S.E. Thomas, A.R. Martin, D. Raybone, J.T. Shawcross, K.L. Ng, P. Beech, J.C. Whitehead, Non thermal plasma aftertreatment of particulates - theoretical limits and impact on reactor design, Society of Automotive Engineers "Spring" Fuels & Lubricants Meeting, Paris, 2000, SAE Paper 2000-01-1926.

[2] S.E. Thomas, J.T. Shawcross, R. Gillespie, D. Raybone, A.R. Martin, The role of NO selective catalysts in the plasma enhanced removal of NOx and PM from diesel exhausts., Society of Automotive Engineers: Non-Thermal Plasma Emission Control Systems, 2001, SP-1639.

[3] B.G. Wicke, C. Wong, K.A. Grady, Comb. & Flam. 66 37 (1986).

[4] R.E. Mitchell, R.J. Kee, P. Glarborg, M.E. Coltrin, Twenty-Third Symposium (International) on Combustion. The Combustion Institute, 1990, 1169-1176.

[5] F.J. Wright, The oxidation of soot by O atoms, 15th International Symposium on Combustion. The Combustion Institute, 1979, 1449.

[6] N.M. Laurendeau, Prog. Energy Combust. Sci. 4 221 (1978).

[7] R. Backreedy, J.M. Jones, M. Pourkashanian, A. Williams, Far. Disc. Chem. Soc. 119 385 (2001).

[8] I.M. Bews, A.N. Hayhurst, S.M. Richardson, S.G. Taylor, Comb. & Flam. 124 231 (2001).

[9] W. Choi, M.T. Leu, J. Phys. Chem. A. 102 7618 (1998).

[10] A.R. Martin, J.T. Shawcross, J.C. Whitehead, in preparation (2003).

[11] R.J. Kee, F.M. Rupley, J.A. Miller, Chemkin-II: A Fortran Chemical Kinetics Package for the Analysis of Gas Phase Chemical Kinetics. Sandia National Laboratory, 1991.

[12] A.C. Gentile, M.J. Kushner, J. Appl. Phys. 78 2074 (1995).

[13] A.C. Gentile, M.J. Kushner, J. Appl. Phys. 78 2977 (1995).

[14] W.L. Morgan, B.M. Penetrante, Comp. Phys. Comm. 58 127 (1990).

[15] B.G. Wicke, K.A. Grady, Comb. & Flam. 69 185 (1987).

[16] R. Dorai, K. Hassouni, M.J. Kushner, J. Appl. Phys. 88 6060 (2000).

[17] R. Dorai, M.J. Kushner, J. Phys. D: Appl. Phys. 35 2954 (2002).

[18] M.F.R. Mulcahy, B.C. Young, Carbon 13 115 (1975).

Analysis of plasma-generated radicals on polymer surfaces

B. Finke, A. Meyer-Plath[1], K. Schröder, A. Ohl

Institut für Niedertemperatur-Plasmaphysik, Greifswald, Germany

Abstract
Plasma functionalisation in gas phases like ammonia allows to equip polymer surfaces with amino functional groups. An important question of this functionalisation consists in the limited knowledge about heterogeneous interface reactions, especially radical formation and subsequent reaction processes. Useful analytical methods comparable to those available for gas phase reactions are scarce. Here we report on investigations of plasma generated C-radicals by NO-labelling, showing similar effects for different plasmas.

1. Introduction

For novel applications of plasma functionalised polymer surfaces, progress in quality of surface functionalisation is desirable with respect to selectivity and efficiency. Polymer surface radicals created during the plasma process by bond scission play a prominent role for heterogeneous surface reactions and give rise to post – process oxidation.
Several papers deal with the investigation of radical formation in plasma treated polymers. Kuzuya et al. [1] studied plasma induced surface radicals of polyethylene (PE) by ESR. Another group [2] used diphenyl-picrylhydrazyl (DPPH) as radical scavenger for the same purpose. This liquid phase reaction has some disadvantages such as altering the surface only by the DPPH solution. Holländer et al. [3] investigated the formation and subsequent reaction of VUV- and hydrogen plasma generated radicals on surfaces of polyethylene (PE), polypropylene (PP) and polystyrene (PS) by using the scavenger nitrogen monoxide NO. The gaseous NO belongs to the few natural and reactive compounds with a lone electron and is therefore particularly suitable for a radical verification. Plasma generated primary, secondary and tertiary carbon radicals react with NO in a different way (see fig. 1). The produced nitrogen and/or oxygen containing functional groups can be differentiated by X-ray photoelectron spectroscopy (XPS) using the N1s region by analysis of their chemical shift. Radical concentrations are linearly correlated to the added nitrogen by reaction with NO. The present work studies surface radicals on polystyrene generated by cw and pulsed microwave-excited plasmas in Ar and NH_3.

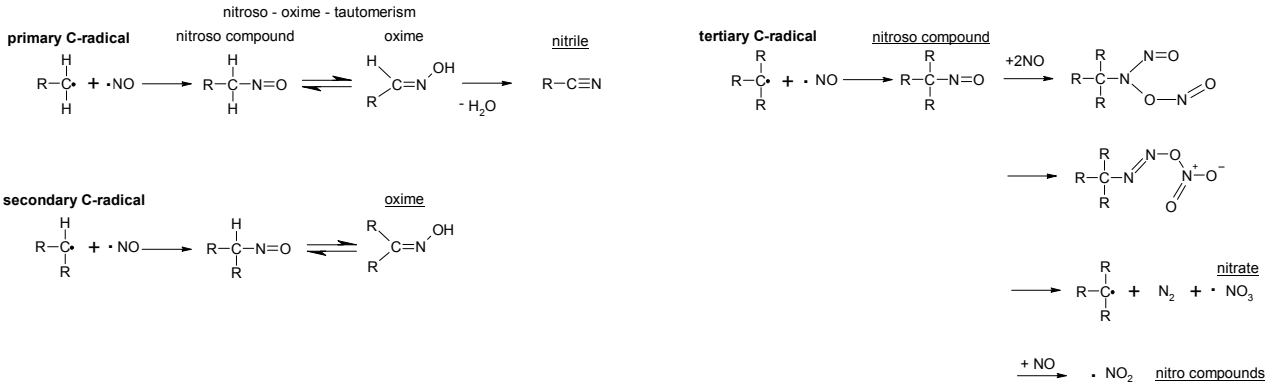

Fig. 1: Reaction of different C-radicals with NO after [3]

2. Experimental

2.1 Processing

Surface functionalisation processes are extremely sensitive to process contaminations. For this reason extraordinary diligence was set to a clean process environment. The experiments were performed in a UHV cluster tool which combines clean plasma reactors with *quasi in situ* XPS analysis and gas phase derivatisation [4]. After switching off the plasma, the samples were transported via the UHV-transfer system

[1]present address: *Bundesanstalt für Materialprüfung und –forschung, Berlin, Germany*

to the XPS and the derivatisation chamber, respectively. The separately pumped UHV-transfer system ($p = 10^{-8}$ mbar) ensures contamination free sample exchange between the three subsystems. In order to avoid wall contamination, the UHV-plasma reactor (base pressure: circa 10^{-7} mbar) was kept all the time free of oxygen-containing gases. Oxygen impurities are known to reduce the nitrogen functionalisation efficiency [5]. Several additional techniques have been applied to reduce the residual contamination level of oxygen and for our purposes also nitrogen, as much as possible. Nonetheless, a small but noticable nitrogen contamination was verified on Ar-plasma treated PS surfaces without NO-derivatisation (see fig. 3). The MW plasmas were generated in surface-wave-sustained (SWS) mode forming a radially-spread plasma glow of 22 cm in diameter in close contact to the MW-coupling window. Their thickness varied with pressure, being about 2 cm at the standard pressure of 0,1 mbar (NH_3-plasma) and 1 mbar (Ar-plasma) respectively. The polymer samples were treated in the afterglow 9 cm below the active plasma zone.
Experiments were carried out in continuous wave (cw) and in pulsed (pp) plasma mode. In the pp mode, the *effective* treatment duration, i.e. the product of duty cycle and *total* treatment duration was kept constant at 9.6 s (1 ms pulse / 100 ms pause). The gas flow rate was 15 sccm NH_3 and 20 sccm Ar, respectively. A detailed study of the excitation mode is given in [6].

2.2 Surface Diagnostics

A special measuring procedure was employed to analyse radicals after having reacted with NO both *in situ* and *ex situ* by means of X-Ray Photoelectron Spectroscopy (XPS). The results of the quasi *in situ* XPS (EA125 U5, OMICRON, Taunusstein, Germany, unmonochromatic Mg-K_α-line) surface analysis were combined with high resolution measurements of the *ex situ* XPS (Axis Ultra, KRATOS, Manchester, GB). The ascertained *in situ* XPS values were calibrated by the *ex situ* values of the high quality machine. In fig. 2 and 4, examples are given for the achieved quality of a peak fit performed in this manner. Quantification of the amino groups was achieved *ex situ* via fluorine surface density after derivation reaction with trifluoro-methylbenzaldehyde (TFBA) [7,8]. The radical verification was carried out with NO at 400 mbar and ambient temperature in a stainless steel derivatisation chamber for 1 h. 5 minutes were needed for the sample transport from the reactor to the derivatisation chamber.

2.3 Experimental procedure

First investigations were realised with a pure Ar-plasma. Meta stable Ar-species are known to efficiently create surface radicals on polymers. For the pure Ar-plasma, no nitrogen contribution from the plasma process should be considered in a clean plasma reactor. But as mentioned above, it´s not as simple as that (see 2.1). The slight nitrogen incorporation could be clearly identified by XPS. However, the attained knowledge on the quenching NO reaction allowed to extend the radical quantification method to surfaces that were subjected to nitrogen–containing plasmas.
The **procedures** are characterised by the following schemes:

A) Ar-plasma

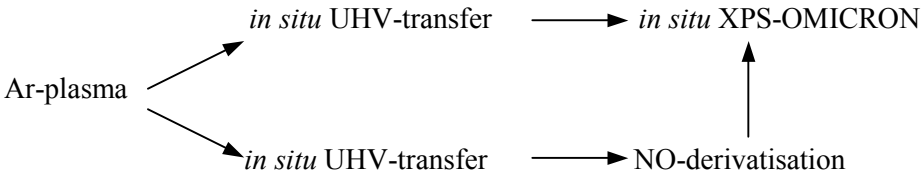

B) NH_3-Plasma a means of amino functionalisation and radical proof

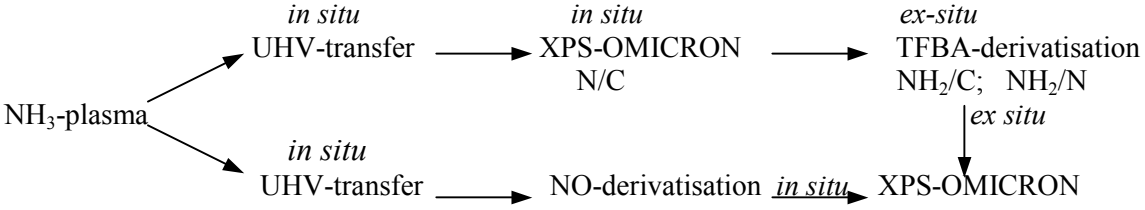

ex situ XPS-KRATOS (high resolution)

According to the schemes, the plasma experiments with and without NO based radical verification were carried out parallel. That means every "normal" Ar- or NH_3-plasma treatment was accomplished by a second, identical experiment, which includes the NO-derivatisation procedure. Polystyrene (PS) was investigated (FalconTM tissue culture dishes, Becton-Dickinson, NJ,USA) and used without further chemical cleaning.

3. Results and discussion

3.1 Analysis of plasma generated surface radicals

Radical creation efficiencies were very similar for cw Ar- and NH_3-plasmas. Quenching reactions with NO were used to explain the formation of different nitrogen-containing functional groups and their derivation from primary, secondary and tertiary carbon radicals. The reaction products for instance amines, oximes, nitroso and nitro compounds, nitrites and nitrates appear at significantly different chemical shifts in the XPS N1s region and were determined by peak fitting, following a formal procedure similar to that suggested by [3]. Conclusions on the concentration of radicals were possible, in our case as difference of the N/C concentrations after the plasma process without and with NO-derivatisation.

3.1.1 Ar-plasma

Comparison between the peak fitting of the XPS-KRATOS and the XPS-OMICRON *in situ* measurements for one and the same sample with NO-derivatisation are exemplified in fig. 2 and fig. 4. Certain differences between *in situ* and *ex situ* XPS spectra become generally apparent. Especially the $–NO_2$ and $–NO_3$ peaks disappear *ex situ* by exposure to air. This cannot be explained until now.

Fig. 2: *ex situ* XPS Kratos measurement of the N1s peak **with** NO-derivatisation (PS; 35s cw Ar-plasma).
The peak fit procedure applied below were derived from such highly-resolved scans. While the peak position was exactly allotted, the peak width was not considered.

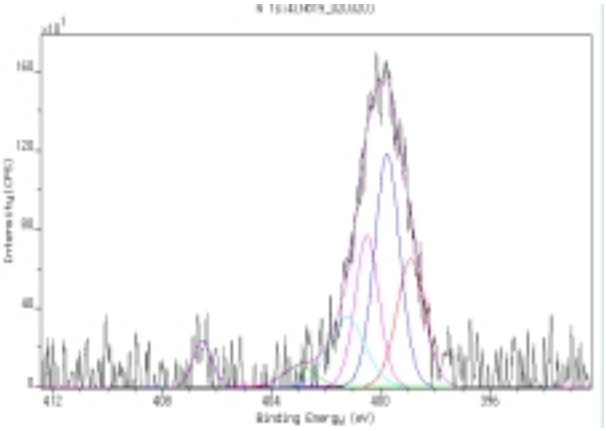

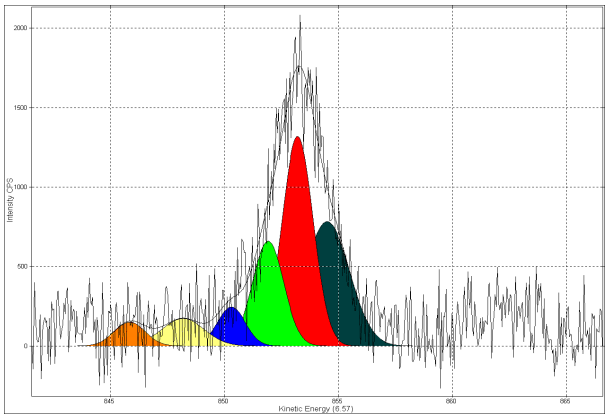

Fig. 3: *in situ* XPS measurement of the N1s peak **without** NO-derivatisation (PS; 35s cw Ar-plasma).
The reactor wall contamination leads to the N1s peak.

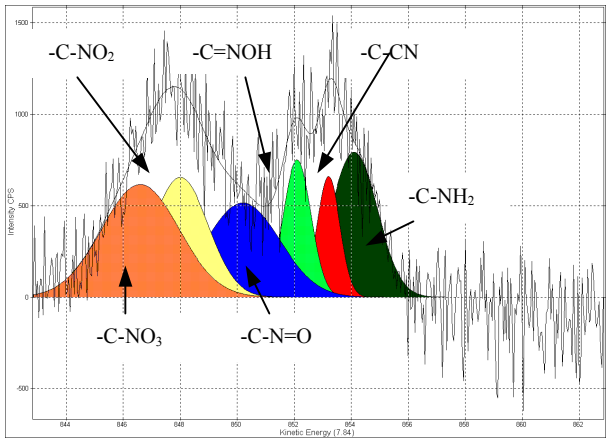

Fig. 4: *in situ* XPS measurement of the N1s peak **with** NO-derivatisation (PS; 35s cw Ar-plasma).

Interestingly a PS-surface after cw Ar-plasma treatment without *in situ* NO-derivatisation (fig. 3) shows N1s peaks for nitrogen in different binding states - a sign for residual reactor contamination. After NO-derivati-

sation a second broad peak appears at binding energies of 403 – 408 eV which can be assigned to the reaction products of tertiary C-radicals with NO.
The formal peak fit shows the following results:
For primary and secondary radicals reaction products are amines –C-NH_2, nitriles –C-CN and oximes –C=N-OH >>> N1s peak in the XPS spectrum between 397 eV and 402 eV
For tertiary radicals reaction products are nitroso –C-N=O and nitro compounds –C-NO_2 as well as nitrates –C-NO_3 >>> a second N1s peak between 403 eV and 408 eV

A more detailed picture arises by quantification of the possible nitrogen functionalities (fig. 5) and drawing comparison of the presented bands.

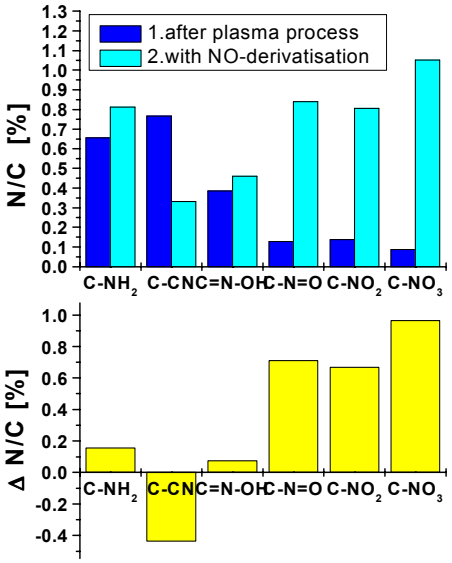

Fig. 5: Detection of surface radicals (PS, 35s cw Ar-plasma, *in situ* N1s-XPS)

Comparison of NO-derivated and not derivated polystyrene:
The available species like amines, nitriles, oximes, nitroso and nitro compounds, nitrites and nitrates were generated in an Ar-plasma in a dimension up to circa 1 % N/C each.
Clearly the differences of the fitted peak areas ΔN/C show the predominant formation of approximately 2.3 % tertiary radicals/C. In parallel to that conclusion a comparative calculation of the whole nitrogen content N/C after NO-derivatisation minus N/C after plasma treatment of XPS measurements results in good agreement 2.2 % radicals/C.
Obviously, the existence of primary and secondary C-radicals is questionable, because the markers are only small for these functional groups and even negative in the case of the nitriles –C-CN.

3.1.2 NH_3-plasma
The procedure of radical verification for the cw Ar-plasma could be successfully transferred to cw and pulsed NH_3-plasma. Fig. 6 and 7 show the peak fit of the N1s bands of polystyrene treated with 40 s cw NH_3-plasma first after the plasma process and second with NO-derivatisation. Analogous results for a pulsed NH_3-plasma are given in fig. 8 and 9. The measured, not NO derivatisated N1s XPS peaks (fig. 6 and 8) at approximately 399 eV characterise the accomplished plasma process, in this case the amino functionalisation. Note that tertiary radicals are really not marked here. However C-radicals are present as shown after NO-derivatisation. The NH_3-plasma process therefore appears to be a clean process. After NO-derivatisation additional to the known first peak a second N1s peak appears at circa 405 eV in the XPS spectrum (fig. 7 and 9). Radical creation processes seem to be very similar to the Ar-plasma, but there exists also appreciable differences in quantity (see fig. 10).

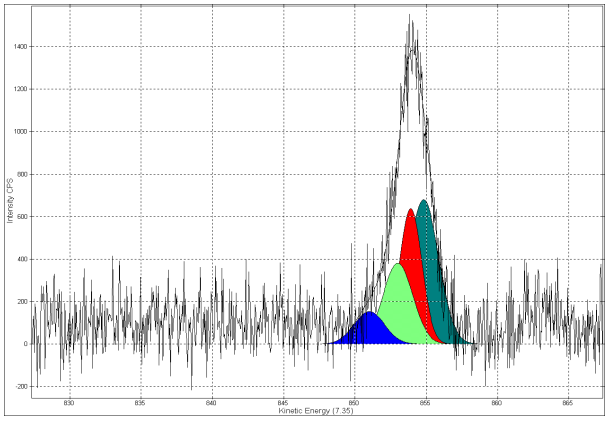

Fig. 6: *in situ* XPS measurement of the N1s peak **without** NO derivatisation (PS; 40 s cw NH_3-plasma).

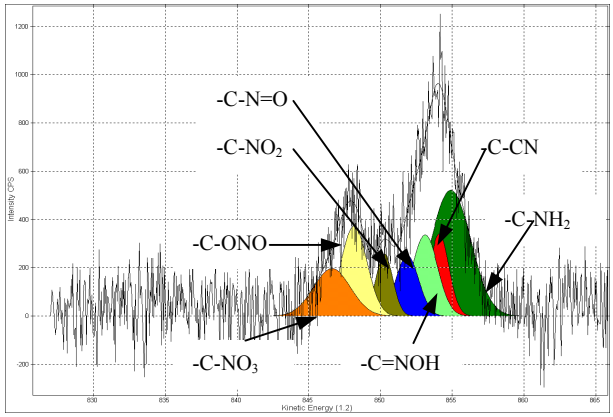

Fig. 7: *in situ* XPS measurement of the N1s peak **with** NO derivatisation (PS; 40s cw NH_3-plasma)

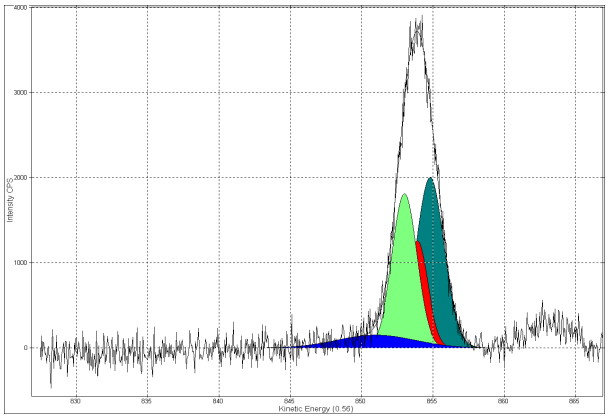

Fig. 8: *in situ* XPS measurement of the N1s peak **without** NO derivatisation (PS; 10s eff. pulsed NH_3-plasma)

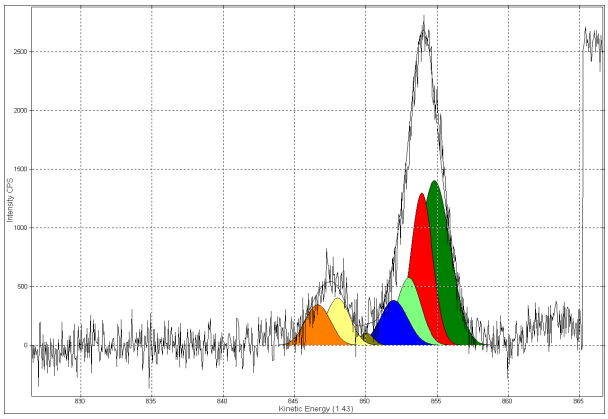

Fig. 9: *in situ* XPS measurement of the N1s peak **with** NO derivatisation (PS; 10s eff. pulsed NH_3-plasma)

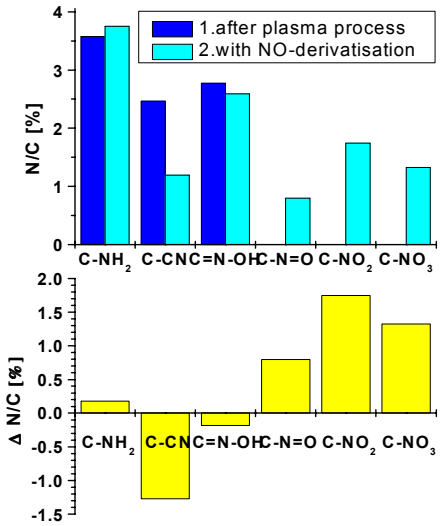

Fig. 10: Detection of surface radicals (PS; 40 s cw pulsed NH_3-plasma, *in situ* N1s XPS

Comparison of NO-derivated and not derivated polystyrene, activated with a cw NH_3-plasma are given in fig. 10. Nitrogen containing functional groups were generated in an cw-NH_3-plasma in a dimension up to circa 4 % N/C. The difference of the fitted peak areas ΔN/C shows the predominant formation of approximately 3.8 % tertiary radicals/C.
Obviously, here as in the case of the Ar-plasma the existence of primary and secondary C-radicals is questionable.
First results were obtained with a pulsed NH_3-plasma exhibiting nitrogen containing functional groups in a dimension up to 11-12 % N/C. The nitrogen entry is considerable higher in a pulsed than in the cw NH_3-plasma mode. But it is also known that the NH_2-efficiency and -selectivity is lower than in the cw-plasma mode [6]. Further investigations are necessary in this case.

Nevertheless, the amino functionalisation may be not affected by the NO derivatisation. That is surprisingly, because NO could react with NH_2-groups. From the experiment it is known that 50 % of the surface nitrogen are NH_2-groups.That can be also observed in an Ar-plasma.

3.2 Post Plasma Processes

An accompaniment of the amino functionalisation processes are the post-plasma processes with oxygen. This may be ascribe also the effect of tertiary radicals.

It can be expected, that the storage stability of functionalised polymer surfaces can profit from a derivatisation with the scavenger NO. First results show, that the ageing of derivatised polymers is less pronounced. Post plasma processes appear to be less expressed after NO-derivatisation.

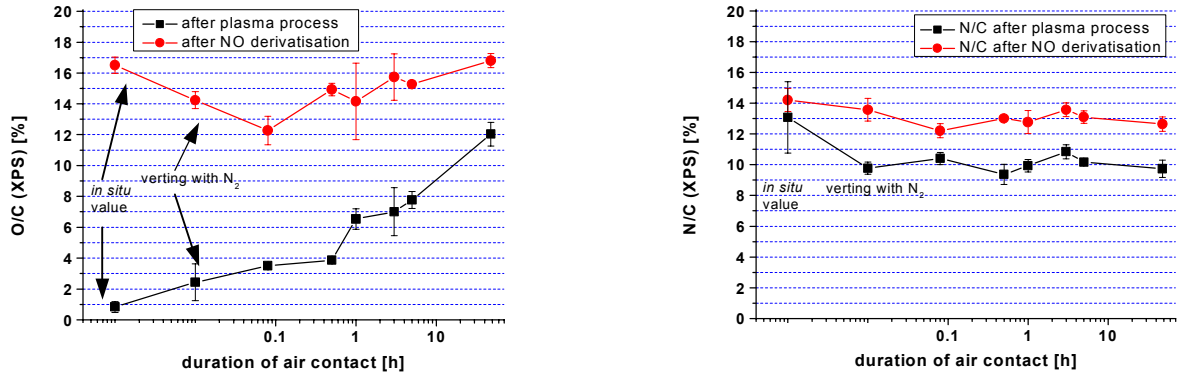

Fig. 12: Storage stabilisation of polystyrene after derivatisation with the radical scavenger NO.

4. Summary

Quenching reactions with NO were applied to investigate the formation of different nitrogen and / or oxygen containing functional groups and their derivation from primary, secondary and tertiary carbon radicals. Radical creation processes seem to be very similar in an Ar- and NH_3-plasma in the cw mode. It could be demonstrated that under the represented conditions tertiary radicals are expected to be predominatly formed. The amino group could react with NO, that doesn´t seem to be the case.

Acknowledgements

The authors thank U. Kellner, G. Friedrichs, U. Lindemann and D. Jasinski for excellent technical assistance. Financial support by the federal ministry for education and research (FKZ: 13N8054) is gratefully acknowledged.

References

[1] M. Kuzuya, T. Yamashiro, Sh. Kondo, M. Sugito, and M. Mouri, Macromolecules **31**, (1998) 3225-29.
[2] F. Poncin-Epaillard, B. Chevet, J.C. Brosse, J. Appl. Polym. Sci. **53**, (1994) 1291-1306.
[3] R. Wilken, A. Holländer, and J. Behnisch, Macromolecules **31**, (1998) 7613-7617; Surf. Coat. Technol. **116-119**, (1999) 991-95.
[4] A. Ohl, W. Schleinitz, A. Meyer-Sievers, A. Becker, D. Keller, K. Schröder, and J. Conrads, Surf. Coat. Technol. **116-119**, (1999) 1006.
[5] R. Förch, N.S. McIntyre, R.N.S. Sodhi, and D.H. Hunter, J. Appl. Polymer Sci. **40**, (1990) 1903.
[6] A. Meyer-Plath, K. Schröder, and A. Ohl, Vacuum (2002) in press.
[7] P. Favia, M. V. Stendardo, and R. d´Agostino, Plasmas and Polymers **1**(2) (1996) 91-112.
[8] K. Schröder, A. Meyer-Plath, D. Keller, W. Besch, G. Babucke, and A. Ohl, Contrib.plasma Phys. **41**,(2001)6, 562 – 572.

Investigation of nanosecond pulsed Dielectric Barrier Discharges in various gas mixtures

A. Khacef, J. M. Cormier and J. M. Pouvesle

GREMI, Université d'Orléans, 14 rue d'Issoudun, B.P. 6744, 45067 Orléans Cedex 2, France
e-mail : ahmed.khacef@univ-orleans.fr

Abstract

For a better understanding of the reaction kinetics in complex media like diesel and gasoline engine exhaust, pulsed dielectric barrier discharge (DBD) in high repetition rate regime and low energy per pulse deposition were investigated into gas mixtures with composition more and more complex: from N_2-C_3H_6 mixture to N_2-NO-O_2-C_3H_6-H_2O-CO-CO_2 mixture simulating diesel engine exhaust.
Analysis of gas composition at the outlet of the plasma reactor revealed a variety of by-products depending on the inlet gas. Acetaldehyde (CH_3CHO), formaldehyde (CH_2O), methanol (CH_3OH), formic acid (CH_2O_2), methyl nitrate (CH_3ONO_2), formic acid (CH_2O_2), nitromethane (CH_3NO_2), and nitrous acid (HONO) are the main by-products observed.
Results show that NOx removal improves with increasing specific energy deposition. For exemple, in the case of simulated diesel exhaust, 60% of NOx have been removed at 26 J/l with a W-value less than 30 eV.

1. Introduction

Air pollution is becoming a serious problem as a result of combustion waste from stationary and automotive engines. As a potent technology, the non-thermal plasma (NTP) process has been studied extensively to remove air pollutants such as NOx, SOx, and volatile organic compounds (VOC) in the exhaust gas stream under atmospheric pressure.

NTP that has a low gas temperature and a high electron temperature can be produced by a variety of electrical discharge methods (pulsed corona discharge, barrier discharge, and dc discharge) [1-3] or electron beam irradiation [4-5]. Pulsed corona and dielectric barrier discharge (DBD) techniques are two of the more commonly used methods for producing electrical discharge plasmas. Regarding their intrinsic properties DBDs appear very well adapted to treat large gas quantities with relatively low energy cost. In these plasmas, the electrons do not react directly with the NOx molecules. The kinetic energy of the electrons is deposited mainly into the background gas molecules like N_2, O_2, and H_2O. The most useful deposition of energy is associated with the production of N, O, and OH radicals through electron-impact dissociation. These radicals are the active species of the plasma that eventually lead to the chemical conversion of NOx. Due to the presence of H_2O and O_2, plasma processing of NOx is dominantly oxidative resulting primarily in NO_2 and some extent in HNO_2, HNO_3. Also, hydrocarbons in exhausts have been found to play an important role in the NOx removal processes.

This paper will present the results of an extensive series of experiments aimed towards understanding the effect of gas composition on the NOx conversion chemistry in plasma. Pulsed dielectric barrier discharges in high repetition rate regime (up to 200 Hz) and low energy per pulse deposition (35 mJ/pulse) were investigated into gas mixtures with composition more and more complex (from N_2-C_3H_6 mixture to N_2-NO-O_2-C_3H_6-H_2O-CO-CO_2 mixture simulating diesel engine exhaust).

2. Experimental set-up

The experimental system consists of a continuous flow gas generation system, laboratory-scale dielectric barrier discharge (DBD) reactor, and a gas detection system (Figure 1). The system was described in detail previously [6] and is briefly described for clarity.

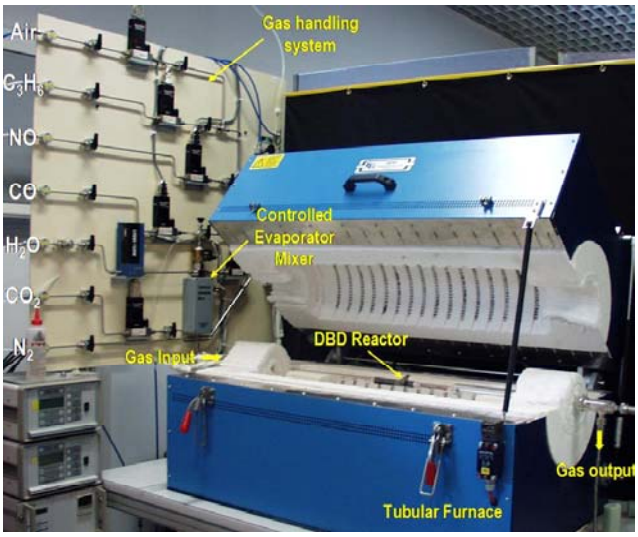

Figure 1: Schematic diagram of the experimental set-up.

Synthetic gas containing mixtures of O_2, N_2, NO, C_3H_6, CO, CO_2, and H_2O were prepared in a gas handling system. The gas composition was controlled with calibrated high-precision mass flow controllers. Water vapor with controlled concentrations was added to the gas mixture using a controlled evaporator mixer CEM®. It consists of a liquid flow control, a carrier gas control and a mixing chamber for liquid and carrier gas with heat exchanger for total evaporation. This device can provide a high reproducibility and a very stable water vapor flow. After mixing in the manifold, the gas then passes through a temperature-controlled line which preheats the gas and prevents condensation.

The DBD reactor (wire to cylinder type) was made of a quartz tube with 12 mm inner diameter and 1 cm wall thickness. The inner electrode was made of a 0.9 mm diameter tungsten wire and the other was a brass mesh. The length of the outer electrode can be adjusted and then determines the active volume of the DBD reactor. The results presented in this paper were obtained with a plasma volume of about 16 cm^3.

The DBD reactor is powered by a homemade high-voltage power supply. This pulse generator is capable of delivering high voltage pulses (up to 150 kV open circuit voltage) into 80 ns (FWHM) pulses and short rise times (40 ns) at variables repetition rates (up to the kHz). The fast voltage rise time allows achieving significant overshoot of breakdown voltages (several kV/ns) and allowing working at larger reduced field values (E/n) than in AC-conventional DBDs.

The electrical energy deposition in the plasma reactor was measured with a capacitive circuit. The input energy density, Joules per liter (J/l), is the ratio of the power deposited into the gas to the gas flow rate at standard conditions (25°C and 1 atm). Experimental conditions are listed in table 1

Discharge pulse energy	35 mJ/pulse
Discharge voltage	20 kV
Repetition rate	Up to 200 Hz
Gas flow rate	4 and 16 l/min

Table 1: Experimental conditions

The major gaseous components as NO, NO_2, CO, CO_2, and C_3H_6 were analyzed online and quantified using Fourier transform infrared absorption spectrometer (FTIR) equipped with a heated 10m-multiple pass absorption cell. An electrochemical NOx analyzer was also used for monitoring continuously NO, NO_2, NOx as well as CO levels in the gas stream.

3. Experimental results

The first set of experiments examined plasma processing of C_3H_6 (500 ppm) in N_2, and NO (500 ppm)-C_3H_6 (500 ppm) in N_2. Figure 2 shows the typical Fourier Transform Infrared (FTIR) spectra illustrated the plasma processing effect on these mixtures at room temperature and for an energy deposition of 27 J/l.

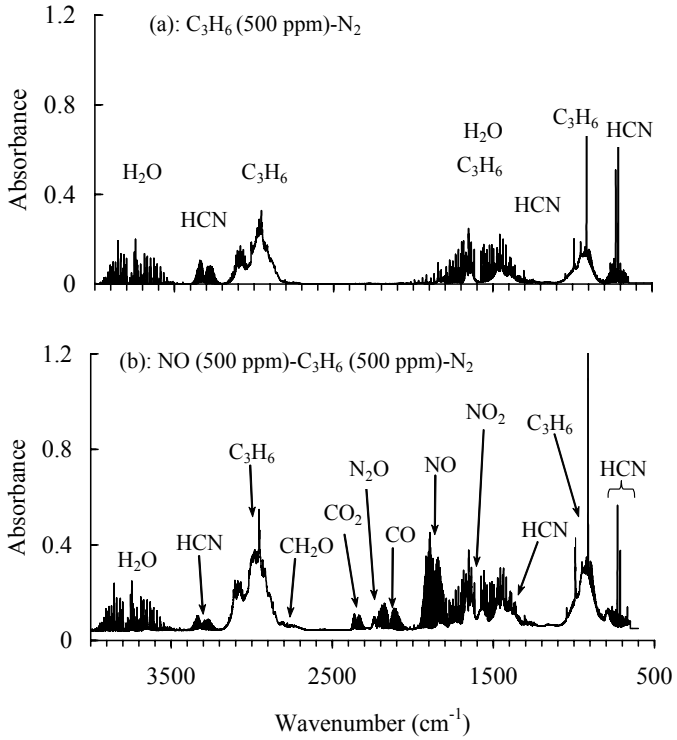

Figure 2: Typical FTIR spectra produced by plasma processing (27 J/l) of (a) C_3H_6 (500 ppm)-N_2 and (b) NO (500 ppm)-C_3H_6 (500 ppm)-N_2.

In the case of C_3H_6-N_2 mixture 50% of propene was converted at energy density of 53 J/l. This conversion leads to the production of hydrogen cyanide (HCN). When 500 ppm of NO was added to N_2-C_3H_6 mixture (case b), oxidation processes take place and NO_2, CO, CO_2 formaldehyde (HCHO) and nitrous oxide (N_2O) were observed.

Figure 3 shows the concentrations of C_3H_6, CO, NO, and NO_2 as a function of energy deposition. The NO to NO_2 oxidation is very weak (< 2%) and NO could be chemically reduced into nitrogen (N_2). The consumption of propene increases with increasing input energy. In that case, at energy deposition of about 53 J/l the measured reduction of C_3H_6 concentration is about 18%. This partial oxidation of propene lead to the production of a small amount of CO (30 ppm), CH_2O (15 ppm) and CO_2 (8 ppm).

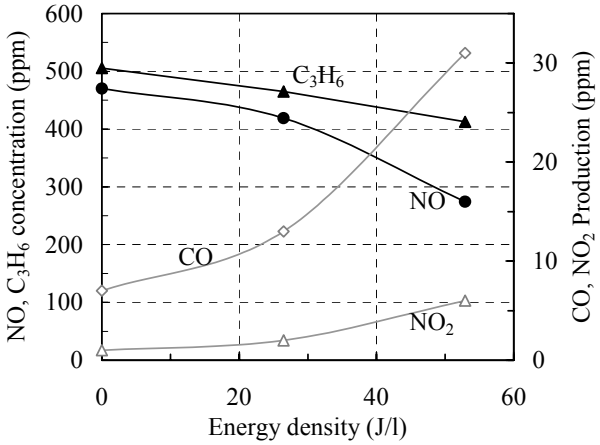

Figure 3: NO, NO_2, CO, and C_3H_6 output concentrations as a function of energy deposition. Inlet gas contains 500 ppm NO, 500 ppm C_3H_6, and balance N_2.

In the second set of experiments we study the following mixtures: O_2 (10%)-C_3H_6 (500 ppm)-N_2 and O_2 (10%)-C_3H_6 (500 ppm)-NO (500 ppm)-N_2. Figure 4 shows typical FTIR spectrum of plasma processing (27 J/l) effect on mixture without NO.

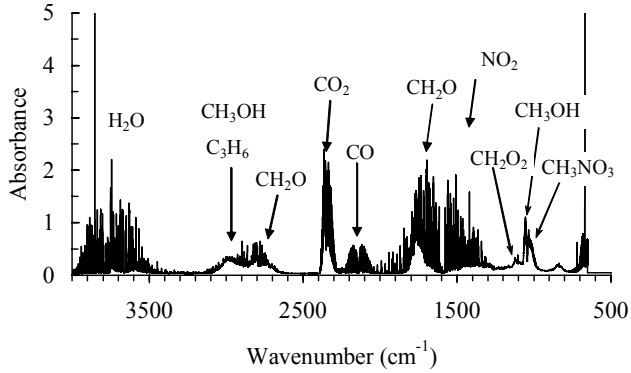

Figure 4: Typical FTIR spectrum produced by plasma processing (27 J/l) of O_2 (10%)-C_3H_6 (500 ppm)-N_2.

When NO was added to this mixture the spectra show a similar behavior and exhibit a high intensity signal in the absorption band of NO_2. Briefly, when the O_2 concentration is higher than 5% the plasma gas phase chemistry is initiated mainly by the production of oxygen radicals via electron induced dissociation of O_2. The dissociation of O_2 promotes the gas-phase oxidation of NO to NO_2. It is well known that when hydrocarbon is added to the gas mixture, NO to NO_2 oxidation is enhanced by large extent as the amount of hydrocarbon increase. The hydrocarbon act as a getter of O and OH radicals, with the resulting products reacting with O_2 to yield peroxy radicals (HO_2) which efficiently convert NO to NO_2.

As expected under these oxygen rich conditions, in addition of the main products of the plasma (NO_2, CO, and CO_2), the plasma partially oxidizes the hydrocarbons. Formaldehyde (CH_2O), methanol (CH_3OH), methyl nitrate (CH_3ONO_2), formic acid (CH_2O_2), and nitrous acid (HONO) are formed. This data are consistent with previously published results [14, 30].

Figure 5 shows CO, CO_2, and NO_2 concentration as well as C_3H_6 conversion rate as a function of energy deposition. At the maximum energy deposition used in that study (53 J/l), the NO to NO_2 conversion was ≈ 90%. The consumption of propene increases with increasing input energy. The reduction of C_3H_6 concentration is about 62%. Formaldehyde is one of the major by-products of the partial oxidation of propene in these plasmas. Carbon products could be quantified as follow: 36.2% CH_2O, 19% CO, 11.3% CO_2 and 33% "others". "Others" represents the by-products like formic acid and methyl nitrate which were not quantified in that study. When CO and CO_2 were added to the O_2-C_3H_6-NO-N_2 mixture no significant changing in the spectrum was observed.

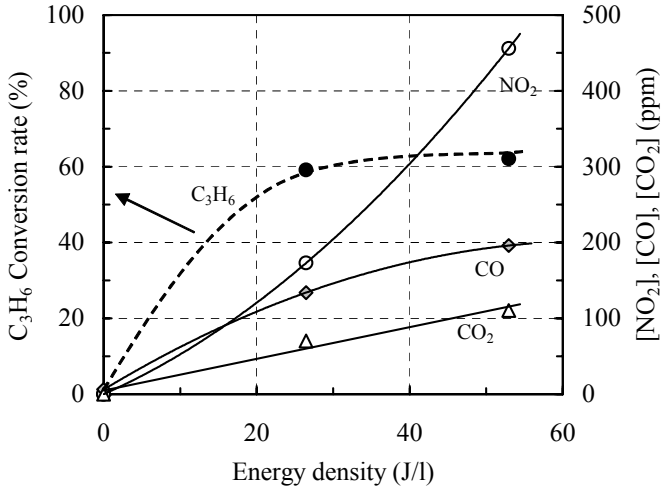

Figure 5: NO_2, CO, CO_2 output concentrations and C_3H_6 conversion rate as a function of energy deposition. Inlet gas contains 10% O_2, 500 ppm NO, 500 ppm C_3H_6, and balance N_2.

In the following section, experiments using gas mixture simulated diesel engine exhaust were conducted at two gas temperatures (150°C and 300°C). The treatment was performed at flow rate of 16 l/min with the same electrical conditions than presented before. The composition of the simulated diesel engine exhaust was: 12% O_2, 10% H_2O, 500 ppm CO, 10% CO_2, 300 ppm NO, 300 ppm C_3H_6, and N_2 as balance. In these humid mixtures, OH radicals produced from water vapor by the plasma plays a major role in the NOx removal chemical reactions. Output NO and NO_2 concentrations and NOx removal rate as a function of energy deposition is shown in figure 6. With increasing energy deposition, the NO concentration decreases while that of NO_2 initially increases (maximum at ≈8 J/l) and then decreases. This phenomenon could be explained by reactions between NO_2 and OH radicals leading to the formation of R-NOx compounds (R=hydrocarbon radicals).

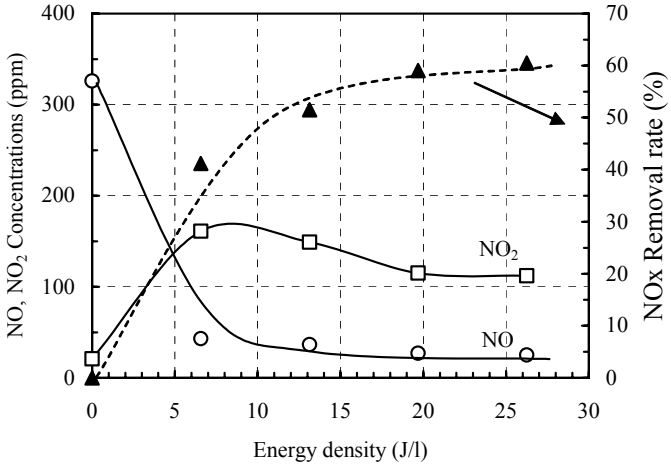

Figure 6: NO, NO_2 concentrations and NOx destruction rate as a function of input energy density in plasma processing of simulated diesel engine exhaust at 150°C.

The NOx (sum of individual concentrations of NO and NO_2) removal efficiency significantly increases with increasing input energy density. Approximately 60% of NOx were removed by the DBD discharge at energy density of about 26 J/l. The products of hydrocarbons processing are those reported commonly in the homogeneous gas phase processing of diesel exhaust containing propene [7, 9]. These by-products are acetaldehyde (CH_3CHO), propylene oxide (C_3H_6O), formic acid (CH_2O_2), methyl nitrate (CH_3ONO_2), and nitromethane (CH_3NO_2). Acetaldehyde and nitromethane were detected by Gas Chromatography coupled with Mass Spectrometer. To our knowledge CH_3NO_2 have not been observed in any other reported experiments. However that specie was predicted as a major by-product from propene induced NO to NO_2 conversion by Shin et al [10].

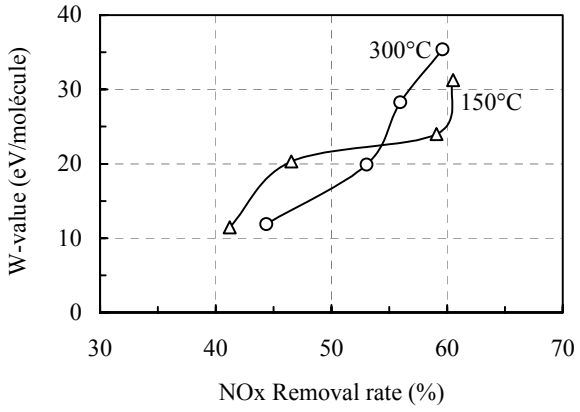

Figure 7: Energy cost as function of NOx removal rate in plasma processing of simulated diesel engine exhaust at 150°C and 300°C.

Energy cost has been used for the evaluation of system performance in gas cleaning using a discharge

plasma system. The efficiency of these processes can be quantified by W-values [11]. W-values (eV/molecule) are the amount of energy required to remove one molecule of the compound. The lower values correspond to more efficient processes. The W-values as a function of NOx-removal rates in simulated diesel engine exhaust at 150°C and 300°C are shown in figure 7. This figure illustrates how the important parameters - the NOx removal efficiency and energy cost per removed molecule - are strongly correlated. At high temperature (300°C), W-value increase rapidly with NOx-removal. Below energy density of about 15 J/l, it appears that the plasma processing of diesel is much more efficient at high temperature. About 45% of NOx are removed with W-value around 12 eV. At higher energy density (26 J/l) and lower gas temperature (150°C), NOx removal efficiency of about 60% was obtained with an energy cost less than 30 eV/molecule. Assuming an engine with a load of 100 kW and an exhaust gas flow rate of 100 l/s, this plasma treatment will correspond to a consumption of about 2.6% of the engine energy output.

Summary

Pulsed dielectric barrier discharge plasma processing of gas mixtures with composition more and more complex (from N_2-C_3H_6 mixture to N_2-NO-O_2-C_3H_6-H_2O-CO-CO_2 mixture simulating diesel engine exhaust) was performed at relatively low energy deposition. The nature of the by-products produced and the effect of gas composition on the NOx conversion chemistry in plasma were studied as a function of energy density deposition and gas temperature. For example, NOx removal efficiency of about 60% was obtained with an energy cost less than 30 eV/molecule in the case of simulated diesel engine exhaust.

Under oxygen rich conditions, in addition of the main products of the plasma (NO_2, CO, and CO_2), acetaldehyde (CH_3CHO), formaldehyde (CH_2O), formic acid (CH_2O_2), methyl nitrate (CH_3ONO_2), nitromethane (CH_3NO_2), methanol (CH_3OH), and nitrous acid (HONO) could be are formed.

References

[1] D. Evans, L. A. Rosocha, G. K. Anderson, J. J. Coogan, and M. J. Kushner, J. Appl. Phys. 74(9), (1993)
[2] B. M. Penetrante, M. C. Hsiao, J. N. Bardsley, B. T. Merrit, G. E. Vogtlin, P. H. Wallman, A. Kuthi, C. P. Burkhart, and J. R. Bayless, Pure & Appl. Chem. 68(5), (1996)
[3] S. Masuda and H. Nakao, IEEE Trans. Ind. Appl. 26, (1990)
[4] Non-thermal Plasma Techniques for Pollution Control, part A and B, ed B. M. Penetrante and S. E. Schultheis (New York: Springer-Verlag), (1993)
[5] N. W. Frank, Radiat. Phys. Chem. 45, (1995)
[6] A. Khacef, J. M. Cormier, and J. M Pouvesle, J. Phys. D: Appl. Phys. 35, (2002)
[7] R. Dorai and M. J. Kushner, SAE Paper 1999-01-3683, (1999).
[8] J. Hoard and M Lou Balmer, SAE Paper 982429, (1998)
[9] B. M. Penetrante, R. M. Brusasco, B. T. Merritt, W. J. Pitz, G. E. Vogtlin, M. C. Kung, H. H. Kung, C. Z. Wan, and K. E. Voss, SAE Paper 982508, (1998).
[10] H. H. Shin and W. S. Yoon, SAE Technical Paper Series No. 2000-01-2969, (2000)
[11] V. Puchkarev, A. Kharlow, M. Gundensen and G. Roth, Proc. of 12th IEEE Pulsed Power Conference, Monterey CA, June 27-30, (1999)

Characteristics of a plasma jet ignitor

J. Caillard[1], C. de Izarra[2], O. Vallée[2] and L. Brunet[1]

[1]*GIAT Industries, 7 route de Guerry, F-18023 Bourges Cedex, France*
[2]*LASEP Faculté des Sciences, Site de Bourges Université d'Orléans, rue Gaston Berger BP 4043 18028 Bourges Cedex France*

Abstract
From previous studies on electrothermal launchers, GIAT Industries (France) has developed a micro-torch system for ignition using plasmas. A transient electric arc is generated between two electrodes connected to a capacitor bank in a polymer cell in order to produce an ablation of the polymer surface, leading to a highly chemically reactive plasma jet at the exit of the torch nozzle. The spectroscopic investigation is performed using atomic emission spectroscopy : excitation temperature has been obtained with a Boltzmann plot and electron density has been measured with the Stark width of H_α Balmer line coming from the ablated polymer: the electron density level is high ($> 10^{18}$ cm^{-3}). By considering an elementary thermodynamical plasma model, it was possible to determine a value of the pressure of the emitting area at the micro-torch nozzle; its value is about 160 MPa.

The plasma jet produces a strong pressure perturbation. It has been experimentally showed that this pressure perturbation is a detonation in agreement with the theoretical model of Sedov-Taylor. The overpressure values obtained from spectroscopic data are in agreement with the overpressure given by the Sedov-Taylor model.

1. The micro-torch igniter

The micro-torch system presented in figure 1 was designed by GIAT Industries [1] with a scaling made according to similar systems operating with higher energy values. The basis concept of this one shot plasma device is to generate an electric arc between two electrodes in a polymer cell in order to produce an ablation of the polymer surface, leading to a highly chemically reactive plasma jet at the exit of the torch nozzle.

The micro-torch has an axisymmetric geometry with an axial brass cathode and a steel body used as an anode. The torch nozzle has a diameter of 4 mm and the polymer cell a 2 mm hole. The polymer to be ablated (POM: PolyOxyMetyl-acetal) is a cylinder having the same axis as the micro-torch system. In addition, a copper wire (diameter: 0.15 mm) is used to initiate the electrical discharge.

The electrical power supply is a low energy energy capacitor bank (1.5 kJ) operating at the maximum voltage of 500 V. The typical duration of the transient plasma jet is about 1 ms, driven by the typical times of the electrical capacitor bank.

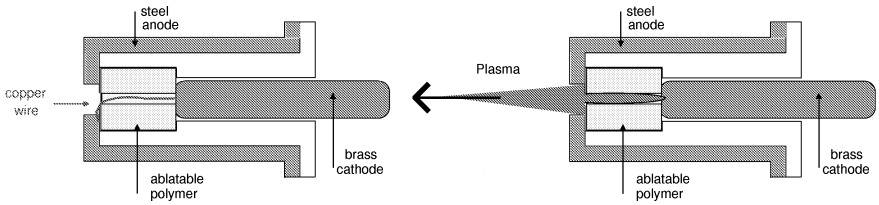

Figure 1: Schematic drawing of a micro-torch system (cut along the axis). Left figure: before the capacitor bank discharge and right figure: during the capacitor bank discharge with the plasma jet at the exit of the torch nozzle.

2. Emission spectroscopy investigation

Spectroscopic data acquisitions are performed with a Chromex monochromator of the Ébert-Fastié type having a focal length of 0.5 m and a 1200 grooves/mm grating operating in the first order. Photodetection is provided with a Princeton Applied Physics OMA equipped with a CCD matrix array having 256 rows of 1024 pixels. In the first spectroscopic order, the detector covers a spectral range of 45 nm.

In order to study the time evolution of a spectral area in the visible range, the CCD array is controlled using a kinetic mode. In this mode, only a number n of rows are illuminated during an exposure time t_e. At the end of the exposure time, these n rows are shifted in the CCD array such that it is also employed as a fast storage memory. The shift of each row is accomplished during a time t_s depending on the kind of CCD controller. In our case, the shortest time shift available is t_s=6 μs. The number of lines illuminated is n=2, and the exposure time t_e=15 μs; these values have been chosen using a trade off between time resolution and signal level. To summarize, data acquisition allows a spectral area to be sampled every $t_e + n \times t_s$=27 μs. Since the typical time of discharge is about 600 μs, the sampling rate is sufficient to obtain a time resolution of the spectral emission of the discharge.

The transient plasma jet created by the discharge is observed side-on at the exit of the torch nozzle. An image of the plasma jet is formed using a lens (focal length of 75 mm) on the tip of a 200 μm diameter optical fiber connected to the monochromator entrance. The fact that the light collected by the optical fiber corresponds to an averaged value of the plasma emissivity across the torch nozzle diameter must be highlighted.

Data acquisition is triggered using a fast time response ($\approx 6\,\mu$s) photodiode (Texas Instruments TSL 252), illuminated by the transient plasma jet.

In all experimental spectra, emission lines of neutral copper are always predominant, and may be used to obtain a temperature value. Figure 2 gives a typical spectral region with Cu_I lines and its evolution over time. At the beginning of the discharge, the Cu_I atomic lines at 515.5 nm and 521.8 nm present a typical self-absorption shape and, consequently, their overall intensity cannot be used directly to obtain a temperature value. However, this self-absorption give useful information concerning the geometry of the emitting source: it can be considered as a hot emitting area surrounded by a cold copper gas mainly coming from the exploded wire. Over time, the line shapes lose their self-absorption shape, meaning that the emitting area is either colder or more homogeneous, or else that the density of the copper ejected from the capillary tube decreases. In this case, the line intensities can be used to build a Boltzmann's plot[2]. The neutral copper lines observed in our spectra are:

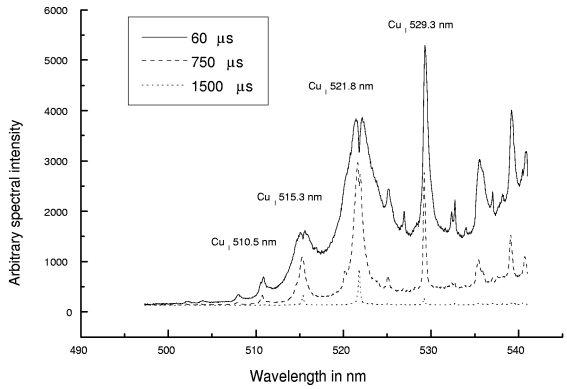

Figure 2: Time evolution of emission spectra for POM material

510.5 nm, 515.5 nm, 521.8 nm and 529.3 nm with transition probabilities [3, 4, 5] known with a rather large associated error. When POM is ablated, Boltzmann's plot gives a temperature of around 10000 K, decreasing over time to 9000 K. It is obvious that the torch emission is not steady. First of all, the copper wire explodes and is ejected from the torch. The plasma is generated. The emission reaches a maximum very rapidly. Thereafter, the spectral emission drops slowly to approach a relatively long light emission at approximately 10 % of the maximum value. The peak current and the maximum spectral emission appear at the same time.

Since the Stark effect is well characterized for atomic hydrogen and the transitions fall within a convenient region of the optical spectrum, the Balmer series is frequently used for line shape analysis. Usually, the H_β (486.1 nm) line has a rather characteristic and broad profile, and is far less sensitive than the H_α. In our plasma, the H_β line profile is complicated by many lines in this spectral region and it is impossible to obtain a tem-

perature estimation. Thus, our analysis focuses on the more prominent H_α (656.3 nm) which Stark broadening gives a direct measurement of the electronic density.

In the spectral the spectral range from 630 nm to 680 nm presents two kinds of emission: lines from the neutral atomic iron resulting from the vaporization of the anode steel and the Balmer α line of hydrogen (H_α). As for the copper, we can obtain the arc plasma temperature from the slope of Blotzmann's plot using iron lines emission [6].

The electronic temperatures were inferred from Boltzmann plots of the iron emission lines observed on the blue wing of the H_α line. The electron densities were inferred from Stark broadened H_α emission lines. In the range from N_e $=10^{13}$ to 10^{20} e/cm^3 the different theories (Kepple-Griem [7], Sholin-Dmura-Lisitsa or Ispolatov-Oks [8]) are very close.

For each data acquisition, temperature and electron density are measured. The figure 3 presents the evolution of the electronic density as a function of the temperature. In the case of a singly ionized plasma in local thermodynamic equilibrium, the electronic density N_e is given by:

$$N_e^2 = CT^{3/2} \exp\left(-b/T\right)$$

where C is a constant.

Fitting experimental results with an analogous mathematical model ($N_e^2 = CT^a \exp\left(-b/T\right)$) gives $a = 1.518 \pm$ 0.055; consequently, Saha's law is valid, and finally, the plasma produced is in local thermodynamic equilibrium. As Saha's law is verified, the density of neutral species (N_0) can be found. For this, a straightforward thermodynamical model of plasma must be used. By considering a 10000 K argon plasma in local thermodynamical equilibrium with electronic density of about $5\,10^{18}\,\text{cm}^{-3}$, the density of neutral species is about N_0 $=3\,10^{21}\,\text{cm}^{-3}$. Using Dalton's law we obtained an over pressure in plasma jet of about 160 MPa. This pressure is considerable, and it will be compared in the following section to the over pressure obtained using a blast wave model.

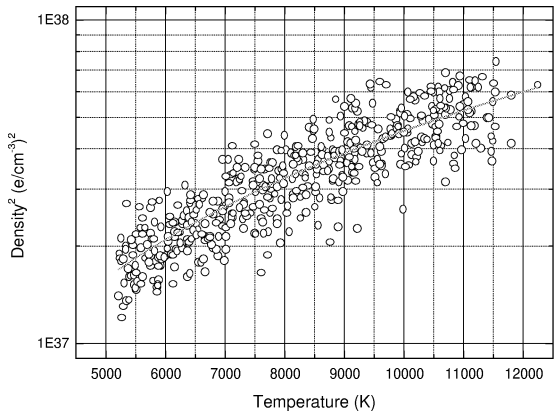

Figure 3: Square of the electronic density as a function of the temperature $N_e^2 = f(T)$

3. Investigation of the overpressure generated by the micro-torch

It was decided to investigate the strong overpressure perturbation generated by the micro-torch system by applying the modified Sedov-Taylor model [9, 10] in an ideal gas.

In the case of the spherical blast wave described by the Sedov-Taylor model, an energy E is deposited instantaneously in an ideal gas of specific mass ρ. The initial energy E is localized in a point taken for reference, and produces a spherical blast wave of radius R from the center which time evolution is [11, 12]:

$$R(t) = \beta \left(\frac{E}{\rho}\right)^{1/5} t^{2/5} + v_s t, \tag{1}$$

where β is a constant and v_s is the sound velocity at ambient pressure.

The experimental investigation of the overpressure perturbation is made by using three pressure sensors disposed on the same plan along a line. The ranges between sensors and between first sensor and the nozzle of the torch are known. The radius of the blast wave front, which is assumed to be the distance from the bore exit to the shock measured along the axis, was measured (sensor position) of time. The over pressure value and the blast wave flight time were directly given by the pressure sensor.

According to the Sedov-Taylor model, the blast wave is supposed follow two mains equations. The first one gives the flight time of the blast wave front (equation (1)), and the second gives the pressure variation on the blast wave radius as function of time [9]:

$$p_2 = C^{te} t^{-6/5}. \tag{2}$$

Experimental data are compared with theoretical blast wave equations (1), (2). The experimental evolution of the blast wave front as a function of time is in good agreement with theoretical predictions (see figure 4). In addition, the comparison of the experimental over pressure is also in good agreement with the Sedov-Taylor model (see figure 5).

Since the Sedov-Taylor blast wave model is showed to be valid, we can easily determine the over pressure as a function of the radial distance by combining equations (1) and (2). Figure 6 shows that the pressure level at the micro-torch nozzle ($\approx$ 175 MPa at the distance r=1 mm) and the pressure found by using Dalton's law (see above) are in good agreement.

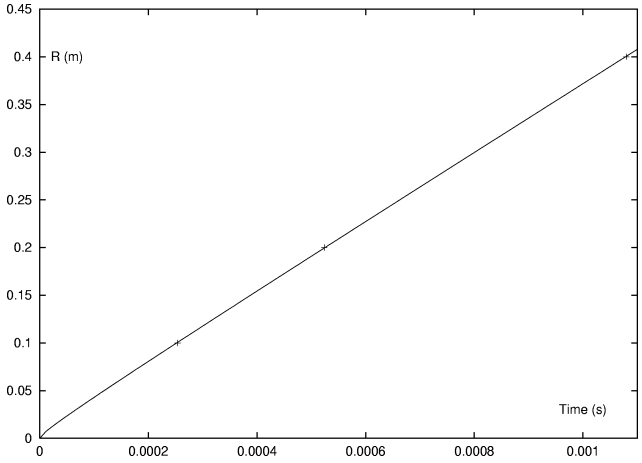

Figure 4: Experimental data for the time dependence of the blast wave front radius R. The solid line is a fit of equation (1).

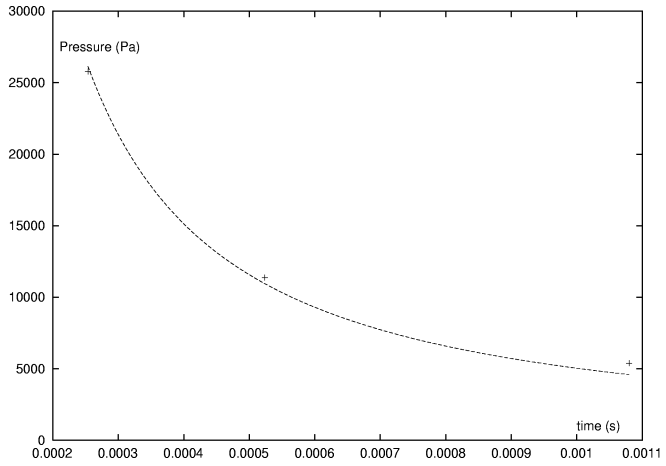

Figure 5: Experimental data giving the over pressure as a function of time on the blast wave front(2).

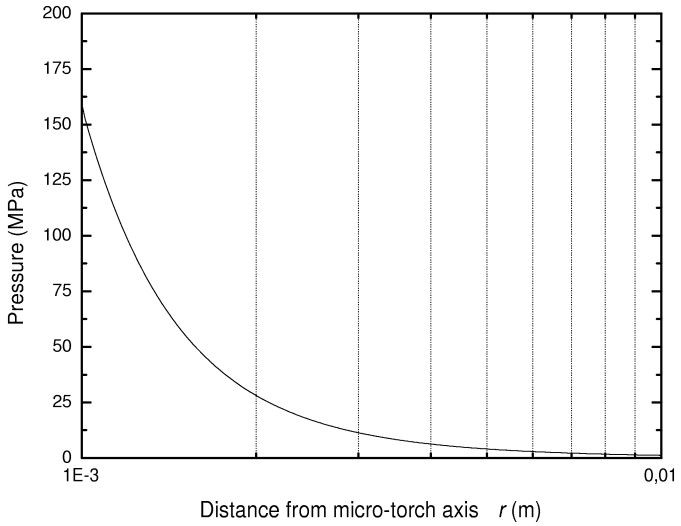

Figure 6: Evolution of the pressure as a function of the radial distance from the micro-torch nozzle (1) (2).

4. Conclusion

In this experimental study, the time evolution of the emission spectra in a micro-torch plasma jet is obtained. All spectra are dominated by the presence of the strong emission lines of the neutral metallic elements mainly coming from the electrodes materials (iron and copper). The presence of diatomic molecular bands such as C_2 Swan bands is not clearly established, mainly because the presence of the strong neutral copper lines that decrease the dynamic range of the optical detector.

The temperature determination from Boltzmann plots is only available at the end of the discharge, because of very strong self-absorption of atomic copper lines at the beginning of the discharge. This self-absorption decreases with time. The reasons of self-absorption are many and should be deeply studied. The hydrogen H_α emission line is easily observed and is employed to measure the electronic density.

Electronic density values are relatively high ($> 10^{18}\,\mathrm{cm}^{-3}$) leading to a plasma in local thermodynamic equilibrium, and allowing to determine the pressure inside of the plasma jet with Dalton's law. This pressure is approximately 160 MPa. In addition, the study of the over pressure generated by the transient arc discharge

shows that it is successfully described with a blast wave model.The notion of blast wave from each discharge (from 1 kJ to 20 kJ) scale as expected for a strong shock resulting from instantaneous energy deposition at a point. In accordance with this model, the pressure of the blast wave front and its velocity are determined. The pressure value obtained by spectroscopy and the pressure value estimated using the modified Sedov-Taylor model are in good agreement.

References

[1] Brevet GI : FR9711836
Composant d'allumage pour composition pyrotechnique ou charge propulsive.

[2] M. Sassi, L. Pierre, J. Bénard and C. Cahen,
Calcul et mesure de la température d'un plasma à l'aide des raies d'émission du cuivre, *J. Phys. III France*, April, 127-141 (1994).

[3] O.E. Hankins, M.A. Bourham, J. Earnhart, and J.G. Gilligan,
Visible light emission measurements from a dense electrothermal launcher plasma, *IEEE Transactions Magnetics*, Vol. 29, n^o 1, January (1993).

[4] A. Bielski
A critical survey of atomic transition probabilities for Cu$_I$, *J. Quant. Spectrosc. Radiat. Transfer*. Vol 15, 463-472 (1975).

[5] M. Biemont
Probabilités de transition dans la configuration $3d^{10}(^1S)$ nl de Cu$_I$ et identifications dans le spectre solaire, *Bulletin de la Société Royale des Sciences de Liège*, 42^e année, n^o 5-6, 206-217 (1973).

[6] NIST Data base
http://physics.nist.gov/cgi-bin/AtData/lines_form

[7] H.R. Griem
Spectral line broadening by plasma, New York : Academic Press (1974).

[8] J.E. Touma, E. Oks, S. Alexio, A Derevianko
Review of advanced generalized theory for Stark broadning of hydrogen lines in plasmas with tables, *J. Quant. Spectrosc. Radiat. Transfer*. Vol 65, 543-571 (2000).

[9] G. I. Taylor,
The formation of a Blast Wave by a Very Intense Explosion, *Proc. R. Soc. London.*, A201, 159-174 (1950).

[10] L. Sedov,
Similarity and Dimensional Methods in Mechanics Academic Press New York (1969).

[11] C. de Izarra, Jean Caillard and O. Vallée,
Transition from the Sedov-Taylor solution up to the sound wave, *Modern Physics Letters B*, Vol. 16, No. 3 (2002) 69-72.

[12] J. Caillard,
Etude spectroscopique de l'interation entre un plasma et un matériau (Spectroscopic investigation of the interaction between a plasma and a material), PhD Thesis, Orleans university, France (2001).

Direct determination method of a global apparatus function in UV OH spectrum thermometry

H. Rabat, C. de Izarra

LASEP: *Laboratoire d'Analyses Spectroscopiques et d'Energétique des Plasmas*
Faculté des Sciences, Site de Bourges Université d'Orléans, rue Gaston Berger BP 4043 18028 Bourges Cedex France

Abstract
In a previous paper [1], we have presented a new method to carry out the rotational temperature from the UV OH band at 306.357 nm (transition $A^2\Sigma, \nu = 0 \rightarrow X^2\Pi, \nu' = 0$) frequently observed in hot gases containing oxygen and hydrogen (flames, arc plasmas). The method is mainly based on a calibration of the height of 3 unresolved groups of lines obtained by performing a numerical simulation of OH spectrum for different temperatures and for different widths of gaussian apparatus functions. In this paper, we underline that the apparatus function needed to carry out the temperature with the method described in the reference [1] is not only the pure optical apparatus function of the optical spectroscopic device commonly measured by employing a laser line, but must include the broadening effects of the rotational lines. At least, we propose a numerical method to determine a global apparatus function needed to apply the temperature determination method presented in the paper by de Izarra [1].

1. Introduction

In a previous paper [1], we have presented new method to carry out the rotational temperature of OH radicals, by considering the sensitivity against the temperature of the amplitude of two unresolved groups of lines for the UV OH band at 306.357 nm (transition $A^2\Sigma, \nu = 0 \rightarrow X^2\Pi, \nu' = 0$) frequently observed in hot gases containing oxygen and hydrogen (flames, arc plasmas).

Using reference data [2], a Dirac synthetic spectrum has first been computed for a given temperature T. Then, to produce a synthetic spectrum, the Dirac spectrum has been convoluted [3] with a normalized gaussian apparatus function

$$G(\lambda) = \frac{2}{\Delta\sqrt{\pi}} \exp\left(-\frac{(\lambda - \lambda_0)^2}{(\Delta/2)^2}\right)$$

where Δ represents the full width at 1/e of the maximum located at the wavelength λ_0. A set of about 2000 synthetic spectra has been computed for the temperature varying from 600 K to 9000 K with 200 K stepped and for Δ varying from 0.02 nm to 0.98 nm with 0.02 nm stepped.

Figure 1 gives a plot of synthetic spectra for an apparatus function with Δ=0.1 nm and for a rotational temperature varying from 1000 K to 8000 K with 1000 K stepped. All the synthetic spectra have been normalized against the intensity of the group of unresolved rotational lines G_{ref} (see figure 1) at ≈309 nm which appears to be the relative strongest group of unresolved lines when the rotational temperature is lower than 4000 K. The ratios G_0/G_{ref} and G_1/G_{ref} for different values of temperature T and apparatus function width Δ are given in the reference [1].

The determination of a temperature from an experimental spectrum needs to precisely know the apparatus function width Δ corresponding to the numerical simulation. If we consider the simulation process used to compute synthetic spectra (figure 2), it is obvious that the apparatus function width Δ corresponds to a global apparatus function, and both includes the broadening effects of the rotational lines and the apparatus function of the optical and spectroscopical devices. Consequently, the experimental determination of the parameter Δ with a laser line is a mistake and does not correspond to the global apparatus function employed in the numerical simulation. For that reason, it is necessary to propose a method to carry out the parameter Δ from experimental spectra.

2. Study of the UV OH Spectra

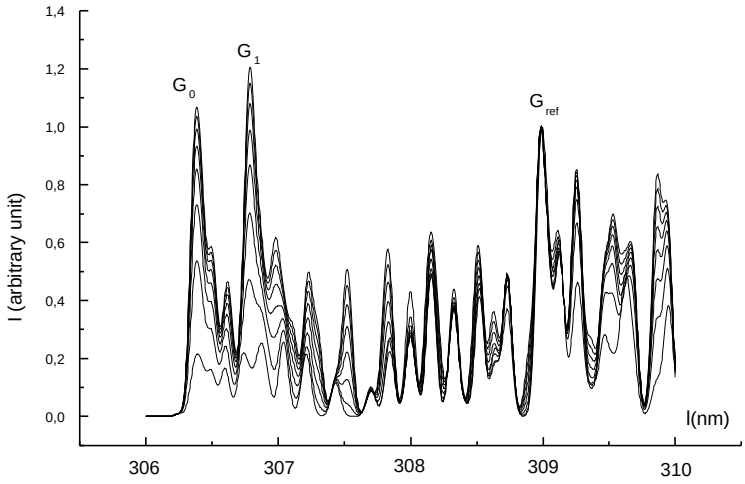

Figure 1: Plot of the UV OH spectrum for the rotational temperature varying from 1000 K to 8000 K, 1000 K stepped ($\Delta = 0.1\,nm$).

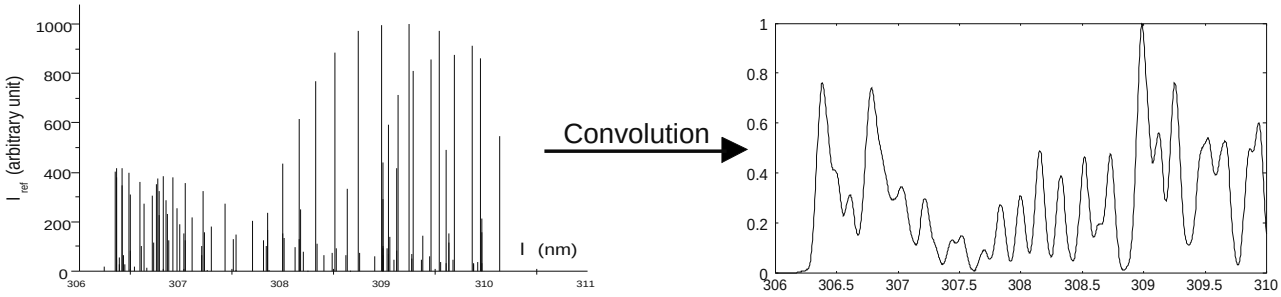

Figure 2: Simulation process used to produce a synthetic spectrum with a convolution of an impulse Dirac spectrum and a global apparatus function Δ.

2.1. Evolution of the spectrum with the temperature

Figure 1 gives a plot of UV OH synthetic spectra for an constant apparatus function (Δ=0.1 nm) and for various rotational temperature. The OH band in this wavelength range shows a red degradation with four main band heads R_1, R_2, Q_1 and Q_2 at respectively 306.537 nm, 306.776 nm, 307.844 nm and 308.986 nm. When the temperature is lower than 4000 K, the group of unresolved rotational lines Q_2 at ≈309 nm appears to be the relative strongest group of unresolved lines [1] and this band can be easily isolated in order to give useful informations. That's why all the synthetic spectra have been normalized against the intensity of this band that for clearness we'll name later on the G_{ref} line.

As shown in Figure 1, the width of lines seems to be independent of temperature value. Indeed, in the temperature range 1000-6000 K, broadening of the spectral lines results mainly from the convolution of the emission spectrum with the apparatus function, which is supposed to be gaussian [4]. To support this assertion, Figure 3 is a plot of half width at 0,7 in height of the G_{ref} line for various apparatus function as a function of the temperature. It is the half width to the low wavelength which is considered because the shape of this line is not symmetric.

The value of the half width for a given apparatus function is not thoroughtly constant. It increases lightly about less than 10% for apparatus functions between 0.02 to 0.5 nm with an increase of 8000 K of the temperature. This difference is reduced when, at one and the same time, the apparatus function is lower than 0.4 nm

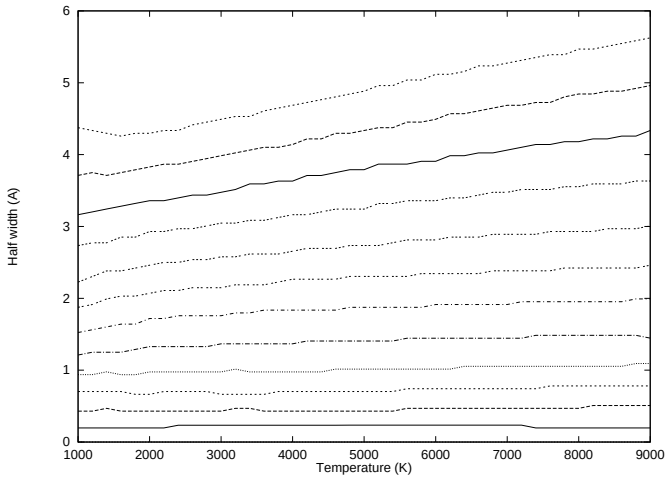

Figure 3: Plot of half width at 0.7 of the Q_2 band at 309 nm for the global apparatus function varying from 0.06-0.72 nm, in 0.06 nm steps, as a function of the temperature.

and the temperature is lower than 6000 K, but it should be taken into account in the error calculation.

2.2. Evolution of the spectrum with the apparatus function

The Figure 4 below shows the shape of the UV OH spectrum for a given temperature as a function of the apparatus function. More this latter increases, more the groups of unresolved lines are broadened. From about 0.5 nm, the width of the G_{ref} line is relatively important but spectra of this shape resulting from a poor resolution are rarely used because they are not interesting for spectroscopy analysis.

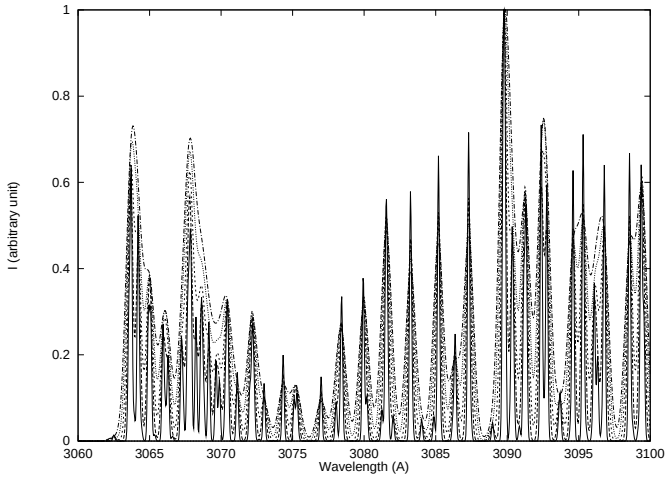

Figure 4: Plot of the UV OH spectrum for the global apparatus function varying from 0.1-0.5 nm, in 0.1 nm steps (T=3000 K).

3. Apparatus function method determination

3.1. Principle

The method presented in this paper allows the determination of the global apparatus function from a UV OH spectrum. In a first step, the equation of the global apparatus function against the half width of the G_{ref} line

must be find for a given height. The value of half width at 1/e can't be used because it is too low in the band. Its evolution as a function of the apparatus function is not linear in the 0.02-0.98 nm range because of the convolution, when its broadening is too important, the value of the half width is not purely corresponding to the G_{ref} line. This evolution stays linear from about 0.7 of the maximum of the line. From this, the choice of the height is free, and three different heights (0.7, 0.8 and 0.9) will be considered. The fact to have three different heights, hence three equations, will allow to be more accurate by making the average of the three found values of the global apparatus function.

Using the data from the synthetic spectra provided by the computer simulation of de Izarra, a computer program has been realized in QuickBasic. The principle is to calculate from a spectrum the difference between the wavelength where the intensity of the G_{ref} line is maximum (=1 a.u.), and the wavelengths where the intensity is 0.7, 0.8 and 0.9 a.u. in this same line. This operation is repeated for global apparatus functions going to 0.02 nm to 0.98 nm, in 0.02 nm steps for a defined temperature and, finally, for rotational temperatures varying from 1000-9000 K, in 200 K steps. For each height, we have 40 curves (for each temperature) of the apparatus function as a function of the half width. The equation of the average curve is the wanted equation and the 1000 K and 9000 K curves give the error boxes of the average curve introduced by the weak increase of the half width with the temperature which has been shown previously.

3.2. Equations

The obtained curves for heights of 0.7, 0.8 and 0.9, are presented in Figures 5 to 7 and the corresponding three order polynomial equations in the Table 1. For each figure, the average curve is in the middle, the 1000 K curve above and the 9000 K curve below.

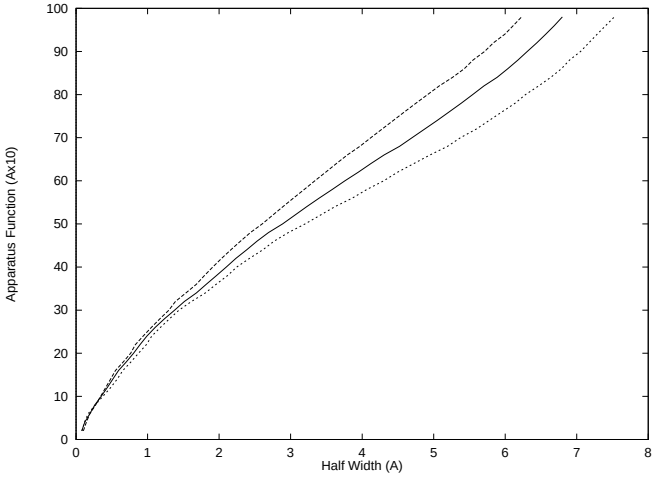

Figure 5: Plot of the global apparatus function as a function of the half width at heights of 0.7.

4. Check of the method

A Balmer lamp gives an emission spectrum of OH at low pressure. In that case, the Doppler broadening are very low and can be neglected. Thus, the measure of the global apparatus function corresponds to the optical apparatus function which is the principal broadening effect of this spectrum. Then, a comparison between the optical apparutus functions measured with a mercury lamp and a Balmer lamp enables to check the method.

The measures of apparatus fonctions are made on a spectroscopic acquisition chain. The monochromator is of Baush & Lomb type with a focal lenght of 2 m and it has a 1200 grooves/mm grating working in the first order. Photodetection is made with intensified controller model 1455 of Princeton Instrument with a single line of 770 intensified pixels of a matrix CCD possessing a internal Peltier cooler, and it is linked to a detector controller model 1461. A 100 mm silicium lens is used to focalise the light into the entrance slit of the monochromator. The width of the slit is fixed to 50 μm.

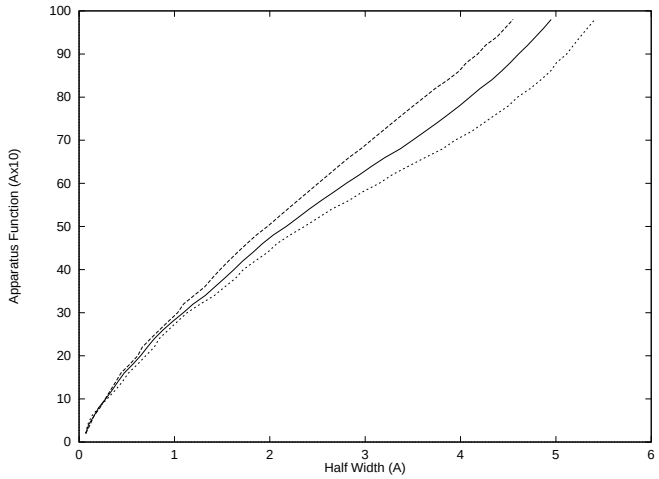

Figure 6: Plot of the global apparatus function as a function of the half width at the height of 0.8.

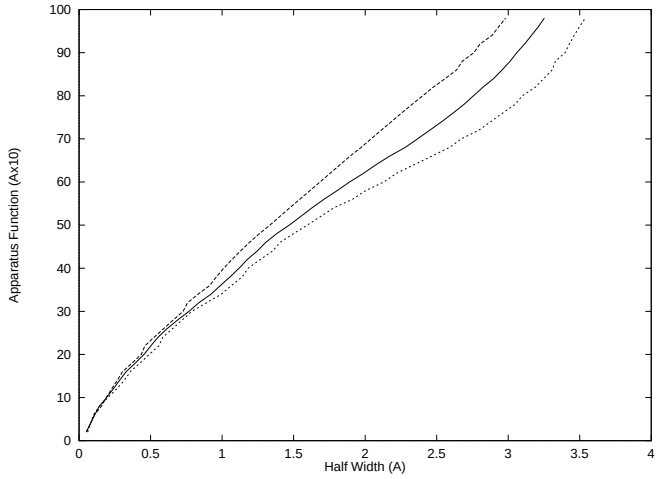

Figure 7: Plot of the global apparatus function as a function of the half width at the height of 0.9.

Table 1: Equations of the global apparatus function (Δ) as a function of the half width W (nm) for three different heights.

Height (a.u.)	**Equations**
	Δ(1000 K)=0.028W^3-0.341W^2+2.582W+0.154
0.7	Δ=**0.029**W^3**-0.352**W^2**+2.458W+0.179**
	Δ(9000 K)=0.0285W^3-0.361W^2+2.385W+0.157
	Δ(1000 K)=0.058W^3-0.519W^2+3.281W+0.129
0.8	Δ=**0.0698**W^3**-0.604**W^2**+3.225W+0.125**
	Δ(9000 K)=0.0704W^3-0.639W^2+3.178W+0.0941
	Δ(1000 K)=0.179W^3-1.042W^2+4.74W+0.114
0.9	Δ=**0.252**W^3**-1.397**W^2**+4.827W+0.0749**
	Δ(9000 K)=0.264W^3-1.548W^2+4.866W+0.011

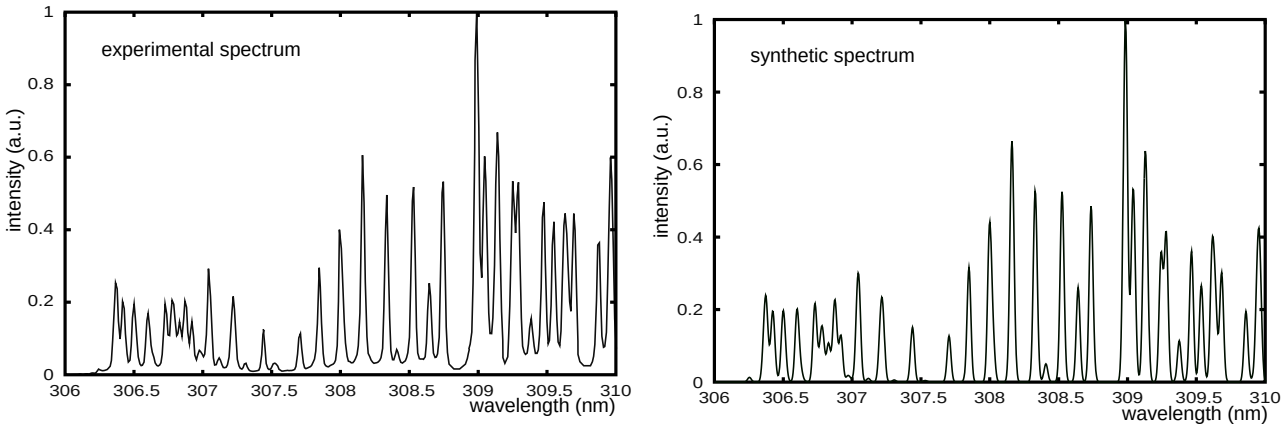

Figure 8: Plots of the UV OH spectra experimental and synthetic for a rotational temperature about 1200 K and for $\Delta = 0.04\,nm$.

In a first step, the apparatus function is measured with a mercury lamp which has two characteristic lines at 435.833 nm and 546.073 nm. These ones are fitted by gaussian functions and the widths at 1/e of these functions give an optical apparatus function about (0.042$\pm$0.003) nm on an average. In a second step, we used a Balmer lamp (Figure 8). The apparatus function is determined from the emission UV OH spectrum provided by this lamp and from the equations founded previously. Its value is about (0.039$\pm$0.003) nm. The comparison between the two values allows to validate the direct determination method of a global apparatus function in UV OH spectrum.

Figure 8 presents a comparison between an experimental spectrum obtained with our balmer lamp and a synthetic spectrum computed with $T = 1200K$ and $\Delta = 0.04nm$. This temperature value has been found by checking the superposition of the normalized experimental spectrum with the different synthetic spectra. The ratios G_0/G_{ref} and G_1/G_{ref} have been used to support the determination of the rotational temperature. It is clear that there is a good agreement between the experimental and the synthetic spectra.

5. Conclusion

This paper has presented a original method to determine the apparatus function of a spectroscopic device from the UV OH spectrum. The found results are equivalent to the experimental methods. A possible application of this work is to use the equations for simulation way with for final aim the elaboration of an 'OH molecular pyrometer', actually studied in our research group.

References

[1] de Izarra C 2000 *UV OH Spectrum used as a molecular pyrometer J. Phys. D: Applied Phys.* **33** 1697-1704

[2] Diecke G H and Crosswhite H M 1961 *J.Q.S.R.T.* **2** 97

[3] de Izarra C 2000 *Computer simulation of the UV OH band spectrum International Journal of Modern Physics C* **11** No5 987-998

[4] Pellerin S, Cormier J M, Richard F, Musiol K, Chapelle J 1996 *A Spectroscopic Diagnostic Method Using UV OH Band Spectrum*, J. Phys. D: Appl. Phys. **29** 726-739

Self-organizing entrainment in transitional thermal plasma plume

Luděk Krejčí[1], Vladimír Dolínek[1], Václav Němička[2], Jan Hlína[2]

Institute of Thermomechanics AS CR, Dolejskova 5, 182 00 Praha 8, Czech Republic
Institute of Electrotechnical Engineering AS CR, Dolejskova 5, 182 00 Praha 8, Czech Republic

Abstract
The paper presents evidence of controlling role of plasma column self-organization in the entrainment of external medium (air) into the transitional thermal plasma plume. The analysis is based on the fact that the transport of thermal energy through the plume transiting to turbulence reflects unambiguously the dynamic phenomena controlling the process evolution. The discussion of the nature of the interrelations among the plume entrainment and heat transport processes suggests how and when the entrainment is performed.

Introduction and Motivation
In many advanced technologies thermal energy needed for their realization is supplied from transitional thermal plasma plumes. However the effective utilization of plasmas under such conditions is often limited owing scanty understanding of phenomena which should control them.

The main objective of our investigations is to grasp and describe these phenomena. However the dynamics of a complex system of non-linear dynamic processes which controls the plasma plume transition forms a dynamics of its own which can be understood only from a holistic description of the whole history of process evolution.

Our experimental evidence [1][2][3] indicated, that such holistic description is unambiguously and sensitively reflected by the history of thermal energy transport taking place in the plume core. It is described by a thermodynamic portrait of the transition process [2] which enables us to disclose what is the underlying nature of the system evolution that leads to strong interdependence of events and to resulting process complexity – what governs the transition in essence. This clue event is the plasma column self-organization [4]. And the gained knowledge base suggests also, how the self-organized energy separation controls directly the transport of heat through the plume which it transiting to turbulence [5].

However, not only the energy transfer but also the mass transport phenomena – the entrainment of external media into the plasma column primarily – represent the direct consequences of underlying column dynamics. The interrelations of these complex processes are controlled at the same time by the evolution of morphology of an ensemble of organized structures produced by all of self-organizing dynamic systems [6]. The morphology of these pattern systems, identified by specific identification procedure of a CCD camera pictures [7] controls obviously both the energy separation as well as the entrainment of external media into the plasma column and determines in such a manner the interrelations between the heat and mass transport through the plume.

In the following text an insight into the mechanism of interplay of these events is presented. However, the nonlinear interactions of the individual phenomena of the dynamic system studied preclude that these detailed observations can be "condensed" into a sole picture of the process. Under such conditions our insight can explain why there is variability or what typical pattern can emerge only – not what the particular outcome of a particular system will be.

Experiments and discussion of their results
The task of experiments was to obtain the data describing the behavior of distinct events taking part in the plume transition and on the basis of their confrontations to gain the responses which can be used in characterizing the complex plume transition phenomena.

The data characterizing the plume dynamics are presented in the form of thermodynamic portraits of the plume transition process [5]. They are represented by the relationships between the core cusp stagnation point heat flux on the plume geometric axis at the distance of 15 mm from the arc heater exit plane and by the plume power data in the arc heater outlet plane. These portraits enable us to disclose not only what is the underlying nature of the system evolution but also what governs the transition in essence. As stated above, this clue event is the plasma column self-organization. A self-organizing process characterizes itself by a specific type of its sensitivity to process initial conditions. Such a process exhibits in the course of reproduced experiments (under slight, randomly established initial conditions) in the process phase diagram

(in the thermodynamic portrait of the transition) different traces which during the process evolution intersect gradually in several process controlling states – in the process milestones [4]. The self-organization also induces and controls the energy separation in the column which markedly changes the energy generation process and the arc chamber thermal balance. As this takes place the arc power loss is clearly driven to attain a constant value at higher flow rates while the corresponding arc power tends to be fully used for plume power enhancement only [5]. And differences in the courses of transition processes in "flapping" and resonance "stabilized" plumes are produced by different evolution of energy separation in the plasma column.

The description of the experimental equipment and the methodics used in the heat flux measurements may be found elsewhere, e.g. in [1]. We will give only facts needed for understanding the text. The experiments have been performed in the plumes in which during an experiment the front sensitive surface of the heat flux probe was exposed in a gradual manner to the flow conditions from the laminar to the turbulent ones. As this takes place, the arc heater was working at constant arc current of 150 A and the argon flow rates varied from 10 to 150 slm. The plasma plume issuing from the arc chambers – which were 24 and 44 mm long – through an exit ring anode orifice of 8 mm diameter. The operation of the total heat flux measuring probe is based on on-line analysis of the unsteady conduction in a copper cylinder of 6 mm dia. mounted flush with the front surface of the probe. Temperature signals from the sensor are processed in an analog circuit in which the inverse heat conduction problem is solved and the heat flux history on the probe face is obtained. The body of informations gained show, that both of the known types of the thermal plasma transition processes [2][3] are represented among the data obtained. The "flapping" transitional plume issued from the arc chamber length of 24 mm; the plumes "stabilized" by the acoustical resonance in the arc chamber cavity issued from the arc chamber of 44 mm length. The turbulent flow – but not the fully developed one – has been attained in the plumes issued both from the arc chamber of 24 and 44 mm at the flow rate of 150 slm.

The needed air entrainment data were obtained by the use of a simple, home made sampling probe feeding the gas sample to the flue gas analyzer Testo 325/1 in which the proportion of O_2 in the sample was determined. The water cooled body of the probe – schematic on Fig. 1 – having the same outer diameter as the body of the calorimeter used is provided by draining hole of 1,5 mm diameter. Next the sample enters the water jacketed part of the sampling tube through which is directly drawn to the gas analyzer. The analysis is based on electrochemical principle; the sensor used can supply the required data of the proportion of O_2 in the sample with the accuracy of ± 0.2 % Vol at the resolution of 0.1 % Vol in 120 s.

The experimental arrangement and the evaluation procedures used during the investigations of the dynamic patterns appearing in the self-organizing plasma plume in the course of its laminar-turbulent transition is described in detail in [7]; we present only inevitable information here. In the course of experiments a fast shutter CCD camera was used. The camera was equipped with a rotating mirror situated between the CCD chip and objective lens. The regime of multiple camera exposures was used to record a sequence of 8 shots with exposure times 1 μs and interval between the exposures 10 μs. The evaluation procedure was based on the correlation analysis of vectors the components of which are defined either as intensities of the same pixels in the succeeding pictures or the intensities recorded by the pixels in the neighborhood of each point of the plasma plume image. The results show, that the images of plasma plumes include regions characterized by various correlations between the succeeding images of the plasma plume. It is possible to identify both the regions where the correlations is very high (the value of the correlations coefficient is close to +1) and the regions related probably to turbulent structures characterized by the negative correlations coefficients close to –1.

The results of experiment obtained in the course of the plume heat transport and air entrainment investigations are presented in Figs 2 – 4. A series of thermodynamic portraits of the heat transport through the plume reflect the evolution of the plume dynamics in the course of self-organized transition processes. The self-organization drives in the course of different experiments the corresponding branches of the process through several fixed process controlling thermodynamic states. The plumes issued from the arc chambers of 44 and 24 mm lengths exhibit two readily distinguishable courses of events (Fig. 2). In the evolution of the "flapping" plume one process phase is "missing" in comparison with the case of resonance "stabilized" plume. The reason is in different arc heater working conditions in which the full energy separation in the plasma column starts [8]. Under such condition the arc chamber power loss attains a value which does not change further while the corresponding arc power increase is then fully used to plume power enhancement. In both cases such state starts under the conditions of maximum measured heat flux – at the plume net

powers of 2.0 and 3.3 kW (at 30 and 60 slm mass flow rates) issuing from the chambers 24 and 44 mm. It suggests, that the plume power enhancement manifests itself in scattering of self-organized structures which results in the decrease of measured plume heat flux. However, the strong decrease of the plume heat flux taking place in these, pre-turbulent phases of the transition process results not only from the fact that the heat flux probe face is struck by small amount of scattered fragments of the self-organized structures but also from the effect of increased entrainment of external environment into the plume through these fragments – Fig. 3a, 3b and 4c, 4d, probably.

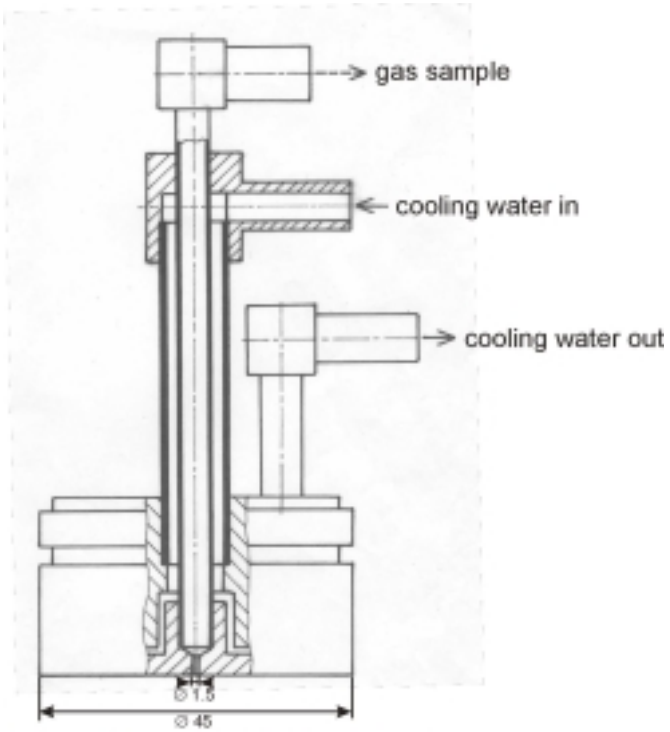

Fig. 1 Schematic of sampling probe

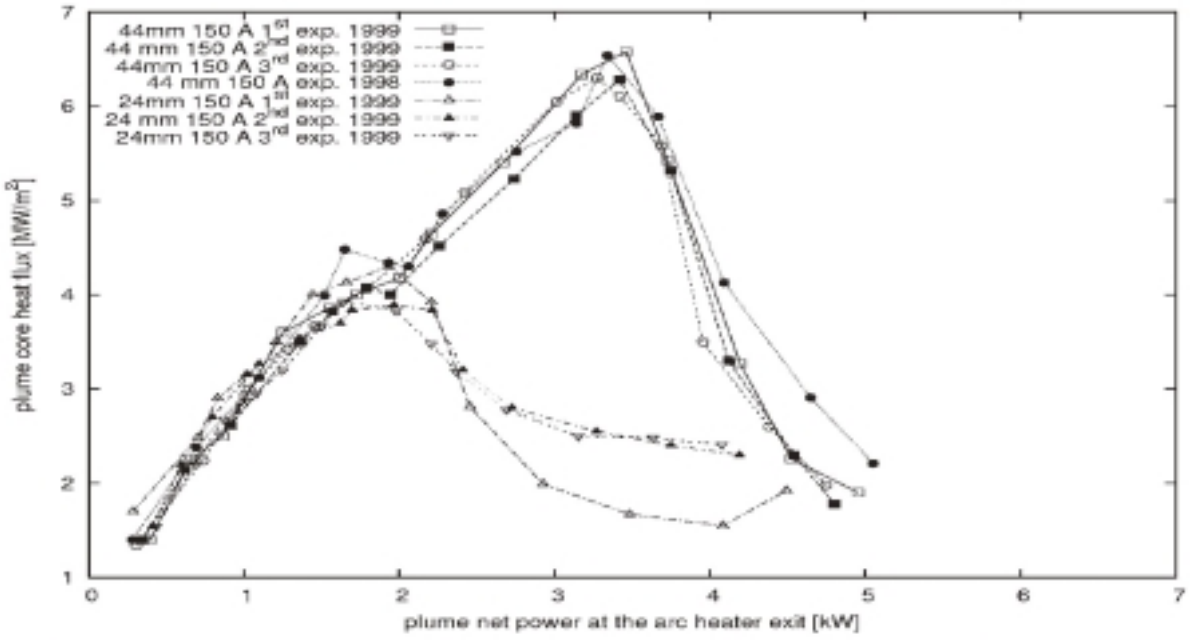

Fig. 2 Local thermodynamic portraits of plasma plume net power transitions

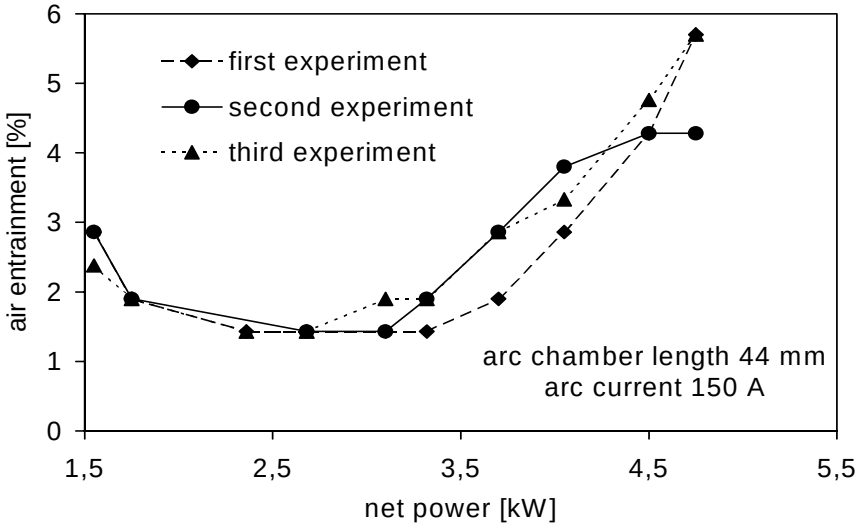

Fig. 3a) Resonance stabilized plume

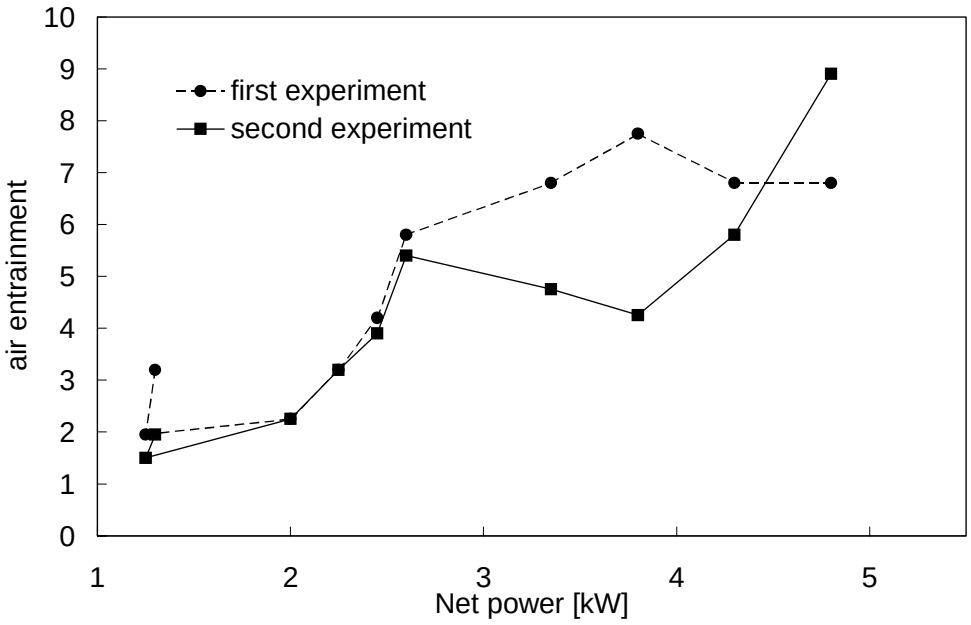

Fig. 3b) “Flapping” plume

3a), 3b) Local arc entrainment during plume transition

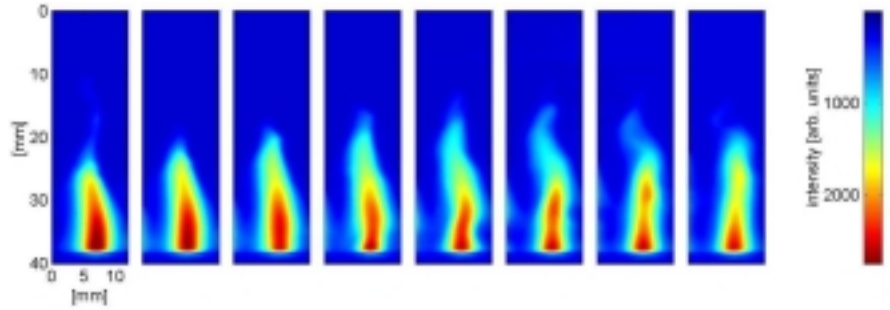

Fig. 4a) Original image sequence for gas flow rate of 40 slm (plume net power 2,68 kW)

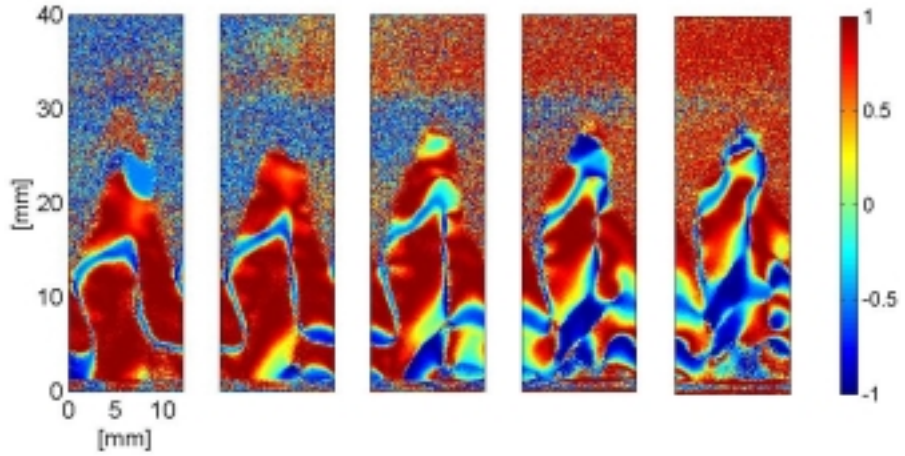

Fig. 4b) Analysis of the sequence shown in Fig. 4a) using temporal correlations

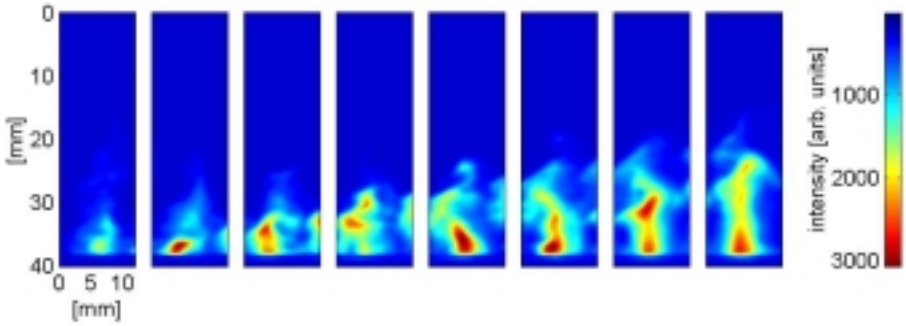

Fig. 4c) Original image sequence for gas flow rate of 100 slm (plume net power 4,05 kW)

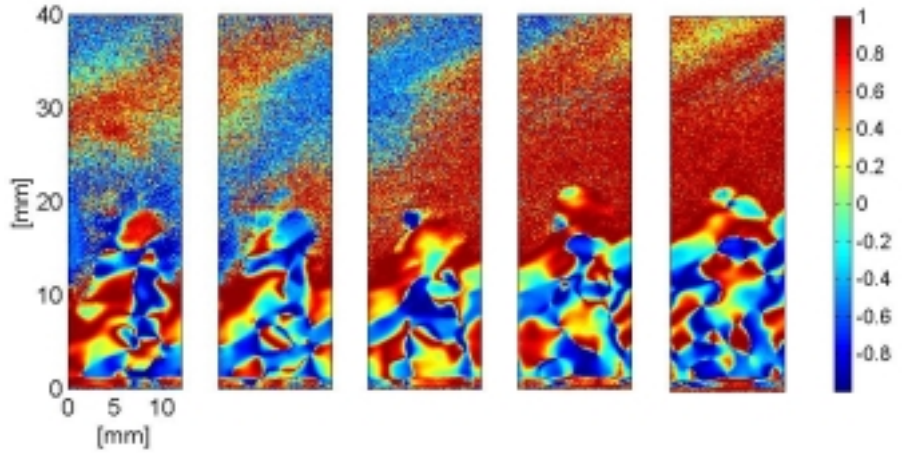

Fig. 4d) Analysis of the sequence shown in Fig. 4c) using temporal correlations

Fig. 4 Motion of self-organized structures in a argon plasma column arc chamber length 44 mm, arc current 150 A

On the other hand, as the self-organized structures develop – at low flow rate values – at 20 slm in the flapping and at 50 slm in the resonance "stabilized plume – the "large" segments – Fig. 4b – shield the hot column interior and striking the heat flux sensor face increase appreciably the heat flux transported through the resonance stabilized plume. It is not the case of "flapping" plume, however as there does not exist a possibility to control the energy separation consecutively as it is in foregoing case [8].

Summaring the piece of knowledge presented it is clear that the behavior of the plasma plumes in the course of their transition to turbulence can no longer be understood in terms of the behavior of the individual events – or the other way round, the distinct phenomena e.g. the entrainment can be understood only from the properties of the dynamic behavior of the entire system. However, such an assertion concern only a set of particular states – of the process "milestones" – which are almost not sensitive to process initial conditions and which exhibit remarkable reproducibility both of dynamic as well as of thermal behavior of the transitional plasma column. This fact is on the one hand employed e.g. just in detailed investigations of the external environment entrainment into the plasma column; on the other hand it represents the main obstacle in searching for a suitable turbulence model used for entrainment computing.

References

[1] L. Krejčí, V. Dolínek, L. Šára, V. Němička and J. Hlína – Energy Transport Enhancements in a Transitional Thermal Plasma Plume. IEEE Transactions on Plasma Science. **25**, 860–863 (1997).

[2] L. Krejčí, V. Dolínek, P. Sopuch, V. Němička and J. Hlína – Nonlinear Convective Heat Transfer in a Transitional Plasma Plume. In: Heat and Mass Transfer under Plasma Conditions. Annals of the New York Academy of Sciences. **891**, 333–339 (1999).

[3] L. Krejčí, V. Dolínek, P. Sopuch, V. Němička and J. Hlína – Resonance in a Transitional Plasma Plume, in: Heat and Mass Transfer under Plasma Conditions. Annals of the New York Academy of Sciences. **891**, 442–448 (1999).

[4] Luděk Krejčí, Vladimír Dolínek, Pavel Sopuch, Václav Němička, Jan Hlína – Self-organization in Thermal Plasma Plume. Proc. of the XXV Int. Conf. on Phenomena in Ionized Gases. Nagoya. **3**, 149–150 (2001).

[5] L. Krejčí, V. Dolínek, P. Sopuch, V. Němička, J. Hlína – Energy Separation in Transitional Plasma Plume. XIV. Int. Conference on Gas Discharges and their Applications. Liverpool. Proc. 240 (2002).

[6] I. Prigogine – From Being to Becoming. W. H. Freeman, San Francisco (1980).

[7] V. Němička, J. Hlína, J. Šonský – Identification of Dynamic Patterns in CCD Camera Records of Thermal Plasma Jets. Symposium TPP–7, Thermal Plasma Processes. Strasbourg (2002).

[8] L. Krejčí, V. Dolínek, V. Němička, J. Hlína – Thermodynamic Control of Laminar-Turbulent Transition in High Temperature Gas Plumes. Paper in preparation for 20th European Symposium on Applied Thermodynamics. Bad Neuenahr (2003).

Acknowledgement

The authors would like to recognize the efforts of Mrs. Jana Lahovská in technical preparation of the manuscript. The work was supported by the Grant Agency of the Czech Republic (Grants No. 202/99/0389 and 202/02/0113) and partly by the Grant Agency of the Academy of Sciences of the Czech Republic (Grant No. A1057001). We are grateful for these supports.

Transfer of Plasma results to different reactors and substrates

V. Sciarratta, D. Hegemann, M. Müller, U. Vohrer, C. Oehr
Fraunhofer Institute for Interfacial Engineering and Biotechnology, Nobelstrasse 12, 70569 Stuttgart, Germany

Abstract
RF plasma polymerization of acrylic acid enables the formation of polyacrylic-like layers containing carboxylic groups on different substrates. The stable layers with high functionalities are deposited. Furthermore the processes can be up-scaled.

KEY WORDS: plasma deposition, pulse plasma, acrylic acid.

1. INTRODUCTION

For industrial application it is required that plasma results obtained successfully with small scale reactors and for particular substrates can be transferred to larger systems and different materials.
Recently we succeeded in creating stable polyacrylic-like ultrathin and thin coatings containing carboxylic-groups on polypropylene [1] with the help of RF continuous plasma. In the present work we investigated the possibility to obtain similar thin layers by means of pulse plasma and tried to understand the rule of the equivalent power in these processes. As second purpose it was attempted to generate the same coatings also on polycarbonate, polyethylene and polystyrene. At last it was tried to find a semi-empirical law to transfer the results to other reactors, in our case from a small round reactor to a bigger reactor "DIN A3" [2]. For all plasma-derived layers, stability tests were carried out. Characterization of the plasma-modified substrates was performed by using fluorescence spectroscopy in combination with derivatization techniques and FTIR (Fourier Transformation Infrared Spectroscopy). The thickness of the polymer films was analyzed by AFM (Atomic Force Microscopy).

2. EXPERIMENTAL

2.1. Materials

The polypropylene film (PP) without additives, used in these studies, was supplied by Alkor Folien GmbH Germany and had a thickness of 50 µm. polystyrene and polycarbonate (144C, Makrolon 2405), in the form of object slides were used without further purification. Low molecular weight polyethylene film, 25 µm thick, was washed with acetone before using. Acrylic acid (AAc) was obtained from Fluka with >99 % purity and was used as received. The silicon wafers, needed for determination of the layer thickness via AFM, were preventively washed with ethanol and partially masked with a temperature stable adhesive tape during the plasma deposition.
thioninacetate (THA, Sigma), ethanol (EtOH, Chromatographie Handel Müller) and chloride acid (HCl, Fluka), needed for the fluorescence labeling, were also used without further purification.

2.2. Plasma deposition apparatus

The plasma experiments in pulse mode and in continuous mode with different substrates (polyethylene, polycarbonate, polystyrene, Si wafer, titanium, nickel free steel), were performed by means of a round symmetrical parallel plate (200 mm diameter) reactor. The discharge was confined between the electrodes by a glass vessel. The gas flow and monomer vapors was introduced through the "hot" electrode towards the substrates. The lower electrode was grounded and served as substrate holder. The shown experiments in the round reactor, were carried out with continuous and pulse RF discharge (duty time 1 ms, dead time 2 ms up to 9 ms) at different input powers. Plasma coatings were carried out by means of continuous and pulse plasma with discharge times up to 30 min.
For the pulse plasma experiments, the average Power $P_{equivalent}$ delivered to the system was calculated using the following expression:

$$P_{equivalent} = P_{CW} \frac{t_{on}}{t_{on} + t_{off}}$$

where $\frac{t_{on}}{t_{on} + t_{off}}$ is defined as duty cycle.

In a first step, the surfaces of the PP samples were cleaned/activated with hydrogen plasma (H_2 flow 4 sccm, pressure 0.05 mbar, time 5 s) and afterwards, a mixture of hydrogen/acrylic acid (AAc flow ca. 1 sccm, total pressure 0.1 mbar) plasma was introduced. Plasma duration time and dead time T_{off} were varied.
In order to reproduce the same plasma experiments obtained in [1], a larger "DIN A3" parallel plate reactor (290x390 mm^2) [2] was adapted. The activation/carrier gas as well the monomer were introduced by means of a gas shower through the hot electrode in the plasma chamber, providing a homogeneous flow and diffusion.
As in the round reactor, also in the "DIN A3" reactor, the surfaces of polypropylene samples were cleaned/activated by means of hydrogen plasma (H_2 flow 10 sccm, pressure 0.05 mbar, time 5 s) and subsequently treated with a hydrogen/acrylic acid (AAc flow ca. 2.5 sccm, total pressure 0.1 mbar) plasma. The activation/treatment discharge power was varied.
Both reactors enable power input with a minimum of losses, even in pulse mode.

2.3. Characterization Techniques

2.3.1. Fluorescence spectroscopy
Fluorescence intensities were measured with a spectrometer (Spectrapro 275, Acton Research Corporation) after fluorescence derivatization of the carboxylic groups with thionin acetate (THA) and ethanol as described in [3, 4]. The concentration of chemically bounded fluorescence groups was determined using a calibration curve. The excitation wavelength of THA was 594 nm, the emission was measured at 618 nm.

2.3.2. Infrared spectroscopy
HATR (horizontal attenuated total reflection) spectroscopy was performed with a Perkin Elmer FTIR Spectrometer (Spektrum 1000). A 45° ZnSe crystal was used; spectra were scanned 32 times between 4000 and 650 cm^{-1} with a resolution of 1 cm^{-1}. Prior to each set of analysis, the ZnSe crystal was cleaned with ethanol and dried with nitrogen. During the measurements the HATR mirrors compartment was purged with nitrogen to reduce water adsorption; the samples were pressed with a graduated pressure clamp to improve a reproducible contact to the ZnSe crystal.

2.3.3. Thickness measurements by AFM
Thickness measurements are necessary to estimate carboxylic groups concentration in plasma deposited layers. These were carried out by means of a Park Scientific Autoprobe CP microscope. The analyzed silicon wafers were partly covered with a temperature stable adhesive tape during the plasma deposition. To analyze the thickness of the plasma polymers, the adhesive tape was removed with caution. The sample surface was aligned in the AFM such that the boundary between the plasma polymer coated and uncoated wafer was beneath the AFM tip.

2.3.4. Stability tests
The treated samples were tested with different polar and non-polar solvents: they were immersed in bi-distilled water, ethanol, 10% twen solution, isopropanol, and mono-ethyl-diethyl-ether and stirred for 30 min at room temperature. Moreover a long time stability was executed by immersion of a thionin acetat derivatized sample in ethanol for 10 days. No change in carboxylic group concentration and in layer morphology were detected applying these tests.

3. RESULTS AND DISCUSSION
Deposition of acrylic-like layers containing carboxylic groups, by means of lab-scale plasma reactors is often difficult to reproduce in industrial scale, since it depends on various plasma parameters. In this section it will be shown how input power mode, substrate materials, form and volume of reactors influence these processes and how it is possible to transfer them to larger reactors.

3.2.1. Dependence on equivalent input power and dead times in pulse plasma
With the objective to investigate the effectiveness of pulse plasma compared to continuous wave, and studying the dependence on input power and pulse ratio, a new set of experiments in the round reactor were carried out. The plasma parameters as in the previous paper [1] were used: the treatment time was 30 min.
Input power $P_{equivalent}$ and on/off pulse ratios between 1/2 ms and 1/9 ms were varied. For continuous wave plasma the input power was also changed between 16 W and 34 W.
In Figure 1 the fluorescence measurements of carboxylic group concentrations for different input power and pulse ratio are reported. For lower continuous power inputs (plasma power input deficiency region) [5], the plasma is no longer

stable and consequently, the formation of powder in the chamber was observed. A poor adhesion of deposited layers is correlated with this effect.

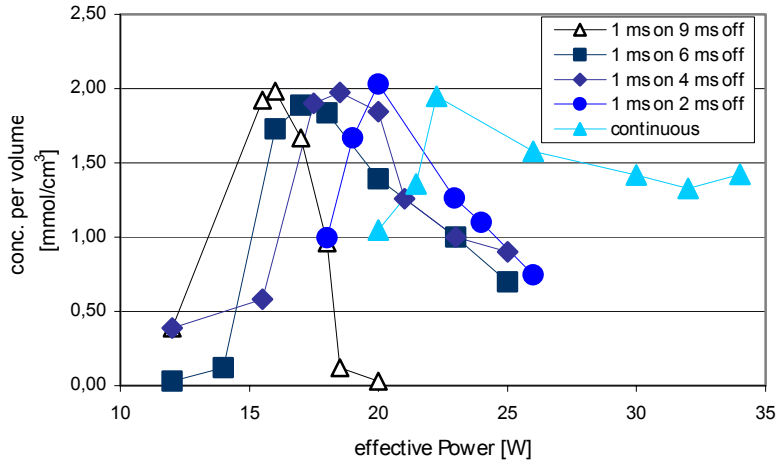

Figure 1: Dependence of COOH concentration on dead times and effective power.

Clearly, it appears that for a fixed pulse ratio varying the equivalent power, a maximum in carboxylic groups is achieved. These maxima depend on dead times: for shorter dead times a higher energy is required. In continuous mode further increased energy is necessary.
Moreover, the maximum concentration values are, within experimental uncertainty, comparable, independent of power on/off ratios and of plasma mode.
To explain these surprising and outstanding results, we have to consider two wave forms with dead times 4 ms and 9 ms as depicted in Figure 2.

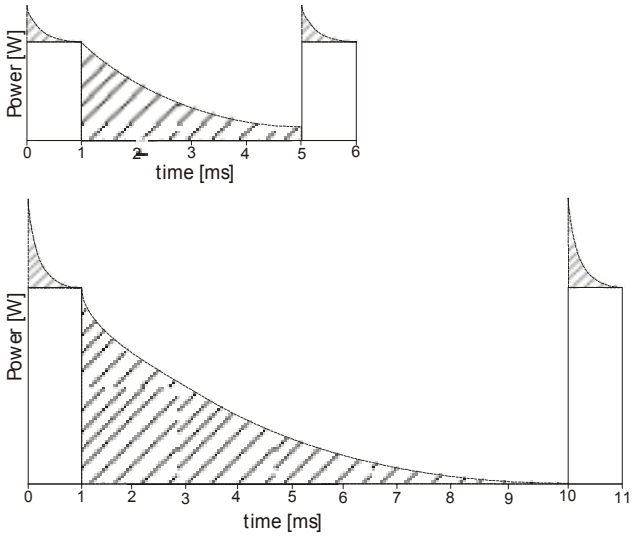

Figure 2: comparison between ideal and experimental pulse sequence at 1/4 ms and 1/9 ms ratios.

So, in order to reproduce the same experiments with different pulse ratios in an ideal case (see whole curves in Figure 2) the equivalent power $P_{equivalent}$ has to remain constant, it results that:

$$P_{equivalent1/9} = \frac{1}{10} P_{Max1/9} = P_{equivalent1/4} = \frac{1}{5} P_{Max1/4}$$

$$P_{Max1/9} = 2P_{Max1/4}$$

Hence it might be assumed that at 1/9 ms a double input power is needed to obtain comparable conditions as at 1/4 ms (after glow).
In the real case however, the pulses have a form as depicted in Figure 2 with dashed curves.
When the generator is switching on, a spike occurs and this is clearly higher for higher maximal powers. When the generator is switching off, the plasma discharge remains for a certain time on. Considering the areas below the dashed curves, it appears evident that with longer dead times a larger input energy is introduced. Consequently, to achieve equal results at longer dead times, a lower equivalent power $P_{equivalent}$ is required.
Furthermore it could be supposed that in continuous mode a lower energy to activate/ support plasma polymerization to avoid the fragmentation of carboxylic groups is necessary. But, during the on-period, in pulse mode, the electron density responsible for the existence of H^+ and for the building free radicals is higher than in continuous mode [6]. Therefore a greater input power in continuous wave is required . These suppositions are confirmed by the results presented in Figure 1.

3.2.2. Transfer to different substrates

Functionalization by means of carboxylic groups is not restricted to polypropylene but it can be extended to other substrates. In our experiments we also used successfully polycarbonate, polyethylene, polystyrene, as well as Si wafer, titanium or nickel free steel.
For the achievement of these treatments, it is important to match the necessary activation energy in order to create free radicals for every substrate.
All the samples were stirred in bi-distilled water for 30 minutes and then dried. Infrared spectra, registered before and after washing, show no changes. In all spectra a new peak at 1715 cm^{-1} appears and it demonstrates that carboxylic groups on the surfaces are present and chemically bounded. Furthermore, three peaks emerge: a broad band with center at about 3000 cm^{-1} is typical for -OH bridges stretching oscillations; another band likewise broad band appears between 2700 and 2500 cm^{-1}, characteristic for carbon acid dimers is the result of combination oscillations of C-O stretchings and O-H deformations. At last, a broad band between 1315 and 1280 cm^{-1} but not always good discernable, to attribute to C-O stretching oscillations is also expected.
All samples, apart from polystyrene, were also analyzed by means of fluorescence coupling [4,5] and the carboxylic groups were detected.
For Si wafer, titanium, and steel we presume that an oxide layer already present on the surface of materials can contribute to the formation of O-H Bridges.

Up-scaling to different reactors

With the aim of transferring the successful experiments of the round reactor to the “DIN A3” one, or in general to another reactor with different forms or volumes, it is important to consider some plasma parameters as well as electrical connections, monomer inlet and pump system. The generator was connected via a matchbox and a V/I Probe in the middle of the “hot” electrode ensuring an homogeneous power input and minimizing the reflected power. The lower electrode was grounded centrally maintaining the system as best as possible symmetrical. The monomer, in our case acrylic acid, was introduced in the round reactor, directly in the middle of the powered electrode, confining a polymerization process only between the electrodes. Therefore, the samples (75 mm in diameter) situated in the middle of the lower electrode were met perpendicular from all the possible plasma created species.
For this reason the “DIN A3” reactor was chosen: a shower system ensured that plasma particles encountered the rectangular samples (240 x 340 mm^2) in a similar way as in the round reactor.
In both reactors the rest gases were exhausted through three tubes by means of a vacuum pump, providing also uniform monomer/activation gas flows in the plasma chamber. Also the distance between electrodes is a consistent parameter to obtain stable plasma polymer with high carboxylic-groups concentration. This variable was also investigated; it was found when maintaining all other plasma parameters fixed, a maximum in COOH concentration at 80 mm distance was reached. This value was hold constant in both plasma systems.
A parameter which depends directly on the flow rate is the residence time τ of a gas molecule, that is the mean time it remains in the process chamber before being pumped away. If the volume of the chamber is V and S is the pump rate then:

$\tau = V/S = pV/pS = pV/Qp_o$

where Q is the flow rate of the molecular gas, p is the pressure in the reactor and p_o is the atmosphere pressure.
If we suppose to have a hydrogen flow of 4 sccm in the round reactor with the pressure p = 0.054 mbar and a plasma volume V = 2513 cm^3 = 2.513 l, the residence time results τ_{round} = 2 s. In the "DIN A3" reactor the plasma chamber has a volume of V = 9726 cm^3 = 9.726 l about 4 times bigger than the round one. This implies that in order to maintain the residence time τ constant also in the " DIN A3" reactor, it is necessary to increase the hydrogen flow rate of a factor 4 at the same pressure.
Similar considerations can also be made for the monomer, acrylic acid: for the experiments carried out in the round reactor the acrylic acid flow was about 1sccm at a pressure of p = 0.032 and consequently a flow of ca. 4 sccm in the "DIN A3" was required. Unfortunately acrylic acid has a relative low vapor pressure at room temperature (3,8 hPa at 20 °C) . The two possible solutions to maintain the pressure constant were either to heat up the monomer or to throttle the vacuum system. The second alternative was chosen because a higher monomer temperature could cause a polymerization of acrylic acid in the system before it reached the plasma chamber. The monomer flow was set to about 2.5 sccm and the hydrogen to 10 sccm (in an ideal case the flow should be Q_{AAc} = 4 sccm and Q_{H2} = 16 sccm).
In figure 1was shown that the polymerization process, in pulse or in continuous mode, is only possible within some input power regions, in which the carboxylic group concentration reaches a maximum. We focused our attention on the process in continuous mode at 22 W with a maximum of COOH-groups concentration being reached. At this input power reactor an optimal matching is achieved in the round and we attempt to reproduce the same results also with the "DIN A3" reactor.
Hence, in order to applicate the same input energy, it is important to correlate the discharge power to the glow discharge volume or to the glow discharge surface (because, in our case, the distance between electrodes is kept constant).
For the round reactor, the input power density $D_{round} = W_{round} / A_{round}$ = 22 / 314.12 = 0.07 W/cm^2, where A_{round} is approximated to the area of the electrode. Since the density value has to remain constant in both systems and the area "DIN A3" electrode is A_{A3} = 1131 cm^2, the input power should be around 80 W. In table 1 the results of plasma polymerization experiments are reported in the round and the "DIN A3" reactor with three different deposition times at 22 W and 80 W, respectively.

	Plasma treatment time [min]	Film thickness after washing [nm]	-COOH group concentration [10^{-9} mol/cm^2] (fluorescence)	-COOH group concentration [10^{-4} mol/cm3]
Untreated PP	-	-	0	0
AAc plasma coated PP in a round reactor	10	176 ± 7	26 ± 3	14 ± 2
	20	285 ± 9	37 ± 4	13 ± 2
	30	394 ± 8	53 ± 5	13 ± 2
AAc plasma coated PP in a DIN A3 reactor	10	177 ± 19	30 ± 3	17 ± 2
	20	265 ± 25	46 ± 5	17 ± 2
	30	379 ± 7	60 ± 6	16 ± 2

Table1: ESCA, fluorescence and thickness measurements results of samples treated in the round and "DIN A3" reactor with different deposition times

It appears that in both reactors homogeneous comparable layers can be produced: considering fluorescence measurements, the carboxylic group concentration of the volume growths with the deposition time, that means the density of the functionalities remains constant in the bulk.

4. CONCLUSIONS

We can conclude that for the formation of acrylic-like layers with a very high concentration of carboxylic groups, according to our findings, a pulsed plasma is not necessarily required to modify PP substrates.
These layers are stable and can also be deposited on different substrates.
As described RF plasma polymerization with acrylic acid can successfully be performed in different reactors regarding certain plasma parameters.

5. REFERENCES

1 V. Sciarratta, U. Voher, D. Hegemann, M. Müller, C. Oehr, Surf. Coat. Technol. (2003) in press
2 D. Hegemann, H. Brunner, C. Oehr, Surf. Coat. Technol. **142-144** (2001) 849-855
3 V.B. Ivanov, J. Behnisch, A. Holländer, F. Mehdorn and H. Zimmermann, Surf. Interf. Anal., **24** (1996) 257-262
4 J. Behnisch, F. Mehdorn, A. Holländer, H. Zimmermann Surf. Coat. Technol., **98** (1998) 875-878
5 H. Yasuda, Plasma Polymerization, Academics Press, Inc. (1985) 298-301
6 A. Brockhaus, St. Behle, A. Georg, A. Schwabedissen, Ch. Soll, J. Engemann, Contrib. Plasma Phys. **39** (1999) 5. 399-409

An Efficient Model For Inductively Coupled Multi-component Plasmas

G. Wenig[1], P. Scheubert[1], P. Awakowicz[1]

[1] *Institute for Physics of Electrotechnology, Munich University of Technology, Munich, Germany*

Abstract
An efficient model for inductively coupled plasma sources is presented. It unifies physical accuracy with computational efficiency. The plasma is divided into bulk and sheaths with separate models for each region. For sheath regions a compact model is used. It takes the particle fluxes as input parameters and gives back the plasma variables at the cut edge between bulk and sheath. For the plasma bulk a drift-diffusion-model is applied. Model results are in excellent agreement with full hydrodynamical calculations.

1. Introduction

Most technological applications of low pressure low temperature gas discharges rely on plasma chemical processes. Prominent examples are given by semiconductor manufacturing or surface coating technology, e. g. These plasmas often contain more than one neutral and ionic species. Inductively coupled plasma sources (ICPs) offer high electron densities and low ion energies at the same time. Therefore, they are well-suited for many, especially sensitive, applications. In order to optimize such processes, a detailed knowledge about the discharge characteristics such as spatial profiles of particle densities or particle fluxes towards the walls is desired. Furthermore, the dependence of the discharge properties on external parameters like neutral gas pressure or input power is of great interest. This information can be obtained by an intimate interplay between diagnostics on the one and modelling and simulation on the other hand. With respect to simulation, two partially opposed major goals are physical accuracy and computational efficiency. In this paper, a model for inductively coupled plasma sources with more than one positive ionic species is presented which satisfies these two demands.

2. An Efficient Two Fluid Plasma Model

Fluid models are commonly applied to describe inductively coupled plasma sources. They consider the plasma as a mixture of two fluids (electrons and ions), which are described by a set of conservation equations. Fluid models can be divided into hydrodynamic models and drift-diffusion-models. The hydrodynamic models use a full momentum balance, whereas the drift-diffusion-models simplify the momentum balance by neglecting the influence of the particle's inertia. Hydrodynamic models can describe the transport properties of all species in a plasma, including the plasma boundary sheaths, e.g. [1]. This however requires a large computational effort, which can be reduced by applying a drift-diffusion-model. Models of this class, however, cannot describe the transport properties of ions in the sheath correctly, as ion transport is dominated by inertia there. In order to gain computational efficiency without sacrificing physical accuracy, in this work a drift-diffusion-model for the plasma bulk was combined with a compact model for the sheaths.
This compact model takes the fluxes of all species as input parameters [2]. It gives back the values of the plasma parameters at the cut edge between sheath and bulk. These values are used as boundary conditions by the bulk module, which in turn delivers updated values for the fluxes. In this way the calculation of a self-consistent solution for the whole discharge is possible.

2.1. Plasma Bulk Model

In the plasma bulk, conservation of mass is considered for all species,

$$\frac{\partial n_k}{\partial t} + \nabla \cdot \vec{j}_k = G_k(T_e), \qquad (1)$$

where $k = e$ for the electrons and $k = i$ for the ions. Here, n_k is the particle number density and j_k the corresponding particle current density. Particle generation of species k is described by the generation rate $G_k(T_e)$, which depends on the electron temperature T_e. The current densities are given by the drift-diffusion-approximation,

$$\vec{j}_k = \frac{q_k n_k}{m_k n_k}\vec{E}_{amb} - \frac{1}{m_k n_k}\nabla n_k k_B T_k . \qquad (2)$$

Here, k_B denotes Boltzmann's constant, q_k the charge and m_k the mass of species k. The collision frequencies n_k describe elastic collisions with neutral atoms. The ambipolar electric field is $\vec{E}_{amb}$.
Additionally, conservation of energy is considered for the electrons:

$$\frac{\partial n_e e}{\partial t} + \nabla \cdot \vec{\Gamma}_e = q_e \vec{E}_{amb} \cdot \vec{j}_e - P_c + P_h . \qquad (3)$$

Here, $e = \frac{3}{2} k_B T_e$ is the mean electron energy. Energy losses by collisions with neutral particles are described by P_c. The heating of the plasma is accounted for by P_h. The electron energy current density $\vec{\Gamma}_e$ consists of a convective and a thermal conductivity contribution:

$$\vec{\Gamma}_e = \frac{5}{2} k_B T_e \vec{j}_e - \frac{5}{2}\frac{n_e k_B T_e}{m_e n_e}\nabla k_B T_e . \qquad (4)$$

The ambipolar electric field $\vec{E}_{amb}$ is derived from an electrostatic potential Φ, which in turn can be calculated from Poisson's equation,

$$\Delta\Phi = -\frac{1}{e_0}(q_e n_e + \sum q_i n_i) , \qquad (5)$$

where the sum runs over all ionic species.

2.2 Plasma Boundary Sheath Model

In the plasma boundary sheath, ion transport is governed by inertia. Therefore, the compact model presented below is based on the full hydrodynamic equations for ions. Due to their small mass, the electrons can be described by the drift-diffusion-approximation in the sheath region as well.

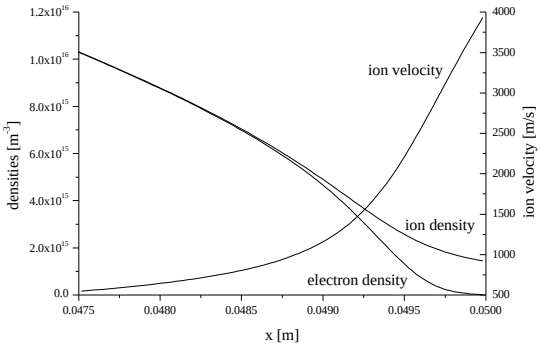

Figure 1: Profiles of particle densities and ion velocity in front of a conducting wall

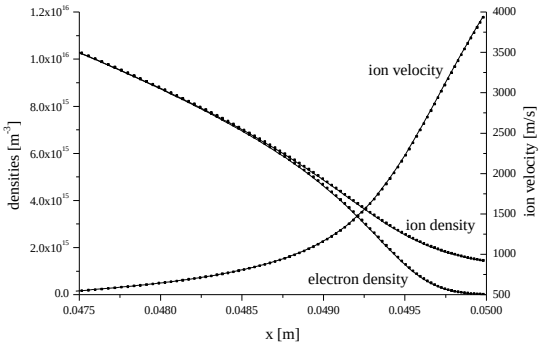

Figure 2: Comparison between full (symbols) and reduced (lines) sheath simulation

The case of a plasma with one single positive ionic species may serve as a starting point for the derivation of the compact modell. Fig.1 shows the sheath region of an argon plasma at $p = 10$ Pa and $T_e = 19300$ K as obtained by a hydrodynamic simulation of the discharge. The discharge length is 10cm and only the last 2.5mm in front of a conducting wall at $x = 0.05$ m are shown. The lines indicate density and velocity profiles as obtained from a hydrodynamic simulation of the whole discharge. In a first step, the goal is a hydrodynamic simulation of the sheath region only, without solving the equations for the bulk. It is assumed that the particle fluxes from the bulk into the sheath are known. They serve as input parameters for the sheath model. The missing three boundary conditions at the cut edge are derived as follows: As the plasma bulk must be quasi-neutral, the electron and ion densities approach each other away from the wall. Therefore, the density gradients can be equated with each other at x= 0.0475m,

$$\frac{\partial n_e}{\partial x} = \frac{\partial n_i}{\partial x} . \qquad (6)$$

Furthermore, the ion velocity profile flattens out towards the bulk, i.e. the curvature vanishes,

$$\frac{\partial^2 v_i}{\partial x^2} = 0. \tag{7}$$

This is due to the disparity between the relevant length-scales, namely the Debye-length for the sheath and the ion mean free path or the reactor dimension for the bulk. This scale is typically at least one order of magnitude larger than the Debye-length. Finally, one has to define the cut-edge between bulk and sheath. The use of the Bohm criterion is not adequate here, as it does not judge the relative importance of ion inertia. Therefore, we track beginning space charge separation and define the cut edge by the relation

$$\frac{n_i}{n_e} = 1 + a, \tag{8}$$

where a is a positive real parameter. Reasonable values are given by $a = 10^{-3}...10^{-2}$. The results of the hydrodynamic simulation of the sheath only are shown by the lines in fig. 2. By comparison with the full solution (symbols in fig. 2) one concludes that the above approximate boundary conditions introduce small errors only. From here, one derives the sheath compact model consisting of a small algebraic system of equations. This will be sketched below, a complete derivation can be found in [3]. From the necessary five algebraic equations, two are delivered by equating the prescribed values of the particle fluxes with their model expressions. Two more equations are obtained by further exploring the above boundary conditions with the help of the stationary fluid equations: In the stationary case the fluid equations express the ion density and velocity gradient as functions of the plasma variables. These functions can be inserted into the boundary conditions, yielding two more algebraic equations between the unknowns at the cut edge. The last equation is given by the definition of the cut edge which remains unaltered.

For the case of multiple positively charged ionic species, the model is generalized as follows: As before, the model uses the electron particle flux and the fluxes of all ionic species as input parameters and equates them with the corresponding model expressions. In eq. (6) the single ion density is replaced by the total ion particle density, leading to

$$\frac{\partial n_e}{\partial x} = \sum \frac{\partial n_i}{\partial x}, \tag{9}$$

where the sum again runs over all ionic species. The same replacement transforms eq. (8) into

$$\sum n_i \Big/ n_e = 1 + a, \tag{10}$$

with the meaning of the parameter a unaltered. Furthermore the model assumes that the velocity curvature of all ionic species vanishes at the cut edge. For S ionic species we thus have $2S+3$ unknowns and just as many algebraic equations. The solution of the algebraic equations delivers the cut edge parameters in a computationally very efficient manner.

As an example, the sheath region of an argon-helium-plasma with $p = 20\,\text{Pa}$ and $T_e = 22500\,\text{K}$ is shown in fig. 3.

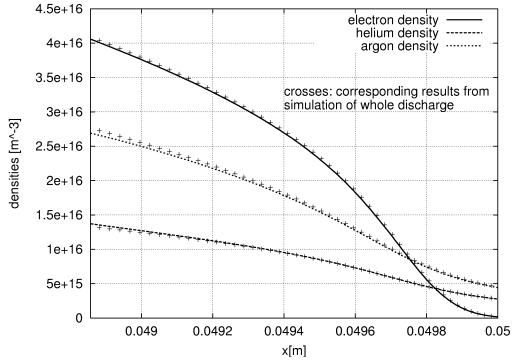

Figure 3: Comparison between full (symbols) and reduced (lines) sheath simulation for the argon-helium-plasma

The symbols indicate the particle density profiles as obtained from a hydrodynamic simulation of the whole discharge. The full lines show the results of the simulation of the sheath region only. As for the case of one ionic species, the results of the reduced model are in excellent agreement with the full solution. The largest discrepancy is visible for the argon ion density. Tab. 1 compares the values of the plasma variables at the cut edge as obtained by full hydrodynamic simulation and the sheath compact model.

Table 1: Comparison of values of the plasma variables at cut edge from simulation of the whole discharge and the sheath model.

	Whole discharge	Sheath model	Error [%]
Electric field [V/m]	940	960	2.10
Electron density [m^{-3}]	$4.10 \cdot 10^{16}$	$4.06 \cdot 10^{16}$	1.00
Helium ion density [m^{-3}]	$1.35 \cdot 10^{16}$	$1.37 \cdot 10^{16}$	1.46
Argon ion density [m^{-3}]	$2.80 \cdot 10^{16}$	$2.69 \cdot 10^{16}$	3.93
Time consumed	~ hours	~ seconds	

The last column in tab. 1 lists the absolute values of the relative error between the hydrodynamic solution of the whole discharge and the values computed by the sheath compact model. The largest deviation occurs for the argon ion densitiy and amounts to roughly 4 %. Compared to the enormous increase in computational efficiency an error as small as this is easily acceptable.

2.3. Electrodynamic Model

Inductively coupled plasmas are heated by externally applied rf fields. In order to calculate these fields self-consistently along with the plasma parameters, an electrodynamic model [4] derived from Maxwell's equations is used. If all quantities vary harmonically in time with an angular frequency w, the induced rf electric field $\vec{E}$ is described by the partial differential equation

$$\Delta\vec{E} + k^2\vec{E} = iwm_0\vec{j} \text{ with } k^2 = e_r\frac{w^2}{c_0^2} - iwm_0 s \ . \tag{11}$$

Here, c_0 denotes the vacuum speed of light, m_0 the permeability of free space and e_r the relative dielectric constants of the reactor materials. The current density in the coils is given by $\vec{j}$. Finally, s describes the electrical conductivity of the different regions. For the conducting reactor walls infinite conductivity is assumed. The conductivity of the plasma is described by the cold plasma approximation [5]

$$s = n_e\frac{n_e e^2}{m_e(n_e^2 + w^2)} - iw\frac{n_e e^2}{m_e(n_e^2 + w^2)}. \tag{12}$$

The power density deposited in the plasma is then given by

$$P_h = \frac{1}{2}\Re\{s\}|\vec{E}|^2 \ . \tag{13}$$

3. Results

Results are presented for cylindrical reactor vessel with a radius of 75mm and a height of 100mm. The reactor is operated at an rf frequency of 27.12 MHz. The following figures show electron density profiles along a radial cutline at half the reactor height.

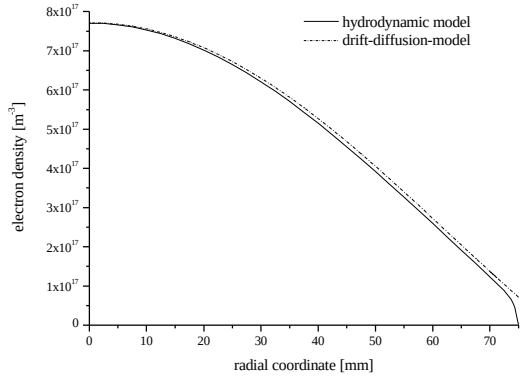

Figure 4: Radial profile of electron density as obtained by hydrodynamic (full line) and drift-diffusion-modell(dashed line) for a coil current of 16.0 A.

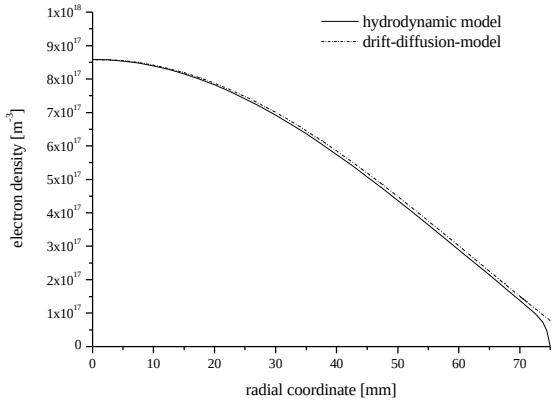

Figure 5: Radial profile of electron density as obtained by hydrodynamic (full line) and drift-diffusion-modell(dashed line) for a coil current of 16.7A

Fig. 4 and 5 show radial profiles of the electron density for a helium plasma at 20 Pa. The coil currents are 16.0A and 16.7A, respectively. The axis of symmetry corresponds to $r = 0$ mm, the reactor wall is situated at $r = 75$ mm. In both figures the solid line represents the results of a full hydrodynamic calculation. The dashed line was obtained by a drift-diffusion calculation in combination with the boundary sheath model sketched above. The value $a = 10^{-3}$ was used. Both model predictions are in excellent agreement. The conceptual difference between both models becomes visible in front of the reactor wall. The hydrodynamic model resolves the steep gradient of the electron density in the boundary sheath. This requires a very fine computational grid in front of the walls and increases the computational demand. In the drift-diffusion-model, however, the boundary sheath is treated by the compact model. This especially means that the small spatial extension of the sheath is neglected. The boundary of the computational domain is now actually defined implicitly by eq. (8) and differs from the reactor dimension by the geometrical extension of the sheath. In the simulation, however, this difference is neglected and the boundary of the computational domain is re-defined by the reactor wall. This leads to the small differences between both models. These differences can be controlled by varying the cut edge parameter a .

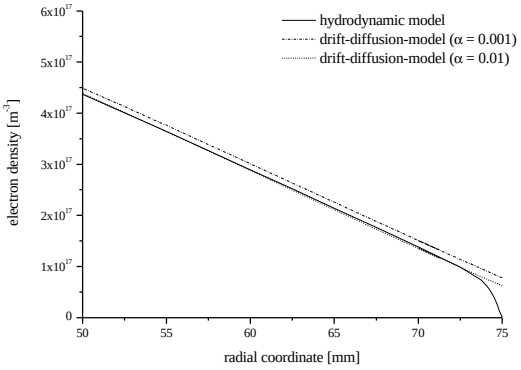

Figure 6: Variation of electron density profile with cut edge parameter a .

Fig. 6 shows two electron density profiles obtained from the drift-diffusion-model for $a = 10^{-3}$ and $a = 10^{-2}$, respectively. The curve for $a = 10^{-2}$ can hardly be distinguished from the hydrodynamical results, whereas the curve for $a = 10^{-2}$ shows the deviations discussed above. This improvement in agreement is due to the fact that a larger value of a corresponds to a definition of the cut edge closer to the reactor wall.

4. Conclusion

A new approach to modelling inductively coupled plasmas has been presented. Here, the plasma bulk is described by a drift-diffusion-model. The plasma boundary sheaths are represented by an efficient compact model which can handle various positive ionic species. This compact model consists of a small system of algebraic equations from which the plasma variables at the cut edge can be calculated in dependence of the particle fluxes into the sheath. This compact model has been proven to yield results in good agreement with much more expensive hydrodynamic calculations.

5. Acknowledgement

The authors wish to thank the Dr. Johannes Heidenhain-Stiftung for their support.

References

[1] P.Scheubert, U.Fantz, P.Awakowicz, H.Paulin; J. Appl. Phys., **90**, 2 (2001).
[2] M.Kratzer, R.-P.Brinkmann; 27th Intl. Conf. on Plasma Science, p. 163 (2000).
[3] G.Wenig, P.Scheubert, P.Awakowicz; Surf. and Coat. Techn, *accepted for publication.*
[4] E.F. Jaeger, L.A.Berry, J.S. Tolliver, D.B.Patchelor; Phys. Plasmas, **2**, 6 (1995).
[5] I.P.Shkarofsky, T.W.Johnston, M.P.Bachynski; The Particle Kinetics of Plasmas, Addison-Wesley (1996).

Comparison between two different torches to inject a suspension to produce thin perovskite coatings

C. Monterrubio-Badillo, H. Ageorges, T. Chartier, J. F. Coudert and P. Fauchais

Laboratoire SPCTS-UMR-CNRS 6638, Université de Limoges, Faculté des Sciences et Techniques, 123 avenue Albert Thomas, 87060 LIMOGES CEDEX, FRANCE.

Abstract

When plasma spraying $LaMnO_3$ perovskite very often decomposition occurs. Thus the purpose of this work is to study the phases present in coatings obtained by injecting a suspension of sumicrometric $LaMnO_3$ perovskites powders (d_{50} = 1 μm) in a direct current d.c. plasma jet produced with two different plasma torches (laboratory torch and PT F4 torch) working with different plasma forming gases : Ar (45,8 slm) and Ar/He (44/10, 43/20 and 30/20 slm). The process consists in mechanically injecting a well dispersed stable suspension of submicrometric perovskite particles in a dc plasma jet. In the process, large suspension droplets (~300 μm) are sheared into tiny ones (a few μm) by the plasma jet flow. Then the solvent is evaporated and the particles melt resulting in perovskite droplets of about 1 μm impacting on the substrate. These coatings will be used as cathodes for the SOFCs (Solid Oxide Fuel Cells). Best results are obtained by injecting a stable suspension in an Ar plasma forming gas when increasing its mass flow rate (with both types of torch). This is due to the higher momentum transfer towards particles and the lower heat transfer to reduce their decomposition.

1. Introduction

Semiconducting oxides (perovskites) based on $LaMnO_3$ doped with SrO and CaO, are most often used as cathode material for the solid oxide fuel cells (SOFCs), [1] due to their high electrical conductivity and their compatibility with the solid electrolyte, generally yttria doped-zirconia [2]. Solid oxide fuel cells are promising candidates for future systems because of their high energy conversion efficiencies and low environmental hazards. Many investigations have been carried out with regard to the choice of materials and processing techniques. However, there are few processes that can be used to fabricate high performance cells quickly and inexpensively. Plasma spraying is a promising candidate for such a process [3]. Until now, only thick coatings (> 100 μm) of perovskite have been elaborated using d.c. plasmas, by injecting, with a carrier gas, micrometric particles in the plasma flow [4]. But it is not possible to inject too small particles (<5 μm) without drastically perturbing the plasma jet by the high carrier gas flow rate necessary to give particles a sufficiently high momentum. In addition, the coatings with nanometric to submicrometric grain sizes exhibit unique properties due to their different physical and chemical properties (electric, dielectric and photoelectric properties) in comparison with coatings having coarse grain sizes [5], thus they are attractive for various high performance applications (such as fuel cell).

The plasma spray process to obtain perovskite thin films is more attractive because of its fast deposition rate and easy masking for deposition of patterned structures, compared with other films formation processes such as electrochemical vapor deposition, chemical vapor deposition, and sputtering. Therefore, the plasma spray process is being considered as a means to reduce manufacturing costs. Coatings of perovskite oxide, may change in chemical composition compared to that of the initial powder and exhibit chemical heterogeneity due to the material volatility in the plasma jet [6]. These problems must be avoided in order to obtain a high electrical conductivity of the cathodes and match the thermal expansion coefficients, as required for SOFCs. The aim of this work is the production of thin coatings (10 to 20 μm) of perovskite with a minimal decomposition by injecting a suspension with submicrometric particles (d_{50} < 1 μm) dispersed in a solvent (ethanol). The principal objective of this study is to compare the difference between two plasma torch types (laboratory torch and industrial torch) with their injection systems of the perovskite suspension. In particular, the following items are investigated :

- The effect of the two different plasma torches on the composition of perovskite coatings.
- The effect of the composition of plasma gases on the composition and morphology of collected particles in flight.

2. Experimental

2.1 Starting materials

La_2O_3 (d_{50} = 24 µm) and MnO_2 (d_{50} = 3.32 µm) powders supplied by CERAC with a high-purity grade (99.99 %) were weighed in stoichimetric proportions and finely ground and thoroughly mixed by attrition milling during 4 hours. The mixture was sintered at 1100 ^{o}C for 6 hours in air. The sintered material was subsequently broken up and finely ground again by attrition milling. The particles obtained after milling have a size distribution in the range 0.1 to 2 µm, with a d_{50}= 0.8 µm, Figure 1a, and a prismatic shape, Figure 1b. The suspension was prepared by adding perovskite powders into an ethanol solution with a dispersant [7]. The solvent allows the solubility of the organic dispersant and the well dispersed particles result in a homogeneous stable suspension.

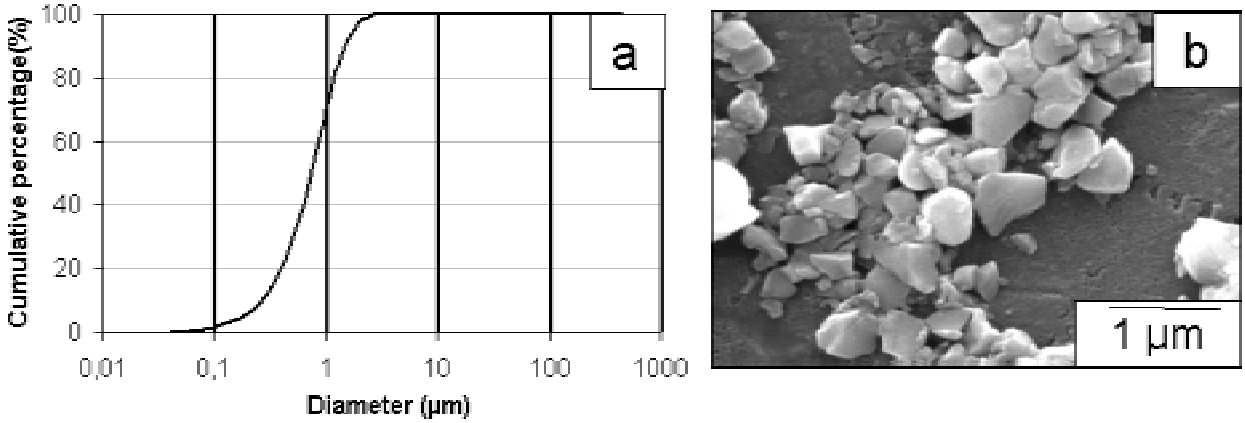

Figure 1. a) Particle size distribution of a perovskite powder elaborated by sintering and b) morpgology of the milled perovskite powder.

Physical properties of the milled perovskite powder are shown in Table 1 and the characteristics of the suspension in Table 2.

Table 1 Physical properties of $LaMnO_3$ perovskite powder

Powder	D_{50} (µm)	D_{90} (µm)	S (m^2/g)
$LaMnO_3$	0.8	1.5	4.2

Table 2 Characteristics of the perovskite suspension

Suspension	wt % of powder	wt % dispersant	Viscosity (mPa.s)
$LaMnO_3$	20	0.4	12

2.2 Plasma Spraying Set-ups

Figure 2 presents a scheme of the experimental system in the configuration used for collecting the splats and films in air. Atmospheric Plasma Spraying (APS) is achieved with conventional d.c. plasma guns with a 6 mm internal diameter anode-nozzle to produce thin films [8]. This process consists in a mechanical injection of a liquid suspension in the plasma jet produced by two different plasma torches. One torch, made in the laboratory, has a copper anode with a rather long nozzle where the suspension is injected internally while the other one is an industrial PTF4 torch where the suspension is injected externally.

The mechanical injection creates calibrated droplets with controlled velocity and flow rate. The torch working parameters have been adjusted according to the liquid injection by using different plasma gas mixtures and arc currents. It is worth to note that, for the same input parameters, both torches with the same anode nozzle i.d. have different voltages, those of the PTF4 torch being systematically higher (by 4 to 10 V according the plasma gases).

The $LaMnO_3$ perovskite suspension is injected in plasma jets obtained with different plasma forming gases in both torches: Ar (45.8 slm) and Ar/He with three different mixtures of gases (44/10, 43/20 and 30/20 slm) corresponding to different enthalpies and mass flow rates (see Figure 3 and Table 3, respectively). The arc current used to create the plasma jet is fixed at 300 A in order to limit the jet enthalpy, because of the extreme sensitivity of the perovskite powder to high temperatures, promoting its decomposition. Other

parameters were kept constant: stand off distance 40 mm, injection pressure 0.4 MPa, torch cooling water flow rate 16.5 slm at a pressure of 0.16 MPa.

The investigation of the behavior of the particles in the plasma jet requires their collection in flight at different distances from the torch-nozzle exit (Figure 2). This is achieved by passing once, at a controlled velocity, through the plasma jet a glass plate disposed at the extremity of a pendulum. The collected particles or splats are used to determine their molten state or morphology. However, in order to achieve a sufficiently thick coating for X-ray diffraction (XRD), the substrate (a 316 stainless steel plate) needs to be passed 30 times through the plasma (keeping the torch fixed).

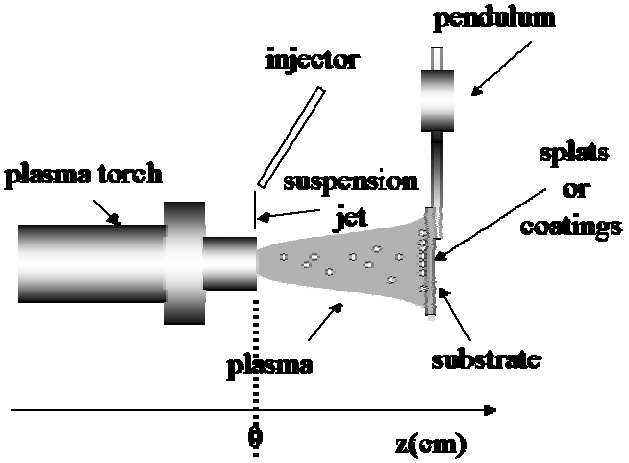

Figure 2. Plasma spray set-up

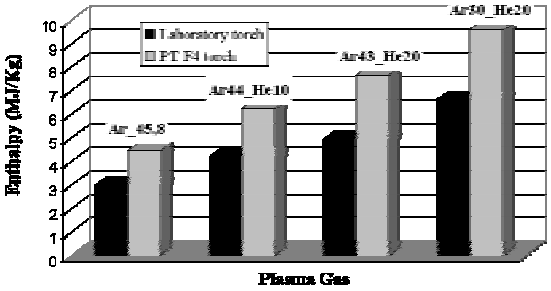

Figure 3. Enthalpy of different plasma gases used

Table 3. Thermal Spray Parameters

	Laboratory torch				PT F4 torch			
Conditions	**1**	**2**	**3**	**4**	**1**	**2**	**3**	**4**
Current (A)	300	300	300	300	300	300	300	300
Voltage (V)	27.7	34.0	38.1	38.2	31.8	41.7	48.1	43.9
Ar (slm)	45,8	44	43	30	45,8	44	43	30
Ar (g/s)	1.36	1.3	1.28	0.89	1.36	1.3	1.28	0.89
He (slm)	----	10	20	20	----	10	20	20
He (g/s)	0	0.029	0.059	0.059	0	0.029	0.059	0.059
Mass flow rate (g/s)	1.36	1.33	1.33	0.95	1.36	1.33	1.33	0.95

2.3 Characterization and Analysis

The microstructure and morphology of particles, splats and coatings were examined by scanning electron microscopy SEM, (Phillips XL 30). All the images obtained were made with secondary electrons (SE). The energy Dispersive Spectroscopy EDS, (LINK ISIS 300) was used to analyze the distribution of chemical elements in samples. The X-Ray diffraction (XRD, Cu Kα) was used to determine the phases present in powders and coatings, the spectra being recorded on a Siemens diffractometer. To determine the particle size distribution a Cilas Laser granulometer was used.

3. Results

3.1 Splats Collection, Morphology and Composition

Figure 4a and 4c show the morphology of collected splats and particles with Ar (45 slm) as plasma gas (arc current of 300A), with the laboratory and PTF4 torches, respectively. The particles correspond to molten ones which have cooled down, impacted on the plate in a plastic state and stuck to it but have not deformed. It can be seen that, with the laboratory torch, a high percentage of non molten or partially molten particles is found, however with the PTF4 torch all particles are well melted due to the higher enthalpy (see figure 3). But, when helium is added to the plasma gas, all particles are well melted in both torches at all plasma conditions. However, differences in morphologies and particle diameters are observed. Figures 4b and 4d show splats and particles collected with an Ar/He (44/10 slm) plasma gas with both torches, splats collected

result from well molten particles. Figure 4b, shows fingered splats with a diameter in the range of 5 to 10 µm whereas splats obtained with the PTF4 torch are disk shaped and their diameter is in the range of 1 to 5 µm. With the others Ar/He plasma forming gases, the particles collected are also well melted.
Figure 4e, shows an EDS analysis of the collected splats with Ar as the plasma forming gas and a PTF4 torch (Figure 4c); manganese, lanthanum and oxygen elements are present in all splats. This confirms that the perovskite phase is present in melted particles. Ca, Si and Mg are elements of the glass plate used to collect splats and Au detection is due to the metalization. The Figure 4f shows a fractured surface of perovskite coating collected at 40 mm of nozzle exit, obtained with the PTF4 torch working with Ar (45 slm). It can be observed, the tiny spherical particles incorporated in the coating, which could correspond to the small particles collected with the splats (see Figure 4a, b, c and d).

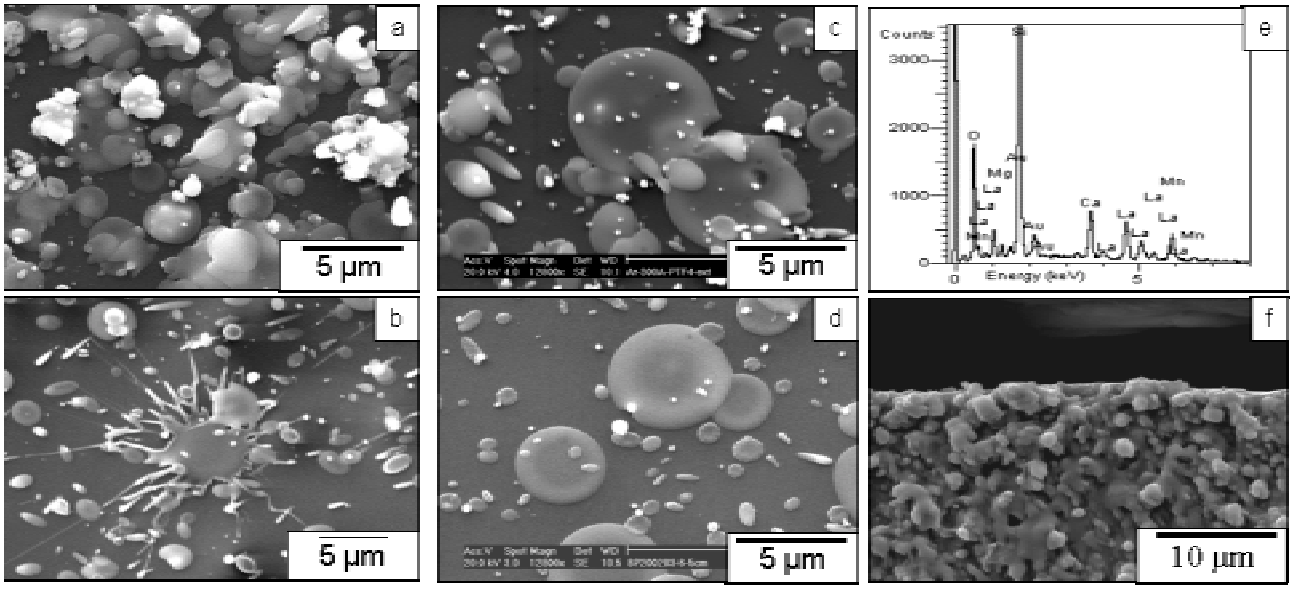

Figure 4. Splats collected on glass plates at 40 mm of the nozzle exit, with the laboratory torch: a) with Ar (45.8 slm), b) with Ar/He (44/10 slm) and with PTF4 torch: c) with Ar (45.8 slm), d) with Ar/He (44/10 slm); e) EDS analysis of the splats collected in figure 4c; f) fractured surface of a perovskite coating, sprayed with the PTF4 torch at 40 mm with Ar (45 slm).

3.2 Obtained Phases in Coatings with both types of torches

Figure 5a, shows the cross section of a perovskite coating (obtained with Ar as plasma forming gas and a PTF4 torch) on an yttria stabilized zirconia (YSZ) plasma sprayed coating, starting from an YSZ suspension, which is used as electrolyte. The perovskite thickness is 20 µm aproximately. The film exhibits sufficient porosity to be used as cathode for the fuel cells. Figure 5b shows a magnification of the interface of $LaMnO_3$ and YSZ films where a good adherence of the two films can be observed.
To study the phases present in the perovskite deposits, stainless steel substrates without zirconia have been used to avoid the superposition of YSZ peaks with those of perovskite. Figures 6a and 6b show the phases obtained in coatings when a perovskite suspension is sprayed with laboratory and PTF4 torches respectively. $LaMnO_3$ and La_2O_3 are present in coatings and with the PTF4 torch a higher percentage of decomposition of perovskite is observed whatever may be the plasma forming gas used (probably due to the higher enthalpy compared to that of the laboratory torch). In cases of the figure 6b, substrate peaks appears because the thickness of the substrate is lower than in case 2, 3 and 4.

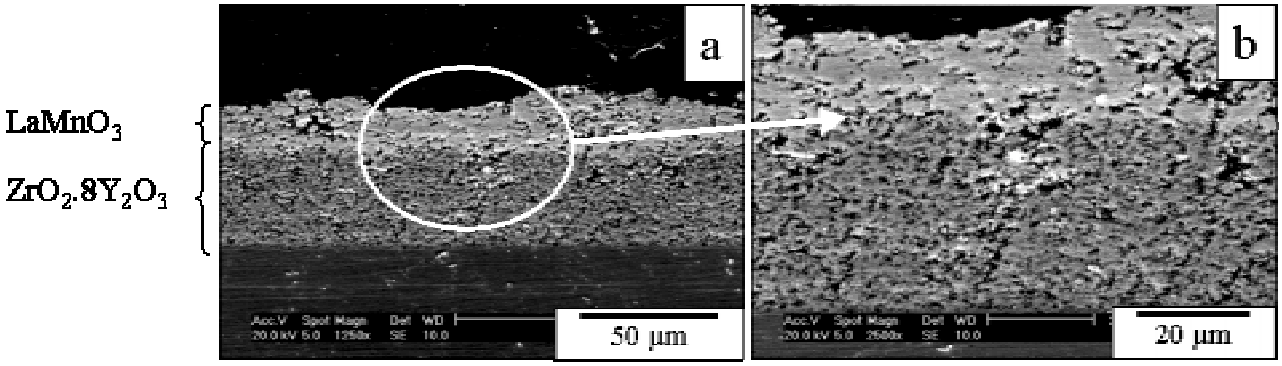

Figure 5. a) Cross section of a $LaMnO_3$ film on a YSZ electrolyte film plasma sprayed and b) magnification of the interface $LaMnO_3$ and YSZ films.

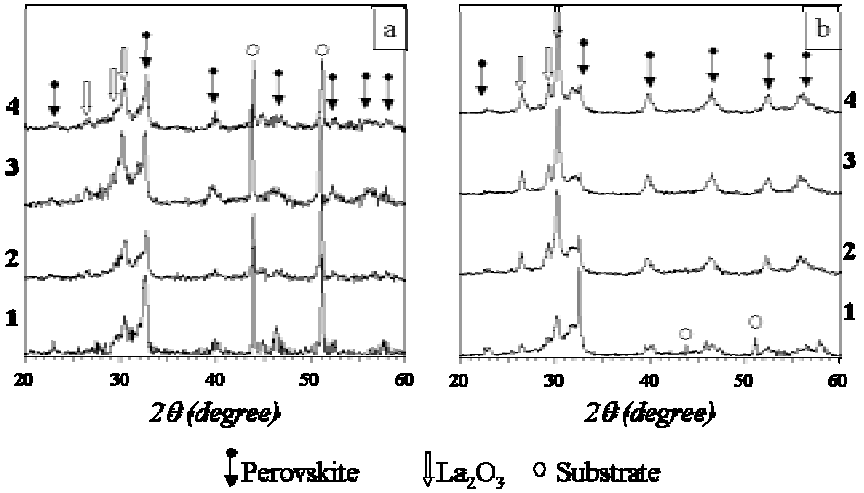

Figure 6. XRD of perovskite coatings obtained with a) the laboratory torch and b) the PTF4 torch. Conditions: 1) Ar (45.8 slm), 2) Ar/He (44/10 slm), 3) Ar/He (43/20 slm) and 4) Ar/He (30/20 slm).

The phases present in deposits are composed of $LaMnO_3$ with a La_2O_3 phase, MnO_2 is not present due to its high degree of volatilisation, its melting temperature being only 1840°C. A mechanism of the particles treatment in the plasma jet was proposed by Wittman et al [8] in which the first step in the occurring phenomena is the destruction, in about 1 µs, of the initial suspension drop (~ 300 µm) into numerous smaller droplets (~ 1 µm) upon penetration into the plasma, secondly the vaporization, in times of the µs order, of the solvent of those smaller droplets followed by the melting of the resulting agglomerates of submicrometric particles during their flight in the plasma jet. In the case of perovskite, evaporation of manganese occurs during the last step.

To synthesize the results obtained by X-ray diffraction, a quantitative analysis of the phases present in the coatings was carried out. Figure 7 shows the decomposition percentage of the perovskite phase in the plasma jet according to the conditions described in Table 3 with both types of torches.

The percentages of decomposition obtained with the laboratory torch are smaller than those obtained with the PTF4 torch for all different plasma forming gases. The results are in good conjunction with the enthalpy of the plasma jets (see figure 3), except for the first condition that corresponds to a pure argon plasma gas.

The variations of the spray parameters have shown that the perovskite decomposes, which is especially the case when H_2 is added to the plasma gas [9]. A careful adjustement of the plasma gas parameters is necessary to inject a suspension into the hot core of the plasma in order to have a minimum decomposition of the perovskite and achieve a sufficient particles melting in the plasma jet. It has been shown that the particles decomposition depends strongly on the spray parameters such as the type of the plasma torch, gas composition and gas enthalpy.

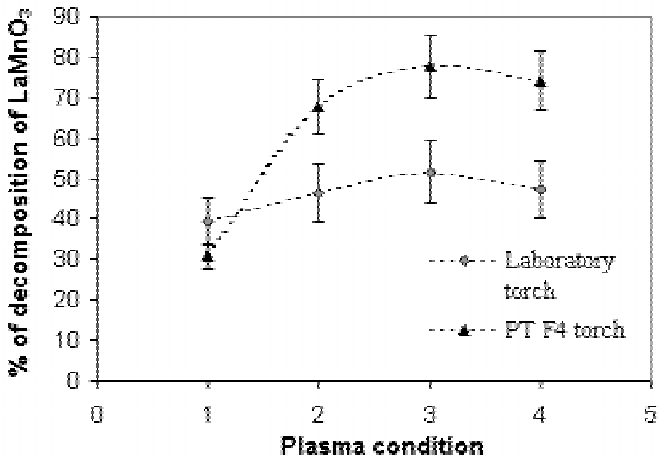

Figure 7. Comparison of the decomposition percentage of perovskite particles in the plasma jets, produced by laboratory and PTF4 torches.

Conclusions

A $LaMnO_3$ perovskite suspension was injected mechanically in a d.c. plasma jet with two types of torches (laboratory and PTF4 torches) to produce thin films (~20 μm). The plasma forming gases have been varied in order to obtain a perovskite thin coating without decomposition. Nevertheless, perovskite decomposition has been found in coatings. So, in the future, a perovskite rich in manganese and also a higher mass flow rate of gases will be consider, in order to obtain a coating with a good homogeneity in chemical composition after the thermal spray process.

References

[1] B.C.H. Steele, Materials for IT-SOFC stacks 35 years R&D: the inevitability of gradualness??, Solid State Ionics **134** (2000) 3-20.

[2] O. Yamamoto, Solid oxide fuel cells: fundamental aspects and prospects, Electrochimica Acta, **45** (2000) 2423-2435.

[3] S. Takenoiri, N. Kadokawa, and K. Koseki, Development of metallic substrate supported planar solid oxide fuel cells fabricated by plasma spaying, J. of Thermal Spray Technology, **9**(3) (2000) 360-363.

[4] H. Tsukuda, A. Notomi, and N. Hisatome, Application of Plasma Spraying to Tubular-Type Solid Oxide Fuel Cells Production, J. Thermal Spray Tech., **9**(3) (2000) 364-368.

[5] J. Karthikeyan, C.C. Berndt, S. Reddy, J.-Y. Wang, A. H. King, and H. Herman, Nanomaterial deposit formed by dc plasma spraying of Liquid Feedstocks, J. Am. Ceram. Soc., **81** (1) (1998) 121-128.

[6] K. Okumura, Y Aihara, S. Ito, S Kawasaki, Development of the Thermal Spraying-Sintering Technology for Solid Oxide Fuel Cells, J. of Thermal Spray Technology **9**(3) (2000) 354-359.

[7] C. Monterrubio-Badillo, T. Chartier, H. Ageorges, J.F. Coudert, and P. Fauchais, Preparation of stable suspensions of perovskites for plasma spraying, accepted in Materials Science Forum, Trans Tech Publication, Switzerland (2003).

[8] K. Wittmann, "Study of the elaboration of thin films by plasma spraying" (in French), Ph. D. Thesis 2001, University of Limoges.

[9] M. Lang, R. Henne, S. Schaper, G. Schiller, Development and characterization of vacuum plasma sprayed thin film Solid Oxide Fuel Cells, J. Thermal Spray Tech., **10** (4) (2000) 618-625.

Self-consistent kinetic approach to stratified regimes of plane and spherical glow discharges

A.V. Fedoseev, G.I. Sukhinin

Institute of Thermophysics, Novosibirsk, Russia

In the paper, a self-consistent model of stratified low-pressure argon glow discharge in plane and spherical geometries is presented. The model includes:

1. The non-local Boltzmann equation in two-term approximation for isotropic part of electron energy distribution function (EEDF) written in total energy–space coordinate representation

$$\frac{1}{r^n}\frac{\partial}{\partial r}\left[\frac{r^n U}{3H(U)}\frac{\partial}{\partial r}f_0(\varepsilon,r)\right]=\frac{\partial}{\partial\varepsilon}\left[2\frac{m}{M}U^2N_gQ^d(U)f_0(\varepsilon,r)\right]+\sum_k UN_gQ_k^{in}(U)f_0(\varepsilon,r)-\sum_k(U+U_k^{in})N_gQ_k^{in}(U+U_k)f_0(\varepsilon+U_k^{in},r), \quad (1)$$

where n=0 for plane geometry and n=2 for spherical one.

2. The non-stationary continuity equation in drift approximation for ions

$$\frac{\partial n_i}{\partial t}+\frac{1}{r^n}\frac{\partial}{\partial r}(r^n n_i\mu_i E)=n_e\nu_I, \quad (2)$$

$\nu_I(r)$ is the direct ionization frequency, μ_i is ion mobility coefficient.

3. Poisson equation for self-consistent electric field

$$\mathrm{div}\vec{E}=4\pi e_0(n_i-n_e) \quad (3)$$

The iterative numerical procedure for the solution of the striation problem is used. At the first step, to obtain the first approximation of distribution function f_0^0(r,U), the parabolic equation (1) is solved in some proposed electric field $E^0(r)$. From the f_0^0(r,U), the electron density distribution $n_e^0(r)$ and the ionization frequency $\nu_I^0(r)$ are obtained. With the help of Eqs.(2-3), new approximation of electric field E(r) is found and the procedure is repeated until successive iterations of electric field are converged. Usually ten iterations are enough for the procedure of convergence, and the final electric field distribution E(r) does not depend on the initial approximation of $E_0(r)$. However the voltage drop is kept constant.

It was found that the iterative process converges only for the case of moving striations. In plane discharge, the solution for ion density and electric field are looked for in the form $n_i=\overline{n}_i(\mathrm{v}_i t+r)$, $E=\overline{E}(\mathrm{v}_i t+r)$, with the striation velocity $\mathrm{v}_i=-\alpha\mu_i E_0$, $0\geq\alpha\leq 1$. For spherical case these relations are more complex. In Figs. 1-2, example of self-consistent field distribution and striation length is presented.

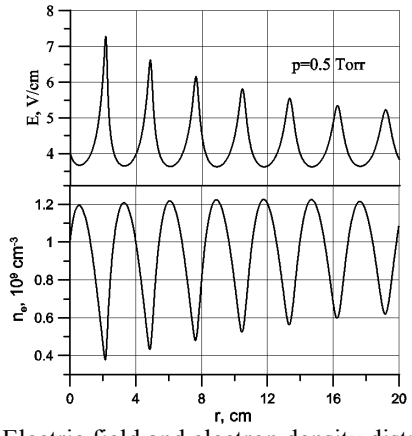

Fig.1. Electric field and electron density distributions in plane striated argon glow discharge.

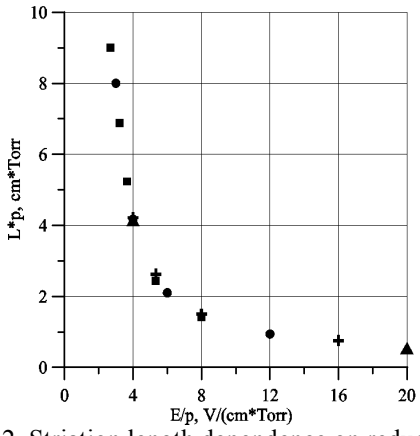

Fig.2. Striation length dependence on reduced electric field in plane glow discharge.

It is found that for argon pressures p>1.5 Torr striation are damped due to energy losses in elastic collisions. For spherical case, the averaged electric field radial distribution varies inversely proportional to the distance from anode, r, and is modulated with striations. The radius of n-th striation obeys the law $r_n\approx r_1\beta^n$.

Acknowledgements

Financial support for this work was partly provided by the International Science and Technology Center under Grant No 1425.

Comparison of stainless steel coatings alumina reinforced by plasma spraying different size mechanofused particles

R. Cuenca Alvarez, H. Ageorges, A. Grimaud and P. Fauchais

Laboratoire SPCTS-UMR 6638, Université de Limoges, Faculté des Sciences et Techniques
123 avenue Albert Thomas, 87060 LIMOGES CEDEX, FRANCE

Abstract
Two different size distributions of stainless steel particles, with mean particle sizes of 126 µm (big: B) and 65 µm (small: S), coated by an alumina shell obtained by the Mechanofusion process (MF) were plasma sprayed in air (APS) to produce coatings with a ductile matrix reinforced by alumina particles uniformly distributed. The morphology of the splats collected onto non preheated and 300°C preheated substrates, the microstructures and micro hardnesses of coatings were analyzed.
Two types of splats are observed depending on the substrate temperature and the molten state of particles at impact. On cold substrates, the splats are extensively fingered. On preheated substrate at 300°C, with fully melted particles the alumina and stainless steel (SS) splats, almost disk shaped, are layered while with particles in a plastic state alumina pieces are randomly distributed around a SS splat. The occurrence of un-melted particles is important with the big ones. Thus the coatings obtained with small composite particles and sprayed on substrate preheated at 300°C exhibit a uniform distribution of alumina and a higher hardness (370 $\pm$ 43 HV5) than that of SS starting from the same particles size distribution (270 $\pm$ 22 HV5). With big composite particles due to the presence of unmelted particles coating hardness is slightly below that of pure SS starting from small particles.

1. Introduction
The mechanical properties of plasma sprayed metallic coatings depend strongly on the feedstock powder characteristics such as the particle shape, size and purity [1]. However these properties can be improved when composite raw powders are used to achieve composite coatings by the combining hardness of ceramics and the ductility of metals or alloys, provided that the ceramic phases are uniformly distributed within the coatings.
A variety of methods exist for the composite powders production for example agglomeration, chemical cladding, organic bonding and mechanical alloying [3-5]. However, the interest of using a mechanical route, such as the Mechanofusion (MF) process, is sustained by the lower cost of the technique and the fact that no additives are necessary [6-9]. The final characteristics of the mechanofused powder depend on the phenomena that take place during the MF processing, such as compression, attrition, frictional shearing and rolling. When two different particles, in terms of chemical composition and size distribution, are MF processed, the finest particles (guest particles) agglomerate on the coarser ones surface (host particles) with no need for binders [6]. Then, the resulting mechanofused composite particles can be used to achieve the composite coatings.
The aim of this paper is to evaluate the influence of two different stainless steel (316L) particle size distributions coated with an alumina shell of about the same thickness on the resulting splat morphologies and coating hardness.

2. Experimental Procedure
2.1. Composite particles preparation
The composite particles are prepared using an in-laboratory designed mechanofusion set-up, described elsewhere [8], with an internal diameter of 100 mm and a height of 30 mm. Four sets of powdered mixtures are analyzed to display the influence of the loading conditions on the oxide shell formation. Two host particle size distributions with mean particle size of 65 (S = small particles) and 126 µm (B = big particles) are considered. They result from the gas atomization of austenitic stainless steel (Fe +19wt.% Cr + 11wt.% Ni). The guest particles are from an alumina powder (CR6 from Baikowski Chimie, France) with a mean particle size of 1.0

μm. The powder loading conditions are summarized in Table 1. After mechanofusion processing, the resulting bigger particles are mesh sieved between 100 - 200 μm.

Table 1: Set of conditions of powdered mixtures.

Set name	Host particles		Guest particles
	316 Stainless Steel Particle Size Distribution [μm]		Mass Ratio of Al_2O_3 Powder/Stainless steel Powder [wt %]
B10	Big particles	-140 + 100	6.25
B20			11.77
S10	Small particles	-90 + 45	6.25
S20			11.77

2.2. Plasma spraying set-up

The mechanofused particles are sprayed using a d.c. plasma gun working in air (APS) with the spraying parameters listed in Table 2. The thoriated tungsten cathode is 10 mm in diameter with a conical tip (40° cone angle). The gun anode/nozzle is made of OFHP copper and has a conical shape (40° cone angle) followed by a cylindrical duct 7 mm in internal diameter and 28 mm in length. The particles are injected perpendicularly to the plasma jet axis through a 1.8 mm i.d. injector located 3 mm upstream of the gun nozzle exit.

Cast iron disk shaped substrates (25 mm in diameter and 15 mm in height) are used for splat collection and for the coating tests. The splats are collected onto non preheated and 300°C preheated substrates. All the substrates used for the splat collection are polished with SiC paper, then with diamond abrasives to achieve a final mean roughness of 0.02 - 0.05 μm (Ra). The substrates for coatings are grit blasted with a suction type machine using a corundum powder (400 μm mean particle size) at 0.4 MPa. The resulting mean roughness is Ra = 6.7 $\pm$ 0.6 μm.

Table 2. Plasma spraying parameters.

	Big Particles	Small Particles
Arc current, [A]	500	500
Voltage, [V]	57	57
Gun thermal efficiency, [%]	56	56
Argon flow rate, [slm]	45	53
Hydrogen flow rate, [slm]	15	7
Spray distance, [mm]	90	100

Note: the carrier gas flow rate was adjusted to achieve a mean particle trajectory making an angle of 3.5° with the torch axis.

2.3. Sample characterization

Changes of the composite particles induced by the mechanofusion process are followed by X-ray diffraction (XRD, Cu-Ka radiation, model D-5000, Siemens), scanning electron microscopy (SEM, model XL30, Phillips), energy dispersive spectroscopy (EDS, Oxford, Link ISIS) and laser granulometry (Malvern, Mastersizer Hidro2000). The raw and mechanofused powder samples for SEM are embedded in a Mecaprex resin, ground and polished following the standard procedures. The cross sections of coated substrates are ground and polished as the powder samples. Surfaces for SEM examination are metallized with gold.

3. Results and Discussion

3.1. Composite particles

The morphology and cross sections of stainless steel-Al_2O_3 mechanofused-composite particles are illustrated in fig. 1. After the MF processing, for the two types of stainless steel particle size distributions, the fine alumina particles are uniformly distributed at the surface of stainless steel particles as shown in fig. 1a. The thickness of the alumina layer depends of the Al_2O_3 ratio to stainless steel mass ratio as given in Table 1 (alumina

corresponds to the gray color as detected by EDS analysis). the views of the cross sections of the mechanofused particles (Figs. 1b and 1c) show that the alumina shell mean thickness attains about 4.8 $\pm$ 0.4 µm for B20 and S20 powders set whereas for the B10 and S10 powders it is in the range of 3.35 $\pm$ 0.25 µm.

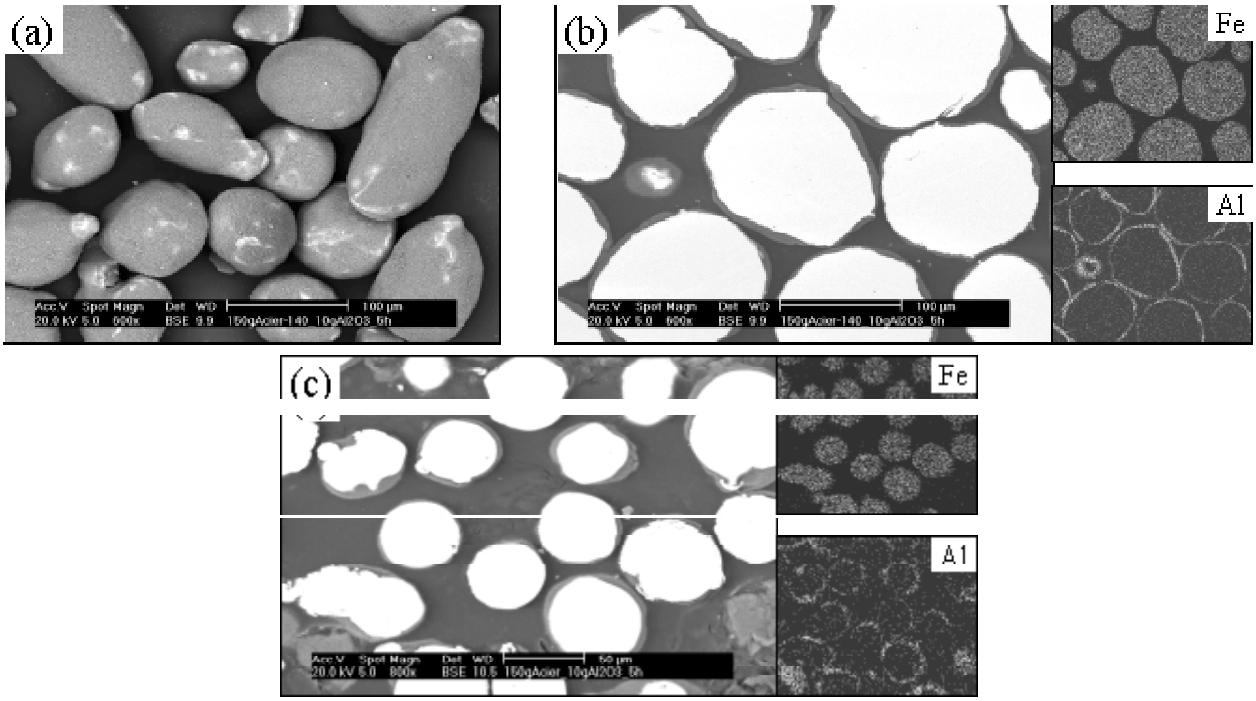

Figure 1. (a) An example of the typical morphologies of composite particles (B20) obtained by the mechanofusion process. Cross sections showing the elements distribution in white color as detected by EDS mapping analysis for the (b) big (B10) and (c) small particles (S10).

3.2. Splats collection

The splat morphologies of small and big composite particles are almost the same for a given temperature of the substrate surface. As it has been previously observed [9], on "non-preheated" substrates, the splats are extensively fingered (figs. 2a and 2b) whereas those collected onto 300°C preheated substrates (figs. 2c and 2d) become more circular. Each splat is composed of alumina and stainless steel too but depending of the particle size, when particles are fully molten before their impact, alumina is either distributed on or under the stainless steel splats, or scattered in small pieces and randomly dispersed over the stainless steel splat (fig. 2e) when the melting is poor. Moreover when collecting the composite particles in flight within the plasma jet, the fully melted ones exhibit a spherical shape with a cap made of alumina while the poorly melted ones have alumina pieces distributed all around the steel core. For the first two cases, calculations [10] have shown that the center of gravity of melted small composite particles with a cap is decentred by less than 2 µm, while with coarse particles it is by less than 0.1 µm. Thus small particles with caps can be considered as heterogeneous ones. In the plasma jet core where the gas velocity is much higher than that of particles the molten alumina shell is entrained at the front edge of the particles. In the plasma plume, when the gas velocity becomes lower than that of particles, due to their heterogeneity particles rock and the alumina shell is now at the particle tail behind the stainless steel. On the contrary, coarse particles behave as perfect spheres and due to their inertia, outside the plasma core, they keep the alumina cap in front of them.

For the third case of splats (fig. 2e), the alumina dispersion is due to the fact that the stainless steel particles are in a plastic state while the alumina shell still retains a semi-solid state in the plasma jet and brokes into pieces due to the large difference of expansion coefficients between both materials ($17x10^{-6}K^{-1}$ for stainless steel and $8x10^{-6}K^{-1}$ for alumina).

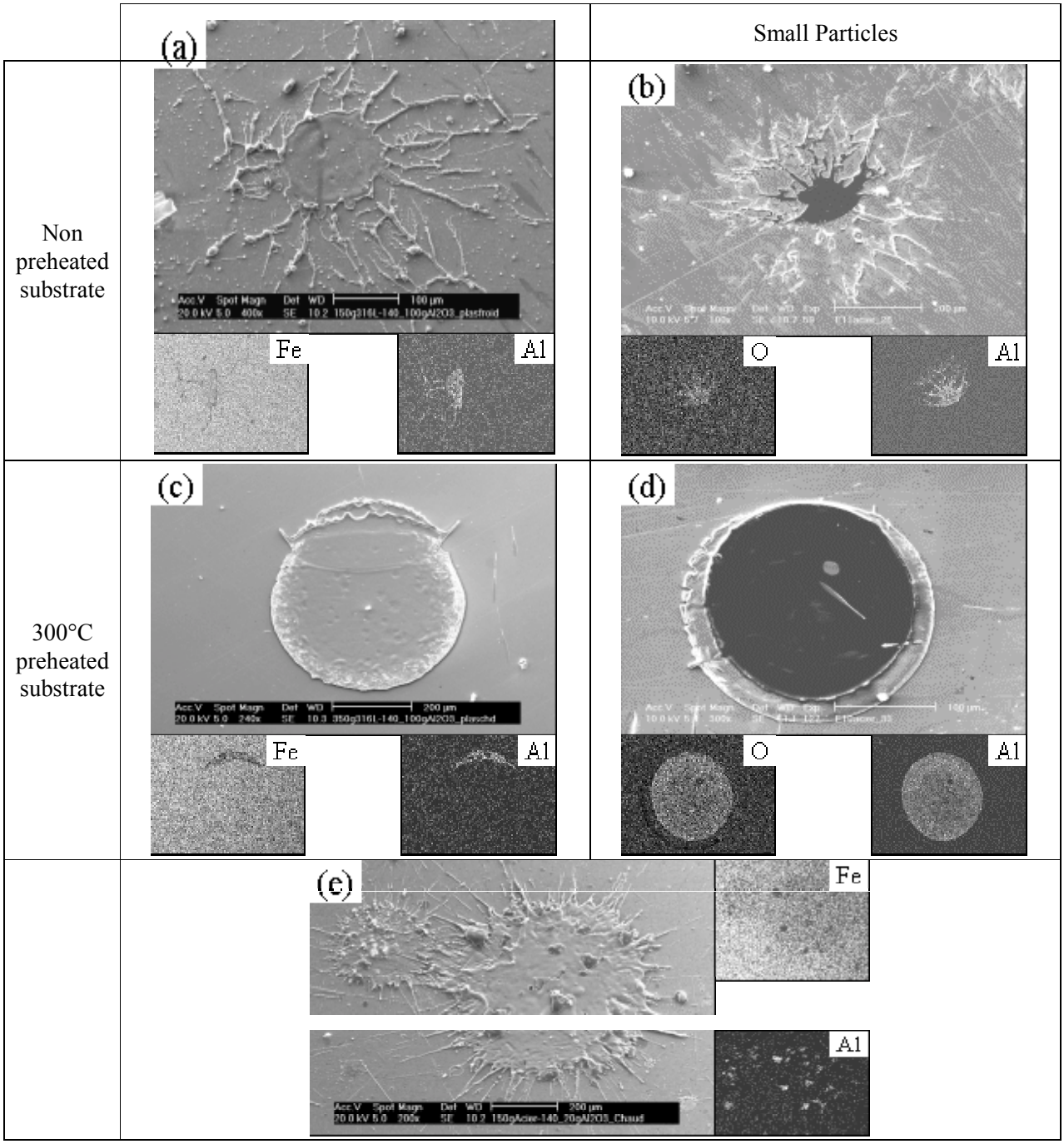

Figure 2: Views of splat morphologies showing in white color the alumina distribution as detected by EDS analysis. Big composite particles collected onto a (a) cold and (c) 300°C preheated substrates. Small composite particles collected onto a (b) cold and (d) 300°C preheated substrates. (e) Splat morphology corresponding to particles which still retains a semi-solid state in the plasma jet with the alumina shell broken into pieces.

3.3. Coatings formation

Typical coating microstructures from the mechanofused big and small particles exhibit a dense lamellar structure with a dark phase randomly distributed within the stainless steel matrix corresponding to the alumina phase detected by EDS analysis. In the Fig. 3a, the coatings resulting from powders with a small particle size distribution exhibit, a uniform distribution of alumina, with a rather dense and fine microstructure. However, in the coatings made with the big particle size distribution, it can be observed a coarse stainless steel particle surrounded by an alumina layer. It is thus clear that big particles do not completely melt during their flight within the plasma jet. To check the influence of particle melting, plasma spraying of coarse particles was performed with a high carrier gas flow rate (8 slm) to limit their residence time in the hot gases and thus their melting. Fig. 4 shows a view of a non melted composite particle collected in flight and which is composed of a stainless steel core covered by pieces of alumina as detected by EDS analysis.

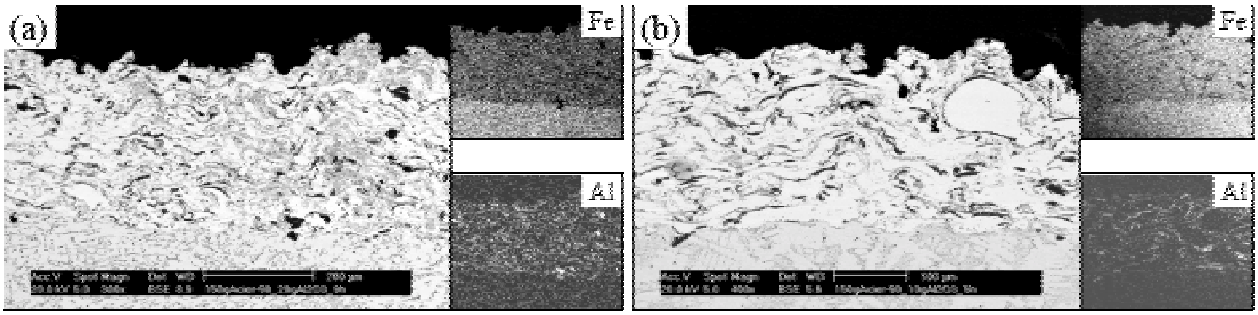

Figure 3. SEM micrographs of typical microstructures of the resulting plasma sprayed coatings from (a) smaller and (b) bigger stainless steel-Al_2O_3 mechanofused powders and their corresponding EDS mapping analysis for Iron (Fe) and Aluminium (Al) in white color .

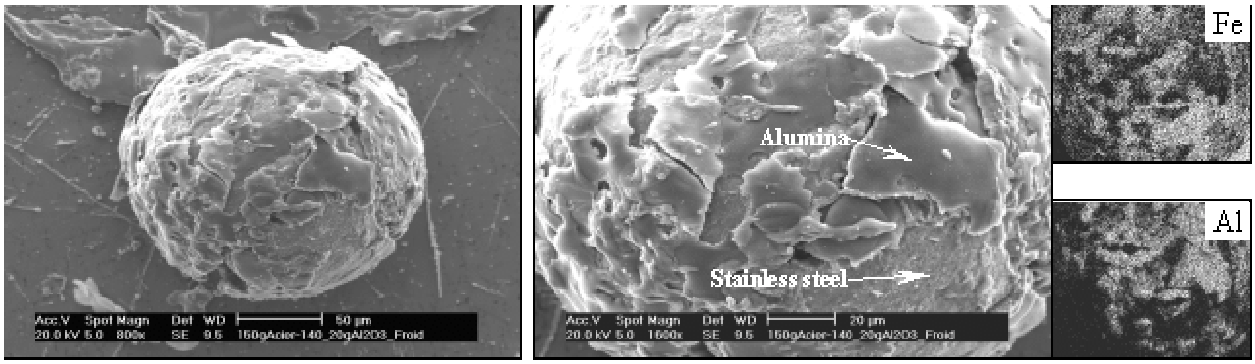

Figure 4. SEM micrographs of a non melted composite particle collected at the impact with a mirror polished substrate.

The hardness of coatings sprayed with small composite particles attains 370 ±43 HV5 and is higher than that reported for pure stainless steel deposits made with particles with a mean particle size of 60 µm (270 ±22 HV5) [6]. Due to the uniformly distributed alumina within the coating, its hardness is increased by the dispersion strengthening of the hard phase. However with coarse composite particles, the hardness attained is lower than that obtained with small composite particles and is almost the same as that of pure stainless steel deposits. This is due to the poorly melted particles at impact resulting in non uniformly scattered alumina pieces and rather poor contact between lamellae.

4. Conclusions

Mechanofusion process is an effective means to control the plasma spray deposit microstructure especially when covering small stainless steel particles (mean particle size of 65 µm) with an alumina shell of few µm in thickness.

The high energy input of the mechanofusion process is directed towards the creation of an alumina shell via the agglomeration of alumina particles with a very fine size (1 μm) on stainless steel particles (either –140 μm + 100 μm or –90 μm +45 μm). It is likely that the mechanofusion process activates the agglomeration of the fine alumina particles on the stainless steel ones, provided the difference in particle size distributions is large.
When spraying composite particles with a particle size distribution between 45 and 90 μm, alumina splats, uniformly distributed, are found embedded in a dense steel matrix enhancing its mechanical properties such as hardness as compared with coatings obtained from pure stainless steel particles with about the same size. With big composite particles (mean particle size = 126 μm) which melting is poor, the coating hardness is lower than that of pure stainless steel of small sizes (~60 μm). Work is in progress to improve big particles melting.

Acknowledgements
R. Cuenca-Alvarez thanks CONACyT-Mexico and SFERE-France for their financial support to conduct his postgraduate studies.

References
[1] S. Sampath, J. Matejicek, C.C. Berndt, H. Herman, A.C. Léger, M. Vardelle, P. Fauchais: Plasma sprayed zirconia : Relationships among particle parameters, splat formation and deposit generation – Part II. Microstructure and properties, in Thermal Spray : Practical Solutions for Engineering Problems, (Ed) C.C. Berndt, (Pub.) ASM International, Materials Park, OH, USA, (1996) p.629-636.

[2] P. Fauchais, A.C. Léger, M. Vardelle: Formation of plasma sprayed oxide coatings, in Proceedings of the Julian Szekely Memorial Symposium on Materials Proceesing (Ed) H.Y. Shon, J.W. Evans, D. Apelian, (Pub) TMS, USA, (1997) p.571-592.

[3] E. Kubel: Powders dictate thermal spray coating properties, Advanced Materials and Processes Vol. 12 (1990), p.24-32.

[4] C. Moreau, S. Dallaire: Plasma spraying of carbon-coated TiC powders in air and inert atmosphere, in Thermal Spray: Research and Applications, (Ed) T. F. Bernecki, (Pub.) ASM International, Materials Park, OH, USA, (1990) p.747-753.

[5] M. Fukumoto, I. Okane: Application of mechanically alloyed composite powders to the thermal plasma spraying, in Thermal Spray: International Advances in Coatings Technology, (Ed) C.C. Berndt, (Pub.) ASM International, Orlando, Fl, USA, (1992) p. 595-600

[6] T. Yokoyama, K. Urayama, M. Naito, M. Kato: The Angmill mechanofusion system and its applications, KONA Vol. 5 (1987), p. 59-68.

[7] H. Ageorges, P. Fauchais: Oxidation of stainless steel particles with and without an alumina shell during their flight in a plasma jet, High Temperature Materials Processes Vol. 4 (2000) p. 323-327.

[8] R. Cuenca Alvarez, H. Ageorges, P. Fauchais, P. Fournier, A. Smith: The effect of mechanofusion process and planetary-milling on composite powder preparation: agglomeration and fragmentation, accepted in Materials Science Forum, Trans Tech Publications, Switzerland (2003).

[9] H. Ageorges, P. Fauchais: Plasma spraying of stainless steel particles coated with an alumina shell, Thin Solid Films 370 (2000) p.213-222.

[10] R. Cuenca-Alvarez, H. Ageorges, P. Fauchais: Stainless steel coatings alumina reinforced by plasma spraying mechanofused particles, accepted in Proceedings of the International Thermal Spray Conference and Exposition, ASM International, Orlando, Fl, USA, (2003).

Influence of stepwise ionization in a Hall thruster

L. Garrigues[1, †], J. Bareilles[1], G.J.M. Hagelaar[1], C. Boniface[1], J.P. Boeuf[1],
S. Roche[2], J. Bretagne[2], M. Touzeau[2] and D. Pagnon[2]

[1] *Centre de Physique des Plasmas et Applications de Toulouse, Université Paul Sabatier, 118 route de Narbonne, 31062 Toulouse cedex 4, France*
[2] *Laboratoire de Physique des Gaz et des Plasmas d'Orsay, Université de Paris Sud, Campus Universitaire d'Orsay, 91405 Orsay cedex, France*

Abstract
The effect of indirect ionization on the discharge properties in a Hall thruster is examined in this paper. We use a two-dimensional hybrid model where ionization from excited states as well as direct electron impact ionization is taken into account. The contribution of stepwise is obtained using an un-coupled collisionnal radiative model. We also show comparisons between measurements and calculations of the density distribution of xenon excited states in the thruster.

1. Introduction

Stationary Plasma Thrusters – SPTs (or Hall thrusters) are efficient electric thrusters for satellite stationkeeping. In SPTs, a discharge is created between two coaxial dielectric cylinders by ionizing a flux of neutral atoms (xenon). Neutral atoms (mass flow rate of 5 mg/s) are injected at one end of the channel, while electrons are emitted from a hollow cathode located outside the channel. The typical length of the channel is 2.5 cm, with internal and external radii of 3.5 cm and 5 cm respectively. Due to the low pressure in the channel (few mTorr), a radial magnetic field is necessary to confine electrons to efficiently ionize the gas. The magnitude of the applied magnetic field is such that the motion of ions is not affected by the magnetic field. A potential drop around 300 V is applied between the anode located in the bottom of the channel and the external cathode. The electric field is distributed in the zone of low electron conductivity and high magnetic field. Ions generated in the channel see most of the applied voltage and are accelerated to energies close to 300 eV, providing the thrust. Many satellites have been launched in the last 3 decades, essentially in the former Soviet Union, with Hall thrusters on board. The space vehicle SMART-1 will be launched around the moon by Ariane V soon with one PPS1350 on board used as orbit transfer for the first time [1].
Although Hall thrusters have been studied since the beginning of the 60's by Russian scientists, the physics of the engine is far from been completely understood. A research group has been created in France in 1996 associating laboratories from CNRS, CNES, SNECMA and ONERA to study the physics of the engine with experimental and modeling research activities [2], [3]. A testing facility is based in Orléans (France) with a SPT equipped with a set of electric and optical diagnostics [2], [4]. Extensive results have been obtained for the spatial and temporal distributions of the optical emission of the plasma within the thruster channel [4]. In parallel to experiments, a two-dimensional axisymmetric model of the discharge in the channel and the near outside regions has been developed. This code combines fluid equations for the electron transport and particle description for both ion and neutral species. In the paper described in Ref. [3], the ionization from the ground state of xenon is only considered. We have taken into account the ionization from excited xenon states to examine the influence of the stepwise ionization on the discharge properties. The contribution of these excited states is obtained from an un-coupled collisionnal radiative model [4], [5] which is able to give the distribution of the metastable and excited levels densities.
The discharge and collisionnal radiative models are briefly described in section 2. Stepwise ionization effect and comparisons between calculated and measured xenon excited states densities are presented section 3.

2. Description of the models

We first give a brief description of the transient hybrid two-dimensional model of the discharge. The collisionnal radiative (CR) model is discussed in the second part of this section.

2.1. Discharge model

† email : garrigues@cpat.ups-tlse.fr, tel : +33.5.61.55.62.43, fax : +33.5.61.55.63.32

A hybrid, axisymmetric two-dimensional model of the thruster has been used. The magnetic field, which is a input of the simulation code, is calculated with an external software. The transport of heavy particles, xenon atoms and ions is described with a particle model where the trajectories of macro-particles representing large number of ions or neutrals are followed. The particle model has been largely described in the paper of Hagelaar *et al.* [3].
The electric field is deduced from the electron momentum equation, assuming quasineutrality (the plasma density is deduced from ion transport). Electron collisions with neutral atoms are not sufficient to explain the transport of electrons across the large radial magnetic field and the observed plasma conductivity in the exhaust region. Anomalous conduction across the magnetic field lines has been attributed to electron-wall collisions or to field electric field fluctuations. Ref. [3] gives a description of the treatment of anomalous conductivity in the model.
In Ref. [3], only ionization from the ground state of xenon atoms was taken into account. In the present paper we study the possible contribution of stepwise ionization and its influence on the model results. We have simplified the problem by extracting information about the total ionization from an un-coupled collisionnal-radiative (CR) model (see below). In practice, we decompose the ionization in two contributions, a first one due to the direct ionization from the fundamental level ($1s_0$ – Paschen notation) and a second one corresponding to the indirect ionization of excited levels. We assume a local equilibrium such that for a given triplet (n_e, T_e, n_a), where n_e is the electron density (equal to ion density – quasineutral plasma), T_e is the electron temperature and n_a the neutral atom density, we estimate the total contribution to the ionization using the CR model results. The CR results have been tabulated so that knowing (n_e, T_e, n_a) at a given location and at a given time in the thruster (from the hybrid 2D model) we can deduce the density of xenon excited states (especially the $2p_5$, $2p_6$, and $3p_6$ levels which will be compared with experimental measurements) and the contribution of stepwise ionization at the same location and time. We have also modified the electron energy equation with a supplementary term of energy loss for the electrons due to the effect of indirect ionization. The idea is to consider a fictive excited state level Xe* with a mean threshold of excitation of few eV. Results show that varying the threshold of excitation between 2 and 4 eV does not influence the results presented in section 3.

2.2. The collisionnal radiative (CR) model
This numerical model solves a set of kinetic equations relative to the excited states of xenon atoms. We consider that the various excited states are produced and quenched by inelastic and superelastic electron-atom collisions; deexcitation due to radiative transitions or collisions with walls are also taken into account. The system of master equations governing the time evolution of the excited species is the following :

$$\frac{dN_i}{dt}=\sum_j C^e_{ji}.N_j.n_e-N_i\left[\sum_j C^e_{ij}.n_e+\sum_{j<i}(1-\Lambda_{ij}).A_{ij}+C^e_{ion,i}.n_e\right]+\sum_{j>i}(1-\Lambda_{ji}).A_{ji}.N_j\pm\sum_{k,l}K^{hp}_{kl}.N_k.N_l-\gamma_i.N_i/\tau_i \qquad (1)$$

where n_e is the electron density and N_i the density of level i. $C^e_{ji}=\int v.f(u).\sigma_{ji}(u)du$ is the electron impact excitation coefficient for the transition $j\rightarrow i$ and $C^e_{ion,i}$ the ionisation coefficient of the level i. $f(u)$ is the electron energy distribution function (EEDF) normalized to 1. σ_{ji} is the electron impact cross section for the transition $j\rightarrow i$. A_{ij} is the Einstein coefficient for the transition $i\rightarrow j$. We can also take into account the self-absorption by introducing a calculated factor ($1-\Lambda_{ij}$) [6]. K^{hp}_{kl} is the rate coefficient of collisions between heavy particles k and l. γ_i is the destruction probability of metastables at the walls, which is taken to be 99%. τ_i is the equivalent lifetime for diffusion and destruction of metastable levels at these walls.
The cross sections for the following processes have been introduced in the model [4], [5] :

- electronic excitation from the fundamental level [7]
- electronic excitation from excited states [7], [8]
- simple and double ionisation [9] [10]
- Penning ionisation

The data from radiative transitions (transition probabilities, oscillator strengths) are from Refs [11], [12]. A detailed description of the model is given in Refs [4], [5].

A parametric study of the contributions to ionisation versus the neutral xenon density (10^{12} – 10^{14} cm^{-3}), the electron density (10^{9} – 5×10^{12} cm^{-3}) and the electron temperature (1 – 50 eV) has been achieved. The main results are the following :

- xenon ionization is mainly obtained through electron collision with ground state xenon atoms as well as 1s (metastable and radiative), 3d, 3-6s and 4-5p levels of neutral xenon
- the contribution of the fundamental level depends strongly on the electron density : it decreases when n_e increases due to stepwise ionisation, especially from the metastable level
- the electron temperature has a smaller influence
- neutral density is also important when electron density is high because of self-absorption of emission lines particularly of resonance lines

Looking at the creation and destruction rates of the different levels, we come to the conclusion that it is possible to reduce the entire xenon scheme to only a few levels, which are the following : ground state, 1s, 2p, 3d, 3-6s, and 4-5p.

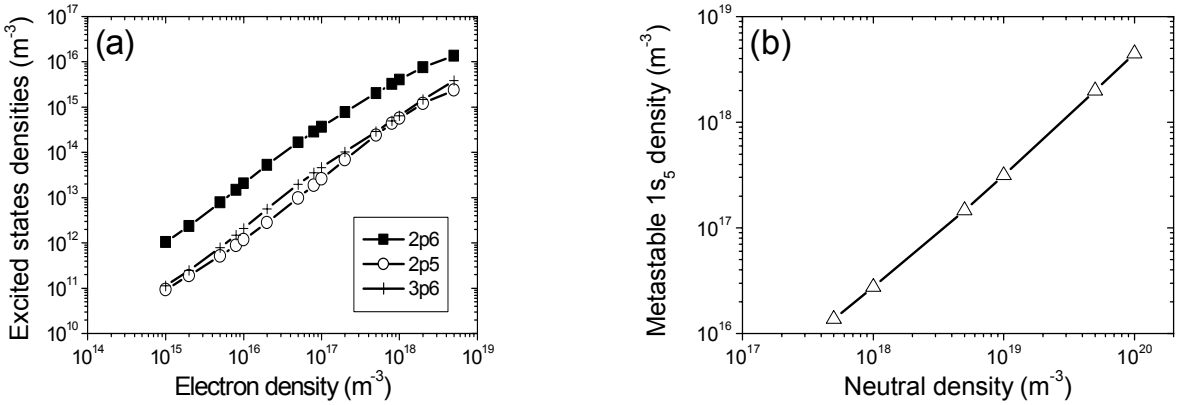

Figure 1 : (a) excited states densities as a function of the electron density in log-log scale for a given neutral density of 10^{19} m^{-3} and an electron temperature of 10 eV; (b) metastable density as a function of the neutral density (log-log scale) for an electron density of 5×10^{17} m^{-3} and an electron temperature of 10 eV.

The influence of the electron and neutral densities, and electron temperature on the densities of $1s_5$, $2p_5$, $2p_6$, and $3p_6$ levels have also been examined. Summarizing,

- the densities of the 2p and 3p levels depend linearly in log-log scale of the electron density as wee can see Fig. 1a. The effect of the electron temperature is not dominant, the population of the excited states is quasi constant for a temperature greater than 10 eV.
- the contribution of the neutral fundamental state on the $1s_5$ population is clearly shown Fig. 1b. Varying the electron temperature between 10 and 50 eV multiply only by a factor 2 the metastable density. For electron density superior to 5×10^{17} m^{-3}, the $1s_5$ level density decreases due to the formation of the 6p level.

3. Results and discussion

We examine the influence of the stepwise ionization in the sub-section 3.1. and we compare calculations with experimental results in sub-section 3.2. The inner and outer ceramics of the SPT are respectively positioned at r=3.45 cm and r=5 cm. The channel length is 2.5 cm. The calculation domain is a box of 8 cm x 8 cm with the inside channel and the near outside region. The coil current is 4.5 A, the xenon mass flow rate is 5 mg/s and the potential fall 300 V in nominal conditions. The neutral backpressure inside the facility is 2.5 mPa. We average the simulation results over a time duration of 3 ms.

3.1. Influence of the stepwise ionization on the discharge properties

In a Stationary Plasma Thruster, most of the ionization occurs in the high magnetic field region close to the exhaust plane. The plasma density is maximum (on the order of 10^{18} m^{-3}) a few mm before the exhaust plane (Fig. 2a). Xenon is injected at the end of the channel and the xenon atom density is maximum (typically 10^{20} m^{-3}) in the anode region. The xenon density (Fig. 2b) is strongly depleted (below 10^{18} m^{-3}) in the exhaust region where the electron temperature (Fig. 2c) is large and most of the ionization occurs.

The contribution of direct ionization to the total ionization is shown on Fig. 2d. The contribution of direct ionization to the source term (number of electron-ion pairs generated per unit volume per unit time) will be

refereed to as S_{direct}. When S_{direct} reaches 1, the indirect contribution is negligible ; when S_{direct} tends to 0, ions are essentially created by stepwise ionization. We must keep in mind that our model is quasineutral, i.e. the electron density is everywhere equal to the ion density. Comparing Figs. 2a and 2d, we conclude that the contribution of the indirect ionization from the excited and metastable levels is essentially influenced by the electron density and not by the electron temperature (in the range of value considered in the SPT) in agreement with the output data calculated by the CR model (see sub-section 2.2). We clearly see a region where the direct ionization source term S_{direct} is low (typically 30-40 %). This zone covers a large area concentrated between the anode and the maximum of ionization. In the outside zone, where the electron density (and so the ion density) is minimum, the contribution of stepwise ionization is negligible.

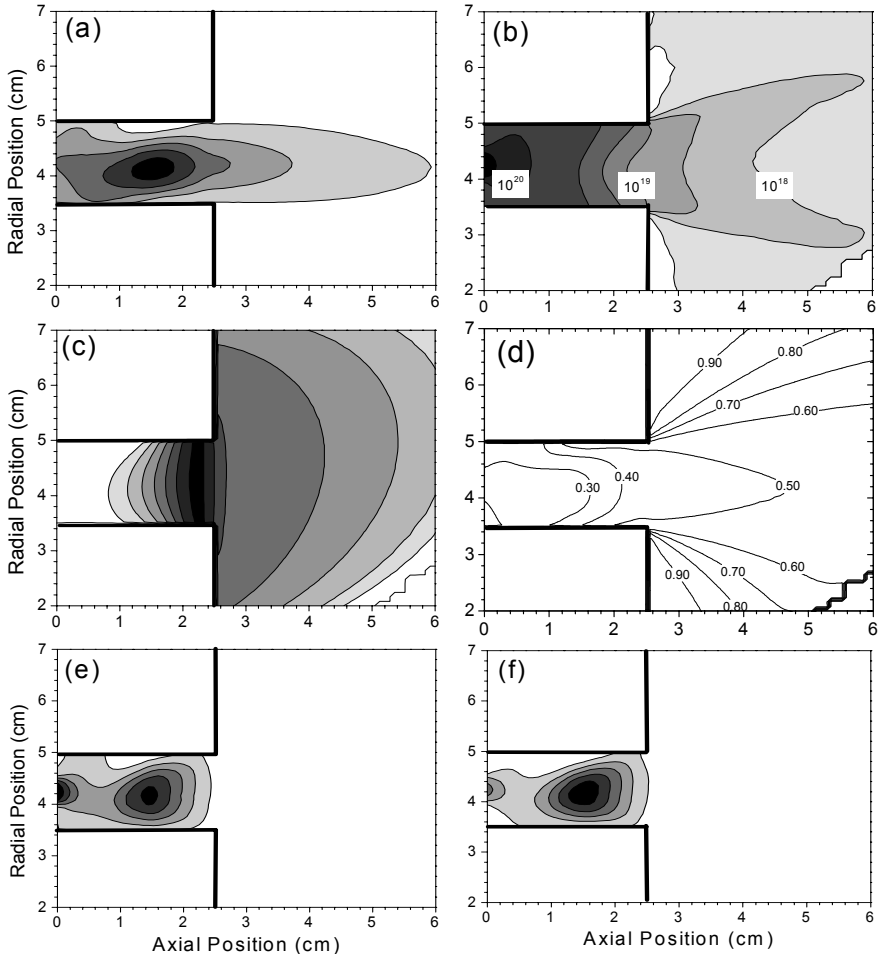

Figure 2 : (a) plasma density distribution in the thruster (each interval of gray scale corresponds to 2×10^{17} m^{-3}) ; (b) neutral atom density distribution in log-scale covering 3 decades; (c) electron mean energy in the thruster from 5 to 20 eV (each interval corresponds to 2 eV) ; (d) contribution S_{direct} of the direct ionization source term ; (e) contours of constant ion source term with stepwise ionization (each interval of gray scale corresponds to 10^{23} m^{-3} s^{-1}) ; (f) contours of constant ion source term without stepwise ionization (same scale than fig. 2e). The channel is located on the left-hand side of the plots the exhaust is at axial position 2.5 cm and the anode is at x=0.

We have reported Fig. 2e the ion source term including stepwise ionization. The maximum is located around the center of the channel and reaches 6×10^{23} m^{-3} s^{-1}. We observe a region of non-negligible ion source term upstream the peak, according to fig. 2a. The density of the metastable level $1s_5$ reaches 2×10^{18} m^{-3} in the anode zone. This is because the atom density is much larger in the anode region than in the exhaust region. The peaks of density of $2p_5$, $2p_6$, and $3p_6$ levels are respectively 2.2×10^{15} m^{-3} for both $2p_5$ and $3p_6$ states and 1.5×10^{16} m^{-3} for $2p_6$ state, that is only a few percent of the total ion density (with a maximum of 1.2×10^{18} m^{-3} – see fig. 2a). The excited states $2p_5$, $2p_6$ and $3p_6$ are produced in the same zone as the maximum of ionization source term. Finally, the total ion source term excluding the stepwise ionization is presented fig. 2f. The maximum is located in the same zone as in fig. 2e, but we note that the ion source is less spread out than when indirect ionization is taken into account, especially in the anode region.

It is interesting to note that if we calculate the total ion current leaving the domain with and without stepwise ionization, we obtain 3.4 A in both cases. The main reason is that the electron mean energy is large enough under nominal operating conditions of the thruster (300 V) to ionize ground state xenon atoms.
We also looked at the effect of the stepwise ionization for lower applied voltage. In the range of 100-200 V, due to the lower electron mean energy, the ionization of the neutral mass flow rate from the fundamental state becomes difficult and the discharge is not initiated. Experimental voltage-current characteristic gives discharge current on the order of 4 A at low voltage [2]. Taking into account the indirect ionization does not change the calculations results because the electron density is too low to populate the xenon excited states and to ionize them. We can therefore conclude that the omission of stepwise ionization in previous models is not responsible from the observed discrepancy between calculations and experiments at low voltage, and that other phenomena must be invoked (see, e.g. [13]) to explain the fact that the models cannot describe the low voltage part of the current-voltage characteristics.

3.2. Comparisons with experimental results

We present figure 3a the densities of the $2p_5$, $2p_6$ and $3p_6$ levels calculated with the two-dimensional discharge model and integrated over the radial direction. We have reported figure 3b the emission intensity obtained on the PIVOINE facility in Orléans using a system of optical fibers distributed on the outer ceramic [2], [4].

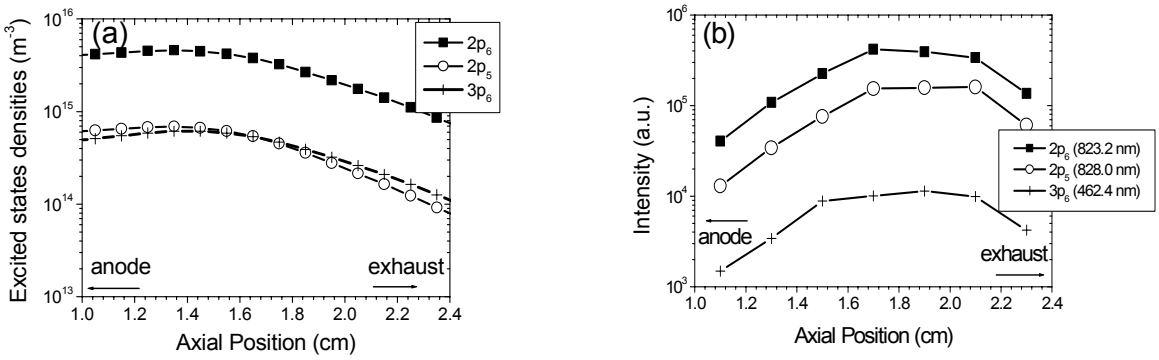

Figure 3 : (a) axial profiles in log-scale of the densities of the $2p_5$, $2p_6$ and $3p_6$ levels obtained with the two-dimensional code ; (b) emission intensity of the 828.0 nm, 823.2 nm and 462.4 nm lines obtained experimentally [4].

Under SPT conditions, the local emission spectroscopy is simply related to the excited states densities [4]. Calculations show a maximum of excited states densities typically 1 cm downstream the exhaust, while the emission is observed in a region nearby (between 5 and 8 mm) the exit. If the density of the $2p_6$ level is large in the channel of the engine, as observed experimentally, comparisons between experiments and calculations of the densities of $2p_5$ and $3p_6$ states present discrepancies. Simulations give the same value for the densities of $2p_5$ and $3p_6$ levels, whereas the intensity variations of the transitions at 828.0 nm and at 462.4 nm differ from more than one order of magnitude. Calculated densities are in agreement with input data extracted from the CR model (see Fig. 1). In the model presented here, we use a simplified method where the excited states density is deduced from an un-coupled CR model assuming local equilibrium. The observed discrepancies may be due to the fact that the transport of excited species is neglected in this simplified model.

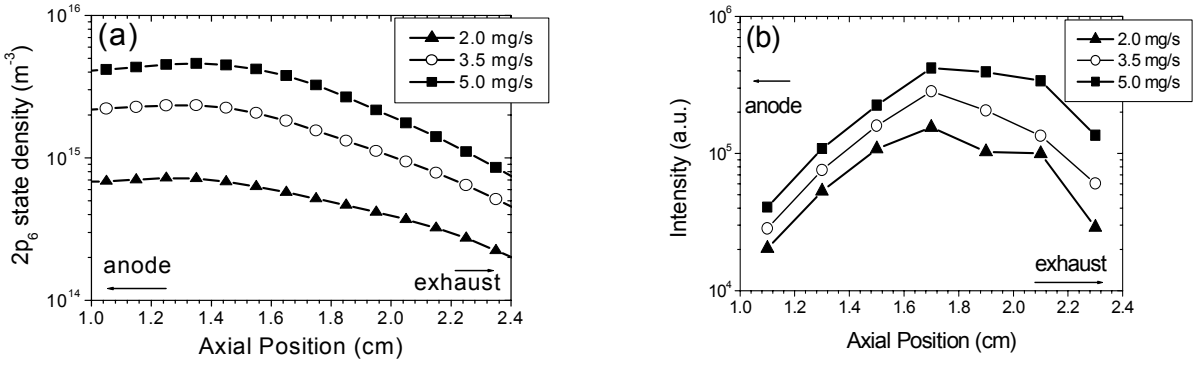

Figure 4 : (a) axial profiles of the $2p_6$ density obtained with the two-dimensional code ; (b) emission intensity at 823.2 nm obtained experimentally for three different mass flow rates of xenon [4].

We end this section with a study of the influence of the mass flow rate in the 2-5 mg/s range, on the density of the $2p_6$ state (see Fig. 4). The applied voltage is 300 V. The modeling and experimental results confirm that the intensity of the $2p_6$ level depends on the xenon mass flow as expected. However, the influence of the Xe debit is much more pronounced in the calculations. The location of the excitation region is not strongly affected by the xenon flow rate if we compare the axial position of the maximums of density and emission.

4. Conclusions

This paper presents a study of the influence of stepwise ionization from xenon excited states on the discharge properties and shows comparisons between calculated densities of $2p_5$, $2p_6$ and $3p_6$ levels with spectroscopy emission in a Hall thruster. Input data for the two-dimensional model of the plasma are extracted from a un-coupled CR model where the species densities had been tabulated as a function of the triplet (n_e, T_e, n_a). Results show that stepwise ionization can reach 60-70 % in the region located between the anode side and the center of the channel. Nevertheless, the total ion current leaving the thruster is the same with and without taking into account the stepwise ionization. This result shows that, for a large enough electron energy, the mechanism of direct ionization from the ground state is sufficient to ionize the neutral flux injected. For low applied voltages, indirect ionization is negligible because the excited states are not populated due to the low electron density. The current-voltage characteristic is not strongly affected by stepwise ionization and we can conclude that stepwise ionization is not responsible for the discrepancy between models and experiments in the low voltage part of the I-V characteristics. The discharge properties are more sensitive to the abnormal electron transport as we have observed in Ref. [3].

Both models and experiments lead to $2p_6$ densities significantly larger than the $2p_5$ and $3p_6$ densities but the $3p_6$ level is significantly less populated than the $2p_5$ in the experiments, which is not the case in the model predictions. The location of the calculated maximums of excited species densities in the channel is deeper than in the measurements. The thruster model presented in this paper uses the results of an external CR model assuming local equilibrium. Some of the discrepancies between model and experiments may be due to the fact that the transport of excited states is not taken into account in this simplified approach (i.e. the excited species densities only depend on the local values of the electron density, temperature, and neutral atom density).

Acknowledgments

This work is supported by the GDR CNRS/CNES/SNECMA/ONERA n° 2232 "Propulsion à Plasma pour Systèmes Spatiaux".

References

[1] G. Saccoccia, *"European Electric Propulsion Activities and Programmes"*, 37th AIAA Joint Propulsion Conference and Exhibit, Salt Lake City, UT, 2001, paper AIAA-2001-3228.

[2] M. Touzeau *et al.*, Plasma Phys. Control. Fusion **42**, B323 (2000).

[3] G.J.M. Hagelaar, J. Bareilles, L. Garrigues, and J.P. Boeuf, J. Appl. Phys. **91**, 5592 (2002) ; G.J.M. Hagelaar, J. Bareilles, L. Garrigues, and J.P. Boeuf, J. Appl. Phys. **93**, 67 (2003).

[4] S. Roche, *"Analyse par Spectroscopie Optique de l'Emission de Plasma des Propulseurs à Effet Hall – Application à l'Erosion des Céramiques"*, Thèse de Doctorat, Université Paris XI (2001).

[5] P. Leray *et al.*, *"Spectroscopic Emission Spatially Resolved along a SPT Channel"*, 2nd Spacecraft Propulsion Conference, Noordwijk, vol. ESA SP-398, p. 347 (1997).

[6] P.J. Walsh, Phys. Rev. **116**, 511 (1959).

[7] V. Puech and S. Mizzi, J. Phys. D : Appl. Phys. **24**, 1974 (1991).

[8] H.W. Drawin, *"Collision and transport cross sections"*, E.U.R. – C.E.A. – F.C. Report, p. 383 (1967).

[9] D. Rapp and P. Englander-Golden, J. Chem. Phys. **43**, 1464 (1965).

[10] D. Marthur and C. Badrinathan, Phys. Rev. A **35**, 1033 (1987).

[11] M. Aymar and M. Coulombe, Atom. Nucl. Data Tables **21**, 540 (1978).

[12] M.H. Miller and A.R. Roig, Phys. Rev. A **8**, 480 (1973).

[13] S. Barral *et al.*, *"Wall Material Effects in Stationary Plasma Thrusters II : Wall Conductivity Theory"*, submitted to Physics of Plasma (2002).

Calculations of Hall thruster lifetime using a two dimensional hybrid model

L. Garrigues[†], J. Bareilles, G.J.M. Hagelaar, C. Boniface and J.P. Boeuf

Centre de Physique des Plasmas et Applications de Toulouse, Université Paul Sabatier,
118 route de Narbonne, 31062 Toulouse cedex 4, France

Abstract
We present in this paper self-consistent simulations of the discharge properties in Hall thrusters with a two-dimensional hybrid model. Understanding the parameters controlling the beam divergence and wall sputtering to optimize the lifetime of the thruster is an important issue. The influence of the magnetic field distribution on the properties, performance and lifetime of the thruster are discussed.

1. Introduction

Stationary Plasma Thrusters – SPTs (or Hall thrusters) provide economic advantage for satellite stationkeeping compared with conventional chemical thrusters (arcjets or resisto-jets). Orbit control missions require a high specific impulse and a low thrust. Due to the high specific impulse, Hall thrusters offer the advantage of reducing the mass of propellant on board on commercial telecommunication satellites (typically 500 kgs for a satellite of 3.5 tons) and so the launch cost. Manufacturers use the gain in propellant mass to increase the payload on new spacecrafts. At the present time, 25 satellites are equipped with Hall thrusters for satellite station keeping [1]. New missions such as deep space applications are now in consideration using 50 kW SPT [2]. Electric thrusters such as Hall thrusters use xenon as propellant. A discharge is created in a cylindrical channel – about 3 cm long and 2 cm wide – by ionization of the xenon flux (density on the order of 10^{19} m^{-3}) by electrons coming from a cathode located outside the engine. Xenon ions, accelerated by the plasma field, provide the thrust. The originality of SPTs is due to the fact the ions are extracted from the thruster without accelerating grids. The accelerating field in the plasma is induced by a drop in the electron conductivity associated with the presence of a transverse magnetic field generated by external coils. Ions are ejected from the channel with velocities on the order of 20 km/s in the exhaust region for a 300 V applied voltage.
The thrusters operating conditions and performance are very sensitive to the magnetic field topology. An efficient engine requires a high level of ionization and ion acceleration must be performed with minimum wall erosion. In modern SPTs, the magnetic circuit consists of two systems of magnetic coils and poles – external and internal. This magnetic system creates a quasi-radial magnetic induction in the exhaust region [3]. Magnetic screens surrounding the accelerating channel allow adjustment of the magnetic gradient in the exhaust region and reduction of the B field magnitude in the anode region [4]. The configuration of the magnetic field lines is convergent and approximately symmetric with respect to the mid surface between the channel walls. The potential drop along the B field lines is small and the equipotential contours tend to line up with the B field lines. The electric field therefore focuses the ion beam in the axial direction [5]. In this paper, we examine the effect of the magnetic field configuration on the thruster regime using a two-dimensional model of the discharge and a freeware code to calculate the magnetic field topology. These models are briefly described in section 2. The influence of the magnetic field on the ion beam properties, on the wall erosion and on the discharge current oscillations is presented section 3 and we conclude in section 4.

2. Description of the models

We begin with a short description of the transient hybrid two-dimensional model of the discharge. We then present the calculation of the magnetic field.

2.1. Discharge modeling

The hybrid model of the discharge is axisymmetric and two-dimensional. This model includes the channel and the exhaust regions, a few centimeters away from the exhaust plane. The model assumes quasineutrality of the plasma. The electric field is deduced from the current continuity equation. Electrons are considered as a fluid while a particle model is used to describe the transport of neutral atoms and ions. The ionization rate

[†] email : garrigues@cpat.ups-tlse.fr, tel : +33.5.61.55.62.43, fax : +33.5.61.55.63.32

is obtained from the electron energy equation assuming a maxwellian electron distribution function. As in many magnetized plasma, the question of electron transport across the magnetic field lines is not clear and "anomalous electron transport" must be invoked to explain the observed electron current. The anomalous transport in the thruster channel has been attributed to electron-wall collisions by many authors, while Bohm diffusion seems to play an important role in the region outside the channel. The model uses empirical parameters (which are adjusted to match the experimental results) to describe this anomalous transport [6]. The model provides the space and time variations of the electric potential, neutral and ion densities, ion velocity distribution function, and the performance of the engine. A complete description of the model and the numerical technique can be found in the paper of Hagelaar *et al.* [6].
In the present paper, the calculation of the erosion rate of the channel walls due to ion bombardment has been included. The erosion rate (eroded thickness per unit time) is :

$$R=\frac{\Gamma_i m_w}{\rho_w}\langle Y(E)C(\theta)\rangle\,, \qquad (1)$$

where Γ_i is the total incident ion flux, m_w is the mean mass of the wall particles, ρ_w is the mass density of the wall material, and the triangular brackets indicate averaging over the incident ions (ion flux). The sputtering yield Y represents the number of eroded particles per incident ion. The correction factor C accounts for the effect of the angle of incidence θ (defined with respect to the radial direction). Empirical formula for the sputtering yield Y and experimental measurements for the correction factor C are deduced from Refs. [7], [8].
The model has been recently improved to describe complex and realistic magnetic field configurations including structures with a zero magnetic field. The calculation domain is divided in four zones limited by the magnetic fields lines passing through the point of zero magnetic field. In each zone, the electron equations are solved separately. The solutions for the zones containing the anode and the cathode are implicitly coupled, so that a total voltage drop can be applied in the current conservation equation. The other zones are connected explicitly. In the zones where the field lines entirely close themselves on the outer or inner walls, the total current in the current conservation equation is taken to be zero.

2.2. Magnetic field modeling

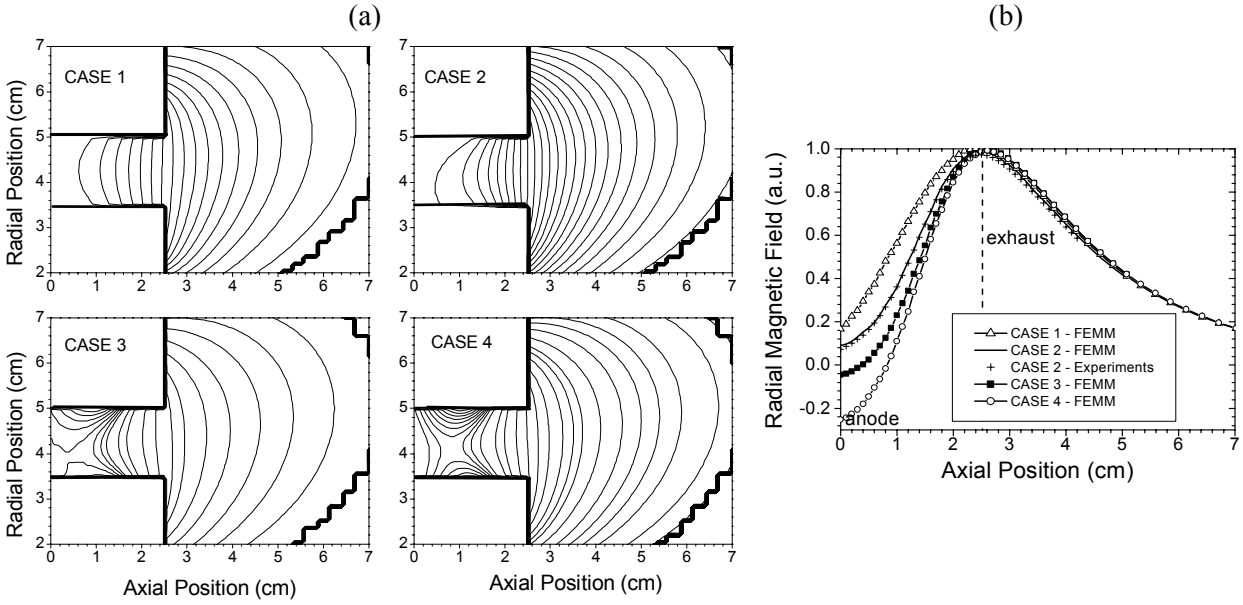

Figure 1 : (a) SPT100 magnetic field lines calculated with FEMM for 4 different configurations of the magnetic circuit. The channel is located on the left-hand side of the plots between the radial positions 3.45 and 5 cm ; the exhaust is at an axial position of 2.5 cm ; (b) axial variations of the calculated radial magnetic field strength at the thruster channel median for different configurations. Measurements for the SPT100-ML are also plotted for CASE 2 [11].

We use the FEMM (Finite Elements Method Magnetic) freeware code [9] to calculate the magnetic field distribution for a given arrangement of the magnetic circuit. This user-friendly software solves Maxwell's

equation for the magnetic vector potential in a cylindrically symmetric geometry with the finite element method. The details of the magnetic circuit and material properties and the current through the coils are inputs of the magnetic field code. We neglect the possible effect of the plasma current on the total magnetic induction. Different geometry of the magnetic circuit have been designed to generate different magnetic field topology with different axial gradients of the radial magnetic field. We extrapolate the calculated B field on the triangle mesh used by FEMM on the two-dimensional grid of the discharge code.
The magnetic field lines are plotted fig. 1a for four different topologies and for a SPT100 (100 mm of external diameter). The inner and outer ceramics of the SPT are respectively positioned at r=3.45 cm and r=5 cm. The channel length is 2.5 cm. Note that the magnetic field in the region outside the channel and the magnetic field lens are practically the same in all configurations. We clearly see the presence of a region of zero magnetic field in the anode region for CASES 3 and 4. A supplementary coil, positioned behind the anode, with a negative coil current was used to create a zone of low magnetic field inside the channel [10].
CASE 2 corresponds to the standard configuration of the magnetic field of the SPT100-ML studied in the PIVOINE facility [11]. The calculated and measured magnetic fields (see Fig. 1b) for this configuration are in good agreement (the coil current in the model has been adjusted to obtain a good match of the maximum field near the exhaust plane).
Variations around this configuration have been obtained by modifying the magnetic circuit. CASE 1 exhibits a larger magnetic field magnitude in the channel and a smaller gradient than CASE 2. The radial magnetic field goes through zero in the anode region and changes sign in a zone of a few millimeters in CASE 3 and 1 cm in CASE 4. The width of the region of large magnetic field is also smaller for CASES 3 and 4 ; this is correlated with the existence of a zero magnetic field region (the region of large magnetic field is pushed toward the exhaust when the point of zero magnetic field is shifted away from the anode).

3. Results and discussion

We first discuss the influence of the magnetic field topology on the thruster properties and performance (3.1). The thruster wall erosion is estimated for different magnetic field configurations (3.2). Finally, the effect of the magnetic field on the oscillations of the discharge current is presented in sub-section 3.3.

3.1. Ion beam properties

The typical conditions are the following : the applied voltage is 300 V and the xenon mass flow rate is 5 mg/s. The gradient of electron temperature is set to zero on the anode while the temperature is fixed to a few eV on the cathode line. As we said in section 2., the difficulty concerns the abnormal electron conductivity in the direction perpendicular to the magnetic field and we use empirical parameters to quantify this effect. The influence of the parameters characterizing anomalous conductivity on the thruster properties has been described in the papers of Hagelaar *et al.* [3]. Comparisons between simulations and experimental results concerning the performance and the amplitude of the current oscillations [12] have allowed us to adjust ours empirical parameters to give the best fit between experiment and simulations in the SPT100 engine. We used the same values for these parameters in the present paper and for the 4 configurations of CASES 1 to 4. This seems reasonable since the magnetic field magnitude is almost the same in the region outside the channel where Bohm diffusion is important. Moreover, in the channel region near the exhaust plane, where the electron-wall collisions play an important role, the intensity of the magnetic induction is very similar in the 4 cases.
We have plotted in figure 2 the time-averaged spatial distributions of the ionization source term (gray scale) and the electric potential (contour lines) for CASES 1 to 4. The zone of high intensity of the magnetic field and low electron conductivity controls the spatial profile of the electric potential. Changing the width of the high magnetic field region influences the electric field distribution. The potential drop inside the channel is concentrated within a few millimeters in CASE 2 and 1 centimeter in CASE 1. The low field region on the anode side extends to 2 centimeters in the case with a zero magnetic field (CASE 3 and 4). An important part of the potential drop occurs in the region outside the channel in all cases, but the exact ratio of the potential drop inside and outside the channel is different for each case and, as expected, depends on the magnetic field distribution. The potential drop outside the channel represents 44 % and 59 % of the applied voltage in CASES 1 and 4 respectively.
The electron energy is deposited deeper in the channel for larger widths of the region of large magnetic field as it can be deduced from the ionization source term distributions plotted in Fig. 2. A zero magnetic field topology leads to a more complex structure of the ionization rate. In the region around the location of the

point of zero magnetic field the electron mobility is larger and the ionization rate decreases (see e.g., CASE 4). In the regions where the magnetic field lines are closed on the channel walls the electron mean energy and ionization source term drop. In all cases, we see a second ionization peak in front of the anode injector. The results in that region are sensitive to the boundary condition that is used for the energy equation (zero energy gradient or fixed energy). A zero energy gradient is imposed in this paper, but a fixed low electron energy would lead to a much smaller ionization rate in that region. Unfortunately, this boundary condition is rather arbitrary (although zero energy gradient seems reasonable), and there are no clear experimental data on the electron energy in this zone. Morozov and Savelyev estimate the magnitude of ionization to a relatively small value (~10 % of the maximum rate) [5]. However, we find that the influence of the boundary condition for the electron energy on the anode is not crucial for the SPT performance. The performance is characterized by typically 3 parameters. We define the thrust T as the force in reaction to the acceleration of ions, the specific impulse I_{sp} as the impulse per unit weight (directly proportionnal to ion beam mean axial velocity if the gas in fully ionized) and the total efficiency η as the kinetic power over the electrical injected power.

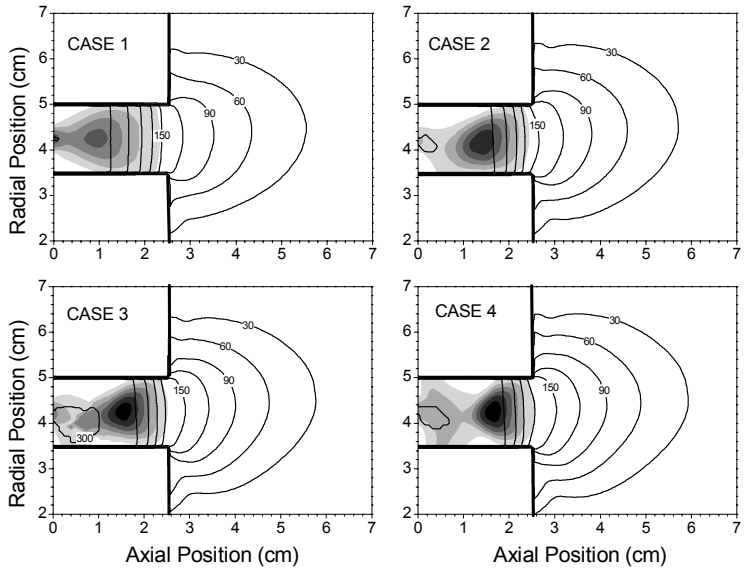

Figure 2 : Time-averaged spatial profiles of the electric potential (contours) and the ionization source term (gray scale). The contours are equally spaced with intervals of 30 V. The gray scale is linear, the intervals correspond to 10^{23} m^{-3} s^{-1}.

An efficient Hall thruster requires efficient ionization of the neutral flow and efficient axial acceleration of the ions (i.e. through a potential as close as possible to the total applied potential). The model results show that the total efficiency η (~50 %), the thrust T (80 mN) and the specific impulse I_{sp} - 1600 s - are almost the same for the different cases. To explain this high level of performance, we can look at the propellant utilization η_u (i.e. the part of xenon flux ionized) and beam energy η_E efficiency (associated to the mean energy of the ion beam compared to the potential drop). The ion production zone is clearly separated from the acceleration region (look at the position of the maximum of ion production compared to the potential fall), and ions are therefore efficiently extracted from the channel thruster, with η_E on the order of 80 %. The neutral flow is efficiently ionized since we obtain typically an efficient propellant utilization efficiency η_u of 90 %. We must note that in the calculations presented here, we assumed that neutrals created by ions recombination on the walls are thermalized and emitted with a temperature of 500 K. In the case of magnetic configurations with a zero B-field, the ion current striking the channel walls can reach values as high as 1 A (only 0.4 A in CASE 2). This is a consequence of fact that ions produced in the regions where the magnetic field lines are closed on the walls are lost to the walls.

3.2. Wall sputtering and lifetime

Figure 3 exhibits the calculated inner wall erosion rate as a function of axial position. Although the ion flux to the walls is larger deeper in the channel, the ion energy flow is much larger in the exhaust region because ion acceleration takes place in the last cm before the exhaust plane. The length of the eroded zone and the intensity of the erosion strongly depend of the configuration of the B field. A zone of 1 cm is eroded in CASE 1, only 3 mm in CASE 4. After 1000 hours of thruster operation, the maximum of material eroded in the exit plane reaches 0.5 mm for CASE 1 and only 0.08 mm for CASE 4.

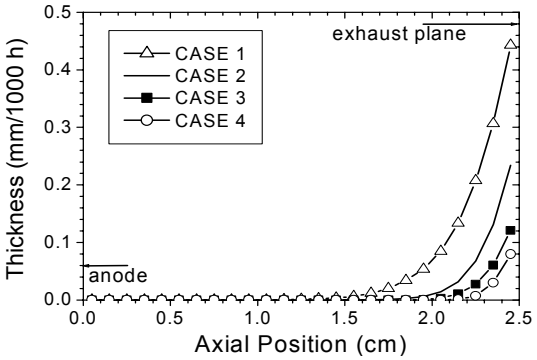

Figure 3 : Calculated erosion rate of the inner channel wall.

The length of erosion is directly connected to the positions of the source term combined with the electric potential fall. In CASE 1, the ion production and acceleration regions cover a large area of the channel, in contrast to CASE 4. A smaller electric potential drop inside the channel leads to a serious decrease in the erosion rate because of the smaller energy of the ions impacting the walls. The mean energy of ions striking the ceramics is 110 eV in CASE 1 and 80 eV in CASE 4 in the exhaust plane. Since the sputtering yield is very sensitive to the ion energy in this energy range, relatively small changes in ion energy may have dramatic consequences for the wall erosion. These results provide a quantitative confirmation of the intuitive fact that the thruster lifetime increases when a larger part of the potential drop is outside the channel. A magnetic field structure with a zero B field topology allows a reduction of the width of the large magnetic field region inside the channel and leads to good performance with improved lifetime (as observed experimentally on the PPS® 1350 [13]).

3.3. Discharge current oscillations

We present on figure 4, the discharge current as function of time for both CASES 1 and 4. The model results show a smaller amplitude of the low frequency oscillations in CASE 4 compared with CASE 1. This is associated with a smaller width of the region of large radial magnetic field in our model calculations. This feature has also been observed in the ATON Hall thruster [14] where the magnetic field also goes through zero in the channel. Note that current oscillations in the range of 100-200 kHz is also observed especially in CASE 4 where the low frequency oscillations is less pronounced. This oscillation has already been described in Ref. [6].

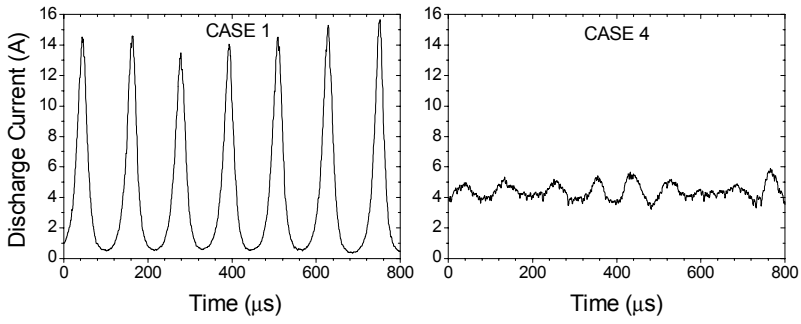

Figure 4 : Discharge current as a function of time for CASES 1 and 4.

4. Conclusions

This paper is dedicated to the study of some aspects of the sensitivity of the SPT properties to the B field configuration using a two dimensional hybrid model. Different magnetic topologies with different widths of the region of large magnetic field near exhaust have been studied, keeping constant the maximum magnetic field intensity and magnetic lens. The results show that the ratio of potential drop inside and outside the channel is controlled by the magnetic field distribution and it has consequences for the thruster wall erosion and lifetime, and on the beam divergence. This is an important aspect of SPTs which is not thoroughly discussed in the literature and we think that more systematic experiments are needed to clarify this point. Systematic measurements of the part of potential inside and outside the channel (e.g. through Laser Induced Fluorescence experiments) would be very useful to confirm the effects predicted by the model. This would also help to validate the simulation results which depend on some adjustable parameters.

The transient behaviour of the thruster, briefly discussed in this paper, also shows that the amplitude of the low frequency current oscillations decreases when the B field configuration exhibits a zero field in the anode region. This stability is associated with a smaller width of the region of large radial magnetic field in the calculations. This feature has also been observed in the ATON Hall thruster [14] where the magnetic field topology presents a zero-B field configuration.

Acknowledgments

This work is supported by the GDR CNRS/CNES/SNECMA/ONERA n° 2232 "Propulsion à Plasma pour Systèmes Spatiaux". Part of this work was also directly supported by SNECMA.

References

[1] E. Britt and J. McVey, *"Electric Propulsion Activities in U.S. Industries"*, 38th AIAA Joint Propulsion Conference, Indianapolis, IN, 2002, paper AIAA-02-3559.

[2] D. Manzella, R.S. Jankosvsky, and R.R. Hofer, *"Laboratory Model 50 kW Hall Thruster"*, 38th AIAA Joint Propulsion Conference, Indianapolis, IN, 2002, paper AIAA-02-3676.

[3] V. Kim, Journal of Propulsion and Power **14**, 736 (1998).

[4] F. Scortecci, A. Serra, A. DiGianvito, and M. Andrenucci, *"Experimental Investigations of a Laboratory Model Hall Thruster"*32th AIAA Joint Propulsion Conference, Lake Buena Vista, FL, 1996, paper AIAA-96-2707.

[5] A. I. Morozov and V. V. Savelyev, in : *Reviews of Plasma Physics*, Vol. 21, ed. B. B. Kadomtsev and V. D. Shafranov (Consultants Bureau, New York, 2000) pp 203-391.

[6] G.J.M. Hagelaar, J. Bareilles, L. Garrigues, and J.P. Boeuf, J. Appl. Phys. **91**, 5592 (2002) ; G.J.M. Hagelaar, J. Bareilles, L. Garrigues, and J.P. Boeuf, J. Appl. Phys. **93**, 67 (2003).

[7] N. Matsunami, Y. Yamamura, Y. Itikawa, N. Itoh, Y. Kazumata, S. Miyagawa, K. Morita, R. Shimizu, and H. Tawara, Atomic Data and Nuclear Data, **31**, 1 (1984).

[8] Y. Garnier, V. Viel, J.F. Roussel, and J. Bernard, J. Vac. Sci. Technol. A **17**, 3246 (1999).

[9] FEMM version 3.1, by D. Meeker, 2002 (http://femm.berlios.de).

[10] D. Valentian, A. Morozov, and A. Bugrova, *"Plasma Accelerator of Short Length with Closed Electron Drift"*, SNECMA Patent n° US5475354 (1995).

[11] V. Lago, personnal communication (2002).

[12] J. Bareilles, G.J.M. Hagelaar, L. Garrigues, C. Boniface, J.P. Boeuf, and N. Gascon, *"Critical Assessment of a 2D model of Hall Thrusters - Comparisons with Experiments"*, 28th International Electric Propulsion Conference, Toulouse, France, 2003, paper IEPC-03-184.

[13] M. Lyszyk, E. Klinger, O. Sécheresse, J.P. Bugeat, D. Valentian, A. Cadiou, T. Beltan, and C. Gelas, *"Qualification Status of the PPS® 1350 Plasma Thruster"*35th AIAA Joint Propulsion Conference, Los Angeles, CA, 1999, paper AIAA-99-2278.

[14] M. Touzeau *et al.*, Plasma Phys. Control. Fusion **42**, B323 (2000).

Studies of micrometric splats obtained by suspension d.c. plasma spraying

J. Fazilleau[1], C. Delbos[1], J-F. Coudert[1], P. Fauchais[1], A.Denoirjean[1], L. Bianchi[2], K. Wittmann-Ténèze[2]

[1]*Laboratoire Science des Procédés Céramiques et Traitements de Surface, Université de Limoges, Limoges, France*
[2]*Commissariat à l'Energie Atomique, Le Ripault, France*

Abstract
The formation and morphology of micrometric splats of stabilized zirconia collected on glass and stainless steel substrates have been studied. Splats result from direct current (d.c.) plasma spraying of a suspension of nanoparticles of stabilized zirconia. A system based on a pendulum allows in-flight particles collection at different distances from the injection point. In our process, as in classical plasma spraying, the material of the substrate as well as its temperature play a very important role in the shape of splats The particles and splats size distribution is measured by means of image analysis and an estimation of the average flattening ratio is made from measurements of splats thickness.

1. Introduction

In conventional d.c. plasma spraying, particles with a size between 10 and 100µm are injected into the plasma jet by using a carrier gas in order to obtain coatings with a thickness of at least 50µm formed by layering lamellae (splats) resulting from the spreading of molten particles. These splats have typically a diameter close to 100µm for a thickness of 1µm [1].
The injection of ceramic suspensions containing submicronic particles (a few tens to a few hundreds of nanometers) in a d.c. plasma jet is a new process which allows to achieve thin coatings (thickness between 1 and 100µm) with a fine microstructure. It results from the fact that the molten droplets of ceramic are in the range 0.1 to a few µm in diameter instead of a few tens of µm for classical spraying. The resulting splats are thus one to two orders of magnitude smaller than in classical plasma spraying. Previous studies of this process allowed to evaluate the influence of the different spray parameters such as standoff distance, current intensity, plasma gas composition, nozzle internal diameter, suspension solvent and suspension load on the state of collected splats. These preliminary works allowed to determine different sets of working conditions [2]. They have shown that the big suspension drops (~300 µm) injected with a momentum high enough to penetrate within the plasma jet are sheared (in times ~ 1µs) by the plasma jet in tiny droplets in the µm size range. The suspension solvent is then evaporated (in the µs time range) and the resulting ceramic agglomerates are melted and accelerated towards the substrate.
There is a great interest in obtaining thin dense stabilized zirconia coatings, in order to deposit electrolytes in SOFCs for instance. The injection of an yttria-stabilized zirconia suspension in a d.c. plasma jet is an interesting way to achieve thin nanostructured stabilized zirconia coatings with a deposition rate almost as high as that of a conventional spray process.
The formation and morphology of micrometric or submicrometric splats of stabilized zirconia have been studied on glass and stainless steel substrates with smooth surfaces (Ra<0.1 µm).

2. Experimental procedure

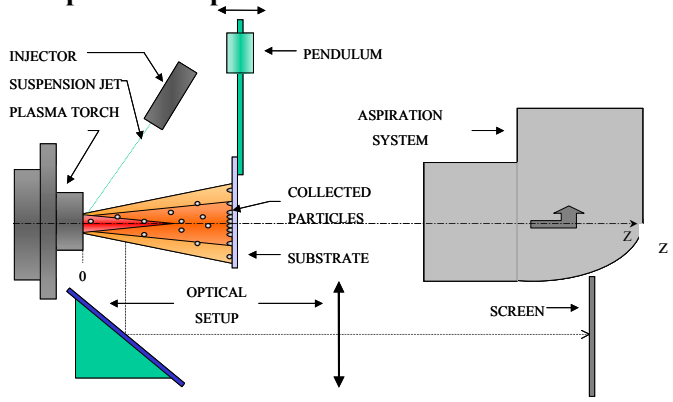

Fig 1 : Experimental set-up

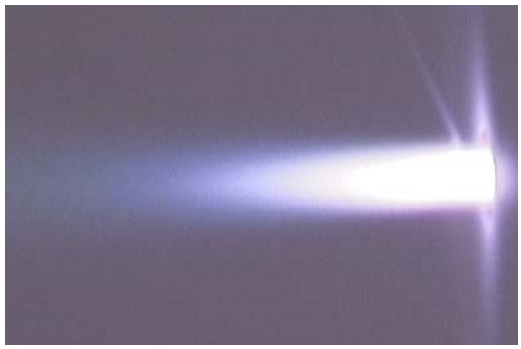

Fig 2 : Liquid injection in the plasma jet

The experimental set-up consists in a d.c. plasma torch (PTF4 type), an injection system for the suspension, a furnace for substrate preheating and a pendulum to collect in-flight particles (Fig.1).
The d.c. plasma torch is operated at 400 or 500A with an Ar/H_2 (45/15 slm) mixture as plasma forming gas and a 6 mm internal diameter nozzle. During all experiments, the characteristics of the plasma torch (arc current intensity and voltage, torch thermal efficiency and gas specific enthalpy) are measured and recorded with a specifically developed computer code.

The injection system is composed of a tank, in which the suspension is stored, and an injector consisting in a stainless steel tube with, at its extremity, a calibrated injection hole which is manufactured by electro-erosion. Suspension is mechanically injected by controlling, with compressed air, the pressure of the liquid in the tank, the pressure of injection being monitored with a gauge. The injector axis is aimed at the nozzle exit, in such a way that the suspension flow penetrates the plasma at counter-flow and targets the nozzle axis (Fig.2).

The ceramic powder used is zirconia doped with 13 wt% yttria (Tosoh TZ-8Y). It has a specific surface area of 13 m^2/g and a mean crystallite size of 25 nm. The solvent used is ethanol. The suspension must have a low viscosity and a good stability to be compatible with the process. A suitable dispersant, which adsorbed on the particles surface, allows an effective dispersion of the powder in the solvent. The dispersant used is a phosphate ester. It acts by a combination of electrostatic and steric repulsions.
After weighing the dispersant, solvent is added and the mixture is stirred until the liquid becomes clear. The zirconia powder is then added and the use of an ultrasonic probe to break the powder agglomerates is the last step to obtain the desired suspension. The mean agglomerated particle size in the suspension is 500 nm and the majority of particles has a size ranging between 100 nm and 2 µm. The rheological studies show that suspensions containing 2 wt% of dispersant display the minimum viscosity of 3.5 mPa.s.
The suspension has a loading of 7 wt% and is injected with the previously described injector. To study the in-flight phenomena acting within the plasma on the initial suspension drops (estimated with the help of a C.C.D camera to be about 300 µm in diameter), particles are collected at different distances downstream of the injection point which correspond to different residence times of particles in the plasma jet.
The pendulum can be positioned relatively to the nozzle exit along the z-axis (Fig.1). Its velocity depends principally on its mass, length and the angle from which it is thrown. Thus, by controlling its velocity and position, a substrate collects different quantities of particles after their treatment in the plasma at different distances downstream of the injection point. The collecting time corresponds to a few milliseconds. The resulting samples are analyzed with a Scanning Electron Microscope (SEM), an Atomic Force Microscope (AFM) and an Interferometric Microscope (IM) in order to observe the collected particle or splat morphologies.

The furnace used for substrate preheating is composed of 2 copper blocks, each of them being electrically heated up to a maximum power level of 250 W. The plate is maintained in this heating device before being thrown at the extremity of the pendulum for the particles collection . The space between the two copper blocks is adjustable. The whole device is insulated by glass wool. A K type thermocouple allows to control the temperature of the copper blocks, which is recorded together with the characteristics of the plasma torch. Knowing the oven temperature, the rise in substrate temperature is determined numerically instead of experimentally because of practical difficulties (moving system, low thickness from a few tenths to a few mm of the heated plate).

3. Results related to the influence of the substrate parameters

3. 1 Glass substrates

The first experiments were made with glass substrates (Ra =0.02 µm). The oven temperature was fixed at 500°C and then substrates were heated during different times corresponding to different temperatures. The flying plate collected particles during about 3 ms. Different collecting distances were tested. The results presented below correspond to the distance where collected particles are fully molten and spread the best.
At 500 A, no change in splats morphology can be observed whatever the glass temperature could be between 20 °C and 480°C. A new experiment (Fig.3) was made at 400A and only a slight effect is observed:

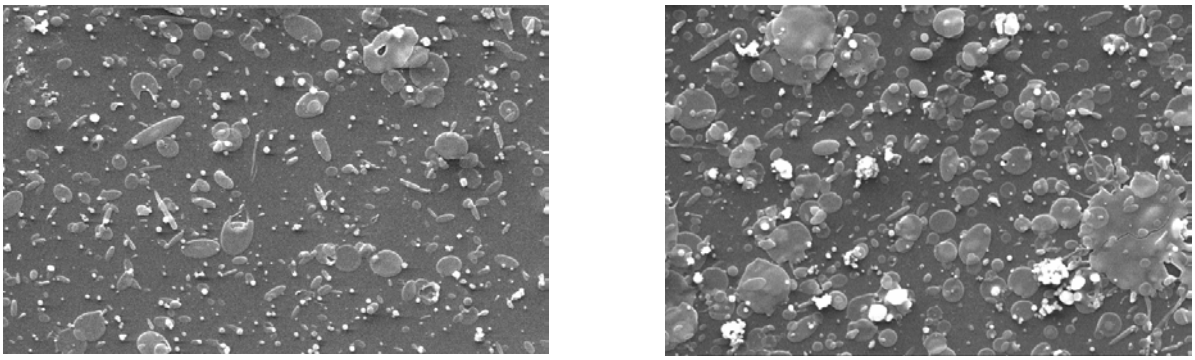

Glass substrate at T=20°C Glass substrate heated at T=400°C

Fig 3: zirconia particles collected on glass substrates I=400A (× 10000). ⟷ 5μm

More particles are collected when the substrate is heated at 400°C and they spread better. With the substrate preheated at 400°C, results comparable to those observed on cold substrates with an arc current intensity of 500 A are obtained with a lower current intensity of 400A. No clear explanation has been found for this behaviour.

3.2 Stainless steel substrates

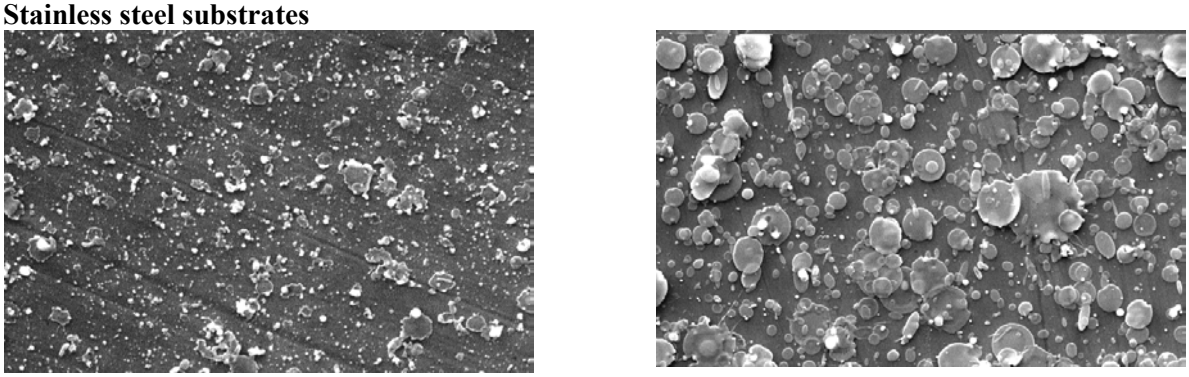

Stainless steel substrate at T=20°C Stainless steel substrate heated at 400°C

Fig 4 : zirconia particles collected on polished stainless steel substrates I=500A (× 10000). ⟷ 5 μm

There is a clear effect of the influence of the substrate temperature on splat morphologies and splats number when the substrate used is made of stainless steel (Fig.4). No preheating leads to few collected splats which are irregularly shaped. A preheating temperature of 400°C for stainless steel substrates leads to disk shaped splats, with a much better spreading. It can be been explained by a better wetting [3], but it is very likely due to the desorption of condensates and aggregates at the substrate surface when the critical temperature called transition temperature is reached [4,5].

4. Results from particles analysis

4.1 Image analysis of collected particles

When the splats collection is made far from the injection point, only spheroidized particles are obtained on the plate. Those are the particles injected which have cooled down, due to their low thermal inertia, and are mostly in a plastic state after having been fully melted in the plasma jet and which impact velocity is now too low for their spreading. Image analysis can be made from the S.E.M photos of different samples collected on the plates (Fig.5,6). Particles with sizes from below 100 nm to 2 μm are observed with a mean size of 200 nm. 65% of particles have a size below 200 nm but they only represent 5% of the collected weight. Particles with a size over 500 nm are only 5% in number but they represent 60% in weight.

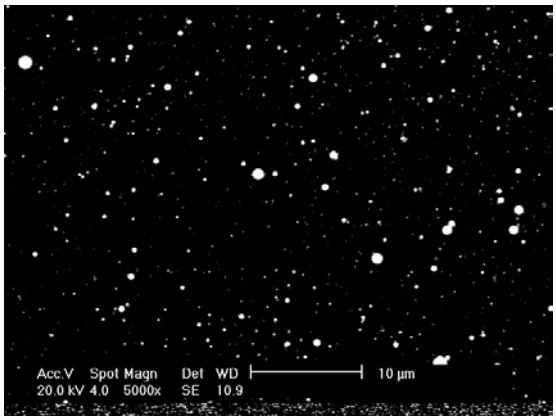

Fig 5 :collection of particles far from the injection point for image analysis. ⟷ 10 µm

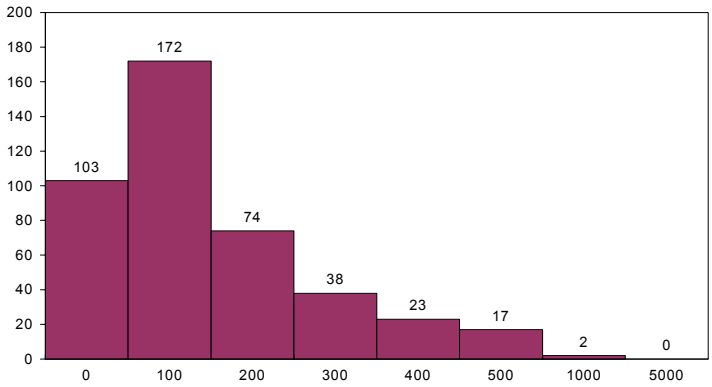

Fig 6: number of collected particles evolution with their size

4.2 Estimation of splat thicknesses

From splats collection, on glass substrates at good spraying distances (where quite dense coatings can be achieved), the observation is made with an interferometric microscope (IM) and an atomic force microscope (AFM) in order to obtain the 3 dimensional (3D) representation of splats and to measure their diameters and thicknesses.

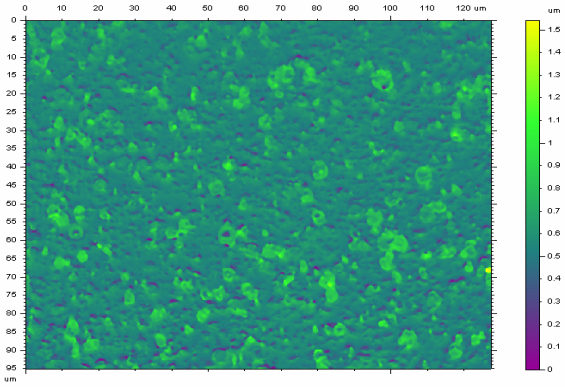

Fig 7 : map of a 127.7*95.3 µm zone obtained with the interferometric microscope

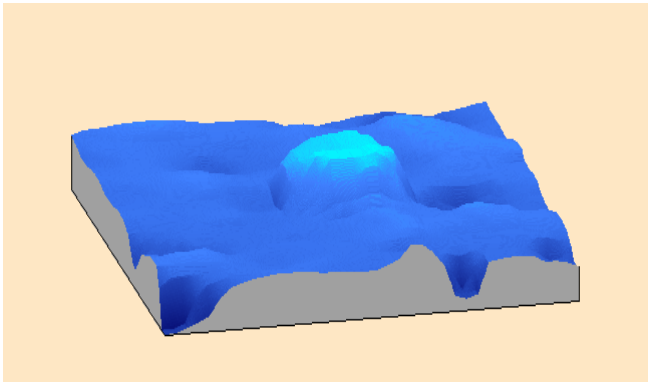

Fig 8 : 3D imaging of an yttria stabilized zirconia splat (D=2µm, h=300nm) thanks to the interferometric microscope

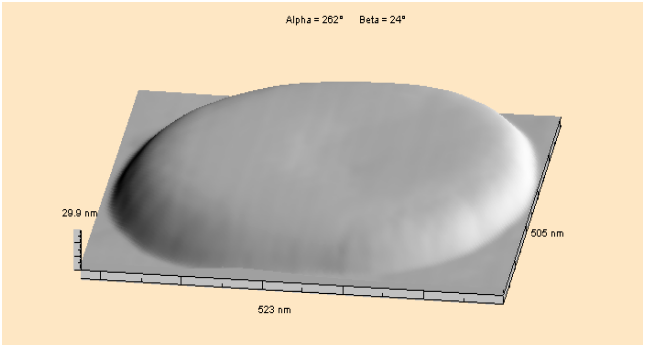

Fig 9 : 3D imaging of a YSZ splat with AFM (D=0.5 µm, h=30 nm)

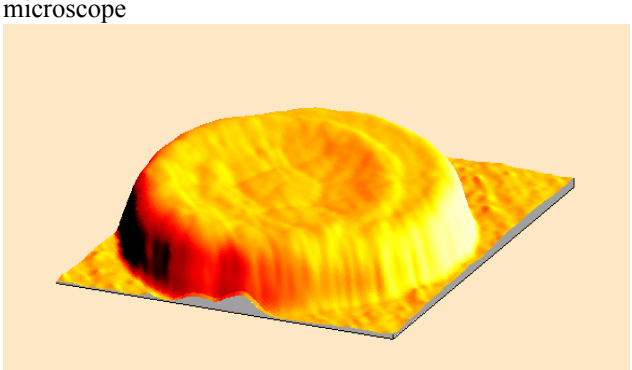

Fig 10 : 3D imaging of a YSZ splat with AFM (D=0.8 µm, h=60 nm)

With the interferometric microscope only the biggest splats (diameter over 1µm) can be observed accurately (Fig.7,8), while the atomic force microscope allows to see smaller splats with more details (Fig.9).
Most of the splats observed have a more or less regular cylindrical shape (Fig.10). The profiles from splats (Fig.11) were taken at the middle of the most regular splats and then their mean diameter D and thickness h were measured.

When considering splats as perfect cylinders, initial diameter of the impacting spherical particle can be calculated from the formula:

$d = \sqrt[3]{1.5 * D^2 * h}$ (1) and the flattening ratio $\xi = \frac{D}{d}$ (2) can be deduced.

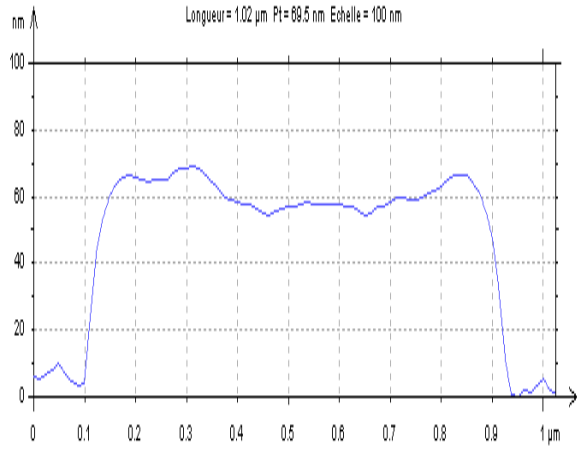

Fig 11 : Example of a profile taken from the splat represented in Fig. 10.

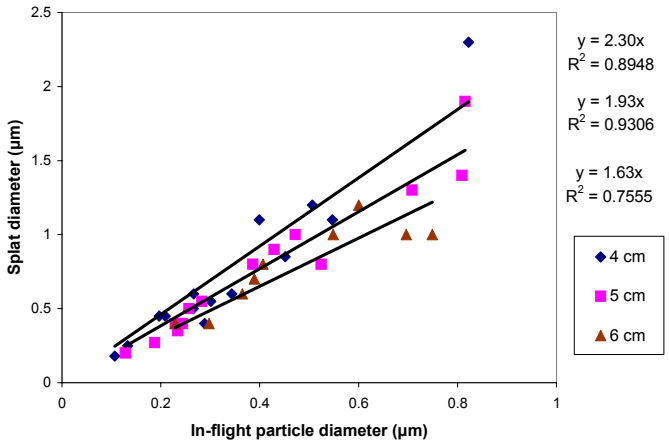

Fig 12 : Estimation of the flattening ratio for different distances downstream of the injection point

With the interferometric microscope the splat diameters considered are in the range 1.8-4.6 µm with their thicknesses varying from 0.17 µm to 0.35 µm while with the atomic force microscope the splat diameters are in the range 0.2-1.9 µm with their thicknesses between 25 nm and 280 nm. The corresponding flattening ratio is between 1.3 and 2.8. As it could be expected, the mean value of ξ decreases when the collection distance from the injection point increases (Fig.12). At 4cm a mean value of 2.30 is obtained for ξ while it is only 1.93 at 5cm and 1.63 at 6cm.

The values of ξ obtained with our process are less than those obtained for bigger particles used in classical spraying [6]. Such values can be explained by lower Reynolds and Weber numbers of particles. The Madjeski's formula $\frac{3\xi^2}{We} + \frac{1}{\mathrm{Re}}\left(\frac{\xi}{1.2941}\right)^5 = 1$ can be used to try to determine the impacting particles speed. A mean value of ξ=2 results in equation $\frac{12}{We} + \frac{8.8}{\mathrm{Re}} = 1$. Neglecting the surface energy term at impact (high We) leads to Re=8.8. Besides, a resolution of the whole equation leads for a 1µm diameter particle at a temperature of 3200 K (assuming that ρ=5700 kg.m^{-3}, µ=0.034 Pa.s, σ=0.5 N.m^{-1}) to an impact velocity v_p of 68 m/s (Re=11.4, We=52.7) while for a 500 nm particle v_p=122 m/s (Re=10.2, We= 84.8). A value of Re~10 is then obtained for our particles. But during flattening We diminishes very fast and so surface tension forces will play a key role on the particle flattening especially at its end. This oversimplified calculation gives indication about particle velocities which are lower than in classical spraying which can be due to the plasma quenching by the solvent evaporation and also the Knudsen effect for these small particles. Moreover, according to particles sizes their thermal inertia is low and as soon as the spray distance increases after an optimal distance, as shown by collected splats and particles, their cooling is very important and ξ decreases. With a mean value of ξ=2 the thicknesses predicted by formulas (1) and (2): $h = \frac{d_p}{1.5\xi^2}$ are h=80 nm for d_p= 500 nm and h=30 nm for d_p= 200 nm which is in good agreement with experimental results.

The images from AFM show that splats have a microstructure similar to that of splats obtained in classical spraying (Fig.13), with microcolumns growing perpendicularly to the substrate with column sizes between 20 and 100 nm for a 1µm diameter splat. However the size distribution of the columns is not as regular as in classical spraying showing that the cooling is not uniform all over the splat surface. In classical spraying the column mean size is between 100 to 400 nm depending on the splat cooling rates.

Besides, x-ray diffraction analysis made on coatings show that our 13wt% yttria-stabilized zirconia crystallizes under the cubic form.

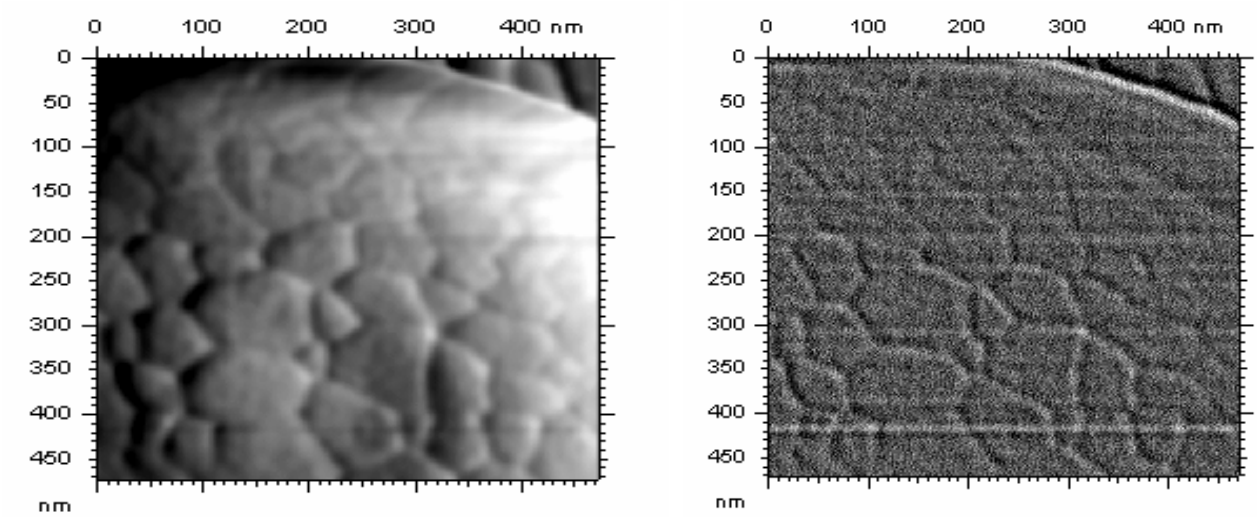

Fig 13 : view of the top of a splat (diameter of 1μm) showing a columnar structure

Conclusion

Nanometric particles have been d.c. plasma sprayed by injecting them as a suspension in ethanol. The formation and morphology of the resulting micrometric splats of stabilized zirconia on smooth surfaces (Ra<0.1 μm) have been studied for glass and stainless steel substrates. The substrate material as well as its temperature play a very important role in the shape of splats in our process as in classical plasma spraying. At low temperatures (T~300K), splats are close to disk shaped on a glass substrate and fingered and exploded with many holes on a stainless steel substrate. At a higher temperature of 670 K, only disk shaped splats are observed on both types of substrates. They are well spread and there is no flagrant difference between glass and stainless steel substrates for splats formation. The image analysis on glass substrates has been made, showing that the majority of molten impinging particles have a size below 1μm but particles over 500 nm in diameter represent more than 50% of the deposited weight. Interferometric microscopy and atomic force microscopy allowed to measure the diameter and thickness for splats corresponding to these molten particles. The flattening ratio was found to be around 2, depending on the spraying distance, corresponding to a mean thickness of 80 nm for an impacting particle size of 500 nm. Splats crystallize in a cubic structure and it was observed that for splats of diameter close to 1μm crystallization occurs under the form of microcolumns growing perpendicularly to the substrate.

References

[1] P.Fauchais, A. Vardelle, B.Dussoubs; “Quo vadis thermal spraying?”; J. Thermal Spray Technology; 10 (1); 2001; 44-66.

[2] K.Wittmann, J.Fazilleau, J.-F. Coudert, P.Fauchais, F.Blein, “A new process to deposit thin coatings by injecting nanoparticles suspensions in a D.C plasma jet”, in Proc. of Int. Thermal Spray Conf.; (ed) E.Lugscheider; (pub.) DVS Düsseldorf, Germany; 2002; 519-522.

[3] S.Kuroda, P.Blazdell; “Suspension plasma spraying of ceramics using an ink jet printer”; in Proc. of Int. Thermal Sporay Conf.; (ed) E.Lugscheider; (pub.) DVS Düsseldorf, Germany.; 2002; 539-543.

[4] M.Fukumoto, E.Nishioka and T.Matsubara, Surface and Coatings Technology; 120-121 (1999); 131-137

[5] S.Sampath, X.Jiang; “Splat formation and microstucture development during plasma spraying: Deposition temperature effects”; Materials Science and Engineering A; 304-306; 2001; 144-150.

[6] L.Bianchi, “D.C. and R.F. plasma spraying of ceramic coatings: mechanism of the formation of the first layer and its link with coatings properties” (in French). Ph.D. University of Limoges, France (1995)

DC plasma spray elaboration of fine structured coatings by ceramic liquid suspension injection

C. Delbos [1], J. Fazilleau [1], J.F. Coudert [1], P. Fauchais [1], L. Bianchi [2], K. Wittmann-Ténèze [2]

[1] *Science des Procédés Céramiques et Traitements de Surface, Limoges, France*
[2] *Commissariat à l'Energie Atomique, Le Ripault, France*

Abstract
This paper is devoted to the production of thin coatings (5<e<100 µm) finely structured. This is achieved by direct current (d.c.) plasma spraying of ceramic suspensions containing submicronic Yttria Stabilised Zirconia (YSZ) and Al_2O_3 particles. The suspensions are either separately or simultaneously injected into a d.c. plasma jet. The spray parameters, influencing the structure of collected splats have been previously studied and this paper is devoted to the coating growth and the achievement of a multi layered coating.

1. Introduction

Many thermal spray techniques are available to work out nanostructured coatings such as Thermal Plasma Chemical Vapor Deposition (TPCVD) [1], pneumatic Suspension Plasma Spraying (SPS) [2], High Velocity Oxy-Fuel guns [3] with agglomerated nanoparticles, Thermal Plasma Spray Pyrolysis (TPSP) [4], Thermal Plasma Flash Evaporation [5] or Hypersonic Plasma particle Deposition (HPPD) [6]. But none of them permits to achieve coatings rapidly, easily and economically.
The objective of the present study is the production of thin coatings with a wide thickness range (5 µm to 100 µm) and a fine structure, meeting the following requirements: a high deposition rate and a cost price as close as possible to those of plasma spraying and of course an easy implementation on existing installations. This is achieved with a new process designed at the SPCTS laboratory [7] [8], where ceramic suspensions containing submicronic particles (a few tens nm) of Yttria Stabilised Zirconia (YSZ) and Al_2O_3, are mechanically injected either separately or simultaneously in a d.c. plasma jet. First, the influence of spray parameters on the structure of splats collected on glass plates is studied in order to determine the best adapted working conditions. Second, the coating growth and the influence of different parameters such as the substrate surface conditions, plasma generation conditions and spray pattern are studied.

2. Experimental method

The SPCTS laboratory experimental set-up consists in a PTF4 (Sulzer Metco) plasma torch, a mechanical injection system for the suspension, a pendulum to collect in-flight particles and a substrate holder to realise coatings by the overlapping of beads at the same location (Fig.1).
The d.c. plasma torch is operated between 300A and 500A with Ar/H2 (45/15 slm) or Ar/H2/He (24/9/30 slm) mixtures as plasma forming gases. The nozzle internal diameter used is 6 mm. During all experiments, the characteristics of the plasma torch (arc current intensity, voltage, thermal efficiency and plasma specific enthalpy) are measured and recorded with a specifically developed computer code.

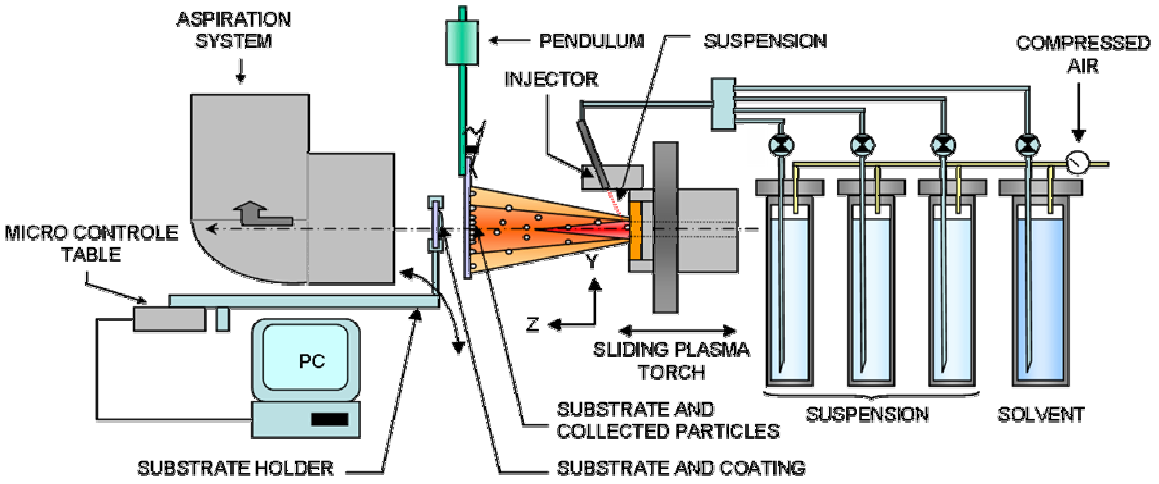

Figure 1: Laboratory experimental set-up.

The injection system is composed of tanks (Fig.1) in which the suspensions and the solvent are stored and an injector consisting in a stainless steel tube with a laser-machined nozzle in order to obtain a calibrated injection hole. The suspension is injected thanks to the pressure of the liquid in the tank, controlled with compressed air, and monitored with a gauge. The injector is positioned directly onto an especially designed ring fixed on the torch nozzle, in such a way that the suspension particles penetrate the plasma at counter-flow and targets the centre of the plasma flow at the nozzle exit.
The zirconia powder used is doped with 13 wt% yttria (Tosoh™ TZ-8Y). It has a specific surface area of 13 m2.g-1 and the mean crystallite size is 25 nm. The alumina powder (Baïkowski™ CR125) has a specific area of 105 m2.g-1. In both cases the solvent used is ethanol. The suspension must have a low viscosity and a good stability to be compatible with the process. A density of 1 vol % has been chosen for the both ceramic suspensions. A suitable dispersant which adsorbs on the particles surface allows an effective dispersion of the powder in the solvent. The dispersant used is a phosphate ester. It acts by a combination of electrostatic and steric repulsions. The stability of the suspensions is longer than one month.
The pendulum is used to study the influence of the operating parameters on the morphology of individual splats. It can be positioned relatively to the system {plasma torch + liquid injector} along the z-axis (see Fig.1), with a precision of 1 mm. Its velocity depends principally on its mass, length and the angle from which it is thrown. Thus, by controlling its velocity and position, the glass plate collects different quantities of particles after their treatment in the plasma at different distances downstream of the injection point. For a single pass, the collecting time corresponds to approximately 3 milliseconds. The resulting samples are analyzed with a Scattering Electron Microscope (SEM) in order to observe the collected particle morphologies in SE (Secondary Electron) and BSE (Back Scattering Electron) modes.
A substrate holder is used to realise coatings by overlapping beads at the same location. It is composed of a sliding arm, which is moved by a computer controlled Micro-Contrôle® table (200 passages, time between two successive passages (1.25 s) and velocity (0.7 $m.s^{-1}$)). For a single pass, the collecting time corresponds to approximately 30 milliseconds. In the same way as for the pendulum it can be positioned relatively to the distance z. In this case, the substrates used are made of stainless steel 316L. The resulting coatings are vacuum impregnated and polished before their cross sections are observed by SEM. This study is done to understand the spray parameters influence on coating elaboration in order to optimize them before an industrial test.

3. Influence of the operating parameters on the morphology of individual splats

The first parameter studied with the pendulum was the influence of the particle collection distance at a current intensity of 500A with an Ar/H2 (45/15 slm) mixture and for a 6 mm nozzle internal diameter (Table 1). In this paper only two collection distances are discussed, the optimal one (d1) for which the best results are observed, and the coating one (d2) such as, d1< d2. In fact the coatings were not manufactured at the optimal distance d1, because the collection time of the substrate holder for one passage is ten times longer than that of the pendulum and a coating requires hundreds of passages. As the substrate is not cooled, the thermal strains are too important and, at the optimal collection distance d1, the coating can't relax the strains, and part of it peels off.

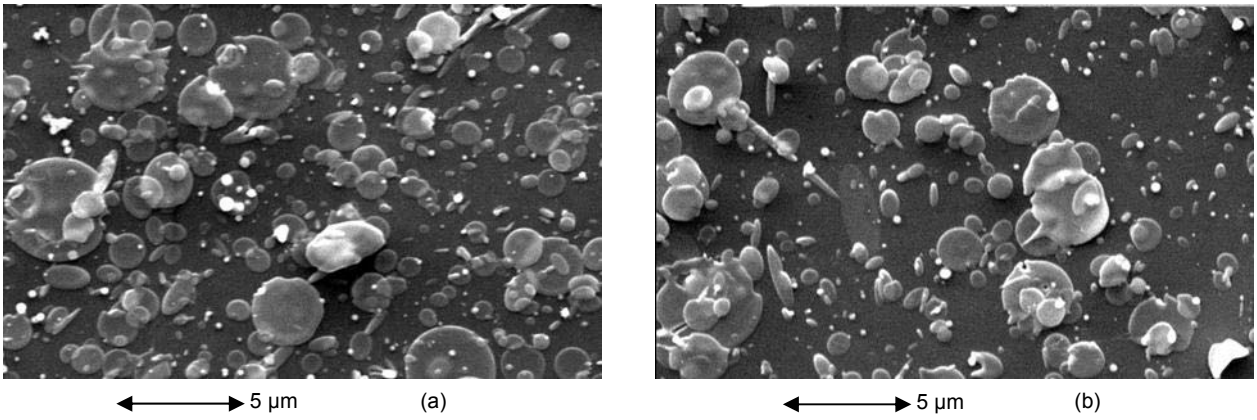

Figure 2: For a 6 mm internal diameter nozzle, an Ar-H_2 (45-15 slm) plasma gas, an arc current of 500 A, and with a suspension containing 1 vol% of YSZ, splats and spherical particles collected, at different distances, a) d1 close to nozzle exit, b) d2>d1.

The results obtained with YSZ particles are shown in Fig.2. For the distance d1 several layers of piled splats and few tiny spheroidized particles, already partially solidified are observed, but as the distance of collection increases, fewer particles are collected with more spherical tiny ones due to the jet expansion and the molten particles fast cooling due to their low thermal inertia.
The Al_2O_3 results are shown in Fig.3. The trend is obviously the same, except the fact that the alumina is more difficult to melt. Consequently at the d2 collection distance (d2=d1+10 mm), the particles are much less spread onto the substrate.

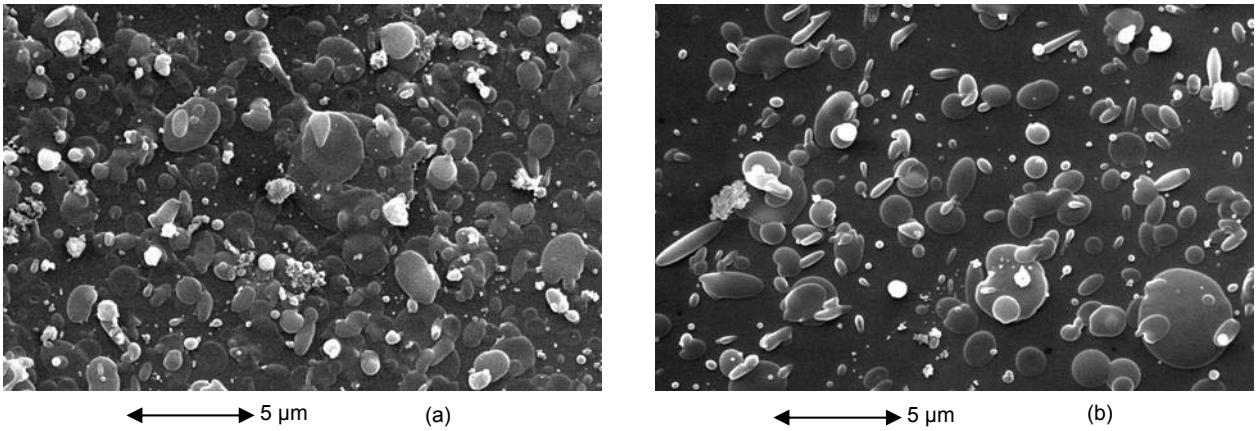

Figure 3: For a 6 mm internal diameter nozzle, an Ar-H_2 (45-15 slm) plasma gas, an arc current of 500 A, and a suspension containing 1 vol% of Al_2O_3, splats and spherical particles collected, at different distances, a) d1 close to nozzle exit, b) d2>d1.

The second parameter studied was the influence of the plasma gas composition at the d1 particle collection distance and a current intensity of 500A. The new plasma gas studied is a ternary mixture composed of Ar (24 slm), H_2 (9 slm) and He (30 slm) which represent 3/5 of an Ar/H2 (45/15) mixture mass flow rate (Table 1). The results obtained with YSZ particles (Fig.4.a) didn't show significant differences with those obtained with a binary gas mixture (see Fig.2.b). The collected particles are numerous, well molten and spread.

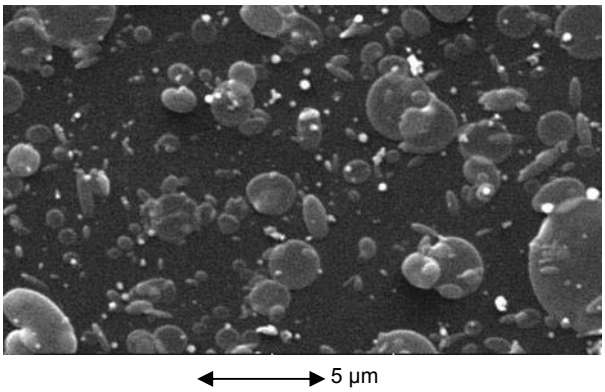

Figure 4: Splats and spherical particles collected for a 6 mm internal diameter nozzle, a d2 collection distance, an Ar/H_2/He (24/9/30 slm) plasma gas, an arc current of 500 A, and a suspension containing 1 vol% of YSZ.

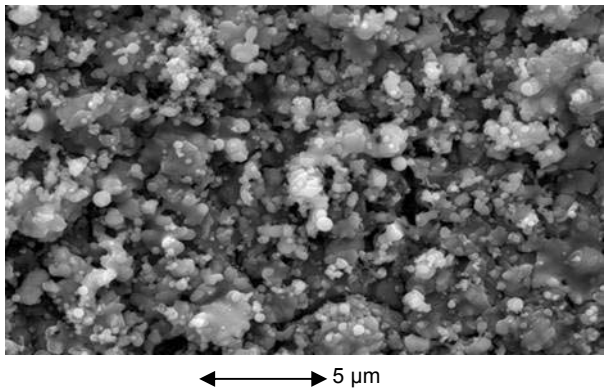

Figure 6: Coating corresponding to 2 overlapping beads at the same location, for a 6 mm internal diameter nozzle, a d2 collection distance, an Ar/H_2 (45/15 slm) plasma gas, an arc current of 500 A, and a suspension containing 1 vol% of YSZ.

Plasma gas composition	Current intensity (A)	Arc voltage (V)	Specific Enthalpy (MJ/kg)
Ar/H_2 (45/15 slm)	500	60.5	13.96
Ar/H_2/He (24/9/30 slm)	500	58.2	23.7

Table 1: Experimental plasma characteristics for a 6 mm nozzle internal diameter for two plasma gas mixtures.

Lastly, the particle collection of a YSZ and Al_2O_3 mixed suspension was studied, at a current intensity of 500A with an Ar/H2 (45/15 slm) mixture and a 6 mm nozzle internal diameter (Fig.5). As it can be seen, the molten particles of YSZ and Al2O3 are not miscible and layer very well.

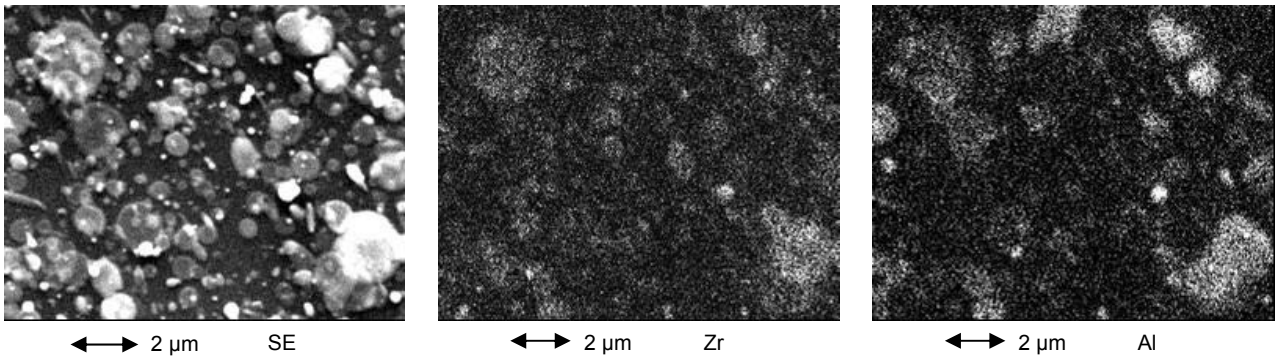

Figure 5: Particles collected at d1 particle collection, for a 6 mm internal diameter nozzle, an Ar-H_2 (45-15 slm) plasma gas, an arc current of 500 A, and a suspension containing a mix (50 vol%/50 vol%) of YSZ and Al_2O_3 (1 vol%).

4. Influence of the operating parameters on coatings

The set-up used to achieve beads layering is far to be optimal because spraying is performed relatively close to the torch nozzle exit (stand-off distance 2 or 3 times shorter than in classical spraying). Thus, even when using the stand-off distance d2, and especially when spraying refractory materials such as zirconia or yttria, it results in a very fast heating of successive passes and substrate, with important temperature gradients (up to 2000 K/mm). Besides, such high temperature gradients generate stresses within coatings, especially at the coating substrate interface, stresses which are relaxed by cracking. This cracking relaxation is more catastrophic in our conditions due to the smooth substrates. In classical plasma spraying, as soon as the zirconia coating temperature increases micronic particles travelling in the periphery of the plasma jet stick to the pass surface and create defects. This is what is observed in Fig.6, representing two successive passages of the torch on a not preheated substrate. In all cases and whatever are the experimental conditions chosen (gas mixtures, suspension composition, collection distances), the same trend is observed. A first layer composed of well spread and layered splats with a few tiny rounded particles at the top covered by a second layer at the top of which spheroidized tiny particles are numerous. This is due to the substrate travelling in front of the plasma flow (Fig.7). During the first pass, only the molten particles travelling in the plasma jet flow centre adhere onto the not preheated substrate, only a few of the finest particles partially solidified, from the periphery of the plasma jet sticking to it, because of the low substrate temperature. During the second pass, the first layer is hot enough for the spheroidized particles to stick on it (Fig.6). The overlapping of molten and unmolten particles is partially responsible of porosity. Consequently the surface temperature is a crucial parameter for the realization of dense coatings. When before the two successive passages of the plasma torch the substrate is preheated, by ten successive passages of the torch without suspension injection, spheroidized particle stick on even during the first pass and more tiny particles (< 1 µm) cover the layered splats. The contact of the first layer with the substrate is worst and it is leads to a detachment of the coating (Fig.8.a).

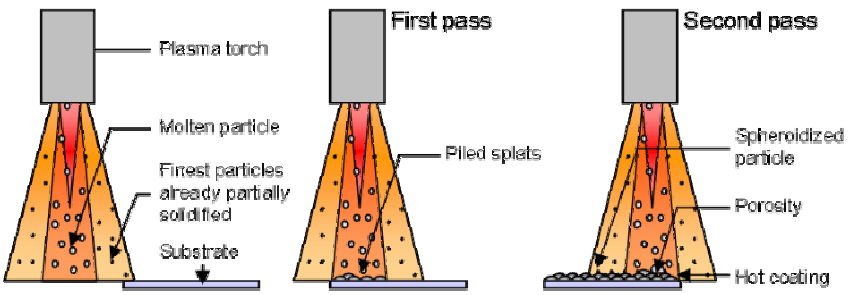

Figure 7: Mechanism proposed for the coating growth.

Some parameters were studied in order to understand the mechanism of the coating growth and confirm the results obtained for individual splats, such as the preheating of the substrate and the plasma gas composition. Experiments were performed at a current intensity of 500A, with a 6 mm nozzle internal diameter at the d2

collection distance and an YSZ suspension (Fig.8 and Fig.9). The coatings on stainless steel 316L substrates were elaborated by 200 successive passages of the substrate holder.

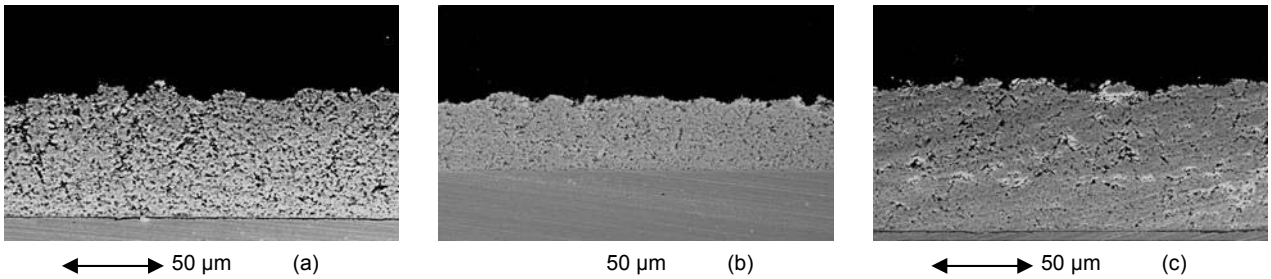

Figure 8: YSZ coatings for a 6 mm internal diameter nozzle, an arc current of 500 A, a) with an Ar-H_2 (45-15 slm) plasma gas with a 10 successive passages preheating, b) with an Ar-H_2 (45-15 slm) plasma gas and without preheating, c) with an Ar-H_2-He (24-9-30 slm) plasma gas and without preheating.

For a binary plasma gas composition and without preheating (Fig.8.b and Fig.9.b), relatively dense YSZ coatings can be achieved, with a thickness of 40 µm. Nevertheless when the substrate surface is preheated (Fig.8.a and Fig.9.a), the porosity and the thickness of the coating are more important, and some adhesion defects can be observed at the interface. It seems that porosities correspond to locations where more tiny spherical particles can be observed (see Fig.9.a).

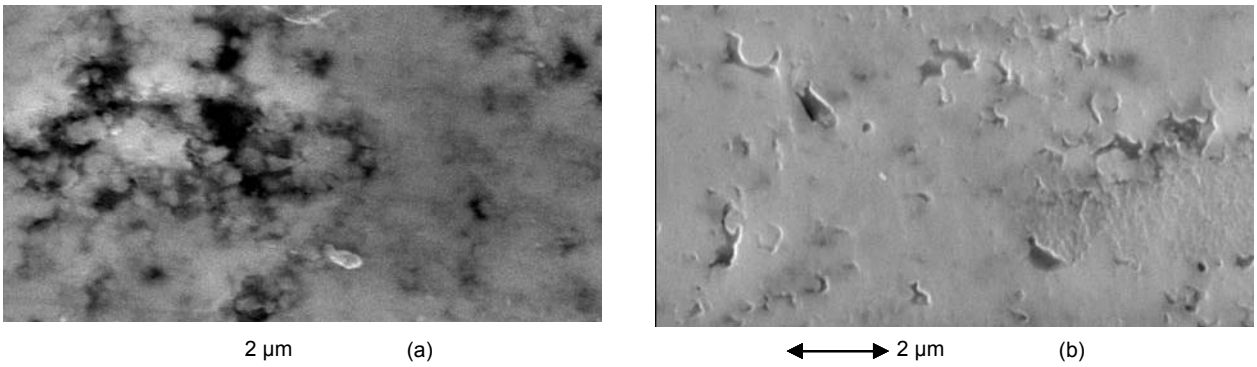

Figure 9: YSZ coating for a 6 mm internal diameter nozzle, an arc current of 500 A, a) with an Ar-H_2 (45-15 slm) plasma gas and without preheating, b) with an Ar-H_2 (45-15 slm) plasma gas with preheating by 10 successive passages of the torch with no particles.

The use of the ternary plasma gas composition with no preheating also leads to a relatively dense coating. Moreover the thickness is twice that achieved with the binary plasma gas mixture. This can be explained both by less air engulfment within the plasma jet for a ternary plasma gas composition, reducing its cooling and its higher enthalpy promoting particles melting. This results in higher coating deposition efficiency.
In the same conditions which permit the production of relatively dense YSZ coating, that is to say with a binary plasma gas composition, a current intensity of 500A and a collection distance of d2, the Al_2O_3 coatings achieved is very porous as shown in Fig.10 which exhibits one of the part of the coating that keeps the entire structure all over its height. The other parts of the coating correspond only to the base of the structure that still stick to the substrate.

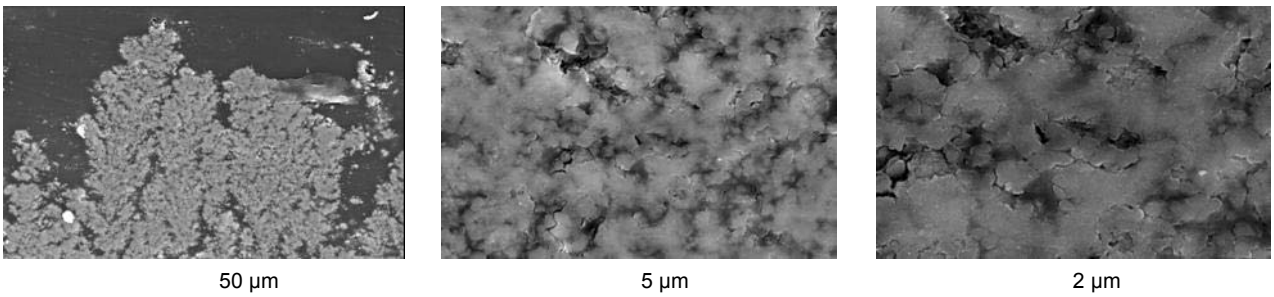

Figure 10: Al_2O_3 coating for a 6 mm internal diameter nozzle, an arc current of 500 A, with an Ar-H_2 (45-15 slm) plasma gas and a collection distance of d2. Pictures taken with different enlargements.

In the case of an alumina-YSZ mixed injection (Fig.11), the same spraying distance d2 could not be used for the coating production, the stresses at the coating-substrate interface being not accommodated. As a consequence the coating was sprayed at a farther distance d3. As for the alumina coating, the observed structure is porous but conserved all along the entire coating (despite that this longer stand-off distance should have enhanced the weakening phenomena of the coating due to the particle cooling, especially the alumina ones). At this distance the YSZ particles are still molten whereas the alumina ones are already in a plastic state. YSZ cements the alumina particles in a porous structure. This result seems interesting for the production of porous structures.

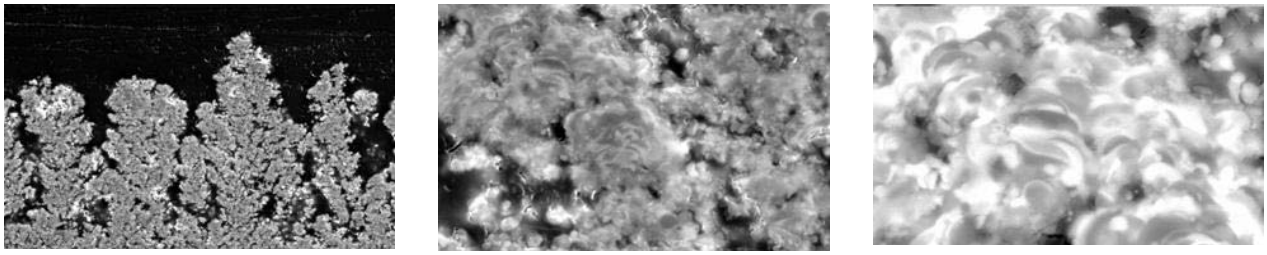

Figure 11: YSZ-Al_2O_3 mixed coating for a 6 mm internal diameter nozzle, an arc current of 500 A, with a Ar-H_2 (45-15 slm) plasma gas and a collection distance of d3. Pictures taken with different enlargements.

5. Conclusions

The injection of ceramic suspensions in a d.c. plasma jet is promissing for the realisation of dense or porous thin coatings. The process is quickly adaptable at low costs to all industrial d.c. plasma spray equipments. Yet the first results proved that it can be used to elaborate thin layers (with a thickness from 5 to 100 µm), with a high deposition rate (15 µm.m^2/h). These layers are made by layering splats having a size one to two orders of magnitude smaller than that obtained in classical d.c. plasma spraying. The next step of this study, is to control the surface temperature and reduce the fine almost solidified particles sticking between successive layers.

References

[1] S.P. Lu, J. Heberlein, E. Pfender, "Process study of thermal plasma chemical vapor deposition of diamond, Part I: substrate material, temperature and methane concentration" Plasma Chem. & Plasma Proc., 12 (1992) 35-53.

[2] E. Bouyer, M. Müller, N. Dignart, F. Gitzhofer, M. Boulos, "Suspension plasma spraying for powder preparation", Progress in Plasma Processing of Materials, (1997) 751-759.

[3] M.L. Lau, H. Jiang, W. Nüchter, E.J. Lavernia, "Thermal spraying of nanocrystalline Ni coatings", Phys. Stat. Sol., A166 (1998) 257-268.

[4] J. Karthikeyan, C.C. Berndt, J. Tikkanen, S. Reddy, H. Herman, "Plasma spray synthesis of nanomaterial powders and deposits", Mater. Sci. Eng., A238 (1997) 275-286.

[5] Y. Takamura, K. Hayasaki, K. Terashima, T. Yoshida, "The role of radicals and clusters in thermal plasma flash evaporation process", Plasma Chem. & Plasma Proc., 16 (1996) 141S-156S.

[6] N. Rao, B. Micheel, D. Hansen, J. Heberlein, P. Mc Murry, S. Girshik, "Synthesis of nano-phase silicon, carbon and silicon carbide powders using a plasma expansion process", J. Materials Res, 10 (8) (1997) 2073-2084.

[7] J. Fazilleau, C. Delbos, J.F. Coudert, P. Fauchais, L. Bianchi, "Study of the injection of a zirconia suspension in a D.C. plasma jet" in progress in Plasma Processing of Materials, (eds.) P. Fauchais and J. Amouroux, (pub.) Begell House N.Y., USA, to be published in (2003).

[8] K. Wittmann, J. Fazilleau, J-F. Coudert, P. Fauchais, F. Blein, "A new process to deposit thin coatings by injecting nanoparticles suspensions in a d.c. plasma jet", Proc. of ITSC 2002, (ed.) E. Lugsheider, (pub.) DVS, Düsseldorf, Germany, (2002) 519-522.

Design of a DBD wire-cylinder reactor for NO_x emission control – Experimental and simulation approach

A. Vincent, M. Moscosa-Santillan, J. Amouroux

Laboratoire de Génie des Procédés Plasma et Traitement de Surface, Université Pierre et Marie Curie, Paris, France

Abstract

A DBD wire-cylinder reactor was designed for NO_x removal from a exhaust gas mixture. The NO conversion has been investigated as a function of main parameters like HV electrode material, catalytic layer on the dielectric surface, initial NO concentration and gap reactor. Isotopic labelling analysis revealed that atomic oxygen produced is the main responsible of the mixture reactivity. Hence, a CSTR-in-series model with multiple injections of atomic oxygen has been proposed in order to explain relationship between reactor parameters and results. Optimisation of model parameters has permitted to fit experimental and simulation with an maximum absolute error of 5 %.

1. Introduction

The removal, based on electrical discharge in non-thermal plasma reactor, of nitrogen oxides from exhaust gases has been the object of several previous works[1,2,3]. The restrictive regulations in order to reduce pollution from motor vehicles exhaust gases permit the development of new processes for NO_x reduction. Some of these are : dielectric barrier discharge (DBD), corona discharge and in a recent study, a photo-trigged reactor has been used with this propose. In a previous work, a first study on DBD systems has been accomplished[4], this study concerned the electrical characterisation of a DBD wire-cylinder reactor as well as the influence of operating parameters and by-products analysis (essentially aldehydes and R-NO_x). For this study, the reactor was used to remove the NO contained in an O_2(10%), CO_2((10%), H_2O(5.4%), C_3H_6(1000 ppm), NO(max. 1000 ppm) and N_2(balance) gas mixture. Characterization and quantification of by-products was realized by Gas Chromatography coupled with Mass Spectrometry (GC-MS). Isotopic oxygen introduced in the inlet flow helped to elucidate the reaction mechanisms conducting to the formation of by-products. Analysis revealed that atomic oxygen produced by electronic impact over O_2, CO and CO_2 molecules is the main responsible of the mixture reactivity. So, a complete mechanism of involved reactions was proposed from O^{18} isotope experiments. Moreover, for each experiment, the electrical characterization of the discharge was carried out using a numerical oscilloscope. This way, measurement of voltage, current intensity, electrical power and electrical charge of the plasma pulses were determined. A correlation was proposed between discharge electrical power and atomic oxygen formed.

In this framework, the aim of this article is to develop a mathematical model in order to understand the relationship between operation parameters (inlet flow rate, inlet composition, electrical energy density, electrical gap) and reactor results (NO_x conversion, stability time, reactor performance). In the first part the experimental set-up is described. Then, reactor characteristics and behaviour are presented in two parts : hydrodynamics of reactor and reaction pathway retained. This basis permits to chose a mathematical model consisting in a cascade of continuous stirred tank reactor (CSTR) with multiple injections of atomic oxygen. Since atomic oxygen injection is intermittent, the mathematical model is intrinsically dynamic. Optimisation of model parameters has permitted to fit experimental and simulation with a maximum absolute error of 5 %. So, the simplified model showed a good agreement with the experimental results. Finally, the robustness of mathematical model was tested introducing some parameter variations (gas flow inlet and electrical gap) and confronting each time model and experimental results.

2. Experimental set-up

The reactor is a cylindrical dielectric tube, a alumino-silicate tube of 15mm and 21mm of internal and external diameters respectively. The high voltage electrode is a 6 or 8 mm diameter copper screw (gap=2.5 or 1.5mm) and the grounded electrode is a sheet of copper. Energy is supplied by a “Calvatron SG2” high voltage 44kHz AC supply. So, applied voltage is comprised between 9 and 15kV peak to peak. Figures 1 and

2 represent the experimental set-up. Instrumentation of the reactor comprises four inlet electronic flowmeters, a GC-MS device (Gas Chromatography–Mass Spectrometry) for outlet gas mixture analysis, a Quintox infrared gas analysers for measuring NO, NO_2, CO, CO_2, O_2, SO_2 concentrations and finally a numerical oscilloscope in order to characterise electrical discharge.

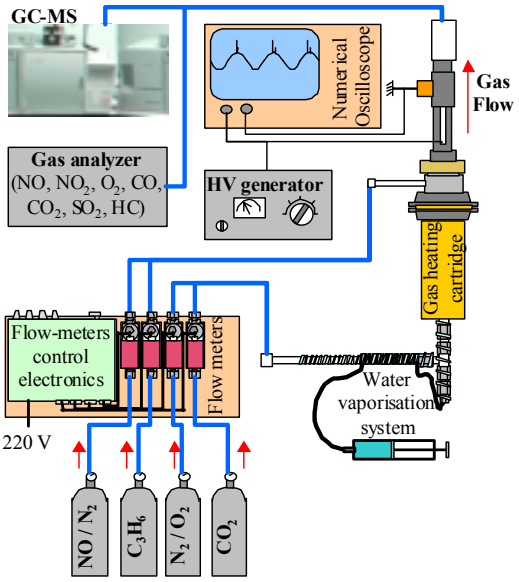

Fig. 1 Experimental set-up of the wire-cylinder reactor, gas feeding system and analysis apparatus.

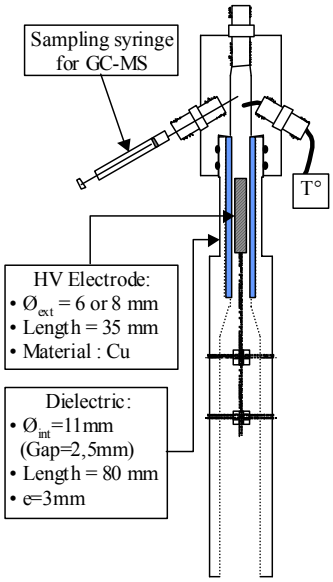

Fig. 2 Detailed schema of the wire-cylinder reactor.

The reactor is fed with a gas mixture at atmospheric pressure. Each gas (except water steam) is introduced in the reactor using electronic mass flow-meter. Inlet gas mixture containing O_2(10%), CO_2(10%) and N_2(balance) are introduced in a heating cartridge while NO (250 to 1000 ppmv) and C3H6(1000 or 2000 ppmv) are introduced after this stage. A motorized syringe pusher introduces H_2O (5,4%) in a heated 1/8" diameter and 2 meters long stainless steel tube. Vaporized water is then mixed with pre-heated gas mixture. The total gas flow is about 12.9 NL.min-1. Gas mixture temperature is measured by a thermocouple at 3cm after the discharge zone.

3. Simulation an modelling of reactor

Hydrodynamics of reactor is presented in order to justify application of a stirred pattern model. Then, we suggest the use of a simple reaction pathway to describe the transformation of main chemical components. Since mathematical model describes complex relationship (electrical, magnetic, chemical and diffusional characteristics), model constants are not only kinetic and they represent the degree of freedom of the model. So, their optimisation permits to fit model and experimental results. The basis of model design are explained at once, an analogy is made between electrical characteristics and model parameters in order to transform actual operating conditions in simple model inlets. Finally, results of simulation and comparison to experimental results are presented as a function of NO concentration, inlet flow rate and electrical gap.

3.1 Hydrodynamic behaviour of DBD reactor

The cylindrical geometry of the reactor and flow pattern suggest the use of a plug flow reactor (PFR) model. However, taking into account dimensions of the HV electrode and by extrapolation of hydrodynamic results obtained in a squared section reactor for a cylindrical configuration[5]. It can be proposed the hydrodynamic behaviour showed in figure 3. Spontaneous stirring observed is explained by the presence of electrical wind caused by discharge, which is responsible of great mobility of reaction species. The electrical wind produce an important retro-mixing in the reactor.

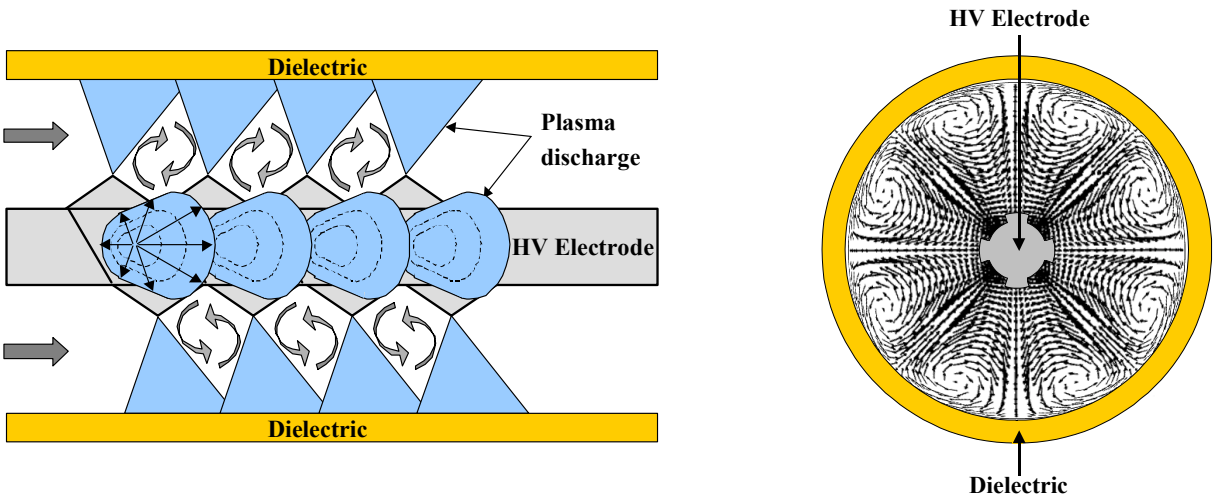

Fig. 3 Longitudinal **[a]** and radial **[b]** reactor sections presenting recycling zones and a stirred behaviour of the wire-cylinder reactor.

Hydrodynamic phenomena of convection and shearing endured by the gas mixture when it crosses longitudinally the reactor, justify the model choice for the reactor description as a cascade of continuous stirred tank reactor (n-CSTR). Figure 4 schematises correspondence between the wire-cylinder reactor and the system of serial CSTR cascade considered in simulation.

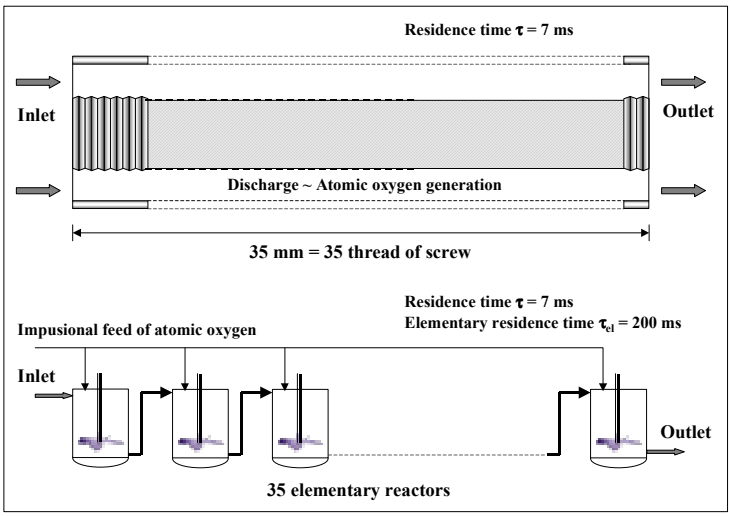

Fig. 4 Equivalence between DBD reactor and the serial CSTR system

3.2 Reaction pathway and design considerations

In order to simulate effects of electrical discharge on the reactor operation, some hypotheses were used based on experimental observations. First, it was considered that the atomic oxygen created by discharge is the main responsible of the mixture reactivity. Second, the electron impulsion flow creates an impulsion flow of atomic oxygen. Finally, a simplified reaction pathway, consisting in three reactions and shown below, was used to provide a global comprehension of the reactor behaviour.

$NO + O \rightarrow NO_2$	$r_1 = k_1 P_{NO} P_O$	Oxidation
$2O \rightarrow O_2$	$r_2 = k_2 P_O^2$	Destruction
$NO_2 + O \rightarrow NO + O_2$	$r_3 = k_3 P_{NO2} P_O$	Reduction

As it was explained before k_i are not kinetic constants but model constants taking into account different phenomena. So, these parameters must to be calculated and optimised. From these hypotheses, the electrical discharge represents a direct variation of the concentration of atomic oxygen in each elementary reactor. To characterize electrical discharge, the electric impulse duration is determined analysing electrical signal in a numeric oscilloscope and the impulse period is calculated directly from the frequency. Due to the short duration of the electric impulse (10 ns) with regard to the period (22 ms), we can consider the impulse as instantaneous. In consequence, the impulse can be translated like an instantaneous injection of atomic oxygen to each elementary reactor. Subsequently, the oxygen injection extent is calculated directly from the energy density.

Once reactor model is proposed, the reactions that govern system behaviour must be settled down. For a multi-component feed for a perfectly mixed tank, the mass balance for component *j* would be as shown in equation 1.

$$\frac{d(C_{jo}^{k}V^{k})}{dt} = F_{i}^{k}C_{ji}^{k} - F_{o}^{k}C_{jo}^{k} + r_{j}^{k}V^{k} \qquad (1)$$

where F^k is volume flow (inlet or outlet) of *j* component, $C_{ji}^{\ k}$ is the concentration of *j* species in the inlet stream of k^{th} reactor, $C_{jo}^{\ k}$ is the concentration of *j* species in the outlet stream of k^{th} reactor, V^k is the elementary reactor volume and r_j^k is the reaction of rate of the generation of component *j*.

Inlet conditions in k^{th} reactor are obtained directly from outlet conditions from previous reactor. Nevertheless, in the case of atomic oxygen, the inlet term is a time function expressed as,

$$C_{Oi}^{k} = C_{Oo}^{k-1} + C_{Oimp}^{k}(t) \qquad (2)$$

where $C_{Oimp}^{\ k}(t)$ term traduces atomic oxygen injection. So, this term is a discrete function expressed by equation 3 and $C_{Oo}^{\ k-1}$ is atomic oxygen flow from $k\text{-}1^{th}$ reactor

$$C_{Oo}^{k}(t)\begin{cases} = \Delta C_{Oinj}^{k} & t = mT_{inj} \\ = 0 & t \neq mT_{inj} \end{cases} \qquad (3)$$

For a system with *n* components, there are *n* component balances. The total mass balance and component balances are not independent. Generally, the mass balance and *n-1* component balances are used. However, in our case, the total mass balance equation is not used in reason of low concentration of reaction species (max. 1000 ppm). So, it was applied a mass balance for each component only for the minority species. The result is a system of n-ordinary differential equations.

The well-known 4th order Runge-Kutta method was used to determine the evolution of concentrations as a function of time along the reactor. Table 1 summarizes experimental parameters used in simulation. With the aim of adjust experimental data and modelling results, optimisation of parameters was carried out using model constants.

Table 1. Experimental DBD reactor conditions used in modelling and simulation

Inlet flow	20 $L.min^{-1}$	Gap	1.5 mm
Gas speed	5.4 $m.s^{-1}$	Reactor length	35 mm
Residence time	6.5 ms	Electrical period	22 µs
NO concentration	250 – 1000 ppm_V	O concentration	Pulsed injection
O_2 concentration	10 $\%_V$	N_2 concentration	Balance

3.3 Simulation results

Each reactor simulation implies solution of the 35X3 system of ordinary differential equations as a function of time. That means a discrete integration in the reactor length and a continuous integration in the time. Moreover, initial conditions (t=0) are fixed as: reactor concentrations for all components are equal to inlet concentration. So, a time of integration large enough must be applied in order to find the pseudo-steady state

mode in outlet (fig. 5), typical values of final time for integration are 8 seconds. The final cyclic pseudo-steady state point in figure 5 represents only one experimental data.

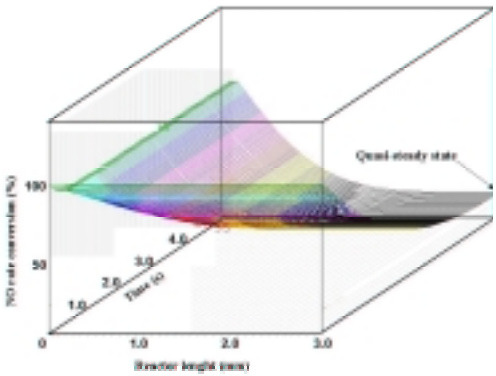

Fig. 5 NO conversion vs. reactor length and time for $C_{NOinitial}$=250ppmv and 40 J.L-1.

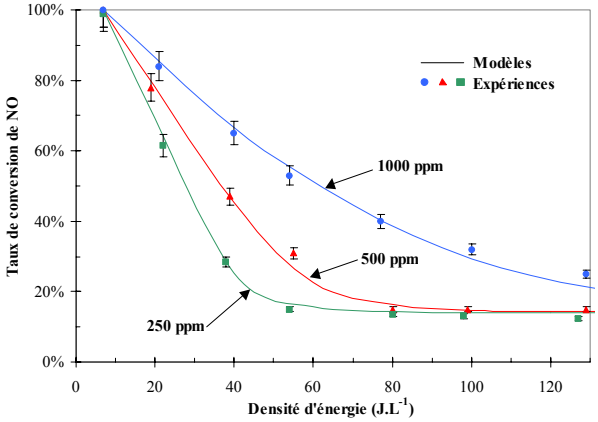

Fig. 6 NO conversion vs. electrical energy density for different NO initial concentrations.

Hence, parameter optimisation on k_i values has been made in order to adjust experimental results of NO conversion as a function of electrical energy density. This has been made for an initial NO concentration of 250ppmv. The k_i values describe some internal process but they are supposed to be independent of NO concentration or inlet flow. Then, robustness of k_i values were tested for different NO concentration (250 to 1000ppmv) and for different inlet flows (6.5 and 12.9 NL.min-1). Simulation and experimental data are compared in the case of three concentrations (fig. 6) and two inlet flows (fig. 7). In the case of electrical gap a simple theoretical correction in the correlation between oxygen impulse intensity and electrical energy density is needed. Actually, this correlation is a straight line and the electrical gap is directly proportional to the slope. The results of this last simulation are shown in figure 8. In general, a good agreement between simulation and experimental is verified, so the CSTR cascade model describes in a pertinent way the DBD wire-cylinder reactor.

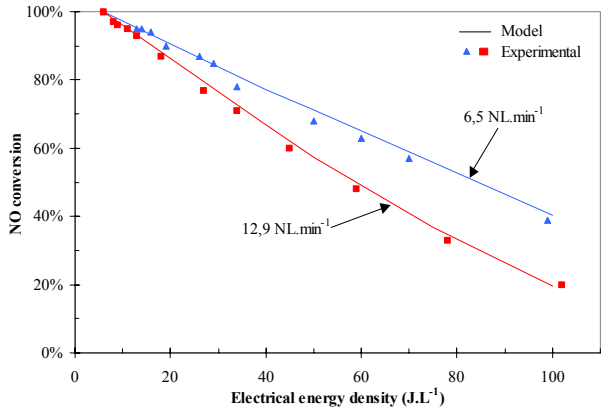

Fig. 7 NO conversion vs. electrical energy density for different inlet flow.

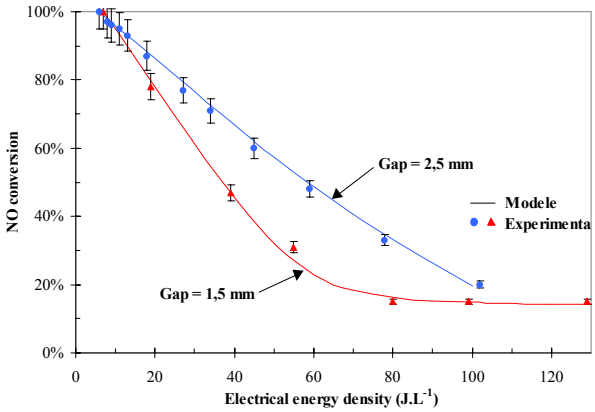

Fig. 8 NO conversion vs. electrical energy density for different electrical gap.

4. Conclusion

In this work, the behaviour of a wire-cylinder DBD reactor was simulated. The validation of mathematical model permits to understand the role of reactor characteristics and operative electrical parameters on the formation of the atomic oxygen. This one been the main responsible of chemical mixture reactivity.

Impulse characteristic of electrical discharge and effects the electrical wind on the reactor streamline suggested a dynamic macroscopic model based on a cascade of 35 elementary stirred reactors. A discrete atomic oxygen flow is introduced in every elementary reactor to represent the formation of active species by the electrical discharge.

The model has been tested on a kinetic pathway representing the processes of formation and destruction and of the atomic oxygen and the oxidation of the NO molecule. The knowledge of reaction pathway, acquired

by O^{18} isotopic analysis, permitted us to propose a simplified model of three reactions. The physico-chemical characteristics of reactions in non-thermal plasma (transport phenomena, excitation levels, thermal gradients…) have been taken implicitly into account in the model by the use of apparent model constants (k_i). However, the role of water was not introduced and that forbidden the approach of mass balances to nitrous and nitric acids.

In order to simulate the DBD wire-cylinder reactor, Mathematical model considers physical (elementary reactor volume, inlet stream composition, inlet flow…) and electrical characteristics (injected atomic oxygen flow in every elementary reactor according to the electrical density of energy, the electrical gap, the electrical duty…). Model results are in good agreement with experimental ones. Actually, maximum absolute error can be estimated to 5% and for almost 95% of experimental data, model error is lower than experimental standard deviation. Some interesting results can be obtained from these simulations, like delay to the establishment of a pseudo-steady state (10 ms), length of the reactor performance (maximum NO_x conversion) and evolution of concentration of main species (NO, NO_2 and O°). This model permits has understanding of complex phenomena present in tea reactor and open interesting ways in design and extrapolation of DBD reactors applied to pollution solutions.

References

[1] M. Baeva, A Pott and J. Ulhenbusch, Plasma Sources Scie. Technol. **11** (2002) 135-141.
[2] B. Eliasson and U. Kogelshatz, IEEE Trans. Plasma Sci **19** (1991) 309-323.
[3] A.A. Fridman, A. Petrousov, J. Chapelle, J. Phys. III France **4** (1994) 1449-1465.
[4] A.Vincent, F. Daou, E. Francke, S. Cavadias, J. Amouroux, ISPC-15 Orléans France (1995).
[5] J.Q. Feng, *Journal of Applied Physics* **86**(5) (1999) 2412-2418.

Selective deposition of fluorocarbon films on Al versus SiO_2 surfaces in high density plasmas

A. Tserepi, P. Bayiati, E. Gogolides, K. Misiakos

Institute of Microelectronics-NCSR "Demokritos", POB 60228, 153 10 Aghia Paraskevi, Attiki, Greece

Abstract

Plasma-deposited fluorocarbon coatings have found a variety of applications, as they modify the surface properties of the materials on which they are deposited. The present work focuses on the selective deposition of fluorocarbon (FC) films on metal surfaces, and more specifically on aluminum, versus SiO_2 surfaces, in order to obtain surfaces of distinctly different wettability. The process selectivity was optimized through proper selection of the deposition conditions, mainly gas mixture composition and deposition time, and was quantified by means of contact angle measurements on Al and SiO_2 surfaces.

1. Introduction

Plasma-induced formation and deposition of polymer films on surfaces is an important issue in etching plasmas; for example, it allows selective etching of a SiO_2 layer over a Si or Si_3N_4 underlayer, while it provides side wall passivation necessary for anisotropic high-aspect ratio Si etching. In fact, the majority of the current research effort relative to fluorocarbon etching plasmas invests in understanding plasma-surface interactions in order to improve etching performance mainly for selective SiO_2 over Si etching or for high aspect-ratio Si etching [1-3]. In both of the aforementioned processes, deposition of FC layers of appropriate thickness and chemical composition is of vital importance to the etch selectivity. In particular, a general trend is observed, that is the thickness of the FC film present on a surface is inversely proportional to the etch rate of the substrate material [2-5]. This has been demonstrated and used for explaining the SiO_2-to-Si and SiO_2-to-Si_3N_4 selective etching. However, analogous studies concerning selective deposition on other materials such as metals and consequent modification of their surface properties are rare in the literature.

The present work focuses on the selective deposition of fluorocarbon (FC) films on metal surfaces, specifically on aluminum, over SiO_2 surfaces, in order to obtain surfaces of distinctly different wettability. Since polymer layers on surfaces are easily formed in fluorocarbon discharges with high concentrations of radical CF_x species, fluorocarbon gases such as C_4F_8 and mixtures of CHF_3/CH_4 were used in our experiments, in high density plasmas known for their overwhelming polymerization ability. For the selection of conditions appropriate for selective deposition of FC films on Al over SiO_2, plasma parameters such as plasma power, bias voltage, electrode temperature, gas pressure and composition were varied, while etch rates of SiO_2 were measured in-situ by laser interferometry. We find that conditions which provide highly selective etching of SiO_2 over resist materials are also appropriate for selective deposition of FC films on Al surfaces. The modified wettability of SiO_2 and Al surfaces exposed to FC plasmas is characterized by contact angle measurements, which are used to demonstrate the selectivity of the deposition process. If, finally, the obtained wettability of the plasma-modified metal surface can be electrostatically switched from a hydrophobic to a hydrophilic state, such FC films preferentially deposited on metal (Al) surfaces can be employed for fluid transport in microfluidic devices (with Al pads patterned along a channel built on a SiO_2 substrate) [6].

2. Experimental

The high-density plasma reactor used in this work is an Alcatel (MET, Micromachining Etch Tool) Inductively Coupled Plasma etcher, consisted of a load-lock and an ultra-high vacuum (10^{-6} mbar) main chamber. A one-loop ring-shaped antenna is supplied by a 0-2000 W rf (13.56 MHz) source, and it generates the plasma through a 150-mm in diameter cylindrical alumina dome. The plasma diffuses from the

generation area in the process chamber, where samples are introduced for processing, loaded on an anodized aluminum holder (100 mm in diameter) mechanically clamped on a chuck. The chuck is located at a distance of 20 cm downstream from the ICP source and allows the sample to be biased and cooled during processing. The sample can be biased independently from the plasma source with a 300 W maximum rf (13.56 MHz) source. Biasing the processing electrode enables to control the ion energy independently from the production of the plasma. A helium pressure of 12 mbar is applied on the backside of the sample holder to provide good thermal conduction between the sample and the chuck. The temperature of the chuck is controlled by circulation of liquid nitrogen and simultaneous heat supply through six heaters, in order to achieve temperature regulation at a desired set point. Good thermal contact between the sample holder and the sample is achieved by means of a thermal paste. The electrode temperature is fixed at values between 0 and –50 ºC in this study.

For this study, the fluorocarbon gases C_4F_8 and mixtures of CHF_3/CH_4 are used, while the substrates to be processed are SiO_2, Al, and AZ 5214 commercial photo-resist. During plasma processing with the above gases, deposition occurs on the reactor walls. Therefore, before each experiment, the processing chamber is thoroughly cleaned using a O_2 or O_2/SF_6 plasma to remove fluorocarbon films from surfaces previously exposed to polymerizing plasmas. After the cleaning, the reactor is reconditioned under the process conditions for 2 min. Plasma parameters, such as the gas pressure and composition, the electrode temperature, the process time, the rf plasma power and bias voltage, are varied. In some experiments, a pretreatment of the sample surfaces prior to deposition is also carried out using Ar and O_2 and its effect on the wetting properties of the surfaces before and after deposition is investigated. The etching or deposition rates on SiO_2, Al, and resist surfaces are measured in real-time by means of in-situ laser (650 nm) interferometry.

The wettability of the treated samples is characterized by contact angle measurements using a GBX Digidrop system. The system allows automatic loading of single droplets on the surfaces under investigation and measurements of *static* contact angles are performed through observation of the droplet (and its reflection) at nearly right angles with respect to the sample surface. For static contact angle measurements in this work, 4μl droplets of de-ionized water are placed on the treated surface. The same system allows also measurement of the contact angle in the *dynamic* mode, where a droplet of increasing or decreasing volume is loaded on the surface, during which process the advancing and receding contact angles as well as the contact angle hysterisis are measured. If a voltage difference is applied between the droplet (through the droplet-depositing syringe) and the substrate, the modification of the contact angles in the presence of an electric field (electrowetting) can be observed.

3. Results and Discussion

3.1. Etching and deposition in C_4F_8 plasmas

3.1.1 Effect of electrode temperature

Numerous investigations of the SiO_2 etching mechanism in high density etching tools have shown that the SiO_2 etching rate can be quite different depending on the bias voltage developed during the etching process [4, 5]. In specific, as the bias voltage increases, the fluorocarbon film deposition regime is followed by the fluorocarbon suppression regime and finally by the oxide sputtering regime, since deposition and etching have different dependencies on the energy of the ions bombarding the surface. In our work, we used the electrode temperature as the tuning parameter which could induce the transition from etching to deposition, as the temperature determines the rate of desorption of products from surfaces, and thus determines the balance between etching and deposition, when the other plasma parameters are fixed. We conducted experiments in C_4F_8 plasmas, at substrate temperatures from 0 down to -50^{o}C. These experiments demonstrated that, on all of the tested surfaces, etching is followed by deposition that occurs at a rate inversely proportional to temperature. The interferometric signals shown in Fig. 1 correspond to a constantly changing top layer thickness on a resist film, as a function of the electrode temperature. In detail, the sinusoidal signals corresponding at T=15 and –20 ºC indicate etching of the resist film up to an end-point, whereas the sinusoidal signal corresponding at T=-50ºC indicates a fluorocarbon film being continuously deposited on the resist surface. Etching and deposition rates determined from such interferograms are shown

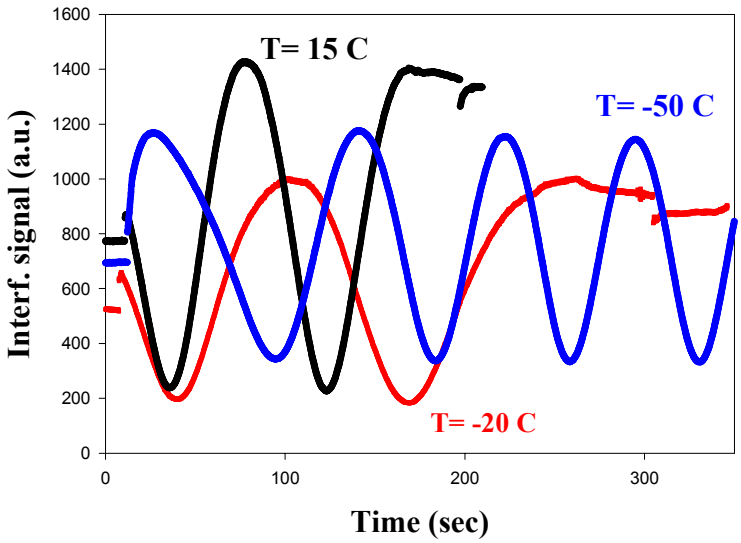

Fig. 1. Interferometric signals from a resist surface (AZ5214) exposed to a C_4F_8 high density plasma, at different electrode temperatures. Two of the signals (T=15 ºC and –20 ºC) indicate etching, while the signal at T=-50ºC indicates deposition of FC film.

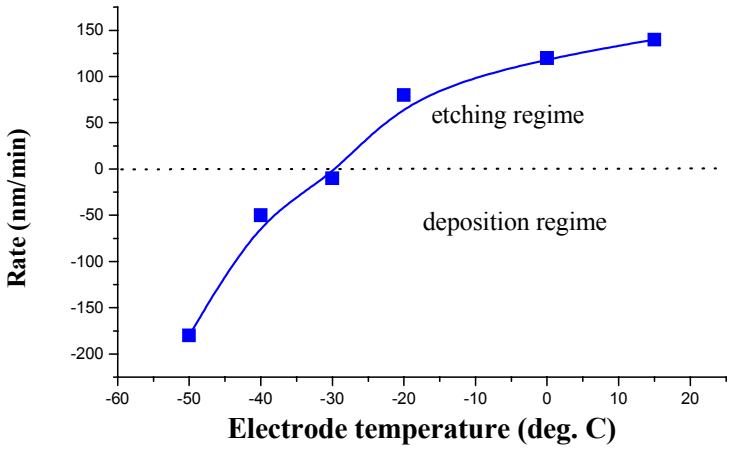

Fig. 2. Etching and deposition rates of a resist (AZ5214) surface exposed to a C_4F_8 high density plasma as a function of the electrode temperature.

in Fig. 2 for a resist material as a function of electrode temperature, indicating the transition from etching to deposition as the temperature decreases.

Similar experiments performed on a SiO_2 film indicated that etching of SiO_2 takes place at lower temperatures (e.g. at -40 °C) compared to that of a resist layer. This is attributed to the fact that a SiO_2 surface consumes more CF_x radicals than a resist surface, thus there are fewer species available for deposition on a SiO_2 surface. Therefore, etching dominates deposition in the case of a SiO_2 surface at temperatures at which deposition takes place on a resist surface. For aluminum surfaces, deposition rates of FC films can be estimated from similar interferograms, and are shown on Table I together with deposition rates on a resist surface. Deposition rates are found to increase as temperature decreases, as shown previously in Fig. 1, and are higher on aluminum than on resist surfaces (see Table I). The latter indicates that conditions that provide selective etching of SiO_2 to resist are also appropriate for FC deposition preferentially on aluminum compared to SiO_2. For example, exposure of surfaces to a C_4F_8 plasma at -40 °C leads to etching of a SiO_2 surface (E.R.= 230 nm/min), deposition on a resist surface (deposition rate= 50

nm/min), and even higher deposition on an Al surface (D.R. =130 nm/min). Therefore, this temperature is appropriate for selective deposition on Al versus SiO_2 surfaces. Furthermore, the selectivity of SiO_2/resist etching can be used as a guide to the selection of appropriate conditions for selective deposition on Al to SiO_2 surfaces. However, contact angle measurements on Al and SiO_2 surfaces exposed to such conditions (-40 C, 1500W, 10 mTorr, -250 V_{bias}) for 1 min or more showed a small difference (smaller than 10°) in the surface hydrophobicity. Therefore, a wider space of plasma conditions was searched for better results.

Table I. Deposition rates of FC films on Al and photo-resist surfaces in C_4F_8 plasmas

Deposition rate (nm/min)		Temperature (ºC)
Al metal	AZ 5214 resist	
90	10	-30
130	50	-40
200	180	-50

To achieve highly selective Al/SiO_2 deposition, various plasma conditions were investigated. The C_4F_8 pressure was varied in the range 1-5 mTorr, the rf power was varied from 1000 to 1800 Watt, the bias voltage from –100 Volts to -150 Volts, and the electrode temperature range from -20 ^oC to 15 ^oC. For the conditions investigated, the selectivity increased with the power, while it decreased with the temperature and the pressure. An experiment which was conducted under the best conditions (1 mTorr, 1800 W, -100V, -20 ^oC) gave a SiO_2/resist selectivity of 2.4. Aluminum and SiO_2 surfaces exposed to such plasma conditions during 1 min exhibited a drastic change of the wetting properties; the contact angle on a treated SiO_2 surface increased to 78º, while that of Al surface increased to 85º. Thus, Al exceeded SiO_2 in hydrophobicity, however at a low degree, presumably due to the fact that deposition of even a thin FC film on the SiO_2 surface is sufficient to cause significant modification of the wetting properties of the SiO_2 surface. The measured difference in contact angle between Al and SiO_2 modified in C_4F_8 plasmas was not big enough to allow exploitation of this difference for fluid control in microfluidic devices based on the electrowetting effect.

3.1.2 Effect of surface pretreatment in non-polymerizing plasmas

In an effort to enhance the selectivity in the Al/SiO_2 deposition, a second set of experiments was designed to elucidate the role of the surface condition prior to the FC deposition. The Al and SiO_2 surfaces were pretreated in O_2 and Ar plasmas for a short time (15 s). The effect of pretreatment on the final contact angles is shown in Fig. 3. For pretreatment with a high bias voltage applied to the electrode, the Al surface

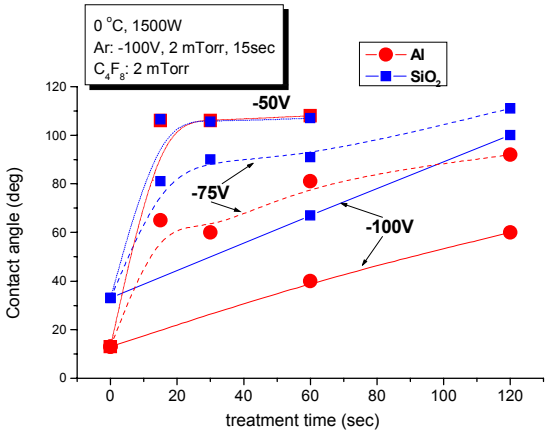

Fig.3a. Water contact angle as a function of treatment time in C_4F_8 after a pretreatment in Ar (15 s, bias voltage –100 V) for various values of the treatment bias voltage.

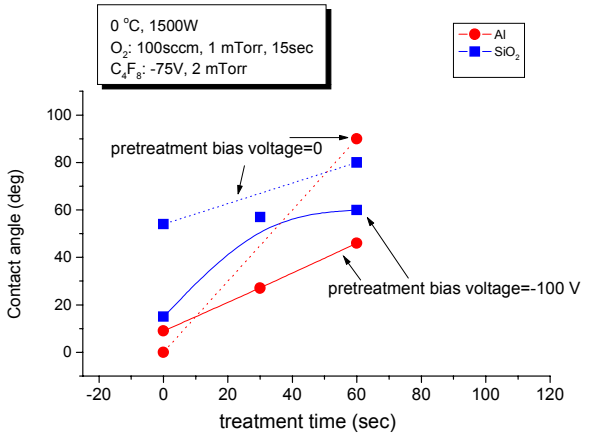

Fig.3b. Water contact angle as a function of treatment time in C_4F_8 after a pretreatment in O_2 (15 s) for different values of the pretreatment bias voltage

remains always more hydrophilic than the SiO_2 surface for treatment times as long as 60 s, in contrast to the previously presented results in the absence of surface pretreatment. Only in the case that the pretreatment is carried out at zero bias voltage, the Al surface becomes more hydrophobic (10º difference in contact angle) after a 60 s treatment in C_4F_8 plasmas (Fig. 3b).

The observed behavior can be explained by the fact that application of a high bias voltage in the pretreatment contributes to the reduction of the oxidized layer on Al. As a result, a clean Al surface characterized by a high sputtering yield is obtained, and thus during subsequent exposure in polymerizing plasmas, sputtering dominates deposition on this surface. Consequently, a surface less hydrophobic than that without the pretreatment is obtained. On the contrary, for the pretreatment without bias, the Al surface retains its surface oxide, a fact that allows after C_4F_8 treatment (60 s) a final surface more hydrophobic than a SiO_2 surface exposed to the same treatment. Certainly, the surface wetting properties should be evaluated for different treatment times, in order to achieve enhanced selectivity.

3.2. CHF_3/CH_4 etching and deposition experiments

In these series of experiments, we used mixtures of CHF_3/CH_4 in various proportions of the two gases. All the measurements of etch rates and selectivity were carried out at a total pressure of 3 mTorr, plasma rf power 1500 W, bias voltage –150 V and at low temperatures (0 and –20 °C). As shown in Figure 4, the selectivity increases as the mixture becomes richer in CH_4, and it reaches a value of about 5 and 7 at 0 °C and –20 °C, respectively. When the content of CH_4 in the gas mixture is higher than 21%, selective deposition of a fluorocarbon film is observed on the resist (AZ5214), whereas the silicon oxide is still etched. We argue that around this CH_4 percentage FC films would be deposited preferentially on Al to SiO_2 surfaces.

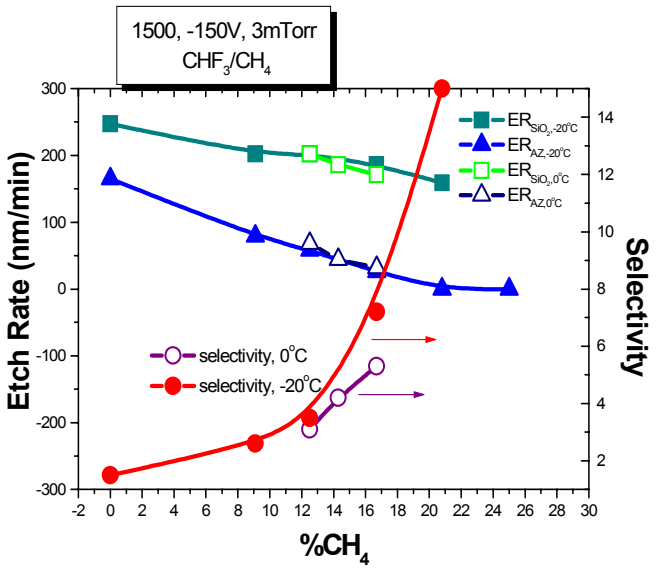

Fig. 4. SiO_2 and resist etch rates and the selectivity as a function of the CH_4 percentage in a CHF_3/CH_4 high density plasma.

Surfaces of silicon dioxide and aluminum were exposed to a plasma containing 79% CHF_3 and 21%CH_4, under the conditions that gave the best selectivity (Pressure=3 mTorr, P=1500 W, V_{bias}=-150 V, T=-20 °C). The plasma exposure time was varied between a few seconds to a few minutes. Subsequently, we determined the water contact angle to verify the hydrophobic character of the treated surfaces. As shown in Figure 5, both substrates exhibit surface modification and indeed a hydrophobic behavior even after a few seconds exposure to CHF_3/CH_4 plasmas. In fact, surfaces become hydrophobic within 15 sec of plasma exposure. However, there is a difference in contact angle between the two surfaces, with a highest value of about 10 degrees for 30-45 sec of plasma exposure time. As shown in the figure, after 1 min of plasma exposure both surfaces exhibit the same contact angle. This result is surprising since, under the conditions used in these experiments, etching occurs on SiO_2 surfaces. However, studies in the literature [2, 3, 5] have

shown that a (thin) fluorocarbon film is deposited even on etched SiO_2 surfaces, through which etching proceeds, in high density plasmas (this is often called "the fluorocarbon suppression regime"). If the deposited layer grows thicker than a certain value, the modified SiO_2 surface properties become indistinguishable from those of the modified Al surface. Therefore, in order to achieve good selectivity for deposition between SiO_2 and Al surfaces, we should restrict the plasma exposure time for the surfaces to 30-45 sec.

Figure 6 shows how the contact angle changes with the content of CH_4 in the gas mixture, for 45 sec of deposition time (Pressure=3 mTorr, P=1500 W, V_{bias}=-150 V, T=0 ^oC). For a 27% CH_4 in the mixture, the difference in contact angles of Al and SiO_2 is as high as 30 degrees. This difference seems satisfactory for allowing fluid control through electrowetting, exploitable in microfluidic devices.

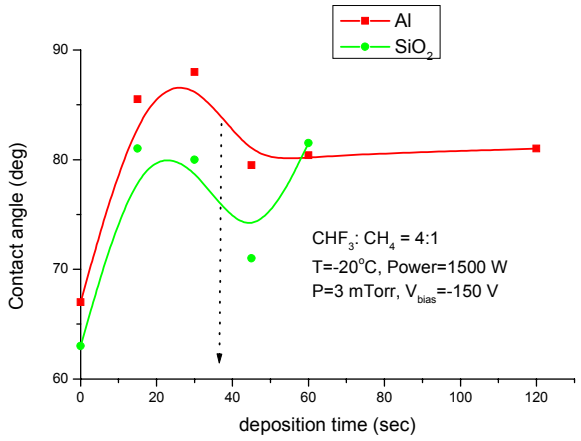

Fig.5. Evolution of the SiO_2 and Al surface properties with treatment time in a CHF_3/CH_4 (4:1) plasma.

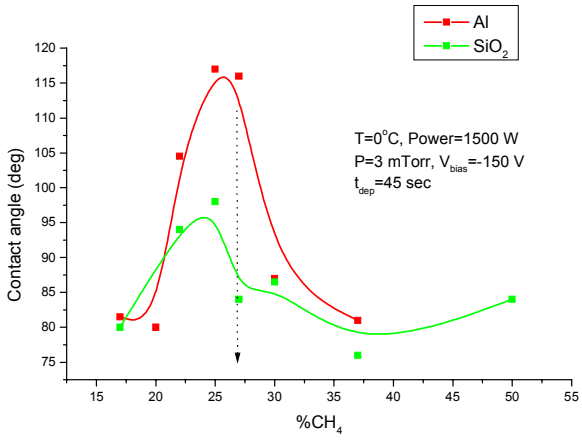

Fig. 6. Dependence of the Al and SiO_2 contact angle of water on the CH_4 percentage in the CHF_3/CH_4 plasma.

4. Conclusions

Differential hydrophobicity of Al and SiO_2 surfaces was achieved through preferential deposition of FC film on these surfaces, by means of C_4F_8 and CHF_3/CH_4 high density plasmas. Conditions ensuring high SiO_2/resist selectivity were found to be appropriate for selective deposition of FC films on Al versus SiO_2. However, a (thin) fluorocarbon film is also deposited on SiO_2 surfaces even at conditions where SiO_2 is etched, thus limiting the selectivity. Therefore, the treatment time must be short enough (30-40 s) such that the SiO_2 surface stays less hydrophobic than an Al surface. The best results are obtained so far in CHF_3/CH_4. The condition of the surface prior to deposition is found to be essential to the outcome of the treatment.

Future work includes measurements of the FC film thickness on SiO_2 and Al surfaces as a function of the treatment time as well as of the gas composition. In addition, the chemical composition of the deposited films will be studied in order to gain more understanding and possibly to further improve the differentiation between Al and SiO_2 surfaces with respect to their wetting properties.

Acknowledgements: This work was partially supported by a European Growth project "Microprotein" No G5RD-CT-2002-00744.

References

[1]. G. Oerlein, *Surface Science* **386**, 222 (1997); and G. Oerlein *et. al*., *J.Vac. Sci. Technol. A* **12**(2), 333 (1994).

[2]. L.Rolland, M.C. Peignon, Ch. Cardinaud, G. Turban, *Microel. Engin.* **53**, 375 (2000).

[3]. M. Matsui, T. Tatsoumi, M. Sekine, *J. Vac. Sci. Technol. A* **19**(4), 1282 (2001).

[4]. M. Schaepkens, T.E. F.M. Standaert, N.R. Rueger, P.G.M. Sebel, G.S. Oerhlein, J.M. Cook, *J. Vac. Sci. Technol. A* **17**(1), 26 (1999).

[5]. N. R. Rueger, J.J. Beulens, M. Schaepkens, M.F. Doemling, J.M. Mizra, T.E. F.M. Standaert, G.S. Oerhlein, *J. Vac. Sci. Technol.* A **15**(4), 1881 (1997).

[6]. M. Pollack, R. Fair, A. Shenderov, *Appl. Phys. Lett.* **77**(11), 1725 (2000).

Nozzle shape and plasma jet generated by a cutting plasma torch

A. Rodríguez-Yunta, C. Pardo, J. González-Aguilar and M.A.G. Calderón

Department of Applied. Physics. University of Cantabria. Santander. Spain

Plasma arc cutting is a process of metal cutting by a plasma jet, that it is widely used because of its high productivity and ability to cut practically all metals. In order for the plasma jet to provide a fast and high quality cut, a narrow supersonic plasma jet must be generated, with a high energy density to be able of a fast melting of the work-piece material. Also the force exerted on work-piece by the plasma jet must be high enough to remove the molten material quickly to avoid dross formation. This is made possible by a special nozzle, through wich the plasma is blown out of the torch. The nozzle creates a narrow highly concentrated plasma flow and also provides the high velocity of the plasma jet. By the other side the nozzle is one of the most vulnerable parts of the torch due to its exposure to extremely high heat fluxes.

In this work we use a theoretical model to study the effect of the nozzle shape on the plasma jet properties. The model is based on a set of one fluid conservative equations for mass density, momentum and energy taking into account compressible effects of the working gas under the usual simplifications of local thermodynamic equilibrium (LTE) and axial symmetry, but with the three momentum components. This kind of models had shown to be in good agreement with experimental data [1,2]. So, the model allows us to study the details of the flow and to make predictions on arc voltage, heat transfer to the workpiece, force and pressure exerted by the plasma jet on the material at the cutting zone.

This numerical model is applied to a conventional air plasma cutting torch with different nozzle orifice shapes. The obtained results show different torch performances for the same minimum diameter, current and total gas mass flow. A comparison of the plasma jet properties, as energy and momentum flows, wideness and double arcing risk, is given for several nozzle shapes.

[1] J. González-Aguilar, C. Pardo, A. Rodríguez-Yunta, and M. A. G. Calderón, "A theoretical study of a cutting plasma torch", IEEE Trans. Plasma Sci., 27, pp. 264-271, (1999)

[2] P.Freton, JJ Gonzalez, A.Gleizes F Camy Peyret, G. Caillibotte and M.Delzenne. "Numerical and experimental study of a plasma cutting torch". J.Phys.D: Appl.Phys. 35, pp 115-131, (2002)

Analysis of Optical Emission Spectroscopy from arcs for plasma vitrification of hazardous wastes

A. Rodríguez-Yunta, C. Pardo, R. García Sánchez and M.A.G. Calderón

Department of Applied. Physics. University of Cantabria. Santander. Spain

Plasma vitrification has been demonstrated as a safe, eficient, cost-efective technology for the treatment of wastes, including hazardous wastes. In this process, a problem is the volatilisation of some elements, as heavy metals or radioactive isotopes, which escape from the final vitrified product, generating secondary ashes that need to be treated again. There is currently significant interest in the development of a real-time monitoring technology for radioactive or trace metals pollution in the stack exhaust of high temperature processes such as those used for waste remediation, power production, and manufacturing.

A promising approach for achieving a practical on-line monitoring, is the atomic emission spectroscopy of the atmospheric pressure plasma generated in the furnace. The optical radiation emited by the plasma from which the metals are identified and quantified, can improve the understanding of the plasma parameters. Measurements are needed of electron temperature, electron density, neutral gas temperature, spatial profiles of these parameters, and their relationship to trace metals atomic emission strengths. Questions of the degree of thermal equilibrium in the plasma need to be answered, as well as plasma conductivity, and the effect of gas composition and particle loading. Spectroscopic measurements of the optical plasma radiation can provide much of the information that is needed.

In this work emission spectra in the range 350-1100 nm were recorded during the vitrification of waste with a system of twin plasma torches operated at an average power of 30 kW. The obtained spectra are rich in atomic lines and diatomic molecular bands superimposed on a blackbody continuum. The detailed properties of the spectra show a strong dependence with the operating conditions and with the feeding of waste and vitrifying agents.

The species concentrations in the plasma were obtained by comparison of the experimental spectra with synthetic ones generated by computer. A complete model based on Saha–Boltzmann and molecular dissociation equilibrium relationships, is used to calculate the plasma properties, as the emission and self-absorption of light. After a normalization of the experimental and theoretical results we are able to obtain data on Temperatures and element concentrations from a set of selected line-to-line and line-to-continua ratios

Using this results, spectroscopy diagnosis could be very useful to have a control on-line of the process. The spectroscopic observation of the intense light emitted by the plasma column can be used to estimate on line the chemical element ratios in the reactor atmosphere. Furthermore, the spectroscopy measurements also provide estimations for the plasma and melted material temperatures. These data can be used to control and study the vaporisation of selected hazardous elements.

Excitation Mechanism of High-Frequency Instability in Anode Layer of Plasmatron

A. Smakhtin, V. Rybakov

Department of Space Electrical Engines and Power Plants, Moscow Aviation Institute (State Technical University), Moscow, Russia

A plasma source for solving different plasma chemistry problems that has enjoyed the widest application is a plasmatron. The reason is that the plasmatron, using the arc discharge in a number of working gases and vapours, has high efficiency and ling-term reliability.

However, variety of instabilities of the plasmatron operating mode set limit on its technical parameters. Each type of these instabilities, distinguished by the inherent frequency and intensity of electromagnetic oscillations, has its own the excitation mechanism.

The excitation mechanism of electromagnetic high-frequency instability considered in this paper is due to the formation of the solid negative electrical charge inside the anode layer of the plasma arc. The kindred instability is exhibited by an experimental approach in different technical systems using the plasma arc. For example, under appropriate conditions this type of instability is in the magnetic plasma dynamic (MPD) thruster. This process is called as the limiting operating conditions of the MPD thruster.

As known there is a double electrical layer near the arc anode where electro-neutralization of the plasma is broken. The thickness of this layer is equal to near the Debye's length. This fact allows to consider the anode layer of the plasma arc as an ordinary vacuum-diode. In this case a quasi-neutral plasma column is defined as the cathode. Hereafter we shall use the term "anode current" to mean "discharge current" as it is conventional to call in literature about the vacuum-diode.

The calculating method of the electronic emission from the plasma column volume takes into account both the temperature radial distribution of the plasma column and the Maxwell's electronic speed distribution in each point of plasma volume. The emission current, issuing from each point of plasma cathode, involves electrons with a collision mean free path is longer than a distance from this point to the anode. In other words, the emission or cathode current involves electrons from Maxwell's "tail" only.

The calculation shows that the electronic emission current from the plasma column increases with increasing of the anode current. The pace of emission increasing is more rapid than the same parameter of the anode current. The emission current becomes more the anode current starting with some value. This operating mode of the vacuum-diode is called as a virtual cathode. When the emission current is higher than the current corresponding to Child-Langmuir law the solid negative charge emerges in the anode layer. In this case there is a potential well between the plasma column and the anode of the plasma arc. As it is in the vacuum-diode this electrical potential distribution is not stable and this mode of plasma arc operation is accompanied by electromagnetic high frequency instability of plasma arc.

The analysis of this excitation problems shows that the situation when the emission current is greater than the anode current reveals itself more effective with decreasing of the plasma column density. This fact has been confirmed experimentally by different scientific teams.

Characterisation of a Double Inductively Coupled Plasma Reactor

P. Messerer[1], B. Boenigk[1], P. Awakowicz[1],

[1] *Institute for Physics of Electrotechnology, Munich University of Technology, Munich, Germany*

Abstract
Due to the need in medical technology for dry sterilisation processes with non toxic agents, a low pressure radio frequency driven plasma reactor was developed. In order to implement a radially and axially homogenous sterilisation plasma, the concept of the inductively coupled plasma (ICP) was transfered into a double ICP (DICP) with two rf antennas, one on top the other on bottom. In order to characterize the DICP plasma under various conditions and to correlate plasma parameters to sterilisation efficiency, investigations with a Langmuir probe system, optical emission spectroscopy (OES) and a energy mass spectrometer (EMS) were completed with a coupled hydrodynamic-electrodynamic simulations of this plasma.

1. Introduction

In contrast to the needs of the semiconductor industry for a two dimensional homogeneous plasma process, plasma sterilisation has to deal with three dimensional medical items like implants, syringes or surgical instruments. Sterilisation is defined as a reduction of spores by a factor of 10^6. Since it is known that a combination of uv light and reactive radicals are necessary for fast sterilisation processes, a double inductive coupled plasma reactor has been developed which combines a reasonable homogenous plasma in voluminous vessels with high uv intensity caused by a high electron density. Additional to sterilisation, the functionality of medical items has not to be influenced, especially the ability to treat the objects without harming the materials while fulfilling the high demands of medicine to inactivate germs and spores by a factor of one million. In some occasions a modification of the material is desirable. As an example artificial joints are made of ultra high weight polyethylene (UHMWPE). This material is exposed to wear of friction. Therefore a hardening of the surface would improve the quality. Experiments with gel analysis show that between 2% and 6% of the material show cross linking which hardens the surface, whereas after sterilising with electron beams a cross linking of about 50% can be observed. This would make the whole material brittle. Another important material is polylactide. This material is used for dissolvable screws, nails etc. in fracture treatment and must not be altered to guarantee a constant rate of dissolution. First tests have shown that polylactide screws could be sterilised without any modification of the properties.
As a second step it was interesting to find the reactions, which are responsible for sterilisation process. Therefore the plasma parameters had to be evaluated and correlated to the results of many sterilisation experiments under various conditions. The Langmuir probe was used to measure the radial profiles of electron density and mean electron energy. The energy mass spectrometer was applied to investigate the flux of the heavy particles towards the wall. The optical emission spectroscopy (OES), as a non intrusive measurement system, was used to find the gas temperature and the amount of uv radiation inside the plasma chamber.

2. Set-up of the reactor

The DICP is a improvement of the known concept of the ICP. The chamber has a diameter of 40 cm and a height of 20cm. The power is generated by a 13,54 MHz rf-generator with an adjustable power between 0 W and 5 kW. The rf coil at the bottom of the chamber complements the rf coil on top. In this way a more even distribution of the power input can be reached. A sketch of the set-up can be seen in fig. 1. The typical pressure range is from 5 Pa to 20 Pa for sterilisation experiments. The diagnostic consists of a Langmuir probe at the side wall, a fibre optic to focus the emissions to a 1/2m spectrometer

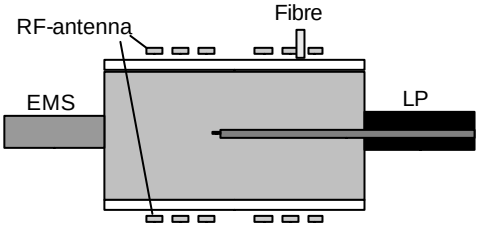

EMS: Energy-mass-spectrometer (ions + neutrals)
LP : Langmuir probe (electron density, mean electron energy and potentials)
Fibre: Optical wave guide + spectrometer+intens. CCD (gas temperature,UV-light)

Figure 1. Set-up of the DICP

connected to an intensified camera and an energy mass spectrometer almost opposite to the Langmuir probe with an optical resolution of 0.04 nm.
The EMS is operated in neutral and ion detection mode in order to collect the number density of the neutrals and the ion fluxes at the wall. Of special interest are the ions since they gain energy in the plasma sheath and the reactive radicals because of their high reactivity. While the ions are easily detectable, the measurement of the radicals poses some difficulties. Here, the method of ionisation threshold mass spectrometry (ITMS) [3] was used.
The OES was used to measure the spectra in the uv range from 180 nm to 400 nm. It is known from literature that the range below 250 nm is most effective [4] for sterilisation purposes. In addition, the shape of some rotational bands of nitrogen were recorded, allowing to evaluate the rotational temperature of the heavy particles which may be identified with the gas temperature under special circumstances.
With the Langmuir probe it is possible to retrieve spatial distributions of the following plasma parameters: the mean electron energy, the electron, the floating and the plasma potential.

3. Langmuir probe

Plasma modelling reveals that the density along the z-axis is by far more homogeneous with both coils. To strengthen this result, radially resolved measurements have been performed. The spatial distribution of the electron density at three rf power values can be seen in figure 2. A constant value of the electron density

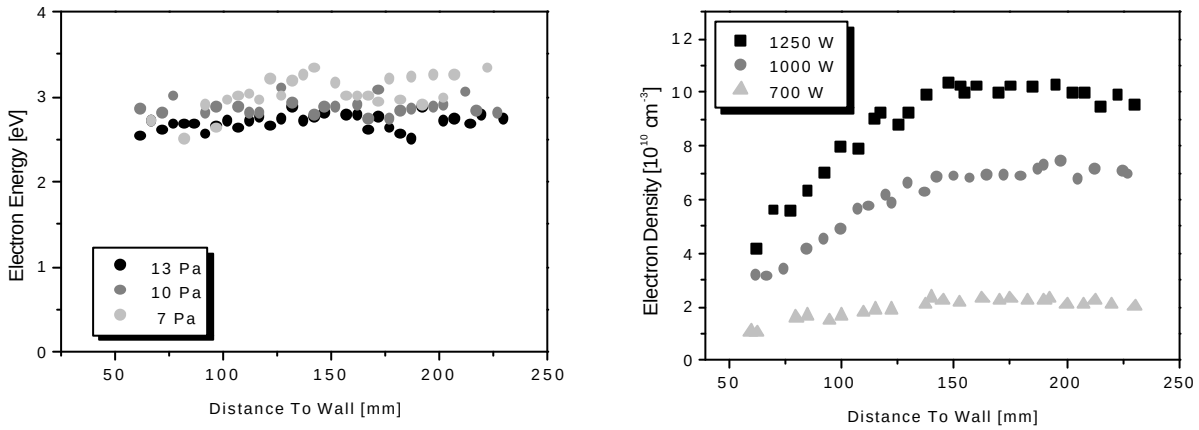

Figure 2: Mean electron energy (left) and electron density (right)

reaches up to a radius of 10 cm, which is half of the radius of the chamber. Sterilisation experiments show a much wider area, almost up to the chamber wall, of constant sterilisation efficiency. This is due to the strong dependency of the UV radiation on the electron energy, given in fig. 2. The mean electron energy remains, in contrast to the electron density, constant almost up to the chamber wall.

4. Optical emission spectrometry

One of the most important factors in the treatment of medical materials is the temperature of the heavy particles. Most of the materials, like polylactide and UHMWPE, will change their properties when the temperature exceeds even low limits of about 70 °C. In order to adjust the rf power input the gas temperature was measured. By adding a small amount of nitrogen and by evaluating the v'=0 – v''=2 rotational band of the second positive system of nitrogen, the shape of the band was compared to calculated profiles, which are very sensitive to the gas temperature [2]. Because of redistribution of the exited levels of the molecular nitrogen, this

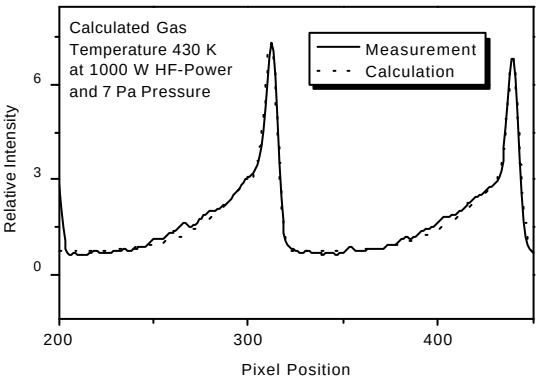

Figure 3: Estimation of the gas temperature

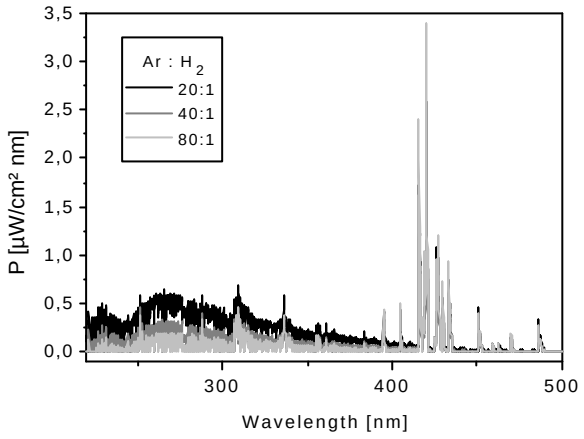

Figure 4: UV radiation in a hydrogen argon plasma

method will only give an upper limit of the gas temperature in mixtures of nitrogen and argon. The temperatures found for the used sterilisation plasmas were below the limit of 430K (fig. 3).
Due to heavy particle collisions of Ar and N_2, the profile of the N_2 rotational band is altered and the temperature derived from this procedure is overestimated. Therefore the real gas temperature seems to be even lower.

The uv radiation is responsible for the fast sterilisation of the materials. Results from such measurements show some amount of uv light in the range below 250 nm, which proved to be the main part of the sterilisation process (fig. 4). The DNA of most bacteria, like B. subtilis, can be broken by high energy radiation. The threshold of the wavelength is at 250 nm, below which sterilisation is good. An exception is A. niger with its black outer layer which protects the DNA from the uv light. This spore can be inactivated with light quanta with even higher energy.

5. Energy mass spectrometry

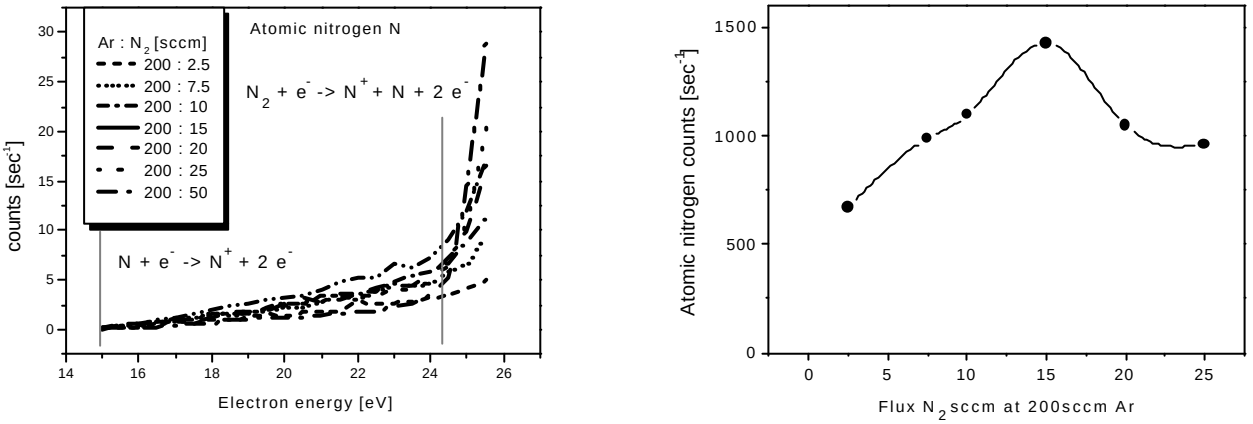

Figure 5: Atomic nitrogen at different concentrations of nitrogen in argon

The EQP 500 (Hiden Technologies) was used for ionisation threshold mass spectrometry (ITMS). The EQP 500 can detect neutral particles. To do that these particles have to be ionised. This is done with two filaments right after the orifice of the instrument. An electron beam with an adjustable energy is directed towards the incoming particles. Due to the interactions with these electrons, the heavy particles are ionised. By varying the energy of the electron beam inside the EQP, used to ionise the radicals inside the instrument, it is possible to detect radicals. It is necessary to adjust the ionising electron beam current inside the EMS in order to gain a detectable signal and to minimise the dissociation of the

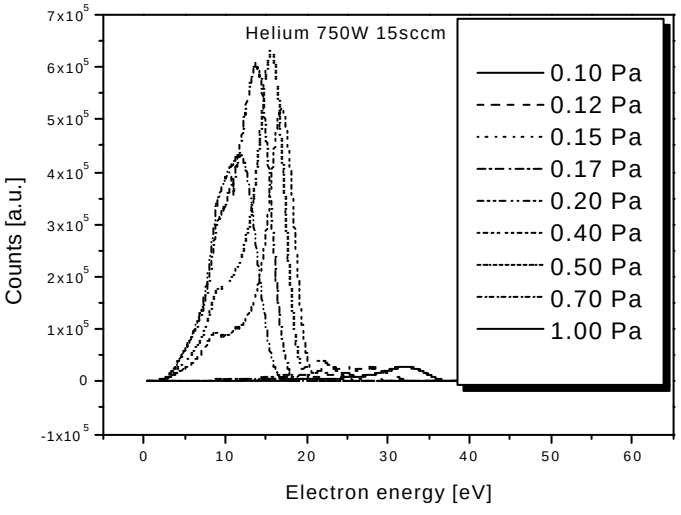

Figure 6: Ion energy of helium at various pressures

radicals (fig. 5). Nitrogen radicals interacting with electrons of an energy less than 14.5 eV are not ionised while electrons with an energy above 24.3 eV can dissociate molecular nitrogen. Nitrogen dissociated inside the EQP 500 would erroneously be counted as radicals. The measurements with different mixtures of nitrogen and argon revealed that the maximum of the flux of radicals to the wall coincides well with a maximum of sterilisation efficiency. This does not state that the radicals are responsible for the sterilisation of the objects but it is a hint that the parameters for a good sterilisation are the same as the parameters which are advantageous for the production of atomic nitrogen in an argon nitrogen plasma.

With respect to sterilisation, another important species are the ions, because they transport kinetic energy of to the substrate. Therefore a first assumption about the sterilisation process was, that the ions take major part by bombarding the objects. The typical energy of ions reaching the wall is 8 to 10 eV, depending partially on the pressure and the gas mixture. Experiments with very low pressure in a helium plasma could produce ions with energies up to 50 eV (see fig. 6). No further experiments were conducted in this direction because the sterilisation is most effective at pressures one magnitude above, at 10 Pa. But a controlled surface modification may be possible with adjusted ion energies.

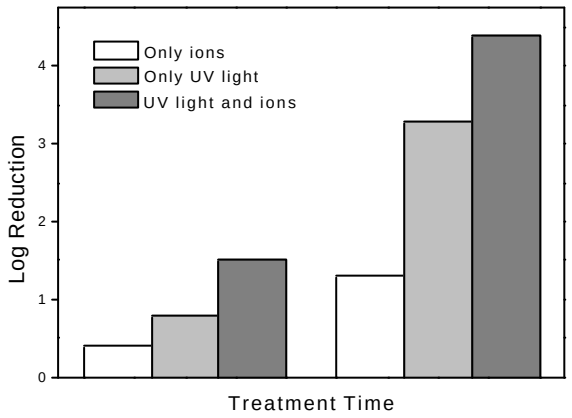

Figure 7: Logarithm of the Reduction of spores (b. subtilis) at different times split up into the parts of UV light and ions.

In order to investigate the influence of the various mechanisms separately an ion beam experiment was set up. The beam was directed onto B. subtilis endospores located on a steel plate. The same experiment was then conducted with uv light from the DICP added, and finally with both, uv light and the ion beam in operation. The results can be seen in fig 7 with treatment times of 5 minutes and 30 minutes at a fixed ion flux density of 10^{14} s^{-1} cm^{-2}. This flux density is around two orders of magnitude below the ion flux density in the DICP. Despite the fact that uv light is the main effect in plasma sterilization, the ions are needed to reach the high reduction rate which is necessary in medical, pharmaceutical and in food applications.

6. Simulation

The measurements can only be done on some locations inside the chamber. For a two dimensional characterisation of the DICP, an in-house hydrodynamic-electrodynamic model was used. The ion transport properties are described by a full hydrodynamic model including the sheath regions. Due to their small mass, the drift diffusion approximation was applied for the electrons. The rf energy input is described by an electrodynamic model derived from Maxwell´s equations [1].

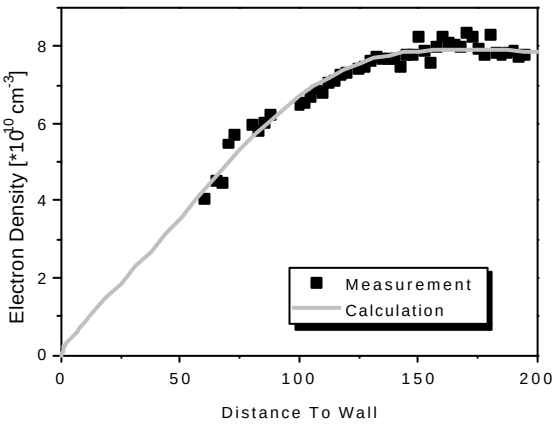

Figure 8: Simulation of mean electron density

From Langmuir probe measurements the radial peak electron density was taken and a coil current was chosen to match the density in measurement and simulation. The neutral gas temperature derived by the OES was taken as input parameter. The calculated electron density could then be compared to the results of the Langmuir probe measurements. Fig 8 shows one measurement in comparison to a simulation. Measured and calculated data are in good agreement.

Further is it possible to calculate the ion density and ion velocity profiles, as well as the induced power density distribution in the chamber. Especially the spatial distribution of the power input into the chamber is of importance when the reactor has to be scaled up. Simulation in interplay with diagnostics can synergetically simplify the construction of newly shaped chambers. The shape and dimensions of the reactor chamber or the antennas can be customised to produce the desired discharge characteristics.

7. Conclusion

While the profile of the electron density cannot be used to describe the profile of the sterilisation rate it is an important part of the characterisation of the plasma. The measurements in combination with a hydrodynamic and electrodynamic simulation of the plasma inside the chamber produced a consistent picture of the parameters everywhere in the reactor chamber. Alternate processes for different applications, like surface modification, can now be developed faster with the knowledge of the state of the plasma in all three dimensions. The future construction of customised plasma reactors is greatly simplified by the simulation of the plasma parameters. Together with the knowledge of the sterilisation process reactors of desired properties can be constructed more efficiently.

8. Acknowledgement

The authors wish to thank the Frauenhofer Institute for Process Engineering and Packaging IVV in Freising for the microbiological preparation and evaluation of the test samples and the Bundesministerium für Bildung und Forschung for funding under contract numbers 13N7681, 13N7607.

References

[1] P. Scheubert, H. Paulin, U. Fantz, P. Awakowicz, J. Appl. Phys. Vol. 90, No 2 (2001) 587-598
[2] K. Behringer, Plasma Phys. Control. Fusion 33, 9, (1991) 997-1028
[3] P. Pecher, thesis, Univ. Bayreuth (1997)

Structure and properties of the intermetallic Ti-Al type surface layers produced on titanium alloy.

T. Wierzchoń[1], M.Ossowski[1], E. Łunarska[2]

[1] *Warsaw University of Technology,Faculty of Materials Science and Engineering,02-507 Warsaw, . Wołoska 141, POLAND*
[2] *Institute of Physical Chemistry, Polish Academy of Sciences, 01-224 Warsaw, Kasprzaka 44/52, POLAND*

Alloys composed of intermetallic phases of the Ti-Al system belong to the group of new materials that show unique physical, chemical and mechanical properties. Unfortunately, their susceptibility to brittle fracture, poor plasticity and the occurrence of fatigue cracking observed within a wide temperature range greatly restrict their practical applications of these alloys. Therefore, attempts are being made at developing methods for producing surface layers of these materials on titanium alloys, which are characterized by a high strength, good corrosion resistance, and a low density but unfortunately a low resistance to friction.
A prospective line is the production of composite layers of the Al_2O_3 + $TiAl_3$ + TiAl + Ti_3Al type by combining (in a way justified from the point of view of the cost involved) various surface engineering methods, such as vacuum evaporation technique of aluminium and the glow discharge assisted treatments.
The paper specifies the conditions under which composite surface layers of the Ti-Al intermetallic phases with a top Al_2O_3 layer are produced on the two-phase Ti6Al2Cr2Mo titanium alloy by using a multiplex process enhanced by the glow discharge phenomenon. The results of examination of the structure, chemical and phase composition and properties, such as corrosion and friction wear resistance of these layers are presented. The composite layers of the Al_2O_3 + $TiAl_3$ + TiAl + Ti_3Al types have a surface hardness of the order of 1600HV0.05 and a good resistance to corrosion and frictional wear.
This multiplex technique, developed in the present study, permits producing surface composite layers of the diffusion character with a precisely specified structure and chemical and phase composition, tailored to suit the increasing use of titanium alloys in industry.

Plasma Parameters During High Power Pulsed Magnetron Sputtering

J. Alami[1], J.T. Gudmundsson[2,3], J. Böhlmark[1], K.B. Gylfason[2,3] and U. Helmersson[1]

[1] *Department of Physics, Linköping University, SE-581 83 Linköping, Sweden*
[2] *Department of Electrical and Computer Engineering, University of Iceland, IS-107 Reykjavik, Iceland*
[3] *Science Institute, University of Iceland, Dunhaga 3, IS-107 Reykjavik, Iceland*

Abstract

We report on Langmuir probe measurements of high power pulsed magnetron discharge. Space and time-dependent plasma parameters are obtained as functions of the process parameters. It is shown that the electron density of a pulsed magnetron plasma, in the substrate vicinity, is three orders of magnitude (10^{18}-10^{19} m^{-3}) higher than that of a d.c. magnetron discharge. The electron temperature evolution was measured by a triple probe, and found to be in the 0.2-3.1 eV range.

1. Introduction

In a conventional d.c. magnetron sputtering the power density is limited by the thermal load on the target. In unipolar pulsing, the power supply operates at zero power level and then pulses to a high level for a short period each cycle. Plasma density in conventional d.c. magnetron sputtering is known to be no more than 10^{15}-10^{16} m^{-3} at ~ 5-10 cm [1] from a metal target, with an ionisation fraction of 1-10% [2]. For the high power unipolar pulsed magnetron sputtering used in this work, density was measured to be three orders of magnitude higher than in a d.c. discharge [3] and with an ionisation fraction of 30-70 % [4]. The magnetron in this case was pulsed with a unipolar pulse wave of 50-100 μs pulse length and 11 J pulse energy. Furthermore, it was shown that the electron energy probability function (EEPF) exhibits a bi-Maxwellian distribution with a cold electron group having an electron temperature T_c=1.1 eV and a hot electron group with T_h=1.9 eV [5]. Langmuir probe measurement is a common technique to investigate plasma parameters such as electron temperature, plasma and floating potential, plasma density, and electron energy density function (EEDF). It allows for understanding the plasma dynamics as well as indicating how to control plasma species, in highly ionised plasmas, for specific film growth purposes. The aim of this work is to investigate the spatial and temporal evolution of both the plasma density and the electron temperature and compare these with measurements for a d.c. plasma.

2. Experimental setup

The measurements were made for a balanced magnetron discharge that has a tantalum (Ta) target with a diameter of 150 mm. The target functions as the cathode and is located inside a stainless steel sputtering chamber of radius R = 24 cm and height L = 75 cm. The cathode is driven by a pulsed power supply that delivers up to 3 MW peak power (2500 V and 1200A) at a repetition frequency of 50 Hz. The pulse length is in the range of 50 – 100 μs (Fig. 1). In this work, measurements were made with an average power of 550 W corresponding to pulse energy of 11 J. As a discharge gas, argon of purity 99.9997% and pressure of 0.5, 5, and 20 mTorr was. Target current, target voltage, and Langmuir probe current and voltage were monitored by a Tektronix TDS 520 C (500 MHz, 1 Gs/s) oscilloscope. The target voltage was measured using a Tektronix P6015 high voltage probe (1000 × attenuation) and the target current by a Tektronix CT-04 high current transformer (20 KA peak current and bandwidth 20 MHZ) and a TCP202 current probe (15A ac/d.c. and bandwidth 50 MHz).

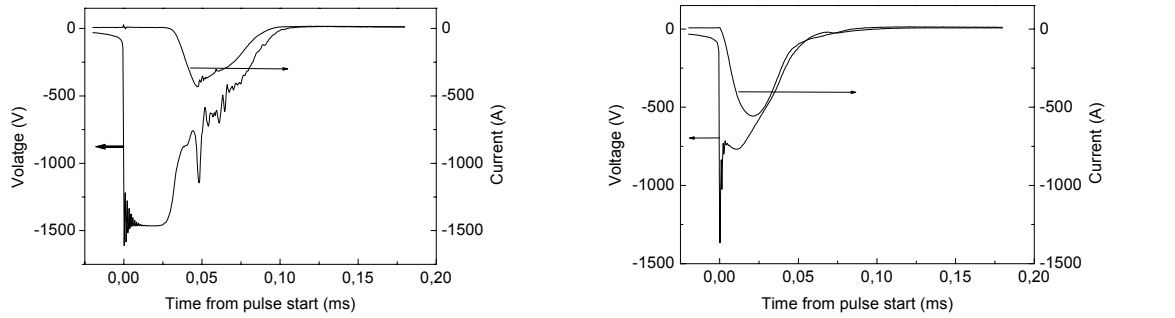

(a) (b)

Figure 1 Target current and voltage versus time from initiating the pulse for (a) 0.5 mTorr and (b) 20 mTorr argon discharge

Plasma parameters were measured using a cylindrical Langmuir probe consisting of a tungsten wire of length l_{pr}= 5.0±0.5 mm and diameter 0.10±0.01 mm. The probe holder is an alumina tube with an outer radius r_{prh}=0.5 mm and a length l_{prh}= 19 mm. The probe is made in such a way that $r_{prh} << l_{pr}$ and r_{pr}, r_{prh}, $\lambda_{De} << \lambda_e \sim$ 10 mm [6]. Here λ_{De} ~14 – 100 μm is the Debye length and λ_e ~ 10 mm is the electron mean free path. The probe was placed perpendicular to the discharge axis, and thus to the electric and magnetic field lines. The Langmuir probe current is determined by measuring the voltage over a resistor (R=10 Ω). The measured voltage together with the probe bias voltage are displayed on an oscilloscope, and collected in a computer. The computer stores the data for later analysis, and controls the power supply that gives the probe bias voltage.

For the Langmuir probe measurements to be valid, the error caused by the magnetic field strength must be minimized [6]. The probe was positioned 4 – 28 cm from the target along the centre line. Time resolved probe measurements were taken for 1000 μs at 2 μs intervals from the start of the pulse for each bias voltage, starting from –15 V and ending at +10 V with a stepping voltage of 0.1 V. For each time value the I–V data was recorded and analysed. First the measured I–V curve was smoothed by convoluting it with a Blackman window [8], then the first and second derivative of the I –V curve was calculated and the EEDF $g_e(\varepsilon)$ was found. The EEDF is given by the Druyvesteyn formula as [9]:

$$g_e(V) = \frac{2m}{e^2 A_{pr}} \left(\frac{2eV}{m}\right)^{\frac{1}{2}} \frac{d^2 I_e}{dV^2} \tag{1}$$

The electron energy ε is given in equivalent voltage (V) units. The plasma potential V_{pl} is the voltage where the second derivative of the electron current I_e is zero, and the floating potential V_{fl} is where the probe draws equal ion and electron currents. The electron density n_e is determined as:

$$n_e = \int_0^\infty g_e(\varepsilon) d\varepsilon \tag{2}$$

To determine the electron temperature, we applied the triple probe [7]. Fig. 2 shows a scheme of the measurement setup; three separate Langmuir probes of identical to the one used for density measurements placed 2 mm apart. An important requirement of the triple probe technique is that all of the Langmuir probes are immersed in plasma sample volumes of identical character. Otherwise a different I-V characteristic exists at each probe and a complete set of measured quantities for a single I-V characteristic is not obtained. P_2 is left floating while a constant voltage is applied to P_1 and P_3.

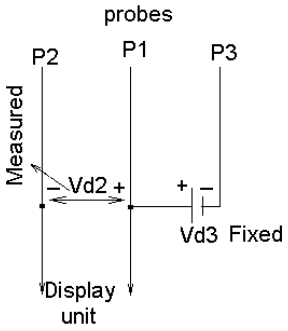

Figure 2 Direct display system utilizing the triple probe

V_{d2} is related to V_{d3} and T_e by the following relation [7]:

$$\frac{1-\exp(-eVd_2/KT_e)}{1-\exp(eVd_3/KT_e)}=\frac{1}{2} \tag{3}$$

To ensure the collection of the saturation current V_{d3} has to be large enough ($eV_{d3} \cong 3kT_e$) but not too large so as to minimize the probe shadowing. We choose this to be 9 V. Equation (3) simplifies to give the electron temperature as [10]:

$$T_e \cong eV_{d2}/\ln 2 \tag{4}$$

To measure the ion current, a negatively biased (-50 V) flat probe, a metal disk of 2 cm in diameter equipped with a guard ring was used.

3. Experimental results and discussion

Electron density was measured at different distances from the Ta target using the Langmuir probe, along the middle axis. Fig. 3(a) shows the electron density as a function of time from initiation of the pulse, for various distances from the Ta target. The density curves with two density peaks. At 4 cm from the sputtering target the first density peak is measured to be $1.2\text{x}10^{19}$ m^{-3} some 42 μs after the pulse start. At 9 cm, the peak value is $1.1\text{x}10^{19}$ m^{-3} after 102 μs and at 13 cm a density peak of $0.6\text{x}10^{19}$ m^{-3} is reached after 166 μs. The same behaviour is seen for the ion current, i.e. the further from the metal target the measurement is done the later the current peak appears indicating a flow of electrons and ions away from the target.

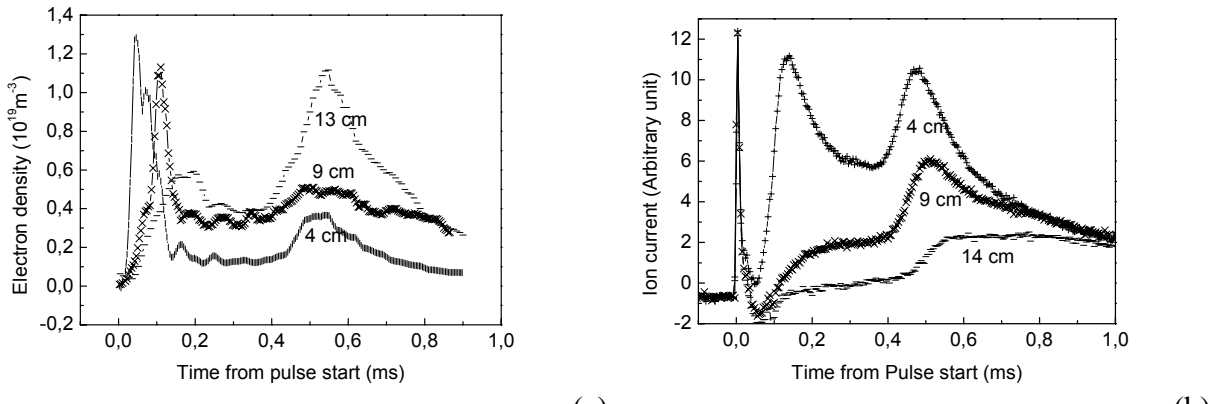

(a) (b)

Figure 3. (a) Electron density at different distances away from a Ta sputtering target measured using a Langmuir probe (b) Ion current for the same system measured by a flat probe in Ar discharge at 20 mTorr and average power 550W.

In Fig. 3(a) a second density peak appears at approximately 0.56 ms after initiation of the pulse. It appears roughly independently of the distance from the sputtering target, in this range. Also, the second electron density peak is higher than the first one the further away from the sputtering target the measurement is done. We relate the formation of more than one peak to ion acoustic solitary waves that propagate through the plasma. We assume that dense plasma is created next to the target during the pulse. This high density of ions and electrons leads to a compressive wave train that propagates into a less dense plasma similar to what was reported by Ikezi *et al*. [11]. The character of the electron and ion density pulse is believed to follow the predictions of the Korteweg-de Vries equation, with respect to the shape and velocity of the solitary waves, although the magnetization of electrons may have to be considered [12]. In Fig. 3(b) the corresponding ion current peak is shown to appear earlier the closer to the sputtering target the measurement is done. An ion current peak is also measured right at the beginning of the pulse. Ehiasarian *et al*. [13] showed that the majority of the charged particles at this point are ions of the working gas, Ar^+. The corresponding electron density measurements are very unstable during these first 10 μs of the pulse and further analysis of the signal here is left for future work.

Electron temperature was measured at different positions underneath the Ta target using the triple probe technique. Fig. 4(a) shows the temporal and along the axis electron temperature evolutions for 20 mTorr Ar pressure and a pulse energy of 11 J. It shows that, while the pulse is on, the electron temperature reaches it's maximum of about 2.8 eV. This decreases sharply as the pulse is switched off and reaches a value of 0.2 eV after just 80 μs from the pulse start. The electron temperature then increases again to about 0.5 eV and then decreases more slowly to 0.1-0.2 eV and stabilises at this value.

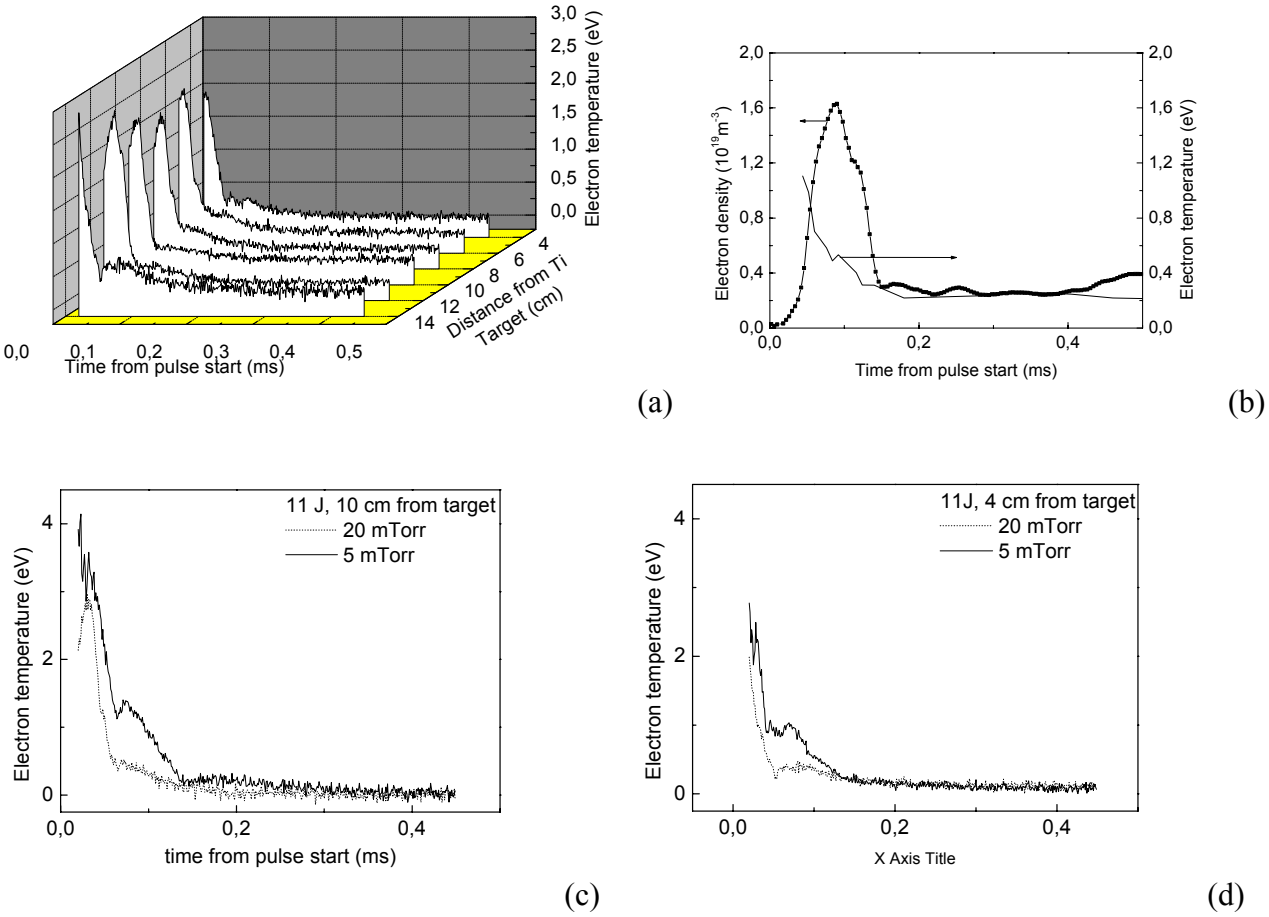

Figure 4. Electron temperature versus time from initiation of the pulse. (a) temporal and along the axis evolution for 20 mTorr Ar pressure and 11 J pulse energy. (b) Temperature decreases as density increases (c) For 5 and 20 mTorr, 10 cm from the target and (d) 4 cm from target.

Fig. 4(b) shows the electron temperature and electron density as functions of time from initiation of the pulse. We note that the electron temperature decreases as the plasma density increases. Fig. 4(c) shows the electron temperature versus time. We see that increasing the magnetron power results in a decrease in the electron temperature. One can also see the effect of the delayed high-energy tale, corresponding to a second electron temperature increase at about 0.8 ms from the pulse start. It is shown to peak at 1.8 eV for the 5 mTorr plasma and is almost non-existing for the higher pressure one, indicating that the 20 mTorr plasma not only has a higher electron density but is also the colder of the two plasmas. This is confirmed in Fig. 4(d) where the measurements were made at 4 cm bellow the target. Fig. 4(d) shows also that the electron temperature at this distance is lower than that measured 10 cm from the target.

Conclusion

Using higher power pulsed magnetron sputtering, we demonstrated that very high plasma density, up to 1.3 10^{19} m^{-3} is achieved 10 cm from a Ta target, which is three orders of magnitude higher than that of a d.c. plasma. The discharge was shown to be cold with average electron temperature well beneath 0.5 eV. A second density peak was shown 0.56 ms after pulse initiation

Acknowledgment

This work was supported by the Swedish Foundation for Strategic Research, the Swedish Research Council, and the University of Iceland Research Fund. Many thanks to Dr. Leif Samuelsson for technical help. The Company Chemfilt R & D AB is acknowledged for the use of the power supply.

References

[1] D.J. Field, S. K. Dew and R. E. Burrell, J. Vac. Sci. Technol. A **20** (2002) 2032
[2] C. Christou and Z.H. Barber, J. Vac. Sci. and Technol. A **18** (2000) 2897
[3] J.T. Gudmundsson, J. Alami and U. Helmersson, App. Phys. Lett. **78** (2001) 3427
[4] V. Kouznetsov, K. Macák, J. M. Schneider, U. Helmersson and I. Petrov, Surface and Coating Techn. **122** (1999) 290-293
[5] J.T. Gudmundsson, J. Alami and U. Helmersson, Surface and Coating Techn. **161** (2002) 249-256
[6] V.A Godyak, in: O. Auciello (Ed.), Plasma-Surface Interactions and Processing of Materials, Kluwer Academic Publishers, Dordrecht, 1990, pp. 95-134
[7] Sin-Li Chen and T. Dekigucgi, J. appl. Phys. **63** (1965) 2363
[8] J.T. Gudmundsson, Smoothing of the IV Langmuir probe characteristic, Memorandum no. UCB/ERL M97/38, Electron Research Laboratory, University of California, Berkeley, 1997.
[9] M.J. Druyvesteyn, Z. Phys **64** (1930) 781
[10] C.Riccardi, G. Longoni, G. Chiodini and M. Fontanesi, Rev. Sci. Inst **72** (2001) 461
[11] H. Ikezi, R. J. Taylor, and D. R. Baker, Phys. Rev. Lett., 25, (1970) 11-14
[12] K. B. Gylfason, J. Alami, U. Helmersson and J. T. Gudmundsson, to be submitted for publication
[13] A.P. Ehiasarian, R. New, W. -D. Münz, L. Hultman, U. Helmersson, V. Kuznetsov, Vacuum **65** (2002) 147-154

Model of the Plasma Movement and Walls Erosion in the Hollow Accelerator Channel

R. Chuyan, N. Avdeenko, S. Khartov, J. Zikeeva

Department of Space Electrical Engines and Power Plants, Moscow Aviation Institute (State Technical University), Moscow, Russia

One of the most popular plasma accelerator is the stationary plasma accelerator with lingering annular channel, external magnetic field and circular (Hollow) electron current. These accelerators are used in the different technological plants for the surface finish, in the several physical plants etc. In this report we try to create the complex mathematical models for investigation of plasma and its components in the accelerators channel.

One of the head problem of this accelerator is problem channel walls erosion. Part of the fast ions by this acceleration scheme inevitable fall to the channel walls and knock some atoms of walls material out. The channel walls erosion is head process, which limited the accelerators lifetime.

The complex of model consist of some connected blocks and based on statistic experimental data, reflecting the process of ions creation in the magnetic field.

1. Block of ions creating process simulation in the acceleration channel in the area of increasing magnetic field.
2. Block of ions' motion simulation in the acceleration channel up to channel boundaries and also out of them if they come out into the external space.
3. Block of ions' interaction with channel's walls (neutral atoms knocking out from walls' material).
4. Block of channel boundaries from changing simulation and re-calculation of the interaction.
5. Block of neutral particles(knocked out from the walls) motion simulation and their interaction with channel walls.

In the report the results of modeling are leaded.

Ions distribution function in the acceleration channel and in the external space and lifetime performances should be obtained as a result of simulation.

Developed method with some corrections and additions can be used for other types of accelerators.

Model of ions creation in the acceleration channel based on the local probe measurement. In the model there is the possibility to correct the initial distribution using results of experiment dealing with stationary plasma thruster (SPT-100) wearing under long-time lifetime tests. But at the that time this method is universal and can be used with some corrections for another of accelerator's models.

By calculation only single-charged ions sputtering action has been taken into account. Such assumption is correct as far as the share of double- and more charged ions in the discharge of the modern accelerators models is not more then 10%.

The structure and main blocks of mathematical model for particles motion in the accelerator's channel and out of it are developed.

The developed model and the software, created on its base, permit to calculate ion creations process, charged and neutral particles motion inside the channel and out of it, their interaction witch channel's walls, to built vector diagram of "dust" exhausting, to calculate channel wall profile change as a dependence on time and to determine thruster's life time.

Large-scale surface wave discharges in N_2-O_2

V. Guerra, E. Tatarova and C. M. Ferreira

Centro de Física dos Plasmas, Instituto Superior Técnico, 1049-001 Lisboa, Portugal

Abstract
In this work we present a theoretical investigation of a large-scale, slot antenna excited surface wave plasma source operating at $\omega/2\pi = 2.45$ GHz ($p = 2$ Torr) in $N_2 - O_2$ mixtures. The spatial distribution of the species of interest and the total electric field spatial variation are calculated and analysed for the discharge zone of the plasma source. The importance of $N_2(X,v)$ and of the electronically excited metastable states $N_2(A)$ and $N(^2D)$ is pointed out.

1. Introduction

Gas discharges operating in nitrogen-oxygen mixtures are used in many plasma-based technologies as, for example, cold sterilization of medical devices or removal of nitrogen oxides (NO_x) from flue and exhaust gases. Furthermore the kinetic processes occurring in low-temperature plasma of atmospheric gases N_2, O_2 and their mixtures are presently the subject of many investigation due to their importance in atmospheric and ionospheric physics. In this respect plasma sources based on microwave propagation are of interest for a new generation of large-scale plasma based technologies.
In this work we report a theoretical investigation on a large area slot antenna excited plasma source operating at 2.45 GHz and $p = 2$ Torr in N_2-O_2 gas mixtures. The plasma is created by surface waves propagating radially and azimuthally along the interface between the plasma and a quartz dielectric plate located at the top wall of a large diameter cylindrical metal camera. The electric field intensity exponentially decreases from the interface thus the plasma source can be separated in two parts. The first one is the active discharge zone close to the interface and the second one is the remote, electric field-free, plasma. The theoretical analysis is made for the active zone. The discharge is sustained by the discrete pure TM_{33} surface mode, which is the proper mode of the system considered. The Maxwell equations and dispersion equation are solved in order to obtain the 2D electric field pattern in a fixed $r - \varphi$ plane in the discharge zone. The electron Boltzmann equation is solved in the local approximation, coupled with a set of rate balance equations describing the production and loss of the most important neutral and charged heavy particles, such as vibrationally excited ground-state N_2 and O_2 molecules, N_2 and O_2 electronically excited states, N and O atoms, NO and O_3 molecules, and the different positive ions present in the discharge. The calculations provide the spatially averaged concentrations of the different species in the discharge zone and the 3D distributions of the electric field and electronic excitation rate coefficients.

2. Theoretical model

In the present model, the real camera geometry is simplified to a vertical wave-guide of an arbitrary cross-section (radius R) short-circuited at its top wall by a metal wall (Fig. 1) [1,2]. A dielectric plate of thickness d and permitivitty ε_d fills the upper region of the wave-guide entirely. The discharge plasma (where surface waves sustain and propagate) below is supposed to be homogeneous with electron density N_e. Weakly damped free oscillations of the kind $\propto \exp(-i\omega t)$ with a complex frequency $\omega = \omega' - i\omega''$ are considered. At fixed geometry and plasma parameters such oscillations can exist only for some discrete values of the complex frequency corresponding to the various eigenmodes. The waves form a resonant eigenmode satisfying the boundary conditions and the plasma "sticks" to some discrete density values.
Such a structure can support pure transverse magnetic (TM) and transverse electric (TE) modes, respectively. Pure TM modes are considered in the present model. In each medium, i.e. plasma and dielectric, the electric filed (ρ, φ, z) components are follows:

$$E_r(\mathbf{r},t) = \frac{1}{k_\tau} J_m'(k_\tau \rho)(\cos m\varphi)\frac{d\xi(z)}{dz}\exp(-i\omega t)$$

$$E_\varphi(\mathbf{r},t) = \frac{1}{\rho k_\tau^2} J_m(k_\tau \rho)(-m\sin m\varphi)\frac{d\xi(z)}{dz}\exp(-i\omega t)$$

$$E_z(\mathbf{r},t) = J_m(k_\tau \rho)(\cos m\varphi)\xi(z)\exp(-i\omega t) \quad (1)$$

Here, the transverse wave number k_τ depends only on the camera geometry and mode indices, and for a TM_{mn} mode it is $k = U_{mn}/R$, where U_{mn} is the n-th root of the m-th Bessel function J_{mn}, i.e., $J_{mn}(U_{mn}) = 0$. In order to fulfil also the boundary conditions at the plasma dielectric interface the transverse field distributions and thus the transverse wave numbers in both media must coincide. Therefore they have the same value in the plasma and dielectric and this value depends only on the cross-section geometry, mode type and mode indices. The function *ξ(z)* describing the axial field distribution is:

$$\xi(z) = E_{01}\exp(\gamma z) + E_{02}\exp(-\gamma z)$$

Here $\gamma_d = -\left[k^2 - \varepsilon_d \omega^2/c^2\right]^{1/2}$ and $\gamma_{pl} = -\left[k^2 - \varepsilon_{pl}\omega^2/c^2\right]^{1/2}$ are the axial propagation constants in the respective medium, i.e., dielectric and plasma. The relative plasma permittivity is

$$\varepsilon_{pl} = 1 - \frac{\omega_{pl}^2}{\omega(\omega + i\nu_{en})},$$

where $\omega_{pl} = e(N_e/\varepsilon_o m_e)^{1/2}$ is the electron plasma frequency (m_e and e being the electron mass and charge respectively). At $z = +\infty$ the wave must decay exponentially along z in the plasma, so that E_{02} must be zero. Assuming that surface wave propagates on the r-φ plane and is evanescent along z- direction, the dispersion equation is obtained, as usual, from the continuity of the transverse electric and magnetic field components on the plasma dielectric interface

$$(\gamma_d/\varepsilon_d)\tanh(\gamma_d d) = \gamma_{pl}/\varepsilon_{pl}.$$

The discharge part of the model is coupled to the discharge electrodynamics through the electron density (in the discharge zone where SWs propagates) at which TM_{33} mode appears. The absolute value of the electric field E_{01} (from now on denoted simply as E_0) can be obtained by solving the electron and heavy-particle kinetics for the spatially averaged populations of the most important neutral and charged species in the discharge region. The kinetic scheme considered is described in detail in [3,4], but a brief outline is given below. The electron energy distribution function is determined by solving the homogeneous Boltzamnn equation in the usual two-term expansion in spherical harmonics, taking into account elastic collisions, excitation and de-excitation of the rotational levels, inelastic and superelastic collisions of electrons with $N_2(X, v)$ and $O_2(X, v')$ molecules, inelastic collisions for excitation of electronic states and ionization of N_2 and O_2. The Boltzmann equation is coupled to a system of rate balance equations describing the kinetics of the vibrationally excited molecules $N_2(X, 0 \le v \le 45)$ and $O_2(X, 0 \le v \le 15)$, which include the processes of excitation and de-excitation of vibrational levels by electron impact (e – V processes), the vibration-vibration (V – V) and vibration-translation (V – T) energy exchange processes ($N_2 - N_2$, $N_2 - O_2$, $O_2 - O_2$, $N_2 - N$, $N_2 - O$, $O_2 - O$), the vibrational deactivation of $N_2(X, v)$ molecules at the wall and dissociation and re-association mechanisms of N_2. The vibrational distribution function of $N_2(X, v)$ molecules is still coupled to the kinetics of electronically states of N_2, and to those of NO, N and O species. The averaged concentrations of the heavy-particles are obtained by solving the corresponding system of master equations for their populations. Besides the manifold of vibration levels $N_2(X\ ^1\Sigma_g^+, v)$ and $O_2(X\ ^3\Sigma_g^-, v')$, the species to be considered are the most populated electronic states of N_2 ($A\ ^3\Sigma_u^+$, $B\ ^3\Pi_g$, $C\ ^3\Pi_u$, $a'\ ^1\Sigma_u^-$, $a\ ^1\Pi_g$, $w\ ^1\Delta_u$, $a''\ ^1\Sigma_g^+$) and O_2 ($a\ ^1\Delta_g$, $b\ ^1\Sigma_g^+$), the atoms N(^4S, ^2D, ^2P) and O(^3P), the molecular species NO($X\ ^2\Pi_r$) and O_3, and the ions N_2^+, N_4^+, O_2^+, O^+, NO^+ and O^-. The kinetics of the metastable atomic species N(^2D, ^2P) was not considered in [3,4], and was added in this work. For the case of pure nitrogen the kinetics of the atomic metastable states is described in [5]. For the mixture it is worth to mention the reactions of formation and destruction of NO, $N(^2D) + O_2 \rightarrow NO + O$ and $N(^2D) + NO \rightarrow N_2 + O$. As it will be seen below, this later reaction can give a significant contribution to the destruction of NO. The maintenance reduced electric field is determined using the requirement that under steady-state conditions the total rate for ionization must compensate exactly for the total rate of electron loss.

The system of equations just described allows the determination of the spatially averaged concentrations of the different heavy-particles, as well as the absolute value of the electric field E_0. Using this value in the set of equations (1) we have then the 3-D values for the electric field in the discharge zone. For the pressures of interest in this work, the homogeneous Boltzmann equation can subsequently be solved in each point in space for the local electric field given by (1), providing the 3-D distribution of the electron excitation, dissociation and ionization rate coefficients.

3. Results and discussion

The computed resonance frequencies (R = 11 cm, d = 1 cm, ε_d = 3.78) of experimentally observed TM_{33} mode as a function of the electron density and electron-neutral collision frequencies are shown in Fig.2. The resonance and the plasma frequencies are normalized to the mode cut-off frequency in the dielectric region, i.e., $\omega_0 = ck/\sqrt{\varepsilon_d}$ .The calculated dispersion curves of TM_{33} mode, for two significantly different values of electron-neutral collision frequency, $\nu_{en} = 10^8$ (solid lines) and $\nu_{en} = 10^{10}$ s^{-1} (dashed lines), are presented. As seen, the resonance frequencies are lower for higher collision frequencies and the effect of collisions is more pronounced at lower electron densities.

According to the dispersion equation, and keeping in mind a real situation when the microwave radiation frequency is 2.45 GHz, the TM_{33} mode is satisfied when the electron density N_e is 9.0×10^{11} cm^{-3} and the attenuation coefficient α is 2.00 cm^{-1}. The corresponding radial and azimuthal variations of the electric field components (at a fixed axial position z=const) are depicted on Fig. 3 and 4 respectively. The intensity of the electric field components is normalized to the value of the field E_0 at the plasma-dielectric interface.

Figure 5 shows the 2-D relative concentration of the $N_2(C\ ^3\Pi_u)$ state, for the conditions of figures 3 and 4, in a mixture of 95% N_2 – 5% O_2. The calculated value of E_0 is E_0 = 130 V/cm. The spatial distribution of the population of this strongly radiative state can be obtained directly from the Boltzmann equation, by assuming that it is mainly created by direct electron impact, $e + N_2(X) \rightarrow e + N_2(C)$, and destroyed by its radiative decay to the $N_2(B\ ^3\Pi_g)$ state, $N_2(C) \rightarrow N_2(B) + h\nu$. If this is the case, the concentration $[N_2(C)]$ in each position **r** is simply proportional to $n_e(\mathbf{r})C_X^A(\mathbf{r})$, where $C_X^A(\mathbf{r})$ denotes the rate coefficient for excitation of $N_2(C)$ from $N_2(X)$ calculated from the Boltzmann equation. In this figure the structure of the TM_{33} mode is clearly identified. However, at the present stage this figure must be considered only as indicative, since our calculations indicate that the remaining mechanisms of excitation of $N_2(C)$, namely the pooling through reaction $N_2(A) + N_2(A) \rightarrow N_2(X) + N_2(C)$ and the stepwise excitation $e + N_2(A) \rightarrow e + N_2(C)$, are also contributing significantly to populate the $N_2(C)$ state.

Finally, figure 6 shows the spatially averaged calculated concentration of NO molecules as a function of the relative concentration of O_2 in the mixture. As it is seen from this figure, for the conditions of this investigation the fractional population of NO can be close to 1%. As largely discussed in [3,4], NO molecules are created by reaction

$$N_2(X, v) + O \rightarrow NO + N \qquad (2)$$

and destroyed by the reverse reaction

$$NO + N \rightarrow N_2(X, v) + O\ . \qquad (3)$$

However, our present results indicate also a strong coupling between the kinetics of $N(^2D)$ metastables and NO molecules. As a matter of fact, NO is further created and destroyed very effectively in collisions that form and destroy $N(^2D)$ atoms as well, respectively via

$$N_2(A) + O \rightarrow NO + N(^2D) \qquad (4)$$

and

$$NO + N(^2D) \rightarrow N_2(X) + O. \qquad (5)$$

Processes (4) and (5) are very similar to (2) and (3), and seem to suggest that, together with nitrogen vibrations, atomic and molecular metastable states can play an important role in the overall discharge kinetics.

References

[1] H. Sugai, I. Ghanashev and M. Nagatsu, *Plasma Sources Sci. Technol.* **7** (1998) 192-205.
[2] I. Ghanashev, M. Nagatsu and H. Sugai, *Jpn. J. Appl. Phys.* **36** (1997) 337-344.
[3] V. Guerra and J. Loureiro, *Plasma Sources Sci. Techol.* **6** (1997) 373-385.
[4] V. Guerra and J. Loureiro, *Plasma Sources Sci. Techol.***8** (1999) 110-124.
[5] V. Guerra, E. Tatarova and C. M. Ferreira, *Vacuum* **8** (2003) 171-176.

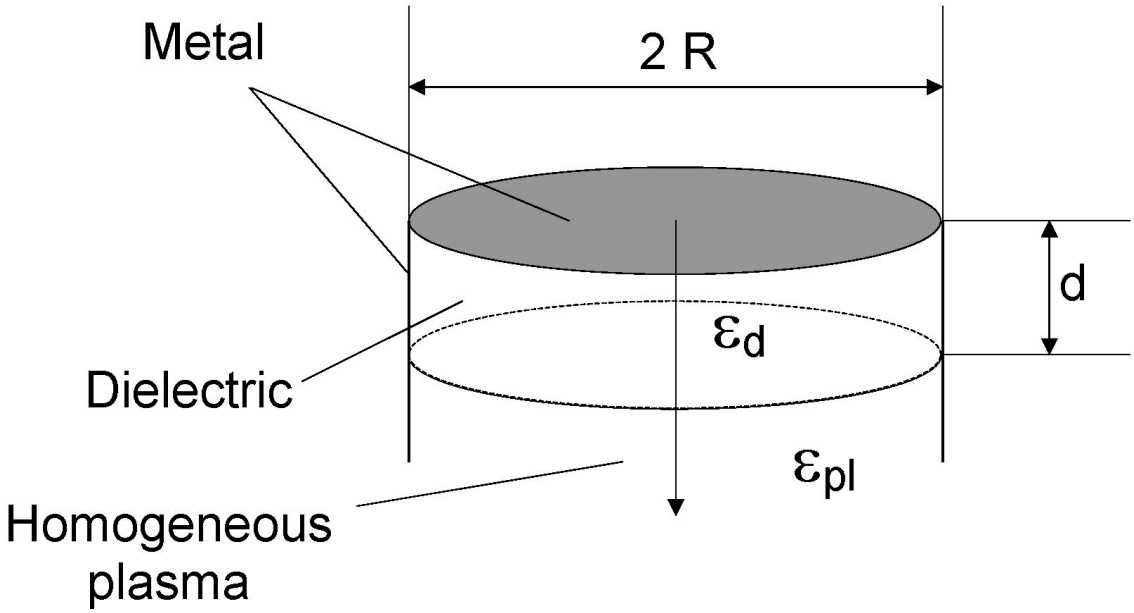

Fig. 1

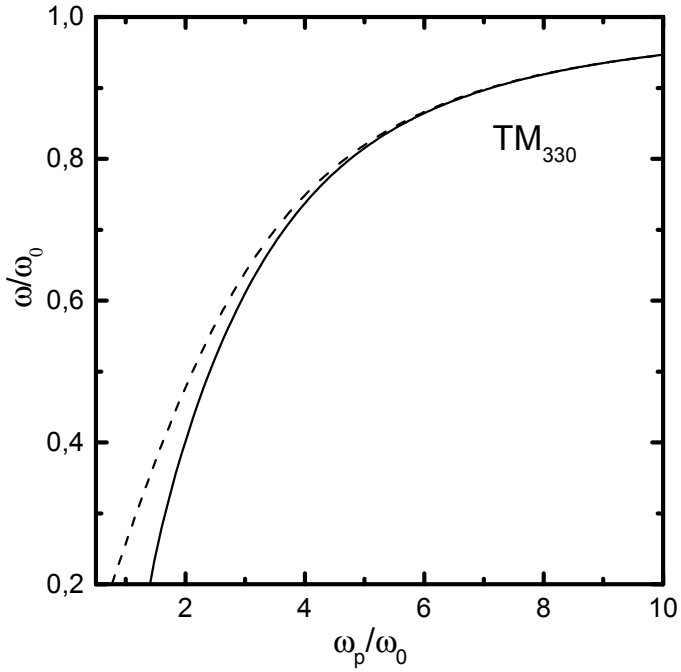

Fig. 2: Calculated resonance frequencies of the experimentally observed TM_{33} mode as a function of the electron density and for $\nu_{en} = 10^8$ (solid lines) and $\nu_{en} = 10^{10}$ s^{-1} (dashed lines),

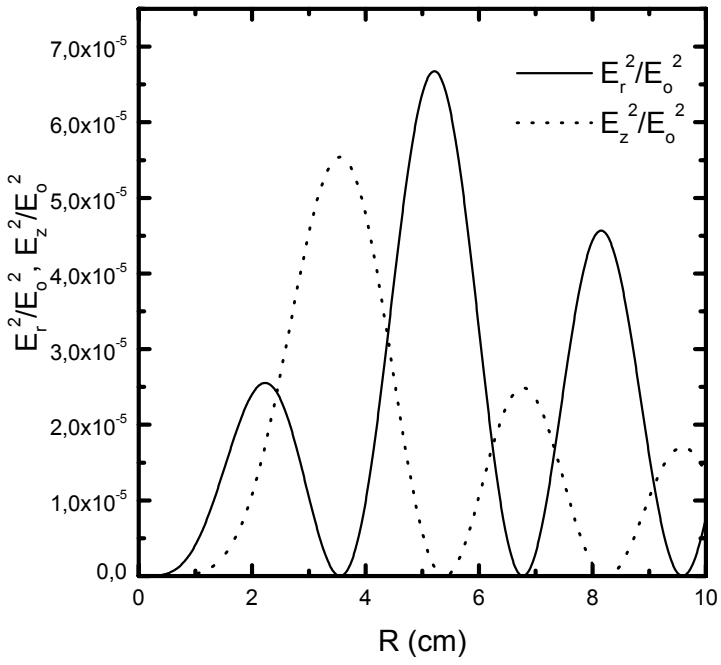

Fig. 3 relative radial variations of the electric field components (at a fixed axial position z=const).

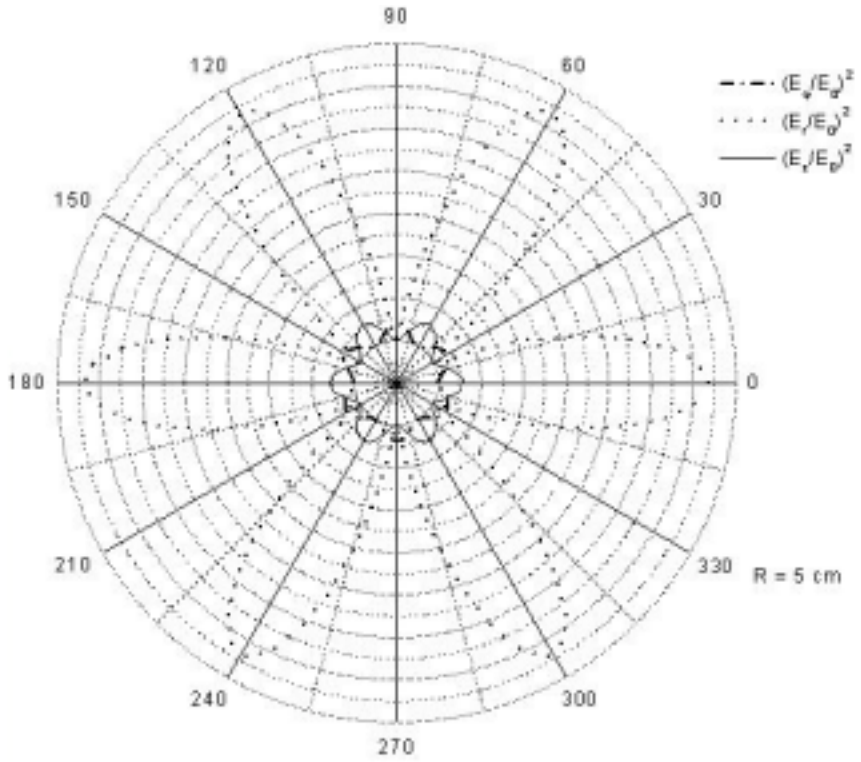

Fig. 4 relative azymuthal variations of the electric field components (at a fixed axial position z=const).

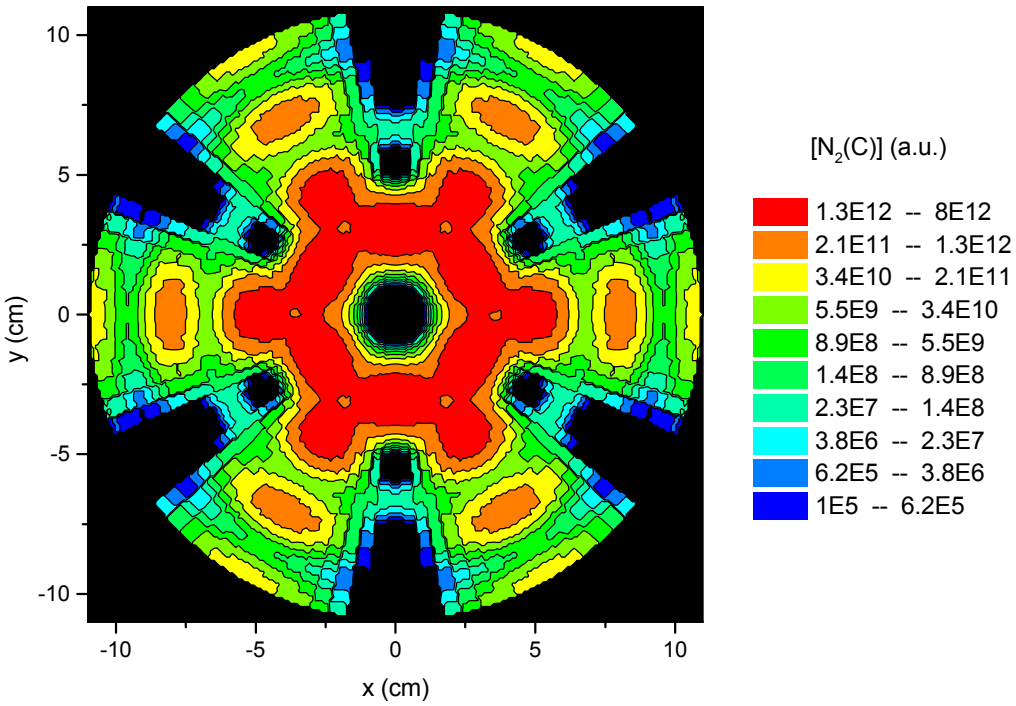

Fig. 5: 2-D distribution of the population of the radiative $N_2(C\ ^3\Pi_u)$ state, for a mixture 95% N_2 – 5% O_2.

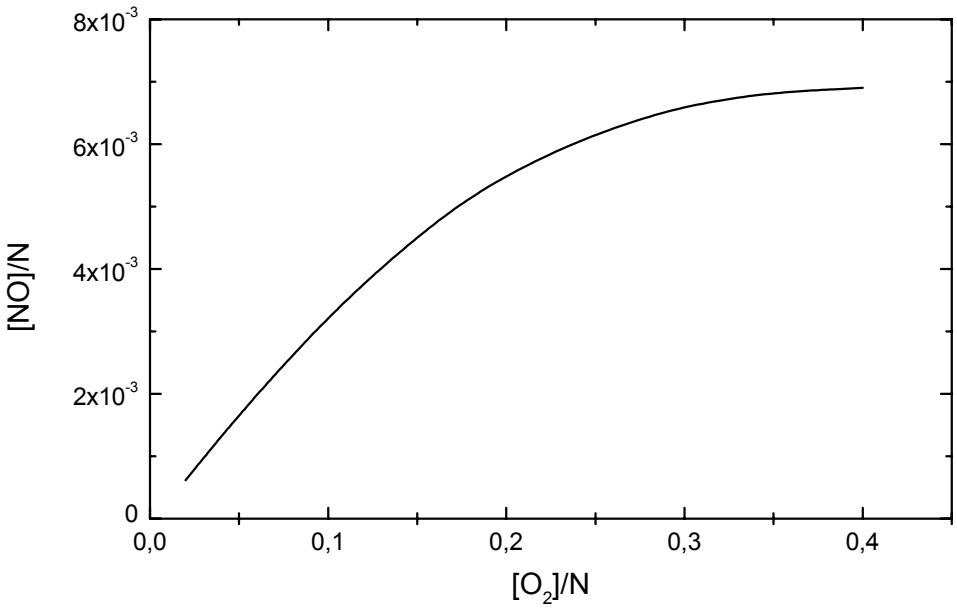

Fig. 6: Relative concentration of NO molecules as a function of the mixture composition.

Initial growth of Cu-nanoparticles in plasmas studied by Mie-ellipsometry

G.Gebauer, T.Galka, J.Winter

Institute for Experimental Physics II, Faculty for Physics and Astronomy
Ruhr-University Bochum, D-44780 Bochum
gg@plas.ep2.ruhr-uni-bochum.de

Plasma generated nanoparticles play an important role in modern materials technology, in catalyses and, for instance, in astrophysics. The development of measuring systems for the study of the transition from macromolecules to coagulated nanoparticles makes it possible to gain insight in to the growth process of nanoparticles and consequently allows their process control.
Nanoparticles of metals are vital for high catalytic activity. Copper particles, for example, are known to enhance the catalytic activity and selectivity of ZnO in hydration and dehydration reactions e.g. methanol synthesis and play an important role in solid-oxide fuel cells [1].
The particle size, the size-distribution and the dielectric properties of the nanoparticles are measured by Mie-ellipsometry [2][3][4]. Careful analyses of the ellipsometric angles Psi and Delta allows to push the sensitivity down to a few 10 nm particles size. We have analyzed the initial phase of Cu-nanoparticles growth in Ar capacitively coupled RF-plasmas. Reactive Cu-atoms required for the growth of particles are eluted from the upper Cu-electrode by DC-sputtering. The lower electrode is divided into several circular segments, which are insulated electrical from each other. The particle enclosure and the growth process is controlled by applying different potentials on these segments.

[1] J.Hambrock, Chemical Communications, **1**, P68, (2002).
[2] Y.Hayashi, Japan Journal of Applied Physics , **33**, L476 (1994).
[3] G.Swinkels, Proefschrift, Technische Universiteit Eindhoven, (1999).
[4] G.Gebauer, Dissertation, Ruhr-University Bochum, (2001).

Lifted flame stabilisation by a nanosecond pulsed DBD discharge

R. Delorme[1], P. Vervisch[1]

[1] *UMR 6614 CORIA CNRS, Saint Etienne du Rouvray, France*

Abstract

In this study, we have realized a burner using a CH_4-air premixing which allows to easily obtain a lifted flame at some centimetres from the exit of the injector. Two electrodes, on which we apply pulsed voltage (rising-time of 10ns, 15 to 25 kV), are placed perpendicularly to the direction of the flame in order to form a streamers sheet near the exit of the injector. When the discharges occur, we observe the catching of the flame base by the streamers sheet whereas this base flame was before a few centimetres above this streamers sheet.

1. Introduction

One of the most problems of the industrial burners or engines concerns the stabilisation of the lean flames which are lifted far from the exit of the gas injectors and thereby, they become very sensible with external or internal perturbations in the flow. Non-equilibrium gas discharge which leads to radicals production can be a solution for flame stabilisation. In different types of electrical discharges, pulsed discharges are the most attractive since the major part of the energy released in the discharge concerns gas internal degrees of freedom.
The choice of Dielectric Barrier Discharge (also named silent discharge) has been made for several reasons :

- in DBD, the electrodes aren't directly in contact with the gas in which this discharge occurs. The lifetime of these electrodes depends on neither the nature nor the flow of the gas. The contamination of the gas with evaporated electrode material is impossible [1]
- a wire-to-wire discharge allows us to generate a plane of streamers perpendicularly to the direction of the flame and so a height's referential for the flame base
- the DBD is a non-equilibrium high-pressure gas discharge which generates energetic electron with 1-20 eV, low excited atomic and molecular species, free radicals and excimer with several eV energy [2]
- the dielectric avoids the spark breakdown between the two electrodes
- the DBD can work at atmospheric pressure, at low pressure or at high pressure.

In the case of a wire-to-wire DBD, the distribution of the streamers is quasi-uniform all along the space between the two wires whereas in the case of a classical discharge between two wires, there are privileged points where the discharges occur due to the inhomogeneity of the material constituting the electrodes.
We often use high-voltage nanosecond pulse generator in the studies realized at our laboratory. In fact, the rise time of the high voltage pulse is a fundamental parameter for the energy of the created electrons. In such discharge, a propagation front (a streamer) crosses the gap from the high-voltage electrode to the low-voltage electrode with high velocity. In the head of this streamer, the electric field has high intensity and this leads to gas ionization, dissociation and excitation [3]. This electric field in the head of the streamer depends on the rising time of the high-voltage pulse : the narrowest the pulse is, the highest the electronic energy is [4].

2. Experimental set-up

The burner is realized in a ceramic tube presenting an internal diameter of 4,7 mm ± 0,05 mm, this tube is sealed into a vertical support made of cordierite. The gas injection allows to choose a premixed or non-premixed flow. In these experiments, the gas injection is always a non-premixed flow of Methane controlled by a Brooks flow-meter model GT-1355 with an Inox 316 model R-6-15-B float ball. This flow-meter has a range of measure comprised between 0 to 2020 l/h of Methane with a precision of 5% full range. With this burner, we can easily obtain a lifted flame at some centimetres from the injector exit.
The discharge system is constituted by two thin wires (diameter 0,1 mm) inserted into two parallel ceramic tubes (external diameter 2 mm) with a gap of 21 mm axis to axis. This gap corresponds to the diameter of the

base of the flame with the maximum used flowing velocity of 14 $m.s^{-1}$. These two tubes take place into a support in order to have a strictly parallel plane of streamers. The width of the discharge sheet is about 40 mm. This discharge system is mounted on a vertical displacement which have a range of 55 mm. This possibility of height variation is useful for the placement of the discharge sheet at any position in the flame or upstream of the flame. The Fig.1. presents this discharge system.

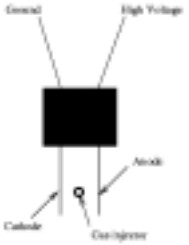

Fig.1. : Scheme of the discharge system

The nanosecond pulsed discharge, between these two electrodes across the dielectric, is generated by an home-made Marx generator, for which the electrical scheme is presented in the Fig.2., linked with a continuous power supply.

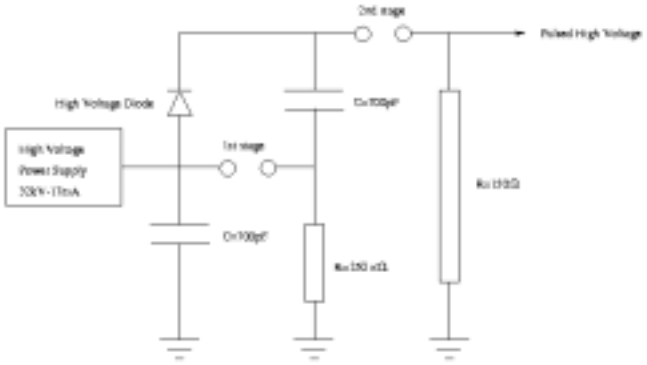

Fig.2. : Electrical scheme of the Marx generator

The principle of this Marx generator is simple, the two capacitors are charged in parallel by the 0-32 kV, 0-17 mA power supply. When the capacitors are sufficiently charged, the dielectric gas (Nitrogen in our case) in the first stage becomes ionized and so conducting. As the potential across the second stage gap is twice the charging voltage, the dielectric gas in the second stage allows the breakdown and an high-voltage pulse is created with the typical characteristics showed in Fig.3.. This signal is obtained by the mean of 500 pulses at a 200 Hz running. This generator can have a maximum repetition rate up to 300 Hz.

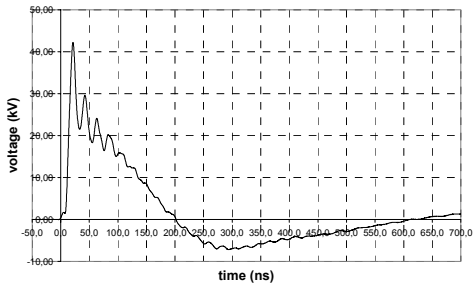

Fig.3. : Typical characteristic of the high-voltage pulse obtained with the Marx generator in the Methane flame

The digital oscilloscope Tektronix TDS-7104 (1 GHz, 4 channels, 10 Gsamples/s, 500 kpoints on 4 channels) allows to have minimal time resolution of 400 ps/point when all the channels are used. The voltage is measured with a capacitive probe Effitech with a time resolution below 1 ns. The measure of the current is realized with a pulse current transformer Stangenes 0.5-1.0 (rise time of 10 ns) between the cathode and the

ground. These two probes are linked to the oscilloscope. The set-up of this experiment is showed in the Fig.4..

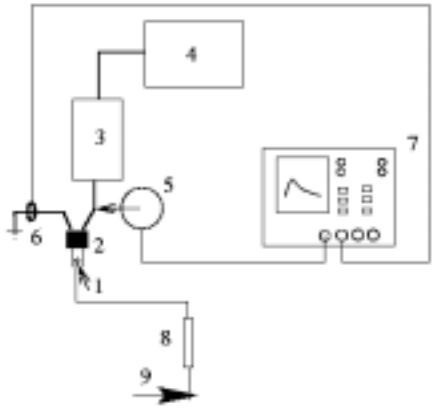

Fig.4. : Experimental set-up of the stabilisation of a lifted flame : **1**. Burner, **2**. Discharge System, **3**. Marx Generator, **4**. High-voltage power supply, **5**. Capacitive probe Effitech, **6**. Pulse current transformer Stangenes, **7**. Digital oscilloscope Tektronix TDS-7104, **8**. Flow-meter Brooks GT-1355, **9**. Methane Inlet

3. Results and discussion

The home-made burner allows to have various flowing velocities from laminar flame to high velocity lifted flame up to at least 35 $m.s^{-1}$ (Reynolds number of 10000) without extinguishing. But in the case of stabilisation, a limit appears due to the maximal discharge gap usable with our Marx generator. This gap measures 21 mm and the maximum flowing velocity corresponding to the base flame diameter is equal to 14 $m.s^{-1}$. In the Table.1., the different flowing velocities used are presented with their associated Reynolds number.

Table.1. : Flowing velocities face to the Reynolds number associated

Flowing Velocity ($m.s^{-1}$)	Reynolds Number
9,7±0,7	2976±244
10,8±0,8	3307±271
11,9±0,8	3638±298
12,9±0,9	3968±395
14,0±1,0	4299±352

The minimum number of Reynolds in this table is greater than the limit of the turbulent comportment who is 2320 in cylindrical tubes. The flame is so a turbulent flame far from the transitional speed.
In the first experiments, the flame was lifted a few centimetres above the plane delimitated by the two electrodes before the discharges apply. When the discharges occur, we observe the catching of the flame base by the streamers sheet. This catching can be seen in the Fig.5., on the left side the flame without discharge and on the right side with discharge for the same flowing velocity.

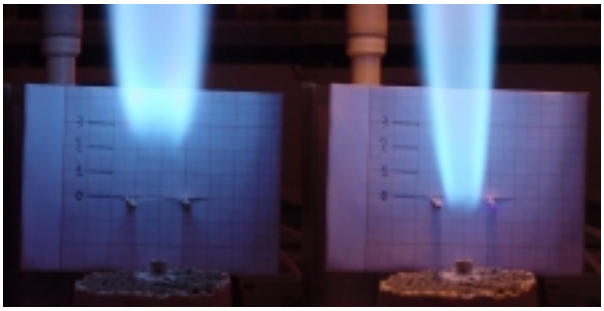

Fig.5. : Catching of the methane flame by the streamer sheet

With this catching, the flow of the injected gases in comparison with the case without streamers can be increased.
With this arrangement, the cathode current and so the injected energy in the discharge can be measured. Their characteristic are showed in Fig.6.. The signals are obtained by the mean on 500 pulses at a frequency of 200 Hz.

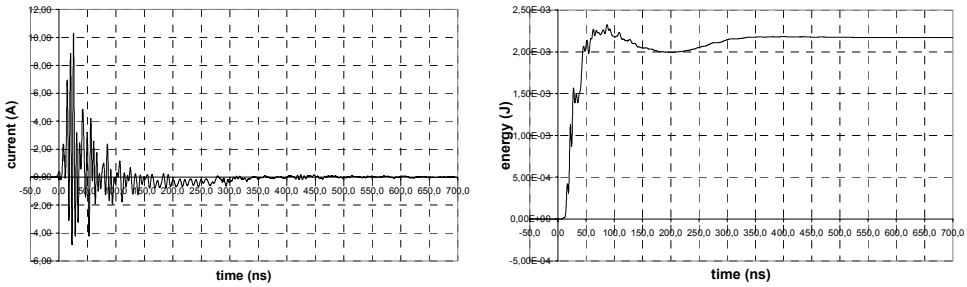

Fig.6. : Typical characteristic of the cathode current and the injected energy obtained with the Marx generator in the Methane flame

The characteristics of this discharge are 42 kV max., 26 A max., 23 mJ max..
With

$$Q = \int_0^{t\max} I dt \,, \qquad (1)$$

the calculated number of charges injected in the discharge is typically 0,02 µC.
The discharge characteristics change drastically according to the streamer sheet position in comparison with the flame position. The variation of the injected energy in the streamers according to the position in the flame can be seen in the Fig.7.. The signals are obtained by the mean on 500 pulses at a frequency of 200 Hz.

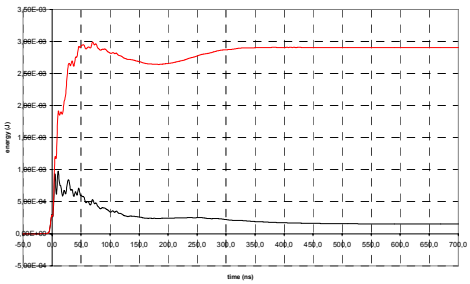

Fig.7. : Typical characteristics of the injected energy according to the position of the streamer sheet in the Methane flame: upper curve in the flame, lower curve below the flame

The choice of the criteria of the flame stabilisation by the streamers sheet can be easily solved by the direct measurement of the injected energy in the streamers (the digital oscilloscope allows this measure). This minimal energy has been chosen equal to 2-3 mJ (in the case of 40 kV discharges), this value corresponds to a good catching of the base flame.
With this criteria, the experiment consists on the flow measurement in the case of streamer discharge for some streamer repetition frequency and for some initial flows of methane. The different repetition frequencies usable with the Marx system are in the range from 1 Hz to 250 Hz, the different methane flowing velocities are in the range from 9,7 $m.s^{-1}$ (the minimal flowing velocity to lift the flame) to 14 $m.s^{-1}$ (the maximal flowing velocity corresponding to the base flame diameter equal to the electrodes gap). The Fig.8. presents the results of this experiment.

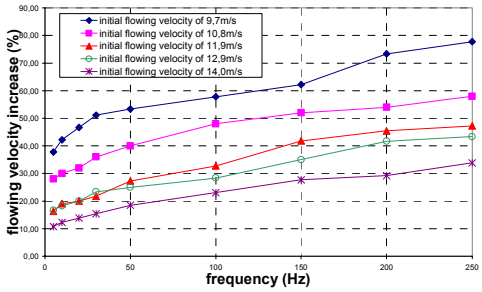

Fig.8. : Characteristics of the flowing velocity increase according to the streamer repetition frequency

The different curves present the flowing velocity increase for 5 cases of initial flowing velocities (the values are in the Table.1.) according to the streamer repetition frequency. In fact, for a same lift height, the flowing velocity can be increased by the specified percentage showed in the Fig.8. in keeping with the corresponding streamer repetition frequency. The flowing velocity increase has a quasi-linearly evolution according to the streamer frequency repetition. With this type of discharges at 250 Hz, the injected power in the streamers is equal to 0,75 W.
The difference between the minimum and the maximum increase of the flowing velocity is showed in the Fig.9..

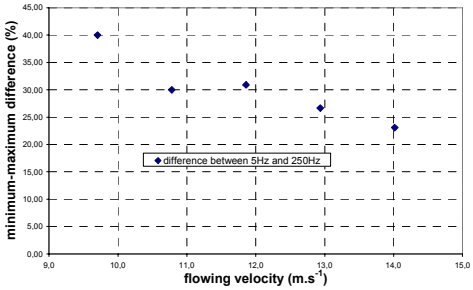

Fig.9. : Characteristic of the minimum-maximum efficiency difference according to the initial flowing velocity

This figure presents, for each initial flowing velocity of the Table.1., the difference between the flowing velocity increase at low frequency (5 Hz) and the flowing velocity increase at high frequency (250 Hz). This difference decreases with the increase of the initial flowing velocity. The repetition streamer frequency seems to be the most important factor to the stabilisation of lifted flame, especially in the case of high flow velocities. From these characteristics, an extrapolated mean value of the flowing velocity increase according to the frequency can be calculated, this value is equal to (0,13 ± 0,03)%/Hz.
Furthermore, a change in the brightness of this diffusion flame appears as soon as the discharges begin, the flame front between the combustion gas and the air forms a cone who presents an lower angle than in the case without discharges. The flame velocity seems so to be higher when the discharges occur, this flame velocity would be measured in the future[5].

4. Conclusion

In this study, we have seen that the stabilisation by nanosecond streamer discharges in double DBD running is possible. The effect of these discharges on the flowing velocity allows to have up to 80% of increase at constant distance between the exit of the injector and the base of the flame. The discharges power contribution in the total power of a such flame of methane is quasi-negligible (less than 1 W) in comparison with the burner power (10 $kW.m^{-3}$). The major objective for the improvement of this lifted flame stabilisation system rests on the possibility of high frequency discharges (more than 1 kHz) in the case of high flowing velocities. The use of such discharges system in industrial burner seems to be a good opportunity if the rise in frequency is feasible.

References

[1] Lifetime investigation of excimer UV sources, Jun-Ying Zhang, Ian W. Boyd - Applied Surface Science. **296-299**, 168 (2000).

[2] Dielectric barrier discharge - properties and applications, Xueji Xu - Thin Solid Films. **237-242**, 390 (2001).

[3] Chemical reactions and ignition initiation in hydrocarbon-air mixtures by high-voltage nanosecond gas discharge, N.L. Aleksandrov, N.B. Anikin, E.M. Bazelyan, D.V. Zatsepin, S.M. Starikovskaia, A.Yu. Starikovskii – 32nd AIAA Plasmadynamics and Lasers Conference and 4th Weakly Ionized Gases Workshop, 11-14 June 2001/Anaheim, CA. AIAA 2001-2949.

[4] Pulsed breakdown at high overvoltage : development, propagation and energy branching, S.M. Starikovskaia, N.B. Anikin, S.V. Pancheshnyi, D.V. Zatsepin, A.Yu. Starikovskii – Plasma Sources Science and Technology. **344-355**, 10 (2001).

[5] Instantaneous Flame-Stabilization Velocities in Lifted-Jet Diffusion Flames, L. Muñiz, M.G. Mungal - Combustion and Flame. **16-31**, 111 (1997).

A pulsed UV source with a nanosecond streamer discharge in DBD running in a Ar-H_2 mixture

R. Delorme[1], P. Vervisch[1]

[1] *UMR 6614 CORIA CNRS, Saint Etienne du Rouvray, France*

Abstract

In this study, we have realized a pulsed DBD radiating source running in a Ar-H_2 mixture which can be suitable in particular in the wavelength region where usual Xenon and Mercury lamp are less efficient. The derived spectrum is a quasi-constant continuum from 188 nm to 350 nm with nevertheless a peak near 205 nm (uncorrected of the detection system spectral response). This radiation is associated with the dissociative transition of H_2 ($a^3\Sigma_g^+ \rightarrow b^3\Sigma_u^+$).

1. Introduction

Most of the commercial lamps, like Xenon or Mercury lamps, have discontinuous spectra with some typical radiations usable for a spectrometer calibration for example. As the emission of these lamps is continuous regarding the time, the utilization of this lamps is very easy and they have proved their qualities for emission measurements. But, in the case of absorption measurement in UV, a pulsed source prevents the contribution of the self emission of the studied medium especially if this one is strongly emissive. Furthermore, a feature less wavelength spectrum is more appropriate for absorption measurements in molecular bands especially in the UV range.

The use of a pulsed Dielectric Barrier Discharge (also named silent discharge) in a cylindrical configuration is of interest for several reasons :

- in cylindrical double DBD, the electrodes aren't directly in contact with the gas in which the discharge occurs. So the electrodes lifetime is increased. The contamination of the gas by evaporated electrode material is avoid [1]
- the construction of the discharge system is easy and is cheaper in comparison with other sources such excimer lasers
- the cylindrical configuration with a wire-to-wire discharge allows us to generate a plane of streamers in the axis of the cylinder
- the DBD is a non-equilibrium high-pressure gas discharge which generates energetic electron with 1-20 eV, low excited atomic and molecular species, free radicals and excimers with several eV energy [2]. These excimers can convert electron kinetic energy into UV radiation [3]
- non-toxic materials or gases are used in our configuration in comparison with some UV sources found in the literature [4], [5]. There is no risk for the environment and for the users
- the DBD can work at atmospheric pressure whereas the excimer lamps are usually sealed at low-pressure with all the disadvantages linked like the fragility of these lamps.

In the case of a wire-to-wire cylindrical DBD, the distribution of the streamers is quasi-uniform all along the space between the two wires whereas in the case of a corona discharge between two wires, there are privileged points where the discharges occur due to the inhomogeneity of the material constituting the electrodes.

We have realized, some years ago, a DBD source running with a power supply delivering 7 kV at 20 kHz [6]. In this source, the discharge is initiated between two fine metallic straight lines of 400 mm length painted on a quartz tube of 5 mm of diameter and 1 mm of thickness. This source was running in Ar to produce the third continuum of Ar_2* excimer. The brightness of this source was too low to perform absorption measurement in an emissive medium. To overcome this difficulty, another power supply has been developed to generate nanosecond high voltage pulses. Indeed, nanosecond high voltage discharges are more suitable since higher electric field can be applied. The large electric field energizes large number of electrons to high energy level. Those numerous energetic electrons lose very little energy in collision with gas atoms

and molecules because the electron mass is very small in comparison to typical molecular mass. So the major part of their energy contributes to generate a large amount of excited states in the medium [7] [8].

2. Experimental set-up

The discharge cell is shown in Fig.1. It consists of a 260 mm length ceramic tube. The outer diameter is 11,9 mm for 1,95 mm thick. The length of discharge is l=130 mm. The tube has two opposite by diameter grooves in which are placed two fine wires (diameter 0,1 mm). The thickness of these wires is important because the electric field generated depends on the electrode curvature radius. The lowest the radius is, the highest the electric field is. The gap between the two electrodes is about 11 mm ± 0,5 mm. The windows are in MgF_2 due to their high transmittivity for λ>128nm [6].
The gases flows are adjustable for each gas, the typical range of Argon flow is from 0 to 20 l/min and that of Hydrogen is from 0 to 15 l/min. In fact, the Argon's flow is higher than the Hydrogen's, the best efficiency for a intense radiation is with 4 l/min of Argon and some tenth of litre of Hydrogen. The pressure at the outlet gas tube is ambient pressure.

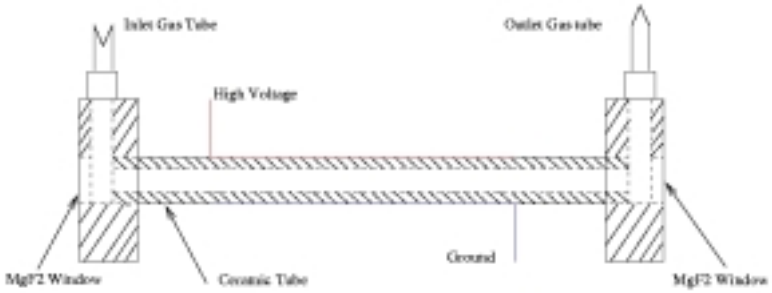

Fig.1. : Scheme of the discharge cell

The nanosecond pulsed discharge, between these two electrodes across the dielectric, is generated by an home-made Marx generator, for which the electrical scheme is presented in the Fig.2., linked with a continuous power supply.

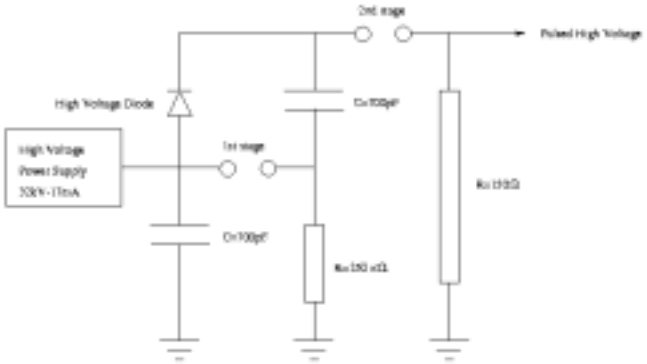

Fig.2. : Electrical scheme of the Marx generator

The principle of this Marx generator is simple, the two capacitors are charged in parallel by the 0-32 kV, 0-17 mA power supply. When the capacitors are sufficiently charged, the dielectric gas (Nitrogen in our case) in the first stage becomes ionised and so conducting. As the potential across the second stage gap is twice the charging voltage, the dielectric gas in the second stage allows the breakdown and an high-voltage pulse is created with the typical characteristics showed in Fig.3.. This pulse has a typical rise-time below 10 ns (in this pulse, the rise-time is 8,9 ns), the FWHM of this signal is quite 40 ns knowing that the signal showed in Fig.3. is obtained by the mean on 64 pulses. This generator can have a maximum repetition rate up to 300 Hz.

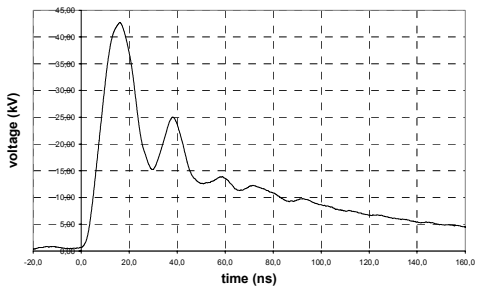

Fig.3. : Typical characteristic of the high-voltage pulse obtained with the Marx generator in Hydrogen and Argon

The discharge cell is imaged on the entrance slit of a Jobin-Yvon THR-1000 spectrometer (focal length 1000 mm, aperture f/7.5 , grating with 4320 grooves/mm) on which is mounted a fast photomultiplier Philips XP-2020Q linked with a digital oscilloscope Tektronix TDS-7104 (1 GHz, 4 channels, 10 Gsamples/s, 500 kpoints on 4 channels) which allows us to have minimal time resolution of 400 ps/point when all the channels are used. The voltage is measured with a capacitive probe Effitech with a time resolution below 1ns. The current measure is realized with a pulse current transformer Stangenes 0.5-1.0 (rise time of 10 ns) between the cathode and the ground. These two probes are linked to the oscilloscope. The mixture of the Argon and the Hydrogen is realized upstream the discharge cell. The control of the grating's displacement is realized by a Spectralink (displacement precision 0,001 nm in wavelength). The experimental set-up is showed in the Fig.4..

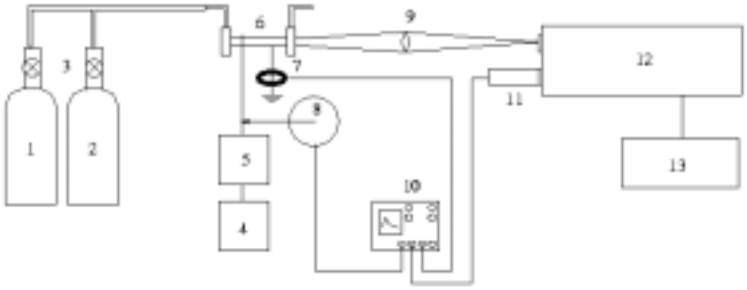

Fig.4. : Experimental set-up of the UV source : **1**. Argon, **2**. Hydrogen, **3**. Flow meters, **4**. High-voltage power supply, **5**. Marx generator, **6**.Discharge cell, **7**. Pulse current transformer Stangenes, **8**. Capacitive probe Effitech, **9**. UV Lens, **10**.Digital oscilloscope TDS-7104, **11**. Photomultiplier Philips XP-2020Q, **12**. Monochromator Jobin-Yvon THR-1000, **13**. Spectralink

3. Results and discussion

With this arrangement, the cathode current and so the injected energy in the discharge can be measured. Their characteristic are showed in Fig.5.. The signals are obtained by the mean on 64 pulses.

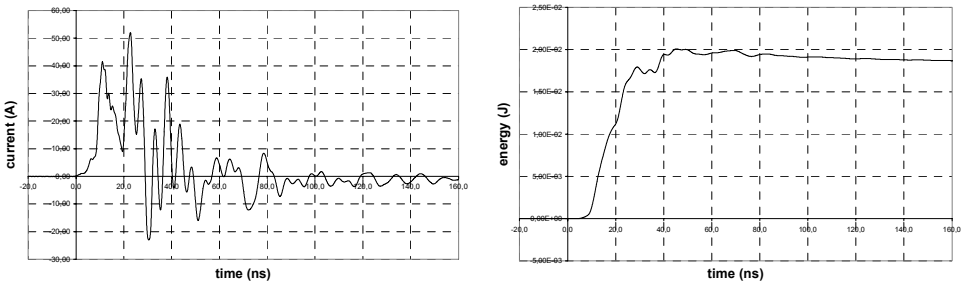

Fig.5. : Typical characteristic of the cathode current and the injected energy obtained with the Marx generator in Hydrogen and Argon

The characteristics of this discharge are 42 kV max., 50 A max., 20 mJ max..

With

$$Q = \int_0^{t_{max}} I dt \,, \tag{1}$$

the calculated number of charges injected in the discharge is typically 0,5 µC.

The O_2 Schumann-Runge bands of ambient air strongly absorb VUV radiation. So, the wavelength range studied in this experiment starts from 185 nm and stops at 350 nm due to the grating used. The Schumann-Runge bands can be clearly seen in the spectrum up to 195 nm due to their absorption.
The generation of a continuous spectrum in wavelength with this source has been obtain after some tries with other gases added to the Argon. The Hydrogen is the only gas which permits us to success in our research.
The technique for the realization of a spectrum in this range with a pulsed source is quite different than in the case of continuous source. In continuous source, generally, a continuous photomultiplier is used and the signal is send to a drawing table or a recorder. The grating's monochromator is displaced all along the wavelength range in one time with a constant velocity and the spectrum is easily obtained. But in our case, the fact that this source is a pulsed source doesn't allow us to use this technique. The digital oscilloscope has a function of curve recorder called Fast Frame. With a program, it is possible to extract the features of this curve like the maximum, the minimum, the area between two cursors, etc... Fig.6. shows a typical characteristic of the impulsional photomultiplier signal response in the case of a detected radiation, the interesting part due to the radiation is gated within the vertical cursors. On this figure, the signal noise is due to electromagnetic perturbations induced by the proximity of the Marx generator which is bad isolated. Here the signal level detected by the photomultiplier is far from the detection limit since typical voltage value is about 10 V.

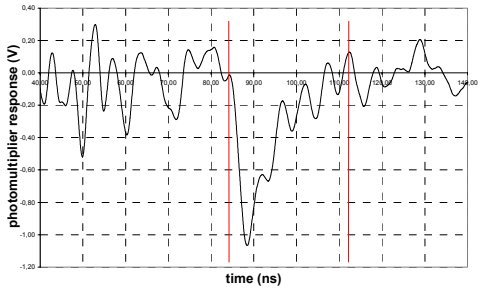

Fig.6. : Typical characteristic of the photomultiplier signal response

Fig.7. presents the spectral behaviour of this source filled by an Argon and Hydrogen mixture. Present results were performed with a 0,01 nm spectral resolution.

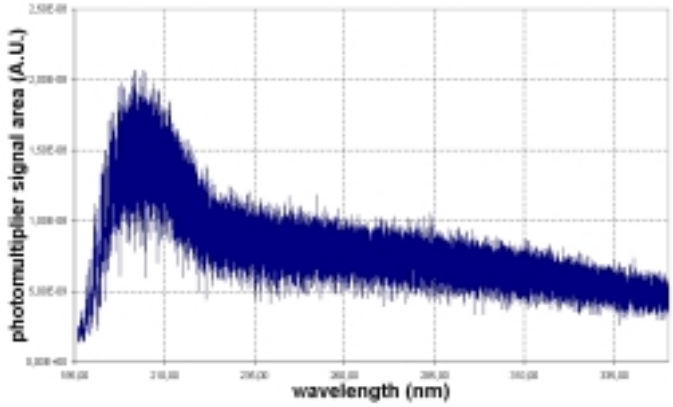

Fig.7. : Spectrum of the pulsed UV source in DBD running in Argon and Hydrogen

The noisy aspect of this spectral behaviour is due to the generation principle of the radiations. Between each pulse generated by the Marx generator, the level signal fluctuates. This fluctuation is one of the parameters which would be resolved in the optimisation of the source. The derived spectrum has a quasi-continuous

aspect regarding the wavelength behaviour from 185 nm to 350 nm with nevertheless a peak near 205 nm. With our system, a delay appears between the rise's beginning of the high voltage pulse and the detection of the radiation, this delay is equal to 95 ns. It is necessary to cut out from this delay, the photomultiplier's delay of optical-electrical conversion equal to 28 ns and the delay of signal transmission from the photomultiplier to the digital oscilloscope (7 meters of cable : 42 ns). The final temporal shift between the rise's beginning of the high-voltage pulse and the detection of the radiation is equal to 25 ns. The duration of this detection signal depends on the rate of Hydrogen in Argon, in the case of the mixture who presents the maximum effect, this duration is equal to 15 ns. This type of spectrum has been also realized with Fast Ionization Wave at a pressure of 10 Torr by Pancheshnyi [9].

This spectrum is issue from the dissociative transition of H_2 ($a^3\Sigma_g^+ \rightarrow b^3\Sigma_u^+$) which presents a continuum from 160 nm to 500 nm [10], [11]. Fig.8. presents this transition.

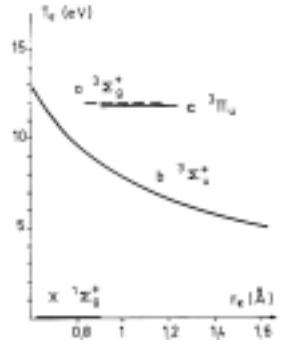

Fig.8. : Electronic states of Hydrogen (— metastable ---- radiative) [11]

In pulsed DBD, some electrons have sufficient energy to overlap the energetic range of the Argon metastable excitation cross section as showed in Fig.9..

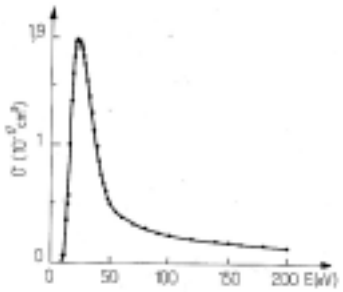

Fig.9. : Argon metastable excitation effective section [11], [12], [13]

In our configuration, the $a^3\Sigma_g^+$ level is over populated by excitation transfer with metastable level of Argon as showed in equation (2).

$$Ar\ (^3P_2, {}^3P_0) + H_2 \xrightarrow{k_{2Q}} Ar + H_2^* \qquad (2)$$

4. Conclusion

This study shows the interest of this nanosecond pulsed UV source to generate a quasi-continuum spectrum from 185 nm to 350 nm due to the dissociative transition of H_2 ($a^3\Sigma_g^+ \rightarrow b^3\Sigma_u^+$). The use of a pulsed Dielectric Barrier Discharge in a cylindrical geometry allows to have several possibilities of tests like the kind of gas injected, the flow of these gases, the electrical characteristics of the discharge... The only limitation is the detection of radiations below 180 nm which imposes to realized an arrangement under vacuum in order to avoid the Schumann-Runge bands. Several tests are in progress to enhance the source efficiency and stability, in particular, by delaying the mixture with a buffer gas to limit the collisional quenching of the concerned excited states.

References

[1] Lifetime investigation of excimer UV sources, Jun-Ying Zhang, Ian W. Boyd - Applied Surface Science. **296-299**, 168 (2000).
[2] Dielectric barrier discharge - properties and applications, Xueji Xu - Thin Solid Films. **237-242**, 390 (2001).
[3] High-intensity sources of incoherent UV and VUV excimer radiation for low-temperature materials processing, U. Kogelschatz, H. Esrom, J.-Y. Zhang, I.W. Boyd - Applied Surface Science. **29-36**, 168 (2000).
[4] Efficient excimer Ultraviolet sources from a dielectric barrier discharge in rare-gas/halogen mixtures, J.-Y. Zhang, I.W. Boyd - Journal of Applied Physics. **633-638**, 80 (2) (1996).
[5] Efficient XeI* excimer ultraviolet sources from a dielectric barrier discharge, J.-Y. Zhang, I.W. Boyd - Journal of Applied Physics. **1174-1178**, 84 (3) (1998).
[6] Spectroscopic methods applied to plasmas and high enthalpy media, Pascal Boubert – Thesis (in French) at University of Rouen (France), 1999.
[7] Chemical reactions and ignition initiation in hydrocarbon-air mixtures by high-voltage nanosecond gas discharge, N.L. Aleksandrov, N.B. Anikin, E.M. Bazelyan, D.V. Zatsepin, S.M. Starikovskaia, A.Yu. Starikovskii – 32nd AIAA Plasmadynamics and Lasers Conference and 4th Weakly Ionized Gases Workshop, 11-14 June 2001/Anaheim, CA. AIAA 2001-2949.
[8] Pulsed breakdown at high overvoltage : development, propagation and energy branching, S.M. Starikovskaia, N.B. Anikin, S.V. Pancheshnyi, D.V. Zatsepin, A.Yu. Starikovskii – Plasma Sources Science and Technology. **344-355**, 10 (2001).
[9] Dynamics of the Excitation of Electronic States of H_2 Molecules in a Fast Ionization Wave, S.V. Pancheshnyi, S.M. Starikovskaia, A.Yu. Starikovskii. Plasma Physics Reports. **393-397**, Volume 25, n°5 (1999).
[10] Quenching Cross-Sections for Electronic Energy Transfer Reactions Between Metastable Argon Atoms and Noble Gases and Small Molecules, L.G. Piper, J.E. Velazco, D.W. Setser. Journal Chemical Physic. **3323**, 59 (1973).
[11] Atomes et Molécules Métastables dans les gaz ionisés, J.L. Delcroix, C. Matos Ferreira, A. Ricard. Centre National de la Recherche Scientifique.
[12] O.P. Bochkova, N.B. Ghernysheva. Optical Spectroscopy. **341** (1972).
[13] J.W. Dreyer, D. Perner. Journal Chemical Physic. **3164**, 61 (1974).

Optical emission spectroscopy (OES) and phase-conjugate degenerate four-wave mixing spectroscopy (PC-DFWM) in investigations of local thermal equilibrium plasma

K.Dzierzega[1,2], S.Zielinska[1], S.Pellerin[2], K.Musiol[1], and Ch. de Izarra[2]

[1] *M. Smoluchowski Institute of Physics, Jagiellonian University, ul.Reymonta 4, 30-059 Kraków, Poland.*
[2] *LASEP, Université d'Orléans - Antenne de Bourges, Rue Gaston Berger BP 4043, 18028 Bourges, France.*

Abstract: The non-intrusive optical emission spectroscopy (OES) and degenerate four-wave mixing (DFWM) spectroscopy, in the backward phase-conjugate (PC) geometry, have been used in local studies of low-temperature plasma generated in a free-burning arc. The semi-empirical model of the PC-DFWM that relates DFWM signal intensity and plasma parameters has been worked out and successfully applied to plasma diagnostics and line profile measurements.

1. Introduction

The concept of local thermodynamic equilibrium (LTE) plays the crucial role in research of atmospheric-pressure thermal plasmas. That is because the knowledge of one parameter, i.e. electron temperature, allows for determination of all other plasma parameters what is particularly simple in case of one component plasma. However, in order to take advantage of the LTE, first the state of plasma must be verified experimentally. This, in turn, requires two independent parameters to be measured with reasonable spatial and, in the case of pulsed plasmas, temporal resolution.

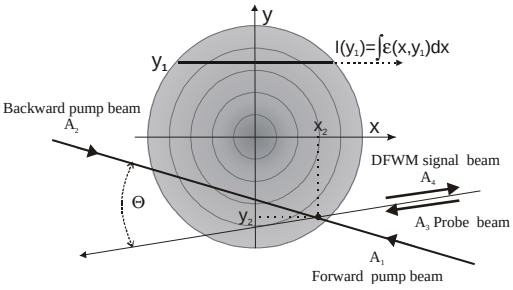

Figure 1. Principles of the OES and the PC-DFWM spectroscopy.

Investigations of the atmospheric arc plasma are mostly based on the OE spectroscopy. A simple experimental set-up and non-intrusive measurement are its major advantage. On the other hand, only intensity integrated along a line of sight can be directly measured and local values of emission coefficient can be obtained exclusively for layers either homogeneous or with cylindrical symmetry by Abel inversion. The legitimacy of application of the OE spectroscopy is questionable in studies of the vicinity of electrodes where plasma symmetry strongly depends on the position of the cathode spot on the electrode surface as is the case for free burning arcs. Moreover, this region of the discharge is highly influenced by the flow rate of gas and deviations from the LTE state have been already reported by many authors [6, 7]. All of these observations were carried out using the OE spectroscopy. In the light of the foregoing discussion alternative and complementary methods are necessary for comprehension of plasma processes.

The application of high spatial and temporal resolution laser-based methods such as laser induced fluorescence, laser collision induced fluorescence or saturation spectroscopy to investigate dense plasmas is impossible because of the relatively high elastic and inelastic collision rates and high photon emission of the plasma. The signal to be detected would be destroyed either by velocity changing collisions or the non-radiative decay of the excited atoms or would disappear in the background of the strong plasma radiation. Application of Thomson scattering method, well established in the field of Tokamak plasmas, however leads to strong plasma disturbance and can result in misinterpretation of the results as it has been recently showed by Murphy [1].

We developed the PC-DFWM method in application to low-temperature plasma with electron collisions to be the dominant processes responsible for depopulation and line broadening. We report on investigations of an argon plasma generated in a free-burning arc using PC-DFWM method at the wavelength corresponding to the 4*s*[3/2]^{o}-4*p*'[1/2] ArI transition (696.543 nm). DFWM spectroscopy with high spatial resolution was used to measure the Stark shift of the line and, independently, to obtain the plasma temperature. The latter was determined using the relationship between DFWM signal intensity and plasma parameters assuming LTE. The results of plasma diagnostics obtained by PC-DFWM methods are compared with those obtained using the OES as described by Pellerin *et al.* [6] and Pokrzywka *et al.* [8].

2. Degenerate four-wave mixing in application to plasma studies

Degenerate four-wave mixing (DFWM) is a nonlinear optical process involving three laser beams of frequency w, which interact through the nonlinearity of a medium to generate a fourth, signal beam, at the same frequency.

We deal with DFWM in the backward phase-conjugate (PC) geometry where the probe beam of amplitude A_3 crosses the two counter-propagating (forward and backward of amplitudes A_1 and A_2, respectively) pump laser beams at an angle q (see Fig. 1). Such configuration satisfies the phase-matching relations for all angles q and makes the spatial resolution of the method to be limited only by dimension of the laser beams. The signal beam, phase-conjugated to one of the incident laser beams, is highly collimated and so can be readily distinguished from the plasma radiation. Moreover, the Doppler broadening effect is significantly reduced because only atoms resonantly interacting with all laser beams contribute to the signal.

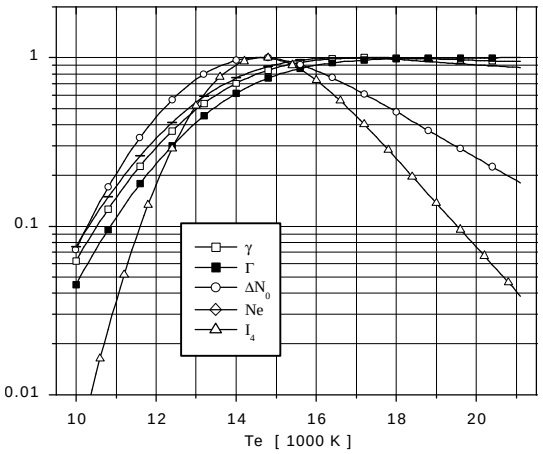

Figure 2. Temperature dependence of atomic and plasma parameters as well as DFWM signal intensity calculated for atmos. pressure argon plasma in LTE. The relative values are shown.

The details concerning the model of PC-DFWM as applied to thermal plasma are given in thesis by Bratasz [2]. Briefly, it assumes the PC-DFWM configuration for an open two-level system of resonance frequency w_0, in an optically thin medium. It considers three laser beams of arbitrary intensity and of linear and parallel polarizations interacting as in Fig.1. The standard formalism of the time dependent density matrix was used to calculate the total polarization of the system irradiated by laser beams. The atom is described by the dipole moment m of the considered transition while an influence of the plasma is described by coherence, g, and population, G, decay rates.

Under above assumptions and for laser beams of equal intensities a semi-empirical expression for the PC-DFWM signal intensity, I_4, has been derived and it reads:

$$I_4(d) \propto (m\,\Delta N_0)^2 \,\frac{\Gamma}{g}\left(\frac{1}{1+d^2}\right)^p \left(\frac{I}{I_{sat}}\right)^p \qquad (1)$$

The p-index equals 3 at low laser intensity limit in accordance with other works, for instance of Abrams *et al*. [3]. On the other hand, at intermediate (close to the saturation intensity) and high laser intensities, the p strongly depends on the pulse shape. And it can vary between 0 and -1. In Eq.(1) we denote laser intensity $I = e_0 c h^2 A^2/2m^2$, the saturation intensity $I_{sat} = e_0 c h^2 g\Gamma/2m^2$ and the dimensionless laser detuning $d = (w_0 - w)/g$. The g and G decay rates in the case of a medium dominated by electron collisions are expressed as

$$g = \frac{N_e}{2}\left(k_1(T) + k_2(T) + k_{el}(T)\right), \qquad \Gamma = \frac{N_e}{2}\,\frac{k_1(T)\,k_2(T)}{k_1(T) + k_2(T)}. \qquad (2)$$

The temperature dependent rate coefficients, $k_n(T)$ and $k_{el}(T)$, stand for the electron velocity averaged cross sections for depopulation of level n and inelastic electron collisions, respectively. Finally DN_0 stands for the equilibrium population difference in the absence of laser beams while N_e denotes electron density. The depopulation rate coefficients, $k_n(T)$ for the involved ArI levels have been calculated by Pokrzywka [4]. DN_0 and N_e as a function of electron temperature T were calculated under conditions of atmospheric-pressure argon plasma in the LTE and their relative values are presented in Figure 2 together with coherence, g, and population, G, decay rates. The p-index was experimentally determined based on the saturation curve (signal intensity versus laser intensity for d=0) to be 0 at intermediate laser intensities over about one order of magnitude of the saturation parameter (I/I_{sat}). The temperature dependence of the PC-DFWM signal intensity, I_4, was then calculated using Eqs.(1) and (2) and is shown in Figure (2). It is characterized by a local maximum at plasma temperature around 14700 K.

There are some reasons to use high instead of low laser intensities for determination of plasma temperature: 1) the PC-DFWM signal is stronger therefore the sensitivity of the method is higher, 2) the signal is almost independent on the laser intensity what results in smaller uncertainties due to possible laser intensity fluctuations, and 3) due to the large power broadening (larger than expected Stark shift of the

investigated line) the PC-DFWM signals measured at a given laser frequency and at different plasma regions can be directly compared without corrections for the Stark shift of the spectral line.

3. Experimental arrangement

The experimental setup is presented in Figure 3. Details concerning the experimental arrangement can be found in the paper by Dzierzega *et al*. [5]. Briefly, the arc discharge was generated between a conical thoriated-tungsten cathode tip and an anode in the form of a disc. The arc was operated in argon at atmospheric pressure and powered by current of 100 A and the flow of argon was maintained at 4l/min.

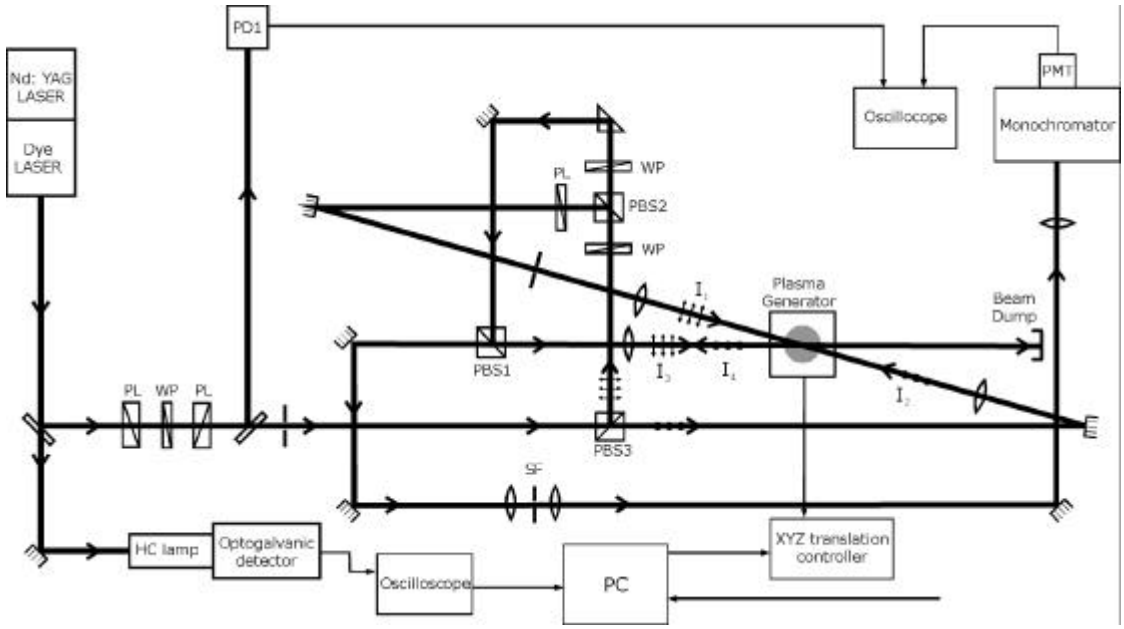

Figure 3. Experimental setup.
PD – photodiodes, WP – waveplates, PL – polarizers, PBS – polarizing beam splitter cubes, PMT – photomultiplier tube.

A tunable dye laser was pumped by the second harmonic of a Nd:YAG laser with 10 Hz repetition rate. The dye laser provided 8 ns pulses of about 10 mJ energy with a spectral bandwidth less than 0.03 cm^{-1}. The output beam of the dye laser was split into three laser beams of equal intensities with the backward pump beam polarized perpendicularly to the other two beams. The 500 mm focal length lenses were used to focus the laser beams at the plasma symmetry axis with a waist diameter of less than 0.2 mm. Two counter-propagating pump beams crossed with the probe beam at an angle of 300 mrad. The generated PC-DFWM signal I_4, propagated backwards along a probe beam path. It was then transmitted through a polarizing beam splitter cube and so separated from the probe beam reflections. The prism monochromator discriminated the signal from the background of plasma light. The signal detection was performed with a fast photomultiplier placed behind the exit slit of the monochromator and directly connected to a digital oscilloscope. The dye laser wavelength was calibrated with an argon hollow-cathode lamp (HC) using an optogalvanic detection system. Signals were averaged over 25 to 100 laser shots and then integrated over a time period of 30 ns.

4. Results

4.1. Spatial distribution of the PC-DFWM signal at high laser intensities

The measurements were performed with laser power density set as to satisfy condition of $p = 0$ in entire plasma volume being investigated. Figure 4 shows the relative PC-DFWM signal intensity versus the distance from the cathode tip, i.e. along the arc axis. This axial distribution reveals maximum at about 2.5 mm from the cathode which we consider as the maximum signal for argon plasma in the LTE (see Fig.2). Assuming LTE all along plasma axis the plasma temperature was then determined it ranges from about 12000 K et the anode side up to 19500 K in the vicinity of the cathode (see Figure 4).

Similar measurements of the PC-DFWM signal intensity distributions were performed in direction perpendicular to the arc axis at different distances from the cathode tip (see Figure 5). These profiles reveal off-axis maxima when measured close to the cathode. However, these maxima are lower than predicted by the theoretical model assuming LTE what we attribute to deviation of our plasma from the LTE in these regions, as it was already observed by many authors, for instance by Haidar [6] and Pellerin *et al.* [7]. At the

edge of the plasma column (about 2mm apart from the axis) the PC-DFWM signal intensity drops by a factor of 10 with respect to the maximum value. This, in turn, corresponds to plasma temperature about 11500 K as can be inferred from Figure 2.

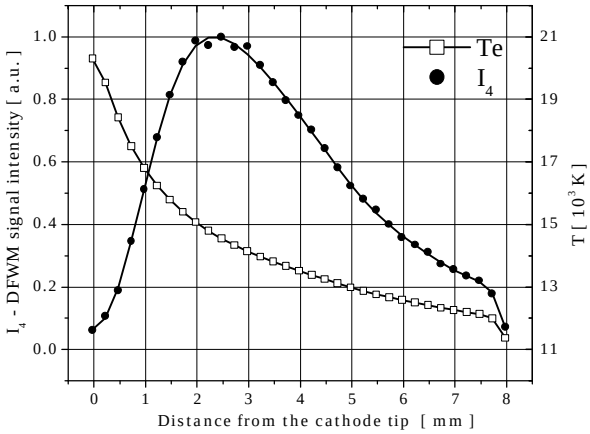

Figure 4. The axial distribution of the PC-DFWM signal intensity (I_4), and electron temperature (T) as determined from the above signal distribution and LTE plasma model.

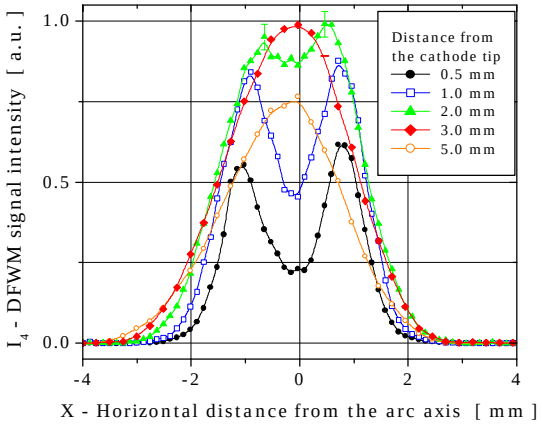

Figure 5. The axial distributions of the PC-DFWM signal intensity measured at different distances from the cathode tip. Arc discharge operated at 100 A and Ar flow maintained at 4l/min.

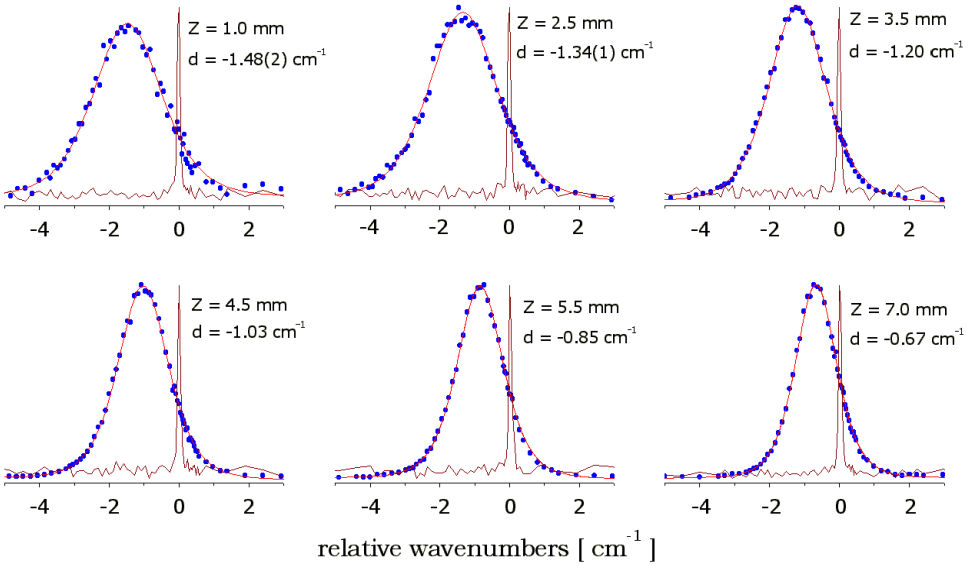

Figure 6. The spectral profiles of the PC-DFWM signals measured at different distances from the cathode tip and at low intensities of laser beams.

4.2. Stark profile measurements at low laser intensities

The other method commonly used in thermal plasma diagnostics is by measuring the Stark profile parameters of spectral lines which are independent on the plasma model assumed. These measurements are almost exclusively based on the OES and so the same problems with data analysis are encountered as already discussed.

We propose the PC-DFWM spectroscopy as the new method in studies of Stark profiles. The PC-DFWM spectrum was simultaneously measured with the HC spectrum at low laser intensity and then it was fitted with the Lorentzian profile to the third power according to Eq.(1). The line shift, d, was determined with uncertainty of 0.01 cm^{-1} as the difference between the fitted resonance frequency and frequency of the maximum of the HC spectrum. Unlike the Stark shifts, the measured line widths were influenced by laser (even at low laser intensities), and their determination needs first a few measurements at different laser intensities and next the real Stark width can be determined as the extrapolation to the zero laser intensity. Figure 6 shows the PC-DFWM spectra measured at different distances from the cathode and on the arc axis. The experimental data points are shown together with the fitted profiles (red curves) and the HC signal intensity.

Figure 7a shows the Stark shifts determined at different plasma regions as a function of electron density while Figure 7b presents the same but normalized (to N_e=10^{23}m^{-3}) Stark shifts, d_n, versus plasma temperature. All data below 12000 K correspond to the region of plasma edge (from at least 1.5 mm from the plasma axis). The significant change of d_n below 12000 K only indicates underestimation of electron densities for these Stark shifts and so the departure of our plasma from the LTE state.

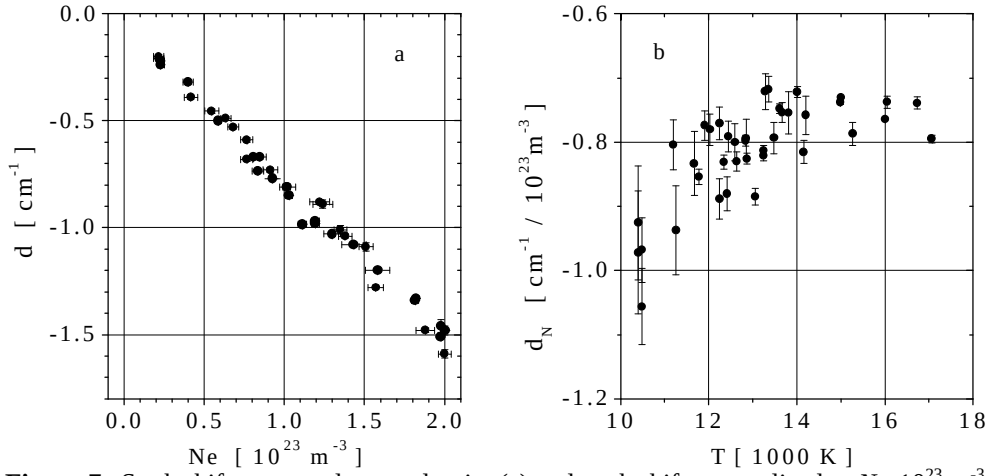

Figure 7. Stark shifts versus electron density (a) and stark shifts normalized to N_e=10^{23} m^{-3} versus electron temperature (b).

4.3. Comparison with optical emission spectroscopy results

The same plasma was studied using OES. Plasma column was observed side-on and at different distances from the cathode tip. Argon line profiles and continuous emission were measured at various chordal positions to perform Abel inversion. Plasma diagnostic was performed by various methods applied to ArI, ArII and ArIII lines assuming LTE state [6, 8]. For example, the total intensity of a spectral line is a function of one parameter: namely the temperature, and always reaches maximum value at so called norm temperature. This fact is a principle of the Larentz-Fowler-Milne method of temperature determination, and was already used for plasma diagnostic by the PC-DFWM method.

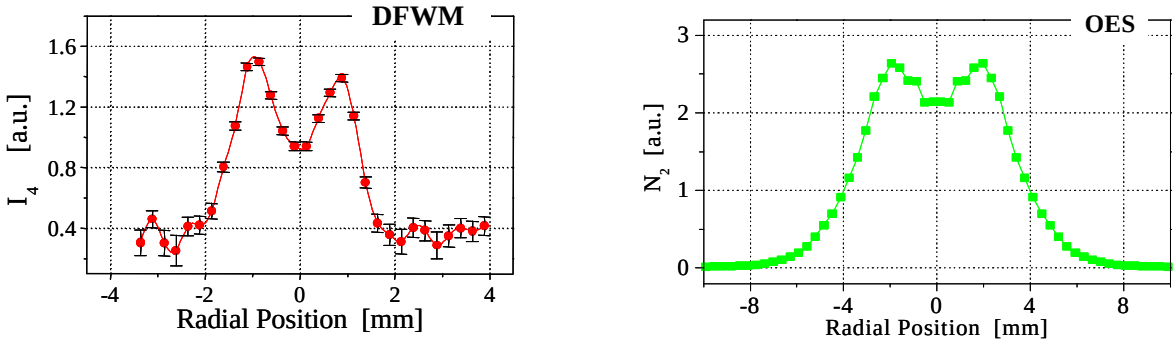

Figure 8a. Radial distributions of DN_0 and N_2 obtained using DFWM and OES methods
Arc discharge operated at 90 A and Ar flow maintained at 4l/min; z=0.75mm from the cathode tip.

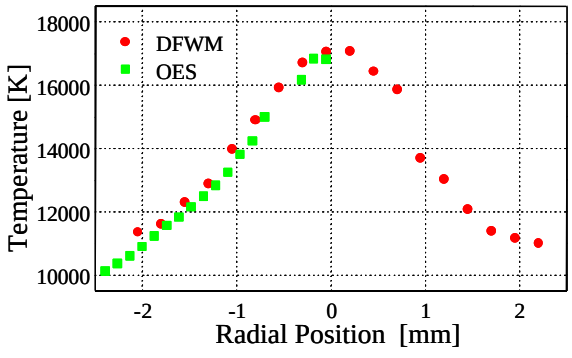

Figure 8b. Radial plasma electron temperature distributions obtained using DFWM and OES methods
Arc discharge operated at 90 A and Ar flow maintained at 4l/min; z=0.75mm from the cathode tip.

Comparison of radial distributions of PC-DFWM signal intensity I_4 and N_2 obtained by OES method measured at distance z=0.75mm from the cathode tip in an arc discharge operating in pure argon (4l/min) at 90A is shown in Figure 8a. The corresponding plasma electron temperature distributions are shown in Figure 8b. It must be noted that the good symmetry observed by OES is due to the Abel process that impose a forced symmetrisation of the data. Nevertheless, the final temperature obtained with these two methods agree very well (on the error bars), even if the DFWM method underlines a real asymmetry of the plasma column.

Moreover, we observed that intensity of the off-axis maximum for neutral argon lines, varies with the distance from the cathode tip, and remains constant for distances greater than approximately 2.5mm. Very similar observations are done with the DFWM spectroscopy [See Figure 5]. From our extended analysis, one can conclude that the arc plasma near the cathode tip shows radial dependence of the physical equilibrium state. Particularly, the Olsen-Richter (O.-R.) graph based on ArI and ArII lines [6, 8], shows that, in the hot core, close to the arc axis, the plasma is in the LTE state, and in the outer zones, the plasma state deviate from the LTE state at p=1atm.

For plasma column layers (slices) closer to the cathode tip, deviation from the LTE state begins at smaller distance from the axis and for higher temperature, even if the electron density is greater than $1.5\times10^{23}m^{-3}$. This deviation from the LTE state decreases with the axial distance from the cathode tip and practically vanishes for z>3mm. It can be caused by an overpopulation of the ArI ground state, that may be quite high. The dominating impact on the ArI ground state overpopulation is the inward transport of the ground state atoms into the plasma column due to the fast flow of the plasma near the tip. Our theoretical estimations of the ArI ground state overpopulation give results consistent with experiment [8].

5. Conclusions

We have reported on the application of the degenerate four-wave mixing (DFWM) method to Stark width and shift measurements of the 696.543 nm ArI line in LTE arc plasma. The DFWM spectroscopy has been used not only for line profile measurements but also for plasma diagnostics.

The DFWM signal is originate from a very limited region of the medium (only due to the dimensions of the laser beams) and so makes the DFWM method to be the method of high spatial resolution. This feature is especially important when one compares the DFWM to an optical emission spectroscopy (OES). The latter one commonly used in plasma investigations directly gives only some global, spatially integrated parameters and their local values are calculated under assumption of the axial symmetry of the plasma column and applying the abel inversion procedure.

At high laser intensities, the relationship between the PC-DFWM signal intensity and plasma temperature has been experimentally determined and then used in plasma investigations. The results of plasma diagnostics by DFWM have been compared to those by commonly used OES method. Particularly, our studies of free-burning argon arc plasma show spatial dependence of plasma state both using the PC-DFWM and OES. In the main core we can conclude that our plasma is in the LTE state and deviates at outer zones and that deviation starts to be significant at smaller distances from the axis in the cathode region.

In the range of low laser intensities the measured line profile is approximated by the Lorentzian profile to the third power with the line width depending on laser intensity and with negligible Doppler broadening. The results of this work imply the DFWM method to be reliable in Stark profiles studies, and especially in the determination of the Stark shift. The method can be particularly recommended in the case of elements with large Doppler broadening and for plasmas with the lack of symmetry. The DFWM method with its high spatial and temporal sensitivity can serve as an excellent tool for further plasma investigations.

References

[1] A.B.Murphy; Phys.Rev.Lett. **89**, 025002 (2002).
[2] £.Bratasz; Thesis (Krakow) (2002).
[3] R.L.Abrams and R.C.Lind; Opt. Lett. **2**, 94 and **3**, 205 (1978).
[4] B.Pokrzywka; Physica Scripta; **66**, 437-443 (2002).
[5] K.Dzierzega, L.Bratasz, S.Pellerin, B.Pokrzywka and K.Musiol; Phys.Scripta **67**, 52-58 (2003).
[6] S.Pellerin, K.Musio³, B.Pokrzywka, J.Chapelle; J.Phys.D. **27**, 522-530 (1994).
[7] J.Haidar; J.Phys.D **28**, 2494-2504 (1995).
[8] B.Pokrzywka, K.Musiol, S.Pellerin, E.Pawelec, J.-M.Cormier and J.Chapelle, CRAS **327**-4 Serie II.b, 391-398 (1999)

Plasma conversion of waste, which is not useable for gasification

D. Bendix[1], D. Hebecker[2]

[1] *BHF Verfahrenstechnik GmbH, Markranstädt OT Kulkwitz, Germany*
[2] *Department of Engineering Sciences, Martin - Luther – University Halle – Wittenberg, Merseburg, Germany*

Abstract

Plasma waste conversion has established applications in special fields or single situations of waste conversion. A new application field for plasma technology could be the conversion of waste material, which is not suitable for gasification or hinders the efficiency of incineration plants. According to this investigation, a plasma plant was in operation for six months parallel to the rotary kiln of an incineration plant. It has been shown that there is no aspect, which would exclude this technology from industrial applications in general.

1. Introduction

Modern incineration plants are designed to process nearly all kinds of municipal and industrial waste. They are able to feed-in about 15% of the primary energy, energy included in the waste material, as electrical energy. The reasons for these low conversion rates are mainly economical. An increase of the conversion rate would lead to a super proportional increase of investment costs because of the mixture of hot offgas after the incineration process. An increase of the efficiency would be possible, if almost only waste material that includes no materials that forms species which lead to high temperature corrosion would be incinerated. Better conditions for a higher conversion rate offer technologies, which produce in their first step a highly energetic offgas by dosage of the oxygen supplier understoichimetric. The high energy gas can be used in motors, turbines or combined processes. Such technologies are economically feasible, when they are specialized to limited sorts of waste materials. The conversion of waste materials, which are segregated after such a waste separation, could be a new application field for plasma technology.

2. Plasma technology for waste conversion

During the last 20 years, plasma technology has been applied to a limited area in the field of waste conversion. Since 1984 the plasma plant of the Swedish company ScanDust has recycled about 600.000t of filter dust from stainless steel production and about 300.000t of metals has been recovered. World wide, about 30 plants for plasma waste conversion have been put online since 1992. The application fields of these plants are niche-application (like filter dust and slag conversion, the disposal of medical waste), single application (conversion of a byproduct of a chemical plant) or temporary tasks (disposal of halogenated hydrocarbons, disposal of military waste). In these applications plasma technology has shown that it has reached an evolutionary level, which would allow a wider range of industrial use. Otherwise, they have shown some difficulties in the operation of plasma waste conversion systems. There are some publications, which show using emission analyses, that plasma waste converters have the potential to produce dioxins and furans in higher concentrations than conventional techniques [01, 02]. An unexpectedly high concentration of dioxins and furans were also analyzed in the offgas of a small plasma reactor for waste conversion (on a laboratory scale) at the Martin – Luther – University. The radically change of the reactor atmosphere, the specific energy input and the mixing conditions of the model substance and reaction partners made only negligible changes in the concentration of dioxins and furans in the offgas. During the continuing search for other explanations for these unexpected concentrations, the specifics of this plasma-chemical waste conversion technology – the energy input by plasma jets – became the focus of the investigation. There are many publications that describe the movements of the anodic arc attachment in DC – plasma torches as the cause of unwanted phenomena in plasma spraying. The movement of the anodic arc attachment can be documented by voltage / current traces, by high - frequency changes of noise and light intensity of the plasma jet and by the erosion traces on the anode [03, 04]. The movement of the anodic arc attachment leads to a high – frequency change of the specific enthalpy and velocity of the plasma jet. Although the average

energy input would lead to the desired condition, which seems to be favorable for the process, the conditions in parts of the reactor close to the minima or maxima of the energy input could be favorable to the formation of unwanted species. Increasing the frequency and decreasing the amplitude will help to decrease the influence of the oscillations. This was achieved by a change of the power supply and some changes in the geometry of the plasma torch [05]. The schematic of the "back flow plasma torch" and the power supply can be seen in Figure 1. This combination generates a plasma jet with a lower amplitude and a higher frequency of the enthalpy fluctuations in comparison to a conventional plasma torch.

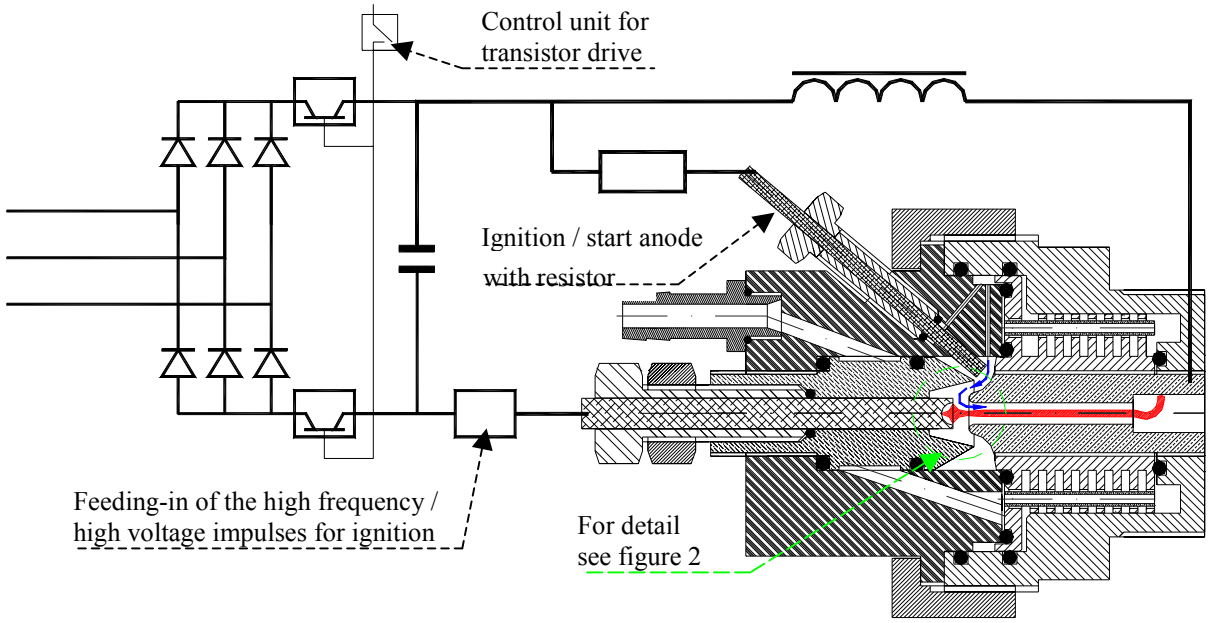

Figure 1 schematic of the "back flow plasma torch" and the power supply

Conventional power supplies for DC – plasma torches are built on the basis of thyristors. Since the possibility for closed loop control of the desired values with this technology is dependent on the commercial power frequency, the minimum damping period is in the range of 10ms. By using diodes and transistors for the power rectification, a minimum control time in the range of 0,1ms can be reached. The frequency of the fluctuations as a result of the movement of the anodic arc attachment is in the range of 1kHz. The power supply can now change the power input for the arc about 10 times during one large movement of the arc. The purpose of changes in the geometry of the plasma torch was to stabilize the arc as long as possible in the centerline of the anode and to decrease the erosion rate of the cathode material with the combination of reasonable cathode material (standard tungsten rods) and oxygen containing plasma gases.

Figure 2 shows the result of the evolution process of the design of the cathodic region. The swirling plasma gas (tangentially input) has a strong turnaround by decreasing the diameter of the passage. According to the conservation of the torsional momentum, the rotational speed of the plasma gas increases. An additionally strong axial symmetric swirl will be generated. In result of this axial symmetric swirl (shaped like a torus), there should be a velocity component inside the arc in the opposite direction of the global flow. That's why the torch was named "back flow plasma torch". A local limited axial symmetric area with a strong cooling of the arc will be formed in consequence of the flow regime. Furthermore a decrease of the arc diameter in this region can be observed (marked as $d_{arc\text{-}min}$). One effect of this is the aerodynamic focusing of the arc on the symmetry axis. Another effect is the generation of a secondary swirl close to the cathodic arc attachment. If the tungsten rod is new (flat top) this secondary swirl creates conditions for an increase of the erosion rate. As a result of this erosion a pit is formed. If the pit is deep enough, the gas volume in the secondary swirl is fixed, the mass transfer from the gas volume in the secondary swirl to the ambient gas will rapidly decrease. The concentration of tungsten vapor or volatile tungsten oxides will reach

equilibrium and the erosion of the cathodic material will be drastically decreased. Only during the arc ignition will tungsten be eroded until equilibrium is reached for the fixed gas in the secondary swirl.

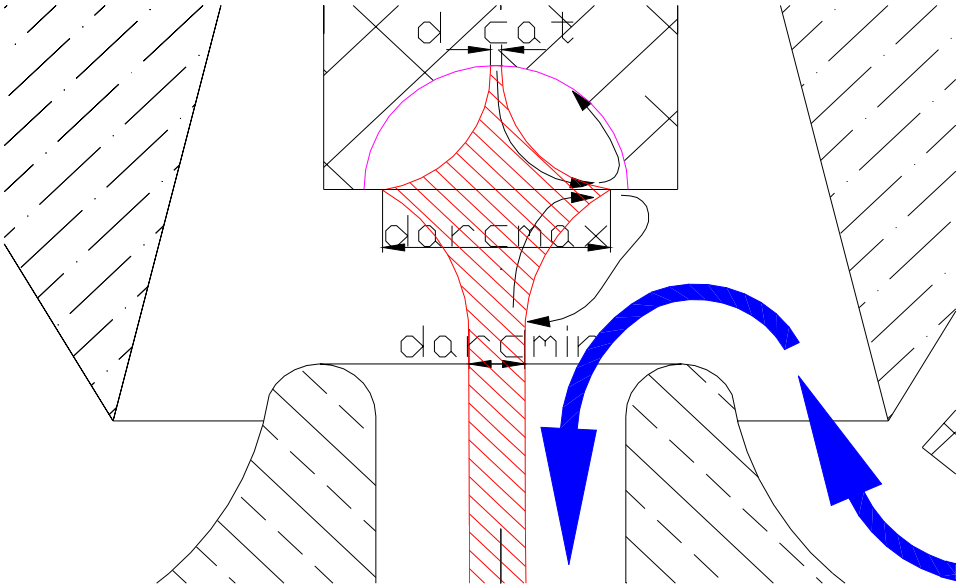

Figure 2 schematic of the cathodic region of the "back flow plasma torch"

The torch was tested with several plasma gases (mixtures: 10-100% N_2, 0-50% CO_2, 0-30%O_2, 0-15% water steam) with variation of the plasma gas volume flux and the DC-current. Figure 3 shows the power output (included in the plasma jet, P_{output}) and the power input (current x voltage, P_{input}) as functions of the plasma gas volume flux (1-5m³/h) and the current (30-100A) with nitrogen as plasma gas.

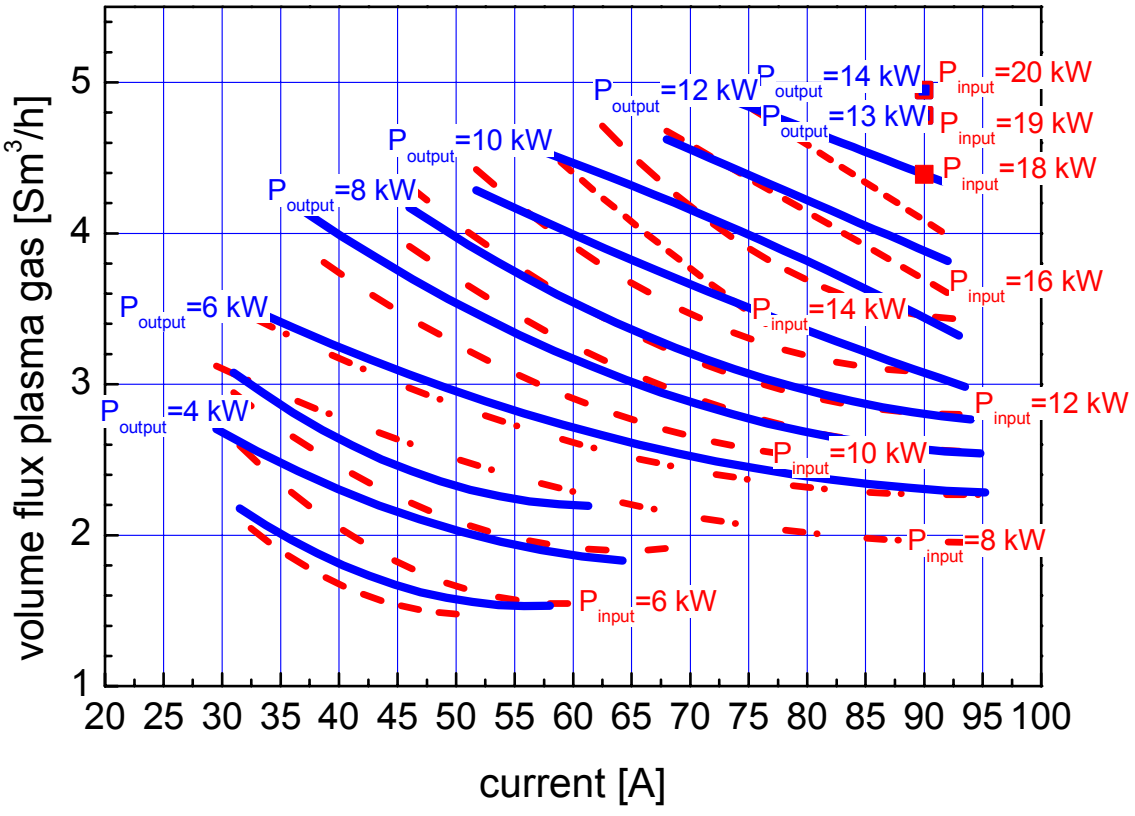

Figure 3 power output and power input
as functions of the plasma gas volume flux and current with nitrogen as plasma gas

A plasma plant with three back flow plasma torches parallel to the rotary kiln of an incineration plant was in operation for six months. The schematic of the plasma plant can be seen at Figure 4.

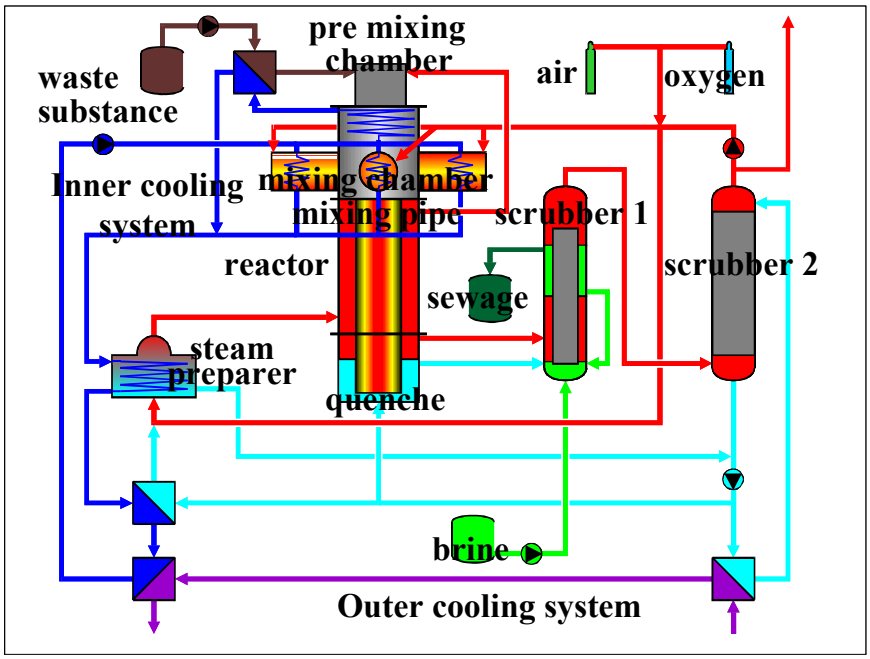

Figure 4 schema of the plasma plant

The waste substances (used organic solvents like propanol and trichloroethylene) are sprayed preheated into the pre mixing chamber. There they comes in contact with the reaction partners (and forms so the reaction system). In the mixing chamber the reaction system encounters the three plasma jets. After passing through a gas cooled SiC – reactor the reaction system is cooled down in the quench. After cleaning and further cooling in two scrubbers, most of the gas will be emitted, another part of the offgas is used as plasma gas and the third part of the offgas is conditioned with oxygen or air and steam to cool the reactor and to form with the model substance the reaction system in the premixing chamber. The mass flux of the waste substance was up to 35 kg/h, and the energy input was in the range of 4 to 15 kW per plasma torch. The plasma plant has shown that it is possible to convert highly chlorinated waste materials (like trichloroethylene) into harmless substances in compliance with all German emission limits. After 50 hours of operation the complete plant was disassembled. Investigation of the wear phenomena has shown that the interval for changing the anodes (this is easy to do in 2 to 3hours of work) should be 50 hours. The wear state of all other parts would allow continued operation. Figure 5 shows cathode and the cross section of an anode after 50 hours of operation time.

Figure 5 cathode new and after 50 hours of operation and the cross section of a anode after 50 hours of operation

3. Inclusion of the plasma technology in the energetic use of waste material

The use of this plasma plant parallel to the rotary kiln of an incineration plant for six months has shown that plasma waste conversion technology has reached a level of evolution, which would allow inclusion of plasma technology in the energetic use of waste materials. Municipal solid waste and industrial waste (in the following named as waste) are of interest for the energetic use. Landfilling is still the predominant way of disposal. In Germany, about 40% of the waste is used energetic or substantial (paramount in biologic - mechanical systems). Good conditions for a high efficiency energetic use offer technologies, which produce a high energetic offgas by dosage of the oxygen supplier understoichimetric in the first step and which use the high energetic gas in the second step in motors, turbines or combined processes. In Germany, there are three gasification technologies in commercial use for the conversion of ungraded municipal waste, which all have financial problems that hinder expansion. Such technologies have better favorable economical, if they are specialized on limited sorts of waste materials. The conversion of waste materials, which are segregated after such a waste separation, could be a new application field for plasma technology.

Operational data of gasification plants in comparison to conventional incineration plants would be convincing to show, that the integration of plasma technology has the potential to increase the efficiency of the energetic use of waste material. The comparison of incineration plants and gasification technology is still not serious, because the existing incineration plants are the result of a 100 years of extensive commercial experience – gasification plants are still the object of research and development. That's why it is more important to use data from real incineration plants, although there are still some unanswered questions left as well. The published data of the modern incineration plant Velsen (Germany, commissioned in 1998, [07]) and the experiences of the 6-month operation time of the plasma plant should be used for the discussion of the sense of plasma technology integration to improve the efficiency of the energetic use of waste. In 2001 206,319t of waste (m_{waste}) with an average heating value of 9,287kJ/kg (Hu_{waste}) were incinerated in the incineration plant Velsen. Besides this, energetic inputs were electrical energy ($P_{el.WI}$=29,527MWh), natural gas (14,637MWh for the catalysts) and fuel oil (392,975l to run up and rack out). A special valuation of the different kinds of energy can be spared, because the only useful energy was electrical energy (2001: $P_{el.netto}$=91,828MWh) and the fraction of fossil fuel (P_{fossil}) is small in comparison to the amount of energy input. The efficiency can be defined as:

$$\eta_{el.\,netto} = \frac{(\dot{m}_{waste} \bullet Hu_{waste} + P_{fossil} + P_{el.\,WI} - \dot{Q}_{offgas} - \dot{Q}_{reactor})\eta_{SP} - P_{el.\,WI}}{\dot{m}_{waste} \bullet Hu_{waste} + P_{fossil}} = 16.7\% \qquad (01)$$

Although the thermal losses of the offgas ($Q_{offgas} \approx 0{,}11 Q_{input}$) and reactor ($Q_{reactor} \approx 0{,}12 Q_{input}$) are average values compared to other thermal plants, the efficiency ($\eta_{el.netto}$) is rather low in comparison to power plants. The reason for this is the low efficiency of the steam process (η_{SP}), which is the result of the low live steam parameters (p=4MPa, T=673K). These low live steam parameters are chosen to diminish high temperature corrosion. The high temperature corrosion would be the result of the heat exchanger material reacting with some species (HF, HCl and other), which is inevitable if ungraded waste was incinerated. If waste materials (χ_{sep}), which include ineligible concentrations of precursors for the formation of species, which restrict the live steam parameters, could be disposed off in a separate way (plasma technology), the efficiency of the steam process in the incineration plant could be increased. The equation for the calculation of the efficiency of the energetic use of waste would have the following structure:

$$\eta_{el.\,netto} = \frac{(\dot{m}_{waste} \bullet Hu_{waste} + P_{fossil} + P_{el.\,WI} - \dot{Q}_{offgas} - \dot{Q}_{reactor})(1-\chi_{sep})\eta_{SP} - (P_{el.\,WI}(1-\chi_{sep}) + \chi_{sep}\,\dot{m}_{waste}\,\varsigma)}{\dot{m}_{waste} \bullet Hu_{waste} + P_{fossil}(1-\chi_{sep})} \qquad (02)$$

The experiments with the plasma plant have shown, that with a specific energy input (ς) of about 1kWh/kg a satisfactorily conversion rate can be reached. Figure 5 was calculated by using this data.

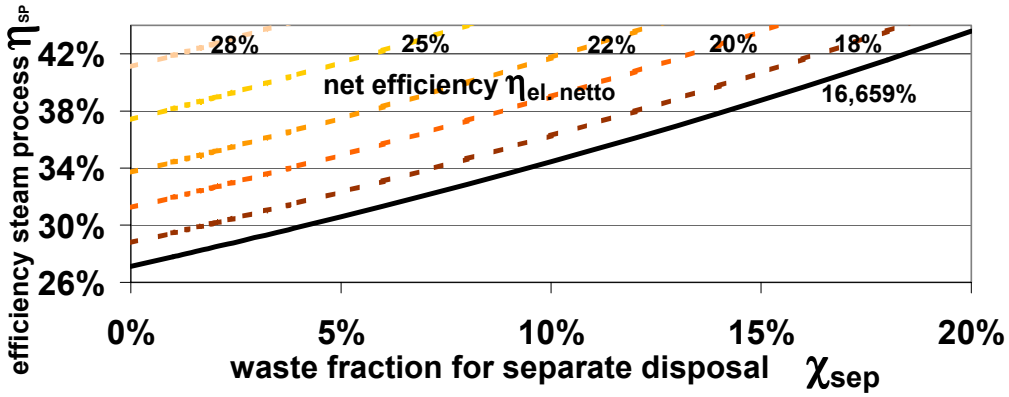

Figure 5 increase of the efficiency by inclusion of a separate disposal

The waste material is not homogenous. With the implementation of the separate gathering of material that can be recycled, the quantity of the waste was decreased and the composition had changed. In some countries the waste delivered to landfills or incineration plants is analyzed year by year to find out the efficiency of the separate gathering [08]. Published data of this "waste analyses" shows that in the atomic composition of the waste there are only about 3% elements, which restrict the live steam parameters. It is clear, that it is not possible to separate only these elements. Now investigations of the developer of incineration plants and waste separation / gathering systems have to show the coherence between the fraction that must be converted separately and scope for increasing the efficiency of the steam process in the incineration plant.

According to the present state of investigation, an increase of the efficiency by the energetic use of waste materials is anticipated by the inclusion of plasma technology in the waste conversion. The project was granted by "Deutsche Bundesstiftung Umwelt" Az:07061/02.

References

[01] *Environment Australia, 1997. Appropriate Technologies for the Treatment of Scheduled Wastes, Review Report Number 4* - November 1997. Canberra, Australia http://www.ea.gov.au/industry/chemicals/swm/swtt/plasma.html

[02] *Non-Stockpile Chemical Weapons Citizens Coalition* November 1999 http://www.cwwg.org/nsmitretek.html

[03] Z. Duan, L. Beall, M.-P. Planche, J. Heberlein, E. Pfender, M. Stachowicz *Arc Voltage Fluctuations as an Indication of Spray Torch Anode Condition* in *Thermal Spray: A United Forum for Scientific and Technological Advances*, Proceedings of the 1st United Thermal Spray Conference, edited by C.C. Berndt (ASM International, Ohio; Indianapolis, Indiana; 1997) pp.407-411

[04] J. F. Couder, M. P. Planche, P. Fauchais, *Characterization of D.C. Plasma Torch Voltage Fluctuations,* Plasma Chemistry and Plasma Processing Vol. 16 No. 1 1996 p. 211

[05] D. Bendix, D. Hebecker, *Energy release in the Plasma torch reactor to the conversion of toxic waste*, in *Progress in plasma processing of materials 1999* : proceedings of the fifth International Thermal Plasma Processes Conference, St. Petersburg, Russia, July 13-16, 1998, ed.: Pierre Fauchais, Jacques Amouroux. - New York [u.a.] : Begell House, 1999 ISBN: 1-567-00126-2

[06] D. Bendix, T. Bergmann, D. Hebecker, A. Schweigel *Generation of a Plasma Plant for Conversion of Halogenated Waste - final report of a research project founded by DBU*, Markranstädt OT Kulkwitz, 2001 (original in German)

[07] *Environmental statement 2001* of the operating company of the Velsen waste disposal plant (original in German, see also: http://www.ava-velsen.de)

[08] W. Hauer, H. Goldschmid, T. Herzfeld *Scrap waste analyses in Lower Austria 2001/2002* Korneuburg, August 2002, (original in German)

Multiphase processes at recovery of metals from halogenides by pulsed electron beam.

Kondratev N.A., Pushkarev A.I., Remnev G.E., Pushkarev M.A.

Research Institute of High Voltages, Tomsk, Russia.

Abstract

The results of experimental study of plasmachemical processes which are flowing past at injection of a high-current pulsed electron beam in a mixture of the gases $SiCl_4 + Ar + H_2$ and $SiCl_4 + O_2 + H_2$ are introduced. It is shown that in chain reaction initiated by high – current pulsed electron beam optimum conditions of formation nanosize powders are realized.

1. Introduction.

The analysis of plasmochemical processes which take place in gases at injection of pulsed high-current electron beam (HCEB) has shown, that the requirements which realized at stimulation of gases, are favorable to organize of chain and catalytic processes [1-3]. Thus the energy of HCEB constitutes small part of a total energy expended on carrying out of reaction. The unique properties of plasma generated at affecting of pulsed electron beam (a high scale of no equilibrium, homogeneous stimulation of large bulks of gas at high pressures, high speed of stimulation), allow realizing new physical principles of initiation of chemical reactions. To them the dissociation of oscillating - activated molecules, chain plasmochemical processes, plasma - catalytic reactions etc is referred. In plasmochemical processes of decomposition of industrial gases (CS_2, SO_2, CO_2, NO_2) and oxidation of hydrocarbons the power inputs of electron beam did not exceed 30% of dissociation energy of source molecules [1-3]. At recovery of tungsten from tungsten hexafluoride under HCEB affecting the power inputs of a electron beam did not exceed 5% of a dissociation energy WF_6 [4].

2. Experimental setup.

In report the results of analysis of dissociating processes of silicon tetrachloride gas-phase under affecting by pulsed HCEB are introduced. Parameters of electron beam - maximal electrons energy 500 keV, beam current in a maximum 6 kA, pulse duration at half-maximum 60 ns, pulsed frequency 2 Hz, current density on an input of a reactor no more than 0.4 kA/cm^2. The plasmochemical reactor is realize as a tube with an inside diameter 90 mm and length 300 mm, total volume 3 liters. Injection of electron beam in a reactor from butt end through a aluminium metal foil with thickness 130 microns. For definition of mix proportion of source gas mixture and products of reaction we have used a mass spectrometer MX-7304 and chromatograph GCHF18.3. An energy deposition of electron beam in gas and amount of energy allocated in reaction was measured on a pressure jump in a reactor [5,6]. Reactor beforehand pumped off up to pressures about 10^{-2} Torr and warmed up to 60°C, then filled up with studied gas.

3. Experimental study of $SiCl_4$ dissociation.

Variations of gas composition in a reactor with increasing of beam current pulses number are presented on fig.1 (mixture 30 Torr $SiCl_4$ + 120 Torr H_2 + 300 Torr Ar). The composition of mixture is determined by a mass spectrometer. With increasing of shots number the loss of silicon tetrachloride and creation of hydrogen chloride is recorded. In bulk of reactor the sad-colored powder was produced, which after letting-to-air in a reactor obtained white color. X-ray structure analysis of a powder has shown, that it is amorphous SiO_2.At beaming a mixture 30 Torr $SiCl_4$ + 120 Torr H_2 + 300 Torr Ar the energy HCEB which absorbed in gas, compounded 100 J for a one shot and was equaled of energy absorbed in a reactor, which filled argon or nitrogen at pressure more than 600 Torr. Let's estimate power inputs of an electron beam on dissociation of silicon tetrachloride. At a loss $SiCl_4$ on 40% for 30 shots (see fig.1) at 1 shot dissociates no less than $4.6 \cdot 10^{19}$ molecules of silicon tetrachloride (gravity $SiCl_4$ at 20°C and 200 Torr is equals to $2.15 \cdot 10^{-3}$ g/cm^3 [7]). As shown in proceeding [8], only about 20 % of electrons energy with energy more than 30 eV is spent for dissociative ionization. Is admissible, that the electrons interact only

with silicon tetrachloride, then the power inputs HCEB on dissociation of a one molecule $SiCl_4$ will make no more than 1.9 eV (upper bound).

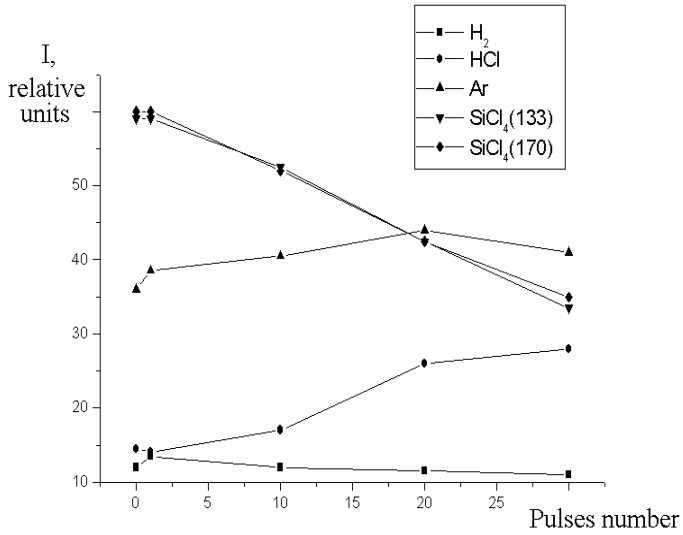

Fig.1 - Dependence of components content of a mixture in plasmachemical reactor as function of exposure.

The reason of anomalously low power inputs, it is essential smaller then dissociation energies of silicon tetrachloride (6.6 eV) at affecting a electron beam, is passing chain reactions in plasmachemical process. In jobs [9,10] for an explanation of low power inputs on dissociation CS_2, also is significant smaller than dissociation energies of carbon disulphide, the ion - radical mechanism is proposed, which one is initiated by process of dissociative adhesion of secondary electrons of beam to molecules O_2 and CS_2. CS radicals, generated at it, and atomic oxygen, reacting with source carbon disulphide, produce accordingly atomic oxygen and radicals CS, constructing a chain reaction.

In our case, at the expense of dissociation of silicon tetrachloride by electronic shock:

$$SiCl_4 + e \rightarrow Si + 4Cl \qquad (1)$$

and dissociative adhesion of low-energy electrons:

$$SiCl_4 + e \rightarrow SiCl^-_4 \rightarrow Si + 4Cl \qquad (2)$$

The atomic chlorine is formed, which initiates reactions in a mixture with molecular hydrogen. The major reactions are (similar to low-temperature homogeneous reacting of chlorine with hydrogen [9,11]):

$$Cl + H_2 = HCl + H + 0.05\ eV \qquad (3)$$

$$Cl + Cl + M = Cl_2 + M + 2.5\ eV \qquad (4)$$

$$H + Cl_2 = HCl + Cl + 2\ eV \qquad (5)$$

$$H + HCl = H_2 + Cl - 0.05\ eV \qquad (6)$$

The displacement of chlorine in $SiCl_4$ on hydrogen with formation trichlorosilane takes place at temperature 400°C at the presence of catalysts (aluminum or zinc) [7]. At injection HCEB in a mixture of silicon tetrachloride with hydrogen the temperature of gas increased not higher than 50°C, therefore loss $SiCl_4$ in reacting $SiCl_4 + H_2 = SiHCl_3 + HCl$ or $SiCl_4 + H \rightarrow SiHCl_3 + HCl$ or $SiCl_4 + H_2 \rightarrow SiH_2Cl_2 + HCl$ and so in our requirements is improbable. Chlorsilane was not detected in reaction products just after injection of HCEB. Other products of reaction, which one could enter to reacting with $SiCl_4$ in our

requirements and to reduce to its loss, are not formed. Therefore ion - radical mechanism of a chain reaction at injection HEB in gas-phased $SiCl_4$ will not be realized.

At analysis of making mechanisms of a chain reaction in our experiments are necessary to take into account the ion - cluster mechanism proposed in operation [12] for explanations of low energy expenditures on dissociation of methane on hydrogen and carbon at affecting pulsed - periodic microwave pseudo-corona discharge. Indirect endorsement of clusters formation in bulk of reactor is forming centers of the ruby laser ray dispersion at passing through bulk of a reactor (formation of a "track" of a laser beam in bulk of reactor) after injection of an electron beam. In a source working mixture "track" of a laser beam was not observed. Investigation of acoustical waves damping, which formed in a reactor at injection of a electron beam, has shown, that the absorption coefficient at a dissipation of a electron beam in vapor-phase silicon tetrachloride 12-19 times more, than calculation value under the formula which is taking into account damping of harmonic motions in a self-contained cylindrical reactor [6]. In a fig. 2 the dependence of an acoustical oscillating energy absorption coefficient in a reactor from pressure for different gases is presented.

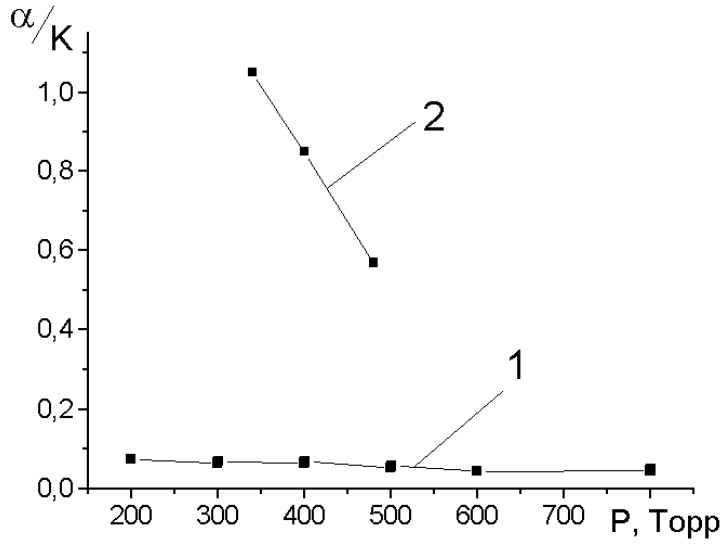

Fig .2 - Dependence of a normalized absorption coefficient of sound in reactor as a function of pressure. 1- Ar, O_2, N_2; 2 - $SiCl_4$.

For comparison of absorption coefficients in different gases the magnitude of coefficient was normalized on coefficient taking into account thermal properties of gases [6]. The dots in figure 2 will correspond to experimental data, curve 1 - to calculation under the formula which is taking into account absorption at reflex from butt ends of a reactor and side walls at propagation along a reactor [6]. For nitrogen, argon and oxygen the discrepancy of calculation and experimental values does not exceed 30%. The curve 2 will correspond to experimental values of an absorption coefficient at generation of acoustical waves in vapor-phase silicon tetrachloride. The considerable increasing of an absorption coefficient thus can be conditioned by formation of clusters in a reactor at injection of an electron beam.

The specific enthalpy of tearing off silicon atom from a metallic cluster equal 4.1 eV, is less than a dissociation energy of a one molecule $SiCl_4$. Therefore energy, selected at formation of a cluster from metallic silicon, is not enough for disintegrating $SiCl_4$ molecules that condense on this cluster. Combined exothermal reactions energy (3-5) and energy of formation of a metallic silicon cluster is most likely for dissociation of silicon tetrachloride molecules.

The carried out studies of dissociation of vapor-phase tetrachloride of silicon and the measuring of power inputs have shown, that at injection of a high-current pulsed electron beam the chain reaction will be realized. The joint action of the ion - cluster mechanism of a chain reaction and dissociation of oscillating - activated molecules with participation of disintegrating product in a exothermal reaction is most likely, because other mechanisms of making of chain process in our case can not explain balance of energy between power inputs on direct recovery of silicon and indispensable power inputs taking into account of number of the dissociated molecules $SiCl_4$ and dissociation energy of tetrachloride of silicon

4. Experimental study of SiO_2 nanoparticle.

It is shown in our experiments that in chain reaction initiated by high – current pulsed electron beam in a mixture of the gases $SiCl_4 + O_2 + H_2$ optimum conditions of formation nanosize powders are realized. In figure 3 the photograph of SiO_2 nanosize powders for mixture of the gases 140 Torr O_2 + 210 Torr H_2 and 1.5 ml $SiCl_4$ after one shot of high – current pulsed electron beam is shown. The photograph on transmission electron microscopy is obtain. The bar chart of this SiO_2 nanoparticle in fig.4 is shown.

.

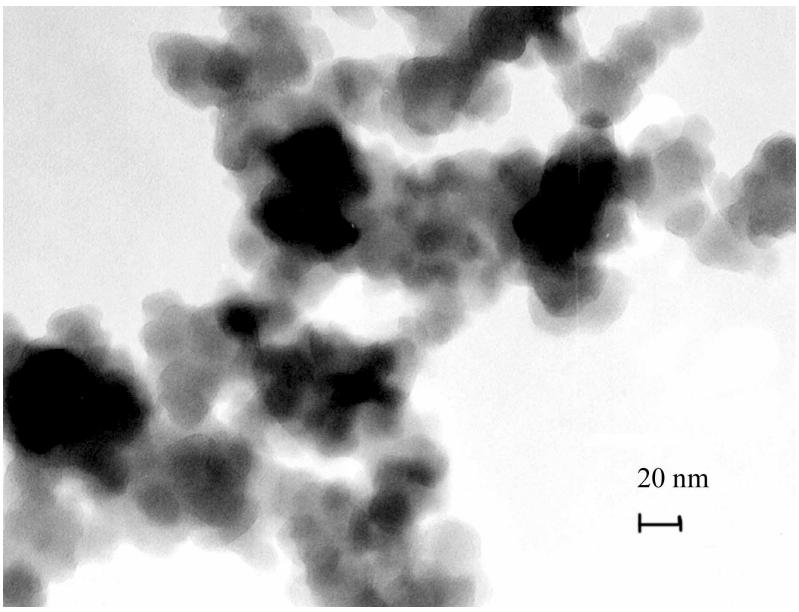

Fig.3.- Photograph of SiO_2 nanosize powders after one shot of high – current pulsed electron beam formed.

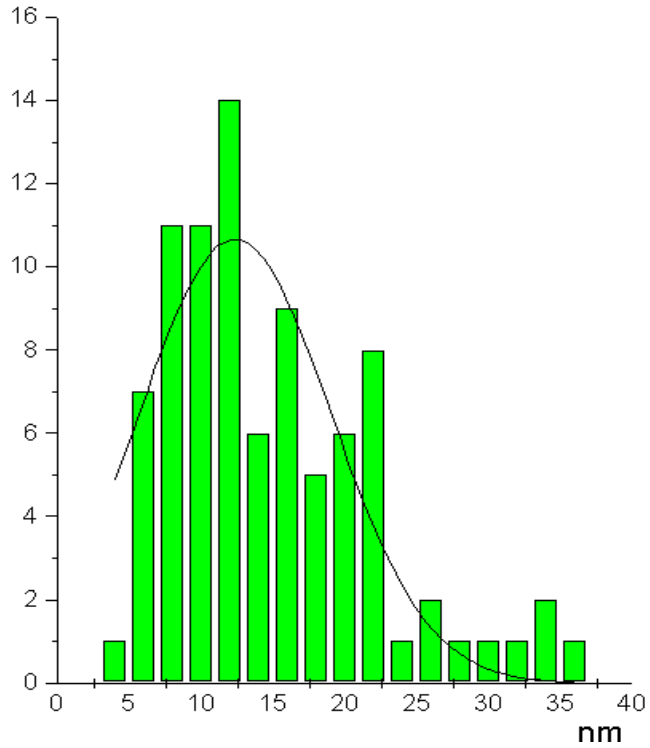

Fig.4. The bar chart of SiO_2 nanoparticle (one shot).Gaussian fit: mean 12.3 nm, sd 6.7 nm.

Specific sguare of SiO_2 nanosize powders is 42 m^2/g. Composition of this powders in atom percent is: 63.62% O, 36.14% Si, 0.2% K, 0.11% Pb, 0.11%Al. In figure 5 the selected area diffraction pattern of SiO_2 nanosize powders for mixture of the gases 140 Torr O_2 + 210 Torr H_2 and 1.5 ml $SiCl_4$ after one shot of high – current pulsed electron beam is shown. Evidently this nanosize powders is amorphous.

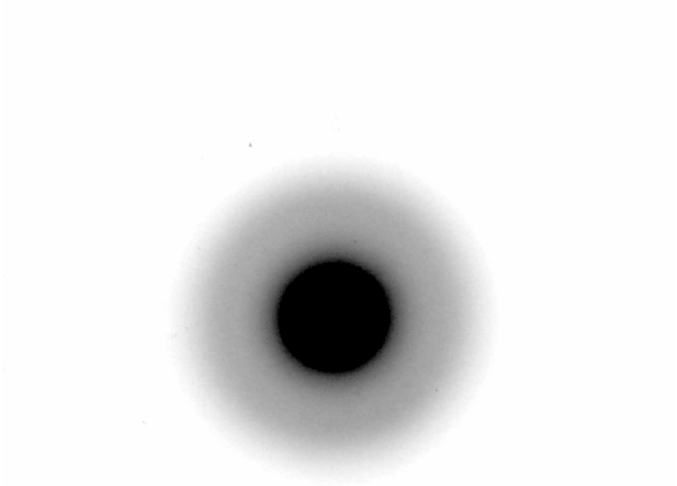

Fig. 5. Selected area diffraction pattern of SiO_2 nanosize powders.

Size of SiO_2 nanosize powders after second injection of a electron beam increased. In figure 6 the photograph of SiO_2 nanosize powders for mixture of the gases 140 Torr O_2 + 210 Torr H_2 and 1.5 ml $SiCl_4$ after ten shot of high – current pulsed electron beam is shown.

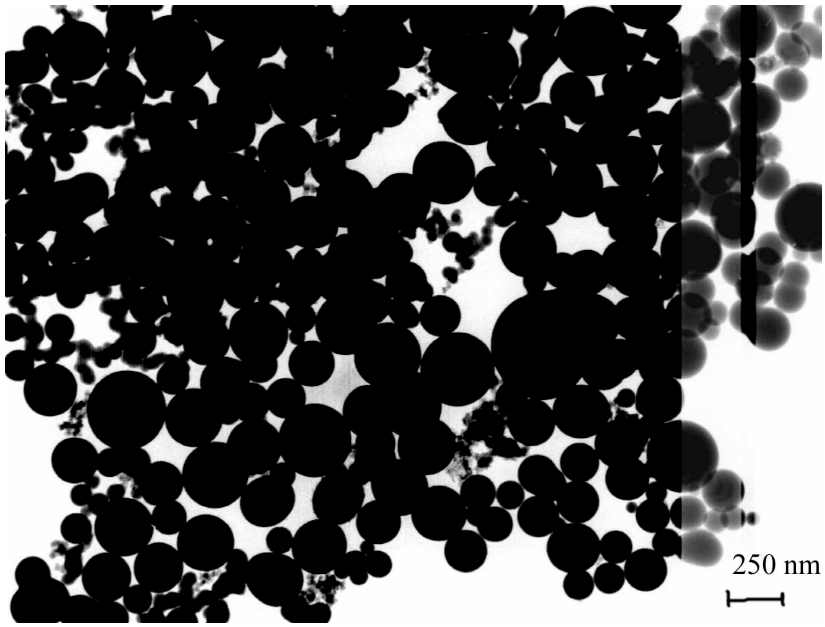

Fig.6.- Photograph of SiO_2 nanosize powders after ten shot of high – current pulsed electron beam formed.

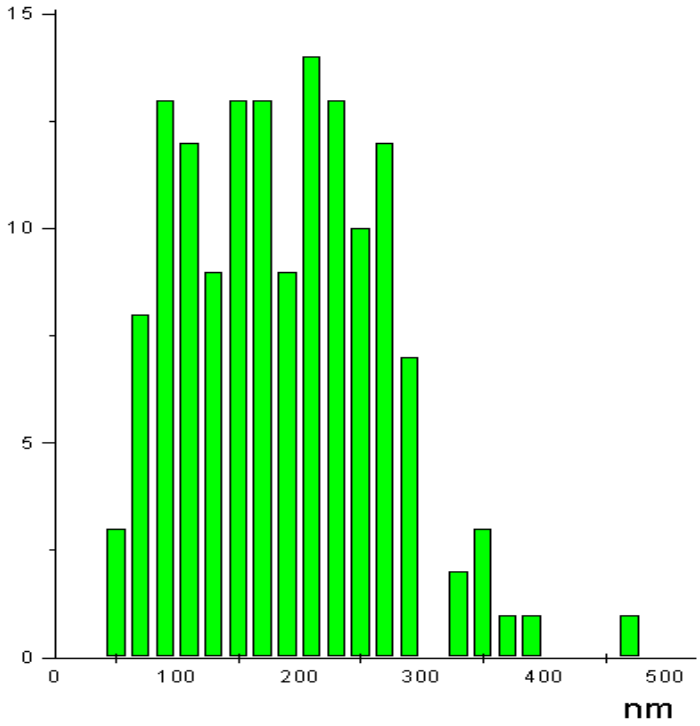

Fig.7. The bar graph of SiO_2 nanoparticle (ten pulsed).

5. Summary

The analysis of known mechanisms of chain reactions (radical mechanism, ion - molecular mechanism, catalytic mechanism and ion - cluster mechanism) demonstrates, that at time of halogenides recovery the considerable contribution is brought by energy of additional exothermal reactions and energy selected at coagulation of silicon atoms. It is illustrated, that in a chain reaction, initiated by a high-current pulsed electron beam, the optimum condition for forming nanosize particles will be realized.

References

[1] Denisov G.V., Novoselov U.N., Tkachenko R.M. The letters in JTF. 1998, v.24, is.4. p. 52.
[2] Novoselov U.N., Rishov V.V., Syslov A.I. The letters in JTF, 1998. v.24, is.19. p. 40.
[3] Ikegaki T., Seino S., Oda Y., Matsuda T., Imada G., Jiang W., and Yatsui K. // Proceedings of 13th International Conference on High-Power Particle Beams (BEAMS 2000), Nagaoka, Japan, June 25-30, 2000.
[4] Remnev G.E., Pushkarev A.I., Pushkarev M.A. and other Informations of high schools. Physics. 2001, n. 5. p.33.
[5] Pushkarev A.I., Pushkarev M.A., Zhukov L.L., Syslov A.I. Informations of high schools. Physics. 2001. n. 7. p.91.
[6] Pushkarev A.I., Pushkarev M.A, Remnev G.E. Acoustic Physics, 2002, v.48, n. 2, p. 220-224.
[7] Lapidus I.I., Niselson L.A. Tetrahlorosilan and trichlorosilane M: Chemistry, 1970, 126 p.
[8] Rishov V.V., Jastremskiy A.G. Plasma physics. 1978, v.4, is.6. p.1262.
[9] Eletsky A.V. Successes of physical sciences. 1981, v.134. n. 2. p.237
[10] Denisov G.V., Novoselov U.N., Syslov A.I. etc. Magazine of technical physics. 2001, v.71. is.1. p.136.
[11] Kondratiev V.N., Nikitin E.E. Chemical processes in gases. M: science, 1981, 264 p.
[12] Babaritsky A.I., Demansky M.A., Demakin S.A. etc. High energy Chemistry. 1999, v.33. n. 1. p.49.

Gas influence on the arc shape in MIG-MAG welding

S.Zielinska[1], S.Pellerin[2], K.Dzierzega[1], K.Musiol[1], Ch. de Izarra[2] and F.Briand[3]

[1] Institute of Physics, Jagellonian University, ul. Reymonta 4, 30-459 Krakow, Poland
[2] LASEP, Fac. des Sciences-Bourges, Universit d'Orlans, BP 4043, 18028 Bourges Cedex France
[3] CTAS - Air Liquide Welding, Rue des Epluches, Saint Ouen l'Aumone, France

Abstract
The type of the applied shielding gas has a strong influence on quality of the welding process. In particular, increase of the percentage of carbon dioxide in argon, results in increase of the transition current while changing from the globular to spray mode of metal transfer. In order to explain this phenomenon, the arc shape was investigated at different mixtures of argon and carbon dioxide in the shielding gas. As a result, we conclude that there is a limit of the percentage of relative concentration CO_2/Ar beyond which the shape of the arc is significantly modified.

1. Introduction

MIG ("Metal Inert Gas")/MAG ("Metal Active Gas") are the welding processes that utilize arc plasma between a consumable solid metal electrode and a weld pool. The upper wire-electrode, liquid metal transferring inside arc and weld pool are protected against air by inert gas flux in the case of the MIG welding, or active gas in the case of the MAG welding. These welding methods are used in all sectors of activity to assemble all grades of metal (ferric and non-ferric) in all positions. The schematic description of the welding torch is presented in Figure 1.

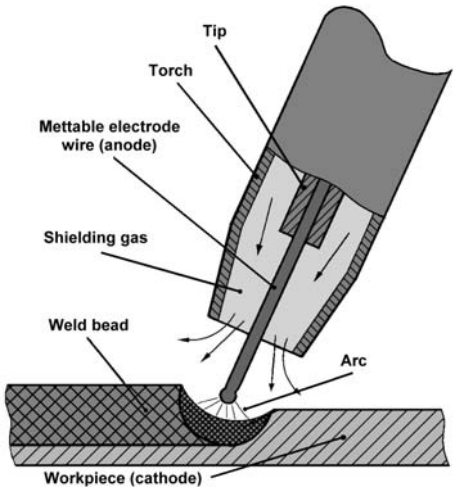

Figure 1: The welding torch

The most frequently used gases or gas mixtures are argon or/and helium in the MIG welding and carbon dioxide as well as various mixtures of these gases with CO_2, H_2, O_2, N_2 in the MAG welding. The MIG-MAG welding is usually performed with reverse-polarity direct current, where the melting electrode serves as an anode, what assures better arc stability.

The wire melting and the metal transfer in the arc can take place in three fundamental ways [1, 2]: short-circuit transfer ("short-arc"), transfer by large drop ("globular transfer") and axial spray transfer ("spray-arc"). The mode of the transfer depends on shielding gas type, dimensions and compositions of the wire electrode, electrode extension, arc voltage and current, and wire speeds. These three modes are characterised by different

arc stability, weld penetration, sputter of the melted metal, gas consumption and quantity of fume. Each of these modes has different applications, operating conditions and welding quality:

- In the ”short-arc” transfer, metal is deposited by series of short circuit resulting from regular contact between the electrode and weld pool. This type of transfer proceeds for low current intensity and relatively low arc voltage. After arc ignition, the tip of wire is being melt due to he resistance heating, and leads to the droplet formation. For these conditions, the electrode melting rate is not sufficient for the droplet detachment, and so melted metal is transferred from the wire to the workpiece during the contact period. Due to the relatively small heat transfer, short-circuit gas metal arc welding is used to weld thin metal plates in all positions.

- As the welding current is increased and the arc voltage is greater than in short-circuit mode, the melting rate rises and becomes fast enough to allow formation of large droplets. Then the pendant droplet size exceeds the electrode diameter and one observes metal transfer by large droplets (”globular transfer”). The electromagnetic force, gravity and other forces lead to drop detachment without contact between electrodes at a frequency of only few hertz. In general, globular transfer mode is difficult to use in practice because it is unstable and accompanied by considerably weld sputter.

- A gradual increase of the current intensity and arc voltage accelerates the melting rate of the wire electrode and subsequent transition to the axial spray transfer mode (”spray-arc”) is observed. The droplets have a diameter smaller than the wire’s diameter and a tapering tip forms at the end of the electrode. When the arc current exceeds a given limit (transition current), the frequency of the droplet detachment increases sharply to the value over 100Hz. This mode insures maximum arc stability and minimum spatter.

2. Shielding gas effect

The type of shielding gas has a major importance in the welding process. Good detachments of the formed droplets, and their correct transfer to the cathode, have a significant stake for the quality of welding. This phenomenon depends on the properties and composition of the plasma around the electrode. In particular, the gradient of voltage at a given current, and thus the power injected from plasma, strongly depend on gas used. The metal transfer mode is also affected by the chemical activity of shielding gas. Argon is the basic gas for MIG welding, but admixtures of oxidising elements increase the possibility of the cathodic emission and improve the stability of arc.

The behaviour of the pendant attached droplet is determined by the current distribution inside, it means by the magnitude and sign of the induced behaviour electromagnetic force: the Lorentz force can act either as a force of detachment (if current lines diverge) or on the other hand, as a force attaching the droplet to the wire electrode (if current lines converge) [3, 4]. In the latter case, a repelled metal transfer was observed during welding process using CO_2 as shielding gas [5]. Detailed calculations made by Haidar [6] indicate that depending on welding conditions, the axial component of the electromagnetic force can perform this double function, and its radial component is the dominant detaching force and is responsible for the transition from the globular to the spray transfer mode.

Rhee & Kannatey-Asibu [7] studied modifications of the droplet diameter and droplet transfer frequency for various compositions of the shielding gas. Changing CO_2/Ar ratio in the shielding gas, they measured the transition current from globular to spray transfer mode. In general the higher quantity of CO_2, the higher transfert current is observed, as far as the mode of spray transfer becomes unrealisable. There are different explanations of the observed phenomenon, in particular:

- As a result of the increased O_2 concentration and so larger oxidation of the electrode surface than under the pure argon, the amount of alloying elements vapours increases what decreases the rate of the droplets formation and disturb their detachment by giving rise to vapour-recoil force [8].

- An influence of the repulsive electromagnetic force is reinforced by the addition of molecular gases such as O_2, H_2 or CO_2 and would increase with concentration and dissociation energy of considered molecular

additives [8]. Rhee & Kannatey-Asibu observed the metal transfer to be similar for helium and carbon dioxide. The arc column is not attached to the entire droplet, probably as a result of relatively high ionisation energy of helium and additional energy required for dissociation in the case of carbon dioxide.

- Kim & Eagard [5] postulated the cathode jet to be responsible for the repelling force (proportional to the square of the current in the case of Tungsten Inert Gas (TIG) welding) and observed repelled metal transfer mode with helium and carbon dioxide shielding gases.

On the other hand, in the case of CO_2, the surface tension coefficient of the molten metal changes under influence of the chemically active gas (both oxygen and carbon decrease the surface tension coefficient for steel). Thus, in principle, it should be easier to obtain spray transfer, but the experiments show that it takes place only for small addition of CO_2. Moreover, the transition current increases considerably along with CO_2 concentration.

The shielding gas effect on welding process is a phenomenon that has been not completely understood. In this work, the arc shape was observed during the MIG-MAG welding for various relative concentrations of argon and carbon dioxide in the shielding gas mixtures.

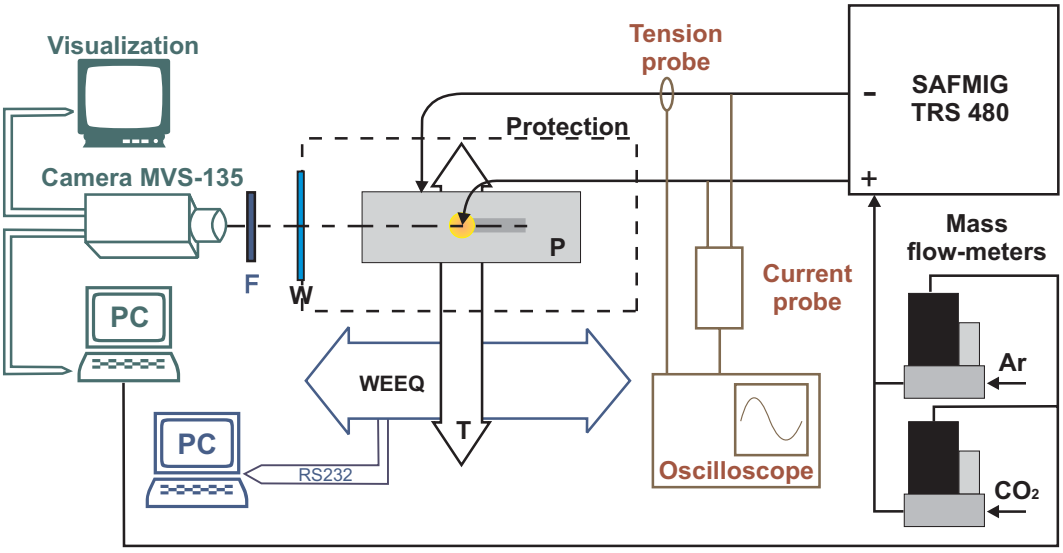

Figure 2: Experimental set-up
[T - Manual moving table; WEEQ - Step-by-step moving table]
[F - Interference filter; P - Metallic plate; W - Glass window]

3. Experimental procedures

The scheme of the experimental system is presented in Figure 2. Its main part is the welding set SAFMIG 480 TRS PLUS [9] equipped with the SAFMIG 480 TR 16 kit [10]. The welding was performed at reverse-polarity (wire-anode, workpiece-cathode) direct current. The wire-anode used in our experiments was a mild steel consumable electrode (AWS A5.17) with a diameter of 1.2 mm.

Two moving tables were used. The first, a micrometric table driven by step motor, ensured the displacement of the mild steel metal plate in the welding direction with horizontal velocity 4 mm/sec. The second, a manually driven table, was used for moving in the direction perpendicular to the previous one. The welding torch was fixed on the third table that can be displaced manually in vertical direction, in order to adjust the arc length by modifying the distance between electrodes.

The gas was provided by two cylinders of the industrial gas. All types of gas mixtures can be considered, but for this study, we used a mixture based on argon and carbon dioxide. Two mass flow-meters allow measurement and control of gas flow.
The measurements of voltage between the electrodes and arc current were carried out by a differential voltage probe St500-3 (FRANAISE D'INSTRUMENTATION) and current probe (Hall effect transducer) LEM LT 500-S. These electrical characteristics were stored using numerical oscilloscope LECROY LT584L.

The observation of the arc and the recordings of the pictures' sequences, were performed with fast camera FASTCOM MVS-135 [11], equipped with photodiodes matrix (512×512 pixels) manufactured in CMOS technology. The registration frequency and exposure time depend on the size of recorded images: to increase the speed of the camera, one must decrease active surface of the photodiode matrix, but within the limit fixed by arc dimensions. A narrow bandwidth interferential filter centred at 466 nm in front of the camera's objective was used to limit the spectral bandwith [Figure 2].

4. Experimental conditions

The power supply set was used in the constant current mode. The configuration of the power supply SAFMIG was identical for all measurements and corresponded to the spray transfer mode for pure argon shielding gas. The wire feed rate was fixed to 9 m/min. The distance between the contact-tube and the metal plate amounted to 20mm. The thickness of the workpiece was 8 mm for all measurements. The chemical composition of the wire material and metal plate is given in Table 1. For the described experiments, shielding gases used were pure argon and various mixtures of argon and carbon dioxide (in the range 0.8 to 15.4% CO_2) with total flow rate about 20l/min.

	C	Si	Mn	Cr	Ni	Mo	P	S	Cu
Metal plate	0.14-0.22	0.05-0.15	0.40-0.65	0.05	0.30	-	0.04	0.30	0.30
Wire	0.09	0.35	1.07	0.02	0.06	0.04	0.01	0.01	0.16

Table 1: Chemical composition of the metal plate and welding wire.

In each welding processes the average welding current intensity (for stable welding process without arc initiation characteristic) was about 318 A. On the other hand, the average value of the voltage changed depending on composition of gas mixture: for pure argon, it was of 36V; for the mixture with 0.8% CO_2: 32.7V and increased until to 40.4V for the mixture with 15.4% CO_2 [Figure 3].

The camera was operated at the frequency of 157.2 pictures/sec (6.4ms between two pictures), according to an active size of the photodiode matrix of 120×120pixels. All observations were carried out with blue interference filter to limit light intensity.

5. Results

The observations carried out show that the type of gas has a significant influence on a plasma column shape [Cf. Figure 4].

In the case of pure argon at an average current of 318 A the arc column has a form similar to that observed in the case of the spray-arc mode of metal transfer [12]. The arc shape is almost not modified in a presence of a small admixture of CO_2 in the mixture of shielding gas [Figure 4]. Then the arc is very stable, what ensures great effectiveness and good quality of welding. The end of the wire was tapered and completely surrounded by the arc, in accordance with description of this mode of molten metal transfer presented in other articles [1, 5, 13, 14]. According to the results observed by Rhee [7] the break-up stream length becomes shorter and the size of the droplets increase with CO_2 concentrations.

On the other hand, the arc voltage decreases abruptly when only 0.8% CO_2 is added [Figure 3]. The difference between the arc voltage for pure argon shielding gas and for small CO_2 concentration (less than 3%) amounts to 3 V what suggests a drop of plasma resistance. Higher CO_2 concentration in argon shielding gas results in gradual increase of the arc voltage and, subsequently welding resistance in the arc and arc energy.

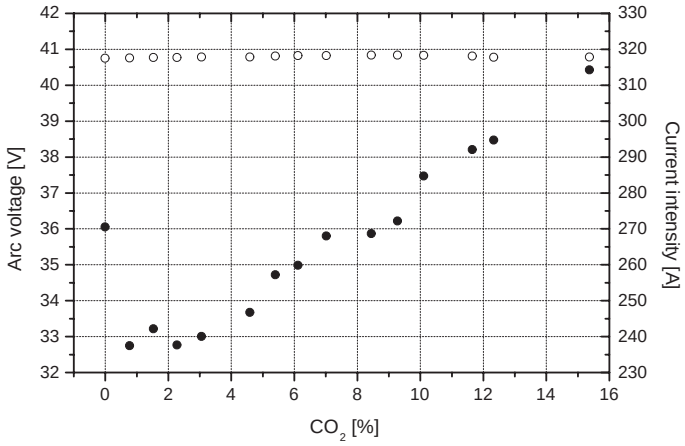

Figure 3: Arc current and voltage as a function of CO_2 concentration in gas mixture.
[● - Arc voltage; ○ - Current intensity]

When the amount of CO_2 in the shielding gas exceeds 9%, one can clearly observe detachment of droplets. The arc loses stability, produces sputter and intensive fume formation. The arc shape is significantly modified (longer and more diffusive) when the percentage of CO_2 exceeds 12%. The molten metal transfer completely changed: large droplets are formed at the end of the electrode as a result of the transition to the globular transfer mode.

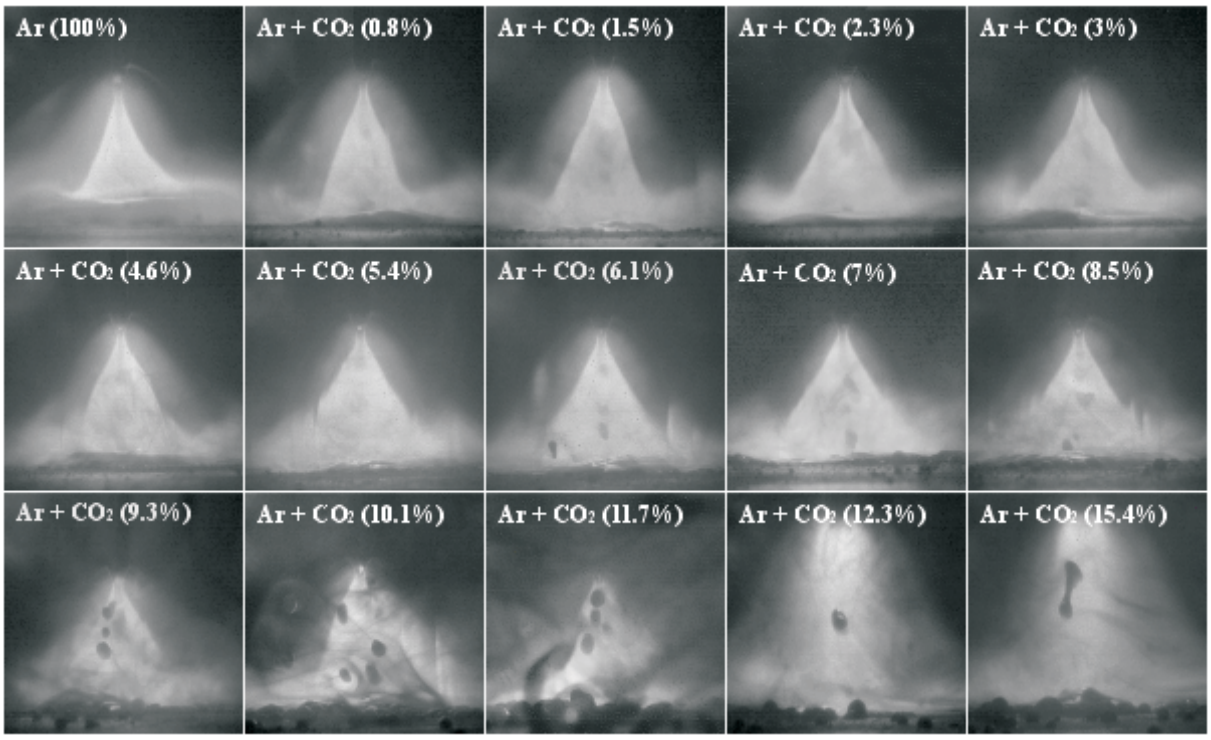

Figure 4: Arc shape for different gas mixture

4. Conclusion

We have proposed one method for welding arc visualization using a fast camera and narrow bandwidth interference filter to limit the light intensity. All measurements were carried out at the same welding current intensity (318 A) and experimental arrangements. The observations of the arc shape during MIG-MAG welding process

have been investigated for 15 different gas mixtures: pure argon, Ar+0.8% CO_2, Ar+1.5% CO_2, Ar+2.3% CO_2, Ar+3% CO_2, Ar+4.6% CO_2, Ar+5.4% CO_2, Ar+6.1% CO_2, Ar+7% CO_2, Ar+8.5% CO_2, Ar+9.3% CO_2, Ar+10.1% CO_2, Ar+11.6% CO_2, Ar+12.3% CO_2, Ar+15.4% CO_2).
The experimental results show that, under our assumed conditions:

- The shape of welding arc strongly depends on CO_2 concentration in the Ar shielding gas: for small relative concentrations, the arc column shape corresponds to the one observed in the case of the spray-arc transfer mode, but the metal transfer is highly modified when the percentage of CO_2 exceeds 12%.
- CO_2 as an admixture to Ar shielding gas changes current-voltage characteristics of the welding arc: small additions of this gas changes the arc shape only in minor way but lead to a significant decrease of arc voltage;
  The further increase of CO_2 concentration causes gradual increase of arc voltage, what might result from the increase of arc resistance, energy and its length as well (visible for larger carbon dioxide quantity in figure 4).

References

[1] Lancaster J. F., "The Physics of Welding", 1st edition, Pergamon Press, Paris, 1984.

[2] Lesnewich A., "Control of Melting Rate and Metal Transfer in Gas-Shielded Metal-Arc Welding. Part II - Control of Metal Transfer", Welding Journal **37** [1958] 418s-425s.

[3] Nemchinsky V. A., "The effect of the type of plasma gas on current constriction at the molten tip of an arc electrode", J. Phys. D **29** [1996] 1202-1208.

[4] Waszink J. H., Graat L. H. J., "Experimental Investigation of the Forces Acting on a Drop of Weld Metal", Welding Journal **62** [1983] 108s-116s.

[5] Kim Y-S., Eagar T. W., "Analysis of Metal Transfer in Gas Metal Arc Welding", Welding Journal **72** [1993] 269s-278s.

[6] Haidar J., "An analysis of the formation of metal droplets in arc welding", J. Phys. D **31** [1998] 1233-1244.

[7] Rhee S., Kannatey-Asibu E., "Observation of Metal transfer during Gas Metal Arc Welding", Welding Journal **71**[1992] 381s-386s.

[8] Jacobsen N., "Monopulse investigation of drop detachment in pulsed gas metal arc welding", J. Phys. D **25** [1992] 783-797.

[9] Safmig 330TRS Plus/Safmig 480TRS Plus - Inst. de scurit d'emploi et d'entretien, documentation technique SAF/Air Liquide Welding, Rf. 8695-273 [1999]

[10] Kit Safmig 480TR 16 - Instruction de scurit d'emploi et d'entretien , documentation technique Air Liquide, Rf. 8695-044 [1999]

[11] MVS-135 Hardware Technical documentation, FastCom Technology S.A. [2000]

[12] F.Briand, "La maitrise du soudage MIG/MAG Pulse" Air Liquide/C.T.A.S [1998].

[13] Kim Y-S., McEligot D. M., Eagar T. W., "Analyses of Electrode Heat Transfer in Gas Metal Arc Welding", Welding Journal **70** [1991] 20s-31s.

[14] Jones L. A., Eagar T.W., Lang H. J, "Images of a Steel Electrode in Ar-2%O2 Shielding during Constant Current Gas Metal Arc Welding", Welding Journal **77** [1998] 135s-140s.

Wear resistance of Al_2O_3 and Cr_2O_3 coatings deposited by water-stabilized plasma spraying

J. Nohava[1], P. Chráska[1]

[1] *Materials Engineering Department, Institute of Plasma Physics AS CR, Prague, Czech Republic*

Abstract

Plasma sprayed ceramic coatings are known for their excellent wear resistance [1]. In our recent work, the influence of water-stabilized plasma torch (WSP®) on the wear properties of gray alumina and cromia coatings was studied. Two methods for determination of wear resistance WSP® sprayed coatings were combined: wet slurry abrasion test and scratch test. Fractographic analysis of the damaged samples was used to determine the main wear mechanisms and to justify superior wear resistance of cromia coating.

1. Experimental setup

WSP® plasma torch was used for spraying of gray alumina (Al_2O_3+3% TiO_2 wt.), cromia (Cr_2O_3) and metal coatings. High temperature in the WSP® plasma torch (approx. 25 000K) allowed to use large grain size powders leading to high deposition rates. The coatings were deposited on rectangular mild steel substrates of 2.5 to 4 mm thickness. The substrates were grit-blasted prior to the deposition. The list of sprayed samples is given in Tab. 1.

Tab. 1 – List of samples.

Sample label	Coating	Powder grain size [μm]	Density of the coating [g/cm^3]
AL	Al_2O_3	-63 +40	3.7
CR	Cr_2O_3	-90 +45	5.2
NI	Ni	-140 +100	8.4
NC	Ni+20% Cr wt.	-140 +100	7.4
ST	AISI 316L	-140 +100	6.9

Two methods for determination of wear resistance of plasma sprayed coatings were combined: wet slurry abrasion test according to ASTM G75-95 and scratch test. The wet slurry abrasion test was performed on a specially designed apparatus, schematically depicted on Fig. 1. The abrasion resistance is determined by using the measured mass loss of a standard-shaped block, driven in a reciprocating motion by a rotating crank, riding in the bottom of a tray containing the slurry. A direct load of 22.4N is applied to the block. The interior of the tray has a flat-bottomed or truncated "V" shape formed by the filler, that confines the slurry particles to the path taken by the wear block. At one end of each stroke, the block is lifted off the lap by a cam action for sufficient time to allow fresh slurry material to flow under the block. The block holder is made of plastic, as are the trays, so that electrolysis inherent in some slurries is minimized. The distance run by the block within one rotation is 400mm.

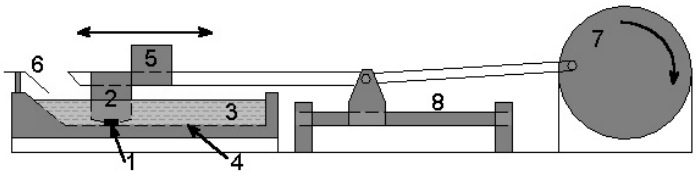

Figure 1 – Wear test machine layout: (1) sample, (2) sample holder, (3) slurry, (4) neoprene lap, (5) dead weight, (6) block lifting cam, (7) rotating wheel, (8) direct drive.

Four rectangular samples in dimensions of (12x25)mm are tested simultaneously in four parallel trays. The wear test consists of four consecutive 2h-runs (distance of 2304m). After each run the samples are rinsed in water, cleaned in ultrasonic bath in ethanol, dried and weighted so that weight loss can be calculated. The cumulative weight loss is divided by coating's density and cumulative volume loss is obtained. Damage of the coating is expressed in the wear rate ***w***, which is defined as the loss of material volume per unit distance [2]. The average wear rate was determined as a coefficient of linear regression

fitted to cumulative volume loss vs. distance experimental data. Wear resistance of a coating can then be quantified as a reciprocal value of the wear rate ***w***.

Scratch test was performed on a CSEM® Revetest scratch tester. In a scratch test, Rockwell C-type indenter is sliding on the coating under continuously increasing load, causing damage to the coating and removal of the coating material. The scratch test was carried out on the as-sprayed coating in plane perpendicular to spraying direction. The length of the scratch was 10mm and the normal load was smoothly and continuously increased from 0 to a maximum value of 100N during each scratch test. Scratching speed was set to 10mm/min and the indenter tip was wiped with ethanol before each scratch test.
Damaged surfaces of AL and CR samples subjected to both wet slurry abrasion and scratch tests were examined in scanning electron microscope (SEM) JEOL JSM 840A and JEOL JSM 5510LV in secondary and backscattered electrons modes. Analysis of damaged surfaces of the wear test samples after every run enabled to study the structure of the coating in depth and trace the changes in morphology during the abrasion tests.

2. Results

Wet slurry abrasion test results

The results of wet slurry abrasion test are plotted in Fig. 2. The most wear resistant coating was the cromia coating with the average wear rate of $0.55\times10^{-2}mm^3/m$. The average wear rate of gray alumina was $1.24\times10^{-2}mm^3/m$, i.e. more than two times higher than that of cromia coating.
The average rate of metal coatings (AISI 316L, NiCr20 and Ni) are higher than wear rates of both gray alumina and cromia coatings. However, the AISI 316L steel coating has wear rate comparable to that of gray alumina coating ($\boldsymbol{w}=1.32\times10^{-2}mm^3/m$). Nickel coating exhibited the highest wear rate, with average value of $2.87\times10^{-2}mm^3/m$.

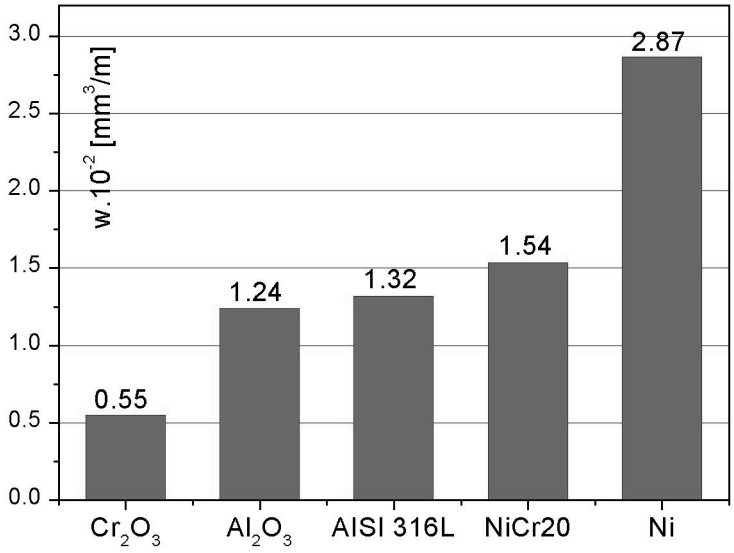

Figure 2 – Wear rates for different types of WSP® sprayed coatings.

Surface morphology of the coatings sprayed by WSP®

The typical morphology of the as-sprayed gray alumina and cromia coatings is shown on Figs. 3a, b. Both gray alumina and cromia coatings exhibited typical splat morphology. Thickness of the splats was in the range of 2 to 10μm.

Several differences in morphology between gray alumina and cromia coatings were found:

- the cromia coating contained less spherical particles than gray alumina coating,
- in some cases crystallization of melted cromia particles on the substrate surface lead to formation of fine, randomly oriented microstructure (see Fig. 3b).

Two types of microstructure inside of the splats were found:

- columnar, predominant in Al_2O_3 splats, reported also by other authors [3, 4] – see Fig. 3c,
- fine with randomly-oriented grains (predominant in Cr_2O_3 splats – see Fig. 3d),
  - the dimensions of the fine grains were in the range of 1 to 5μm.

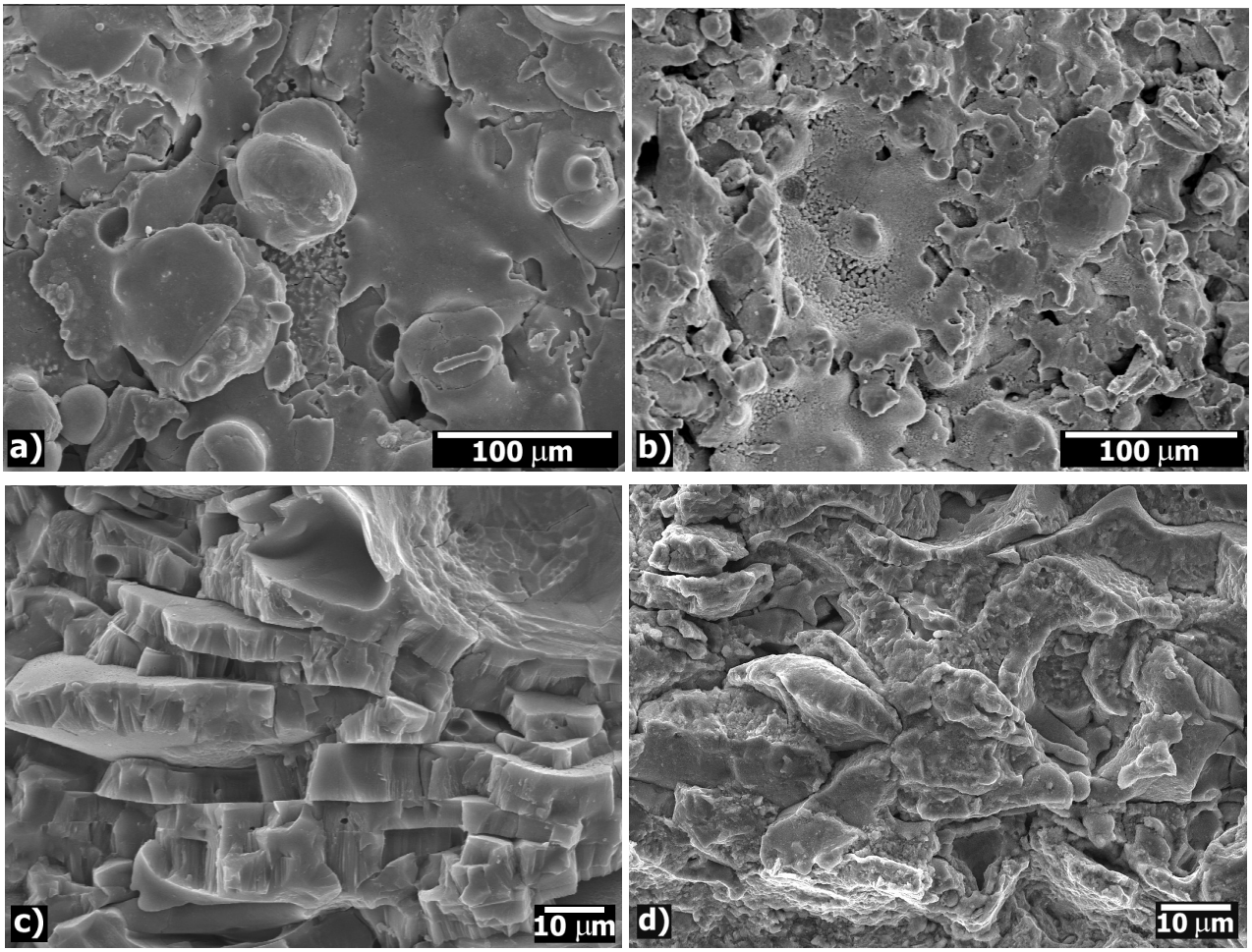

Figure 3 – The surface of Al_2O_3 coating **(a)** and Cr_2O_3 coating **(b)** sprayed by WSP® before the wear tests. Microstructure inside of **(c)** Al_2O_3 and **(d)** Cr_2O_3 splats.

Fractographic analysis of samples subjected to wear and scratch tests

After the first 2-h cycle of the wear test, the damaged surface of both types of coatings exhibited grooves parallel to the direction of the sample sliding movement. The span between grooves was approximately 100μm. At magnification from 1000× to 5000×, dense net of microcracks in splats, intersplat cracks [5] and smoothened edges of splats were observed. The residues of fractured splats had dimensions in plane perpendicular to the spraying axis from 20 to 50μm whereas the splat dimensions in the same plane prior to wear tests were up to 150μm.

Typical morphology of the damaged surface is presented on Figs. 4a, 4b. In several cases voids created by pull-out of spherical particles were found. The abrasive particles did not penetrate in the interior of such voids and the non-damaged splat structure of the coating [6] was observed. It was thus proved that the structure inside the coating is identical to that on the surface of the coating.

The damaged surfaces of both gray alumina and cromia coatings after the second, third and fourth 2-h cycle exhibited the main morphological features as observed after the first cycle, i.e. a dense net of microcracks in splats, delamination and smoothened edges of splats. Average dimensions of the residues of fractured splats after the later cycles were smaller than the dimensions of such residues formed in preceding cycles.

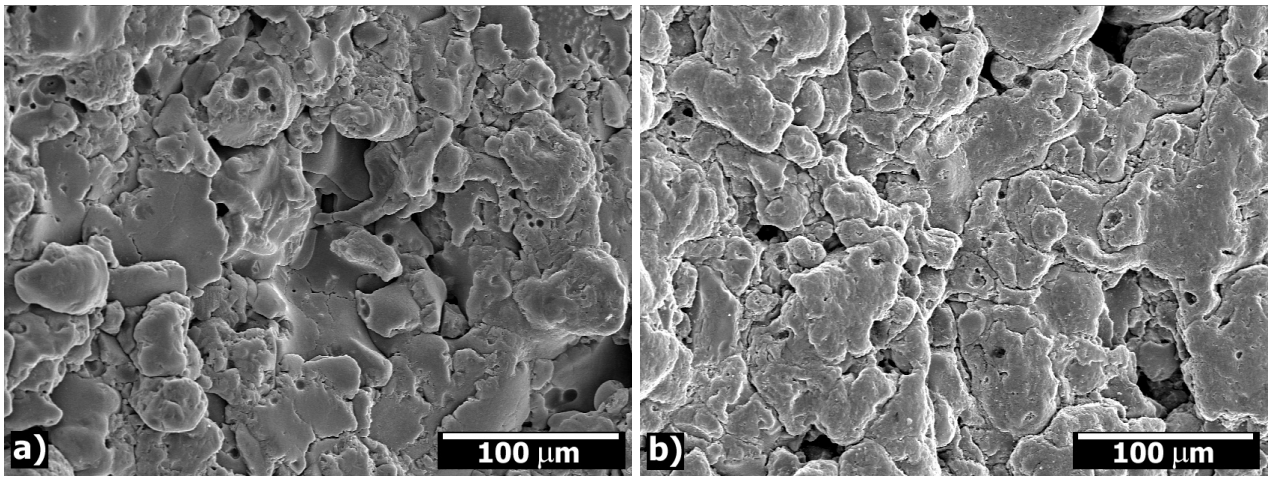

Figure 4 – SEM image of the damaged surface of Al_2O_3 coating **(a)** and Cr_2O_3 coating **(b)** after 4 hours of the wear test.

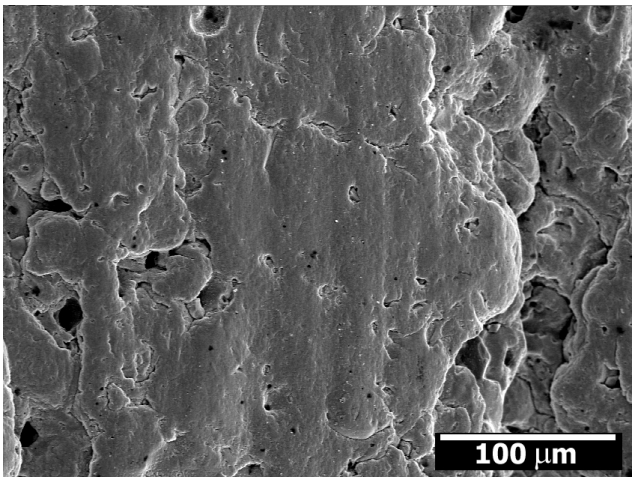

Figure 5 – SEM image of a flat area on the damaged surface of the cromia coating after 6 hours of the wear test.

During the second and third 2-h cycle large areas (2-D dimensions up to few hundreds of micrometers) with only minor vertical variation were created in the Cr_2O_3 coating (see Fig. 5). Such areas were not observed on the damaged surface of the gray alumina coating.

After the third cycle complete removal of the gray alumina coating from substrate was observed in several areas. It was decided in such cases to abandon the fourth cycle of the test because it would yield non-relevant values of the wear rate.

Fractographic analysis of the scratch test results

The results of the scratch test on the AL (gray alumina) and CR (cromia samples) served for SEM evaluation of the damaged surfaces and consequent determination of the main wear mechanisms of the ceramic coatings sprayed by WSP®.

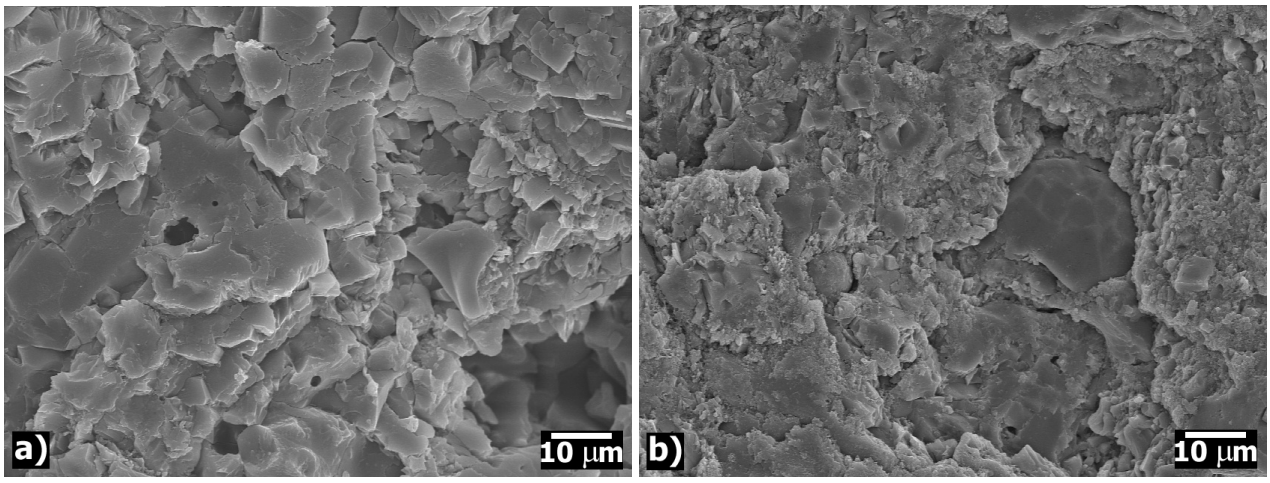

Figure 6 – SEM image of the interior of the scratch on **(a)** Al_2O_3 coating, **(b)** Cr_2O_3 coating.

The fractographic analysis of scratches on AL and CR samples confirmed the results of the fractographic analysis of the coatings subjected to the wear tests. The main morphological features found were:

- microcracks in splats,
- splats delaminated from neighboring splats and spherical particles,
- debris from the fractured splats re-deposited in the scratch.

However, several significant differences between the scratch morphology on the gray alumina and cromia coatings were found:

- the net of microcracks in the gray alumina splats was more dense than that in the cromia splats.
- the residues of fractured splats were in dimensions of approx.:
  - 10 to 30μm in the case of gray alumina coating (Fig. 6a),
  - 2 to 10μm in the case of cromia coating (Fig. 6b).

3. Discussion

The results of the wet slurry abrasion tests confirmed excellent wear resistance of the WSP®-sprayed Al_2O_3 and Cr_2O_3 coatings: cromia coating has the lowest wear rate, followed by gray alumina coating [7, 8]. The metal coatings exhibited higher wear rates than the ceramic coatings. The AISI 316L steel coating has wear rate comparable to that of gray alumina coating and can thus be considered for wear resistant applications, too. The results of the wear tests proved that WSP® can be used for spraying of large area wear resistant protective coatings such as cromia or gray alumina.

Direct comparison of the wear rates of WSP®-sprayed coatings with the results of other authors is difficult to carry out due to various experimental methods used by different authors. However, a good agreement between wear resistance of atmospheric plasma sprayed alumina and cromia determined by rubber wheel test [9] and WSP®-sprayed gray alumina and cromia coatings determined by slurry abrasion test was found (see Tab. 2).

Tab. 2 – Volume loss of alumina a cromia coatings deposited by different spraying techniques.

Coating	Volume loss in [mm^3] (atmospheric plasma spraying) [9]	Volume loss in [mm^3] slurry abrasion test (WSP®)
Al_2O_3	89.7	42.6
Cr_2O_3	22.3	18.6

The SEM analysis lead to determination of the main wear mechanisms of the WSP®-sprayed ceramic coatings:

- pull-out of spherical particles, thus creating areas with high stress concentration, susceptible to fracture [10],
- delamination and removal of entire splats [11],
- splat fracture and consecutive removal of the splat residues.

The different wear rates of cromia and gray alumina coatings are believed to be due to different internal microstructure of the splats. The gray alumina splats exhibit mainly columnar microstructure whereas cromia splats reveal fine and randomly oriented microstructure. Formation of microcracks perpendicular to the surface of the splats, which may result in splat fracture, is more favorable in the columnar microstructure. Fine and randomly oriented microstructure of cromia splats prevents formation and growth of vertical microcracks due to higher energy needed for crack propagation through the splat. The microcrack in cromia splat is forced to alternate its propagation plane, which is energy consuming process.

Removal of coatings material in the case of fine, randomly oriented microstructure is realized by smaller particles (corresponding to the size of microstructural units, i.e. 1 to 10μm) than removal of the material with columnar microstructure. The fine and randomly oriented microstructure of cromia splats resulted in superior wear resistance of cromia coating compared to gray alumina coating.

The removal of the gray alumina coating is thus supposed to be faster, which resulted in wear rate higher than that of the cromia coating.

4. Conclusion

Wet slurry abrasion and scratch tests of coatings sprayed by WSP® proved that this spraying technique can successfully be applied for deposition of wear resistant coatings. Due to high throughput and high temperature is this technique suitable for spraying of various large grain powders on large areas allowing complete melting of powder particles. The wear resistance of protective WSP®-sprayed coatings is comparable to that of coatings sprayed by other technologies and in some cases may be even higher. Wear

rates of the WSP®-sprayed coatings in ascending order were (see Fig. 2): Cr_2O_3, Al_2O_3, AISI 316L, Ni20Cr, Ni.

Fractographic analysis of the coatings damaged by wet abrasion and scratch tests allowed to identify the main morphological features of WSP®-sprayed gray alumina and cromia coatings. Comparison of the main wear mechanisms with wear mechanisms of coatings sprayed by other technologies indicated that both wear mechanisms are similar. Different micromorphology features and wear mechanisms lead to explanation of different wear rates of gray alumina and cromia coatings.

Acknowledgements

The authors deeply appreciate the collaboration with Karel Voleník from the Institute of Plasma Physics and Jan Siegl from the Dept. of Materials at the Czech Technical University (Prague) who was helpful in evaluation of the fractographic analysis. The work was supported by GA CR grant no. 106/01/0094.

References

[1] Pawlowski, L.: The science and engineering of thermal spray coatings. John Wiley & Sons Ltd, West Sussex, UK, 1995, 414 p.

[2] Wielage, B. – Steinhauser, S. – Schnick, T. – Nickelmann, D.: Characterization of the Wear Behavior of Thermal Sprayed Coatings. Journal of Thermal Spray and Technology. 8, 4 (1999).

[3] Xie, Y. – Hawthorne, H. M.: The damage mechanisms of several plasma-sprayed ceramic coatings in controlled scratching. Wear 1999. Vol. 233-235, pp. 293-305.

[4] Damani, R. J. – Rubeša, D. – Danzer, R.: Fracture toughness, strength and thermal shock behaviour of bulk plasma sprayed alumina – effects of heat treatment. Journal of the European Ceramic Society 2000. Vol. 20, pp. 1439-1452.

[5] Li, J. – Zhang, Y. – Huang, J. – Ding, C.: Mechanical and Tribological Properties of Plasma-Sprayed Cr_3C_2-NiCr, WC-Co, and Cr_2O_3 Coatings. Journal of Thermal Spray and Technology 1998. Vol. 7, No. 2, pp. 242-246.

[6] Richard, C. S. – Lu, J. – Béranger, G. – Decomps, F.: Study of Cr_2O_3 Coatings Part I: Microstructure and Modulus. Journal of Thermal Spray and Technology 1995. Vol. 4, No. 4, pp. 342-346.

[7] Leivo, E. M. – Vippola, M. S. – Sorsa, P. P. A. – Vuoristo, P. M. J. – Mantyla, T. A.: Wear and Corrosion Properties of Plasma Sprayed Al_2O_3 and Cr_2O_3 Coatings Sealed by Aluminum Phosphates. Journal of Thermal Spray and Technology 1997. Vol. 6, No. 2, pp. 205-210.

[8] Pantelis, D. I. – Psyllaki, P. – Alexopoulos, N.: Tribological behaviour of plasma-sprayed Al_2O_3 coatings under severe wear conditions. Wear 2000. Vol. 237, pp. 197-204.

[9] Knuuttila, J. – Ahmaniemi, S. – Mantyla, T.: Wet abrasion and slurry erosion resistance of thermally sprayed oxide coatings. Wear 1999. Vol. 232, pp. 207-212.

[10] Hawthorne, H. M. – Erickson, L. C. – Ross, D. – Tai, H. – Troczynski, T.: The microstructural dependence of wear and indentation behaviour of some plasma-sprayed alumina coatings. Wear 1997. Vol. 203-204, pp. 709-714.

[11] Westergard, R. – Axén, N. – Wiklund, U. – Hogmark, S.: An evaluation of plasma sprayed ceramic coatings by erosion, abrasion and bend testing. Wear 2000. Vol. 246, pp. 12-19.

On the HMDSO dissociation paths in an Ar-fed expanding thermal plasma

M. Creatore, Y.Barrell, M.C.M. van de Sanden

Equilibrium and Transport in Plasmas, Department of Applied Physics
Eindhoven University of Technology, P.O.Box 513, Eindhoven, The Netherlands

Abstract
Recently, it has been reported on the use of the expanding thermal plasma (ETP), a remote configuration, for the deposition of carbon-free dense SiO_2 films by means of hexamethyldisiloxane (HMDSO)/O_2 mixtures, at a very competitive growth rate of 7-10 nm/s. Because of its geometry, the ETP configuration has also proven its suitability for studies concerning the fragmentation paths of the HMDSO molecule and the reactions occurring in the plasma phase. In this framework, very recent results obtained by means of a very sensitive, high spectral resolution- absorption technique, Cavity Ring Down Spectroscopy, are presented.

Introduction
Organosilicon-based Plasma Enhanced Chemical Vapour Deposition (PECVD) is nowadays widely spread in the technological fields where $SiC_xH_yO_z$ films are employed, as IC/MEMS devices, optics, tribology, and packaging [1]. It is the possibility of tuning and controlling the degree of organic/inorganic character that eventually allows tailoring the physical-chemical properties of the coating (density, refractive index, dielectric constant, surface energy, internal stress, hardness…). However, this technology, mainly aimed to find out the "right recipe" for the film at competitive deposition rates, is not accompanied yet by a clear picture of the plasma phase reactions and the species responsible of the deposition process.
Recently [2-3], it has been claimed that the Expanding Thermal Plasma (ETP) leads to an entirely step-by-step chemistry-controlled deposition process (e.g., no ion bombardment involved), due to the geometrical separation between the plasma source and the deposition chamber.
In this paper we address the expanding thermal plasma (ETP) technique as a simplified approach to get better insight into the hexamethyldisiloxane (HMDSO) chemistry. In this framework, a very sensitive plasma diagnostic tool, as Cavity Ring Down (CRD) Spectroscopy, has been coupled to the ETP set-up. Absorption measurements of CH_3 and CH radicals, coupled with Mass Spectrometry investigations, have pointed out to the HMDSO dissociation mechanism.

Experimental
The ETP [4,5] is an example of remote plasma: plasma production, active species transport and substrate surface treatment (deposition/etching) are geometrically separated. Its advantage over other conventional remote plasma sources is that the downstream properties have no influence on the plasma production zone, due to the huge pressure difference between the two zones. This means that, for example, we can change the deposition precursors flow rates and/or the working pressure without affecting the plasma source characteristics. The Ar (Φ_{Ar}=25-100 sccs) plasma is ignited in a dc cascaded arc, operating at currents (I_{arc}) of 25-75 A and pressure range of 0.15-0.4 bar. The thermal plasma expands supersonically through a nozzle into the deposition chamber kept at the pressure (P_{vessel}) of 0.1-0.3 mbar. At 5 cm from the arc outlet, the HMDSO is injected in the plasma by means of a ring. Because of the expansion, the electron temperature drops to about 0.3 eV [6]: electron-induced molecule dissociations are very unlikely to occur and the chemical activity in the ETP deposition chamber is dominantly controlled by the (Ar^+, e^-) flow from the arc; furthermore, ion bombardment can be neglected.
CRDS and Mass Spectrometry (MS) measurements have been performed. CRDS, an absorption technique which is rapidly spreading as a diagnostic tool for the plasma phase investigation is highly sensitive, as it is characterized by a long effective path length due to high reflectivity (>0.99) of the mirrors defining the cavity. The principle of this technique and one of its applications when coupled to the ETP set-up, can be found in Refs. [7, 8] (see Figure 1a). In this paper we report on CH and CH_3 radicals. CH absorption has been detected within the 430.1 nm system ($A^2\Delta$ (v=0)←$X^2\Pi$ (v=0)) [8] and CH_3 at 216.6 nm ($\widetilde{B}^2A_1 \leftarrow \widetilde{X}^2A_2$, 214 -218 nm [9]). The broad spectrum, due to the pre-dissociative state of CH_3, is shown in Figure 1a. The detection region for the radicals is 3 cm above the substrate, placed at a distance of 60 cm from the nozzle.

MS investigation has been performed by means of an AccuQuad Residual Gas Analyser 200D (resolution of 10 pts/amu and detection sensitivity of 10^{-17} A), placed at the side of the substrate holder, at about 5 cm lower than the substrate.

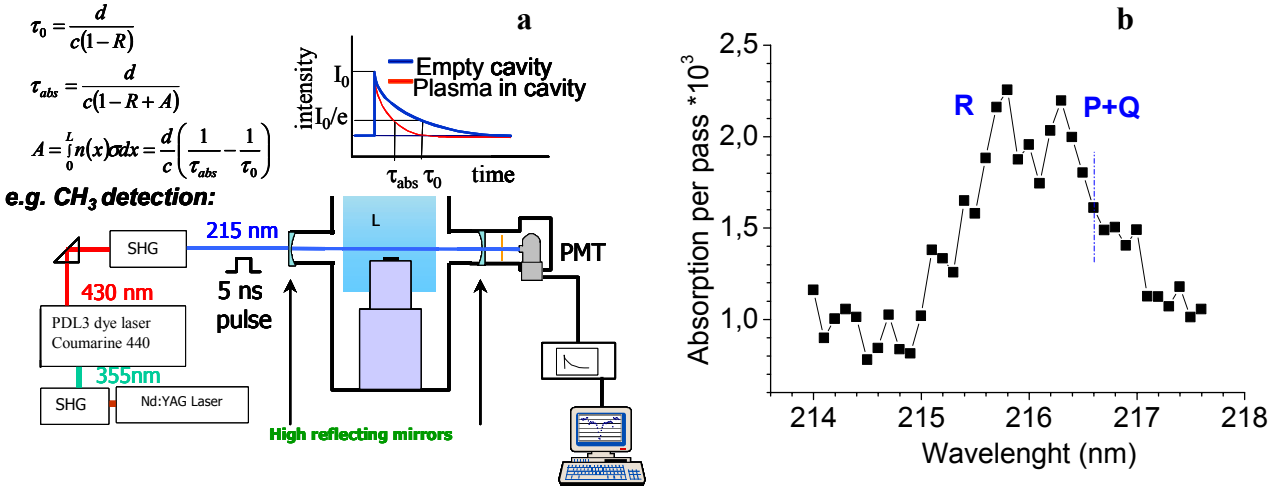

Figure 1: a) Cavity Ring Down Spectroscopy (and its principles) coupled to the ETP set-up. The particular case of CH_3 absorption is shown. b) Broad spectrum of CH_3 radical, due to its pre-dissociative character.

Results

In order to understand the dissociation paths of the HMDSO molecule in an expanding Ar plasma (Scheme I), the absorption of CH_3 radical has been measured by means of Cavity Ring Down Spectroscopy (CRD). The methyl radical, in fact, is a direct product of one of the possible dissociation routes which $[HMDSO]^+$ can undergo. The HMDSO reacts with an Ar^+ by means of charge exchange, which is then followed from a fast dissociative recombination with an electron.

Scheme I- Dissociative paths for the HMDSO molecule in an expanding thermal plasma

$$Me_3SiOSiMe_3 + Ar^+ \rightarrow [Me_3SiOSiMe_3]^+ + Ar$$

$$[Me_3SiOSiMe_3]^+ \xrightarrow{e^-} \begin{cases} Me_3SiO + SiMe_3 \rightarrow Me + Me_2SiO + SiMe_3 \\ Me_3SiOSiMe_2CH_2 + H \\ Me_3SiOSiMe_2 + Me \end{cases}$$

Figure 2 reports the measured CH_3 density divided by the total HMDSO density, e.g., the amount of methyl groups detected per HMDSO molecule. This ratio is compared, always in Figure 2, with the amount of Ar^+ available (from Langmuir probe measurements) per HMDSO molecule. One can conclude that the CH_3 production is leveled by the Ar^+ availability.

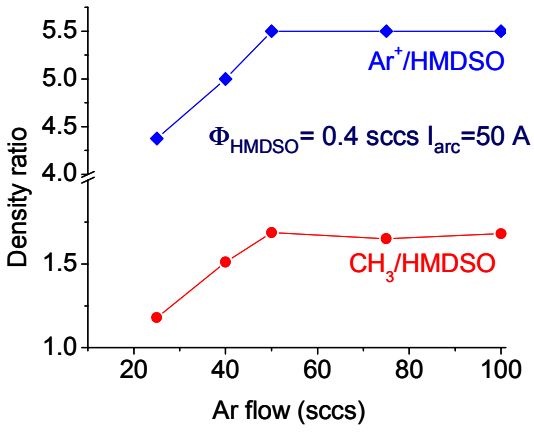

Figure 2: Ar^+/HMDSO density ratio compared with CH_3/HMDSO density ratio, as a function of the Ar flow rate.

Figure 3 reports the measured CH_3 density per HMDSO molecule, as a function of the arc current. When compared to the amount of Ar^+ available per HMDSO molecule, the CH_3/HMDSO decreases as the arc current increases, i.e., as more Ar^+ per HMDSO molecule are available.

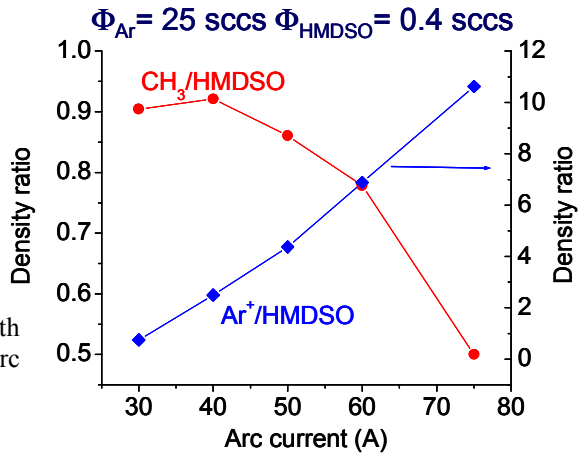

Figure 3: Ar^+/HMDSO density ratio compared with CH_3/HMDSO density ratio, as a function of the arc current.

The CH_3 radical can undergo dissociation as well, if enough Ar^+ are available. In particular, CH_3 can dissociate to give CH, according to Scheme II.

Scheme II- Dissociative path for the CH_3 radical in an expanding thermal plasma

$$CH_3 + Ar^+ \rightarrow CH_3^+ + Ar$$

$$CH_3^+ \xrightarrow{e^-} CH + H + H$$

The CH radical was monitored as a function of the arc current and its density is reported in Figure 4.
The CH density increases as function of the arc current, as more Ar+ are available for the path described in Scheme II.

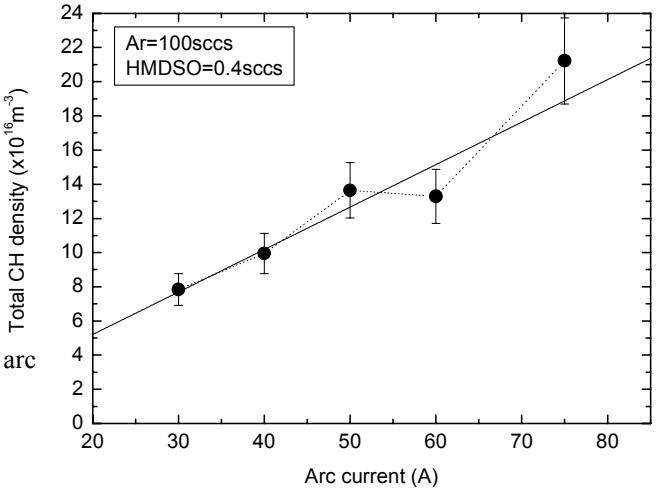

Figure 4: CH radical density as a function of the arc current.

The data shown in Figure 3 and 4 point out to dissociation paths of the HMDSO molecule where the formation of CH_3 radicals are involved. However, they cannot provide information whether the scission occurs at the Si-C bond or at the Si-O bond. Mass spectrometry studies were, therefore, performed in condition of similar Ar^+ produced (according to the arc efficiency and to the data collected by means of Langmuir probe) and amount of HMDSO available (at 50 A from 25 sccs Ar, the efficiency in Ar^+ production is estimated around 10% and the HMDSO injected downstream was 2 sccs). In these experimental conditions, we can highlight the most probable dissociation mechanism for the HMDSO molecule.

Figure 5 compares the ratio of the intensity of the 173 amu peak-to-the intensity of the HMDSO parent ion (*m/e*=147) when the plasma is off or on. The mass 173 amu corresponds to the $Si^+(CH_3)_3$ detected in the mass spectrometry, which corresponds to the neutral species $Si(CH_3)_4$ or to the radical $Si(CH_3)_3$, if this is characterized by a very low sticking probability, so that it can survive to the walls during its path to the mass spectrometer.

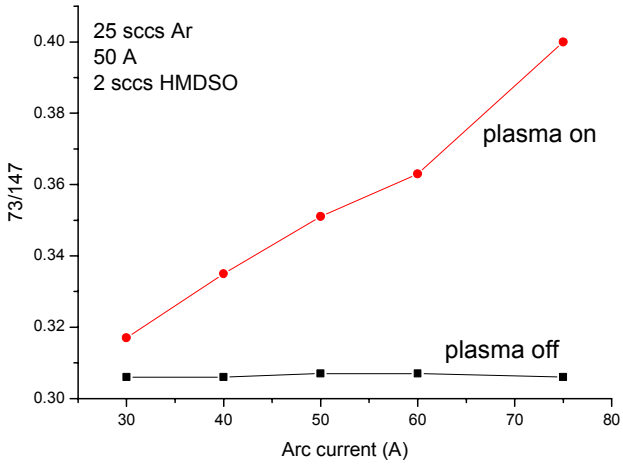

Figure 5: 73 amu signals normalized to the HMDSO parent ion (147 amu) as a function of the arc current, in the gas (plasma off) and in the plasma phase.

When this ratio is higher in the plasma phase, we can argue that the $SiMe_3$ radicals are also produced in the plasma phase (beside the MS), thus, suggesting that the preferred HMDSO dissociation route is at the Si-O bond.

Conclusions

The coupling of CRDS and MS to the ETP set-up looks promising in order to get better insight into the HMDSO dissociation paths. Under mild arc conditions (e.g., Φ_{Ar}=25 sccs, I_{arc}=50 A) the Si-O bond is preferred in the dissociative recombination of the $[HMDSO]^+$with an e^-. This shows totally different dissociation paths when comparing the ETP chemistry with more conventional plasma system, e.g., capacitively coupled, where the Si-C is unstable under electron impact.

Acknowledgements

The authors would like to thank M.J.F. van de Sande, J. Jansen, H. de Jong, B. Hüsken for their skilful technical assistance. This work is part of the research supported by a Marie Curie fellowship of the 5th Framework European Community Programme under Contract Number HPMF-CT-2001-01299.

References

[1] A. M. Wrobel, M. R. Wertheimer, in *Plasma Deposition, Treatments and Etching of Polymers*, R. d'Agostino ed., Academic Press Inc., Boston, (1990)

[2] M. Creatore, M.F.A.M. van Hest, J. Benedikt, M.C.M. van de Sanden, *MRS Material Research Society Proceedings* 715, 101 (2002)

[3] M. Creatore, M. Kilic, K. O'Brien, R. Groenen, M.C.M. van de Sanden, *Thin Solid Films* 427(1-2), 137 (2003)

[4] J.W.A.M. Gielen, W.M.M. Kessels, M.C.M. van de Sanden, D.C. Schram, *J. Appl. Phys.* 82, 2643 (1997)

[5] J.W.A.M. Gielen, M.C.M. van de Sanden, D.C. Schram, *Appl. Phys. Lett.* 69, 152 (1996)

[6] M.C.M. van de Sanden, J.M. de Regt, D. C. Schram, *Plasma Sources Sci. Technol*. 3, 511 (1994)

[7] K. W. Busch, M. A. Busch (Eds.), "Cavity Ring Down Spectroscopy: An Ultratrace-Absorption Measurement Technique" (American Chemical Society, 1999)

[8] R. Engeln, K.G.Y. Letourneur, M.G.H. Boogaarts, M.C.M. van de Sanden, D.C. Schram, *Chem. Phys. Lett.* 310, 405 (1999)

[9] P. Zalicki, Y. Ma, R.N. Zare, E.H. Wahl, J.R. Dadamio, T.G. Owano, C.H. Kruger, *Chem. Phys. Lett.* 234, 269 (1995)

Expanding thermal plasma for low-k dielectrics deposition

M. Creatore, Y.Barrell, W.M.M. Kessels, M.C.M. van de Sanden

Equilibrium and Transport in Plasmas, Department of Applied Physics
Eindhoven University of Technology, P.O. Box 513, Eindhoven, The Netherlands

Abstract
As the need for low-k dielectrics in the ULSI technology becomes urgent, the research primarily focuses on the deposition of novel materials with appropriate electrical properties and on the challenges concerning their integration with later processing steps. In this framework we introduce the expanding thermal plasma as a novel remote technique for the deposition of low-k organo-silicate glass materials from argon/oxygen/hexamethyldisiloxane mixtures.

Introduction
As the device dimensions of the ULSI chips shrink [1,2], it is necessary to reduce propagation delays, cross-talk noise between metal wires and power dissipation due to RC coupling. This is the reason why Cu (lower resistivity) has substituted Al and the research is now focused on the inter-metal dielectric (IMD) materials, which should have a dielectric constant lower than the one of SiO_2 in order to reduce the capacitance.
The spin-on deposition (SOD) has been the first to be adopted (IBM: SILK, k=2.65). On the other hand, chemical vapour deposition (CVD) is nowadays acknowledged for the possibility of using existing toolsets. Moreover, when the choice for a low-k dielectric falls on the siloxane (OSG) class, simpler process integration is expected because of the chemical structure similar to SiO_2.
Among the materials investigated, carbon-doped SiO_2 (SiOC) is considered a promising candidate in the 0.13 μm technology and beyond. The origin of the low dielectric constant of SiOC films has been investigated in literature [3] and mainly attributed to the decrease of the ionic component of the dielectric constant due to the replacement of Si-O bonds with $Si\text{-}CH_3$ bonds. Moreover, the presence of terminal groups increase the porosity, which inevitably decrease k. Also, a change in the dipolar component of the k value has to be considered since the $Si(O)_4$ tetrahedron is symmetric and does not have a dipolar component, while the insertion of methyl groups induces asymmetry, which promotes dipole generation.
The introduction of organic terminal groups in the silica network reduces necessarily the density of the dielectric, but also affects other properties. This brings up challenges on how to integrate the dielectric characteristics with later processing steps. In general, the main issue is related to the mechanical stability of the film, affected by the porosity. Residual gases from etch/ash processes can be trapped in the pores. High levels of porosity can lead to moisture uptake, which eventually leads to degradation of the dielectric constant. Films, which are mechanically weak, are prone to damage during processes, which induce stress (e.g., CMP, assembly, thermal processes…), and they are quite sensitive to wet/dry clean chemicals.
These considerations lead to conclude that a "successful" dielectric is a balance of material properties: the introduction of C-containing groups in the SiOSi network is limited by the negative impact of the porosity on the mechanical strength. In general, it has been observed [2] that the best compromise between electrical (k value) and mechanical (hardness) properties is obtained when deposition is performed from precursors with 2 Si-O and 1 Si-C bonds per Si atom. Two examples are DMOMS $(CH_3O)_2SiH(CH_3)$ and DEMS $(CH_3CH_2O)_2SiH(CH_3)$. The films deposited by these precursors shows a k value in the range of 2.75-2.95, as measured at 1 MHz and hardness around 1-3 GPa. Therefore, hexamethyldisiloxane (HMDSO) may not appear suitable as deposition precursor, due to the high $Si\text{-}CH_3$: Si-O bond ratio, which could lower far beyond the density of the film, and thus its mechanical stability. However, the expanding thermal plasma (ETP) set-up allows selecting different fragmentation paths for HMDSO, which eventually can be turned to the progressive cleavage of Si-C bonds. Therefore, the tuning of the process parameters, as it will be shown later, allows tailoring the organic functionalities in the film.

Experimental
The ETP (Figure 1) is an example of remote plasma [4,5]: plasma production, active species transport and substrate surface treatment (deposition/etching) are geometrically separated. Its advantage over other conventional remote plasma sources is that the downstream properties have no influence on the plasma

production zone, due to the huge pressure difference between the two zones. This means that, for example, we can change the deposition precursors flow rates and/or the working pressure without affecting the plasma source characteristics. The Ar (Φ_{Ar}=25-100 sccs) plasma is ignited in a dc cascaded arc, operating at currents (I_{arc}) of 25-75 A and pressure range of 0.15-0.4 bar. The thermal plasma expands supersonically through a nozzle into the deposition chamber kept at the pressure (P_{vessel}) of 0.1-0.3 mbar. At 5 cm from the arc outlet, the HMDSO is injected in the plasma by means of a ring. Because of the expansion, the electron temperature drops to about 0.3 eV [6]: electron-induced molecule dissociations are very unlikely to occur and the chemical activity in the ETP deposition chamber is dominantly controlled by the (Ar^+, e^-) flow from the arc; furthermore, ion bombardment can be neglected. O_2 was injected through the nozzle.

C-doped SiO_2-like films were deposited at a substrate temperature of 50°C on *c*-Si (100) having a resistivity of 7-21 Ω·cm. The dielectric constant at 1 MHz was obtained by a C-V meter on metal-insulator-semiconductor (MIS) structures. The values were confirmed by means of the Hg probe. Hardness/Young modulus values were obtained by means of nano-indentation measurements. Spectroscopic ellipsometric measurements (Woollam M-2000F rotating compensator ellipsometer, 245 – 1000 nm) were carried out on the deposited films in order to evaluate their optical constants and thickness.

Film chemical characterization was carried out by means of X-ray Photoelectron Spectroscopy, after sputtering with Ar ions in order to remove the carbon contamination due to sample exposure to the ambient air.

Plasma characterization was carried out by means of Cavity Ring Down Spectroscopy (CRDS) [7,8] and Mass Spectrometry (MS). In the first case, radicals could be detected 3 cm above the substrate (which is placed at a distance of 60 cm from the nozzle). MS investigation of the background gas has been performed by means of an AccuQuad Residual Gas Analyser 200D (resolution of 10 pts/amu and detection sensitivity of 10^{-17} A), placed at the side of the substrate holder, at about 5 cm lower than the substrate.

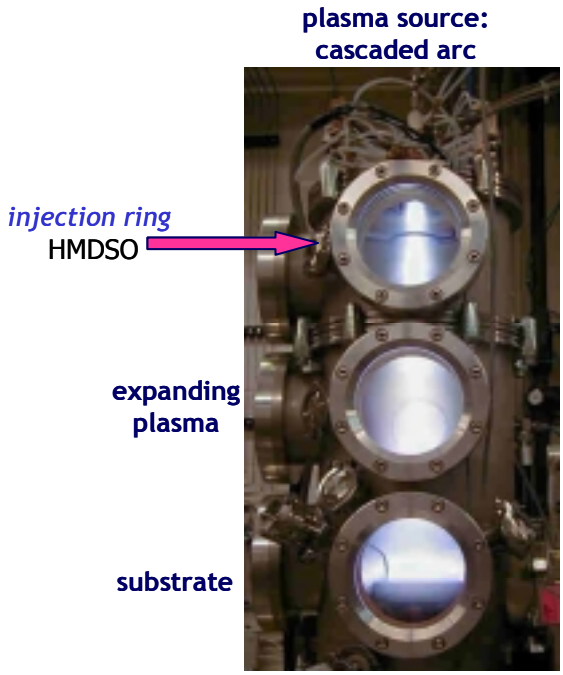

Figure 1: The expanding thermal plasma set-up.

Results

As already mentioned in the Introduction, the ETP set-up leads to a more rationalized approach to the deposition process, since the downstream properties have no influence on the plasma parameters. The HMDSO molecule dissociates in expanding Ar plasma [9,10], according to Scheme I: first, a charge exchange with an Ar ion occurs, followed from a fast dissociative recombination with an electron.

Scheme I- Dissociative paths for the HMDSO molecule in expanding thermal plasma

$$Me_3SiOSiMe_3 + Ar^+ \rightarrow [Me_3SiOSiMe_3]^+ + Ar$$

$$[Me_3SiOSiMe_3]^+ \xrightarrow{e^-} \begin{cases} Me_3SiO + SiMe_3 \rightarrow Me + Me_2SiO + SiMe_3 \\ Me_3SiOSiMe_2CH_2 + H \\ Me_3SiOSiMe_2 + Me \end{cases}$$

Figure 2a shows the depleted (e.g., consumed) HMDSO flow rate, as a function of the arc current, i.e., the Ar^+ flow rate as calculated from Langmuir probe measurements. The consumed HMDSO flow is proportional to the Ar ion flow, which emanates from the arc. Figure 2b compares the ratio of the intensity of

the 173 amu peak-to-the intensity of the HMDSO parent ion (*m/e*=147) when the plasma is off or on, as a function of the arc current. The mass 173 amu corresponds to the $Si^{+}(CH_3)_3$ detected in the mass spectrometry, which relates to the neutral species $Si(CH_3)_4$ or to the radical $Si(CH_3)_3$, if this is characterized by a very low sticking probability, so that it can survive to collisions with walls during its path to the mass spectrometer. When this ratio is higher in the plasma phase, we can argue that $SiMe_3$ radicals are also produced in the plasma phase (beside the MS), thus, suggesting that the preferred HMDSO dissociation route is at the Si-O bond.

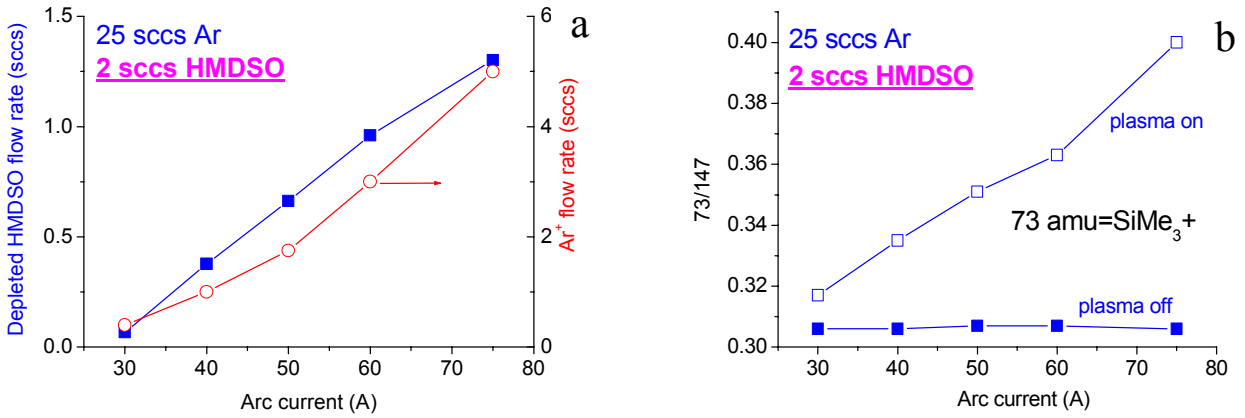

Figure 2: a) Depleted HMDSO flow rate as a function of the arc current. The Ar ion flow rate (as calculated from Langmuir probe measurement) has been reported for comparison. b) 73 amu signals normalized to the HMDSO parent ion (147 amu) as a function of the arc current, in the gas (plasma off) and in the plasma phase.

From Figure 2 it appears clear that the most favourite dissociation path occurs at the Si-O bond, in conditions where the HMDSO flow rate is similar to the Ar^{+} flow rate. These conditions, however, will presumably lead to the "wrong" film stoichiometry, as the film will be oxygen-deficient. XPS analysis of the films deposited in the same experimental conditions reported in Figure 2 show that the composition varies a little with the arc current and it can be expressed as $SiC_1O_{0.6}$.

In order to rebuild the SiOSi network, it is therefore necessary to "dilute" HMDSO in O_2. Figure 3a shows the depleted HMDSO and O_2 flow rates, as a function of the O_2 addition. Figure 3b, in particular, shows that the HMDSO depletion is "almost" independent from the O_2 depletion: even in the presence of O_2, Ar^{+} "prefers" to react with HMDSO, presumably due to the very low reaction constant of the charge exchange reaction of Ar^{+} with O_2 ($4.6 \cdot 10^{-11}$ cm^3/s). However, we cannot neglect, for the moment, reactions of HMDSO fragments with O_2.

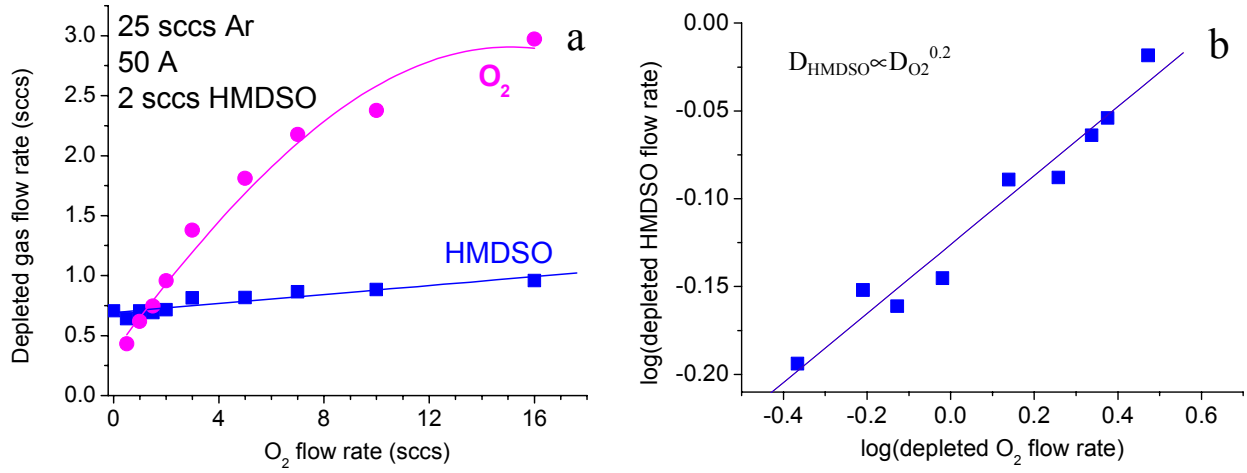

Figure 3: a) Depleted HMDSO and O_2 flow rate as a function of the added O_2 flow. b) Logarithm plot of the depleted HMDSO flow rate as a function of the depleted O_2 flow rate.

Films deposited in the above-mentioned conditions do show a refractive index (as measured at 633 nm), which decreases as a function of the O_2 flow rate and reaches values below 1.46 (thermal silica), as shown in Figure 4a. Since films deposited even at high dilution of HMDSO in O_2 still contain carbon (Figure 5), we can conclude that the low refractive index is due to the presence of porosity. Figure 4b reports the imaginary part of the dielectric function, which is correlated with the presence of carbon in the film, as the absorption in the low wavelength range witnesses: the absorption in the film decreases as the O_2 addition increases.

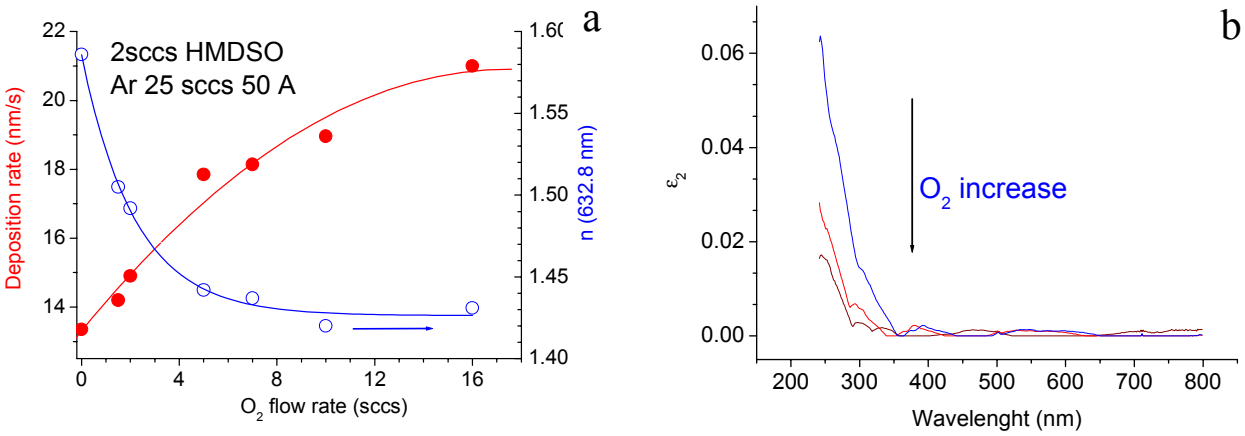

Figure 4: a) Deposition rate and refractive index of the deposited films as a function of the O_2 flow rate. b) Imaginary part of the dielectric function as a function of the O_2 flow rate.

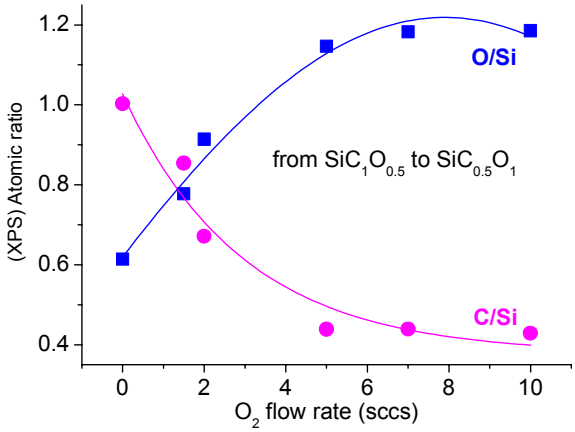

Figure 5: Chemical composition of the deposited films as a function of the O_2 flow rate, as determined from XPS measurements.

Films deposited in these conditions reach a dielectric constant if 3.44±0.15 for O_2=10 sccs. However, as the chemical composition suggests, the films are expected to be mechanically weak due to the fact that they are still deficient in oxygen content. The films show a hardness of 0.4 GPa and a modulus of 4-4.5 GPa.

We can conclude from this first investigation that a higher dilution of HMDSO in O_2 is necessary. In particular, by keeping constant the Ar ion flow rate expanding from the arc and decreasing the HMDSO flow rate, more Ar^+ per HMDSO molecule will be available. We could, therefore, use these Ar^+ in a selective way in order to "strip" methyl groups from the HMDSO molecule and O_2 for controlling the inorganic SiOSi structure.

Figure 6 shows reports the measured CH_3 density divided by the total HMDSO (0.4 sccs) density, e.g., the amount of methyl groups detected per HMDSO molecule. This ratio is compared, always in Figure 6, with the amount of Ar^+ available (from Langmuir probe measurements) per HMDSO molecule. One can conclude that the CH_3 production (stripping) is leveled by the Ar^+ availability.

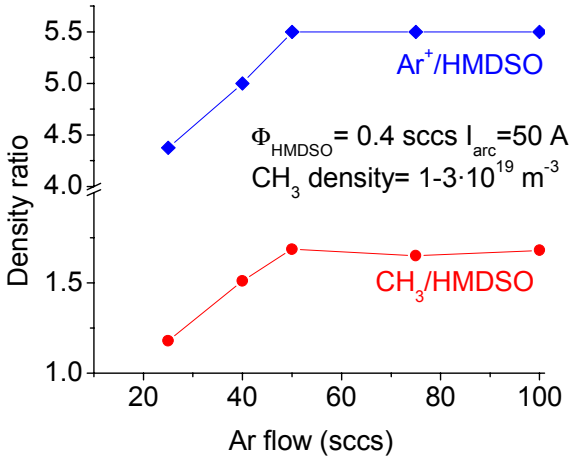

Figure 6: Ar^+/HMDSO density ratio compared with CH_3/HMDSO density ratio, as a function of the Ar flow rate.

Figure 7a shows the refractive index as a function of the O_2 flow rate: the *in situ* values are found lower than the *ex situ* measurements due to the water up-take when porous films are exposed to ambient air. Figure 7b shows the dielectric constant as a function of the O_2 addition, which reaches a value as low as 2.9. The hardness and modulus of these films are 1GPa and 10 GPa, respectively.

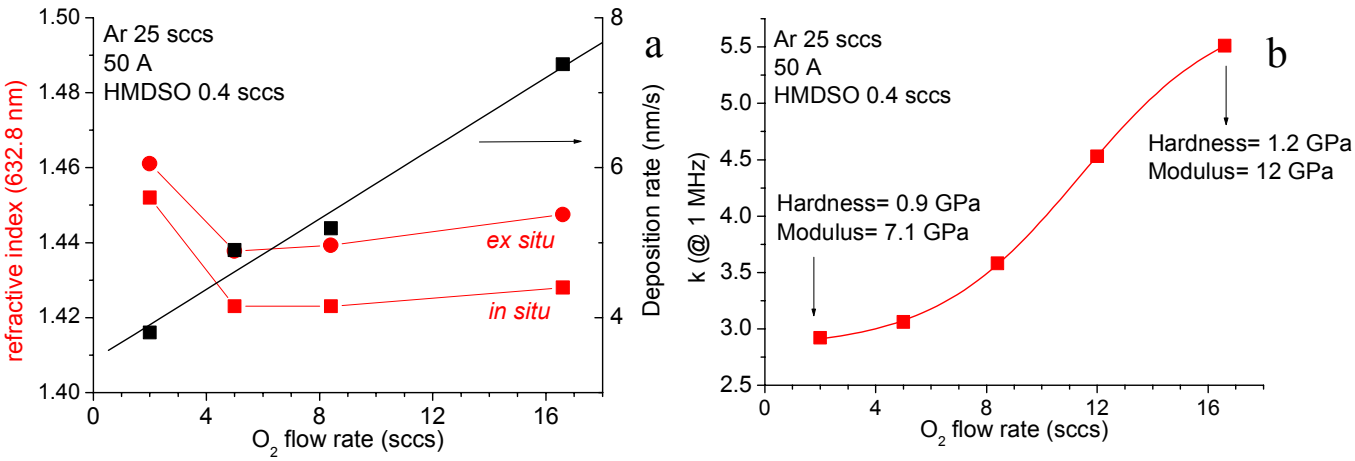

Figure 7: a) Deposition rate and refractive index of the deposited films as a function of the O_2 flow rate. b) Dielectric constant (as measured at 1 MHz) as a function of the O_2 flow rate. The hardness and modulus values are also reported.

Conclusions

Low-dielectric constant films were deposited by means of the expanding thermal plasma set-up: a minimum of 2.9, as measured at 1MHz, was found with an acceptable hardness of 1 GPa. The investigation of the plasma phase by means of Cavity Ring Down Spectroscopy and Mass Spectrometry has been helpful for tailoring the organic/inorganic content of the deposited films.

The future work will deal with a better insight into the deposition of low-k materials and their further characterization (e.g., porosity evaluation).

Acknowledgements

The authors would like to thank H. de Jong for the measurements on the MIS structures and M.J.F. van de Sande, J. Jansen, B. Hüsken for their skilful technical assistance. Nathan Kemeling (ASMI) is acknowledged for the dielectric constant measurements by means of the Hg probe and for the hardness/modulus measurements. M. C. Burrell (General Electric, Research and Development Centre) is acknowledged for

providing the XPS results. This work is part of the research supported by a Marie Curie fellowship of the 5th Framework European Community Programme under Contract Number HPMF-CT-2001-01299.

References

[1] *MRS Bulletin* 22(10) (1997)
[2] *Semiconductor International*, June 2002
[3] J.Y. Kim, M.S. Hwang, Y.-H. Kim, H.J. Kim, Y. Lee, *J.Appl.Phys.* 90(5), 2469 (2001)
[4] J.W.A.M. Gielen, W.M.M. Kessels, M.C.M. van de Sanden, D.C. Schram, *J. Appl. Phys.* 82, 2643 (1997)
[5] J.W.A.M. Gielen, M.C.M. van de Sanden, D.C. Schram, *Appl. Phys. Lett.* 69, 152 (1996)
[6] M.C.M. van de Sanden, J.M. de Regt, D. C. Schram, *Plasma Sources Sci. Technol*. 3, 511 (1994)
[7] K. W. Busch, M. A. Busch (Eds.), "Cavity Ring Down Spectroscopy: An Ultratrace-Absorption Measurement Technique" (American Chemical Society, 1999)
[8] R. Engeln, K.G.Y. Letourneur, M.G.H. Boogaarts, M.C.M. van de Sanden, D.C. Schram, *Chem. Phys. Lett.* 310, 405 (1999)
[9] M. Creatore, M. Kilic, K. O'Brien, R. Groenen, M.C.M. van de Sanden, *Thin Solid Films* 427(1-2), 137 (2003)
[10] M.Creatore, M.F.A.M. van Hest, J. Benedikt, M.C.M. van de Sanden, *MRS Proc.* 715, 101 (2002)

The $N_2(A^3S_u^+)$ density produced in atmospheric-pressure nitrogen streamers: experimental determination by time-resolved emission spectrometry.

M.Šimek

Institute of Plasma Physics, Department of Pulse Plasma Systems,
Academy of Sciences of the Czech Republic, Za Slovankou 3, 18221 Prague , Czech Republic

Abstract
Newly developed spectrometric method was applied to determine absolute densities of $N_2(A^3\Sigma_u^+)$ metastable species produced by positive streamers. Streamers were generated in high-purity, atmospheric-pressure nitrogen with NO traces by applying short, high-voltage pulses to wire anode in coaxial wire-cylinder electrode geometry. The $N_2(A^3\Sigma_u^+)$ densities in the range 10^{14}-10^{15} [cm^{-3}] were found close to the central wire anode during early post-discharge time.

1. Introduction
In the physics and chemistry of non-equilibrium nitrogen or N_2-O_2/air discharges, the fundamental role is played by the lowest electronically excited and metastable $A^3\Sigma^+_u$ state of N_2. Except for a very long (~2s) radiative lifetime, the $N_2(A^3\Sigma^+_u)$ molecule possesses enough energy (~6 eV) to initiate many energy transfer and chemical reactions [1]. Recently, we have proved that the post-discharge populations of $NO(A^2\Sigma^+)$ and $N_2(^3\Pi,^5\Pi)$ states in atmospheric-pressure nitrogen streamers have a common $N_2(A^3\Sigma^+_u)$ precursor [2,3]. The experimental evidence is based on the fact that the intensity of $N_2(C^3\Pi_u \rightarrow B^3\Pi_g)$, second positive system (2.PG) emission varies quadratically with the intensity of the $NO(A^2\Sigma^+ \rightarrow X^2\Pi)$ system (NO-γ) and on the study of the $N_2(C^3\Pi_u, v=0\text{-}4)$ state vibrational distributions during both discharge and post-discharge phases. An independent confirmation of the former scheme was provided through the observation of the $N_2(C''^5\Pi_u \rightarrow A'^5\Sigma_g^+)$ Herman infrared (HIR), $N_2(C'^3\Pi_u \rightarrow B^3\Pi_g)$ Goldstein-Kaplan (GK), and $N_2(B^3\Pi_g \rightarrow A^3\Sigma_u^+)$ first positive (1.PG) systems populated by the $N_2(A^3\Sigma_u^+)$ energy pooling as well. The quantitative $N_2(A^3\Sigma^+_u)$ determination is obviously the next step for further study of nitrogen streamer properties.
To determine absolute $N_2(A^3\Sigma^+_u)$ densities we applied newly developed method suitable to investigate atmospheric-pressure nitrogen streamers [4,5]. The method originates from the correlation of emission intensities of the $NO(A^2\Sigma^+)$ and $N_2(C^3\Pi, C''^5\Pi)$ states observed in a decaying streamer channel with the $N_2(A^3\Sigma^+_u)$ state evolution through a simplified kinetic model:

- $N_2(A^3\Sigma_u^+)+N_2(A^3\Sigma_u^+) \rightarrow N_2+N_2(C^3\Pi_u)$ & $N_2(C^3\Pi_u) \rightarrow N_2(B^3\Pi_g) + h\nu_{2.PG}$,
- $N_2(A^3\Sigma_u^+)+N_2(A^3\Sigma_u^+) \rightarrow N_2+N_2(C''^5\Pi_u)$ & $N_2(C''^5\Pi_u) \rightarrow N_2(A'^5\Sigma_g^+) + h\nu_{HIR}$,
- $N_2(A^3\Sigma_u^+)+NO(X^2\Pi) \rightarrow N_2+NO(A^2\Sigma^+)$ & $NO(A^2\Sigma^+) \rightarrow NO(X^2\Pi) + h\nu_\gamma$.

Assuming atmospheric-pressure, post-discharge conditions under which the excitation of $N_2(C''^5\Pi_u, C^3\Pi_u)$ and $NO(A^2\Sigma^+)$ states is governed by the above mentioned energy transfer processes, one can expect that $NO(A^2\Sigma^+, X^2\Pi)$ and $N_2(C''^3\Pi_u, C^3\Pi_u, A^3\Sigma_u^+)$ populations go rapidly towards the steady-state which is determined by a balance between the pooling, resonant transfer, radiative and quenching processes. A stationary solution of corresponding rate equations then provides simple correlation between $NO(X^2\Pi)$, $NO(A^2\Sigma^+)$, $N_2(C^3\Pi_u)$ and $N_2(A^3\Sigma^+_u)$ state densities. The diagnostic procedure is then based on the modelling of NO-γ and N_2-2.PG emissions controlled by $N_2(A^3\Sigma^+_u)$ species through the pooling and resonant energy transfer reactions, and on establishing suitable calibration procedure [4]. Figure 1 shows synthetic bands occurring in the region of Δv=-1,-2 sequences of N_2-2.PG system. Each of synthesised band components contributes to the final spectrum with a specific weight, which depends on $N_2(A^3\Sigma^+_u)$ density. An example of the spectrometric representation of $N_2(A^3\Sigma^+_u)$ density through the blend of NO-γ and N_2-2.PG emissions is given in figure 2. All spectra shown in figure 2 were normalised so as to equal 2.PG-(0,1) band intensities. Finally, the concentration of $N_2(A^3\Sigma^+_u)$ metastables can be determined from experimental data by analysing time evolutions and relative intensities of emissions driven by the pooling and resonant energy transfer

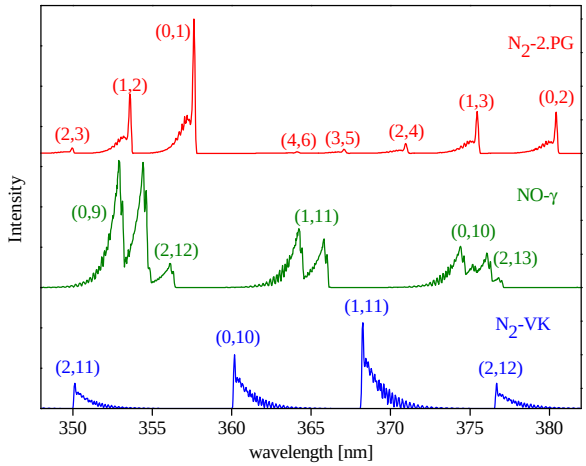

Figure 1: Synthetic bands of N_2-2.PG, N_2-VK and NO-γ systems.

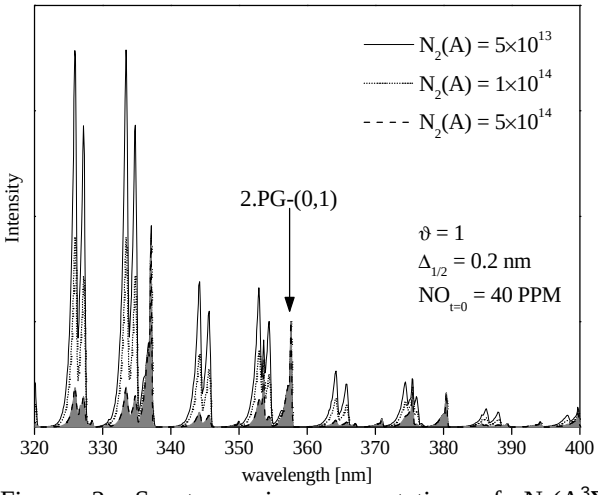

Figure 2: Spectroscopic representation of $N_2(A^3\Sigma_u^+)$ concentration via N_2-2.PG, N_2-VK and NO-γ emissions.

reactions [5]. The application of the method requires that concentrations of predominant $N_2(A^3\Sigma^+_u)$ quenchers are known and stable during the acquisition of spectrometric data. This can be fulfilled by adding a well defined quantity of an efficient $N_2(A^3\Sigma^+_u)$ quencher to the nitrogen stream so that the influence of the trace impurities (O_2, H_2O) as well as of species produced during the discharge phase (mainly $N_2(X,v\geq5)$ and $N(^4S)$ atoms) remains minor or not competitive. The former is well fulfilled, in our case, by adding small quantity of NO to the main N_2 stream and by limiting the amount of energy ($\leq 10^{-3}$ Wh/l) that is dissipated in the discharge volume [5].

2. Experimental setup

Investigated streamers (see figure 3) were generated in coaxial wire-cylinder geometry at atmospheric pressure in high-purity nitrogen with quantified NO traces. The experimental corona device consists of an Ag-coated Cu central wire anode (2r = 0.75 mm) and a grounded stainless-steel cylinder (2R=56 mm). The pulsed high-voltage power supply with maximum ratings, 100 kV/1kA/ 7 ns rise time/ ~100 ns fall time, delivers up to 2 J per pulse with up to a 10 Hz repetition rate at atmospheric pressure into the discharge volume ~ 1500 cm^3. Stable flow of nitrogen with defined quantity of NO is maintained by Bronkhorst mass flow controllers. The GA-60 flue gas analyser equipped with electrochemical cells was used to monitor volumetric concentration of nitrogen oxides (NO and NO_2).

The ISA JobinYvon and Chromex spectrometric systems, equipped either with multi-channel detectors or with a photon-counting system monitored the emission coming out along the symmetry axis of the discharge through quartz optics and colour glass filters. High time resolution has been obtained by synchronising the data acquisition systems with HV circuitry for the corona discharge. Because streamer parameters alter during the propagation between electrodes and the strongest emission can be expected from the high field region, we focused on emission generated close to wire anode (indicated by white dash circle in figure 3). The space resolution in radial direction was obtained by using a collection system composed of two lenses and three apertures.

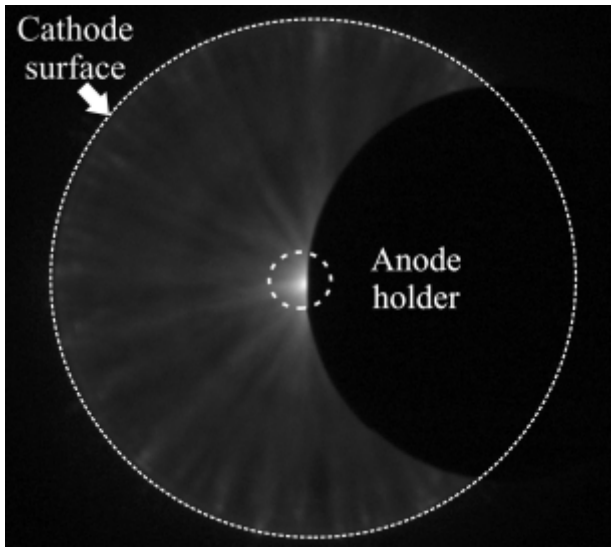

Figure 3: Digital photograph of the discharge area registered by a fast CCD camera.

3. Results

In order to follow time evolution of emission intensities we used two complementary data acquisition approaches. The first approach makes use of an ICCD detector, fixing the delay of the CCD intensifier opening gate with respect to the master trigger controlling corona pulsing. Multichannel ICCD spectra were used to evaluate relative emission intensities of selected molecular bands at given post-discharge time. The second approach uses PMT with a multichannel

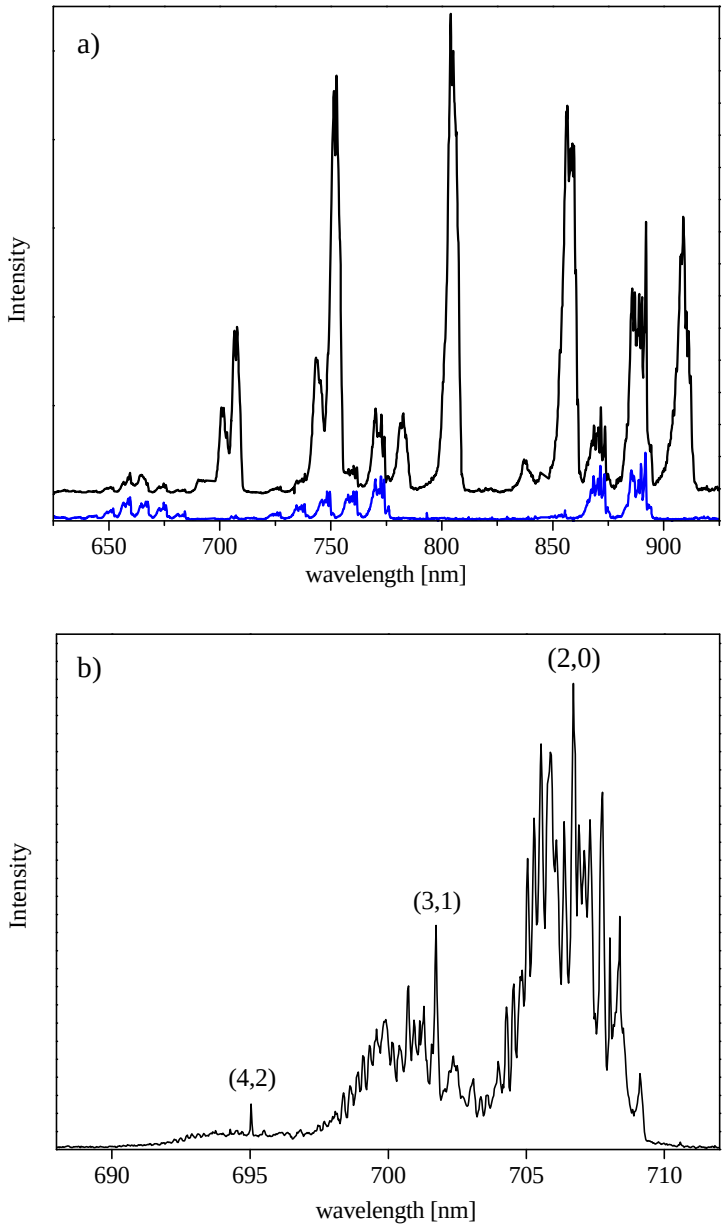

Figure 4: Characteristic streamer-induced emission observed in high-purity nitrogen at atmospheric pressure. Spectra acquired by multichannel ICCD data acquisition technique show a) the blend of bands of N_2-1.PG and N_2-HIR systems in the VIS-NIR spectral region and b) the $\Delta v=2$ sequence of N_2-HIR systems. Lower (blue) trace in the upper figure acquired as a discharge average, other (black) traces acquired without time resolution.

photon-counting system to obtain "continuous" time courses at fixed wavelengths. In the case of the photon-counting technique we selected appropriate wavelengths and entrance/exit slit widths of monochromator in order to obtain bandwidths well matching selected peaks. Finally, the composition of the gas mixture after passing the discharge chamber was studied by means of the flue gas (NO_x) analyser.

A number of ICCD spectra were taken during the post-discharge period to evaluate relative emission intensities between selected bands. Basically, data were acquired in two regimes; a) by fixing the initial N_2+NO composition (and all other discharge conditions) and varying the delay of the ICCD gate with respect to the corona HV pulse onset, and b) by fixing the ICCD gate and varying the NO concentration in the mixture.

Characteristic examples of ICCD spectra obtained in VIS-NIR spectral region from the discharge in high purity nitrogen are shown in figure 4. The upper trace in figure 4a (acquired without any time resolution) is given by the superposition of N_2-HIR and N_2-1.PG emissions. The lower blue trace (acquired as the average over the 150 ns discharge period) is given exclusively by N_2-1.PG emission, which is excited by streamer head electrons. Because N_2-HIR emission is excited exclusively by the pooling energy transfer, the square root of its intensity ($\ddot{O}(I^{HIR})$) describes relative evolution of $N_2(A^3\Sigma^+_u)$ density. To obtain $\ddot{O}(I^{HIR})$ curves, we utilised HIR emission occurring via the $\Delta=+2$ sequence, which is shown with better spectral resolution in figure 4b. The normalisation of relative $\ddot{O}(I^{HIR})$ curves was performed by analysing the $(I^{2.PG}/I^{g})$ intensity ratio of N_2-2.PG and NO-γ emissions [4,5]. Resulting normalised $\ddot{O}(I^{HIR})$ curves, obtained for several N_2+NO mixture compositions, are shown in figure 4.

4. Conclusions

The potential of the spectrometric method to determine $N_2(A^3\Sigma^+_u)$ metastable concentrations was investigated in the environment controlled by specific energy transfer processes. The method is based on the N_2-2.PG, N_2-VK, N_2-HIR and NO-γ emission analysis and its performance was inspected by analysing post-

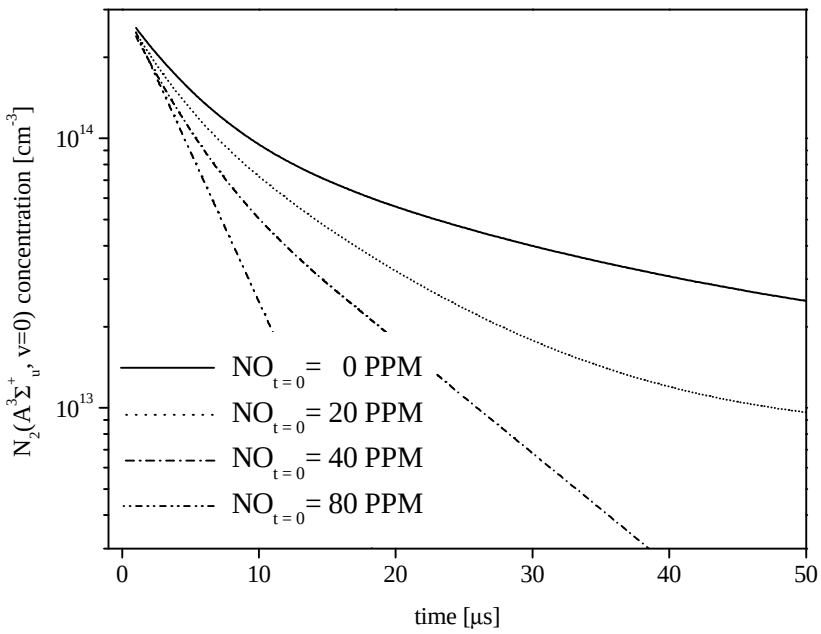

Figure 4: The $N_2(A^3\Sigma_u^+)$ concentrations determined through normalised $\ddot{O}(I^{HIR})$ curves. The time on the *x*-axis means the delay t_D between the onset of the HV corona pulse and the centre of an opening gate for the MSA counting channels.

discharge emission induced by pulsed positive streamers generated in coaxial wire-cylinder geometry in high-purity nitrogen with quantified NO traces.

After verification that all necessary conditions for correct application of the method were satisfied, we evaluated concentrations of $N_2(^3\Sigma^+_u)$ metastables from spectroscopic data acquired close to the central wire anode.

According to the method, the aggregate concentration of $N_2(A^3\Sigma^+_u)$ metastable species in the two lowest v=0,1 vibrational levels reaches as much as $\sim 5\times10^{14}$ [cm^{-3}] during early post-discharge time (~1 μs). Our data represent, to our knowledge, the first experimentally determined $N_2(A^3\Sigma^+_u)$ densities produced by nitrogen streamers at high (atmospheric) pressure, which are reported in the literature.

Acknowledgements

This work was supported by the Grant Agency of the Academy of Sciences of the Czech Republic under contract GAAV 1043102.

References

[1] M.F. Golde - Reactions of $N_2(A^3\Sigma_u^+)$, Int.J.Chem.Kinet. **20,** 75 (1988).

[2] M. Šimek, V. Babický, M. Clupek, and P. Šunka - Observation of N_2 Herman infrared system in pulsed positive streamer induced emission at atmospheric pressure, J.Phys.D:Appl.Phys. **34,** 3185 (2001).

[3] M. Šimek, S. DeBenedictis, G. Dilecce, V. Babický, M. Clupek, and P. Šunka - Time and space resolved analysis of $N_2(C^3\Pi_u)$ vibrational distributions in pulsed positive corona discharge J.Phys.D:Appl.Phys. **35,** 1981 (2002).

[4] M. Šimek - Determination of $N_2(A^3\Sigma_u^+)$ metastable density produced by nitrogen streamers at atmospheric pressure: 1. Design of diagnostic method, Plasma Sources Sci. Technol. submitted (2003).

[5] M. Šimek - Determination of $N_2(A^3\Sigma_u^+)$ metastable density produced by nitrogen streamers at atmospheric pressure: 2. Experimental verification, Plasma Sources Sci. Technol. submitted (2003).

Absorption measurements of OH radical in sterilization plasma by means of Cavity Ring Down Spectroscopy

M. Creatore[1], R. Groenen[1], R. De Mitri[2], F. Rossi[2], M.C.M. van de Sanden[1]
[1] *Department of Applied Physics, Eindhoven University of Technology, Eindhoven, The Netherlands*
[2] *Institute for Health and Consumer Protection, Joint Research Centre, Ispra, Italy*

Abstract
A highly sensitive laser-aided diagnostic tool, Cavity Ring Down Spectroscopy (CRD) is used to study the OH (integrated) absorption in a MW (2.45 GHz) sterilization plasma, operating at a power of 500-1500 W and fed by O_2/H_2 mixtures. Two different groups of lines of the broad OH absorption were detected: their intensity ratio gives a good indication of the rotational temperature of the radical, in general very close to the gas temperature.

1. Introduction

Plasma-based techniques to achieve sterilization represent an alternative, safer and versatile (especially indicated for moisture- and heat- sensitive polymer-made devices) route to conventional techniques, as those using autoclaves, ovens or wet chemicals (e.g., ethylene oxide). The main reason for using plasmas in sterilization is the presence of highly reactive species (more reactive than "conventional" chemicals), which have been identified in ultraviolet radiation and radicals. It is still unclear whether and how radicals or photons play a fundamental role in the destruction of micro-organisms; yet, a rationalization of these processes is necessary in order to develop more efficient plasma-aided sterilization tools.
In this framework, preliminary investigation has been carried out on a MW (2.45 GHz) sterilization plasma, operating at a power of 500-1500 W and fed by O_2/H_2 mixtures. A highly sensitive laser-aided diagnostic tool, Cavity Ring Down Spectroscopy (CRD) [1,2] which is commonly-used at Eindhoven University of Technology [3,4,5], has been coupled to the reactor in order to detect the absorption of the OH radical (3064 Angstrom system, $A^2\Sigma^+$ (v=0)-$X^2\Pi$ (v=0)).

2. Experimental

Figure 1 shows the CRD spectroscopy set-up (and its principles) coupled with the MW reactor. CRD requires an optical cavity defined by two highly reflective mirrors (>99%). A laser pulse (5 ns) is produced using the Nd-YAG laser-pumped dye laser (PDL2 Spectra Physics) and sent into the optical cavity. The laser pulse undergoes hundreds of reflections in the cavity and a detector, placed behind the cavity, records the succession of pulses transmitted from the cavity after each round trip. Because the intensity of the pulse confined within the cavity undergoes attenuation at each round trip (a combination of losses caused by the mirrors themselves, as well as scattering and absorption from the *sample* present in the cavity), the detector records a waveform with a time decay theoretically fitted by an exponential. The time required for the intensity to decay to 1/e of its original value is defined as ring down time. Its value is related only to mirror losses (as shown in Figure 1) when the cavity is empty (τ_0), e.g., in our case no plasma or no OH is present. In the presence of an absorbing species (e.g., OH) the ring down time decreases to τ_{abs}. The absorption of the species can be, therefore, calculated from the measured ring down times and the length of the cavity.
The detection region for the radicals is 7 cm from the microwave source. Depending on the operative pressure, the OH absorption has been sampled in the glow (low pressure regime) or in the immediate afterglow (high pressure regime).
The two plano-concave mirrors (radius of curvature of 100 cm) are mounted on the reactor and bellows allow for fine adjustment; the cavity length is 97 cm. An Ar flow is supplied to protect the mirrors from possible contamination due to H presence. For an empty vessel a ringdown time of ≈400 ns has been recorded. At the exit of the dye laser a 2 mJ light pulse is obtained with a bandwidth of 0.28 cm^{-1}. The frequency of the output beam is then doubled, from 616 nm to 308 nm, by means of a KDP (Potassium Deutero-Phospate) crystal. A LabView program controls the wavelength stepping of the dye laser and reads out the transients via a GPIB interface. For every wavelength 64 transients are averaged and the average is then fitted to an exponential decay function.

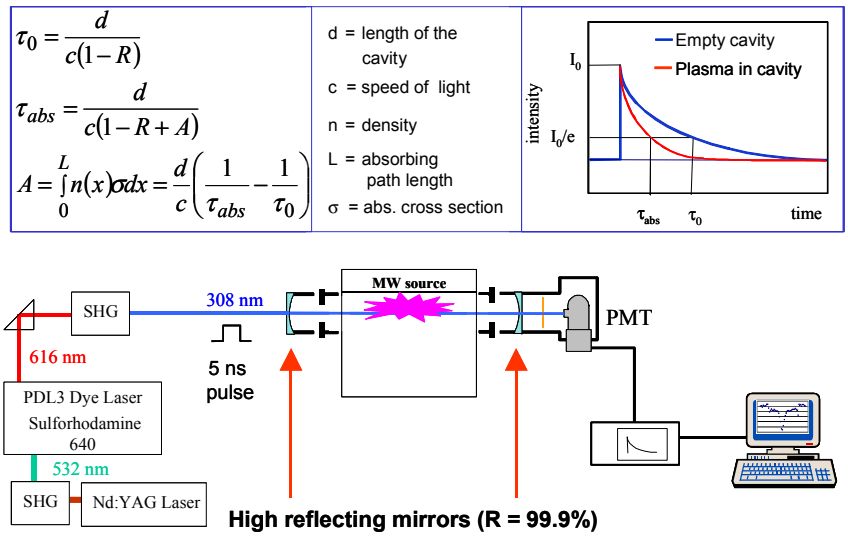

Figure 1: Cavity Ring-Down Spectroscopy set-up coupled with the MW source. Principles of CRDS are also reported.

3. Results and Discussion

The OH system which has been investigated is the 3064 Angstrom system, $A^2\Sigma^+$ (v=0)-$X^2\Pi$ (v=0). According to literature [6,7], the UV OH spectrum can be used as a *molecular pyrometer*, namely, the rotational temperature of OH can be determined as a function of the experimental conditions and approximated to the gas temperature in the plasma. Therefore, two different regions for OH absorption were monitored: the $I0_2$ lines (3064.95 and 3065.10 Angstrom) belonging to the G_0 group and the $I2_3$ lines (3081.54, 3081.62 and 3081.66 Angstrom) belonging to the G_2 group. These regions are shown in Figure 2.

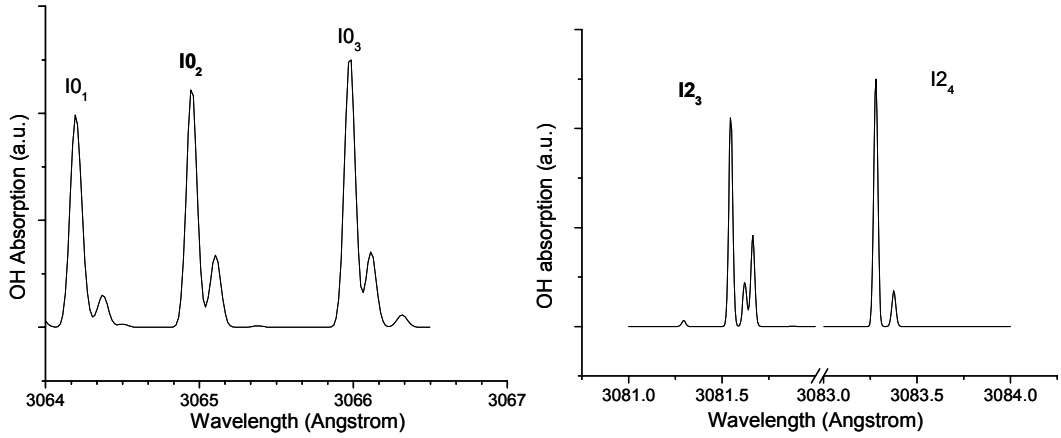

Figure 2: OH band spectra in the two regions chosen for the data acquisition, the G0 and G2 groups.

The OH (integrated) absorption is studied as a function of the different experimental parameters, e.g., power, pressure and gas feed composition (H_2/O_2 mixtures). Figures 3 and 4 show that OH production increases with the power as molecule dissociation becomes more efficient. As the pressure increases, the absorption decreases, probably due to the fact that the discharge becomes more confined, e.g., the CRD starts detecting in the afterglow region. At 350 mTorr (not shown), the absorption becomes quite noisy and estimated around $2 \cdot 10^{-5}$ per pass. The error is estimated around $5 \cdot 10^{-6}$ for the absorption measured in the G_0 group and $1 \cdot 10^{-6}$ for the absorption measured in the G_2 group. Figure 4 shows also the good agreement between the two data series, as collected in different OH absorption regions.

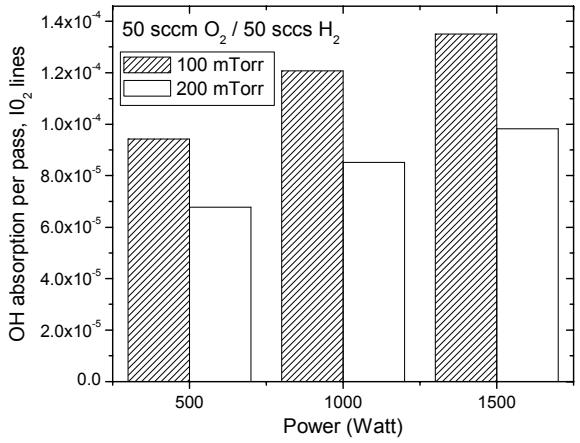

Figure 3: OH integrated absorption (from measurements on the $I0_2$ lines) as a function of the power, for two different pressure values, at constant gas feed composition.

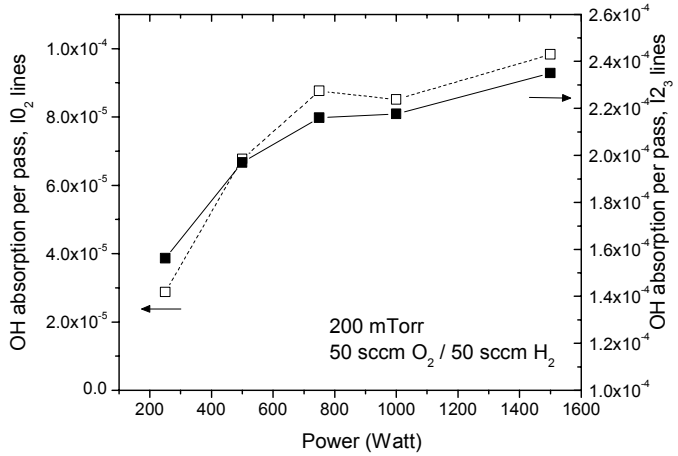

Figure 4: OH integrated absorption (from measurements on the $I0_2$ lines and $G2_3$ lines) as a function of the power, at constant pressure and gas feed composition.

Figure 5 shows the OH absorption as a function of the total flow rate. Any interpretation of this outcome is affected by the error on the absorption measurement, which is estimated around $5 \cdot 10^{-6}$. In Figure 6 the effect of the gas flow rate ratio on the OH absorption is shown. Again, a good agreement between the two data series as collected in different OH absorption regions, is found out. The OH production appears to reach a maximum at about H_2:O_2=0.3, which could be explained in terms of better dissociation efficiency of H_2 molecule compared with O_2 molecule.

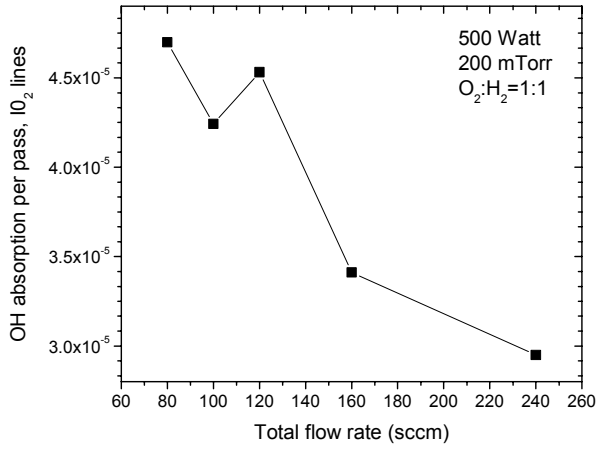

Figure 5: OH integrated absorption (from measurements on the $I0_2$ lines) as a function of the total gas flow rate, at constant pressure and power.

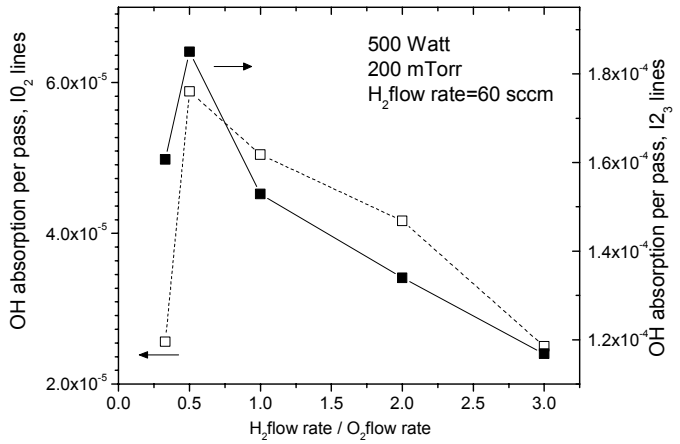

Figure 6: OH integrated absorption (from measurements on the $I0_2$ lines and $I2_3$ lines) as a function of the gas flow rate ratio, at constant H_2 flow rate, pressure and power.

From the ratio of the integrated absorption recorded in the two spectral regions it is possible to estimate the rotational temperature of the OH radicals. Simulations of the two spectral regions by means of the LIFBASE program [8] were run at different rotational temperatures, and the ratio $A(I0_2)/A(I2_3)$ was then calculated. The experimental ratio, as calculated from the absorption values reported in Figure 4 for the power series, was then compared with this simulation and rotational temperatures values were then determined and shown in Figure 7. The rotational temperature is found to increase with the power and the error is estimated around 150 K.

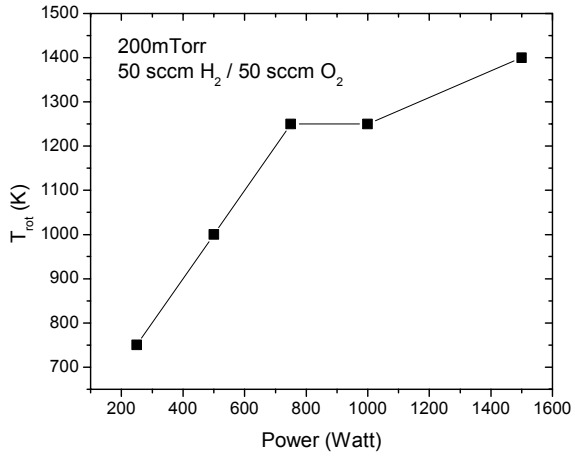

Figure 7: Rotational temperature of the OH radical, as calculated from the ratio of the integrated absorption lines ($I0_2/I2_3$), shown in Figure 4, as a function of the power.

4. Conclusions

The OH (integrated) absorption is studied as a function of the different experimental parameters, e.g., power, pressure and gas feed composition (H_2/O_2 mixtures) using a highly sensitive laser-aided diagnostic tool, Cavity Ring Down Spectroscopy (CRD). OH production increases with the power as molecule dissociation becomes more efficient. As the pressure increases, the absorption decreases, probably due to the fact that the discharge becomes more confined, e.g., the CRD starts detecting in the afterglow region. The OH production appears to reach a maximum at a gas feed composition of about $H_2:0_2=0.3$, which could be explained in terms of better dissociation efficiency of H_2 molecule compared with O_2 molecule. The rotational temperature of the OH radicals is found to increase with the power and the error is estimated around 150 K.

Acknowledgements

The authors gratefully acknowledge Dr. Richard Engeln for the fruitful discussions on Cavity Ring Down Spectroscopy.

References

[1] A. O'Keefe, D.A.G. Deacon - Rev. Sci. Instrum. **59**, 2544 (1988).
[2] K.W. Busch, M.A. Busch - Cavity Ring Down Spectroscopy, American Chemical Society, (1999).
[3] R. Engeln, G. von Helden, A.J.A. van Roij, G. Meijer - J. Chem. Phys. **110**, 2732 (1999).
[4] R. Engeln, K.G.Y. Letourneur, M.G.H. Boogarts, M.C.M. van de Sanden, D.C. Schram - Chem. Phys. Lett. **310**, 405 (1999).
[5] M.G.H. Boogarts, P.J. Bocker, W.M.M. Kessels, D.C. Schram, M.C.M. van de Sanden - Chem. Phys. Lett. **326**, 400 (2000).
[6] S. Pellerin, J.M. Cormier, F. Richard, K. Musiol, J. Chapelle - J. Phys. D.: Appl. Phys. **29**, 726 (1996).
[7] C. de Izarra - J. Phys. D.: Appl. Phys. **33**, 1697 (2000).
[8] LIFBASE: Database and Simulation Program (v 1.6), J. Luque and D.R. Crosley, SRI International Report MP 99-009 (1999).

Emission spectroscopy of pulse diaphragm discharge in water

A. Brablec[1], P. Slavíček[1], M. Šimor[2], P. Sťahel[1], D. Trunec[1], M. Černák[2]

[1] *Department of Physical Electronics, Masaryk University, Brno, Czech Republic*
[2] *Faculty of Mathematics, Physics and Informatics, Comenius University, Bratislava, Slovakia*

Abstract
The main object of the contribution is to report an extension of earlier papers focused on a more detailed study of the physical pulse diaphragm discharge properties and H_2O plasma parameters. Namely, for various solutions (NaCl, $FeCl_2$, $NaNO_3$ and others) the electron number density calculated from H_α spectral line profile as a function of solution conductivity and speed of cord movement for fixed applied voltage, diameter of hole in the dielectric diaphragm, thickness of the diaphragm were measured.

1. Introduction

Preliminary results on physical characteristics of pulsed underwater diaphragm electrical discharge [1, 2] have shown that the discharges burning in tap water, water-chelaton solutions, and some other water-based solutions can be used as a potential atmospheric-pressure H_2O - plasma source for surface activation various material in the form of fabrics, films, fibers, etc. The discharge burning at atmospheric pressure can substitute low-pressure plasma sources [3 - 6], when atmospheric pressure on-line surface treatments of polymer products with the low added value in large amounts are required.

Underwater pulsed corona discharges generated in liquid water matrix at atmospheric pressure have been demonstrated to be effective in the production of hydrated electrons and hydroxyl radicals [7 - 11, 13, 15]. Following the pioneering work of Clements et al. [7] on pulsed streamer corona generated using point-to-plane geometry of electrodes in water, various types of underwater electrical discharges producing hydrated electrons and hydroxyl radicals in liquid water-based media have been tested for the removal of low levels of non biodegradable organic pollutants from ground water and industrial waste water [14]. Very few results, however, have been published on interactions of the active species generated in pulsed electrical discharges in water with polymer materials [1, 15, 17].

In contrast to other types of underwater electrical discharges, in diaphragm electrical discharge the discharge plasma is not in a direct contact with the metallic electrodes, which helps to eliminate potential problems with electrode oxidation and erosion due to a direct contact of the electrodes with highly reactive H_2O plasma.

While in [1] and [2] the common features and chemical effects including hopeful application of this discharge for surface treatment of polymer materials are presented and discussed, the main object of the present paper is to report a more detailed study of the discharge physical properties. Using optical emission spectroscopy the electron number densities have been determined from broadening of hydrogen lines (H_α) vs. solution conductivity, frequency of high voltage pulses, speed of fiber movement for fixed applied voltage, diameter of the hole in dielectric diaphragm, and the diaphragm thickness.

2. Experimental set-up

The atmospheric pressure H_2O-plasma was generated using the diaphragm discharge arrangement described in more detailed in [1]. Its schematic drawing is shown in Fig.1. The discharge occurred in the vicinity and inside of the hole in the diaphragm made from a plexiglas desk (in the following the diameter of the diaphragm and its thickness are denoted as R and h), which was inserted in the gap between two metallic planar electrodes in conductive water - based solution. Several salts as NaCl, $FeCl_2$, $NaNO_3$, KBr, maleic acid were tested with five different conductivities σ. One of the electrodes was connected with a HV pulse power supply. The power supply of variable voltage U consisted of 60 kV DC source, a low inductance storage capacitor of 3 nF capacitance, and a rotating double spark gap similar to that described in [12]. The double spark gap was used to separate the charging and discharging phases of the storage capacitor. The polyester cord threads moved in the hole with a speed v from 16 to 64 mm/s. The HV pulse power supply was operated at fixed frequencies f = 20, 28, 35, and 43 Hz. As illustrated by Fig.2, many bubbles and turbulence are observed near the plasma channel. The discharge plasma took the form of streamers propagating on the thread surface to the distance of several millimetres from the diaphragm.

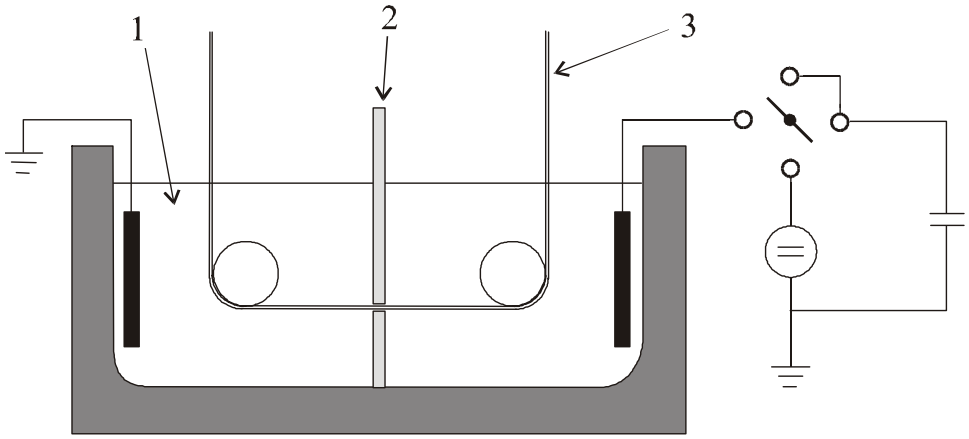

Fig.1: A schematic block drawing of the experimental set-up driven by the HV pulse power supply using the double spark gap: 1 - water based solution, 2 - plexiglas diaphragm, 3 - treated fiber.

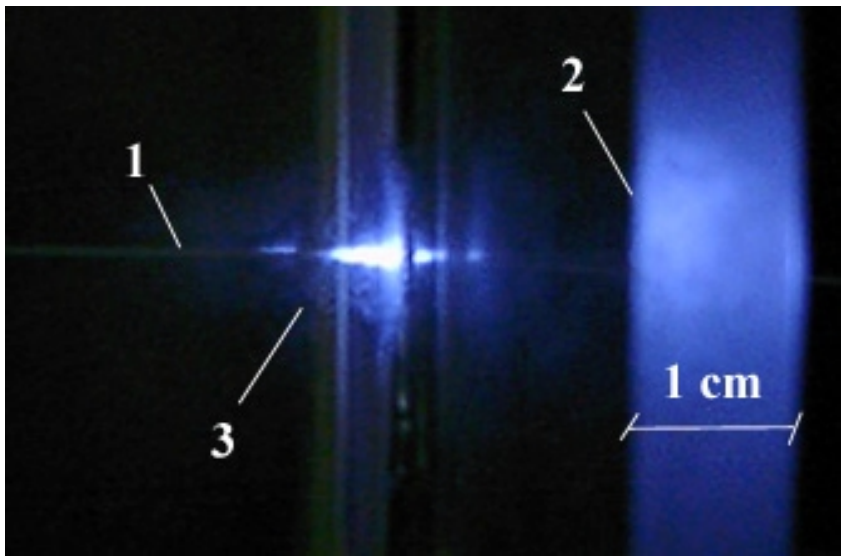

Fig.2: The snapshot of the discharge channel: 1 - treated fiber, 2 - plexiglas diaphragm, 3 - discharge.

Spectral analysis of the light emitted by the discharge was done using TRIAX 550 spectrometer by Jobin - Yvon with the CCD detector (cooled by liquid nitrogen, 2000 x 800 pixels) using a grating with 1200 gr/mm.

3. Results and discussion

To determine electron temperatures and densities the standard Griem's table (which takes into account the impact broadening by electron and quasi-static broadening by ions) of H_α line profile [17] and the procedure for data processing presented in [1] were used. The effect of individual parameters of the experimental set-up on the electron number density is summarised in Tabs.1 - 3. The electron density changes from 1.10^{16} cm^{-3} to 1.10^{18} cm^{-3} while the electron temperature was practically constant $\approx 4.10^4$ K in all experimental conditions studied. The error of the measured electron density was less than 5 %. The error of electron temperature was much higher, which is due to the weak dependence of the line profile on the electron temperature.

For different rate constants for reactions of OH radicals with ions and compounds used in the previous contributions [1, 2], the KBr solution (the rate constant for Br^{-1} is 1100 while for Cl^{-1} the rate constant is 430 in units of 10^7 l $mol^{-1}s^{-1}$, taken from [11]) was also measured. Moreover, maleic acid, which has been used treatment of polymer materials, was also tested.

It was found that for lower conductivity (less than 100 μS/cm) the electron number density changes slightly from 4.7 – 5.1 10^{16} cm^{-3}. It is interested that the electron number density is about 2 times higher for the solution with Br^{-1} ions than for solutions with Cl^{-1} ions (see the ratio of rate constants given above). Next, in case of maleic acid the electron density is relatively high (see the last line in Tab.1).

Salt	conductivity[a] [μS/cm]					frequency[b] [Hz]			
	100	200	300	400	500	20	28	35	43
NaCl	4.0	9.1	15.6	12.0	22.0	15.6	16.8	59.2	71.0
$FeCl_2$	4.1	5.9	12.0	15.3	20.9	12.0	13/7	19.2	18.6
$NaNO_3$	3.4	8.7	11.5	16.8	23.5	11.5	14.5	16.1	19.2
KBr	5.2	18.5	20.5	24.4	44.0				
Maleic Acid	6.2	16.5	33.0	51.3	48.5				

Table 1: The electron number density in 10^{16} cm^{-3} vs. conductivity and frequency for different water - based solutions of salts with treated fiber. Other parameters are fixed: U = 40 kV, h = 2 mm, R = 1.2 mm, v = 33 mm/s, a) f = 20 Hz, b) σ = 300 μS/cm.

Salt	speed [mm/s]							
	16	33	49	64	77	97	120	140
NaCl	7.7	15.6	10.7	9.1	10.2	16.8	42.1	58.9
$FeCl_2$	9.0	12.0	9.9	10.5	17.9	17.0	72.1	53.9
$NaNO_3$	10.6	11.5	13.3	11.3	14.7	15.9	21.6	31.4

Table 2: The electron number density in 10^{16} cm^{-3} vs. speed of treated fiber for selected water - based solutions of salts with treated fiber. Other parameters are fixed: U = 40 kV, h = 2 mm, R = 1.2 mm, f = 20 Hz, σ = 300 μS/cm.

U [kV]	conductivity[a] [μS/cm]					thickness[b] [mm]			diameter[c] [mm]			
	100	200	300	400	500	2	3	4	1.2	1.5	2.0	2.5
40	4.0	9.1	15.6	12.0	22.0	1.2	4.7	8.6	15.6	4.5	1.2	1.1
45	4.6	20.4	80.3	16.5	51.7	10.8	8.6	7.4	80.3	5.9	10.8	6.1
50	5.1	21.4	96.5	43.5	57.4	21.1	24.5	13.3	96.5	12.2	21.1	6.7
55	6.9	63.8	104.7	71.4	77.5	32.1	64.4	28.1	104.7	15.9	32.1	19.8

Table 3: The electron number density in 10^{16} cm^{-3} vs. conductivity, thickness and diameter of the diaphragm for various input voltage, water - based solution of NaCl and for fixed parameters as follows: f = 20 Hz, v = 33 mm/s, a) h = 2 mm, R = 1.2 mm, b) R = 2 mm, σ = 300 μS/cm, c) h = 2 mm, σ = 300 μS/cm.

In a contrast to the previous measurement [2], where surprisingly no OH bands were observed in the emission spectra at 305 - 311 nm, in these experiments the OH lines have been found. Their intensities, however, were low and comparable with the noise. The rotational temperature of OH radicals changed from 950 to 1600 K for parameters given in Tabs.1 - 3. For high level of noise the errors were not lower than 30 %.

If a higher electron number density corresponds to the higher production of OH radicals, the electron number density could be taken as a parameter that characterises chemical efficiency of the discharge. Of course, this conclusion should be supported with simultaneous measurements of OH radicals and surface properties of treated fibers. From the Tabs.1 - 3 one can deduce that the electron number density increases with increasing voltage and frequency. This is valid for all solutions. In case of $FeCl_2$ and $NaNO_3$ it seems that the electron number density increases with increasing conductivity σ. Among used salts and parameters

of the experimental set-up the solution with NaCl has produced the highest values of electron density 1 x 10^{18} cm^{-3} for σ = 300 μS/cm, U = 55 kV, f = 20 Hz, v = 33 mm/s, h = 2 mm, and R = 1.2 mm.

It is evident that the present experiments, even if many measurements were realised, do not cover all experimental possibilities. Also, as indicated the results in Tabs.1 - 3, some results deviate from the expected trends. It evokes possible problems, e.g. for the diaphragm with diameter of hole below 1 mm there is difficult to realise the precise diaphragm with given thickness and diameter. For example it was observed that the discharge changes its colour. Or, as shown in Tabs.1-3, the electron number density depends significantly on conductivity of solution.

The visual appearance of the discharge indicate that the discharge mechanism is identical with those described in [22, 23] where, however, diaphragm discharges without any fibrous dielectric material, such as a PES cord thread were studied. A general picture of the discharge development is relatively complicated since the water vapour generated there is mixed with air bubbles trapped in cavities inside the cord thread. In such a way a gas-filled region inside the hole and in its immediate vicinity is formed. Neglecting a voltage drop on the water layers between both electrodes and the diaphragm, nearly whole HV pulse applied to the electrodes appears on the gas region surface, resulting in its electrical breakdown and creation of a highly conductive plasma streamers propagating along the cord thread surface.

The physical picture (see also [1]) indicates that all gas discharge processes occur in a water vapour/air mixture with dependence on the conductivity, parameters of the diaphragm and chemical composition of the solution used. It is possible that because of a complex chemistry involved in the generation and decay of various radicals in atmospheric pressure plasmas [11], the solution chemical composition can have a significant effect on the radicals densities and, consequently, on chemical effects of the discharge plasma. Also, at the moment we have no plausible explanation for the observed sensitivity of H_α line to composition of the solution used. Such effects apparently can result from a very complex chemistry of the active species in water vapour plasma. A detailed study of the discharge plasma chemistry is beyond the scope of this article and could be an interesting subject for some future studies.

Acknowledgement
This work has been financially supported by grant 202/01/P017, 202/03/0708 of Grant Agency of the Czech Republic, research intent CEZ J07/98:143100003 funding by the Ministry of Education of the Czech Republic.

References

[1] A. Brablec, P. Slaviíček, P. Sťahel, T. Čižmár, D. Trunec, M. Šimor, M. Černák, Czech. J. Phys. **52** (2002) Suppl. D491.
[2] M. Šimor, H. Krump, I. Hudec, J. Ráhel, A. Brablec, M. Černák, Acta Physica Slovaca (2003) submitted.
[3] C. M. Chan, T. M. Ko and H. Hiraoka, Surface Sci. Reports **24** (1996) 1.
[4] S. Okazaki et al. E.C. Chemical Co., Ltd., JP 34425092 (1992).
[5] N. J. Chou et al.: US 5,019,210 (1991).
[6] U. Hayat: GB 9124467 (1993).
[7] J. S. Clements, M. Sato and R. H. Davis, IEEE Trans. Ind. Appl. **IA-23** (1987) 224.
[8] S. A. Slobodskoi et al, Vopr. Technol. Ulavlivania i Pererab. Prod. Koksovania, (1978) 71.
[9] A. K. Sharma, B. R. Locke, P. Arce and W. C. Finney, Hazardous Waste & Hazardous Materials **10** (1993) 209.
[10] D. R. Grimonpre, A. K. Sharma, W. C. Firney, B. R. Locke, Chem. Engineering Journal **82** (2001) 189.
[11] P. Lukeš, Ph.D. Thesis, Prague 2001.
[12] Šunka, V. Babický, M. Člupek, P. Lukeš, M. Šimek, J. Schmidt, M. Černák, Plasma Sources Sci. Technol. **8** (1999) 258.
[13] P. Šunka, V. Babický, M. Člupek, K. Koláček, P. Lukeš, M. Řípa, M. Černák: in *Proc. of 18th Symp. Plasma Physics and Technology*, 1997, Prague, p.144.
[14] P. Šunka, Physics of Plasmas **8** (2000) 2587.
[15] M. Mikula, J. Panák, and V. Dvonka, Plasma Sources Sci. Technol. **6** (1997) 179.
[16] M. Šimor, M. Černák, H. Krump, J. Hudec, M. Štefečka: in *Proc. of XXV Int. Conf. on Phenomena in Ionised Gases*, **4**, 2001, Nagoya, p. 63.

[17] H. R. Griem: Spectral line broadening by plasmas, Academia Press, New York, 1974.
[18] W. D. Harkins and A. Feldman, J. Am Chem. Soc. **44** (1992) 2665.
[19] E. M. Drobishevhii, Yu. A. Dunyajev, S. I. Rozov: Zh. Trkh. Phys. **43** (1973) 1217.
[20] I. E. Boguslavskii, E. V. Krivickii, V. N. Petrishenko: Elektron. Obrob. Mater. **183** (1995) 33.

Efficiency of ozone production by non-thermal electrical discharges in synthetic air – comparative study

M. Šimek[1], M.Clupek[1], S. Pekárek[2], J.Rahel[3], M. Šimor[3] and M.Cernák[3]

[1]*Institute of Plasma Physics, Department of Pulse Plasma Systems, Academy of Sciences of the Czech Republic, Za Slovankou 3, P.O.Box 17, 18221 Prague , Czech Republic*
[2]*Czech Technical University Prague, Faculty of Electrical Engineering, Technická 2, 166 27 Prague 6, Czech Republic*
[3]*Institute of Physics, Comenius University, Mlýnská dolina F2, 85215 Bratislava, Slovakia*

Abstract
The work focuses on the experimental determination and critical comparison of ozone formation efficiencies by several non-equilibrium discharges in synthetic air at atmospheric pressure. The experiments were performed in one site by using identical gas handling system, as well as the same instrumentation used for sampling and analysis of the discharge products. We found the maximum ozone concentrations ~2000 PPM. The highest ozone yield and the lowest energy cost reached ~80 g/kWh and ~20 eV/O_3, respectively.

1. Introduction

To reduce the cost of ozone based technologies (*e.g.*, treatment of drinking and wastewater, decomposition of hazardous organic wastes, medical applications) the design of efficient ozone generators has always been the focus of many researchers. Even though industrial ozonizers based on electrical discharges are in use for a long time, the design of an ideal plasma-chemical ozonator is a difficult task. To produce ozone from air efficiently, an ozonator should produce, first of all, large quantities of oxygen atoms at reasonable cost. When nitrogen is present in the feeding gas, the ozone production can not be separated from the generation of nitrogen oxides. Taking into account the mechanism of ozone formation from air [1] it is therefore obvious that for efficient ozone production it is necessary to suppress the excessive production of nitrogen atoms. Due to the fact that ozone loss processes are significantly enhanced by increasing the gas temperature [2] then to reduce ozone destruction channels it is necessary to keep the temperature as low as possible.
This work focuses on the experimental determination and comparison of ozone formation efficiencies by several non-equilibrium discharges in synthetic air at atmospheric pressure. Similar efficiency studies are usually performed for one single ozonator. Therefore it is often difficult to compare directly results obtained on one ozonator type presented by different research groups, and it is even more difficult to compare results concerning different ozonator types. It is usually because of various methodologies used for ozone concentration and energy density measurements. We eliminated the most important drawbacks by applying identical methodology to investigate different ozone-generating devices. The experiments were performed in one site by using identical gas handling system, as well as the same instrumentation used for sampling and analysis of the discharge products [1].

2. Experimental setup

The efficiency of ozone production was determined for five different plasma generators, namely for:

- pulsed positive corona discharge in wire-cylinder geometry (PPCD) [1],
- DC hollow needle-to-plate discharge enhanced by the gas flow (GFCD) [2],
- low-current DC gliding discharge (DCGD) [3],
- surface dielectric barrier discharge (SDBD) [4],
- diffuse coplanar surface discharge (DCSD) [5].

The experimental PPCD device (figure 1a), consists of an Ag-coated Cu central wire anode and a grounded stainless-steel cylinder. The pulsed high-voltage (HV) power supply with maximum ratings, 100 kV/1kA/ 7 ns rise time/ ~ 100 ns fall time, delivers up to 2 J per pulse with up to a 10 Hz repetition rate at atmospheric pressure into the discharge volume ~ 1500 cm^3. The power supply is connected to the discharge chamber through the diagnostic interface. The matching of the discharge chamber to the power supply and formation of the HV pulse is accomplished by means of the resistive load.

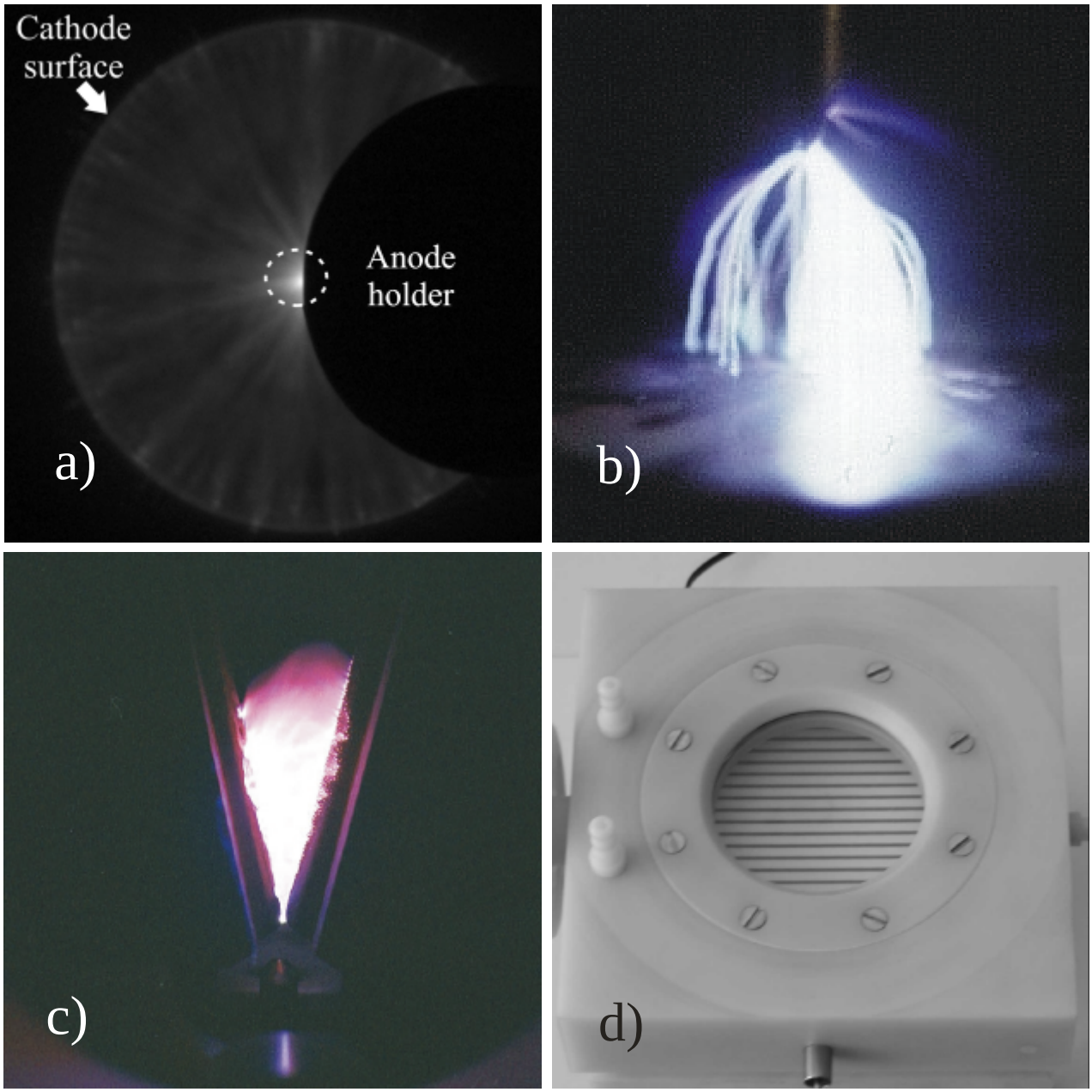

Figure 1. Photographs of experimental discharge devices: a) PPCD, b) GFCD, c) DCGD and d) reactor for both SDBD and DCSD discharges with currently inserted SDBD electrode system.

The second discharge tested for ozone generation is a needle to plate corona discharge. Classical DC corona is not suitable for efficient ozone generation with reasonable production rate. To achieve this aim it is necessary to enhance both the discharge power and air flow through the discharge region. For this purpose we used the gas flow through the needle electrode [2]. The electrode arrangement of this GFCD device (figure 1b) consists of stainless steel needle situated perpendicularly to the stainless steel disc. The needle is used as an anode and the disc as a grounded cathode. The outer and inner diameter of the needle is 1.2 mm and 0.7 mm respectively. The tip of the needle is sharpened at an angle 15°. The distance between the tip of the needle and the disc electrode is 3.2 mm. Both electrodes are placed inside a quartz tube. The air into the discharge is supplied through the needle only. A DC regulated HV power supply provides voltage up to 10 kV.

The DCGD device (figure 1c) consists of two diverging electrodes placed in a fast gas flow created by the nozzle [3]. When powered with sufficient voltage (several kV), the breakdown occurs in the point of a minimum distance between the electrodes and the plasma filament is carried away in the direction of the gas

flow increasing its length. The gliding discharge period can be roughly divided into three phases. The first breakdown or ignition phase is characterized with a fast decrease of electrode voltage simultaneously with an increase of the discharge current (followed with an increase of the gas temperature). The second intermediate phase is characterized with rather slow changes of all discharge parameters. The third extinction phase is characterized with a thermodynamic instability of the plasma filament with fast decrease of the gas temperature and discharge current. As soon as the length of the plasma filament reaches certain value, the filament snaps and the current is interrupted. Consequently, the electrode voltage increases as long as a new breakdown occurs initiating a next discharge cycle.

The SDBD device consists of two electrodes separated by a 100x100 mm^2 alumina dielectric plate. The thickness of alumina plate is 0.5 mm. The alumina plate has a discharge electrode on its upper surface and an induction electrode on its lower surface. The discharge electrode consists of 21 interconnected parallel strips made from tungsten. The induction tungsten electrode serves to produce a tangential electric field component on the upper dielectric barrier surface. The electrode system is energized by a sinusoidal HV (up to 6 kHz and 8 kV peak-to-peak). This arrangement produces a stable surface discharge starting from both edges of each strip electrode and covering uniformly the ceramic surface [4].

The electrode arrangement of DCSD device consists of two parallel strip-like molybdenum electrodes embedded in alumina using a green tape technique. The thickness of the ceramic layer between the plasma and electrodes is 0.4 mm. A sinusoidal high-frequency HV (1-15 kHz, up to 10 kV peak-to-peak) was applied between the electrodes. Such an electrode geometry and discharge energization arrangement generates visually almost uniform plasmas in air (or in nitrogen) at atmospheric pressure. The discharge consists of numerous H-shaped elementary discharges developing with a high intensity and running on the electrode system surface along the embedded strip electrodes. The density and the movement velocity of the elementary discharges increase with the gap voltage [5].

The O_3 and NO_x concentrations were monitored outside the discharge chamber by a non-dispersive UV absorption technique and by electrochemical cells, respectively. The pyrex probe (30 cm long, 6 mm i.d.) and Teflon tube (1.5 m long, 4 mm i.d.) was used for sampling the discharge products at the end of the discharge region with a constant speed of 1 l/min. The API 450 and API450M (Advanced Pollution Instrumentation) non-dispersive UV photometric O_3 analyzers were used to determine the ozone concentrations in the discharge products. Both instruments use mercury line 254 nm as the light source for the absorption and selective MnO_2 ozone scrubber that minimizes the influence of other potential absorbers. Covering ranges from 0-1000 and 0-5000 PPM respectively, the two analyzers assured high precision over several orders of O_3 concentration measurements. The GA-60 flue gas analyzer (Madur Electronics) equipped with electrochemical cells (O_2, CO, SO_2, NO, NO_2) was used to monitor volumetric concentration of nitrogen oxides covering ranges from 0-5000 and 0-800 PPM for NO and NO_2 respectively. Linearity of the NO sensor was verified in the range 0-900 PPM by defined mixture of Pulmonix® forte (Messer Austria, 900 PPM NO in N_2, with main impurities H_2O< 3 PPM, O_2<1 PPM and NO_2<1PPM).The production of ozone and NO_x was investigated as a function of energy density delivered to the discharge volume.

3. Results and conclusions

For each single measurement (*i.e.,* for given airflow and discharge conditions), the discharge ran continuously for 20-30 minutes until a steady-state ozone level had been indicated by both ozone analyzers. After each single measurement, the discharge was turned off until ozone monitors reported zero ozone level. Then the new discharge conditions and/or airflow were fixed and the discharge turned on again for the new measurement. Following such a procedure we found detected ozone and NO_x levels highly reproducible. Ozone generation was investigated for typical operation conditions, *i.e.* for conditions that were determined by the capability of available power supplies to assure stable and long-lasting discharge. For explored range of parameters we found the maximum ozone concentrations approaching 2000 PPM. From ozone concentration measurements we evaluated the ozone production, yield and production energy cost. Calculated ozone production and yield (figure 2) reached as much as 1 g/h and 80 g/kWh, the minimum ozone production energy cost (figure 3) approached 20 eV/O_3. Figure 2 and figure 3 do not show results obtained for the gliding discharge because corresponding numbers are significantly out of the range covered by other discharges. In the case of DCGD, the ozone generation was inspected, for fixed electrode geometry; in the energy density range 0.1-0.3 Wh/l. Calculated DCGD ozone yield does not exceed 0.1 g/kWh. In the case of DCGD ozone production energy cost, the minimum value does not go below ~9×10^3 eV/O_3.

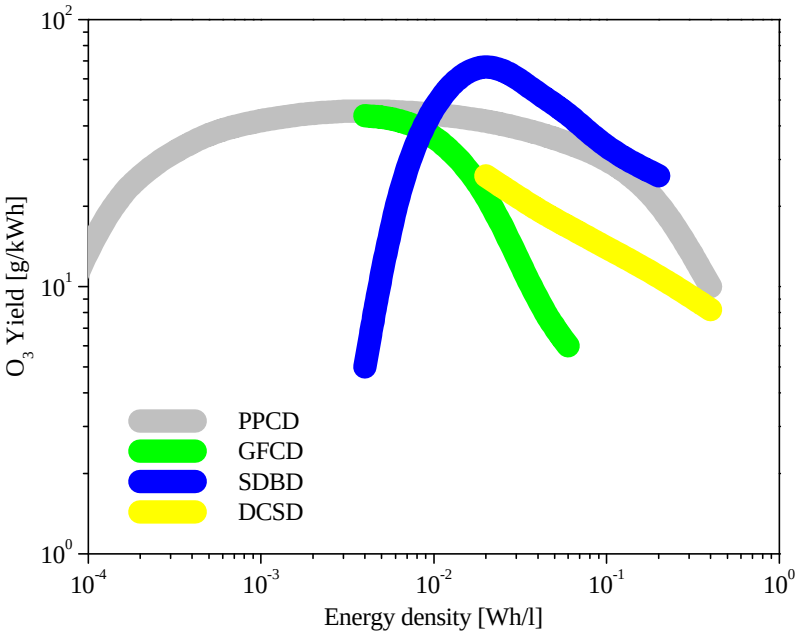

Figure 2. Ozone yield versus energy density

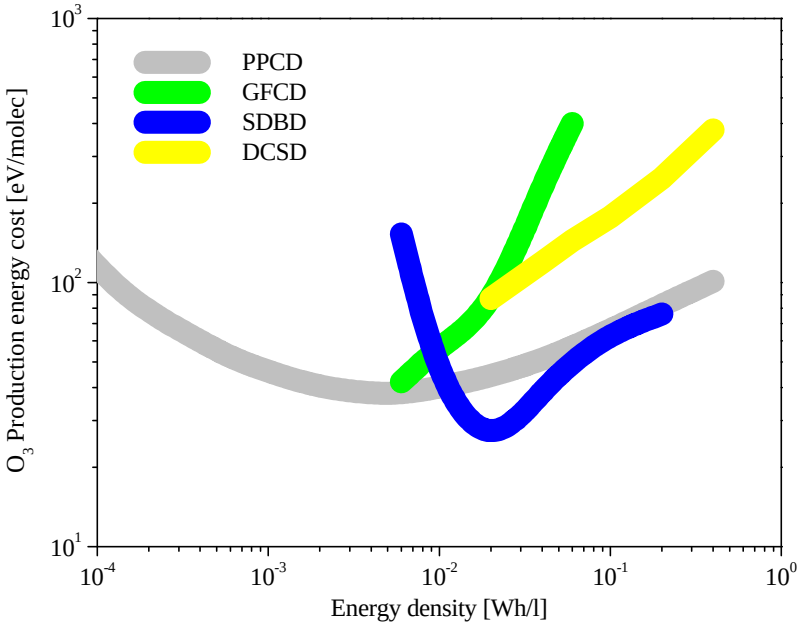

Figure 3. Ozone production cost versus energy density

Efficiency of ozone formation was explored for several non-equilibrium plasma generators in atmospheric pressure synthetic air in a wide range of applied energy densities by appropriately combining the discharge parameters and airflow rate. From the ozone concentration measurements, we evaluated ozone production, yield and production energy cost. Both the ozone production yield and energy cost show quite large variations. The best performance from the point of view of ozone generation efficiency show plasma generators based on streamers homogenously distributed either over the dielectric surface (SDBD) or inside the inter-electrode space (PPCD). Lower performance then shows the GFCD plasma generator based on self-repetitive streamers localized in a relatively small part of the whole reactor volume. The lowest efficiency then shows the DCGD plasma generator, which is based on one predominant plasma filament. The DCSD device is supposed to have a performance similar to the performance of the SDBD device. Measured DCSD characteristics are however significantly below the SDBD numbers. Unfortunately, for given electrode design and the energization, we were not able to obtain the DCSD characteristics at low energy densities. An attempt to decrease energy density resulted in large discharge instability (with streamers covering only randomly varying fraction of the electrode surface). Another kind of instability limited the inspection of the GFCD device towards low energy densities. With increasing air-flow rate (decreasing energy density), a regular discharge burning was progressively replaced by irregular bursts of pulses, or even with the discharge blow-out.

The performance of all generators is strongly limited by the presence of nitrogen oxides ($NO+NO_2$). For the SDBD, DCSD and PPCD devices we always observed the quantity of NO_2 species comparable with detected ozone levels, while NO species remained bellow the detector sensitivity. For the GFCD and DCGD devices, NO species can be detected. The former results are not surprising as a distributed dissipation of electrical power

(through well distributed plasma filaments) prevents an excessive heating of the gas. On the other side, a local release of energy through one (or few) plasma filament leads to the local increase of the gas temperature (ΔT=50-250 K in the case of the GFCD, ΔT=500-1500 K in the case of the DCGD) and consequently to the enhanced decomposition of ozone molecule through both thermal and plasma-induced (NO_x) chemical processes.

Acknowledgements

This work was supported by the Grant Agency of the Academy of Sciences of the Czech Republic under contract GAAV 1043102. It was also partially supported by the research program No: J04/98:212300016 "Pollution control and monitoring of the Environment" of the CTU in Prague.

References

[1] M.Šimek, M.Clupek - Efficiency of ozone production by pulsed positive corona discharge in synthetic air, J.Phys.D:Appl.Phys. 35, 1171 (2002).
[2] S.Pekárek, V.Kríha, M.Šimek, R.Bálek, F.Hanitz - Hollow needle-to-plate electrical discharge at atmospheric pressure, Plasma Sources Sci. Technol. 8, 513 (1999).
[3] M.Šimek - A spectroscopic study of DC gliding discharge in nitrogen, Proceedings ISPC 14 vol.2, 1045 (1999).
[4] J.Ráhel´, M.Šimor, M.Cernák, M.Štefecka, Y.Imahori, M.Kando - Surf.Coat.Technol. in press (2002).
[5] M.Šimor, J.Ráhel´, P.Vojtek, A.Brablec, M.Cernák - Atmospheric-pressure diffuse coplanar surface discharge for surface treatments, Appl. Phys. Lett. 81, 2716 (2002).

Energy dissipation of cold reactive particles on surfaces

J. Winter, J. Berndt, D. Diesing*

Institut für Experimentalphysik II, Ruhr-Universität-Bochum, 44780 Bochum, Germany
**Institut für Schichten und Grenzflächen 3, Forschungszentrum Jülich, 52425 Jülich, Germany*
e-mail: d.diesing@fz-juelich.de

Abstract

We analyse the energy dissipation of cold reactive neutrals (Ar*) on surfaces using metal-insulator-metal (MIM) tunnel junctions. By this means we detect and perform energy spectroscopy of hot charge carriers injected into the metal bulk. This process occurs in addition to and in competition with the well known secondary electron emission into the vacuum. MIM sensors may be used as very sensitive detectors for excited and/or reactive cold species in a plasma environment.

Introduction

Depending on the plasma parameters metastable excited neutrals can be a very prominent species in the plasma. They can thus play an important role in the electron particle balance of discharges, influence the electron energy distribution function (EEDF) and, via the ionisation balance, the electric fields. When ions, excited neutral species or reactive radicals strike a surface, the particles are usually de-excited and/or a chemical bond is formed (chemisorption). If the excess energy between initial and final state exceeds the work function of the material (minimum energy required to emit an electron from the solid), electrons can be emitted into the vacuum. A prominent example is the de-excitation of metastable atoms on metal surfaces. This is especially important for plasmas where the secondary electron emission from the metal electrodes plays a key role in the maintenance of the discharge. For some systems this process has been well investigated, e.g. for Ar* on pure metal surfaces [1,2]. In addition to the electron emission into the vacuum an accompanying process is the electronic excitation of the metal. Excited defect electrons or excited electrons with energies below the work function can be injected into the bulk of the electrode. In this paper we investigated the latter processes for the first time by exposing a metal / insulator / metal junction (further called MIM) to the spatial afterglow of a surface wave sustained discharge producing Ar* metastable atoms predominantly in the $3p^5\,4s^1$ state [3].

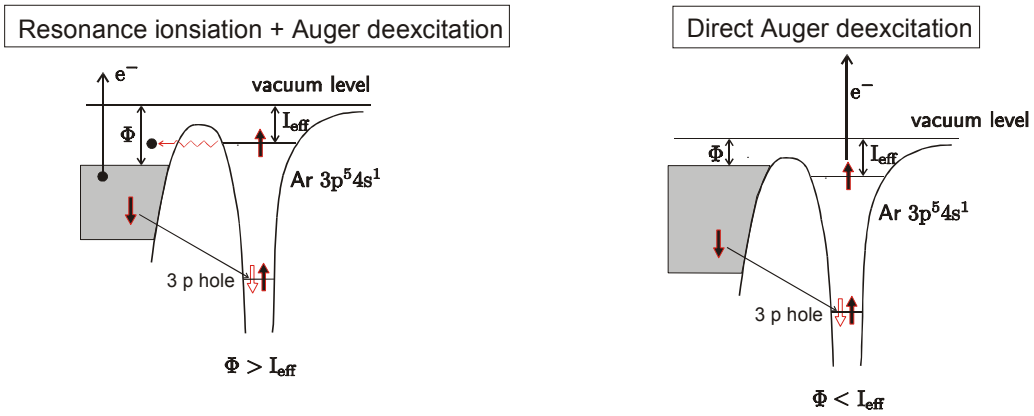

Fig. 1 : Schematic view of the two basic de-excitation schemes of metastable atoms at metal surfaces. Left view graph: Workfunction bigger than first ionization potential. Second view graph: Workfunction smaller than first ionization potential.

The basic processes of de-excitation of excited species approaching a metal surface, namely resonance ionisation and subsequent Auger de-excitation or direct Auger deexcitation are shown in more detail in fig. 1 at the example of the Ar $3p^5 4s^1$ excited metastable state [1].

In a potential energy diagram the potential well of the excited metastable (filled electronic states are represented by bold arrows) is separated from the metal bulk by a thin potential barrier. In the case of resonance ionisation the excited electron of the metastable atom (for Ar: 4 s^1) tunnels into the unoccupied states of the metals conduction band. Subsequently the resulting Ar^+ ion is neutralised by an electron from the conduction band of the metal. The excess energy of this process is disposed to an Auger process in the metal (left view graph of fig.1). In the case of direct Auger de-excitation an electron emission into the metal is not possible. The first step in this process is the transfer of an electron from the conduction band of the metal to the metastable atom. Subsequently the resulting Ar^- ion is neutralised by an Auger process in the atom. The excess energy in this scheme is transferred to the free electron originating from the Ar atom.

Auger de-excitation is the most probable process on adsorbate covered metal surfaces and on (111) noble metal surfaces [4] . It occurs when the work function Φ of the material is smaller than the effective ionisation energy I_{eff} of the metastable atom. In any of the two de-excitation schemes an excited defect electron remains in the metal. Practically nothing is known so far about the excited defect electrons produced by metal – metastable interactions. It is known from 2 photon photoemission experiments that the lifetime of excited defect electrons or electrons embraces a range of several 10 fs [5]. The corresponding mean free path is in the order of 20-30 nm. Defect electrons produced at the surface can thus be transported into the metal bulk within a range of this mean free path.

This point is exploited in our new approach for the detection and spectroscopy of the metastable caused excitation. As a sample we use a 20 nm thick gold film which is separated by a 2.3 nm thick oxide film from a 30 nm thick aluminium electrode. The excited defect electrons stemming from the afterglow / gold interface migrate to the inner gold / oxide interface of the MIM layer system. Here they can tunnel into the aluminium electrode and can thus be detected as a tunnel current.
This process is illustrated in more details in figure 2. Ar metastables striking the gold surface produce excited defect electrons. These defect-electrons migrate to the oxide / gold interface. There they can be neutralised by electrons originating from the aluminium which are tunnelling through the oxide layer to the gold film. A competing process for this neutralisation is the de-excitation of the defect electron by an Auger process. The partitioning between neutralisation by tunnelling and Auger de-excitation can be tuned by the bias voltage applied to the MIM system. For defect electrons with weak excitation energy the neutralisation by tunnelling can be prohibited by a small bias voltage. In this case the defect electrons in the gold film do not find corresponding electrons in the aluminium electrode. Consequently the detected tunnel current must decrease. If the bias voltage is increased and the Fermi level of the aluminium is lower than the energetic level of the hottest defect electron the metastable induced tunnel current should reduce to zero (bottom view graph in figure 2) .

It should be mentioned that the application of a bias voltage induces a DC tunnel current. To distinguish this DC current from the current induced by the metastables it is necessary to work with a chopped gas beam.

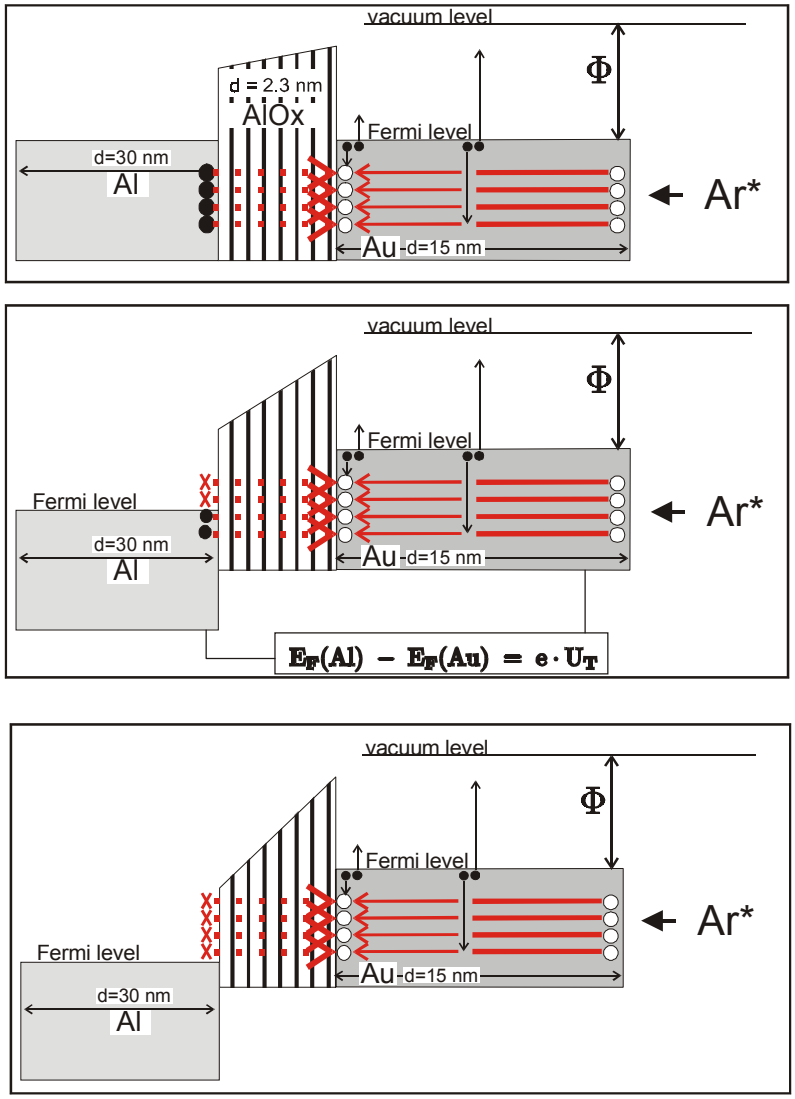

Fig. 2 : Energy level diagramm of a MIM tunnel junction in contact with metastable Argon atoms. Open circles represent defect electrons, closed circles represent electrons. Top view graph: Applied tunnel voltage 0 V. Middle view graph: Small tunnel voltages decrease the metastable induced tunnel current. Bottom view graph: The threshold voltage reduces the metastable induced tunnel current to zero.

Experimental set-up

Figure 3 shows a sketch of the experimental set up. A surface wave produced discharge is used as source for metastable noble gas atoms. The discharge is produced in a quartz tube of 10 mm inner diameter and 12 mm outer diameter by a travelling surface wave (2.45 GHz), which is excited by a Waveguide-Surfatron. The quartz tube is surrounded by a metal cylinder with a diameter of 5 cm. A microwave generator (Marconi signal source type 6056B) is driving a Thomson-CSF TH 2404 Klystron at 2,45 GHz, which supplies the power (ranging up to 1 kW) to the launcher. The transmitted and reflected powers, are measured with two HP 436 A powermeters. The gas flows through the quartz tube are regulated by mass flow controllers (MKS flowmeters), allowing a maximum flow rate of 500 sccm. The upstream pressure is measured by a pressure transducer (Baratron® type 626 A), and ranges from 1 to 3 mbar, depending on the flow rate. Downstream the quartz tube is penetrating through an O-ring seal into a vacuum vessel which is pumped by a turbomolecular pump with a pumping

speed of 1600 l/s. Depending on the gas flow, the pressure in the reaction chamber ranges between 10^{-2} and 10^{-4} mbar. The MIM-detector (together with a chopper disc) is placed in this reaction chamber approximately 5 cm from the end of the glass tube

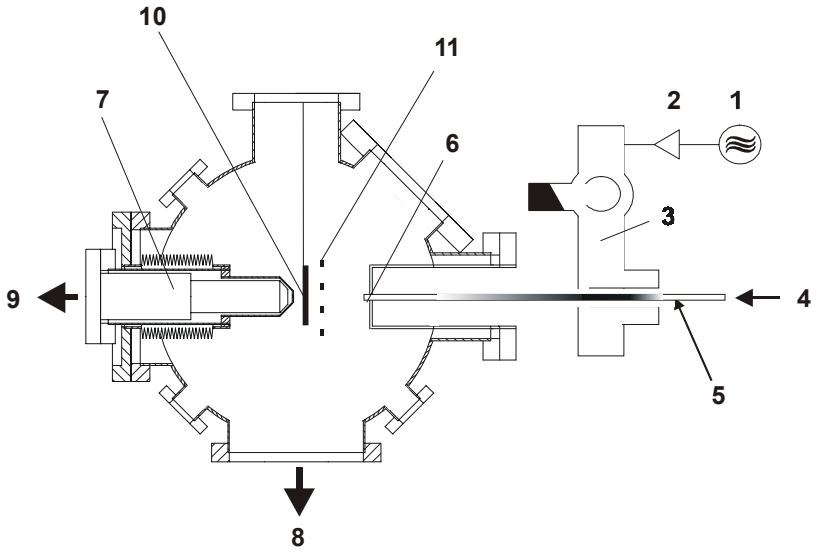

Fig. 3 : Experimental Set-up - 1. Microwave Generator, 2. Klystron and Pre-amplifier (+70 dB), 3. Waveguide-Surfatron, 4. Gas inlet, 5. Quartz tube (d_{in}=10 mm, d_{out} = 12 mm), 6. Post-discharge / Plasma, 7. Mass Spectrometer, 8. Turbopump (1500 l/s), 9. Turbopump (50 l/s), 10 MIM-detector, 11 chopper disk

An important property of surface wave sustained discharges is that the plasma length and thus the distance from the discharge to the substrate/ MIM-detector is not fixed. It depends on several parameters, such as gas mixture, total tube pressure and the applied power. In the present experiment the active plasma zone is ending about 30 cm before the end of the glass tube. Close to the end of the glass tube we have installed three metal grids. By applying appropriate voltages to these grids ions and electrons are prevented from reaching the MIM-detector.

The metal / insulator / metal layer system is produced in three steps. A 30 nm thick aluminium base electrode is evaporated an a glass slide in a high vacuum chamber. A localised anodic oxidation is performed in an electrochemical droplet cell. The procedure is described in detail elsewhere [6,7]. The gold electrode is evaporated across the aluminum / aluminum oxide layer and contacted by additional gold pads. In previous experiments we investigated the lateral conductivity of 20 nm thick gold, copper and aluminium films in contact with Ar afterglows [8]. No sputtering effects could be found. The conductivity of the films remained unchanged. The temperature at the sample position was found to be close to room temperature [9]. In the present experiments the conductivity of the gold electrode was controlled permanently during the experiments.

The samples used in the experiment have a preferential 111 orientation of the gold surface. These surfaces show a band gap at energies above the Fermi level. Thereby an electron injection normal to the surface on 111 terraces is not possible [10]. We therefore do not expect a remarkable amount of resonance ionisation processes. Moreover the gold film was not sputtered before exposure to the metastable atoms. Thereby a submonolayer coverage with oxygen cannot be excluded. There are several reports in literature that molecular adsorbates suppress the process of resonance ionization [11].
The tunnel currents were detected using an in house developed potentiostat [6] containing an autoranging current voltage converter. The sample was galvanostatically separated from the

vacuum chamber. The chopper disk enabled a 33 % beam on time and a 66 % beam off time for the clear distinction between DC tunnel current and chemically induced tunnel current.

Experimental results:

In figure 4 typical examples for the transient shape of metastable induced tunnel currents are shown at different bias voltages. The right side view graphs show the internal band structure of the MIM system. The left side figures show the AC component of the tunnel current as a function of time.

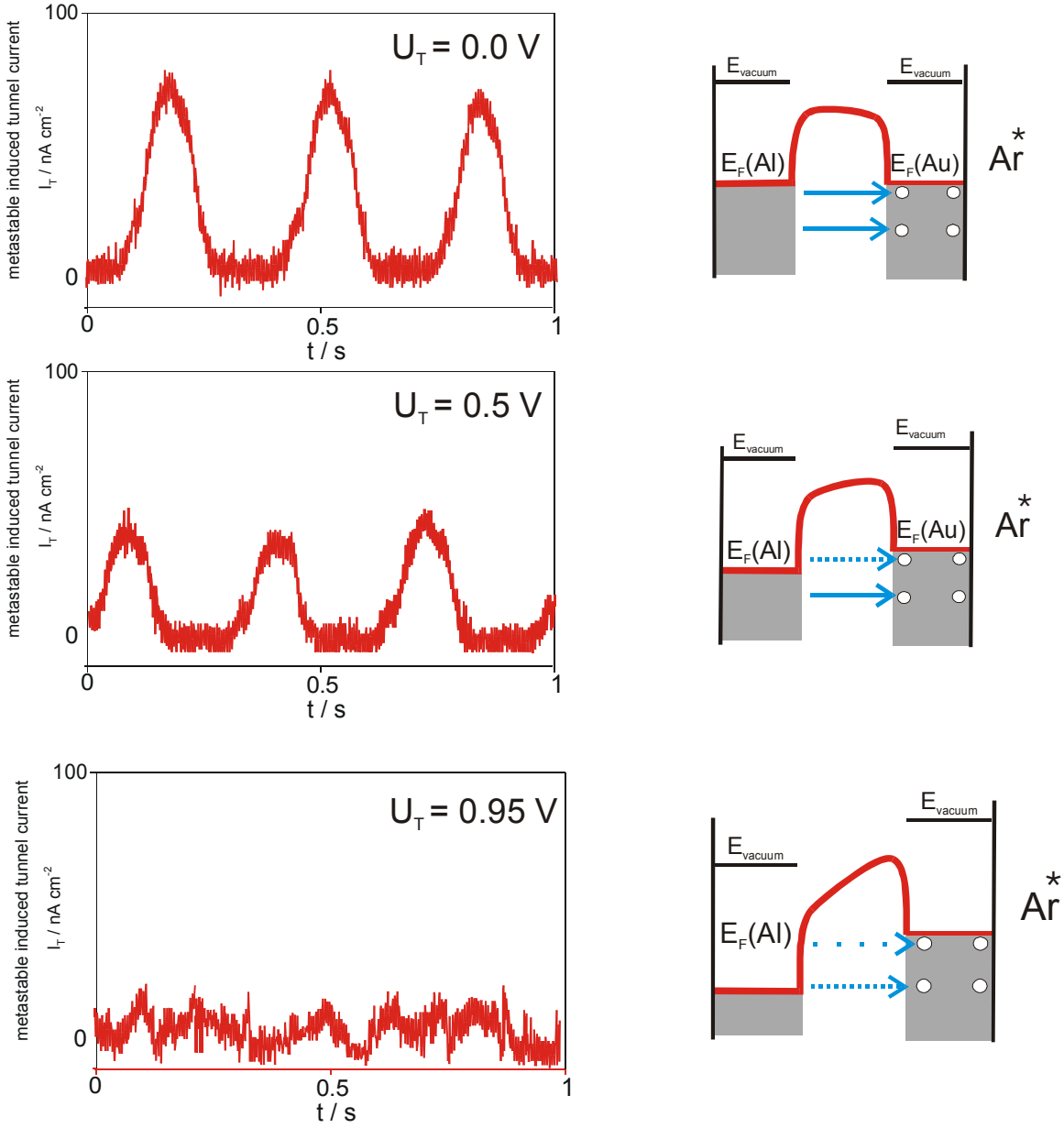

Figure 4: Left side view graphs show the AC part of the tunnel current for different bias voltages. The right side view graphs show the corresponding change of the internal band structure of the MIM system due to the bias voltage.

The typical shape results from the geometric design of the chopper disk leading to an asymmetric signal. At a tunnel voltage of 0 V (means Fermi level of the aluminum and the gold electrode on the same level) 70 nA peak to peak current density can be detected. The peak to peak signal drastically depends on the bias voltage. For a bias voltage of 0.5 Volts the metastable induced tunnel current is reduced by almost a factor of 2. The signal parishes nearly completely at a bias voltage of 0.95 V. This means that the excited defect electrons have at least an energy of 0.95 eV.

Conclusion

It could be shown that tunnel junctions with thin (d < 3 nm) oxide films are stable in the spatial afterglow of a surface wave sustained discharge. Plasma induced tunnel currents in the order of several 10 nA could be easily detected by using an optimized current voltage converter. We could not observe an electron injection from the afterglow into the MIM junction. The transient shape of the induced tunnel current depends on parameters as chopper frequency and gas flow. This clearly shows that the tunnel currents are not induced by electrons or photons emitted from the discharge. MIM sensors are obviously a new sensitive diagnostics for fluxes of metastables.

Acknowledgement: The presented work is supported by the Deutsche Forschungs-gemeinschaft in the SFB 616 Teilprojekt A3. The authors wish to thank Dr. Klaus Georg Tschersich (ISG4, research center Jülich) for intensive discussions on gas beams.

References:

[1] F.B. Dunning, P. Nordlander and G.K. Walters, Phys. Rev. B 44 (1991) 3246
[2] W. Sesselmann, H. Conrad, G. Ertl, J. Küppers, B. Woratschek and H. Haberland, Phys. Rev. Lett. 50 (1983) 446
[3] J. Berndt, K. Makasheva, H. Schlüter, Plasma Sources Sci. Technol. 11 (2002) 208
[4] W. Sesselmann, B. Woratscheck, J. Küppers, G. Ertl and H. Haberland, Phys. Rev. B 35 (1987) 8348
[5] M. Bauer, S. Pawlik and M. Aeschlimann, Chem. Phys. 205 (1996) 127
[6] A.W. Hassel and D. Diesing, Electrochem. Comm. 4 (2002) 1
[7] A.W. Hassel and D. Diesing, Thin Solid Films 414 (2002) 296
[8] D. Diesing, J. Berndt, D. Douai and J. Winter, Thin Solid Films 409 (2002) 243
[9] H. Kersten, D. Rohde and J. Berndt , Thin Solid Films 377 (2000) 585
[10] A. Goldmann, V. Dose and G. Borstel, Phys. Rev. B 22 (1985) 1971
[11] F. Bozso, J.T. Yates, J. Arias, H. Metiu, J. Chem. Phys. 78 (1983) 4256

Ablation Plasma Ion Implantation Processing of 10-20 Nanometer Layered-Materials

R.M. Gilgenbach, B. Qi, M.C. Jones, Y.Y. Lau, A. Lazarides

Intense Energy Beam Interaction Lab
Nuclear Engineering & Radiological Sciences Department
University of Michigan - Ann Arbor, MI 48109-2104 - USA

G.L. Doll - Advanced Materials R & D
Timken Research - The Timken Corporation
Canton, OH 44706-0930 - USA

We report a novel technique for deposition and implantation of 10-20 nm layers of metals by Ablation Plasma Ion Implantation (APII). This process is based upon KrF laser ablation of a solid, metal target. The ablated ions are accelerated to a substrate by a negative voltage of magnitude up to 10 kV. In principle, ions can be ablated and accelerated from any solid target material. When the target is oriented parallel to the substrate, one obtains ion-beam-assisted-deposition (IBAD) of thin films; Ti thin films are 10's of nm thick with an implanted damage layer of 15 nm in Si substrates. For target orientation perpendicular to the substrate, pure ion implantation is achieved with Ti implantation-damage layers some 20 nm deep in Si and no overlying film. The perpendicular orientation reduces arcing and particulate deposition on the substrate. Extensive plasma diagnostics have been performed on the ablation plasma utilizing resonant laser interferometry and Langmuir probes, yielding total ion populations in the range of 10 14 per pulse. Implanted ion doses were estimated by electrical diagnostics and materials analysis including, X-Ray Energy Dispersive Spectroscopy (XEDS) and X-Ray Photoelectron Spectroscopy (XPS), yielding implanted doses in the range 10 12 per square cm per pulse. This yields an ion-utilization efficiency on the order of 10% over the implanted area.

* Research supported by The National Science Foundation

Investigation of pulsed Oxygen/organosilicon plasmas created in a low pressure inductively coupled plasma

A. Bousquet[1], A. Granier[1], A. Goullet[1], G. Cartry[1], C. Leteinturier[1], A. Rousseau[2]

[1] *Institut des Matériaux Jean Rouxel, CNRS-Université de Nantes, Nantes, France.*
[2] *Laboratoire de Physique des Gaz et des Plasmas, CNRS-Université de Paris Sud, Orsay, France.*

Abstract

The time behaviour of Ar (750nm), O (844nm), OH (306nm), H (486nm) and CO (296nm) emissions has been studied by time-resolved optical emission spectroscopy in pulsed oxygen/tetraethoxysilane (TEOS) plasmas. In TEOS/O_2 1:9 mixture, the O and H lifetimes are deduced from the time variations of their intensities normalised to the Ar line intensity. O and H lifetimes are found to be equal to 17 and 23ms, respectively, which means that they are active and long time species and can thus interact with the surface in plasma-off time. A different time behaviour has been observed for O in pure O_2 (τ_O = 5ms) and has been related to a drop of their loss probability on the reactor walls from 0.06±0.01 in pure O_2 to 0.02±0.01 upon TEOS addition.

1. Introduction

New technological applications of low-pressure plasma often demand precise control of the plasma parameters in order to optimize various process characteristics. A promising approach is the use of pulsed plasmas, which allows to enhance some wanted species. For example, for the deposition of Teflon-like films, it was shown that using a plasma pulsed with a short plasma-on time, the fragmentation of the feedstock gas was reduced yielding a film composition much closer to Teflon than with a continuous plasma [1]. In oxygen/organosilicon plasmas, pulsed plasma can be used to emphasize the action of oxygen atoms, which are known to be responsible for the oxidation of hydrocarbon compounds and then to improve the quality and the roughness of the film [2]. Pulsed plasma can also be used to increase the neutral to ion flux ratio on the substrate in order to reduce the compressive stress in the deposited film [3]. In this context, we have studied by time-resolved optical emission spectroscopy the different active species created in pulsed oxygen/tetraethoxysilane (TEOS) plasma.

The work presented hereafter was performed in pulsed oxygen/TEOS plasmas created in a low-pressure reactor, operated at 13.56 MHz. In continuous plasma mode, both plasma and film properties have been deeply investigated as a function of the organosilicon to oxygen flow rate ratio [4]. Inorganic transparent and hard SiO_2-like films are obtained in oxygen-rich plasmas whereas the plasma polymerized $SiO_xC_yH_z$ films obtained in organosilicon-rich plasmas are soft and absorbent in UV.

2. Experimental setup and diagnostic

Helicon reactor. The pulsed experiments were carried out in a helicon reactor, described previously [5]. In brief, it is composed of a source, a Pyrex tube surrounded by a helicon antenna, and a diffusion chamber, where the silicon substrate is located. The base pressure of the reactor is less than 7.10^{-4} Pa. The oxygen and argon are introduced on the top of the source, whereas TEOS was injected via a gas ring located in the diffusion chamber, 8cm above the substrate. The organosilicon flow rate was controlled by MKS 500C massflow. To achieve good operating conditions, liquid TEOS was heated at 40°C. Experiments were performed in pure oxygen and in a TEOS/O_2 1:9 mixture. In both conditions, the total gas flow was fixed at 16 sccm, which corresponds to a pressure of 2.5mTorr before the plasma ignition.

The magnetic field (60G) inside the source is generated by an electromagnet coil around the antenna. The radio-frequency (13.56MHz) power is capacitively coupled up to about 100W and inductively coupled at higher powers. The plasma is generally operated in the inductive mode using a rf power of 300W. In pulsed mode, the power is 100% rectangular-wave modulated with a modulation frequency

varied from 1 to 500 Hz. The duty cycle, defined as the T_{on} period to the total period ratio, is varied from 14 to 50%.

Time-resolved optical emission spectroscopy. The light emitted by the discharge was sampled through a quartz window, using an optical fiber. The emission spectrum was detected by a Jobin-Yvon monochromator (HR460) equipped with two gratings (2400 and 1200 g/mm gratings used for the 180-420 and 420-850 nm spectral range, respectively) and a photomultiplier (R928 Hamamatsu). Argon was used as an actinometer.
For each pulsed condition, an emission spectrum was first recorded in the spectral range 180-850nm, with a resolution of 0.3 nm in order to locate the exact position of the maximum intensity of the line. Then, the temporal variations of the intensity at this fixed wavelength, were recorded during the plasma-on period using a digital oscilloscope (TDS 340).. The time behaviour of Ar^* (750nm), O^* (844 and 777nm), H_β (486nm), OH^* (306nm) and CO^* (296nm) emissions were more especially studied. Whatever the plasma conditions, the decay time of Ar line measured when the plasma is switched off is less than 50 µs. This time is expected to be close to the characteristic switch off time of both the generator and the detection system.
Experiments were carried out with the optical fiber positioned in the mid-height of diffusion chamber, so that the collected light is emitted from the plasma located between the injection ring and the substrate-holder.

The actinometry principle. The collected light intensity is given by : $I = C_{exp}.C(\lambda).A.[M^*]$, where C_{exp} is a geometrical parameter which accounts for the observed volume and the solid angle of the emission, $C(\lambda)$ is the spectral response of the system, A is the probability of the radiative transition, and $[M^*]$ is the concentration of the excited state of the M species.
The actinometry principle is to record the intensities of the studied species M and of an actinometer A. This actinometer is a gas introduced in a low and known concentration in the studied plasma. It is chosen to not react with the other gas. Actinometry can be used if several hypotheses are verified:
(1) The actinometer addition doesn't modify the discharge.
(2) The excited species M* and A* are produced by direct electron impact from their fundamental state. The excitation coefficient denoted K_{exc}, depends on the electron temperature and on the excitation cross section.
(3) The excited species is lost by radiative emission.
If these hypotheses are fulfilled, the intensity ratio can be related to the concentration ratio as follows :

$$\frac{I_M}{I_A} = \frac{C(\lambda_M)}{C(\lambda_A)} \cdot \frac{\lambda_A}{\lambda_M} \cdot \frac{K_{exp}{}^M}{K_{exp}{}^A} \cdot \frac{[M]}{[A]}$$

To get free from the electron temperature and from the excitation cross section, the actinometer has to be chosen so that the excitation threshold and excitation cross sections are similar for A and M. To monitor the oxygen atom concentration in oxygen plasmas, several authors have shown that the argon line at 750 nm, and the oxygen line at 844 nm were the best suited [6]. Nevertheless, if using these lines is necessary, it is not sufficient and actinometry can be invalid, for instance when the oxygen dissociation degree is low and the mean electron energy is high [7].

3. Results in oxygen plasmas
Figure 1 displays the time variations of Ar* line intensity. The initial spike, corresponding to the plasma breakdown, occurs after around 90µs and the emission reaches stability after about 100µs. The same plasma stabilization time is observed in all explored pulsed conditions. The observed initial peak corresponds to a rise of the Ar excitation coefficient, related to a higher electron temperature for the plasma breakdown [7].
The excited oxygen atoms can be created upon electron impact on either O or O_2 :
(1) $O + e^- \rightarrow O^* + e^-$ direct excitation of atomic oxygen
(2) $O_2 + e^- \rightarrow O^* + O + e^-$ dissociative excitation of O_2

Since molecular oxygen is the feedstock gas, its concentration is high before the plasma ignition. If reaction (2) is the dominant one, then the emission intensity is expected to increase as fast as the

electron density when the power is switched on. Figure 2 shows the temporal behaviour of the O*(844nm) to Ar*(750nm) intensity ratio measured in pure O_2 plasma for different modulations. At long power-off periods ($t_{off} \geq 75$ms), I_O/I_{Ar} is close to zero at the intercept. This behaviour suggests that the excited $O(3p^3P)$ atomic oxygen is not significantly created by dissociative excitation of O_2 but mainly by direct excitation of atomic oxygen.

When the same experiment is carried out at 50W, namely in the capacitively coupled plasma, I_O/I_{Ar} is weak and almost independent of the time. In these plasma conditions, the electron density is not high enough to efficiently dissociate O_2 into oxygen atoms so that the excited atoms are mainly produced by dissociative excitation of O_2. In addition, it can be noted that the I_O/I_{Ar} value measured at 50W is very close to the value measured at the intercept at 300 W (e.g. in inductive mode). Hence, it can be concluded that the initial value of I_O/I_{Ar} corresponds to the dissociative excitation of O_2, whereas the slower rise of I_O/I_{Ar} is due to the direct excitation of atomic oxygen, which is slowly produced. After several milliseconds, it reaches a stable value equal to the one obtained in continuous mode.
As the power-off period is decreased below 75ms, the value of I_O/I_{Ar} measured at the intercept increases, due to the increase in the residual atomic oxygen concentration which is only partially lost during the plasma-off period.

The same experiments were performed with the oxygen line at 777 nm. In all the pulsed plasma conditions, the intercept value of the O*(777nm) to Ar*(750nm) intensity ratio was always significant. In other words, $O(3p^5P)$ (the upper state of the 777nm transition) is always created in significant amount by dissociative excitation of O_2, which agrees with all the studies devoted to actinometry in oxygen plasmas [6-7].

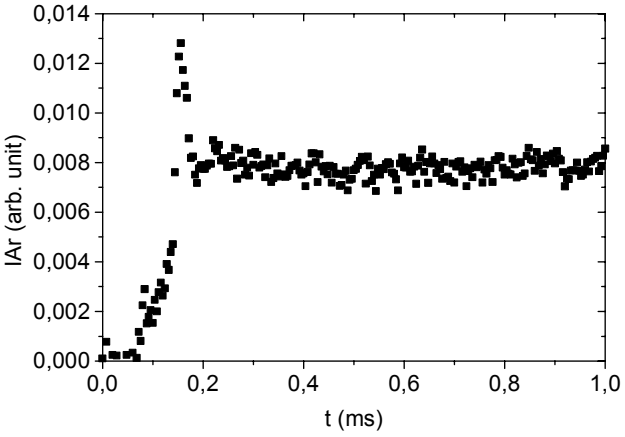

Figure 1: Argon line (750 nm) intensity in an inductively coupled O_2 plasma pulsed at 1Hz 2.5 mTorr-300W, t_{on}=130ms and t_{off}=860ms.

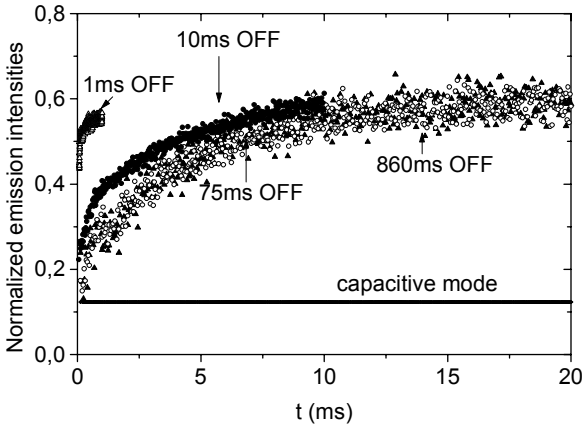

Figure 2: Normalized emission intensity of O in pulsed O_2 plasma for different conditions:*
(—) capacitive mode (50 W)
(symbols) : inductive mode (300 W) :
(Δ) $t_{on}=t_{off}$=1ms ; (●) $t_{on}=t_{off}$=10ms ;
(○) t_{on}=25ms, t_{off}=75ms ; (▲) t_{on}=130ms, t_{off}=860ms

At 1Hz, I_O/I_{Ar} can be modeled by an exponential law [7]:

$$\frac{I_O}{I_{Ar}} = \left(\frac{I_O}{I_{Ar}}\right)_{max}\left[1-\exp\left(-\frac{t}{\tau_O}\right)\right] \quad (3) \quad \text{and} \quad \ln\left[1-\left(\frac{I_O}{I_{Ar}}\right)\Big/\left(\frac{I_O}{I_{Ar}}\right)_{max}\right] = -\frac{t}{\tau_O} \qquad (1)$$

where τ_O is the rise-time of oxygen atoms.

The rise-time was assumed to be equal to the decay-time, which is likely to be reasonable in the case in low-pressure plasmas where gas-phase recombination is unimportant [7]. However, we can notice that at higher pressure (around 50 Pa), experiments carried out in both plasma-on and plasma-off periods by laser induced fluorescence have shown that the decay-time of O atom in O_2 plasma is much higher than the rise-time [2]. Hence, the lifetime deduced from relation (1), represented in figure 3, is likely to be a minimum value.

The oxygen atom lifetime τ_O is found to be equal to 5ms. By using the Chantry formalism [8] to describe the diffusion of O to the reactor walls, the atom recombination probability on the reactor walls, denoted γ_O, can be deduced from the oxygen lifetime. A value of 0.06±0.01 is found, corresponding to those already obtained in continuous mode [9], and in the same order of those reported in the literature [7]. This value is much higher than those measured in spatial post discharges [10]. However, it has been shown [11-15] that loss probabilities are largely higher on surfaces submitted to ion bombardment (continuous discharges and pulsed discharges) than on surfaces not submitted to ion bombardment (spatial post discharge).

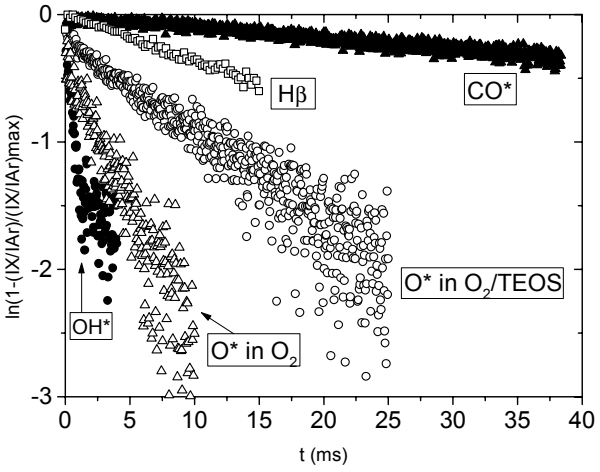

Figure 3: Time variations at 1Hz (t_{on}=130ms, t_{off}=860ms) of different species plotted under the form of Relation (1) in pure O_2 plasma : (Δ) O, and in O_2/TEOS plasmas : (○) O*, (●) OH*, (□) H_β, (▲) CO**

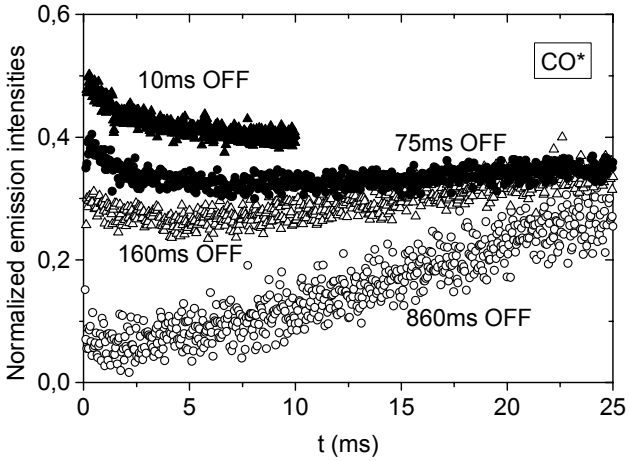

Figure 4: Normalized emission intensity of CO in TEOS/O_2 1:9 plasma (300W) for different modulation conditions :*
(▲) t_{on}=t_{off}=10ms ; (●) t_{on}=25ms / t_{off}=75ms ;
(Δ) t_{on}=25ms, t_{off}=160ms; (○) t_{on}=130ms, t_{off}=860ms.

3. Results in O_2/TEOS plasmas

All the results presented hereafter were obtained in a TEOS/O_2 1:9 plasma operated in the inductive mode (2.5mTorr – 300W). The optical fiber was located on the diffusion chamber. Previous measurements carried out by mass spectroscopy in a continuous plasma created in the same mixture, power and pressure conditions, have shown that more than 95% of the TEOS molecules were dissociated and that H_2, H_2O, CO and CO_2 were the main stable by-products of the dissociation and oxidation reactions [16]. Since these species are stable molecules, they are only lost by pumping. Their lifetimes are expected to be equal to the residence time in the reactor, which was estimated to be 330ms. We followed O*, CO*, OH* and H_β emissions by time-resolved optical emission spectroscopy.

3.1. Oxygen atoms

The time variation of I_O/I_{Ar} measured at 1 Hz is plotted in Figure 3. I_O/I_{Ar} and τ_O (17ms) are both higher than in the O_2 plasma, which indicates a higher oxygen concentration, and corresponds to a lower value of the O-atom loss probability γ_O (= 0.02). The same trends have already been observed in the case of continuous

plasmas [5]. As TEOS is added, new radicals are created and compete with O at the reactive sites of the surface. The oxygen loss rate drops so that its lifetime and its concentration in the plasma rise.

3.2. CO molecules

Figure 4 shows that the initial value of the normalized CO* emission rises when the plasma-off time drops. It is zero only for a time-off (860 ms) much higher than the residence time. Hence, it can be concluded that CO* is produced by electron impact upon the stable CO molecule.

3.3. OH radicals

The normalized OH* intensity behaviour, plotted in figure 5, is very different. For all the pulse frequencies investigated, its initial value is very low and it reaches its steady state value within a few ms. Hence, it can be concluded that OH* is not significantly created from a stable species but from OH radicals. The OH lifetime, determined using the method previously described for O, is equal to 1ms, which confirms that OH is a very reactive species.

3.4. H_β time variation

The time behaviour of the normalized H_β line for the different modulation conditions are plotted in figure 6. $I_{H\beta}/I_{Ar}$ time variations strongly depend on the rf-on time and rf-off time conditions. When the rf-off time is equal to 860ms, namely when all the stable species created by the plasma have disappeared during the rf-off time, $I_{H\beta}/I_{Ar}$ is almost zero at the intercept. Hence, H_β is not created by dissociative excitation of TEOS. This result was expected, since the electron energy threshold for this reaction was measured to be equal to 17eV by Kurunczi et al [17]. Since the electron temperature in O_2/TEOS 9:1 plasma was measured to be about 4eV [5], H_β emission by dissociative excitation of TEOS is not efficient.

When the rf-off time is decreased to 160 or 75ms, the value of $I_{H\beta}/I_{Ar}$ at the intercept increases, which can be attributed to the presence of residual H atoms from the previous pulse or emission of H_β by dissociative excitation of H_2 and/or H_2O. Since the rise time of H_β is equal to 23ms, which is much smaller than the residence time, it is likely that H_β is mainly created upon excitation of H.

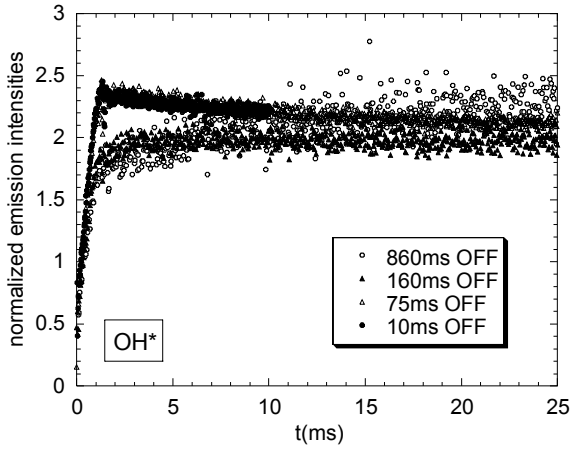

Figure 5: Normalized emission intensity of OH in TEOS/O_2 1:9 pulsed plasma (300W) for different modulation conditions :*
(●) $t_{on}=t_{off}=10ms$; (Δ) $t_{on}=25ms$, $t_{off}=75ms$;
(▲) $t_{on}=25ms$, $t_{off}=160ms$; (○) $t_{on}=130ms$, $t_{off}=860ms$

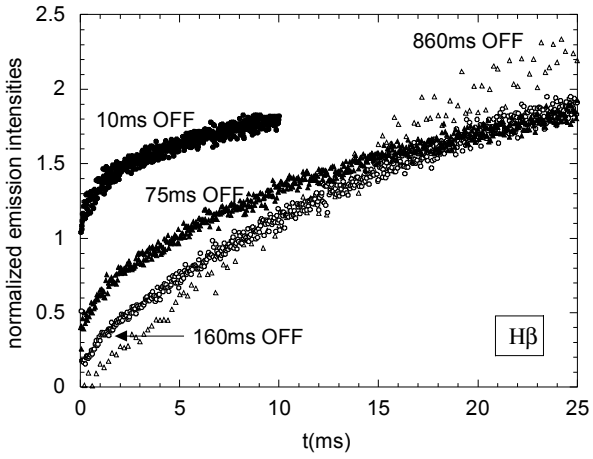

Figure 6: Normalized emission intensity of H_β in TEOS/O_2 1:9 pulsed plasma(300W) for different modulation conditions :
(●) $t_{on}=t_{off}=10ms$; (Δ) $t_{on}=25ms$, $t_{off}=75ms$;
(○) $t_{on}=25ms$, $t_{off}=160ms$; (Δ) $t_{on}=130ms$, $t_{off}=860ms$

Conclusion

Time-resolved optical emission spectroscopy is a suitable method to determine species kinetics in pulsed plasma and to verify the actinometry validity. This technique was used to determine the relative importance of the different mechanisms of the species creation. The oxygen atom loss probabilities on the reactor walls are determined to be: 0.06 in pure O_2 and 0.02 in TEOS/O_2 1:9 plasmas. This difference

may be due to a saturation of reactive sites on the walls by new radicals coming from TEOS dissociation. The lifetimes of studied species were also determined and give indications on the plasma composition for both power-on and power-off period.

References

[1] Kenneth K.S.Lau, Karen K. Gleason – J. of Fluorine Chem. **104**, 119 (2000).
[2] A. Georg, J. Engemann and A. Brockhaus – J. Phys. D: Appl. Phys. **35**, 875 (2002).
[3] C. Charles, R. Boswell – J. Appl. Phys. **84**, 1 (1998).
[4] K. Aumaille, C. Vallée, A. Granier, A. Goullet, F. Gaboriau, G.Turban – Thin Solid Films **359**, 188 (2000).
[5] A. Granier, F. Nicolazo, C. Vallée, A. Goullet, G. Turban, B. Grolleau – Plasma Sources Sci. Technol. **6**, 147 (1997).
[6] R.E. Walkup, K.L. Saenger and G.S. Selwyn, J. Chem. Phys. **84**, 2668 (1986)
[7] J.P. Booth, N. Sadeghi – J. Appl. Phys. **70**, 611 (1991).
[8] P. J. Chantry – J. Appl. Phys. **62** (4), 1141 (1987).
[9] C. Vallée, "Low temperature deposition of thin silicon dioxide films from oxygen/organosilicon plasma in a rf helicon reactor", Ph. D., January 19th 1999.
[10] Greaves J C et Linnett J W *Transactions of the Faraday Society* **55** 1355-1361 (1959)
[11] Magne L, Coitout H, Cernogora G et Gousset G *J. Phys. III France* **3** 1871-1889 (1993)
[12] Pagnon D, Amorim J, Nahorny J, Touzeau M et Vialle M *J. Phys. D : Appl. Phys.* **28** 1856-1868 (1995)
[13] Cartry G., Magne L. et Cernogora G., J. Phys. D.: Appl. Phys. **32**, L53-L56 (1999)
[14] Rousseau A., Cartry G. et Duten X., J. Appl. Phys. **89** 2074-2078 (2001)
[15] Tserepi A. and Miller T.A., J. Appl. Phys. **77** 505 (1995)
[16] K. Aumaille, "Comparative study of thin film deposition processes from organosilicon plasmas: TEOS, HMDSO and HMDSN", Ph. D., December 11th 2000.
[17] P. Kurunczi, A. Koharian, K. Becker, K. Martus, Contrib. Plasma Phys. **36**, 723 (1996).

Mass Spectroscopy Study of the Formation of Ammonia in Iron Nitrocarburizing Process by Using a dc Glow Discharge

H.R.T Silva, P. Egert[1], A.S. da Silva Sobrinho, A. Casaril, and C.V. Speller

Materials Sc. Laboratory/EMC/UFSC - 88040-900 - Florianópolis - SC - Brazil
[1]Environmental Engineering - Unisul - 88130-000 - Florianópolis - SC - Brazil

Mass spectroscopy was used to study the evolution of the ammonia formed during the iron nitrocarburizing process by using a dc glow discharge in different $N_2/H_2/CH_4$ gas concentration mixtures. The experiments were performed in two different configurations [1-2]: the volume configuration was used to collect ammonia that is formed in all the reactor volume, including that formed in the sample surface, while the surface configuration was used to enhance the collection of ammonia formed on the plasma/sample surface interface. The technique proved to be an efficient tool to investigate the mechanism of the physical chemistry of the plasma nitrocarburizing process. Results obtained using the surface configuration showed that the formation of ammonia in the nitrocarburizing process present a maximum for nitrogen rich gas mixture (about 75% N_2 - 22% H_2 - 3% CH_4) that decreases as the treatment time increases, giving rise to a new maximum in hydrogen rich gas mixture (about 22% N_2 - 75% H_2 - 3% CH_4). This shows that the ammonia formation is related with the formation of the compound layer, probably by a mechanism similar to that proposed by Szabo and Wilhelm [3] for the nitriding process. In the case of volume configuration where the collected gas contain ammonia formed in all plasma reactor (reactor walls and sample surface), the results show a very broad maximum for the ammonia, which is the convolution of the two maximum: one for the ammonia formed in the hot sample surface (high nitrogen consumption) and the other one for the stoechiometric ammonia formed in the reactor walls (high hydrogen consumption).

References:

[1] Egert, P., Maliska, A. M., Silva, H. R. T., Speller, C. V., *Surface and Coatings Technology*, 122, (1), 33-38, 1999.
[2] Maliska, A. M., Egert, P., Souza, A. R., Speller, C. V., Klein, A. N. *Journal of Materials Science*, 32, 6375-6382, 1997.
[3] Szabo, A. and Wilhelmi, H., *Plasma Chemistry and Plasma Processing* 4 (2), 89-105, 1984.

Preparation of hard coatings employing non-equilibrium plasma under atmospheric and reduced pressure

V. Valinčius, P. Valatkevičius, L. Marcinauskas

Plasma Processing Laboratory of Lithuanian Energy Institute, Kaunas, Lithuania

Abstract
The plasma spray system has been developed for deposition of wide range of coatings. Two types of plasma torches were developed for operating by feeding air, nitrogen or hydrocarbon containing gases mixed with dispersed particles using the possibility of injection directly into the reacting arc zone. Thick and thin carbon containing films suitable for further plasma treatment and diamond phase nucleation process have been deposited employing non-equilibrium atmospheric and reduced pressure plasma.

1. Introduction

Due to distinctive characteristics of plasma, low temperature plasma flows and jets have been widely used in a variety of fields: plasma chemistry, metallurgy, material processing, waste treatment, laser and space technology and the scientific research goals. Plasma technology processes take place at high temperatures of gas flows created by the specific equipment. Usually, gas retains its dielectric properties there, however, with certain amount of electrons it becomes a conductor and a suitable power source creates in it the electric current, even electric arc discharge.

Amorphous carbon films appeared as very important means for technological applications, presenting a variety of unique properties. Among of the applications plasma polymerization [1,2] and diamond phase nucleation in micro channels of high electrical conductivity of hydrocarbon films [3,4,5] should be mentioned. The creation of suitably arced coatings for that purposes is a very important task, because microarcing plays an essential role in the initiation of electric breakdown that enable and influence diamond nucleation. Despite the large amount of scientific work, several aspects of the deposition process, especially in the conditions of atmospheric pressure, are still a matter of controversy.

The plasma spray deposited diamond and hard ceramic coatings are attractive in many fields of industry. It is well known that high or low pressures are required for synthesis of them. During last years, significant progress has been made in the development of atmospheric pressure plasma technology. There appeared a possibility to realize plasma deposition of diamond, diamond like carbon and other hard coatings under atmospheric or slightly reduced pressure conditions [6,7,8].

We conclude that synthesis of plasma polymeric coatings in atmospheric pressure plasma possibly can be performed in two ways: 1) synthesis of polymer coatings directly in atmospheric pressure plasma jet under effect of ion bombardment and with presence of the catalyst; and 2) treatment and polymerisation of earlier deposited coatings employing low-pressure discharge.

In the first case reactive species, generated by the dissociation of gas precursors, react with heated injected particles and the resulting material splats to form the chemical compounds of polymeric precursors. Reactions may occur in flight with the solid and liquid species (the flight time is about $1 \cdot 10^{-3}$ s), and at the splat surface. The second case is based on different methods of release of energy in the local areas of coatings, such as external irradiation of precursor by concentrated beams of electrons, ions, photons, stress, etc. In that case especially prepared coatings are necessary.

However the essential condition in both cases is a synthesis of coatings suitable for the further treatment process. The early deposited coatings could be prepared by low temperature non-equilibrium plasma at atmospheric pressure employing two different approaches: 1) plasma enhanced spray deposition of coatings using partly or fully melted phase of dispersed particles, and 2) plasma chemical condensation of films employing evaporated substances. In the last case raw materials used can be compounds that make up the coating itself. So, the deposition of the carbon film suitable for the further plasma treatment and diamond phase nucleation process is in the main focus of present studies, where coating samples were formed employing the direct plasma spraying technology. In present paper we report on the technology of forming such coatings employing plasma jet at atmospheric and reduced pressure on the metallic, silicon, quartz glass or ceramic-based material. The ingredients are introduced directly into reactive arc zone. The condensed-phase preparation of coatings can be realized at conditions of both, equilibrium and non-equilibrium plasma.

The plasma technique is also used for activation of the substrate surface and sprayed species, which reaches the surface in liquid or vapour phase. Plasma nonequilibrity plays a very important role in film formation therefore the distribution of electron temperature and density is analyzed here.

2. Experimental equipment and technical details

Experimental installation (Fig.1.) consists of the power, gas and cooling systems, plasma torch (PT), feeders, measuring devices, auxiliaries and airing devices. The PT and gas dynamic system was modified so, that major part of dispersed carbon particles and jet forming gas were supplied directly into the reacting zone of arc. This allows forming very active vapour and melted particles jet in no reacting gas plasma, which could condense and adhere on the especially prepared substrate surface. The thickness of coatings may be adjusted in wide range due to ratio of the flow rate of evaporated and melted particles.

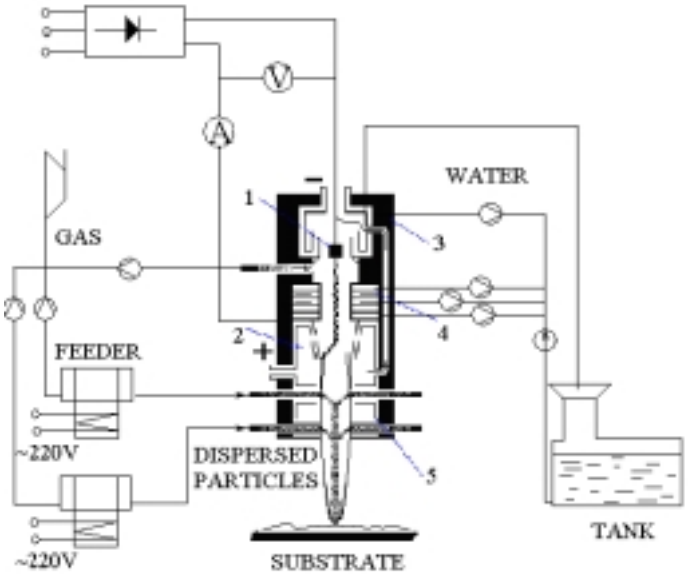

Fig. 1. The schematic presentation of plasma system for deposition of coatings in reduced and atmospheric pressure. 1 – cathode, 2 – anode, 3 – cooling rings, 4 – gas injection rings, 5 – injection of dispersed particles

Two constructions of plasma sources were used. The first one – a linear dc PT of 35 kW of power with hot cathode and step-formed anode with tangential gas injection was designed especially to produce non-equilibrium plasma jet. The schematic presentation of the PT is shown in Fig. 2. It consists of a cathode junction 1 with hafnium emitter, insulation-injection rings 3, and cathode-coupled section for arcing 4, neutrode 5, and step-formed anode 6. In the case when magnetic stabilization of flow is necessary, the magnetic coil may be useful. Each ring 3 contains blowholes of tangential air supply (G_1, G_3 and G_3) for the arc stabilization and to obtain a possibility to introduce the stock and plasma forming gas directly into the arc. The G_1 under investigation is of the order of 0,54 – 1,27, G_3 – 1 – 3,45, and G_5 – 1 – 3,45 10^{-3} kg·s^{-1}. At the constant total gas flow, G_1, G_2 and G_3 are defined as diverse ones. The current can be varied in the range of 150 - 200 A in the experiments described here. The voltage drop depends on the gas flow rate and gas composition and ranges from 180 to 250 V.

One of the simplest and acceptable ways to influence the arc for production of non-equilibrium plasma was the injection of thin stream of gas circular directly into different cross section of rechargeable chamber. The mass flow of the source gases as air or nitrogen was regulated by mass flow controllers. The flow in the air lines was controlled by diaphragm and differential pressure gauge with electrical output signal. The nitrogen flow rate was controlled by critical jet up to maximum of 3.5 10^{-3} kg·s^{-1}.

The voltage-current characteristics of the plasma torch are slowly decreasing and may be presented analytically in the following way:

$$\frac{Ud_2}{I} = c\left(\frac{I^2}{Gd_2}\right)^m \cdot \left(\frac{d_2}{I}\right)^{0,5} \cdot \left(\frac{G_1}{G}\right)^{-0,12}, \qquad (1)$$

where U is voltage, I - the arc current, G - the flow rate, d - exhaust nozzle diameter, m=0,8.

The efficiency coefficient η is calculated according:

$$\frac{1-\eta}{\eta} = c\left(\frac{I^2}{Gd_2}\right)^m \cdot \left(\frac{G_1}{G}\right)^{0,12} \cdot \left(\frac{G}{d_2}\right)^{0,2} \cdot \frac{d_2}{I} \cdot \left(\frac{l}{d_2}\right)^{0,95}, \quad (2)$$

where l - the characteristic arc distance, $c = 0{,}71 \cdot 10^{-4}$, $m = 0{,}8$.

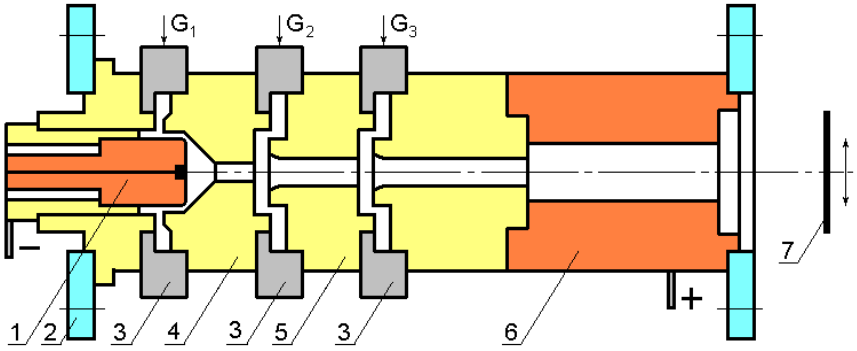

Fig. 2. Plasma torch for deposition of coatings. Explanation see in the text.

Before being introduced into working gas, the dispersed particles is mixed in vibrating feeders with controlled dosage. The gas and powder were injected trough a 4,5 mm diameter cylindrical tube with a flow rate about $0{,}4 \cdot 10^{-3}$ kg·s^{-1}. The distance between the plasma torch and substrate was equal to 0,09-0,12 m ($x/d \approx 12$).

Stainless steel sheets, silicon plate, ceramics and quartz glass tubes have been used as substrate. The substrate was cooled by air or water so, that surface temperature couldn't exceed 650 K. During deposition, the substrate was rotated and its linear velocity was equal to 5 m·s^{-1}. The surface of the substrate was nitrogen cooled during all process of deposition. Simultaneously, the plasma torch moved horizontally and parallel to the substrate with a velocity equal to $(3\text{-}5) \cdot 10^{-3}$ m·s^{-1}.

The propane-butane gas was injected into non-equilibrium nitrogen plasma to get carbon-containing the plasma forming flow. A mixture of propane-butane gases is fed into the space between the two electrodes at $(0{,}15 - 0{,}45) \cdot 10^{-3}$ kg·s^{-1} (at 10^5 Pa and 293 K). For deposition thick films carbon particles are added to air carrier gas. The aluminum layer on metallic surface is deposited for subsequent synthesis of hard coating and for protection of metal surface from oxidation during deposition process.

To estimate the charged particle flux and temperature in the jet effluent, double planar Langmuir probe was placed in the exhaust plasma jet. The probes are circular, water cooling, of $4 \cdot 10^{-3}$ m diameter and made of oxygen free copper. The edges of the probe are shielded off by a ceramic (Al_2O_3) coating.

For large area application the similar of new types of plasma sources were developed. The other PT, 5 kW of power, consisting of similar parts, was designed and specially constructed to improve plasma spray quality employing high velocity plasma jet. PT fitted with an orifice used to generate the supersonic plasma jet. Plasma forming gas was injected only tangential in two places. The latter plasma source has been placed in a vacuum chamber together with its belonging auxiliaries. A series of films were deposited with different N_2 and dispersed carbon particles flow rates each for 100 s duration.

3. Results and discussion

The plasma jet parameters at the exhaust nozzle of plasma torch were also strongly regulated and fixed. Results of plasma diagnostics showed that temperature and velocities profiles in plasma jet are axi-symmetrical and parabolic shaped. The diameter of the jet slightly increases.

An electron flux of 5 x 10^{13} particles cm^{-2}·s^{-1} was collected on the probe when 100 V to the floating potential positively biased it. The electron temperature was several times of magnitude higher than temperature of heavy particles (Fig.3.). The electron density (Fig.4.) in the plasmas under our investigation is of the order of $10^{16} - 10^{17}$ cm^{-3} and the temperature is 0,5 – 1,8 eV.

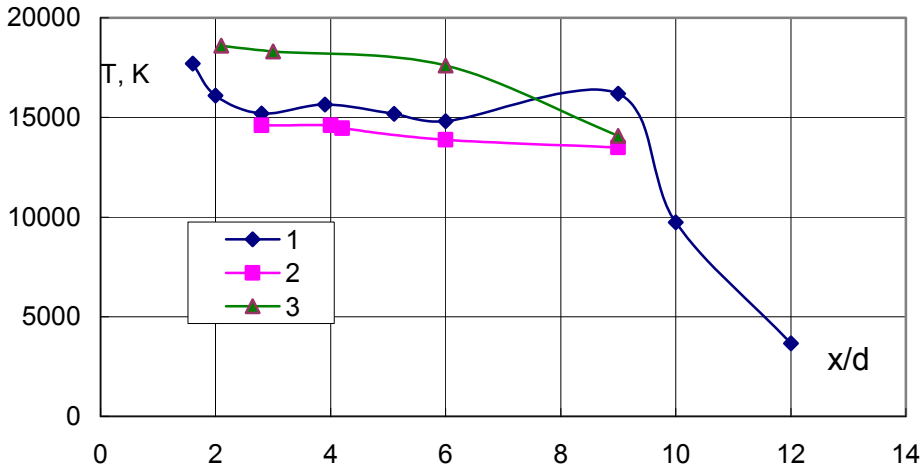

Fig. 3. Distribution of electron temperature in plasma jet. 1,2 – PT developed by authors, 3 – PT of Sankt-Petersburg colleagues

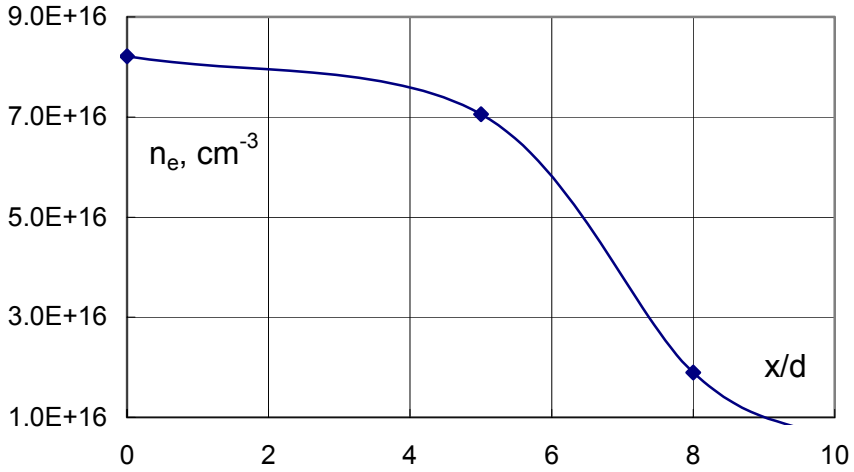

Fig. 4. The electron density as a function of distance

The subject of this paper is the application of plasma spray torch for deposition of carbon derivative coatings on metal and ceramic substrates of different configuration and composition. In the present study carbon derivative films were formed from carbon containing gas, carbon dispersed particles and their mixtures by the direct plasma spraying technology with or without evaporation of solid fraction.

In many cases coatings have been deposited without any sub layer and intermediate layers. At first the deposition process was performed according to our previously developed methods [9,10], when dispersed particles were injected into the plasma jet inside or outside the stream reactor, connected to the exhaust nozzle of PT. Carbon containing coatings were thick and rough. SEM images allow investigation of the film morphology and estimation of deposition rate as function of plasma forming gas rate and location of injection place. From the SEM studies, on the samples it can be observed that the coating consists of large ($(5 – 10)\cdot10^{-6}$ m) different shaped (spherical, hollow, broken, sphere within a sphere, tubular, and some other irregular shaped) particles (Fig.5a.). After modification of plasma source, when there appeared a possibility to inject particles simultaneously with plasma forming gases directly into the reaction zone of arc, the view has substantially changed (Fig.5b). Dispersed particles have evaporated and after transportation to the substrate they condensed again on the cold surface of substrate. The particles size on the coating could be changed by the change of arc length, its electric parameters, also plasma jet parameters. By the way the dissociation and ionization of substances is possible and the rest particles become as highly activated. The high velocity of plasma accelerates ions and heavy particles, which take part in film growth and the DC self-bias between the plasma and the substrate has been rapidly quenched on reaching the growing film. Because

of the shock, so activated particles impacts the surface atoms passing a part of energy to them. In that reason, atoms of the growing film become also activated and amorphous carbon is deposited on the surface.
Upon propane-butane addition, the film growth rate in the central area of the deposits initially increases from 50 to $150 \cdot 10^{-6}$ m/h. With further increasing gas flow rate, the film growth rate drops again while the material particles in the layer start to deteriorate. The structure of the film is fine and homogeneous; particles on the film become a streamline shape (Fig. 6.).

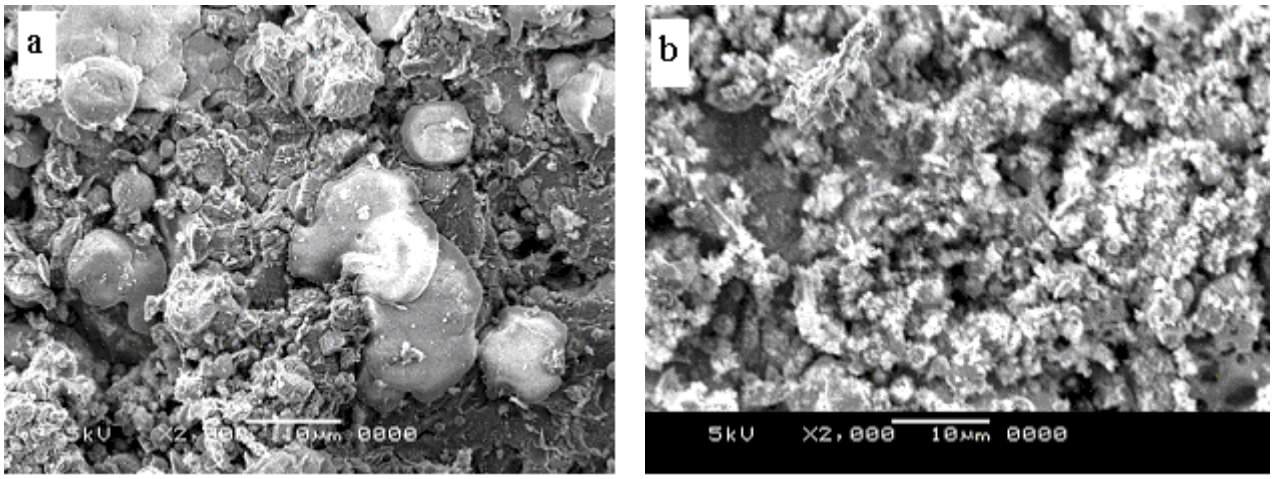

Fig. 5.The surface structure view of carbon coatings. a) dispersed particles injected in the stream reactor; b) particles injected directly into reaction zone of arc

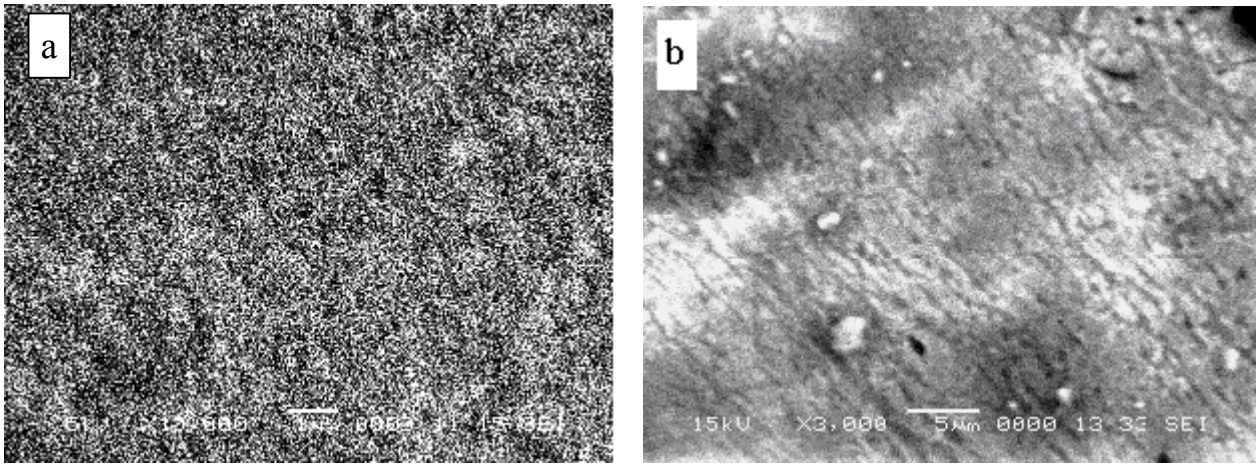

Fig. 6. The surface structure view of carbon coatings in the support of propane-butane gases. a) dispersed particles and gas injected into the reaction arc zone; b) the same, after additional plasma treatment at reduced pressure

Based on the results of the present study, the structural properties of deposited films on different surfaces (Fig.6.) display their suitability for further polymerization and diamond nucleation processes. For reproducible plasma deposition of fine carbon derivative coatings as a recipe could be given the use of special plasma torch with injection of dispersed carbon particles and propane-butane gases into the reaction zone of arc. SEM images of films grown with propane-butane and N_2 mixture of, respectively, 6 and 91% illustrated that propane-butane gas addition to the process gas mixture affects the film morphology. Films grown with no added propane-butane gas are predominantly faceted and twinning, while with addition of these gas the coating became even structure distribution with facets approaching ~10-50 nm in size. The addition of dispersed carbon particles into process mixture promotes the growth of large type of surface particles features.
The variation of N_2 or hydrocarbons containing gas flow rate has only low influence to the film growth rate. Significant film growth increases increasing dispersed particles injection rate and reaches the maximal value of 1 $\mu m \cdot s^{-1}$ in a 35 kW DC arc jet system operating with N_2/propane-butane at atmospheric pressure. The deposition rate in vacuum chamber employing 5 kW DC arc jet system was less than 0.1 $\mu m \cdot s^{-1}$ at the pressure of 10^{-3} Pa operating with the same gas mixture. Hardness values of deposited films estimated

employing Vicker's identification technique were in the range of 10,9 to 12,5 GPa. Films deposited employing 5 kW plasma spray system at reduced pressure after additional plasma treatment showed the 15,7 – 18,4 GPa hardness.

Conclusions

Finally we note that the present work supports the suggestion that DC plasma jet correlates with deposition of high quality hard coatings suitable for further plasma treatment, plasma polymerization, microarcing and diamond phase nucleation in microchannels of high electrical conductivity.

The DC-arc jet provides an excellent environment for plasma assisted deposited of thick and thin hard amorphous carbon films. Shape and size of particles on deposited coatings strongly depend on the localization of injection place. Fine-grained structures obtained after injection of dispersed particles directly into the reaction zone of the arc.

Significant differences in size and shape were observed during deposition process when carbon particles were injected directly into the arc together with non-reacting gas.

Carbon film particles deposited on quartz glass surface with addition of propane gases, assume the minimal size and streamline shape.

Acknowledgement

This work was supported by Lithuanian State Science and Studies Foundation.

References

[1] H. Dong, T. Bell – Surf. Coat. Technol. **111,** 1 (1999).
[2] H. Biederman, D. Slavinska – Surf. Coat. Technol. **125,** 1-3 (2000).
[3] M. Ibm-Charaa, M. Jaouen, J. Delafond, L. Pranevicius – Diamond and Related Mat. **5**, 2 (1996).
[4] L. Pranevicius, L.L. Pranevicius, M. Jaouen, J. Delafond, H. Gonnordb – Lithuanian Mater. Sci. **2,** 3 (1996).
[5] S.P. Bugaev, K.V. Oskomov, N.S. Sochugov, A.D. Korotajev – Surf. Coat. Technol. **96,** 1 (1997).
[6] S.E. Babayan, J.Y. Jeong, A. Schutze, V.J. TU, M. Moravey, G.S. Selwyn and R.F. Hicks – Plasma Sources Sci. Technol. **10**, (2001).
[7] J. M. Larson, M. T. Swihart and S. L. Girshick – Diamond Relat. Mater. **8**, 10 (1999).
[8] S. K. Jr. Baldwin, M. Zhao, T. G. Owano and C. H. Kruger – Diamond Relat. Mater. **6**, 2-4 (1997).
[9] V. Valincius, P. Valatkevicius, L.L. Pranevicius, D. Milcius – Lithuanian Mater. Sci. **1**, 6 (1998).
[10] L. Pranevicius, L.L. Pranevicius, P. Valatkevicius, V. Valincius – Surf. Coat. Technol. **123**, 2-3 (2000).

Plasma Chemistry of Fullerenes and Carbon Nanotubes Production

Eletskii Alexander V.Bezmelnitsyn, R.Dubrovskii

Russian Research Center "Kurchatov Institute"
Kurchatov Square 123182 Moscow Russia
Phone: (+7)095-1967280 Fax: (+7)095-1967280 Email: eletskii@imp.kiae.ru

Plasma chemistry aspects of fullerenes and carbon nanotubes (CNT) production in arc discharge plasmas are reviewed. Two main ways of thermal decomposition of graphite, resulting in fullerene (nanotubes) containing soot generation are considered and compared in detail. The first one is the arc discharge with graphite electrodes in helium, where the soot is generated as a result of thermal decomposition of graphite anode (Kraetchmer scheme). The second one is based on usage of an arc plasmatron, where small size amorphous graphite particles are admitted. The conditions favorable for fullerenes and carbon nanotubes formation in plasma are analyzed on the basis of experimental data. The kinetics of vaporization of a small size carbon particles in plasma medium is investigated theoretically, on the basis of the heat conductivity equation with taking into account the temperature dependence of the heat conductivity coefficient.
The work is supported by the CRDF through the REC "Plasma".

Correlation of Optical Emission Parameters and ZnO:Al Film Properties in Reactive Magnetron Sputtering from Ceramic and Metallic Targets

T. Wallendorf[1], S. Marke[1], Ch. May[2*], J. Strümpfel[2]

1: IfU GmbH Privates Institut für Umweltanalysen, Lichtenau, Germany, www.ifu.de
2: VON ARDENNE ANLAGENTECHNIK GMBH, Dresden, Germany, www.ardenne-at.de
*: now with Fraunhofer Institute for Photonic Microsystems IPMS Dresden, Germany, www.ipms.fhg.de

Abstract

Aluminium doped zinc oxide (ZAO) layers are used as transparent conductive layer (TCO) in thin film solar modules. A significant cost reduction of TCO thin film production is expected by use of much less expensive metallic alloy targets.

The preparation of ZAO films with good TCO properties from ceramic targets with low amounts of oxygen gas inlet is well established due to low effort of process control means.

ZAO films with good TCO properties can also be deposited from metallic target in the transition mode of the reactive sputter process. To control the discharge in the transition mode by adding varying amounts of oxygen gas using a combination of a Plasma Emission Monitor PEM®05 and a fast optical emission spectrometer AOS-4, which allows multi wavelength control was applied.

The optical emission spectroscopy investigations were carried out in DC mode with metallic and ceramic targets at varying discharge power and gas pressure. The properties of the ZAO films obtained are correlated with optical emission data. It was investigated, if the optical emission parameters obtained in ceramic target process can be used as a measure for the control of the reactive metallic target process.

Introduction

Aluminium doped zinc oxide films (ZAO) are used as combined window and contact layer for thin film solar modules [1, 2, 3]. Commonly these films are DC sputtered from ceramic ZAO targets [4, 5]. However, a reduction of the high deposition costs can be expected, if reactive sputtering of metallic alloy targets will be applied. To deposit high quality TCO coatings special requirements are needed to stabilize the process. It has been shown that single wavelength Plasma Emission Monitoring (PEM) can be used to meet this requirements [6].

In further works we have shown that dual wavelength control by use of a simple intensity ratio can be used to improve the stability and reproducibility of the process parameters, which results in high transparency and low resistivity of the films grown [7, 8]. For this dual

wavelength control we successfully used a combination of an AOS spectrometer produced by IfU GmbH and a PEM®05 Plasma Emission Monitor which is produced by VON ARDENNE ANLAGENTECHNIK GmbH.

The AOS 4 spectrometer is a fast optical measurement system, based on AOTF technology, where the wavelength is selected by a fast switching Acousto Optical Filter [9]. Its wavelength calibration is stable over several years due to special internal stabilization. The robust design works without any moving parts and combines a wide wavelength range of 250-800 nm with an excellent wavelength resolution of 0.5nm@800nm and 0.05nm@250nm. The random wavelength access is carried out by full electronic control within a few milliseconds maintaining both, wavelength resolution and wavelength range.

The AOS 4 spectrometer supports 3 modes of operation:

Spectral scanning mode (called spectrum mode): The spectrum mode delivers complete intensity information from a wavelength range. The wavelength range is scanned by stepping through with acquisition time of minimum 5 milliseconds per step. Characteristic emission lines can be found in the spectrum using an automatic peak search tool. An advanced emission library tool based on data from the N.I.S.T. library [10] supports the identification of the lines found in the spectrum.

Chronogram / time tracking mode: The chronogram mode uses the advantage of fast random wavelength access. The AOS spectrometer control software supports the quasi simultaneous watching of up to 16 spectral emission lines with an acquisition time of down to 5 milliseconds each. The total time resolution depends from the number of selected emission lines. This mode is connected with an analog output, which can be set to values calculated by a user defined algorithm from the measured intensities. The chronogram mode can be used to monitor or to control a plasma process.

Microchronogram mode: The microchronogram mode combines the fast random wavelength access with a fast acquisition of the photomultiplier signal. It is specially intended for investigation of pulsed plasma applications. The measurement can be triggered by an external digital or analog signal, which may be derived from the pulse plasma power supply voltage or from the plasma power generator. The AOS spectrometer control software allows to take optical data from up to 16 preselected wavelength's, with a time resolution of downto 200ns.

Experimental

In [7] we have shown that dual wavelength control can easily be established with a combination of the AOS spectrometer and a PEM®05 Plasma Emission Monitor in DC and MF power supply mode as well. As the preparation of ZAO films with good properties using ceramic target is well established, it seems to be worth to compare the plasma emissions coming from a ceramic target process and from a metallic target process.

For our experiments we used the same setup and diagnostics for the films grown, as in [6]. We have shown that the metallic target allows to cover the complete film property range from totally metallic via transition to totally oxygenic behaviour only by controlling the reactive gas flow. The transition range has been investigated more detailed using metallic targets.

In a second step we recorded spectra from the plasma emissions using ceramic targets. As it has been shown in earlier work, very small amounts of oxygen have to be added to the discharge region to obtain the optimum in film properties without advanced process control.

Results

An emission spectrum of the metallic target magnetron discharge taken under single wavelength control is shown in fig 1. The operating condition are choosen close to metallic mode, where the transparency of the films grown is zero.

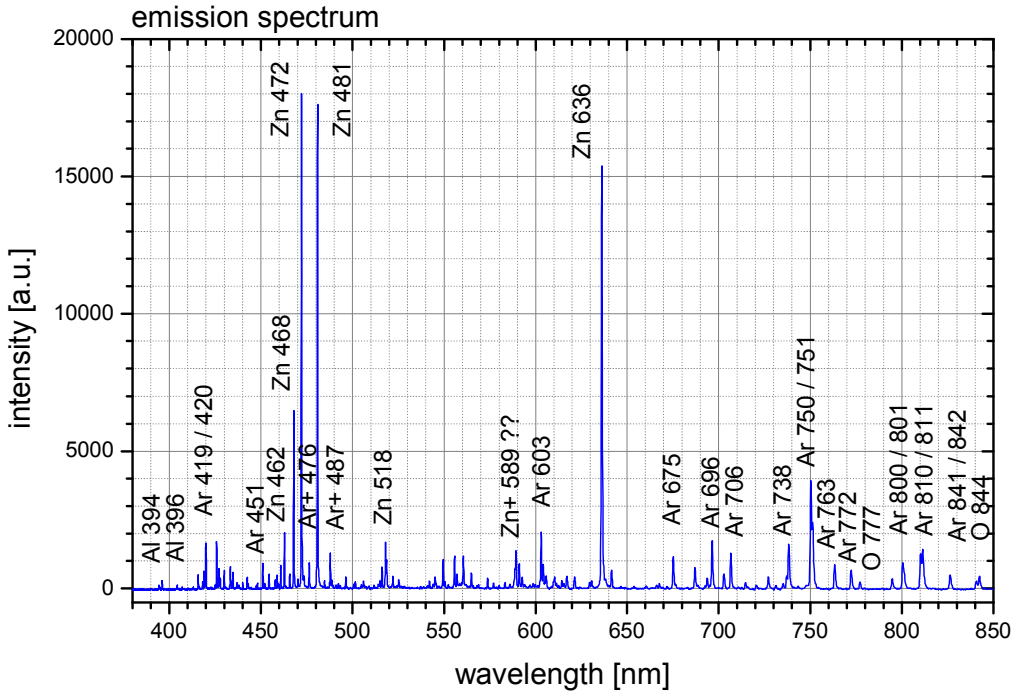

Fig. 1 Visible part of an emission spectrum taken with AOS under near metallic conditions with small amounts of oxygen

The most interesting emission lines have been selected and coordinated to the following specimen using data from the N.I.S.T. emission line library [10]:

Al	394, 396 nm
Ar	419, 420, 451, 603, 675, 696, 706, 738, 750, 751, 763, 772, 800, 801, 810, 811, 841 and 842 nm
Ar+	413, 454, 461, 476, and 488 nm
O	777 and 844 nm
Zn	307, 328, 330, 334, 462, 468, 472, 481, 518 and 636 nm
Zn+	491, 492 nm, overlayed with Ar+ emission lines, 589nm

A quiet intensive emission line at 589nm was identified as single charged Zn^+ ion line using the N.I.S.T. library. As the ionisation degree of the magnetron discharge may be low, only

very few ion lines could be observed. Considering the remarkable intensity of this 589nm line it may be used to monitor the ionic Zn^+ species.

To investigate the behaviour of different emission lines the AOS was used in chronogram mode. Following emission lines have been selected to be viewed under film deposition experiments with varied discharge set point:

Ar	750 nm
O	777 nm
Zn	472, 481, 636 nm
GND	657.5 nm, where no emission lines have been observed.

For the deposition experiments in metallic mode we used a simple ratio of the intensities from the O 777 and the Zn 636 emission line. As it has been shown in [6] the AOS output signal is highly sensitive to the mode of operation and allows the adjustment of the setpoint needed for deposition of ZAO films with TCO properties by reactive sputtering.

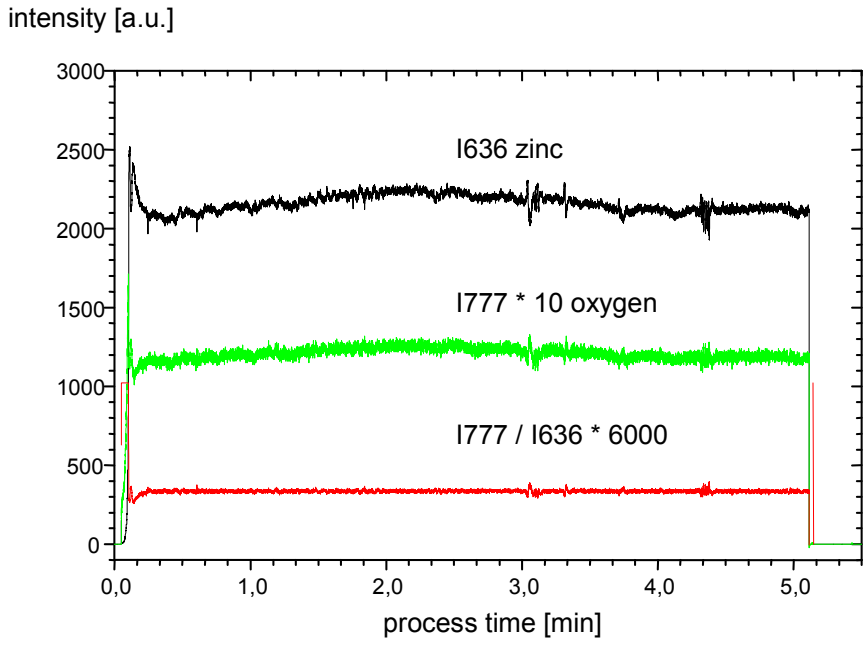

Fig. 2 Chronogram taken during the process dual wavelength control using AOS and PEM.

Fig. 4 shows a chronogram taken during the process control of the deposition of a ZAO layer under dual wavelength control. Plasma power was turned on at process time = 3 seconds. Approximately at 15 seconds the discharge had been stabilized to the setpoint (65% are related to S =325 digits due to signal conversion from digital to analog). There are changes in intensity visible at both emission wavelength 636nm and 777nm, but the ratio was held very constant.

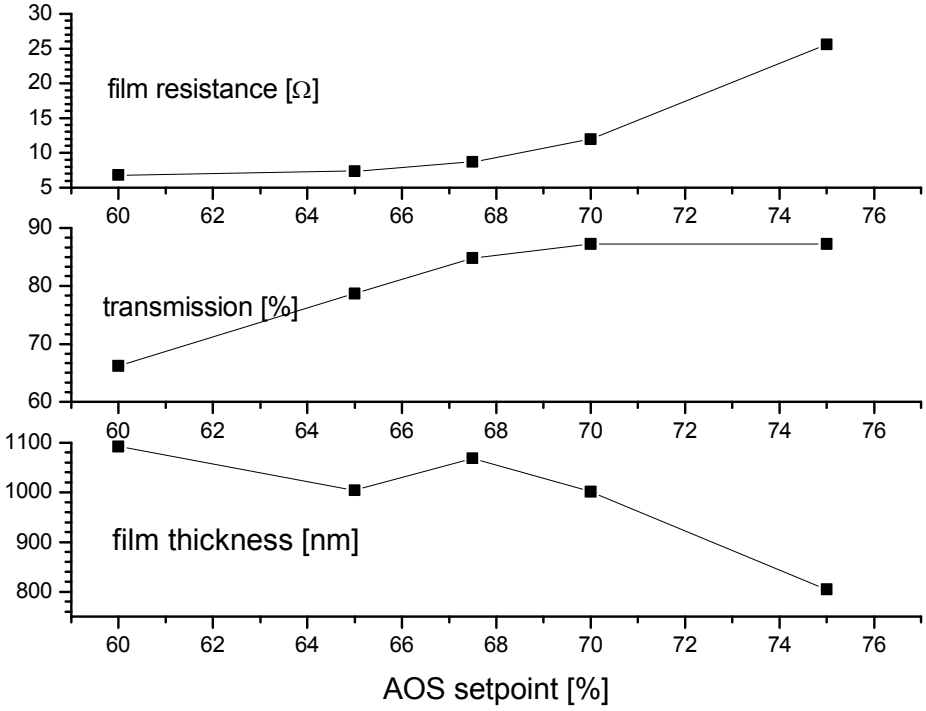

Fig. 3 Properties of ZAO layers grown at room temperature from metallic target with dual wavelength control

In fig. 2 there are shown properties of films grown with different AOS setpoints from metallic target. Higher values for the AOS setpoint correspond to higher content of Oxygen in the gas. The best film of this series was deposited at a gas pressure of 2.7 μbar with an AOS setpoint equal to 67.5%. Its transmission was as high as 84.8% with a film resistance of 871μΩcm.

Several film deposition experiments have been carried out with ceramic target. During deposition we recorded several emission spectra. The point of interest was to determine the intensity of the O 777 line. For this collection of emission data we used the same optical setup as for the optical measurements from metallic target.

target	Ar flow	O_2 flow	Remarks	Ar 763 counts	O 777 counts	O / Ar ratio
metallic	300 sccm	140 sccm	metallic films	930	103	0.11
metallic	300 sccm	188 sccm	very good TCO films	960	115	0.12
metallic	300 sccm	200 sccm	oxide films	960	245	0.26
ceramic	300 sccm	1 sccm	very good TCO films	13400	90	0.0007
ceramic	300 sccm	10 sccm	R > 300 Ω oxide films	13400	350	0.0261

Tab. 1 Selected optical emission data from ceramic and metallic target

The intensity of the O 777 line was very small in all experiments carried out with ceramic target. Only if large amounts of oxygen of 30 sccm are added to the gas discharge, a remarkable intensity of the O 777 line could be observed. At these reactive gas flows the properties of the films obtained are strongly oxygenic already. Selected emission data from both targets are shown in tab. 1.

As it can be seen in the right column, the intensity ratio measured from ceramic and from metallic target do not agree. The idea of using the plasma emission intensities from ceramic target as a reference value for metallic target set-point optimisation is not valuable for Aluminium doped Zinc Oxide layers.

Conclusion

ZAO layers can be produced from metallic targets by reactive magnetron sputtering. This process is expected to be much less expensive in the case of mass production due to low target costs and higher deposition rates.

The advanced process control needed for the metallic process can be established with a combination of a fast scanning AOS spectrometer and a PEM®05 plasma emission monitor using a simple ratio calculated from emission lines of the reactive gas and the metal used.

The optical emissions for the optimum ZAO properties set-point of the metallic target process cannot be optimised using the optical emissions from the the optimum set-point of the ceramic target process.

References

[1] M. Powalla and B. Dimmler, Proc. 17th Europ. Photovolt. Solar Energy Conf., München, (2001), 983

[2] V. Probst et al., Proc. 17th Europ. Photovolt. Solar Energy Conf., München, (2001), 1005

[3] J. Müller et al., Proc. 17th Europ. Photovolt. Solar Energy Conf., München, (2001), 2876

[4] R. Menner, R. Schäffler, B. Sprecher, and B. Dimmler, Proc. 2nd World Conf. PV Solar Energy Conv., Wien, (EC JRC Ispra, 1998), 660-663.

[5] A.E. Delahoy and M Cherny, Mat. Res. Soc. Symp. Proc. 426 (1996), 467.

[6] C. May, R. Menner, J. Strümpfel, M. Oertel and B. Sprecher: Deposition of TCO films by reactive magnetron sputtering from metallic Zn:Al alloy targets, Surf. Coat. Technol. 169-170C (2003) 514-518

[7] T. Wallendorf, S. Marke, Ch. May, J. Strümpfel, Optical investigations in a PEM controlled reactive magnetron sputter process for aluminium doped zinc oxide layers using metallic alloy targets, Conf. on Plasma Surface Engineering, Garmisch-Partenkirchen, Germany, 2002, in press

[8] T. Wallendorf, S. Marke, C. May, J. Strümpfel, Time Resolved Optical Investigation in a MF Driven Reactive Magnetron Sputter Process for ZnO:Al Layers using Metallic Alloy Targets, to be published on the CIP 2003, Antibes, France

[9] V. Shogun, A. Tyablikov, E. Shelyhmanov, M. Abachev, W. Scharff, T. Wallendorf: Application of an acousto-optic spectrometer for plasma etching process quality control, Surf. Coat. Technol. 74-75 (1995) 571-574

[10] N.I.S.T. Atomic Spectra Database, http://physics.nist.gov/cgi-bin/AtData/main_asd

Diagnostics of dust structures in a gas discharge plasma

Olga S. Vaulina, Oleg F. Petrov and Vladimir E. Fortov

Institute for High Energy Densities, Russian Academy of Sciences, Moscow, Russia

Dusty plasma consists of neutral gas, ions, electrons, and micron-sized particles (dust grains). The particles are typically charged negatively in gas-discharge plasmas. The combined effect of interaction between the particles and the ambient plasma as well as between the particles themselves leads to the formation of various complex plasma states ranging from "gaseous plasma" to "liquid plasma" (or plasma fluid) and "plasma crystals". These states are distinguished by the level of ordering in the particle system. Since the particles can be visualized and analyzed at the kinetic level, complex plasmas are recognized as valuable model system for the study of phase transitions and other collective processes including transport properties and wave phenomena. Results are presented for a set of experiments performed in different types of gas-discharge plasma.

Effective structural (pair correlation function) and transport (diffusion constant) characteristics of the system of microparticles (dusty plasma) have been measured in a set of experiments in dc- and rf gas-discharge plasmas. The comparison between these measurements and numerical simulations were used for complex plasma diagnostics. Specifically, the effective coupling parameter, which mainly governs structural and dynamical properties of the system, was determined for different experimental conditions. The application of these measurements to estimate the particle charge and the plasma screening length is discussed.

First we report on the experiment performed in dc discharge plasma. More details about the experimental apparatus can be found for example in Ref. [1]. The basic plasma parameters were: Ne gas at pressure p = 0.4-1 Torr, the current I = 3 mA, the electron temperature $T_e \approx$ 2-5 eV, plasma number density $n_i \sim n_e \sim 5\times10^9$ cm^{-3}. Basic purpose of these experiments was to study the properties of dust structures in a state close to gaseous one. The diffusion constant measurements were performed for small iron particles with the radius a = 1-3 μm, which formed quasi 3D cloud even in gravity conditions. The measured particle temperature was practically independent of neutral pressure, $T_p \approx 1$ eV. The interparticle distance was slightly decreasing from $\Delta \approx 250$ μm at $p \approx$ 56 Pa to $\Delta \approx 190$ μm at $p \approx$ 128 Pa. The effective coupling parameters Γ^* retrieved from these measurements as a function of neutral pressure were obtained. The complex plasma was in a weakly coupled "gaseous" state in this case as Γ^* was in the range from ~10 to ~20.

We studied dynamics of small (a =1-2.5 μm) aluminum oxygen (Al_2O_3) particles in a single dust lay, which was formed above the ground electrode of rf- discharge (P = 10-40 Pa, the power W= 2-7 W, $T_e \approx$ 1-3 eV, n_i ~ 10^9 cm^{-3}) in argon. The effective coupling parameters were also estimated. Nevertheless the application of our three-dimensional simulation for analysis of effective characteristics can be not valid in this case.

This work was financially supported by the INTAS, Grant No.2000-0522 and No.2001-0391.

References:

1. A. M. Lipaev *et al*., JETP **85**, 1110 (1997).

Imaging Emission Spectroscopy of Atmospheric Pressure Carbon Dioxide Microwave Discharge using an Acousto Optical Tunable Filter

S. Marke[1], Th. Oberreuther[2], T. Wallendorf[1], Ch. Wolff[2]

1: IfU GmbH Privates Institut für Umweltanalysen, Lichtenau (Germany), www.ifu.de
2: University Dortmund, Fachbereich Chemietechnik, Dortmund (Germany), www.uni-dortmund.de

Abstract

Carbon dioxide is a waste gas which disturbs the atmospheric thermal equilibrium of our planet. Therefore techniques for reducing the industries Carbon dioxide emission plays an increasing role worldwide.

A special technique was developed to activate the Carbon dioxide. Due to low reactivity of the Carbon atom depending on the oxidation number of +IV thermal activation methods are not expected to work efficiently. A microwave plasma (up to 6kW) at atmospheric pressure allows the efficient activation of Carbon dioxide continuously up to flow rates of 10 m³/hr.

Optical emission spectroscopy is used to investigate the aggregation of Carbon atoms to specimen containing up to four Carbon atoms. An Imaging Spectrometer based on Acousto Optical Tuneable Filter technology is used to visualize the spatial distribution of excited particles inside of the plasma source. Especially the Oxygen emission at 777.3 nm and the C_2-band head at 516.5 nm were investigated varying the gas flow and discharge power.

Introduction

Causing the green house effect Carbon dioxide becomes a really interesting raw material for chemical synthesis. Carbon dioxide is a molecule with low reactivity [1]. Therefore plasma activation is good chance to prepare the CO_2 molecule for following chemical and plasma chemical reactions.

The observation of CO_2 activation was carried out by **o**ptical **e**mission **s**pectroscopy (OES). First experiments were performed with an AOS 4 (**a**cousto**o**ptic **s**pectrometer) [2] produced by IfU GmbH, Germany. The most important emission structures of activation process were determined. In second step the spatial distribution of excited particles inside of the plasma was recorded by imaging spectroscopy based on AOTF-technique (**a**cousto**o**ptic **t**unable **f**ilter) [3] to visualise the efficiency of activation in plasma volume [4].

The experiments were carried out at the University of Dortmund, Germany, in a special developed plasma synthesis reactor. The plasma activation was supplied by micro wave and could be performed at a pressure ranging from some mbar up to somewhat more than atmospheric pressure. It was possible to handle flow rates up to 10m^3/h.

Experimental

Plasma Synthesis Reactor

The plasma synthesis reactor is divided into three main parts (fig.1): the plasma source, the reaction tube and the reactor head. By using the CYRANNUS® I plasma source from Iplas GmbH, Germany, it is possible to activate carbon dioxide continuously up to flow rates of 10 m³/h and a microwave power up to 6 kW. The maximum flow rate of the plasma source in inefficient mode is 200 m^3/h. Causing the high flow rates the CO_2 activation inside of the plasma source has to perform at atmospheric pressure [5].

The gas supply of the reactor can handle five different gases simultaneously. Besides Carbon Dioxide during all experiments also Argon, Methane, Hydrogen, Ethene, Nitrogen, and Butadiene were used as reaction partners to enforce chemical conversions in the reaction tube. The gas inlets could be switched between three positions: before the plasma source (complete activation of reaction partners), directly after the plasma source (partial activation and additional cooling) or in reaction tube (partial activation and first reaction partner contact near the catalysators). In reaction tube there is a possibility to place some catalysators. Causing the high temperatures only pure metals are useful established.

Inside of the reactor head a cooling system and the outlet for gas chromatic analysis is realised.

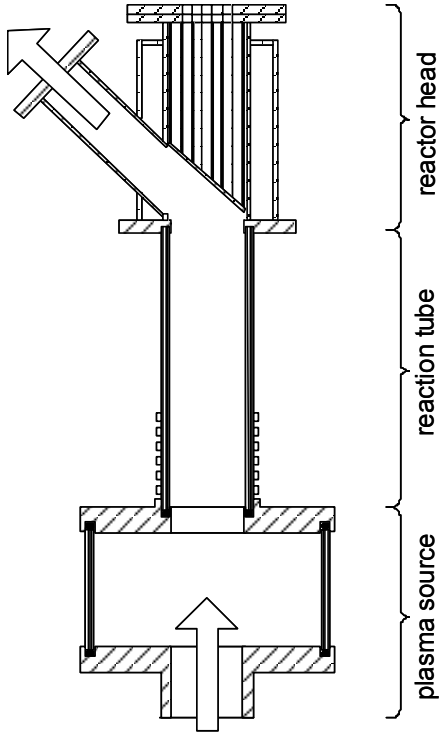

figure 1: plasma synthesis reactor

The measurement of plasma emission was possible at the plasma source and at the beginning of the reaction tube. All here represented spectroscopic measurements were performed only at the plasma source. For better realisation of imaging spectroscopy the ring of plasma source was modified with parallel arranged holes (fig.2). The emitting light is forming parallel light beams between plasma source and imaging spectrometer.

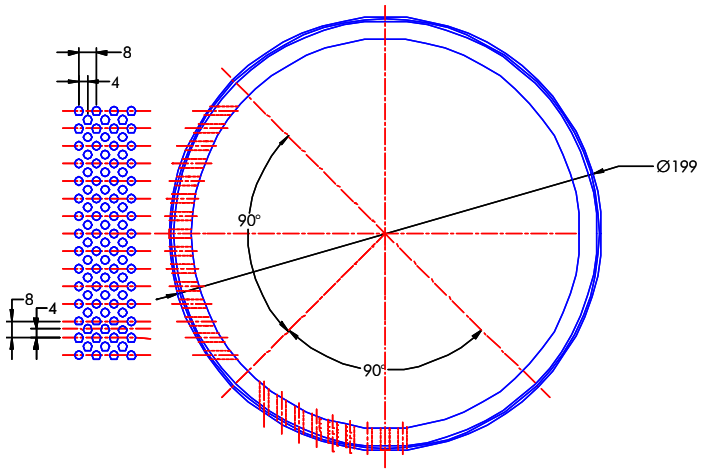

figure 2: preparation of plasma source ring for imaging spectroscopic diagnostics

Acoustooptic Imaging Spectroscopy

Through exploitation of the two-dimensional aperture of the AO spectrometer, it becomes to prosecute possibly imaging spectroscopy. Similar applications are already known for the NIR and IR range. The use in UV/VIS range demands special requests to all components of the AO spectrometer, e.g. the radio frequency driver, the AO crystal and the belonging optical components. To use a quartz crystal in UV/VIS range a particular adaptation is necessary [3].

The resonance condition for the diffraction of the light wave depends strongly on the angles of the propagation direction of the light wave and the propagation direction of the ultrasound wave as well as the crystal orientation [2]. The incoming linear polarised light beam is diffracted into two partial beams: **n**ot tuned **o**rdinary (NO – same polarisation, broad band light) and **t**uned **o**rdinary (TO – vertical rotated polarisation, narrow band light at resonance wavelength). In case of divergent light complies the resonance condition at different places in the crystal with same ultrasound frequency for different wavelengths. The reproduction of a single wavelength image can take place only deficiently. Therefore, divergence and dispersion of the ray of light must be as small as possible in the entire spectral range. This demands high requests at all optical components. In and out coupling objectives are achromatically (non disperse) and from high quality. An accurate mapping of approximately 150x300 pixels can be guaranteed with in the spectral range from 400 nm till 800 nm. The transmission wavelength bandwidth has excellent 0.5nm in the near infrared at 800nm, and 0.15nm in the near UV at 400nm, respectively. The millisecond random wavelength access of the AO spectrometer system is seen as an essential benefit against commonly used interference filter technology. The sampling time for a single wavelength image is 120 milliseconds

As first result the measurements at continuous light emitters appear that the contrast (TO - to NO beam) which is precipitated of the final polariser is not enough, in order to extract the wavelength separated picture. The intensity of the TO beam consists of one small spectral range only, $T(\lambda)\approx 0$, besides $T(\lambda-\Delta\lambda<\lambda<\lambda+\Delta\lambda)>0$, and that of the NO beam of the entire spectral range:

$$\int i(\lambda)d\lambda = \int T(\lambda)i(\lambda)d\lambda + \int [1-T(\lambda)]i(\lambda)d\lambda$$

$$I_{ges} = I_{TO} + I_{NO}$$

The pictures of both partial beams are overlapping, because the integral intensity is approximately equal at continuous light sources. In the present arrangement (fig.3), the TO beam possesses an diffraction angle of approximately 2° to the NO beam. Therefore, an optical diaphragm system is brought in here to suppress the disturbing NO beam additionally.

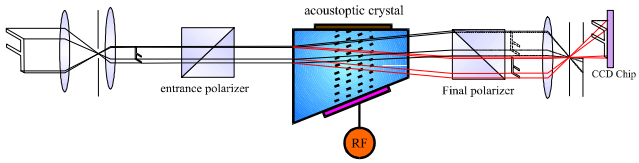

figure 3: optical arrangement of imaging spectrometer

Results

Optical Emission Spectroscopy

At atmospheric pressure there were found following specimen in emission spectrum (fig.4): C, C_2, C_3, C_4, O, H, OH and CH [6,7].

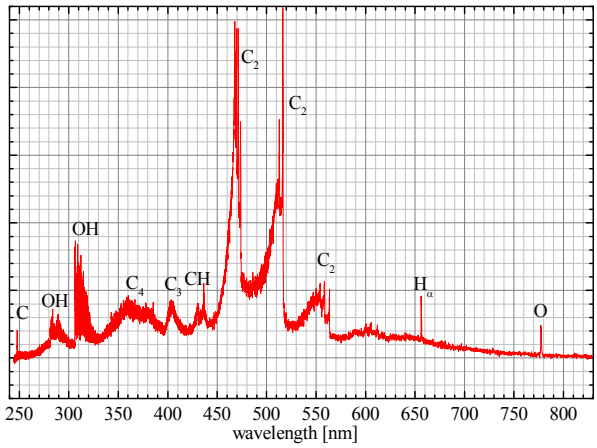

figure 4: typical emission spectrum of CO_2 activation at atmospheric pressure adding Hydrogen containing raw materials

A chance to get valuable products is the addition of natural gas to carbon dioxide to produce synthesis gas which is a gas mixture of hydrogen and Carbon Monoxide:

$$CH_4 \Leftrightarrow C + 2H_2 \qquad +84\ kJ/mole$$

$$CO_2 \Leftrightarrow C + O_2 \qquad +406\ kJ/mole$$

$$2C + O_2 \Leftrightarrow 2CO \qquad -246\ kJ/mole$$

$$CH_4 + CO_2 \Leftrightarrow 2CO + 2H_2 \qquad +244\ kJ/mol$$

In this reaction system the formation of soot and water can also be observed. These side products decrease the conversion rates and the yield of synthesis gas strongly and are strongly to be avoided. In case of oversupplying Hydrogen this effect is increasing and it is visible in emission spectrum by increase of the OH bands in UV at 280 nm to 330 nm. To produce

stoichiometric synthesis gas the hydrogen content should be reduced. In this case the disturbing OH bands are missing (fig. 5).

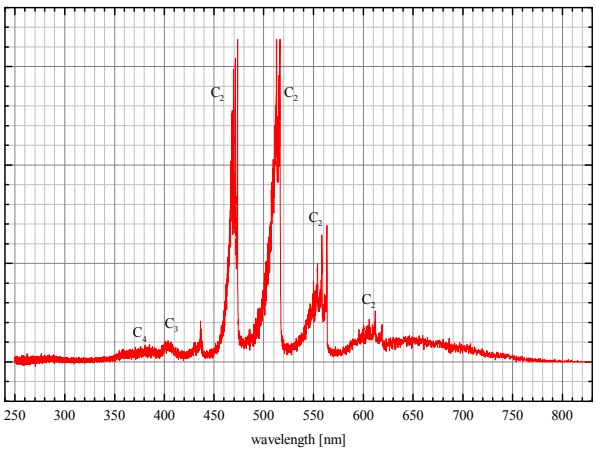

figure 5: typical spectrum of synthesis gas production at atmospheric pressure

Imaging Spectroscopy

During the experiments with natural gas ($Ar/CO_2/CH_4$-mixture) the emissions of Oxygen (777.3 nm), C_2 (516.5 nm) and the H_α-line (656.2nm) were investigated. The plasma volume was observed through the hole mask in plasma source ring (fig.6).

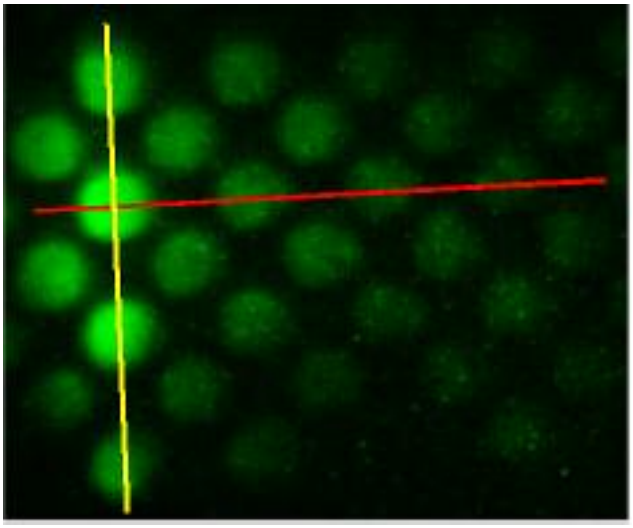

figure 6: spatial distribution of the C_2 band head emission at 516.4nm through the hole mask of the plasma source

The mathematical interpretation of following results was done in radial direction (redline in fig. 6) and in main stream direction (yellow line in fig.6). Firstly a three dimensional visualization with mathematical diameter correction was enforced.

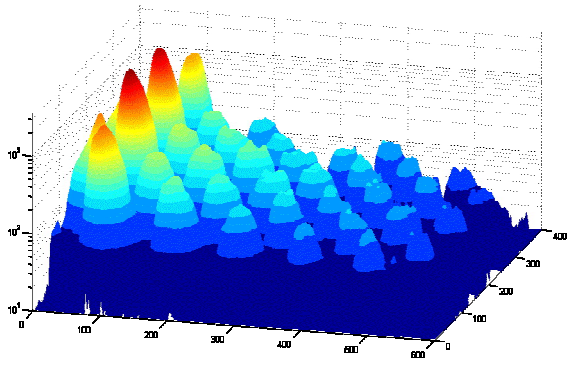

figure 7: intensity distribution of the O-Triplets during the Methan experiments

The radial specimen distribution shows an essentially smaller inhomogeneity, as which of the gone ahead pure CO_2 activation experiments (fig.8). This circumstance improves the efficiency of the entire system so.

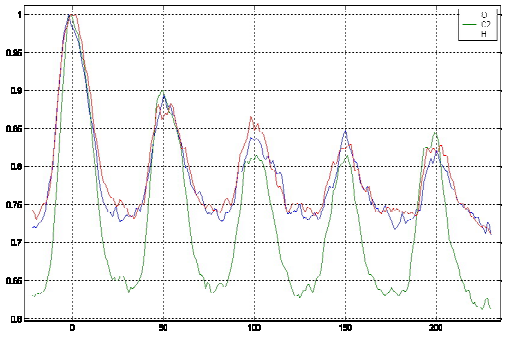

figure 8: radial distribution of exited specimen

The behaviour of Hydrogen and Oxygen in main stream direction is quiet similar. This results from the fact that both atoms can decompose relatively easy. (binding energy: C-H: 3.5EV; OC-O: 5.5eV). Atomic carbon is set free in both cases (CH_4, CO_2), only in a second step and isn't available immediately for the recombination to C_2. Therefore the emission of the C_2 start more slowly than the emission of H and O at the source entrance (fig.9).

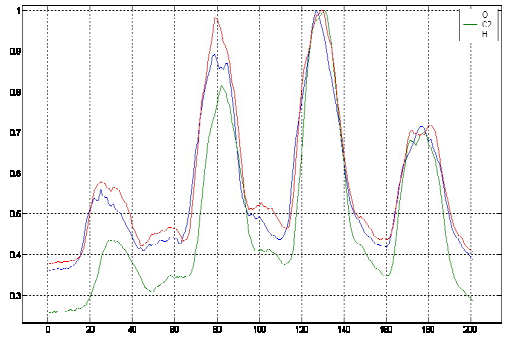

figure 9: distribution in main stream direction of exited specimen

Clear postponements of the maximum C_2 Excitation appears through variation of the gas composition. With low argon content, one finds circumstances the pure CO_2 activation similarly. An increase of the argon content leads to one noticeable shift of the stimulation-maximum to the stream exit and can be used with it as optimisation value (fig.10).

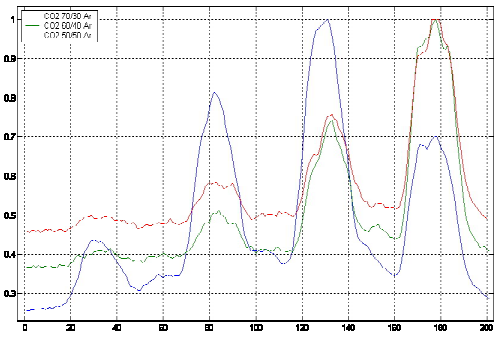

figure 10: distribution of C_2-emissions in main stream direction at different streaming conditions

The argon content a drastic influence to the radial distribution of the C_2 emission. An inferior Ar content leads here to better homogeneity (fig.11). These are best conditions for an upscaling to an industrial application without any Argon.

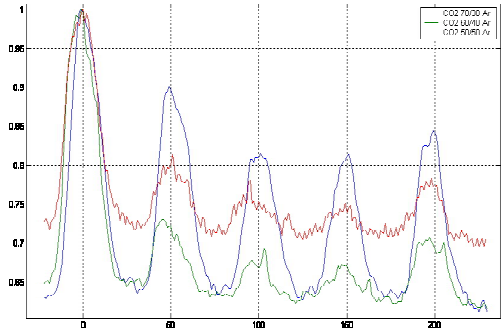

figure 11: radial distribution of C_2-emissions at different streaming conditions

Conclusion

The presented plasma activation of Carbon Dioxide adding Methane is able to produce synthesis gas, a 1:1 mixture of CO and H_2. The developed plasma synthesis reactor can handle up to 10 m^3/h gas flow.

Acoustooptic imaging spectroscopy is a useful method to investigate large area or volume plasma phenomena. The simultaneous capture of whole images at a single wavelength and the fast access to another wavelength allows a fast sampling of time and spatial resolved distributions of excited specimen in plasma volume.

In present work it was shown that CO_2 plasma activation for chemical synthesis can be optimised by imaging emission spectroscopy.

Acknowledgement

The financial support by the German Bundesministerium für Bildung und Forschung BMBF, project fund 13N7687/2 is gratefully acknowledged

References

[1] Kraus, M. ;Eliasson,B.; Wokaun,A.; Kogelschatz,U, *„CO_2 Reforming of methane by the combination of dielectric-barrier“*, Phys. Chem. Chem. Phys., 2001, 3, p. 294-300

[2] Aronson, L. B.; *„Electro-optic tuning and sidelobe control in acoust-optic filters”*, Optics Letters Vol. 20 (1995) No.1, S. 46-48

[3] V. Shogun, A. Tyablikov, E. Shelyhmanov, M. Abachev, W. Scharff, T. Wallendorf: *„Application of an acousto-optic spectrometer for plasma etching process quality control“*, Surf. Coat. Technol. 74-75 (1995) 571-574

[4] Potts, H.; Hugill, J; *„Studies of high-pressure, partially ionized plasma generated by 2.45GHz microwaves“*; Plasma Sources Sci. Techn. 9 (2000) 18-24

[5] Eliasson,B.; Kogelschatz,U., *Nonequilibrium Volume Plasma Chemical Processing*, IEEE Trans. Plasma Sci., 1991, 6, p. 1063-1077

[6] Pearse, R.W.B.; Gaydon, A.G.; *„The Identification of molecular spectra“*, 1963,Chapman & Hall LTD London,

[7] Lide, D. R.; „*Handbook of Chemistry and Physics“*;1995; CRC Press, 10-1 ff

Control of energy input at ignition of fuel-air mixtures by nanosecond discharge

S.A.Bozhenkov, E.I.Mintoussov, S.M.Starikovskaia, S.V.Pancheshnyi, A.Yu.Starikovskii

Physics of Nonequilibrium Systems Laboratory, Moscow Institute of Physics and Technology, Dolgoprudny Moscow Region, Russia

Abstract

The present work is devoted to the details of the energy input control in nanosecond discharge. The discharge is used for the ignition of hydrogen-air and methane-air mixtures in a temperature range of 800-2200 K. Gas mixture is heated by the shock wave. We represent results of the energy input measurements in the fast ionisation wave at different gas temperatures. Possibilities to decrease significantly the temperature threshold of the ignition using gas discharge are analysed.

1. Introduction

Process of combustion is described from the point of view of chemical kinetics as a chain mechanism. Chain propagation in a condition of high temperatures takes place at a high velocity. The slowest stage is the initiation of a chain which is often combined with increased activation energy. For this reason, the reaction rate is in fact higher with artificial chain initiation [1]. For example, for hydrogen-oxygen combustion at a pressure of 1 atm and temperature of 750 K reaction rate for the process $O_2+M=O+O+M$ is about of 10^{-40} cm^3/s, which is extremely low value. Reaction of the dissociation have an extremely high activation energy (59380 K for the mentioned reaction [2]), so, they become efficient at higher temperatures. In a region of low temperatures gas discharge low temperature nonequilibrium plasma can be used as an efficient source of the radicals for the chain reaction initiation.

In this paper, the homogeneous ignition method is discussed, which is fast in comparison with the characteristic times of combustion processes and gas dynamics. The method is based on the use of a nanosecond high-voltage discharge in the form of a fast ionization wave (FIW) producing atoms, radicals, and excited molecules. The fast ionization wave originates at very high – hundreds of percent – overvoltage on the electrode system, that is the case where the voltage, at the moment of the discharge initiation, significantly exceeds the threshold of the initiation of a stationary glow discharge. From the point of view of the experiment, this means a high rate of voltage rise: 1 kV/ns and higher. A typical pulse amplitude is tens - hundreds of kV and a duration is 10-100 ns. The most distinctive features of this type of discharge are the high propagation velocity (10^9-10^{10} cm/s), the good reproducibility of the discharge parameters, and the spatial homogeneity over a large gas volume. The fact that electric fields behind the discharge front are high enough and may be used for the gas dissociation is also of a great importance. These properties may be interesting for different applications, such as hypersonic combustion or the ignition of lean mixtures. A review of our papers concerning the kinetic approach to this discharge is given in [3].

2. Experiment

The apparatus used to investigate the fast homogeneous ignition of combustible mixtures (Figure1) consists of a shock tube (ShT), discharge cell (DC) connected to the shock tube, the gas evacuation and supply system, the system of discharge initiation, and the diagnostic system.

The shock tube is made of stainless steel and has a square cross section of 25x25 mm with a 1.6 m working channel length. The high pressure cell (HPC) length is 60 cm. There are 2 pairs of diagnostic optical windows along the stainless steel working channel. The windows were aligned with respect to inner shock tube walls and walls were polished to decrease disturbances of flow. The last section of the shock tube is made from a transparent dielectric material. We used two different sections in our experiments. The first one is made from a 10 mm thick quartz plates surrounded by an organic glass 20 mm in thickness and has twelve quartz optical windows for an emission output. The second one is made from an organic glass and has eight optical windows (6 of them are made from quartz and 2 are made from MgF_2). Both sections have 25x25 mm the inner square cross-section and are 20 cm in length. The results were the same for both sections, therefore we shall not specify which of sections was used. The uniform nanosecond discharge in the form of the fast ionization wave was organized in the dielectric section; the end plate (EP) of the shock tube is a high-voltage

electrode of the discharge system; the electric circuit is closed via grounded stainless steel driven section of the shock tube.

The nanosecond discharge initiation was synchronized with the reflected shock wave coming to the observation point (point A in the figure) by means of a microsecond pulse generator (PG). To obtain high-voltage pulse we used Marks-type generator. The GIN-9 high voltage Marks generator (HVG) consists of 10~stages. To provide the spark gap operation, the pulsed voltage generator is filled with nitrogen at a pressure of 3 atm, which provides a starting voltage range from 100 to 160 kV. To sharpen the voltage impulse coming from the generator to the discharge gap, a forming ferrite line of wave resistance Z=40 Ohm is used. At the forming line output, the voltage rise rate is 8 kV/ns, which provides the formation of gas discharge in the form of a fast ionization wave in the dielectric section of the shock tube.

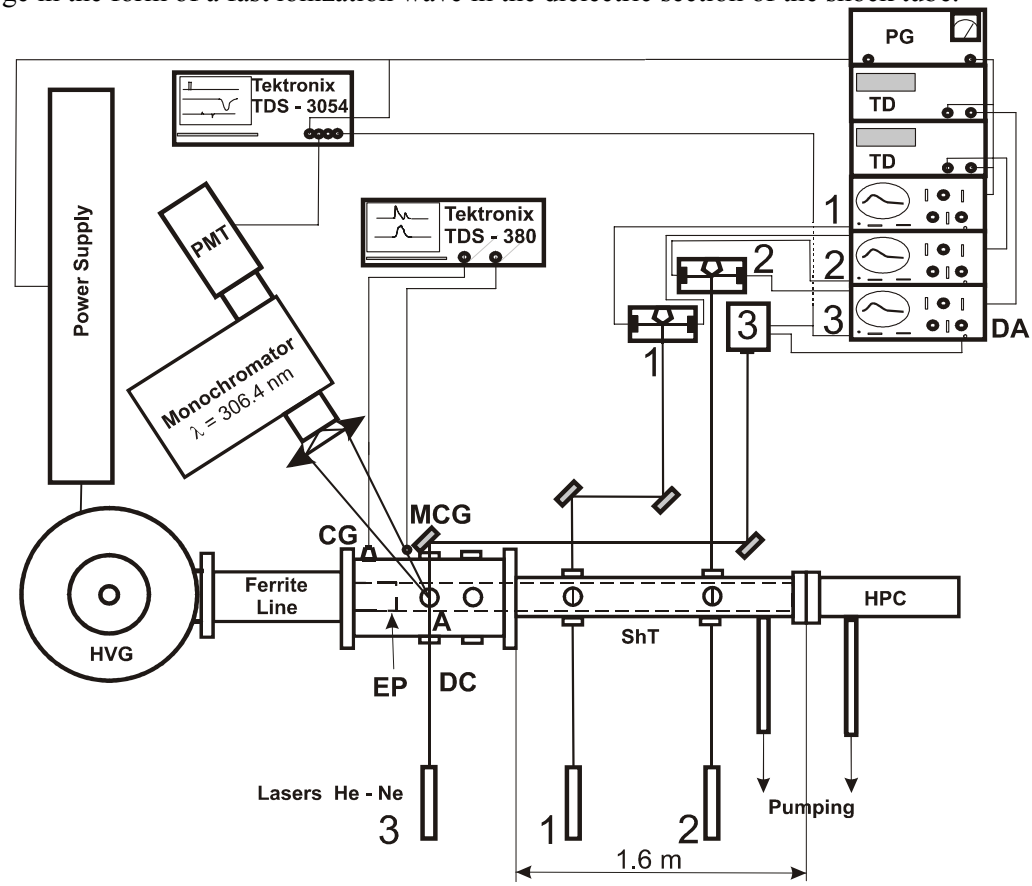

Figure 1. Experimental setup

To evacuate the system, rotary and diffusive pumps were used. Having been pumped the system was filled with investigated gas mixture. We used gas mixtures of methane or hydrogen with air or oxygen diluted with Ar or He in order to reach the desired pressure and temperature behind the reflected shock. The initial pressure in the driven section was varied from 5 to 40 Torr. Dilution by Ar or He increased the specific heat ratio, and allowed higher temperatures to be reached behind the reflected shock wave. He, dry air, or CO_2 were used as driver gases. In some experiments special perforated flow plate was inserted between high pressure section and driven section before the diaphragm. This plate allowed us to decrease the shock wave velocity at the same initial conditions.

Diagnostic system consists of three parts. They are the system monitoring shock wave parameters, the system monitoring the nanosecond discharge electrical parameters and the system registering ignition. The system monitoring the shock wave parameters includes the system measuring the incident and reflected shock wave velocity by the laser schlieren technique and the system controlling the initial pressure. The schlieren system consists of 3 He-Ne lasers mounted along the shock tube at different points and 3 pairs of photodiodes with differential analysers (DA); the time delays between points 2-1 and 1-3 along the tube were registered by time-delay analyzers (TD) and monitored by the Tektronix TDS3054 oscilloscope. From the initial gas mixture composition, the initial pressure and velocity of the incident shock wave, we determined the pressure, gas density and temperature behind the reflected shock wave by solving the conservation laws, assuming a full relaxation and no chemical reactions. Thermodynamic data were taken from [4].

The system monitoring the nanosecond discharge electrical parameters includes a calibrated magnetic current gauge (MCG) to control current pulse and a capacitance gauge (CG) over the high-voltage electrode to monitor the high-voltage pulse shape and amplitude. We placed an additional capacitive gauge near the observation point (12 cm apart from the CG) to measure the velocity of the discharge development. The signals from electrical gauges were monitored by using a Tektronix TDS~380 oscilloscope. All cables were additionally screened and oscilloscopes were placed into the shielded room to diminish high-frequency electrical noise.

The combustion process was investigated by using emission spectroscopy. Emission originating due to the combustion process was monitored in the direction perpendicular to the shock tube axis at a distance of 55 mm from the end plate (point A) with the use of a MDR-23 monochromator (1.2 nm/mm, 1.2 m focal length, 1200 1/mm, LOMO), a FEU-100 photomultiplier (MELZ), and a Tektronix TDS3054 oscilloscope. The observation point is rather far from the end plate. To decrease influence of boundary layers it is more usual for kinetic measurements to be made in the vicinity of end plate. However we had to choose position of the observation point in such way to avoid electric field disturbances caused by high voltage electrode. We measured the OH emission (306.4 nm) in a wide range of experimental conditions: mixtures of various compositions, temperature variations from 750 to 2250 K, pressure variations from 0.3 to 2.3 atm. The same experiments were repeated under a discharge action, at high-voltage pulse amplitude variations from 100 to 160 kV on the electrode and a pulse duration of about 30-40 ns at a half-height of an amplitude (FWHM). For all the cases, the ignition delay time τ_{ign} was determined as a time delay between the last physical action (that is, the reflected shock wave signal in a case of autoignition or the discharge initiation when the nanosecond discharge being used) and the start of OH emission. The ignition delay decreases under the action of the FIW. The operating time of our shock tube was about of t_{max} = 400-500 μs. In the figures we have represented all obtained points, even those for which ignition delay time $\tau_{ign}>t_{max}$, to give reference points for the comparison with the ignition by the nanosecond discharge.

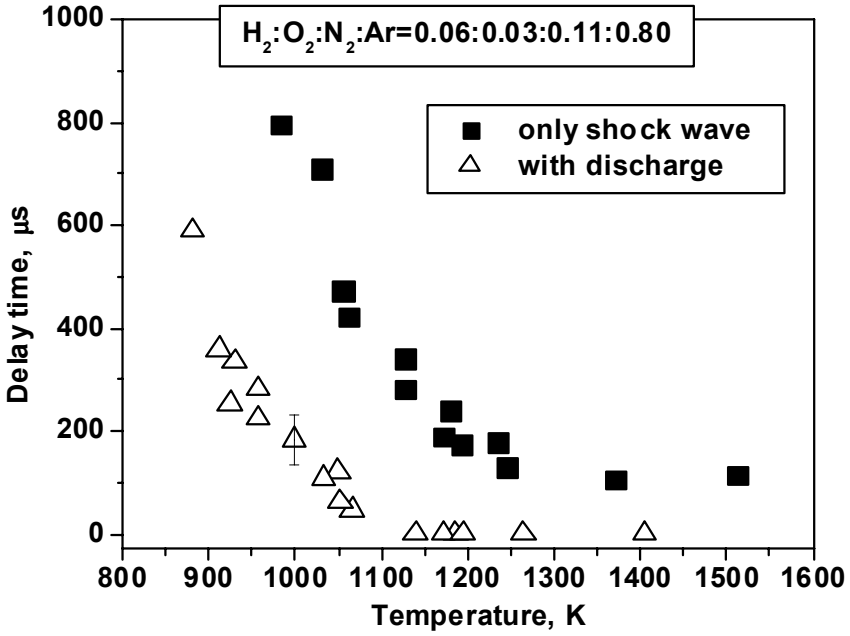

Figure 2. Ignition time delay *vs* temperature for hydrogen-air stoichiometric mixture diluted with Ar

It is very important to analyse the power input into plasma during the discharge. To do that we developed special technique based on the measurements of voltage signal in two adjacent points along the discharge cell together with the current signal. All signal are registered synchronously with the time resolution of 2 ns. To obtain the total energy input, the integration by time takes place.

3. Results of the experiment. Ignition delay.

We determined the dependence of ignition delay upon the temperature at fixed voltage U=160 kV. The measured time delays of the ignition of the H_2-air-Ar mixture are shown in Figure 2. The decrease in time delay for ignition under the action of plasma and the decrease of the temperature threshold (minimum temperature where the ignition is possible) are clearly seen. For example, at T=1000 K, the energy input in

the discharge decreases the ignition delay time by a factor of 4.8, from 860 to 140 μs. It should be noted that in this figure and in the next figures devoted to the experimentally measured ignition delay, zero delay time means some conventional value. We were not able to measure delay time less than 2 μs, which actually gives the typical duration of the electrical noise from the discharge. The numerical analysis of the ignition delay time and comparison with the experiment is described in [5].

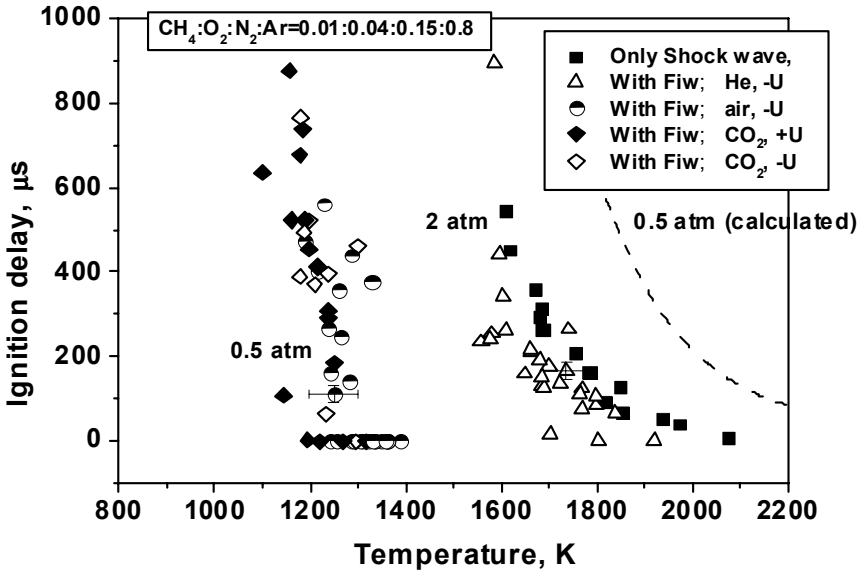

Figure 3. Ignition time delay *vs* temperature for methane-air stoichiometric mixture diluted with Ar

We observed the same tendency for ignition delay for methane-air mixture (Figure 3). He, air or CO_2 were used as high pressure chamber gases, and this is indicated in the Figure. The ignition delay time changes dramatically under the action of the discharge. We were able to provide the ignition of highly diluted methane-air mixture at a pressure of 0.3-0.5 atm and a temperature of 1100-1200 K. The dashed line on the right represents calculated autoignition delay time for the initial pressure of 0.5 atm, it was impossible to get these parameters in our experiments.

3. Results of the experiment. Energy input.

From the Figure 3 it is clear that for the initial pressure of 2 atm and initial temperature within the range of 1600-1900 K the shift in the ignition delay is relatively low. At the same time experiments at a pressure of 0.5 atm demonstrate significant (about of 700 K) shift in the ignition threshold.

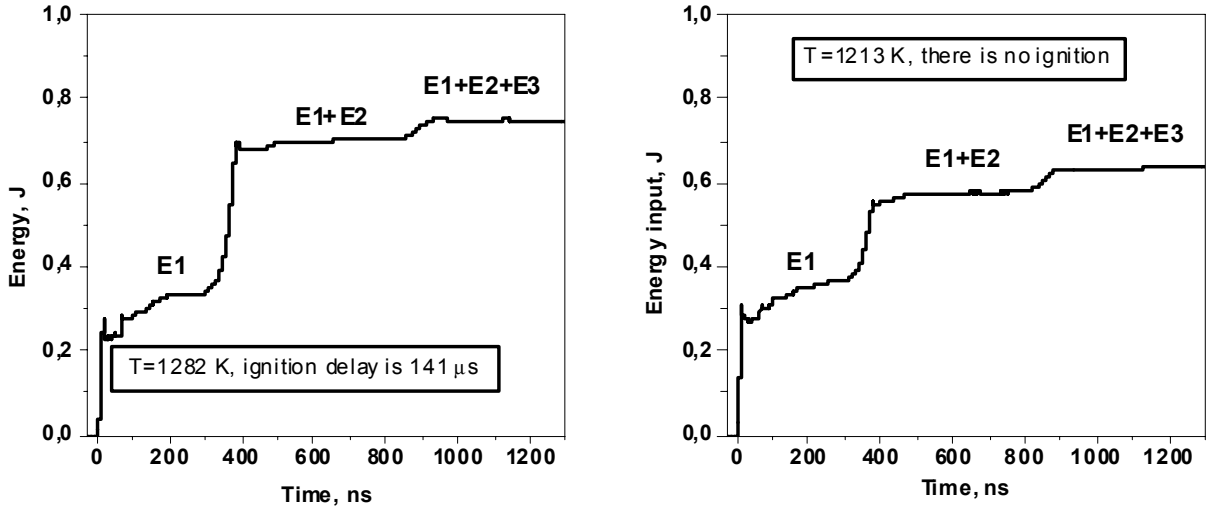

Figure 4. Typical energy input into plasma of the discharge *vs* time

To understand the reason we analysed the energy input into the plasma under the action of a nanosecond high-voltage discharge. All experiments were performed for the mixture mentioned in the Figure 3. Typical energy input in the experiment *vs* time is represented in the Figure 4. We obtained one or two pulses reflecting form the high-voltage generator and coming back to the discharge cell, so, the total energy input consisted of three separated in time portions: the first one, marked as E1 in the Figure, and one or two from reflected pulses, E2 and E3 respectively. It is interesting that the energy input in experiments with ignition is practically the same as in the experiments without ignition.

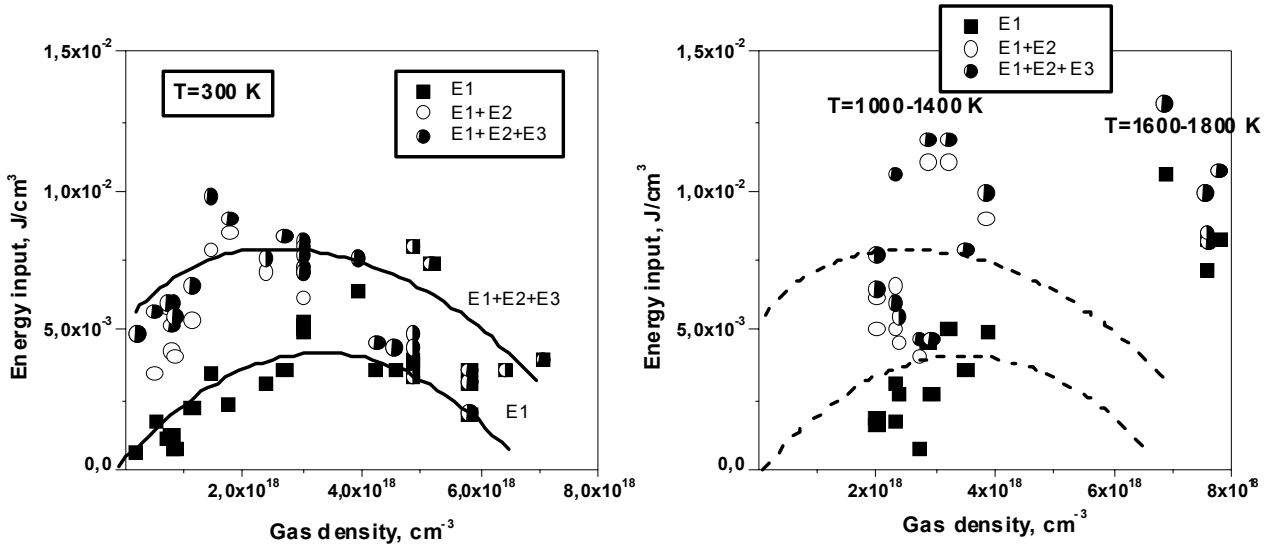

Figure 5. The energy input *vs* gas density. Comparison of the energy input at ambient and high temperature

We compared the energy input at ambient temperature and at combustion temperatures in the same methane-air mixture diluted with argon. The results are represented in the Figure 5, "cold" experiments in the left graph, and high temperature experiments in the right one. As for the "cold" experiments, the behavior of the energy input dependence upon the gas density is qualitatively the same is in well-known experiments on the energy input in repetitive high-voltage nanosecond discharge (see, for example, [6]). From these experiments it is known that the nanosecond discharge propagates uniformly in space within the region of this cupola-shape dependence. With the density increase discharge loses its uniformity and transforms to a streamer corona.

At the high temperatures we obtain practically the same values of the energy input at given gas density. The only difference is the strong data scattering for the E2 and E3 (that is for the energy input in reflected pulses).

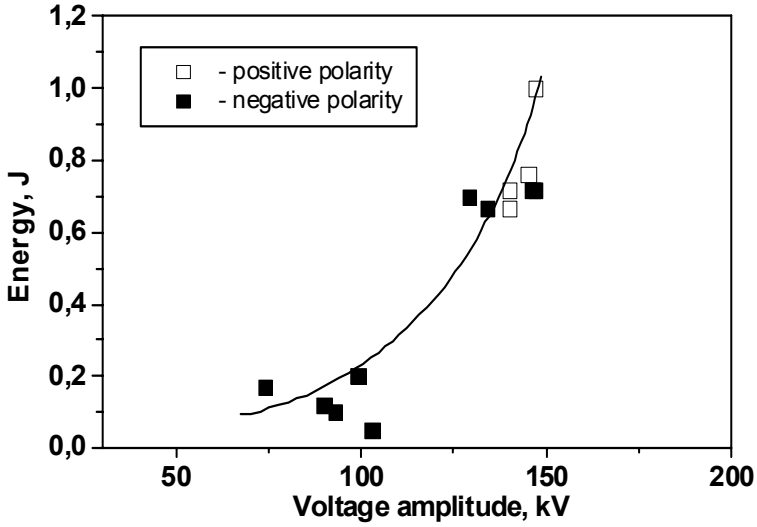

Figure 6. The energy input *vs* voltage amplitude on the high-voltage electrode

We used different voltage amplitudes of the high-voltage pulse to initiate the discharge, and total energy input upon the voltage peak value on the high-voltage electrode is represented in the Figure 6. The gas parameters are the following: gas number density is (2-3)x10^{18} cm^{-3}, temperature is 1000-1400 K. In spite of the fact that we have difference of the order of magnitude between the energy input in the discharge all this experiments have not dramatic difference in the ignition delay time dependence upon pressure. To understand this fact we have to analyse the dynamics of voltage and current in the discharge cell to make a conclusion about electric field value and efficiency of radicals production.
In part, coming back to the Figure 5, it was possible to conclude from such an analysis, that at high pressure (and, consequently, at relatively high gas densities) we have not nanosecond uniform discharge. We have made the detailed analysis of results which correspond to the group of points T=1600-1800 K. Oscillograms of the current and voltage rather fit to those in the nanosecond pulsed corona. So, we concluded that, even higher initial energy input for the temperature range of 1600-1800 K does not lead to significant shift in ignition delay time because of too gas high densities for the uniform nanosecond discharge development at given experimental conditions. To decrease the ignition delay significantly under those experimental conditions it is necessary, for example, to increase the amplitude of the high voltage pulse.

5. Acknowledgements

This work was partially supported under grants No. 01-02-17785, 02-03-33376, and 02-02-99305 of the Russian Foundation for Basic Research; Projects No.1474 and No1440 of International Science and Technology Center; grant YSF 2001/1-138 of INTAS; and by Award No. MO-011-0 of the U.S. Civilian Research and Development Foundation (CRDF).

6. Conclusions

So, the experimental scheme for testing the ignition delay time under the successive action of a shock wave and a nanosecond discharge is described. The shift in the ignition time delay is obtained experimentally for hydrogen-air and methane-air stoichiometric mixtures diluted with Ar.
Energy input into a gas due to the action of nanosecond gas discharge is analysed for the ambient gas temperature and for the temperature range of 1000-1800 K for the methane-air-argon mixture. It was demonstrated that such an analysis provides additional tools to analyse and to optimise the ignition by pulsed nanosecond discharge.

References

[1] T.O. See You, N. Ext June, I.N. Taormina - We. Hope. You. Enjoy. **22**, 6 (2003).
[1] N.N.Semenov. “Some problems relating to chain reactions and to the theory of combustion” – Nobel prize lecture (1956).
[2] S.M.Starikovskaia, N.B.Anikin, S.V.Pancheshnyi, D.V.Zatsepin, A.Yu.Starikovskii. – Plasma Sources Sci. Technol. **10**, 344 (2001).
[3] S.A.Losev – in: Chemistry of Plasma (B.M.Smirnov, ed.) – Atomizdat Press, **14**, 1 (1987).
[4] V.P.Glushko (ed.) – Thermodynamical properties of individual species. M: Nauka Publ. (1978)
[5] S.A.Bozhenkov, S.M.Starikovskaia, A.Yu.Starikovskii - 16th European Conference on Atomic and Molecular Physics af Ionized Gases. 14-18 July 2002, Grenoble, France. **1**, 131, (2002).
[6] S.M.Starikovskaia, N.B.Anikin, S.V.Pancheshnyi, A.Yu.Starikovskii – in: “Selected Research Papers on Spectroscopy of Nonequilibrium Plasma at Elevated Pressures” (Ochkin, V.N., ed.) – Proc. of SPIE **4460**, 63 (2002).

Inhomogeneous Burgers equation as a model of fluctuations in electric arcs

É. Moreau, O. Vallée & C. de Izarra

LASEP *: Laboratoire d'Analyse Spectroscopique et d'Energétique des Plasmas*
Faculté des Sciences, Site de Bourges Université d'Orléans, rue Gaston Berger BP 4043
18028 Bourges cedex France

Abstract

The purpose of this paper is to describe a relatively unused approach in plasma physics, but which allows to apprehend fluctuations and turbulence phenomena in electric arcs. The Burgers equation is considered as a simplified model of the Navier-Stokes equation to treat fluctuations of a velocity field plunged in a fluctuating field of strength. This point of view arises as an alternative method to numerical simulations.

1 Introduction

In 1939, J.M.Burgers introduced his famous equation (see [1]) which turned out to be an useful model in many fields of physics : growth of interfaces, driven diffusion, flame fronts or directed polymers [2, 3] ...

The first idea of this equation was to progress in the comprehension of turbulent flows. As we will see later, Burgers equation contains several similarities with the Navier-Stokes equation, and this will allow the description of a velocity field in time and space. This way of using the Burgers equation, relatively unused in comparison to fluid equations for numerical simulations, is the starting point of our approach. One of the reason leading to the present study is the rather small time necessary to obtain results in comparison to the time of computation. Among the most comprehensive codes treating electric arcs, we can underline the ESTET 3.4 CFD code developed by Delalondre & al.[4, 5]. Some important results have been found from this numerical computations of about 100 hours of CRAY computer corresponding to 0.01 second of real time. This comes from the fact that, in magnetohydrodynamic model (MHD), many Partial Derivative Equations (PDE) have to be taken into account, and this is in this context that arises our approach, which should allow to simplify calculations while treating fluctuation problems.

The paper is built as follow : in the next section, generalities about the Burgers equation are presented. The treatment of fluctuation problems is described in the third section. Then a conclusion will resume the mains ideas and will give a survey to the continuation of this work.

2 The Burgers equation

The initial value problem of the Burgers equation for the velocity field u is presented in the following form :

$$\left| \begin{array}{l} \partial_t \mathbf{u} + (\mathbf{u}.\nabla)\mathbf{u} - \nu\ \nabla^2\mathbf{u} = \mathbf{f}(\mathbf{r},t) \\ \mathbf{u}(\mathbf{r},0) = \varphi(\mathbf{r}) \end{array} \right. \tag{1}$$

with an evolution term $\partial_t u$, an advective term $(u.\nabla)u$, a diffusive term $\nu\ \nabla^2 u$, $\mathbf{f}(\mathbf{r},t)$ a the term of forces, and where ν stands for the viscosity.

So we use this equation as a simplified model of Navier-Stokes equation, where the term of force represents all forces which are linkable to fluctuations : it can be as well a pressure gradient than exterior force or Maxwell term (Laplace force). This is a non linear diffusion equation, where no-linearitie can be evaluate, as for Navier-Stokes equation, by the way of the Reynolds number Re, which is proportional to $1/\nu$. However, on the contrary to shock models, the diffusive term does not have to be neglected, because turbulence does not appear only in the inviscid limit $\nu \to 0$. So we have an equation which is closely related to Navier-Stokes equations.

We use now the well known Hopf-Cole transformation (HC) [6] from which the Burgers equation may be transformed into a linear PDE :

$$\mathbf{u}(\mathbf{r},t) = -2\nu \frac{1}{\psi(\mathbf{r},t)} \nabla\psi(\mathbf{r},t). \tag{2}$$

This leads to the heat equation with a source term, which is easier to handle than the Burgers equation.

3 Analytic resolution of a fluctuation problem

We present here the analytical resolution of the Burgers equation for two different terms of force. First we examine the case of a constant force as a random variable, where we show that we obtain the result in term of Airy functions. Then the case of a time dependent force is studied, by the way of two equivalent methods. We restrict the solution to this problem to one dimension.

3.1 Constant force

Let us consider the following Burgers equation with a constant force

$$\left| \begin{array}{l} \partial_t u + u\partial_x u - \nu\ \partial_{xx} u = f \\ u(x,0) = \varphi(x) \end{array} \right. \tag{3}$$

where f is a random variable which represents for example the effect of the electric field. It means that for one realisation of f we have one solution u_f obeying the previous equation.

At all events, the HC transformation leads to the heat equation with a linear source term proportional to x :

$$\partial_t \psi(x,t) = \nu\ \partial_{xx}\psi(x,t) - \frac{fx}{2\nu}\psi(x,t). \tag{4}$$

This equation being linear with respect to ψ, it can be solved by a variable separation method such as $\psi(x,t) = \Phi(t)\theta(x)$. From this, the analytic expression of the velocity field $u(x,t)$ can be obtained. We first have :

$$\frac{\dot{\Phi}(t)}{\Phi(t)} = \nu \frac{\theta''(x)}{\theta(x)} - \frac{fx}{2\nu}; \tag{5}$$

where the dot indicates the derivative with respect to t, and the prime $'$ the derivative with respect to x. Then, for the time variable we find $\Phi(t) = e^{rt}$ and for the space variable, we recognize the Airy differential equation :

$$\theta'' - \frac{f}{2\nu^2}\left(x + \frac{2\nu r}{f}\right)\theta = 0. \tag{6}$$

The solution is found by putting $X = \left(\frac{f}{2\nu^2}\right)^{1/3}(x + \frac{2\nu r}{f})$,

$$\theta(X) = a_1 Ai(X) + a_2 Bi(X). \tag{7}$$

But $Bi(X) \to \infty$ as $X \to \infty$, then we would have $u \to \infty$, so we get $a_2 = 0$. Thus the solution of (4) now reads

$$\psi_f(x,t) = a_1 e^{rt} Ai\left[\left(\frac{f}{2\nu^2}\right)^{1/3}\left(x + \frac{2\nu r}{f}\right)\right]. \tag{8}$$

However, this solution leads to a stationary solution for the velocity field u, but we can avoid this situation by developing $\psi_f(x,t)$ on the Airy functions basis [7], with the conditions :

$$\psi(0,t) = 0 \quad \text{and} \quad \lim_{x\to+\infty} \psi(x,t) = 0\ .$$

Then we choose r such as $\left(\frac{f}{2\nu^2}\right)^{1/3}\frac{2\nu r}{f}$, is a zero of the Airy function. Noting Ω the countable set of values taken by r, we obtain successively :

$$\psi_f = \sum_{\Omega} \Phi_r(t)\theta_{r,f}(x) = \sum_{\Omega} a_r e^{rt} Ai[X_{r,f}] \; ; \tag{9}$$

and :

$$u_f = -2\nu \frac{\sum_{\Omega} a_r \left(\partial_x X_{r,f}\right) e^{rt} Ai'[X_{r,f}]}{\sum_{\Omega} a_r e^{rt} Ai[X_{r,f}]} \; . \tag{10}$$

Then, since $u_f(x,t)$ is the fluctuating quantity, we are able to compute mean quantities as :

$$\begin{array}{l} \langle u(x,t)\rangle_f \\ \langle u(x,t)u(x',t')\rangle_f, \; \ldots \\ \langle \partial_x u(x,t)\rangle_f \end{array} \tag{11}$$

These quantities appear in particular in the $k-\epsilon$ model, via the diffusion turbulent term, the viscous dissipation term,... This resolution is treatable in three dimensions.

3.2 Time-dependent force

Fluctuations may arise also under the action of a random force, such as Langevin force, and taking the form of a time-dependent function in the Burgers equation :

$$\left| \begin{array}{l} \partial_t u + u\partial_x u - \nu \, \partial_{xx} u = f(t) \\ u(x,0) = \varphi(x) \end{array} \right. \tag{12}$$

An interesting theorerical result resides in the possibility of solving analytically this equation by two different methods.

Time Space Transformation method : The Time Space Transformation method (TST) have been used to solve the Schrödinger equation with a linear potential [8]. Now, the HC transformation applied to (12) leads to :

$$\partial_t \psi = \nu \, \partial_{xx}\psi - \frac{1}{2\nu}\big[x f(t) + c(t)\big]\psi, \tag{13}$$

which is nothing but a Schrödinger equation with an imaginary time, and with a linear potential. Then, the TST method for (13) is composed by a transformation of the form

$$\psi(x,t) = \Phi(y,t) e^{x \int f(t)\mathrm{d}t}, \tag{14}$$

followed by the shifting of variables

$$\mathrm{TST} \left| \begin{array}{l} y = x + \iint f(t)\mathrm{d}t \\ t' = t \end{array} \right. \tag{15}$$

Just notice that in the case of a Langevin force, the term $\int f(t)\mathrm{d}t$ has to be taken either from the Itô point of view, or from the Stratonovich's one.[10]

From these transformations, we arrive to a well known heat equation :

$$\partial_{t'} \Phi(y,t') = \nu \, \partial_{yy} \Phi(y,t'). \tag{16}$$

Thus, from a given initial condition and inverting the latest transformations according to :

$$\Phi(y,t') \rightarrow \Phi(x,t) \rightarrow \psi(x,t) \rightarrow u(x,t), \tag{17}$$

we can express analytically the velocity field. We can also note that the solution is only defined when we have imposed an initial condition.

The Orlowsky-Sobczyk method (OS) This method [9] enable to proceed directly from an inhomogeneous Burgers equation with a force term $f(t)$, to an homogeneous Burgers equation. Then the Hopf-Cole transformation yields to the heat equation.

Let us start again with the equation :

$$\left| \begin{array}{l} \partial_t u + u\partial_x u - \nu\, \partial_{xx} u = f(t) \\ u(x,0) = \varphi(x) \end{array} \right. \tag{18}$$

The OS method will consist on to carry out the following shifting of variables :

$$\mathrm{OS} \left| \begin{array}{l} y = x - \iint f(t)\mathrm{d}t \\ t' = t \\ v(y,t') = u(x,t) - \int f(t)\mathrm{d}t \end{array} \right. \tag{19}$$

where $v(y,t')$ is the new velocity. These transformations lead to

$$\partial_{t'} v + v\partial_y v - \nu\, \partial_{yy} v = 0. \tag{20}$$

The expected equation is then obtained from the HC transformation. We arrive as for TST method to the heat equation

$$\partial_{t'} \Phi(y,t') = \nu\, \partial_{yy} \Phi(y,t'). \tag{21}$$

Giving us an initial condition, we go up to the analytic expression of the velocity field according this time to :

$$\Phi(y,t') \rightarrow v(y,t') \rightarrow v(x,t) \rightarrow u(x,t)\ . \tag{22}$$

The two latest methods (TST and OS) can be compiled by the following commutative diagram, where IBE means the Inhomogeneous Burgers Equation, HBE the Homogeneous Burgers Equation and $Heat - S$ the heat equation with a source term.

$$\begin{array}{ccc} IBE : f(t) & \xrightarrow{OS} & HBE \\ {\scriptstyle HC}\downarrow & & \downarrow{\scriptstyle HC} \\ Heat - S & \xrightarrow[TST]{} & Heat \end{array}$$

FIG. 1 – Commutative diagram showing the equivalence between the two methods.

4 Conclusion

We have shown that the analytical solution of Burgers equation allows the treatment of fluctuations. We started from the inhomogeneous Burgers equation presenting the same non-linearities as the Navier-Stokes equation. From this, two axes have been developed :

(i) From a mathematical point of view, we have seen the possibility to simplify the Burgers equation (into the heat equation with a source term) and solving it for particular values of the force. The complete solution depends narrowly on the form of this term. For a time dependent force $f(t)$, we have obtained the heat equation by two methods (Eq. (16) and (21)). These methods have been then gathered into a commutative diagram.

(ii) These results have led to the study of fluctuations, by mean of appropriate terms. Naturally, the resolution of the Burgers equation, by the nature itself of this equation, allows the study of fluctuations of a velocity field when the system is plunged into a fluctuating field of force.

An interesting work would consist now on studying the case of an elastic force in order to treat the trajectory of an arc column. The calculations are under way and should be achieved soon.

Références

[1] J. M. BURGERS, *The non linear diffusion equation* (Reidel, Boston, 1974).

[2] E. MEDINA, T. HWA & M. KARDAR, Phys. Rev. A, **55**, 2924 (1985), And all included references.

[3] -U. FRISCH, & J. BEC, arXiv :nlin.CD/0012033 (2001)
-*Les Houches 2000 : New Trends in Turbulence* M. Lesieur, ed. Springer **EDP**-Sciences.

[4] C. DELALONDRE & AL, EDF report, **HE-44/99/020A**.

[5] C. DELALONDRE & AL, Proceeding of the 14^{th} ISPC Vol.1 (321-326) (1999).

[6] E. HOPF : Commun. Pure Appl. Math. **3**, 201-212 (1950).
J.D. Cole : Q. Appl. Math. **9**, 225-232 (1951).

[7] O. VALLÉE & M. SOARES, *Les fonctions d'Airy pour la physique*, Ed. Diderot (1998).

[8] M. FENG, Phys. Rev. A, **64**, 034101 (2001) , and references therein.

[9] H. J. WOSPAKRIK & F. P. ZEN, arXiv : solv-int/9812014 v1 (1998).

[10] H. RISKEN, *The Fokker-Planck equation, second edition*, Spinger (1989).

Theoretical and experimental investigation of the component content of active particles generated by barrier discharge in dry and wet air in the remote chamber

I.A. Soloshenko[1], V.V. Tsiolko[1], V.Yu. Bazhenov[1], A.G. Terentyeva[1], A.I. Shchedrin[1], A.V. Ryabtsev[1], A.I. Kuzmichev[2]

[1]*Dept. Gas Electronics, Institute of Physics of National Academy of Sciences of Ukraine, Kiev, Ukraine*
[2]*Dept. Electron Device, National Technical University of Ukraine "Kiev Polytechnical Institute", Kiev, Ukraine*

Abstract
In the present work detailed theoretical and experimental studies of the plasma-chemical reactor, which consists of two parts: 1) generator of active particles based on volume barrier discharges; 2) work chamber, are accomplished for widely used plasma generating medium – dry and wet air. It is shown that the essential amount of active molecules, such as O_3, H_2O_2, N_2O_5, HNO_3, HNO_2, NO_3, is possible in work chamber volume with concentrations depending on flow rate and water vapor percentage.

1. Introduction

In the last ten years nonthermal discharges at one atmosphere pressure find more and more applications in the technology. Particularly, possibilities of the use of corona and barrier discharges for efficient cleaning of industrial gases from nitrogen oxides NO_x and N_xO_y, sterilization of medical articles, in modification of surface features of polymer materials and chemical warfare agent decontamination were demonstrated. For solving the last three tasks the most optimal is the use of plasma-chemical reactor, which consists of two parts: 1) generator of active particles based on one or several discharges; 2) – work chamber with relatively big volume containing articles or materials to be processed. Such design enables elimination of the influence of processed articles on the discharge operation regime and, consequently, on the component content of active particles.

Purpose of the present work consists in theoretical and experimental investigation of the component content and concentration of active particles in work chamber of developed by us reactor of the type mentioned above at the use of ambient air with various humidity as working medium. Calculations were performed both for the discharge gap, where formation and decomposition of radicals and molecules occurred under action of electrons, and for the chamber, where only chemical reactions between the particles formed in the discharge took place.

2. Experimental setup and methods of measurements

Generation of active particles was performed in sixteen volume barrier discharges placed evenly on top wall of work chamber made of polymethylmethacrylate with 80 liters volume (430x430x430 mm). Internal chamber walls were covered by glass plates for diminishing losses of active particles. The active particles formed in the discharges came to the chamber, where articles to be processed were placed, and then left the chamber via the system of filters through the hole placed in a center of the chamber bottom plane. Air was supplied to the discharges via the system for moistening/desiccation, which enabled relative humidity (RH) variation in 20-90% range at temperature 20-22^{0}C. Volume rate of air purge could be adjusted in range 1-8 l/min (at that transient time of working medium in barrier discharge volume changed in range 5÷0.6 s, and linear velocity of particles at entrance to the chamber – in range 1.5÷12 cm/s). For performing optical measurements of the component content windows made of KU-1 quartz were placed at side walls of the chamber at distances of 65, 215 and 365 mm from top chamber wall. For powering the discharges high-voltage AC source with 15 kV maximum amplitude and 400 Hz frequency was used. Total active power introduced into the discharges comprised 120 W, and specific power value was 1.5 W/cm^3.

For researches of mixture component content in the chamber absorption spectroscopy method was implemented with the use of hardware-software complex based on monochromator MDR-23 (having 0.1 nm spectral resolution). Detection of light beams was performed by means of photomultiplier tube (PMT) FEU-100. For measuring digitized values of PMT electric signal specially developed hardware-software complex with 16-bit conversion and 11025 Hz sampling rate was used. NO_3 concentration was calculated

from measurements of absorption by this component at wavelengths $\lambda = 662$ nm and 623 nm. Component concentrations of O_3, NO_3, N_2O_5, HNO_3, HNO_2, H_2O_2, HO_2NO_2 were calculated from measurements of total absorption curve in wavelength range 200-300 nm. For that purpose values of component densities were chosen by means of automatic curve fitting software, so that resulting absorption curve would coincide with measured one. Use of such method was possible due to fact that characters of spectrum dependencies of absorption cross sections for studied components in wavelength range 200-300 nm are essentially different. For validation the method, O_3 concentration values obtained by procedure described above were compared with results on O_3 concentration measurements by its absorption at 296.5 nm wavelength, when it was possible to neglect absorption contributed by the other components. O_3 concentration values obtained by two those methods coincided with precision of concentration measurement (that is, scatter values for different measurements). Precision of the measurements was not worse than 5% for ozone, and 10-15% for the other components. Absorption cross sections for O_3, NO_3, N_2O_5, HNO_3, HNO_2, HO_2NO_2, H_2O_2 were taken from references given in [1].

3. Methods of numeric modeling the plasma component content in barrier discharge and work chamber

As it was already noted in the introduction, the most optimal plasma-chemical reactor for many technological tasks is one consisting from two independent parts – generator of active particles based on the discharges at atmosphere pressure and work chamber intended for placement of articles to be processed. Such design leads to significant complication of the calculations, because it is necessary at first to calculate component content of active particles in the discharge space, and then to take into account changes of content and concentrations of particles immediately in the chamber only due to chemical reactions. The second complexity of the calculations results immediately from specificity of barrier discharge, which represents a set of filamentary micro-discharges stochastically spread in space and time between the electrodes, so that each of micro-discharges has ~10^{-8} s duration and ~0.1 mm diameter. Normally [2], at determining concentrations of particles in discharge, initially plasma kinetics is calculated in separate current channels of micro-discharges, and then after time of the order of diffusion time value (~10^{-3} s) averaging of concentrations of all components over the whole discharge space is performed. In such approach there exists a set of parameters (dimensions, density per discharge electrode square unit and rate of formation the current channels) that are not well known and essentially depend on design of the discharge space and gas type. Such parameters are usually fitting ones.

Calculations represented in the present work are based on another approach, in which power introduced into the discharge is immediately averaged over the discharge volume. In such approach valid consideration is assured for the processes, that are linear on specific power, and also for non-linear processes with typical reaction time longer than diffusion time ($\tau > 10^{-3}$ s). This condition is fulfilled good enough in the system under study, because typical durations of chemical reactions between dissociation products in current channels normally exceed 10^{-2} s. Advantage of such approach consists in the absence of free parameters, and thus exactly this approach was used in our calculations. At performing the calculations, processes at barrier discharge electrodes and those at work chamber walls were not taken into consideration.

In calculations of the plasma component content and concentrations of molecules and radicals formed in barrier discharge volume, kinetic equation were used as follows:

$$\frac{dN_i}{dt} = S_{ei} + \sum_j k_j N_j + \sum_{j,l} k_{jl} N_j N_l + \ldots \qquad (1)$$

Here N_i are concentrations of molecules and radicals; k_j, k_{jl} are rate constants of molecular processes; S_{ei} is rate of formation of the products of electron-molecular reactions, which was calculated from the equation:

$$S_{ei} = \frac{W}{V}\frac{1}{\varepsilon_{ei}}\frac{W_{ei}}{\sum_j W_{ej} + \sum_j W_j}. \qquad (2)$$

W is power introduced into barrier discharge; V is barrier discharge volume. W_{ej} is specific power spent for electron-molecular process of non-elastic scattering with threshold energy ε_{ej}:

$$W_{ei} = \sqrt{\frac{2q}{m}} n_e N_i \varepsilon_{ei} \int_0^\infty \varepsilon Q_{ei}(\varepsilon) f(\varepsilon) d\varepsilon, \qquad (3)$$

where $q = 1.602 \cdot 10^{-12}$ Erg/eV; m and n_e are electron mass and concentration; Q_{ei} is cross section of respective non-elastic process; $f(\varepsilon)$ is electron energy distribution function (it was calculated from Boltzman equation). W_i is specific power spent for heating the gas:

$$W_i = \frac{2m}{M_i}\sqrt{\frac{2q}{m}} n_e N_i \int_0^\infty \varepsilon^2 Q_i(\varepsilon) f(\varepsilon) d\varepsilon \,, \qquad (4)$$

where M_i is mass of respective type of molecules, Q_i is transport scattering cross section.
Electron distribution function was calculated from Boltzman equation in two-term approximation [3].

$$\frac{1}{n_e N}\left(\frac{m}{2e}\right)^{1/2} \varepsilon^{1/2} \frac{\partial(n_e f_0)}{\partial t} - \frac{1}{3}\left(\frac{E}{N}\right)^2 \frac{\partial}{\partial \varepsilon}\left(\frac{\varepsilon}{\sum_i \frac{N_i}{N} Q_i} \frac{\partial f_0}{\partial \varepsilon}\right) - \qquad (5)$$

$$-\frac{\partial}{\partial \varepsilon}\left[2\sum_i \frac{m}{M_i}\frac{N_i}{N} Q_i \varepsilon^2 \left(f_0 + T\frac{\partial f_0}{\partial \varepsilon}\right)\right] = S_{eN}$$

where ε is energy (eV); T is gas temperature (eV); e is electron charge; E is electric field strength; N is total concentration of the molecules; N_i is concentration of respective type of the molecules; m is electron mass; S_{eN} and S_{ee} are integrals of non-elastic collisions of electrons with neutral particles and electrons, respectively.
The integral of non-elastic collisions of electrons with gas molecules was chosen in form

$$S_{eN} = \sum_i \frac{N_j}{N}\left[(\varepsilon - \varepsilon_i) Q_{ei}(\varepsilon + \varepsilon_i) f_0(\varepsilon + \varepsilon_i) - \varepsilon Q_i(\varepsilon_i) f_0(\varepsilon)\right], \qquad (6)$$

Q_{ei} are cross sections of excitation and ionization of O_2 and N_2 molecules with threshold energy ε_j.
Electron-electron scattering was not taken in consideration, because, as it was shown by our test calculations, at fulfilling inequality $n_e/N \le 10^{-6}$ e-e scattering does not have significant effect on rate constants of electron-molecular processes. Absence of e-e scattering integral in equation (5) leads to fact that stationary electron distribution function becomes independent on electron concentration. For that reason, for determining densities of neutral plasma components there is no necessity to solve kinetic equations for electrons and ions. It was assumed in the calculations that electric field in the discharge did not change in space and time, and it was taken to be equal 20 kV/cm, which is mean field value in barrier discharge on air, as it follows from [4]. At solving equations (1) 105 elementary processes were taken in consideration. Equations (1) were solved together with Boltzman equation by numerical techniques analogous to [3].

At second stage of the calculations it was assumed that the whole mixture acquired in barrier discharge volume (excluding charged plasma components) comes to work chamber in spatially uniform way with rates:

$$S_{ir} = \frac{N_{i\tau}}{\tau_r}\frac{V_r}{V_a}, \qquad (7)$$

where τ_r and V_r are pump-through time and volume of barrier discharge space, respectively, $N_{i\tau}$ are concentrations of particular components of the mixture in time point τ_r, V_a is work chamber volume.
Calculation of concentrations of molecules and radicals in work chamber was performed on a basis of equations:

$$\frac{dN_i}{dt} = S_{ir} - S_{ia} + \sum_j k_j N_j + \sum_{j,l} k_{jl} N_j N_l + \ldots \qquad (8)$$

Here $S_{ia} = \frac{N_i}{\tau_a}$ is rate of coming the plasma components out of work chamber due to gas purge, τ_a is time of gas purge through work chamber.

4. Results of numeric modeling of the component content of active particles in work chamber volume

In Fig.1 calculated values of concentrations of gas mixture components in work chamber with dry (20% RH, light bars) and wet (80% RH, black bars) air for purge rates of 2, 4 and 8 l/min. Such purge rates correspond to average time of mixture presence in the chamber of 40, 20 and 10 minutes, and average time of mixture presence in barrier discharge volume of 2.5, 1.25 and 0.5 s, respectively. As one can see from Fig.1, concentrations of particular components of the mixture possess different dependencies on purge rate. For that reason, by varying purge rate one can change ratio between concentrations of particular components in rather wide range.

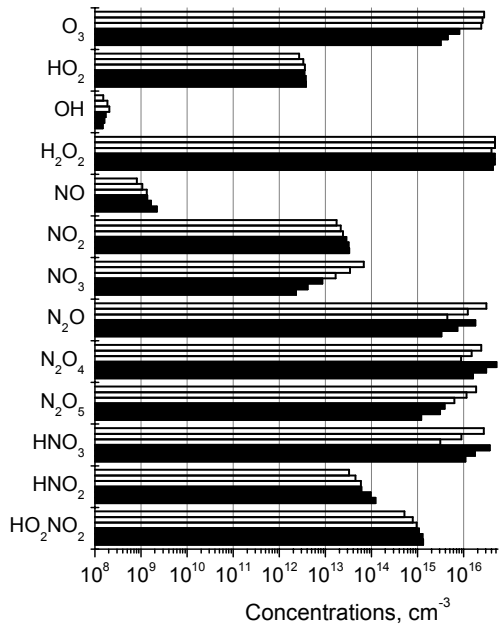

Fig.1. Calculated quasi-stationary concentration values of gas mixture components in work chamber in dry (20% RH, light bars) and wet (80% RH, black bars) air at purge rates 2, 4 and 8 l/min (purge rate increases from top to bottom).

In Fig.2 temporal dependencies of the component concentrations of gas mixture in work chamber with dry (20% humidity) air for 8 l/min purge rate are presented. Mentioned concentrations have practically linear dependence on time in the interval before approximately 1 minute. It is due to fact that the rate of their coming from the discharge does not change in time, and chemical reactions in the chamber volume do not have enough time to change ratios between concentrations of the components. Thus, only after big enough time interval ($\tau >> 1$ min) quasi-stationary values of the component concentrations are reached, that gives evidence to steady in time income of these components, that is, the income is determined by processes of carrying the molecules out of barrier discharge volume. Ozone concentration reaches its

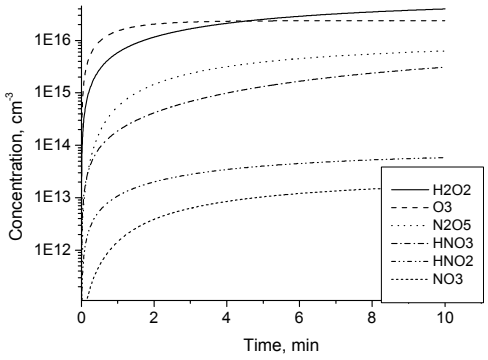

Fig.2. Calculated dependencies of component concentrations of H_2O_2, O_3, N_2O_5, HNO_3, HNO_2, NO_3 in work chamber on time at 8 l/min purge rate of dry air (20% RH)

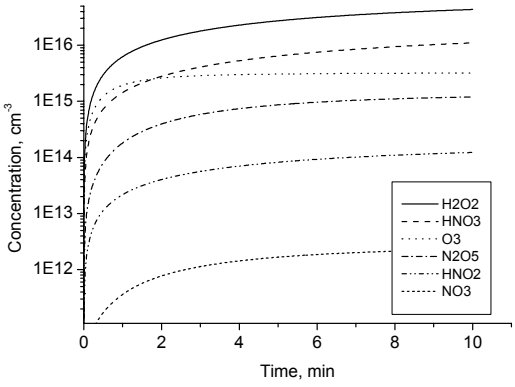

Fig.3. Calculated dependencies of component concentrations of H_2O_2, O_3, N_2O_5, HNO_3, HNO_2, NO_3 in work chamber on time at 8 l/min purge rate of wet air (80% RH).

quasi-stationary value for the time of about 100 – 250 s. Hydrogen peroxide concentration is practically independent on time, because in our calculations it is limited by value of saturated vapor concentration.

At increase of air humidity (Fig.3) concentrations of acid components (HNO_3, HNO_2) grow up due to increase of concentration of hydrogen-containing molecules in the mixture. At that ozone concentration decreases by about one order of magnitude due to fact that in barrier discharge volume increase of ozone decomposition at collisions with OH and HO_2 molecules occurs. For the same reason NO_3 concentration decreases in wet air, and since main channel of N_2O_5 formation is represented by reactions with NO_3 participation, N_2O_5 concentration is respectively decreased.

5. Experimental results for dry air (RH≈25%)

Measurements of component concentrations of O_3, NO_3, N_2O_5, HNO_3, HNO_2, H_2O_2, HO_2NO_2 in the chamber were performed at three volume rates of the purge (8, 4 and 2 l/min) at distances of 65, 215 and 365 mm from top wall of the chamber. HO_2NO_2 was not detected in any operation regime of the setup. It agrees with fact that calculated values of HO_2NO_2 concentration do not exceed $1\cdot10^{15}$ cm^{-3}, and sensitivity threshold of measuring technique does not exceed that value. The experiments have shown that characters of the dependencies of quasi-stationary concentrations of O_3, N_2O_5, HNO_3, HNO_2, NO_3 in the chamber on purge rate are in good agreement with calculated ones: concentrations of O_3, NO_3, N_2O_5, HNO_3 grew up with decrease of purge rate, and HNO_2 concentration decreased at that. However, for correct comparison of experimental results with calculated ones, one should determine, to which extent an assumption about uniform distribution of active particles in work chamber volume is fulfilled. Measurements of concentrations of active particles in three cross sections of the chamber have demonstrated the following. Heterogeneity of the distribution of measured densities of the particles on the chamber height is minimum at 8 l/min supply rate (minimum scatter about 10% was observed for O_3, and maximum about 30-40% - for HNO_2), and increases essentially with the rate decrease, reaching 200-300% for NO_3 and N_2O_5 at 2 l/min supply rate. As it was shown by experiments with smoke supply to gas route, such character of the dependence of homogeneity of particle distribution in the chamber volume on purge rate, first of all, is due to peculiarities of the process of mixing active particles coming from the discharges with air in the chamber. It was determined that at low rates of air supply (1-2 l/min) process of filling the chamber by active medium in the first approximation can be imagined as motion of gas "plunger" from top to bottom. That is, mixing of active particles with air occurred only in top part of the chamber, and then formed mixture moved downward and extruded residual air out of the chamber. But in case of volume supply rate of 8 l/min flows of active particles passed through the whole chamber due to higher initial velocity, then they were reflected from the bottom and returned to the chamber, thus providing good mixing of active particles with air present in the chamber volume. Thus, one can see that the most correct comparison of calculated and experimentally measured concentration values is possible at high purge rate.

Fig.4 exhibits dependencies of averaged over chamber height densities of O_3, NO_3, N_2O_5, HNO_3, HNO_2 on time for 8 l/min purge rate. (Starting values of component concentrations in Figs. 4 and 5 correspond to sensitivity thresholds of measuring technique.) One can see from the figure that, as in case of calculations (see Fig.2), concentrations of all components practically reach quasi-stationary values in short time. Concentrations of O_3 and HNO_3 comprise $2.6\cdot10^{16}$ cm^{-3} and $2.6\cdot10^{15}$ cm^{-3}, respectively, and are essentially higher than densities of other components. Comparison of experimental data with calculated ones at 10-th minute shows that discrepancies between theoretical and experimental concentration values do not exceed 5% for O_3 and 25-100% for HNO_3, NO_3, HNO_2. In case of N_2O_5, the difference is essentially greater - experimentally measured concentrations are lower than calculated ones approximately by factor of 20. The most probable reason of the discrepancy between theory and experiment may consist in intensive precipitation of N_2O_5 at surfaces of the chamber walls, because their temperature is lower than that of dinitrogen pentoxide sublimation (32.4^0C). Another essential difference between experimental results and the theory is the absence of H_2O_2 in the chamber, although calculated values of hydrogen peroxide concentration are $\geq 5\cdot10^{16}$ cm^{-3}, which is almost one order of magnitude higher than sensitivity threshold of used measuring technique.

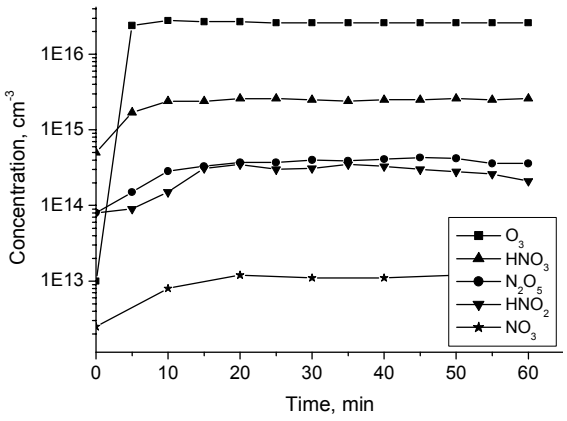

Fig.4. Dependencies of experimentally measured concentrations of O_3, HNO_3, N_2O_5, HNO_2, NO_3 averaged over the chamber volume on time at 8 l/s purge rate of dry air (RH≈ 25%).

6. Experimental results for wet air (RH ≈ 80 %).

As in the case of dry air, heterogeneity of distribution of component concentrations of O_3, NO_3, N_2O_5, HNO_3, HNO_2 on chamber height is minimum at 8 l/min and increases essentially at rate decrease down to 2 l/min. However, homogeneity degree is worse than in previous case. Particularly, for the rate of 8 l/min maximum difference in concentration values of NO_3, N_2O_5, HNO_3, HNO_2 measured at top and middle windows comprised about 100% (at that homogeneity of O_3 distribution remained high enough – concentration difference in those cross-sections did not exceed 10%). Unlike previous case, at the use of wet air and purge rates of 8 and 4 l/min hydrogen peroxide was also detected. In Fig.5 the dependencies of averaged over top part of the chamber (only measurements at top and middle windows were considered) component concentrations of O_3, NO_3, N_2O_5, HNO_3, HNO_2, H_2O_2 on time for 8 l/min purge rate are given. One can see from the figure that component concentrations of O_3, HNO_3, NO_3, N_2O_5, HNO_2 reach their quasi-stationary values till 10-20 minutes of filling the chamber. Hydrogen peroxide concentration reaches quasi-stationary value $\approx 8 \cdot 10^{16}$ cm^{-3} only at 55-60 min after the start of chamber filling. Comparison of theoretical and experimental data at 10-th minute shows that agreement between calculated and measured component concentration values of O_3, NO_3, N_2O_5, HNO_3, HNO_2 in case of wet air is essentially worse than that in case of dry air. Whereas theoretical and calculated concentrations of N_2O_5, HNO_2 and NO_3 differ approximately twice, in case of O_3 and HNO_3 this difference is significantly more. Particularly, theoretical values of O_3 concentration are about 6 times less than experimental ones. As to HNO_3, on the contrary, theoretically obtained concentration values are 6-7 times higher than measured ones. The most possible reason for such effect may be increased HNO_3 exit out of the chamber volume at air humidity growth due to solving nitrogen acid molecules in water layer at chamber walls.

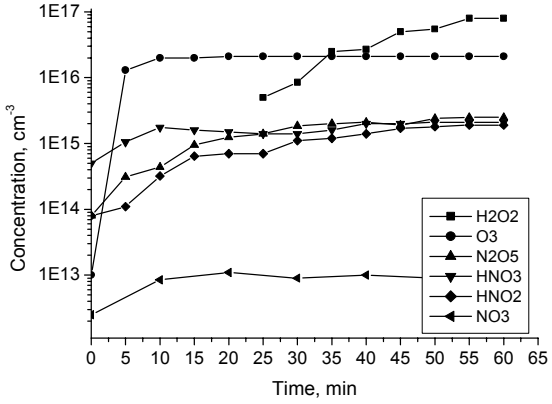

Fig.5. Dependencies of experimentally measured concentrations of H_2O_2, O_3, N_2O_5, HNO_3, HNO_2, NO_3 averaged over volume of upper half of the chamber on time at 8 l/s purge rate of wet air (RH≈80%).

7. Conclusions

Accomplished comparison of calculated and experimentally measured concentrations of O_3, NO_3, N_2O_5, HNO_3, HNO_2, H_2O_2 in the work chamber at different air humidity shows that proposed by us approach to calculation of concentration of the particles in most cases gives good agreement between the theory and the experiment. Noticeable discrepancies observed in certain cases may be reasonably explained by factors that can not be correctly taken into account in the theory. The most important of those is the influence of discharge electrode surfaces and work chamber walls, and inhomogeneity of component distribution in the chamber.

References

[1] JPL Publication 00-3

[2] I. Stefanovic, N.K. Bibinov, A.A. Deryugin, I.P. Vinogradov, A.P. Napartovich and K. Wiesemann *Plasma Sources Sci. Technol.* **10,** 406 (2001)

[3] Ann C. Gentile, Mark J. Kushner *Journal Appl. Phys.* **78** (3), 2074 (1995)

[4] D. Braun, V. Gibalov and G. Pietsch *Plasma Sources Sci. Technol.* **1,** 166 (1992)

Prediction of droplets desolvation in an rf inductively coupled plasma

Yanguang Shan, J. Mostaghimi

Centre for Advanced Coating Technologies
Department of Mechanical and Industrial Engineering, University of Toronto, Canada

Abstract
A mathematical model for the desolvation of solvent droplets has been implemented into a time-dependent rf-ICP code. Plasma-droplet interactions and droplets collisions are considered. Simulations have been performed for various droplet sizes under typical ICP operating conditions. Effects of the local cooling, droplets collisions, central gas flow rate and plasma power, as well as sample uptake rate have been investigated. Some results agree quite well with the experiment.

1. Introduction

In ICP atomic spectrochemical analysis, the samples are commonly introduced into the ICP as an aqueous aerosol via a spray. Studies [1-3] have shown that the efficient desolvation process can significantly improve the overall performance of the spectrometry. Signal fluctuations due to individual incompletely desolvated droplets can be significant [4-9]. Each incompletely desolvated droplet affects the plasma ionization and excitation within 1-2 mm of the droplet, acting as a local heat sink [9]. The region near desolvated analyte particles is also affected [7]. A few numerical studies have been done by several groups to study the droplets desolvation in an ICP [10-12]. These studies have led to a better understanding of the desolvation process. However, these models deal with the plasma temperature and velocity and the droplets desolvation and trajectories separately. The coupling effect of the droplets desolvation and trajectories on the plasma gas was not included. The droplet-droplet collisions, which may lead to coalescence of droplets, also were not considered. In this paper, we present a mathematical model to study droplet desolvation and trajectories within the ICP torch. This model is based on the spray model used in KIVA II [13-15]. It was implemented into a two-dimensional, time-dependent radio frequency ICP code. Interactions between plasma gas and the droplets injection as well as droplet-droplet collisions are included.

2. Mathematical models

Mathematical models of the rf-ICP have been very successful in predicting plasma properties and in studying a variety of plasma phenomena. The model used in this paper was developed by Mostgahimi *et al*. and the details of this model can be found elsewhere [16].

2.1. Spray model

To simulate the behavior of the spray droplets, a droplet probability distribution function is defined.

$$f = f(\vec{x}, \vec{v}, r, T_d, t) \tag{1}$$

where $\vec{x}$ is the droplet position, $\vec{v}$ is the droplet velocity, r is the equilibrium radius of droplet, T_d is the droplet temperature which is assumed to be uniform within the droplet.The time evolution of f is obtained by solving the spray equation.

$$\frac{\partial f}{\partial t} + \nabla_{x_i} \cdot (f\dot{\phi}_i) = \dot{f}_{coll} \tag{2}$$

where x_i are $\vec{x}, \vec{v}, r, T_d$, and ϕ_i are $\vec{v}$ $\vec{F}$, R, $\dot{T}_d$ which are time change rates of x_i for an individual droplet. The expressions for $\vec{F}$, R, and $\dot{T}_d$ will be given later. $\dot{f}_{coll}$ is the source term due to droplet collisions.

2.2. Droplets collisions

When a large number of droplets travel in a flow, there exists a possibility that the droplets may collide. During collisions, droplets may coalesce or graze each other depending on droplets' properties. In droplet collision model, collisions are considered only when a pair of parcels (each parcel contains a number of droplets with same properties) locate in the same computational cell [21]. The droplets within the same parcels are not allowed to collide since they are moving with the same velocity. The probability that no collision occurs between the droplets of this pair of parcels is calculated as following

$$P_{nocoll} = e^{I_{coll}\Delta t} \tag{3}$$

where I_{coll} is the collision frequency the larger droplet experiences, given by

$$I_{coll} = \frac{N_1}{V_c}\pi(r_1 + r_2)^2\left|\vec{v}_1 - \vec{v}_2\right| \tag{4}$$

where N_1 is the number of droplets in the parcel with the smaller radius droplets, V_c is the volume of the computational cell. To specify the collision types, the collision impact parameter b is defined [13].

$$b = \sqrt{xx}(r_1 + r_2) \tag{5}$$

where xx is a random number, b_{cr} is the critical impact parameter. b_{cr} is given by

$$b_{cr}^2 = (r_1 + r_2)^2 \min(1.0, \frac{2.4g(\gamma)}{We_d}) \tag{6}$$

$$g(\gamma) = \gamma^3 - 2.4\gamma^2 + 2.7\gamma \quad (\gamma = r_2 / r_1, r_1 \le r_2) \tag{7}$$

$$We = \frac{\rho_d\left|\vec{v}_1 - \vec{v}_2\right|^2 r_1}{\sigma(\overline{T_d})} \qquad (\overline{T_d} = \frac{r_1^3 T_{d_1} + r_2^3 T_{d_2}}{r_1^3 + r_2^3}) \tag{8}$$

If the impact parameter is less than the critical impact parameter, then the droplets coalesce. If the impact parameter is greater than the critical impact parameter, then the droplets in the parcel pair just graze. In this case, droplets maintain their sizes and temperatures but undergo velocity changes in the resulting semi-elastic collision. The velocities of droplets after collision are given by

$$\vec{v}_1^{'} = \frac{r_1^3\vec{v}_1 + r_2^3\vec{v}_2 + r_2^3(\vec{v}_1 - \vec{v}_2)\dfrac{b - b_{cr}}{r_1 + r_2 - b_{cr}}}{r_1^3 + r_2^3} \tag{9}$$

$$\vec{v}_2^{'} = \frac{r_1^3\vec{v}_1 + r_2^3\vec{v}_2 + r_1^3(\vec{v}_2 - \vec{v}_1)\dfrac{b - b_{cr}}{r_1 + r_2 - b_{cr}}}{r_1^3 + r_2^3} \tag{10}$$

2.3. Trajectories of individual droplets

To simulate droplet trajectories, we assume: (1) the droplet is spherical; (2) the gas film around the droplet is quasi-steady and has uniform physical properties; (3) the pressure around the droplet is uniform; (4) the droplet surface is under thermal equilibrium state; (5) no droplet dispersion since the plasma gas is assumed to be laminar, and (6) rarefied gas effects are neglected.

The governing equations for the motion of a droplet can be expressed as

$$\frac{d\vec{x}}{dt} = \vec{v} \qquad \text{and} \qquad \frac{d\vec{v}}{dt} = \vec{F} \tag{11}$$

The aerodynamic drag force is given by the expression

$$\vec{F} = \frac{3}{8}\frac{\rho_g}{\rho_d}\frac{\left|\vec{u} - \vec{v}\right|}{r}(\vec{u} - \vec{v})C_D \tag{12}$$

where ρ_g and ρ_d are the densities of surrounding gas and droplet respectively, $\vec{u}$ and $\vec{v}$ are the velocities of surrounding gas and droplet respectively. The drag coefficient C_D is given by

$$C_D = \begin{cases} 0.424 & \mathrm{Re}_d > 1000 \\ \dfrac{24}{\mathrm{Re}_d}(1 + \dfrac{1}{6}\mathrm{Re}_d^{2/3}) & \mathrm{Re}_d \le 1000 \end{cases} \tag{13}$$

$$\mathrm{Re}_d = \frac{2\rho_g\left|\vec{u} - \vec{v}\right|r}{\mu_g(\overline{T_g})}, \ \overline{T_g} = \frac{T_g + 2T_d}{3} \tag{14}$$

The evaporation of the droplet results in a change of droplet radius and droplet temperature. The rate of droplet radius change R is given by the Frossling correlation [20]

$$R = -\frac{(\rho D)_{dg}(\overline{T}_g)}{2\rho_d r}\frac{Y_1^* - Y_1}{1 - Y_1^*}Sh_d \tag{15}$$

where Y_1^* is the liquid vapor mass fraction at the droplet surface, Y_1 is the liquid vapor mass fraction in the gas. $(\rho D)_{dg}$ is the liquid vapor diffusivity in gas. We use the formula suggested by R. B. Bird *et al.* [17] to estimate the liquid vapor diffusivity in plasma gas. The Sherwood number is given by

$$Sh_d = (2.0 + 0.6\,\mathrm{Re}_d^{1/2}\,Sc_d^{1/3})\frac{\ln(1+B_d)}{B_d} \tag{16}$$

$$Sc_d = \frac{\mu_g(\overline{T}_g)}{(\rho D)_{dg}(\overline{T}_g)}\ ,\ B_d = \frac{Y_1^* - Y_1}{1 - Y_1^*} \tag{17}$$

The surface mass fraction Y_1^* is given by

$$Y_1^*(T_d) = \frac{W_1}{W_1 + W_0\left(\frac{p_g}{p_v(T_d)} - 1\right)} \tag{18}$$

where W_0 is the local average molecular weight of all species except the liquid vapor; $p_v(T_d)$ is the equilibrium vapor pressure at T_d.

The rate of droplet temperature change is determined by the energy balance equation.

$$\rho_d \frac{4}{3}\pi r^3 c_d \dot{T}_d - \rho_d 4\pi r^2 R L_d(T_d) = 4\pi r^2 Q_d \tag{19}$$

where c_d is the liquid specific heat, $L_d(T_d)$ is the latent heat of vaporization, and Q_d is the rate of heat conduction to the droplet surface per unit area. Q_d is given by the Ranz-Marshall correlation [20].

$$Q_d = \frac{K_{gas}(\overline{T}_g)(T_g - T_d)}{2r}Nu_d \tag{20}$$

$$Nu_d = (2.0 + 0.6\,\mathrm{Re}_d^{1/2}\,\mathrm{Pr}_d^{1/3})\frac{\ln(1+B_d)}{B_d} \tag{21}$$

$$\mathrm{Pr}_d = \frac{\mu_g(\overline{T}_g)c_p(\overline{T}_g)}{K_g(\overline{T}_g)} \tag{22}$$

2.4. Coupling source terms and initial and boundary conditions

The exchange of mass, momentum, and energy between plasma gas and the spray are given by following.

$$S_c{}^s = \sum_{N=1}^{NP}\frac{dm_d}{dt}\delta(\vec{x} - \vec{x}_d) \tag{23}$$

$$\vec{S}_m{}^s = \sum_{N=1}^{NP}\frac{d(m_d\vec{v})}{dt}\delta(\vec{x} - \vec{x}_d) \tag{24}$$

$$S_E{}^s = \sum_{N=1}^{NP}\frac{d(m_d h_d)}{dt}\delta(\vec{x} - \vec{x}_d) \tag{25}$$

The spray is continuous and the initial properties (sizes, velocities, temperatures) of injected droplets are specified, then distributions of these properties are calculated according to appropriate distribution functions. Two types of droplet size distribution are available: (1) mono-disperse distribution and, (2) x-squared distribution. The temperatures of all injected droplets are same. Whenever a liquid droplet impinges on a rigid wall, we assume it completely evaporates near the wall, and there is no heat transfer between the droplet and the torch wall. The plasma model was solved using the SIMPLER algorithm [18].The method used for solving the spray equation is based on the ideas of Monte Carlo method and of discrete particle method [13]. The parcels are introduced into the computation domain during the time of injection. Each parcel is composed of a number of droplets with same location and properties. We sample randomly from

assumed probability distributions that govern droplet properties at injection and droplet behavior after injection. To realize this method, the continuous distribution f is replaced by a discrete distribution $f^{'}$.

$$f^{'} = \sum_{p=1}^{NP} N_p \delta(\vec{x} - \vec{x}_p)\delta(\vec{v} - \vec{v}_p)\delta(r - r_p)\delta(T_d - T_{d\,p}) \tag{26}$$

The discrete distribution is then simulated stochastically by tracking the parcels' positions and properties in the solution domain.

3. Results

The plasma is operated at 1.0 kW power and 0.9 l/min central flow rate, Sample uptake rate is 1 ml/min. The inner diameter of the center tube is 1.0 mm. Other operating parameters are same as those in Table 1 in Ref. [9]. The operating parameters used in this paper are same as the above description unless mentioned.

3.1. Desolvation profiles for mono-disperse droplets

Desolvation profiles of mono-disperse solvent droplets are shown in Fig. 1. A train of mono-disperse droplets are introduced into the plasma in this calculation. It can be seen from Fig. 1 that the desolvation rate sharply increases after the droplets reaching above the load coil where the maximum gas temperature on the torch axis is predicted by models and experiments. The profiles also show that the height in the ICP where vaporization begins for a particular size of droplets is almost fixed. This characteristic is helpful to improve the precision of the ICP spectrometry.

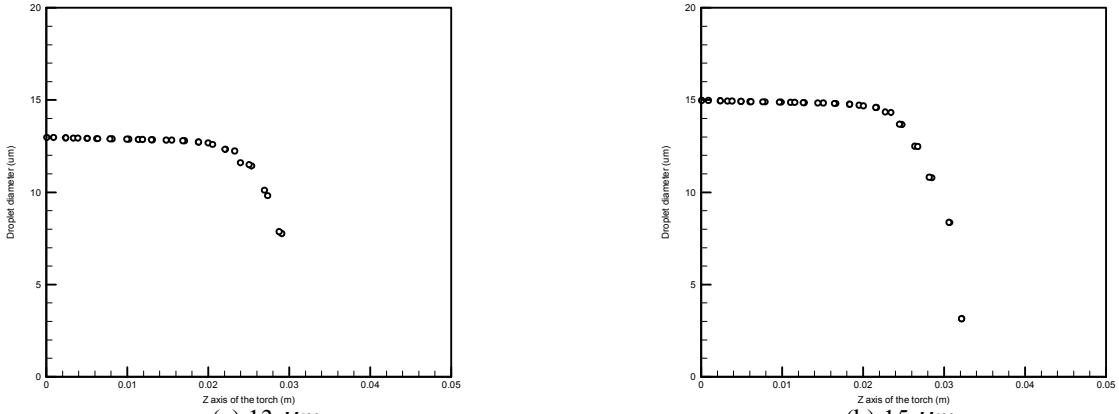

(a) 13 μm (b) 15 μm

Figure 1 Desolvation profiles for mono-disperse droplets

3.2. Effects of the local cooling and droplets collisions on droplets desolvation

Figure 2a shows the desolvation profile of a train of 13 μm mono-disperse droplets without considering the local cooling effect. Compare it with Fig. 1a (the cooling effect is included), it is obvious that the local cooling effect leads to a delay of droplets desolvation. The height of complete desolvation for 13 μm mono-disperse droplets increases from 3.4 mm ALC (Above the Load Coil) to 9.2 mm ALC when the cooling effect is considered.

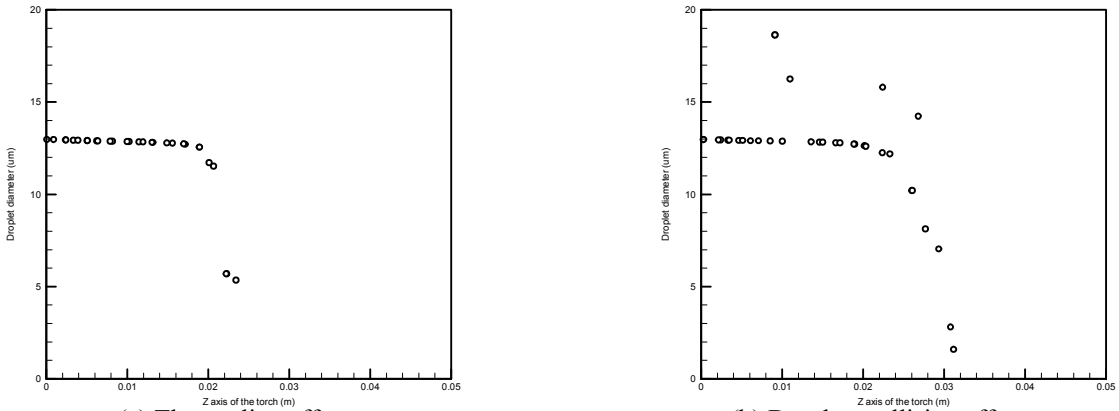

(a) The cooling effect (b) Droplets collision effect

Figure 2 Effect of the local cooling and droplets collisions on droplets desolvation

Fig.2b shows the desolvation profile of mono-disperse (13 μm) droplets with considering droplets collisions. Compare it with Fig. 1a (droplets collisions are not included), it can be seen the droplets coalescences are predicted. The height of complete desolvation for droplets increases from 9.2mm ALC to 11.2 mm ALC due to droplets collisions. The effect of droplets collisions is slight compared to the effect of local cooling.

3.3. Height of complete desolvation for droplets of different initial diameters

Heights of complete desolvation for mono-disperse droplets of different initial diameters are presented in Fig. 3a, Fig. 3b. The central gas flow rates are 0.8 l/min, 0.9 l/min respectively. For 1 kW ICP, the experimental prediction of the height of complete desolvation for a 14.8 μm diameter droplet is 11.4 mm ALC [9]. The model here predicts a height of 10.9 mm ALC for a train of 14.8 μm mono-disperse droplets to be completely evaporated. When we compare Fig. 3a here with Fig. 10a in Ref. [9] and Fig. 3b here with Fig. 10b in Ref. [9], it is found that the prediction results by the simulation agree quite well with the experimental results. The differences between simulation results and experimental results are probably due to an inaccurate prediction of plasma fields and an inaccurate calculation of the cooling effect. For a fixed sample uptake rate, the cooling effect could be over estimated for smaller droplets while underestimated for bigger droplets. Besides possible inaccurate predictions of models, the operating conditions for the experiment and the simulation are not exactly same. The experiment determined the minimum diameter of the droplets at the exit of the spray chamber that survive at a particular height in the plasma by introducing a distribution size of droplets while the simulation determined the height of complete desolvatation for a train of mono-disperse droplets.

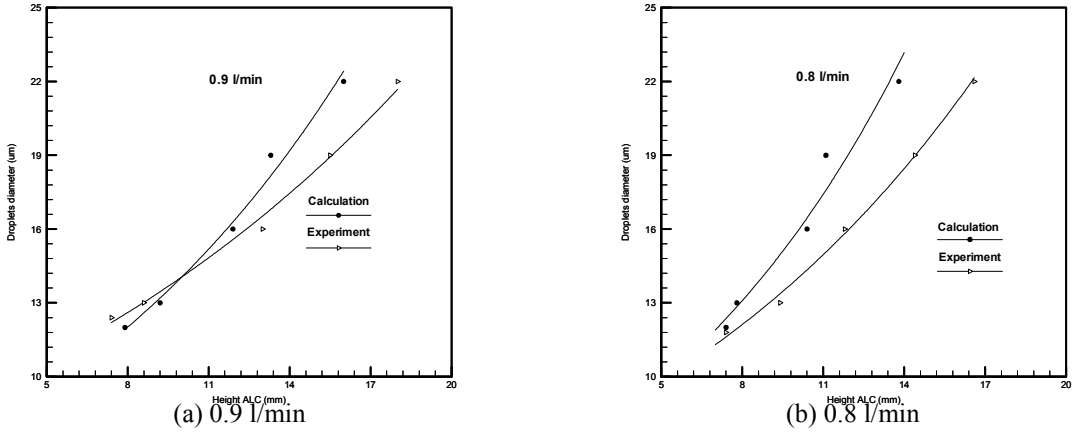

(a) 0.9 l/min (b) 0.8 l/min

Figure 3 Height of complete desolvation for droplets of different initial diameters

3.4. Effects of central gas flow rate and plasma power on the desolvation

Fig. 4a and Fig. 4b show the effects of central gas flow rate and plasma power on the height of complete desolvation for 15 μm mono-disperse droplets. It is seen from Fig. 4a that the height of complete desolvation increases as the central gas flow rate increases. This is because the increasing of central gas flow rate leads to further cooling of the plasma center temperature. As can be expected, the height of complete desolvation for droplets decreases when the power of ICP increases.

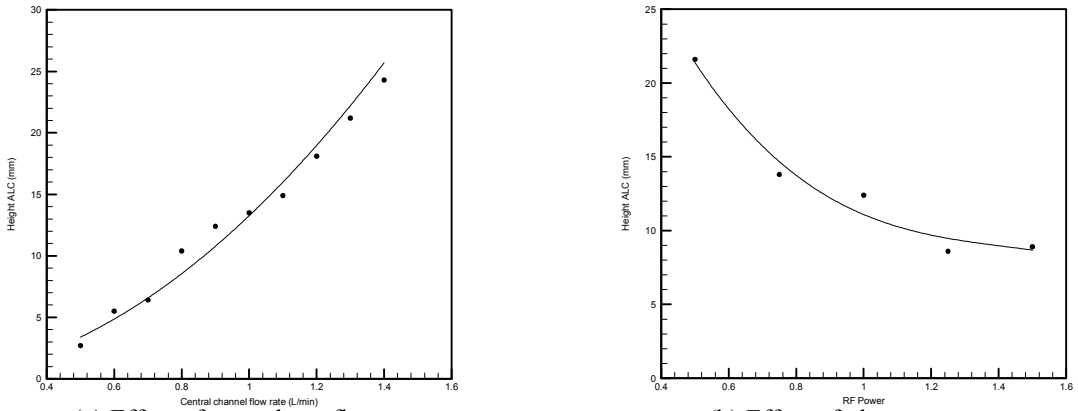

(a) Effect of central gas flow rate (b) Effect of plasma power

Figure 4 Effect of central gas flow rate and plasma power on the desolvation

3.5. Effect of sample uptake rate on the desolvation

The effects of central flow rate and ICP power on droplets desolvation are widely reported both numerically [11] and experimentally [9]. However, little consideration is put on the effect of sample uptake rate on the desolvation of droplets. As mentioned previously and reported in reference [7], the local cooling can significantly affect the plasma conditions and droplets desolvation. It is reasonable to conclude that the sample uptake rate, acting as the main cooling source, could affect the desolvation of droplets. Fig. 5 shows the effect of sample uptake rate on the desolvation of droplets. It can be seen the relationship between sample uptake rate and droplets desolvation height is nearly linear. The increase of sample uptake rate can lead to a delay of droplets desolvation.

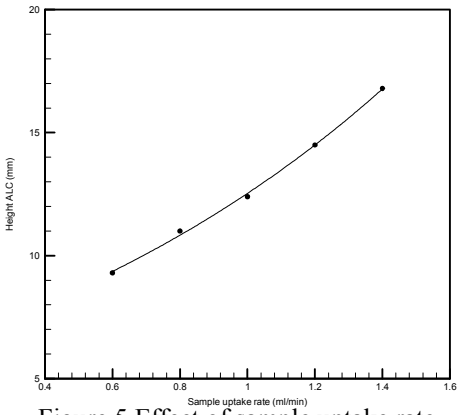

Figure 5 Effect of sample uptake rate

4. Conclusion

A mathematical model was developed to study desolvation of solvent droplets within ICP. The model is used to predict the height of complete desolvation for mono-disperse droplets within the rf-ICP. Calculations have been performed for various droplet sizes under a variety of ICP operating conditions. Effects of the local cooling, droplets collisions, central gas flow rate and plasma power, as well as sample uptake rate have been investigated. It is found that the local cooling effect can greatly delay droplets desolvation. It is also found that: as the droplet size increase, the height of complete desolvation for droplets increases; as the central gas flow rate increase, the height of complete desolvation for droplets increases; as the ICP power increase, the height of complete desolvation for droplets decreases. The predicted heights of complete desolvation for different droplet diameters in a 1 kW ICP operated at different central gas flow rates are compared with experimental results. The agreement is quite good. It is also concluded that the sample uptake rate can be a factor affecting the droplets desolvation process. Increasing of sample uptake rate can delay the droplets desolvation.

References

[1] J. A. Koropchak, D. H. Winn, Anal. Chem., 58 (1986) 2558.
[2] K. A. Vermeiren, P. D. P. Taylor, R. Dams, J. Anal. At. Spectrom., 2 (1987) 383.
[3] A. R. Eastgate, R. C. Fry, G. H. Gower, J. Anal. At. Spectrom., 8 (1993) 305.
[4] M. T. Ciceroneo, P. B. Farnsworth, Spectrochim. Acta Part B, 44 (1989) 897.
[5] J. W. Olesik, L. J. Smith, E. J. Williamsen, Anal. Chem., 61 (1989) 2002.
[6] S. E. Hobbs, J. W. Olesik, Anal. Chem., 64 (1992) 274.
[7] S. E. Hobbs, J. W. Olesik, Spectrochim. Acta Part B, 48 (1993) 817.
[8] J. C. Fister III, J. W. Olesik, Spectrochim. Acta Part B, 46 (1991) 869.
[9] J. W. Olesik, J. C. Fister III, Spectrochim. Acta Part B, 46 (1991) 851.
[10]J. A. Horner, G. M. Hieftje, Spectrochim. Acta Part B, 53 (1998) 1235.
[11]J. A. Horner, S. A. Lehn, G. M. Hieftje, Spectrochim. Acta Part B 57 (2002) 1025.
[12]C. M. Benson, S. F. Gimelshein, D. A. Levin, A. Montaser, Spectrochim. Acta Part B 56 (2001) 1097.
[13]A. A. Amsden, P. J. O'Rourke, T. D. Butler, KIVA-II. Los Alamos National Laboratory report LA—11560-MS, May 1989.
[14]A. A. Amsden, KIVA-3. Los Alamos National Laboratory report LA—12503-MS, March 1993
[15]A. A. Amsden, KIVA-3V. Los Alamos National Laboratory report LA-UR-97-698, 1997.
[16]J. Mostaghimi, K. C. Paul, and T. Sakuta, J. Appl. Phys.**,** 83 (1998) 1898.
[17]R. B. Bird, W. E. Stewart, and E. N. Lightfoot, Transport Phenomena, (1960) 505.
[18]S. V. Patankar*,* Numerical Fluid Flow and Heat Transfer, McGraw-Hill, New York, 1980.
[19]J. W. Olesik, S. E. Hobbs, Anal. Chem., 66 (1994) 3371.
[20]G. M. Faeth, Prog. Energy Combust. Sci. 3, (1977) 191.
[21]P. J. O'Rourke. Collective Drop Effects in Vaporizing Liquid Sprays, Ph.D. thesis 1532-T, Princeton University, 1981.

Influence of different wall materials on the vibrational population of molecular hydrogen

U. Fantz[1], S. Meir[1,2] and B. Heger[2]

[1] *Lehrstuhl für Experimentelle Plasmaphysik, Universität Augsburg, Universitätsstr. 1, D-86135 Augsburg, Germany*
[2] *Max-Planck-Institut für Plasmaphysik, EURATOM Association, Boltzmannstr. 2, D-85748 Garching, Germany*

Abstract
Optical emission spectroscopy provides a tool to determine the vibrational population in the ground state of hydrogen molecules up to relative population densities $n(v)/n(v=0) > 1\%$, i.e. the first four to five vibrational levels. The vibrational temperature in hydrogen plasmas changes if an additional surface is placed into the discharge. Results for quartz, copper, aluminium, tungsten and graphite are presented and a dependence on the surface temperature is observed. A correlation with the atomic hydrogen density is discussed.

1. Introduction

The vibrational population in the ground state of hydrogen molecules ($H_2(v)$) is an important parameter in hydrogen plasmas. One example is the formation of negative ions (H^-) due to the dissociative attachment process which is resonant with v=4 for H_2 and v=6 for D_2. Other examples are the enhancement of ionisation and dissociation rates and the modification of the electron energy distribution function. In order to calculate the vibrational distribution both electron impact collisions and heavy particle collisions have to be considered. This includes electron impact excitation in electronically excited states followed by spontaneous emission which causes re-distributions of vibrational populations in the ground state. Furthermore, the vibrational population can be affected by wall collisions, either directly ($H_2(v)$ + wall $\rightarrow$ $H_2(w)$) or by recombining hydrogen atoms/ions ($H_{ads\ or\ gas} + H_{ads} \rightarrow H_2(v)$, Langmuir-Hinshelwood or Eley-Rideal mechanism). For these processes the data base is scarce and often not determined from plasma-material interaction experiments.
The paper reports on investigations of the vibrational populations of hydrogen and deuterium molecules in low pressure plasmas where an additional surface is placed into the plasma chamber. Several materials (steel, quartz, aluminium, copper, tungsten and graphite, all of them plasma treated) are tested in two types of discharges, i.e. microwave and radio-frequency plasmas. To obtain a possible correlation with surface temperature, the substrate holder can be cooled actively. The atomic hydrogen density is determined as well as the electron density and electron temperature. Thus, a dependence of measured vibrational populations on plasma parameters can be discussed also.

2. Experiments and diagnostic method

Two different types of plasma experiments were used to study plasma wall interaction with respect to a modification of the vibrational population of hydrogen molecules. One necessary experimental requirement was to have a homogeneous plasma in direct contact with an additional surface. For diagnostic purposes, lines of sight should be arranged to be parallel to the surface with the possibility to vary the distance to the surface. Furthermore, the surface should be large enough to satisfy predominant observation of surface processes in proportion to volume processes. Since laboratory plasmas are general limited by chamber walls, mostly steel surfaces, different configurations were chosen: a surface wave excited microwave plasma (Duo-Plasmaline®) with chamber walls far away from the plasma generation volume and an inductively coupled plasma source (ICP) with a plasma being always in contact with chamber walls. The geometry is shown in Fig. 1. In both experiments, the plasma is directly in contact with a quartz surface, in consequence of the plasma generation, i.e. the coupling of the generator power into the chamber volume.
The microwave plasma, based on the principle of the Duo-Plasmaline® (f = 2.45 GHz, $P_{max} = 2 \times 1.2$ kW), has a cylindrical symmetry which provides axial homogeneous and radial variable plasma parameters [1]. The cylindrical chamber is 420 mm in diameter and 700 mm in length. The plasma column is about 300 mm long, the radius varies from about 30 mm to vessel dimensions, depending mainly on pressure. As the plasma is investigated along the axis, the large vessel dimensions reduce effects of the wall material (high-grade steel) on the observed plasma volume. However the central column is a quartz tube and the plasma is always in direct contact with this quartz surface, as sketched in Fig. 1. Electron temperatures and densities of 2 - 4 eV and 0.5 - 5 $\times$ 10^{17} m^{-3}, respectively, can be achieved, depending on pressure (6 to 100 Pa) and the

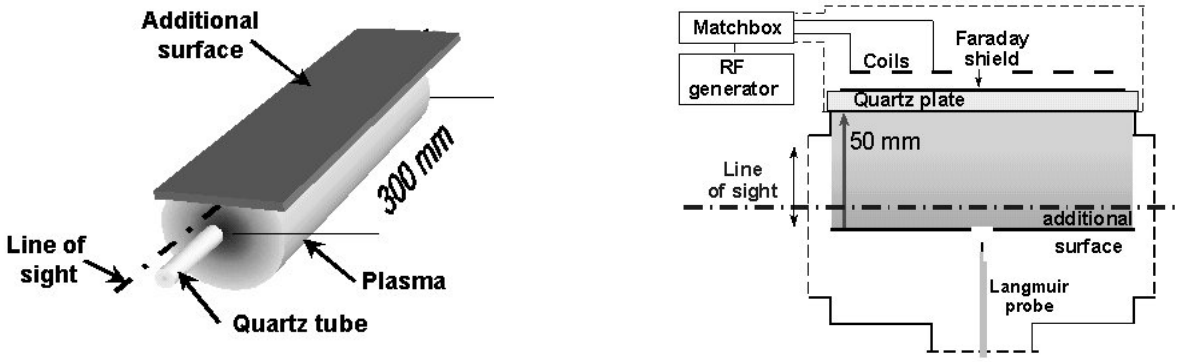

Figure 1. Geometry and lines of sight for both plasma experiments. Left: surface wave excited microwave plasma. Right: planar inductively coupled plasma.

percentage of helium admixture. Gas temperatures range from 550 K at low pressure to 750 K at high pressure. The line of sight for diagnostic purposes is arranged to be parallel to the central axis (homogeneous plasma) at a distance of 20 mm to the quartz tube and 6 mm to an optionally exposed surface which has typically a size of 300 × 70 mm. Since the surfaces are exposed to the plasma the surface temperature is assumed to be in equilibrium with the gas temperature of the plasma. The large area and the long path of the line of sight directly above the surface should guarantee a maximum signal for the measurements.

The planar inductively coupled plasma source (f = 27.12 MHz, P_{max} = 600 W) is 150 mm in diameter and 100 mm in height [2]. To avoid capacitively coupling a Faraday shield is placed between the coils and the quartz plate. The plasma is heated mainly below the quartz plate. The chamber walls (high-grade steel) are water cooled. As a consequence the plasma in the ICP interacts with cooled steel surfaces and a hot quartz plate. This has to be kept in mind when discussing the effect of additional surfaces in the chamber on the vibrational population of hydrogen. However, relative variations of vibrational populations with several surfaces should be reliable and steel and quartz are investigated first. Due to planar coils and cylindrical symmetry of the chamber, the plasma parameters were homogeneous above an additional surface located in the center of the discharge (Fig. 1). Langmuir probe measurements are carried out through a hole (10 mm in diameter) in the additional surface along the z-axis of the reactor. Electron temperatures and densities are 2 - 5 eV and 10^{16} -10^{18} m^{-3}, respectively, due to a wide pressure range (1 -100 Pa) and a variation in input power. Gas temperatures are 450 – 800 K. The additional surface is 150 mm in diameter and can be cooled actively to 300 K, otherwise the surface temperature reaches gas temperature. Because of large diagnostic windows, which are 80 mm in height, the lines of sight for diagnostics can be arranged to be parallel to the surface with variable distance to the surface. Measurements are taken every 5 mm from 1 - 40 mm.

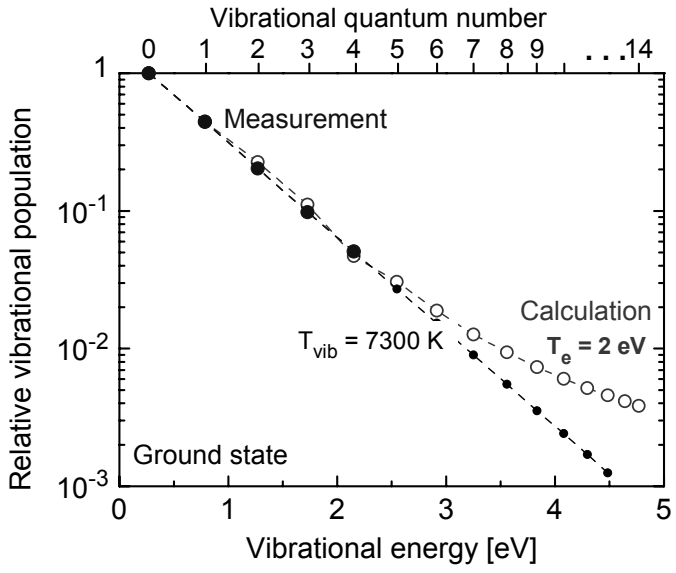

Figure 2. Boltzmann plot for relative vibrational populations of molecular hydrogen. Open symbols: collisional radiative model. Filled symbols: populations accessible by measurements. Small filled symbols: population according T_{vib}.

The spectroscopic method for determination of the ground state vibrational population is based on the measurement of the radiation of the Fulcher transition and the application of the Franck - Condon principle. It was already established for H_2 and D_2 in laboratory plasmas as well as in fusion edge plasmas [3, 4]. Beneath Franck - Condon factors, branching ratios, effective lifetimes, vibrationally resolved excitation rate coefficients as well as quenching corrections are considered for the interpretation of the radiation. It has to be mentioned that this method is sensitive for the first four (five) ground state vibrational levels of H_2 (D_2). For these levels the vibrational distribution is

characterised by a vibrational temperature $T_{vib}(X)$. However, it is not expected that vibrational levels higher than quantum number four (five) follow this Boltzmann distribution. It is well known, that electron impact excitation to the first electronically excited states in the singlet system ($B\,^1\Sigma_u^+$ and $C\,^1\Pi_u$) followed by spontaneous emission into the ground states leads to an overpopulation of higher vibrational quantum numbers. These volume processes can be described in simplified collisional radiative models. The result of such a calculation is shown in Fig. 2, together with a population according to a vibrational temperature (small filled symbols) [5]. The comparison shows, that the assignment of a $T_{vib}(X)$ to the first four to five quantum numbers is justified. The vibrational populations which are accessible with this simplified diagnostic method are shown for clarity by the filled symbols. It should be noticed that all results presented here refer to variations in vibrational populations of these first four to five levels. In order to obtain changes in higher vibrational states other diagnostic techniques must be applied, such as active laser diagnostics.

3. Results

For the investigations of the influence of additional surfaces on the vibrational population of hydrogen molecules, a gas mixture of 10%H_2 in helium was chosen. Helium was used to enhance electron temperature and electron density in comparison with pure hydrogen discharges. Thus, the intensity of the Fulcher band emission increases. Additionally, the molecular density decreases and consistently depopulating heavy particle collisions of molecules are reduced. To obtain a change in vibrational populations due to interaction with surfaces, mixing heavy particle collisions (volume processes) should be diminished as much as possible. Furthermore, the mean free path of the molecules, which penetrate from the surface into the plasma, should be in the range of some millimetres. This should be fulfilled for pressures below 20 Pa.

In the Duo-Plasmaline® the influence of steel, quartz, tungsten and graphite on the vibrational population of hydrogen and deuterium, characterised by $T_{vib}(X)$, was measured as a function of the discharge pressure. A comparison with plasmas without an additional surface is presented in Fig. 3. The pressure was varied from 6 to 100 Pa which yields molecular densities of 7×10^{19} to 1×10^{21} m^{-3}. The isotopes show similar dependence on pressure and materials. Except for graphite, $T_{vib}(X)$ ranges from 4600 to 6800 K (H_2) and 3000 to 4500 K (D_2). Furthermore, the isotopes show similar vibrational population densities, which is manifested in lower temperatures for D_2 due to lower energy separation of D_2 in comparison to H_2. Above a pressure of 20 Pa an enhancement of $T_{vib}(X)$ by the additional surface ($T_s \approx 500$ K) is clearly observed. Since the plasma is always in contact with the quartz tube only a relative enhancement with respect to quartz is measured. The fact that even the additional quartz surface leads to an increase of $T_{vib}(X)$ could lead to the statement that this variation is due to a change in plasma parameters, i.e. increase of electron temperature and decrease of electron density before the surface. However the radiation of a helium line remains stable. A considerable enhancement is observed in case of a carbon surface (graphite). Graphite is of special interest for investigations on plasma wall interaction for fusion experiments. In hydrogen plasmas chemical erosion of carbon occurs due to the bombardment of atoms and low energy ions. Hydrocarbons are released from the surface and penetrate into the plasma. Radiation of radicals such as CH and C_2 can be used to monitor the formation. In the underlying experiment the evaluation of the measured CH radiation yields a methane

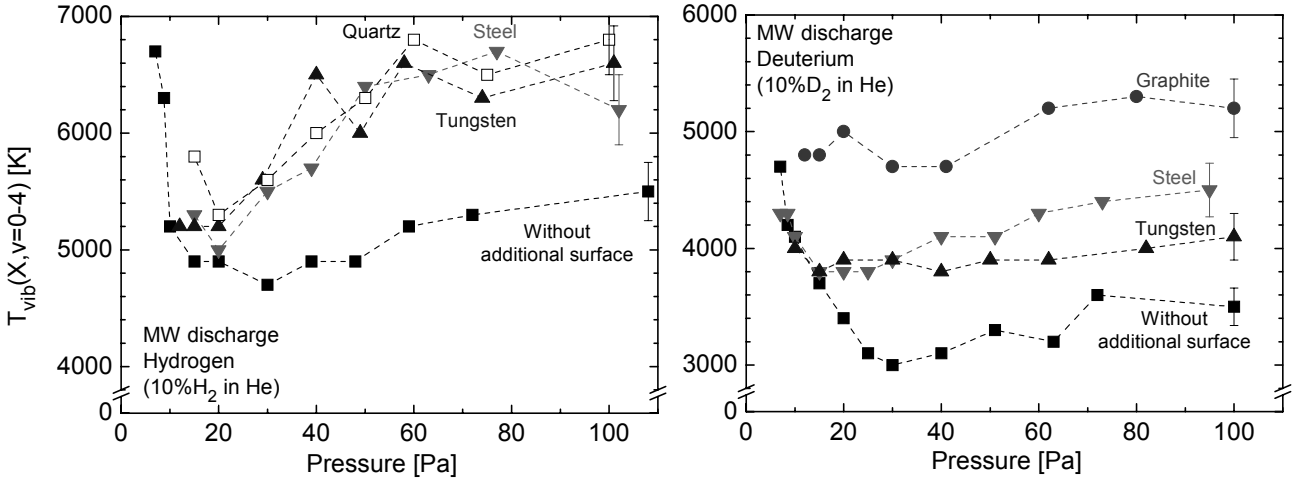

Figure 3. Vibrational temperatures in the microwave discharge with and without additional surfaces in hydrogen (left) and deuterium (right) plasmas as a function of discharge pressure.

density in the plasma of one percent. Since C_2 radiation is detected, higher hydrocarbons, such as the C_2H_y family are also present. As a consequence the enhancement in the vibrational population of hydrogen could be due to dissociation of hydrocarbons in the plasma. Measurements of vibrational population of hydrogen in methane plasmas indicated higher $T_{vib}(X)$ than in hydrogen plasmas under same conditions[6].

The inductively coupled plasma source provides the advantage to obtain spatially resolved vibrational populations and offers a comparison of surfaces at gas temperature with actively cooled surfaces (T_s = 300 K). Since the experiments run with similar gas mixture and discharge pressure electron temperatures and densities are comparable. Therefore, the relative dependence of the vibrational population on the additional surface is expected to be identical. However, in contrast to the Duo-Plasmaline®, the plasma is always directly in contact with cooled chamber walls, i.e. steel surfaces. First of all the profile of vibrational temperature in an empty chamber was measured at a pressure of 10 Pa and 5 Pa. Data were taken each 5 mm, covering a range of –35 to +35 mm from the discharge centre (z = 0). Flat profiles are obtained for both pressures, the temperatures are $T_{vib}(X)$ = 5000 K at 10 Pa and $T_{vib}(X)$ = 2800 K at 5 Pa with an error of approximately 500 K. Gas temperature is 560K and 500 K for 10 Pa and 5 Pa, respectively. Profiles of the atomic hydrogen density are obtained from the analysis of the absolute value of the radiation of the Balmer line, i.e. H_y, based on a collisional radiative model. Details of such an analysis are given in [7]. The atomic densities are in the range of some 10^{18} m^{-3} increasing a factor of three from a pressure of 5 to 10 Pa. Furthermore, a profile is observed, i.e. the density increases towards the coupling region, i.e. the quartz plate. Since the profile is given by diffusion, the slope in density can be used to yield the atomic hydrogen flux in the centre of the discharge [8]. Thus, a atomic hydrogen flux of $\Gamma_H = 2.6\times10^{21}$ $m^{-2}s^{-1}$ is obtained (10 Pa). For 5 Pa the slope indicates a lower flux but the small increase in density yields high error bars. Therefore, further measurements are carried out at the gas pressure of 10 Pa.

For reference, steel and quartz were tested first. At a distance of 5 mm from the surface no influence of steel on the vibrational population of hydrogen was measured. Active cooling of the surface yields the same results within the error bars. A large enhancement of $T_{vib}(X)$, from 5000 K to 8400 K, was detected in case of quartz (T_s = 560 K). It has to be mentioned that the surface was taken from the manufacturer and was exposed approx. one hour to the hydrogen plasma before the measurements have been started. Previous investigations indicate a time dependence, on a scale of several hours plasma operation, on the results. The longer the quartz surface was exposed to the plasma, the lower is the influence on $T_{vib}(X)$. The quartz plate at the top of the chamber is assumed to be in a steady state, full plasma operation time was several weeks.

Cooper, aluminium and tungsten surfaces lead to similar results as for the additional steel surface, i.e. no influence on $T_{vib}(X)$ in the plasma due to these metallic surfaces is observed at 5 mm distance. However, $T_{vib}(X)$ increases from 5500 K to 6500 K if the temperature of tungsten decreases, from 560 K to 300 K, respectively. This enhancement is clearly outside the error bars of the measurements. In case of graphite, the enhancement is much larger, i.e. from 6700 K to 9000 K or even higher, since the method is not sensitive for these high temperatures. Thus, similar statements for the material dependence are obtained in both plasma experiments, with the additional information that graphite temperature is an important parameter. This might be correlated to additional chemical processes, the formation of hydrocarbons, which can occur in contrast to metallic surfaces. However, in case of chemical erosion processes, it is known that the carbon flux from a graphite target has a maximum around 800 K. This means, less hydrocarbons are released from the surface at 300 K graphite temperature than at 560 K. It should be mentioned that the graphite material investigated in both experiments is pressed polycrystalline carbon, commonly used in fusion experiments. However, the surface is modified due to plasma treatment, i.e. the eroded hydrocarbons are re-deposited and form amorphous hydrocarbon films (a-C:H).

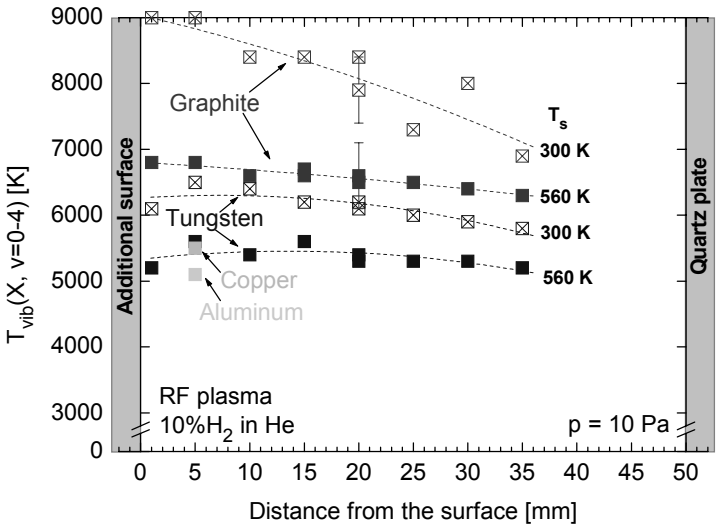

Figure 4. Spatially resolved vibrational temperatures of hydrogen in the ICP discharge with several additional surfaces.

For graphite and tungsten at 560 K and 300 K spatially resolved results are presented in Fig. 4. For comparison, the measured data for copper and aluminium at 560 K is shown also. In order to clarify the geometric set-up, the location of the additional surface and of the quartz plate are indicated. Except for graphite at 300 K, the profiles of $T_{vib}(X)$ are relatively flat. The large enhancement of $T_{vib}(X)$ for short distances from the graphite surface at 300 K indicate direct surface processes followed by collisions in the plasma volume. From the point of view of the surface the number of adsorbed atomic hydrogen particles can vary with substrate temperature. In case of the recombination of two particles, either the particles are adsorbed both, i.e. the Langmuir-Hinshelwood mechanism, or one atom in the gas phase recombines with a adsorbed atom, i.e. Eley-Rideal mechanism. Both processes depend on substrate temperature and the latter in particular on the atomic hydrogen density. The surface itself should be saturated with adsorbed particles, which is a reasonable assumption.
The atomic hydrogen densities are determined by optical emission spectroscopy, i.e. the analysis of the H_γ radiation, at a distance of 5 mm from the surface. In comparison to an empty chamber the density ($n_H = 3\times10^{18}$ m^{-3}) decreases a factor of 1.5 by implementing the metallic surfaces. In case of graphite, the density increases and the highest density is observed using the quartz surface ($n_H = 6\times10^{18}$ m^{-3}). The decrease in substrate temperature of tungsten does not affect the atomic hydrogen density, however an enhancement of a factor of 1.5 is measured for graphite. This is explained by different reflection coefficients for the materials being also a function of substrate temperature. Comparing these results with the variation of $T_{vib}(X)$ a correlation can be obtained, i.e. the higher the atomic hydrogen density the larger is the enhancement of $T_{vib}(X)$. This might indicate that the formation of molecules by the Eley-Ridal mechanism is preferred for the formation of already vibrationally excited hydrogen molecules.

4. Conclusions

The influence of several materials on the vibrational population of hydrogen in two types of hydrogen discharges was measured by optical emission spectroscopy. This diagnostic method offers an easy and fast method to determine the vibrational population of the first four to five quantum numbers which was characterised by a vibrational temperature. Since in both discharges, the plasma is always in contact with a quartz surface and, additionally, in one case, with cooled steel surfaces, only relative variations are obtained. For metallic surfaces, such as steel, cooper, aluminium and tungsten, which are exposed additionally to hydrogen and deuterium plasmas no change in $T_{vib}(X)$ was detected at low pressures, within the error bars of the method. Of course, the surfaces themselves were plasma treated and it was assumed that the substrate temperature is close to the gas temperature ($T_s \cong 600$ K). For tungsten, a decrease of substrate temperature leads to an enhancement of $T_{vib}(X)$. The largest effect was obtained in case of quartz. However, additional investigations have shown that the absolute value depends on the plasma exposure time of quartz. Furthermore, polycrystalline graphite surfaces, which are chemically active due to the chemical erosion process, were investigated. This surface has the highest influence on $T_{vib}(X)$ depending also on substrate temperature. Spatially resolved measurements showed the strongest influence near the target. This might be explained by the formation of hydrocarbons which penetrate into the plasma and dissociate in already vibrationally excited hydrogen molecules. A correlation of $T_{vib}(X)$ influenced by an additional surface with the atomic hydrogen density could be noticed.
These investigations on plasma wall interaction show clearly that the vibrational population of hydrogen molecules can be influenced by surfaces. As a consequence it is not sufficient to consider just plasma volume processes for plasma modelling. Detailed investigations on a dependence on material and substrate temperature have to follow to provide a data base for these kind of processes. Thus predictions of $H_2(v)$ will be improved which is necessary for example to increase negative hydrogen ion densities in plasmas.

References

[1] E. Räuchle - J. Phys. **IV** France 8, Pr7-99 (1998).
[2] P. Scheubert, U. Fantz, P. Awakowicz, H. Paulin - J. Appl. Phys.**90** 587 (2001).
[3] U. Fantz, B. Heger - Plasma Phys. Control. Fusion **40**, 2023 (1998).
[4] U. Fantz, D. Reiter, B. Heger, D. Coster - J. Nucl. Mater**. 290 – 293**, 367 (2001).
[5] D. Wünderlich, U. Fantz - IPP Report, IPP **10/18** (2001).
[6] U. Fantz, S. Meir - ECA **25A**, 273 (2001).
[7] K. Behringer, U. Fantz - NJP **2** 23 (2000).
[8] U. Fantz, H. Paulin - Physica Scripta **T91** 43 (2001).

Can Langmuir Probe be used for the Diagnosis of Atmospheric Thermal Plasmas with Gas Motion?

M T C Fang, J L Zhang and J D Yan

Department of Electrical Engineering and Electronics
The University of Liverpool, Liverpool L69 3GJ, UK

Abstract

The disturbance caused by the insertion of a Langmuir probe into a 5mm long, free burning 200A argon plasma at atmospheric pressure is investigated. It has been found that the disturbances are so severe that probe measurements cannot refer to an undisturbed plasma. The difficulties in interpreting the results of a sweeping probe are also discussed.

1. Introduction

This paper is concerned with the use of Langmuir probes in free burning, thermal plasmas at atmospheric pressure. The temperature range of interest is from 25,000K to 10,000K. Due to the interaction of the current sustaining the discharge with its own magnetic field a maximum velocity of around 150m/s on the axis of the discharge can be attained. The length of the discharge does not usually exceed 1cm. In such a hostile environment, the survival of the probe requires that the residing time of a probe is sufficiently short in order to avoid electron emission and ablation of the probe. Sweeping probes are therefore often used [1].

It is well-known that the derivation of the plasma parameters from probe measurements solely depends on the theoretical model with which the probe V-I characteristics are interpreted. A necessary condition for the meaningful use of probes is that the plasma is not disturbed sufficiently far away from the probe surface (usually a probe diameter). This is in fact the starting assumption of any probe theory. Earlier theory on probes in high pressure plasmas up to 1975 has been summarised by Chung et al [2]. Much work on probes assumes collision dominated space charge sheath (although it can be thin [2]) and the plasma is weakly ionised. The latter decouples the fluid dynamic aspects of the problem from the electrical characteristics of the flow. Thus, gas velocity and heavy particle temperature are assumed to be known although electron temperature may be different from that of heavy particles under the influence of the probe bias [2, 3]. The effects of ionisation and chemical reactions within the region of electrical disturbance are usually not considered.

The application of probes to the thermal plasma conditions indicated above has an added complexity. That is that the Debye length is usually smaller than the smallest mean free path calculated using LTE composition for the temperature range of interest. Thus, the space charge sheath is collisionless. The matching of a collisionless space charge sheath with a collision dominated quasi-neutral pre-sheath is extremely difficult. It can only be done if a kinetic approach is adopted for the region (commonly known as the Knudsen layer, [4]) between the continuum pre-sheath and the collisionless sheath. However, this is yet to be done for probes.

The objective of the paper is to investigate by computer simulation the validity of the necessary condition for the application of probes to flowing thermal plasmas within the temperature range of interest. Attention is paid to the thermal and fluid dynamic disturbances caused by a spherical probe situated on the arc axis. The probe surface temperature is assumed at the melting temperature of the material and a non-slip velocity boundary condition is imposed along the surface. Since sweeping probes are often used, we also investigate the characteristic time required for the plasma and probe to reach steady state.

This paper is not concerned with the situation where the use of Langmuir probes is restricted in the region near a wall or the probe being flush with a large cold electrode (e.g. [5,6]). For such an arrangement, the presence of a probe does not introduce additional thermal and fluid dynamic disturbances.

The paper is organised as follows. In Section 2, we present the temperature and velocity fields of a 200A free burning arc in argon in the absence and in the presence of a spherical probe. The time required for the plasma and the probe to reach steady after the insertion of a probe is investigated in Section 3. Finally, in Section 4 appropriate conclusions are drawn.

2. The Influence of the Probe on the Temperature and Velocity Fields

The arc burns in a 5mm gap between a shaped cathode and a water-cooled copper anode (Figure 1). The argon gas is fed in through an annular nozzle at a fixed flow rate of 10*l/min*.

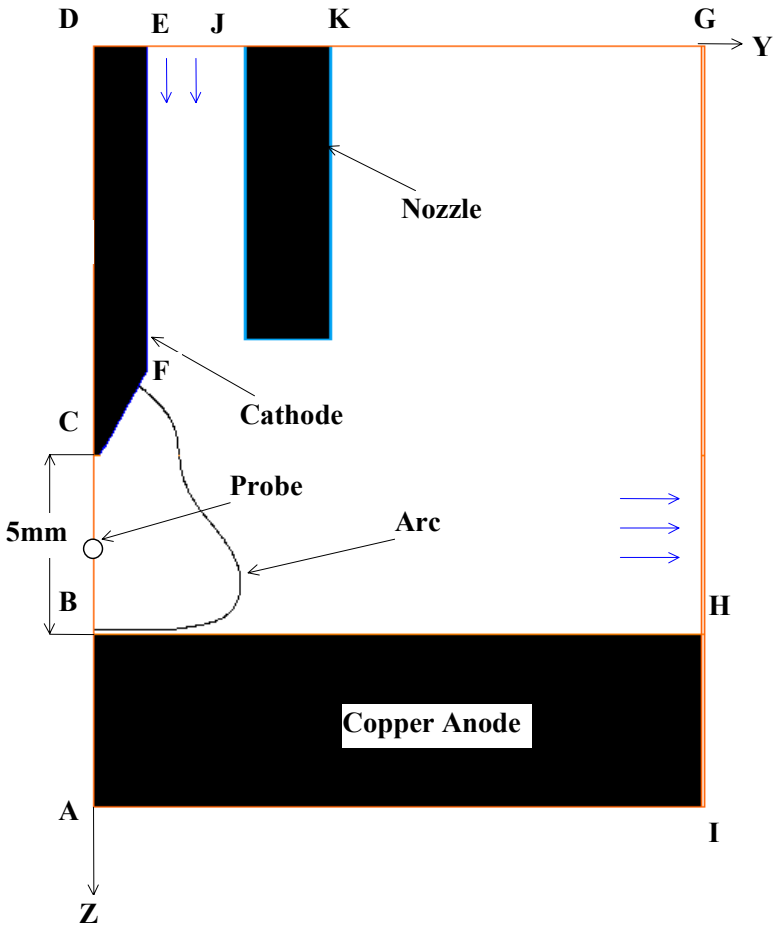

Figure 1 Schematic diagram showing the electrodes, nozzle and the dimensions. The same length scale is adopted.

The axisymmetric arc under LTE and steady state can be described by the conservation equations, which can be written in the following form:

$$\nabla \bullet \left(\rho \Phi \vec{V}\right) - \nabla \bullet \left(\Gamma_{\Phi} \nabla \Phi\right) = S_{\Phi} \tag{1}$$

where Φ is the dependent variable, ρ is the gas density, and $\vec{V}$ is the velocity vector. The source term S_{Φ} and the diffusion coefficients Γ are given in Table 1 where all symbols have their conventional meaning.

Table 1

Equation	Φ	Γ	S_{Φ}
mass of mixture	1	0	0
z-momentum	w	μ	$-\partial P/\partial z + J_r B_\theta$+ viscous terms
r-momentum	v	μ	$-\partial P/\partial r - J_z B_\theta$+ viscous terms
enthalpy	h	k/c_p	$\sigma E^2 - q + dP/dt$ + viscous dissipation

The electrical field is obtained by solving the current continuity equation:

$$\nabla \cdot (\sigma \nabla \varphi) = 0 \tag{2}$$

where φ is the electrical potential.

The net radiation loss per unit time and volume, q, is calculated by a semi-empirical radiation transport model [7]. The transport model requires the net emission coefficients, which are given by Menart et al. [8]. Transport properties as a function of temperature and pressure are provided by Murphy [9]. The boundary conditions required for solution are listed in the Table 2.

Table 2 Boundary Conditions

	DE	EJ	KG&GH	BH	BC	CD	Probe surface
v	---	0	$\partial v/\partial n = 0$	v=0	$\partial v/\partial y = 0$	---	v=0
w	---	w_{in}	$\partial w/\partial n = 0$	w=0	$\partial w/\partial y = 0$	---	w=0
h	---	T=500K	$\partial h/\partial n = 0$	T=1355K	$\partial h/\partial y = 0$	---	T=1355K
φ	$\partial\varphi/\partial z = j_0/\sigma$	$\partial\varphi/\partial z = 0$	$\partial\varphi/\partial n = 0$	φ=const	$\partial\varphi/\partial y = 0$	$\partial\varphi/\partial y = 0$	$\partial\varphi/\partial n = 0$

Where j_0 is the total current divided by the cross section of the uniform section of the cathode and n denotes the normal direction to a surface.

PHOENICS [10] is used to solve the conservation equations and the current continuity equation. The temperature and axial velocity fields are shown in Figure 2. The highest temperature, 27,000K, is near the cathode and the maximum axial velocity is about 130m/s. The calculated temperature is in good agreement with that measured [11], thus gaining confidence in computed results.

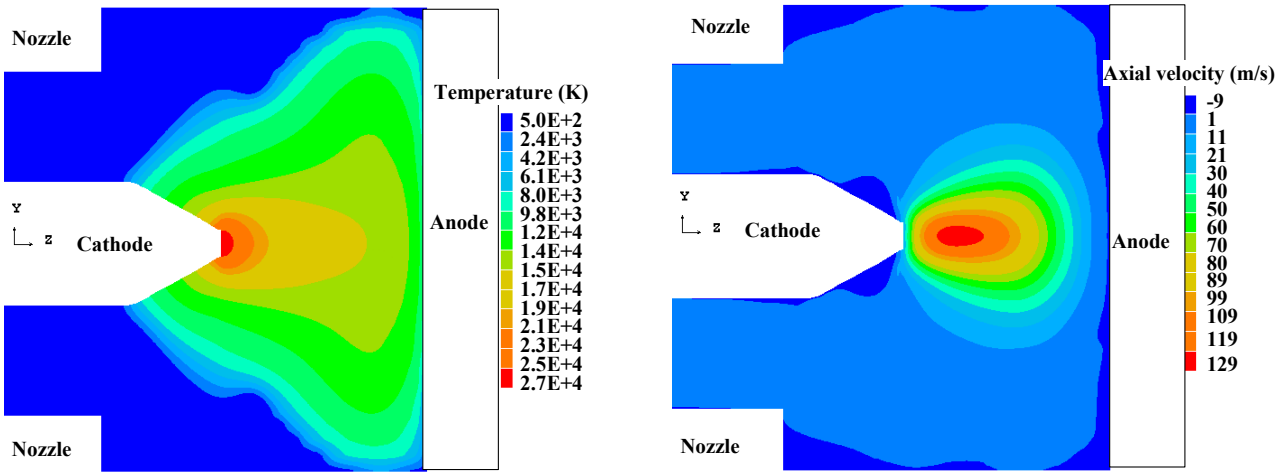

Figure 2 Temperature and axial velocity fields of a free burning argon arc at 200A.

The influence of a probe inserted in such an arc discharge is investigated by placing a spherical probe of radius of 0.125mm made of copper on the arc axis, which is 2.5mm away from the cathode tip. The surface temperature of the probe is set at 1,355K and the non-slip condition for velocity along probe surface is imposed. The computed results with a probe inserted are given in Figure 3, which shows severe disturbance affecting a large part of the arc, especially the velocity field. A detailed comparison of axis temperature and velocity in the absence of a probe with those in the presence of a probe is shown in Figure 4. The thermal disturbance in the upstream region of the probe extends 3 probe diameters from the probe surface. The size of the thermal disturbance downstream of the probe is twice that of the upstream. The disturbance on the velocity field is even more severe, which extends to the cathode and anode region. It is therefore obvious that

the disturbance caused by the presence of a probe is not localised, and, hence, the very foundation for the application of Langmuir probes does not exist for the thermal plasma under investigation. Since there are no "localised" un-disturbed upstream conditions, the use of the knowledge of the local plasma parameters in the absence of a probe to estimate the thermal, viscous and electrical boundary layer thickness would be in serious error.

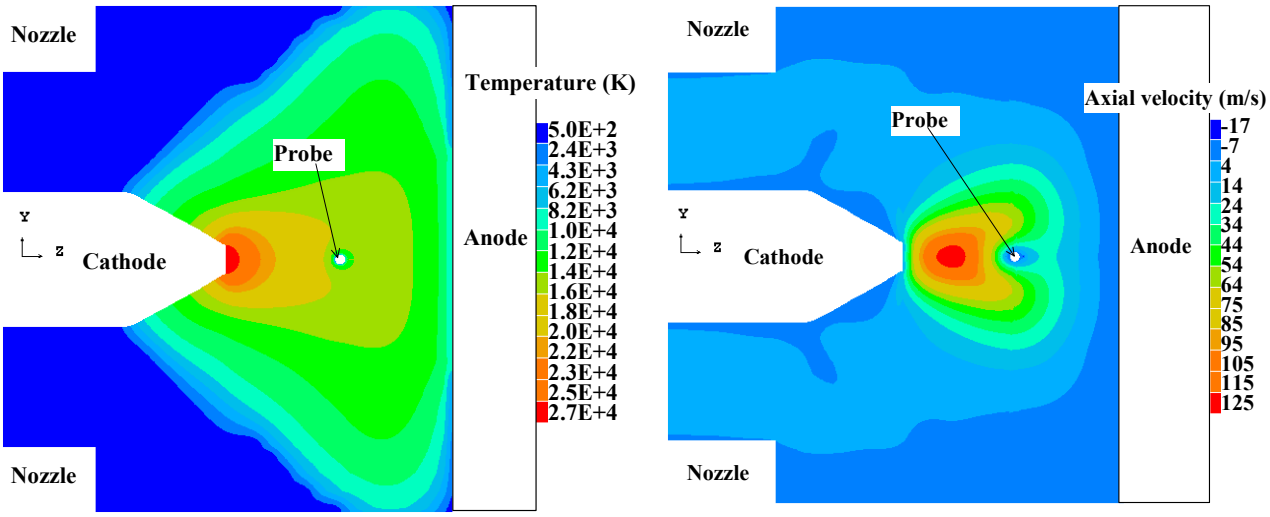

Figure 3 Temperature and axial velocity fields of a free burning arc at 200A with a spherical probe inserted on the axis.

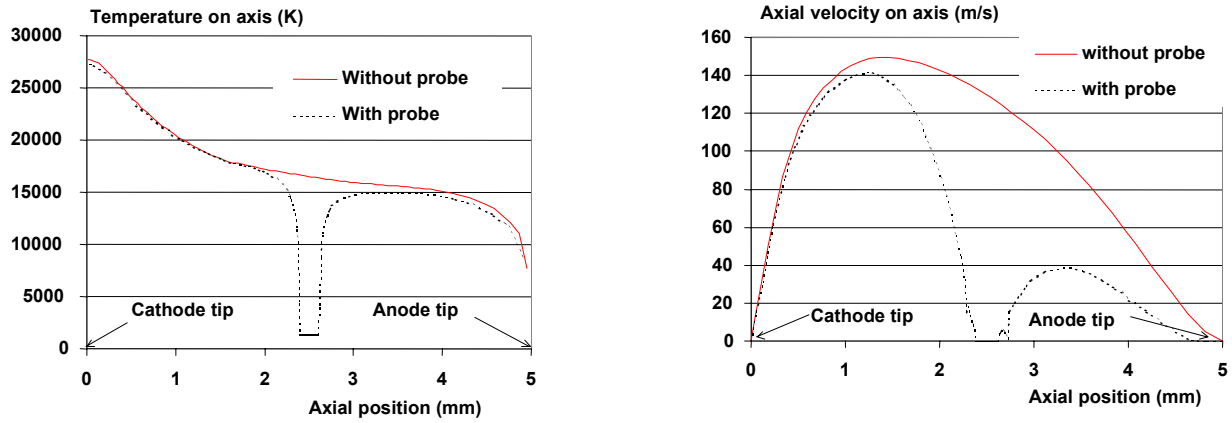

Figure 4 Thermal and fluid dynamic disturbances caused by the insertion of a spherical probe of radius of 0.125mm.

It is not surprising that the insertion of a probe could cause such a severe disturbance. The temperature boundary conditions imposed along the probe surface force the surrounding gas to become electrically non-conducting, which deprives Ohmic input in the region. This further reduces the temperature close to the probe. The increase in gas density due to the reduced temperature results in a decrease in velocity. Thus, the energy convected into the near probe region from high temperature upstream region is reduced. Through thermal conduction and the effects on the velocity field the cooling effects due to the probe spread into neighbouring regions, thus resulting in a severe disturbance extending to the whole arc.

The results shown in Figures 3 and 4 are obtained by assuming that the whole system is still in local thermal equilibrium. LTE assumption would no longer be valid in the region where temperature is below 8,000K. This renders the situation even more complex. However, for the demonstration of the effects of the insertion of a probe the LTE model serves the purpose.

3. On the Use of a Sweeping Probe

The use of a sweeping probe is necessary in practice in order to avoid the destruction of the probe by the high temperature plasma. The interpretation of the results obtained by a sweeping probe requires, in addition to the assumption of localised disturbance, that the plasma and the probe are in quasi-steady state when the probe sweeps across an arc cross section. The validity of this assumption is investigated by observing the transients caused by the insertion of a cylindrical probe into a uniform flow perpendicular to the probe. The upstream temperature and velocity correspond to the local un-disturbed conditions given in figure 2. Typical results are shown in Figure 5. The time required to obtain the steady state solution is approximately 4-5ms, which is comparable to the residing time of the probe in the arc. It is therefore unlikely that a quasi-steady state could be established on every point of the trajectory of the sweeping probe. The current method of computing the time required for the establishment of steady state tends to underestimate the time as the disturbance caused by the probe affects the whole arc.

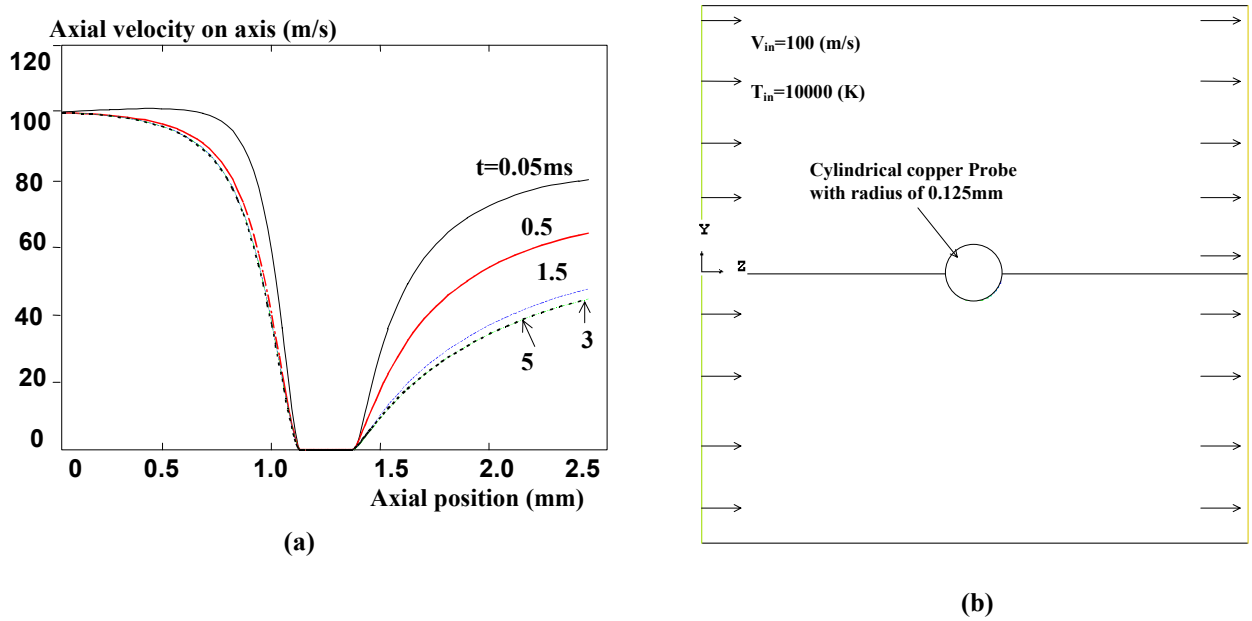

Figure 5 (a) The change of axis velocity after the insertion of a probe at t=0. (b) The simulation domain which is twenty times of the probe radius.

4. Conclusions

The application of Langmuir probe for the measurement of plasma parameters requires that the disturbance caused by the probe be localised. The validity of this very basis for the interpretation of Langmuir probe characteristics has been examined by using computer simulation. It has been found that, for the thermal plasma conditions under investigation, the presence of the probe severely affects the temperature and velocity fields of the whole arc. It is therefore not possible to refer probe measurements to an un-disturbed plasma. Probe measurements in the fringes of arc plasmas (such as anode boundary layer) may be feasible. The added difficulty in elucidating the characteristics of a sweeping probe is that the plasma and the probe are not in quasi-steady state.

Acknowledgement

The work forms a part of a research programme supported by the Science and Engineering Research Council of the UK. Valuable discussions with Emeritus Professor E Pfender of the University of Minnesota and with Professor M S Benilov of Universidale da Madeira, Portugal, are gratefully acknowledged. However, our discussions with Professor Benilov do not imply that he agrees with our conclusions.

Reference

[1] A E F Gick, M B C Quigley and P H Richards, J Phys D: Appl. Phys., **6**, 1941 (1973).
[2] P M Chung, L Talbot and K J Touryan, Electrical probes in stationary and flowing plasmas, Spring-Verlag, New York, (1975).
[3] M S Benilov, J Phys D: Appl. Phys., **33**, 1683 (2000).
[4] K-U Riemann, J Phys D: Appl. Phys, **25**, 1432 (1992).
[5] E Leveroni and E Pfender, Rev Sci Instrum., **60**, 3744 (1989).
[6] M Tanaka and M Ushio, J Phys D: Appl. Phys, **32**, 906 (1999).
[7] J F Zhang, M T C Fang and D B Newland, J. Phys. D, Appl. Phys., **20**, 368 (1987).
[8] J Menart, J Heberlein and E Pfender, Plasma Chemistry and Plasma Processing. **16**, 245S (1996).
[9] A B Murphy, Private communication.
[10] Phoenics is supplied by CHAM which is based at Bakery House, 40 High Street, Wimbledon Village, London, SW19 5AU, UK.
[11] Private communication, C Fanara, Cranfield University, UK.

FTIR spectrometry of argon/hexane plasma during the deposition of Ag/C:H films

P. Hlídek[1], H. Biederman[2], D. Slavínská[2], J. Kousal[2]

[1] *Institute of Physics, Charles University, Prague, Czech Republic*
[2] *Department of Macromolecular Physics, Charles University, Prague, Czech Republic*

Abstract
DC unbalanced magnetron was employed for the deposition of composite Ag/C:H (hard plasma polymer) films. Gaseous phase products of the discharge were characterized by FTIR spectrometry. Absorption bands of C_2H_2, CH_4 and C_2H_4 were identified for the working gas argon/*n*-hexane. For the case of working gas argon/*n*-hexane/air CO, CO_2, HCN, CH_4 and C_2H_2 were found. Only CO lines were observed in emission spectra. Non-equilibrium of rotational and vibrational states became evident from these spectra.

1. Introduction

Tunable diode laser absorption spectroscopy (TDLAS) and Fourier transform infrared (FTIR) spectroscopy are the most common techniques for infrared diagnostics of plasma. Because of its high sensitivity and resolution power, TDLAS can detect molecules in very low concentrations (including direct detection of short living intermediate species). This method is very useful for investigation of chemical reactions in plasma. On the contrary, FTIR is able to monitor much wider spectral region but with lower sensitivity and usually with much worse spectral resolution. Monitoring of stable end-products of reactions by FTIR spectroscopy gives indirect information about reactions in the plasma.

Applications of FTIR spectroscopy for detection of many various species in plasma or in discharges have been reported (see [1] for a review). This technique has been used for investigation of hydrocarbon plasma as well [2-6]. Methane CH_4 and acetylene C_2H_2 are the most abundant products detected. Spectral resolution is an important parameter; the resolution in the order of 10^{-3} cm^{-1} or better is used in high-resolution FTIR or laser spectroscopy of molecules. The necessary equipment is not common in laboratories not specialized in this field. In the most cases, FTIR spectroscopy is routinely used for characterization of liquid or solid samples. A resolution of the order of several cm^{-1} is adequate for this purpose. On the other hand, a high resolution measurement is time-consuming (investigated object can change its properties) and problem with signal/noise ratio appears in the case of low sample concentrations. Therefore resolution of 1 cm^{-1} or several cm^{-1} is often used for plasma diagnostics [2,4-6]. Of course, the better resolution the higher peak intensity of the narrow rovibrational bands; computer modelling (taking into account apparatus function of the spectrometer and correct parameters of absorption lines) has to be used for determination of molecule concentration [5].

Nanometer-sized metallic particles in various matrixes have been studied extensively in recent years because of their interesting properties and their possible applications. From the spectroscopic point of view, effects like surface enhanced Raman scattering (SERS) and surface enhanced infrared absorption (SEIRA) in systems containing silver particles are well-known. Composite material Ag/C:H based on polymer-like hydrocarbon matrix is one of many investigated systems containing silver nanoparticles. The composite materials can be prepared by a plasma polymerization with simultaneous metal sputtering, e.g. using a planar magnetron [7-9]. In our experiments the working gas was a mixture of argon and *n*-hexane vapour. Properties of the deposited films depend on concentration, size and shape of silver inclusions. Recently we reported dependence of deposition rate and properties of the films on the coverage of the silver electrode (i.e. magnetron target) by solid products of reactions in gaseous phase [10]. We employed both *in situ* and *ex situ* infrared spectrometry for characterization of the films deposited on mirror substrates (infrared reflection – absorption spectroscopy IR RAS) or on silicon wafers (transmittance measurements). In this paper we report infrared transmittance and emission measurements of the gaseous phase during the film deposition.

2. Experimental

Plasma polymerization and co-sputtering of silver proceed in a small vacuum chamber (inner diameter 190 mm, volume 4.7 dm^3). The silver target (diameter 75 mm) is a component of an unbalanced magnetron equipped with a ring of ceramic permanent magnets and with a mild steel magnetic circuit [11]. The chamber was pumped by rotary and diffusion pumps, pressure was measured by MKS Baratron 626 gauge and the

discharge was powered by an Advanced Energy MDX500 DC supply. Typical parameters of the discharge were: mixture of argon and n-hexane vapour as the working gas (air added in some cases); typical total flow rate 5 ccm(STP)/min., total pressure 3 – 30 Pa; current 0.1 A, power 30 – 45 W. Films were deposited on glass substrates and silicon wafers for IR transmittance measurement. The substrates were placed on a holder at a distance 80 mm from the magnetron target. Before each deposition the silver target was cleaned mechanically by an emery paper, washed by ethanol and additionally cleaned by an intensive sputtering in argon plasma (magnetron current 0.5 A for 5 minutes).
The infrared spectra were measured by Bruker IFS 66S spectrometer (beamsplitter KBr, detector MCT with cutoff wavenumber 800 cm^{-1}, the best resolution 0.15 cm^{-1}). The vacuum chamber was equipped with two KRS5 windows protected against film deposition by conical-shaped covers. Both transmittance and emission measurements were performed using focusing optics. The focus was localised in the centre of the chamber, 20 mm above the substrate. The transmittance spectra of the films were measured *ex situ* several minutes after the samples were taken out of the chamber.

3. Results and discussion

Absorption in gaseous phase

In our previous deposition experiments we usually used pressures 1 – 2 Pa. However, the higher pressure in the chamber the better spectra can be obtained. The spectra measured at the pressure 4 Pa of the mixture argon : *n*-hexane = 85 :15 with spectral resolution 0.2 cm^{-1} and 2 cm^{-1}, respectively, are shown in Fig. 1. The spectra for the total pressure 30 Pa in Fig.2 measured with resolution 0.2 cm^{-1} give more informations. About 80 - 90 % hexane is decomposed in the discharge. Absorption bands of methane CH_4, acetylene C_2H_2 and ethylene C_2H_4 can be distinctly recognized in the spectra. Methane, acetylene, carbon monoxide CO, carbon dioxide CO_2 and hydrogen cyanide HCN were identified in the discharge products for mixtures argon/hexane/air. HITRAN molecular spectroscopic database [12] was used for the identification. The absorption bands created by overlapping of many molecular transitions (not resolved in our spectra, e.g. 729 cm^{-1} for acetylene, 712 cm^{-1} for hydrogen cyanide or 3018 cm^{-1} for methane) are the most distinct lines for resolution 2 cm^{-1}. The strongest simple rovibrational lines of the small molecules can be seen in the spectra measured with 0.2 cm^{-1} as well.

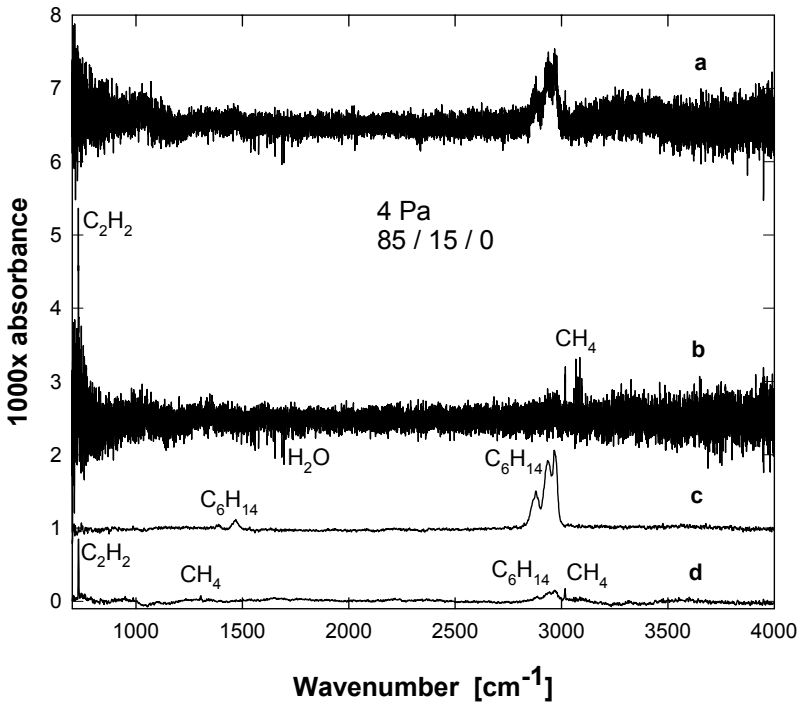

Fig.1. Absorption spectra of the gaseous phase measured with resolution 0.2 cm^{-1} (curves a,b) and 2 cm^{-1} (c,d) without the discharge (a,c) and during the discharge (b,d). The total pressure 4 Pa, composition argon : hexane = 85 : 15, discharge current 0.1 A, input power 32 – 36 W. Time of measurement 5 minutes in all cases.

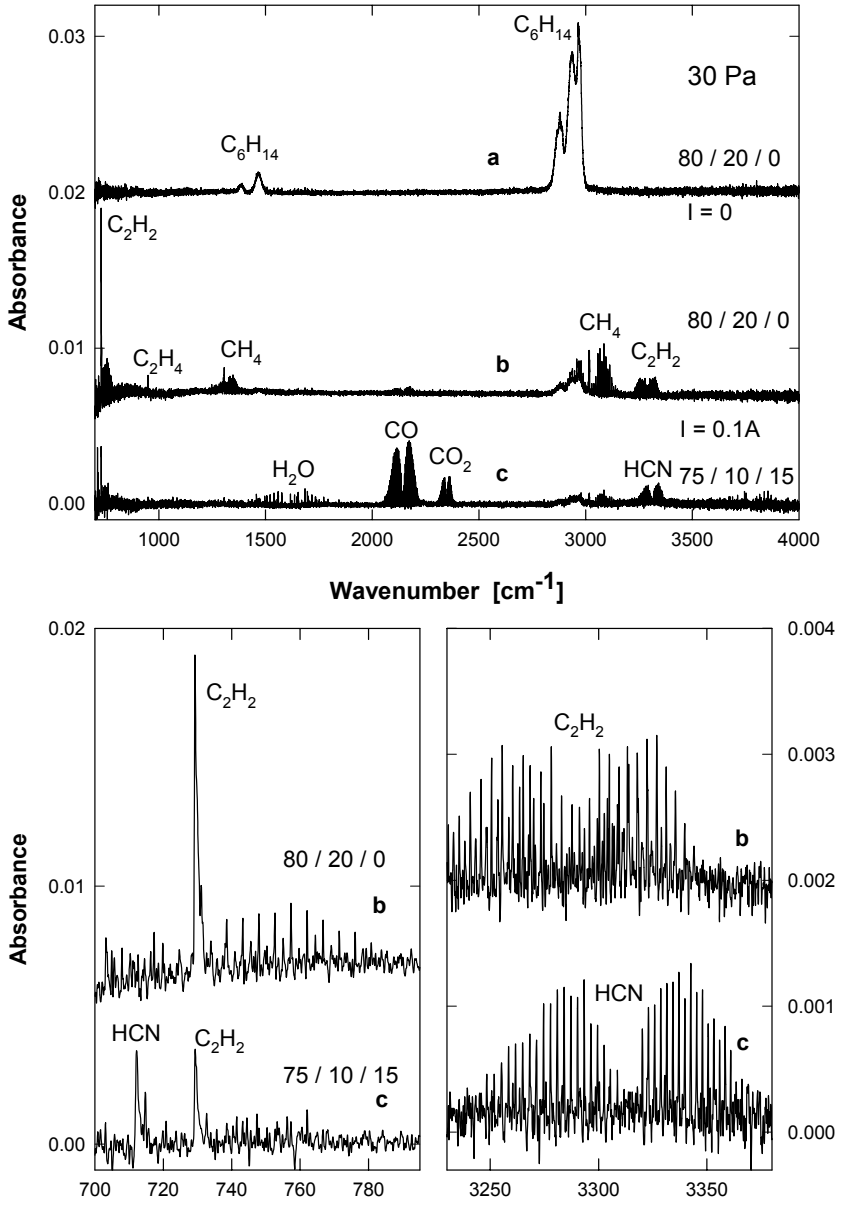

Fig. 2. Absorption spectra of the gaseous phase without discharge (a) and during the discharge (b, c). The composition of the gas is shown in the form argon / hexane / air. Total pressure is 30 Pa, electric current 0.1 A.

Emission of IR radiation by CO

We observed a line emission in the range 2000 – 2200 cm^{-1} superimposed on a background continuous room temperature thermal radiation. The absorption in this range (see Fig. 3a) is due to rovibrational transitions from the lowest vibrational state ν=0 of CO molecules to the first excited one ν=1 with the change of rotational quantum number $\Delta J=-1$ (branch P) and $\Delta J=+1$ (branch R). The emission corresponds to the inverse transitions from ν=1 to ν=0 (e.g. spectra d, h in Fig. 3), but a relatively strong contribution of transitions from ν=2 to ν=1 can be recognized in many spectra (e.g. c, i in Fig. 3). The vibrational temperature can be estimated to be higher than 2000 K if we take value 1/2 for the ratio of intensity of the transitions from higher vibrational level (from ν=2 to ν=1) to the intensity of transitions from ν=1 to ν=0. The estimation is based on Boltzmann distribution function taking into account that matrix elements for transition ν=2 to ν=1 are almost twofold than those for ν=1 to ν=0 transitions. On the contrary, the rotational temperature does not differ from 300 K remarkably. It should be emphasized that the emitted radiation was collected from the space near the substrate, relatively far from the magnetron electrode.

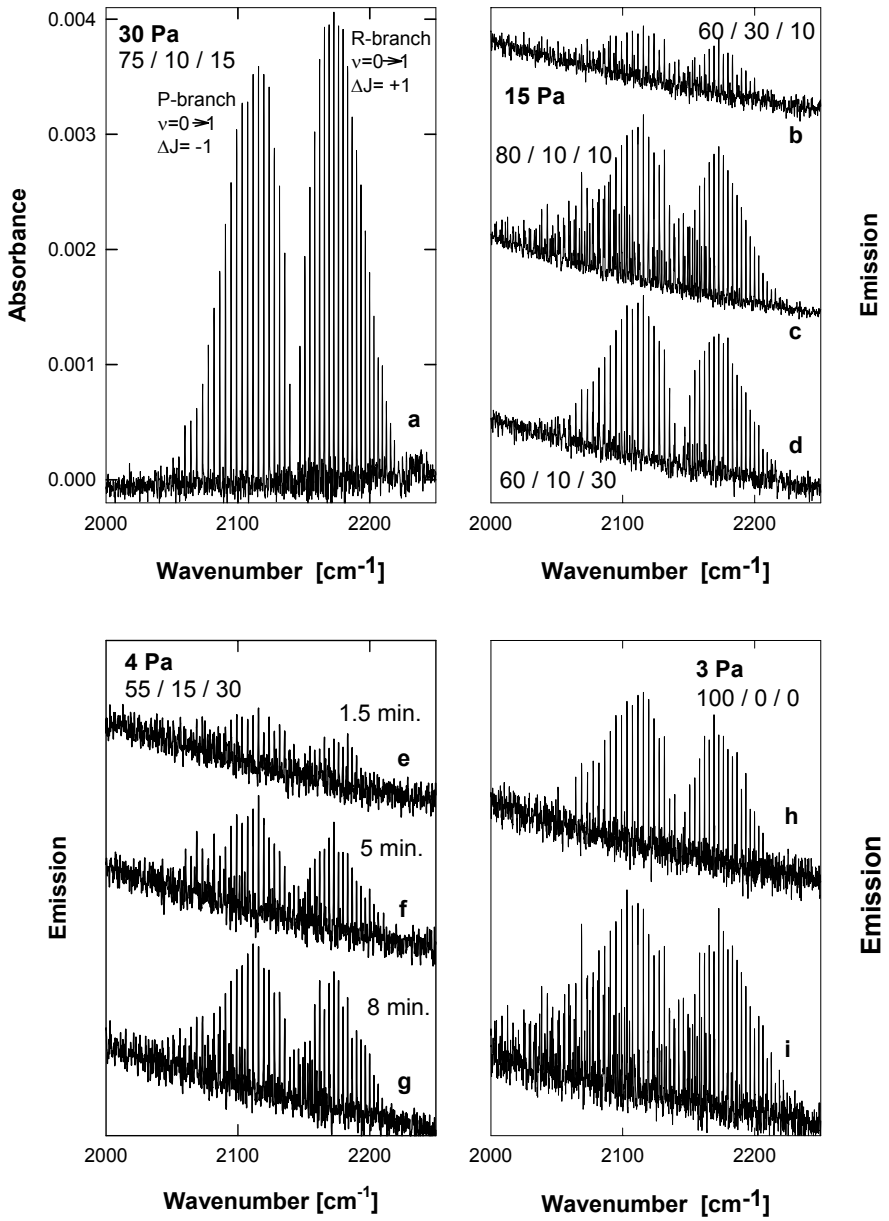

Fig. 3. Absorption and emission of carbon monoxide. Spectra a – d were recorded for various gas mixtures. Spectra e, f, g illustrate an evolution of the emission during one deposition. Spectra h, i were collected during initial stage of target cleaning in argon discharge with current 0.5 A (h - target with thick carbon cover, i - mechanically cleaned target); this emission was disappearing during several minutes.

The emission spectra are changing during the discharge on the time scale of minutes. Their intensity increases at lower pressures with air excess in the mixture (curves e, f, g in Fig. 3). On the contrary, their weakening or gradual vanishing is observed for *n*-hexane-rich mixtures. It seems that hexane and/or products of its reactions suppress all emission transitions (spectrum b), while air inhibits only transitions from the higher vibrational states $\nu = 2$ (spectrum d).

Spectra of the films

"Surface enhanced infrared absorption" (SEIRA) is well-known effect observed in various systems containing nanoparticles of some metals, including silver. Absorption bands caused by vibrations of atomic groups placed tightly near the metallic inclusions and with dipole moment perpendicular to the surfaces of metal particles are greatly enhanced. It is also the case of the composite films Ag / C:H. Vibration spectra of the deposited films were deduced from the transmittance measurements. Silicon substrate absorption was

subtracted and a subjectively chosen background correction was performed to eliminate contributions of an antireflection effect and a broad absorption tail of the silver – plasmon absorption with maximum in the visible region. The treated spectra are shown in Fig.4. Time of deposition was 10 minutes and the silver target of magnetron was cleaned before each deposition. All spectra were measured immediately (in 5 minutes) after removing the sample out of the chamber. A decrease of deposition rate with increasing pressure is considerable: from 30 nm/min for total pressure 4 Pa to 3 nm/min for 15 Pa.

As shown in our previous *in situ* investigation of samples deposited at a pressure 1 – 2 Pa, the spectra are very quickly changing just during first several minutes when the films are exposed to the ambient air. Namely the following absorption bands strengthen:

a) bands near 830 cm^{-1} (carbonate ions CO_3^{2-} bonded to silver particles with their plane parallel to metallic surface),

b) broad band around 1400 cm^{-1} (symmetric stretching of carboxylate ions OCO^- bonded to silver particles) and around 1550 cm^{-1} (antisymmetric stretching of the same ions),

c) bands in region from 1950 cm^{-1} to 2200 cm^{-1} (various types of carbonyl bonding to the silver).

Aging in the air (time scale days or weeks) caused some changes in the spectra:

1) carbonate groups oriented planparallel to the silver inclusions surface vanish,

2) absorption of carboxylate groups is strongly increased,

3) type of carbonyl bonding to silver is changed (possibly from a bridge configuration on the surface of Ag-inclusions to a linear one and/or to cations Ag^+ dispersed in the polymer matrix).

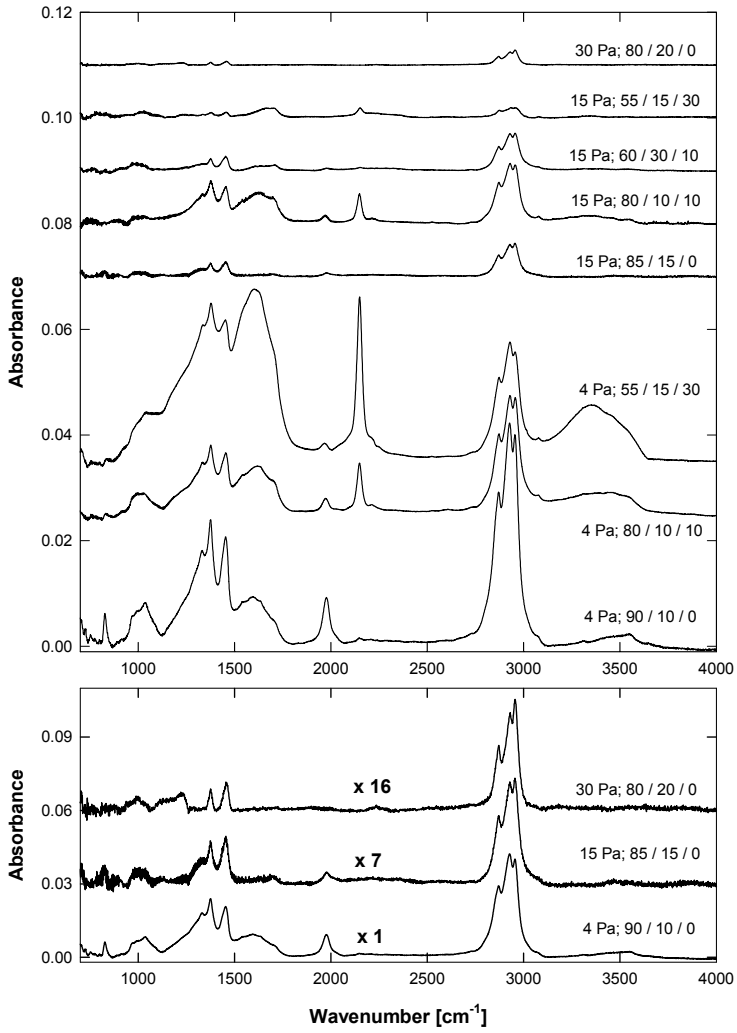

Fig. 4. Absorption spectra of the deposited films. The spectra are shifted in the upper part and normalized and shifted in the lower part of the figure. Total pressure and composition of the input gaseous mixture (argon/hexane/air) is given for the respective curves.

Similar bands are observed in the films deposited using the mixture argon/*n*-hexane/air. The effect of adding air into the gas mixture for discharge resembles the long-time aging of the films deposited from argon/*n*-hexane mixture. There is an exception: the films deposited in the mixture argon/*n*-hexane/air reveal much more intensive antisymmetric stretching band OCO^- ions. This can be explained by orientation of carboxylate groups which become more inclined relatively to the silver particle surface. It may be a consequence of a changed surface geometry and composition resulting from a higher oxidation of the silver inclusion surfaces.

It seems that role of the silver particles in the observed spectra becomes less important with increasing the total pressure. Absorption bands caused by hydrocarbons constituting polymer matrix prevail in these films. The absorption of CH_3 groups (near 2960 cm^{-1}) becomes stronger comparing to CH_2 groups (2930 cm^{-1}). This may be caused by creation of shorter molecular chains at higher pressures. Moreover, deposition rate is reduced substantially as mentioned above.

Another question is the incorporation of nitrogen in the films. Gaseous phase spectra showed a production of HCN in the discharge containing air. Unfortunately, the observed broad band infrared absorption (typical for disordered systems like plasma polymers) is not able to resolve oxygen- and nitrogen-containing groups because of an overlap of characteristic wavenumbers (e.g. OH and NH stretching above 3000 cm^1 or many possible types of vibrations in spectral region 1500 – 1700 cm^{-1}).

Conclusions

About 80 - 90 % *n*-hexane is decomposed in the discharge. The most IR-active gaseous products of reactions in plasma are methane CH_4 and acetylene C_2H_2 for gaseous mixture argon/hexane. The absorption of carbon monoxide CO, carbon dioxide CO_2, hydrogen cyanide HCN, acetylene C_2H_2 and methane CH_4 was observed in the discharge spectra in the mixture argon/*n*-hexane/air. Remarkable non-equilibrium between vibrational and rotational states occupation was found in the emission spectra of carbon monoxide. It depends not only on composition of the mixture but also on the cover of the magnetron target by solid products of plasma reactions. Rate of deposition of the films becomes lower with increasing total pressure. Spectra of the films deposited from mixture argon/*n*-hexane/air reveal some similar features to the aged films of Ag/C:H.

Acknowledgement. This work was supported by Ministry of Education of Czech Republic: program BM MSM 113200002 and project COST 527.40.

References

[1] Y. Segui, P. Raynaud, Plasma Diagnostic by Infrared Absorption Spectroscopy, in *Plasma Processing of Polymers,* eds. R. d'Agostino et al., Kluwer Academic Publisher 1997, p. 81.
[2] T. Mitomo, T. Ohta, E. Kondoh, K. Ohtsuka, J. Appl. Phys. **70**, 4532 (1991).
[3] C. Campargue, M. Chenevier, L. Fayette, B. Marcus, M. Mermoux, A. J. Ross, Appl. Phys. Lett. **62**, 134 (1993).
[4] Ch. Deschenaux, A. Affolter, D. Magni, Ch. Hollenstein, P. Fayet, J. Phys.D: Appl. Phys. **32**, 1876 (1999).
[5] M.F.A.M. van Hest, A. de Graaf, M.C.M. van de Sanden, D. C. Schram, Plasma Sources Sci. Technol. **9**, 615 (2000).
[6] C. Domingo, T. de los Arcos, A. Ainetschian, M. M. Sanz, I. Tanarro, Vibrational Spectroscopy **30**, 157 (2002).
[7] H. Biederman, L. Martinů, Plasma polymer – metal composition films, in *Plasma Deposition, Treatment and Etching of Polymer,* ed. R. d'Agostino, Academic Press, Boston 1990.
[8] H. Biederman, Y. Osada, *Plasma Polymerization Processe,* Elsevier, Amsterdam 1992.
[9] P. Hlídek, H.Biederman, H. Boldyryeva, D. Slavínská, Proc. of ISPC 15, vol.VI, Orleans, July 9-13, 2001, p. 2373.
[10] H. Boldyryeva, P. Hlídek, H. Biederman, D. Slavínská, A. Choukourov, Proc 4th Int. Conf. Coatings on Glass, Braunschweig, November 3 – 7, 2002, p. 323.
[11] H. Biederman, V. Stundžia, D. Slavínská, J. Glosík, Vacuum **57**, 415 (1999).
[12] L. S. Rothman et al., J. Quant. Spectrosc. Radiat. Transfer **60**, 665 (1998).

In situ-EDXRD Study of Nucleation and Growth of Tungsten and Molybdenum Disulfide Films Deposited by Reactive Magnetron Sputtering

V. Weiß, R. Mientus*, I. Sieber, K. Ellmer

Hahn-Meitner-Institut, Solare Energetik, D-14109 BERLIN, Glienicker Str. 100
phone: ++49-30-80622770, fax: ++49-30-80622434, e-mail: ellmer@hmi.de
** Opto-Transmitter-Umweltschutz-Technologie e.V., Köpenicker Str. 325b, 12555 BERLIN, Germany*

Energy dispersive X-ray diffraction (EDXRD) is a well-established method for the investigation of phase changes of powdered materials under high pressure and/or high temperature [1]. Recently, this technique was introduced by us for the in situ-investigation of thin film growth during reactive magnetron sputtering [2].
In the present work this method is used for the investigation of nucleation and growth of thin molybdenum and tungsten disulfide films, which are of interest as absorber materials for thin film solar cells [3]. These semiconducting materials belong to the class of layer-type van der Waals compounds, like graphite or mica.
For these experiments an situ-magnetron sputtering chamber was installed at a bending magnet beam line of the synchrotron radiation source DESY-HASYLAB in Hamburg (Germany). White synchrotron light hits at a small angle the growing film on a silicon substrate. The diffracted beam, observed under diffraction angles between 3 and 10 ° exits the chamber via a Kapton foil and is energy analyzed by a high purity Ge detector. The whole diffraction spectrum can be measured in short data collection times of between 10 to 30 sec, thus allowing time-resolved growth studies.
The balanced magnetron sputtering source at a distance of 6 cm from the substrate was excited either by DC or RF (13,56 MHz). For the characterization of the film growth the following quantities are used, which can be extracted from the EDXRD spectra:

- pattern of the diffraction peaks (phases, texture)
- energetic positions of the peaks (lattice constant, mechanical strain and stress)
- width and form of the diffraction lines (grain size, micro stress in the grains).

Furthermore, the fluorescence lines of Mo or W can be used to monitor in situ the growth rate of the films (in atoms/cm^2).
We found, that the growth of the layer-type compounds depends significantly on the deposition conditions, especially on the deposition rate and on the substrate temperature. At low growth rates and/or high temperatures the films exhibit a pronounced (001) texture, where the van der Waals planes are oriented parallel to the substrate surface. By varying the total sputtering pressure it was investigated if the energy of the sputtered or reflected particles (neutral argon) contributes significantly to the growth mode. It turned out, that the energy of the particles does not influence the film formation to a large extend in the pressure region investigated (0.5 to 9 Pa). At high deposition rates and/or low substrate temperatures the growth starts again with the (001) orientation. But after some 10 nm a texture cross-over occurs and a combined (100)(101) texture dominates the EDXRD spectra, where the van der Waals planes are vertically oriented, leading to a pronounced dentritic film structure. It is assumed that the vertically oriented lamella originate at defects (dislocations, stacking faults), which are likely to be formed in these materials due to the weak van der Waals bonding along the (001) direction. Due to the much higher growth rate along the (100) direction compared to the (001) direction, this cross-over can not be reversed once it occured.
In order to prepare (001)-textured films of these van der Waals compounds the orientations of the nuclei have to be preserved up to the desired film thickness by a low growth rate at high temperatures. The EDXRD method is a powerful tool for the in situ-investigation of thin film growth. The EDXRD results are complemented by morphological results obtained by scanning and transmission electron microscopy.

1 B. Buras and L. Gerward, Progr. Crystal Growth Charact. **18,** 93-138 (1989).
2 K. Ellmer, R. Mientus, V. Weiß, and H. Rossner, Nucl. Instr. Meth. Phys. Res. A **467-468,** 1041-1044 (2001).
3 H. Tributsch, Ber. Bunsengesell. Phys. Chem. **81,** 362-369 (1977).

Composite films with plasma polymer matrix prepared by rf magnetron sputtering

H. Biederman[1], Y. Pihosh[1], J. Kousal[1], D. Slavínská[1], P. Hlídek[2] and M. Trchová[3]

[1]*Department of Macromolecular Physics, Charles University, Faculty of Mathematics and Physics, Prague, Czech Republic*
[2]*Institute of Physics of Charles University, Prague, Czech Republic*
[3] *Institute of Macromolecular Chemistry, Academy of Sciences of the Czech Republic, Prague, Czech Republic*

Abstract
Composite films were deposited by rf co-sputtering of Ag or SiO_2 and PTFE or PE(PP) targets, respectively. Characteristics of sputtered Ag/hydrocarbon plasma polymer films correspond to the properties of composite metal/dielectric films. Composite SiO_x/fluorocarbon plasma polymer films reveal various wettability (static contact angle of water from 41° to 68 °) and hardness (from 3100 N/mm^2 to 720 N/mm^2). Composite SiO_x/hydrocarbon plasma polymer films have similar properties - the hardness seems to be generally lower.

1. Introduction
Composite films with plasma polymer matrix have been studied for several decades [1,2]. In the most cases – metal/plasma polymers have been in the center of the attention [1-3]. These can be prepared by several techniques – one of them is co-sputtering from composite metal/polymer target. Metal/fluorocarbon plasma polymer films [1-3] and metal/hydrocarbon plasma polymer were prepared using Pt-10 %Rh or Au or Cu/PTFE composite target [4]. In the other case Ekonol - (trade name of Carborundum Co) that is an aromatic polyester was used instead of PTFE [4].
More complex composites such as SiO_x/fluorocarbon plasma polymer were prepared by ion beam co-sputtering [5] and by plasma polymerization [6,7]. The intention was to apply the composite films mainly as protective coatings. Recently, these films were deposited using rf magnetron equipped with a composite SiO_2/PTFE target [8]. Composite films SiO_x/hydrocarbon plasma polymer or a-C:H prepared by plasma polymerization of HMDSO and a hydrocarbon gas have been investigated [9-11]
In this contribution rf co-sputtering from the two magnetrons equipped with Ag or SiO_2 and PTFE (Polytetrafluoroethylene) or PE (Polyethylene) and PP (Polypropylene) targets, respectively, was used in order to prepare composite films Ag/hydrocarbon plasma polymer, SiO_x/fluorocarbon plasma polymer and SiO_x/hydrocarbon plasma polymer. Deposition processes and basic characterization of the composite films are discussed below.

2. Experimental
The composite films were deposited in argon as a working gas at a pressure 5 Pa and a flow rate 25 cm^3 (STP)/min. The experimental set-up consists of two balanced magnetrons 78 mm in diameter each, sitting next to each other with the 90 mm distance between their centres. Ag and PE (PP); SiO_2 and PTFE (Goodfellow LTD); SiO_2 and PP (Goodfellow LTD), targets in the form of the disks were placed on the top of respective magnetrons.
The substrates were located 40 mm above the magnetrons. The specially designed substrate-holder enabled us to move (oscillate) the substrates in a horizontal plane above the magnetrons and thus to deposit the films with improved thickness homogenity in contrast to the previous case [8].
The parameter that controls the amount of respective component (Ag and PP, SiO_x and PTFE and etc.) in the film, is the deposition rate of the respective material given by the applied power to the magnetron. The deposition rate of each magnetron was controlled by quartz crystal microbalance heads (QCM) sitting above the magnetrons at the same level as the substrates. The calibration measurement was carried out earlier and it is described in [8].
The films were characterized by X-ray Photoelectron Spectroscopy (XPS), Fourier Transform Infrared Spectroscopy (FTIR), Atomic Force Microscopy (AFM), microhardness, and static contact angle of water.
Wettability was examined on composite films deposited on glass substrates. The contact angle of the water drops (about 2 mm in diameter) was measured with a contact angle meter (self built) by a sessile drop method at a temperature 18-20 °C in the air. The contact angle was measured in the the static mode when the

constant time (1 min) passed after dropping of water. The average angle values have been estimated from the three different points measured in the middle of the samples.
XPS measurements were performed using Kratos Axis 165 apparatus in a monochromatic Al K_α hybridmode, which means that both electrostatic and magnetic lenses were used.
The FTIR-RAS was performed on Nicolet Impact 400 spectrometer. For this measurement the films were deposited on Au precoated glass substrates. The film hardness was measured by an ultra-microindenter Fischerscope H-100 B.

3. Results and Discussion

Composite Ag/hydrocarbon plasma polymer

The films Ag/sputtered PP were deposited at 5 Pa of Ar, flow of Ar cm^3STP/min and powers ranging from 3 to 15 W for Ag and 30 to 60 W for PP targets, respectively. The films were deposited on glass substrates and carbon foils supported by Cu grid for TEM measurements.
Morphology of composite films Ag/sputtered PP or PE resembles those found for Ag/hydrocarbon plasma polymer prepared by dc magnetron sputtering of Ag in a working gas mixture of Ar and n-hexane[12] i.e. the film consists from Ag clusters embedded in a hydrocarbon plasma polymer matrix. The same optical anomalous absorption was found and dc electrical behavior. The dc electrical conduction increases with the filling factor f (volume fraction ratio) of Ag by several orders of magnitude revealing the percolation threshold approx. at f =0.4. The films are futher considered for antibacterial effects.

Composite SiO_x/fluorocarbon plasma polymer

The most attention was paid to composite SiO_x/fluorocarbon plasma polymer films. The deposition parameters are shown in Table 1.

Table 1. The deposition conditions.

Parameter	Value
Pressure of working gas: p	5 Pa
Flow rate of working gas: F	25 ccmSTP/min
Working gas	Ar
Power delivered to the magnetron with SiO_2 target: P_{SiO2}	25-160 W
Power delivered to the magnetron with PTFE target: P_{PTFE}	35-145 W
Deposition time: t	20 min
Substrate-target distance: d	4 cm

The deposition experiments were performed at different ratios of the applied powers to the magnetrons (P_{PTFE}/P_{SiO2}) (see Tab.1) at a constant oscillation velocity of the substrates.
The static contact angle of water measured on the resulting composite films increases steadily from 41° for film prepared at a power ratio P_{PTFE}/P_{SiO2} = 1/12 to the value 68° for film prepared at P_{PTFE}/P_{SiO2} = 10/1 (the contact angle on silica is ~27° and on PTFE it is ~109°). As it can be seen from Fig.1 the hardness values were found from 3100 N/mm^2 (1 mN load) to 720 N/mm^2 (1 mN load) in the above mentioned range of the power ratio. The films are rather smooth according to AFM – the roughness R_a is between 2 and 6 nm.
The infrared spectra of the fluorocarbon films are shown in Fig. 2. The spectra of the films prepared at the low P_{PTFE}/P_{SiO2} contain mainly the absorption bands coming from silicon-oxygen bond formations. The intensive asymmetric Si-O-Si as well as less intensive O-H, Si-O stretching vibrations are detected at 1080 cm^{-1} , 950 cm^{-1} and 795 cm^{-1} [13], respectively (see Fig. 2A, B).
With increasing PTFE content in the investigated samples, the asymmetric and symmetric CF_2 bands appear at 1230 cm^{-1} and 1150 cm^{-1}, respectively (Fig. 2C). At the moderate fluorocarbon concentrations the contributions from both SiO_x and CF_2 vibrations produce the total peak envelope in the range 900-1200 cm^{-1} (see Fig.2C). The following increase of fluorocarbon content leads to the disappearance of SiO_x response. Thus, only peaks related to CF_2 contributions are dominant over the whole spectrum (see Fig. 2D). In

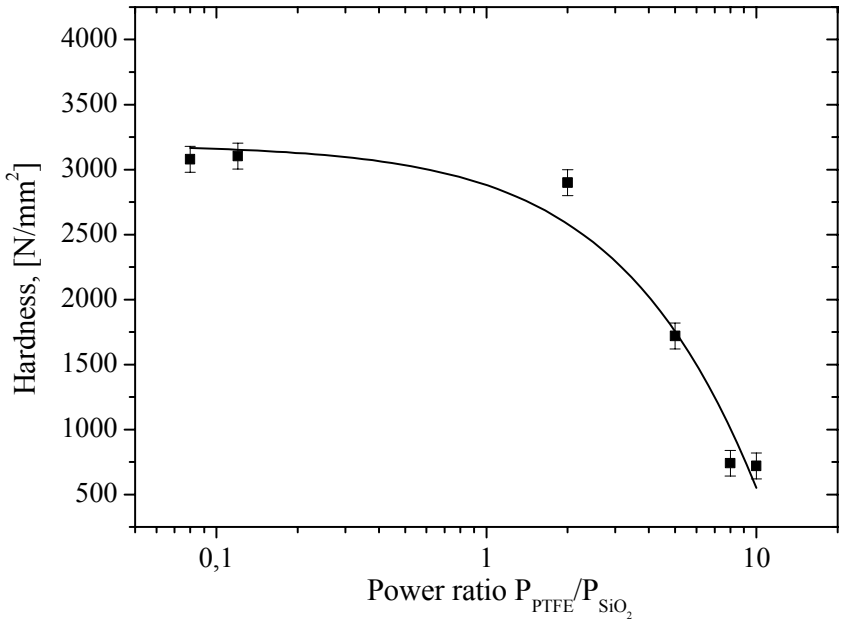

Fig.1. The dependence of film hardness on the applied power ratio.

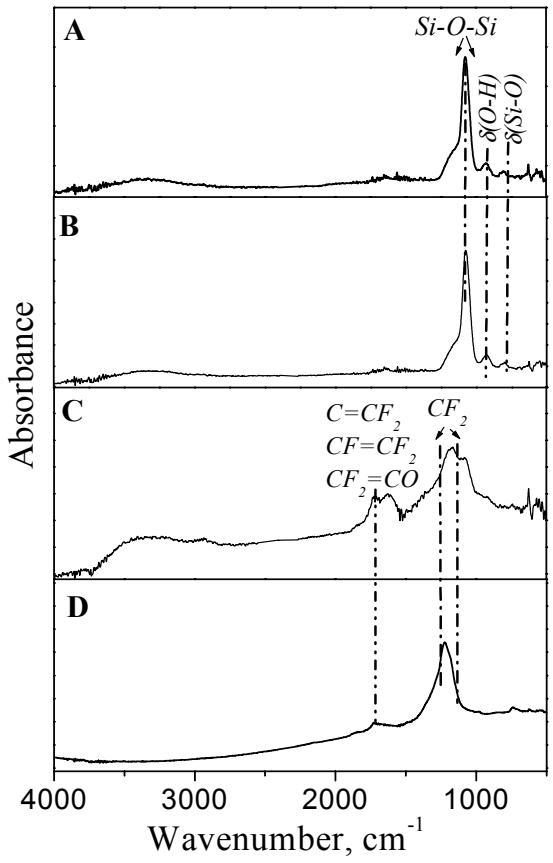

Fig.2. FTIR spectra of the films deposited at different P_{PTFE}/P_{SiO2} power ratios: 0.08 (A), 0.5 (B), 2 (C), 10 (D).

addition, the peaks corresponding to C=CF, $CF=CF_2$, CF=O vibration groups contribute to the FTIR spectrum.

The elemental composition obtained by XPS analysis is shown in Fig.3. One can see that the samples prepared at power ratios from P_{PTFE}/P_{SiO2} = 1/12 to P_{PTFE}/P_{SiO2} = 1/2 are composed from the two distinct components SiO_x and a fluorocarbon plasma polymer that is very deficient in fluorine (C:F ~ 4). However, part of carbon is likely bonded also to oxygen as may be seen from high resolution C1s spectra. It has been formerly observed that in some composite films with fluorocarbon plasma polymer matrix – namely gold/fluorocarbon plasma polymer the deficiency in fluorine increases with the increase of gold concentration and also it increases from the film bulk towards the surface [1]. In addition during the deposition process a reaction between Si and F may be expected that leads to creation of SiF_4 that is volatile at a room temperature and is removed from the reactor by pumps. This may also explain remarkable decrease of Si for power ratios P_{PTFE}/P_{SiO2} = 2/1 and 5/1 and occurence of only traces of Si for 8/1. The decrease of fluorine concentration is also seen. For power ratio 10/1 sudden increase of F was found that is not yet explained. Therefore these films prepared at higher ratios of powers (fluorocarbon dominated) can be viewed as a very oxidised fluorocarbon plasma polymers deficient in fluorine. However, some post deposition oxidation especially on the sample surface my happen at ambient atmosphere when transferring the samples for XPS measurements.
High resolution Si2p spectra show the peak at 103.5 eV that indicates that Si is bonded to oxygen. No Si-F bonding environments at higher binding energies or Si-C at lower energies was found. This suggests together with some AFM and EFM observations that especially for power ratios P_{PTFE}/P_{SiO2} from 1/12 to 1 the structure of the composite film is not homogenous but has a heterogeneous character probably regions of SiO_x dispersed in a fluorocarbon plasma polymer matrix that is also partly oxidised. However, bulk

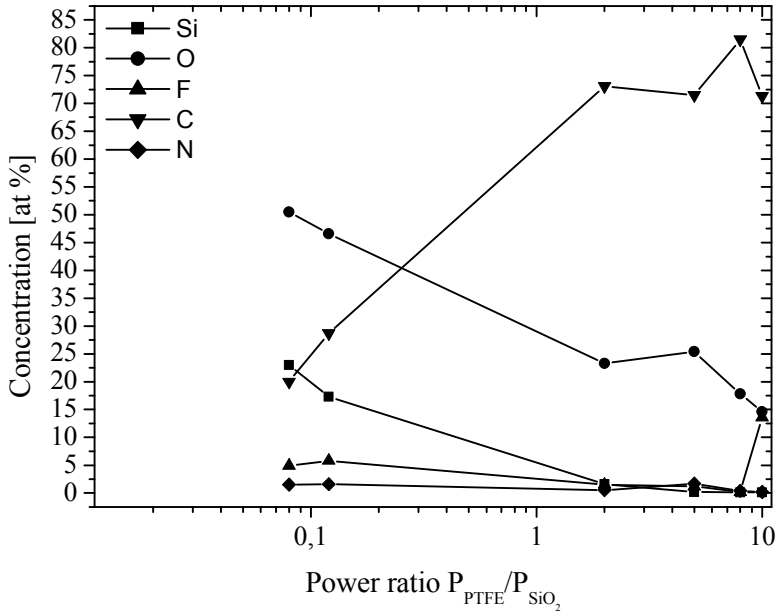

Fig.3. XPS elemental composition of composite SiO_x/fluorocarbon plasma polymer

elemental profiles by RBS/ERDA will be attempted in order to confirm if the XPS surface analyses is valid for the whole bulk of the film.

Composite SiO_x/hydrocarbon plasma polymer
These films were deposited as described above. The infrared data showed similar results as those for SiO_x/fluorocarbons. AFM observations showed similar roughness as before – the films are more or less smooth. Static contact angle is presented in Fig.4. It changes from 33° to 80° and this reflects the ratio of SiO_x and

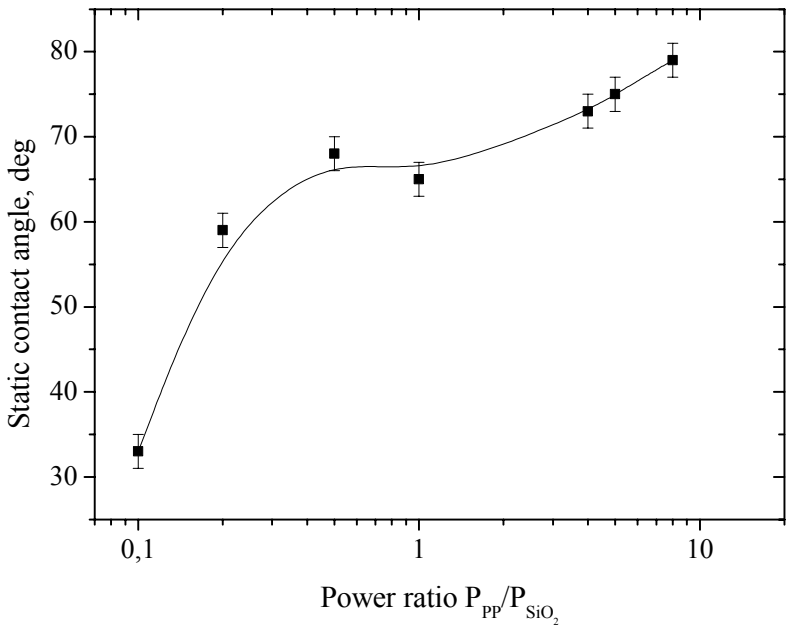

Fig.4. The dependence of static contact angle on the applied power ratio

hydrocarbon plasma polymer components in the composite. The hardness measured at the load 1 mN was found from 1000 N/mm^2 to 1800 mN/mm^2 .

4. Conclusions

Composite films with plasma polymer matrix were prepared by rf magnetron sputtering. Sputtered PP or PE films containing silver were found to be a type of composite Ag/hydrocarbon plasma polymer films. Composite films SiO_x/fluorocarbon plasma polymer were found to have very likely a heterogeneous structure. Contact angle of water increases from 41 ^{o} (high SiO_x contents) to 68 ^{o} (low SiO_x contents). Hardness decreases from 3100 N/mm^2 to 720 N/mm^2. Composite films prepared by co-sputtering of PP and SiO_2 possess various hardness (in the range from about 1000 N/mm^2 to 1800 N/mm^2) and vettability (static contact angle from 33 ^{o} to 80^o).

Acknowledgements

This work was supported partly by the grant OC 527.10(COST 527) and partly by Kontakt ME 553 and also by the Research Program BM MSM 113200002, all from the Czech Ministry of Education, Youth and Sports of the Czech Republic. The authors are grateful to Dr. A Hollander and A. Choukourov for XPS measurements on SiO_x/plasma fluorocarbon films. They are also indebted to Dr. J. Zemek for helpful discussions and to Dr. M. Kormunda and Z. Soukup for hardness measurements.

References

[1] H. Biederman and L. Martinů: Plasma polymer - Metal Composite Films. In: Plasma deposition, treatment and etching of polymers, Ed. R. d´ Agostino. Academic Press , Boston, 1990, p.269

[2] H. Biederman, and Y. Osada., Plasma Polymerization Procesess. Elsevier, Amsterdam, 1992.

[3] H. Biederman and Holland L., Nucl. Instr. and Methods **212,** 497 (1983).

[4] Roy R.A., Messier R. and Krishnaswami S.V., *Thin Solid Films* **109,** 27 (1983).

[5] A. Banks, S.K. Rutledge, J.A. Dever, P.D. Hambourger, P. Walters, E.J Bruckner, 39th Annual Technical Conference SVC paper 83, 1996, p. 431.

[6] A. Hozumi, H. Sekoguchi, N. Kakinoki, O. Takai, J. Mater.Sci. **32,** 4253 (1997).

[7] T. Shirafuji, Y. Miyazaki, Y. Hayashi, and S. Nishino, Plasmas and Polymers **4,** 57 (1999)

[8] A. Choukourov, Y. Pihosh, V. Stelmashuk, H. Biederman, D. Slavinska, M. Kormunda and L. Zajíčková, Surf. and Coat. Technol.**151-152**, 214 (2002).

[9] L. Zajíčková, P. Dvořák, V. Buršiková, V. Peřina, A. Macková, V. Navrátil, J. Janča, 15th Internacional Symposium on Plasma Chemistry, Volume **1**, 2001, p.133.

[10] M. Grischke, A. Hiecke, F. Morgenweck, H. Dimigen, Diamond and Related Materials **7**, 454 (1998).
[11] A. Grill, Diamond and Related Materials **8,** 428 (1999).
[12] H. Biederman, P. Hlídek, J. Zemek, D. Slavínská, J. Ježek, P. Zakouřil, and J. Glosík, Vacuum **46** , 1414(1995)
[13] M. Trchova, J. Zemek and K. Jurek, "Photoelectron and infrared spectroscopy of semi-insulating silicon layers," *J. Appl. Phys.,* **82** (7), 3519 (1997).

“From acoustic waves to the gas temperature in a point-to-plane dielectric barrier discharge in air at atmospheric pressure”

M. Dhainaut[1], E. Odic[2], Ph. Béquin[3], Ph. Herzog[4], M.Goldman[1], A. Goldman[1], Ph. Dessante[2] and C. Karimi[2]

1 Laboratoire de Physique des Gaz et des Plasmas (Université Paris-Sud / CNRS) Equipe Décharges Electriques et Environnement, SUPELEC, F-91192 - Gif sur Yvette cedex (France)

2 Service Electrotechnique et Electronique Industrielle, SUPELEC, F-91192 - Gif sur Yvette cedex (France)

3 Laboratoire d'Acoustique de l'Université du Maine - UMR CNRS 6613 - F 72085 - Le Mans cedex 9 (France)

4 Laboratoire de Mécanique et d'Acoustique - UPR 7051 - F 13402 - Marseille cedex 20 (France)

Abstract

Acoustic waves produced by the filamentary discharges developing in a point-to-plane dielectric barrier discharge in air at atmospheric pressure are used for an evaluation of the mean gas temperature in the discharge volume at its lowest level, just before the ignition of new filamentary discharges. Of crucial importance for the chemistry developed by the discharge, as it is typically the case for ozone production, this temperature exhibits values for instance ranging from room temperature to 780 K while the plasma temperature varies between 450 K and 1020 K.

References

[1] A. Chelouah, E. Marode, G. Hartmann and S. Achat, "A new method for temperature evaluation in nitrogen discharge", J. Phys.D : Appl. Phys. **27** (1994).

[2] B. Eliasson, U. Kogelschatz and P. Baessler, "Dissociation of O_2 in N_2/O_2 mixtures", Letter to the Editor, J. Phys. B: At. Mol. Phys., **17** (1984).

[3] M. Petit, N. Jidenko, A. Goldman, M. Goldman, and J-P. Borra, "A numerical treatment for electrical characterization of dielectric barrier discharges", Review of Scientific Instruments, **73,** 7 (2002).

[4] M. Fitaire, “Bruits Acoustiques des Arcs Electriques”, dans l’Arc Electrique et ses Applications, Club EDF- Arc Electrique – Tome 1, Ed. du CNRS (1984).

[5] E. Marode, S. Samson, D. Djermoune, N. Deschamps, and M. Touzeau, R. De Souza, “Time resolved Temperature Measurements and Computation of Streamer Air Discharge and Diffusion Controlled Chemistry”, J. Adv. Oxid. Technol., **4**, 3 (1999).

[6] M. Dhainaut , E. Odic, M. Goldman, A. Goldman, and C. Karimi, “Dependence of the oxidation properties of a dielectric barrier discharge in air on the plasma and gas temperatures”, Proc. 8th International Symposium on High Pressure Low Temperature Plasma Chemistry, HAKONE VIII, Estonia, **1** (2002).

1 Introduction

A thermal macroscopic equilibrium is obtained in a plasma reactor when a balance is reached between the heat input and the heat losses.

Let us here consider the case of dielectric barrier discharges traditionally used for ozone production. Heat losses depend on the external parameters such as the feed gas (air) temperature, flow rate, velocity and injection mode on the one hand, and as the reactor walls and dielectric barrier thermal conductivities on the other hand. Note that a feedback mechanism of the electrodes and of the dielectric temperatures on the electrical and physical properties of the discharge is often observed. The heat input comes from the energy injected in the discharge. In a dielectric barrier discharge, the gaseous gap is alternatively heated and cooled. When the discharge parameters, such as the injected energy, its current characteristics, its plasma temperature, its gaseous products concentrations, exhibit steady state values, a local thermal equilibrium is reached. The plasma temperature can be evaluated through rotational temperature measurements performed inside the transient filamentary streamers by means of emission spectroscopy [1], but the reactive volume temperature is periodically evolving between an upper limit, the plasma temperature measured during the emissive phase, and a lower limit, the neutral gas temperature just before the occurrence of any filamentary discharge. Focussing on a filamentary discharge developing in a gaseous gap with a 10 kHz repetition rate, it is worthy of note that the plasma phase (≈ 100 ns duration) only represents 0.1% of the period duration.

Since the time scale for ozone formation at atmospheric pressure is higher (5-15 µs) [2], the temperatures to be taken into account for the reactions kinetics are intermediate between both of the two limit values.
Results presented in this paper correspond to an attempt to evaluate the lower limit value for different repetition rates of the current pulses of the discharge, i.e. different local thermal conditions, through the analysis of the acoustic waves emitted by the filamentary discharges. The current interpulse duration will be controlled, independently of the applied electrical field value, by using pulsed high voltage signals with different repetition rates.

2 Experimental set-up and measurements

2.1 Experimental set-up

A schematic block diagram of the complete experimental set-up is given in Fig. 1. Three groups of measuring devices take place around the discharge cell itself, allowing the simultaneous monitoring, each one with its own time resolution constant, of the (i) discharge voltage/current signals, (ii) plasma temperature and (iii) discharge acoustic signal.

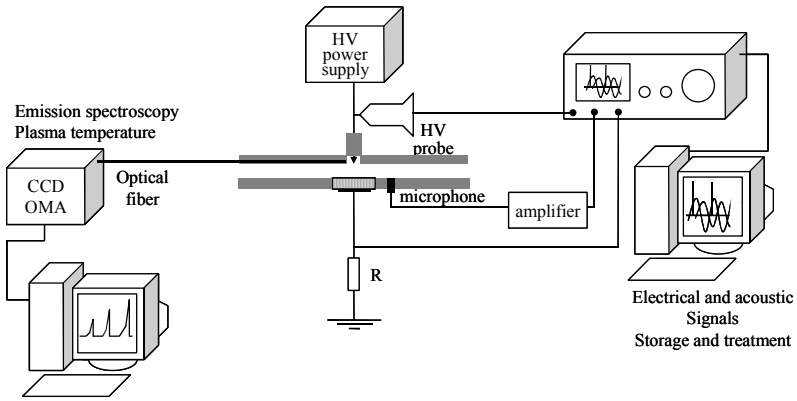

Figure 1 : Experimental set-up

The discharge reactor (Fig. 2) consists of a point-to-plane electrode system (Fig. 2). The high field electrode (point of ~ 50 µm radius of curvature) made of stainless steel is connected to the high voltage power supply. The plane grounded electrode made of brass is covered with a dielectric barrier (alumina-silicate ceramics 3 mm thickness). The gas gap length between the active electrode and the dielectric barrier surface is fixed to 2 mm. Experiments are performed in ambient air at room temperature.

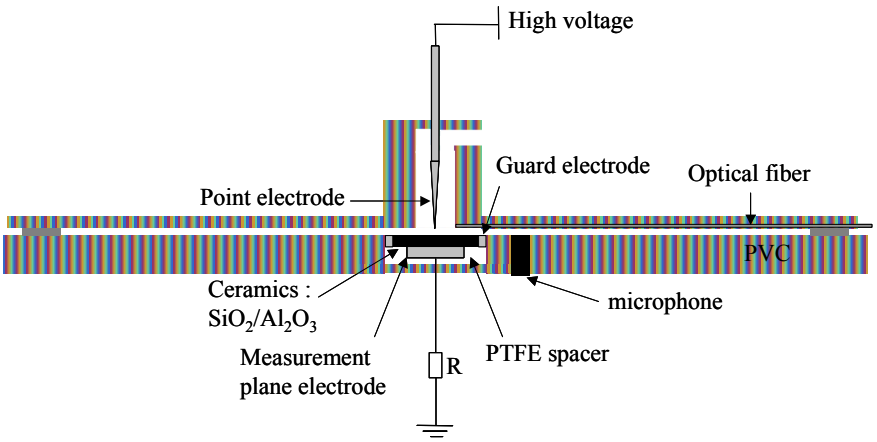

Figure 2 : Discharge reactor

2.2 Electrical measurements

Electrical measurements are carried out using a Lecroy LC347A 500 MHz - 2 GS/s numerical oscilloscope. A Lecroy 1000:1 100 MHz high voltage probe provides the voltage signal $v_1(t)$ applied to the high field

electrode. The measurement brass plane electrode is connected to ground through a 50 Ω resistor ; so the discharge current signal corresponds to the time resolved voltage $v_2(t)$ obtained on this resistor. The dielectric surface is limited by a guard electrode connected to ground. For the study of the discharge current signal itself, an accurate electrical analysis is realized with a numerical data treatment [3] which after eliminating the capacitive current, allows a fine analysis of the active components of the discharge current : the pulsed current and the pseudo continuous current - sometimes qualified of synchronous current (synchronous with the applied voltage).

2.3 Temperature measurements

Temperature measurements are performed by emission spectroscopy using a CCD detector coupled to an Optical Multi-channel Analyzer (OMA). This technique allows the evaluation of the rotational temperature reached in the filamentary discharge plasmas developing in air at atmospheric pressure by the excited molecular nitrogen. The $C^3\Pi_u$ excited state used for this purpose is produced through direct electron impact with the nitrogen molecule in its fundamental state :

$$e + N_2(X^1\Sigma_g^+) \rightarrow N_2(C^3\Pi_u) + e \qquad (1)$$

As this transition is quasi-instantaneous in our working conditions, the population distribution on the rotational level of the $C^3\Pi_u$ state can be considered as representative of the population distribution on the rotational level of the $X^1\Sigma_g^+$ state. Due to quenching effects with the neutral gas, the molecular excited state has, at atmospheric pressure, a lifetime of the order of 0.5 ns. The radiative desexcitation corresponding to the $0 \rightarrow 1$ band of the second positive system, i.e. the transition

$$N_2(C^3\Pi_u) \rightarrow N_2(B^3\Pi_g) + h\nu \qquad (2)$$

is used to determine the rotational temperature of the $C^3\Pi_u$ state, and by identification, the rotational temperature of the fundamental state, i.e. the neutral gas temperature. These measurements so provide an evaluation of the temperature of the plasma gas itself, in the filamentary discharge, where thermodynamic equilibrium does not exist.

2.4 Acoustic measurements

For measuring the acoustic pressure, a Brüel and Kjaer (B&K) 1/4 inch condenser microphone type 4938 (pressure field response) is used with a B&K microphone amplifier (Nexus). The microphone is flush-mounted and measures the actual sound-pressure level at the plate surface.

3 Results - Discussion

3.1 The acoustic signals

In a first approach, the interpulse duration is chosen long enough to minimise overlapping effects of the acoustic signal from a period to the following one. This is obtained with a pulsed voltage signal working at low frequency (≈ 3.5 kHz) and inducing the development of a single discharge channel per period, to which a single current pulse is associated, as it can be seen in Fig. 3.

Now focussing on the acoustic wave signal, it is worthy of note that this signal is resulting from the overlapping of the source phenomenon with reflection waves : as a matter of fact, the first overpressure peak is associated to the primary acoustic wave, the following overpressure peaks corresponding to reflection waves strongly dependent on the geometry of the upper part of the reactor. Furthermore, in the same figure, one can observe that the magnitude of the first overpressure peak is linked to the amplitude I of the current pulse. This first phenomenon here observed in unstable conditions will be now more systematically investigated for a steady state discharge regime.

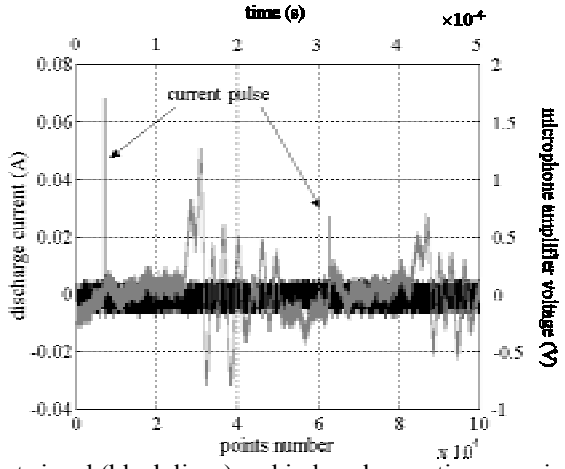

Figure 3 : Discharge pulsed current signal (black lines) and induced acoustic wave signal (grey lines). Acoustic pressure A_a(Pa) = 2.61 × microphone amplifier voltage (V). (V_p = 6.4 kV, F = 3.5 kHz, ambient air atmospheric pressure).

3.2 The acoustic signal as a function of the discharge current at a fixed "low" frequency (3.5 kHz)

For a same discharge repetition rate, governed by the pulsed high voltage repetition rate and inducing the development of a single discharge per period, one can increase the current pulse amplitude I by increasing the peak voltage amplitude V_p. When plotting the overpressure magnitude ΔP, i.e. the acoustic wave amplitude A_a, as a function of the current pulse amplitude I, as shown in Fig. 4, a linear correlation is obtained.

A consistent theoretical and experimental work has been done in the years 1980 on the acoustic emissions of atmospheric pressure arc discharges [4]. The acoustic equations are obtained from a first order expansion of the fundamental equations of dynamics for neutral particles. Assuming the neutral particles gas as an ideal gas, adiabatic conditions and first-order of the acoustic quantities, a propagation equation for the pressure can be obtained by use of the set of linearized acoustic equations (continuity, Euler and Fourier equations) in which the source terms appear :

$$\nabla^2 P - \frac{1}{c^2}.\frac{\partial^2 P}{\partial t^2} = -\frac{\gamma - 1}{c^2}.\frac{\partial H}{\partial t} + \mathrm{div}\vec{F} - \frac{\partial Q}{\partial t} \quad (3)$$

where P, Q, F and H are respectively the acoustic pressure perturbation, the particle mass source term, the vector force per unit volume and the energy per unit volume dissipated by Joule effect, c being the adiabatic sound speed and γ the specific heat ratio (7/5 for diatomic gases). This equation shows that three different mechanisms can potentially induce the excitation of acoustic waves : momentum transfer, energy transfer and mass transfer. It is stated by the authors that, in the case of atmospheric pressure arc discharges, energy transfer is predominating, namely through thermal transfer. The acoustic wave magnitude A_a can so be correlated to the energy transferred to the discharge according to the following equation :

$$A_a = K \times \frac{M}{k_B T_g} \times \frac{\partial H}{\partial t} \quad (4)$$

where M is the mass of gas in which the arc is burning, T_g the initial temperature of this mass of gas, k_B the Boltzmann's constant and K a constant proportionality coefficient.

Experiments on arcs burning in air performed at atmospheric pressure by Fitaire et al. [4] permitted to obtain a linear correlation between the acoustic wave amplitude A_a and the electric power (transferred to the discharge) derivative ∂W/∂t, assuming that cathode and anode voltage drops are not modified by an applied voltage modification. The theoretical approach was so validated by the experiments.

Coming back to our results of Fig. 4, it is noticeable that for the discharge regime under investigation, the characteristics of the current pulses are very similar : whatever the amplitude value I, constant values of rise time (≈ 10 ns) and amplitude/duration ratio are observed, with a current pulse duration never exceeding 100 ns. In turn, comparing our experiments results obtained in a thermodynamic non-equilibrium system at atmospheric pressure to the arc experimental results, it can be assumed :

(i) since all filamentary discharges here under consideration propagate with negligible voltage drops and for very akin onset voltage values, that the amplitude I of the current pulses of our non disruptive discharges can be here assimilated, with a K' factor proportionality, to the arc discharge $\partial W/\partial t$ power term.

(ii) since a linear correlation can be found between A_a and I, that the overpressure wave corresponding to the acoustic wave may be attributed to a local transient temperature variation.

Adapted to our experimental conditions, the Fitaire's equation may be written :

$$A_a = K.K' \times \frac{M}{k_B T_g} \times I \qquad (5)$$

implying that the gas volume involved in the discharge propagation is remaining constant, i.e. that the gas mass M and temperature T_g value remain constant for the pulsed current amplitude I range investigated. Plasma temperature values obtained by spectroscopic measurements in the vicinity of the point electrode range from 420 K to 480 K with increasing values of I. The transient heating of the gas gap volume by the discharge propagation is balanced by different cooling mechanisms : slow phenomena (conduction, diffusion) enhanced by the electrical wind effects, and rapid phenomena such as an adiabatic expansion [5]. The relaxation time (here ≈ 280 µs) is widely sufficient in this case (3.5 kHz case) to allow a cooling of the gas down to room temperature (300 K).

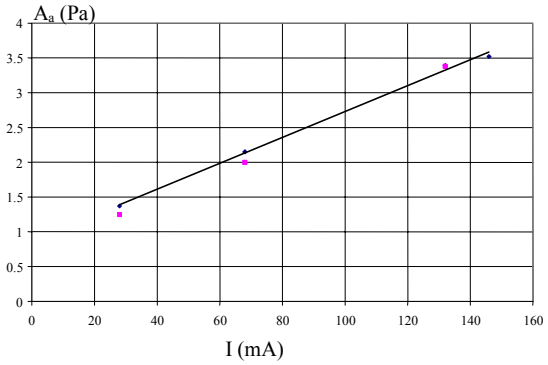

Figure 4 : Evolution of the acoustic wave magnitude A_a as a function of the current pulse amplitude I (F = 3.5 kHz, ambient air atmospheric pressure).

3.3 Effect of the frequency

Different working conditions have been investigated, adjusted through the high voltage pulsed signal frequency and a control of the current pulses amplitude ; the corresponding electrical and physical experimental data are summed up in Table 1. Increasing the frequency for a constant pulsed current amplitude ideally leads to reduce the cooling phase duration while keeping a same heat input phase. As a result, the mean temperature of the point-to-plane gas gap will increase, leading to :

(i) an increase of the local plasma temperature when the discharge will develop in this medium (injecting its own thermal contribution in a pre-heated gas)

(ii) to a decrease of the magnitude of the overpressure wave due to the decrease of the variation between plasma temperature and neutral gas temperature at the end of the relaxation phase.

Table 1 : Electrical and physical parameters of the discharge for 4 working points.

Frequency F (kHz)	Pulsed current amplitude I (mA)	Acoustic pressure A_a (Pa)	Plasma temperature T_{pl} (K)
3.5	140	3.38	480
15	50/140	1.7	540
30	225	2.7	920
50	225	1.3	1020

This is illustrated by Fig. 5 which shows that for equivalent current pulses, the acoustic pressure decreases when the high voltage frequency is raised. Note that the 3.5 kHz point (blank mark in Fig. 5) is calculated

using an extrapolation of the linear curve of Fig. 4. In other respects, the 15 kHz case in Table 1 exhibits a non consistent acoustic pressure value because two types of current pulses were obtained during two consecutive periods, so prohibiting a proper treatment of the acoustic signal.

Now focussing on the 50 kHz case, frequency condition for which thermal effects are not negligible [6], one can apply the equation (5) using as a constant coefficient the one found for the 3.5 kHz case (neutral gas temperature reference being room temperature). The gas gap temperature so calculated reaches 780 K, which is lower than the plasma temperature near the point electrode (1020 K). So it can be inferred that in the 50 kHz case, ozone is mainly produced in the volume surrounding the discharge channel and not inside the volume of the discharge channel between two current pulses. In the other cases, both possibilities seem to be valid.

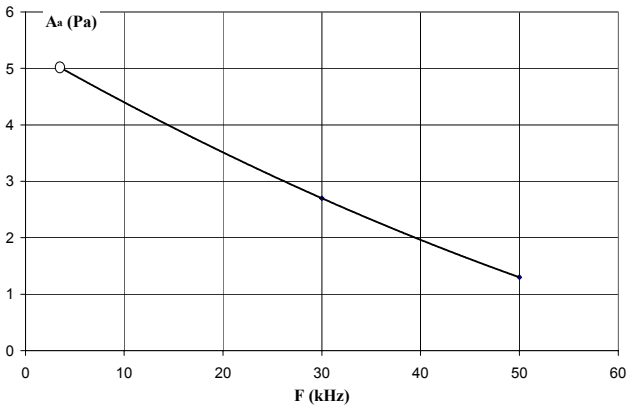

Figure 5 : Evolution of the acoustic wave magnitude A_a as a function of discharge frequency F (I = 225 mA, ambient air atmospheric pressure).

4 Conclusion

The paper shows how lower values of the temperature in the volume of intermittent electrical discharges in air at atmospheric pressure can be determined during their non emissive phases by means of acoustic pressure measurements, while emission spectroscopy allows to get upper values with the determination of rotational temperatures during their emissive phases. This is of particular interest for gas phase chemical reactions kinetics, such as ozone formation/destruction kinetics.
So, using pulsed high voltage signals of frequencies ranging from 3.5 kHz to 50 kHz, we were able to obtain a significant concentration of ozone with temperatures inside the discharge channels always higher than for instance 780 K, temperature of the gas at the end of the relaxation phase, immediately preceding the development of a filamentary discharge. It is typically a case for which it can be concluded that ozone formation reactions can only take place externally to the discharge volume and not in it during the time intervals between successive intermittent discharges.

Acknowledgements
The authors wish to thank Professor M. Fitaire for fruitful discussions.

Epitaxial Growth of Doped and Undoped Zinc Oxide Films on Sapphire Substrates: Influence of Substrate Orientation and Pretreatment

G. Vollweiler, K. Ellmer

Hahn-Meitner-Institut, Solare Energetik, D-14109 BERLIN, Glienicker Str. 100
phone: ++49-30-80622770, fax: ++49-30-80622434, e-mail: ellmer@hmi.de

Aluminium-doped zinc oxide (ZnO:Al) films have been grown on c-plane (001) and a-plane (110) sapphire by RF magnetron sputtering from a ceramic target. The films grew epitaxially, even at room temperature. However, the crystalline quality depends both on the substrate temperature as well as on the sapphire orientation. The best films, proved by X-ray diffraction (rocking curves and pole figure measurements) were grown on (110)-oriented sapphire in the temperature range 473 to 773 K. The minimum rocking curve half width was about 0.75°. By Rutherford backscattering analysis it could be shown, that the films exhibit a significant variation of the defect density over the film thickness. The highest density, as expected, is observed at the interface sapphire/ZnO:Al. Films grown on (001)-oriented sapphire have higher rocking curve half widths (about 1.3°) and exhibit sometimes two types of domains in the same film rotated by 30°.

Low temperature plasma treatment on the empress tree seeds observed through pH factor

N. Puač[1], S. Živković[2], Z. Giba[3], D. Grubišić[2] and Z.Lj. Petrović[1]

[1]*Institute of Physics, POB 68, 11080 Zemun, Serbia and Montenegro*
[2]*Institute for Biological Research "Siniša Stanković", 29. novembra 142, 11060 Belgrade, Serbia and Montenegro*
[3]*Institute of Botany, Faculty of Biology, University of Belgrade, Takovska 43, 11000 Belgrade, Serbia and Montenegro*

Abstract
In this paper we present result of studies of low-temperature plasma treatment of Empress tree (*Paulownia tomentosa* Steud.) seeds. Treatments were carried out in capacitively coupled RF discharge for various powers given by RF power supply and various pressures. Significant improvement of germination was achieved and optimal plasma treatment conditions were determined. Decreasing of pH values of treated samples implied deposition of some bioactive nitrogenous compounds in/on seed coat.

1. Introduction

There are different types of pretreatments (chemical, mechanical or physical) for seeds that have small percentage of germination. Low-temperature plasma treatment is a serious alternative due to high efficiency, low consumption of power. Also, this treatment is environmentally friendly. Increasing percentage of seed germination is very important for fundamental studies and for practical use. In addition, such studies may provide further understanding of biochemical and biophysical processes involved in seed germination.
In this paper we present result of studies of low-temperature plasma treatment of *P. tomentosa* seeds. The treatments were carried out in low pressure non-equilibrium RF discharges previously used for treatment of polymers and wool fibers. The reactor was designed in such a way to minimize the energy of ions that hit the surface exposed to the plasma so the geometry is cylindrical with a large ratio of areas of central, powered and outer grounded electrode. Special probes were designed to monitor voltage and current immediately before the discharge and power was calculated from those measurements.
Our goal was to determine the influence of glow discharge parameters (power given by RF power supply, pressure and treatment time) on germination of seeds and to find optimum procedure for plasma treatment. Treatments were carried out in air and argon plasma. After determining optimal plasma treatment conditions, pH values of treated samples under these conditions were measured. This enabled us to establish some of the mechanisms responsible for improvement of germination.

2. *Paulownia tomentosa* Steud.

Empress tree seeds belong to the group of light-requiring seeds. To induce germination of empress tree seeds it is necessary to illuminate the samples with red light (λ=660 nm). On the other hand light with wavelength of λ=730 nm inhibits germination. Photoreceptor responsible for plant germination is phytochrome, which changes its conformation and initiate germination when illuminated.
Germination process of *P. tomentosa* consists of three stages. The first stage is imbibition where distilled water was added to the seeds and then seeds were held in dark for 72 hours. After that, samples were irradiated with pulse (5 min) of red light (λ=660 nm) and the second phase of phytochrome activity started. This phase lasts for three days and after that begins the last phase-radical elongation. Seed samples were held at constant temperature of 24 ± 1 °C at all time.
One of the main reasons for using empress tree seeds was short process of germination, small dimensions (approximately 4x3 mm) and the fact that it is not liable to pathogen attack and infections. Also, very important was the fact that characteristics of this seed is well known and what effect does different factors, like

temperature, light [1,2] and organic nitrates [3] have on seeds. Figure 1. shows the electron scanning microscopy *of P. tomentosa.*

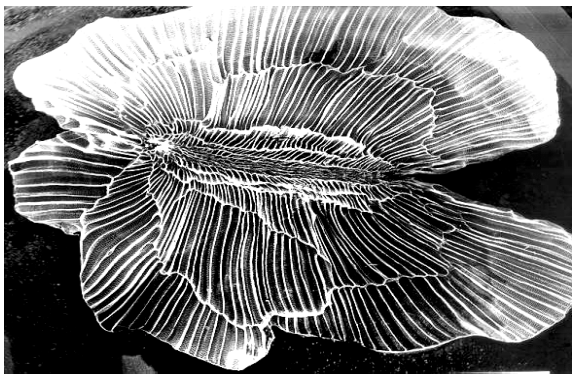

Figure 1. *Paulownia tomentosa* electron scanning microscopy

3. Experimental

Glow discharge treatment was carried out in capacitively coupled, radio-frequency (13.56 MHz) induced air and argon plasma. RF system used in this experiment is highly asymmetric and therefore the sheath potential against the walls of reactor is very small and damage by ion bombardment is minimal so organic products and natural fibers may be treated [4]. It consists of a constant RF power supply, matching box, vacuum pump, chamber, gas supply with appropriate pressure gauges, current and voltage probes, digital oscilloscope and computer as shown in Fig. 2. The chamber is a cylinder made of stainless steel with central electrode (14 mm in diameter) which is the powered electrode and the wall (37 cm in diameter) which is the grounded electrode. At the bottom of the chamber there is a flat platform (33 cm long and 24.5 cm wide) where we put the samples. Stability of the system is very important and was checked before every treatment. It was maintained by adjusting matching box so the reflected power would be minimal.

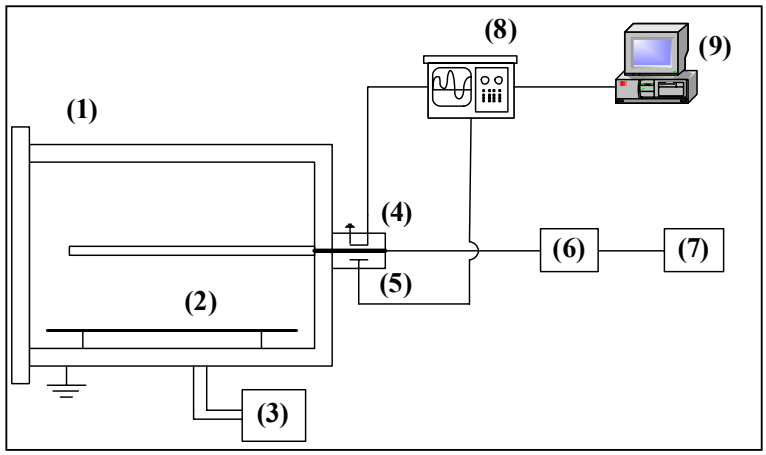

Figure 2. Experimental setup: (1) discharge chamber; (2) platform; (3) vacuum system; (4) current probe; (5) voltage probe; (6) matching box; (7) RF power supply; (8) digital oscilloscope; (9) PC

The experiments were performed by using the Empress tree seeds. Tree different groups of seeds were used: the first, which germinates up to 25 %, after 5 min of red light pulse, the second, which germinates up to 40 % after 5 min red light pulse, and the third, which germinates up to 80 % after the same light treatment. Lots of 100

seeds were placed in 6 cm diameter petri dishes before plasma treatment. Four petri dishes were set on the platform and treated by air or argon low temperature plasma. Power was maintained at constant levels of 50 W, 100 W, 200 W and pressure of 200 mTorr for different treatment times. In addition, for power of 100 W treatments were also carried out for pressures of 100 mTorr and 400 mTorr. One control group were samples of seeds held under a constant pressure of 200 mTorr without igniting plasma. This was the vacuum control group. Also, for every set of conditions (power, pressure, type of gas), 400 untreated seeds were used for control group and their percentage of germination was determined. After the plasma treatment seeds were imbibed with 2 ml of distilled water. Germination was counted seven days after the light treatment. All experiments were repeated 2 times, each with 3-5 replicates. The data points represent means; standard errors are not shown since they never exceeded 3%. Also, pH values of treated seeds were determined. Germination of seeds, counting of germinated seeds and determining of pH values of treated samples was done at the Institute for Biological Research "Siniša Stanković".

4. Results and discussion

Plasma treated samples have a higher percentage of germination than the untreated samples. The curves for the power of 50 W and 200 mTorr and for the vacuum control sample are shown in Fig.3. Untreated control group of this set of samples germinate up to 3%. Percentage of germination for treated seeds is increased for shorter treatment times while for longer treatment times it is decreasing. The other curve representing vacuum control is almost constant at the untreated control group value and it shows that vacuum has almost no effect on seed germination.

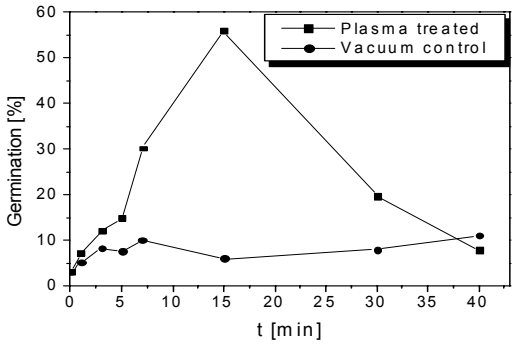

Figure 3. Germination curve for a constant power of 50 W and a constant pressure of 200 mTorr.

We can see that germination curve increases, reaches its maximum value and then decreases. For longer treatment times and higher powers given by RF power supply germination curve falls to zero. Fig. 4. shows germination curves for constant powers of 100 W and 200 W and pressure of 200 mTorr. The percentage of germination for control groups for the samples used are 25 % and 23 % for power of 100 W and 200 W, respectively. Obviously, we can see that with the increasing power given by RF power supply maximum of germination curve shifts towards shorter times. This implies that the overall effect of plasma is proportional to the integral effect of the flux of particles reaching its surface. Also, plasma treatment by ion bombardment damages the seed's surface and therefore after longer treatment times seeds cannot germinate.

If we reduce pressure, germination curve widens and for the same power given by RF power supply we have a larger range of times where germination is increased. Inhibition in this case occurs only for the longest treatments times. For larger pressures germination curve is narrow, maximum occurs for shorter treatment times and inhibition is significant even for 5 min treatments (see Fig. 5.). Control group values for both pressures is 77.25 % and feed gas was air.

One set of samples (2 Petri dishes) was covered by a glass cover (square shape, 10 cm wide, 30 cm long and 2.5 cm high) and was treated at the same time with another set of samples (2 Petri dishes) which was uncovered. In Fig. 6. we show germination curves for both cases. The glass cover, obviously, shielded the samples and the total flux of particles reaching the surface was smaller than in the case of uncovered samples. Therefore, the curve representing the covered samples is wider, for shorter treatment times less stimulation occurs, but, in this case, the seed survived longer treatment times. On the other hand, glass cover prevented UV photons from reaching the surface so maintenance of a relatively high improvement indicates the importance of active radicals from the plasma.

Besides air we have also used argon as the feed gas and the curves representing data for these two gases are shown in Fig. 7. Both curves are normalized to their control group values. For argon the percentage of germination for the control group is 59 % and for air it is 25 %. The stimulation for argon is much smaller than for air. This implies that there is another mechanism, besides ion bombardment of seed surface, involved in improving germination.

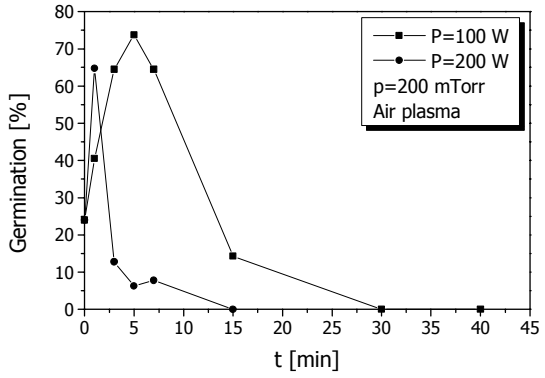

Figure 4. Germination curves for a constant power of 100 W and 200 W a constant pressure of 200 mTorr.

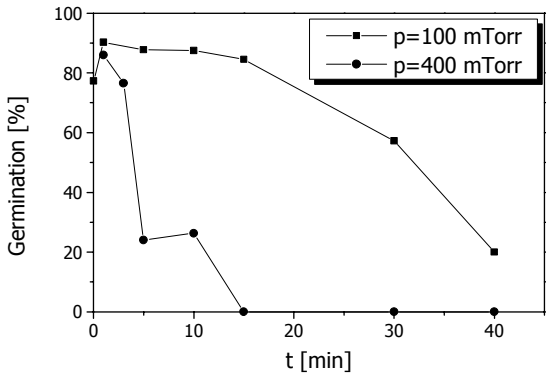

Figure 5. Germination curves for constant power of 100 W and pressures of 100 mTorr and 400 mTorr.

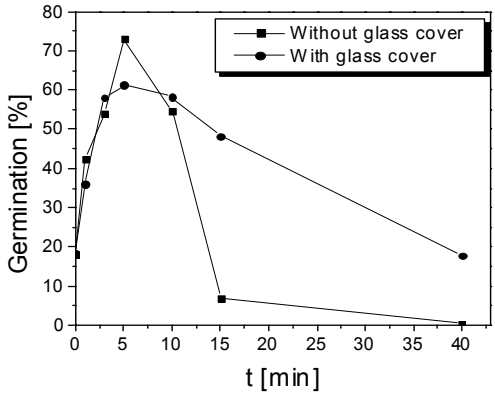

Figure 6. Germination curves for a constant power of 100 W and a constant pressure of 200 mTorr. Control group value: 18.25 %

Interaction between active species from plasma and seeds surface leads to a change of seed's surface topography. This implies that plasma treatment causes the destruction of surface layer and it also activates the surface. Activated surface is now capable of bonding active nitrogenous compounds. These compounds reduce pH values of samples and play important role in increasing the germination of seeds [5,6].
In Fig 8. we show pH values of samples treated by air and argon plasma for power of 100 W and pressure of 200 mTorr. pH values measured one hour after imbibition started decreases with increasing treatment times. pH of the samples treated by air plasma reduces from 6.8 (1 min treatment) to 3.8 (40 min). We should expect that for longer times percentage of germination should be at a maximum. However, that is not the case and the reason is significant damage of seed and its germ due to ion bombardment.

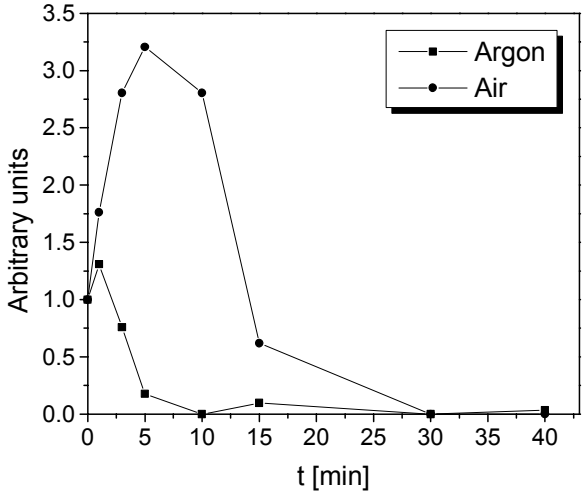

Figure 7. Normalized germination curves for air and argon at a constant pressure of 200 mTorr and a constant power of 100 W.

In case of argon plasma decrement of pH is not so significant and this concurs with germination curve for argon plasma. For 1 min treatment pH=6.8 and decreases to 4.8 for 40 min treatment. This small change in pH values of samples treated by argon plasma can be explained either with the fact that argon used in this experiment is not completely clean or the fact that there is some effect of vacuuming on pH factor. Also, it is not impossible that

argon metastables are the active species which can interact with surface of seeds and change pH values. Control in Fig 8. represents pH value of distilled water.

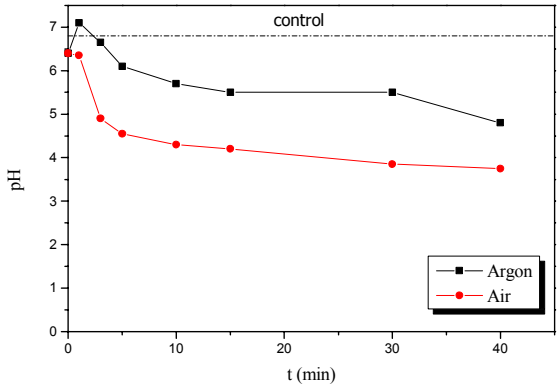

Figure 8. The pH of water solution in which seeds were imbibed after air and argon plasma pretreatments.

5. Conclusion

Percentage of germination of seeds used in the present study is increased by non-equilibrium RF plasma treatment. The effect increases with pressure and power, so it seems that the overall effect is proportional to the total flux of reactive particles reaching the surface.

Stimulatory effect on germination of seeds *P. tomentosa* treated by low temperature plasma can be explained by several mechanisms. The first mechanism is etching of seed's surface by ion bombardment. Damaged surface is now better absorbent of water and gases necessary for germination. This is not the main mechanism but can be relevant for seeds with hard surfaces.

Activation of surface is very important because plasma treatments can change physical and chemical characteristics of seed's surface and therefore change its dormancy. Activated surface is now capable of bonding active nitrogenous compounds. Although there is no direct evidence, generation and deposition of nitrogenous oxides in/on the seed coat [3] may be the clue for understanding the stimulatory effect of air-derived cold plasma in *P. tomentosa* seed germination.

6. References

[1] Grubišić D., Arch. Biol. Sci., **27**, 7 (1975)
[2] Grubišić D., R. Konjević, Physiol. Plant., **86**, 479 (1992)
[3] Grubišić D., Z. Giba , R. Konjević, Photochem. and Photobiol., **56**, No. 5, 629 (1992)
[4] Radetić M., B. Tomčik, N. Puač, Z.Lj. Petrović, *Contributed papers,* XX SPIG, (2000)
[5] Giba Z., D. Grubišić, S. Todorović, L. Sajc, Ž. Stojaković, R. Konjević, Plant Growth Reg. **26**, 175 (1998)
[6] Giba Z., D. Grubišić,S. Todorović, R. Konjević, Yugoslav. Physiol. Pharmacol. Acta. **34**, No. 2, 447 (1998) (also available on web site http://www.ippa.bg.ac.yu)

Influence of chemical non-equilibrium on the simulation of a D.C. plasma jet

I. Choquet, A. Boussagol, P. Nylén

University of Trollhättan/Udevalla, Box 957, 461 29 Trollhättan, Sweden

This paper presents a comparison of the numerical simulations of a d.c. plasma jet (similar to [1]) assuming chemical equilibrium and chemical non-equilibrium. The calculations are done with the 3D commercial computational fluid dynamics code Fluent [2].

Numerical simulations can be of great help in the optimization of plasma spraying conditions for a specific material. The quality of the coating is indeed governed by the particle parameters before impact (such as temperature, molten state, velocity, and size), and thus the plasma-particle interaction. The prediction of the plasma flow field is thus essential. The plasma jet is generally simulated assuming, as in [1], that the plasma is:

- optically thin,
- in thermal equilibrium, and
- in chemical equilibrium.

In this work, we investigate the influence of chemical non-equilibrium, while keeping the assumption of local thermal equilibrium as well as optically thin plasma. Arc root fluctuations are not considered and, therefore, the flow is assumed to be in steady state. We study an argon plasma jet flowing into a cold air environment and simulate numerically two cases:

- The reference test case is at chemical equilibrium.
  The gas flow is then supposed to be made of two (also three) gases: the plasma-forming gas and the ambient gas (also the powder carrier gas). The thermodynamic and transport properties of the gas mixture are calculated using mixing laws and the data of pure gases derived from kinetic theory in [3].
- The test case with chemical non-equilibrium.
  We then retain the chemical species with a number density larger than $10^{21} m^{-3}$ in the range of temperature we consider (from 300 to 15000K) at atmospheric pressure. Concerning the air for instance we take into account N_2, O_2, NO, N, O, N^+, O^+, Ar, Ar^+, and the electrons. The forward reaction rates are expressed in an Arrhenius form. The equilibrium constants of reaction have the following temperature dependence:

$$K(T) = \exp\left[AT + B + C\ln\left(\frac{10^4}{T}\right) + \frac{D}{T} + \frac{E}{T^2} \right],$$

  where A, B, C, D and E are constants characteristic of the chemical species involved in the chemical reaction under consideration.
  The transport coefficients of the pure gases are, as for the reference test case, derived from kinetic theory with the same order in the expansions. The collision cross sections are taken from the data base T&Twinner [4]. The reaction rates and transport coefficients are implemented in the Fluent code in the form of 'user defined functions'.

The density, velocity, and temperature flow fields computed for these two test cases are then compared and the assumptions concerning chemical equilibrium and non-equilibrium are discussed.

[1] A. Boussagol, G. Mariaux, E. Legros, A. Vardelle, P. Nylen, 3-D - Modeling of a D.C. plasma jet using different commercial CFD codes, ISPC15, **3**, p. 1015, (2001).
[2] Fluent user guide, Fluent Incorporaed, Evanston, III, U.S.A., (1996).
[3] . I. Boulos, P. Fauchais, E. Pfender, - Thermal plasmas. Fundementals and applications, Vol. 1, Plenum Press, (1994).
[4 T&Twinner, ADEP - Banque de données de l'Université et du CNRS.Ed Direction des Bibliothèques des Musées et de l'Information Scientifique et Technique, France (2001).

Derivation of an inviscid hydrodynamic/diffusion limit for an arc discharge of moderate pressure

Isabelle Choquet[1], Brigitte Lucquin-Desreux[2]

[1] *University of Trollhättan/Uddevalla, Box 957, 461 29 Trollhättan, Sweden*
[2] *Laboratoire d'Analyse Numérique, Univ. Pierre et Marie Curie, 16 rue Clisson, F-75013 Paris.*

Abstract
In this paper we study a partially ionized plasma that corresponds to the plasma column of an arc discharge of moderate pressure. We derive an inviscid hydrodynamic/diffusion limit from a system of Boltzmann type transport equations modeling that plasma problem. The original property of this system is that impact ionization is a leading order collisional process. As a consequence, there is no evolution equation governing the density of electrons.

1. Introduction

This work is concerned with the derivation, from a kinetic framework, of an inviscid diffusion/hydrodynamic limit for a plasma problem. Let us recall that the case of a binary gas mixture can be found in [1] for instance. The ternary gas mixture corresponding to a very weakly ionized plasma, such as a glow discharge where ionization occurs very seldom, is studied in [2].
Here, we consider the partially ionized plasma investigated in [3]. Its electrons, ions and neutral molecules are subject to elastic binary collisions as well as ionization and recombination reactions. We assume that the ionization level is several orders of magnitude larger than in [2]. It lies within the range 10^{-3} to 10^{-1}, which corresponds to an arc discharge problem. A typical arc discharge, investigated in [4] for instance, consists of electrodes interacting with a thermal plasma through non-equilibrium boundary layers. Here we do not consider the cathode and anode layers, and focus the study on the modelling of the plasma column. We assume that impact ionization-recombination dominates radiative ionization-recombination, excluding thus very high pressure arc discharges. The activation energy Δ of ionization reactions is supposed to be constant and given by the impacting electron.
We start this study from a system of Boltzmann type transport equations governing the distribution functions of electrons, ions and neutral molecules. This system, presented in section 2, is coupled through collision operators that involve three collisional processes: i) elastic binary collisions where at least one particle is neutral (Boltzmann), ii) elastic binary collisions between charged particles (Fokker-Planck), and iii) inelastic collisions with impact ionization and its reverse recombination. Notice that the study of charge carriers giving rise to impact ionization can be found in [5] for semiconductor devices.
This system is scaled in section 3, based on its two small parameters. The first parameter ϵ measures the relative smallness of the electron mass with respect to the neutral particles. The second parameter δ measures the ionization level of the plasma. For an arc discharge we have $\delta \approx \epsilon$. The main consequence of this scaling is that impact ionization gets a leading order collisional process.
A macroscopic limit is then derived in section 4.

2. A system of Boltzmann equations modelling an arc discharge

We study a gas partially ionized whose electrons, ions and neutral molecules are subject to elastic binary collisions as well as ionization and recombination reactions. To that purpose, we assume that:
• (**2.1**) *The external forces applied to the particles do not depend on the velocity variable, excluding thus magnetized plasmas.*
• (**2.2**) *The interaction potentials associated with the nonreactive collisions only depend on the distance between the particles.*

• (**2.3**) *Radiative ionization and recombination are negligible, excluding thus very high pressure arc discharges.*
• (**2.4**) *The activation energy of impact ionization reactions is given by the electron, and not by the neutral particle.*
• (**2.5**) *The charge level of ions is of order one.*
To avoid confused notations, we restrict the presentation of this study to a single neutral species and the related single charged ion species. The extension of the forthcoming results to several molecular species characterized by masses of similar order of magnitude, and to ions of charge $Z < 10$ is indeed straightforward. We thus investigate the following system of Boltzmann transport equations:

$$\begin{aligned}
&\partial_t f^e + v_e \cdot \bigtriangledown_x f^e + \frac{F_e}{m_e} \cdot \bigtriangledown_{v_e} f^e = (\partial_t f^e)_c \ , \\
&\partial_t f^i + v_i \cdot \bigtriangledown_x f^i + \frac{F_i}{m_i} \cdot \bigtriangledown_{v_i} f^i = (\partial_t f^i)_c \ , \\
&\partial_t f^n + v_n \cdot \bigtriangledown_x f^n + \frac{F_n}{m_n} \cdot \bigtriangledown_{v_n} f^n = (\partial_t f^n)_c \ .
\end{aligned} \tag{1}$$

The indexes e, i and n denote quantities associated with electrons, ions and neutral particles, respectivelly. The distribution functions $f^\alpha = f^\alpha(t, x, v_\alpha)$, where $\alpha = e, i, n$, depend on time $t \geq 0$, space $x \in I\!R^3$ and velocity $v_\alpha \in I\!R^3$. F_α represents the external forces acting on the paticle α of mass m_α; it satisfies the assumption 2.1.
The system of Boltzmann equations (1) is coupled through the collision operators $(\partial_t f^\alpha)_c$. These operators involve three collisional processes detailed below: i) elastic binary collisions where at least one particle is neutral, ii) elastic binary collisions between charged particles, and iii) inelastic collisions with ionization and its reverse recombination. Thus

$$(\partial_t f^\alpha)_c = Q^{\alpha\alpha}(f^\alpha, f^\alpha) + Q^{\alpha\beta}(f^\alpha, f^\beta) + Q^{\alpha\gamma}(f^\alpha, f^\gamma) + Q^{\alpha,ir}(f^\alpha, f^\beta, f^\gamma), \tag{2}$$

where the superscript *ir* stands for ionization-recombination, and $\alpha, \beta, \gamma = e, i, n$ with $\alpha \neq \beta \neq \gamma \neq \alpha$.
Let us first consider binary elastic collisions between the two particles α and β. When one of these particles (or both) is neutral, the binary collisions are described by Boltzmann operators of the form:

$$Q^{\alpha\beta}(f^\alpha, f^\beta)(v_\alpha) = \int_{I\!R^3 \times S^2_+} \sigma^{\mathcal{B}}_{\alpha\beta} \ |v_\alpha - v^\star_\beta| \Big(f^{\alpha\prime} f^{\beta\prime}_\star - f^\alpha f^\beta_\star \Big) d\Omega \ dv^\star_\beta \ , \tag{3}$$

where $\alpha = n$ and $\beta = e, i, n$ or $\alpha = e, i, n$ and $\beta = n$. The distribution functions $f^{\alpha\prime}$ and $f^{\beta\prime}_\star$ stand for $f^\alpha(t, x, {v_\alpha}')$ and $f^\beta(t, x, v^{\star\prime}_\beta)$, respectivelly. S^2 is the unit sphere of $I\!R^3$ and $S^2_+ := \Big\{ \Omega \in S^2; (v_\alpha - v^\star_\beta) \cdot \Omega > 0 \Big\}$. The post-collisional velocities ${v_\alpha}'$ and $v^{\star\prime}_\beta$ are defined from the pre-collisional velocities v_α and $v^\star_\beta$ by:

$${v_\alpha}' = v_\alpha - 2 \ \frac{\mu_{\alpha\beta}}{m_\alpha} \Big((v_\alpha - v^\star_\beta) \cdot \Omega \Big) \Omega \quad \text{and} \quad v^{\star\prime}_\beta = v^\star_\beta + 2 \ \frac{\mu_{\alpha\beta}}{m_\beta} \Big((v_\alpha - v^\star_\beta) \cdot \Omega \Big) \Omega, \tag{4}$$

where $\mu_{\alpha\beta} = m_\alpha m_\beta / (m_\alpha + m_\beta)$ is the reduced mass. From assumption 2.2, the scattering cross section $\sigma^{\mathcal{B}}_{\alpha\beta}$ is a function of two variables: $\sigma^{\mathcal{B}}_{\alpha\beta} = \sigma^{\mathcal{B}}_{\alpha\beta}(\mathcal{E}, \chi)$, where $\mathcal{E} = \mu_{\alpha\beta} |v_\alpha - v^\star_\beta|^2$ is the reduced kinetic energy and χ denotes the angle $\Big(\frac{v_\alpha - v^\star_\beta}{|v_\alpha - v^\star_\beta|}, \Omega \Big)$. While the former belongs to $I\!R_+$, the latter lies within the range $[0, 1]$.
Elastic collisions between two charged particles α and β are modelled by Fokker-Planck-Landau operators:

$$\begin{aligned}
Q^{\alpha\beta}(f^\alpha, f^\beta)(v_\alpha) = \frac{\mu^2_{\alpha\beta}}{m_\alpha} \ \bigtriangledown_{v_\alpha} \cdot \int_{I\!R^3} &\sigma^{\mathcal{F}}_{\alpha\beta} \ |v_\alpha - v^\star_\beta|^3 \ S(v_\alpha - v^\star_\beta) \\
&\times \Big(\frac{1}{m_\alpha} \bigtriangledown_{v_\alpha} f^\alpha \ f^\beta_\star - \frac{1}{m_\beta} \bigtriangledown_{v^\star_\beta} f^\beta_\star \ f^\alpha \Big) \ dv^\star_\beta \ ,
\end{aligned}$$

where $\alpha, \beta = e, i$ and $\bigtriangledown_{v_\alpha} f^\alpha = (\bigtriangledown f^\alpha)(v_\alpha)$. $S(w)$ is the matrix $S(w) = \mathbf{Id} - \frac{w \otimes w}{|w|^2}$ where $\mathbf{Id}$ is the identity matrix. Here, due to assumption 2.2, the scattering cross section for grazing collisions $\sigma^{\mathcal{F}}_{\alpha\beta}$ only depends on the reduced kinetic energy: $\sigma^{\mathcal{F}}_{\alpha\beta} = \sigma^{\mathcal{F}}_{\alpha\beta}(\mathcal{E})$.
From assumption 2.3, radiative ionization and recombination are supposed to be negligible. The ionization process we shall consider is thus impact ionization. Its mechanism can be schematized by the following direct and reverse reactions:

$$e + A \xrightarrow{\sigma^d} e + e + A^+ \qquad \text{and} \qquad e + A \xleftarrow{\sigma^r} e + e + A^+ ,$$

where e represents an electron, A^+ a single charged ion, and A the related neutral atom. σ^d and σ^r stand for the direct and reverse reaction cross sections. They are supposed to be positive. Applying the principle of detailed balance, we assume in the sequel that these cross sections are linked through $\sigma^d = \mathcal{F}_0\ \sigma^r$, where $\mathcal{F}_0$ is a positive constant. The ionization-recombination operators are then given by:

$$\begin{aligned} Q^{e,ir}(f^e, f^i, f^n) = &\int_{I\!R^{12}} \sigma^r\ \delta_v\ \delta_{\mathcal{E}} \left(f^{e\prime}\ f^e_\star\ f^i - \mathcal{F}_0\ f^e\ f^n \right) dv_e{}'\ dv^\star_e\ dv_i\ dv_n \\ &+2 \int_{I\!R^{12}} \sigma^{r\prime}\ \delta_{v'}\ \delta_{\mathcal{E}'} \left(\mathcal{F}_0\ f^{e\prime}\ f^n - f^e\ f^e_\star\ f^i \right) dv_e{}'\ dv^\star_e\ dv_i\ dv_n, \end{aligned} \tag{5-a}$$

$$Q^{i,ir}(f^e, f^i, f^n) = \int_{I\!R^{12}} \sigma^r\ \delta_v\ \delta_{\mathcal{E}} \left(\mathcal{F}_0\ f^e\ f^n - f^{e\prime}\ f^e_\star\ f^i \right) dv_e\ dv_e{}'\ dv^\star_e\ dv_n, \tag{5-b}$$

$$Q^{n,ir}(f^e, f^i, f^n) = \int_{I\!R^{12}} \sigma^r\ \delta_v\ \delta_{\mathcal{E}} \left(f^{e\prime}\ f^e_\star\ f^i - \mathcal{F}_0\ f^e\ f^n \right) dv_e\ dv_e{}'\ dv^\star_e\ dv_i. \tag{5-c}$$

Due to assumption 2.4, the reverse reaction cross section writes $\sigma^r = \sigma^r(v_e{}', v^\star_e, v_i; v_e, v_n) = \sigma^r(v_e{}', v^\star_e; v_e)$, and $\sigma^{r\prime} = \sigma^r(v_e, v^\star_e; v_e{}')$. $\delta_{\mathcal{E}}$ and δ_v hold for the energy and momentum conservation during the ionization-recombination process:

$$\begin{aligned} \delta_{\mathcal{E}} : &\qquad m_e|v_e|^2 + m_n|v_n|^2 = m_e(|v_e{}'|^2 + |v^\star_e|^2) + m_i|v_i|^2 + 2\Delta, \\ \delta_v : &\qquad m_e v_e + m_n v_n = m_e(v_e{}' + v^\star_e) + m_i v_i, \end{aligned} \tag{6}$$

where the ionization energy Δ is a constant.
Notice that the factor 2 in Eq. (5-a) is a consequence of the indistinguishability of electrons. This indistinguishability and the principle of detailed balance imply that $\sigma^r(v_e{}', v^\star_e; v_e) = \sigma^r(v^\star_e, v_e{}'; v_e) = \sigma^r(v_e, v^\star_e; v_e{}')$.
The reference values of the problem are now introduced in order to scale the system of Boltzmann transport equations (1).

3. Scaled system of Boltzmann equations

We first introduce the reference dimensions of the problem (such as time t_0, length x_0) in order to scale the previous system. In that aim, let ϵ denote the parameter measuring the relative smallness of the electron mass with respect to the neutral particle:

$$\epsilon = \sqrt{\frac{m_e}{m_n}} = \sqrt{\frac{m_e}{m_i + m_e}} << 1.$$

We assume that:

• (**3.1**) *Electrons, ions and neutral species have temperatures of the same order of magnitude* T_0.

Their reference velocities $(v_\alpha)_0$ will be defined from the thermal velocity, $(v_\alpha)_0 = \sqrt{kT_0/m_\alpha}$, with $\alpha = e, i, n$, k being the Boltzmann constant. Consequently, we obtain the following ordering:

$$(v_n)_0 = \sqrt{1-\epsilon^2}\ (v_i)_0 = \epsilon\ (v_e)_0.$$

Besides, we shall choose $x_0 = t_0\ (v_e)_0$ as reference length. The reference time t_0 is specified later on.

• (**3.2**) *The densities of the charged particles have the same order of magnitude:* $(\rho_e)_0 = (\rho_i)_0$.

We introduce a second parameter measuring the ionization level,

$$\delta = \frac{(\rho_e)_0}{(\rho_n)_0} = \frac{(\rho_i)_0}{(\rho_n)_0},$$

where $(\rho_n)_0$ is the typical density of neutral particles. The distribution function scales are determined from the previous characteristic quantities according to $(f^\alpha)_0 = (\rho_\alpha)_0 (v_\alpha)_0^{-3}$ where $\alpha = e, i, n$.

• (**3.3**) *The force field F_α with $\alpha = e, i, n$, derives from a potential and is relatively weak, i.e. the force term $(F_\alpha m_\alpha^{-1}) \cdot \bigtriangledown_{v_\alpha} f^\alpha$ involved in (1) is supposed to be of lower order than the collision operator $(\partial_t f^\alpha)_c$.* The force scale is related to the length scale by $(F_\alpha)_0 = kT_0 x_0^{-1}$.

To specify the typical values of the elastic collision operators $Q^{\alpha\beta}$ we assume that:

• (**3.4**) *The interaction potentials associated with binary elastic collisions between the various species of charged particles have the same order of magnitude: $\sigma^{\mathcal{F}}_{\alpha\beta} = \sigma^{\mathcal{F}}_0$ for any $\alpha, \beta = e, i$. A similar property is supposed to apply to elastic binary collisions involving a neutral particle (or two), thus: $\sigma^{\mathcal{B}}_{n\alpha} = \sigma^{\mathcal{B}}_{\alpha n} = \sigma^{\mathcal{B}}_0$ where $\alpha = e, i$ or n.*

The variables involved in (1)-(2) can now be expressed in dimensionless variables as:

$$t = t_0\ \bar{t}\ , \quad x = x_0\ \bar{x}\ , \quad v_\alpha = (v_\alpha)_0\ \bar{v}_\alpha\ , \quad f^\alpha = (f^\alpha)_0\ \bar{f}^\alpha\ , \quad \ldots\ .$$

Further details can be found in Ref [3]. In the sequel we shall only use reference values and dimensionless variables. To simplify the notations, the bar above dimensionless variables will therefore be omitted from now on.

We now need to specify the characteristic time t_0. We first notice that choosing the time scale $t_0 = \tau_{en} = \epsilon^2 \tau_{ir} = \delta\ \tau_{ee}$ while $\delta \to 0$, we recover the dimensionless system studied in [2]. This corresponds to a very weakly ionized plasma, such as a glow discharge, where ionization occurs very seldom and the ionization level δ lies within the range 10^{-8} to 10^{-5}, such that $\delta << \epsilon$.

In an arc discharge, the ionization level lies within the range 10^{-3} to 10^{-1}, implying that $\delta \approx \epsilon$.

• (**3.5**) *We thus assume in the present study that: $t_0 = \tau_{en} = \epsilon\ \tau_{ir} = \delta\ \tau_{ee}$* and $\delta = \epsilon$.

The scaled version of the system of Boltzmann transport equations writes then,

$$\begin{aligned}
&\partial_t f^e + v_e \cdot \bigtriangledown_x f^e + F_e \cdot \bigtriangledown_{v_e} f^e = Q^{en}_\epsilon(f^e, f^n) \\
&\qquad\qquad + \epsilon\ \left[Q^{ee}(f^e, f^e) + Q^{ei}_\epsilon(f^e, f^i) + Q^{e,ir}(f^e, f^i, f^n)\right], \\
&\partial_t f^i + \frac{\epsilon}{\sqrt{1-\epsilon^2}} \left(v_i \cdot \bigtriangledown_x f^i + F_i \cdot \bigtriangledown_{v_i} f^i\right) = \frac{\epsilon}{\sqrt{1-\epsilon^2}}\ Q^{in}_\epsilon(f^i, f^n) \\
&\qquad\qquad + \epsilon\ Q^{i,ir}(f^e, f^i, f^n) + \epsilon^2\ \left[\frac{1}{\sqrt{1-\epsilon^2}}\ Q^{ii}(f^i, f^i) + Q^{ie}_\epsilon(f^i, f^e)\right], \\
&\partial_t f^n + \epsilon\ \left(v_n \cdot \bigtriangledown_x f^n + F_n \cdot \bigtriangledown_{v_n} f^n\right) = \epsilon\ Q^{nn}(f^n, f^n) \\
&\qquad\qquad + \epsilon^2 \left[Q^{ne}_\epsilon(f^n, f^e) + \frac{1}{\sqrt{1-\epsilon^2}}\ Q^{ni}_\epsilon(f^n, f^i) + Q^{n,ir}(f^e, f^i, f^n)\right].
\end{aligned} \tag{7}$$

In this system, collisions of electrons, ions and neutral particles with neutral particles are leading order collisional processes, as in any weakly ionized plasma. However, contrary to the very weakly ionized

problem studied in [2], the leading order operators of neutral particles and ions are also coupled with electrons. Besides, the collision operators for elastic electron collisions Q^{ee} and ionization $Q^{e,ir}$ have now the same order of magnitude. But the main novelty comes from the ionization-recombination operator for ions, which is here among the leading order operators.

The properties of the collision operators, required to derive the hydrodynamic/diffusion limit, are studied in [3].

4. Inviscid hydrodynamic/diffusion limit

To derive the macroscopic limit, we start from the dimensionless system (7) and replace the collision operators $Q_\epsilon^{\alpha\beta}$ by their expansions with respect to ϵ (cf. Ref. [3] for more details). Then we introduce the diffusion scaling of small parameter ϵ: $t \to \epsilon^2 t$, $x \to \epsilon x$, and obtain:

$$
\begin{aligned}
&\partial_t f_\epsilon^e + \epsilon^{-1}\left(v_e \cdot \bigtriangledown_x f_\epsilon^e + F_e \cdot \bigtriangledown_{v_e} f_\epsilon^e\right) = \epsilon^{-2}\, Q_0^{en}(f_\epsilon^e, f_\epsilon^n) \\
&\qquad + \epsilon^{-1}\left[Q_1^{en}(f_\epsilon^e, f_\epsilon^n) + Q_0^{ei}(f_\epsilon^e, f_\epsilon^i) + Q^{ee}(f_\epsilon^e, f_\epsilon^e) + Q^{e,ir}(f_\epsilon^e, f_\epsilon^i, f_\epsilon^n)\right] \\
&\qquad + Q_2^{en}(f_\epsilon^e, f_\epsilon^n) + Q_1^{ei}(f_\epsilon^e, f_\epsilon^i) + \epsilon\left[\, Q_3^{en}(f_\epsilon^e, f_\epsilon^n) + Q_2^{ei}(f_\epsilon^e, f_\epsilon^i)\right] + \mathcal{O}(\epsilon^2), \\
&\partial_t f_\epsilon^i + v_i \cdot \bigtriangledown_x f_\epsilon^i + F_i \cdot \bigtriangledown_{v_i} f_\epsilon^i \\
&\qquad = \epsilon^{-1}\Big[Q_0^{in}(f_\epsilon^i, f_\epsilon^n) + Q^{i,ir}(f_\epsilon^e, f_\epsilon^i, f_\epsilon^n)\Big] + Q^{ii}(f_\epsilon^i, f_\epsilon^i) + Q_0^{ie}(f_\epsilon^i, f_\epsilon^e) \\
&\qquad + \epsilon\left[\, \tfrac{1}{2}\, Q_0^{in}(f_\epsilon^i, f_\epsilon^n) + Q_2^{in}(f_\epsilon^i, f_\epsilon^n) + Q_1^{ie}(f_\epsilon^i, f_\epsilon^e)\right] + \mathcal{O}(\epsilon^2), \\
&\partial_t f_\epsilon^n + v_n \cdot \bigtriangledown_x f_\epsilon^n + F_n \cdot \bigtriangledown_{v_n} f_\epsilon^n = \epsilon^{-1}\, Q^{nn}(f_\epsilon^n, f_\epsilon^n) \\
&\qquad + Q_0^{ne}(f_\epsilon^n, f_\epsilon^e) + Q_0^{ni}(f_\epsilon^n, f_\epsilon^i) + Q^{n,ir}(f_\epsilon^e, f_\epsilon^i, f_\epsilon^n) + \epsilon\, Q_1^{ne}(f_\epsilon^n, f_\epsilon^e) + \mathcal{O}(\epsilon^2).
\end{aligned}
\tag{8}
$$

Next, we expand the solutions in powers of ϵ: $f_\epsilon^e = f_0^e + \epsilon\, f_1^e + \epsilon^2\, f_2^e + \mathcal{O}(\epsilon^3)$ and $f_\epsilon^\alpha = f_0^\alpha + \epsilon\, f_1^\alpha + \mathcal{O}(\epsilon^2)$, with $\alpha = i, n$. Then, we insert these expansions in the system (8) and identify terms of equal powers of ϵ. This leads to systems of equations of order ϵ^{-2}, ϵ^{-1}, ϵ^0, etc, to be successively solved (these systems are also detailed in Ref. [3]).

From the lower order systems we prove that:

• The equilibrium distribution functions of neutral particles f_0^n and ions f_0^i are Maxwellians characterized by the same mean velocity u and temperature T.

• The equilibrium distribution function of electrons is the centered Maxwellian of temperature T_e.

• The electron density ρ_e is governed by the ion density ρ_i, the density of neutral particles ρ_n and the electron temperature T_e, according to:

$$
\rho_e = \frac{\mathcal{F}_0\ \rho_n}{\rho_i}\ (2\pi T_e)^{3/2}\ \exp\Big(-\frac{\Delta}{T_e}\Big)\ . \tag{9}
$$

Notice that this relation can be compared to a Saha law generalized to a plasma characterized by two temperatures: a temperature for heavy particles and another temperature for light particles.

Then we introduce the conservative variable $\mathbf{u} = (\rho_n, \rho_i, \rho_n u, \rho_n E, \rho_e E_e)$: $I\!R^3 \times I\!R^+ \to \mathcal{U}$ where $\mathcal{U}$ denotes the open set $\big\{\mathbf{u} \in I\!R^7, \rho_n \in I\!R^+, \rho_i \in I\!R^+, \rho_n u \in I\!R^3, T \in I\!R^+, T_e \in I\!R^+, \big\}$. The density ρ_n, the momentum $\rho_n u$ and the energy $\rho_n E = \rho_n(|u|^2 + 3T)/2$ of neutral particles are defined such that:

$$
\begin{pmatrix} \rho_n \\ \rho_n u \\ \rho_n E \end{pmatrix} = \int_{I\!R^3} \begin{pmatrix} 1 \\ v_n \\ \frac{1}{2}|v_n|^2 \end{pmatrix} f_0^n(v_n) dv_n \tag{10}
$$

The ion density ρ_i and the electron internal energy $\rho_e E_e = \frac{3}{2}\rho_e T_e$ are defined by:

$$
\rho_i = \int_{I\!R^3} f_0^i(v_i)\ dv_i \quad \text{and} \quad \rho_e E_e = \frac{1}{2}\int_{I\!R^3} |v_e|^2\ f_0^e(v_e)\ dv_e\ . \tag{11}
$$

Using these notations we successively establish the solvability conditions for defining the first order corrective terms $f_1^\alpha(v_\alpha)$, with $\alpha = n, i$, and the second order corrective term $f_2^e(v_e)$ (refer to [3] for more details). These conditions give the inviscid hydrodynamic/diffusion system governing the time evolution of the neutral particle and ion densities ρ_n and ρ_i, the velocity u and the temperature T of the heavy particles, and the electron temperature T_e. This inviscid hydrodynamic/diffusion system derived from Eq. (8) is:

$$
\begin{aligned}
&\partial_t \rho_n + div(\rho_n u) = 0, \qquad t > 0,\ x \in I\!R^3,\\
&\partial_t \rho_i + div(\rho_i u) = \rho_i\ Y^{ir},\\
&\partial_t(\rho_n u) + div[\rho_n (u \otimes u)] + \bigtriangledown_x(\rho_n T) - \rho_n F_n = 0,\\
&\partial_t(\rho_n E) + div[\rho_n u\,(E + T)] - \rho_n u \cdot F_n = 0,\\
&\partial_t T_e + u \cdot \bigtriangledown_x T_e + \frac{2T_e^2}{3T_e + 2\Delta}\left(div\,(u) - \frac{1}{\rho_e} \bigtriangledown_x \left[\rho_e D_1\Big(\frac{\bigtriangledown_x \rho_e}{\rho_e} - \frac{F_e}{T_e}\Big) + \rho_e D_2 \frac{\bigtriangledown_x T_e}{T_e}\right]\right)\\
&\qquad\qquad = \left(1 + \frac{\rho_i}{\rho_e}\right)\ \frac{2T_e^2}{3T_e + 2\Delta}\ Y^{ir},
\end{aligned}
$$

with the energy $E = \frac{1}{2}\ |u|^2 + \frac{3}{2}\ T$. The diffusion coefficients are

$$
\begin{aligned}
D_1 &= \int_{I\!R^3} M_{0,T_e}(v_e)\ \Psi_1(|v_e|)\ v_e \otimes v_e\ dv_e\ ,\\
D_2 &= \int_{I\!R^3} M_{0,T_e}(v_e)\ \Big[\Big(\frac{3}{2} + \frac{\Delta}{T_e}\Big)\ \Psi_1(|v_e|) + \Psi_2(|v_e|)\Big] v_e \otimes v_e\ dv_e\ .
\end{aligned}
$$

The ionization-recombination source term Y^{ir} and the functions Ψ_1 and Ψ_2 are detailed in [3]; M_{0,T_e} is the normalized and centered Maxwellian for electrons. This system is supplemented by the closure relation defining the electron density (9).
We thus observe that due to the important difference in masses between heavy particles and ions, and to the collisions with impact ionization, this inviscid macroscopic limit does not lead to the standard Euler equations for a plasma problem. An important property of this new macroscopic model is that the electron density is governed by a generalized Saha law rather than a conservation equation.

The extension of this study to a viscous plasma flow is under progress.

References

[1] Degond, P., Lucquin-Desreux, B. *Transport coefficients of plasmas and disparate mass binary gases*, Transport Theory and Stat. Phys., Vol. 25, No. 6, pp. 595-633 (1996).

[2] P. Degond, A. Nouri, C. Schmeiser, *Macroscopic models for ionization in the presence of strong electric fields*, Rapport Interne 99-02, MIP, Université Paul Sabatier (1999).

[3] Choquet, I., Lucquin-Desreux, B. *Hydrodynamic limits for an arc discharge of moderate pressure*, in preparation.

[4] Wendelstorf, J., *Ab initio modelling of thermal plasma gas discharges (electrics arcs)*, PhD. Thesis, Carolo-Wilhelmina University, Germany, Dec. 2000.

[5] Choquet, I., Degond, P., Schmeiser, C. *Hydrodynamic limits for charge carriers giving rise to strong ionization in semiconductors*, Transport theory and statistical physics (TTSP), to appear.

Expanding Thermal Plasma Deposition of Hydrogenated Amorphous Carbon Films

J. Benedikt, R.V. Woen, M.C.M van de Sanden

Department of Applied Physics, Eindhoven University of Technology, Eindhoven, The Netherlands

Abstract
Ar/C_2H_2 expanding thermal plasma (ETP) is used for hydrogenated amorphous carbon (a-C:H) deposition. The ETP plasma is able to produce good quality a-C:H (hardness 14 GPa) at very high growth rates (up to 70 nm/s) without ion bombardment involved. The remote nature of the plasma is suitable for the study of plasma chemistry by means of laser spectroscopy and mass spectroscopy in combination with plasma chemistry modelling. The reactive species in ETP are identified and their role in the growth is discussed.

Introduction
As summarised recently by Robertson [1] most of the good quality a-C:H films (and diamond-like carbon films in general) prepared by plasma enhanced chemical vapour deposition techniques requires an ion bombardment (ion energy typically 100 eV) during the growth. This presence of ion bombardment leads to a growth process that is physical in nature and the chemical identity of the growth precursors is suppressed.
On the contrary, good quality a-C:H films are grown by means of Ar/C_2H_2 ETP without ion bombardment involved. In the remote part of the ETP the electron temperature is low and the plasma behaviour is ruled by the heavy particle kinetics, e.g. hydrogen abstraction or ion induced reactions [2]. In other words the generation of precursors for growth is dominated by the chemistry and not by physical processes such as electron impact dissociation or ionisation in direct plasmas. The chemistry in remote plasmas could therefore be more selective and lead to the dominant production of one specific precursor. These conditions can possibly leads to different material properties allowing e.g. to achieve better electronic properties.
For understanding the growth mechanism under Ar/C_2H_2 ETP conditions it is essential to study plasma chemistry. Cavity Ringdown Spectroscopy (CRDS) and Mass Spectrometry (MS) was used to measure densities of hydrocarbon radicals (C, CH and C_2), consumption of acetylene gas and production of stable molecules (C_4H_2, C_6H_2). Next to it, also broadband absorption was observed and can be most probably assign to the C_2H radical and C_2H functional group in C_4H_2 molecule. Remote nature of the ETP is very suitable for successful modelling of obtained results. Simple plug down model was build and has shown very good agreement with experimental results. The influence of plasma composition on the film properties (determined by single wavelength ellipsometry) will be discussed.

Experimental Setup
A schematic view of the deposition system is shown in Fig.1. A cascaded arc creates Ar plasma (0.2-0.5 bar), which expands into a low-pressure vessel (0.3 mbar). This expansion is first supersonic and than, after the shock, subsonic [2]. Because of this high pressure difference between the arc and the vessel, there is no influence of the conditions in the vessel on the performance of the arc, and the amount of argon ions and electrons, emanating from the arc is fully determined by cascaded arc settings (argon gas flow and applied arc current). Acetylene is injected into the ETP beam and different radicals (and ions) are created. The substrate holder is positioned 60 cm downstream from the nozzle where the deposition takes place. The temperature of the substrate is well-controlled ($\Delta T < 10°C$ when exposed to plasma) [3] and is kept at 250°C. Pressure in the reactor is not kept constant and increases slightly (up to 10% of its starting value) with increasing acetylene flow. The setup is described in more detail elsewhere [3,4,5].
The CRDS setup is described in Refs. [6,7]. All the measurements were done 30 mm above the substrate with the laser beam crossing the ETP axis. Saturation effects are checked carefully in all the measurements. It should be noted that with CRDS line integrated densities are obtained. It is assumed that all the species have similar radial density profiles. The details of the CRDS measurements and the description of the CRDS principle are given elsewhere [6,7,8].

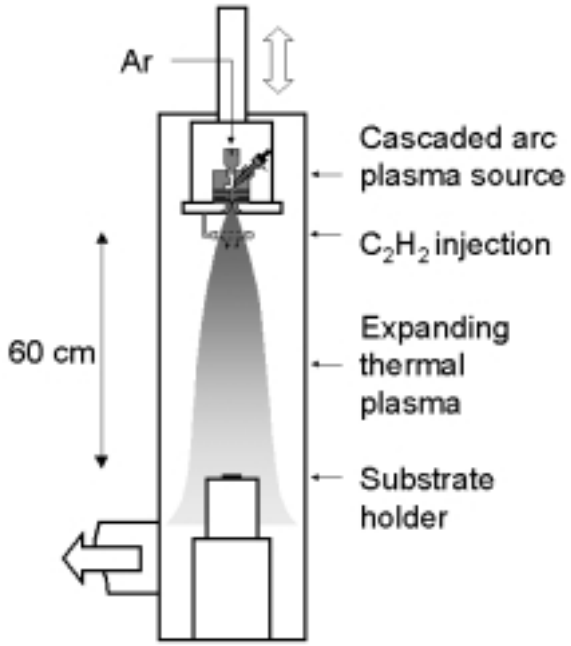

Fig. 1: Experimental Setup

Results and discussion

Experimental results

The MS measurement of acetylene and diacetylene in the background of the plasma at the arc current of 48A are shown in Fig. 2. Since arc current is fixed, also the amount of argon ions and electrons emanating from the cascaded arc is constant. Than varying the acetylene flow into the reactor, we vary the $C_2H_2/(Ar^+,e^-)$ ratio. At small acetylene flows all the acetylene is consumed in the plasma and transformed into different reaction products. On the contrary for high acetylene flows the consumption is saturated and does not increase as demonstrated by the fact that the difference between measurement at plasma off and plasma on conditions is constant. The C_4H_2 measurement shows absence of diacetylene for small acetylene flows and saturated values for high acetylene flows.

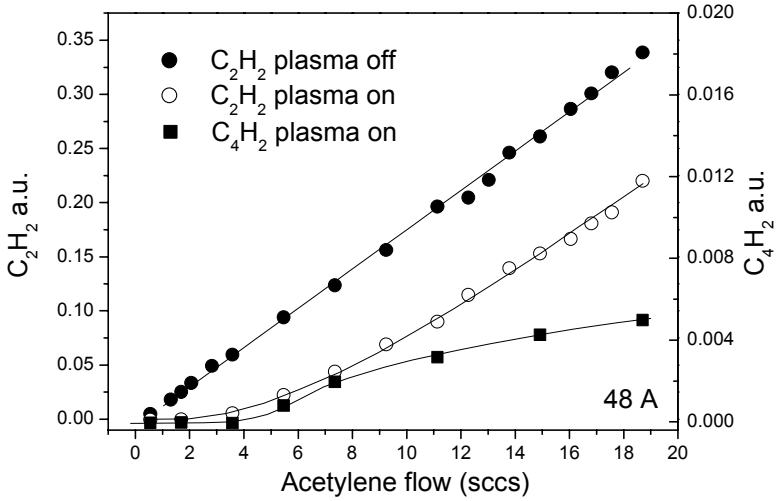

Fig. 2: Mass spectrometry measurement of C_2H_2 and C_4H_2 molecules as function of acetylene flow at fixed arc current of 48A. No C_4H_2 was observed under plasma off conditions.

To understand the results in Fig. 2 we need first to discuss the dissociation process of the acetylene injected. The first step is a charge transfer reaction between acetylene and an argon ion [9]:

$$Ar^+ + C_2H_2 \rightarrow Ar + C_2H_2^{+,r,v} \qquad k_1 \approx 4.2 \times 10^{-16}\ m^3/s \qquad (1)$$

This step is followed by a dissociative recombination of the molecular ion with an electron [10]:

$$C_2H_2^{+,r,v} + e^- \rightarrow C_2H^* + H \qquad k_2 \approx 3 \times 10^{-13}\ m^3/s \qquad (2)$$
$$\rightarrow CH^* + CH^*$$
$$\rightarrow C_2 + H + H$$

Since we are dealing with remote plasma and the reaction rate constants k_{CE} and k_{DR} are relatively large, for low acetylene flows there are more argon ions than acetylene molecules and acetylene can be fully consumed in reaction (1). On the contrary for high acetylene flows all the argon ions and electrons are consumed in reaction (1) leaving some acetylene unconsumed. The constant acetylene consumption at high acetylene flows indicates that polymerisation does not take place in the plasma chemistry. It was already argued, that C_2H radical is the dominant product of reaction (2) [11]. Main source reaction for the diacetylene molecule is than the reaction of C_2H radical with acetylene [12]:

$$C_2H + C_2H_2 \rightarrow C_4H_2 + H \qquad k_3 \approx 1.3 \times 10^{-16}\ m^3/s \qquad (3)$$

The C_4H_2 molecule is a stable molecule and will most probably not react with acetylene. Since C_2H production is limited by amount of available argon ions and electrons the C_4H_2 measurements saturates at high acetylene flows.

In Fig. 3 the C metastable state, CH and C_2 radicals absorption together with broadband absorption (BBA) are shown as measured by CRDS. The CH, C_2 and C radicals are created in a secondary reaction of C_2H radical with another argon ion and electron pair:

$$Ar^+ + C_2H^{e,r,v} \rightarrow Ar + C_2H^{+,r,v} \qquad (3)$$

$$C_2H^{+,r,v} + e^- \rightarrow CH^* + C^* \qquad (4)$$
$$\rightarrow C_2^* + H(n=1,2,\ldots)$$

This reaction takes place only when there are enough Argon ions and electrons in the plasma (two Argon ions and two electrons per acetylene molecule are needed). For this reason the highest C, CH and C_2 absorption is measured at low acetylene flows.

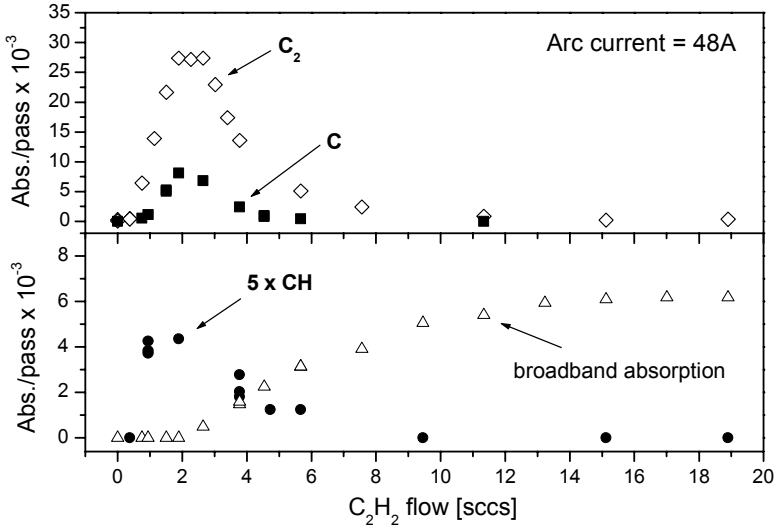

Fig. 3: C, CH, C2 and broadband absorption (BBA) as measured by CRDS.

Modelling of the plasma chemistry

The geometry of the expanding thermal plasma with the nozzle and injection ring followed by the expansion region allows modelling of the plasma chemistry with a rather simple plug-down 1D-model [13]. To the reactions mentioned above the loss processes of C [14], CH [15] and C_2 [16] radicals has to be added:

$C + C_2H_2 \rightarrow$ products $\quad k_4 \approx 2.8 \times 10^{-16}$ m^3/s (4)

$CH + C_2H_2 \rightarrow$ products $\quad k_5 \approx 3 \times 10^{-16}$ m^3/s (5)

$C_2 + C_2H_2 \rightarrow$ products $\quad k_6 \approx 1$ to 5×10^{-16} m^3/s (6)

More details about the model can be found in [17]. Comparison of experimental results (C_2 radical, C_4H_2 molecule) and modelling is shown in fig. 4:

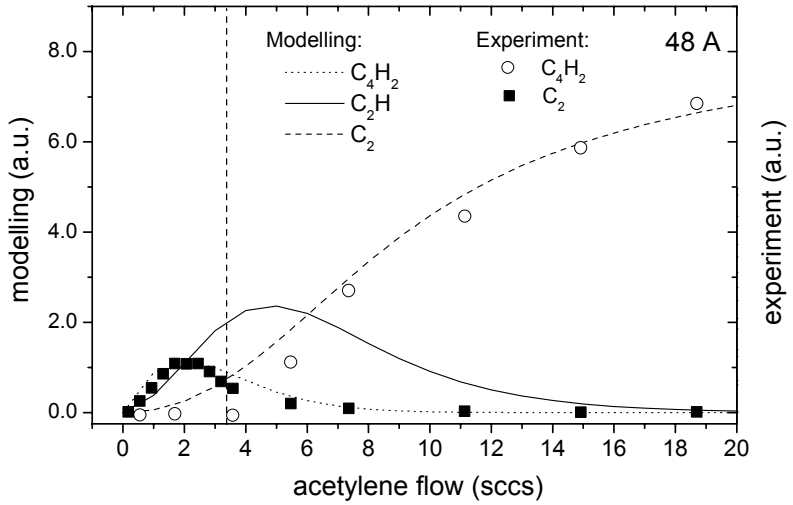

Fig. 4: Comparison of experimental and modelled result. Vertical dashed line indicates argon ion and electron flow used in the model.

Argon ion (and electron) flow was used as a variable parameter. The value of 3.3 standard cubic centimetres per second (sccs) gave the best agreement between the measurements and the model. Both experimental results and modelling shows, that ETP beam composition changes as the $C_2H_2/(Ar^+,e^-)$ ratio changes. At low flows mainly C, C_2 and CH radicals reach the substrate, at higher flows with ratio close ore slightly higher than unity C_2H radical is dominant species in the beam. At very high acetylene flows the radicals react away in the gas phase and C_4H_2 molecules arrives to the substrate.

Broadband absorption

A broadband absorption (BBA) was observed together with C, CH and C_2 absorption (in the wavelength regions 248nm, 431nm and 517nm). Its values at 248 nm and 431 nm as a function of acetylene flow are shown in Fig. 5. It is clear that more than one species contributes to the BBA since it behaves differently at different wavelengths (seen also at 517 nm). The most remarkable change is around 5 sccs of acetylene flow, where the plasma chemistry model predicts highest C_2H radical density. The BBA measured at the wavelength of 248 nm has the feature around 5 sccs much less pronounced and resemble more the C_4H_2 data. Insert in Fig. 5 shows BBA as function of wavelength at highest acetylene flow of 18.7 sccs. It shows exponential dependence with exponent of –6.4. Similar BBA behaviour (with exponents ranging between –2.7 and –9.2) was observed in flames in not sooting conditions [18] and was attributed to aromatic functionalities or chromophoric groups containing not more than two aromatic rings.

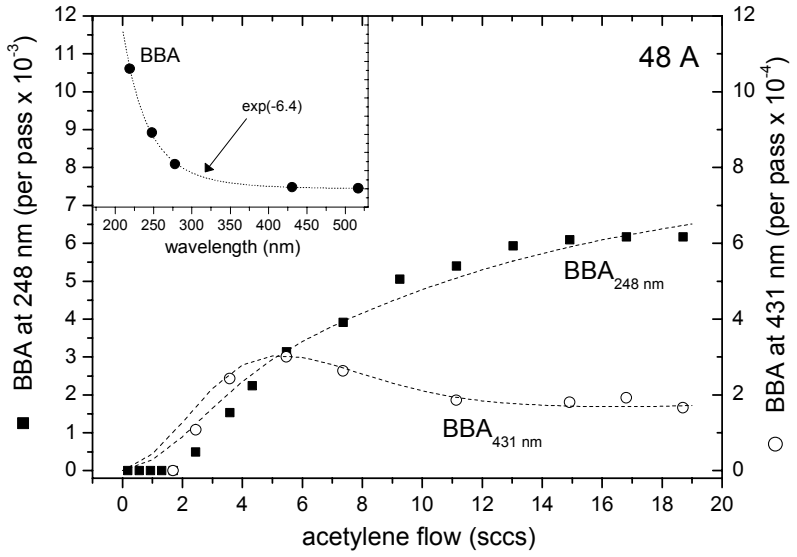

Fig. 5: BBA at two different wavelengths. Dashed lines were constructed as combination of C_2H and C_4H_2 densities as predicted by the model. Insert shows BBA at highest acetylene flow as function of the wavelength.

On the basis of obtained experimental data, modelling and the fact that -C≡C-H group is a chromophoric group we suggest that this group is a cause of BBA in our Ar/C_2H_2 ETP. Than both C_2H radical and C_4H_2 molecule can contribute to BBA. The supporting argument is the fact, that we were not able to detect any of reported spectral features of the C_2H radical or C_4H_2 molecule [19], probably due to broadening of their spectra as a result of their high ro-vibrational excitation.

A-C:H films growth

Fig. 6 shows refractive index and film growth rate as determined by real-time in situ single wavelength ellipsometer. It was shown that in the case of our a-C:H films the refractive index is the measure of mechanical properties of the films [4]. The dashed line indicates the argon ion and electron flow given by the model.

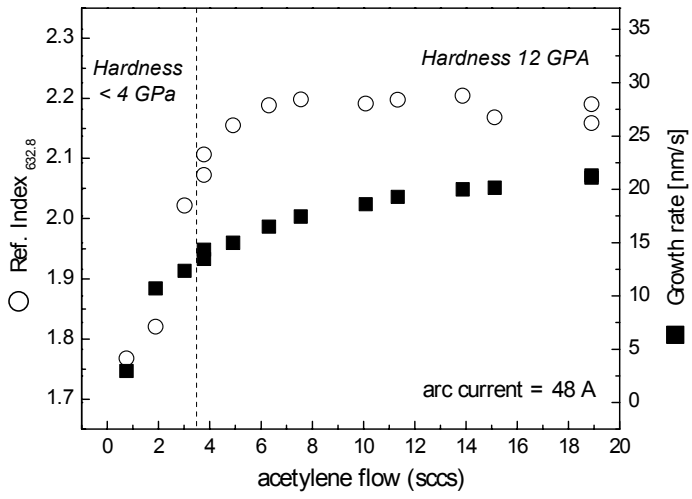

Fig. 6: Refractive index and growth rate of a-C:H films as determined by real-time in-situ single wavelength ellipsometer.

Comparing now ETP beam composition with results in Fig. 6 we can conclude that first C, CH and C_2 radicals do not lead to the deposition of hard a-C:H films. Second that highest refractive index is reached at the acetylene flow in which C_2H density above the substrate is expected to be maximal. Third good quality a-C:H films are also grown under the conditions, where C_4H_2 molecules are dominant in the ETP beam and, next to it, BBA scales very well with the film growth rate, both indicating that C_4H_2 molecules contribute to the film growth. As a deposition mechanism of C_4H_2 molecule we suggest its braking under impact onto the plasma activated surface into two C_2H radicals.

Acknowledgement
The authors would like to thank M.J.F. van de Sande, J.F.C. Jansen, A.B.M. Hüskens and H.M.M. de Jong for their skilful technical assistance. Fruitful discussions with D.C.Schram and R.A.H. Engeln are acknowledged. This work is part of the research program of the "Stichting voor Fundamenteel Onderzoek der Materie" (FOM). Part of this work was done in the frame of NATO Science for Peace project No. 974354.

References
[1] J. Robertson, Mater. Sci. Eng., R **37**, 129 (2002).
[2] M.C.M. van de Sanden, R.J. Severens, W.M.M. Kessels, R.F.G. Meulenbroeks and D.C. Schram, J. Appl. Phys. **84,** 2426 (1998).
[3] J.W.A.M. Gielen, W.M.M. Kessels, M.C.M. van de Sanden, D.C. Schram, J. Appl. Phys. **82**, 2643 (1997).
[4] J.W.A.M. Gielen, P.R.M. Kleuskens, M.C.M. van de Sanden, L.J. van Ijzendoorn, D.C. Schram, E.H.A. Dekempeneer, J. Meneve, J. Appl. Phys. **80**, 5986 (1996).
[5] J.W.A.M. Gielen, M.C.M.van de Sanden, P.R.M. Kleuskens, D.C. Schram, Plasma Sources Sci. Technol. **5**, 492 (1996).
[6] R. Engeln, K.G.Y. Letourneur, M.G.H. Boogaarts, M.C.M. van de Sanden, D.C. Schram, Chem. Phys. Lett. **310**, 405 (1999).
[7] J. Benedikt, M. Wisse, R.V. Woen, R. Engeln, M.C.M. van de Sanden, to be published
[8] K.W. Busch, M.A. Busch, *Cavity Ringdown spectroscopy* (Am. Chem. Society, 1999).
[9] M. Tsuji, H. Kouno, K. Matsumura, T. Funatsu, Y. Nishimura, J. Chem. Phys. **98**, 2011 (1993).
[10] P.M. Mul, J.W. McGowan, Astr. Phys. J. **237**, 749 (1980).
[11] J. W. A. M. Gielen, M. C. M. van de Sanden, P. R. M. Kleuskens and D. C. Schram, Plasma Sources Sci. Technol. **5**, 492 (1996).
[12] H. van Look, J. Peeters, J. Phys. Chem **99**, 16284 (1995).
[13] M.C.M. van de Sanden, J.M. de Regt and D.C. Schram, Plasma Sources Sci. Technol. **3**, 501 (1994).
[14] D. Chastaign, P.L. James, I.R. Sims, I.W.M. Smith, Phys. Chem. Chem. Phys. **1**, 2247 (1999).
[15] R. Guadagnini, G.C. Schatz, S.P. Walch, J. Phys. Chem. A **102**, 5857 (1998).
[16] H. Reisler, M.S. Mangir, C. Wittig, J. Chem. Phys. **73**, 2280 (1980).
[17] J. Benedikt, R. V. Woen, S. L. M. van Mensfoort, V. Perina, J. Hong, M. C. M van de Sanden, Diam. Rel. Mater. (2003) to be published
[18] C. Buchta, A. D'Alessio, A. D'Anna, G. Gambi, P. Minutolo, S. Russo, Planet. Space Sci. **43**, 1227 (1995).
[19] N.S. Smith, Y. Bénilan, P. Bruston, Planet. Space Sci. **46**, 1215 (1998).

Aerosol Production by Dielectric Barrier Discharges in air at atmospheric pressure

N. Jidenko[1], J.-P. Borra[1]

1 Laboratoire de Physique des Gaz et des Plasmas (CNRS –Univ. Paris XI)
Equipe Décharges Electriques et Environnement, SUPELEC, France

Abstract
This work focuses on sub-micrometer aerosol production in DBD by nucleation in air of very locally saturated vapour produced when filamentary discharges reach the surface. Two hypotheses on the source of condensable vapours (sublimation by Joule effect or ion sputtering) are discussed by comparison of aerosol frequency (part/s) for constant electrical energy flux, related to constant charge per filament with different surface temperatures. Then, the air flow rate is varied to discuss of competition between production and collection in this plane-to-plane DBD arrangement.

1. Introduction

As already observed with point to plane arrangements in clean air at atmospheric pressure, either with metallic electrodes polarised in DC or with AC Dielectric Barrier Discharges (DBD), the increase of the applied voltage induces the same succession of the same electrical discharge regimes (auto-stabilisation, glow, filamentary streamer and spark). Whatever the symmetry and the polarisation waveform, i.e. whatever the geometry and the related distribution of filaments in time and space are, production of nanometer aerosol is observed when filamentary discharges reach the surface [4, 5, 6]. Particles are produced by gas to particle conversion i.e. nucleation of sursaturated vapour produced either (i) from surfaces by plasma-surface interaction in carefully conditioned air at atmospheric pressure, (as proven by size distribution measurements and chemical analysis of particles electro-precipitated on the electrodes [10] as well as collected in the effluents of DBD [5]) ; or (ii) from combustion like mechanisms in depollution plasmas of Volatile Organic Compounds (polluted air), where condensable species are produced by plasma-gas interaction in volume [5, 6]. This paper focuses on surface erosion in clean air characterised by particles frequency between 10^2 and 10^9 part/s (with a few l.p.m), depending on geometry, humidity and voltage in terms of experimental parameters and related to the impulse component of the electrical power injected in the plasma (P_{imp}) and on gas flow rate for dilution factor.

$P_{imp} = \frac{1}{nT}\int_{nT} i_{imp}(t).u(t).dt$, $i_{imp}(t)$: impulse current, u(t): applied voltage, T: period and n: an integer.

To deal with the origin of vapour from surfaces submitted to filamentary discharges, sublimation by Joule effect and/or on ion sputtering in the spot can still be considered because the energy flux is related to both charge per filament and ionic sputtering as well as to the spot temperature at the feet of the filament and sublimation. To check the mechanism of production, we work with silent discharges (plane to plane), where the discharges only occur in numerous micro-discharges (filaments) [1-3] so that all the electrical power is injected in the gap through impulse filamentary discharges i.e. power and energy flux on surface (in $Watt.m^{-2}$ or $J=.s^{-1}.m^{-2}$) are directly proportional. The reduction of the discharge gap length enables us to reduce the charge per filament and to control independently the surface temperature, as experimentally observed [5] and confirmed by considerations about the ratio d/ε_r (d: gap and ε_r: relative dielectric permitivity [7]). Assuming that the kinetic energy of ions reaching the plane is related to charge per filament, this short gap configuration allows us to carefully control the surface temperature via heat exchanges on surfaces for constant electrical energy flux i.e. the "decoupling" of kinetic energy (assumed to be related to charge per filament) and surface temperature.

In the first part, from particle production rate (part/s) versus electrical characteristics and from aerosol size distributions, we confirm the nucleation mechanism induced by interaction of filamentary discharges with dielectric plane in a plane-to-plane geometry. Two hypotheses on the source of condensable vapours (sublimation by Joule effect or ion sputtering) are discussed versus surface temperature by particle production rate measurement during the transient initial phase to reach the quasi-steady-state surface temperature and particle production rate (QSS). Then, when surface temperature is stable at the QSS the air flow rate is varied. Results are coherent with a competition between production and collection in the DBD arrangement considered as an AC Electro Static Precipitator, as already described by [5, 9, 10].

2. Experimental set-up

The dielectric media is a single stage of honeycomb monolith between two plane electrodes constitutes the discharge cell. Their area is about 3 cm2. The discharge gap (pore diameter) measures 1 mm. The electrical discharges occur in numerous filaments distributed in time and space.
A 1 to 60 kHz signal is derived from a function generator, fed through a 2 kW amplifier, and then stepped up with a high voltage transformer. This sinusoidal AC high voltage is applied across the cell electrodes and measured by high voltage probe. The current crossing the cell is measured through a 50 Ω adaptive line to prevent from deformation and reflection. Dry air flows are controlled with mass flow controllers between 1 and 3 L/min. Using an oscilloscope (LeCroy LC374A, 500 Mhz, 2 Gs/s), both current and tension are treated as described in previous paper [8]. The current measured is an influence or displacement current underestimated in our conditions (represents only 85% to 95% of the current crossing the gap).

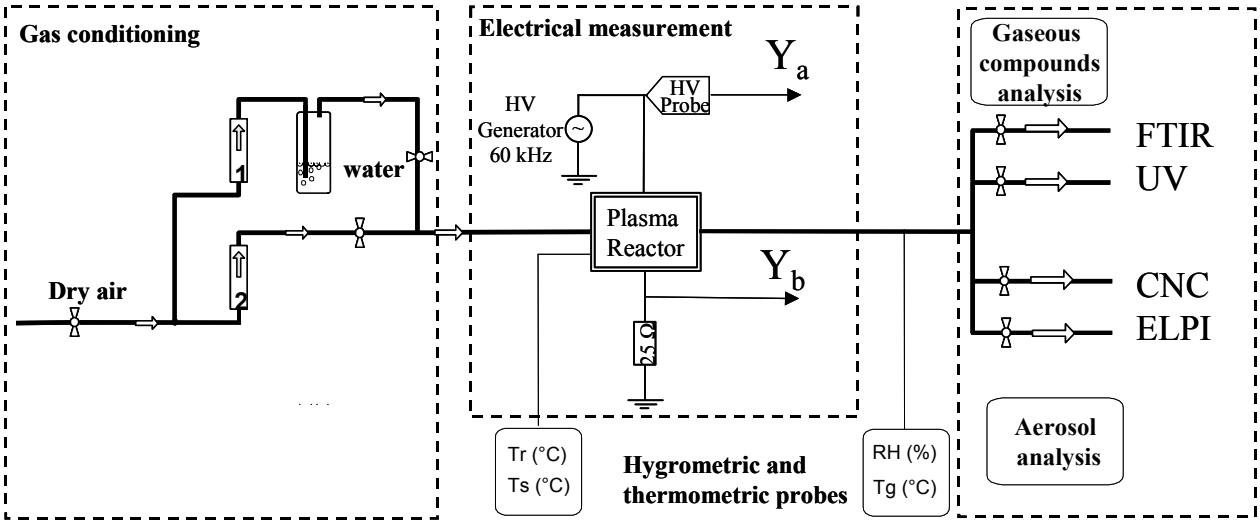

Figure 1: Experimental set-up

The aerosol concentration in the outlet gas is characterised by a Condensation Particle Counter (model CPC 3022 TSI) for all the particles whose diameter are higher than 5 nm. An Electrical Low Pressure Impactor (ELPI Dekati) gives its size distribution with 11 trays between 30 nm and 10 µm. The outlet gas and the metallic electrode temperatures (Tg and Te) are measured with thermocouples in order to evaluate the mean dielectric surface temperature (Ts). Tg and Te depend on gas flow rate and on thermal exchanges around the dielectric. The more representative temperature to deal with Ts, is the Te of the metallic electrode less than 200 µm from the dielectric surface.

3. Results and discussion

3.1 Quasi-steady state equilibrium

For a given operating condition (frequency 60kHz, peak to peak voltage from 12 kV to 17 kV, air flow rate 2 L/min), when the quasi-steady state equilibrium is reached, the concentration of particles as well as all the characteristic temperatures are related to the impulse component of the electrical power injected in the plasma (depending on the applied voltage). On Figure 2, the aerosol frequency (number of particles per second) at the output of the reactor is plotted versus the energy flux on surface (ϕ_e=P/S where P the input power and S is the area of an electrode, expressed in Joule by cm^2 per second or Watt /cm^2).

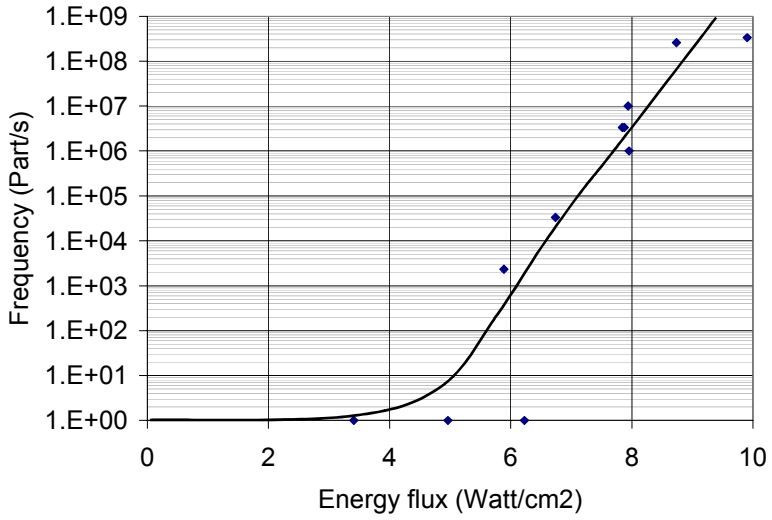

Figure 2: Aerosol frequency (part.s-$^{1)}$ at the reactor output versus energy flux (J/s.cm^2)

The first remark lies on the existence of a threshold effect when dealing with particle production rate versus impulse input power. This has never been observed in longer gap, probably because of the higher minimum impulse energy flux per filament reaching the plane on longer distances. Assuming that the kinetic energy of ions reaching the plane ("pushed" by the primary streamer charge density) is related to charge per filament measurements, this apparent electrical threshold would tend to support ions sputtering rather than sublimation effect (even with small filaments with lower charge per filament than 10 pC/filament, the aerosol production is null); but for lower energy fluxes than the apparent threshold value reported on figure 2, and constant charge per filament lower than 10 pC/filament with different surface temperatures (controlled by heat exchanges), this threshold energy is rather related to a corresponding threshold surface temperature of 140°C with alumino-silicate and 160°C with aluminium oxides dielectric barriers, in air at atmospheric pressure (cf. Fig 4b).

3.2 Nucleation confirmed by aerosol size distribution

Prior to any discussion about the mechanism of vapour production through ion sputtering or sublimation we first confirmed from aerosol size distribution that the nano-particle production arises from nucleation i.e. from gas-to-particle conversion (90 % of the aerosol is smaller than 30 nm, [8]). The operating conditions are: gas flow rate Q=3 L/min, peak-to-peak applied voltage Vpp=17 kV, input power P=30 Watt and temperature of the metallic electrodes Te=170 °C. In those conditions, the aerosol concentration is about 2^{E7} part/cm^3. The aerosol size distribution in plotted on Figure 3, the different trays are in dashed line and the real size distribution is in dotted line.

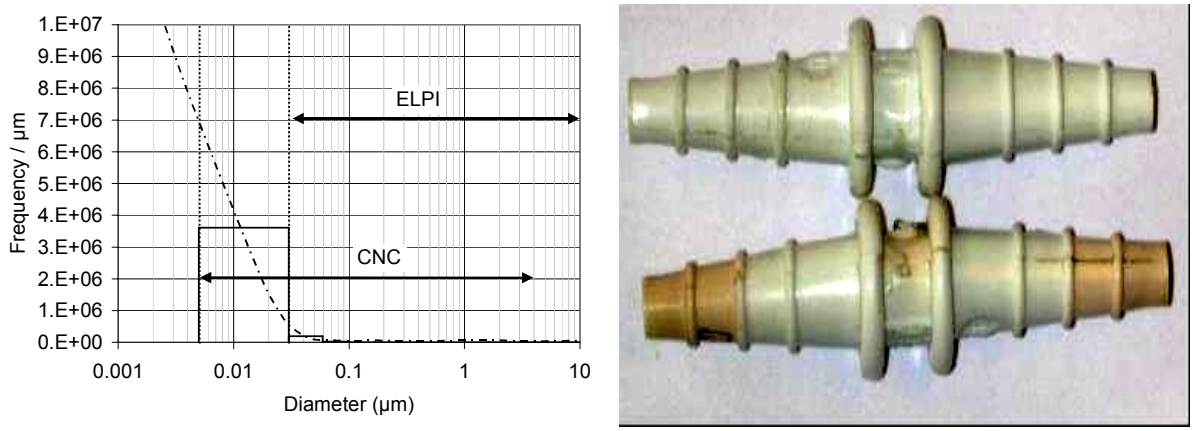

Figure 3: Aerosol size distribution and picture of the tube connector before (above) and after (below) the reactor

Three major arguments tend to show that this vapour comes from the dielectric planes and is produced by plasma-surface interaction: (i) the same phenomenon is observed in different clean gases (without volatile organic compound, such as N_2). The gas does not seem to be important for the particles production. (ii) The gas flow rate does not modify neither aerosol size distribution nor aerosol frequency (for gas flow rate higher than 2 l.p.m as discussed in §3.4). This means that the vapour concentration is not modified by the gas flow rate because if it would come from condensable species created by interaction plasma gas, the partial pressure (inversely proportional to the gas flow rate) and thus the frequency of nucleation and size distribution would be affected. So the vapour and the subsequent nucleated nano particles do not seem to be produced in the volume but locally before homogenisation of the concentration in the whole reactor volume (constant aerosol frequency independently of dilution); iii) after few tens hours of work the air connector at the output is coated by particles of the same colour than the dielectric (see picture of the lower connector in figure 3).

3.3 Transient state: Influence of the surface temperature

When the DBD is turned on, the mean surface temperature evolves from ambient to a final equilibrium temperature depending on the discharge current and on thermal exchanges around the dielectric, while both electric characteristics and the temperature of neutral species in filaments are constant. It is thus possible to discuss about the transition observed in § 3.1 with an energy flux nearly constant. Figure 4 a) depicts the evolution of electrode temperature (dotted line) and particles frequency (dashed line) since the lighting on to the quasi-steady-state (Q=2 L/min, Vpp=14.2 kV, Ps=7 Watt/cm^2). On the right is plotted the aerosol frequency versus the temperature for the transient initial phase (dotted line) and the aerosol frequency at the quasi-steady-state (dashed line). The discrepancy between the final steady states (temperatures and aerosol frequencies) can be explained by taking into account different thermal conditions (ambient temperature 20 °C and 26 °C and dielectric thickness 150 µm and 300 µm).

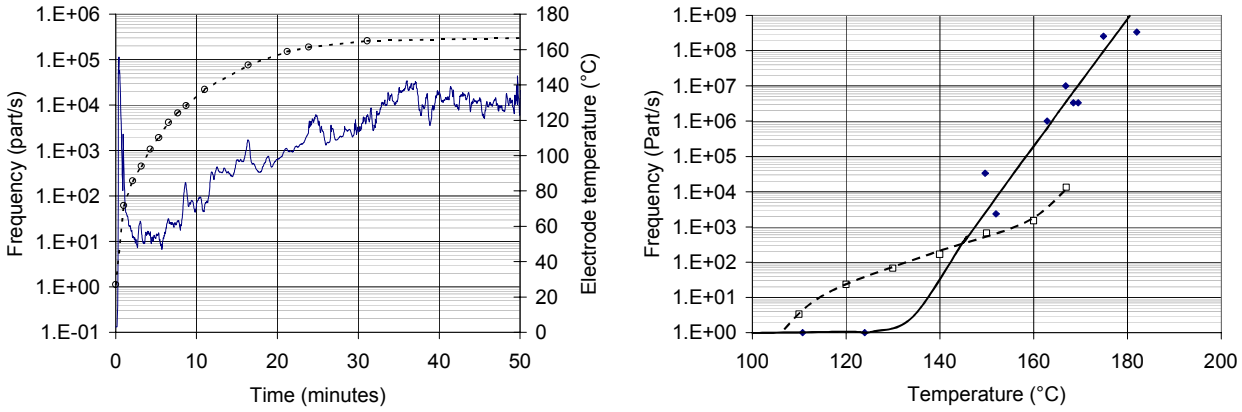

Figure 4: (a+b) Evolution of aerosol concentration and electrode temperature

- At first, when the discharge is switched on, there is a particle's puff. This initial puff can come from the suspension of unadherent particles already deposed on surfaces.

- Then the production of nucleated particles follows the mean surface temperature. For lower electrode temperature than 110°C there is no particle counted at the output. This temperature is different than the transition one at the QSS (140°C) because of the heat dynamic: the difference between surface and electrode temperatures is higher during the transient state than during the quasi steady state (the thermal capacitance of the metallic electrodes slows the temperature rising).

    - Aerosol frequency dependence on surface temperature for constant filament properties tends to support the sublimation process rather than ionic sputtering for the vapour production. For a constant energy flux related to constant charge per filament, the production of particles evolves with the mean surface temperature that is the more reliable measured temperature to deal with the spot temperature at the feet of the filament. This is confirmed by another experience, starting of the QSS and observing the evolution of the concentration and the temperature with an external cooling. The diminution of the surface temperature without modifying the energy flux and the related filament properties, induces a decrease of aerosol frequency.

Even if the mean surface temperature (less than 500 K) is under dielectric fusion temperature (about 2 000 K), one has to emphasise that this mean temperature results on thermal energy transfers to the surface occurring through the spots. Thus, this mean surface (temperature characterised through Te measurements), is related to individual thermal contribution of single filaments multiplied by the number of filament per second. However the spots last about 20 ns and on a surface of about 0.01 mm^2 so the local temperature is probably above sublimation temperature of the surface with the corresponding energy flux per filament estimated from 10^9 to 10^{16} J/s.m2 in our conditions, even if only a part of this total energy flux per filament is involved in heating of the surface.

3.4 Gas flow rate influence: 5 phases between production and the output of the reactor

The gas flow rate changes transit time and surface temperature without modifying significantly the plasma conditions. On Figure 5, the evolutions of the aerosol frequency with the gas flow rate (between 1 and 3 L/min) are plotted for four voltages (from 14 kV to 15.5 kV).

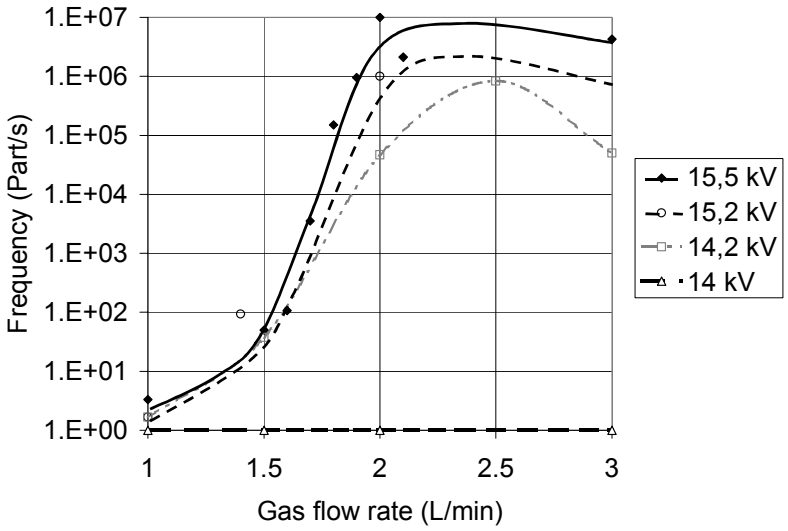

Figure 5: Aerosol frequency versus gas flow rate for different voltages

Except for the lower voltage, where there is no aerosol at the output whereas the input power is about 15 Watt (i.e. 5 Watt/cm^2) all the curves have the same shape. The output aerosol frequency increases with the gas flow rate until a maximum frequency depending on the input power. After this maximum the output aerosol frequency decreases.

- For the lower voltage, there is no aerosol at the output whereas the input power is about 15 Watt i.e. 5 Watt/cm^2 probably because surface temperature lies under the threshold temperature discussed in §3.1.
- At 1 L/min there is no aerosol whatever the energy flux or the electrode temperature are, probably related to longer transit time of charged particles in the polarised gap enabling collection of particles, as discussed below.
- The shape of aerosol frequency versus gas flow rate could be explained by the fact that even if there is no aerosol counted at the output, production of aerosol could occur in the reactor. Actually, between the production of vapor by the interaction of filament on the surface and the output of the reactor there are at least five phases: nucleation, growth, transport, charge, and exit/collection. Nucleated aerosol is produced as described before. Once created, they can grow by heterogeneous nucleation and coagulation. Then the ions produced by the discharges can charge the particles. So that they can be collected on the surfaces by electro-precipitation mechanism like. Before the maximum aerosol frequency (for low air flow rate), longer transit times allow the growth, the charge and the electrostatic collection of all the particles formed: the electrostatic force is dominant. But with transit time smaller than 10 ms (gas flow rate > 1.5 l.p.m), particles have less time to grow up, to get charged and to be collected: the training force becomes greater than electrostatic one. After the maxima, nearly constant aerosols frequencies are observed independently of the gas flow rate; this means that all the particles produced can reach the output of the

reactor without being collected because nearly only a dilution effect is dominant. Nevertheless, the small decrease of aerosol frequency can be explained by a better surface cooling all the more noticeable at lower voltages inducing lower energy and resulting heat fluxes on surfaces and lower surface temperature.

As a conclusion, surface temperature can modify vapour production, transport through thermophoresis, charge, Brownian and coulombian coagulation, as well as the reduced field (~E/P). Thus, for a given energy flux and related charge per filament, the dielectric surface temperature and residence time play on each process involved in the sequence from vapour production to exit of nucleated aerosol from the reactor (vapour production, nucleation, growth, charge and transport i.e. exit/collection).

4. Conclusion

Even if under certain conditions no particle is counted at the output of the reactor whereas the discharge mode is filamentary, it seems that filamentary discharges always produce particles. “Small filaments” (charge per filament from 1 to 100 pC/filament) produced by DBD in shorts gaps does not prevent from nucleated aerosol production. This tends to show that with “small filaments”, either (i) the kinetic of ions reaching the plane is still higher that the minimum kinetic energy required for ion sputtering or (ii) the sublimation is the dominant process to account for vapours arising from plasma-surface interaction in the feet of the filament when it reaches the plane. Moreover, this sublimation hypothesis is supported by the reported effects of surface temperatures (related to spot temperature) on nucleated aerosol frequency.

Then, from flow rate influence for a given energy flux and related charge per filament, the dielectric surface temperature and residence time play on each process involved in the sequence from vapour production to exit of nucleated aerosol from the reactor (vapour production, nucleation, growth, charge and transport i.e. exit/collection). Nevertheless, great experimental efforts have still to be done so as to define surface temperature influence on vapour production and/or charging, growing and collection after the production during the transit time in the reactor.

However, silent discharges at atmospheric pressure could be used either as nano-particles production tool or as well as filtering devices for particle collection.

References

[1] U. Kogelschatz et al. "From ozone generators to flat television screens: history and future potential of dielectric-barrier discharges"; Pure Appl. Chem., Vol 71 , No 10; pp 1819-1828; 1999

[2] K V Kozlov et al. “ Spatio–temporally resolved spectrometric diagnostics of the barrier discharge in air at atmospheric pressure ”; J. Phys. D: Appl. Phys 34; pp 3164-3176; 2001

[3] Hammer T., “Application of plasma technology in environment” Contrib. Plasma Phys., 39 441-462 (1999)

[4] JP Borra et al. “Electrical Discharge regimes and aerosol production in point-to-plane DC high-pressure cold plasmas: aerosol production by electrical discharges” J aerosol Sci Vol 29 No5/6 pp 661-674 1998

[5] L. Parissi et al. : Electrical discharge for environmental purposes; ed Raizers book; pp279-312; 1999

[6] N. Jidenko et al. “Volatile organic compounds depollution by dielectric barrier discharge in porous media”; Hakone VIII; pp 364-368; 2002

[7] V. I Gibalov et al.«The development of dielectric barrier discharges in gas gaps and on surfaces »; J. Phys. D: Appl. Phys 33; pp 2618-2636; 2000

[8] M. Petit et al. "Electrical characterization of gas discharges using a numerical treatment. Application to dielectric barrier Discharges" review of scientific instruments; Vol 73, No 7; pp 2705-2712; 2002

[8] W.C.Hinds, Aerosol technology - Properties, behavior, and measurement of airborne particles , Wiley, New York, 1982

[9] S. Masuda et al. « Boxer charger – a novel charging device for high resistivity powders », Conf. Rec. IEEE/IAS ANN. MEETING, Vol 1B, pp. 16, 1978

[10] Pauleau « Thèse de l’université de Pau et des pays de l’Ardour » n°102, 1980

Influence of the discharge regime on the dust formation in dielectric barrier discharge

C. Jimenez[1], C. Khamphan[2], N. Gherardi[1], P. Segur[2], F. Massines[1], L. Boufendi[3]

[1] *Laboratoire de Génie Electrique, Université Paul Sabatier, Toulouse, France*
[2] *Centre de physique des Plasmas et de leurs Applications, Université Paul Sabatier, Toulouse, France*
[3] *Groupe de Recherche sur l'Energétique des Milieux Ionisés, Université d'Orléans, Orléans, France*

Abstract
The influence of the dielectric barrier discharge regime on the dust nucleation and growth is studied in a plasma formed in a $N_2/SiH_4/N_2O$ mixture at atmospheric pressure. Two kinds of dielectric barrier discharges are compared : the filamentary and the glow discharges. The formation of large aggregates is more important and more rapid and reactive gases dissociation is quicker in the case of a filamentary discharge. However kinetics of formation of particles seem to be the same in the two regimes.

1. Introduction

Whatever the pressure, the use of silane in a plasma easily leads to the formation of powders or particles. This formation was first considered as disastrous in particular in micro-electronics industry where dust contamination can severely reduce the yield and performance of fabricated devices. Also the effort essentially aimed at avoiding particle growth in order to control the contamination level in industrial reactors. Since thirty years more and more studies have been led and some positive aspects of dusty plasmas have progressively emerged and now particles are not anymore considered as only unwanted pollutants. Control of the properties of plasma produced particles allows the development of new technologies or new materials [1,2,3].

The aim of this study is to understand the particles formation in a silane plasma containing an oxidizing gas, at atmospheric pressure. After a brief description of the experimental set-up and the discharges used, results will be presented and discussed.

2. Experimental set-up

The discharge is produced between two parallel and rectangular electrodes, both covered by a dielectric layer (alumina). A silicon wafer, used as a substrate, is placed on the lower electrode (figure 1).
After a primary vacuum of 10^{-1} Pa is achieved, the vessel is filled to atmospheric pressure (10^5 Pa) with a mixture of N_2, SiH_4 and N_2O . During the discharge, gases are introduced laterally, on one side of the reactor. The pressure is maintained constant by slight pumping. The flow of each gas is controlled by mass flow controller. An alternative voltage is applied to the electrodes. The frequency is about few kHz and the amplitude reaches 10kV. The discharge current is measured thanks to a 50Ω resistance in series with the mass electrode.

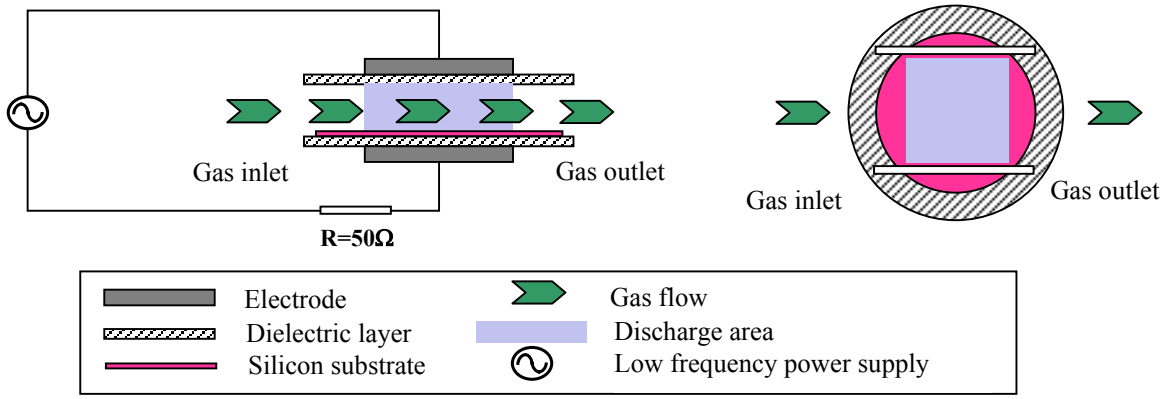

Figure 1 : schematic diagram of the reactor

Some of the particles formed during the discharge deposit on the substrate. Ex-situ analysis by optical or scanning electron microscopy allow to determine the size and the localization of these particles.
As the gas flow injector is on one side of the discharge, the decomposition of the reactive gases and particles growth can be studied relatively to their residence time in the discharge.
The gas phase is studied by optical emission spectroscopy (OES). Measurements are made through a quartz window using an optical fiber and a 27cm focal length monochromator (SPEX 270M) equipped with a 1200 lines mm^{-1} grating coupled to an intensified CCD camera (Jobin Yvon, i-spectrum one).This system works in the range of 200-800nm with a wavelength resolution of 1nm. A collimator system allows a space resolution in the discharge equal to 5mm. The acquisition of spectra was synchronized to the discharge current, permitting time resolution.
Appearance of particles in the gas phase is studied by laser light scattering. A laser diode (Stocker Yale, Lasiris SNF 501-L, 680nm, 70mW) is used. The beam is focused and pass trough one side of the discharge to the other, in the opposite way of the gas flow. When the beam meets a cloud of particles, a part of the light is scattered and detected at 90° by the same equipment as for OES.
Powders deposited on the substrate are studied by optical and Scanning Electron Microscopy (SEM).

3. Two kinds of discharges

At atmospheric pressure, two kinds of dielectric barrier discharges can develop : the glow discharge and the filamentary one.
The glow discharge is characterized by the appearance of a single discharge canal covering the whole surface of the electrodes. We observe a single current peak by half period of the applied voltage (figure 2b). It lasts a few hundreds of microseconds.
On the contrary, during a filamentary discharge, a large numbers of micro-discharges develop simultaneously and randomly in the gap. Each micro-discharge has a diameter of about 100µm and lasts a few tens of nanoseconds. In a half period of the applied voltage many current peaks can be observed, each one corresponding to the sum of the currents through the filaments developing at the same moment between the electrodes (figure 2a).

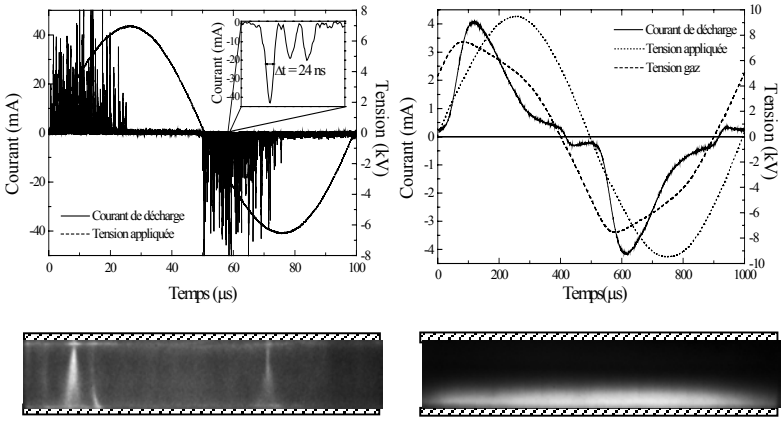

Figure 2 : electrical characteristics and photographs (10ns exposure time) of (a) a filamentary discharge and (b) a glow discharge

In some specific conditions of gas flow and excitation frequency, it is possible to obtain, by simply increasing the applied voltage, a low power filamentary regime (30mW/cm² at 10.5kV), a glow discharge (0.4W/cm² at 11.5kV) and a high power filamentary regime (1.2W/cm² at 15kV). The comparison of the powder formation in these three discharges allows to distinguish the influence of the discharge regime, glow or filamentary, and the power on the formation and growth of particles.

4. Observations on the substrate

The sample obtained with a glow discharge presents a whitish band of 0.5cm at 1cm from the gas inlet. Nevertheless, powders cannot be observed with optical microscope.

Whatever the power, filamentary samples look much more dusty, with a high concentration of powders even at the first beginning of the discharge area (0.5mm). Analysis with optical microscope leads to the conclusion that these powders are in fact aggregates of smaller particles. The smallest particle discernible with the optical microscope is 1µm in diameter.
We can also conclude that the glow discharge does not form such big particles, whereas the filamentary discharges create powders of about 1µm in diameter.

Analysis of these samples with a Scanning Electron Microscope confirms these observations.
On the filamentary sample obtained at high frequency, big clusters of particles can be observed. These aggregates grow rapidly up to 800nm at 2.5mm from the beginning of the discharge area (figure 3, a and b). Then they disappear suddenly : the deposit is only made of an accumulation of small grains of about 40 nm in diameter (figure 3c).

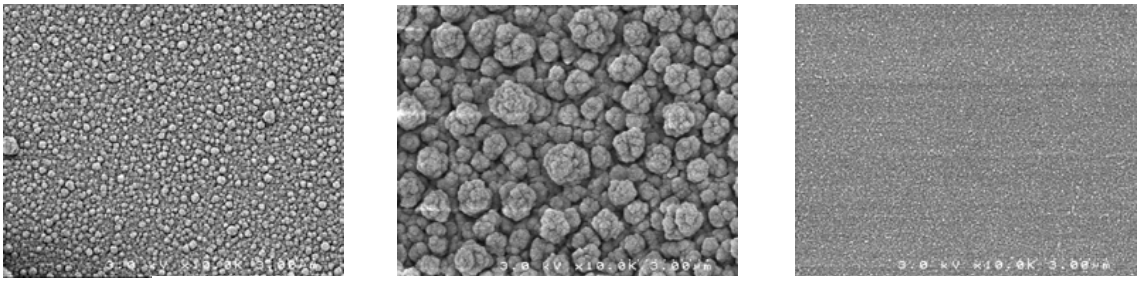

(a) (b) (c)

Figure 3 : SEM photographs of the surface of a high power filamentary sample at different distance from the beginning of the discharge area : (a) at 1.25mm, (b) at 1.75mm, (c) at 4.75mm.

Observations have also been made with a sample obtained with a glow discharge. They lead to the same behavior as the one observed on a filamentary substrate : the size of the grains quickly increases when moving from the gas inlet and then reduces (figure 4). However the size of the aggregates is much smaller (150-200nm) with a glow than with a filamentary discharge. This explains the fact that it was not possible to observe them with the optical microscope. Moreover, the kinetics of clusters and particles formation is much less rapid in a glow discharge than in a filamentary one : about 2 times more discharges are necessary to obtain the clusters with the maximum size. Another point is the fact that in the glow discharge, deposit growth is accelerated when there is no more large aggregates on the substrate.
A common point between the two discharges is that the elementary grain constituting the aggregates at the beginning of the discharge area or the deposit at the end has the same size for the two regimes that is to say, about 40 nm in diameter.

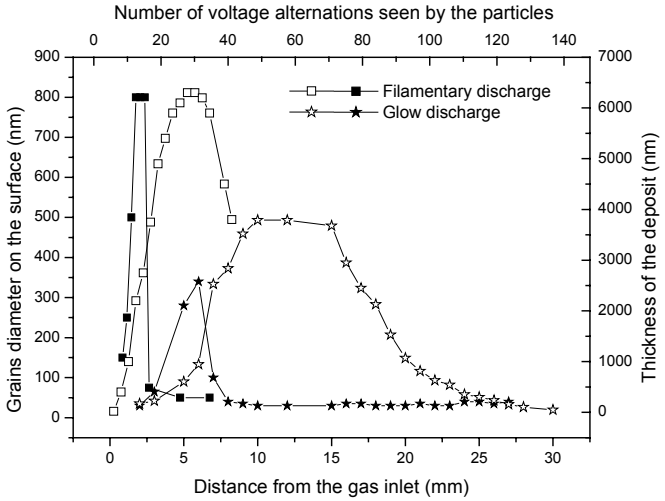

Figure 4 : Grains diameter (full symbol) and thickness of the deposit (open symbol) in a glow (star) and in a high power filamentary (square) discharge determined by analysis of the SEM photographs.

5. Study of the gas phase

5.1. Glow discharge

Experiment of laser light scattering in a $N_2/SiH_4/N_2O$ mixture has been carried out during a glow discharge (figure 5 a and b).

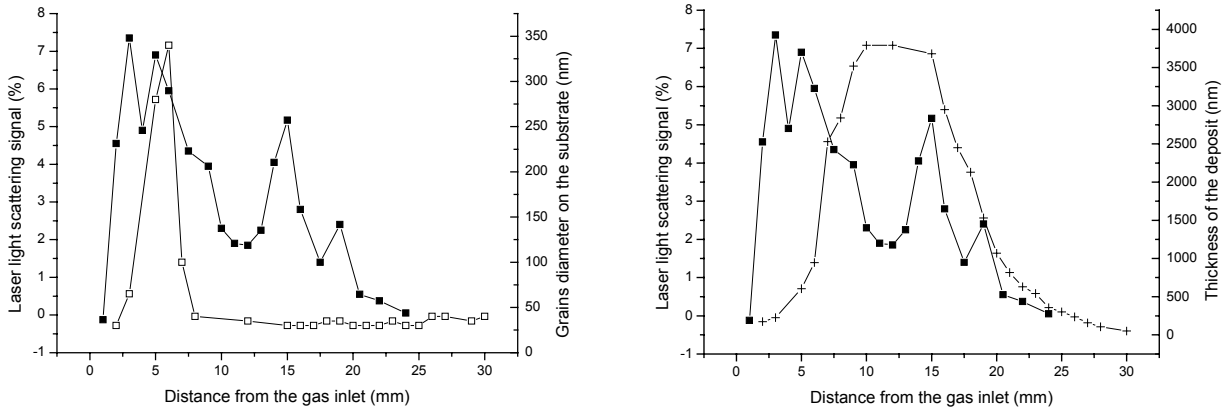

Figure 5 : laser light scattering in a glow discharge (full square) and (a) diameter of the aggregates on the surface (open square) in the $N_2/SiH_4/N_2O$ mixture, (b) thickness of the deposit (cross).

We observe that the scattering intensity reaches its maximum at about 3mm from the gas inlet. That means that about twenty half periods of the voltage are necessary to create the maximum number of particles which have a size large enough to diffuse the laser light.

Scattering intensity is proportional to the particle radius to the power of 6 and to the particle density. So, even a little change in the particle radius leads to an important variation of the scattering intensity. The fact that the scattering signal never varies significantly leads to the conclusion that in the gas phase, particles have roughly the same size (40 nm as we can observe on the SEM photographs). So the scattering variation is mainly attributed to a change in particle density. The scattering intensity has been compared with the diameter of the aggregates on the substrate surface (figure 5a). We observe that the region of the largest aggregates on the substrate is not linked with the maximum intensity of laser light scattering. This means that these aggregates are not formed in the gas gap but on the surface of the substrate. Scattering signal decreases as the thickness of the deposit increases : a possible explanation is that particles created in the gas gap are consummated on the surface to form the deposit more rapidly than they are created which induces a decrease of laser scattering. The scattering peak at 15mm can be due to the fact that the discharge pulls particles from the surface.

The decomposition of the gases during the glow discharge is studied in a N_2/SiH_4 mixture by OES. The excitation conditions and N_2 and SiH_4 flows are the same as previously. Decomposition of the gases is studied in terms of the distance from the gas inlet, that is to say as a function of the number of discharges seen by the gases (figure 6a).

Emissions of Si (251-253nm), SiN (401nm), SiH/SiN (412nm) and NH (336nm) have been observed.

Si and SiN radicals are created in important quantity at the very first beginning of the discharge area. More interactions may be needed to create SiH or SiN species, that could explain the delay needed to reach the maximum intensity of emission. Radiative state of NH ($NH(A^3\Pi)$) can be obtained by four main ways described by equations 1, 2, 3 and 4 :

$$SiH_4 + N(^2D) \rightarrow SiH_3 + NH \quad \text{Eq. 1}$$

$$SiH_x + N(^4S) \rightarrow SiH_{x-1} + NH \quad (x=1,2,3) \quad \text{Eq. 2}$$

$$NH + N_2(A^3\Sigma_u^+) \rightarrow NH(A^3\Pi) + N_2 \quad \text{Eq. 3}$$

$$N(^2D) + H(^2S) \rightarrow NH(A^3\Pi) \quad \text{Eq. 4}$$

So, the emission amplitude of NH depends on SiH_x, N or H densities. Atomic nitrogen is essentially created by electronic dissociation of N_2 and dissociative recombination of N_2^+. As nitrogen is the main gas, atomic nitrogen must be produced all along the discharge, whatever the distance from the inlet. Moreover, hydrogen comes essentially from silane dissociation. So the variations of NH emission are mainly linked to the

variations of SiH_x densities. Beyond 8mm from the gas inlet, all the emissions are decreasing. That means that the radicals linked to the dissociation of silane are consummated to form powders in the gas phase or a deposit on the substrate, or are transformed in other radicals.
The inter-electrode gap can also be divided in two regions. The first one goes from the gas inlet to 8mm : in this region the silane radicals are numerous. In the second region beginning around 8mm from the inlet, silane radicals have drastically reduced.

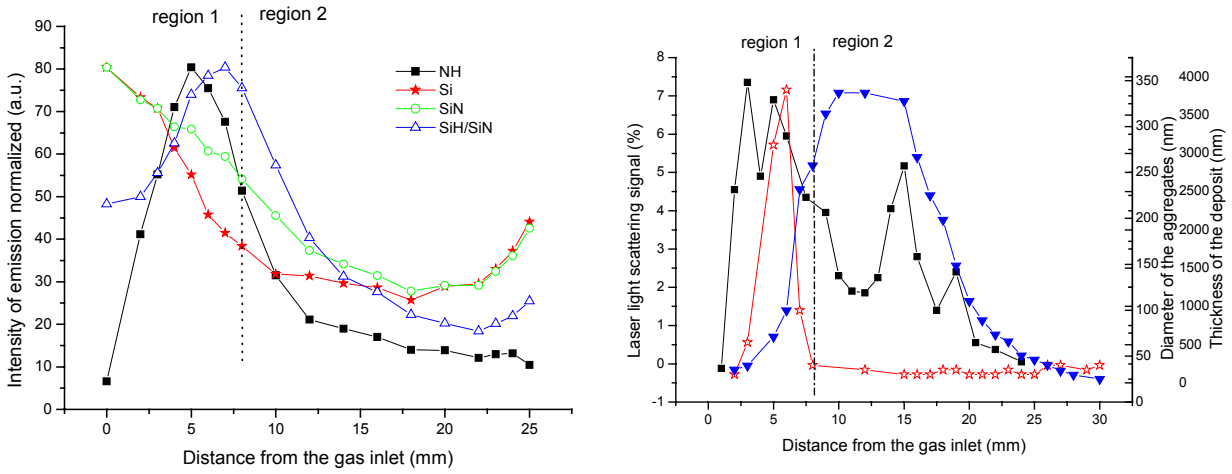

Figure 6 : (a) evolution of emissions intensity as a function of the distance from the gas inlet ; Si at 251-253nm (full star), SiN at 401nm (open circle), SiH/SiN at 412nm (open triangle), NH at 336nm (full square)
(b) comparison of OES, laser light scattering (square), diameter of the aggregates (star) and thickness of the deposit (triangle).

The different observations made with laser light scattering, OES and SEM can be correlated. One discharge is enough to create Si, SiH, SiN radicals but the particles density increases up to 4mm. This delay can be attributed to the time needed to form a particle large enough to induce laser light scattering. For larger distance, particles begin to arrive at the substrate surface and aggregate. This happens in the region 1, where there is a large quantity of silane radicals which act like binding agents between the particles (figure 6). When there is no more binding agents, particles that arrive on the surface do not bind together and the size of the structures on the surface is much smaller (40nm).

5.2 Filamentary discharge
Similar experiments have been undertaken for the high power filamentary discharge.
Figure 7a shows the results of OES in a the N_2/SiH_4 mixture. The same behavior as the one in glow discharge can be observed : two regions can be distinguished, the first one being correlated with a high presence of silane radicals and the second one with an important decrease of these species. The first region is correlated with the presence of large aggregates on the surface, wich confirms the role of binding agent of SiH_x radicals (figure 7b). As we can see on the SEM photographs, a large amount of powders are created and rapidly fixed on the substrate : at 1.7 mm, deposit is constituted by large aggregates (800nm) of smaller particles (40nm). Beyond 3mm, particles on the surface have the same size of 40nm. As laser light scattering signal does not vary drastically, we can again conclude that the signal is rather proportional to the density of particles than to a change in their size (figure 7b). The signal increase is comparable to that of the glow discharge, but the peak width is smaller. The scattering signal grows up like the deposit thickness, therefore scattering intensity seems to be controlled by the creation rate of particles and not by their loss on the surfaces. So many particles are created that their deposit on the substrate does not influence the scattering signal. Beyond 4mm, density of particles decreases : they are sufficiently numerous to make the deposit grow for 2mm more. And then both scattering intensity and thickness decrease.

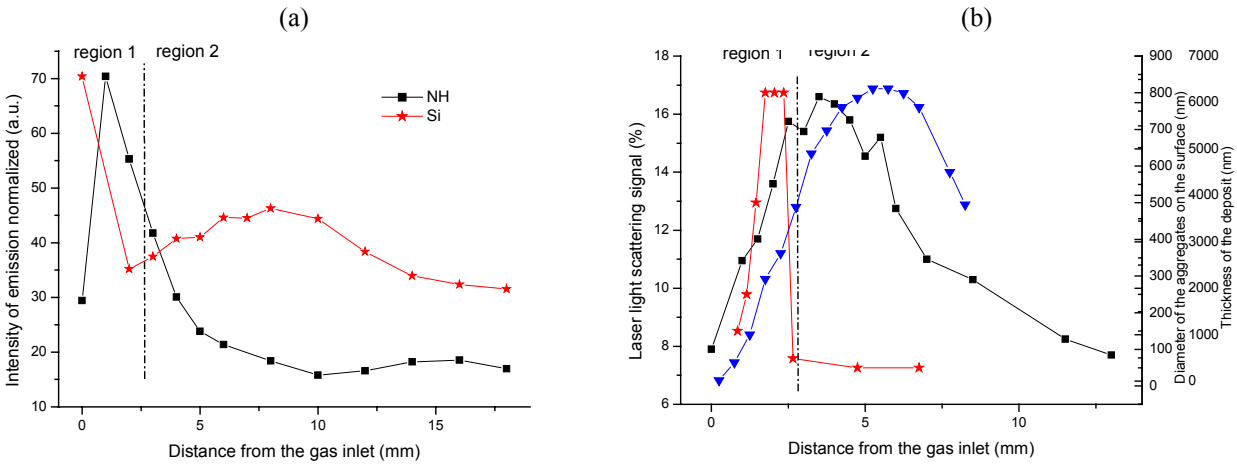

Figure 7 : (a) evolution of emissions intensity as a function of the distance from the gas inlet ; Si at 251-253nm (full star), NH at 336nm (full square)
(b) comparison of laser light scattering intensity (square), diameter of the aggregates (star) and thickness of the deposit (triangle)

7. Conclusion

Whatever the power delivered by the filamentary discharge, the quantity of big powders (about 1µm) produced in this kind of discharge is more important than in a glow discharge. However, the same two regions can be defined in the two regimes : at the beginning of the discharge area, important presence of SiH_x radicals, playing the role of binding agent, seems to lead to the formation of large aggregates of particles on the surface of the deposit ; farther in the discharge, these radicals have disappeared and the deposit is made of powders of 40nm in size that are not linked together. In another hand, dissociation of reactive gases, growth of aggregates and deposit are 2 to 3 times more rapid in the case of the high power filamentary discharge. Then the slowdown of the mechanism allows to get an area without powder at the really entrance of the discharge in the glow discharge case. As laser light scattering experiments show, formation of powders seem to happen as quickly in the glow discharge than in the filamentary. An explanation could be that filamentary discharge form more powders and that these powders are more rapidly driven on the surfaces.

References

[1] A. Bouchoule et al – Dusty plasmas : physics, chemistry and technological impacts in plasma processing, Bouchoule, John Wiley&sons, LTD
[2] H. Kersten, H. Deutsch, E. Stoffels, W.W. Stoffels, G.M.W. Kroesen, International Journal of Mass Spectrometry, **223-224** (2003) 313-325
[3] P. Roca i Cabarrocas, P. Gay, A. Hadjadj, Journal of Vaccum Science and Technology A, **14**, 2, (1996)

Electrotechnical approach of a process based on glow dielectric barrier discharge

N. Naudé, J-P Cambronne, N. Gherardi, F. Massines

Laboratoire de Génie Electrique de Toulouse, Université Paul Sabatier, Toulouse, France

Abstract

The aim of this work is to improve the working domain of a glow dielectric barrier discharge at atmospheric pressure (GDBD) thought a better understanding of the power supply and the discharge coupling. A model of the GDBD and its power supply is presented. This model is based on the use of equivalent electrical circuits and is taking into account the main phenomena of the GDBD and the main parasitic elements of the power supply. It permits to have a general view of the process and to study the influence of the electrical circuit and its parasitic elements on the discharge and on the working domain.

1. Introduction

Because of their homogeneity, GDBD are very interesting for surface treatment. Industrial processes using a few amount of reactive gases diluted in N_2 to reach the atmospheric pressure would be very useful. One of the main difficulties to reach that goal is that a GDBD at atmospheric pressure in nitrogen can only be obtained on limited working domain. This domain depends of the excitation form and the electrical characteristics of the power supply. The development of an industrial process supposes an optimization of the coupling between the discharge and the power supply. A possible approach to achieve this goal consists in developing an electrical model of the power supply and the GDBD [1]. After a brief description of the experimental set-up, we will describe the modeling of the GDBD and of its power supply, then we will study the working domain of the GDBD as well as one reason of destabilization of the GDBD.

2. Experimental set-up

The experimental arrangement used for this study is shown in figure 1. GDBD are generated between two parallel plane electrodes, coated on ceramic plates, to which an a.c. high voltage is applied in the frequency range from 200 Hz to 20 kHz with a magnitude up to 24 kV peak to peak. The discharge is obtained in an atmospheric pressure of nitrogen. To limit impurities, a pumping system is used to reach a secondary vacuum (10^{-6} mbar). The electrodes are rectangular with the dimension of 10 mm in length and 60 mm in width. The gap between the two electrodes is currently 1 mm. A flow of nitrogen in the direction of the electrode width is used to renew the gas and eliminate the species etched from the surface.

The power supply is made of a low frequency generator providing the reference signal which is then amplified by a linear amplifier whose output is applied to the primary winding of a transformer, the discharge system being connected with its secondary. The discharge current, I_d, is measured via a 50 Ω resistance connected to the ground in series with the discharge by a 2 GHz bandwidth digital oscilloscope. The applied voltage, V_{ps}, is measured by a high voltage probe. The voltage applied to the gas, V_g, is calculated from I_d and V_{ps}.

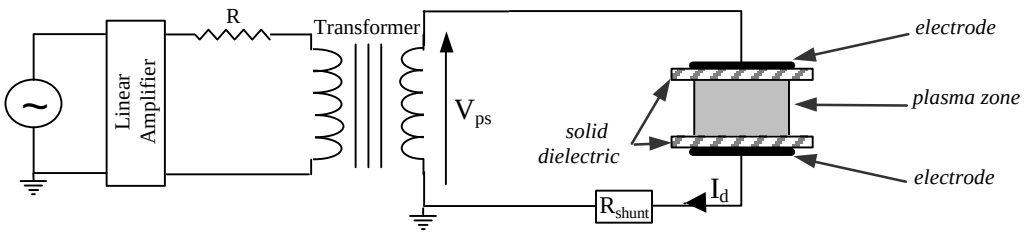

Fig. 1 : Schematic diagram of the experimental set-up

3. Power supply model

The figure 2 presents the model of the power supply experimentally studied [3]. The principal element of the power supply is the transformer. Indeed, the amplifier can be modelled by a constant gain.

This model is composed of six elements : R_T is the resistance of the copper winding, X_T accounts for the flux leakage, R_M represents the core loss of the magnetic core material due to hysteresis, X_M is the magnetizing inductance and finally C_1 and C_2 model the coupling capacitor of the primary and secondary windings.

In order to determine this parameters, we realized different tests without connecting the GDBD to the power supply. We measured the impedance seen from the primary with the secondary with no-load then in short-circuit. To measure the impedance (modulus and argument) in high frequency (from 50 kHz to 1 MHz), we used an impedance analyzer (HP 4284A). As the magnetic circuit (modelled by X_M and R_F) is nonlinear, it is necessary to determine its parameters for nominal conditions : the reference signal is amplified by the linear amplifier whose output is applied to the primary winding of the transformer. Therefore, to measure the impedance in low frequency (from few Hz to 50 kHz), we determined the impedance (modulus and argument) from experimental measures of the primary current (measured by a current probe) and voltage (measured by a differential probe voltage).

To check the validity of this model, the measured and calculated free and short-circuit impedance of the transformer seen from the primary have been compared (fig. 4). This model fairly describe the behavior of the transformer until 300 kHz. This model permits to consider the inductive and capacitive parasitic elements of the power supply (mainly of the transformer [2]) as well as the parasitic elements of measurement (high voltage probe, current measurement).

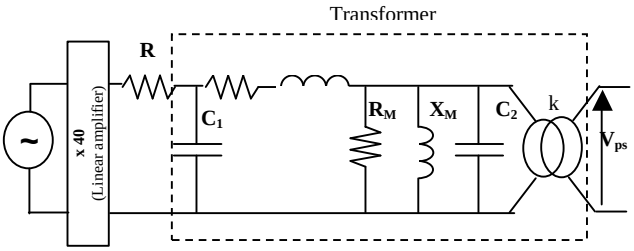

Fig. 2 : Electrical equivalent circuit of the power supply

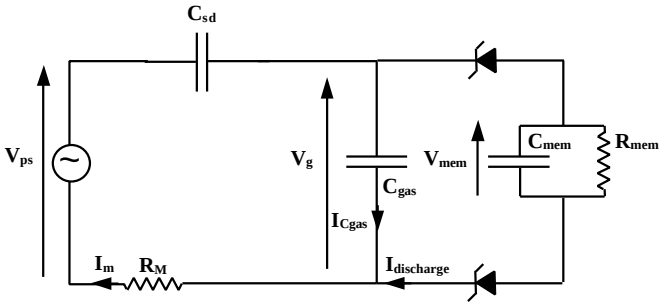

Fig. 3 : Electrical equivalent circuit of the discharge

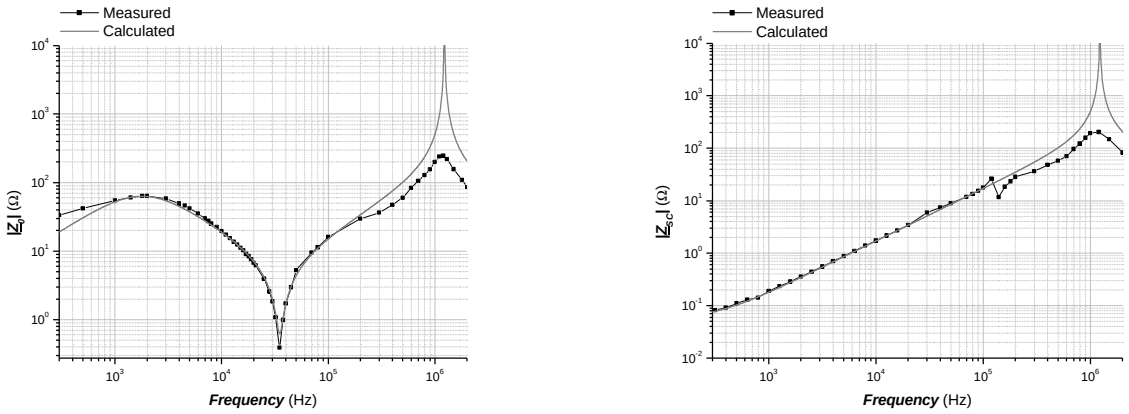

(a) (b)

Fig. 4 : Comparison between experimental and simulated of the modulus of free and short-circuit impedance

4. Electrical glow dielectric barrier discharge model

Unlike the models usually used in plasma, this model based on electrical components is macroscopic. The figure 3 present the electrical schema of the GDBD experimentaly studied (fig. 1). It does not directly describe the physics of the discharge but it holds account of it. However, it calculate in a simple way and with very short calculating times the discharge current and voltage, which are also measured. The

interest of this electrical circuit is to model in a simple way the discharge by using elements having a physical signification.

C_{sd} and C_{gas} capacitors model respectively the dielectric layer and the gas gap between the two electrodes. When the discharge is in off-state, the gas behave like an insulator, and the system can be modelled as the C_{gas} capacitor.

The two zeners diodes model the breakdown of the GDBD in nitrogen (Townsend breakdown). The choice of diodes to model breakdown is not trifling, in fact the effect of avalanche observed in the semiconductors [5] is comparable with gas avalanches occurring during the Townsend breakdown in the case of the GDBD. The figure 5 represents the layout of the discharge current according to the gas voltage for one period. During the rise of discharge current (fig. 6), the characteristic is exponential and can be modeled by the inverse characteristic of a diode. The inverse characteristic of a diode is defined by three parameters, which determine the equation 1. BV symbolize the reverse breakdown voltage, IBV the current at the reverse breakdown voltage and NBV the reverse breakdown ideality factor. In fact, NBV determine the slope of the characteristic of the discharge current according to the gas voltage. The lower NBV is, the quickest the discharge current increases is.

Finally, the elements C_{mem} and R_{mem} have been introduced to describe a specific behavior of GDBD : as shown in figure 7, for a given voltage amplitude, higher the frequency is lower the breakdown voltage is. Previous studies explained this by the fact that the gas remains excited from a discharge to the following one. The specie responsible of the memory effect is $N_2(A^3\Sigma_U^+)$ metastable which are created during a discharge and partly quenched between two discharges [4]. If the frequency increases the time between two discharges decrease then the metastables are less destroyed which induces a decrease of the breakdown voltage. In our model, during the discharge, the C_{mem} capacity is charged (equivalent to the creation of $N_2(A^3\Sigma_U^+)$ metastables) whereas between two discharges, the C_{mem} capacity discharge in R_{mem} resistance (destruction of $N_2(A^3\Sigma_U^+)$ metastables).

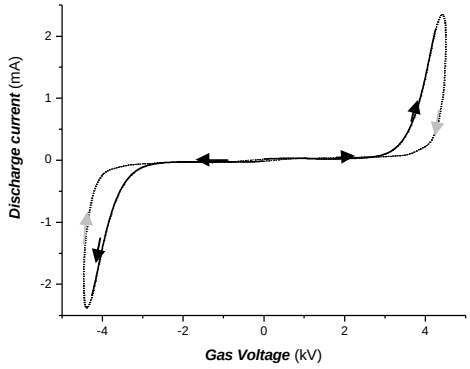

Fig. 5 : Discharge current versus gas voltage during one period (f=2 kHz, V_{ps}=15 kV_{pk-pk})

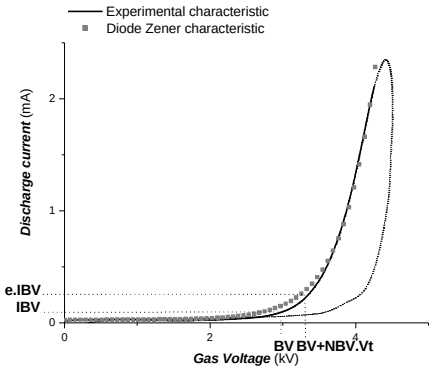

Fig. 6 : Rise of the discharge current (2 kHz, 15 kV_{pk-pk})

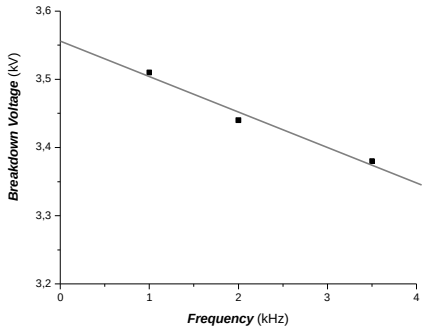

Fig. 7 : Breakdown voltage versus frequency (V_{ps}=13 kV_{pk-pk})

$$i(t)=IBV\times\exp\left(\frac{-V-BV}{NBV\times\frac{k\cdot T}{q}}\right) \qquad \text{Eq. 1}$$

To check the validity of this model, the calculated and measured discharge current have been compared for excitation frequencies ranging from 1 and 4 kHz and for sinusoidal or triangular voltages. As example, figure 8 shows the results of simulations and experiment concerning the waveforms of the discharge current (I_d), the applied voltages (V_{ps}). Then, all the model component values being fixed, the model fairly describe the GDBD electrical behavior.

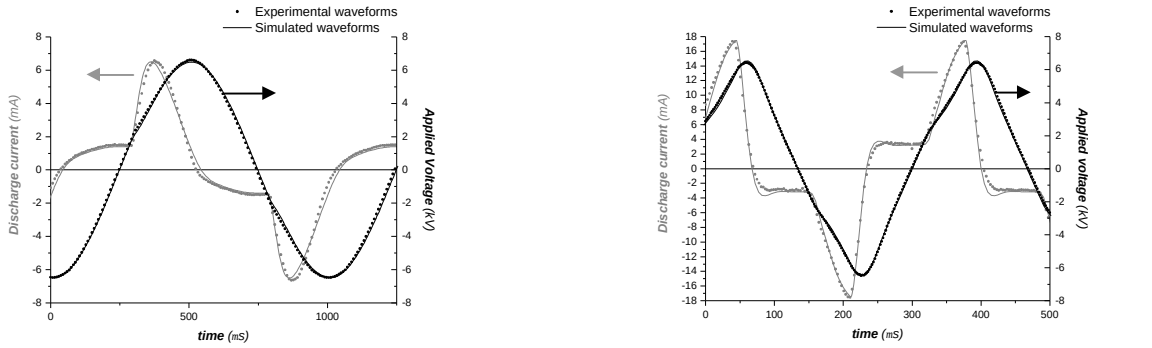

(a) (b)

Fig. 8 : Comparaison between experimental and simulated waveforms for sinusoïdal voltage (a) V_A=13 kV_{pk-pk} and f=1 kHz, and triangular voltage (b) V_A=13 kV_{pk-pk} and f=3 kHz,

5. Working domain of GDBD and destabilization

The GDBD works only for a limited range of amplitude and frequency of the applied voltage [6]. The fact of being slightly apart from these limits of operation is characterized by the propagation of instabilities in the glow discharge, instabilities which lead to a pure filamentary discharge if the amplitude or the frequency of the applied voltage is increased even higher.

When the frequency is too much increased, pulses are observed in the rise of the current. These pulses develop too slowly to be streamers [7]. As shown figure 11, when the frequency increases, the current increases more quickly, it involves a reduction of NBV (fig. 12). As described previously [7], for frequencies higher than 3 kHz, the speed of the current rise allowing to keep a glow discharge is limited. The figures 13 represents the experimental and simulated discharge current and applied voltage during a destabilization for a frequency of 5 kHz. To understand this behavior, it is necessary to carefully consider the variation of the power supply load due to the discharge development.

During the ignition of the discharge, the load seen by the power supply varies [7]. In fact, if no discharge occurs (part a in figure 9), the current is defined by equation 2. When the gas voltage reaches the breakdown voltage, the current increases quickly and stops while the gas voltage becomes constant (part b in figure 9). The rise of the current is controlled by the ionization occurring in the discharge [6]. After the rise of the discharge current (part c in figure 9), the calculated gas voltage (eq. 4 and fig. 10) is constant thus all the voltage fluctuations are applied on C_{sd} and the current is defined by equation 3. During the rise of the current, the load seen from the power supply varies from $(C_{sd}.C_{gas})/(C_{sd}+C_{gas})$ to C_{sd} (eq. 2 and 3). Higher is C_{sd}/C_{gas} ratio larger the load variation is.

The destabilization in high frequency comes from a too fast variation of the load seen from the power supply that involve oscillations [7] of the electrical circuit (parasitic elements). In order to limit the risks of destabilizations in the rise of the glow discharge current, there are two solutions : act on the speed of this variation (which depends on the conditions of excitation of the GDBD, therefore of the frequency) or on the amplitude (which depends on the ratio of the capacitors C_{sd} and C_{gas}). A solution to limit the risks of destabilization in high frequency, is to reduce the C_{sd}/C_{gas} ratio. For that, we can decrease the gas gap (to increase the value of C_{gas}) or decrease the value of C_{sd} (by using a dielectric which have lower relative permittivity or increase the thickness of the dielectric). The figure 14 represents the simulated discharge current for low and high C_{sd}/C_{gas} ratio all the other parameters being constant. For a C_{sd}/C_{gas}=7.5, we observe a pulse in the rise of the discharge current whereas in the case of the lower ratio C_{sd}/C_{gas}=3.6, the discharge current do not comprise pulses. The reduction of this ratio permits to increase the working domain of the GDBD in term of maximum frequency. This has been checked experimentally by determine the working domain of the GDBD for low and high C_{sd}/C_{gas} ratio (fig. 15). It is interesting to notice that a reduction in a factor 2 of the C_{sd}/C_{gas} ratio permits to increase GDBD working domain as presented figure 15 of a factor 6.

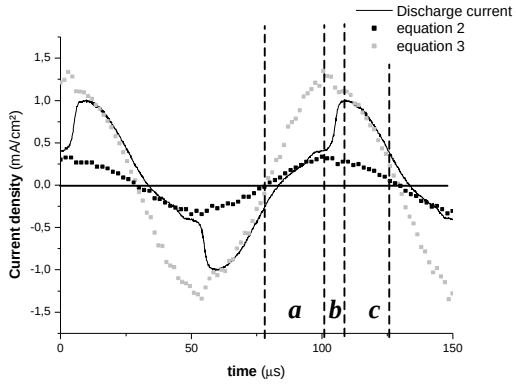

Fig. 9 : Calculated current from equations 2 and 3 compared with the discharge current (f=10 kHz and Vps=15 kV_{pk-pk})

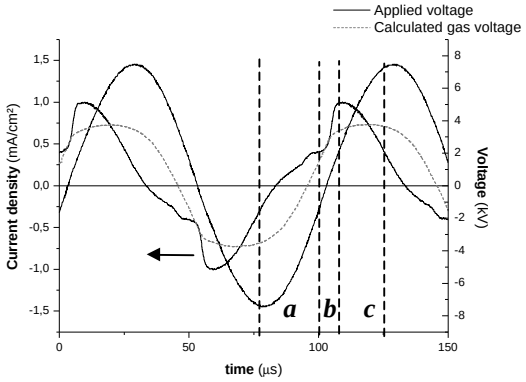

Fig. 10 : Example of discharge current and gas voltage (f=10 kHz and Vps=15 kV_{pk-pk})

$$i(t)=\frac{C_{sd}\cdot C_{gas}}{C_{sd}+C_{gas}}\times\frac{dV_{ps}(t)}{dt} \quad \text{Eq. 2}$$

$$i(t)=C_{sd}\times\frac{dV_{ps}(t)}{dt} \quad \text{Eq. 3}$$

$$V_{gas}(t)=V_{ps}(t)-\frac{1}{C_{sd}}\times\int i(t).dt+K \quad \text{Eq. 4}$$

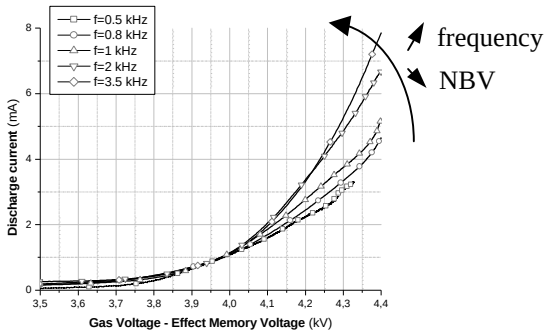

Fig. 11 : Measured evolution of discharge current around breakdown versus gas voltage for different frequency

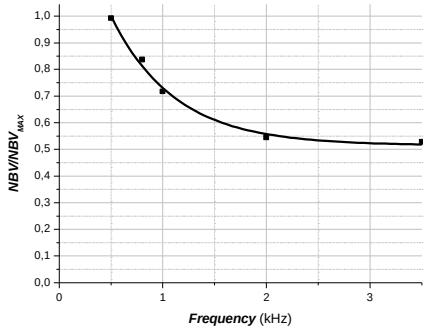

Fig. 12 : NBV value calcultated from fig. 9 results

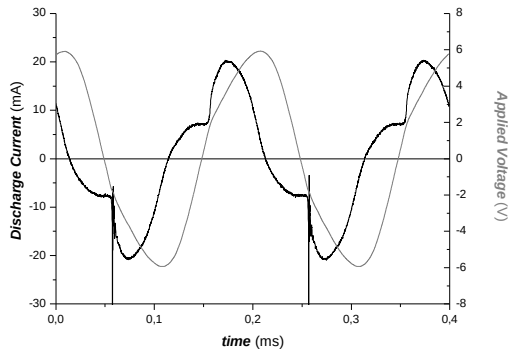

(a)

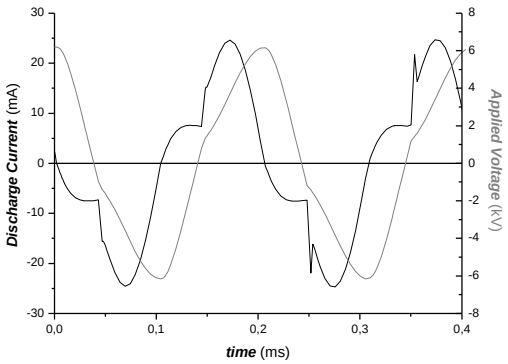

(b)

Fig. 13 : Discharge current and applied voltage during the high frequency destabilization (f=5 kHz, V_{ps}=13 kVcc) (a) experimentals waveforms, (b) simulated waveforms

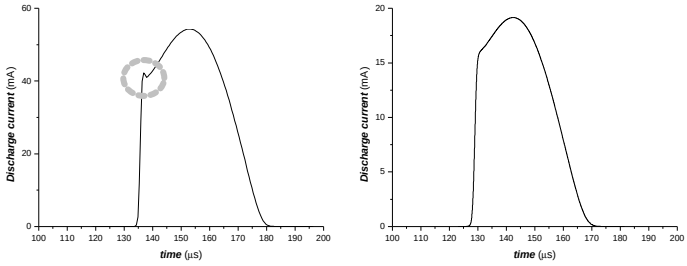

(a) (b)

Fig. 14 : Simulated discharge current for high (a) and low (b) C_{sd}/C_{gas} ratio (V_{ps}=16 kV_{pk-pk}, f=8 kHz and NBV=6200)

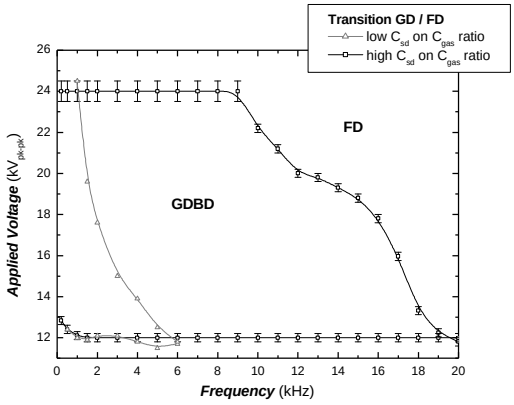

Fig. 15 : Comparison of the domains for low and high C_{sd}/C_{gas} ratio

6. Conclusion

Glow dielectric barrier discharge and its power supply have been modeled. This model based on electrical components permits to have a general point of view of the process and it fairly describes the GDBD electrical behavior. It has been first show that decreasing the C_{sd}/C_{gas} ratio permits to significantly increase the working domain of the GDBD, a reduction in a factor 2 of the C_{sd}/C_{gas} ratio (from 7,5 to 3,6) permits to increase GDBD working domain of a factor 6 and the maximum frequency of a factor 3.

This electrical model can be used as predictive one to study different power supply, and to define the type of excitation that produces a maximal ignition time of the discharge and a maximum transmitted power which will determine the treatment rate. It is also an interesting tool for the power supply design and the process optimization. This will be checked soon.

Acknowledgements

The authors wish to thanks the Air Liquide society for their financial support and A. Boulanger for its technical support.

References

[1] Evolutionary electrical model of homogeneous discharge, N. Naudé, F. Massines, J-P Cambronne – to be published in : Proc. 10th European Conference on Power Electronics and Applications, Toulouse (2003)

[2] Multiwinding transformers: a successive refinement method to characterize a general equivalent circuit, *A. Schellmanns, K. Berrouche, Keradec-JP*, IMTC 1998 Conference Proceedings, pp. p.717-22 vol.2

[3] Prise en compte de l'alimentation et de l'interface de mesure dans la modélisation électrotechnique d'une décharge homogène, N. Naudé, J-P Cambronne, F. Massines, Electrotechnique du Futur 2001 (Nancy), p. 249-254

[4] Gherardi N., Gouda G., Gat E., Ricard A. and Massines F., *Plasma Sources Sci. Technol.*, **9**, 340-6 (2000)

[5] Physique des semi-conducteurs et des composants électroniques, Masson, Henry Mathieu.

[6] Croquesel E., Gherardi N., Martin S. and Massines F., Boundary of the Glow Regime at Atmospheric Pressure in a Nitrogen Dielectric Barrier Discharge. In: *Proc. 7th Int. Symp. On High Pressure Low Temperature Plasma Chemistry*, ed. By H.-E. Wagner, J. F. Behnke, and G. Babucke, Greisfswald, 2000, pp. 88-92

[7] Two different origins for the destabilization of a glow dielectric barrier discharge in nitrogen, N. Gherardi, E. Croquesel, N. Naudé, P. Veis, F. Massines – Proc. Hakone VIII (2002)

Study of Chemical Species Generation within a RF Excited Diglyme Plasmas

C. C. P. Rita, M. A. Algatti*, R. P. Mota, R. Y. Honda,
M. E. Kayama, E. C. Rangel and N. C. Cruz

Universidade Estadual Paulista "Júlio de Mesquita Filho", Faculdade de Engenharia, Departamento de Física e Química, Av. Ariberto Pereira da Cunha 333, Pedregulho, 12516-410, Guaratinguetá, SP, Brazil
*Corresponding author: (e-mail: algatti@feg.unesp.br, phone:(+55 12)31232841

Abstract
This paper deals with the study of the fragmentation process of $CH_3O(CH_2CH_2O)_2CH_3$ diethylene glycol dimethyl ether (diglyme) molecule in low-pressure RF excited plasma discharges utilizing mass spectrometry. The results showed that for a fixed pressure, the increase of the RF power coupled to the plasma chamber from 5 to 45 W produced a plasma environment very reactive that reduces the population of the heavier chemical species and increases the population of the lighter one.

Keywords: Molecular fragmentation, Mass spectrometry, Diglyme Plasmas, Biomaterials

1. Introduction

Materials processing using low-pressure RF excited plasmas are of great importance in many current scientific and technological issues encompassing microelectronics, optical and biomaterials industries [1-10]. The main reason is that within such kind of plasmas electrons may attain an energy excess of some eV in comparison with the heavy particles present in the discharge. This unusual thermal non-equilibrium situation is very profitable in molecular fragmentation through electronic impact. This feature of such plasmas gives rise to a very reactive chemistry in a relative cold environment [4-8] whose kinetics is not easily controlled. Therefore is of paramount importance to set many plasma diagnostics in order to probe the trends of chemical species as well as the electrons behavior for different plasma parameters such RF power coupled to the plasma chamber, gas pressure, gas flux and so on [11-14].

In the field of biomaterials science and technology, plasma polymerized polyethylene glycol dimethyl ether is a material that has been keeping the attention of the scientific community due to its non-fouling properties [15-19]. If the appropriate plasma parameters are set these films may be synthesized keeping a molecular structure quite similar to the polyethylene oxide-like (PEO-like) with the advantage that these films are not soluble in water. The aqueous solubility of PEO makes it less appropriate in many biomaterials applications. In order to retain the monomer structure within the plasma deposited films and consequently its functionality, many different issues have been addressed in recent literature as for instance the film deposition under low mean RF power level by controlling the power supply on/off ratio [11,20], the decreasing of monomer residence time and consequently the reduction of its interaction with the plasma environment [20], the cooling of substratum with liquid nitrogen [13], the energy reduction of the ions reaching the substratum [14], and so on.

In order to set the appropriate experimental parameters that would result customized film structures in plasma polymerization of PEO-like coatings this paper deals with the study of the RF power dependence of different chemical species resulting from diglyme fragmentation for different values of the pressure inside the plasma reactor. The trends of chemical species were followed by mass spectrometry [21,22].

2. Experimental Setup and Plasma Diagnostics

The glow discharges were generated by a RF power supply operating in the range from 5 to 45 W in $CH_3O(CH_2CH_2O)_2CH_3$ (diglyme) atmospheres ranging from 16 Pa (120 mTorr) to 40 Pa (300 mTorr) within a stainless steel cylindrical, 210 mm of internal diameter and 225 mm long, parallel plate electrodes plasma reactor. This reactor is provided with eight lateral entrances, positioned at the mid plane between the electrodes, that may be used for setting optical, electrical and mass diagnostics and the low (mechanical pump) and high (turbo-molecular pump) vacuum systems. The vacuum inside the plasma chamber is

monitored by pirani™ (thermocouple) and penning™ (inverse magnetrom) gauges. The turbo-molecular pump is coupled to the chamber through a gate valve and is used for cleanness purposes. The pressure is pumped down to 1.33 x 10^{-4} Pa (10^{-6} Torr), being the chamber purged with argon several times before each running of the experiment. The inner side of the plasma chamber was polished up to the optical quality (roughness of 0.5 microns or less) in order to minimize the retention of impurities and facilitate the cleaning process. The plasma chamber walls were heated with a temperature- controlled belt in order to minimize the monomer's condensation as well as the humidity. Diglyme was placed inside a stainless steel bottle and was fed into the plasma chamber through a needle valve. The plasmas were excited by a RF power supply operating in 13.56 MHz whose output intensity could be varied from 0 to 300 W (Tokyo HY-Power model RF-300™). The RF power was coupled to the plasma reactor through an appropriate matching network (Tokyo HY-Power model MB-300™) that allows one to minimize the reflected RF power. The mass spectrometry was realized using a mass spectrometer and energy analyzer (Hiden Analytical model EQP-300™), operating in the mass and energy range from 1 to 300 amu and from 0 to 100 eV respectively. The background mass spectra with the plasma turned off were carried out at the same pressure conditions of each diglyme plasma polymerization processes. These spectra allowed one to control the number of chemical species resulting from the fragmentation within the mass spectrometer as well as to control the presence of contaminants resulting from the plasma chamber cleaning process. The block diagram of the experimental setup is presented in figure 1.

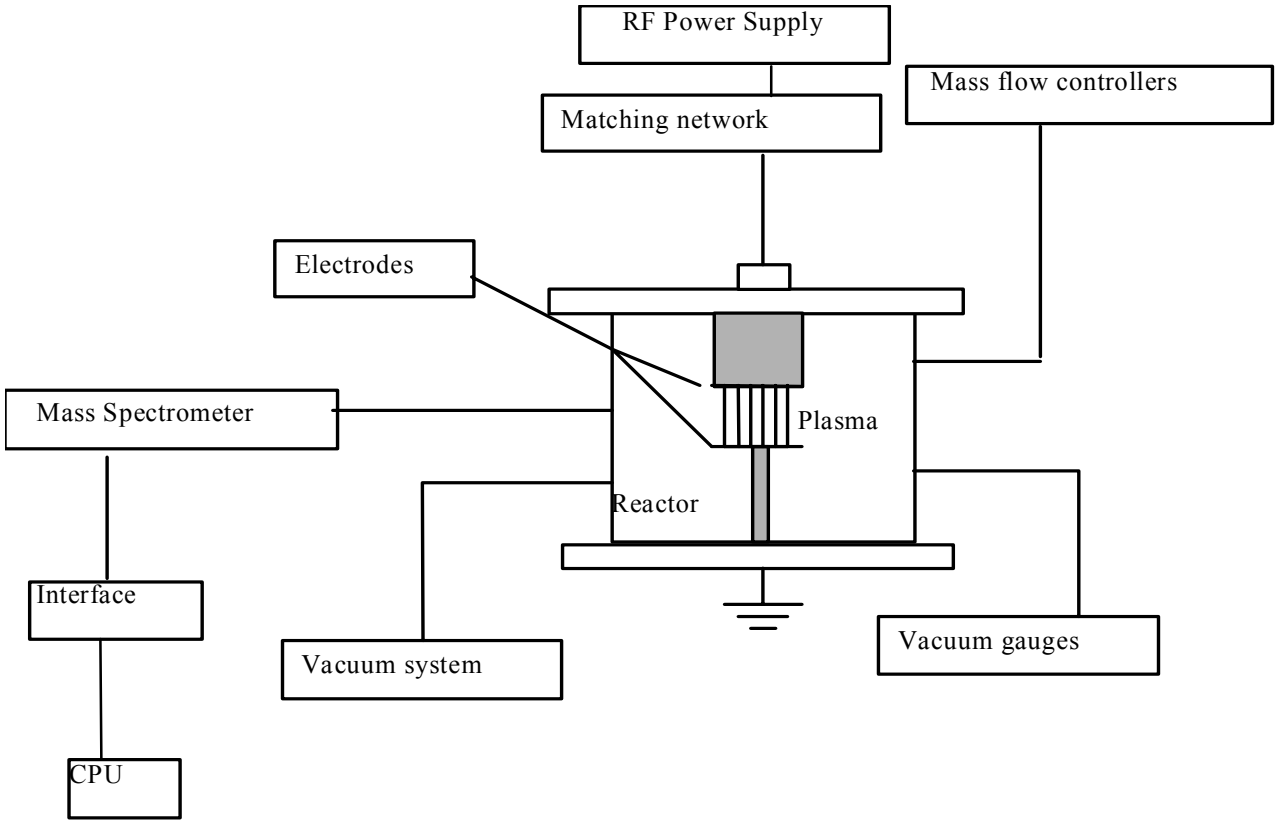

Figure 1. Block diagram of the experimental setup used in plasma polymerization of diglyme for different values of pressure and RF power coupled to the reactor.

The photograph of the stainless steel plasma chamber with the mass spectrometer coupled to it is shown in figure 2.

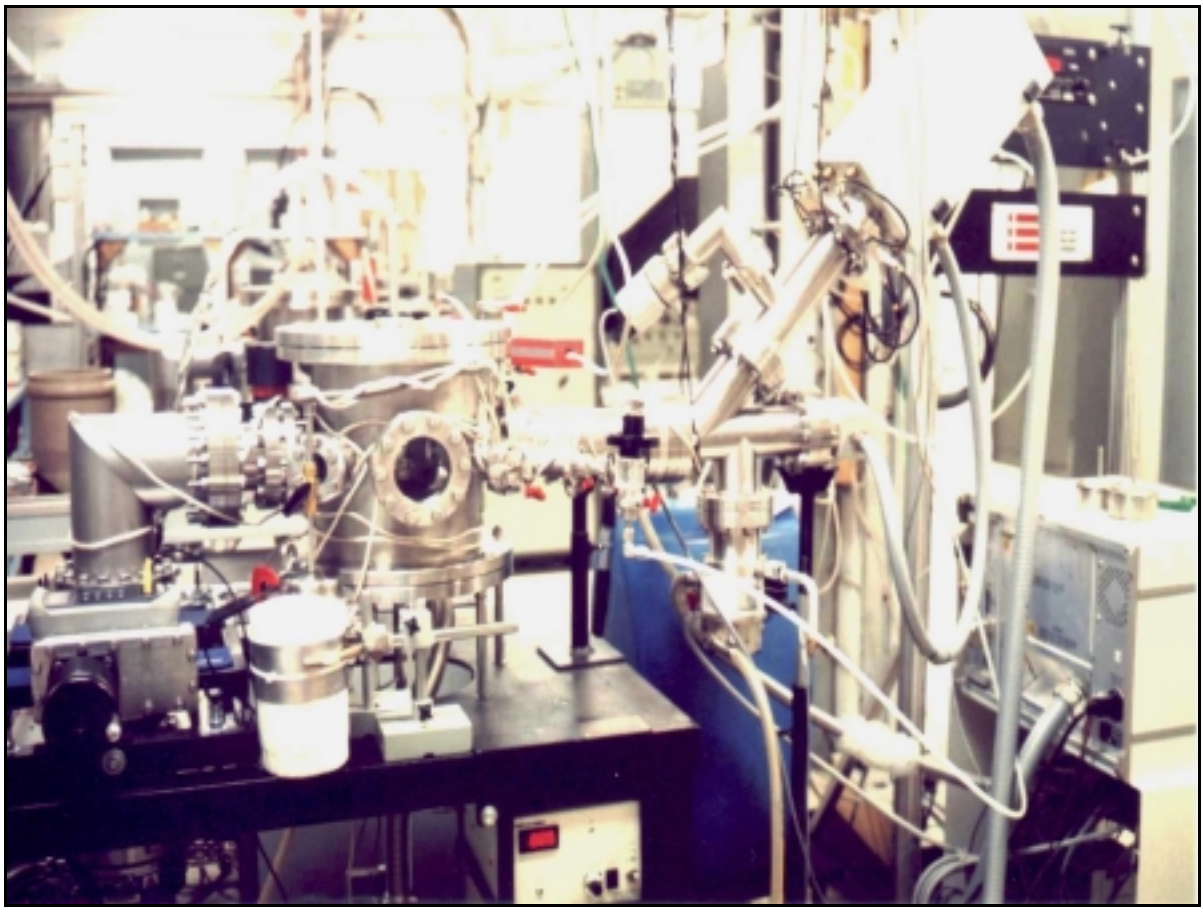

Figure 2. Photograph of the experimental setup used in plasma polymerization of diglyme for different values of pressure and RF power coupled to the reactor.

3. Results and Discussions

It is presented in table 1 all possible primary fragments of diglyme molecule (134 amu) resulting from the disruption of the chemical bonds between carbon-carbon and carbon-oxygen atoms. Since the molecule is central symmetric to the oxygen atom located in ethylene-glycol group one may identify only four different points of molecular disruption involving the above mentioned chemical bonds which results the fragments listed in table 1.

Table 1. Primary Diethylene glycol dimethyl ether fragments

fragment	chemical structure	mass (amu)
1	CH_3	15
2	CH_3O	31
3	CH_3OCH_2	45
4	$CH_3OCH_2CH_2$	59
5	$CH_3OCH_2CH_2O$	75
6	$CH_3OCH_2CH_2OCH_2$	89
7	$CH_3OCH_2CH_2OCH_2CH_2$	103
8	$CH_3OCH_2CH_2OCH_2CH_2O$	119

It may be pointed out that all the molecular fragments presented in table 1, with the exception of the number 8 (119 amu), may result from secondary or higher fragmentation process of the heavier fragments of the diglyme molecule. The number of possibilities contributing for the population of a fragment increases inversely proportional to its mass. From the point of view of the non-fouling characteristic of the plasma deposited diglyme films the ethylene-glycol structure, e.g., CH_2CH_2O (44 amu), is one the most important

structure to be retained within the film composition if one wants to keep its functionality [4,21,22]. Therefore is important to keep under control the plasma parameters that enhance the presence of heavier fragments within the discharge.

Figure 3 shows typical mass spectra of neutrals and ions resulting from a RF excited diglyme plasma taken at a pressure of 12.6 Pa (95 mTorr) and 5 W of RF power coupled to the plasma chamber. It may be seen the presence of several primary fragments of diglyme molecule resulting mainly from inelastic electronic collisions. It also may be appreciated that the number of neutrals is much higher than the ions due the low degree of ionization of such kind of discharges.

Figure 4 shows the RF power dependence of diglyme fragments within the plasma, for a fixed pressure of 13.3 Pa (100 mTorr). It can be seen that as the RF power coupled to the plasma chamber increases the concentration of heavier species decreases indicating the predominance of electronic inelastic collisions resulting in molecular fragmentation. It also can be appreciated that the concentration of lighter species like CH (13 amu), H (1 amu), and O (16 amu) increases with the increasing of the RF power. This result is in close agreement with the decreasing of the concentration of heavier species within the plasma discharge.

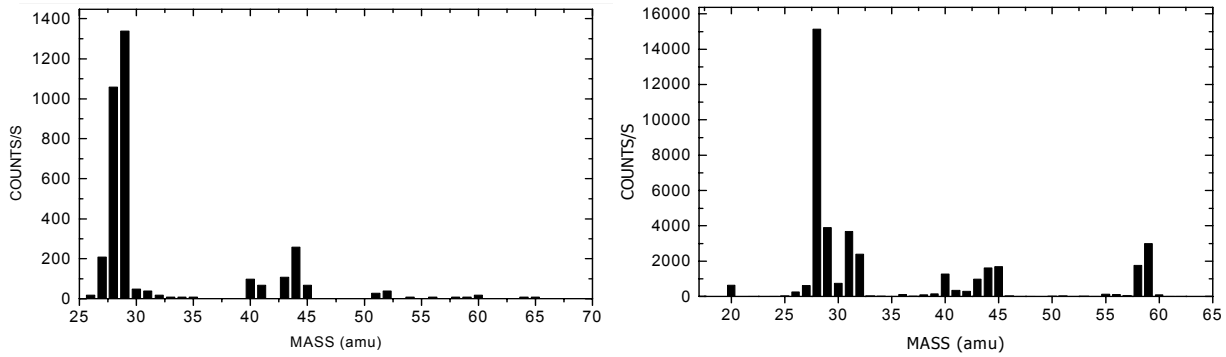

Figure 3. Typical mass spectra of ions (left) and neutrals (right) of RF excited diglyme plasmas taken at 12.6 Pa and 5 W of pressure and RF power respectively.

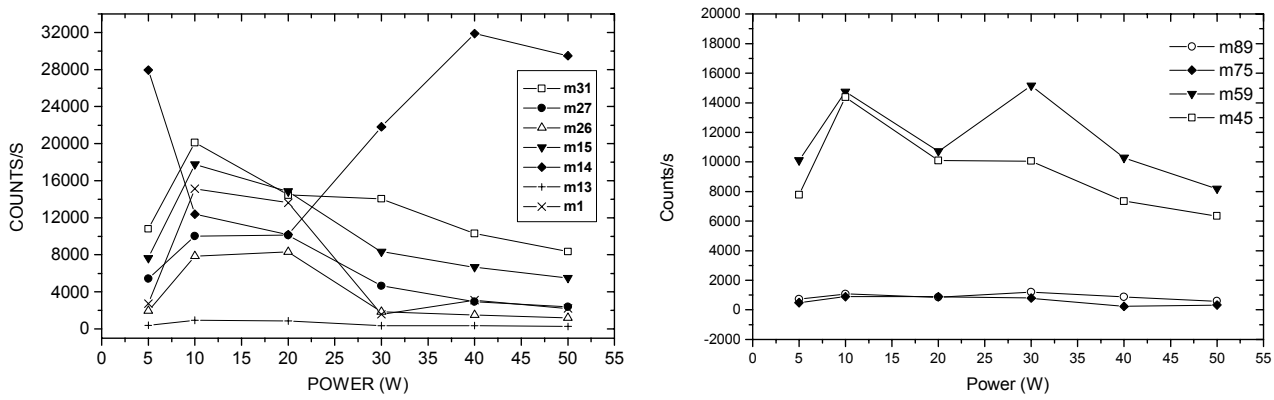

Figure 4. Power dependence of diglyme fragments products at a fixed pressure of 13.3 Pa.

4. Conclusions

One can conclude from the presented results that the operation of the plasma reactor at low RF power levels is appropriate if one wants to preserve the monomer functionality since it enhances the predominance of heavier chemical species within the discharge. The control of the plasma reactivity would be improved if one used a RF power supply whose output could be modulated by a square waveform in order to vary the plasma on/off ratio. This approach was already used with great success in current literature for others monomers [11,20]. The presented results also showed the effectiveness of mass spectrometry as plasma diagnostic for monitoring the diglyme plasma polymerization process.

Acknowledgments

The authors would like to thank FAPESP, (Fundação de Amparo à Pesquisa do Estado de São Paulo) for financial support and José Benedito Galhardo for technical assistance during the plasma chamber construction.

References

[1] – A. Bogaerts, E. Neyts, R. Gijbels and J. van der Mullen, Spectrochimica Acta **B57**, 609-658, (2002).
[2] R. J. Shul and S. J. Pearton (eds.) Handbook of Advanced Plasma Processing Techniques, Springer Verlag, Berlin, Germany, (2000).
[3] P. K. Chu, J. Y. Chen, L. P. Wang and N. Huang, Mat. Science and Engineering Reports **36**, 143-206, (2002).
[4] – R. d'Agostino, P. Favia and F. Fracassi (eds.) Plasma Processing of Polymers, NATO ASI series E: Applied Sciences vol. 346, Kluwer Academic Publishers, Dordrecht, The Netherlands, (1997).
[5] - N. Inagaki, Plasma Surface Modification and Plasma Polymerization, Technomic Publishing Company, Inc., Lancaster, USA, (1996).
[6] – H. Biederman and Y. Osada, Plasma Polymerization, Plasma Technology, vol. 3, Elsevier, Amsterdam, (1992).
[7] - R. d'Agostino (ed.) Plasma Deposition, Treatment and Etching of Polymers, Academic Press, Inc, San Diego, USA, (1990).
[8] - H. Yasuda, Plasma Polymerization, Academic Press, Inc., New York, USA, (1985).
[9] - B. D. Ratner and D. G. Castner (eds.) Surface Modification of Biomaterials, Plenum Press, New York, USA, (1997).
[10]– B. D. Ratner, A. S. Hoffman, F. J. Shoen and J. E. Lemons (eds.) Biomaterials Science: An Introduction to Materials in Medicine, Academic Press, San Diego, USA, (1996).
[11]– G. Cicala, M. Creatore, P. Favia, R. Lamendola and R. d'Agostino, App. Phys. Lett. **75**, 37-39, (1999).
[12]– P. Favia and R. d'Agostino, Surf. Coat. Technol. **98**, 1102-1106, (1998).
[13]– H. Biederman and D. Slavínská, Surf. Coat. Technol. **125**, 371-376, (2000).
[14]– R. Itatani, Plasm. and Ions, **1**, 37-44, (1998).
[15]– S. K. Hendricks, K. Kwok, M. Shen, T. A. Horbett, B. D. Ratner and J. D. Bryers, J. Biomed. Mater. Res. **50**, 160-170, (2000).
[16]– M. N. Mar, B. D. Ratner and S. S. Yee, Sensors and Actuators B **54**, 125-131, (1999).
[17]– C. S. Kwok, T. A. Horbett and B. D. Ratner, J. Control. Release **62**, 301-311, (1999).
[18]– G. P. Lopez, B. D. Ratner, C. D. Tidwell, C. L. Haycox, R. J. Rapoza and T. A. Horbett, J. Biomed. Mater. Res. **26**, 415-439, (1992).
[19]– N. A. Alcantar, E. S. Aydil and J. N. Israelachvili, J. Biomed. Mater. Res. **51**, 343-351, (2000).
[20]- C. Oehr, M. Müller, B. Elkin, D. Hegemann and U. Vohrer, Surf. Coat. Technol. **116-119**, 25-35, (1999).
[21]- E. F. Antunes, A. R. Bigansolli, M. A. Algatti, R. P. Mota, R. Y. Honda, J. C. Teixeira, M. E. Kayama, E. C. Rangel and N. C. Cruz, Study of the chemical reactions on low pressure RF excited diglyme plasmas using mass spectrometry and optical spectroscopy. In: A. Bouchoule, J. M. Pouvesle, A. L. Thomann, J. M. Bauchire and E. Robert, editors. Proceedings of the 15th International Symposium on Plasma Chemistry, vol. 6. Orléans, France, pp. 2317-2322, (2001).
[22] R. P. Mota, A. R. Bigansolli, E. F. Antunes, E. C. Rangel, N. C. Cruz, R. Y. Honda, M. A. Algatti, E. A. Aramaki and M. E. Kayama, Optical and structural properties of PEO-like plasma polymers, Mol. Cryst. Liq. Cryst. **374**, 415-420, (2002).

Bacterial Adhesion onto Plasma Modified Polymer Surfaces

G. Z. Gadioli, E. C. Rangel, R. Y. Honda, M. C. Pereira, N. C. Cruz

Department of Chemistry and Physics, UNESP, Guaratinguetá, Brazil

Bacterial adhesion onto polymers used in prosthesis and clinical devices is of great concern. For instance, the most efficient solution to overcome the biofilm formation onto silicone voice prosthesis is by surgically substituting the prosthesis. In many cases, such replacement has to be done ever three months. Therefore, surface modifications to prevent bacteria attachment are highly desirable. In this sense, plasma treatment is of particular interest because it allows strong surface modifications without altering bulk properties.

The present work describes an investigation on the adherence of *Escherichia coli* onto silicone (SI) and polyurethane (PU) surfaces as-received and after exposure to SF_6 or O_2 plasmas.

Treatments were performed in a vacuum chamber by applying radiofrequency power (13,56 MHz) to two external electrodes. During the treatments the chamber was continuously pumped by an 18-m^3/h rotary vane pump. The admission of the gases was controlled by needle valves while the chamber pressure was monitored by a Pirani gauge. After the treatments the samples were immersed for 24 hours in water contaminated with *E. coli*. Afterwards they were individually taken to an ultrasonic bath for 5 minutes in 5 ml of sterile water. The rising water was inoculated in agar EAM in Petri dishes and incubated for 24 hours at 37°C. The number of colony forming units (CFU) was counted using pictures taken of the dishes.

Some of the results obtained are shown in figure 1. According to the figure, one can be observed that the exposure to any of the plasmas caused the decrease of bacterial adhesion. It is interesting to mention that the contact angles, θ, immediately after the exposure to O_2 and SF_6 plasmas were, respectively, 20° and 140° for silicone and 40º and 135º for polyurethane samples while both pristine materials presented θ around 110°. Therefore, the results show no straight relationship between surface wettability and bacterial adhesion. Further studies are under development to clarify the real effect of plasmas on the surfaces causing the inhibition of biofilm formation.

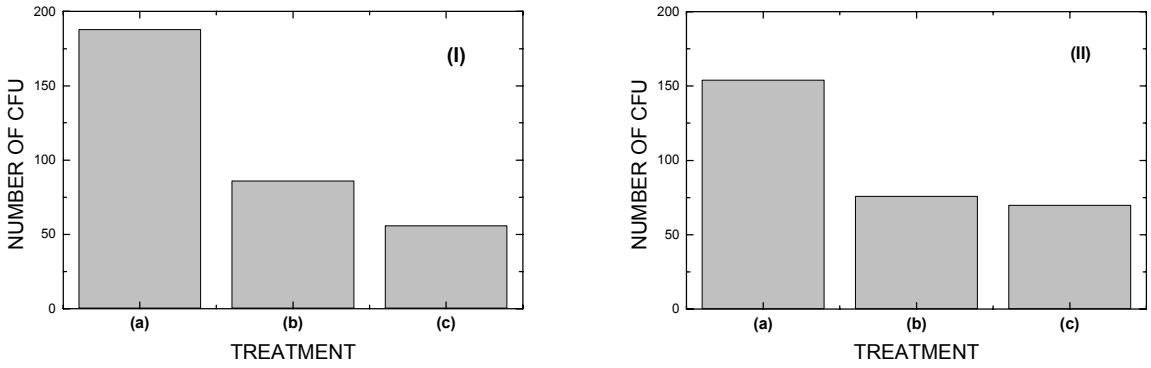

Figure 1 – Number of colonies forming units obtained from (I) polyurethane and (II) silicone surfaces as-received (a), and after exposure to O_2 (b) or SF_6 (c) plasmas.

The authors thank Fapesp for financial support.

Glow Dielectric Barrier Discharge for nitrogenous functions grafting on polymer surfaces

Nicolas Gherardi, Eric Croquesel and Françoise Massines

Laboratoire de Génie Electrique de Toulouse, Université Paul Sabatier, Toulouse, France

Abstract
The aim of this work is to confirm the understanding of the mechanisms governing the obtaining of atmospheric pressure glow dielectric barrier discharge (GDBD) in rare gases and to study the effect of GDBD in various atmospheres on the polypropylene surface activation.

1. Introduction

In order to improve surface energy and adhesion of polypropylene film, corona treatments in atmospheric air are often used in the industry. However, such a process leads to surface transformations based on oxygen chemistry and presents a lack of homogeneity. An alternative process is to treat the film with a Glow Dielectric Barrier Discharge (GDBD) in a controlled atmosphere. It is now well known that the GDBD structure from the anode to the cathode depends strongly on the atmosphere in which the discharge is ignited. In He, the discharge is a subnormal glow one while in nitrogen, it is closer to a Townsend one. The mechanisms responsible for these discharge structures are closely related to the metastable properties in these two gases. This knowledge has been extended to another rare gas, argon, in order to check the validity of these conclusions. By adding some hundreds ppm of ammonia in argon, a GDBD can be obtained. The characteristics of this GDBD are compared to He and N_2 GDBD ones. Then, the different atmospheres used (He, He/N_2, N_2, N_2/NH_3, Ar/NH_3) are compared relative to their effect on a polypropylene film, taking into account the amount of energy dissipated in the discharge during the treatment.

2. Experimental set-up

The discharge is ignited between two ceramic-coated electrodes, in a "roll-to-roll" configuration (figure 1) allowing online treatment with film speeds up to 500 cm/min. The treatment duration of the polypropylene film can be as low as 0.5 sec. The gas gap can be varied from 1 to 5 mm. To ascertain control of the treatment atmosphere, the cell is kept inside a vessel which is pumped down to 1 Pa before introducing of the desired gas up to 10^5 Pa. The gases used are N60 Air Liquide quality with less than 1 ppm of impurities. In order to continuously renew the atmosphere, a gas flow can be added (up to 6 slpm), maintaining the atmospheric pressure by a slight pumping. The electrical excitation is a sinusoidal voltage ranging from 0 to 24 kV peak to peak. The frequency can be adjusted between 200 Hz and 35 kHz, independently of the voltage amplitude.

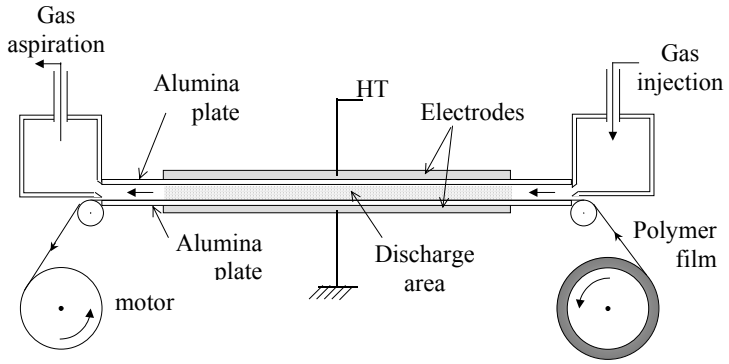

Figure 1: experimental set-up

The discharge is analysed by electrical measurements and through the light emitted (short exposure time photography and spectroscopy). The discharge current is measured through a 50 Ω resistor in series with the grounded electrode. The current and the voltage applied to the electrodes are visualized on a numerical oscilloscope (Tektronix 784A - 1GHz). The gas voltage actually applied on the gas and the power dissipated in the discharge are deduced from these two measurements via calculations detailed elsewhere [1]. The discharge light is observed through a quartz window. An optical lens is used to obtain the image of the plasma on the intensifier of a CCD camera (PRINCETON Instruments LN/CCD-1100-PB/UVAR) for recording photographs. A pulse generator, which is triggered by the power supply used to excite the discharge, governs the intensifier. An adjustable delay is introduced via the programmable pulse generator to synchronize the intensifier with the discharge current. Exposure time varies from 10 ns to 1µs.

The polymer is a 20 µm thick polypropylene (PP) film of capacitor grade. The surface transformations are characterized by static contact angle measurements and X-ray Photoelectron Spectroscopy.

3. Results

3.1. Discharge features

As it has already been written elsewhere [2], glow discharge properties depend on the main gas in which the discharge is ignited. Hence, the discharge current of a GDBD depends on the atmosphere. Comparing GDBD in He and in N_2 with the same power supply frequency, it appears that although there are some similarities in the two gases (the current is composed of only one peak per half cycle and the duration of this peak is in the range of microseconds, which is very long compared to a micro-discharge one), the current peak is 5 times higher in He than in N_2 while its duration is 5 times shorter in He [2]. Figures 2 shows that the gas voltage variations with time during the discharge also depend strongly on the atmosphere. In He (Figure 2a), as soon as breakdown occurs, the gas voltage, V_g, decreases and reaches a value close to 0 at the end of the discharge peak. On the other hand, in N_2 (Figure 2b), the gas voltage continues to increase after the breakdown and stays high until the end of the current peak, which corresponds to the instant at which the voltage delivered by the power supply, V_a, is maximum.

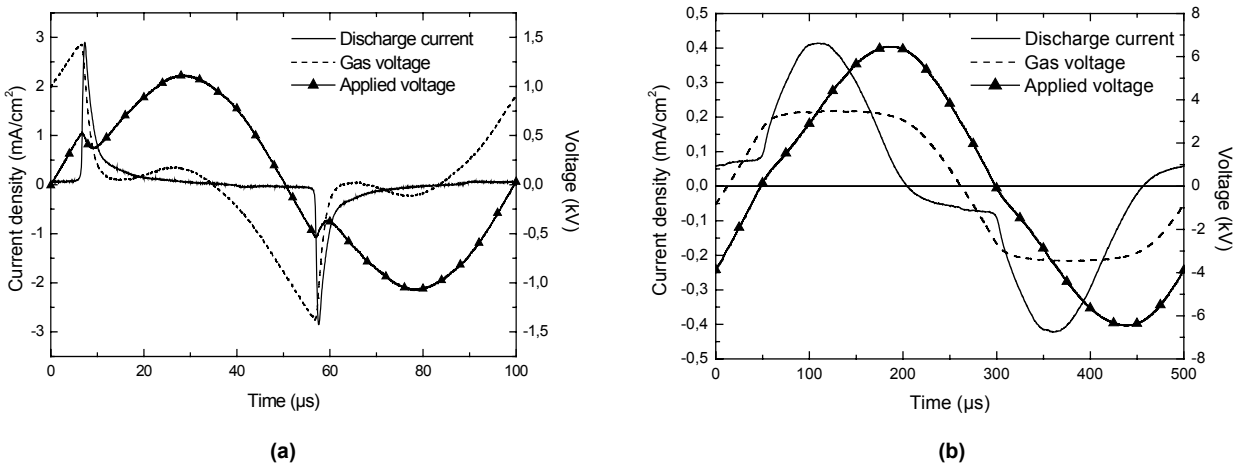

Figure 2: Discharge current, gas voltage and applied voltage of a GDBD (a) in He and (b) in N_2

The associated light distribution in the gas gap presents also some differences. Figure 3 represent 10 ns exposure time photography taken at the maximum of the GDBD current peak in the two atmospheres. In the two gases there is only one discharge canal covering uniformly the whole electrode surfaces.

Nevertheless, the light distribution depends on the gas nature. In He (Figure 3a), three areas can be distinguished: from the anode to the cathode, there is first a large luminous area, then a dark space and finally a highly luminous zone near the cathode. Such a structure is that of a glow discharge [3], the three areas being respectively a positive column, a Faraday dark space, and cathode and negative glows which cannot be separated at high pressure. This structure, which is that of a low-pressure glow discharge, is not observed in N_2 in which the light is localised close to the anode (Figure 3b).

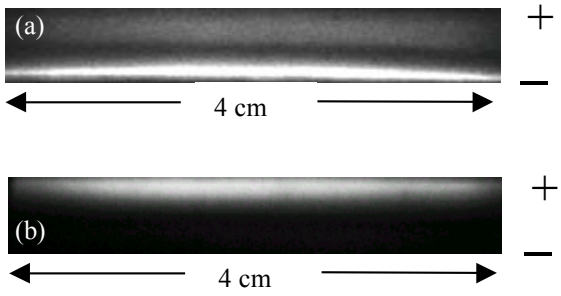

Figure 3: 10 ns exposure time photographs of the gas gap during a GDBD in He (a) in N_2 (b)

Some comparisons with numerical models developed by P. Ségur team [4,5] allow showing that these differences are due to the fact that the GDBD in He is a subnormal discharge close to a normal glow discharge, while the GDBD in N_2 is a subnormal discharge close to a Townsend discharge.

The mechanisms responsible for the obtaining of the GDBD have been discussed previously [2]. A critical point is that the memory effect from one discharge to the following one has to be high enough in order to have a high seed electron density. In the glow case (GDBD in He), the memory effect is based on electrons and ions trapped in the positive column while in the Townsend case (GDBD in N_2), the metastables which stay in the gas create electrons through cathode secondary emission. This last effect is possible in N_2 due to the long lifetime of the $N_2(A)$ (as long as there is not too much additive gas which quenches $N_2(A)$). This is not possible in He because even in pure He, at atmospheric pressure, the He(2^3S) metastables interact very rapidly to form the He_2 excimer [6]. Penning ionisation plays also an important role in He by lowering the breakdown field. Indeed, He(2^3S) metastable state is able to ionise almost every other gases. In a mixture of He/N_2, Penning ionisation on N_2 is very efficient and then a GDBD can be obtained up to 1.6 % of N_2 added [7]. When the percentage of N_2 becomes higher, the discharge physics changes and the discharge is no longer a glow one. It has to be pointed out that even in "pure" He, it has been shown that Penning ionisation occurs between He metastables and impurities present in the vessel, coming from the residual air, from the filling gas impurities and from the gaseous products desorbed or etched from the surface. Some optical measurements have shown that N_2 is one of these main impurities [8].

This being understood, it is of interest to see how the discharge develops in another gas. Ar has been chosen in order to confirm some of the previous conclusions. The first result is that in pure Ar, using a millimetric gas gap and in the frequency range used here (up to 35 kHz), we did not succeed to obtain of a GDBD covering uniformly the entire electrode surfaces, which is in accordance with the literature [9]. We attribute that to the fact that as in He, Ar metastables have a very short lifetime at atmospheric pressure due to the formation of Ar_2 [10]. Then these metastables cannot induce a secondary emission which lasts long enough to play a role like in N_2. Moreover, unlike He(2^3S), Ar(4^3P) (11.55 eV and 11.7 eV) cannot ionise the impurities which still exist in the vessel, as for instance N_2 (ionisation potential: 15.6 eV).

Then, the Penning ionisation has to be enhanced by the adding of an appropriate gas. This can be for example acetone [11], methanol (IP: 10.85 eV), oxygen peroxide (IP: 10.9 eV), or ammonia (IP: 10.15 eV). Although ammonia does not seem to be the most efficient considering the ionisation potential, it has been chosen here, the aim being the grafting of nitrogenous functions on polymer. By adding some 100 ppm of NH_3, a GDBD can actually be obtained. Its electrical characteristics are represented in figure 4 and a 1 µs exposure time photography taken at the maximum current peak is shown in figure 5. As it could be envisaged by comparing the metastable properties of Ar(4^3P) and He(2^3S), the GDBD in an Ar/NH_3 mixture is similar to the one obtained in He or He/N_2 mixture. Indeed, the current peak is high and narrow, and the gas voltage decreases during the current peak, which is the signature of the formation of the cathode fall. However, one can note that the gas voltage drop is not as marked as in He, which indicates that the cathode fall is may be less contracted. This could be attributed to the less efficient Penning ionisation as compared to He. The photography taken at the maximum current peak (figure 5) confirms the fact that the obtained

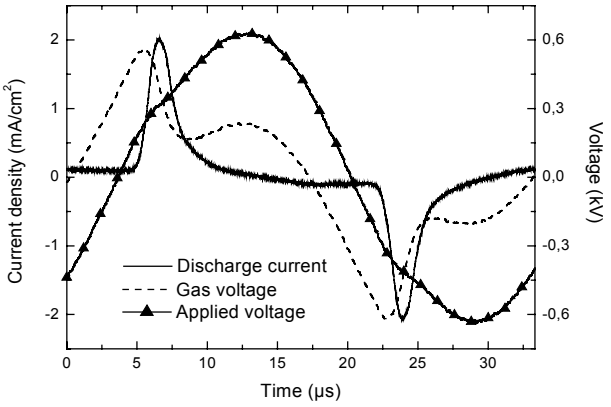

Figure 4: Discharge current, gas voltage and applied voltage of a GDBD in Ar/NH_3

discharge has a structure similar to the one in He, with three distinct areas: the positive column, the Faraday dark space and the cathode and negative glows which cannot be distinguished at high pressure. The thicknesses of these areas are similar to He ones.

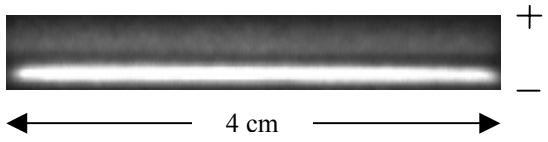

Figure 5: 1 µs exposure time photographs of the gas gap (4 mm) during a GDBD in Ar/NH_3

3.2. Surface transformations

Gas	Gap (mm)	Voltage (kV_{pk-pk})	Frequency (kHz)	Surface power density (W/cm^2)	Volume power density (W/cm^3)
He	5	3	10	0.15	0.3
He + 1% N_2	5	3	10	0.15	0.3
N_2	1	13	2	0.45	4.5
N_2 + 80 ppm NH_3	1	13	2	0.41	4.1
Ar + 370 ppm NH_3	4	1.2	30	0.11	0.28

Table 1: Discharge conditions used for the polypropylene surface treatment

The discharge conditions used for the surface treatments are shown in table 1. In figure 6, all the water contact angle results are reported as a function of the energy density dissipated in the gas during the treatment. The discharge energy density is the calculated mean power density multiplied by treatment duration. In all the cases, the water contact angle decreases with increasing the energy dissipated in the gas during the treatment. However, the optimum water contact angle, the energy for which this angle is reached, and the kinetics of the decrease, depend on the atmosphere used.

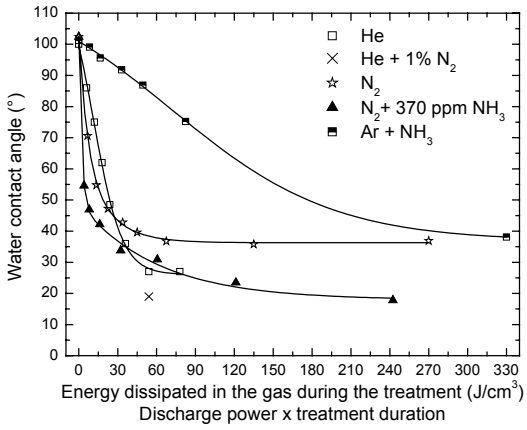

Figure 6: Water contact angle vs. energy dissipated in the gas during the treatment for the different discharge atmospheres

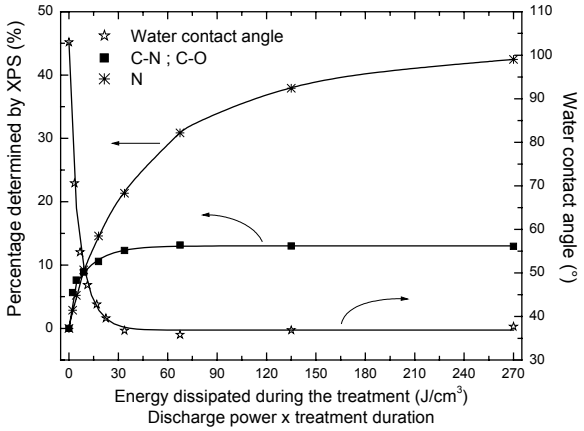

Figure 7: Correlation between water contact angle measurements and chemical composition determined by XPS, for N_2 GDBD treatment

3.2.1. GDBD in He, He/N_2 and N_2

Comparing the results obtained in He and N_2, it appears that the GDBD in He is more efficient than the one in N_2. In He, the water contact angle reaches 28° with 54J/cm^3 dissipated in the gas while GDBD in N_2 leads to a water contact angle of 37° with 68J/cm^3 dissipated in the gas. This can be surprising taking into account the fact that He is a non-reactive gas. In fact, XPS measurements after He and N_2 GDBD treatments show that He GDBD incorporates N atoms like a N_2 GDBD (table 2 [7]). This rather high N incorporation has been attributed to the creation of N_2^+ ions through Penning ionisation in He GDBD [12], the N_2 coming from the residual air present in the gas cell, the filling gas impurities and from the gaseous products which the plasma desorbs or etches from the surface. Considering a few ppm of N_2 in He, the relative contribution of Penning ionisation becomes as high as the direct ionisation [2], and about 10^{11} cm^{-3} N_2^+ ions are created [13]. Moreover, the recombination of N_2^+ ions with the surface is an exothermic reaction, which has a high probability of being dissociative ($N_2^+ + e_{surface} \rightarrow 2N + 4eV$ [14]), and the energy released is high enough to break polypropylene chemical bonds. Therefore, the N due to N_2^+ recombination at the surface efficiently reacts with the polypropylene surface, because radicals are created at the same time and the same place in the gas and on the polymer. The effect is enhanced if a small amount of N_2 is added in He. Indeed, the minimum angle reached after the treatment decreases from 28° in "pure" He to 19° in a mixture of He added with 1% of N_2.

Treatment	C (%)	O (%)	N (%)	Water contact angle (°)
Untreated polypropylene	100	0	0	102
GDBD N_2	71	4	25	37
GDBD He	87	4	9	28

Table 2: Chemical composition of the polypropylene surface determined by XPS and associated water contact angle for the N_2 and He treatments

Another surprising point is that 25% of N grafted by N_2 GDBD leads to a water contact angle of 37° when only 9% of N grafted by He GDBD leads to a lower value of the water contact angle (28°). This may be due to the transformation depth induced by the two discharges. Indeed, N_2 GDBD leads to a very deep incorporation of N atoms in the polymer, up to more than 6nm [15]. As He is a gas known for its crosslinking properties, it can be suggested that He GDBD leads to a grafting which is more localised on the top surface of the polymer. Moreover, it has been shown [15] than the water contact angle measured after a GDBD treatment in N_2 is not correlated with the percentage of N atoms grafted on the polymer but with the amount of C-N functions (amines). Indeed, the water contact angle decreases when the percentage of C-N grafted functions increases and saturates when this percentage saturates, even if heavy nitrogened functions (C-C≡N, N-C≡N et N_2C=O) are still incorporated (figure 7). By looking at the decomposition of N1s XPS peak, for a water contact angle of 38° (25% of N), 32% of the N bonds are amine bonds, which means that 8% of atoms are N atoms in amino groups. The fact that 9% of N atoms grafted by He GDBD is enough to have such a low water contact angle may be due to the fact that these N atoms are mainly grafted under amine forms. This will be checked in the near future by making a decomposition of the C peak following He GDBD treatment.

3.2.2. GDBD in Ar/NH_3 and N_2/NH_3

In Ar/NH_3 mixture, the kinetics of the decrease of the water contact angle is very slow. However, the fact that the discharge is a glow one clearly shows that Penning ionisation occurs between Ar metastable and NH_3, and so that NH_3^+ and NH_4^+ ions are created [16]. Then, the water contact angle results indicate that these ions would be much less efficient than N_2^+ ions for the incorporation of N atoms. This may be due to the fact that the recombination of NH_x^+ ions with electrons from the polymer surface is not sufficiently exothermic to break a chemical bond on the polypropylene and then to lead to the production of radicals on the polymer and in the gas, at the same instant and the same place, as it occurs in He GDBD.

The addition of NH_3 in the N_2 GDBD has an interesting effect. Indeed, despite the very small amount of NH_3 added (80 ppm), the water contact angle that can be reached is lowered compared to N_2 GDBD, especially for long treatment duration (fig 6). In fact, it looks as if the kinetics of decrease observed with N_2/NH_3

treatment is the convolution of the N_2 kinetics and the Ar/NH_3 one. However, looking at the very strong N incorporation occurring in N_2 GDBD, the fact that the water contact angle still continues to decrease in N_2/NH_3 has to be related to the incorporation of functions different to those grafted by N_2 GDBD. As in N_2 GDBD, the water contact angle is connected to the amount of C-N functions grafted on the polymer, and as NH_3 would preferentially lead to the formations of amino groups [17], this lowering of the water contact angle in N_2/NH_3 mixture may be caused by a higher incorporation of these amino groups compared to the N_2 GDBD. Obviously, this has to be checked by doing some XPS measurements on these treatments.

4. Conclusion

Atmospheric pressure glow dielectric barrier discharge can be generated in argon if Penning ionisation is enhanced by the adding of an appropriate gas. Ammonia can be used for that purpose, the $Ar(2^3P)$ metastable states being able to ionise it. The GDBD in Ar/NH_3 mixture is then similar to the one in He, i.e. a subnormal glow close to a normal glow discharge.

GDBD in various atmospheres (He, He/N_2, N_2, N_2/NH_3, Ar/NH_3) have been compared relative to their efficiency on polypropylene wettability. Taking into account the energy dissipated in the gas during the treatment, it appears that the GDBD in He/N_2 mixture is the most efficient discharge to lower the water contact angle. In fact, N_2 GDBD grafts much more N atoms than He GDBD, but the associated water contact angle is higher. This result may be attributed to two phenomena: (i) N is bonded deeper in the material with N_2 GDBD than with He GDBD, due to the crosslinking ability of He (ii) He GDBD grafts mainly amino groups while N_2 GDBD leads to higher valency nitro bonds for long treatment durations. GDBD in Ar/NH_3 mixture is the least efficient discharge, but the adding of NH_3 in N_2 GDBD increases the N_2 GDBD efficiency, probably due to a higher level of amino grafting.

References

[1] F. Massines, Ph. Decomps, C. Mayoux, *Proc. 4th Int. Symp. On High Pressure Low Temperature Plasma Chemistry, HAKONE IV*, Bratislava (1993) p. 141

[2] F. Massines, N. Gherardi, P . Ségur, C. Khamphan, A. Ricard, *Surf. Coat. Technol.,* in press

[3] Raizer Y.P., *in: Gas discharge physics*, Springer-Verlag, Berlin (1991)

[4] F. Massines, R. Ben Gadri, Ph. Decomps, A. Rabehi, P. Ségur, C. Mayoux, *J. Phys. D: Appl. Phys* **38**, 2950 (1998)

[5] P. Ségur and F. Massines, *Proc. 13th Int. Conf. On Gas Discharge and their Applications, GD2000,* Glasgow (2000) p. 15

[6] G. Meyers, A. Cunningham, *J. Chem. Phys.* **67**, 247 (1977)

[7] F. Massines, G. Gouda, N. Gherardi, M. Duran, E. Croquesel, *Plasmas and Polymers* **6**, 35 (2001)

[8] A. Ricard, Ph. Decomps, F. Massines, *Surf. Coat. Technol.* **112**, 1 (1999)

[9] S. Okazaki, M. Kogoma, M. Hueara, Y. Kimura, *J. Phys. D : Appl. Phys.* **26**, 889 (1993)

[10] J.B. Leblond, F. Collier, F. Hoffbeck, P. Cottin, *J. Chem. Phys.* **74**, 6242 (1981)

[11] S. Okazaki, M. Kogoma, H. Uchiyama, *Proc. 3rd Int. Symp. High Pressure Low Temperature Plasma Chemistry, Hakone III,* Strasbourg (1991) p. 101

[12] T.D. Märk and H.J. Oskam, *Phys. Rev. A* **4,** 1445(1971)

[13] Yu. B. Golubovskii, V.A. Maiorov, J. Behnke, J.F. Behnke, *Proc. 8th Int. Symp. High Pressure Low Temperature Plasma Chemistry, Hakone VIII,* Puhajarve (2002) p. 48

[14] E. Marode, *J. Appl. Phys.* **46**, 2005 (1975)

[15] E. Croquesel, F. Massines, E. Gat, C. Reynaud, Tran Minh Duc, G. Rames-Langlade, *Proc. 15th Int. Symp. Plasma Chemistry, ISPC 15,* Orléans (2001) p. 2355

[16] M.J. Kushner, *J. Appl. Phys* **71**, 4173 (1992)

[17] S. Ben Rejeb, M. Tatoulian, F. Arefi Khonsari, N. Fisher Durand, A. Martel, J.F. Lawrence, J. Amouroux, F. Le Goffic, *Analytica Chimica Acta* **376**, 133 (1998)

Probabilistic modeling of the spot displacements on a high-pressure arc cold cathode

Sylvain Coulombe

CRTP/Department of Chemical Engineering, McGill University, Montréal, Québec, Canada

Abstract
A probabilistic model for the description of the type-A cathode spot (*macro-spot*) displacement dynamic is applied to a high-pressure rotating arc configuration for which experimental observations exist. Such system shows a $1/f^{\sim 1}$ (flicker noise) signature in the arc voltage signal for cathode surface conditions leading to arc anchoring. The cathode spot displacement conditions leading to such signature and computer simulations of the principal figures of interest (arc elongations, Fourier spectrum, and erosion trace) are presented.

1. Background

The dynamic of the arc attachment points on the electrodes is, in general, seen as detrimental to the operation of high-pressure arcs. Of particular interest with low current arc systems is the cathode macro-spot dynamic (the type-A spot [1]). The very existence of spots on non-refractory cathodes is associated with the requirements for a self-sustaining operation [2] and thus, such spots are essential. An obvious drawback of these requirements is the cathode erosion phenomenon leading to the release of copious amounts of metallic vapors into the arc. The movement of the cathode spot is erratic, and shows periods of momentarily attachment over confined regions (local diffusion) and jumps over longer distances (re-strike events). The later are a source of significant arc elongations causing arc voltage and temperature variations. The arc length elongations between re-strike events lead to the characteristic "saw-teeth" in the voltage signal. The local diffusion events add a high-frequency noise component to this signal.

The arc elongation dynamic associated with the electrode attachment effects is particularly problematic for the plasma spraying process since the thermal and acceleration history of the particles is affected, which in turns affects the uniformity of the coating. In plasma torches, the gas dynamics add to the arc attachment effects, leading to stronger instabilities. A significant research effort is now dedicated to the development of tools to monitor those instabilities and to relate them to the coating quality ([3] and references therein). A less significant effort is dedicated to the understanding of the relationship between the surface state and the movement of the arc attachment points, which lead to arc length and voltage fluctuations. Experimental observations made in our laboratory ([4,5] and references therein) revealed the intimate relationship between the contamination state of the cathode surface (i.e. electron emissive properties) and the erosion rate and smoothness of the cathode spot displacement. Arc anchoring conditions observed with copper cathodes in an argon or argon+nitrogen plasma gas atmosphere are associated with a $1/f^{1}$ voltage fluctuations signature while conditions leading to a smooth movement of the cathode spots (ex. Ar + 1vol% CO arc on Cu cathode) are associated with a white noise signature.

We recently presented a probabilistic modeling approach for the description of the cathode spot displacement dynamic [6]. We then demonstrated the ability of the model to qualitatively reproduce the experimentally obtained voltage signature for a range of cathode surface conditions giving rise to smooth and anchoring arc movements. We now present the results obtained for conditions leading to a *1/f* signature.

2. Description of the model

The probabilistic cathode spot displacements model was described in detail in a recent study [6] and only the essential details are presented here. A rotating arc geometry consisting of a center anode surrounded by a concentric water-cooled cathode is considered (figure 1). In such an arrangement, the attachment of the arc on the anode is confined to a plane while the cathode spot displacements are not as constrained. In a real experimental arrangement, the arc gap is small (a few mm) and the arc is forced into a rotating motion through the use of a magnetic field or tangential gas injection. Our model geometry for the cathode surface consists of an elongated rectangue where the shortest direction corresponds to the axis of the electrode assembly while the longest, to the azimuthal direction (the direction along the main arc motion). The arc

rotation is modeled assuming a uniform movement of the anode attachment (constant velocity) while the cathode spot is allowed to diffuse locally and jump in re-strike events. The arc elongations are thus only due to cathode spot displacements.

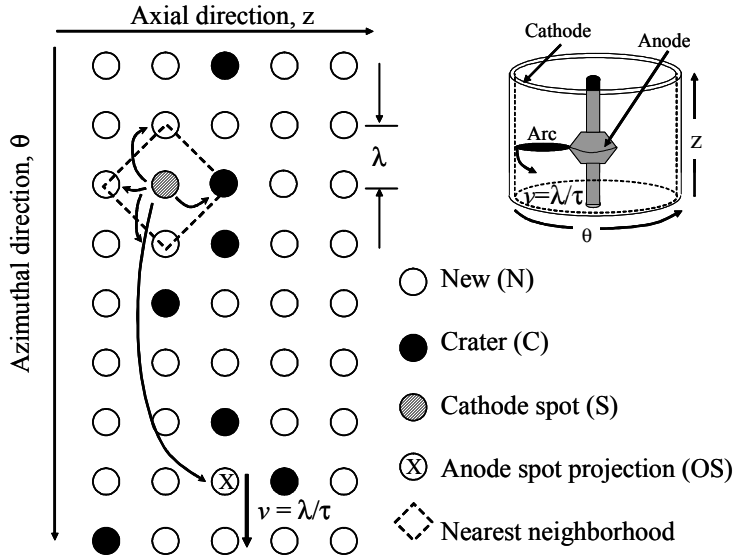

Figure 1. Schematic of the arc gas heater assembly and model geometry

The cathode spot has a residence time τ at a given location on the model surface (characteristic burning time). After this lapse of time, the new location of the cathode spot is predicted using a probabilistic scheme: i) the spot has a probability p_S to stay at the current location and burn for another time period τ. ii) the spot has a probability p_N to diffuse locally and move a distance λ (characteristic diffusion distance) to a neighboring lattice position located in either one of the cardinal directions. iii) the spot jumps with a probability p_J to the current position of the anode attachment point projected on the cathode lattice. The total probability is normalized: $p_{TOT} = p_S + p_N + p_J = 1$. In the present study, we assume $p_N = 4p_S$ with equal diffusion probabilities in each cardinal directions. The later assumption implies that the probability for the cathode spot to move into one of the local neighboring sites equals its probability to stay at the present location. This definition of probabilities is introduced in order to reproduce a local random diffusion process. A uniformly distributed random number $0 \le R \le 1$ is drawn after each time step τ and the actual event that takes place is determined using the following decision scheme:

Jump under the anode attachment point if:	$R \le p_J$
Move one λ North if:	$p_J < R \le p_J + p_S$
Move one λ South if:	$p_J + p_S < R \le p_J + 2p_S$
Moves one λ East if:	$p_J + 2p_S < R \le p_J + 3p_S$
Moves one λ West if:	$p_J + 3p_S < R \le p_J + 4p_S$
Stay at current location if:	$p_J + 4p_S < R \le 1$

Periodic boundary conditions are used to close the computational domain and thus, reproduce the cylindrical geometry of the cathode surface. The calculated arc elongation corresponds to the linear distance between the actual cathode spot position and the anode spot position projected onto the cathode plane. The frequency signature of the arc elongations dynamic is obtained by calculating its frequency power spectrum (FPS). The "depth" of the erosion trace is calculated by adding the number of times the cathode spot visited a given location on the model lattice. Numerous arc rotations are used in order to reproduce the erosion trace left on the cathode surface. The dimensions of the model cathode surface lattice are 101λ x 2048λ (axial and azimuthal directions).

3. Results and discussion

In [6] we determined the conditions leading to a *1/f* arc elongation dynamic: $p_J = p_N + p_S = 0.5$, meaning that in a displacement event the cathode spot is as likely to diffuse locally than to jump in the arc movement direction in a re-strike event. Those conditions are used in the present study.

Arc Elongation dynamic

Figure 2 presents the temporal evolution of the normalized arc elongation (top) and the corresponding power frequency spectrum calculated for one arc passage over the cathode surface. The arc elongation signal consists in a series of "saw-teeth" (low frequency) on top of which is added a weak higher frequency signal. The saw-teeth are characteristic of the momentarily arc anchoring on the cathode surface between re-strike events which leads to a stretching of the arc, thus a voltage increase, as the anode attachment point moves. The arc length increases in an essentially linear fashion before to suddenly shrink to its nominal length (arc gap distance) in a re-strike event. The higher frequency component of the signal is attributed to the local diffusion of the cathode spot between re-strike events. This simulated signal, though considerably less noisy than experimentally obtained ones [4], is nevertheless is good qualitative agreement.

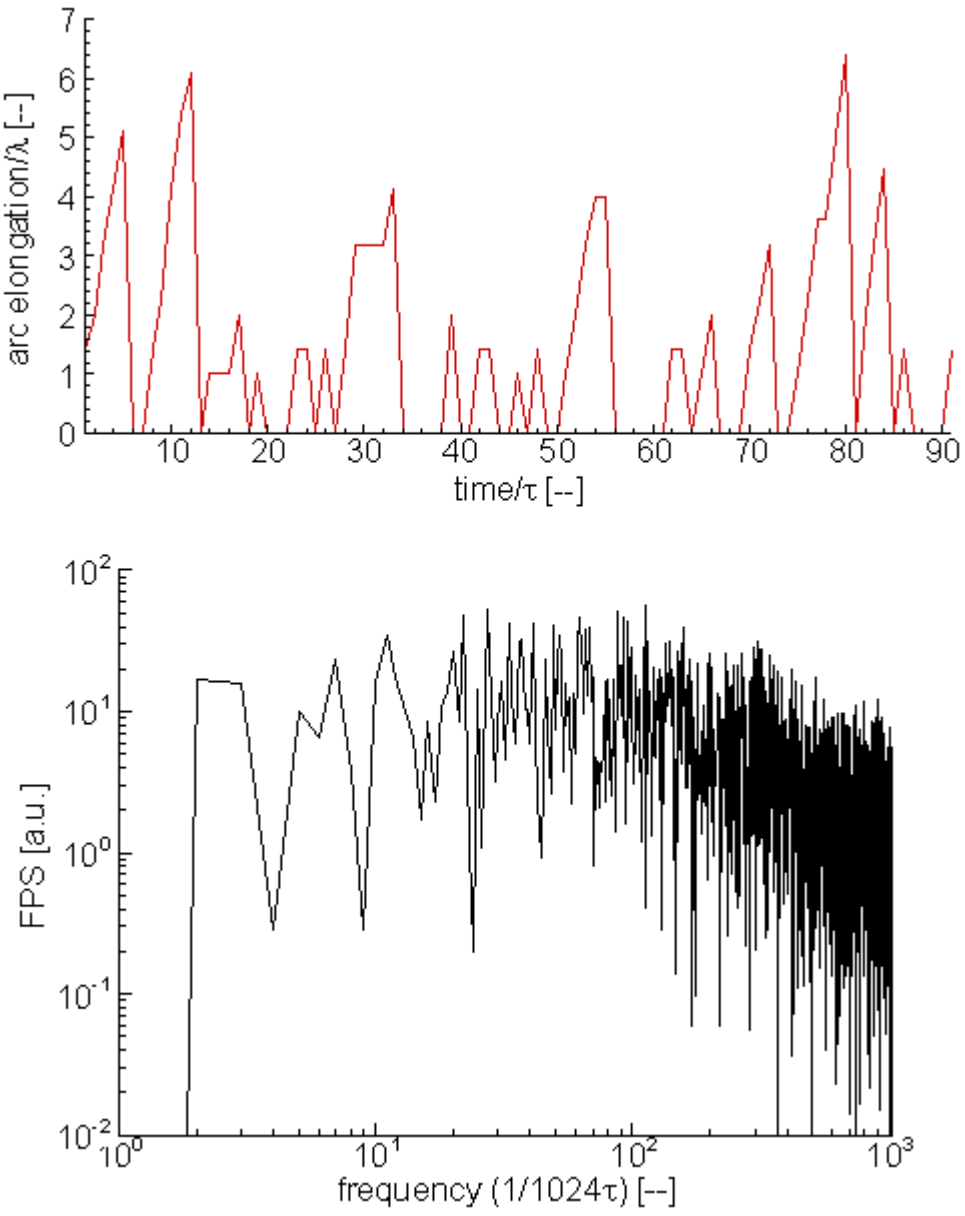

Figure 2. Closed-up view of the simulated temporal evolution of the arc elongation and corresponding Fourier spectrum obtained for conditions leading to a *1/f* signature (p_J=0.5, p_S=0.1) and one arc passage.

Figure 3 reveals the cathode spot displacements over a few time steps. The anode rotation plane is defined by $z = 51\lambda$. The cathode spot momentarily wanders out of the anode rotation plane before to jump back to this plane in a re-strike event. It is important to note that this jumping condition corresponds to a re-strike event at the minimum anode-cathode distance and thus, was not arbitrarily chosen. Without such condition, the cathode spot drifts out of the anode rotation plane causing an increase of the *rms* arc length and eventually, leaves the cathode surface. For the conditions leading to a *1/f* signature, the cathode spot rarely wanders more than 2-3λ out of the anode rotation plane before to jump in a re-strike event. As the jumping probability decreases, significantly more wandering out of the plane of rotation is observed [6].

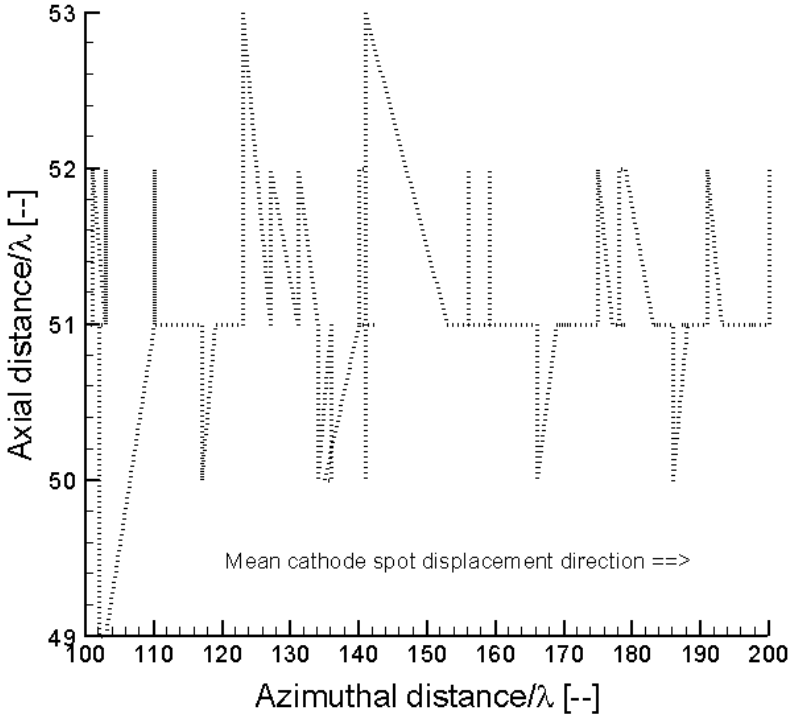

Figure 3. Close-up view of the simulated cathode spot displacements (p_J=0.5, p_S=0.1).

Erosion trace

The local diffusion of the cathode spot between re-strike events leads to the formation of an erosion trace on the cathode surface. Figure 4 shows a close-up view of the simulated erosion trace left by the cathode spot following respectively, 1 (top) and 10000 (bottom) arc passages. The gray scale used is such that the lighter the gray tone at a given location on the model cathode lattice, the higher the number of times the cathode spot visited this specific location. To some extent, this contour plot can be interpreted as the erosion trace where the gray tone represents the local depth of the trace. The depth of the erosion trace is obviously more significant in the anode rotation plane. When the jumping probability is increased, the cathode spot residence time in a given area of the surface decreases and thus, the extent of local damage to the surface is less significant [6].

4. Concluding comments

The results presented in this study complement our initial investigation of the type-A cathode spot (*macro-spot*) displacement dynamic in high-pressure arc systems. We attributed the experimentally observed *1/f* electrical signature (flicker noise) to the cathode spot dynamic and showed that this signature can be qualitatively reproduced using a simple probabilistic displacement model which uses local displacement rules based on the cathode surface conditions. This tool will potentially find a useful application in the monitoring and control of the cathode erosion process.

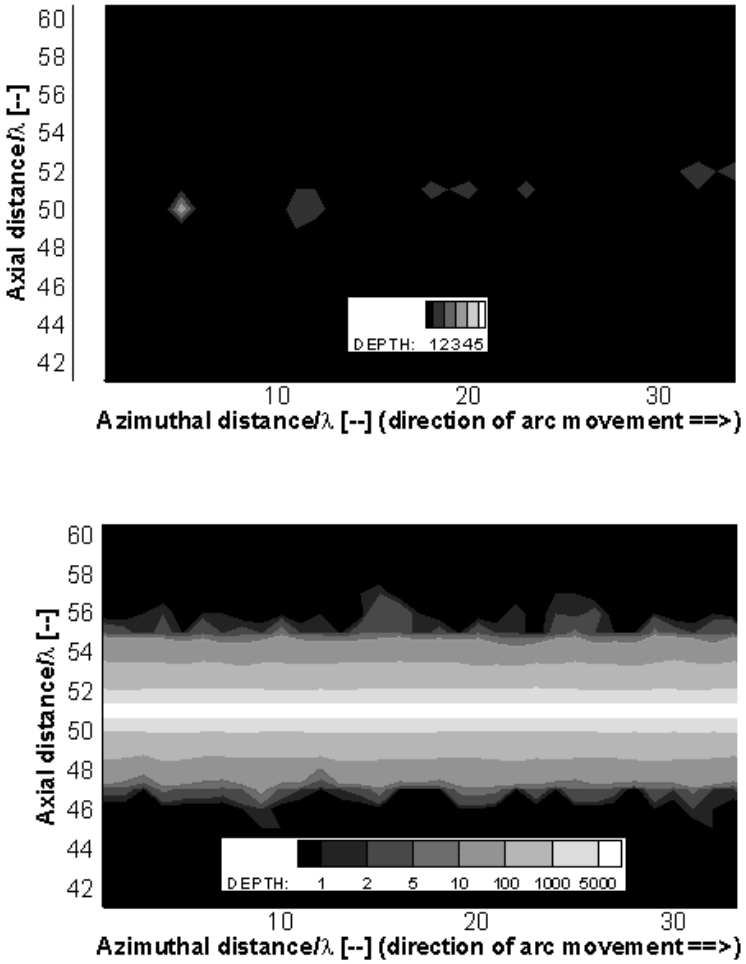

Figure 4. Closed-up view of the simulated erosion trace left on the model cathode surface for *1/f* conditions (p_J=0.5, p_S=0.1). Top: 1 arc passage. Bottom: 10000 arc passages.

Acknowledgments

The author wishes to acknowledge the financial support from McGill University and the National Science and Engineering Research Council (NSERC) of Canada through the Discovery and Canada Research Chairs Programs.

References

[1] B. Jüttner – J. Phys. D: Appl. Phys. **34**, R103 (2001).
[2] S. Coulombe, J. –L. Meunier – Plasma Sources Sci. Technol. **6**, 508 (1997).
[3] L. Leblanc, C. Moreau C - J. Thermal Spray Technol. **11**, 380 (2002).
[4] N. Desaulniers-Soucy, J. –L. Meunier - J. Phys. D: Appl. Phys. **28**, 2505 (1995).
[5] R. N. Szente, R. J. Munz, M. G. Drouet – Plasma Chem. Plasma Process. **7**, 349 (1987).
[6] S. Coulombe – J. Phys. D: Appl. Phys. **36**, 686 (2003).

Modeling of a low-pressure chlorine plasma sustained by electromagnetic surface waves

L. Stafford[1], F. Vidal[2], J. Margot[1], & M. Chaker[2]

[1] *Groupe de physique des plasmas, Université de Montréal, Montréal, Québec Canada*
[2] *INRS-Énergie, Matériaux et Télécommunications, Varennes, Québec, Canada*

Abstract
This paper reports the results of a model aiming to describe the characteristics of a chlorine high-density plasma. The model allows in particular to determine the pressure-dependence of the concentration of neutral and charged species. Comparison of this model to experimental measurements achieved in a high-density plasma sustained by an electromagnetic surface wave shows an excellent agreement for the neutral atomic and molecular species. As far as charged species are concerned, the model reproduces well experiments for atomic chlorine ions and electrons, but some discrepancy occurs for molecular positive ions and negative ions. The cause of this discrepancy remains to be clarified but might result from an underestimation of the creation rates of Cl_2^+ and Cl^-. The results also demonstrate that diffusion can be ignored above 1 mTorr.

1. Introduction

Chlorine- and fluorine-containing plasmas are routinely used for the etching of a vast class of materials, including materials with novel applications such as ferroelectrics [1-2]. While intense research efforts are devoted to the use of such plasmas for etching purpose, there is comparatively little information available concerning the gas-plasma phase and its interaction with surfaces. However, to be efficient, the optimization of etching processes requires a good understanding of the discharge chemistry. In addition, while high-density plasmas (i.e. low pressure plasmas (1 mTorr or so) with relatively high ionization degrees) are now finding their way as the most promising solution for the next generation of integrated circuits, important efforts still need to be devoted to the development of models that would allow optimizing the characteristics of such discharges in complex chemistries.

In this context, we have developed a 1-dimensional fluid model describing a high-density chlorine plasma. Among other quantities, the model allows to determine the radial structure of the plasma, including various neutral and charged species in the pressure regime ranging from 0.1 to 10 mTorr (in the following, gas pressure means pressure in the vessel before plasma ignition). The calculated densities of electrons, Cl, Cl_2, Cl^+, Cl_2^+ and Cl^- are compared to experimental measurements achieved in a low-pressure surface-wave sustained plasma.

2. Overview of the model

The model is based on fluid equations, in which the particle balance equations for electrons, Cl, Cl_2, Cl^+, Cl_2^+ and Cl^- are solved together with the corresponding flux equations and the energy balance equation. For simplicity, the model is isothermal, which means that power deposition is considered as spatially uniform. In addition, since chlorine is an electronegative gas, a simple quasi-neutral model cannot be used so that the plasma sheath needs to be treated in detail by solving Poisson's equation. In these conditions, the set of equations to be solved takes the following form

$$\frac{\partial n_k}{\partial t} + \nabla \cdot \mathbf{J}_k = S_k , \tag{1}$$

$$\mathbf{J}_k = \pm n_k \mu_k \mathbf{E} - D_k \nabla n_k , \tag{2}$$

$$P_V = \bar{n}_e \Theta , \tag{3}$$

$$\nabla \cdot \mathbf{E} = e\left(-n_e - n_{Cl^-} + n_{Cl_2^+} + n_{Cl^+}\right)\Big/\varepsilon_0 , \tag{4}$$

where k=1-6 indicates one of the 6 species considered, n_k being the density of the species k, $\mathbf{J_k}$ its flux, S_k its source term (volume creation minus volume losses), D_k and μ_k its free diffusion coefficient and mobility, $\mathbf{E}$ the space-charge electric field, P_V the average power absorbed by the plasma per volume unit and Θ the average power dissipated per electron [3]. In chlorine plasmas, the parameter Θ depends on the cross-section average values of both neutral atomic and molecular chlorine densities and on the electron temperature T_e. It

is calculated by summing all the power losses for electrons. In the range of pressures considered here, only inelastic collisions such as ionization and excitation play a significant role. A list of reactions affecting the electron power loss in chlorine discharges with their corresponding rate is given in [4]. Note that under steady-state conditions, Θ is also equal to the average power absorbed per electron [5].

In cylindrical coordinates, Eq. (1) can be written as

$$\frac{\partial n_k}{\partial t} + \frac{1}{r}\frac{\partial (r J_{kr})}{\partial r} + \frac{\partial J_{kz}}{\partial z} = S_k \,. \tag{5}$$

To avoid the problem of solving a 2-D model, the axial contribution of the flux in Eq. (5) is treated as an adjustable constant of the form $-(D_a/\Lambda^2)n_k$ where D_a is taken as the classical ambipolar diffusion coefficient and Λ an axial diffusion length. Such an approach allows to address in an approximate but simple way problems in which axial diffusion cannot be neglected, for example when the plasma is subjected to a magnetic field.

The radial component of equation (2) can be expressed as

$$J_{kr} = \pm n_k \mu_k E_r - D_k \frac{\partial n_k}{\partial r}\,, \tag{6}$$

while neglecting the axial component of the electric field in Poisson's equation (4) yields

$$\frac{1}{r}\frac{\partial (r E_r)}{\partial r} = \frac{e}{\varepsilon_0}\left(-n_e - n_{Cl^-} + n_{Cl_2^+} + n_{Cl^+}\right). \tag{7}$$

The source terms appearing in Eq. (5) are generally expressed as

$$S_k = \sum_j \beta_j n_k n_j\,, \tag{8}$$

where summation is performed on all the reactions involving a density change of the species k. For example, in the case of electrons

$$S_e = \beta_1 n_e n_{Cl_2} + \beta_2 n_e n_{Cl} + \beta_3 n_e n_{Cl_2} + \beta_4 n_e n_{Cl^-} - \beta_5 n_e n_{Cl_2^+} - \beta_6 n_e n_{Cl_2}\,, \tag{9}$$

where the coefficients β_j are given in Table 1, together with the whole reaction set considered in the model.

No	Mechanism	Reaction	Rate (cm^3/s)
(1)	Electron-impact ionization of Cl_2	$Cl_2 + e \rightarrow Cl_2^+ + 2e$	$\beta_1 = 9.214\times10^{-8}\exp(-12.9/T_e)$
(2)	Electron-impact ionization of Cl	$Cl + e \rightarrow Cl^+ + 2e$	$\beta_2 = \sqrt{T_e/12.96}\,\exp(-12.96/T_e)\sum_{i=0}^{5} a_i \left[\log(12.96/T_e)\right]^i$
			$a_0 = 1.419\times10^{-7}$ $a_1 = -1.864\times10^{-8}$ $a_3 = 3.306\times10^{-8}$
			$a_4 = -3.54\times10^{-9}$ $a_5 = -2.915\times10^{-8}$
(3)	Dissociative ionization of Cl_2	$Cl_2 + e \rightarrow Cl^+ + Cl + 2e$	$\beta_3 = 3.881\times10^{-8}\exp(-15.5/T_e)$
(4)	Electron-impact detachment	$Cl^- + e \rightarrow Cl + 2e$	$\beta_4 = 2.627\times10^{-8}\exp(-5.375/T_e)$
(5)	Dissociative recombination	$Cl_2^+ + e \rightarrow 2Cl$	$\beta_5 = 5.1\times10^{-7}(0.025/T_e)^{0.43}$
(6)	Dissociative attachment	$Cl_2 + e \rightarrow Cl^- + Cl$	$\beta_6 = 3.69\times10^{-10}\exp\left(\sum_{i=1}^{5} a_i/T_e^i\right)$ $a_1 = -1.68$;
			$a_2 = 1.457$; $a_3 = -0.44$; $a_4 = 0.0572$; $a_5 = -0.0026$
(7)	Ion-ion recombination	$Cl_2^+ + Cl^- \rightarrow Cl_2 + Cl$	$\beta_7 = 5\times10^{-8}$
(8)	Ion-ion recombination	$Cl^+ + Cl^- \rightarrow 2Cl$	$\beta_8 = 5\times10^{-8}$
(9)	Polar dissociation	$Cl_2 + e \rightarrow Cl^- + Cl^+ + e$	$\beta_9 = 8.549\times10^{-10}\exp(-12.65/T_e)$
(10)	Charge transfer	$Cl^+ + Cl_2 \rightarrow Cl_2^+ + Cl$	$\beta_{10} = 5.4\times10^{-10}$
(11)	Electron-impact dissociation	$Cl_2 + e \rightarrow 2Cl + e$	$\beta_{11} = 3.80\times10^{-8}\exp(-3.824/T_e)$

Table 1: Reactions considered in the model and corresponding rates (from [6,7])

The equation system is solved using usual boundary conditions

$$J_{kr}(0)=0;\ n_i(R+\delta)=0;\ J_{er}(R)=\frac{1}{4}\sqrt{\frac{8T_e}{\pi m_e}}n_e(R);\ J_{Clr}(R)=\frac{\gamma}{4}\sqrt{\frac{8T_n}{\pi m_{Cl}}}n_{Cl}(R);\ J_{Cl_2r}(R)=-\frac{1}{2}J_{Clr}(R)\,, \qquad (10)$$

where R is the vessel radius, n_i the total positive ion density, T_n the neutral temperature and γ the surface recombination coefficient characterizing the interaction of Cl with the wall. The value of γ depends on the wall characteristics. For example, in the case of anodized aluminum, γ is equal to 0.15 [8,9].

3. Results of the model and comparison with experiments

The model was tested through comparison with experimental data obtained from a high-density plasma produced by an electromagnetic surface wave at 190 MHz in a cylindrical structure made of two abutting cylinders of different diameter [6]. This plasma can be subjected to an axial magnetic field B_0. Details on the plasma reactor and diagnostics can be found in [6,10]. Measurements of the neutral density of atomic and molecular chlorine were performed using mass spectrometry and actinometry on Cl_2 molecules according to the zero-power extrapolation technique suggested by Donnelly [11]. The total ion density was determined by electrostatic probe and the Cl^+/Cl_2^+ ratio by ion mass spectrometry. The negative ion density was measured by laser photodetachment and ion acoustic waves. Finally the electron density was calculated using the neutrality condition.

In its present state of development, since the model is one-dimensional and isothermal, it does not allow to fully take into account the whole complexity of the reactor geometry and of the spatial distribution of species. Testing of the model was thus performed by comparison of the cross-section average densities of the various species with the experimental values in the larger of the two cylinders (processing chamber, R=14 cm). The parameters used for calculations were chosen to match the experimental conditions presented in reference [6]: P_V = 2.5 mW/cm^3 (250 W absorbed power), T_n = 300 K, Λ=150 cm, B_0 = 900 G.

3.1. Characteristics of neutral species

Figure 1 presents the Cl_2 dissociation degree τ_d as a function of the gas pressure for different values of the Cl surface recombination coefficient γ. It can be seen that for all values of γ, τ_d is decreasing with increasing pressure. In addition, when the surface recombination coefficient increases, the dissociation degree decreases as noticed in [7,12-13]. In our experimental conditions, the value of γ that provides the best agreement with the experimental data is found to be 0.02. This value lies between those of pure anodized aluminum (γ~0.15) and pure quartz (γ~0.008) [9,14]. Figure 1 shows that for γ=0.02, even in the moderate power conditions investigated, the dissociation degree exceeds 80% when operating at or below 1 mTorr while it decreases at about 25% at 10 mTorr. A similar decrease of the dissociation degree was also observed in [15,16].

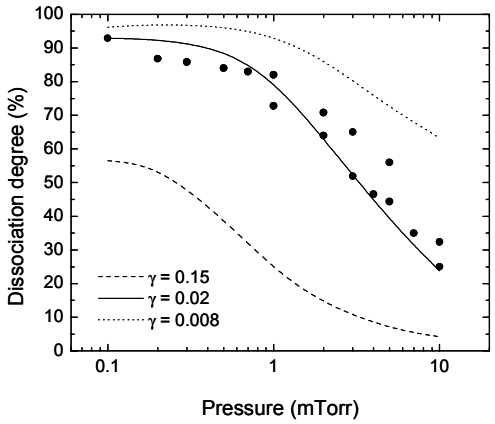

Fig. 1: Dissociation degree as a function of the gas pressure for different values of the surface recombination coefficient γ. The full circles correspond to the experimental values.

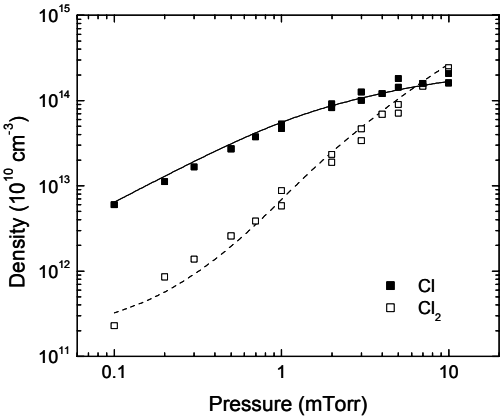

Fig. 2: Density of atomic and molecular chlorine neutrals as a function of the gas pressure for γ=0.02. The full and dotted lines correspond to the calculated densities of Cl and Cl_2 respectively.

The dependence on the gas pressure of the atomic and molecular chlorine neutral densities is presented in Fig. 2. These data were deduced from Fig. 1 assuming a gas temperature of 300 K as discussed in [6]. Clearly, at low pressure, the plasma is dominated by Cl while as soon as the pressure exceeds about 7 mTorr, Cl_2 takes advantage over Cl. Clearly, the model reproduces very well the experimental values, thereby indicating that for neutral species, the use of a 1-D isothermal model is quite suitable.

3.2. Characteristics of charged particles

Figure 3 shows the Cl and Cl_2 positive ion densities as a function of the gas pressure. The model predicts that Cl^+ increases up to a pressure of about 0.5 mTorr and then decreases like p^{-2}. As for Cl_2^+, its density increases with p, significantly up to 1 mTorr and slowly above this pressure. Overall Cl^+ dominates the positive ion population below 1 mTorr while the main ion species is Cl_2^+ above a few mTorr. Comparison with the experimental results shows an excellent agreement for the Cl^+ population. However, the model does not correctly predict the pressure dependence of the Cl_2^+ density, the experimental data showing a nearly pressure-independent behavior.

Figure 4 shows the electron and negative ion densities as a function of the gas pressure. As can be seen, the negative ion density is much smaller than the electron density at lower pressure, while Cl^- becomes the dominant negative charge carrier at higher pressure (i.e. above 2 mTorr). However, the model strongly underestimates the negative ion population in the lower pressure region while it slightly overestimates it at higher pressure.

It is worth mentioning that both model and experiment yield a similar pressure-dependence of Cl^+ and electrons on one hand, and of Cl^- and Cl_2^+ on the other hand. In addition, over the whole range of pressures investigated, the absolute values of Cl^+ and electrons are very close each other. The densities of Cl^- and Cl_2^+ are also very similar except at very low pressure for the calculated values. Similar observations were reported in [17]. In order to understand the reasons of this behavior, we have investigated the importance of the various reactions in the particle balance equations (1).

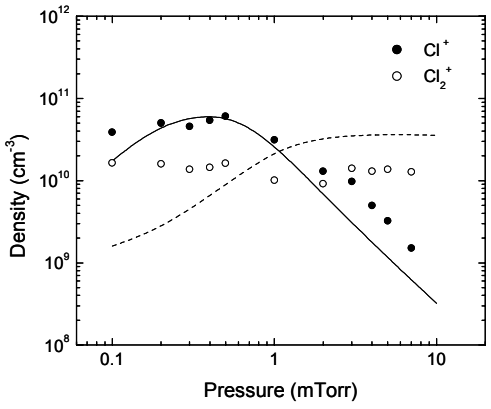

Fig. 3: Density of atomic and molecular positive chlorine ions as a function of the gas pressure. The full and dotted lines correspond to the calculated densities of Cl^+ and Cl_2^+ respectively.

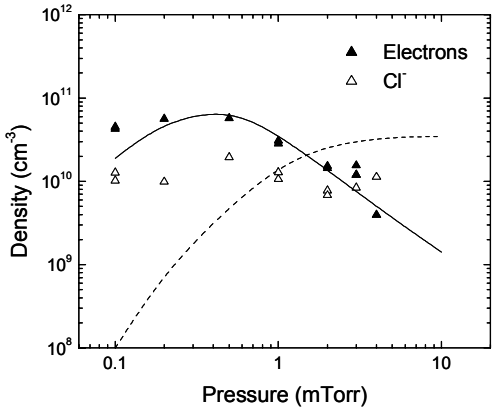

Fig. 4: Density of electrons and negative chlorine ions as a function of the gas pressure. The full and dotted lines correspond to the calculated densities of electrons and Cl^- respectively.

Figures 5a to 5d shows the volume creation and loss rates (i.e. the number of particles created or lost per volume and time unit) of Cl^+, e^-, Cl^- and Cl_2^+ through the various mechanisms that appear in Table I. In the case of Cl^+ (Fig. 5a), the creation is clearly governed by electron-impact ionization, while polar dissociation is everywhere negligible. On the other hand, the main losses occurring in the plasma volume are due to charge transfer, ion-ion recombination being lower by at least one order of magnitude over the whole range of pressures investigated. Charge transfer is however ignored in most publications. A close analysis of the results presented in Fig. 5a shows that volume creation and losses do not exactly balance each other. The difference is taken into account by the diffusive term $\nabla \cdot \mathbf{J}_k$ appearing in Eq. (1). Interestingly, for Cl^+, this term is positive at lower pressure, thereby representing a net loss term (when averaged over the radius, the

flux is directed towards the wall), while at higher pressure, it becomes negative (i.e. on the average the flux is directed inwards). A similar behavior is observed for electrons as can be seen in Fig. 5b. Indeed, the total creation term (mainly electron-impact ionization) is larger than the loss terms (dissociative recombination + attachment) at lower pressure, while the reverse situation occurs at higher pressure. In addition, note that the contribution of detachment to the creation term is negligible over the whole range of pressures investigated.

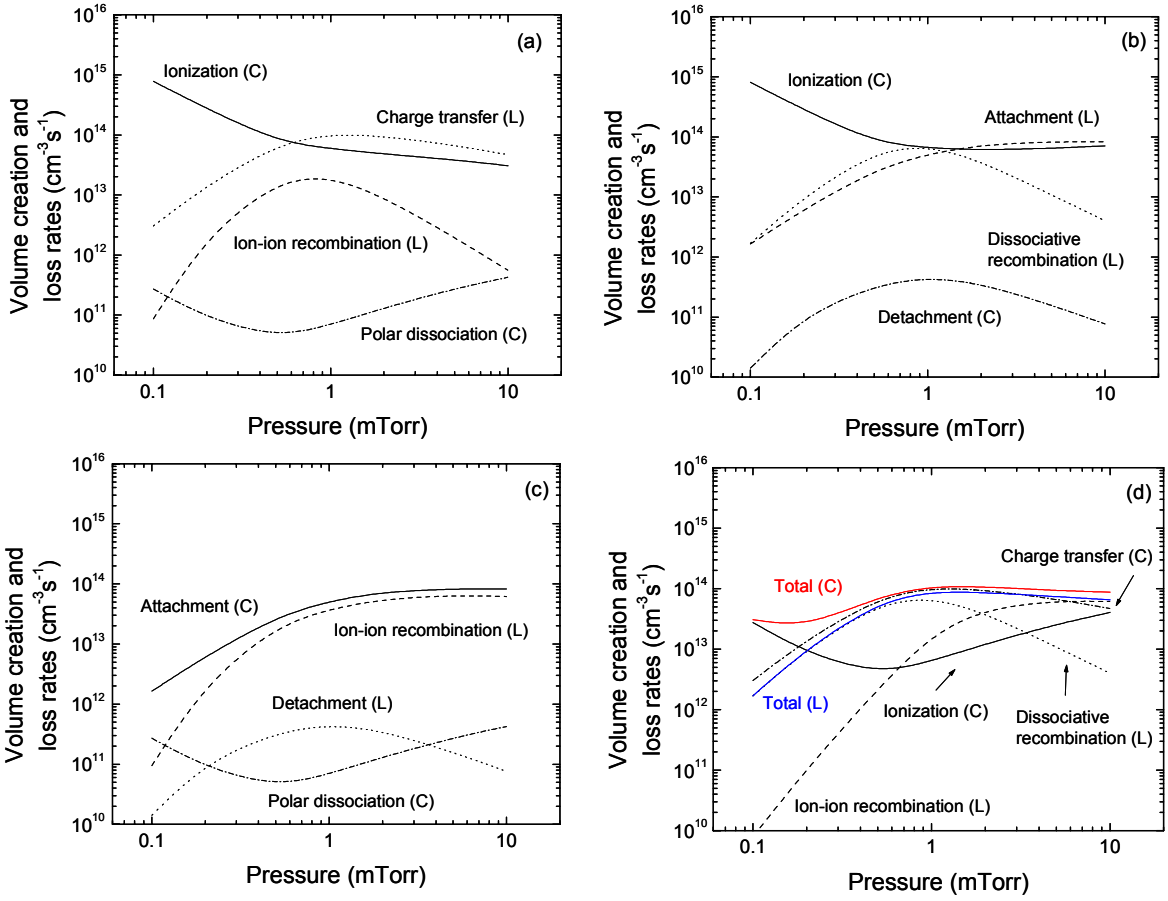

Fig. 5: Pressure dependence of the volume creation and loss rate of charged species through various mechanisms. (a) Cl^+, (b) electrons, (c) Cl^-, (d) Cl_2^+

Figure 5c shows the results obtained for negative ions. In this case, creation is largely dominated by attachment and volume losses by ion-ion recombination, the other mechanisms playing only a minor role. It can also be seen that creation is everywhere larger than losses, the difference being compensated by an outward diffusive term. However, the relative weight of this term with respect to volume losses is less important than for Cl^+ and electrons. In the case of Cl_2^+ (Fig. 5d), the situation appears a little bit more complex. For this reason, we also show on Fig. 5d the total volume creation and loss terms. Creation is essentially governed by charge-transfer except at very low pressure (0.1 mTorr) where electron-impact ionization dominates. The volume losses are mainly due to dissociative recombination below 2 mTorr and to ion-ion recombination beyond. Note that for Cl_2^+ the diffusive term is also outward.

It is quite remarkable in Figs. 5a to 5d that the creation rate shows a similar pressure dependence for Cl^+ and electrons on one hand, and for Cl_2^+ and Cl^- on the other hand. Since the total volume losses behave similarly with pressure for the 4 species, it is suspected that the pressure dependence of the creation rate is the key factor explaining the final pressure dependence of the densities. That would explain why molecular chlorine ions closely follow negative ions both theoretically and experimentally. In these conditions, the discrepancy observed between model and experiments for Cl_2^+ and Cl^- might be resulting from an underestimation of either the Cl_2^+ or the Cl^- creation in the lower pressure region. This remains however to be investigated in more detail before definitely concluding.

Finally, one notes from Figs. 5a to 5d that the total creation and volume losses become very similar above a typical pressure value of 1 mTorr. This indicates that under the conditions investigated here, the diffusion processes can reasonably be ignored when one is interested by plasmas operating above such a pressure. This allows considerable simplification of modeling.

4. Conclusion

The fluid model that was developed for describing a high-density chlorine plasma reproduces very well a number of observed characteristics. In particular, the pressure dependence of the dissociation degree and the absolute value of the Cl and Cl_2 neutral density are correctly described by the model. As for the charged species, the density of Cl^+ and electrons is correctly predicted. However, the model underestimates the density of Cl_2^+ and Cl^- in the lower pressure region.

Acknowledgments

The authors gratefully acknowledge the financial support of Micronet (Network of Centers of Excellence in Microelectronics), the Natural Sciences and Engineering Research Council of Canada (NSERC) and the Fond Québécois de la Recherche sur la Nature et les Technologies (FQRNT).

References

[1] L. Stafford, J. Margot, O. Langlois & M. Chaker, submitted to J. Vac. Sci. Technol. A
[2] D. S. Wuu, F. C. Liao, N. H. Kuo, R. H. Horng & M. K. Lee, Jpn. J. Appl. Phys. Part I 39, 2068 (2000)
[3] F. Vidal, T.W. Johnston, J. Margot, M. Chaker & O.Pauna, IEEE Trans. Plasma Sci. 27, 727 (1999)
[4] C. Lee & M.A. Lieberman, J. Vac. Sci. Technol. A 13, 368 (1995)
[5] C. M. Ferreira & M. Moisan, Phys. Scr. 38, 382 (1988)
[6] L. Stafford, J. Margot, M. Chaker & O. Pauna, J. Appl. Phys. 93, 1907 (2003)
[7] G. I. Font, I. D. Boyd & J. Balakrishnan, J. Vac. Sci. Technol. A 16, 2057 (1998)
[8] L. D. B. Kiss & H. H. Sawin, J. Electrochem. 139, 1414 (1992)
[9] G. P. Kota, J. W. Coburn & D. B. Graves J. Vac. Sci. Technol. A 16, 270 (1998)
[10] J. Margot, F. Vidal, M. Chaker, T. W. Johnston, A. Aliouchouche, M. Tabbal, S. Delprat, O. Pauna & D. Benhabib, Plasma Sources Sci. Technol. 10, 556 (2001)
[11] V. M. Donnelly, J. Vac. Sci. Technol. A 14, 1076 (1996)
[12] C. Lee & M. A. Lieberman, J. Vac. Sci. Technol. A 13, 368 (1995)
[13] S. C. Deshmukh & D. J. Economou, J. Appl. Phys. 72, 4597 (1992)
[14] S. C. Deshmukh & D. J. Economou, J. Vac. Sci. Technol. B 11, 206 (1993)
[15] M. V. Malyshev & V. M. Donnelly, J. Appl. Phys. 88, 6207 (2000)
[16] G. A. Gaddy, S. F. Webb & R. Blumenthal, Appl. Phys. Lett. 71, 3206 (1997)
[17] M. V. Malyshev & V. M. Donnelly, J. Appl. Phys. 90, 1130 (2001)

Modeling particle formation in a dielectric barrier discharge at atmospheric pressure in $SiH_4/N_2O/N_2$

C. Khamphan[1], A. Dollet[3], P.Ségur[1], C. Jimenez[2], M.C. Bordage[1] and F. Massines[2]

[1] *Centre de Physique des plasmas et de leurs Applications de Toulouse(CPAT), UMR CNRS n°5002*
[2] *Laboratoire de Génie électrique de Toulouse(LGET), UMR CNRS n°5003*
Université Paul Sabatier, 118,route de Narbonne ,31062 Toulouse Cedex France
[3] *Institut de Science et de Génie des Matériaux et Procédés, UPR CNRS 8521,Tecnosud, 66100 Perpignan, France*

Abstract
This article is devoted to the understanding of the gas-phase chemistry in a glow dielectric barrier discharge at atmospheric pressure in a $N_2/N_2O/SiH_4$ mixture. The main goal of this work is to identify the particle precursors. A detailed chemical kinetics model based on homogeneous nucleation is used, and it is found that SiO and SiH_2O species play an important role in the initiation of the clustering mechanism.

1. Introduction

Dielectric barrier discharges (DBD) at atmospheric pressure are widely used for surface treatment, depollution or ozone production. These discharges are usually filamentary in nitrogen but, under some specific conditions, a glow discharge can be obtained [1]. This feature is very interesting for surface purposes. The addition of SiH_4 and N_2O in nitrogen DBDs enables specific chemical functions to be grafted on a polymer surface, thus enhancing wettability. Nevertheless, particles form in the gas phase during the process and this is a limitation for such applications. Furthermore, experimental observations made in LGET show that particle formation is greater in a filamentary discharge than in a glow discharge [2]. Since there is a great advantage in avoiding particle formation, it is important to understand why clustering depends on discharge regime. Our aim is to identify the main powder precursors by means of numerical modeling, and to determine the different clustering processes involved in filamentary and glow discharges.
As a first step towards this, we studied the primary chemistry occurring in a glow dielectric barrier discharge in a mixture of $N_2/N_2O/SiH_4$. A brief description of the numerical model and chemical clustering mechanism used is made, and the first results obtained are presented.

2. Description of the model

2.1 Numerical modeling

The discharge was obtained between two plane parallel electrodes coated with a dielectric layer (Al_2O_3). An alternating voltage of about $11kV_{pk-pk}$ was applied. The frequency was 4 kHz.
The numerical model of the discharge is presented in detail elsewhere [3], therefore only a brief description will be given here. Our one-dimensional electrical model is based on the solution of the continuity equations for every species (electrons, ions and excited states) coupled to the Poisson equation. This model is used to describe the transport of electrons, ions and early products of electron impact processes (ionization, dissociations, excitation).
A zero-dimensional model was added to the electrical one in order to study the kinetics of heavy neutral particles. This zero-dimensional model consists in solving the space-integrated convection diffusion equation:

$$\frac{\partial \overline{N}_k(t)}{\partial t} = \overline{S}_k(t) \qquad \text{(Eq.1)}$$

where $\overline{N}_k(t)$ is the space-averaged density of species k and $\overline{S}_k(t)$ is a source or sink term due to chemical reactions.

2.2 Chemical kinetics

The glow discharge was produced in a mixture of nitrogen with a few ppm of silane and nitrous oxide. The chemistry occurring in a nitrogen glow discharge has already been studied in another work [3]. The initial set of reactions listed in nitrogen was completed by accounting for the chemistry of silane and nitrous oxide.

The one-dimensional electrical model includes 16 neutral species, 15 charged species and 5 excited states. The electron impact reactions include electronic excitation, ionization, dissociation and attachment. The corresponding reactions rates were determined using a numerical solution of the equilibrium form of the Boltzmann equation, and appropriate cross sections sets found in the literature. The model also includes electron-ion recombinations, ion-ion neutralization, ion-neutral reactions, reactions between neutral species and reactions with metastable states.

The reaction scheme describing the early stages of silane oxidation is mainly based on the work of Kushner in SiH_4 [4] and in a SiH_4/N_2O mixture [5].

The clustering mechanism considered in this study is based on the work of Suh et al [6] who built a model describing particle formation during low pressure silane oxidation.

In the model of Suh et al, the clustering of SiO and SiO_2 occurs through four main pathways : SiO self-clustering, insertion of SiH_2O and its dimer into SiO clusters, SiO_2 self-clustering and insertion of HSiOOH and its dimer into SiO_2 clusters (see table 1). Suh et al calculated the related reaction rates at 0.8 Torr by using the QRRK theory[7]. However, since we operated at atmospheric pressure, we must carefully make use of the rate constants reported by Suh et al.

In the case of unimolecular decomposition reactions (reactions 1-9, 20-28, see table 1), the rate constant increases with pressure up to the high pressure limit k_∞. Suh et al. reported the high pressure limit rate constants for these reactions together with the related correction factors taking into account pressure dependence. For correction factors close to one, we can assume that the rate constants are equal to the corresponding high pressure limits at atmospheric pressure. This is the case for most of the unimolecular reactions except reaction 1. For this reaction, the rate constant at atmospheric pressure was extrapolated from data published by Zachariah et al. [8].

For bimolecular reactions leading to dissociation of the intermediate complex (reactions 10-19, 29-38 table 1), the pressure dependence is inverted compared to unimolecular reactions (that is, the rate coefficient is pressure independent at low pressure and inversely proportional to the pressure at high pressure[7]). Since we had no reliable information about the value of the rate constants at atmospheric pressure, we used the low pressure limit constant as a first approximation. Further more, a few QRRK calculations made by ourselves showed that these reactions rates should remain more or less in this pressure domain at P=1atm. All reactions selected are presented in table 1, with the corresponding values of the rate constants.

It must be mentionned that another clustering pathway has been reported in [9], which consists in the self-clustering of SiH_2O. No accurate kinetic data were available to calculate the corresponding rate constants. For this reason, this clustering pathway was not considered in this work, neither in [6], but further investigation will be required to conclude that it is negligible or not.

3. Results

3.1 Electrical characteristics

Figure 1 shows the time evolution of the measured electrical characteristics: discharge current, applied and gas voltages. Figure 2 presents the electrical characteristics obtained from the model.

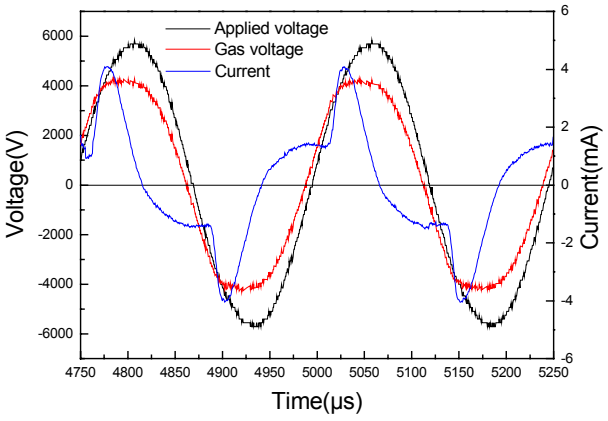

Figure 1 : Measured discharge current, applied voltage and gas voltage

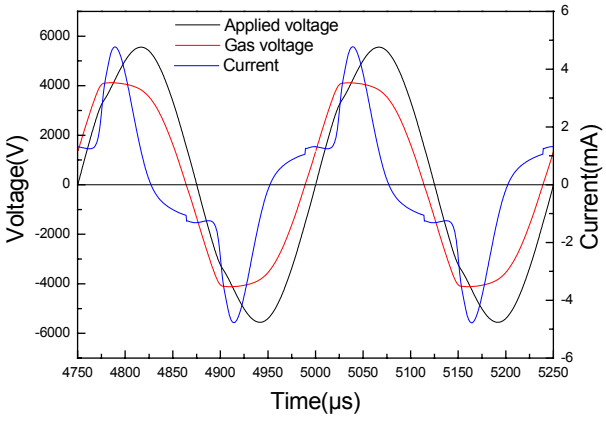

Figure 2 : Calculated discharge current, applied voltage and gas voltage

The good agreement (shape and amplitude) between calculated and measured values indicates that realistic physical mechanisms are included in the model.

3.2 Results of the kinetic model

Figures 3 to 7 present the species concentration calculated by using the kinetic model over sixty periods (which is equivalent to 120 discharges). Figure 3 is related to the clustering of SiO while figure 4 concerns the clustering of SiO_2.

There are two main pathways for SiO polymerization: SiO self-clustering and insertion of SiH_2O and $(SiH_2O)_2$ into SiO clusters. SiO, SiH_2O and $(SiH_2O)_2$ concentrations are rather high: about $10^{11}cm^{-3}$, $10^{13}cm^{-3}$ and $10^{12}cm^{-3}$ respectively (figure 5). This means that powder formation can be efficiently initiated via SiO clustering.

On the other hand, clustering of SiO_2 is found to be quite inefficient (figure 4). $(SiO_2)_n$ clusters are formed by SiO_2 self-clustering and insertion of HSiOOH and $(HSiOOH)_2$ into SiO_2 clusters. We can observe that SiO_2 creation is very slow (figure 4) and that HSiOOH concentration is rather low compared to SiH_2O and $(SiH_2O)_2$ (figure 5). $(HSiOOH)_2$ concentration is even lower and was not represented on the figure. Hence, it seems rather unlikely that particle formation could be significantly initiated from SiO_2 clustering reactions.

Based on the above remarks, SiO and SiH_2O appear as the most probable particle precursors, and the particle created in the gas phase mostly result from $(SiO)_n$ clusters.

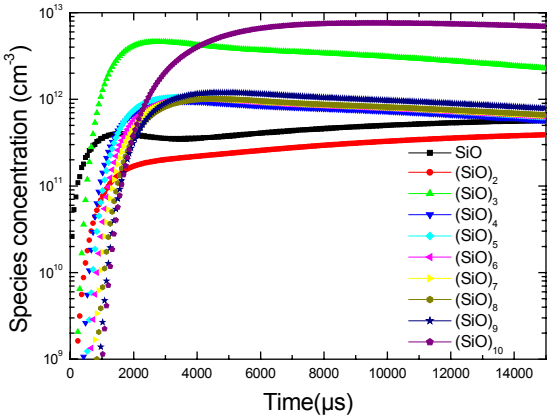

Figure 3 : Time-dependent concentrations of $(SiO)_n$ clusters (over 60 periods)

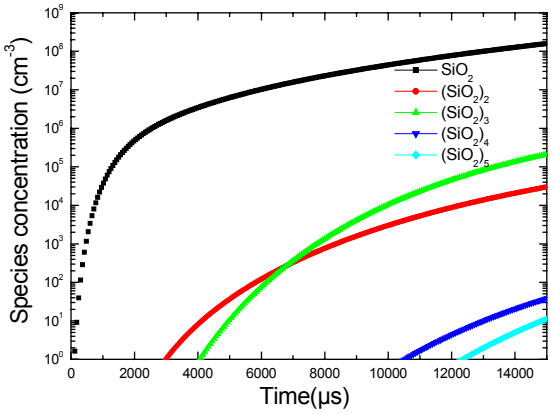

Figure 4 : Time-dependent concentrations of $(SiO_2)_n$ clusters (over 60 periods)

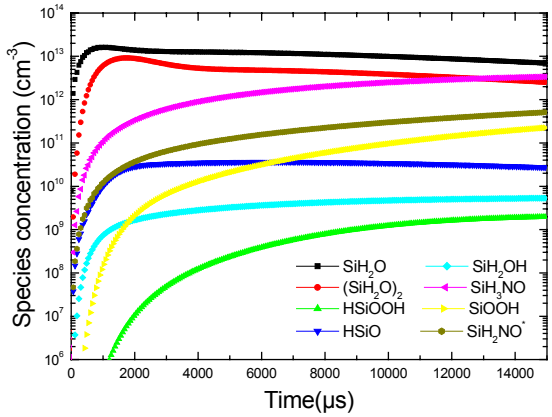

Figure 5 : Time-dependent concentrations of oxidized species of silane (over 60 periods)

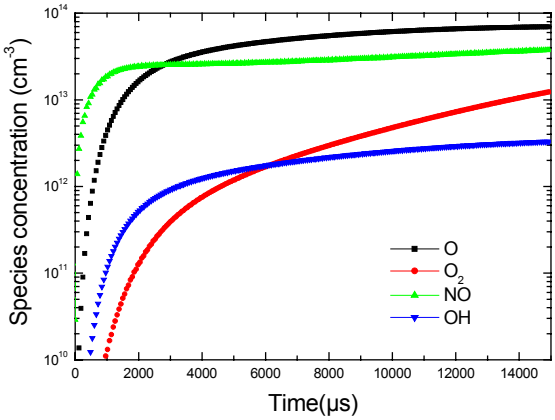

Figure 6 : Time-dependent concentrations of O, O_2, NO and OH (over 60 periods)

In figure 6, the time variations of the oxidizing species concentrations (O, O_2, OH, NO) are presented. The densities of O and NO are quite high. NO is mainly created by collision of N_2O with the nitrogen metastable state $N_2(A^3\Sigma_u^+)$ the density of which is high in the discharge (between $2.10^{12}cm^{-3}$ and $2.10^{13}cm^{-3}$) (Eq.2). Then, NO reacts with atomic nitrogen to produce oxygen (Eq.3).

$$N_2(A^3\Sigma_u^+) + N_2O \rightarrow N + NO + N_2 \quad \text{(Eq.2)}$$

$$N + NO \rightarrow O + N_2 \quad \text{(Eq.3)}$$

As a result, creation of oxidizing species by electronic dissociation of N_2O is very weak.
The high density of NO leads to the creation of SiH_3NO and SiH_2NO^* via the following reactions:

$$SiH_3 + NO + N_2 \rightarrow SiH_3NO + N_2 \quad \text{(Eq.4)}$$

$$SiH_2 + NO \rightarrow SiH_2NO^* \quad \text{(Eq.5)}$$

This result is rather surprising because our experimental results have shown that there is no nitrogen in the deposited layer. Chu et al [10] pointed out that the dissociation of SiH_2NO^* into $SiO+NH_2$ would be highly exothermic, then it would be possible that the molecules dissociate. However, no data are available and this dissociation pathway was not taken into account in our model.
In figure 7, concentrations of SiH_2, SiH_3, SiH_4 and Si_2H_6 are plotted. SiH_2 and SiH_3 radicals are created by collision between SiH_4 and $N_2(A^3\Sigma_u^+)$ (Eq.6-7), and also by electronic dissociation of silane (Eq.8-9). Oscillations on the densities of SiH_2 and SiH_3 confirm this strong connection with the discharge.

$$N_2(A^3\Sigma_u^+) + SiH_4 \rightarrow SiH_2 + H_2 + N_2 \quad \text{(Eq.6)}$$

$$N_2(A^3\Sigma_u^+) + SiH_4 \rightarrow SiH_3 + H + N_2 \quad \text{(Eq.7)}$$

$$e^- + SiH_4 \rightarrow SiH_2 + 2H + e^- \quad \text{(Eq.8)}$$

$$e^- + SiH_4 \rightarrow SiH_3 + H + e^- \quad \text{(Eq.9)}$$

Si_2H_6 is mainly formed by the following reaction:

$$SiH_4 + SiH_2 \rightarrow Si_2H_6 \quad \text{(Eq.10)}$$

The time variation of the nucleation rate is presented in figure 8. The nucleation rate is defined as the rate at which particles containing more than ten silicon atoms are created. We can observe that this rate is maximum after about 48 discharges. This result is in rather good agreement with measurements [2].

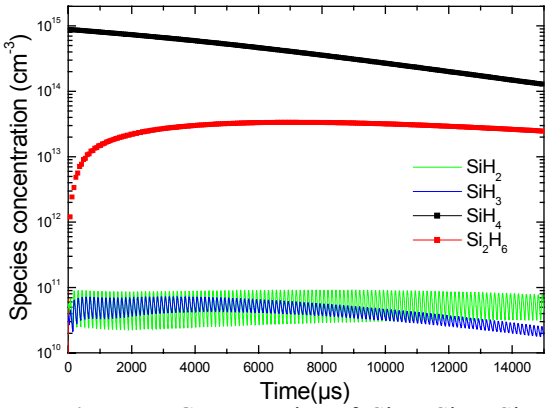

Figure 7 : Concentration of SiH_2, SiH_3, SiH_4 and Si_2H_6 (over 60 periods)

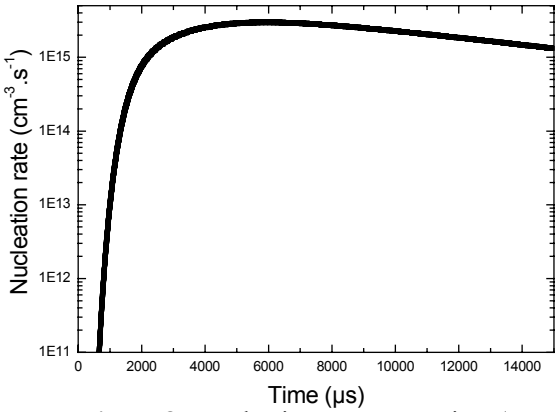

Figure 8 : Nucleation rate versus time (over 60 periods)

3.3 Discussion

The above results show the most probable clustering pathways in the case of the homogeneous nucleation model developed by Suh et al. However, it would be interesting to compare the results obtained with a heterogeneous model (ie., a model based on ion-induced nucleation). Indeed, in figure 9, we note that electron density is high while electric field is low between two discharges. At this time, electron attachment on particles is likely to occur.

Another drawback of our model is that we only considered chemistry in the gas phase, but surface chemistry might significantly influence the concentration of species in the gas phase. Surface reactions will be included in our model in the future.

4. Conclusion

In this paper, the preliminary results of our model of particle formation in a mixture of $N_2/N_2O/SiH_4$ at atmospheric pressure have been presented. The clustering mechanism is based on the work done by Suh et al [6]. Using this clustering mechanism, we found that SiO and SiH_2O were the most probable powder precursors.
In future studies, this model will be coupled with an aerosol model in order to study growth and coagulation of the primary clusters. The next step of our work is to introduce this chemical kinetics mechanism into our model of filamentary discharge. The kinetics involved in a filamentary discharge is likely to be very different. The energy injected is highly localized and many reactive radicals are then created in the filament, which will probably induce rapid cluster growth.

Acknowledgment

The authors are grateful to S.L.Girshick and M.R.Zachariah for providing their thermochemical data.

References

[1] P.Ségur and F. Massines, Proc. 13th Int. Conf. on Gas Discharges and their applications (GD2000), 15
[2] C.Jimenez, C.Khamphan, N.Gherardi, P.Ségur, F.Massines, L.Boufendi, Proceedings of this conference
[3] C.Khamphan, P.Ségur, F.Massines, M.C.Bordage, N.Gherardi, Y.Cesses, Proceedings of this conference
[4] M.J. Kushner, J.Appl.Phys. **63(8)** (1988), 2532
[5] M.J. Kushner, J.Appl.Phys. **74(11)** (1993), 6538
[6] S.M.Suh, M.R.Zachariah and S.L.Girshick, J. Vac. Sci. Technol. A **19(3)** (2003), 940
[7] P.R. Westmoreland, J.B. Howard, J.P. Longwell and A.M. Dean, AIChE Journal, **32** (12) (1986), 1971
[8] M.R.Zachariah and W.Tsang, Aerosol Science and Technology **19** (1993), 499-513
[9] J.O.Chu, D.B.Beach, R.D.Estes and J.M.Jasinski, Chem. Phys. Lett. **143** (1998) 135
[10] C.J.Giunta, J.D.Chapple-Sokol and R.G.Gordon, J.Electrochem.Soc. **137** (1990) 3237

Table 1. Clustering reactions included in the model. Rate constants are in the form $k_{formard} = A.\exp(-E_a / RT)$

	Reaction	A(cm^3 mol s)	Ea(cal/mol)
SiO self-clustering			
1	$(SiO)_2 \leftrightarrow SiO + SiO$	1.38E+14	49580
2	$(SiO)_3 \leftrightarrow (SiO)_2 + SiO$	3.78E+15	53160
3	$(SiO)_4 \leftrightarrow (SiO)_3 + SiO$	1.49E+14	36670
4	$(SiO)_5 \leftrightarrow (SiO)_4 + SiO$	2.73E+14	51020
5	$(SiO)_6 \leftrightarrow (SiO)_5 + SiO$	2.88E+14	46920
6	$(SiO)_7 \leftrightarrow (SiO)_6 + SiO$	2.88E+14	46920
7	$(SiO)_8 \leftrightarrow (SiO)_7 + SiO$	2.88E+14	46900
8	$(SiO)_9 \leftrightarrow (SiO)_8 + SiO$	2.88E+14	46950
9	$(SiO)_{10} \leftrightarrow (SiO)_9 + SiO$	2.88E+14	46920
SiO clustering by $(SiH_2O)_m$ (m=1 or 2)			
10	$SiO + (SiH_2O)_m \leftrightarrow (SiO)_{m+1} + mH_2$	2.00E+13	0.0
11	$(SiO)_2 + (SiH_2O)_m \leftrightarrow (SiO)_{m+2} + mH_2$	2.00E+13	0.0
12	$(SiO)_3 + (SiH_2O)_m \leftrightarrow (SiO)_{m+3} + mH_2$	3.00E+13	0.0
13	$(SiO)_4 + (SiH_2O)_m \leftrightarrow (SiO)_{m+4} + mH_2$	1.00E+14	0.0
14	$(SiO)_5 + (SiH_2O)_m \leftrightarrow (SiO)_{m+5} + mH_2$	1.00E+14	0.0
15	$(SiO)_6 + (SiH_2O)_m \leftrightarrow (SiO)_{m+6} + mH_2$	1.00E+14	0.0
16	$(SiO)_7 + (SiH_2O)_m \leftrightarrow (SiO)_{m+7} + mH_2$	1.00E+14	0.0
17	$(SiO)_8 + (SiH_2O)_m \leftrightarrow (SiO)_{m+8} + mH_2$	1.00E+14	0.0
18	$(SiO)_9 + SiH_2O \leftrightarrow (SiO)_{10} + H_2$	1.00E+14	0.0
19	$SiH_2O + (SiH_2O)_2 \leftrightarrow (SiO)3 + 3H_2$	3.00E+13	0.0
SiO_2 self-clustering			
20	$(SiO_2)_2 \leftrightarrow SiO_2 + SiO_2$	1.91E+16	85670
21	$(SiO_2)_3 \leftrightarrow (SiO_2)_2 + SiO_2$	4.97E+17	95810
22	$(SiO_2)_4 \leftrightarrow (SiO_2)_3 + SiO_2$	1.25E+17	94550
23	$(SiO_2)_5 \leftrightarrow (SiO_2)_4 + SiO_2$	6.10E+17	94780
24	$(SiO_2)_6 \leftrightarrow (SiO_2)_5 + SiO_2$	5.78E+17	94570
25	$(SiO_2)_7 \leftrightarrow (SiO_2)_6 + SiO_2$	3.32E+17	92050
26	$(SiO_2)_8 \leftrightarrow (SiO_2)_7 + SiO_2$	3.83E+17	93530
27	$(SiO_2)_9 \leftrightarrow (SiO_2)_8 + SiO_2$	3.33E+17	93530
28	$(SiO_2)_{10} \leftrightarrow (SiO_2)_9 + SiO_2$	3.74E+17	93530
SiO_2 clustering by $(HSiOOH)_m$ (m=1 or 2)			
29	$SiO_2 + (HSiOOH)_m \leftrightarrow (SiO_2)_{m+1} + mH_2$	2.00E+13	0.0
30	$(SiO_2)_2 + (HSiOOH)_m \leftrightarrow (SiO_2)_{m+2} + mH_2$	2.00E+13	0.0
31	$(SiO_2)_3 + (HSiOOH)_m \leftrightarrow (SiO_2)_{m+3} + mH_2$	3.00E+13	0.0
32	$(SiO_2)_4 + (HSiOOH)_m \leftrightarrow (SiO_2)_{m+4} + mH_2$	1.00E+14	0.0
33	$(SiO_2)_5 + (HSiOOH)_m \leftrightarrow (SiO_2)_{m+5} + mH_2$	1.00E+14	0.0
34	$(SiO_2)_6 + (HSiOOH)_m \leftrightarrow (SiO_2)_{m+6} + mH_2$	1.00E+14	0.0
35	$(SiO_2)_7 + (HSiOOH)_m \leftrightarrow (SiO_2)_{m+7} + mH_2$	1.00E+14	0.0
36	$(SiO_2)_8 + (HSiOOH)_m \leftrightarrow (SiO_2)_{m+8} + mH_2$	1.00E+14	0.0
37	$(SiO_2)_9 + HSiOOH \leftrightarrow (SiO_2)_{10} + H_2$	1.00E+14	0.0
38	$HSiOOH + (HSiOOH)_2 \leftrightarrow (SiO_2)3 + 3H_2$	3.00E+13	0.0
Particle formation(n+m≥11,n=9 or 10,m=1 or 2)			
39	$(SiO)_{10} + SiO \rightarrow particle$	1.60E+13	0.0
40	$(SiO)_n + (SiH_2O)_m \rightarrow particle$	1.60E+13	0.0
41	$(SiO_2)_{10} + SiO_2 \rightarrow particle$	1.60E+13	0.0
42	$(SiO_2)_n + (HSiOOH)_m \rightarrow particle$	1.60E+13	0.0

Comparative Study Of Polypyrrole And Polythiophene Thin Films Obtained By Continuous Wave-PECVD, Pulsed-PECVD And Hot Filament-CVD

L. Martin[1], K. Gleason[2], S. Borrós[1]*

[1]*Materials Science Laboratory, Institut Químic de Sarrià-Universitat Ramón Llull, Barcelona, Catalonia, Spain*

[2] *Massachusetts Institute of Technology, Chemical Engineering Department, Cambridge ,MA, USA*

s.borros@iqs.url.edu

Abstract

The agressivity of CW-PECVD is of such magnitude that not even working with low power, PPy-like and films are obtained. In order to improve the structure, morphology and properties of PPy and PTh, pulsed-PECVD and HFCVD were used. With pulsed-PECVD, almost all aspects are improved. With HF-CVD the catalytic effect of the filament results in the co-deposition of tungsten oxide. With the information given by AFM, XPS and IR techniques, a comparative study of the films is attained.

.

1. Introduction

Conventional polymers consist of chains with a regular repeat unit but polymers obtained by plasma-enhanced chemical vapor deposition (PECVD) tend to form non regular three-dimensional cross-linked networks. The use of continuous wave-PECVD (CW-PECVD) produces a continuous ion bombardment of the growing film that can result in the formation of trapped free radicals in the film. Upon exposure to atmosphere, these free radicals can be oxidized leading to changes in the film structure and properties. In the polimerization of polypyrrole (PPy) and polythiophene (PTh) by CW-PECVD this changes show up mainly in the formation of C=O and –OH[1-4]. To reduce the formation of oxygenated groups, pulsed-PECVD can be used[5]. In this technique, electrical power is repeatedly turned on and off, making it easier to modulate plasma excitation to favor deposition from reactive neutral species rather than from ions. An alternative to PECVD is hot filament-CVD (HFCVD). RecentlyHFCVD[6-8] has been use successfully to develop fluorocarbon films with very close structure to bluk polymer. In this technique, pyrolisis of the monomer is achieved using a resistively heated filament. Then, polimerization reactions take place on the cooled surface of the substrate. The absence of plasma excitation in HFCVD minimizes the potential structural damage of the film from ion bombardment and electron irradiation.

In a previous work done by our research group[9], it was demonstrated that pyrrole is a more labile monomer than thiophene. For this reason, polymers derived from thiophene show closer structure to monomer than those derived from pyrrole. Also, the agressivity of CW-PECVD makes it impossible, even working with low power,to obtain PPy-like films because the main structure of the monomer is broken by the irradiation. These films have a poor doping capacity and therefore the exhibit a low conductivity upon doping[10]. Furthermore, the growth rate of PPy is much slower than that of PTh. This means that a greater amount of time is needed in the case of PPy to obtain pin-hole free films. In order to improve the structure (presence of C=O and OH, N/C or S/C ratios...), morphology (thickness, roughness, grain size and aspect, porosity...) and properties (conductivity upon doping, solubility, adherence to substrate, thermal stability...) of PPy and PTh, pulsed-PECVD and HFCVD were used.

2. Experimental section

Plasma-polymerized films were prepared using pyrrole (Sigma, as supplied) and thiophene (Sigma, as supplied) by radio-frequency plasma polymerization.

2.1 Plasma reactor system

The plasma polymerisation apparatus consists of a stainless steel discharge vessel (diameter 30 cm; width 25 cm). The RF power supply (27MHz) is capacitively coupled to the internal electrode. The vapour container with the monomer is attached to the deposition chamber through a vacuum cock and a needle valve. The reactor chamber was evacuated to a base pressure of 0,15 mbar and then the chamber was filled with monomer vapour until the pressure reached the desired level. 10 minutes later, when the pressure was stabilized, the power source was turned on. The films were deposited onto cleaned and degreased glass slides.

2.2. Hot Filament Reactor

Hot Filament enhanced polymerization was done in a stainless steel vessel (diameter 20 cm, 15 cm width). The hot filament is heated using a DC power supply. The distance between the filament and the sample was varied between 2 and 3 cm during the experiments. Temperature was measured with a pyrometrer. The reactor pressure was evacuated to a base pressure of 0.5 torr and the the chamber was filled with monomer vapour. Pressure was then kept automatically at 0.5 torr.

Films were deposited on oriented silicon wafers. The wafers were continously cooled inside the reactor at 25ºC using a recirculation bath. Nicrom and tungstene filaments were tested.

2.3 Infrared Spectroscopy

For IR studies specimens were scraped from the glass substrate and pelletized after mixing with KBr; these pellets were used to record IR spectra.. For recording IR spectra we used a FTIR Nicolet Magna 560 under identical conditions.

2.4 AFM

The surface morphology of the films has been studied with a Nanoscope III (Digital Instruments, Santa Barbara, CA) equipment with an extended electronic module. All images were collected on tapping mode and treated with Nanoscope software. The images for the morphological studies had a scan size of 5 m x 5 m. For thickness measurements images of a scan size of 10 m x 10 m were done onto scrapped films.

2.5 XPS

The XPS analysis were performed using a Perkin Elmer PHI 5500 spectrometer. The operating conditions were as follows: the X-ray source [Al K (1486.6eV)] was operated at a power of 350W. The spectrometer was operated in the fixed analyser transmission mode at a pass energy of 23.50 eV and a take off angle of 45ºC. The base pressure in the sample chamber was maintained below $5x10^{-9}$ Torr. Total spectral acquisition times per sample were typically 10-15 minutes. Spectral analyses were carried out using Multipak software for quantification and peak-fitting. The energy scale of the spectra is corrected to the C-H (1s) at 285.0 eV.

3. Results

3.1.-Deposition Rate

The deposition rate of the films has been calculated from thickness measurements done using the AFM technique onto scrapped films at different deposition times over a range between 30 seconds and 1 hour (fig 1).

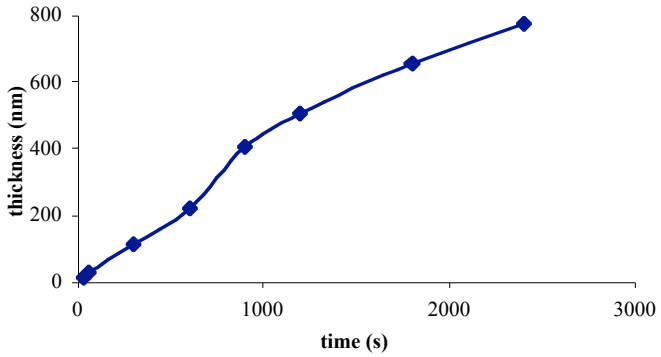

Fig. 1. Calculation of the deposition rate of polythiophene (continuous plasma, 10W, 0.4mbar of monomer pressure)

For all the samples, the power was maintained at 10 W (and 15kHz for the pulsed plasma) and the monomer pressure at 0.4 mbar. The results are summarized in table 1.

Table 1. Deposition rate of different samples

Sample	Monomer	Type of plasma	Deposition Rate (nm·min-1)
PyrC	Pyrrole	Continuous	11.5
PyrP	Pyrrole	Pulsed	2.2
ThioC	Thiophene	Continuous	21.4
ThioP	Thiophene	Pulsed	4.8

The fact that pyrrole is more labile than thiophene explains its lower deposition rate. Instead of activating the pyrrole, the exposition of the monomer to the RF power has a predominant effect of breaking its bonds and forming stable molecules such as CH_4 that leave the system without depositing onto the substrate. For this reason, after 1 hour of deposition, PPy films are absolutely transparent whereas PTh films present a brownish colour.

On the other hand, as it could be expected, the use of pulsed plasma greatly decreases the deposition rate.

3.2.-Morphology

The images obtained with AFM (fig. 2) show that pulsed plasma polymerized films have better morphological characteristics.

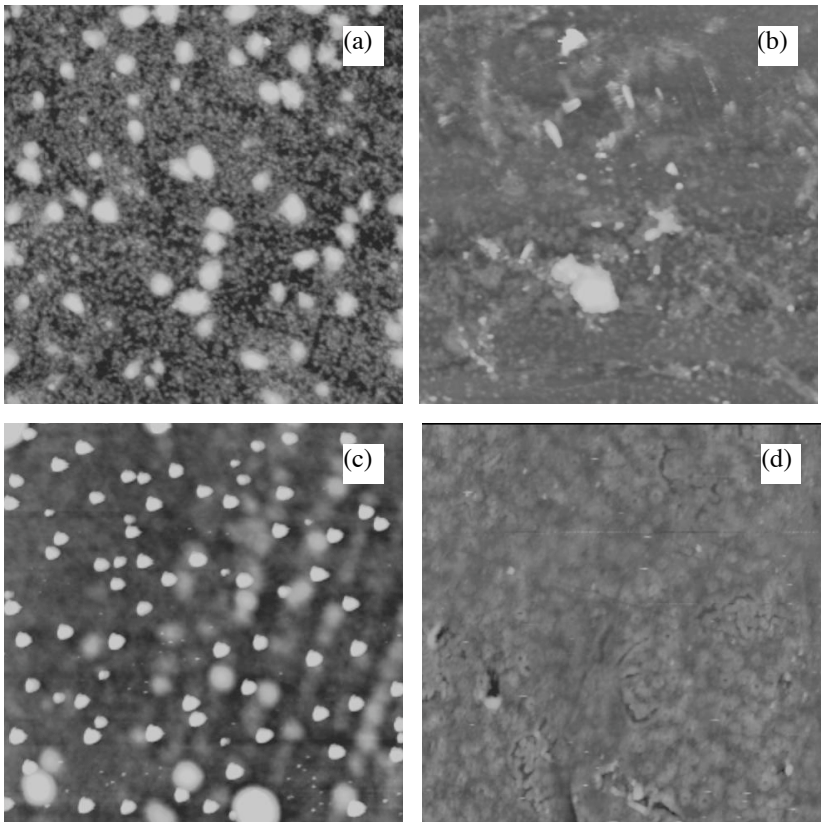

Fig.2. AFM images, 5□m x 5□m, of (a) PyrC, (b) PyrP, (c) ThioC and (d) ThioP

The effect of the use of pulsed plasma can be seen in the first place in the reduction of the roughness. Roughness measurements were performed on several images taken from the same sample in order to assure homogeneity. PPy films reduce their roughness from 4.85 nm to 2.99 nm and PTh show a greater reduction from 5.52 nm to 1.84 nm. However this reduction is not very impresive. The effect that has a greater impact on the visual appearance of the films is the reduction in grain size combined with a narrower distribution of grain size (fig.3), which provides these films with greater uniformity.

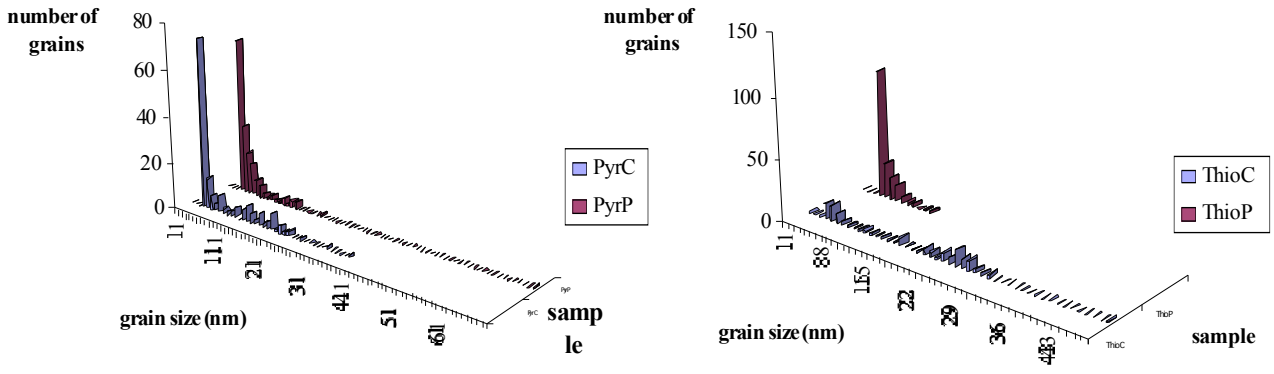

Fig 3. Grain size distribution

In continuous plasma films the size distribution is less uniform because the grain growth versus nuclei formation ratio is greater than in the pulsed plasma films. This affirmation is supported by the fact that the number of grains increases when pulsed plasma is applied. In PyrC the average number of grains is 156 and in PyrP is 160 and this trend is even stronger with thiophene films, with ThioC having 114 grains and ThioP 176. Also, as it can be seen in figures 2 and 3, continuous plasma films present bigger grains.

3.3.-Composition

The use of continuous plasma produces two negative effects on the chemical structure of the films. The first one is that the constant ion bombardment of the growing film that results in some extent in the formation of trapped free radicals in the film. Upon exposure to atmosphere, these free radicals react with oxygen forming C=O and O-H moieties. The second one is that the constant irradiation produced by the glow discharge can lead to a massive bond cleavage thus breaking completely the monomer structure.

Both effects are clearly present in the plasma polymerization of pyrrole which is, as mentioned above, a more labile monomer. The structure of PPy and PTh films was investigated by IR and XPS. The IR spectra of PyrC samples consist of broad peaks due to the inhomogeneities in the structure. It should be noted also the presence of absorption peaks at 2930-2800 cm^{-1} (assigned to O-H stretching), 1750-1650 cm^{-1} (C-O stretching) and 1099 cm^{-1} (C-O-C asymmetrical stretching). This is consistent with XPS results which reveal an oxygen content of 36 %. Furthermore, the C/N ratio (which has been widely used as a fragmentation indicator) is 5.2, due to the loss of nitrogen atoms from the monomer structure.

The PyrP sample shows an IR spectrum with more defined peaks, revealing a more uniform structure. This is a direct consequence of the mild character of pulsed plasma, which is responsible for the ring retention. Another effect is the reduction in the formation in trapped free radicals. As a consequence, there is a reduction of the peaks of the oxidized forms (C=O, O-H and C-O-C). XPS results which reveal an oxygen content of 8 % and a C/N ratio of 4.6.

On the other hand, as thiophene is a less labile monomer, it was expected that its oxygen content would be inferior. This was demonstrated with the XPS spectrum (fig. 4), where a content of 13.4% was revealed.

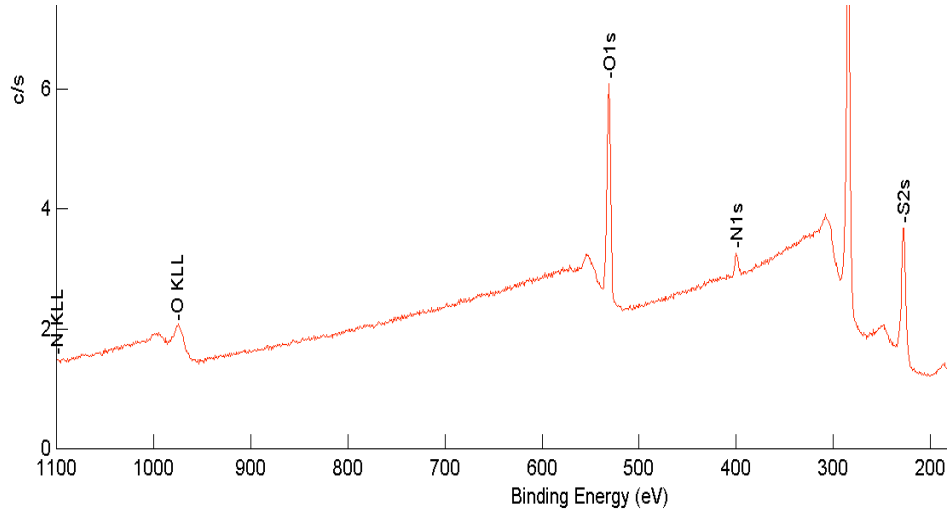

Fig. 4. XPS survey scan of ThioC

Regarding the IR spectra, the same effect as with pyrrole is observed: broad peaks when using continuous plasma versus narrow peaks and reduction of oxidized forms peaks when using pulsed plasma.

3.4.-Hot filament CVD

The use of Nicron filament did not give any film formation.even when filament was heated until 550C. Using tungstene film growing is observed at filament temperatures higher than 500ºC. The deposition rate was clearly higher (200nm/min) than when plasma polymerization was used. The HFCVD also leads to rougher films formation.

However unclear IR spectra resulted from the analysis of the films obtained. Significant signals corresponding to organic moieties could not be detected.

The XPS analysis showed the same trend. Intense signals corresponding to tungstene (W) and oxygen (O) were detected. The intensity of the W signal increased with the filament temperature.

It seems that a tungstene oxide film is deposited together with the polymeric film. The rate of such deposition is directly related with filament temperature.

4. Conclusions

To obtain monomer-like films without aging effects (oxidation of free radicals), the use of pulsed plasma CVD is recommended. However pulsed plasma polymerization has a slower deposition rate. Nevertheless, when very uniform films are desired, this technique is to be used because it enables better morphological characteristics.

5.-References

(1) S. Eufinger, W. J. van Ooij, and T. H. Ridgway, Journal of Appl. Pol. Sci., **61**, 1503 (1996)

(2) Y. Iriyama and M. Hanawa, Polymer Journal, **33**, 419, (2001)

(3) W.Kim, J. Wong, Molecular Crystals and Liquid Crystals. 247, 321 (1994)

(4) Short, Robert D.; Goruppa, A., Special Publication - Royal Society of Chemistry, **263** (Emerging Themes in Polymer Science), 119-133 (2001)

(5) L.M.H.Groenewoud, G.H.M. Engbers, J.G.A.Terlingen, H. Wormeester, J. Feijen. Langmuir. **16**. 6278-6286 (2000).

(6) K.K. Lau, J. A. Caufield, K.K. Gleason, Chem. Mater., **12**, 3032 (2000).

(7) Gleason, Karen K. Chemical vapor deposition of fluorocarbon polymer thin films on various substrates. Massachusetts Institute of Technology, USA. 97-US7511(9742356), 56. WO. 5-5-1997.

(8) H. PG. Pryce Lewis, J.A. Caufield, K.K. Gleason, Langmuir, **17**, 7652, (2001).

(9) Borros, S.; Diago, M. P.; Esteve, J.; Agullo, N. *Materials Research Society Symposium Proceedings.* **2002**, *725*, 225-230.

(10) R.K.Sadhir, K.F. Schoch. Thin Solid Films. **223**. 154-160 (1993).

INFLUENCE OF PLASMA POLYMERIZED CARBON BLACK IN THE IN-RUBBER PROPERTIES OF FILLED COMPOUNDS

N. Tricás[1], E. Vidal-Escales[1], S. Borrós[1*], M.Gerspacher[2]

[1]Material Science Lab. – Institut Químic de Sarrià (Universitat Ramon Llull)
Via Augusta 390, 08017 Barcelona (Spain).
[2] Sid Richardson Carbon Black Co. Fort Worth Research Center
4825 N.Freeway Fort Worth,Texas 76106.

Abstract

Composites make possible to obtain performance-improved materials, one example are filled polymers. The main factor involved in the final properties is the interaction between phases. Thus, surface modification of one of the components encourages us to obtain high performance composites. In this work cold plasma was used to change the surface characteristics of carbon black (CB). Many analytical techniques were used to evaluate the modified surface and filler treated samples were mixed and tested in terms of mechanical and viscoelastic properties.

Introduction

A CB filled elastomer can be regarded as a composite characterized by a "rubbery" continuous phase and a particulate "rigid" dispersed phase. The continuous phase is therefore responsible for the "rubbery" behavior of the composite, but the filler plays a specific and important role. The changes provoked by the presence of the filler in polymeric composites have been studied since a long time ago [1-3].

Polymer-filler interaction is known to be important to obtain good performance rubber materials and the approach of considering polymer composites as two interpenetrated networks is becoming popular. The polymer-filler interaction starts when the formulation components (polymer, curing agents and fillers) are introduced in the mixer to obtain a homogenous material that will be cured later. To obtain a good filler dispersion the polymer and the filler need to have some affinity for each other. Several techniques have been used to elucidate the CB conductive network structure; this is an important aspect as the majority of rubber compound properties are related to the CB dispersion degree [4-6]. In addition poor dispersion can itself give rise to certain detrimental effects. These effects can be summarized as follows: reduced product life, poor performance in service, poor product appearance, poor processing characteristics, raw-material waste and high finished product rejection rates. These inadequacies are generally result of the presence of rather large, undirspersed agglomerates that can act as failure-initiating flaws [7].

However it is worth to point out that filler particles tend to agglomerate forming clusters due to the filler-filler interaction, which can be also described as a poor micro-dispersion of the filler in the polymeric matrix. Some filler particles are not even separated during the compounding process while others come together especially during vulcanization or when exposed to high temperatures, this process is known as flocculation. A large difference between the polymer and the filler surface energy as well as a short filler-filler distance could result into high agglomeration. This agglomeration is strain and temperature dependent, as a consequence it has and important role in the mechanical and viscoelastic properties [8].

During the last 50 years many studies of CB as reinforcement filler have been published, many of them were focused on the morphology of the blacks (particle size and structure), [9,10]. However it has been admitted that the unique property that distinguishes CB from other fillers is its characteristic surface activity. Although surface activity is a poor defined term, it includes all the physico-chemical properties of the material, which can alter the behavior, the kinetics and the processes in which this material is involved. In a physical sense, variations in the surface activity determine the adsorptive capacity and energy of adsorption,

[1] Corresponding Author: Tel. +34 93 267 20 00; Fax. +34 93 205 62 66; E-mail: s.borros@iqs.edu

and therefore it represents the type and quantity of interactions that surface molecules can establish with their surroundings. The importance and some techniques to measure this property have already been described in a previous paper [11].

Two main factors seem to be involved in the surface activity level. One is CB's surface morphology, which is acquired during the filler formation process in the reactor. The presence of different amounts of crystalline and amorphous carbon domains on CB's surface, affect its energy distribution and consequently its surface activity [12] The effect of this parameter in the rubber-filler interaction has been studied in a previous work [13]. The other factor is the CB's surface chemical composition that can be responsible for changes on the surface polarity. Many authors consider that the presence of functional groups on CB is almost negligible [14]. Techniques such as plasma polymerization can be used to tailor this property introducing different functional groups that could improve both the reaction and interaction with the polymer matrix.

As a result of the above discussion the aims of this work are focused on CB surface chemistry modification in order to change the filler-filler as well as the polymer-filler interaction. The resulting filler has been characterized in terms of chemical composition and surface energy by means of different analytical techniques such as Raman Spectroscopy, Inverse Gas Chromatography, Thermal Programmed Desorption and Thermogravimetric studies. Finally, the changes that modification of CB surface energy provokes on the final properties of vulcanized filled compounds have been evaluated.

Experimental

Materials

The used CB was an experimental grade supplied by Sid Richardson Carbon Black Co, with a specific area of 121 m^2g^{-1} and a CDBP of 102 $cm^2/100g$.

Plasma treatment

In order to coat CB particles with a polymeric layer it was treated in a bell-jar cold plasma reactor at a frequency of 27 MHz and a power supply of 50 W. Pressure was maintained at 1mbar before the monomer gas was introduced in the reactor. The monomer used was acrylic acid, giving the plasma a light purple color. When the gas was introduced in the reactor the pressure increased up to 2mbar. Samples were treated for 4 hours.

Thermal Programmed Decomposition (TPD)

Modified and regular CB was submitted to a controlled increase of temperature inside an oven. A flow of helium carried the components inside a mass spectrum were the components that are desorbed from the sample or thermally destroyed can be detected. In order to place the sample inside the oven, a quartz vial with 30mg of CB is introduced in a quartz tube connected with the helium source and the mass spectrometer. To analyze CB samples temperature was increased from 30ºC to 600ºC at 10ºC/min. Helium flow was set at 60 cm^3/min.

Raman Spectroscopy

Raman spectra in order to study the CB surface morphology were performed at the Texas Christian University, Fort Worth. In order to perform the analysis, CB is compressed in a steel-stainless mold to achieve a uniform and smooth surface. Afterwards the spectrum is obtained. During the analysis a motor rotates the sample (14.000 r.p.m.), in order to avoid thermal decomposition due to the laser incidence.

Thermogravimetrical Assays

The Thermogravimetric Assay equipment was a Mettler Toledo TG50. Conditions are described in a previous paper [15].

Inverse Gas Chromatography

Measures were performed at infinite dilution with different polar and apolar probes to obtain the dispersive and specific component. N_2 was used as a carrier gas. Column temperature was 160ºC. Column length was 25 cm. CB was sieved between 250 and 300 μm. previous to column filling.

Low frequency viscoelastic properties

In order to study the CB behavior in rubber compounds at low strain results were obtained testing samples at 1Hz and 30ºC with strain measurements from 0.1 to 10% strain.

Bound Rubber

Approximately one gram of compound is weighted in a steel-stainless cage (25x25x50mm). The cage is introduced in a 200 ml beaker and covered with toluene for three days. The solvent is stirred for half an hour twice a day. After this period the cage is dried to constant weight.

Results and Discussion

The nature of the modified surface after the plasma treatment was evaluated. However, it is worth to point out, that first visual analysis gave evidence that changes on the surface had taken place inside the reactor. Already after 30 minutes of treatment both the inside of the reactor and the sample container were found to be sticky, which is one of the most common properties of polymers obtained by cold plasma polymerization.

On the other hand, CB surface polarity also presented clear differences. When untreated CB was introduced in a beaker containing water, the filler stayed on the liquid surface due to their differences in polarity and finally sank slowly. This was not the case of treated samples that sank almost immediately after they were introduced in the water. This effect could probably be due to an increase of the filler polarity by acrylic acid polymerization on its surface reinforcing the idea of successful surface modification. Moreover acrylic acid has a high water adsorption capacity that would facilitate the sinking process.

CB Surface Analysis

TPD

The abundance of different ions was screened during the increasing temperature ramp. These ions were mainly produced due to acrylic acid thermal desorption (mz= 27, 55, 72) and polyacrylate major decomposition ion (mz= 44) due to the decarboxylation of the polymer. Results for a modified sample were compared with an untreated sample and the analysis of the wool that holds the vial inside the quartz tube. For the ions resulting from the acrylic acid desorption a slight increase was observed near acrylic acid evaporation temperature (141ºC). Fig. 1 shows the case for mz = 27. On the other hand, when mz=44 abundance is analyzed a considerably increase of this ion is observed. The abundance of this fragment starts to rise from 150 ºC achieving a constant level, however it is above 500 ºC when the level of this ion increases steeply, fig. 2.

Therefore it can be said that the polymerization reaction took successfully place in the reactor since much higher levels are observed for the decarboxilation process than for thermal desorption even though some acrylic acid monomers may also be present (scales differ in one order of magnitude).

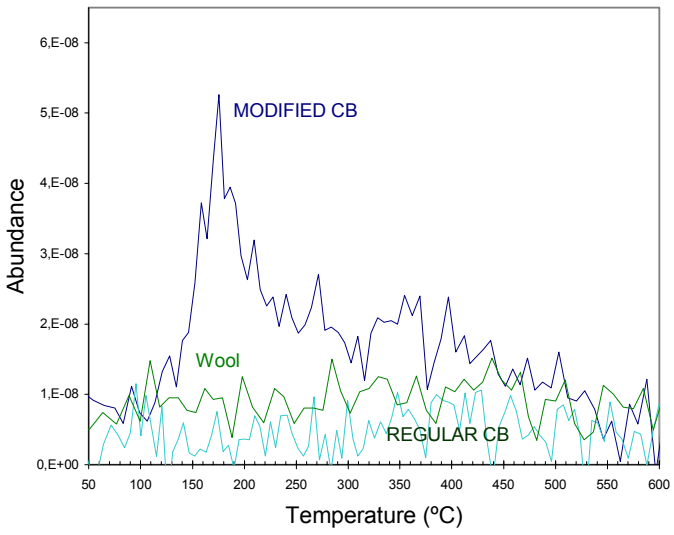

Fig.1 Acid acrylic desorption during TPD analysis

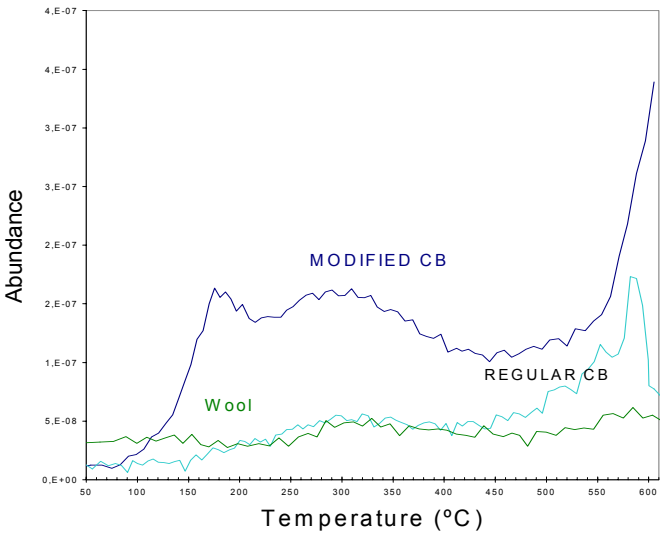

Fig.2 *Polyacrylate* decomposition during TPD analysis

Raman Spectroscopy

The Raman Spectrum of the regular and modified were obtained in order to evaluate any possible change in their surface structure since this technique allows to determine the amount of crystalline structure on CB. The values obtained from the spectrum were the same for both samples. None of the chemical changes were reveled by Raman spectroscopy suggesting that the bulk structure of the acrylic acid treated CB remained substantially unchanged and comparable to that of untreated CB, in contrast with the surface functionalization as already shown by TPD. Therefore, the temperature in the reactor was low enough to maintain the filler surface structure unaltered and only the chemical composition was changed during the treatment.

Thermogravimetrical Assays

Using samples that had been modified during different lengths of time (2 and 4 hours) a linear correlation between the weight loss and the plasma treatment duration was established, obtaining as expected higher weight loss for longer treated samples.

This technique can also be used to study surface activity by means of T15% (temperature when CB has lost a 15% of its weight) as shown in other literature works [11,13]. In this case the modified CB shows a higher T15% (590ºC) than the regular CB (568ºC), showing that surface activity had been modified. However, for T50% (temperature when CB has lost a 50% of its weight) the values were very close only differing 2ºC. This is an indication that the plasma treatment had only affected the surface (T15%) while the bulk part of CB remained unmodified (T50%).

Inverse Gas Chromatography

Inverse gas Chromatography is also used to study surface activity but it also allows dividing this parameter in two components, the dispersive and the specific one. The first is due to Van der Waals forces caused by carbon atoms interaction and the second is related with the interaction of specific chemical groups such as acids in our case. For the modified CB there was a dramatic change in the dispersive component. While the regular experimental grades showed values close to other CB grades with similar specific surface area (N-110 and N-220), the modified CB presented a lowe value that would correspond to CB's of much lower specific surface areas (around $20 m^2 g^{-1}$). Values are shown in table 1. This result was attributed to the presence of the acidic groups on the surface of CB.

Table 1. Dispersive component for several CB grades

CB grade	Dispersive component (mJ/m2)
N-110	580
N-220	575
Regular CB	608
Modified CB	250

Table 2. Specific component for several CB grades

CB grade	Dispersive component (mJ/m2)
N-110	156
N-220	----
Regular CB	143
Modified CB	82

However the same result was obtained for the specific component when a higher value was expected for basic probes, such as tetrahydrofurane, due to the presence of the acid groups. It is also worth to mention that CB modified for 2 and 4 hours presented practically identical results probably due to the complete coverage of CB particles. Several hypotheses to understand this phenomenon have been presented. Due to the high level of coverage with the plasma polymer the particles could trend to agglomerate together and preferably interact among themselves than with the injected probes. This process could be facilitated by the high pressures present inside the column at a 40cm3ml-1 flow. Moreover this high degree of coverage would give a completely new surface rather difficult to compare by IGC with the original CB surface.

In concluding the results so far show that CB surface has been strongly changed in terms of chemical composition shown by, TPD, TGA and IGC while its inner structure remains as the original filler. These facts present the cold plasma technique as a good treatment to obtain chemical changes on CB.

In-Rubber Properties

Both regular and modified CB were mixed at 50 phr with natural rubber. Low frequency dynamic properties, which give an idea of the filler-filler interaction and Bound Rubber, which is more related with polymer-filler rubber were determined.

Low frequency dynamic properties

This test shows the behavior of the filler network by means of G' and G'' modulus. The higher interaction between the filler particles the higher value for both parameters since it would be more difficult to break the CB network inside the polymer. High elastic modulus (G') is beneficial for the material performance contrary to high loss modulus (G'') that provokes high hysteresis due to the dissipated heat. In this case modified CB show a higher value for both modulus showing a higher interaction between CB particles (fig. 3 and 4).

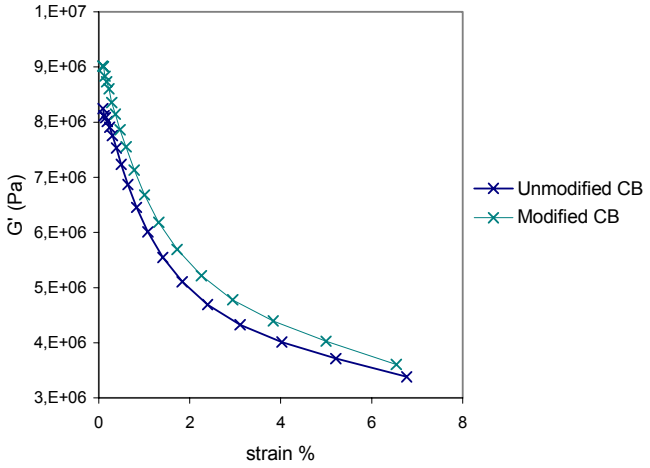

Fig.3 Elastic Modulus (G')

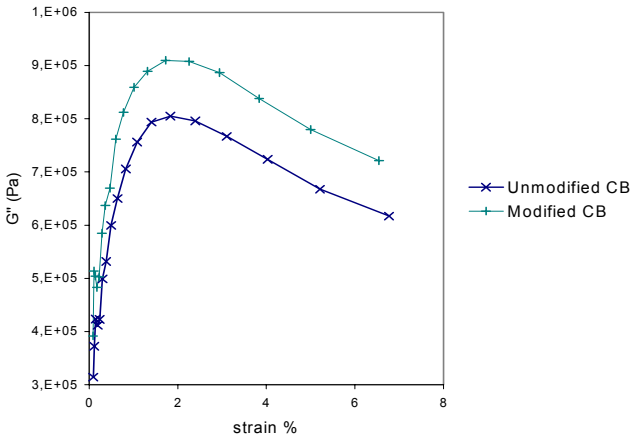

Fig.4 Loss Modulus (G'')

This would be in agreement with the hypothesis made from the IGC results showing a high degree of CB coating by a polymer film. As a result CB surface would be prevented to interact with the polymer chains leading to a higher filler-filler and probably to a lower filler-polymer interaction.

Bound Rubber

Plasma modified CB presented lower bound rubber level (46%) than the original filler (55%). This indicates that the chemical surface modification treatment had also affected the polymer filler interaction in agreement with the G' and G'' values. However, is difficult to compare this value with other CB since as it has been shown before the filler surface has been completely covered by the polymer and consequently the new surface does not resemble CB nature anymore.

Conclusions

Cold plasma has been presented as a suitable technique in order to modify the chemistry of CB surface without affecting CB bulk properties. Among other analytical techniques, TPD, TGA and Raman Spectroscopy have been presented as very useful techniques to characterize the plasma modified filler surface. From the surface activity point of view a diminishing of both the dispersive and specific component has been detected by means of IGC. On the other hand, G' and G'' obtained values show an increase of the filler-filler interaction causing a higher agglomeration of the filler inside the polymer. The obtained results show that CB has been completely covered by a polymer film forbidding CB surface to play any role in the polymer matrix. Nevertheless these results show that it is possible to selectively change CB surface chemistry. This should encourage to work with different monomers as well as with different plasma conditions in order to achieve tailored CB's to obtain high performance materials based on specific polymer-filler interaction.

References

[1] A.R. Payne, Rubber Chem. Technol. 39, 365 (1966)
[2] A.I. Medalia, Rubber Chem. Technol., 52, 437 (1978)
[3] Gerspacher, M.; O'Farrell, C.P.; Yang, H. H. Elastomerics (1990), 122(11), 23-30
[4] Leclere Ph., Lazzaroni R., Gubbels F., Calberg C., Dubois Ph., Jerome R., Bredas J.L., Mater. Res. Soc. Symp. Proc., 475-480 (1997)
[5] Coran A.Y. and Donnet J.B., Rubber Chem. Technol., 65(5), 973-97 (1992)
[6] O'Farrell C.P., Gerspacher M. and Nikiel L., Kautsch. Gummi Kunstst., 53, 701 (2000)
[7] W.H. Hess, Rubber Chem. Technol. 64, 386 (1991)
[8] S. Wolff and M.-J. Wang, Rubber Chem. Technol. 65, 329 (1992)
[9] J.A. Alaya, W. M. Hess, A.O. Dotoson and D.A Joyce, Rubber Chem. Technol., 46, 897 (1990)
[10] A.C. Pater and K.W. Lee, Elastomerics 122, 14 (1990).
[11] N. Tricás, E. Vidal-Escales and S. Borrós, Affinidad 500, 337 (2002)
[12] A. Schröder, M. Klüppel, J.Heidberg and R.H Schuster, Carbon, 40(2), 207 (2002)
[13] N. Tricás, E. Vidal-Escales, S. Borrós, M.Gerspacher, Composites Science and Nanotechnology 65, 1155 (2003)
[14] M. Gerspacher, C.P. O'Farrell, Tire Technology International, 43 (1999)
[15]E. Vidal-Escales and S.Borrós, "Influence of carbon black surface activity on vulcanization reaction", Presented in the Savannah Spring RubberMeeting of the ACS (2002)

Thermal electron attachment to MoF_6, ReF_6, and WF_6

Jeffrey F. Friedman[1], Thomas M. Miller[2], Amy E. Stevens Miller[3], and A. A. Viggiano[2]

[1] *Department of Physics, University of Puerto Rico, Mayaguez, Puerto Rico, USA*
[2] *Air Force Research Laboratory, Space Vehicles Directorate, Hanscom AFB, Massachusetts, USA*
[3] *ChemMotif, Inc., Suite 211, 60 Thoreau Street, Concord, Massachusetts, USA*

Abstract
An experimental study has been made of thermal electron attachment to MoF_6, ReF_6, and WF_6 using a flowing-afterglow Langmuir-probe apparatus. The experiment is a thorny one because the molecules tend to form oxide impurities on feedline surfaces and because of thermal decomposition of MoF_6 on surfaces as the gas temperature is increased. The electron attachment rate constant for MoF_6 is $(2.3 \pm 0.5) \times 10^{-9}$ cm^3 s^{-1} and forms MoF_6^- exclusively for 297-385 K. The rate constant increases with temperature up to the point where decomposition becomes apparent. Electron attachment to ReF_6 occurs with a rate constant of $(2.4 \pm 0.5) \times 10^{-9}$ cm^3 s^{-1} at 297 K. WF_6 attaches electrons so weakly that it is difficult to measure the attachment rate constant at room temperature (ca. 10^{-12} cm^3 s^{-1}). Molecular structure calculations have been carried out for MoF_6 to aid in understanding the electron attachment process.

1. Introduction

It is often assumed that hexafluorides attach electrons efficiently because SF_6 is well known to do so, and indeed is widely used as an electron scavenger in plasmas and in electrical devices. But the transition-metal fluorides appear to be different. For one thing, their electron affinities have been calculated to be quite large—over 5 eV for MoF_6, compared to EA(SF_6) = 1.05 eV.

Electron beam studies of negative ion formation in MoF_6 and ReF_6 were carried out by Stockdale et al. many years ago, with an electron energy resolution of about 0.1 eV [1]. Electron attachment to MoF_6 near zero energy was found to produce mostly MoF_6^-, with some MoF_5^-. Electron attachment to ReF_6 near zero energy was found to produce mostly ReF_6^-, with very small amounts of ReF_5^- and ReF_3^-.

Stockdale et al. [1] also studied negative ion formation in the main-group hexafluorides SeF_6 and TeF_6, which are interesting because Se and Te lie directly below S in the periodic table. They found very weak signals from electron attachment to SeF_6, yielding the SeF_5^- ion exclusively, and no electron attachment at all to TeF_6, under essentially zero-pressure (single collision) conditions. The negative ions SeF_6^- and TeF_6^- exist, and can be produced by charge transfer from SF_6^-, but are not formed in single collisions with free electrons [1]. Jarvis et al. [2] have studied electron attachment to SeF_6 and TeF_6 under an atmospheric pressure of N_2 at 300 K and found that these pressures were adequate to stabilize the parent ions of SeF_6 and TeF_6, though some dissociative electron attachment takes place, producing SeF_5^- and TeF_5^-. Rate constants of $(8.0 \pm 1.2) \times 10^{-10}$ and $(8.2 \pm 1.1) \times 10^{-11}$ cm^3 s^{-1} were measured (in 1 atm N_2) for SeF_6 and TeF_6, respectively, values which are orders of magnitude below the attachment rate for SF_6 (2.3×10^{-7} cm^3 s^{-1}). Earlier work with SeF_6 and TeF_6 was discussed in [1] and [2].

We have used a flowing afterglow Langmuir probe (FALP) apparatus to study electron attachment to MoF_6, ReF_6, and WF_6, *viz*.,

$$MoF_6 + e^- \rightarrow MoF_6^- + 5.4 \text{ eV} \quad (1)$$

$$ReF_6 + e^- \rightarrow ReF_6^- + \sim 4.2 \text{ eV} \quad (2)$$

$$WF_6 + e^- \rightarrow WF_6^- + 3.5 \text{ eV} \quad (3)$$

in a helium buffer gas at 133 Pa. The respective energies released in the above reactions (the electron affinities of the molecules) were taken from Refs. 3-6. Some limited information is presented here as to the temperature dependence of the rate constants. In addition, the ion-molecule reaction

$$Ar^+ + MoF_6 \rightarrow MoF_5^- + F + Ar + 1.1\ eV \qquad (4)$$

was studied, for reasons that will be explained below. The energy released in this reaction was calculated from the heats of formation of the reactants.

2. Flowing-Afterglow Langmuir-Probe Experiment

The FALP apparatus is sketched in Fig. 1. Reactions take place in a weak plasma in a fast flow of helium carrier gas along the length of a flow tube (from left to right in the figure). Knowing the velocity of the flowing plasma allows us to convert the distance scale into a time scale and deduce reaction rate constants. In the FALP, a cylindrical, movable Langmuir probe is used to measure the electron density along the axis of the flow tube. In absence of an electron-attaching gas the only loss of electron density is through ambipolar diffusion to the walls of the flow tube. When an electron-attaching gas is added to the flow tube, the electron density decays much more rapidly, to the point where eventually a pure positive-ion/negative-ion plasma obtains. The FALP method [7] and this particular instrument at the U. S. Air Force Research Laboratory [8] have been described previously.

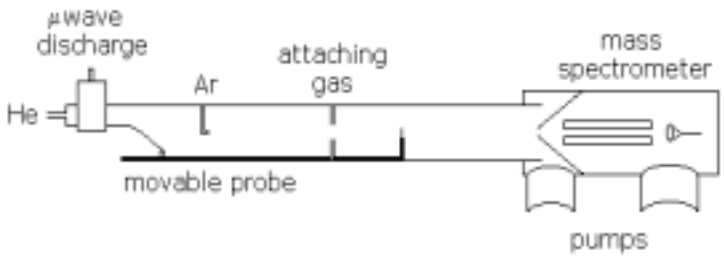

Fig. 1. A sketch of the FALP apparatus.

Helium gas flows in the FALP at typically 16 std. L min^{-1}, giving a bulk gas velocity of 63 m s^{-1} in a flow tube of 3.6-cm radius, at 133 Pa pressure and room temperature. The electron/He^+ source in the FALP is a 3.45-GHz microwave discharge at the upstream end of the flow tube. The discharge additionally creates metastable-excited He^*, which are undesirable because suprathermal electrons would be released in the reaction zone when reactant neutrals are Penning ionized by the He^*. Because of this, a small flow of 60 std. cm^3 min^{-1} of Ar gas is injected into the flow tube 10 cm downstream of the discharge for the purpose of deexciting the He^* via Penning ionization with Ar, well ahead of the reaction zone. Electrons created in the discharge and in Penning ionization thermalize readily in the He carrier gas prior to the reaction zone. The Ar also removes He_2^+ by ion-molecule reaction yielding Ar^+. Thus, following Ar reaction the plasma consists of electrons, He^+, and Ar^+, undergoing ambipolar diffusion.

Halfway down the flow tube, the electron attaching gas under study is added through a 3-radial-needle port with a known flow rate resulting in a known concentration n_r in the flow tube. At this point, the electron density $n_e(0)$ has been adjusted to be in the range 0.8-3 x 10^9 cm^{-3} : small enough that $n_e(0) << n_r$, so that first-order kinetics holds, and small enough that electron-ion recombination is negligible. (Thermal electron-ion recombination rate constants are only significant for molecular ions, such as those produced in ion-molecule reactions with the gas under study. However, since the recombination rate depends on the

square of the plasma density, that rate is entirely negligible at the low plasma densities used in the electron attachment experiments, provided the electron attachment rate constant is larger than ca. 10^{-10} cm^3 s^{-1}.)

The decay in the electron density following addition of the gas under study is due to the coupled effects of ambipolar diffusion and electron attachment. The solution to the relevant rate equation is [7,8]

$$n_e(t) = n_e(0)\,(\nu_a - \nu_D)^{-1}\,[\nu_a \exp(-\nu_a t) - \nu_D \exp(-\nu_D t)], \qquad (5)$$

where ν_a is the electron attachment frequency, ν_D is the diffusion loss frequency, and t is the reaction time. The electron attachment rate constant is k_a and is equal to $\nu_a\, n_r^{-1}$. The diffusion loss frequency ν_D is equal to the ambipolar diffusion coefficient divided by the square of the diffusion length characteristic of the apparatus, and is measured directly from the electron density decay along the flow tube axis in absence of the electron-attaching gas. The reaction time t is the distance between the gas inlet port and the movable Langmuir probe, divided by the plasma velocity. The plasma velocity (typically 100 m/s) is measured by pulse-modulating the microwave discharge and timing the arrival of the disturbance on the Langmuir probe, at different distances in the reaction zone. The plasma velocity as measured on the flow tube axis is greater than the bulk gas velocity by a factor of about 1.6 because of the way the parabolic velocity profile of the gas in laminar flow overlaps the fundamental diffusion mode of the plasma.

The Langmuir probe in these experiments is 25 μm in diameter, 4 mm long, and is made of tungsten. The diameter is much smaller than the plasma sheath diameter as required by orbital-limited cylindrical probe theory. Furthermore, the He pressure is kept low enough (usually 133 Pa) that the collisionless-sheath condition is satisfied. The probe potential is swept from about -2 to 2 V around the local plasma potential, and the current collected is typically a few μA. The electron-attracting portion of the probe I-V characteristic is parabolic in shape, as indicated by probe theory. A plot of the square of the probe current yields a straight line; the slope of this line is readily determined and yields the electron density at the position of the probe along the axis of the flow tube. Hysteresis in the probe characteristic is eliminated by cleaning the probe in the plasma to white-hot appearance through application of a high bias voltage (100-200 V).

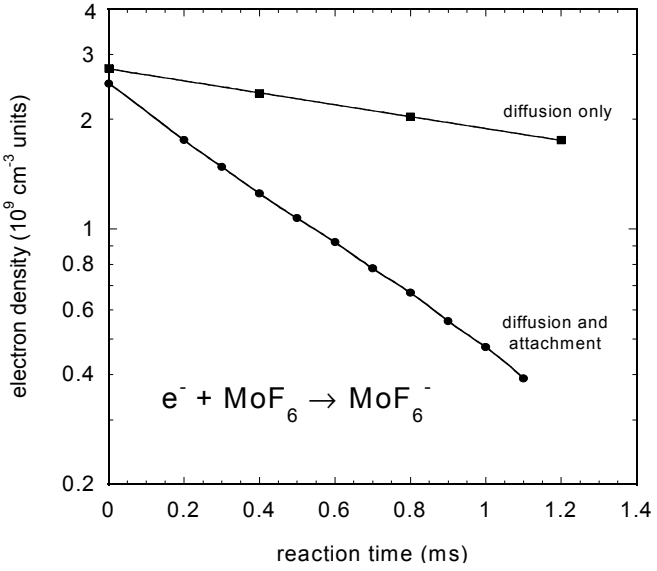

Fig. 2. Data obtained at 297 K for electron attachment to MoF_6 in 133 Pa of He gas and 13 ppmv of MoF_6.

We note that only relative electron densities are needed in electron attachment measurements, and the major uncertainty is the probe surface area. This uncertainty is mainly due to the question of where current collection terminates at the boundary between probe and a coaxial glass support. The relative electron density measurements are estimated uncertain to ±10%. The absolute electron attachment results are estimated uncertain to ±25%. The major uncertainty in the latter figure is measurement of the flow rates of the He, Ar, and electron-attaching gas. An example of the data obtained is shown in Fig. 2.

As electron attachment proceeds, the negative charge in the plasma becomes increasingly composed of negative ions. However, ambipolar diffusion is still determined by electron diffusion to the walls of the flow tube because of the high mobility of electrons. Negative ions are confined by the space charge field to the axial region of the flow tube as long as the electron density is at least 1/100th that of the negative ions. Eventually, the space charge field collapses and the plasma becomes a negative-ion/positive-ion plasma.

The data shown in Fig. 2 were obtained for a case where the negative ions are stable enough that thermal electron detachment will not take place at the temperatures of the measurement. If the electron detachment energy of the negative ion is low enough, thermal electron detachment will take place, and that process would have to be taken into account in the rate equations used to analyze the decay in the electron density [9].

At the downstream end of the flow tube there is an orifice leading to a high-vacuum region where an rf quadrupole mass spectrometer is used to determine the ion products and branching fractions for the electron attachment reactions studied.

3. Experimental Results

A. MoF_6

Electron attachment experiments with MoF_6 (reaction 2) were problematic because of decomposition on the walls of the feedlines carrying the neat vapor into the FALP flow tube. Decomposition apparently occurred in reaction with water vapor adsorbed on feedline surfaces, as evidenced by the appearance of oxides $MoOF_4^-$ in the attachment mass spectrum at very low flow rates. Higher flow rates of reactant results in only MoF_6^- in the mass spectrum. Positive-ion mass spectra were also obtained and did not show oxides; the spectra consisted almost entirely of MoF_5^+, even at low flows of reactant, from reaction of MoF_6 with the plasma ions Ar^+ (and some He^+).

There is some indication that the oxide attaches electrons more readily than does MoF_6. At very low flow rates of reactant, with $MoOF_4^-$ dominating the mass spectrum, the apparent rate constant was larger by a factor of ~2. With larger flow rates of reactant, and only MoF_6^- in the mass spectrum, a rate constant of $(2.3 \pm 0.5) \times 10^{-9}$ cm^3 s^{-1} was measured at 297 K in 133 Pa of He gas. This rate constant corresponds to an attachment efficiency on the order of 1%. At 340 K and 385 K, rate constants of $(2.9 \pm 0.6) \times 10^{-9}$ and $(3.5 \pm 0.8) \times 10^{-9}$ cm^3 s^{-1} were measured, respectively. These data may be said to be described by an activation energy of 47 meV over this very narrow temperature range. At higher temperatures, the apparent electron attachment rate constant fell in magnitude in a rapid manner characteristic of thermal decomposition. However, the bond enthalpy $D(MoF_5\text{-}F)$ is about 3.3 eV (using available heats of formation), so the decomposition is probably taking place on the walls of stainless steel feedlines, which travel half the length of the FALP flow tube inside of the heated region. The decomposition problem requires further study.

The reaction of Ar^+ with MoF_6 (reaction 4) was studied in order to use positive ion mass spectra as a diagnostic for the oxide and decomposition issues raised above. A rate constant of $(1.8 \pm 0.4) \times 10^{-9}$ cm^3 s^{-1} was measured for this reaction. An F atom was released in the reaction, as we have seen for other Ar^+ reactions with single-center hexafluorides [10].

B. ReF_6

We have studied electron attachment to ReF_6 (reaction 2) only at 297 K thus far. A rate constant of (2.4 ± 0.5) × 10^{-9} cm^3 s^{-1} was measured, comparable to that for MoF_6. The temperature dependence of the rate constant has not been studied at this writing.

C. WF_6

WF_6 was found to attach electrons so weakly that it is difficult to measure the attachment rate constant at room temperature (ca. 10^{-12} cm^3 s^{-1}). Even the ion product of the reaction is unclear when the attachment rate constant is so low, because ion-molecule reactions, which may be orders of magnitude faster, obscure the attachment mass spectrum. At this writing, it appears that WF_6^- is the product of attachment. WF_5^-, along with oxide impurities, appears in the attachment mass spectra at very low flow rates of WF_6. Production of WF_5^- is said to be approximately 4 eV endothermic [5], but appears in the attachment mass spectra at low flows of WF_6. However, as with MoF_6, oxides produced in the feedlines complicate the data analysis. The apparent rate constant for electron attachment to WF_6 increases rapidly with temperature, reaching about 2 x 10^{-10} cm^3 s^{-1} at 522 K. No decomposition problem was noted with the WF_6 gas. The apparent activation energy for electron attachment is ~0.3 eV.

It would be appropriate at this point to explain why the attachment rate constants for the single-center hexafluorides span so many orders of magnitude. But the information available is inadequate to do so. The usual picture of attachment is that the free electron becomes temporarily trapped in a resonant state of the parent anion in the continuum (the only way to explain the large size of attachment cross sections), and then the anion is stabilized either collisionally or radiatively, or autodetaches. The question of the size of the attachment cross section or rate constant is then tied up in the number of resonant states available to the electron and to the autodetachment width, plus the likelihood of collisional stabilization [11].

3. Calculations Using Density Functional Theory

We used the Gaussian-98W program package [12] to investigate the molecular structures of neutral and anionic MoF_6, primarily to obtain estimates of the energetics of the electron attachment process. We hope to be able to present some results of calculations for ReF_6 and WF_6 by the time of the meeting. The calculations should be viewed as tests of how well the Gaussian-98W program package can handle molecules for which a relativistic treatment would be more appropriate. Calculations of the total energies of the parent molecules and fragments were carried out using density functional theory, in particular Becke's three parameter hybrid functional denoted by B3LYP [13], which includes the Lee, Yang, and Parr correlation functional, which contains both local and non-local terms [14]. The Hamiltonian is non-relativistic, but the basis set denoted by LANL2DZ contains effective core potentials incorporating mass-velocity and Darwin relativistic effects [15].

The MoF_6 neutral and anion molecules were geometry-optimized using the B3LYP/LANL2DZ functional and basis set, and a harmonic frequency analysis was performed at the same level of theory to give the zero-point energies (ZPE). The vibrational frequencies were not scaled in calculating the ZPE. ZPE corrections were then applied to the total energies to give 0 K values. The results are given in Table 1. The B3LYP/LANL2DZ geometry optimization yielded an Mo-F bond length of 1.871 Å, which may be compared with the experimental result of 1.820 Å [16]. (The Re-F bond length is very similar, 1.832 Å [16].) The adiabatic electron affinity of MoF_6 was calculated from the difference in 0 K total energies of MoF_6 and MoF_6^-.

4. Conclusions

A flowing-afterglow Langmuir-probe apparatus was used to study electron attachment to MoF_6, ReF_6, and WF_6 in 133 Pa of helium gas. Measurement of electron attachment rate constants and ion products of attachment is difficult with these gases is difficult because they tend to form metal oxides on the surfaces of feedlines, and the oxides appear to attach electrons at least as efficiently as do the parent molecules. Furthermore, if the electron attachment reaction is very inefficient, as it is with WF_6, subsequent ion-

molecule reactions may obscure the actual ion product of electron attachment. Nevertheless, we conclude that MoF_6 and ReF_6 attach electrons with similar rate constants at 297 K, $(2.3 \pm 0.5) \times 10^{-9}$ and $(2.4 \pm 0.5) \times 10^{-9}$ cm^3 s^{-1}, respectively. The rate constant for MoF_6 is seen to increase with temperature.

Table 1. Total energies and zero-point energies (ZPE) for MoF_6 and MoF_6^-, in hartree units, calculated at the B3LYP/LANL2DZ level of theory, and the electron affinity (EA) derived from these calculations.

molecule	ZPE[a]	total energy[b] (0 K)
MoF_6	0.01376	-666.78340
MoF_6^-	0.01548	-666.97450

Present calculation, EA(MoF_6) = 5.20 eV
Ref. 3 calculation, EA(MoF_6) = 5.37 eV

The parent anion is the sole ion product of attachment in both cases. WF_6 attaches electrons at such a low rate at 297 K as to be immeasurable (a rate constant on the order of 10^{-12} cm^3 s^{-1}), but the rate constant increases rapidly with temperature to the point that the reaction is about 0.1% efficient at 522 K. Electronic structure calculations were carried out using density functional theory for neutral and anionic MoF_6. The calculated EA(MoF_6) is quite high (5.2 eV) and agrees with earlier estimates. The reaction between Ar^+ ions and MoF_6 was studied as a diagnostic for MoF_6 decomposition. The reaction produces $MoF_5^+ + F$, with a rate constant of $(1.8 \pm 0.4) \times 10^{-9}$ cm^3 s^{-1}.

References

[1] J. A. D. Stockdale, R. N. Compton, and H. C. Schweinler, J. Chem. Phys. **53**, 1502 (1970).
[2] G. K. Jarvis, R. A. Kennedy, and C. A. Mayhew, Int. J. Mass Spectrom. **205,** 253 (2001).
[3] E. Miyoshi, Y. Sakai, A. Murakami, H. Iwake, H. Tersashima, T. Shoda, and T. Kawaguchi, J. Chem. Phys. **89**, 4193 (1988).
[4] H. Dispert and K. Lacmann, Chem. Phys. Lett **45**, 311 (1977).
[5] L. N. Sidorov, A. Y. Borshchevsky, E. B. Budny, and V. D. Butsky, Chem. Phys. **71**, 145 (1982).
[6] P. M. George and J. L. Beauchamp, Chem. Phys. **36**, 345 (1979).
[7] D. Smith and P. Spanel, Adv. At. Mol. Phys. **32,** 307 (1994).
[8] T. M. Miller, A. E. S. Miller, J. F. Paulson, and X. Liu, J. Chem. Phys. **100,** 8841 (1994).
[9] T. M. Miller, R. A. Morris, A. E. S. Miller, A. A. Viggiano, and J. F. Paulson, Int. J. Mass Spectrom. Ion Processes **135,** 195 (1994).
[10] T. M. Miller, J. F. Friedman, A. E. S. Miller, and John F. Paulson, J. Phys. Chem. **98**, 6144 (1994).
[11] A. Chutjian, A. Garscadden, J. M. Wadehra, Phys. Rep. **264**, 393 (1996).
[12] M. J. Frisch, et al., Gaussian 98W, Revision A.7, Gaussian, Inc., Pittsburgh PA, 1998.
[13] A. D. Becke, J. Chem. Phys. **98,** 5648 (1993).
[14] C. Lee, W. Yang, and R. G. Parr, Phys. Rev. B **37**, 785 (1988).
[15] P. J. Hay and W. R. Wadt, J. Chem. Phys. **82**, 270 (1985); W. R. Wadt and P. J. Hay, ibid. **82**, 284 (1985); P. J. Hay and W. R. Wadt, ibid. **82**, 299 (1985).
[16] D. R. Lide, Editor, *Handbook of Chemistry and Physics*, 78th Ed. (CRC Press, Boca Raton, 1997), Sect.9, pp. 20-21.

Locomotive wheel tire measurements database analysis timed for 2002

S.V.Antipovsky[1], P.P.Ivanov[1], V.E.Isakaev[1], E.Kh.Isakaev[1], S.A.Kobzev[2], V.I.Moldaver[2], O.A.Sinkevich[1] and A.S.Tyuftyaev[1]

[1]*Associated Institute for High Temperatures, Russian Academy of Sciences*
[2]*Moscow Railways*

Abstract

In order to improve the wheel life Moscow Railways use during the last 5-7 years a plasma technology for local surface hardening and nitriding of wheel flanges. Simultaneously the gathering of monthly measured data concerning the change in tires and flange thickness and kilometers of run for a great body of plain and plasma treated wheel sets was going on. The effect of the plasma treatment is analyzed using the measured data from the database.

1. Introduction

The resource of locomotive wheels is a great headache on the railways. They lose the regulated profile, mainly the flange thickness, due to the wear and must undergo the truing operation on the lathe. So during the exploitation process the diameter of the wheel goes down to the allowed limit. To save the bulk of wheel from wasting the outer part of wheel being under heavy duty is made as separate tire of 90 mm in thickness while the wheel diameter is 950 mm. When the tire loses the half of its initial thickness it is changed. These 45 mm of the tire thickness represent the tire resource what we mean speaking about the wheel resource. Even more exactly under "wheel resource" we mean the run of the locomotive until the change of tire, while looking further for the fate of the bulk of wheel is practically beyond the reach.

The wheel flange going thin was the most frequent cause of wheel failure, the driving force to introduce the plasma technology. It was only natural at the beginning to pay the main attention to the flange wear, evaluating the increased wheel life due to plasma treatment using the specific flange wear per 1000000 km as a criterion [1]. This criterion is easy to calculate knowing the run of the locomotive and the value of previous month measurement. The raw data from the database in an atomized form is suitable for this job. But it is more convenient to use a data model based on aggregated data units – measurement cycles, several sequential measurements between two truings. This data model excludes the greater part of fluctuations caused by data input errors. The same criterion used in this data model gets a solid and smoothed character. Easy, beautiful and convincing criterion of comparison in the measurement cycles data model is the number of truings per million kilometers of run. According to our database plasma treated wheel sets have this number half as much as plain wheel sets [1] (see Table 1).

Table 1. A comparison of plasma treated wheel sets with plain ones by the number of truings per 1 million km

	Number of measurement cycles in selection	Total run of selected wheel sets, 1000000 km	Total number of truings in selection	Number of truings per 1000000 km
Plain wheel sets	40580	1905.882	18056	9.47
Plasma treated wheel sets	5635	451.423	2158	4.78

But in spite of all convincing nature of the figures in the last column they don't prove ultimately the advantages of using the plasma technology to improve the field-performance characteristics of wheel sets of the rolling stock. The conditions of exploitation are different for engine houses of Moscow Railways, the tracks being rectilinear over the plains and with many curves through the mountains. The allowed minimal thickness of flange depends on the regulated velocity of motion of trains. These factors influence on the truing frequency not only through the objective variation of the intensity of wear but also through the subjective differences in the maintenance policy.

So we leave behind the easy solutions while in the long run as we pointed earlier the wheel resource is determined by the tire thickness going down due to the tread wear and during the truing process. For the

assessment of wheel resource a specific loss of the tire thickness per 10000 kilometers of run may be used as a criterion. This criterion has a sense only for the aggregated data such as a sequence of measurement cycles including at least one truing process because the truing is responsible for the most of loss of the tire thickness. We used this criterion in [1] too, selecting wheel sets having at least two measurement cycles. In those circumstances it had to be considered as a differential parameter. But time is going on and more data comes to the database, and we hope that the specific loss of the tire thickness per 10000 kilometers of run may be handled as an integral criterion based on the whole history of the separate tire from the mounting to dismounting (or that the situation is closer to this ideal one).

Regrettably the data coming from engine houses to our database has not the quality we would like it to have. There is a lack of the fullness of coverage, there are many errors, the locomotives emerge from nowhere and others disappear leaving no good-by message. But statistics goes through because of the really great number of measured data.

The wheel sets covered in the database are characterized (for the current analysis) by the number of measurement cycles, by initial and final tire thickness making the total loss of thickness and the total run. Those initial and final tire thickness values are not always maximal and minimal allowed ones, regrettably. Once more the hope is on the quantity of data - now the database contains 370 000 measurements concerning 19400 wheel sets.

2. Analysis

There are factors having an influence on the wheel life: lubrication, special profiling, and the flange thickness at the beginning of service. The skill is needed in the analysis to single one influence from the other lot. Actually other methods of improvement of the wheel life are friendly to the plasma treatment – the best results are provided using the lubrication over plasma-hardened surface. In this analysis we selected plasma treated and plain wheel sets in groups without distinction by above-mentioned factors. But we couldn't ignore the great difference between diesel and electric engines concerning the intensity of the wheel wear. The Table 2 justifies this approach.

Table 2. Specific loss of the tire thickness per 10000 kilometers of run for diesel and electric engines (without distinction between plasma treated and plain wheel sets).

Engine	Number of wheel sets in selection	Average loss of tire thickness, mm	Average run, km	Specific loss of the tire thickness per 10000 kilometers of run
Diesel	6989	9.2	65 675	3.03
Electric	5084	11.7	172 569	1.25

So further we are dealing with 4 groups of wheel sets: plasma treated and plain wheel sets for diesel and electric engines. The bold-faced averaging in the considered 4 groups of wheel sets all over the database results in the Table 3 and Fig. 1.

Table 3. Specific loss of the tire thickness per 10000 kilometers of run for plain and plasma treated wheel sets under diesel and electric engines.

Engine	Type of wheel set	Number of wheel sets in selection	Average loss of tire thickness, mm	Average run, km	Specific loss of the tire thickness, mm/10000 km of run
Diesel	Plain	5604	8.9	58 193	3.40
	Hard.	1385	10.4	95 945	1.59
Electric	Plain	4084	11.4	157 523	1.39
	Hard.	1000	13.1	234 016	0.68

The Table 3 shows that the number of data units in the considered selections nearly equal for diesel and electric engines and that the number of plasma treated wheel sets make a quarter of the number of plain ones. Wheel sets under electric engines have the greater average loss of tire thickness and more than twice average run per measurement cycle compared with ones under diesel engines. The explanation of this fact may be that the electric engines are used exclusively as main-line locomotives while the diesel engines are

used as local shunting engines. The last case is characterized by less run and more maneuvering, more use of brakes.

Table 3 and Fig. 1 show very favorable influence of the plasma treatment on the specific loss of the tire thickness per 10000 km of run – the main criterion of wheel resource according to the earlier mentioning.

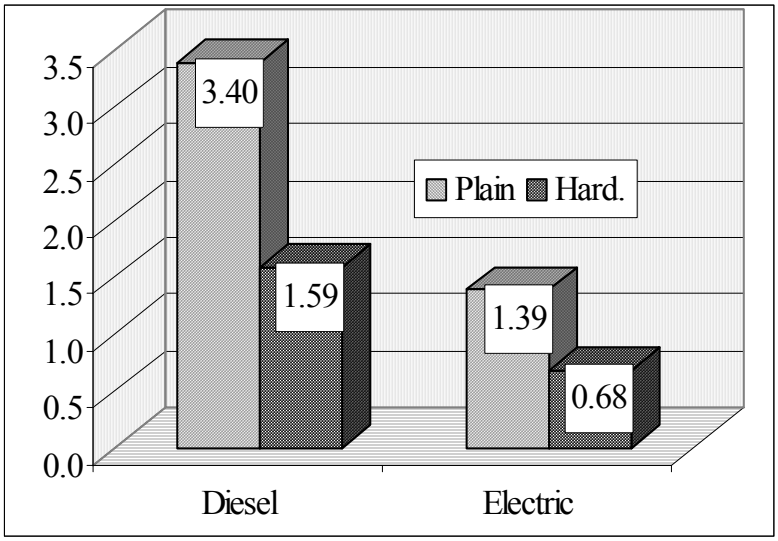

Fig. 1. Specific loss of the tire thickness per 10000 kilometers of run for plain and plasma treated wheel sets under diesel and electric engines.

The value of the specific loss of the tire thickness is diminished more than two times. This is true both for diesel and electric engines. This is true when diesel and electric engines are considered in one group together. The results of the averaging in this case are presented in the Table 4.

Table 4. Average run (R) and specific loss of the tire thickness per 10000 kilometers of run (S) for plain and plasma treated wheel sets.

	R, km	S, mm/10000 km of run
Plain	100 066	2.54
Hard.	153 837	1.20

Nothing unexpected is here after comparing two last columns of tables 3 and 4.

Following two figures illustrate the 4-group approach and the current state of our database. Fig. 2 shows that the majority of wheel sets is represented by one measurement cycle, the number of wheel sets being inversely proportional to the number of measurement cycles. The number of wheel sets under diesel engines (blank-marked) is greater than under electric engines (triangle-marked). The number of plain wheel

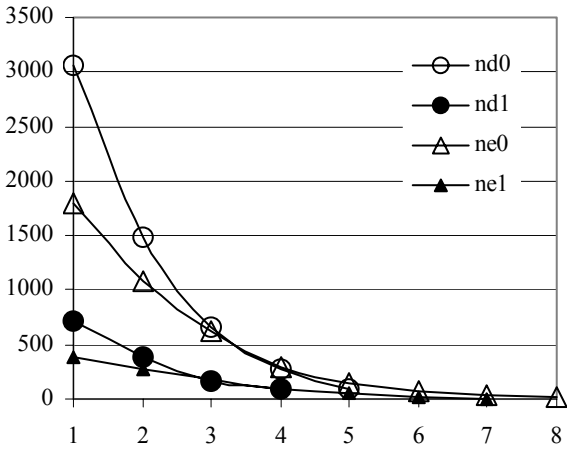

Fig. 2 Number of wheel sets in database as a function of number of measurement cycles for the following selections:
nd0-plain wheel sets, diesel engine
nd1-plasma treated wheel sets, diesel engine
ne0-plain wheel sets, electric engine
ne1-plasma treated wheel sets, electric engine

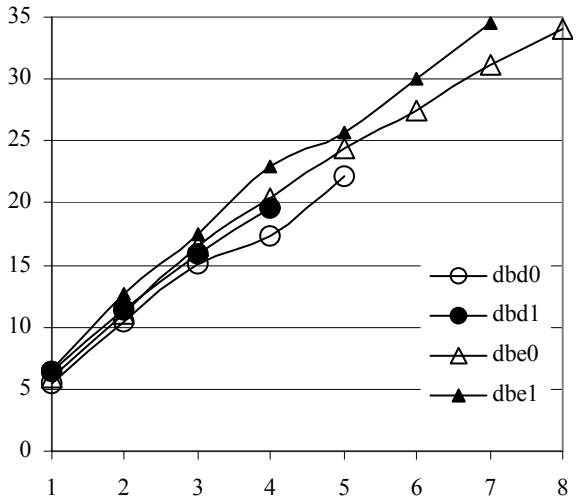

Fig. 3 Loss of tire thickness versus the number of measurement cycles for the following selections:
nd0-plain wheel sets, diesel engine
nd1-plasma treated wheel sets, diesel engine
ne0-plain wheel sets, electric engine
ne1-plasma treated wheel sets, electric engine

sets (circle-marked) is greater than the number of plasma treated ones (black-marked). Fig. 3 shows practically linear dependence between the number of measurement cycles and averaged loss of tire thickness with the derivative 4÷5 mm per measurement cycle. There is no distinction between any of groups.

Fig. 4 shows the time-varying results of specific loss of tire thickness per 10000 km run analysis displayed along the number of measurement cycles axis. As in the fig. 2 diesel engines are marked by circles and electric engines by triangles, plain wheel sets are marked blank and plasma treated ones are marked black.

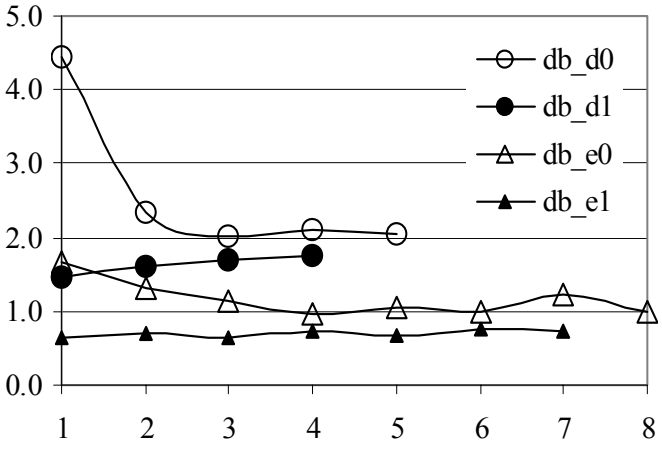

Fig. 3 Specific loss of tire thickness per 10000 km run versus the number of measurement cycles for the following selections:
db_d0-plain wheel sets, diesel engine
db_d1-plasma treated wheel sets, diesel engine
db_e0-plain wheel sets, electric engine
db_e1-plasma treated wheel sets, electric engine

The curves end at different points of abscissa due to lack of data to make a good statistics. The longest life as expected with good reason from the earlier mentioning have wheel sets under electric engines. One point less of the curves for plasma treated wheel sets compared with plain ones is due to the fact that they are outnumbered 4 times by the latters.

Plasma treatment until now is performed mainly for new wheel sets. The wheel sets identified as plasma treated ones in the considered selections actually keep their quality only until the first truing. After the truing the hardened layer is usually lost. Very seldom are they hardened second time. No wonder that the difference between the plasma hardened and plain wheel sets is maximal at the first measurement cycle disappearing altogether at the end of service.

For the plain wheel sets specific loss at the first measurement cycle exceeds the average value more than twice. This phenomenon, especially well pronounced for diesel engines, was amply discussed in our earlier publications [2]. On the contrary, the curves for plasma treated wheel sets show the tendency to be constant or to some growth. The mutual annihilation of two tendencies – the enhanced intensity of wear of new wheel sets with great initial flange thickness and the diminished intensity of wear of plasma treated wheel sets – is the trustworthy explanation of the behavior of latters.

3. Long-lived wheel sets

An interesting aspect of the wheel life problem is the direct measurement of the wheel run between the mounting and dismounting of separate tire. Due to some stochastic nature of measurements under industrial environment it is not easy to locate full-length working wheel sets in the database. A possible approach is to select them having initial and final tire thickness in the vicinity of allowed maximal and minimal values. These values are 75 and 40÷36 mm for diesel engines and 90 and 45 mm for electric engines. The results of averaging among the long-lived wheel groups in 4 groups are presented on the Table 5.

Table 5. Characteristics of the most long-lived plain and plasma treated wheel sets under diesel and electric engines.

Engine	Type of wheel set	Number of wheel sets in selection	Average loss of tire thickness, mm	Average run, km	Specific loss of the tire thickness, mm/10000 km of run	Average service time, year
Diesel	Plain	39	34	96229	4.05	2.70
	Hard.	19	37	147826	2.87	3.56
Electric	Plain	145	35	256 811	1.98	2.97
	Hard.	21	38	419 104	0.95	3.84

The figures on the Table 5 may be considered as a direct measurement of the run and service time of separate tire or a very close approximation to them after comparing the values of average loss of tire thickness with allowed ones – 45 mm for electric engines and 37 mm for diesel engines. The hope of

improvement is there for the characteristics of electric engines, and they are most interesting too because they are truly determined by wear and not by whatsoever it may be as in the case of diesel shunting engines.

Concerning the advantage of plasma treated wheel sets compared with plain ones it appears with greatest evidence in specific loss of the tire thickness per 10000 km of run for main-line locomotives. In this aspect quasi-direct measurement results of the Table 5 are in full agreement with purely statistical results of the Table 3.

4. Conclusions

For any selections of plain and plasma treated wheel sets the plasma treatment halves the specific loss of the tire thickness per 10000 km of run.

The perspective of the further improvement of the wheel life comes from the fact that up to now only new wheel sets are subjected to the plasma treatment, and in the group of so called "plasma treated wheel sets" this quality disappears for the second and further measurement cycles.

References

[1] S.V.Antipovsky, E.Kh.Isakaev, P.P.Ivanov, A.S.Tyuftyaev and G.A.Zhelobtsova, Influence of plasma treatment on the resource of railway wheels, 15th International Symposium on Plasma Chemistry, Orlean, France, 9-13 July 2001.

[2] E.Kh. Isakaev, V.M. Amelin, S.V. Antipovsky, P.P. Ivanov, A.A. Troitsky, A.S. Tyuftyaev, A.E. Yablonsky, Plasma hardening and nitriding of railway wheels: field-performance of first 18000 plasma treated wheel sets, Proc. of the XIII Int. Conf. on Gas Discharges and their Applications, Glasgow, UK, Sept.3-8, 2000, pp. 1017-1020.

New application of plasma technology for the surface hardening of steel products

E.I.Gontaruk[1], M.V.Illichev[2], E. Kh.Isakaev[2], O.A.Sinkevich[2], A.S.Tyuftyaev[2] and G.A.Filippov[3]

[1]*Oskol Electrometallurgy Integrated Plant*
[2]*Associated Institute for High Temperatures, Russian Academy of Sciences*
[3]*Bardin Institute for Ferrous Metals*

Abstract

Plasmatron with expanding anode channel used successfully for the hardening and nitriding railway wheel flanges, for the plasma treatment of rollers of the transport rollgang of the hot-saw workbench at the rolling mill, for the recovering of worn railway frogs using a plasma coating by the Mn-Cr-Ni powder in multiple layers with abrasive cleaning between them and a riveting of every single layer to eliminate residual stresses

1. Introduction

The problem of enhancement of resistance to metal fatigue and wear resistance of products of heavy engineering industry and ferrous metallurgy is becoming more important due to ever increasing demands to the reliability and durability of constructions and to the quality of articles. The conventional methods of volumetric hardening of construction components made of steels and alloys are approaching to the limits of their capability. Besides the production of massive details is characterized by complex manufacture and the need of replacement of components (rollers, transporting rollers, railway wheels and so on) [1]. So the promising way to the enhancement of working durability of steel products is the use of modern plasma technologies for the surface hardening and the coating [2].

These technologies make a new quality of the surface and enhance its properties keeping the properties of the bulk of the product unchanged, allow the recovering of worn items by means of plasma coating up to nominal geometry followed by subsequent surface hardening using highly concentrated heating sources (laser, electron beam, plasma)

The hardening of the ordinary material coating spares the expensive alloyed steels and other deficit materials, enhances the resource and reliability of the mechanisms, makes the production less power-hungry and solves many problems of the repair. The effective method of surface treatment is the use of low temperature plasma.

Fig. 1 Layout of the plasmatron with expanding channel of the outlet electrode (C – cathode, A – anode, I – insulating insertion).

A new technological process may reckon for the industrial application having stable output parameters and economic efficiency of the using the end product. So the optimization was performed for the construction parameters of the plasmatron with expanding channel of the outlet electrode [3], mainly the determination of the optimal angle of expansion (see Fig. 1). In the expanding channel the arc interacts with the gas flow in a different way compared with cylindrical channel. The drastic increase of the inlet velocity of the expanding channel intensifies the heat transfer between the arc and the cold gas. Main parameters of gas flow (the velocity, Mach number) are monotonous along the channel. The experimental investigations and field testing of this plasmatron prove it to be a stable device with enhanced resource and reliability [4].

2. Hardening of railway wheels.

The technology is developed for the hardening of wheel sets allow the simultaneous treatment of both flanges of wheel set in one pass. Over the whole treated area and in depth uniform structures appear characteristic of the hardening with smooth transition to the bulk of metal providing the strength of traction between the hardened layer and the bulk of metal [5]. Compared with the earlier technology using two pass plasma treatment this one makes in one pass deeper and wider (up to 70 mm) hardened layer with enhanced mechanical properties. The test results for wheel steel samples after these two technologies are presented in the Table 1.

The plasmatron of this kind has found many applications: for cutting copper molds of continuous casting devices and for the hardening and nitriding wheel sets for railway rolling stock. The technology developed for the hardening of wheel sets allow the simultaneous treatment of both flanges of wheel set in one pass. Over the whole treated area and in depth uniform structures appear characteristic of the hardening with smooth transition to the bulk of metal providing the strength of traction between the hardened layer and the bulk of metal [5]. Compared with the earlier technology using two pass plasma treatment this one makes in one pass deeper and wider (up to 70 mm) hardened layer with enhanced mechanical properties. The test results for wheel steel samples after these two technologies are presented in the Table 1.

Table 1 Dimensions and properties of the hardened area of the wheels treated using the old and newly developed technologies

Technology	Number of passes	Sample	Hardened layer thickness, mm	Average hardness of the treated area, HB	Microhardness, kg/mm^2		Impact strength		Components of the destruction work						Wear resistance	Delayed destruction
					Hardened layer	Transitional area	KC, J/cm^2	$\Delta KC/KC^0*L$	A_C, J/cm^2	$\Delta A_C / A_C*L$	Ap, J/cm^2	$\Delta Ap/ Ap*L$	A_Σ, J/cm^2	$\Delta A_\Sigma/ A_\Sigma$	mm^3	$\Delta t_{дл}//Vp*10^4$, min/mm/min
Old	2	No1	1.7	282	604	457	30.1	1.8	7.2	0.9	22.1	0.4	29.3	0.8	0.29	220/7.6
New	1	No2	4.0	435	599	500	11.7	0.4	3.3	0.75	15.7	0.4	19	0.7	0.17	450/1.6

The investigations show that the depth and the hardness measured in longitudinal and transversal directions in the hardened layer of the sample No2, treated by this technology, are greater compared with the ones measured in the sample No1 hardened by means of the previous technology. The average value of the hardness of the plasma treated area of the sample No2 is 435 HB, while the corresponding value of the sample No1 is no more than 282HB. Besides the hardness of the treated area of the sample No2 shows substantially greater stability compared with the one of the sample No1. The scatter of the hardness values of the treated area of the sample No2 is in the range 363÷530, while the corresponding range for the sample No1 is greater - 217÷499HB.

The lower hardness of the sample No1 is due to the two-pass hardening. This is proved by two overlapping areas ("tracks") on the surface. During the second pass the thermal unhardening of the previously hardened layer is going on (see Fig. 2).

Less stable hardness of the plasma treated area of the sample No1 may be also the result of lesser surface and depth of the hardened layer providing the greater share of transient areas in the dispersion of hardness values.

Impact strength of both samples is less compared with the original sample. The reduction is greater for the sample No2 first of all due to the greater thickness of the hardened layer. But the reduction may be caused by the higher level of hardness of the sample No2.To take this factor into account the evaluation was made of the change of impact strength per one unit of the thickness of the hardened layer:

$$(KC^0-KC^Y)/(L*KC^0) \quad (1)$$

where KC^0 - impact strength of the original sample, KC^Y - impact strength of the hardened metal, L - the thickness of the hardened layer.

It turned out that the change of the impact strength is caused not only by the increased hardness of the treated layer. The hardness bound change of impact strength is less for the sample No2 (0.4) than for the sample No1 (1.8). Additional factors are the peculiarities of the structural state of the hardened layer.

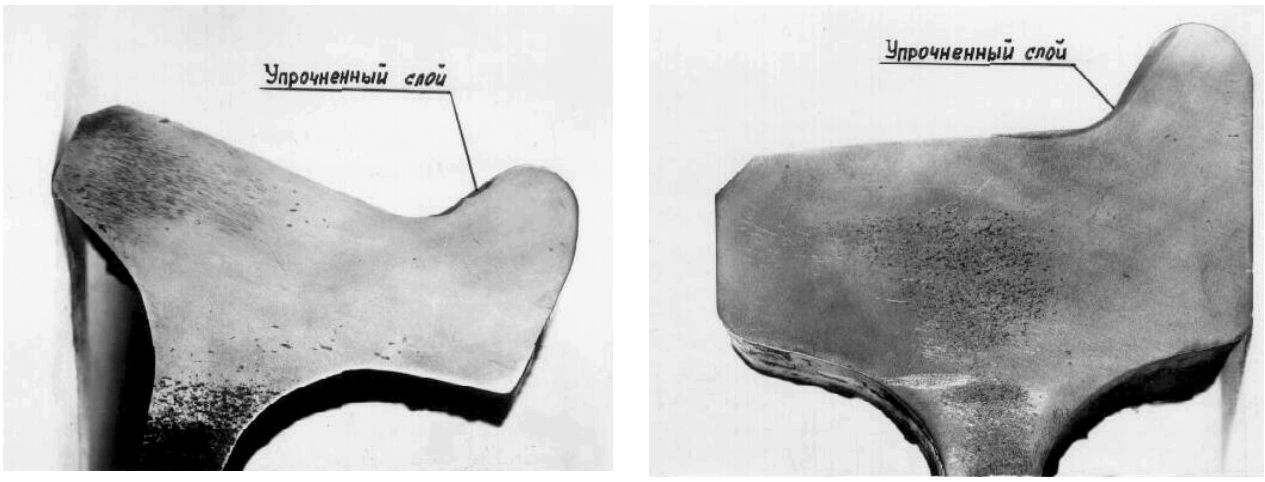

Fig. 2 Transversal ground edges of wheels hardened using the old (No1) and newly developed technology (No2).

Absolute values of the destruction work and its components for the hardened metal are not the same for the samples No1 and No2. But the specific values of the total destruction work A_{Σ}, of the crack creation work A_C and of the crack propagation work Ap, evaluated using expression (1) like criteria, are much alike for the greater values of the hardened layer thickness of the sample No2.

Wear test of the hardened layer was performed using "Skoda-Savin" device and plain-disc layout under the load 85H with the counter body made as disc of hard alloy Vidia XX 30 mm in diameter and 2.5 mm in thickness rotating at 675 rpm. The creation time of the wear hole was 270 s. The volume of the hole produced during the test time served as a measure of wear. Tests have shown that wear resistance of the second sample is twice as much as of the first one.

Test on the delayed destruction is capable to locate the week areas in the metal structure. This test was performed using the static stress a little less than the yield stress in the corrosive and hydrogen environment according to [6]. Besides this test allows the assessment of the frail destructibility of metal when hydrogenated.

Test has shown that the delay time of the crack creation in the hardened area of the sample No2 is greater two times compared with the sample No1. Average velocity of crack propagation Vp in the hardened area of this sample approximately 5 times less than in the sample No1.

So the newly developed technology makes the hardened layer of higher level of mechanical properties and of the resistance to wear uniformly distributed across the width of the treated surface. The analysis of field-performance characteristics of plain and plasma treated wheel sets shows the increase of the wheel life 2 times [7].

3. Hardening of rollgang rollers

The experience got in the broad band hardening of wheel steel was helpful for the development of the technology of hardening the rollers of transport rollgang of the hot-saw workbench of the Rolling Mill 700 of Oskol electrometallurgy integrated plant. The plasma treatment installation was modificated to fit the configuration and dimensions of the rollers. Two transport rollers 360 mm in diameter with barrel length 500 mm were delivered by the plant and were subjected to the plasma coating with chrome alloy.

In order to enhance the resistance of rollers to wear the heavy duty area in the central part of barrel 200-250 mm in width was subjected to plasma hardening. The roller was rotating during the process, and the plasmatron was moving along the roller. Two options were tested – the treatment in two bands 50 mm in

width overlapping by 3 mm and the treatment in two separate bands with the gap 3 mm between. The metal was heated up to ~1200 ^{0}C, to exclude the melted layer on the roller surface. The cooling was provided by the heat transfer to the bulk of roller and by air cooling of the surface. The hardness of rollers was measured before and after the hardening, and the corresponding values are 40.6HRC and 51HRC. The values of hardness measured along the roller are uniform in the 3 mm gap option, and in the overlapped option the tempering of the previously hardened layer occurs, so the hardness falls down to the original hardness of the coating.

The plasma treated rollers were installed into the rollgang section after the stationary saw for hot cutting immediately beside the first group of cages sequentially (Fig. 3).

The field testing was going on during 13.5 months (see Table 2). The actual surface wear was measured after 4.5 months of operation. The wear of the overlapped-option hardened roller was 1.95 mm; the wear of gap-option hardened roller was 1.75 mm, while non-treated rollers No 3, 4 have shown the corresponding values of wear 1.8 and 4.55 mm. The wear of the roller No 3 is close to the one of plasma treated rollers. The explanation is in the vicinity of hardened rollers overtaking a part of the load on them. The roller has substantially greater wear compared with hardened rollers, more so that it was coated only 1 month before the measurement. After 13.5 months of operation the second measurement was performed showing the wear for hardened rollers 5.5 mm, for non-hardened roller No 3 – 5.8 mm and for No 4 – 8.3 mm, worth to note that the roller No 3 was coated in 5 months before the measurement.

It turns out that the plasma hardening made the wear of transport rollers 1.5-2 times lower.

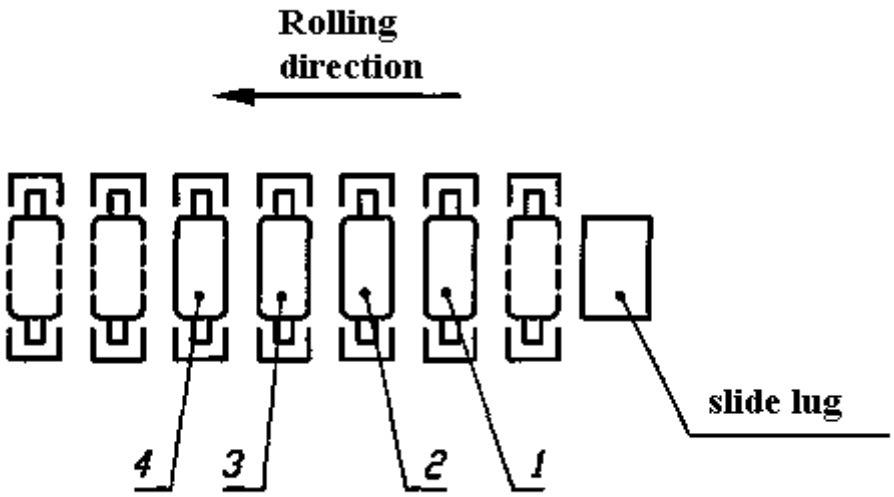

Fig. 3 Layout of the placement of rollers in the rollgang section: No1 – hardened with overlap, No2 – hardened with gap, No3 and No4 – non-hardened.

Table 2. Development of radial wear (mm) of hardened and non-hardened rollers in the course of time.

Time, month	Hardened		Non-hardened	
	No1	No2	No3	No4
4.5	1.95	1.75	1.80	4.55*
13.5	5.50	5.50	5.80**	8.30

* - the coating 1 month before the measurement

** - the coating 5 month before the measurement

4. Recovering of railway frogs

The recovering of the products of manganese steel (Hadfield steel) using plasma coating is not an easy job due to the peculiarities of properties of this steel: its structure is not stable enough during the heating and cooling processes. Its thermophysical properties – low heat conductivity and high coefficient of thermal expansion – are unfavorable enhancing its aptitude to the creation of thermal cracks [8].

Several methods are used to recover the worn products of Hadfield steel: acetylene-oxygen torch, electric arc, semiautomatic coating by powder wire, automatic arc coating under flux and so on. A method of

the explosive hardening is used to treat the surface of the new products before putting them into operation and after recovering the worn ones [9]. But the methods known up to now don't enhance substantially the resource of the recovered products, and further investigations on this line are needed.

Most important is the problem of the resource enhancement for railway frogs made of Hadfield steel. It is a commonplace that the resource of a frog cast of manganese steel is many times less than one of a railway switch as a whole. The life of the frog is limited mainly by the wear of the core between the sections from 20 to 40 mm. Depending on working conditions, wear tolerances are in the range 6-8 mm. The manufacture cost of these frogs is high (the content of manganese is high). Besides the change of worn frogs at the track is very expensive operation because the traffic is to be cut.

The properties of the coating layer material regardless of the method used depend mainly on the depth of melting of substrate and of the intensity of mixing of layer and substrate metals. Greater the depth and more intensive the mixing – worse layer properties.

Among of the most effective ways for surface hardening and coating of steel products are plasma treatment and plasma coating. For these operations a plasmatron is designed with expanding anode channel [10]. A powder is injected into argon which is simultaneously transporting, plasma forming and protecting gas. A coating of a real piece of new frog was performed using a Mn-Cr-Ni powder in multiple layers with abrasive cleaning between them and a riveting of every single layer to eliminate residual stresses [11].The core of the frog is wedge-shaped therefore during the coating process the amplitude of plasmatron motion is to be controlled according the layout sketched in the Fig. 4

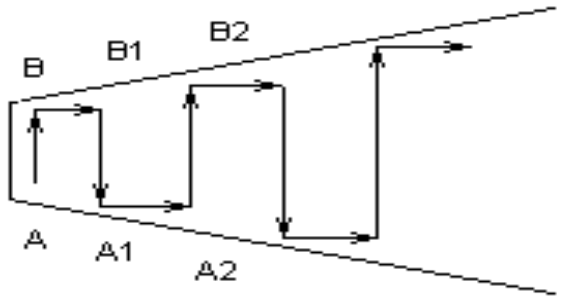

Fig.4. Layout of the plasmatron motion during the coating process

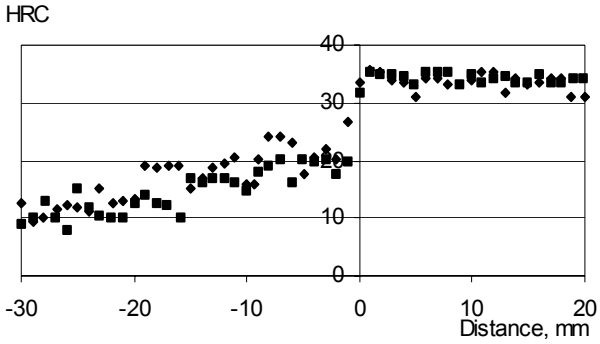

Fig. 5 Hardness HRC versus the depth in the layer and the substrate.

The coating was performed under the following parameters of technological regime: work current I=90-160 A, U=30-40 V, flow rate of argon G=1 m^3/hour, transversal motion velocity of plasmatron Vp=20mm/min, onward velocity of plasmatron Von=10mm/min, flow rate of the powder 0.2-0.3 g/s. The total thickness of the layer comes to 20-22 mm. The balance is made by the frog wear 6-8 mm after taking it from the track, besides there are surface defects to be eliminated.

The hardness HRC was measured 20 mm deep in the layer and 30 mm deep in the substrate (fig. 5). According to the plot at the depth 30 mm of substrate the measured hardness is 9-12 HRC. Towards the boundary the hardness grows evenly up to 17-20 HRC. At the distance ~2 mm from the boundary the hardness increases sharply up to 32-34 HRC. Further on along the thickness of layer the hardness stays constant at the level 32-35 HRC.

Two frogs recovered using the plasma technology were field-tested at the tracks of Moscow Railways. The first one was taken out fully worn after withstanding 115 million tonne brutto of load (worth to note that the new frog is expected to stand for 60 millions tonne), the second one withstood 144 millions tonne and was sanctified to continue the field-testing.

Conclusions

Plasma technology using the plasmatron with expanding channel of the outlet electrode enhances the quality of the surface treatment due to the elevated depth and width of the hardened layer.

Field-testing of the hardened railway wheels and rollgang rollers proves their doubled resource due to the plasma treatment.

Broad range investigations were performed of the plasma coated layer over manganese steel.

References

[1] A.P. Semyonov, I.B. Kovsh, I.M. Petrova et al., Methods and devices for the hardening the surfaces of the details of machines using concentrated energy flows, Moscow, Nauka (1992), p. 404 (in Russian).

[2] P.P. Ivanov, E.Kh. Isakaev, V.I. Izotov et al., An efficient method of the surface plasma hardening of railway wheels, Steel, No 1(2000), pp. 63-66 (in Russian).

[3] E.Kh. Isakaev, R.R. Grigor'yants, N.O. Spector, A.S. Tyuftyaev, Influence of the expansion angle of the outlet electrode on the plasmatron characteristics, Teplofizika vysokikh temperatur, 32, No 4 (1994) pp. 627-637(in Russian).

[4] E.Kh. Isakaev, A.S. Tyuftyaev.// Influence of the throat geometry on the arc characteristics in the cutting plasmatron, Welding industry. No7. 1994. p.23-26(in Russian).

[5] Illichev M.V., Isakaev E.Kh., Alekseeva L.E. and Filippov G.A. An influence of plasma treatment parameters on the structure and properties of treated zone of railway wheel sets// Proc. of the III Int. Conf. on Plasma Physics and Plasma Technology. Minsk. Belarus. Sept. 18-22. 2000. P.551-553.

[6] Izotov V.I., Pozdn'akov V.A., Filippov G.A. Observing and explaining the creation mechanism of frail micro cracks in a ferrite-perlite tube steel under tensile load in hydrogen environment // FMM. 2001. v. 91. No5. P.84-90(in Russian).

[7] Illichev M.V., Isakaev E.Kh., Ivanov P.P., Tyuftyaev A.S. Influence of the plasma hardening on the railway wheel tire resource // Proceedings of the conference on the Low temperature plasma physics LTPP-2001, Petrozavodsk, 2001, p. 209-214(in Russian).

[8] Morozovskaya E.H. Automatic coating over high manganese content austenite steel// Automatic welding, 1961, No3. P.32-41(in Russian).

[9] Deribas A.A. Explosive hardening of manganese steel.//Physics of combustion and explosion. No3, 1966, p. 11-14(in Russian).

[10] Illichev M.V., Isakaev E.Kh., Zhelobtsova G.A., Katarzhis V.A., Spektor N.O., Filippov G.A., Effective method of coating copper substrate with wear resistant refractory layer, // Proceedings of the conference on the Low temperature plasma physics LTPP-2001, Petrozavodsk, 2001(in Russian).

[11] Sagalevich V.M. Methods of elimination of welding deformations and stresses, "Mashinostroyenie" 1974, 248 p(in Russian).

Determination of Basic Parameters of Hot Gas Mixture Free Jet

J. Gregor[1], I. Jakubová[1], T. Mendl[1], V. Sember[2], J. Šenk[1]

[1]Department of Electrical Power Engineering FEEC TU Brno
Purkynova 118, 612 00 Brno, e–mail: jakubova@feec.vutbr.cz
[2]Institute of Plasma Physics, Academy of Sciences of the Czech Republic
Za Slovankou 3, Praha, Czech Republic

Abstract
In the paper the basic parameters of free jet in the "hot" zone just after the output of the arc heater and in the "cold" zone far from the output are studied. The determination of the water vapour flow rate and the total output momentum in the "hot" zone is based on spectroscopic measurements and calculation by means of conservation equations. In the "cold" zone the contact measuring methods (thermocouple, pressure sensor) in combination with calculation method are used.

1. Introduction

Temperature, velocity and composition are the most important parameters of hot gas free jet. The choice of measuring methods and instruments depends on many technical circumstances and demands, and it is influenced especially by the expected range of measured values. In the hot region near the arc heater output the method of optical emission spectroscopy is used to determine the temperature. Just after this hot region (T<10000 K) the molecular spectroscopy and schlieren methods are favourable for the jet investigation. The condition in the region with lower temperatures (T<2500 K, far from the arc heater output) enable the utilization of thermocouples and cooled dynamic pressure sensors for measurements of temperature and velocity fields in the jet plume. In this paper the results of investigation of hot and cold parts of jet plume are described.

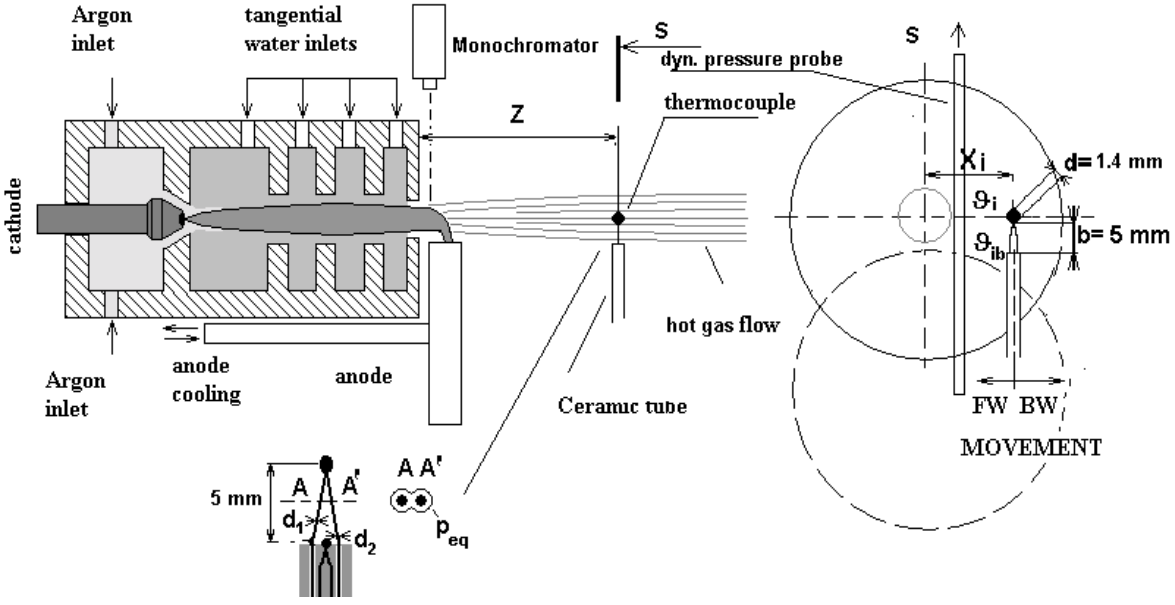

Fig.1 Scheme of the experimental device with hybrid water-argon plasma torch

2. Experimental and Measuring Arrangement

The arc in the arc heater is stabilised and cooled by the steam evaporated from the surrounding water swirl (Fig. 1). Water stabilised torch was modified by adding argon into the chamber. The main parameters of the experimental device were: output orifice diameter 5.6 mm, arc current 300 A, arc voltage 230 V (input power 69 kW), efficiency 0.55, argon flow rate 0.346 $.10^{-3}$ $kg.s^{-1}$.

The spectroscopic measurements were performed using the monochromator Jobin Ivon HR320 (Czerny-Turner configuration, f=0.32 m) with a grating of 1200 grooves per mm and with linear photodiode array.

Temperature distribution in the cold zone of jet plume was measured by Ir-IrRh thermocouple in ceramic protective tube. The thermocouple was inserted into the gas flow perpendicularly to its axis at the distance

z=365 mm from the output orifice (Fig. 1). The velocity field was measured by means of cooled dynamic pressure sensor inserted into the jet plume.

3. Output Parameters of the Arc Heater

The initial parameters of the jet at arc heater output are calculated by means of continuity, momentum, and energy equations using spectroscopically measured temperature distribution. From the continuity equation we obtain the total flow rate through the arc heater output orifice

$$G_M = \int_0^{r_T} \rho_M[T(r)].v(r)2\pi r dr \,. \tag{1}$$

From the momentum equation the initial momentum of plasma flow rate can be expressed

$$G_M.v_{out} = \int_0^{r_T} \rho_M[T(r)].v^2(r)2\pi r dr \,. \tag{2}$$

The energy equation can be written as

$$\eta UI = \int_0^{r_T} \{\ \rho_M[T(r)].v(r)\left[(h_M[T(r)] - h[373]) + \frac{v^2(r)}{2}\right]\}2\pi r dr + G_{WV} l \tag{3}$$

where $G_M = G_{Ar} + G_{WV} = G_{Ar}\left(1 + \frac{x_{WV}\rho_{WV}}{x_{Ar}\rho_{Ar}}\right)$; $x_{WV} + x_{Ar} = 1$ for the arc heater output.

G[kg.s^{-1}] is mass flow rate, ρ[kg.m^{-3}] specific mass, T[K]temperature, v[ms^{-1}] velocity, r[m] radial co-ordinate, η[-] efficiency, UI[W] input power, h[J.kg^{-1}] enthalpy, l[J.kg^{-1}] evaporation heat of water, x[-] molar fraction, lower indexes *M, T, out, Ar, WV* denominate values related to Ar+H_2O mixture, output orifice, argon, and water vapour.

The evaluation of the temperature distribution from spectroscopic measurements is based on Boltzmann diagram that uses relative emission coefficients of spectral lines of the same species and the same stage of ionisation [1]. The two groups of ArII lines were selected in the spectral regions around 420 nm and 482 nm. The obtained temperature profile at the arc heater output is given in Fig. 2.

The approximation of temperature radial profile by parabolic dependence obtained by means of the least squares method

$$T(r) = T_0 - (T_0 - T_T)\frac{r^2}{r_T^2}, \quad 2rdr = -\frac{r_T^2}{T_0 - T_T} dT \tag{4}$$

makes it possible to transform the integration over the co-ordinate r to the integration over the temperature T

$$G_M = \frac{\pi r_T^2 M}{T_0 - T_T} \int_{T_T}^{T_0} \rho_M(T) a_M(T) dT \tag{5}$$

$$G_M.v_{out} = \frac{\pi r_T^2 M^2}{T_0 - T_T} \int_{T_T}^{T_0} \rho_M(T) a_M^2(T) dT \tag{6}$$

$$\eta UI = \frac{\pi r_T^2 M}{T_0 - T_T} \int_{T_T}^{T_0} \rho_M(T) a_M(T)[h_M(T) - h_M(373)]dT + \frac{\pi r_T^2 M^3}{2(T_0 - T_T)} \int_{T_T}^{T_0} \rho_M(T) a_M^3(T) dT + G_{WV}\left[l + c_{pH_2O}(373 - 300)\right], \tag{7}$$

where a_M [m/s] is velocity of sound in heated gas, T_0 is the maximum temperature. This change of variables makes the solving of equation system easier because the integrals of thermodynamic quantities in equations (5), (6), and (7) can be calculated by the program for calculation of thermodynamic properties of gas mixtures [2]. Using the values UI=69000 W, ηUI=37950 W, G_{Ar}=0.346.10^{-3}kg.s^{-1} measured on the arc heater and the values T_0=18052 K, T_T=7930 K obtained from spectroscopic measurements (Fig. 2) the unknown values of water vapour flow rate G_{WV}=0.1903.10^{-3} kg.s^{-1} (G_{WV}/G_{Ar}=0.55), $G_M v_{out}$=1.21kg.m.s^{-2}, M=0.705, and v_{out}=2260 m.s^{-1} were obtained from the equation system (5), (6), (7). The process of calculation is given in Fig. 3.

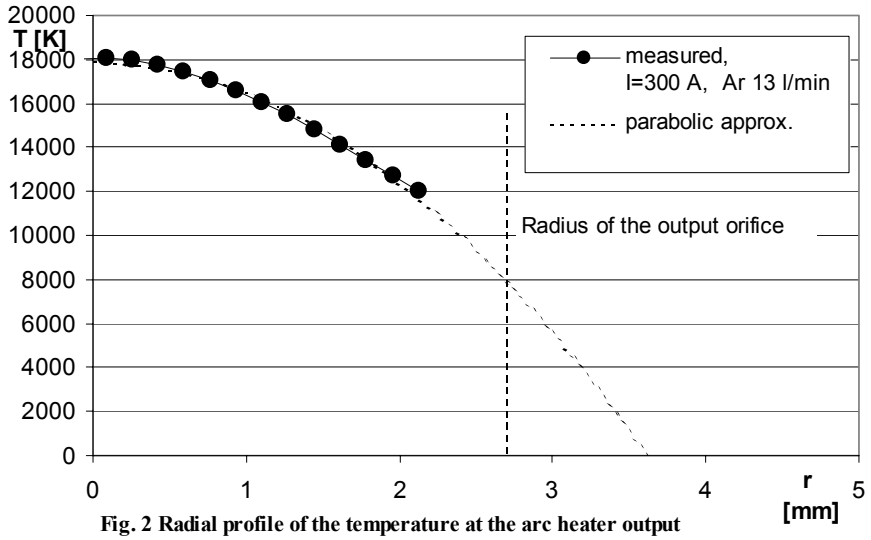

Fig. 2 Radial profile of the temperature at the arc heater output

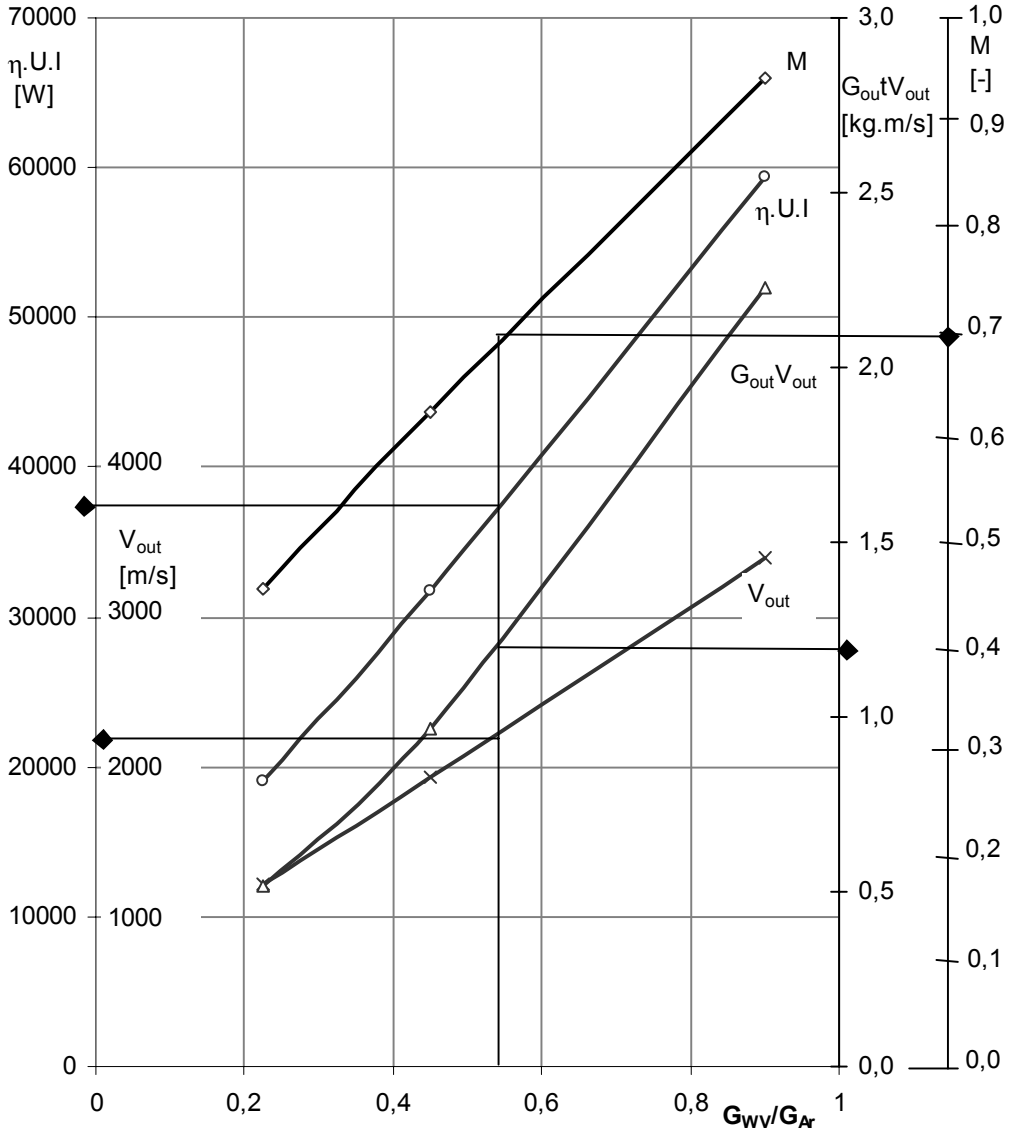

Fig. 3 The dependence of the calculated output quantities of the arc heater on the relation G_{WV}/G_{Ar}

4. Investigation of the Cold Part of the Jet Plume

The temperature distribution in the cold part of the free jet was determined by thermocouple inserted into hot gas. This measured temperature may differ from the real gas temperature because of energy loss by radiation and by heat conduction through the leads. These differences can be corrected using energy balance equation for thermocouple tip and the leads as it is shown in [3]. The corrected temperature profile with velocity profile measured by dynamic pressure sensor at z=365 mm are given in Fig. 4. The profiles were approximated by Gaussian distribution

$$\frac{T(r,z)-T_\infty}{T_{MAX}(z)-T_\infty}=e^{-\ln 2\left(\frac{r}{b_T}\right)^2}, \qquad \frac{v(r,z)}{v_{MAX}(z)}=e^{-\ln 2\left(\frac{r}{b_V}\right)^2} \tag{8}$$

where T_∞ is the temperature of the surrounding environment.

This substitution enables to determine the Prandtl number in the jet Pr = $(b_V/b_T)^2$=0.676 which is in very good agreement with the values given in [4], [5] for cylindrically symetrical jet. The determination of concetration of components in the gas mixture is based on the assumption that far from the output the components are completely mixed and the molar mass M_ρ of them is constant in the investigated temperature interval (T<2500 K). Then the molar fraction sum of the whole cross-section $\sum x_k$=1can be expressed by means of the component flow rates G_k

$$\frac{R}{p\int_{A(z)}\frac{v(r,z)}{T(r,z)}dA}\left[\frac{G_M}{M_{\rho M}}+\frac{G_{ON}(z)}{M_{\rho ON}}\right]=1. \tag{9}$$

From the momentum transfer law within the jet we obtain

$$k_t(z).G_M v_{OUT}=\frac{\int_{A(z)}\frac{v^2(r,z)}{T(r.z)}dA}{\int_{A(z)}\frac{v(r,z)}{T(r.z)}dA}\left[G_{WV}+G_{Ar}+G_{ON}(z)\right] \tag{10}$$

where R [J.kmol^{-1}.K^{-1}] is universal molar constant, p [Pa] pressure, M_ρ [kg.kmol-1] molar mass , $A(z)$ [m^2] the cross-section of jet in the distance z from the output , $k_t(z)$ [-] expresses the momentum loss and index ON means the values related to air.

Solving the equation system system (9), (10) for the gained output quantities of the arc heater and the determined quantities of the investigated cross-section at z=365 mm we obtain the values of the air flow rate $G_{ON}(365)=6.23.10^{-2}$kgs^{-1} and the coefficient of momentum radial loss $k_T(365)$=0.776.

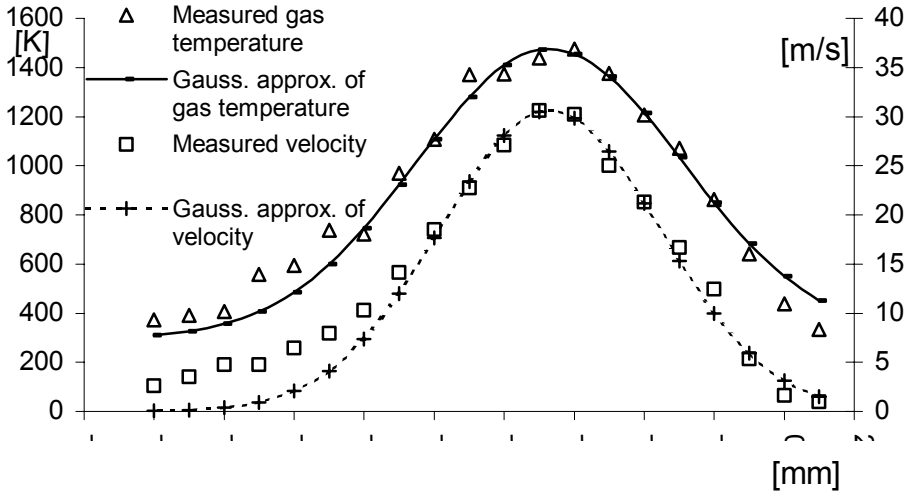

Fig. 4 Measured temperature and velocity profiles at z=365 mm approximated by gaussian curve

5. Conclusion

The calculated flow rates confirm our assumption that the shares of H_2O vapour (0,3 %) and Ar (0,6 %) in the total flow rate of the jet far from the arc heater output are very small. They are smaller than the relative content of this admixtures in atmosferic air at normal condition (it is 1,3 % Ar and 0,94 % H_2O vapour).
The significance of this insubstancial quantity is in the fact, that the flow rate $G_M=G_{WV}+G_{Ar}$ is the carrier of the original momentum of the jet.

References

[1] V. Sember - Czechoslovak Journal of Physics, vol.52(2002), suppl. D, D643-D650.
[2] Programme ADEP University of Limoges.
[3] J. Gregor, I. Jakubova , T. Mendl, J. Senk, V. Kopecky - Czechoslovak Journal of Physics, vol. 52(2002), suppl. A, 2192 A A1- A6.
[4] H. Schlichting - Theory of Boundary Layer(in German). Verlag G. Braun, Karlsruhe, BRD, 1965.
[5] B.E. Launder, D.B. Spalding - Mathematical Models of Turbulence. Academic Press, London & New York, 1972.

Plasma-deposited polyimide precursor monomers: preparation and optical study of thin coatings

G. Maggioni[1,2], A. Quaranta[1,2], E. Negro[1,2], S. Carturan[1,3] and G. Della Mea[1,2]

[1] *INFN - Legnaro National Laboratories, Legnaro, Padua, Italy*
[2] *Department of Materials Engineering and Industrial Technologies, University of Trento, Povo, Trento, Italy*
[3] *Department of Physics, University of Trento, Povo, Trento, Italy*

Abstract
Different polyimide precursor monomers are deposited by Glow Discharge-induced Sublimation (GDS) in order to characterize the deposition process and to study the structure of the deposited coatings in terms of molecular damage and aggregation. The deposition process has been characterized with plasma sampling mass spectrometry and by measuring the time evolution of the deposition rate. The films have been studied by FT-IR and UV-Vis fluorescence. The results have been compared with vacuum-evaporated thin films.

[1] A. Quaranta, S. Carturan, G. Maggioni, P. M. Milazzo, U. Abbondanno, G. Della Mea, F. Gramegna, U. Pieri - IEEE Trans. Nucl. Sci. **48**, 219 (2001).
[2] A. Quaranta, A. Vomiero, S. Carturan, G. Maggioni, G. Della Mea, - accepted for publication in Synthetic Met. (2002).
[3] M. Hasegawa, K. Horie - Prog. Polym. Sci. **26**, 259 (2001).
[4] G. Maggioni, S. Carturan, V. Rigato, G. Della Mea - Surf. Coat. Technol. **142-144**, 156 (2001).
[5] G. Maggioni, S. Carturan, A. Quaranta, A. Patelli, G. Della Mea - Chem. Mater. **14**, 4790 (2002).
[6] M.A.R. Alves, E. da Silva Braga, A. Fissore, L. Cescato - Vacuum **49**, 213 (1998).
[7] G. Maggioni, S. Carturan, D. Boscarino, G. Della Mea, U. Pieri – Mater. Lett. **32**, 147 (1997).
[8] NIST Mass Spec Data Center, S.E. Stein, director, "IR and Mass Spectra" in NIST Chemistry WebBook, NIST Standard Reference Database Number 69, Eds. P.J. Linstrom and W.G. Mallard, July 2001, National Institute of Standards and Technology, Gaithersburg MD, 20899 (http://webbook.nist.gov).

1. Introduction

Fluorescent coatings are widely used in several application fields ranging from optical gas sensors to nuclear and high energy radiation detectors. Several techniques are currently employed in their manufacturing, such as liquid phase epitaxy, dip coating and the sol-gel method. The application of these fluorescent coatings in nuclear physics puts some limitations in the choice of the materials, which must be radiation-resistant, mechanically stable and low-weight. Fluorinated polyimides are a class of very interesting materials; they have already been used as highly transparent and radiation-resistant matrices in plastic scintillators [1,2]; moreover, these polymers are intrinsically fluorescent, as reported by Hasegawa and Horie in their recent review [3].

Recently, a solvent-free deposition technique, based on glow discharge-induced sublimation, has been developed for the preparation of thin organic coatings [4]. This method is based on a weakly ionized glow discharge produced with a standard radio frequency magnetron sputtering equipment. Low energy gas ions impinge on the solid precursor leading to the sublimation of the organic molecules and to their subsequent condensation onto the substrate.

This work is a feasibility study about the deposition of polyimide precursor monomers, both fluorinated and non-fluorinated, through glow discharge-induced sublimation (GDS). One of its previous applications is the successful growth of a thin coating of 3-hydroxyflavone employed as a wavelength shifter in a Cherenkov light detector for astrophysics [5].

Several precursor monomers have been selected for this work: 4,4'-(Hexafluoroisopropylidene)di-phthalicanhydride (6FDA), 3,4,3',4'-biphenyltetracarboxylic dianhydride (BPDA), 3,3'-diaminodiphenylsulfone (3,3'-DDS), 2,4,6-trimethyl-m-phenylenediamine (TMPD) and 4,4'-(Hexafluoroisopropylidene) dianiline (6FDAm). The plasma deposition of these monomers has been characterized by plasma sampling mass spectrometry while their deposition rate has been monitored with a quartz crystal thickness sensor. So as to better characterize the deposition process and the properties of the films, thin monomer coatings have also been deposited through vacuum evaporation (VE) to compare the

novel GDS deposition procedure with a standard thermal evaporation process. The chemical structure of the GDS and VE coatings has been studied by FT-IR analysis. In order to achieve a better understanding on both the aggregation states of the organic compounds in the coatings and on the molecular integrity after the deposition, UV-visible fluorescence analysis has been performed on both VE and GDS coatings. Fluorescence spectra have been also collected from the monomers dissolved in liquid THF at different concentrations in order to obtain the isolated molecule emission features to be compared with those collected from the coatings.

2. Experimental

6FDA, 3,3'-DDS and 2,4,6-TMPD were obtained from Lancaster at 99%, 98% and 98% purity, respectively; s-BPDA was obtained from Acros Chemicals at 97% purity; 6FDAm was obtained from Acros Organics at 98% purity. All the chemicals were used without further purification. In Fig. 1 are reported the chemical structures of the organic molecules studied in these experiments.

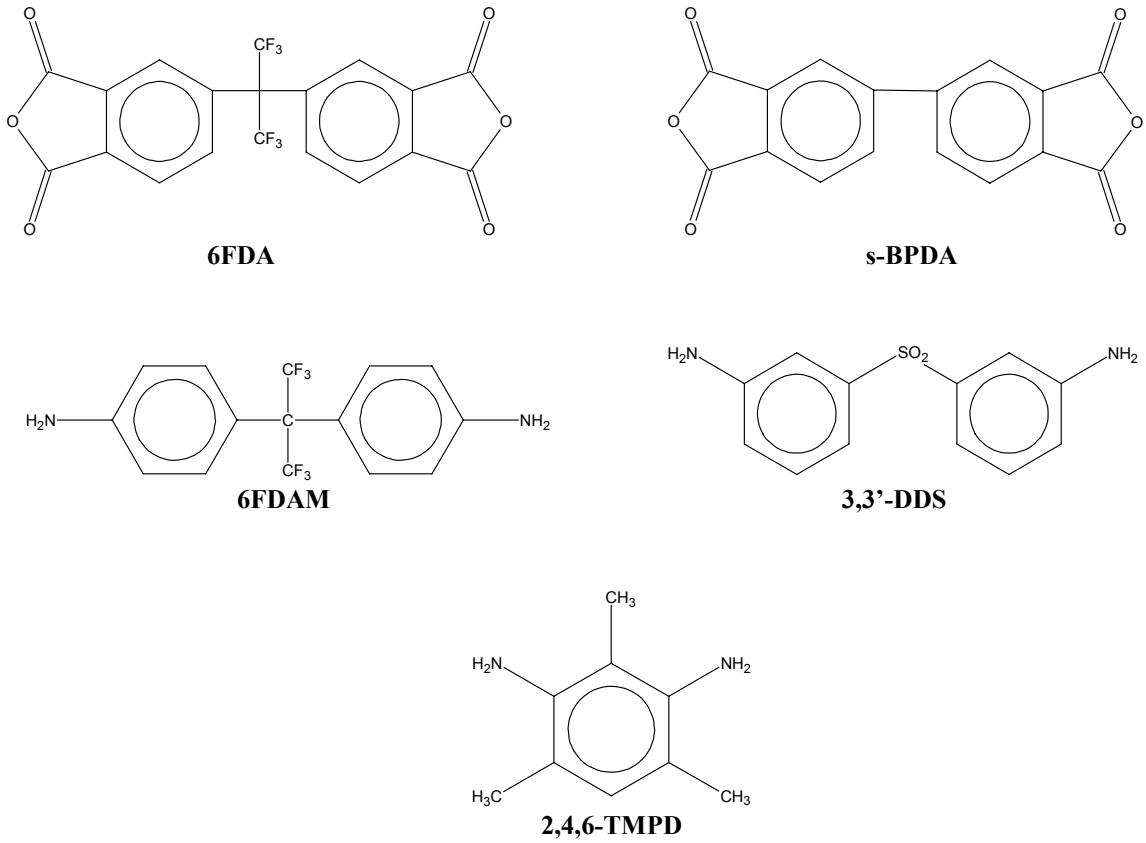

Figure 1. Chemical structure of 4, 4'-hexafluoroisopropylidene diphthalic anhydride (6FDA), 3,3',4,4'-biphenyltetracarboxylic acid dianhydride (s-BPDA), 4,4'- hexafluoroisopropylidene dianiline, (6FDAm), 3,3'-diaminodiphenyl sulfone (3,3'-DDS), 2,4,6 trimethyl m-phenylenediamine (2,4,6-TMPD).

The experimental apparatus used for the glow discharge deposition consisted in a stainless steel vacuum chamber evacuated by a turbomolecular pump to a base pressure of 10^{-4} Pa and equipped with a 1-inch cylindrical magnetron sputtering source connected to a radio frequency power generator (600 W, 13.56 MHz) through a matching box. The organic powders were put on the surface of an aluminum target, placed on the sputtering source. The glow discharge feed gas used in all the depositions was a 95% argon – 5% oxygen gas mixture. The oxygen gas was added to argon in order to promote the removal of the carbon-rich surface layer which is formed on the organic compound target owing to the ion bombardment [6]. The pressure inside the chamber was measured through a capacitance gauge. Typical values of rf power, target DC self-bias and working pressure were in the ranges 10-20 W, -20 to –200 V and 5.00±0.05 Pa, respectively. A quadrupole mass spectrometer (Hiden Analytical, model PSM 001) was connected to the deposition chamber through an electrically grounded sampling orifice (100 μm diameter) and evacuated by a turbomolecular pump to a base pressure of 10^{-6} Pa. The monomers were deposited on silicon substrates

lapped on both surfaces. The film thickness and deposition rate were measured by a quartz crystal microbilance.
Vacuum evaporated (VE) coatings were prepared with an apparatus specifically designed for the evaporation of organic compounds [7]. The powders were placed in copper crucibles wrapped with heating wires in a stainless steel vacuum chamber evacuated by a turbo molecular pump to a base pressure of 5×10^{-4} Pa. All the monomers were evaporated on silicon substrates, with the exception of TMPD due to its heat-induced molecular decomposition with the release of highly volatile molecular fragments.
FT-IR spectra of the samples were recorded using an evacuated Jasco FT-IR 660 Plus spectrometer with a resolution of 4 cm^{-1}. The transmittance spectra in the 4000-400 cm^{-1} range were collected from both the VE and the GDS coatings. KBr pellets containing the organic compounds were also inspected to obtain reference spectra.
The deposited films underwent fluorescence analysis at room temperature using a Jasco FP-770 spectrofluorometer equipped with a 150-W xenon lamp. The emitted light was collected at right angle from the sample surface. The data were corrected taking into account the spectral responsivity of the detection system (emission monochromator plus photomultiplier). So as to achieve a better understanding of the fluorescence behaviour of the molecules, emission spectra were also collected from liquid solutions prepared by dissolving each chemical in THF at two different concentrations, namely 10^{-2} and 10^{-4} M. These two concentrations were chosen in order to identify the fluorescence emission of insulated molecules and of fluorescent aggregates.

3. Results

The deposition rate of the different monomers follows a nearly exponential decay law which can be fitted by the expression

$$\log D = \log D_0 - Bt \qquad (1)$$

where D is the deposition rate in molecules cm^{-2} s^{-1} and t is the deposition time. The calculated values of $\log D_0$ and B are reported in Table 1.

Table 1: Deposition parameters for the different monomers. The first two rows refer to the GDS deposition, while the last row reports the vacuum evaporation rate. The temperatures for the vacuum evaporation procedure are also reported (T_{evap}). 6FDA powder sublimated completely in a few seconds when T_{evap} was reached.

Monomer	BPDA	6FDA	3,3'-DDS	6FDAm
log D_0	15.2	15.5	15.6	15.9
B (s^{-1})	$1.54\text{x}10^{-3}$	$1.61\text{x}10^{-3}$	$6.22\text{x}10^{-3}$	$1.96\text{x}10^{-3}$
T_{evap} (°C)	245	205	158	155
VE evap rate (molecules/cm^2s)	$1.4\text{x}10^{14}$	-	$1.1\text{x}10^{14}$	$2.2\text{x}10^{14}$

As far as TMPD is concerned, its deposition rate was nearly constant for about 500 s; afterwards it decayed following a nearly exponential law.

3.1 Dianilines

The dianilines mass spectra collected during the depositions show a different peak distribution and intensity with respect to the fragmentation patterns reported in literature [8]. In Fig. 2 is reported the TMPD mass spectrum; the molecular ion peak at 150 m/z shows a relative intensity with respect to the other fragmentation peaks lower than in the literature spectrum. 6FDAm mass spectrum exhibits a very small molecular ion peak together with other features not reported in literature, among which a peak at 69 m/z corresponding to the CF_3- group is noteworthy. Moreover, 3,3'-DDS shows neither the molecular ion peak nor any other fragment peak appearing in the literature spectrum. Among the different signals, a peak at 64 m/z ascribed to the SO_2 was visible.
FT-IR spectra of GDS, VE and KBr-dispersed samples exhibit nearly the same peak distribution with some little differences among them. The FT-IR spectrum of the TMPD sample deposited via GDS exhibits a small, sharp peak at 2160 cm^{-1}, which can be ascribed to the C≡C stretching vibration. The FT-IR spectrum collected from the GDS-deposited film of 3,3'-DDS shows a lower relative intensity between the peaks

placed at 1295 and 1150 cm^{-1}, ascribed to the C-SO_2-C stretching modes, and the peaks placed at 1600 and 1625 cm^{-1}, ascribed to the stretching vibration of the benzene rings. Moreover, a new small peak at 2210 cm^{-1} appears, due to the C≡N stretching vibration.

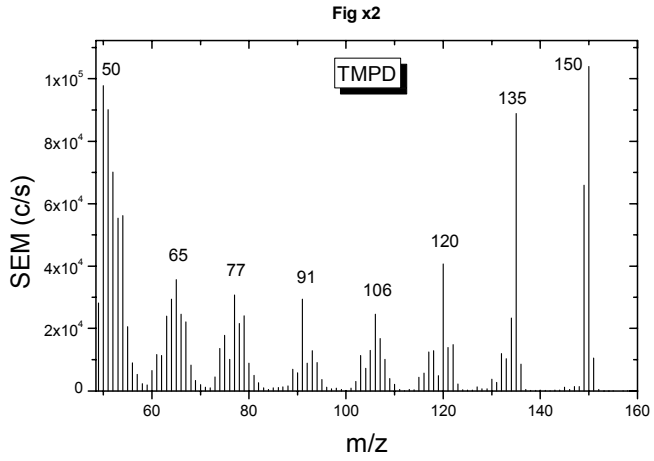

Figure 2: Mass spectrum of TMPD collected during the GDS deposition process.

As far as the fluorescence spectra are concerned, in Table 2 the main peaks collected from dianilines in liquid THF, VE and GDS samples are reported. In general, the fluorescence spectra obtained under UV excitation of the THF-dissolved and VE samples exhibit two kind of peaks: the former is placed at lower wavelengths and is ascribed to the isolated molecule, while the latter is placed at higher wavelengths, features a lower intensity and is probably due to dimers or aggregates. Some bathochromic shift can be observed owing to the different polar environments. Only the spectrum collected from the VE sample of 6FDAm shows a very faint band at 530 nm.

Table 2. Fluorescence peaks observed for the different dianiline samples.

Sample	THF (10^{-4} M)	THF (10^{-2} M)	VE	GDS
TMPD	335 nm (monomer) 415 nm (dimer)	340 nm (monomer) 415 nm (dimer) 475 nm (aggregates)	-	490 nm
6FDAm	330 nm (monomer) 420 nm (dimer/aggregates)	335 nm (monomer) 420 nm (dimer/aggregates)	330 nm (monomer)	500 nm 580 nm (shoulder)
3,3'-DDS	385 nm (monomer)	385 nm (monomer) 530 nm (very faint)	345 nm (monomer) 372 nm (monomer in more polar environment)	440 nm

GDS films show broad, faint emission bands at longer wavelengths. These fluorescence features are not directly connected to any of the emission peaks observed in THF-dissolved or VE samples.

3.2 Dianhydrides

The mass spectra of 6FDA and BPDA do not exhibit the molecular ion peaks and most of the high m/z features appearing in the literature spectra. In the case of 6FDA, the peaks corresponding to the CF_3- group at 69 m/z can be spotted.

As far as the FT-IR spectra are concerned, all the main molecule absorption peaks are visible in both VE and GDS samples. There is a significant broadening of these peaks in the latter with respect to VE and KBr samples.

In Table 3, the main fluorescence peaks collected from THF-dissolved, VE and GDS samples are reported.

6FDA exhibits two different emission features in THF at 10^{-4} and 10^{-2} M. In the first case two peaks are visible; the former is placed at 312 nm and is due to the monomer, while the latter is placed at 380 nm and is probably due to a dimer. In the second case only a broad band at 415 nm can be observed. On the other hand, the fluorescence spectrum of the VE sample shows a peak at 322 nm together with a structured band placed at about 500 nm. While the first peak can be clearly assigned to the undamaged monomer, the second band can be ascribed to some kind of aggregate formed during the condensation on the substrate. Finally, the fluorescence spectrum of the GDS sample shows a broad, faint band at 580 nm.
On the other hand, BPDA always exhibits the monomer emission peak, with some indication of dimer/aggregate formation in the GDS sample.

Table 3. Fluorescence peaks observed in the different dianhydride samples.

Sample	THF (10^{-4} M)	THF (10^{-2} M)	VE	GDS
BPDA	357 nm (monomer) 435 nm (dimer)	370 nm (monomer) 444 nm (dimer)	362 nm (monomer)	360 nm (monomer) 480 nm (faint emission)
6FDA	312 nm (monomer) 380 nm (dimer/aggregates)	415 nm (aggregates)	322 nm (monomer) 500 nm (aggregates)	580 nm

4. Discussion

The evolution of the deposition rates shown by the monomers during the GDS process points out the different mechanisms involved in the damage of the target. The exponential decrease observed after a few tens of seconds from the beginning of the deposition is ascribed to the progressive formation of a carbonised surface layer made of non-volatile species which cannot be removed from the target surface and hinder the further sublimation of the organic compound. The faster is the formation of the blocking layer, whose growth is only delayed by the reaction with the active oxygen species present into the plasma, the faster is the decaying rate. As far as TMPD is concerned, a possible interpretation of the different behaviour shown by this molecule is that the strong sublimation of integer species together with the emission of volatile fragments delay the formation of the blocking layer, which takes a much longer time (more than 500 seconds) than in the other chemicals.
Examining the VE-deposition procedure, 6FDAm, 3,3'-DDS and BPDA follow a similar pattern undergoing a gradual evaporation over a few minutes with comparable deposition rates, while 6FDA and TMPD suddenly "burst", evaporating completely in a matter of seconds once they reach a critical temperature. But while 6FDA deposits on the target surface, TMPD does not. This effect can be explained by supposing that the latter molecule undergoes a chemical decomposition on reaching the critical temperature, giving rise to the formation of very volatile fragments which do not adsorb on the substrate. From this fact, it can be concluded that the GDS deposition process allows to prepare coatings of organic compounds showing heat-induced decomposition during the standard thermal evaporation in vacuum.

4.1 Dianilines

The presence of the molecular ion peaks in the TMPD and 6FDAm mass spectra points out that the emission of undamaged monomer molecules takes place during the plasma-induced sublimation, so that their deposition onto the substrate can be expected. On the other hand, a further molecular fragmentation due to the interactions of the molecules with the plasma gives rise to ion peaks not appearing in the literature. It is possible to infer from this fact that weakly-damaged non-volatile molecules could adsorb on the substrate surface, becoming embedded in the film structure. FT-IR spectra points out that the GDS films are constituted mainly by integer molecules. This fact can be deduced by the presence of all the main fingerprint peaks, whose relative intensities correspond to those shown by the undamaged compounds. However, the presence of the features arising from the C≡C triple bond in the TMPD spectrum evidences that damaged molecules are also embedded into the film.
In the case of 3,3'-DDS, the absence of the molecular ion peak in the mass spectrum can be ascribed to the lower deposition rate of this chemical; the result is that in the deposition chamber the molecular concentration is lower than the detection limit of the mass spectrum analyzer. However, from the FT-IR spectra it can be deduced that the GDS-deposited 3,3'-DDS film is mainly made of undamaged molecules,

with some damaged structures as it is pointed out by the relative intensities between the stretching peaks corresponding to the SO_2 group and to the benzene rings. Besides, in the spectra is clear the presence of a feature ascribed to a $C \equiv N$ bond.
In the analysis of the film structure, UV-Vis spectroscopy plays an important role since it deals mainly with the delocalized molecular orbitals of the aromatic groups. Therefore, the fluorescence spectra can give more information both on the structure of the molecule as a whole and on its chemical surroundings. In fact, even if the mass spectra and/or the FT-IR spectroscopy give indications that GDS films are constituted by integer molecules, all the fluorescence spectra exhibit features which cannot be directly ascribed to the molecular orbitals of the undamaged, isolated molecules. On the other hand, the fluorescence spectra collected from VE films show the characteristic features of the monomers or the aggregates as observed in THF solutions.
At present, the nature of the new optically-active structures present in the GDS films is not clear. It must be pointed out that in the GDS deposition process the energy provided by the impinging ions gives rise to the formation of highly energetic species together with molecular fragments, which can produce a film structure different from the one obtained by means of a thermally-activated process like vacuum evaporation. In particular, the combination of energetic and weakly damaged molecules can induce the growth of molecular aggregates with new optical properties.

4.2 Dianhydrides
As far as 6FDA and BPDA are concerned, the absence of the molecular ion peak in the mass spectra can be attributed once again to the fact that the molecular emission rate during the GDS deposition process is below the detection limit of the mass analyzer. In fact, FT-IR spectra exhibit all the main molecular features, suggesting that the plasma-grown films are made of undamaged molecules for the most part. Moreover, the concentration of damaged structures is below the FT-IR detection limit, owing to the absence of any new peak.
The UV-Vis fluorescence emission spectra shows that the GDS-deposited 6FDA film exhibits a broad band centered at 580 nm, while the VE sample shows the monomer main peak together with a new feature at about 500 nm. This behavior can be ascribed, as for dianilines, to the formation of new optically-active molecular structures into the GDS-deposited coating. Moreover 6FDA, like 6FDAm, exhibits new fluorescence bands in VE samples. This finding can be explained with a more pronounced fragility of this kind of molecules caused by the $C(CF_3)_2$- group.
On the other hand, BPDA is the only monomer among those studied in this work that shows the molecular fluorescence peak in GDS films, thus confirming that undamaged molecules are deposited even in the absence of the molecular ion peak in the mass spectrum. In a previous work [5] the 3-hydroxyflavone dye molecule was deposited using the GDS procedure as an integer molecule, which preserved its optical properties. Therefore it can be concluded that some molecules, probably those characterized by a rigid structure, can be deposited via GDS to obtain films sharing the same optical properties of the isolated molecules.

5. Conclusions
Different organic thin films have been produced by means of the novel glow discharge-induced sublimation procedure. The deposition rate decreases with the time owing to the formation of a carbonaceous layer on the powder target surface which hinders further molecule sublimation.
From the analysis of mass and FT-IR spectra it can be deduced that the deposited films are mainly made of undamaged molecules with some weakly damaged structures. Moreover, the UV-Vis spectroscopy analysis evidences that the GDS deposition process gives rise to the formation of molecular structures with new optical properties compared to the starting monomers. This effect can be ascribed to a combination of energetic impinging monomers and damaged structures which form different kind of optically-active aggregates. The only exception is BPDA, which exhibits the monomer fluorescence features, indicating that it preserves its molecular structure also from the point of view of the electronic molecular orbitals.

Acknowledgements
This research was financially supported by the Fifth Commission of Istituto Nazionale di Fisica Nucleare (ASTHICO project).

The Method for Evaluation of Energy Processes in Intensively Blasted Electric Arc

J. Heinz[1], M. Hrabovsky[2], I. Jakubova[1], J.Senk[1]

[1]*Brno University of Technology, Faculty of Electrical Engineering and Communication, Purkynova 118, 612 00 Brno, Czech Republic*

[2]*Institute of Plasma Physics. ASCR, Za Slovankou 3, P.O Box 17, 18221, Prague, Czech Republic*

The contribution presents a mathematical-physical model of intensively blasted electric arc burning in anode channel of arc heater. The model is used for evaluation of measurements on experimental arc plasma generator with argon as working gas. The calculation procedure based on mass and energy conservation equations and Ohm's law enables to determine the temperature and velocity fields and energy flows in the blasted electric arc. Main input data (arc current and voltage, mass flow rate of working gas, energy losses of the arc heater's anode channel etc.) were obtained from measurement on the arc heater described in [1].
For calculation purposes the whole channel area is divided into two zones - electrical arc zone and heated zone. In the heated zone temperature dependencies of thermodynamic quantities are rather simple (constant or linear) and the energy equation can be expressed in simpler way, while in the arc zone the non-linear temperature dependencies must be taken into account. The radial temperature profile in arc zone is approximated by modified parabolic dependence, and in heated zone by Gaussian distribution.
According to Reynolds number quantity, the gas flow is supposed to be laminar or nearly laminar. During the solution procedure of equation system it was found that the oscillations of the arc position and volume may be interpreted as local turbulence and can be included into thermal conductivity as its turbulence component.
By means of the mathematical-physical model the measurements on the experimental arc heater in the range of current values 80-200 A and flow rate 22 g/s are investigated. The obtained results of theoretical-experimental investigation enable to evaluate the energy flows (convection, conduction and radiation) from arc. The distribution of the anode channel losses (radiation, heat transfer to channel walls) and their dependency on arc current can be judged.

[1] J. Gregor et al.- In Proceedings of SAP&ETEP, part I, pp 364-367, Lodz (Poland). 1993.

Carbon nanotubes from the thermal plasma dissociation of C_2Cl_4

D. Harbec[1], J.-L. Meunier[1], L. Guo[1], R. Gauvin[2]

[1]*CRTP / Department of Chemical Engineering, McGill University, Montreal, Quebec, Canada*
[2]*Department of Mining, Metals and Material Engineering, McGill University, Montreal, Quebec, Canada*

Abstract
Carbon nanotubes (CNT) are produced using a 100 kW dc non-transferred plasma torch and C_2Cl_4 as carbon precursor. Catalytic metallic nanoparticles are generated *in situ* using the tungsten metal vapours emitted by the electrode erosion process. Large quantities of multi-wall (MWNT), single-wall nanotubes (SWNT) and spherical onion-like carbon structures are observed under FE-SEM and TEM. Preliminary results are given here on the effect of some process parameter and electrode erosion.

1. Introduction

Carbon nanotube (CNT) structures are presently showing a vast interest throughout the scientific community and are finding their way into commercial applications. Applications particularly in the field of advanced materials are however strongly restrained not only by the price of CNT, but more importantly by the availability of large quantities of this material. A scalable approach for the synthesis of the fullerene cage-like molecules of C_{60} and C_{70} using a plasma torch based on the dissociation of tetrachloroethylene (C_2Cl_4) was described in previous ISPC conferences [1-4]. This paper presents an extension of the work on fullerenes to the nucleation and growth of carbon nanotubes. The objective of the project is first to demonstrate the possibility of large-scale production of CNT using thermal plasma torch technology [5], and to provide the design parameters enabling a scale-up to industrial power levels of the plasma torch system. These studies include an experimental component and modeling of the flow/energy/particle nucleation fields for a better understanding of the synthesis reactor.
As in fullerene experiments, the CNT growth is performed using a 100 kW non-transferred plasma torch. Long single-wall (SWNT) and multi-wall (MWNT) nanotubes were grown in various sections of the reactor. One key aspect of CNT synthesis is the need for nanoparticles of metal catalyst acting as a seed to anchor the tube structure and favouring growth at the tube-metal interface. Many techniques are pre-seeding the growth region with the nanoparticles of metal catalyst, while the conventional graphite arc technique uses metal particles imbedded within the anode and evaporated along with the carbon electrode [6-7]. One constraint of the graphite arc technique is the lack of independent control of the metal nanoparticle nucleation zone and the concentration/temperature fields of the carbon precursor species, these being coupled by the electrode erosion process and resulting local plasma composition responsible for the species concentration fields [6]. A plasma torch system provides some flexibility in trying to separate and provide a better *in-situ* control through the use of a catalyst nucleation zone followed by a CNT growth zone on the catalyst particles. We use in this study a simple and efficient method to induce such a two-step process by first producing metal vapour that condenses into nanoparticles within the plasma stream at a position of the carbon precursor injection. For simplicity of production and efficiency in generating the metal only in a vapour state within the plasma stream, we simply use the electrode erosion products within the plasma torch as the metal vapour source.

2. Experimental Setup

The water-cooled reactor (Figure 1) has a cylindrical geometry (ID=40 cm) and the flexibility to modify the length of the expanding plasma flame with a movable water-cooled disk plate (ID=36 cm) up to a possible total reactor length of L=100 cm. A quartz window provides optical access to the plasma jet for spectroscopy measurements. A 100kW non-transferred D.C. plasma torch is used for the dissociation of C_2Cl_4 injected in the torch nozzle with 20 slpm of helium or argon as the carrier gas. C_2Cl_4 is fed at flow rates of 0.15-0.54 mol/min at a temperature of 200°C ± 10°C. Helium or Argon are used as the plasma forming gas at 225 slpm for helium or 100 slpm for argon. Table 1 gives a summary of these experimental conditions. In the experiments presented in this paper, thoriated tungsten was used as electrode material and the erosion process within the plasma torch acted as the source of tungsten nanoparticles. A graphite cylinder of 30 cm long is added around the plasma jet in order to extend the hot section of the reactor and limit by-product formation by avoiding cold gas entrainment within the plasma jet. The operating pressure inside the reactor

is set at a value between 200 torr and 1 atm. It is controlled using a water-sealed vacuum pump and an automatic proportional valve. The chlorinated exhaust from the pump is treated through a packed column in which a caustic solution shower absorbs the chlorine gas. Observations of CNT were done using FE-SEM and TEM. Typical run durations were of 5 minutes.

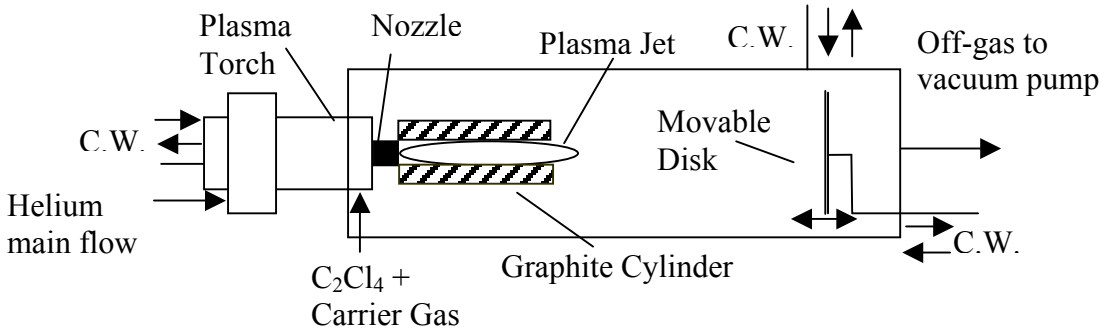

Figure 1: Experimental setup (C.W.=cooling water)

Table 1: Experimental conditions for fullerene/ nanotube soot production in present paper

Conditions	**Plasma-Forming Gas**	
	Helium	**Argon**
Torch Power (kW)	30 to 65	30
Main plasma gas flow rate (slpm)	225	100
C_2Cl_4 feed rate (mol/min)	0.15	0.15
Carrier Gas flow rate (slpm)	20	20
Reactor Pressure (torr)	200, 500	200
Reactor Length (cm)	100	100
Run Duration (min)	5	5

3. Results and Discussion

-3.1 Nucleation of Tungsten Nanoparticles

The plasma torch was designed with an inside diameter of the C_2Cl_4 injection nozzle that is enlarged with regards to the torch flow outlet at the downstream electrode (Figure 2). Modeling of the main plasma flow field indicated a recirculation zone is created with local cooling of the plasma stream. The thoriated tungsten electrodes generate tungsten vapours upstream of the injection nozzle within the plasma torch. The quench of the plasma stream occurring within the injection nozzle provides a nucleation zone into which tungsten nanoparticles acting as a catalyst for CNT nucleate. Depending on the operating conditions, carbon soot containing CNT condenses or grows within the nozzle at various positions upstream or downstream of the C_2Cl_4 injection and are collected either as a coating on the nozzle walls and/or downstream within the reactor itself. It was observed at the lower pressure for example that 10% of the total collected soot is condensed in the upstream region.

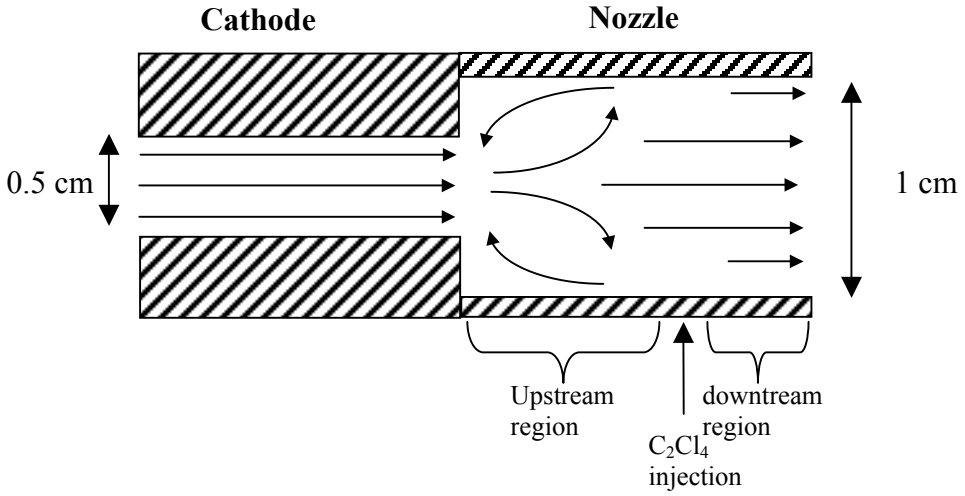

Figure 2: Sketch of the cathode/nozzle geometry and velocity streamlines

Tests were preliminary performed using helium as plasma-forming gas, 55 kW torch power and 200 torr reactor pressure. The resulting mixture of tungsten nanoparticles and carbon collected in the upstream region

of the nozzle was observed under FE-SEM and EDX (Figure 3a and b respectively). All electron microscopy images presented here are performed on raw unpurified samples.
The tungsten nanoparticles were found well-distributed within the carbon material which shows a cauliflower appearance at low magnification. The EDX spectrum confirmed that these nanoparticles are made of tungsten. The spectrum also shows the presence of chlorine in the sample coming from the chlorinated carbon precursor.

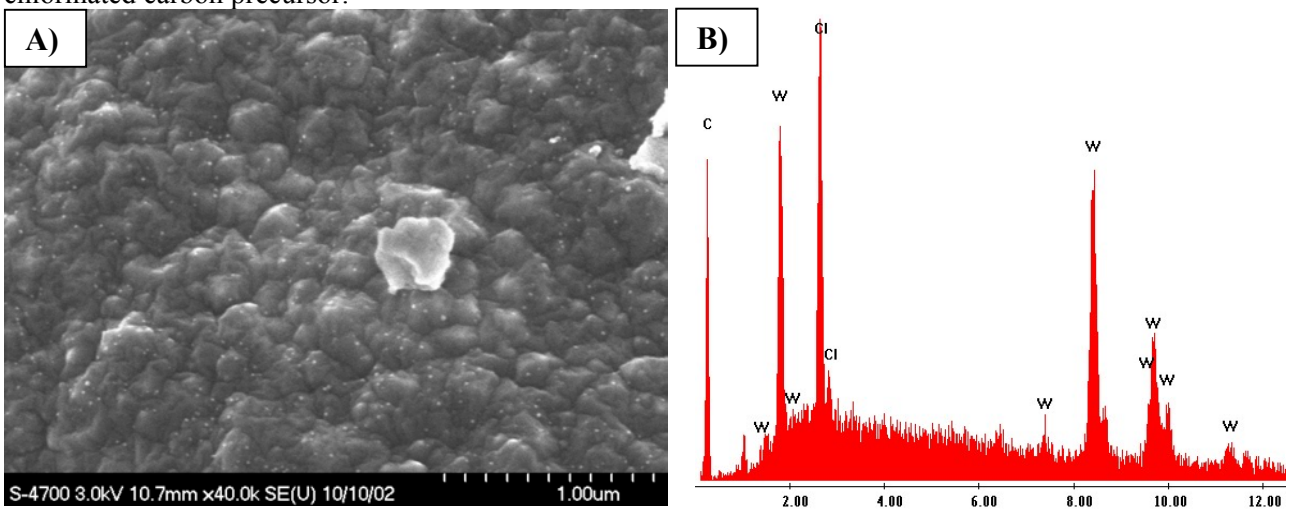

Figure 3: A) FE-SEM image showing nucleated tungsten nanoparticles (white dots, ϕ<20nm) well dispersed within the carbon deposit on the nozzle walls. B) EDX elemental analysis confirming the tungsten nature of these particles.

-3.2 Formation of CNT

At higher magnification using the FE-SEM, a well-distributed and high concentration of CNT can be seen in the carbon deposit within the nozzle. Both the deposit and CNT form a very stable structure in the nozzle during torch operation. Figure 4a,b respectively show that they are long (up to the 50 μm scale) and have relatively uniform diameters (≅20 nm range).

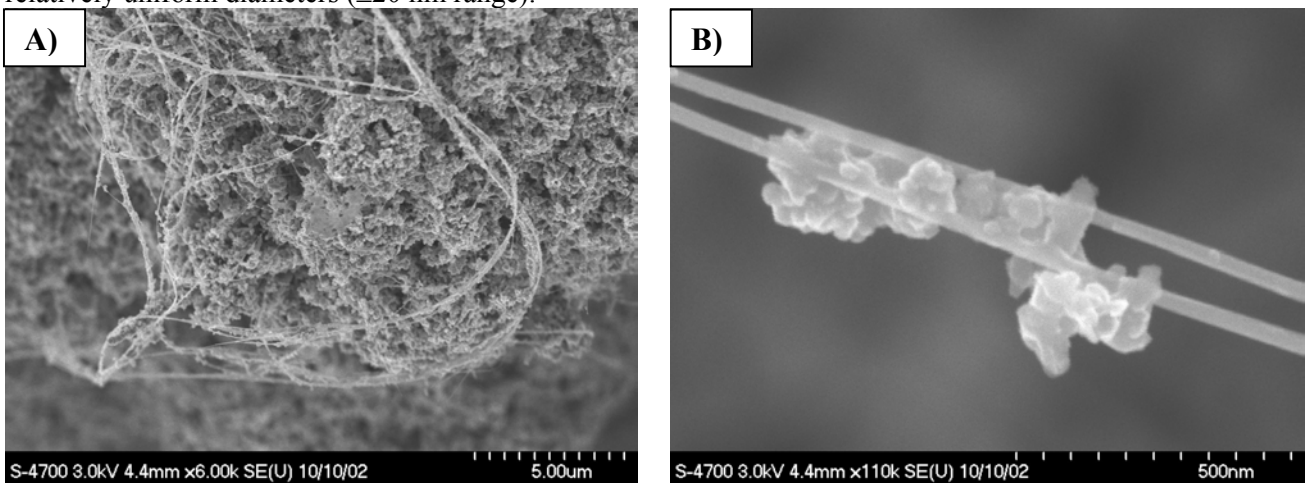

Figure 4: A) Large concentration of long and well-distributed CNT. B) Close-up of CNT with typical diameter in the 20-50 nm range.

Such structures are well distributed throughout the region upstream of the C_2Cl_4 injection at the lower reactor pressure, the downstream section typically showing larger CNT diameters. Increasing reactor pressure tends to push the smaller diameter CNT downstream of the nozzle towards the plasma tailflame. Under TEM, nanoparticles of tungsten having diameters in the 10-20 nm range are found encapsulated in the tip of the CNT (Figure 5a). The majority of the CNT observed correspond to MWNT, while a smaller fraction is seen as SWNT. Also present in large quantities are spherical onion-like carbon structures. The SWNT have diameters of 2-3 nm, while MWNT are characterized by an external diameter around 15-20 nm and internal diameters of 2-3 nm. One can see in Figure 5a that tungsten particles are effectively observed at the tip of the CNT, confirming that the tungsten vapours from the erosion process effectively promote CNT formation. A transitional metal at the CNT interface prevents an early closure and promotes an efficient elongation of the

carbon structure. The observations presented here indicate an excess of carbon to catalyst particles in the CNT synthesis region, and a size of the catalyst particles that seem to promote MWNT. The catalyst being produced by the electrode erosion process in the present experiment, section 3.3 shows the evolution of the erosion rate of the plasma torch.

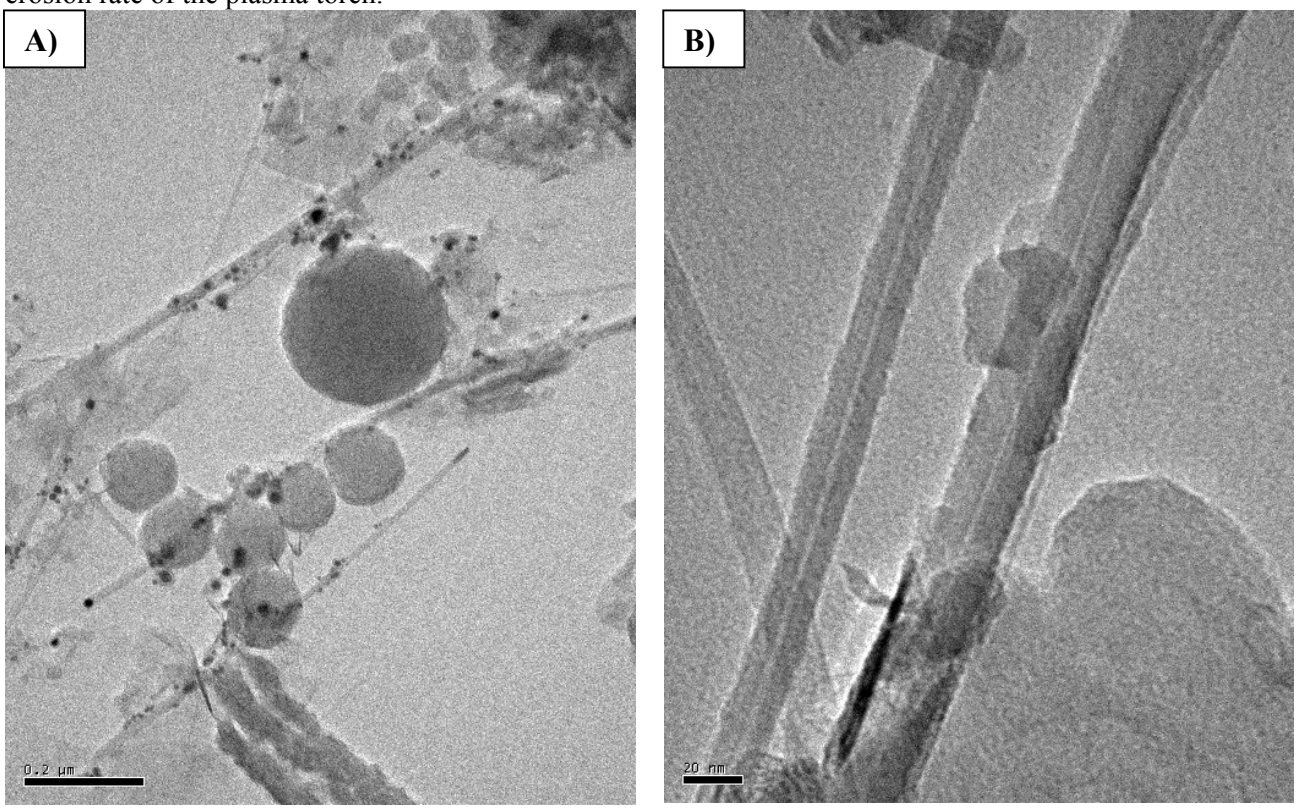

Figure 5: TEM images on carbon deposits collected in the nozzle after 5 minutes of operation using 55 kW torch power, 225 slpm helium, 0.15 mol/min C_2Cl_4 and 200 torr reactor pressure. Figure A shows tungsten particles (black dots) and a relatively large amount of spherical onion-like carbon structure. Figure B: close-up of some CNT structures. Scale lines: in A: 200 nm; in B: 20 nm.

-3.3 Erosion Rates of the Torch Electrodes

The relative quantity of available catalyst particles plays a crucial role in CNT growth and yield. Low quantities will yield by-products such as premature closed dome structures, whereas larger quantities will increase metal-carbon interfaces and yield more efficiently CNT [8-9]. Erosion rate experiments on the tungsten electrodes were thus performed at different torch currents in order to provide some knowledge and control on the amount of catalytic nanoparticles that can be provided into the system. The cathode for this evaluation was weighted before and after each experiment and erosion rate was calculated according to the duration of the experiment and the arc current used. Table 2 indicates the torch conditions used in this study and the values of current associated which each condition. Figure 6 presents the cathode erosion rates for the various torch conditions in Table 2. These are expressed in mass eroded/Coulomb of electric charge passing (10^{-5} mg/C) through the electrode during each experiment.

Table 2: Torch currents associated with their respective gas and power conditions

Torch Conditions	Current (Amps)
100 slpm Argon @ 30 kW	375
225 slpm Helium @ 30 kW	160
225 slpm Helium @ 45 kW	240
225 slpm Helium @ 55 kW	290
225 slpm Helium @ 65 kW	350

Depending on the torch current condition, the quantity of tungsten available in the system lies from 0.01% to 0.1% of the carbon fed. The plasma torch electrodes are made of tungsten to minimize erosion at higher power and to sustain the chlorine gas environment. One can see from Figure 6 that higher torch power provides enough electrode heating to reach thermionic "hot cathode" emission and relatively low erosion rate. On the contrary, the low power of 30kW in He is below a lower limit for this cathode arrangement having a tubular geometry. The cathode emission process in this case is most probably in the thermo-field "cold-cathode" mode leading to a strong increase of the erosion rate.

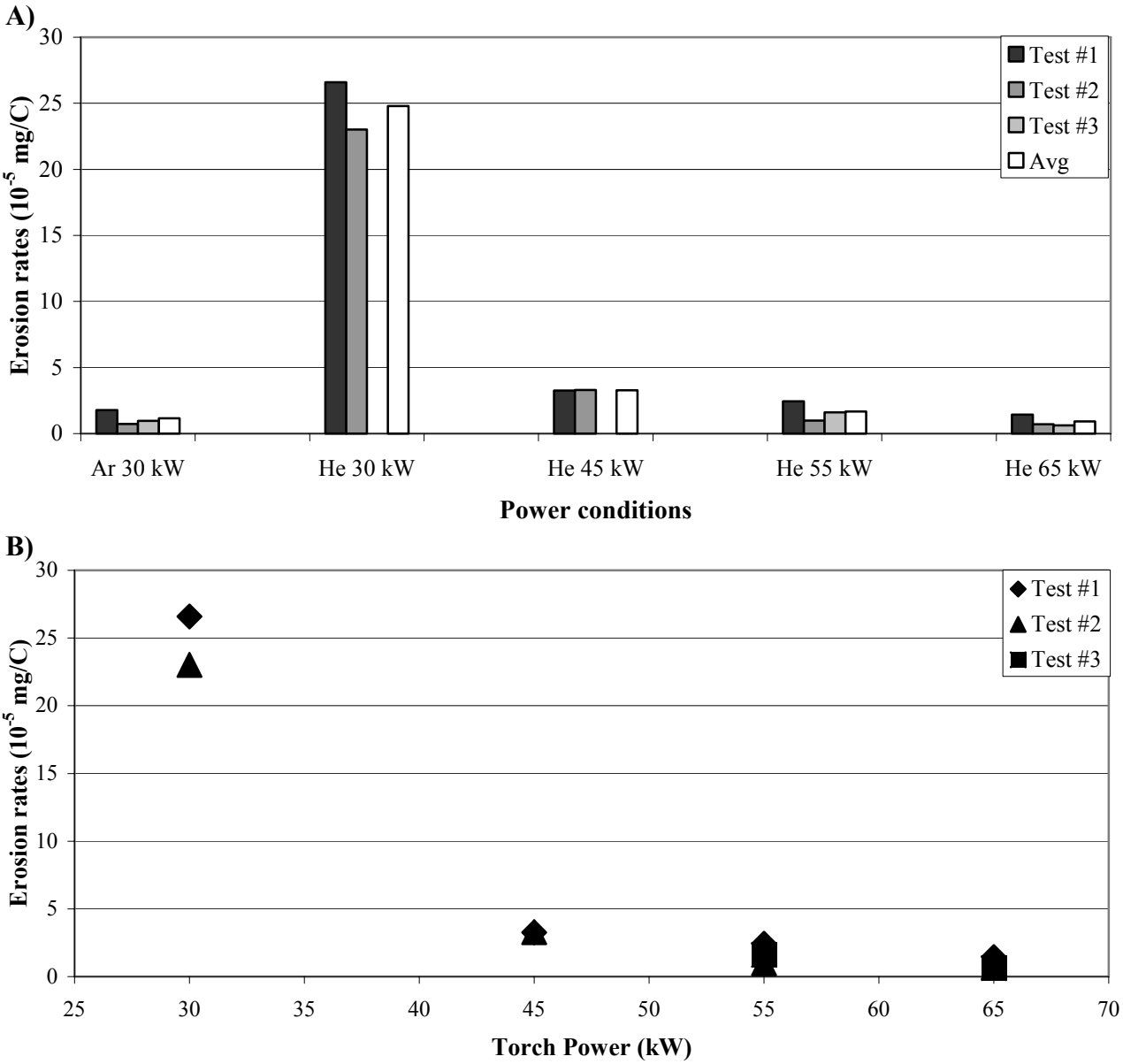

Figure 6: A) Erosion rate versus plasma conditions. B) Erosion rate versus torch power using 225 slpm of helium

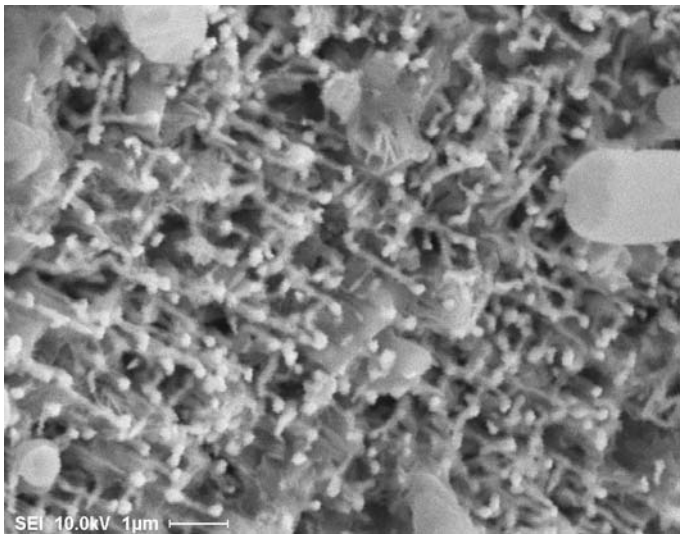

Figure 7: CNT produced at 500 torr pressure in the reactor on the movable disk.

-3.4 Effect of Reactor Pressure

In graphite arc systems, CNT are produced at pressures typically higher than fullerenes, for example in the 500-600 torr range [6-7,9]. The results presented above indicate CNT found in the upstream region of the nozzle when operating at 200 torr, while no CNT is observed further downstream in the reactor for this pressure. At 500 torr, observations made using FE-SEM revealed the absence of CNT in the upstream region of the nozzle, but their presence at the exit section of the nozzle and on the movable disk. The increase of pressure allowed the growth of CNT of comparable size and morphology to the ones produced at lower pressure, but in this case produced in the exit section of the nozzle. CNTs are also collected on the movable disk in the reactor. Some, as shown in Figure 7, are typi-

cally shorter (≅1μm long) than those seen in the nozzle itself and seem to have grown from the plate surface itself. The observations above suggest that an increase of reactor pressure produces flow and thermal conditions for catalyst nucleation with good adherence and CNT growth to occur further downstream in the nozzle and within the reactor. Soot accumulation within the nozzle gradually tends to a degradation of the plasma jet conditions. The transfer of CNT synthesis outside of the torch nozzle strongly favours implementation of a continuous process.

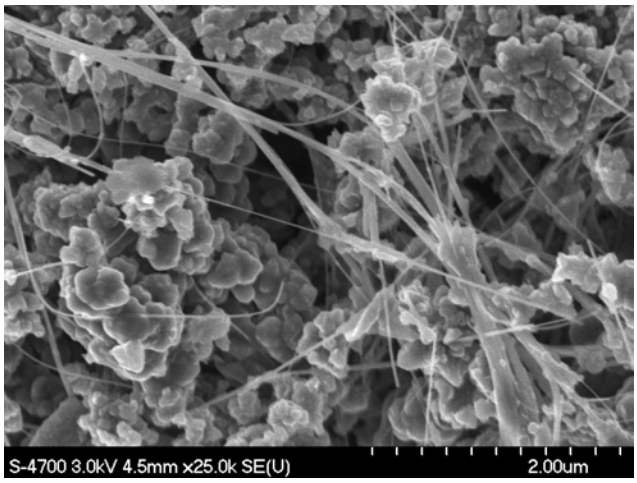

Figure 8: CNT's and soot collected using argon experimental conditions (Table 1)

-3.5 Tests in Argon

Typically, the carbon arc system does not provide conditions for fullerenes and CNT yields in argon. This is strongly linked to the physics of the arc-surface interaction leading to a small amount of carbon vapours being produced. Hence, this limitation should not necessarily be applicable to a plasma torch system aimed at separating plasma and atomic carbon production. Tests using argon as the plasma-forming gas were hence performed in view of the economical aspect of argon over helium. Conditions stated in Table 1 were used. The preliminary observations using FE-SEM (Figure 8) indicate important amounts of CNT are effectively produced; the concentration was fairly uniform in the torch nozzle deposit (upstream and downstream) and in fact appears to be higher in argon than for helium (Figure 3). This affirmation remains of preliminary nature at this time since soot was not analyzed for CNT quantification yet.

4. Conclusion

FE-SEM, TEM and EDX observations demonstrated the potential for a scale increase in CNT production using C_2Cl_4 as a carbon precursor in a process that could operate under a continuous production regime. In these demonstration experiments, the catalyst particles are generated *in situ* from the electrode erosion of a 100 kW D.C. plasma torch. The new process enables the synthesis of SWNT, MWNT, and onion-like spherical carbon structures. The CNT structures are produced both in helium or argon environment. At present, the experiments were limited to the use of thoriated tungsten electrodes showing low erosion rates. A change of the electrode material to thermo-field electrodes showing good catalyst behaviour such Ni/Co is expected to improve the CNT yield. The present study shows that CNT production is shifted downstream from the C_2Cl_4 injection nozzle at higher reactor pressure and using argon over helium as plasma-forming gas.

4. References

[1] J.-F. Bilodeau, T. Alexakis, J.-L. Meunier, P.G. Tsantrizos, Proc. of ISPC-13, Beijing August 18-22, 1618-1623 (1997).
[2] J.-F. Bilodeau, T. Alexakis, J.-L. Meunier, P.G. Tsantrizos, J. Phys. D : Appl. Phys, **30**, 2403-2410 (1997).
[3] T. Alexakis, P.G. Tsantrizos, Y.S. Tsantrizos, Appl. Phys. Lett. **70**, 2102-2104 (1997).
[4] D. Harbec, J.-L. Meunier, T. Alexakis, B. Cicek, M. Pacheco, M. Razafinimanana, Proc. of ISPC-15, Orléans, France, July 9-13, 2001, v. 7, 2757-2752.
[5] D. Harbec, J.-L. Meunier, "Method for producing carbon nanotubes using a thermal plasma torch", U.S. Patent appl. number 60/426,407 (2002).
[6] A. Huczko, H. Lange, T. Sogabe, J. Phys. Chem. A., **104** (46), 10708-10712 (2000).
[7] P. Bernier, W. Maser, C. Journet, A. Loiseau, M. Lamy de la Chapelle, S. Lefrant, R. Lee, J.E. Fisher, Carbon, **36**, 675-680 (1998).
[8] T. Guo, P. Nilkolaev, A. Thess, D.T. Colbert, R.E. Smalley, Chem. Phys. Lett., **243**, 49-54 (1995).
[9] M. Pacheco, Ph.D. thesis, CPAT, Univ. Paul-Sabatier, Toulouse, France, (2003).

Time evolution of laser-induced plasmas for various pulse durations and laser fluences

S. Laville[1], B. Le Drogoff[1], F. Vidal[1], M. Chaker[1], T. W. Johnston[1], J. Margot[2], M. Sabsabi[3], O. Barthélemy[2]

[1] *INRS-Énergie, Matériaux et Télécommunications, Varennes, Québec, Canada*
[2] *Département de physique, Université de Montréal, Montréal, Québec, Canada*
[3] *IMI, Conseil National de Recherches du Canada, Boucherville, Québec, Canada*

Abstract
The time evolution of a plasma produced by laser ablation of an aluminum target in ambient air at atmospheric pressure is investigated both experimentally and numerically. The space-averaged plasma temperature and electron density as a function of time are compared for (i) three laser pulse durations (100 fs, 270 ps and 8 ns) at a fluence of 20 J/cm^2 and (ii) for laser fluences up to ~30 J/cm^2 for 100 fs pulses. For fairly early times (< 1 μs), the plasma averaged temperature increases with the laser pulse duration and fluence, while for longer times the temperature is nearly independent of these parameters. The electron density also appears to be nearly independent of the plasma initial conditions for times greater than ~100 ns. Using our code, the results of which are in good agreement with experiments, this general behavior can essentially be explained by plasma's radiative losses and the work done on the ambient air for expansion.

1. Introduction

Laser Induced Plasma Spectroscopy (LIPS) is a spectrochemical analysis method based on the measurement of impurity line intensities emitted by plasmas created by laser-induced ablation from a target (for a review of LIPS, see Ref. [1,2]). While LIPS is already successfully used in several applications, there is a constant demand for improving the lower limit of detection of trace impurities. A step toward this goal is to improve our knowledge and understanding of the laser-created plasma characteristics as a function of the laser parameters such as pulse duration, laser energy per surface (fluence), wavelength, etc.

Several authors have investigated the influence of the laser parameters on the plasma emission, temperature and electron density (see [1-3] for ns pulses only). The conclusion which emerges from these investigations is that, for sufficiently short delays (typically less than a few hundred of nanoseconds), early temperature values increase with the fluence and pulse duration [4,5], while at later times the fluence has little influence on the temperature. Similar observations have been reported for the electron density as a function of the fluence. However, electron density has not been systematically investigated as a function of the pulse duration (except in [5] where 100 fs and 8 ns pulses were compared). Although these general trends emerge clearly from the experimental studies, to our knowledge the basic reasons for this behavior have not yet been discussed.

The main goals of this paper are to present measurements of the time dependence of the space-averaged plasma properties (temperature and electron density) for various pulse durations and laser fluences, and to compare the results with those of a numerical model. The objective of the modeling is to give a realistic interpretation of our measurements and to obtain physical insight. The code used here is a one-dimensional fluid model which is similar to the one used in our previous work [6-8]. The code includes a self-consistent treatment of hydrodynamics, laser energy absorption and interaction with the ambient medium. A novel feature of the code used here is the radiative cooling of the expanding plasma, which proves to play a major role in the plasma evolution.

We have considered three pulse durations (τ): one in the ultrashort regime (100 fs), one in the intermediate-pulse regime (270 ps) and one in the usual long-pulse regime (8 ns) for a laser fluence of 20 J/cm^2. We have also considered fluences from somewhat above the ablation threshold (~0.1 J/cm^2) [9] to ~30 J/cm^2 for a pulse duration of 100 fs. Our investigations were carried out using solid aluminum targets in air at atmospheric pressure and a 0.8 μm laser wavelength (Ti:Sapphire) for the 100 fs and 270 ps pulses, and a 1.064 μm laser wavelength (Nd:YAG) for the 8 ns pulse.

2. Experimental

All the measurements presented in this paper were performed at room temperature in air at atmospheric pressure. For the 100 fs and 270 ps pulses considered here the beam was focused on the target at an incidence angle of 20° from the normal using a quartz lens (f = 50 cm). The emission spectrum (from which the electron density and temperature were extracted) was measured by observing the aluminum plasma perpendicularly to the target surface, i.e., along the expansion axis of the plasma, using a gateable intensified charge-coupled device (Andor ICCD) coupled to a 50 cm Czerny-Turner spectrometer (Spectra Pro 500i, Acton Research Company) equipped with a 3600 gr/mm grating. Time-resolved emission spectra were obtained by controlling the time delay, denoted t_d (i.e., the time at which the plasma emission starts to be recorded), with respect to the laser pulse and the integration time (following the time delay, t_d), by means of an EG&G delay generator. The ICCD dark current was automatically removed from the emission signal for each measurement. The measurements consisted in accumulating the data for 100 successive laser shots. More details are given in Ref. [5]. The setup for the 8 ns pulse measurements is explained in Ref. [10].

The shape of the lines used for the diagnostics is well fitted by a Voigt profile, which suggests that self-absorption is negligible for the lines considered in this study. The peak intensity, the full width at half maximum (FWHM), and the center wavelength of each line were determined together with the continuum emission for each emission spectrum recorded. The excitation temperature and the electron density determined in our study are space integrated.

3. The numerical model

The code used here is a one-dimensional fluid model which includes a self-consistent treatment of: (i) absorption of the laser energy, (ii) hydrodynamics, (iii) thermal conduction, (iv) electron-ion energy coupling (implying that the ion temperature and the electron temperature are treated separately), (v) shock wave generation in ambient air and (vi) radiative transfer and losses at the interface between plasma and air.

Fluid equations for the conservation of mass, momentum and energy are solved through a one-dimensional Lagrangian scheme. The model also includes a realistic equation of state in order to describe thermodynamic properties (pressure and internal energy as a function of density and temperature) over the various states of the matter ranging from solid to plasma. In this paper, we have described the ablation step using the equation-of-state model QEOS (Quotidian Equation Of State) [11] while SESAME [12] is rather used for the expansion phase.

A particular feature of the code used for this paper is that radiative transfer and losses to the ambient medium are taken into account. Difficulties linked to the solution of equation of radiative transfer lead us to use the diffusion (or Eddington) approximation in which the radiative energy flux is proportional to the gradient of the radiative energy density u_v [13]. We have checked that the radiative energy flux thus obtained is always much smaller than the free streaming value cu_v (where c is the speed of light), this being a necessary condition for the validity of the diffusion approximation. We have used ten energy groups for photons, the absorption coefficient for each photon energy group being given by tables of Ref. [14]. Particle inter-diffusion between the plasma and the air has been neglected because the characteristic time scale for the diffusion process is much longer than that considered here.

The expansion of laser plasma plumes into the ambient gas is realistically an axisymmetric two-dimensional problem, but a full code for such a problem would be very costly and cumbersome for the long time scale of interest here (~10 μs). At very early times, one can assume roughly one-dimensional Cartesian expansion as long as the expansion distance is smaller than the focal spot diameter. At very late times, long after the laser has finished, the expansion can be reasonably considered as hemispherical expansion [15]. We ran the code with both geometries which can be seen as two limiting cases. The two cases are shown in Fig. 1, where the spot size on the flat target and the energy gives the fluence. In the spherical case the spot size has the same area on a hemispherical surface.

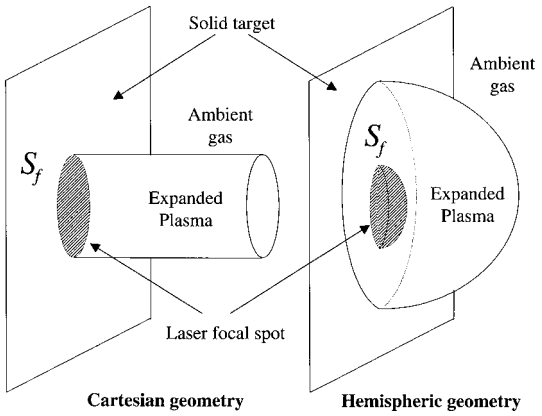

Fig. 1: The two plasma expansion geometries (Cartesian and hemispherical) used in our one-dimensional simulations.

4. Results

The plasma expansion is typically followed over times ranging from 100 ns to a few tens of μs. For light detection delay times shorter than 100 ns, the signal-to-noise (line-to-continuum) ratio is too small (i.e., the continuum emission dominates the lines) to provide useful spectroscopic information to determine the plasma properties. For longer delays (i.e., typically more than a few tens of μs, dependently of the emitted species of interest and of the pulse duration), the plasma emission has decreased so much as to be too small to provide usable results.

In order to make a comparison of the simulation results with our space-integrated measurements, we have replicated the experimental procedure on the model by integrating the appropriate line intensity emitted by each portion of the plasma. (We assumed that the plasma is optically thin for the lines considered and that the direction of observation has no importance.) We have then extracted from this space-averaged line signal the values used to infer the temperature and the electron density using the same methods as those used for treating the experimental data. To calculate the appropriate species densities, we solved the Saha equations and used as input parameters the atom density and the plasma temperature provided by the code.

4.1. Average plasma temperature as a function of the pulse duration

The average temperature was determined using a Boltzmann plot for a set of eight atomic lines of Fe(I) (element initially present with a concentration de 0.7% in the aluminum target). For optically thin plasmas, the intensity of a given line depends of the population of the excited level. For a plasma at LTE, the Boltzmann law links the total density to emitted species density (neutrals or ions).

Figure 2 shows the plasma space-averaged temperatures obtained from our measurements and from our code as a function of time, for the three pulse durations τ = 100 fs, 270 ps and 8 ns, and for the single fluence of 20 J/cm^2. A comparison of the measurements for all the pulse durations considered here shows that at early times, the plasma temperature is larger for longer pulses. Nevertheless, for sufficiently late times (more that a few microseconds), we observe that the laser pulse duration has little influence on the plasma temperature. At about 10 μs, the obtained temperatures for all pulse durations reach the common value 4000-5000 K, and therefore all the temperatures decrease together.

In Fig. 2, the code results are seen to agree well with measurements for the pulse durations presented here, considering the estimated experimental errors (about 20 %). For the average temperature, the choice of the expansion geometry proved to be irrelevant, since very similar results have been obtained in both cases. This result suggests that the calculation of the average temperature does not require a full two or three dimensional treatment and can be done using a one-dimensional model, as the one used here. The temperatures predicted by our model are however somewhat lower (a few percent) than the experimental results, for all times presented here. These discrepancies probably result from an overestimation in the code of the plasma radiative losses, due to the validity limits of the diffusion approximation for the plasma

studied and also from the opacities used, which could be underestimated. One observes a significant divergence of the temperatures obtained for the different laser pulses at short times. The fact that the temperature is initially higher for longer pulses is a consequence of the absorption of the laser energy in the expanding plasma. For short pulses, laser energy absorption occurs near solid density in strong electron density gradients and is less efficient for that reason [8]. The decrease of the temperature with time is naturally due to the fact that when the laser pulse has ended, no more energy is being supplied to the plasma which can then only cool down. In our simulations, the plasma can lose energy by pushing the ambient air (pressure forces work) and by emitting radiation. Radiative cooling rate decreases rapidly with decreasing plasma temperature. This is the main reason why the average temperatures evolves asymptotically in the same way for all pulse durations. This effect also explains why the temperature does not depend on the expansion geometry even though the spatial profiles differ considerably when considering one geometry or the other.

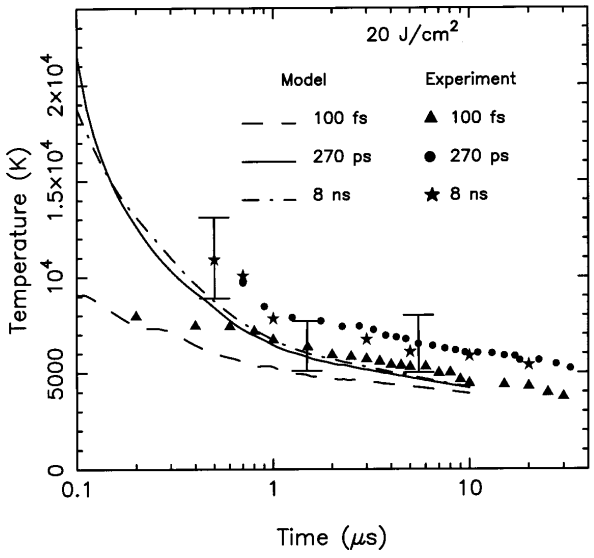

Fig. 2: Plasma space-averaged temperature as a function of time for several pulse durations. The simulation results were obtained using the Cartesian or hemispherical plasma expansion geometry. The laser fluence is 20 J/cm^2.

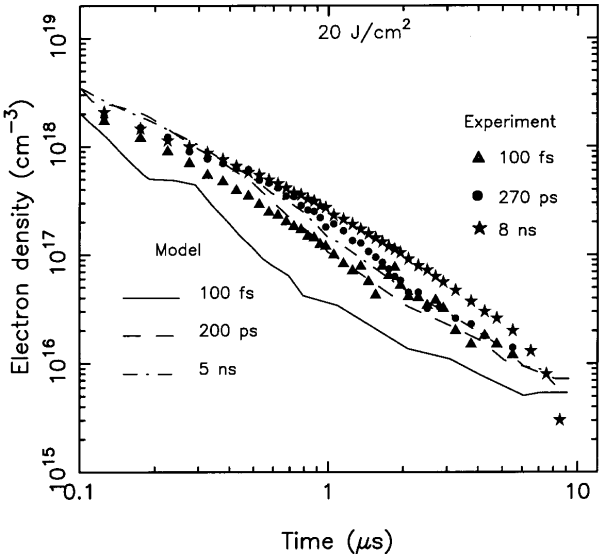

Fig. 3: Plasma space-averaged electron density for several pulse durations. The simulation results were obtained using the hemispherical plasma expansion geometry for the same laser parameters as in Fig. 2.

4.2. Average electron density as a function of the pulse duration

The average electron density was determined by using the Stark effect broadening formula $\Delta\lambda_{1/2} \approx 2Wn_e$, where $\Delta\lambda_{1/2}$ is the full width at half maximum of the Stark broadened line profile, n_e is the electron density and W is the electron impact parameter [16]. The Al II line at λ = 281.62 nm and the neutral Mg line at λ = 285.21 nm have both been used for determining the electron density [5].

Figures 3 shows the plasma electron density obtained from our measurements and from our code as a function of time, for the three same pulse durations as those used for temperature measurements (Fig. 2). A comparison of the electron density obtained for the various pulse durations shows that the plasma electron densities are so similar that we can conclude that for the delays considered here, the plasma electron density does not depend on the laser pulse duration. Typically, the electron density decreases quickly with time from a few 10^{18} cm^{-3} at 100 ns until a few 10^{15} cm^{-3} at 10 μs. This behavior was expected, since we have shown earlier that the temperature weakly depends on the pulse duration.

One observes in Fig. 3 good agreement between the measurements and the simulation results. As for the temperature, shown in Fig. 2, the electron density weakly depends on the expansion geometry chosen in the

simulations although the dependence upon this choice is more significant for the electron density than for the temperature. In Fig. 3 the hemispherical expansion geometry was selected since a somewhat better agreement with experiments is obtained than for the Cartesian geometry.

4.3. average plasma temperature as a function of the laser fluence

We investigate here the influence of the laser fluence on the average temperature for a given pulse duration. Since the temperatures given by our model are very similar for delays higher than a few hundreds of nanoseconds, whatever may be the pulse duration, we will only show results obtained for a 100 fs pulse.

Figure 4 shows the temperature as a function of the laser fluence obtained at several delays (t_d = 1, 5, 10 μs) after the laser pulse for a pulse duration of 100 fs.

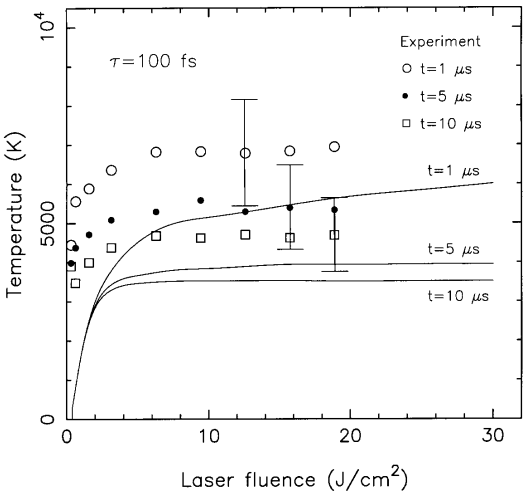

Fig. 4: Space-averaged temperature as a function of the laser fluence obtained from measurements and from simulations (full lines) at the delays t_d = 1, 5 and 10 μs after the laser pulse for a 100 fs pulse. Estimates of the experimental uncertainties are shown for each pulse duration.

One observes in Fig. 4 that the plasma temperature increases with the laser fluence and reaches a saturation value that depends on the observation delay. As the delay decreases, the temperature saturation value increases and occurs at an increasing fluence. This behavior is in agreement with other experimental investigations. In particular, in Ref. [4], it is shown that the temperature of a plasma created by ablation of a steel target with a 140 fs pulse increases with the laser fluence for delays of the order of 1 μs. In [3], experiments show that the temperature and electron density of steel plasmas are nearly independent of the laser fluence beyond a few microseconds, for 15 ns pulse.

In the framework of our model, the saturation of the temperature as a function of the fluence is basically due to the rapid increase of the radiation emission with the temperature. As the fluence increases, the plasma temperature tends to increase since more energy is absorbed in the plasma. However, radiative cooling strongly restricts this temperature increase. The temperature saturation values obtained from the simulations for the given delays are in qualitative agreement with measurements although, as mentioned in Sec. 4.1, the temperatures given by the code are always slightly underestimated. Moreover, the threshold fluence at which the saturation value is obtained is smaller in the experiments than in the code. The latter discrepancies could be simply due to the different definitions used for the fluence for radial Gaussian pulses since one notes that multiplying the experimental fluences by a numerical factor of about 4 (which could result from an overestimation of the focal spot diameter by a factor of 2) in Fig. 4 would improve the agreement.

5. Conclusion

In this paper, we have presented both measurements and results from our simulation code for the time-evolution of aluminum plasmas induced by laser ablation in ambient air at atmospheric pressure. The

simulations show that, for sufficiently long delays (typically more than a few hundred nanoseconds), the laser pulse duration and fluence have little influence on the temperature and the electron density obtained. This behavior, which is in agreement with experiments, can essentially be explained by an increase of the plasma radiative losses with the plasma temperature, and does not occur when radiation loss is neglected.

We have also observed that for short delays, the temperature increases with the laser pulse duration and the fluence while the electron density weakly depends on the pulse duration. Using our code, this observed behavior can be explained by the more efficient absorption of long pulses with respect to short pulses, which results in an initially hotter plasma. Despite the assumptions made in our one-dimensional model (simplified treatment of geometry rather than a full two-dimensional treatment, no exchange between the plasma and ambient air, etc.), the simulation results obtained are in good agreement with our experimental results and literature. Nevertheless, the calculated mean temperature seems to be slightly underestimated for long delays (more than a few microseconds) in comparison with experiments, which can be explained mainly by overestimation of the radiative losses in our model. It is interesting to note that the choice of the expansion geometry has little affects on the results obtained for space-average quantities. More insight in the plasma properties will be provided by taking into account the radial expansion in the framework of a two-dimensional model.

Acknowledgments
The authors gratefully acknowledge the financial support of the Natural Science and Engineering Research Council of Canada (NSERC) under Strategic Grant No. 21898-98.

References

[1] D.A. Rusak, B.C. Castle, B.W. Smith, J.D. Winefordner, Crit. Rev. in Anal. Chem. **27**, 257 (1997).
[2] V. Majidi, M.R. Joseph, Crit. Rev. in Anal. Chem. **23**, 143 (1992).
[3] R. Sattmann, V. Sturm, and R. Noll, J. Phys. D: Appl. Phys. **28**, 2181 (1995).
[4] K.L. Eland, D.N. Stratis, T. Lai, M.A. Berg, S.R. Good, and S.M. Angel, Appl. Spectrosc. **55**, 279 (2001).
[5] B. Le Drogoff, J. Margot, M. Chaker, M. Sabsabi, O. Barthélemy, T.W. Johnston, S. Laville, F. Vidal, and Y. von Kaenel, Spectrochimica Acta B **56**, 987 (2001).
[6] F. Vidal, T.W. Johnston, S. Laville, O. Barthélemy, M. Chaker, B. Le Drogoff, J. Margot, M. Sabsabi, Phys. Rev. Lett. **86**, 2573 (2001).
[7] F. Vidal, S. Laville, T.W. Johnston, O. Barthélemy, M. Chaker, B. Le Drogoff, J. Margot, M. Sabsabi (2001), Spectrochimica Acta B **56**, 973 (2001).
[8] S. Laville, F. Vidal, T.W. Johnston, O. Barthélemy, M. Chaker, B. Le Drogoff, J. Margot, and M. Sabsabi, Phys. Rev. E **66**, 066415 (2002).
[9] B. Le Drogoff, F. Vidal, Y. von Kaenel, M. Chaker, T.W. Johnston, S. Laville, M. Sabsabi, and J. Margot, J. of Appl. Phys. **89**, 8247 (2001).
[10] M. Sabsabi, P. Cielo, Applied Spectroscopy **49**, 499 (1995).
[11] R.M. More, K.H. Warren, D.A. Young, and G.B. Zimmerman Phys. Fluids 31, Phys. Fluids **31**, 3059 (1988).
[12] K. Trainor, *SESAME Computer Library of Los Alamos National Laboratory*, report No. UCID-18574-82-2 (1982).
[13] Y.B. Zel'dovich, Y.P. Raizer, *Physiscs of Shock Waves and High-Temperature Hydrodynamics Phenomena* (Academic, New York, 1967).
[14] N. H. Magee, Jr., J. Abdallah, Jr., R. E. H. Clark, *et al*., Astronomical Society of the Pacific Conference Series (Astrophysical Applications of Powerful New Databases, S. J. Adelman and W. L. Wiese eds.) **78**, 51 (1995).
[15] Y.-I. Lee, T. L. Thiem, G.-H. Kim, Y-Y. Teng, J. Sneddon, Appl. Spectrosc. **46**, 1597 (1992).
[16] H. R. Griem, *Plasma Spectroscopy* (McGraw Hill, New York, 1964).

Temperature Effects in Nucleation and Transport of Particles in Silane Plasmas

U. Bhandarkar, S. Warthesen, S. Girshick, U. Kortshagen

Department of Mechanical Engineering, University of Minnesota, Minneapolis, USA

ABSTRACT

Novel properties of nanoparticles can be exploited if they can be generated to meet specific requirements. Towards this end, we have developed models to understand the growth and transport of particles in plasmas. In this contribution we discuss how the gas temperature of the discharge can be utilized to control nucleation as well as diffusive and thermophoretic transport in such plasmas. The results give valuable clues on methods to control particle size and direct their transport.

I. INTRODUCTION

For a long time particle formation in plasmas has been considered mainly as a contamination process that needed to be avoided. However, more recently a more favorable view of particles in plasmas has emerged with the realization that if particles are tailor-made to meet certain specifications, their novel properties can be exploited. One such example is the plasma deposition of silicon thin films that are used in the manufacture of solar cells. Amorphous hydrogenated silicon films – a standard material for thin film solar cells – are susceptible to light induced defect creation that leads to a deterioration of the solar cell efficiency on exposure to sunlight [1]. Roca i Cabarrocas and co-workers [2, 3, 4] have claimed that nanostructured silicon thin films deposited using a capacitive plasma show improved electronic properties due to the inclusion of silicon clusters (less than 1 nm in size) and nanoparticles in the 1-3 nm size range. The most significant aspect of the improved properties is that these films show increased stability against light-induced defect creation and are thus promising materials for solar cells.

However, the generation of particles with required size and composition is in itself insufficient. For maximum benefit, it is also necessary to selectively transport the nanoparticles once they have been generated. For example, Fontcuberta *et al.* [3] have claimed that the thermophoresis effect can be used effectively to transport particles in the 1-3 nm size range to the substrate.

This leads us to the conclusion that it is necessary to obtain a thorough understanding of particle growth and transport processes in plasmas. Significant experimental progress has been achieved in recent years. A particularly important observation is that particle formation in plasmas can be delayed with an increase in the neutral gas temperature [5, 6]. Similarly, the above stated example of thermophoresis is extremely important for transporting particles towards a surface. To help understand these processes from a fundamental point of view we are developing models to study the formation and transport of particles in low-pressure plasmas. In this contribution we describe recent progress on two models that were developed to address the above problems. A quasi 1-D plasma chemistry/particle model is used to study the delay of particle nucleation with increasing gas temperature. Particle transport is studied with a Monte Carlo code.

II. Plasma Chemistry/Particle Model

Our plasma chemistry/particle model is a quasi 1-D model (0-D with a diffusive loss term) that comprises three different modules coupled in a self-consistent scheme. These modules are:

1) A chemistry module that describes the clustering of silicon hydride species with up to ten silicon atoms. A detailed description of this module is available in a previous publication [7]. Silicon hydride species with more than ten silicon atoms are considered to be “particles” and are assumed to form irreversibly. Such particles form the source term for the next module.

2) A particle growth module that solves for the growth of particles due to coagulation and surface reactions. This model divides a particle volume range spanning six orders of magnitude into 180 sections based on a logarithmic scale. Such "sectional models" are common in the aerosol literature [8]. Our present module also takes into account the charging of particles in the plasma and the corresponding effect on coagulation. The basis of this model without surface growth has been described in ref. [9].

3) A plasma module that is coupled to both the modules described above. This module utilizes the plasma quasi-neutrality condition and also solves for the balance of positive ions and input power into the plasma. As a result we obtain plasma parameters such as electron density, positive ion density and the electron temperature.

Diffusion and pumping constitute loss terms for neutral silicon hydride clusters and particles. Diffusion coefficients are calculated using Chapman-Enskog theory [10] and assuming one predominant species in the background gas mixture (usually Ar and silane). Positive ions and positively charged particles are subject to ambipolar diffusion whereas the anions and negatively charged particles are assumed to be trapped in the plasma.

This model was used to study the effect of gas temperature on the nucleation of particles. To this end, we simulated the experiments performed by Boufendi *et al.* [5] using a capacitive discharge at 117 mTorr pressure utilizing an Ar-SiH_4 mixture in the ratio 96.2:3.8. Gas temperatures used were 20 ^{o}C, 80 ^{o}C and 120 ^{o}C. The authors used Laser Induced Particle Explosive Evaporation (LIPEE) to study the onset of nucleation as a function of gas temperature. This technique relies on evaporating small particles using an intense laser beam and measuring the emitted radiation. Using a simple model they concluded that the emission was proportional to the fourth power of the particle size. Figure 1 shows the results of the LIPEE experiments, which clearly show a delay of the LIPEE signal with increasing gas temperature. We used our model to study mechanisms that had previously been proposed as potential explanations for this effect, such as quenching of vibrationally excited species that propagate fast clustering [6], the temperature dependence of electron attachment to form anions [11], and gas density related effects [12]. In addition, we paid particular attention to the temperature dependence of diffusive losses and the surface growth of newly formed sub-nanometer particles. To distinguish between the contribution of previously proposed mechanisms and that of diffusion and surface growth, we performed two sets of calculations at the higher temperatures (i.e., 80 ^{o}C and 120 ^{o}C), one set wherein all calculations were carried out at the prevailing gas temperature (called "complete") and another set where the diffusion coefficients of all species and particles were calculated assuming a temperature of 20 ^{o}C while all other reaction rates were calculated at the prevailing gas temperature (called "fixed-D"). We found that the "complete" set of calculations led to a dramatic drop in particle density as gas temperature increased, whereas the "fixed-D" set showed only a small difference for the three gas temperatures. This immediately points to the fact that the temperature dependence of diffusion

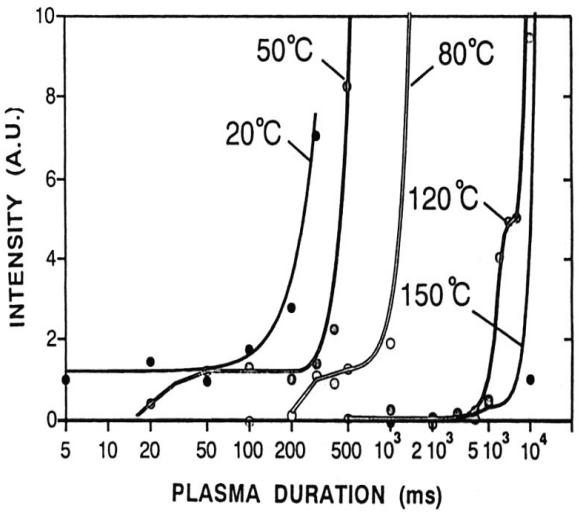

Figure 1: Temperature dependence of particle generation in 3.8 % silane in argon, 117mToorr from Ref 1.

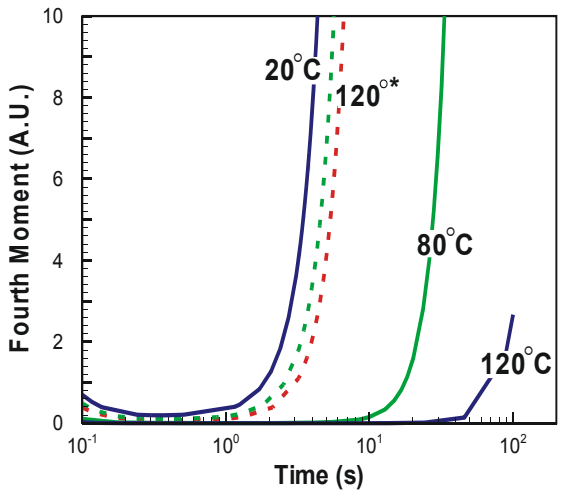

Figure 2: Simulated LIPEE signal for the same conditions as in Figure 1. Dotted lines represent "fixed-D" simulations, while solid lines indicate the "complete" results

coefficients plays a key role in the particle growth process since the only difference between the two sets is the manner of calculation of the diffusion coefficient. This is convincingly shown by comparing the simulations to the experimental data. We calculated the fourth moment of our simulated particle size distribution (Fig. 2) for comparison with the experimental LIPEE signal (Fig. 1). The "complete" simulations show qualitatively the same delay of nucleation as the experiments, while the agreement in the "fixed-D" calculation is poor.

A simple explanation for the drastic effect is as follows. Small particles in the sub-nanometer regime can be charged negative, neutral or even positive. The neutral and positive fractions are liable to be lost by diffusion whereas the negative fraction is trapped. To remain completely trapped in the plasma the particles need to achieve a "safe" size of around 2-3 nm at which point most of the particles become negatively charged. An increase in gas temperature (T_g) leads to an increase in the diffusion constant (D) of surface growth radicals as well as the subnanometer size particles ($D \propto T_g^{3/2}$). The increased loss rates of surface growth radicals slows the growth of particles to the safe size during which time the particles also experience an increase in loss rate due to an increase in their own diffusion coefficients. This dual effect of slower growth rate and faster loss rate leads to an exponential decrease in the particle concentrations that can participate in further growth processes. Thus temperature dependent diffusion plays a crucial role in the growth and transport of sub-nanometer particles and can be an effective tool to control particle sizes.

III. Monte Carlo Transport Simulations

To explore the transport of nanoparticles in a plasma a Monte Carlo transport model was developed. The Monte Carlo approach utilizes random numbers and probabilities to simulate individual collisions between a nanoparticle and surrounding plasma species. The nanoparticle velocity and position are recorded in time, and statistics are gathered over large numbers of particles to indicate general transport trends. The system modeled is a parallel plate reactor with gradients existing in the axial direction between the two electrodes, and the domain is modeled as radially infinite. The plasma species included in the model are electrons, positive ions, and neutral gas molecules. The electron and ion density profiles are determined by a fluid model and are undisturbed by the nanoparticles. The gas velocity profile is treated as one-dimensional stagnation-point flow, and is also unaffected by the presence of nanoparticles. Nanoparticles are assumed to be spherical and interaction among particles is not considered. The algorithm used in this Monte Carlo code is simply to move a particle in space for time *dt*, according to its known velocity components, then to simulate an instantaneous collision resulting in the transfer of momentum and/or charge to the nanoparticle.

The probability of a particle traveling for time *dt* between collisions is represented by a randomly generated number, R_1. The time between collisions is recalculated after each collision according to Equation 1.

$$dt = -\ln(1 - R_1)\left(\frac{1}{\nu_{\max}}\right) \qquad (1)$$

The maximum collision frequency, ν_{max}, is the sum of collision frequencies for a nanoparticle with each of the three plasma species. The electron-particle collision frequency is proportional to the electron current to the particle. This is determined by applying orbital motion limited (OML) theory, assuming that the nanoparticle behaves as a spherical probe. The particle potential required for this calculation is a function of particle charge. The collision frequency for an ion and a charged nanoparticle is calculated similarly, using the equation for ion current to a spherical probe [13]. Langevin collision rates are applicable to ion-molecule collisions, and thus are used to calculate charged particle-neutral molecule and neutral particle-ion collision rates [11]. One tenth of the Langevin collision rate is used in the simulation since the Langevin rate is an upper bound, which tends to overestimate collision rates by roughly an order of magnitude [7]. The collision frequency between neutral species is calculated using the Lennard-Jones collision diameter and potential in an equation for bimolecular reaction rates, treating the nanoparticles as large molecules [11].

After a particle has traveled for time *dt*, an instantaneous collision is simulated. A random number is generated to determine which species is colliding with the nanoparticle, based on their respective collision

frequencies. Collisions with an electron or an ion result in a transfer of one charge unit, neglecting the ion drag force. The charge on a particle is not allowed to exceed a calculated maximum charge based on the particle size [14]. When the nanoparticle collides with a neutral gas molecule, the result is a transfer of momentum between the species, changing the particle velocity components. In a momentum transfer collision, it is necessary to determine the direction and velocity of the incoming gas molecule. A gas molecule colliding with the particle is assumed to have traveled one gas mean free path since its last collision. Thus, the density and energy of the possible collision partners are determined by using the gas temperature at a location one mean free path from the nanoparticle, in any direction surrounding the particle. The temperature at this location is provided by the temperature profile. The probability of the nanoparticle being hit from a specific direction is proportional to the gas density calculated in that location. The pre-collision speed of the molecule is assigned as the average velocity of a Maxwellian distribution, $(8k_BT_g/\pi m_g)^{1/2}$, using the gas temperature at the appropriate location.

The location on the particle surface where the collision occurs is also based on probability and determined by using a random number. The reflection of the gas molecule off the surface can be either diffuse or specular (a ratio of 9:1, respectively, is applied here [15]). In a diffuse collision, the direction of the departing gas molecule is again determined through the use of random numbers. In a specular reflection, the angle of reflection is equal to the angle of incidence. The post-collision velocity of the particle is determined by conserving momentum and energy.

Diffusion is inherent in this method, and under conditions of pure diffusion (constant temperature and no directed gas flow), the particle is equally likely to be hit by a gas molecule from any direction, and the energy of the molecules, relating to the amount of momentum transferred, is the same regardless of their position. Thermophoresis is incorporated when a temperature gradient exists. The density of molecules is greater on the colder side of the particle; thus collisions from this side are more probable. However, the energy of the molecules on the hot side of the particle is higher, thus more momentum will be transferred to the particle from a gas molecule approaching from this direction. The net momentum transfer pushes particles towards lower temperatures. Gas drag is incorporated by adding a velocity component (varying spatially) to the gas molecules in the direction of gas flow, increasing the net momentum transfer in that direction. The electrostatic force is incorporated during the time between collisions. The velocity components of a charged nanoparticle change as it is accelerated by the electric field. The algorithm of moving the particle then allowing a collision to occur, is repeated for one nanoparticle until it has reached the upper or lower plate, or until the desired amount of time is simulated.

Using this code, we study the transport of particles in the 1-10 nm size range in the presence of temperature gradients. The parameters applied to the Monte Carlo transport model simulate the experimental conditions used by Fontcuberta *et al.* in a study of polymorphous film production [3]. In this study, the temperature gradient was varied between the upper and lower electrodes of a parallel plate reactor while holding other parameters constant, and the resulting film was characterized. At 1400 mTorr, with a gas flow rate of 140 sccm hydrogen and 3 sccm silane, the temperature of the film substrate was held, in almost every case, at 450 K while varying the temperature of the second electrode. The electrode separation distance was most commonly set to 2 cm. At weak (or positive) temperature gradients, deposited films were characterized as polymorphous and were found to contain nanocrystallites around 3 nm in diameter. As the strength of the temperature gradient increased, a critical temperature gradient of -50 K/cm was observed above which the resulting films no longer exhibited the properties of polymorphous films. This result has been partially attributed to the thermophoretic effect, that a strong temperature gradient will overcome the gas drag force to transport particles away from the hot film substrate, thus preventing their deposition.

A series of simulations have been carried out to investigate the transport properties under these conditions. In this series, the nanoparticles of interest are those deposited in the film. The following results consider only neutral particles since negatively charged particles are electrostatically trapped in the plasma, and are thus unavailable for deposition. Positively charged particles are not considered in this series. Figure 3 is a diagram of the model domain, describing the simulation input parameters. Nanoparticles are assigned the density of bulk silicon, 2.33 g/cm^3, and are initially distributed randomly between the upper and lower electrodes. Within a simulation time of 5 milliseconds, many particles have left the discharge by reaching

either the upper cold electrode or the lower electrode, the latter representing deposition of the particle into the film. Figure 4 shows the fraction of particles deposited on either electrode as the temperature gradient is varied, for particles of 1, 3, and 10 nm in diameter. Each symbol is an average over hundreds of particles, and lines connecting the symbols are drawn to guide the eye.

At weak (or zero) temperature gradients, particles of all sizes show relatively small preference for one electrode over the other. As the magnitude of the temperature gradient is increased, the particles are more likely to have been deposited on the cold (upper) electrode, indicating that the thermophoretic force has transported particles away from the hot substrate towards the cold electrode. This trend is most drastic for 10 nm particles, and the effect decreases with decreasing particle size. 1 nm particles are transported almost equally to both electrodes for all temperature gradients, showing only a slight variation in their distribution with the changing thermophoretic force. However, thermophoretic velocity is independent of size [14]. Gas drag is also included, but has a negligible effect on particle transport under these conditions. This indicates that Brownian diffusion, a size dependent transport mechanism, plays a large role in the transport of the smallest nanoparticles. For 3 nm particles, diffusion causes some particles to move against the thermophoretic force, but the influence of the thermophoretic effect is still apparent. Simulation results agree with those indicated by the experiments in ref. [3], that the transport of particles 3 nm and larger are controlled through the adjustment of the gas temperature gradient. Considerably fewer particles are deposited in the film as the temperature gradient becomes stronger. However, thermophoresis does not significantly influence the transport of 1 nm particles, which are dominated by diffusion.

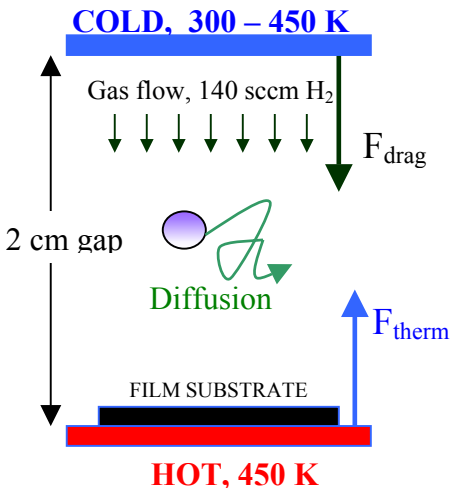

Figure 3: Simulation parameters

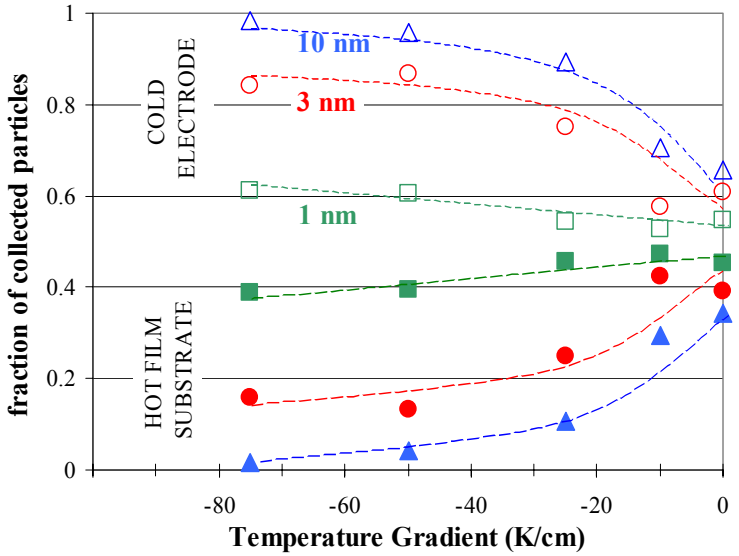

Figure 4: Distribution of collected particles after 5 ms, as a function of temperature gradient, for particles of various diameters. Open symbols: collection by the cold upper electrode. Closed symbols: nanoparticle deposition in film

IV. CONCLUSION

A quasi one-dimensional plasma chemistry/particle model has been developed to explore the experimentally observed temperature dependence of nucleation onset time. The simulations indicate that, with increasing temperature, an increased diffusion loss of surface growth radicals and sub-nanometer particles slows the growth of particles, thus delaying the onset of nucleation. The effect of temperature gradient has been studied in regards to particle transport using a one-dimensional Monte Carlo simulation, under the conditions of polymorphous film growth. These simulations indicate that thermophoresis can indeed be a dominant transport mechanism for particles larger than a few nanometers in size. However, as particle size decreases, diffusion becomes the dominant transport mechanism. These numerical investigations provide insight into the experimentally observed importance of both temperature and the presence of a temperature gradient, in controlling particle nucleation, growth, and transport in a low-pressure plasma.

V. ACKNOWLEDGMENTS

This work is supported in part by NSF through grant ECS 9731568 and through IGERT grant DGE-0114372 and by the Minnesota Supercomputing Institute.

VI. REFERENCES

[1] Staebler, D.L. and C.R. Wronski. *Appl. Phys. Lett.*(1976), **31,** p. 292.

[2] P. Roca i Cabarrocas, S. Hamma, P. St'ahel, C. Longeaud, J. P. Kleider, R. Meaudre, and M. Meaudre. In *14th European Photovoltaic Solar Energy Conference, Barcelona, June 1997,* pages 1-4, Bedford, UK, (1997). H.S. Stevens and Associates.

[3] A. Fontcuberta i Morral and P. Roca i Cabarrocas. *Thin Solid Films* (2001), **383**(1,2), 161-164.

[4] P. Roca i Cabarrocas, A. Fontcuberta i Morral, and Y. Poissant. *Thin Solid Films* (2002), **403-404**, 39-46.

[5] L. Boufendi, J. Hermann, A. Bouchoule, B. Dubreuil, E. Stoffels, W. Stoffels, and M. L. de Giorgi. *J. Appl. Phys.* (1996), **76**, 148.

[6] A. A. Fridman, L. Boufendi, T. Hbid, B.V. Potapkin, and A. Bouchoule. *J. Appl. Phys.* (1996), **79**(3), 1303.

[7] U. V. Bhandarkar, M. T. Swihart, S.L. Girshick, and U. R. Kortshagen. *J. Phys. D: Appl. Phys.* (2000), **33**(21), 21731-2746

[8] F. Gelbard, Y. Tambour, and J. H. Seinfeld. *Journal of Colloid and Interface Science* (1980), **76**(2), 541.

[9] U. Kortshagen and U. Bhandarkar. *Phys. Rev. E,* (1999), **60**(1), 887-898.

[10] R. C. Reid, J. M. Prausnitz, and T. K. Sherwood. The Properties of Gases and Liquids, chapter 11. Mc-Graw Hill, New York, 3rd Edition (1977).

[11] J. Perrin, O. Leroy, and M. C. Bordage. *Contrib. Plasma Phys.* (1996), **36**(1), 3-49.

[12] S. Warthesen, U. Bhandarkar, U. Kortshagen, and S. Girshick. *MRS Symp. Proc.* (2002), **715**, 31-36.

[13] A. Bouchoule, editor. Dusty Plasmas; Physics, Chemistry and Technological Impacts in Plasma Processing. John Wiley and Sons LTD, Chichester (1999).

[14] W. Hinds. Aerosol Technology; Properties, Behavior, and Measurement of Airborne Particles. John Wiley and Sons, Inc. New York (1999), p. 33.

[15] P. S. Epstein. *Phys. Rev.* (1924), **23**, 710.

Transport of nitrogen atoms in pure molecular nitrogen at atmospheric pressure

M. Ganciu [1,2], J. Orphal [3], M. Vervloet [3], A.-M. Pointu [1], M. Touzeau [1]

[1]*Laboratoire de Physique des Gaz et des Plasmas, CNRS, Université Paris-Sud, Orsay, France*
[2]*National Institute for Laser, Plasma and Radiation Physics, Plasma Department, Magurele, Bucharest, Romania*
[3]*Laboratoire de Photophysique Moléculaire, CNRS, Université Paris-Sud, Orsay, France*

A new type of discharge [1] (high purity N_2 at atmospheric pressure, point-point electrodes in a special configuration, some 10 kV fast pulses of some 10 kHz, flow rate ≈ 500 cm^3/sec) able to generate a large flux of nitrogen atoms at atmospheric pressure, proved the possibility to transport nitrogen active species over long distances (more than 10 meters in a polyamide tube with an internal diameter of 6 mm). We report investigations concerning the mechanism that is responsible for this transport.

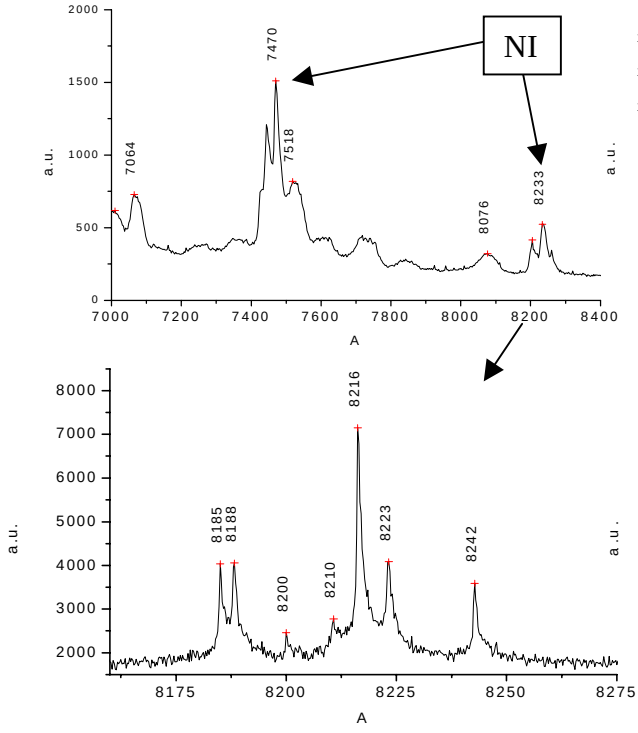

Fig 1. Emission spectrum of the discharge

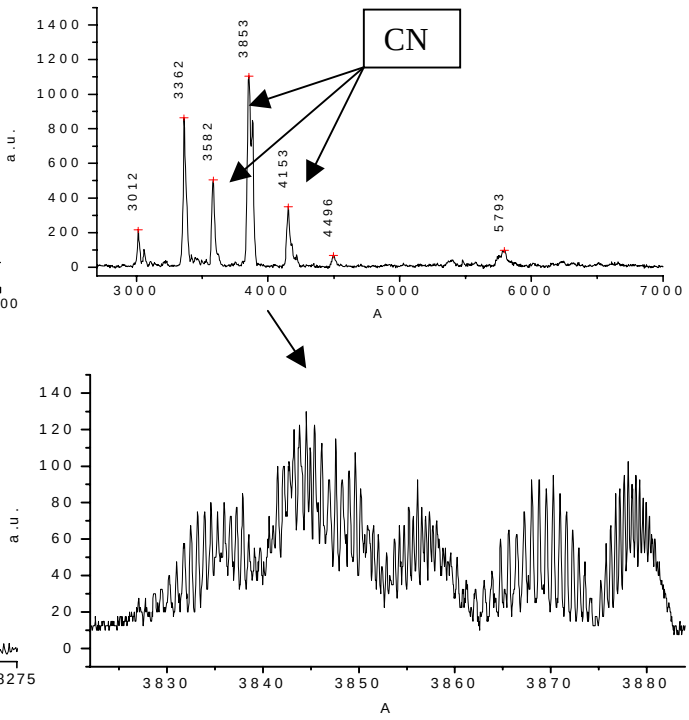

Fig 2. Emission spectrum of the post-discharge (1 m from the discharge)

Nitrogen atom concentrations are estimated by measuring the O_3 concentration when O_2 is introduced in the post discharge flow. For an N_2 (N50 purity) flux of about 500 cm^3 s^{-1}, using 15 W average power of applied electrical pulses, a nitrogen atom concentration of about 4×10^{14} cm^{-3} was estimated in the afterglow at 20 cm from the discharge. This measurement is compared with classical NO titration. The role of tube material, length, and internal diameter for nitrogen atom transport is discussed. The results are in agreement with main N atom losses by volume recombination and with the hypothesis that, at high pressure the surface recombination coefficient for N atoms is reduced [2]. The temperature of the post-discharge is about 300 K as shown by the CN rotational band (0-0) contour. A simple model of nitrogen atom transport is presented.

[1] Mihai Ganciu, Johannes Orphal, Michel Vervloet, Anne-Marie Pointu, and Michel Touzeau, 55th Gaseus Electronics Conference, 15-18 October 2002, Minneapolis, MN

[2] Steven F. Adams and Terry A. Miller, Plasma Sources Sci. Technol. **9**, 248 (2000)

Hydrogenated Silicon Thin Films With Nanocrystalline Inclusions Deposited In Low Pressure SiH_4:He:H_2-Plasmas

S. Thompson[1], C.R. Perrey[2], T.J. Belich[3], U. Kortshagen[1], C.B. Carter[2], and J. Kakalios[3]

[1]*Department of Mechanical Engineering, University of Minnesota, Minneapolis, MN 55455 USA*
[2]*Department of Materials Science, University of Minnesota, Minneapolis, MN 55455 USA*
[3]*School of Physics and Astronomy, University of Minnesota, Minneapolis, MN 55455 USA*

Abstract
Hydrogenated amorphous silicon thin films with nanocrystalline inclusions are synthesized via an RF capacitively coupled discharge using a mixture of helium and hydrogen diluted silane. Films with an increasingly nanocrystalline morphology show improvements in the optical absorption coefficient Urbach slope. However despite a sharpening of the band tail states, photosensitivity measurements indicate significant light-induced defect creation.

1. Introduction

One of the most promising materials for application in cost effective, efficient photovoltaic cells is plasma deposited hydrogenated amorphous silicon (a-Si:H). Amorphous silicon films can be deposited over large areas and have a higher optical absorption coefficient for visible light than that of crystalline silicon. However, extended illumination of a-Si:H solar cells results in the formation of metastable defects [1], known as the Staebler-Wronski effect, thereby dramatically decreasing the efficiency of the photovoltaic device. Hydrogenated amorphous silicon thin films with nanocrystalline inclusions (a/nc-Si:H), also sometimes referred to as "polymorphous", have attracted considerable attention recently due to reports of superior electronic properties combined with an improved resistance to light-induced defect formation [2-7].

In this study, a/nc-Si:H films are deposited by a radio frequency (RF) plasma enhanced chemical vapor deposition (RF-PECVD) using a mixture of helium and hydrogen diluted silane. Conditions are similar to those reported by Roca i Cabarrocas *et al.* [2, 5] in that they are at the edge of powder formation. In comparison, a-Si:H films are deposited by the same process without hydrogen dilution at a lower pressure and lower RF power. The optical absorption coefficient Urbach slope and the photoconductivity of the films are presented and discussed in relation to analysis of the structural morphology of the films obtained by high-resolution transmission electron microscopy (HRTEM).

2. Experimental Details

A series of films was synthesized using an RF (13.56 MHz) capacitively coupled plasma discharge. The schematic of the reactor is shown in Figure 1. The upper electrode is the RF powered showerhead electrode, through which the gas enters the chamber. The substrates rest on the lower grounded electrode. The electrode area is 200 cm^2. Both electrodes are independently heated to allow for control of the temperature gradient for the process. The various samples were synthesized under the conditions described in Table 1. The a/nc-Si:H films were deposited with an RF electrode temperature T_{RF} = 250^{0}C and substrate temperature T_S=250^{0}C. Nominally amorphous samples were deposited with T_S = 250^{0}C and an unheated RF electrode.

Table 1: Deposition conditions and resulting material

Pressure (mTorr)	Flow Rate SiH_4:He (5:95) (sccm)	Flow Rate H_2 (sccm)	Power (W)	Material
1800	40	100	20	a/nc-Si:H
1450	40	100	20	a/nc-Si:H
250	30	0	5	a-Si:H
100	19	0	5	a-Si:H

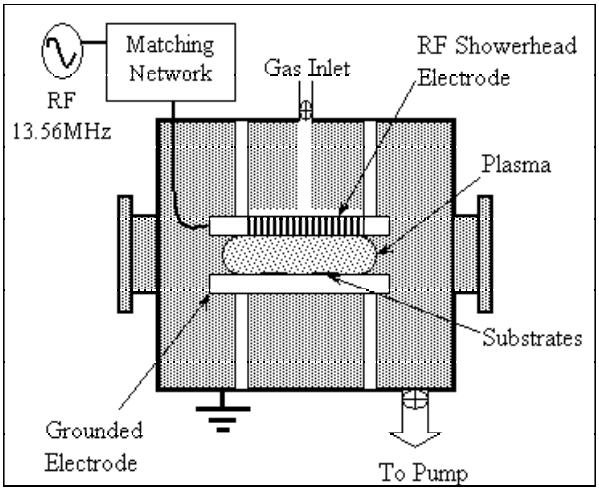

Figure 1: Schematic of RF capacitively coupled plasma reactor chamber

For the purpose of transmission electron microscopy (TEM) studies films with an approximate thickness of 100 Å were deposited on cleaved NaCl substrates. These films were floated off in distilled water and "caught" on a 3 mm copper TEM grid [8]. These samples were then allowed to dry in a dessicator and subsequently analyzed using a Philips CM30 TEM operating at 300 kV.

For the optical absorption coefficient and photoconductivity measurements, films with an approximate thickness of 3000 Å were deposited on Corning 7059 substrates. Two coplanar chromium electrodes either 2 or 4 mm apart were then evaporated onto the film samples. The optical absorption coefficient α of the samples was obtained by the constant photocurrent method (CPM). CPM measurements were performed at room temperature after dark annealing the samples at 170^0C for 1 hour. A tungsten-halogen light source was directed through a monochromator and focused on the sample. A bias of 10 V was applied to one electrode, and the photocurrent was measured from the other. At each incident photon energy hν, the light intensity striking the sample was adjusted to maintain a uniform value of the photocurrent. Thus any dependence of the photo-excitation intensity on the recombination lifetime is eliminated from the measured photocurrent. The optical absorption spectra are acquired by relating the photocurrent to the incident light intensity relative to the transmitted light intensity and film thickness.

The Tauc optical gap E_g is determined from the CPM spectra. The density of states in amorphous semiconductors varies continuously with energy, from a large density of filled or empty states, termed the conduction and valence bands, respectively, to an exponentially decreasing density of strained bond states tailing into the mobility gap, known as the valence and conduction band tails. Additionally, dangling bond states residing in the middle of the mobility gap can either accept or promote photo-excited charge carriers. The absence of a sharp gap in the density of allowed states in amorphous semiconductors results in a smoothly varying spectral dependence of the absorption coefficient. One common technique for extracting the optical gap from the wavelength dependence of the absorption spectrum involves constructing a 'Tauc plot'. In using Fermi's Golden Rule for calculating the absorption coefficient, one assumes that valence band to conduction band absorption predominates, that the density of occupied and empty states varies parabolically with energy, and that there is a constant momentum matrix element connecting optical transitions between bands. In this case, it can be shown that there is a linear relationship between $\alpha^*h\nu$ and the square of the incident photon energy $h\nu$, given by:

$$(\alpha^*h\nu)^{1/2} = B(h\nu - E_g). \quad (1)$$

Figure 2 shows a Tauc plot of the 1800 mTorr sample obtained using CPM. The data is well described by the Tauc expression, with an intercept value of 1.74 eV, the Tauc gap E_g. The absorption coefficient data

that tails off for photon energies less than E_g represents photon absorption due to band tail to band optical transitions. In this case the absorption coefficient can be expressed as

$$\alpha = \alpha_0 \, exp \, [(hv\text{-}E_1)/E_0] \tag{2}$$

where E_1 and α_0 are independent of both thermal and structural disorder. The value E_0 is referred to as the Urbach slope, which reflects the exponentially decreasing density of band tail states. With larger densities of strained Si-Si bonds, the band tail states extending into the mobility gap will be broader corresponding to a large value of the Urbach slope E_0. Therefore E_0 is sometimes used as a figure of merit for the intrinsic order in amorphous semiconductor films.

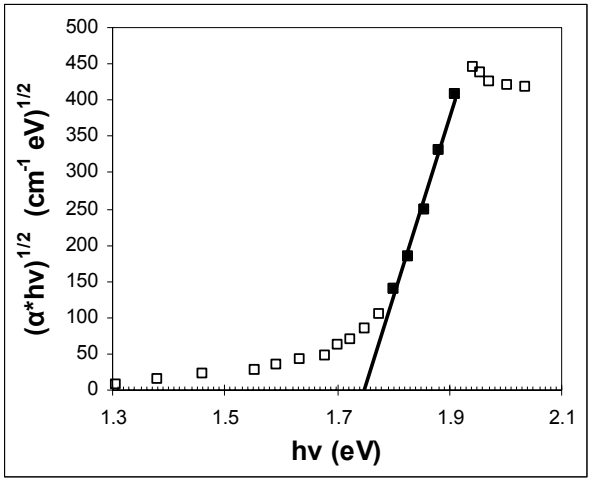

Figure 2: Tauc plot for the 1800 mTorr a/nc-Si:H sample showing a Tauc optical gap *Eg* of 1.74 eV.

The Staebler-Wronski effect was investigated through measurements of the photoconductivity and photosensitivity as a function of light exposure time (light soaking). The photoconductivity σ_{ph} is determined by the measured photocurrent divided by applied voltage and geometric factors. The photosensitivity is defined as the photoconductivity normalized by the dark conductivity: σ_{ph}/σ_d. Prior to measurement, the films were dark annealed at 177 ^{0}C for two hours and cooled at a controlled rate of one degree per minute. These measurements were performed under vacuum at 47 ^{0}C under ~100 mW/cm^2 of heat-filtered white light from a tungsten-halogen lamp.

3. Results

The identification and characterization of amorphous or nanocrystalline materials is a developing field. There are many techniques available for the analysis of structure and medium range order in the TEM [9-11]. The phenomena of scattering from ordered regions with dimensions comparable to the unit cell are still being understood. For this study, displaced-aperture dark-field (DADF) imaging is used to survey the crystalline material in the specimens [8].

A bright-field (BF) TEM image of the a/nc-Si:H sample deposited at 1800 mTorr is shown in Figure 3A. Several dark features are visible on the surface of the film; DADF was used to examine these features. Using DADF regions that satisfy the Bragg diffraction condition at the position of the aperture will appear bright [8]. Two such DF images using different objective aperture positions are shown in Figures 3B and 3C. Here, crystalline particles approximately 5 nm in size are apparent in an amorphous matrix; one such particle is noted in Figure 3B by an arrow.

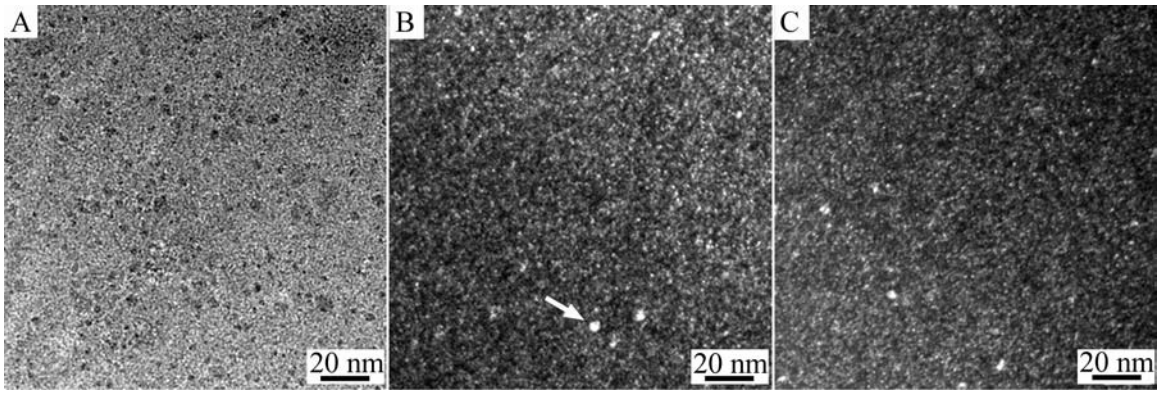

Figure 3: TEM images of the a/nc-Si:H sample deposited at 1800 mTorr. (A) is a bright-field image of a typical region of the film, showing irregular contrast not necessarily indicative of the presence of crystalline material. (B) and (C) are dark-field images using different objective aperture positions. In these images crystalline material appears bright, making crystals approximately 5 nm in size apparent. One such crystal is noted in (B) by an arrow.

A similar analysis is applied to the nominally a-Si:H sample deposited at 250 mTorr. Here, the BF image in Figure 4A shows some uneven contrast features. These are likely due to thickness variations in the film associated with the nature of the NaCl substrate. To examine evidence of crystallinity in the film, the DADF technique was again used. Figures 4B and 4C are images from different objective aperture positions. The lack of bright regions of contrast in these images suggests that if any crystallites are present, they are likely smaller than ~1 nm.

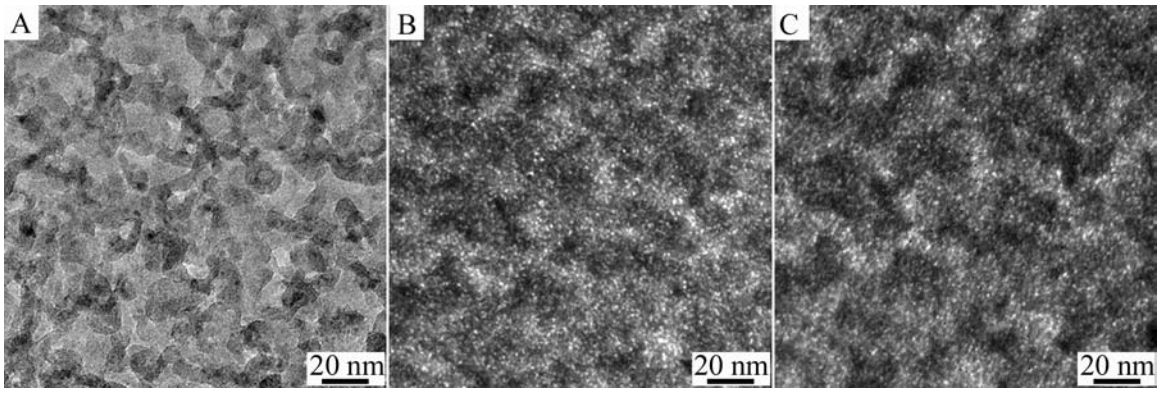

Figure 4: TEM images of the a-Si:H sample deposited at 250 mTorr. (A) is a bright-field image of the film, while (B) and (C) are dark-field images formed from different objective aperture positions. The contrast in the dark-field images suggest that if there is crystalline material present, it is approximately 1 nm or less in size. The contrast features in (A) are likely due to the NaCl substrate used for deposition.

Measurements of the optical absorption spectra Urbach slopes and Tauc optical gaps are presented in Table 2. In comparison to the a-Si:H sample deposited at 250 mTorr, the a/nc-Si:H samples deposited at 1450 mTorr and 1800 mTorr show a slightly smaller Urbach energy and a shrinking optical gap. This is consistent with other studies of a/nc-Si:H films [3].

The 100 mTorr film has an Urbach slope and Tauc gap comparable to a-Si:H, while the 250, 1450, and 1800 mTorr films have larger Urbach slopes and wider optical gaps. Though the 250 mTorr film was deposited with silane diluted only in He, not H_2, its similar optical properties to the 1450 and 1800 mTorr films (grown with H_2 dilution) suggest that there may possibly be ~ 1nm crystallites present in this film. Further studies of these films' properties are presently under way.

Table 2: Comparison of Urbach slope, Urbach energy, and Tauc optical gap of the samples

Pressure (mTorr)	Material	E_o (eV)	T_o (K)	E_g Tauc (eV)
1800	a/nc-Si:H	0.051	598.6	1.74
1450	a/nc-Si:H	0.054	625.8	1.77
250	a-Si:H	0.063	730	1.78
100	a-Si :H	0.038	438	1.69

The photoconductivity measurements as a function of light-exposure time for the 250, 1450, and 1800 mTorr samples are shown in Figure 5. It appears that the kinetics of light-soaking is similar for the three samples. All three films begin with a photoconductivity of a similar magnitude. But saturation occurs sooner for the 1450 and 1800 films in comparison to the 250 film. Not shown is the data for the 100 mTorr film, which had a photoconductivity magnitude and decay comparable to the other films.

Photosensitivity measurements as a function of light exposure time are shown in Figure 6. The a/nc-Si:H 1800 and 1450 mTorr films both show an initial magnitude of photosensitivity that is 2 and 5 times larger compared to the 250 mTorr film, which is in turn a factor of 4 higher than the 100 mTorr film. Additionally, the magnitude of the total decrease of the photosensitivity is smaller for the 250 mTorr film.

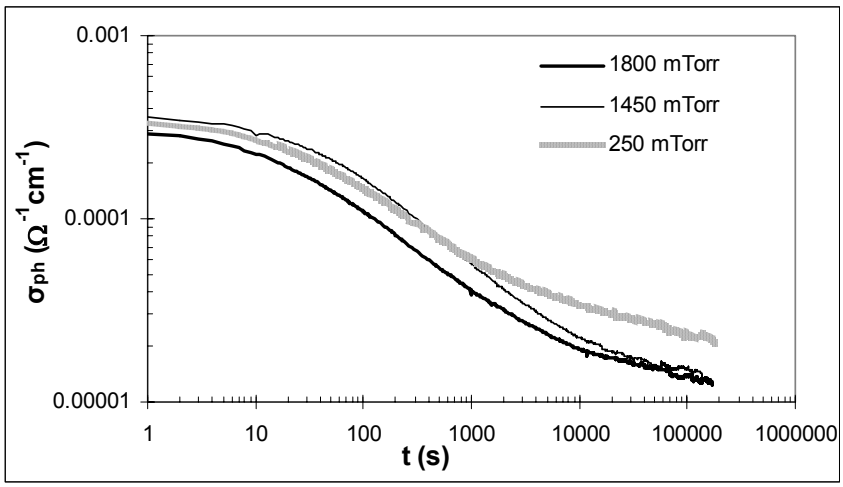

Figure 5: Photoconductivity σ_{ph} of the 1800 mTorr, 1450 mTorr, and 250 mTorr film samples measured against light-exposure time at 47 ^{0}C.

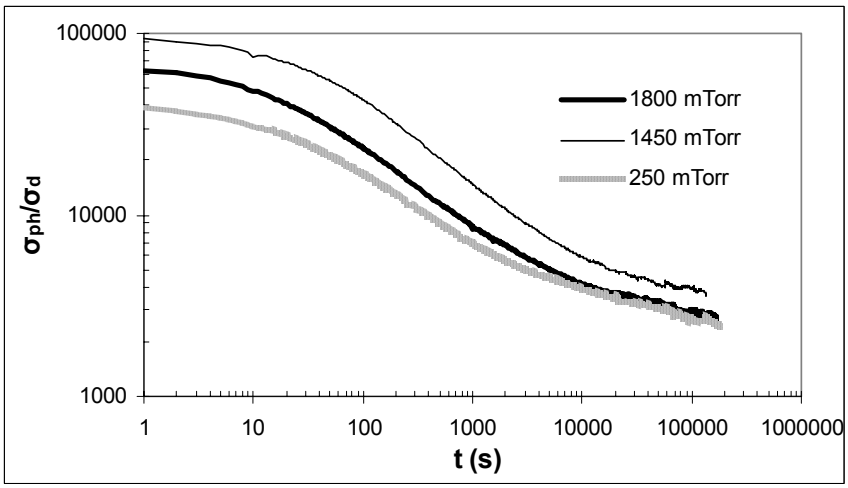

Figure 6: Photosensitivity σ_{ph}/σ_d as a function of light exposure for the 1800, 1450, and 250 mTorr films measured at 47 ^{0}C.

4. Discussion

Several characteristic of the a/nc-Si:H films are comparable with those observed for the a-Si:H film, specifically the Urbach slope and the Tauc optical gap. The Urbach slope of the optical absorption spectra reflects the band-tail density of states. A slight improvement of the Urbach slopes for the a/nc-Si:H films in comparison to the a-Si:H films could correspond to a reduction in the density of strained bonds. Although all three films show a decrease in both the photoconductivity and photosensitivity with extended light illumination, consistent with the Staebler-Wronski effect [1], there exist differences in the magnitude of this effect. The initial values of the photosensitivity of the films with nanocrystalline morphology, the 1450 and 1800 mTorr samples, are 5 and 2 times larger than that of the 250 mTorr sample. But the magnitude of the decrease in the photosensitivity over light-exposure time is larger for the a/nc-Si:H samples as well. Additionally, the a/nc-Si:H films saturate more quickly than the a-Si:H films. It possible that the nanocrystalline morphology of the a/nc-Si:H in comparison to the a-Si:H film is responsible for the variation in electronic properties and the increased rate of light-exposure saturation.

5. Conclusions

Hydrogenated amorphous silicon thin films with nanocrystalline inclusions have been deposited by RF-PECVD. Despite the inclusions of nanocrystallites, the a/nc-Si:H films show electronic properties comparable to the nominally amorphous film. Additionally, the a/nc-Si:H films do display a Staebler-Wronski effect and no significant enhancement of transport properties is observed.

Acknowledgements

This work is supported by NSF under IGERT grant DGE-0114372. TJB and JK are primarily supported by NREL/AAD-9-18668-13. ST, TJB, JK, and UK acknowledge partial support by the NSF MRSEC DMR-0212302. CRP and CBC acknowledge support from the 3M Hetzer Endowed Chair.

References

1. Staebler, D.L. and C.R. Wronski, *Reversible Conductivity Changes in Discharge-Produced Amorphous Si.* Appl. Phys. Lett., 1976. **31**: p. 292.
2. Roca i Cabarrocas, P., A. Fontcuberta i Morral, and Y. Poissant, *Growth and optoelectronic properties of polymorphous silicon thin films.* Thin Solid Films, 2002. **403-404**: p. 39.
3. Butte, R., et al., *Some electronic and metastability properties of a new nanostructured material: Hydrogenated polymorphous silicon.* Philos.Mag. B, 1999. **79**(7): p. 1079.
4. Longeaud, C., et al., *Properties of a new a-Si:H-like material: Hydrogenated polymorphous silicon.* J. Non Cryst. Solids, 1998. **227-230**: p. 96-99.
5. Fontcuberta i Morral, A. and P. Roca i Cabarrocas, *Shedding light on the growth of amorphous, polymorphous, protocrystalline and microcrystalline silicon thin films.* Thin Solid Films, 2001. **383**(1-2 Feb): p. 161-164.
6. Butte, R., et al., *Structural, optical and electronic properties of hydrogenated polymorphous silicon films deposited at 150 degree C.* Journal of Non-Crystalline Solids, 2000. **266 (A)**: p. 263-268.
7. Fontcuberta i Morral, A., H. Hofmeister, and P. Roca i Cabarrocas, *Structure of plasma-deposited polymorphous silicon.* Journal of Non-Crystalline Solids, 2002. **299-302 April**: p. 284-289.
8. Williams, D.B. and C.B. Carter, *Transmission Electron Microscopy*. 1996, New York: Plenum Press.
9. Voyles, P.M., et al., *Experimental Methods and Data Analysis for Fluctuation Microscopy.* Materials Research Society Symposium Proceedings, 2001. **589**: p. 155-160.
10. Gibson, J.M., M.M.J. Treacy, and D. Loretto, *Electron Speckle and Higher-Order Correlation Functions from Amorphous Thin Films.* Materials Research Society Symposium Proceedings, 1997. **455**: p. 349-356.
11. Cheng, J.-Y., et al., *Ion-implanted amorphous silicon studied by variable coherence TEM.* Materials Research Society Symposium Proceedings, 2001. **589**: p. 247-252.

Plasma – catalyst of combustion of low-reactive coals

Petrov S.V., Saakov A.G.

RPE TOPAS Ltd., Kiev, Ukraine

The consistent current trend is to deterioration of the quality of coals supplied to heat-electric generation plants, which is associated with increase in their ash and moisture content, decrease in volatile yield and combustion heat. Contrary to forecasts, this promotes growth of consumption of oil fuel (gas), especially at the coal-dust heat-electric generation plants, used for kindling of boilers and stabilization of burning of the coal dust even under rated loading. In this case, the combined combustion of fuel oil and coal, especially in kindling the coal-dust boilers, results in deterioration of all indicators of power-generating plants, i.e. increase in combustible loss, decrease in gross efficiency of a boiler, growth of yield of nitrogen oxides, increase in high-temperature corrosion of heating surfaces and ejection of sulphur dioxide, as the initial sulphur content of fuel oil is, as a rule, several times higher than that of the coal. In addition, vanadium pentoxide, which is an active carcinogen, is evolved in combustion of fuel oil.

Traditional methods for decreasing the consumption of fuel oil at heat-electric generation plants (increase in dust milling dispersity, high preheating of the air mixture and secondary air, etc.), used to improve fuel ignition and burning stabilization, have exhausted themselves. Therefore, a radical increase in the efficiency of utilization of fuel can be related only to development and mastering of absolutely new technologies. The plasma technology seems to hold the highest promise among the alternative technologies available for solving the above problems. This technology provides a substantial increase in cost effectiveness and improvement in environmental indicators of power-generating plants working with solid fuel.

As shown by numerical estimations, relative energy power of an electric lighter, related to the heat power of a gas stove burner, is 0.001 %, relative power of an electric candle is 0.01 %, relative power of the plasma torch in ignition of the fuel oil flame is 0.05 %, and that in ignition of the coal dust flame is 0.5-1.0 %.

Using such combined plasma-coal torch devices, it is possible to realize different sophisticated energy fuel-utilization technologies. They include:

- plasma ignition of the coal-dust flame (fuel oil free kindling of boilers, lighting of the coal-dust flame, stabilization of the liquid slag yield in furnaces with liquid slag removal);
- electric-thermochemical preparation of fuel (ETCPF) for combustion;
- coal distillation;
- plasma-steam coal distillation, production of synthesis gas;
- integrated processing of low-grade solid fuels in plasma reactors;
- processing of coal production wastes – coal slime.

The coal slime has hardly had any substantial application up to now, because of its high ash content and special requirements for its further utilization. It contains the Fe, Si, Al and Mg compounds, as well as other impurities. The use of plasma allows implementation of the waste-free technology for production of valuable products from a high-ash (low-grade) carbon raw materials. Thus, the air-water plasma conversion of coal provides a high-calorific synthesis gas containing the hydrogen and CO mixture at a temperature of 1500 ^{o}C, whereas an expensive ferrosilicium and fibrous warmth-keeping materials can be produced from a molten slag after reduction in the plasma reducing reactor.

Therefore, the use of plasma allows development of the waste-free and environmentally clean technologies which lead to reduction of import of scarce power supplies.

Tests of the combined plasma-coal torch devices at the Coal Energy Technology Center proved the high efficiency of lighting of the coal-dust flame.

Radical and Ion Behavior in Inductively Coupled, GEC Reference Cell C_4F_8/Ar Discharges.

Harold M. Anderson, Geoff Courtin, Marcus Barela

Department of Chemical and Nuclear Engineering
University of New Mexico, Albuquerque, New Mexico, USA 87131

Abstract

Diode laser absorption spectroscopy (DLAS), UV/visible absorption spectroscopy (UV/VIS), ion energy analysis and Langmuir probe measurements were performed to characterize both the fluorocarbon radical and ion behavior in inductively coupled C_4F_8/Ar discharges. The interpretation of these results is that the neutral radicals CF_2 and CF are key participants in the oxide etch process and that there is an ion flux and a reactant flux limiting regime in the etch, dependent on the C_4F_8/Ar ratio.

1. Introduction

The increased complexity of developing plasma processes for etching 300 mm wafers with critical feature sizes approaching 0.1 μm dimensions is fueling the need for more advanced plasma models that can aid in designing processes without costly experimentation. Before these models currently under development can be put to use, the predictive capability of the models must be verified by diagnostic measurements. One of the most challenging plasma etching operations is selective oxide etching using fluorocarbon based gases. The primary focus of this report is on diode laser gas phase density measurements of CF_x, SiF_x, CO_x and C_xF_y species made in the UNM GEC/ICP Reference Cell using DLAS and UV/VIS absorption spectroscopy. Concurrently, ion behavior was studied by ion energy analysis and Langmuir probe measurements. The work concentrated on etching of blanket bulk oxide and PR wafers in a tool parameter space defined by source power, bias power and pressure and correlating these results to radical and ion behavior in inductively coupled C_4F_8/Ar discharges. The work involved generating sets of statistically designed experiments used to characterize the gas phase plasma chemistry over a wide reactor operational parameter space. Routine post-etch measurements for etch rate and selectivity were performed. Diluting the C_4F_8 with Ar was used to illustrate the effect that greater ion current has on the etch rate. The interpretation of these results strongly suggest that the neutral radicals are key participants in the oxide etch process and that there is an ion flux and a reactant flux limiting regime in the oxide etch process window dependent on the C_4F_8/Ar ratio.

2. Technical details

A liquid nitrogen cooled diode laser based absorption spectroscopy system was used for these studies. The temperature of the diode and the current through the diode determines the wavelength of emission from the diode laser. With the diode temperature regulated, the current can be ramped to sweep the laser wavelength across a region of interest. Wavelength modulation spectroscopy (WMS) was used to increase the detection sensitivity [1]. This method involves simultaneously modulating the current ramp with a small sinusoidal wave. A lock-in amplifier is then used to demodulate the signal from the detector. This places the signal at a frequency above most of the laser and detector noise. The increased signal-to-noise ratio results in detection sensitivity that is usually limited by "accidental" etalons, which arise from multiple reflections off surfaces encountered by the primary beam. For the work presented here, the laser current was modulated at 50 kHz. The resulting high

frequency absorption signal was monitored with a lock-in amplifier set to observe at the second harmonic of the modulation frequency (100 kHz). A schematic of the detection system is shown in Figure 1. The processed signal from the detector resulted in a second derivative of the absorption spectrum due to demodulation at the second harmonic. This method has the added advantage that a single pass through the plasma is usually sufficient, eliminating the need for multipass optics. This method has previously been used in the past to successfully monitor fluorocarbon concentrations [2,3].

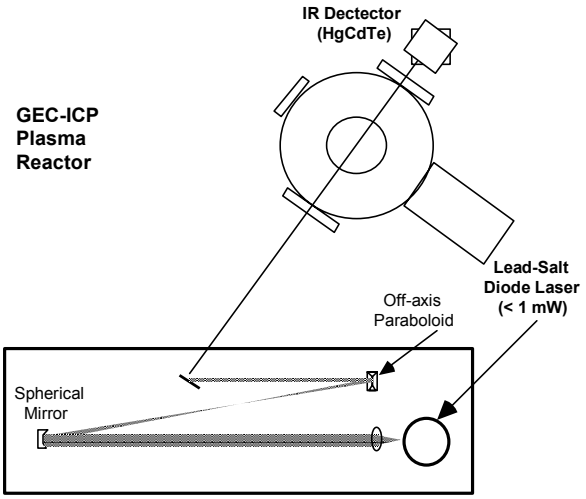

Figure 1 Schematic of GEC-ICP Cell and diode laser apparatus.

Diodes with a frequency around 1230 cm^{-1} were used for CF, CF_2 and COF_2 detection, diodes with a frequency around 870 cm^{-1} were used for SiF and SiF_2 detection, diodes with a frequency around 2120 cm^{-1} are used for CO detection and a diodes with a frequency around 1185 cm^{-1} are used for C_2F_4 detection. Details about the calibration of the absorption signal to absolute concentration of these species can be found in a previous work [4]. UV/VIS absorption measurements were made with a gated Xenon flash lamp and a Cetac EP-2000 spectrometer for comparison against diode laser measurements. Langmuir probe measurements were made with a conventional negatively biased single tip probe used to collect ion current. Ion energy analysis was performed using a high-resolution micro-engineered retarding field energy analyzer with sub-micron dimensions [5].

In the blanket oxide and blanket PR etch experiments using the GEC reference cell, the power was varied from 200 to 500 W, pressure was varied from 5 to 25 mTorr, and the bias was varied from 20 to 150 W power. The gas flow rate was maintained at 26.1 sccm and the wafer chuck temperature was maintained at 20^o C. The experiments were conducted using a central composite experimental design and the results are depicted as a response surface plot.

3. Results

Oxide etching in the inductively coupled GEC Cell is dominated by bias power rather than source power in pure C_4F_8. This is illustrated in figure 2 below which shows that at low bias power there is net deposition of polymer, while at high bias powers there is rapid etching of the oxide surface. However, the real variable that drives the oxide etch process is bias voltage rather than bias power, since bias voltage determines ion energy striking the surface. Langmuir probe measurement of the ion current density was used to estimate the bias voltage at the wafer at which this transition took place. For C_4F_8, this transition occurs at ~ 60 eV (75 W bias power) in the GEC Cell. The conversion was made based on a correlation made by Doemling, et al. [6] who showed that V_{DC} measured from

probe data as V_{DC}=P/ICD*A is the same as the self bias voltage measured directly using a wafer probe. In the above expression, P is the RF bias power, ICD is the ion current density and A is the area of the wafer.

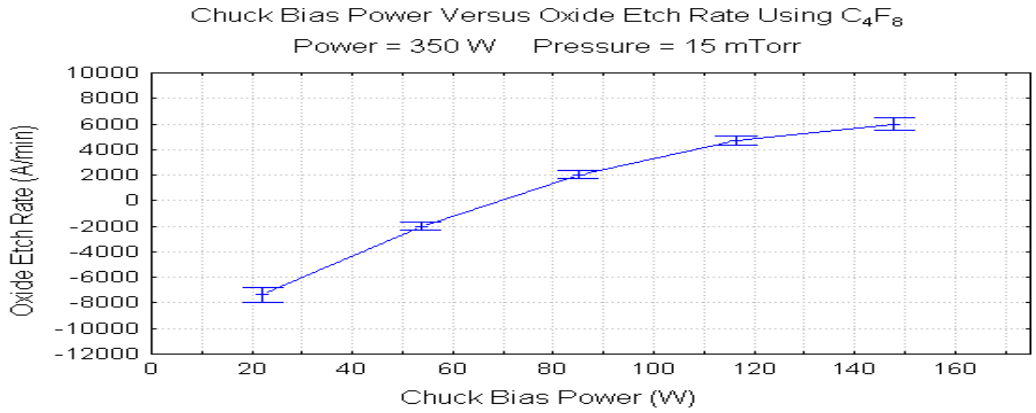

Figure 2. Oxide etch rate in C_4F_8 as a function of the chuck bias power.

DLAS has shown that C_4F_8 is largely dissociated to first form C_2F_4 (shown in figure 3), then further dissociate to form CF_2 and CF in the discharge. Over an oxide surface, CF_2 and CF are consumed in the oxide etch process, but only when the bias power is sufficient to keep the oxide surface clean through energetic ion bombardment. At higher bias powers (125 W) where oxide etching is fast (~600 nm/min.), CF_2 appears to be the key radical for the etch process since ~50 percent (2.7-3.0 mTorr in a 15 mTorr C_4F_8 discharge) is consumed. This is illustrated in figure 4 below. These values were obtained by comparing the CF_2 concentrations over non-reactive wafer surfaces versus blanket oxide wafer surfaces undergoing etching. CF is shown to display a similar trend, but its concentration is an order of magnitude less than CF_2. Also of interest to note, C_2F_4 has a similar trend with respect to bias power and active etching. Under high bias power and active etching, the concentration of C_2F_4 is also reduced by ~50 percent from those shown in Figure 3.

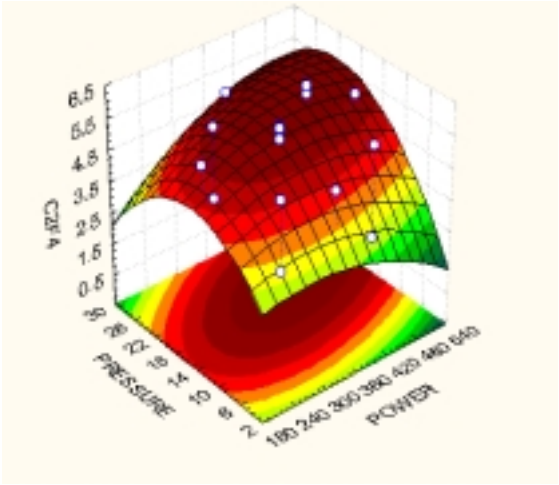

Figure 3 C_2F_4 concentration (mTorr) as a function of pressure and power in a 15 mTorr C_4F_8 discharge. Bias power constant at low setting (i.e. no etching).

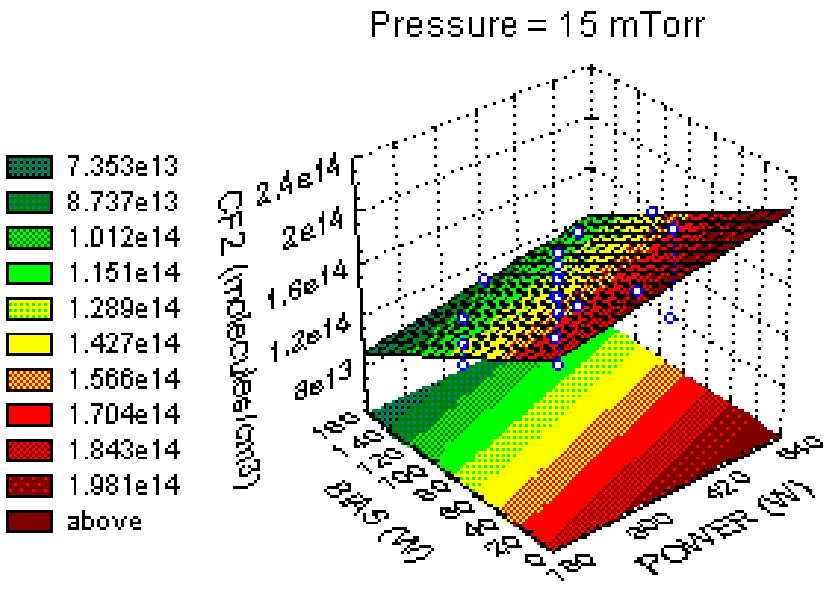

Figure 4. Oxide etch rate CF_2 behavior for bias versus power.

Given the fact that CF_2 is present in an order of magnitude greater concentration than CF, the CF_2 radical appears to be the primary radical constituent driving the oxide etch process. With both C_2F_4 and CF_2 concentrations depressed to only about 20 percent each of the total gas pressure, and with CF concentrations on the order of 1 percent or less, the remainder of the total gas pressure must be made up of etch product species like SiF, SiF_2, CO and COF_2. Previous measurements of CO concentrations by DLAS in the GEC Cell under steady-state blanket oxide etch conditions place the CO concentration at approximately 2 mTorr under relatively comparable etch conditions. Given the necessity of having to have a stochiometric balance for the evolution of SiO_2 etch products during the etch process, the appearance of CO in these quantities during active oxide etching appears to be in rough balance with the loss of CF_2 and C_2F_4 due to the underlying consumption of CF_2 during the etch process. C_2F_4 is presumably not directly consumed by etching, but its equilibrium concentration appears to be perturbed by the consumption of CF_2. However, this active participation of CF_2 in the etch process appears to only take place when the oxide surface is kept clean by energetic ion bombardment. CF, by merit of its order of magnitude lower concentration than that of CF_2, cannot be driving the oxide etch process in and of itself. There simply isn't enough CF available to account for the anticipated mass balance between reactant species and etch products.

Over a PR surface, neither CF_2 nor CF concentrations vary as a function of PR etch rate. Consequently, they do not appear to be involved in the PR etch mechanism. However, PR etching is also critically dependent on bias power. PR films etch presumably due to energetic ion bombardment that degrades the PR film, making it liable to attack by fluorine.

As C_4F_8 is diluted in Ar, the etch rate is first significantly enhanced by the additional ion current density provided by Ar, up to about a 20/80 dilution as shown in Figure 5. Beyond 80% the decline in etch rate is even more precipitous. DLAS measurements of CF_2 and CF concentrations show a near linear decline as the Ar fraction is increased from 0 to 80%, and CF_2 falls to less than 1 mTorr at 80% Ar dilution. Further increases in Ar show that CF_2 declines to the point such that these reactants for the oxide etch process could not sustain the etching rate. The interpretation of these results is that the neutral radicals CF_2 and CF are key participants in the oxide etch process and that there is an ion flux and a reactant flux limiting regime in the oxide etch process window dependent on the C_4F_8/Ar ratio. These regimes are illustrated in figure 5.

Langmuir probe measurements of ion density in this study show a significant increase in ion density in pure Ar as opposed to C_4F_8, and Li, et al. [7] have shown that at 90% Ar dilution of C_4F_8 more than 70% of the ion flux is attributable to Ar ions. This suggests that there is considerable synergism between Ar and C_4F_8 over that range, but the lack reactive flux beyond the 80-90% Ar range means the normal reactive ion process is surpressed. In the regime from 0 to 60% Ar in C_4F_8, there are sufficient fluorocarbon ions to keep the oxide surface clean and allow for continued etching, but the etch rate appears to be constrained by the overall lower ion density and ion flux to the surface. The function of this ion flux to the surface is consistent with a surface cleaning role for ions, keeping fluorocarbon deposits at a minimum and allowing for reaction of CF_2 radicals with a clean oxide surface, as has been suggested by Li, et al. [7]. Although the reactor used in this study is different from the inductive reactor used by Li, et al. [7], the etching performance of the GEC Cell is quite similar and adds to the credibility of this mechanism. In the no or low Ar addition regime, low ion flux (but energetic nonetheless) allows a finite thickness of fluorocarbon film to be present on the oxide surface, and this film constrains etching by interfering with CF_2 radical interaction with oxide bonds.

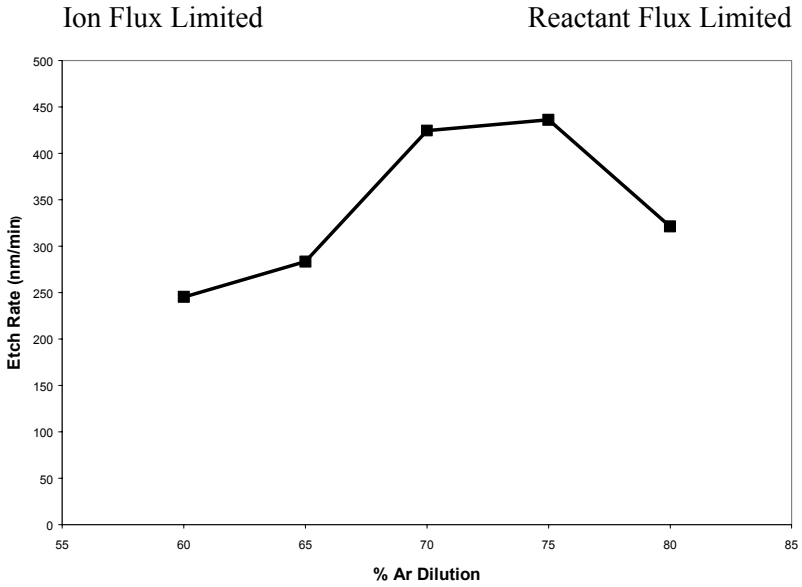

Figure 5. Etch rate versus Ar dilution for C_4F_8 (power 350W, bias power 100 W, pressure 20 mTorr)

4.0 Conclusions

The etch mechanism for both oxide and PR films has been clarified and the importance of CF, CF_2 and F to the etching of both these films has been established. C_4F_8 dissociation has been quantitatively characterized through the major electron impact, dissociation pathways involving C_2F_4 intermediates and CF and CF_2 radicals. The role of energetic ion bombardment in oxide etching has been clarified and it is clearly shown that fluorocarbon etching of oxide is not strictly ion driven. Rather, there is a regime in the reactive ion etching of oxide surfaces is ion flux limited and one that is neutral reactant flux limited, dependent on the dilution of the fluorocarbon with Ar. The role of CF_2 and CF neutral radicals in this complex interaction has been quantified by DLAS spectrometry.

This project was funded by SEMATECH and NSF.

References

[1] D. S. Bomse, A. C. Stanton and J. A. Silver, *Appl. Opt.* **31**, 718 (1992)

[2] H. C. Sun, E. A. Whittaker, Y. W. Bae, C. K. Ng, V. Patel, W. H. Tam, S. Mcguire, B. Singh and B. Gallois, *Appl. Opt.* **32**, 885 (1993)

[3] D. B. Oh, A. C. Stanton, H. M. Anderson and M. P. Splichal, *J. Vac. Sci. Technol.* B, **13**, 954-961 (1995)

[4] W.L. Perry, K. Waters, M. Barela, and H.M. Anderson, "Oxide Etch Behavior in a High-Density, Low-Pressure, Inductively-Coupled C_2F_6 Plasma:Etch Rates, Selectivity to Photoresist, Plasma Parameters and CF_x Radical Densities,", *J. Vac. Sci. Technol. A.,* 19, 2272-2281 (2001).

[5] M.G. Blain, J.E. Stevens and J.R. Woodworth, "High-Resolution Sub-Micron Retarding Field Energy Analyzer for Low Temperature Plasma Analysis," Applied Physics Letters, 75(25), 3923-3925 (1999).

[6] M.F. Doemling, N.R. Rueger, G.S. Oehrlein, and J.M. Cook, "Photoresist Erosion Studied in an Inductively Coupled Plasma Reactor Employing CHF_3," J. Vac. Sci. Technol. B **16**(4) (1998), 1998.

[7] Li, X., X Hua, L. Ling, G. S. Oehrlein, M Barela, and H.M. Anderson, Fluorocarbon-Based Plasma Etching of SiO2: Comparison of C_4F_6/Ar and C_4F_8/Ar Discharges, *J. Vac. Sci. & Technol. A.* 20, 2052-2063 (2002).

Anode Attachment Stability and Anode Heat Fluxes for High Intensity Arcs With Argon and Nitrogen Gas Flow Parallel to the Anode

T. Iwao[1], P. Cronin[2], D. Bendix[3], and J. Heberlein[2]

[1] JSPS Research Fellow, University of Minnesota and Chuo University, Minneapolis, USA
[2] Department of Mechanical Engineering, University of Minnesota, Minneapolis, USA
[3] Department of Engineering Sciences, Martin-Luther-University Halle-Wittenberg, Merseburg, Germany

Abstract

The motion of the anode attachment and the heat flux to the anode have been determined for a configuration where the arc axis is perpendicular to the anode surface with the plasma gas flowing along the arc axis, and with lateral injection of different gases parallel to the anode surface. The arc is stabilized by a constrictor except for a gap of 10 mm between the constrictor and the anode. The constrictor channel diameter is 10 mm, the arc current is 100 A, the plasma gas flow rate is 5 slpm of argon, and the lateral gas flow rate is 0 to 25 slpm, with argon or nitrogen gas injected laterally. High-speed videography and calorimetric measurements of the anode cooling water temperature rise have been used to characterize the anode attachment. The results show that different modes of anode attachment exist, including a steady deflected anode root, a randomly fluctuating attachment, and a periodically fluctuating attachment. When the anode spot appears, the lateral gas leads to an arc voltage increase. The total anode heat transfer changes with different lateral gas flow rates and for the different attachments modes. This effect may be explained by lateral gas flow causing a convective heat loss from the arc to the chamber walls.

1. Introduction

The arc - anode attachment and anode heat fluxes play an important role for the anode erosion characteristics and the anode lifetime. A better knowledge of these phenomena is required to optimize the anode performance. It had been shown previously that operation modes of plasma spray torches depend on the thickness of the cold gas boundary layer between the arc column and anode surface. The well known restrike and takeover patterns were correlated to end-on images taken with a video camera of high time resolution[1]. In this study we have addressed the question of the interaction of the arc with an anode when there is a cold gas flow parallel to the anode surface forming a cold boundary layer and leading to a constant motion of the anode attachment with a corresponding fluctuation in plasma power. This situation is encountered in many applications of non-transferred plasma torches such as plasma spraying where the fluctuation in plasma jet power can have a detrimental influence on the quality of the produced coating.

In this paper, the motion of the anode attachment and the heat flux to the anode have been determined for a configuration where the arc axis is perpendicular to the anode surface with the plasma gas flowing along the arc axis, and with lateral injection of different gases parallel to the anode surface.

2. Experimental Apparatus

The experimental apparatus of a DC plasma torch with lateral gas flow is shown in Fig.1. The arc is generated between a rod shaped cathode and a water-cooled flat anode situated perpendicularly to the arc axis. An assembly of water-cooled constrictor segments, each separated by ceramic discs, surrounds the arc. A gap between the constrictor and the anode allows observation and control of the fluid dynamic boundary layer in the stagnation region. The entire assembly is housed in a controlled atmosphere chamber. The distance between the cathode and anode is sufficiently large to minimize the effect of the cathode jet. The lateral gas distributor provides the parallel gas flow along the anode surface to deflect the arc. While the relation between the elastic modulus of the arc and arc voltage measurements were investigated[2,3], there are few reports[4] about the relation between the arc voltage, the attachment region and unstable arc modes for different lateral gases. The parallel gas flow to the anode surface from the lateral gas distributor cools the arc in the boundary layer leading to a constriction of the arc and to a deflection. A description of the oscillating phenomena requires diagnostic experiments with high time resolution. The voltage and current traces are recorded with a high-speed oscilloscope and correlated to the images of a color CCD camera with an exposure time as low as 222 μs, and with a high framing rate video system with frame rates at 4,500 frames per second. Appropriate zoom lenses, tele-microscopic lenses and neutral density filters allow matching to experimental conditions and provide the necessary optical resolution. The arc is stabilized by a constrictor except for a gap of 10 mm between the constrictor and the anode. The constrictor channel diameter is 10 mm, arc current is 100 A, the plasma gas flow rate is 5 slpm of argon, the lateral gas flow rate is 0 to 25 slpm of argon or nitrogen, and the background atmosphere in the chamber is argon with a pressure of 0.1 MPa. The high-speed videography and calorimetric measurements of the anode cooling water temperature rise have been used to characterize the anode attachment.

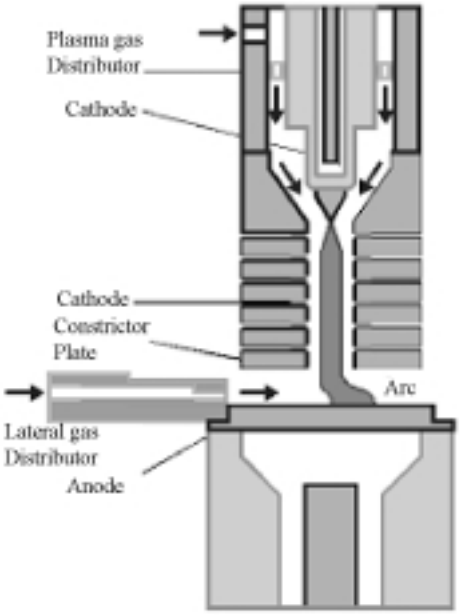

Fig.1 Experimental Apparatus of Plasma Torch

3. Arc Mode and voltage

Figure 2 (a) and (b) show the arc appearance mode as function of the lateral gases of argon and nitrogen, respectively. The mode 0 shows the stable attachment. Mode 1 shows a constriction of the arc in front of the anode. This mode is only observed with nitrogen. Mode 2 shows the lateral gas flow deflecting the arc. Mode 3 shows the appearance of a cold boundary layer. Mode 4 shows the appearance of an extended cold boundary layer and of an anode spot. Mode 5 shows the anode spot instability appearing.

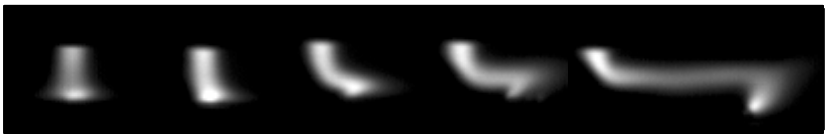

0slpm Mode 0 | 15slpm Mode 2 | 18slpm Mode 3 | 20slpm Mode 4 | 25slpm Mode 5

(a) Argon

0slpm Mode 0 | 5slpm Mode1 | 10slpm Mode 2 | 15slpm Mode 3 | 16slpm Mode 4 | 18slpm Mode 5

(b) Nitrogen

Fig.2 Arc Mode.

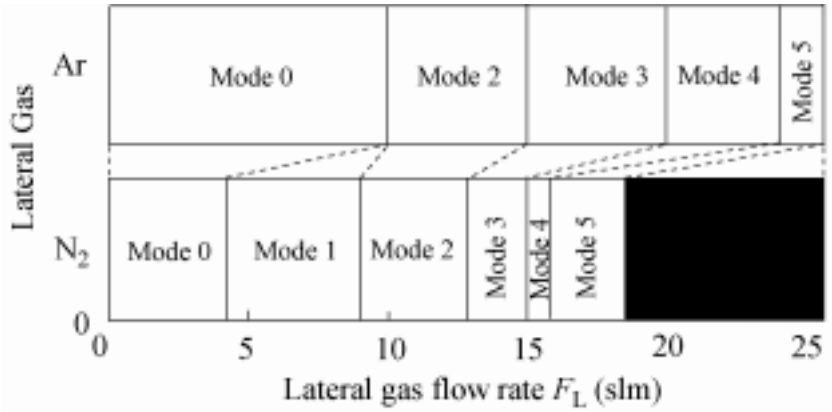

Fig.3 Relation of arc mode between current and lateral gas flow rate.

When the lateral gas flow increases from 4 slpm to 8 slpm, the arc constricts when the lateral gas is nitrogen. However, when the lateral gas is argon, there is little change in the arc diameter. When the lateral gas flow increases from 10 slpm of argon, and 9 slpm of nitrogen, the arc is deflected. A cold boundary layer appears when the flow rate reaches 15 slpm of the argon or 13 slpm of the nitrogen. An extended cold boundary layer and anode spot appears when the lateral gas flow reaches 20 slpm of argon or at 16 slpm of nitrogen. At these flow rates, the anode spot remains stationary and the arc becomes longer. The arc attachment becomes unstable when the flow rate reaches 24 slpm of argon or 17 slpm of nitrogen. The arc is extinguished when the nitrogen flow rate reaches 19 slpm. Figure 3 shows the arc mode as a function of lateral gas flow rate. Before the anode spot appears, the lateral gas just deflects the arc. However, after the arc spot appears, the effect of lateral gas increases. While the arc mode 4 and 5 can exist from 20-25 slpm in the case of argon as lateral gas, it can only exist from 16 to 18 slpm in the case of nitrogen. Also, the arc is longer with argon than with nitrogen. While the arc with nitrogen is extinguished immediately after the appearance of mode 5, the arc is not easily extinguished with argon flow.

4 Correlation of arc voltage and mode

Figure 4 shows the average, maximum and minimum values for the arc voltage as a function of the lateral gas flow rate. The voltage remains constant as long as there is no mode change or no movement of the attachment spot. Beginning of the arc attachment movement by increasing the lateral gas flow rate is seen also by voltage fluctuations. A change from mode 4 to mode 5 (attachment instability) is accompanied by a change in the maximum value for the voltage from 51.1 V to 56.2 V for a change of the lateral gas flow rate from 23 to 25 slpm in the case of argon flow, and from 52.9 to 54.5 V for an increase in the nitrogen flow rate from 16 to 17 slpm. There is a much smaller change in the average voltage. It can be seen that a similar deflection of the arc is obtained for a mass flow of 0.6 g/s of argon and 0.38 g/s of nitrogen. This is an indication that the deflection of the arc is not only due to the lateral gas momentum but also due to the higher energy losses encountered with the lateral flow of the molecular gas.

Figure 5 shows a voltage trace for conditions when a mode 5 attachment is established (100 A, 5 slm argon as plasma gas, 25 slm argon as lateral gas). It is seen that the voltage can remain constant for about 20 ms, but this period is followed by three restrikes in about 10 ms. In previous experiments under the approximately the same conditions, a restrike frequency of about 230 Hz has been measured [3]. It is clear from the present measurements that there is a random component in the restrikes. Also the magnitude of the voltage jump during the restrike can vary, being 3 V at location A in Fig. 5, 3.9 V at location B, 4.4 V at C and 6 V at D. Figure 6 shows the high speed images during the different restrike events. It is apparent that the time required for the arc to establish an upstream attachment in the case of a restrike is about 0.67 ms.

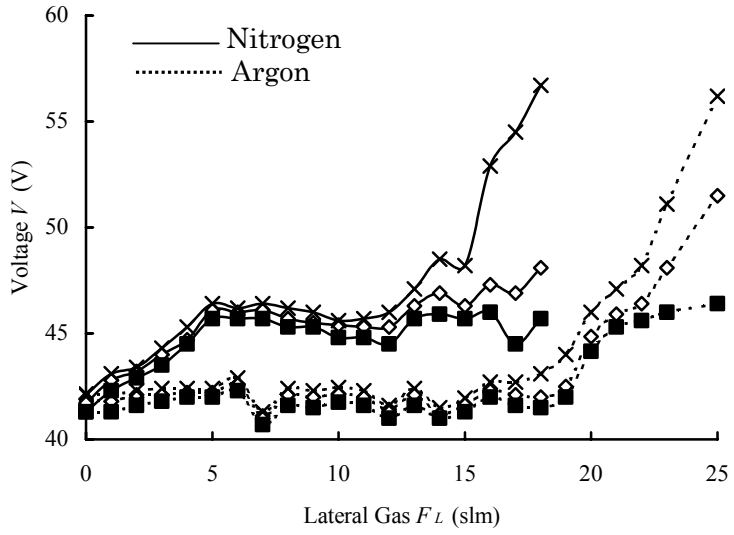

Fig.4 Voltage as functions of lateral gas.
(◇:Average, ■:Minimum, ×:Maximum)

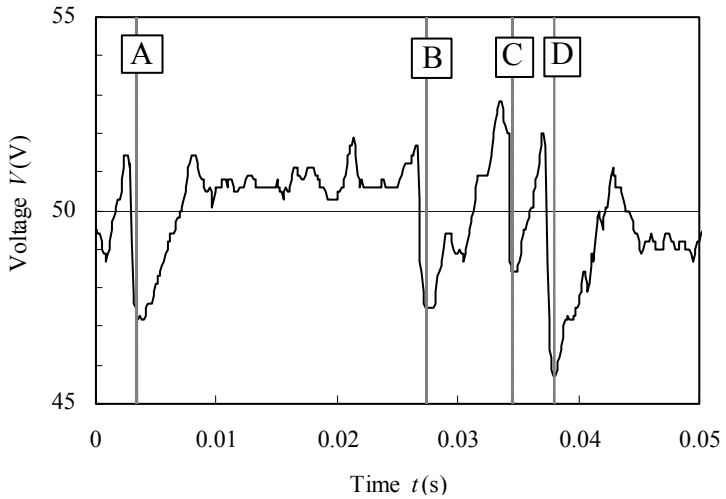

Fig.5 Correlation of restrike time and arc voltage.

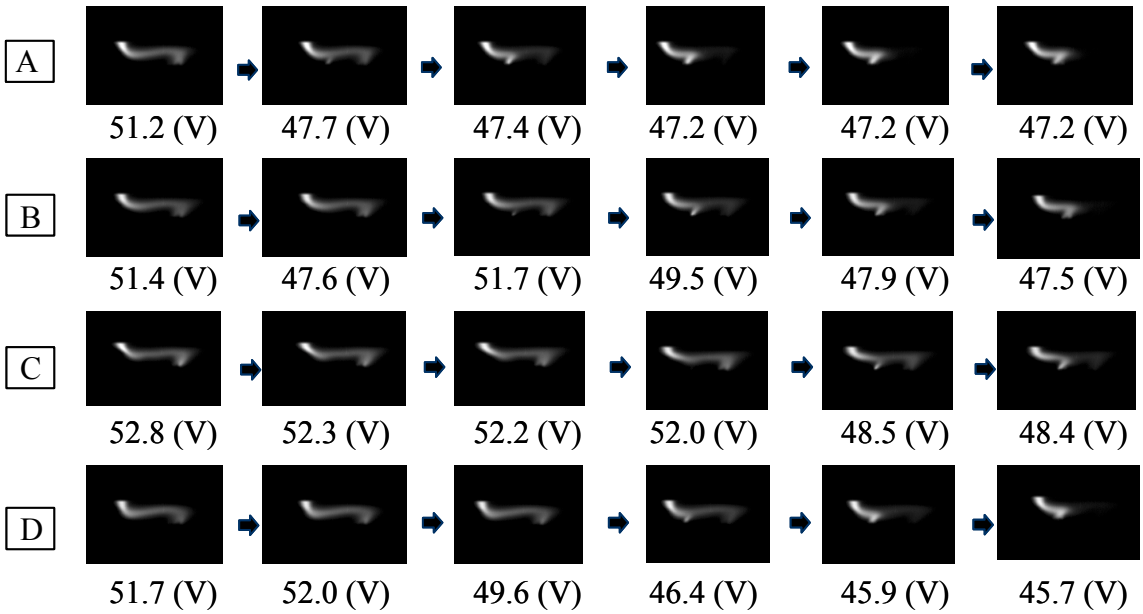

Fig.6 Arc mode with restrike.

5 Heat flux to anode

Figure 7 shows the total heat transfer to the anode as a function of the lateral gas flow rate for the two gases. The heat transfer shows a slight decrease with increasing lateral argon gas flow rate, indicating a convective loss from the arc to the chamber walls. With nitrogen, an initial increase is noticed during the period of arc constriction (mode 1). This increase in heat transfer indicates that the voltage increase during arc constriction and the associated increase in dissipated power are largely transferred to the anode.

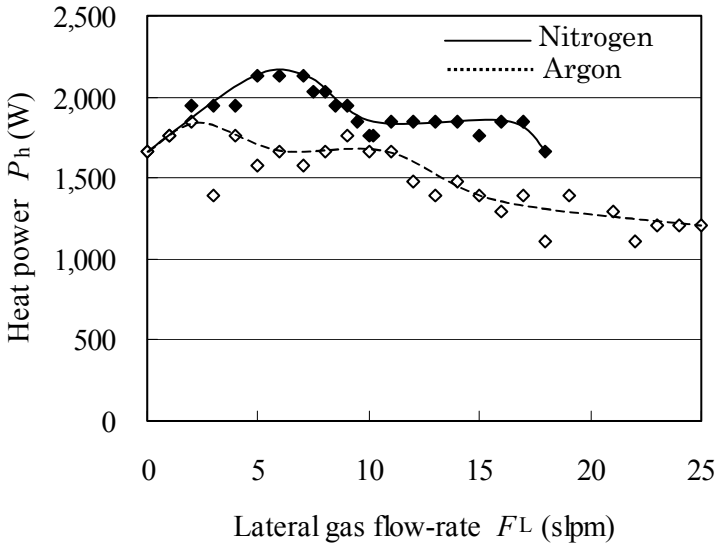

Fig.7 Heat flux to the anode.
(◆:Nitrogen,◇:Argon)

6. Summary

A lateral gas flow can result in distinctly different appearances of the arc-anode attachment, going with increasing mass flow from a diffuse to a constricted attachment, to a deflection and the establishment of an extended cold boundary layer between the deflected arc and the anode, and finally an instable attachment. The transitions occur at lower mass flow rates when nitrogen is the laterally blown gas compared with argon. An attachment mode change is accompanied by an increase in arc voltage in the case of nitrogen, but only an extended boundary layer build-up leads to a significant increase in arc voltage in the case of lateral argon flow. Arc instabilities usually lead to arc extinction in the case of nitrogen flow, and to voltage fluctuations with no specific periodicity in the case of argon. Anode heat fluxes initially rise with increasing lateral nitrogen flow indicating transfer of the increased energy dissipation to the anode. A further increase of the lateral flow leads to a decrease in heat transfer for nitrogen as well as for argon, indicating an energy loss to the surrounding chamber walls.

Acknowledgments

This research was supported by the National Science Foundation. (Grant No. CTS-0225962)

References

[1] Z. Duan and J. Heberlein, JTST, ASM, Vol.11(1), March 2002, pp.44-51.
[2] T. Inaba, H.Oi, M.Endo, Proc. of Korea-Japan Symp.on Electrical Discharge and High Voltage Engineering, Kumi, Korea, May 1996, pp. 220-223.
[3] S. I. Tanaka, A. Ito, T. Kameda, T. Iwao, T. Inaba, Y. Miyashita, ISPC-15, Vol.III, Orleans, France, July 2001, pp.833-839.
[4] R. Hartmann, J. Heberlein, ISPC-15, Vol.II, Orleans, France, July 2001, 2001, pp.497-502.

Low –Temperature Plasma Synthesis of Single-Crystal Silicon Nanoparticles

A. Bapat[1], U.Kortshagen[1], S.Campbell[2], C.Perrey[3] C.Barry Carter[3]

[1] *Department of Mechanical Engineering, University of Minnesota, Minneapolis, USA*
[2] *Department of Electrical and Computer Engineering, University of Minnesota, Minneapolis, USA*
[3] *Department of Chemical Engineering and Material Science, University of Minnesota, Minneapolis, USA*

Abstract

Nanoparticles have attracted considerable interest for a wide array of potential applications [1]. Discrete, freestanding silicon nanoparticles are highly desirable for the fabrication of novel microelectronic devices. We employ a high-density inductive RF plasma in SiH_4 diluted in Helium and Argon for production of nanoparticles. Characterisation using Transmission Electron Microscopy (TEM) and X-Ray Energy Dispersive Spectroscopy (XEDS) suggests presence of defect-free crystalline particles.

1. Introduction

Amorphous silicon has been used for a wide variety of electronic applications including thin film transistors and energy conversion devices. However, these devices suffer strongly from defect scattering and recombination. Single-crystal semiconductor nanoparticles with their high carrier velocities and longer recombinative lifetimes are expected to be well suited for device fabrication. Potential applications of crystalline silicon nanoparticles as a substitute for amorphous silicon in optical and quantum effect electronic devices, have led to intense research efforts in that direction (see ref. [1] and references therein). These efforts mainly focused on particles in the 2-10 nm range for their unique confinement effects and ease of production. As a prominent example, microelectronic memory devices have already been built using silicon nanocrystals in this size range [2].

Out of a variety of synthesis methods, gas-phase synthesis of nanoparticles has been widely used for electronic applications due to the high degree of purity that can be achieved. A variety of gas-phase processes such as inert gas condensation [3], flame synthesis [4], furnace flow reactors [5] and thermal plasma particle synthesis [6] have been proposed for nanoparticle synthesis. These processes are relatively efficient in the synthesis of particles, however, they often produce either agglomerates or nanoparticles with broad size distributions that require post-synthesis size selection [2, 7].

The ability of plasmas to create highly monodisperse particles has been demonstrated on multiple occasions [8]. The monodispersity of the particle formation in silane plasmas can be explained by the fact that nanoparticles formed in the plasma scavenge precursors needed in the formation of new nuclei. After an initial nucleation and growth phase the nanoparticles seem to grow only by surface deposition. The particles get negatively charged due to the higher mobility of electrons as compared to ions in the discharge. This helps prevent agglomeration of particles once they reach a size of approximately 10 nm and carry enough negative charge [9]. The large electron mobility also leads to a negative charging of the reactor walls that cause the negatively charged particles to be trapped in the plasma region [8, 10].

Nanocrystals with size of the order of a few tens of nanometers having a monodisperse size distribution would be best suited for use with present day commercial lithography tools. A method for synthesizing single crystal, non-agglomerated silicon nanoparticles would be highly desirable, especially if particles can be remotely created and deposited on any kind of substrate. This could enable deposition on insulating substrates allowing high signal speeds or on other versatile substrates such as plastics. Recently several groups studying the formation of silicon particles in silane plasmas have reported generation of monodisperse, non-agglomerated distributions of particles [8,11-14]. However, particles observed in these studies were amorphous or polycrystalline.

Several studies of particle synthesis in low-temperature plasmas that focused on crystalline particles showed small crystallites, usually 2-5 nm in size [15-18]. In the present paper, we describe a synthesis route that allows the production of highly oriented, single-crystalline nanoparticles in the size range 20-80 nm.

2. Experimental set-up

Contrary to most studies reported, we employ a high-density inductively coupled low-pressure RF plasma for this work. This kind of plasma is known to produce plasma densities about one to two orders of magnitude higher than those of capacitively coupled plasmas [19] that were used in most of the aforementioned studies. Figure 1 is a schematic of the experimental setup. The inductive plasma is generated in a Pyrex tube with 5.1 cm inner diameter and 23 cm length. RF power of 150-200 W at 13.56 MHz is applied to a 5-turn induction coil. In the inductive mode, a bright ellipsoidal plasma forms inside the induction coil with an estimated local power deposition of 0.75-1 W/cm^3 . The Pyrex tube is attached to a high vacuum chamber. Particles are extracted through a 1mm orifice and deposited on amorphous carbon support film grids for transmission electron microscopy (TEM) at the end of the vacuum chamber. The process gas is 5% silane diluted in helium that can further be diluted by argon. During the plasma process, an operating pressure of 500-800 mTorr is maintained in the Pyrex tube. The total gas flow rate is 3.5-4 sccm. The pressure in the high vacuum chamber generally rises from 10^{-7} to 10^{-5} Torr during the deposition process. The plasma-on time normally is between 60-90 seconds. During this time, particles are likely negatively charged and trapped in the plasma. When the plasma is turned off, the particles are extracted through the extraction orifice by gas drag and are deposited on the TEM support films. A mask in front of the TEM gridholder permits the selective exposure of grids to varying plasma conditions and thus allows for a comparative study. A load lock system is employed to allow faster processing of substrates.

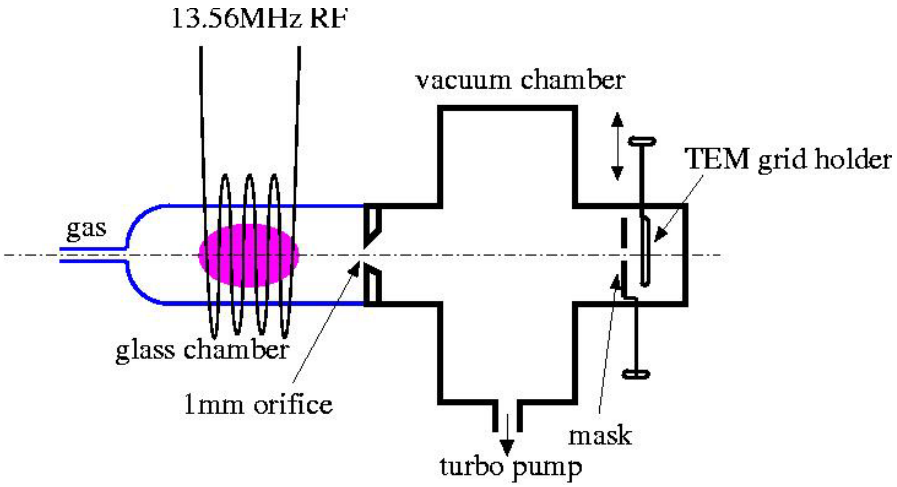

Figure 1: Sketch of Experimental Setup

Using this setup, experiments were conducted for varying plasma conditions in order to study the effect of plasma parameters on the particle formation process. TEM analysis was performed to study the particles deposited. The results presented here are only for a specific set of conditions, which lead to the formation of monodisperse crystalline particles. Process conditions for all results cited here were 0.72 sccm of silane (5%) in helium (95%) and 3 sccm of argon, leading to a total pressure of 700 mTorr, and a RF power input of 100 W applied for 90 seconds.

3. Preliminary findings

From preliminary studies performed, some trends can be inferred of the effect of plasma parameters on particle formation. The particle concentration is found roughly proportional to the silane partial pressure. Longer plasma-on times, higher power density, and higher total gas pressure favor formation of single crystal particles. Preliminary estimates of gas temperature in the plasma predict temperature values of the order of 1300K at the discharge center. Negatively charged particles are trapped in the plasma and can be assumed to reach at least the local gas temperature and then undergo a rapid annealing process leading to crystallization.

4. TEM analysis of deposited particles

Deposits of the nanoparticles on TEM support grids were examined using a Philips CM30 and JEOL 3010 TEMs; both were operated at 300 kV. The CM30 is equipped with a X-ray energy dispersive spectrometeter (XEDS) for chemical analysis. In order to image individual nanoparticles in the scanning electron microscope (SEM), the specimen was coated with Pt to enhance conductivity. All SEM studies utilized a Hitachi S900 field-emission SEM.

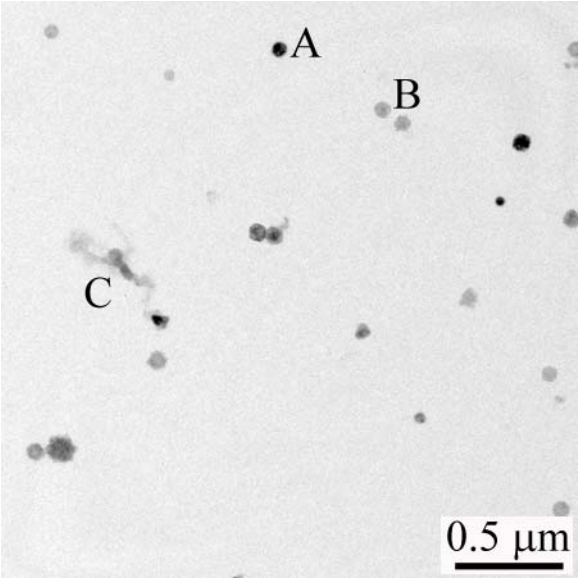

Figure 2: Bright field TEM image illustrating the spatial distribution of the nanoparticle deposit. The particle "A" is strongly diffracting and appears dark, while the particles at "B" are not in an appropriate diffracting orientation. A polycrystalline agglomerate is in the region "C."

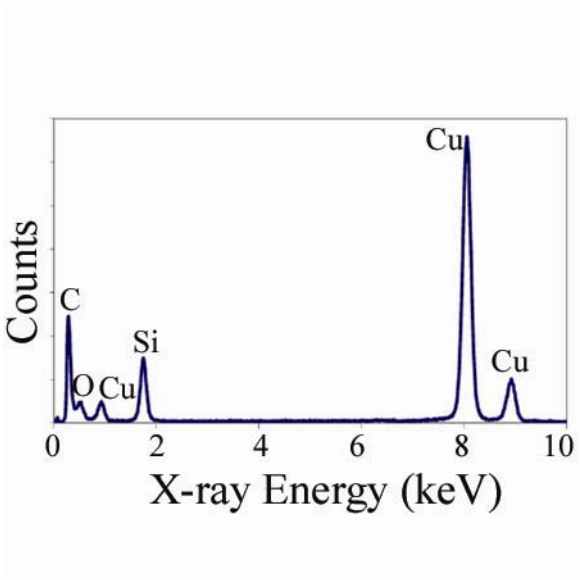

Figure 3: X-ray energy dispersive spectra showing the chemical species present. The Si and O peaks originate from the nanoparticles, and the Cu and C are from the TEM support grid and film, respectively.

Figure 1 is a bright-field (BF) TEM image of a typical area of the deposit. The size distribution of single-crystal nanoparticles is fairly uniform, with an average diameter of approximately 75 nm. Some particles in this image, such as the particle denoted "A," are in an appropriate crystallographic orientation to diffract strongly and appear dark. Conversely, the particles labeled "B" are not in a diffracting orientation and appear lighter. A polycrystalline agglomerate is noted in the region "C." The chemical identity of the deposit was confirmed using XEDS. The spectra resulting from the deposit is shown in Figure 2. The Si and O signals originate from the nanoparticles, while the Cu and C are from the TEM support grid and film, respectively.

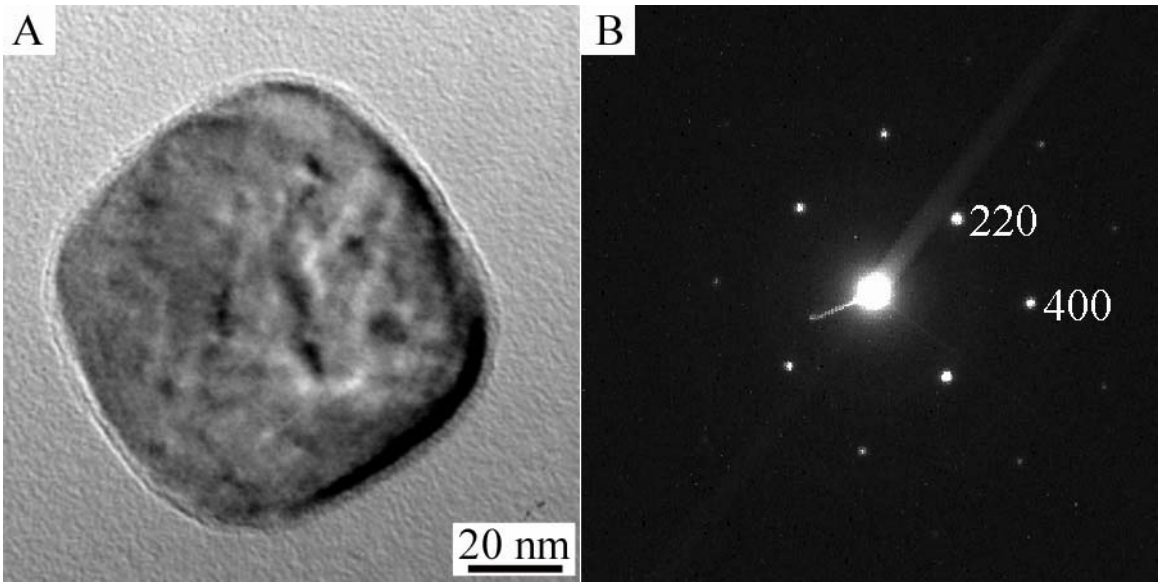

Figure 4: TEM observations of a nanoparticle with a "rounded square" appearance. (A) is a bright-field image of an individual nanoparticle, and (B) is the corresponding selected area diffraction pattern. This pattern is consistent with [001] single crystal Si.

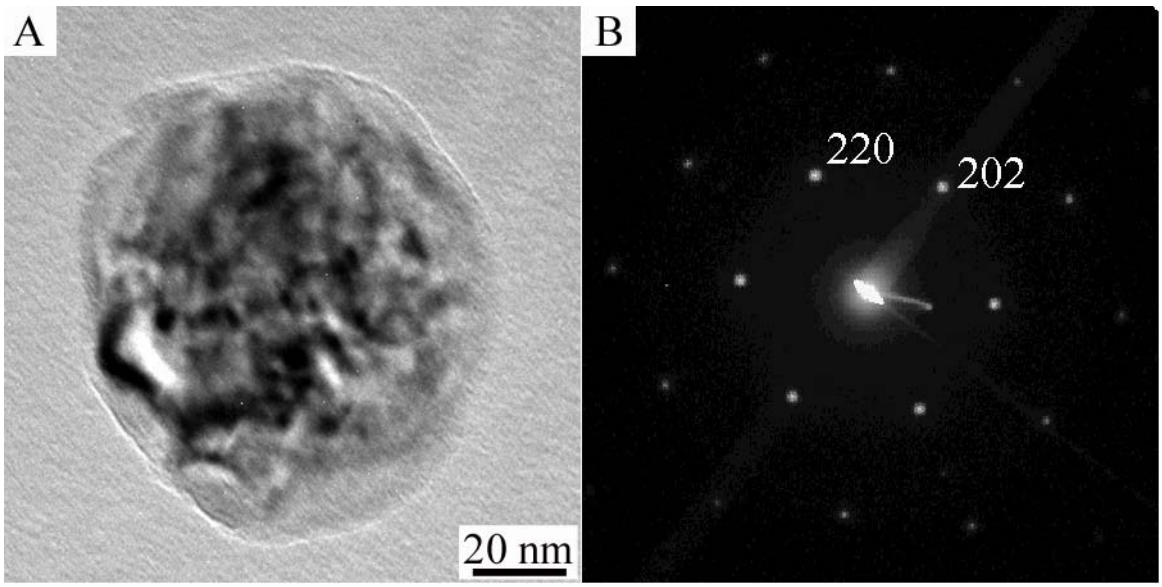

Figure 5: TEM observations of a nanoparticle with a "smoothed hexagon" appearance. (A) is a bright-field image of an individual nanoparticle, and (B) is the corresponding selected area diffraction pattern. This pattern is consistent with $[\bar{1}11]$ single crystal Si.

The use of the TEM for characterization of the nanoparticles provides the ability to identify the shape and crystallographic features of individual particles. Examination of nanoparticles at higher magnifications reveals shapes classified as "highly oriented." Figure 3A is a BF TEM image of a nanoparticle that has a "rounded square" appearance, while Figure 4A shows a particle with a "smoothed hexagon" appearance. Figures 3B and 4B are the selected-area diffraction (SAD) patterns from each particle. These diffraction patterns correspond to single-crystal diamond-cubic Si with [001] and $[\bar{1}11]$ orientations, respectively. Additionally, an amorphous surface layer is visible on each particle; this surface layer is likely an oxide layer.

Because the TEM images three-dimensional structures in two dimensions, the three-dimensional character of the nanoparticles can be difficult to discern solely from these images [20]. Imaging at different degrees of tilt has shown that the surface of the nanoparticles is not uniform and contains ledges and ridges [21]. Additionally, the apparent shape of the nanoparticles changed as the tilt was varied [21]. These obser-

vations agree with the TEM results, since the nanoparticles have different projected shapes when viewed along various crystallographic axes. The non-uniform surface of the nanoparticle will contribute to the contrast features visible in the TEM images [20].

5. Conclusion

In this paper we demonstrate a low-temperature plasma synthesis process for producing single-crystal silicon nanoparticles in the size range 20-80 nm. The XEDS and SAD analysis from the TEM confirm that the nanoparticles are crystalline diamond cubic Si of a highly oriented character. Future efforts are directed in the direction of better control of particle distribution with varying plasma parameters, modeling of particle trajectories in the plasma gas flow and electrical characterization of nanoparticles as a step towards building nanoparticle-based electronic devices.

Acknowledgements

This work was supported in part by NSF under grant CTS-9876224 and by the MRSEC Program of the National Science Foundation under Award Number DMR-0212302. CRP and CBC acknowledge Prof. Stan Erlandsen for access to the FESEM and Chris Frethem for technical assistance, and Dr. Markus Lentzen and Prof. Knut Urban at IFF-IMF in Jülich for access and assistance with the HRTEM.

References

[1] F. E. Kruis, H. Fissan, A. Peled, J. Aerosol Sci. **29**, 511-535 (1998).
[2] M. L. Ostraat et al., Applied Physics Letters **79**, 433-435 (Jul 16, 2001).
[3] H. Hahn, R. S. Averback, J. Appl. Phys. **67**, 113 (1990).
[4] M. R. Zachariah, M. I. Aquino, R. D. Shull, E. B. Steel, Nanostruc. Mater. **5**, 383-392 (1995).
[5] K. Deppert, J.-O. Bovin, J.-O. Malm, L. Samuelson, J. Crystal Growth **169**, 13-19 (1996).
[6] N. P. Rao et al., J. Aerosol Sci. **29**, 707 (1998).
[7] R. P. Camata, H. A. Atwater, K. J. Vahala, R. C. Flagan, Applied Physics Letters **68**, 3162-3164 (1996).
[8] A. Bouchoule, L. Boufendi, Plasma Sources Sci. Technol. **3**, 293 (1994).
[9] U. Kortshagen, U. Bhandarkar, Phys. Rev. E **60**, 887 (1999).
[10] J.L. Dorier et al., IEEE Trans. Plasma Sci. **24**, 101 (1996).
[11] A. Bouchoule, L. Boufendi, Plasma Sources Sci. Technol. **2**, 204 (1993).
[12] L. Boufendi, A. Bouchoule, Plasma Sources Sci. Technol. **3**, 263 (1994).
[13] C. Courteille et al., J. Appl. Phys. **80**, 2069 (1996).
[14] Y.Watanabe, M. Shiratani, Jpn. J. Appl. Phys. **32**, 3074 (1993).
[15] A. F. i. Morral, R. Brenot, E. A. G. Hamers, R. Vanderhagen, R. R. i. Cabarrocas, Journal of Non-Crystalline Solids **266-269**, 48-53 (2000).
[16] G. Viera, S. Huet, M. Mikikian, L. Boufendi, Thin Solid Films **403**, 467-470 (2002).
[17] C. Courteille, J.-L. Dorier, J. Dutta, C. Hollenstein, A. A. Howling, J. Appl. Phys. **78**, 61 (1995).
[18] S. Oda, Adv. Colloid Interfac. Sci. **71-72**, 31-37 (1997).
[19] M. A. Lieberman, A. J. Lichtenberg, (1994).
[20] D. B. Williams, C. B. Carter, Transmission Electron Microscopy: A Textbook for Materials Science (Plenum Press, New York and London, 1996).
[21] A. Bapat, U. Kortshagen, S. Campbell, C. R. Perrey, and C. B. Carter. “Synthesis of Crystalline Silicon Nanoparticles in Low-Pressure Inductive Plasmas." Materials Research Society Proceedings, **737**, 2002, F1.10.

Radial distribution of species derived from the introduction of N_2 and O_2 in the helium plasma produced by the axial injection torch

R. Álvarez[1], M.C. Quintero[1], A. Rodero[1], Z. Pokorna[2]

[1] *Department of Physics, University of Córdoba, Córdoba, Spain*
[2] *Department of Physical Electronics, Masaryk University, Czech Republic*

Abstract

The effect of the introduction of species as nitrogen and oxigen in the helium microwave induced plasma created by the axial injection torch is radially studied by means of the Abel inversion procedure. The spectrum was scanned for atomic and ionic lines together with rotational bands of neutral and ionic molecules of such species. No ionic lines of any specie were detected at any plasma condition, neither were rotational bands of oxygen.

1. Introduction

Due to the high ionization potential of He, the He plasma produced by the axial injection torch (Torche à Injection Axiale or TIA)[1] is very useful as an excitation source for analytical chemistry [2]. The mixtures of helium with molecular gases are of great interest for a number of technological applications that take into account both physical and chemical processes. These plasmas are rich in active components, such as O, N and excited metastable species, which favour the different plasmochemical processes wich are necessary for such applications.

The different species present in the plasma, their radial distribution [3], and the possible mechanisms of creation and destruction have been studied. In order to do so, different percentages of N_2 and O_2 were introduced in the helium plasma produced by the TIA. The obtained results have been compared with those obtained with helium as the only component of the plasma gas, where the N_2 and O_2 are present in the TIA due to diffusion from the air surrounding the plasma.

2. Experimental

The axial injection torch produces a small (~1 mm diameter and 10-20 mm long) and very stable microwave plasma. It can operate with atomic and molecular gases, including air, which makes it a very versatile plasma. Its operating conditions range from 300 to 2000 W of incident microwave power and from 0.5 to 15 L min^{-1} of flow-rate of the plasma gas. In the present work, the plasma working conditions are 4 L min^{-1} of total gas flow-rate and 600 W of incident MW power.
The experimental set-up used in this work is aimed to the obtention of emission lines of the plasma for different lateral positions. Once these data are obtained, an Abel inversion can be performed on them in order to obtain the radial distribution of the emission intensity of the measured line. In Table 1 can be found the technical description of the instruments used in the set-up. The image of the flame produced by the plasma

Table 1: Technical description of the components of the experimental set-up

Microwave launcher	TIA (Montreal University)
Microwave generator	GPM 12K T/t (SAIREM) at 2.45 GHz
Material of the nozzle	Brass
Monochromator	THR-1000 (Jovin-Yvon) Grating 1200 grooves mm^{-1} Dispersion: Typically 0.8 nm mm^{-1} at λ=500nm Computer-controlled Spectralink system
ICCD camera	Flamestar 2 (La Vision)
Flow controller	Mass flow controllers FC280 Dynamass control system (Tylan General)

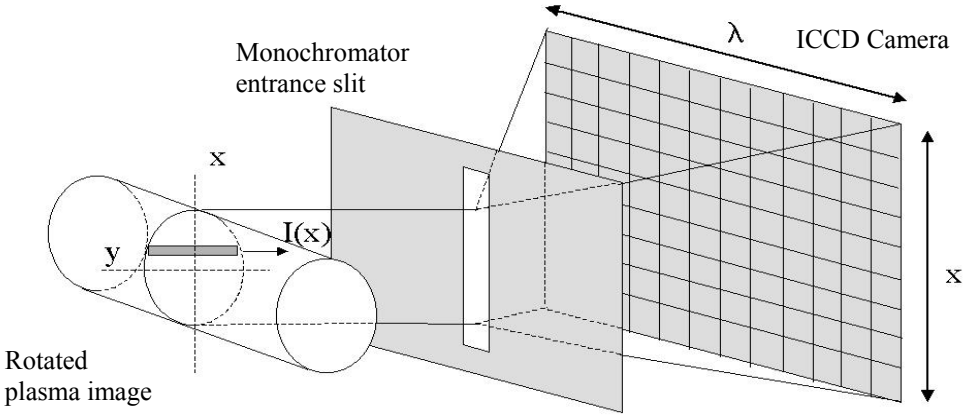

Fig. 1: The image of the flame, rotated 90º and integrated in the y-axis is dispersed in wavelength by the monochromator.

generator device is carried to the entrance slit of the monochromator by an optical system consisting of two convergent lenses and a Dove prism. The prism rotates the image 90º, allowing the selection of a transversal slice of the plasma, which is then focussed on the slit. The image of the slice is then dispersed in wavelength by the monochromator and focussed on the bidimensional array of photosensitive pixels of an intensified CCD camera. With this set-up, then, each row of the camera pixels collects an emission spectrum for a different lateral position of the discharge, and each column a lateral distribution of emission intensity for a different wavelength, as is shown in Fig. 1.

3. Data treatment

The measured emission intensity data are integrated along the plasma depth in the line-of-sight direction. The Abel inversion provides the radial distribution of the emission coefficient of a spectral line, $\varepsilon(r)$, from the lateral distribution of such integrated intensity, $I(x)$:

$$\varepsilon(r) = -\frac{1}{\pi}\int_r^R \frac{I'(x)}{\sqrt{x^2 - r^2}}\,dx \qquad (1)$$

where R is the plasma radius and $I'(x)$ is the first derivative of $I(x)$ respect to x. In order, eq. (1) has to be discretized. In this work the Hankel-Fourier method to Abel-invert discrete sets of data has been used, which was found in a previous paper to be more accurate than other methods present in the literature [3]. The $I(x)$ distributions were then Abel-inverted, and the radial distribution of the emissivity of such lines was obtained. The error of the Abel inversion is higher the closer to the plasma centre the radial positions are. This error has been calculated previously [3], yielding a relative error for the results of less than 8% for radial positions $r > 0.2\,R$.

4. Measurements and results

The measurements were performed for an input microwave power of 600 W and a constant gas flow-rate of 4 L min^{-1}. Five different plasma gas compositions were used in this work: pure helium, helium with 0.5% nitrogen added, helium with 2.5% nitrogen added, helium with 0.5% oxigen added and helium with 2.5% oxigen added. At each plasma condition, the emission spectra of the plasma was scanned in order to find atomic (N, O) or ionic (N^+, O^+) lines, and molecular (N_2, O_2) or ionized molecular (N_2^+, O_2^+) bands. Whichever was the plasma gas composition, only four of these eight species were found in the plasma: N, N_2, N_2^+ and O.

No ionic species from nitrogen nor from oxigen were detected in the discharge. This was to be expected, as although the helium ionization energy (24.587 eV) is higher than that of the oxygen (13.62 eV) and nitrogen (14.53 eV), the energy values of the excited levels of the O^+ and N^+ ions are still above the He ionization

energy [4], which probably causes these species to be mainly in their ground states, hence explaining the lack of emission from these species in our plasma.

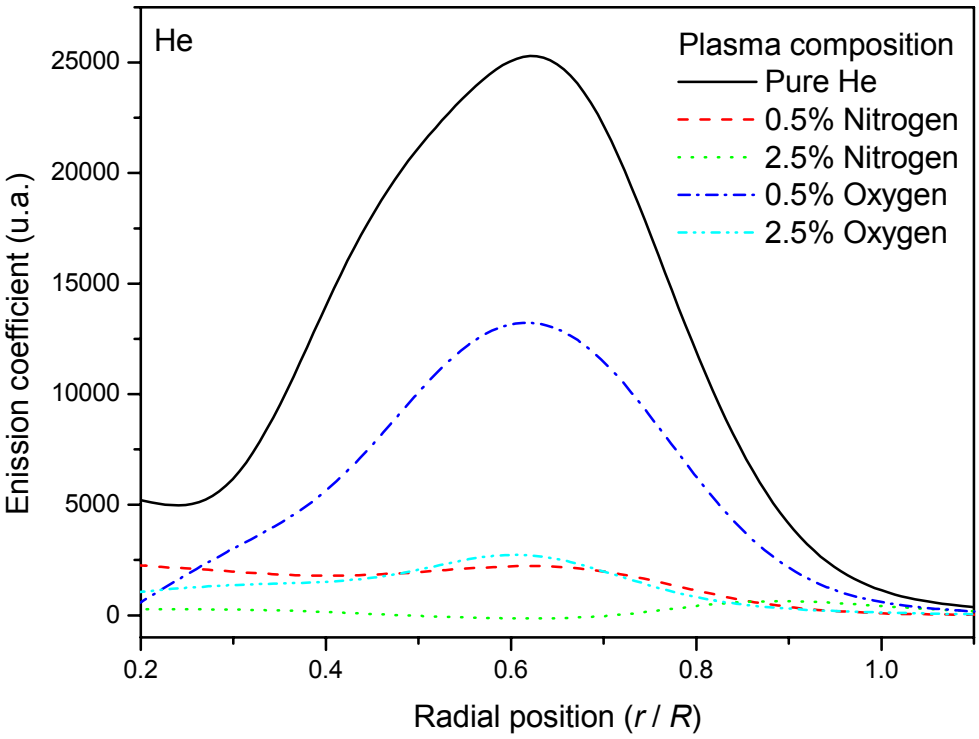

Fig. 2: Radial distributions of the emission coefficient of the 587.6 nm He line for different plasma gas compositions.

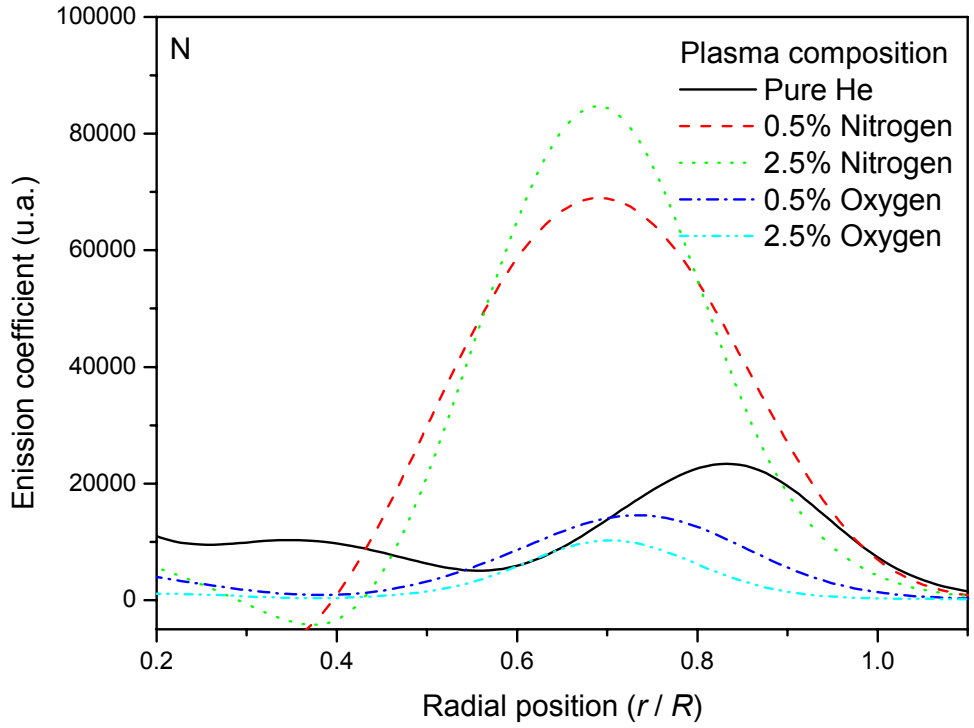

Fig. 3: Radial distributions of the emission coefficient of the 749.9 nm N line for different plasma gas compositions.

In the He-N_2 mixture a great profussion of N_2 and N_2^+ molecular bands were observed. In the He-O_2 mixture, however, no molecular bands (O_2, O_2^+) were detected. This behaviour was also found when the plasma gas is

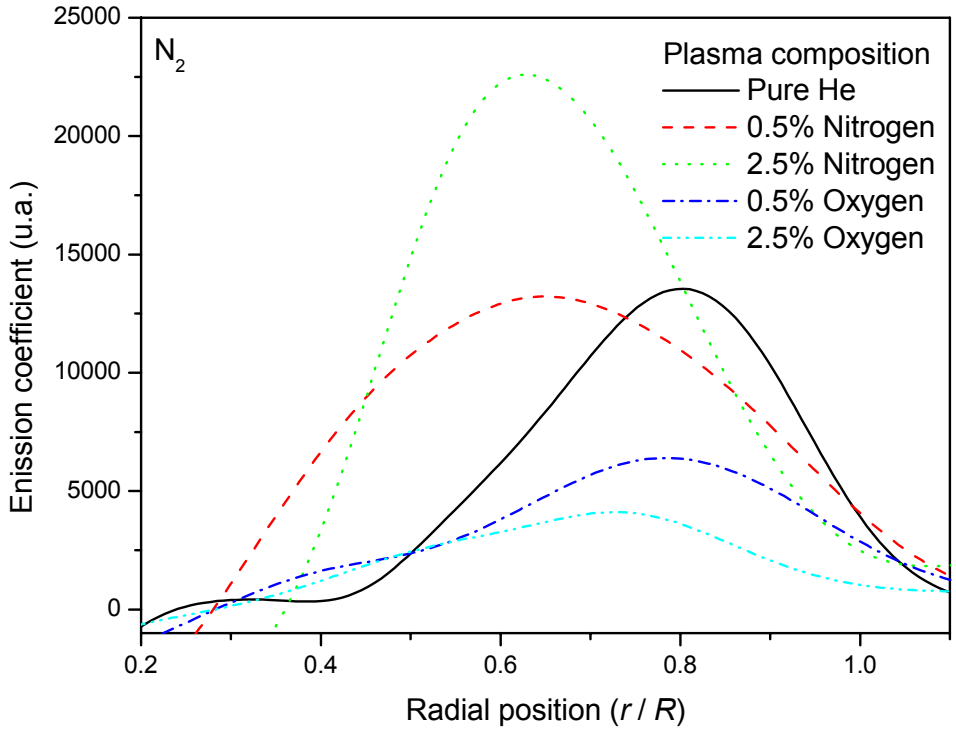

Fig. 4: Radial distributions of the emission coefficient of the 357.7 nm N_2 rotational bandhead for different plasma gas compositions.

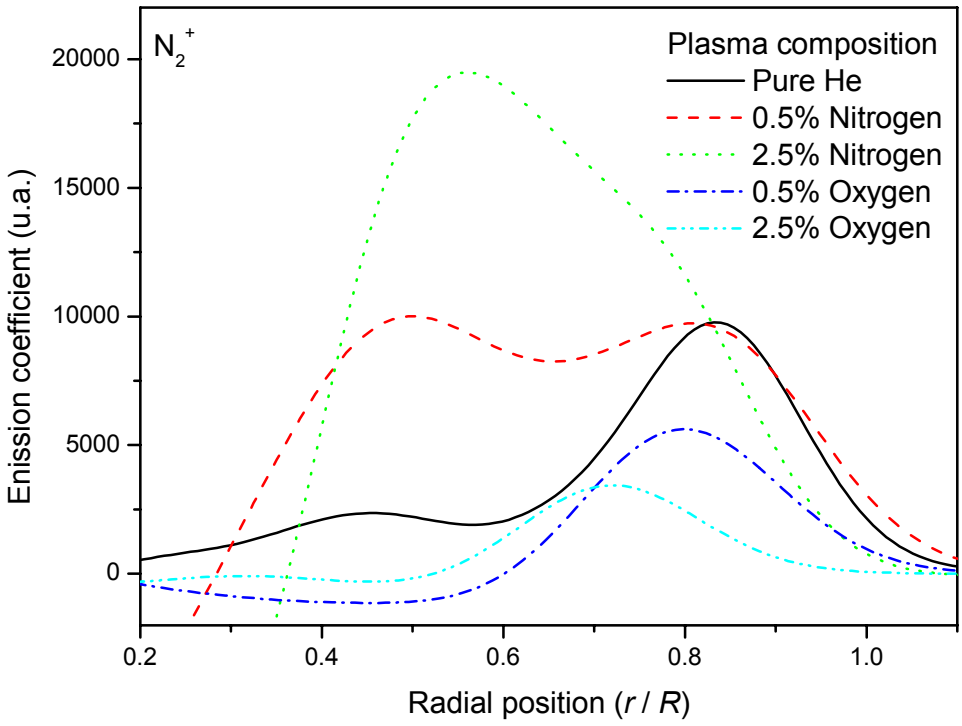

Fig. 5: Radial distributions of the emission coefficient of the 391.4 nm N_2^+ rotational bandhead for different plasma gas compositions.

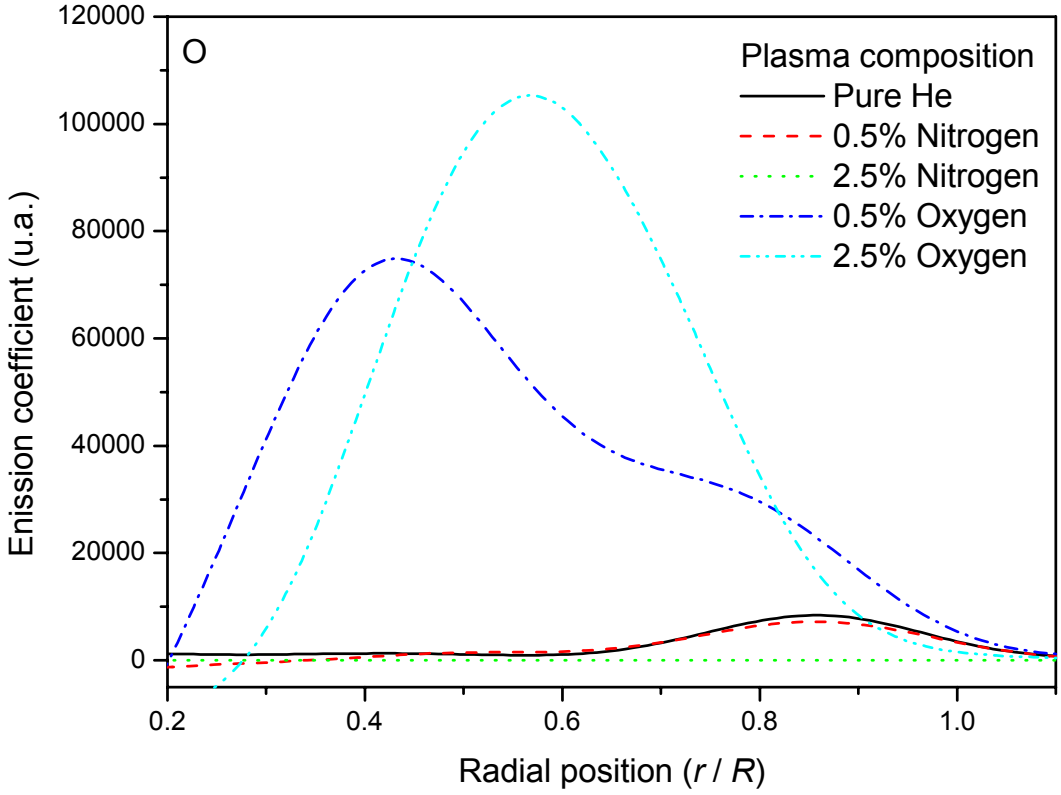

Fig. 6: Radial distributions of the emission coefficient of the 777.2 nm O line for different plasma gas compositions.

pure helium, i.e. when the molecular gases come from the surrounding air that enters the discharge. The radial distributions of emission intensity of the measured species and that of a helium line are represented in Figs. 2 to 6 for every composition of the plasma gas.

5. Discussion of the results

The lack of O_2^+ can be explained by taking into account the charge transfer mechanisms proposed by Ricard [5] for a helium plasma, where molecular oxigen interacts with the ionized helium present in the plasma in these ways:

$$\begin{aligned} He^+ + O_2 &\rightarrow O_2^+ + He \\ He^+ + O_2 &\rightarrow O^+ + O + He \end{aligned} \qquad (2)$$

The occurrence ratio of these two processes is 0.03 and 0.97 respectively. As the most favoured process is, by far, the second one, this could explain the fact that no O_2^+ molecular bands were observed, while a number of atomic oxygen lines could be detected.
As to the lack of N_2^+ molecular bands, the charge transfer processes for molecular nitrogen are similar to that of molecular oxigen [5]:

$$\begin{aligned} He^+ + N_2 &\rightarrow N_2^+ + He \\ He^+ + N_2 &\rightarrow N^+ + N + He \end{aligned} \qquad (3)$$

but not the occurrence ratios, which are in this case of 0.4 and 0.6 respectively. This could explain the fact that N_2^+ bands were detected, but not O_2^+ bands, which have an occurrence ratio of only 0.03.

There is still another difference between N_2 and O_2 introduction: N_2 bands are visible all over the TIA spectrum, while no O_2 band could be measured, although the introduced quantities were the same for both gases. This is probably due to the difference in their respective dissociation energies, being 9.76 eV for N_2 and around half of that (5.12 eV) for O_2, which might indicate that O_2 is completely dissociated in the TIA plasma.

In Fig. 2 the radial distributions of a helium line are presented for every plasma gas composition. It can be seen that the line intensity decreases with the introduction of gases to the plasma, decreasing more with the added gas concentration, and being higher the decrease with oxygen than with nitrogen. This behavior can be explained if its taken into account that the dissociation energy of these gases is lower than the energy of the helium excited levels, the oxygen dissociation energy being lower than that of nitrogen.
Figs. 3 to 5 show radial distribution of nitrogen lines (N, N_2 and N_2^+ respectively), and a similar behaviour can be seen in all of them: the emission increases with the percentage of nitrogen introduced in the plasma and decreases with the percentage of oxygen. In the absence of extra nitrogen, the maxima of the distributions are close to the plasma edge, as the nitrogen comes then from the surrounding air. When nitrogen is introduced in the discharge, the radial position of the maxima shift towards the plasma centre.
In Fig. 6 can be seen the radial distribution of the atomic oxygen line for every plasma gas composition. The relative increase of the emission coefficient of this line is high when compared with the increase in the nitrogen lines. A reason for this could be the fact that, as can be seen when comparing the reaction rates of eq. 2, atomic and ionic oxygen are the main oxygen species present in the TIA plasma; not appearing molecular species and not existing enough energy to excite the ionized oxygen, atomic oxygen is the most excited oxygen specie.

References

[1] M. Moisan, G. Sauve, Z. Zakrzewski, J. Hubert, Plasma Sources, Sci. Technol. **3** 584 (1994).
[2] A. Rodero, M.C. Quintero, A. Sola and A. Gamero, Spectrochim. Acta, Part B **51** 467 (1996).
[3] R. Álvarez, A. Rodero and M.C. Quintero, Spectrochim. Acta, Part B **57** 1665 (2002).
[4] M. Capitelli, C.M. Ferreira, B.F. Gordiets, A.I. Osipov, *Plasma Kinetics in Atmospheric Gases*, Springer-Verlag (2000).
[5] A. Ricard, *Reactive Plasmas*, SFV Paris, France (1996).

Acknowledgements

This work was supported by the Spanish Ministry of Science and Technology within the framework of Project PPQ 2001-2537

Destruction of carbon tetrachloride in a microwave plasma produced at atmospheric pressure by the axial injection torch

S. Rubio, A. Rodero, M.C. Quintero

Department of Physics, University of Córdoba, Córdoba, Spain

Abstract
A novel plasma method and its application for destruction of carbon tetrachloride, using a moderate-power (several hundred watts) microwave torch discharge in atmospheric-pressure flowing helium are presented. This method can be extended to any other VOCs. The dependence on the destruction efficiency percentage was obtained for different values of the plasma conditions. The results show destruction and removal efficiencies greater than 99.999%.

1 Introduction

Some volatile organic compounds (VOCs), such as carbon tetrachloride (CCl_4) or trichloroethylene (C_2HCl_3), are typical emission gases of semiconductors and paint industries. These gases must be removed from the clean rooms not only to increase the product yield but also to protect human health. Specially, carbon tetrachloride has shown evidence of being very toxic in the water and a human carcinogen and teratogenic agent [1].

Therefore, efficient methods of destruction of these gases, which emitted to the atmosphere cause environmental problems, are in great demand. Different technologies have been investigated for decomposing the VOCs: catalytic oxidation and combustion, thermal decomposition, carbon adsorption and condensation.

Recently, several thermal and non-thermal plasma technologies have proved their potential for efficient removal of gaseous pollutants, including volatile organic compounds [2]. These plasmas are characterised by the electrons in the plasma having a higher energy than the ions or atoms and molecules, and this higher energy of the electrons can produce sufficient active chemical radicals and secondary electrons that decompose the pollutants molecules.

Non-thermal plasma techniques represent a new generation of air emission control technology that potentially could treat large-volume emissions containing dilute concentrations of pollutants. This work is focused on the study and optimisation of a destruction method of carbon tetrachloride (CCl_4), using a microwave plasma discharge. This system is a torch structure that produces a very stable high pressure (atmospheric) plasma flame at 2.45 GHz. Some modifications over the original design were made to obtain the maximum destruction percentage, like a reaction chamber design to isolate and analyse the products after destruction in the plasma.

A wide range of concentration of CCl_4 was studied, achieving destructions and removal efficiencies greater than 99.999% using an applied microwave power from 300 to 1000 W. This range of power is the one used by conventional microwave ovens.

2 Experimental set-up

The plasma was produced by the axial injection torch (Torche à Injection Axiale or TIA) [3]. This device provides a free expanding microwave plasma more resistant to impedance changes -that are caused by the introduction of samples- than other microwave plasmas [4].

A reactor was designed to be coupled to the wave-guide, in order to isolate and analyse the gases resulting from the destruction [5]. Gas samples can be taken from the reactor to be analysed by gas chromatography.

The conjunction TIA + Reactor is a good device to be applied to the destruction of volatile organic compounds.

The VOCs to be destroyed were introduced in the plasma by previously mixing them with the main gas, helium. The gas was saturated with CCl_4 vapour by forcing helium through a glass tube submerged in liquid CCl_4 at ambient temperature. The volumes of CCl_4 delivered into the plasma were determined by accurately measuring the weight differences before and after each experiment.

The concentration of CCl_4 in the final mixture was regulated by remixing with helium, before introduce the gas into the plasma. These concentrations were calibrated previously by gas chromatography.

The three main parameters and their variation range used in this work are:

- Total flow (helium + CCl_4 vapour) from 0.5 to 2.5 L/min.
- CCl_4 concentration of the gas from 0.01 to 10 %.
- Microwave applied power from 300 and 1000 W.
- Different internal diameters of the nozzle of the torch, in order to increase the energy efficiency.

A scheme of the experimental set-up is presented in Fig. 1.

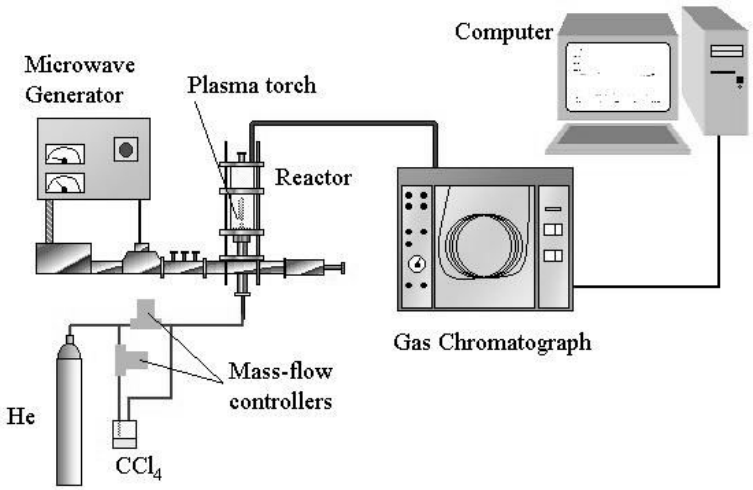

Fig. 1: Experimental set-up.

The gas mixture can then be led out through the exhaust in a fume hood via a $CaCO_3$ fluidised bed, to absorb the VOCs and their discharge products [6].

3 Carbon tetrachloride analysis

Quantitative analysis of CCl_4 was performed using an Agilent4890D gas chromatograph equipped with an electron capture detector (ECD) and a flame ionisation detector (FID). A calibration curve was generated in order to characterise the responses of these detectors to the analyte concentration. This calibration curve was carefully chosen to widely cover the concentration range of the samples injected.

The carbon tetrachloride mass density was measured before and after entering the plasma in order to compute the correspondent destruction and removal efficiency percentage (%DRE) from its standard definition [7]:

$$\%DRE = \left(\frac{W_{in} - W_{out}}{W_{in}} \right) \times 100 \qquad (1)$$

where W represents the weight of CCl_4 in the reactor chamber and the *in* and *out* subscripts denote the quantity before and after being processed.

Energy efficiency was calculated in terms of g(VOC)/kWh, as the mass of CCl_4 destroyed per hour, divided by the microwave power applied.

4 Results and discussion

The destruction of carbon tetrachloride depends on the plasma parameters, such as the electron density and the gas temperature. It is also very important to take into account the residence time of the CCl_4 in the plasma, that is computed as a function of the plasma volume. This volume and plasma parameters depend on the plasma conditions, i.e. the injected microwave power and the gas flow.

Destruction percentage was calculated for every different conditions of the TIA, such as gas flow, applied microwave power, and concentration of CCl_4. Different internal diameters of the nozzle of the torch were studied too.

The main gas flow is a fundamental parameter for the operation of the TIA. The gas flow affects considerably the destruction because the residence time of the CCl_4 in the plasma depends on the velocity of

the gas in the exit of the nozzle, and a high value of the flow reduces the residence time. Therefore it is interesting to obtain an optimum gas flow, which maintains stable the plasma in the reaction chamber and at the same time achieves good destruction percentages.

A fixed quantity of CCl_4 was destroyed using different flows of He, between 0.5 and 4.0 L/min. We can prove that the efficiency of destruction decreases when the total flow increases. But in this result two parameters are playing the same role: when the gas flow increases the time of residence decreases, and the concentration of CCl_4 decreases too (if a fixed mass of CCl_4 is used). Both effects produce a decrease of %DRE, so it is necessary study them separately.

4.1 Dependence of destruction efficiency with total flow

In order to study this dependence of %DRE when the total flow is changed, we have to maintain constant the concentration of CCl_4, which implies that the mass of CCl_4 must be increased as the flow of helium increases. We can observe only the dependence on the gas flow, if we have always the same concentration of CCl_4. This value is measured on-line by gas chromatography.

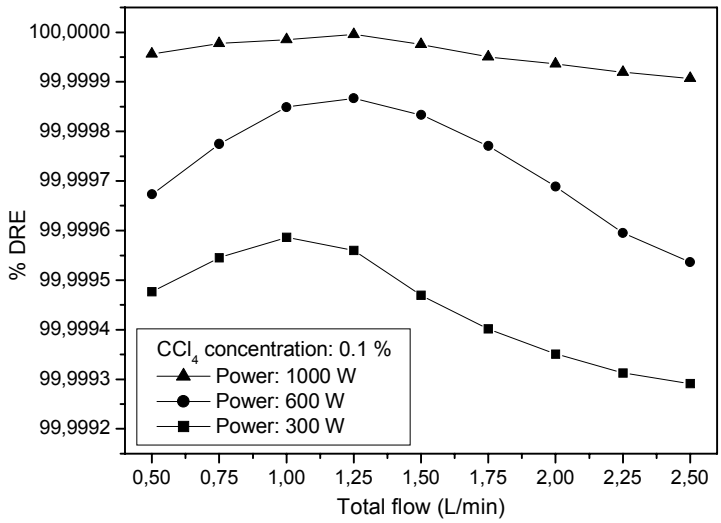

Fig. 2: Dependence of the %DRE with the gas flow for a fixed concentration of CCl_4, and three different applied microwave powers.

In fig. 2 it is shown a study with a concentration of 0.1 % of CCl_4. The total flow was changed and the %DRE measured for each value. Three applied microwave powers were used in this graph where we can observe that higher microwave powers achieve better destruction efficiencies. However the study of the influence of the applied microwave power will be discussed below.

It can be seen that there is an optimum gas flow value where the CCl_4 destruction is maximum. In this point the plasma has the best conditions to destroy a particular CCl_4 concentration with an applied microwave power. The %DRE decreases at higher values of helium flow. This is due to the decrease of the plasma gas temperature and to the reduction of the plasma volume, which implies lower residence times of the CCl_4 in the plasma.

On the other hand, the lowest flows of helium do not achieve the best destruction percentage because the TIA does not work correctly with total flows below 0.7 L/min.

4.2 Dependence of destruction efficiency with CCl_4 concentration

Another important parameter to characterise the destruction capability of this set-up, is the concentration of CCl_4 in the gas mixture used to generate the plasma. We have observed that higher destruction percentages were obtained when higher CCl_4 concentrations were used. This result implies that more CCl_4 molecules are decomposed, using a given energy and total flow, when CCl_4 concentration increases.

Similar results have already been found by T. Yamamoto [8] and B.M. Penetrante [9] and they suggested that secondary decomposition of CCl_4 could be induced by fragments of ions and radicals, from the initial decomposition of carbon tetrachloride.

Thus, if the concentration is higher, the quantity of molecules and collisions increases and the destruction efficiency is improved. It must exist a limit to this effect, but it is necessary very high concentrations, which is not possible because this value depends on the saturation of the gas with vapour of CCl_4, and we observe that concentrations above 20% are not possible.

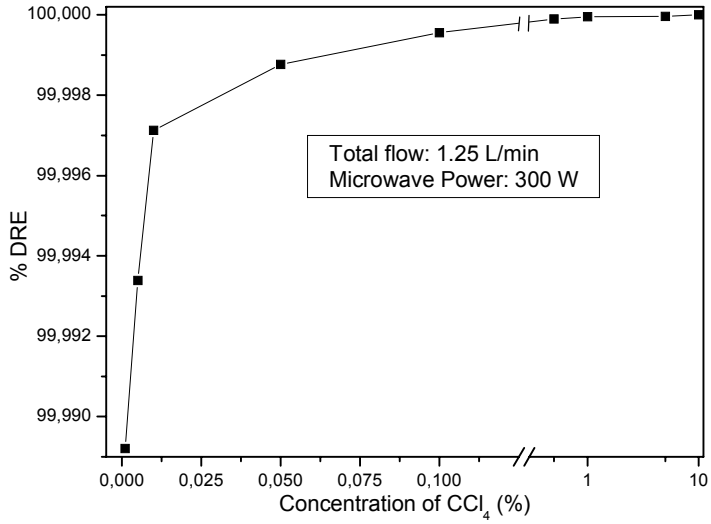

Fig. 3: Dependence of the %DRE with the applied microwave power for different CCl_4 concentrations.

Our data support this theory and in fig. 3 it is represented efficiency versus concentration of CCl_4, using a fixed total flow (1.25 L/min) and a constant applied microwave power of 300 W.

Higher concentrations seem to be the best solution because the energy efficiency is maximum. However lower concentration are of remarkable importance in some applications, such as the removal of air pollution. In this case, a good destruction percentage can be obtained by increasing the applied microwave power or decreasing the total flow. So it is possible to find the best conditions to destroy any quantity of CCl_4 with the proposed plasma-reactor system.

4.3 Dependence of destruction efficiency with applied microwave power

The electron energy increases when the microwave energy increases. Thus, the destruction capability improves when higher microwave power is used, but the energy efficiency decreases. We cannot use energies higher that are used in the actual method of processing, if we want show this system as novel.

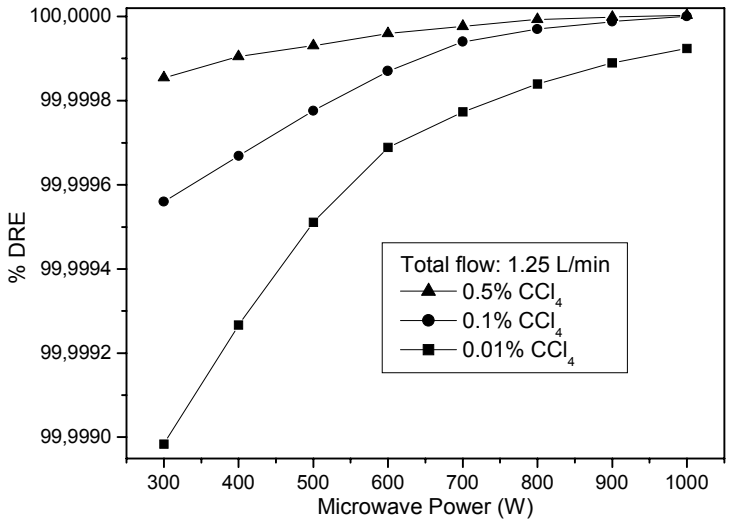

Fig. 4: Dependence of the %DRE with the CCl_4 concentration in the plasma gas.

In fig. 4 the dependence of the %DRE with the microwave power was studied using a helium flow rate of 1.25 L/min and different applied microwave powers, for three separate CCl_4 concentrations. These results clearly show that the %DRE increases as the microwave power until this raises 900 W, where the destruction efficiency exceeds 99.9998% for the highest concentrations. Beyond this value of injected power, no significant improvement of the %DRE was observed.

These results show 99.99985 % of destruction is obtained with 1000 W at 0.1 %. The same percentage is obtained with 400 W at 0.5 %. The conclusion is that we need lower microwave power to destroy the same percentage of CCl_4 if higher concentrations are introduced. The maximum possible concentration is given by the saturation of CCl_4 in helium.

4.4 Different cross-sections of the nozzle

Reduced energy efficiencies can be calculated from previous results, but in this set-up it is possible to achieve great values of this parameter only by changing the nozzle where the plasma is coupled.

We have already said that the destruction efficiency depends on plasma volume and residence time, but these parameters depend directly on the velocity of the gas in the exit of the nozzle. Thus, if we use a higher cross-section in the nozzle, a higher quantity of mass of CCl_4 will be destroyed with the same destruction percentage, because a higher flow is necessary to maintain the same velocity of gas in the nozzle, if we maintain a fixed concentration of CCl_4 in the gas.

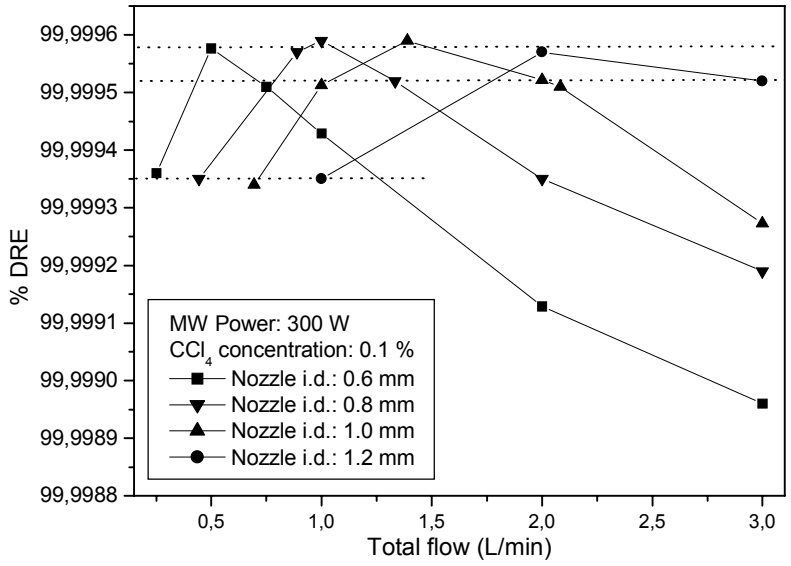

Fig. 5: Comparison of the destruction capabilities of four different nozzles of the TIA. "i.d." means "internal diameter"

Fig. 5 compares the results of experiments of 0.1 % of CCl_4 with four different internal diameters of the nozzles. The dash dot lines link points with the same velocity of gas in the nozzle, and we observe that these points have the same destruction and removal efficiency. This demonstrates that %DRE depends strongly on the velocity of the gas in the exit of the nozzle.

It is possible to observe that higher flows of helium+CCl_4 are necessary if we use higher internal diameters of the nozzle. If the system is completely scalable with internal diameters of 3 mm, flows above 15 L/min can be used. An application of these diameters would be the industrial treatment.

Energy efficiencies over 500 g/kWh were achieved in our apparatus with destruction and removal efficiencies above 99.999%.

Hence, it is necessary to say that the results previously presented, made in a laboratory scale, were measured using a nozzle with a small diameter, 0.8 mm of internal diameter. However, in an industrial processing, it would be interesting use bigger cross-sections.

5 Conclusions

This paper shows the effects of microwave power, gas flow rate, and CCl_4 concentration on decomposition efficiency:

- The conjunction TIA plus reactor seems to be a promising device to VOCs destruction.CCl_4 decomposition increases with microwave power supplied.
- At fixed CCl_4 concentrations and applied microwave power, its decomposition efficiency decreases as the gas flow rate increases.
- The decomposition efficiency was slightly higher with higher CCl_4 concentrations, which implies that more CCl_4 molecules are decomposed for a given energy when CCl_4 concentration is higher. This suggests that secondary decomposition of CCl_4 can be induced by some fragment ions and radical from the initial decomposition of CCl_4 [8,9].
- Energy efficiencies above 500 g/kWh can be achieved using higher cross-sections of the nozzle of the torch. The destruction efficiency depends on the velocity of the gas in the exit of the nozzle. More mass is destroyed per minute when higher cross-sections are used.
- It can be found the best parameters to maximize the destruction efficiency, for every concentrations of CCl_4.This method is useful in industrial processes, if we use higher internal cross-sections of the nozzle and the necessary flows and watts to destroy all that is needed.

6 References

[1] Halogenated solvent cleaners. Emission control technologies and cost analysis, Radiant Corporation, Noyes Data Corporation, Park Ridge, NJ (1990).

[2] T. Oda, T. Takahashi, K. Tada: *IEEE Trans. On Industry Apps.* **35** (1999) 373-379.

[3] M.Moisan, G.Sauvè, Z.Zakrzewski, J.Hubert: *Plasma Sources Sci. Technol* **35** (1994) 584.

[4] A. Rodero, M.C. Quintero, A. Sola and A. Gamero: *Spectrochim. Acta* Part B **51** (1996) 467.

[5] A. Rodero, M.C. Quintero, S. Rubio, C. Lao, A. Gamero: Spanish Patent nº: P200201328

[6] J. Chang, T. Myint, A. Chakrabarti and A. Miziolek: *Jpn. J. Appl. Phys*, **36** (1997) 5018.

[7] C.R. Brunner: *Hazardous air emission from incinerators*. Chapman and Hall, New York (1985).

[8] T. Yamamoto and S. Futamura: *Combust. Sci. and Tech.*, **133** (1998) 117.

[9] B.M. Penetrante, et al.: *Plasma Sources Sci. Technol.* **6** (1997) 251-259

Acknowledgements: This work was supported by the Spanish Ministry of Science and Technology within the framework of Project PPQ 2001-2537.

A Spectroscopic Characterization of Microwawe Discharges

M. Semerad[1], A. Hrdlicka[1], M. C. Quintero[2], R. Álvarez[2], A. Rodero[2]

[1] *Laboratory of Atomic Spectrochemistry, Faculty of Science, Masaryk University, Brno, Czech Republic*
[2] *Department of Applied Physics, University of Cordoba, Cordoba, Spain*

Abstract
The aim of this work is to present the results of the spectroscopic caracterization made on two microwave plasma torch discharges with different construction geometry: the Axial Injection Torch (Torche à Injection Axiale or TIA) studied at the Cordoba University, and a microwave plasma torch used at the Masaryk University. Various discharge parameters have been measured for various operating conditions, such as different microwave power inputs and presence or not of extra H_2O in the discharge.

1. Introduction

Plasmas used in analytical chemistry are characterized mainly in order to relate their fundamental parameters with their analytical capability. Such characterizations are usually performed with the plasma working with a pure plasma gas, this is, with no analytes added. However, the introduction of liquid samples in the discharge causes some water to enter the plasma (unless the sample is not a dilution in water), which might modify the plasma parameters and hence its analytical capability. In this work the effect of the introduction of water in a microwave induced argon plasma has been studied. For that purpose two main plasma parameters such as the electron density (n_e) and the gas temperature (T_g) have been measured in two different microwave plasma torches. Both torches receive the input power via a waveguide, which enables them to stand more power that torches fed via a coaxial cable.

The TIA (Fig.1) provides a very stable plasma that can operate over a very wide range of operating conditions, (viz. incident powers between 150 and 3000 W, and gas flow-rates between 1 and 15 l min^{-1}),

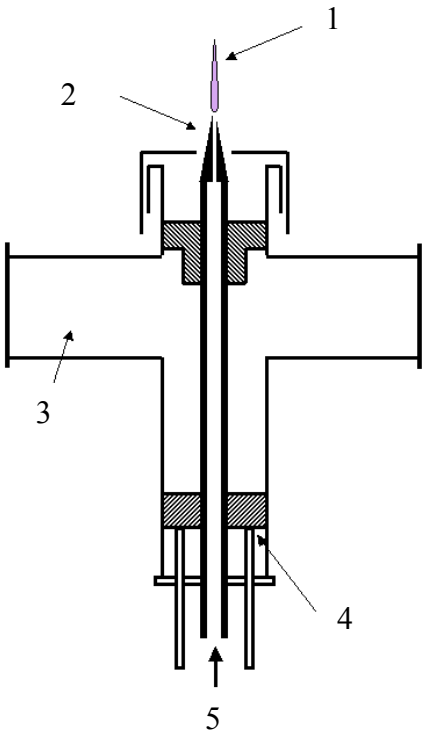

Fig.1: Scheme of the TIA
1- Plasma; 2- Nozzle; 3- Waveguide; 4- Moveable plunger; 5- Gas

Table 1: Description of the instruments used in the TIA set-up.

Microwave launcher	TIA (Montreal University)
Microwave generator	GPM 12K T/t (SAIREM) at 2.45 GHz
Maximum generator power output	2000 W
Forwarded power	300–1000 W
Material of the nozzle	Brass
Argon flow rate	3.5 l min^{-1}
Monochromator	THR-1000 (Jovin-Yvon) Grating 1200 grooves mm^{-1} Dispersion: Typically 0.8 nm mm^{-1} at λ=500nm Computer-controlled Spectralink system
ICCD camera	Flamestar 2 (La Vision)
Flow controller	Bronkhorst mass flow controllers IB31 control unit (Iberfluid Instruments)

with no additional cooling. It requires no dielectric tube to hold the plasma and can operate with any type of gas, whether atomic (He, Ar) or molecular (O_2, N_2, air). The TIA therefore seems to be a promising alternative to the ICP as an excitation source for atomic and molecular spectroscopy; in fact, it has been experimentally found to provide strong emission lines for non-metals such as S(II) and halogens such as F(I), with helium as the plasma gas. Spectroscopic investigation of this discharge with helium as the working gas was described in [1]. The other microwave plasma discharge (Fig.2) has been studied at the Department of Physical Electronics of the Masaryk University at Brno as an environment for synthesis of boron nitride [2], and is actually being used as a plasma source for spectroscopic analysis.

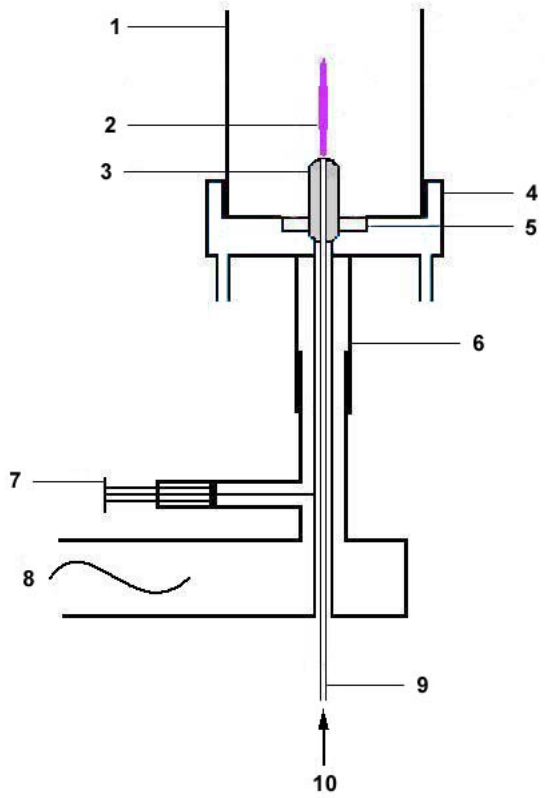

Fig. 2: Scheme of the Brno torch:
1- Wire shield; 2- Plasma torch; 3- Brass nozzle; 4- Aluminum holder; 5- Boron nitride underlay; 6- Cylindrical waveguide; 7- Movable plunger; 8- Waveguide; 9- Sample delivery quartz tube; 10- Argon input.

Table 2: Overview of technical parameters for the Brno torch.

MW generator working frequency (Muegge)	2.45 GHz
Maximum generator power output	2000 W
Forwarded power	300–1000 W
Reflected power	10–80 W
Inner diameter of the quartz tube	2.3 mm
Material of the nozzle	Brass
Argon flow rate	3.5 l min^{-1}
Sample flow rate	1.2 $cm^3.min^{-1}$
Nebulizer	Meinhard concentric
Scanning the spectra	Optical cable
Monochromator (Jobin-Yvon)	TRIAX 320, CCD detector

Rotational temperatures were measured from molecular species present in the discharge (OH and N_2^+) and T_g could be obtained by calculation of Boltzmann distribution law from the relative intensities of selected emission lines of these species. Electron number density was measured from Stark broadening of the hydrogen emission lines of the Balmer series.

2. Experimental

In order to compare the results obtained with the two different torches, their working parameters have been set as equal as possible. In tables 1 and 2 the technical description of the instruments used in both experimental set-ups can be found. The discharge produced by the TIA is sustained by the 2.45 GHz incident power suplied by the microwave generator, which ranges from 400 to 1000 W. The plasma gas flow was set to 3.5 l min^{-1}. The optical system consists of a Dove prism and two achromatic lenses, which respectively rotate 90º an image of the plasma and focus it at the entrance slit of the monochromator, hence allowing an axial position to be selected. The axial position of the measurements was the maximum emission position, i.e. 1 mm above the tip of the noozle. An intensified CCD camera at the exit of the monochromator was used for measuring the spectra. The water was introduced in the discharge by making the 15% of the argon flow through distilled water.

As to the measurements on the microwave plasma torch from Brno, the microwave plasma discharge is generated by means of the 2.45 GHz generator (Muegge) that delivers a maximum power of 2 kW. The plasma originates above the nozzle of the laboratory-constructed applicator. The same plasma gas and the same flow rate as the ones used with the TIA (argon, 3.5 l min^{-1}) flows through the inner quartz tube, and the discharge is also operated at a forward power of 400–1000 W, with a low reflected power (10–80 W). The radiation emitted from the plasma was collected using an optical fibre onto the entrance slit of a TRIAX monochromator (Jobin-Yvon) provided with a CCD detector. Spectra acquisition and treatment were performed by means of SPECTRAMAX software. When water was introduced, it was delivered into the Meinhard concentric nebulizer with the Scott spray chamber, which has a pump uptake rate of 1.2 cc min^{-1} and a nebulization efficiency of approx. 5%.

3. Spectroscopic measurement.

Rotational temperature measurement

The gas temperature measurement is performed frequently as an integral part of discharge investigation. Various techniques have been developed for this purpose (Langmuir probes, thermocouples, pyrometers); however, under the MW operating conditions only one approach is usually applied in the field of spectral methods. This techniques supports on the fact that the neutral gas temperature is taken to be nearly the same as rotational temperatures calculated from molecular spectra of some species (N_2, N_2^+, OH, CN…), because of the highly favourable exchange of energy between the kinetic energy of heavy particles and the internal rotational – vibrational states of the molecular species involved [1, 3].

In order to measure the gas temperature in the TIA plasma, seven lines of the R-branch of the first positive system (0-0) of the rotational band of the N_2^+ ionic molecule have been measured. The correlation of the Boltzmann plot is $R^2 \sim 0.7$ without adding water and $R^2 \sim 0.6$ when the water is introduced. No OH bands could be detected in this plasma.
In the plasma torch used in Brno, the gas temperature was determined from the relative intensities of the OH rotational lines (band 306.4 nm, branch Q_1). An important remark for this calculation is that one must select only the OH rotational lines of the Q_1 branch with rotational quantum number up to 13/2, which ensures the obtainment of reliable temperature (cold OH group). On the contrary, higher energy lines provide considerably higher temperatures, which are related to OH as a product of e.g. water dissociation (hot OH group) [4].

The R-branch of N_2^+ was measured too, but for this plasma torch the band does not provide good correlation in the Boltzmann plot ($R^2 \approx 0.2$-0.5), even if these lines are quite distincted in the spectra. That is why the Q_11, Q_12, Q_14, Q_15 and Q_16 OH lines were used, as described above. They are measurable and usable under any of the studied conditions and the correlation of their Boltzmann plot for this plasma is much better ($R^2 > 0.9$).

Electron density measurement:

Electron number density was measured from Stark broadening of the hydrogen H_β (486.13 nm) emission line, using the presence of hydrogen in the discharge. Lorentzian part of the line profile was calculated from this equation [3]:

$$\Delta\lambda_L = \frac{(\Delta\lambda_0)^2 - (\Delta\lambda_G)^2}{\Delta\lambda_0} \quad (1)$$

where $\Delta\lambda_0$ is the FWHM and $\Delta\lambda_G$ is the instrumental and Doppler broadening.

In the case of the Brno plasma, the H_β was observable in the discharge spectra both with and without water nebulization. However, in the case of the TIA, the emission intensity of the H_β line was too low to provide good measurements of the electron density. This problem was solved by making use of a previous calibration between the FWHM of the H_β and the H_α [1], which presents a higher emission intensity in the TIA discharge. Hence, from the FWHM of the H_α line it was obtained the FWHM of the H_β line, and from it, using the previous equation, its Lorentzian part $\Delta\lambda_L$.

The electron number density [m^{-3}] can then be calculated from the Czernichowsky and Chapelle formula [3]:

$$\log n_e = 22.578 + 1.478 \log \Delta\lambda_L - 0.144(\log \Delta\lambda_L)^2 - 0.1265 \log T_e \quad (2)$$

where $\Delta\lambda_L$ is in nanometers and the estimated electron temperature T_e is of 15000 K for the Brno plasma and of 20000 K for the TIA plasma. This values have been taken on basis of the respective MW discharge properties [1, 3]. However, the Czernichowsky and Chapelle formula is not very sensitive to small changes in the T_e.

4. Results

The values of the electron density for the two plasma torches, with and without water added to the discharge, are represented in the figure 3 as a function of the supplied microwave power. The first result that can be seen in the figure is that the n_e increases with the introduction of water for whatever the suplied power value or the plasma torch used. It can also be seen that the n_e increases with the power in the case of the TIA,

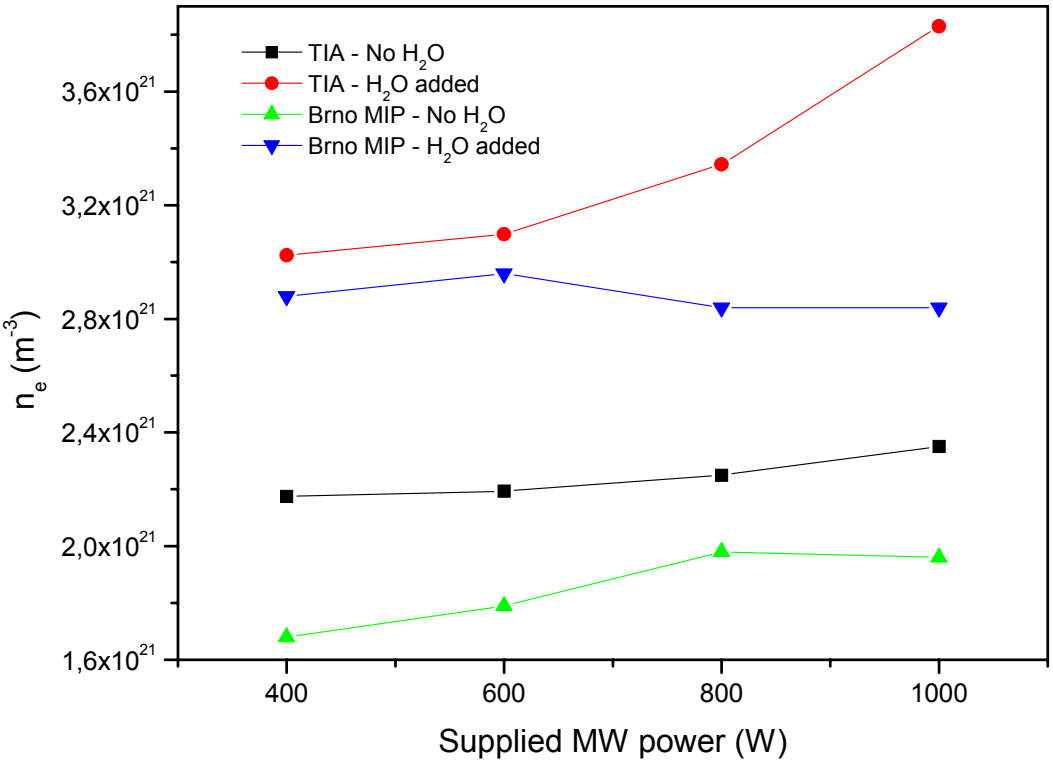

Fig. 3: Variation of the electron density with the suplied power for different torches, with and without adding water

although such variation is not so clear in the Brno plasma. The n_e values obtained for the TIA are above that of the Brno torch, although the order of magnitude of the results is the same in both torches.

The measured gas temperature values are depicted in Fig. 4, where, as in Fig. 3, there are the values corresponding to both torches, with and without adding water to the discharges, as a function of the supplied power. As the electron density, this parameter is also increased with the introduction of water for every possible case. However, the variation of the T_g with the supplied power is not as clear as that of the n_e in the case of the TIA, and the same happens for the Brno plasma. Furthermore, water makes the correlation of the Boltzmann plot to decrease in the calculation that uses the N_2^+ band, which difficults the apreciation of any dependence. The values of this parameter are higher for the TIA plasma than for the Brno plasma, which is not very conclusive due to the difference in the method of obtention of the T_g for the two plasmas.

5. Conclusions

The plasma parameters measured in this work, i.e. the electron density and the gas temperature, have been found to clearly increase when a small percentage of water is introduced in the discharge, not depending on the type of microwave plasma torch studied. This result implies that the introduction of water in a microwave discharge as a result of the introduction of liquid analytical samples is, rather than the cause of a decreasement of the analytical power of the discharge, a way of improving the plasma excitation capability. This increase of the parameters with the water presence may be related to the behavior of polar water molecules as a good MW energy absorber, followed by their dissociation on OH radicals and hydrogen, water products which would then transfer their energy to the other species present in the plasma. In the case of the TIA, no traces of OH were found, which suggests that in that plasma the OH radicals are dissociated, being hydrogen the cause of the increasement in the n_e and T_g values. The T_g and the n_e seem to increase with the supplied power, although that dependence is not always so clearly seen when water enters the discharge. The plasma produced by the TIA shows higher values of its parameters than the Brno plasma, although the order of magnitude of the measured parameters in both torches is the same.

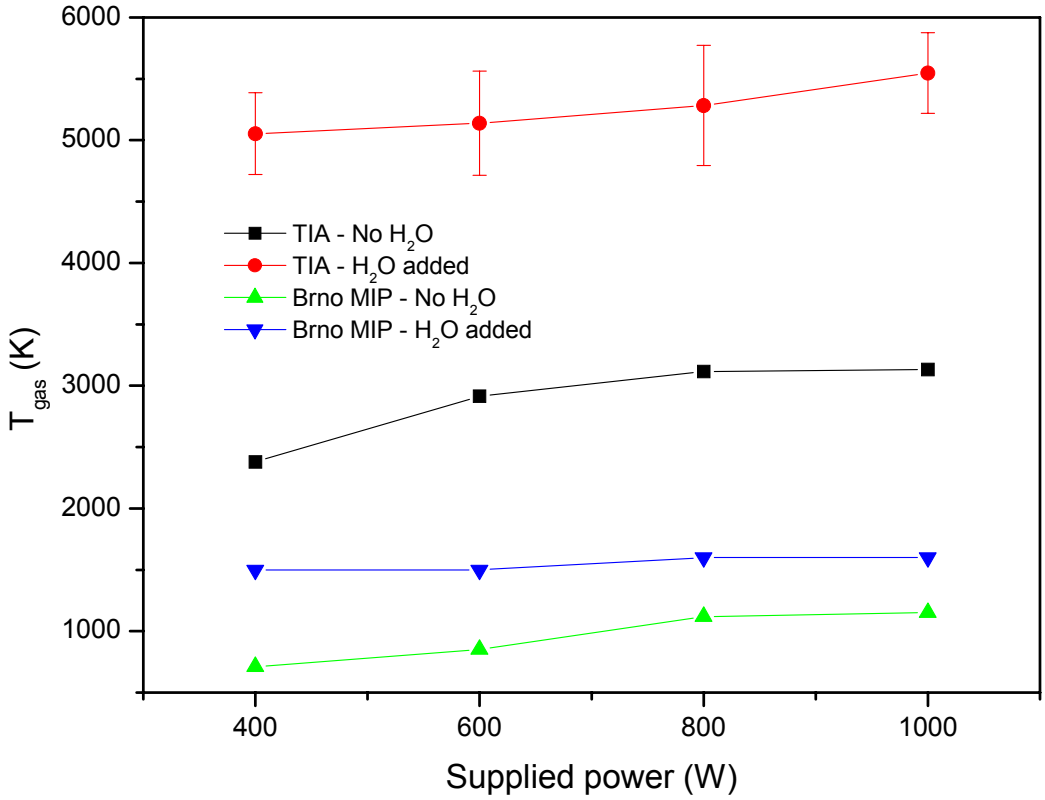

Fig. 4: Variation of the gas temperature with the suplied power for different torches, with and without adding water

References

[1] A. Rodero, M.C. Quintero, A. Sola y A. Gamero, *Spectrochim. Acta Part B* **51** 467 (1996).
[2] V. Kudrle, J. Janca, V. Brozek, CHISA 2000, Prague, Czech Society of Chemical Engeneering 178 (2000).
[3] P. W. J. M. Boumans, *Inductively Coupled Plasma Emission Spectroscopy, Part II*, J. Wiley&Sons, N.Y. (1987).
[4] J. Janca, J. Teply, C. Tesar, M. Dressler, *High Temp. Material Processes* **1** 73 (1997).

Acknowledgements

This work was supported by the Spanish Ministry of Science and Technology within the framework of Project PPQ 2001-2537

Drag Coefficients for Spheres in Supersonic Argon Plasma Flow

A. Blais, A. Sirois, B. Jodoin

Department of Mechanical Engineering, University of Ottawa, Ottawa, Canada

Supersonic plasma flows are found in many industrial applications. They are generally obtained in Low Pressure Plasma Spraying (LPPS) processes, using plasma torches operated at reduced pressure. Plasma spray coatings benefits from the reduced pressure, higher velocities, and longer heating zone that exist in the supersonic core of the plasma jet [1,2]. This configuration accelerates particles to high impact speed. It leads to a higher density of the deposit than usual coating processes and less contamination due to the reduced operating pressure. Many different coatings have been successfully obtained using this technique [3]. Experimental and theoretical studies have been conducted to develop diagnostic tools and to characterize the supersonic plasma jet [4]. Those studies aimed at a better understanding of the various phenomena occurring in the supersonic plasma jet.

Because of the complexity of the supersonic plasma flow, one common goal of all the theoretical models developed is to get a complete and detailed model. Such a model should be able to predict the entire flow field and its interaction with the injected particles and the substrate. While many authors have focused their work on the prediction of the flow field in the plasma torch, others have developed models to predict the flow behavior in the free jet outside the torch. At the present time, those models are becoming more and more useful as predicting tools for the entire flow field. However, little work has been done so far regarding the injected particles behavior in the supersonic flow. Furthermore, all the modeling work done so far uses the drag coefficient (C_D) for spherical particles as measured in supersonic air flow. The fact that a different gas is used and that it is in plasma state has never been considered in the drag coefficients used to predict the particles trajectories. Since the time history of the in-flight particles is of crucial importance to predict the impact temperature and velocity of the particles, this drag coefficient may have a major influence in the prediction of the process performance.

The present work focuses on the prediction of the drag coefficients of spherical particles in a supersonic argon plasma. The approach used is to model a solid sphere injected in a supersonic argon plasma jet and to predict the plasma flow field around the particle to obtain the drag coefficient of the particle. The model is validated extensively with results from the literature on supersonic cold flows. The drag coefficient predicted by the model for supersonic cold flows is able to capture the proper physics and predict the drag coefficient within a few percent of error. The plasma model is then used to predict the drag coefficient in supersonic argon plasma flows for various Mach number and different pressures. A chemical non-equilibrium model is used, solving the mass, momentum, energy and species equations.

It is found that the drag coefficient is strongly influenced by the specific heat ratio, even at low temperature. Therefore, C_D is a function of the plasma temperature and pressure for a specific Mach number. It is also found that for supersonic flows, the drag coefficient is not function of the Reynolds number and that the drag force is mainly due to the pressure force on the particle created by the shock wave in front of the particle. It is expected that these new drag coefficients will help improve modeling the plasma-particle interactions in supersonic argon plasmas.

[1] R. Henne, V. Borck, V. Siebold, D. Mayr, W. Reush, M. Rahmane, G. Soucy and M.I. Boulos, "Converging-Diverging Nozzles for Improved Atmospheric Plasma Spraying", Proceedings of 3rd European Conference on Thermal Plasma Processing, VDI Berichte, Aachen, Germany, 1995, pp. 247-267

[2] M. Rahmane, G. Soucy, M.I. Boulos and R. Henne, "Diagnostics of D.C. Plasma Jets Generated with Laval Anodes", Proceedings of the 1995 National Thermal Spray Conference (Houston,TX), Vol. 1, ASM International, Materials Park, OH, 1995, pp. 157-162

[3] H. Tahara, N. Uda and K.-I. Onoe, "Discharge Features in a Steady-State Nitrogen Arcjet with an Expansion Nozzle", IEEE Transactions on Plasma Science, Vol. 22, No. 1, 1994, pp. 58-64

[4] S.C. Snyder, G.D. Lassahn and L.D. Reynolds, "Direct Measurement of Gas Temperature and Gas Velocity Profiles in Sonic and Supersonic Argon-Helium Plasma Jets", Proceedings of the 11th International Symposium on Plasma Chemistry and Plasma Processing, Vol. 1, International Organising Committee of the 11th International Symposium on Plasma Chemistry, Loughborough, England, UK, 1993, pp. 386-391

Synthesis of carbon single wall nanotubes by a microwave plasma torch

O. Smiljanic, F. Larouche, X. Sun, J.-P. Dodelet, B.L. Stansfield

INRS-Énergie, Matériaux et Télécommunications, Varennes, Québec, Canada

Abstract

Single wall carbon nanotubes have been produced via a gas-phase process using a plasma torch to dissociate a carbon-containing gas. Two different microwave plasma torches have been used successfully. Results show that both the plasma temperature and the temperature gradient play important roles in determining the efficiency of the process.

1. Introduction

The enormous interest in carbon nanotubes is due to the exceptional properties of these structures as well as the innovative applications which could arise[1,2]. Despite this potential, which could produce a technological revolution, progress in the field is slowed by the lack of raw material, due to the inadequate methods of synthesis (laser ablation, electric arc, CVD). The production of nanotubes in large quantities is thus an objective sought by many laboratories around the world. There exist two forms of carbon nanotubes: those with multiple walls (MWCNTs) and those with a single wall (SWCNTs). This latter form is much more interesting than the MWCNTs because of their properties. On the other hand, the level of production of SWCNTs is only a few grams per day, with prices approximately 1000$/g. A breakthrough in production technology is thus necessary to realize the many applications of SWCNTs.

Our objective is to demonstrate that there is an alternative to the existing methods for SWCNT synthesis: an approach based on the use of a plasma torch. As a first step, we have shown that the synthesis by plasma torch produces a product comparable to that produced by laser ablation and electric arc, the two most popular methods. As a second step, we have tested different torch configurations to solve certain problems, and finally we have studied the important parameters influencing the synthesis of SWCNTs.

2. Principle

The fact that the carbon and the catalyst are in solid form is a principal disadvantage of the laser and arc methods. In principle, these are discontinuous processes, because the carbon block must be changed once it is used up. In addition, the vaporization of graphite requires a lot of energy (716.6 kJ/mol), thus requiring a powerful laser or arc for a small rate of production, which partially explains the high cost of nanotubes produced by these methods. We have thus replaced the solid source by a gaseous one. Instead of using graphite, we use a carbon-containing gas, and an organometallic molecule containing carbon and metal as the catalyst: ferrocene. Other metallocenes exist, such as nickelocene and cobaltocene, which might be more efficient, but we have chosen in our experiments to use ferrocene because it is not as toxic as nickelocene or cobaltocene. Since the ultimate aim is the large scale production of nanotubes, it is difficult to foresee such a production using carcinogenic materials. The advantage of using a carbon-containing gas is the small amount of energy we need to supply to atomize it; for methane it is only 80 kJ/mol. Thus, the power necessary to produce the building blocks required for building the SWCNTs in a high temperature plasma is ten times smaller than in the case of laser or arc techniques. In addition, by using a carbon-containing gas the process can be continuous, which would favor the implementation of a large-scale industrial process.

Compared to the CVD methods, a significant advantage is provided by the plasma, which does the work of decomposing the gas, whereas in the CVD approach the role of the catalyst is double: the decomposition of the gas and the assembly of the nanotubes. In addition, in the CVD methods, the majority of the gas (greater than 90%) passes through the reactor without reacting with the catalyst particles, which thus requires a recirculation of the unreacted gas to avoid a loss of efficiency.

3. Methodology

We have tested two different types of microwave plasma torches: a tubular design where the plasma is generated within the body of the torch, and an axial design (the TIA)[3]. The schematic showing the operation of the first design is shown in Figure 1 (left). The mixture of carbon-containing gas, ferrocene and argon is injected into the torch and atomized by the plasma. In this way, the basic building blocks for the formation of the nanotubes (C_2, carbon clusters, atoms and clusters of metal) are created. The exhaust from the plasma is injected into a furnace at 900°C, where the growth of the nanotubes takes place. The deposits containing the nanotubes are collected from the walls of the reactor. The sheath gas is used to protect the plasma tube by forming a gaseous layer between the plasma and the wall. We also count on this layer to prevent the formation of carbon deposits on the surface. We have also injected the gaseous mixture at the exhaust of the torch to avoid the formation of deposits on the plasma tube.

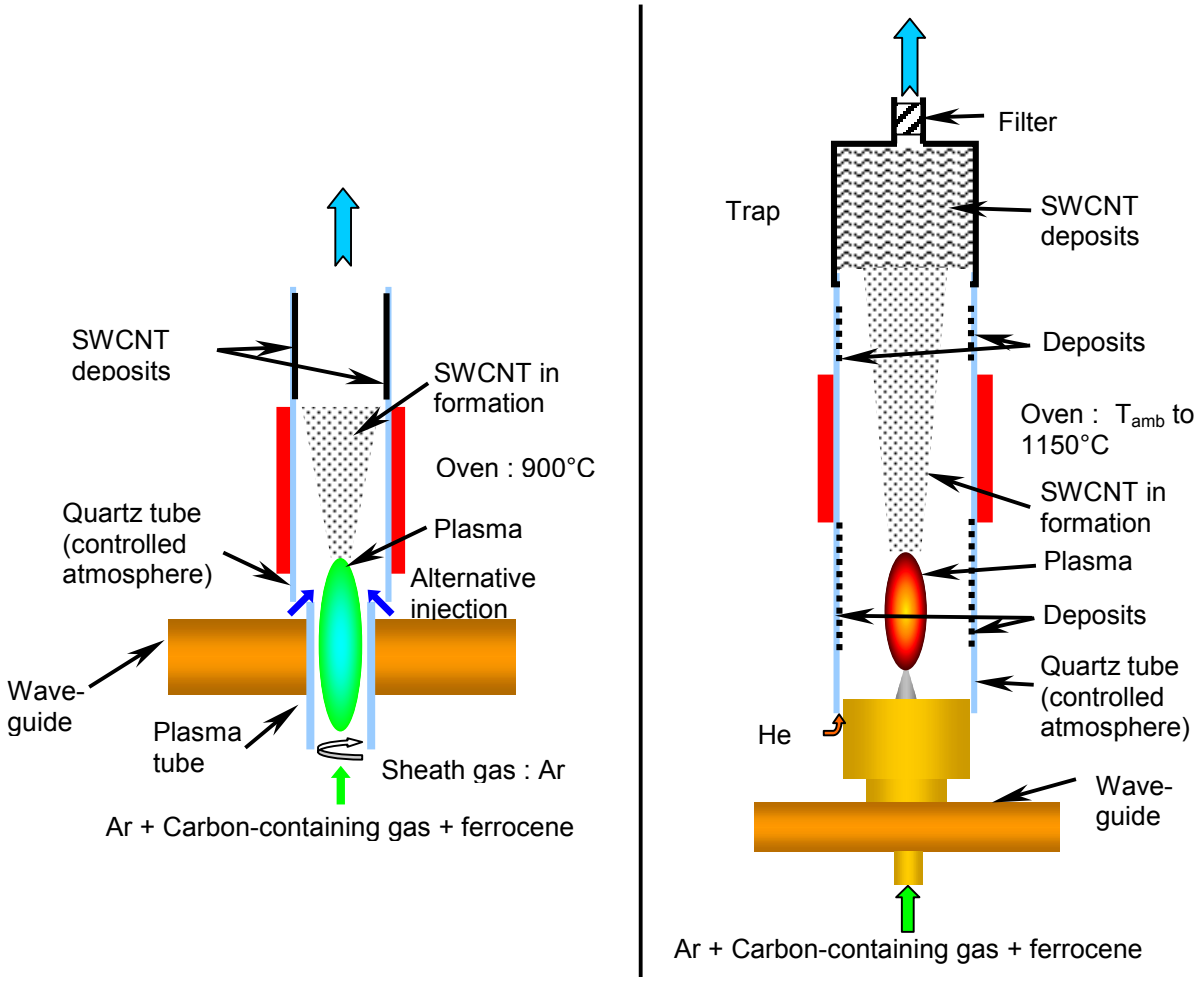

Figure 1 : (Left) Schematic showing the growth of single wall nanotubes in a tubular plasma torch. (Right) Overall view of the process based on the TIA.

In the second approach, the plasma is produced outside the structure of the torch, which has the advantage of making the torch less sensitive to carbon deposits (Figure 1 right). The plasma torch decomposes the carbon-containing gas and the ferrocene, again producing the building blocks necessary for fabricating the nanotubes. The other important points in the process are the control of the temperature gradient between the flame and the furnace and the temperature of the latter. To achieve this, the furnace is placed at a variable height above the torch. In addition, in order to minimize the carbon deposits on the

quartz tube, and to control the flow and the thermal gradient, helium is injected around the torch next to the quartz tube. The deposits form inside the quartz tube, at the exhaust from the furnace and in the downstream trap.

The operation of the torch is controlled by computer using Labview. We have used ethylene as the carbon-containing gas, with a throughput of 50 sccm. The program adjusts the argon throughput to obtain the desired metal to carbon ratio, typically 2%. The system is operated at atmospheric pressure, but under a controlled atmosphere of argon and helium. The furnace temperature is measured by an optical pyrometer. The samples are analysed by scanning electron microscopy (SEM), transmission electron microscopy (TEM), as well as by Raman scattering. The Raman spectra were taken using an irradiation wavelength of 782 nm.

To compare the samples, we have established what we call a quality factor Q. The main criterion used in the literature is the ratio between the peaks related to the graphitic structure (G) and the disorder (D): G/D. This allows us to determine the degree of graphitisation in the sample, and thus indicates its quality. To complement this criterion, we have added to this the ratio between the highest peak of the radial breathing mode (B) and the disorder peak (D): B/D. Figure 2 shows the relative positions of these peaks.

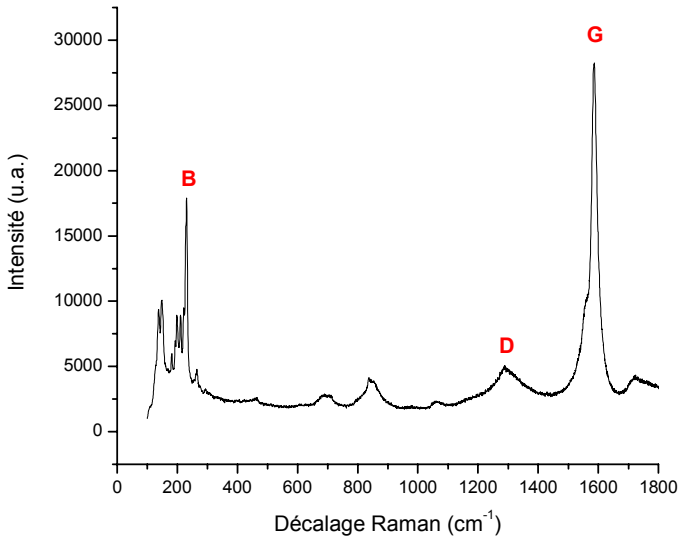

Figure 2 : Typical Raman spectrum of a sample containing a large proportion of nanotubes. The peaks G, D and B represent the graphitic peak, the peak related to the disorder, and the peak related to the nanotube diameter, respectively.

This latter ratio indicates the proportion of nanotubes in the deposit, but does not alone provide information on the overall quality. In practice, we should take into account the degree of graphitisation, the amount of disordered structures, and the proportion of nanotubes in the sample, to obtain a criterion representative of the quality. Thus, we have combined these two ratios G/D and B/D to obtain a parameter Q indicating the overall quality of the sample :

$$Q = \frac{G}{D} \cdot \frac{B}{D} = \frac{G \cdot B}{D^2}$$

The height of each peak is determined with respect to the background, which allows us to have a quality factor Q which is zero when there are no nanotubes in the sample, since in this case B=0. We have compared our results obtained using this parameter to our SEM observations, and we find a good qualitative correlation. The margin of error between samples is of the order of 20%. Emission spectra of the plasma were obtained using a ½ meter spectrograph (Acton Research) equipped with a grating having 1200 lines/mm, coupled to an ICCD multichannel detector (Andor). The resolution of this system is about 0,050 nm.

4. Results : the tubular plasma torch

We have tested two configurations with this set-up : with injection of the carbon-containing gas and the ferrocene either upstream or downstream from the plasma source. The aim was to stop the formation of carbon deposits in the plasma tube, which hinder a good coupling between the microwaves and the plasma.

When the mixture is injected upstream, a good production of nanotubes is obtained (Figure 3). We see in Fig.3a that the unrefined samples are basically composed of cords of single wall nanotubes (several of which combine to form a larger bundle), mixed with nanometer-size particles. The diameter of the cords is of the order of 20 nm, and the length exceeds 1 μm. In Fig.3b, we see clearly that the tubes are single wall, having diameters of the order of 1.5 nm. The tubes are surrounded by a matrix composed of amorphous carbon and nanoparticles of the catalyst having diameters of 1 to 3 nm. Thus, the nanoparticles of the catalyst, which are necessary for the formation of the nanotubes, are created spontaneously in-situ. The typical quality factor of the samples for this configuration is 11. Unfortunately, deposits form inside the plasma tube, and prevent good coupling between the microwaves and the plasma; this results in a degradation of the latter with time, and ultimately extinction after 15 or 20 minutes. We have thus attempted to inject the carbon-containing mixture downstream from the plasma source, at the exhaust of the torch.

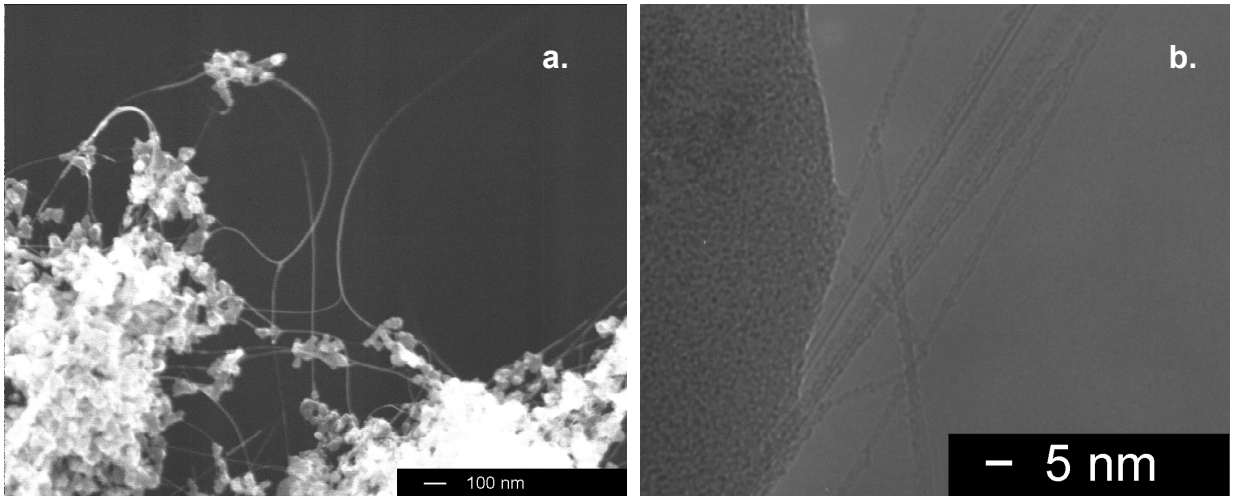

Figure 3 : a. SEM image of the deposits obtained with the tubular torch, with injection of the mixture upstream of the plasma source. b. TEM image of the same deposit.

In this case, SWCNTs are also obtained, but in a much lower proportion than in the previous case. The quality factor obtained for this configuration is only 1.8. Since the plasma is much less intense downstream from the source region, the temperature which the mixture attains must be lower than in the previous case. Since the temperature gradient is a key element in the gas phase synthesis of SWCNTs[4,5], the plasma temperature is very important, since it determines the initial point for the temperature drop. The importance of the temperature gradient as well as the growth temperature were verified in experiments with the TIA source.

5. Résults : the TIA

Emission spectroscopy of the flame allowed us to verify the presence of certain species necessary for the formation of single wall nanotubes. We were also able to determine certain important parameters defining the temperature profile during the growth of the nanotubes. The Swan band of C_2 is very intense, indicating that a significant density of these molecules is present in the plasma. The presence of atomic hydrogen in the plasma is confirmed by the observation of the H_α (656.3 nm) line; this indicates that at least some of the organic molecules are dissociated . Unfortunately, the H_β line could not be clearly distinguished from the background ; the width of this line is dominated by Stark broadening for our plasma, and it could have been used to calculate the plasma density. The fact that the H_α line is present, while that of H_β is not, is

somewhat mysterious, and will be studied further. We have also confirmed the presence of the following lines of FeI, thus indicating that the ferrocene is at least partially dissociated: 426.0 ; 427.1 ; 428.2 ; 430.7 and 432.5 nm. Finally, a spectroscopic analysis of the flame indicated no presence of the radical CH; the (0,0) band of CH, with band head at 431.4 nm, the most intense band, is absent. This last observation suggests a dissociation scenario for the ethylene in the plasma.

The presence of the C_2 molecules and the atomic hydrogen, and the absence of CH radicals in the plasma, suggests that the ethylene is dissociated by one of the following paths:

- $C_2H_4 \rightarrow C_2 + 4H$
- $C_2H_4 \rightarrow C_2 + 2H_2$
- $C_2H_4 \rightarrow C_2 + xH + yH_2$

We have not been able to determine whether the hydrogen is produced directly in the atomic form or in the form of molecules. The measurement of radiation from atomic hydrogen could also be due to the dissociation of the molecular hydrogen by the plasma.

The temperature of the flame is an important parameter in the process, since it largely determines the rate of dissociation of the carbon-containing gas and the ferrocene, as well as fixing initial point of the temperature gradient. We have determined the temperature of the flame during the synthesis of the nanotubes by analysing the spectrum of the (0,0) Swan band, taking into account the resolution of our instrument[6]. We obtain a rotational temperature of the C_2 molecules to be 5000 ± 1000 K. The uncertainty is relatively large, since it is strongly dependent on the spectral resolution of the system, which is relatively poor in our case.

We first studied the effect of the furnace temperature on the quality of the deposit (Fig. 5a.) in order to determine the optimum temperature for nanotube synthesis by our process. To do this, we placed the furnace both around and above the flame. Secondly, we placed the furnace only above the flame, to produce a greater temperature drop (Fig. 5b.) ; this enabled us to study the influence of the temperature gradient on the growth of the SWCNTs.

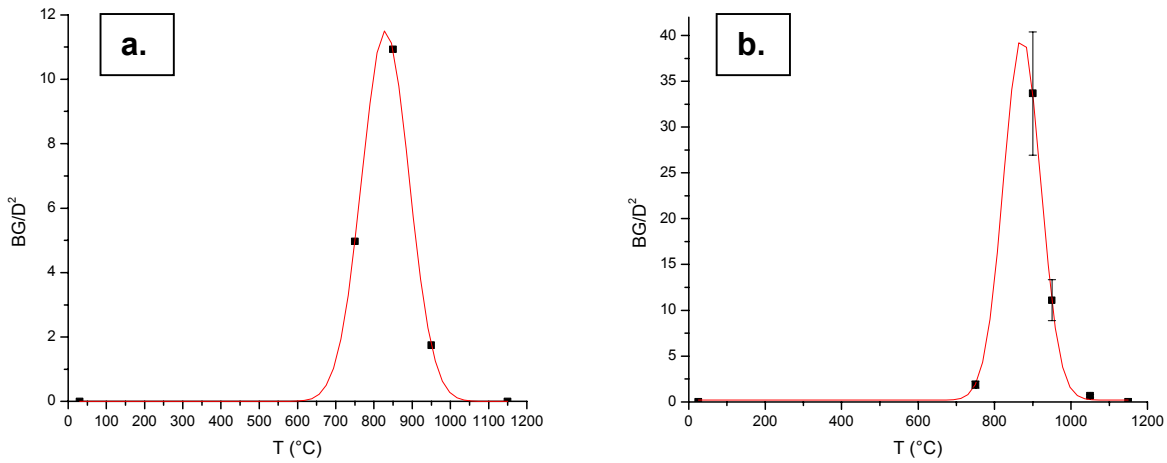

Figure5 : a. Influence of the furnace temperature on the growth of the SWCNTs, with the furnace around the flame (Q_{max} = 12). b. Influence of the furnace temperature on the growth of the SWCNTs with the furnace above the flame (Q_{max} = 40).

We see from Fig.5 that the temperature has an important influence on the quality of the sample ; there is an operational window around 850°C. These results are compatible with those from experiments on the production of nanotubes by pulsed laser ablation, where the presence of the nanotubes is related to the furnace temperature. Below 800°C and above 1400°C, the deposits don't contain nanotubes. It should be noted that the metal used as catalyst in our case is iron, whereas a mixture of nickel and cobalt is used in most laser experiments, which has an influence on the growth temperature[7].

The experiments carried out with the flame in the furnace produced deposits of relatively poor quality (Q = 12 at most), even at the optimum temperature, showing that the temperature is not the only

important parameter. By raising the furnace above the flame, we allow the plasma to cool more rapidly, thus establishing a larger temperature gradient at the exhaust of the torch. This gradient has an important effect, as can be seen in Fig. 5b, where the quality of the deposit is significantly increased. This improvement is seen for deposits recovered from all the regions in the reactor. For maximum production of SWCNTs, an optimum combination of temperature and temperature gradient must be established. In the case of the electric arc or continuous laser (CO_2), the heat in the arc plasma or in the laser-heated plasma is sufficient to maintain a temperature level high enough for the growth of nanotubes. To attain the temperature gradient in the arc, the graphite electrodes as well as the chamber are cooled, whereas for the continuous laser it is the ambient gas which provides such control. In the case of the pulsed laser, the gradient is formed naturally between the plasma and the furnace since the pulse is very brief (a few ns), and it produces little matter or heat. In summary, to increase the efficiency of our process, one must create the proper temperature gradient, all the while maintaining the particles at the optimum temperature, approximately 850°C, during the growth.

6. Conclusion

By comparing the quality factors obtained for the two torches, with different configurations, we can extract essential information about the growth of SWCNTs in a plasma torch. On the one hand, the plasma temperature must be sufficiently high, since it dissociates the carbon-containing gas and also determines the initial point of the temperature gradient. In the case of downstream injection in the tubular torch, the carbon-containing mixture is injected at the exhaust of the torch, where the plasma is less intense, resulting in a sample of poorer quality. On the other hand, although the temperature drop has an influence on the quality of the product, one cannot go below the growth temperature of the SWCNTs.

References

1. Harris, P. J. F, Carbon nanotubes and related structures: new materials for the 21st century, 1999
2. Saito, R., Dresselhaus, G., and Dresselhaus, M. S., Physical properties of carbon nanotubes, 1998
3. M. Moisan, G. Sauve, Z. Zakrzewski, and J. Hubert, Plasma Sources Science and Technology, 584-592, (1994)
4. M. Castignolles, A. Foutel-Richard, A. Mavel, J. L. Cochon, D. Pigache, A. Loiseau, and P. Bernier **Nanotube 2002**, (2002)
5. D. Laplaze, L. Alvarez, T. Guillard, J. M. Badie, and G. Flamant, Carbon **40**, 1621-1634, (2002)
6. S. Pellerin, K. Musiol, O. Motret, B. Pokrzywka, and J. Chapelle, Journal of Physics D: Applied Physics, 2850-2865, (1996)
7. O. Jost, A. A. Gorbunov, J. Moller, W. Pompe, X. Liu, P. Georgi, L. Dunsch, M. S. Golden, and J. Fink, Journal of Physical Chemistry B **106**, 2875-2883, (Mar. 2002)

Carbon Nanostructure Growth by Short-Wavelength Laser Ablation

Y. Suda[1], K. Utaka[1], M.A. Bratescu[1] and Y. Sakai[1]

[1] *Graduate School of Engineering, Hokkaido University, Sapporo, 060-8628, Japan*
a-suda@eng.hokudai.ac.jp

Abstract
Multi-walled carbon nanotube (CNT) was synthesized by short-wavelength laser ablation technique employing a metal-catalyzed graphite target. Focused ArF excimer laser (λ=193 nm) beam was irradiated on the target, then carbon and metal cluster vaporized and formed to CNT inside quartz tube operating at 1000°C. Transmission electron microscopy showed that the CNT was about 20 nm in diameter and more than 1 μm in length. Y-junction structure of the CNT was also observed.

1. Introduction

As carbon nanotube (CNT) shows unique structural and electronic properties, it is widely studied for applications of field emitter, electronic device and so on. Especially for the application of future electronic devices, CNT is used as quantum dots and molecular-scale wires connecting between the dots [1]. It is well known that laser ablation of metal-catalyzed graphite in Ar gas ambient is to synthesize CNT with a high yield [2]. However, the growth mechanism of CNT is not fully understood.

In the present study, we used ArF excimer laser (λ=193 nm) for CNT growth. As the short-wavelength laser generates more energetic carbon particles than infrared laser does, it is supposed that CNT growth process is different between them. It is possible to consider the growth mechanism in terms of behavior of ablated clusters. This difference is also expected to produce interesting nano-materials such as nanoballons [3]. To analyzed the CNT properties, transmission electron microscopy (TEM) and Raman spectroscopy was used. The CNT formation mechanism is discussed.

2. Experimental set-up

The present CNT growth set-up (AL039, SUGA Co., Ltd.) has basically the same configuration as that by Guo et al [4]. A schematic diagram of the set-up is illustrated in Fig. 1. It consists of a quartz tube (60 mm inner diameter, 620 mm length), an electrical furnace (360 mm length) operating at 1000ºC, and an ArF excimer laser. Inside of the tube, a target was mounted at 130 mm ahead of the rear end of the furnace and spun at 40 rpm. A water-cooled collector was mounted on the backside of the target. The temperature distribution inside of the tube is shown in Fig. 1 (b). The operating temperature is 1000ºC in the area of ~100 mm at the center of the furnace and decreases down to 600ºC at the front end. A 20-mm diameter graphite target containing 1 at. % Ni (TOYO TANSO Co., Ltd.) was used. However, in our analysis of the target by X-ray photoelectron spectroscopy (XPS), Fe and Y as well as Ni were detected. The laser beam (ArF excimer laser, LAMBDA PHYSIK COMPex 205: wavelength=193 nm; pulse duration=20 ns; fluence=3 J/cm^2; repetition rate=10 or 50 Hz) entered through a quartz window and was focused to the area of 1×5 mm^2 on the target surface. Ar gas flowed along the tube inner wall with a flow rate of 750 sccm, which was introduced from the window side, and pumped out through a butterfly valve by a rotary pump. Ar gas pressure was kept at 500 Torr. Although carbon soot was deposited on the area from (1) to (6) in Fig. 1, most soot was deposited on area (3). The soot was dispersed in ethanol using ultrasonic cleaner and collected on a metal mesh for TEM (JEM-2000FX, JEOL. Co., Ltd.) and Raman spectroscopy (Renishaw, Co., Ltd.) analysis.

3. Results and discussion

3. 1. TEM observation of carbon nanotube and Y-junction structure

After laser ablation of the target for 60 min., carbon soot was deposited mainly on area (3) of the inner tube wall. At the present moment, we are interested in the position where the carbon soot deposited. In previous reports by other groups, most carbon soot was obtained on a collector just located behind the target when a long-wavelength laser (e.g. YAG laser, λ=532 nm) was used [2, 4]. However, in the present experiment,

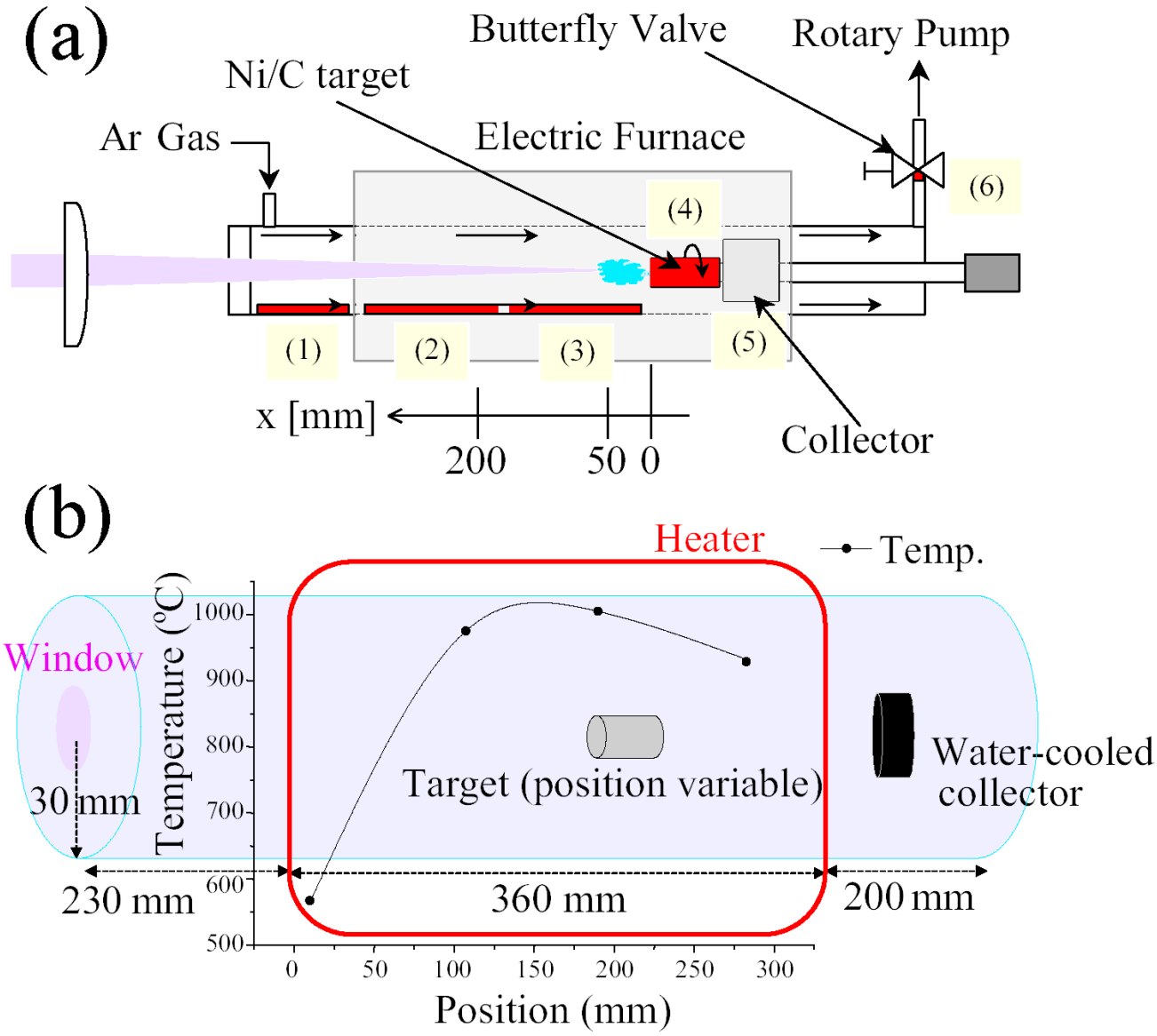

Figure 1. (a) A schematic diagram of the set-up. Parenthetic number shows the deposition area of carbon soot. (b) Temperature distribution inside the tube along the x-axis.

considerable amount of soot was obtained on the area in front of the target. To explain this difference, we have the following speculation.

Generally, as the laser light wavelength for ablation shortens, the size of carbon clusters (C_n^+) decreases and the kinetic energy of C_n^+ increases [6, 7]. In the ArF excimer laser ablation, the size of C_n^+ was mainly n=1-3 [6], and the kinetic energy of C_n^+ was ~80 eV at the laser fluence of 3 J/cm^2 [7]. This energy is much higher than that of heavier clusters. It may be reasonable that the lighter C_n^+ flew farther from the target against the direction of Ar gas flow and was deposited on area (3). However, the heavier C_n^+ is dragged backward by the Ar gas flow and is deposited on area (4)-(6).

Fig. 2 shows the TEM micrographs of the soot. It is clearly shown that many CNTs were synthesized. These tubes were approximately 20 nm in diameter and longer than 1 μm in length. The magnified photograph (b) reveals that the tube is of multi-wall structure with several layers. The spacing between tube walls is ~1 nm and several times larger than that shown in Ref. 5. The yield of CNT growth was high, and almost no catalytic metal particle was observed. It is interesting that CNT does not contain any catalytic particles. This was confirmed by XPS (ESCA-3400, Shimadzu Co., Ltd.) and EDX (Energy Dispersive X-ray Analyzer, H-700, JEOL. Ltd) analysis.

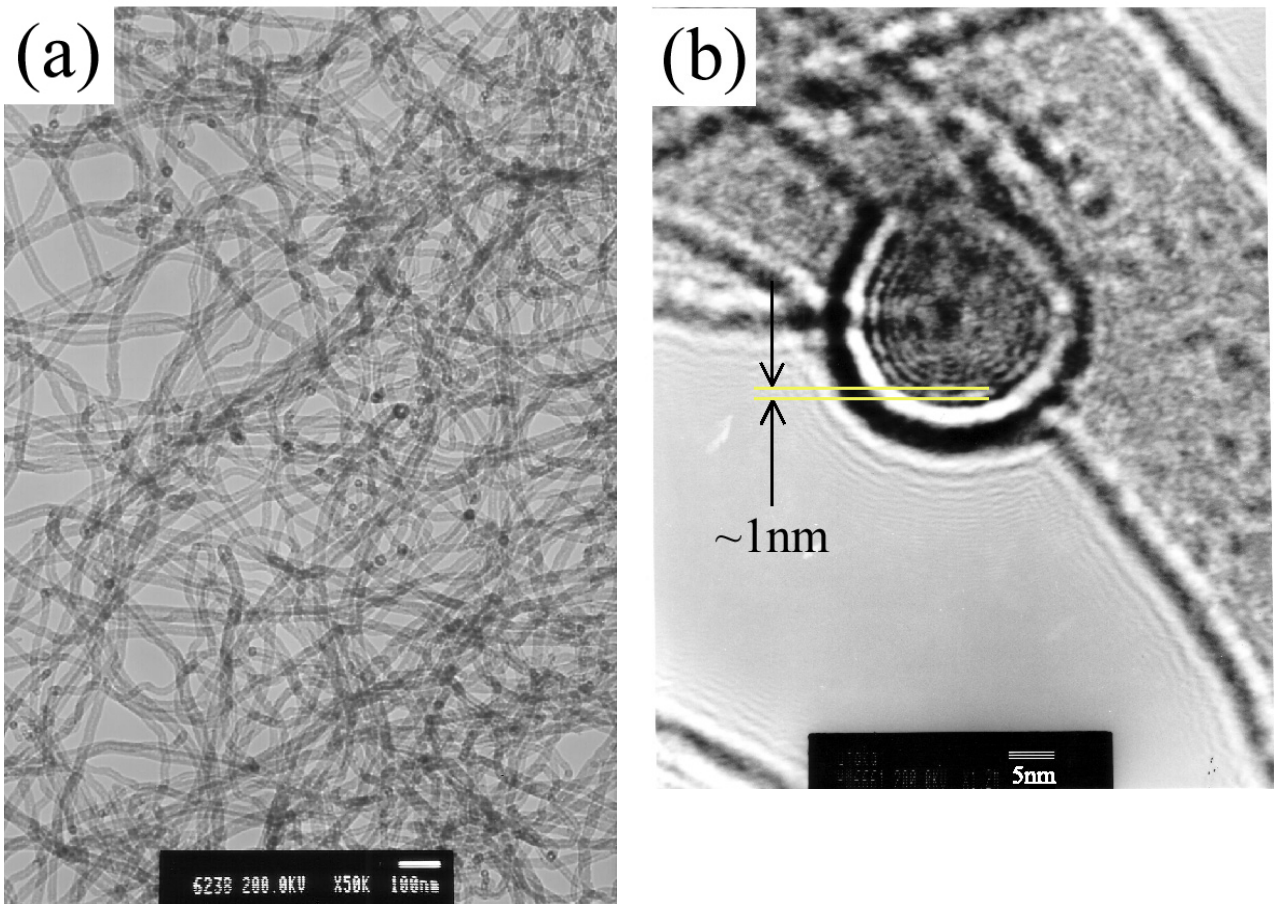

Figure 2. TEM micrographs of the soot deposited on area (3).

Some CNT contained Y-junction structure as shown in Fig. 3. The junction occurs at every several hundreds nm along the axial direction of CNT. At the junction, the axial direction bent, and very short branch grew out from the CNT stem. And it is clear that the hollow part of CNT was not so long and terminated by the wall like "bamboo gnarl". These structure are similar to that synthesized in a thermal chemical vapour deposition (CVD) system [8]. It was confirmed that this junction appeared when thiophene (C_4H_4S) was included in CH_4 gas. However, in the present experiment, we did not contain any sulfur in the graphite target. Further study to understand the Y-junction growth mechanism is required.

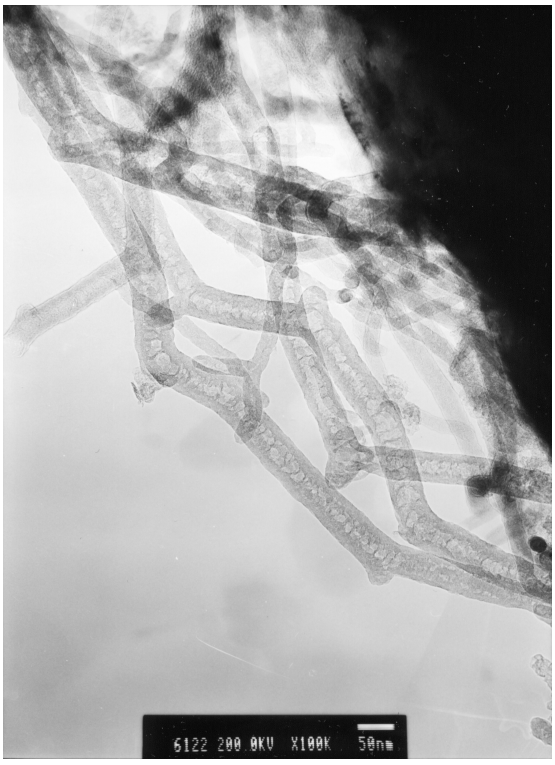

Figure 3. Y-junction structure of CNT.

3. 2. Raman Characterization

Raman spectroscopy is a convenient and strong tool for analysing CNT structure, for instance, diameter and chirality. Raman spectra of the carbon soot containing CNT supported on a metal mesh for TEM were shown in Fig. 4. Two peaks appear clearly and show the graphite structure. One peak that locates around 1581 cm^{-1} is called "G peak", which originates from the in-plane bond-stretching motion of pairs of sp^2 carbon atoms. The other peak that locates around 1360 cm^{-1} shows a breathing mode of six-fold graphite ring called "D (disordered) peak" [9]. As the D

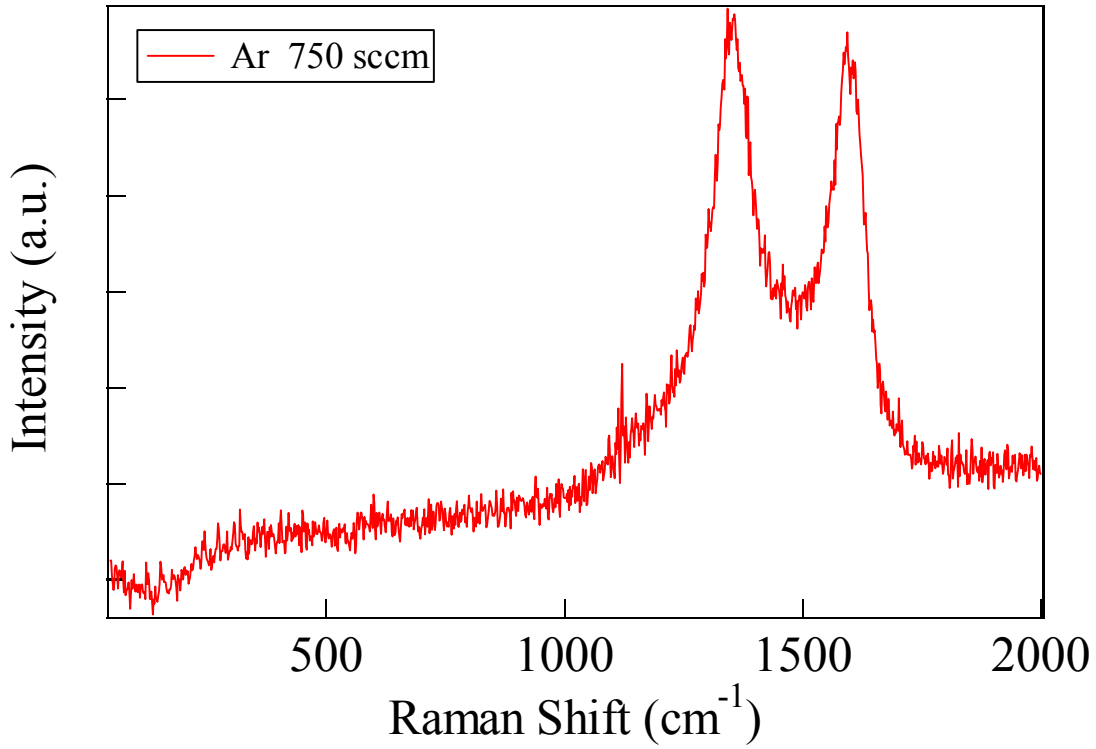

Figure 4. Raman spectra of the carbon soot

mode is forbidden in perfect graphite, the appearance of this peak shows that CNT contains some defect in crystalline structure. In this case, the ratio of D peak intensity to G peak one (I_D/I_G) is ~1, which is a similar value to that of multi-walled CNT synthesized in a plasma enhanced CVD system [11].

3. 3. Effect of ArF laser repetition frequency on CNT linearlity

To obtain high-quality CNT, we tried to increase the laser repetition rate. TEM micrograph of CNT synthesized at a repetition rate of 50Hz is shown in Fig. 5. Relatively long and linear CNT as well as graphite nano-balloon are obtained as shown in Fig. 5 (a). The CNT deposited on area (5) of low temperatures (a water-cooled collector), where the temperature is estimated to be 700ºC from the temperature distribution in Fig. 1 (b), shows similar feature to that synthesized at the rate of 10 Hz, which was deposited at the high temperature area (3).

It is speculated that CNT was formed in gas phase containing carbon and catalytic metal clusters below their eutectic temperature [10]. It may be important to increase the laser repetition rate, since successive energy input would heat up the ablated plasma and contribute to the stability and confinement of the plasma.

4. Conclusions

CNT was successfully synthesized in an electric furnace operating at 1000ºC by laser ablation technique with a short-wavelength pulsed laser (ArF). We confirmed that the CNT structure was multi-walled tubes by TEM and Raman spectroscopy. It was capable to improve the CNT structure (e.g. linearity) by increasing the laser repetition rate. We should study further to find the optimum synthesis condition of CNT.

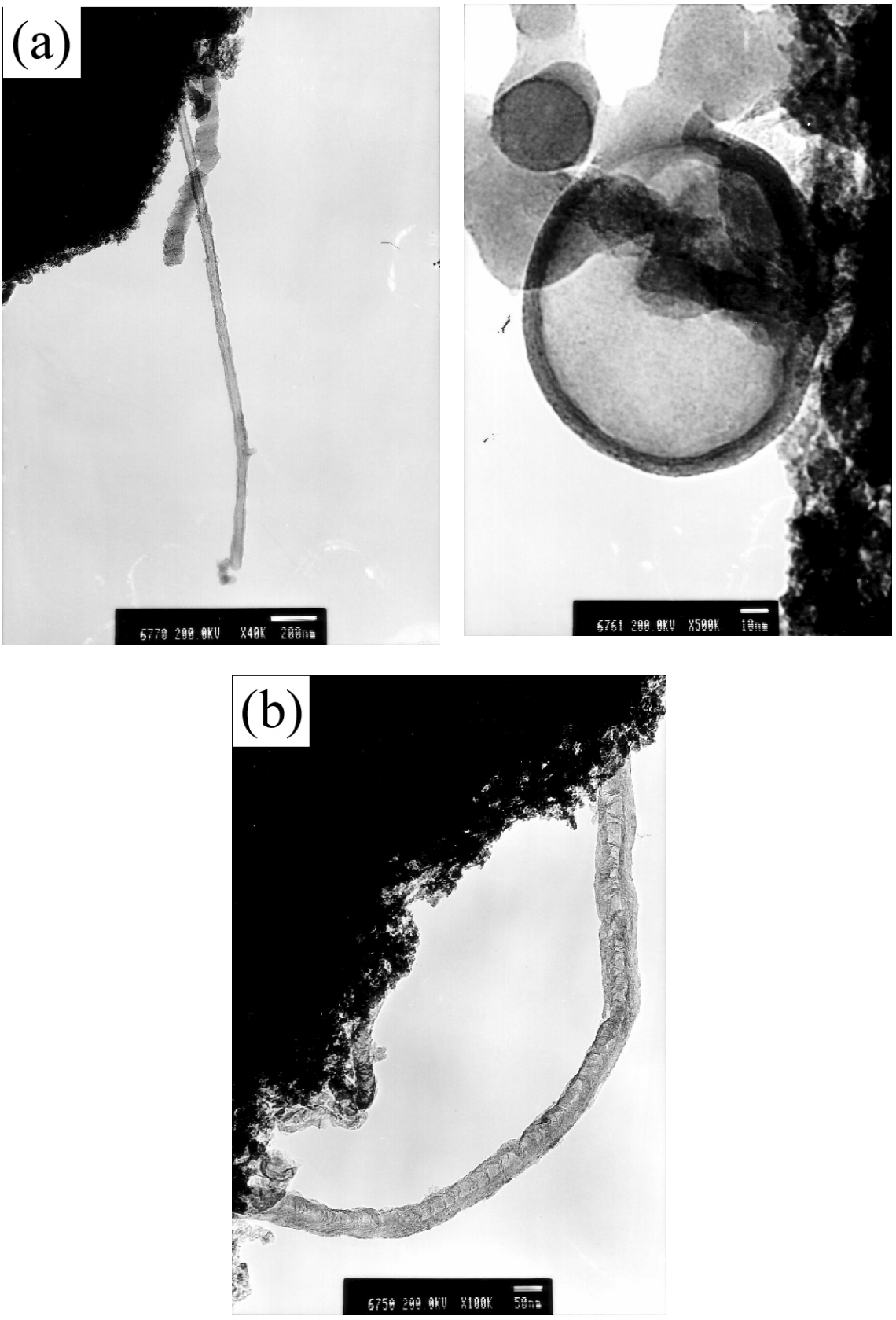

Figure 5. TEM micrographs of CNT deposited at various areas. (a) area (3). (b) area (5) where the temperature is around 700^{o}C.

References

[1] Nathan R. Franklin, Yiming Li, Robert J. Chen, Ali Javey, and Hongjjie Dai, "Patterned growth of single-walled carbon nanotubes on full 4-inch wafers", Appl. Phys. Lett., **79** (2001) 4571

[2] A. Thess, R. Lee, P. Nikolaev, H.J. Dai, P. Petit, J. Robert, C.H. Xu, Y.H. Lee, S.G. Kim, A.G. Rinzler, D.T. Colbert, G.E. Scuseria, D. Tomanek, J.E. Fischer, R.E. Smalley, "Crystalline Ropes of Metallic Carbon Nanotubes", Science, **273** (1996) 483

[3] S. Komatsu, Y. Shimizu, Y. Moriyoshi, K. Okada, M. Mitomo, "Nanoparticles and nanoballoons of amorphous boron coated with crystalline boron nitride", Appl. Phys. Lett., **79** (2001) 188

[4] T. Guo, P. Nikolaev, A. Thess, D.T. Colbert, R.E. Smalley, "Catalytic growth of single-walled carbon nanotubes by laser vaporization", Chem. Phys. Lett., **243** (1995) 49

[5] M.S. Dresselhaus, G. Dresselhaus and Ph. Avouris (Eds.), Carbon Nanotubes Synthesis, Structure, Properties, and Applications, Springer, 2001, p. 66

[6] J.J. Gaumet, A. Wakikusa, Y. Shimizu, Y. Tamori, "Energetics for Carbon Clusters Produced Directly by Laser Vaporization of Graphite – Dependence on Laser Power and Wavelength", J. Chem. Soc. Faraday Trans., **89** (1993) 1667

[7] D.H. Lowndes, V.I. Merkulov, A.A. Puretzky, D.B. Geohegan, G.E. Jellison, Jr, C.M. Rouleau, T. Thundat, "Amorphous Diamond Films Deposited by Pulsed-Laser Ablation: The Optimum Carbon-Ion Kinetic Energy and Effects of Laser Wavelength", Mater. Res. Soc. Symp. Proc., **526** (1998) 325

[8] Hongwei Zhu, Lijie Ci, Cailu Xu, Ji Liang and Dehai Wu, "Growth mechanism of Y-junction carbon nanotubes", Diamond and Relat. Mater., **11** (2002) 1349

[9] A.C. Ferrari and J. Robertson, "Interpretation of Raman spectra of disordered and amorphous carbon", Phys. Rev. B, **61** (2000) 14095

[10] H. Kataura, Y. Kumazawa, Y. Maniwa, Y. Ohtsuka, R. Sen, S. Suzuki, Y. Achiba, "Diameter control of single-walled carbon nanotubes", Carbon, **38** (2000) 1691

[11] C.J. Lee, J.H. Park and J. Park, "Synthesis of bamboo-shaped multiwalled carbon nanotubes using thermal chemical vapor deposition", Chem. Phys. Lett., **323** (2000) 560

Acknowledgement

The authors thank to Prof. H. Sugawara in Hokkaido University for fruitful discussion about laser ablation plasma, K. Suzuki in Nihon University for support of Raman spectroscopy analysis and Prof. T. Shibayama and K. Sugawara in Hokkaido University for support of TEM observation. This study is supported in part by Nissan Science Foundation.

Characterization of polypropylene surface treated by atmospheric pressure ejected plasmas for adhesion improvement

Y.H.Choi[1], Y.H. Kim[1], J.H.Kim[1], K.H.Paek[2], W.T. Ju[2], and Y.S.Hwang[1]

[1] *Department of Nuclear Engineering, Seoul National University, Seoul, Korea*

[2] *Plasnix Co.Ltd. , Seoul, Korea*

Abstract

An atmospheric pressure ejected plasma(APEP) source has been developed to enhance the surface characteristics such as adhesion of polypropylene surface. With different gas species and compositions in the plasma source, surface characteristics as well as plasma properties are measured by optical emission spectroscopy(OES), X-ray photoelectron spectroscopy(XPS) and atomic force microscopy(AFM). Maximum lap shear strengths of about 4MPa are obtained in helium plasmas without any additional reactive gases such as O_2 or N_2.

References

[1] M. D.Green, F. J. Guild, R. D.Adams, International Journal of Adhesion & Adhesives **22**(2002) ,pp.81-90.

[2] M. Zenkiewicz, J. Adhesion Sci. Technol., Vol. **15**, N.1(2001), pp. 63-70

[3] C. Muhlhan, H. Nowack, Surface and Coating Technology **98** (1998), pp.1107-1111.

[4] M.R. Wertheimer et al., Adhesion Promotion Techniques, K. L. Mittal and A. Pizzi,eds., Marcel Dekker Inc,. New York (1999) , pp.139.

[5] F. Massines ,G. Gouda, N.Gherardi, M.Duran, and E.Croquesel, Plasmas and polymers, vol.**6**(2001), pp35-49

[6] J. Kurdi, M. Tatoulian, J. Amouroux and F. Arefi-Khonasari, Proceedings of the14th International Symposiim on Plasma Chemistry, Volume **4**

[7] D. Briggs, Surface analysis of polymers by XPS and Static SIMS, chap.3, Cambridge University Press (1998)

1. Introduction

Polypropylene has been widely used in many different industries including automotive industry since it has good mechanical properties, light weight, low cost and readily-recyclable characteristics. However, it has inherently low surface energy so that its applicability has been limited by the difficulty in painting, coating, bonding, and metalization. To improve surface properties such as good bondability, pre-treatment of polypropylene surface has been studied. Not only wet chemical processes but also dry physical (or chemical) processes such as flame treatment, corona discharge, low pressure or atmospheric pressure plasma treatments are intensively studied and developed[1-5]. Among them, the atmospheric pressure plasma pre-treatment is considered to be most promising in real industrial applications since it is an environmentally preferential dry process applicable to in-line processes without any expensive vacuum system.

In this study, an atmospheric pressure ejected plasma source has been developed to modify the polypropylene surface for better adhesion property. To treat arbitrary shaped objects as well as flat shaped

ones the plasma source in plasma ejection configuration has been favored to the configuration of dielectric barrier discharge (DBD) plasma source. The main purpose of the study is to asses the mechanisms responsible for the increased adhesion as a result of atmospheric pressure plasma ejected plasma treatment.

To evaluate adhesion properties, bonding strengths are measured with lap shear strength tests and correlated with the change of plasma properties such as plasma radical line intensity measured by optical emission spectroscopy(OES). Also the chemical or physical changes of plasma-treated polypropylene surface are examined to understand improved bondability by X-ray photoelectron spectroscopy (XPS), secondary ion mass spectroscopy (SIMS)and atomic force microscopy (AFM), respectively.

2. Experimentals

2.1 Test material preparations

Two kinds of Homo-polypropylene (5mm thickness bulk) with other surface roughness (R_{rms}=110nm, $R_{rms=}$30nm) are prepared and cutted by pieces of 25.4×110×5 mm which are referred to ASTM3163-96. Before the plasma treatment, polypropylene surface is cleaned by acetone solution to remove the contaminant such as oil and dusts.

2.2 Plasma treatments

The schematics of overall experimental setups and the structure of the atmospheric pressure ejected plasma source are shown in Figs.1 and 2, respectively. Power electrode is made of aluminum with tapered-shape as shown in the fig.2 and ground electrode of 32mm inner diameter is made of stainless steel. Between them, boron-nitride insulator is inserted to generate the glow-like plasmas without arc channel. Atmospheric pressure plasmas are generated between two axial electrodes by applying RF power to the power electrode at the frequency of 27.12MHz up to 1kW. Generated plasmas are ejected from the discharge region along with the direction of gas flow. Discharge gases (helium and argon) mixed with a small amount of reactive gas (N_2 or O_2) are injected into the discharge region through the mass flow controller. Treatment distance between plasma source and polypropylene surface is defined as L as shown in Fig.1.

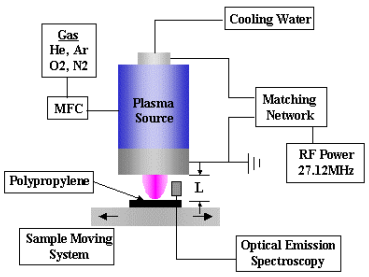

Fig.1 Schematics of overall experimental setup

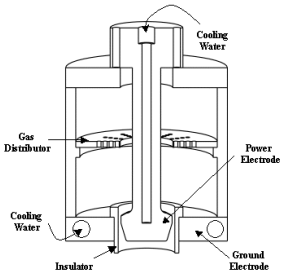

Fig.2 Structure of the atmospheric pressure ejected plasma source

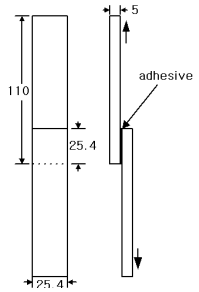

Fig.3 Assembled specimen for lap shear strength test with dimension

2.3 Adhesion Strength Tests

Adhesion strength is evaluated by the lap shear strength test, which is carried out using Instron Tensile Test Machine, at a pull-off speed of 1mm/min. Two polypropylene specimens treated by plasmas are adhered to each other immediately after plasma treatments using cyanoacrylate adhesive and stored at room temperature in air for 24 hours to ensure fully hardening between adherent and adhesive. Polypropylene assembly

adhered to cyanoacrylate adhesive for the lap shear strengrh test is shown in Fig.3. Tests for lap shear strength are performed as referred to ASTM3163-96. Each data points are averaged values of five identical measurements and error bars are obtained from the standard deviation of them.

2.4 Plasma Charaterizations

Plasma properties such as radical line intensity with gas compositions are diagnosed with a personal computer (PC) plug-in type spectrometer of AVS-PC2000S-ISA from Avantes with the spectral resolution of 0.4nm. And gas temperatures are measured by thermocouple. Principal emission lines of radicals in this experiment are summarized in Table.1.

Table.1 Principal emission lines

Species	Emission lines (nm)
He^* (3s→2p)	706.5
O^* (3p→3s)	777.2
N_2^+ ($B^2\Sigma_u \rightarrow X^2\Sigma_g$)	391.4
N_2^*($C^3\Pi_u \rightarrow B^3\Pi_g$)	337.1
Ar^* (4p→4s)	750.3

2.5 Surface Characterizations

The evolution of the surface characteristics is monitored by X-ray photoelectron spectroscopy(XPS) and Secondary ion mass spectroscopy (SIMS). The XPS study is performed with a VG-Scientific ESCALAB 250 spectrometer with monocromatized Al Kα X-ray source (1486.6eV) at Korea Basic Science Institute. Chemical compositions (atomic percent,%) are determined from the broad-scan XPS spectra with sensitivity factors for each atom. The SIMS study is performed with PHI 7200 TOF-SIMS/SALI with 8keV Cs+ ion source at Korea Institute of Science and Technology.

Changes of Surface morphology before and after plasma treatments are measured by SPA-400, Seiko Instrument with contact mode whose scan size is 50μm with 1line/sec scanning speed. Surface roughness values are expressed in terms of R_{rms} that is averaged roughness of three independent measurements for each specimen.

3. Experimental Results and Discussions

3.1 He plasmas with N_2 or O_2 gases

Lap shear strength variations with N_2 or O_2 flow rate (0.25%~6 %) for fixed helium flow rate of 5slm are shown in Fig.4. Maximum lap shear strength is obtained in helium plassma without N_2 or O_2. A small amount (0.25%) of N_2 or O_2 additoin to helium leads to the sharp decrease of lap shear strength. As shown in Fig.5 and 6, He^* line intensity and N_2^+/N_2^* line intensity ratio are also decreased with N_2 or O_2 addition. Because the N_2^+/N_2^* line intensity ratio represent the mean electronic temperature[6], high bondability in helium plasma in the absence of N_2 or O_2 can be related to the high population of He^* generated by high energy electrons. High energy He^* can contribute to bondability via excitation of polymer suface and creation of excited atoms or molecule such as O^* or N_2^* near the polypropylene suface. A small amount of oxygen or nitrogen added to helium plasmas results in the negative effects on the adhesion from the viewpoint of generating high energy He^*. Chain scission effect on the surface through helium plasma

treatment is verified as shown in Fig.7. Breaking of C-H bonds by plasma radicals and removal of hydrogen atoms from surface are confirmed by the decreased H/C ratio. This is so called creation of polymer radicals by plasma treatments, which leads to the absorption of excited species(O*, N_2^*) to the polypropylene surface.

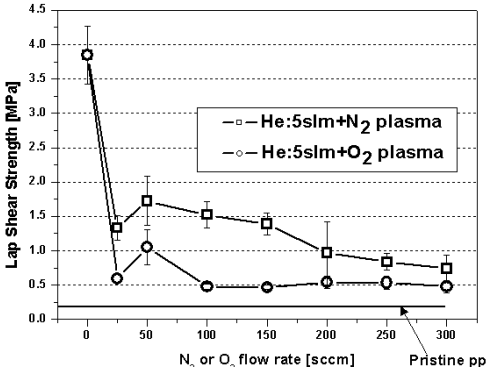

Fig.4 Lap shear strength variaions with N_2 or O_2 flow rate in fixed helium flow rate: Power:200W, He:5slm Frequency:27.12MHz, L:2mm, Treatment time:20sec

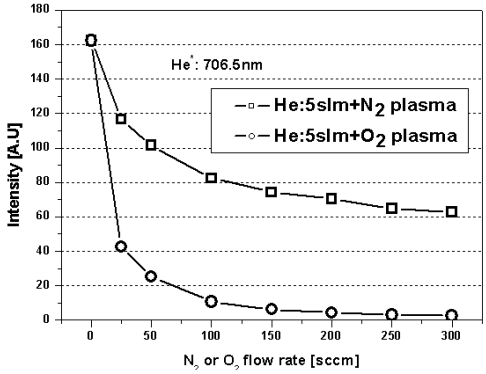

Fig.5 He^* line intensity variation in discharge region with N_2 or O_2 flow rate: Power:200W. He:5slm. Frequency:27.12MHz

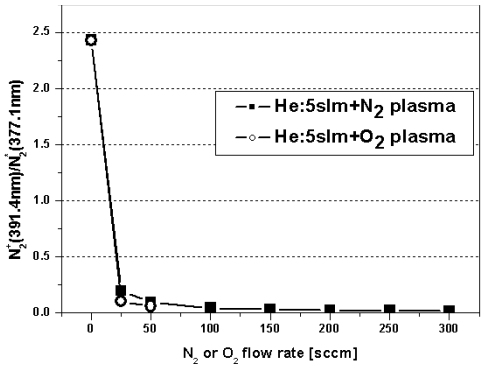

Fig.6 N_2^+(391.4nm)/N_2^*(337.1nm) line intensity ratio variations with N_2 flow rate:Power:200W, He:5slm, Frequency:27.12MHz

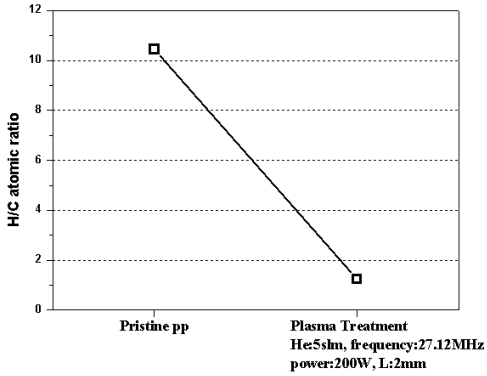

Fig.7 Variation of C/H ratio with He=5sm Plasma treatment (from SIMS results)

As shown in Table.2, high oxygen content on the surface is obtained in helium plasmas without N_2 or O_2. Figure 8 shows that C ls peak of polypropylene treated with helium plasma is expanded toward higher binding energy level corresponding to the ether (C-O), carbonyl (C=O) and ester (O=C-O) fucnctional groups which are favorable to adhesion [7]. From these results, generation of oxygen or nitrogen functoinal groups on the surface takes place sufficiently under ambient condition without additional injection of oxygen or nitrogen gases as reactive additives, which is contrary to vacuum-based plasma treatment. Variations of atomic percent with gas compositions are summarized in Table.2

Table.2 Atomic percent variations with gas compositions : Power:200W, Frequency:27.12MHz, L:2mm, Treatment time:20sec

	C	N	O	(N+O)/C
Pristine pp	93.519	0.096	6.386	0.07
He:5slm	74.993	1.941	23.066	0.33
He:5slm+N2:50sccm	84.191	2.339	13.47	0.19
He:5slm+N2:200sccm	89.589	0.643	9.768	0.12
He:5slm+O2:50sccm	79.78	0.929	19.292	0.25
He:5slm+O2:200sccm	92.218	0.514	7.268	0.08

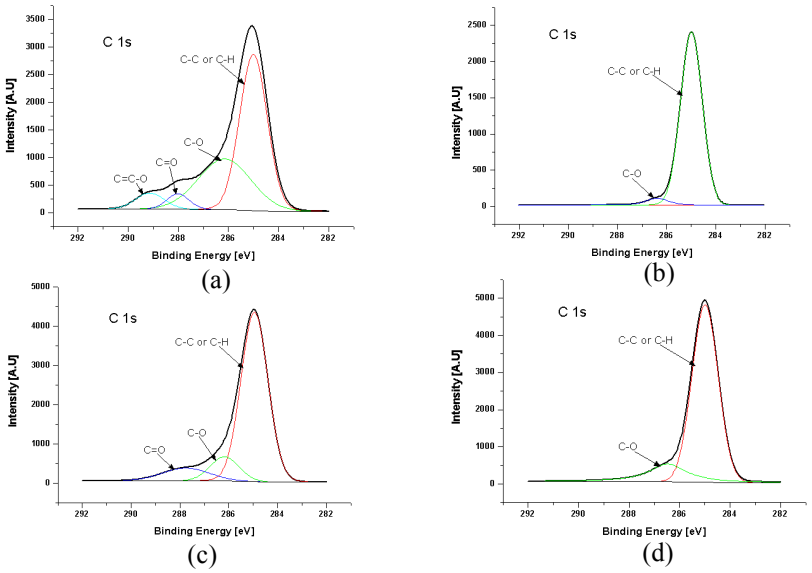

Fig.8 XPS C 1s spectra for (a) pristine pp (b) He:5slm (c) He:5slm+N_2:50sccm (d)He:5slm+N_2:200sccm,Power:200W, Frequency:27.12MHz, L:2mm,

For two kinds of polypropylene having different surface roughness, variations of lap shear strengths with different treatment times are shown in Fig.9. Surface roughnesses of two polypropylenes are 30nm and 110nm respectively, measured by AFM contact mode. As shown in Fig.9, steeper increase in lap shear strength with treatment time is observed in polypropylene having surface roughness of R_{rms}=110nm. Therefore, surface roughness can be considered as another important factor leading to the increase of adhesion. As shown in Fig.10, surface roughness of polypropylene treated by helium plasma without reactive gas is increased from 30nm to 50nm. Maximum adhesion in helium plasma can be explained not only by high population of He^* in discharge region, but also by rough surface imparted during the helium plasma treatment.

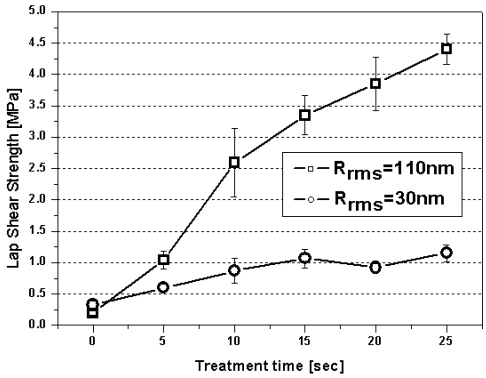

Fig.9 Lap shear strength variations with treatment time : Power:200W, Frequency:27.12MHz, L:2mm, He:5slm

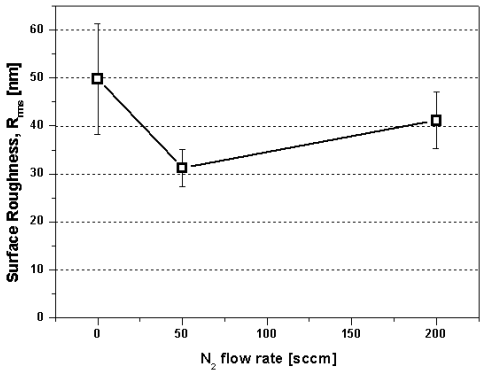

Fig.10 Surface roughness variations with N_2 flow rate : Power:200W, Frequency:27.12MHz, L:2mm, He:5slm

3.2 He/Ar plasmas

Due to the thermal problem, operations of He+Ar plasmas are limited at the relatively lower power level of less than 150W and with longer treatment distance of L=5mm. As shown in Fig.11, lap shear strength and gas temperature are increased as fractions of Ar gases are increased, and simultaneously ejection lengths of plasmas becomes longer.

OES measurements of Fig.12 show the decrease in He^* and Ar^* line intensity as the Ar/(Ar+He) ratio

increased. But lap shear strengths show completely opposite trend. Therefore, the increase of bondability with the increased Ar/(Ar+He) ratio cannot be explained only with high energy metastable species such as He^*. And XPS measurements for He+Ar plasmas shown in Table.3 do not provide any significant increase of oxygen and nitrogen concentrations on the surface. Putting above results altogether, bondability improvement with Ar/(Ar+He) ratio more likely seems to be combined effects of other factors such as gas temperature and plasma ejection length.

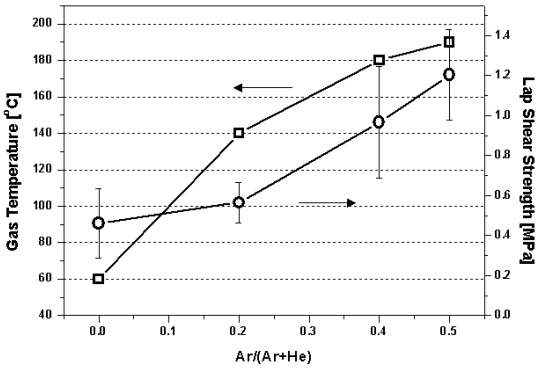

Fig.11 Variations of lap shear strength and gas temperature with Ar/(Ar+He) ratio: Power:150W, Frequency:27.12MHz, L:5mm, Treatment time:20sec

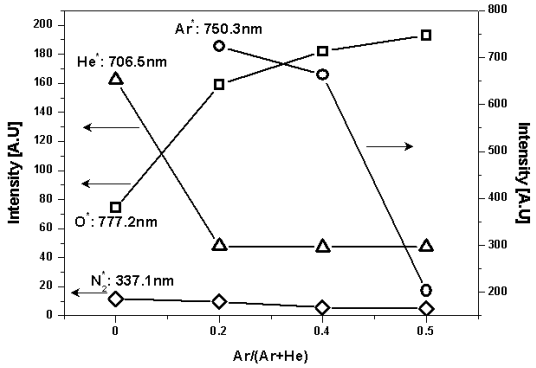

Fig.12 Variations of optical emission with Ar/(Ar+He) ratio :Power:150W, Frequency:27.12MHz

Table.3 Atomic percent variations with gas compositions : Power:150W, Frequency:27.12MHz, Distance:5mm, Treatment time:20sec

	C	O	O/C
Pristine pp	93.519	6.386	0.07
He:4slm+Ar:1slm	91.521	8.106	0.089
He:3slm+Ar:2slm	92.341	7.659	0.083

Unit: Atomic percent, %

4. Conclusions and future work

Experimental results and future work can be summarized as followings:

(1) Maximum lap shear strength in helium plasma without adding reactive gases such as N_2 or O_2, which is correlated with high He^* line intensity instead of other reactive radicals. High energy He* seems to play an important role on adhesion improvement in He plasmas and need to be provided by maintaining good plasma discharge conditions.

(2) Surface roughness is another factor affecting the adhesion as shown in helium plasma tests.

(3) Increases of gas temperature and ejection length of plasma, induced by adding Argon gas to He gas as discharge gases, are identified to be another parameters to improve adhesion characteristics, which is identified from higher lap shear strength in spite of low He^* line intensity when Ar gas is added. But gas temperature effect is not verified yet and further studies are needed.

(4) Plasma characteristics such as electron densities and temperatures with different gas compositions may provide clues to understand adhesion improvements, which will be studied more in detail.

Self-consistent chemical and thermal non-equilibrium modelling of Ar-N_2 induction thermal plasma with a reaction chamber

Yasunori Tanaka and Tadahiro Sakuta

Department of Electrical and Electronic Engineering, Kanazawa University, 2-40-20, Kodatsuno, Kanazawa 920-8667, JAPAN

Abstract

A self-consistent two-dimensional thermally and chemically non-equilibrium model for Ar-N_2 inductively coupled thermal plasma (ICTP) was developed. Transport and thermodynamic properties were self-consistently calculated at each iteration step using the local particle composition, heavy particle temperature and electron temperature. Spatial particle composition distribution in the plasma torch and the reaction chamber was derived by solving simultaneously the mass conservation equation of each particle, considering diffusion, convection and production terms including thirty reactions.

1. Introduction

The inductively coupled thermal plasma (ICTP) can be found in various technology fields such as materials processing, plasma waste destruction and plasma spraying, because of its high temperature and high reaction activity [1]. Up to now, numerical modelling of such an ICTP has been made to understand the plasma internal state in detail on the assumption of local thermal equilibrium (LTE) in steady state [2, 3]. The use of this model enables us to understand the transport of mass, momentum, energy, gas flow and temperature fields in the ICTP. However, further understanding of reactions and particle density distributions in the ICTP has greatly been required for advanced material processings at non-LTE state. For this purpose, we have so far developed a one-temperature chemical non-equilibrium modelling [4, 5], in which reaction rates were considered for each of reactions. However, in some experimental cases, electron temperature T_e has been found to be higher than heavy particle temperature T_h especially near the wall of the ICTP, which means thermal non-equilibrium exists there. The thermally non-equilibrium can also affect the distribution of radicals and excited particles. Some two-temperature models for thermal plasma have been developed until now. However, many of the models are not self-consistent because they used transport and thermodynamic properties under equilibrium condition, and/or they neglected chemical non-equilibrium effect for example. Thus, a self-consistent model including thermal and chemical non-equilibrium effects has been greatly desired in the plasma material processing field. In this paper, a two-dimensional thermally and chemically non-equilibrium model for Ar-N_2 ICTP is proposed considering reaction rates and difference between electron and heavy particle temperatures. First, the proposed plasma model and the governing equations used are interpreted. Secondly, Ar-N_2 ICTP simulation is made by three different models i.e., the present two-temperature chemically non-equilibrium (2T-NCE) model, a one-temperature chemical equilibrium (1T-CE) model [3], and a one-temperature chemically non-equilibrium (1T-NCE) model [5]. Finally, by comparison of the results calculated by the three different methods, the effect of chemical and thermal non-equilibrium in the Ar-N_2 ICTP was discussed.

2. Modelling of Ar-N_2 induction thermal plasma

2.1. Hypothesis

In the present calculation, the followings were assumed in Ar-N_2 ICTP: (i) There are only seven particles Ar, Ar^+, N_2, N_2^+, N, N^+ and electron in Ar-N_2 ICTP. All the species are in the ground state. (ii) All the heavy particles has the same temperature with a Maxwellian energy distribution function. On the other hand, the electron energy distribution function also follows Maxwell-Boltzmann law, although its mean energy is not always the same to that of heavy particles. (iii) Electrons lose their energies through elastic collisions with heavy particles and through inelastic collisions involving ionization and dissociation reactions. However, inelastic collisions involving electronic, rotational and vibrational excitations are not taken into account in the present work. (iv) The reaction heat is supplied from or transferred to the electron kinetic energy if the electron is concerned with the reaction. (v) The plasma has an axissymetric structure. (vi) The optically thin assumption is established, and thus the effect of light absorption is negligible. (vii) Pressure in the ICTP is around the atmospheric pressure. (viii) All the particles moves together with gas flow.

2.2. Governing equations

On the basis of the hypothesis mentioned in the previous section, the Ar-N_2 ICTP behavior can be expressed by the governing equations described in Tab.1.

Tab. 1. Governing equations.

Mass conservation:

$$\frac{\partial \rho}{\partial t} + \frac{\partial (\rho u)}{\partial z} + \frac{1}{r}\frac{\partial (r\rho v)}{\partial r} = 0 \tag{1}$$

Momentum conservation:

$$\begin{aligned}\frac{\partial (\rho u)}{\partial t} &+ \frac{\partial (u\rho u)}{\partial z} + \frac{1}{r}\frac{\partial (rv\rho u)}{\partial r} \\ &= -\frac{\partial p}{\partial z} + 2\frac{\partial}{\partial z}\left(\eta \frac{\partial u}{\partial z}\right) \\ &+ \frac{1}{r}\frac{\partial}{\partial r}\left[\eta r\left(\frac{\partial u}{\partial r} + \frac{\partial v}{\partial z}\right)\right] + \mu_0 \sigma \Re[\dot{E}_\theta \dot{H}_r^*]\end{aligned} \tag{2}$$

$$\begin{aligned}\frac{\partial (\rho v)}{\partial t} &+ \frac{\partial (u\rho v)}{\partial z} + \frac{1}{r}\frac{\partial (rv\rho v)}{\partial r} \\ &= -\frac{\partial p}{\partial r} + \frac{\partial}{\partial z}\left[\eta\left(\frac{\partial v}{\partial z} + \frac{\partial u}{\partial r}\right)\right] \\ &+ \frac{2}{r}\frac{\partial}{\partial r}\left(\eta r \frac{\partial v}{\partial r}\right) - 2\eta\frac{v}{r^2} + \mu_0 \sigma \Re[\dot{E}_\theta \dot{H}_z^*]\end{aligned} \tag{3}$$

Translational energy conservation of heavy particle:

$$\begin{aligned}\frac{\partial (\rho h')}{\partial t} &+ \frac{\partial (u\rho h')}{\partial z} + \frac{1}{r}\frac{\partial (rv\rho h')}{\partial r} \\ &= \frac{\partial}{\partial z}\left(\lambda_{\mathrm{h}}^{\mathrm{tr}}\frac{\partial T_{\mathrm{h}}}{\partial z}\right) + \frac{1}{r}\frac{\partial}{\partial r}\left(r\lambda_{\mathrm{h}}^{\mathrm{tr}}\frac{\partial T_{\mathrm{h}}}{\partial r}\right) \\ &+ \sum_{j\,(j\neq \mathrm{e})}^{N}\left[\frac{\partial}{\partial z}\left(\rho D_j' h_j' \frac{\partial Y_j}{\partial z}\right) + \frac{1}{r}\frac{\partial}{\partial r}\left(r\rho D_j' h_j' \frac{\partial Y_j}{\partial r}\right)\right] \\ &- \sum_{\ell\,(\beta_{\mathrm{e}\ell}^{\mathrm{f}}\beta_{\mathrm{e}\ell}^{\mathrm{r}}=0)}^{L}\Delta Q_\ell + E_{\mathrm{eh}}\end{aligned} \tag{4}$$

Energy conservation of electron:

$$\begin{aligned}\frac{\partial}{\partial t}\left(n_{\mathrm{e}}\frac{5}{2}\kappa T_{\mathrm{e}}\right) &+ \frac{\partial}{\partial z}\left(un_{\mathrm{e}}\frac{5}{2}\kappa T_{\mathrm{e}}\right) + \frac{1}{r}\frac{\partial}{\partial r}\left(rvn_{\mathrm{e}}\frac{5}{2}\kappa T_{\mathrm{e}}\right) \\ &= \frac{\partial}{\partial z}\left(\lambda_{\mathrm{e}}^{\mathrm{tr}}\frac{\partial T_{\mathrm{e}}}{\partial z}\right) + \frac{1}{r}\frac{\partial}{\partial r}\left(r\lambda_{\mathrm{e}}^{\mathrm{tr}}\frac{\partial T_{\mathrm{e}}}{\partial r}\right) \\ &- \frac{\partial}{\partial z}\left(\frac{1}{m_{\mathrm{e}}}\frac{5}{2}\kappa T_{\mathrm{e}}\Gamma_{\mathrm{ez}}\right) - \frac{1}{r}\frac{\partial}{\partial r}\left(r\frac{1}{m_{\mathrm{e}}}\frac{5}{2}\kappa T_{\mathrm{e}}\Gamma_{\mathrm{er}}\right) \\ &- \sum_{\ell\,(\beta_{\mathrm{e}\ell}^{\mathrm{f}}\beta_{\mathrm{e}\ell}^{\mathrm{r}}\neq 0)}^{L}\Delta Q_\ell + \sigma\dot{E}_\theta\dot{E}_\theta^* - P_{\mathrm{rad}} - E_{\mathrm{eh}}\end{aligned} \tag{5}$$

Mass conservation of species j (for N, $\mathrm{N^+}$, $\mathrm{N_2^+}$, $\mathrm{Ar^+}$):

$$\begin{aligned}\frac{\partial (\rho Y_j)}{\partial t} &+ \frac{\partial (u\rho Y_j)}{\partial z} + \frac{1}{r}\frac{\partial (rv\rho Y_j)}{\partial r} \\ &= \frac{\partial}{\partial z}\left(\rho D_j' \frac{\partial Y_j}{\partial z}\right) + \frac{1}{r}\frac{\partial}{\partial r}\left(r\rho D_j' \frac{\partial Y_j}{\partial r}\right) \\ &+ m_j \sum_{\ell=1}^{L}(\beta_{j\ell}^{\mathrm{r}} - \beta_{j\ell}^{\mathrm{f}})\left(\alpha_\ell^{\mathrm{f}}\prod_{i=1}^{N} n_i^{\beta_{i\ell}^{\mathrm{f}}} - \alpha_\ell^{\mathrm{r}}\prod_{i=1}^{N} n_i^{\beta_{i\ell}^{\mathrm{r}}}\right)\end{aligned} \tag{6}$$

Maxwell equation by vector potential:

$$\frac{\partial^2 \dot{A}_\theta}{\partial z^2} + \frac{1}{r}\frac{\partial}{\partial r}\left(r\frac{\partial \dot{A}_\theta}{\partial r}\right) - \frac{\dot{A}_\theta}{r^2} = \bar{i}\mu_0\sigma\omega\dot{A}_\theta \tag{7}$$

$$\dot{H}_z = \frac{1}{\mu_0}\frac{1}{r}\frac{\partial}{\partial r}(r\dot{A}_\theta), \quad \dot{H}_r = -\frac{1}{\mu_0}\frac{\partial \dot{A}_\theta}{\partial z} \tag{8}$$

$$\dot{E}_\theta = -\bar{i}\omega\dot{A}_\theta \tag{9}$$

Reaction heat per unit volume and time:

$$\Delta Q_\ell = \psi_{\mathrm{reac}\ell}\left(\alpha_\ell^{\mathrm{f}}\prod_{i=1}^{N} n_i^{\beta_{i\ell}^{\mathrm{f}}} - \alpha_\ell^{\mathrm{r}}\prod_{i=1}^{N} n_i^{\beta_{i\ell}^{\mathrm{r}}}\right) \tag{10}$$

Translational enthalpy of heavy particles:

$$h' = \sum_{j\neq \mathrm{e}} Y_j h_j', \qquad h_j' = \frac{1}{m_j}\left(\frac{5}{2}kT_{\mathrm{h}}\right) \tag{11}$$

Energy transfer from electron to heavy particles:

$$E_{\mathrm{eh}} = \sum_{j\neq \mathrm{e}}\frac{3}{2}\kappa(T_{\mathrm{e}} - T_{\mathrm{h}})\frac{4m_j m_{\mathrm{e}}}{(m_j + m_{\mathrm{e}})^2} n_j n_{\mathrm{e}} \pi\bar{\Omega}_{\mathrm{e}j}\bar{v}_{\mathrm{e}j} \tag{12}$$

$$\bar{v}_{\mathrm{e}j} = \sqrt{\frac{8\kappa T_{\mathrm{e}}(m_{\mathrm{e}} + m_j)}{\pi m_{\mathrm{e}} m_j}} \tag{13}$$

Relation between mass density and mass fraction:

$$n_j = \frac{\rho Y_j}{m_j} \tag{14}$$

Equation of state:

$$\rho = \frac{p}{\dfrac{Y_{\mathrm{e}}}{m_{\mathrm{e}}}\kappa T_{\mathrm{e}} + \displaystyle\sum_{j\neq \mathrm{e}}\frac{Y_j}{m_j}\kappa T_{\mathrm{h}}} \tag{15}$$

Quasi-neutrality:

$$\frac{Y_{\mathrm{e}}}{m_{\mathrm{e}}} = \frac{Y_{\mathrm{Ar^+}}}{m_{\mathrm{Ar^+}}} + \frac{Y_{\mathrm{N_2^+}}}{m_{\mathrm{N_2^+}}} + \frac{Y_{\mathrm{N^+}}}{m_{\mathrm{N^+}}} \tag{16}$$

Balance of mass fraction:

$$Y_{\mathrm{Ar}} = Y_{\mathrm{Ar}}^{\mathrm{TOT}} - Y_{\mathrm{Ar^+}} \tag{17}$$

$$Y_{\mathrm{N_2}} = Y_{\mathrm{N_2}}^{\mathrm{TOT}} - Y_{\mathrm{N}} - Y_{\mathrm{N^+}} - Y_{\mathrm{N_2^+}} \tag{18}$$

Admixture ratio $\mathrm{N_2}$ to Ar:

$$Y_{\mathrm{N_2}}^{\mathrm{TOT}} = \frac{m_{\mathrm{N_2}} Q_{\mathrm{N_2}}}{m_{\mathrm{Ar}} Q_{\mathrm{Ar}} + m_{\mathrm{N_2}} Q_{\mathrm{N_2}}} \tag{19}$$

$$Y_{\mathrm{Ar}}^{\mathrm{TOT}} = 1.0 - Y_{\mathrm{N_2}}^{\mathrm{TOT}} \tag{20}$$

Effective diffusion coefficient of heavy particle:

$$D_j' = \frac{1 - Y_j}{\displaystyle\sum_{k\neq j}\frac{x_i p \Delta_{ij}^{(1)}}{\kappa T_{\mathrm{h}}}} \tag{21}$$

Electrical conductivity:

$$\sigma = \frac{e^2}{\kappa T_{\mathrm{e}}}\frac{n_{\mathrm{e}}}{\displaystyle\sum_{j\neq \mathrm{e}} n_j \Delta_{\mathrm{e}j}^{(1)}} \tag{22}$$

Viscosity:

$$\eta = \sum_{j=1}^{N}\frac{m_j n_j}{\displaystyle\sum_{i=1}^{N} n_i \Delta_{ij}^{(2)}} \tag{23}$$

Translational thermal conductivity of heavy particle:

$$\lambda_{\mathrm{h}}^{\mathrm{tr}} = \frac{15}{4}\kappa\sum_{i\neq \mathrm{e}}\frac{n_i}{\displaystyle\sum_j \xi_{ij} n_j \Delta_{ij}^{(2)}} \tag{24}$$

Translational thermal conductivity of electron:

$$\lambda_{\mathrm{e}}^{\mathrm{tr}} = \frac{15}{4}\kappa\frac{n_{\mathrm{e}}}{\displaystyle\sum_j \xi_{\mathrm{e}j} n_j \Delta_{\mathrm{e}j}^{(2)}} \tag{25}$$

$$\frac{1}{\Delta_{ij}^{(1)}} = \frac{3}{8}\sqrt{\frac{\pi\kappa T_{\mathrm{h,e}}(m_i + m_j)}{2m_i m_j}}\frac{1}{\pi\bar{\Omega}_{ij}^{(1,1)}} \tag{26}$$

$$\frac{1}{\Delta_{ij}^{(2)}} = \frac{5}{16}\sqrt{\frac{\pi\kappa T_{\mathrm{h,e}}(m_i + m_j)}{2m_i m_j}}\frac{1}{\pi\bar{\Omega}_{ij}^{(2,2)}} \tag{27}$$

$$\xi_{ij} = 1 + \frac{(1 - m_i/m_j)(0.45 - 2.54 m_i/m_j)}{(1 + m_i/m_j)^2} \tag{28}$$

where t: time (s), r: radial position (m), z: axial position (m), u: axial flow velocity (m/s), v: radial flow velocity (m/s), ρ: mass density ($\mathrm{kg/m^3}$), p: pressure (Pa), T_{h}: heavy particle temperature (K), T_{e}: electron temperature (K), P_{rad}: radiation loss ($\mathrm{W/m^3}$), n_j: number density of species j ($\mathrm{m^{-3}}$), Y_j: mass fraction of species j, x_j: mole fraction of species j, m_j: mass of species j (kg), Γ_{er}, Γ_{ez}: radial and axial electron flux due to ambipoler diffusion ($\mathrm{1/m^2/s}$), α_ℓ^{f}, α_ℓ^{r}: rate coefficients of forward and backward reaction ℓ, respectively, $\beta_{j\ell}^{\mathrm{f}}$, $\beta_{j\ell}^{\mathrm{r}}$: stoichiometric number of species j in forward and backward reaction ℓ, μ_0: permeability of vacuum (H/m), κ: Boltzmann constant (J/K), $\dot{A}_\theta$: vector potential (V·s/m), ω: angular frequency of coil current (rad/s), $\dot{E}_\theta$: electric field strength (V/m), $\dot{H}_z$: axial magnetic field strength (A/m), $\dot{H}_r$: radial magnetic field strength (A/m), $\bar{i}$: complex index ($\bar{i}^2 = -1$), $\psi_{\mathrm{reac}\ell}$: reaction heat for reaction ℓ (J), $\pi\bar{\Omega}_{ij}^{(1,1)}$: momentum transfer collision integrals ($\mathrm{m^2}$), $\pi\bar{\Omega}_{ij}^{(2,2)}$: viscosity collision integrals ($\mathrm{m^2}$), Q_{Ar}: Ar gas flow rate ($\mathrm{m^3/s}$), $Q_{\mathrm{N_2}}$: $\mathrm{N_2}$ gas flow rate ($\mathrm{m^3/s}$), N: total number of species, L: total number of reactions.

2.2.1. Energy conservation equation of heavy particle in two-temperature state

In two-temperature state, electron energy conservation equation should be separately treated from that of heavy particles. Moreover, in chemically non-equilibrium condition, energy transfer due to diffusion should be explicitly considered. Energy conversion through reactions also needs to be taken into account with considering whether the reaction is related with electron energy or not.
Equation (4) shows the translational energy conservation equation of heavy particle. In this equation, h' is the total translational enthalpy of heavy particles defined by Eq.(11). The left hand side of Eq.(4) includes the energy change and the energy transfer by convection. On the right hand side of Eq.(4), the first and second terms are the thermal conduction terms, the third is the energy transfer due to diffusion of heavy particles, the fourth is the energy conversion by the reactions, and the last term is the energy conversion between electron and heavy particle through elastic collision. In a conventional LTE or 1T-CE model, which is the extremely simplified model, the thermal conductivity has the translational, internal and reactional terms implicitly [1], which includes diffusion, excitation and reaction effect. However, in the two-temperature and chemical non-equilibrium (2T-NCE) condition, the thermal conductivity cannot have internal and reactional terms implicitly because the local particle composition is not determined only by temperature, and then they should be calculated with considering effect of diffusion, convection and reactions. Thus, translational thermal conductivity of heavy particles $\lambda_{\mathrm{h}}^{\mathrm{tr}}$ are used in the first and second terms, and the third and the fourth terms are added on the right hand side in Eq.(4) at the same time. In the fourth term, ΔQ_ℓ is the reaction heat per unit volume and time. This is defined by Eq.(10) considering reaction rates. For the heavy particle energy conservation, ΔQ_ℓ for reaction ℓ is summed unless there are electrons in both left and right sides in reaction equation. The energy conversion between electron and heavy particle through elastic collision E_{eh} is calculated through Eq.(12).

2.2.2. Electron energy conservation equation

Equation (5) indicates the electron energy conservation equation. In this equation, we took into account the heat conduction by electrons, the energy transfer by ambipoler diffusion, reaction heat, joule heating, radiation loss and the energy conversion between electron and heavy particle through elastic collision as described on the right hand side. The ambipoler diffusion terms were calculated through $\mathbf{\Gamma}_{\mathrm{e}} = -\rho D_{\mathrm{a}} \boldsymbol{\nabla} Y_{\mathrm{e}}$ where D_{a} is the ambipoler diffusion coefficient. In the present calculation, approximation $D_{\mathrm{a}} \sim 2D_{\mathrm{Ar^+}}$ was used because the electron are produced mainly by Ar ionization and difference between T_{e} and T_{g} is small in the wide area.

2.3. Reaction rates

Table 2 summarizes reactions in an Ar-N_2 plasma. Thirty reactions including the fifteen forward reactions in Tab.2 and their backward reactions were taken into account. The reaction rate α_ℓ^{f} for forward direction was given by Arrhenius' law $\alpha_\ell^{\mathrm{f}} = a_\ell T^{b_\ell} \exp(-c_\ell/T)$ where a_ℓ, b_ℓ and c_ℓ are constants. The values of a_ℓ, b_ℓ and c_ℓ for the reactions 1–9 in Tab.2 were given by Dunn [7]. For the tenth reaction, i.e. Ar three body recombination reaction, the reaction rate α_{10}^{f} were given by Owano et al.[8]. The reaction rate of the eleventh reaction α_{11}^{f} was computed using the collision cross section [9]. Others were predicted from values of the reactions 1–9. The reaction rates α_ℓ^{r} for the backward direction were calculated by the relationship $\alpha_\ell^{\mathrm{r}} = K_\ell(T)\alpha_\ell^{\mathrm{f}}$ where $K_\ell(T)$ is the equilibrium constant. The quantity $K_\ell(T)$ was calculated using internal partition functions and reaction heat $\psi_{\mathrm{reac}\ell}$. Here, the dependent temperature T in the above corresponds to T_{e} if one of colliding particles is the electron, but otherwise T_{h}. This dependent temperature for each reaction is indicated in Tab.2.

2.4. Transport properties

Transport properties such as electrical conductivity σ, viscosity η, translational thermal conductivity of heavy particle $\lambda_{\mathrm{h}}^{\mathrm{tr}}$, thermal conductivity of electron $\lambda_{\mathrm{e}}^{\mathrm{tr}}$ and effective diffusion of heavy particle D'_j were calculated at each position in the calculation space at each iteration step using the local particle composition, T_{h} and T_{e} derived. These transport properties were obtained by the first order approximation of Champman-Enskog method through Eqs.(21)–(28). Radiation loss P_{loss} was calculated taking account of atomic and ionic spectral lines and continuous spectrum including bremsstrahlung and recombination radiation. The absorption effect was not taken into account in the present calculation.

2.5. Calculation space and calculation conditions

Figure 1 shows the configuration of the ICTP system [5, 6] treated in this calculation. The ICTP system is composed of the plasma torch and the reaction chamber. The plasma torch on the left hand side in Fig.1 has two coaxial quartz tubes with a 330 mm length. The inner tube has an inside diameter of 70 mm. An eight turn

Tab. 2. Reactions taken into account in the present calculation.

Nº	Reaction			a_ℓ	b_ℓ	c_ℓ	Reaction heat $\psi_{\mathrm{reac}\ell}$ (eV)	Dep.Temp. for forward	Dep.Temp. for backward
1	$N_2 + N_2$	→	$N + N + N_2$	4.98×10^{-9}	−1.5	113260	9.759	T_h	T_h
2	$N_2 + N$	→	$N + N + N$	2.49×10^{-8}	−1.5	113260	9.759	T_h	T_h
3	$N_2^+ + N$	→	$N_2 + N^+$	1.30×10^{-19}	0.5	0	−1.047	T_h	T_h
4	$N_2^+ + e$	→	$N + N$	2.49×10^{-8}	−1.5	0	−5.821	T_e	T_h
5	$N^+ + e + e$	→	$N + e$	2.29×10^{-20}	−4.5	0	−14.534	T_e	T_e
6	$N_2^+ + N_2 + e$	→	$N_2 + N_2$	6.07×10^{-34}	−2.5	0	−15.580	T_e	T_h
7	$N_2^+ + N + e$	→	$N_2 + N$	1.66×10^{-35}	−2.5	0	−15.580	T_e	T_h
8	$N^+ + N_2 + e$	→	$N + N_2$	6.07×10^{-34}	−2.5	0	−14.534	T_e	T_h
9	$N^+ + N + e$	→	$N + N$	1.66×10^{-35}	−2.5	0	−14.534	T_e	T_h
10	$Ar + e$	→	$Ar^+ + e + e$	-	-	-	15.760	T_e	T_e
11	$Ar + Ar$	→	$Ar^+ + e + Ar$	-	-	-	15.760	T_h	T_e
12	$N_2 + Ar$	→	$N + N + Ar$	2.49×10^{-8}	−1.5	113260	9.759	T_h	T_h
13	$N_2 + Ar^+$	→	$N + N + Ar^+$	2.49×10^{-8}	−1.5	113260	9.759	T_h	T_h
14	$N_2^+ + Ar + e$	→	$N_2 + Ar$	1.66×10^{-35}	−2.5	0	−15.580	T_e	T_h
15	$N^+ + Ar + e$	→	$N + Ar$	1.66×10^{-35}	−2.5	0	−14.534	T_e	T_h

induction coil is installed around the plasma torch. The reaction chamber on the right hand side is made of SUS304 with a tapered shape. All the wall of the plasma torch and the chamber are cooled by water.

For this instrument, the calculation was performed in the *z*-*r* two-dimensional cylindrical space as hatched in Fig.1. This space was divided into 92×66 grids. The T_h of the inner wall side of the torch was determined by the thermal conduction through the 1.0 mm thick quartz. Non-slip condition was required at all the wall surface. The cold gas with T_h=T_e of 300 K is supplied along the inside quartz tube as a sheath gas from the area (*z*[mm], *r*[mm]) = (0,60)–(0,65). Its gas flow rate was set to 100/2.5 slpm for Ar/N_2 mixture. At outlet of *z*=910 mm, it was assumed that the gas flow and heat transfer occurs freely. The vector potential at any wall was calculated considering the coil current and the eddy current inside the plasma [2]. Input power into plasma is fixed at 27 kW. Pressure at (*z*, *r*)=(0,0) is set to 101 325 Pa. The SIMPLE method was adopted to solve simultaneously the governing equations described in the previous section. Steady state solution was obtained for the above condition.

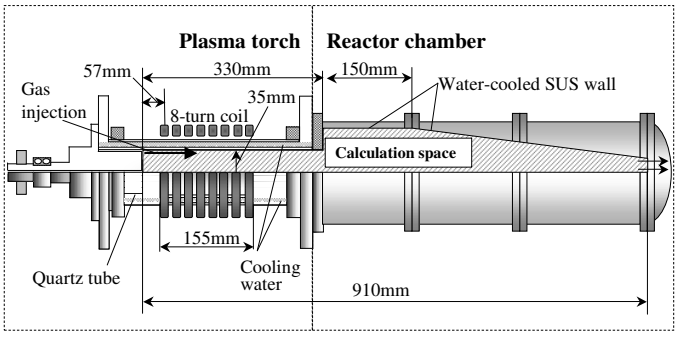

Fig. 1. Plasma torch configuration and calculation space.

3. Calculation results

3.1. Three different models for thermal plasma simulation

We have already developed a one-temperature chemical equilibrium (1T-CE) model [3] and a one-temperature chemically non-equilibrium model (1T-NCE) [5, 6]. In the present work, a two-temperature chemically non-equilibrium (2T-NCE) model is developed as described in the prior section.

The 1T-CE model corresponds to the LTE model in which chemical equilibrium is established under one-temperature condition. In this case, particle composition can be easily and previously calculated as a function of one-temperature through Gibbs free energy minimization method or Saha's equations, and then transport and thermodynamic properties depends only on one-temperature T(1T-CE) if the pressure is fixed. Thus, particle composition distribution was derived only from T(1T-CE) at each position of thermal plasma. The 1T-NCE model takes account of chemically no-equilibrium effect, in which reaction rates, convection and diffusion effect on particle composition distribution is considered. In this case, particle composition at each position was derived through mass conservation of each of species j as described in Eq.(6). Transport and thermodynamic properties depend on not only one-temperature T(1T-NCE) but also particle composition at each of position in thermal plasma. Thus, temperature and particle composition distributions are influenced by this chemical non-equilibrium effect. However, electron temperature is assumed to be the same to heavy particle temperature. The 2T-NCE model, the present work model, does not assume chemical equilibrium condition, and the electron temperature is not assumed to the same to the heavy particle temperature. For this model, transport and thermodynamic properties depend on local particle composition, T_e and T_h. In this

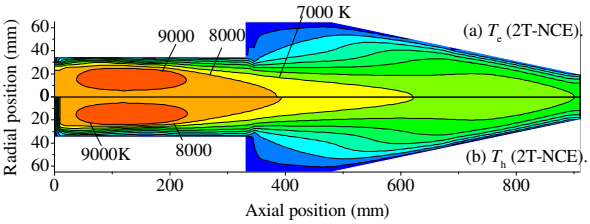

Fig. 2. Isocontours for electron temperature and heavy particle temperature by two-temperature chemical non-equilibrium model.

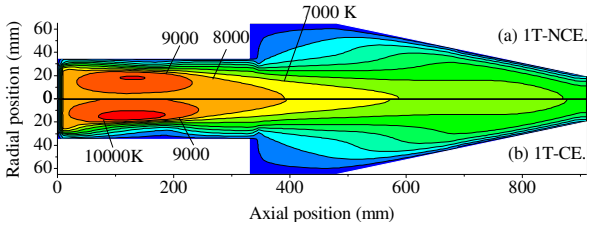

Fig. 3. Isocontours for temperature by one-temperature models.

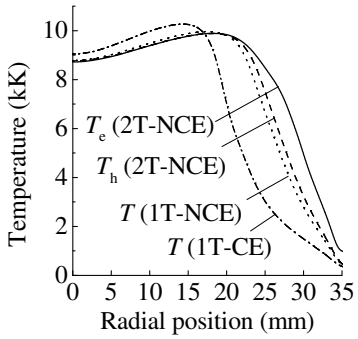

Fig. 4. Radial temperature distributions at axial position of 155 mm by different models.

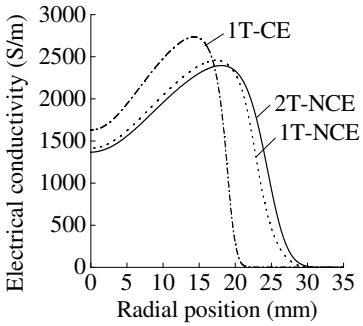

Fig. 5. Radial distributions of electrical conductivity at axial position of 155 mm by different models.

section, calculation results by these three models are compared to study the effect of chemically and thermally non-equilibrium.

3.2. Distributions of temperature and electrical conductivity

Figures 2 (a) and (b) demonstrates the two-dimensional distributions of T_e and T_h, respectively, by the 2T-NCE model. In the plasma torch, it should be noted that T_e is higher than T_h near the wall. This is because electric field strength $|\dot{E}_\theta|$ is high there, and also the energy conversion between the electron and heavy particles is low due to small collision frequency between them. On the other hand, in the reaction chamber, T_e is almost equal to T_h because of low electric field strength. For comparison, isothermal contours by 1T-CE and 1T-NCE models are also indicated in Figs.3(a) and (b). From these figure, it can be seen that the 1T-CE model predicts higher temperature around (z, r)=(155,15) and lower temperature around the torch wall than the 1T-NCE and 2T-NCE models. Figure 4 shows the radial distributions of T_e and T_h by the 2T-NCE model, T by the 1T-NCE and T by the 1T-CE model at axial position z=155 mm where $|\dot{E}_\theta|$ is highest. Radial temperature profile by the 1T-CE model is apparently narrower than that by the NCE models. This results from the fact that the 1T-CE model does not take into account radial diffusion of electron, which occurs particularly near the wall. On the other hand, temperature profile by the 1T-NCE model is similar to T_h by the 2T-NCE model. However, it should be noted that T_e is by 2000 K higher than T_h and T by the 1T-NCE model at r >22 mm.

Figure 5 represents radial distribution of electrical conductivity σ by the three models. It is found that σ by the 1T-NCE model has a peak around r=20 mm, while that by the 1T-CE model is around r=15 mm. This also arises from the fact that electron density in the NCE models has plainer radial distribution profile due to diffusion. The 2T-NCE model predicts a little higher σ around r >22 mm than that by the 1T-NCE. This is attributed to the high T_e by to high electric field near the wall.

From the above results, it can be found that chemical non-equilibrium substantially affects the temperature and electrical conductivity distribution.

3.3. Particle density distribution

For the advanced material processings, distribution of radicals such as the electron and the active atomic particles is of great importance to be understood. Figure 6 shows the electron density distribution by the three different models. The 1T-CE model has higher electron density n_e around (z,r)=(150,15) than the NCE models. However, the 1T-CE model predicts lower n_e near the wall. This is again attributed to no account of diffusion

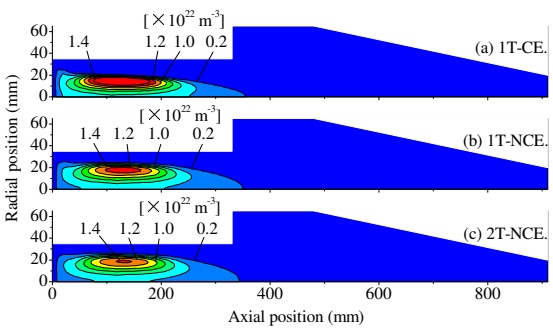

Fig. 6. Isocontours for electron density predicted by different models.

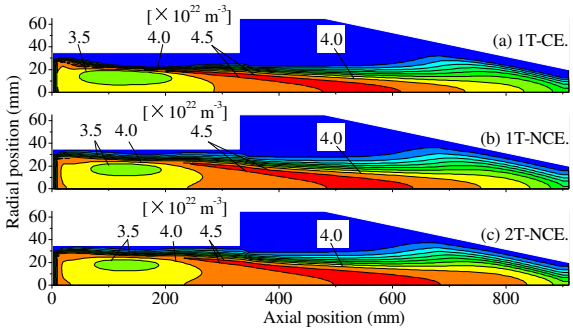

Fig. 7. Isocontours for nitrogen atom density predicted by different models.

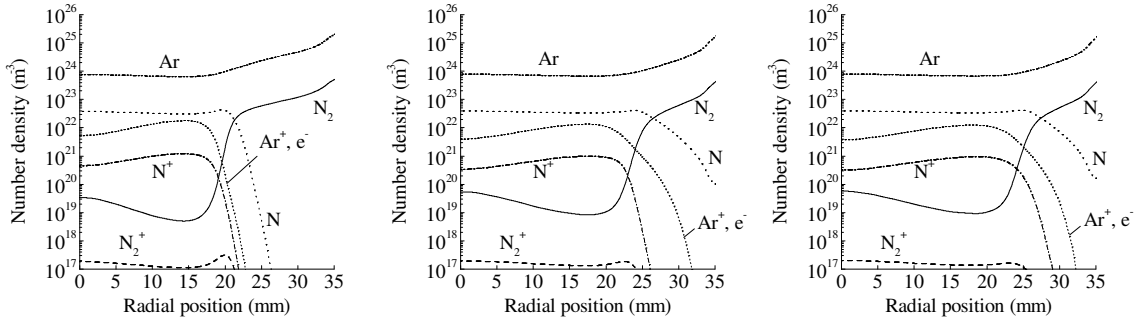

(a) 1T-CE model. (b) 1T-NCE model. (c) 2T-NCE model.

Fig. 8. Radial distribution of particle composition at axial position of 155 mm by three different models.

effect in the 1T-CE model. On the other hand, the 1T-NCE model has a similar electron density distribution to the 2T-NCE model although the 2T-NCE model has higher one near the wall.

Nitrogen atom density distribution is indicated in Fig.7. The existence of nitrogen atom is extended to the reaction chamber. The NCE models simulate wider radial distribution profile than the 1T-CE model. Figure 8 shows radial distribution of particle composition at an axial position of 155 mm. From this figure, it is seen that the two NCE models predict similar composition distributions. However, the 1T-CE model has much lower density of electron, nitrogen atom, and ions at $r > 22$ mm. For the simulation of spatial distribution of particle density, it is proved that chemical non-equilibrium effect cannot be negligible rather than thermal non-equilibrium effect in this calculation condition.

4. Conclusions

A self-consistent chemical and thermal non-equilibrium model for Ar-N_2 inductively coupled thermal plasma (ICTP) was developed considering effects of diffusion, convection, reaction rates in two-temperature state, without the local thermal equilibrium (LTE) assumption. As a result, it was found that chemical equilibrium state substantially affects the distribution of the particle composition and the temperature rather than thermally non-equilibrium effect. This deviation among the LTE and non-equilibrium models mainly arises from the diffusion in the radial direction. Therefore, the diffusion effect should be considered for accurate understanding in such the plasma processing condition treated in the present paper.

References

[1] M.I.Boulos, P.Fauchais, E.Pfender - Thermal Plasmas, Fundamentals and Applications, **I**, Plenm Press (1994).
[2] J.Mostaghimi, M.I.Boulos - Plasma Chem. Plasma Process, **9**, 25 (1989).
[3] Y.Tanaka, T.Sakuta - J. Phys. D: Appl. Phys., **35**, 2149 (2002)
[4] Y.Tanaka, T.Sakuta - J. Phys. D: Appl. Phys., **35**, 468 (2002)
[5] Y.Tanaka, T.Sakuta - Joint Int. Plasma Symp. of 6th APCPST, 15th SPSM, OS2002 & 11th KAPRA, No.204 (2002)
[6] Y.Tanaka, T.Sakuta - Plasma Sources Sci. & Tech., **12**, 69 (2003)
[7] M.G.Dunn and K.A.Lordi - AIAA Journal, **8**, 339 (1970).
[8] T.G.Owano, C.H.Kruger, R.A.Beddini - AIAA Journal, **31** 75 (1993).
[9] A.V.Phelps - J. Phys. Chem. Ref. Data, **20**, 557 (1991).

NOx and Soot Reduction Using Dielectric Barrier Discharge and Selective Catalytic Reduction in Diesel Exhaust

Min Suk Cha, Young-Hoon Song, Jae-Ok Lee, and Seock Joon Kim

Emission Control Group, Korea Institute of Machinery & Materials, Daejeon, Korea

Abstract

A combined De-NOx technique of non-thermal plasma and selective catalytic reduction (SCR) using NH_3 has been investigated to remove NOx from a 300 hp marine diesel engine exhaust under low temperature conditions (100–200 ^oC). As results, De-NOx efficiency for combined process was increased from 20 to 80 % at 100 ^oC compared to SCR sole process. From the measurement of smoke-meter, over 45 % of PM were reduced and the size distribution of PM was significantly altered after plasma process.

1. Introduction

Recently, we are faced with the elevated regulation of NOx from combustion exhaust gases, because it caused smog, an acid rain, and a respiratory disease. Available technologies for aftertreatment of NOx, for instance, are three-way catalyst and selective catalytic reduction (SCR) used for gasoline engines and stationary combustion systems, respectively. However, since the three-way catalyst should be operated in stoichiometry, it can not be adopted to lean burn engines such as diesel engines. For a SCR technique especially using NH_3 as a reducing agent, though it shows a good performance for oxygen contained flue gases, there is the limitation of operating temperature – normally its operating temperature is above 300 ^oC, so that de-NOx efficiencies are quite poor in low temperature range. In this reason, NH_3 SCR can not be used for low temperature flue gases in many stationary combustion systems as well as mobile engines which have a stop-and-go features. In these regards, catalytic processes combined with non-thermal plasma can be considered as one of the promising candidate for treating NOx from lean burn engines with low temperature exhaust, and recently many of researchers had a interest on this field [1-4]. Another main hazardous product in diesel engines is particulate matter (PM), which is generally formed from soot particles. Since diesel engines are operated with a diffusion flame, soot particles are inevitable.

In the present study, we investigated the effects of non-thermal plasma combined with conventional NH_3 SCR process on NOx treatment in marine diesel engine exhaust with emphasis on the increasing de-NOx efficiencies in low temperature range, i.e., 100-200 ^oC. The principles and illustrative test results of the combined De-NOx process of SCR and plasma techniques were well introduced in recent researches [1, 2]. A dielectric barrier discharge (DBD) was considered as the source of non-thermal plasma. We designed and constructed a planar type DBD, which showed a good performance even in humid and highly sooting conditions. Fundamental investigations, such as NO to NO_2 conversion characteristics with DBD, the effects of additives were also made with a simulated gas. In addition, the size variation and reduction of PM with the DBD reactor will be discussed.

2. Experiment

To investigate the basic characteristics of a non-thermal plasma and SCR processes, we first considered a lab-scale experiment with a diesel exhaust-like simulated gas. Figure 1 shows the schematic of lab-scale experimental setup. The apparatus consisted of a gas supply system, a mixing and preheating unit, a constant temperature furnace, a DBD reactor and a power supply, a SCR reactor, and measurement systems. To simulate a diesel exhaust, mass flow controllers were used for compressed air, N_2, CO_2, NO, and C_3H_6. Here, propylene was used for representing unburned hydrocarbons and the effect of water vapor was not considered for simplicity. The gas compositions are listed in Table 1, which correspond to 25 % load condition in marine diesel engine used in the present study. The flowrate of ammonia, as a reducing agent in SCR process, was also controlled with MFC, and it was fixed as much as the amount of NOx. Total flow-rate of simulated gas was fixed at 20 slpm for lab-scale test.

To identify the effects of operating temperature on each process, the DBD and SCR reactors were located in the constant temperature oven. The simulated gas was mixed and heated up to target temperature within the mixing and preheating unit, then it was introduced to the DBD reactor. The composition of gas was measured by Fourier transform infrared spectroscopy (FTIR, vector33, Bruker) at three different points – the inlet and outlet of the DBD reactor, and the outlet of the SCR reactor. These three points represent an initial condition,

the effects of plasma, and the role of a catalyst, respectively.

Table 1 Composition of diesel exhaust-like simulated gas

O_2 [%]	CO_2 [%]	NOx [ppm]	HC [ppm]
17.6	4.35	550	116

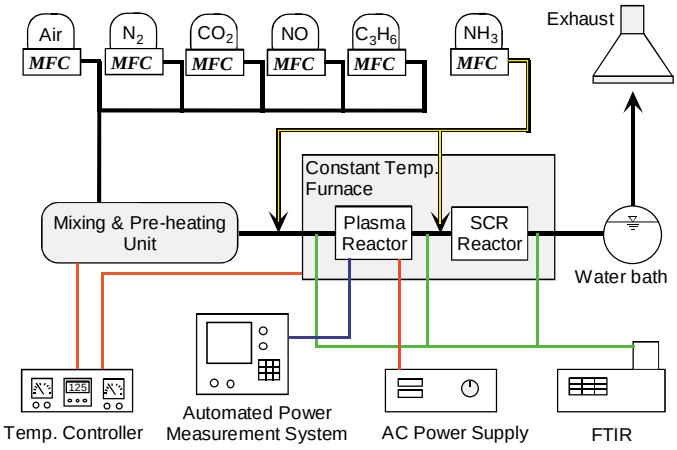

Fig. 1 Schematic of lab-scale experimental setup.

As shown in Fig. 2, the dielectric barrier discharge (DBD) reactor, which was constructed by stacking up a planar electrode together with spacers for gas flow, was used as a non-thermal plasma source. The planar electrode consisted of two α-Al_2O_3 ceramic plates bonded each other. At one of the attached surface, a silver paste was coated. AC power supplies with 60Hz and 10kHz frequencies were used separately for the lab-scale test and a pilot-scale test, respectively to supply adequate electric power in each experiment. The delivered electric power was measured by automated power measurement system using a charge-voltage diagram (Lissajous diagram) [5] with an additional capacitor of 2 μF. For SCR process, commercialized NH_3 SCR catalyst (SK Corp.) was used.

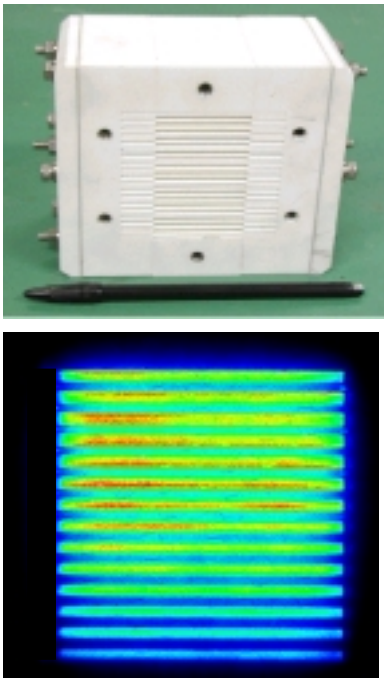

Fig. 2 Planar type DBD reactor and discharge images with ICCD camera.

Fig. 3 Pilot-scale plasma/SCR combined system with marine diesel engine.

To investigate the practical applicability of the plasma/SCR combined process to real diesel exhaust, 300 hp rating marine diesel engine (Yanmar) was used. 100 Nm^3/h was bypassed from a main exhaust stream, while the total flow-rate is about 1,000 Nm^3/h at full load condition. Note that at this flow-rate Q = 100 Nm^3/h,

space velocities are *S.V.* = 4,500/h and 450,000/h for the catalyst and the plasma reactor, respectively. NOx removal efficiencies were also measured with the FTIR spectrometer.

3. Results and Discussion

Effects of Non-thermal Plasma on NOx

In general, important chemical reactions relating to NO and NO_2 are as follows.

$$NO + N \rightarrow N_2 + O \quad (1)$$
$$NO + O + M \rightarrow NO_2 + M \quad (2)$$
$$NO + O_3 \rightarrow NO_2 + O_2 \quad (3)$$
$$NO + OH + M \rightarrow HNO_2 + M \quad (4)$$
$$NO + HO_2 \rightarrow NO_2 + OH \quad (5)$$
$$NO_2 + N \rightarrow N_2O + O \quad (6)$$
$$NO_2 + OH + M \rightarrow HNO_3 + M \quad (7)$$
$$NO_2 + O \rightarrow NO + O_2 \quad (8)$$

As can be seen in Eqs. 1-8, radicals or molecules such as O, O_3, OH, N, and HO_2 are needed in the reactions. Since non-thermal plasma was known to make lots of chemically active species, we used a DBD as the source of radicals.

In N_2/O_2 mixtures, much of input energy could be used for O_2 dissociation rather than N_2 dissociation [6]. Furthermore since Eq. 1 is relatively slow reaction, the reactions relating to N radical can not be considered for simplicity. In the present lab-scale experiment, we did not consider the effects of H_2O. In this regard, Eqs. 2, 3, and 8 can be important reactions. These O and O_3 involved reactions are composed with the oxidation of NO to NO_2 and the backward conversion of NO_2 to NO. In this point of view, one can conceive that at certain thermodynamic state including a concentration and temperature the reactions can be equilibrated, i.e., NO to NO_2 conversion can be saturated with the input power of plasma.

Figure 4 shows NO to NO_2 conversion efficiencies along with a SED (specific energy density) defined as input energy per the unit volume of a gas to be treated, i.e., SED = input power for plasma generation/gas flow-rate. Here, the rectangle and circle symbols indicate simulated mixtures with and without HC (C_3H_6), respectively, and conversion efficiency was defined by the volume fraction of NO_2 for the total amount of NOx. As shown in the figure, for the case without HC, NO_2 conversion rate is relatively insensitive to SED demonstrating saturated feature at about 13 %. However, owing to the addition of HC, the production of NO_2 is significantly increased, for instance 45 % of NO is oxidized to NO_2 at SED = 200 kJ/m^3. It is to be noted that the change of total amount of NOx ($NO + NO_2$) was negligible for both conditions, meaning that with the sole process of non-thermal plasma NOx can not be reduced to nitrogen.

The increase of NO to NO_2 conversion efficiency with the addition of propylene can be explained as follows. Propylene can be partially oxidized with the aid of O radical, and through this partial oxidation lots of reactive species can be produced with a chain reaction [7]. Chemical reactions relating these species are

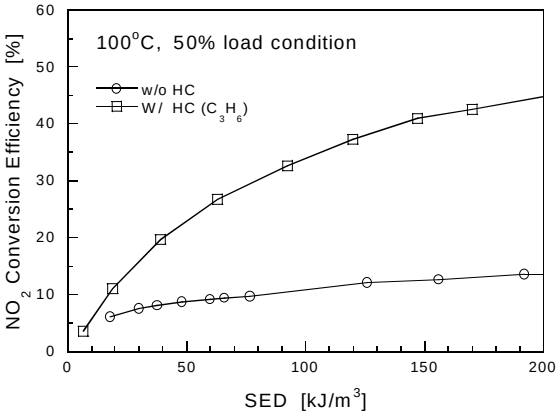

Fig. 4 NO_2 conversion rate with SED for 50 % load condition.

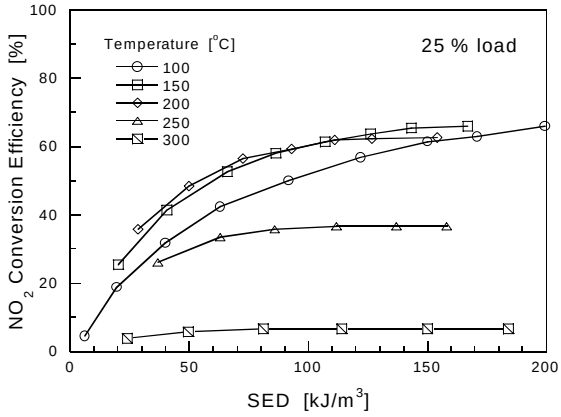

Fig. 5 NO_2 conversion rate with various operating temperatures for 25 % load condition.

$$NO + CH_3O_2 \rightarrow NO_2 + CH_3O \quad (9)$$
$$NO + O_2C_2H_4OH \rightarrow NO_2 + OC_2H_4OH. \quad (10)$$

Above reactions are known as faster than Eqs. 2, 3. Furthermore in defect of O radical, the backward reaction of NO_2 to NO in Eq. 8 can be decreased. In this reason, high conversion efficiency can be obtained with the addition of HC. In Fig. 5, we plotted NO to NO_2 conversion efficiencies for various operating temperatures with the simulated gas of 25 % load condition. As can be seen, at 150 and 200 ^oC NO_2 conversion exhibits its optimum, while the conversion became deteriorated as the temperature increases. It partly because the temperature sensitive characteristic of reaction 8 than Eqs. 2, 3, 9, and 10, i.e., NO_2 to NO conversion reaction prevail over the NO oxidation at high temperatures.

Characteristics of Plasma/SCR Combined Process

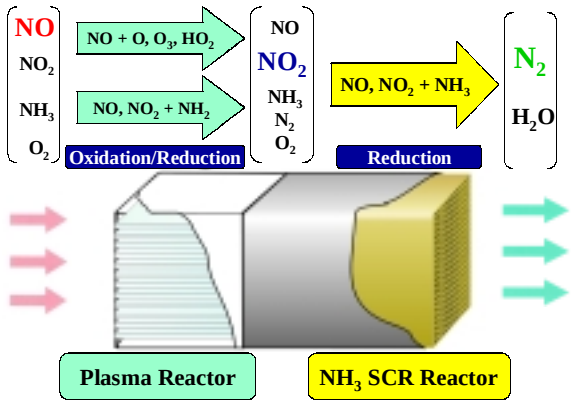

Fig. 6 Concept of plasma/SCR hybrid system.

As discussed in the previous section, NOx can not be reduced to nitrogen with non-thermal plasma process in the presence of oxygen. Some portion of NO was oxidized to NO_2 demonstrating negligible change of the total amount of NOx. In this regard, NH_3 SCR process was adopted after the plasma process to achieve the full reduction of NOx. In Fig. 6, the concept of plasma/SCR combined process was depicted. As shown in the figure, plasma and SCR reactors are connected in series. In combustion flue gases, over 90 % of NOx consisted of NO. A plasma reactor converts NO to NO_2 at certain amount. Some portion of NO can be reduced by NH_2 radical within the plasma reactor. Then $NO+NO_2$ reduced to N_2 in NH_3 SCR reactor, since NO_2 or $NO+NO_2$ mixture could be more easily reduced at low temperature [1]. Above arguments will be elaborated later.

Chemical reactions concerning NOx reduction in NH_3 SCR process are

$$4NO + 4NH_3 + O_2 \rightarrow 4N_2 + 6H_2O \quad (11)$$
$$6NO + 8NH_3 \rightarrow 7N_2 + 12H_2O \quad (12)$$

However, for the mixture of $NO+NO_2$, the below overall reaction is known as a dominant mechanism [1].

$$NO + NO_2 + 2NH_3 \rightarrow 2N_2 + 3H_2O \quad (13)$$

In addition, when NH_3 was injected before a plasma reactor, NH_2 radical produced from NH_3 by a plasma process also affects to NOx [1].

$$NH_2 + NO \rightarrow N_2 + H_2O \quad (14)$$
$$NH_2 + NO_2 \rightarrow N_2O + H_2O \quad (15)$$

From the reaction 15, undesirable N_2O formation occurred through a plasma process, however, in the present experiment, N_2O leakage can not be detected after SCR reactor.

Since over 90 % of NOx can be reduced to N_2 above 250 ^oC using a NH_3 SCR process, to identify synergetic effects with plasma process operating temperatures were varied from 100 to 200 ^oC. In Fig. 7, we plotted NOx reduction rates for the non-thermal plasma, the NH_3 SCR, and the plasma/SCR combined processes. As shown in the figure, for the plasma sole process with SED = 84 kJ/m^3, about 30 % of NOx is removed irrespective of temperature through Eqs 14 and 15. On the contrary, for the SCR sole process, it shows significant dependence on temperature. At 100 ^oC, NOx reduction rate is about 20 %, while it reaches about 85 % at 200 ^oC. However, the NOx reduction rate is dramatically changed for plasma/SCR combined process

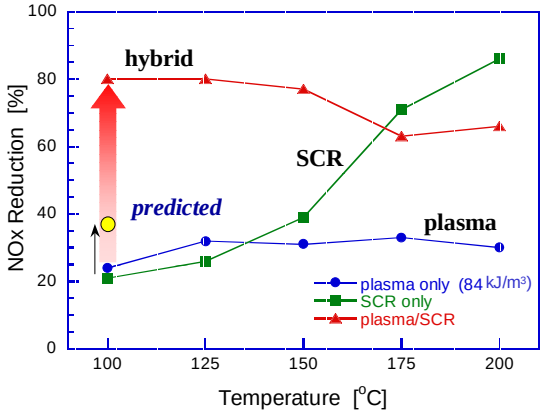

Fig. 7 NOx reduction efficiencies for various processes.

in relatively low temperature. About 80 % of NOx can be reduced through the plasma/SCR combined process in the temperature range of 100-150 °C. As depicted in Fig. 7 for 100 °C, the arithmetic sum of NOx reduction rate for plasma/SCR combined process is about 36 %, i.e., 20% (plasma) + 80% (remained portion of NOx relative to the initial amount after plasma reactor) × 20% (SCR performance) = 36%. While it reaches at 80% for combined process demonstrating synergetic effect of combining two processes. To clarify the synergetic result, we investigated de-NOx efficiencies for SCR sole process with NO and NO_2 separately. As results, NO_2 can be more easily reduced at low temperature compared to NO. In this reason, converted NO_2 within the plasma reactor can raise a reduction rate in SCR process. It is to be noted that a NOx reduction rate for a mixture of NO+NO_2 showed its optimum at around $[NO_2]/[NOx]$ = 0.4 to 0.6, which is agree with Eq. 13. However, de-NOx performance of combined process was deteriorated compared to SCR process over 170 °C. Through a parametric test with additives, we concluded that this result was originated from the HC addition. It was found that HC can serve as a reducing agent in catalytic process, while it reduced NO_2 to not N_2 but NO.

NOx Removal in Diesel Engine Exhaust

To investigate the applicability of the combined process in diesel engine exhaust, we construct the 100 Nm^3/h rating pilot-scale plasma/SCR combined system as shown in Fig. 3. The plasma reactor operated excellently with highly humid and sooting condition. Since the NO to NO_2 conversion in plasma reactor was mainly related to the amount of HC addition as well as input powers, first we investigated NOx reduction rates of combined system for various input powers and HC addition. Figure 8 shows the NOx reduction efficiencies along with the normalized C_3H_6 concentration for various input power conditions at 100 °C. As results, since de-NOx efficiency is saturated at about 80%, we chose the combination of SED = 40 kJ/m^3, which corresponds to 1.1 kW input power with flow-rate of 100 Nm^3/h, and $[C_3H_6]$ = 1.5[NOx] = 800 ppm as an operating condition. Note that to determine an operating condition in commercial applications the comparison of fuel cost between making electricity with engine and supplying HC should be made.

Figure 9 shows the NOx reduction rate for plasma/SCR combined system together with SCR sole process along with operating temperatures. Generally, combined process exhibits superior performance to SCR sole process. For instance, at 100 °C 20% NOx reduction occurs with SCR sole process, while 80% of NOx can be reduced with plasma/SCR combined system. Furthermore, contrary to the results in Fig. 7, even at 200 °C 90% of NOx is reduced with combined system, while 55% reduction is obtained using the SCR sole process. It is to be noted that the portion of converted NO_2 in total NOx is in the range of 60 – 70% as shown in Fig. 9.

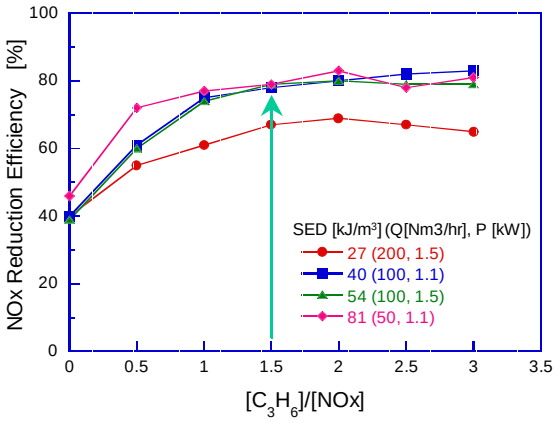

Fig. 8 NOx reduction efficiencies for various operating conditions.

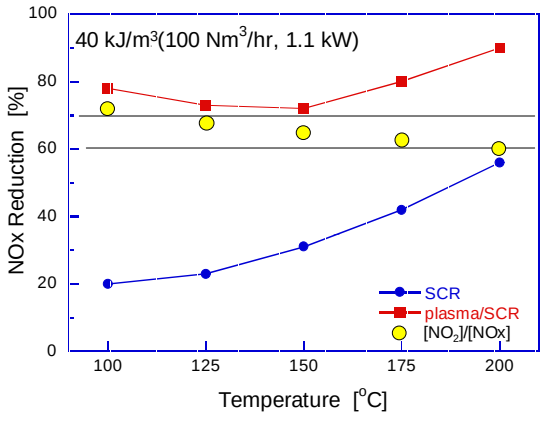

Fig. 9 NOx reduction efficiencies for SCR and combined system together with the percentage of $[NO_2]/[NOx]$ along with temperature.

To apply the combined system to the full-scale 300 hp rating diesel engine exhaust, we estimate the power consumption of the plasma reactor to be 5-6 kW approximately. This power can cover about 500 Nm^3/h, which can be enough for a warming up period considering that the exhaust flow-rate is about 1,000 Nm^3/h at full load. Since the estimated power corresponds to 2 % of the engine power, and moreover the plasma reactor should be turned off after exhaust temperature increases, probably the operating cost of the plasma reactor does not matter in practical applications. In addition, the degradation of catalyst from unwanted byproduct such as ammonium nitrate can be fixed by occasional high temperature (>250^oC) operations.

Effects of Non-thermal Plasma on PM

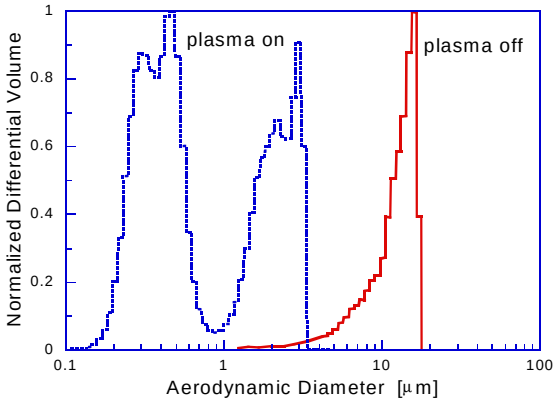

Fig. 10 Effect of plasma on the size distribution of PM in diesel exhaust.

Through the present pilot-scale test, it was also found that the present planar type DBD can be effective to change the emission characteristics of PM. The size distribution and blackness of PM were measured at the outlet of the plasma reactor using a particle size analyzer and a smokemeter, respectively. Figure 10 shows the size variation of PM. As shown in the figure, the initial distribution pattern (solid line) is significantly altered by the plasma process (dotted line). With the aid of the plasma process the average size of PM is quite reduced to the order of 1 μm demonstrating the double peak of its distribution. While the average size is in the order of 10 μm for the untreated PM. Since the reduction of average size means the increase of total surface area of PM, this result can be helpful to a continuously regenerative DPF system, which used NO_2 as an oxidizing agent for PM. Furthermore, 45% reduction in the blackness can be observed with the plasma process. From the above results, we can conceive that through the plasma reactor mass reduction can be possible as well as its average size reduction. However, at present, detailed mechanism of PM reduction is not clear, and further investigation will be a future study.

4. Concluding Remarks

Non-thermal plasma process combined with conventional NH_3 SCR process was successfully applied to the marine diesel engine exhaust. To treat 550 ppm of NOx from the diesel engine, we chose the flow-rate of 100 Nm^3/hr, electric power of 1.1 kW (SED=40 kJ/m^3), and 800 ppm C_3H_6 addition among the various optimal operating conditions. As results, de-NOx efficiencies for combined process were increased from 20 to 80 % and from 55 to 90% at 100 and 200 ^oC, respectively compared to SCR sole process. We estimated that the power consumption is about 2 % of engine power.

In addition to the NOx reduction, we found that PM in the diesel exhaust, mainly consisted of soot, was affected by the plasma process. From the measurement of smoke-meter, over 45 % of PM were reduced after plasma process. Furthermore, the size of PM is significantly decreased. It suggested that the non-thermal plasma process can be a viable method for PM reduction or assisted one for other DPF systems.

Acknowledgement: This work was supported by National Research Lab. program of the Korean Ministry of Science and Technology and Clean Energy program of the Korea Energy Management Corporation/R&D center.

References

[1] S. Bröer and T. Hammer - *Appl. Catalysis B* **28**, 101 (2000).
[2] J. Hoard and M. L. Balmer – SAE paper 982429 (1998).
[3] T. Hammer – SAE paper 2000-01-2894 (2000).
[4] J. Hoard, P. Liang, M. L. Balmer – SAE paper 2000-01-2895 (2000)
[5] R. Feng, G. S. P. Castle, and S. Jayaram - *IEEE Trans. Ind. App*. **34**, 563 (1998).
[6] B. M. Penetrante – NATO ASI series G **34**, 65 (1993).
[7] E. A. Filimonova, Y. Kim, S. H. Hong, and Y.-H. Song - *J. Phys. D: Appl. Phys*. 35, 2795 (2002).

Comparison of PFCs Decompositions between Glow and Streamer Mode in Dielectric Barrier Discharges

Yongho Kim, Kwan-Tae Kim, Min Suk Cha, Young-Hoon Song, and Seock Joon Kim

Emission Control Group, Korea Institute of Machinery and Materials, Daejeon, Korea

Abstract

Using a dielectric barrier discharge (DBD), CF_4 removal characteristics are investigated for a N_2 streamer discharge and a He glow discharge. The optimal concentration of oxygen was ranged 500 ppm ~ 1 % for treating 500 ppm of CF_4. In N_2 streamer discharge, CF_4 can be more easily removed with 3 mm discharge gap, compared with 1 mm discharge gap. Helium glow was the most efficient one to remove CF_4. Experimental results were compared in view of an effective plasma volume.

1. Introduction

Perfluorocompounds (PFCs), such as CF_4 and NF_3, have been widely used in a semiconductor industry as a plasma etching gases. Since these PFCs are known to cause a greenhouse effect intensively, there has been a growing interest in reducing PFCs emissions. Among various PFCs decomposing techniques, a dielectric barrier discharge (DBD) is considered as one of a promising candidate because it has been successfully used for generating ozone (O_3) and decomposing nitrogen oxide (NO). In NO decomposition, energetic streamers in DBD produce numerous radical species, such as O and N in air. The O radicals oxidize NO to NO_2 ($NO + O \rightarrow NO_2$). The N radicals reduce NO to N_2 ($NO + N \rightarrow N_2 + O$). In CF_4 decomposition, however, CF_4 rarely reacts with radical species, even though dissociated fluorine compounds, such as CF_3, CF_2, and CF, show a good reactivity with O radicals [1, 2]. For a successful CF_4 decomposition, therefore, an electron interaction with CF_4, *primary reaction*, is essentially needed in advance of a radical reaction with CF_4, *secondary reaction*. Table 1 shows a CF_4 decomposing mechanism by the DBD plasma, where an electron is represented by "e".

Table 1. CF_4 decomposition mechanisms by DBD plasma [1]

Primary Reaction		Secondary Reaction		
$e + CF_4 \rightarrow CF_3 + F^-$	: 4.8 eV (1)	$CF_3 + O \rightarrow COF_2 + F$	: 3.16×10^{-11} cm^3s^{-1}	(4)
		$COF_2 + O \rightarrow CO_2 + F_2$	: 5.30×10^{-11} cm^3s^{-1}	(5)
$e + CF_3 \rightarrow CF_2 + F^-$	: 3.0 eV (2)	$CF_2 + O \rightarrow CFO + F$	: 2.17×10^{-11} cm^3s^{-1}	(6)
		$CFO + O \rightarrow CO_2 + F$	: 4.98×10^{-11} cm^3s^{-1}	(7)
$e + CF_2 \rightarrow CF + F + e$	: 4.55 eV (3)	$CF + O \rightarrow CO + F$	: 1.24×10^{-11} cm^3s^{-1}	(8)
		$CO + O \rightarrow CO_2$	: 6.52×10^{-11} cm^3s^{-1}	(9)

A first work in this experiment was to find how many primary reactions are associated with the streamer mode in DBD. Considering secondary reaction, finding the optimal concentration of oxygen was next. Finally, influences of an *effective plasma volume* (= plasma volume / reactor volume) on the CF_4 decomposition were studied by means of (1) varying a discharge gap distance of DBD reactor and (2) a glow mode operation with a helium gas.

2. Experimental Methods

Figure 1 shows the schematics of a coaxial-cylinder DBD reactor. A quartz tube with 27 mm diameter and 350 mm length was employed as a dielectric barrier. Outside of this quartz tube, a grounded mesh electrode was wrapped. The quartz tube and the mesh electrode was cooled by a flowing water. An inner metal electrode with 23 mm diameter was water cooled as well. A discharge gap distance between inner rod and outter quartz was 3 mm. Through the discharge gap, a nitrogen gas was supplied with 2 slpm. A 1000 ppm of an oxygen was added as for an O radical sources. Initial CF_4 concentration was fixed at 500 ppm. AC voltage, fixed at 10 kHz, was applied to the inner rod electrode. During this experiment, external electric power was varied from 0.75 kW to 1.5 kW. A discharge voltage and a current were measured with

Oscilloscope (LeCroy). A discharge power delivered into the DBD reactor was measured by means of the Lissajou diagram method. A FTIR (Brooker) was used for the measurements of species concentrations.

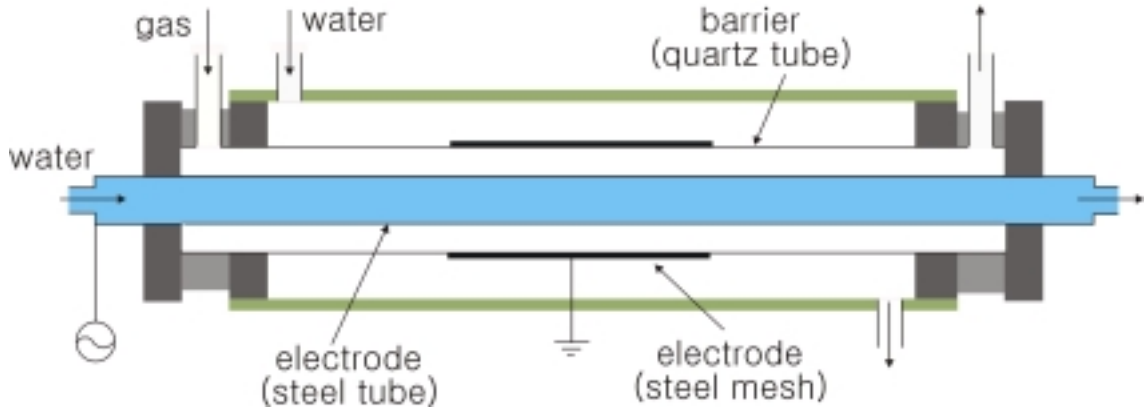

Figure 1. Schematic diagram of a coaxial-cylinder DBD reactor.

3. Results and Discussion

CF_4 Decomposition with Streamer in DBD

Figure 2(a) shows CF_4 removal efficiencies for various input powers in a pure nitrogen discharge (solid line) and a nitrogen discharge with 0.1 % of oxygen (dashed line). Each DBD reactor volume was filled with filamentary streamers at a tested input power from 0.75 to 1.5 kW. With these streamer discharges, 500 ppm of CF_4 was removed linearly with increasing input power. In a pure nitrogen discharge (solid line), 8.6 % of CF_4 was removed at 0.75 kW and 23.2 % at 1.5 kW. Considering 2 slpm of the nitrogen gas, a discharge energy density was reached up to 34 MJ/m^3 at input power of 1.5 kW. Though a great amount of discharge energy was delivered into the DBD reactor volume, the decomposition efficiency of CF_4 was quite low in streamer operation. Noting a similar dissociation rate between N_2 and CF_4, inefficient CF_4 decomposition can be caused by a poor *effective plasma volume* (= plasma volume / reactor volume) of streamer. In a nitrogen discharge with 0.1 % of oxygen (dashed line), about 10 % enhancement of removal efficiency was obtained. Though O radical does not react with CF_4 molecule directly, O radical can oxidize CF_3 to COF_2 (reaction 4, in Table 1). Owing to the stabilization of CF_3 by O radical, the recombination of CF_3 with F can be decreased, as a result, decomposition efficiency of CF_4 was increased. From the FTIR spectrum shown in Fig. 2, COF_2 is further oxidized by another O radical (reaction 5, in Table 1) and then it is converted into CO_2, of which spectra was increased during the oxidation process.

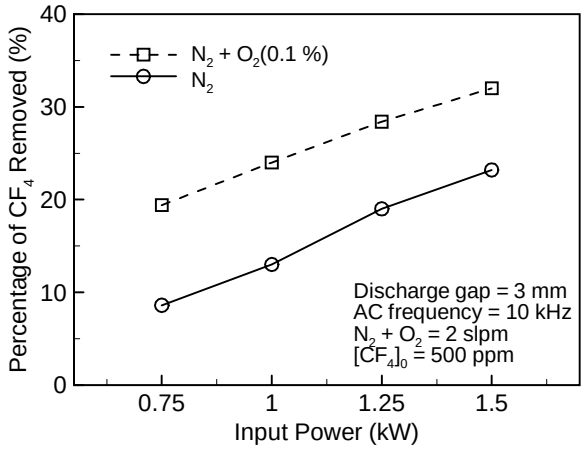

Figure 2(a). CF_4 removal in N_2 and N_2+O_2.

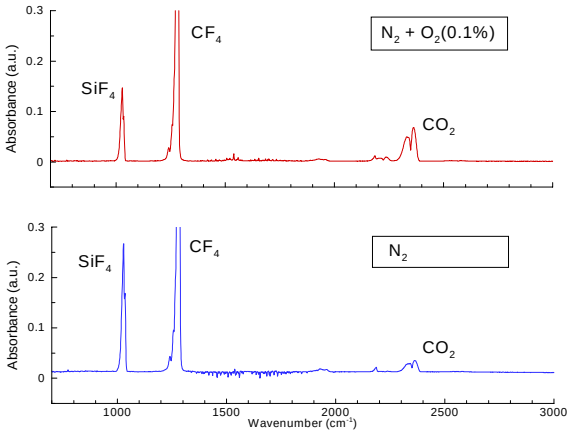

Figure 2(b). FTIR spectrum at 1.5 kW input power.

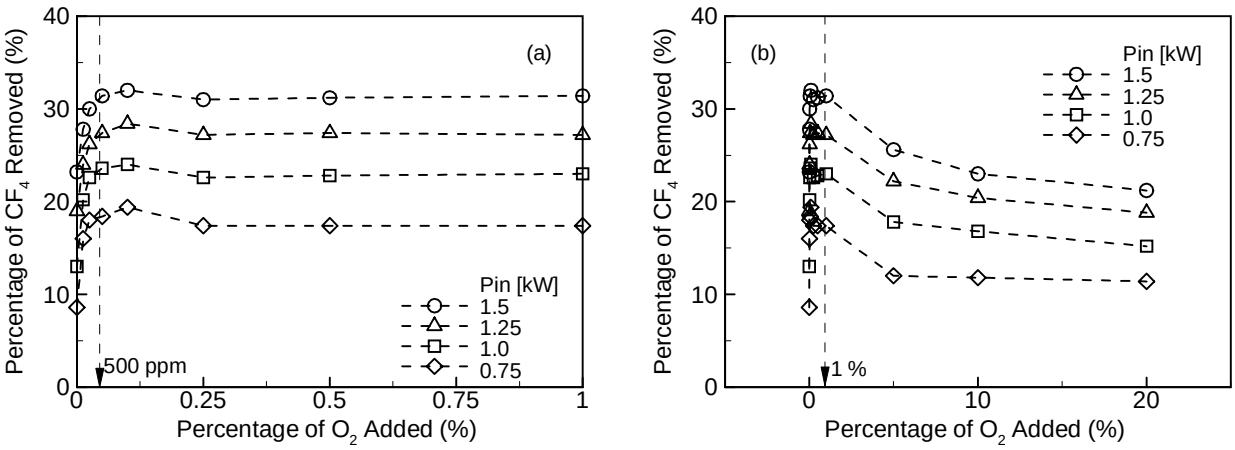

Figure 3. Percentage of CF_4 removed for various oxygen concentrations.

To find the optimal concentration of oxygen, which means the minimization of the recombination as well as the maximization of CF_4 decomposition, we investigated the effect of O_2 concentration. In Fig. 3(a), as O_2 concentrations increase until it reaches 500 ppm, CF_4 removal was gradually increased. For instance, at input power 1.5 kW (circle symbol), CF_4 removal reached 32 % at O_2 = 500 ppm, compared with 23 % at O_2 = 0 ppm. For further increase of O_2 in the range of 500 ppm ~ 1 %, CF_4 removal characteristics were insensitive to O_2 concentration. On the other hand, as O_2 concentrations increase over 5 %, CF_4 removal was decreased as decreased as shown in Fig. 3(b). Decreasing electron density due to excessive oxygen molecules can cause to decrease primary reactions of CF_4.

To clarify the dependence of initial CF_4 concentration, removal characteristics were investigated for various initial CF_4 concentrations. For all tested conditions, the amount of O_2 addition was fixed at 0.1 %. In Fig. 4(a), the removed CF_4 concentrations increased linearly with increasing initial CF_4 concentrations in the range of 100 ~ 500 ppm. Consequently, at the same input power, the same removal efficiency can be obtained regardless of initial CF_4 concentrations, shown in Fig. 4(b). This result means that electron density in streamer could be already enough to decompose both 100 ppm and 500 ppm of CF_4. At a given input power, the same effective plasma volume can result in the same decomposition efficiency even for different initial CF_4 concentrations. Moreover, it can also be considered that increasing input power plays a role to increase effective plasma volume rather to increase electron density.

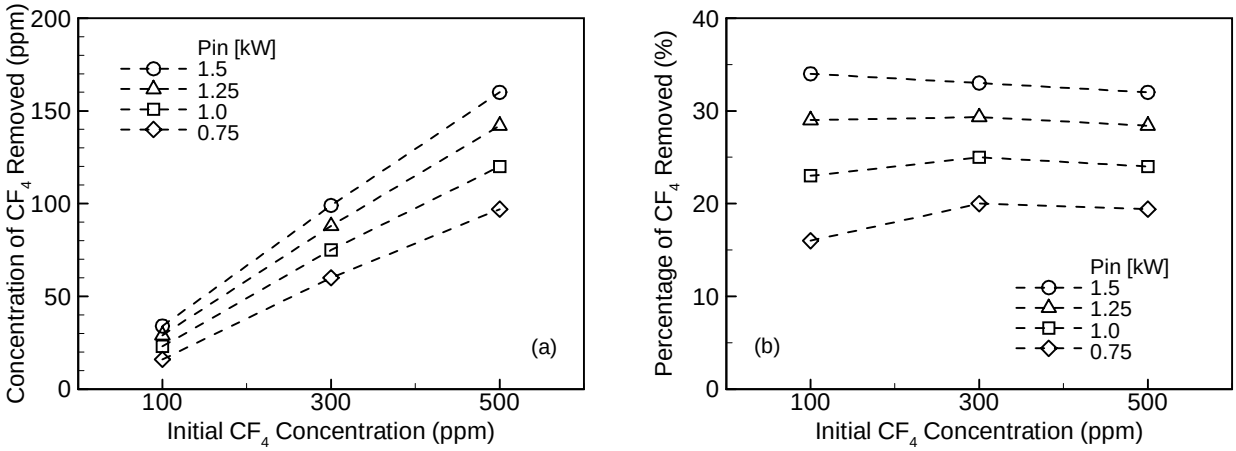

Figure 4. (a) Concentration of CF_4 removed, (b) percentage of CF_4 removed for different initial CF_4 concentration

Influences of Effective Plasma Volume on CF_4 Decomposition

Maintaining experimental conditions as the same as those in previous one, at first, discharge gap distance (*d*) of DBD reactor was reduced from 3 mm to 1 mm. In *d* = 1 mm operation, streamers were also observed to

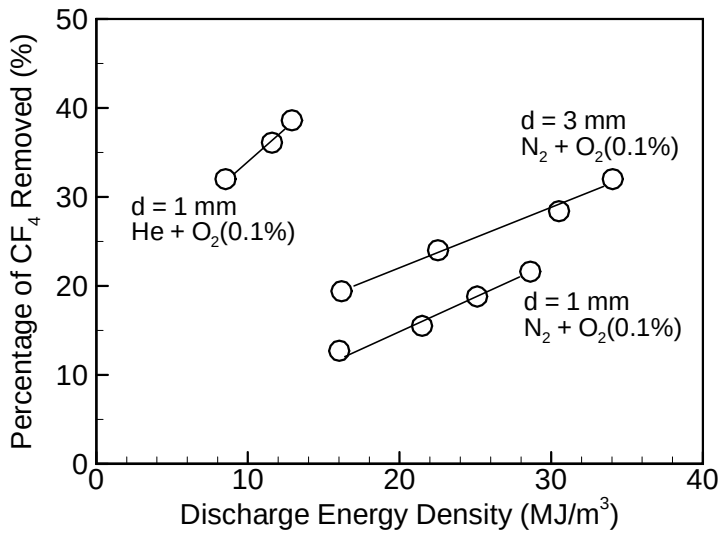

Figure 5. CF_4 removal for d = 3 and 1 mm, and for N_2 and He

fill up DBD reactor. In Fig. 5, CF_4 removal efficiencies are plotted as a function of discharge energy density in unit of J/m^3. As can be seen in Fig. 5, CF_4 removal efficiencies in d = 1 mm were decreased, compared with d = 3 mm. To analyze this experimental result, an effective plasma volume (V_s/V_r) was employed, which was originally derived by Rosocha [3] with considering an energy balance, $\varepsilon_r V_r = \varepsilon_r V_s$. Here, ε_r is total discharge energy per unit volume, V_r is a reactor volume, ε_s is streamer energy per unit volume, and V_s is a streamer volume. Defining the effective plasma volume as $F = V_s/V_r = \varepsilon_r/\varepsilon_s$, a ratio of F at d = 3 mm (F_3) to F at d = 1 mm (F_1) was represented as follows;

$$\frac{F_3}{F_1} = \frac{\varepsilon_{r,3}/\varepsilon_{s,3}}{\varepsilon_{r,1}/\varepsilon_{s,1}} \sim \left(\frac{\varepsilon_{r,3}}{\varepsilon_{r,1}}\right)\left(\frac{E_{s,1}}{E_{s,3}}\right).$$

In the above expression, we assumed ε_s mainly depends on average electric field at discharge gap, E_s. Measuring a discharge power using a Lissajou diagram, $\varepsilon_{r,3}$ was a little greater than $\varepsilon_{r,1}$. For instance, $\varepsilon_{r,3}$ = 23 kJ/ m^3 at 1 kW input power, compared with $\varepsilon_{r,1}$ = 22 kJ/ m^3. To estimate E_s, a gas gap voltage, V_g, was manipulated with applied voltage, V_a, and discharge current, I_d [4]. At 1 kW input power, Fig. 6 shows the measured V_a, I_d, and evaluated V_g at (a) d = 3 mm and (b) d = 1 mm, respectively. Though applied voltage at d = 1 mm was greater than that at d = 3 mm ($V_{a,1} > V_{a,3}$), the gas gap voltages evaluated for both cases were same ($V_{g,1} \sim V_{g,3}$). Based on the V_g measurement, we could estimate E_s ($=V_g/d$) for both cases, and we found $E_{s,1} \sim 3E_{s,3}$. Considering measured ε_r and evaluated E_s together, it could be concluded that F_3 is greater than F_1 in this experiment. An enhanced effective plasma volume ($F_3 > F_1$) can make the primary reaction of CF_4 increase, which result in higher CF_4 removal.

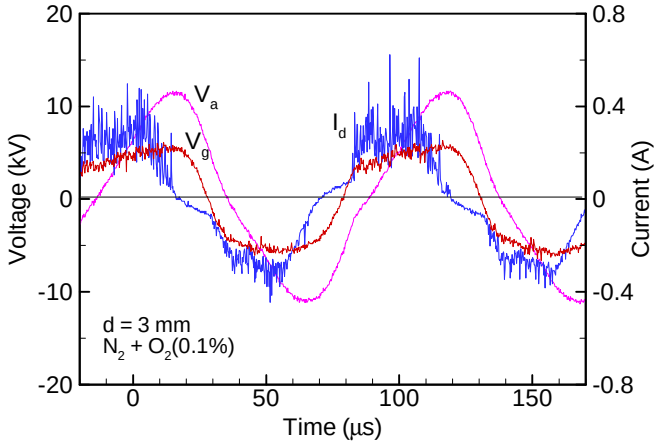

Figure 6(a). Waveforms of V_a, I_d, and V_g measeured at d = 1 mm

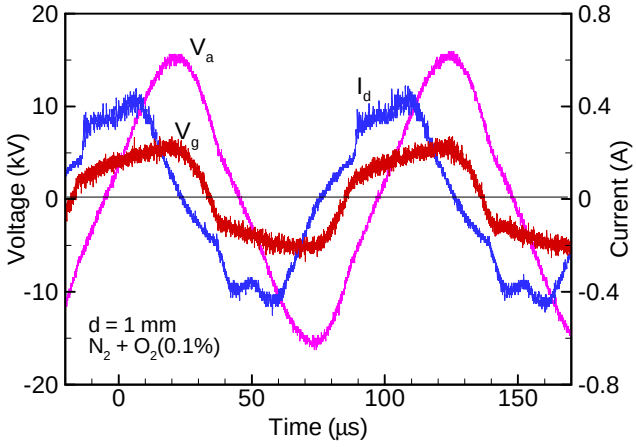

Figure 6(b). Waveforms of V_a, I_d, and V_g measeured at d = 1 mm

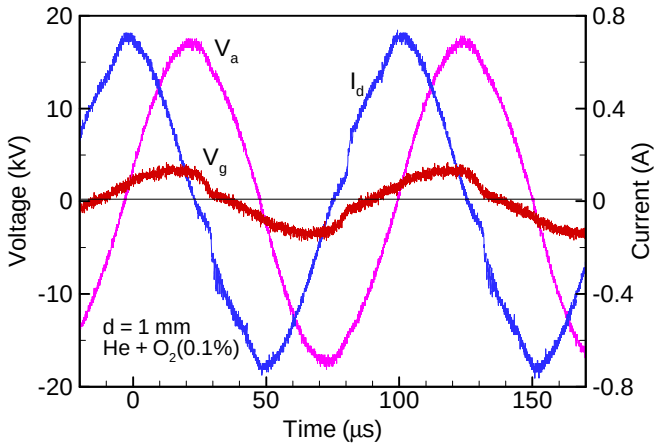

Figure 6(c). Waveforms of V_a, I_d, and V_g measeured at He discharge

Recently, there has been a growing interest in atmospheric glow discharge (AGD). Compared with streamer discharge, a spatial uniformity of AGD was one of merit for surface treatment of materials. In this CF_4 removal process, AGD is considered as a promising one because it has higher effective plasma volume. In this work, a N_2 gas was replaced with a He gas at d = 1 mm reactor. As shown in Fig. 6(c), the discharge current of He plasma did not show any current spike. Helium glow discharge with higher effective plasma volume resulted in higher CF_4 removal, as shown in previous Fig. 5.

4. Conclusion

Using a dielectric barrier discharge (DBD), CF_4 removal was examined for a streamer operation in N_2 and a glow operation in He. About 20 % of CF_4 was removed by the streamer discharge in N_2, spending 34 MJ/m^3. It was revealed that a primary reaction in streamer discharge, such as $e + CF_4 \rightarrow CF_3 + F$, is not so probable. Oxygen radical, reacting with CF_3, was helpful to inhibit a recombination (CF_3 + F), and resultantly to enhance CF_4 decomposition efficiency. However, excessive oxygen made an electron density decrease. An optimal concentration of oxygen was ranged from 500 ppm to 1 %, with which 30 % of CF_4 was removed in streamer discharge. Finally, influences of an *effective plasma volume* (= plasma volume / reactor volume) on the CF_4 decomposition were studied by means of (1) varying a discharge gap distance of DBD reactor and (2) a glow mode operation with a helium gas. As a result, higher effective streamer volume at d = 3 mm DBD caused enhanced CF_4 removal than d = 1 mm DBD in nitrogen. Helium glow was the most efficient one to remove CF_4 due to its highest effective plasma volume.

References

[1] S. J. Yu and M. B. Chang, "Oxidative Conversion of PFC via Plasma Processing with Dielectric Barrier Discharges," Plas. Chem. Plas. Proc., **21** (3), 311 ~ 327 (2001).

[2] M. Kogoma, T. Abe, and K. Tanaka, "PFCs Abatement System by the Atmospheric Pressure Glow Plasma," Proc. 8th Int. Sym. High Pressure Low Temperature Plasma Chemistry, Puhajarve, Estonia, 303 ~ 307 (2002).

[3] L. A. Rosocha, "Processing of Hazardous Chemicals using Silent-Electrical-Discharge Plasmas," Chap. 11 in *Plasma Science and the Environment* (AIP Press, New York, USA, 1997).

[4] F. Massines, A. Rabehi, P. Decomps, R. B. Gadri, P. Segur, and C. Mayoux, "Experimental and Theoretical Study of a Glow Discharge at Atmospheric Pressure Controlled by Dielectric Barrier," J. Appl. Phys., **83** (6), 2950 ~ 2957 (1998).

Plasma Synthesis of Spherical Titanium Dioxide from Titanium Nitride

S.-M. Oh[1], D.-W. Park[2], and T. Ishigaki[1]

[1] *Advanced Materials Laboratory, National Institute for Materials Science, Tsukuba, Japan*
[2] *Department of Chemical Engineering, Inha University, Incheon, Korea*

Abstract

Titanium dioxide was synthesized by in-flight oxidation of titanium nitride using inductive thermal plasma. The structure and phase composition of products depended mainly on the oxygen flow rate, and the formation mechanism of TiO_2 was investigated. The reaction was carried out initially by surface oxidation and melting, leading to core-shell structured composites with TiN cores and oxidized shells. At higher O_2 flow rate, the composites changed to anatase single crystal by rapid solidification of TiO_2 melts.

1. Introduction

Titanium dioxide has been used for a pigment, photovoltaic solar cell, photo-catalyst, gas sensor, biosensor, and optical material because of its high refraction index(>2.5), good photocatalytic activity, high resistance against chemical attack, and thermal stability. Recently, it has been a subject of interest as a photo-catalyst[1] or photonic crystal[2]. To improve the photocatalytic activity under visible light, the modification of TiO_2 has been tried to control by introduction of metal or reduction of TiO_2[3-6]. As a photonic crystal, highly ordered macroporous materials(inverse opals) or self-assembled opal-like structures[7], mono-dispersed single crystal TiO_2 spheres have been required. Many researchers reported that the structure, phase composition, and morphology relating to the key properties might be strongly influenced by synthetic conditions and additive compounds, but the mechanism was not yet cleared[8,9]. Titanium dioxide has been industrially produced by chloride and sulphate process, and recent research on the preparation of the powder tends toward sol-gel method[10,11], flame synthesis[4,12], sputtering[3], and plasma synthesis[5,6,13,14].

The present work is based on the thermal plasma process to prepare spherical titanium dioxide particles from titanium nitride particles. The purpose of this study is to prepare mono-dispersed spherical titanium dioxide and determine the main process parameter on the structure, phase composition, and morphology. We investigate the formation mechanism of anatase and rutile, and the effect of additive hydrogen in thermal plasma.

2. Experimental procedures

Fig. 1 shows the schematic diagram of experimental apparatus for preparation of TiO_2 powder by in-flight oxidation of titanium nitride. The water-cooled plasma torch(Model PL-50, TENKA Plasma System Inc., Canada) connected to a 2 MHz radio frequency power supply(Nihon Koshuha Co. Ltd., Japan) and attached a water-cooled cylindrical reactor. A water-cooled probe for injection of raw material was injected into the center of the plasma torch along the axis. As source materials, titanium nitride powder with diameter of ave. 28 ? (Nippon New Metal Co., Japan) was injected into plasma plum through the water-cooled probe using carrier gas, and the feed rate was adjusted to be about 1.5 g/min by controlling the motor speed of the powder feeder. Ar+He, Ar+O_2, or Ar+H_2 plasma was generated by mixing He, O_2, or H_2 in Ar-sheath gas, respectively. As the carrier gas, pure Ar was used in Ar+O_2 plasma, while Ar+O_2 mixing gas was used in Ar+He or Ar+H_2 plasma. The total flow rate of central and sheath gases were typically 30 l/min and 90 l/min, and the reactor pressure was controlled to about 500 torr because the filter could easily be blocked with product

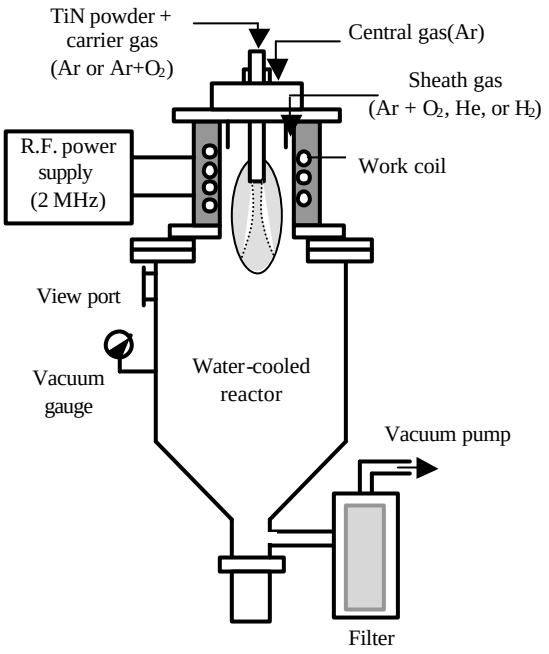

Fig. 1. Schematic diagram of a thermal plasma reactor for preparation of TiO_2 powder.

powders. The detailed experimental conditions were listed in Table 1.

Table 1 Experimental conditions

Plasma power	25kW, 40 kW
Pressure	500 torr
Plasma gas	Ar - 30 l/min
Sheath gas (total 90 l/min)	Ar + O_2(0 - 17.5 l/min) Ar + He(0 - 10 l/min) Ar + H_2(0 – 10 l/min)
Carrier gas (total 5 l/min)	Ar + O_2(0 – 2.5 l/min)
powder feed	1.5 g/min

The oxidized products were collected mainly at the reactor wall, and residual powders in exhausted gases were collected by porous metal filter. An X-ray diffractormeter(CuKa, RINT 2000, Rigaku, Japan) was used to analyze the phase compositions and particle size. Particle morphology was observed on the optical microscope and scanning electron microscope(Model S-5000, Hitachi, Japan). The internal structure of oxidized products was investigated for the cross-sectioned samples, which were embedded in polymer resin and polished with diamond paste. Micro Raman spectroscopy(NR-1800, JASCO, Japan) was used for structural analysis with a liquid nitrogen cooled CCD detector using a 100 mW Ar^+ laser.

3. Results and discussion

The synthesized powders typically consisted of micron sized bigger particles and nano-sized smaller particles: the bigger grained powders are solidified from molten species, while the smaller grained powders are derived by solidification of vaporized species. Two groups of particles could be separated from each other by sedimentation treatment after ultrasonic dispersion in a solvent where bigger powders easily sediment in short time. Fig. 2 shows the X-ray diffraction patterns of the bigger powders and smaller powders synthesized at a different O_2 flow using Ar-O_2 plasma. At a low O_2 flow rate(a), the diffraction pattern of bigger powders shows the peaks corresponding to TiN and rutile including Ti_4O_7[JCPDS 18-1402]. As the O_2 flow rate was increased, the peaks showed only the lines corresponding to TiO_2 in which anatase phase was dominated as shown in b. With the increasing O_2 flow rate, the anatase to rutile transformation might be promoted by increased exothermic reaction heat and heat transfer from plasma plum, but rutile phase was decreased. It is noted that the formation of anatase and rutile is strongly influenced by ambient oxygen pressure. Small powders are composed only of anatase and rutile regardless of O_2 flow conditions, and the size is calculated to be 50 nm by using peak patterns of Fig. 2c and d The nanopowders of anatase and rutile were derived by rapid solidification of gas mixture of TiO(g) and TiO_2(g), which are vaporized from the oxidized melts. At a higher O_2 flow rate, anatase content increased because the TiO_2(g) species dominate in the gas mixture as shown in Fig. 3.

Fig. 3 shows the chemical equilibrium compositions calculated for the systems of TiN/O_2 using the computer-based numerical method[15] in which Gibbs free energy is assumed to be minimum. In the low oxygen input system(a), Ti_4O_7 as well as TiO_2(rutile) with condensed phase exists at a range of temperature up to their boiling point. At a higher temperature of over 3000 K, TiO(g) is more stable than TiO_2(g) species, and it may cause the formation of the oxygen defect structure. With an increasing the oxygen input, TiO_2(g) become main product at the temperature range of 3000 K to 4200 K, while TiO(g) species is stable at the higher temperature exceeding 4200 K. It is interesting to note that the gas phase composition depends on the oxygen input condition, and the formation of nanopowder is derived by rapid quenching of mixture of TiO(g) and TiO_2(g) clusters.

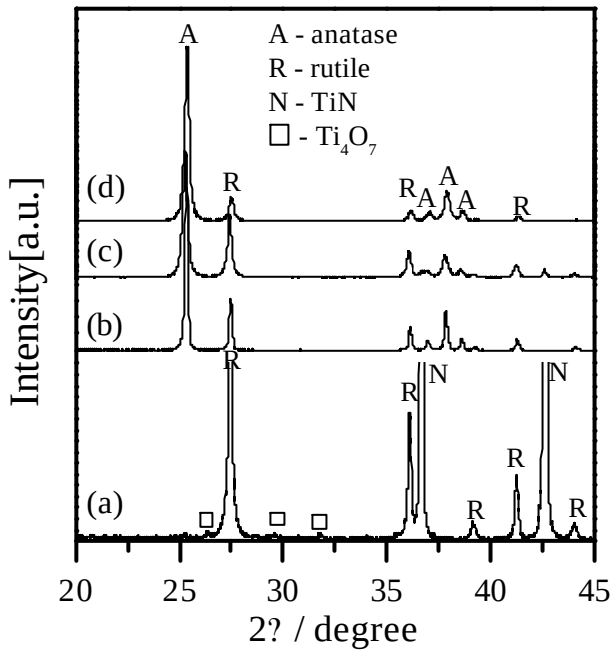

Fig. 2. X-ray diffraction patterns of separated powders from as-produced powders: (a, b) bigger powders; (c, d) smaller powder; (a, c) O_2 – 2.5 l/min; (b, d) O_2 – 17.5 l/min.

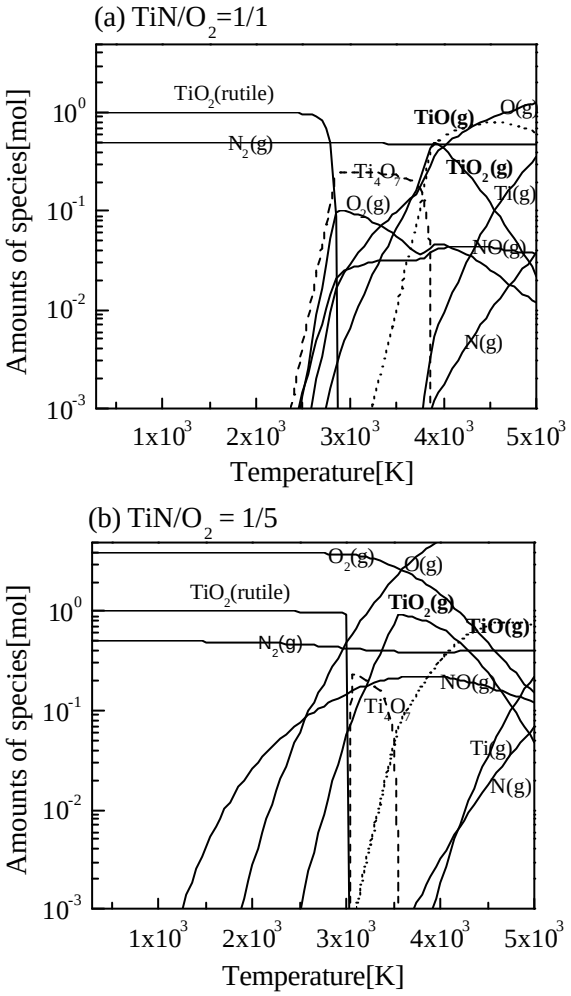

Fig. 3. Chemical equilibrium compositions calculated at different O_2 input conditions in TiN/O_2 systems.

Fig. 4 shows optical micrographs of raw powders and bigger powders synthesized at a different O_2 flow rate. The change of the color to black, blue, yellow, white, or transparent is relating to the degree of oxidation. The cross-section view in Fig. 4b reveals that the bigger powders formed of core-shell structured composites, TiN cores and oxidized shells, because the surface of the powders is rapidly oxidized to TiO_2 melts but oxygen did not fully diffused into TiN cores under low O_2 input conditions. The partially oxidized spherical powders consisted mainly of rutile as shown in Fig. 5, and the formation of rutile is attributed to the oxygen diffusion from molten TiO_2 shell into core because creation of oxygen vacancies enhance the formation of rutile[4]. With the increasing oxygen flow rate, the core-shell structured composites were more spherodized and reduced in size by enhanced oxidation and vaporization. At higher oxygen input conditions, mono-dispersed spherical crystals with diameters of several micrometers were produced as shown in Fig. 4c.

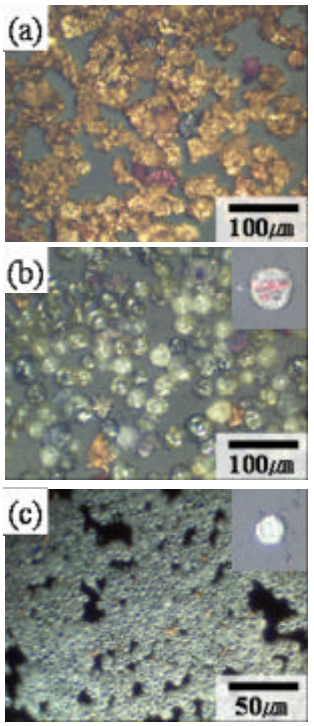

Fig. 4. Optical micrographs of raw powder(a) and oxidized powders(b,c): (b) O_2 – 2.5 l/min, (c) O_2 – 10 l/min.

The content of rutile was shown in Fig. 5 in which the relative weight fraction of rutile, excluding TiN, was calculated by using X-ray diffraction patterns. The rutile content of synthesized powders rapidly decreased with the increasing oxygen flow rate, and it implies that the formation of anatase and rutile is influenced mainly by oxygen flow rate. It is elucidated that the surface of the powders is rapidly oxidized and melted along the plum stream then the partially molten composites are rapidly solidified to anatase or rutile depending on the oxygen content in the melts. At low oxygen input, the molten surface of core-shell composites rapidly solidified to oxygen defect structure by diffusion of oxygen into the cores of composites, and TiN and TiO sub-oxides remain in the cores of composites. With the increasing oxygen flow rate, the powders become fully oxidized and melted, leading to anatase single crystal by rapid solidification under the oxygen rich atmosphere. For the smaller powders,

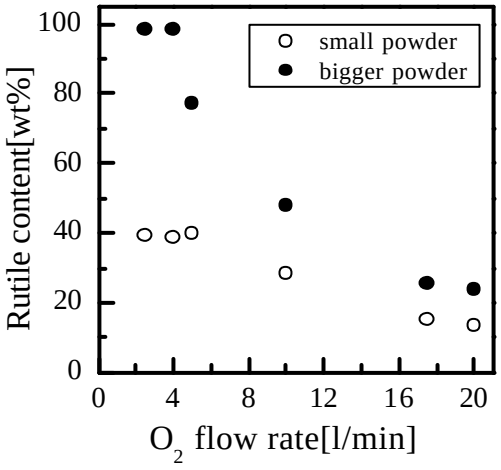

Fig. 5. Weight fractions of rutile for the powders synthesized by Ar-O_2 plasma.

anatase and rutile nanopowders are derived by quenching of the gas mixture of TiO(g) and TiO_2(g) species at high temperature as shown in Fig. 3. The formation mechanism of anatase and rutile was suggested that the anatase is formed by solidification of the oxygen-rich gas mixture under higher O_2 input conditions, while the rutile is derived from the oxygen-deficient gas mixture.

Raman spectra reveal the structure of the powders synthesized at different O_2 flow rate by Ar-O_2 plasma. At the low O_2 flow rate of 4.0 l/min, the peaks correspond to that of rutile as shown in Fig. 6a. The shifting and broadening of the spectrum is attributed to oxygen vacancies or lattice strain by rapid solidification[16,17]. The spectrum of the powder synthesized at the high O_2 flow of 20 l/min shows the peaks corresponding to the single crystal of anatase as in b[16,17]. It is similar to the results observed with X-ray diffraction as shown in Fig. 2.

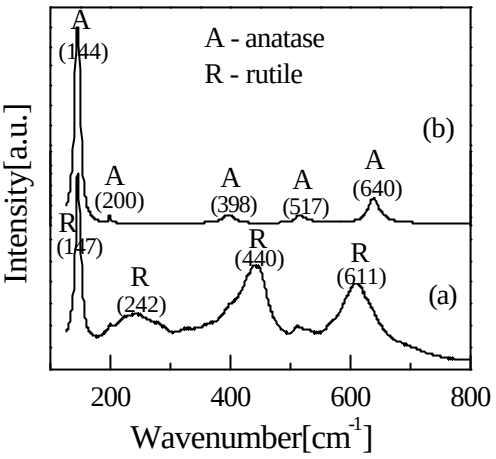

Fig. 6. Raman spectra of synthesized powders: (a) O_2 – 4.0 l/min and (b) O_2 – 20 l/min.

Fig. 7 shows the SEM images of separated powders from as-produced powders synthesized at the O_2 flow rate of 20 l/min. The bigger powders were well spherodized by solidification of TiO_2 melts, and the size significantly reduced by enhanced vaporization. The fully spherodized powders are associated to the anatase phase as shown in Fig. 6b. This has led us to conclude that the spherical single anatase crystal was synthesized by rapid solidification of fully oxidized TiO_2 melt under higher O_2 input conditions. In the case of gas phase synthesis, spherical nanopowders were grown from mixtures of TiO(g) and TiO_2(g) clusters, and the powders were evenly distributed by homogeneous nucleation and growth.

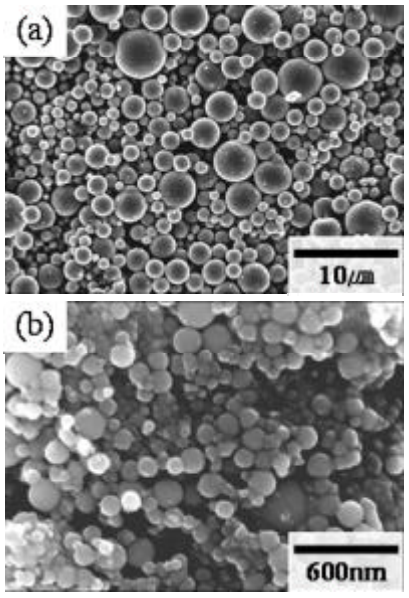

Fig. 7. SEM images of typical prolducts synthesized under higher O_2 input conditions: (a) bigger grained powder, (b) smaller grained powder.

To investigate the effect of H_2 addition, hydrogen was mixed into Ar-sheath gas, and oxygen injected into the center probe with the flow rate of 1 l/min. Fig. 8 shows the X-ray diffraction patterns of separated powders form as-produced products by Ar-H_2 plasma and Ar-He plasma. The patterns for bigger powders synthesized at low O_2 flow rate by Ar-He plasma reveal the peaks corresponding to TiN, rutile, and Ti_4O_7[JCPDS 18-1402]. The formation of rutile and TiO sub-oxides must have been caused by the ambient oxygen deficiency. Introduction of H_2 enhanced the reduction of partially oxidized powders, leading to ?-Ti_3O_5[JCPDS 40-0806], Ti_2O_3[JCPDS 10-0063], and $TiO_{0.34}N_{0.74}$[JCPDS 44-0951] as shown in (b). The pattern for nanopowders synthesized by Ar-He plasma shows the peaks corresponding to anatase and rutile in (c), because the powders are derived by the quenching of gas mixtures vaporized from TiO_2 melts. By introduction of hydrogen, the X-ray pattern reveals only the peaks corresponding to rutile , and the formation of pure rutile is attributed to the oxygen deficient clusters.

Fig. 9 shows a model for in-flight oxidation of TiN by thermal plasma. The surface of raw powders is rapidly oxidized and melted, because the m.p. of oxidized particle gets lower than that of TiN. Partial oxidization of the surface cause the powders to form core-shell structured composites, TiN cores and oxidized melts, and vaporized species forms nanopowder by rapid quenching. Under lower O_2 input conditions, the composites consist of TiN and black colored rutile, because oxidized molten shells is slightly reduced by oxygen diffusion into cores. With the increasing O_2 flow rate, the core is re-oxidized and transformed itself to yellow rutile or white grey anatase. Under higher O_2 input conditions, the powders are fully oxidized and melted, leading to spherical anatase crystals by rapid solidification. Nanopowder is derived from the gas mixtures which are consisted of TiO(g) and TiO_2(g) clusters, and the composition depends on the ambient oxygen

pressure. It was demonstrated that the formation of rutile phase is attributed to ambient oxygen deficiency because TiO(g) clusters are more stable than TiO_2(g) clusters under low O_2 input conditions.

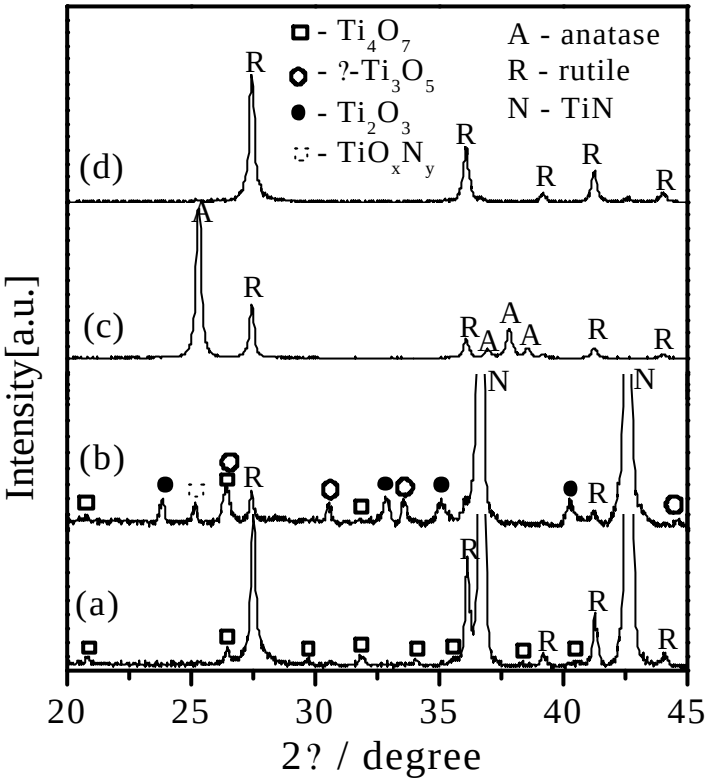

Fig. 8. X-ray diffraction patterns of powders synthesized by Ar-He plasma(a,c) and Ar-H_2 plasma(b,d): (a,b) bigger powders and (c,d) smaller powder.

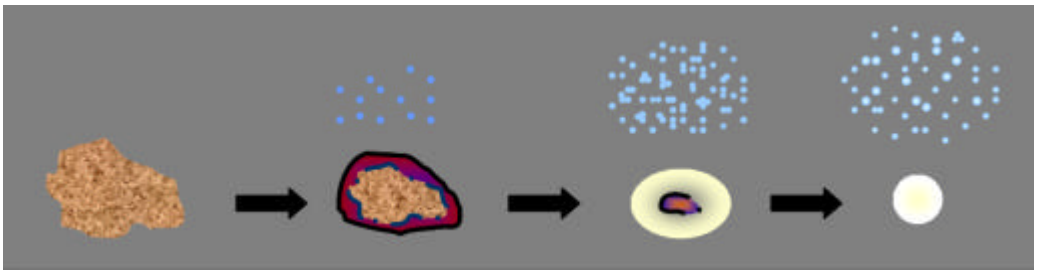

Fig. 9 Schematic model of preparation of spherical TiO_2 powders by in-flight oxidation of TiN powders.

4. Conclusions

We have synthesized spherical titanium dioxide from titanium nitride powders using r.f. thermal plasma. The products consisted of bigger grained powders and small grained powders: the bigger powders are derived by solidification of oxidized melts, and the smaller powders were derived by rapid solidification of vaporized species. Under low O_2 input conditions, the core-shell structured composites, TiN cores and oxidized shells, were produced by partial oxidization of surface. The composites were dominated by rutile because oxidized melts easily reduce to oxygen defect structures by the oxygen diffusion from oxidized shells to TiN cores. With the increasing oxygen flow rate, the composites became fully oxidized and melted to TiO_2 melts, leading to spherical anatase single crystals. The vaporized species from the oxidized surface

caused the formation of nanopowders with diameter of ave. 50nm, and the formation mechanism of nanopowders is associated to the composition of gas mixtures of TiO(g) and TiO_2(g). Under higher O_2 input conditions, TiO_2(g) species is more stable than TiO(g), thus the oxygen-rich clusters grow to anatase nanopowder. Introduction of hydrogen enhanced the reduction of TiO_2 species and the formation of oxygen-deficient clusters, leading to rutile nanopowder.

References

[1] A.Fujishima, T.N.Rao, and D.A.Tryk, *J. Photochemistry and Photobiology C: Photochemistry Review*, **1**, 1 (2000).
[2] M.Lanata, M.Cherchi, A.Zapettini, S.M.Pietralunga, and M.Martinelli, *Opt. Mater*. **17**, 11 (2001).
[3] R.Asahi, T.Morikawa, T.Ohvaki, K.Aoki, Y.Taga, *Science*, **293**, 269 (2001).
[4] S. Vemury and S. E. Pratsinis, *J. Am. Ceram. Soc.*, **78**, 2984 (1995).
[5] S.-M.Oh, S.-S.Kim, J.E.Lee, T.Ishigaki, and D.-W.Park, *Thin Solid Films*, in press.
[6] Y.-L.Li and T.Ishigaki, *Chem. Phys. Lett*., **367**, 561(2003).
[7] J.C.Knight and P.St.J.Russel, *Science*, **296**, 276 (2002).
[8] D.Beydoun and R.Amal, *Mater. Sci. Eng*., **B94**, 71 (2001).
[9] J.A.Gamboa and D.M.Pasquevich, *J. Am. Ceram. Soc*., **75,** 2934 (1992).
[10] C.C. Wang and J.Y. Ying, *Chem. Mater.*, **11**, (1999) 3113.
[11] T.L.Hanley, V.Luca, I.Pickering, and R.F.Howe, J. *Phys. Chem. B*, **106**, 1153(2002).
[12] H.D.Jang and S.-K.Kim, *Mater. Res. Bull*., **36**, 627(2001).
[13] S.-M.Oh, J.-G.Gong, and D.-W.Park, *J. Chem. Eng. Jap.*, **34**(2), 283 (2001).
[14] Y.L.Li and T.Ishigaki, *Chem. Mater*., **13**(5), 1577 (2001).
[15] G.Eriksson and K.Hack, "Chemsage Version 4.01", GTT Technologies, Herzogenrath, Germany, (1998).
[16] T.L.Hanley, V.Luca, I.Pickering, and R.F.Howe, J. *Phys. Chem. B*, **106**, 1153(2002).
[17] J.C.Parker and R.W.Siegel, *J. Mater. Res*., **5**(6), 1246(1990).

Numerical simulation of dielectric barrier-controlled glow discharge at atmospheric pressure

Dezhen Wang and Yanhui Wang

State Key Laboratory of Materials Modification by Laser, Ion and Electron Beams, Department of Physics, Dalian University of Technology, Dalian 116023, China

The space and time distributions of the electric field and the electron and ion densities, as well as the time evolutions of the discharge current density and the surface charge density of the dielectric layer in He dielectric barrier-controlled glow discharge at atmospheric pressure are calculated by solving one-dimensional continuity and momentum equations for electron and ion coupled to the current continuity equation. The properties of uniform atmospheric pressure glow discharge under the conditions of different driving frequency, voltage or dielectric layer are discussed and analyzed. When the driving frequency is high enough, a large number of ions are trapped and the induced space charge field makes a great many electrons stay in the discharge volume. These seed electrons lead to a Townsend discharge at atmosphere pressure. The structure of this discharge is similar to that of low- pressure glow discharge, i.e. there exist four specific regions: the cathode fall, the negative glow, the Faraday dark space and the positive column. The discharge current becomes small with decreasing the applied voltage amplitude. The secondary electron emission from the dielectric layer makes the discharge current increase. The thicker the dielectric layer is or the smaller the permittivity is, the smaller the discharge current is.

[1] S. Kanazawa, M. Kogoma, T. Moriwaki and S. Okazaki, *J. Phys. D: Appl. Phys.* 21, 838(1988)

[2] T. Yokoyama, M. Kogoma, T. Moriwaki and S. Okazaki, *J. Phys. D: Appl. Phys.* 23, 1125(1990)

[4] J. R. Roth, P. P. Tsai, C. Liu, M. Laroussi and P. D. Spence, *One Atmosphere Uniform Glow Discharge Plasma*, U.S. patent 5, 414.304 (1995)

[5] P. P. Tsai, L.C. Wadsworth and J. R. Roth, *Textile Res. J.* 67, 359(1997)

[6] R. B. Gadri, J. R. Roth., T. C. Montie etc., *Surface and Coatings Technology* 131**,** 528 (2000)

[7] F. Massines, A. Rabehi, P. Decomps, R. B. Gadri, P. Segur and C. Mayoux, *J. Appl. Phys.* 83, 2950 (1998)

[8] F. Massines and G. Gouda, *J. Phys. D: Appl. Phys.* 31, 3411(1998)

Drilling of a Deep Hole by Means of Electro Discharge Machining with a Composite Electrode

S. Kumagai[1], N. Misawa[1], M. Akamatsu[1], K. Takeda[1] and E. Abdukarimov[2]

[1] *Department of Machine Intelligence and Systems Engineering, Akita Prefectural University, Honjo, JAPAN*
[2] *Arifov Institute of Electronics, Tashkent,UZBEKISTAN*

Abstract
A new electro discharge machining system employing a composite electrode fabricated a narrow and deep hole (diameter: 0.70 mm, depth: 150 mm) in a steel block. The composite electrode was a metal rod wearing a dielectric pipe jacket. The dielectric jacket prevents secondary discharges occurring between the sidewalls of the rod electrode and the fabricated hole, attaining a fabrication of a deep and narrow hole. The system design and setup, the operation, and the machining performance were described.

1. Introduction

A development of drilling of a narrow and deep hole in a metal contributes greatly to an extensive field of molding and assembly industries. One method to fabricate a narrow and deep hole in a metal is an electro discharge machining (EDM) utilizing transient arc discharges occurring between a work piece (drilled metal) and a tip of a metal electrode. Transient arc discharges inflict thermal shocks and intense impulse waves on the work piece, producing a hole and a waste metal. Working fluid injected from the rotating pipe-shaped electrode to the drilling portion has significant roles to maintain electrical insulation between the work piece and the electrode during arc-extinguishing, and to exhaust a waste metal. Dielectric oil is commonly used as working fluid. The waste metal makes negative effects reducing electrical insulation between the side of the formed hole and the side of the electrode. In addition to this, exhausting the waste metal requires a high pressure (up to 10 MPa) because of the small electrode bore diameter. Unexhausted waste metal reduces the drilling speed and accuracy, as well as the durability of the electrode. Oil disposal and inflammability, and its carbonization resulting from discharges reduce a function of the EDM method. New EDM drilling system being capable of overcoming faults of the above system has been developed. This system employs a special electrode wearing a dielectric jacket (composite electrode). The EDM system with a composite electrode may attain a high-speed, high-operationality, and low-cost fabrication of a narrow and deep hole. However, practical techniques for the system operation are insufficiently developed. A theoretical approach to a principle of the system, an evaluation of the machining speed and accuracy, and an optimization of the system operation are implemented.

2. Composite Electrode EDM System

2. 1. System Concept

EDM systems for a fabrication of a narrow and deep hole in a metal produce transient arc discharges at the drilling portion. The conventional EDM systems employ a metal pipe as an electrode and dielectric oil as working fluid. Fig. 1 shows drilling diagrams of the conventional and the composite electrode EDM systems. Both the electrodes rotate during the operation. The composite electrode is a rod electrode wearing a dielectric pipe jacket. Water is used as working fluid in the composite electrode EDM system. Water flows in a clearance between the rod electrode and the dielectric jacket in order to suppress uncontrolable arc discharges, to exhaust the waste metal, and to quench the discharge-drilling portion. Because a larger cross-section of water flow is possible compared to pipe electrodes, the composite electrode EDM system requires a lower pressure for pumping water. Electrical insulation between the side of the fabricated hole and the side of the electrode is steadily maintained. Thus, negative effects of a waste metal are restricted to the minimum.

2. 2. System design and setup

2. 2. 1. Elements of composite electrode

EDM allows transient arc discharges across a small gap between the work piece and the electrode, causing a fusion and/or a fragmentation of a metal work pieces and simultaneously causing a wear of the electrode. The distance between the tips of the electrode and the jacket shortens with developing the drilling. Thus, the jacket needs to move upward to maintain a specified distance between the tips of the electrode and the work

piece. The schematic diagram indicating the movements of the electrode and the jacket is shown in Fig. 2. The jacket is subjected to very severe atmosphere (high electrical stress, high temperature, and high reactivity) and should have low friction factor and high flexibility. Polytetrafluoroethylene (PTFE) is most likely to meet the above requirements [1] and is therefore employed as the jacket material. The distance between the tips of the electrode and the jacket is maintained during the drilling. A low-wear electrode facilitates a control of the jacket upward movement. Thus, a stiff and non-brittle electrode is suitable to this EDM system. Generally, copper, tungsten, or tungsten alloys are used as electrode materials of hole-fabrication EDMs. Tungsten rod is chosen because it is reported to be the most resistant to discharge-wear in the above electrode materials [2]. The diameter of obtainable tungsten rod electrodes is over 0.30 mm. The composite electrode consisting of tungsten rod (diameter: 0.30 mm, Nilaco Corporation, Japan) and PTFE jacket (bore diameter: 0.41 mm, external diameter: 0.56 mm, Zeus Industrial Products Inc., USA) is used.

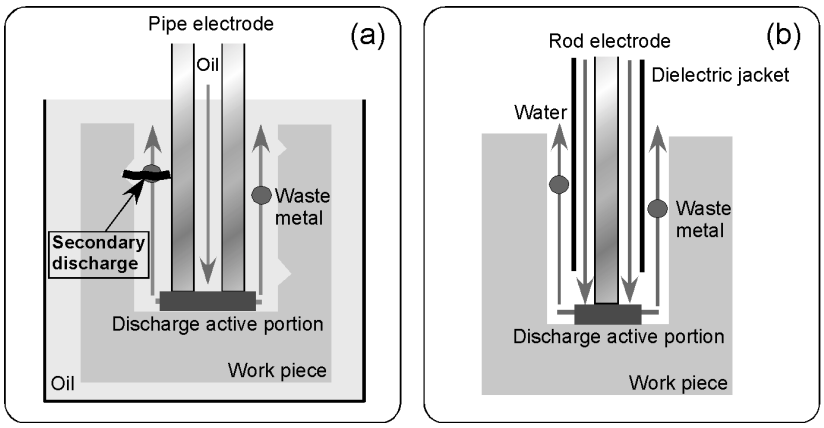

Fig. 1. Diagrams of convetional and composite electrode EDMs for a fabrication of a deep hole in a metal. (a) conventional EDM, (b) composite elctrode EDM.

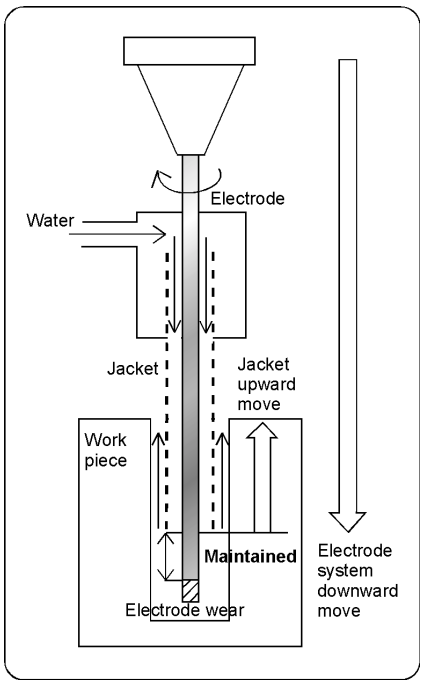

Fig. 2. Movements of the electrode and the jacket in the composite electrode EDM sysem.

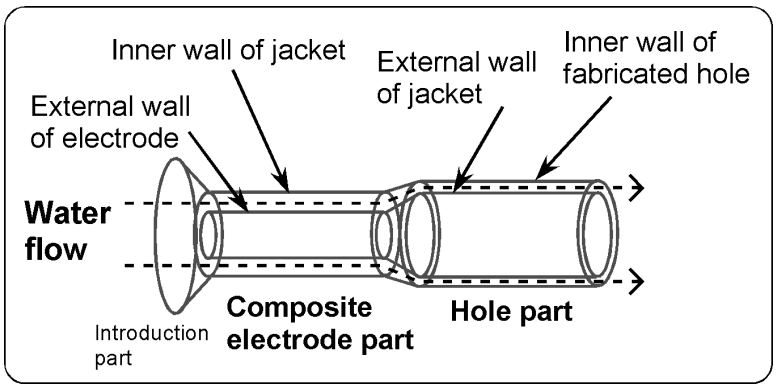

Fig. 3. A model of water flow in the composite electrode EDM system.

2. 2. 2. Required water pressure to exhaust waste metal

Working fluid of water is imposed to exhaust a waste metal produced as a byproduct of drilling and to quench a drilling portion. In the composite electrode EDM system, water flows first between the electrode sidewall and the jacket inner wall, then flows between the jacket external wall and the inner wall of the fabricated hole. The water flow rate and the related water pressure sufficient to exhaust a waste metal and quench a drilling portion should be understood. A series bi-cylinder model simplifies the path of water flow in the composite electrode EDM system (see Fig. 3). For fluid passing through a bi-cylinder, the relation between flow rate Q and pressure P is formulated (1) [3].

$$Q = \frac{\pi P}{8\eta l}\left\{(r_o^4 - r_i^4) - \frac{(r_o^2 - r_i^2)^2}{\ln(r_o / r_i)}\right\} \quad (1)$$

where, r_i, r_o, and l are radius of the inner cylinder, radius of the external cylinder, and length of the bi-cylinder. η is viscosity coefficient of fluid. When the actual dimensions and physical constants are given (electrode diameter: 0.3 mm, bore diameter of jacket: 0.41 mm, external diameter of jacket: 0.56 mm, length of jacket: 200 mm, viscosity coefficient of water: 0.00101 kg/(ms)), the relation between $Q_{comp.elec.}$ (m*l*/s) and $P_{comp.elec.}$ (MPa) for the composite electrode part is expressed by (2).

$$Q_{comp.elec.} = 0.076 P_{comp.elec.} \tag{2}$$

The equation (2) is verified by measuring the flow rate Q as a function of water pressure P. Fig. 4 shows the theoretical line based on (2) and the measurement result. The measurement result is consistent with the theory at 0-1 MPa. A higher water flow rate is observed than theoretically predicted at > 1 MPa. An expansion of PTFE pipe exposed to high pressure would be a primal reason. The actual water flow in the composite electrode exceeds the theoretical one, providing a margin safety in the system design.

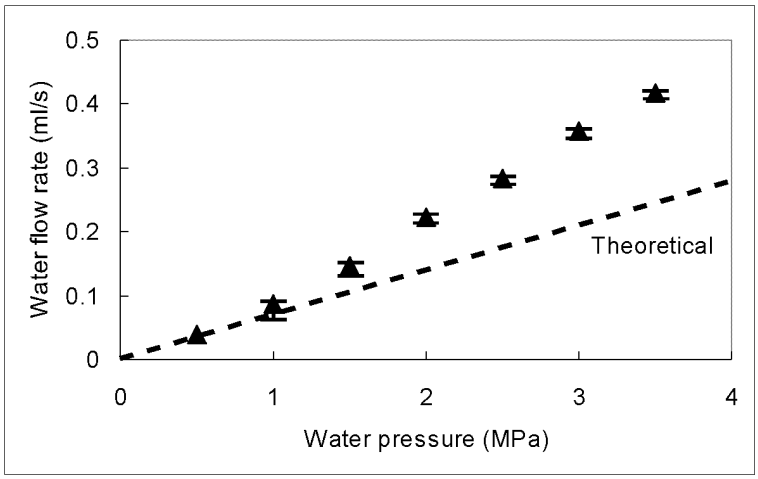

Fig. 4. A relation between water flow rate and pressure of the composite electrode. The theretical line is based on a bi-cylindrical model. Electrode diameter: 0.30 mm, bore diameter of jacket: 0.41 mm, external diameter of jacket: 0.56 mm, length of jacket: 200 mm, viscosity coefficient of water: 0.00101 kg/(ms)

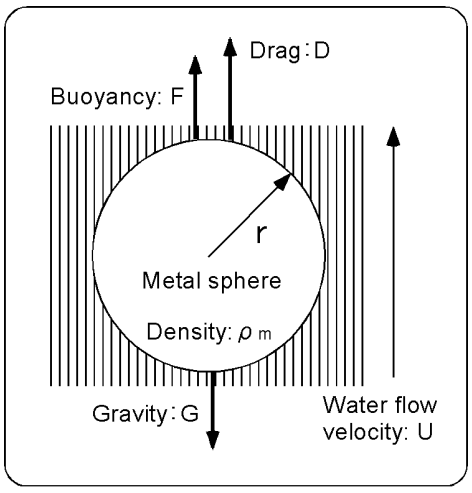

Fig. 5. A dynamic model of an exhaust of a waste metal assumed to be sphere.

A waste metal produced as a byproduct of drilling is exhausted through a clearance between the external wall of the PTFE jacket and the inner wall of the fabricated hole. While the waste metal is in water flow, it is assumed to be subject to dynamics presented in Fig. 5. For an upward movement of the waste metal assumed to be sphere (for an exhaust), the equation (3) should be satisfied.

$$D + F > G \tag{3}$$

D: drag, F: buoyancy, and G: gravity for metal sphere are written by the equation (4)-(6).

$$D = 6\,\pi\,\eta_w\,rU \tag{4}$$
$$F = 4\rho_w\,\pi\,r^3 g/3 \tag{5}$$
$$G = 4\rho_m\,\pi\,r^3 g/3 \tag{6}$$

where, η_w, r, and U are viscosity coefficient of water, radius of metal sphere, and water flow velocity, respectively. ρ_w, ρ_m, and g are density of water, density of metal, and gravitational constant, respectively. The equations (3)-(6) provide a condition for an exhaust of the waste metal (7).

$$U > \frac{2g(\rho_m - \rho_w)r^2}{9\eta_w} \tag{7}$$

The radius of the waste metal is actually measured to be 10-50 μm using a microscope, and is supposed to be 50 μm. The density of the waste metal is supposed to be 10000 kg/m^3 (Fe: 7860 and Cu: 8930 kg/m^3). The exhaust of the waste metal in the conditions given in the above should satisfy (8).

$$U > 0.0485 \text{ (m/s)} \tag{8}$$

In order to obtain the water flow velocity in the hole part U_{hole}, the depth and the diameter of the fabricated hole should be determined. Because the jacket pipe of which external diameter and length are respectively 0.55 mm and 200 mm is employed, the diameter and the depth of the hole are respectively assumed to be 0.70 mm and 150 mm. Under the given conditions, the relation between Q_{hole} (m*l*/s) and P_{hole} (MPa) for the hole part is

$$Q_{hole} = 0.373 P_{hole} \tag{9}.$$

The pressure generated by a pump is allocated to the composite electrode and the hole parts which are connected in series. The water flow rate in the composite electrode $Q_{comp.elec.}$ is equal to that of the hole part Q_{hole}. The equations (2) and (9) indicate that the most pressure is allocated to the composite electrode part. The relation between the water flow velocity in the hole part U_{hole} in unit m/s (= Q_{hole}/S_{hole}, S_{hole}: cross-section of water flow) and whole the pressure applied to the composite electrode part and the hole part P_{total} (MPa) is written by (10).

$$U_{hole} = 0.459 P_{total} \tag{10}$$

This equation suggests that at least water pressure 0.1 MPa is required for an exhaust of a waste metal.

2. 2. 3. Required water pressure to quench drilling portion

A drilling portion is quenched by water flow and, therefore, the quenching efficiency is strongly dependent on the water pressure. If the quench during the EDM system is simplified to an energy conversion, the required water flow rate can be correlated with the quenching ability. It is assumed that electricity energy provided from discharges is converted to thermal energy for water temperature increase without energy loss. The range of temperature increase of water T is assumed to be 25-95 ˚C. In addition to this, the discharge conditions are assumed to be voltage 100 V, current 1 A, and therefore power W, 100 W or J/s. A specific heat of water c is 4.18 J/(˚Cg). The required water flow for quenching Q_q in unit m*l/s* is calculated by (11).

$$Q_q = W/(Tc) \tag{11}$$

Q_q is calculated to be 0.342 m*l*/s. Using the equation (8), the water pressure required in the above-supposed conditions is estimated to be 0.9 MPa. The water pressure sufficient both to exhaust a waste metal and to quench a discharge-drilling portion is estimated to be ~1 MPa. But, it should be noted that higher water pressure promote an exhaust of a waste metal and quenching of a drilling portion

2. 2. 3. Power source equipment

In general EDMs, pulse voltage is applied to a gap between the work piece and the electrode. In this study, pulse-on 142 V for 112 μs and pulse-off 58 V for 5 μs are repeatedly applied to the gap in an open circuit using a pulse power source (5T, Sankyo Engineering Inc., Japan). This pulse voltage form creates the highest current level in the above power source. The pulse-off interval is necessary to extinguish arc, preventing excessive current leading to a circuit short and producing transient arc discharges suitable to EDMs. It should be noticed that the employed power source possesses a utility to stop voltage application when electrical insulation in the gap is extremely reduced (the voltage allocated to the gap is < 33 V). This utility protects a circuit short of the power source.

3. Operation Conditions Consideration

Other conditions to be determined for the system operation are water flow rate (water pressure), a polarity, a distance between the tips of the electrode and the jacket, and threshold gap voltage. An electrode movement (approaching or leaving the work piece) controls arc discharges during general EDMs. A determination of approaching or leaving is dependent on the voltage across the gap between the work piece and the electrode. When the gap voltage is higher than the threshold voltage level, the electrode approaches the work piece to generate arcs. When lower, the electrode leaves the work piece to extinguish arcs and to inhibit excessive current. This threshold gap voltage is determined to be ~90 V, which is the highest level in the system. A higher threshold gap voltage can fabricate a larger diameter-hole. The composite electrode requires a clearance for jacket insertion. Furthermore, it mitigates a deformation of the electrode tip or an insulating deposition at the electrode tip, both causing a cessation of drilling. However, a higher threshold voltage includes a negative profit of a lower drilling speed. On ahead, water pressure sufficient to exhaust a waste metal and to quench a drilling portion is estimated to be ~1 MPa. But, a higher water pressure is better for an efficient exhaust of a waste metal and an efficient quench of a drilling portion. The pressure test demonstrates that the PTFE jacket can resist water pressure up to 3.5 MPa. The water flow rate at 3.5 MPa is 0.42 m*l*/s (measured), referring to Fig. 2. A drilling test is performed to carbon steel (S50C) to find a better polarity. Table 2 shows the electrode wear rate and the drilling speed of the tungsten electrode as a cathode (-) or an anode (+). The results imply that the electrode-cathode polarity (40 %) is suitable to the composite electrode EDM system. The distance between the tips of the electrode and the jacket is also optimized to be 7.0 mm after several trials. The conditions determined for a fabrication of a narrow and deep hole by means of the composite electrode EDM system is determined as presented in Table 2.

Table 1. Wear rate and drilling speed of tungsten electrode (Elec.) at different polarity. The tests are carried out for 10 min. 40 % indicates 40 mm electrode wears for 100 mm hole fabrication. Work piece (WP) is carbon steel (S50C).

Polatity	Elec.: -, WP: +	Elec.: +, WP: -
Electrode wear rate	40 %	> 1000 %
Drilling speed	0.51 mm/min	0.59 mm/min

Table 2. Conditions determined for a steady operation of the composite electrode EDM system.

Item	Description
Electrode	Tungsten rod (diameter: 0.30 mm)
Jacket	PTFE pipe (bore diameter: 0.41 mm, external diameter: 0.56 mm)
Water flow rate (water pressure)	0.42 m*l*/s (3.5 MPa)
Polarity	Electrode: -, Work piece: +
Output voltage	Pulse, on 142 V for 112 μs and off 58 V for 5 μs.
Threshold gap voltage	~90 V (If gap voltage < 33 V, no output)
Distance between electrode and jacket tips	7.0 mm

4. Drilling performance of the composite electrode EDM system

Drilling to a rectangular steel block of which height is 150 mm is attempted under the conditions determined in Table 2. One of well-used carbon steels (S50C) is selected as the sample block. The current level during the drilling is maintained to be ~0.6 mA. The distance between the tips of the electrode and the jacket is constantly controlled to be 7.0 mm. Tap water (~100 μS/cm) is used as working fluid. When an undesirable deformation or an insulating deposition occurs at the tip of electrode leading to a cessation of drilling, the defective portion is cut and removed. Fig. 6 shows the depth and the electrode wear as a function of the operating time. A high linearity is observed in the data of the depth and the electrode wear. The average drilling speed is 0.37 mm/min and the average electrode wear rate is 92.7 % (the electrode wears 92.7 mm for 100 mm-depth hole). Fig. 7 shows a cross-sectional view of the fabricated hole. A good circle (diameter: 0.7 mm) is observed at the inlet of hole. But, the circle in the block enlarges (0.9-1.0 mm) and deforms to oval with the depth. The tungsten electrode is rotating during the drilling at 400 rpm for an aid of maintaining transient arc discharge. When the electrode is inserted in the fabricated hole, a force spent for a downward movement of the electrode enhances the electrode vibration. The electrode vibration caused by the rotation is tried to be restricted to the minimum. But, the vibration is likely to be a primal reason of the hole deformation. An insufficiency of the water flow rate (pressure) is a predominant reason. The electrode tip is not covered with the PTFE dielectric jacket. A residual waste metal induces more intense and more

geometrically non-uniform discharges at the tip of the electrode. The output voltage form, the threshold gap voltage, and the distance between the electrode and the jacket tips can control the electrode vibration and the undesirable discharge mode. The conditions preferred to a steady and safe drilling is chosen so far. But, a higher-speed and a higher-accuracy drilling require resetting of the above-presented items. An employment of a narrower tungsten rod to increase water flow rate is also one solution and seem interesting in upgrading the composite electrode EDM system.

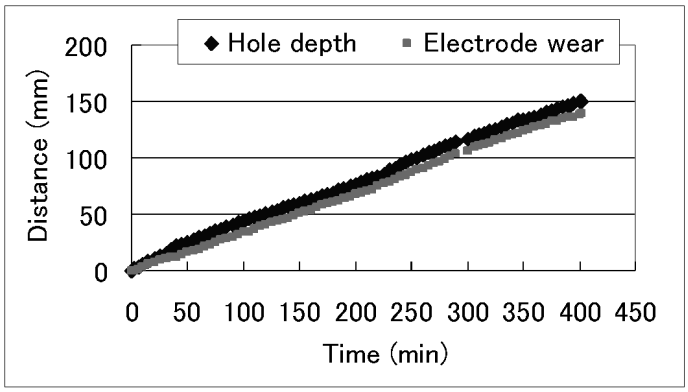

Fig. 6. Time variations of the hole depth and the electrode wear during the composite electrode EDM for carbon steel (S50C). The average drilling speed is 0.37 mm/min and the average electrode wear rate is 92.7 %.

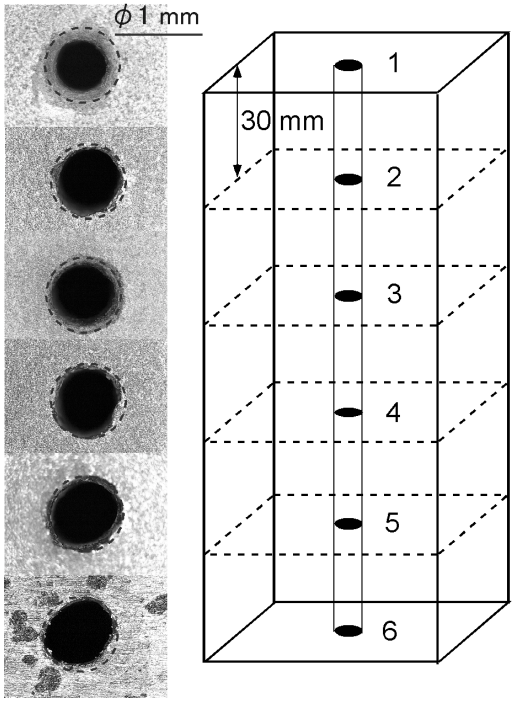

Fig. 7. The appearance of hole fabricated in the composite electrode EDM system. The fabracation process is shown in Fig. 6.

5. Conclusions

New EDM system with a composite electrode that is tungsten rod (diameter: 0.3 mm) wearing PTFE pipe jacket (bore diameter: 0.41 mm, external diameter: 0.56 mm) fabricated a narrow and deep hole in carbon steel block (S50C). The depth, the inlet diameter, and the outlet diameter of the fabricated hole are 150, 0.7, and 1.0 mm, respectively. The electrode wear and the drilling speed are 92.7 % and 0.37 mm/min, which are recorded under the steady and safe system operation. Tap water, flowing in a clearance between the sidewall of the electrode and the inner wall of the jacket, can be used as working fluid. The system concept, setup, and operation principle are in detail mentioned. A further improvement of the operation conditions is considered in regard to the output voltage form, the threshold gap voltage, and the distance between the electrode and the jacket tips. Those are likely to be relevant to the speed and the accuracy of the composite electrode EDM system.

Acknowledgement

This study was performed as a part of the project "H14 Sokkogata Chiiki Shinsei Konsosiamu Kenkyu Kaihatsu Jigyo" sponcered by Ministry of Economy, Trade and Industry of Japan. The authors appreciate the cooperation members of Collaboration and Industrial Advanced Fasclity of Honjo-Yuri, Sanei Kikai Inc., and Kobayashi Kogyo Inc. (all in Honjo, Japan) for thier experimatal supports and technical advice.

References

[1] F. Kurihara, *Polymeric Materials -How to Use-*, Nikkan Kogyo Shinbunsya, 231 (1988). *in Japanese*

[2] N. Saito, H. Mohri, T. Takawashi, and M. Furuya, *Electrical Discharge Machining Technology*, Nikkan Kogyo Shinbunsya, 41 (1997). *in Japanese*

[3] The Japan Society of Mechanical Engineers, *Mechanical Engineering Enchiridion*, A5-76 (1987). *in Japanese*